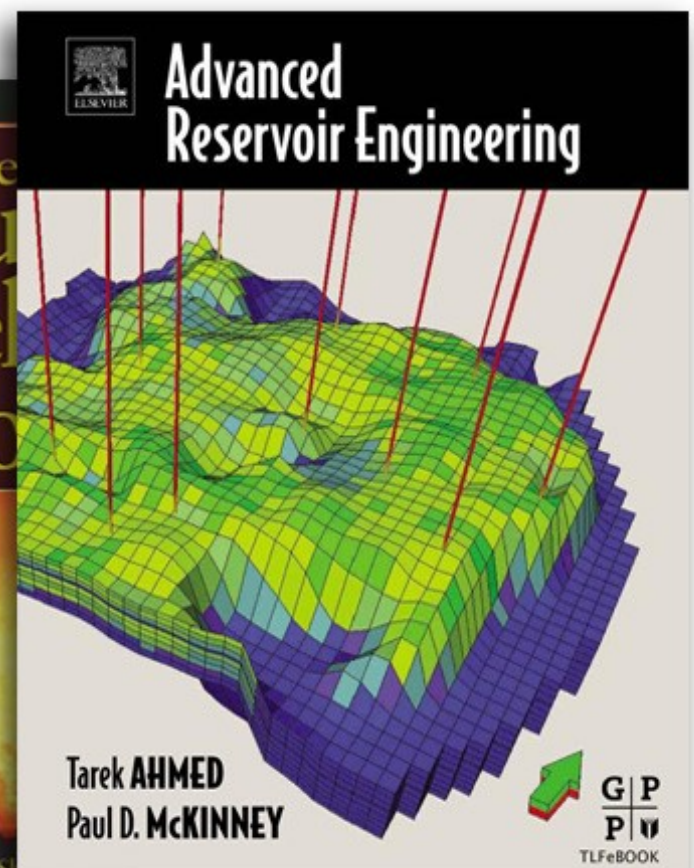
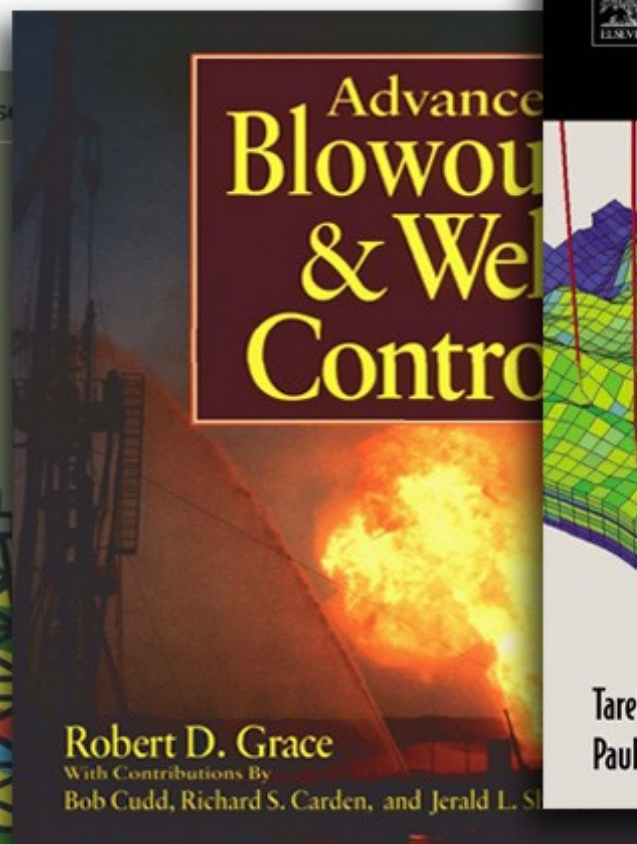
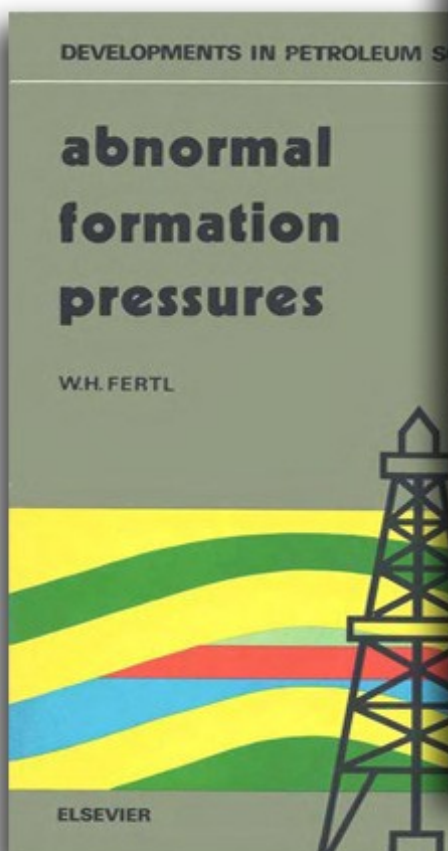




**ALL OF THE PETROLEUM ENGINEERING EBOOKS**  
**in**  
**www.nafti.ir/ebook**



# Reservoir Stimulation

## Contents

### Preface: Hydraulic Fracturing, A Technology for All Time

Ahmed S. Abou-Sayed..... P-1

### Chapter 1 Reservoir Stimulation in Petroleum Production

Michael J. Economides and Curtis Boney

1-1.	Introduction .....	1-1
1-1.1.	Petroleum production .....	1-1
1-1.2.	Units .....	1-3
1-2.	Inflow performance .....	1-3
1-2.1.	IPR for steady state .....	1-4
1-2.2.	IPR for pseudosteady state.....	1-5
1-2.3.	IPR for transient (or infinite-acting) flow .....	1-5
1-2.4.	Horizontal well production .....	1-6
1-2.5.	Permeability anisotropy .....	1-10
1-3.	Alterations in the near-wellbore zone .....	1-11
1-3.1.	Skin analysis .....	1-11
1-3.2.	Components of the skin effect .....	1-12
1-3.3.	Skin effect caused by partial completion and slant.....	1-12
1-3.4.	Perforation skin effect.....	1-13
1-3.5.	Hydraulic fracturing in production engineering.....	1-16
1-4.	Tubing performance and NODAL* analysis.....	1-18
1-5.	Decision process for well stimulation.....	1-20
1-5.1.	Stimulation economics .....	1-21
1-5.2.	Physical limits to stimulation treatments.....	1-22
1-6.	Reservoir engineering considerations for optimal production enhancement strategies.....	1-22
1-6.1.	Geometry of the well drainage volume .....	1-23
1-6.2.	Well drainage volume characterizations and production optimization strategies ....	1-24
1-7.	Stimulation execution .....	1-28
1-7.1.	Matrix stimulation .....	1-28
1-7.2.	Hydraulic fracturing .....	1-18

### Chapter 2 Formation Characterization: Well and Reservoir Testing

Christine A. Ehlig-Economides and Michael J. Economides

2-1.	Evolution of a technology .....	2-1
2-1.1.	Horner semilogarithmic analysis .....	2-1
2-1.2.	Log-log plot.....	2-2
2-2.	Pressure derivative in well test diagnosis.....	2-3
2-3.	Parameter estimation from pressure transient data .....	2-7
2-3.1.	Radial flow.....	2-7
2-3.2.	Linear flow.....	2-9

2-3.3.	Spherical flow .....	2-10
2-3.4.	Dual porosity .....	2-11
2-3.5.	Wellbore storage and pseudosteady state .....	2-11
2-4.	Test interpretation methodology .....	2-12
2-5.	Analysis with measurement of layer rate .....	2-14
2-6.	Layered reservoir testing .....	2-15
2-6.1.	Selective inflow performance analysis .....	2-15
2-6.2.	Analysis of multilayer transient test data .....	2-16
2-7.	Testing multilateral and multibranch wells .....	2-16
2-8.	Permeability determination from a fracture injection test .....	2-17
2-8.1.	Pressure decline analysis with the Carter leakoff model .....	2-17
2-8.2.	Filter-cake plus reservoir pressure drop leakoff model (according to Mayerhofer <i>et al.</i> , 1993) .....	2-21

## Chapter 3 Formation Characterization: Rock Mechanics

M. C. Tiercelin and J.-C. Roegiers

3-1.	Introduction .....	3-1
	Sidebar 3A. Mechanics of hydraulic fracturing .....	3-2
3-2.	Basic concepts .....	3-4
3-2.1.	Stresses .....	3-4
3-2.2.	Strains .....	3-5
	Sidebar 3B. Mohr circle .....	3-5
3-3.	Rock behavior .....	3-6
3-3.1.	Linear elasticity .....	3-6
	Sidebar 3C. Elastic constants .....	3-8
3-3.2.	Influence of pore pressure .....	3-8
3-3.3.	Fracture mechanics .....	3-9
3-3.4.	Nonelastic deformation .....	3-11
3-3.5.	Failure .....	3-11
3-4.	Rock mechanical property measurement .....	3-12
3-4.1.	Importance of rock properties in stimulation .....	3-12
3-4.2.	Laboratory testing .....	3-13
3-4.3.	Stress-strain curve .....	3-14
3-4.4.	Elastic parameters .....	3-15
3-4.5.	Rock strength, yield criterion and failure envelope .....	3-19
3-4.6.	Fracture toughness .....	3-19
	Sidebar 3D. Fracture toughness testing .....	3-20
3-5.	State of stress in the earth .....	3-21
3-5.1.	Rock at rest .....	3-22
3-5.2.	Tectonic strains .....	3-23
3-5.3.	Rock at failure .....	3-23
3-5.4.	Influence of pore pressure .....	3-25
3-5.5.	Influence of temperature .....	3-26
3-5.6.	Principal stress direction .....	3-26
3-5.7.	Stress around the wellbore .....	3-26
3-5.8.	Stress change from hydraulic fracturing .....	3-27
3-6.	In-situ stress management .....	3-28
3-6.1.	Importance of stress measurement in stimulation .....	3-28
3-6.2.	Micro-hydraulic fracturing techniques .....	3-28

3-6.3.	Fracture calibration techniques .....	3-34
3-6.4.	Laboratory techniques .....	3-34

## Chapter 4 Formation Characterization: Well Logs

Jean Desroches and Tom Bratton

4-1.	Introduction .....	4-1
4-2.	Depth .....	4-2
4-3.	Temperature .....	4-2
4-4.	Properties related to the diffusion of fluids .....	4-3
4-4.1.	Porosity .....	4-3
4-4.2.	Lithology and saturation .....	4-5
4-4.3.	Permeability .....	4-6
	Sidebar 4A. Permeability-porosity correlations .....	4-8
4-4.4.	Pore pressure .....	4-10
4-4.5.	Skin effect and damage radius .....	4-11
4-4.6.	Composition of fluids .....	4-12
4-5.	Properties related to the deformation and fracturing of rock .....	4-13
4-5.1.	Mechanical properties .....	4-13
4-5.2.	Stresses .....	4-15
4-6.	Zoning .....	4-24

## Chapter 5 Basics of Hydraulic Fracturing

M. B. Smith and J. W. Shlyapobersky

5-1.	Introduction .....	5-1
5-1.1.	What is fracturing? .....	5-1
5-1.2.	Why fracture? .....	5-4
5-1.3.	Design considerations and primary variables .....	5-6
	Sidebar 5A. Design goals and variables .....	5-7
5-1.4.	Variable interaction .....	5-9
5-2.	In-situ stress .....	5-9
5-3.	Reservoir engineering .....	5-10
5-3.1.	Design goals .....	5-11
	Sidebar 5B. Highway analogy for dimensionless fracture conductivity .....	5-11
5-3.2.	Complicating factors .....	5-12
5-3.3.	Reservoir effects on fluid loss .....	5-13
5-4.	Rock and fluid mechanics .....	5-13
5-4.1.	Material balance .....	5-13
5-4.2.	Fracture height .....	5-14
5-4.3.	Fracture width .....	5-15
5-4.4.	Fluid mechanics and fluid flow .....	5-15
5-4.5.	Fracture mechanics and fracture tip effects .....	5-16
5-4.6.	Fluid loss .....	5-17
5-4.7.	Variable sensitivities and interactions .....	5-18
5-5.	Treatment pump scheduling .....	5-20
5-5.1.	Fluid and proppant selection .....	5-21
5-5.2.	Pad volume .....	5-21
5-5.3.	Proppant transport .....	5-23
5-5.4.	Proppant admittance .....	5-24
5-5.5.	Fracture models .....	5-25

5-6.	Economics and operational considerations .....	5-26
5-6.1.	Economics .....	5-26
5-6.2.	Operations .....	5-27

## Appendix: Evolution of hydraulic fracturing design and evaluation

K. G. Nolte .....	A5-1
-------------------	------

## Chapter 6 Mechanics of Hydraulic Fracturing

Mark G. Mack and Norman R. Warpinski

6-1.	Introduction .....	6-1
6-2.	History of early hydraulic fracture modeling .....	6-2
6-2.1.	Basic fracture modeling .....	6-2
6-2.2.	Hydraulic fracture modeling .....	6-3
	Sidebar 6A. Approximation to the Carter equation for leakoff .....	6-6
	Sidebar 6B. Approximations to Nordgren's equations .....	6-6
	Sidebar 6C. Radial fracture geometry models .....	6-8
6-3.	Three-dimensional and pseudo-three-dimensional models .....	6-8
	Sidebar 6D. Field determination of fracture geometry .....	6-10
6-3.1.	Planar three-dimensional models .....	6-11
	Sidebar 6E. Lateral coupling in pseudo-three-dimensional models .....	6-12
	Sidebar 6F. Momentum conservation equation for hydraulic fracturing .....	6-13
	Sidebar 6G. Momentum balance and constitutive equation for non-Newtonian fluids .....	6-14
6-3.2.	Cell-based pseudo-three-dimensional models .....	6-16
	Sidebar 6H. Stretching coordinate system and stability analysis .....	6-20
6-3.3.	Lumped pseudo-three-dimensional models .....	6-23
6-4.	Leakoff .....	6-25
6-4.1.	Filter cake .....	6-25
6-4.2.	Filtrate zone .....	6-26
6-4.3.	Reservoir zone .....	6-26
6-4.4.	Combined mechanisms .....	6-26
6-4.5.	General model of leakoff .....	6-27
6-4.6.	Other effects .....	6-27
6-5.	Proppant placement .....	6-28
6-5.1.	Effect of proppant on fracturing fluid rheology .....	6-28
6-5.2.	Convection .....	6-28
6-5.3.	Proppant transport .....	6-29
6-6.	Heat transfer models .....	6-29
6-6.1.	Historical heat transfer models .....	6-30
6-6.2.	Improved heat transfer models .....	6-30
6-7.	Fracture tip effects .....	6-30
	Sidebar 6I. Efficient heat transfer algorithm .....	6-31
	Sidebar 6J. Verification of efficient thermal calculations .....	6-32
6-7.1.	Linear elastic fracture mechanics .....	6-32
	Sidebar 6K. Crack tip stresses and the Rice equation .....	6-33
6-7.2.	Extensions to LEFM .....	6-34
6-7.3.	Field calibration .....	6-35
6-8.	Tortuosity and other near-well effects .....	6-36
6-8.1.	Fracture geometry around a wellbore .....	6-36
6-8.2.	Perforation and deviation effects .....	6-36

6-8.3.	Perforation friction.....	6-37
6-8.4.	Tortuosity.....	6-37
6-8.5.	Phasing misalignment.....	6-38
6-9.	Acid fracturing.....	6-40
6-9.1.	Historical acid fracturing models.....	6-40
6-9.2.	Reaction stoichiometry.....	6-40
6-9.3.	Acid fracture conductivity.....	6-41
6-9.4.	Energy balance during acid fracturing.....	6-42
6-9.5.	Reaction kinetics.....	6-42
6-9.6.	Mass transfer.....	6-42
6-9.7.	Acid reaction model.....	6-43
6-9.8.	Acid fracturing: fracture geometry model.....	6-43
6-10.	Multilayer fracturing.....	6-44
6-11.	Pump schedule generation.....	6-46
	Sidebar 6L. Approximate proppant schedules.....	6-47
6-12.	Pressure history matching.....	6-48
	Sidebar 6M. Theory and method of pressure inversion.....	6-48

## Chapter 7 Fracturing Fluid Chemistry and Proppants

Janet Gulbis and Richard M. Hodge

7-1.	Introduction.....	7-1
7-2.	Water-base fluids.....	7-1
7-3.	Oil-base fluids.....	7-6
7-4.	Acid-based fluids.....	7-7
7-4.1.	Materials and techniques for acid fluid-loss control.....	7-7
7-4.2.	Materials and techniques for acid reaction-rate control.....	7-8
7-5.	Multiphase fluids.....	7-8
7-5.1.	Foams.....	7-9
7-5.2.	Emulsions.....	7-9
7-6.	Additives.....	7-10
7-6.1.	Crosslinkers.....	7-10
	Sidebar 7A. Ensuring optimum crosslinker performance.....	7-13
7-6.2.	Breakers.....	7-14
	Sidebar 7B. Breaker selection.....	7-16
7-6.3.	Fluid-loss additives.....	7-16
7-6.4.	Bactericides.....	7-18
7-6.5.	Stabilizers.....	7-18
7-6.6.	Surfactants.....	7-19
7-6.7.	Clay stabilizers.....	7-19
7-7.	Proppants.....	7-19
7-7.1.	Physical properties of proppants.....	7-19
7-7.2.	Classes of proppants.....	7-21
	Sidebar 7C. Minimizing the effects of resin-coated proppants.....	7-22
7-8.	Execution.....	7-22
7-8.1.	Mixing.....	7-22
7-8.2.	Quality assurance.....	7-23
	Acknowledgments.....	7-23



## Chapter 8 Performance of Fracturing Materials

Vernon G. Constien, George W. Hawkins, R. K. Prud'homme and Reinaldo Navarrete

8-1.	Introduction .....	8-1
8-2.	Fracturing fluid characterization.....	8-1
8-3.	Characterization basics .....	8-2
8-4.	Translation of field conditions to a laboratory environment.....	8-2
8-5.	Molecular characterization of gelling agents.....	8-2
8-5.1.	Correlations of molecular weight and viscosity.....	8-2
8-5.2.	Concentration and chain overlap .....	8-3
8-5.3.	Molecular weight distribution.....	8-4
8-5.4.	Characterization of insoluble components.....	8-5
8-5.5.	Reaction sites and kinetics of crosslinking .....	8-5
8-6.	Rheology.....	8-6
8-6.1.	Basic flow relations .....	8-7
8-6.2.	Power law model .....	8-7
8-6.3.	Models that more fully describe fluid behavior.....	8-8
8-6.4.	Determination of fracturing fluid rheology.....	8-10
8-6.5.	Rheology of foam and emulsion fluids.....	8-12
8-6.6.	Effect of viscometer geometry on fluid viscosity .....	8-15
8-6.7.	Characterization of fluid microstructure using dynamic oscillatory measurements..	8-16
8-6.8.	Relaxation time and slip.....	8-17
8-6.9.	Slurry rheology.....	8-17
8-7.	Proppant effects.....	8-19
8-7.1.	Characterization of proppant transport properties.....	8-19
8-7.2.	Particle migration and concentration .....	8-21
8-8.	Fluid loss.....	8-22
8-8.1.	Fluid loss under static conditions.....	8-23
8-8.2.	Fluid loss under dynamic conditions .....	8-24
8-8.3.	Shear rate in the fracture and its influence on fluid loss .....	8-25
8-8.4.	Influence of permeability and core length.....	8-26
8-8.5.	Differential pressure effects.....	8-26

## Chapter 9 Fracture Evaluation Using Pressure Diagnostics

Sunil N. Gulrajani and K. G. Nolte

9-1.	Introduction .....	9-1
9-2.	Background .....	9-2
9-3.	Fundamental principles of hydraulic fracturing.....	9-3
9-3.1.	Fluid flow in the fracture .....	9-3
9-3.2.	Material balance or conservation of mass .....	9-4
9-3.3.	Rock elastic deformation .....	9-4
	Sidebar 9A. What is closure pressure? .....	9-6
	Sidebar 9B. Pressure response of toughness-dominated fractures.....	9-9
9-4.	Pressure during pumping .....	9-10
9-4.1.	Time variation for limiting fluid efficiencies .....	9-12
9-4.2.	Inference of fracture geometry from pressure .....	9-12
9-4.3.	Diagnosis of periods of controlled fracture height growth.....	9-14
9-4.4.	Examples of injection pressure analysis.....	9-15
	Sidebar 9C. Pressure derivative analysis for diagnosing pumping pressure.....	9-16
9-4.5.	Diagnostics for nonideal fracture propagation .....	9-18

	Sidebar 9D. Fluid leakoff in natural fissures.....	9-23
9-4.6.	Formation pressure capacity .....	9-24
9-4.7.	Pressure response after a screenout.....	9-27
9-4.8.	Fracture diagnostics from log-log plot slopes .....	9-28
9-4.9.	Near-wellbore effects .....	9-30
	Sidebar 9E. Rate step-down test analysis—a diagnostic for fracture entry.....	9-32
9-5.	Analysis during fracture closure.....	9-34
9-5.1.	Fluid efficiency .....	9-34
9-5.2.	Basic pressure decline analysis.....	9-37
9-5.3.	Decline analysis during nonideal conditions.....	9-38
9-5.4.	Generalized pressure decline analysis .....	9-42
	Sidebar 9F. <i>G</i> -function derivative analysis .....	9-43
9-6.	Pressure interpretation after fracture closure.....	9-45
9-6.1.	Why linear and radial flow after fracture closure? .....	9-46
9-6.2.	Linear, transitional and radial flow pressure responses .....	9-48
	Sidebar 9G. Impulse testing.....	9-49
9-6.3.	Mini-falloff test.....	9-50
9-6.4.	Integration of after-closure and preclosure analyses.....	9-50
9-6.5.	Physical and mathematical descriptions.....	9-51
9-6.6.	Influence of spurt loss.....	9-53
9-6.7.	Consistent after-closure diagnostic framework .....	9-54
9-6.8.	Application of after-closure analysis.....	9-56
9-6.9.	Field example .....	9-57
9-7.	Numerical simulation of pressure: combined analysis of pumping and closing .....	9-59
9-7.1.	Pressure matching .....	9-60
9-7.2.	Nonuniqueness .....	9-60
9-8.	Comprehensive calibration test sequence.....	9-61

## Appendix: Background for hydraulic fracturing pressure analysis techniques

Sunil N. Gulrajani and K. G. Nolte.....	A9-1
---	------

## Chapter 10 Fracture Treatment Design

Jack Elbel and Larry Britt

10-1.	Introduction .....	10-1
	Sidebar 10A. NPV for fixed costs or designated proppant mass .....	10-2
10-2.	Design considerations .....	10-3
10-2.1.	Economic optimization.....	10-3
10-2.2.	Treatment optimization design procedure .....	10-3
10-2.3.	Fracture conductivity.....	10-4
10-2.4.	Dimensionless fracture conductivity.....	10-6
10-2.5.	Non-Darcy effects .....	10-8
10-2.6.	Proppant selection .....	10-8
10-2.7.	Treatment size .....	10-9
10-2.8.	Fluid loss .....	10-10
10-2.9.	Viscosity effects .....	10-11
	Sidebar 10B. Fluid exposure time.....	10-12
10-2.10.	Injection rate .....	10-13
10-3.	Geometry modeling .....	10-14
	Sidebar 10C. Geometry models.....	10-14
10-3.1.	Model selection.....	10-15



10-3.2.	Sources of formation parameters .....	10-16
	Sidebar 10D. In-situ stress correlation with lithology .....	10-16
10-4.	Treatment schedule .....	10-17
	Sidebar 10E. Fracturing economics sensitivity to formation permeability and skin effect ...	10-17
10-4.1.	Normal proppant scheduling .....	10-18
10-4.2.	Tip screenout .....	10-21
10-5.	Multilayer fracturing .....	10-24
10-5.1.	Limited entry .....	10-24
10-5.2.	Interval grouping .....	10-25
10-5.3.	Single fracture across multilayers .....	10-25
10-5.4.	Two fractures in a multilayer reservoir .....	10-26
10-5.5.	Field example .....	10-28
	Sidebar 10F. Fracture evaluation in multilayer zones .....	10-28
10-6.	Acid fracturing .....	10-30
10-6.1.	Acid-etched fracture conductivity .....	10-31
	Sidebar 10G. Acid-etched conductivity .....	10-32
10-6.2.	Acid fluid loss .....	10-33
	Sidebar 10H. Fluid-loss control in wormholes .....	10-34
10-6.3.	Acid reaction rate .....	10-35
10-6.4.	Acid fracturing models .....	10-36
10-6.5.	Parameter sensitivity .....	10-36
10-6.6.	Formation reactivity properties .....	10-41
10-6.7.	Propped or acid fracture decision .....	10-41
10-7.	Deviated wellbore fracturing .....	10-42
10-7.1.	Reservoir considerations .....	10-43
10-7.2.	Fracture spacing .....	10-45
10-7.3.	Convergent flow .....	10-45
10-7.4.	Fracturing execution in deviated and horizontal wells .....	10-47
10-7.5.	Horizontal well example .....	10-49

## Chapter 11 Fracturing Operations

J. E. Brown, R. W. Thrasher and L. A. Behrmann

11-1.	Introduction .....	11-1
11-2.	Completions .....	11-1
11-2.1.	Deviated and S-shaped completions .....	11-1
11-2.2.	Horizontal and multilateral completions .....	11-2
11-2.3.	Slimhole and monobore completions .....	11-2
11-2.4.	Zonal isolation .....	11-2
	Sidebar 11A. Factors influencing cement bond integrity .....	11-3
	Sidebar 11B. Coiled tubing–conveyed fracture treatments .....	11-6
11-3.	Perforating .....	11-8
11-3.1.	Background .....	11-8
	Sidebar 11C. Estimating multizone injection profiles during hydraulic fracturing ..	11-9
	Sidebar 11D. Propagating a microannulus during formation breakdown .....	11-11
11-3.2.	Perforation phasing for hard-rock hydraulic fracturing .....	11-11
11-3.3.	Other perforating considerations for fracturing .....	11-14
11-3.4.	Frac and packs and high-rate water packs .....	11-16
11-3.5.	Fracturing for sand control without gravel-pack screens .....	11-16
	Sidebar 11E. Calculation of minimum shot density for fracture stimulation .....	11-17
11-3.6.	Extreme overbalance stimulation .....	11-18

11-3.7.	Well and fracture connectivity .....	11-18
11-4.	Surface equipment for fracturing operations.....	11-19
11-4.1.	Wellhead isolation .....	11-19
11-4.2.	Treating iron .....	11-19
11-4.3.	High-pressure pumps.....	11-22
11-4.4.	Blending equipment .....	11-23
11-4.5.	Proppant storage and delivery.....	11-23
11-4.6.	Vital signs from sensors .....	11-24
11-4.7.	Equipment placement .....	11-26
11-5.	Bottomhole pressure measurement and analysis .....	11-26
11-6.	Proppant flowback control .....	11-29
11-6.1.	Forced closure .....	11-30
11-6.2.	Resin flush .....	11-30
11-6.3.	Resin-coated proppants.....	11-30
11-6.4.	Fiber technology.....	11-30
11-7.	Flowback strategies .....	11-30
	Sidebar 11F. Fiber technology .....	11-31
11-8.	Quality assurance and quality control.....	11-32
11-9.	Health, safety and environment .....	11-32
11-9.1.	Safety considerations.....	11-32
11-9.2.	Environmental considerations.....	11-33

## Appendix: Understanding perforator penetration and flow performance

Phillip M. Halleck .....	A11-1
--------------------------	-------

## Chapter 12 Post-Treatment Evaluation and Fractured Well Performance

B. D. Poe, Jr., and Michael J. Economides

12-1.	Introduction .....	12-1
12-1.1.	Fracture mapping techniques .....	12-1
12-1.2.	Pressure transient analysis .....	12-6
12-2.	Post-treatment fracture evaluation .....	12-10
12-2.1.	Wellbore storage dominated flow regime .....	12-11
12-2.2.	Fracture storage linear flow regime.....	12-11
12-2.3.	Bilinear flow regime .....	12-11
12-2.4.	Formation linear flow regime .....	12-13
12-2.5.	Pseudoradial flow regime.....	12-14
12-2.6.	Pseudosteady-state flow regime .....	12-15
12-3.	Factors affecting fractured well performance .....	12-16
12-3.1.	Non-Darcy flow behavior.....	12-16
12-3.2.	Nonlinear fluid properties .....	12-20
12-3.3.	Fracture damage and spatially varying fracture properties.....	12-21
12-3.4.	Damage in high-permeability fracturing .....	12-25
12-3.5.	Heterogeneous systems.....	12-26
12-4.	Well test analysis of vertically fractured wells.....	12-27
12-4.1.	Wellbore storage dominated flow analysis .....	12-28
12-4.2.	Fracture storage linear flow analysis.....	12-28
12-4.3.	Bilinear flow analysis .....	12-29
12-4.4.	Formation linear flow analysis .....	12-29
12-4.5.	Pseudoradial flow analysis.....	12-29
12-4.6.	Well test design considerations.....	12-30

12-4.7. Example well test analyses .....	12-31
12-5. Prediction of fractured well performance.....	12-39

## Chapter 13 Introduction to Matrix Treatments

R. L. Thomas and L. N. Morgenthaler

13-1. Introduction .....	13-1
13-1.1. Candidate selection .....	13-1
Sidebar 13A. The history of matrix stimulation .....	13-2
13-1.2. Formation damage characterization.....	13-3
13-1.3. Stimulation technique determination .....	13-3
13-1.4. Fluid and additive selection.....	13-3
13-1.5. Pumping schedule generation and simulation .....	13-3
13-1.6. Economic evaluation.....	13-4
13-1.7. Execution .....	13-4
13-1.8. Evaluation.....	13-4
13-2. Candidate selection .....	13-4
13-2.1. Identifying low-productivity wells and stimulation candidates .....	13-4
Sidebar 13B. Candidate selection field case history .....	13-6
13-2.2. Impact of formation damage on productivity.....	13-6
13-2.3. Preliminary economic evaluation.....	13-7
13-3. Formation damage characterization.....	13-8
Sidebar 13C. Formation damage characterization field case history.....	13-9
Sidebar 13D. Fluid and additive selection field case history .....	13-10
13-4. Stimulation technique determination.....	13-10
13-5. Treatment design.....	13-11
13-5.1. Matrix stimulation techniques.....	13-11
13-5.2. Treatment fluid selection .....	13-12
13-5.3. Pumping schedule generation and simulation .....	13-19
Sidebar 13E. Placement study case histories.....	13-29
13-6. Final economic evaluation.....	13-32
13-7. Execution .....	13-32
13-7.1. Quality control .....	13-32
13-7.2. Data collection .....	13-34
13-8. Treatment evaluation .....	13-35
13-8.1. Pretreatment evaluation .....	13-35
13-8.2. Real-time evaluation .....	13-35
13-8.3. Post-treatment evaluation.....	13-37

## Chapter 14 Formation Damage: Origin, Diagnosis and Treatment Strategy

Donald G. Hill, Olivier M. Liétard, Bernard M. Piot and George E. King

14-1. Introduction .....	14-1
14-2. Damage characterization.....	14-1
14-2.1. Pseudodamage.....	14-2
14-2.2. Pseudoskin effects and well completion and configuration .....	14-3
14-3. Formation damage descriptions .....	14-4
14-3.1. Fines migration.....	14-4
14-3.2. Swelling clays .....	14-6
14-3.3. Scales.....	14-6
14-3.4. Organic deposits.....	14-7
14-3.5. Mixed deposits .....	14-8

14-3.6.	Emulsions .....	14-9
14-3.7.	Induced particle plugging .....	14-9
14-3.8.	Wettability alteration .....	14-10
14-3.9.	Acid reactions and acid reaction by-products .....	14-11
14-3.10.	Bacteria .....	14-11
14-3.11.	Water blocks .....	14-12
14-3.12.	Oil-base drilling fluids .....	14-13
14-4.	Origins of formation damage .....	14-13
14-4.1.	Drilling .....	14-13
14-4.2.	Cementing .....	14-21
14-4.3.	Perforating .....	14-21
14-4.4.	Gravel packing .....	14-22
14-4.5.	Workovers .....	14-22
14-4.6.	Stimulation and remedial treatments .....	14-23
14-4.7.	Normal production or injection operations .....	14-24
14-5.	Laboratory identification and treatment selection .....	14-26
14-5.1.	Damage identification .....	14-26
14-5.2.	Treatment selection .....	14-28
14-6.	Treatment strategies and concerns .....	14-31
14-6.1.	Fines and clays .....	14-33
14-6.2.	Scales .....	14-34
14-6.3.	Organic deposits .....	14-35
14-6.4.	Mixed deposits .....	14-35
14-6.5.	Emulsions .....	14-36
14-6.6.	Bacteria .....	14-36
14-6.7.	Induced particle plugging .....	14-36
14-6.8.	Oil-base drilling fluids .....	14-37
14-6.9.	Water blocks .....	14-37
14-6.10.	Wettability alteration .....	14-38
14-6.11.	Wellbore damage .....	14-38
14-7.	Conclusions .....	14-39

## Chapter 15 Additives in Acidizing Fluids

Syed A. Ali and Jerald J. Hinkel

15-1.	Introduction .....	15-1
15-2.	Corrosion inhibitors .....	15-2
15-2.1.	Corrosion of metals .....	15-2
15-2.2.	Acid corrosion on steel .....	15-2
15-2.3.	Pitting types of acid corrosion .....	15-3
15-2.4.	Hydrogen embrittlement .....	15-3
15-2.5.	Corrosion by different acid types .....	15-3
15-2.6.	Inhibitor types .....	15-4
15-2.7.	Compatibility with other additives .....	15-4
15-2.8.	Laboratory evaluation of inhibitors .....	15-5
15-2.9.	Suggestions for inhibitor selection .....	15-5
15-3.	Surfactants .....	15-5
15-3.1.	Anionic surfactants .....	15-6
15-3.2.	Cationic surfactants .....	15-6
15-3.3.	Nonionic surfactants .....	15-6
15-3.4.	Amphoteric surfactants .....	15-7

15-3.5.	Fluorocarbon surfactants .....	15-7
15-3.6.	Properties affected by surfactants .....	15-7
15-3.7.	Applications and types of surfactants .....	15-9
15-4.	Clay stabilizers .....	15-11
15-4.1.	Highly charged cations .....	15-11
15-4.2.	Quaternary surfactants .....	15-12
15-4.3.	Polyamines .....	15-12
15-4.4.	Polyquaternary amines .....	15-12
15-4.5.	Organosilane .....	15-13
15-5.	Mutual solvents .....	15-13
15-5.1.	Adsorption of mutual solvents .....	15-14
15-5.2.	Chlorination of mutual solvents .....	15-14
15-6.	Iron control additives .....	15-14
15-6.1.	Sources of iron .....	15-14
15-6.2.	Methods of iron control .....	15-15
15-7.	Alcohols .....	15-16
15-8.	Acetic acid .....	15-18
15-9.	Organic dispersants .....	15-18
15-10.	Organic solvents .....	15-18
15-11.	Diversion .....	15-18
15-12.	Additive compatibility .....	15-19
15-13.	Facility upsets following acid stimulation .....	15-19
15-13.1.	Discharge requirements .....	15-19
15-13.2.	Prevention of facility upsets .....	15-20

## Chapter 16 Fundamentals of Acid Stimulation

A. Daniel Hill and Robert S. Schechter

16-1.	Introduction .....	16-1
16-2.	Acid-mineral interactions .....	16-2
16-2.1.	Acid-mineral reaction stoichiometry .....	16-2
16-2.2.	Acid-mineral reaction kinetics .....	16-4
	Sidebar 16A. Calculating minimum acid volume using dissolving power .....	16-5
	Sidebar 16B. Relative reaction rates of sandstone minerals .....	16-8
16-2.3.	Precipitation of reaction products .....	16-10
	Sidebar 16C. Geochemical model predictions .....	16-11
16-3.	Sandstone acidizing .....	16-13
16-3.1.	Introduction .....	16-13
16-3.2.	Acid selection .....	16-13
16-3.3.	Sandstone acidizing models .....	16-13
	Sidebar 16D. Comparison of acid volumes for radial and perforation flow .....	16-16
16-3.4.	Permeability response .....	16-19
16-4.	Carbonate acidizing .....	16-19
16-4.1.	Distinctive features .....	16-19
16-4.2.	Wormholes .....	16-20
16-4.3.	Initiation of wormholes .....	16-21
16-4.4.	Acidizing experiments .....	16-23
	Sidebar 16E. Optimum injection rate for initiating carbonate treatment .....	16-26
16-4.5.	Propagation of wormholes .....	16-27

## Appendix: Advances in understanding and predicting wormhole formation

Christopher N. Fredd	A16-1
----------------------	-------

### Chapter 17 Carbonate Acidizing Design

J. A. Robert and C. W. Crowe

17-1.	Introduction	17-1
17-2.	Rock and damage characteristics in carbonate formations	17-1
17-2.1.	Rock characteristics	17-1
17-2.2.	Damage characteristics	17-2
17-3.	Carbonate acidizing with hydrochloric acid	17-2
17-3.1.	Introduction	17-2
17-3.2.	Historical background	17-2
17-3.3.	Reactivity of carbonate minerals with hydrochloric acid	17-3
17-3.4.	Acidizing physics	17-4
	Sidebar 17A. Wormhole initiation and propagation	17-6
17-3.5.	Application to field design	17-7
	Sidebar 17B. Acidizing case study	17-8
17-4.	Other formulations	17-9
17-4.1.	Organic acids	17-9
17-4.2.	Gelled acids	17-10
17-4.3.	Emulsions	17-11
17-4.4.	Microemulsions	17-11
17-4.5.	Special treatments	17-12
17-4.6.	Self-diverting acid	17-12
	Sidebar 17C. Examples of special treatments	17-13
	Sidebar 17D. Placement using self-diverting acid	17-13
17-5.	Treatment design	17-14
17-5.1.	Candidate selection	17-14
17-5.2.	Pumping schedule	17-14
17-5.3.	Additives	17-14
17-5.4.	Placement	17-14
17-6.	Conclusions	17-14
	Acknowledgments	17-15

### Chapter 18 Sandstone Acidizing

Harry O. McLeod and William David Norman

18-1.	Introduction	18-1
18-2.	Treating fluids	18-1
18-2.1.	Hydrochloric acid chemistry	18-2
18-2.2.	Chemistry of hydrofluoric acid systems	18-2
18-3.	Solubility of by-products	18-4
18-3.1.	Calcium fluoride	18-5
18-3.2.	Alkali fluosilicates and fluoaluminates	18-5
18-3.3.	Aluminum fluoride and hydroxide	18-5
18-3.4.	Ferric complexes	18-5
18-4.	Kinetics: factors affecting reaction rates	18-6
18-4.1.	Hydrofluoric acid concentration	18-6
18-4.2.	Hydrochloric acid concentration	18-6
18-4.3.	Temperature	18-7



18-4.4.	Mineralogical composition and accessible surface area .....	18-7
18-4.5.	Pressure .....	18-7
18-5.	Hydrofluoric acid reaction modeling .....	18-7
18-6.	Other acidizing formulations .....	18-8
18-6.1.	Fluoboric acid .....	18-8
18-6.2.	Sequential mud acid .....	18-10
18-6.3.	Alcoholic mud acid .....	18-11
18-6.4.	Mud acid plus aluminum chloride for retardation .....	18-11
18-6.5.	Organic mud acid .....	18-11
18-6.6.	Self-generating mud acid systems .....	18-12
18-6.7.	Buffer-regulated hydrofluoric acid systems .....	18-12
18-7.	Damage removal mechanisms .....	18-12
18-7.1.	Formation response to acid .....	18-13
18-7.2.	Formation properties .....	18-13
18-7.3.	Formation brine compatibility .....	18-13
18-7.4.	Crude oil compatibility .....	18-14
18-7.5.	Formation mineral compatibility with fluid systems .....	18-14
18-7.6.	Acid type and concentration .....	18-16
18-8.	Methods of controlling precipitates .....	18-18
18-8.1.	Preflush .....	18-18
18-8.2.	Mud acid volume and concentration .....	18-18
18-8.3.	Postflush or overflush .....	18-18
18-9.	Acid treatment design considerations .....	18-19
18-9.1.	Selection of fluid sequence stages .....	18-20
18-9.2.	Typical sandstone acid job stages .....	18-20
18-9.3.	Tubing pickle .....	18-20
18-9.4.	Preflushes .....	18-20
18-9.5.	Main fluid stage .....	18-21
18-9.6.	Overflush stage .....	18-21
18-9.7.	Diversion techniques .....	18-22
18-9.8.	Typical sandstone acid job stages .....	18-22
18-10.	Matrix acidizing design guidelines .....	18-23
18-10.1.	Calculations .....	18-24
18-10.2.	Flowback and cleanup techniques .....	18-25
18-11.	Acid treatment evaluation .....	18-26
18-12.	Conclusions .....	18-27

## Chapter 19 Fluid Placement and Pumping Strategy

J. A. Robert and W. R. Rossen

19-1.	Introduction .....	19-1
19-2.	Choice of pumping strategy .....	19-1
19-2.1.	Importance of proper placement .....	19-1
19-2.2.	Comparison of diversion methods .....	19-2
19-2.3.	Fluid placement versus injection rate .....	19-3
19-2.4.	MAPDIR method .....	19-3
19-3.	Chemical diverter techniques .....	19-4
19-3.1.	Historical background .....	19-4
19-3.2.	Diverting agent properties .....	19-4
19-3.3.	Classification of diverting agents .....	19-4
19-3.4.	Potential problems during diversion treatment .....	19-5

19-3.5.	Laboratory characterization.....	19-6
19-3.6.	Modeling diverter effects.....	19-7
19-3.7.	Field design.....	19-9
19-4.	Foam diversion.....	19-10
19-4.1.	Historical background.....	19-10
19-4.2.	Foam mechanisms.....	19-10
19-4.3.	Foam behavior in porous media.....	19-12
19-4.4.	Foam diversion experiments.....	19-14
19-4.5.	Modeling and predicting foam diversion.....	19-15
19-4.6.	Application to field design.....	19-16
19-5.	Ball sealers.....	19-18
19-6.	Mechanical tools.....	19-19
19-7.	Horizontal wells.....	19-20
19-7.1.	Optimal treatment.....	19-20
19-7.2.	Placement techniques.....	19-22
19-8.	Conclusions.....	19-23
	Acknowledgments.....	19-24

## Chapter 20 Matrix Stimulation Treatment Evaluation

Carl T. Montgomery and Michael J. Economides

20-1.	Introduction.....	20-1
20-2.	Derivation of bottomhole parameters from wellhead measurements.....	20-1
20-3.	Monitoring skin effect evolution during treatment.....	20-1
20-3.1.	McLeod and Coulter technique.....	20-1
20-3.2.	Paccaloni technique.....	20-2
20-4.	Prouvost and Economides method.....	20-4
20-4.1.	Deriving skin effect during treatment.....	20-4
20-4.2.	Determining reservoir characteristics before treatment.....	20-4
20-5.	Behenna method.....	20-5
20-6.	Inverse injectivity diagnostic plot.....	20-5
20-7.	Limitations of matrix treatment evaluation techniques.....	20-5
	Sidebar 20A. Example calculation of the Prouvost and Economides method.....	20-6
	Sidebar 20B. Example application of the Hill and Zhu method.....	20-7
20-8.	Treatment response diagnosis.....	20-8
	Sidebar 20C. Production indications for matrix stimulation requirements.....	20-10
20-9.	Post-treatment evaluation.....	20-11
20-9.1.	Return fluid analysis.....	20-11
20-9.2.	Tracer surveys.....	20-11
20-10.	Conclusions.....	20-12

## References

Chapters 1–12.....	R-1
Chapters 13–20.....	R-45

Nomenclature.....	N-1
-------------------	-----

# Preface: Hydraulic Fracturing, A Technology For All Time

Ahmed S. Abou-Sayed, ADVANTEK International

I was quite pleased when my friend Joseph Ayoub at Schlumberger Dowell approached me to write the preface for the third edition of *Reservoir Stimulation*. It is indeed a pleasure and a compliment to be associated with the distinguished list of individuals contributing to this volume. As an active member of this close-knit community for the past 25 years, I have enjoyed working with most of the 47 contributing authors. These outstanding scientists and engineers have carried the technology of hydraulic fracturing forward to its current high state.

This third edition is an updated classic reference for well stimulation—or in today's lingo, well performance enhancement technology—that includes not only hydraulic fracturing but also an expanded treatment of well acidizing and chemical treatment as well as formation damage migration. *Reservoir Stimulation* covers the topics necessary for understanding the basis and practical aspects of treatment design and execution. It addresses the scientific fundamentals, engineering considerations and operational procedures of a job. Pre- and post-treatment analyses, job monitoring and economic elements of the various injectivity and productivity enhancement processes are well presented.

Before I get into a technical discussion of the volume's contents, let me share with the reader a bit of history and my personal point of view of the future. I am not trying to preempt the excellent contents compiled by the volume's editors, Michael Economides and Ken Nolte. The two editors have succeeded in bringing to the reader an integrated account of the objectives, mechanics and implementation of the well and reservoir aspects of productivity enhancement. Other significant contributions that helped bring *Reservoir Stimulation* to the reader came from Joseph Ayoub and Eric Nelson, who provided continual technical advice and reviewed the contents for technical accuracy, and Bob Thrasher, who with utter competence and, I must say, sheer patience and persistence pulled this treatise together

by managing the various chapters from the vast array of contributors.

A leading contributor, however, to this publication's success is Michael Economides, who, over the last two decades, has contributed substantially to the integration of reservoir performance into well stimulation technology and design. He has proficiently filled this gap in practice with his thorough work related to performance prediction and evaluation. Michael provides the continuous thread that gives the volume its integrated form.

The other leading contributor is Ken Nolte, who presents a compelling story that puts forward the history of hydraulic fracturing technology in the Appendix to Chapter 5. He describes its evolution from the late 1940s from his vista, easily scoring a true bull's-eye. His towering work since the mid-1970s affords him a unique view of the technological progress that he helped shape.

What further insight can I add to the views of these two? I guess you can call it the maverick's view. I will be informal and hope my anecdotal style will not offend any serious student of the subject. What follows is my view of this fascinating technology, which has renewed itself many times since its inception and has contributed substantial financial benefits to the oil and gas industry.

During the late 1970s, considered the banner years of fracturing technology advances, there was a saying often used in jest by most of us working on fracturing:

“When everything else fails, frac it.”

How true this has been; a lot of “fraccing” was done for well stimulation in those days and since. We now speak more appropriately about improved well performance, downhole flow integrity and enhanced productivity or injectivity. How did we get here?

During the late 1940s, fracturing was a timid technique. In the 1950s, its proliferation took place. In the 1960s, we aimed at understanding what we were

doing. The 1970s was a time to expand, quantify and optimize our procedures. In the 1980s, we worked to influence the outcome through monitoring and real-time engineering. Now in the 1990s, it has been the time for new frontiers. And in the middle of all that, we have managed environmental cleanup via injection.

Since its inception in 1946, hydraulic fracturing technology has been tapped by the oil and gas industry to solve a variety of problems and provide answers to a multitude of difficult issues. These issues cover the areas of enhanced well productivity (by far the most significant utilization), improved well injectivity, storage and environmental remediation.

Three watershed phases have contributed to the widespread technological advances. The first phase coincided with the quick development of well stimulation techniques in the late 1940s and early 1950s by the pioneering operating and service companies. The second phase of prolific advances occurred in the mid-1970s, when the national energy policy makers directed their attention and crucial U.S. government funding to developing tight gas sands and unconventional energy resources. In the early to mid-1980s, the most significant advances better adapted the technology for use in stimulating medium- to high-permeability (i.e., prolific) reservoirs. The economic payout to the industry has increased rapidly at each phase of development and with every successful treatment. Ken Nolte provides the details in the Appendix to Chapter 5.

In each phase, the producers and service companies have collaborated to provide innovative and cost-effective approaches to problems. During the infancy of development, slow but consistent progress improved low-rate well productivity by pumping better materials and using progressively more reliable equipment.

During the 1960s, the emphasis shifted to understanding the fracturing process and increasing its effectiveness by enhancing the quality of the pumped materials (i.e., fluids and proppants) as well as by developing chemical additives, including acid fracturing.

In the mid-1970s, massive hydraulic fracturing replaced an ill-fated attempt to use a nuclear device to fracture a tight gas reservoir (the Gas Buggy experiment, part of Project Plowshare, which was designed to develop peaceful uses of nuclear explosive technology). The need for creating the massive hydraulic fractures required to unlock the vast

amount of gas trapped in tight sands and unconventional reservoirs gave impetus to the development of sophisticated fluids (e.g., crosslinked gels), tougher proppants (e.g., bauxite and lower density ceramics) and large-volume pumping equipment and proppant handling capacity. More in-depth analysis of fracturing processes and vastly improved monitoring and analysis techniques were necessary during this period for optimizing treatments.

During the last decade of the twentieth century, the technology has pushed forward in more uncharted waters. Examples of the new directions are horizontal and complex well fracturing for reservoir management (part of what Ken Nolte refers to as reservoir plumbing). Others applications include refracturing, frac and pack treatments for sand control and, finally, a class of operations termed environmental fracturing, which includes produced water disposal, drilling cuttings injection and soil reclamation by crush and inject technology.

The new generation of hydraulic fracturing applications is associated with additional operational costs, in contrast to revenue-enhancing well stimulation work. However, in the final analysis these new applications are extremely beneficial and essential to achieving industry's goals of protecting the environment and moving toward zero emission of exploration and production waste. They have been easy extensions of the know-how. That the underlying understanding of conventional hydraulic fracturing operations, and the tools and techniques developed, has been instantly applicable to these areas is a tribute to the innovation and robustness of the hydraulic fracturing technologists. They saw the opportunities as ways to expand their horizons and, let us not forget, sometimes preserve their jobs.

Now, what about the present volume? *Reservoir Stimulation* consists of 20 chapters with numerous sidebars and appendixes prepared by authors of indisputably high reputation and respected as experts in their fields. The list contains operating company researchers, practitioners, scientists from academic and national laboratory institutions as well as field operations staff. The latter group offers unique insight on how the technologies are operationally implemented in the real world. As such, the contents of this volume provide a balanced view and offer something for everyone. This integrated knowledge approach makes *Reservoir Stimulation* a must read for engineers and geoscientists working with well stimulation

technology, from mechanical stimulation (fracturing) through chemical treatments (acidizing).

The reader must view this volume as a confirmation and accurate account of the larger context of the exciting progress that has been made in the field of hydraulic fracturing and well stimulation. Recent emphasis has focused on fluid and proppant development, field equipment for mixing and pumping materials, highly sophisticated (but simple to use) interpretation techniques or monitoring treatment parameters, and computers that monitor, provide feedback and control the fracture. The available hardware enables real-time redesign during pumping.

Efforts also have been made, prior to job design and execution, to thoroughly characterize reservoir qualities and properties for the optimization of stimulation treatment design and better economic results. Logging tools are used for lithology, permeability, stress and natural fracture detection. Detection of the created fracture azimuth and length received attention with the development of techniques such as passive borehole seismic methods, crosswell tomography, tiltmeters and hydraulic impedance tests.

The myriad techniques available for in-situ stress magnitude and azimuth determination include core relaxation, differential strain curve analysis, microfracturing and wellbore breakouts. Results of well tests and mini-fracture treatments are used readily in fracture treatment designs.

The development of accurate downhole pressure gauges with digital memory provides a detailed account of fluid pressure at the fracture inlet and assists on-site redesign and post-treatment analysis. Recent efforts are directed at the development of downhole gauges that transmit pressure, flow rate and fluid rheology data in real time. Such gauges are now in service in well monitoring and testing applications.

Simpler techniques, such as using the annulus or a tubing-based manometer, have been highly successful. These applications are limited operationally to wells with large-diameter casing and tubing and by rig cost. Coiled tubing operations may reduce this limitation and expand the application of real-time downhole pressure monitoring.

Fluids now are available with excellent shear sensitivity and high-proppant carrying capacities for use at high temperatures and flow rates. Additives such as borates make it possible to design fluids that have low frictional or viscosity properties while traveling down

the well tubulars, only to become viscous after turning the corner of well perforations into the formation.

What comes next in this ever-changing world of well stimulation and performance enhancement? Current emphasis by the service industry in fluid development is on providing cleaner fluids to the user community. Such fluids maintain the designed fracture conductivity, improve the treatment economics and extend fracturing applications to higher permeability reservoirs.

Intermediate-density ceramic proppants are stronger and lighter, so they can be carried farther into the fracture at greater depths. Extensive efforts are directed at obtaining a more thorough understanding of proppant transport mechanisms. Monitoring techniques and proppant placement and distribution are conducted using multiple-isotope radioactive tagging.

More sophisticated logging tools and interpretation algorithms are adding the ability to track the location of several pumped stages. This development has improved the understanding of how to design more effective fracture treatments and has prompted an emphasis on fracture containment.

Pumping and surface handling equipment have progressed substantially ahead of the other technologies, and more advances are under way. The availability of new-generation blenders, offshore gelling and crosslinking of fluids on the fly, and high-pressure-high-flow-rate pumps and intensifiers provides the industry with the capacity to execute and control the most complicated fracture. Emphasis must also be directed toward zone isolation techniques and the hardware to conduct large stimulation jobs in long, complex wells.

As the hardware side of the technology (materials and equipment) developed at a rapid pace over the last two decades, the software side (modeling, monitoring and interpretation) also moved forward. The U.S. government, Gas Research Institute (GRI) and academic communities with consulting company support are delivering design codes with varying degrees of sophistication to the industry. Some of the codes are field based and used extensively for the optimization and redesign of fracture treatments. Computer hardware advances and experience-based intelligence software must provide a window of opportunity for broader and more effective use of modeling developments.

The results of the current software and hardware advances are manifested in a growing area of application, refracturing and simultaneous multiple-job execution. In an economically successful effort, the Prudhoe Bay Unit Operating Partners took advantage of these advances in technology to refracture many wells in Alaska North Slope fields such as Kuparuk. Previous jobs, performed in the mid-1980s, were based on the standard approaches and supplies of that time. The refracturing process systematically and consistently used the latest technology and materials, including progressively bigger proppants, more aggressive designs and a better knowledge base of the reservoir characteristics. The success of refracturing treatments between 1988 and 1995 was most significant in wells where the original design parameters, materials or execution was below the current standard. The result has been an additional 50 million barrels of reserves and a much needed 50,000 B/D of oil production from the North Slope. The industry will see more refracturing efforts emerge worldwide.

Fracturing technology has also been applied to horizontal and highly deviated wells. The advent of this type of fracturing posed challenges to operators. Well-to-fracture conductivity affects treatment pressure, premature screenouts, proppant flowback and well productivity. The pumping of sand slugs, high-overpressure perforating, dynamic formation breakdown and fracture initiation are among the most successful methods for improving well connection and reducing fracture cornering and tortuosity in the near-wellbore region.

In economically sensitive fields, the use of S-shaped wells instead of highly deviated wells is gaining increased acceptance when fracture stimulations are planned. This approach, used successfully by BP Amoco in the North Sea Ravenspurn field, avoids many of the difficulties of fracturing and producing deviated wells. It also minimizes the effect of any near-wellbore tortuosity on treatment pressure, proppant flowback and production efficiency.

More complex issues face the horizontal well stimulation industry. Multiple fracturing perpendicular to the borehole provides the most attractive hydrocarbon sweep and reserve recovery. However, fracturing along the borehole is operationally easier but may have to be executed using multiple treatments through perforated intervals in long horizontal wells. The industry must sort through these competing

issues and arrive at satisfactory design and optimization criteria.

Criteria for the completion, perforation, zonal isolation and design of job stages for extended reach, horizontal, multilateral, openhole and high-rate wells are needed to help produce a material difference in the productivity of fractured or acidized horizontal wells. Innovative techniques are required for executing multiple jobs within a horizontal well without excessive cost while minimizing interference of the created fractures. Monitoring techniques for proppant placement, production logging and downhole pressure profiling also are desirable, if not necessary, for job optimization.

A new chapter was opened with the application of hydraulic fracturing technology for sand control in producing soft and unconsolidated formations. This technology involves sequential, uninterrupted fracturing and gravel-pack operations through downhole gravel-pack hardware. The first application of the frac and pack technique was implemented in 1985 for well stimulation at west Sak, a heavy-oil reservoir on the North Slope. The treatment was successful, but the heavy-oil development was halted owing to the price collapse and drop in global oil economics.

Finally, operators recently began development of deepwater reservoirs using frac and pack technology in the Gulf of Mexico. The technique has almost eliminated the chronic high positive skin factor (20–30) normally associated with gravel-pack operations. Well productivity has increased 2 to 3 times and skin factors are reduced to almost zero or below, while complete sand control is maintained. These treatments will grow in number and magnitude as deeper water is conquered and higher well productivity is a must.

In this context, let us review the contents of this volume.

The third edition begins with an introductory chapter by Michael Economides and Curtis Boney. They discuss the inflow performance of regular, horizontal and complex wells in combination with various reservoirs. This chapter lays the groundwork for assessing the need for well stimulation, its applicability and expected rewards. Finally, the authors address reservoir engineering considerations for optimal production enhancement strategies.

In Chapter 2, the other Dr. Economides joins Michael. Christine Ehlig-Economides and Michael



Economides present the well testing methodology and pressure transient analysis used to characterize formations and describe the status of well damage.

The well-recognized rock mechanics engineers Mark Thiercelin and Jean-Claude Roegiers (known as “JC”) authored Chapter 3. They present a well-thought-out treatment of rock mechanics—the characterization of the box containing recoverable hydrocarbons. Their work details the theoretical components describing rock behavior and reactions under the loads and stresses generated by E&P operations. The presentation is thorough and on a high fundamental level, while providing insight into the practical application of this specialty in a useful and tractable fashion.

Jean Desroches and Tom Bratton describe in Chapter 4 how to use well logs and other geophysical information to obtain pertinent properties of the rock formation for effective treatment design. In addition to the conventional, routine properties such as porosity, permeability and saturation, they cover the estimation of pore pressure, formation tests, skin effect and damage extent, in-situ stress and other mechanical properties. An interesting treatment of predicting in-situ rock stress and strength from logs is presented.

In Chapter 5, Mike Smith (the pipe-smoking half of the well-known Nolte-Smith duo) and my dear late friend Jacob Shlyapobersky collaborated to lay down for the reader the basics of hydraulic fracturing. This is a pragmatic chapter that serves well as a primer for new engineers searching for a quick appreciation of the factors with an impact on fracture design. Its value is further enhanced by the historical perspective written as the aforementioned Appendix by Ken Nolte.

Mark Mack joins Norm Warpinski of Sandia National Laboratories in Chapter 6 to provide a comprehensive treatment of the mechanics of hydraulic fracturing and discuss the science behind the technology. The chapter reflects their massive contributions to the understanding, through extensive field observation efforts, of the phenomena and processes involved in hydraulic fracturing. The theoretical and practical knowledge collected throughout their illustrative careers is well represented.

Chapter 7 exposes the reader to the materials pumped in the well during stimulation treatments. Janet Gulbis and Richard Hodge have written a rigorous, but easily read, discussion of the chemical and rheological aspects of stimulation fluids and proppants. They cover fluid additives, including fluid-loss

control materials, crosslinking agents, breakers, surfactants, clay stabilizers and bactericides, and describe their appropriate uses.

The performance of fracturing materials, a subject that has seen tremendous advances in the last 20 years, is presented in Chapter 8 by Vern Constien, George Hawkins, Bob Prud’homme and Reinaldo Navarrete. The chapter outlines techniques for measuring and designing the necessary rheology for fracturing fluids and treatment chemicals. The authors also discuss the important topic of propped fracture conductivity and proppant flowback and the impact of fluid rheology on both. Damage resulting from polymer loading is also covered in this chapter.

Sunil Gulrajani and Ken Nolte discuss the latter’s favorite topic of fracture evaluation using pressure diagnostics in Chapter 9. These techniques, when first introduced in 1978, provided quantitative tools for assessing the nature, extent and containment of the hydraulic fracture. They subsequently established the basis for efforts toward real-time diagnostics and control of the well treatment progress. The authors examine the mathematical foundation of the diagnostic technique, including an accompanying Appendix, provide field verification examples and present means of integrating this approach with other evaluation tools, well measurements and field observations.

Jack Elbel and Larry Britt collaborated in Chapter 10 to present the art and science of fracture treatment design. The inclusion of economic analysis as the first step in the design optimization process, along with the authors’ vast experience with treatment design and field implementation, offers a unique glimpse of this essential process. Staff from the operating divisions (or asset teams, in today’s lingo) will find this material readily applicable for both hydraulic fracturing and acidizing treatments. The subject matter is well organized with simple recommendations that can be followed without great effort.

Ernie Brown, Bob Thrasher and Larry Behrmann use Chapter 11 to introduce the reader to the operational procedures and completion considerations necessary for successful field execution of well stimulation treatments. Their discussion includes vertical, deviated and S-shaped wells, in addition to wells with more complex geometries. Factors that have an impact on quality assurance, technologies for treatment monitoring and operational integrity during job execution are all addressed in detail. Field instrumentation, real-time analysis and recommended remedi-

ation actions during execution are presented in a logical sequence. The Appendix by Phillip Halleck thoroughly reviews perforator penetration and its relation to permeability damage.

In Chapter 12, Bob Poe and Michael Economides discuss post-treatment evaluation and well performance prediction. The authors also present applications of fracture-mapping techniques, production logging and pressure transient analysis. The chapter concludes this half of the volume on the salient aspects of hydraulic fracturing technology for well stimulation.

The second set of chapters is dedicated to the technology of chemical stimulation and formation damage mitigation using chemical treatments. It begins with the introduction of matrix treatment (acidizing) by chemical means by Ron Thomas and Lee Morgenhaler. Both authors are highly experienced in their topic, as reflected by the thoroughness of the information in Chapter 13. The initial overview of using a candidate selection advisor walks the reader through the process in a simple and able manner. They also provide an interesting historical progression of the technology. In addition to candidate selection, the authors cover fluid selection, treatment placement and operational processes as well as treatment economics. The discussion is well supported by the introduction of case histories and process flow charts, and the theme of advice is clear throughout the chapter.

Don Hill, George King, Olivier Liétard and Bernard Piot discuss formation damage in Chapter 14. Covered thoroughly are the origin and diagnosis of formation damage along with suitable treatment strategies for its mitigation and elimination. Various mechanisms and stages of the formation damage process are presented in a logical sequence. Damage causes are identified for drilling, completion (i.e., casing, cementing, perforating and gravel packing), stimulation, and production and injection operations.

Chapter 15 covers damage removal materials and their impact on well performance and integrity. Syed Ali and Jerry Hinkel explain the association of treatment materials and damage types for recommended stimulation processes. The discussion is both comprehensive and concise, providing the practicing engineer with a useful guide for assessing the impact of chemical treatment additives and production chemistry on formation deliverability and well productivity.

Professors Dan Hill and Bob Schechter explain the fundamentals of acid stimulation in Chapter 16. This

scientifically rigorous treatment of the subject summarizes extensive research results with great clarity. The implications of pumping procedures and fluid chemistry on well stimulation results are thoroughly presented for the reader. Acidizing of both sandstone and carbonate rock is covered. The subjects of wormhole formation and permeability enhancement in the acid injection path are discussed, with an additional treatment of wormhole formation in the Appendix by Chris Fredd.

The subject of carbonate acidizing is well served in Chapter 17 by Joel Robert and Curtis Crowe. The chapter includes a detailed discussion of the reaction of hydrochloric acid with carbonate rocks. Placement and diversion techniques are highlighted along with case studies and field illustrations.

Harry McLeod and W. David Norman present an authoritative treatment of sandstone acidizing in Chapter 18. The authors share their thorough knowledge of the theoretical and practical aspects of this subject. Treatment fluids, reaction kinetics and modeling, and damage removal mechanisms are covered. The effective discussion of acid staging, diverting and operational procedures will guide the practicing engineer in successfully planning job execution.

Joel Robert and Bill Rossen continue the operational theme in Chapter 19. They discuss pumping strategies, diversion techniques, foam treatments, ball sealers and mechanical tools. Horizontal well acidizing is specifically addressed.

In the final chapter, Carl Montgomery and Michael Economides address matrix stimulation treatment evaluation. Several analysis methods are presented and critiqued. The authors also provide sharp insights into the comparative analytical tools used for treatment monitoring and diagnostics. Chapter 20 ends with a process diagram of job treatment evaluation and an assessment of production logging and tracer methods as evaluation tools.

So here you have it, a technology for all time and all places, a money-making endeavor and a challenging engineering effort that is made easier with references such as this volume.

The third edition of *Reservoir Stimulation* will be, like its two predecessors, on the desk of every practicing engineer and technologist working on well stimulation, whether the concern is hydraulic fracturing, acidizing or chemical treatment. The tradition established by the previous editions is continued and further expanded in the present version. The pleasure

I had in reading through the vast amount of knowledge imbedded in the 20 chapters more than makes up for the strange hour at which I am working on these final thoughts. I hope the reader will find this volume as stimulating (no pun intended), educational and useful as I believe it to be and will recognize and utilize the contributions and know-how of its authors to achieve his or her goals.

Good reading.

# Reservoir Stimulation in Petroleum Production

*Michael J. Economides, University of Houston*

*Curtis Boney, Schlumberger Dowell*

## 1-1. Introduction

Reservoir stimulation and artificial lift are the two main activities of the production engineer in the petroleum and related industries. The main purpose of stimulation is to enhance the property value by the faster delivery of the petroleum fluid and/or to increase ultimate economic recovery.

Matrix stimulation and hydraulic fracturing are intended to remedy, or even improve, the natural connection of the wellbore with the reservoir, which could delay the need for artificial lift. This chapter outlines stimulation techniques as tools to help manage and optimize reservoir development.

Understanding stimulation requires understanding the fundamental issues of petroleum production and the position and applicability of the process.

### 1-1.1. Petroleum production

Petroleum reservoirs are found in geologic formations containing porous rock. Porosity  $\phi$  is the fraction of the rock volume describing the maximum possible fluid volume that can be stored.

Petroleum, often referred to in the vernacular as oil or gas depending on the in-situ conditions of pressure and temperature, is a mixture of hydrocarbons ranging from the simplest, methane, to long-chain hydrocarbons or complex aromatics of considerable molecular weights. Crude oils are frequently referred to as paraffinic or asphaltenic, depending on the dominant presence of compounds within those hydrocarbon families.

The phase behavior of petroleum hydrocarbons is usually greatly simplified, separating compounds in the gaseous phase from those in the liquid phase into two pseudocompounds (oil and gas). The bubble-point pressure  $p_b$  of the mixture becomes important. If the reservoir pressure is greater than this value, the fluid is referred to as undersaturated. If the reservoir pressure is below  $p_b$ , free gas will form, and the

reservoir is known as saturated or two phase. Gas reservoirs exist below the dewpoint pressure.

Petroleum reservoirs also always contain water. The water appears in two forms: within the hydrocarbon zone, comprising the interstitial or connate water saturation  $S_{wc}$ , and in underlying water zones, which have different magnitudes in different reservoirs. The connate water saturation is always present because of surface tension and other adhesion affinities between water and rock and cannot be reduced.

The underlying water, segregated from hydrocarbons by gravity, forms a gas-water or oil-water contact that is not sharp and may traverse several feet of formation because of capillary pressure effects. The water may intrude into the hydrocarbon zone as a result of perturbations made during petroleum production.

The ideas of porosity and connate water saturation are coupled with the areal extent of a reservoir  $A$  and the reservoir net thickness  $h$  to provide the hydrocarbon volume, referred to as initial-oil-in-place or initial-gas-in-place:

$$V_{HC} = Ah\phi(1 - S_{wc}). \quad (1-1)$$

Because oil and gas production rates in the petroleum industry are accounted in standard-condition volumes (e.g., standard pressure  $p_{sc} = 14.7$  psi or 1 atm [ $1 \times 10^5$  Pa] and standard temperature  $T_{sc} = 60^\circ\text{F}$  [ $15.6^\circ\text{C}$ ]), the right-hand side of Eq. 1-1 is divided by the formation volume factor for oil  $B_o$  or for gas  $B_g$ .

Wells drilled to access petroleum formations cause a pressure gradient between the reservoir pressure and that at the bottom of the well. During production or injection the pressure gradient forces fluids to flow through the porous medium. Central to this flow is the permeability  $k$ , a concept first introduced by Darcy (1856) that led to the well-known Darcy's law. This law suggests that the flow rate  $q$  is proportional to the pressure gradient  $\Delta p$ :

$$q \propto k\Delta p. \quad (1-2)$$

The fluid viscosity  $\mu$  also enters the relationship, and for radial flow through an area  $2\pi rh$ , Eq. 1-2 becomes

$$p - p_{wf} = \frac{q\mu}{2\pi kh} \ln \frac{r}{r_w}, \quad (1-3)$$

where  $p_{wf}$  and  $r_w$  are the bottomhole flowing pressure and wellbore radius, respectively.

Equation 1-3 is also well known and forms the basis to quantify the production (or injection) of fluids through vertical wells from porous media. It is perhaps the most important relationship in petroleum engineering.

The permeability  $k$  used in Eq. 1-3 is absolute, implying only one fluid inhabiting and the same fluid flowing through the porous medium. This is, of course, never true for oil or gas flow. In the presence of another fluid, such as connate water, an effective permeability is in force, which is usually symbolized by a subscript (e.g.,  $k_o$ ) and always implied. The effective permeability in a reservoir is smaller than the absolute permeability, which may be measured in a laboratory on cores extracted from the reservoir.

If more than one fluid flows, relative permeabilities that are functions of the fluid saturations are in effect:

$$k_{ro} = \frac{k_o}{k}, k_{rw} = \frac{k_w}{k} \text{ and } k_{rg} = \frac{k_g}{k}, \quad (1-4)$$

where  $k_{ro}$ ,  $k_{rw}$  and  $k_{rg}$  are the relative permeabilities and  $k_o$ ,  $k_w$  and  $k_g$  are the effective permeabilities of oil, water and gas, respectively.

Equation 1-3, in conjunction with appropriate differential equations and initial and boundary conditions, is used to construct models describing petroleum production for different radial geometries. These include steady state, where the outer reservoir pressure  $p_e$  is constant at the reservoir radius  $r_e$ ; pseudosteady state, where no flow is allowed at the outer boundary ( $q = 0$  at  $r_e$ ); and infinite acting, where no boundary effects are felt. Well-known expressions for these production modes are presented in the next section.

Regardless of the mode of reservoir flow, the near-well zone may be subjected to an additional pressure difference caused by a variety of reasons, which alters the radial (and horizontal) flow converging into the well.

The skin effect  $s$ , which is analogous to the film coefficient in heat transmission, was introduced by Van Everdingen and Hurst (1949) to account for these phenomena. Fundamentally a dimensionless number, it describes a zone of infinitesimal extent that causes a steady-state pressure difference, conveniently defined as

$$\Delta p_s = \frac{q\mu}{2\pi kh} s. \quad (1-5)$$

Adding Eqs. 1-3 and 1-5 results in

$$p - p_{wf} = \frac{q\mu}{2\pi kh} \left( \ln \frac{r}{r_w} + s \right), \quad (1-6)$$

where the  $p_{wf}$  in Eq. 1-6 is different from that in Eq. 1-3. A positive skin effect requires a lower  $p_{wf}$ , whereas a negative skin effect allows a higher value for a constant rate  $q$ . For production or injection, a large positive skin effect is detrimental; a negative skin effect is beneficial.

Two extensions of Eq. 1-6 are the concepts of effective wellbore radius and the important productivity (or injectivity) index.

With simple rearrangement and employing a basic property of logarithms, Eq. 1-6 yields

$$p - p_{wf} = \frac{q\mu}{2\pi kh} \ln \left( \frac{r}{r_w e^{-s}} \right). \quad (1-7)$$

The

expression  $r_w e^{-s}$  is the effective wellbore radius, denoted as  $r_w'$ . A positive skin effect causes the effective wellbore radius to be smaller than the actual, whereas a negative skin effect has the opposite result.

A second rearrangement yields

$$\frac{q}{p - p_{wf}} = \frac{2\pi kh}{\mu [\ln(r_e / r_w) + s]}. \quad (1-8)$$

The left-hand side of Eq. 1-8 is the well productivity (or injectivity for  $p_{wf} > p$ ) index.

The entire edifice of petroleum production engineering can be understood with this relationship. First, a higher  $kh$  product, which is characteristic of particular reservoirs, has a profound impact. The current state of worldwide petroleum production and the relative contributions from various petroleum-producing provinces and countries relate intimately with the  $kh$  products of the reservoirs under exploitation. They can range by several orders of magnitude.

There is virtually nothing that a petroleum engineer can do to substantially alter this situation. Mature petroleum provinces imply that following the exploitation of far more prolific zones is the exploitation of increasingly lackluster zones with small  $kh$  values, which characterize more recently discovered formations.

A second element of mature fields is reservoir pressure depletion, the effect of which can be seen readily from Eq. 1-8. Although the right-hand side of the equation may be constant, even with a high  $kh$ , the production rate  $q$  will diminish if  $p - p_{wf}$  is reduced. For a constant  $p_{wf}$ , reduction in the reservoir pressure  $p$  has this effect.

The role of the petroleum production engineer, who must deal with the unalterable  $kh$  and pressure of a given reservoir, is to maximize the productivity index by reducing the skin effect and/or the required bottomhole flowing pressure to lift the fluids to the top. Maximizing the productivity index by reducing the skin effect is central to the purpose of this volume and constitutes the notion of stimulation; reducing the bottomhole flowing pressure leads to artificial lift (both gas and pump assisted). Finally, the bottomhole flowing pressure may have an allowable lower limit to prevent or retard undesirable phenomena such as sand production and gas or water coning.

### 1-1.2. Units

The traditional petroleum engineering oilfield units are not consistent, and thus, most equations that are cast in these units require conversion constants. For example,  $1/(2\pi)$  in Eq. 1-3 is appropriate if SI units are used, but must be replaced by the familiar value of 141.2 if  $q$  is in STB/D (which must be multiplied also by the formation volume factor  $B$  in RB/STB);  $\mu$  is in cp;  $h$ ,  $r$  and  $r_w$  are in ft; and  $p$  and  $p_{wf}$  are in psi. Table 1-1 contains unit conversion factors for the typical production engineering variables.

For unit conversions there are two possibilities. Either all variables are converted and then two versions of the equation exist (one in oilfield and a second in SI units), or one equation is provided and the result is converted. In this volume the second option is adopted. Generally, the equations are in the traditional oilfield units predominant in the literature.

**Table 1-1. Unit conversions for petroleum production engineering.**

Variable	Oilfield Units	SI Units	Conversion (multiply oilfield units)
Area, $A$	ft <sup>2</sup>	m <sup>2</sup>	$9.29 \times 10^{-2}$
Compressibility, $c_t$	psi <sup>-1</sup>	Pa <sup>-1</sup>	$1.45 \times 10^{-4}$
Length	ft	m	$3.05 \times 10^{-1}$
Permeability, $k$	md	m <sup>2</sup>	$9.9 \times 10^{-16}$
Pressure, $p$	psi	Pa	$6.9 \times 10^3$
Rate (oil), $q$	STB/D	m <sup>3</sup> /s	$1.84 \times 10^{-6}$
Rate (gas), $q$	Mscf/D	m <sup>3</sup> /s	$3.28 \times 10^{-4}$
Viscosity, $\mu$	cp	Pa-s	$1 \times 10^{-3}$

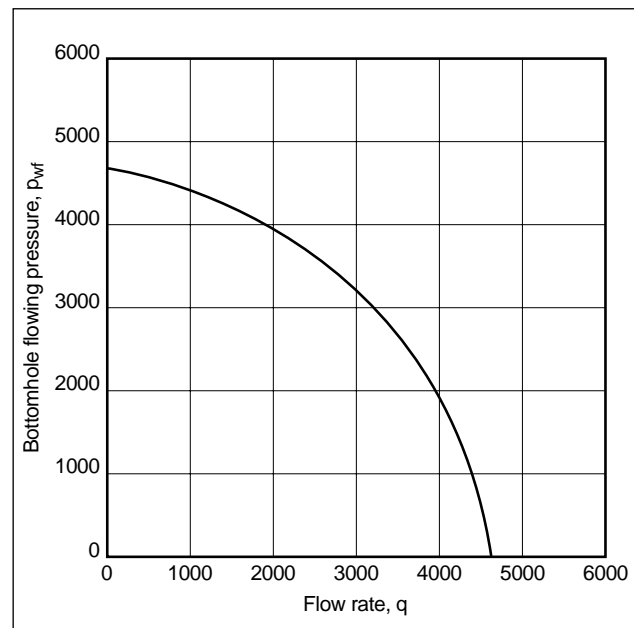


**Figure 1-1.** The inflow performance relationship relates the production rate to the bottomhole flowing pressure.

## 1-2. Inflow performance

The well production or injection rate is related to the bottomhole flowing pressure by the inflow performance relationship (IPR). A standard in petroleum production, IPR is plotted always as shown in Fig. 1-1.

Depending on the boundary effects of the well drainage, IPR values for steady-state, pseudosteady-state and transient conditions can be developed readily. In the following sections, the relationships for the three main flow mechanisms are presented first for vertical and then for horizontal wells. The



expressions, almost all of which are in wide use, are in oilfield units. A complete outline of their development is in Economides *et al.* (1994).

### 1-2.1. IPR for steady state

Equation 1-6 can be converted readily to a steady-state expression by simply substituting  $p$  with  $p_e$  and  $r$  with  $r_e$ . Thus, in oilfield units and with simple rearrangements, the IPR for oil is

$$q = \frac{kh(p_e - p_{wf})}{141.2B\mu[\ln(r_e/r_w) + s]} \quad (1-9)$$

A plot of  $p_{wf}$  versus  $q$  forms a straight line, the vertical intercept is  $p_e$ , and the flow rate at the horizontal intercept (i.e., at  $p_{wf} = 0$ ) is known as the absolute open-flow potential. The slope is, of course, constant throughout the production history of the well, assuming single-phase flow, and its value is exactly equal to the reciprocal of the productivity index.

For gas, the analogous expression is approximately

$$q = \frac{kh(p_e^2 - p_{wf}^2)}{1424\bar{\mu}\bar{Z}T[\ln(r_e/r_w) + s]} \quad (1-10)$$

where  $\bar{Z}$  is the average gas deviation factor (from ideality),  $T$  is the absolute temperature in °R, and  $\bar{\mu}$  is the average viscosity.

Equation 1-10 has a more appropriate form using the Al-Hussainy and Ramey (1966) real-gas pseudo-pressure function, which eliminates the need to average  $\mu$  and  $Z$ :

$$q = \frac{kh[m(p_e) - m(p_{wf})]}{1424T[\ln(r_e/r_w) + s]} \quad (1-11)$$

For two-phase flow, production engineers have used several approximations, one of which is the Vogel (1968) correlation, which generally can be written as

$$\frac{q_o}{q_{o,max}} = 1 - 0.2 \frac{p_{wf}}{p} - 0.8 \left( \frac{p_{wf}}{p} \right)^2 \quad (1-12)$$

$$q_{o,max} = \frac{AOFP}{1.8}, \quad (1-13)$$

where  $q_o$  is the oil production rate,  $q_{o,max}$  is the maximum possible oil rate with two-phase flow, and  $AOFP$  is the absolute open-flow potential of single-phase oil flow.

The usefulness of the Vogel approximation is that it can be used to predict the oil production rate when free gas flows (or is present) although only oil properties are employed. For steady state, Eqs. 1-12 and 1-13 can be combined with Eq. 1-9:

$$q_o = \frac{k_o h p_e \left[ 1 - 0.2 \frac{p_{wf}}{p_e} - 0.8 \left( \frac{p_{wf}}{p_e} \right)^2 \right]}{254.2 B_o \mu_o [\ln(r_e/r_w) + s]} \quad (1-14)$$

The subscript  $o$  is added here to emphasize the point that oil properties are used. The subscript is frequently omitted, although it is implied. Although neither Eq. 1-11 (for gas) nor Eq. 1-14 (for two-phase flow) provides a straight-line IPR, all steady-state IPRs provide a stationary picture of well deliverability. An interesting group of IPR curves for oil is derived from a parametric study for different skin effects, as shown in Fig. 1-2.

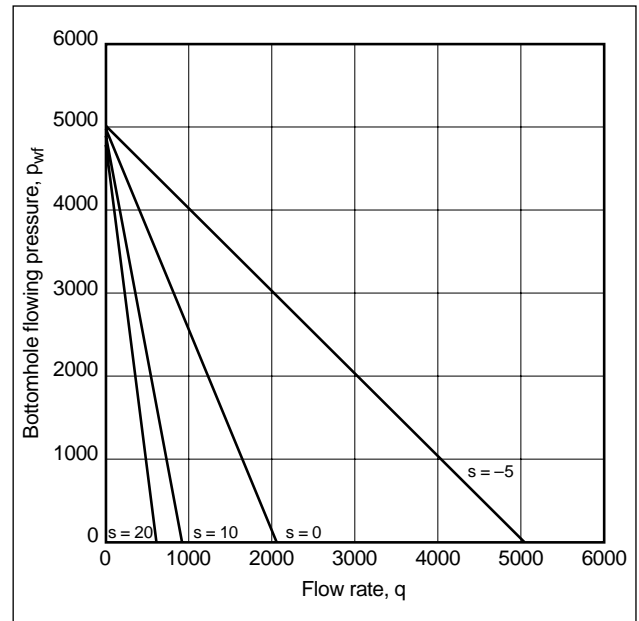


**Figure 1-2.** Variation of the steady-state IPR of an oil well for different skin effects.

- Example of steady-state IPR: skin effect variation  
Suppose that  $k = 5$  md,  $h = 75$  ft,  $p_e = 5000$  psi,  $B = 1.1$  RB/STB,  $\mu = 0.7$  cp,  $r_e = 1500$  ft and  $r_w = 0.328$  ft. Develop a family of IPR curves for an undersaturated oil reservoir for skin effects from  $-5$  to  $20$ .

### Solution

Using Eq. 1-9 and substituting for the given variables:

$$q = 3.45 \left( \frac{5000 - p_{wf}}{8.43 + s} \right).$$

Figure 1-2 is a plot of the family of IPR curves. For a reasonable  $p_{wf} = 2000$ , the flow rates at  $s = 20, 0$  and  $-5$  are approximately 365, 1230 and 3000 STB/D, respectively, showing the extraordinary impact of a negative skin effect.

### 1-2.2. IPR for pseudosteady state

At first glance, the expression for pseudosteady-state flow for oil,

$$q = \frac{kh(\bar{p} - p_{wf})}{141.2B\mu[\ln(0.472r_e/r_w) + s]}, \quad (1-15)$$

appears to have little difference from the expression for steady state (Eq. 1-9). However, the difference is significant. Equation 1-15 is given in terms of the average reservoir pressure  $\bar{p}$ , which is not constant but, instead, integrally connected with reservoir depletion.

Material-balance calculations such as the ones introduced by Havlena and Odeh (1963) are required to relate the average reservoir pressure with time and the underground withdrawal of fluids.

Interestingly, the productivity index for a given skin effect is constant although the production rate declines because  $\bar{p}$  declines. To stem the decline, the production engineer can adjust the  $p_{wf}$ , and thus, artificial lift becomes an important present and future consideration in well management. Successive IPR curves for a well producing at pseudosteady state at different times in the life of the well and the resulting different values of  $\bar{p}$  are shown in Fig. 1-3.

The analogous pseudosteady-state expressions for gas and two-phase production are

$$q = \frac{kh[m(\bar{p}) - m(p_{wf})]}{1424T[\ln(0.472r_e/r_w) + s]} \quad (1-16)$$

$$q = \frac{kh\bar{p} \left[ 1 - 0.2 \frac{p_{wf}}{\bar{p}} - 0.8 \left( \frac{p_{wf}}{\bar{p}} \right)^2 \right]}{254.2B\mu[\ln(0.472r_e/r_w) + s]}. \quad (1-17)$$

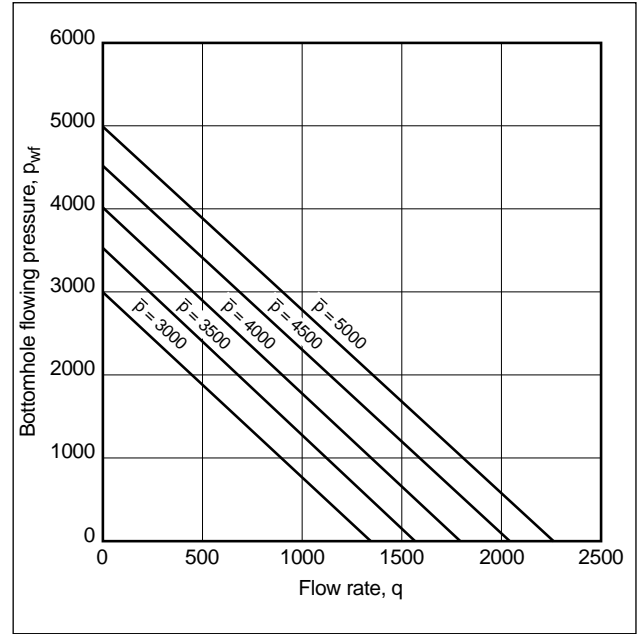


**Figure 1-3.** Variation of the pseudosteady-state IPR for an oil well for declining reservoir pressure.

- Example of pseudosteady-state IPR: effect of average reservoir pressure

This example repeats the preceding “Example of steady-state IPR: skin effect variation” (page 1-4) for  $s = 0$  but allows  $\bar{p}$  to vary from 5000 to 3000 in increments of 500 psi.

### Solution

Using Eq. 1-15 and substituting for the given variables (including  $s = 0$ ):

$$q = 0.45(\bar{p} - p_{wf}).$$

In the Fig. 1-3 family of IPR curves for different values of  $\bar{p}$ , the curves are parallel, reflecting the constant productivity index. (This type of construction assumes that oil remains undersaturated throughout; i.e., above the bubblepoint pressure.)

### 1-2.3. IPR for transient (or infinite-acting) flow

The convection-diffusion partial differential equation, describing radial flow in a porous medium, is

$$\frac{\partial^2 p}{\partial r^2} + \frac{1}{r} \frac{\partial p}{\partial r} = \frac{\phi \mu c_t}{k} \frac{\partial p}{\partial t}, \quad (1-18)$$

where  $c_t$  is the total system compressibility,  $p$  is pressure,  $t$  is time, and  $r$  is radial distance. This equation, in wide use in many other engineering fields, provides a well-known solution for an infinite-acting reservoir producing at constant rate at the well.

Using dimensionless variables (for oil, in oilfield units) for pressure and time, respectively:

$$p_D = \frac{kh\Delta p}{141.2qB\mu} \quad (1-19)$$

$$t_D = \frac{0.000264kt}{\phi\mu c_t r_w^2}. \quad (1-20)$$

For  $r = r_w$  (i.e., at the well) a useful approximate form of the solution in dimensionless form is simply

$$p_D = \frac{1}{2}(\ln t_D + 0.8091). \quad (1-21)$$

Equation 1-21 provided the basis of both the forecast of transient well performance and the Horner (1951) analysis, which is one of the mainstays of pressure transient analysis presented in Chapter 2.

Although Eq. 1-21 describes the pressure transients under constant rate, an exact analog for constant pressure exists. In that solution,  $p_D$  is replaced simply by the reciprocal of the dimensionless rate  $1/q_D$ .

The dimensioned and rearranged form of Eq. 1-21, after substitution of the natural log by the log base 10, is

$$q = \frac{kh(p_i - p_{wf})}{162.6B\mu} \left( \log t + \log \frac{k}{\phi\mu c_t r_w^2} - 3.23 \right)^{-1}, \quad (1-22)$$

where  $p_i$  is the initial reservoir pressure. The skin effect can be added inside the second set of parentheses as  $0.87s$ .

As previously done for the pseudosteady-state IPR, gas and two-phase analogs can be written:

$$q = \frac{kh[m(p_i) - m(p_{wf})]}{1638T} \left( \log t + \log \frac{k}{\phi\mu c_t r_w^2} - 3.23 \right)^{-1} \quad (1-23)$$

$$q = \frac{kh p_i \left[ 1 - \frac{p_i}{p_{wf}} - \left( \frac{p_i}{p_{wf}} \right)^2 \right]}{254.2B\mu \left( \log t + \log \frac{k}{\phi\mu c_t r_w^2} - 3.23 \right)}. \quad (1-24)$$

Transient IPR curves can be generated for each instant in time as shown in Fig. 1-4.

- Example of transient IPR

Using the variables of the previous two examples and  $\phi = 0.25$ ,  $c_t = 10^{-5} \text{ psi}^{-1}$  and  $p_i = 5000$  psi, develop transient IPR curves for  $t = 3, 6$  and 36 months. The time in Eq. 1-22 must be entered in hours. Assume  $s = 0$ .

**Solution**

Using Eq. 1-22 and substituting for the given variables:

$$q = \frac{3(5000 - p_{wf})}{\log t + 4.19}.$$

Figure 1-4 is a graph of the three transient IPRs. The expected flow rate declines for a constant  $p_{wf} = 2000$ . The flow rates at 3, 6 and 36 months are 1200, 1150 and 1050 STB/D, respectively. The 36-month calculation is unrealistic because it is unlikely that a well would remain infinite acting for such long period of time. Thus, a pseudosteady-state IPR with a  $\bar{p}$  intersection at a point below  $p_i$  is most likely in effect at that time.

## 1-2.4. Horizontal well production

Since the mid-1980s horizontal wells have proliferated, and although estimates vary, their share in the

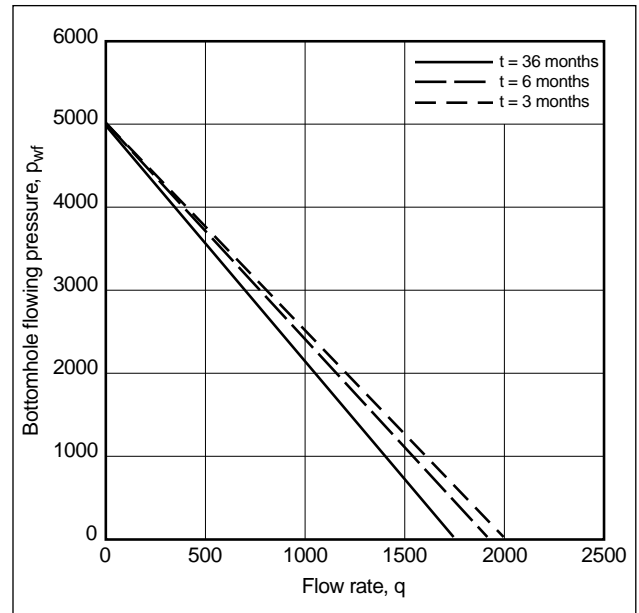


**Figure 1-4.** Transient IPR curves for an oil well.

production of hydrocarbons will probably reach 50% or more.

A model for a constant-pressure ellipse at steady-state production was introduced by Joshi (1988) and augmented by Economides *et al.* (1991):

$$q = \frac{k_H h (p_e - p_{wf})}{141.2 B \mu \left( \ln \left[ \frac{a + \sqrt{a^2 - (L/2)^2}}{L/2} \right] + \frac{I_{ani} h}{L} \ln \left[ \frac{I_{ani} h}{r_w (I_{ani} + 1)} \right] \right)}, \quad (1-25)$$

where  $L$  is the horizontal well length and  $k_H$  is the horizontal permeability. The latter is the same as that used in all vertical well deliverability relationships. The subscript distinguishes it from the vertical permeability  $k_V$ , which is related to the index of the horizontal-to-vertical permeability anisotropy  $I_{ani}$ :

$$I_{ani} = \sqrt{\frac{k_H}{k_V}}. \quad (1-26)$$

The large half-axis  $a$  of the horizontal drainage ellipse formed around a horizontal well within an equivalent radius  $r_{eH}$  is

$$a = \frac{L}{2} \left\{ 0.5 + \left[ 0.25 + \left( \frac{r_{eH}}{L/2} \right)^4 \right]^{1/2} \right\}, \quad (1-27)$$

where  $r_{eH}$  is the equivalent radius in a presumed circular shape of a given drainage area. Equation 1-27 transforms it into an elliptical shape.

Equation 1-25 can be used readily to develop a horizontal well IPR and a horizontal well productivity index.

A comparison between horizontal (Eq. 1-25) and vertical (Eq. 1-9) productivity indexes in the same formation is an essential step to evaluate the attractiveness or lack thereof of a horizontal well of a given length over a vertical well. Such comparison generally suggests that in thick reservoirs (e.g.,  $h > 100$  ft) the index of anisotropy becomes important. The smaller its value (i.e., the larger the vertical permeability), the more attractive a horizontal well is relative to a vertical well. For thinner formations (e.g.,  $h < 50$  ft), the requirements for good vertical permeability relax.

A skin effect can also be added to the horizontal well deliverability of Eq. 1-25, inside the large

parentheses in the denominator and multiplied by the scaled aspect ratio  $I_{ani} h/L$ .

For gas and two-phase flow, Eq. 1-25 can be adjusted readily by the transformations (compared with Eq. 1-9) shown in Eqs. 1-11 and 1-14.

For pseudosteady state, a generalized horizontal well production model, accounting for any positioning of a well laterally and vertically within a drainage, was presented by Economides *et al.* (1996). The basic model in Fig. 1-5 has reservoir dimensions  $x_e$ ,  $y_e$  and  $h$ , horizontal well length  $L$  and an angle  $\phi$  between the well projection on the horizontal plane and  $x_e$ .

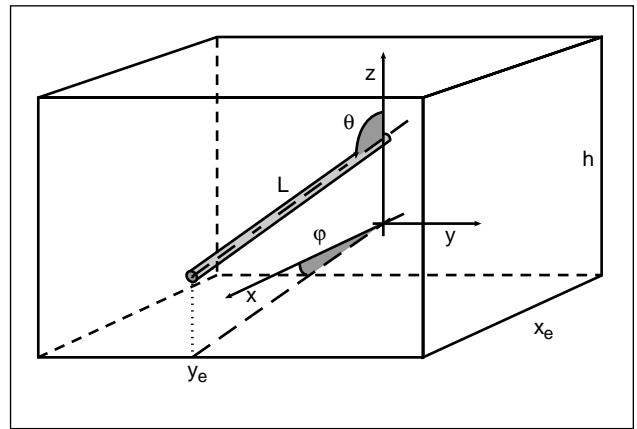


**Figure 1-5.** Generalized well model for production from an arbitrarily oriented well in an arbitrarily shaped reservoir (Economides *et al.*, 1996).

The solution is general. First, the pseudosteady-state productivity index  $J$  is used:

$$J = \frac{q}{\bar{p} - p_{wf}} = \frac{k x_e}{887.22 B \mu \left( p_D + \frac{x_e}{2\pi L \sum s} \right)}, \quad (1-28)$$

where the reservoir permeability  $k$  is assumed to be isotropic throughout (it is adjusted later) and  $x_e$  is the well drainage dimension. The constant allows the use of oilfield units; the productivity index is in STB/D/psi. The summation of the skin effects  $\sum s$  accounts for all damage and mechanical skin effects. Finally, the dimensionless pressure is

$$p_D = \frac{x_e C_H}{4\pi h} + \frac{x_e}{2\pi L} s_x. \quad (1-29)$$

Equation 1-29 decomposes a three-dimensional (3D) problem into one two-dimensional term and one one-dimensional term. The first term on the right-hand side accounts for horizontal positioning effects, with  $C_H$  as a shape factor. The second term accounts for both the reservoir thickness (causing a distortion of the flow lines) and the additional effects from vertical eccentricity in the case that the well is not positioned at the vertical middle of the reservoir.

The vertical effects skin effect  $s_x$  is (after Kuchuk *et al.*, 1988)

$$s_x = \ln\left(\frac{h}{2\pi r_w}\right) - \frac{h}{6L} + s_e, \quad (1-30)$$

where  $s_e$  is the vertical eccentricity skin:

$$s_e = \frac{h}{L} \left[ \frac{2z_w}{h} - \frac{1}{2} \left( \frac{2z_w}{h} \right)^2 - \frac{1}{2} \right] - \ln \left[ \sin \left( \frac{\pi z_w}{h} \right) \right], \quad (1-31)$$

where  $z_w$  is the elevation from the bottom of the reservoir. For a well at the vertical middle,  $s_e = 0$ .

- Example calculation of  $s_x$  for two thicknesses  
Assume that  $L = 2000$  ft and  $r_w = 0.328$  ft. Calculate  $s_x$  for  $h = 50$  ft and  $h = 200$  ft.

#### Solution

Using Eq. 1-30 for  $h = 50$  ft:

$$s_x = \ln \frac{50}{(2)(3.14)(0.328)} - \frac{50}{(6)(2000)} = 3.2.$$

For  $h = 200$  ft,  $s_x = 4.6$ . This calculation suggests that for thicker reservoirs the distortion of the flowlines has relatively more severe detrimental effects.

Figure 1-6 provides values for  $s_x$  for a range of reservoir thicknesses and a centered well ( $r_w = 0.4$  ft).

For the case of a vertically eccentric well, Fig. 1-7 provides values for  $s_e$  for various levels of eccentricity. The values in Fig. 1-7 are the same for symmetrical eccentricity; i.e.,  $s_e$  is the same for  $z_w/h = 0.1$  and  $0.9$ . At  $z_w/h = 0.5$ ,  $s_e = 0$ , as expected.

To account for the position of the well in the horizontal plane, a series of shape factors is presented in Table 1-2. Although the solution pre-

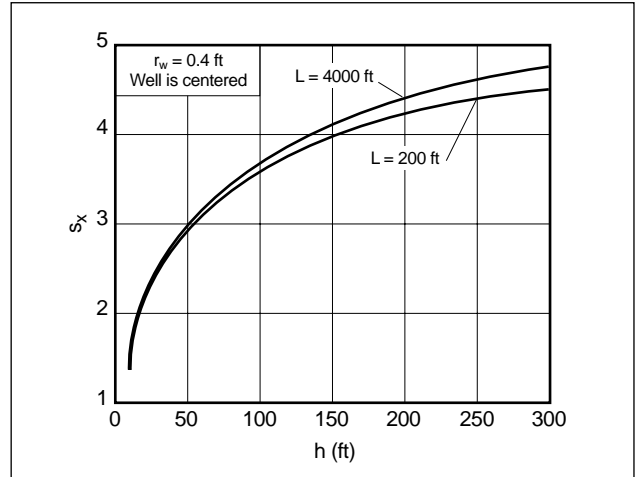


Figure 1-6. Vertical effects skin effect for a horizontal well (Economides *et al.*, 1996).

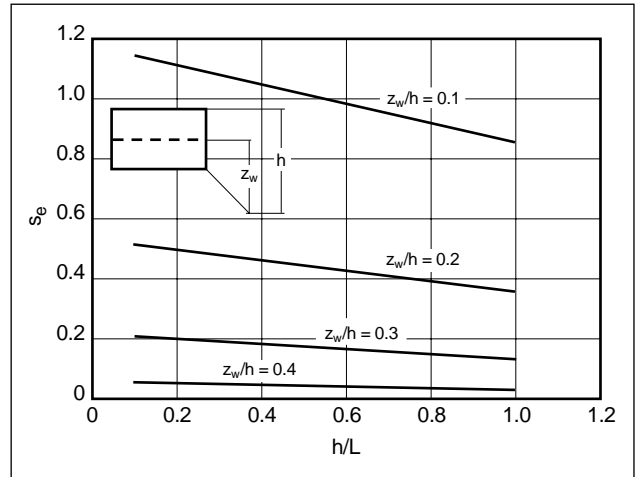
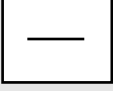
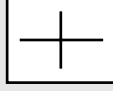
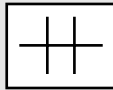
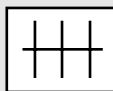
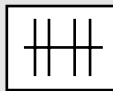
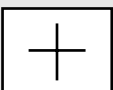
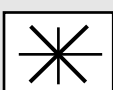
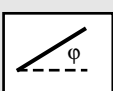


Figure 1-7. Vertical eccentricity skin effect (Economides *et al.*, 1996).

sented by Economides *et al.* (1996) is general and a computer program is available, the library of shape factors in Table 1-2 is useful for quick approximations (in the style of the classic Dietz [1965] factors for vertical wells). Multiple horizontal well configurations are also included.

- Example calculation of horizontal well productivity index: comparison with a vertical well  
Assume that  $L = 2000$  ft,  $x_e = y_e = 2700$  ft,  $h = 200$  ft,  $r_w = 0.328$  ft,  $B = 1$  RB/STB and  $\mu = 1$  cp. The well is in the vertical middle (i.e.,  $s_e = 0$ ). Permeability  $k = 10$  md. For this example, the productivity index is calculated for an isotropic reservoir. However, the permeability of most reservoirs is not isotropic between the vertical and horizontal planes, resulting in a consid-

**Table 1-2. Shape factors for well productivity (Economides *et al.*, 1996).**

		$L/x_e$	$C_H$				$C_H$
	$x_e = 4y_e$	0.25	3.77		$x_e = y_e$ $L_x/x_e = 0.4$	$L_y = 2L_x$	1.10
		0.5	2.09			$L_y = L_x$	1.88
		0.75	1.00			$L_y = 0.5L_x$	2.52
		1	0.26				
	$x_e = 2y_e$	0.25	3.19		$x_e = y_e$ $L_x/x_e = 0.4$	$L_y = 2L_x$	0.79
		0.5	1.80			$L_y = L_x$	1.51
		0.75	1.02			$L_y = 0.5L_x$	2.04
		1	0.52				
	$x_e = y_e$	0.25	3.55		$x_e = y_e$ $L_x/x_e = 0.4$	$L_y = 2L_x$	0.66
		0.4	2.64			$L_y = L_x$	1.33
		0.5	2.21			$L_y = 0.5L_x$	1.89
		0.75	1.49				
		1	1.04				
	$2x_e = y_e$	0.25	4.59		$x_e = y_e$ $L_x/x_e = 0.4$	$L_y = 2L_x$	0.59
		0.5	3.26			$L_y = L_x$	1.22
		0.75	2.53			$L_y = 0.5L_x$	1.79
		1	2.09				
	$4x_e = y_e$	0.25	6.69				
		0.5	5.35				
		0.75	4.63				
		1	4.18				
	$x_e = y_e$	0.25	2.77				
		0.5	1.47				
		0.75	0.81				
		1	0.46				
	$x_e = y_e$	0.25	2.66				
		0.5	1.36				
		0.75	0.69				
		1	0.32				
	$x_e = y_e$ $L/x_e = 0.75$	0	1.49				
		30	1.48				
		45	1.48				
		75	1.49				
		90	1.49				

erable reduction in the productivity index, as shown in the next section.

### Solution

From the “Example calculation of  $s_x$  for two thicknesses” (page 1-8),  $s_x = 4.6$ , and from Table 1-2 for  $x_e = y_e$  and  $L/x_e = 2000/2700 \approx 0.75$ ,  $C_H = 1.49$ .

Using Eq. 1-29:

$$p_D = \frac{(2700)(1.49)}{(4)(3.14)(200)} + \frac{(2700)(4.6)}{(2)(3.14)(2000)} = 2.59,$$

and using Eq. 1-28:

$$J_H = \frac{(10)(2700)}{(887.22)(1)(1)(2.59)} = 11.7 \text{ STB / D / psi.}$$

The productivity index of a vertical well in the same formation, under pseudosteady-state conditions and assuming that the well is in the center of the square reservoir, is

$$J_v = \frac{kh}{141.2B\mu \ln(0.472r_e / r_w)}.$$

The drainage area is  $2700 \times 2700$  ft, resulting in  $r_e = 1520$  ft. Thus,

$$J_v = \frac{(10)(200)}{(141.2)(1)(1) \ln[(0.472)(1520) / (0.328)]} = 1.84 \text{ STB / D / psi.}$$

The productivity index ratio between a horizontal and a vertical well in this permeability-isotropic formation is  $11.7/1.84 = 6.4$ .



### 1-2.5. Permeability anisotropy

From dealing with vertical wells, petroleum engineers learned to generally ignore the concept of permeability anisotropy and refer to reservoirs as having permeabilities equal to 0.1, 3, 100 md, etc., as if permeability were a scalar quantity.

Although it has been known for a long time that permeability has different values in different directions (i.e., it is a vector) and although the impact of such anisotropy is recognized in waterflooding and even in the spacing of wells, for production from a single vertical well it is of little concern. Muskat (1937), in one of his many early contributions, suggested that the permeability affecting vertical well production is

$$\bar{k} = \bar{k}_H = \sqrt{k_x k_y}, \quad (1-32)$$

where  $\bar{k}$  is the average permeability, which for a vertical well is equal to the average horizontal permeability  $\bar{k}_H$ , and  $k_x$  and  $k_y$  are the permeabilities in the  $x$  and  $y$  directions, respectively.

Although the “average” permeability in Eq. 1-32 could equal 10 md, this value could result because the permeabilities in the  $x$  direction and  $y$  direction are both equal to 10 md or because  $k_x = 100$  md and  $k_y = 1$  md. Horizontal-to-horizontal permeability anisotropy of such magnitude is rare. However, permeability anisotropies in the horizontal plane of 3:1 and higher are common (Warpinski, 1991). Logically, a horizontal well drilled normal to the maximum rather than the minimum permeability should be a better producer.

Suppose all permeabilities are known. Then the horizontal well length, wellbore radius and reservoir dimensions can be adjusted. These adjusted variables, presented by Besson (1990), can be used instead of the true variables in predicting well performance with the model in Section 1-2.4:

$$\text{Length:} \quad L' = L\alpha^{-1/3}\beta \quad (1-33)$$

$$\text{Wellbore radius:} \quad r'_w = r_w \frac{\alpha^{2/3}}{2} \left( \frac{1}{\alpha\beta} + 1 \right), \quad (1-34)$$

where

$$\alpha = \sqrt{\frac{(k_x k_y)^{1/2}}{k_z}} \quad (1-35)$$

$$\beta = \left( \sqrt{\frac{k_y}{k_x}} \cos^2 \varphi + \sqrt{\frac{k_x}{k_y}} \sin^2 \varphi \right)^{1/2} \quad (1-36)$$

$$x' = x \frac{\sqrt{k_y k_z}}{\bar{k}} \quad (1-37)$$

$$y' = y \frac{\sqrt{k_x k_z}}{\bar{k}} \quad (1-38)$$

$$z' = z \frac{\sqrt{k_x k_y}}{\bar{k}} \quad (1-39)$$

$$\bar{k} = \sqrt[3]{k_x k_y k_z}. \quad (1-40)$$

- Example of horizontal well productivity index in an anisotropic reservoir

Repeat the calculations in “Example calculation of horizontal well productivity index: comparison with a vertical well” (page 1-8) but with  $k_x = 20$  md,  $k_y = 5$  md (the average horizontal permeability is still 10 md) and  $k_z = 1$  md. Assume that the well is parallel to the  $x_e$  boundary; i.e., the angle  $\varphi = 0$ .

#### Solution

From Eqs. 1-35 and 1-36,  $\alpha = 3.16$  and  $\beta = 0.707$ , respectively. The horizontal well length is then adjusted using Eq. 1-33 and becomes 964 ft. The wellbore radius is adjusted using Eq. 1-34 and becomes 0.511 ft. The reservoir dimensions  $x_e$ ,  $y_e$  and  $h$  are adjusted using Eqs. 1-37 through 1-39 and become 1304, 2608 and 432 ft, respectively.

The vertical effect skin effect from Eq. 1-30 is 4.85. The adjusted reservoir dimensions become  $2x_e = y_e$ . The adjusted penetration ratio  $L/x_e$  remains the same (0.75). Thus, from Table 1-2 the shape factor is 2.53.

Using Eq. 1-29 for dimensionless pressure and substituting with the adjusted variables:

$$p_D = \frac{(1304)(2.53)}{(4)(3.14)(432)} + \frac{(1304)(4.85)}{(2)(3.14)(964)} = 1.65,$$

and using Eq. 1-28, the productivity index becomes

$$J = \frac{(4.63)(1304)}{(887.22)(1)(1)(1.65)} = 4.12 \text{ STB/D/psi},$$

representing a 65% reduction from the value of 11.7 STB/D/psi calculated in the preceding “Example calculation of horizontal well productivity index: comparison with a vertical well” for the isotropic case.

### 1-3. Alterations in the near-wellbore zone

The skin effect  $s$  is intended to describe alterations in the near-wellbore zone. One of the most common problems is damage to the permeability that can be caused by practically any petroleum engineering activity, from drilling to well completions to stimulation itself. As mentioned in Section 1-1.1, the skin effect is a dimensionless number that can be obtained from a well test, as explained in detail in Chapter 2.

The nature of radial flow is that the pressure difference in the reservoir increases with the logarithm of distance; i.e., the same pressure is consumed within the first foot as within the next ten, hundred, etc. If the permeability of the near-wellbore zone is reduced significantly it is entirely conceivable that the largest portion of the total pressure gradient may be consumed within the very near wellbore zone. Similarly, recovering or even improving this permeability may lead to a considerable improvement in the well production or injection. This is the role of matrix stimulation.

#### 1-3.1. Skin analysis

Figure 1-8 describes the areas of interest in a well with an altered zone near the wellbore. Whereas  $k$  is the “undisturbed” reservoir permeability,  $k_s$  is the permeability of this altered zone.

The Van Everdingen and Hurst (1949) skin effect has been defined as causing a steady-state pressure difference (Eq. 1-5). Skin effect is mathematically dimensionless. However, as shown in Fig. 1-8, it reflects the permeability  $k_s$  at a distance  $r_s$ . A relationship among the skin effect, reduced permeability and altered zone radius may be extracted. Assuming

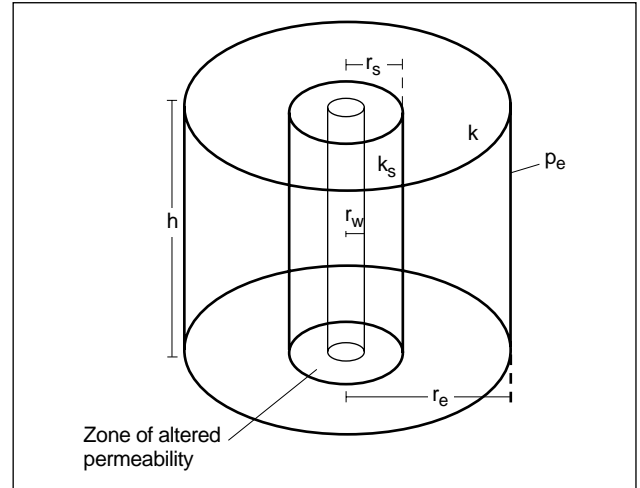


Figure 1-8. Zone of altered permeability  $k_s$  near a well.

that  $p_s$  is the pressure at the outer boundary of the altered zone, from Eq. 1-9 the undamaged relation is

$$q = \frac{kh(p_s - p_{wf,ideal})}{141.2B\mu \ln \frac{r_s}{r_w}}, \quad (1-41)$$

and if damaged,

$$q = \frac{k_s h(p_s - p_{wf,real})}{141.2B\mu \ln \frac{r_s}{r_w}}, \quad (1-42)$$

using the respective values of undamaged ideal and damaged real bottomhole flowing pressure.

Equations 1-41 and 1-42 may be combined with the definition of skin effect and the obvious relationship

$$\Delta p_s = p_{wf,ideal} - p_{wf,real} \quad (1-43)$$

to obtain

$$\Delta p_s = \frac{141.2qB\mu}{h} \ln \left( \frac{r_s}{r_w} \right) \left( \frac{1}{k_s} - \frac{1}{k} \right). \quad (1-44)$$

Equations 1-44 and 1-5 can then be combined:

$$s = \left( \frac{k}{k_s} - 1 \right) \ln \frac{r_s}{r_w}, \quad (1-45)$$

which is the sought relationship. This is the well-known Hawkins (1956) formula.

Equation 1-45 leads to one of the best known concepts in production engineering. If  $k_s < k$ , the well is damaged and  $s > 0$ ; conversely, if  $k_s > k$ , then  $s < 0$  and the well is stimulated. For  $s = 0$ , the near-well-bore permeability is equal to the original reservoir permeability.

Certain well logs may enable calculation of the damaged radius, whereas pressure transient analysis may provide the skin effect and reservoir permeability. Equation 1-45 may then provide the value of the altered permeability  $k_s$ .

Frick and Economides (1993) postulated that in the absence of production log measurements, an elliptical cone is a more plausible shape of damage distribution along a horizontal well. A skin effect expression, analogous to the Hawkins formula, was developed:

$$s_{eq} = \left( \frac{k}{k_s} - 1 \right) \ln \left[ \frac{1}{I_{ani} + 1} \sqrt{ \frac{4}{3} \left( \frac{a_{sH,max}^2}{r_w^2} + \frac{a_{sH,max}}{r_w} + 1 \right) } \right], \quad (1-46)$$

where  $I_{ani}$  is the index of anisotropy and  $a_{sH,max}$  is the horizontal axis of the maximum ellipse, normal to the well trajectory. The maximum penetration of damage is near the vertical section of the well. The shape of the elliptical cross section depends greatly on the index of anisotropy.

The skin effect  $s_{eq}$  is added to the second logarithmic term in the denominator of the horizontal well production expression (Eq. 1-25) and must be multiplied by  $I_{ani}h/L$ . One obvious, although not necessarily desirable, way to offset the effects of damage is to drill a longer horizontal well.

### 1-3.2. Components of the skin effect

Matrix stimulation has proved to be effective in reducing the skin effect caused by most forms of damage. However, the total skin effect is a composite of a number of factors, most of which usually cannot be altered by conventional matrix treatments. The total skin effect may be written as

$$s_t = s_{c+\theta} + s_p + s_d + \sum pseudoskins. \quad (1-47)$$

The last term in the right-hand side of Eq. 1-47 represents an array of pseudoskin factors, such as phase-dependent and rate-dependent effects that

could be altered by hydraulic fracturing treatments. The other three terms are the common skin factors. The first is the skin effect caused by partial completion and slant. It has been well documented by Cinco-Ley *et al.* (1975a). The second term represents the skin effect resulting from perforations, as described by Harris (1966) and expounded upon by Karakas and Tariq (1988). The third term refers to the damage skin effect.

Obviously, it is of extreme importance to quantify the components of the skin effect to evaluate the effectiveness of stimulation treatments. In fact, the pseudoskin effects can overwhelm the skin effect caused by damage. It is not inconceivable to obtain skin effects after matrix stimulation that are extremely large. This may be attributed to the usually irreducible configuration skin factors.

### 1-3.3. Skin effect caused by partial completion and slant

Figure 1-9 is relevant to Cinco-Ley *et al.*'s (1975a) development. Table 1-3 presents the pseudoskin factors caused by partial penetration and slant. To use them, it is necessary to evaluate several dimensionless groups:

$$\text{Completion thickness} \quad h_{wD} = h_w/r_w \quad (1-48)$$

$$\text{Elevation} \quad z_{wD} = z_w/r_w \quad (1-49)$$

$$\text{Reservoir thickness} \quad h_D = h/r_w \quad (1-50)$$

$$\text{Penetration ratio} \quad h_{wD}' = h_w/h. \quad (1-51)$$

The terms  $h_D$ ,  $h_{wD}$ ,  $z_{wD}/h_D$  and  $h_{wD}\cos\theta/h_D$  must be known to evaluate the skin effect.

As an example, assume  $h_D = 100$ ,  $z_{wD}/h_D = 0.5$  (midpoint of the reservoir) and  $h_{wD}\cos\theta/h_D = 0.25$  ( $\theta = 60^\circ$ ,  $h_w/h = 0.5$ ). For this case,  $s_{c+\theta} = 5.6$  (from Table 1-3). If the penetration ratio is reduced to 0.1, the skin effect increases to 15.5.

It is apparent that this skin effect alone could dwarf the skin effect caused by damage. The skin effect resulting from the partial penetration length  $h_{wD}'$  may be unavoidable because it typically results from other operational considerations (such as the prevention of gas coning).

From Table 1-3 and for full penetration it can be seen readily that a deviated well, without damage, should have a negative skin effect. Thus, a small skin effect or even one equal to zero obtained from

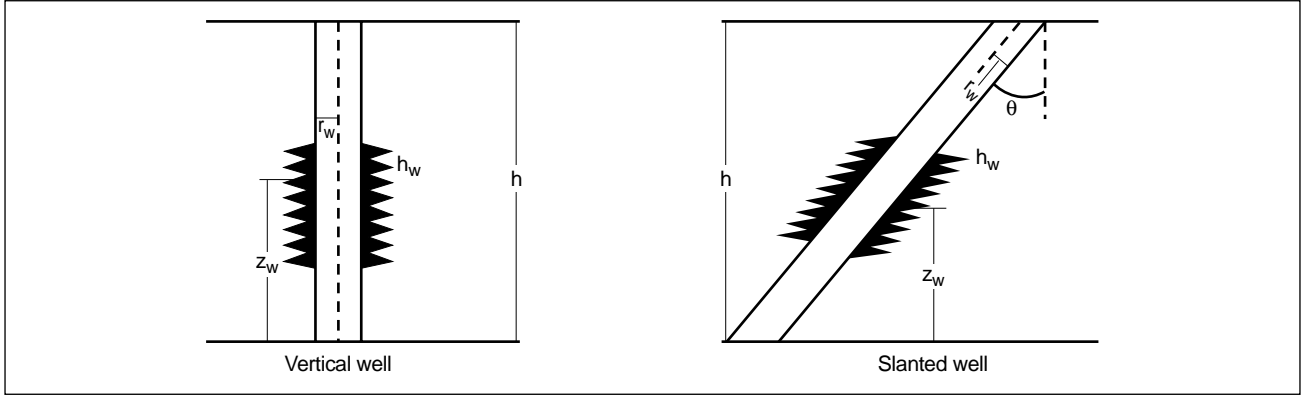


**Figure 1-9.** Geometry for partial and off-centered completions and slant skin effects (Cinco-Ley et al., 1975a).

a well test in a highly deviated well may mean considerable damage. Removal of this damage with appropriate stimulation could increase the deviated well production (or injection) considerably.

### 1-3.4. Perforation skin effect

Karakas and Tariq (1988) developed a procedure to calculate the skin effect caused by perforations. This skin effect is a composite involving the plane-flow effect  $s_H$ , vertical converging effect  $s_V$  and wellbore effect  $s_{wb}$ :

$$s_p = s_H + s_V + s_{wb} \quad (1-52)$$

The pseudoskin factor  $s_H$  is given by

$$s_H = \ln \frac{r_w}{r'_w(\theta)}, \quad (1-53)$$

where  $r'_w(\theta)$  is the effective wellbore radius and is a function of the perforation phasing angle  $\theta$ :

$$r'_w(\theta) = \begin{cases} l_p/4 & \text{when } \theta = 0 \\ \alpha_\theta(r_w + l_p) & \text{when } \theta \neq 0 \end{cases} \quad (1-54)$$

where  $l_p$  is the length of the perforation and  $\alpha_\theta$  is a phase-dependent variable and can be obtained from Table 1-4.

The vertical pseudoskin factor  $s_V$  can be calculated after certain dimensionless variables are determined:

$$h_D = \frac{h}{l_p} \sqrt{\frac{k_H}{k_V}}, \quad (1-55)$$

where  $h$  is the distance between perforations and is exactly inversely proportional to the shot density;

$$r_{pD} = \frac{r_{perf}}{2h} \left( 1 + \sqrt{\frac{k_V}{k_H}} \right), \quad (1-56)$$

where  $r_{perf}$  is the perforation radius; and

$$r_{wD} = \frac{r_w}{l_p + r_w}. \quad (1-57)$$

The vertical pseudoskin effect is then

$$s_V = 10^a h_D^{b-1} r_{pD}^b, \quad (1-58)$$

where  $a$  and  $b$  are

$$a = a_1 \log r_{pD} + a_2 \quad (1-59)$$

$$b = b_1 r_{pD} + b_2. \quad (1-60)$$

The values of the constants  $a_1$ ,  $a_2$ ,  $b_1$  and  $b_2$  are given in Table 1-5 as functions of the phasing angle  $\theta$ .

Finally, the wellbore skin effect  $s_{wb}$  can be approximated by

$$s_{wb} = c_1 e^{c_2 r_{wD}}. \quad (1-61)$$

The constants  $c_1$  and  $c_2$  can be obtained from Table 1-6.

As an example, assume  $r_w = 0.406$  ft,  $l_p = 0.667$  ft,  $h = 0.333$  ft (3 shots per foot [spf]),  $k_H/k_V = 3$ ,  $r_{perf} = 0.0208$  ft [0.25 in.] and  $\theta = 90^\circ$ .

From Eq. 1-54 and Table 1-4,  $r'_w(\theta) = 0.779$  ft, and thus from Eq. 1-53,  $s_H = -0.65$ . From Eqs. 1-55, 1-56 and 1-57, the dimensionless variables  $h_D$ ,  $r_{pD}$  and  $r_{wD}$  are equal to 0.86, 0.05 and 0.38, respectively. From Eq. 1-59 and Table 1-5,  $a = 2.58$ , and from Eq. 1-60 and Table 1-5,  $b = 1.73$ . Then, from

Table 1-3. Pseudoskin factors for partially penetrating slanted wells (Cinco-Ley <i>et al.</i> , 1975).											
$\theta_w$ (°)	$z_{wD}/h_D$	$\frac{h_{wD}\cos\theta_w}{h_D}$	$s_{\theta+c}$	$s_c$	$s_{\theta}$	$\theta_w$ (°)	$z_{wD}/h_D$	$\frac{h_{wD}\cos\theta_w}{h_D}$	$s_{\theta+c}$	$s_c$	$s_{\theta}$
<b><math>h_D = 100</math></b>						<b><math>h_D = 100</math> continued</b>					
0	0.95	0.1	20.810	20.810	0	0	0.6	0.5	2.430	2.430	0
15			20.385	20.810	-0.425	15			2.254	2.430	-0.176
30			18.948	20.810	-1.861	30			1.730	2.430	-0.700
45			16.510	20.810	-4.299	45			0.838	2.430	-1.592
60			12.662	20.810	-8.147	60			-0.466	2.430	-2.897
75			6.735	20.810	-14.074	75			-2.341	2.430	-4.772
0	0.8	0.1	15.809	15.809	0	0	0.5	0.5	2.369	2.369	0
15			15.449	15.809	-0.36	15			2.149	2.369	-0.175
30			14.185	15.809	-1.623	30			1.672	2.369	-0.697
45			12.127	15.809	-3.682	45			0.785	2.369	-1.584
60			8.944	15.809	-6.864	60			-0.509	2.369	-2.879
75			4.214	15.809	-11.594	75			-2.368	2.369	-4.738
0	0.6	0.1	15.257	15.257	0	0	0.625	0.75	0.924	0.924	0
15			14.898	15.257	-0.359	15			0.778	0.924	-0.145
30			13.636	15.257	-1.621	30			0.337	0.924	-0.587
45			11.583	15.257	-3.674	45			-0.411	0.924	-1.336
60			8.415	15.257	-6.842	60			-1.507	0.924	-2.432
75			3.739	15.257	-11.517	75			-3.099	0.924	-4.024
0	0.5	0.1	15.213	15.213	0	0	0.5	0.75	0.694	0.694	0
15			14.854	15.213	-0.359	15			0.554	0.694	-0.139
30			13.592	15.213	-1.620	30			0.134	0.694	-0.560
45			11.540	15.213	-3.673	45			-0.581	0.694	-1.275
60			8.372	15.213	-6.841	60			-1.632	0.694	-2.326
75			3.699	15.213	-11.514	75			-3.170	0.694	-3.864
0	0.875	0.25	8.641	8.641	0	0	0.5	1	0	0	0
15			8.359	8.641	-0.282	15			-0.128	0	-0.128
30			7.487	8.641	-1.154	30			-0.517	0	-0.517
45			5.968	8.641	-2.673	45			-1.178	0	-1.178
60			3.717	8.641	-4.924	60			-2.149	0	-2.149
75			0.464	8.641	-8.177	75			-3.577	0	-3.577
0	0.75	0.25	7.002	7.002	0	<b><math>h_D = 1000</math></b>					
15			6.750	7.002	-0.251	0	0.95	0.1	41.521	41.521	0
30			5.969	7.002	-1.032	15			40.343	41.521	-1.178
45			4.613	7.002	-2.388	30			36.798	41.521	-4.722
60			2.629	7.002	-4.372	45			30.844	41.521	-10.677
75			-0.203	7.002	-7.206	60			22.334	41.521	-19.187
						75			10.755	41.521	-30.766
0	0.6	0.25	6.658	6.658	0	0	0.8	0.1	35.840	35.840	0
15			6.403	6.658	-0.249	15			34.744	35.840	-1.095
30			5.633	6.658	-1.024	30			31.457	35.840	-4.382
45			4.290	6.658	-2.447	45			25.973	35.840	-9.867
60			2.337	6.658	-4.32	60			18.241	35.840	-17.599
75			-0.418	6.658	-7.076	75			8.003	35.840	-27.837
0	0.5	0.25	6.611	6.611	0	0	0.6	0.1	35.290	35.290	0
15			6.361	6.611	-0.249	15			34.195	35.290	-1.095
30			5.587	6.611	-1.023	30			30.910	35.290	-4.380
45			4.245	6.611	-2.365	45			25.430	35.290	-9.860
60			2.295	6.611	-4.315	60			17.710	35.290	-17.580
75			-0.451	6.611	-7.062	75			7.522	35.290	-27.768
0	0.75	0.5	3.067	3.067	0	0	0.5	0.1	35.246	35.246	0
15			2.878	3.067	-0.189	15			34.151	35.246	-1.095
30			2.308	3.067	-0.759	30			30.866	35.246	-4.380
45			1.338	3.067	-1.729	45			25.386	35.246	-9.860
60			-0.082	3.067	-3.150	60			17.667	35.246	-17.579
75			-2.119	3.067	-5.187	75			7.481	35.246	-27.765

**Table 1-3. Pseudoskin factors for partially penetrating slanted wells (Cinco-Ley et al., 1975) continued.**

$\theta_w$ (°)	$z_{wD}/h_D$	$h_{wD}\cos\theta_w$ $h_D$	$s_{\theta+c}$	$s_c$	$s_{\theta}$	$\theta_w$ (°)	$z_{wD}/h_D$	$h_{wD}\cos\theta_w$ $h_D$	$s_{\theta+c}$	$s_c$	$s_{\theta}$
<b><math>h_D = 1000</math> continued</b>						<b><math>h_D = 1000</math> continued</b>					
0	0.875	0.25	15.733	15.733	0	0	0.6	0.5	4.837	4.837	0
15			15.136	15.733	-0.597	15			4.502	4.837	-0.335
30			13.344	15.733	-2.389	30			3.503	4.837	-1.334
45			10.366	15.733	-5.367	45			1.858	4.837	-2.979
60			6.183	15.733	-9.550	60			-0.424	4.837	-5.261
75			0.632	15.733	-15.101	75			-3.431	4.837	-8.268
0	0.75	0.25	14.040	14.040	0	0	0.5	0.5	4.777	4.777	0
15			13.471	14.040	-0.569	15			4.443	4.777	-0.334
30			11.770	14.040	-2.270	30			3.446	4.777	-1.331
45			8.959	14.040	-5.081	45			1.806	4.777	-2.971
60			5.047	14.040	-8.993	60			-0.467	4.777	-5.244
75			-0.069	14.040	-14.109	75			-3.458	4.777	-8.235
0	0.6	0.25	13.701	13.701	0	0	0.625	0.75	1.735	1.735	0
15			13.133	13.701	-0.568	15			1.483	1.735	-0.252
30			11.437	13.701	-2.264	30			0.731	1.735	-1.004
45			8.638	13.701	-5.063	45			-0.512	1.735	-2.247
60			4.753	13.701	-8.948	60			-2.253	1.735	-3.988
75			-0.288	13.701	-13.989	75			-4.595	1.735	-6.330
0	0.5	0.25	13.655	13.655	0	0	0.5	0.75	1.508	1.508	0
15			13.087	13.655	-0.568	15			1.262	1.508	-0.246
30			11.391	13.655	-2.264	30			0.528	1.508	-0.980
45			8.593	13.655	-5.062	45			-0.683	1.508	-2.191
60			4.711	13.655	-8.944	60			-2.380	1.508	-3.888
75			-0.321	13.655	-13.976	75			-4.665	1.508	-6.173
0	0.75	0.5	5.467	5.467	0	0	0.5	1	0	0	0
15			5.119	5.467	-0.348	15			-0.206	0	-0.206
30			4.080	5.467	-1.387	30			-0.824	0	-0.824
45			2.363	5.467	-3.104	45			-1.850	0	-1.850
60			-0.031	5.467	-5.498	60			-3.298	0	-3.298
5			-3.203	5.467	-8.670	75			-5.282	0	-5.282

**Table 1-4. Dependence of  $\alpha_{\theta}$  on phasing.**

Perforating Phasing (°)	$\alpha_{\theta}$
0 (360)	0.250
180	0.500
120	0.648
90	0.726
60	0.813
45	0.860

**Table 1-5. Vertical skin correlation coefficients.**

Perforating Phasing (°)	$a_1$	$a_2$	$b_1$	$b_2$
0 (360)	-2.091	0.0453	5.1313	1.8672
180	-2.025	0.0943	3.0373	1.8115
120	-2.018	0.0634	1.6136	1.7770
90	-1.905	0.1038	1.5674	1.6935
60	-1.898	0.1023	1.3654	1.6490
45	-1.788	0.2398	1.1915	1.6392

Eq. 1-58,  $s_V = 1.9$ , and from Eq. 1-61 and Table 1-6,  $s_{wb} = 0.02$ .

The total perforation skin effect obtained with Eq. 1-52 is equal to 1.3 for this example.

- Combination of damage and perforation skin effect  
Karakas and Tariq (1988) showed that the damage and perforation skin effect can be approximated by

$$(s_d)_p = \left( \frac{k}{k_s} - 1 \right) \left[ \ln \frac{r_s}{r_w} + s_p \right] = (s_d)_o + \frac{k}{k_s} s_p, \quad (1-62)$$

where the perforations terminate inside the damage zone ( $l_p < l_d$ ),  $r_s$  is the damage zone radius, and  $(s_d)_o$  is the equivalent openhole skin effect

**Table 1-6. Variables  $c_1$  and  $c_2$ .**

Perforating Phasing (°)	$c_1$	$c_2$
0 (360)	1.6E-1	2.675
180	2.6E-2	4.532
120	6.6E-3	5.320
90	1.9E-3	6.155
60	3.0E-4	7.509
45	4.6E-5	8.791

(Eq. 1-45). If, for example,  $l_p = 1.2$  ft ( $r_s = 1.606$  ft) and the permeability reduction ratio  $k/k_s = 5$ , from Eq. 1-62 and the perforation skin effect calculated in the previous section,  $(s_d)_p = 12$ .

Karakas and Tariq (1988) also showed that the damage skin effect for perforations terminating outside the damaged zone can be approximated by

$$(s_d)_p = s_p - s'_p, \quad (1-63)$$

where  $s'_p$  is the perforation skin effect evaluated at the modified perforation length  $l'_p$  and modified radius  $r'_w$ :

$$l'_p = l_p - \left(1 - \frac{k_s}{k}\right) l_d \quad (1-64)$$

$$r'_w = r_w + \left(1 - \frac{k_s}{k}\right) l_d. \quad (1-65)$$

The quantities  $l'_p$  and  $r'_w$  are used instead of  $l_p$  and  $r_w$ , respectively, to calculate  $s_p$  as presented in Section 1-3.4.

Assume that in the previous example  $l_d = 0.4$  ft, which makes the modified length  $l'_p$  and modified radius  $r'_w$  equal to 0.347 and 0.726 ft, respectively. From Eq. 1-63,  $(s_d)_p = 1$ , which is a marked decrease from the value calculated for the length of the damage larger than the length of the perforations.

### 1-3.5. Hydraulic fracturing in production engineering

If removal of the skin effect by matrix stimulation and good completion practices does not lead to an economically attractive well, the potential benefit

from hydraulic fracturing is illustrated by revisiting “Example of steady-state IPR: skin effect variation” (page 1-4). With permeability equal to 5 md, the reduction in the skin effect from 10 to 0 (e.g.,  $p_{wf} = 2000$  psi) results in production rates of 560 and 1230 STB/D, respectively, and this difference of 670 STB/D is clearly an attractive target for matrix stimulation. However, at a permeability of 0.05 md, all rates would be divided by 100, resulting in an incremental production of only 6.7 STB/D.

Interestingly, for  $k = 0.05$  md, reducing the skin effect to  $-5$  leads to a poststimulation production rate equal to 30 STB/D and an incremental production rate (over the  $s = 10$  case and  $k = 0.05$  md) of about 25 STB/D. Such an equivalent skin effect can be the result of hydraulic fracturing.

A great portion of this volume is devoted to this type of stimulation, its fundamental background and the manner with which it is applied in petroleum engineering. Here, hydraulic fractures are presented as well production or injection enhancers.

Prats (1961), in a widely cited publication, presented hydraulic fractures as causing an effective wellbore radius and, thus, an equivalent skin effect once the well enters (pseudo)radial flow. In other words, the reservoir flows into a fractured well as if the latter has an enlarged wellbore. Figure 1-10 is Prats' development graphed as the dimensionless effective wellbore radius  $r_{wD}'$  versus the relative capacity parameter  $a$ .

The dimensionless relative capacity parameter has been defined as

$$a = \frac{\pi k x_f}{2 k_f w}, \quad (1-66)$$

where  $k$  is the reservoir permeability,  $x_f$  is the fracture half-length,  $k_f$  is the fracture permeability, and  $w$  is the fracture width.

The dimensionless effective wellbore radius is simply

$$r_{wD}' = \frac{r'_w}{x_f} = \frac{r_w e^{-s_f}}{x_f}. \quad (1-67)$$

Thus, if  $x_f$  and  $k_f w$  are known (as shown later in this volume, this is the essence of hydraulic fracturing), then Fig. 1-10 enables calculation of the equivalent skin effect  $s_f$  that the well will appear to have while it flows under pseudoradial conditions. Cinco-

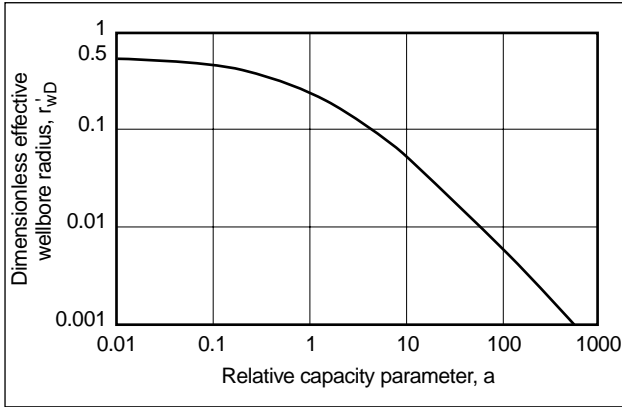


**Figure 1-10.** Dimensionless effective wellbore radius of a hydraulically fractured well (Prats, 1961).

Ley and Samaniego-V. (1981b) later introduced a direct correlation for  $s_f$  (Fig. 1-11).

Graphed on the x-axis of Fig. 1-11 is the dimensionless fracture conductivity  $C_{fD}$ , which is simply

$$C_{fD} = \frac{k_f w}{k_f x} \quad (1-68)$$

and is related to Prats' relative capacity by

$$C_{fD} = \frac{\pi}{2a} \quad (1-69)$$

The following example illustrates the impact of a hydraulic fracture on well production.

- Example calculation of production from a hydraulically fractured well

Using the variables in "Example of steady-state IPR: skin effect variation" (page 1-4) but with  $k = 0.5$  md, demonstrate the production improvement from a hydraulic fracture at  $C_{fD} = 5$  and  $x_f = 500$  ft. Also, compare this result with the pretreatment production if  $s = 10$  and after a matrix stimulation, assuming that all skin effect is eliminated ( $s = 0$ ). Use  $p_{wf} = 2000$  psi.

#### Solution

The IPR for this well is simply

$$q = 0.345 \left( \frac{5000 - p_{wf}}{8.43 + s} \right).$$

Using Fig. 1-11 (Fig. 1-10 can also be used) and  $C_{fD} = 5$ :

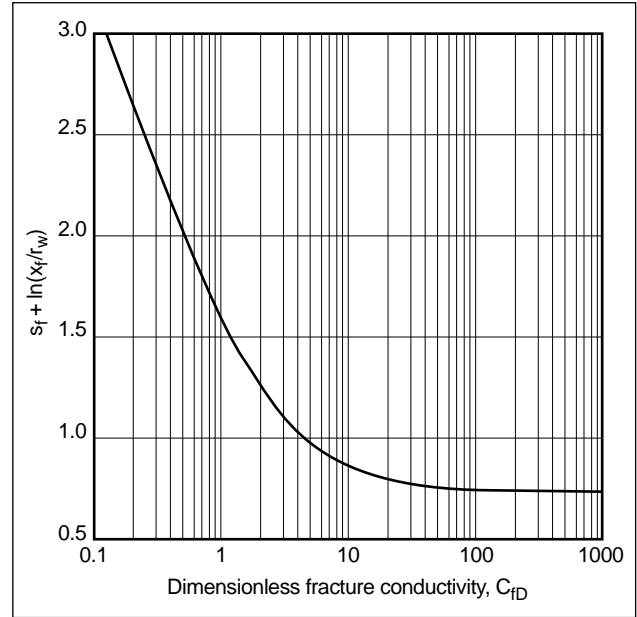


**Figure 1-11.** Equivalent fracture skin effect (Cinco-Ley and Samaniego-V., 1981b).

$$s_f + \ln \frac{x_f}{r_w} = 0.9,$$

which for  $x_f = 500$  ft and  $r_w = 0.328$  ft gives  $s_f = -6.4$ .

The production rates at pretreatment ( $s = 10$ ), after matrix stimulation ( $s = 0$ ) and after fracturing ( $s = -6.4$ ) are 56, 123 and 518 STB/D, respectively.

- General requirements for hydraulic fractures

What general requirements should be expected from the design of hydraulic fractures? As discussed in later chapters of this volume, the execution of a hydraulic fracture should provide a fracture length and propped width, and selection of the proppant and fracturing fluid is crucial for fracture permeability. Because of physical constraints the resulting values may not be exactly the desired ideal values, but certain general guidelines should permeate the design.

The dimensionless fracture conductivity  $C_{fD}$  is a measure of the relative ease with which the reservoir (or injected) fluid flows among the well, fracture and reservoir. Obviously, in a low-permeability reservoir even a fracture of narrow width and relatively low permeability results de facto in a high-conductivity fracture. The limiting value is an infinite-conductivity fracture, which mathemati-



cally implies that once fluid enters the fracture it is instantaneously transported into the well. Thus, in low-permeability reservoirs, the length of the fracture is critical and the design must consider this requirement. The longer the fracture, subject to the economic constraints of its execution, the more desirable it is.

Conversely, for high-permeability reservoirs, as shown by Eq. 1-68, to increase  $C_{fD}$  requires increasing the  $k_f w$  product. Thus, maximizing conductivity must be the major result from the design. Arresting the length growth and inflating the fracture are means to accomplish this purpose. A process involving tip screenout (TSO) has been developed, exactly to effect such a fracture geometry.

- Optimal fracture conductivity

With advent of the TSO technique especially in high-permeability, soft formations (called frac and pack), it is possible to create short fractures with unusually wide propped widths. In this context a strictly technical optimization problem can be formulated: how to select the length and width if the propped fracture volume is given. The following example from Valkó and Economides (1995) addresses this problem, using the method derived by Prats (1961).

- Example of optimal fracture conductivity

Consider the following reservoir and well data:  $k = 0.4$  md,  $h = 65$  ft,  $r_e/r_w = 1000$ ,  $\mu = 1$  cp,  $p_e = 5000$  psi and  $p_{wf} = 3000$  psi. Determine the optimal fracture half-length  $x_f$ , optimal propped width  $w$  and optimal steady-state production rate if the volume of the propped fracture is  $V_f = 3500$  ft<sup>3</sup>. Use a value of 10,000 md for the fracture permeability  $k_f$ , taking into account possible damage to the proppant, and assume that the created fracture height equals the formation thickness. Use the Cinco-Ley and Samaniego-V. (1981b) graph (Fig. 1-11), which assumes pseudoradial flow.

#### Solution

The same propped volume can be established by creating a narrow, elongated fracture or a wide but short one. In all cases the production rate can be obtained from Eq. 1-9, which with the incorporation of  $s_f$  takes the form

$$q = \frac{kh\Delta p}{141.2B\mu \left( \ln \frac{r_e}{r_w} + s_f \right)}.$$

Obviously, the aim is to minimize the denominator.

This optimization problem was solved by Prats (1961) for steady-state flow. He found the maximum production rate occurs at  $a = 1.25$  ( $C_{fD} = 1.26$  from Eq. 1-69). For this value of  $a$ ,  $r_w'/x_f = 0.22$  from Fig. 1-10 and Eq. 1-66 gives

$$x_f/w = 0.8k_f/k = 0.8 \times 10,000/0.4 = 20,000.$$

Using  $V_f = 2whx_f$  with this  $x_f/w$  ratio,

$$x_f^2 = 20,000V_f/2h = (20,000 \times 3500)/(2 \times 65),$$

and  $x_f = 730$  ft; hence,  $w = x_f/2000 = 0.037$  ft = 0.44 in. From  $r_w' = 0.22 x_f$  and  $r_w = 0.33$  ft, Eq. 1-7 gives  $r_w'/r_w = e^{-s} = 490$ , and  $s = -(\ln 490) = -6.1$ .

For  $p_e = 5000$  psi and  $p_{wf} = 3000$  psi, the optimized production rate is

$$q = \frac{(0.4)(65)(2000)}{(141.2)(1)(\ln 3000 - 6.2)} = 204 \text{ STB/D}.$$

It is necessary to check if the resulting half-length is less than  $r_e$  (otherwise  $x_f$  must be selected to be equal to  $r_e$ ). Similarly, the resulting optimal width must be realistic; e.g., it is greater than 3 times the proppant diameter (otherwise a threshold value must be selected as the optimal width). In this example both conditions are satisfied.

This example provides an insight into the real meaning of dimensionless fracture conductivity. The reservoir and the fracture can be considered a system working in series. The reservoir can deliver more hydrocarbons if the fracture is longer, but with a narrow fracture, the resistance to flow may be significant inside the fracture itself. The optimal dimensionless fracture conductivity  $C_{fD,opt} = 1.26$  in this example corresponds to the best compromise between the requirements of the two subsystems.

## 1-4. Tubing performance and NODAL\* analysis

The inflow performance relationships described in Section 1-2 provide a picture of the pressure and rates that a reservoir with certain characteristics (permeability, thickness, etc.), operating under certain

conditions (pressure, mode of flow), can deliver into the bottomhole of a well. The fluid must traverse a path from the bottom of the well to the top and then into surface equipment such as a separator. Figure 1-12 describes such a path, which consists of several segments, joints and valves, all of which cause a pressure drop. NODAL analysis considers the reservoir/wellbore system and uses calculations of the pressure loss across each segment to predict the production rate and identify any restrictions that may reduce the hydrocarbon flow rate.

At its simplest manifestation, for a given wellhead pressure, tubing performance allows calculation of the required bottomhole flowing pressure to lift a range of flow rates to the top. The total pressure drop in the well consists of the hydrostatic and friction pressure drops.

Several correlations for tubing performance are in use in the petroleum industry (Beggs and Brill, 1973; Hagedorn and Brown, 1965). Brown (1977), in a widely used work, outlined the procedure for pressure drop calculations in production strings as shown

in Fig. 1-13 for two wellhead flowing pressures. As the flow rate increases (on the right side of the curves) the required bottomhole flowing pressure increases, reflecting higher friction pressures at the higher rates. On the left side of the curves, the peculiar shape is due to liquid holdup; lower rates do not have sufficient momentum to purge liquid accumulation in the well, resulting in an unavoidable increase in the hydrostatic pressure.

The correlations to calculate the required pressure drops take full account of the phase behavior of the, almost always, two-phase oil and gas mixture. An increase in the wellhead pressure ordinarily results in a disproportionate increase in the bottomhole pressure because the higher pressure level in the tubing causes a more liquid-like fluid and a larger hydrostatic pressure component (density is higher).

Combining the tubing performance curve, often known in vertical wells as the vertical lift performance (VLP), with an IPR provides the well deliverability at the determined bottomhole flowing pressure (Fig. 1-14).

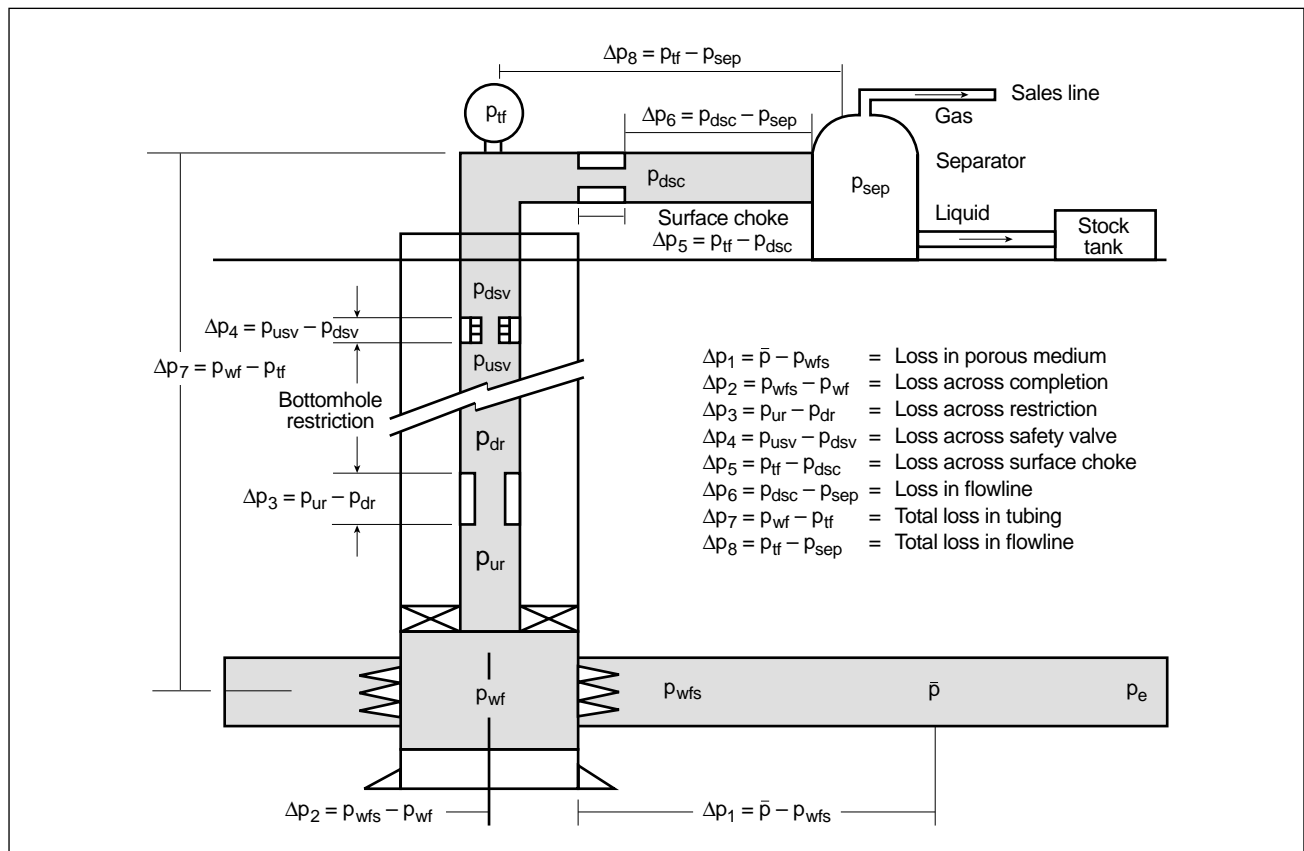


**Figure 1-12.** Well hydraulic system.  $p_{dr}$  = downstream restriction pressure,  $p_{dsc}$  = pressure downstream of the surface choke,  $p_{dsv}$  = pressure downstream of the safety valve,  $p_{sep}$  = separator pressure,  $p_{tf}$  = tubing flowing pressure,  $p_{ur}$  = upstream restriction pressure,  $p_{usv}$  = pressure upstream of the safety valve,  $p_{wfs}$  = wellbore sandface pressure.

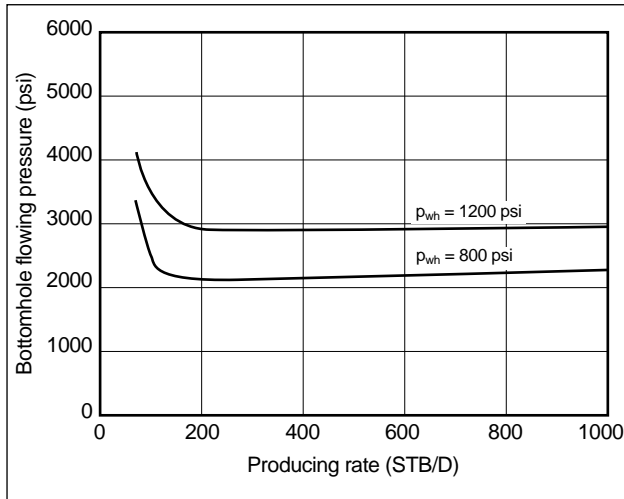


**Figure 1-13.** Vertical lift performance (also known as tubing intake) curves for two values of wellhead flowing pressure  $p_{wh}$ .

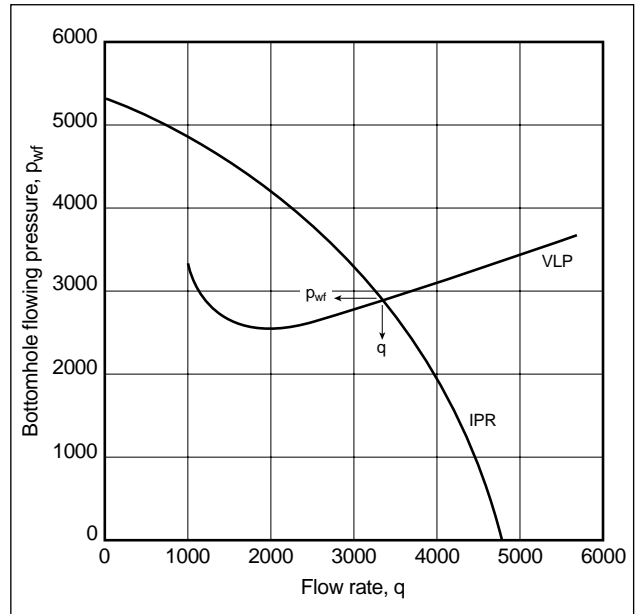
NODAL analysis is one of the most powerful tools in production engineering. It can be used as an aid in both the design and optimization of well hydraulics and IPR modification. Figure 1-15 shows one of the most common uses of NODAL analysis. The well IPR is plotted with three VLP curves (e.g., each corresponding to a different wellhead pressure—and perhaps a different artificial lift mechanism—in the case of an oil well or a different tubing diameter in a gas well). The three different production rates over time can be balanced against the incremental economics of the various well completion options.

Figure 1-16 demonstrates a single VLP but three different IPRs (e.g., each corresponding to a different hydraulic fracture design). Again, the incremental benefits over time must be balanced against the incremental costs of the various fracture designs.

The use of NODAL analysis as an engineering investigative tool is shown in Fig. 1-17. Suppose that several perforations are suspected of being closed. A calculation allowing several different scenarios of the number of open perforations and comparison with the actual flow rate can provide a convincing answer to the problem.

## 1-5. Decision process for well stimulation

To be done properly, the engineering exercise of the decision process for well stimulation requires considerable knowledge of many diverse processes. Few



**Figure 1-14.** IPR and VLP curves combined for the prediction of well deliverability.

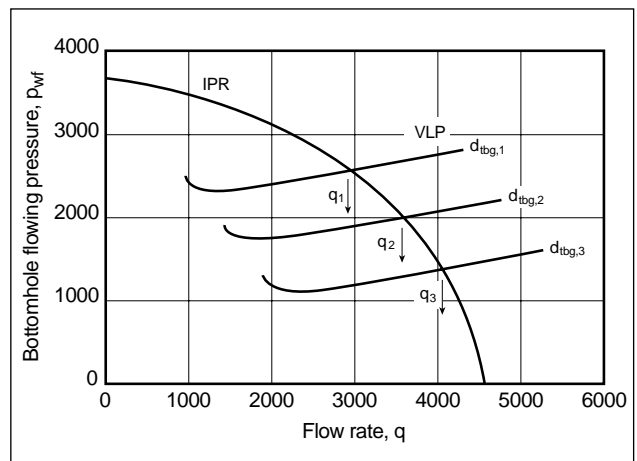


**Figure 1-15.** VLP curve variation for different tubing diameters ( $d_{tbg}$ ) and the effect on well deliverability.

activities in the petroleum or related industries use such a wide spectrum of sciences and technologies as well stimulation, both matrix and fracturing. This volume is intended to present these technologies and their interconnections.

As with many engineering processes, stimulation must culminate in the design, selection of the specific treatment and, of course, selection of candidate wells. To choose among the various options, of which one is to do nothing, a means for an economic comparison of the incremental benefits weighted against the costs is necessary.

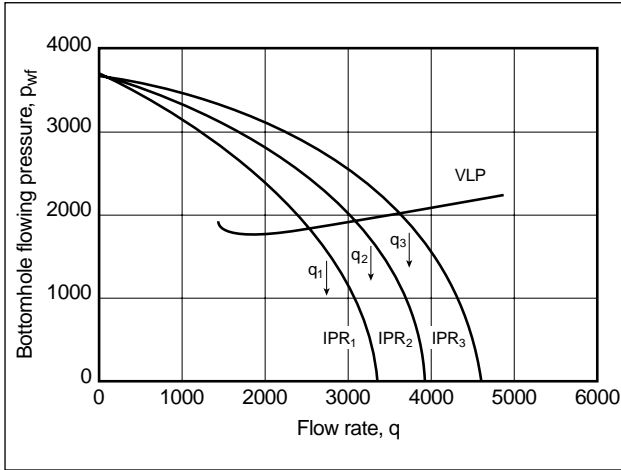


**Figure 1-16.** IPR curve variation (e.g., for different skins) and the effect on well deliverability.

### 1-5.1. Stimulation economics

Because the whole purpose of stimulation is to increase the value of the producing property through an accelerated production rate or increased recovery, economics should be the driver in deciding whether to conduct the stimulation, what type of stimulation to do and which various aspects of the treatment to include.

Several economic indicators can be used to show the value of stimulation. Because of the wide variety of operating conditions, companies may not have a single indicator for the “answer” in all stimulation investments. Although the common ground in economics is profit, in many petroleum activities liquidity, risk and corporate goals may make it necessary to choose investments that differ from the ultimate maximum value of a project.

The oldest indicator used in oil production is pay-out time, which is the amount of time necessary to recoup the money invested. If the actual time is less than the required time, the investment is considered attractive:

$$\sum_{n=1}^n \Delta \$_n - cost = 0, \quad (1-70)$$

where  $\Delta \$_n$  is the incremental revenue (minus the incremental expenses and taxes that are due to operations),  $n$  is the time period increments (e.g., years) in which it is received, and  $cost$  consists of the total expenses associated with the stimulation. This indicator does not provide for the time value of money

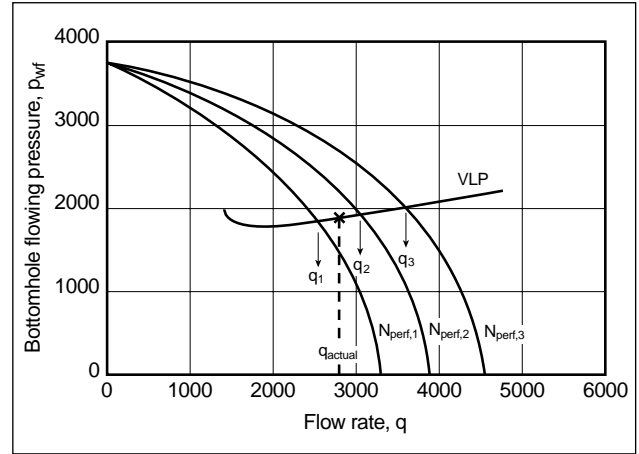


**Figure 1-17.** Well diagnosis (e.g., for unknown number of open perforations  $N_{perf}$ ) using a comparison of predicted versus actual IPRs.

or the net value (profit) for the operator; rather, it is a measure of liquidity or how fast the investment will be recovered.

The indicator can be adjusted to show the time value of money (discounted payout), the hurdle rate necessary for the company to invest or both factors. The hurdle rate is the annualized percentage of return that must be achieved to make the project as good an investment as the average company investment. The discounted payout is

$$\sum_{n=1}^n \frac{\Delta \$_n}{(1+i)^n} - cost = 0. \quad (1-71)$$

The interest (hurdle) rate  $i$  is the indicator that suggests when the investment will be returned without lowering the corporate investment returns and accounting for inflation (time value of money).

When the full stream of cash flows for the projected relative life of the project is used, an indicator called net present value (NPV) is defined as

$$NPV = \sum_{n=1}^n \frac{\Delta \$_n}{(1+i)^n} - cost. \quad (1-72)$$

NPV gives a dollar value added to the property at present time. If it is positive, the investment is attractive; if it is negative, it means an undesirable investment. NPV is the most widely used indicator showing a dollar amount of net return.

To get an indicator on relative profitability against more global investments such as stocks, bonds and corporate profits, the rate of return (ROR) is used.

ROR is simply varying  $i$  to get an NPV equal to zero. That value of  $i$  is the ROR. The limitation in using the ROR indicator is that it does not provide a mechanism of how the cash comes in (cash flow versus time).

In Fig. 1-18 there are two investment possibilities. A has the highest NPV for small interest rates but falls off quickly with increasing rates, whereas B has a smaller NPV with low rates but remains flatter as rates rise. This means that A makes more money, but as interest rates rise its return is hurt more than that for B. B pays the money back with a better ROR, even if it has a smaller NPV at low interest rates.

Another indicator of investment profitability is the benefits to cost ratio (BCR):

$$BCR = \frac{NPV}{cost}, \quad (1-73)$$

which shows the relationship of relative return for a given investment (cost) size. BCR is a good indicator if there are more investment opportunities than money to invest.

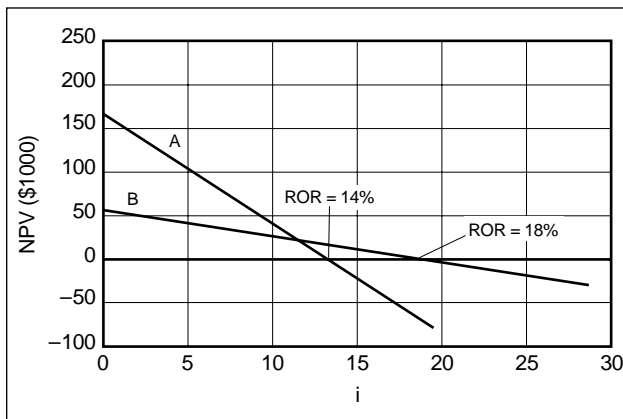


**Figure 1-18.** Determination of the rate of return for projects A and B.

### 1-5.2. Physical limits to stimulation treatments

Physical limits are dominant aspects for stimulation treatment decisions as often as economic indicators. For the well, these include the following:

- Maximum allowable treating pressure limits injection rates and the type of treating fluids.
- Tubular size limits rates and pipe erosion.

- Well location size limits the equipment and materials that can be used.
- Tubular integrity prevents or limits the type of treatments that can be employed without compromise.
- Completion tools and their location limit where the treatment is placed and the magnitude of the rates and volumes.
- Zonal isolation is whether the zone can be isolated from other intervals through perforating and/or pipe integrity limitations.

Typical reservoir constraints are

- production failures: water or gas coning or influx, formation sanding
- physical location of the zones and their thicknesses: pay zone qualities limit or dictate treatments.

## 1-6. Reservoir engineering considerations for optimal production enhancement strategies<sup>†</sup>

Cost-effective production improvement has been the industry focus for the past several years. Fracturing, stimulating, reperforating and recompleting existing wells are all widely used methods with proven results in increasing the NPV of old fields. Now reentry drilling is generating high interest for the potential it offers to improve recovery from damaged or depleted zones or to tap into new zones at a generally low cost. Applied to mature reservoirs, all these strategies have the advantage of starting with a fair to good reservoir description as well as a working trajectory to the target formation. Even when a new well is drilled, the decision whether to drill a vertical, slanted or horizontal well and how to complete the productive interval can profoundly effect the well's productivity and the size of the volume drained by the well. Today's technology also entertains multiple branches from a main trunk, which may be a newly drilled or existing well.

<sup>†</sup> This section by Christine Ehlig-Economides, Schlumberger GeoQuest.

### 1-6.1. Geometry of the well drainage volume

The geometry of the well drainage volume depends on the well trajectory within the productive zone, neighboring wells, geometry of hydraulic fractures, nearby reservoir limits and reservoir flow characteristics. Areas drained by an isolated well in an effectively infinite reservoir are diagrammed in Figs. 1-19a and 1-19b. A vertical well creates a circular cylinder pressure sink whereas a hydraulically fractured well creates a pressure sink in the shape of a finite slab with dimensions defined by the formation thickness and the total fracture length. With adequate vertical permeability the horizontal well drainage area is similar to that of a vertical fracture, with the total fracture length equal to that of the horizontal well. The extent of the effective drainage area is approximately defined by the locus of points equidistant from the surface of the pressure sink associated

with the well. This forms a circle for a vertical well; an approximate ellipse is formed for hydraulically fractured and horizontal wells.

Wells drilled in a square pattern impose a square drainage area. For vertical wells, this is similar to the circular effective drainage shape (Fig. 1-19c), but for horizontal wells, the equivalent drainage efficiency corresponds to an elongated area. As a rule of thumb, the length of the horizontal well drainage area can be as long as the length of the horizontal well plus one diameter of the comparable vertical well drainage area. For the case in Fig. 1-19d, one-half as many horizontal wells of the length shown could be used to drain the same pattern, as shown in Fig. 1-20a. With longer horizontal wells, even fewer are required.

Figure 1-20b shows another consideration. If the vertical well pattern does not take the direction of maximum horizontal stress  $\sigma_{H,max}$  into account,

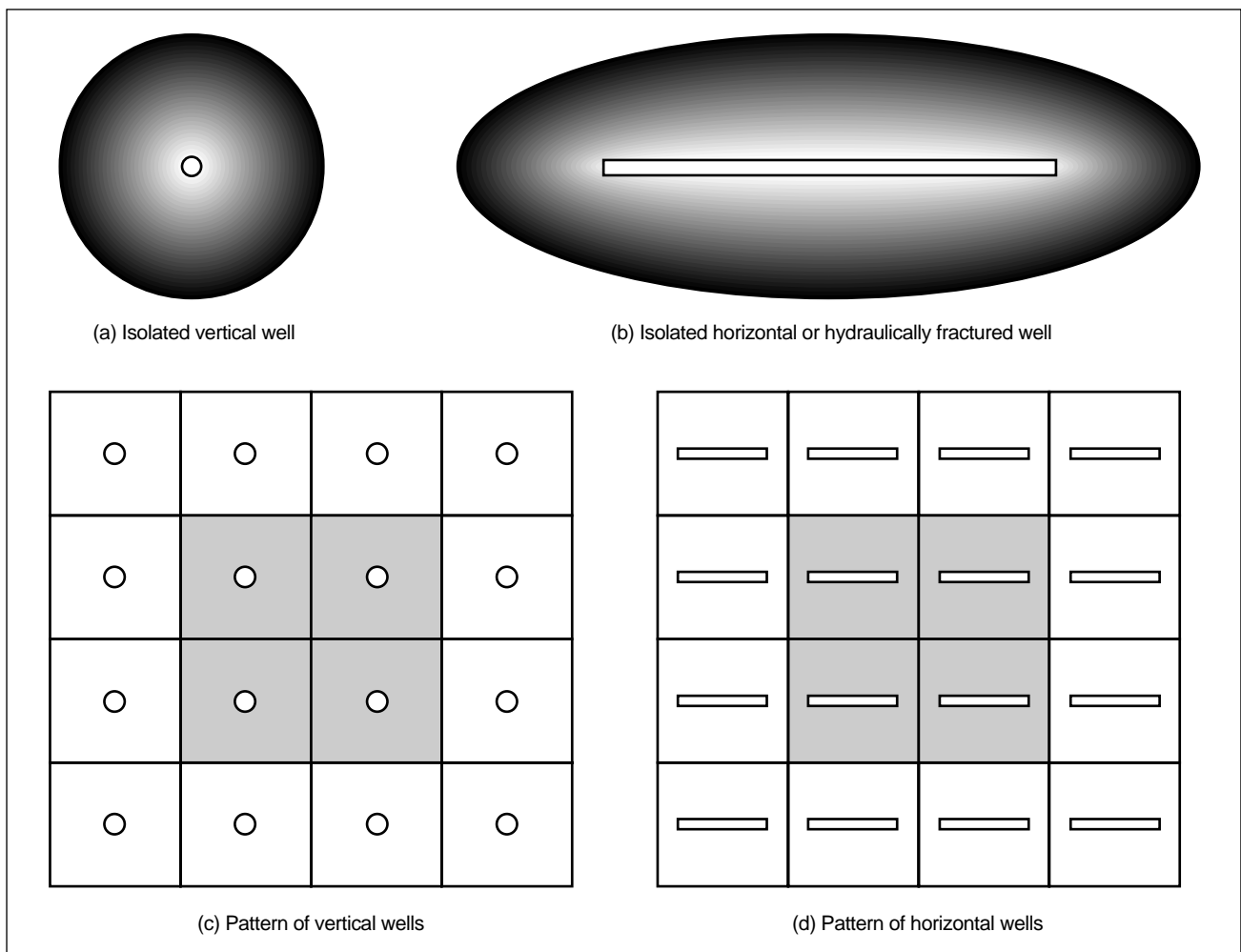


**Figure 1-19.** Drainage areas for single and multiple vertical and horizontal wells.

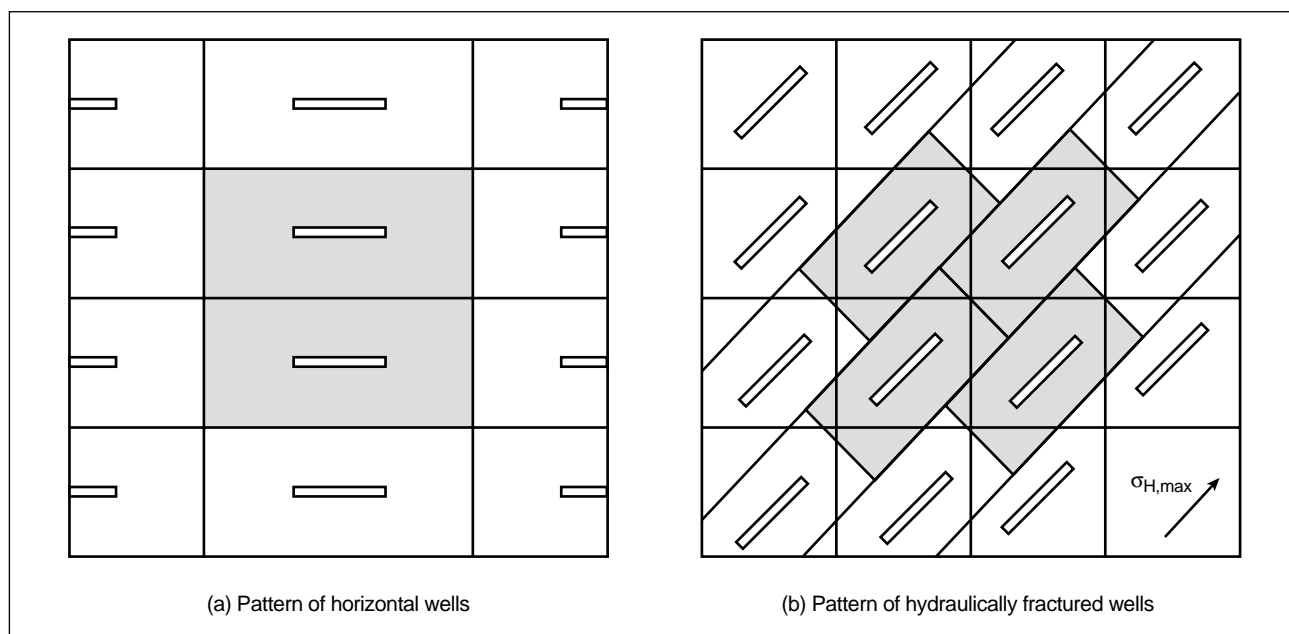


**Figure 1-20.** Drainage areas resulting from (a) longer horizontal wells draining more area per well and (b) hydraulically fractured wells in a square pattern that is not in line with the direction of maximum stress.

hydraulically fracturing the wells may result in unplanned drainage geometries.

### 1-6.2. Well drainage volume characterizations and production optimization strategies

Figures 1-19 and 1-20 assume that the reservoir is homogeneous and isotropic over vast areas. In reality, typical reservoir geology is much more complex. Formation flow characteristics may favor one well geometry over others. The chart in Fig. 1-21 summarizes production optimization strategies for a series of 10 common well drainage volume characterizations. The chart addresses five potential well paths: conventional vertical, hydraulically fractured vertical, slanted, horizontal and hydraulically fractured horizontal. For any one of the drainage volume characterizations, well path options are shown in block diagrams.

Laminated reservoirs (chart row 4 on Fig. 1-21) are a good starting point to understanding the information in the chart. The chart distinguishes layered from laminated by defining a reservoir as layered if the recognized sands are thick enough to be targeted by a horizontal well. If not, the reservoir is classed as laminated. In general, laminated reservoirs have poor vertical permeability. A horizontal well is not

an option in this case because the productivity would be severely penalized by the low vertical permeability, and in a thick formation, a horizontal well may not even produce the entire formation thickness. A vertical well—barefoot, perforated and gravel packed, or gravel packed—can provide excellent productivity in formations with moderate mobility. A slanted well can produce a marginal increase in productivity over a vertical well.

In very high mobility laminated reservoirs (such as turbidites), a frac and pack may provide sand control and the means to bypass near-wellbore damage. However, in a low-mobility reservoir, hydraulically fracturing the well is preferred over any other option because it provides an effective planar sink, greatly increasing the well productivity. For thin and laminated reservoirs, hydraulic fractures in a horizontal well may be the optimal choice because the longer well provides greater reach that increases the drainage volume of the well and the hydraulic fractures enable horizontal flow to the well through the entire formation thickness. Hydraulic fractures in a horizontal well can be planned either as longitudinal, by drilling the well in the direction of maximum horizontal stress, or as transverse, by drilling the well in the direction of minimum stress.

Horizontal wells offer particular advantages in naturally fractured reservoirs (chart row 5 on Fig. 1-21)

Drainage Volume Characterization	Well Path				
	Vertical well	Hydraulically fractured vertical well	Slanted well	Horizontal well	Hydraulically fractured horizontal well
1. Thick and homogeneous, no gas cap or aquifer			$k_v/k_H \geq 0.1$ 	$k_v/k_H \geq 0.1$ 	 Longitudinal $Q_{Hmax}$ Transverse $Q_{Hmax}$
2. Thick and homogeneous, with gas cap and/or aquifer	Gel treatment 	Small fracture 	Not recommended: risk of premature gas or water production	Closely spaced parallel wells preferred 	Not recommended: risk of premature gas or water production
3. Layered			$k_v/k_H \geq 0.1$ preferred over vertical	Stacked parallel wells, with branch flow conformance 	 $Q_{Hmax}$
4. Laminated		Hydraulic fracture preferred 		Not recommended: risk of disappointing productivity/recovery owing to low vertical permeability	 $Q_{Hmax}$
5. Naturally fractured		Prop natural fractures 		Horizontal well to normal to fractures preferred 	Reopen natural fractures 
6. Naturally fractured under waterflood	Plug fractures connected to injector 	Water injection wells 	Closely spaced short parallel wells normal to fractures 	Water injection wells 	Not recommended: risk of premature water breakthrough
7. Structural compartment	Moderate mobility 	High mobility Frac and pack 		Drain each with one or more wells 	Maximum stress oriented by faults  $Q_{Hmax}$
8. Stratigraphic compartment		High mobility Frac and pack 		Drain each with one or more wells 	Hydraulic fracturing may apply in high-mobility cases
9. Elongated compartment		$Q_{Hmax}$ Low mobility 	Multiple well paths starting from single main trunk 	Single well traversing multiple channels 	$Q_{Hmax}$ Low mobility 
10. Attic compartments	Not preferred	Not preferred	Single well traversing multiple beds 	One well per bed drilled on strike preferred 	Not preferred

**Figure 1-21.** Production optimization strategies. Completion options include perforating, gravel packing and stimulation in combination with an applicable strategy.



when they are drilled normal to the fracture planes. Locating natural fractures and determining their orientation is crucial to developing the best well design in these formations. Hydraulic fracturing places proppant in a series of natural fractures, which typically results in a propped fracture that is parallel to the natural fractures. A horizontal well normal to natural fractures usually provides better productivity than hydraulic fracturing.

Although natural fractures usually are subvertical (nearly vertical), shallower reservoirs and overpressured zones may have subhorizontal (nearly horizontal) fractures open to flow. Vertical and slanted wells are a reasonable choice in these cases. Injection of proppant into horizontal fractures in overpressured zones keeps them open after production lowers the pore pressure. Otherwise, the weight of the overburden tends to close horizontal natural fractures. Likewise, high-pressure injection can reopen natural fractures in depleted zones or natural fractures that were plugged during drilling.

Moving up the chart to the layered reservoirs in row 3 offers an opportunity to address the importance of conformance control. The conventional vertical well commingles production from multiple layers. Productivity and storage capacity contrasts can result in the differential depletion of layers that are not in hydraulic communication vertically other than at the well. In this case, when the production rate is reduced or the well is shut in, crossflow occurs in the wellbore as the higher pressure layers recharge the depleted zones. Another risk of commingled production is that downdip water or updip gas will advance to the well, resulting in early breakthrough of unwanted fluids in the most productive layer or layers. In this case the oil in the lower productivity layers is bypassed. Reentry drilling offers a modern solution by targeting the bypassed oil with a horizontal well.

Strategies for conformance control begin with perforating with a higher shot density in the lower productivity layers. Hydraulic fracturing in layered reservoirs can be useful for conformance control, especially if the treatment is phased to target contrasting zones separately. Unphased, ill-designed hydraulic fracture treatments can be detrimental to production by opening up the high-productivity zones and aggravating the productivity imbalance.

A single horizontal well is not an option for a layered reservoir because it produces from only one

layer, but stacked reentry laterals are a highly effective strategy. In the latter design, the length of the lateral can be roughly inversely proportional to the layer's flow capacity. A slanted well offers a less expensive strategy for boosting productivity in a layered reservoir. By designing the trajectory with more drilled length in less productive layers, some conformance control can be achieved. However, if early water breakthrough occurs in the higher productivity layer, it is generally much easier to shut off production in one of the stacked laterals than in a midlength portion of the slanted well.

Hydraulic fracturing in slanted wells is performed typically in offshore wells that commonly follow the same deviation used to reach the reservoir location from a platform. These fractures are typically frac and pack treatments designed for sand control. Because the deviated trajectory may be detrimental to the fracture treatment design, some operators direct the trajectory downward to nearly vertical before passing through the productive formation if hole stability problems do not preclude this approach.

At the top row of the chart in Fig. 1-21 are thick, homogeneous formations. Any of the well path options may be applied for these reservoirs. Mobility extremes may favor hydraulic fracturing, whereas moderate mobility allows using less expensive, conventional vertical well completions. A slanted well may be more cost effective than hydraulic fracturing or a horizontal well, provided that the ratio of vertical to horizontal permeability is not too small. Hydraulic fractures along a horizontal well can compensate for a productivity reduction caused by low vertical permeability in a thick reservoir.

Thick reservoirs with overlying gas or underlying water pose special production problems for which chart row 2 on Fig. 1-21 illustrates some important points. In vertical wells, a strategy to delay bottomwater breakthrough is to perforate near the top of the productive interval. However, the pressure gradient resulting from radial flow toward the well is sufficient to draw the water upward in the shape of a cone. Once the water reaches the deepest perforations, water may be preferentially produced because the water mobility may be greater than oil mobility for low-gravity crudes (owing to the higher oil viscosity) and/or there may be considerable energy to support water production because of a strong bottomwater drive. Once water breakthrough occurs,

there may be little further rise of the cone, and additional oil production will be at an increasing water cut and marginal. One strategy to produce additional oil is to plug back the well above the top of the cone and reperforate. Another is to try to inject gel radially below the perforations. At times, water breakthrough is delayed or avoided with gel injection, and the shape of the cone is widened in any case so that a greater volume of oil is displaced toward the perforations.

A horizontal well drilled near the top of the oil zone above bottomwater produces a pressure gradient normal to the well, and the bottomwater will rise in the shape of a crest instead of a cone. The crest-shaped water advance displaces oil in its path, leading to greater oil recovery than with a vertical well by virtue of the flow geometry. Ehlig-Economides *et al.* (1996) discussed strategies for production enhancement under a strong bottomwater drive. Previous work cited from the literature has analytical estimates for breakthrough time and indicates that recovery efficiency is independent of the production rate under a strong bottomwater drive. Ehlig-Economides *et al.* showed that the relationship between recovery and the spacing of parallel horizontal wells is

$$r_v = 0.5236 \frac{h}{x_e} \sqrt{k_H/k_V} \left( \frac{3z_w/h - 0.5}{2.5} \right), \quad (1-74)$$

that recovery efficiency is a simple function of the half-spacing between wells:

$$qt_{BT} = \frac{\pi r N}{3} \frac{h}{2x_e} \sqrt{k_H/k_V} \quad (1-75)$$

and that the optimal half-spacing between wells is

$$x_{e,opt} = h \sqrt{k_H/k_V}. \quad (1-76)$$

In these three equations,  $r_v$  is the fraction of the well drainage volume occupied by the crest at the time of water breakthrough. For the optimal well spacing from Eq. 1-76 and a well standoff from the oil-water contact  $z_w$  approximately equal to the thickness of the oil column  $h$ , the maximum water-free oil recovery (assuming piston-like displacement) is  $\pi/6 = 0.5236$ . In this case, the optimal interwell spacing is most likely too close for conventional well drilling but may be economical if the laterals can be drilled from a common main trunk.

Interestingly, the same conditions that penalize a horizontal well in a reservoir without overlying gas or underlying water (thick zone, low vertical permeability) favor the horizontal well if overlying gas or underlying water is present. This also illustrates designing the well spacing to be close enough to cause interwell interference. The interwell or inter-lateral interference is beneficial in this case because it both accelerates production and enhances recovery.

Another case that may favor close parallel lateral spacing is in chart row 6 on Fig. 1-21. Although orienting a horizontal well normal to natural fractures boosts well productivity, this approach may risk early water breakthrough, especially in reservoirs under waterflood. Injecting water opposite of a bank of parallel laterals drilled at sufficiently close spacing may allow them to withdraw oil from the matrix rock before the injected water front advances to the production wells. Water may be injected above fracturing pressure to boost injectivity. When horizontal or multilateral wells are not economically justified, the likely short-circuiting of water between vertical well injector/producer pairs may be plugged by gel, thereby forcing the displacement process into the matrix rock.

The remaining rows 7 through 10 on the chart are reminiscent of 3D reservoir geometries. Although conventional vertical wells do not address a 3D reservoir geometry, hydraulically fractured and horizontal wells do, and knowledge of structural and stratigraphic reservoir heterogeneities can greatly improve the design of these wells.

Structural compartmentalization (chart row 7 on Fig. 1-21) results from faults that may not be visible in seismic data interpretations. Even if faults are clearly indicated in the seismic data, only dynamic data derived from formation or well tests or longer term production history matching can establish whether the faults are sealing or conductive. Stratigraphic compartmentalization (chart row 8) is a result of depositional processes. Facies with considerable contrasts in flow characteristics may serve as buffers or flow conduits that act as first-order controls on well productivity and ultimate hydrocarbon recovery. Both structural and stratigraphic heterogeneities may be complicated by diagenetic processes occurring at a later time.

Horizontal wells can target one or more reservoir compartments, and multibranch wells enable shut-off of a branch that produces unwanted gas or water. In

tight reservoirs with considerable faulting, the faults may be associated with natural fractures that can be targeted with horizontal wells, or they may provide reliable information on the maximum stress direction that is essential for planning hydraulic fractures in vertical or horizontal wells.

Stratigraphic limits (chart row 8 on Fig. 1-21) may account for additional reservoir compartmentalization, both vertically and areally. In some cases the reservoir sands may be too thin to be individually identified in a seismic data cross section, but they may have sufficient areal extent to be visible in seismic attribute maps for a structural horizon. In that case, horizontal wells may be an ideal strategy for producing thin formations and for reaching multiple sands.

Chart row 9 on Fig. 1-21 refers to elongated compartmentalization. Although these diagrams depict fluvial reservoir geology, elongated reservoirs can also occur in heavily faulted formations. In either case, the apparent drilling strategies depend on the objective for the well. For example, the well direction can be planned to stay in an elongated reservoir body or to intersect as many reservoir bodies as possible. The latter case implies drilling in the direction normal to the elongation, which for a fluvial reservoir means drilling normal to the downslope direction at the time of deposition. Another approach may be a multibranch well designed to target channels identified with borehole seismic measurements in the horizontal trunk well.

Hydraulic fracturing offers different challenges and possibilities. First, unlike a well trajectory plan, the direction of the hydraulic fracture is not a design choice. Rather, the fracture propagates normal to the direction of minimum stress. A hydraulic fracture may propagate into isolated sand bodies not contacted by the drilled well trajectory, but in other cases the fracture propagation may be inhibited by facies changes or structural discontinuities, and a screenout may occur. In general, drilling solutions may be more flexible in elongated reservoir systems.

The last chart row on Fig. 1-21 is for the special geometry of the attic compartment. In this case, steeply dipping beds may be in contact with an updip gas cap, downdip aquifer or both. One strategy is to drill a horizontal well that passes through several of the beds and stays sufficiently below the updip gas and above the downdip water. Although this seems to be an efficient approach, it suffers from a signifi-

cant disadvantage in that flow is commingled among the layers, and when gas or water breakthrough occurs it interferes with production from other layers. The better strategy may be to drill multiple horizontal wells, each on strike and staying in a specific bed. The advantage to this strategy is that each of the wells is optimal in its standoff from the gas-oil or oil-water contact, thus delaying multiphase production as long as possible, and in its productive length within the formation, thus maximizing productivity.

## 1-7. Stimulation execution

A good understanding of job execution is necessary for making decisions on the applicability and risk of various treatments. As with any well work, basic safety procedures must be developed and followed to prevent catastrophic failure of the treatment, which could result in damage to or loss of the well, personnel and equipment. Specific standards and operating procedures have been developed for stimulation treatments, which if followed can lead to a safe, smooth and predictable operation. Chapters 11 and 19 fully detail execution concerns.

### 1-7.1. Matrix stimulation

Matrix stimulation, mainly acidizing, is the original and simplest stimulation treatment. More than 40,000 acid treatments are pumped each year in oil and gas wells. These treatments (Fig. 1-22) typically involve small crews and minimal equipment. The equipment usually consists of one low-horsepower, single-action reciprocating pump, a supply centrifugal and storage tanks for the acid and flush fluids. Blending equipment is used when solids are added to the treatment.

The most common process is for the fluids to be preblended at the service company facility and then transported to the location. This allows blending small volumes accurately, controlling environmental hazards. The fluids are then pumped with little effort or quality risk.

### 1-7.2. Hydraulic fracturing

Unlike matrix stimulation, fracturing can be one of the more complex procedures performed on a well (Fig. 1-23). This is due in part to the high rates and



**Figure 1-22.** Matrix stimulation treatment using a coiled tubing unit, pump truck and fluid transport.

pressures, large volume of materials injected, continuous blending of materials and large amount of unknown variables for sound engineering design.

The fracturing pressure is generated by single-action reciprocating pumping units that have between 700 and 2000 hydraulic horsepower (Fig. 1-24). These units are powered by diesel, turbine or electric engines. The pumps are purpose-built and have not only horsepower limits but job specification limits. These limits are normally known (e.g., smaller plungers provide a higher working pressure and lower rates). Because of the erosive nature of the materials (i.e., proppant) high pump efficiency must be maintained or pump failure may occur. The limits are typically met when using high fluid velocities and high proppant concentrations (+18 ppg). There may be numerous pumps on a job, depending on the design.

Mixing equipment blends the fracturing fluid system, adds the proppant and supplies this mixture to the high-pressure pumps. The slurry can be continuously mixed by the equipment (Fig. 1-25) or batch mixed in the fluid storage tanks. The batch-mixed fluid is then blended with proppant in a continuous stream and fed to the pumps.



**Figure 1-23.** This large fracturing treatment used 25,000 hydraulic horsepower and 1.54 million gal of fracturing fluid to place 6.3 million lbm of propping agent. The job lasted 11 hours.



**Figure 1-24.** One thousand hydraulic horsepower pumping unit.



**Figure 1-25.** For this fracturing treatment, propping agent was introduced into the fracturing fluid via conveyors to the blender. The blender added the propping agent to the continuously mixed fracturing fluid (creating a slurry) and discharged the slurry to the high-pressure pumping equipment.

# Formation Characterization: Well and Reservoir Testing

Christine A. Ehlig-Economides, Schlumberger GeoQuest  
Michael J. Economides, University of Houston

## 2-1. Evolution of a technology

The evolution of well and reservoir testing has gone through three important milestones, each of which shaped both the manner with which well tests are interpreted and the information that can be extracted from them. These three major developments are the semilogarithmic straight line (Horner analysis), log-log diagnostic plot and log-based derivative. They are briefly outlined in the following text.

### 2-1.1. Horner semilogarithmic analysis

Using the semilogarithmic approximation of the solution of the partial differential equation (Eq. 1-18) shown in Chapter 1 and employing the superposition principle, Horner (1951) presented the mainstay for buildup analysis, which, appropriately, was named after him.

Presuming infinite-acting radial flow, the expression for the shut-in pressure  $p_{ws}$  in psi is

$$p_{ws} = p_i - \frac{162.6qB\mu}{kh} \log \frac{t_p + \Delta t}{\Delta t}, \quad (2-1)$$

where  $p_i$  is the initial reservoir pressure in psi,  $q$  is the rate during the flowing period in STB/D,  $B$  is the formation volume factor in RB/STB,  $\mu$  is the viscosity in cp,  $k$  is the permeability in md,  $h$  is the reservoir thickness in ft,  $t_p$  is the producing (flowing) time in hr, and  $\Delta t$  is the time since shut-in in hr.

A semilogarithmic plot of  $\log[(t_p + \Delta t)/\Delta t]$  versus  $p_{ws}$  should form a straight line (Fig. 2-1) with the slope equal to

$$m = -\frac{162.6qB\mu}{kh}, \quad (2-2)$$

from which the unknown  $k$ , or  $kh$  if  $h$  is also not known, can be determined. Although from a visual observation several straight lines through the data are generally plausible, the question of which of them is the correct one is resolved in the next section.

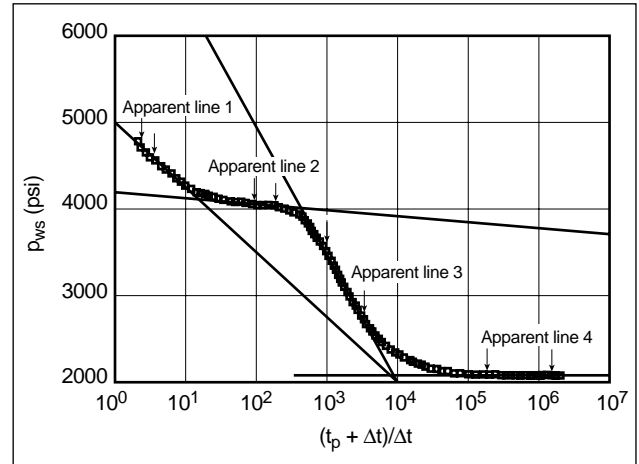


**Figure 2-1.** Analysis of pressure buildup data on a semilog plot. Arrows denote beginning and end of semilog linear trends.

From the extension of the correct straight line to  $t = 1$  hr, the value of the pressure  $p_{1hr}$  can be extracted, and the Horner analysis suggests that the skin effect  $s$  can be calculated by

$$s = 1.151 \left( \frac{p_{1hr} - p_{wf}(\Delta t=0)}{m} - \log \frac{k}{\phi \mu c_i r_w^2} + 3.23 \right). \quad (2-3)$$

The value of  $p_{wf}(\Delta t=0)$  is the last value of the bottomhole flowing pressure,  $m$  is the slope of the line,  $\phi$  is the porosity (unitless),  $c_i$  is the total compressibility in  $\text{psi}^{-1}$ ,  $r_w$  is the wellbore radius in ft, and the constant 3.23 is to account for oilfield units and the conversion from  $\ln$  to  $\log$ .

For a drawdown (flowing) test the analogous semilogarithmic straight-line equation is

$$p_{wf} = p_i - \frac{162.6qB\mu}{kh} \left( \log t + \log \frac{k}{\phi \mu c_i r_w^2} - 3.23 + 0.87s \right) \quad (2-4)$$

and for skin effect

$$s = 1.151 \left( \frac{p_i - p_{1hr}}{m} - \log \frac{k}{\phi \mu c_i r_w^2} + 3.23 \right). \quad (2-5)$$

Two reasons make buildup tests far more popular (and reliable) than drawdown tests:

- Both solutions imply constant rate  $q$ . Although this is difficult to accomplish for drawdown, for buildup the rate is constant and, simply, equal to zero. Rate fluctuations before the buildup can be “smoothed” by defining an equivalent production time as

$$t_p^* = \frac{N_p}{q_{last}}, \quad (2-6)$$

where  $N_p$  is the cumulative production and  $q_{last}$  is the last flow rate. Equation 2-6 can be shown to be a reasonable approximation, fundamentally based on the superposition principle.

- The initial reservoir pressure  $p_i$  required for the drawdown analysis (Eq. 2-5) is rarely known with certainty, especially in a new formation. Buildup analysis not only does not require  $p_i$ , it can determine its value.

At infinite shut-in time (i.e., at  $(t_p + \Delta t)/\Delta t = 1$ ), the straight line on the Horner plot should intercept the pressure at  $p_i$  (for a new reservoir).

The problem with semilogarithmic constructions from both drawdown and buildup data is that the correct straight line (i.e., which data fall on it) is often difficult to identify, as can be seen readily in Fig. 2-1. This dilemma was resolved by the second major development in modern well testing.

## 2-1.2. Log-log plot

H. J. Ramey and his coworkers introduced the log-log plot as a means to diagnose the well pressure transient response. The first of these landmark papers is by Agarwal *et al.* (1970).

Figure 2-2 presents some of the common pressure response patterns for a well test. Early-time wellbore storage effects manifest themselves with a unit slope on the log-log plot. Figure 2-2 contains two sets of curves. The first set, to the left, represents reduced

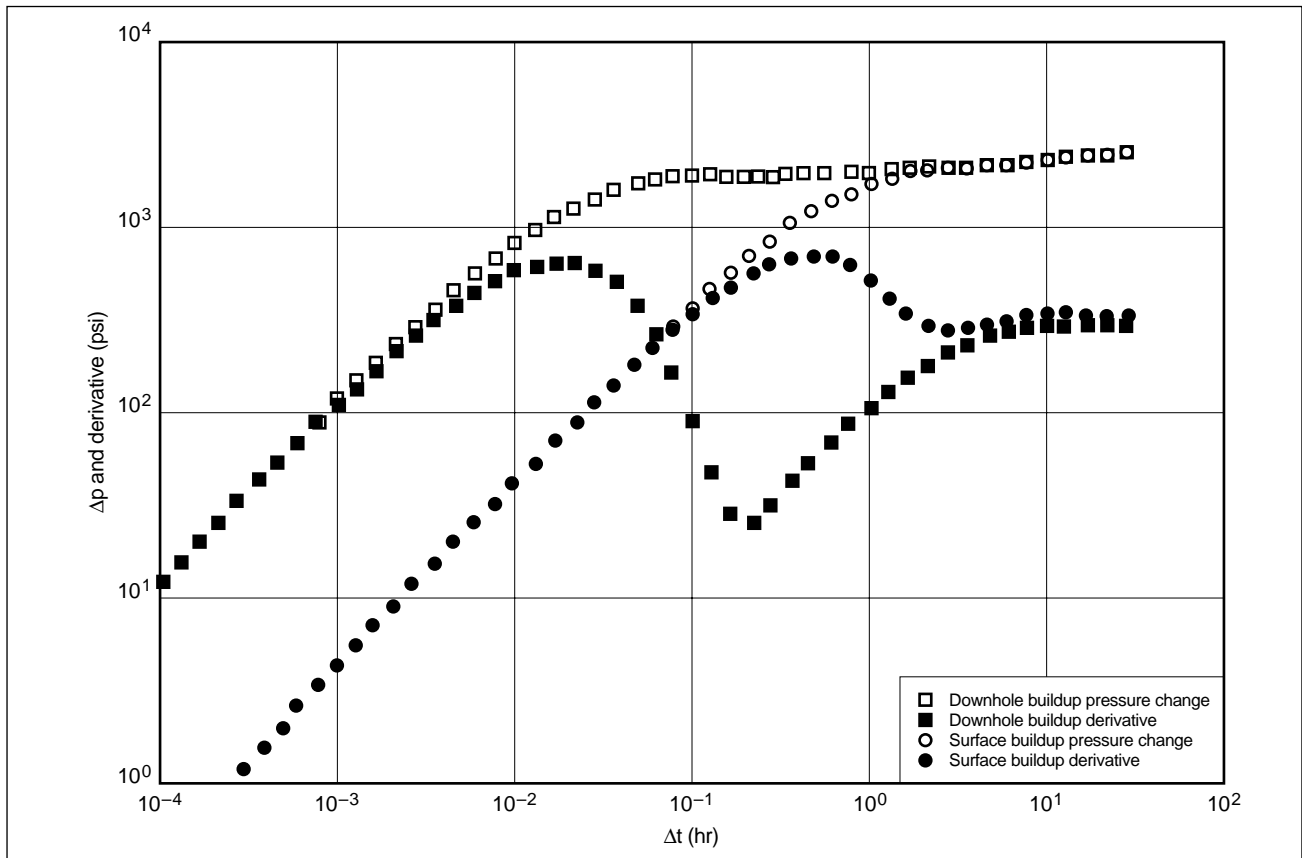


Figure 2-2. Log-log plot of pressure buildup data.

wellbore storage that can be accomplished with a downhole shut-in for pressure buildup. The second set is the response with surface shut-in or a draw-down test. The upper curve in both sets is the pressure response; the bottom is the pressure derivative. The latter is explained and justified in the next section. Although the reader is not yet familiar with other pressure/pressure derivative responses, the minimization of wellbore storage effects may reveal certain early-time patterns that are otherwise distorted or totally masked by uncontrolled, lengthy wellbore storage effects.

Mathematically, the relationship of dimensionless pressure  $p_D$  (which is exactly proportional to the real  $\Delta p$ ) versus dimensionless time  $t_D$  during dominant wellbore storage effects is

$$p_D = \frac{t_D}{C_D}, \quad (2-7)$$

where  $C_D$  is the dimensionless wellbore storage coefficient (defined in Section 2-3.5).

Agarwal *et al.* (1970) also suggested a rule of thumb according to which infinite-acting radial flow would be separated from the end of wellbore storage effects by  $1\frac{1}{2}$  log cycles of time. Data from after this transition period can be plotted on the semilogarithmic plot and analyzed as suggested in the previous section.

Thus, well test analysis became a technology consisting of diagnosis using the log-log plot in a pattern recognition exercise to find the beginning of the correct straight line followed by the semilogarithmic plot for permeability and skin effect determination.

For the drawdown log-log diagnostic plot, the appropriate variables to plot are  $p_i - p_{wf}$  versus  $t$  (again,  $p_i$  is most likely unknown) and for buildup the far more convenient  $p_{ws} - p_{wf}(\Delta t = 0)$  versus  $\Delta t$ .

There are three problems with the log-log plot of pressure difference versus time, and they affect both the likelihood of Horner analysis and the unique determination of other reservoir and well variables:

- Well tests are usually shorter than required to enter fully developed infinite-acting radial flow. This is particularly true for low-permeability reservoirs, and in such cases the use of Horner analysis would be inappropriate.
- Other geometries or reservoir and well features such as fractures and dual-porosity systems may affect the test response. In such cases, Horner

analysis would not be appropriate for the interpretation of even a long test.

- Different reservoir features may result in practically indistinguishable pressure responses, especially in reasonably short well tests. Therefore, there is the issue of uniqueness in the interpretation.

Type-curve matching by superimposing relatively short-duration field data over the mathematical model solutions has been attempted but with frequent problems of uniqueness. The technique involves plotting the mathematical (dimensionless) solution to a problem and the real data in identical log-log formats. Keeping the axes parallel, the data are matched with a portion of the solution and the overlying coordinates are determined. From the relationships between the mathematical and real variables, missing parameters such as permeability, porosity or fracture length are calculated. Type-curve matching has not been proved to be a particularly successful exercise, especially because it is not sensitive to changes in pressure. These changes can denote important phenomena—but with subtly different responses.

It is in this environment that the pressure derivative emerged.

## 2-2. Pressure derivative in well test diagnosis

When the dimensionless pressure  $p_D$  is differentiated with respect to the natural logarithm of dimensionless time  $t_D$ , then

$$\frac{dp_D}{d(\ln t_D)} = t_D \frac{dp_D}{dt_D} = t_D p'_D, \quad (2-8)$$

where  $p'_D$  is the dimensionless pressure derivative with respect to dimensionless time  $t_D$ .

The use of this particular form of pressure derivative represents a major advancement in pressure transient analysis. It was first presented to the petroleum literature by Bourdet *et al.* (1983). Figure 2-3 represents the complete solution of Gringarten *et al.*'s (1979) work for an infinite-acting reservoir, complemented by the pressure derivative as developed by Bourdet *et al.* (1983).

During wellbore storage effects, the dimensionless pressure is related to dimensionless time and dimen-



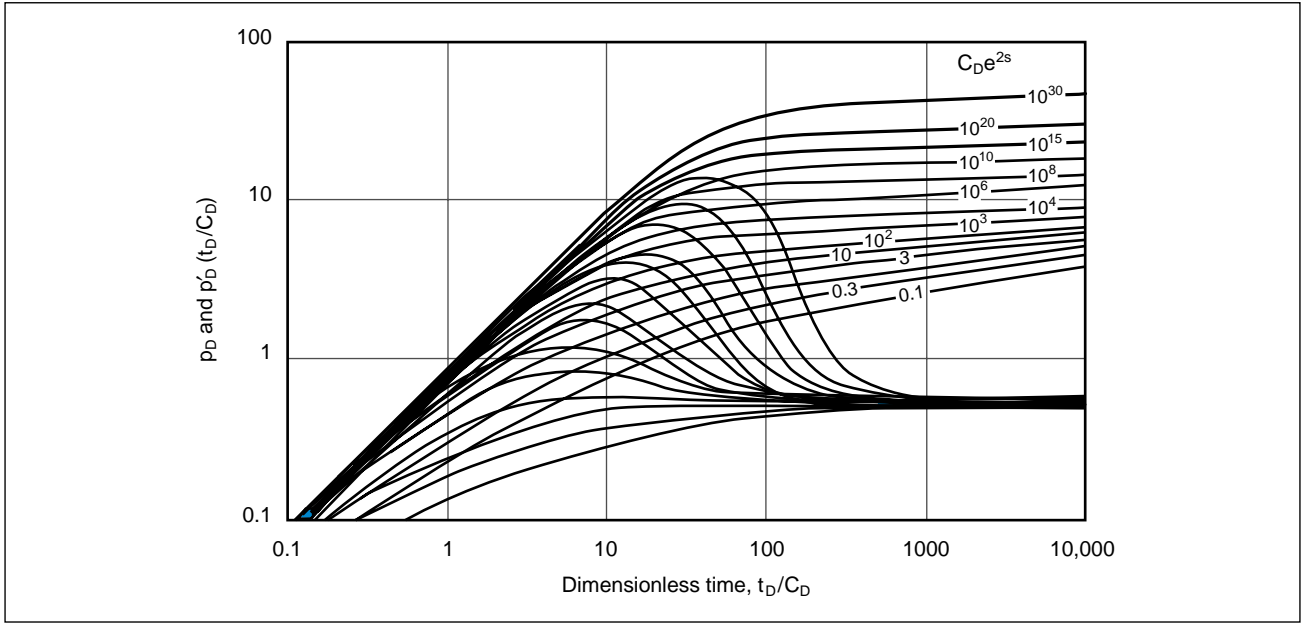


**Figure 2-3.** Dimensionless type curves for pressure drawdown and derivative for an infinite-acting reservoir with wellbore storage and skin effect (see discussion of type-curve use in Bourdet et al., 1983).

sionless wellbore storage by Eq. 2-7, which, when differentiated and combined with Eq. 2-8, yields

$$dp_D/d(\ln t_D) = t_D p'_D = t_D/C_D. \quad (2-9)$$

On log-log paper, this shows a unit straight line exactly as does the dimensionless pressure.

During the radial flow period and when the semi-logarithmic approximation is in effect (Eq. 1-19),

$$dp_D/d(\ln t_D) = t_D p'_D = 0.5, \quad (2-10)$$

and, thus, the dimensionless derivative curve at late time approaches a constant value equal to 0.5.

In general, if

$$p_D \sim t_D^m, \quad (2-11)$$

where  $m$  is equal to 1.0 for wellbore storage, 0.5 for linear flow and 0.25 for bilinear flow, then

$$dp_D/d(\ln t_D) = t_D (dp_D/dt_D) \sim m t_D^m, \quad (2-12)$$

which on log-log coordinates implies that the derivative curve is parallel to the pressure curve departed vertically by  $\log m$ .

The derivative is useful in pressure transient analysis, because not only the pressure curve but also the pressure derivative curve must match the

analytical solution. More importantly, the derivative is invaluable for definitive diagnosis of the test response. Although pressure trends can be confusing at “middle” and “late” times, and thus subject to multiple interpretations, the pressure derivative values are much more definitive. (The terms early, middle and late time are pejorative expressions for early-, midway- and late-appearing phenomena. For example, wellbore storage effects are early, fracture behavior is middle, and infinite-acting radial flow or boundary effects are late.) Many analysts have come to rely on the log-log pressure/pressure derivative plot for diagnosing what reservoir model is represented in a given pressure transient data set. To apply this method of analysis, the derivative of the actual pressure data must be calculated. A variety of algorithms is available. The simplest is to calculate the slope for each segment, using at least three time intervals. More sophisticated techniques also may be contemplated.

Patterns visible in the log-log and semilog plots for several common reservoir systems are shown in Fig. 2-4. The simulated curves in Fig. 2-4 were generated from analytical models. In each case, the buildup response was computed using superposition. The curves on the left represent buildup responses, and the derivatives were computed with respect to the Horner time function.

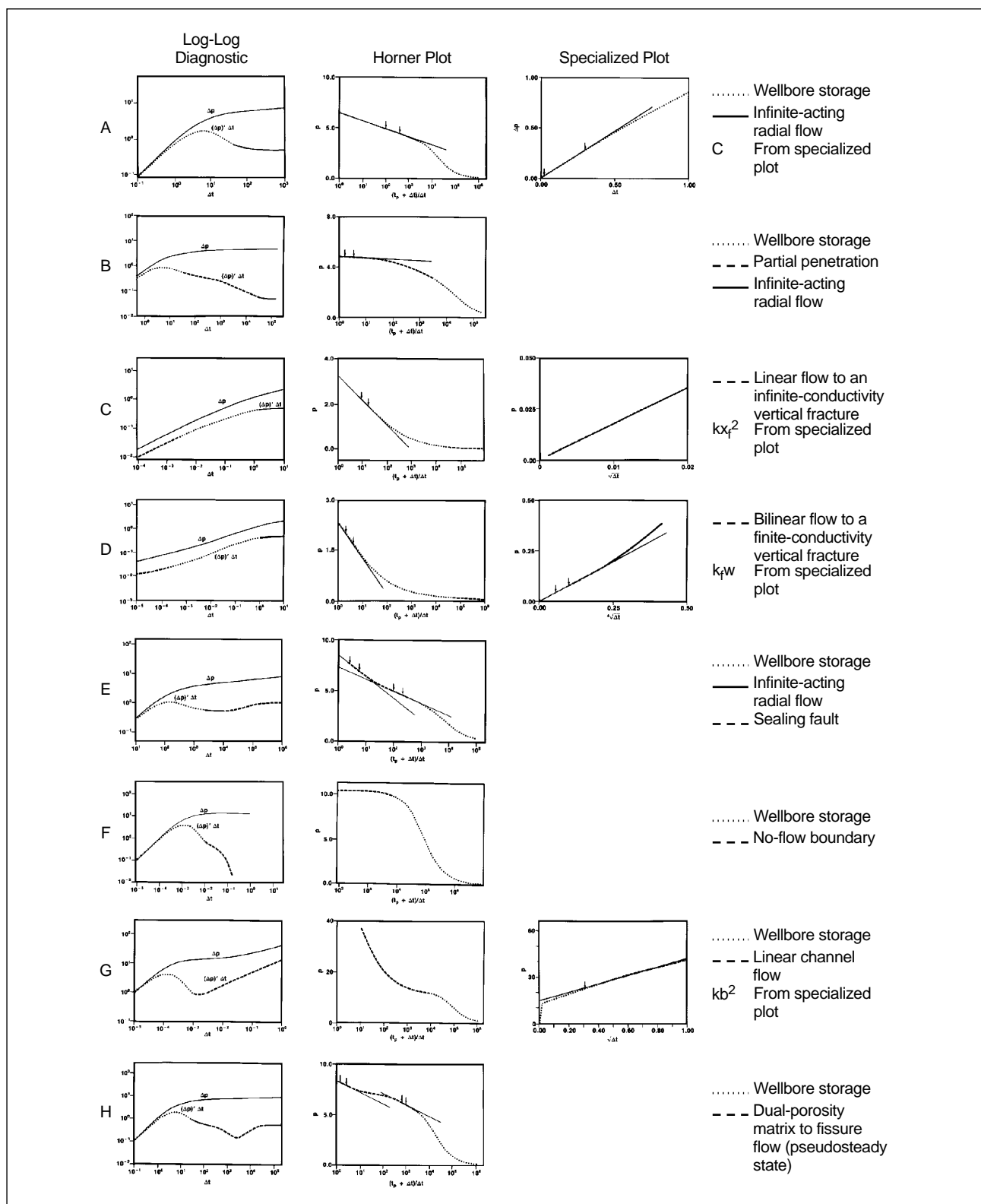


Figure 2-4. Log-log and semilog plots for common reservoir systems.

Patterns in the pressure derivative that are characteristic of a particular reservoir model are shown with a different line, which is also reproduced on the Horner plot. In cases where the diagnosed behavior can be analyzed as a straight line with a suitable change in the time axis, the curves are shown as specialized plots in the third column. Determination of the lines drawn on the Horner plots for each example was based on the diagnosis of radial flow using the derivative.

Example A illustrates the most common response, a homogeneous reservoir with wellbore storage and skin effect. The derivative of wellbore storage transients is recognized as a hump in early time (Bourdet *et al.*, 1983). The flat derivative portion in late time is easily analyzed as the Horner semilog straight line. In example B, the wellbore storage hump leads into a near plateau in the derivative, followed by a drop in the derivative curve to a final flat portion. A plateau followed by a transition to a lower plateau is an indication of partial penetration (Bilharz and Ramey, 1977). The early-time plateau represents radial flow in an effective thickness equal to that of the interval open to flow into the partially penetrating wellbore. Later, radial flow streamlines emanate from the entire formation thickness. The effects of partial penetration are rarely seen, except in tests that employ a downhole shut-in device or the convolution of measured downhole flow rates with pressure (Ehlig-Economides *et al.*, 1986).

Examples C and D show the behavior of vertical fractures (see Chapter 12). The half-slope in both the pressure change and its derivative results in two parallel lines during the flow regime representing linear flow to the fracture. The quarter-sloping parallel lines in example D are indicative of bilinear flow. During linear flow, the data can be plotted as pressure versus the square root of  $\Delta t$ , and the slope of the line in the specialized plot is inversely proportional to  $\sqrt{kx_f^2}$ , where  $x_f$  is the vertical fracture half-length in ft. During bilinear flow, a plot of pressure versus the fourth root of  $\Delta t$  gives a line with the slope inversely proportional to  $\sqrt[4]{k(k_f w)}$ , where  $k_f$  is the fracture permeability in md and  $w$  is the fracture width in ft.

Example E shows a homogeneous reservoir with a single vertical planar barrier to flow or a fault. The level of the second derivative plateau is twice the value of the level of the first derivative plateau, and the Horner plot shows the familiar slope-doubling effect (Horner, 1951). Example F illustrates the

effect of a closed drainage volume. Unlike the draw-down pressure transient, which sees the unit slope in late time as indicative of pseudosteady-state flow, the buildup pressure derivative drops to zero (Proano and Lilley, 1986).

When the pressure and its derivative are parallel with a slope of  $\frac{1}{2}$  in late time, the response may be that of a well in a channel-shaped reservoir (Ehlig-Economides and Economides, 1985), as in example G. The specialized plot of pressure versus the square root of time is proportional to  $kb^2$ , where  $b$  is the width of the channel.

Finally, in example H the valley in the pressure derivative is an indication of reservoir heterogeneity. In this case, the feature is due to dual-porosity behavior (Bourdet *et al.*, 1984).

Figure 2-4 clearly shows the value of the pressure/pressure derivative presentation. An important advantage of the log-log presentation is that the transient patterns have a standard appearance as long as the data are plotted with square log cycles. The visual patterns in semilog plots are enabled by adjusting the range of the vertical axis. Without adjustment, much or all of the data may appear to lie on one line, and subtle changes can be overlooked.

Some of the pressure derivative patterns shown are similar to those characteristic of other models. For example, the pressure derivative doubling associated with a fault (example E) can also be an indication of transient interporosity flow in a dual-porosity system (Bourdet *et al.*, 1984). The abrupt drop in the pressure derivative in the buildup data can indicate either a closed outer boundary or a constant-pressure outer boundary resulting from a gas cap, aquifer or pattern injection wells (Proano and Lilley, 1986). The valley in the pressure derivative (example H) could be an indication of a layered system instead of dual porosity (Bourdet, 1985). For these cases and others, the analyst should consult geological, seismic or core analysis data to decide which model to use for interpretation. With additional data, there may be a more conclusive interpretation for a given transient data set.

An important use for pressure/pressure derivative diagnosis is at the wellsite. The log-log plot drawn during transient data acquisition can be used to determine when sufficient data have been collected to adequately define the infinite-acting radial flow trend. If the objective of the test is to determine permeability and skin effect, the test can be terminated once the derivative plateau is identified. If hetero-

geneities or boundary effects are detected in the transient, the test can be run longer to record the entire pressure/pressure derivative response pattern required for analysis.

## 2-3. Parameter estimation from pressure transient data

The patterns identified in pressure transient data are easily recognized either by their shape or their derivative slope on the log-log diagnostic plot. Each of these patterns reflects a flow geometry in the reservoir, which, when identified, enables the computation of well and/or reservoir parameters. Ehlig-Economides (1995) summarized various computations based on flow regime equations.

### 2-3.1. Radial flow

Radial flow is illustrated by the flow streamline geometries shown in Fig. 2-5. In each case, radial flow is characterized by flow converging to a line at the center of a circular cylinder. The parameters sensed from radial flow are permeability, skin effect and reservoir pressure. In addition, the onset time for radial flow indicates the effective radius of the cylinder to which the flow converges, and the departure time from radial flow indicates the distance to whatever feature serves as an obstacle to continued radial flow propagation of the pressure signal in the formation.

Analysis of the radial flow regime quantifies the permeability in the plane of convergent flow (normal to the line source or sink). On a semilogarithmic plot of pressure versus elapsed time, the reservoir perme-

ability can be determined from a rearrangement of Eq. 2-2:

$$k = \frac{1.151\alpha_p q B \mu}{m h}, \quad (2-13)$$

where  $m$  is the absolute value of the slope of a semi-log line. The unit conversion constants in this and other equations are provided in Table 2-1.

For vertical wells, horizontal (bedding plane) permeability is determined from radial flow. Natural fractures and depositional features such as cross-bedding give rise to a preferential flow direction or permeability anisotropy in the bedding plane. In these cases, the horizontal permeability determined from analysis of the radial flow regime is actually the geometric mean of the maximum permeability  $k_x$  directed parallel to the principal permeability axis and of the minimum permeability  $k_y$  directed perpendicular to it, as given by  $\sqrt{k_x k_y}$ .

Figure 2-5a shows radial flow toward a portion of the vertical wellbore. This occurs initially when the well only partially penetrates the formation, when the well is only partially completed in the formation thickness or when drilling or completion damage restricts flow to the well. In time, the radial flow expands through the entire thickness, as in Fig. 2-5b.

For horizontal wells, the radial flow regime about the well (Fig. 2-5c) represents the geometric mean of the horizontal permeability  $k_H$  (or  $\sqrt{k_x k_y}$ ) and the vertical permeability  $k_V$  (or  $k_z$ ), given by  $\sqrt{k_H k_V}$ , or, more precisely,  $\sqrt{k_y k_z}$  (if the well is oriented parallel to the principal permeability axis). For this case, the equation for the slope of the semilog line is

$$\sqrt{k_y k_z} = \frac{1.151\alpha_p q B \mu}{m_{epr} L_p}, \quad (2-14)$$

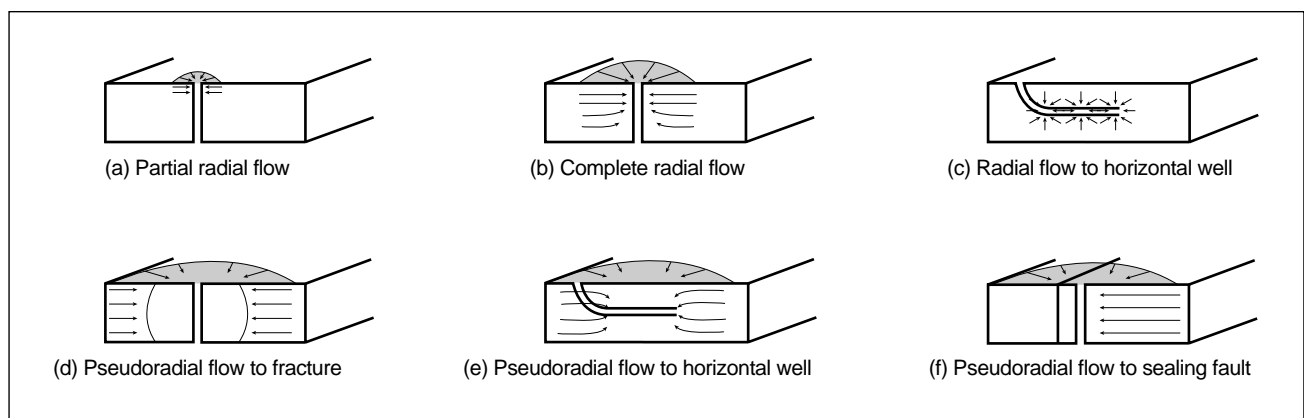


Figure 2-5. Radial flow geometries.

**Table 2-1. Unit conversion factors and constants.**

Quantity	Oilfield Unit	SI Unit
Production rate, $q$	STB/D	m <sup>3</sup> /s
Formation thickness, $h$	ft	m
Permeability, $k$	md	m <sup>2</sup>
Viscosity, $\mu$	cp	Pa·s
Pressure difference, $\Delta p$	psi	Pa
Pressure, $p$	psi	Pa
Radius, $r$	ft	m
Fracture half-length, $x_f$	ft	m
Fracture width, $w$	in.	cm
Fracture stiffness, $s_f$	psi/in.	Pa/m
Distance to sealing fault, $L$	ft	m
Channel width, $b$	ft	m
Productive length, $L_p$	ft	m
Time, $t$	hr	s
Porosity, $\phi$ (fraction)	Unitless	Unitless
Total system compressibility, $c_t$	psi <sup>-1</sup>	Pa <sup>-1</sup>
Porosity-compressibility-thickness product, $\phi c_t h$	ft/psi	m/Pa
Wellbore storage, $C$	bbl/psi	m <sup>3</sup> /Pa
Skin effect, $s$	Unitless	Unitless
$\alpha_p$	141.2	$1/(2\pi) = 0.1592$
$\alpha_t$	0.000264	1
$\alpha_c$	24	1
$\alpha_{ff}$	4.06	$1/(2\sqrt{\pi}) = 0.2821$
$\alpha_{hf}$	4.06	0.2821
$\alpha_{bf}$	44.1	0.3896
$\alpha_{pp}$	2453	0.0049
$\alpha_f$	0.000148	0.7493
$\alpha_{cf}$	8.168	$1/(\sqrt{\pi}) = 0.5642$

where the subscript *ep* refers to early pseudoradial.

Pseudoradial flow refers to radial flow converging to an effective wellbore radius  $r_w'$  larger than the well, such as to a vertical (hydraulic) infinite-conductivity fracture ( $r_w' = x_f/2$ ) or to a horizontal well ( $r_w' = L_p/4$ , where  $L_p$  is the productive length). These cases are illustrated in Figs. 2-5d and 2-5e, respectively. Pseudoradial flow can also occur after the pressure signal has propagated beyond one or more sealing boundaries (faults or stratigraphic limits), as illustrated in Fig. 2-5f.

The shaded zones in each of the flow regime diagrams depict the approximate volume traversed by the expanding pressure disturbance. The time of departure from a flow regime trend on the pressure derivative  $t_{dep}$  corresponds to the distance  $d$  to whatever flow barrier inhibits continued radial expansion of the pressure perturbation according to the following equation:

$$d = 2 \sqrt{\frac{\alpha_i k t_{dep}}{\phi \mu c_i}} \quad (2-15)$$

When the transient response ends with a level derivative, the test radius of investigation is computed with Eq. 2-15, with  $t_{dep}$  equal to the elapsed time associated with the last data point. An upward departure from a level pressure derivative trend corresponds to a flow barrier at distance  $d$ . A downward departure corresponds to an increase (outside a radius of  $d$ ) in  $k$ ,  $kh$ ,  $k/\mu$  or  $kh/\mu$  or to a constant-pressure boundary.

The permeability in Eq. 2-13 is in the direction of the reservoir feature found at distance  $d$ . For a horizontal well, departure from early radial flow occurs when the pressure signal reaches a bed boundary. A deflection for the bed boundary more distant from the well will occur if the borehole is much closer to one bed boundary. When the position of the well is known between bed boundaries, the departure time(s) can be used to compute vertical permeability (Eq. 2-15).

The onset of pseudoradial flow corresponds to a distance computed with Eq. 2-15 of 10 times the effective radial flow radius, or  $10r_w'$ , for hydraulically fractured and horizontal wells. For massive hydraulic fractures and long horizontal wells, the onset of radial flow does not appear for a considerable length of time. Similarly, the onset of radial flow following the identification of slope doubling resulting from a barrier corresponds to a radius 10 times the distance between the well and the barrier. The onset of radial flow after evidence of intersecting barriers to flow corresponds to about 10 times the distance from the well to the barrier intersection, and the level of the derivative above that observed before evidence of the nearest flow barrier increases inversely with the sine of the angle between the barriers.

Logically, the permeability computed from the radial flow regime (Eq. 2-13) corresponds to the average permeability between the radii corresponding to the onset to and the departure from radial flow.

The skin effect computed from radial flow (Eq. 2-3) depends on the effective radius of the flow. For example, the skin effect computed from radial flow to a partial penetration or completion corresponds to the mechanical skin effect along the flowing interval, but the skin effect computed later based on radial flow in the entire formation thickness includes the sum of skin effect components corresponding to mechanical skin effect and an apparent skin effect caused by vertical flow convergence. Similarly, the skin effect computed from pseudoradial flow corresponds to an apparent skin effect dominated by the stimulation effect associated with a larger effective wellbore.

The average reservoir pressure is determined from pressure buildup test data by extrapolating the radial flow trend to a Horner time of 1 on a Horner plot. The extrapolated pressure  $p^*$  is used to determine average pressure when the approximate drainage shape is known using the Matthews, Brons, Hazebroek (MBH) analysis described in Earlougher (1977).

### 2-3.2. Linear flow

Linear flow is the second most commonly observed flow regime. It is characterized by entirely parallel flow in the formation and can result either because of the well completion or trajectory geometry or because of outer reservoir boundaries. Figure 2-6a illustrates linear flow to a vertical fracture plane, and Fig. 2-6b shows linear flow to a horizontal well. Both of these flow regimes occur before pseudo-radial flow, and their duration is dependent on the fracture half-length, or the productive length in the case of a horizontal well. Figure 2-6c shows linear flow resulting from the elongated shape of the reservoir. This can be observed in wells located between parallel faults or in elongated sands such as fluvial or deep marine channels. Linear flow can also occur to a shallow horizontal fracture or a thin high-permeability bed.

The portion of the data exhibiting a linear flow trend (half-slope derivative) can be analyzed by plotting pressure against the square root of time. The equation for the slope of the straight-line portion of pressure versus the square root of time is as follows for linear flow to a fracture:

$$x_f \sqrt{k} = \left( \frac{\alpha_{lf} qB}{m_{lf} h} \right) \left( \frac{\mu}{\phi c_i} \right)^{1/2} \quad (2-16)$$

for linear flow to a horizontal well:

$$L_p \sqrt{k} = \left( \frac{\alpha_{hl} qB}{m_{hl} h} \right) \left( \frac{\mu}{\phi c_i} \right)^{1/2} \quad (2-17)$$

and for linear flow inside an elongated reservoir:

$$b \sqrt{k} = \left( \frac{\alpha_{cf} qB}{m_{cf} h} \right) \left( \frac{\mu}{\phi c_i} \right)^{1/2} \quad (2-18)$$

Each of these equations relates permeability and the width of the linear flow ( $x_f$  for the vertical fracture,  $L_p$  for the horizontal well and  $b$  for the elongated reservoir). The permeability affecting linear flow analysis is in the direction of the linear flow streamlines.

In addition to Eqs. 2-16 through 2-18, departure from linear flow corresponds to the following equations for a vertical fracture:

$$t = \frac{\phi \mu c_i x_f^2}{16 \alpha_x k_x} \quad (2-19)$$

and for a horizontal well:

$$t = \frac{\phi \mu c_i L_p^2}{64 \alpha_x k_x} \quad (2-20)$$

Each of these equations also relates permeability and the width of the linear flow. Thus, when the linear flow regime and a departure from it are identified in the transient data, both parameters can be estimated.

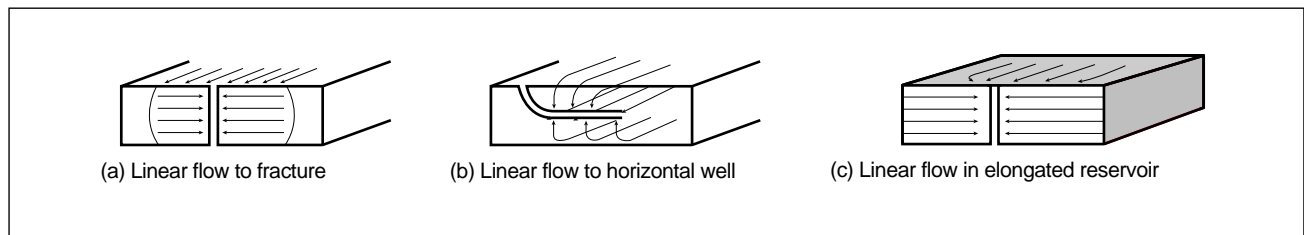


**Figure 2-6.** Linear flow geometries.

For a well in an elongated reservoir,

$$t = \frac{\pi\phi\mu c_i d^2}{16\alpha_i k_x}, \quad (2-21)$$

where  $d$  corresponds to the distance between the well and a barrier or a constant-pressure boundary normal to the reservoir elongation. Equation 2-21 enables calculation of the distance  $d$ .

For finite-conductivity hydraulic fractures, bilinear flow, as shown in Fig. 2-7, may occur before or instead of linear flow. The slope of the straight line on a plot of pressure versus the fourth root of elapsed time relates to fracture parameters as the following:

$$k_f w \sqrt{k} = \left( \frac{\alpha_{bf} q B \mu}{m_{bf} h} \right)^2 \left( \frac{1}{\phi \mu c_i} \right)^{1/2}. \quad (2-22)$$

The time of departure from bilinear flow is dependent on the fracture half-length, as for linear flow according to Eq. 2-19, when the departure is concave down toward radial flow. If linear flow follows bilinear flow, Eq. 2-19 applies only for the departure from linear flow. Bilinear flow involves the fracture conductivity  $k_{fw}$ , fracture half-length and reservoir permeability  $k_y$ . After bilinear flow, if linear flow appears and a departure from it, then fracture conductivity, fracture half-length and reservoir permeability can all be determined by Eqs. 2-16, 2-19 and the following:

$$\frac{k_f w}{k x_f} = \left( \frac{\pi}{3} \right) \frac{m}{1.151} \left( \frac{1}{\Delta p_{int}} \right), \quad (2-23)$$

where  $\Delta p_{int}$  is the difference in the pressure intercept.

Unfortunately, for horizontal wells and hydraulically fractured vertical wells, sufficient flow regime variation for complete analysis is typically lacking. Many well tests exhibit only linear or bilinear flow transients in fractured wells. Horizontal well tests usually do not exhibit linear flow, rendering ambiguous the distinction between early radial flow regimes and pseudoradial flow.

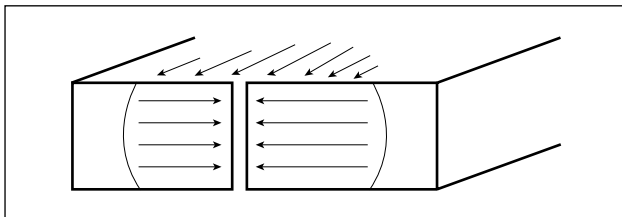


**Figure 2-7.** Bilinear flow to a hydraulic fracture.

### 2-3.3. Spherical flow

Spherical and hemispherical flow regimes are illustrated in Fig. 2-8 as streamlines converging to a point. These flow regimes appear in partially penetrated and partially completed wells. The parameters sensed by spherical flow are the spherical permeability, given by  $k_{sph} = \sqrt{k_H k_V}$ , and the distances between the flowing interval and the bed boundaries.

The spherical flow plot is pressure versus the reciprocal of the square root of elapsed time. The equation for determining the spherical permeability from the straight-line portion of a spherical flow plot is

$$k_{sph} = \left( \frac{\alpha_{pp} q B \mu}{m_{pp}} \sqrt{\phi \mu c_i} \right)^{2/3}. \quad (2-24)$$

In addition, the departure from spherical flow caused by the nearest bed boundary to the flowing interval occurs at the time satisfying the following:

$$t = \frac{\phi \mu c_i z_w^2}{36 \alpha_i k_V}, \quad (2-25)$$

where  $z_w$  is the elevation of the midpoint of the perforations from the bottom of the reservoir.

For hemispherical flow that occurs after the nearest bed boundary has been sensed, the constant in Eq. 2-21 is 18 in place of 36.

A test can be designed to observe spherical flow in a pilot hole prior to drilling a horizontal well. This strategy enables determination of the formation vertical permeability, which, in turn, enables much more accurate forecasts of the horizontal well productivity. In some cases such a test may discourage drilling the horizontal well if the expected productivity is not sufficient to justify it. Further, conducting the pilot hole test enables a more meaningful interpretation of a subsequent test in the horizontal well because parameters determined from the pilot hole test do not have to be redetermined from the horizontal well test.

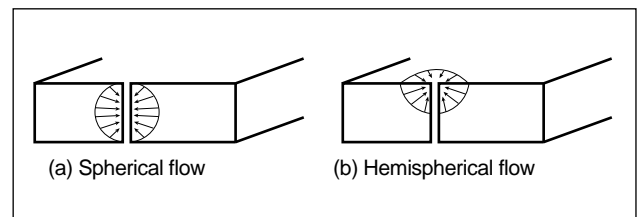


**Figure 2-8.** Spherical and hemispherical flow geometries.

### 2-3.4. Dual porosity

Dual-porosity flow behavior results when reservoir rocks contain distributed internal heterogeneities that have highly contrasting flow characteristics such that flow occurs mainly in a high-permeability formation feature that accounts for a small fraction of the formation storativity. Examples are naturally fractured reservoirs and laminated systems with thin high-permeability layers.

The two commonly observed dual-porosity transient trends are shown in examples E and H in Fig. 2-4. Example E illustrates transient dual-porosity behavior typical of highly laminated systems, which is virtually impossible to distinguish from a sealing fault without additional information. In example H, which shows pseudosteady-state dual-porosity behavior typical of naturally fractured formations, a valley-shaped drop in the pressure derivative signals recharge from matrix rock into the natural fractures. Dual-porosity behavior can appear during any of the flow regimes and complicates transient analysis.

Recognizing and characterizing dual-porosity flow behavior is extremely important to reserves estimation, trajectory planning for deviated and horizontal wells, and stimulation design and post-treatment evaluation.

The two parameters that characterize dual-porosity systems are the storativity ratio  $\omega$  and the interporosity flow parameter  $\lambda$ . For pseudosteady-state dual porosity, the time of the onset of dual-porosity behavior  $t_{on}$  is a function of both parameters:

$$t_{on} = \frac{\phi \mu c_t r_w^2}{\alpha_i k} \frac{7\omega^2}{\lambda(1-\omega)} \left( \ln \frac{1}{\omega} \right)^2. \quad (2-26)$$

Similarly, the time of the end of dual-porosity behavior  $t_{end}$  is

$$t_{end} = \frac{\phi \mu c_t r_w^2}{\alpha_i k} \frac{(1-\omega)}{7\lambda}, \quad (2-27)$$

and the time of the valley minimum  $t_{min}$  is given by Bourdet *et al.* (1983) as

$$t_{min} = \frac{1}{2} \left( \frac{\phi \eta c_t}{\alpha_i k} \right) \left( 1 + \omega^{\frac{1}{1-\omega}} - \omega^{\frac{\omega}{1-\omega}} \right). \quad (2-28)$$

When two of these three times can be identified in the pressure derivative response,  $\omega$  and  $\lambda$  can be estimated.

Dual-porosity reservoirs are likely to exhibit highly anisotropic flow behavior. Highly laminated systems usually have considerable contrast in horizontal and vertical permeability, whereas naturally fractured systems usually have a preferential flow direction oriented parallel to the natural fractures. Laminated formations favor vertical wells; horizontal wells are particularly attractive in naturally fractured reservoirs. Because natural fractures are usually sub-vertical and oriented with the stress field, the maximum permeability and maximum stress directions are usually closely aligned, resulting in enormous implications for hydraulic fracture design and trajectory planning in deviated wells.

Observance of dual-porosity transients should trigger additional measurements or analysis to establish the direction and magnitude of the implicit permeability anisotropies.

### 2-3.5. Wellbore storage and pseudosteady state

Wellbore storage and pseudosteady state both result from fluid compression or expansion in a limited volume. For wellbore storage the control volume is the wellbore; for pseudosteady state it is the reservoir drainage volume. Both these cases are sensitive mainly to two parameters, fluid compressibility and the control volume, but other factors determine their onset and duration. Both are recognized by a unit-slope trend in the pressure derivative.

For wellbore storage, the pressure change and the derivative coincide with a unit-slope trend on the log-log diagnostic plot in early time. The derivative typically departs below the pressure change and appears as a hump during the transition to reservoir-dominated flow regimes. This is typically the first flow regime observed in any test, and it usually dominates the transient response. The wellbore storage coefficient can be computed from the straight-line portion of the plot of pressure change versus elapsed time using the following equation (the line must pass through the origin on the plot):

$$C = \frac{qB}{\alpha_c m_c}. \quad (2-29)$$

The duration of wellbore storage can be reduced by designing buildup tests with downhole shut-in. Other factors affecting wellbore storage duration are perme-



ability (duration increases for low permeability) and skin effect (duration increases for a higher positive skin effect). Because heterogeneities or flow geometries located inside the radius of investigation of the pressure signal at the time of the end of wellbore storage are masked by wellbore storage, it is important to minimize this phenomenon.

Pseudosteady state is observed only in drawdown tests. In buildup tests, pseudosteady state behavior is distorted by superposition, which causes a downturn in the derivative that is indistinguishable from the effect of a constant-pressure boundary. The time of the onset of pseudosteady state is a function of the shape and magnitude of the drainage area and the position of the well within it. Modern flow regime analysis of the transient behavior observed in the pressure derivative before the onset of pseudosteady state enables characterization of the well and drainage boundary geometry, which, in turn, enables quantification of the average reservoir pressure.

## 2-4. Test interpretation methodology

Interpretation of transient test data involves the following steps:

- data processing
- model diagnosis
- flow regime analysis
- nonlinear regression.

In the data processing step, the data for analysis are extracted from the complete data set as a series of one or more transients, each of which is a response to a single step change in the surface rate. The transient data are reduced, usually with a routine designed to sample or filter the data logarithmically in elapsed time since the surface rate change. Poor-quality data may be excluded in this step.

For model diagnosis, the pressure change and its derivative are computed from the data for a single transient, incorporating all recent surface rate changes in the superposition time used for data differentiation. For multirate tests, the data from more than one transient can be plotted together on the log-log diagnostic plot by dividing the pressure change

and derivative data for each transient by the rate change that initiated the transient. Reservoir-dominated flow regime derivative transients plotted in this manner should overlaid each other, and differences in the pressure change trends are a sign of rate-dependent skin effects. It is also possible to confirm the accuracy of the surface rate sequence.

In flow regime analysis, the parameters associated with each flow regime identified on the log-log diagnostic plot are computed using the techniques and equations outlined in Section 2-3.

The parameters estimated from the flow regimes serve as a starting point for the nonlinear regression step. The objective of this step is to find a match for the entire transient response. To do this, a model must be selected that accounts for all identified flow regimes.

- Example post-treatment test in a hydraulically fractured well

This example illustrates a transient test response following a hydraulic fracture treatment in a high-permeability reservoir. Figure 2-9 is a log-log diagnostic plot of the drawdown data, obtained with a downhole pressure-measuring device. The flow regimes identified in the transient response are wellbore storage, bilinear flow and radial flow. The flow rate from this well was more than 3600 STB/D.

From the unit slope in the early-time portion, the wellbore storage constant  $C$  is computed as 0.0065 bbl/psi. From the radial flow portion, the reservoir permeability  $k$  is computed as 12.5 md and the radial skin effect is equal to  $-4.3$ . Then, from the bilinear flow portion, the product  $k_f w$  is estimated as 1900 md-ft. From Fig. 1-11 a trial-and-error procedure is indicated. Assuming  $x_f = 100$  ft (the designed length), dimensionless fracture conductivity  $C_{fD} = (1900)/(12.5)(100) = 1.5$  and from Fig. 1-11,  $s_f + \ln(x_f/r_w) = 1.3$ . Because  $r_w = 0.328$  ft, the calculated fracture half-length is 90 ft, which is close enough. With these as starting parameters, an initial simulation for the transient response is compared to the data in Fig. 2-10. Nonlinear regression allows the well and reservoir parameters to vary until an optimized match is found for the entire response, as shown in Fig. 2-11. The final parameter estimates are  $C = 0.005$  bbl/psi,  $k = 12$  md,  $x_f = 106$  ft and  $C_{fD} = 1.6$ .

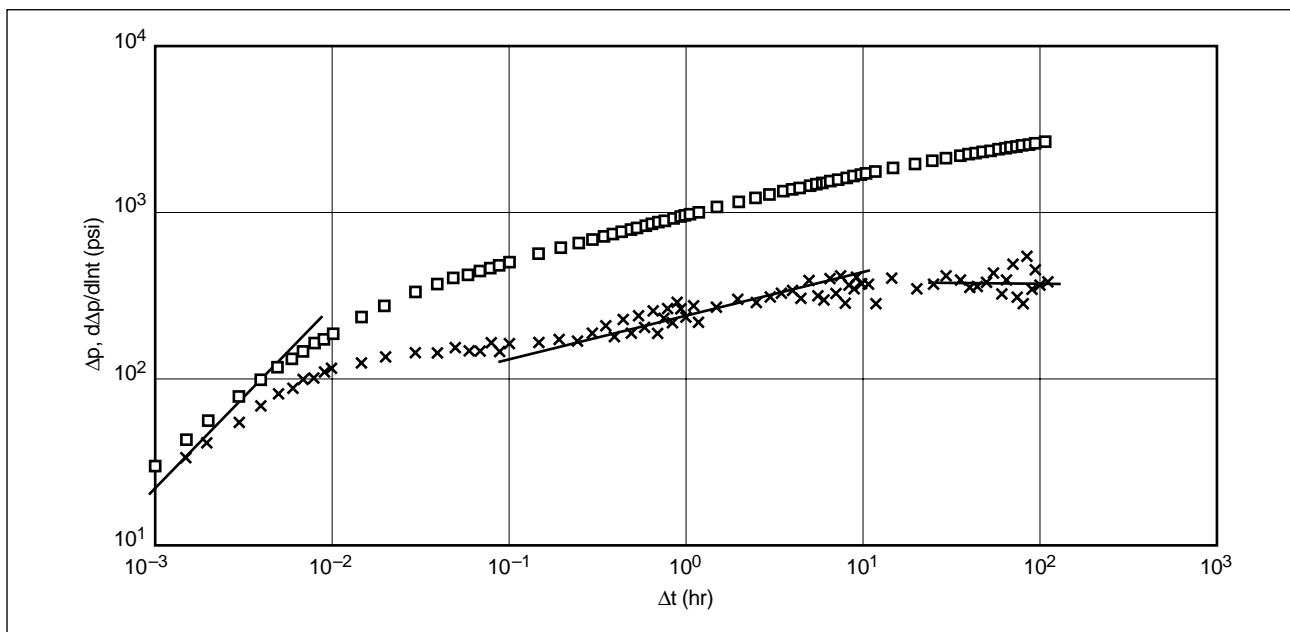


**Figure 2-9.** Log-log diagnostic plot of post-treatment test after hydraulic fracturing.

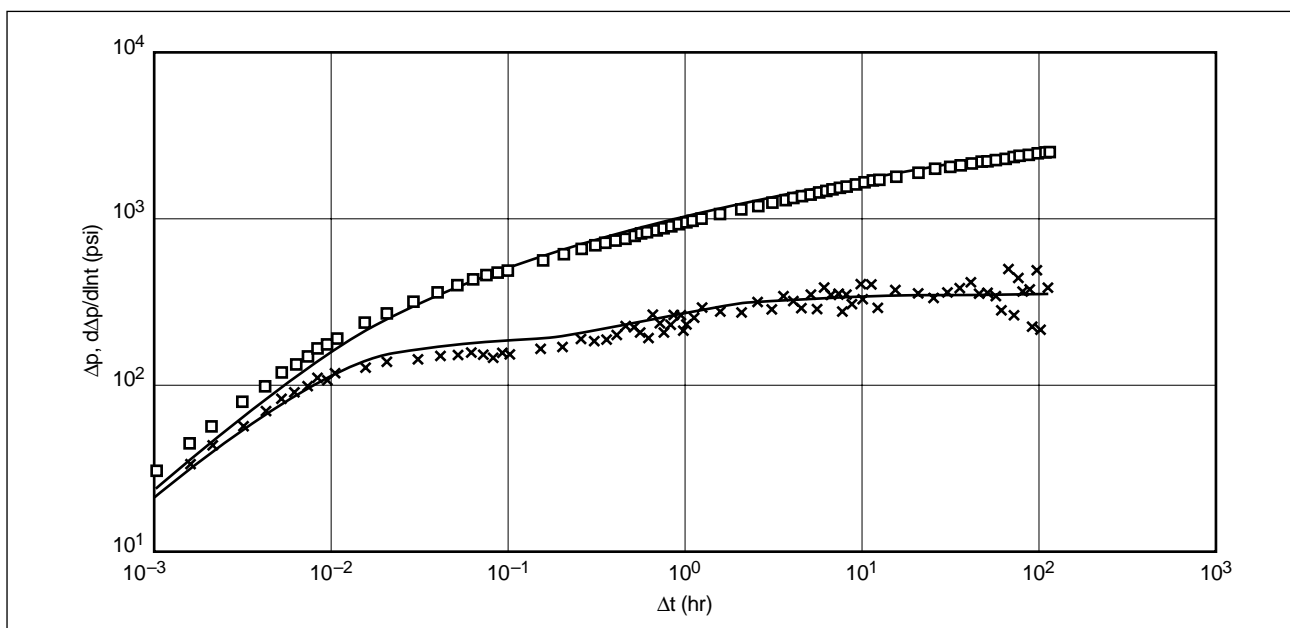


**Figure 2-10.** Initial match with post-treatment test data.

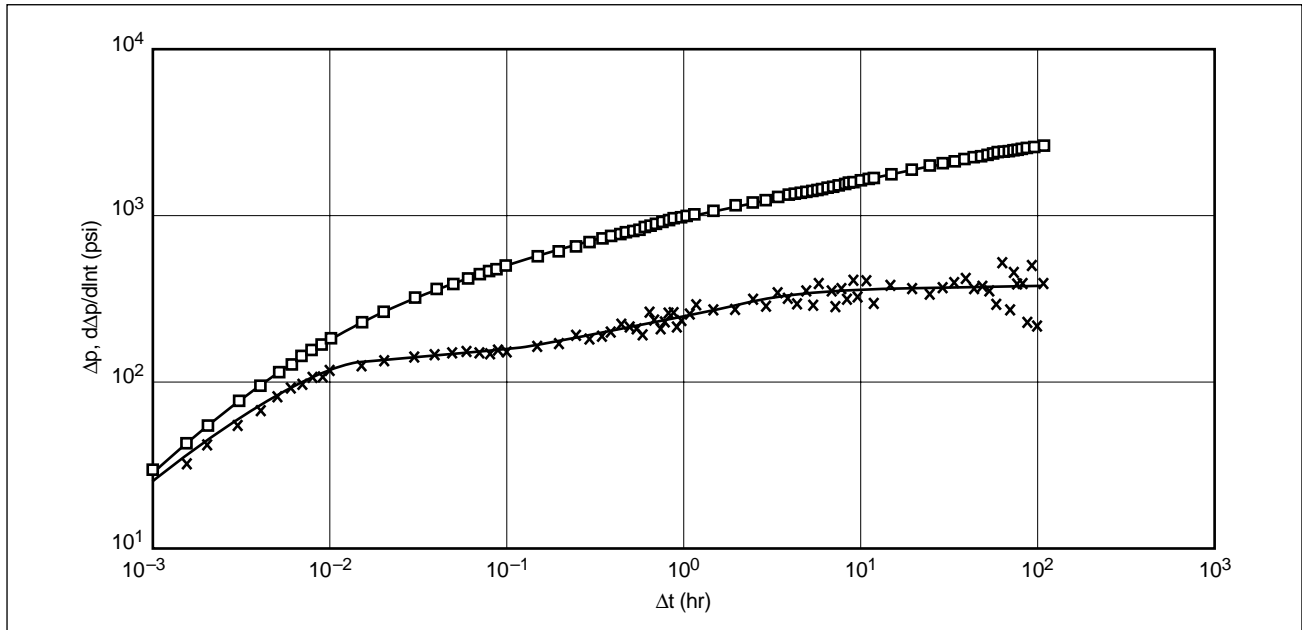


**Figure 2-11.** Final match with post-treatment test data.

## 2-5. Analysis with measurement of layer rate

When downhole shut-in is not an option, a buildup test with surface shut-in can be dominated for much of the test duration by wellbore storage. An alternative in Fig. 2-12 to the conventional buildup test is designed to acquire downhole measurements of both flow rate and pressure using a production logging tool. The best data acquired with such tests are during drawdown, but additional data processing is required for model diagnosis. In this case an analog for the pressure change is the rate-normalized pressure (RNP), computed as the ratio of the pressure change to the flow rate change for data acquired at the same instant in time. The pressure change (flow rate change) is the difference between the bottom-hole pressure (flow rate) measured at any elapsed time  $t$  since the start of the test transient and the bottom-hole pressure (flow rate) measured at the start of that transient. The analog for the pressure derivative is the deconvolution derivative, computed as a derivative of the RNP, or the convolution derivative, which accounts for superposition effects caused by each change in the continuously acquired downhole rate. Both computations account for superposition resulting from recent changes in the surface rate, and

each can be used for model diagnosis in the same fashion as the pressure change and derivative are used. This data acquisition and processing technique reduces the duration of wellbore storage in a draw-down test by the same amount as downhole shut-in does in a buildup test.

Some wells with commingled flow from several layers are equipped with sliding sleeves. This enables

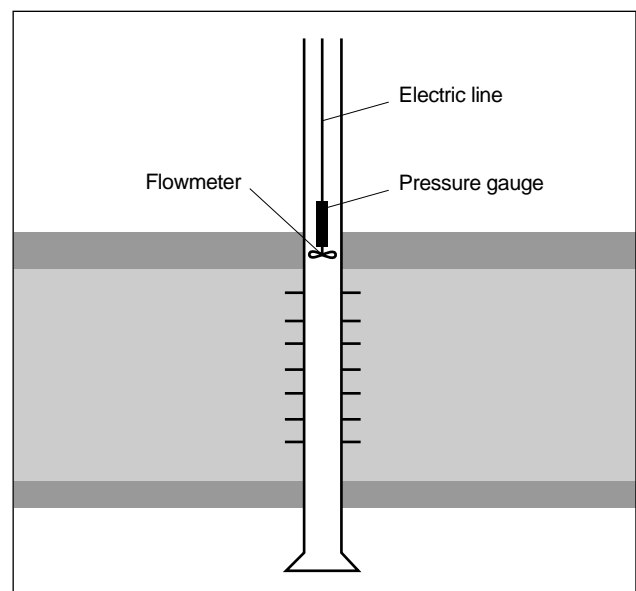


**Figure 2-12.** Acquisition of transient flow rate and pressure data.

flow from a particular layer to be shut off by shutting the sleeve. Such completions allow a more direct test of the layer, as diagrammed in Fig. 2-13. The figure shows two flowmeters spaced above and below the flow ports of the sliding sleeve. The flowmeter above the sleeve opening measures the flow rate  $q_2$  from layers 2 and 3, and the lower flowmeter measures the flow rate  $q_1$  from layer 3 only. A simple subtraction,  $q_2(t) - q_1(t)$ , enables direct measurement of the flow from the layer, which can be used in the RNP analysis described in the previous paragraph.

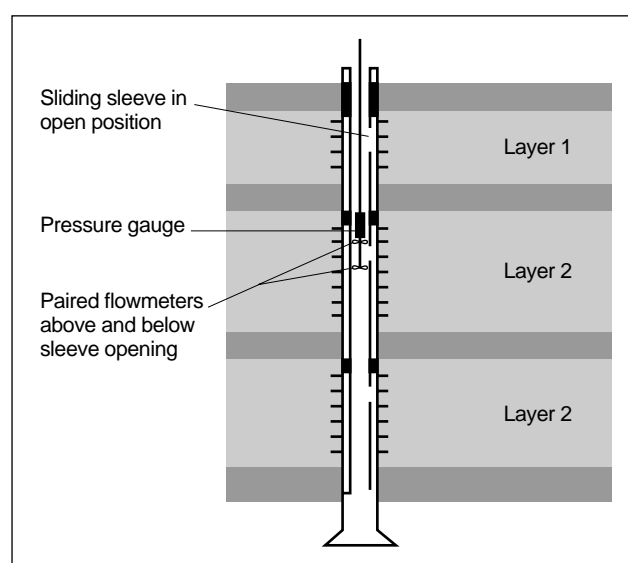


**Figure 2-13.** Acquisition of transient flow rate and pressure data for a single layer in a commingled completion.

## 2-6. Layered reservoir testing

Layered formations pose special problems for reservoir management that can be best addressed with a layer-by-layer characterization of reservoir parameters. The multilayer transient test is designed to provide the average pressure, productivity index, and well and reservoir parameters for two or more layers commingled in a common wellbore. When a contrast in performance is apparent in commingled layers, this test can determine whether the contrast is due to large variations in layer  $kh$  values or to large variations in skin effect. In the former case, there may be implications for waterflood vertical displacement efficiency. In the latter case, there may be a work-over treatment that would improve the performance of layers with higher skin factors. Alternatively, the

test may show which layer skins have been lowered by a recent stimulation treatment.

The sequence of the multilayer transient test is the key to its success. This test merges stabilized and transient flow rate and pressure measurements using a production logging tool. A typical test sequence is illustrated in Fig. 2-14. Beginning with the well shut-in, a flow rate survey is acquired, and then the tool is positioned above the lowest layer. After a brief pause while the sensors equilibrate to the wellbore conditions at this depth, the flow rate is increased at the surface while leaving the tool stationary at this depth. When flow and pressure have stabilized at radial, pseudosteady-state or steady-state conditions, or when the desired behavior has been observed, another flow rate survey is acquired. Then the tool is positioned above the next lowest layer to repeat the same procedure at this depth, taking care to acquire the stabilized profile data after the same length of time following the rate change as for the first measurement sequence. When stationary measurements have been acquired above each of the intervals of interest and stabilized flow surveys have been acquired for at least three surface flow rates, the tool is positioned for an optional final buildup test. The final tool position is optional; it is worthwhile to position the tool where wellbore crossflow could occur while the well is shut in.

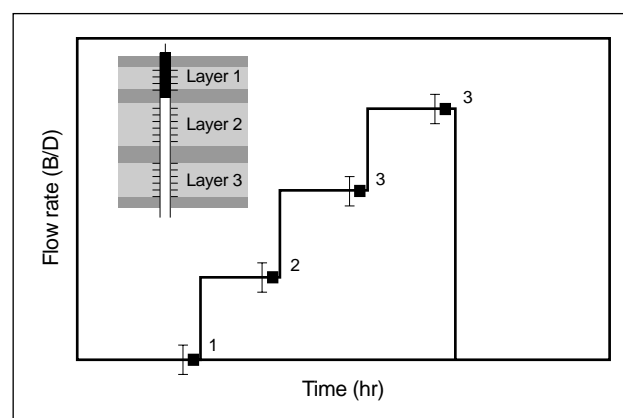


**Figure 2-14.** Test sequence for a multilayer transient test.

### 2-6.1. Selective inflow performance analysis

Selective inflow performance (SIP) analysis extends the concepts of flow-after-flow or isochronal tests to multiple layers. Each time a flow profile is acquired,

subtracting the flow rate measured above a layer from that measured below it gives the flow rate to or from that layer. For SIP analysis, an inflow performance plot of datum pressure versus layer flow rate provides the layer average pressures and productivity indices, as shown in Fig. 2-15. For oil wells, the slope of each line is the reciprocal of the layer productivity index  $J$ . For gas wells, a quadratic fit of the data provides, for each layer tested, the productivity index and an estimate of the coefficient  $D$  associated with the rate-dependent skin effect caused by turbulent flow near the wellbore. In water injection wells, SIP analysis can be useful for estimating the formation parting pressure in each layer.

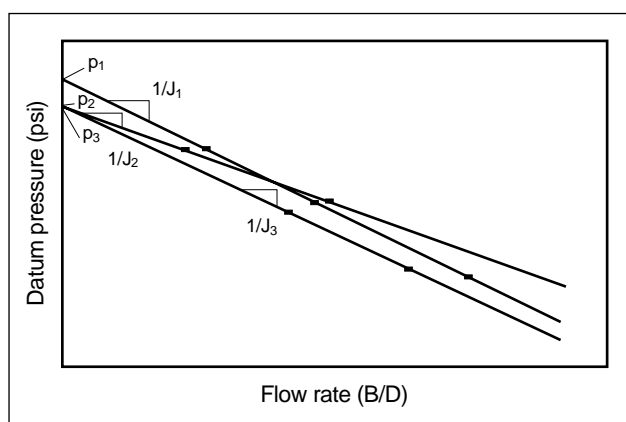


**Figure 2-15.** Selective inflow performance analysis.

### 2-6.2. Analysis of multilayer transient test data

Multilayer transient data analysis begins with the transient flow rate and pressure data acquired above the lowest reservoir layer. The RNP is computed, as indicated previously, as the ratio of the pressure change to the flow rate change for data acquired at the same instant in elapsed time since the start of the transient. The log-log plot of RNP and its derivative can be used to select a model for the transient behavior of the lowest reservoir layer. Then, analogous procedures to those used for single-layer drawdown tests with measured bottomhole pressure and flow rate are applied to estimate parameters for observed flow regimes and to refine these estimates using nonlinear regression. Once a suitable match between the measured data and a model is found, the parameters used to generate the match provide an interpretation for the lowest reservoir layer.

The analysis then proceeds to the next lowest reservoir layer. Diagnosis of the model for this and shallower reservoir layers is more difficult than for the lowest layer. Again, the RNP and its derivative are computed, but this time the behavior observed is that of the lowest two layers combined. To see the behavior of the next lowest layer by itself requires additional processing. However, by assuming that the model for the second layer is similar to that of the lowest layer, parameters for the second layer model can be estimated. Again, nonlinear regression is used to refine the estimates, this time using a two-layer model with the parameters for the lowest layer held fixed in the model.

The analysis of succeeding layers continues in this bottom-to-top fashion. Each time, the model for the behavior includes an additional layer. This procedure has been labeled the sequential interpretation method. Once all the layer parameters have been estimated, a simultaneous interpretation can be performed for all layers. In this case, the nonlinear regression uses all the transients and a model for all the layers. This step refines the parameter estimates and, because it uses data covering a longer period of time than any single transient, may account for external boundary effects that are too distant to be apparent in a single transient.

## 2-7. Testing multilateral and multibranch wells

Multilateral wells and, more generally, multibranch wells have two or more well paths branching from a common main trunk as in Fig. 2-16. Dual completion strings may segregate production from the well paths, but this limits the number of branches. Otherwise, the flow from the branches is commingled in the main trunk. If the branch departures from the main trunk are separated, then the flow rate can be measured as

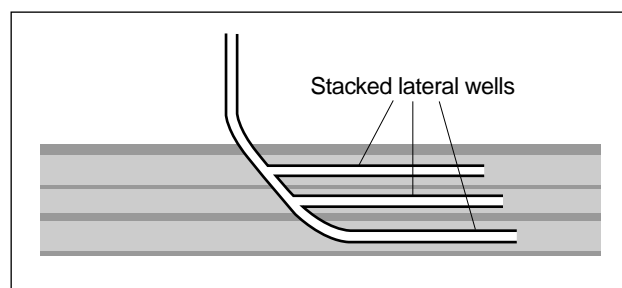


**Figure 2-16.** Multibranch well with stacked horizontal branches commingled in an inclined trunk section.

previously discussed, by the difference above and below the branch or inside a sliding sleeve in the main trunk, where applicable. Alternatively, a test sequence analogous to the multilayer transient test with data acquired in the main trunk above each branch (Fig. 2-17) enables the analysis of each branch, with SIP analysis providing the branch productivities and transient analysis providing a set of model parameters for each branch. If the branch departures are not separated, the flow rate measurement must be acquired in the branch. Permanent pressure and flow rate sensors installed in the branch could also provide a means to test the branch.

Model selection for a branch depends on the trajectory geometry of the branch, which can be vertical, slanted or horizontal. Karakas *et al.* (1991) published an interpretation for a series of tests in a bilateral well.

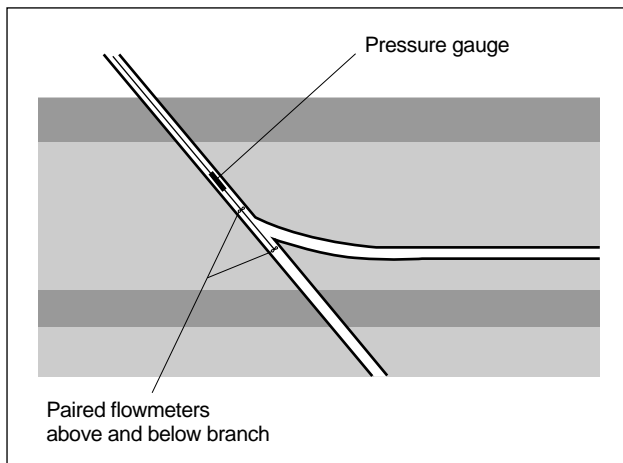


**Figure 2-17.** Transient data acquisition in a multibranch well.

## 2-8. Permeability determination from a fracture injection test<sup>†</sup>

Fracture injection tests, called also calibration treatments, consist of injecting a known amount of the fracturing fluid into the formation, shutting down the pumps and observing the decline of the pressure in the wellbore. It is assumed that up to the end of injection time  $t_e$ , the injection rate  $i$  into one wing is constant. After injection, the pressure in the wellbore declines because the fluid is leaking off from the created fracture and the fracture faces are approaching

each other, relaxing the elastic force exerted on the formation. The decrease of the induced stress results in decline of the wellbore pressure. Because the whole process is controlled by fluid leakoff, pressure decline analysis has been a primary source of obtaining the parameters of the assumed leakoff model.

The polymer content of the fracturing fluid is partly intended to impede fluid loss into the reservoir. The phenomenon is envisioned as a continuous buildup of a thin layer (the filter cake) that manifests the ever increasing resistance to flow through the fracture face. In reality, leakoff is determined by a coupled system, of which the filter cake is only one element. In the following, pressure decline analysis is introduced as it pertains to the modeling of fluid loss (see Chapters 6 and 9) along with another method coupling filter-cake resistance and transient reservoir flow.

### 2-8.1. Pressure decline analysis with the Carter leakoff model

A fruitful formalism dating back to Howard and Fast (1957) is to consider the combined effect of the different fluid-loss mechanisms as a material property. According to this concept, the leakoff velocity  $u_L$  is given by the Carter equation:

$$u_L = \frac{C_L}{\sqrt{t}}, \quad (2-30)$$

where  $C_L$  is the leakoff coefficient in  $\text{ft}/\text{min}^{1/2}$  and  $t$  is the time elapsed since the start of the leakoff process. The integrated form of Eq. 2-30 is

$$\frac{V_L}{A_L} = 2C_L \sqrt{t} + S_p, \quad (2-31)$$

where  $V_L$  is the fluid volume that passes through the surface  $A_L$  during the time period from time zero to time  $t$ . The integration constant  $S_p$  is called the spurt-loss coefficient. It can be considered the width (extent) of the fluid flowing through the surface instantaneously at the beginning of the leakoff process. The two coefficients,  $C_L$  and  $S_p$ , can be determined from laboratory tests.

Application of Eqs. 2-30 and 2-31 during fracturing can be envisioned assuming that the given surface element “remembers” when it has been opened to fluid loss and has its own zero time, which may be different from location to location on a fracture surface.

<sup>†</sup> This section by Professor Peter Valkó, Texas A&M University.

A hydraulic fracture injection may last from tens of minutes up to several hours. Points at the fracture face near the well are opened at the beginning of pumping, whereas points at the fracture tip are younger. Application of Eq. 2-31 necessitates tracking the opening time of the different fracture face elements. If only the overall material balance is considered, then Carter's concept is used:

$$V_i = V + 2Ar_p(\kappa C_L \sqrt{t} + S_p), \quad (2-32)$$

where  $V_i = it$  is the total injected volume for one wing with a fracture volume  $V$ ,  $A$  is the surface area of one face of one wing, and  $r_p$  is the ratio of permeable area to total fracture area (see Figs. 2-18 and 2-19 for detail). The variable  $\kappa$  is the opening-time distribution factor. Clearly, the maximum possible value of  $\kappa$  is 2. The maximum is reached if all the surface opens at the first moment of pumping.

Nolte (1979, 1986a) postulated a basic assumption leading to a remarkably simple form of material balance. Assuming that the fracture surface evolves according to a power law, then

$$\frac{A}{A_e} = \left( \frac{t}{t_e} \right)^\alpha, \quad (2-33)$$

with the exponent  $\alpha$  constant during the injection period.

Considering the opening-time distribution factor, Nolte realized that it is a function of the exponent  $\alpha$ , only

$$\kappa = g_0(\alpha). \quad (2-34)$$

The function  $g_0(\alpha)$  can be determined by an exact mathematical method and is given by Meyer and Hagel (1989):

$$g_0(\alpha) = \frac{\alpha \Gamma(\alpha) \sqrt{\pi}}{\Gamma\left(\frac{3}{2} + \alpha\right)}, \quad (2-35)$$

where  $\Gamma(\alpha)$  is the Euler gamma function. A remarkable fact concerning the  $g_0(\alpha)$  function is that its values for two extremely departing values of the exponent  $\alpha$ , namely at one-half and unity, differ only slightly:  $g_0(1/2) = \pi/2 \cong 1.57$  and  $g_0(1) = 4/3 \cong 1.33$ .

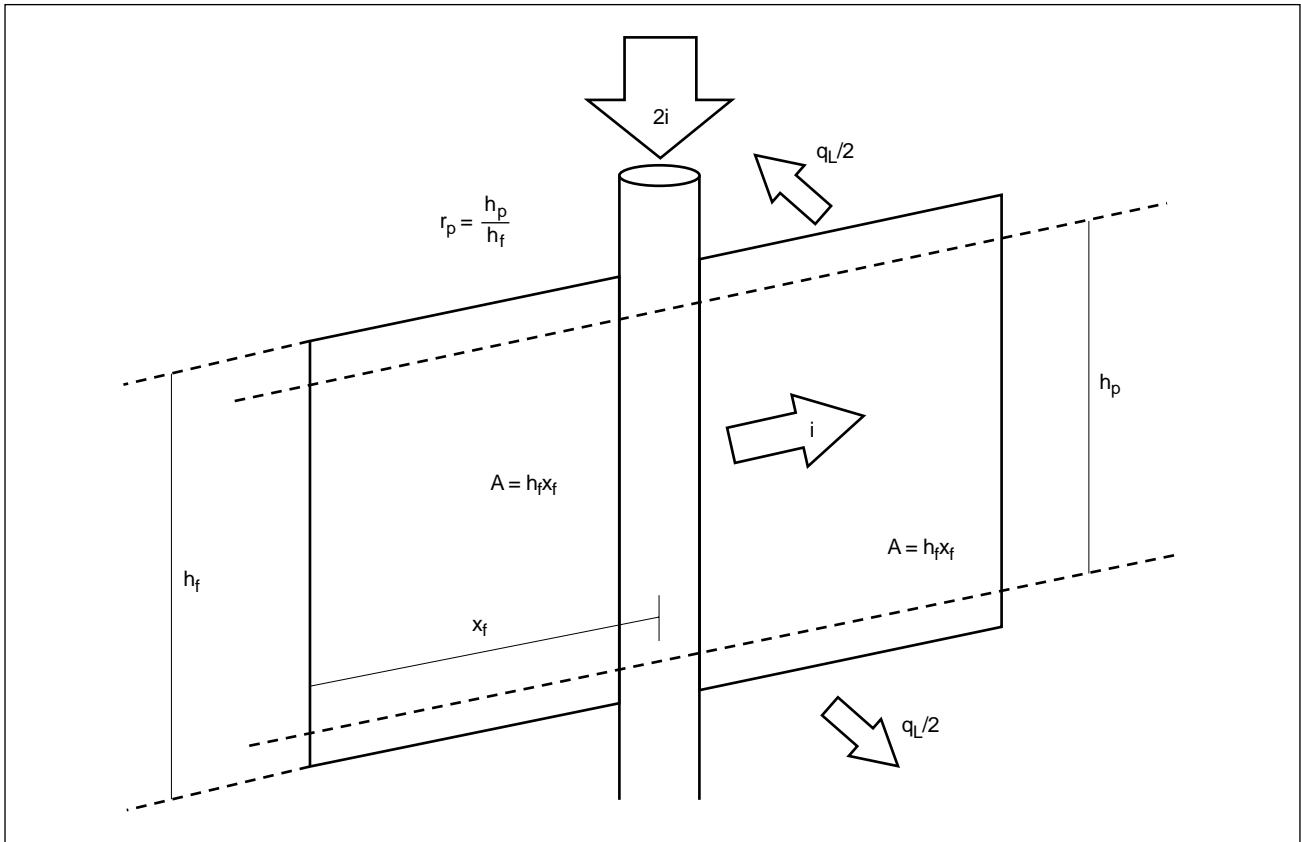


**Figure 2-18.** Basic notation for PKN and KGD geometries.  $h_p$  = permeable height,  $h_f$  = fracture height and  $q_L$  = rate of fluid loss.

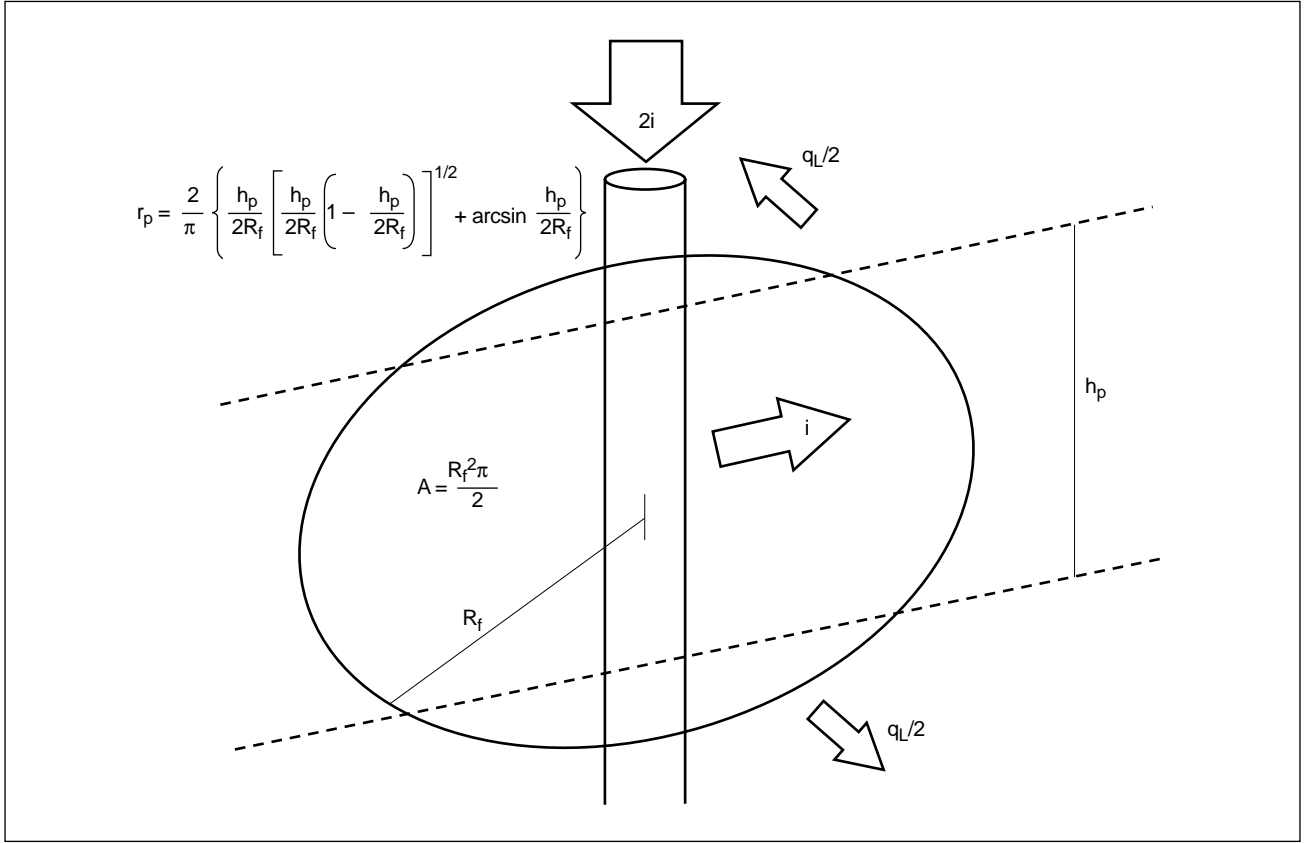


**Figure 2-19.** Basic notation for radial geometry.

If the fracture area is assumed to remain constant after the pumps are stopped, at the time  $t_e + \Delta t$  the volume of the fracture is

$$V_{t_e+\Delta t} = V_i - 2A_e r_p S_p - 2A_e r_p g(\alpha, \Delta t_D) C_L \sqrt{t_e}, \quad (2-36)$$

where dimensionless time is defined as

$$\Delta t_D = \frac{\Delta t}{t_e} \quad (2-37)$$

and the two-variable function  $g_0(\alpha, \Delta t_D)$  is the following mathematical expression (Valkó and Economides, 1995):

$$g(\alpha, \Delta t_D) = \frac{4\alpha \sqrt{\Delta t_D} + 2\sqrt{1+\Delta t_D} \times F\left[\frac{1}{2}, \alpha; 1+\alpha; (1+\Delta t_D)^{-1}\right]}{1+2\alpha}. \quad (2-38)$$

The function  $F[a, b; c; z]$  is the hypergeometric function, available in tabular form (Abramowitz and Stegun, 1989) or computing algorithms.

The average fracture width at time  $\Delta t$  after the end of pumping is

$$\bar{w}_{t_e+\Delta t} = \frac{V_i}{A_e} - 2r_p S_p - 2r_p C_L \sqrt{t_e} g(\alpha, \Delta t_D). \quad (2-39)$$

Hence, time variation of the width is determined by the  $g(\alpha, \Delta t_D)$  function, length of the injection period and leakoff coefficient but is not affected by the fracture area.

The fracture closure process (i.e., decrease of average width) cannot be observed directly. However, from linear elastic theory the net pressure is known to be directly proportional to the average width as

$$p_{net} = s_f \bar{w}, \quad (2-40)$$

where  $p_{net} = p - p_c$  and  $p_c$  is the closure pressure. The significance of the closure pressure is described in Chapters 5, 6 and 9. The fracture stiffness  $s_f$  is a proportionality constant for the fracture geometry measured in psi/ft, and it plays a similar role as the constant in Hooke's law. Its form depends on the fracture geometry, which may be PKN, KGD or radial (fracture geometries are described in Chapter 6). In petroleum engineering literature, its inverse  $1/s_f$  is



also called the fracture compliance. Expressions of  $s_f$  for common fracture geometries are in Table 2-2.

Table 2-2. Proportionality constant $s_f$ for different fracture geometries.		
PKN	KGD	Radial
$\frac{2E'}{\pi h_f}$	$\frac{E'}{\pi x_f}$	$\frac{3\pi E'}{16R_f}$

The combination of Eqs. 2-39 and 2-40 yields

$$p = \left( p_c + \frac{s_f V_i}{A_e} - 2r_p s_f S_p \right) - (2r_p s_f C_L \sqrt{t_e}) \times g(\alpha, \Delta t_D) = b_N + m_N \times g(\alpha, \Delta t_D), \quad (2-41)$$

so that a plot of  $p$  versus  $g(\alpha, \Delta t_D)$  has a slope  $m_N$  and intercept  $b_N$  at  $g = 0$ .

Equation 2-41 suggests that the pressure variation in the shut-in period is governed mainly by the leakoff coefficient, and a plot of wellbore pressure versus  $g(\alpha, \Delta t_D)$  values results in a straight line provided that the fracture area  $A_e$ , proportionality constant  $s_f$  and leakoff coefficient  $C_L$  do not vary with time. Under these assumptions the pressure behavior will depart from the linear trend only when the fracture finally closes.

The expression in Eq. 2-41 is the basis of Nolte's pressure decline analysis. The technique requires plotting the wellbore pressure versus the values of the  $g$ -function, as first suggested by Castillo (1987). The  $g$ -function values should be generated with the exponent  $\alpha$  considered valid for the given model and rheology. Other choices for  $\alpha$  (e.g., involving the estimated efficiency of the fracture) are discussed in Chapter 9. A straight line is fitted to the observed points.

For a plot of pressure falloff data from a fracture injection test versus the  $g$ -function, Eq. 2-41 implies that the closure pressure  $p_c$  must lie on the line fitted through the data. Hence, independent knowledge of the closure pressure, which can be determined from the step rate test described in Chapter 9, helps to identify which part of the falloff data to use for the straight-line fit.

The slope of the straight line is denoted by  $m_N$  and the intercept by  $b_N$ . From Eq. 2-41, the slope is related to the unknown leakoff coefficient by

$$C_L = \frac{(-m_N)}{2r_p \sqrt{t_e} s_f}. \quad (2-42)$$

The intercept  $b_N$  of the straight line at zero shut-in time provides an expression for the spurt-loss coefficient:

$$r_p S_p = \frac{V_i}{2A_e} - \frac{b_N - p_c}{2s_f}. \quad (2-43)$$

The first term in Eq. 2-43 can be interpreted as the gross width that would have been created without any fluid loss minus the apparent leakoff width  $w_L$ . Depending on the fracture geometry, expressions for  $s_f$  can be substituted into Eqs. 2-42 and 2-43, resulting in the expressions for  $C_L$  in Table 2-3 and for  $s_f$  and  $w_L$  in Table 2-4. Tables 2-3 and 2-4 show that calculation of the leakoff coefficient depends on the fracture geometry.

Table 2-3. Leakoff coefficient $C_L$ for different fracture geometries.		
PKN	KGD	Radial
$\frac{\pi h_f}{4r_p \sqrt{t_e} E'} (-m_N)$	$\frac{\pi x_f}{2r_p \sqrt{t_e} E'} (-m_N)$	$\frac{8R_f}{3\pi r_p \sqrt{t_e} E'} (-m_N)$

- PKN fracture geometry

For PKN geometry, the leakoff coefficient can be determined from Eq. 2-42 because  $s_f$  is dependent on the fracture height, which is a known quantity. Similarly, the spurt-loss coefficient and the apparent leakoff width can be computed from Eq. 2-43 using the expressions in Table 2-4.

- KGD and radial fracture geometries

For KGD geometry,  $s_f$  is dependent on the fracture half-length  $x_f$ ; for radial geometry, it is dependent on the fracture radius  $R_f$ . If the spurt loss is negligible, then  $x_f$  or  $R_f$  can be determined from the expressions in Table 2-5, and, in turn, the leakoff coefficient can be computed from the appropriate expression in Table 2-3. This analysis procedure was introduced by Shlyapobersky *et al.* (1988a). If the spurt loss cannot be neglected, the more detailed analysis procedures in Chapter 9 must be used.

If the closure pressure is not determined independently, straightforward analysis with the

**Table 2-4. Spurt-loss coefficient and apparent leakoff width for different fracture geometries.**

	PKN	KGD	Radial
$S_p$	$\frac{V_i}{2r_p x_i h_i} - \frac{\pi h_i (b_N - p_c)}{4r_p E'}$	$\frac{V_i}{2r_p x_i h_i} - \frac{\pi x_i (b_N - p_c)}{2r_p E'}$	$\frac{V_i}{\pi R_i^2} - \frac{8R_i (b_N - p_c)}{3\pi r_p E'}$
$w_L$	$\frac{\pi h_i (b_N - p_c)}{4r_p E'}$	$\frac{\pi x_i (b_N - p_c)}{2r_p E'}$	$\frac{8R_i (b_N - p_c)}{3\pi r_p E'}$

**Table 2-5. Fracture extent from the no-spurt-loss assumption.**

PKN	KGD	Radial
$x_i = \frac{2E'V_i}{\pi h_i^2 (b_N - p_c)}$	$x_i = \sqrt{\frac{E'V_i}{\pi h_i (b_N - p_c)}}$	$R_i = \sqrt[3]{\frac{3E'V_i}{8(b_N - p_c)}}$

$g$ -function plot relies on correct identification of the portion of the data through which the line should be fitted. As with Horner analysis of pressure buildup data, the success of this plot is undermined if—for whatever reason—identification is not straightforward. More details on this analysis are provided in Chapter 9.

## 2-8.2. Filter-cake plus reservoir pressure drop leakoff model (according to Mayerhofer *et al.*, 1993)

Carter's bulk leakoff model is not the only possible interpretation of the leakoff process. Other models have been suggested, but one reason why such models have not been used widely is that it is difficult to design a calibration test interpretation procedure that is standardized (i.e., the results of which do not depend too much on subjective factors of the interpreter). The Mayerhofer *et al.* (1993) method overcomes this difficulty. It describes the leakoff rate using two parameters that are physically more discernible than the leakoff coefficient to the petroleum engineer: the reference resistance  $R_0$  of the filter cake at a reference time  $t_0$  and the reservoir permeability  $k_r$ . To obtain these parameters from an injection test, the reservoir pressure, reservoir fluid viscosity, formation porosity and total compressibility must be known.

Figure 2-20 is a schematic of the Mayerhofer *et al.* model in which the total pressure difference between the inside of a created fracture and a far point in the

reservoir is shown with its components. Thus, the total pressure drop is

$$\Delta p(t) = \Delta p_{face}(t) + \Delta p_{piz}(t) + \Delta p_r(t), \quad (2-44)$$

where  $\Delta p_{face}$  is the pressure drop across the fracture face dominated by the filter cake,  $\Delta p_{piz}$  is the pressure drop across a polymer-invaded zone, and  $\Delta p_r$  is the pressure drop in the reservoir.

In a series of experimental works using typical hydraulic fracturing fluids (e.g., borate- and zirconate-crosslinked fluids) and cores with permeability less than 5 md, no appreciable polymer-invaded zone was detected. At least for crosslinked fluids, the second term on the right side of Eq. 2-44 can be ignored:

$$\Delta p(t) = \Delta p_{face}(t) + \Delta p_r(t). \quad (2-45)$$

Using the Kelvin-Voigt viscoelastic model for description of the flow through a continuously depositing fracture filter cake, Mayerhofer *et al.* (1993) gave the filter-cake pressure term as

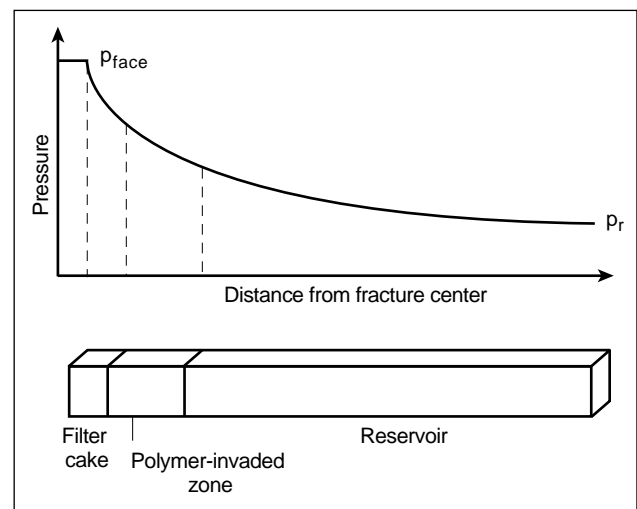


**Figure 2-20. Filter-cake plus reservoir pressure drop in the Mayerhofer *et al.* (1993) model.**

$$\Delta p_{face} = \frac{R_0}{r_p A} \sqrt{\frac{t}{t_0}} \frac{q_L}{2}, \quad (2-46)$$

where  $R_0$  is the characteristic resistance of the filter cake, which is reached during reference time  $t_0$ . The flow rate  $q_L$  is the leakoff rate from one wing of the fracture. In Eq. 2-46, it is divided by 2, because only one-half of it flows through area  $A$ .

The pressure drop in the reservoir can be tracked readily by employing a pressure transient model for injection into a porous medium from an infinite-conductivity fracture. For this purpose, known solutions such as the one by Gringarten *et al.* (1974) can be used. The only additional problem is that the surface area increases during fracture propagation. Therefore, every time instant has a different fracture length, which, in turn, affects the computation of dimensionless time.

The transient pressure drop in the reservoir is

$$\Delta p_r(t_n) = \frac{\mu_r}{2\pi k_r h_f} \sum_{j=1}^n (2q_j - 2q_{j-1}) p_D[(t_n - t_{j-1})_D], \quad (2-47)$$

where  $h_f$  is the ratio of the leakoff area to the characteristic length (given as  $r_p h_f$  for PKN and KGD geometries and as  $r_p \pi R_f/2$  for radial geometry),  $\mu_r$  is the reservoir fluid viscosity, and  $p_D$  is the dimensionless pressure function describing the behavior of the reservoir (unit response).

The factor 2 must be used in Eq. 2-47 in front of  $q_j$  because  $q$  is defined as the leakoff rate from one wing. In petroleum engineering literature, however, dimensionless pressure is defined using the total flow into (from) the formation.

Substituting Eqs. 2-46 and 2-47 into Eq. 2-45 obtains

$$\Delta p(t_n) = \frac{R_0}{2r_p A_n} \sqrt{\frac{t_n}{t_e}} q_n + \frac{\mu_r}{\pi k_r h_f} \sum_{j=1}^n (q_j - q_{j-1}) p_D[(t_n - t_{j-1})_D], \quad (2-48)$$

where the end of pumping is selected as the characteristic time for the filter-cake resistance. A simple rearrangement yields

$$q_n = \frac{\Delta p(t_n) - \frac{\mu_r}{\pi k_r h_f} \left[ -q_{n-1} p_D(t_n - t_{n-1}) + \sum_{j=1}^{n-1} (q_j - q_{j-1}) p_D[(t_n - t_{j-1})_D] \right]}{\frac{R_0}{2r_p A_n} \sqrt{\frac{t_n}{t_e}} + \frac{\mu_r p_D[(t_n - t_{n-1})_D]}{\pi k_r h_f}}. \quad (2-49)$$

Equation 2-49 can be used both in hydraulic fracture propagation and during fracture closure. It allows determination of the leakoff rate at the time instant  $t_n$  if the total pressure difference between the fracture and the reservoir is known, as well as the history of the leakoff process. The dimensionless pressure solution  $p_D[(t_j - t_{j-1})_D]$  has to be determined with respect to a dimensionless time that takes into account the actual fracture length at  $t_n$  (not at  $t_j$ ).

The injection test interpretation processes data given as  $(t_n, p_n)$  pairs with  $n > n_e$ , where  $n_e$  is the index of the first time point after shut-in. For the consideration of dimensionless pressure, the early-time approximation can be used for an infinite-conductivity fracture:

$$p_D[(t_n - t_{j-1})_D] = \sqrt{\frac{\pi k}{c_{it} \mu_r \phi x_{fn}^2}} (t_n - t_j). \quad (2-50)$$

The leakoff rates are strongly connected to the observed pressure changes according to

$$q_j = \frac{A_e (p_{j-1} - p_j)}{s_f \Delta t_j} \quad (2-51)$$

for  $j \geq n_e + 2$ .

Combining Eqs. 2-50 and 2-51 with Eq. 2-48 obtains for  $n > n_e + 2$ :

$$\begin{aligned} p_n - p_r &= \frac{R_0 t_n^{1/2}}{2t_e^{1/2}} \frac{p_{n-1} - p_n}{s_f r_p \Delta t_n} \\ &+ \frac{1}{k_r^{1/2} s_f r_p} \left( \frac{\mu_r}{\pi c_f \phi} \right)^{1/2} \left[ \sum_{j=n_e+3}^n \left( \frac{p_{j-1} - p_j}{\Delta t_j} - \frac{p_{j-2} - p_{j-1}}{\Delta t_{j-1}} \right) (t_n - t_{j-1})^{1/2} \right] \\ &+ \frac{1}{k_r^{1/2} A_e r_p} \left( \frac{\mu_r}{\pi c_f \phi} \right)^{1/2} \left[ q_1 t_n^{1/2} + \sum_{j=2}^{n_e+2} (q_j - q_{j-1}) (t_n - t_{j-1})^{1/2} \right]. \end{aligned} \quad (2-52)$$

During fracture propagation, the leakoff rates  $q_j$  for  $j = 1, \dots, n_e + 1$  are not known exactly (nor are any values for  $t_j$  in this period). Therefore, some kind of assumption is required to proceed.

The key assumption is that for these purposes the first  $n_e + 1$  leakoff rates can be considered equal:

$$q_j = q_{app} \quad (2-53)$$

for  $j = 1, \dots, n_e + 1$ .

In fact, it is more convenient to work not with the average leakoff rate but with the apparent leakoff width defined by

$$w_L = \frac{(1-\eta)V_i}{A_e} = \frac{q_{app}}{A_e} t_e, \quad (2-54)$$

where  $\eta$  is the fluid efficiency.

The apparent leakoff width can be estimated from the Nolte-Shlyapobersky method as shown in Table 2-4. Then Eq. 2-52 leads to

$$p_n - p_r = \frac{R_0 t_n^{1/2}}{2 t_e^{1/2}} \frac{p_{n-1} - p_n}{s_f r_p \Delta t_n} + \frac{1}{k_r^{1/2} s_f r_p} \left( \frac{\mu_r}{\pi c_i \phi} \right)^{1/2} \left[ \frac{p_{n+1} - p_{n+2}}{t_n - t_{n+1}} \left( t_n - t_{n+1} \right)^{1/2} + \sum_{j=n_e+3}^n \left( \frac{p_{j-1} - p_j}{\Delta t_j} - \frac{p_{j-2} - p_{j-1}}{\Delta t_{j-1}} \right) \left( t_n - t_{j-1} \right)^{1/2} \right] + \frac{1}{k_r^{1/2} A_e r_p} \left( \frac{\mu_r}{\pi c_i \phi} \right)^{1/2} \left[ q_{app} t_n^{1/2} - q_{app} \left( t_n - t_{n+1} \right)^{1/2} \right]. \quad (2-55)$$

In terms of the apparent leakoff width and after rearrangement, Eq. 2-55 becomes

$$\frac{(p_n - p_r) \Delta t_n}{(p_{n-1} - p_n) t_e^{1/2} t_n^{1/2}} = \frac{R_0}{2 s_f r_p t_e} + \frac{1}{k_r^{1/2} s_f r_p} \left( \frac{\mu_r}{\pi c_i \phi} \right)^{1/2} \frac{\Delta t_n}{(p_{n-1} - p_n) t_e^{1/2} t_n^{1/2}} \times \left[ \frac{p_{n+1} - p_{n+2}}{\Delta t_n + 2} \left( t_n - t_{n+1} + 1 \right)^{1/2} + \sum_{j=n_e+3}^n \left( \frac{p_{j-1} - p_j}{\Delta t_j} - \frac{p_{j-2} - p_{j-1}}{\Delta t_{j-1}} \right) \left( t_n - t_{j-1} \right)^{1/2} \right] + \frac{w_L}{k_r^{1/2} r_p} \left( \frac{\mu_r}{\pi c_i \phi} \right)^{1/2} \frac{t_n^{1/2} - \left( t_n - t_{n+1} + 1 \right)^{1/2}}{(p_{n-1} - p_n) t_e^{3/2} t_n^{1/2}} \Delta t_n. \quad (2-56)$$

Introducing the notation

$$d_j = \frac{p_{j-1} - p_j}{\Delta t_j}$$

$$y_n = \frac{p_n - p_r}{d_n t_e^{1/2} t_n^{1/2}}$$

Eq. 2-56 takes the form

$$y_n = \frac{R_0}{2 s_f r_p t_e} + \frac{1}{k_r^{1/2} s_f r_p} \left( \frac{\mu_r}{\pi c_i \phi} \right)^{1/2} \left[ \frac{d_{n+2} \left( t_n - t_{n+1} + 1 \right)^{1/2}}{d_n t_e^{1/2} t_n^{1/2}} + \sum_{j=n_e+3}^n \frac{(d_j - d_{j-1}) \left( t_n - t_{j-1} \right)^{1/2}}{d_n t_e^{1/2} t_n^{1/2}} \right] + \frac{w_L}{k_r^{1/2} r_p} \left( \frac{\mu_r}{\pi c_i \phi} \right)^{1/2} \frac{1 - \left( \frac{t_n - t_{n+1} + 1}{t_n} \right)^{1/2}}{t_e^{3/2} d_n}. \quad (2-57)$$

The Mayerhofer *et al.* method is based on the fact that Eq. 2-57 can be written in straight-line form as

$$y_n = b_M + m_M (c_1 x_{1,n} + c_2 x_{2,n}) \quad (2-58)$$

for  $n > n_e + 2$ , where

$$x_{1,n} = \left[ \frac{d_{n+2}}{d_n} \left( \frac{t_n - t_{n+2}}{t_e t_n} \right)^{1/2} + \sum_{j=n_e+3}^n \frac{d_j - d_{j-1}}{d_n} \left( \frac{t_n - t_{j-1}}{t_e t_n} \right)^{1/2} \right] \quad (2-59)$$

$$x_{2,n} = \frac{1 - \left( 1 - \frac{t_{n+1}}{t_n} \right)^{1/2}}{t_e^{3/2} d_n}. \quad (2-60)$$

The coefficients  $c_1$  and  $c_2$  are geometry dependent and discussed later. Once the  $x$  and  $y$  coordinates are known, the  $(x,y)$  pairs can be plotted. The corresponding plot is referred to as the Mayerhofer plot. A straight line determined from the Mayerhofer plot results in the estimate of the two parameters  $b_M$  and  $m_M$ . Those parameters are then interpreted in terms of the reservoir permeability and the reference filtercake resistance. For the specific geometries, the coefficients  $c_1$  and  $c_2$  as well as the interpretation of the straight-line parameters are as follows.

- PKN geometry

$$y_n = \left( \frac{R_0}{r_p} \right) \left( \frac{\pi h_f}{4 E' t_e} \right) + \frac{h_f}{k_r^{1/2} r_p} [c_1 x_{1,n} + c_2 x_{2,n}]$$

$$c_1 = \left( \frac{\pi \mu_r}{4 (E')^2 \phi c_i} \right)^{1/2} \quad c_2 = \frac{w_L}{h_f} \left( \frac{\mu_r}{\pi \phi c_i} \right)^{1/2}$$

$$k_{r,M} = \left( \frac{h_f}{r_p m_M} \right)^2 \quad R_{0,M} = \frac{4 E' t_e}{\pi h_f} r_p b_M$$

- KGD geometry

$$y_n = \left( \frac{R_0}{r_p} \right) \left( \frac{\pi x_f}{2 E' t_e} \right) + \frac{x_f}{k_r^{1/2} r_p} [c_1 x_{1,n} + c_2 x_{2,n}]$$

$$c_1 = \left( \frac{\pi \mu_r}{(E')^2 \phi c_i} \right)^{1/2} \quad c_2 = \frac{w_L}{x_f} \left( \frac{\mu_r}{\pi \phi c_i} \right)^{1/2}$$

$$k_{r,M} = \left( \frac{x_f}{r_p m_M} \right)^2 \quad R_{0,M} = \frac{2 E' t_e}{\pi x_f} r_p b_M$$

- Radial geometry

$$y_n = \left( \frac{R_0}{r_p} \right) \left( \frac{8R_f}{3\pi E' t_e} \right) + \frac{R_f}{k_r^{1/2} r_p} [c_1 x_{1,n} + c_2 x_{2,n}]$$

$$c_1 = \left( \frac{16^2 \mu_r}{3^2 \pi^3 (E')^2 \phi c_t} \right)^{1/2} \quad c_2 = \frac{w_L}{R_f} \left( \frac{\mu_r}{\pi \phi c_t} \right)^{1/2}$$

$$k_{r,M} = \left( \frac{R_f}{r_p m_M} \right)^2 \quad R_{0,M} = \frac{3\pi E' t_e}{8R_f} r_p b_M$$

- Example interpretation of fracture injection test  
Table 2-6 presents pressure decline data, and Table 2-7 presents reservoir and well information for this example. The closure pressure  $p_c$  determined independently is 5850 psi.

**Table 2-6. Example pressure decline data.**

$\Delta t$ (min)	$p_{ws}$ (psi)
0.2	7550.62
0.4	7330.59
0.6	7122.36
0.8	6963.21
1.0	6833.39
1.2	6711.23
1.4	6595.02
1.6	6493.47
1.8	6411.85
2.0	6347.12
2.2	6291.51
2.4	6238.43
2.6	6185.85
2.8	6135.61
3.0	6090.61
3.2	6052.06
3.4	6018.61
3.6	5987.45
3.8	5956.42
4.0	5925.45
4.2	5896.77
4.4	5873.54
4.6	5857.85
4.8	5849.29
5.0	5844.81
5.2	5839.97
5.4	5830.98
5.6	5816.30
5.8	5797.01
6.0	5775.67

**Table 2-7. Example reservoir and well information.**

Permeable height, $h_p$	42 ft
Reservoir fluid viscosity, $\mu_r$	1 cp
Porosity, $\phi$	0.23
Total compressibility, $c_t$	$2 \times 10^{-5}$ psi <sup>-1</sup>
Reservoir pressure, $p_r$	1790 psi
Plane strain modulus, $E'$	$8 \times 10^5$ psi
Pumping time, $t_e$	21.75 min
Injected volume (two wing), $2V_i$	9009 gal
Closure pressure, $p_c$	5850 psi
Geometry	Radial

Figure 2-21 is a plot of the data in Cartesian coordinates and also shows the closure pressure. The  $g$ -function plot in Fig. 2-22 is created using  $\alpha = \%$ , which is considered characteristic for the radial model.

From the intercept of the straight line is obtained the radial fracture radius  $R_f = 27.5$  ft. (The straight-line fit also provides the bulk leakoff coefficient  $C_L = 0.033$  ft/min<sup>1/2</sup> and fluid efficiency  $\eta = 17.9\%$ .) The ratio of permeable to total area is  $r_p = 0.76$ .

Figure 2-23 is the Mayerhofer plot. From the slope of the straight line ( $m_M = 9.30 \times 10^7$ ) is obtained the apparent reservoir permeability  $k_{rapp} = 8.2$  md and the true reservoir permeability  $k_r = 14.2$  md. The resistance of the filter cake at the end of pumping ( $t_e = 21.2$  min) is calculated from the intercept ( $b_M = 2.5 \times 10^{-2}$ ) as the apparent resistance  $R_{0,app} = 1.8 \times 10^4$  psi/(ft/min) and the true resistance  $R_0 = 1.4 \times 10^4$  psi/(ft/min).

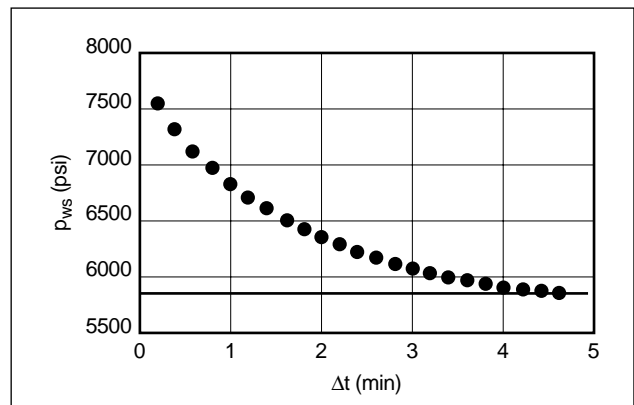


**Figure 2-21.** Example of bottomhole pressure versus shut-in time.

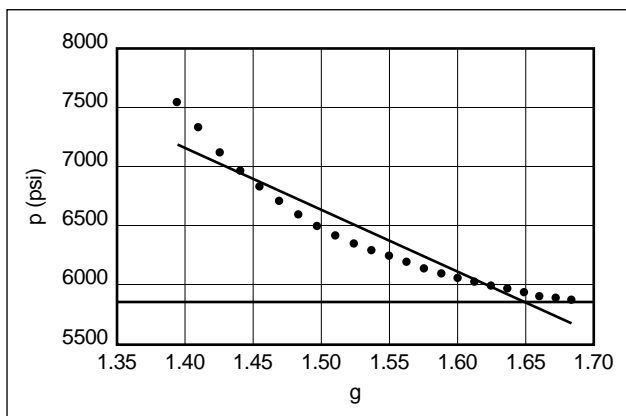


**Figure 2-22.** Example g-function plot.

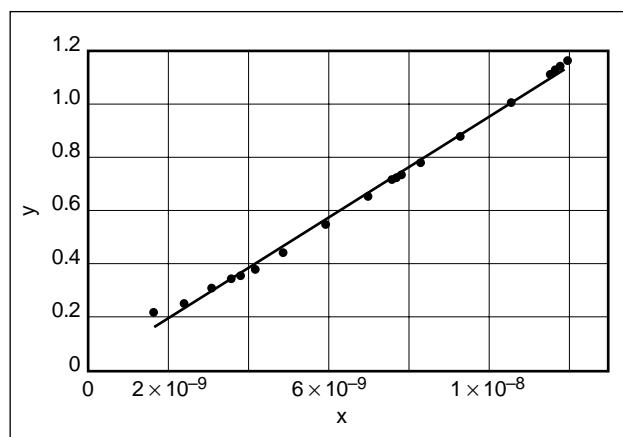


**Figure 2-23.** Example Mayerhofer plot with radial geometry.

# Formation Characterization: Rock Mechanics

*M. C. Thiercelin, Schlumberger Dowell*

*J.-C. Roegiers, University of Oklahoma*

## 3-1. Introduction

The National Academy of Sciences defines rock mechanics as “the theoretical and applied science of the mechanical behavior of rock; it is that branch of mechanics concerned with the response of the rock to the force fields of its physical environment.” From this definition, the importance of rock mechanics in several aspects of the oil and gas industry can easily be understood. The fragmentation of rock governs its drillability, whereas its mechanical behavior influences all aspects of completion, stimulation and production. However, not until recently has this particular aspect of earth sciences started to play a predominant role in energy extraction. The impetus was to explain, qualitatively and quantitatively, the orientation of fractures (Hubbert and Willis, 1957), some unexpected reservoir responses or catastrophic failures (e.g., less production after stimulation and pressure decline in wells surrounding an injection well; Murphy, 1982), casing shear failure (Nester *et al.*, 1956; Cheatham and McEver, 1964), sand production (Bratli and Risnes, 1981; Perkins and Weingarten, 1988; Morita *et al.*, 1987; Veeken *et al.*, 1991; Kooijman *et al.*, 1992; Cook *et al.*, 1994; Moricca *et al.*, 1994; Geilikman *et al.*, 1994; Ramos *et al.*, 1994), rock matrix collapse during production (Risnes *et al.*, 1982; Pattillo and Smith, 1985; Smits *et al.*, 1988; Abdulraheem *et al.*, 1992) and borehole stability problems (Gnirk, 1972; Bradley, 1979; Guenot, 1989; Santarelli *et al.*, 1992; Ong and Roegiers, 1993; Maury, 1994; Last *et al.*, 1995).

The significant contribution as far as the orientation of fractures is concerned was provided by the work of Hubbert and Willis (1957; see Sidebar 3A), which indicates ever-increasing differences between vertical and horizontal stresses within the earth’s crust. Until then, all design considerations were based on the assumption that an isostatic state of stress prevailed everywhere.

As deeper completions were attempted, borehole collapses and instabilities became more common and often led to expensive remedial measures. The primary cause of these problems is instabilities caused by large tectonic forces. The concepts developed by mining engineers that rocks are far from being inert were found applicable (Cook, 1967; Hodgson and Joughin, 1967). Rocks are quite receptive to disturbances, provided that some energy limits are not exceeded. If critical energies are exceeded, dynamic failure is likely to occur, such as rock burst or casing collapse. In addition, the importance of inherent discontinuities (e.g., faults, fissures) was realized (Goodman, 1976), especially as highly conductive conduits. From this broader understanding of the role of rock deformation, research focused on definition of the pertinent parameters required to properly characterize the targeted formations. Cores were taken not only for the determination of permeability, porosity and lithology, but also to run mechanical tests under simulated downhole conditions. Downhole tools were developed to better characterize the formation in situ.

There will always remain some uncertainties on the relevance of laboratory-determined parameters to the field situation, either because of the disturbance a core sample suffers during the coring and handling process or because of scale effects. There are also limitations on the use of simple constitutive laws to predict rock behavior for heterogeneous, discontinuous, time-dependent and/or weak formations. Studies are currently being conducted on these issues, and our understanding and predictive capability of downhole rock behavior can be expected to continue to progress.

This chapter briefly summarizes some of the most important aspects of rock mechanics to characterize the mechanical behavior of reservoirs and adjacent layers, as applied to the stimulation process.

### 3A. Mechanics of hydraulic fracturing

Hubbert and Willis (1957) introduced several key concepts that explain the state of stress underground and its influence on the orientation of hydraulic fractures. Reviewed here are the fundamental experiments that Hubbert and Willis performed to validate these concepts.

#### State of stress underground

The general state of stress underground is that in which the three principal stresses are unequal. For tectonically relaxed areas characterized by normal faulting, the minimum stress should be vertical with the injection pressure less than that of the overburden. In areas of active tectonic compression and thrust faulting, the minimum stress should be vertical and equal to the pressure of the overburden (Fig. 3-20). The hydraulic fractures should be horizontal with injection pressures equal to or greater than the pressure of the overburden.

To demonstrate these faulting conditions, Hubbert and Willis performed a sandbox experiment that reproduces both the normal fault regime and the thrust fault regime. Figures 3A-1 and 3A-2 show the box with its glass front and containing ordinary sand. The partition in the middle can be moved from left to right by turning a hand screw. The white lines are plaster of paris markers that have no mechanical significance. As the partition is moved to the right, a normal fault with a dip of about 60° develops in the left-hand compartment, as shown in Fig. 3A-1. With further movement, a series of thrust faults with dips of about 30° develops in the right-hand compartment, as shown in Fig. 3A-2.

The general nature of the stresses that accompany the failure of the sand is shown in Fig. 3A-3. The usual conven-

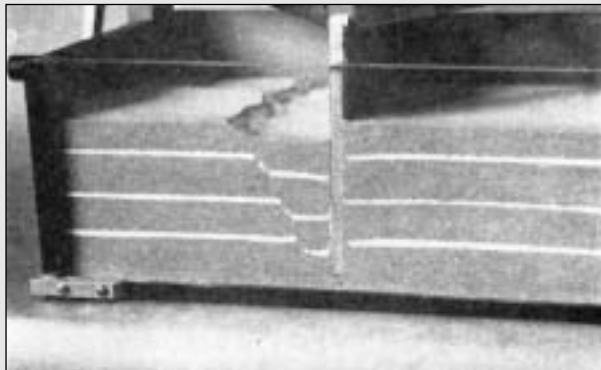


Figure 3A-1. Sandbox experiment showing a normal fault.

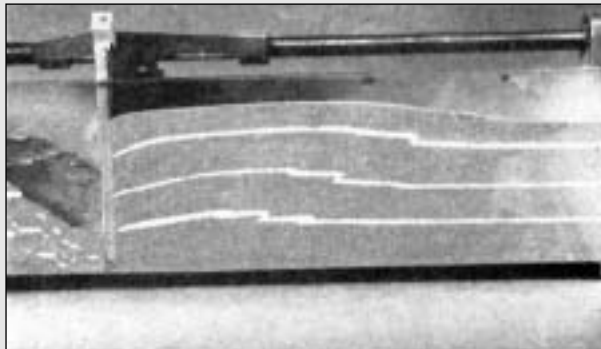


Figure 3A-2. Sandbox experiment showing a thrust fault.

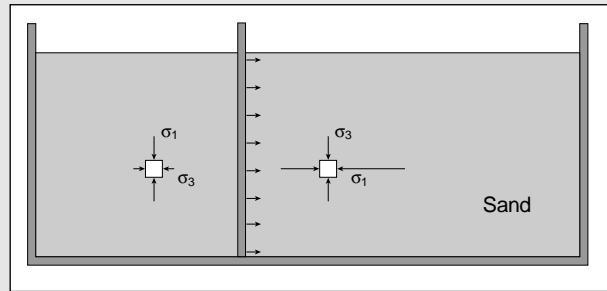


Figure 3A-3. Approximate stress conditions in the sandbox experiment.

tion is adopted of designating the maximum, intermediate and minimum principal effective stresses by  $\sigma_1'$ ,  $\sigma_2'$  and  $\sigma_3'$ , respectively (here taken as compressive). In the left-hand compartment,  $\sigma_3'$  is the horizontal effective stress, which is reduced as the partition is moved to the right, and  $\sigma_1'$  is the vertical effective stress, which is equal to the pressure of the overlying material minus the pore pressure. In the right-hand compartment, however,  $\sigma_1'$  is horizontal, increasing as the partition is moved, and  $\sigma_3'$  is vertical and equal to the pressure of the overlying material minus the pore pressure. The third type of failure, strike-slip faulting, is not demonstrated in the sandbox experiment.

Next, the combination of shear and normal stresses that induce failure must be determined. These critical effective stress values can be plotted on a Mohr diagram, as shown in Fig. 3A-4. The two diagonal lines form the Mohr envelopes of the material, and the area between them represents stable combinations of shear stress and normal effective stress, whereas the area exterior to the envelopes represents unstable conditions. Figure 3A-4 thus indicates the stability region within which the permissible values of  $\sigma_n'$  and  $\tau$  are clearly defined. The stress circles can then be plotted in conjunction with the Mohr envelopes to determine the conditions of faulting. This is illustrated in Fig. 3A-4 for both normal and thrust faulting. In both cases, one of the principal effective stresses

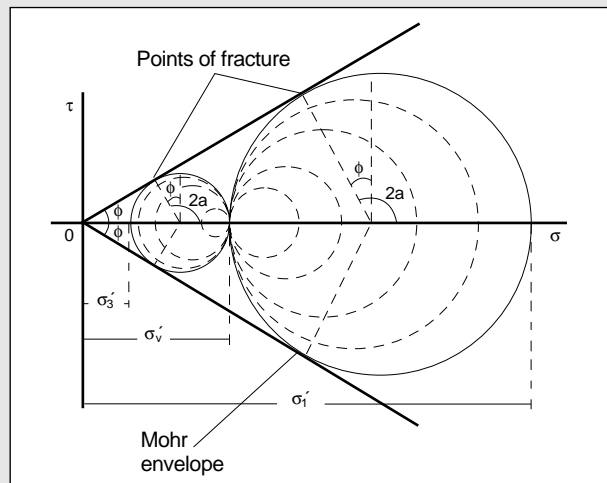


Figure 3A-4. Mohr diagram of the possible range of horizontal stress for a given vertical stress  $\sigma_v'$ . The horizontal stress can have any value ranging from approximately one-third of the normal stress, corresponding to normal faulting, to approximately 3 times the vertical stress, corresponding to reverse faulting.



### 3A. Mechanics of hydraulic fracturing (continued)

is equal to the overburden effective stress  $\sigma_v'$ . In the case of normal faulting, the horizontal principal stress is progressively reduced, thereby increasing the radius of the stress circle until the circle touches the Mohr envelopes. At this point, unstable conditions of shear and normal effective stress are reached and faulting occurs on a plane making an angle of  $45^\circ + \phi/2$  with the minimum stress. For sand with an angle of internal friction of  $30^\circ$ , the normal fault would have a dip of  $60^\circ$ , which agrees with the previous experiments. The minimum principal effective stress would reach a value at about one-third of the value of the overburden effective stress (Eq. 3-58). For the case of thrust faulting, the minimum principal stress would be vertical and remain equal to the overburden pressure while the horizontal stress is progressively increased until unstable conditions occur and faulting takes place on a plane making an angle of  $45^\circ + \phi/2$  with the minimum principal stress or  $45^\circ - \phi/2$  with the horizontal. For sand, this would be a dip of about  $30^\circ$ , which again agrees with the experiment. Failure occurs when the maximum horizontal effective principal stress reaches a value that is about 3 times the value of the overburden effective stress (Eq. 3-59). The intermediate stress, which is the minimum horizontal stress, is not defined by this process.

From these limiting cases and for a fixed effective vertical stress  $\sigma_v'$ , the effective horizontal stress may have any value between the extreme limits of  $\frac{1}{3}$  and 3 times  $\sigma_v'$ .

#### Orientation of hydraulic fractures

The second important contribution of Hubbert and Willis' work concerns the orientation of hydraulic fractures. When their paper was presented, technical debate was occurring on the orientation of hydraulic fractures. A theoretical examination of the mechanisms of hydraulic fracturing of rocks led them to the conclusion that, regardless of whether the fracturing fluid was penetrating, the fractures produced should be approximately perpendicular to the axis of minimum principal stress.

To verify the inferences obtained theoretically, a series of simple laboratory experiments was performed. The general procedure was to produce fractures on a small scale by injecting a "fracturing fluid" into a weak elastic solid that had previously been stressed. Ordinary gelatin (12% solution) was used for the solid, as it is sufficiently weak to fracture easily, molds readily in a simulated wellbore and is almost perfectly elastic under a short-time application of stresses. A plaster of paris slurry was used as the fracturing fluid because it could be made thin enough to flow easily and once set provided a permanent record of the fractures produced. The experimental arrangement consisted of a 2-gal polyethylene bottle, with its top cut off, used to contain a glass tubing assembly consisting of an inner mold and concentric outer casings. The container was sufficiently flexible to transmit externally applied stresses to the gelatin. The procedure was to place the glass tubing assembly in the liquid gelatin and after solidification to withdraw the inner mold leaving a "wellbore" cased above and below an open-hole section.

Stresses were then applied to the gelatin in two ways. The first way (Fig. 3A-5) was to squeeze the polyethylene container laterally, thereby forcing it into an elliptical cross section and producing a compression in one horizontal direction and an extension at right angles in the other. The minimum principal stress was therefore horizontal, and vertical fractures should be expected, as observed in Fig. 3A-6. In other experiments, the container was wrapped with rubber tubing stretched in tension, thus producing radial compression and vertical extension. In this case, the minimum principal stress was vertical, and a horizontal fracture was obtained.

From these analyses and experiments, Hubbert and Willis concluded that

- the state of stress, and hence the fracture orientations, is governed by "incipient failure" (i.e., faulting) of the rock mass
- in areas subject to active normal faulting, fractures should be approximately vertical
- in areas subject to active thrust faulting, fractures should be approximately horizontal.

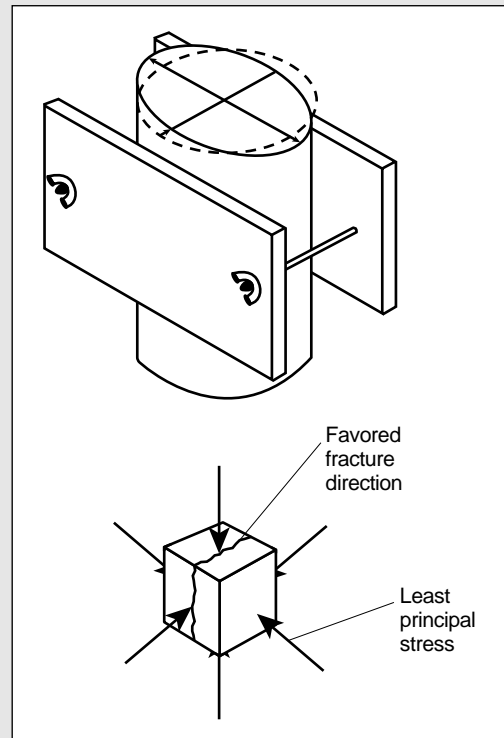


**Figure 3A-5.** Experimental arrangement for producing the least stress in a horizontal direction.



**Figure 3A-6.** Vertical fracture produced under stress conditions illustrated in Fig. 3A-5.

## 3-2. Basic concepts

### 3-2.1. Stresses

In considering a randomly oriented plane of area  $\Delta A$  centered on a point P within a body across which a resultant force  $\Delta F$  acts (Fig. 3-1), the stress vector  $\sigma$  at that point is defined as

$$\sigma = \lim_{\Delta A \rightarrow 0} \left[ \frac{\Delta F}{\Delta A} \right]. \quad (3-1)$$

Therefore, this quantity is expressed as a force per unit area. In geomechanics, by convention, compression is taken to be positive because the forces prevailing in the earth are usually compressive in nature. This resultant stress  $\sigma$  can be decomposed into a normal component  $\sigma_n$  and a shear component  $\tau$ . The shear component tends to “shear” the material in the plane  $\Delta A$ . It should be realized that an infinite amount of planes can be drawn through a given point varying, by the same token, the values of  $\sigma_n$  and  $\tau$ . The stress condition, therefore, depends on the inclination. Consequently, a complete description of a stress must specify not only its magnitude, direction and sense, but also the direction of the surface upon which it acts. Quantities described by two directions, such as stresses, are known as second-order tensors.

In a two-dimensional (2D) situation, if  $\sigma_x$ ,  $\sigma_y$  and  $\tau_{xy}$  are known (Fig. 3-2), the stress state on any plane with normal orientation at an angle  $\theta$  from Ox can be derived using the following expressions:

$$\sigma_n = \sigma_x \cos^2 \theta + 2\tau_{xy} \sin \theta \cos \theta + \sigma_y \sin^2 \theta \quad (3-2)$$

$$\tau = \frac{1}{2} (\sigma_y - \sigma_x) \sin 2\theta + \tau_{xy} \cos 2\theta. \quad (3-3)$$

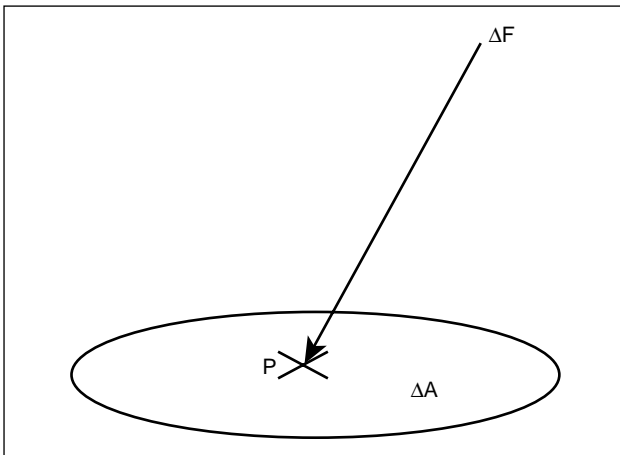


Figure 3-1. Force on a point P.

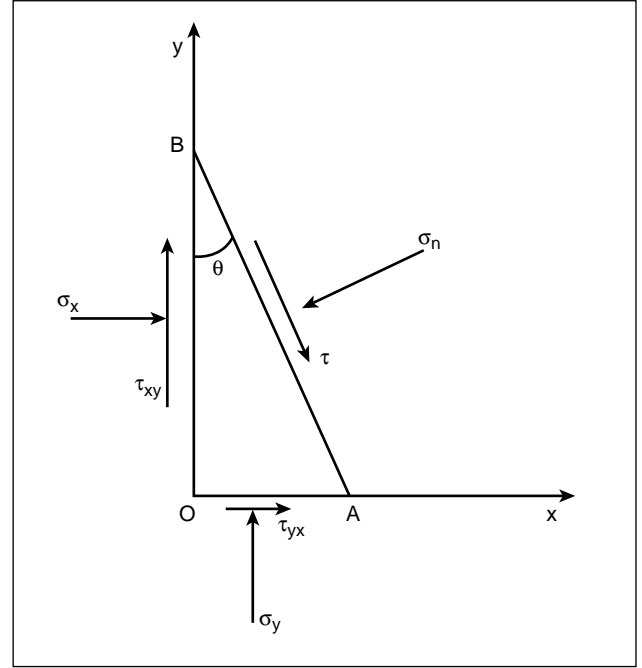


Figure 3-2. Two-dimensional decomposition of normal and shear stresses.

These expressions are obtained by writing equilibrium equations of the forces along the  $\sigma_n$  and  $\tau$  directions, respectively. The moment equilibrium implies that  $\tau_{xy}$  is equal to  $\tau_{yx}$ . There always exist two perpendicular orientations of  $\Delta A$  for which the shear stress components vanish; these are referred to as the principal planes. The normal stresses associated with these planes are referred to as the principal stresses. In two dimensions, expressions for these principal stresses can be found by setting  $\tau = 0$  in Eq. 3-3 or, because they are the minimum and maximum values of the normal stresses, by taking the derivative of Eq. 3-2 with respect to the angle  $\theta$  and setting it equal to zero. Either case obtains the following expression for the value of  $\theta$  for which the shear stress vanishes:

$$\theta = \frac{1}{2} \arctan \left( \frac{2\tau_{xy}}{\sigma_x - \sigma_y} \right) \quad (3-4)$$

and the two principal stress components  $\sigma_1$  and  $\sigma_2$  are

$$\sigma_1 = \frac{1}{2} (\sigma_x + \sigma_y) + \left[ \tau_{xy}^2 + \frac{1}{4} (\sigma_x - \sigma_y)^2 \right]^{1/2} \quad (3-5)$$

$$\sigma_2 = \frac{1}{2} (\sigma_x + \sigma_y) - \left[ \tau_{xy}^2 + \frac{1}{4} (\sigma_x - \sigma_y)^2 \right]^{1/2}. \quad (3-6)$$

If this concept is generalized to three dimensions, it can be shown that six independent components of the stress (three normal and three shear components) are needed to define the stress unambiguously. The stress vector for any direction of  $\Delta A$  can generally be found by writing equilibrium of force equations in various directions. Three principal planes for which the shear stress components vanish—and, therefore, the three principal stresses—exist.

It is convenient to represent the state of stress at a given point using graphical methods. The most widely used method is the Mohr representation described in Sidebar 3B. Other useful quantities are stress invariants (i.e., quantities that do not depend on the choice of axes). For example, the mean stress  $\sigma_m$ :

$$\sigma_m = \frac{1}{3}(\sigma_x + \sigma_y + \sigma_z) = \frac{1}{3}(\sigma_1 + \sigma_2 + \sigma_3) \quad (3-7)$$

and the octahedral shear stress  $\tau_{oct}$ :

$$\tau_{oct} = \frac{1}{3}[(\sigma_1 - \sigma_2)^2 + (\sigma_1 - \sigma_3)^2 + (\sigma_2 - \sigma_3)^2]^{1/2} \quad (3-8)$$

are two stress invariants typically used in failure criteria.

### 3-2.2. Strains

When a body is subjected to a stress field, the relative position of points within it is altered; the body deforms. If these new positions of the points are such that their initial and final locations cannot be made to correspond by a translation and/or rotation (i.e., by rigid body motion), the body is strained. Straining along an arbitrary direction can be decomposed into two components, as shown in Fig. 3-3:

- elongation, defined as

$$\epsilon = \lim_{l \rightarrow 0} \frac{l - l^*}{l} \quad (3-9)$$

- shear strain, defined as

$$\gamma = \tan(\psi), \quad (3-10)$$

where  $\psi$  is the change of angle between two directions that were perpendicular prior to straining.

Consequently, strain (which is either a ratio of lengths or a change of angle) is dimensionless. Because stresses are taken as positive in compression, a positive longitudinal strain  $\epsilon$  corresponds to a decrease in length, and a positive shear strain  $\gamma$  reflects an increase in the angle between two directions that were

### 3B. Mohr circle

Equations 3-2 and 3-3 can be used to derive  $\sigma_n$  and  $\tau$  as a function of  $\sigma_1$  and  $\sigma_2$  (effective stresses are considered):

$$\sigma_n = \frac{1}{2}(\sigma_1 + \sigma_2) + \frac{1}{2}(\sigma_1 - \sigma_2)\cos 2\theta \quad (3B-1)$$

$$\tau = -\frac{1}{2}(\sigma_1 - \sigma_2)\sin 2\theta. \quad (3B-2)$$

The angle  $\theta$  is the angle at which the normal to the plane of interest is inclined to  $\sigma_1$ . These expressions provide the equation of a circle in a  $(\sigma_n, \tau)$  plane, with its center located on the axis at  $\frac{1}{2}(\sigma_1 + \sigma_2)$  and of diameter  $(\sigma_1 - \sigma_2)$  (Fig. 3B-1). This circle is known as the Mohr circle and contains all the information necessary to determine the two-dimensional stress state at any orientation in the sample. The intersection of this circle with the horizontal axis determines the maximum and minimum values of the normal stresses at a point in the material. The apex represents the maximum value of the shear stress. For a three-dimensional state of stress, similar circles can be constructed for any two orthogonal directions.

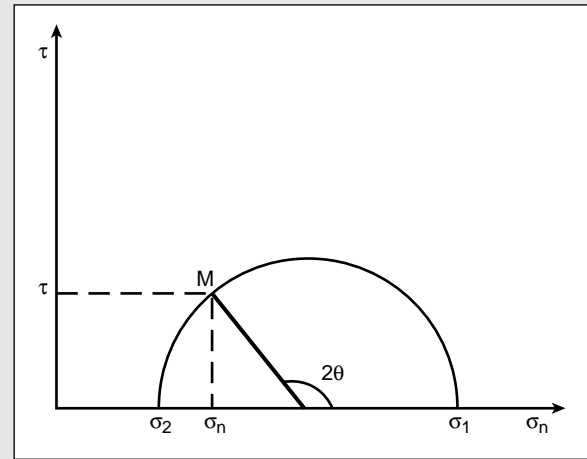


**Figure 3B-1.** The coordinates of point M on the Mohr circle are the values of normal stress and shear stress across a plane with the normal oriented at  $\theta$  to the direction of maximum principal stress.

perpendicular initially. Just as in the case of stresses, principal strains can be defined as longitudinal strain components acting on planes where the shear strains have vanished. It should be pointed out that the analogy between stress and strain analyses is not completely valid and that equilibrium equations and compatibility equations have to be satisfied respectively for the stresses and for the strains. These relations put some restrictions on the local variation of stress and strain in the neighborhood of a point. For example, compatibility equations ensure that the strained body remains continuous and that no cracks or material overlaps will occur. For further details on stresses and strains, the reader is referred to the classic works by Love (1927),

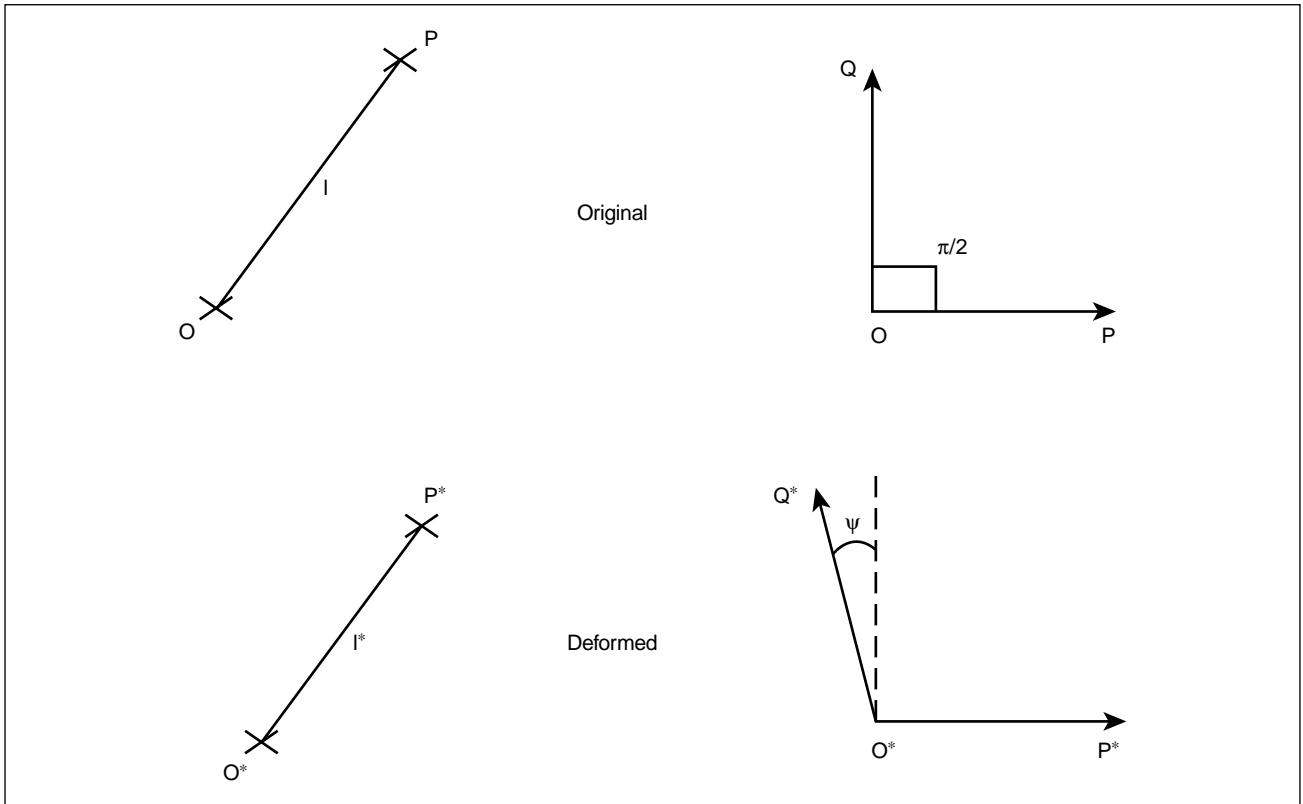


**Figure 3-3.** Normal and shear strain components.

Timoshenko and Goodier (1970) and Muskhelishvili (1953).

### 3-3. Rock behavior

When a rock specimen or an element of the earth is submitted to load, it deforms; the higher the stress level, the more strain the rock experiences. It is an important aspect of rock mechanics, and solid mechanics in general, to determine the relationship between stress and strain (i.e., the constitutive equations of the material under consideration). Various theories have been developed to describe, in a simplified way, this relationship. The simplest one is the theory of elasticity, which assumes that there is a one-to-one correspondence between stress and strain (and, consequently, that the behavior is reversible). Because this is usually the assumed case in hydraulic fracturing, most of the simulation models use the theory of elasticity. Other theories have been developed to better take into account the complex behavior of rock, especially in compression. For example, the theory of plas-

ticity is particularly useful for predicting the stress concentration around a wellbore or the behavior of soft materials during reservoir depletion.

#### 3-3.1. Linear elasticity

To introduce the theory of linear elasticity, let us consider a cylindrical sample of initial length  $l$  and diameter  $d$ . The sample shortens along the loading direction when a force  $F$  is applied to its ends (Fig. 3-4). According to the definitions in the previous section, the axial stress applied to the sample is

$$\sigma_1 = \frac{4F}{\pi d^2} \quad (3-11)$$

and the axial strain is

$$\epsilon_1 = \frac{l - l^*}{l}, \quad (3-12)$$

where  $l^*$  is the resultant length.

Linear elasticity assumes a linear and unique relationship between stress and strain. The consequence of uniqueness is that all strain recovers when the

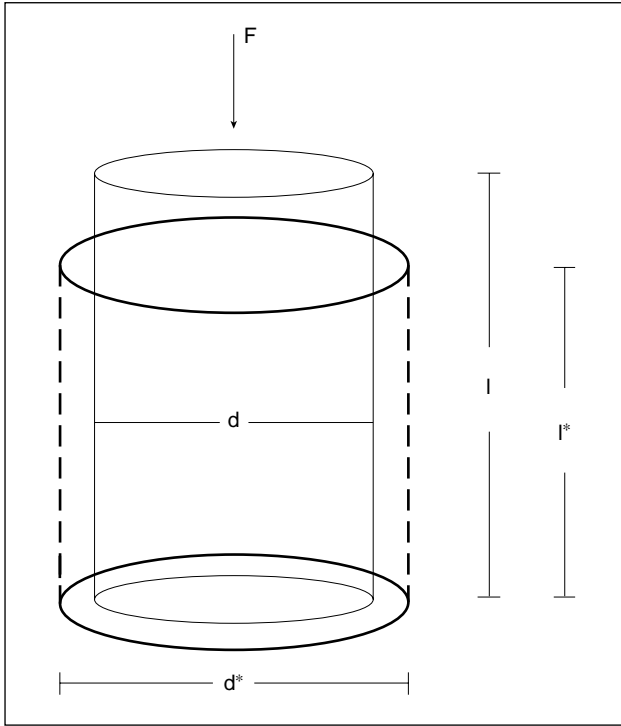


**Figure 3-4.** Sample deformation under uniaxial loading.

material is unloaded. In the case of a uniaxial compression test, this means that

$$\sigma_1 = E\varepsilon_1. \quad (3-13)$$

The coefficient of proportionality  $E$  is Young's modulus.

When a rock specimen is compressed in one direction, not only does it shorten along the loading direction, but it also expands in the lateral directions. This effect is quantified by the introduction of an additional constant (Poisson's ratio  $\nu$ ), defined as the ratio of lateral expansion to longitudinal contraction:

$$\nu = -\frac{\varepsilon_2}{\varepsilon_1}, \quad (3-14)$$

where

$$\varepsilon_2 = \frac{d - d^*}{d}, \quad (3-15)$$

where  $d^*$  is the new diameter.

The negative sign is included in Eq. 3-14 because, by convention, expansion is considered negative and

Poisson's ratio, by definition, is a positive quantity. These stress-strain relations can be generalized to full three-dimensional (3D) space by

$$\begin{aligned} \varepsilon_x &= \frac{\sigma_x}{E} - \frac{\nu}{E}(\sigma_y + \sigma_z) \\ \varepsilon_y &= \frac{\sigma_y}{E} - \frac{\nu}{E}(\sigma_x + \sigma_z) \\ \varepsilon_z &= \frac{\sigma_z}{E} - \frac{\nu}{E}(\sigma_x + \sigma_y) \\ \gamma_{xy} &= \frac{1}{G}\tau_{xy}; \gamma_{yz} = \frac{1}{G}\tau_{yz}; \gamma_{xz} = \frac{1}{G}\tau_{xz}, \end{aligned} \quad (3-16)$$

where the shear modulus  $G$  is

$$G = \frac{E}{2(1 + \nu)}. \quad (3-17)$$

Another coefficient that is commonly used is the bulk modulus  $K$ , which is the coefficient of proportionality between the mean stress  $\sigma_m$  and volumetric strain  $\varepsilon_V$  during a hydrostatic test. In such a test, all three normal stresses are equal and, consequently, all directions are principal. For this case:

$$\sigma_m = K\varepsilon_V; \varepsilon_V = \frac{\Delta V}{V}; K = \frac{E}{3(1 - 2\nu)}, \quad (3-18)$$

where  $V$  is the rock volume and  $\Delta V$  is its variation.

In isotropic linear elasticity, only two elastic constants are independent. For example, and as discussed previously, the shear modulus  $G$  and the bulk modulus  $K$  can be written as functions of  $E$  and  $\nu$ . The most commonly used constants in reservoir applications are defined in Sidebar 3C.

Elasticity theory can be extended to nonlinear and anisotropic materials. A nonlinear elastic material does not have a linear relationship between stress and strain, but recovers all strain when unloaded. An anisotropic material has properties that differ in different directions. A common type is transverse anisotropy, which applies to materials that have a plane and an axis of symmetry (the axis of symmetry is the normal to the plane of symmetry). This is particularly suited for bedded formations where the bedding plane is the plane of symmetry. These materials, which exhibit the simplest type of anisotropy, are characterized by five elastic constants.

### 3C. Elastic constants

Two independent constants characterize isotropic linear elastic materials. Several different conditions can be considered and specific equations can be derived from the three-dimensional elasticity relations (Eq. 3-16):

#### Unconfined axial loading

Specified:  $\sigma_x$  or  $\varepsilon_x$ , with  $\sigma_y = \sigma_z = 0$

$$E = \sigma_x / \varepsilon_x \quad (3C-1)$$

$$\varepsilon_y = \varepsilon_z = -\nu \varepsilon_x \quad (3C-2)$$

$$E = 2(1 + \nu)G, \quad (3C-3)$$

where  $E$  is Young's modulus,  $\nu$  is Poisson's ratio, and  $G$  is the shear modulus.

#### Hydrostatic (isotropic) loading

Specified:  $\sigma_x = \sigma_y = \sigma_z$  and  $\varepsilon_x = \varepsilon_y = \varepsilon_z$

The volumetric strain  $\varepsilon_v$  is equal to  $\varepsilon_x + \varepsilon_y + \varepsilon_z$ .

$$K = \sigma_x / \varepsilon_v = E / 3(1 - 2\nu), \quad (3C-4)$$

where  $K$  is the bulk modulus.

#### Plane strain loading (all x-y planes remain parallel)

Specified:  $\varepsilon_z = 0$ , with the added constraint that  $\sigma_y = 0$

$$E' = \sigma_x / \varepsilon_x \quad (3C-5)$$

$$E' = E / (1 - \nu^2) = 2G / (1 - \nu), \quad (3C-6)$$

where  $E'$  is the plane strain modulus used in fracture width models.

#### Uniaxial (laterally constrained) strain

Specified:  $\varepsilon_y = \varepsilon_z = 0$

$$C = \sigma_x / \varepsilon_x = E(1 - \nu) / [(1 + \nu)(1 - 2\nu)] = K + \frac{4}{3}G \quad (3C-7)$$

$$\sigma_z = \sigma_y = [\nu / (1 - \nu)] \sigma_x, \quad (3C-8)$$

where  $C$  is called the constrained modulus and is used for earth stresses and plane compressive seismic waves.

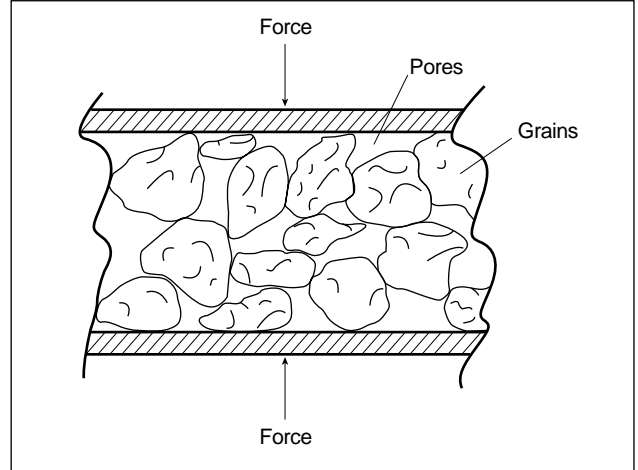


**Figure 3-5.** Load sharing by pore pressure. Total stress = pore pressure + effective stress carried by the grains.

- An increase of pore pressure induces rock dilation.
- Compression of the rock produces a pore pressure increase if the fluid is prevented from escaping from the porous network.

When the fluid is free to move, pore pressure diffusion introduces a time-dependent character to the mechanical response of a rock: the rock reacts differently, depending on whether the rate of loading is slow or fast compared with a characteristic time that governs the transient pore pressure in the reservoir (itself governed by the rock deformation).

Hence, two limiting behaviors must be introduced: drained and undrained responses. One limiting case is realized when a load is instantaneously applied to a porous rock. In that case the excess fluid pressure has no time to diffuse and the medium reacts as if it were undrained and behaves in a “stiff” manner. On the other extreme, if the pressurization rate is sufficiently slow and excess pressure areas have ample time to drain by diffusion, the rock is “softer.” The stiffening effect is more important if the pores are filled with a relatively incompressible liquid rather than a relatively compressible gas.

In 1923, Terzaghi first introduced the effective stress concept for one-dimensional consolidation and proposed the following relationship:

$$\sigma' = \sigma - p, \quad (3-19)$$

where  $\sigma$  is the total applied stress,  $\sigma'$  is the effective stress governing consolidation of the material, and  $p$  is the pore pressure. However, Biot (1941, 1956a) proposed a consistent theory to account for the coupled

### 3-3.2. Influence of pore pressure

Pore fluids in the reservoir rock play an important role because they support a portion of the total applied stress. Hence, only a portion of the total stress, namely, the effective stress component, is carried by the rock matrix (Fig. 3-5). Obviously, this effective stress changes over the life of the reservoir. In addition, the mechanical behavior of the porous rock modifies the fluid response. Two basic mechanisms highlight this coupled behavior (e.g., Detournay and Cheng, 1993):

diffusion/deformation processes that are observed in elastic materials. Such a strong coupling is due to the fact that any change in pore pressure is accompanied by variation in the pore volume; hence, it affects the overall mechanical response of the rock. This poroelastic material behavior is similar to that of an elastic solid when the stresses in Eq. 3-16 are replaced by the following effective stresses:

$$\sigma' = \sigma - \alpha p. \quad (3-20)$$

This relation rigorously governs the deformation of a porous medium, whereas failure is controlled by Terzaghi's (1923) effective stresses in Eq. 3-19 (Rice, 1977; Rudnicki, 1985). The poroelastic constant  $\alpha$  varies between 0 and 1 as it describes the efficiency of the fluid pressure in counteracting the total applied stress. Its value depends on the pore geometry and the physical properties of the constituents of the solid system and, hence, on the applied load. It is related to the undrained Poisson's ratio  $\nu_u$ , drained Poisson's ratio  $\nu$  and Skempton (1960) pore pressure coefficient  $B$ , defined as

$$B = \frac{\Delta p}{\Delta \sigma}, \quad (3-21)$$

where  $\Delta p$  represents the variation in pore pressure resulting from a change in the confining stress  $\Delta \sigma$  under undrained conditions. From these variables:

$$\alpha = \frac{3(\nu_u - \nu)}{B(1 - 2\nu)(1 + \nu_u)}. \quad (3-22)$$

Only in the ideal case, where no porosity change occurs under equal variation of pore and confining pressure, can the preceding expression be simplified to

$$\alpha = 1 - \frac{K}{K_s}, \quad (3-23)$$

where  $K$  is the bulk modulus of the material and  $K_s$  is the bulk modulus of the solid constituents. Typically, for petroleum reservoirs,  $\alpha$  is about 0.7, but its value changes over the life of the reservoir. The poroelastic constant  $\alpha$  is a scalar only for isotropic materials. It is a tensor in anisotropic rocks (Thompson and Willis, 1991). Another important poroelastic parameter is the poroelastic stress coefficient  $\eta$ , defined as

$$\eta = \alpha \frac{(1 - 2\nu)}{2(1 - \nu)}, \quad (3-24)$$

which describes the in-situ stress change caused by injection and/or production. This is addressed later in the chapter.

### 3-3.3. Fracture mechanics

Fracture mechanics studies the stability of preexisting defects that are assumed to pervade a continuum. These inclusions induce high stress concentrations in their vicinity and become the nucleus for crack initiation and/or propagation. Historically, Griffith (1921, 1924) established the foundation of fracture mechanics; he studied propagation by considering the energy used in various parts of the fracturing process.

Griffith's original treatment expressed the condition that the total energy is unchanged by small variations in the crack length. The different approach presented here states that the energy that is consumed by the creation of new surfaces should be balanced by the change in the potential energy of the system:

$$dW_{elas} + dW_{ext} + dW_s + dW_{kin} = 0, \quad (3-25)$$

where  $dW_{elas}$  represents the change in elastic energy stored in the solid,  $dW_{ext}$  is the change in potential energy of exterior forces,  $dW_s$  is the energy dissipated during the propagation of a crack, and  $dW_{kin}$  is the change in kinetic energy. Energy dissipated as heat is neglected. To proceed further, it is assumed that the energy  $dW_s$  required to create the new elementary fracture surfaces  $2dA$  is proportional to the area created:

$$dW_s = 2\gamma_F dA, \quad (3-26)$$

where  $\gamma_F$  is the fracture surface energy of the solid, which is the energy per unit area required to create new fracture surfaces (similar to the surface tension of a fluid). The factor 2 arises from the consideration that two new surfaces are created during the separation process. The propagation is unstable if the kinetic energy increases; thus,  $dW_{kin} > 0$  gives

$$G_e > 2\gamma_F, \quad (3-27)$$

where the strain energy release rate  $G_e$  is defined as

$$G_e = - \frac{d(W_{elas} + W_{ext})}{dA}. \quad (3-28)$$

The onset of crack propagation, which is referred to as the Griffith criterion, is

$$G_e = 2\gamma_F. \quad (3-29)$$

Another approach was developed by Irwin (1957). He demonstrated that, for a linear elastic material, the magnitude of the stresses in the vicinity of a stress-free crack follows an  $r^{-1/2}$  relationship (Fig. 3-6):

$$\sigma_{ij} = -\frac{K_I}{\sqrt{2\pi r}} f_{ij}(\theta) + \dots, \quad (3-30)$$

where  $K_I$  is referred to as the stress intensity factor for the opening mode of deformation of the fracture,  $f_{ij}(\theta)$  represents a bounded function depending only on the angle  $\theta$  referenced to the plane of the crack, and  $r$  is the distance from the point of interest to the tip of the fracture. The negative sign is included because, by convention, tensile stresses are negative.

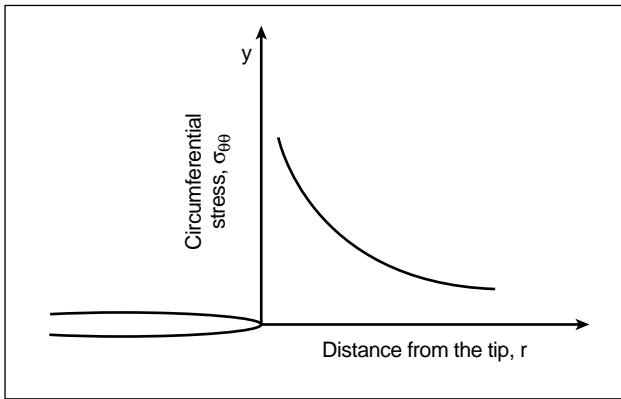


**Figure 3-6.** Stress concentration near the tip of a crack.

The width  $w$  near the tip of a stress-free crack is also a function of the stress intensity factor:

$$w = \frac{8(1-\nu^2)}{E} K_I \sqrt{\frac{r}{2\pi}}. \quad (3-31)$$

In Eq. 3-31, plane strain is assumed.

The stress intensity factor is a function of the loading parameters and of the geometry of the body. Hence, length is included in the unit to express  $K_I$ . A fracture propagates when  $K_I$  reaches a critical value, known as the critical stress intensity factor  $K_{Ic}$  or fracture toughness. For a perfectly elastic material,  $K_{Ic}$  is a material property. It must be evaluated experimentally. Experimental results show that for short crack lengths,  $K_{Ic}$  increases with crack length. When this scale effect is observed,  $K_{Ic}$  cannot be considered a material property. This behavior is discussed in more detail in Section 3-4.6.

The unit for  $K_{Ic}$  is pressure times the square root of length. Fracture toughness is a measure of the resis-

tance of the rock to crack propagation. It must not be confused with the tensile strength of the rock  $T_o$ , although these two properties can be related by the following formula:

$$T_o = \frac{K_{Ic}}{\sqrt{\pi a_c}}, \quad (3-32)$$

where  $a_c$  is a length scale (e.g., flaws or grain size) characteristic of the rock under consideration.

Irwin's (1957) approach is similar to Griffith's (1921, 1924). It can be demonstrated that, for an isotropic and linear elastic material, the stress intensity factor is related to the strain energy release rate by

$$G_e = \frac{1-\nu^2}{E} K_I^2. \quad (3-33)$$

As an example of this application to hydraulic fracturing, the stress intensity factor for a uniformly pressurized crack subjected to a far-field minimum stress  $\sigma_3$  is

$$K_I = (p_f - \sigma_3) \sqrt{\pi L}, \quad (3-34)$$

where  $p_f$  is the pressure in the crack,  $L$  is the half-length of the crack, and plane strain is assumed. During propagation, the net pressure  $(p_f - \sigma_3)$  is therefore

$$(p_f - \sigma_3) = \frac{K_{Ic}}{\sqrt{\pi L}}. \quad (3-35)$$

Using Sneddon's (1946) solution, the width at the wellbore  $w_w$  is

$$w_w = \frac{K_{Ic}}{\sqrt{\pi L}} \frac{4(1-\nu^2)L}{E}. \quad (3-36)$$

A propagation criterion based on the stress intensity factor is easily implemented in fracture propagation codes. However, the concept of fracture surface energy does not imply linear elasticity and can be used for fracture propagation in nonlinear materials where the strain energy release rate is replaced with the  $J$ -integral (Rice, 1968).

Stress intensity factors are not limited to opening modes. Other modes exist (Irwin, 1957) to analyze 3D fracture propagation in complex stress fields (e.g., propagation from inclined wellbores) where the fracture changes direction during propagation. Finally, fracture mechanics has also been used to explain brittle rock fracture in compression (Germanovich *et al.*, 1994).



For further details on fracture mechanics, the reader is referred to Cherapanov (1979), Kanninen and Popelar (1985) and Atkinson (1987).

### 3-3.4. Nonelastic deformation

As discussed in the next section, most rocks exhibit nonreversible deformations after unloading, or at least a nonunique relationship between stress and strain. This means that rocks are not perfectly elastic materials, and a number of theories have been developed to model such behaviors. They include the theory of plasticity, damage mechanics and time-dependent analysis (creep). As an example, the theory of elasto-plasticity is briefly described.

Figure 3-7 shows the stress-strain relationship of a cylindrical ideal sample. From O to point A, the relation between stress and strain is linear, and the slope of the curve is Young's modulus  $E$ . The stress-strain relation does not change if the sample is unloaded in this region. This is the region where the theory of elasticity applies. Beyond point A, the slope of the curve decreases. Moreover, if the sample is unloaded in this region, say at point B, the unloading portion does not follow the same path as the loading portion

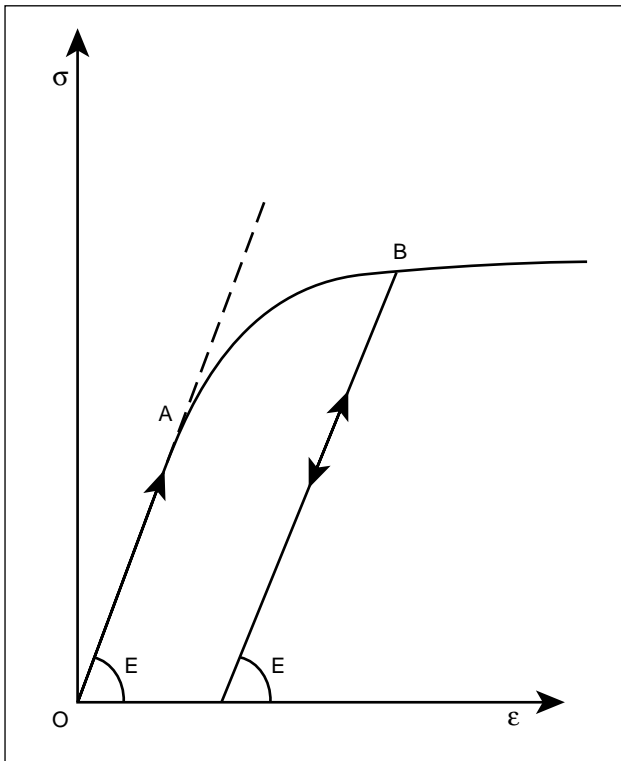


**Figure 3-7.** Stress-strain relationship for an elasto-plastic material with strain hardening. OA = elastic, AB = plastic.

but is perfectly linear with a slope  $E$ . At zero stress, part of the deformation has not been recovered. This represents the plastic strain component in the theory of elasto-plasticity. Point A is actually the initial yield stress of the rock. During reloading, the sample behaves as a perfectly elastic solid up to point B, which is the new yield stress. The increase of yield stress with an increase of plastic strain is called strain hardening, and the decrease of yield stress with an increase of plastic strain is called strain softening. A perfectly plastic material is a material with no strain hardening or softening. As shown in this example, the yield stress is a function of the loading history of the rock if the rock hardens or softens.

In elasto-plasticity, part of the strain is predicted by the theory of elasticity; i.e., any strain increment associated with a stress increment is the sum of an elastic component and a nonelastic component:

$$d\epsilon = d\epsilon_e + d\epsilon_p, \quad (3-37)$$

where  $d\epsilon$  is the total strain increment,  $d\epsilon_e$  is the elastic strain increment, and  $d\epsilon_p$  is the plastic strain increment. Contrary to the elastic strain component, the plastic strain component cannot be recovered during unloading. Predicting the plastic strain increment requires a yield criterion that indicates whether plastic deformation occurs, a flow rule that describes how the plastic strain develops and a hardening law.

The yield criterion is a relationship between stresses that is used to define conditions under which plastic deformation occurs. In three dimensions, this is represented by a yield function that is a function of the state of stress and a hardening parameter:

$$f(\sigma_1, \sigma_2, \sigma_3, h) = 0. \quad (3-38)$$

The hardening parameter  $h$  determines the evolution of the yield curve with the amount of plastic deformation of the material. Elasto-plastic deformation with hardening is important in the study of the stability of formations prone to sanding. Weak sandstones usually show hardening behavior, which can be close to linear hardening. For further details on elasto-plasticity, the reader is referred to Hill (1951) and Chen and Han (1988).

### 3-3.5. Failure

A failure criterion is usually a relationship between the principal effective stresses, representing a limit

beyond which instability or failure occurs. The Terzaghi effective stress is used in failure criteria. Several types of criteria have been proposed in the literature and have been used for various applications. The more popular criteria include the following:

- Maximum tensile stress criterion maintains that failure initiates as soon as the minimum effective principal stress component reaches the tensile strength  $T_o$  of the material:

$$\sigma_3 - p = -T_o. \quad (3-39)$$

- Tresca criterion expresses that failure occurs when the shear stress  $(\sigma_1 - \sigma_3)/2$  reaches the characteristic cohesion value  $C_o$ :

$$\sigma_1 - \sigma_3 = 2C_o. \quad (3-40)$$

- Mohr-Coulomb criterion expresses that the shear stress tending to cause failure is restricted by the cohesion of the material and by a constant analogous to the coefficient of friction times the effective normal stress acting across the failure plane:

$$\tau = C_o + \tan(\phi)(\sigma_n - p), \quad (3-41)$$

where  $\phi$  is the angle of internal friction and  $C_o$  is the cohesion. The Mohr-Coulomb failure criterion can be rewritten in terms of the principal stresses to give  $\sigma_1$  at failure in terms of  $\sigma_3$ :

$$\sigma_1 - p = \sigma_c + N_\phi(\sigma_3 - p), \quad (3-42)$$

where the coefficient of passive stress  $N_\phi$  is

$$N_\phi = \tan^2\left(\frac{\pi}{4} + \frac{\phi}{2}\right). \quad (3-43)$$

The uniaxial compressive strength then becomes

$$\sigma_c = 2C_o\sqrt{N_\phi}. \quad (3-44)$$

In a  $((\sigma_n - p), \tau)$  plane, this criterion is a straight line of slope  $\tan\phi$  and intercept  $C_o$ . A rock fails as soon as the state of stress is such that the criterion is met along one plane, which is also the failure plane. Using the Mohr circle graphical representation described in Sidebar 3B, this means that the state of stress at failure is represented by a Mohr circle that touches the failure envelope. The point of intersection can be used to determine the angle  $\theta$  between the normal to the failure plane and the direction of  $\sigma_1$ , as shown in Fig. 3-8. It can be shown that

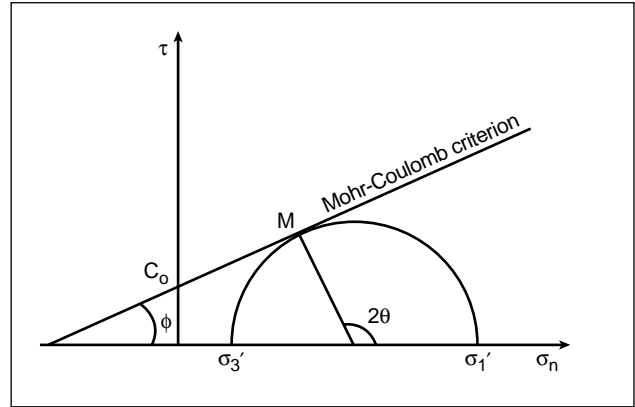


**Figure 3-8.** Graphical representation of a state of stress at failure.

$$\theta = \frac{\pi}{4} + \frac{\phi}{2}. \quad (3-45)$$

- Mohr failure envelope is a generalization of the linear Mohr-Coulomb criterion. An example of a more general model is the following nonlinear model:

$$\sigma_1 - p = \sigma_c + A(\sigma_3 - p)^n, \quad (3-46)$$

where  $A$  and  $n$  are obtained experimentally. The failure envelope can also be constructed graphically (see Section 3-4.5).

As shown here, the Tresca and Mohr-Coulomb criteria do not include the influence of the intermediate stress  $\sigma_2$ . Experimental evidence shows they are, in many cases, good approximations. However, there are other criteria that include the effect of  $\sigma_2$ .

## 3-4. Rock mechanical property measurement

### 3-4.1. Importance of rock properties in stimulation

Most of the hydraulic fracture propagation models assume linear elasticity. The most important rock parameter for these models is the plane strain modulus  $E'$ , which controls the fracture width and the value of the net pressure. In multilayered formations,  $E'$  must be determined in each layer, as the variation of elastic properties influences the fracture geometry. Elastic and failure parameters are also used in stress models to obtain a stress profile as a function of depth and rock properties. These profiles are important for esti-

imating the stress variation between layers and, consequently, the geometry of hydraulically induced fractures. The parameters involved are Young's modulus, Poisson's ratio, the poroelastic coefficient and the friction angle. The poroelastic stress coefficient  $\eta$  controls the value of stress changes induced by pore pressure changes that result from depletion, injection or fracture fluid loss.

The role of fracture toughness in hydraulic fracturing has been the subject of investigation in recent years (Shlyapobersky, 1985; Thiercelin, 1989; Cleary *et al.*, 1991; Johnson and Cleary, 1991; Advani *et al.*, 1992; SCR Geomechanics Group, 1993; Valkó and Economides, 1994). Laboratory measurements give values of  $K_{Ic}$  of the order of 1000 psi/in.<sup>1/2</sup> (at least in the absence of confining pressure), whereas fracture propagation models indicate that  $K_{Ic}$  must be at least 1 order of magnitude larger to influence fracture geometry. These results are, however, a function of fracture geometry and pumping parameters. Shlyapobersky (1985) suggested that in-situ fracture toughness, often referred to as apparent fracture toughness, can be much greater than laboratory values because of scale effects. These effects include the influence of heterogeneities, discontinuities (Thiercelin, 1989), large-scale plasticity

(Papanastasiou and Thiercelin, 1993) and rock damage (Valkó and Economides, 1994). In-situ determination is, however, difficult to achieve.

Finally, rock failure must be considered in evaluating the long-term stability of the rock around the fracture or at the wellbore. In particular, in weak formations (chalk or weak sandstones) part of the rock collapses if the drawdown pressure is too high.

### 3-4.2. Laboratory testing

Uniaxial and triaxial tests are considered the most useful tests in the study of mechanical rock properties. The difference between them resides in the presence or absence of confining pressure applied to the specimen. A typical triaxial testing system is shown schematically in Fig. 3-9. It subjects a circular cylinder of rock to an axisymmetric confining pressure and a longitudinal or axial load. Generally, these loads are similar to the in-situ state of stress. Relationships between the mechanical properties of the rock and the degree of confinement are obtained by performing a series of tests using different stress and pore pressure conditions. Also, if the rock is anisotropic, an additional series of tests should be performed using differ-

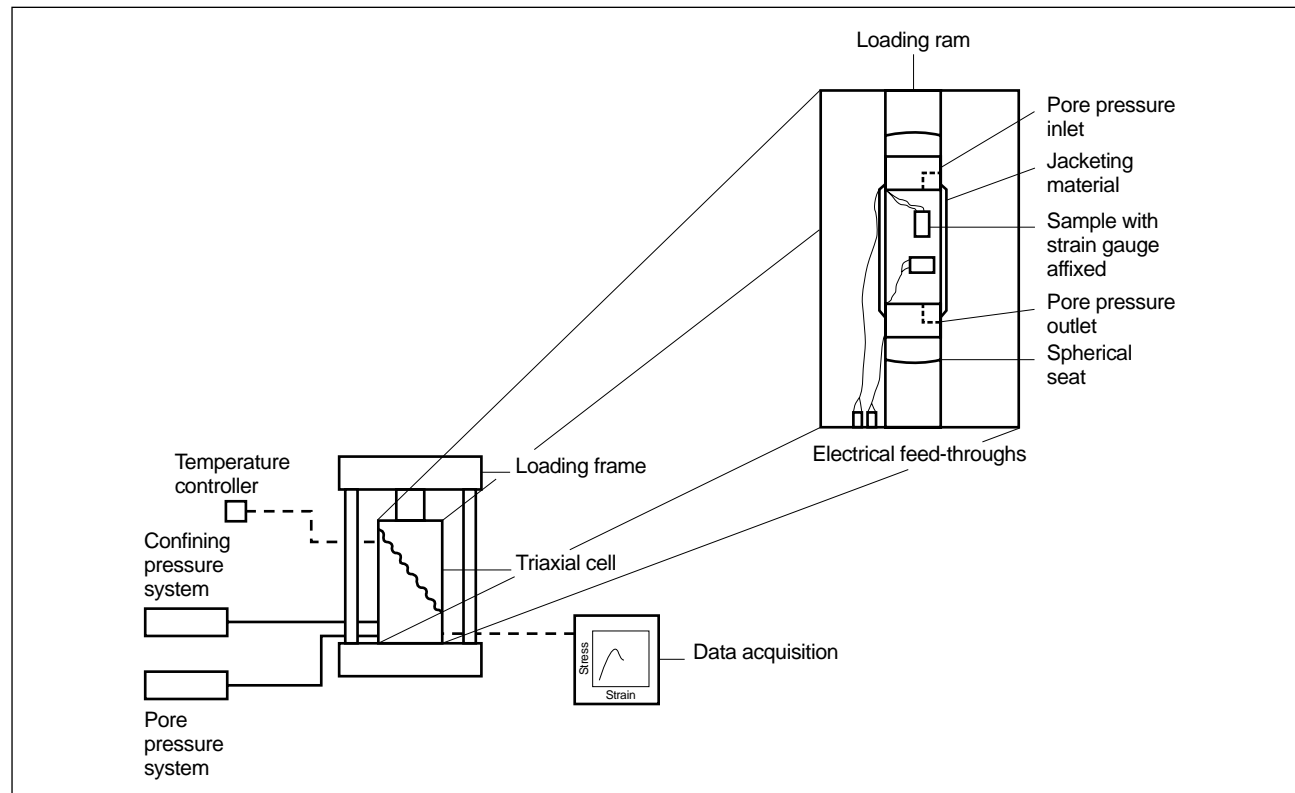


**Figure 3-9.** Triaxial testing configuration.

ent orientations of the cylinder axis with respect to the plane of anisotropy. During the course of the test, the primary information recorded is the deformation versus load relationships (Fig. 3-10), from which both Young's modulus and Poisson's ratio can be found. Because these primary elastic constants depend on confining stress, temperature, pore saturation and pressure, it is extremely important that the laboratory environment encompass the representative field situation to obtain representative data.

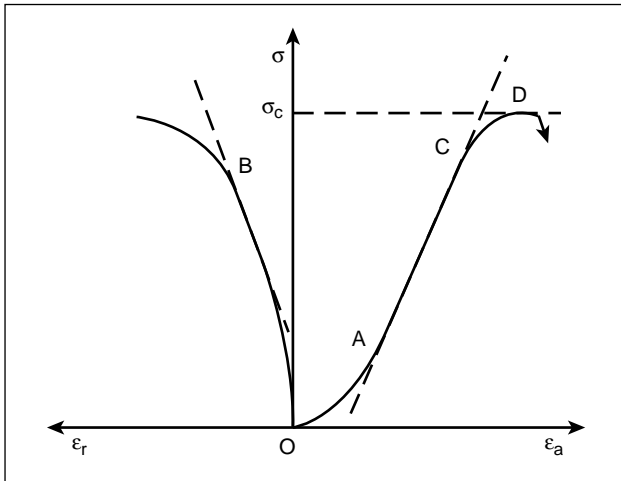


**Figure 3-10.** Stress-strain curves.

The importance of good specimen preparation cannot be overemphasized, and the International Society of Rock Mechanics (ISRM) recommended procedures that must be followed (*Rock Characterization Testing and Monitoring*; Brown, 1981). The end faces must be parallel; otherwise, extraneous bending moments are introduced, making correct interpretation of the results more difficult. In addition, because of the mismatch between the rock properties and those of the testing platens, shear stresses that develop at the rock/platen interfaces create an additional confinement immediately adjacent to the specimen ends. This dictates the use of specimens with a length:diameter ratio of at least 2 or the use of appropriate rock inserts or adaptive lubricant. The loading rate should also be maintained between 70 and 140 psi/s to avoid dynamic effects. Finally, some rock types (such as shales) are sensitive to the dehydration of natural pore fluids; care must be taken to preserve their integrity by avoiding drying cycles and contact with air during specimen recovery, storage and test preparation.

### 3-4.3. Stress-strain curve

Figure 3-10 presents a typical stress-strain relationship for rocks. The test is conducted under constant confining pressure  $p_c$  and constant axial strain rate. Measurements include the values of axial stress, axial strain and radial strain. When confining pressure is applied to the sample, the origin of the stress-strain plot is usually translated to remove the influence of hydrostatic loading on the stress and strain (i.e., the axial stress is actually the differential  $\sigma_a - p_c$ ).

During the initial stages of loading, from O to point A, the rock stiffens. This nonlinear regime is probably due to the closing of preexisting microcracks pervading the specimen. This particular region of the stress-strain curve is a signature of the stress history undergone by the rock specimen during past geologic time, including the coring process. This characteristic is discussed later as applied to in-situ stress determinations.

As the load increases further, the stress-strain curve becomes linear (from point A to point B); this is the portion of the stress-strain curve where the rock behavior is nearly elastic. If unloading occurs in this region, the strain returns almost to zero, usually along a different path. This effect is called hysteresis and indicates that some energy dissipates during a cycle of loading and unloading.

When the rock specimen is loaded beyond point B, irreversible damage sets in. It is shown by a decrease of the slope of the stress versus radial strain curve. At this stage, the damage is not seen on the axial strain. At point C, the axial strain also becomes nonlinear, and large deformations eventually occur. If the rock is unloaded in this region, permanent strains at zero stress are observed. Point D is the maximum load that the rock can sustain under a given confining pressure. Rock failure (i.e., when the sample loses its integrity) occurs at about this point. Some rocks, especially those with high porosity, may not exhibit a maximum peak stress but continue to carry increasing stress (i.e., continue to harden).

Another interesting rock characteristic is revealed by the volumetric strain, defined as the change in volume with respect to the original specimen volume. For a triaxial test, the volumetric strain of the cylindrical specimen is  $\epsilon_a + 2\epsilon_r$ , where  $\epsilon_a$  is the axial strain and  $\epsilon_r$  is the radial strain. As seen on Fig. 3-11, the volumetric strain versus axial stress can reverse its trend upon reaching point E; i.e., the rock specimen

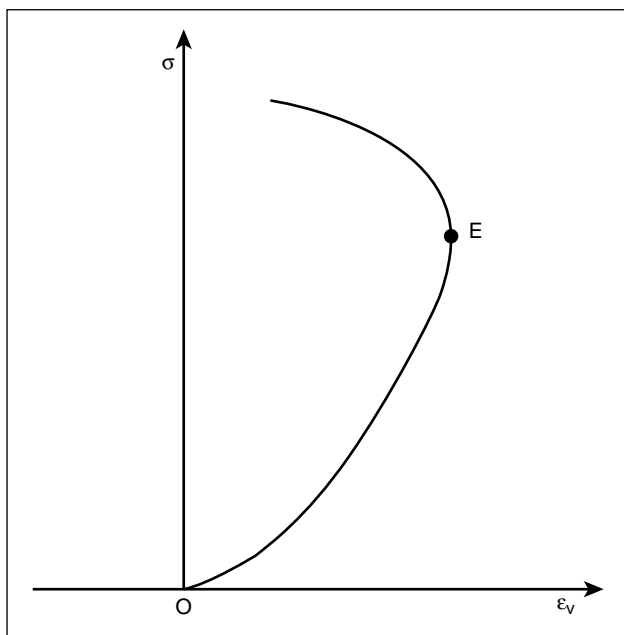


**Figure 3-11.** Axial stress versus volumetric strain.

starts to increase in volume under additional compressive load. This is referred to as dilatancy.

Dilatancy is responsible for the nonlinearity that is observed in the radial strain and consequently in the variation of volume. It is due either to the creation of tensile cracks that propagate in a direction parallel to the axis of loading (in that case, point B shown in Fig. 3-10 is distinct from point C) or to frictional sliding along rough surfaces and grains (in that case, point B is close to point C). Soft rocks under confining pressure could show a decrease in volume instead of an increase, because of compaction. This is typical of chalk and weak sandstones. Compaction in cohesive rocks requires the destruction of cohesion, which could create a sanding problem during production. Finally, if the framework of elasto-plasticity is used, point B is the initial yield point. If the nonelastic component of the variation of volume is negative, the rock is dilatant; otherwise, the rock is compactant.

Brittle rocks and ductile rocks must also be differentiated. Brittle rocks are characterized by failure prior to large nonelastic deformation. Low-porosity sandstones and hard limestones are typical brittle rocks. Ductile rocks are characterized by the absence of macroscopic failure (i.e., theoretically, the rock will yield indefinitely). Salt, young shales and very high permeability sandstones are typical ductile rocks. These behaviors, however, are functions not only

of rock type but also confining pressure, loading rate and temperature, with a general transition from brittle to ductile behavior with an increase in confining pressure, increase in temperature and decrease in loading rate. Moreover, in porous rocks (e.g., sandstones, shales), a transition from dilatant to compactant behavior with confining pressure is also observed.

### 3-4.4. Elastic parameters

As discussed previously, rocks are not perfectly elastic. Especially in soft rocks, it could well be difficult to find a portion of the stress-strain curves that exhibits nearly elastic behavior. On the other hand, the knowledge of elastic parameters is of great importance for engineering applications, and assuming, as a first approximation, that the rock behaves as an elastic material has significant advantages.

There are two main approaches to elastic parameter determination. The first one is to find elastic parameters that can be used to predict as close as possible the behavior of the rock along an expected loading path. These parameters do not measure the real elastic component of the rock but approximate the rock behavior. This is the approach used in engineering design, although the assumption underlying the measurement must be kept in mind. The other approach is to develop a test procedure that measures, as close as possible, the elastic component of the strain. This approach is useful if a correlation is sought between downhole measurements made using sonic tools and core measurements. Because of the variety of approaches that can be used, it is essential to always mention how elastic properties have been measured.

Elastic property measurement can be made under static conditions or under dynamic conditions. The ratio of the dynamic to static moduli may vary from 0.8 to about 3 and is a function of rock type and confining stress. In most cases, this ratio is higher than 1 (e.g., Simmons and Brace, 1965; King, 1983; Cheng and Johnston, 1981; Yale *et al.*, 1995). Possible explanations for these differences are discussed in the following. Static elastic properties, as measured in the laboratory during sample loading (see the following section), are generally assumed more appropriate than dynamic ones for estimating the width of hydraulic fractures. Knowledge of dynamic elastic properties is, however, required to establish a calibration procedure to estimate static downhole properties from downhole

measurements, which are obtained essentially from sonic tools (see Chapter 4).

- Static elastic properties

Static elastic properties are usually measured using the equipment described in Section 3-4.2. For classification purposes, the ISRM proposed the following recommended procedures that use, for the measurement of Young's modulus, the axial stress–axial strain curve measured during the loading of the sample (Brown, 1981) (Fig. 3-12):

- tangent Young's modulus  $E_t$ —the slope at a stress level that is usually some fixed percentage of the ultimate strength (generally 50%)
- average Young's modulus  $E_{av}$ —determined from the average slopes of the generally straight-line portion of the curve
- secant Young's modulus  $E_s$ —usually the slope from zero stress to some fixed percentage of the ultimate strength (generally 50%).

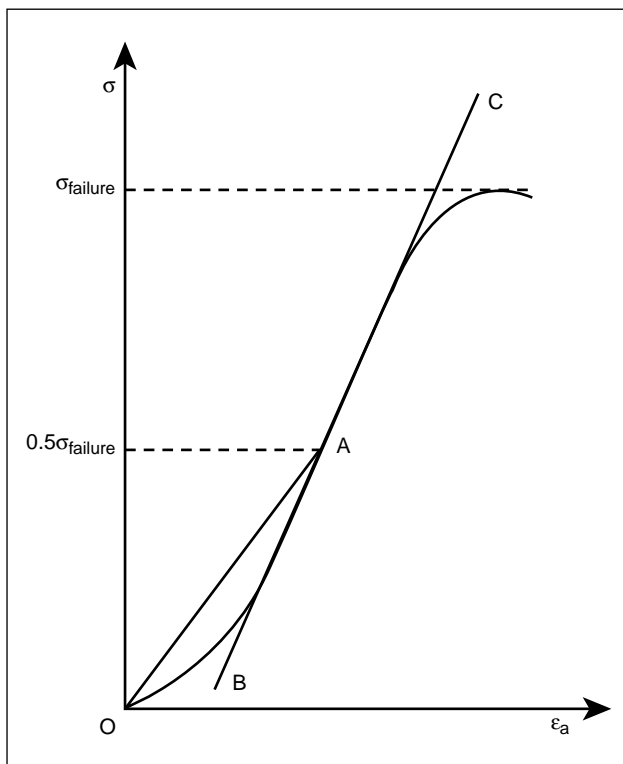


**Figure 3-12.** ISRM-recommended methods to measure Young's modulus:

- derivative of the stress-strain curve at point A is  $E_t$ , measured at 50% of the ultimate strength
- slope of the straight line BC is  $E_{av}$
- slope of the straight line OA is  $E_s$ .

Poisson's ratio is determined using similar methods and the axial strain–radial strain curve.

These elastic constants must be adjusted to the proper reservoir conditions for design purposes. Moreover, for stimulation purposes an approach that requires failure of the sample is not necessary. The best method is either to use the average modulus or to measure a tangent modulus at a state of stress near the expected downhole effective state of stress. The average value simulates the effect of the width, causing stresses that are maximum at the fracture face and decay to zero away from the face. Ideally, the sample must be tested in a direction normal to the expected hydraulic fracture plane (i.e., in the horizontal direction if the fracture is expected to be vertical). The best way to reproduce downhole conditions is probably to apply a confining pressure equal to the effective downhole mean pressure  $(\sigma_h + \sigma_v + \sigma_H)/3 - p$ , where  $\sigma_h$ ,  $\sigma_v$  and  $\sigma_H$  are the minimum horizontal stress, vertical stress and maximum horizontal stress, respectively. The tangent properties are then measured using an incremental increase of the axial load. Terzaghi's effective stress is used here rather than the Biot effective stress concept because the tangent properties are essentially controlled by this effective stress (Zimmerman *et al.*, 1986).

The second approach utilizes small unloading-loading cycles that are conducted during the main loading phase. If the cycle is small enough, the slope of the unloading stress-strain curve is close to that of the reloading stress-strain curve (Fig. 3-13, Hilbert *et al.*, 1994; Plona and Cook, 1995). This leads to the measurement of elastic properties that are close to the actual ones and also close to the value determined using ultrasonic techniques. It is also important to perform these measurements at the relevant confining pressure and axial stress.

- Elastic properties determined using sonic measurements

Sonic measurements are conveniently used to determine the elastic properties under dynamic conditions in the laboratory. These properties are also called dynamic elastic properties. To obtain them, a mechanical pulse is imparted to the rock specimen, and the time required for the pulse to traverse the length of the specimen is determined. Then, the velocity of the wave can be easily calculated. Again, these measurements should be performed under simulated

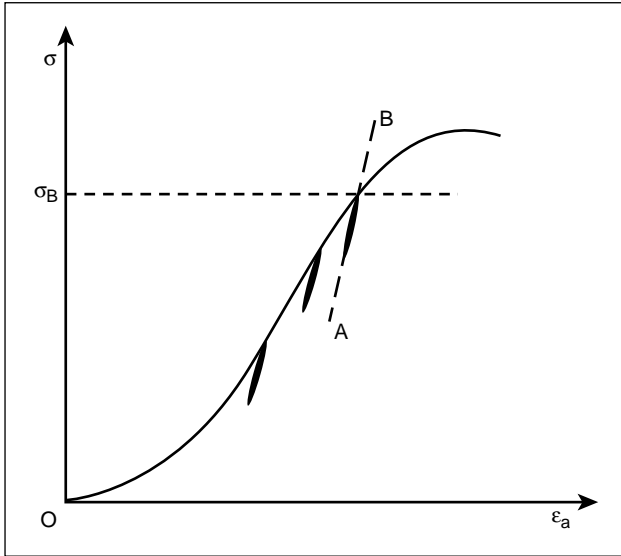


**Figure 3-13.** Young's modulus measured using small cycles (Hilbert *et al.*, 1994). Young's modulus at  $\sigma_B$  is the slope of line AB.

downhole conditions and can be conducted during triaxial compression tests (Fig. 3-14).

As also discussed in Chapter 4, two types of elastic body waves can be generated: compressional (also called *P*-waves) and shear (*S*-waves). Elastic wave theory shows that the velocities of *P*- and *S*-waves ( $u_P$  and  $u_S$ , respectively) are related to the elastic constants through the following relationships (in dry rocks):

$$u_P = \left[ \frac{C_{dyn}}{\rho} \right]^{1/2} = \left[ \frac{K_{dyn} + \frac{4}{3} G_{dyn}}{\rho} \right]^{1/2}$$

$$= \left[ \frac{E_{dyn}(1 - \nu_{dyn})}{\rho(1 + \nu_{dyn})(1 - 2\nu_{dyn})} \right]^{1/2} \quad (3-47)$$

$$u_S = \left[ \frac{G_{dyn}}{\rho} \right]^{1/2} = \left[ \frac{E_{dyn}}{2\rho(1 + \nu_{dyn})} \right]^{1/2}, \quad (3-48)$$

where  $\rho$  refers to the mass density of the rock specimen and the relationship between the various elastic moduli is as in Sidebar 3C. The subscript *dyn* refers to dynamic, as the values of the elastic constants obtained by dynamic techniques are in general higher than those obtained by static methods. This difference is now believed to be due mainly to the amplitude of the strain, with the very low amplitude dynamic measurements representing the actual

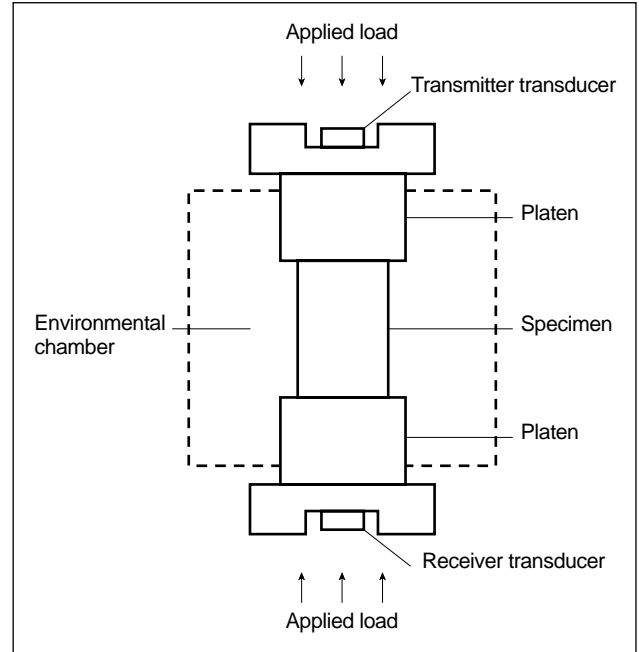


**Figure 3-14.** Ultrasonic pulse measurement.

elastic component of the rock (Hilbert *et al.*, 1994; Plona and Cook, 1995). Because of poroelastic effects and rock heterogeneity, the acoustic velocity is also a function of wave frequency. But in dry rocks, the influence of the frequency appears to be of second order compared with that of the strain amplitude (Winkler and Murphy, 1995). Consequently, when the dynamic and static small-amplitude loading/unloading measurements are compared, their values agree quite well (Fig. 3-15; Plona and Cook, 1995).

Correlations can be established between static and dynamic moduli (Coon, 1968; van Heerden, 1987; Jizba and Nur, 1990). Coon demonstrated that the coefficient of correlation can be improved if consideration of the lithology is included. These correlations allow an estimation of large-amplitude static in-situ values from log data where core data are not available (see Chapter 4). Figure 3-15 suggests another procedure in which a corrective factor is found by the ratio of the loading to unloading tangent moduli for low-amplitude static tests.

- Scale effects in elastic properties

The elastic properties of rock are scale dependent, as are any rock properties. This means that the value of an elastic parameter that is determined on a laboratory sample may be quite different of that of a rock mass, mainly because of the presence of

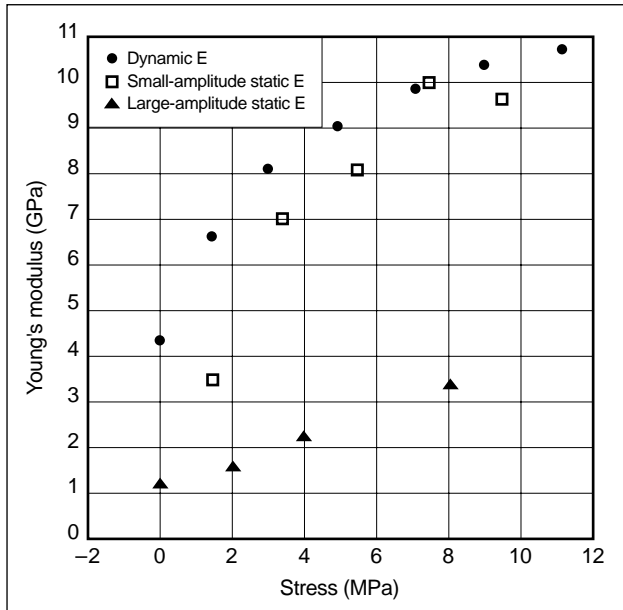


**Figure 3-15.** Dynamic versus static Young's modulus measurements (after Plona and Cook, 1995).

discontinuities in the rock mass. Various approaches are being developed to take this phenomenon into consideration (Schatz *et al.*, 1993). An alternative is to determine the properties downhole, as described in the next section. However, downhole measurements are usually limited to a scale on the order of 3 ft, whereas a large fracture involves a scale on the order of 100 ft. Rock imperfection on this scale can be mapped by a combination of wellbore seismic and sonic measurements.

- Elastic properties determined using downhole measurements

Downhole measurements are made to estimate the elastic properties. Dynamic log measurements are described in detail in Chapter 4. Other techniques include direct downhole static measurements and inversion of the pressure response obtained during a micro-hydraulic fracturing test. A direct downhole static measurement requires measuring the deformation of a small portion of the wellbore during pressurization. This can be done by using downhole extensimeters (Kulhman *et al.*, 1993). Usually this technique yields only the shear modulus  $G$ . Pressure inversion techniques (Piggott *et al.*, 1992) require

a fracture propagation model to invert the pressure response in terms of elastic properties. The geometry and mechanical assumptions of the fracture propagation model must be as close as possible to the actual situation. If the fracture propagates radially, this technique can extract an estimate of the plane strain modulus  $E'$  (Desroches and Thiercelin, 1993).

- Poroelastic properties

For isotropic rocks, it is generally recommended to conduct tests that measure the volumetric response of the sample, as poroelastic effects are volumetric ones. Three tests are usually made to measure the five properties that characterize an isotropic poroelastic material. All three tests involve hydrostatic loading but differ on the boundary conditions applied to the pore fluid. For the drained test, the fluid in the rock is maintained at constant pressure; for the undrained test, the fluid is prevented from escaping the sample; and for the unjacketed test, the pore pressure is maintained equal to the confining pressure. The reader is referred to Detournay and Cheng (1993) for further information. Presented here is the determination of  $\alpha$ , which, with knowledge of the drained Poisson's ratio, allows determination of the poroelastic stress coefficient  $\eta$ , which is probably the most important poroelastic parameter for hydraulic fracturing applications. This measurement is conducted using the drained test, in which the volume change of the sample  $\Delta V$  and the volume change of the pore fluid  $\Delta V_f$  are measured as a function of an incremental increase of the confining pressure. The value of  $\alpha$  is then given by the following relation:

$$\alpha = \frac{\Delta V_f}{\Delta V}. \quad (3-49)$$

As for the elastic properties, the test must be conducted with a confining pressure close to the downhole mean stress. These properties must be tangent properties and, for practical purposes, are a function of the Terzaghi effective stress. Mathematical consideration and experimental results confirm that poroelastic properties are controlled by the Terzaghi effective stress (Zimmerman *et al.*, 1986; Boutéca *et al.*, 1994).



### 3-4.5. Rock strength, yield criterion and failure envelope

The strength of a rock is the stress at which the rock fails (i.e., the rock loses its integrity). This strength obtained with a uniaxial test is called the uniaxial compressive strength  $\sigma_c$  (UCS). The overall strength of rocks is a relationship between the principal effective stress components (in the sense of Terzaghi, see Section 3-3.5). This relationship is called the failure criterion, and its graphical representation is called the failure envelope.

To obtain the failure envelope of a particular rock type, a series of triaxial tests should be performed under different confining pressures until failure of the specimen occurs for each condition. There are various ways to represent the failure envelope. The classic approach in rock mechanics is to plot the effective stresses at failure for each test using a Mohr circle representation (see Sidebar 3B) of diameter  $(\sigma_{failure}' - \sigma_3')$ , where  $\sigma_{failure}'$  represents the ultimate strength of the specimen measured under confinement  $\sigma_3'$  (Fig. 3-16). The envelope of these circles is a locus separating stable from unstable conditions. It should be emphasized that the failure of rocks occurs when the matrix stresses reach a critical level; hence, the failure envelope represents a relationship between the “effective” stress levels. Therefore, the knowledge of such a characteristic can also be used to put some limits on the allowable variation of the reservoir pore pressure during production. Indeed, a change in pore pressure corresponds to a translation of the pertinent Mohr circle along the normal stress axis.

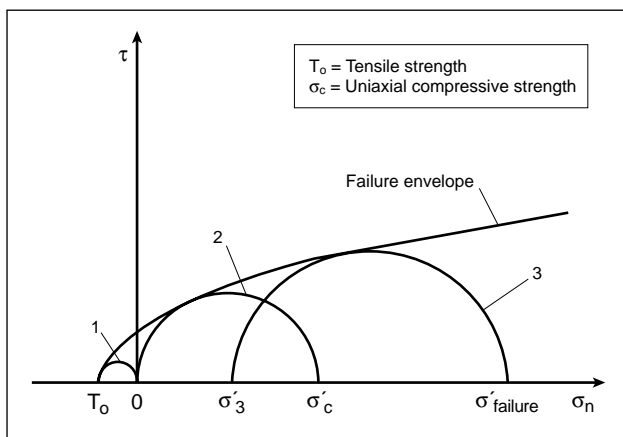


**Figure 3-16.** Failure envelope. 1 = Mohr circle corresponding to uniaxial tensile test; 2 = Mohr circle corresponding to uniaxial compressive test; and 3 = Mohr circle corresponding to triaxial test with effective confining stress  $\sigma'_c$  and failure stress (i.e., ultimate strength)  $\sigma'_{failure}$ .

A specific case is the study of pore collapse. Pore collapse is usually not associated with a sudden loss of integrity and therefore has to be detected from the initial yield envelope rather than the failure envelope. In some instances, yield can be initiated under isotropic loading (Fig. 3-17). The portion of the yield curve that shows a decrease of the shear stress at yield as a function of the confining pressure is characteristic of compactant materials. This usually occurs with poorly consolidated rocks. In cohesive materials compaction is associated with pore collapse and consequently with cohesion loss. This is a potential failure mechanism of the matrix that could lead to the production of formation particles (e.g., sanding).

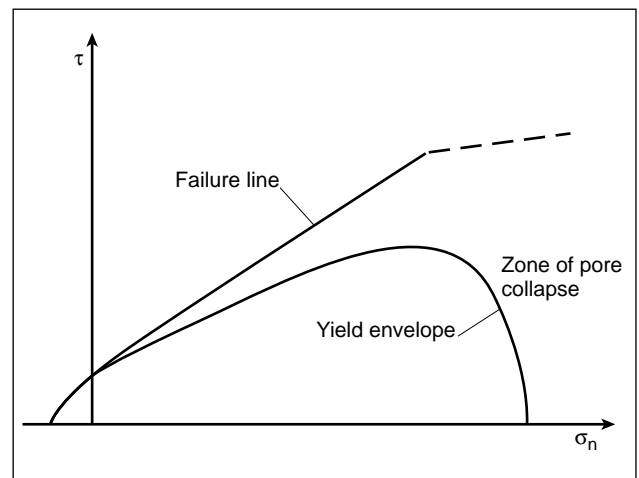


**Figure 3-17.** Failure and initial yield envelopes for poorly consolidated sandstones.

### 3-4.6. Fracture toughness

Determining the value of fracture toughness requires using a sample that contains a crack of known length. The stress intensity factor, which is a function of the load and sample geometry, including the length of the preexisting crack, is then determined. Testing measures the critical load and, therefore, the critical stress intensity factor  $K_{Ic}$  at which the preexisting crack is reinitiated. Another approach is to measure the fracture surface energy and use Eq. 3-33. An example using a simple geometry is discussed in Sidebar 3D. Testing the sample under downhole conditions is also required because fracture toughness increases with effective confining pressure and is affected by temperature. Various sample geometries have been proposed, but the most practical ones from an engineering point

### 3D. Fracture toughness testing

To illustrate the measurement of fracture toughness and the influence of a crack on material behavior, a bar of unit thickness containing a central crack of length  $2L$  is considered (Fig. 3D-1). Although this is a simple geometry, in practice such an extension test is difficult to conduct. The crack length is supposed to be small compared with the bar width and the width small compared with the bar length. The stress intensity factor for this geometry is given by

$$K_I \approx \sigma \sqrt{\pi L} \left(1 - \frac{L}{2b}\right) \left(1 - \frac{L}{b}\right)^{-1/2}, \quad (3D-1)$$

where  $\sigma$  is the stress applied to the sample (i.e.,  $F/2b$ ).

Figure 3D-1 also shows a plot of the load versus displacement curve. The load increases to the point where the crack starts to propagate. During stable crack propagation, the load decreases. If the sample is unloaded at this stage, the load-displacement curve exhibits a slope different from the one obtained during initial loading. However, the displacement is recovered upon complete unloading. This behavior is fundamentally different from that of elasto-plasticity, and a perfectly brittle behavior is exhibited. The change of slope is not a material property but is due to the increased length of the crack. It can, therefore, be used to estimate the crack length.

The critical stress intensity factor is the value of  $K_{Ic}$  when the crack starts to propagate:

$$K_{Ic} \approx \frac{F_c}{2b} \sqrt{\pi L} \left(1 - \frac{L}{2b}\right) \left(1 - \frac{L}{b}\right)^{-1/2}, \quad (3D-2)$$

where  $F_c$  is the critical load.

It can also be demonstrated that the area OAB in Fig. 3D-1 corresponds to the energy  $dW_s$  that was dissipated to propagate the crack from  $2L$  to  $(2L + 2\Delta L)$ . The strain energy release rate is, therefore, the dissipated energy divided by the created surface area  $2\Delta L$ :

$$G_o = \frac{dW_s}{2\Delta L}. \quad (3D-3)$$

A similar approach can be used if the crack is propagated to the sample end; in that case:

$$G_o = \frac{dW_s}{2b}, \quad (3D-4)$$

where  $dW_s$  corresponds to the area under the load-displacement curve and the initial crack length is assumed to be small compared with the sample width (i.e.,  $\Delta L \cong b$ ). Using this approach, there is no need to measure crack length. For linear elastic behavior:

$$G_o = \frac{1 - \nu^2}{E} K_I^2. \quad (3D-5)$$

The load-displacement curve shown in Fig. 3D-1 can also be used to determine the process zone behavior (Labuz *et al.*, 1985).

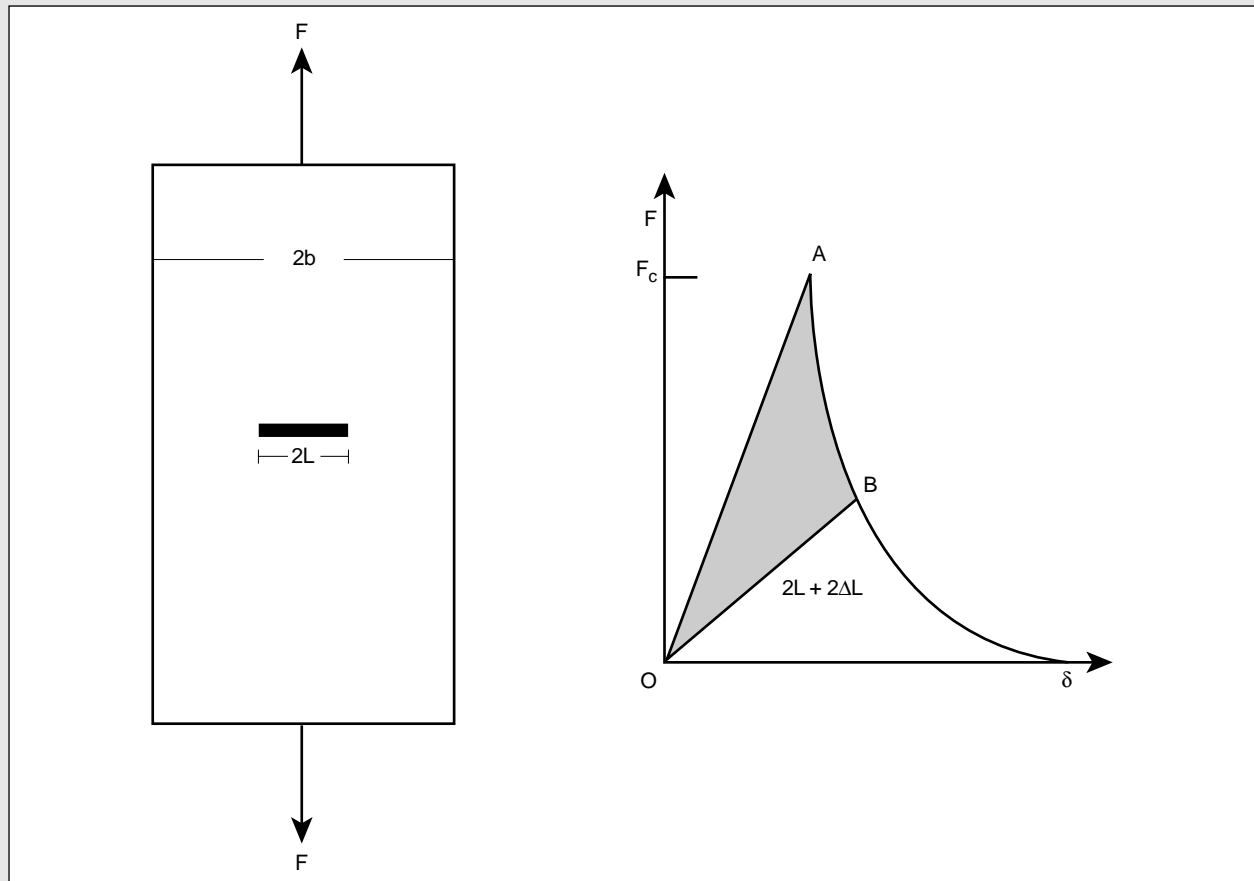


**Figure 3D-1.** Fracture toughness measurement. The shaded area on the left of the plot represents the energy required to propagate the crack from  $2L$  to  $(2L + 2\Delta L)$ .

of view are those based on core geometries (Ouchterlony, 1982; Thiercelin and Roegiers, 1986; Zhao and Roegiers, 1990; ISRM Commission on Testing Methods, 1988, 1995).

However, the existence of very large stress values near the tip of the crack makes it difficult to develop a rigorous test configuration because a cloud of micro-cracks is created ahead of the crack tip. This is commonly referred to as the process zone (Swanson and Spetzler, 1984; Labuz *et al.*, 1985). The extent of this nonlinear region must be limited so that it does not reach the edge of the laboratory sample. Also, this process zone must be relatively small compared with the size of the crack if linear elastic calculations are to be valid (Schmidt, 1976; Schmidt and Lutz, 1979; Boone *et al.*, 1986).

The development of the process zone is one of the causes of the scale effects that are observed in fracture toughness testing; i.e., the determined value of fracture toughness increases with sample size. Modeling of process zone behavior can be conducted using the information obtained during tensile failure of a specimen (see Sidebar 3D). Modeling can also give some insight on the tip behavior of large-scale hydraulic fractures (Papanastasiou and Thiercelin, 1993).

### 3-5. State of stress in the earth

The propagation and geometry of hydraulic fractures are strongly controlled by the downhole state of stress. In particular, it is generally accepted that the degree of fracture containment is determined primarily by the in-situ stress differences existing between layers. In the absence of a meaningful stress contrast, other mechanisms such as slip on bedding planes (Warpinski *et al.*, 1993) and fracture toughness contrast (Thiercelin *et al.*, 1989) can have a role. Moreover, hydraulic fractures propagate, in most cases, normal to the minimum stress direction. Consequently, knowledge of the minimum stress direction allows prediction of the expected direction of the hydraulic fracture away from the wellbore.

Stresses in the earth are functions of various parameters that include depth, lithology, pore pressure, structure and tectonic setting. A typical example from the Piceance basin in Colorado (Warpinski and Teufel, 1989) is shown in Fig. 3-18. The stress regime in a given environment depends, therefore, on regional considerations (such as tectonics) and local considerations (such as lithology). Understanding the interac-

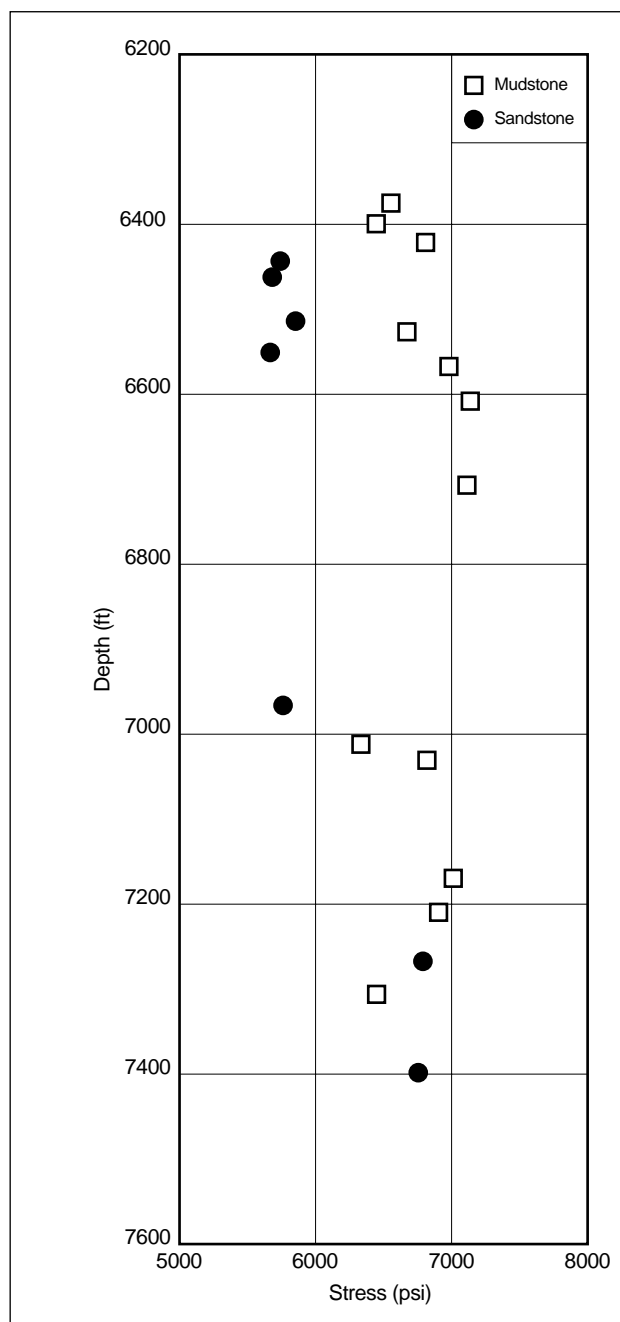


**Figure 3-18.** Stress profile for Well MWX-3 (Warpinski and Teufel, 1989).

tion between regional and local considerations is important as it controls the stress variation between layers. In some stress regimes the adjacent layers are under higher stress than the pay zone, enhancing fracture height containment; in others, the adjacent layers are under lower stress than the pay zone, and fracture propagation out of the zone is likely, limiting lateral fracture penetration. Key regional stress regimes and

the consequences of these regimes on the local state of stress in a reservoir are reviewed in the following. These regimes lead to the introduction of simple stress models that allow making rough estimates of the stress profile as a function of depth and rock properties. These models can also be used to obtain a calibrated stress profile from log and stress measurement information, as shown in Chapter 4. The influence of the variation of temperature and pore pressure on the state of stress is also analyzed. Finally, the influence of industrial intervention on the state of stress is presented. Intervention includes drilling a hole and depleting or cooling a formation.

### 3-5.1. Rock at rest

One stress regime is when the rock is under uniaxial strain conditions (i.e., there is no horizontal strain anywhere). To estimate the state of stress that is generated under this regime, it is assumed that the rock is a semi-infinite isotropic medium subjected to gravitational loading and no horizontal strain.

Under these conditions, the vertical stress is generated by the weight of the overburden and is the maximum principal stress. Its magnitude, at a specific depth  $H$ , is estimated by

$$\sigma_v = \int_0^H \rho(H)g dH, \quad (3-50)$$

where  $\rho$  is the density of the overlying rock masses and  $g$  is the acceleration of gravity. The value of this stress component is obtained from the integration of a density log. The overburden gradient varies from about 0.8 psi/ft in young, shallow formations (e.g., Gulf Coast) to about 1.25 psi/ft in high-density formations. Assuming that quartz has a density of 165 lbm/ft<sup>3</sup>, the overburden gradient ranges between the well-known values of 1.0 and 1.1 psi/ft for brine-saturated sandstone with porosity ranging between 20% and 7%, respectively.

With uniaxial strain assumed, the other two principal stresses are equal and lie in the horizontal plane. If they are written in terms of effective stress, they are a function of only the overburden:

$$\sigma'_h = K_o \sigma'_v, \quad (3-51)$$

where  $K_o$  is the coefficient of earth pressure at rest and  $\sigma'_h$  is the minimum effective horizontal stress. Assumptions about rock behavior can be used to estimate

values of  $K_o$ . However, stress predictions using these assumptions must be used with great caution and may not be applicable in lenticular formations (Warpinski and Teufel, 1989). Nevertheless, they are useful for understanding the state of stress in the earth and can be used as a reference state (Engelder, 1993).

With the assumption of elasticity and for the boundary conditions outlined previously,  $K_o$  is

$$K_o = \frac{\nu}{1-\nu}, \quad (3-52)$$

and the relationship between the total minimum horizontal stress  $\sigma_h$  and the overburden  $\sigma_v$  is, after re-arranging and using the Biot effective stress for  $\sigma'$ ,

$$\sigma_h = \frac{\nu}{1-\nu} \sigma_v + 2\eta p. \quad (3-53)$$

The dependence of horizontal stress on rock lithology results from the dependence of Poisson's ratio  $\nu$  on rock lithology. In most cases, the model predicts that sandstones are under lower stress than shales as  $K_o$  in sandstones and shales is about equal to  $\frac{1}{3}$  and  $\frac{1}{2}$ , respectively. The use of Eq. 3-53 to obtain stress profiles in relaxed basins is presented in Section 4-5.2. More complex elastic models that are associated with this stress regime have been developed to consider rock anisotropy (Amadéi *et al.*, 1988) and topography (Savage *et al.*, 1985).

For purely frictional materials,  $K_o$  can be approximated by  $(1 - \sin\phi)$  (Wroth, 1975), which gives the following relationship for the total stresses:

$$\sigma_h \approx (1 - \sin\phi)\sigma_v + \sin(\phi)p, \quad (3-54)$$

where  $\phi$  is the angle of internal friction of the rock (Eq. 3-41), of the order of 20° for shales and 30° for sandstones. In this expression, the Terzaghi effective stress concept prevails because this case involves frictional behavior.

This equation implies that rocks with a high value of friction angle are under lower stress than rocks with low value of friction angle; i.e., in general, sandstones are under lower stress than shales. The observation that models based on elasticity and models based on frictional behavior give the same trend of stress contrast always occurs, although the fundamental assumptions for these models have nothing in common.

For purely viscous materials (salt),  $K_o$  is simply equal to 1 and the state of stress is lithostatic (Talobre, 1957, 1958):

$$\sigma_h \approx \sigma_v \quad (3-55)$$

(a lithostatic state of stress as such does not require the uniaxial strain condition, and therefore, it defines a stress regime by itself).

Over geologic time, rock experiences, in various combinations and degrees, diverse mechanical behaviors and various events. Behaviors include elastic, frictional and viscous behaviors, and events include the occurrence of tectonic strain, variation of pore pressure and temperature, erosion and uplift. As reviewed by Prats (1981), these mechanisms lead to deviations from these simple reference states, some of which are briefly reviewed here.

### 3-5.2. Tectonic strains

Tectonic stresses and strains arise from tectonic plate movement. In this section, the notion of tectonic strain is introduced, which is a quantity added to or subtracted from the horizontal strain components. If incremental tectonic strains are applied to rock formations, these strains add a stress component in an elastic rock as follows:

$$d\sigma_h \approx \frac{E}{1-\nu^2} d\epsilon_h + \frac{E\nu}{1-\nu^2} d\epsilon_H \quad (3-56)$$

$$d\sigma_H \approx \frac{E}{1-\nu^2} d\epsilon_H + \frac{E\nu}{1-\nu^2} d\epsilon_h, \quad (3-57)$$

where  $d\epsilon_H$  and  $d\epsilon_h$  are the (tectonic) strains with  $d\epsilon_H > d\epsilon_h$ . The resulting stress increments are not equal, with  $d\sigma_H > d\sigma_h$ , where  $d\sigma_H$  is the stress increment generated in the  $d\epsilon_H$  direction and  $d\sigma_h$  is the stress increment generated in the  $d\epsilon_h$  direction. These relations are obtained by assuming no variation of the overburden weight and provide a dependence of stress on Young's modulus  $E$ . This means that the greater the Young's modulus, the lower the horizontal stress if the strains are extensive and the higher the horizontal stress if the strains are compressive. To understand this mechanism, the different layers can be compared to a series of parallel springs, the stiffness of which is proportional to Young's modulus as depicted in Fig. 3-19. This model is actually a good qualitative description of the state of stress measured in areas in which compressive tectonic stresses occur. The model can account for situations where sandstones are under higher horizontal stress than adjacent shales (Plumb *et al.*, 1991; see also Chapter 4). The overburden stress

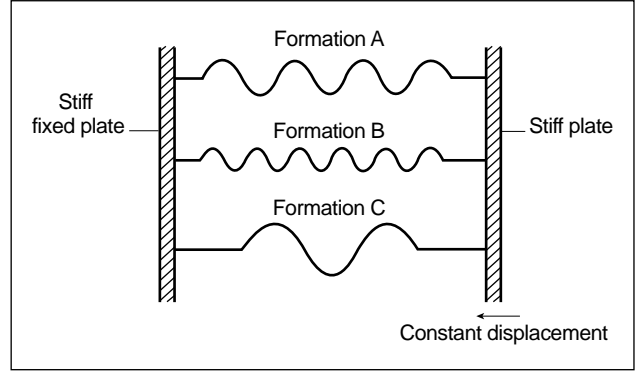


**Figure 3-19.** By analogy, the stiffer the spring, the more load it will carry.

is a principal stress but not necessarily the maximum. The state of stress described in this section cannot be considered to define a particular stress regime (although one could speak of compressional stress regime) as it does not define a reference state. Only if the strains are high enough for the rock to fail are reference states obtained, as discussed in the next section.

### 3-5.3. Rock at failure

If the strains are high enough, the rock fails either in shear or in tension. Three stress regimes can be defined if the rock fails in shear. These stress regimes are associated with the three classic fault regimes (Anderson, 1951): normal, thrust and strike-slip fault regimes (Fig. 3-20). Stresses can be estimated by the adapted shear failure model. The simplest shear failure model that applies to rocks is the Mohr-Coulomb failure criterion. A stress model based on this criterion assumes that the maximum in-situ shear stress is governed by the shear strength of the formation (Fenner, 1938). Hubbert and Willis (1957) used this criterion and sandbox experiments in their classic paper on rock stresses and fracture orientation (see Sidebar 3A). As presented in Eq. 3-42, the Mohr-Coulomb failure criterion can be written to give  $\sigma_1$  at failure in terms of  $\sigma_3$ . In sandstones and shales,  $N_\phi$  is about equal to 3 and 2, respectively.

If failure is controlled by slip along preexisting surfaces, the compressive strength  $\sigma_c$  can be assumed negligible. However, a residual strength may still exist. The angle of internal friction  $\phi$  is usually measured by using ultimate strength data as a function of the confining pressure obtained during triaxial testing. This angle can also be measured by using residual

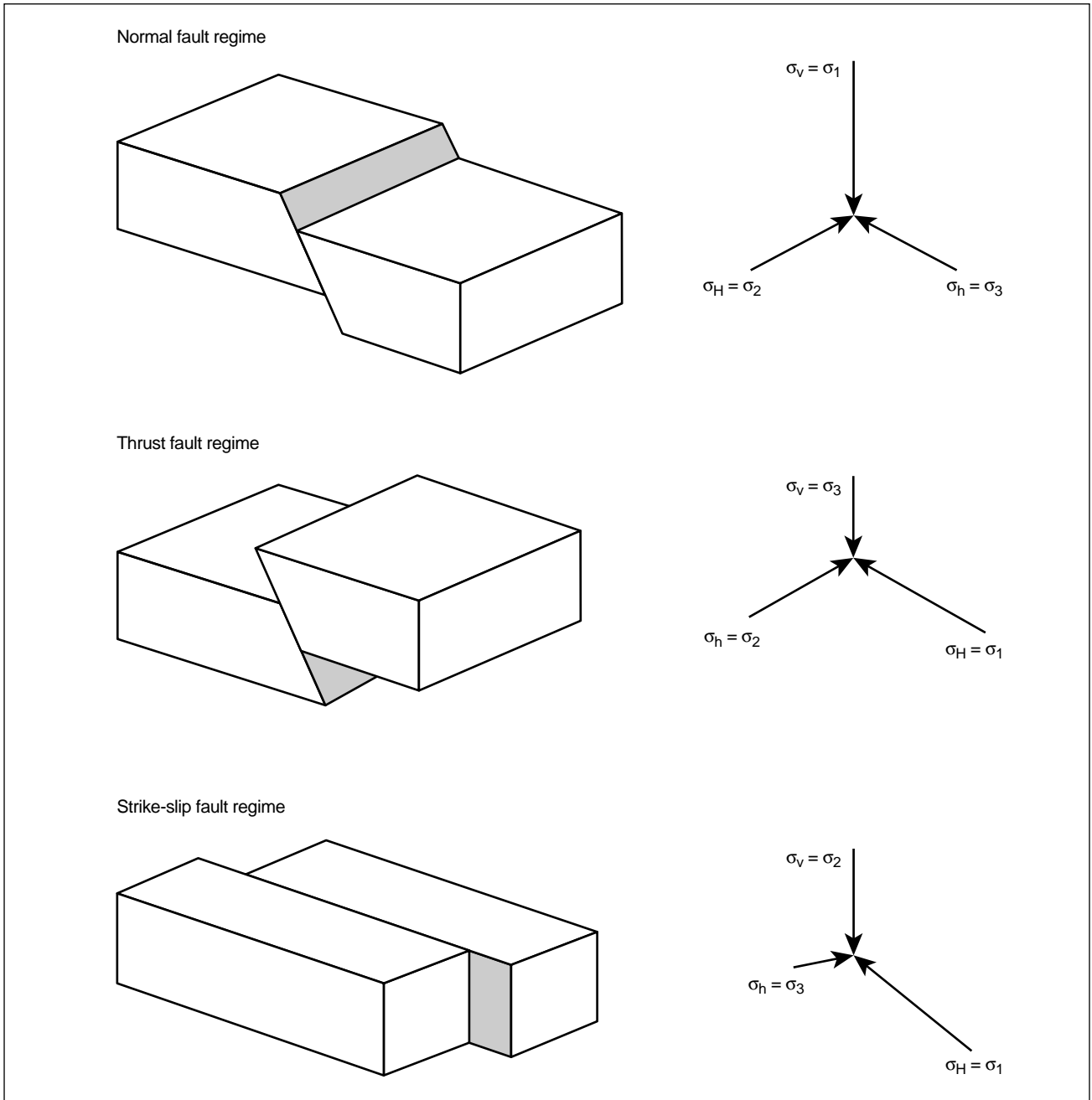


**Figure 3-20.** The three fault regimes (Anderson, 1951).

strength data as a function of the confining pressure obtained during triaxial testing once the sample has failed. Using the residual angle of friction rather than the angle of internal friction in a failure stress model should be more consistent with the assumption that the minimum stress is controlled by friction along pre-existing planes. Generally, the residual angle of friction is smaller than or equal to the internal angle of friction.

If the formation is in extension (i.e., normal fault regime, Fig. 3-20), the vertical stress is the maximum principal stress. The minimum principal stress is in the horizontal plane and is therefore  $\sigma_h$ . Equation 3-42 becomes

$$\sigma_h - p \approx \frac{1}{N_\phi} (\sigma_v - p), \quad (3-58)$$

in which the effect of strength is neglected. An equation similar to Eq. 3-51 can be retrieved. However, if the rock is at failure, the coefficient of proportionality cannot be considered as a coefficient of earth stress at rest. The most surprising and confusing result is that, in practice, Eqs. 3-53 and 3-58 give similar predictions, especially if, in the elastic model,  $\alpha$  is assumed equal to 1. The coefficient of proportionality in sandstones and shales is, whether elasticity or failure is assumed, about equal to  $\frac{1}{3}$  and  $\frac{1}{2}$ , respectively. This similarity has been demonstrated in more detail for one area of East Texas by Thiercelin and Plumb (1994b).

If the formation fails under compressive tectonic strain, the maximum principal stress is in the horizontal plane and is therefore  $\sigma_H$ . In the thrust fault regime, the minimum principal stress is the vertical stress (Fig. 3-20):

$$\sigma_H - p \approx N_\phi (\sigma_v - p). \quad (3-59)$$

In this case,  $\sigma_h$  is the intermediate principal stress and is equal to or greater than the vertical stress. Horizontal hydraulic fractures could be achieved.

Thus, the principal stresses can be estimated and ordered by looking at the fault regime. In practice, these considerations must be checked with downhole measurements, as the state of stress may deviate from the expected ordering of stresses because of stress history. These models assume that the fault plane was created under the current tectonic setting; i.e., the normal to the fault plane makes an angle  $(\pi/4 + \phi/2)$  with the direction of the maximum principal stress. Pre-existing faults can be reactivated under a state of stress that differs from the one that created them. A Mohr-Coulomb stability criterion can still be applied, but Eq. 3-42 must be modified to take into consideration that the fault plane orientation was not induced by the current state of stress.

Another stress regime is associated with tensile failure. Tensile failure is sometimes observed downhole, although it appears to contradict the general compressional regime of the earth. This mode of failure simply states that  $\sigma_3 - p = 0$  (by neglecting the tensile strength of the rock) and may be suspected if it is observed from downhole images that the normal to the plane of the preexisting fractures is the direction of minimum stress. This condition can occur in extensional regions with overpressured zones (where the pore pressure tends to be the value of the minimum

stress component) or when the in-situ stress ratio is too large. As the rock is close to a uniaxial state of stress, this regime can occur only in rocks with a compressive strength high enough to avoid normal faulting (as a rule of thumb, the uniaxial compressive stress must be equal to or greater than the effective overburden stress). This condition is achieved for tight gas sandstones in some areas of the Western United States and East Texas.

Failure models also have an important role in providing bounds for the in-situ stress. They represent a limit state above which the rock is unstable in the long term. In the extension regime in particular, it is unlikely that a minimum stress value below the value predicted by the failure model can be obtained.

### 3-5.4. Influence of pore pressure

It is of interest to understand what happens when depleting or injecting into a reservoir. Elastic models with uniaxial strain conditions can be applied with some confidence, as the variation of stresses occurs over a short period of geologic time, although it is always necessary to double check the assumptions because failure models could well be the real physical mechanism, as shown in the following.

If the material behaves elastically, and assuming uniaxial strain conditions, Eq. 3-53 gives

$$d\sigma_h = 2\eta dp. \quad (3-60)$$

The range of  $2\eta$  is approximately between 0.5 and 0.7. Geertsma (1985) demonstrated the applicability of this model to stress decrease during depletion.

A failure model can also be applied. For example, Eq. 3-58 gives

$$d\sigma_h = \frac{N_\phi - 1}{N_\phi} dp. \quad (3-61)$$

If the coefficient of friction is  $30^\circ$ , the coefficient of proportionality is 0.67. As previously, a strong similarity exists between the predictions from the elastic and failure models. To use a failure model, however, requires checking that the effective state of stress satisfies the failure criterion prior to and during the variation of pore pressure. The effective stresses increase during depletion, although the total minimum stress  $\sigma_h$  decreases.

Field data generally support the predictions of these models and show that variation in the minimum stress

ranges from 46% to 80% of the change in pore pressure (Salz, 1977; Breckels and van Eekelen, 1982; Teufel and Rhett, 1991).

### 3-5.5. Influence of temperature

Temperature variation also changes the state of stress (Prats, 1981). Cooling happens during uplift or the injection of a cool fluid. This induces an additional stress component in the horizontal plane, which using the uniaxial strain assumption again is

$$d\sigma = \frac{E\alpha_T}{1-\nu} dT, \quad (3-62)$$

where  $dT$  is the temperature variation and  $\alpha_T$  is the linear thermal expansion coefficient. In this case, an influence of Young's modulus on the state of stress is also obtained. Cooling the formation reduces the normal stress; hence, cool-water injection could lead to tensile fracturing of the formation in the long term.

### 3-5.6. Principal stress direction

Figure 3-20 indicates the expected direction of the minimum stress as a function of the fault regime (Anderson, 1951). In practice, it is observed that at shallow depths the minimum principal stress is the vertical stress; i.e., a hydraulic fracture is most likely to occur in a horizontal plane. The transition between a vertical minimum principal stress and a horizontal minimum principal stress depends on the regional situation. In an extension regime, however, the minimum stress direction can be expected to be always in the horizontal plane, even at shallow depths. This is usually not observed, probably because of the existence of residual stresses and because vertical stress is usually the minimum principal stress at shallow depths. In normally pressured sedimentary basins, the minimum stress is most probably in the horizontal plane at depths greater than 3300 ft (Plumb, 1994b).

Stress rotation may also occur because of topology. However, at great depths, rotation is induced mainly by fault movement. In some situations, overpressurization has been observed to generate a change in the ordering of stress, with the value of the minimum horizontal stress higher than that of the vertical stress. Finally, changes in structural or stratigraphic position can locally affect the stress direction dictated by the

far-field stress and the stress value. An example is the stress field at the top of the Ekofisk formation, where the maximum principal horizontal stress is oriented perpendicular to the structure contour around Ekofisk dome (Teufel and Farrell, 1990).

### 3-5.7. Stress around the wellbore

So far, only the far-field stress components resulting from geologic contributions or reservoir production have been considered. In addition, the magnitude and orientation of the in-situ stress field can be altered locally, as a result of excavation. These induced stresses usually result in large stress concentrations, differing significantly from the original values. Drilling a borehole, for example, distorts the preexisting stress field. The following expressions can be obtained for the stresses around the wellbore, where  $\sigma_x$  and  $\sigma_y$  are principal stresses in the x-y plane,  $p_w$  is the wellbore pressure,  $r_w$  is the wellbore radius, and  $r$  is the distance from the center of the well (Fig. 3-21):

$$\begin{aligned} \sigma_r &= \frac{1}{2}(\sigma_x + \sigma_y) \left\{ 1 - \frac{r_w^2}{r^2} \right\} + \frac{1}{2}(\sigma_x - \sigma_y) \left\{ 1 - \frac{4r_w^2}{r^2} + \frac{3r_w^4}{r^4} \right\} \cos 2\theta + p_w \frac{r_w^2}{r^2} \\ \sigma_\theta &= \frac{1}{2}(\sigma_x + \sigma_y) \left\{ 1 + \frac{r_w^2}{r^2} \right\} - \frac{1}{2}(\sigma_x - \sigma_y) \left\{ 1 + \frac{3r_w^4}{r^4} \right\} \cos 2\theta - p_w \frac{r_w^2}{r^2} \\ \tau_{r\theta} &= -\frac{1}{2}(\sigma_x - \sigma_y) \left\{ 1 + \frac{2r_w^2}{r^2} - \frac{3r_w^4}{r^4} \right\} \sin 2\theta. \end{aligned} \quad (3-63)$$

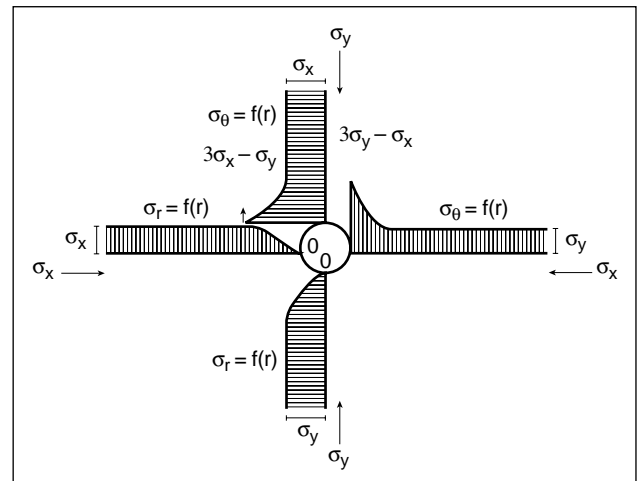


**Figure 3-21.** Stress concentration around a circular hole in the absence of wellbore pressure.



To derive these expressions, it is assumed that the rock remains linear elastic, the borehole is drilled parallel to one of the principal stress directions, and the wellbore fluid pressure  $p_w$  does not penetrate the rock (e.g., because of the presence of mudcake). At the borehole wall (i.e.,  $r = r_w$ ), the following expressions are obtained:

$$\begin{aligned}\sigma_r &= p_w \\ \tau_{r\theta} &= 0 \\ \sigma_\theta &= (\sigma_x + \sigma_y) - 2(\sigma_x - \sigma_y)\cos 2\theta - p_w.\end{aligned}\quad (3-64)$$

Considering only the directions parallel and perpendicular to the minimum stress direction (i.e.,  $\theta = 0$  and  $\theta = \pi/2$ , respectively), these expressions further simplify:

$$(\sigma_\theta)_{\theta=0} = 3\sigma_y - \sigma_x - p_w \quad (3-65)$$

$$(\sigma_\theta)_{\theta=\pi/2} = 3\sigma_x - \sigma_y - p_w. \quad (3-66)$$

As an example, consider the case of 3000-psi wellbore pressure in equilibrium with the pore pressure of the reservoir and values of 3500 psi for  $\sigma_x$  and 5000 psi for  $\sigma_y$ . The equations lead to maximum values for the effective tangential stress ( $\sigma_\theta - p$ ) of 5500 psi in compression ( $\theta = 0^\circ$ ) and 500 psi in tension ( $\theta = 90^\circ$ ). The latter result indicates the possibility for the occurrence of tensile failure in a direction perpendicular to the minimum stress, solely as a result of drilling the borehole.

A hydraulic fracture is induced by increasing the wellbore pressure  $p_w$  up to the point where the effective tangential stress ( $\sigma_\theta - p$ ) becomes equal to  $-T_o$ . If  $\sigma_x = \sigma_h$ , this happens at  $\theta = 90^\circ$  (where the stress concentration induced by the far-field state of stress is minimum), which means that fracture initiates in a direction perpendicular to the minimum horizontal stress direction. Fracture initiation at the breakdown pressure  $p_{if}$  is, therefore, obtained when (Hubbert and Willis, 1957)

$$p_{if} = 3\sigma_h - \sigma_H + T_o - p. \quad (3-67)$$

These induced stresses diminish rapidly to zero away from the wellbore. Consequently, they affect the pressure to induce a fracture, but not the propagation of the fracture away from the wellbore wall.

If the wellbore fluid penetrates the formation, poroelastic effects must be taken into account to calculate the stress concentration around the wellbore. In partic-

ular,  $\sigma_\theta$  at the wellbore becomes a function of time if  $\sigma_x$  is not equal to  $\sigma_y$  (Detournay and Cheng, 1988). The long-time solutions are

$$(\sigma_\theta)_{\theta=0} = 3\sigma_y - \sigma_x - p_w + 2\eta(p_w - p) \quad (3-68)$$

$$(\sigma_\theta)_{\theta=\pi/2} = 3\sigma_x - \sigma_y - p_w + 2\eta(p_w - p). \quad (3-69)$$

If the wellbore fluid pressure is higher than the far-field pore pressure, poroelastic effects increase the stress concentration at the wellbore. The initiation pressure (Haimson and Fairhurst, 1969) is obtained from Eq. 3-69, with  $(\sigma_\theta - p_w) = -T_o$ :

$$p_{if} = \frac{3\sigma_h - \sigma_H + T_o - 2\eta p}{2(1 - \eta)}. \quad (3-70)$$

A typical value of  $\eta$  is 0.25.

These equations are used in Section 3-6.2. Finally, plasticity effects reduce the stress concentration at the wellbore. Particularly in highly plastic rocks, the tangential stress at the wellbore never becomes tensile. In this case, fracture could initiate in shear (Papanastasiou *et al.*, 1995).

### 3-5.8. Stress change from hydraulic fracturing

Two effects are considered in this section. The first one addresses the increase of minimum stress because of the poroelastic effect. During the fracturing process, fracturing fluid leaks into the formation. This leakage induces a pore pressure increase around the fracture that results in dilation of the formation and, therefore, an increase of the minimum stress in this region. For a 2D crack in an infinite sheet, the increase of minimum stress as a function of time is (Detournay and Cheng, 1991)

$$\Delta\sigma_3 = \eta(p_f - p)f(\tau_c), \quad (3-71)$$

where  $p_f$  is the fracturing fluid pressure and  $\tau_c$  is a characteristic time given by

$$\tau_c = \frac{2tkG(1 - \nu)(v_u - v)}{\alpha^2\mu(1 - 2\nu)^2(1 - v_u)L^2}, \quad (3-72)$$

where  $G$  is the shear modulus,  $k$  is the permeability,  $t$  is the time,  $\mu$  is the viscosity, and  $L$  is the fracture half-length.

The function  $f$  varies between 0 and 1 as  $\tau_c$  increases from 0 to infinity. The value of the characteristic time at which poroelastic effects can start to influence the state of stress around the fracture is about  $10^{-3}$ . In reservoir rocks where  $\eta$  is equal to about 0.25, poroelastic effects are important when the net pressure and characteristic time are high. This effect decreases if a high-pressure drop occurs at the fracture face. High-pressure drops happen, for example, when a good fluid-loss control agent is used. Poroelastic effects eventually disappear when injection is stopped and the excess pore pressure dissipates into the formation.

The second effect is the stress increase caused by opening of the fracture. This effect remains if the fracture is held open by proppant (Warpinski and Branagan, 1988; Palmer, 1993). An upper bound for the stress increase once injection has been stopped is the value of the net pressure at shut-in, but in practice, because the in-situ proppant concentration at shut-in is about one-half of its compacted concentration, it could be about 50% of this value. This effect can be significant for short and wide fractures, where crack-tip screenout induces a large net pressure (of the order of 1000 psi) at the end of the job. It has been proposed that this mechanism strengthens weak formations and, therefore, decreases the risk of sanding.

## 3-6. In-situ stress measurement

### 3-6.1. Importance of stress measurement in stimulation

The value of the minimum stress is one of the most important parameters in hydraulic fracturing. At typical reservoir depths, the fracturing pressure is a strong function of the minimum stress (or closure pressure). With some pumping regimes, the value of the net pressure, which is the fracturing pressure minus the closure pressure, could be quite small compared with the closure pressure. The net pressure is the most robust and usually the only parameter that is available for obtaining information on fracture geometry. An error in closure stress measurement can lead to a significant error in the estimation of the net pressure and, consequently, the fracture geometry. Because of the small value of the net pressure compared with the minimum stress, knowledge of the in-situ state of stress at depth also gives insight into the expected treatment pressures.

It is also generally accepted that the degree of fracture containment is determined mainly by the in-situ stress differences between layers, although, as mentioned in the previous section, other mechanisms can play a role in the absence of a meaningful stress contrast. Knowledge of the stress variation between the pay zone and the adjacent layers is therefore essential for predicting the extent that the fracture grows out of the zone.

Fracturing from inclined or horizontal wellbores has also brought new requirements for determination of the far-field in-situ stress because it controls the complex stress field that is generated near the wellbore. The efficiency of a fracturing treatment is a function of wellbore inclination with respect to the principal stress direction and magnitude (Martins *et al.*, 1992a; Pearson *et al.*, 1992).

Finally, the amount of stress confinement influences the rock properties (elasticity, strength and permeability).

Several methods are regularly used in the petroleum industry to estimate the magnitude and orientation of in-situ stress at depth. Some of them rely on field data interpretations, whereas others rely on core measurements. Techniques based on wellbore images and sonic logs are presented in Chapter 4.

### 3-6.2. Micro-hydraulic fracturing techniques

Fracturing techniques are commonly used to measure the minimum stress. The micro-hydraulic fracturing technique is certainly the most reliable technique if conducted properly, although it could be used in conjunction with other methods for added completeness. This technique uses the pressure response obtained during initiation, propagation and closure of a hydraulically induced fracture to accurately determine the state of stress. Because stresses are functions of rock properties, it is quite important to ensure that the test provides a measure that is representative of a given lithology. Small-scale hydraulic fractures are usually required, especially if the measurements will be correlated with log or core information. However, the fracture must be large compared with the wellbore radius to measure the far-field minimum stress component, and a fracture with a size of 5–15 ft is a good compromise. At this scale, a tool that includes a gamma ray sonde is recommended for accurate placement with regard to lithology. Analysis of the sonic and gamma ray logs should be made prior to testing

to decide on the location of the most appropriate lithologies for the tests. It is recommended to select locations that span lithologies with different values of Poisson's ratio and Young's modulus if the objective of the measurement is to establish a complete stress profile (see also Chapter 4).

To perform a micro-hydraulic fracture in an open-hole, the selected test interval is isolated from the surrounding well using a packer arrangement (Fig. 3-22). Fluid is then injected in the interval at a constant flow rate. During injection, the wellbore is pressurized up to the initiation of a tensile fracture. Initiation is usually recognized by a breakdown on the pressure versus time record, hence the name breakdown pressure (Fig. 3-23). In practice, breakdown is not always obtained. Initiation could also occur prior to breakdown. After the initial breakdown, injection should continue until the pressure stabilizes. Injection is then stopped and the pressure allowed to decay. The fracturing fluid is usually a low-viscosity fluid for low-permeability zones or a drilling mud for zones with higher ranges of permeability. Usually less than 100 gal is injected into the formation at flow rates ranging from 0.25 to 25 gal/min. The amount of fluid and the injection rate used during fluid injection are preferably selected to achieve a predetermined fracture size at the end of the test. This approach, however, requires the use of a fracture propagation model to estimate the fracture geometry during propagation and closure.

Several injection/fall-off cycles are performed until repeatable results are obtained (Fig. 3-24; Evans *et al.*, 1989). The most accurate stress measurements are made using downhole shut-off devices, downhole pumps and downhole pressure gauges. A downhole shut-off tool is used to shut in the straddle interval and minimize any wellbore storage effects (Warpinski *et al.*, 1985). This is required because careful monitoring of the shut-in behavior is used to determine the minimum stress. Downhole pumps have the advantage of minimizing wellbore storage during pumping and shut-in (Thiercelin *et al.*, 1993). Low-storage tools enable the effective control of fracture propagation and analysis of the pressure response in great detail.

- Estimating minimum stress

Various techniques are used to estimate the magnitude of the least principal stress. The simplest one is to take the instantaneous shut-in pressure (ISIP) as an approximation of the minimum stress (Fig. 3-23). However, errors of the order of hundreds of psi or

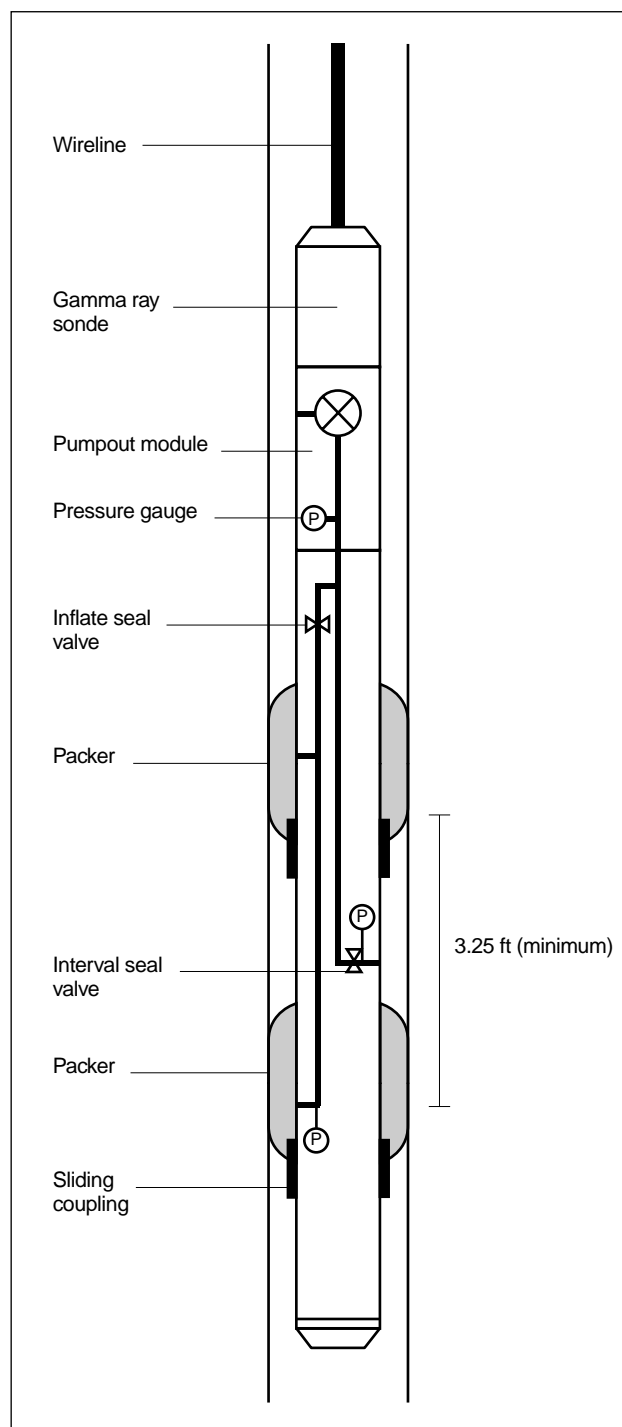


**Figure 3-22.** Wireline stress tool.

more may result when using this approach, especially for zones that develop significant net pressure or in a porous formation. Recently, techniques to determine the closure pressure have replaced the ISIP as a measure of the minimum principal stress. Conceptually, the closure pressure is the pressure at

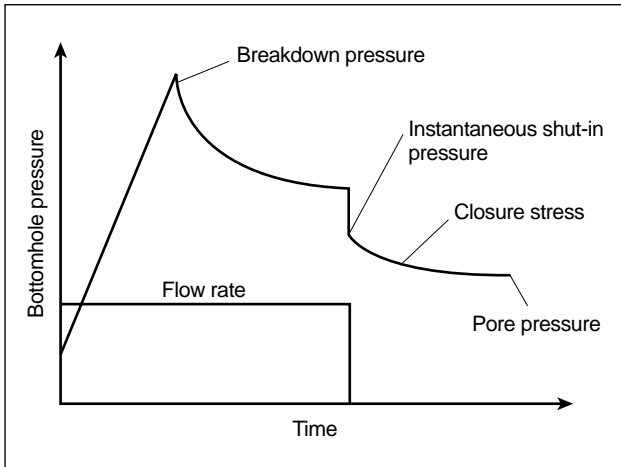


**Figure 3-23.** Downhole pressure during a micro-hydraulic fracturing test.

which the fracture would close completely in the absence of fracture face irregularities (e.g.,  $w_w = 0$  in Eq. 3-36).

In the broadest sense, the techniques involve plotting the pressure decline after shut-in on specialized plots that accentuate a slope change when closure occurs. The pressure decline, after creating an unproped fracture, can exhibit different and identifiable behaviors, as discussed in Chapter 9. These pressure behaviors are the result of various events that include height growth closure, fracture extension after shut-in, fracture recession, transition through closure pressure, consolidation of filter-cake and face irregularities, reservoir linear flow and pseudoradial flow. It is generally difficult to analyze pressure decline because the transitional pressure response through most of these various

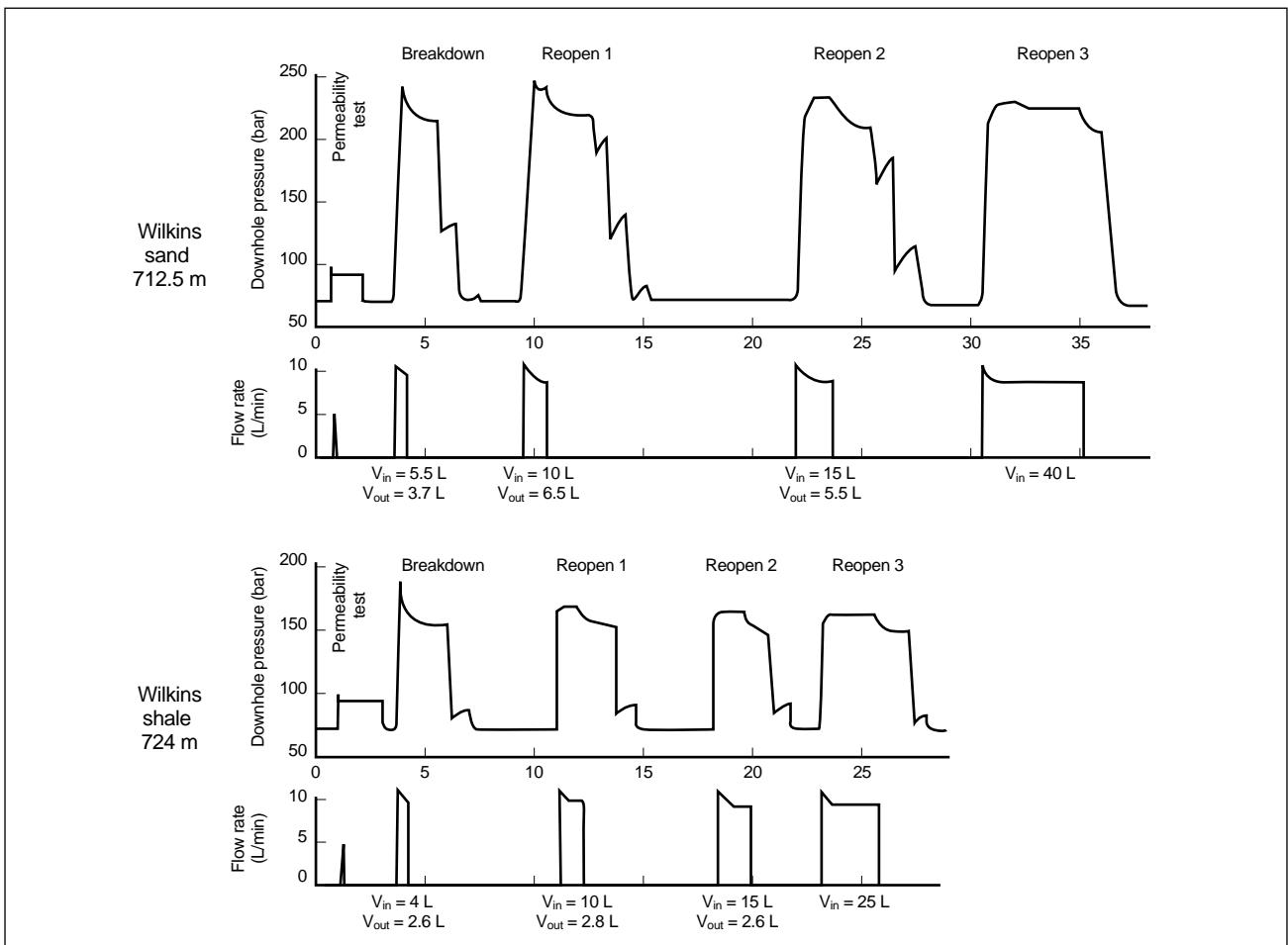


**Figure 3-24.** Pressure and injection rate record obtained into a sand and immediately underlying shale (Evans et al., 1989).

behaviors can be featureless. Therefore, lacking a robust, comprehensive prediction model for these behaviors, no combination of specialized plots provides a reliable tool for extracting closure pressure from decline data. The exception appears to be specialized plots for closure governed by reservoir-controlled fluid loss. These plots can provide detectable slope changes during several of the transition periods. In permeable formations, where the fracturing fluid leaks off from the fracture face, closure pressure is inferred when the pressure decline deviates from a linear dependence on the square root of shut-in time or the square root of the sum of shut-in time and injection time  $t_i$  (Fig. 3-25; Nolte, 1982, 1988a).

An improved representation of fluid loss is provided by the  $G$ -plot, which is discussed in Section 9-5. Castillo (1987) introduced use of the  $G$ -plot for closure inference along with specialized functions for the pressure (i.e., linear pressure for wall cake-controlled fluid loss, square root for filtrate-controlled fluid loss and logarithm if the resistance of the movement of the reservoir fluid controls fluid loss). Additional examples of the  $G$ -plot-based method are given by Shlyapobersky *et al.* (1988b). Although the  $G$ -plot provides a firmer foundation than the square-root plot, its derivation does not consider the well-established additional fracture extension and recession after shut-in (see Section 9-5).

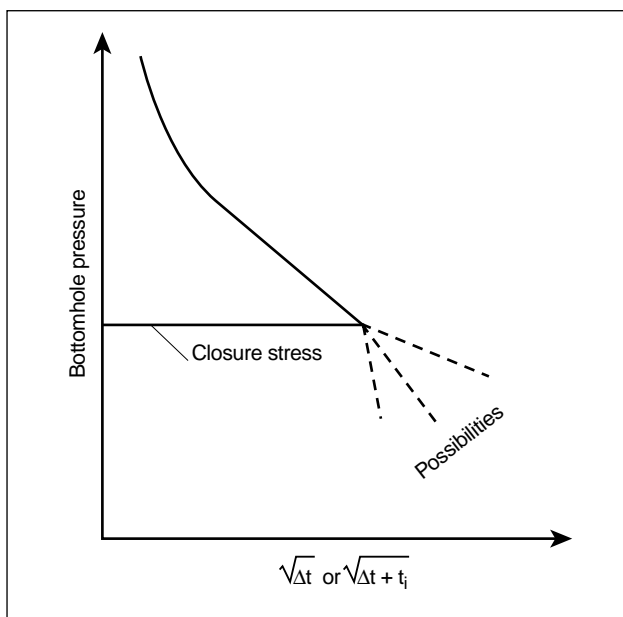


**Figure 3-25.** Pressure decline analysis (Nolte, 1982, 1988a).

To overcome the ambiguity of decline analysis, the pump-in/flowback (PI/FB) test was developed (Nolte, 1979). This test, illustrated in Fig. 3-26, provides a robust, unique signature when correctly executed. The flowback period essentially involves flowing fluid out of the fracture at a constant rate, usually between one-sixth and one-quarter of the injection rate. The initial interpretation assumed that closure occurred at the inflection point above the intersection point shown on Fig. 3-26b. Subsequently, Shlyapobersky *et al.* (1988b) suggested that closure occurred at the onset of the linear response, which is below the intersection point shown in Fig. 3-26b. Their basis was that linear response corresponds to wellbore storage only (i.e., when the fracture is closed). Plahn *et al.* (1997) pro-

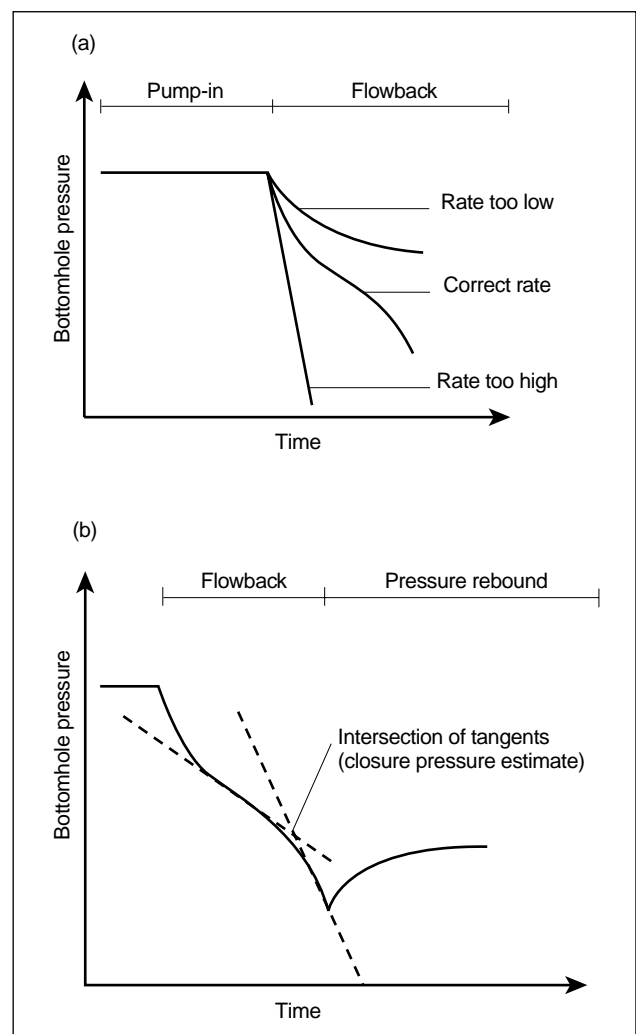


**Figure 3-26.** Flowback and pressure rebound: (a) influence of flowback rate on pressure response (Nolte, 1982, 1988a) and (b) recommended approach for closure pressure estimation (Plahn *et al.*, 1997).

vided a study of the PI/FB test using a comprehensive model that couples the wellbore, fracture growth and recession, and the reservoir. They recommended the intersection of tangents illustrated on Fig. 3-26b and demonstrated that this was precisely the case for low fluid loss and an ideal frictionless fluid; i.e., the curved parts of the pressure response during flowback result from pressure gradients that develop as a result of fluid flow within the fracture either to the fracture tip or to the wellbore.

The PI/FB test has another feature, the pressure rebound that is observed once the well has been shut in to end the flowback period. During rebound, the fluid in the fracture flows into the well until equalization between the well pressure and the pressure within the fracture occurs. Nolte (1982) suggested that the maximum pressure value of the rebound was a lower bound for the closure pressure (i.e., the pressure equilibrated into the closed but conductive fracture).

Plahn *et al.* (1997) also investigated the rebound of the PI/FB test. They found that generally most of the fracture remained open during flowback and the initial rebound phase and that the characterizing behavior resulted from pinching of the fracture width at the wellbore because of the reversed flow. After shut-in of the reversed flow, reopening of the pinched fracture permitted pressure equalization between the wellbore and the fracture (i.e., pressure rebound). They concluded that even when the flowback phase is continued to below the second straight dashed line on Fig. 3-26b and is dominated by wellbore storage, the rebound pressure can

exceed the closure pressure; however, for cases with meaningful fluid loss to the formation, the rebound pressure is generally below the closure pressure. For the preferred arrangement of straddle packers and downhole shut-in, wellbore storage becomes small and the second straight line approaches a vertical line. In low-permeability formations, the pressure rebound tends toward the closure pressure (Fig. 3-27) (Thiercelin *et al.*, 1994). The observation of pressure rebound is also a quality control test as it demonstrates that a fracture was created without bypassing the packers.

A companion test to estimate the closure pressure is the step rate test (Fig. 3-28; see the Appendix to Chapter 9). During a step rate test, the injection is increased by steps up to the point that the pressure response indicates that a fracture is extending (i.e., the extension pressure). The indication is a slope change, with the decrease in  $dp/dq$  reflecting

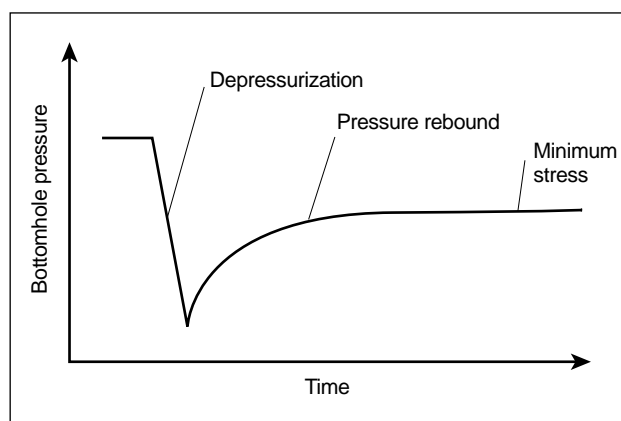


**Figure 3-27.** Pressure rebound in a low-permeability formation.

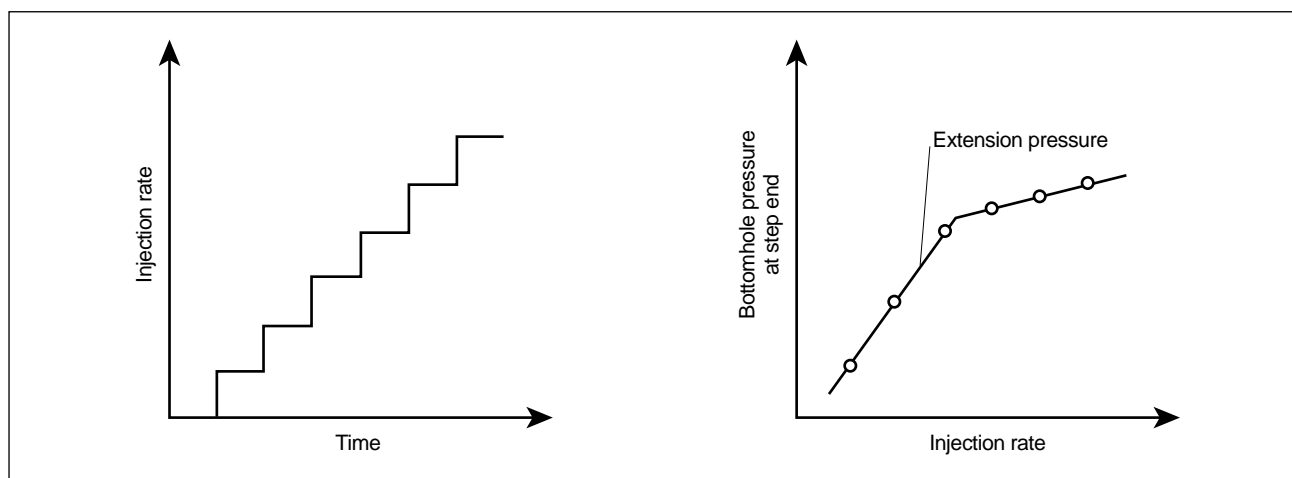


**Figure 3-28.** Step rate test (Nolte, 1982, 1988a).

increased injectivity as the extending fracture exposes an increasing fluid-loss area and storage volume. Successful execution of the test ensures that a fracture was created, which is a necessary quality control for permeable formations where the pump-in/shut-in response for a nonfractured reservoir can be mistaken for fracture propagation and closure. Obviously, a clear indication that a fracture was created is a necessary condition for closure pressure determination. The extension pressure also provides an upper bound on the closure pressure to assist in planning and analyzing subsequent tests. The step rate and rebound tests are discussed again in Section 3-6.3.

In low-permeability formations, Lee and Haimson (1989) proposed using statistical analysis procedures with an exponential pressure-time decay method.

Modeling shows that the stress estimated by fracturing can be in error by  $\eta(p_f - p)$  because of poroelastic effects (Detournay and Cheng, 1991), where  $p_f$  is the fracture propagation pressure. An estimation of the characteristic time of the process allows estimating whether these poroelastic effects are important. In practice, they are negligible in low-permeability formations (i.e., shales) but may become significant in millidarcy-permeability formations unless a high flow rate and/or high-viscosity fluids are used (Boone *et al.*, 1991) or fluid-loss control agents are added.

Finally, inversion of the pressure response (Piggott *et al.*, 1992) is probably the most powerful technique in situations where the fracture geometry is not too complex and the fluid and rock are well characterized. This method uses a fracture propagation model to invert the pressure response obtained during propagation and closure of the fracture. To be successful, the model must use assumptions on fracture propagation and closure that represent fairly well the governing in-situ conditions. For example, radial geometry is usually appropriate for a microfracturing interpretation. The inversion of microhydraulic fracturing data is, however, more complex if conducted for an inclined or horizontal borehole, in which case planar fractures are an exception rather than a rule.

- Estimating maximum horizontal stress

Attempts have also been made to determine the maximum horizontal stress component from the fracture initiation pressure. This stress measurement

is less accurate because it depends strongly on assumed rock behavior near the wellbore. In addition, the breakdown pressure magnitude is highly dependent on the pressurization rate. For example, the initiation pressure depends upon whether the formation behaves elastically or inelastically. Initiation pressure depends also on the diffusion of fracturing fluid into the formation, leading to a dependence on the pressurization rate (Haimson and Zhongliang, 1991). However, bounds on the initiation pressure value can be obtained (Detournay and Cheng, 1992) using Eqs. 3-67 and 3-70.

The subsequent analysis presented in this chapter assumes that the material behaves in a linearly elastic manner and that the pressurization rate is low enough to use a long-time solution for the prediction of initiation pressure. It is also assumed that the wellbore is vertical, the overburden pressure is a principal stress, and the fracture initiates vertically. If the fluid is nonpenetrating, the initiation pressure is given by Eq. 3-67.

For the injection cycles that follow the first injection cycle, the initiation pressure corresponds to reopening the fracture, and so  $T_o$  in Eq. 3-67 is effectively equal to zero. As  $\sigma_h$  was determined from the closure, this formula can be used to estimate the intermediate stress  $\sigma_H$ .

Equation 3-70 applies when the fracture fluid diffuses in the rock. This is the preferred equation for predicting or interpreting the initiation pressure for low-pressurization rates. For low-porosity rocks (such as hard limestones),  $\eta = 0$  and the value of the initiation pressure is

$$p_{if} = \frac{3\sigma_h - \sigma_H + T_o}{2} \quad (3-73)$$

if the fracturing fluid fully penetrates the microcracks. In particular, if  $\sigma_h + T_o < \sigma_H$ , the initiation pressure is less than the minimum stress. A breakdown pressure may not appear, and care must be taken to differentiate between the initiation pressure and the maximum pressure. If  $\eta$  is equal to 0.5, Eq. 3-70 gives a prediction similar to Eq. 3-67. For reservoir rocks,  $\eta$  is equal to about 0.25. It can be seen from these equations that using a nonpenetrating fluid increases the breakdown pressure, and if the fluid penetrates preexisting microcracks, it is easier to break nonporous formations (where  $\eta = 0$ ) than porous formations (for rocks exhibiting the same tensile strength).

However, the estimate of  $\sigma_H$  using Eq. 3-67 or Eq. 3-70 could be quite poor, especially if the assumption of linear isotropic elasticity does not apply or the wellbore is not aligned with a principal stress direction.

### 3-6.3. Fracture calibration techniques

Whereas the micro-hydraulic fracturing method is intended for measuring almost at a point in the formation, large-scale fracture analysis requires characterizing the “average” stress over larger sections (e.g., 30 ft). The average stress is termed closure pressure.

For this purpose, fluid volumes greater than that for the microfracture are used to determine closure pressure, especially when a precise stress profile is not available. Consequently, the fracture must be large enough for making the measurement of closure pressure on a rock volume that is representative of the complete zone. The methods used for determining the closure pressure with these larger fractures are similar to those for micro-hydraulic fracturing. However, the closure pressure determination becomes more complex, with the possibility of multiple closures resulting from stress variations within the reservoir. In particular, shut-in decline tests could be quite difficult to interpret and a combination of the step rate and flow-back tests is recommended. The procedures also differ slightly because of the larger amounts of fluid involved and the resulting higher net pressure. With these larger fractures, an apparent breakdown pressure could be observed but must not be interpreted for maximum horizontal stress determination, even in an openhole situation. One variation presented by Wright *et al.* (1995) consists of a multiple, discrete injection during the shut-in decline phase. Large-scale tests are also discussed in Sidebar 9A.

### 3-6.4. Laboratory techniques

- Anelastic strain recovery

The anelastic strain recovery (ASR) method requires access to oriented core samples. The method is based on the relaxation that a rock core undergoes following its physical detachment from the stressed rock mass (Teufel, 1983). The recovered strains are measured in various directions, and the principal strain axes are determined. These principal directions are assumed to be the same as the principal

axes for the in-situ stresses. The recovered strains generally include an instantaneous, elastic part that is impossible to detect (because it occurs as soon as the drill bit passes the particular depth) and a time-dependent, inelastic component. A typical ASR curve is shown in Fig. 3-29.

The ASR method relies on strain measurements made on cores retrieved from their downhole environment by conventional procedures. Therefore, strains corresponding to the initial elastic recovery, as well as part of the inelastic portion, are lost because of the finite time it takes to bring the oriented core to the surface. The interpretation requires an assumption regarding the relationship existing between the time-dependent strain and the total strain. The suggestion of direct proportionality made by Voight (1968) is typically employed. The relative magnitude of strain recovery in the different directions is used as an indication of the relative stress magnitudes, and the absolute magnitudes are related to the known overburden stress.

- Differential strain curve analysis (DSCA)

Differential strain curve analysis (DSCA) relies on strain relaxation as an imprint of the stress history and considers the consequence of this relaxation (Siegfried and Simmons, 1978; Strickland and Ren, 1980). This approach assumes that the density and distribution of the resulting microfracturing are directly proportional to the stress reduction the core

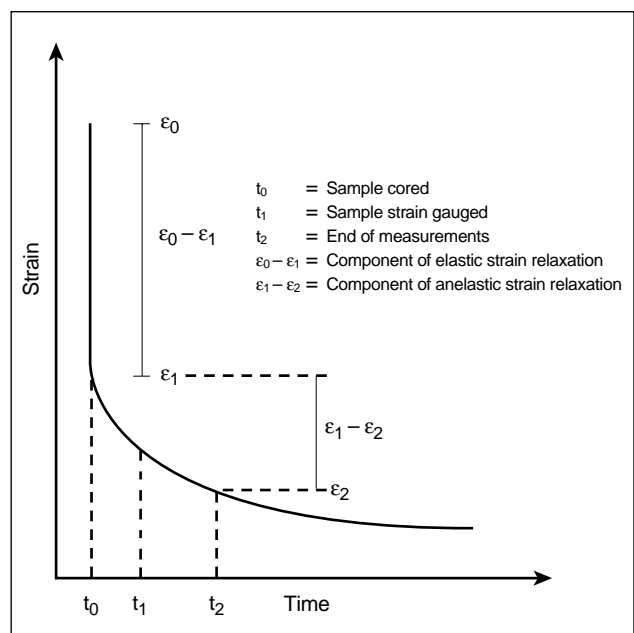


Figure 3-29. ASR curve.



sustained. Hence, if the microcrack-distribution ellipsoid could be delineated, it may reveal the pre-existing stress condition. The existence of pervading microdiscontinuities plays an important role in the beginning of the loading cycle, as it introduces a “softening” element. Consequently, accurate strain measurements in various directions should make possible anisotropic characterization of the microcracking, which can be related to measurement of the preexisting stress state. A typical DSCA curve is shown in Fig. 3-30.

The results of DSCA yield the orientation of the three principal stresses. The stress magnitudes can only be indirectly calculated by knowing the elastic constants and the overburden as for ASR. To determine the in-situ stress state, only six strain measurements are theoretically required on any oriented

core. However, as can be seen from Fig. 3-31, standard tests are run using twice as many strain gauges. This duplication allows several combinations of solutions; hence, statistical data analysis methods can be used. The resulting standard deviation is a good measure of the confidence possible in the results.

Although ASR and DSCA seem to be based on the same fundamental phenomenon, differences may occur in the results. This is usually the case when a particular rock formation has been subjected during its geologic history to a stress field large enough to induce a microcracking pattern that overshadows the one resulting from the present unloading. DSCA reflects the sum of whatever happened in the stress history of the rock, whereas ASR is limited to its present state of stress.

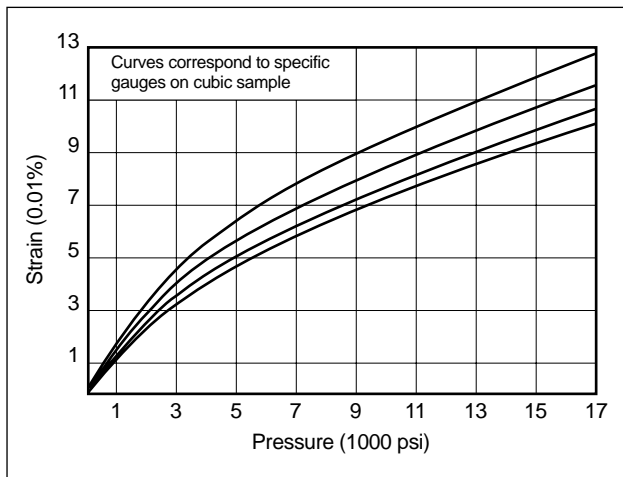


**Figure 3-30.** DSCA plots.

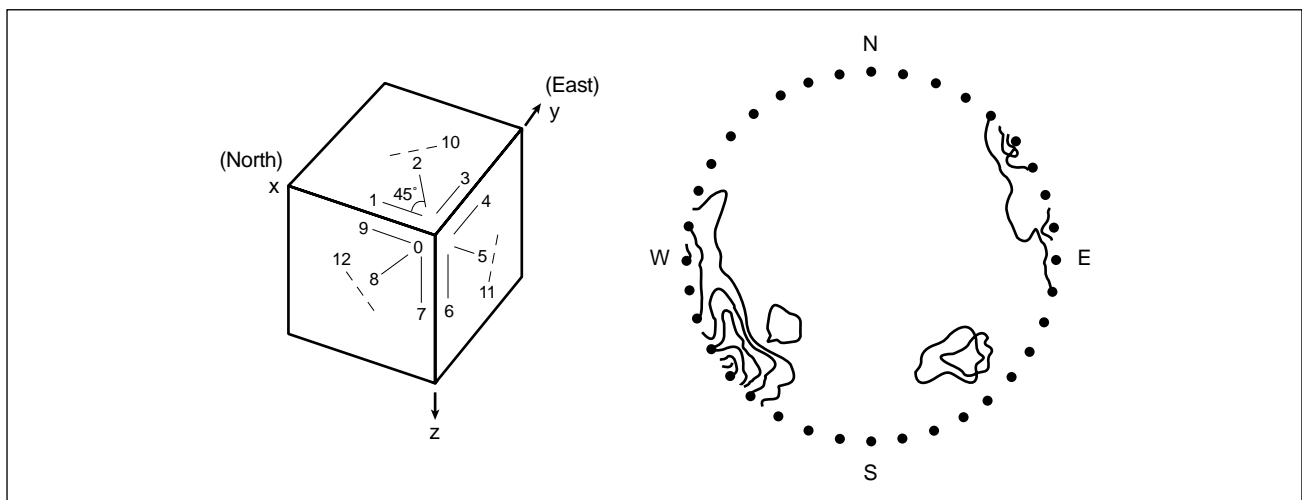


**Figure 3-31.** Gauge pattern and typical results plotted on a polar stereonet for DSCA.

# Formation Characterization: Well Logs

*Jean Desroches, Schlumberger Dowell*  
*Tom Bratton, Schlumberger Sugar Land Product Center*

## 4-1. Introduction

The purpose of this chapter is to describe, strictly in the context of reservoir stimulation, the use of geophysical information (commonly referred to as logs) to obtain a description of the formation affected by a stimulation treatment. The entire process of classic formation evaluation for the determination of hydrocarbon reserves is out of the scope of this volume. A fundamental difference between these two processes is that all properties are required not only for the hydrocarbon-bearing formations (pay zones) but also for the adjacent formations (bounding layers).

The output of the process described in this chapter is a model of the formation to be stimulated. The model consists of a series of planar, parallel layers or beds, with known properties for each layer. Each property in a layer is either a constant, averaged property or a linear function of depth (e.g., pore pressure) (Fig. 4-1).

To construct the model, estimates first must be obtained of the relevant properties in each layer. These properties are in two broad classes: properties relevant to the diffusion of fluid in the formation and properties relevant to the deformation of the forma-

tion. Sections 4-4 and 4-5, respectively, discuss the various means of determining these properties.

All that is then necessary is to transform the data gathered into a consistent model. The first step for this process is to fill any data gaps by relying on geologic information. Each depositional basin has its own “style,” characterized by unique properties. Moreover, the succession of layers is not arbitrary, but obeys worldwide a logic that is captured by the notion of sequence (e.g., sand/shale sequence, limestone/marl sequence) (Wagoner *et al.*, 1930; Friedman and Sanders, 1978). Combining information characterizing the basin with information from the relevant sequence makes it possible to estimate missing data or interpolate between data points with an educated guess or correlation. This process is particularly crucial for the determination of lithology, pore pressure and stress profiles. The need for a model based on a basin and field perspective is emphasized throughout this chapter. This approach also clearly indicates the need for bringing geological expertise into the picture.

Once a complete description versus depth is achieved, the boundaries of the layers to be considered are defined (i.e., zoning), which is also guided by geologic information. Section 4-6 discusses the zoning process.

An important aspect stressed throughout this chapter is the calibration of geophysical data. Apart from the most basic properties, such as porosity and water saturation, geophysical information requires calibration with laboratory data. Again, the notion of basin and sequence is useful: the calibration procedure is usually portable within the same sequence in the same basin. In other words, if no core samples have been tested for a particular well, results from other cores taken in the same formation and basin may be used, albeit with some caution.

In this chapter, it is assumed that the geophysical information comes from the well to be stimulated. The porting of geophysical information from one well to another is not addressed.

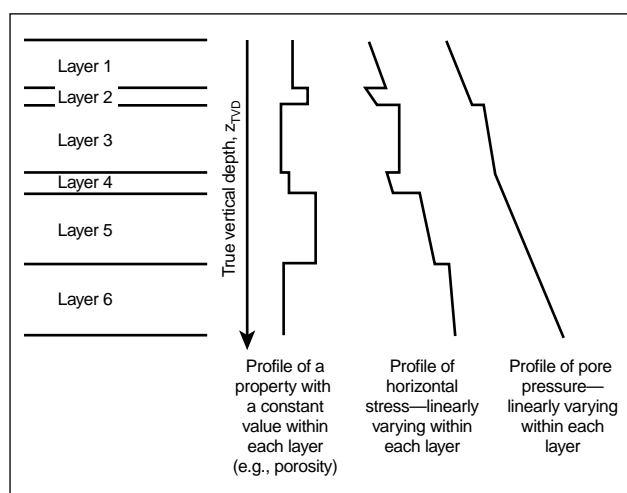


**Figure 4-1.** Model of the earth in the vicinity of the formation to be stimulated.

## 4-2. Depth

The several types of “depths” used in the oil field impact the building of the final representation of the reservoir to be stimulated. True vertical depth (TVD) is, as its name indicates, the depth measured along the vertical. Given a zero reference point, it is unique. Measured depth (MD) is the distance measured along the wellbore trajectory (which is never exactly vertical). It is not unique, because it depends on the way it is measured. MD during drilling is measured by the length of pipe that has gone into the ground. MD at wireline logging time is measured by the length of cable that has gone into the ground. Finally, logging-while-drilling (LWD) data are logged versus time, which complicates the issue because several measurements can be assigned to the same depth.

Special care must be taken to ensure that all log measurements are referenced to a single measured depth. The reference depth is usually from a gamma ray log or that of an imaging tool for complex reservoirs. However, the conversion of MD to TVD must be reliable because MD is required to compute the fluid friction and fluid displacement, but TVD is required to design the treatment placement. For example, fracture height is related to properties in TVD, not in MD. At any point along the wellbore trajectory, an increase of the true vertical depth  $\Delta TVD$  is related to an increase of measured depth  $\Delta MD$  by

$$\Delta TVD = \Delta MD \cos \theta, \quad (4-1)$$

where  $\theta$  is the deviation of the well from the vertical at that point. Integration of Eq. 4-1 along the wellbore trajectory allows the conversion between MD and TVD.

In the context of this chapter, formation beds have a constant thickness, but their boundaries may make an angle  $\delta$  with the horizontal. The angle  $\delta$  is called the dip of the formation. It is convenient to present logs versus true bed thickness (TBT) as an imaginary line perpendicular to the bed boundaries (Fig. 4-2). This presentation is useful for comparing logs acquired in deviated wells in a dipping reservoir. An increase of the true bed thickness  $\Delta TBT$  is related to an increase of measured depth by

$$\Delta TBT = \frac{\Delta MD [\cos(\theta + \delta)]}{\cos \delta}. \quad (4-2)$$

Layer thicknesses, therefore, relate to properties in TBT. For horizontal beds, TVD and TBT coincide. A schematic of the effect of a deviated well path on the presentation of a log in MD, TVD and TBT is presented in Fig. 4-2.

## 4-3. Temperature

The temperature of the formation is critical for the performance of both matrix stimulation products and hydraulic fracturing fluids.

The mud temperature acquired at wireline logging time is typically used for an estimate of the formation

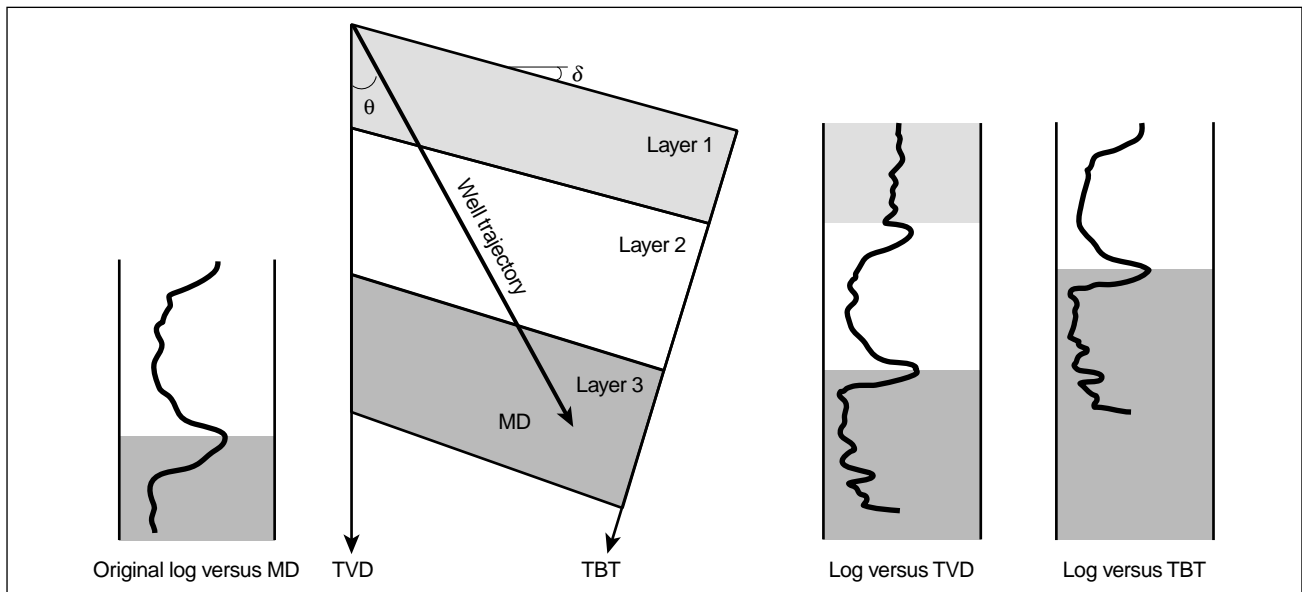


**Figure 4-2.** The effect of wellbore deviation and dipping beds on the presentation of logs.

temperature. It yields only a lower bound of the formation temperature and can underestimate the formation temperature by as much as 30°F [15°C]. Wireline temperature is, however, the only continuous temperature measurement.

Discrete point measurements of temperature can be obtained during fluid sampling with formation testers. The temperature of the sampled fluid is continuously monitored during sampling to yield the most accurate temperature measurement currently available.

Another good estimate of reservoir temperature is the bottomhole temperature recorded by a slickline-conveyed gauge after perforation and initial flow of the formation.

## 4-4. Properties related to the diffusion of fluids

The diffusion of fluids is governed by porosity, permeability, pore pressure and the fluid types in the formation. This section introduces means for determining these parameters from logs. Lithology and saturation are discussed because that information is used to infer permeability, but fluid viscosity and compressibility cannot be obtained from logs.

### 4-4.1. Porosity

Porosity is the fraction of the total formation volume that is not occupied by solid rock (i.e., filled with formation fluid). The common symbol for porosity is  $\phi$  and the measurement unit is either the volume fraction (range from 0 to 1) or percent (from 0 to 100). The porosity of formations can vary from nearly zero for evaporites to up to 40% for unconsolidated formations (e.g., shales or sandstones) and even higher for chalk or diatomite.

Porosity is a cornerstone of formation analysis. It is measured through several geophysical methods, for which the principles and assumptions of each are presented. The conveyance method of the measuring tool is irrelevant: the principles apply to both wireline and LWD tools. The subsequent processing of the data is not addressed in detail in this chapter (see Quirein *et al.*, 1986).

Porosity is classically divided into two groups:

- Primary porosity consists of the original space between the grains that form the rock matrix or the

space present within sedimentary particles at the time of deposition.

- Secondary porosity consists of the space that was created by tectonic forces creating microcracks and water dissolution creating cavities.

The distinction between primary and secondary porosity is important insofar that porosity is used in many correlations to develop a first estimate of other properties (e.g., rock strength or permeability). The correlations rely mostly on the primary porosity, not the secondary porosity.

Another important distinction is that of the total porosity  $\phi_{total}$  and effective porosity  $\phi_{eff}$ . The total porosity is the volume not occupied by solid rock. However, part of the volume of total porosity is occupied by fluid that cannot move (i.e., bound water). The effective porosity is the volume occupied by moveable fluids, and it is the porosity of interest for most oilfield applications. A notable exception is the use of  $\phi_{total}$  for all reservoir calculations involving transient flow.

A final concern is that no open- or cased hole log measures porosity directly. Rather, a property related to porosity is what is measured. This is why a combination of porosity measurements is preferred for estimating  $\phi_{eff}$ . Which measurements are used varies depending on the lithologic sequence and possibly the geologic province.

- Porosity from density

Density tools measure the electron density of a formation, which is extremely close to its bulk density  $\rho_b$  (Tittman and Wahl, 1965). Density is a shallow measurement (i.e., the depth of investigation is typically 0.5 ft), and the volume of rock sampled is usually within the flushed zone (i.e., the zone in the vicinity of the wellbore where the formation fluids have been displaced by mud filtrate).

If the density of the matrix components  $\rho_{ma}$  and that of the pore fluid  $\rho_f$  are known, the total porosity from density can be found by volume balance:

$$\phi_D = \frac{\rho_{ma} - \rho_b}{\rho_{ma} - \rho_f}, \quad (4-3)$$

where  $\rho_{ma}$  is determined from the lithology and  $\rho_f$  is taken as that of the mud filtrate, which is obtained from charts as a function of temperature, pressure and salinity. If there is gas present,  $\phi_D$  overestimates the total porosity.

- Porosity from neutron

Neutron tools measure an index of how much hydrogen is present in the formation (Allen *et al.*, 1967). It is also a shallow measurement (i.e., the depth of investigation is typically 1 ft). If no hydrogen is in the rock matrix and the hydrogen index of the fluid is known, the neutron porosity  $\phi_N$  obtains a measure of the total porosity.

Water and liquid hydrocarbons have similar hydrogen indices; therefore,  $\phi_N$  is insensitive to the presence of oil in the sampled volume. However, if gas is present,  $\phi_N$  underestimates the total porosity.

The deviation of  $\phi_N$  and that of  $\phi_D$  from the total porosity tend to be in opposite directions. One example, mentioned previously, is their opposite behavior in the presence of gas. A simple average of  $\phi_N$  and  $\phi_D$  yields a good estimate of the effective porosity:

$$\phi_{eff} \equiv \frac{1}{2}(\phi_N + \phi_D). \quad (4-4)$$

- Porosity from sonic

The presence of pore fluid increases the rigidity of the rock over the case where porosity is truly empty (i.e., “moon dry samples”). Moreover, most of the attenuation of the sonic waves in a porous formation comes from the fluid (Biot, 1956b, 1956c). If the elastic properties of the solid and the fluid are known, and therefore the traveltimes in these media, an estimate of the total porosity can be computed:

$$\phi_s = A \frac{\Delta t - \Delta t_{ma}}{\Delta t_f - \Delta t_{ma}}, \quad (4-5)$$

where  $A$  is a constant and  $\Delta t$  denotes the measured transit time of a sonic wave in the formation. The transit time in the matrix  $\Delta t_{ma}$  is known from the lithology. Because sonic is a shallow measurement (i.e., the depth of investigation is typically 1 ft), the fluid in the pore space is usually approximated by the mud filtrate, the properties of which are known functions of the temperature, pressure and salinity. However, the sonic porosity  $\phi_s$  is a strong function of the properties of the fluid in the pore space. Therefore, if the fluid in the sampled pore space contains hydrocarbons,  $\phi_s$  can deviate significantly from the total porosity.

The value of  $\phi_s$  is of particular interest because it is sensitive primarily to the primary porosity, not to the secondary porosity.

- Porosity from nuclear magnetic resonance

Nuclear magnetic resonance (NMR) tools measure the relaxation time of protons. The porosity measured by NMR tools is similar to  $\phi_N$  but is influenced primarily by moveable fluids.

Extracting porosity from NMR measurements requires complex processing. However, NMR-measured porosity has two major advantages. First, because it is influenced primarily by moveable fluids, it is extremely close to  $\phi_{eff}$ , and second, it yields excellent estimates of porosity in shaly (i.e., clay-bearing) formations, which are typically challenging for estimating porosity (Minh *et al.*, 1998).

- Porosity from resistivity

Porosity can also be estimated from resistivity measurements. If the resistivity of the rock matrix is assumed to be infinite compared with that of the fluid, the conductivity of the formation is proportional to the porosity.

The formation factor  $F$  is introduced as a ratio:

$$F = \frac{R_o}{R_w}, \quad (4-6)$$

where  $R_o$  is the resistivity of the formation 100% saturated with brine of resistivity  $R_w$ .

Archie (1942) postulated that the formation factor is related to the total porosity by the relation

$$F = \frac{a}{\phi^m}, \quad (4-7)$$

where  $a$  and  $m$  are constants depending on the type of formation. For example,  $a = 0.62$  and  $m = 2.15$  for clean sandstones.

Therefore, if  $R_w$  is known (e.g., from water “catalogs,” samples or spontaneous potential [SP] measurements), an estimate of the total porosity of the formation can be obtained by equating Eqs. 4-6 and 4-7:

$$\phi = \left[ \frac{aR_w}{R_o} \right]^{1/m}. \quad (4-8)$$

This technique is not recommended, because it is greatly affected by the fluid saturation and conductive minerals in the matrix.

- Final estimate of porosity

As mentioned previously, the best estimate of porosity is obtained from a combination of logs, using synergistic processing that accounts for the

response of each tool and is tailored to the geologic environment. If such a processed porosity estimate is not available, the simple average of  $\phi_D$  and  $\phi_N$  in Eq. 4-4 is a good first-order estimate of  $\phi_{eff}$  in noncomplex environments, and the porosity from NMR yields a good estimate in more complex environments.

#### 4-4.2. Lithology and saturation

Lithology and saturation are primary inputs for designing matrix acidizing treatments. Lithology is also part of the more general information that must be considered to build a stress model (see Section 4-5.2). For hydraulic fracturing, saturation is used to estimate the compressibility of the formation fluid for computing the compressibility-controlled leakoff.

- Saturation

Water saturation  $S_w$  is the fraction of the pore volume occupied by water. By definition,  $1 - S_w$  is the fraction of the pore volume occupied by hydrocarbons. Also of interest is the irreducible water saturation  $S_{wi}$ , which is the fraction of the pore volume occupied by water bound to the formation.

Special attention is devoted in formation evaluation to both porosity and saturation because their product defines the volume of hydrocarbons in the reservoir. Similarly for reservoir stimulation, these are important quantities because they indirectly govern the flow of water-base fluids in a porous medium filled with both water and hydrocarbons. The relative permeability to water is linked to the saturation (see Section 4-4.3). The total compressibility of the formation fluids, which is used for the determination of leakoff during hydraulic fracturing treatments, is also computed using the saturation.

The value of  $S_w$  is obtained mainly through resistivity measurements. In a clean formation (i.e., a formation without shales or other conductive minerals), all the conductivity of the formation is associated with the brine in the pore space. Conductivity is the reciprocal of resistivity.

For the true resistivity of the formation  $R_t$ , which is beyond the disturbances associated with the wellbore, Archie (1942) derived experimentally that

$$R_t = \frac{R_w A}{\phi^m S_w^n}, \quad (4-9)$$

where  $A$ ,  $m$  and  $n$  are constants that are functions of the formation.

Because resistivity is usually measured at different depths of investigation, it is possible to measure both the resistivity of the flushed zone  $R_{xo}$ , where all movable fluid has been displaced from the formation by mud filtrate, and the resistivity of the virgin formation  $R_t$ , far from the wellbore. The following expression is thus useful because it is independent of the porosity:

$$S_w = \left( \frac{R_{xo}/R_t}{R_{mf}/R_w} \right)^\alpha, \quad (4-10)$$

where  $R_{mf}$  is the known resistivity of the mud filtrate and  $\alpha$  is typically assigned a value of  $\frac{2}{3}$ .  $R_w$  can be determined from water catalogs, samples or SP measurements.

If conductive minerals (e.g., clay minerals) are in the formation, their effect can be accounted for by several weighted-average techniques, especially for shaly formations (Poupon *et al.*, 1970). For complex cases, the best estimate of  $S_w$  is determined by lithological analysis, as discussed in the following.

- Lithology

The goal of a lithological analysis is to obtain a volumetric distribution of the minerals and fluids in the formation as a function of depth. The concept is first explained in this section with the example analysis of a sand/shale sequence. The concept is then generalized to any kind of formation.

Historically, much work was devoted to sand/shale sequences (e.g., 40 papers in *Shaly Sands*, 1982). The simplest form of lithological analysis in such formations is a shaliness indicator—i.e., an indicator of the volumetric ratio of clay minerals to clean sand.

The crudest shaliness indicator is based on gamma ray measurement. If all natural radioactivity in a sand/shale sequence is assumed to come from clay minerals, high gamma ray values (>90 API units) indicate a shale (i.e., almost exclusively clay minerals), low gamma ray values (<20 API units) indicate a clean sandstone, and values in between indicate a mixture of clay and sand.

This scale can be further refined by introducing a simple response equation of a gamma ray tool. For example,

$$GR_{API} = 15[K_2O]. \quad (4-11)$$

This linear equation relates quantitatively the gamma ray count to the concentration of potassium oxide ( $K_2O$ ) in percent. For a simple mineralogical model, such as quartz and a potassium-bearing clay mineral, the ratio of quartz to clay can be determined with the help of this equation.

Tools based on different physical principles are sensitive to different combinations of atoms or minerals. Each tool response  $TR$  can be characterized by an equation, not necessarily as simple as Eq. 4-11, but which can always be cast in a form involving the volumetric fraction of  $n$  minerals and at least one fluid volumetric fraction  $V_f$ :

$$TR = f(V_{mineral}^1, V_{mineral}^2, \dots, V_{mineral}^n, V_f), \quad (4-12)$$

where  $V_{mineral}^i$  is the volumetric fraction of mineral  $i$ . The equations can be linear or nonlinear. Each tool output yields one equation similar to Eq. 4-12 with the volume fractions of  $n$  minerals and the formation fluids to form a system of usually nonlinear equations solved on a depth level by depth level basis (usually every 6 in.) for the various volume fractions (Quirein *et al.*, 1986).

Obviously, assumptions must be made about which minerals are in the formation. First, more minerals than there are equations cannot be solved for, so the smaller the number of logs, the more limited the number of minerals. Second, no unique set of minerals explains the response of a set of tools to a formation. Several sets of minerals can equally well fit the set of logs with very different results. A mineralogical model for the formation must be identified before lithological analysis is conducted. The mineralogical model must be validated by a geologist familiar with the area before any credit may be given to the lithological output.

Although a lithological analysis output (see the example in Fig. 4-3) is an extremely useful tool for building a pressure profile or stress model, it consists of only volumetric outputs. The analysis output cannot be interpreted without extreme caution for mechanical properties, zones that are hydraulically connected, etc.

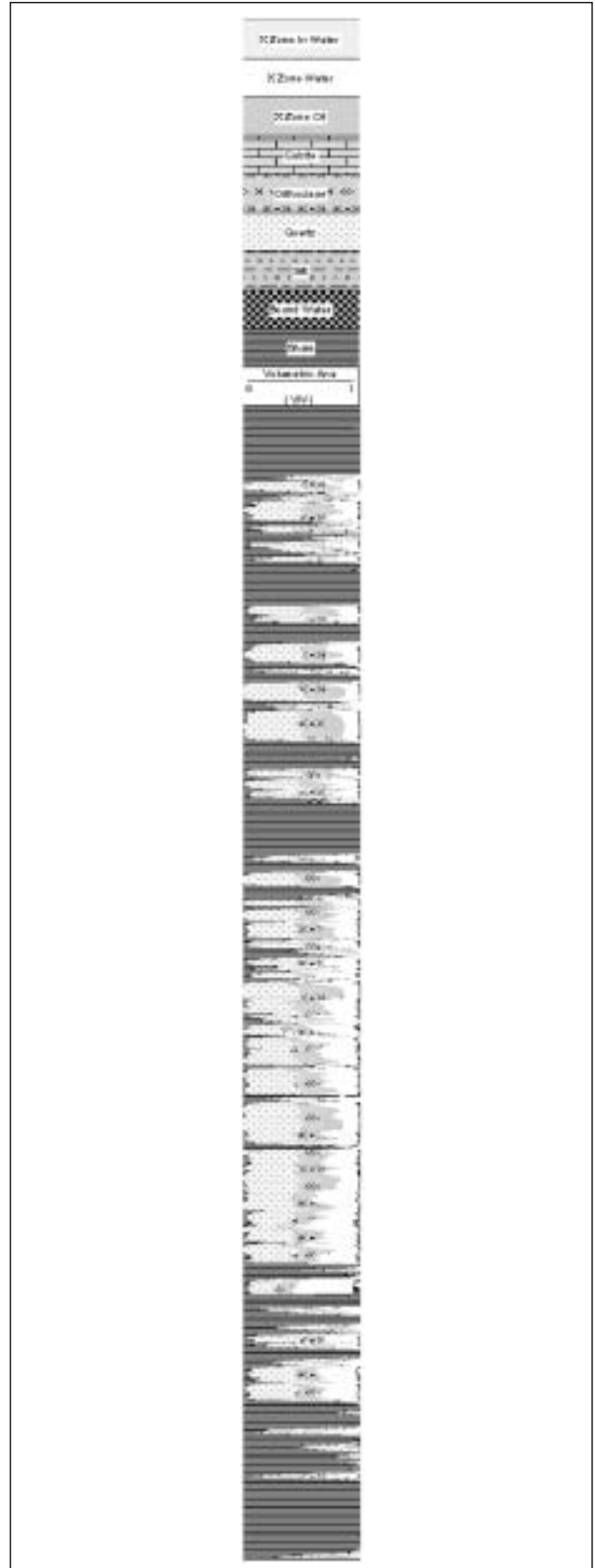


**Figure 4-3.** Example of lithological analysis.

### 4-4.3. Permeability

Permeability is a measure of the ease with which fluids can flow through a formation. The S.I. permeability unit is  $\text{m}^2$ , but the customary oilfield unit is the millidarcy (md).

Permeability is a tensor, and its value depends on the orientation of the flow. In the absence of extensive natural fractures or fissures or large horizontal stress anisotropy, the permeability  $k_H$  parallel to the bedding of the formation, which is horizontal in the model of the earth assumed here, can be considered isotropic, and the horizontal flow has no preferred direction. In the presence of natural fractures or large horizontal stress anisotropy, however, permeability can vary horizontally and the horizontal flow will have a preferred direction. The permeability perpendicular (i.e., vertical) to the bedding  $k_V$  is usually at least 1 order of magnitude smaller for sandstone reservoirs. For laminated sandstone reservoirs, it can be more than 2 orders of magnitude smaller. In some carbonate reservoirs, however,  $k_V$  can be equal to or larger than  $k_H$ . If no precision is given, the permeability of interest is  $k_H$ . For specific problems,  $k_H$  and  $k_V$  and even the horizontal components of  $k_H$  may be required. For vertical wells,  $k_H$  is sufficient to describe practically all production or injection phenomena. For horizontal or multibranch wells, any contrast in  $k_H$  will also have an impact on production or injection.

When several fluids are present, it is customary to introduce relative permeabilities. If  $k$  is the absolute (or “total”) permeability of the formation for a single fluid, the relative permeability to water  $k_{rw}$  is

$$k_{rw} = \frac{k_w}{k}, \quad (4-13)$$

where  $k_w$  is the effective permeability of the formation to water. Similarly, the relative permeability to oil  $k_{ro}$  relates the effective permeability to oil  $k_o$  to the total permeability  $k$  by

$$k_{ro} = \frac{k_o}{k}. \quad (4-14)$$

Relative permeabilities typically depend on the water saturation of the formation  $S_w$  (Fig. 4-4) (Amyx *et al.*, 1960). For example, the Park-Jones relations yield

$$k_{rw} = \left( \frac{S_w - S_{wi}}{1 - S_{wi}} \right)^m \quad (4-15)$$

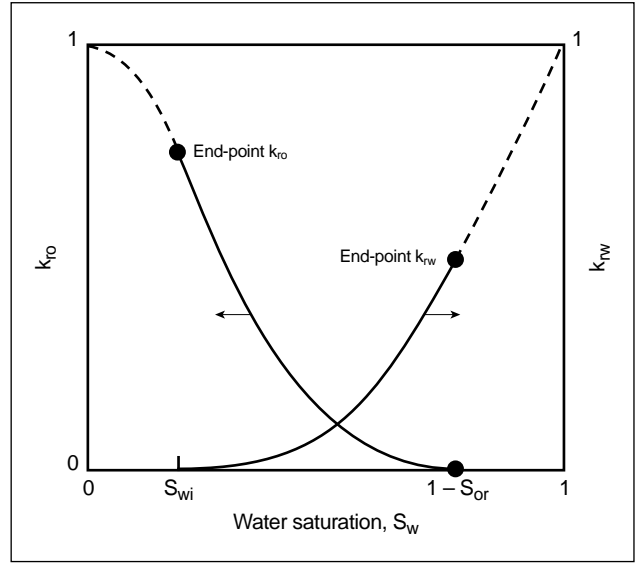


**Figure 4-4.** Typical variation of relative permeability as a function of water saturation (Dake, 1982). The curves simply and practically describe the simultaneous flow of oil and water through a porous medium.  $S_{or}$  = residual oil saturation.

$$k_{ro} = \frac{(1 - S_w)^a}{(1 - S_{wi})^b}, \quad (4-16)$$

where  $m$  is typically 3, whereas  $a$  and  $b$  must be determined by calibration (e.g., on core data). The permeabilities to water and to oil are then calculated simply by multiplying the total permeability  $k$  by the relative permeabilities of the sequence of interest to water and oil, respectively.

The irreducible water saturation  $S_{wi}$  can be obtained for hydrocarbon-bearing formations either from laboratory measurements on cores or NMR measurements (*The Log Analyst*, 1996, 1997); it is assigned a value of 1 in non-hydrocarbon-bearing formations.

In the context of reservoir stimulation, fluid displacement is usually treated like piston displacement. Therefore, the so-called end-point permeabilities are important (i.e., permeability of the formation to oil at irreducible water saturation and permeability of the formation to water at maximum water saturation). The end-point permeabilities can be very different. For candidate selection and subsequent treatment evaluation, the permeability of interest is that of the formation to native hydrocarbons. For the design and execution of a stimulation treatment, however, interest is in the permeability of the formation to water injection because water-base fluids are usually injected into the formation.



Permeability to the native mobile reservoir fluids can be estimated either by indirect or direct measurements. Direct measurements (formation testing) provide discrete measurements of permeability. Indirect measurements provide a continuous log of permeability that must be calibrated with the direct individual measurements (e.g., on cores or through formation testing).

- Indirect measurements

The following indirect measurements related to permeability require calibration, usually on cores, to a water zone. However, they are the best means for interpolating permeability between direct permeability measurements.

- Correlation to porosity and water saturation

Porosity is an obvious quantity to relate to permeability because interconnected porosity is required to have permeability. Several equations that relate permeability to porosity (e.g., Carmen, 1983; Wylie and Rose, 1950; Timur, 1968) are of the following form:

$$k = C \frac{\phi^x}{S_{wi}^y}, \quad (4-17)$$

where  $C$  is a constant that is a function of the rock type and grain size of the granular material. The exponents  $x$  and  $y$  are a function of the sequence of interest, and porosity estimation is as covered in Section 4-4.1.

It must be emphasized that calibration is absolutely necessary and that the calibration is specific to both the sequence and the lithology. Once expressions have been calibrated for a particular sequence, however, they also provide good continuous estimates of permeability within the field. Sidebar 4A is a practical example that illustrates the caution necessary when using a permeability-porosity correlation.

- Permeability from lithology and porosity

Permeability is governed by a length scale  $\Lambda$  that corresponds to the size of the dynamically connected pores (i.e., pores that permit fluid flow) (Herron *et al.*, 1998).

For high-permeability formations (i.e., >100 md), a good estimate of permeability is provided by the  $k$ -lambda model:

$$k = C\Lambda^2\phi^m, \quad (4-18)$$

#### 4A. Permeability-porosity correlations

Three well-know relations of permeability and porosity are

$$\text{Labrid (1975)} \quad \frac{k_i}{k} = \left( \frac{\phi_i}{\phi} \right)^3 \quad (4A-1)$$

$$\text{Lund and Fogler (1976)} \quad \frac{k_i}{k} = \exp \left[ 7.5 \times \frac{(\phi_i - \phi)}{0.08} \right] \quad (4A-2)$$

$$\text{Lambert (1981)} \quad \frac{k_i}{k} = \exp [45.7 \times (\phi_i - \phi)]. \quad (4A-3)$$

These equations correlate a change in permeability to a change in porosity in sandstones. For an assumed initial formation porosity  $\phi_i$  of 0.2 and permeability  $k_i$  of 20 md, if the porosity  $\phi$  after an acid job is 0.28, then the three correlations give values for the new permeability  $k$  of 55, 36,000 and 774 md, respectively.

Clearly, proper choice and calibration of a permeability-porosity correlation for the sequence of interest are necessary.

where the constants  $C$  and  $m$  again depend on the type of formation. For lower permeability formations, corrections must be made to obtain a first-order estimate of permeability. The  $k$ -lambda model in Eq. 4-18, therefore, is best used for high-permeability formations.

$\Lambda$  is a length scale that is difficult to measure. However, it is inversely proportional to the surface area of the pores  $S$  divided by the volume of the pores  $V$ , which is a ratio measured by NMR tools. This makes  $k$ -lambda permeability a good method for estimating permeability from NMR measurements in high-permeability formations (Herron *et al.*, 1998).

Also, the values of both  $S$  and  $V$ , and therefore  $\Lambda$ , can be measured for single minerals. If a mineralogical analysis of the formation has been made (see “Lithology” in Section 4-4.2),  $\Lambda$  can be estimated using a volumetric average of  $\Lambda$  for each constituent mineral. The better the quality of the lithology estimate, the better the resulting permeability estimate. In particular, this approach performs best when geochemical logging is used to determine the lithology (Herron *et al.*, 1998).

- Permeability from the Stoneley wave

When a pressure pulse is emitted within a wellbore, a guided wave called a Stoneley wave is readily propagated along the wellbore. The wave travels along the wellbore and pushes fluid through the mudcake into the formation. As the fluid is mobilized in the formation, it alters the

attenuation and frequency response of the formation. This effect was modeled by Biot (1956b, 1956c). If the mudcake is considered an elastic membrane, an estimate of the permeability of the formation to water can be computed (Brie *et al.*, 1998).

The formation must have a minimum of 12% porosity and low to medium permeability (1 to 100 md) for the best results. This is a shallow permeability measurement, typically limited to the invaded zone. If gas is in the invaded zone, the results are erratic.

Although permeability from the Stoneley wave is an indirect measurement, it is closely related to a true permeability measurement. Again, calibration is important because the measurement is sensitive to the elastic properties of the mudcake, which are unknown.

- Direct measurements

- Formation testers

To measure permeability, formation testers hydraulically isolate the part of the formation to be tested. During drawdown, fluid is withdrawn from the formation at a controlled rate. Pressure is then allowed to rebound to an equilibrium value (i.e., buildup). Both the drawdown and buildup are analyzed to estimate the permeability of the formation.

Formation testers can be divided into two groups on the basis of the resulting permeability measurement: tools with a single probe and tools with multiple probes or a packer and probe assembly (Fig. 4-5).

Single-probe tools press a probe against the wellbore wall to achieve a hydraulic seal. A small amount of fluid, usually mud filtrate, is

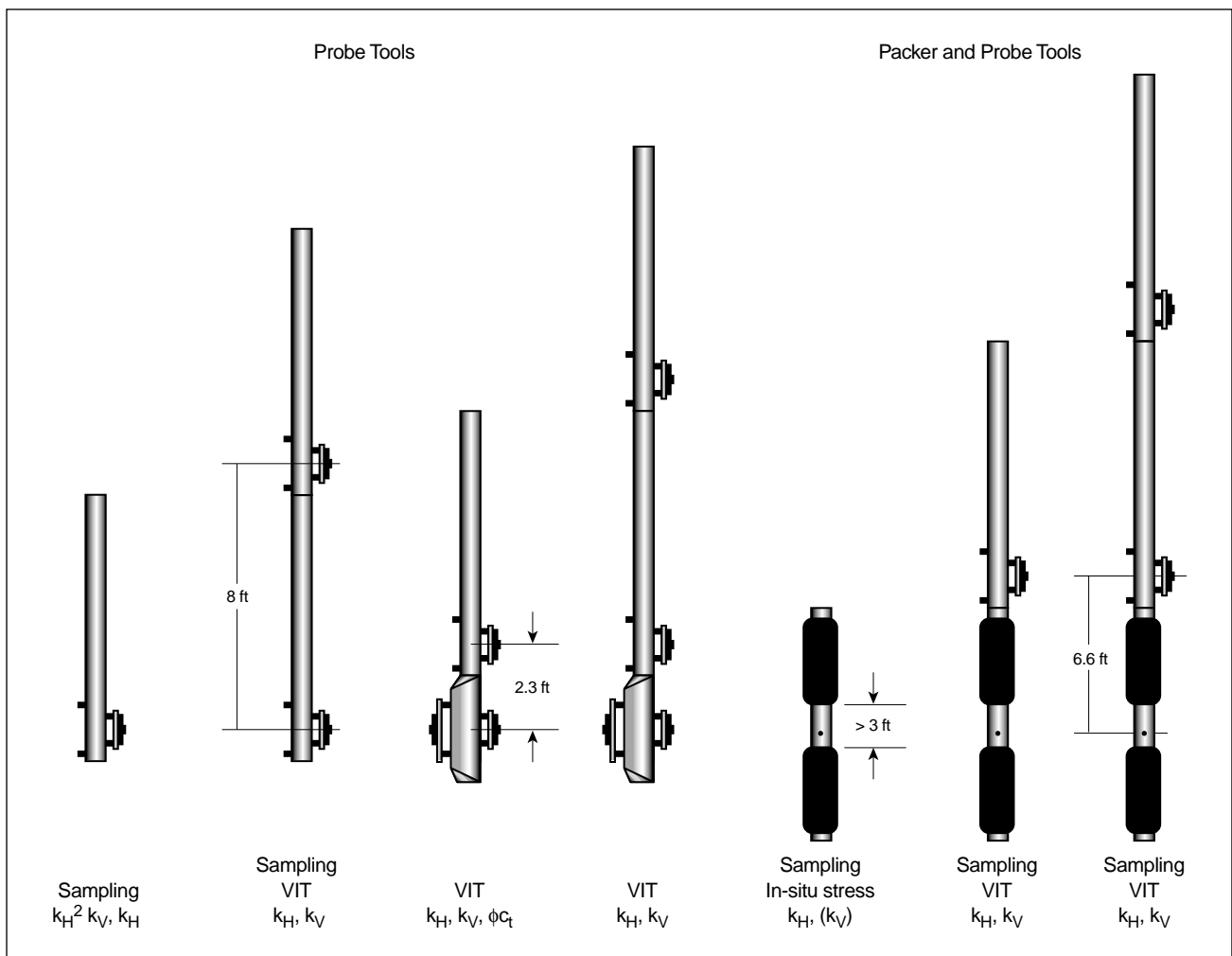


**Figure 4-5.** Probe tools and packer and probe tools. VIT = vertical interference testing.

withdrawn during drawdown. The steady-state pressure drop at the sink probe  $\Delta p$  is given by

$$\Delta p = \frac{\mu q}{2\pi k_H} \times \frac{C}{r_p} K\left(\sqrt{1 - \frac{k_v}{k_H}}\right) \quad \text{for } k_v < k_H \quad (4-19)$$

$$\Delta p = \frac{\mu q}{4k_H} \times \frac{C}{r_p} \quad \text{for } k_v = k_H \quad (4-20)$$

$$\Delta p = \frac{\mu q}{2\pi\sqrt{k_v k_H}} \times \frac{C}{r_p} K\left(\sqrt{1 - \frac{k_H}{k_v}}\right) \quad \text{for } k_v > k_H, \quad (4-21)$$

where  $C$  is a shape factor accounting for the curvature of the wellbore,  $\mu$  is the fluid viscosity (usually that of the mud filtrate),  $q$  is the rate of fluid withdrawal,  $r_p$  is the radius of the probe, and  $K(\eta)$  is the complete elliptical integral of the first kind of modulus  $\eta$  (Wilkinson and Hammond, 1990).  $K(\eta)$  can be approximated by  $\pi/2(1 + 1/4\eta^2 + \eta^4)$ . The expression for the isotropic case  $k_H = k_v$  is typically used to compute an estimate of  $k_H$ .

Once drawdown is stopped, the pressure bounces back to the formation pressure (see Section 4-4.2). In addition to  $\mu$ , the expression governing the pressure behavior now also includes the formation porosity  $\phi$  and the total compressibility  $c_t$  of the fluid in the formation.

Drawdown and buildup permeability estimates are usually different. For small drawdown volumes (i.e., of the order of 20 cm<sup>3</sup>), use of the drawdown portion of the test is preferred for estimating the permeability of the formation. Then, a measure of the horizontal permeability  $k_H$  to water can be obtained.

Permeability tests conducted with single-probe tools are commonly performed because they are simple, quick and reliable. Moreover, these tests provide a good relative indicator of formation permeability. The volume of investigation is of the order of a few feet.

In the multiple-probe configuration of a formation tester tool, several probes are used, separated by several meters. A pressure pulse is sent through one probe, and the response of the formation is monitored at the location of the other probes. This method enables the determination

of both  $k_H$  and  $k_v$  (Zimmerman *et al.*, 1990; Pop *et al.*, 1993).

In the packer and probe configuration, a straddle packer is used to isolate part of the formation to withdraw what can be large volumes of fluids. The response of the formation is monitored by a probe several feet above the packer. This configuration also enables the determination of both  $k_H$  and  $k_v$ , especially in high-permeability formations that require a large-volume withdrawal to create a pressure response measurable at the probe.

The obvious advantage of the multiple-probe tools and packer and probe tools is that they produce  $k_H$  and  $k_v$  estimates. However, the radius of investigation into the formation is also much larger than with a single-probe tool (i.e., at least 3 times the spacing between the probes), which departs from a discrete point measurement. In particular, the viscosity and compressibility terms in the equations governing the flow correspond to those of the formation fluid. These extra parameters must be determined to estimate the permeability. Thus, the design of formation tests using multiple-probe and packer and probe tools is critical for obtaining representative data (Goode *et al.*, 1991).

#### – Well tests

The same procedure as that used for formation testing is used during well testing. The well is flowed at a constant rate during drawdown before it is shut in and pressure buildup observed (see Chapter 2).

Well testing has a much larger volume of investigation and produces an estimate of a composite  $k_H$ . This composite value is crucial for the economic evaluation of stimulation treatments. However, for matrix stimulation, especially fluid placement and diversion, knowledge of the permeability within each layer is essential, hence the need for continuous measurements of permeability by the methods outlined here.

### 4-4.4. Pore pressure

Pore pressure is the pressure of the fluid in the formation. After production, its value can differ significantly from one layer to the next within a sequence.

It is a necessary input for designing matrix stimulation treatments of multiple layers, if only to account for and potentially take measures to control crossflow between zones. The pore pressure also strongly influences the state of stress in a formation (by as much as 50%) and is therefore a critical piece of information for designing hydraulic fracturing treatments.

- Pore pressure measurement

In addition to being measured by well tests, pore pressure is measured by formation testers. Once a seal has been achieved between the formation tester and the formation, fluid is withdrawn from the formation to lower the pressure in the tester to below the far-field pore pressure. Flow is then stopped, and if the formation has sufficient permeability, the formation will flow to equilibrate the tester with the bulk of the formation. The pressure in the tester will rise until a plateau is reached. The pressure corresponding to the plateau is taken as an estimate of the pore pressure.

In low-permeability formations (<1 md), two effects can have an impact on the pressure measurement. First, the formation may not supply enough fluid in a short enough time to equilibrate with the tester. In this case, the measurement may be aborted before a meaningful plateau is reached. Second, even if a plateau is reached, it may indicate equilibrium with the higher local pore pressure induced by overbalance drilling (Fig. 4-6). This effect is commonly referred to as supercharging (Phelps *et al.*, 1984; Lane, 1993). It is therefore a reasonable practice to question pore pressure measurements associated with a mobility that is less than 1 md/cp.

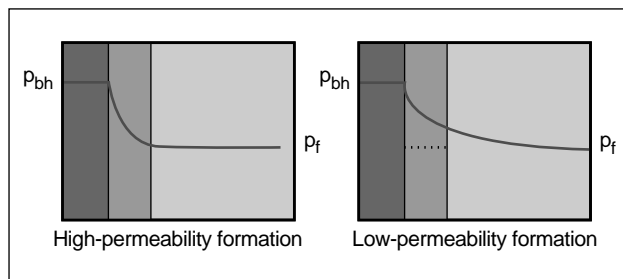


**Figure 4-6.** In high-permeability formations, the fluid leaking through the mudcake dissipates easily with no significant increase in formation pressure. In low-permeability zones, the fluid leaking through the mudcake cannot dissipate easily. In this latter case, the pressure measured immediately behind the mudcake is higher than the true formation pressure.  $p_{bh}$  = borehole pressure,  $p_f$  = far-field pore pressure.

- Pressure profiles

Because pore pressure is a point measurement, there are gaps between the measurements. The gaps can be filled by building pressure profiles.

If there are several fluids in the formation (e.g., a mixture of water, oil and gas), only one of them is mobile and continuous across the pore space. This fluid is called the continuous fluid. Under static conditions (i.e., no flow), pressure changes as a function of depth result from gravity only. In other words, the pressure changes are a function of the density of the continuous fluid in the formation:

$$\frac{dp}{dz_{TVD}} = \rho_f g, \quad (4-22)$$

where  $p$  is the pore pressure,  $z_{TVD}$  is the true vertical depth,  $\rho_f$  is the density of the continuous fluid, and  $g$  is the acceleration of gravity.

A normally pressured reservoir consists of formations where  $p$  is close to a reference pressure given by a continuous column of brine up to the surface, which corresponds to a pressure gradient between 0.43 and 0.45 psi/ft in oilfield units:

$$p(z_{TVD}) \approx \int_0^{z_{TVD}} \rho_{brine} dz, \quad (4-23)$$

where  $\rho_{brine}$  is the density of the brine. An over-pressured reservoir consists of formations where  $p$  is much larger than the reference pressure, and an underpressured reservoir exhibits values of  $p$  that are much smaller than the reference pressure.

In simple virgin (i.e., unproduced) reservoirs, all the permeable zones are equilibrated with each other, and the pore pressure measurements plotted versus TVD should form a straight line with a slope given by the density of the continuous fluid in the formation. The straight line can be used to interpolate the pore pressure values between the point measurements. The slope will change depending on the fluid, which enables the determination of fluid contacts (Fig. 4-7) (Stewart *et al.*, 1982; Desbrandes and Gualdrón, 1988).

In developed reservoirs or those with complex structures, building pressure profiles requires many pore pressure measurements. The identification of gradients is a powerful tool for detecting discontinuities in pore pressure that most likely correspond to discontinuities in permeability and discontinuities in stress magnitudes.

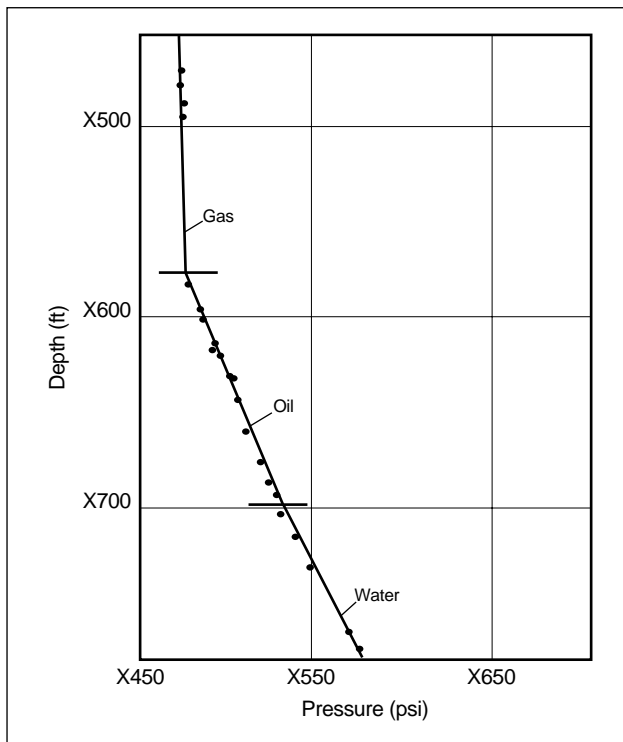


**Figure 4-7.** A vertical pressure profile defines fluid types and fluid contact levels.

#### 4-4.5. Skin effect and damage radius

Skin effect is a measure of the damage inflicted to the formation permeability in the vicinity of the wellbore. Damage may result from drilling and completion processes or the production of formation fluids. The skin effect can therefore vary during the life of a well.

For candidate selection and subsequent treatment evaluation, the skin effect of interest is that related to flow from the formation (i.e., the production skin effect). For the design and execution of a stimulation treatment, however, the skin effect of interest is that related to the injection of treatment fluids into the formation. Production skin and injection skin effects can be very different. The damage radius is an estimate of how far the damage extends into the formation. Skin effect and damage radius are important inputs for the design of matrix stimulation because they affect the type and volume of matrix fluids required and the diversion techniques for fluid placement (see Chapter 19). However, these parameters are difficult to obtain, and no current method is fully satisfactory. The following methods provide crude estimates.

- Skin effect

There are several means for measuring the production skin effect. At logging time, the production skin effect is measured by formation testing. It is, however, extremely dependent on the geometry of the test (Frimann-Dahl *et al.*, 1998). Selective well testing measures an integrated value of the production skin effect over the zones of interest at the time the well test is conducted. There is currently no means to continuously measure production skin effect.

It is even more difficult to estimate the injection skin effect. The injection skin effect can be obtained at logging time by conducting injection testing with a packer and probe configuration of the tester. Using Stoneley wave measurements together with permeability estimates is a potential means for determining the injection skin effect continuously. However, with current technology, the injection skin effect is a parameter that requires calibration.

- Damage radius

For a vertical well drilled with conductive mud, an invasion profile can be computed from resistivity logs (Souhaite *et al.*, 1975). Resistivity logs provide resistivity measurements at several depths of investigation (e.g., 10, 20, 30, 60 and 90 in.). Provided that there is a resistivity contrast between the mud filtrate and virgin formation fluid, each resistivity measurement reflects how much the formation fluid was displaced by mud filtrate. The resulting invasion profile does not strictly correlate to a drilling-induced damage profile, but it is a reasonable first-order estimate. This technique can be extended to nonvertical wells by including the effect of dip between the wellbore and the formation (Anderson *et al.*, 1996).

There are currently no geophysical means to measure the location of damage resulting from the production of formation fluids, although time-lapse gamma ray may correlate with the buildup of radioactive scale.

#### 4-4.6. Composition of fluids

Although there are indirect logging means for determining the composition of formation fluids, they are limited basically to distinguishing among water (brine), gas and oil (e.g., Schiuma *et al.*, 1997). Some conclusions can be made about the type of oil by measuring its specific density through pressure profiling (see Section 4-4.4).

The only reliable method for determining the composition of fluids downhole is to collect uncontaminated fluid samples for laboratory analysis. Sampling is best achieved with formation testers (see “Formation testers” in Section 4-4.3). For example, the MDT\* Modular Formation Dynamics Tester can measure both the resistivity and optical properties of the flowing fluid to distinguish between uncontaminated formation fluid and the invading water- or oil-base drilling mud or mud filtrate. For more information on fluid sampling, see Hashem *et al.* (1997) and Akram *et al.* (1998).

### 4-5. Properties related to the deformation and fracturing of rock

As presented in Chapters 3 and 5, the geometry of a hydraulic fracture depends strongly on both the mechanical properties of the rock formation, which describe how the formation will deform under a change in stresses, and the stresses acting on the formation. The mechanical properties of the formation and the in-situ stresses are not independent. A difference in mechanical properties between two adjacent formations usually leads to a difference in the in-situ stresses. Except for the simplest situations, at least a qualitative model must be used to explain the relationship between the formation mechanical properties and stresses.

#### 4-5.1. Mechanical properties

- Elastic properties

The only tool that responds to the elastic properties of the formation is the sonic. When a pressure pulse is created in a wellbore filled with fluid, the complex phenomena that occur at the boundary between the wellbore and the formation result in the propagation of several types of waves into the

formation (Paillet and Chang, 1991). The two types of waves of interest for estimating the elastic constants of a medium are compressional waves (*P*-waves) and shear waves (*S*-waves). The sonic tool measures the characteristic propagation speed of the *P*- and *S*-waves.

In an isotropic medium, only the two elastic constants of the shear modulus  $G$  and Poisson's ratio  $\nu$  are independent. They are related to the velocity of propagation of a *P*-wave  $u_P$  and that of an *S*-wave  $u_S$  by

$$G = \rho_b u_S^2 \quad (4-24)$$

$$\nu = \frac{2u_S^2 - u_P^2}{2(u_S^2 + u_P^2)} \quad (4-25)$$

The propagation velocity can be replaced with the time  $\Delta t$  it takes a wave to travel a fixed distance  $d$  (e.g., between a source and a receiver):

$$G = \rho_b \frac{d^2}{\Delta t_S^2} \quad (4-26)$$

$$\nu = \frac{\frac{1}{2} \left( \frac{\Delta t_S}{\Delta t_C} \right)^2 - 1}{\left( \frac{\Delta t_S}{\Delta t_C} \right)^2 - 1} \quad (4-27)$$

where  $\Delta t_S$  and  $\Delta t_C$  are the *S*-wave and *P*-wave traveltimes, respectively.

Young's modulus  $E$  is related to the two constants by

$$E = 2G(1 + \nu) \quad (4-28)$$

These equations deserve a few comments. First, a measurement of  $\rho_b$  is required. Second, good-quality compressional and shear wave velocity measurements are crucial for the determination of  $E$  and  $\nu$ . In particular, both the compressional and shear waves must travel in the undisturbed formation to yield a realistic estimate of  $\nu$ —in other words, “deep” measurements of  $u_P$  and  $u_S$  are essential. A combination of sonic logs recorded with different sources (e.g., monopole and dipole) may therefore be necessary to ensure the quality of the compressional and shear wave velocity estimates. For zones where the shear velocity is not known, synthetic traveltimes can be generated from lithological analysis, but these values must be used with caution. Third, because  $G$  is obtained

more directly, it should be considered the primary elastic parameter in correlations, as discussed subsequently.

The result of sonic processing—in consideration of other effects, such as that from fluids in the vicinity of the wellbore—is a continuous estimate versus depth of the elastic properties of an isotropic linear elastic material. However, wave propagation is a phenomenon of small strain with a large strain rate. Rock formations appear stiffer in response to an elastic wave than in a rock mechanics laboratory test, where much larger strains are applied at a lower strain rate. In fact, the weaker the rock, the larger the difference between the elastic properties derived from acoustic measurements (i.e., the so-called dynamic properties) and those derived from laboratory experiments (i.e., static properties). It is believed that the difference results not so much from the applied strain rate as the amount of strain applied to the rock (Hilbert *et al.*, 1994; Plona and Cook, 1995). Nevertheless, there is not a one-to-one correspondence between elastic properties measured by sonic logs and those measured by laboratory experiments, which more closely approximate the behavior during fracturing.

The sonic and rock mechanics communities debate which set of measurements represents the appropriate elastic properties of materials, and a similar concern applies to which measurements of Young's modulus and Poisson's ratio should be used to model hydraulic fracturing.

Work by Papanastasiou (1997), together with experimental evidence from van Dam *et al.* (1998), shows that the relevant Young's modulus for hydraulic fracturing is the unloading modulus measured during laboratory experiments. The value of the unloading modulus lies between that of the classic tangent modulus measured with laboratory tests of cores and that of the modulus determined with sonic measurements (Hilbert *et al.*, 1994; Plona and Cook, 1995).

For Poisson's ratio, there is not much difference between the loading and unloading values of Poisson's ratio determined on cores. Moreover, the difference between Poisson's ratio measured in the laboratory and that determined by sonic tools, with the provisions listed previously, is not large, provided that no compaction occurred during the laboratory test. If compaction occurs, a purely elastic model is no longer valid.

Thus, values determined for Poisson's ratio are usually valid. The data for Young's modulus should be reviewed.

Several correlations are used to estimate static elastic properties from dynamic elastic properties (e.g., Coon, 1968; van Heerden, 1987; Jizba and Nur, 1990; Morales, 1993). The correlations were developed by comparing elastic properties from laboratory tests on core samples to elastic properties determined from sonic logs run in the cored wells. From a plot of dynamic versus static data for several wells in a specific formation, a cloud of points was obtained and a curve fitted to it. Most of the correlations are a variant of

$$static = (A \times dynamic^\alpha) + B, \quad (4-29)$$

where *static* is the static elastic property and *dynamic* the corresponding dynamic elastic property. The constants *A*,  $\alpha$  and *B* are determined;  $\alpha$  is commonly assigned a value of 1.

For clean sandstones, correlations have been developed between the porosity and the ratio of dynamic Young's modulus and static loading Young's modulus. At very low porosity (<5%), the ratio is close to 1, whereas it is close to 10 at 40% porosity.

The correlations can be used to obtain first estimates of the static Young's modulus and Poisson's ratio of a formation from dynamic measurements. If the correlation used was developed from data from rocks belonging to a sequence (e.g., sand/shale turbidite) similar to that of the formation—or, even better, from rocks belonging to the same basin as the formation—the resulting elastic properties can be considered representative. Otherwise, a calibration point should be identified (e.g., by conducting a fracture calibration test; see Section 9-7). Even with a reliable correlation, calibration is critical for determining Young's modulus, and the results may completely rescale the Young's modulus profile. Poisson's ratio in this situation usually is unchanged.

The preferred method for obtaining a continuous log of elastic properties for hydraulic fracturing is to calibrate the sonic processing output with good-quality results of core tests (i.e., to determine a specific correlation) (see Section 3-4.4). The cores should be from the reservoir section and its bounding layers to fully represent the sequence. The tests should be conducted at a confining pressure simi-

lar to that in the formation downhole and with a controlled pore pressure similar to that in the reservoir. Both the loading and the unloading Young's moduli and Poisson's ratios should be measured. The dynamic versus static properties are then plotted for each formation to select the appropriate scaling function; e.g., is the ratio between the dynamic and static properties constant throughout the sequence, or is it a function of porosity, of vertical depth, of lithology, etc.? The resulting calibration is usually applicable within the field (e.g., Edimann *et al.*, 1998).

- Fracture toughness, strength and friction angle

The three parameters of fracture toughness, strength and friction angle  $\phi$  are of interest because they are all related to the failure of rocks. However, no geophysical measurements are directly sensitive to any of the three. Strength and friction angle are routinely measured on cores, but fracture toughness is much more difficult to measure in the laboratory (see Section 3-4.6).

Fracture toughness and friction angle are fairly consistent within a particular rock type, provided that it is consolidated. Tables can be used (Senseny and Pfieffe, 1984; Atkinson and Meredith, 1987; Plumb, 1994a) to provide first estimates of their values.

A number of factors affect the fracturing resistance or toughness and the scale of the processes (see Section 6-7). If fracture toughness is defined as a material parameter, it is not scale dependent (Vliet, 1999), and its effect on hydraulic fracturing is small (Desroches *et al.*, 1993), which in turn allows some error in its determination. However, an apparent toughness can be used to include several processes occurring in the vicinity of the tip of a fracture propagating in soft materials, especially in unconsolidated sandstones (Ayoub *et al.*, 1992b). In that case, the so-called fracture toughness is purely a calibrated parameter (see Section 5-4.5 and Sidebar 9B) that does not have much in common with the true fracture toughness of the material.

For sandstones, the unconfined compressive strength (UCS) of the rocks can also be estimated from correlation with sonic data (e.g., Kowalski, 1975).

The friction angle can also be estimated using correlations with physical properties such as porosity (e.g., Plumb, 1994a) but with less success.

Indeed, the key is the lithology, not a particular physical property.

- Soft formations

The deformation of soft formations is difficult to describe with linear elasticity. Several approaches have been proposed, such as modified elasticity (Franquet and Economides, 1999), for which Young's modulus and Poisson's ratio are functions of the state of stress, and plasticity (e.g., Papanastasiou, 1997; Nikolaevskiy and Economides, 2000). These approaches require additional parameters that cannot be determined by current geophysical methods.

## 4-5.2. Stresses

The state of stress in the earth is one of the major factors influencing the geometry of a hydraulic fracture. The state of stress can be described by three principal stresses that are perpendicular to each other: maximum principal stress  $\sigma_1$ , intermediate principal stress  $\sigma_2$  and minimum principal stress  $\sigma_3$ . Because the principal stress directions are orthogonal, the direction of two principal stresses automatically describes the direction of all of them. However, the description is complete only when the order is known (Fig. 4-8).

A complete description of the state of stress is best illustrated by an example of a nominal reservoir at depth (>2000 ft). The weight of the sediments, or the overburden stress  $\sigma_v$ , is usually one of the principal stresses. The two other principal stresses are therefore horizontal. The azimuth of the minimum horizontal stress  $\sigma_h$  completes the description of the orientation of the stresses, because the maximum horizontal stress  $\sigma_H$  is horizontal and orthogonal to  $\sigma_h$ . What is missing is the order of the stresses. Is  $\sigma_v$  the maximum principal stress  $\sigma_1$ , in which case  $\sigma_h$  is the minimum principal stress  $\sigma_3$  and  $\sigma_H$  is the intermediate principal stress  $\sigma_2$ ? Or is  $\sigma_v$  the minimum principal stress, or even the intermediate principal stress? Each of these cases corresponds to a different stress regime, as subsequently discussed. A complete description of the state of stress is of particular importance because hydraulic fractures propagate perpendicular to the minimum principal stress. If  $\sigma_3$  is horizontal, a vertical fracture will be created; if  $\sigma_3$  is vertical, a horizontal fracture will be created; if  $\sigma_3$  is inclined, an inclined fracture normal to it will be created.



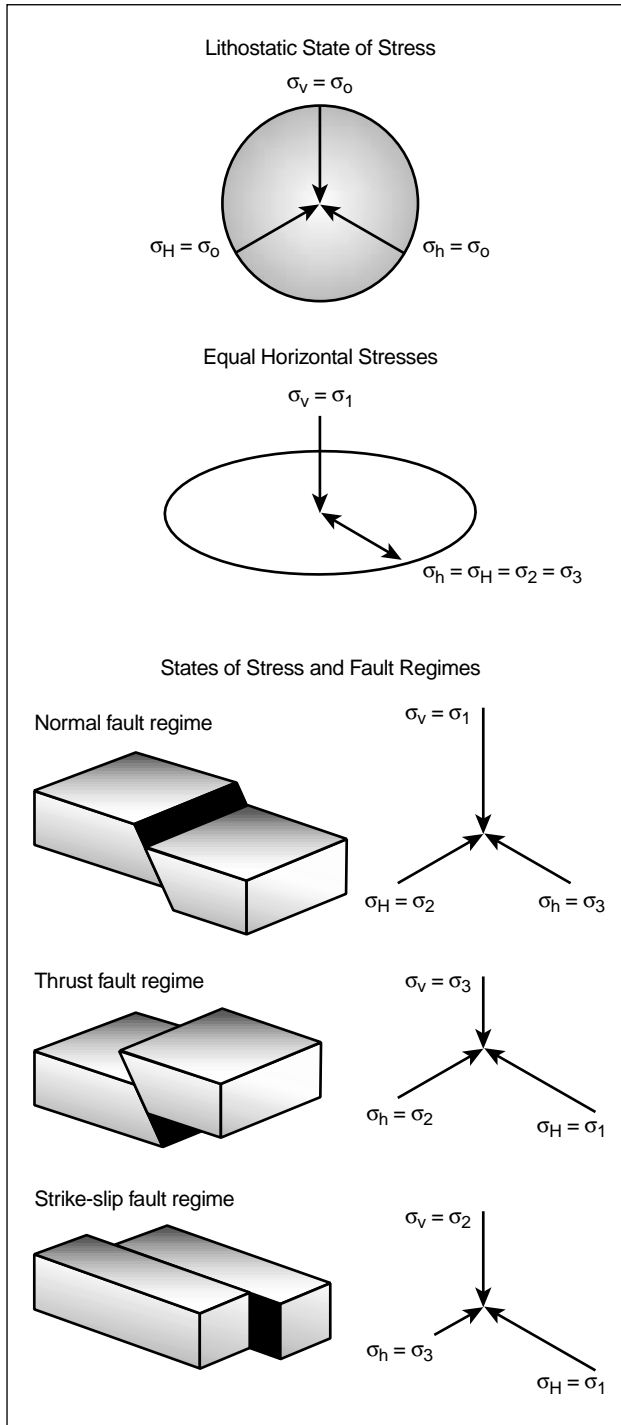


**Figure 4-8.** Stress regimes and order of stresses  $\sigma_o$  = equal-stress constant.

For hydraulic fracturing applications, the recommended methodology for determining the stresses is as follows. This approach is restricted to reservoirs at depths greater than 2000 ft because the overburden is

most likely a principal stress, provided that the location is not near a major fault.

- The value of  $\sigma_v$  is determined first.
- Second, the orientation of  $\sigma_h$  is determined. This could be a consideration in planning the drainage pattern of the reservoir. But more importantly, the orientation of the principal stresses can vary significantly from one layer to the next and thereby enhance hydraulic fracture containment.
- Finally, the value of the minimum stress as a function of depth is determined and compared with that of the overburden to determine which stress is  $\sigma_3$ .

For some cases in a thrust-faulted basin, especially in carbonates with strongly contrasting elastic properties, the order of the stresses can differ from one layer to the next, strongly affecting the treatment.

In other words, not only is the magnitude of  $\sigma_h$  of concern, but also the orientation and order of the principal stresses. For shallower formations ( $\leq 2000$  ft), the situation can be more complex because the overburden is not necessarily a principal stress.

- Determination of overburden

The overburden is the weight of the column of sediments. Although it is not measured directly, it can be easily computed as the integral over depth of the bulk density:

$$\sigma_v(z_{TVD}) = \int_0^{z_{TVD}} \rho_b dz. \quad (4-30)$$

However,  $\rho_b$  is rarely measured up to the surface more than once in the lifetime of a field (i.e., for seismic profiling). Research may be necessary to obtain an estimate of  $\rho_b$  between the top of the log and the surface. Furthermore, for deepwater projects, the significant affect of the water column on  $\sigma_v$  must be included.

- Stress orientation

The orientation of the principal stresses can be determined using diverse resources. The popular approaches are discussed here.

- World stress map

If no information is available for the well or field, the world compilation of stress orientations can be consulted (e.g., see the World Stress Map site on the World Wide Web at <http://www-wsm.physik.uni-karlsruhe.de/>).

However, most of the data are from the analysis of deep seismicity, which occurs at much greater depths than typical oilfield wells.

- Geologic maps

A geologic map of the field should be examined to see if major faults have been identified. In the vicinity of the faults, the principal stresses have most likely rotated to align themselves parallel to the fault surface (e.g., Barton and Zoback, 1994).

- Shear anisotropy

Shear waves are polarized waves and are therefore sensitive to differences in the elastic properties of the material in the direction perpendicular to their travel path. If the properties are sufficiently different, shear waves polarized in one direction will travel significantly faster than those polarized in the orthogonal direction (Fig. 4-9). If the rock formation contains a population of defects that have a uniform distribution of orientation, the defects that are normal to  $\sigma_H$  are under more stress than those normal to  $\sigma_h$ . A shear wave traveling vertically and polarized parallel to  $\sigma_H$  will therefore travel faster than a shear wave polarized perpendicularly to  $\sigma_H$ .

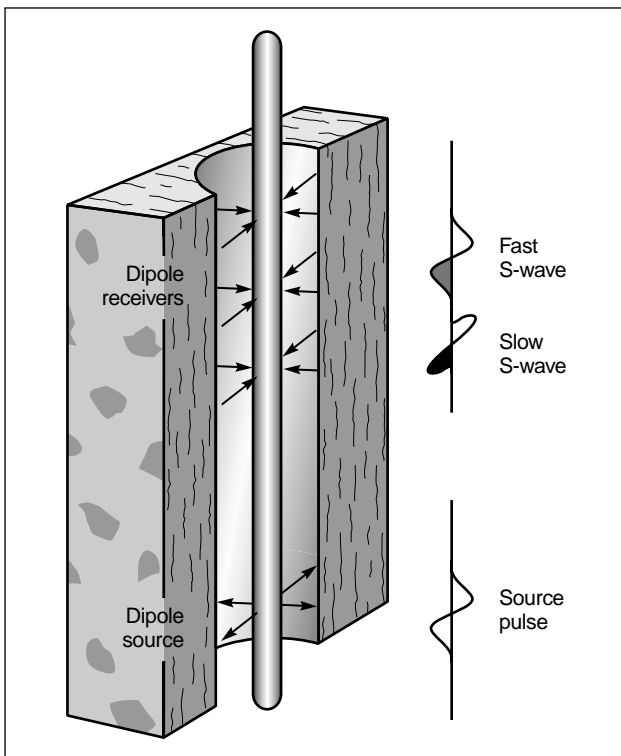


**Figure 4-9.** Relation between the polarization of shear waves and stresses.

A dipole sonic tool can be run in the wellbore to measure the velocity of shear waves polarized in an orthogonal arrangement. From these data, the azimuth of the fastest shear wave can be extracted. In a well close to vertical, the azimuth corresponds to the direction of  $\sigma_H$  (Endo *et al.*, 1996).

One question that often arises is whether the anisotropy measured from the slow and fast shear directions is induced by the stress contrast or the intrinsic properties of the medium. In a vertical well, most of the anisotropy is due to stress effects and can readily be related to the direction of the far-field stresses (Endo *et al.*, 1996). This is not necessarily the case in horizontal or deviated wells, and the use of shear anisotropy to infer stress directions is not recommended in these situations.

Processing dipole sonic data for anisotropy analysis is challenging. As a rule, the azimuth of the fast shear wave that is reported on the logs should be fairly stable regardless of the rotation of the tool. If this is not the case, the rotation of the tool—not a formation property—was measured. In addition, the uncertainty window reported around the azimuth should be tight (i.e., less than 5° on each side). These simple quality control measures identify most of the poor-quality data. The fast shear azimuth computed from good-quality shear anisotropy data provides a robust estimate of the azimuth of the maximum horizontal stress  $\sigma_H$  in a vertical well (Fig. 4-10).

- Wellbore breakouts

The presence of a wellbore in the formation generates a local change in the stresses, a process referred to as stress concentration (see Section 3-5.7). When the pressure in the wellbore falls below a certain level, the formation may fail in compression or shear, and wellbore breakouts can form (Zoback *et al.*, 1985; Plumb and Cox, 1987). The breakout is symmetrical and bi-wing (Fig. 4-11). In a vertical well, interpretation is straightforward because the azimuth of the breakout corresponds to the azimuth of  $\sigma_h$  if  $\sigma_h$  is a principal stress direction. In deviated or horizontal wells, the location of breakouts is a function of the ratio of stresses  $(\sigma_2 - \sigma_3)/(\sigma_1 - \sigma_3)$  and the orientation of the wellbore with respect

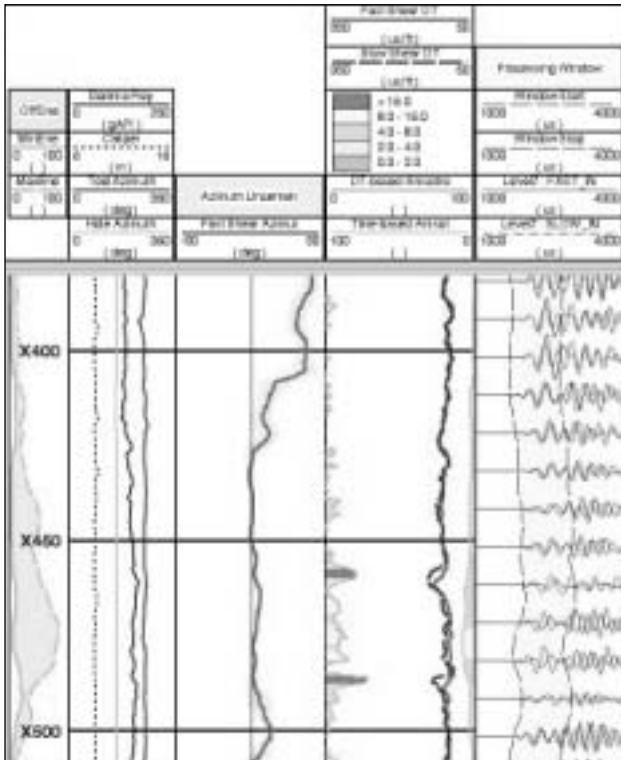


**Figure 4-10.** Stress direction log obtained by the analysis of shear wave anisotropy. The orientation on track 3 changes between the lower section (X425 and below) and the upper section.

to the stresses. Processing is required (Cesaro *et al.*, 1997), and in some cases it can identify both the orientation of the stresses and the ratio between them.

The simplest way to detect breakouts is to examine the log track recorded by a four-arm caliper (Fig. 4-12) (Plumb and Hickman, 1985). More sophisticated imaging logs can also be used (Fig. 4-13). Special care must be taken not to misidentify features such as key seating and overreaming as breakouts. For more information on the identification of breakouts, see Bratton *et al.* (1999) and Maury *et al.* (1999).

Simple interpretation assumptions are used to infer stress magnitudes from breakouts (Cesaro *et al.*, 1997). However, currently no technique reliably infers the stress magnitudes from the presence of breakouts alone.

#### – Drilling-induced fractures

Because of the stress concentration resulting from the presence of the wellbore, tensile stresses may be generated at the borehole wall

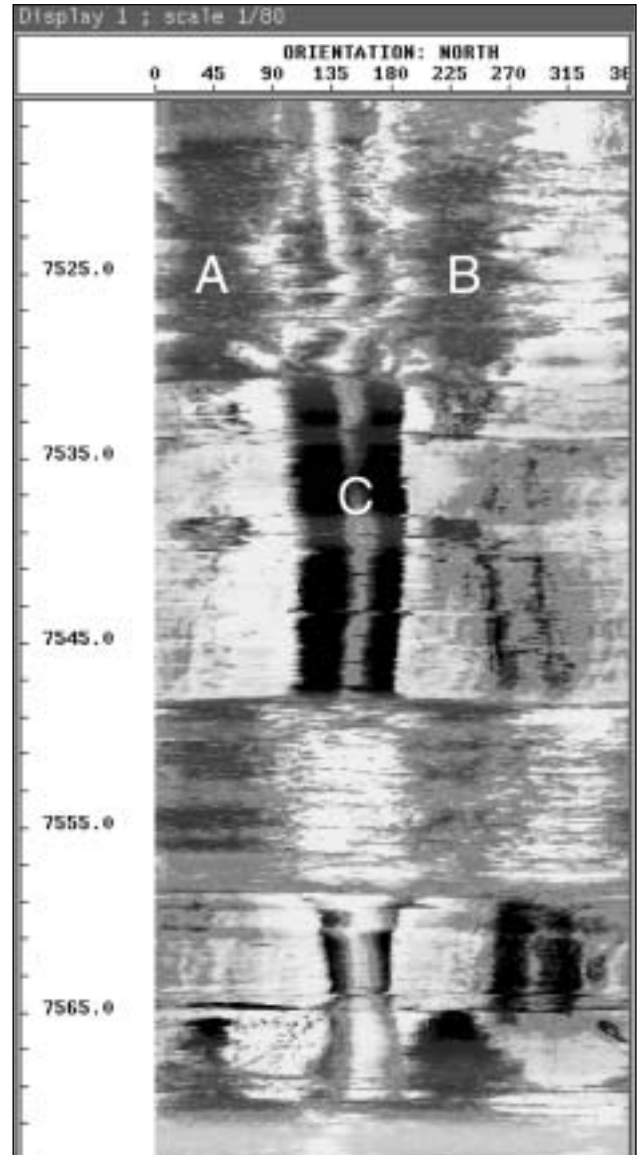


**Figure 4-11.** Reflectance image showing breakouts (A and B) and drill collar wear (C) in an interbedded sandstone and shale. The breakout width varies with the rock strength and increases with depth below 7565 ft.

when the pressure in the wellbore rises above a certain level. If the resistance of the rock is reached, drilling-induced fractures will be created. These readily identifiable fractures occur parallel to the wellbore axis in two sets, 180° apart (Fig. 4-14). They can be continuous or discontinuous; the latter are called en echelon fractures.

Drilling-induced fractures are shallow and conductive, which makes them obvious on electrical imaging logs, such as that recorded by the

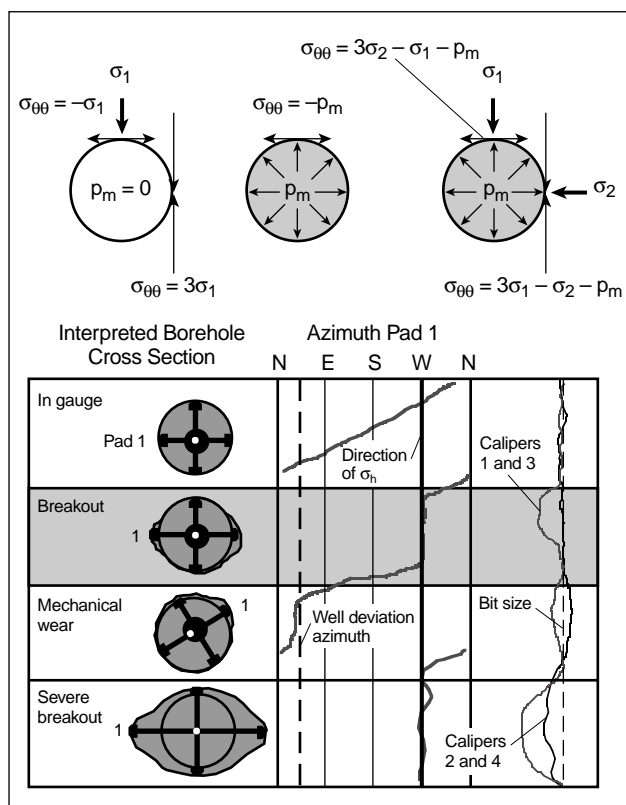


**Figure 4-12.** Interpretation of calipers for breakouts and the stress direction.  $\sigma_{\theta\theta}$  = circumferential stress,  $p_m$  = mud pressure in the wellbore.

FMI\* Fullbore Formation MicroImager. They are distinguished from natural fractures because the fracture sets parallel the wellbore, in some cases for hundreds of feet.

In a vertical well, drilling-induced subvertical fractures occur in the direction of the maximum horizontal stress. In deviated and horizontal wells, en echelon fractures are observed. An analysis similar to that conducted for breakouts can yield stress ratios and stress directions (Wiprut and Zoback, 1998).

A final check consists of verifying that any breakouts occur  $90^\circ$  from drilling-induced fractures.

#### – Tests on cores

The recovery of cores introduces nonlinear effects because of the brutal change of stress (i.e., unloading) to which the cores were subjected. Anelastic strain recovery (ASR) or differential strain analysis (DSA) may yield the direction of the principal stresses (see Section 3-6.4) (Voigt, 1968; Siegfried and Simmons, 1978;

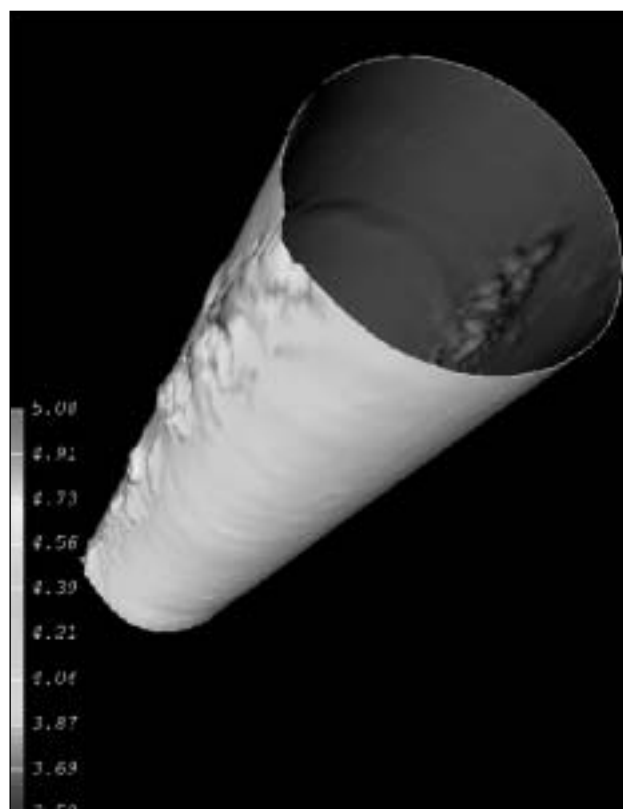


**Figure 4-13.** Three-dimensional (3D) computer model of a 2-ft section of an 8½-in. diameter borehole constructed from UBI\* Ultrasonic Borehole Imager transit-time data. The ridges on the right and left sides are breakout elongations resulting from stress-induced wellbore failure.

Strickland and Ren, 1980). In the case of hard rocks, fast unloading of the core creates a population of defects (i.e., microcracks) related to the stress field at the time of coring (i.e., the current state of stress). Provided that the population of defects is dominant in the sample, which is usually the case, the DSA technique will yield information on the current state of stress. This technique also provides the order of the principal stresses, making it extremely useful when it is suspected that the vertical stress is not a principal stress or not the maximum principal stress.

#### – Population of natural fractures

This technique does not provide information about the current state of stress and therefore is not useful unless the fractures were created by the current state of stress. The state of stress changes often and significantly at the geologic time scale. The current state of stress, which is of interest for hydraulic fracturing, is typically

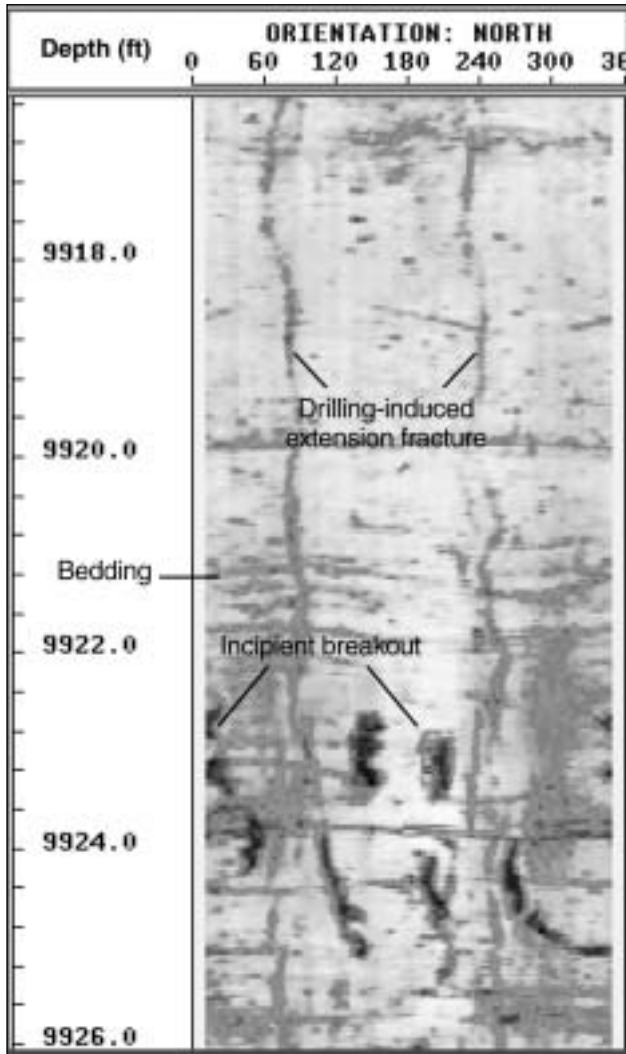


**Figure 4-14.** Drilling-induced extension fractures in sandstone in the Travis Peak formation, Wascom field, East Texas.

different from that at the time of creation of the fractures in the formation.

– Hydraulic fracture diagnostics

Microseismicity or tiltmeters (e.g., Warpinski, 1994) (see Section 12-1.1) can provide an estimate of the azimuth of a hydraulic fracture. Because a hydraulic fracture propagates perpendicular to the minimum principal stress, its diagnostics provide information about the direction of the minimum principal stress, albeit after the fact.

- Measurement of the minimum principal stress

The minimum principal stress acting on a formation can be measured only discretely and indirectly.

Laboratory analysis of cores (see the previous mention of DSA and ASR) can provide from strain measurements the ratio of effective stresses acting on the formation at the time the core was taken. These techniques are discussed in detail in Section 3-6.4.

Stress measurements using the micro-hydraulic fracturing technique (Haimson, 1993) can be conducted in open- or cased holes. As also discussed in Section 3-6.2, the tests measure the pressure at which a 3- to 10-ft fracture opens or closes to produce an estimate of the minimum total stress acting on the formation (Desroches and Kurkjian, 1999) averaged over a height of several feet. Another advantage of the technique is that bounding layers can also be tested.

Closure pressure determined from a hydraulic fracturing calibration treatment is also an estimate of the minimum total stress acting on the formation. The difference from the previous technique is that the measurement is averaged over a much larger volume of rock and usually corresponds to the pay zone. Provided that the averaging is taken into account, the minimum principal stress values yielded by both the micro-hydraulic fracturing technique and hydraulic fracturing calibration agree (e.g., Desroches and Woods, 1998) with the exception of complex situations. Pressure derivative analysis of the calibration treatment can also provide the average minimum total stress for the bounding layer, allowing the primary height growth of the fracture (see Sidebar 9C).

- Measurement of intermediate principal stress

The intermediate principal stress is always inferred from a relation that involves at least the minimum principal stress (Haimson and Huang, 1989; Ito and Hayashi, 1991; Guo *et al.*, 1993). Obtaining a good estimate of the intermediate principal stress is difficult. It is mentioned only because it was once popular to use the breakdown pressure for the calculation (Hubbert and Willis, 1957). However, more recent work on the breakdown process (Detournay and Carbonell, 1994) shows that the breakdown pressure provides unreliable estimates and should not be used in the analysis of stresses.

- Continuous estimate of minimum principal stress versus depth

As for the other properties mentioned in this chapter, the goal is to obtain a stress profile (i.e., a con-

tinuous description) of the value and orientation of the minimum principal stress over the zone of interest. To generate the best continuous description from the information available, geologic information must also be used.

The three-step procedure proceeds from the general to a particular case. First the global basin perspective is used to determine the most likely stress regime acting on the formation. A mathematical model (also called a stress model) is chosen in the second step to represent the variation of the stresses across the sequence of interest comprising the pay zone and bounding layers. The model is selected and calibrated using stress measurements and formation properties. It provides stress data for the design of hydraulic fracturing treatments for the sequence of interest. Finally, after a calibration treatment, further refinement based on lithology yields the stress variations in the layers to be stimulated.

#### – Stress regimes

An assessment of the stress regime establishes the expected cause for bed-to-bed stress variations through the formation and helps to identify a mathematical model for defining the stress profile.

Five states of stress may be defined in terms of the principal stresses (Fig. 4-8) (Engelder, 1993).

The simplest case consists of all three principal stresses being equal (i.e., lithostatic state of stress). This can occur in materials with little or no shear strength, such as poorly consolidated shales, or in materials that flow, such as salt. It may also be approached in extremely overpressured sediments. This state of stress is not widely documented because stress is usually not measured in these materials.

The second simplest case occurs in regions where the two horizontal stresses are equal and less than the vertical stress of the overburden. This regime may be expected in basins located in quiet, intraplate settings.

For the remaining cases, the three principal stress magnitudes differ significantly. In-situ stress measurements and borehole image analysis concur to indicate that this is the most likely situation. Unequal horizontal stresses can be attributed to tectonic forces or effects that result from the presence of a geologic feature (e.g., a fold or fault).

Depending on the ordering of the stresses, three cases are defined:

- $\sigma_v$  is the maximum principal stress  $\sigma_1$ : normal fault regime
- $\sigma_v$  is the minimum principal stress  $\sigma_3$ : thrust fault regime
- $\sigma_v$  is the intermediate principal stress  $\sigma_2$ : strike-slip fault regime.

Stress measurements from around the world also indicate that pore pressure, lithology and the position of the layer within the structure (e.g., Whitehead *et al.*, 1987; Thiercelin and Plumb, 1991; Aleksandrowski *et al.*, 1992) are factors influencing variation of the stresses in sedimentary rocks. Typically, pore pressure changes induce stress changes that are greater than those associated with lithology, tectonic setting and structural or stratigraphic position.

The stress regime is extremely important. Depending on the stress regime, identical lithologic structures can induce very different stress contrasts. For example, in a typical sand/shale sequence (Fig. 4-15A), the shales bear higher stresses than the sandstones in a relaxed tectonic setting, whereas the sandstones bear higher stresses than the shales in a compressive tectonic setting (Fig. 4-15B).

#### – Mathematical stress models

For the tectonic setting of the basin, the most likely of the five states of stress described previously is identified. The probable state of stress guides the ordering of the stresses and selecting

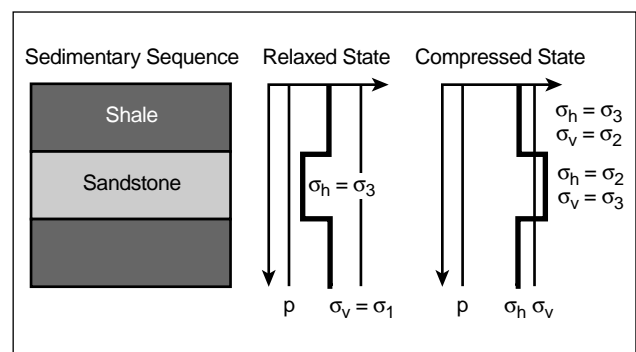


**Figure 4-15A.** Schematic stress profiles through a bedded sand/shale sequence show the two end-member stress profiles observed in sedimentary rocks. The relaxed-state profile is most frequently observed. The compressed-state profile is expected wherever significant horizontal strain is present.



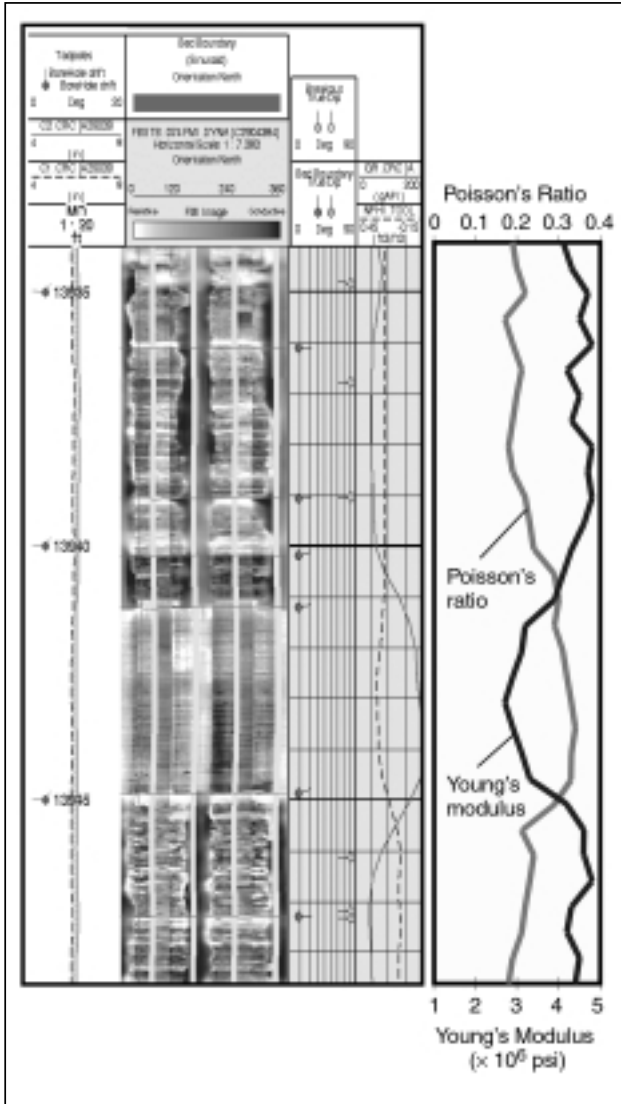


**Figure 4-15B.** Lithology-controlled breakouts, indicating a compressed state.

the stress model that provides a continuous description of the minimum horizontal stress as a function of depth over the zone of interest.

For the simplest, lithostatic case:

$$\sigma_h(z_{TVD}) = \sigma_H(z_{TVD}) = \sigma_v(z_{TVD}) = \int_0^{z_{TVD}} \rho_b(z) dz. \quad (4-31)$$

For the case in which the equal horizontal stresses are less than the vertical stress, the model can be either the uniaxial model or the friction failure model, with failure computed between the horizontal stress and the vertical stress.

For the remaining three cases of unequal horizontal stresses, it is appropriate to use either the poroelastic stress model or a friction failure model, with failure computed between the minimum and maximum principal stresses and the ordering coming from the faulting regime.

To select the stress model, measurements of the magnitude of the minimum principal stress are required for several points in the considered sequence. Two measurements are the absolute minimum.

The methodology defines the coefficient of earth stress  $K$  as the ratio between the effective vertical stress  $\sigma_v'$  and the effective minimum horizontal stress  $\sigma_h'$ :

$$K = \frac{\sigma_h'}{\sigma_v'}, \quad (4-32)$$

which is approximated, to the first order, by

$$K^* = \frac{\sigma_h - p}{\sigma_v - p}, \quad (4-33)$$

where  $p$  is the pore pressure (Fig. 4-16).

$K^*$  is plotted with respect to the variables  $v$ ,  $E$ , true vertical depth  $z_{TVD}$ ,  $\phi$  and  $p$ . Strong correlation among  $K^*$ ,  $v$  and  $p$  favors using the uni-

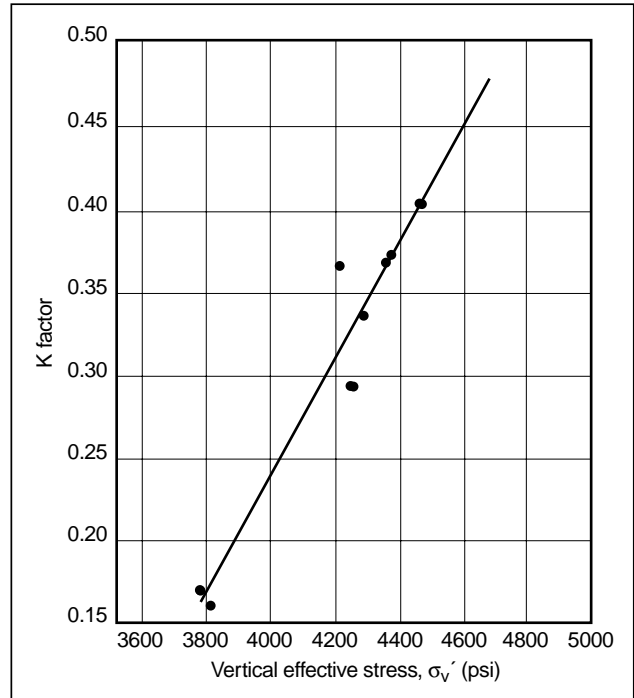


**Figure 4-16.**  $K$  factor ( $= (\sigma_h - p)/(\sigma_v - p)$ ) as a function of vertical effective stress (equivalent to  $z_{TVD}$ ) (Morita et al., 1998).

axial model. A continuous profile of  $\sigma_h$  is obtained by using the following equation with the Biot constant  $\alpha$  as an ad hoc potentially lithology-dependent calibration parameter:

$$\sigma_h = \frac{\nu}{1-\nu}(\sigma_v - \alpha p) + \alpha p. \quad (4-34)$$

Use of this model is reasonable for low-porosity, low-permeability sandstones, shales and carbonates.

Strong correlation among  $K^*$ ,  $\nu$ ,  $E$  and  $p$  favors using the poroelastic model. Indeed, a significant effect of Young's modulus suggests tectonic activity. A continuous profile of  $\sigma_h$  is obtained by using the following equation:

$$\sigma_h = \frac{\nu}{1-\nu}(\sigma_v - \alpha p) + \alpha p + \frac{E}{1-\nu^2}\epsilon_h + \frac{\nu E}{1-\nu^2}\epsilon_H, \quad (4-35)$$

where the minimum tectonic strain  $\epsilon_h$  and maximum tectonic strain  $\epsilon_H$  are the primary calibration factors (i.e., adjusted first with  $\alpha = 1$ ) and  $\alpha$  is the secondary calibration parameter adjusted once the tectonic strains are adjusted. The amount and sign of the tectonic strains must be compatible with the geologic setting. For example, negative strains are not possible in a compressive environment. This model applies in lithologies similar to those applicable to Eq. 4-34.

Strong correlation among  $K^*$ , the friction angle  $\phi$  and  $p$  (but not  $\epsilon$  or  $\nu$ ) favors use of the incipient failure model:

$$\sigma_h = \frac{1}{N_\phi}(\sigma_v - p) + p \quad (4-36)$$

$$N_\phi = \tan^2\left(\frac{\pi}{2} + \frac{\phi}{4}\right), \quad (4-37)$$

where  $N_\phi$  is the coefficient of passive stress. This model is appropriate for medium- to high-porosity sandstones (15% and greater) and clay-supported rocks, particularly in regions of normal (or growth) faulting. The friction angle of these rocks does not vary greatly, so this setting yields only small variations of the stresses as a function of lithology.

Correlation among  $K^*$ ,  $\phi$  and  $p$  with departure from Eq. 4-37 suggests use of the purely frictional model:

$$\sigma_h = (1 - \sin\phi)\sigma_v + (\sin\phi)p. \quad (4-38)$$

This model is appropriate in high-porosity, high-permeability sandstones, chalks and shales. It corresponds to rock at rest if the rock compacts. There are no calibration parameters in the models governed by friction except for the friction angle. Calibration is conducted by modifying the friction angle.

The effect of pore pressure variations (through either depletion or water flooding; see Section 3-5.7) and temperature variations can also be added to the selected model (e.g., Perkins and Gonzales, 1984). Another effect that can be considered is stress relaxation; it reduces the difference between the minimum and maximum stresses (e.g., Prats, 1981), especially in shales. Once the stress model is built, it usually is portable within the same sequence in the same basin, provided that significance differences in pore pressure and possibly in temperature are taken into account.

The methodology advocated in this chapter relies on physical processes underlying the mathematical form of the model selected to build a stress profile. Other mathematical forms can be selected, but without geologic confirmation, the portability of the stress profile to another well is not likely.

#### – Stress profile adjustment after a calibration treatment

As mentioned previously, the analysis of a calibration treatment yields an average of the minimum stress acting on the pay zone (called the closure pressure) and possibly a value of the average stress contrast between the pay zone and the bounding layer in which the fracture may have grown.

If only the stress acting on the pay  $\sigma_{PZ}$  is available, the model-based stress profile can be scaled or shifted to honor its value at depth. If the stress acting on a bounding layer  $\sigma_{BL}$  is also available, further calibration can be performed. It is preferable to modify the parameters of the mathematical model to honor these stress values, but the parameters may not be available at the time of the calibration treatment. If this is the case, a lithology-based stress interpolation can be used as follows.



One of the formation properties can usually be identified as representative of the difference in stresses (e.g., the percentage of dolomite in a carbonate sequence or the volume of clay in a sand/shale sequence). For this property  $A$ ,  $A_{PZ}$  and  $A_{BL}$  are its values in the pay zone and the bounding layers, respectively, and the stresses in the vicinity of the pay zone may be estimated as a linear function of  $A$ :

$$\sigma(z_{TVD}) = m \times A(z_{TVD}) + b, \quad (4-39)$$

where the linear regression constants are

$$m = \frac{\sigma_{BL} - \sigma_{PZ}}{A_{BL} - A_{PZ}} \quad (4-40)$$

$$b = \sigma_{PZ} - m \times A_{PZ}. \quad (4-41)$$

This approach has been successfully applied for both sand/shale (Miller and Smith, 1989; Smith *et al.*, 1989) and carbonate sequences.

## 4-6. Zoning

Most of the models used in reservoir stimulation require defining zones with constant, or possibly linearly varying, properties within each zone. Once all the required properties have been collected, the logs must be zoned into distinct zones that will be the final input to the stimulation process. If parallel, horizontal beds are assumed, the zones must ultimately be defined in TVD. If the beds are not parallel or not horizontal, more complicated and ad hoc transformations must be made, but these adjustments are outside the scope of this chapter.

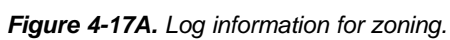
Zoning can be done subjectively by hand or objectively in a manner called log squaring, which was developed for formation evaluation (Trouiller *et al.*, 1989; Serra and Andreani, 1991). Log squaring uses the response functions of the tools introduced in “Lithology” in Section 4-4.2. However, it is not directly applicable to reservoir stimulation because it considers only the classic measurements used in formation evaluation (e.g., porosity, density, resistivity). It ignores pore pressure, permeability, mechanical properties and stresses, which are integral to the zoning process considered here. Furthermore, because no response equation exists yet for these latter properties, the zones output by log squaring must be manually refined.

A simple solution is to consider as many zones as there are significant changes. But this is not practical because more than 100 zones could be defined and only a limited number of zones can be considered. Therefore, broader zones must first be defined. The first step is to decide which property, or set of properties, should guide the definition of zones. In sand/shale sequences, for example, the volume of clay is a primary guide, whereas in carbonate sequences, the percentage of dolomite is a good primary guide. However, permeability barriers (usually associated with pore pressure and hence stress changes), changes in elastic properties and changes in the stresses should also be considered. The set of properties selected to guide the zoning process must also reflect the geologic understanding that guided choosing the model for the stresses. Determination of the leakoff height is also part of the zoning process. The zones must be defined in a consistent manner so that the leakoff coefficient determined from a calibration treatment is meaningful for the remainder of the sequence.

A zoning example is presented in Fig. 4-17. This sand/shale sequence reservoir has strong variations in permeability and pore pressure because of water flooding. The main properties selected to define zones were the separation between sands and shales and the profile of pore pressure. More zones were added to consider sharp changes in Young’s modulus, which resulted in the definition of 25 zones. Zoning for formation evaluation would have been significantly different, reflecting the analyst’s different point of view.

Once the zones have been defined, they must be populated with a constant value (or possibly linearly varying, for pore pressure and stresses). For thin beds with significant contrast, taking the peak value is preferred, whereas for thick beds, taking an average away from the bed boundaries is preferred.

Finally, most log measurements sample the formation to only a few feet from the wellbore. The zoning process described here, however, populates zones with a constant value along the bed extension, ignoring any heterogeneity along the bed. The constancy may be arbitrary, especially for geologic environments known to typically have lateral variations of properties (e.g., channels, bar sands). Crosswell tomography (Warpinski *et al.*, 1998b) shows that formation properties can vary significantly along a bed in less than 50 ft of horizontal displacement. Yet knowledge of the geologic environment is the only qualifier of the information developed from the zoning process.



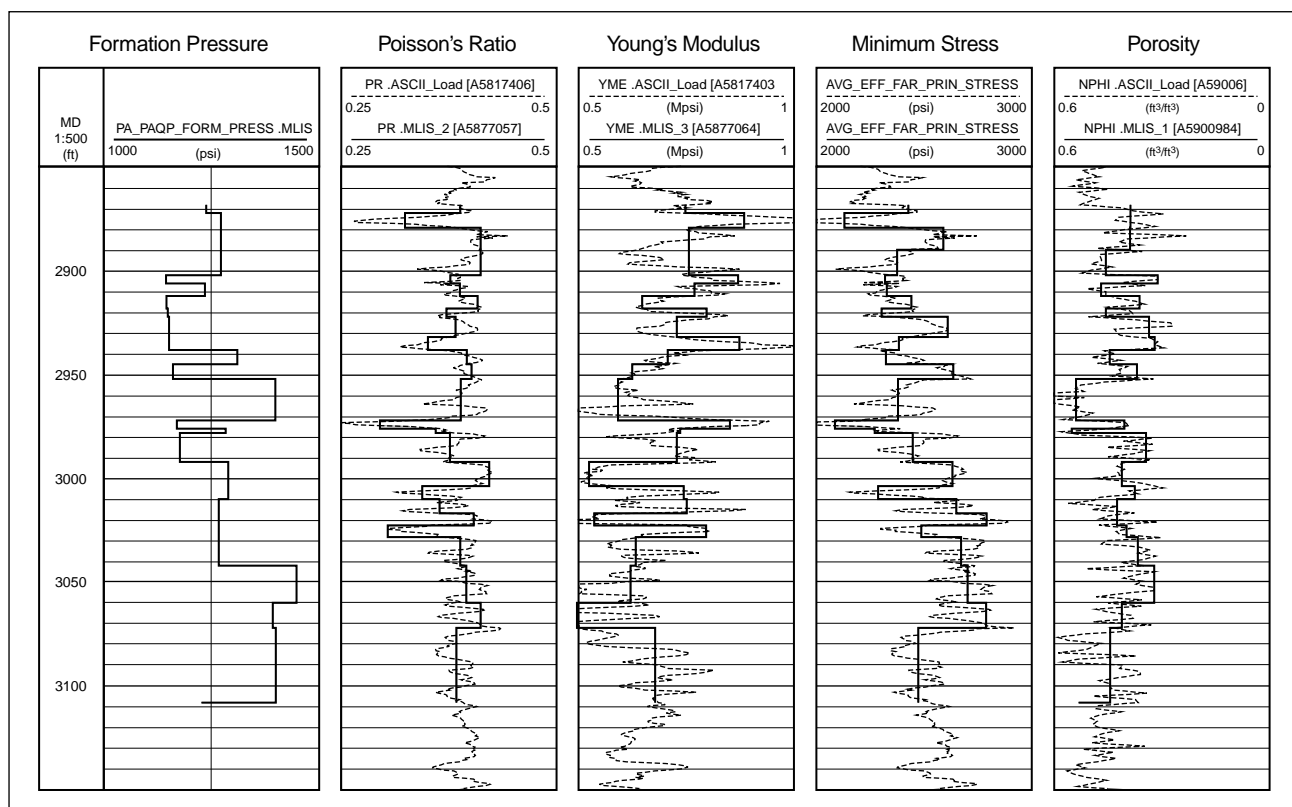


**Figure 14-17B.** Corresponding zoned formation model.

# Basics of Hydraulic Fracturing

*M. B. Smith, NSI Technologies, Inc.*

*J. W. Shlyapobersky,<sup>†</sup> Shell E&P Technology Co.*

## 5-1. Introduction

Since its introduction, hydraulic fracturing has been, and will remain, one of the primary engineering tools for improving well productivity. This is achieved by

- placing a conductive channel through near-wellbore damage, bypassing this crucial zone
- extending the channel to a significant depth into the reservoir to further increase productivity
- placing the channel such that fluid flow in the reservoir is altered.

In this last instance, the fracture becomes a tool for true reservoir management including sand deconsolidation management and long-term exploitation strategies. As first visualized (see the Appendix to this chapter), the concept of hydraulic fracturing was quite straightforward. This visualization is described in the following, and in general, for reasonably simple geology, the basic physics of fracturing is straightforward and well established. Complexity arises from two directions: geologic reality and the inherent multidisciplinary nature of the fracturing process.

Historically, the control of fracturing has rested with drilling and operations groups owing to the nature of field procedures using pumps, packers, pressure limits, etc. However, the final results (and thus design) are dominantly a production engineering exercise, and fracturing cannot be removed from intimate contact with reservoir engineering. At the same time, designing a treatment to achieve the desired results is also intimately connected with rock mechanics (which controls fracture geometry; see Chapters 3 and 4), fluid mechanics (which controls fluid flow and proppant placement inside a fracture; see Chapter 6) and the chemistry that governs the performance of the materials used to conduct the

treatment (see Chapters 7 and 8). However, the design must also be consistent with the physical limits set by actual field and well environments. Also, treatments must be conducted as designed to achieve a desired result (i.e., full circle to the critical role of operations). Proper treatment design is thus tied to several disciplines:

- production engineering
- rock mechanics
- fluid mechanics
- selection of optimum materials
- operations.

Because of this absolutely essential multidisciplinary approach, there is only one rule of thumb in fracturing: that there are no rules of thumb in fracturing.

The multidisciplinary nature, along with the difficulty in firmly establishing many of the design variables, lends an element of art to hydraulic fracturing. This is not to say that the process is a mystery nor is it to say that for most cases the basic physics controlling the process is not defined (see Chapter 6). It simply says that the multitude of variables involved, along with some uncertainty in the absolute values of these variables, makes sound engineering judgment important.

### 5-1.1. What is fracturing?

If fluid is pumped into a well faster than the fluid can escape into the formation, inevitably pressure rises, and at some point something breaks. Because rock is generally weaker than steel, what breaks is usually the formation, resulting in the wellbore splitting along its axis as a result of tensile hoop stresses generated by the internal pressure. The mechanics of this process are described in Section 3-5.7, and the simple idea of the wellbore splitting like a pipe (shown as a cartoon in Fig. 5-1) becomes more complex for cased and/or perforated wells and

<sup>†</sup> Deceased

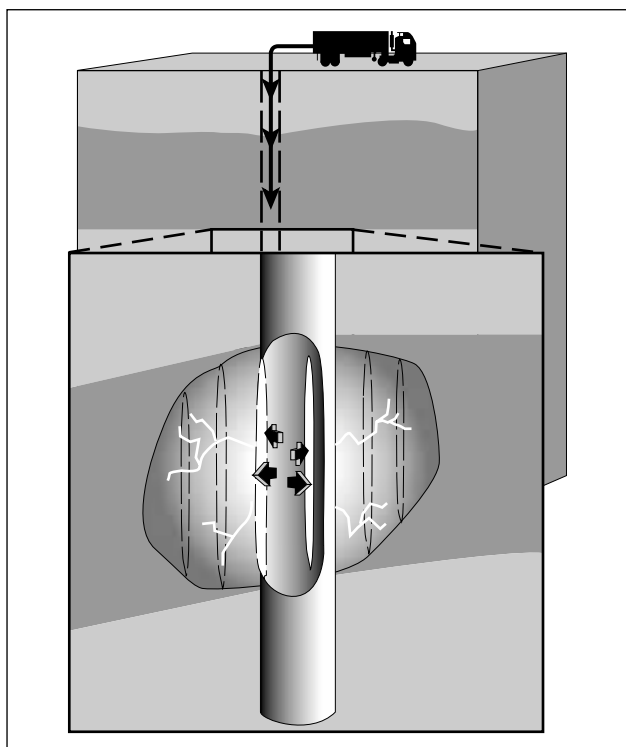


**Figure 5-1.** Internal pressure breaking a vertical wellbore.

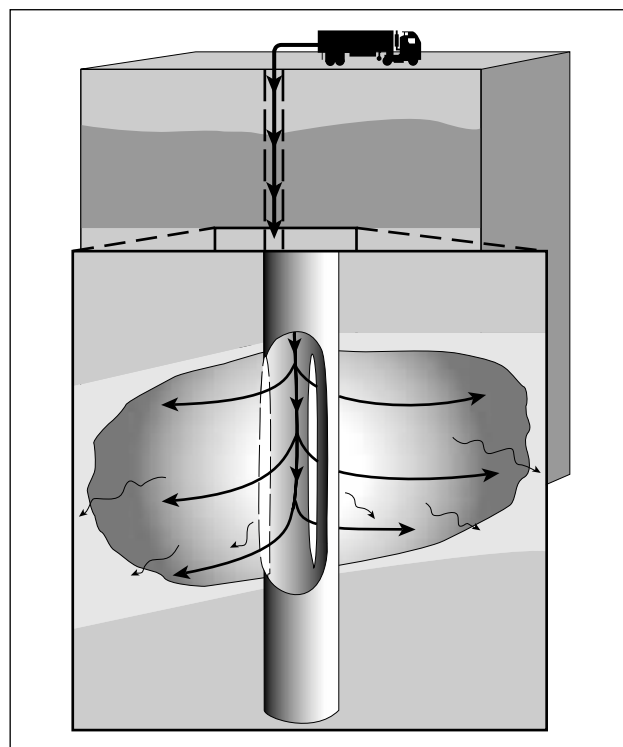


**Figure 5-2.** Cross-sectional view of a propagating fracture.

nonvertical wells. However, in general, the wellbore breaks—i.e., the rock fractures—owing to the action of the hydraulic fluid pressure, and a “hydraulic” fracture is created. Because most wells are vertical and the smallest stress is the minimum horizontal stress, the initial splitting (or breakdown) results in a vertical, planar parting in the earth.

The breakdown and early fracture growth expose new formation area to the injected fluid, and thus the rate of fluid leaking off into the formation starts to increase. However, if the pumping rate is maintained at a rate higher than the fluid-loss rate, then the newly created fracture must continue to propagate and grow (Fig. 5-2). This growth continues to open more formation area. However, although the hydraulic fracture tremendously increases the formation flow area while pumping, once pumping stops and the injected fluids leak off, the fracture will close and the new formation area will not be available for production. To prevent this, measures must be taken to maintain the conductive channel. This normally involves adding a propping agent to the hydraulic fluid to be transported into the fracture. When pumping stops and fluid flows back from the well, the propping agent remains in place to keep the fracture

open and maintain a conductive flow path for the increased formation flow area during production. The propping agent is generally sand or a high-strength, granular substitute for sand (see Section 7-7). Alternatively, for carbonate rocks, the hydraulic fluid may consist of acid that dissolves some of the formation, leaving behind acid-etched channels extending into the reservoir.

After the breakdown, the fracture propagation rate and fluid flow rate inside the fracture become important. They are dominated by fluid-loss behavior. As introduced by Carter (1957) and discussed in the following (and in Chapters 6 and 9), the fluid-loss rate  $q_L$  from a fracture can be expressed as

$$q_L \approx \frac{2C_L A}{\sqrt{t - \tau}}, \quad (5-1)$$

where  $C_L$  is the fluid-loss coefficient,  $A$  is an element of the fracture area (i.e., increased inflow area),  $t$  is time measured from the start of pumping, and  $\tau$  is the time when each small area element of a fracture is created or opened. As a direct consequence of this relation, the highest rate of fluid loss is always at the fracture tip. Newly created fracture area exists at that

point ( $t - \tau = 0$  in the denominator), making  $q_L$  instantly infinite.

Initially, fracture penetration is limited, and hence fluid loss is high near the wellbore. For that reason, the first part of a hydraulic fracture treatment consists of fluid only (no proppant); this is termed the pad. The purpose of a pad is to break down the wellbore and initiate the fracture. Also, the pad provides fluid to produce sufficient penetration and width to allow proppant-laden fluid stages to later enter the fracture and thus avoid high fluid loss near the fracture tip. After the pad, proppant-laden stages are pumped to transport propping agent into the fracture. This chapter describes the process for propped fracture treatments; acid fracture treatments are discussed in Section 10-6.

However, because fluid loss to the formation is still occurring, even near the well, the first proppant is added to the fluid at low concentrations. The proppant-laden slurry enters the fracture at the well and flows toward the fracture tip (Fig. 5-3). At this point, two phenomena begin. First, because of the higher fluid loss at the fracture tip, slurry flows through the fracture faster than the tip propagates, and the proppant-laden slurry eventually overtakes the fracture tip. Next, because of fluid loss, the proppant-laden slurry stages lose fluid (but not proppant) to the formation.

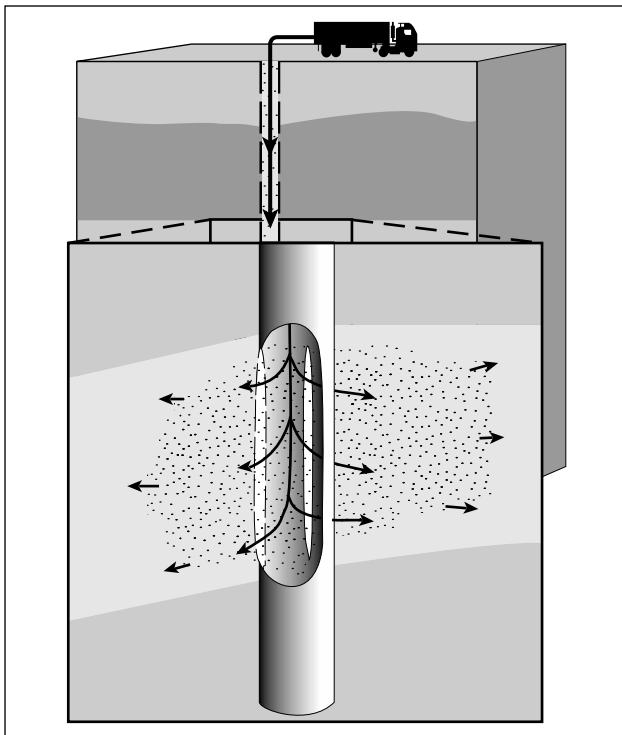


**Figure 5-3.** *Introducing proppant into the fracture.*

Thus, proppant concentration (i.e., volume fraction of solid proppant) increases as the slurry stages dehydrate. The pump schedule, or proppant addition schedule, must be engineered much like handicapping horse races, but with no single winner. Rather, all stages should finish at the right place, at the right time, with the right final proppant concentration. The pad should be completely lost to the formation, and the first proppant stage should be right at the fracture tip (which should be at the design length).

As the proppant slurry stages move down the fracture, they dehydrate and concentrate. Slurry stages pumped later in the treatment are pumped at a higher concentration. These stages are not in the fracture for long prior to the treatment end (i.e., prior to shut-down) and are thus exposed to less fluid loss and less dehydration. Ideally, the first proppant stage pumped reaches the fracture tip just as the last of the pad fluid is lost into the formation (a correctly handicapped race), and this first stage has concentrated from its low concentration to some preselected, higher final design concentration. Meanwhile, the slurry concentration being pumped is steadily increased to the same final design concentration. At treatment end, the entire fracture is filled with the design concentration slurry. Design considerations for the final concentration are discussed later in this section and in detail in Section 10-4.

The preceding description might be termed a “normal” design, where the entire fracture is filled with a uniform, preselected, design proppant concentration just as the treatment ends. If pumping continues past that point, there would be little additional fracture extension because the pad is 100% depleted. Continued pumping forces the fracture to become wider (and forces the pressure to increase) because the increased volume simply acts like blowing up a balloon. In some cases the additional propped width that results may be desirable, and this procedure is used purposely. This is termed tip-screenout (TSO) fracturing.

At the conclusion of the treatment, the final flush stage is pumped. This segment of a treatment consists of one wellbore volume of fluid only and is intended to sweep the wellbore clean of proppant (Fig. 5-4). The well is generally then shut-in for some period to allow fluid to leak off such that the fracture closes on and stresses the proppant pack. Shut-in also allows temperature (and chemical breakers added to the fluid while pumping) to reduce

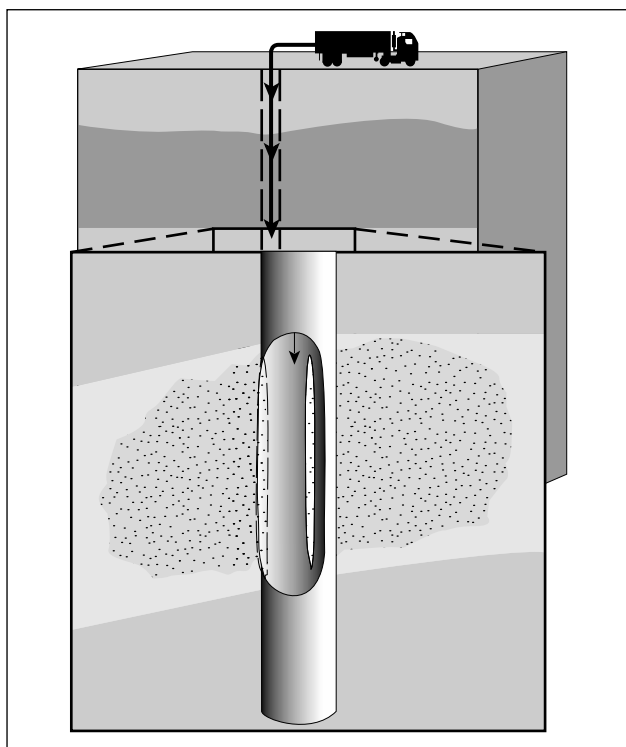


**Figure 5-4.** Flushing the wellbore to leave a propped fracture.

the viscosity of the fracturing fluid (see Section 7-6.2). Ideally, this process leaves a proppant-filled fracture with a productive fracture length (or half-length  $x_f$ ), propped fracture height and propped fracture width (which determines the fracture conductivity  $k_{fw}$ ). Here,  $x_f$  is the productive fracture half-length, which may be less than the created half-length  $L$  or less than the propped length.

### 5-1.2. Why fracture?

Hydraulic fracture operations may be performed on a well for one (or more) of three reasons:

- to bypass near-wellbore damage and return a well to its “natural” productivity
- to extend a conductive path deep into a formation and thus increase productivity beyond the natural level
- to alter fluid flow in the formation.

In the third case, fracture design may affect and be affected by considerations for other wells (e.g., where to place other wells and how many additional wells to drill). The fracture becomes a tool for reservoir management. Although these three motivations

are addressed separately in this section, they frequently overlap.

- **Damage bypass**

Near-wellbore damage reduces well productivity. This damage can occur from several sources, including drilling-induced damage resulting from fines invasion into the formation while drilling and chemical incompatibility between drilling fluids and the formation. The damage can also be due to natural reservoir processes such as saturation changes resulting from low reservoir pressure near a well, formation fines movement or scale deposition. Whatever the cause, the result is undesirable. Matrix treatments (discussed in Chapters 13 through 20) are usually used to remove the damage chemically, restoring a well to its natural productivity. In some instances, chemical procedures may not be effective or appropriate, and hydraulic fracture operations are used to bypass the damage. This is achieved by producing a high-conductivity path through the damage region to restore wellbore contact with undamaged rock.

- **Improved productivity**

Unlike matrix stimulation procedures, hydraulic fracturing operations can extend a conductive channel deep into the reservoir and actually stimulate productivity beyond the natural level.

All reservoir exploitation practices are subject to Darcy’s law:

$$q \approx \frac{kh}{\mu} \frac{\Delta p}{\Delta x} \left( \frac{A}{h} \right), \quad (5-2)$$

where the all-important production rate  $q$  is related to formation permeability  $k$ , pay thickness  $h$ , reservoir fluid viscosity  $\mu$ , pressure drop  $\Delta p$  and formation flow area  $A$ . Reservoir exploitation revolves around manipulating this equation. For example, pressure drop may be increased by using artificial lift to reduce bottomhole flowing pressure, water injection to increase or maintain reservoir pressure, or both. For other cases, in-situ combustion or steam injection is used to reduce reservoir fluid viscosity and thus increase productivity. For fracturing, as pictured in Fig. 5-5, operations are on the formation area in the equation, with the increased formation flow area giving the increased production rate and increased present value for the reserves. (Strictly speaking, it is the

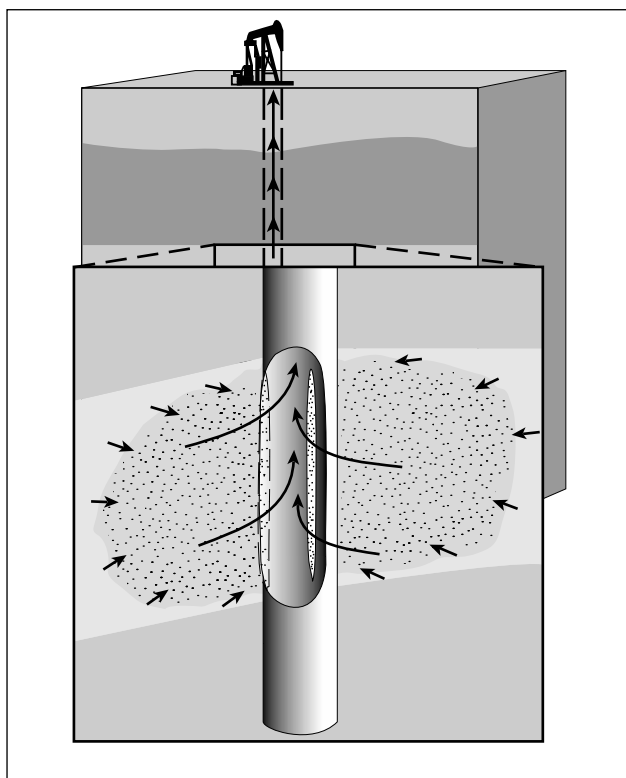


**Figure 5-5.** Increased flow area resulting from a fracture.

flow shape that is altered, as discussed in detail in Chapter 1.)

This is the classic use of fracturing, to increase the producing rate by bypassing near-wellbore formation damage or by increasing exposure of the formation area and thus stimulating well performance beyond that for no damage. For a single well, treatment design concentrates on creating the required formation flow area to yield increased production at minimal cost. More formally, the design should optimize economic return on the basis of increased productivity and treatment cost.

- Reservoir management

Along with improving well productivity, fractures also provide a powerful tool for altering reservoir flow. In combination with the other parts of field development, the fracture becomes a reservoir management tool. For example, creating long fractures in tight rock ( $k < 0.1$  md) enables field development with fewer wells. However, even fewer wells are required if the fracture azimuth is known and the wells are located appropriately (e.g., not on a regulatory-required square pattern). The actual philosophy shift for fracturing, from

accelerating production from a single well to reservoir management, occurred with the application of massive stimulation treatments in tight gas formations (see Appendix to this chapter). Although outwardly a traditional application of fracturing to poorer quality reservoirs, these treatments represented the first engineering attempts to alter reservoir flow in the horizontal plane and the methodology for well placement (e.g., Smith, 1979).

Fracturing for vertical inflow conformance (i.e., reservoir management) was successfully used in the Gullfaks field (Bale *et al.*, 1994), where selective perforating and fracturing were used to optimize reserve recovery and control sand production while maintaining (but not necessarily increasing) the required production rates. This is illustrated in Fig. 5-6, where the bottom, low-permeability Rannoch-1 zone was perforated to create a propped fracture that extends up and into the high-permeability ( $>1000$ -md) Rannoch-3 zone. Without fracturing, the entire zone can be perforated, and a low drawdown allows a significant production rate on the order of 20,000 STB/D, sand free. However, sand production is triggered by water breakthrough in the high-permeability zone (from downdip water injection). The resulting wellbore enlargement caused by sand production acts to stimulate production from the high-permeability zone. To stop sand production, draw-

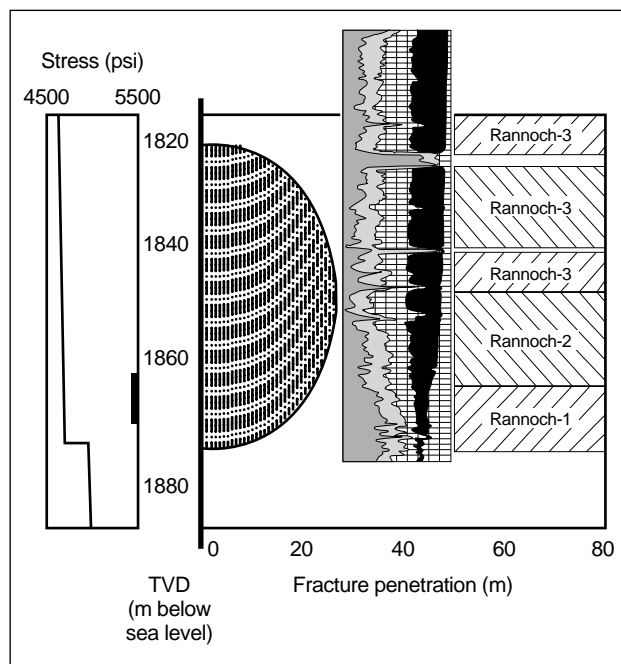


**Figure 5-6.** Fracturing for vertical inflow conformance.



down must be reduced even more. The production is then essentially 100% water coming from the stimulated high-permeability zone, and the well must be abandoned. This further diminishes production from the large reserves found in the deeper zones with lower permeability.

Open- or cased hole gravel packing could be used to eliminate the sand production. However, such completions are less than satisfactory for two reasons. First, the deeper, lower permeability zones can significantly benefit from stimulation. Second, significant scaling occurs with water breakthrough and quickly plugs the gravel pack.

The fracturing tool selected to manage the Gullfaks field is termed an indirect vertical fracture completion (IVFC). The IVFC accomplishes several goals:

- Some (although choked) production is achieved from the main zone to enable the well to reach minimum productivity standards.
- Production from the lower, moderate-permeability zone is stimulated, maximizing reserves from this zone.
- Greater drawdown is allowed because the weak high-permeability rock is separated from the perforations, and greater drawdown increases the total rate and significantly increases recovery from the lower zones.
- If the upper high-permeability zone has sand production tendencies (as is typically the case), then producing this zone via the fracture totally avoids the need for sand control.
- Any potential for water breakthrough in the high-permeability zone is retarded, and post-water-breakthrough oil production is significantly increased.

To achieve these goals, fracture conductivity must be tailored by synergy between the reservoir and fracture models. Too much conductivity accelerates production and the time to water breakthrough from the high-permeability main zone. Also, too much conductivity, because of surface or tubular limits for the production rate, restricts drawdown on the lower zones, and the desired, more uniform vertical production profile is not achieved. The fracture design goal is not to simply accelerate the rate but to achieve maximum reserves recovery with no sacrifice of rate

(as compared with a simple completion in which the entire zone is perforated).

Another example of reservoir management is waterflood development utilizing fractures and a “line drive” flood pattern (i.e., one-dimensional [1D] or linear flow from injection fractures to production fractures). Knowledge of the fracture azimuth, combined with conductive fractures (or correctly controlled injection greater than the fracture pressure) results in improved sweep efficiency and enables more efficient field development.

### 5-1.3. Design considerations and primary variables

This section introduces the primary variables for fracture design. Sidebar 5A summarizes how the design variables originate from treatment design goals.

As mentioned previously, fracturing was controlled historically by operational considerations. This limited its application because fracturing is dominantly a reservoir process, and hence why a reservoir is fractured and what type of fracture is required should be dominated by reservoir engineering considerations. The permeability  $k$  becomes the primary reservoir variable for fracturing and all reservoir considerations. Other, so-called normal reservoir parameters such as net pay and porosity dominate the economics and control the ultimate viability of a project but do not directly impact how the fracturing tool is employed. As discussed in Chapter 12, postfracture productivity is also governed by a combination of the fracture conductivity  $k_f w$  and  $x_f$ , where  $k_f$  is the permeability of the proppant in the fracture,  $w$  is the propped fracture width, and  $x_f$  is the fracture penetration or half-length. These variables are controlled by fracturing and therefore identify the goals for treatment design.

The productive fracture half-length  $x_f$  may be less than the created (or the created and propped) half-length  $L$  because of many factors (see Section 12-3). For example, the fracture width near the tip of a fracture may be too narrow to allow adequate propped width. As another example, vertical variations in formation permeability, or layering, can cause the apparent productive length  $x_f$  to be less than the actual propped length (Bennett *et al.*, 1986). Similarly, this also makes the fracture height  $h_f$  important in several ways (Fig. 5-7):

## 5A. Design goals and variables

This discussion briefly summarizes the design goals of hydraulic fracturing that provide a road map for the major design variables.

### Design goals

Design goals result from Darcy's law (Eq. 5-2), in which the dimensionless term  $A/(\Delta x h)$  is defined by flow conditions and equals  $\ln(r_e/r_w')$  for steady-state flow (as discussed in Chapter 1). For steady-state flow, Prats (1961) showed that a fracture affects productivity through the equivalent wellbore radius  $r_w'$  and that  $r_w'$  is related to the fracture half-length or penetration  $x_f$  by the dimensionless fracture conductivity ( $C_{fD} = k_{fW}/kx_f$ ). Cinco-Ley *et al.* (1978) extended these concepts for transient flow with the relation among  $x_f$ ,  $r_w'$  and  $C_{fD}$  shown in Fig. 5-11 for pseudoradial flow (where the pressure-depletion region  $\gg x_f$  but is not affected by external boundaries). Thus, the primary design goals are fracture half-length or penetration and the fracture conductivity  $k_{fW}$ , with their relative values defined by  $C_{fD}$ .

### Design variables

Design variables result from material balance, rock mechanics and fluid mechanics considerations.

The material balance is (Eqs. 5-10 through 5-12)

$$V_i = V_i - V_{Lp}; \quad V_i = 2Lh_i\bar{w}, \quad V_i = q_i t_p \quad \text{and} \quad V_{Lp} \approx 6C_L h_L L \sqrt{t_p} + 4Lh_L S_p, \quad (5A-1)$$

where  $C_L$  and  $S_p$  are fluid-loss parameters that can be determined by the results of a fluid-loss test (Fig. 5A-1) for which the filtrate volume divided by the exposed area  $V_L/A = S_p + 2C_L\sqrt{t}$ . Combining the relations in Eq. 5A-1 gives Eq. 5-13:

$$L \approx \frac{q_i t_p}{6C_L h_L \sqrt{t_p} + 4h_L S_p + 2\bar{w}h_i},$$

where fracture penetration  $L$  is related to pump rate, fluid loss, height, width, etc.

Next is the elasticity equation (Eq. 5-14):

$$w_{max} = \frac{2p_{net}d}{E'},$$

where  $p_{net} = p_f - \sigma_c$ , and width is related to net pressure as a function of modulus and geometry and the pressure required to propagate the fracture (Eq. 5-21):

$$p_{sp} = (p - \sigma_c) \text{ at tip} \propto K_{lc-apparent} \sqrt{1/d}, \quad (5A-2)$$

where  $d$  is the characteristic fracture dimension and generally is the smaller dimension between  $h_f$  and  $L$ .

Third is the fluid flow equation (Eqs. 5-15 through 5-19), in which Eq. 5-15 ( $dp_{net}/dx = 12\mu q/h_f w^3$ ) is combined with the width equation:

$$p_{net} \approx \left[ \frac{E'^3}{h_f^4} \{ \kappa \mu q_i L \} + p_{net tip}^4 \right]^{1/4}, \quad (5A-3)$$

where the pressure drop down the fracture is related to viscosity, pump rate, fracture length (and thus to fluid loss), etc. The net pressure distribution gives the fracture width distribution and thus the final propped fracture width (i.e.,  $k_{fW}$ ). Hence the primary design variables are  $C_L$ ,  $h_L$ ,  $S_p$ ,  $h_f$ ,  $E'$ ,  $K_{lc-apparent}$ ,  $q_i$ ,  $\mu$  and  $\sigma_c$ .

### Optimum design

The optimum design results from maximizing revenue  $\$(r_w')$  minus the costs  $\$(x_f, k_{fW})$  by using the preferred economic criteria.

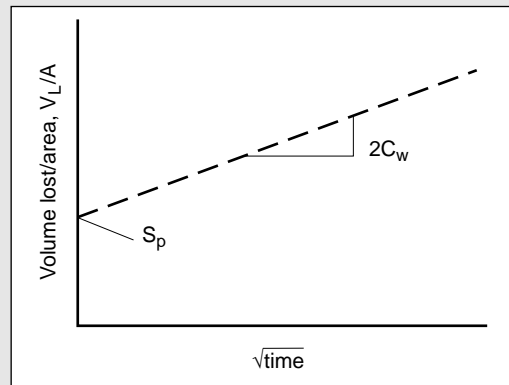


**Figure 5A-1.** Ideal laboratory fluid-loss data for spurt loss  $S_p$  and the wall-building or filter-cake fluid-loss coefficient  $C_w$ . If the total fluid loss is dominated by the filter cake, then the total fluid-loss coefficient  $C_L = C_w$ .

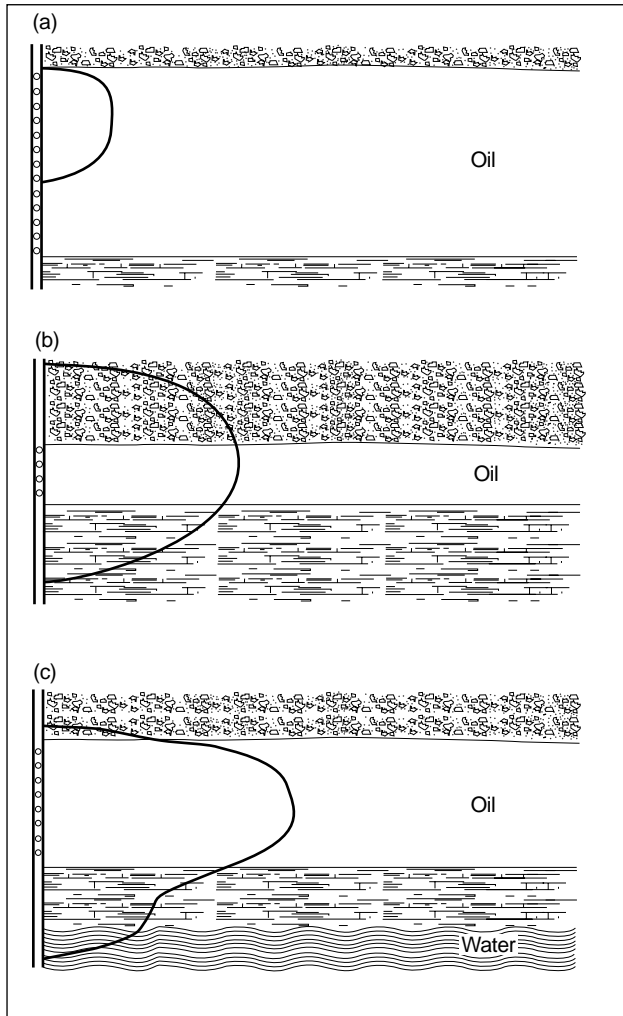


**Figure 5-7.** The importance of fracture height.

- In Fig. 5-7a, the fracture is initiated near the top of the interval, and  $h_f$  is not large enough to contact the entire zone, which is clearly an important reservoir concern.
- In Fig. 5-7b, the fracture grew out of the zone and contacted mostly nonreservoir rock, diminishing  $x_f$  relative to the treatment volume pumped.
- In Fig. 5-7c, the fracture grew downward past the oil/water contact and if propped would possibly result in unacceptable water production.

In all these cases, as discussed in Section 5-4.2, fracture height growth is controlled by rock mechanics considerations such as in-situ stress, stress gradients, stress magnitude differences between different geologic layers and differences in strength or fracture toughness between different layers. All these

rock mechanics considerations are related to the net pressure  $p_{net}$ :

$$p_{net} = p_f - \sigma_c, \quad (5-3)$$

where  $p_f$  is the pressure inside the fracture and  $\sigma_c$  is the minimum in-situ stress (or fracture closure pressure).

For an ideal, homogeneous zone, closure pressure is synonymous with the minimum in-situ stress. However, such ideal conditions do not exist. Stress is a point value, and stress varies from point to point. For realistic in-situ conditions, closure pressure reflects the pressure where the fracture is grossly closed, although the pressure may still be greater than the minimum in-situ stress at some points. For zones that are only slightly nonhomogeneous, the closure pressure represents a zone-averaged stress over the fracture. However, other conditions may be more complex. Consider the three-layer case of two low-stress sandstone intervals with a thick interbedded shale. The correct closure pressure may be the zone-averaged stress over the two low-stress zones, without including the higher stress interbedded zone.

The fracture width is also of major importance for achieving the desired design goals. Typically, this is expressed as the product of fracture permeability times fracture width; i.e.,  $k_f w$  is the dimensional conductivity of the fracture. Figure 5-8 is an ideal wellbore/fracture connection for a propped fracture that is intended to bypass near-wellbore formation damage. To achieve the desired production goals, a narrow fracture must, at a minimum, carry the flow that

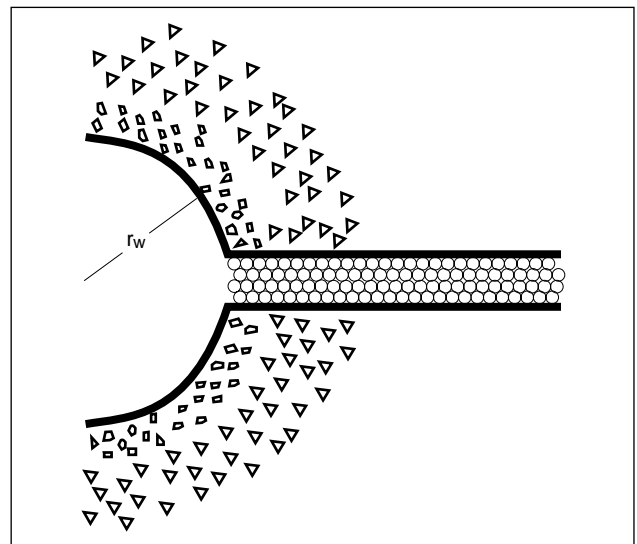


**Figure 5-8.** An ideal wellbore/fracture connection for a propped fracture that is intended to bypass near-wellbore formation damage.

would have been produced through the entire wellbore circumference (had there been no damage). The fracture conductivity  $k_f w$  must be greater than  $2\pi r_w k$ , where  $r_w$  is the wellbore radius. For higher permeability formations that can deliver high rates with sufficient fracture permeability, fracture width and any variables that affect width become important. As discussed in the following and in Section 6-2, width is controlled by the fracture dimensions ( $h_f$  and  $L$ ), net pressure inside the fracture acting to open and propagate the fracture, and another property, the modulus or stiffness of the rock.

As implied by the term hydraulic fracturing, fluid mechanics is an important element in fracturing. The two dominant fluid mechanics variables, injection (pump) rate  $q_i$  and fluid viscosity  $\mu$ , affect net pressure inside the fracture (and thus width) and largely control transport and the final placement of proppant in the fracture. These variables also have a role in controlling the volume of fluid lost to the formation during pumping. For example, high pump rates reduce the total fluid loss because for a given volume pumped there is less time for fluid loss to occur.

Another key factor of a good design is selection of the fluid and proppant systems with performance characteristics (e.g.,  $\mu$ ,  $C_L$ ,  $k_f$ ) that best meet the requirements for the fracture treatment (i.e., material selection). In addition, the performance variables for the materials must be properly characterized. Fluids and proppants are addressed in Chapter 7, and their performance is discussed in Chapter 8.

Finally, all the design parameters must be molded to be compatible with existing well conditions (i.e., operational considerations). For example, it does little good to complain that the detailed design and analysis done in planning a treatment for an existing well call for a high pump rate of 60 bbl/min when the wellbore conditions limit the maximum allowable pump rate to one-half that rate. Clearly, for new wells the operational considerations (detailed in Chapter 11) should be an integral part of planning for the drilling and completion process (e.g., well trajectory for extended reach wells) (Martins *et al.*, 1992c).

### 5-1.4. Variable interaction

It is clear that with major design considerations coming from multiple disciplines, the variables will react, interact and interconnect in multiple ways and

that many of these interactions will be contradictory or incompatible. This is discussed later, but an example is as follows. Consider a case where reservoir goals require a long fracture. With deep penetration into the pay zone, getting good proppant transport down a long fracture clearly requires high fluid viscosity. However, high viscosity increases the net pressure inside the fracture. This reacts with the stress difference between the pay and the overlying and underlying shales and causes height growth, resulting in less penetration than desired, and thus less viscosity is required.

Inherent contradictions controlling fluid selection abound:

- Good viscosity is required to provide good proppant transport, but minimal pipe friction is also desirable to reduce surface pump pressure.
- The fluid system is expected to control fluid loss, but without damage to the formation or fracture permeability.
- Performance at high temperature, for long periods of time, is required from a fluid system that does not cost much.

## 5-2. In-situ stress

In-situ stress, in particular the minimum in-situ stress (termed the fracture closure pressure for nonhomogeneous zones, as discussed earlier) is the dominant parameter controlling fracture geometry. It is discussed in detail in Chapter 3. For relaxed geologic environments, the minimum in-situ stress is generally horizontal; thus a vertical fracture that formed when a vertical wellbore broke remains vertical and is perpendicular to this minimum stress. Hydraulic fractures are always perpendicular to the minimum stress, except in some complex cases, and even for those cases any significant departure is only at the well. This occurs simply because that is the least resistant path. Opening a fracture in any other direction requires higher pressure and more energy.

The minimum stress controls many aspects of fracturing:

- At very shallow depths or under unusual conditions of tectonic stress and/or high reservoir pressure, the weight of the overburden may be the minimum stress and the orientation of the hydraulic fractures will be horizontal; for more

normal cases, the minimum stress is generally horizontal and the maximum horizontal stress direction determines whether the vertical fracture will run north–south, east–west, etc.

- Stress differences between different geologic layers are the primary control over the important parameter of height growth (Fig. 5-9).
- Through its magnitude, the stress has a large bearing on material requirements, pumping equipment, etc., required for a treatment. Because the bottom-hole pressure must exceed the in-situ stress for fracture propagation, stress controls the required pumping pressure that well tubulars must withstand and also controls the hydraulic horsepower (hhp) required for the treatment. After fracturing, high stresses tend to crush the proppant and reduce  $k_f$ ; thus, the stress magnitude dominates the selection of proppant type and largely controls postfracture conductivity.

Therefore, the detailed design of hydraulic fracture treatments requires detailed information on in-situ stresses. An engineer must know the magnitude of the minimum in-situ stress for the pay zone and over- and underlying zones and in some cases must know the direction for the three principal stresses. For a simple, relaxed geology with normal pore pres-

sure, the closure stress is typically between 0.6 and 0.7 psi/ft of depth (true vertical depth, TVD). More generally, as discussed in Chapter 3, the minimum stress is related to depth and reservoir pressure by

$$\sigma_c \cong K_o(\sigma_v - p_r) + p_r + T, \quad (5-4)$$

where  $K_o$  is a proportionality constant related to the rock properties of the formations (possibly to both the elastic properties and the faulting or failure properties),  $\sigma_v$  is the vertical stress from the weight of the overburden,  $p_r$  is the reservoir pore pressure, and  $T$  accounts for any tectonic effects on the stress (for a relaxed, normal fault geology,  $T$  is typically small).  $K_o$  is typically about  $\frac{1}{2}$ . For fracture design, better values are required than can be provided by such a simple relation, and methods of measuring or inferring the in-situ stress are discussed in Chapters 3 and 4. For preliminary design and evaluation, using Eq. 5-4 with  $K_o = \frac{1}{2}$  is usually sufficient.

### 5-3. Reservoir engineering

As previously mentioned, because the ultimate goal of fracturing is to alter fluid flow in a reservoir, reservoir engineering must provide the goals for a design. In addition, reservoir variables may impact the fluid loss.

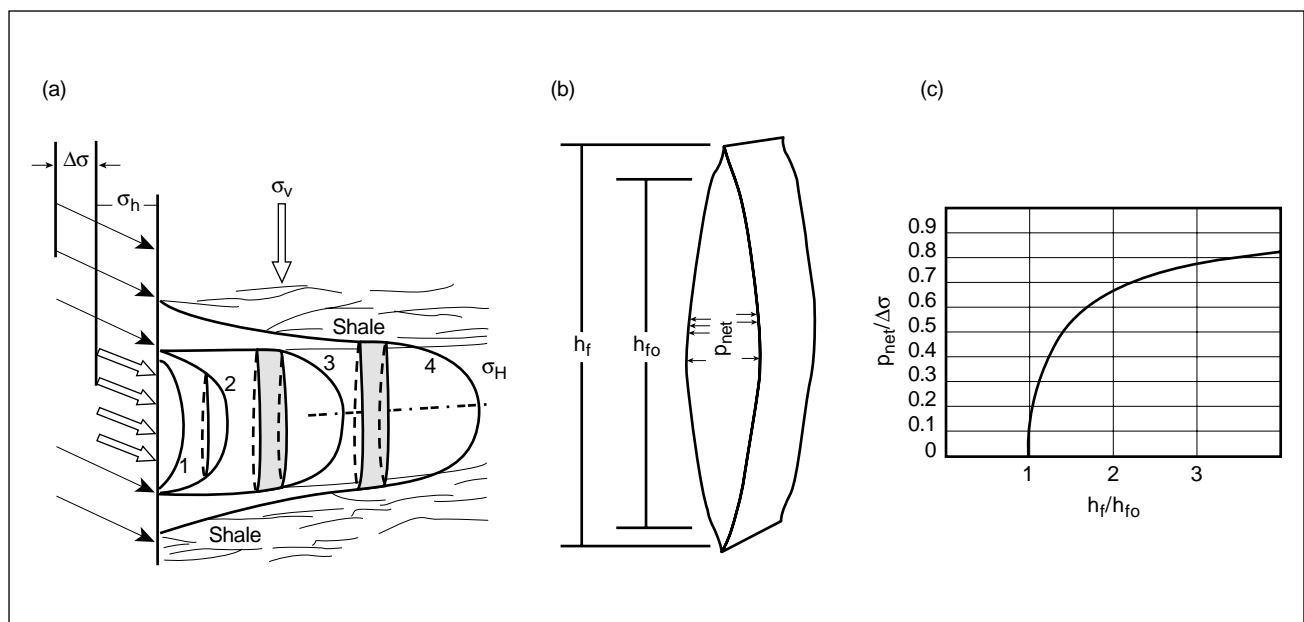


**Figure 5-9.** Fracture height growth. (a) Idealized fracture profile of the relation of fracture geometry to in-situ stresses.  $\sigma_h$  = minimum horizontal stress,  $\sigma_H$  = maximum horizontal stress. (b) Typical fracture vertical cross section illustrating the relation of the total fracture height  $h_f$  to the "original" fracture height  $h_{fo}$ . (c) Theoretical relation among  $h_f/h_{fo}$ ,  $p_{net}$  and the in-situ stress difference  $\Delta\sigma$  (Simonson et al., 1978).

### 5-3.1. Design goals

Historically, the emphasis in fracturing low-permeability reservoirs was on the productive fracture length  $x_f$ . For higher permeability reservoirs, the conductivity  $k_f w$  is equally or more important, and the two are balanced by the formation permeability  $k$ . This critical balance was first discussed by Prats (1961), more than 10 years after the introduction of fracturing, with the important concept of dimensionless fracture conductivity  $C_{fD}$ :

$$C_{fD} = \frac{k_f w}{k x_f}. \quad (5-5)$$

This dimensionless conductivity is the ratio of the ability of the fracture to carry flow divided by the ability of the formation to feed the fracture. In general, these two production characteristics should be in balance. In fact, for a fixed volume of proppant, maximum production is achieved for a value of  $C_{fD}$  between 1 and 2, as discussed in Chapters 1 and 10, with an analogy to highway design in Sidebar 5B.

Prats also introduced another critical concept, the idea of the effective wellbore radius  $r_w'$ . As shown in Fig. 5-10, a simple balancing of flow areas between a wellbore and a fracture gives the equivalent value of  $r_w'$  for a propped fracture (qualitative relation only):

$$r_w' \approx \frac{2}{\pi} x_f. \quad (5-6)$$

However, this simple flow area equivalence ignores the altered pore pressure field around a linear

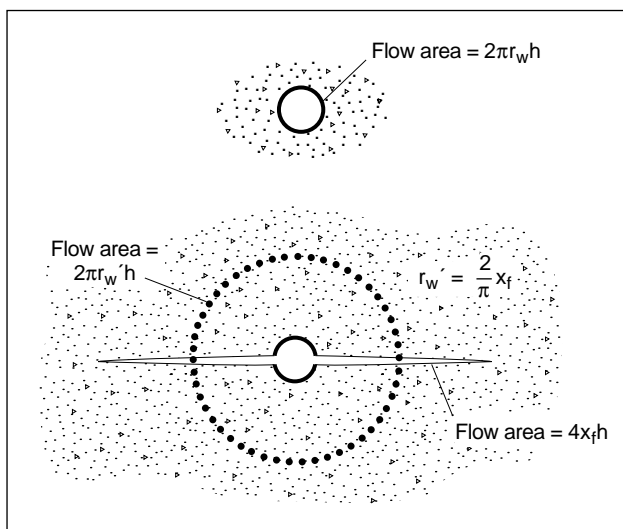


Figure 5-10. Equivalent wellbore radius  $r_w'$ .

fracture and also assumes infinite conductivity. Prats correctly accounted for the pressure distribution around a fracture and provided a general relation between dimensionless conductivity and  $r_w'$  for steady-state conditions (see Chapter 1). The relation shows that for infinite-conductivity fractures, the upper limit on  $r_w'$  is slightly less than that from the flow area balance in Eq. 5-6. For infinite  $k_f w$ , Prats found

$$r_w' = 0.5x_f. \quad (5-7)$$

Cinco-Ley *et al.* (1978) later integrated this into a full description of reservoir response, including tran-

#### 5B. Highway analogy for dimensionless fracture conductivity

A simplistic analogy for dimensionless fracture conductivity  $C_{fD}$  is a highway system. The numerator of this dimensionless variable is  $k_f w$ , which is the capacity of the highway or the ability of the highway to carry traffic. The denominator is  $kx_f$ ; this is the ability of the feeder roads to supply traffic to the highway.

The famous old U.S. highway known as Route 66 ran, for much of its length, across sparsely populated areas where feeder roads were few, narrow and far between. The ability of the feeder road network to supply traffic to the highway was limited (similar to the conditions existing when a propped hydraulic fracture is placed in a formation with very low permeability). In this case, the width, or flow capacity, of the highway is not an issue ( $k_f w$  does not have to be large). What is needed (and was eventually built) is a long, narrow (low-conductivity) highway.

As a comparison, consider Loop 610, the "superhighway" surrounding the city of Houston. The feeder system is located in a densely populated area, and the feeder roads are numerous and wide. Here, the width, or flow capacity, of the highway is critical. Making this highway longer has no effect on traffic flow, and the only way to increase traffic flow is to widen (i.e., increase the conductivity of) the road. This is obviously analogous to placing a fracture in a higher permeability formation, with the postfracture production limited by the fracture width (or, more accurately, limited by  $k_f w$ ).

If  $C_{fD}$  is the ratio of the ability of a highway to carry traffic to the ability of the feeder system to supply that traffic to the highway, clearly a highway should be engineered to approximately balance these conditions. That is, a  $C_{fD}$  value  $> 50$  is seldom warranted, because a highway would not be constructed to carry 50 times more traffic than the feeder system could supply. In the same way, a value of 0.1 makes little sense. Why construct a highway that can only carry 10% of the available traffic? In general, an ideal value for  $C_{fD}$  would be expected to be about 1 to result in a balanced, well-engineered highway system.

A balance of about 1 is certainly attractive for steady-flow traffic conditions that may exist through most of the day. However, during peak traffic periods the feeder system may supply more traffic than normal, and if this rush hour or transient traffic period is a major consideration, then a larger ratio of  $C_{fD}$  may be desirable. Thus, a  $C_{fD}$  of 10 may be desirable for peak flow (transient) periods, as opposed to a  $C_{fD}$  value of approximately 1 for steady-state traffic conditions.

sient flow. For pseudoradial flow, Cinco-Ley *et al.* expressed  $r_w'$  as a function of length and  $C_{fD}$  (Fig. 5-11).

The chart in Fig. 5-11 (equivalent to Prats) can be used (when pseudoradial flow is appropriate) as a powerful reservoir engineering tool to assess possible postfracture productivity benefits from propped fracturing. For example, the folds of increase (FOI) for steady-state flow can be defined as the postfracture increase in well productivity compared with prefracture productivity calculated from

$$FOI = \frac{\ln(r_e / r_w) + s}{\ln(r_e / r_w')}, \quad (5-8)$$

where  $r_e$  is the well drainage or reservoir radius,  $r_w$  is the normal wellbore radius, and  $s$  is any prefracture skin effect resulting from wellbore damage, scale buildup, etc. An equivalent skin effect  $s_f$  resulting from a fracture is

$$s_f = -\ln(r_w' / r_w) \quad (5-9)$$

for use in reservoir models or other productivity calculations. Equation 5-8 provides the long-term FOI. Many wells, particularly in low-permeability reservoirs, may exhibit much higher (but declining) early-time, transient FOI. The preceding relations are for transient pseudoradial flow before any reservoir boundary effects; the case for boundary effects is discussed in Section 12-2.6.

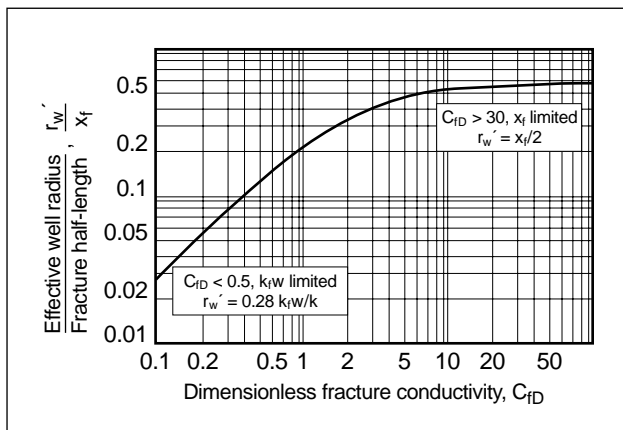


**Figure 5-11.** Equivalent wellbore radius as a function of dimensionless fracture conductivity and fracture length.

### 5-3.2. Complicating factors

These principal concepts give a straightforward method for predicting postfracture production; however, complications can reduce postfracture productivity below the levels expected or give better productivity than that calculated. The major complications include non-Darcy (or turbulent) flow, transient flow regimes, layered reservoirs and horizontal permeability anisotropy (particularly any natural fissure permeability).

For high-rate wells, non-Darcy or turbulent flow can be an important factor that causes an increased pressure drop along the fracture. This creates an apparent conductivity that is less than the equivalent laminar flow conductivity. The apparent  $C_{fD}$  is also reduced and productivity is less than that expected. Another complicating effect that can reduce productivity from expected levels is formation layering, where a fracture is in multiple layers with significantly different values for porosity, permeability or both. Unlike radial flow into a wellbore, average values of permeability and porosity do not apply, and for layered formations, postfracture performance falls below simple calculations based on average permeability (Bennett *et al.*, 1986). These and other effects are discussed in Section 12-3.

For lower permeability formations and for some time period, postfracture performance is dominated by transient flow (also called flush production) as discussed by Cinco-Ley *et al.* (1978). For transient conditions, reservoir flow has not developed into pseudoradial flow patterns, and the simple  $r_w'$  relations are not applicable. In the example in Fig. 5-12, pseudoradial flow did not develop until about 48 months. During the prior transient flow regimes,

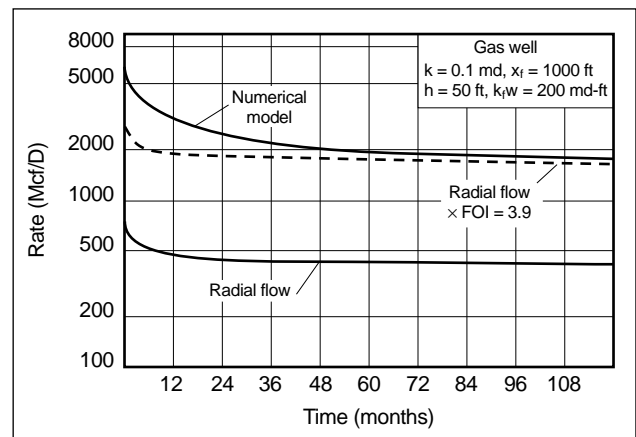


**Figure 5-12.** Late development of pseudoradial flow.

productivity was better than that predicted from the pseudoradial flow  $r_w'$ . The duration of the transient flow period is a function of permeability,  $C_{fd}$  and  $x_f^2$  such that for moderate- to high-permeability wells the period is too short to have practical significance for fracture design. However, it may be important for postfracture well test analysis. For low-permeability wells with long fractures, transient flow may dominate most of the productive well life.

### 5-3.3. Reservoir effects on fluid loss

Reservoir properties such as permeability to reservoir fluid, relative permeability to the fracturing fluid filtrate, total system compressibility, porosity, reservoir fluid viscosity and reservoir pressure all play a role in fluid loss while pumping (see Section 6-4). Thus, certain reservoir information is required for treatment design, as well as for specifying design goals.

## 5-4. Rock and fluid mechanics

Rock and fluid mechanics (along with fluid loss) considerations control the created fracture dimensions and geometry (i.e., fracture height  $h_f$ , length  $L$  and width  $w$ ). These considerations all revolve around the net pressure  $p_{net}$  given by Eq. 5-3. However,  $p_{net}$ , which controls  $h_f$  and  $L$ , is itself a function of  $h_f$  and  $L$ , and the various physical behaviors connecting height, net pressure, width, etc., interact in many ways. This makes simple statements about the relative importance of variables difficult or impossible. However, the basic physical phenomena controlling fracture growth are understood and are well established.

### 5-4.1. Material balance

The major equation for fracturing is material balance. This simply says that during pumping a certain volume is pumped into the earth, some part of that is lost to the formation during pumping, and the remainder creates fracture volume (length, width and height). It is the role of fracture models to predict how the volume is divided among these three dimensions. The volume pumped is simply

$$V_i = q_i \times t_p, \quad (5-10)$$

where  $q_i$  is the total injection rate and  $t_p$  is the pumping time for a treatment. Equally simple, the fracture volume created during a treatment can be idealized as

$$V_f = h_f \times \bar{w} \times 2L = \eta \times V_i, \quad (5-11)$$

where  $h_f$  is an average, gross fracture height,  $\bar{w}$  is the average fracture width,  $L$  is the fracture half-length or penetration, and  $\eta$  is the fluid efficiency. Finally, as discussed by Harrington *et al.* (1973) and Nolte (1979), the volume lost while a hydraulic fracture treatment is being pumped can be approximated by

$$V_{Lp} \cong 6C_L h_L L \sqrt{t_p} + 4L h_L S_p, \quad (5-12)$$

where  $C_L$  is the fluid-loss coefficient (typically from 0.0005 to 0.05 ft/min<sup>1/2</sup>),  $h_L$  is the permeable or fluid-loss height, and  $S_p$  is the spurt loss (typically from 0 to 50 gal/100 ft<sup>2</sup>). Because material balance must be conserved,  $V_i$  must equal  $V_{Lp}$  plus  $V_f$ , and Eqs. 5-10 through 5-12 can be rearranged to yield

$$L \cong \frac{q_i t_p}{6C_L h_L \sqrt{t_p} + 4h_L S_p + 2\bar{w} h_f}, \quad (5-13)$$

showing a general relation between several important fracture variables and design goals.

Modeling of hydraulic fracture propagation in low- to medium-permeability formations typically shows an average width of about 0.25 in. ( $\pm 50\%$ ) over a fairly wide range of conditions (e.g., Abou-Sayed, 1984). Using this value, the effect of the primary variables height  $h_f$  and fluid-loss coefficient  $C_L$  on fracture penetration  $L$  are investigated in Fig. 5-13. This is for a simple case of a constant 0.25-in. fracture width. Figure 5-13a shows length as a strong, nearly linear function of  $h_f$ ; e.g., doubling  $h_f$  cuts fracture penetration by 50%. For similar conditions, Fig. 5-13b shows that the fluid-loss coefficient is not as important; e.g., doubling  $C_L$  reduces  $L$  by only about 20%. However, with fracturing, such simple relations are never fixed. As seen in Fig. 5-13c, for a higher loss case, doubling  $C_L$  from 0.005 to 0.01 reveals a nearly linear relation between  $C_L$  and  $L$ , just as for height in Fig. 5-13a. Basically, for Figs. 5-13a and 5-13b, the loss term (first term in the denominator of Eq. 5-13) is small compared with the fracture volume term (third term in the denominator). Therefore, the fluid loss is relatively low and fracture



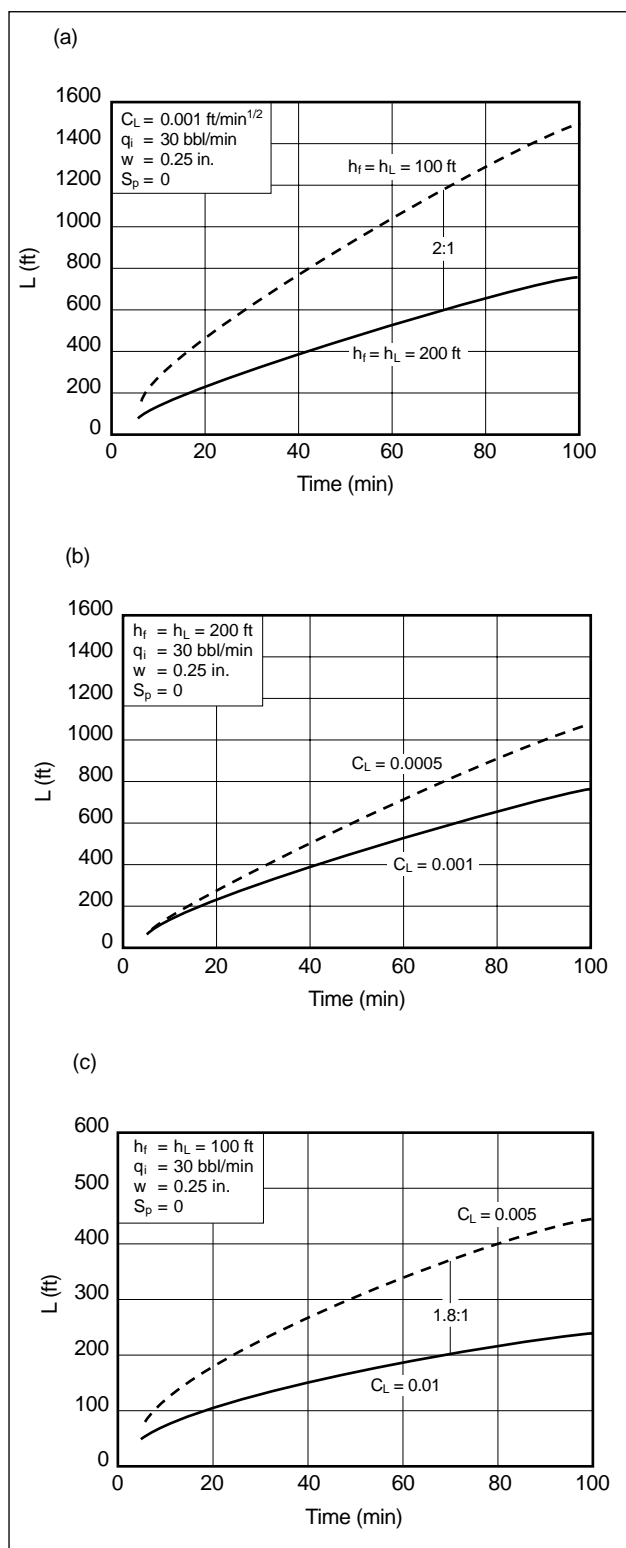


Figure 5-13. Effect of  $h_f$  and  $C_L$  on  $L$ .

fluid efficiency ( $\eta$ , as defined in Eq. 5-11) is high. In Fig. 5-13c, the loss term is large compared with the volume term (high loss and low efficiency), and the loss coefficient becomes the dominant variable, with  $L$  less sensitive to variations in  $h_f$  or equivalently  $\bar{w}$  if it varies from the fixed value of 0.25 in.

## 5-4.2. Fracture height

Equation 5-13 demonstrates that fracture height  $h_f$  and fluid-loss height  $h_L$  are important parameters for fracture design. Loss height is controlled by in-situ variations of porosity and permeability. Fracture height is controlled by the in-situ stresses, in particular by differences in the magnitude or level of stress between various geologic layers. More formally, height is controlled by the ratio of net pressure to stress differences  $\Delta\sigma$ , as illustrated in Fig. 5-9, where  $\Delta\sigma$  is the difference between stress in the boundary shales and stress in the pay zone. Ignoring any pressure drop caused by vertical fluid flow, the relation among fracture height, initial fracture height,  $p_{net}$  and  $\Delta\sigma$  can be calculated as demonstrated by Simonson *et al.* (1978). This relation is included in Fig. 5-9c.

For cases when  $p_{net}$  is relatively small compared with the existing stress differences (e.g., less than 50% of  $\Delta\sigma$ ), there is little vertical fracture growth and the hydraulic fracture is essentially perfectly confined. This gives a simple fracture geometry (Fig. 5-14a) and increasing net pressure (Fig. 5-14b). For cases when  $p_{net}$  is much larger than the existing stress differences, vertical fracture height growth is essentially unrestrained. Again, the geometry is a fairly simple radial or circular fracture (Fig. 5-14c) and declining net pressure (Fig. 5-14b).

For more complex cases when  $p_{net}$  is about equal to  $\Delta\sigma$ , fracture geometry becomes more difficult to predict, and significant increases in height can occur for small changes in net pressure. Also, for this case, the viscous pressure drop from vertical flow retards fracture height growth (see Weng, 1991), and the equilibrium height calculations in Fig. 5-9 are no longer applicable.

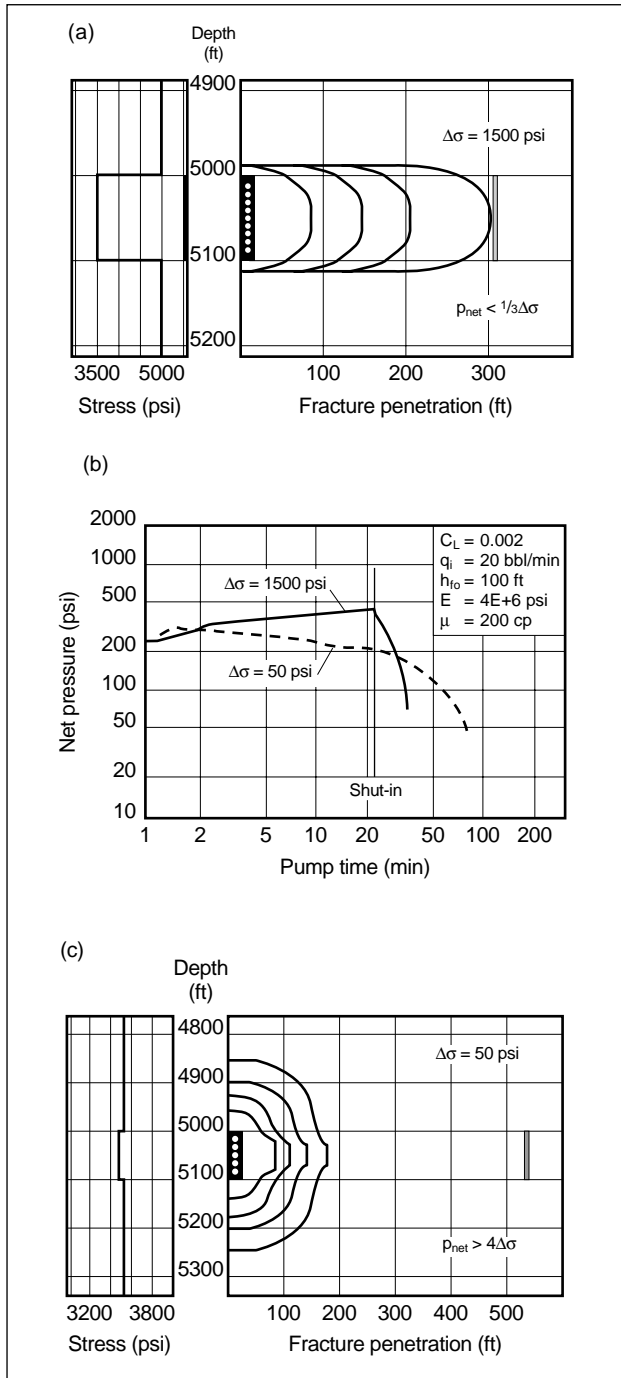


Figure 5-14. Relationship of  $p_{net}$  to stress differences.

### 5-4.3. Fracture width

Consider a slit in an infinite elastic media (i.e., the earth). Also consider that the slit is held closed by a fracture closure stress but is being opened by an internal pressure equal to the closure stress plus a net pressure  $p_{net}$ . Under these conditions (discussed in

detail in Chapter 6), the slit opens into an elliptical shape, with a maximum width

$$w_{max} = \frac{2p_{net}d}{E'}, \quad (5-14)$$

where  $E'$  is the plane strain modulus ( $E' = E/(1 - \nu^2)$ ),  $\nu$  is Poisson's ratio and typically equals about 0.2), and  $d$  is the least dimension of the fracture. For a confined-height fracture with a tip-to-tip length greater than  $h_f$ ,  $d$  equals  $h_f$ . This shows a direct relation between net pressure and width and introduces an important material property, the plane strain modulus. However, because typically  $\nu^2 < 0.1$ , the plane strain modulus seldom differs from Young's modulus  $E$  by a significant amount.

### 5-4.4. Fluid mechanics and fluid flow

The major fluid flow parameters are the fluid viscosity (resistance to flow)  $\mu$  and injection rate  $q_i$ . The rate also effects the pump time and hence is important to fluid-loss and material-balance considerations, as discussed previously. Both parameters are critical for proppant transport, and both parameters also affect net pressure and thus affect fracture height and width.

As an example, consider a Newtonian fluid flowing laterally through a narrow, vertical slit (i.e., fracture) (Fig. 5-15). For laminar flow (the general case for flow inside hydraulic fractures), the pressure drop along some length  $\Delta x$  of the slit is

$$\frac{\Delta p_{net}}{\Delta x} = \frac{12\mu q}{h_f w^3}. \quad (5-15)$$

Assuming a simple case of a long, constant-height and -width fracture with two wings and zero fluid loss (i.e., the flow rate in each wing is  $q = q_i/2$ ) and also assuming zero net pressure at the fracture tip,

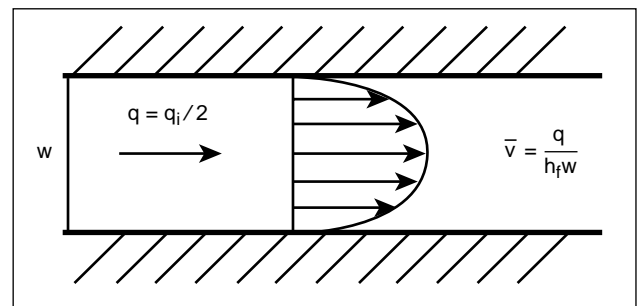


Figure 5-15. Fluid flowing laterally through a narrow vertical fracture.

Eq. 5-15 is integrated from the fracture tip back to the wellbore to give

$$p_{net} = \frac{6\mu q_i L}{h_f w^3}. \quad (5-16)$$

For this long, confined-height fracture,  $h_f$  is the minimum fracture dimension for Eq. 5-14, and the fracture width and net pressure are related by

$$p_{net} = \frac{E'w}{2h_f}. \quad (5-17)$$

Combining the two equations gives the proportionality

$$w \propto \left\{ \frac{\mu q_i L}{E'} \right\}^{1/4}. \quad (5-18)$$

The exponent of  $1/4$  for this simple fracture geometry and for Newtonian fluids implies that the fracture width is virtually constant; e.g., doubling the pump rate from 20 to 40 bbl/min increases the width only by about 20%. The same effect is found for all the variables in Eq. 5-18. Generally, for non-Newtonian fluids, the exponent is approximately  $1/3$ .

This relationship for fracture width can also be used with Eq. 5-17 to give net pressure expressed as

$$p_{net} = \frac{E'^{3/4}}{h_f} \{ \kappa \mu q_i L \}^{1/4}, \quad (5-19)$$

where  $\kappa$  is a constant (see Eq. 6-11) to provide an equality for this expression.

Thus, as a result of viscous forces alone, net pressure inside the fracture develops as a function of the modulus, height and  $(q\mu)^{1/4}$ . From the nature of this relation, however, it is clear that modulus and height are much more important in controlling net pressure than are pump rate and viscosity, the effect of which is muted by the small exponent for the relation.

#### 5-4.5. Fracture mechanics and fracture tip effects

The fluid mechanics relations show  $p_{net}$  related to modulus, height, fluid viscosity and pump rate. However, in some cases, field observations have shown net pressure (and presumably fracture width) to be greater than predicted by Eq. 5-19 (Palmer and Veatch, 1987). In such cases the fluid viscosity has a smaller effect on fracture width than predicted by Eq. 5-19. This is probably because the simple rela-

tion in Eq. 5-16 assumes no net pressure at the fracture tip; i.e., fracture tip effects or fracture propagation effects are ignored. When tip effects are taken into account, the fracture width is affected by both fluid viscosity and tip effects (Shlyapobersky *et al.*, 1988a, 1988b). As shown by Nolte (1991), tip effects can be approximated by considering the net pressure within the tip region to equal  $p_{tip}$  (as opposed to zero) in Eq. 5-16. For a positive tip pressure, the net pressure equation becomes

$$p_{net} \approx \left[ \frac{E'^3}{h_f^4} \{ \kappa \mu q_i L \} + p_{tip}^4 \right]^{1/4}, \quad (5-20)$$

where  $p_{tip}$  is the pressure required at the fracture tip to open new fracture area and keep the fracture propagating forward. This simple relationship serves to illustrate that there are always two components to net pressure: a viscous component and a fracture tip-effects component. The relative magnitude of the two effects varies from case to case, and because of the small exponent, the combined effects are much less than the direct sum of the individual effects. For example, when the viscous component and the tip component are equal, the net pressure is increased by only 20% over that predicted when one of the components is ignored.

- Fracture toughness and elastic fracture mechanics

The fracture tip propagation pressure, or fracture tip effect, is generally assumed to follow the physics of elastic fracture mechanics. In that case, the magnitude of the tip extension pressure  $p_{tip}$  is controlled by the critical stress intensity factor  $K_{Ic}$  (also called the fracture toughness). Fracture toughness is a material parameter, and it may be defined as the strength of a material in the presence of a preexisting flaw. For example, glass has a high tensile strength, but the presence of a tiny scratch or fracture greatly reduces the strength (i.e., high tensile strength but low fracture toughness). On the other hand, modeling clay has low strength, but the presence of a flaw or fracture does not significantly reduce the strength. Laboratory-measured values for the material property  $K_{Ic}$  show toughness ranging from about 1000 to about 3500 psi/in.<sup>1/2</sup>, with a typical value of about 2000 psi/in.<sup>1/2</sup>. These tests (after Schmidt and Huddle, 1977; Thiercelin, 1987) include a range of rock types from mudstones and sandstones to

carbonates and consider confining pressures from 0 to 5000 psi.

From elastic fracture mechanics, for a simple radial or circular fracture geometry with a penetration of  $L$ , the fracture tip extension pressure is

$$p_{tip} = K_{Ic} \sqrt{\frac{\pi}{48L}}, \quad (5-21)$$

and it decreases as the fracture extends. For even a small fracture penetration of 25 ft, this gives a tip extension pressure of 29 psi, whereas viscous pressures (Eq. 5-19) are typically 10 or more times larger. Thus normal linear elastic fracture mechanics considerations indicate that fracture mechanics, or the tip extension pressure, generally plays a negligible role for hydraulic fracturing.

- Apparent fracture toughness

Field data typically show fracture extension pressure to be greater than that given by Eq. 5-21, with 100 to 300 psi as typical values and even higher values possible. This difference is due to several behaviors not included in elastic fracture mechanics calculations. One important (and long-recognized) consideration is that the fracturing fluid never quite reaches the fracture tip; i.e., there is a “fluid lag” region at the tip that increases the apparent toughness and tip pressure (Fig. 5-16). In other cases, tip pressure may be even greater. Other tip phenomena include nonelastic rock deformation near the fracture tip and tip plugging with fines, with these mechanisms acting alone or in conjunction with the fluid flow and/or fluid lag

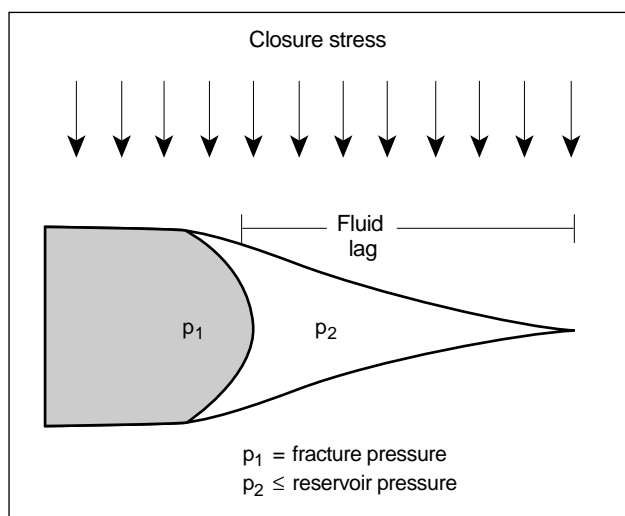


**Figure 5-16.** Unwetted fracture tip (fluid lag).

phenomena. Tip phenomena are discussed in detail in Chapters 3 and 6.

Measured values for tip extension pressure that are higher than predicted from laboratory-measured rock toughness  $K_{Ic}$  can be accounted for in hydraulic fracture calculations through the use of the effective, or apparent, fracture toughness  $K_{Ic-apparent}$  (Shlyapobersky, 1985). In practice, because  $K_{Ic-apparent}$  is not a material constant, the tip effects should be defined or calibrated by fracturing pressure data for a particular situation (see Sidebar 9B).

### 5-4.6. Fluid loss

As seen from the material balance (Eq. 5-13), fluid loss is a major fracture design variable characterized by a fluid-loss coefficient  $C_L$  and a spurt-loss coefficient  $S_p$ . Spurt loss occurs only for wall-building fluids and only until the filter cake is developed. For most hydraulic fracturing cases, the lateral (and vertical) extent of the fracture is much greater than the invasion depth (perpendicular to the planar fracture) of fluid loss into the formation. In these cases, the behavior of the fluid loss into the formation is linear (1D) flow, and the rate of fluid flow for linear flow behavior is represented by Eq. 5-1.

This assumption of linear flow fluid loss giving the  $C_L/\sqrt{t}$  relation has been successfully used for fracturing since its introduction by Carter (1957). The relation indicates that at any point along the fracture, the rate of fluid loss decreases with time, and anything that violates this assumption can cause severe problems in treatment design. For example, fluid loss to natural fissures can result in deep filtrate invasion into the fissures, and the linear flow assumption may no longer be valid. In fact, for the case of natural fissures if net pressure increases with time, the fluid-loss rate can increase, and treatment pumping behavior may be quite different from that predicted. The total fluid loss from the fracture is controlled by the total fluid-loss coefficient  $C_L$ , which Howard and Fast (1957) decomposed into the three separate mechanisms illustrated in Fig. 5-17 and discussed in Section 6-4.

The first mechanism is the wall-building characteristics of the fracturing fluid, defined by the wall-building coefficient  $C_w$ . This is a fluid property that helps control fluid loss in many cases. For most fracturing fluid systems, in many formations as fluid loss

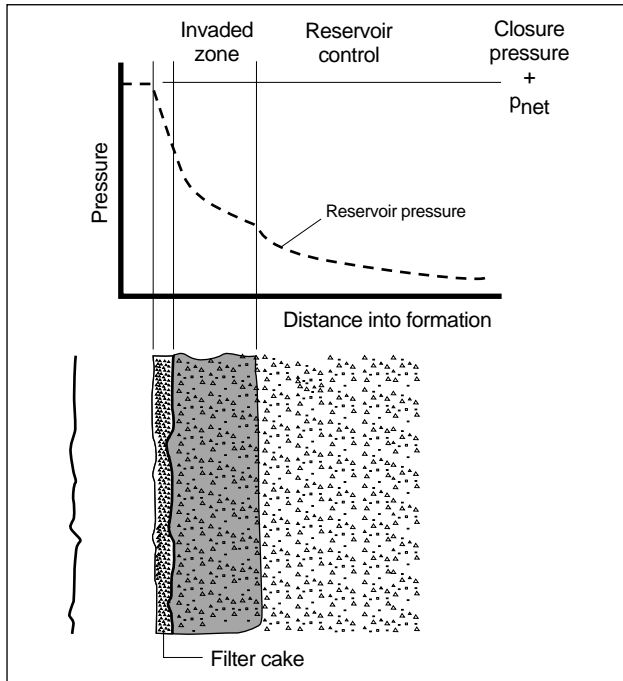


**Figure 5-17.** The three regions of fluid loss.

occurs into the formation, some of the additives and chemicals in the fluid system remain trapped on or near the formation face, forming a physical filter-cake barrier that resists fluid loss.

Outside of the filter cake is the invaded zone, which is the small portion of the formation that has been invaded by the fracturing fluid filtrate. This mechanism is the filtrate effect, or invaded zone effect, and it is characterized by the viscosity or relative permeability control coefficient  $C_v$ . As discussed in Chapter 6,  $C_v$  can be calculated, and this parameter is governed by the relative permeability of the formation to the fracturing fluid filtrate  $k_{fil}$ , the pressure difference  $\Delta p$  between the pressure inside the fracture (i.e., closure pressure +  $p_{net}$ ) and the reservoir pressure, and the viscosity of the fracturing fluid filtrate  $\mu_{fil}$ . This mechanism is usually most important in gas wells, where the invading fluid has much higher viscosity than the reservoir fluid being displaced, or where relative permeability effects produce a filtrate permeability that is much less ( $< k/10$ ) than the permeability to the reservoir fluid. Other cases are where a clean fluid is used such that no filter cake develops or for fracturing high-permeability wells where no filter cake develops and high-viscosity crosslinked gel may be lost to the formation (i.e.,  $\mu_{fil}$  is very high).

For fluid to leak off from the fracture, the reservoir fluid must be displaced. This sets up some resistance to fluid loss, and this reservoir effect is characterized by the compressibility coefficient  $C_c$ . As discussed in Chapter 6, the parameter for this calculation is governed by a pressure difference  $\Delta p$  between the pressure inside the fracture (i.e., closure pressure +  $p_{net}$ ) and the reservoir pressure, permeability to the movable formation fluid  $k$ , total system compressibility for the reservoir  $c_r$ , and the viscosity of the reservoir fluid (gas or oil)  $\mu$ . This parameter is usually more important for a liquid-saturated reservoir (low compressibility and relatively high reservoir fluid viscosity) and when a filter cake does not develop.

Each of these three mechanisms provides some resistance to fluid loss, and all three act as resistors in series (although the fluid-loss coefficient itself is defined in terms of conductance, or the inverse of resistance). The three mechanisms variously combine in different situations to form the total or combined fluid-loss coefficient  $C_L$ , which is used for fracture design (see Chapter 6). This clearly complex situation makes it desirable to measure fluid loss from field tests (just as permeability must be measured from field flow, buildup tests or both) whenever possible (see Chapter 9).

#### 5-4.7. Variable sensitivities and interactions

The complexity of hydraulic fracture design comes from the interactions of the major design variables ( $h_f$ ,  $E$ ,  $\Delta\sigma$ ,  $K_{Ic}$  and  $C_L$ ) and that different variables affect different aspects of fracturing in different ways. As discussed in Section 5-4.1 concerning the sensitivity of fracture penetration to  $h_f$  and  $C_L$ , the importance of various variables can change from case to case. Several examples of this are discussed here.

- Net pressure

The magnitude of net pressure for a specific fracture treatment is a major concern, because the ratio of net pressure to stress differences between the pay zone and bounding zones controls fracture height. Also, net pressure directly controls width. However, what controls net pressure varies significantly from case to case.

In the case of hard-rock formations (i.e., formations with values for Young's modulus of  $2 \times 10^6$  psi or greater) with height confinement and for

treatments pumping viscous fluids at normal fracturing rates, the viscous term of the net pressure equation dominates any fracture tip effects. Toughness or tip effects become important for cases where fracture height is unconfined (e.g., radial or circular fractures) or for very soft rocks (e.g., formations such as unconsolidated sands with  $E \leq 0.5 \times 10^6$  psi). For treatments using low-viscosity fluid or pumping at very low rates, the viscous term of the net pressure equation becomes small, and fracture toughness becomes a dominant parameter. Although many cases fall into one of these extremes, neither effect should be overlooked for the prudent application of fracturing.

The magnitude of net pressure may also be controlled by in-situ stress differences between the pay and the bounding layers. Consider a case where barrier zones (e.g., formations with higher closure stress) surround the pay zone (Fig. 5-9) and further assume that because of either viscous or toughness effects,  $p_{net}$  increases to the level of the stress differences. Massive height growth then begins, and only very small increases in the net pressure are possible. Net treating pressure is now controlled directly by  $\Delta\sigma$  and is essentially independent of both fluid viscosity and apparent fracture toughness effects. This case is illustrated in the next section.

- Fracture height and net pressure

For a fracture with significant stress barriers and in a formation with a medium to high value for the modulus, the viscous term in Eq. 5-20 controls the net treating pressure. In such a case,  $p_{net}$  becomes a strong function of fracture height. However, as illustrated in Fig. 5-9, fracture height  $h_f$  is controlled by net pressure. To put it in another form, fracture height is a function of fracture height. As discussed in Chapter 6, this is where fracture models become important.

As an example, consider the case of a thin ( $h = 25$  ft) sandstone pay zone in a hard-rock formation ( $E = 5 \times 10^6$  psi). Further assume that this zone is surrounded by shales with an in-situ stress 1000 psi greater than the stress in the sand, making them what would normally be considered good barriers to vertical fracture growth. As seen in Fig. 5-18a, even for pumping a moderate (50-cp) viscosity fluid at a moderate rate, net pressure immediately jumps to a level slightly greater than

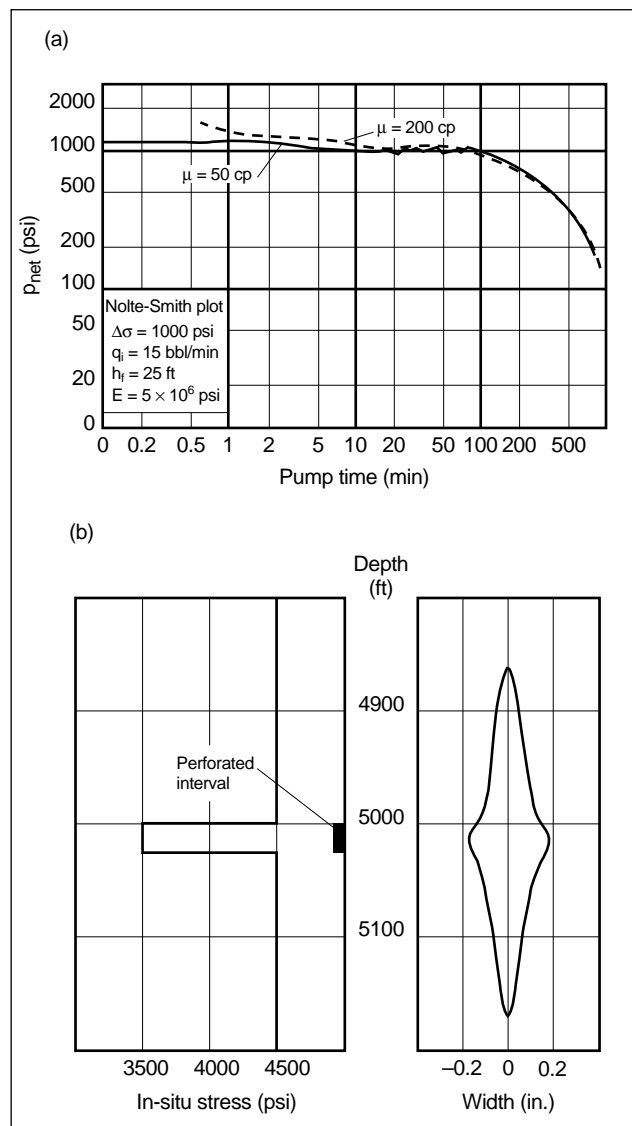


**Figure 5-18.** Height growth example in a hard-rock formation.

1000 psi (i.e.,  $\Delta\sigma$  is controlling  $p_{net}$ ), and extensive height growth occurs. Because  $\Delta\sigma$  is controlling the allowable net pressure, increasing the fluid viscosity fourfold has essentially no effect on net pressure after the first few minutes. The vertical fracture width profile plotted in Fig. 5-18b shows that for  $p_{net}$  about equal to  $\Delta\sigma$ , fracture width in the bounding layers may be too small for proppant admittance. This is discussed in the subsequent section on proppant admittance.

Now consider the same case but with a 50-ft thick sandstone section. As seen in Fig. 5-19,  $p_{net}$  stays below  $\Delta\sigma$  for the 50-cp fluid case and little

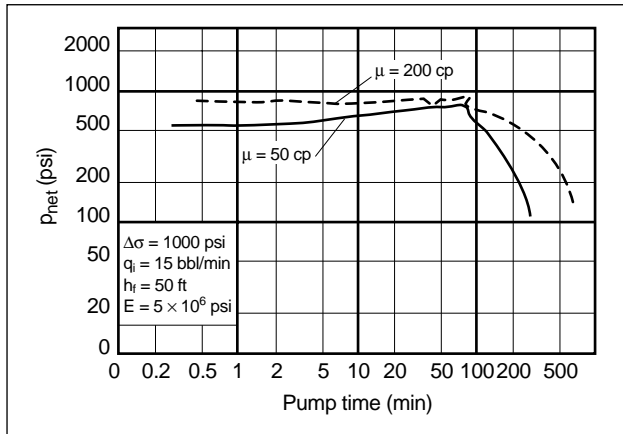


**Figure 5-19.** Height growth example in a thicker hard-rock formation.

height growth occurs. For a more viscous (200-cp) fluid, net pressure again approaches the stress difference of 1000 psi, and again extensive height growth occurs. These examples show that fracture height is a function of fracture height.

Finally, consider the original ( $h = 25$  ft) case again, but assume this is a soft-rock (unconsolidated sand with  $E < 0.5 \times 10^6$  psi) zone. Further assume that because of high permeability, fluid loss is much greater than for the previous two cases. Figure 5-20 shows  $p_{net}$  is much less than  $\Delta\sigma$ , with essentially no height growth. Also, the flat nature of the net pressure behavior in the Nolte-Smith log-log plot of  $p_{net}$  versus time indicates that fracture tip effects are dominating net pressure behavior, as expected from Eq. 5-20. Chapter 9 discusses net pressure behavior and the means to determine the controlling conditions.

- Fluid viscosity

Fluid viscosity provides an example of how variables affect different parts of the fracturing process in different ways. Consider a case of radial fracture growth in a soft rock ( $E < 1 \times 10^6$  psi). Toughness dominates  $p_{net}$  and fracture width, and viscosity becomes unimportant in controlling fracture geometry. However, viscosity can remain a critical consideration for proppant transport if a long fracture is desired and for fluid-loss control.

Further assume this case is a very high permeability formation, such that only a short fracture is required. Thus, high viscosity is not required for proppant transport. However, in this very high

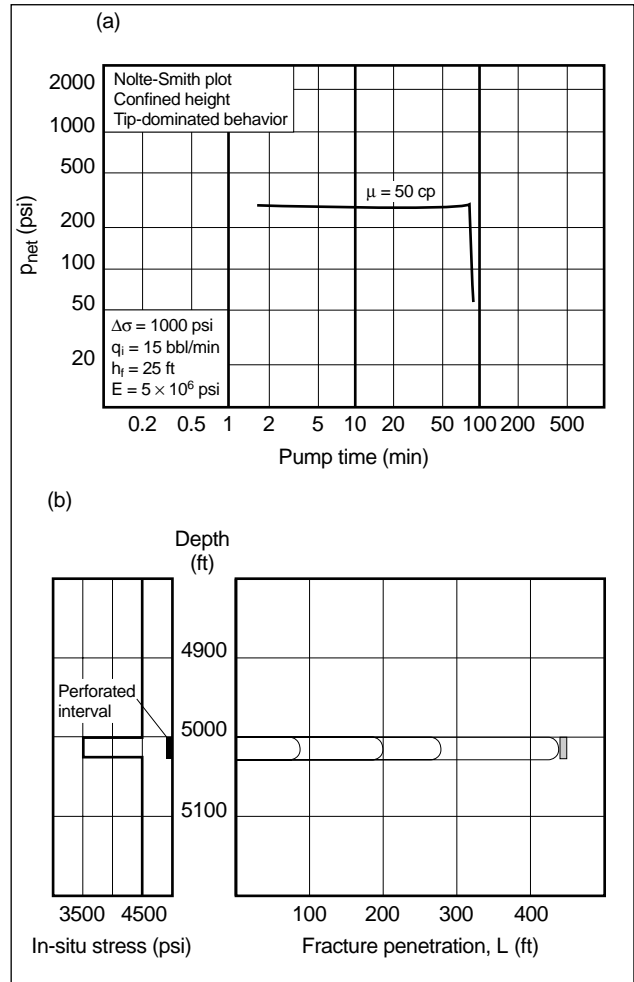


**Figure 5-20.** Height growth example in a soft-rock formation.

permeability formation it is probable that the fracturing fluid cannot build a filter cake to control fluid loss, and the only fluid-loss control will come from the viscosity (or invaded zone) effect  $C_v$  (see Section 5-4.6). Viscosity is therefore a major factor for fluid selection, despite having no effect on geometry and not being critical for proppant transport.

## 5-5. Treatment pump scheduling

The fracture design process involves reservoir engineering to define the  $x_f$  and  $k_{fw}$  goals. It involves rock mechanics to consider the possibility of obtaining a desired fracture geometry. It includes fluid mechanics considerations to confirm that the required proppant transport is possible and rheology to determine if the required fluid properties are pos-

sible. It also includes material selection and on-site operational considerations as discussed in Section 5-6. The product of this process is a treatment pump schedule. This includes the pad volume necessary to create the desired fracture penetration, along with acid or proppant scheduling to achieve the desired postfracture conductivity. For propped fracturing, pump scheduling includes fluid selection, proppant selection, pad volume, maximum proppant concentration to be used and a proppant addition schedule. After the design goals and variables are defined, the proppant addition schedule is usually obtained by using a fracture simulator, although for many cases analytical calculations based on fluid efficiency are also easily implemented. Chapter 10 provides additional detail for treatment design.

### 5-5.1. Fluid and proppant selection

Fracturing materials are discussed in Chapter 7, and their performance characterization is discussed in Chapter 8. The major considerations for fluid selection are usually viscosity (for width, proppant transport or fluid-loss control) and cleanliness (after flow-back) to produce maximum postfracture conductivity. Other considerations that may be major for particular cases include

- compatibility with reservoir fluids and reservoir rock
- compatibility with reservoir pressure (e.g., foams to aid flowback in low-pressure reservoirs)
- surface pump pressure or pipe friction considerations
- cost
- compatibility with other materials (e.g., resin-coated proppant)
- safety and environmental concerns (see Chapter 11).

Proppant selection must consider conductivity at in-situ stress conditions (i.e., the effect of stress on proppant permeability  $k_p$ ). Proppant size must also be considered. In general, bigger proppant yields better conductivity, but size must be checked against proppant admittance criteria, both through the perforations and inside the fracture (see Section 5-5.4). Finally, the maximum in-situ proppant concentration at shut-in must be selected, as it determines how much of the hydraulic width created by the fracture treatment will be retained as propped width once the fracture closes.

### 5-5.2. Pad volume

For a treatment using viscous fluid, the fluid carries the proppant out to the fracture tip. For these cases the pad volume determines how much fracture penetration can be achieved before proppant reaches the tip and stops penetration in the pay zone. Once the pad is depleted, a fracture may continue to propagate into impermeable layers until the proppant bridges in low-width areas. Thus, pumping sufficient pad to create the selected length is critical. For treatments using very low viscosity fluid (i.e., “banking”-type treatments), proppant settles out of the fluid and essentially replenishes the pad. The pad volume must only be sufficient to open enough fracture width for proppant admittance, and the carrying capacity of the fluid, as opposed to the pad volume, determines the final propped length.

On the other hand, too much pad can in some instances be even more harmful, particularly for cases requiring high fracture conductivity. The fracture tip continues to propagate after pumping stops, leaving a large, unpropped region near the fracture tip. Significant afterflow can then occur in the fracture, carrying proppant toward the tip and leaving a poor final proppant distribution. This afterflow occurs because the widest section of the fracture is near the wellbore at shut-in, and most of the proppant pumped is stored there. However, the highest fluid-loss rates are near the fracture tip. Thus, proppant-laden slurry continues to flow toward the tip of the fracture. Afterflow continues until either the fracture closes on the proppant, stopping proppant movement, or until proppant-laden slurry reaches the fracture tip. At that point the slurry dehydrates and stops any additional fracture propagation. Ideally, of course, it is better to have the proppant at the fracture tip at shut-in and thus minimize afterflow.

An ideal schedule for a normal treatment (as opposed to subsequently discussed TSO designs) is one where the pad depletes and proppant reaches the fracture tip just as the desired fracture penetration is achieved and also just as pumping stops. This is the sequence in Figs. 5-2, 5-3 and 5-4.

The critical parameter of the pad volume or pad fraction  $f_{pad}$  is related directly to the fluid efficiency for a treatment (Nolte, 1986b). This relation from Sidebar 6L gives the pad volume expressed as a fraction of the entire treatment volume:



$$f_{pad} \approx \frac{1 - \eta}{1 + \eta}. \quad (5-22)$$

That is, a treatment with an expected efficiency  $\eta$  of 50% would require a pad fraction of about  $\frac{1}{3}$ . As discussed in Chapter 9, the efficiency for a specific formation and fluid system can be determined by a calibration treatment.

This discussion of pad volume has so far concentrated on the fluid-loss aspects of the pad volume; i.e., the pad is pumped first to serve as a sacrificial stage of the treatment to enable the fracture to penetrate into permeable formations. This important effect of the pad volume may be the critical aspect governing the size of the pad for most applications. However, hydraulic fracturing is complicated, in that most things are done for at least two reasons, which applies to pad volume specification. The second purpose of the pad volume is to create sufficient fracture width to allow proppant to enter the fracture (see Section 5-5.4 on proppant admittance). Even for a case of very low fluid loss, some minimum pad volume is required. Both of these aspects of the pad volume must always be considered for treatment design.

- Propped width

A major design goal is fracture conductivity  $k_f w$ , which consists of proppant pack permeability and propped fracture width. Proppant permeability  $k_f$  is a function of the proppant selected, in-situ stress and residual damage from fluid additives (see Chapter 8). Propped width is controlled by the treatment design.

The effective propped width  $w_{p-eff}$  is a function of the average fracture width  $w_f$  at shutdown (i.e., hydraulic width at the end of pumping a treatment), proppant concentration  $C$  in the fracture at that time (i.e., giving the ideal propped width  $w_p$ ) and the volume of proppant  $w_{lost}$  that is lost on the faces of the fracture to embedment, gel residue, etc. (usually expressed as lbm/ft<sup>2</sup> “lost”). In terms of these parameters, the effective propped width can be expressed as

$$w_{p-eff} = w_p - w_{lost} = w_f \times F - w_{lost} \quad (5-23)$$

$$F = \frac{C}{(8.33 \times \gamma_{prop} + C) \times (1 - \phi)}, \quad (5-24)$$

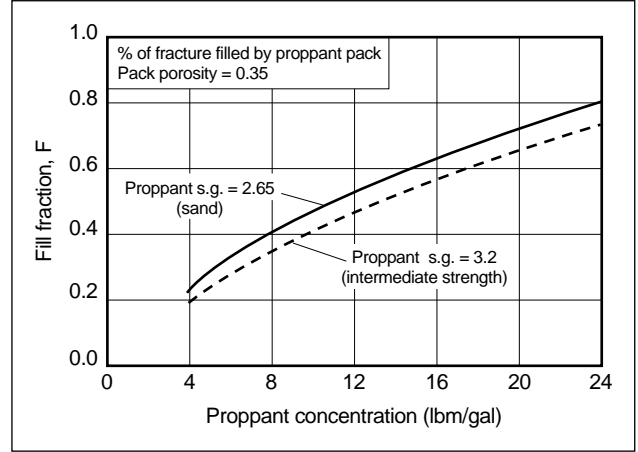


Figure 5-21. Fill fraction versus proppant concentration.

where  $F$  is the fill fraction (Fig. 5-21), the constant 8.33 converts the units to lbm/gal,  $\gamma_{prop}$  is the specific gravity (s.g.) of the proppant,  $C$  is the final in-situ proppant concentration at shut-in expressed as pounds of proppant per fluid gallon (ppg), and  $\phi$  is the porosity of the proppant pack, typically about 0.35.

Increasing the concentration from 8 ( $F \approx 0.4$ ) to 16 ppg ( $F \approx 0.6$ ) significantly increases the propped fracture width (50% increase in the fill fraction). However, this large increase in propped width is accomplished at the expense of additional risk to the job and to the well, because of either surface mechanical problems or an unexpected total screenout somewhere in the fracture or in the near-wellbore region between the well and the far-field fracture (see the discussion of tortuosity in Section 6-6). In practice, most treatments use a maximum concentration of about 8 to 14 ppg, although concentrations of 20 ppg have been pumped.

Another manner of increasing propped width is to increase fracture width. Theoretical and numerical models generally show that the fracture width, while the fracture is growing, is relatively insensitive to the controllable job variables of pump rate and fluid viscosity. For a simple fracture geometry, width is proportional to rate and viscosity raised to a small power. For Eq. 5-18 with the exponent  $\frac{1}{4}$ , doubling the pump rate increases fracture width by only 18%, at the expense of significant pipe friction and surface

pressure increases. Viscosity is easily increased by an order of magnitude (e.g., 10 times increase in  $\mu$  increases the width by 77%), but only at the expense of using more fluid additives and with additional conductivity damage potentially negating the extra width.

Thus, the hydraulic fracture width is fairly fixed ( $\pm 50\%$ , at least in terms of the treatment's controllable parameters), and the proppant fill fraction has a practical limit of about 0.5 ( $\pm 0.1$ ). Without TSO designs (discussed in the following) the final, effective propped width is almost fixed by nature. The goal for a normal fracture design is then to achieve a required  $k_{fW}$  within these limits, with proppant concentration, proppant selection and fluid selection allowing a large range of values.

- Tip-screenout designs

As mentioned previously, as long as a fracture is free to propagate, the hydraulic fracture width is relatively insensitive to the controllable treatment parameters of fluid viscosity and pump rate. If more conductivity is required than can be achieved from a normal design, the only effective manner to increase the propped width is to stop the fracture from propagating but to continue to pump. This technique has come to be called TSO fracturing (Smith *et al.*, 1984).

For a normal treatment, the pad volume is designed to deplete just as pumping stops. What would happen if pumping simply continued beyond that time? If the pad is depleted, then proppant-laden slurry will be located everywhere around the fracture periphery. If there is fluid loss, then this slurry will dehydrate and leave packed proppant around the periphery. Even with no fluid loss, the proppant may bridge in the narrow fracture width around the periphery, particularly in places where the width is extremely narrow as a result of the fracture penetrating a boundary layer. In either case, any additional propagation is restricted and further pumping causes an increase of net pressure and thus an increase of fracture width. TSO designs are discussed in detail in Chapter 10.

### 5-5.3. Proppant transport

Several modes of proppant settling can occur while proppant is being transported into a hydraulic frac-

ture (see Section 6-5). First is what may be termed simple or single-particle settling. Behavior of this type is governed by Stokes law, in which the velocity of a single particle falling through a liquid medium is

$$v_{fall} = 1.15 \times 10^3 \frac{d_{prop}^2}{\mu} (\gamma_{prop} - \gamma_{fluid}), \quad (5-25)$$

where  $v_{fall}$  is the settling rate in ft/s,  $d_{prop}$  is the average proppant particle diameter in in.,  $\mu$  is the fluid viscosity in cp, and  $\gamma_{prop}$  and  $\gamma_{fluid}$  are the specific gravity of the proppant and the fluid, respectively. The settling rate, and thus the efficiency with which proppant can be transported into the fracture, is directly related to the fluid viscosity. This is usually the main consideration for how much viscosity is required for a fracture treatment. However, there are additional considerations for calculating settling following Stokes law. At low proppant concentrations (e.g., less than 1 or 2 ppg) particles may clump, producing an apparent diameter greater than the actual particle diameter and accelerating settling. Higher particle concentrations act to increase the slurry viscosity and retard settling (also known as hindered settling). The pump rate is also an important parameter controlling proppant transport for simple settling by Stokes law.

As shown in Fig. 5-22, for a Newtonian fluid the distance  $D$  a proppant particle is transported into a fracture, before that particle can fall from the top of

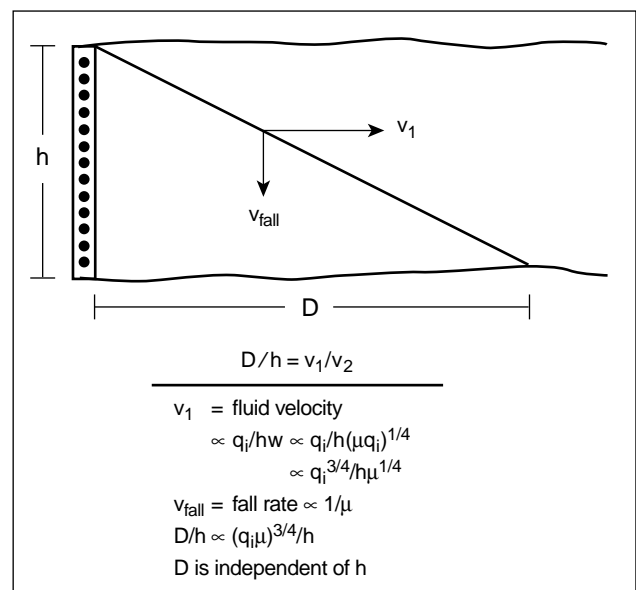


Figure 5-22. Stokes law.

the fracture to the bottom, is related to  $(q_i\mu)^{3/4}$ . This distance is independent of the fracture height and, more significantly, shows that for some given transport distance, less viscosity can be used at higher pump rates. This relation can be important for higher temperature applications, where fluid viscosity can degrade significantly with time. At higher rates (and hence shorter pump times), less viscosity is required for proppant transport. Also, the fluid is exposed to the high formation temperature for less time, so the fluid system maintains better viscosity. In general, considering how fluid viscosity degrades down a fracture, including the effect of proppant concentration increasing the effective slurry viscosity, and considering the non-Newtonian nature of most fracturing fluids, if a fracturing fluid retains 50- to 100-cp viscosity (at reservoir temperature and at a shear rate of  $170 \text{ s}^{-1}$ ) at the end of the fracture treatment, it will provide essentially perfect proppant transport (Nolte, 1982).

The next mode of proppant settling is termed convection, and it was probably first included in fracture modeling in the context of a fully three-dimensional (3D) planar model by Clifton and Wang (1988). This type of settling is controlled by density differences (i.e., buoyancy) between two fluids. For example, a proppant-laden fluid stage with an 8-ppg concentration has a slurry density of 11.9 lbm/gal (s.g. = 1.44). If this slurry is placed directly next to a clean fluid stage with a density of 8.5 lbm/gal (s.g. = 1.02), the heavier slurry will tend to sink and override the lighter clean fluid, simply carrying the proppant toward the bottom of the fracture. However, a treatment does not normally follow clean pad fluid with a heavy 8-ppg slurry. Rather, the treatment increases proppant concentration slowly to account for fluid-loss effects and mitigate convection effects. Only near the end of pumping (when the need for transport decreases), when the initial proppant stages have undergone significant dehydration, can a significant density difference begin to develop. In general, rigorous numerical modeling of this phenomena shows convection is not a major factor during pumping (Smith *et al.*, 1997). If excessive pad is used, such that a large unpropped region of the fracture exists after shut-in, convection can occur during the shut-in after flow, with potentially significant adverse effects on the final proppant placement.

The third effect on proppant transport is termed migration (see Chapter 6). In brief, a viscoelastic

fluid (which describes most fracturing fluid systems) flowing down a channel imparts a normal force to particles entrained in the fluid such that the particles tend to migrate to and concentrate in the center of the channel. For low average concentrations, this can result in a center core of high-proppant-concentration slurry, with a region of essentially clean fluid on either side. This heavier core of concentrated slurry tends to fall owing to its greater density, carrying the entrained proppant toward the bottom of the fracture at a faster rate than for a dispersed slurry (Nolte, 1988b).

Finally, any calculations for proppant settling must consider geologic reality. Detailed examinations of hydraulic fractures both at the wellbore using television cameras (Smith *et al.*, 1982) or away from wells in mineback tests (see Warpinski, 1985) show something other than the smooth fracture walls assumed for settling calculations. Small shifts and jogs of the fracture probably have no significant impact on fluid flow or on lateral proppant transport into the fracture. However, these small irregularities could significantly impact settling. Calculations for proppant settling that ignore these effects will be a worst-case scenario.

#### 5-5.4. Proppant admittance

Proppant admittance is critical to hydraulic fracturing in two forms: entrance to the fracture through perforations and entrance of proppant into the fracture itself. These effects were recognized early, and the original fracture width models were used primarily for determining a pad volume that would allow admittance by generating a fracture width greater than  $2.5d_{prop}$ , where  $d_{prop}$  is the average proppant particle diameter. Before these models, operators were reluctant to pump significant volumes of pad as it was considered expensive and potentially damaging.

The laboratory data in Fig. 5-23 (Gruesbeck and Collins, 1978) illustrate two important ideas:

- A minimum perforation diameter is required for proppant to flow through the perforations.
- Minimum perforation diameter is a function of the slurry concentration.

At low concentrations (e.g., 1 ppg), the perforation hole diameter must be only slightly greater than that of the proppant particles. The required hole diameter increases with concentration until at about 6 ppg

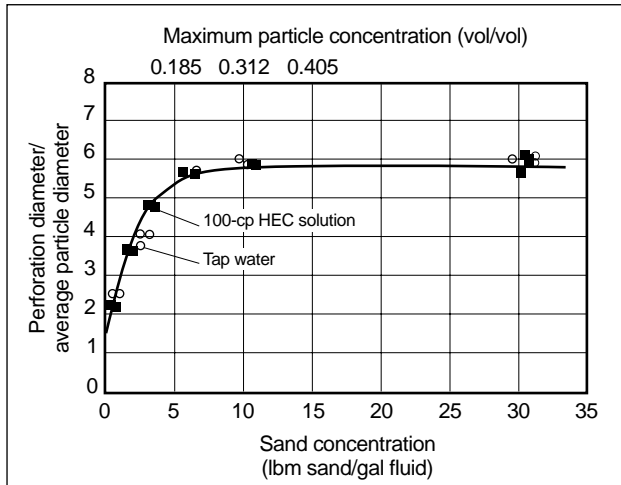


**Figure 5-23.** Proppant admittance through perforations (Gruesbeck and Collins, 1978).

(solid volume fraction of about 0.20), the perforation hole diameter must be 6 times the average particle diameter.

This same trend applies for slurry flow down a narrow fracture. An approximate proppant bridging or proppant admittance criteria can be derived by calculating an equivalent hydraulic radius for a narrow slot,  $r_{hyd} = w/2$ , where  $w$  is the average width of the fracture. For a round perforation hole, the hydraulic radius is  $d/4$ , where  $d$  is the perforation hole diameter. Equating the two hydraulic radius values shows that  $2w$  is equivalent to the diameter of a round hole. Using this along with two lines fitting the data of Gruesbeck and Collins leads to an approximate admittance criteria for a hydraulic fracture:

- For a proppant solid volume fraction  $f_v$  less than 0.17, the average width must be greater than  $(1 + 2f_v/0.17) \times d_{prop}$ .
- For  $f_v$  greater than 0.17, the average width must be greater than  $3d_{prop}$  (i.e., a width greater than three proppant grain diameters).

This approximate correlation also compares well with other experimental data from proppant-laden slurry flowed through a narrow slot (van der Vlis *et al.*, 1975), although the correlation may be optimistic for low proppant concentrations. As shown in Table 5-1, the behavior for bridging in a fracture is similar to bridging in perforation holes. At low proppant concentrations, the average fracture width must be only slightly greater than the average particle diameter. As the proppant concentration increases toward

**Table 5-1. Proppant admittance criteria.**

Proppant <sup>†</sup> Concentration (lbm proppant/gal fluid)	$\bar{w}/d_{prop}$	
	Experimental Bridge Formation <sup>‡</sup>	Correlation Bridge
0.5 to 2	1.8	1.15 to 2.0
2 to 5	2.2	2.0 to 3.0
5 to 8	2.6	3.0

<sup>†</sup> Sand as proppant  
<sup>‡</sup> Data from van der Vlis *et al.* (1975)

6 to 8 ppg, the required average fracture width increases to  $3d_{prop}$ .

This critical width is important to the hydraulic fracturing process. Should proppant enter a part of the fracture where sufficient width does not exist, the proppant will bridge and no longer flow down the fracture. Additional slurry flowing in this direction will cause proppant to pile up, dehydrate and block that part of the fracture. Should this occur near the wellbore, possibly as a result of some form of near-wellbore width restriction (see tortuosity discussion in Section 6-8), a total screenout can result with serious consequences for the success of the fracture treatment.

### 5-5.5. Fracture models

Clearly, developing a final treatment pump schedule must consider many options. The interactive roles of the various major variables ( $h_f$ ,  $E$ ,  $C_L$ ,  $K_{Ic-apparent}$ ,  $\mu$  and  $q_i$ ) must be considered along with the various roles of fluid viscosity for net pressure, width, proppant transport and fluid loss. In addition, the design must consider the various roles of the pad volume concerning fluid loss and creating fracture width. Fracture simulators, or fracture placement models, provide the means to handle this complexity and to consider the interaction of the multitude of variables. For this reason, a final schedule is generally developed using a fracture geometry model. However, as discussed in Section 5-5.2, Sidebar 6L and Section 10-4, in many instances an acceptable pump schedule can be developed more simply for a treatment on the basis of the expected fluid efficiency (as determined from a calibration treatment). The use of a properly calibrated fracture geometry model also enables the consideration of multiple scenarios for designing the

optimum treatment for a specific application. This approach is briefly discussed in Section 5-6.1.

## 5-6. Economics and operational considerations

The preceding discussion covers most of the technical aspects of hydraulic fracturing (reservoir engineering, fluid mechanics, rock mechanics, etc.) and reviews the complex interactions that exist between the various, often competing design variables. However, to complicate things further, hydraulic fracturing and treatment design are generally governed by—or are at least sensitive to—two final considerations: economics and field operations.

### 5-6.1. Economics

At the most basic level, hydraulic fracturing is about time and money: “economics.” Given reasonable geologic continuity, a single well would, given sufficient time, drain an entire reservoir. However, the operating costs of maintaining a well over the decades required to accomplish this drainage would probably make the entire operation unattractive from a commercial viewpoint. Alternatively, a single well

with a large hydraulic fracture may drain the reservoir much faster, making the economics much more attractive despite the additional cost of the treatment. Carrying this forward, 2, 10 or 100 or more wells could be drilled and/or fractured. Between these extremes is the optimum plan, which is the number of wells, number of fractured wells or both that maximize the economic value of the production compared with the development capital costs and the ongoing operating costs.

As a simple example, the process (at least for a single well) could proceed as pictured in Fig. 5-24 (Veatch, 1986). First, reservoir engineering calculations provide a production forecast for various combinations of fracture half-length  $x_f$  and conductivity  $k_f w$  (including the case of no fracture at all). Based on some future price forecast, this allows calculation of a present value, which is the future revenue from the production less future operating costs and discounted back to the present. Hydraulic fracturing calculations based on fluid loss, fracture height, etc., are used to determine the treatment volumes required to generate various combinations of fracture length and propped fracture width, and these calculations are easily converted into estimated treatment costs. Some form of net revenue economic analysis is then used to determine the best type of proppant, desired

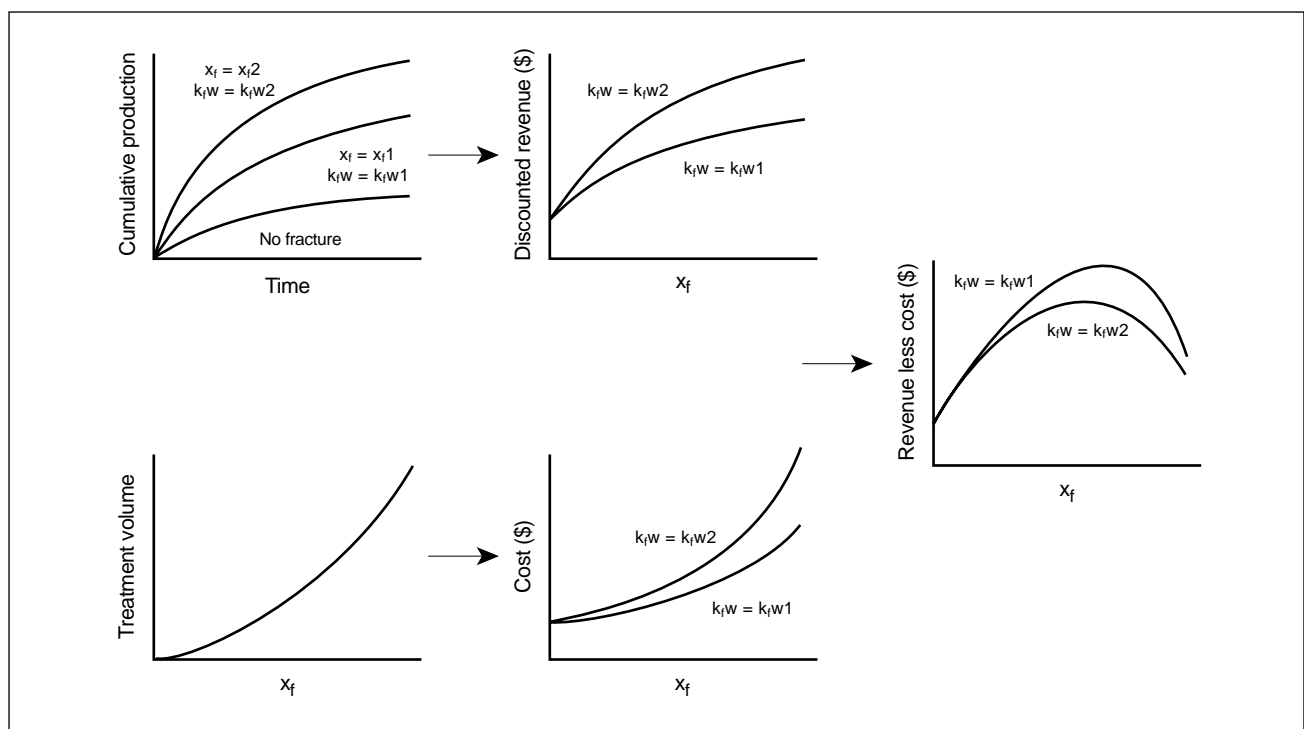


Figure 5-24. Veatch (1986) economics diagrams.

fracture length and other requirements for the optimum treatment.

There are, of course, many variations of this basic process. For example, full-cycle economics includes drilling and other completion costs, along with fracture treatment costs, in determining the optimum fracture design. This type of analysis is usually appropriate in any case involving multiple wells (e.g., should a resource be developed using 10 wells with huge fractures or 20 wells with smaller or no fracture treatments?). Point-forward analysis, on the other hand, considers only the fracture treatment costs (because drilling and other completion costs are already expended) and is most appropriate for working over existing wells.

## 5-6.2. Operations

As discussed in the preceding section, economics provides the final design consideration for hydraulic fracturing, whereas field conditions provide the practical limits within which the design must fit. Even beyond defining these limiting conditions, however, any design is only as good as its execution; thus the treatment must be pumped as designed. Field operations and operational considerations impact hydraulic fracturing in two ways:

- prefracture condition of the wellbore, quality of the cement job, perforations, pressure limits, etc., with these considerations defining practical limits that the design must meet
- quality assurance and quality control (QA/QC) before and during the actual treatment.

These operational considerations are discussed in Chapters 7 and 11, with some of the major items highlighted in the following.

- Wellbore considerations

Some of the major wellbore considerations for hydraulic fracturing include

- size and condition of wellbore tubulars
- quality of the cement job for zonal isolation
- perforations
- wellbore deviation.

During a hydraulic fracture treatment, the predicted surface pressure  $p_{surf}$  and the hydraulic horsepower required for a treatment are related

to the hydrostatic head of the fluid in the wellbore  $p_{head}$  and the pipe friction  $p_{pipe\ friction}$ :

$$p_{surf} = \sigma_c + p_{net} + p_{pipe\ friction} - p_{head} \quad (5-26)$$

$$hhp \propto q_i \times p_{surf}. \quad (5-27)$$

Pipe friction is a major term, and thus the size of the well tubulars has a strong influence on allowable pump rates (because pipe friction is typically related to  $v^e$ , where  $v = q_i/A$  is the flow velocity down the tubing, and  $e$  is typically about 1.1 to 1.7). Also, the strength and condition of the tubulars (along with the associated wellhead equipment) set an allowable surface pressure and thus indirectly set an allowable injection rate. In addition, the size, type and condition of the wellbore tubulars may limit (or prohibit) future work-over and recompletion opportunities.

A critical aspect of wellbore considerations is a good cement job around the casing or liner to provide zonal isolation. In general, a fracture grows where nature dictates, and the engineer has little control over fracture height growth. The only control possible is the ability to specify where the perforations are placed and the fracture initiates. If that ability is compromised by a poor cement sheath around the casing that allows the perforations to communicate directly with an undesired interval, then even this minimal level of control is lost, and the hydraulic fracture treatment may be seriously compromised.

Another important consideration is the perforations that allow the fluid to leave the wellbore and create the fracture. The number and size of the perforation holes are important for proppant admittance, as discussed briefly in Section 5-5.4 and in detail in Section 11-3.

- Quality assurance and quality control

Quality issues are critical for hydraulic fracturing. After proppant pumping starts, a treatment cannot be stopped because of problems without significantly compromising the design goals. For this time period, everything must work, including the wellbore equipment, pumping and blending equipment and chemicals (i.e., the fluid system). To cite a simple example, if a treatment uses 10 tanks of batch-mixed fluid, and one of the

tanks is bad, then the QA score is a relatively high 90%. However, if the bad fluid is pumped just after proppant addition starts, it may easily cause total failure of the treatment, and if successful treatment is critical to economic success of the well, this causes total economic failure. Typically, this type of failure cannot be overcome without completely redrilling the well (refracturing operations are usually a risky procedure), and thus 90% can be a failing grade for QA.

# Appendix: Evolution of Hydraulic Fracturing Design and Evaluation

*K. G. Nolte, Schlumberger Dowell*

## Overview

This Appendix to Chapter 5 reviews the evolution of hydraulic fracturing design and evaluation methods. Complementary reviews are the application of fracturing by Smith and Hannah (1996) and fracturing fluids by Jennings (1996). This review of design and evaluation considers three generations of fracturing: damage bypass, massive treatments and tip-screenout (TSO) treatments.

The first two generations of fracturing and their links to practices are emphasized because these contributions are not likely well known by the current generation of engineers. The review focuses on propped fracturing and does not explicitly consider acid fracturing. Although the principles governing the mechanics of both are essentially the same, the fluid chemistry for obtaining fracture conductivity is quite different (see Chapter 7). These principles have their roots in civil and mechanical engineering, more specifically in the general area of applied mechanics: solid mechanics for the rock deformation and fluid mechanics for the flow within the fracture and porous media. For the porous media aspects, fracturing evaluation has benefited greatly from the reservoir engineering practices discussed in Chapters 2 and 12.

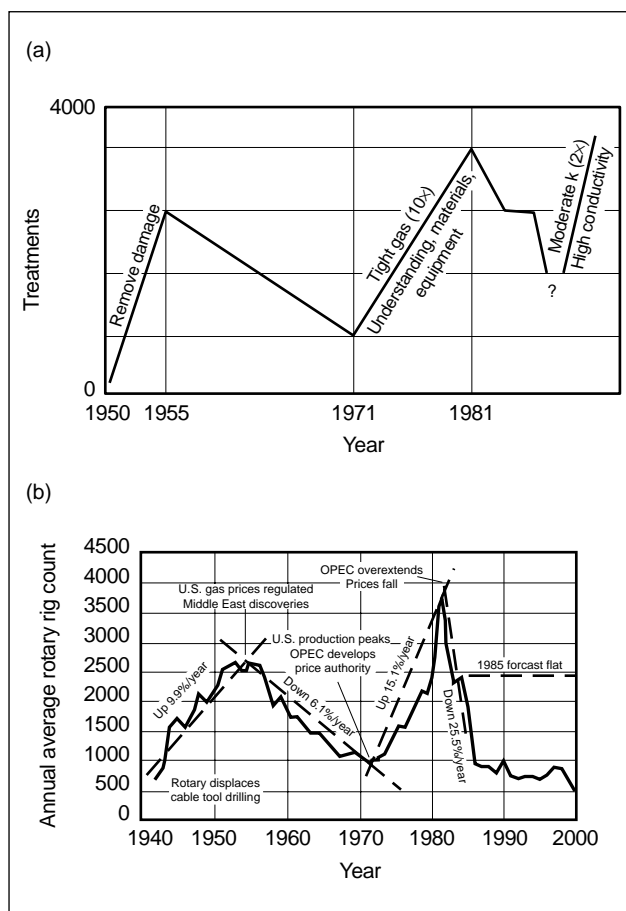
This review reflects the author's perspective and bias in interpreting the impact of past contributions, and therefore parts of this review should be anticipated to raise objections from others with an extensive knowledge of fracturing. In addition to this volume, the Society of Petroleum Engineers (SPE) Monograph *Recent Advances in Hydraulic Fracturing* (Gidley *et al.*, 1989) provides balanced, detailed coverage of the diverse areas of fracturing from the perspectives of more than 30 fracturing specialists.

This review concludes with speculation concerning a future generation, in which fracture design and reservoir engineering merge into fracturing for

reservoir management (i.e., control of both the vertical and horizontal flow profiles within the reservoir). Similar speculation in a 1985 lecture suggested that development of the technical foundation for the TSO generation would quickly bring higher permeability formations into consideration as typical fracturing candidates (i.e., “moderate  $k$  ( $2\times$ )” on Appendix Fig. 1a, with  $2\times$  indicating a target for folds of increase [FOI] in the production rate, in contrast to  $10\times$  for tight gas and massive treatments). However, the advent of this generation was considerably delayed because of two factors that have generally dominated technical considerations during the history of fracturing. These dominating factors are hydrocarbon prices and resistance to trying something new until established practices fail to allow the economic development of a prospect.

The cycles of fracturing activity in Appendix Fig. 1a clearly reflect the timing of the first two fracturing generations. Appendix Fig. 1b identifies economic drivers for corresponding cycles in the U.S. rig count. The first surge of activity resulted when rotary drilling was introduced, which enabled the development of deeper reserves. Fracturing activity followed this trend soon after its commercialization in 1949 because it was found to be an effective, low-cost means of mitigating the resulting drilling mud damage to reservoir sections (i.e., the damage bypass generation). Both drilling and fracturing activities began a long-term decline after 1955 because of degrading prices caused by imported oil and regulated gas prices. Similarly, both activities began a rapid increase at about 1979 as prices increased because the Organization of Petroleum Exporting Countries (OPEC) reduced its oil supplies and a natural gas shortage developed in the United States. The gas shortage, and its 10-fold-plus increase in price, encouraged the development of tight gas reserves and an associated demand for massive fracturing treatments to develop the tight reserves. The failure of past fracturing practices for





**Appendix Figure 1.** (a) Trends in fracturing activity treatments per month (courtesy of K. G. Nolte and M. B. Smith, 1985–1986 SPE Distinguished Lecture). (b) U.S. drilling rig activity shows five major trends (updated from Oil & Gas Journal, 1985).

large treatments spurred a significant research and development effort that beneficially impacted every aspect of fracturing and essentially developed the fracture design and evaluation framework presented in this volume. The industry's rapid contraction during the early 1980s resulted again from OPEC, but this time because of OPEC's failure to maintain artificially high prices. The TSO treatment for creating the very wide propped fractures required for high permeability evolved during this time. This technique allowed the development of a troublesome soft-chalk reservoir in the North Sea by fracturing. However, the significant potential of the TSO generation did not materialize until about 10 years later, when its application was required on a relatively large scale to achieve viable economics for two high-permeability applications: bypassing deep damage in the Prudhoe Bay field and its coupling with gravel

packing to achieve low-skin completions for a significant venture in the Gulf of Mexico.

The potential for a future reservoir management generation was demonstrated in 1994 for the Norwegian Gullfaks field. The potential is to use TSO treatments and indirect vertical fracturing for increased reserves recovery, formation solids control and water management. However, the unique benefits and favorable economics for this different approach to reservoir "plumbing" were slow to materialize because of the industry's comfort with deviated drilling and more traditional completions.

Another observation from this historical perspective is the 1985 forecast of a flat drilling level (Appendix Fig. 1b). However, activity continued to decrease rapidly, to less than one-half of the forecast, and subsequently declined by another one-half. Stable activity levels within the petroleum industry are not seen in the historical cycles and remain the product of wishful thinking.

## The beginning

The concept of hydraulic fracturing within the petroleum industry was developed during the last half of the 1940s within Stanolind (now BP Amoco; e.g., Clark, 1949; Farris, 1953; Howard and Fast's *Hydraulic Fracturing Monograph*, 1970) by building on the industry's experience with injection techniques that had experienced increased injectivity by fracturing: acidizing (Grebe and Stoesser, 1935), squeeze cementing and brine injection wells. A re-issued patent was granted (Farris, 1953, resulting from an initial filing in 1948) that was comprehensive in scope and covered many recognized practices and products: proppant, gelled oil, breakers, fluid-loss additives, continuous mixing, pad-acid fracturing, emulsified acids and the use of packers for fracturing multiple zones. Several aspects of the patent that later became important included the implication that fractures were horizontal and the use of a "low-penetrating" fluid or with viscosity > 30 cp.

The first experimental treatments were performed in 1947 on four carbonate zones in the Houghton field in Kansas (Howard and Fast, 1970). The zones had been previously acidized and were isolated by a cup-type straddle packer as each was treated with 1000 gal of napalm-thickened gasoline followed by 2000 gal of gasoline as a breaker. These unpropped

treatments did not increase production and led to the incorrect belief for some time that fracturing had no benefit over acidizing for carbonate formations.

A subsequent treatment of the Woodbine sand in the East Texas field was highly successful. It consisted of 23 bbl of gelled lease crude, 160 lbm of 16-mesh sand at 0.15 ppa and 24 bbl of breaker (Farris, 1953). Halliburton originally obtained an exclusive license from Stanolind and commercialized fracturing in 1949. Activity rapidly expanded to about 3000 treatments per month by 1955 (Appendix Fig. 1a). Before a universal license was granted to other service companies, water or “river” fracturing became popular in lower permeability areas such as the San Juan basin (C. R. Fast, pers. comm., 1997). As implied by the name, the treatments used river water and sand. The water was outside the definition of a nonpenetrating fluid within the patent’s specified filtrate rate through filter paper or viscosity greater than 30 cp.

## The first generation: damage bypass

Applications of first-generation fracturing were primarily small treatments to bypass near-wellbore drilling fluid damage to formations with permeability in the millidarcy range. An inherent advantage of propped fracturing, relative to matrix treatment for damage removal, is that a fracture opens the complete section and retains a conductive path into the zone. The complete opening overcomes the diversion consideration for matrix treatments (see Chapter 19), but adds the consideration of producing from bottomwater or an upper gas cap. For lower permeability formations, large amounts of produced water are generally not a problem. For higher permeability formations, water production can be significant, which provided the historical preference for matrix treatment in higher permeability applications. However, the precision of fracturing improved significantly, and TSO treatments have been routinely performed in Prudhoe Bay oil columns only 50 ft thick and above very mobile water (Martins *et al.*, 1992b).

The technology for this fracturing generation is summarized in the Howard and Fast (1970) Monograph. The breadth of this volume is shown by its comprehensive consideration of candidate selection (see Chapter 1) and optimal design based on economic return (see Chapters 5 and 10). Other note-

worthy design and evaluation methods from this generation are fracture orientation (horizontal or vertical), in-situ stress and fracture width models, FOI prediction and fracture conductivity in production enhancement.

## Fracture orientation and in-situ stress

The application of mechanics to fracturing was catalyzed by the horizontal orientation of fractures implied in the Stanolind patent and the desire of several operators to avoid paying the nominal patent royalty of \$25–\$125, based on volume (C. R. Fast, pers. comm., 1997). Significant research activity was conducted to show that fractures can be vertical, as is now known to be the general case for typical fracturing conditions. The fracture orientation debate eventually led to a lawsuit that was settled before the trial ended. The settlement accepted the patent and nominal royalty payments and stipulated that other service companies receive a license to practice fracturing. However, the royalty benefits were more than nominal to Stanolind because about 500,000 treatments were performed during the 17-year period of the patent (C. R. Fast, pers. comm., 1997). Key to the favorable settlement for Stanolind was its well-documented demonstration of a horizontal fracture in the Pine Island field (see fig. 7-1 in Howard and Fast, 1970).

The central issue in the orientation debate was the direction of the minimum stress. The pressure required to extend a fracture must exceed the stress acting to close the fracture. Therefore, the fracture preferentially aligns itself perpendicular to the direction of minimum stress because this orientation provides the lowest level of power to propagate the fracture. The minimum stress direction is generally horizontal; hence, the fracture plane orientation is generally vertical (i.e., a vertical fracture). The preference for a horizontal fracture requires a vertical minimum stress direction.

In the following review, the orientation consideration is expanded to also cover the state of stress in more general terms. The stress at any point in the various rock layers intersected by the fracture is defined by its magnitude in three principal and perpendicular directions. The stress state defines not only the fracture orientation, but also the fluid pressure required to propagate a fracture that has operational importance, vertical fracture growth into surrounding formation

layers and stress acting to crush proppant or to close etched channels from acid fracturing. The crushing stress is the minimum stress minus the bottomhole flowing pressure in the fracture. The orientation debate resulted in three papers that will remain significant well into the future.

The first paper to be considered is by Harrison *et al.* (1954). Some of the important points in the paper are that the overburden stress (vertical stress  $\sigma_v$ ) is about 1 psi per foot of depth, fracturing pressures are generally lower than this value and therefore fractures are not horizontal, and an inference from elasticity that the minimum horizontal stress is

$$\sigma_h = K_o \sigma_v, \quad (1)$$

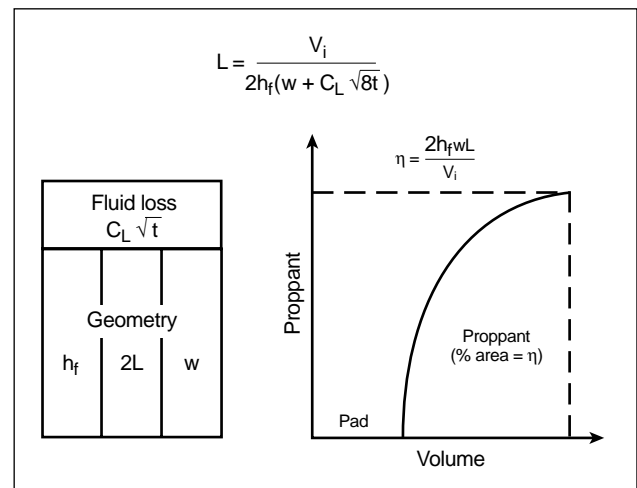
where  $K_o = \nu/(1 - \nu) = 1/3$  for  $\nu = 1/4$  (see Eq. 3-51).

Using Poisson's ratio  $\nu$  of  $1/4$ , Harrison *et al.* concluded that the horizontal stress is about one-third of the vertical stress and therefore fractures are vertical. Appendix Eq. 1 provides the current basis for using mechanical properties logs to infer horizontal stress, with Poisson's ratio obtained from a relation based on the shear and compressional sonic wave speeds (see Chapter 4). Another assumption for Appendix Eq. 1 is uniaxial compaction, based on the premise that the circumference of the earth does not change as sediments are buried to the depths of petroleum reservoirs and hence the horizontal components of strain are zero during this process. Therefore, Appendix Eq. 1 provides the horizontal stress response to maintain the horizontal dimensions of a unit cube constant under the application of vertical stress.

However, there is one problem with this 1954 conclusion concerning horizontal stress. Appendix Eq. 1 is correct for the effective stress  $\sigma'$  but not for the total stress  $\sigma$  that governs fracture propagation:  $\sigma' = \sigma - p$ , where  $p$  is the pore pressure, which also has a role in transferring the vertical stress into horizontal stress as explicitly shown by Appendix Eq. 2. Harrison *et al.* (1954) correctly postulated that shales have higher horizontal stresses and limit the vertical fracture height. The general case of higher stress in shales than in reservoir rocks was a necessary condition for the successful application of fracturing because fractures follow the path of least stress. If the converse were the general case, fractures would prefer to propagate in shales and not in reservoir zones.

Harrison *et al.* also reported the Sneddon and Elliott (1946) width relation for an infinitely extending pressurized slit contained in an infinitely extending elastic material. This framework has become the basis for predicting fracture width and fracturing pressure response (see Chapters 5, 6 and 9). They used the fracture length for the characteristic, or smaller and finite, dimension in this relation. Selecting the length for the characteristic dimension resulted in what is now commonly termed the KGD model. Selecting the height, as is the case for a very long fracture, is termed the PKN model. These models are discussed in the next section and Chapter 6. Harrison *et al.* considered a width relation because of its role in fracture design to determine the fluid volume required for a desired fracture extent.

The role of volume balance (or equivalently, the material balance in reservoir terminology) is an essential part of fracture design and fracture simulation code. As shown schematically on the left side of Appendix Fig. 2, each unit of fluid injected  $V_i$  is either stored in the fracture to create fracture volume or lost to the formation as fluid loss. (However, Harrison *et al.*'s 1954 paper does not discuss fluid loss.) The stored volume is the product of twice the fracture half-length  $L$ , height  $h_f$  and width  $w$ . If the latter two dimensions are not constant along the fracture length, they can be appropriately averaged over the length. The half-length is then obtained by simply dividing the remaining volume, after removing the fluid-loss volume, by twice the product of the



**Appendix Figure 2.** Volume balance for fracture placement (equation from Harrington *et al.*, 1973) (adapted courtesy of K. G. Nolte and M. B. Smith, 1984–1985 SPE Distinguished Lecture).

average height and the average width. The fluid-loss volume depends on the fluid-loss surface area, or a height-length product. Furthermore, as shown on the right side of Appendix Fig. 2, the ratio of stored to total volume is termed the fluid efficiency  $\eta$  and directly affects the proppant additional schedule (Harrington *et al.*, 1973; Nolte, 1986b) (see Sidebar 6L).

The second paper to be discussed from the orientation era is by Hubbert and Willis (1957). The lessons from this paper extend beyond fracturing and into the area of structural geology. This work provides simple and insightful experiments to define the state of in-situ stress and demonstrate a fracture's preference to propagate in the plane with minimum stress resistance. For the latter experiments, the "formation" was gelatin within a plastic bottle preferentially stressed to create various planes of minimal stress.

They also used simple sandbox experiments to demonstrate normal and thrust faulting and to define the state of stress for these conditions (see Sidebar 3A). They showed that  $K_o$ , or equivalently the horizontal stress, within Appendix Eq. 1 is defined by the internal friction angle ( $\phi = 30^\circ$  for sand) and is  $\frac{1}{3}$  for the minimum stress during normal faulting and 3 for the maximum stress during thrust faulting. For the normal faulting case and correctly including pore pressure in Appendix Eq. 1, the total minimum horizontal stress becomes

$$\sigma_h = (\sigma_v + 2p)/3, \quad (2)$$

where  $K_o = \frac{1}{3}$  with  $\phi = 30^\circ$ . For this case the horizontal stress is much less than the vertical stress except in the extreme geopressure case of pore pressure approaching overburden, which causes all stresses and pore pressure to converge to the overburden stress. For the thrust faulting case, the larger horizontal stress (i.e., for the two horizontal directions) is greater than the overburden and the smaller horizontal stress is equal to or greater than the overburden. Both the extreme geopressure case and an active thrust faulting regime can lead to either vertical or horizontal fractures. The author has found Appendix Eq. 2 to accurately predict the horizontal stress in tectonically relaxed sandstone formations ranging from microdarcy to darcy permeability. The accuracy at the high range is not surprising, as the formations approach the unconsolidated sand in the sandbox experiments. The accuracy obtained for microdarcy-permeability sands is subsequently explained.

Hubbert and Willis also provided an important set of postulates: the rock stresses within the earth are defined by rock failure from tectonic action and the earth is in a continuous state of incipient faulting. From this perspective, the stress is not governed by the behavior of the intact rock matrix, but by an active state of failure along discrete boundaries (e.g., by sand grains within fault boundaries, which explains the application of Appendix Eq. 2 to microdarcy-permeability sandstones). This insightful conclusion about the role of failure is at the other extreme of the behavior spectrum from the elastic assumptions that Poisson's ratio (Appendix Eq. 1) governs the horizontal stress and that failure has no effect on the stress. This extreme difference in the assumptions for Appendix Eqs. 1 and 2 is often overlooked because of the similar value of  $K_o = \sim \frac{1}{3}$  obtained in the case of a tectonically relaxed region and Poisson's ratio near  $\frac{1}{4}$ . However, the role of elasticity becomes important in thrusting areas (see Section 3-5.2) because of the difference in horizontal stress resulting for layers with different values of Young's modulus (stiffness). More of the tectonic action and higher levels of stress are supported by the stiffer layers.

Additional considerations for horizontal stress outlined by Prats (1981) include the role of long-term creep. Creep deformation allows relaxation of the stress difference between the overburden and horizontal stresses, thereby enabling the horizontal stress to increase toward the larger vertical stress governed by the weight of the overburden. This effect is well known for salt layers that readily creep and can collapse casing by transferring most of the larger overburden stress into horizontal stress. The role of stress relaxation is an important mechanism for providing favorable stress differences between relatively clean sands governed by friction (i.e., Appendix Eq. 2) with minimal creep and sediments with higher clay content. In the latter case, the clay supports some of the intergranular stresses. The clay structure is prone to creep that relaxes the in-situ stress differences and increases the horizontal stress for a clay-rich formation.

Hence, both clay content and Poisson's ratio produce the same effect on horizontal stress. Because clay content also increases Poisson's ratio, there is a positive correlation of clay content (creep-induced stress) to larger Poisson's ratios (and elastic stress, from Appendix Eq. 1) inferred from sonic velocities. The implication of the correlation is that clay-rich

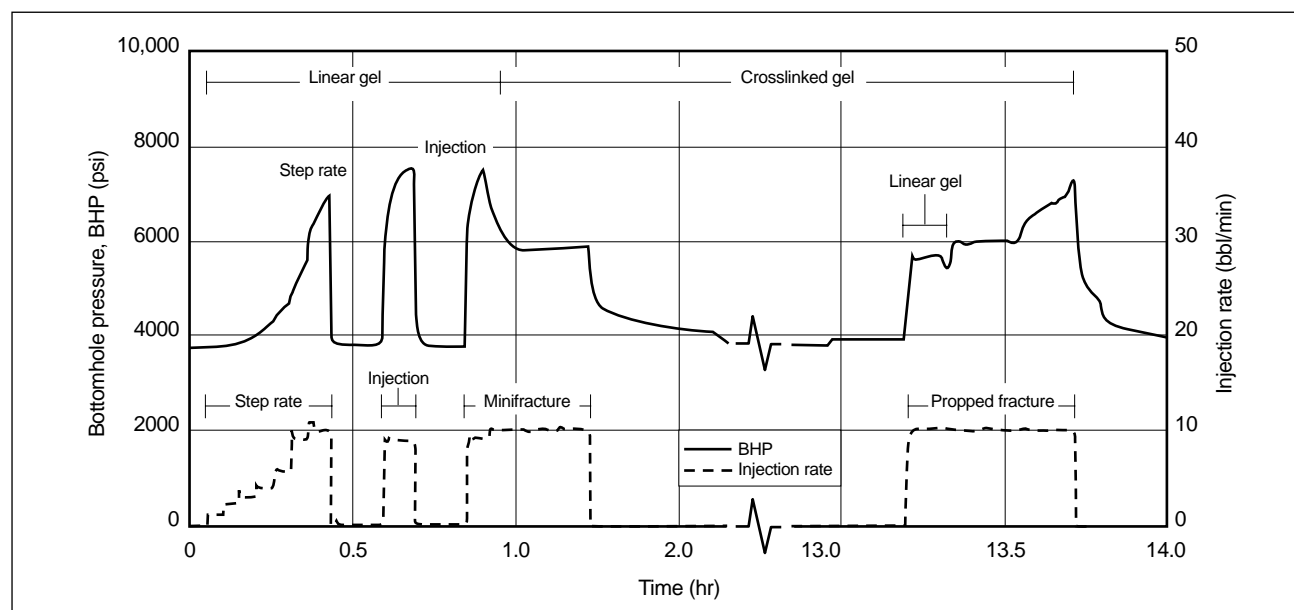
formations can also have horizontal stresses greater than those predicted by either Appendix Eq. 1 or 2, which is consistent with the general requirement to calibrate elastic-based stress profiles to higher levels of stress (e.g., Nolte and Smith, 1981). The correlation of clay and Poisson's ratio links the conclusions of Hubbert and Willis and Prats that horizontal stress is governed primarily by nonelastic effects and the general correlation between the actual stress and elastic/sonic-based stress profiles.

The third significant paper from this period is by Lubinski (1954). He was a Stanolind researcher who introduced the role that poroelasticity can have in generating larger stresses during fracturing. (Poroelasticity could increase horizontal stress and lead to horizontal fractures, as in the Stanolind patent.) Lubinski presented poroelasticity within the context of its analogy to thermoelasticity. His use of the thermal stress analogy facilitates understanding the poroelastic concept because thermal stresses are generally more readily understood than pore stresses by engineers. The analogy provides that when pore pressure is increased in an unrestrained volume of rock, the rock will expand in the same manner as if the temperature is increased. Conversely, when the pore pressure is lowered, the rock will contract as if the temperature is lowered. When the rock is constrained, as in a reservoir, a localized region of pore pressure change will induce stress changes: increasing stress within the region of increasing pore pressure (e.g., from fracturing fluid filtrate or water

injection) and decreasing stress within the region of decreasing pore pressure (e.g., production). The long-term impact of Lubinski's paper is that the importance of poroelasticity increases as routine fracturing applications continue their evolution to higher permeability formations. This is apparent from the thermal analogy—as the area of expansion increases the induced stresses also increase. For poroelasticity, the area of significant transient change in pore pressure increases as the permeability increases (see Section 3-5.8).

Appendix Fig. 3 shows an example of significant poroelasticity for a frac and pack treatment in a 1.5-darcy oil formation. The time line for the figure begins with two injection sequences for a linear-gel fluid and shows the pressure increasing to about 7500 psi and reaching the pressure limit for the operation. During the early part of the third injection period, crosslinked fluid reaches the formation and the pressure drops quickly to about 5600 psi (the native fracturing pressure) and remains essentially constant during the remainder of the injection.

The first two injections, without a crosslinked-fluid filtrate (or filter cake) to effectively insulate the formation (as in the thermal analogy) from the increasing injection pressure, resulted in pore pressure increases of significant magnitude and extent within the formation. The pore pressure increase provides up to a 1900-psi horizontal and poroelasticity stress increase that extends the fracturing pressure beyond the operational limit, leading to the shut-in for the



**Appendix Figure 3.** High-permeability frac and pack treatment (Gulrajani et al., 1997b).

second injection. This increase is about one-third of the native stress. However, during the two subsequent injections the insulating effect of the crosslinked fluid's internal cake and filtrate allows fracture extension within essentially the native stress state. The pressure drop supported by the cake and filtrate is about 1300 psi, as reflected by the rapid pressure decrease after the third injection. This decrease occurs because of the rapid closure and cessation of fluid loss (that activated the pressure drop), which is the same reason that surface pressure decreases at the cessation of injection and loss of pipe friction. The last injection for the proppant treatment is also of interest because of the absence of a poroelastic effect during the initial linear-gel injection. This observation indicates that the insulating effect remained effective from the prior injection of crosslinked fluid.

For a normally pressured and tectonically relaxed area, the maximum increase in horizontal stress before substantial fracture extension is about one-third of the native horizontal stress (Nolte, 1997), as was found for the case shown in Appendix Fig. 3. Also, for any pore pressure condition in a relaxed area, the stress increase will not cause the horizontal stress to exceed the overburden (i.e., cause horizontal fracturing). However, as the example shows, without fluid-loss control, poroelasticity can significantly increase the fracturing pressure and extend it beyond operational limits for high-permeability reservoirs.

## Width models

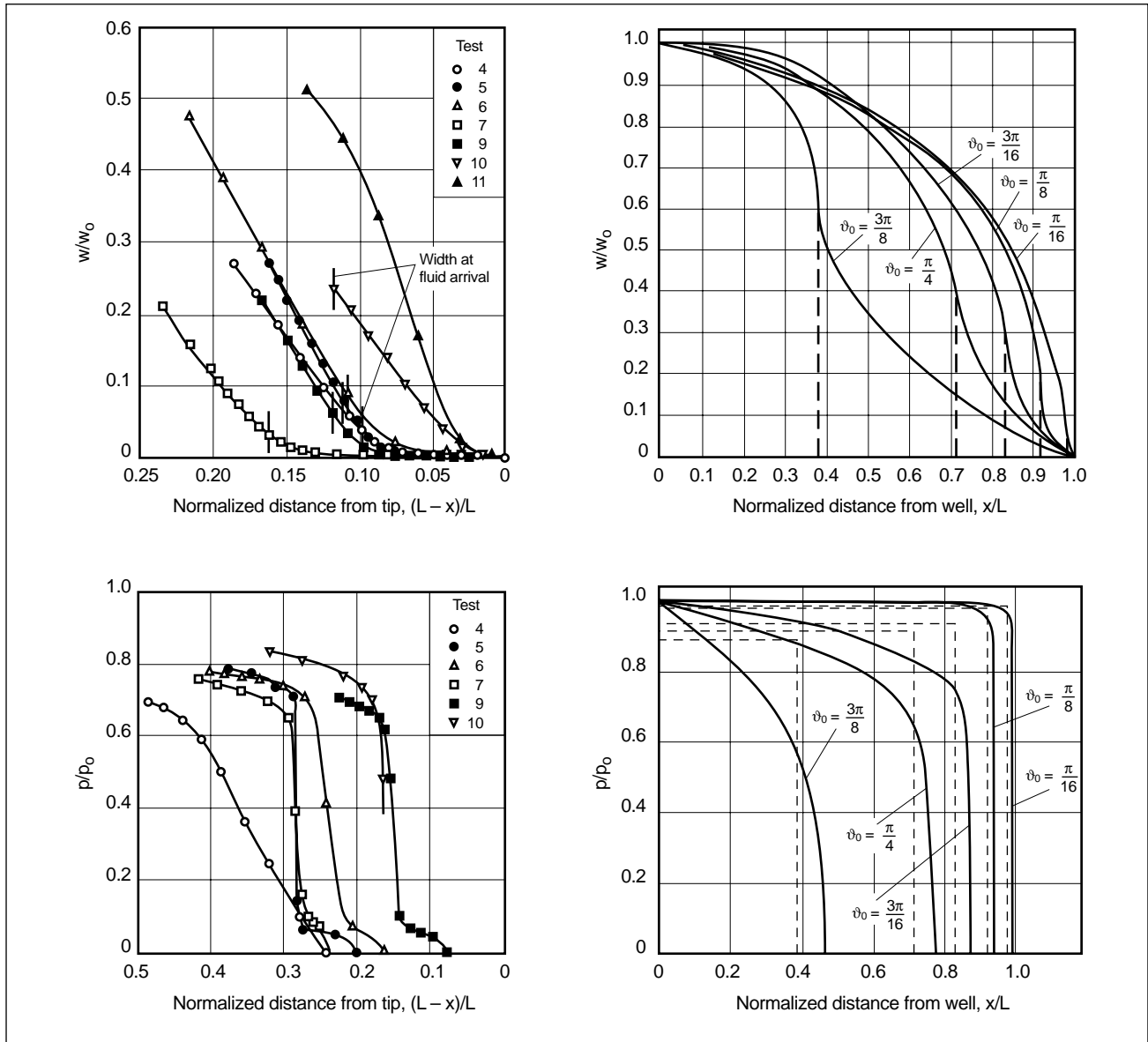
The first rigorous coupling of fluid flow and the elastic response of the formation was reported by Khristianovich and Zheltov (1955). They used a two-dimensional (2D) formulation based on a complex variable analysis. Their formulation was equivalent to the length becoming the characteristic, or smaller, dimension and provides the initial "K" for the KGD width model discussed later and in Chapter 6. In addition to being the first paper to provide the coupling of fluid flow and rock interaction that is the embodiment of the hydraulic fracturing process, the paper also identified the role for a fluid lag region at the fracture tip. This low-pressure region, beyond the reach of fracturing fluid and filling with pore fluid, has a large, negative net pressure and acts as a clamp at the fracture tip. The fluid lag's clamping effect provides the natural means to lower the potentially

large tip-region stresses to a level that can be accommodated by the in-situ condition. The presence of the lag region has been demonstrated by field experiments at a depth of 1400 ft at the U.S. Department of Energy (DOE) Nevada Test Site (Warpinski, 1985).

Appendix Fig. 4 compares the Khristianovich and Zheltov analytical results for width and pressure to the corresponding parameters from the Warpinski field results. For the analytical results, decreasing values of the complex variable angle  $\vartheta_0$  toward the right side of the figure correspond to relatively smaller lag regions and larger differences between the minimum stress and pressure in the lag region (i.e., generally deeper formations). The width profiles clearly show the clamping action at the tip, and the field data appear to be represented by a  $\vartheta_0$  value of about  $\pi/8$  for the analytical cases. Also noteworthy of the experimental results is that tests 4 through 7 with water and test 9 with gel show similar behavior when test 4, which had a relatively low injection rate, is ignored. Tests 10 and 11 were with a gelled fluid and clearly show progressively different behavior from the preceding tests because of the altered tip behavior resulting from prior gel injections and the residual gel filter cakes that fill the fracture aperture after closure. The cakes have the consistency of silicon rubber and functionally provide an analogous sealing affect for subsequent tests.

The practical importance of the lag region cannot be overemphasized. The extent of the region, which is extremely small in comparison with commercial-scale fractures, adjusts to the degree required to essentially eliminate the role of the rock's fracture resistance or toughness (e.g., see SCR Geomechanics Group, 1993) and to isolate the fluid path from all but the primary opening within the multitude of cracks (process zone) forming ahead of the fracture (see Chapters 3 and 6). The field data show the width at the fluid front is well established (i.e., generally greater than 5% of the maximum width at the wellbore) and that fluid enters only a well-established channel behind the complexity of the process zone. These aspects of the lag region provide great simplification and increased predictability for applying commercial-scale hydraulic fracturing processes.

A paper by Howard and Fast (1957), and particularly the accompanying appendix by R. D. Carter, provides the current framework for fluid loss. The paper identifies the three factors controlling fluid loss: filter-cake accumulation, filtrate resistance into



**Appendix Figure 4.** Comparison of Warpinski (1985) field data (left) and Khristianovich and Zheltov (1955) analysis (right).  $w_0$  and  $p_0$  are the wellbore values of width and pressure, respectively;  $x$  is the distance from the well.

the reservoir and displacement of the reservoir fluid (see Fig. 5-17 and Chapters 6 and 8). All three factors are governed by the relation  $1/\sqrt{t}$  (where  $t$  is time) for porous flow in one dimension. The coefficient for this relation was termed the fluid-loss coefficient  $C_L$ . The authors also provided the means to determine the coefficient for all three factors using analytical expressions for the filtrate and reservoir contributions and to conduct and analyze the filtercake experiment, which is now an American Petroleum Institute (API) Recommended Practice.

Also of significance was presentation of the Carter area equation, with area defined as the product of the

height and tip-to-tip length. This equation, based on the assumption of a spatial and temporal constant fracture width, provided the first rigorous inclusion of fluid loss into the fracturing problem (see Chapter 6). Equation 6-18, which is solved by Laplace transformation, is in terms of exponential and complementary error functions and is not “engineer friendly.” This difficulty was soon overcome by developing a table for the more complicated terms in the equation using a dimensionless variable (see Eq. 6-19) that is proportional to the fluid-loss coefficient (loss volume) divided by the width (stored volume) and hence also related directly to the fluid efficiency

$\eta$  illustrated in Appendix Fig. 2. Nomographs for the complete equation were also developed (e.g., figs. 4-17 and 4-18 of the Howard and Fast Monograph). Eventually a simple and approximate expression (Harrington *et al.*, 1973) for the Carter equation provided the basis for fracture design into the 1980s. The approximate expression is based on the relation at the top of Appendix Fig. 2. For these applications, the average width was first determined from either the KGD or PKN model, as discussed in the following.

Another 1957 paper was by Godbey and Hodges (1958) and provided the following prophetic phrases: “By obtaining the actual pressure on the formation during a fracture treatment, and if the inherent tectonic stresses are known, it should be possible to determine the type of fracture induced. . . . The observation of both the wellhead and bottomhole pressure during fracturing operations is necessary to a complete understanding and possible improvement of this process.” These statements anticipated two of the important enablers for the second generation of fracturing: the use of pressure in a manner analogous to well test characterization of a reservoir and employment of a calibration treatment to improve the subsequent proppant treatment (see Chapters 5, 9 and 10).

In 1961 Perkins and Kern published their paper on fracture width models, including the long aspect ratio fracture (length significantly greater than height) and radial model (tip-to-tip length about equal to height) as described in Section 6-2.2. They considered, for the first time, both turbulent fluid flow and non-Newtonian fluids (power law model) and provided validating experiments for radial geometry and the role of rock toughness.

Perkins and Kern also discussed fracture afterflow that affects the final proppant distribution within the fracture. After pumping stops, the stored compression in the rock acts in the same fashion as compressible fluids in a wellbore after well shut-in. After fracture shut-in, fluid flow continues toward the tip until either proppant bridges the tip or fluid loss reduces the fracture width and stored compression to the extent that the fracture length begins to recede toward the wellbore (Nolte, 1991). The magnitude of the fracture afterflow is large compared with the wellbore storage case, as discussed later for Appendix Eq. 4.

The one shortcoming acknowledged by Perkins and Kern was not rigorously accounting for the flow rate change in the fracture required by continuity (i.e., material balance). They assumed that the volumetric flow rate was constant along the fracture’s length, which does not account for the effects of fluid loss and local rates of width change (storage change). This assumption was later addressed by Nordgren (1972), who provided closed-form equations for the bounding cases of negligible fluid loss and negligible fracture storage (i.e., most fluid injected is lost during pumping) for a long-aspect fracture and Newtonian fluid (see Section 6-2.2). The initial letters of the last names of the authors of these two papers form the name of the PKN model.

The remaining paper of historic importance for width modeling is by Geertsma and de Klerk (1969). They used the Carter area equation to include fluid loss within the short-aspect fracture, as previously considered by Harrison *et al.* (1954) and Khristianovich and Zheltov (1955). Their initials coupled with those of the authors of the latter paper form the name of the KGD (or KZGD) width model.

## Reservoir response to a fracture

Until the advent of numerical simulators, production models for a fracture did not consider transient flow effects and were based on the FOI relative to the reservoir’s radial flow response with no damage (skin effect = 0). The increase in production, relative to the case before fracturing, can be significantly greater than the FOI measure because fracturing also bypasses near-wellbore damage. The enhanced stimulation benefit increases as the magnitude of the damage increases. For example, removing a skin effect of about 25 increases production by about a factor of 4, whereas during the first generation a typical FOI target was about 2, relative to zero skin effect.

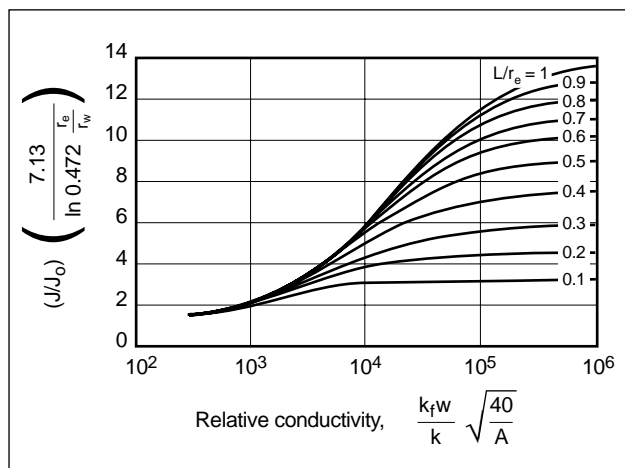
Papers considering finite-conductive fractures began to appear in 1958 and are summarized in chapter 10 of the Howard and Fast (1970) Monograph. Craft *et al.* (1962) considered the combined effects of fracture stimulation and damage bypass. Also of historical interest is that most of this work was performed on analog computers with electrical circuits representing the reservoir and fracture components. Recognition of the role of conductivity was important because the idealized assumption of infinite conduc-



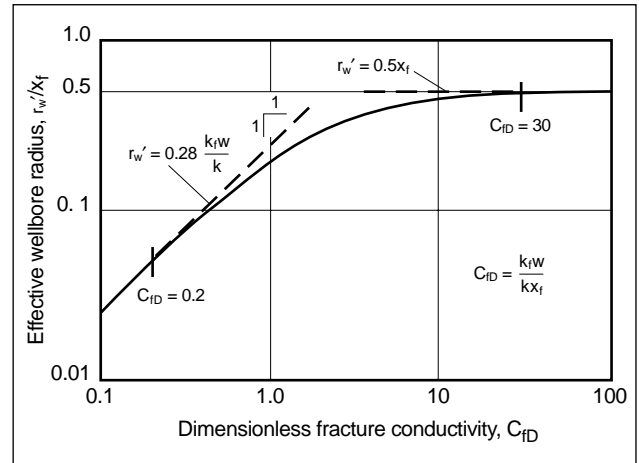
tivity, with no pressure loss in the proppant pack, cannot result from an economics-based optimized treatment. The incremental production increase, by achieving the infinite-acting case, would not offset the operational cost for the additional proppant.

McGuire and Sikora (1960) presented a significant study of the production increase in a bounded reservoir for a fracture with a finite conductivity  $k_f w$  for the proppant pack, where  $k_f$  is the fracture permeability. The boundary and conductivity effects are summarized in the set of pseudosteady-state curves shown in Appendix Fig. 5. The curves reflect different ratios of the fracture length relative to the drainage radius  $r_e$ , with the vertical axis reflecting the FOI as  $J/J_o$  and the horizontal axis reflecting dimensionless conductivity based on the drainage radius. The McGuire and Sikora curves were the primary reservoir tool for fracture design and evaluation until the late 1970s.

Prats (1961) used mathematical analyses to conduct a comprehensive consideration of finite-conductivity fractures with the assumption of steady-state flow (i.e., constant-pressure boundaries). He introduced a dimensionless conductivity  $\alpha$  that is essentially the inverse of the dimensionless fracture conductivity commonly used for transient analyses (i.e.,  $C_{fD} = k_f w / k x_f = \pi / 2\alpha$ ). Prats also introduced the concept of an effective (or apparent) wellbore radius  $r_w'$ . The effective radius allows describing the fracture response in terms of an enlarged wellbore radius within the radial flow equation. This concept is illustrated in Appendix Fig. 6 for pseudoradial flow (adapted from Cinco-Ley and Samaniego-V., 1981b).



**Appendix Figure 5.** McGuire and Sikora (1960) curves for folds of increase ( $J/J_o$ ) in a bounded reservoir of area  $A$  (acres).



**Appendix Figure 6.** Effective wellbore radius versus dimensionless fracture conductivity (Nolte and Economides, 1991, adapted from Cinco-Ley and Samaniego-V., 1981b).

The effective wellbore radius, coupled with the radial flow equation, provides a powerful tool for efficiently calculating the FOI, or negative skin effect, provided by the fracture. Prats also considered fracture face damage (or skin effect) and provided an optimized treatment based on a fixed amount of proppant.

## Treatment optimization

Optimizing a fracture treatment is an essential part of maximizing its benefit (see Chapters 5 and 10). For this reason Prats' (1961) optimization consideration is of historic importance, although proppant volume is generally not a realistic criterion because proppant cost is only part of the investment for a fracture treatment (e.g., Veatch, 1986; Meng and Brown, 1987). Prats' proppant optimization condition at  $C_{fD} = 1.26$  could be a practical target for high-permeability reservoirs; however, this value is about an order of magnitude lower than the optimum case for the long transient period of a very low permeability reservoir.

Additional lessons are also provided by the apparent wellbore concept. The first is that a fracture is equivalent to enlarging the wellbore and not increasing the formation's global permeability. Incorrectly considering a fracture to be a permeability increase can lead to incorrect conclusions concerning reservoir recovery and waterflood sweep. Another insight is the generally favorable economics for an effectively designed and executed fracture. A fracture

treatment is equivalent to excavating a very large diameter borehole (e.g., hundreds of feet in most cases) and therefore is an extremely cost-effective way to provide an equivalent excavation.

The most important optimization lesson is found in Appendix Fig. 6 for the roles of conductivity  $k_{fw}$  (achieved by proppant cost) and fracture penetration (achieved by fluid and other additive costs; see Chapter 7). The figure indicates that as  $C_{fD}$  increases beyond 10, the effective wellbore radius approaches one-half of the fracture length and there are diminishing returns for additional increases in conductivity (i.e., incurring proppant costs without an effective increase in production rate). For this part of Appendix Fig. 6, the effective radius is constrained only by length and is termed the length-limited case. However, increasing both fracture length and conductivity to maintain a constant  $C_{fD}$  achieves the most efficient conversion of length into an effective wellbore radius. This conversion is the basis for effectively fracturing low-permeability formations.

The practical limits for the length-limited case are reaching the drainage radius, increasing conductivity within the limits of achievable fracture width and efficiently extending a fracture when the pressure reaches the formation capacity, as discussed later. As permeability increases, and proportionally decreases  $C_{fD}$ , the ability to increase conductivity becomes the constraint. As  $C_{fD}$  progressively decreases, the conductivity-limited case is reached. The figure indicates that as  $C_{fD}$  decreases below 1, a log-log unit slope is approached that relates  $r_w'$  to  $k_{fw}/k$ , with the obvious absence of an effect from length. When the unit slope is reached, near a value of 0.2, the wellbore drawdown completely dissipates within the fracture before reaching the tip, and the extremities of the fracture cannot provide a production benefit. For the conductivity-limited condition, the production rate can be increased economically only by providing more conductivity  $k_{fw}$ , with an obvious constraint from the available fracture width developed during the treatment. This constraint was significantly extended by the third fracturing generation of TSO treatments, which is discussed toward the end of this Appendix.

## Transition between the first and second generations

By 1961, the design and evaluation tools for most of the next two decades had been established by the contributions discussed. Incremental development of these tools slowed because fracturing was considered a mature technology. Also affecting technical development was the degrading economics for lower quality reserves as oil import-export increased and fracturing activity decreased (Appendix Fig. 1). This condition did not change until the mid-1970s brought natural gas shortages and higher gas prices to the United States. Higher prices produced the incentive to develop extensive regions of tight gas reserves with fractures targeting the  $FOI = 10$  range of the McGuire and Sikora curves (Appendix Fig. 5). Before this period, typical fracturing targets were oil reservoirs with an  $FOI$  of about 2, with  $FOI$  relative to an undamaged wellbore. However the  $FOI = 10$  target required about an order-of-magnitude increase in the volume and cost for a typical treatment and was hence termed massive hydraulic fracturing.

This new target introduced higher temperature reservoirs, typically of tight gas, that generally exceeded the performance limits for fracturing fluid systems. These conditions stretched the so-called mature technology in almost every conceivable way and resulted in a bumpy journey because of the proportionally large economic penalty when a treatment failed to meet expectations. However, reports of successful field development (e.g., Fast *et al.*, 1977) encouraged continued interest in tight gas development.

## Realistic estimate of conductivity

Cooke (1975) reported realistic experiments for characterizing the conductivity of proppant packs. His procedure formed proppant packs from a slurry composed of polymer-based fluids by using a cell with rock faces that allowed fluid loss and the subsequent application of closure stress. The Cooke cell is now a standard apparatus for a fracturing fluid laboratory

(see Chapter 8). The experiments showed that the retained pack permeability could be very small. These results were unexpected because prior testing procedures did not use fracturing fluids or stress levels for deeper gas reserves. The primary difference resulted because the rock acts as a polymer screen at moderate and smaller permeability levels, which significantly increases the polymer concentration remaining within the proppant pack porosity after fracture closure.

Cooke also provided a simple mass-balance relation for this important consideration. The concentration factor for the polymer and other additives remaining in the fracture relative to the original concentration can be expressed as

$$CF = 44 / \langle ppa \rangle, \quad (3)$$

for a typical proppant pack porosity of 0.33 and proppant specific gravity (s.g.) of 2.65. The relation depends on the average concentration  $\langle ppa \rangle$  defined as the total pounds of proppant divided by the total gallons of polymer-based fluid. This relation indicates a polymer concentration increase of 20 or greater for typical treatments at that time (e.g.,  $\langle ppa \rangle$  of 1 to 2 lbm). This unexpected discovery of a significant reduction in retained permeability, coupled with the prior discussion on conductivity and effective wellbore radius, partly explains the difficult transition to massive treatments.

Cooke's pioneering work had obvious effects on proppant schedules for treatments and laboratory testing procedures. Equally important, the work initiated substantial product development activities, as discussed in Chapter 7. These include improved proppants, beginning with Cooke's work on bauxite for high crushing stress, improved breaker chemistry and breaker encapsulation, large reductions of polymer concentration for crosslinked fluids, foams and emulsions, and residue-free viscoelastic surfactant systems. The evolution of fracturing fluid chemistry was reviewed by Jennings (1996).

## Height growth and proppant transport

Simonson *et al.* (1978) presented the mechanics governing fracture growth into a layer with higher stress, complementing the postulate by Harrison *et al.* (1954) concerning the role of stress for height confinement. The analysis considered a three-layer case for two symmetric barriers (i.e., two barriers extending

infinitely above and below the pay section with each barrier having the same magnitude of stress). The three-layer case provided insight into how to adapt more general relations to any number of layers (e.g., Nolte and Smith, 1981; chapter 3 of Gidley *et al.*, 1989). These relations led to the calculations employed in pseudo-three-dimensional (P3D) fracture simulators (see Section 6-3.2).

Novotny (1977) outlined a comprehensive basis for proppant transport calculations and in particular identified the important roles of channel shear rate and fracture closure in determining the ultimate placement of proppant (see Section 6-5.3. Both effects produce more proppant fall. For non-Newtonian fluids, the effective viscosity for sedimentation is determined from the vectorial sum of the shear rate in the channel and that caused by proppant fall (as for stagnant fluid). This sum is generally dominated by the channel flow and is much greater than that for a particle in stagnant fluid (i.e., higher shear rate and lower viscosity). In addition, the closure period prolongs the time for proppant fall and maintains the channel flow to reduce the effective viscosity. Novotny also provided a brief analysis of the volume balance during closure, which is the essential ingredient for the fracturing pressure decline analysis (e.g., Nolte, 1979) that is used for calibration treatments (see Section 9-5).

## Transient reservoir response

The FOI consideration for fracture production was found to be completely inadequate for the substantial period of transient flow that occurs in tight formations (see Section 12-2). The first tool for finite-conductivity transient flow was type curves provided by Agarwal *et al.* (1979). Although these curves were developed from numerical simulators, access to computers was generally outside the reach of most engineers. These and similar type curves became the standard evaluation tool to assess production from a fracture treatment. Type curves were also used for optimizing treatment design. By the mid-1980s, as general access to computers increased, the use of type curves began to decrease accordingly.

Cinco-Ley and Samaniego-V. (1981b) provided several advancements for understanding and quantifying the transient behavior of a reservoir fracture system. In addition to advancing the effective wellbore concept (e.g., Appendix Fig. 6) and type curves, they identified and provided comprehensive descrip-

tions for the distinctive transient regimes resulting from a finite-conductivity fracture (see Section 12-2).

The bilinear flow regime, generally the first to occur during production or a well test, was paramount for bridging the gap between fracture design and subsequent evaluation based on production or well tests. For permeability in the range of  $10\text{ }\mu\text{d}$ , the bilinear period can last on the order of a year or more for a long fracture ( $>2500\text{ ft}$  from the well). During bilinear flow the stabilized pressure drawdown progresses along the fracture length. During this period, it is not possible to determine the length of the fracture from a well test or production data because the total length has not had time to effectively experience the wellbore drawdown. Therefore, a meaningful evaluation for fracture length cannot be obtained until the bilinear period ends and the transient response progresses toward pseudoradial flow (potentially several years). An obvious implication in this case is that a standard well test cannot be used to determine fracture length; the length can be determined only from long-term production data. They also identified another important aspect of bilinear flow that occurs because of the transient flow condition within the proppant pack: the fracture conductivity can be characterized, independent of length and hence most reliably, by the slope of a plot of pressure versus the quarter-root of time.

Recognition of these consequences for bilinear flow also explains the difficult transition to the successful application of massive treatments. Well test interpretations misinformed instead of informed. They indicated relatively short fracture lengths that were assumed to be treatment placement failures and led to the common and contradicting result: how can 1 million lbm of sand be contained in a fracture length of only 100 ft? Much longer propped lengths were later substantiated by production data after the bilinear period had ended (e.g., values of fracture half-length  $x_f > 5000\text{ ft}$ ; Roberts, 1981). Another contribution to incorrect interpretations was ignoring Cooke's (1975) report of very low retained-pack permeability, which led to overly optimistic estimates of conductivity and proportionally pessimistic estimates of length. The coupling of these two factors produced incorrect and negative assessments for many early attempts to establish massive fracturing as a viable means of developing tight gas formations.

These advancements and insight from Bennett *et al.* (1986) for layered formations provide a solid foundation for the reservoir response to fracturing.

## The second generation: massive fracturing

As indicated in the preceding section, the bumpy road to successful massive fracturing also included massive penalties because the cost of a fracture treatment could become equivalent to the well cost. The combined effect of many companies experiencing \$500,000 treatments that did not provide commercial wells resulted in a significant investment for fracturing research. One result of this effort is the SPE Monograph *Recent Advances in Hydraulic Fracturing* (Gidley *et al.*, 1989). The manuscripts for this comprehensive volume, with more than 30 contributors, were completed in 1984, only five years after the 1979 SPE annual meeting provided the first meaningful number of papers from this research effort. The papers presented at this meeting were significant also because they presented a key that enabled the reliable application of massive fracturing and rapid progression of the treatment size record from 2 million lbm in 1979 to more than 7 million lbm by 1986.

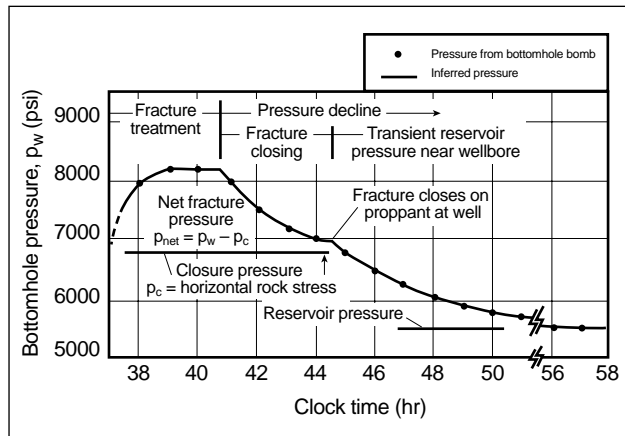
The key was that, for the first time in its 30-year history, fracturing was considered in a framework similar to that used for reservoir characterization. The reservoir framework consists of pressure transient analysis for the flow characteristics, wireline logs for the formation parameters and geophysics for the macroview. The 1979 papers include the following (a different reference year indicates the publication date):

- Logging: Rosepiller (1979) introduced application of the long-spaced sonic tool to infer stress in different layers (see prior discussion of stress concerning Appendix Eq. 2 and Chapter 4). Dobkins (1981) presented improved cased hole logging procedures for inferring the fracture height that were also used by Rosepiller to qualitatively validate his novel use of mechanical property logs.
- Pressure transient analysis (PTA): Nolte and Smith (1981) introduced the role of pumping pressures by

using a log-log plot as a diagnostic tool (similar to PTA practice) for fracture growth characteristics, the role of pressure simulation for quantifying geometry (including height growth) and the role of calibrated stress profiles obtained from mechanical property logs. Nolte (1979) introduced the role of pressure during the postinjection closing period to quantify fluid loss and predict fracture width and length by using a specialized time function in a manner analogous to the Horner plot. The combination of these two papers provided a foundation for the common use of the calibration treatment and pressure-history matching for defining design parameters (see Chapter 9). Appendix Fig. 7 illustrates the fracturing pressure for three distinct phases: pumping, closing and the after-closure period.

- Geophysics: Smith (1979) introduced the role of mapping fracture trajectories by using surface tiltmeters and borehole passive seismic techniques to improve reservoir recovery by the correct placement of infill wells (see Section 12-1).

A companion paper in 1980 showed the synergistic benefit when these individual considerations are unified for tight gas exploitation (Veatch and Crowell, 1982).



**Appendix Figure 7.** Bottomhole fracturing pressure (Nolte, 1982).

## Fracturing pressure: analog of reservoir response

An important component of fracturing pressure analysis is the closure pressure. The closure pressure is the datum for the net pressure that constrains the

width prediction, provides an analog of the reservoir pressure and reflects the height-averaged minimum stress for the pay zone (see Sidebar 9A). The fracture width is proportional to the net pressure. The data in Appendix Fig. 7, one of the first recordings of bottomhole pressure during a treatment, are similar to the reservoir response for an injection test with a pressure increase (pumping) and subsequent falloff (closing). The injection pressure is governed by the evolving fracture geometry, and the closure data are governed by the fluid loss. These two conditions, respectively, enable characterizing the stored and lost components of the volume-balance equation shown in Appendix Fig. 2. After closure, the pressure is independent of the fracture parameters and depends on the reservoir response to the fluid lost during the treatment.

The fundamental analogy between reservoir and fracturing behavior results because a diffusion-type process governs both behaviors. The respective reservoir and fracturing equivalents are  $kh/\mu \rightarrow w^2h/\mu$  (transmissibility), where  $k$  is the permeability,  $h$  is the reservoir thickness,  $w$  is the width, and  $\mu$  is the appropriate fluid viscosity, and  $\phi c_t \rightarrow h/(wE) \propto 1/p_{net}$  (storage capacity of the reservoir), where  $\phi$  is the porosity,  $c_t$  is the total system compressibility, and  $E$  is the formation's elastic modulus. The last expression for storage contains an inverse proportionality to the net fracture pressure  $p_{net}$ . This can be written in terms of the fracture volume  $V_f$ , fluid pressure  $p_f$  and closure pressure  $p_c$ .

$$\frac{1}{V_f} \frac{dV_f}{dp_f} = \frac{1}{p_{net}} = \frac{1}{p_f - p_c} \quad (4)$$

$$\frac{1}{w} \frac{dw}{dp_{net}} = \frac{1}{p_{net}} \text{ for constant } h \text{ and } L. \quad (5)$$

This equation implies that the elastic formation, compressed to contain the fracture's volume, produces a system compressibility analogous to an equal volume of perfect gas at a pressure equal to the fracture's net pressure. The result is a significant storage capacity considering typical conditions with more than 1000 bbl for fracture volume and only hundreds of pounds per square inch for net pressure. The last storage relation, for constant lateral dimensions, is important for a TSO, as discussed later.

## Fracture simulators

Describing a hydraulic fracture produces a significantly more complex role for the diffusive process than the reservoir case because the basic parameter groups change continuously with time, with a nonlinearity for the equivalent permeability, and the far-field elastic coupling between width and pressure produces local parameters that have a general dependence on the pressure everywhere within the fracture's unknown boundaries. For these reasons, fracture simulators that rigorously and robustly couple these parameters in a general manner (see Section 6-3) have not progressed at the same rate as reservoir simulators.

The modeling difficulties led to widespread use of simulators based on P3D assumptions that partially circumvent the far-field elastic-coupling condition. The two most common means were relaxing the lateral coupling in the long direction of the fracture (as for the PKN model) to allow a cellular representation and vertical height growth of the cells (e.g., Nolte, 1982) or prescribing the boundary and width profiles by elliptical segments and a lumped dependence on the governing parameters (e.g., Settari and Cleary, 1986). P3D models, or more precisely P2D models, evolved to include automated proppant scheduling and the temperature-exposure history for polymer and additive scheduling (e.g., Nolte, 1982), acid fracturing (e.g., Mack and Elbel, 1994), economic optimization for treatment design (e.g., Veatch 1986; Meng and Brown, 1987), automated pressure-history matching (e.g., Gulrajani and Romero, 1996; Gulrajani *et al.*, 1997b) and rigorous 2D slurry flow (e.g., Smith and Klein, 1995).

Originally restricted to in-office use, these models merged with on-site fracture monitoring systems to provide treatment evaluation and simulation in real-time mode. An equally important advance was the parallel evolution of process-controlled mixing and blending equipment for reliable execution of more demanding treatment schedules and progressively more complex chemistry that requires precise proportioning (see Chapters 7 and 11).

## Fracture mapping and model validation

An important achievement was the definition of fracture length, height and width by employing passive seismic measurements and tiltmeters in observation

wells (Warpinski *et al.*, 1996; see Section 12-1). The importance of these measurements for fracture design and evaluation cannot be overemphasized. Independent measurements for each component of the fracture volume (Appendix Fig. 2) provide a long-awaited benchmark for validating fracture models.

Like the first generation's failure to find a consensus for width models (e.g., Perkins, 1973), pressure-history matching could not resolve the second generation's conflicting adaptations of the P3D framework (see Chapter 6). The convergence of modeling assumptions failed for several reasons. The first was fundamental to the pressure-matching process and results because of the multitude of opportunities for nonuniqueness. Another reason was the failure to achieve a dominant industry opinion on either the technique or procedures for a specific technique to define closure pressure (e.g., Pahn *et al.*, 1997). This state of affairs allowed selecting a closure pressure procedure to validate particular modeling assumptions and therefore justify relatively arbitrary and ad hoc modeling assumptions. Techniques to determine the closure pressure are discussed in Section 3-6 and the Appendix to Chapter 9.

Because of nonuniqueness in the reservoir response and the basing of reservoir models on overly idealized modeling assumptions for a fracture, the reservoir response cannot generally provide an effective constraint on the achieved fracture length (Elbel and Ayoub, 1991; Nolte and Economides, 1991). Mapping constraints on all three fracture dimensions provide a unique, objective test of the geometry model assumptions (e.g., Gulrajani *et al.*, 1997a) and a basis for rationally judging and selecting the model complexity appropriate for the specific application, available data and simulation resources.

## Treatment design and evaluation

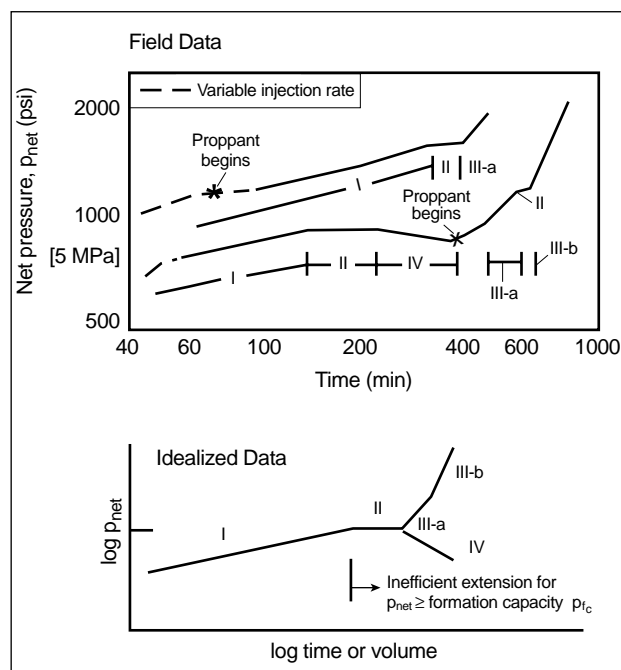
The primary fracture evaluation advance from the massive treatment generation is the calibration treatment performed before the proppant treatment to define placement parameters. Combining the calibration treatment and the purpose-designed TSO treatment produced the primary treatment innovation of the second generation. The calibrated TSO treatment, developed by Smith *et al.* (1984), became the key to the third fracturing generation (discussed later) and essentially removed width as a constraint for the conductivity required to successfully fracture

very high permeability formations. This capability and timing produced the overly optimistic prediction in 1985 for the beginning of the TSO generation, as indicated by Appendix Fig. 1a.

## Transition between the second and third generations

The following paragraphs link several aspects of the massive and TSO generations by using the information available from the diagnostic log-log plot for fracturing in Appendix Fig. 8. Appendix Table 1 lists the interpretations for various slopes exhibited in the figure by the net pressure during fracturing. The data are from two massive treatments in tight gas formations. The top curve is a treatment in the Wattenberg field, the first microdarcy-permeability field development (Fast *et al.*, 1977). The behavior shown by the lower treatment curve, which was designed by this author, provided insight for developing the TSO treatment that enables successfully fracturing darcy-scale oil formations. The treatment related to the lower curve was not particularly successful. However, it was one of the first 2 million lbm treatments and hence functioned better as a “sand-disposal” treatment than a gas-stimulation treatment. The sand was disposed of with 900,000 gal of crosslinked fluid containing 90 lbm/1000 gal of polymer, or approximately 80,000 lbm of polymer.

The marginal success of the treatment is readily understood by considering Appendix Eq. 3. For the treatment average of 2.1 ppa, the equation predicts 1900 lbm/1000 gal crosslinked fluid (in reality, a solid) remaining in the proppant pack porosity after the treatment. However, the size and viscosity for this treatment provided an ideal test condition of how a formation responds to fluid pressure and an excellent illustration for the concept of formation



**Appendix Figure 8.** Log-log diagnostic plot for fracturing (Nolte, 1982).

capacity. The capacity (Nolte, 1982) defines the pressure limit for efficient fracture extension and is analogous to the pressure-capacity rating for a pressure vessel. The cited reference has an unsurprising theme of the negative effects of excesses of pressure, polymer and viscosity.

Three mechanisms for a formation can define its pressure capacity before “rupture” accelerates fluid loss from the formation’s pay zone. The subsequent fluid loss also leaves proppant behind to further enhance slurry dehydration and proppant bridging. Each mechanism is defined by the in-situ stress state and results in a constant injection pressure condition, or zero log-log slope, when the net pressure reaches the mechanism’s initiation pressure. The mechanisms are

**Appendix Table 1. Slopes of fracturing pressures and their interpretation in Appendix Fig. 8.**

Type	Approximate log-log slope value	Interpretation
I	$\frac{1}{8}$ to $\frac{1}{4}$	Restricted height and unrestricted expansion
II	0	Height growth through pinch point, fissure opening or T-shaped fracture
III-a	1	Restricted tip extension (two active wings)
III-b	2	Restricted extension (one active wing)
IV	Negative	Unrestricted height growth

- opening the natural fissures in the formation, governed by the difference in the horizontal stresses
- extending the height through a vertical stress barrier and into a lower stress (and most likely permeable) zone, governed by the difference in the horizontal stress for the barrier and pay zone
- initiating a horizontal fracture component when the pressure increases to exceed the level of the overburden stress.

An important observation for the pressure capacity is that it depends on the in-situ stress state and therefore does not change for the formation in other well locations unless there are significant local tectonic effects. As a result, all future treatments for the field can generally be effectively designed on the basis of only one bottomhole pressure recording and its detailed analysis (see Section 9-4).

The upper curve on Appendix Fig. 8, for the Wattenberg treatment, illustrates the fissure-opening mechanism with the Type II zero slope occurring at a net pressure of 1700 psi. This value provides one of the largest formation capacities ever reported. The fissure opening is preceded by restricted height growth and unrestricted extension (Type I slope) that provide the most efficient mode of fracture extension. Therefore, conditions in this formation are favorable for propagating a massive fracture; not by coincidence, this was the first field successfully developed in the massive treatment generation (Fast *et al.*, 1997), and it provided incentive to continue the development of massive treatment technology. Returning to Appendix Fig. 8, after the period of constant pressure and enhanced fluid loss, a Type III-a slope for a fracture screenout occurs because slurry dehydration forms frictional proppant bridges that stop additional extension (i.e., a generally undesired screenout for a tight formation requiring fracture length over conductivity). After the penetration is arrested, the major portion of the fluid injected is stored by increasing width (see Appendix Eq. 4) and the net pressure develops the unit slope characteristic of storage. The amount of width increase is proportional to the net pressure increase.

The Wattenberg treatment consisted of 300,000 gal of fluid and 600,000 lbm of sand with an average concentration of 2 ppa, similar to the previous example. However, the treatment was successful because a polymer-emulsion fluid with low proppant pack damage was used. After the treatment defined the formation capacity, model simulations indicated that

the required penetration could be obtained by not exceeding the formation capacity. A subsequent treatment designed using 150,000 gal and 900,000 lbm of sand (an average of 6 ppa) became the prototype for the remaining development of the field (Nolte, 1982).

The lower curve on Appendix Fig. 8 is for the aforementioned sand-disposal treatment in the Cotton Valley formation of East Texas. As previously discussed, the treatment provided an opportunity to observe a large range of fracturing behavior with five types of interpretive slopes occurring, including

- Type I indicating extension with restricted height growth
- Type II defining this formation's lowest pressure capacity at 1000 psi for the penetration of a stress barrier
- Type IV, with decreasing pressure, indicating unrestricted vertical growth through a lower stress zone after the barrier was penetrated.

The Type IV condition continued until proppant was introduced. Almost immediately after proppant entered the fracture the pressure increased, most likely because the proppant bridged vertically in the width pinch point formed by the penetrated stress barrier and restricted additional height growth. During the preceding 6-hr period of significant vertical growth, the horizontal growth was retarded. As a result, the very high polymer concentration formed a thick polymer filter cake at the fracture tip that probably restricted further horizontal extension. Thus, the extremities of the fracture were restricted either by proppant or polymer cake, and continued injection was stored by increasing width indicated by the Type III-a unit slope. After a significant increase in pressure, the pressure became constant for a short period at 1200 psi with a Type II slope that probably resulted from opening natural fissures to define a second, higher capacity. Subsequently the slope increased to an approximately 2:1 slope indicated as Type III-b. This latter slope for a storage mechanism indicates that about one-half of the fracture area had become restricted to flow, which could have resulted from one wing of the fracture being blocked to flow near the well because of slurry dehydration from the fissure fluid loss. The wellbore region experiences the largest pressure and is most prone to adverse fluid-loss effects from exceeding a capacity limit.



Subsequent treatments were improved after understanding the formation's pressure behavior as in the Wattenberg case and for this area after understanding the implications of Appendix Eq. 3 for concentrating polymer. In addition, the observation that proppant bridging could restrict height growth was developed for treatments to mitigate height growth (Nolte, 1982). An effective and relatively impermeable bridge can be formed within the pinch point to retard height growth by mixing a range of coarse and fine sand for the first sand stage after the pad fluid.

Smith *et al.* (1984) later sought a means to significantly increase fracture width for the development of a chalk formation within the Valhall field in the Norwegian sector of the North Sea. The additional width was required because laboratory tests indicated the likelihood of substantial proppant embedment into the soft formation that would lead to the loss of effective propped width. Fracturing was considered for this formation because other completion techniques would not sustain production because of chalk flow. The resulting treatment design was based on the behavior on the log-log plot in Appendix Fig. 8 for the sand-disposal treatment: a purpose-designed TSO treatment. For the disposal treatment, they observed that after the initial screenout occurred, 2 million lbm of proppant could be placed, and the net pressure increase indicated that this occurred by doubling the width after the screenout initiated.

Smith *et al.* designed and successfully placed a TSO treatment in which proppant reached the tip and bridged to increase the width by a factor of 2 during continued slurry injection after the purpose-designed TSO occurred. This design, with successful placement of progressively larger propped width increases, became the tool that enabled the development of this formation. The ability to significantly increase the width after screenout results from the large storage capacity of a fracture, as detailed in the discussion following Appendix Eqs. 4 and 5. Additional discussion on the fracture completion in Valhall field and the TSO treatment is in the "Reservoir and Water Management by Indirect Fracturing" section.

As a historical note, a similar concept for a TSO was disclosed in a 1970 patent (Graham *et al.*, 1972), with the bridging material consisting of petroleum coke particles (approximately neutral density to ensure transport to the extremities). The patent's goal was increased width to enable placing larger size proppant in the fracture.

## The third generation: tip-screenout treatments

A proper historical perspective of this third generation requires perspective from the next generations; however, several of its developments are reviewed here. A more comprehensive presentation and reference are by Smith and Hannah (1996).

Demonstration of the ability to routinely place a successful TSO treatment opened the door for effective fracture stimulation of higher permeability formations. Another component for the successful fracturing of high permeability was the continued development of synthetic proppants that can produce a cost-effective 10-fold increase in permeability relative to sand for higher closure stresses (see Chapter 7). Coupling this increase in permeability with the similar increase for propped width achieved by a TSO treatment in a moderate- to low-modulus formation provides about a 100-fold increase in conductivity over a conventional sand fracture. The conductivity increase also translates into a 100-fold increase of the target permeability for fracturing, as implied by Appendix Figs. 5 and 6. The increases for width and conductivity also mitigate nondarcy (or turbulent) flow effects in the fracture for high-rate wells, particularly gas wells (see Sections 10-7.3 and 12-3.1).

However, the anticipated growth rate shown on Appendix Fig. 1a was slowed not only by the unanticipated, extensive contraction of activity in general, but also by two prevailing mind sets: high-permeability formations cannot be successfully fracture stimulated and why fracture a commercial well? Additional field proof for the benefits of a TSO treatment came from two successful programs: a significant improvement over conventional fracture treatments for the Ravenspurn gas field in the southern North Sea (Martins *et al.*, 1992b) and high-permeability applications in the Prudhoe Bay field (Hannah and Walker, 1985; Reimers and Clausen, 1991; Martins *et al.*, 1992a).

## Deep damage

Fracturing in Prudhoe Bay was particularly successful because deep formation damage induced by prior production (i.e., beyond the reach of matrix treatments) facilitated sidestepping the mind set of not applying

fracturing to high permeability. The incremental production from only one year of the fracturing program would have ranked as the 10th largest producing field in the United States (e.g., Smith and Hannah, 1996), without including similar results achieved by another operator in the other half of the field. Another significant aspect of the Prudhoe Bay application is that the fractures were routinely placed in a relatively small oil zone above a rising water zone without entering the water zone (Martins *et al.*, 1992a), which demonstrated that fracturing is a viable, potentially superior alternative to matrix treatments in high-permeability formations. This precise fracturing was achieved by coupling an initial detailed fracture modeling study with a calibration treatment before each proppant treatment.

## Frac and pack

The frac and pack completion consists of a TSO treatment before a conventional gravel pack. During the early 1990s, frac and pack treatments were applied on a limited basis around the world, notably offshore Indonesia. Prior to the TSO treatment era, this technique was tried at various times but without sustained success. The large propped width from a TSO treatment was a necessary ingredient for successful frac and pack applications, as discussed later.

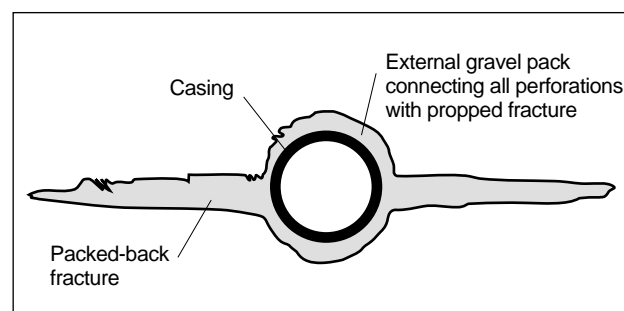
The frac and pack boom was in the Gulf of Mexico. The first successful application began because of economic considerations and therefore overcame the mind set of not fracturing a commercial well. A significant field development was not meeting production expectations because standard gravel-packed completions could not consistently achieve a low skin effect; the skin effect ranged between 7 and 30. The skin effect was 10 after the first frac and pack treatment and progressively decreased to near zero from improvements in the treatment design and the use of larger size proppant (Hannah *et al.*, 1994).

The threefold-plus increase in production rate, by eliminating the skin effect, resulted from more than just adding a TSO treatment to the procedure. An important feature of a frac and pack is reduction of the inherent flow restriction around and through the perforations. The ring of proppant around the casing (Appendix Fig. 9) acts as an excellent external gravel pack for reducing the pressure drop through the perforated region. The ring results from the large TSO

fracture width that mechanically must continue around the wellbore; i.e., if the formation is pushed apart 2 in. over the large surface area of the fracture, the rock around the wellbore must be displaced accordingly. For a well-designed and executed frac and pack, the initiating screenout at the tip is progressively packed back to the well to completely pack the resulting ring.

The continuing success of the initial frac and packs started a rapid conversion to this completion, with the frac and pack becoming the preferred Gulf of Mexico sand control completion. In addition to continued use offshore Indonesia, technology transfer resulted in a wider geographical distribution for this sand control technique (e.g., West Africa, Gulrajani *et al.*, 1997b).

As for other applications of TSO treatments, on-site redesign after a calibration treatment became a standard frac and pack practice. An important observation is that the same analysis procedures and design models introduced for the massive treatments of tight gas formations in the late 1970s were transferred directly to frac and pack treatments in soft formations.



**Appendix Figure 9.** Successfully packed-back TSO treatment.

## Reservoir and water management by indirect fracturing

Another application of TSO treatments is reservoir management. The prototype example for this application was in the Norwegian Gullfaks field (Bale *et al.*, 1994a, 1994b). The reservoir section had a multi-darcy-permeability upper zone that graded downward to a permeability of about 100 md. The standard completion was to perforate and gravel pack the upper zone. However, an edge-water drive would encroach through the high-permeability zone and turn a prolific oil well into an even higher water producer.

A solution was found from the pioneering work of the Valhall TSO treatment discussed for Appendix Fig. 8. This application in the early 1980s was for more than mitigating proppant embedment. The primary objective was for controlling chalk production from the primary producing zone above where the TSO treatment was placed. The upper chalk zone was very soft with high porosity and composed of almost as much oil as chalk. When this zone was put on production, chalk filled the tubing and led to casing collapse. The zone was produced by placing the TSO treatment in the more competent zone below and extending the fracture height into the bottom of the very high porosity formation. This completion enabled chalk-free production from both the upper and lower zones (Smith *et al.*, 1984).

This indirect access to the primary producing zone has come to be known as an indirect vertical fracture completion (IVFC) and is illustrated in Appendix Fig. 10. The technique of perforating and fracturing only from competent sections and producing from incompetent sections is a robust method for controlling the production of formation material and increasing recovery from the lower permeability zones by fracture stimulation. From this perspective, a TSO-IVFC becomes a solids control and reservoir management application (see Section 5-1.2).

The Gullfaks adaptation by Bale *et al.* (1994a) also placed a TSO-IVFC in a lower competent part of the formation. In addition to providing sand control and managing reservoir depletion, it was a water management treatment because it delayed water breakthrough and greatly increased reserves recovery

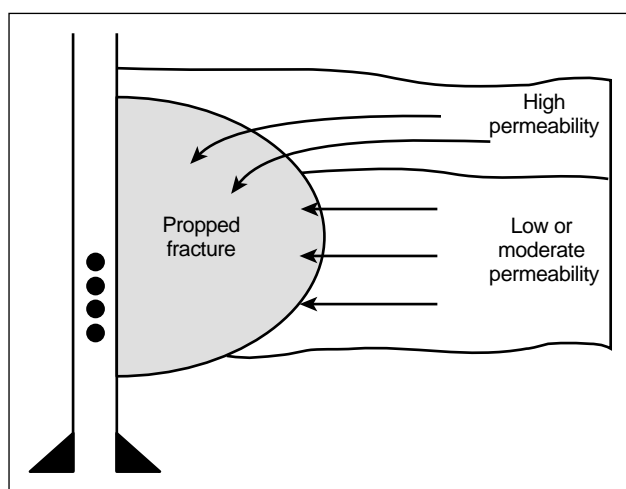
from the lower sections by fracture stimulation and a significant increase in drawdown. This application completes the link between the sand-disposal tight gas treatment in Appendix Fig. 8 to reservoir and water management with the intermediate development of the TSO-IVFC for solids control in the Valhall field.

## Screenless sand control

Another apparent role of the IVFC is to eliminate the need for a screen in many sand-control environments by selecting and perforating only competent sections within or near the unconsolidated sections of the formation. The zone selection method can potentially be enhanced by a sonic log application. This application takes advantage of the generally considered negative effect of near-wellbore refracted and relatively slower waves caused by the wellbore mechanical damage that routinely occurs in weak or highly stressed formations (Hornby, 1993). However, for screenless completions, the negative effect becomes a positive effect because the change in the wave speed for the refracted wave is a direct indication of the state of rock failure around the well, which is caused by the wellbore stress concentration within the in-situ stress field. Therefore, the layers with a minimal near-well change in wave speed relative to the far-field speed are the more competent candidate zones for perforating and applying a TSO-IVFC to achieve screenless formation-material-controlled production.

A second method of achieving a screenless sand-control completion is applied without strategically placed perforations (e.g., Malone *et al.*, 1997). This method couples the proppant ring around the casing from a TSO treatment and proppant with effective flowback control (e.g., fibers, curable-resin-coated proppant or both). The combination with a successful packed-back TSO achieves an external gravel pack of stable proppant (i.e., an external formation-material screen as illustrated by Appendix Fig. 9). Perforation and completion considerations are addressed in Section 11-3.5.

The screenless completion obviously eliminates the cost of the screen and related tools, but more importantly it enables economic development of significant behind-pipe reserves that do not warrant the mobilization and operational costs for a rig on an offshore production platform, as generally required for a standard gravel-pack completion.



**Appendix Figure 10.** Indirect vertical fracture for reservoir management (Bale *et al.*, 1994a).

## A future generation: fracturing and reservoir engineering merger?

The previous discussion of the TSO generation clearly shows the blurring of what can be controlled on the inside and outside of the casing and of what have been the traditional roles of a fracture design engineer and a reservoir engineer. This blurring of past distinctions provides prospects for additional innovations and the advent of a fourth fracturing generation.

### Optimal reservoir plumbing

From a broader viewpoint, the IVFC and strategically placed perforations provide the means to extend optimized plumbing into the reservoir. Optimized plumbing, through a NODAL analysis, is generally practiced only for the surface facilities and within the wellbore. Extended optimization requires additional considerations for designing the plumbing system provided by the fracture in the reservoir and also within the fracture itself.

The outline for these considerations was defined by Bale *et al.* (1994b) for the Gullfaks application. They considered the role of the permeable fracture plane on the reservoir's 3D flow pattern and how tailoring the distribution of conductivity can advantageously affect this flow pattern (e.g., reducing the conductivity as the fracture approaches the high-permeability upper zone to delay water production while increasing the conductivity in the lower permeability zone and applying a large drawdown to accelerate production from this zone; see Section 5-1.2). Therefore, the analysis and design tools have evolved for considering the role of fractures in NODAL analysis for reservoir, formation material and water management.

### Achieving full potential for horizontal wells and laterals

The preceding discussion of the IVFC is in the context of single, essentially vertical wells. The potential for innovative strategies to drain a reservoir increases several fold by adding consideration of horizontal and lateral wells. These highly deviated wellbores are typically placed without cemented casing because of economic considerations and therefore do not generally reach their full potential because they lack an effective technique to remove wellbore damage. The solution

of using cemented casing for effective treatment diversion tends to be overlooked because of an apparent failure to appreciate lifecycle economics or the effectiveness of good cementing techniques (see Chapter 11). Staged fracturing, from correctly placed perforated sections, enables highly effective damage bypass, as demonstrated by the first fracturing generation's rate of 100 treatments per day in 1955.

The general benefit for a horizontal well, particularly with vertical variations of permeability, is magnified by the fracture adding a large vertical permeability component (see Chapters 11 and 12). Simply stated, an extended reach well cannot drain what it is not connected to nor can it efficiently drain what it is isolated from by wellbore damage. The addition of a vertical fracture allows efficient drainage of all isolated sections that the propped fracture reaches. The location of the fracture, or plumbing source, can be specified by correctly placed perforations within a cemented casing and an effective fracture design and execution. Cased hole logging and logging while drilling can be used to identify IVFC target locations for connection to bypassed reserves and management for their exploitation.

### Fracturing for well testing

The after-closure portion of Appendix Fig. 7, labeled "transient reservoir pressure near wellbore," shows the return of the fracturing pressure to the reservoir pressure and demonstrates the well testing potential for any injection above fracturing pressure. This potential for a fracture is ensured by the well-known result that the long-term reservoir response is pseudoradial flow (e.g., Cinco-Ley and Samaniego-V., 1981b) and is the same flow regime used for standard well testing. An attractive aspect of the use of fracturing for testing is that the fracture enhances the likelihood that all the zones are open and captured by the test. This is an important consideration for layered formations and particularly thinly layered zones that can be missed by open perforations. Another attraction of fracturing or injection testing is that the wellbore is generally filled with water that provides minimal wellbore storage and formation volume factor effects.

The long-term radial response following fracture closure was developed and presented in a pair of papers: Gu *et al.* (1993) from the application perspective and Abousleiman *et al.* (1994) from the theoretical perspective. They recognized that the radial

response from fracture injection met the assumptions for a slug (or equivalently an impulse) test and that they could directly apply this developed area of reservoir technology.

Another well-known flow regime for a fracture is pseudolinear flow. Incorporating the analysis of this after-closure flow regime was the last link of the fracturing–pressure analysis chain between the beginning of injection and returning to reservoir pressure. Consideration of this regime by Nolte *et al.* (1997) indicated that the reservoir “memory” of the fracturing event can validate several aspects for analysis of a calibration treatment (e.g., closure time and hence the critical closure pressure, fracture length and hence the fluid-loss coefficient, and the division of fluid loss between normal wall diffusion and tip spurt). Quan-

tifying spurt loss is particularly important for high-permeability formations and is not practically attainable by any other means than after-closure analysis. The after-closure analyses are presented in Section 9-6, and a method to quantify reservoir parameters during the closure period is presented in Section 2-8.

These applications from the reservoir behavior of fracturing complement the 1979 adoption of reservoir methodologies and achieve a direct merging of fracturing into the classic realm of reservoir testing and characterization (see Chapters 2 and 12). Reservoir characterization from a calibration testing sequence to define fracturing parameters provides the ingredients essential for on-site, economics-based treatment optimization.

# Mechanics of Hydraulic Fracturing

*Mark G. Mack, Schlumberger Dowell*

*Norman R. Warpinski, Sandia National Laboratories*

## 6-1. Introduction

The mechanics of hydraulic fracturing is a convenient description of the processes and mechanisms that are important to fracturing technology. Mechanics generally refers to an engineering discipline that is concerned with the mechanical properties of the material under consideration and the response of that material to the physical forces of its environment. Hydraulic fracturing is complicated because it involves four different types of mechanics: fluid, solid, fracture and thermal. In fracturing, fluid mechanics describes the flow of one, two or three phases within the fracture; solid mechanics describes the deformation or opening of the rock because of the fluid pressure; fracture mechanics describes all aspects of the failure and parting that occur near the tip of the hydraulic fracture; and thermal mechanics describes the exchange of heat between the fracturing fluid and the formation. Furthermore, the responses are coupled and depend on each other. To develop tools for the design and analysis of a process as complicated as hydraulic fracturing, it is necessary to build models that describe each of the responses sufficiently. This chapter describes the history and technology associated with these models.

A model of a process is a representation that captures the essential features of the process in a manner that provides an understanding of the process (Starfield *et al.*, 1990). The construction of the model depends on the type of question it is required to answer. The three main types of models are physical, empirical and mechanistic (or analytic). Each has advantages and disadvantages, which are outlined in the following.

- Physical models are scale models of actual processes. The primary advantage of such models is that, by definition, they incorporate the correct assumptions of material behavior. For example, if a fracturing fluid is pumped between a pair of par-

allel rock faces with roughness comparable to fractured rock, no assumptions need to be made about how the fluid behaves rheologically. Instead, how it behaves is simply observed. Unfortunately, physical models are usually expensive to build and use.

In addition, there are major issues of scale-up if the model is significantly smaller than the actual structure. For example, in a model of a bridge, the weight is proportional to the scale factor cubed, but the length of any element is proportional only to the scale factor. Thus, even elements that do not fail in the model may fail in practice. Nevertheless, scale models are useful provided an appropriate dimensional analysis is performed and if the scale factor is not too great (de Pater *et al.*, 1993).

- Empirical models are developed by observation. Typically, laboratory or field data are gathered and combined to create design charts or empirical equations, which can then be used to predict or design future cases. For example, if 100 wells in an area have been fractured with different-size treatments, 6 months of cumulative production could be plotted against treatment size. Provided the scatter is not too great, the production response from a new treatment can be predicted from the historical data.

The advantages of empirical models are that no assumptions need to be made about any behavior and there is no scale effect. The primary disadvantage is low confidence in extrapolation outside the range of the data. The 100-well data set may be useful in the same field, even for treatments slightly larger than any in the data set, but is most likely irrelevant in another area. For an empirical model to be useful, the data must be arranged in terms of suitable dimensionless variables, so that it is as general as possible. For example, the 100-well data set may be useful in a different area provided the results are normalized with respect to permeability and pay thickness. To obtain the right

dimensionless quantities, however, it is generally necessary to have at least some understanding of the mechanics of the physical process being modeled.

- Analytical models are mathematical representations of a physical reality in which the governing mechanics are stated in the form of equations. The equations typically define both physical laws, such as conservation of mass, and constitutive laws, such as elasticity. The former are inviolable laws of nature, whereas the latter are hypotheses of physical behavior that require laboratory work to confirm that they are applicable and to determine the constants in the model.

The major advantages of analytical models are that they may be extrapolated outside the range in which they were developed, provided the various component laws still hold. Thus, if the elastic constant of a spring has been measured, the force required for a given displacement of the spring can be predicted, even for displacements that have not been tested. If the spring is cut in half, the behavior of each half can be predicted. Perhaps the greatest limitation of analytical models, however, is the assumptions that are made in developing the model. For example, it is typically assumed that rock is homogeneous, yet there are many cases where it is fractured or otherwise variable from point to point, and this may not be accounted for in the model.

A simulator is a computational implementation of a model. Many analytical models are tractable only if they are solved numerically, unless a large number of approximations or simplifying assumptions are made. With the widespread availability of computers, it is now generally accepted that better answers may be obtained by numerically solving a more general model rather than by solving a simplified model exactly. Nevertheless, it must be emphasized that useful rules of thumb and relations between quantities can often be developed much more easily using analytic solutions, which provide insight into the relations between parameters affecting the results for more complex conditions. Some of the simplest rules would probably not be “discovered” from a numerical solution without a great deal of effort, if at all. An extensive presentation of analytic-based solutions and approximations for the mechanics of hydraulic fracturing was provided by Valkó and Economides (1996).

Four important reasons for developing and using models of hydraulic fracture treatments are to

- perform economic optimization (i.e., determine what size treatment provides the highest rate of return on investment)
- design a pump schedule
- simulate the fracture geometry and proppant placement achieved by a specified pump schedule
- evaluate a treatment (by comparing the predictions of a model with actual behavior).

In each of these cases, the objective is a quantitative estimate of either the volume of fluid and proppant required to create a fracture with a desired conductivity and geometry or the geometry produced by a specified pump schedule.

## 6-2. History of early hydraulic fracture modeling

### 6-2.1. Basic fracture modeling

Sneddon (1946) and Sneddon and Elliot (1946) developed the solutions for the stress field and pressure associated with static pressurized cracks. They showed that the width of a static penny-shaped (i.e., circular) crack of radius  $R$  under constant pressure is given by the expression

$$w(r) = \frac{8p_{net}R(1-\nu^2)}{\pi E} \sqrt{(1-(r/R)^2)}, \quad (6-1)$$

which describes an ellipsoid, and the volume of the crack  $V$  by

$$V = \frac{16(1-\nu^2)R^3}{3E} p_{net}, \quad (6-2)$$

where the net pressure  $p_{net}$  is defined as the pressure in the crack minus the stress against which it opens,  $\nu$  is Poisson's ratio, and  $E$  is Young's modulus. Sack (1946) showed that the pressure required to extend a crack of radius  $R$  under constant pressure is given by

$$p_{net} = \sqrt{\frac{\pi\gamma_F E}{2(1-\nu^2)R}}, \quad (6-3)$$

where  $\gamma_F$  is the specific fracture surface energy. Equations 6-1 and 6-2 are derived using the theory of linear elasticity, and Eq. 6-3 is derived using linear elastic fracture mechanics. The basis of Eq. 6-3 is that the energy required to create the surface area when a crack is propagated must equal the work done by the

pressure in the crack to open the additional width. A more detailed discussion of fracture mechanics is in Chapter 3. Combining Eqs. 6-2 and 6-3, Perkins and Kern (1961) showed that the pressure for propagation of a radial fracture is

$$p_{net} = \left( \frac{2\pi^3 \gamma_f^3 E^2}{3(1-\nu^2)^2 V} \right)^{1/5} \quad (6-4)$$

Thus, if the fracture volume is known,  $p_{net}$  can be calculated and Eq. 6-2 used to determine  $R$ . For example, if the injection rate  $q_i$  is constant, fluid friction in the fracture is negligible, and there is no leakoff, Eq. 6-4 can be substituted into Eq. 6-2 with the volume  $V$  replaced by  $q_i t$  as

$$q_i t = \frac{16(1-\nu^2)R^3}{3E} \left( \frac{2\pi^3 \gamma_f^3 E^2}{3(1-\nu^2)^2 q_i t} \right)^{1/5}, \quad (6-5)$$

where  $t$  is the time. Rearranging and solving for  $R$ ,

$$R = \left[ \frac{9E q_i^2 t^2}{128\pi \gamma_f (1-\nu^2)} \right]^{1/5} \quad (6-6)$$

Sneddon and Elliot (1946) also showed that for fractures of a fixed height  $h_f$  and infinite extent (i.e., plane strain), the maximum width is

$$w = \frac{2p_{net} h_f (1-\nu^2)}{E} \quad (6-7)$$

and the shape of the fracture is elliptical, so that the average width  $\bar{w} = (\pi/4)w$ . The term  $E/(1-\nu^2)$  appears so commonly in the equations of hydraulic fracturing that it is convenient to define the plane strain modulus  $E'$  as

$$E' = \frac{E}{1-\nu^2}, \quad (6-8)$$

which is used for this chapter. (A plane strain deformation is one in which planes that were parallel before the deformation remain parallel afterward. This is generally a good assumption for fractures in which one dimension [length or height] is much greater than the other.)

## 6-2.2. Hydraulic fracture modeling

Several introductory and key papers published between the late 1950s and early 1970s that developed the foundation of hydraulic fracture modeling approach the problem by making different assumptions concern-

ing the importance of different aspects. Carter (1957) neglected both fluid viscosity effects and solid mechanics and concentrated on leakoff. Khristianovich and Zheltov (1955) made some simplifying assumptions concerning fluid flow and focused on fracture mechanics. Perkins and Kern (1961) assumed that fracture mechanics is relatively unimportant and focused on fluid flow. These three basic models are each described in some detail in following sections.

The first work on hydraulic fracture modeling was performed by several Russian investigators (summarized by Khristianovich *et al.*, 1959). The first reference in English is Khristianovich and Zheltov's (1955) paper. The other major contribution was the work of Perkins and Kern (1961). These models were developed to calculate the fracture geometry, particularly the width, for a specified length and flow rate, but did not attempt to satisfy the volume balance. Carter (1957) introduced a model that satisfies volume balance but assumes a constant, uniform fracture width. This model was used into the late 1970s for determining volume balance, with more realistic width profiles from the aforementioned geometry models to ensure that the fracture width was sufficient for proppant entry. This approach was made obsolete by extensions to the Khristianovich and Zheltov and Perkins and Kern models developed by Geertsma and de Klerk (1969) and Nordgren (1972), respectively. These two basic models, generally known as the KGD and PKN models after their respective developers, were the first to include both volume balance and solid mechanics.

The PKN and KGD models, both of which are applicable only to fully confined fractures, differ in one major assumption: the way in which they convert a three-dimensional (3D) solid and fracture mechanics problem into a two-dimensional (2D) (i.e., plane strain) problem. Khristianovich and Zheltov assumed plane strain in the horizontal direction; i.e., all horizontal cross sections act independently or equivalently, and all sections are identical (Fig. 6-1), which is equivalent to assuming that the fracture width changes much more slowly vertically along the fracture face from any point on the face than it does horizontally. In practice, this is true if the fracture height is much greater than the length or if complete slip occurs at the boundaries of the pay zone. Perkins and Kern, on the other hand, assumed that each vertical cross section acts independently (Fig. 6-2), which is equivalent to assuming that the pressure at any section is dominated by the height of the section rather than the length of



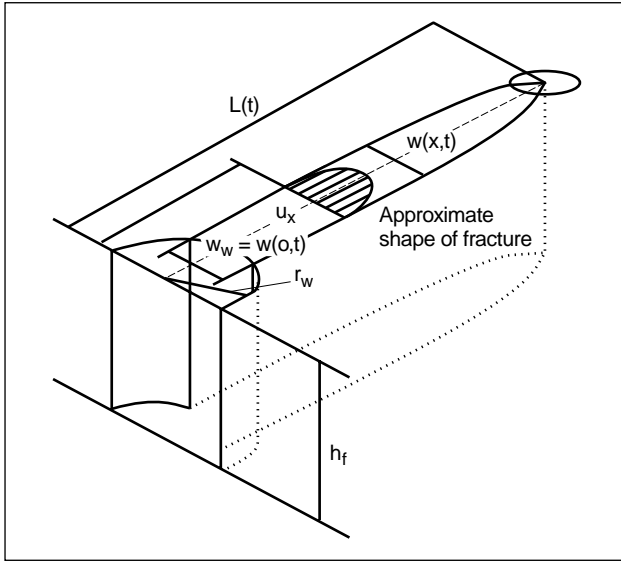


**Figure 6-1.** KGD fracture.

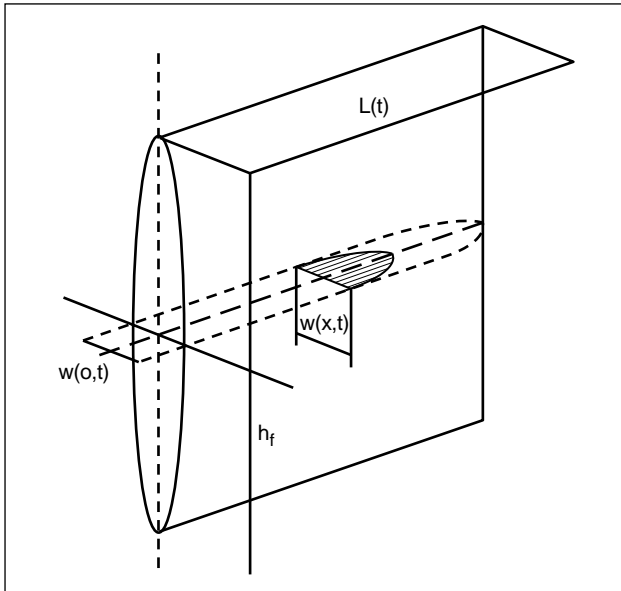


**Figure 6-2.** PKN fracture.

the fracture. This is true if the length is much greater than the height. This difference in one basic assumption of the models leads to two different ways of solving the problem and can also lead to different fracture geometry predictions. In the case of the PKN model, fracture mechanics and the effect of the fracture tip are not considered; the concentration is on the effect of fluid flow in the fracture and the corresponding pressure gradients. In the KGD model, however, the tip region plays a much more important role, and the fluid pressure gradients in the fracture can be approximated.

- Derivation of Perkins and Kern model of a vertical fracture

Perkins and Kern (1961) assumed that a fixed-height vertical fracture is propagated in a well-confined pay zone; i.e., the stresses in the layers above and below the pay zone are sufficiently large to prevent fracture growth out of the pay zone. They further assumed the conditions of Eq. 6-7, as shown in Fig. 6-2, that the fracture cross section is elliptical with the maximum width at a cross section proportional to the net pressure at that point and independent of the width at any other point (i.e., vertical plane strain). Although Perkins and Kern developed their solution for non-Newtonian fluids and included turbulent flow, it is assumed here that the fluid flow rate is governed by the basic equation for flow of a Newtonian fluid in an elliptical section (Lamb, 1932):

$$\frac{dp}{dx} = -\frac{64q\mu}{\pi h_f w^3}, \quad (6-9)$$

where  $p$  is the pressure,  $x$  is the distance along the fracture, and  $\mu$  is the fluid viscosity.

Substituting Eq. 6-7 into Eq. 6-9, replacing the flow  $q$  by one-half of the injection rate ( $q_i/2$ ) and assuming that the flow rate is constant along the fracture length (which implies that both leakoff and storage in the fracture resulting from width increases are neglected) obtains

$$p_{net}^3 dp_{net} = -\frac{4}{\pi} \frac{\mu q_i E'^3}{h_f^4} dx. \quad (6-10)$$

Integrating this expression along the fracture half-length  $L$  obtains, with  $p_{net} = 0$  at the fracture tip,

$$p_{net} = \left[ \frac{16\mu q_i E'^3}{\pi h_f^4} L \right]^{1/4}, \quad (6-11)$$

from which Eq. 6-7 implies that

$$w(x) = 3 \left[ \frac{\mu q_i (L-x)}{E'} \right]^{1/4}. \quad (6-12)$$

In oilfield units (with  $q_i$  in bbl/min and  $w$  in in.), the width at the wellbore ( $x = 0$ ) is

$$w_w = 0.38 \left( \frac{q_i \mu L}{E'} \right)^{1/4}. \quad (6-13)$$

For this model, the average width in the fracture is  $\pi/4$  (about 80%) of the wellbore width. With a

Newtonian fluid, the model width is independent of the fracture height.

Perkins and Kern (1961) noted that the average net pressure in the fracture would greatly exceed the minimum pressure for propagation, calculated by an equation similar to Eq. 6-4, unless the fluid flow rate was extremely small or the fluid had an unrealistically low viscosity. Thus, under typical hydraulic fracturing conditions, the pressure resulting from fluid flow is far larger than the minimum pressure required to extend a stationary fracture. This justifies neglecting fracture mechanics effects in this model. Furthermore, they pointed out that the fracture would continue to extend after pumping stopped, until either leakoff limited further extension or the minimum pressure for fracture propagation was reached.

Several important observations concern this solution:

- assumption of plane strain behavior in the vertical direction
- demonstration that fracture toughness could be neglected, because the energy required to propagate the fracture was significantly less than that required to allow fluid flow along the fracture length
- assumption that leakoff and storage or volume change in the fracture could be neglected
- assumption of fixed height
- no direct provision of fracture length as part of the solution.
- Inclusion of leakoff

Although Perkins and Kern (1961) suggested that their paper could be used in practical applications, they neglected both leakoff and storage of fluid in the fracture. They assumed that some other method would be used to calculate the fracture length, such as that proposed by Carter (1957).

Carter introduced the basic equation for leakoff, which is discussed in detail in Section 6-4. The leakoff velocity  $u_L$  at a point on the fracture wall is

$$u_L = \frac{C_L}{\sqrt{t - t_{exp}}}, \quad (6-14)$$

where  $C_L$  is the leakoff coefficient,  $t$  is the current time, and  $t_{exp}$  is the time at which point  $u_L$  was exposed. Carter introduced a simple mass balance:

$$q_i = q_L + q_f, \quad (6-15)$$

where  $q_L$  is the leakoff rate over the whole fracture and  $q_f$  is the volume rate of storage in the fracture. If the fracture width  $\bar{w}$  is assumed to be constant in both space and time, Eq. 6-15 can be written as

$$q_i = 2 \int_0^{A_f(t)} u_L dA_f + \bar{w} \frac{\partial A_f}{\partial t}, \quad (6-16)$$

where  $A_f$  is the fracture face area. Carter showed that Eq. 6-16 can be rewritten as

$$q_i = 2 \int_0^t u_L(t - \lambda) \frac{\partial A_f}{\partial \lambda} d\lambda + \bar{w} \frac{\partial A_f}{\partial t}. \quad (6-17)$$

Substituting Eq. 6-14 into Eq. 6-17 and using Laplace transformations, he showed that this could be solved to obtain

$$A_f = \frac{q_i \bar{w}}{4\pi C_L^2} \left( e^{s^2} \operatorname{erfc}(S) + \frac{2}{\sqrt{\pi}} S - 1 \right), \quad (6-18)$$

where

$$S = \frac{2C_L \sqrt{\pi t}}{\bar{w}}. \quad (6-19)$$

The fracture wing length  $L$  as a function of time is then obtained by dividing the area by twice the fracture height. Harrington and Hannah (1975) showed (see Sidebar 6A) that Eq. 6-18 could be simplified with little loss of accuracy to

$$A_f = \frac{q_i t}{\bar{w} + 2C_L \sqrt{2t}}, \quad (6-20)$$

which is much easier to work with for simple calculations.

Designs were performed by iterating between the Carter technique to obtain the fracture length as a function of time (Eq. 6-19) and the Perkins and Kern model to determine the width (Eq. 6-13) until a consistent solution was found, and then Eq. 6-11 was used to determine the pressure.

Nordgren (1972) added leakoff and storage within the fracture (resulting from increasing width) to the Perkins and Kern model, deriving what is now known as the PKN model. To add storage and leakoff, the equation of continuity (i.e., conservation of mass) is added to the set of equations (6-7 and 6-9) used by Perkins and Kern:

$$\frac{\partial q}{\partial x} + q_L + \frac{\partial A}{\partial t} = 0, \quad (6-21)$$

## 6A. Approximation to the Carter equation for leakoff

Equation 6-20 was derived by assuming that the exposure time  $t_{exp}$  in Eq. 6-14 is equal to  $t/2$ , for which integration gives the volume lost per unit area of the fracture face as

$$u_L = 2C_L \sqrt{t/2} = C_L \sqrt{2t}. \quad (6A-1)$$

Harrington and Hannah (1975) introduced efficiency as:

$$\eta = \frac{V_f}{V_f + V_L}, \quad (6A-2)$$

where  $V_f$  is the fracture volume,  $V_f$  is the volume of fluid injected, and  $V_L$  is the leaked-off volume, which in terms of Eq. 6-20 becomes

$$\eta = \frac{\bar{w}}{\bar{w} + 2C_L \sqrt{2t}} \quad (6A-3)$$

or

$$\eta = \frac{1}{1 + 2C_L \sqrt{2t} / \bar{w}}. \quad (6A-4)$$

This approximation allows the efficiency  $\eta$  and  $S$  in Eq. 6-19 to be related by

$$\eta = \frac{1}{1 + 0.8S} \quad (6A-5)$$

or

$$S = 1.25 \frac{1 - \eta}{\eta}, \quad (6A-6)$$

which also shows that  $S$  tends to 0 as the efficiency tends to 1 (negligible fluid loss) and that  $S$  tends to infinity for zero efficiency (i.e., negligible fracture volume relative to the fluid-loss volume). An improved approximation for  $\sqrt{2t}$  is in Chapter 9 (i.e.,  $g_0 \sqrt{t}$ , where  $g_0$  is within 5% of 1.5 and varies with efficiency).

where  $q$  is the volume flow rate through a cross section,  $A$  is the cross-sectional area of the fracture ( $\pi w h_f / 4$  for the PKN model), and  $q_L$  is the volume rate of leakoff per unit length:

$$q_L = 2h_f u_L, \quad (6-22)$$

where  $u_L$  is from Eq. 6-14. The cross-sectional area  $A$  is not  $A_f$ , the area of the fracture face. Substituting for pressure in terms of width, similar to the method of Perkins and Kern, Eq. 6-21 can be written as

$$\frac{E'}{128\mu h_f} \frac{\partial^2 w^4}{\partial x^2} = \frac{8C_L}{\pi \sqrt{t - t_{exp}}(x)} + \frac{\partial w}{\partial t}. \quad (6-23)$$

Nordgren solved this equation numerically in a dimensionless form to obtain the width and length as a function of time. The dimensionless time  $t_D$  used in the solution is defined by

$$t_D = \left[ \frac{64C_L^5 E' h_f}{\pi^3 \mu q_i^2} \right]^{2/3} t. \quad (6-24)$$

Dimensionless time  $t_D$  is a stronger function of the leakoff coefficient ( $C_L^{10/3}$ ) than time  $t^1$ .

Because Nordgren's solution was ultimately obtained numerically, it is not possible to express it analytically. However, some useful approximations to the fracture geometry for the limiting cases of high and low efficiency can be obtained (see Sidebar 6B). These expressions provide useful physical insight into the behavior of fractures. For example, the equation for length when leakoff is high (i.e., low efficiency) indicates that the length is determined simply by a mass balance between leakoff and flow into the fracture; i.e., the length increases just fast enough for the leakoff rate to balance the inflow. Analytical extensions to the PKN model that include power law fluids and explicit consideration of the efficiency between the bounding values of 0 and 1 can be obtained.

It is important to reemphasize that even for contained fractures, the PKN solution is valid only when the fracture length is much greater than the height. Typically, if the height is less than about one-third of the total (tip to tip) fracture length, the error resulting from the plane strain assumption is negligible.

## 6B. Approximations to Nordgren's equations

Nordgren (1972) derived two limiting approximations, for storage-dominated, or high-efficiency ( $t_D < 0.01$ ), cases and for leakoff-dominated, or low-efficiency ( $t_D > 1.0$ ), cases, with  $t_D$  defined by Eq. 6-24. They are useful for quick estimates of fracture geometry and pressure within the limits of the approximations. Both limiting solutions overestimate both the fracture length and width (one neglects fluid loss and the other neglects storage in the fracture), although within the stated limits on  $t_D$ , the error is less than 10%.

The storage-dominated ( $\eta \rightarrow 1$ ) approximation is

$$L(t) = 0.39 \left[ \frac{E' q_i^3}{\mu h_f^4} \right]^{1/5} t^{4/5} \quad (6B-1)$$

$$w_w = 2.18 \left[ \frac{\mu q_i^2}{E' h_f} \right]^{1/5} t^{1/5}, \quad (6B-2)$$

and the high-leakoff ( $\eta \rightarrow 0$ ) approximation is

$$L(t) = \frac{q_i t^{1/2}}{2\pi C_L h_f} \quad (6B-3)$$

$$w_w = 4 \left[ \frac{\mu q_i^2}{\pi^3 E' C_L h_f} \right]^{1/4} t^{1/8}. \quad (6B-4)$$

Equation 6B-3 could also be obtained from the approximation in Sidebar 6A, with the fracture width set to zero and  $2\sqrt{2t}$  replaced by  $\pi \sqrt{t}$ , which is more correct. Once the width is determined from Eq. 6B-2 or 6B-4, the pressure can be found from Eq. 6-7.

- Derivation of the Khristianovich–Geertsma–de Klerk model

Khristianovich and Zheltov (1955) derived a solution for the propagation of a hydraulic fracture by assuming the width of the crack at any distance from the well is independent of vertical position (i.e., a rectangular cross section with slip at the upper and lower boundaries), which is a reasonable assumption for a fracture with a height much greater than its length. Their solution includes the fracture mechanics aspects of the fracture tip. They recognized that to solve this problem analytically it was necessary to simplify the solution. They did this by assuming that the flow rate in the fracture is constant and that the pressure in the fracture could be approximated by a constant pressure in the majority of the fracture body, except for a small region near the tip with no fluid penetration, and hence no fluid pressure. This assumption can be made because the pressure gradient caused by fluid flow is highly sensitive to fracture width and therefore occurs primarily in the tip region. The concept of fluid lag remains an important element of the mechanics of the fracture tip and has been validated at the field scale (Warpinski, 1985). They showed that provided this dry region is quite small (a few percent of the total length), the pressure in the main body of the fracture is nearly equal to the pressure at the well over most of the length, with a sharp decrease near the tip.

Using Khristianovich and Zheltov's result that the tip region is very small, Geertsma and de Klerk (1969) gave a much simpler solution to the same problem. Their derivation is outlined in the following.

For a rectangular cross section, the equivalent of Eq. 6-9 is

$$\frac{\partial p}{\partial x} = -\frac{12q\mu}{h_f w^3}, \quad (6-25)$$

which can be written in integral form as

$$p_{net} = \frac{6\mu q_i}{h_f} \int_0^L \frac{dx}{w^3}. \quad (6-26)$$

It can be shown that applying Barenblatt's tip condition (which requires that the fracture tip must close smoothly, as illustrated in Fig. 6-3) implies that the stress intensity factor (see Chapter 3) is zero:

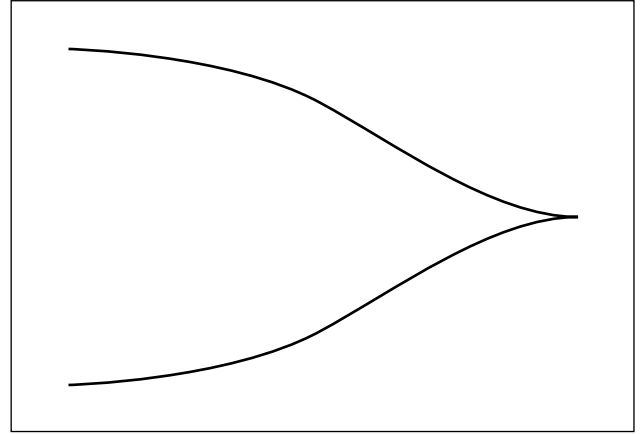


Figure 6-3. Barenblatt's tip condition.

$$\int_0^L \frac{p_{net}(x)dx}{\sqrt{1-(x/L)^2}} = 0. \quad (6-27)$$

The width profile with a small unpressured tip region is close to that obtained for a constant net pressure over the entire fracture, which is equivalent to Eq. 6-7 with  $h_f$  replaced by  $2L$ :

$$w_w = \frac{4}{E'} L p_{net}. \quad (6-28)$$

Solving Eqs. 6-26 through 6-28, they found expressions of the form given by Perkins and Kern (1961):

$$p_{net,w} \approx \left[ \frac{21\mu q_i}{64\pi h_f L^2} E'^3 \right]^{1/4}, \quad (6-29)$$

with the wellbore width given by

$$w_w = \left[ \frac{84}{\pi} \frac{\mu q_i L^2}{E' h_f} \right]^{1/4}. \quad (6-30)$$

For no leakoff, the equations can be solved for length and width, respectively:

$$L(t) = 0.38 \left[ \frac{E' q_i^3}{\mu h_f^3} \right]^{1/6} t^{2/3} \quad (6-31)$$

$$w_w = 1.48 \left[ \frac{\mu q_i^3}{E' h_f^3} \right]^{1/6} t^{1/3}. \quad (6-32)$$

The high-leakoff solution for the PKN model (Eq. 6B-3) also applies to the KGD model, but Geertsma and de Klerk did not provide an explicit width relationship for the KGD model in the case of high leakoff.

Geertsma and de Klerk also extended the model to include fluid leakoff, following Carter's (1957) method. Fluid loss is incorporated by assuming that it has no effect on fracture shape or pressure distribution. The volume of a two-wing KGD fracture is

$$V_f = \frac{\pi}{2} h_f L w_w. \quad (6-33)$$

Performing a volume balance and solution procedure similar to that of Carter, they obtained

$$L = \frac{q_i w_w}{64 C_L^2 h_f} \left( e^{s^2} \operatorname{erfc}(S) + \frac{2}{\sqrt{\pi}} S - 1 \right), \quad (6-34)$$

where

$$S = \frac{8 C_L \sqrt{\pi t}}{\pi w_w}. \quad (6-35)$$

To include the effects of spurt loss  $S_p$ ,  $w_w$  should be replaced by  $w_w + (8/\pi)S_p$ , which is equivalent to the Carter relation with  $w$  replaced by  $\bar{w} + 2S_p$  and  $\bar{w} = \pi w/4$ .

- Assumptions of the PKN and KGD models

Both the PKN and KGD models contain a number of assumptions that are revisited in this section. They assume that the fracture is planar (i.e., that it propagates in a particular direction, perpendicular to the minimum stress, as described in Chapter 3). They also assume that fluid flow is one-dimensional (1D) along the length of the fracture. In the case of the models described, they assume Newtonian fluids (although Perkins and Kern also provided solutions for power law fluids), and leakoff behavior is governed by a simple expression derived from filtration theory (Eq. 6-14). The rock in which the fracture propagates is assumed to be a continuous, homogeneous, isotropic linear elastic solid; the fracture is considered to be of fixed height or completely confined in a given layer; and one of two assumptions is made concerning the length to height ratio of the fracture—i.e., height is large (KGD) or small (PKN) relative to length. Finally, the KGD model includes the assumption that tip processes dominate fracture propagation, whereas the PKN model neglects fracture mechanics altogether.

Since these models were developed, numerous extensions have been made that relax these assumptions, the most important of which are the solutions for power law fluids. These two models

are still used to design treatments and are usually available as options in simulators.

Similar solutions can be derived for radial fractures (see Sidebar 6C).

## 6C. Radial fracture geometry models

Both Perkins and Kern (1961) and Geertsma and de Klerk (1969) considered radial fractures, which grow unconfined from a point source. This model is applicable when there are no barriers constraining height growth or when a horizontal fracture is created.

Geertsma and de Klerk formulated the radial model using the same arguments outlined in "Derivation of the Kristianovich–Geertsma–de Klerk model" (page 6-7). The fracture width is

$$w_w = 2.56 \left[ \frac{\mu q_i R}{E'} \right]^{1/4} \quad (6C-1)$$

and the radial length  $R$  is

$$R = \sqrt{\frac{q_i (4w_w + 15S_p)}{30\pi^2 C_L^2} \left( e^{s^2} \operatorname{erfc}(S) + \frac{2}{\sqrt{\pi}} S - 1 \right)}, \quad (6C-2)$$

where

$$S = \frac{15 C_L \sqrt{\pi t}}{4w_w + 15S_p}. \quad (6C-3)$$

An explicit relationship for pressure can be derived by considering the solution for flow from a point source, in which case the pressure in the fracture is a function of the expression  $\ln(r_w/R)$ , where  $r_w$  is the radius of the wellbore.

The no-fluid-loss approximations for the radial model are

$$w_w = 2.17 \left[ \frac{\mu^2 q_i^3}{E'^2} \right]^{1/9} t^{1/9} \quad (6C-4)$$

$$R = 0.52 \left[ \frac{E' q_i^3}{\mu} \right]^{1/9} t^{4/9}. \quad (6C-5)$$

The large-fluid-loss approximation for radial length is

$$R = \frac{1}{\pi} \left[ \frac{q_i^2 t}{C_L^2} \right]^{1/4}. \quad (6C-6)$$

An expression for width in the case of large fluid loss was not provided but can be found from Eqs. 6C-1 and 6C-6.

## 6-3. Three-dimensional and pseudo-three-dimensional models

The simple models discussed in the previous sections are limited because they require the engineer to specify the fracture height or to assume that a radial fracture will develop. This is a significant limitation, because it is not always obvious from logs and other

data where or whether the fracture will be contained. Also, the fracture height usually varies from the well (where the pressure is highest) to the tip of the fracture. This limitation can be remedied by the use of planar 3D and pseudo-3D (P3D) models.

The three major types of hydraulic fracture models that include height growth are categorized according to their major assumptions.

- General 3D models make no assumptions about the orientation of the fracture. Factors such as the wellbore orientation or perforation pattern may cause the fracture to initiate in a particular direction before turning into a final preferred orientation (perpendicular to the far-field minimum in-situ stress). Simulators incorporating such models are computationally intensive and generally require a specialist to obtain and interpret the results. They are most applicable in research environments, for which they are used for studying details of fracture initiation and near-well complexities such as those discussed in Section 6-8, rather than overall fracture growth. One example of such a study was published by Brady *et al.* (1993). These models are not discussed further in this volume.
- Planar 3D models are based on the assumption that the fracture is planar and oriented perpendicular to the far-field minimum in-situ stress. No attempt is made to account for complexities that result in deviations from this planar behavior. Simulators based on such models are also computationally demanding, so they are generally not used for routine designs. They should be used where a significant portion of the fracture volume is outside the zone where the fracture initiates or where there is more vertical than horizontal fluid flow. Such cases typically arise when the stress in the layers around the pay zone is similar to or lower than that within the pay. This type of model is described in more detail in Section 6-3.1.
- P3D models attempt to capture the significant behavior of planar models without the computational complexity. The two main types are referred to here as “lumped” and cell-based. In the lumped (or elliptical) models, the vertical profile of the fracture is assumed to consist of two half-ellipses joined at the center, as shown in Fig. 6-4. The horizontal length and wellbore vertical tip extensions are calculated at each time step, and the assumed shape is matched to these positions. These models make the

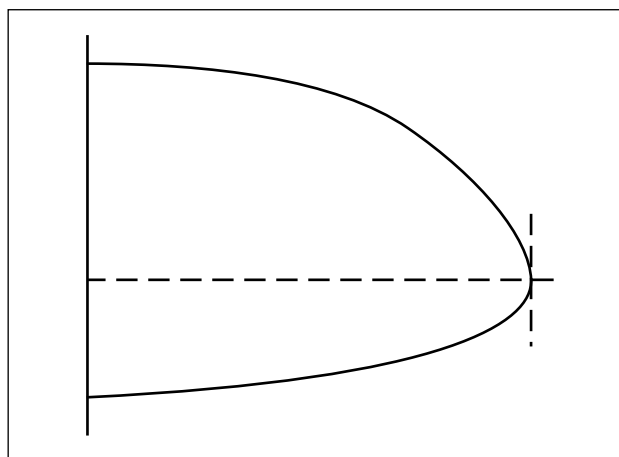


**Figure 6-4.** Conceptual representation of the lumped model.

inherent assumptions that fluid flow is along streamlines from the perforations to the edge of the ellipse and that the streamlines have a particular shape, derived from simple analytical solutions. Cell-based models treat the fracture as a series of connected cells. They do not prescribe a fracture shape, but generally assume plane strain (i.e., each cell acts independently) and do not fully couple the calculation of fluid flow in the vertical direction to the fracture geometry calculation.

In the fixed-height models described previously, no consideration is given to the layers surrounding the fractured zone. The planar and P3D models use data about the properties of the surrounding zones to predict the rate of growth into these zones. For the purpose of this chapter, planar 3D models are defined as those in which calculation of the full 2D fluid-flow field in the fracture is coupled to the 3D elastic response of the rock, and P3D models are defined as those that approximate either the coupling or the 3D elasticity in some manner.

Regardless of which type of model is used to calculate the fracture geometry, only limited data are available on typical treatments to validate the model used. For commercial treatments, the pressure history during treatment is usually the only data available to validate the model. Even in these cases, the quality of the data is questionable if the bottomhole pressure must be inferred from the surface pressure. The bottomhole pressure is also not sufficient to uniquely determine the fracture geometry in the absence of other information, such as that derived from tiltmeters and microseismic data (see Sidebar 6D). If a simulator incorporates the correct model, it should match both

## 6D. Field determination of fracture geometry

Fracture geometry can be determined by using the two techniques of microseismic activity and tiltmeters. Microseisms can be used to locate the fracture, thus providing estimates of its length and height, whereas tiltmeters can provide information about fracture width.

### Microseisms

Although all models of hydraulic fracturing assume that the rock is a continuous medium, it is well known that reservoirs have natural fractures, bedding planes and other weakness features that respond as a noncontinuum. Such features have been used to image hydraulic fractures using seismic techniques.

Hydraulic fractures induce two large changes in the reservoir as they are created. The stress in the surrounding rocks is perturbed because of fracture opening, and the pore pressure is increased as a result of leakoff of the high-pressure fracturing fluid. Both of these features can result in the generation of large shear stresses on many of the weakness planes near the hydraulic fracture, resulting in small shear slippages called microseisms or microearthquakes.

Microseisms generate seismic waves that can be detected by sensitive seismic receivers in nearby wells. As shown in Fig. 6D-1, both compressional waves (*P*-waves) and shear waves (*S*-waves) can be generated by the microseism, and these two waves travel with different velocities. If a receiver can detect both the *P*- and *S*-waves, the time separation can be determined and the distance to the source inferred from

$$d = \frac{u_P u_S}{u_P - u_S} [t_S - t_P], \quad (6D-1)$$

where  $u_P$  and  $u_S$  are the compressional and shear velocities, respectively, and  $t_S$  and  $t_P$  are the shear and compressional arrival times.

The direction in space can be determined by using a tri-axial receiver to examine the amplitude of the *P*-wave. The *P*-wave has the characteristic that its particle motion (how the rock mass vibrates) is aligned with the direction of travel of the wave. By obtaining the orientation of the resultant amplitude vector at any time, the microseism can be traced back to its source.

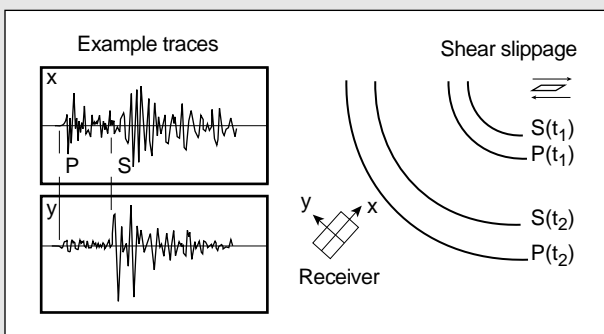


**Figure 6D-1.** Microseismic traces at the receiver resulting from shear slippage.

With multiple seismic receivers, triangulation techniques can be employed and greater accuracy obtained. With either approach, however, the objective is to locate the zone of microseisms surrounding the hydraulic fracture and deduce the size and shape of the fracture from this information.

### Downhole tiltmeters

Width development in a hydraulic fracture results in elastic deformation of the formation. This deformation can be used for fracture diagnostics to provide significant information about fracture height and width and also about formation characteristics.

As a fracture is opened, the deformation of the rock extends for large distances into the reservoir. Although the deformation is small at distances of more than a few tens of feet, highly sensitive tiltmeter devices can measure these small changes in position. A tiltmeter does not actually measure the displacement of the earth, but rather the curvature of the displacement, and it is capable of measuring up to nanoradian resolution (a nanoradian is the angle induced by stretching a line from New York to Los Angeles and raising the New York side by the diameter of a pencil). Tiltmeters have long been used for surface diagnostics of earth movement, but the application of a string of downhole tiltmeters provides highly sensitive fracture data.

Figure 6D-2 shows a schematic of the tilt response of the formation measured in a well offset to the fracture treatment. The characteristic S-shaped curve is typical of tilt, as opposed to strain, and can be simply explained. Straight across from the fracture, the rock is pushed away, but is not tilted on the geometric axis of the fracture, and there is zero tilt. Above the fracture, the earth experiences curvature that is defined as negative for this example. The curvature reaches a maximum at a well-defined point and then decreases to zero as the distance from the fracture increases. The bottom is identical to the top, except that the curvature has the opposite direction and opposite sign.

Two aspects of this distribution are important for diagnostics. First, the locations of the maximum tilt values are a function of the height  $h_f$  of the fracture relative to the distance  $d$  away. Thus, fracture height can be quickly estimated. Second, the amplitude of the tilt is a function of the width of the fracture, so the width during fracturing, and possibly the final propped width, can be estimated as well.

Branagan *et al.* (1996) provided an example of the application of tiltmeters to the calculation of hydraulic fracture geometry.

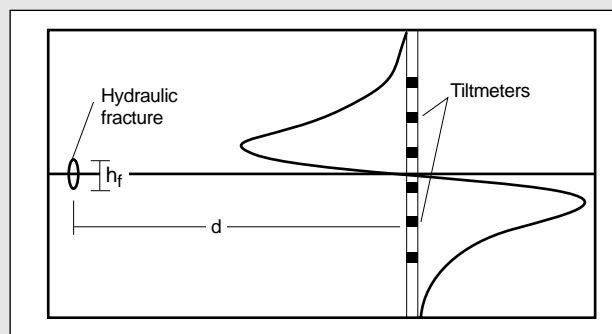


**Figure 6D-2.** Tiltmeter response to hydraulic fracture width.

treating pressure and fracture geometry. These issues are addressed in Section 6-12 and Chapter 9.

### 6-3.1. Planar three-dimensional models

A planar fracture is a narrow channel of variable width through which fluid flows. The fracture geometry is defined by its width and the shape of its periphery (i.e., height at any distance from the well and length). Both the width at any point and the overall shape vary with time. They depend on the pressure distribution, which itself is determined by the pressure gradients caused by the fluid flow within the fracture. Because the relation between pressure gradient and flow rate is highly sensitive to the fracture width (Eq. 6-9), the geometry and fluid flow are tightly coupled. Although the mechanics of these processes are described separately in this section, the complexity of solving any fracture model lies in the close coupling between the different processes. Three separate problems are considered:

- width profile in a fracture of known shape and pressure distribution
- shape of the fracture
- flow of fluid in a fracture of known shape and width (i.e., known geometry).

Hirth and Lothe (1968) and Bui (1977) showed how the pressure and width in a fracture may be related. Basically, the width at any point (x,y) is determined by an integral of the net pressure over the entire fracture, expressed as

$$w(x,y) = \iint_S f(x-x', y-y')(p(x',y') - \sigma(x',y')) dx' dy', \quad (6-36)$$

where  $\sigma$  is the stress.

The details of the elastic influence function  $f$  in Eq. 6-36 are beyond the scope of this volume. Useable forms of Eq. 6-36 can be derived generally only for homogeneous linear elastic materials (see Sidebar 6E). In fracturing applications, the rock is usually also assumed to be isotropic.

The shape of the fracture evolves with time. In essence, the boundary (i.e., the vertical and horizontal tips) moves outward as the fluid provides sufficient energy to fracture the rock at the boundary. More complex tip behavior is discussed subsequently, but in this

section it is assumed that this process is described by linear elastic fracture mechanics (LEFM). If the LEFM failure criterion is exceeded at any point on the fracture periphery, the fracture will extend until the criterion is again met. For simple shapes and pressure distributions, such as ellipses under constant pressure, the criterion can be specified analytically, similar to Eq. 6-3. For more complex shapes and pressure distributions, analytical solutions are not available. In these cases, it can be shown that a relatively simple criterion can be written in terms of the width near the tip and the critical stress intensity factor or fracture toughness  $K_{Ic}$ , which is introduced in Chapter 3:

$$w(x) = \frac{4\sqrt{2}K_{Ic}}{\sqrt{\pi E'}} \sqrt{x}, \quad (6-37)$$

where  $x$  is the distance measured from the tip. Relations between fracture mechanics parameters such as the specific surface energy (used in Eq. 6-3) and the fracture toughness are provided in Chapter 3.

The fluid flow is described by equations for conservation of mass (a general form of Eq. 6-21, including the density  $\rho$  and expressed in terms of velocity  $u$ ):

$$\left( \frac{\partial(\rho w u_x)}{\partial x} + \frac{\partial(\rho w u_y)}{\partial y} \right) + \frac{\partial}{\partial t}(\rho w) + 2\rho u_L = 0, \quad (6-38)$$

which can be written as a vector equation:

$$\nabla \cdot (\rho w \bar{u}) + \frac{\partial}{\partial t}(\rho w) + 2\rho u_L = 0, \quad (6-39)$$

and the conservation of momentum (a general form of Eq. 6-9) is

$$\rho \frac{D\bar{u}}{Dt} = -\nabla p - [\nabla \cdot \tau] + \rho \bar{g}, \quad (6-40)$$

where  $\tau$  is the shear stress and  $\bar{g}$  is the acceleration of gravity.

The first two terms in Eq. 6-38 relate to the spatial change of the mass-flow vector, and the second two terms represent the storage resulting from width increases and leakoff, respectively. Equation 6-40 is a vector equation. The term on the left-hand side is the rate of change of momentum, and the terms on the right-hand side are the pressure, viscous and gravitational forces, respectively. It simply states that a small element of fluid accelerates because of the forces acting on it. This equation can be expanded and then simplified for the geometries of interest in hydraulic frac-



## 6E. Lateral coupling in pseudo-three-dimensional models

Assume that a fracture has a fixed height and that it consists of a number of elements each of constant width over the height (i.e., a KGD fracture). Let the grid points be represented by points  $x_i$  in the center of the elements with corners  $(x_{l,i}, y_{b,i})$ ,  $(x_{r,i}, y_{t,i})$  and  $(x_{r,i}, y_{b,i})$ , as shown in Fig. 6E-1. Crouch and Starfield (1983) developed a boundary element solution technique called the displacement discontinuity method. They showed that the pressure at any point is given by

$$p(x_i) = \sum_k A_{ik} w_k, \quad (6E-1)$$

where  $A_{ik}$  is an influence function of the form

$$A_{ik} = \frac{G}{4\pi(1-\nu)} I(x_{c,i}, y_{c,i}; x_{l,k}, x_{r,k}, y_{b,k}, y_{t,k}), \quad (6E-2)$$

where the influence function  $I$  is defined as

$$I = \frac{[(x_{c,i} - x_{r,k})^2 + (y_{c,i} - y_{t,k})^2]^{1/2}}{(x_{c,i} - x_{r,k})(y_{c,i} - y_{t,k})} - \frac{[(x_{c,i} + x_{l,k})^2 + (y_{c,i} - y_{t,k})^2]^{1/2}}{(x_{c,i} + x_{l,k})(y_{c,i} - y_{t,k})} + \frac{[(x_{c,i} + x_{l,k})^2 + (y_{c,i} + y_{b,k})^2]^{1/2}}{(x_{c,i} + x_{l,k})(y_{c,i} + y_{b,k})} - \frac{[(x_{c,i} - x_{r,k})^2 + (y_{c,i} + y_{b,k})^2]^{1/2}}{(x_{c,i} - x_{r,k})(y_{c,i} + y_{b,k})}. \quad (6E-3)$$

To accurately solve Eq. 6E-1 requires a large number of elements. Also, it is difficult to extend directly to other shapes such as ellipses or for nonconstant heights. To overcome these problems, the equation is modified as follows. The width at any point can be written as

$$w(x_k) = w(x_i) + \Delta w_{ki}, \quad (6E-4)$$

where  $\Delta w_{ki}$  is defined as

$$\Delta w_{ki} = w(x_k) - w(x_i). \quad (6E-5)$$

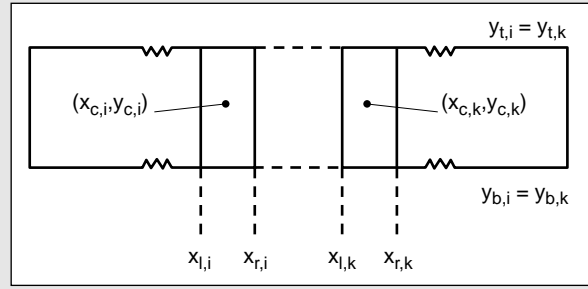


**Figure 6E-1.** Geometry for displacement continuity solution.

Equation 6E-1 can then be written as

$$p(x_i) = p(w_i) + p_{corr}, \quad (6E-6)$$

where

$$p(w_i) = w(x_i) \sum A_{ik} \quad (6E-7)$$

$$p_{corr} = \sum A_{ik} \Delta w_{ki}. \quad (6E-8)$$

The term  $w(x_i) \sum A_{ik}$  thus represents the pressure induced by a fracture of constant width  $w(x_i)$ . For a fracture of infinite length, this pressure would be exact if calculated using the plane strain solution. The term  $p(w_i)$  can therefore be obtained as the sum of the plane strain solution and the effect of two semi-infinite fractures of  $w - w_i$  attached at the tip of each fracture wing.

From Eq. 6E-2, the influence functions decrease with distance from an element. The advantages of the form of Eq. 6E-8 are that the corrections are smallest near the element where the widths are almost the same and that the self-correction is exactly zero by definition. The number of elements required to obtain an accurate solution is significantly reduced, and variable heights and other shapes are easily introduced. Lateral coupling is relatively easy to introduce to the explicit solution method because the pressure correction is simply added before the fluid velocities are calculated.

turing (see Sidebar 6F). For a particular component, such as the  $x$  component, Eq. 6-40 can be written as

$$\rho \frac{Du_x}{Dt} = -\frac{\partial p}{\partial x} - \left( \frac{\partial \tau_{xx}}{\partial x} + \frac{\partial \tau_{yx}}{\partial y} + \frac{\partial \tau_{zx}}{\partial z} \right) + \rho g_x. \quad (6-41)$$

A constitutive law relating the stresses  $\tau$  to the flow rate is required to complete the description of fluid flow. In the case of steady flow in a narrow channel such as a fracture, the full details of the constitutive law are not required, because the narrow fracture width results in the complete dominance of some stress terms. The only terms of interest are the shear stresses induced by velocity gradients across the fracture. In addition, use is made of the lubrication approximation, so flow perpendicular to the fracture wall (the  $z$  direction) is neglected. With these assump-

tions, the equations for the stress in a Newtonian fluid reduce to

$$\begin{aligned} \tau_{xz} &= \tau_{zx} = -\mu \left( \frac{\partial u_x}{\partial z} \right) \\ \tau_{yz} &= \tau_{zy} = -\mu \left( \frac{\partial u_y}{\partial z} \right), \end{aligned} \quad (6-42)$$

and Eq. 6-41 can be written as

$$\rho \frac{Du_x}{Dt} = -\frac{\partial p}{\partial x} + \mu \left( \frac{\partial^2 u_x}{\partial z^2} \right) + \rho g_x. \quad (6-43)$$

For the special case of a narrow channel (Poiseuille flow), where velocity gradients parallel to the flow are small and there is no flow perpendicular to the channel, the time-dependent term simplifies to a partial

## 6F. Momentum conservation equation for hydraulic fracturing

Equation 6-40 is a vector equation, for which a component can be written as

$$\rho \frac{Du_i}{Dt} = -\frac{\partial p}{\partial x_i} - \left( \frac{\partial \tau_{xi}}{\partial x} + \frac{\partial \tau_{yi}}{\partial y} + \frac{\partial \tau_{zi}}{\partial z} \right) + \rho g_i, \quad (6F-1)$$

where  $u$  is the velocity,  $g$  is the gravitational acceleration, and  $i$  is  $x$ ,  $y$  or  $z$ . The term on the left side of Eq. 6F-1 is termed the substantial derivative, which is the rate of change seen by an observer moving with the fluid motion. It can be related to the usual partial derivative (i.e., the rate of change seen by a stationary observer) as

$$\frac{D}{Dt} = \frac{\partial}{\partial t} + u_x \frac{\partial}{\partial x} + u_y \frac{\partial}{\partial y} + u_z \frac{\partial}{\partial z}. \quad (6F-2)$$

Thus, Eq. 6F-2 can be expanded to

$$\begin{aligned} \rho \left( \frac{\partial u_i}{\partial t} + u_x \frac{\partial u_i}{\partial x} + u_y \frac{\partial u_i}{\partial y} + u_z \frac{\partial u_i}{\partial z} \right) \\ = -\frac{\partial p}{\partial x_i} - \left( \frac{\partial \tau_{xi}}{\partial x} + \frac{\partial \tau_{yi}}{\partial y} + \frac{\partial \tau_{zi}}{\partial z} \right) + \rho g_i. \end{aligned} \quad (6F-3)$$

This completely general equation can be simplified for a narrow channel in an impermeable medium. Leakoff does not occur in this case, so components in the  $z$  direction can be neglected. In addition, the flow is assumed to be steady state, so time derivatives can be ignored. In this case, Eq. 6F-3 simplifies to

$$\begin{aligned} \rho \left( u_x \frac{\partial u_i}{\partial x} + u_y \frac{\partial u_i}{\partial y} \right) \\ = -\frac{\partial p}{\partial x_i} - \left( \frac{\partial \tau_{xi}}{\partial x} + \frac{\partial \tau_{yi}}{\partial y} + \frac{\partial \tau_{zi}}{\partial z} \right) + \rho g_i, \end{aligned} \quad (6F-4)$$

for  $i = 1$  or  $2$ . Even for a permeable medium, Eq. 6F-4 is used. In this case, leakoff is treated as a sink term and included in the mass balance, but it is assumed not to affect the equations relating pressure, stress and fluid velocity.

### Newtonian fluids

To make Eq. 6F-4 useful, the stress components must be determined, which is done by assuming a model of fluid behavior. For example, a Newtonian fluid is a model with one parameter, the viscosity  $\mu$ . The stress components are

$$\begin{aligned} \tau_{xx} &= \mu \frac{\partial u_x}{\partial x} + \frac{2}{3} \mu (\nabla \cdot u) \\ \tau_{yy} &= 2\mu \frac{\partial u_y}{\partial y} + \frac{2}{3} \mu (\nabla \cdot u) \\ \tau_{zz} &= 2\mu \frac{\partial u_z}{\partial z} + \frac{2}{3} \mu (\nabla \cdot u) \\ \tau_{xy} &= \tau_{yx} = -\mu \left( \frac{\partial u_x}{\partial y} + \frac{\partial u_y}{\partial x} \right) \\ \tau_{yz} &= \tau_{zy} = -\mu \left( \frac{\partial u_y}{\partial z} + \frac{\partial u_z}{\partial y} \right) \\ \tau_{zx} &= \tau_{xz} = -\mu \left( \frac{\partial u_z}{\partial x} + \frac{\partial u_x}{\partial z} \right). \end{aligned} \quad (6F-5)$$

The first three components of Eq. 6F-5 are the normal stresses, and the last three are the shear stresses. The last term of the normal components is zero for incompressible fluids. In the case of 1D flow between parallel plates, without leakoff, two of the velocity components are identically zero. In addition, conservation of mass implies that the third component cannot vary with position. Hence, all three normal components are identically zero. The equations thus reduce to those for shear flow. Although these assumptions are not strictly true in general, they are used for the flow calculations in hydraulic fracture modeling. It can also be shown that for a narrow channel, the velocity gradients perpendicular to the walls (the  $z$  direction) are much greater than those in the parallel directions. Finally, therefore, the stress components for a Newtonian fluid in a hydraulic fracture can be written as

$$\begin{aligned} \tau_{zx} &= -\mu \left( \frac{\partial u_x}{\partial z} \right) \\ \tau_{zy} &= -\mu \left( \frac{\partial u_y}{\partial z} \right). \end{aligned} \quad (6F-6)$$

Substituting Eq. 6F-6 into Eq. 6F-4 obtains

$$\begin{aligned} \rho \left( u_x \frac{\partial u_x}{\partial x} + u_y \frac{\partial u_x}{\partial y} \right) &= -\frac{\partial p}{\partial x} + \mu \frac{\partial^2 u_x}{\partial z^2} \\ \rho \left( u_x \frac{\partial u_y}{\partial x} + u_y \frac{\partial u_y}{\partial y} \right) &= -\frac{\partial p}{\partial y} + \mu \frac{\partial^2 u_y}{\partial z^2} + \rho g. \end{aligned} \quad (6F-7)$$

For 1D flow along the fracture length, as typically assumed in P3D models, Eq. 6F-7 can be simplified to

$$\frac{\partial^2 u_x}{\partial z^2} = \frac{1}{\mu} \frac{\partial p}{\partial x}. \quad (6F-8)$$

Assuming zero slip (i.e., zero velocity at the fracture wall), the solution to Eq. 6F-8 is

$$u_x = \frac{1}{2\mu} \frac{\partial p}{\partial x} (z^2 - (w/2)^2). \quad (6F-9)$$

Integrating to obtain the average velocity across the channel,

$$\bar{u}_x = \frac{-w^2}{12\mu} \frac{\partial p}{\partial x}. \quad (6F-10)$$

The flow rate per unit height is obtained by multiplying the average velocity by the width  $w$ .

In the case of 2D flow, the left-hand sides of Eq. 6F-7 are zero if inertia may be neglected. In this case for the  $y$  direction, an equation can be formed similar to Eq. 6F-10, except that it includes a gravitational term.

derivative of velocity with respect to time. It is usually assumed that the flow is steady state, which finally obtains

$$\frac{\partial p}{\partial x} = \mu \left( \frac{\partial^2 u_x}{\partial z^2} \right) + \rho g_x \quad (6-44)$$

and a similar equation for the y component.

Equations 6-36 through 6-44 summarize the planar 3D model for Newtonian fluids. Similar results can be obtained for non-Newtonian fluids (see Sidebar 6G). These equations are generally not amenable to analytic solutions, but require a numerical simulation. In addition, although it is relatively straightforward to write the conceptual equations, efficient and robust numerical solutions are difficult to obtain. The primary reasons for this difficulty are the extremely close coupling of the different parts of the solution (e.g., fluid flow and solid deformation), the nonlinear relation between width and pressure, and the complexity of a moving-boundary problem.

The first numerical implementation of a planar model was reported by Clifton and Abou-Sayed (1979). In essence, their approach was to define

a small fracture, initiated at the perforations, divide it into a number of equal elements (typically 16 squares) and then begin solution of the equations. As the boundary extends, the elements distort to fit the new shape. One difficulty with such a solution is that the elements can develop large aspect ratios and very small angles, as shown in Fig. 6-5. The numerical schemes typically used to solve the equations do not usually perform well with such shapes.

A different formulation was described by Barree (1983), and numerous field applications have been reported (e.g., Barree, 1991). It neatly avoids the problem of grid distortion by dividing the layered reservoir into a grid of equal-size rectangular elements, which are defined over the entire region that the fracture may cover. In this case, the grid does not move. Instead, as the failure criterion is exceeded, the elements ahead of the failed tip are opened to flow and become part of the fracture, as shown in Fig. 6-6. Two limitations of this approach are that

- the number of elements in the simulation increases as the simulation proceeds, so that the initial number may be small, resulting in inaccuracy

## 6G. Momentum balance and constitutive equation for non-Newtonian fluids

The definition of a Newtonian fluid is the one-parameter relation between stress and velocity (Eq. 6G-5). In tensor notation, this can be written as

$$\tau_{ij} = -\mu \Delta_{ij}, \quad (6G-1)$$

where  $\Delta$  is the rate of deformation tensor, with components

$$\Delta_{ij} = \frac{\partial u_i}{\partial x_j} + \frac{\partial u_j}{\partial x_i}. \quad (6G-2)$$

The viscosity may be a function of pressure and temperature or other variables, including the history of the fluid, but not of  $\Delta$ . For non-Newtonian fluids, an equation similar to Eq. 6G-1 may be written:

$$\tau_{ij} = -\mu_a \Delta_{ij}, \quad (6G-3)$$

where  $\mu_a$  is a function of  $\Delta$ . For flows of the type of interest in fracturing, it can be shown that  $\mu_a$  may depend only on  $\Delta$  through a relation of the form

$$\mu_a = \mu_a(I_2), \quad (6G-4)$$

where  $I_2$  is the second tensor invariant:

$$I_2 = \sum_i \sum_j \Delta_{ij} \Delta_{ji}. \quad (6G-5)$$

For example, for a power law fluid, the function  $\mu_a$  is

$$\mu_a = K \left| \sqrt{\frac{I_2}{2}} \right|^{n-1} \quad (6G-6)$$

and for a Bingham plastic

$$\mu_a = \mu_0 + \frac{\tau_0}{\sqrt{\frac{I_2}{2}}}. \quad (6G-7)$$

The commonly used consistency index  $K'$  is dependent on the flow geometry and is related to a basic fluid property, the generalized consistency index  $K$  (Eq. 6G-6). For parallel plates (i.e., in a slot), which can represent a fracture, the relationship is

$$K' = K \left( \frac{2n+1}{3n} \right)^n. \quad (6G-8)$$

For a pipe it is

$$K' = K \left( \frac{3n+1}{4n} \right)^n. \quad (6G-9)$$

The maximum difference between the two expressions is less than 4% for all values of  $n$ . For 1D flow of a power law fluid between parallel plates, the average fluid velocity is given by

$$\bar{u}_x = \left( \frac{1}{K} \right)^{1/n} \left( \frac{\partial p}{\partial x} \right)^{1/n} \frac{n}{1+2n} \left( \frac{w}{2} \right)^{\frac{1+n}{n}}. \quad (6G-10)$$

For the special case of the power law exponent  $n = 1$ , this reverts to the equation for a Newtonian fluid, with  $K'$  replaced by the viscosity. Table 6G-1 summarizes useful information for the laminar flow of both Newtonian and power law fluids under different geometries. However, the expressions for pressure drop are not generally applicable for drag-reducing fluids such as those used in hydraulic fracturing.

## 6G. Momentum balance and constitutive equation for non-Newtonian fluids (continued)

Table 6G-1. Summarized expressions for laminar flow of Newtonian and power law fluids.				
	Fluid Type	Pipe	Parallel Plates	Ellipse (zero eccentricity)
Reynold's number ( $N_{Re}$ )	Newtonian	$\frac{\rho u D}{\mu}$	$\frac{2 \rho u w}{\mu}$	$\frac{\pi \rho u w}{2 \mu}$
	Power law	$\frac{8^{1-n} \rho D^n u^{2-n}}{K'_p}$	$\frac{3^{1-n} 2^{2-n} \rho u^{2-n} w^n}{K'_{pp}}$	$\frac{\pi^{2-n} \rho u^{2-n} w^n}{2^n K'_{ell}}$
Hydraulic diameter ( $D_H$ ) Friction factor $\left( f = \left( \frac{D_H}{4L} \Delta p \right) / \left( \frac{1}{2} \rho u^2 \right) \right)$		$\frac{D}{16/N_{Re}}$	$\frac{2w}{24/N_{Re}}$	$\frac{\pi w/2}{2\pi^2/N_{Re}}$
Velocity distribution	Newtonian	$u_r = 2u \left[ 1 - \left( \frac{2r}{D} \right)^2 \right]$	$u_x = \frac{3u}{2} \left[ 1 - \left( \frac{2y}{w} \right)^2 \right]$	$u_x = 2u \left[ 1 - \left( \frac{2y}{w} \right)^2 - \left( \frac{2z}{h_i} \right)^2 \right]$
	Power law	$u_r = \left( \frac{3n+1}{n+1} \right) u \left[ 1 - \left( \frac{2r}{D} \right)^{\frac{n+1}{n}} \right]$	$u_x = \left( \frac{2n+1}{n+1} \right) u \left[ 1 - \left( \frac{2y}{w} \right)^{\frac{n+1}{n}} \right]$	
Pressure drop ( $\Delta p/L$ or $dp/dx$ )	Newtonian	$\frac{128 \mu q}{\pi D^4}$	$\frac{12 \mu q}{h_i w^3}$	$\frac{64 \mu q}{\pi h_i w^3}$
	Power law	$\frac{2^{5n+2} q^n K}{\pi^n D^{3n+1}}$	$\left( \frac{4n+2}{n} \right)^n \frac{2 q^n K}{h_i^n w^{2n+1}}$	See Eq. 6-57
$K'$		$K'_p = K \left( \frac{3n+1}{4n} \right)^n$	$K'_{pp} = K \left( \frac{2n+1}{3n} \right)^n$	—

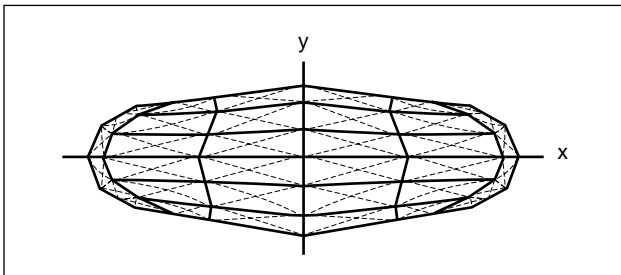


**Figure 6-5.** Planar 3D fracture divided into elements that were initially square.

- the general size of the fracture must be estimated in advance of the simulation to ensure that a “reasonable” number of elements is used.

In addition, this particular implementation has two simplifying assumptions, that a simplified method is used for representing modulus contrasts and a tensile

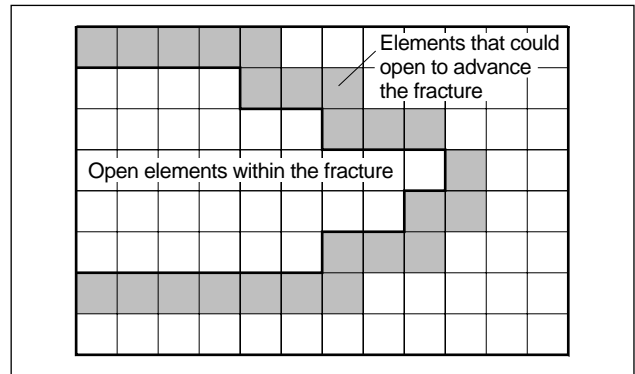


**Figure 6-6.** Fixed-grid solution showing elements open to advance the fracture.

strength criterion is used for fracture extension, rather than a fracture mechanics effect. The failure criterion is used to compare the stress at the center of all boundary elements with the material tensile strength.

If the strength is exceeded, then the element is assumed to open. However, the fracture-induced stress in the material near the tip of a fracture varies with the square root of the distance from the tip. Hence, the failure criterion is grid-resolution dependent.

### 6-3.2. Cell-based pseudo-three-dimensional models

In cell-based models, the fracture length is divided into a number of discrete cells. This is directly analogous to the planar models, except that only one direction is discrete instead of two. Fluid flow is assumed to be essentially horizontal along the length of the fracture, and the solid mechanics is typically simplified by assuming plane strain at any cross section. As in the PKN model, these assumptions make these models suitable primarily for reasonably contained fractures, which are long relative to their height.

These two assumptions allow separating the solid and fracture mechanics solution from the fluid flow as follows. Plane strain implies that each cross section acts independently of any other. In addition, the assumption of 1D fluid flow implies that the pressure in the cross section is always

$$p = p_{cp} + \rho_f g y, \quad (6-45)$$

where  $p_{cp}$  is the pressure along a horizontal line through the center of the perforations and  $y$  is the vertical distance from the center of the perforations. Equation 6-45 is valid only if vertical fracture extension is sufficiently slow that the pressure gradient resulting from vertical flow can be neglected. This assumption that the vertical tips of the fracture are approximately stationary at all times is called the equilibrium-height assumption.

- Solid mechanics solution

With the equilibrium-height assumption, the solid mechanics solution simplifies to the determination of the fracture cross-sectional shape as a function of the net pressure, or  $p_{cp}$ . Simonson *et al.* (1978) derived this solution for a symmetric three-layer case. Fung *et al.* (1987) derived a more general solution for nonsymmetric multilayer cases. Following Fung *et al.* the stress intensity factors at the top and bottom tips  $K_{Ia}$  and  $K_{II}$ , respectively, can be written in terms of the pressure at the center of the perforations  $p_{cp}$  and the closure stresses in the layers  $\sigma_i$  as

$$K_{Ia} = \sqrt{\frac{\pi h_f}{2}} \left[ p_{cp} - \sigma_v + \rho_f g \left( h_{cp} - \frac{3}{4} h_f \right) \right] + \sqrt{\frac{2}{\pi h_f}} \sum_{i=1}^{n-1} (\sigma_{i+1} - \sigma_i) \left[ \frac{h_f}{2} \cos^{-1} \left( \frac{h_f - 2h_i}{h_f} \right) - \sqrt{h_i - (h_f - h_i)} \right] \quad (6-46)$$

$$K_{II} = \sqrt{\frac{\pi h_f}{2}} \left[ p_{cp} - \sigma_v + \rho_f g \left( h_{cp} - \frac{1}{4} h_f \right) \right] + \sqrt{\frac{2}{\pi h_f}} \sum_{i=1}^{n-1} (\sigma_{i+1} - \sigma_i) \left[ \frac{h_f}{2} \cos^{-1} \left( \frac{h_f - 2h_i}{h_f} \right) - \sqrt{h_i - (h_f - h_i)} \right], \quad (6-47)$$

where  $\rho_f$  is the fluid density,  $h_{cp}$  is the height at the center of the perforations, and  $h_i$  is the height from the bottom tip of the fracture to the top of the  $i$ th layer, as shown in Fig. 6-7.

This set of nonlinear equations can be solved by iteration. Assuming that the solution (two vertical tip positions plus the pressure) at one value of  $p_{cp}$  is known, a height increment is assumed. The incremental height growth in the two vertical directions is then calculated such that Eqs. 6-46 and 6-47 are both satisfied, and  $p_{cp}$  to obtain these positions is calculated. Finally, the width profile associated with this solution can be obtained as

$$w(y) = \frac{4}{E'} \left( p_{cp} + \rho_f g (h_{cp} - y) - \sigma_n \right) \sqrt{y(h_f - y)} + \frac{4}{\pi E'} \sum_{i=1}^{n-1} (\sigma_{i+1} - \sigma_i) \left[ (h_i - y) \cosh^{-1} \left( \frac{y}{|y - h_i|} \frac{h_f - 2h_i}{h_f} + \frac{h_i}{|y - h_i|} \right) + \sqrt{y(h_f - y)} \cos^{-1} \left( \frac{h_f - 2h_i}{h_f} \right) \right], \quad (6-48)$$

where  $y$  is the elevation measured from the bottom tip of the fracture.

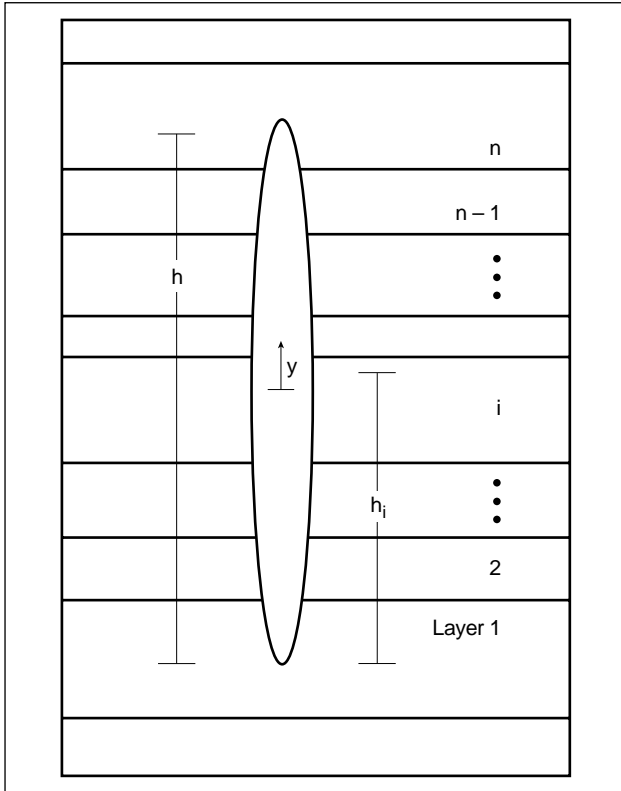


**Figure 6-7.** Definition of variables for the fracture containment problem.

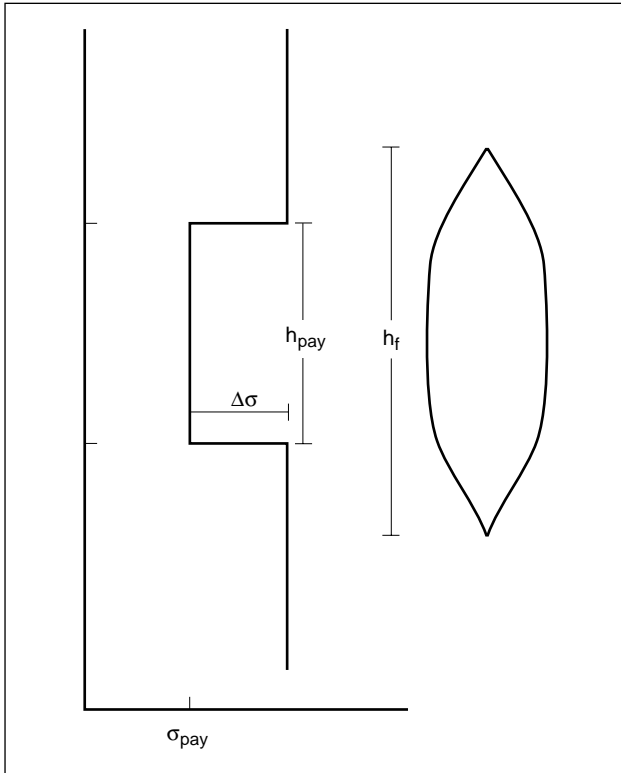


**Figure 6-8.** Simple three-layer height growth problem.

Consider, for example, the symmetric three-layer case shown in Fig. 6-8. If the gravitational component is neglected, so that the problem is symmetric, then the penetrations into the two barriers are equal. In this case, Eq. 6-46 can be simplified significantly and written as (Simonson *et al.*, 1978)

$$K_{Iu} = K_{II} = \sqrt{\frac{\pi h_f}{2} \left[ p_{cp} - \sigma_{pay} - \frac{2\Delta\sigma}{\pi} \cos^{-1} \left( \frac{h_{pay}}{h_f} \right) \right]}, \quad (6-49)$$

where  $\Delta\sigma$  is the difference in stress between the central layer (pay zone) and the surrounding layers, and  $h_{pay}$  and  $\sigma_{pay}$  are the thickness and stress of the pay zone, respectively. Figure 6-9 shows fracture height as a function of net pressure, as calculated by Eq. 6-49.

Although Eq. 6-49 is for a special case, it shows two interesting practical results. First, penetration into the barrier layers occurs at a critical net pressure:

$$p_{net,crit} = \sqrt{\frac{2K_{Ic}^2}{\pi h_f}}. \quad (6-50)$$

For example, if  $K_{Ic}$  is 2000 psi/in.<sup>1/2</sup> and  $h_f$  is 20 ft [240 in.], the critical net pressure for breakthrough

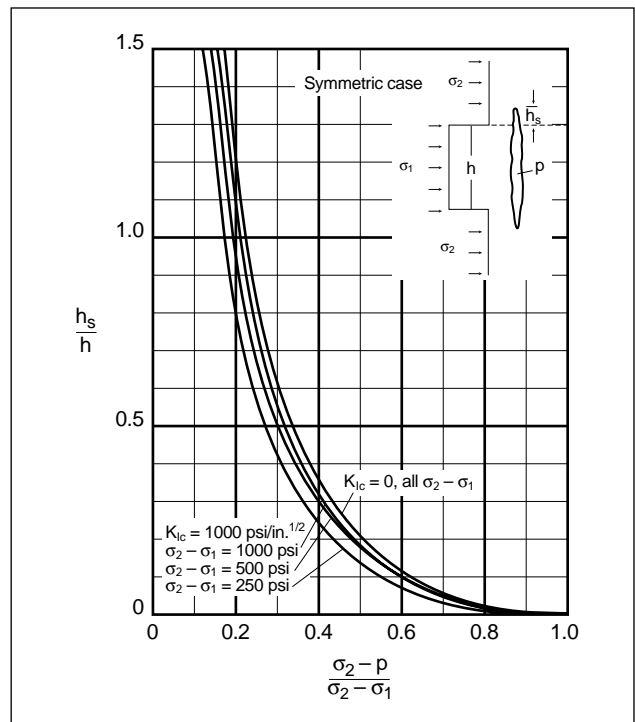


**Figure 6-9.** Fracture height versus net pressure for symmetric barriers.  $h_s$  = penetration into the boundary layer.

is only about 100 psi. Second, the net pressure cannot reach the stress contrast because this would result in infinite fracture height.

In a typical cell-based simulator, a table of these solutions is calculated prior to simulating the fracture evolution rather than at each time step of the calculation, and the relations among width, pressure and height are used to greatly speed up the solution of the fluid flow equations (conservation of mass and momentum).

- Fluid mechanics solution

One of the major differences between planar 3D and P3D models is the fluid flow calculation. The fluid flow model in most P3D models is the same as that introduced by Nordgren (1972) (i.e., a 1D version of the model described for the planar 3D model). In this model, both vertical flow and the variation of horizontal velocity as a function of vertical position are neglected. This results in the inability of typical P3D models to represent several aspects of behavior, namely (Smith and Klein, 1995)

- effect of variations in width in the vertical direction on fluid velocity
- local dehydration, which is approximated as simultaneous dehydration over the entire height of the fracture
- fluid loss after tip screenouts (TSOs), when fluid flow through the proppant pack is ignored
- proppant settling resulting from convection or gravity currents.

The average velocity and width are used (width is replaced by cross-sectional area divided by height) to simplify the conservation of mass (Eq. 6-38 for an incompressible fluid) to

$$\frac{\partial Au}{\partial x} + \frac{\partial A}{\partial t} = -2 \sum_i (u_L h_L)_i, \quad (6-51)$$

where  $u$  is the average cross-sectional velocity and  $u_L$  and  $h_L$  are the leakoff rate (Eq. 6-14) and height in each layer. Similarly, the conservation of momentum simplifies to

$$\frac{\partial p}{\partial x} = -\frac{\partial \tau_{xz}}{\partial z}. \quad (6-52)$$

For a power law fluid with properties  $n$  and  $K$ ,

$$\tau_{xz} = K \left( \frac{\partial u_x}{\partial z} \right)^n. \quad (6-53)$$

Solving Eq. 6-52 with Eq. 6-53 with the no-slip boundary condition (i.e., zero velocity at the fracture wall), the average velocity across the channel is

$$\bar{u}_x = -\text{sgn} \left( \frac{\partial p}{\partial x} \right) \left( \left| \frac{\partial p}{\partial x} \right| / K \right)^{1/n} \frac{n}{1+2n} \left( \frac{w}{2} \right)^{\frac{1+n}{n}}, \quad (6-54)$$

where  $\text{sgn}$  represents the sign of the quantity.

In the special case of a Newtonian fluid,  $n = 1$  and  $\mu = K$ , and Eq. 6-54 becomes

$$\bar{u}_x = -\frac{w^2}{12\mu} \frac{\partial p}{\partial x}. \quad (6-55)$$

To obtain the total flow rate across the height of the cross section, and hence an average velocity for substitution in Eq. 6-51, Eq. 6-54 is integrated from the bottom to the top tip of the cross section:

$$q = \int_{h_f} w(y) \bar{u}_x(y) dy. \quad (6-56)$$

The average velocity is thus determined as

$$u = \frac{q}{A} = -\text{sgn} \left( \frac{\partial p}{\partial x} \right) \Phi \left[ \left( \left| \frac{\partial p}{\partial x} \right| / 2K \right) \left( \frac{A}{h_f} \right)^{1+n} \right]^{1/n}, \quad (6-57)$$

where the channel function  $\Phi$  is

$$\Phi = \left( \frac{h_f}{A} \right)^{\frac{1+2n}{n}} \frac{n}{2+4n} \frac{1}{h_f} \int_{h_f} w(y)^{\frac{1+2n}{n}} dy. \quad (6-58)$$

Relations for the PKN model with power law fluids can be derived following this approach (see Nolte, 1979, 1991).

- Laminar and turbulent flow

When fluid flows between parallel plates at a low rate without leakoff, any fluid element remains a fixed distance from the wall of the channel, except in a small entrance region. This is known as laminar flow. By contrast, in turbulent flow, eddies occur, and fluid is continually mixed. This mixing results in added friction and different flow behavior. The Reynold's number  $N_{Re}$  (defined in Table 6G-1) enables determining whether laminar or turbulent flow will occur. If  $N_{Re}$  exceeds 2100, flow will be turbulent. Inside the fracture,  $N_{Re}$  is typically well below this value, except for particularly thin fluids, such as acid.

– Rheology of fracturing fluids

Fracturing fluids are generally treated as power law fluids, and because they are shear thinning (i.e., viscosity decreases with increasing shear rate),  $n$  is usually less than 1. The effective parameters of the power law model  $K'$  and  $n'$  are typically derived from laboratory measurements (see Chapter 8) over a range of shear rates. For shear-thinning fluids, the apparent viscosity (derived from  $K'$  and  $n'$ ) decreases as shear rate increases, and the viscosity would be infinite at zero shear rate. In reality, limiting low- and high-shear viscosities occur and must be considered.

Fracturing fluid properties change with time and temperature. Typically, exposure to high temperatures reduces fluid viscosity. However, crosslinkers may cause initial viscosity increases prior to the degradation. The effects of temperature and time are included in numerical hydraulic fracture simulators, typically by means of tables of  $K'$  and  $n'$  versus time at a series of temperatures, which are similar to those in service company handbooks.

• Numerical solution of the model

The three basic solutions described for height-growth mechanics (pressure-width-height relation), conservation of mass and conservation of momentum (velocity-pressure relation) are coupled and solved simultaneously. There are several methods by which the coupled equations may be solved, two of which are introduced here. Either a fixed or moving mesh may be used for the two methods, as described previously for planar 3D models. In this section, the explicit finite-difference method is introduced with a grid that moves with the fluid and an implicit method is described. In each case, prior to starting the simulation of the fracture evolution, a table of the pressure-height-width relation (from the equilibrium-height solution) is calculated as described for “Solid mechanics solution” in Section 6.3-2.

For the explicit finite-difference method, the fluid in the fracture at any time is divided into  $n$  elements, each with a cross-sectional area  $A_i$  and bounded by two vertical surfaces at  $x_i$  and  $x_{i+1}$ , moving at velocities  $u_i$  and  $u_{i+1}$ , respectively, as shown in Fig. 6-10. (The grid is numbered such that  $i = 1$  represents the tip to facilitate the addition

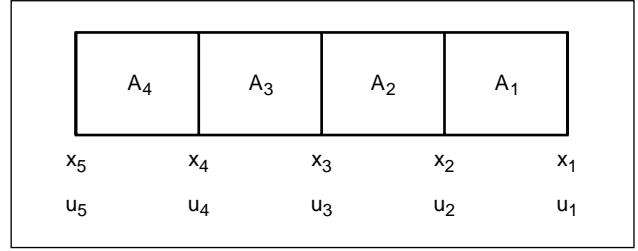


**Figure 6-10.** Fracture divided into elements with positions and velocities defined at grid points.

of new elements at the well, as necessary.) Mass-conservation Eq. 6-51 can be rewritten as

$$\frac{\partial A}{\partial t} = -2 \sum_i (h_L u_L)_i - \frac{\partial A u}{\partial x}, \quad (6-59)$$

with the derivatives replaced by central finite-difference approximations to obtain

$$A_i^{t+\Delta t} = A_i^t - \frac{h}{\Delta x} V_L + A_i^t (u_{i+1} - u_i) \frac{\Delta t}{\Delta x}, \quad (6-60)$$

where  $V_L$  represents the volume leaked off over the element of length  $\Delta x$  in time step  $\Delta t$ . The velocities are calculated at the grid points, and the area is assumed constant in each element. The cross-sectional area can thus be updated from the values of the velocities and areas at the previous time step. Once this has been done, the pressure at each cross section can be obtained from the solid mechanics solution by looking up the pressure in the precalculated pressure-height-width relation table for the corresponding area  $A$ . Pressure gradients can then be calculated using the approximation

$$\left. \frac{\partial p}{\partial x} \right|_i \approx \frac{p_{i-1} - p_i}{(x_{i-1} - x_{i+1})/2} \quad (6-61)$$

and new velocities obtained using Eq. 6-57. Once all the velocities are known at a given time, the positions of the grid points are updated using

$$x_i(t + \Delta t) = x_i(t) + u_i(t + \Delta t) \Delta t. \quad (6-62)$$

This method is known as a Lagrangian method because the grid coordinates move with the fluid. Leakoff causes each element to shrink and possibly even disappear as it penetrates farther into the fracture, limiting the usefulness of this method for modeling hydraulic fracturing treatments. In addition, new elements must continually be added at the wellbore. This makes it difficult to control how



many elements are present at any time or the sizes of the elements. Another approach is to introduce a fixed grid, as discussed for planar 3D models. This has the advantage that the number of elements in the simulation is relatively small near the beginning of the simulation when less accuracy is required and increases as the simulation progresses. Yet another approach is to introduce a moving mesh in which the grid points move at some reasonable velocity, for example, such that the fracture is always divided into a fixed number of equal-size elements (i.e., using a stretching coordinate system; see Sidebar 6H).

One of the primary limitations of explicit finite-difference methods, such as those introduced in the

preceding text, is that the time step used in the calculation may not exceed a critical value to ensure stability. Because only quantities from the previous step are used in moving forward, numerical errors can grow larger from step to step if the time step is too large. In the development of a general hydraulic fracturing simulator using such differencing schemes, the time step must be chosen carefully to avoid stability problems and yet minimize the computation time. A simple stability analysis is in Sidebar 6H.

It has been found that in cases of high leakoff or large widths (such as TSO designs), the critical time step for stability may be too small for efficient solution of the system, limiting the utility of the

## 6H. Stretching coordinate system and stability analysis

### Stretching coordinate system

One way to simplify grid point bookkeeping is to use a stretching coordinate system. If

$$X = \frac{x}{L(t)}, \quad (6H-1)$$

then  $X$  will always remain bounded between 0 and 1 while  $x$  varies between 0 and  $L(t)$ . Placing a grid on  $X$  will fully cover the fracture regardless of the growth characteristics. However, although the gridding is simplified, the complexity of the differential equation is increased. The derivatives are found as

$$\frac{\partial}{\partial x} = \frac{1}{L} \frac{\partial}{\partial X} \quad (6H-2)$$

$$\frac{\partial}{\partial t} = \frac{\partial}{\partial t} - \frac{X}{L} \frac{dL}{dt} \frac{\partial}{\partial X}. \quad (6H-3)$$

Equation 6-59 becomes

$$\frac{\partial A}{\partial t} - \frac{X}{L} \frac{dL}{dt} \frac{\partial A}{\partial X} = -\frac{1}{L} \frac{\partial q}{\partial X} - q_L, \quad (6H-4)$$

and the other equations of the system are similarly transformed.

### Stability analysis

A full stability analysis for a nonlinear system is difficult, but an approximate time-step limitation can be found as follows.

Assume that the pressure gradient can be written as

$$\frac{\partial p}{\partial x} = C_p \frac{\partial A}{\partial x}. \quad (6H-5)$$

In the case of the PKN model, where the fracture height  $h_f$  is fixed,  $C_p = \beta h_f$ , where  $\beta$  is defined by

$$p = \beta w. \quad (6H-6)$$

Substituting Eq. 6H-5 into Eq. 6-59 and applying the chain rule,

$$\frac{\partial A}{\partial t} = \frac{D}{n} A \left[ A^{1+n} \frac{\partial A}{\partial x} \right]^{1/n-1} \left[ A^{1+n} \frac{\partial^2 A}{\partial x^2} + (1+n) A^n \left( \frac{\partial A}{\partial x} \right)^2 \right], \quad (6H-7)$$

where absolute values must be assumed for all quantities, because an error analysis is being performed, and  $D$  is defined as

$$D = \frac{\Phi C_p^{1/n}}{(2Kh_f^{1+n})^{1/n}}. \quad (6H-8)$$

The highest order term in Eq. 6H-7 is

$$\frac{D}{n} A \left[ A^{1+n} \frac{\partial A}{\partial x} \right]^{1/n-1} \left[ A^{1+n} \frac{\partial^2 A}{\partial x^2} \right]. \quad (6H-9)$$

If the derivative is expanded using a central difference approximation, the term in  $A_i$  becomes

$$\frac{-2D}{n(\Delta x)^2} \frac{\partial A}{\partial x} A^{1/n-1} A^{3+1/n}. \quad (6H-10)$$

To investigate the effect of an error introduced into  $A$ ,  $A$  is replaced by  $A(1 + \epsilon)$ , which can be approximated (for small  $\epsilon$ ) as

$$\frac{-2D}{n(\Delta x)^2} \frac{\partial A}{\partial x} A^{1/n-1} A^{3+1/n} \left( 1 + \left( 3 + \frac{1}{n} \right) \epsilon \right). \quad (6H-11)$$

If a time step is taken (discretizing Eq. 6H-7 similar to Eq. 6-59), then the error  $\epsilon$  grows to

$$E = \Delta t \frac{-2D}{n(\Delta x)^2} \frac{\partial A}{\partial x} A^{1/n-1} A^{3+1/n} \left( 1 + \left( 3 + \frac{1}{n} \right) \epsilon \right). \quad (6H-12)$$

For this error to reduce in magnitude, it must be smaller than  $A\epsilon$ , which can occur only if

$$\Delta t < \frac{(\Delta x)^2}{2AC_p C_v}, \quad (6H-13)$$

where the viscosity leakoff control coefficient  $C_v$  is

$$C_v = -\frac{(3n+1)\nu}{\frac{\partial p}{\partial x} n^2}. \quad (6H-14)$$

explicit scheme. An implicit finite-difference scheme, with no time-step limitation, may eliminate this limitation. In essence, implicit and explicit methods can be distinguished by the fact that explicit methods solve for quantities at one time step on the basis of only values at the previous time steps, whereas implicit methods include the use of quantities at the current time. This implies that a set of equations is set up and solved, because the quantities at the current time step must all be found simultaneously. For linear problems, a set of linear equations results, and these are easily solved by standard methods such as gaussian elimination. For the 1D flow problem, the implicit finite-difference formulation yields a tridiagonal system of equations (i.e., a sparse matrix with only three diagonals filled with nonzeros). Highly efficient solution techniques are available to solve such systems (e.g., Carnahan *et al.*, 1969). For nonlinear problems, however, such methods can be complex and are not always much more efficient than explicit methods. Iteration is frequently required, because a nonlinear system is linearized. If the linearization approximation is inaccurate, it must be corrected and resolved.

Another method without the time-step limitation, and which avoids forming a system of equations, is a method using integrated or analytical elements. A similar method to that described in the following was the basis of the commercial time-sharing method made available by Amoco between 1981 and 1983 (Nolte, 1982, 1988a). Consider once again the basic equations of the PKN model with  $x = \phi$  at the tip:

$$w = \frac{2p_{nef}h_f}{E'} \quad (6-63)$$

$$\frac{dp}{dx} = \frac{64q\mu}{\pi h_f w^3}. \quad (6-64)$$

Substituting Eq. 6-64 for  $p$  into Eq. 6-63 obtains

$$\frac{E'}{2h_f} \frac{dw}{dx} = \frac{64q\mu}{\pi h_f w^3}. \quad (6-65)$$

Detailed numerical simulations have shown that the velocity varies much more slowly than the flow rate  $q$  because the reduction in width toward the tip partially compensates for fluid leakoff and storage in the fracture. Instead of the Perkins and Kern

(1961) assumption that  $q$  is constant (Eq. 6-10), replacing  $q$  by  $\pi u h_f w/4$  allows writing Eq. 6-65 as

$$\frac{dw}{dx} = \frac{32\mu h_f}{E' w^2} u \quad (6-66)$$

or

$$w^2 dw = \frac{32\mu h_f}{E'} u dx. \quad (6-67)$$

Integrating over a distance  $\Delta x$  obtains

$$w(x + \Delta x) = \left[ w^3(x) + \int_x^{x+\Delta x} \frac{96\mu h_f}{E'} u dx \right]^{1/3}. \quad (6-68)$$

If the terms under the integral can be assumed to be constant, this simplifies further to

$$w(x + \Delta x) = \left[ w^3(x) + \frac{96\mu h_f}{E'} u \Delta x \right]^{1/3}. \quad (6-69)$$

If the height is not constant and the fluid is non-Newtonian, a similar equation can be written for the cross-sectional area of the fracture by using the power law rheological parameters:

$$A_{i+1}^t = \left[ \left( A_i^t \right)^{n+2} + \frac{(n+2)\pi K h_f^{n+3}}{E' \Phi^n} u^n \Delta x \right]^{1/(n+2)}, \quad (6-70)$$

where

$$\Phi = \frac{n}{h_f(2+4n)} \int_{h_f} \left( \frac{w(y)}{\bar{w}} \right)^{\frac{1+2n}{n}} dy. \quad (6-71)$$

For an analytical solution,  $\Delta x$  would be the entire fracture length (Nolte, 1991), and this would be combined with a tip criterion and a volume-balance equation. The numerical solution proceeds similarly, except that  $\Delta x$  is chosen sufficiently small to obtain an accurate solution. Fluid loss is integrated over the time step, which allows obtaining acceptable accuracy, even with large time steps. The solution method at each time step is as follows:

1. Estimate a tip velocity.
2. For each element, working in from the tip to the well,
  - a. calculate an average fluid velocity based on the velocity at the outer side of the element and the estimated velocity at the inner side (At the first iteration, assume the inner fluid velocity is equal to the outer fluid velocity.)

- b. determine the cross-sectional area at the inner side of the element for the estimated velocity by using Eq. 6-70
  - c. determine the velocity at the inner side such that the leakoff and element volume change during the time step result in a mass balance
  - d. repeat the iteration using the new velocity.
3. Compare the actual flow into the fracture with the wellbore velocity calculated by the iterative scheme in the preceding step.
  4. Refine the estimate of the tip velocity using a Newton-Raphson method until volume balance is achieved, which typically takes two to four iterations.

This method of solving the equations is efficient because the velocity does not vary significantly along the fracture for typical cases. For typical PKN cases with a single fluid, the fracture can be divided into about 10 elements. For non-PKN cases, the grid must be chosen sufficiently fine that the integrand in Eq. 6-68 (which includes effects of fluid rheology and fracture height) is approximately constant in each element (because the solution scheme is derived with the assumption that it is constant).

Regardless of whether a moving- or fixed-grid method is used, usually only a small number of elements (about 10) is necessary to obtain a reasonably accurate solution to the equations described so far. However, other information may be required at a much finer resolution. To achieve this, the schedule is typically divided into a large number of substages (about 100). Quantities such as proppant concentration, fluid temperature and acid concentration can then be tracked on this finer grid. In addition, particularly in acid fracturing, it is desirable to track leakoff and etching on a finer grid. To do this for methods using a moving grid, a second grid that does not move is established. Quantities such as reservoir temperature, proppant bank height and leakoff volume in the reservoir are tracked on this solid-based grid.

- Nonequilibrium-height solution

It was noted in “Solid mechanics solution” in Section 6.3-2 that the assumption of slow height growth allows creating a pressure-height-width table prior to solving the equations of fracture evolution. This so-called equilibrium-height assumption

is quite accurate, provided that the fluid is moving relatively slowly in the vertical direction so that the pressure drop resulting from vertical fluid flow is negligible. This assumption is violated if high-permeability zones are exposed, because fluid must then move rapidly because of the increased leakoff in such layers. Also, if the stress in the surrounding zones is insufficient to confine the fracture and the vertical tips extend quickly, then the fluid must move quickly to fill the resulting fracture. In either of these cases, the pressure gradient resulting from vertical fluid flow may become large, and the equilibrium-height assumption becomes invalid at these locations in the fracture.

To remove this assumption and obtain valid results from a simulator, some restriction must be placed on height growth. For nonequilibrium-height growth, the pressure gradient because of fluid flow in the vertical direction must be approximated, based on the rate of height growth. It is common to base this approximation on the KGD model (e.g., Settari and Cleary, 1982). In Section 6-7 on tip effects, an analytical near-tip solution developed by Lenoach (1994) is discussed that provides an expression for the net pressure of the form

$$p_{net} = E' \left( \frac{2\sqrt{2}(2+n)}{\pi(2-n)} \right) \times \left[ \frac{K}{E' h_f^n} \left( \frac{\cos((1-\beta)\pi)}{\sin(\beta\pi)} \right)^{1+n} \left( \frac{(2n+1)^n}{n(2+n)^n} \right)^{1/(2+n)} u_{tip}^{n/(2+n)} \right], \quad (6-72)$$

where  $u_{tip}$  is the tip velocity and  $\beta$  is  $2/(2+n)$ . As previously noted, for a fracture under constant pressure, the stress intensity factor is related to the net pressure by

$$p_{net} = \frac{K_{Ic}}{\sqrt{\pi h_f/2}}. \quad (6-73)$$

The Lenoach tip solution can be used to obtain an apparent fracture toughness caused by the non-zero tip velocity by combining Eqs. 6-72 and 6-73. This effect can be added to the actual rock toughness, and the sum is used in Eqs. 6-46 and 6-47 instead of the actual rock toughness to determine the fracture height growth. The basic algorithm used to move from one pair of vertical tip positions to another during a time step is as follows:

1. Estimate the top and bottom tip velocities for the cell.
2. Calculate the new fracture tip positions at the end of the time step, using these velocities.
3. Calculate the stress intensity factors from Eqs. 6-46 and 6-47.
4. Determine the excess stress intensity factors (i.e., the calculated value minus the rock toughness).
5. Calculate the velocities required to generate these excess stress intensity factors, using Eqs. 6-72 and 6-73.
6. Compare the velocities with the guessed values and iterate until the correct velocities are found.

One of the advantages of the equilibrium-height models is the speed gained by precalculating a table of the fracture height-pressure relation. Not only is this not possible for the nonequilibrium model, but the iterative process to determine the tip positions can be time consuming. The nonequilibrium-height algorithm should therefore be used only when necessary because of the apparent rapid height growth indicated by the equilibrium-height calculation.

- Lateral coupling

In the description of the solid mechanics solution provided previously, the basic assumption is that individual cross sections act independently (i.e., plane strain in the horizontal direction, or laterally decoupled). This is implicit in the assumption that the pressure and width at any point are uniquely related. In reality, the pressure at any point is dependent not only on the local width, but also on the width distribution over the entire fracture, as discussed in Section 6-3.1 on planar 3D models. This lateral coupling is generally not important, unless the fracture wing length is less than the height. Even then, the fracture geometry will not be significantly different if lateral coupling is neglected, although the pressure response may be underestimated. Lateral coupling can be included in the solutions described previously (see Sidebar 6E).

The effect of lateral coupling during pumping is to increase the pressure at and near the well and to decrease it near the tip. Figure 6-11 shows the evolution of pressure during a treatment for a confined fracture simulated using the KGD, PKN and later-

ally coupled PKN models. The pressure predicted by the laterally coupled model is always higher than either the KGD or PKN solution would predict. It can also be shown that the width at the well is always smaller than that predicted by either of the simple models. The point in Fig. 6-11 where the pressure from the laterally coupled model is lowest (and where the pressures from the KGD and PKN models are equal) corresponds to a square, where the fracture wing length is one-half of the height. The pressure calculated by the laterally coupled model exceeds that predicted by the KGD or PKN model at this time by approximately 40%, which is comparable to the pressure in a radial fracture of similar dimensions.

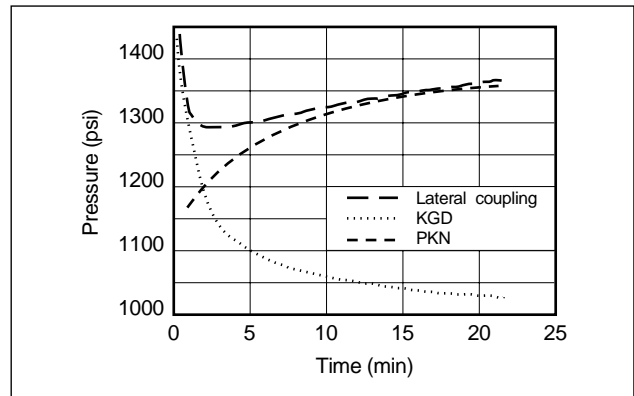


**Figure 6-11.** Pressure record with and without lateral coupling.

### 6-3.3. Lumped pseudo-three-dimensional models

Lumped models are an alternative to cell-based models and were first introduced by Cleary (1980b). Although more details are presented in subsequent paragraphs, it is worthwhile at this point to quote two sentences from the conclusions of his paper: “the heart of the formulae can be extracted very simply by a nondimensionalization of the governing equations; the remainder just involves a good physico-mathematical choice of the undetermined coefficients” and “results could be presented in the usual format of design charts, based on dimensionless groups extracted, . . . [a] more appealing procedure may be to program the solutions for a suitable pocket calculator, with the separately determinable  $\gamma$  or  $\Gamma$  coefficients and job parameters as input.” Although numerous papers have

been presented on the use of this model (e.g., Cleary *et al.*, 1994), which is now on laptop computers rather than pocket calculators, these sentences capture the essence of lumped models in that they are extremely simple models and the key to their successful use is the selection of appropriate coefficients for the problem analyzed.

Like all the models presented previously, the starting point of the lumped model is the set of basic equations defining the hydraulic fracturing process, which are mass conservation (Eq. 6-39), the relation between the distribution of crack opening over the length of the fracture  $2L$ , net pressure distribution (similar to Eq. 6-36) expressed as

$$p_{net}(x) = \int_{-L}^L I(x, x') w(x') dx', \quad (6-74)$$

and conservation of momentum (Eq. 6-40) expressed as

$$\tilde{q} q^{m-1} = -\gamma_4 w^{2n-m+1} \tilde{\nabla} p / \mu, \quad (6-75)$$

where  $\gamma_4$  is the channel factor ( $1/2$  for a Newtonian fluid), and various combinations of the power law factors  $m$  for turbulence and  $n$  enable consideration of both non-Newtonian fluids and turbulent flow.

In the lumped models, these equations are simplified by assuming a fracture shape and adopting a spatial averaging approach to reduce them to ordinary differential equations in time. This approach implicitly requires the assumption of a self-similar fracture shape (i.e., one that is the same as time evolves, except for a length scale). The shape is generally assumed to consist of two half-ellipses of equal lateral extent, but with different vertical extent.

It is instructive to consider some of the lumped equations for the KGD model (Cleary, 1980b). The mass balance is obtained by averaging over the fracture length:

$$\rho(q\bar{w} - Lq_L) = d(\gamma_3 \rho \bar{w} L) / dt, \quad (6-76)$$

where

$$\bar{w} \approx (\gamma_1 p_{net} / E) L \quad (6-77)$$

$$q^m \bar{w}^m \approx \gamma_5^m (\bar{w})^{2n+2} / L^2, \quad (6-78)$$

where

$$\gamma_5^m \equiv \gamma_2 \gamma_4 E / (\gamma_1 \mu), \quad (6-79)$$

which is the 1D form of Eq. 6-75. Equation 6-76 is similar to Eq. 6-15 (based on Carter, 1957) with the

addition of  $\gamma_3$ , and Eq. 6-77 is identical to that of Geertsma and de Klerk (1969) with  $\gamma_3$  replacing  $4(1 - \nu^2)$ . Superficially, these equations are extremely simple, but the values of the  $\gamma$  coefficients are not always obvious and may not be constant. As noted by Crockett *et al.* (1989), these models are extremely general, with the degree of accuracy limited ultimately only by the effort invested in determination of the  $\gamma$  coefficients by detailed simulations, laboratory experiments or field studies.

For more general fracture shapes (i.e., with height growth), it is typically assumed that height growth is governed by a KGD-type solution and length growth by a PKN-type solution (Cleary *et al.*, 1983), although this is not a theoretical limitation of lumped models.

One area in which lumped models have been exploited extensively is in the development of computer software systems to apply and use pressure data during a treatment. Some of the key characteristics and requirements for such a software system are that (Crockett *et al.*, 1989)

- the physics is realistic and general
- execution time is much faster than treatment time to allow repetitive execution for pressure history matching
- the software can use improved estimates of parameters obtained in real time (i.e., during the treatment).

Although these real-time software systems are generally referred to as real-time hydraulic fracture models (e.g., Crockett *et al.*, 1989), the model itself is only a small part of the software and should address the first requirement listed (i.e., realistic and general physics). The second and third requirements are computer hardware and software design constraints. Because lumped models were developed for pocket calculators in 1980, they impose a minimal impact on computer hardware and systems. As computing power continues to improve, it will become possible to run increasingly sophisticated models during treatment execution either at the wellsite or remotely. There are other software design issues, such as robust execution with a wide variety of parameter values, easy import and superposition of actual data on model output, and graphical display, that are required for a useful software system for real-time applications. Discussion of these issues is beyond the scope of this volume.

## 6-4. Leakoff

One of the key issues in designing a fracture treatment is accurate knowledge of how rapidly fluid will leak out of the fracture into the reservoir. Without this information, it would be impossible to design a treatment that provides a specified fracture geometry. Mini-fracture treatments are performed to estimate the leakoff coefficient (see Chapter 9). Equation 6-14 introduced in “Inclusion of leakoff” in Section 6-2.2 is the basic equation of filtration and was first used for fracturing by Carter (1957). He showed that it was applicable for three separate leakoff processes:

- displacement and compressibility of reservoir fluid
- invasion of the formation by filtrate or fracturing fluid
- buildup of an external filter cake.

Williams (1970) divided the leakoff into three time periods, rather than considering the three processes. During the initial period, leakoff is quick, followed by a decreasing leakoff rate and finally a steady-state leakoff rate. In the initial period, filter cake has not formed, so the leakoff rate is controlled by the resistance of the formation to flow of the fracturing fluid. The external filter cake builds during the second period. Finally, the cake stops building, because the high-velocity fluid in the fracture prevents further polymer deposition. This last stage is referred to as dynamic leakoff. Williams lumped all leakoff prior to dynamic leakoff into a quantity he called spurt volume, although spurt loss has since been generally accepted to refer only to the initial high-leakoff period before the cake starts building.

Settari (1985) presented an excellent review of the classic leakoff model, as well as an even more general model of leakoff that represents an excellent framework for leakoff modeling. In the following sections, each of the three processes (displacement and compressibility of reservoir fluid, invasion of the formation by filtrate or fracturing fluid and buildup of filter cakes, either externally on low-permeability rocks or internally on high-permeability rocks) is considered as if it is the only one acting and then in combination. Finally, Settari's general model is summarized.

The fluid-loss derivations in Eqs. 6-82 through 6-91 are for the pressure drop for individual loss mechanisms. For general application, they are in terms of the total pressure drop between the fracture and initial reservoir pressures in Eqs. 6-94 through 6-96 and in oilfield units in Eqs. 8-26 and 8-27.

### 6-4.1. Filter cake

In laboratory filtration experiments performed at constant pressure, the rate of filtration is proportional to the square root of time (see Chapter 8). A model for this process can be derived by assuming that

- the amount of cake deposited is proportional to the volume of fluid  $V_L$  passed through a unit surface area
- cake permeability  $k_{cake}$  is independent of its thickness
- flow through the cake obeys Darcy's law
- pressure drop across the cake  $\Delta p_{cake}$  is constant

to write

$$u_L = \frac{dV_L}{dt} = \frac{k_{cake}}{\mu_{fil}} \frac{\alpha \Delta p_{cake}}{V_L}, \quad (6-80)$$

where  $\mu_{fil}$  is the viscosity of the filtrate and it is assumed that the cake thickness  $L_{cake}$  is proportional to the fluid volume lost; i.e.,  $V_L = \alpha L_{cake}$ . By integrating for  $V_L$ , it can be shown that

$$u_L = C_w / \sqrt{t}, \quad (6-81)$$

where the fluid-loss coefficient through the wall filter cake is

$$C_w = \sqrt{\frac{k_{cake} \alpha \Delta p_{cake}}{2\mu_{fil}}}. \quad (6-82)$$

Carter (1957) proposed that the volume leaked off can then be determined as

$$V_L = 2C_w \sqrt{t} + S_p, \quad (6-83)$$

where  $S_p$  is the volume that leaks off without forming a filter cake and can be interpreted as an integration constant. A more appropriate physical model is to assume that the initial volume that leaks off, without building a cake, is the spurt volume and that Eq. 6-80 applies after the cake is established. This interpretation results in

$$V_L = 2C_w \sqrt{t - t_{sp}} + S_p, \quad (6-84)$$

where  $t_{sp}$  is the spurt time.

Another approach to account for leakoff by using standard petroleum engineering concepts of reservoir permeability and treating the filter cake as a pressure-dependent resistance is outlined in Chapter 2 along with high-permeability conditions (Valkó and Economides, 1997). The following approach to the leakoff coefficient is as presented by Settari (1985).

### 6-4.2. Filtrate zone

The first zone inside the reservoir is called the filtrate zone or invaded zone. It is assumed that

- pressure drop  $\Delta p_v$  across the zone is constant
- filtrate fully displaces the mobile phase(s) within the formation, resulting in piston-like displacement and 100% filtrate saturation
- the fluid and rock are incompressible

to write

$$u_L = \frac{dV_L}{dt} = \frac{k_{fil}}{\mu_{fil}} \frac{\Delta p_v}{L_v}, \quad (6-85)$$

where  $k_{fil}$  is the permeability related to the filtrate and  $L_v$  is the length of the invaded zone. Integrating this equation, with the assumption that

$$L_v = V_L / \phi = \frac{1}{\phi} \int u_L dt, \quad (6-86)$$

where  $\phi$  is the porosity, obtains

$$u_L = \frac{C_v}{\sqrt{t}}, \quad (6-87)$$

where the viscosity control leakoff coefficient  $C_v$  is

$$C_v = \sqrt{\frac{k_{fil} \phi \Delta p_v}{2\mu_{fil}}} \quad (6-88)$$

and the leakoff volume at any time is

$$V_L = 2C_v \sqrt{t}. \quad (6-89)$$

The permeability to the filtrate  $k_{fil}$  reflects the relative permeability of the formation to flow of the filtrate. This effect may be significant when a water filtrate enters a hydrocarbon zone at nearly irreducible water saturation.

### 6-4.3. Reservoir zone

Although the uninvaded reservoir does not contain fracturing fluid, pressure is required to displace the reservoir fluid away from the fracture face. Assuming

- constant pressure drop  $\Delta p_c$  between the filtrate/reservoir interface and the far-field reservoir
- compressible flow with constant total compressibility  $c_t$
- relatively slow movement of the front of the invading fluid
- an infinite reservoir,

the front can be treated as the face of an infinite porous medium, and an analytical solution (Collins, 1961) is used to obtain

$$u_L = \frac{C_c}{\sqrt{t}}, \quad (6-90)$$

where the compressibility control leakoff coefficient  $C_c$  is

$$C_c = \sqrt{\frac{k_r c_t \phi}{\pi \mu_r}} \Delta p_c, \quad (6-91)$$

where  $k_r$  is the permeability of the reservoir rock and  $\mu_r$  is the reservoir fluid viscosity.

### 6-4.4. Combined mechanisms

In practice, all three processes occur simultaneously. The leakoff velocities in Eqs. 6-80, 6-85 and 6-90 must be equal, and the sum of the pressure drops must equal the total pressure difference between the reservoir pressure and the fracturing pressure:

$$\frac{C_t}{\sqrt{t}} = \sqrt{\frac{k_{cake} \alpha \Delta p_{cake}}{2\mu_{fil}(t-t_{sp})}} = \sqrt{\frac{k_{fil} \phi \Delta p_v}{2\mu_{fil}t}} = \sqrt{\frac{k_r c_t \phi}{\pi \mu_r t}} \Delta p_c \quad (6-92)$$

$$\Delta p_{cake} + \Delta p_v + \Delta p_c = \Delta p_{total}, \quad (6-93)$$

where  $C_t$  is the total leakoff coefficient and  $\Delta p_{total}$  is the difference between the pressure in the fracture and the far-field reservoir pressure  $p_r$ . If the spurt volume and time can be neglected, these equations can be combined (Williams *et al.*, 1979) to yield the total leakoff coefficient:

$$C_t = C_{wcv} = \frac{2C_c C_v C_w}{C_v C_w + \sqrt{C_w^2 C_v^2 + 4C_c^2 (C_v^2 + C_w^2)}} \quad (6-94)$$

with the coefficients  $C_w$ ,  $C_c$  and  $C_v$  calculated using the overall pressure difference.

Equation 6-94 is valid only if the cake permeability is independent of pressure. If the cake is highly compressible and the cake permeability is approximately proportional to  $1/\Delta p$ , Nolte (1988a) has shown that the fluid loss is limited either by the cake or the reservoir. In that case, the fluid-loss rate is the minimum of Eq. 6-81, with the pressure drop equal to the total pressure drop, or

$$u_L = \frac{C_{cv}}{\sqrt{t}}, \quad (6-95)$$

where the combined leakoff coefficient is

$$C_{cv} = \frac{2C_c C_v}{C_v + \sqrt{C_v^2 + 4C_c^2}} \quad (6-96)$$

with the coefficients  $C_c$  and  $C_v$  again calculated using the total pressure difference.

#### 6-4.5. General model of leakoff

A great deal of complexity can be added to the leakoff model in an attempt to account for detailed behavior such as the compressibility of the invading fluid and the moving boundary of the reservoir fluid. Given the accuracy with which the other parameters in a hydraulic fracture treatment are known, the inclusion of such effects is generally unnecessary. This section describes modification of the models to incorporate the two effects of the variable pressure difference and changing fluid properties.

The model described in previous sections can be generalized to account for multiple fluids. Settari (1985) showed that the fluid loss in the invaded zone can be described by replacing the term  $C_v$  with an equivalent term:

$$\bar{C}_v = \frac{2C_v^2 \sqrt{t}}{V_L}, \quad (6-97)$$

where  $C_v$  is calculated using the average viscosity and relative permeability of all the filtrate leaked off to the current time, and  $V_L$  is the fluid volume that previously leaked off into the reservoir. Settari also showed that replacing the wall-building coefficient for the fluid under consideration with an equivalent value would account for variations in leakoff behavior between fluids in a treatment. The equivalent value in this case is

$$\bar{C}_w = \frac{2C_w^2 \sqrt{t}}{V_L}, \quad (6-98)$$

where the previously leaked-off fluid volume  $V_L$  has also contributed to wall building.

The critical fluid component affecting wall building is the gel and/or fluid-loss additive concentration. An extension to Settari's model can be derived by considering Eq. 6-80, in which the thickness of the cake is assumed to be proportional not to the volume flowed through the wall but to the volume of gel deposited. Thus, the thickness is proportional not to the time-integrated velocity but to the integral over time of the

product of gel concentration and fluid velocity. In this case, Eq. 6-98 is replaced by

$$\bar{C}_w = \frac{2C_{gel} C_w^2 \sqrt{t}}{M_{gel}}, \quad (6-99)$$

where  $C_{gel}$  is the gel mass concentration in the fluid and  $M_{gel}$  is its specific density. There is an implicit assumption that the term  $C_{gel} C_w^2$  is constant. This assumption is consistent with laboratory work reported by Mayerhofer *et al.* (1991). The viscosity of water decreases with increasing temperature, and this effect on the leakoff coefficient should be included in the fracture model.

#### 6-4.6. Other effects

##### • Pressure evolution during treatment

If an estimate of the leakoff coefficient has been obtained from a mini-fracture decline analysis, then the most likely way to use the simulator would be to enter the total leakoff coefficient derived from the analysis. It is thus assumed that the leakoff behavior during the minifracture is the best representation of what will occur during the main treatment. However, if the leakoff behavior is unknown and is to be determined from fluid and reservoir properties, the best approach is to enter a laboratory-determined wall-building coefficient for each fluid and use the simulator to determine the total leakoff coefficient at each position in the fracture as a function of time and on the basis of the continually evolving pressure difference between the fracture and the reservoir. Except in overpressured reservoirs, the assumption of a constant total pressure difference is generally reasonable. The ratio of leakoff coefficients between the lowest pressure difference during the treatment (when the net pressure is zero and the pressure difference between the closure stress and the reservoir pressure is just  $\Delta p = \sigma_c - p_r$ ) and at the end of pumping (when it is  $\Delta p = p_{net} + \sigma_c - p_r$ ) is given for reservoir-controlled leakoff by

$$\frac{C_c(p_{net} = 0)}{C_c(p_{net} = p_{net,max})} = \frac{\sigma_c - p_r}{p_{net,max} + \sigma_c - p_r} \quad (6-100)$$

and for the wall-building or viscosity-controlled cases by

$$\frac{C_L(p_{net} = 0)}{C_L(p_{net} = p_{net,max})} = \sqrt{\frac{\sigma_c - p_r}{p_{net,max} + \sigma_c - p_r}}. \quad (6-101)$$



If the ratio is close to 1, a constant leakoff model can be used, in which the leakoff coefficients ( $C_c$ ,  $C_v$  and  $C_w$ ) for each fluid in the treatment can be precalculated on the basis of an assumed typical net pressure (e.g., 250 psi). If the effect of pressure changes is large, a variable leakoff model can be used, in which the pressure changes in the fracture are accounted for as the simulation proceeds. In this case, the reservoir component of leakoff  $C_c$  should be determined using a convolution of the pressure history during the treatment.

- Pressure-sensitive leakoff

One of the major assumptions of the analysis in the previous sections is that the permeability remains constant. In fact, many reservoirs may have fissures or other features that may open under the influence of the fracture treatment. The effect of this opening is to increase the leakoff rate (Warpinski, 1991). Pressure-sensitive leakoff is addressed more fully in Chapter 9.

- Poroelasticity and backstress

Chapter 3 discusses the influence of pore pressure on rock mass behavior. Poroelastic effects are changes in stress that occur as a result of changes in pore pressure in the reservoir. As fluid leaks out of the fracture into the reservoir, the affected part of the reservoir dilates, and a “backstress” develops, which increases the effective closure pressure. This effect is generally small, but it may be important in some cases, as discussed by Nolte *et al.* (1993). Chapter 3 provides the solution for a fracture in an infinite, homogeneous medium. Although the additional pressure results in an increased net pressure in the fracture, it generally has little effect on fracture geometry.

## 6-5. Proppant placement

The objective of hydraulic fracturing is to place proppant to provide a conductive path for production. The presence of proppant introduces three important issues in the behavior of fluids in hydraulic fractures:

- effect of proppant on fluid rheology
- convection or gravity currents
- proppant transport.

### 6-5.1. Effect of proppant on fracturing fluid rheology

Generally the viscosity of a proppant-laden slurry  $\mu_{slurry}$  is higher than that of the carrying fluid  $\mu_{base}$  alone. Experimental relations are well established for Newtonian fluids, but much less so for power law fluids. Nolte (1988b) showed that relations for power law fluids could be obtained by using the relations for Newtonian fluids and raising them to the power of  $n$ . For example, the viscosity ratio  $\mu_r$  could be obtained as

$$\mu_r = \frac{\mu_{slurry}}{\mu_{base}} = \frac{1}{(1 - f_v / f_{vM})^{2.5n}}, \quad (6-102)$$

where  $f_v$  is the proppant volume fraction, and  $f_{vM}$  is the maximum fraction for a mobile slurry.

### 6-5.2. Convection

Density differences between fluids may result in the denser fluid flowing under the lighter fluid or the lighter fluid overriding the denser fluid. This phenomenon, known as convection or gravitational flow, is important in many fields, such as saltwater intrusion under fresh water (Badon Ghyben, 1888; Herzberg, 1901). In fracturing, it may be relevant if a high-density slurry stage flows under a previously pumped stage or pad, as well as for other 2D aspects of fluid flow, such as those considered by Clifton and Wang (1988).

The fluid flow equations for a Newtonian fluid can be written as

$$\begin{aligned} u_x &= \frac{-w^2}{12\mu} \frac{\partial p}{\partial x} \\ u_y &= \frac{-w^2}{12\mu} \left( \frac{\partial p}{\partial y} + \rho g \right) \end{aligned} \quad (6-103)$$

and (Eq. 6-38 for incompressible fluids)

$$\left( \frac{\partial(wu_x)}{\partial x} + \frac{\partial(wu_y)}{\partial y} \right) + \frac{\partial w}{\partial t} + 2u_L = 0. \quad (6-104)$$

Substituting Eq. 6-103 into Eq. 6-104 obtains

$$\frac{1}{12\mu} \left( \frac{\partial^2 w^3 p}{\partial x^2} + \frac{\partial^2 w^3 p}{\partial y^2} \right) = \frac{\partial w}{\partial t} + 2u_L - \frac{1}{12\mu} \frac{\partial w^3 \rho g}{\partial y}. \quad (6-105)$$

The last (gravitational) term on the right-hand side of Eq. 6-105 is the convective term. This can be treated as a source term, just as the other two terms are storage or sink terms, resulting from width change and leakoff. Baree and Conway (1994), Unwin and Hammond (1995) and Smith and Klein (1995) showed that this is generally not significant for most properly designed fracturing treatments. Smith and Klein showed that if excess pad was pumped, the fluid flow after pumping stops (i.e., afterflow) could lead to convection until the pad leaked off. Also, Eq. 6-105 shows the extreme sensitivity of convection to fracture width. If the width is large (e.g., in a low-modulus rock), convection may be more critical. Fortunately, such low moduli are usually associated with high permeabilities, in which case TSO designs and rapid leakoff after shut-in effectively prevent convection. Cleary and Fonseca (1992) presented a dimensionless number that reflects the ratio of buoyant and viscous forces. This ratio can be used to estimate the effect of different conditions on the severity of convection.

Finally, Clark and Courington's (1994) and Clark and Zhu's (1994) experiments on convection largely verify the theoretical and numerical results described here.

### 6-5.3. Proppant transport

Hydraulic fracturing produces a conductive channel by placing proppant in a crack created in a pay zone. Hence, an essential consideration in fracturing fluid design is to accomplish proppant transport. The effect of convection on proppant transport was previously discussed. There are two other factors that may impact proppant placement. The first, and most commonly understood, is settling. If a bottle containing a mixture of sand and water is shaken up and then left on a table, the sand will settle out of the water. It can be shown theoretically that the terminal velocity of a single particle far from any walls in a stagnant Newtonian fluid is given by Stokes law:

$$u_{\infty} = \frac{g(\rho_{sol} - \rho_f)d_{sol}^2}{18\mu}, \quad (6-106)$$

where  $\rho_{sol}$  is the solid particle density,  $\rho_f$  is the fluid density, and  $d_{sol}$  is the solid particle diameter.

The assumptions of this equation are of limited applicability in hydraulic fracturing because the fluids are non-Newtonian and the particles are highly con-

centrated and may be close to the channel walls, which causes two effects: hindered settling, which implies that particles get in the way of each other, and clustered settling, in which particles join together, effectively increasing the diameter in Eq. 6-106. Novotny (1977) presented a correlation for the particle velocity  $u_{sol}$  in hindered settling in terms of the volume fraction of solids  $f_v$ :

$$u_{sol} = u_{\infty} F(f_v), \quad (6-107)$$

where

$$F(f_v) = (1 - f_v)^{\beta} \quad (6-108)$$

and the exponent  $\beta$  ranges from 5.5 at low values of  $N_{Re}$  to 2 at high values of  $N_{Re}$ . For power law fluids, a generalized form of Stokes law (Eq. 6-106) is used:

$$u_{\infty} = \left[ \frac{(\rho_{sol} - \rho_f)gd_{sol}^{n+1}}{3^{n-1}18K'} \right]^{1/n}. \quad (6-109)$$

Equation 6-108 can still be used to account for hindered settling. Other correlations have been developed, but a definitive correlation has not appeared in the literature. Many fracturing fluids are designed for almost perfect transport, so the settling rate is usually not important unless the fracture remains open for a long time after pumping stops.

Another effect on proppant placement is fluid migration (Nolte, 1988b) or encapsulation (Cleary and Fonseca, 1992). Fracturing fluids are generally viscoelastic. Although it is beyond the scope of this section to discuss this phenomenon in detail, one of its important effects is to drive proppant to the center of the flow channel. This migration could result in a dense sheet near the center of the channel, surrounded by clear fluid. This has the effect of accelerating particle settling, especially for low proppant concentrations. Unwin and Hammond (1995) presented simulations showing the effect of this migration on proppant placement.

## 6-6. Heat transfer models

The properties of many fracturing fluids show some dependence on temperature. In addition, the rates of the reactions that occur in acid fracturing are dependent on temperature. In a typical fracturing treatment, the fluid is pumped at a temperature signifi-

cantly below the reservoir temperature. As the fluid penetrates farther into the fracture, heat transfer occurs between the fracturing fluid and the rock, resulting in an increase in fluid temperature.

The temperature gradient in the direction perpendicular to the fracture wall is significantly larger than those in other directions, so the temperature gradients in the other directions can be neglected. In addition, heat conduction in the fluid can be ignored because it is small relative to both conduction in the rock and transport of heat with the moving fluid. These assumptions reduce the heat transfer problem to a 1D problem perpendicular to the fracture wall, with conduction through the rock to the fracture face and convection from the rock face into the fluid.

### 6-6.1. Historical heat transfer models

The first significant thermal model for hydraulic fracturing was published by Whitsitt and Dysart (1970). To obtain an analytical solution, they assumed a leakoff rate that varies linearly from zero at the well to a maximum at the fracture tip and accounted for the inhibiting effect of the leakoff, which occurs in the opposite direction to the heat transfer. Unfortunately, the solution they obtained contains an integral that must be evaluated numerically. Two of their more significant contributions are demonstration of the effect of temperature on acid reaction rates for acid fractures and that the temperature in much of the fracture is well below the reservoir temperature, so that fluids could be designed for lower temperatures than previously believed.

Sinclair (1971) obtained a solution to a similar problem, except that he assumed a uniform leakoff rate along the fracture. An example of the results is shown in Fig. 6-12. The significance of this figure is the relatively small fluid heat-up that occurs when the fluid efficiency is low. For an efficiency of 10%, the temperature in the fracture is approximately the inlet temperature over about 80% of the fracture length. At higher efficiencies, a more rapid heat-up occurs, so that about 50% or more of the fracture length is at or close to the reservoir temperature.

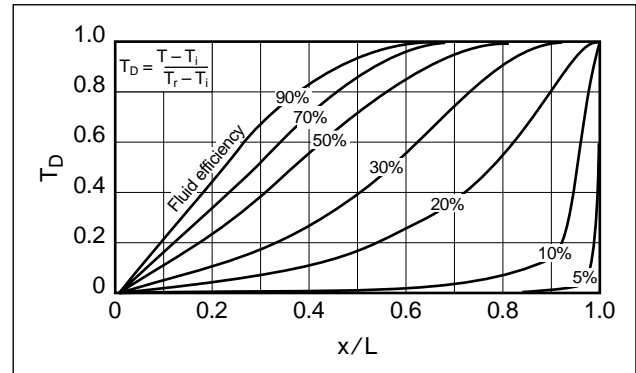


**Figure 6-12.** Temperature profile in a fracture for different fluid efficiencies.  $T_D$  = dimensionless temperature,  $T$  = absolute temperature,  $T_i$  = fluid temperature at the fracture mouth,  $T_r$  = reservoir temperature.

### 6-6.2. Improved heat transfer models

Meyer (1987) developed a solution that accounts for a finite-film, or convective, coefficient for heat transfer between the rock and the fluid and also introduced the power law Nusselt number to determine the value of the convective heat transfer coefficient. This showed that the effect of the finite-film coefficient is to reduce the rate of fluid heat-up.

Kamphuis *et al.* (1993) developed a numerical simulator that accounted for similar effects. One of the advantages of the numerical model is that it allows including more effects, such as variable pump rate during the treatment, and, of more practical importance, calculating temperature changes after shut-in. This model requires the introduction of a calculation grid in the rock.

Another algorithm has been developed to solve the heat transfer problem (see Sidebar 6I). It has many of the advantages of the numerical solution mentioned previously but is extremely computationally efficient. The equation for the fluid temperature is unconditionally stable; i.e., there is no upper limit on the time step. The results of simulation with this method compare favorably with the full numerical solution of Kamphuis *et al.* (see Sidebar 6J).

## 6-7. Fracture tip effects

All fracture models include the effects of rock deformation (width), mass transport and fluid loss in similar ways. However, the failure and opening of the fracture

## 6I. Efficient heat transfer algorithm

Mack and Elbel (1994) presented an efficient algorithm for the calculation of temperature changes in hydraulic fractures.

Consider a semi-infinite rock mass with constant surface flux  $F_0$  starting at time zero. The temperature change of the rock surface  $\Delta T_{surf}$  as a function of time  $t$  is (Carslaw and Jaeger, 1959)

$$\Delta T_{surf} = -C_0 F_0 \sqrt{t}, \quad (6I-1)$$

where

$$C_0 = \frac{2}{k_h} \left( \frac{\kappa}{\pi} \right)^{1/2}, \quad (6I-2)$$

where  $k_h$  is the thermal conductivity of a solid and  $\kappa$  is the thermal diffusivity of a solid.

For a piecewise constant-flux history, Eq. 6I-1 can be generalized to

$$\Delta T_{surf}^n = C_0 \sum_{i=1}^n (F_i - F_{i-1}) \sqrt{t_n - t_{i-1}}, \quad (6I-3)$$

where  $t_i$  and  $F_i$  represent the time and the surface flux, respectively, at the end of the  $i$ th time step. Thus,

$$\Delta T_{surf}^n = T_r^0 - E_n - C_0 F_n \sqrt{\Delta t_n}, \quad (6I-4)$$

where  $T_r^0$  is the initial reservoir temperature,  $\Delta t_n = t_n - t_{n-1}$ , and  $E_n$  represents the effect of all previous time steps, which can be written as

$$E_n = C_0 \sum_{i=1}^{n-1} (F_i - F_{i-1}) \sqrt{t_n - t_{i-1}} - C_0 F_{n-1} \sqrt{\Delta t_n}. \quad (6I-5)$$

Now consider an element of fluid of height  $\partial y$ , length  $\partial x$  and width  $w/2$  that experiences a change in temperature from  $T_{fl}^{n-1}$  at the beginning of a time step to  $T_{fl}^n$  at the end of the step. The quantity of heat required to cause this temperature change is  $\rho_f C_{pfl} w \partial x \partial y (T_{fl}^n - T_{fl}^{n-1})/2$ . Assuming a constant flux over time step  $\Delta t_n$ , this implies that the flux and temperatures over the area  $\partial x \partial y$  are related by

$$(T_{fl}^n - T_{fl}^{n-1}) = \frac{F_n}{D_1} \Delta t_n, \quad (6I-6)$$

where

$$D_1 = \frac{\rho_f C_{pfl} w}{2}. \quad (6I-7)$$

Finally, consider the effect of heat transfer by convection from a rock surface at temperature  $T_{surf}^n$  to fluid at a temperature  $T_{fl}^n$ . If the heat transfer coefficient is  $h$ , the flux is

$$F_n = h(T_{surf}^n - T_{fl}^n). \quad (6I-8)$$

Equations 6I-3, 6I-6 and 6I-8 can be solved for  $T_{fl}^n$ ,  $F_n$  and  $T_{surf}^n$  to yield

$$T_{fl}^n = \frac{T_r^0 - E_n + C_2 T_{fl}^{n-1}}{1 + C_2} \quad (6I-9)$$

$$F_n = \frac{D_1 (T_{fl}^n - T_{fl}^{n-1})}{\Delta t_n} \quad (6I-10)$$

$$T_{surf}^n = T_{fl}^n + \frac{F_n}{h} \quad (6I-11)$$

$$C_2 = (C_0 \sqrt{\Delta t_n} + 1/h) \frac{D_1}{\Delta t_n}. \quad (6I-12)$$

Defining  $D_0$  as  $1/C_0$ ,

$$T_{fl}^n = \frac{h D_0 \Delta t_n (T_r^0 - E_n) + D_1 (h \sqrt{\Delta t_n} + D_0) T_{fl}^{n-1}}{h D_0 \Delta t_n + D_1 (h \sqrt{\Delta t_n} + D_0)}. \quad (6I-13)$$

It has been shown (Kamphuis *et al.*, 1993) that the effect of leakoff on the heat flux is equivalent to reducing the conductivity by the factor

$$\frac{\exp(-P^2)}{1 + \operatorname{erf}(P)}, \quad (6I-14)$$

where  $P = C_0 / \sqrt{k_h}$ .

Meyer (1987) showed that the Nusselt number

$$\frac{hw}{k_{fl}}, \quad (6I-15)$$

where  $k_{fl}$  is the thermal conductivity of the fluid, for non-Newtonian fluids ranges from 6 for  $n' = 0$  to 4.11 for  $n' = 1$ . A Nusselt number of 4.3 is most representative of typical fracturing fluids.

If a fracture treatment is simulated with an explicit finite difference scheme, it is not practical to retain the flux history of each solid grid point because many thousands of time steps may be required to simulate the entire treatment. It has been found that using 5 to 10 steps to represent the flux history is sufficient, provided the time steps are merged in such a way that the overall heat loss from the formation is conserved. This results in an accurate representation of the most recent temperature changes in the simulation, yet retains computational and storage efficiency.

at its tip boundary are addressed in numerous ways. Nevertheless, certain general principles can be described that apply to this region, and different implementations can be considered as modifications of the general principles. If the fracture tip is envisioned as the zone between the fracturing fluid and the undisturbed rock ahead of the fracture, then there are four possible features of this region that must be addressed:

- failure or opening process (normal LEFM)
- disturbed zone in the rock ahead of the fracture tip (damage not incorporated in the LEFM model)
- unwetted zone (fluid lag region)
- disturbed zone along the fracture face (e.g., dilatancy or compaction).

## 6J. Verification of efficient thermal calculations

The paper by Kamphuis *et al.* (1993) includes results for a KGD fracture in sandstone. The parameters are all held constant except for the leakoff coefficient  $C_L$ , which has values of  $4E-5$ ,  $1E-4$ ,  $2E-4$  and  $3E-4$   $m/s^{1/2}$ . Figure 6J-1 compares the results obtained using the method described in Sidebar 6I and those obtained by Kamphuis *et al.* The dimensionless temperatures along the fracture are shown as a function of the leakoff coefficient, with the lowest curve representing the largest leakoff coefficient. The agreement is good, considering the relatively small number of elements (eight) used in this simulation and the relatively coarse nature of the heat transfer algorithm compared to Kamphuis *et al.*'s detailed finite-difference calculations.

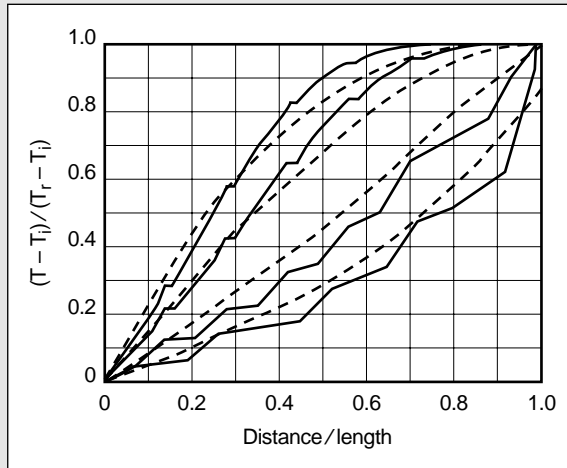


**Figure 6J-1.** Comparison of temperature calculations (solid lines) with the results of Kamphuis *et al.* (1993) (dashed lines).

These four mechanisms are typically neglected or handled in an ad hoc manner because of a lack of understanding and data, particularly on a field scale, about this complex zone.

### 6-7.1. Linear elastic fracture mechanics

Although early studies of fracture in rock used Griffith's (1921) crack theory and surface energy (Barenblatt, 1962; Perkins and Krech, 1968; Friedman *et al.*, 1972), most analyses of rock fracture are now formulated in terms of LEFM. The advantage of LEFM over earlier theories is that it incorporates, within a simple framework, some degree of dissipative energy processes, such as plastic flow and microcracking, when the zone of dissipation is small compared with the fracture length (see plateau region for  $K_{Ic}$  on Fig. 6-13). However, when this zone is not relatively small, energy-release methods should be used, as discussed in Chapter 3.

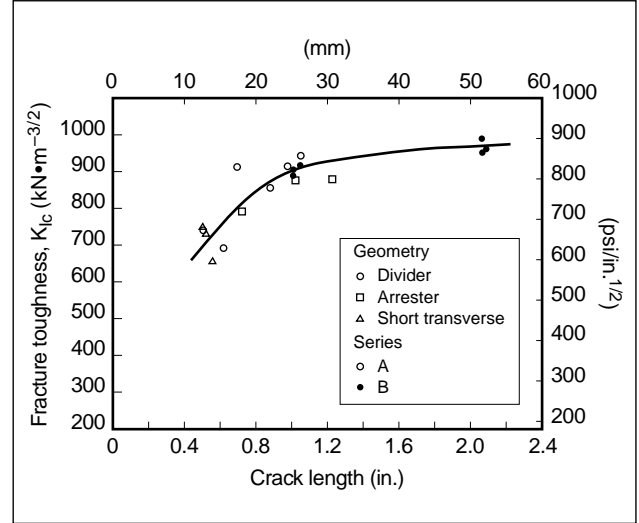


**Figure 6-13.** Scale dependence of fracture toughness in the laboratory (Schmidt, 1976).

#### • Stresses around a crack tip

Irwin (1957) identified three different types of singular stress fields (i.e., stress approaches infinity) around a crack tip and characterized these as Mode I (opening), Mode II (in plane sliding) and Mode III (antiplane sliding). For hydraulic fracture modeling, Mode I is of primary interest, although the other modes come into play in more complicated situations such as fracture turning from deviated wells. For a 2D crack opened by a constant internal pressure, Irwin showed that the stress intensity factor  $K_I$  is simply

$$K_I = \sqrt{\pi L p_{net}}, \quad (6-110)$$

where  $L$  is the crack length and  $p_{net}$  is the net internal pressure opening the crack. Similarly, for a radial crack

$$K_I = 2\sqrt{\frac{R}{\pi}} p_{net}, \quad (6-111)$$

where  $R$  is the crack radius (see Sidebar 6K).

LEFM, as postulated by Irwin, holds that the crack will advance when the value of  $K_I$  exceeds some critical value  $K_{Ic}$  of the material, called the critical stress intensity factor. More commonly known as fracture toughness,  $K_{Ic}$  can be related to the surface energy of previous studies through

$$K_{Ic} = \sqrt{\frac{2E\gamma_F}{1-\nu^2}}, \quad (6-112)$$

## 6K. Crack tip stresses and the Rice equation

Irwin (1957) found that the opening mode of a 2D crack has a singular stress distribution in the near-crack-tip region:

$$\sigma_x = \frac{K_I}{\sqrt{2\pi r}} \cos(\theta/2) [1 - \sin(\theta/2) \sin(3\theta/2)] \quad (6K-1)$$

$$\sigma_y = \frac{K_I}{\sqrt{2\pi r}} \cos(\theta/2) [1 + \sin(\theta/2) \sin(3\theta/2)] \quad (6K-2)$$

$$\tau_{xy} = \frac{K_I}{\sqrt{2\pi r}} \cos(\theta/2) [\sin(\theta/2) \sin(\theta/2)], \quad (6K-3)$$

where  $\theta$  is the angle measured from the crack axis,  $r$  is the distance from the crack tip, and  $K_I$  is the stress intensity factor.

By comparing the stress field given by Eqs. 6K-2 and 6K-3 with the solution of the stress field around the tip of a 2D crack extending from  $-L$  to  $L$ , Rice (1968) showed that  $K_I$  can be calculated as

$$K_I = \frac{1}{\sqrt{\pi L}} \int_{-L}^L p(x) \sqrt{\frac{L+x}{L-x}} dx, \quad (6K-4)$$

where  $p(x)$  is the pressure distribution in the crack. For constant pressure in the crack, Eq. 6K-4 reduces to Eq. 6-110.

For a radial crack, the equivalent equation is

$$K_I = \frac{2}{\sqrt{\pi R}} \int_0^R \frac{rp(r)}{\sqrt{R^2 - r^2}} dr, \quad (6K-5)$$

which, for constant pressure, reduces to Eq. 6-111.

where the specific fracture surface energy  $\gamma_F$  includes localized dissipative effects and can be determined in the laboratory, as discussed in Chapter 3. The attractiveness of this theory is its ability to include all the complicated failure processes in one parameter, which, hypothetically, is a material constant similar to modulus or strength. However, for the general case of dissipative effects, the linear elastic stresses given by Eqs. 6K-1 through 6K-3 may no longer apply near the crack tip.

- Application of fracture toughness to hydraulic fracturing in rocks

Although LEFM is attractive in its simplicity, two questions remain concerning its application to hydraulic fracturing:

- Is  $K_{Ic}$  a material property of rocks and what are its characteristics?
- Does  $K_{Ic}$  require modification for hydraulic fracturing applications?

The first question is difficult to answer because of scaling problems. In the initial application of  $K_{Ic}$  to rocks, Schmidt (1976) showed a clear size effect at small scales, but  $K_{Ic}$  appears to approach a “con-

stant” value as the crack size reaches some threshold value. Figure 6-13 shows example results for Indiana limestone that led Schmidt to conclude that  $K_{Ic}$  is a material constant. However, the small size of the laboratory samples is several orders of magnitude different than that of field-size hydraulic fractures, and size effects, which would invalidate the application of LEFM to this process, cannot be definitely ruled out.

Even without size difficulties, most rock material “constants” (such as Young’s modulus) are not constant and vary with confining stress, temperature, strain rate and the size of the rock mass tested. Similarly, in Schmidt and Huddle’s (1977) work with Indiana limestone, a significant increase of the critical stress intensity factor with confining stress was measured. Thiercelin (1987) confirmed this behavior but also showed that the amount of the increase is strongly dependent on the rock fabric and other factors.

Assuming that  $K_{Ic}$  is a material constant and scaling is not a problem, fracture toughness can be incorporated in a 2D or P3D crack model by integrating Eq. 6K-4 with the model-derived pressure distribution (or using Eq. 6-110 with a weighted-average pressure) to obtain the stress intensity factor  $K_I$ . Even an unwetted region can be included by modifying the pressure distribution used in Eq. 6K-4, as discussed later. For the calculated value of  $K_I$ :

- If  $K_I$  exceeds the input value of  $K_{Ic}$ , the crack is allowed to advance.
- If the value of  $K_I$  is less than or equal to  $K_{Ic}$ , the crack remains in its same position.
- If  $K_I$  becomes negative, the crack must retreat (i.e., the width reduces to zero) until  $K_I$  becomes  $\geq 0$ , as negative values indicate that the internal pressure is insufficient to support the entire crack size.

For field-size hydraulic fractures,  $L$  or  $R$  and  $p_{net}$  are so large that the stress intensity at a hydraulic fracture crack tip is much larger than typical laboratory  $K_{Ic}$  values of 500–2000 psi/in.<sup>1/2</sup>. Hence, it is usually assumed that  $K_{Ic}$  for this normal crack growth process, as understood from the laboratory, is negligible except for small fractures and initial growth. The following sections discuss modifications to this theory.

## 6-7.2. Extensions to LEFM

In the practical application of hydraulic fracturing, the measured net pressures are usually larger than those predicted by models (Shlyapobersky, 1985, 1988a, 1988b; Cleary *et al.*, 1991). Although these high net pressures could be due to better than expected containment, poor measurement of the closure stress, near-wellbore effects, complex fracturing, poor understanding of rheology and many other factors, the general tendency has been to focus on the tip region as the source of these anomalous results. Considerable work on fracture tip effects began after Shlyapobersky (1985) suggested that hydraulic fracture data could be interpreted to show a scale effect on  $K_{Ic}$  for field-size fractures. Since then, three additional major mechanisms have been proposed to account for the high net pressures at the crack tip: fluid lag effects (Jeffrey, 1989; Gardner, 1992; Advani *et al.*, 1993), dilatancy (Cleary *et al.*, 1991) and damage (Yew and Liu, 1993; Valkó and Economides, 1993a).

- Fluid lag region

As applied to hydraulic fracturing, the unwetted zone near the crack tip has pressure less than the closure pressure and hence acts to clamp the fracture tip closed and reduce the stress intensity in the rock. This zone was first introduced by Khristianovich and Zheltov (1955) and successfully used by Geertsma and de Klerk (1969) in modeling 2D fractures. From their initial formulations, it is clear that this unwetted region could have an impact on fracture parameters if it were sufficiently large. In a simple 2D geometry, the application is straightforward, but the size of the unwetted zone and the exact pressure in the zone must be assumed. The pressure within the unwetted region is most likely the reservoir pressure for permeable rocks and could be as low as the vapor pressure of the fluid for impermeable rocks, so limits can be placed on its value. The size of the unwetted region is a more difficult problem and has been the subject of considerable investigation.

Fluid lag can be incorporated into the standard  $K_{Ic}$  form by defining an effective fracture toughness (Jeffrey, 1989):

$$K_{Ic}^{eff} = K_{Ic} + K_{Ic}^{lag}, \quad (6-113)$$

where

$$\begin{aligned} K_{Ic}^{lag} &= 2\sqrt{\frac{L}{\pi}} \int_{L-d}^L \frac{p_{tip}}{\sqrt{L^2 - x^2}} dx \\ &= 2p_{tip} \sqrt{\frac{L}{\pi}} \left[ \frac{\pi}{2} - \arcsin\left(\frac{L-d}{L}\right) \right] \end{aligned} \quad (6-114)$$

for a 2D (KGD) crack, where  $p_{tip}$  is the net pressure (pressure near the tip minus the closure pressure) in the nonwetted region and  $d$  is the fluid lag distance. Typically,  $p_{tip}$  values are between  $-\sigma_c + p_r$  and  $-\sigma_c + p_{vapor}$ , where  $\sigma_c$  is the closure stress,  $p_r$  is the reservoir pressure, and  $p_{vapor}$  is the vapor pressure of the fluid. The fracture propagation criterion now becomes

$$2\sqrt{\frac{L}{\pi}} \int_0^{L-d} \frac{p(t)}{\sqrt{L^2 - x^2}} dx = K_{Ic} + K_{Ic}^{lag}. \quad (6-115)$$

Similar equations can be written for radial cracks (Jeffrey, 1989).

Detailed study of the crack tip has led to the discovery of concepts unique to hydraulic fracturing. Modeling of the crack tip region by the SCR Geomechanics Group (1993; Lenoach, 1995) shows that even when effects of fracture toughness  $K_{Ic}$  are ignored, the consequences of coupled fluid flow and leakoff still result in a singularity at the crack tip. For an impermeable rock, the power of the hydraulic fracture singularity is not  $1/2$  as for the rock behavior in LEFM, but rather  $n/(2+n)$ , where  $n$  is the power law index of the fluid. For permeable rocks, the power of the singularity is  $3n/(4+4n)$ , which is stronger than the impermeable singularity. Thus, an important singularity in stress may exist at the tip even under conditions in which the fracture toughness plays no role. They also made numerical simulations that show that the size of the fluid lag region adjusts to meet the fracture propagation criterion.

Models that determine the size of the unwetted region (Jeffrey, 1989; Gardner, 1992; Yew and Liu, 1993; SCR Geomechanics Group, 1993) generally produce small unwetted lengths, except at small confining stresses. However, only a small region is required near the tip to overshadow the effect from the fracture body. One shallow field experiment (relatively low confining stress) had sizable fluid lag zones (Warpinski, 1985), but no careful field study of fluid lag distances at higher confining stresses has been made. Fracture models where the lag distance is calculated generally show only a

small influence on global fracture parameters; a good example is calculation of the 3D aspects of the lag effect by Advani *et al.* (1993). Earlier in this chapter, it was shown that the dimension that controls fracture width is the smaller one. Hence, the KGD model is most applicable for short fractures and the PKN model for long fractures. Advani *et al.*'s study shows that a similar effect occurs for the fracture mechanics; i.e., the length  $L$  in Eq. 6-114 must be replaced by the fracture height if the fracture length exceeds the height.

- Dilatancy

Although the LEFM concept can include small-scale damage and plasticity within its framework, the possibility exists that the damage zone around a field-size hydraulic fracture could be sufficiently large that the near-tip stress distribution becomes invalid, or other effects could alter the stress distribution. For example, Cleary *et al.* (1991) suggested that the mechanism responsible for elevating crack tip pressures is dilatancy just behind the fracture tip. They postulated that if this dilatancy occurs during the rock failure process, then the fracture width just behind the tip may be pinched slightly by the expanded fracture. Dilatation of material, which is essentially a volumetric expansion caused by failure, cannot be accommodated by the surrounding elastic material, so the rock stress in the near-tip region must increase. Yew and Liu (1993) developed a modified fracture toughness to include dilatation of the material ahead of the crack tip for the case where a plastic zone is created around the tip. An approximate equation for this behavior, in terms of an effective fracture toughness, was given as

$$K_{Ic}^{eff} = K_{Ic} + \frac{144\alpha^2}{\sqrt{3}\pi^2(1+\sqrt{3}\alpha)} \sqrt{\frac{1-\nu}{1+\nu}} \left[ \frac{E-E_t}{\sqrt{EE_t}} \right] K_I, \quad (6-116)$$

where  $\alpha$  is found by solving

$$\tan \phi = \frac{3\alpha}{\sqrt{1-12\alpha^2}}, \quad (6-117)$$

where  $\phi$  is the friction angle and  $E_t$  is the Young's modulus of the plastic material.

Throughout the body of a fracture such dilatancy is negligible, but it could play an important role in the near-tip region, where the width is small. However, numerical simulations of crack growth, assum-

ing the rock experiences dilatant-plastic yielding, (Papanastasiou and Thiercelin, 1993) show no overall increase in the width at the fracture tip because plastic deformation dominates the dilation effect. De Pater *et al.* (1993) tried to identify dilatancy in laboratory tests and through detailed modeling of the fracture tip, but no clear evidence of such behavior was obtained.

- Other behavior: damage- and fluid-induced effects

Another approach to modeling near-tip rock behavior is to use a cumulative damage approach, in which the microcrack damage ahead of the crack forces the undamaged material to accept more of the load. Valkó and Economides (1993a) formulated a fracture model using this approach. Their model scales the damage with the fracture length, which is consistent with the KGD model and applies only to relatively short fractures. This analysis would be applicable for longer fractures if applied to a tip element or with a scaling criterion.

Because most of the modeling efforts associated with hydraulic fracturing deal with either fluid mechanics or rock mechanics, the strong chemical interactions that can affect rock behavior are often forgotten. An extreme example of this effect is the large reduction in strength that can occur as a result of stress corrosion cracking. Similarly, there has been some evidence that the chemistry, rheology or molecular structure may influence tip behavior. Holder *et al.* (1993) conducted laboratory tests in which the inferred fracture toughness values using crosslinked gels were substantially greater than those with linear gels or Newtonian fluids. Dunning (1980) found that surfactants can have a major effect on the crack propagation stress (or, alternatively, the fracture toughness). The effects of pH, total ions, and breakers and other fluid additives can cause additional chemical effects. However, these effects can influence tip failure only in the absence of a fluid lag region or where the fluid penetrates a damaged area ahead of the fracture tip.

### 6-7.3. Field calibration

Obtaining a definitive description of the fracture tip behavior is complex and difficult. From a practical standpoint, because the tip pressure must be consistent with field observations, its magnitude and impact can be estimated using observed pressure data, as dis-



cussed in Chapters 5 and 9. To maintain a credible description of fracture geometry, this should not be an ad hoc procedure. Shlyapobersky *et al.* (1988a, 1988b) proposed a method to calibrate a field-scale effective fracture toughness that assumes that the fracture stops growing soon after shut-in and fluid flow within the fracture stops. By determining an initial shut-in pressure (ISIP) at the time when fracture growth stops (if possible) and the closure stress in the formation, the method measures a value of  $p_{net}$  associated with an open fracture at the end of pumping. Given  $p_{net}$ , the effective fracture toughness is calculated from

$$K_{lc}^{eff} = \alpha_g p_{net} \sqrt{R_{eff}}, \quad (6-118)$$

where  $R_{eff}$  is one-half of the fracture height for a long 2D crack or the crack radius for a penny-shaped crack, and  $\alpha_g$  is a geometry coefficient, which depends on the geometry for a rectangular crack or is 0.64 for a penny-shaped crack.

This and other procedures to define tip effects by field calibration require an accurate measurement of  $p_{net}$  as well as reliable information on the fracture geometry ( $h_f$ ,  $L$  and  $R$ ), fluid flow within the fracture after shut-in and the expected nature of the rock's failure behavior.

## 6-8. Tortuosity and other near-well effects

High near-wellbore friction losses have been observed in fracture treatments, particularly in deviated wells or when the perforations are inadequate or poorly designed. Some attempts have been made to understand the effect of near-wellbore geometry on the placement of hydraulic fractures (Aud *et al.*, 1994) and to develop methods to prevent unplanned screenouts (Cleary *et al.*, 1993; Stadulis, 1995). Near-wellbore friction losses have been attributed to phenomena such as wellbore communication (perforations), tortuosity (fracture turning and twisting), perforation phasing misalignment and induced rock pinching, and multiple fractures (e.g., Stadulis, 1995). These effects have been identified as detrimental to the success of a fracturing treatment because of the increase in net pressure and the increased likelihood of unplanned screenouts caused by the limited fracture width near the wellbore.

### 6-8.1. Fracture geometry around a wellbore

Several researchers have investigated mechanisms related to fracture initiation in vertical and deviated wells. Behrmann and Elbel (1991) and Daneshy (1973) found that the perforation must be oriented within about 10° to 20° of the plane normal to the minimum far-field stress for a fracture to initiate at the perforation and extend. Other experiments show that when the perforations are not oriented in the direction of far-field fracture propagation and the well is deviated, the fractures can be nonplanar or S shaped (Weijers, 1995; El Rabaa, 1989). However, predicting the near-wellbore pressure drop in deviated wells is difficult because of the uncertainty of the near-well fracture geometry.

A symmetric bi-wing planar fracture is generally assumed to develop when a hydraulic fracture treatment is performed. Hydraulic fracture models such as the planar and P3D models described previously do not account for fracture initiation and near-wellbore effects. Apart from multiple fractures, the near-wellbore effects described here have no effect on the overall fracture geometry, except if a near-wellbore screenout is caused by near-wellbore effects. This is in contrast to fracture tip effects (see Section 6-7), which may affect fracture geometry significantly.

The purpose of modeling near-wellbore effects is twofold: to understand the source of near-wellbore screenouts, so that they may be predicted and prevented, and to correctly remove the near-wellbore contribution from the measured “net pressure” so that the remaining net pressure may be interpreted correctly as a characteristic of the overall fracture geometry.

### 6-8.2. Perforation and deviation effects

The three assumed components of near-wellbore pressure loss are friction through the perforation, fracture turning (i.e., tortuosity) and perforation misalignment friction, which are also assumed to be additive:

$$\Delta p_{near\ wellbore} = \Delta p_{pf} + \Delta p_{tort} + \Delta p_{misalign}. \quad (6-119)$$

It is not possible to predict near-wellbore effects, other than friction through perforations. Rather, models for these mechanisms of pressure increase are provided, and each mechanism has one or more parameters, which can be evaluated from field data.

### 6-8.3. Perforation friction

A discussion of perforating requirements for hydraulic fracturing is in Chapter 11. Insufficient or poor perforations can have a significant effect on the execution and evaluation of a fracturing treatment because they affect the breakdown and treating pressure. Improper perforating can result in near-wellbore screenouts if the perforations do not provide an adequate pathway to the main body of the fracture. The equation commonly used to calculate perforation friction implicitly assumes that the perforation is a short cylindrical tunnel (McClain, 1963):

$$\Delta p_{pf} = 0.2369 \frac{q^2 \rho}{n^2 D_p^4 C^2}, \quad (6-120)$$

where  $q$  is the total flow rate,  $\rho$  is the fluid density,  $n$  is the number of perforations,  $D_p$  is the perforation diameter, and  $C$  is the discharge coefficient. The discharge coefficient represents the effect of the perforation entrance shape on the friction pressure.

The effect of perforation friction on fracture treating pressure is usually negligible if the perforations are correctly sized and phased. If this is not the case, perforation friction is assumed to be constant during the entire treatment. When sand slurries are pumped at high differential pressure across the perforations, the pressure drop changes, owing to erosion. There are two effects of erosion on the pressure drop through a perforation: smoothing of the entrance of the perforation, with a resulting increase in the discharge coefficient  $C$ , and an increase in diameter  $D_p$ . Figure 6-14 shows the related evolution of the coefficient of discharge with the perforation geometry (Crump and Conway, 1988). These effects, and their implementation in a fracture simulator, are described in more detail in Romero *et al.* (1995).

Figure 6-15 illustrates the difference between the resulting pressure responses when perforation friction and erosion are included in the calculation and when they are neglected for a PKN geometry model. The pressure increases as expected for a confined fracture, until proppant reaches the perforations. Then the pressure decreases, mainly because of the increase in the discharge coefficient. After about 2000 lbm of sand is injected, the slope becomes positive again, almost paralleling the slope prior to the sand, which indicates a constant discharge coefficient and a slow increase of the perforation diameter.

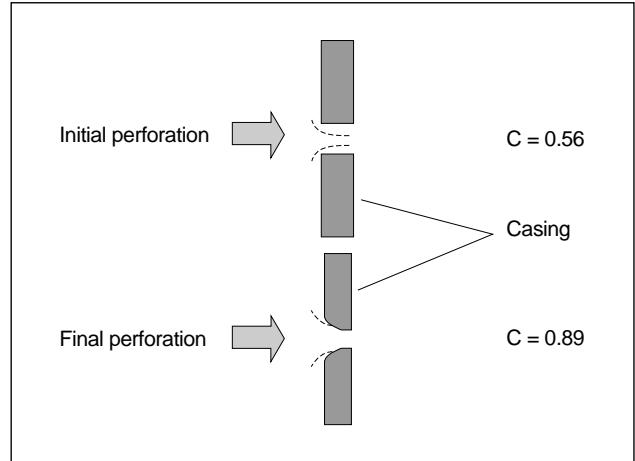


**Figure 6-14.** Evolution of the coefficient of discharge  $C$  with the erosion of entrance (Crump and Conway, 1988).

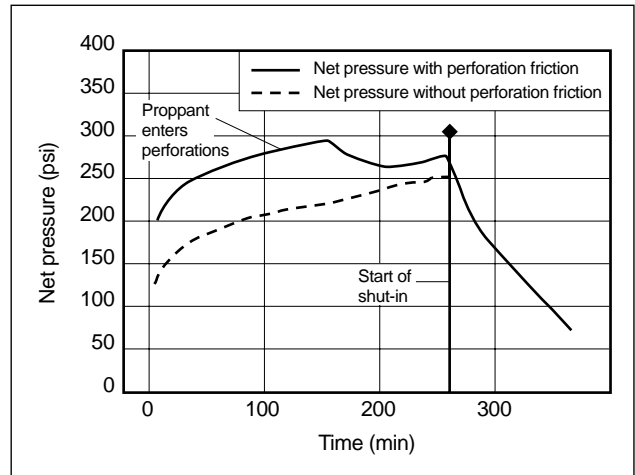


**Figure 6-15.** Effect of perforation friction on measured net pressure.

### 6-8.4. Tortuosity

Tortuosity is defined here as a convoluted pathway connecting the wellbore to the main body of the fracture. Several studies (Aud *et al.*, 1994; Cleary *et al.*, 1993) have identified tortuosity as an important phenomenon that could affect the execution of a fracture treatment when the wellbore and stress fields are misaligned. The simplified schematic of fracture geometry in Fig. 6-16 shows how a fracture may turn and twist to align itself with the preferred fracture plane.

The fracture width is proportional to the difference between the pressure in the fracture and the stress against which the fracture opens. When the fracture

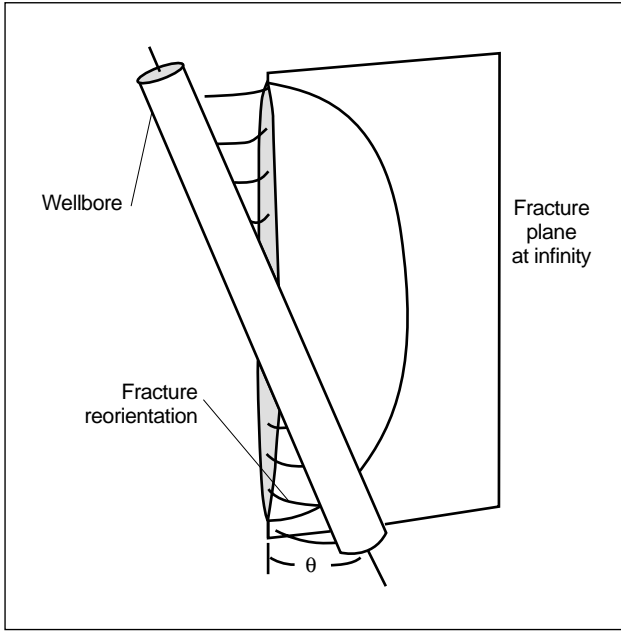


**Figure 6-16.** The fracture twists and turns to align itself with the preferred direction of propagation.

is opening against a stress higher than the minimum in-situ stress, the fracture width is reduced relative to that without turning. If the ratio between the stress against which the fracture is opening and the minimum in-situ stress is higher than about 1.5, the fracture mouth acts as a nozzle, allowing fluid to enter, but with a large pressure drop associated with the pinching of the fracture width at the well. This process of fracture width reduction along the reorientation path restricts flow and could cause near-wellbore screenouts.

The radius of curvature  $R$  of the reorientation path can be determined for a Newtonian fluid as (Romero *et al.*, 1995)

$$R = \lambda \sqrt{\frac{E^3 \mu q}{h_f} \left( \frac{1}{\sigma_{h,min} (\kappa - 1)} \right)^2}, \quad (6-121)$$

where  $\lambda$  is an experimental coefficient,  $q$  is the flow rate,  $\sigma_{h,min}$  is the minimum horizontal stress, and  $\kappa$  is the ratio between the stress against which the fracture is opening and the minimum stress. The coefficient  $\lambda$  is obtained from experimental data (e.g., Abass *et al.*, 1994) or field data and can be considered a fitting parameter.

Fracture simulators such as the planar or P3D simulators discussed previously represent the behavior of the main body of the fracture, but an additional component is required to represent the tortuosity. A model

of the curved path is attached to the main body of the fracture. Equation 6-121 is used to define the shape of the path, and the outer boundary conditions (i.e., width and pressure at the end of the tortuous region) are the conditions at the wellbore, obtained from the simulator without tortuosity. Although the calculated pressure at the well may be higher than that predicted when tortuosity is neglected, the width may be lower because the stress against which the fracture is opening is higher. This may result in screenouts caused by near-wellbore bridging, which can be accounted for in the model by preventing proppant from entering if the width is too small.

The effect of tortuosity is largest near the beginning of the treatment and decreases as the treatment proceeds. This occurs because an increment in the closure stress, relative to that on a planar fracture, has a fixed absolute effect ( $\Delta w$ ) on the width  $w$ . However, the pressure drop is, roughly speaking, inversely proportional to the width cubed, so that a change in width from  $w$  to  $w - \Delta w$  has a much greater effect when  $w$  is small (i.e., when the fracture is first created). The model also shows that the pressure drop caused by tortuosity can be reduced by increasing the fluid viscosity, which has been reported in practice (Aud *et al.*, 1994) as an effective means of preventing near-well screenouts. Both added pump time prior to the introduction of proppant (i.e., increased pad) and increased viscosity may reduce near-wellbore screenouts because they cause the width to be greater in the tortuous region than it would have been. However, these treatment changes can be detrimental to height confinement and proppant placement and permeability in the resulting fracture, so other approaches to mitigate the cause of tortuosity should be considered.

### 6-8.5. Phasing misalignment

Perforating practices (i.e., hole size, spacing and orientation) vary widely. In general, not all the perforations in a well are aligned with the preferred fracture plane. Indeed, it would be quite coincidental for this to be the case, unless special efforts are made to obtain reliable information on the stress directions at a particular well. If  $0^\circ$  phasing is used, the orientation of the perforation to the plane of the hydraulic fracture may be as large as  $90^\circ$ . On the other hand, nearly perfect alignment or  $0^\circ$  phasing causes preferential propagation of one wing of the fracture with limited

penetration of the companion wing because of the pressure drop resulting from flow around the annulus to the nonconnected wing.

Nolte (1988a) pointed out that if the fracture does not initiate at the perforations, the fluid must communicate with the fracture through a narrow channel around the side of the casing. This channel can cause higher treating pressures because of the width restrictions (Fig. 6-17). As with the tortuosity effect discussed previously, this can cause both increased pressure and screenouts because of proppant bridging. Also, proppant may erode the restrictions. The circle in Fig. 6-17 represents a relatively stiff wellbore (casing and cement). If the fluid exits the well through the perforation, it must traverse the microannulus and pass the restriction area before entering the main body of the fracture. A geometry effect occurs as the rock is displaced by a distance  $w$  away from the cement, resulting in a channel around the annulus with a width of  $w^2/8D$  at the fracture entrance (point A in the figure), where  $w$  is the fracture width and  $D$  is the wellbore diameter. In addition, an elastic response (Poisson's effect) occurs in which the fracture opening results in movement of the rock toward the wellbore, reducing the fracture width.

Figure 6-18 shows the displacement (in the direction of the fracture) obtained around the wellbore for a typical case in which the microannulus and fracture are subject to a constant fluid pressure. The negative displacement of the rock at the intersection between the wellbore and the fracture represents the wellbore pinching from the net pressure in the fracture (Poisson's effect). To maintain flow into the fracture through the pinch point, the microannulus must be pressurized to a higher level than the fracture. Figure 6-19 shows the pinching displacement when the net pressure varies

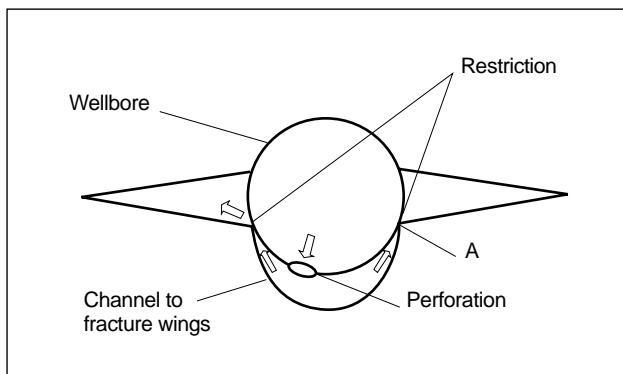


**Figure 6-17.** Nonalignment of perforations and the fracture plane causes pinch points.

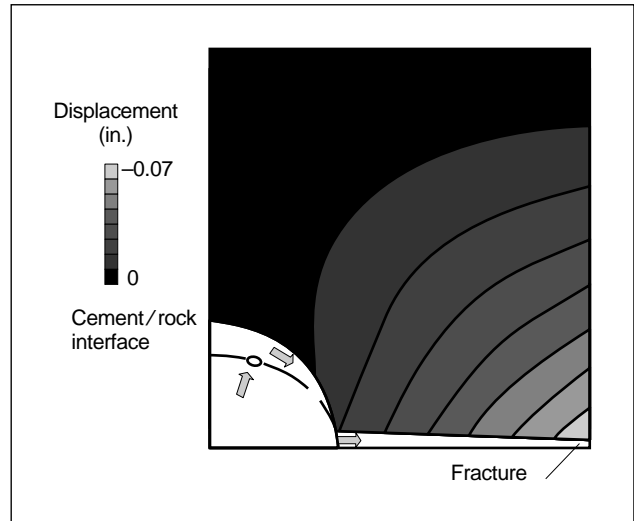


**Figure 6-18.** The displacement field around a fracture shows a tendency to pinch closed at the wellbore.

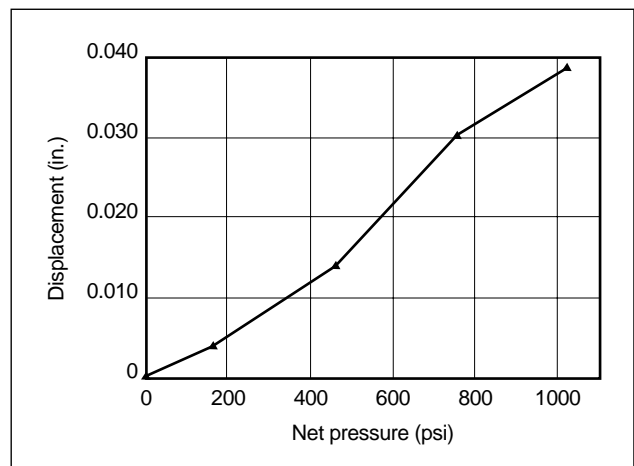


**Figure 6-19.** Evolution of wellbore pinching with increasing net pressure.

from 0 to 1000 psi for a typical case. The effect increases as fracturing pressure increases, in contrast to the tortuosity effect, which decreases as pressure and width increase.

If the pinch point is present when proppant attempts to enter the fracture, bridging may occur, resulting in premature screenout. The fluid travels through the pinch point at a high velocity, and either fluid or slurry may erode the pinch point, provided this occurs before bridging. The degree of erosion is affected by the viscosity of the fluid, proppant concentration and rock strength. The reported effectiveness of proppant slugs (Cleary *et al.*, 1993; Stadulis, 1995) may be due to this erosion. Because the slugs are small, they do

not bridge everywhere, so fluid entry at higher velocity continues and erodes some channels. Even prior to the use of slugs, it was common to inject proppant at low concentration to erode restrictions when high pressures occurred during the fracture initiation stage. In contrast to tortuosity, pinching is increased by large pads and higher net pressures. This may explain why, in some cases, prepad slugs can be injected at low net pressures when the pinching is smaller, but in the main treatment a near-well screenout occurs.

## 6-9. Acid fracturing

Hydraulic fracturing with acid (usually hydrochloric acid [HCl]) is an alternative to propped fractures in acid-soluble formations such as dolomites and limestones. The major difference between acid and propped fractures is that conductivity is obtained by etching the fracture faces instead of by using a proppant to prevent the fracture from closing. Acid fracturing may be preferred operationally because the potential for unintended proppant bridging and proppant flowback is avoided. However, designing and controlling the depth of penetration of the live acid into the formation and the etched conductivity are more difficult than controlling proppant placement. Acid penetration is governed by the chemical reaction between the rock and the fracturing fluid (as opposed to a simple mass balance in propped fractures), and conductivity is determined by the etching patterns formed by the reacting acid (as opposed to being a property of the proppant under a given stress). In both cases, acid fracturing introduces a dependence on rock properties that is not present in propped fracturing. In addition, the properties that acid fracturing design and control depend on are usually more difficult to determine than other formation properties.

The geometry of acid fractures can be determined by the same models used for propped fractures, with the exception of the impact of etched width on the width-pressure relation. However, several additional aspects of acid fracturing must be considered:

- acid transport to and reaction at the rock surface
- heat transfer, because the reaction releases heat, and the reaction rate is temperature sensitive
- leakoff, because acid leakoff behavior is significantly different from that of nonreactive fluids.

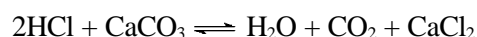
### 6-9.1. Historical acid fracturing models

Williams *et al.* (1979) provided a detailed discussion of acid fracturing models prior to 1980, and Li *et al.* (1993) reviewed some of the more recent work. One of the main drawbacks of most of the early models was that the fracture geometry calculation was separated from the acid reaction calculation to develop analytically tractable solutions. Since then, computer-based models have overcome these limitations, and the preceding models are no longer used. For example, Settari (1993) presented a detailed description of a comprehensive model with the fracture geometry and acid reaction calculations coupled, including a comprehensive leakoff model, coupled heat transfer and the capability to include multiple fluids with varying rheology.

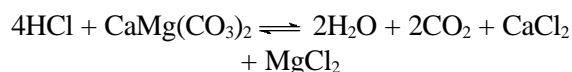
Much of what follows is based on the work described by Settari. Roodhart *et al.* (1993) presented a model in which they developed the heat transfer calculations extensively, using the work of Kamphuis *et al.* (1993). The other factor they included was the effect of the boundary layer thickness for acid reaction developing as the fluid enters the fracture, resulting in a thinner layer near the well and causing a higher etching rate. The aforementioned publications contain extensive lists of references.

### 6-9.2. Reaction stoichiometry

The main chemical reactions of interest in acid fracturing are those between HCl and calcium carbonate (limestone) or calcium-magnesium carbonate (dolomite). The chemical reaction for limestone is written as



and for dolomite as



The first reaction equation indicates that two molecules of HCl react with one molecule of calcium carbonate to form one molecule each of water, carbon dioxide and calcium chloride. The second equation shows that four molecules of HCl react with one molecule of calcium-magnesium carbonate to form two molecules each of water and carbon dioxide and one each of calcium chloride and magnesium chloride.

These so-called stoichiometric equations allow computing the volume of rock dissolved by a given volume of acid. These equations can be used to determine the dissolving power  $X_C$  of the acid, which is the volume of rock dissolved per unit volume of acid reacted. The mass dissolving power (i.e., the mass of rock dissolved per unit mass of acid reacted) is first defined as

$$\beta = \frac{(\text{molecular weight of rock}) \times (\text{rock stoichiometric coefficient})}{(\text{molecular weight of acid}) \times (\text{acid stoichiometric coefficient})} \quad (6-122)$$

For the limestone reaction,

$$\beta = \frac{100.09 \times 1}{36.47 \times 2} = 1.372 \quad (6-123)$$

so that each gram of 100% pure HCl dissolves 1.372 g of rock. To obtain the dissolving power, the masses must be converted to volumes:

$$X_C = \frac{\rho_C \beta C}{\rho_{CaCO_3}}, \quad (6-124)$$

where  $\rho_C$  and  $\rho_{CaCO_3}$  are the densities of the acid solution and calcium carbonate, respectively, and  $C$  is the weight-fraction concentration (e.g., 0.28 for 28% acid). For example, the specific gravity of 28% acid is 1.14, whereas that for 15% acid is 1.07. A complete table of densities is in Williams *et al.* (1979). Applying this calculation for the limestone-HCl reaction,  $X_{15}$  is 0.082, and  $X_{28}$  is 0.161. Similarly, for dolomite the values are 0.071 and 0.141, respectively.

The stoichiometric equations for acid reactions provide a relation for the coupling between fracture geometry and acid spending. Because there are many unknowns in acid fracturing, the modeling can be simplified by neglecting the variation in density of the acid and using that of 10% acid, which is a suitable average for most acid fracture treatments. In this case,  $X_{100}$  can be approximated as  $10X_{10}$  and  $X_C$  as  $CX_{100}$ . Now, consider the volume of a fracture element of cross-sectional area (width times height)  $A$  and length  $\delta x$  in which the acid concentration changes by an amount  $\Delta C$ . The volume of acid spent is  $A \cdot \delta x \cdot \Delta C$ , and the volume  $\Delta A \cdot \delta x$  of rock dissolved is

$$\Delta A_{etch} = X_{100} A \Delta \bar{C}, \quad (6-125)$$

where  $A_{etch}$  is the etched area and  $\bar{C}$  is the average acid concentration in the cross section.

### 6-9.3. Acid fracture conductivity

Acid fracture conductivity is much more poorly understood than propped fracture conductivity. The flow rate through an open channel of width  $w$  is proportional to  $w^3$ . If the etched channel were under no stress, this proportional relation would be used to determine the conductivity of an acid fracture. However, the stress in the reservoir acts to close the channel. If the etching were completely uniform, this closing could be calculated in a manner similar to that used to calculate the width of an elliptical fracture, except that the net pressure is negative. As an approximation, for a uniform etched width, the shape of the resulting closed fracture would be

$$w(z) = w_{etch} - \frac{4\sigma_c}{E'} \sqrt{h_f^2 - z^2}, \quad (6-126)$$

where  $w_{etch}$  is the etched width, and the width is set to zero wherever Eq. 6-126 predicts a negative width. It is apparent from this equation that the width in most of the channel would be much lower than that of an open channel, as most of the channel would have closed completely. This would clearly reduce fracture conductivity significantly.

Fortunately, acid etches the rock surface in a non-uniform manner, because of rock heterogeneity and fingering of the acid through the wider previously etched channels. This results in numerous horizontal “pillars” supporting the channels between them, for which Eq. 6-126 could be used with the fixed fracture height  $h_f$  replaced by the distance between the pillars. It is not practical to model this in detail, because the pattern is not generally known. Because conductivity is higher in formations where numerous small channels occur supported by numerous pillars, uniform etching is not desirable. If, however, the pillars lack the strength to support the additional load required to keep the channels open, some of the pillars will collapse, reducing the conductivity. Fracture conductivity is thus dependent not only on the etching pattern, but also on the rock strength and closure stress. Nierode and Kruk (1973) developed an empirical equation for conductivity:

$$(wk)_{eff} = C_1 \exp(-C_2 \sigma), \quad (6-127)$$

where

$$C_1 = 0.265 wk_{fi}^{0.822} \quad (6-128)$$

$$C_2 = \begin{cases} (13.9 - 1.3 \ln S_{RE}) \times 10^{-3} & 0 \text{ psi} < S_{RE} < 20,000 \text{ psi} \\ (3.8 - 0.28 \ln S_{RE}) \times 10^{-3} & 20,000 \text{ psi} < S_{RE} < 500,000 \text{ psi} \end{cases} \quad (6-129)$$

$$wk_{fi} = 9.36 \times 10^{13} \left( \frac{w_{etch}}{12} \right)^3, \quad (6-130)$$

where  $\sigma$  is the effective stress in psi,  $S_{RE}$  is the rock embedment strength in psi, and  $wk_{fi}$  is the conductivity in md-in. A typographical error in the original paper is corrected in Eq. 6-129.

#### 6-9.4. Energy balance during acid fracturing

The total heat generated (per unit volume) by a change in acid concentration  $\Delta \bar{C}$  is  $\Delta \bar{C} \Delta H$ , where  $\Delta H$  is the heat of reaction. Coupling of the acid and heat transfer models is provided by assuming that all the heat initially increases the fluid temperature, resulting in a fluid temperature change of

$$\Delta T_{fl} = \frac{\Delta \bar{C} \Delta H}{\rho_f C_{pfl}}, \quad (6-131)$$

where  $\rho_f$  is the fluid density and  $C_{pfl}$  is the fluid heat capacity. Section 6-6 describes how heat is transferred between the fluid and the formation. The magnitude of the temperature change resulting from acid reaction may be sufficient to cause the temperature of some fluids to exceed the reservoir temperature. It is thus particularly important to use a numerical temperature calculation when simulating acid fracturing.

#### 6-9.5. Reaction kinetics

Surface reactions such as the acid-rock reactions discussed here are complex, even under laboratory conditions. In general, the liquid-phase reaction between species A and B to form products C and D is governed by an expression of the form

$$r = \xi_f a_A^{n_A} a_B^{n_B} - \xi_r a_C^{n_C} a_D^{n_D}, \quad (6-132)$$

where  $\xi_f$  is the forward rate constant,  $\xi_r$  is the reverse rate constant, and  $a_X$  represents the chemical activity of species X. In the reactions of interest in acid fracturing, reverse reactions are usually much slower than forward reactions and can be neglected. In very dilute systems, the chemical activity is equal to the concentration. It is also usually observed that the reaction

rate constants are functions of temperature, following the Arrhenius equation:

$$\xi_f^T = \xi_f^{T_{ref}} \exp \left( \frac{-\Delta E}{R} \left( \frac{1}{T} - \frac{1}{T_{ref}} \right) \right). \quad (6-133)$$

The acid reaction rate at a surface is thus a complex function of the activities of all species involved in the reaction. Detailed modeling of the reaction in terms of these activities is not required for a hydraulic fracture simulator, because of the large amount of uncertainty in the other parameters. Instead, the reaction rate can be assumed to be governed by the simple equation for the rate of acid consumption  $r$  (Settari, 1993):

$$r = \frac{\partial M_{acid}}{\partial t} = -K_r (C_{wall} - C_{eqm})^m, \quad (6-134)$$

where the temperature-dependent reaction rate constant is

$$K_r = k_0 \exp \left( \frac{-\Delta E}{R} \left( \frac{1}{T} - \frac{1}{T_{ref}} \right) \right), \quad (6-135)$$

where  $M_{acid}$  is the moles of acid per unit rock face area,  $t$  is the time,  $C_{wall}$  is the surface acid concentration,  $C_{eqm}$  is the equilibrium concentration,  $m$  is the order of reaction,  $k_0$  is the reaction rate constant at the reference temperature  $T_{ref}$  (298K [25°C]),  $\Delta E$  is the activation energy,  $R$  is the universal gas constant, and  $T$  is the absolute temperature.

$C_{eqm}$  is generally zero for the reactions of interest.

#### 6-9.6. Mass transfer

Before the reaction can occur at the fracture wall, the acid molecules must be transported to the wall. In a stagnant fluid, diffusion in an ideal case can be described by Fick's law:

$$v_{A,x} = -D_A \frac{\partial C_A}{\partial x}, \quad (6-136)$$

where  $v_{A,x}$  is the velocity of species A,  $D_A$  is the molecular diffusion coefficient,  $C_A$  is the acid concentration, and the derivative represents the concentration gradient. Williams *et al.* (1979) proposed accounting for leakoff by adding a term to the right-hand side of Eq. 6-136, resulting in

$$v_{A,x} = -D_A \frac{\partial C_A}{\partial x} + C_A u_L. \quad (6-137)$$

In flowing fluids, this equation is no longer valid, because acid transport is by convection rather than diffusion. For acid fracture modeling, Eq. 6-136 is simply replaced by

$$v_{A,x} = K_g(C_A - C_{wall}) + (C_A - C_{wall})u_L, \quad (6-138)$$

where the mass-transfer coefficient is

$$K_g = D_{eff}N_{Sh}/w, \quad (6-139)$$

where  $D_{eff}$  is the effective acid diffusion coefficient. The Sherwood number  $N_{Sh}$  is determined from the correlation (Lee and Roberts, 1980)

$$N_{Sh} = \begin{cases} 6.26N_{Sc}^{1/3} & N_{Re} < 1800 \\ 0.001104N_{Re}^{1.153}N_{Sc}^{1/3} & 1800 < N_{Re} < 7000, \\ 0.026N_{Re}^{4/5}N_{Sc}^{1/3} & N_{Re} > 7000 \end{cases} \quad (6-140)$$

where the Reynold's and Schmidt numbers are defined respectively by

$$N_{Re} = \frac{2wv\rho_f}{\mu} \quad (6-141)$$

$$N_{Sc} = \frac{\mu}{D_{eff}\rho_f}. \quad (6-142)$$

### 6-9.7. Acid reaction model

If reaction occurs, the acid concentration varies across the fracture width, and the surface concentration is less than the bulk acid concentration. The surface concentration is such that the amount consumed at the surface is balanced by transport to the surface by diffusion.

The wall concentration for a given bulk concentration is obtained by equating the right-hand sides of Eqs. 6-134 and 6-138 to obtain

$$K_r(C_{wall} - C_{eqm})^m = (K_g + u_L)(\bar{C} - C_{wall}). \quad (6-143)$$

This equation, which is a general model of acid reaction, can easily be solved if  $m = 1$  but is solved iteratively otherwise. If  $K_r$  is very large compared with  $K_g + u_L$ , then Eq. 6-143 is satisfied when  $C_{wall}$  is approximately equal to  $C_{eqm}$ . In this case,  $C_{eqm}$  can replace  $C_{wall}$  on the right-hand side of Eq. 6-143, and Eq. 6-138 can be written as

$$r = \frac{\partial M_{acid}}{\partial t} = -(K_g + u_L)(\bar{C} - C_{eqm}). \quad (6-144)$$

In this case, the reaction rate is termed mass-transfer limited, because the rate at which it occurs is controlled by the rate at which live acid can be brought to the rock surface. Similarly, if  $K_g + u_L$  is very large compared with  $K_r$ , then Eq. 6-143 is satisfied when  $C_{wall}$  is approximately equal to  $\bar{C}$ . In this case,  $\bar{C}$  can replace  $C_{wall}$  on the left-hand side of Eq. 6-143, and Eq. 6-134 can be written as

$$r = \frac{\partial M_{acid}}{\partial t} = -K_r(C_{wall} - C_{eqm})^m. \quad (6-145)$$

Equation 6-145 represents the reaction-rate- or kinetics-limited case in which the rate of acid consumption is limited by the rate at the wall.

### 6-9.8. Acid fracturing: fracture geometry model

The movement of acid perpendicular to the fracture wall is considered in this section. The preceding sections discuss the fluid flow equations typically solved in fracture models. Acid movement within the fracture can be modeled similarly to the movement of proppant. For a fracture simulator to simulate acid fracturing treatments accurately, several specific requirements must be met relating to

- fluid tracking in the fracture and reservoir
- recession of the active fracture length
- effect of etching on the relation between pressure and width.

Although typical fluid flow calculation schemes use a coarse grid (about 10 elements), accurate fluid front tracking can be obtained only by following up to 50 fluid stages. Typical treatments include only about 10 different stages, but stages can be subdivided for better tracking of the large gradients that may occur in acid concentration within a single stage. Also, a finer grid is required to track leakoff volumes into the formation and formation exposure to fluid stages for accurate modeling of the extreme differences in leakoff characteristics and viscosity between acid and nonacid stages.

Acid fracturing treatments are typically designed with sudden changes in flow rate because the different fluids in the treatment have significantly different frictional properties. These sudden changes, as well as the high leakoff that may occur during pumping of the



acid stages, may cause recession of the active fracture length. The simulator must model this recession, which seldom occurs in proppant treatments.

For a confined fracture in a homogeneous isotropic elastic material, the relation between the net pressure and cross-sectional area  $A$  can be written as

$$p_{net} = \frac{2E'}{\pi h_f^2} A. \quad (6-146)$$

A modification to this relation is required to account for dissolution of the rock by acid. Only the elastic area  $A_{elas}$  contributes to the net pressure in the fluid, although the total area  $A$  (where  $A = A_{elas} + A_{etch}$ ) is available as a flow channel and to store the fluid mass.

Mack and Elbel (1994) presented example problems illustrating the effects of some of the features of acid fracturing models.

## 6-10. Multilayer fracturing

Many fracture treatments are performed in settings that result in the formation and extension of nearly isolated fractures in different zones. Frequently it is desirable to fracture multiple zones simultaneously, because treatment of each zone separately would not be practical or would be significantly more expensive. However, the design of treatments for multiple zones requires some special considerations. For example, the amount of each fluid stage entering each zone cannot be controlled by the engineer. Fluid partitioning is important, because it dictates the size of the individual fractures formed. In addition, if the partitioning is unfavorable, premature screenouts may occur in some zones.

Some early work on the propagation of multiple fractures (Lagrone and Rasmussen, 1963; Ahmed *et al.*, 1985; Cramer, 1987; Ben Naceur and Roegiers, 1990) considered fluid partitioning in a limited way (e.g., using a limited representation of the formation or at only a single point in time). In the method described in this section, fluid partitioning is calculated throughout the treatment.

To simulate the simultaneous propagation of multiple fractures, a single-fracture model (either analytical or numerical) is integrated with a set of constraints coupling the individual fractures. For the present, it is assumed that the individual fractures are well separated, with no mechanical interaction or any fluid flow between fractures except via the well. In this case, the fractures can be represented as in Fig. 6-20. Fractures

may open and propagate in  $n$  layers. At any time, the sum of the flow rates into all layers must equal the total injection rate. In addition, the sum of the closure stress in a zone plus the pressure drops through the path from the tip of the fracture in that zone to a reference point in the well must be the same for each fracture. This set of conditions can be expressed as

$$q_i = \sum_{j=1}^n q_{i,j} \quad (6-147)$$

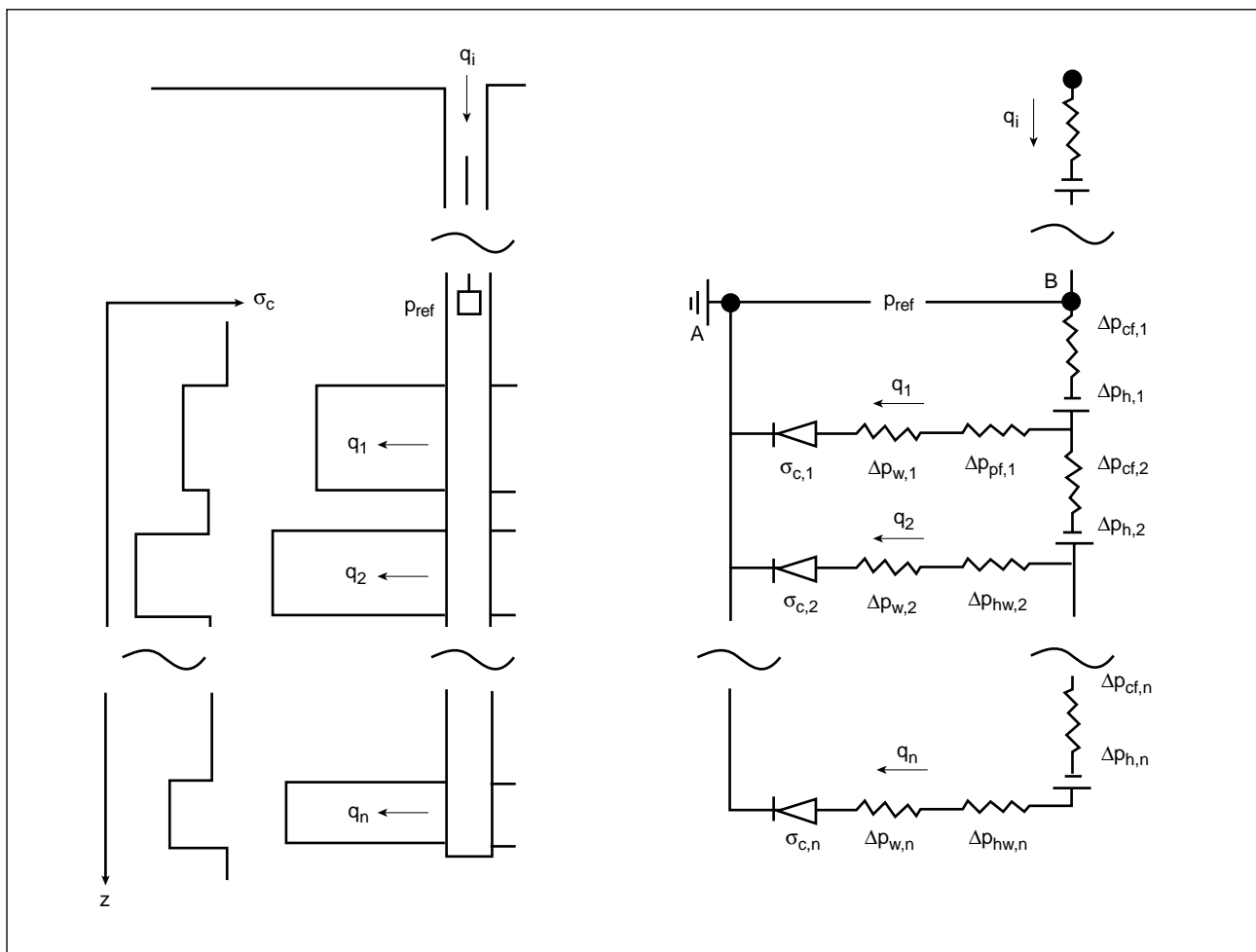
$$p_{ref} = \sigma_{c,j} + \Delta p_{w,j}(q_{i,j}) + \Delta p_{near\ wellbore,i}(q_{i,j}) - p_{h,j} + p_{cf,j}(q_{i,j}), \quad (6-148)$$

which is applied for each fracture. The terms on the right-hand side of Eq. 6-148 represent the closure stress, pressure drop in the fracture, pressure drop in the near-wellbore region including the perforations, hydrostatic pressure and casing friction, respectively. There are thus  $n + 1$  unknowns ( $n$  flow rates  $q_{i,j}$  and reference pressure  $p_{ref}$ ) and  $n + 1$  equations describing the system. Equation 6-148 is highly nonlinear, but the system can nevertheless be solved by standard techniques, as shown by Elbel *et al.* (1992).

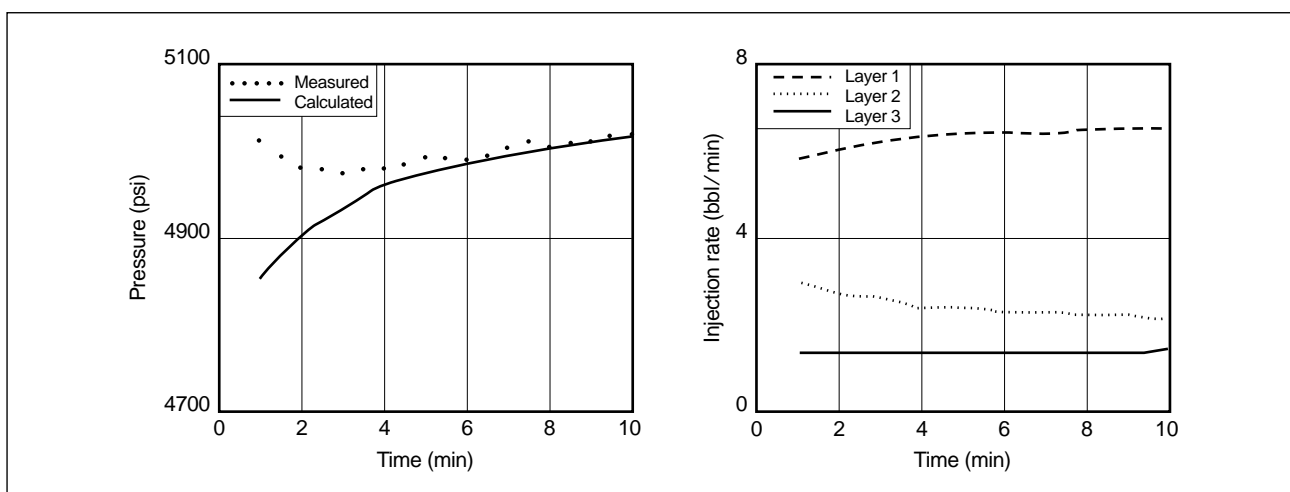
Figure 6-21 shows an example of a multilayer fracture treatment modeled as a set of PKN fractures. The fluid partitioning was measured using a spinner flowmeter, and the downhole pressure was recorded. The model accurately captures the behavior of the system.

Figure 6-22 shows a more complex case. The effect of a screenout in a layer reduces the flow into that layer while increasing it into others. Another interesting effect that the model shows is the effect of crossflow, in which fluid may flow between fractures after pumping ends. If this rate is excessive, proppant may be drawn out of one or more fractures and that flush fluid may be injected into other fractures, impairing near-wellbore fracture conductivity. The crossflow also violates the assumptions of pressure decline analysis, possibly resulting in an incorrect estimate of fluid loss.

Extension of the model to cases with height growth was reported by Mack *et al.* (1992). They showed that significant differences in both fracture geometry and flow partitioning can occur if the P3D representation is used for the individual fractures, because fracture height growth changes the relation between net pressure in the fracture and the flow rate into the fracture. Figure 6-23 shows an example comparing the pressure response and the resulting fracture geometry. In



**Figure 6-20.** Relationships for multiple fractures propagating simultaneously.



**Figure 6-21.** Multilayer fracture treatment modeled as a set of PKN fractures.

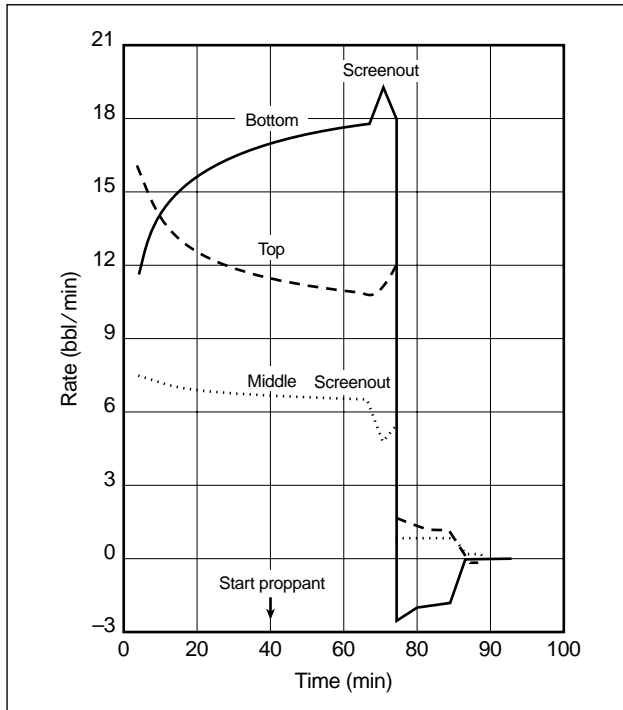


**Figure 6-22.** Fluid rate into three fractures, showing effects of screenout and crossflow.

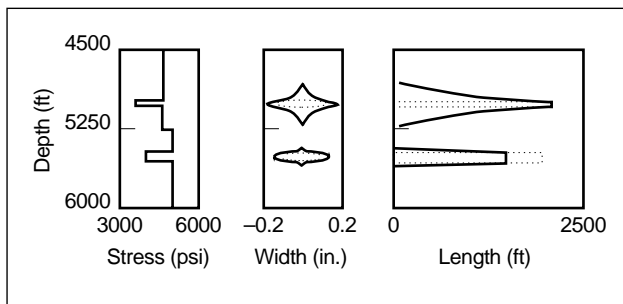


**Figure 6-23.** Pressure response and geometry of fractures modeled with the P3D model.

general, the multiple fractures would not connect into a continuous fracture unless the wellbore were perfectly aligned (e.g.,  $<2^\circ$ ) with the minimum stress directions. Except for this rare case, height growth would be inhibited after the tips overlapped.

## 6-11. Pump schedule generation

It is time consuming to design the schedule required to achieve a fracture of desired length and proppant concentration. One way to simplify the task is to use

an analytical solution such as that described in Sidebar 6L. However, the analytical solutions are generally applicable only for simple (i.e., radial, PKN or KGD) models. Another alternative is to develop a pump schedule generator that uses a numerical simulator. This tool uses the simulator in a so-called inverse mode to determine the schedule. It requires all the formation and fluid data necessary for a forward simulation. Instead of the schedule, however, the desired propped length, minimum and maximum proppant concentrations, and step in concentration between stages are specified. A typical concentration range could be 2 ppg minimum to 12 ppg maximum, with steps of 2 ppg.

To obtain the desired schedule, the simulator is started with a schedule derived from an analytic approximation or a schedule with a small pad stage and an arbitrarily sized slurry stage with the maximum proppant concentration. As the simulation proceeds, the simulation software monitors the leakoff of individual fluid elements in the fracture. As the fluid leaks off, the proppant concentration increases. If the user-specified maximum is exceeded, the simulator adjusts the proppant concentration down to the maximum value and keeps track of how much proppant has to be “converted” conceptually to fluid to maintain this. In addition, the fracture length is tracked and the schedule continually extended until the user-specified length is reached. When the desired length is reached, it is relatively simple to determine how much proppant (if any) is left in each fluid element. This represents the amount of proppant that should be in that element when pumped, providing a design proppant schedule. If proppant does not reach the fracture tip (i.e., some of the pad should have been slurry), this can be accounted for.

There are two issues that make this process more complex than as described. First, as previously noted, proppant affects fluid rheology, so modification of the amount of proppant during the simulation affects the fracture length. This is minimized by repeating the calculation with the schedule generated by the previous iteration as input. Three iterations are usually sufficient to converge on a suitable schedule. A more critical issue is that this method cannot easily account for bridging. Except during the initial small pad stage, there is always proppant everywhere in the simulated fracture, although some of it may later be converted to fluid. Bridging is therefore ignored and accounted for

## 6L. Approximate proppant schedules

**K. G. Nolte**  
Schlumberger Dowell

The facility to approximate proppant schedules for routine and tip screenout (TSO) designs based on fluid efficiency (Nolte, 1986b) is an important design tool. For a specified amount of fluid or proppant, the technique requires an efficiency estimate for the proppant treatment that can be determined from a fracture calibration treatment after an appropriate adjustment for differences in the injection times of the treatments. Efficiency is the ratio of the fracture volume to the injected volume before pumping is stopped. As illustrated on Fig. 6L-1, it defines the area under the ramp addition curve. This scheduling technique is reviewed here and generalized to include the effect of fluid-loss spurt.

Conceptually, spurt loss occurs only during the addition of new fracture area and before proppant reaches the fracture tip and halts fracture extension. Therefore, for normal design practices (see Section 5-1.1), spurt loss  $S_p$  occurs only for the pad fluid and must be isolated from the efficiency  $\eta$  to estimate the pad volume. The modified efficiency  $\eta_c$  excluding spurt, which reflects only the  $C_L$  component of fluid loss, can be found from Nolte (1989) as

$$\eta_c = 1 - \frac{1 - \eta}{\kappa}; \quad \kappa = 1 + \frac{S_p}{g_0 C_L \sqrt{t_s}} \quad (6L-1)$$

$$f_{LS} = \frac{(\kappa - 1)(1 - \eta)}{\kappa} = (1 - \eta) - (1 - \eta_c), \quad (6L-2)$$

where  $\kappa$  is the spurt factor for the case of total fluid loss with spurt relative to the case with no spurt and  $\kappa = 1$ ,  $g_0 \approx 1.5$  (see Chapter 9),  $C_L$  is the leakoff coefficient,  $t_s$  is the time of tip screenout or injection without a screenout, and  $f_{LS}$  is the volume fraction lost to spurt during pumping. Various means for obtaining the value of  $\kappa$  are discussed in Chapter 9.

The pad fraction is defined as the ratio of the pad volume to the total fluid and proppant volume injected during time  $t_s$ . In the absence of spurt loss ( $\kappa = 1$ ), the pad fraction can be expressed in various forms:

$$\begin{aligned} f_p(\eta) &\equiv (1 - \eta)^2 \\ &\equiv \frac{(1 - \eta)}{(1 + \eta)} = \frac{1}{(1 + 2f_{LL})} \equiv \frac{1}{(1 + G^*)}, \end{aligned} \quad (6L-3)$$

where  $f_{LL}$  is the ratio of fracture to loss volume during injection and is equal to  $\eta/(1 - \eta)$ , and  $G^*$  is the decline analysis variable discussed in Chapter 9. The pad relation  $(1 - \eta)^2$  in Eq. 6L-3 gives a smaller value than the relation  $(1 - \eta)/(1 + \eta)$ , which can be alternatively expressed as shown. Numerically simulated pad data fall between the two relations. When the spurt loss becomes significant ( $\kappa > 1$ ), the pad fraction is composed of two components: the first is equivalent to the no-spurt case given by Eq. 6L-3 and uses a value of  $\eta_c$  that excludes spurt loss, and the second is the contribution of spurt using Eq. 6L-2:

$$f_p(\kappa > 1) = f_p(\eta_c) + f_{LS} \quad (6L-4)$$

**Figure 6L-1.** Dimensionless proppant concentration versus dimensionless injected volume.

In addition to the pad, the schedule requires the volume fraction of proppant  $f_v$  to be added following the pad (Nolte, 1986b)

$$f_v(\tau) = f_o \tau^\epsilon; \quad \epsilon = \frac{(1 - f_p - \eta)}{\eta}; \quad 0 < \tau < 1 \quad (6L-5)$$

to approximate a spatially uniform concentration of  $f_o$  at the end of pumping. The dimensionless slurry time  $\tau$  is 0 when proppant addition begins and unity when pumping stops. This definition provides that  $f_p + \tau$  reflects the total time. Equation 6L-5 is illustrated as the curve in Fig. 6L-1, which also shows the division of volume between the pad fraction and the slurry fraction  $f_s$ . The definition of  $\epsilon$  leads to the shaded area under the  $f_v$  curve, which is equal to the efficiency. The remaining area is  $1 - \eta$ , which reflects the ratio of the loss volume to the injected volume.

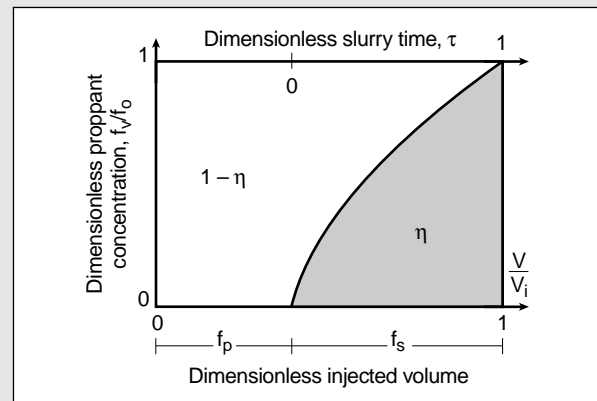
For scheduling a TSO treatment to achieve the final fracture volume  $V_f$  relative to that at screenout  $V_{iso}$ , Nolte's (1990) result can be extended to include spurt:

$$\frac{V_f(\Delta t_D)}{V_{iso}} = 1 + \frac{\Delta t_D}{\eta_{so}} + \frac{1 - \eta_{so}}{\kappa \eta_{so}} \left\{ \frac{g(\Delta t_D)}{g_0} - 1 \right\} \quad (6L-6)$$

$$\eta_p = \frac{\eta_{so}}{1 + \Delta t_D} \frac{V_f(\Delta t_D)}{V_{iso}}; \quad \Delta t_D = \frac{(t_p - t_{so})}{t_{so}} \quad (6L-7)$$

$$g(\Delta t_D) = (1 + \Delta t_D) \sin^{-1} (1 + \Delta t_D)^{-1/2} + \Delta t_D^{1/2}, \quad (6L-8)$$

where  $\Delta t_D$  is the dimensionless time after screenout,  $\eta_{so}$  and  $\eta_p$  are the respective efficiencies at screenout and end of pumping,  $t_p$  is the total pumping time, and  $t_{so}$  is the time at screenout. The term  $g(\Delta t_D)$  is the low-efficiency dimensionless fluid-loss function defined in the Appendix to Chapter 9, which also provides additional TSO relations. Low efficiency is typical for TSO treatments. The ratio of fracture volumes defined by Eq. 6L-6 can be replaced by the ratio of corresponding average widths, as graphically represented in Fig. 10-15 for various efficiency values. For proppant scheduling, the pad volume to achieve the TSO is found by using Eq. 6L-4 with  $\eta_{so}$  and  $f_{LS}$  corrected for spurt by Eqs. 6L-1 and 6L-2. The proppant addition is obtained from Eq. 6L-5 in terms of the final efficiency  $\eta_p$ . From a practical standpoint and to avoid proppant screenout midway in the fracture, the pad can be extended by a low-proppant-concentration stage, as discussed in Section 10-4.2.



only when the final design is simulated. Depending on the required conductivity, proppant of smaller diameter may be used for the treatment.

The method described here can be extended to TSO designs by specifying both the fluid concentrations and the desired areal concentration (e.g., 1 lbm of proppant per square foot of fracture face area). The simulator is run as previously described, except that once the design length is reached, length extension is artificially prevented and pumping continued until the fracture width is sufficient to obtain the desired areal concentration. The design of TSO treatments is discussed in Chapter 10.

## 6-12. Pressure history matching

One of the most difficult and expensive aspects of a well-engineered fracture design is obtaining the input required for the design simulators. Formation data, such as stresses, permeability and elastic properties,

are rarely well known. Obtaining such data is frequently difficult, expensive or both. This section describes a method to obtain data from the postjob analysis of pressure recorded during a treatment.

The only direct output from the formation during a fracture treatment is the pressure history measured during and after pumping the treatment. Chapter 9 discusses the interpretation of these pressure records in detail. However, these analyses can be only quantitatively accurate for relatively simple fracture geometries. This section considers the application of a formal theory of inversion (see Sidebar 6M) to complement qualitative interpretation and to increase the quantitative information available from the pressure record.

Inverse analysis is a method of characterizing a system from its response to an imposed input. In the case of hydraulic fracturing, the system is the reservoir, surrounding layers, the well and all associated parameters. The input is the pumping of a fluid, and the response is the pressure recorded during the treatment. The pressure record is analyzed to extract the proper-

### 6M. Theory and method of pressure inversion

The first step in the application of pressure history inversion is parameterization of the problem. This involves defining which properties are to be determined as well as setting bounds on their values and relations between values of different parameters. For example, it may be assumed that the stress in a layer is between 5000 and 6000 psi and that the stress in a neighboring layer is between 500 and 1000 psi higher. If the parameters are represented by the vector  $\bar{x}$  and the pressure record by  $\bar{p}$ :

$$\bar{p} = F(\bar{x}), \quad (6M-1)$$

where  $F$  represents the mechanics of fracture development and relates the observed pressure to the input parameters. The pressure vector is the sequence of discrete pressures measured during the treatment. The vector  $\bar{x}$  may be a list of selected parameters, such as

$$\bar{x} = [h_f, E', \sigma], \quad (6M-2)$$

indicating that the parameters to be found are the fracture height, Young's modulus and stress, and it is assumed that all other parameters are specified. Symbolically, the inversion process can be written as

$$\bar{x} = F^{-1}(\bar{p}), \quad (6M-3)$$

which is analogous to inverting a matrix to solve a set of linear equations with a known right-hand side. In this case, however, the known vector  $\bar{p}$  is the sequence of pressure readings, the relation is highly nonlinear and cannot be solved directly, and there are many more pressure readings than there are unknown parameters.

Two cases can be distinguished: the measured data defined by

$$\bar{p}_{meas} = F_{meas}(\bar{x}) \quad (6M-4)$$

and the simulated data defined by

$$\bar{p}_{sim} = F_{sim}(\bar{x}). \quad (6M-5)$$

Equations 6M-4 and 6M-5 imply that if a model is used to calculate the pressure data for a given set of parameters, it will generate a pressure record. Similarly, in the field, a pressure record is generated by the system with a set of parameters. The function  $F$  also has subscripts *sim* and *meas* to emphasize that the model is not an exact representation of reality, so even if the correct  $\bar{x}$  is found, the calculated and measured pressures may not agree. For example, if the PKN model is selected to match the data but if significant height growth has occurred, the pressure record generated by the correct  $\bar{x}$  will not match the measured pressure.

The objective of pressure history inversion is to minimize the difference between the measured and calculated pressure records, defined using an error function:

$$\epsilon = \left( \sum_i W_i |P_{sim,i} - P_{meas,i}|^r \right)^{1/r}, \quad (6M-6)$$

where the weighting factors  $W_i$  are typically set to 0 for points to be ignored and to 1 for all other points. The points can also be weighted according to the range of interest. For example, if only the decline period is to be matched,  $W_i$  is set to 0 for all points during pumping. The minimization of  $\epsilon$  can be performed numerically by a routine in a standard numerical library. Essentially, the algorithm consists of selecting a sequence of sets of parameter values until a satisfactory match is obtained, similar to the 1D Newton-Raphson method (Press *et al.*, 1986) for solving a single nonlinear equation.

ties of the formation so that the fracture geometry can be determined.

This approach is common in well testing, and some of the same pitfalls and limitations should be noted. For example, the pressure record should not be assumed to be the only information available. Other information, such as logs, should be used to narrow the expected ranges of parameters or to specify relations between them. In addition, the selection of the model types to be used should be made logically on the basis of other data. This is analogous to well test interpretation (Gringarten *et al.*, 1974), in which diagnostic plots and the knowledge of boundary conditions are used to specify model type (e.g., infinite reservoir versus rectangular bounded reservoir) before using an analysis package to determine the best estimates of permeability, height, etc. If this preanalysis is not done, there is a high risk of obtaining a good match to the pressure history with the incorrect parameters because of the nonuniqueness of the response; i.e., two different sets of inputs may provide the same output pressure. Gulrajani *et al.* (1996) discussed nonuniqueness in detail. Other limitations of pressure history inversion analysis are the ability of the algorithm to represent the mechanics and the time requirements for computer processing if a sophisticated fracture model is used.

Piggott *et al.* (1992) described a method for performing fracturing pressure history inversion to obtain formation properties. These properties can be used in future designs for wells in the same field and also to confirm or refute the assumptions of the design of the pumped treatment. For example, if the postjob application of pressure history inversion analysis indicates that the stresses in the barriers were smaller than expected, resulting in the occurrence of significant height growth, the effect on geometry would be quantified (i.e., significant height growth at the expense of reduced length in the pay zone, possibly reducing production significantly). This information could then be used to adjust predictions for production from that well and to modify input parameters for future well designs. Pressure history inversion applied on a calibration treatment could be used to redesign the main treatment.

A well-characterized data set is desirable for evaluating any pressure history inversion algorithm. Piggott *et al.* used field experiments conducted by the Gas

Research Institute (Robinson *et al.*, 1991) to evaluate a pressure history inversion algorithm. These experiments are ideal for this purpose, because more data were gathered in these wells than in typical commercial wells. Figure 6-24 shows the pressure match obtained by inverting the perforation diameter and the stresses in the layers bounding the pay zone in one well. For comparison, the inverted values of the diameter and stresses are listed in Table 6-1 (Robinson *et al.*, 1991). Gulrajani *et al.* (1996) also presented several field applications of pressure history inversion. These examples show the wide range of applicability of the technique, as well as the quality of the results that can be obtained by its application.

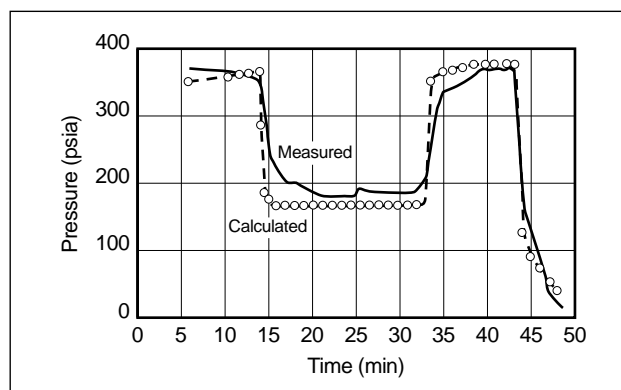


**Figure 6-24.** Pressure match obtained using pressure history inversion (Piggott *et al.*, 1992).

**Table 6-1. Parameters assumed and from data inversion (P3D model single-layer simulation) (Robinson *et al.*, 1991).**

Assumed parameters	
Young's modulus	$8 \times 10^6$ psi
Poisson's ratio	0.3
Fluid-loss height	42 ft
Closure pressure	6300 psi
Number of perforations	35
Leakoff coefficient	$0.0037 \text{ ft/min}^{1/2}$
Initial fracture height	120 ft
Parameters from inversion	
Stress contrast below pay zone	337 psi
Stress contrast above pay zone	186 psi
Perforation diameter	0.18 in.

# Fracturing Fluid Chemistry and Proppants

*Janet Gulbis, Schlumberger Dowell*

*Richard M. Hodge, Conoco*

## 7-1. Introduction

The fracturing fluid is a critical component of the hydraulic fracturing treatment. Its main functions are to open the fracture and to transport propping agent along the length of the fracture. Consequently, the viscous properties of the fluid are usually considered the most important. However, successful hydraulic fracturing treatments require that the fluids have other special properties. In addition to exhibiting the proper viscosity in the fracture, they should break and clean up rapidly once the treatment is over, provide good fluid-loss control, exhibit low friction pressure during pumping and be as economical as is practical. Characterization of these performance properties is addressed in Chapter 8.

Because reservoirs to be stimulated vary markedly in terms of temperature, permeability, rock composition and pore pressure, many different types of fluids have been developed to provide the properties described. The first fracturing fluids were oil-base; in the late 1950s, water-base fluids thickened with guar became increasingly popular. In 1969, the first crosslinked guar treatment was performed. By this time, only about 10% of fracturing treatments were conducted with gelled oil. Currently, more than 65% of all fracturing treatments use water-base gels viscosified with guar or hydroxypropylguar. Gelled oil treatments and acid fracturing treatments each account for about 5% of the total. About 20%–25% of all treatments contain an energizing gas. Additives are also used to enhance viscosity at high temperatures, to break viscosity at low temperatures or to help control leakoff of the fluid to the formation.

This chapter describes the chemistry of commonly used fracturing fluids and additives. In addition, it discusses how the chemistry is practiced at the well-site.

## 7-2. Water-base fluids

Because of their low cost, high performance and ease of handling, water-base fluids are the most widely used fracturing fluids. Many water-soluble polymers can be used to make a viscosified solution capable of suspending proppants at ambient temperature. However, as the temperature increases, these solutions thin significantly. The polymer concentration (polymer loading) can be increased to offset thermal effects, but this approach is expensive. Instead, crosslinking agents are used to significantly increase the effective molecular weight of the polymer, thereby increasing the viscosity of the solution (Fig. 7-1). The specific chemistry and performance of crosslinkers are discussed in more detail in Section 7-6.

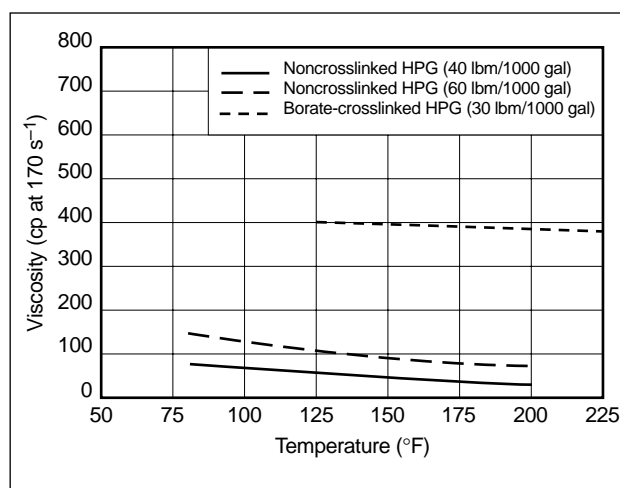


**Figure 7-1.** Effect of temperature and crosslinker on the viscosity of hydroxypropylguar solutions.

One of the first polymers used to viscosify water for fracturing applications was guar gum. Guar is a long-chain, high-molecular-weight polymer composed of mannose and galactose sugars (Whistler, 1959). Polymers composed of sugar units are called polysaccharides. Guar gum comes from the

endosperm of guar beans, which are grown mainly in Pakistan and India. The beans are removed from the bean pod and processed to separate the endosperm from the bean hull and embryo (splits), and the splits are ground into a powder (Fig. 7-2). The guar polymer has a high affinity for water. When the powder is added to water, the guar particles swell and hydrate, which means the polymer molecules become associated with many water molecules and unfold and extend out into the solution. The guar solution on the molecular level can be pictured as bloated strands suspended in water. The strands tend to overlap and hinder motion, which elevates the viscosity of the solution.

The structure of the guar molecule is usually represented as in Fig. 7-3. For a number of years, it was thought that guar consisted of a mannose backbone with galactose side chains on every other mannose unit (one galactose unit to two mannose units). The galactose and mannose sugars differ in the orientation of the OH groups on the ring. Recent studies indicate that the arrangement of galactose units may be more random, with galactose appearing on two or three consecutive mannose units (*Guar and Derivatives*, 1986). Also, the ratio of mannose to galactose may range from 1.6:1 to 1.8:1, instead of 2:1 as indicated in Fig. 7-3.

The process used to produce guar powder does not completely separate the guar from other plant materials, which are not soluble in water. As much as 6% to 10% insoluble residue can be present in guar fluids. Guar can be derivatized with propylene oxide to produce hydroxypropylguar (HPG) (Fig. 7-4). The



**Figure 7-2.** Guar pods, beans, splits and powder.

reaction changes some of the OH sites to  $-O-CH_2-CHOH-CH_3$ , effectively removing some of the crosslinking sites. The additional processing and washing removes much of the plant material from the polymer, so HPG typically contains only about 2% to 4% insoluble residue. HPG was once considered less damaging to the formation face and proppant pack than guar, but recent studies (Almond *et al.*, 1984; Brannon and Pulsinelli, 1992) indicate that guar and HPG cause about the same degree of pack damage.

Hydroxypropyl substitution makes HPG more stable at an elevated temperatures than guar; therefore, HPG is better suited for use in high-temperature ( $>300^\circ\text{F}$  [ $150^\circ\text{C}$ ]) wells. The addition of the less hydrophilic hydroxypropyl substituents also makes

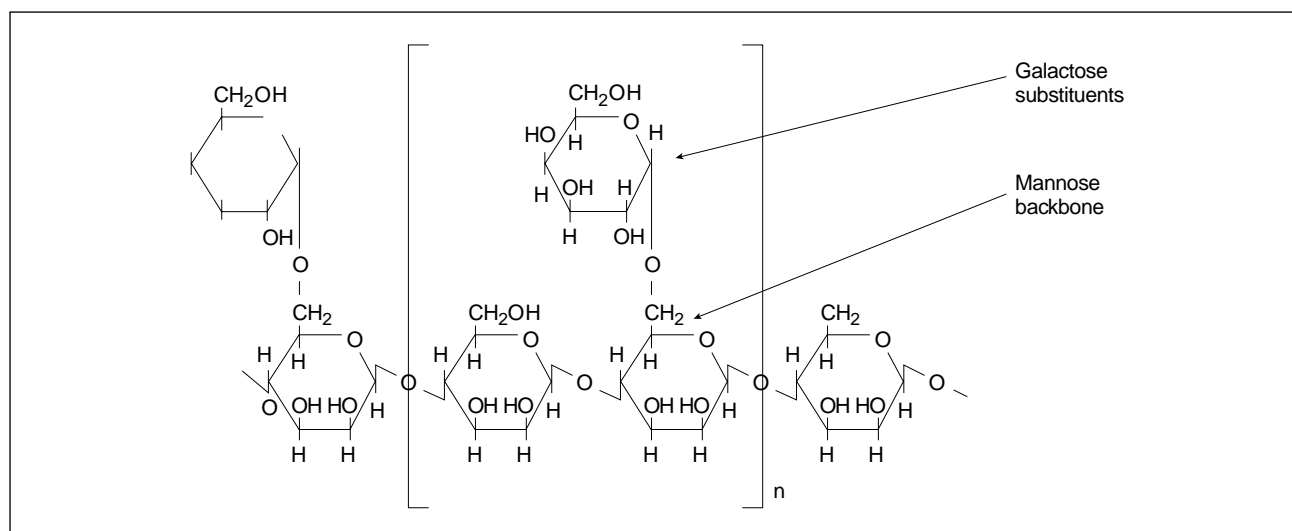


**Figure 7-3.** Structure of guar.



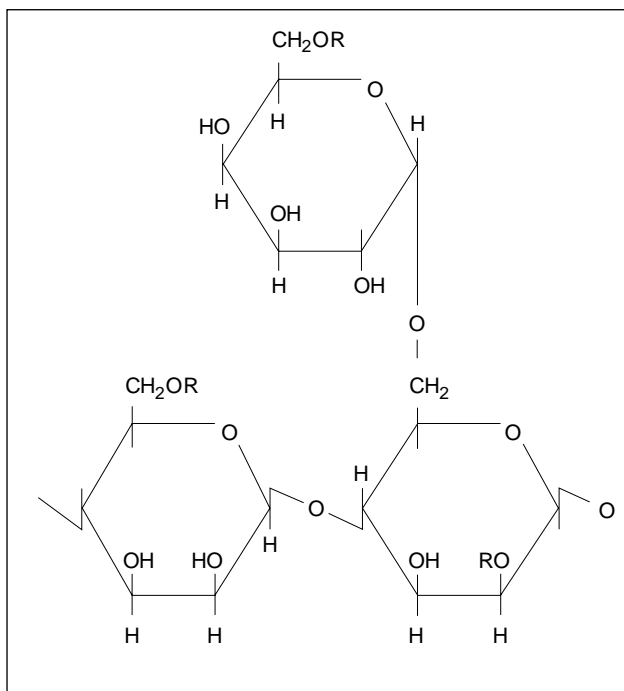


**Figure 7-4.** Repeating-unit structure of hydroxypropylguar,  $R\text{-CH}_2\text{-CHOH-CH}_3$ .

the HPG more soluble in alcohol. A common quality assurance check is to add an equal volume of methanol to the polymer solution. Guar precipitates, while HPG with the standard level of hydroxypropyl substitution does not (Ely, 1985). HPG containing less hydroxypropyl substitution than the standard generally fails the test.

Another guar derivative used in recent years is carboxymethylhydroxypropylguar (CMHPG). This “double-derivatized” guar contains the hydroxypropyl functionality of HPG as well as a carboxylic acid substituent. CMHPG was first used for low-temperature wells (Almond and Garvin, 1984). For these applications, it is usually crosslinked with Al(III) through the carboxy groups. This provides a less expensive fluid than HPG crosslinked with Ti and Zr complexes. More recently, CMHPG has been crosslinked with Zr crosslinker to produce fluids with higher viscosity at high temperatures than those made with comparable amounts of HPG (Hunter and Walker, 1991).

Cellulose derivatives have occasionally been used in fracturing fluids (Carico and Bagshaw, 1978). Hydroxyethylcellulose (HEC) (Fig. 7-5) or hydroxypropylcellulose (HPC) is used when a very clean fluid is desired. These polymers have a backbone

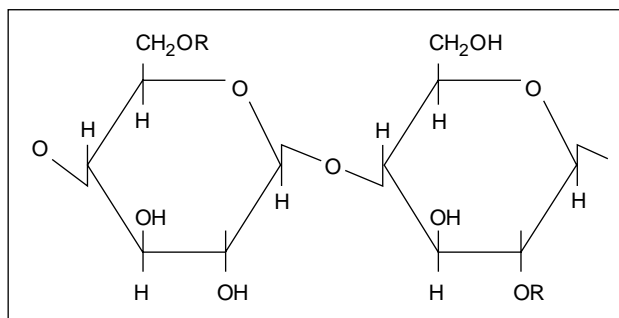


**Figure 7-5.** Repeating-unit structure of hydroxyethylcellulose,  $R\text{-CH}_2\text{CH}_2\text{OH}$ .

composed of glucose sugar units. Although similar to the mannose backbone of guar, there is a significant difference. Guar contains hydroxyl pairs that are positioned on the same side of the sugar molecule (cis orientation). In HEC, the OH groups are on adjacent carbons, but they are on opposite sides of the ring (trans orientation). Because of their close proximity, the cis arrangement for guar is easily crosslinked, whereas the increased separation of the trans arrangement makes HEC more difficult to crosslink. However, HEC can be crosslinked at a pH of 10 to 12 with Zr(IV) (Underdown *et al.*, 1984) or with lanthanides (Dovan and Hutchins, 1993). To crosslink HEC under milder conditions, the carboxymethyl group can be added to make carboxymethylhydroxyethylcellulose (CMHEC), which makes crosslinking with metal ions such as Al(III), Ti(IV) and Zr(IV) possible at a pH of approximately 4 to 6.

Still another type of polymer is xanthan gum (Fig. 7-6). Xanthan is a biopolymer, produced metabolically by the microorganism *Xanthomonas campestris* (Lipton and Burnett, 1976). Xanthan solutions behave as power law fluids even at low shear rates (Kirkby and Rockefeller, 1985), whereas HPG solutions become Newtonian. Clark *et al.* (1985) showed that at shear rates less than  $10\text{ s}^{-1}$  the low-shear properties enable xanthan solutions to suspend sand better than HPG. These properties may increase the future use of xanthan for fracturing, but currently xanthan is more expensive than guar or cellulose derivatives, and it is used less frequently. Davies *et al.* (1991) reported using a different biopolymer, scleroglucan, because of its near-perfect proppant suspension and because it does not require a breaker.

Partially hydrolyzed acrylamide polymers are used as friction-reducing agents. These polymers can be used at low loading (less than 10 lbm/1000 gal) to



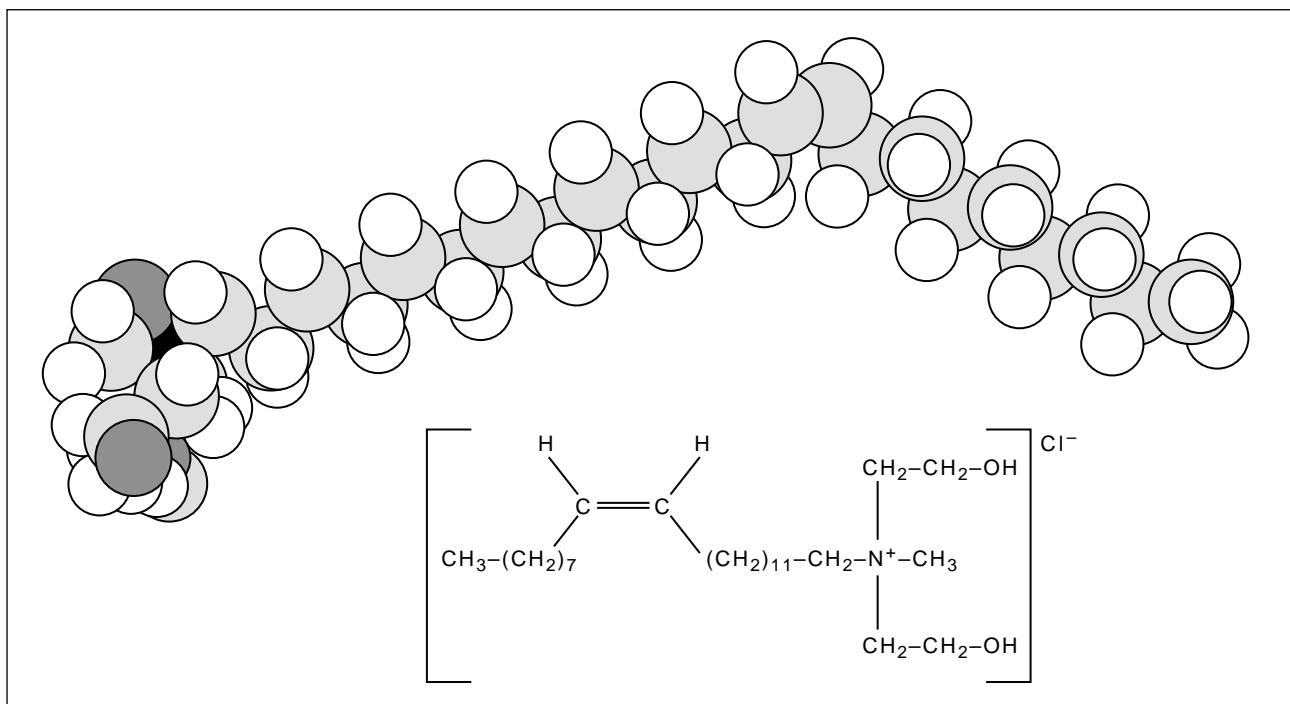


**Figure 7-7.** Molecular and structural formulas for a viscoelastic surfactant thickener.

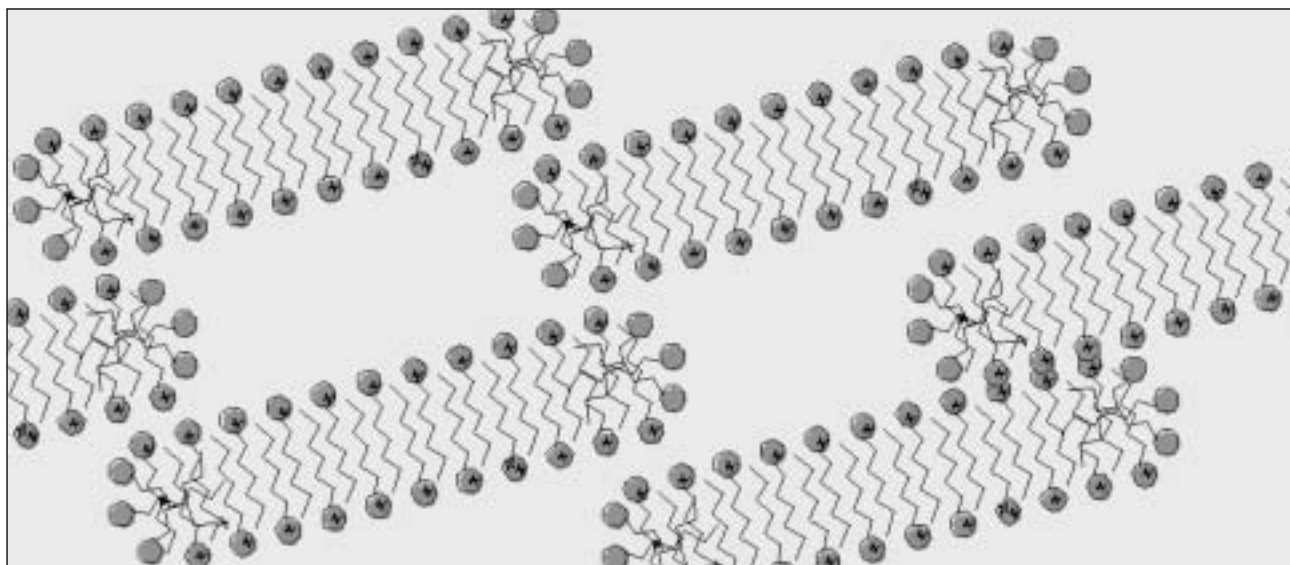


**Figure 7-8.** Micellar association.

pant packs treated with VES fluid systems is >95%. VES systems can also be foamed with nitrogen. No additional foaming agents are required.

### 7-3. Oil-base fluids

Heavy oils were used originally as fracturing fluids, primarily because these fluids were perceived as less damaging to a hydrocarbon-bearing formation than water-base fluids. Their inherent viscosity also makes them more attractive than water (Howard and Fast, 1970). Oil-base fluids are expensive to use and operationally difficult to handle. Therefore, they are now used only in formations that are known to be extremely water-sensitive.

In the 1960s, the industry used aluminum salts of carboxylic acids (e.g., aluminum octoate) to raise the viscosity of hydrocarbon fracturing fluids (Burnham *et al.*, 1980). This improved the temperature stability and proppant-carrying capability of the fluids. In the 1970s, the aluminum carboxylate salts were replaced by aluminum phosphate ester salts. Again, the temperature range of the fluids was extended and proppant transport was enhanced. Today, aluminum phosphate ester chemistry remains the preferred method of gelling hydrocarbons for fracturing purposes. Both methods of thickening oil rely on an “associative” mechanism (Baker *et al.*, 1970). As suggested in Fig. 7-9, interactions between the aluminum complexes and phosphate ester molecules produce a long polymer chain (Burnham *et al.*, 1980).

The R groups shown in Fig. 7-9 are hydrocarbon chains that must be soluble in the oil to be gelled. The soluble R groups keep the aluminum phosphate ester polymer in solution. Generally, the R groups are hydrocarbon chains containing 1 to 18 carbon atoms (Crawford *et al.*, 1973). The R groups have a high affinity for oils such as kerosene and diesel that comprise 12- to 18-carbon (and somewhat higher) chains. Crude oils are composed of a larger number

of different organic compounds and may contain paraffins and asphaltenes. Some high-molecular-weight compounds, especially paraffins and asphaltenes, are not compatible with the aluminum phosphate ester gelling system. Many crude oils may be gelled, but it is good practice to test them prior to attempting to gel on location.

The R groups can be pictured as forming an oil-compatible shield around the polar core of aluminum ions (McKenzie, 1980). Polar species (such as water, acids, bases or salts) are incorporated into the polar core and affect the association of the aluminum ions and phosphate ester groups. These materials can make the gel structure more rigid, or they can destroy the gel structure.

The viscosity of the standard aluminum phosphate ester gel is controlled by varying the quantities of aluminum compound and phosphate ester. To improve high-temperature performance, the viscosity of the gel can be increased by increasing the amount of polymer; however, this results in very high viscosities on the surface, which make it difficult to draw the fluid out of the tanks to the pumps. One approach used is to add part of the gelling materials “on the fly” so that high viscosity is not achieved until the fluid reaches the fracture (Harris *et al.*, 1986; Cramer *et al.*, 1991). On-the-fly addition means that the materials are added to the fluid as the fluid is pumped downhole. Another approach is to maximize thermal stability by carefully controlling the composition of the solution to provide optimum conditions for association of the aluminum and phosphate ester species (Gross, 1993).

Typically, these gels take several hours to form once the chemicals are mixed together. Recent developments in gelled oil chemistry make a true continuous-mix (all materials added on the fly) gelled oil possible. By changing the aluminum source, the aluminum/phosphate ester ratio in the gel and/or the phosphate ester mix (Daccord *et al.*, 1985; McCabe *et al.*, 1990; Huddleston, 1992), a rapidly thickening gel composition can be achieved. With this chemistry, the aluminum source and phosphate ester can be added to the hydrocarbon as it is pumped downhole. The gel is formed on the way to the perforations. The expense of premixing the gel is eliminated, as well as the disposal problem of unused gel.

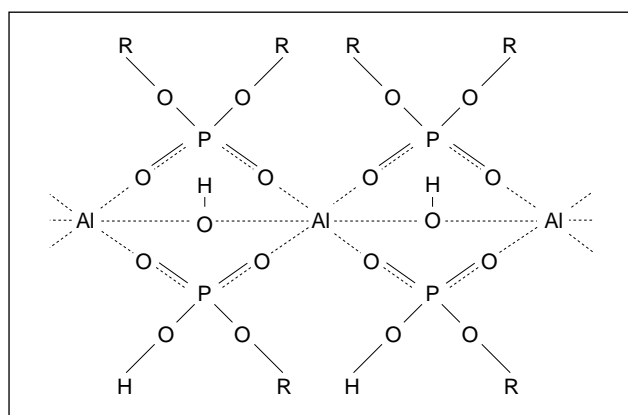


**Figure 7-9.** Proposed structure of the aluminum phosphate ester polymer chain (Burnham *et al.*, 1980).

## 7-4. Acid-based fluids

Acid fracturing is a well stimulation process in which acid, usually hydrochloric acid (HCl), is injected into a carbonate formation at a pressure sufficient to fracture the formation or to open existing natural fractures. As the acid flows along the fracture, portions of the fracture face are dissolved. Because flowing acid tends to etch in a nonuniform manner, conductive channels are created that usually remain when the fracture closes. The effective length of the fracture is determined by the etched length, which depends on the volume of acid used, its reaction rate and the acid fluid loss from the fracture into the formation. The effectiveness of the acid fracturing treatment is determined largely by the length of the etched fracture.

In some cases, especially in carbonates, a choice exists between acid and propped fracturing treatments. Operationally, acid fracturing is less complicated because no propping agent is employed. Also, the danger of proppant screenout and the problems of proppant flowback and cleanout from the wellbore after the treatment are eliminated. However, acid is more expensive than most nonreactive treating fluids.

The major barrier to effective fracture penetration by acid appears to be excessive fluid loss (Nierode and Kruk, 1973). Fluid loss is a greater problem when using acid than when using a nonreactive fluid. The constant erosion of fracture faces during treatment makes it difficult to deposit an effective filter-cake barrier. In addition, acid leakoff is extremely nonuniform and results in wormholes and the enlargement of natural fractures. This greatly increases the effective area from which leakoff occurs and makes fluid-loss control difficult.

### 7-4.1. Materials and techniques for acid fluid-loss control

Various additives and treating techniques have been developed to control acid fluid loss. Among these are particulates (oil-soluble resins and 100-mesh sand) and gelling agents. In general, acid fluid-loss additives have not been used extensively because of performance and cost limitations. As a result, alternate methods of fluid-loss control usually are employed. The most common technique involves the use of a viscous pad preceding the acid. The pad is used to

initiate the fracture and to deposit a filter cake that acts as a barrier to acid leakoff. The ability of a single viscous pad fluid to control fluid loss is questionable. Studies by Nierode and Kruk (1973), Coulter *et al.* (1976) and Crowe *et al.* (1989) show that the filter cake deposited by the pad is quickly penetrated by wormholes resulting from acid leakoff. Once this occurs, the acid fluid loss is identical to that occurring if no pad were used. In recent years, multiple stages of viscous pad have been used to control acid fluid loss (Coulter *et al.*, 1976). In this widely used technique, the fracture is initially created by a gelled pad, after which alternating stages of acid and additional polymer pad are pumped. These additional pad stages are designed to enter and seal wormholes created by the preceding acid. Each alternating pad stage in this treatment is usually equal to or larger than the acid stage that preceded it.

In addition to fluid-loss additives, two-phase fluids (foams and emulsions) have been shown to effectively control fluid loss during acid fracturing treatments. Nierode and Kruk (1973) presented data showing that an acid external emulsion, consisting of an oil inner phase with gelled acid as the outer phase, provides good fluid-loss control. The use of these acid external emulsions in well stimulation has been rather limited. The use of foamed acid is one of the most effective methods for controlling acid fluid loss. Scherubel and Crowe (1978) and Ford (1981) showed that foamed acids provide excellent fluid-loss control. Fluid-loss control is further enhanced by the use of a viscous pad preceding the foamed acid. However, foaming the acid reduces the effective amount of acid available for etching because there is less acid present per unit volume injected. As a result, a high acid concentration (e.g., 28% HCl) should be used in preparing foamed acid to maximize the amount of acid available for fracture etching.

Acid fluid loss can also be reduced by gelling the acid. This method of control has become widely used since the development of more acid-stable thickening agents. Commonly, thickeners include xanthan biopolymers, various acrylamide copolymers and certain surfactants that thicken acid by micellar association.

A gelling agent must be sufficiently stable to allow the gelled acid to retain its viscosity at the treating temperature. However, slow cleanup or actual plugging of the well may result if the viscosity of the

spent acid is too high or if the polymer degrades to form insoluble reaction products. Procedures for evaluating acid gelling agents and the advantages and limitations of various materials were described by Crowe *et al.* (1981). Guar and cellulose base thickeners lack sufficient stability for use in acid at temperatures above 125°F [50°C]. Xanthan biopolymers can be used at temperatures up to 200°F [90°C]; at higher temperatures acrylamide copolymers are generally employed. Certain acrylamide copolymers are stable at high temperatures and do not produce insoluble reaction products. However, acrylamide homopolymers should not be used as acid thickeners. They are rapidly hydrolyzed and combine with calcium to form insoluble precipitates upon spending of the acid.

A number of crosslinked gelled acids have been developed. These systems employ various acid gelling agents and use either polyvalent metal ions or aldehydes as crosslinkers. In general, the crosslinked acids tend to be shear sensitive and are usually unstable at elevated temperatures. Breaking of the crosslinked gel in spent acid also is a problem. It may be claimed that the gel will be broken by acid degradation, and data are usually presented showing a loss of viscosity with time in live acid. However, in actual practice, the acid spends rapidly with no live acid available to degrade the polymer. As a result of their high viscosity, the crosslinked systems present a greater risk of formation damage and have not been widely used.

Certain surfactants can also be used as thickeners for gelling acid (Norman, 1978). These gelling agents thicken acid by forming micelles that associate in chainlike structures and therefore behave much like polymers. Gelled acids of this type are quite shear-stable, because micellar chains reform quickly following shearing. Another advantage of the surfactant thickeners is the low viscosity of the spent acid. These acid thickeners are usually designed to provide considerable viscosity in live acid but to thin during spending. This occurs as the result of the disruption of micellar association brought about by changes in the ionic environment caused by increased concentrations of reaction products formed during spending of the acid. The lowered spent-acid viscosity aids the recovery of treating fluids following the treatment. However, this can also be a disadvantage. Acid fluid loss is dependent largely upon the leakoff viscosity of the spent acid. As a result,

the fluid loss of acid gelled with surfactant-type thickeners, which break during spending, is not significantly different from that of ungelled acid. Only those gelled acids that retain their viscosity during leakoff are capable of providing effective fluid-loss control. Another disadvantage of this gelling agent is the limited temperature range over which it can be used. Although the surfactant itself is stable in acid, it provides little increase in viscosity above 150°F [65°C]. High temperatures disrupt the micellar association responsible for acid viscosity.

#### 7-4.2. Materials and techniques for acid reaction-rate control

Reducing the reaction rate of acid to achieve increased etched fracture penetration is an important consideration. In low- to moderate-temperature wells, retardation is not critical. However, in applications greater than about 250°F [120°C] retardation can be critical to the success of the treatment (Nierode and Kruk, 1973). One of the most common methods of extending live acid penetration involves the injection of a viscous nonreactive pad preceding the acid. The pad reduces the acid reaction rate by increasing the fracture width and by cooling the fracture surfaces. Weak organic acids (acetic or formic acid) are used as retarded acids. These weakly ionized acids react at a much slower rate than HCl, even at very high temperatures. Additives, such as retarders, reduce the reaction rate by forming a protective hydrophobic film on carbonate surfaces that acts as a barrier to slow acid attack or by blanketing carbonate surfaces with a thin layer of carbon dioxide foam. Oil-outside emulsions are the most effective retarders because the external oil phase physically separates the acid from the reactive carbonate surface.

Gelled acids are usually considered retarded. However, the amount of retardation provided by the increased acid viscosity is generally small and can actually accelerate the acid reaction rate under flowing conditions, as shown by examining the data presented by Gdanski and Norman (1986) and Crowe *et al.* (1990).

### 7-5. Multiphase fluids

There are situations in which the properties of standard water-base, oil-base or acid-based fluids can be

enhanced by incorporating a second phase into the fluid. Foams are created by adding gas to the fluid. Emulsions are created by mixing oil and water together. The different systems are described in this section.

### 7-5.1. Foams

A foam is a stable mixture of liquid and gas. To make the mixture stable, a surface-active agent (surfactant) is used. The surfactant concentrates at the gas/liquid interface and lowers the interfacial tension. The surfactant stabilizes thin liquid films and prevents the cells from coalescing.

Pressurized gas (nitrogen or carbon dioxide) in a foam expands when the well is flowed back and forces liquid out of the fracture. Foams accelerate the recovery of liquid from a propped fracture and thus are excellent fluids to use in low-pressure reservoirs. Also, the liquid phase is minimal because foams contain up to 95% by volume gas. In the case of a water-base fluid, foaming the fluid significantly decreases the amount of liquid in contact with the formation. Therefore, foams perform well in water-sensitive formations (Ward, 1984; Ainley, 1983). Foams yield pseudoplastic fluids with good transport properties (King, 1982; Reidenbach *et al.*, 1986). They provide good fluid-loss control in low-permeability formations where the gas bubbles are approximately the size of the rock pore openings (Harris, 1985).

Foams are described by their quality:

$$\text{foam quality} = \frac{\text{gas volume}}{\text{foam volume}} \times 100. \quad (7-1)$$

Originally, foam quality was considered to range from 52% to 95%. Above 95%, the foam usually changes to a mist, with gas as the continuous phase. Below 52%, a stable foam does not exist because there are no bubble/bubble interactions to provide resistance to flow or to gravity separation (Mitchell, 1969). Above 52% gas, the gas concentration is high enough that the bubble surfaces touch.

Stable dispersions of gas in liquid can be prepared with qualities less than 52% (Watkins *et al.*, 1983). It may not be appropriate to call them foams, but they can be used effectively as energized fluids. Viscosifying the liquid phase with a polymer is an effective method for increasing the stability of foams (Wen-

dorff and Ainley, 1981). The thicker the continuous phase, the more difficult it is for the gas bubbles to move together and coalesce. Guar, HPG and xanthan gum have been used as stabilizers. Still, a relatively high quality, although not as high as 52%, is required to maintain dispersion of the gas phase.

A further improvement in foam stability can be achieved by crosslinking the polymer in the aqueous phase (Watkins *et al.*, 1983). The liquid phase then becomes viscous enough to maintain dispersion of the gas bubbles, even at foam quality less than 40%. Thickening the liquid phase also improves foam rheology and fluid-loss control. Proppant concentrations in the foamed fluid are generally lower than the concentration achieved with single-phase, liquid treatments. Therefore, a larger volume of foam may be required to place the desired amount of proppant.

Nitrogen and carbon dioxide are used as energizing gases.  $N_2$  is less dense than  $CO_2$ .  $CO_2$  creates a denser foam and, consequently, lower surface treating pressures because of the increased hydrostatic head in the wellbore. Lower treating pressures reduce pumping costs. On the other hand, because  $CO_2$  is much more soluble in oil and water than  $N_2$ , it takes more  $CO_2$  to saturate the liquid and to create the foam. Reductions in pumping costs may be offset by increases in material costs.

### 7-5.2. Emulsions

An emulsion is a dispersion of two immiscible phases such as oil in water or water in oil stabilized with a surfactant. Emulsion-based fracturing fluids are highly viscous solutions with good transport properties. The higher the percentage of the internal phase, the more resistance there is to droplet movement, resulting in a higher viscosity.

Emulsion-based fracturing fluids have been used for a number of years (Kiel, 1971). The most common fluid, termed polyemulsion, is composed of 67% hydrocarbon internal phase, 33% viscosified brine external phase and an emulsifying surfactant. Viscosifying the aqueous phase improves the emulsion stability and significantly reduces friction pressure during pumping because the polymer acts as a friction reducer. The polymer concentration used is generally 20 to 40 lbm/1000 gal, so the fluid contains only one-sixth to one-third as much polymer as a standard water-base fracturing fluid. The emulsion

usually breaks because of adsorption of the emulsifier onto the formation rock; because so little polymer is used, this type of fluid is known for causing less formation damage and cleaning up rapidly (Roodhart *et al.*, 1986).

Disadvantages of polyemulsions are high friction pressure and high fluid cost (unless the hydrocarbon is recovered). Polyemulsions also thin significantly as the temperature increases, which limits their use in hot wells.

## 7-6. Additives

A fracturing fluid is generally not simply a liquid and viscosifying material, such as water and HPG polymer or diesel oil and aluminum phosphate ester polymer. Various additives are used to break the fluid once the job is over, control fluid loss, minimize formation damage, adjust pH, control bacteria or improve high-temperature stability. Care must be taken when using multiple additives to determine that one additive does not interfere with the function of another additive.

### 7-6.1. Crosslinkers

A number of metal ions can be used to crosslink water-soluble polymers (Conway *et al.*, 1980). Borate, Ti(IV), Zr(IV) and Al(III) compounds are frequently used crosslinkers. The borate compounds (Deuel and Neukorn, 1949) and transition metal complexes (Chrisp, 1967) react with guar and HPG through cis-OH pairs on the galactose side chains to form a complex, as illustrated in Fig. 7-10a. As the

molecules overlap, the complex in Fig. 7-10a can react with other polymer strands to form a crosslinked network (Menjivar, 1984) illustrated in Fig. 7-10b. A species is created with 2 times the molecular weight of the polymer alone. Because each polymer chain contains many cis-hydroxyls, the polymer can be crosslinked at more than one site. Networks with a very high molecular weight develop, especially under static conditions, resulting in highly viscous solutions.

One of the simplest crosslinkers, the borate ion, is used to produce very viscous gels with guar and HPG that can be stable above 300°F. At a pH above 8, borate ions and guar form an extremely viscous gel in a matter of seconds. To maximize the thermal stability of the crosslinked gel, the pH and borate concentration must be increased, with an optimum pH of 10 to 12 depending on the borate compound and borate ion concentration (Harris, 1993). The borate ion  $B(OH)_4^-$  is believed to be the crosslinking species. Regardless of the borate source (boric acid, borate salt or borate complex), a high pH is required to shift the equilibrium and maintain an adequate concentration of borate ions (Prud'homme, 1991):



The fraction of boric acid present at ambient temperature as the effective crosslinking compound,  $B(OH)_4^-$ , is shown in Fig. 7-11 as a function of pH. As illustrated, increasing the pH results in a higher concentration of  $B(OH)_4^-$ . Increasing the temperature reduces the pH, resulting in a lower crosslinker concentration and lower viscosity. Attempting to compensate for the detrimental effects of temperature by increasing the  $H_3BO_3$  concentration can cause syneresis (overcrosslinking) of the gel.

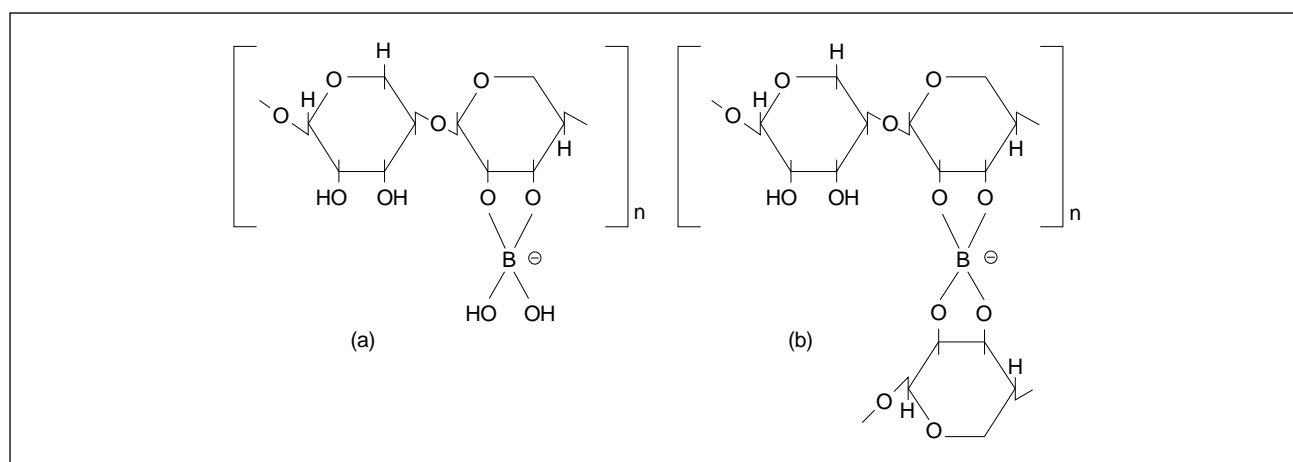
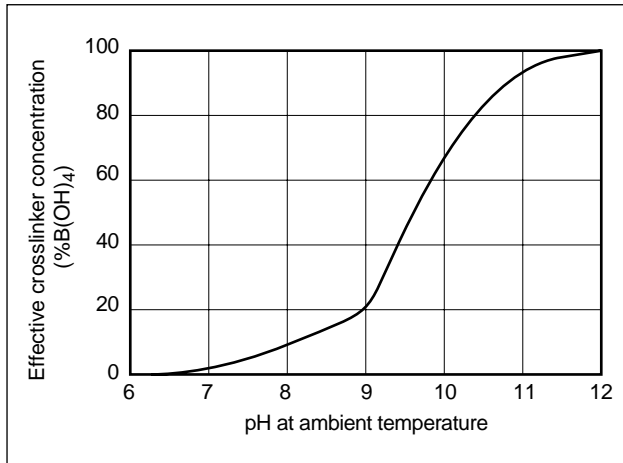


Figure 7-10. Proposed crosslinking mechanism (Menjivar, 1984).





**Figure 7-11.** Borate in concentration as a function of pH.

Transition metal crosslinkers have been developed for high-temperature applications and/or low-pH environments (i.e., CO<sub>2</sub>-energized fluids). Titanium and zirconium complexes have been used most frequently because of their affinity for reacting with oxygen functionalities (cis-OH and carboxyl groups), stable +4 oxidation states (Cotton and Wilkinson, 1972) and low toxicity. The bond formed between the titanium or zirconium complex and the polymer is thermally stable. The upper temperature limit for these gels is 350° to 400°F [150° to 200°C]. It appears that the stability of the polymer backbone, rather than the polymer-metal ion bond, is the limiting factor. Very hot wells (>400°F) can be fractured with these fluids if the treatments are designed to provide adequate cooldown by injecting sacrificial fluid immediately before the fracturing treatment. However, it must be emphasized that rudimentary heat transfer calculations suggest that the cooldown of a formation is only moderate and confined near the well unless fluid leakoff is substantial. The vast majority of the fracturing fluid is likely to be exposed to the static reservoir temperature.

Regardless of the gel composition or viscosity, all fracturing gels thin with shear and heat. However, some gels return to their original state once shear or heat is removed. Typically, borate crosslinking is reversible; crosslinks form and then break, only to form again (Deuel and Neukorn, 1949). If the polymer is not thermally degraded, this reversible behavior continues to accommodate changes in shear rate or temperature. The transition metal-polymer bond is sensitive to shear. High shear irreversibly degrades transition metal-crosslinked fluids (Craigie, 1983). Unlike borate crosslinker, once the bond between the transition metal crosslinker and polymer is broken, it does not reform. Therefore, if the crosslinking rate is very rapid in the high shear region of the tubing, an irreversible loss of viscosity occurs. The effect that tubing shear has on fluid viscosity is illustrated in Fig. 7-12. A fluid that is crosslinked rapidly under unrealistic conditions of low shear is very viscous at high temperatures (curve A). The same fluid crosslinked at high-shear-simulating conditions in the tubing loses much of its viscosity because of shear degradation and behaves like curve C. Other characteristics of commonly used crosslinkers are compared in Table 7-1.

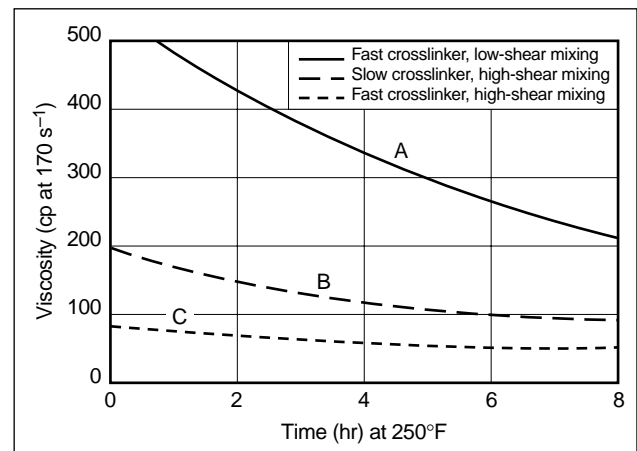


**Figure 7-12.** Effect of shear and crosslinking rate on viscosity.

**Table 7-1. Characteristics of commonly used crosslinkers**

Crosslinker	Borate	Titanate	Zirconate	Aluminum
Crosslinkable polymers	Guar, HPG, CMHPG	Guar, HPG, CMHPG, CMHEC <sup>†</sup>	Guar, <sup>‡</sup> HPG, <sup>‡</sup> CMHPG, CMHEC <sup>†</sup>	CMHPG, CMHEC
pH range	8–12	3–11	3–11	3–5
Upper temperature limit (°F)	325	325	400	150
Shear degraded	No	Yes	Yes	Yes
<sup>†</sup> Low-pH (3–5) crosslinking only				
<sup>‡</sup> High-pH (7–10) crosslinking only				

To avoid the detrimental effects of high shear occurring in the tubing, the crosslinking rate is usually reduced to limit viscosity development until the fluid is near the target zone. In addition to minimizing shear degradation, delaying crosslinking also reduces frictional pressure losses and, therefore, hydraulic horsepower requirements. A number of factors can be manipulated to control the rate of crosslinking. These include fluid temperature and pH, shear conditions, crosslinker type and the presence of other organic compounds that react with the crosslinker. For example, increasing the temperature or pH usually accelerates the crosslinking reaction. Fortunately, some of these parameters can be controlled to slow down the crosslinking reaction so that it does not occur in the high-shear region (generally 500 to 1500 s<sup>-1</sup>) of the tubing, while allowing the bulk of the crosslink reaction to occur in the low-shear region (generally 10 to 200 s<sup>-1</sup>) of the fracture. By manipulating the chemistry, shear degradation and frictional pressure loss can be minimized. The effect of reducing the crosslinking rate on viscosity is illustrated by comparing curves B (delayed crosslinking) and C (rapid crosslinking) in Fig. 7-12. The effects of high shear can be reduced, but not eliminated, by slowing the crosslinking rate (i.e., curve B does not reach the viscosity values of curve A).

A number of techniques can be used to control the reaction rate of the metal ion and polymer. For example, many different organic molecules (ligands) are capable of reacting with the metal ion (crosslinker), which can strongly affect the properties of the ion. Crosslinkers can be delayed by competition

for the metal ion between the polymer and other ligands. A hypothetical titanium complex with two ligands (L) capable of binding at two sites (bidentate) and two ligands (A) capable of binding at one site (monodentate) is illustrated in Fig. 7-13a. On addition to water, complexes of titanium and zirconium form colloidal particles (Fig. 7-13b) (Prud'homme *et al.*, 1989). For crosslinking to occur, polymer molecules must displace the organic compounds at the coordination sites on the surface of the colloidal particles. If the ligands are easy to displace, crosslinking occurs rapidly. If the organic compounds are difficult to displace or are present in a high concentration, crosslinking occurs slowly (Payne and Harms, 1984; Rummo, 1982; Hodge, 1988a, 1988b). Forming slow-reacting complexes to control the crosslinking rate can also be used with borate ions to minimize friction pressure and greatly improve thermal stability (Dawson, 1991).

Slowly dissolving crosslinkers and activators can be used to delay crosslinking. As the crosslinking ion or activator concentration increases, the crosslink density increases, producing a rise in viscosity. Some borate compounds, such as colemanite and ulexite, dissolve slowly in water, producing a controllable crosslinking rate and delaying viscosity development (Mondshine, 1986; Tan *et al.*, 1992). Also, slowly dissolving bases or acids can be used to delay the crosslinking rate of pH-dependent crosslinkers. The pH of the fluid containing the desired concentration of crosslinker begins at a value that does not initiate significant crosslinking. The base or acid dissolves at a controlled rate, producing the desired pH change

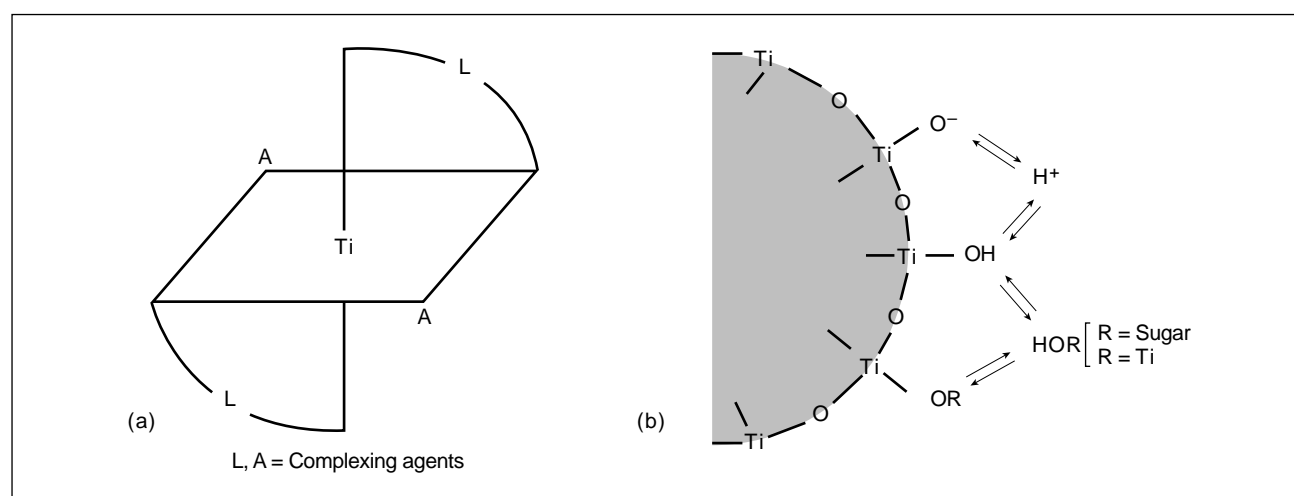


**Figure 7-13.** Hypothetical titanium complex (a) hydrolyzed to a colloidal titanium dioxide particle and (b) providing polymer crosslinking on the particle surface.

and initiating crosslinking. This method can be used to control the crosslinking rate of borate ions by using a rapidly dissolving borate compound, such as boric acid, and a slow-dissolving base, such as CaO or MgO.

When using delayed crosslinkers, viscosity should be building before the fluid reaches the producing interval, although complete crosslinking is not necessary at that time. If complete crosslinking occurs too soon, high friction pressure and shear degradation may result. If crosslinking occurs too slowly, proppant may settle in the wellbore or in the fracture near the wellbore, resulting in poor proppant transport and potential screenout (proppant blocking fluid passage in the fracture). Therefore, considerable effort is spent on location to produce a fluid composition with the desired crosslink time. Unfortunately, as pointed out by Baranet and Ainley (1985) and Hodge and Baranet (1987), commonly used field methods for determining crosslink time may not be reliable. Typically, these methods do not simulate the shear conditions in the tubing during a fracturing treatment and produce a fluid composition that crosslinks too slowly. To avoid the problems associated with overdelayed crosslinked fluids, crosslink times of one-half to three-fourths of the tubing residence time may be recommended (Cawiezel and Elbel, 1990; Aud *et al.*, 1994) or dual-crosslinker systems may be used (Baranet and Ainley, 1985; Royce *et al.*, 1984; Hodge and Baranet, 1987). Dual-crosslinker systems combine a fast crosslinker to ensure adequate viscosity at the perforations and a slow crosslinker accelerated by heating in the fracture to produce a viscous, temperature-stable fluid.

There are many benefits from using a delayed-crosslinking fluid. Delayed crosslinkers produce fluids with better long-term stability at elevated temperatures. In some areas, this has allowed reducing polymer loadings. Also, reducing the friction pressure allows higher injection rates and lower horsepower requirements. However, delayed crosslinking introduces some risk of near-wellbore screenout associated with overdelaying the crosslinking rate. Little or no benefit from avoiding shear degradation is realized for treatments with low wellbore shear rates ( $<300 \text{ s}^{-1}$ ) or short wellbore residence times (time to perforations  $< 60 \text{ s}$ ). In these low-shear and/or shallow jobs, delayed crosslinking to avoid shear degradation is

generally not recommended. Factors to consider in optimizing crosslinker performance are reviewed in Sidebar 7A.

#### 7A. Ensuring optimum crosslinker performance

The composition of crosslinked fluids is carefully optimized to obtain the desired performance (rheology and proppant transport, thermal stability, crosslinking rate, cleanup, etc.). Many factors influencing the performance must be considered during the selection of a fracturing fluid candidate and monitored during on-site preparation. To obtain the best possible performance from a crosslinked fluid, the following issues must be addressed.

##### Crosslinker concentration

Each fluid composition has an optimum range for crosslinker concentration dictated by the type of polymer, polymer concentration and fluid pH. If the crosslinker concentration is too low, the crosslinking rate will be slower and the viscosity development will be lower than anticipated. If the crosslinker concentration exceeds the optimum range, the crosslinking rate will be faster than anticipated and the final viscosity may be much lower because of syneresis. Syneresis is the precipitation of the polymer from solution caused by the collapse of the polymer network. In the most severe cases, "free water" may be observed at ambient sampling conditions. However, detection of syneresis in delayed crosslinking fluids usually requires heating the fluid to the anticipated downhole temperature to fully react all the crosslinker.

##### pH control

All crosslinked fluids have a specific pH range for optimum performance. If this pH is not maintained, the desired crosslinking rate and thermal stability cannot be obtained. To minimize pH variation in crosslinked fluid, buffers are included with the crosslinked fluid. However, gross contamination of the fracturing fluid can overwhelm these buffers and compromise crosslinked-fluid performance. Proper pH control is critical to crosslinked-fluid performance and must be monitored diligently.

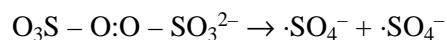
##### Chemical contamination

A variety of common compounds and oilfield products can interfere with the performance of crosslinker compounds. Typically, these contaminants reduce or eliminate crosslinking and produce a fluid with a slow rate of viscosity development (extremely long crosslink time) and significantly lower viscosity. In the most obvious cases, no viscosity increase may be produced by the crosslinker. Among the "naturally" occurring compounds that can be present in mix water are bicarbonate, phosphate and silicates. The source of many of these contaminants is the mix water used to prepare the fracturing fluid. In addition to naturally occurring contaminants, many surfactants, clay stabilizers and foaming agents can interfere with crosslinked-fluid performance. To avoid contamination with incompatible additives, fracture tanks and mixing equipment should be empty and clean before the mix water is loaded and fracturing fluid prepared. Furthermore, substitution of additives should not be approved without compatibility testing (typically, rheology testing at the anticipated fluid temperature).

## 7-6.2. Breakers

Relatively high viscosity fluids are used to transport proppant into the fracture. Leaving a high-viscosity fluid in the fracture would reduce the permeability of the proppant pack to oil and gas, limiting the effectiveness of the fracturing treatment (Penny, 1987; Brannon and Pulsinelli, 1992). Gel breakers are used to reduce the viscosity of the fluid intermingled with the proppant. Breakers reduce viscosity by cleaving the polymer into small-molecular-weight fragments. It has been estimated that fluid loss during the treatment and during closure increases the polymer concentration in the fracture after closure 5–7 times (Penny, 1987) to as much as 20 times (Hawkins, 1988) higher than the surface concentration. The increased polymer concentration causes a major increase in viscosity. For example, the viscosity of an unbroken guar fluid containing polymer at 400 lbm/100 gal (40 lbm/1000 gal gel concentrated 10 times because of fluid loss on fracture closure) has been estimated to be in excess of 1000 poise (Pope *et al.*, 1994). Significant effort has gone into designing breakers to address this problem. Ideally, a gel breaker put into the fluid at the surface should have minimal effect on the gel until pumping ceases (and the fracture closes) and then should react rapidly with the gel. The viscosity of the gel and the molecular weight of the polymer should be significantly reduced to allow rapid cleanup of the sand pack (Almond *et al.*, 1984; Gall and Raible, 1985).

The most widely used fracturing fluid breakers are oxidizers and enzymes. The most common oxidative breakers are the ammonium, potassium and sodium salts of peroxydisulfate ( $S_2O_8^{2-}$ ). Thermal decomposition of peroxydisulfate (persulfate) produces highly reactive sulfate radicals that attack the polymer, reducing its molecular weight and its viscosifying ability:



Free-radical breakers have the potential to create free radicals on the polymer and produce a chain reaction that increases breaker efficiency. Decomposition of persulfate, and therefore reactivity, is very temperature dependent, as is typical of chemical reactions. Thermal decomposition is too slow below about 125°F for persulfates to be used alone, but free-radical generation can be accelerated by the addition of amines (Hinkel, 1981). When the fluid temperature exceeds 125°F, sulfate radical genera-

tion occurs more rapidly. With increased temperature, the breaker becomes too reactive. As little as 0.1 lbm/1000 gal of dissolved persulfate causes rapid viscosity loss above 180°F [80°C]. At high temperatures, the reaction of dissolved persulfate with the polymer generally occurs during pumping rather than after placement of the proppant and closure of the fracture. This undesirable high reactivity of dissolved persulfate at elevated temperatures was a major limitation of these breakers. The introduction of encapsulated breakers, which is discussed later, greatly improved persulfate performance at elevated temperatures.

Certain enzyme breakers of the class hemicellulase are also used to reduce the viscosity of water-base fluids. Enzymes have been in use for some time, but prior to 1994 their use was thought to be limited to a relatively mild environment: pH range of about 3.5 to 8 and temperatures less than about 150°F. Because they are active at ambient temperature, enzymes begin to degrade the polymer immediately upon mixing and under some conditions can be too reactive, like persulfates.

Recent work in the area of conductivity improvement and breakers has led to a broadening of applications for both oxidizers and enzymes. Before the introduction of encapsulated breakers in 1989, only low levels of peroxydisulfate breaker were used for wells above 150°F. Such low levels of breaker were not effective at breaking the highly concentrated gels existing in the pack after closure (Brannon and Pulsinelli, 1992). To significantly improve pack permeability, breaker concentrations 5–10 times higher are required. Encapsulated breakers were developed to allow high concentrations of breaker to be used without compromising fluid viscosity during pumping (Gulbis *et al.*, 1992). In an encapsulated breaker, the active breaker is coated with a film that acts as a barrier between the breaker and the fracturing fluid. The breaker may be released as a result of crushing (Nolte, 1985), osmotic rupture (Wallis *et al.*, 1988) or diffusion of the breaker chemical (Gupta and Cooney, 1992) through the barrier polymer. Any type of breaker, including enzymes and acids, can be encapsulated. Encapsulation is usually expensive, so a mixture of dissolved and encapsulated breakers can be used to achieve the desired level of breaker at the lowest cost. Because temperature has a significant effect on breaker activity and coating permeability, a single encapsulated breaker cannot cover the temper-

ature range of 70° to 300°F [20° to 150°C]. A higher temperature usually requires that the breaker have a less permeable coating, which is achieved by increasing the coating thickness or by using a different barrier polymer. The breaker chemical itself may have to be changed for high-temperature applications. For example, the half-life of persulfate at 160°F [70°C] is about 6.8 hr, but at 200°F it is only about 15 min. Thus, even encapsulated persulfate breakers have limited utility above 200°–225°F [90°–110°C].

Consideration of the theoretical advantages of enzyme breakers has led to a renewed interest in these materials. Enzymes are biocatalysts, meaning they are not used up when they react with guar. Theoretically, a single enzyme molecule can react with many different guar molecules (i.e., turnover rate) so polymer degradation might go on for a longer time and be more complete than with an oxidizer. These enzymes are globular proteins with three-dimensional (3D) structures. They promote reactions with molecules that are able to become properly oriented at the enzyme's 3D active site. Therefore, enzymes are fairly specific in terms of their reactions. In the case of oilfield polymers, an enzyme that catalyzes the hydrolysis of the inter-ring linkages is required. It has been suggested that the most effective enzyme breaker for guar would contain a beta-mannanase for attacking the polymer backbone and an alpha-galactosidase for removing the side chains (Brannon and Tjon-Joe-Pin, 1994). Commercial oilfield enzyme mixtures used in fracturing fluids contain these enzymes. The ratio of mannanase to galactosidase varies.

Recently, enzymes have been identified that are effective up to a pH of about 10, making it possible to use them in high-pH fluids such as borates. Also, it has been found that commercial enzymes retain some level of activity, for at least a short period of time, above 150°F. They can be used at elevated temperatures if the concentration is increased significantly. This is particularly true above 200°F, where higher concentrations are required because of denaturing (permanent loss of the 3D structure) of the enzyme. A mitigating factor is pressure. Enzymes can have increased lifetimes at high pressure (Michels and Clark, 1992), which can reduce the concentration necessary at temperatures of 150°–200°F. As with oxidizers, enzymes can be extremely reactive when first introduced into the

fluid, before it heats up in the reservoir, and premature viscosity loss may result.

Since 1994, enzymes have been used in conditions previously thought impossible. Oxidizers and enzymes are also being used together, which may provide the best performance. Breaker selection criteria are listed in Sidebar 7B. It remains to be seen whether they will evolve to displace the workhorse oxidizers.

Other materials have been considered for use as breakers. Oxidizers that are not as active as persulfates may be used (Misak, 1975). Under controlled conditions, many organic peroxides do not begin to produce free radicals unless the temperature approaches 200°F (Norman, 1968). Unfortunately, these materials are usually hazardous and difficult to handle. Inorganic peroxides, such as  $\text{CaO}_2$ , can also be used (Mondshine, 1993). Inorganic peroxides are controlled-release breakers because of the limited solubility of the inorganic peroxides at high pH. The release of the peroxide ion, and therefore the rate of reaction with the polymer, is pH dependent. Contaminants such as metal ions can rapidly accelerate the decomposition of both organic and inorganic peroxides (Sheppard and Kamath, 1978), which can make their performance unpredictable.

Another category of breaker acts by eliminating crosslinking. A solution of fluoride ions at low pH has been used as an overflush to dissolve filter cake formed from a titanate- or zirconate-crosslinked fluid (Norman *et al.*, 1989).

Acids degrade guar polymers. The release must be controlled, because fracturing fluids for high-temperature formations generally are high pH to achieve the desired stability. A combination breaker/fluid-loss additive was developed using an acid condensation product (Cantu and Boyd, 1988). The material has a particle-size distribution appropriate for a fluid-loss additive and hydrolyzes to slowly release an organic acid. High concentrations of acid are typically required to reduce the pH of the fracturing fluid sufficiently for conductivity improvement, so this type of breaker has not been widely used.

Guar polymers decompose at elevated temperatures because of hydrolysis or reaction with dissolved oxygen, so it would seem that at some temperature breakers would not be necessary. However, the benefits of a high-temperature breaker have been observed even in 300°F wells (McConnell, 1994). The reason breakers are beneficial even at very high

## 7B. Breaker selection

Which type of breaker is the best is currently a topic for much debate. Both of the common types of breakers have strengths and weaknesses.

Selection Criterion	Oxidizers	Enzymes	Comments
Performance at high temperature	+		Oxidizers have been identified for high-temperature applications. Current enzymes have some activity up to 225°F [105°C]. Higher temperature versions will most likely be identified in the future.
Completeness of break		+	Theoretically, enzymes should have the advantage because of their catalytic nature. However, enzyme sensitivity to temperature, pH and other chemicals can significantly shorten the life-time of the enzyme. Under ideal conditions (less than approximately 180°F [80°C], pH 5–8), enzymes break the polymer into smaller fragments than oxidizers do, but there is no information in the literature to document that significant production of simple sugars results.
Duration of breaking		+	Enzymes, unless exposed to extremes of pH or temperature, react with the polymer over a more extended time period (days) than oxidizers (hours).
Fast break	+		A fast break to allow quick turnaround of the well is accomplished much better with oxidizers.
Chemical sensitivity	+	+	Enzymes are highly sensitive to pH, so control of pH within a limited range is necessary for predictable performance. Oxidizers are affected by the presence of curable-resin-coated proppants, whereas enzymes are not.

temperatures may be that thermal decomposition is reduced when the polymer is in highly concentrated form as it is in the closed fracture, or it may be that the breaker causes a faster break and enhances early production.

The breaker situation for oil-base fluids is somewhat different (McKenzie, 1980). Acids and bases are known to rapidly break the aluminum phosphate ester gel. Usually, a slowly soluble acid or base is added to the gel on the fly. Gels break fairly readily at elevated temperatures but can be difficult to break below 100°F [35°C].

### 7-6.3. Fluid-loss additives

Good fluid-loss control is essential for an efficient fracturing treatment. Several types of materials are used to provide fluid-loss control, but the effectiveness of the various types depends on the type of fluid-loss problem: loss to low- or high-permeability matrix or loss to microfractures.

During leakoff into the rock matrix, fluid enters the pore spaces of the rock. Some polymers, such as guar and HPG, are filtered out on the surface of low-

permeability rocks. Fluids containing these polymers are called wall-building fluids because of the layer of polymer and particulates that builds up on the rock. This layer, called a filter cake, is generally much less permeable than the formation. If the fluid contains particulates of the proper size, these particulates tend to plug the pore spaces and enhance the formation of filter cake. The fluid volume lost before an effective cake forms is called spurt loss. Pore-size distribution for the rock matrix varies from formation to formation. Generally, lower permeability formations have smaller pore openings. A 0.1-mD rock may have an average pore diameter of less than 1.0  $\mu\text{m}$  whereas a 500-mD rock may have an average pore diameter of 20  $\mu\text{m}$ . The range of pore size may be quite large, which makes it beneficial for fluid-loss additives to have a wide range of particle sizes so that all pore spaces can be bridged.

In high-permeability formations, polymer and additives may be able to penetrate most pore throats and form an internal filter cake. In this case, most of the resistance to leakoff, and therefore pressure drop, occurs inside the rock, leaving only a small fraction of the total pressure drop in the external cake (Navarrete and Mitchell, 1995). This makes any

external filter cake vulnerable to shear degradation by the fluid. During a fracturing treatment, fluid loss occurs under dynamic conditions (i.e., fluid flows along the face of the formation). Prud'homme and Wang (1993) proposed that the extent to which the thickness of the filter cake grows is controlled by the shear stress  $\tau$  exerted by the fluid at the wall of the cake and the yield stress of the cake. The cake stops growing when the fluid stress becomes equal to the yield stress of the cake, and it starts to erode when the fluid stress is larger than the yield stress of the cake. The yield stress of a polymer cake depends on the polymer concentration and pressure gradient in the cake, whereas the shear stress of the fluid is determined by the rheological properties of the fluid and the shear rate  $\gamma$  at the formation face.

Silica flour has been shown to be an effective fluid-loss additive for helping establish a filter cake. Penny *et al.* (1985) reported a 10-fold reduction in spurt loss for 5- to 100-mD rock when silica flour was used. Navarrete *et al.* (1994) determined that the effectiveness of a particulate fluid-loss additive, such as silica flour, depends on whether it can reach the wall of the rock and avoid being sheared off the surface. This depends on the relative ratio of the force driving the particle toward the wall  $F_y$  and the shear force driving the particle tangentially to the wall  $F_x$ . The chance that a particle will reach the wall and stay there increases as  $F_y/F_x$  increases:

$$\frac{F_y}{F_x} \sim (q_L/d\tau_w). \quad (7-2)$$

The ratio  $F_y/F_x$  increases with

- larger leakoff flux toward the wall ( $q_L$ )
- smaller particle size ( $d$ )
- smaller shear stress ( $\tau_w$ ) of the fluid along the wall.

The shape of a particle plays an important role in its effectiveness to approaching and staying at the wall. Gauthier *et al.* (1971) showed experimentally that axisymmetric particles (rods, platelets, etc.) in a shear flow tend to align their major axis with the flow. Under dynamic conditions, an axisymmetric particle approaches the fracture surface with its major axis parallel to the surface. Once the particle is on the surface, there is little torque exerted on the particle for removal. Therefore, larger aspect ratio axisymmetric particles are better fluid-loss additives than low-aspect-ratio particles.

Deformable particles such as starches are also good fluid-loss additives. Starches are polysaccharides of long chains of glucose molecules, comprising 20%–30% linear amylose molecules and 80%–70% branched amylopectin molecules. They are extracted in granular form from the cells of certain plants, such as potato, maize, wheat and tapioca, which determine their shape and size. Starches can be viewed as soft particles that can deform under pressure or stress. This makes them well suited to produce low-permeability filter cakes, because they can deform and block pore throats or fill in empty spaces, thus reducing the porosity of the cake. On the other hand, the deformability of a starch can play an adverse role when pore throats are too big. In that case, starch penetrates into the formation without reducing spurt loss. Combining starch with particulates can provide an overall fluid-loss additive that reduces spurt and forms a low-permeability filter cake. Starches are considered less damaging than inorganic particles because they degrade naturally or by the addition of amylase enzymes and oxidizers (Williamson and Allenson, 1989).

Oil-soluble resins also can be used to control fluid loss. These materials, when sized properly with an adequate thermal-softening point, can bridge and seal the pore spaces to reduce fluid loss. An advantage that these materials have over silica flour or starches is that they are oil-soluble and dissolve in produced liquid hydrocarbons. On dissolving, formation or proppant-pack damage is minimized. However, oil-soluble resins are considerably more expensive than other types of fluid-loss additives.

Another method for controlling fluid loss is to use dispersed fluids. These fluids are oil-in-water dispersions that contain a fairly small oil concentration and exhibit good fluid-loss control. For low permeability, the dispersed droplets are effective as deformable particles to block pore throats. The dispersion also produces two-phase flow through the filter cake, which significantly reduces its permeability to water. The effectiveness of 5% diesel as a fluid-loss additive has been demonstrated in dynamic tests (Gulbis, 1983; Penny *et al.*, 1985). However, Gulbis pointed out that diesel is not nearly as effective in a dynamic test as in a static test. In a static test, 5% diesel reduced the fluid-loss rate by a factor of 5. In a dynamic test, the reduction was only by a factor of 1.5. A possible explanation for the difference is that dynamic filter cake containing oil is very thin com-

pared with one without oil, indicating that oil has a detrimental effect on cake durability and thickness. Penny *et al.* (1985) and Nolte (1982) also emphasized the fragile nature of filter cakes that contain oil.

Controlling fluid loss to natural fractures that intersect the main fracture is more difficult than controlling fluid loss to the matrix because the openings to be blocked can be larger and can expand from the pressurized filtrate. Solid materials (such as silica flour) can bridge a fracture and plug it off (Hall and Houk, 1983; Wood and Cramer, 1984), but their effectiveness depends on the size of the intersecting fracture. Silica flour smaller than 200 mesh is very useful against microfractures (<50  $\mu\text{m}$  wide), but larger particles (such as 100-mesh sand) are necessary after the macrofracture aperture expands (>50  $\mu\text{m}$  wide). These large particulates also are available as oil-soluble resins.

As stated earlier, the primary purpose of a fracturing treatment is to generate a highly conductive flow channel through the producing formation to the wellbore. Ideally, fluid-loss additives should not damage the permeability of the formation, fracture face or proppant pack. In reality, many of the fluids and additives form long-lasting filter cakes that are not readily removed from the fracture. As demonstrated by Holditch (1979b), a 90% reduction in permeability of the fracture face can be tolerated, because of the linear flow regime caused by the fracture. This is true for relatively low-permeability reservoirs (e.g.,  $k < 5$  mD) where the fracture conductivity is moderate to large and the fracture length is large (invariably longer than 200 ft). Fracture face damage, caused by fluid leakoff, is important in high-permeability fracturing where the fracture length may be as short as 15 ft. This damage is one of the dominant reasons for post-treatment positive skin effects (Mathur *et al.*, 1995). For moderate-permeability reservoirs, the conductivity of the propped fracture, rather than formation permeability, tends to be the limiting factor in long-term productivity. Therefore, formation face damage caused by fluid-loss additives is usually a secondary concern.

#### 7-6.4. Bactericides

Bactericides are added to polymer-containing aqueous fracturing fluids to prevent viscosity loss caused by bacterial degradation of the polymer. The poly-

saccharides (sugar polymers) used to thicken water are an excellent food source for bacteria. Bacteria not only ruin gel by reducing the molecular weight of the polymer, but some can turn the reservoir fluids sour. Once introduced into the reservoir, some bacteria can survive and reduce sulfate ions to hydrogen sulfide ( $\text{H}_2\text{S}$ ), an extremely dangerous gas with a characteristic rotten-egg odor (i.e., sour).

Materials such as glutaraldehyde, chlorophenates, quaternary amines and isothiazoline are used to control bacteria (Ruseska *et al.*, 1982). Usually the materials kill the bacteria, but they do not always inactivate the enzymes they have produced that are responsible for breaking down the polysaccharides. For this reason, it is common practice to add bactericide to fracture tanks before the water is added to ensure that the bacterial enzyme level is kept low. Improvements and changes in bactericides are made so that if a strain develops that is resistant to one type of bactericide, another can be used. Bactericides are not necessary in acid-based or oil-base fracturing fluids.

#### 7-6.5. Stabilizers

Stabilizers are used to prevent degradation of polysaccharide gels at temperatures above 200°F (Thomas and Elbel, 1979). The common stabilizers are methanol and sodium thiosulfate ( $\text{Na}_2\text{S}_2\text{O}_3$ ). Methanol is more hazardous to handle and is used as 5% to 10% of the fluid volume. Sodium thiosulfate is generally used at 10 to 20 lbm/1000 gal. Sodium thiosulfate is the more effective of the two, increasing the viscosity at elevated temperatures by a factor of 2 to 10, depending on the temperature and time of exposure to temperature (Thomas and Elbel, 1979).

The mechanism for these stabilizers is not fully understood. It is believed that they act as oxygen scavengers and prevent the rapid gel degradation caused by dissolved oxygen. Walker *et al.* (1995) studied several oxygen scavengers and found sodium thiosulfate to be the most effective at maintaining gel stability. Sodium thiosulfate must be used in great excess because its reaction with oxygen is not favorable. Other materials that are better oxygen scavengers, such as sodium sulfite and sodium erythorbate, are not good gel stabilizers, apparently because the reaction products also cause gel degradation.

Fluid pH also should be considered in maximizing fluid stability. Guar and its derivatives are hydrolyzed



at low pH, especially at elevated temperatures (>200°F). Therefore, if long-term fluid stability is desired, a high-pH (e.g., 9–11) fluid should be used.

### 7-6.6. Surfactants

A surface-active agent, or surfactant, is a material that at low concentration adsorbs at the interface between two immiscible substances. The immiscible substances may be two liquids, such as oil and water, a liquid and a gas, or a liquid and a solid. The surfactant becomes involved in the interface and lowers the amount of energy required to expand the interface (Rosen, 1972). More detailed information about surfactant structure and function is in Chapter 15.

Some applications for surfactants in fracturing fluids have already been discussed. They are necessary ingredients in foams to promote the formation of stable bubbles. They are used in polyemulsion fluids to stabilize the oil-in-water emulsion. In addition, they are used as surface-tension-reducing agents and formation-conditioning agents (Penny *et al.*, 1983) to promote cleanup of the fracturing fluid from the fracture. Some bactericides and clay-control agents are surfactants.

### 7-6.7. Clay stabilizers

Clays are layered particles of silicon and aluminum oxide averaging 2  $\mu\text{m}$  in size (Moore, 1960). Negatively charged particles result when the charge balance between positive (aluminum) and negative (oxygen) is disrupted through displacement of cations or breaking of the particles. Cations, from solution, surround the clay particle and create a positively charged cloud. Such particles repel each other and are prone to migration (Crowe, 1979). Once clay particles are dispersed, the particles can block pore spaces in the rock and reduce permeability.

Solutions containing 1% to 3% KCl are commonly used as the base liquid in fracturing fluids to stabilize clays and prevent swelling. In addition to KCl, the organic cation tetramethyl ammonium chloride is an effective stabilizer (Himes and Vinson, 1991). All these salts help maintain the chemical environment of the clay particles, but they do not provide permanent protection. More permanent methods for controlling clay migration involve the use of quaternary amines or inorganic polynuclear cations. The latter materials,

such as zirconium oxychloride (Veley, 1969) and hydroxyaluminum (Haskin, 1976), are used primarily in matrix-acidizing treatments to neutralize the surface charge on clays (Thomas *et al.*, 1976). Unfortunately, they have limited compatibility with higher pH fracturing fluids.

Quaternary amines possess a positively charged group that is attracted to the negatively charged clay particle. Once the quaternary amine is attached to the clay particle, the hydrocarbon chain portion extends from the particle, forming an organic barrier and minimizing the cationic cloud. This type of clay stabilizer is used in water-base fracturing treatments.

## 7-7. Proppants

Proppants are used to hold the walls of the fracture apart to create a conductive path to the wellbore after pumping has stopped and the fracturing fluid has leaked off. Placing the appropriate concentration and type of proppant in the fracture is critical to the success of a hydraulic fracturing treatment. Factors affecting the fracture conductivity (a measurement of how a propped fracture is able to convey the produced fluids over the producing life of the well) are

- proppant composition
- physical properties of the proppant
- proppant-pack permeability
- effects of postclosure polymer concentration in the fracture
- movement of formation fines in the fracture
- long-term degradation of the proppant.

### 7-7.1. Physical properties of proppants

The physical properties of proppants that have an impact on fracture conductivity are

- proppant strength
- grain size and grain-size distribution
- quantities of fines and impurities
- roundness and sphericity
- proppant density.

To open and propagate a hydraulic fracture, the in-situ stresses must be overcome. After the well is put on production, stress acts to close the fracture and

confine the proppant. If the proppant strength is inadequate, the closure stress crushes the proppant, creating fines that reduce the permeability and conductivity of the proppant pack. Proppants can be produced from a variety of materials and in a variety of size ranges to meet the conductivity requirements of the fracture design.

The difference between the bottomhole fracturing pressure and bottomhole producing pressure provides an estimate of the maximum effective stress (or closure stress) on the proppant. During flowback and testing operations, the bottomhole producing pressure is usually held constant and at a low value to maximize the production rate. The potential for maximum crushing can occur during flowback and testing operations, when the flowing pressure at the perforations may be low, or initially in the production of a well because the fracture gradient is at its maximum. However, if the well is initially completed and produced at a higher bottomhole pressure and with a nearly constant production rate, the maximum effective stress on the proppant is less. By producing a well in this manner, the stress on the proppant can increase with time, but it never exceeds the bottomhole fracturing pressure. Because the producing pressure is lowest at the well, the effective closure stress is highest at the well, and higher strength proppant can be used as a tail-in segment after the fracture has been packed with a lower strength proppant.

Strength comparisons are shown in Fig. 7-14. The following general guidelines may be used to select proppants based on strength and cost:

- sand—closure stresses less than 6000 psi
- resin-coated proppant (RCP)—closure stresses less than 8000 psi
- intermediate-strength proppant (ISP)—closure stresses greater than 5,000 psi but less than 10,000 psi
- high-strength proppant—closure stresses at or greater than 10,000 psi.

Proppant type and size should be determined by comparing economic benefits versus cost.

Proppants with larger grain sizes provide a more permeable pack because permeability increases as the square of the grain diameter; however, their use must be evaluated in relation to the formation that is propped and the increased difficulties that occur in proppant transport and placement. Dirty formations,

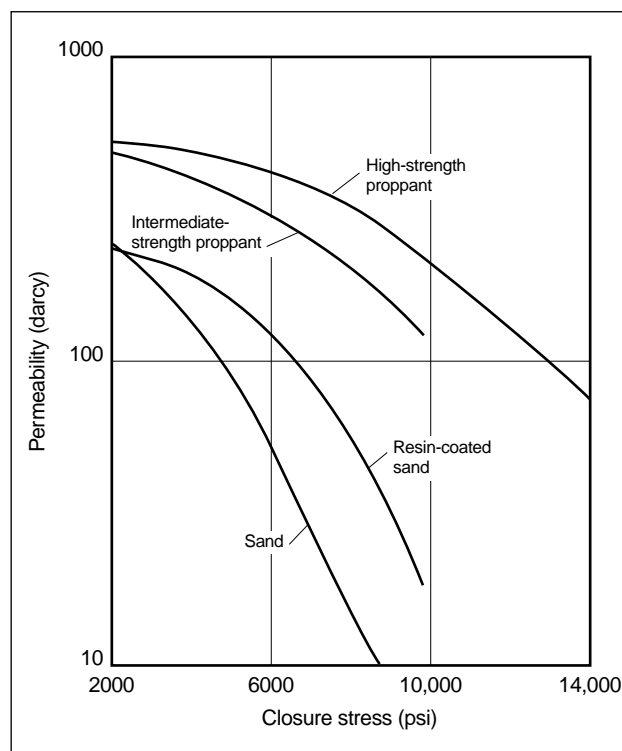


**Figure 7-14.** Strength comparison of various types of proppants.

or those subject to significant fines migration, are poor candidates for large proppants. The fines tend to invade the proppant pack, causing partial plugging and a rapid reduction in permeability. In these cases, smaller proppants, which resist the invasion of fines, are more suitable. Although smaller proppants offer less initial conductivity, the average conductivity over the life of the well is higher and more than offsets the initial high productivity provided by larger proppants (which is usually followed by a rapid production decline).

Larger grain sizes can be less effective in deeper wells because of greater susceptibility to crushing resulting from higher closure stresses (as grain size increases, strength decreases). Larger proppants have more placement problems. Placement problems are twofold—a wider fracture is required for the larger grains, and the particle settling rate increases with increasing size. If the grain-size distribution is such that the mesh range contains a high percentage of smaller grains, the proppant-pack permeability and therefore conductivity are reduced to about that for a pack of the smaller grains.

The roundness and sphericity of a proppant grain can have a significant effect on fracture conductivity.

Proppant grain roundness is a measure of the relative sharpness of the grain corners, or grain curvature. Particle sphericity is a measure of how close the proppant particle or grain approaches the shape of a sphere. If the grains are round and about the same size, stresses on the proppant are more evenly distributed, resulting in higher loads before grain failure occurs. Angular grains fail at lower closure stresses, producing fines that reduce fracture conductivity.

Proppant density has an influence on proppant transport because the settling rate increases linearly with density. Therefore, high-density proppants are more difficult to suspend in the fracturing fluid and to transport to the top of the fracture. Placement can be improved in two ways: using high-viscosity fluids to reduce settling or increasing the injection rate to reduce treatment time and the required suspension time. Also, high-density proppants require more mass of material to fill a given fracture volume.

### 7-7.2. Classes of proppants

Sand is the most commonly used proppant. It is the most economical, is readily available and generally provides sufficient fracture conductivity for closure stresses less than 6000 psi. Its specific gravity is about 2.65. Depending on the overall balance of physical properties, sand can be subdivided into groups:

- northern white sand
- Texas brown sand
- Colorado silica sand
- Arizona silica sand.

American Petroleum Institute (API) standards can be used to similarly qualify and group any sand source.

Resin coatings are applied to sand (usually northern white sand) to improve proppant strength and to reduce flowback during production. Resin-coated sand is stronger than conventional sand and may be used at closure stresses less than 8000 psi, depending on the type of resin-coated sand. At closure stresses greater than 4000 psi and without adverse fluid effects on the resin, resin-coated sand has a higher conductivity than conventional sand. The resin helps spread the stress over a larger area of the sand grain and reduces the point loading. When grains crush, the resin coating helps encapsulate the crushed portions of the grains and prevents them from migrating and plugging the flow channel. In some cases, resin-

coated proppant may be used as an alternative to ISP, which is discussed next. Resin-coated sands have a specific gravity of about 2.55.

The resin coating on some RCPs is cured (at least partially) during the manufacturing process to form a nonmelting, inert film. Proppants processed in this fashion are called precured-resin-coated proppants. The major application for precured-resin-coated proppants is to enhance the performance of sand at high stress levels.

A curable resin coating may also be applied to sand or other types of proppants. The major application of curable-resin-coated proppants is to prevent the flowback of proppants near the wellbore. The curable-resin-coated proppants are mixed and pumped in the later stages of the treatment, and the well is shut in for a period of time to allow the resin to bind the proppant particles together. Theoretically, the RCP cures into a consolidated, but permeable, filter near the wellbore.

Although they provide versatile and reliable performance, RCPs contain components that can interfere with common fracturing fluid additives, such as organometallic crosslinkers, buffers and oxidative breakers. These undesirable interactions have been reported to interfere with the crosslinking of organometallic crosslinkers, suppress fracturing fluid cleanup by consuming oxidative breakers and compromise proppant-pack bonding, leading to reduced permeability, proppant flowback and increased proppant crushing (Dewprashad *et al.*, 1993; Nimerick *et al.*, 1990; Stiles, 1991; Smith *et al.*, 1994). Fiber technology, as discussed in Section 11-6.4, is an alternative technique for proppant flowback problems that introduces no chemical compatibility issues or special curing requirements for time and temperature. Guidelines for minimizing the undesirable effects of RCPs are listed in Sidebar 7C.

ISP is fused-ceramic (low-density) proppant or sintered-bauxite (medium-density) proppant. The sintered-bauxite ISP is processed from bauxite ore containing large amounts of mullite. This is in contrast to a high-strength proppant, which is processed from bauxite ore high in corundum. ISP is generally used at closure stresses greater than 5,000 psi, but less than 10,000 psi. The specific gravity of ISP ranges from 2.7 to 3.3.

High-strength proppant is sintered bauxite containing large amounts of corundum, and it is used at closure stresses greater than 10,000 psi. High-strength

### 7C. Minimizing the effects of resin-coated proppants

To minimize the effects of curable-resin-coated proppant and fluid interactions, the following guidelines are recommended.

- Use fiber reinforcement.
- Minimize the amount of RCP. If proppant flowback control is required, consider alternate materials for addressing the problem. Card *et al.* (1994) described the incorporation of fibers in the proppant pack as a means to prevent flowback.
- Use precured-resin-coated proppants. These materials are cured (at least partially) and are typically less reactive with fracturing fluid additives than fully curable-resin-coated proppants.
- Avoid using curable-resin-coated proppants in conjunction with high concentrations of oxidative breakers. RCPs decrease breaker effectiveness. Conversely, oxidative breakers can compromise the strength development of an RCP. The reactivity of RCPs with oxidative breakers varies, and some RCPs have little effect on breaker activity. Additional breaker may be required when using RCPs to ensure adequate cleanup.
- Always determine the compatibility of the fracturing fluid and the RCP before the treatment. Typically, 30%–60% of the curable-resin coating can be lost to the fluid. Resin loss does not behave in a straightforward manner with changes in temperature or time at temperature. Resin loss increases as exposure to shear increases.
- Never batch mix RCPs in fracturing fluids. Minimize handling of RCPs to keep dust levels low. Solid resin is a good emulsion stabilizer and can create an emulsion with the fracturing fluid that is not miscible in water.

proppant is the most costly proppant. Its specific gravity is 3.4 or greater.

## 7-8. Execution

During the fracturing treatment, fluid chemistry comes together with proppant handling, mixing and pumping equipment to create the desired propped fracture. The field environment is often quite different from the ideal laboratory conditions in which the fracturing fluid or additive was developed. The following sections address the field environment.

### 7-8.1. Mixing

Fluids may be batch mixed or continuously mixed. Batch mixing has slightly different meanings, depending on the fluid prepared. For oil-base fluids,

it means that all ingredients (except fluid-loss additive, breaker and proppant) are blended together in the fracture tanks (typically, 500-bbl capacity) before pumping begins. The tanks are usually mixed the day before pumping because the gel takes several hours to form. A fluid-loss additive and a breaker are added on the fly as the gel is pumped. These materials are added on the fly to prevent the fluid-loss additive from settling out in the fracture tanks or the breaker from prematurely reducing the gel viscosity prior to pumping.

For batch-mixed, water-base fluids, the bactericide, polymer, salt, clay stabilizer, etc., are mixed together before pumping. The polymer is given sufficient time to hydrate in the tanks before the job begins. The pH of the gel is adjusted for optimum crosslinking. Crosslinker is added on the fly in the case of transition metal (Ti and Zr) crosslinkers. Because borate crosslinking occurs only at a high pH, boric acid can be added to the polymer in the tanks, and a base such as NaOH can then be added on the fly to raise the pH and to initiate crosslinking.

As discussed later, batch mixing affords the best opportunity for quality assurance. Unfortunately, it also results in wasted materials. There are always tank bottoms, the fluid that cannot be drawn out of the fracture tanks. Typically, tank bottoms represent at least 7% of the total volume of fluid in the tanks, resulting in the waste of 7% of the batch-mixed chemicals and requiring costly disposal. Also, this fluid must be broken and the fracture tanks should be cleaned. If the job is postponed and the gel degrades because of bacterial action, the entire batch of gel may have to be discarded. From a cost standpoint, continuously mixed fluid is more desirable. In this mode, all materials are added on the fly, so there is no wasted fluid and no unnecessary expense. Polymer slurries (concentrated suspensions of guar or HPG in diesel) were developed so that polymer could be accurately metered and so that it would disperse and hydrate rapidly enough for continuous mixing (Constien *et al.*, 1988; Yeager and Bailey, 1988). This type of operation requires accurate metering of all materials and makes quality assurance more difficult. Techniques for on-site rheology measurement have been developed so that the linear (precrosslinked) gel viscosity can be closely monitored. Because of environmental considerations and disposal costs, most aqueous-based fluids are now continuously mixed.

## 7-8.2. Quality assurance

Testing the components of the fracturing fluid prior to the treatment is the only way to ensure that the fluid used will have the properties expected of it. In the case of a water-base fluid, the mix water must meet certain specifications. It should be relatively free of iron ( $<25\text{-ppm Fe}^{2+}$ ) and other reducing agents that promote gel degradation or catalyze the reaction of peroxydisulfate (persulfate) breakers (Ely, 1985). The pH of the water affects the polymer hydration rate. If the water pH is low, hydration may be rapid and lumping of the gel results. If the water pH is too high, the gel hydrates too slowly. Water temperature also affects hydration rate. Increasing the water temperature causes faster polymer hydration (viscosity development). A sample of polymer from location should be used to prepare a linear (precrosslink) gel with the water from the fracture tanks. Testing should ensure that proper dispersion (no lumps) and hydration (viscosity development) will be obtained on location.

If the proper viscosity can be achieved, crosslinker performance can be evaluated. A fracturing fluid sample containing the appropriate concentration of crosslinker can be heated to accelerate crosslinking and produce a thick gel. In addition to gross crosslinker performance, a measure of how long it will take for the gel to crosslink should be performed (crosslink time). Common on-site tests for measuring crosslink time are the vortex closure test, static stiffness test (Hodge and Baranet, 1987) and falling-ball viscometer method (Cawiezel and Elbel, 1990). In the vortex closure test, polymer solution is stirred in a blender to create a vortex. The crosslinker is added, and the time required for the vortex to close, forming a smooth surface, is termed the vortex closure time. The static stiffness test involves mixing the fluid components together and then pouring the

fluid back and forth between two containers. The time at which the fluid appears very thick (stringy or pours as one mass from container to container) is the crosslink time. The falling-ball viscometer measures the time required for the crosslinked fluid to develop suspending properties. Hodge and Baranet (1987) point out that the vortex closure and static stiffness tests are misleading because the procedures do not simulate the shear the fluids experience in the tubing or the heat-up that occurs in the wellbore. Both factors greatly impact the crosslinking rate and viscosity development. As discussed in Section 7-6.1, the use of dual-crosslinker systems can eliminate the necessity of accurate control of the crosslink time.

Not all potential mix water sources or fracturing fluid additives are compatible. When preparing the test sample with materials from location, all components should be included. Any severe compatibility problems should show up in this test, preferably well before the treatment and in a laboratory setting. To determine how well the fluid will perform at elevated temperatures, a Fann 50 rheology test (see Chapter 8) is usually performed. This preliminary test should reveal problems with the chemicals or problems with the mix water or oil source.

Once the job is in progress, the viscosity of any continuously mixed linear gel should be monitored to quickly identify problems that could develop. Also, a sample of the crosslinked fluid should be inspected periodically. A detailed discussion of quality assurance procedures is provided by Ely (1985).

## Acknowledgments

Curtis Crowe contributed the acid fracturing section. Reinaldo Navarrete updated the fluid-loss section. The proppant section was written originally by Brian Ainley and edited by Bob Thrasher.

# Performance of Fracturing Materials

*Vernon G. Constien, Constien and Associates*

*George W. Hawkins, Schlumberger Dowell*

*R. K. Prud'homme, Princeton University*

*Reinaldo Navarrete, Kelco Oilfield Group*

## 8-1. Introduction

Hydraulic fracturing employs special fluids that are intended primarily to create an appropriate fracture geometry while transporting proppants. Key to the entire exercise is the fluid rheology, which affects the fluid viscosity, its proppant-carrying capability and its propensity for leaking off into the porous medium.

This chapter begins with fracturing fluid characterization, followed by the translation of laboratory-obtained information to field conditions. There is a clear link between the chemistry of fracturing fluids, most of which are polymer solutions with their properties augmented by several additives, and the physical properties expected from these fluids. Rheology and its modeling and control take center stage in the chapter. This includes not only traditional water-base polymer solutions but also complex fluids such as foams. Proppant-transporting slurries are also examined in relative detail with regard to both their rheology and potentially problematic proppant settling. The general discussion of fracturing fluid loss contains some of the classic thinking, especially with regard to laboratory-derived data. This discussion should be read in conjunction with Chapters 9 and 2, which address leakoff modeling and the interpretation of fracturing pressure behavior, which are intimately related phenomena. Finally, damage from fracturing fluids to the formation face and the resulting proppant pack, the first from fracturing fluid leakoff and the second because of unbroken polymer following the treatment, are outlined. These problems are tackled in detail in Chapter 12.

## 8-2. Fracturing fluid characterization

Fracturing fluid additives and fluid systems are characterized for the following purposes:

- additive and system development
- obtaining input data for use in fracture design simulators

- quality control before or during the treatment.

Characterization during the development process for an additive or fluid system is typically used to determine if a new composition is an improvement over an existing system or if it can provide similar performance at a lower cost.

Characterization of fluid systems that obtains representative performance data in critical areas such as rheology, pipe friction pressure, fluid-loss rates, fracture conductivity and formation damage is conducted to obtain data that can be used in fracture design and production simulators.

Characterization of fluid systems at the point of use for quality assurance purposes usually involves methods that can be applied at less than ideal conditions to indicate how the systems are performing. Examples of these tests are provided in Davidson *et al.* (1994), Ely (1985) and Section 7-8 of this volume.

The American Petroleum Institute (API) has developed recommended practices for several of the laboratory characterization methods described in this chapter. An excellent review of laboratory methods is also in the Society of Petroleum Engineers (SPE) Monograph 12, *Recent Advances in Hydraulic Fracturing* (Gidley *et al.*, 1989).

This chapter addresses the characterization methods used for additive and system development and for obtaining input data for use in fracture design simulators. The focus is on the most commonly used fluids: water-base systems utilizing guar or derivatized guar as the polymer viscosifier (see Chapter 7). In general, methods used for water-base fluids can be applied—with appropriate modification—to other fluids such as gelled oils, emulsions and foams.

Whatever the fluid system, a set of data describing the fluid rheology, fluid loss, pipe friction, fracture conductivity and possible formation damage should be determined before the fluid system is used in field operations.

### 8-3. Characterization basics

Before any significant laboratory work to determine fluid system properties is begun, representative material samples of all components must be obtained. These include samples of the water, hydrocarbon and acid. In some instances sampling may require obtaining multiple lots of materials to prepare a composite blend. At a minimum, all materials must be identified by the manufacturer and lot number so that they can be traced back to the point of origin. In the case of proppants, special care must be taken because it is generally difficult to obtain representative samples from any size lot (*Recommended Practices for Testing Sand Used in Hydraulic Fracturing Operations* [RP 56], 1983). This difficulty arises because of size segregation during transport and transfer.

In addition to obtaining representative material samples, calibrating and maintaining the laboratory instruments before and during testing is required. Adherence to the prescribed testing methods is crucial for comparing different systems and avoiding frequent rerunning of the data to obtain an exact match to the testing conditions. Complete records containing material sample and calibration data information are essential for product or system comparisons because the usable lifetime of the data can span several years.

### 8-4. Translation of field conditions to a laboratory environment

The range of conditions that fracturing fluids experience during their use is so diverse and the physical scale so large that the characterization process is usually divided into a series of small-scale tests that simulate key portions of the large, complex physical environment. The scope of the characterization can potentially range from the molecular level to testing fluids in large-scale equipment, which may approach actual mixing, wellbore and fracture dimensions.

The exact details of the characterization method may change depending on the composition of the fluid. For example, oil-base fluids, emulsions and foams may have compressibility or bubble- or drop-size effects that require the determination of properties over a range of pressures.

### 8-5. Molecular characterization of gelling agents

An important set of techniques for the understanding and prediction of fracturing fluid performance involves characterization at the molecular level. As discussed in Chapter 7, water-base fracturing fluids are formulated primarily from guar or derivatized guar polymers. Methods such as intrinsic viscosity measurements, dynamic light scattering, nuclear magnetic resonance (NMR), size-exclusion chromatography (SEC) and freeze-fracture electron microscopy provide information on guar molecular size, crosslinking, degradation mechanisms and gel structure.

Before extensive investigations are made of the properties of fully formulated guar-based fracturing fluid systems, it is worthwhile to consider the properties of the guar itself. Guar is a natural product and, as such, is subject to variation of its properties. Suppliers of oilfield-grade guar blend batches to obtain consistent performance from the materials. However, before an investment is made in the development of a new fluid system, the basic properties of blended representative batches of the base polymer should be determined.

#### 8-5.1. Correlations of molecular weight and viscosity

Guar and its derivatives are the polymers most commonly used in fracturing fluids. Like many polysaccharides, guar is conformationally mobile and adopts a disordered or “random-coil” geometry in dilute solutions.

Viscosity–molecular weight relations for several guar samples were determined by Robinson *et al.* (1982) using dilute solution viscometry and light-scattering measurements. They concluded that guar acts as a random-coil polymer and that the methods commonly used to study synthetic polymers could be used to determine information such as intrinsic chain flexibility.

Intrinsic viscosity  $\mu_i$  is a convenient index of the size or hydrodynamic volume of isolated polymer coils in solution. For random-coil polymer solutions,  $\mu_i$  can be expressed as a function of the end-to-end

distance of a random-coil polymer and the molecular weight. An experimental determination of the intrinsic viscosity is obtained with

$$\mu_i = \left( \frac{\ln \mu_r}{C} \right)_{C=0} = \left( \frac{\ln \mu / \mu_0}{C} \right)_{C=0}, \quad (8-1)$$

where  $C$  is the concentration and the viscosity parameters are defined in Table 8-1.

<b>Table 8-1. Viscosity nomenclature (Kaufman and Falcetta, 1977).</b>	
Solvent viscosity	$\mu$
Shear-rate-independent (zero-shear) viscosity	$\mu_0$
Intrinsic viscosity	$\mu_i = \left( \frac{\ln(\mu/\mu_0)}{C} \right)_{C=0}$
Relative viscosity	$\mu_r = \mu/\mu_0$
Specific viscosity	$\mu_{sp} = \mu_r - 1$
Inherent viscosity	$\mu_{inh} = \frac{\ln(\mu_r)}{C}$

To determine the intrinsic viscosity of a polymer, viscosity measurements are made on a series of dilute samples at very low shear rates. The extrapolation to zero concentration at zero shear is the value of  $\mu_i$ .

The Mark-Houwink equation provides a close approximation of the variation of  $\mu_i$  with molecular weight:

$$\mu_i = K(M_v)^a, \quad (8-2)$$

where the Mark-Houwink coefficient  $K$  in dL/g and the exponent  $a$  are experimentally determined constants for a polymer-solvent system at a specific temperature.  $M_v$  is the viscosity average molecular weight. The value of  $a$  provides an indication of the degree of coiling or extension of the polymer chains. For spheres,  $a = 0$ ; for rigid rods,  $a = 2$ ; and for random chains,  $a \cong 1$ . For guar, values of  $a$  typically have been reported between 0.72 (Robinson *et al.*, 1982) and 0.80 (Sharman *et al.*, 1978).

Data for the Mark-Houwink coefficients for guar and hydroxyethylcellulose (HEC) are listed in Table 8-2.

**Table 8-2. Mark-Houwink coefficients for fracturing fluid gelling agents ( $\mu_i = K(M_v)^a$ ).**

Polymer	$K$	$a$	Reference
HEC	$1.03 \times 10^{-3}$	0.70	Sharman <i>et al.</i> (1978)
Galactomannan	$6.7 \times 10^{-4}$	0.80	Sharman <i>et al.</i> (1978)
Guar	$3.8 \times 10^{-4}$	0.723	Robinson <i>et al.</i> (1982)
Guar	$3.67 \times 10^{-5}$	0.884	Pope <i>et al.</i> (1994)

## 8-5.2. Concentration and chain overlap

The interaction of concentration and the molecular size or weight of the gelling agent is important for understanding the critical concentrations necessary for crosslinking and the shear stability of dilute crosslinked fracturing fluids. As the concentration  $C$  of the gelling agent in solution is increased, the polymer coils begin to interact at a concentration called the critical overlap concentration  $C^*$ . The value of  $C^*$  is determined by measuring the solution viscosity as a function of concentration. The results are plotted as the log specific viscosity  $\mu_{sp}$  versus log polymer concentration (i.e., the Kraemer method). The specific viscosity is used to remove the contribution of the solvent to the bulk viscosity:

$$\mu_{sp} = (\mu_{bulk} - \mu_{solvent}) / \mu_{solvent}. \quad (8-3)$$

As discussed previously, extrapolation to zero polymer concentration provides the intrinsic viscosity  $\mu_i$ . As the polymer concentration is increased from zero,  $C^*$  is indicated by a significant increase in slope.  $C^*$  is also affected by the solvent, other soluble species such as salts and temperature.

$C^*$  is the theoretical minimum concentration at which intermolecular crosslinking is possible. Below  $C^*$ , it is not possible to form chemical crosslinks because the polymer molecules are too far apart. Reaction of the crosslinker below  $C^*$  results predominantly in intrapolymer crosslinks but not interpolymer crosslinks (Menjivar, 1984; Pezron, 1988a, 1988b).

For solutions of polysaccharides,  $C^*$  is about  $4/\mu_i$  (Robinson *et al.*, 1982). Pope *et al.* (1994) determined the relation (Fig. 8-1) between specific viscosity and the concentration and intrinsic viscosity for the high-molecular-weight guar commonly used in hydraulic fracturing. From Fig. 8-1 and the  $\mu_i$  value reported for



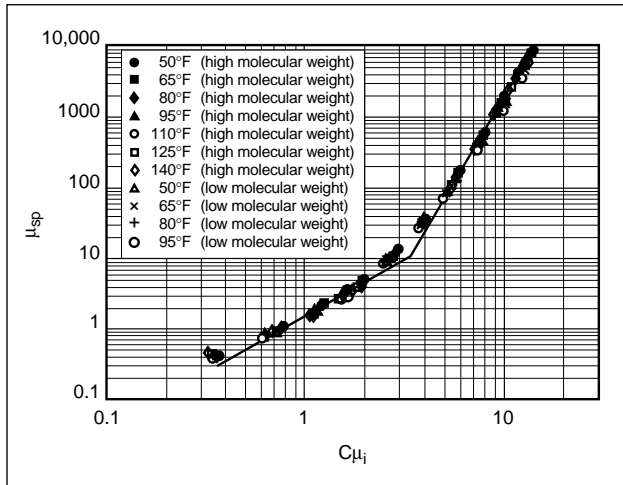


**Figure 8-1.** Relationship between specific viscosity and the concentration and intrinsic viscosity for two molecular weights of guar over a temperature range of 50° to 140°F [10° to 60°C] (Pope et al., 1994).

Pope *et al.*'s guar sample of 15.5 dL/g,  $C^*$  is about 0.21 dL/g, or in terms of common oilfield units, about 17.5 lbm/1000 gal. This value is in good agreement with the lower concentrations of guar used in cross-linked fracturing fluids, which are in the range of 15–20 lbm/1000 gal (Harris and Heath, 1998).

Values for  $\mu_i$  and  $C^*$  for various molecular weights of hydroxypropylguar (HPG) reported by Menjivar (1984) are listed in Table 8-3.

### 8-5.3. Molecular weight distribution

Size-exclusion chromatography (Gall and Raible, 1984, 1985; Sattler *et al.*, 1985; Hawkins, 1986) is a technique for measuring the molecular weight distribution of polymers. Although the application of SEC

to water-soluble polymers is more difficult than for polymers soluble in organic solvents (e.g., polyethylene, polystyrene), useful data can be obtained if care is taken. SEC is a highly effective method for studying the degradation of water-soluble polymers. Its advantage over simple measurements of intrinsic viscosity is that it provides information on the molecular weight distribution in the sample and relative difference between samples for evaluating guar degradation processes.

An example from an SEC analysis of HPG degraded by an ammonium persulfate breaker is shown in Fig. 8-2. This technique is not only useful in laboratory studies, but important for analyzing flowback samples of the fracturing fluid to determine how breakers work in actual field conditions. When

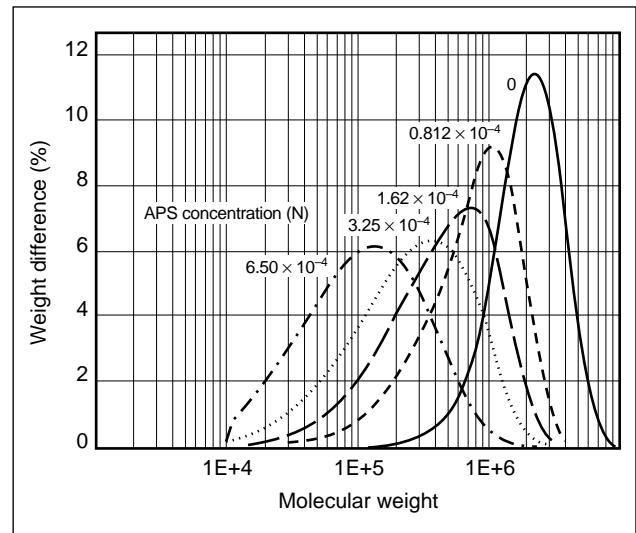


**Figure 8-2.** Molecular weight reduction and broadened distribution of HPG with increasing ammonium persulfate (APS) breaker concentration at 199°F [93°C] for 5 hr.

**Table 8-3. Critical overlap concentration  $C^*$  for several HPG samples (Menjivar, 1984).**

HPG Sample	Intrinsic Viscosity (dL/g)	Critical Overlap Concentration (g/dL)	Estimated Average Molecular Weight
A	18.1	0.19	$3.0 \times 10^6$
B	16.4	0.21	$2.6 \times 10^6$
C	15.9	0.22	$2.5 \times 10^6$
D	15.4	0.22	$2.4 \times 10^6$
E	13.8	0.25	$2.0 \times 10^6$
F	13.3	0.26	$1.9 \times 10^6$
G	12.5	0.27	$1.8 \times 10^6$

the molecular weight (or intrinsic viscosity) and concentration of guar are known, the viscosity can be predicted from a master curve. This information enables estimating the tendency for viscous fingering to occur during flowback of the fracturing fluid (Pope *et al.*, 1994).

#### 8-5.4. Characterization of insoluble components

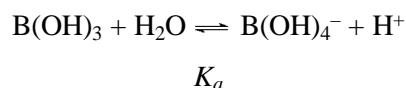
Although molecular size studies of the water-soluble portion of polymers provide much understanding of performance properties such as viscosity, some portions of the guar molecule are not soluble. The insoluble components can be present in the polymers from the beginning, or they can be created during fluid degradation. The insoluble components are difficult to characterize for determining their influence on properties such as fluid loss and fracture conductivity damage. Analysis of the insoluble components of guar is also difficult. For guar systems, insight can be gained through basic elemental analysis (e.g., total carbon, hydrogen and nitrogen) and more complex techniques such as fourier transfer infrared spectroscopy (FTIR). These analyses can also provide information on the change in the galactose:mannose ratio (see Chapter 7 for the guar structure) in the soluble and insoluble guar residues following exposure to breakers or elevated temperatures.

#### 8-5.5. Reaction sites and kinetics of crosslinking

Crosslinking is used to enhance the performance of fracturing fluids by effectively increasing the molecular size of the gelling agent. Figures 8-1 and 8-2 show that viscosity can be increased by increasing the polymer concentration, molecular size or both. For economic and performance reasons (especially for fracture conductivity), it is desirable to use as low a concentration of gelling agent as possible. If the concentration is fixed at a value slightly higher than  $C^*$ , then to achieve high viscosity,  $\mu_i$  (or the volume occupied by the polymer chain) must be increased. Crosslinking the polymer chains together increases the effective size of the species up to a size limited by the stoichiometry of the reaction and the shear to which the fluid is exposed. Shear effects on fluid properties are discussed in Section 8-6.4.

Relatively few studies have identified the actual chemical species involved in the reactions with metal ion crosslinkers and guar or guar derivatives (see Chapter 7). Some borate-crosslinked fracturing fluid systems have been studied using NMR. Using this technique, Jasinski *et al.* (1996) were able to determine the stoichiometries of the borate anion and high-molecular-weight guar to derive the equilibrium constants. The number of borate crosslinks for a gel can be calculated from measurements of the borate-to-monomeric-sugar equilibrium-binding constants. These constants have been measured for model sugars and the borate-to-sugar equilibrium-binding constants used to model gel rheology (Kesavan *et al.*, 1993; Pezron *et al.*, 1988b) and correlate computed crosslink concentrations with the elastic storage modulus  $G'$  (see Section 8-6.7) (Jasinski *et al.*, 1996).

The overall borate ion equilibrium is



with the computed fraction of borate anion versus pH shown in Fig. 8-3. The acid equilibrium constant  $K_a$  of the borate ion equilibrium equation is 9.2.

The multiple equilibria associated with borate ion crosslinking of guar can be calculated from the known equilibrium constants shown in Fig. 8-4. The figure illustrates that as a function of pH value, the concentration of active crosslink sites (denoted as  $\text{A}_2\text{B}^-$ ) changes by over 1 order of magnitude from a neutral pH of 7 to a pH of 9.2. The number of active crosslink sites decreases at very high pH values. The equilibria are also a function of temperature. Increasing temperature produces an exponential decrease in crosslink concentration, as shown in Fig. 8-3. The equilibria enable understanding the mechanism for

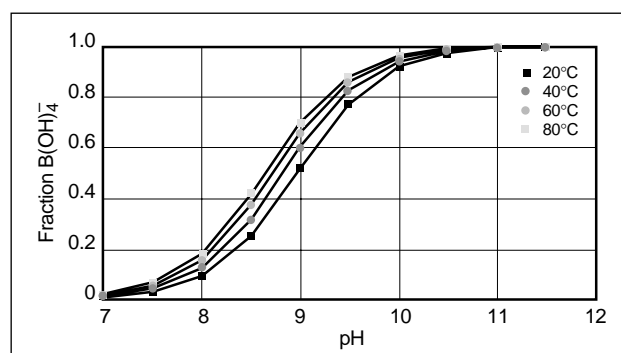


**Figure 8-3.** Borate anion fraction in a 0.01M boric acid solution (= 0.7M NaCl, no guar) versus pH and temperature.

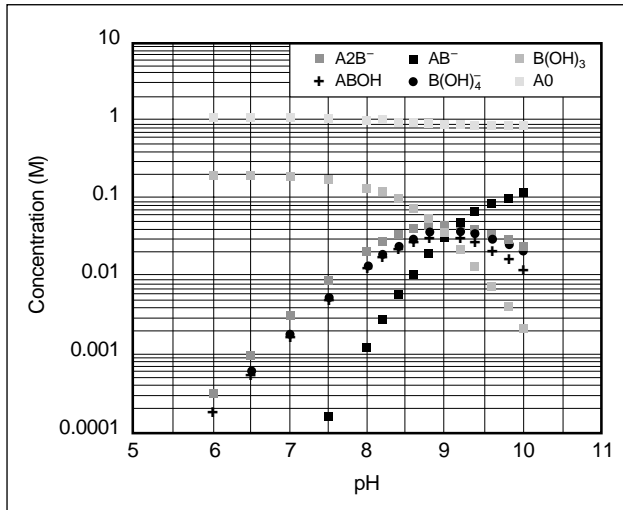


**Figure 8-4.** Species concentrations calculated from the equilibrium model versus pH.  $A_2B^-$  = crosslink site,  $ABO$  = borate in the nonionic form attached to one cis-diol,  $AB^-$  = a borate ion attached to one cis-diol,  $B(OH)_4^-$  = borate ion,  $B(OH)_3$  = neutral boric acid,  $A_0$  = uncomplexed cis-diol.

controlling borate gel rheology. By selecting suitable chemistry to control the concentration of borate ions or the base (pH) in solution (Cawiezel and Elbel, 1990; Nelson *et al.*, 1997; Dawson, 1992), it is possible to produce systems with high viscosity at high temperatures that do not overcrosslink and synerese (i.e., phase separate) while the fluid is heating up to the temperature within the fracture.

## 8-6. Rheology

The most common laboratory evaluations conducted on fracturing fluids are steady-shear rheological measurements. The property that is determined is the apparent viscosity of the fluid as a function of shear rate, temperature, fluid composition and time. These relations are commonly determined in viscometers, such as the rotational concentric cylinder (Fig. 8-5), capillary (Fig. 8-6) and large pipe or slot-flow devices.

The data are usually related to a mathematical model for predicting the fluid viscosity in the various environments that occur in the fracturing process.

Because of the difficulties in evaluating the rheology of fluids containing proppant in small-scale laboratory instruments, most of the slurry rheology data in the industry have been derived from large pipe or slot-flow devices, as discussed in Section 8-6.9.

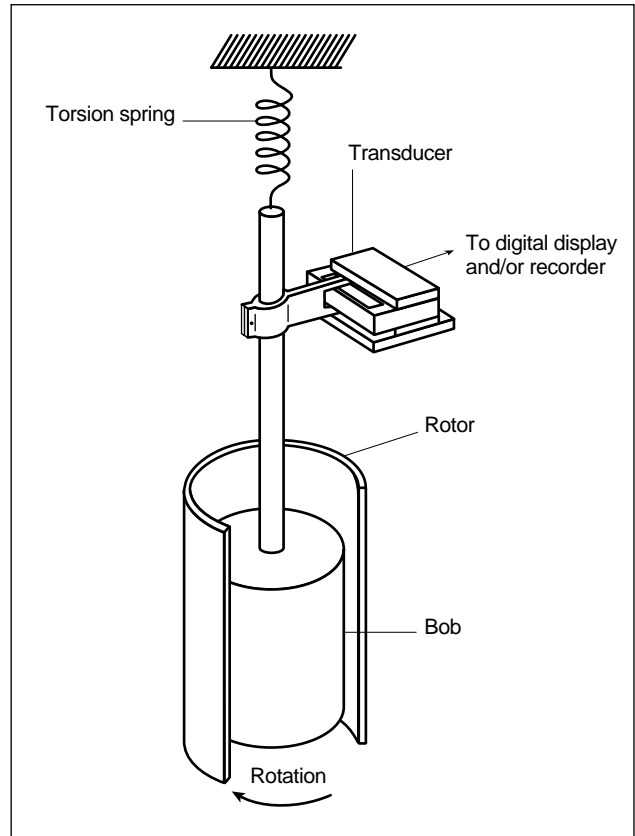


**Figure 8-5.** Rotational concentric cylinder viscometer.

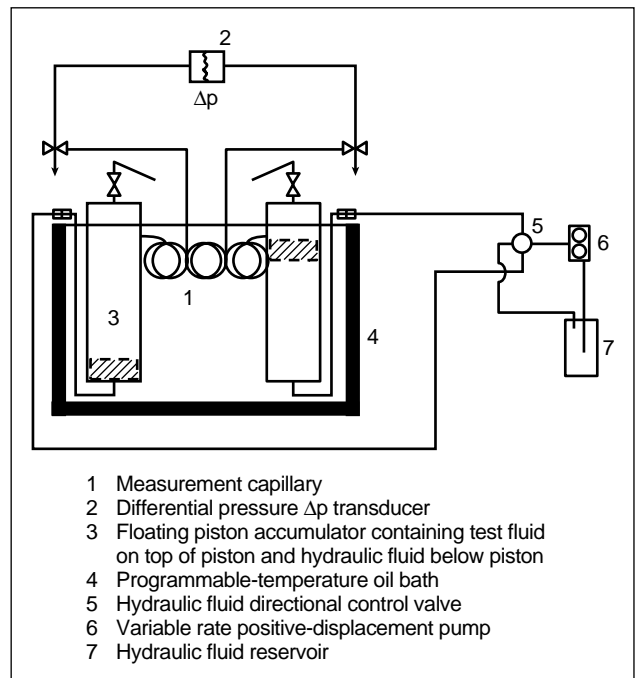


**Figure 8-6.** Reciprocating capillary viscometer.

### 8-6.1. Basic flow relations

Simple viscosity characterizations involve measurements of the stress that results from applying a known shear rate on the fluid. Shear in laminar flow can be thought of as a process in which infinitely thin, parallel planes slide over each other (Fig. 8-7). The shear rate  $\gamma$  is defined as the velocity difference between the planes divided by the distance between the planes:

$$\gamma = \frac{du}{dx} = \frac{u_1 - u_2}{x}. \quad (8-4)$$

The usual rate of shear reported in viscometric experiments is the value at the wall of the instrument and is referred to as the apparent Newtonian or nominal shear rate.

The shear stress  $\tau$  is the shearing force per unit area of surface:

$$\tau = \frac{F}{A}. \quad (8-5)$$

In most measurements, the shear stress is determined by measuring the torque exerted on a measurement bob or by the pressure drop across a tube.

The apparent viscosity  $\mu_a$  is the ratio of the shear stress to the shear rate:

$$\mu_a = \frac{\tau}{\gamma}. \quad (8-6)$$

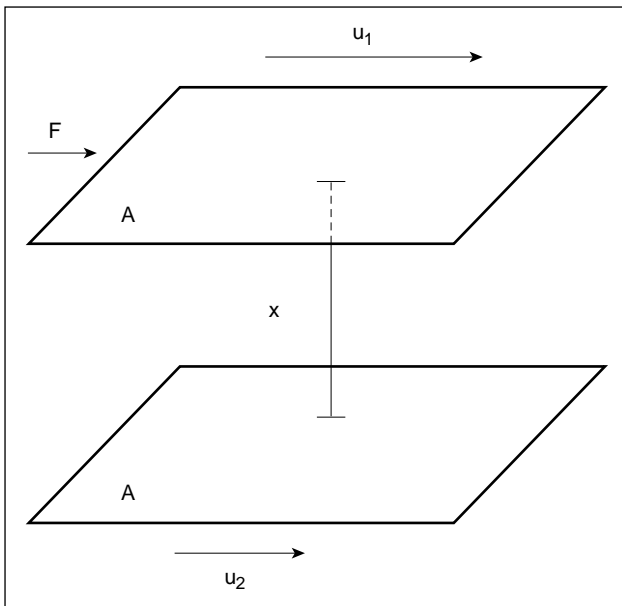


**Figure 8-7.** Shear rate depicted as the difference in velocity between two plates divided by the distance  $x$  between the plates.

Newtonian behavior implies that fluids have a constant viscosity at all shear rates. Water, low-viscosity oils and gas are examples of fluids that exhibit this behavior. Fracturing fluids have predominantly non-Newtonian behavior. This means that the apparent viscosity of the fluid is dependent on the shear that the fluid is experiencing at a specific point. Figure 8-8 illustrates the apparent viscosity of a simple fracturing fluid over a wide range of shear.

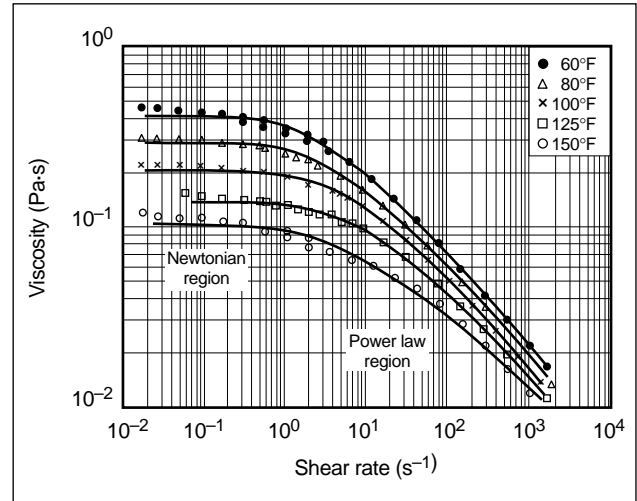


**Figure 8-8.** Shear viscosity of hydroxypropylguar (0.48% in water) (Guillot and Dunand, 1985).

A fracturing fluid will have considerably different values of  $\mu_a$ , depending on the shear that is exerted on the fluid. The non-Newtonian behavior of most fracturing fluids plays a significant role in the friction pressure developed in the tubing and the fracture and also in the ability of the fluid to transport proppant.

Rheological characterization of a non-Newtonian fluid requires that the response of the fluid to changes in shear rate must be determined and related to a model so that the apparent viscosity can be calculated under the different shear conditions in the fracture.

### 8-6.2. Power law model

The power law model is the most widely used model to represent fracturing fluid behavior in fracture design simulators:

$$\tau = K\gamma^n \quad (8-7)$$

$$\mu_a = K/\gamma^{(1-n)}, \quad (8-8)$$

where  $K$  is the consistency index in  $\text{lbf}\cdot\text{s}^n/\text{ft}^2$  or  $\text{kPa}\cdot\text{s}^n$  and  $n$  is the flow behavior index (dimensionless). These relations hold for most fracturing fluids over the range of shear rates in which the fluid displays non-Newtonian behavior. A log-log plot of  $\tau$  versus  $\gamma$  (Fig. 8-9) usually yields a straight line over a portion of the shear range. The slope of the straight-line portion is equal to the behavior index  $n$ , and the value of  $\tau$  at  $\gamma = 1.0 \text{ s}^{-1}$  is equal to the consistency index  $K$ . A log-log plot of  $\mu_a$  versus  $\gamma$  has a straight-line slope of  $n - 1$  when the power law model is applicable per Eq. 8-8 (Fig. 8-8). The slope is zero for Newtonian behavior.

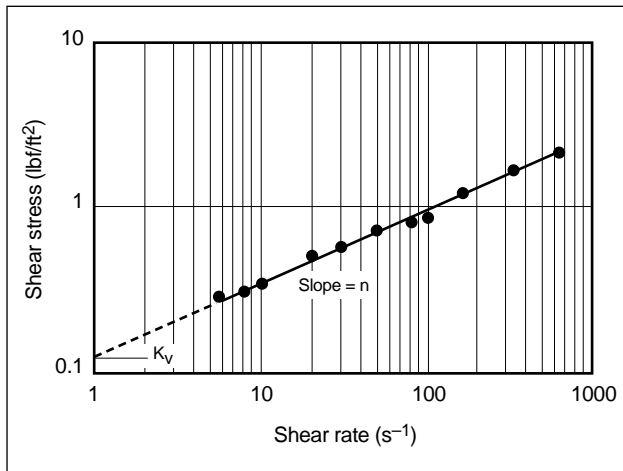


**Figure 8-9.** Determination of power law coefficients from capillary viscometer data.

Fracturing fluid rheology data are usually determined under laminar flow conditions in a rotational concentric cylinder viscometer (Fig. 8-5) and reported in terms of the power law parameters  $n$  and  $K$ . However,  $K$  is dependent on the flow geometry for concentric cylinder devices and is referred to as the viscometer consistency index  $K_v$ . For a power law fluid, the shear rate depends on the value of  $n$  in addition to the flow rate and conduit dimension. As a result, determination of the shear rate is coupled to the determination of  $n$  from the flow data. Savins (1958) overcame the coupling problem by assuming that the shear rate was the same as for a Newtonian fluid. This assumption enables determining the value of  $n$  and a device-independent value of  $K$  (i.e.,  $K_{pipe}$  or  $K_{slot}$ ; Table 8-4) for each flow rate. The corresponding device-independent values depend on the ratio of the actual and apparent Newtonian shear rates, raised to the  $n$ th power. Savin's relations for the

three flow devices are listed in Table 8-4. The device-independent values are used for the general flow equations in Chapter 6. Tables 9.1 and 9.2 in Gidley *et al.* (1989) provide a comprehensive summary of these flow considerations.

**Table 8-4. Viscometer geometry corrections.**

$$K = K_v \left( \frac{B^{2/n}(B^2 - 1)}{n(B^{2/n} - 1)B^2} \right)^{-n}$$

$$K_{pipe} = K \left( \frac{3n+1}{4n} \right)^n$$

$$K_{slot} = K \left( \frac{2n+1}{3n} \right)^n$$

$$\mu_a = \frac{47,880K}{\gamma^{(1-n)}}$$

- $K$  = geometry-independent consistency index ( $\text{lbf}\cdot\text{s}^n/\text{ft}^2$ )
- $K_v$  = consistency index for a concentric cylinder viscometer
- $B$  =  $r_{cup}/r_{bob}$
- $r_{cup}$  = cup inner radius
- $r_{bob}$  = bob radius
- $K_{pipe}$  = consistency index for pipe flow
- $K_{slot}$  = consistency index for slot flow
- $\mu_a$  = apparent viscosity (cp) at a specific shear rate
- $\gamma$  = shear rate ( $\text{s}^{-1}$ )

### 8-6.3. Models that more fully describe fluid behavior

A limitation of a model that uses only  $n$  and  $K$  is its inability to accurately describe the Newtonian region of fluid behavior that generally occurs at both very low and high shear rates. The prediction of viscosity using only high-shear values of  $n$  and  $K$  can vastly overestimate the viscosity at low shear rates.

Because shear rates vary across the fracture width from high at the wall to zero in the center, the viscosity of the fracturing fluid also varies. The viscosity at the wall is much lower than the viscosity in the center of flow. Figure 8-10 is a laser doppler velocimetry (LDV) plot of a fracturing fluid profile in a slot-flow geometry (Lear, 1996). Equation 8-4 implies that the shear rate is proportional to the slope of the flow profile; therefore, Fig. 8-10 indicates a relatively small shear rate over the central portion of the slot. The variations in shear rate and viscosity are important for accurately predicting the fracture width and proppant

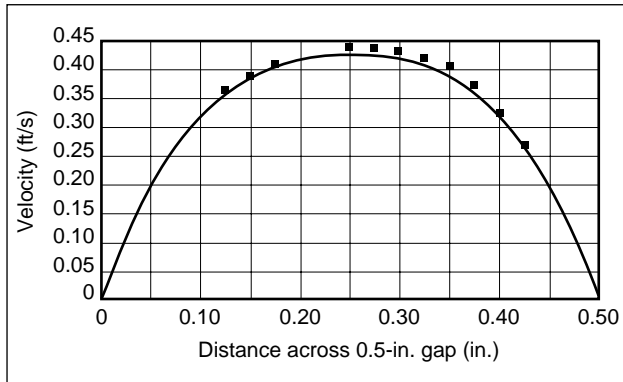


**Figure 8-10.** Laser doppler velocimetry plot of a 35 lbm guar/1000 gal fluid at a flow rate of 40 gpm in a slot-flow geometry (Lear, 1996).

transport. Fracture width is related to the viscosity at the wall whereas proppant transport is related to the viscosity gradient across the slot (Guillot and Dunand, 1985; Kirkby and Rockefeller, 1985; Roodhart, 1985a; Acharya and Deysarkar, 1987). Low-shear viscosity is also important for understanding the cleanup of fracturing fluids within proppant packs (Penny and Jin, 1995; Pope *et al.*, 1994). These effects are discussed in Section 8-7.

To better predict the full range of fracturing fluid viscosity, a rheology model must utilize not only  $n$  and  $K$  but also a zero-shear viscosity term. The Ellis model adds zero-shear viscosity  $\mu_0$  to the power law model to improve viscosity prediction:

$$\frac{1}{\mu_a} = \frac{1}{\mu_0} + \frac{1}{K\dot{\gamma}^{n-1}}, \quad (8-9)$$

where  $n$  and  $K$  are defined from the high-shear data (i.e., power law region; Fig. 8-8).

It is difficult experimentally to obtain both  $\mu_0$  and the high-shear viscosity behavior because of the wide range of torque or pressure drop values that an instrument must be capable of accurately measuring. Guillot and Dunand (1985) used LDV to determine the velocity profile of HPG gels flowing in a tube, which in turn was used to calculate the fluid viscosity. To verify the method, their first step was to compare viscosities measured in a concentric cylinder geometry viscometer and their capillary viscometer (Fig. 8-11). The agreement was good, and the results showed a deviation from power law behavior at shear rates below  $10 \text{ s}^{-1}$ . Guillot and Dunand found that the predicted data from the Ellis model fit the experimentally determined velocity profiles very well (Fig. 8-12).

Similar behavior was observed for fluids viscosified with hydroxyethylcellulose (HEC) (Torrest, 1982; Roodhart, 1985a).

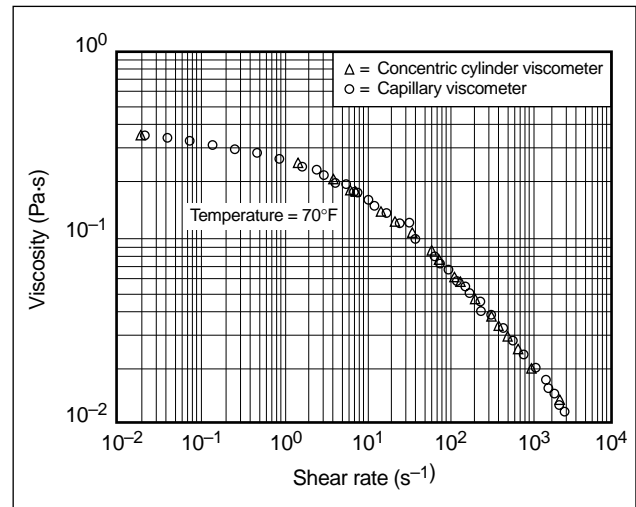


**Figure 8-11.** Effect of shear rate on the viscosity of an HPG aqueous solution (0.48%) (Guillot and Dunand, 1985).

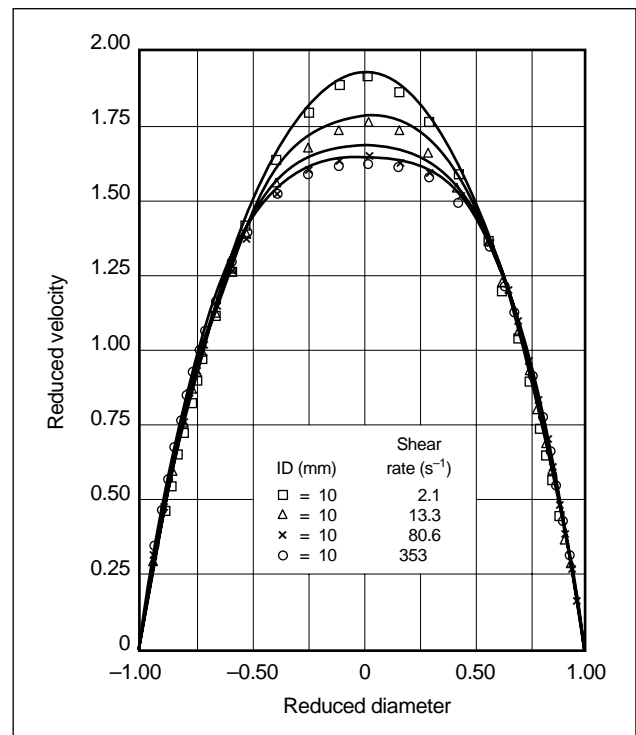


**Figure 8-12.** Measured and predicted velocity profiles of an HPG solution (0.48%) (Guillot and Dunand, 1985).

### 8-6.4. Determination of fracturing fluid rheology

- Shear history and temperature conditioning

During hydraulic fracturing treatments, the fluid experiences wide variations in shear and temperature. The fluid properties in the fracture depend on the chemistry in the formulation and also the history of shear and temperature to which the fluid has been exposed, from initial mixing through final disposition in the fracture. High shear is experienced by the fluid during pumping through the tubulars and perforation tunnels. Once in the fracture, the shear on the fluid is significantly less, but the fluid temperature increases until it eventually reaches formation temperature.

Examples of a shear and temperature history experienced by a fluid for a specific set of conditions and the KGD fracturing model (Table 8-5) are illustrated in Figs. 8-13 and 8-14, respectively.

The shear rate experienced by a specific volume of fluid increases with time. The formation temper-

**Table 8-5. Input data for shear and temperature simulation (KGD model).**

Depth to perforations	8000 ft
Fracture gradient	0.70 psi/ft
Porosity	10%
Permeability	0.10 md
Well spacing	320 acres
Reservoir pressure	4000 psi
Fracture height	300 ft
Shear modulus	$2.4 \times 10^6$ psi
Spurt-loss coefficient	0 gal/ft <sup>2</sup>
Total fluid-loss coefficient	0.002 ft/min <sup>1/2</sup>
Ambient surface temperature	80°F [26°C]
Reservoir temperature	200°F [95°C]
Fluid flow behavior index $n$	0.50
Fluid consistency index $K$	0.02 lbm-s <sup><math>n</math></sup> /ft <sup>2</sup>
Fracture treatment volume	250,000 gal
Pump rate	40 bbl/min
Casing	
OD	5.5 in.
ID	4.67 in.
Shear rate in casing	647 s <sup>-1</sup>
Time at shear in casing	4.24 min

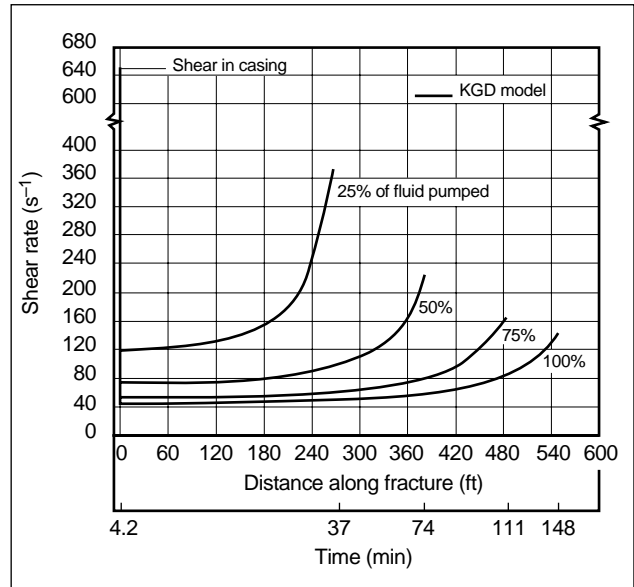


**Figure 8-13.** Shear rate profile during a fracture treatment (Table 8-5) (Worlow, 1987).

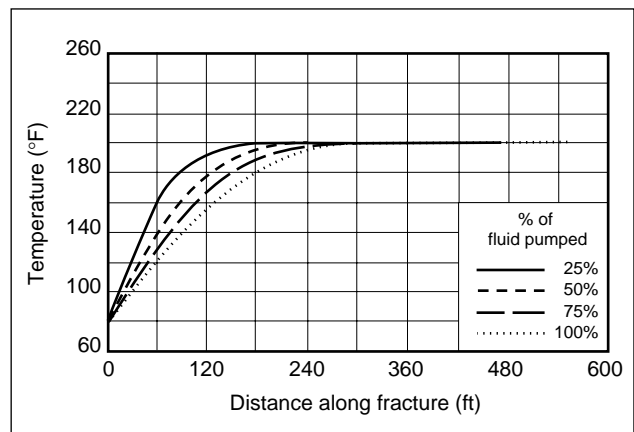


**Figure 8-14.** Temperature profile during a fracture treatment (Table 8-5) (Worlow, 1987).

ature gradient experienced by the fluid as it enters the fracture is highest at the beginning of the treatment and decreases thereafter. As a result, the distance the fluid travels down the fracture before it reaches maximum temperature increases with the total fluid volume pumped (see Section 10-2.9). These are typical trends in the shear and temperature conditions experienced by a fluid. Changing the treatment conditions or the fracturing model can significantly change the predicted values. For example, if the height is reduced by 75% in the example in Table 8-5 (from 300 to 75 ft), the wall shear rate would increase by a factor of 4.

Measurement of the rheological and leakoff properties of a fracturing fluid under all conditions that approach realistic shear and temperature conditions can be an expensive and time-consuming operation. The extent to which field conditions must be simulated depends on the composition of the fluid and the intended use of the data. For example, fluids that do not show time or shear effects on their properties require less elaborate equipment and testing procedures and are easier to scale up to field conditions than fluids that have a strong dependence on shear history. Also, if the intent is to study the effect of shear and temperature on the fluid and to optimize fluid composition for maximum stability, different testing methods may be required than what is appropriate for generating rheological data strictly for fracture design purposes.

Because of the sensitivity of the rheology of crosslinked fluids to their shear and temperature history, considerable efforts have been made to develop industry standard testing methods that will enable comparison of fluid performance data from different laboratories. The API Work Group on Fracturing Fluid Rheology recommended a method that evaluates fluids under fixed tubing and fracture shear history conditions. This method does not intend to represent actual fracturing conditions nor necessarily provide data for fracture design purposes, but rather to establish baseline data for comparing fluid systems.

An example of the effect of shear history on typical crosslinked fluid systems is shown in Fig. 8-15. The data were measured using the device illustrated in Fig. 8-16. The technique maintains the fluid under flowing conditions from the time the crosslinker is added until the test is complete. The test procedure subjects the fluid to a high-shear environment to simulate flow down the tubing or casing followed by a reduced shear rate and increased temperature to simulate fracture conditions. Crosslinker is continuously metered into the fluid at the start of the high-shear conditioning. The equipment for conducting the experiment varies from small laboratory devices to large coiled-tubing devices connected to slot-flow viscometers. These instruments generally provide reproducible results as long as the crosslinker is carefully metered into the fluid under controlled shear conditions. The use of narrow-gap concentric cylinder or small-

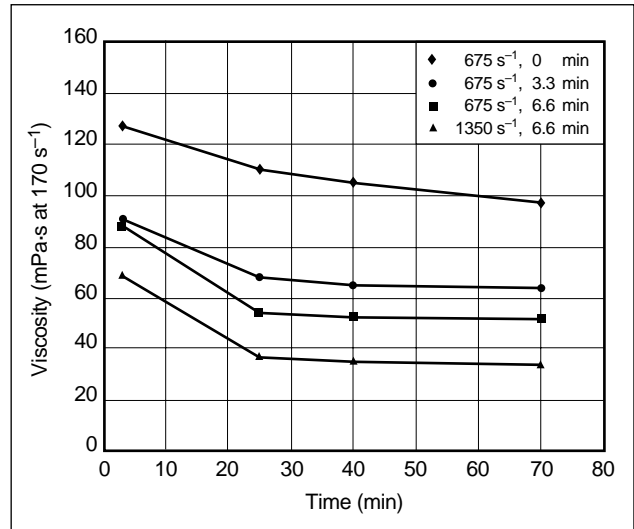


**Figure 8-15.** Effect of shear history during crosslinking of fast-reacting titanate crosslinker (Prud'homme *et al.*, 1989).

diameter capillary viscometers also was found to enhance the reproducibility (Prud'homme, 1986). Several other references (Fan, 1992; Prud'homme *et al.*, 1988, 1989; Prud'homme, 1990) discuss these procedures in detail.

Cameron *et al.* (1990) and Cameron (1993) studied the nonhomogeneous flow character of delayed crosslinked gels and proposed methods for improving the evaluation of fluids with these characteristics.

- Shear effects on fluid rheology

Crosslinked fracturing fluids fall into two distinct categories: gels with reversible crosslinks and gels with irreversible crosslinks. Both types of gels may look equally “solid” or “liquid” in bulk, but the reversibility of the crosslink sites makes profound differences between the flow properties and microstructures of the gels.

Shear affects the rheology of reversible and irreversible gels differently. For guar crosslinked with borate at a guar concentration of 40 lbm/1000 gal, the polymer strand density is almost uniform in space because the concentration is 6 times higher than the critical overlap concentration  $C^*$  (see Section 8-5.2). For this state, shear history effects are minor. For borate gels in the range of 20 lbm/1000 gal, the polymer chains are nearing the value of  $C^*$ . In this regime shear can destabilize the gel and cause shear-induced phase separation. The fluid begins to separate into regions of high and low concentration at a microscopic scale. With



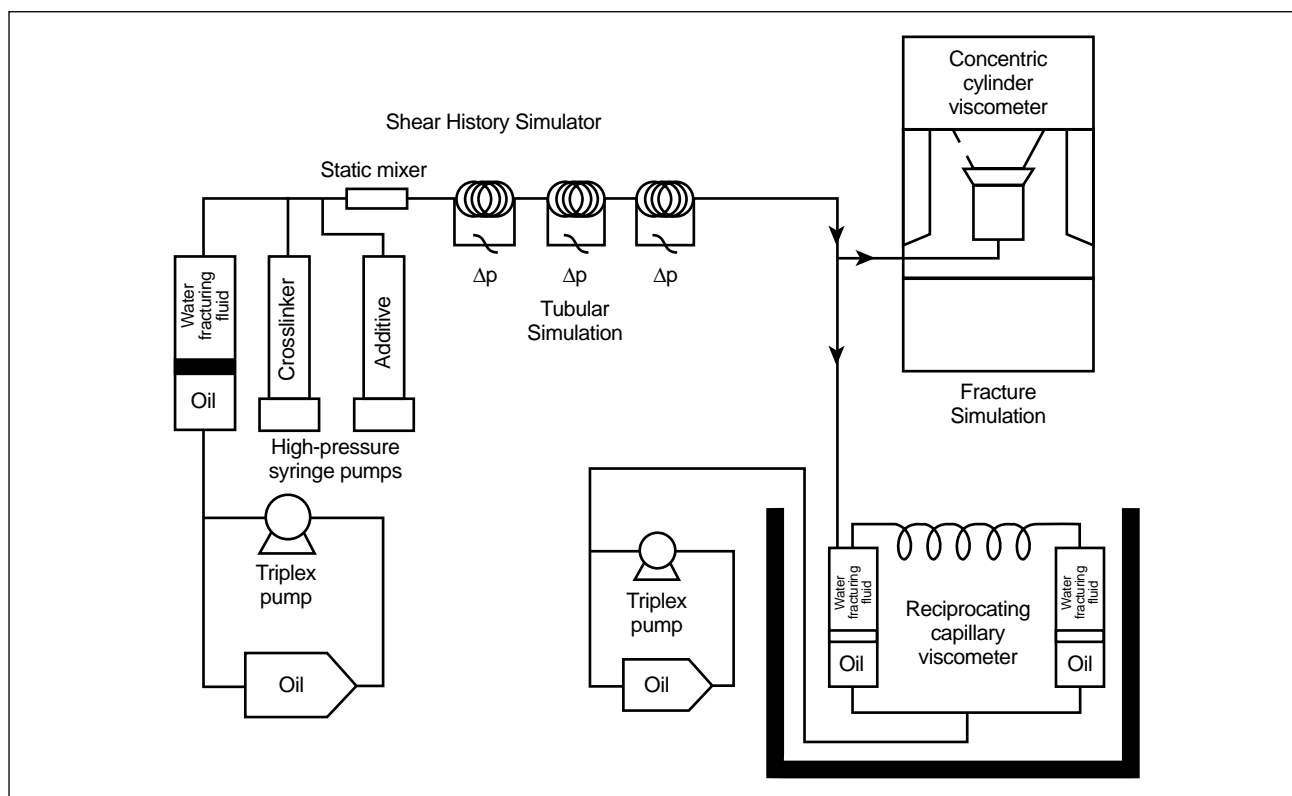


**Figure 8-16.** Tubing shear history simulator plus rotational or reciprocating capillary viscometers (Constien et al., 1986).

only minor segregation, the low-concentration regions fall below  $C^*$ , homogeneous crosslinking is no longer possible, and the gel viscosity drops. Because the borate crosslinks may reform over time, the gel will regain its initial viscosity if the shear is removed. However, the time scale for reequilibration may be on the order of hours. To minimize shear-induced phase separation at polymer concentrations near  $C^*$ , the fluid chemistry can be adjusted to control the crosslinking rate during the time the fluid is exposed to high shear in the tubing or casing. This approach can produce uniform and highly viscous fracturing fluids at low gelling agent concentrations.

Shear also affects the rheology of irreversible titanate and zirconate gels differently. Shear during the crosslinking reaction degrades the gel domains. Under shear, irreversible gel networks break apart into small domains or particles of crosslinked gel. This has been demonstrated by freeze-fracture microscopy on sheared and unsheared titanate-crosslinked HPG gels (Zasadzinski *et al.*, 1987). The texture of a fluid that was crosslinked quies-

cently formed bundles of approximately 25 to 50 molecular chains that aggregated into an open network with pore sizes of 100–250 Å and the appearance of felt. After the fluid was sheared, the gel was broken into fragments. Each fragment acted as a gel particle, and the rheology became that for a suspension of elastic spheres.

To minimize shear damage to the crosslinked structure, delayed crosslinking systems are used to prevent crosslinking during the high-shear-rate flow down the wellbore. However, even in the lower shear environment of the fracture, there are shear rate effects on the ultimate viscosity (Fig. 8-17). Fluids crosslinked in the example in Fig. 8-17 at shear rates between 60 and 87  $\text{s}^{-1}$  show differences in viscosity of 40%.

### 8-6.5. Rheology of foam and emulsion fluids

The viscosity of foams or emulsions is dependent on the volume fraction of the internal phase (known as the quality  $\Gamma$ ), bubble- or drop-size distribution and shape (known together as the texture), interfacial

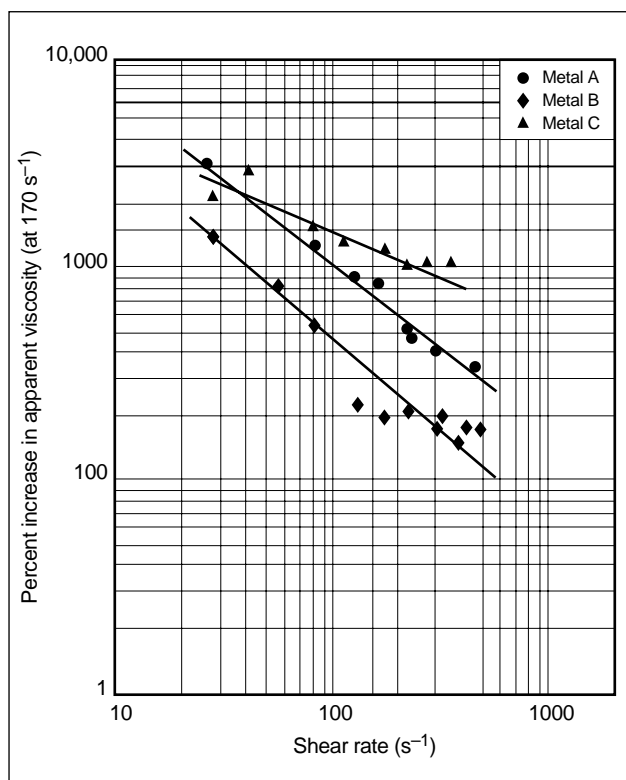


**Figure 8-17.** Effect of shear during crosslinking on apparent viscosity (constant shear on a Fann 39 viscometer for 20 min at 80°F [26°C]) (Conway et al., 1980).

tension and rheological properties of the continuous phase (see Sections 7-5.1 and 7-5.2). Increasing the quality of the foam or emulsion generally increases the viscosity until the concentration of the internal phase reaches a point at which the system is no longer stable. Figure 8-18 illustrates the effect of increasing quality on a simple nitrogen ( $N_2$ ) foam (Cawiezel and Niles, 1987).

The foam texture is dependent on several variables, including the surfactant chemistry, mixing and flow conditions, and pressure (Cameron and Prud'homme, 1989). In general, the finer the bubble or drop size and the narrower the size distribution, the higher the viscosity of the system becomes.

Foams and emulsions have been characterized using several different rheological models, including Herschel-Bulkley, Bingham and power law (Reidenbach *et al.*, 1986; Harris and Reidenbach, 1987; Mitchell, 1971; Wendorff and Ainley, 1981), and a wide variety of experimental methods. One of the difficulties that occurs during testing is that the bubble size and distribution may change with the different shear and temperature conditions experienced by the

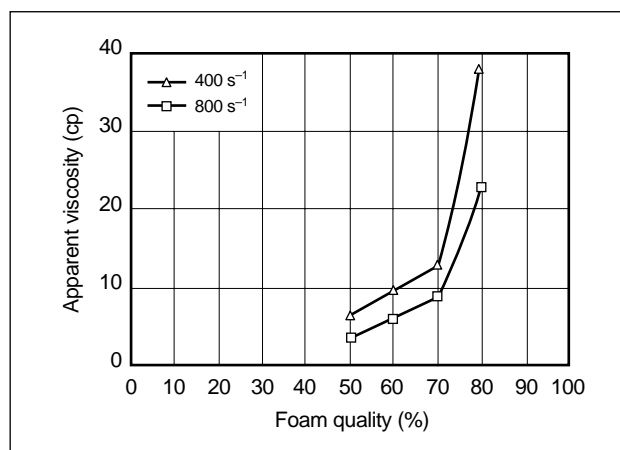


**Figure 8-18.** Apparent viscosity data for  $N_2$  foam with a quality of 50% to 80% at 400- and 800- $s^{-1}$  shear rates (Cawiezel and Niles, 1987).

fluid. The change in bubble or drop size depends on pressure, temperature and shear effects, making the characterization of behavior for these multiphase systems more difficult than for single-phase fluids.

In addition to the standard shear rate and shear stress measurements for viscosity determinations, the volume fraction of the internal phase, bubble- or drop-size distribution and interfacial tension should be characterized and reported for foams and emulsions. These data are required to adequately compare different fluid systems and aid in understanding fluid behavior at various temperature and shear conditions. Unfortunately, in most of the literature on foam or emulsion fluids, data for the bubble or drop size were not obtained. A good example of test results that include drop-size information in addition to pressure drop and flow rate data is by Harris (1985).

Without data relating to the bubble- or drop-size distribution, accurately correcting the pressure drop data during flow for wall slip is difficult. During wall slip, the shear rate of the flow is concentrated and increased at the slip boundary, which can change the bubble or drop and result in a viscosity change for the fluid (Fig. 8-19) (Prud'homme and Khan, 1996).

The equipment used to characterize a foam or emulsion should be selected so that the dispersed drop or bubble size is less than  $1/10$  of the distance between the measurement boundaries. This geometry limitation restricts the use of standard narrow-gap concentric cylinder viscometers for all but the smallest bubble- or drop-size systems. The majority of rheological characterizations have been conducted with either capillary or pipe viscometers with the condi-

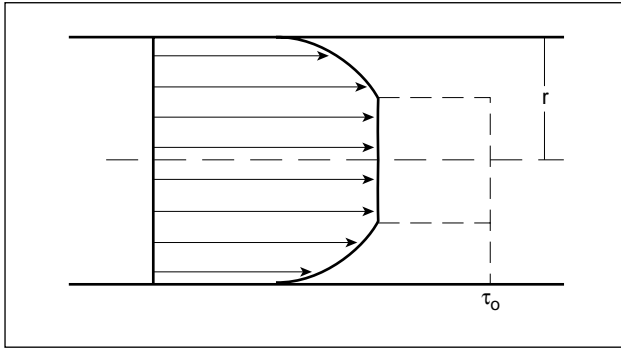


**Figure 8-19.** Flow of foam in a tube. The foam slips at the wall and is in plug flow at the center of the tube, where the shear stress is below the yield stress of the foam  $\tau_0$ .  $r$  = tube radius.

tions made to match the actual fracturing treatment conditions of shear, temperature and pressure as closely as possible. The viscometers are high-pressure circulating systems (Reidenbach *et al.*, 1986; Harris and Heath, 1996) or single-pass pipe viscometers (Harris, 1985; Cawiezel and Niles, 1987; Harris *et al.*, 1995).

One of the more extensive studies of  $N_2$  and carbon dioxide ( $CO_2$ ) foams was conducted by Reidenbach *et al.* (1986). A model for calculating rheological properties based on the foam quality  $\Gamma$ , yield point  $\tau_{yp}$ , and  $n$  and  $K$  for the liquid phase was proposed. The basic equation is

$$\frac{\Delta p D_p}{4L} = \tau_{yp} + K_{foam} \left( \frac{8v}{D_p} \right)^n, \quad (8-10)$$

where  $\tau_{yp}$  is related to the foam quality and gas composition,  $D_p$  and  $L$  are the pipe diameter and length, respectively, and  $\Delta p$  is the pressure drop. The consistency coefficient  $K_{foam}$  was found to be dependent on the liquid-phase consistency coefficient  $K$  and quality:

$$K_{foam} = K e^{(C_1 \Gamma + 0.75 \Gamma^2)}, \quad (8-11)$$

where the constant  $C_1$  varies with the external phase. Typical values for  $\tau_{yp}$ ,  $C_1$  and  $K$  are listed for  $N_2$  and  $CO_2$  foams in Tables 8-6 and 8-7, respectively.

One of the difficulties that typically occurs in relating laboratory-generated data on foams to field-scale tubing is the effect of the pipe diameter on the resulting stress, which may result from texture differences near the pipe wall. Winkler *et al.* (1994) proposed using a volume-equalized power law (VEPL) model as a constitutive flow behavior equation to provide a

**Table 8-6. Parameters for  $N_2$  foams (Reidenbach *et al.*, 1986).**

Foam Quality (%)	True Yield Point (lbf/ft <sup>2</sup> )		
$\Gamma \leq 0.6$	$0.07\Gamma$		
$\Gamma > 0.6$	$0.0002e^{9\Gamma}$		
True Foam Consistency Index (lbf-s <sup><i>n</i></sup> /ft <sup>2</sup> )			
External Phase	<i>K</i>	<i>C</i> <sub>1</sub>	<i>n</i>
Water	0.00002	3.6	1.0
10 lbm HPG/1000 gal	0.00053	2.1	0.75
20 lbm HPG/1000 gal	0.00256	1.7	0.607
40 lbm HPG/1000 gal	0.0152	1.2	0.45

**Table 8-7. Parameters for  $CO_2$  foams (Reidenbach *et al.*, 1986).**

Foam Quality (%)		True Yield Point (lbf/ft <sup>2</sup> )	
$\Gamma \leq 0.6$		$0.042\Gamma$	
$\Gamma > 0.6$		$0.00012e^{8.9\Gamma}$	
True Foam Consistency Index (lbf-s <sup><i>n</i></sup> /ft <sup>2</sup> )			
External Phase	<i>K</i>	<i>C</i> <sub>1</sub>	<i>n</i>
Water	0.00002	4.0	1.0
10 lbm HPG/1000 gal	0.00053	2.6	0.75
20 lbm HPG/1000 gal	0.00256	2.2	0.607
40 lbm HPG/1000 gal	0.0152	1.0	0.45

geometry-independent approach for the prediction of foam properties in pipes at different conditions:

$$\epsilon_s = \frac{\hat{v}}{\hat{v}_l} = \frac{\rho_l}{\rho}, \quad (8-12)$$

where the specific volume expansion ratio  $\epsilon_s$  is defined as the ratio of the specific volume of the foam  $\hat{v}$  to the specific volume of the base liquid  $\hat{v}_l$  and is also equal to the ratio of the liquid density  $\rho_l$  to the foam density  $\rho$ . In terms of the VEPL model, the effective viscosity is (Enzendorfer *et al.*, 1995)

$$\mu_{eff} = K \epsilon_s^{1-n} u^{n-1} D^{1-n} \frac{1}{8} \left( \frac{6n+2}{n} \right)^n. \quad (8-13)$$

Foams with qualities from 30% to 75% were generated in a 40-ppg HPG solution and the pressure was measured in a series of pipe diameters. Figure 8-20 illustrates the shear stress versus volume-equalized shear rate for these foams pumped through four different pipe diameters.

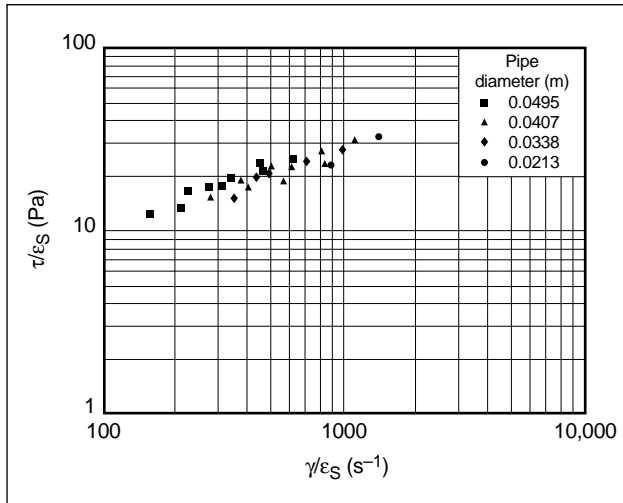


**Figure 8-20.** Volume-equalized wall shear stress versus volume-equalized wall shear rate of 40-ppg HPG foams of quantities from 30% up to 75% at pipe inlet conditions of different pipe sections and a temperature of 68°F [20°C] (Winkler *et al.*, 1994).

Measuring the rheology of crosslinked foams involves many of the same considerations discussed in Section 8-6.4 for single-phase crosslinked fluids. Because crosslinked foams are generally used to transport higher proppant concentrations at higher formation temperatures than foams prepared from linear gels, crosslinked foams should be measured at the temperatures and pressures that represent these conditions (Watkins *et al.*, 1983). The temperature and pressure conditions are important for correctly simulating the quality and texture.

Harris and Heath (1996) used a recirculating flow-loop viscometer to measure borate-crosslinked N<sub>2</sub> foams. The viscosity of the borate-crosslinked foams was predicted by linear regression analysis with a temperature adjustment factor:

$$\text{borate foam viscosity} = m_o T_o (1 + T_o/c) + \mu_{100}, \quad (8-14)$$

where  $m_o = -0.5$ ,  $T_o$  is the offset temperature (i.e., the actual temperature minus 100°F), the factor  $c = 80$ , and  $\mu_{100}$  is the viscosity at 100°F [40°C]. Figures 8-21 and 8-22 are curve fits for foamed borate-crosslinked fluids by this technique.

The viscosity for borate-crosslinked foamed fluids was found to increase with the gas quality and polymer concentration, with a 3- to 10-fold increase over linear foam of the same polymer concentration.

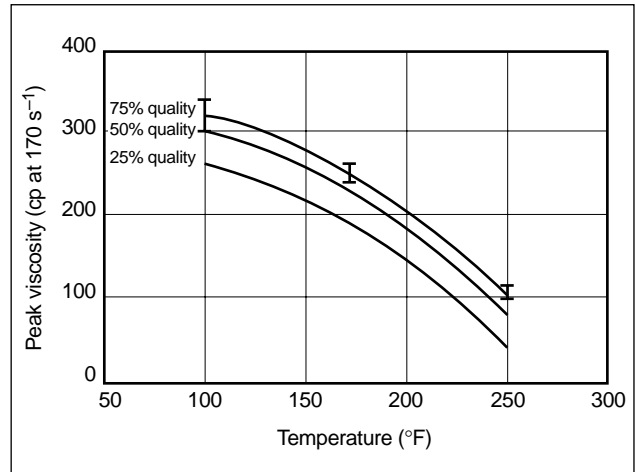


**Figure 8-21.** Curve fit of borate-crosslinked foam with 30 lbm/1000 gal guar.

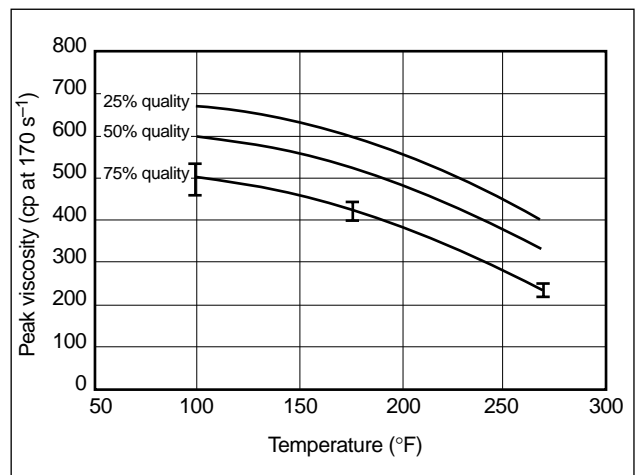


**Figure 8-22.** Curve fit of borate-crosslinked foam with 40 lbm/1000 gal guar.

### 8-6.6. Effect of viscometer geometry on fluid viscosity

In addition to testing fluids with shear and temperature history simulation, understanding the effect of the viscometer geometry on the inferred viscosity of the fracturing fluid is important. For rheological measurements in concentric cylinder viscometers, the more narrow the gap between the rotor and the bob, the more uniform the shear field for non-Newtonian fluids. Harrington *et al.* (1979) illustrated the effect on the shear rate across the gap of a rotational viscometer as a function of the behavior index  $n$ . Fan and Holditch (1993) reported the effects of gap width on the inferred viscosity of several fracturing fluids.

As the gap width increased, the shear stress variation in the gap increased and the average or effective shear rate on the fluid decreased as a function of the width and the behavior index  $n'$  of the fluid. Figure 8-23 illustrates the effect on crosslinked fracturing fluid viscosity of two different bob sizes in a Fann 50 viscometer.

Comparison of data gathered using the same Newtonian wall shear rate in wide- and narrow-gap viscometers finds that the inferred viscosity of the fluid in the wide-gap viscometer is higher because the effective shear rate is lower. Data can be determined independent of the gap width if the experiments are performed using an equivalent volume-averaged shear rate. The volume-averaged shear rate for a power law fluid is determined as follows:

$$\gamma_v = \gamma_b \frac{n'}{(n' - 1) \left[ \left( \frac{r_{cup}}{r_{bob}} \right)^2 - 1 \right]} \left[ \left( \frac{r_{cup}}{r_{bob}} \right)^{2-2/n'} - 1 \right], \quad (8-15)$$

where  $r_{cup}$  is the cup radius,  $r_{bob}$  is the bob radius, and  $\gamma_b$  is the shear rate at the bob:

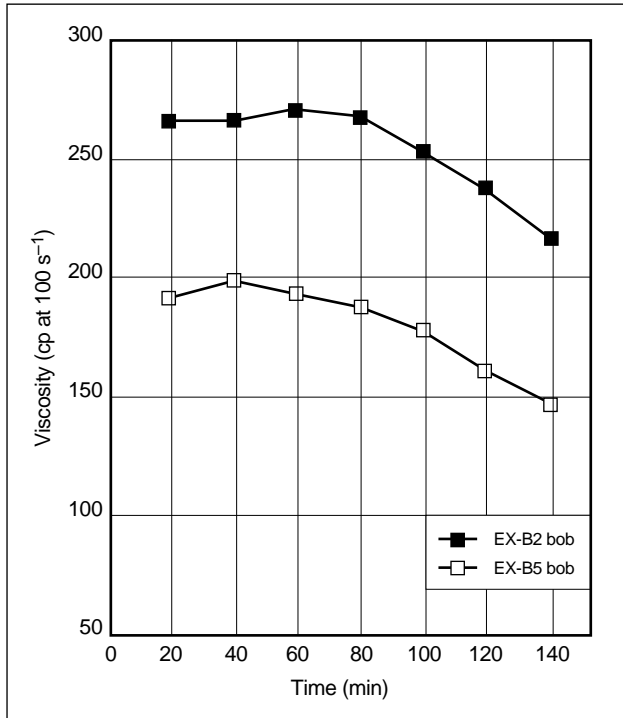


**Figure 8-23.** Viscosity measurements of delayed titanate HPG gel using a nominal shear rate of  $100 \text{ s}^{-1}$  at  $200^\circ\text{F}$  [ $95^\circ\text{C}$ ] and two bob sizes (Fan and Holditch, 1993).

$$\gamma_b = \frac{\pi\omega}{15n' \left[ 1 - \left( \frac{r_{bob}}{r_{cup}} \right)^{2/n'} \right]}, \quad (8-16)$$

where  $\omega$  is the viscometer angular velocity. Equations 8-15 and 8-16 can be applied to Newtonian fluids when  $n' = 1$ .

Figure 8-24 illustrates use of the volumetric average shear rate method to test a titanate-crosslinked fracturing fluid (Fan and Holditch, 1993).

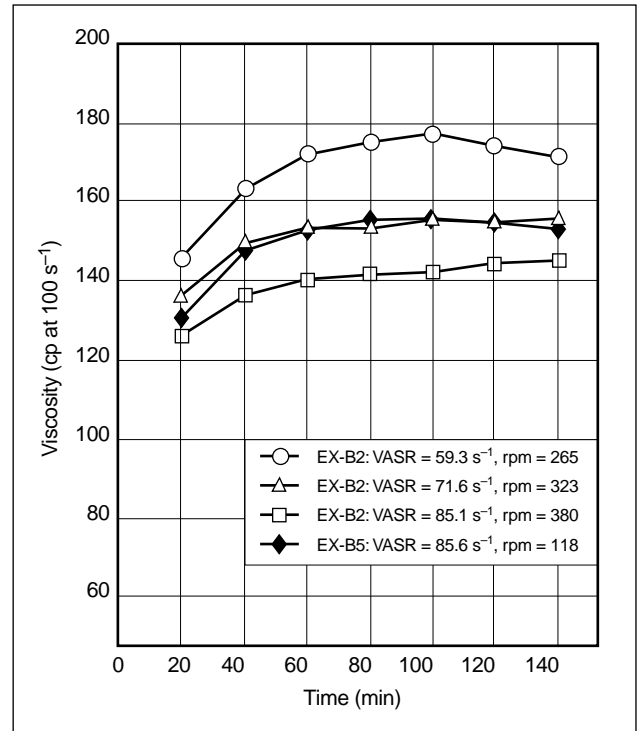


**Figure 8-24.** Comparison of viscosity measurements for delayed titanate HPG gel using the volumetric average shear rate (VASR) method at  $150^\circ\text{F}$  [ $65^\circ\text{C}$ ] (Fan and Holditch, 1993).

### 8-6.7. Characterization of fluid microstructure using dynamic oscillatory measurements

Shear rheology measurements provide the parameters  $n$  and  $K$ . This information is necessary for optimizing fluid stability and viscosity and for predicting laminar flow behavior in fractures. Additional information concerning the microstructure of the fluid can be obtained using dynamic oscillatory rheological measurements. Dynamic oscillatory measurements may be used to evaluate the viscous, linear elastic and

nonlinear elastic (i.e., normal force) properties of polymer fluids. The linear elastic properties, which are known as the elastic storage modulus  $G'$  and viscous loss modulus  $G''$ , are sensitive to changes in polymer structure that may not be observed with steady shear measurements. For example, Prud'homme (1986) used dynamic oscillatory measurements to determine differences in the extent of hydration of guar mixed by two different methods, although the steady shear viscosity measurements were the same. Similarly, Knoll (1985) studied the differences in crosslink density and wall-slip tendencies of fluids that had been dynamically mixed. Several other studies have used dynamic mechanical testing to obtain information on such properties as crosslinking kinetics and the effects of elasticity on proppant suspension capabilities and flow properties (Clark, 1979; Acharya, 1986, 1988; Acharya and Deysarkar, 1987; Menjivar, 1984; Prud'homme, 1985; Clark and Barkat, 1989; Clark *et al.*, 1993; Power *et al.*, 1994; de Kruijf *et al.*, 1993).

### 8-6.8. Relaxation time and slip

The relaxation time of fracturing fluids defines the critical shear rate for reversible behavior. This time can be determined from dynamic oscillatory measurements. Dynamic oscillatory moduli as a function of temperature are shown in Fig. 8-25. If the moduli are fitted to a Maxwell model (i.e., a rheological model for a linear viscoelastic fluid with one time constant and one elasticity constant), the relaxation time

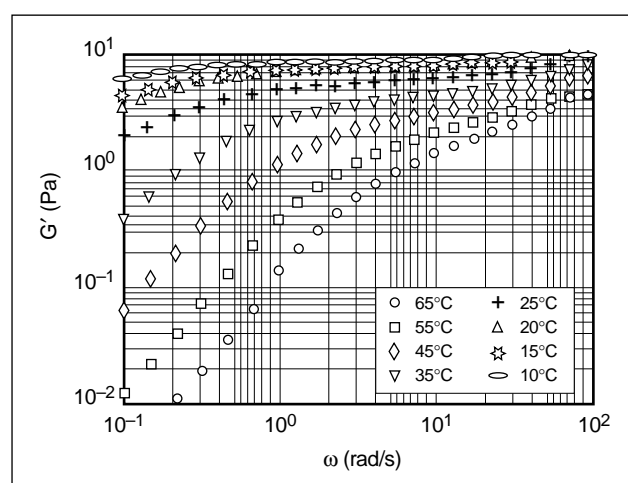


**Figure 8-25.** Storage modulus  $G'$  of 48% by weight HPG crosslinked by 0.12% by weight borax gel at a pH of 9.15 (Kesavan *et al.*, 1993).

constant of the fluid can be obtained. The importance of the time constant is that it can be related to the shear rate for the fluid by the dimensionless Deborah number:

$$De = \frac{\lambda}{t}, \quad (8-17)$$

where  $\lambda$  is the characteristic relaxation time and  $t$  is the characteristic flow time, which is proportional to  $1/\dot{\gamma}$ . If  $De > 1$ , then the relaxation time of the polymer gel is longer than the flow time. In this case, the fluid can not relax and behaves more like an elastic solid than a fluid. As a solid it slips at interfaces rather than flowing as a continuous fluid. The inferred viscosity of a “slipping” fluid depends on the measurement geometry and wall roughness, and hence does not reflect the actual fluid composition and process conditions such as fluid temperature but is an artifact of the testing device.

Measurements from multiple geometries are necessary to separate the effects of slip from the true fluid viscosity (Kesavan *et al.*, 1993). For shear rates such that  $De < 1$ , the fluid will display normal shear thinning viscosity.

### 8-6.9. Slurry rheology

Fluids containing proppant generally account for 20% to 80% of the total volume of a fracturing treatment, yet little rheological data exist for these slurries. Determining the rheology of fracturing slurries is a considerable problem because of the dependence on fluid composition, flow geometry, temperature, time, and proppant size, density and concentration. The majority of instruments used to determine the rheological properties of “clean” fluids are not suited for these studies because their geometry does not accommodate the distance between the flow boundaries (i.e., the gap or slot should be  $>10$  times the particle diameter) or high concentrations (i.e., up to 20 ppa). Also, the proppant must be kept in uniform suspension.

The common means for characterizing fracturing fluid slurries are large slot-flow devices, “wiped-disc” concentric cylinder viscometers and wide-gap concentric cylinder viscometers. Examples of slurry viscosity data are presented in Figs. 8-26 and 8-27 (Ely, 1987).

Gardner and Eikerts (1982) used a large closed-loop pipe viscometer to study crosslinked aqueous fracturing fluids containing proppant in laminar flow.

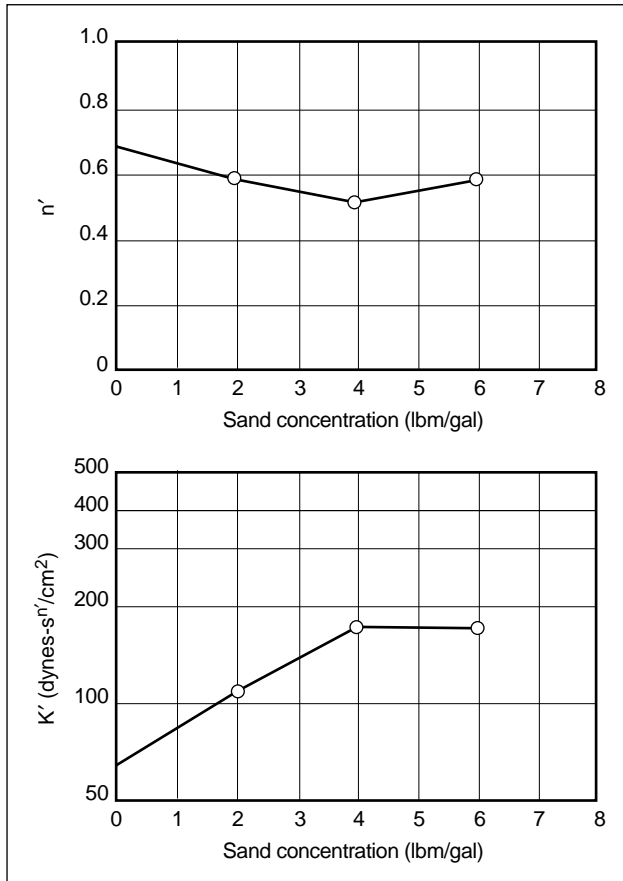


**Figure 8-26.** Flow behavior index  $n'$  and fluid consistency index  $K'$  as functions of sand concentration (Ely, 1987).

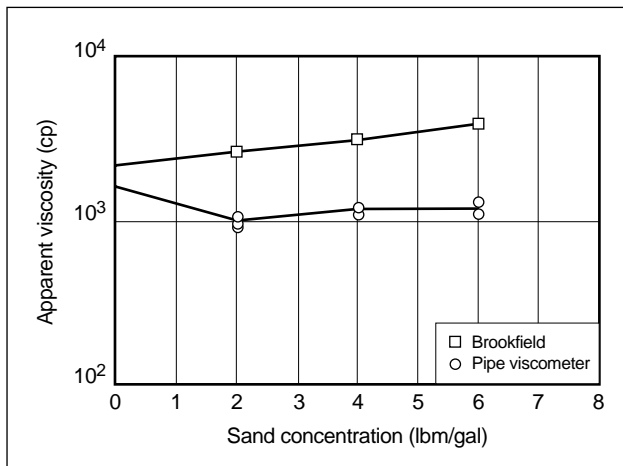


**Figure 8-27.** Apparent viscosity measured with two types of viscometers as a function of sand concentration (Ely, 1987).

They found that the apparent viscosity of a cross-linked fracturing fluid increased up to 230% with the addition of 6 ppa (Fig. 8-28). Their data also indicate

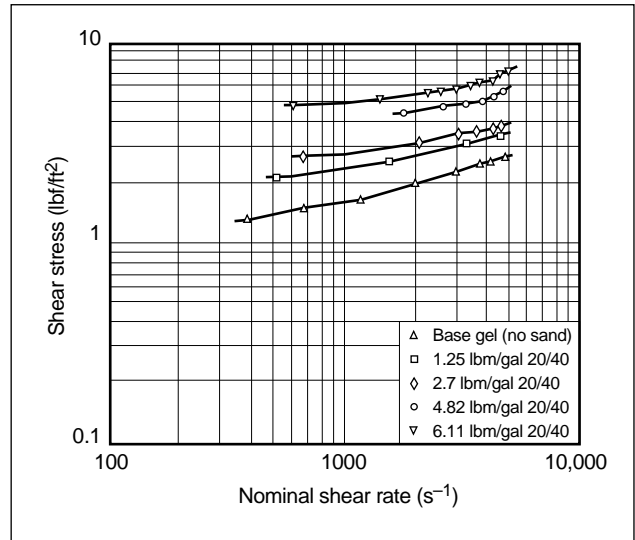


**Figure 8-28.** Effect of proppant on fluid viscosity (Gardner and Eikerts, 1982).

that the apparent viscosity of the fluid at 511 s<sup>-1</sup> with proppant was 2.7 times that predicted by Ford (1960) for a Newtonian fluid with an equivalent proppant concentration. These large effects of proppant are contrary to those expected for shear-thinning fluids (Nolte, 1988b).

In a more extensive work that considered both laminar and turbulent flow, Shah and Lee (1986) studied the relation of friction pressure to proppant concentration and size in four different HPG base fluids in different pipe sizes and correlated the laboratory predictions with field measurements. Shah and Lee's studies illustrate the complexity of characterizing slurry rheology. The friction pressure of fluids containing proppant was found to increase with increasing proppant concentration (Figs. 8-29 and 8-30). The predicted amount of friction pressure increase diminished with turbulent flow rates (e.g., >12 bbl/min).

A relation for the increase in friction pressure in turbulent flow resulting from the presence of proppant is

$$\Delta p_{friction} = (\mu_r)^m (\rho_r)^{(1-m)}, \quad (8-18)$$

where  $\Delta p_{friction}$  is the friction pressure ratio with and without solids,  $\mu_r$  is the ratio of the apparent slurry viscosity to the apparent fluid viscosity,  $\rho_r$  is the ratio of the slurry density to the fluid density, and  $m$  is the log-log slope of the friction plotted versus the Reynold's number. Hannah *et al.* (1983) used  $m = 0.2$  for the equation.

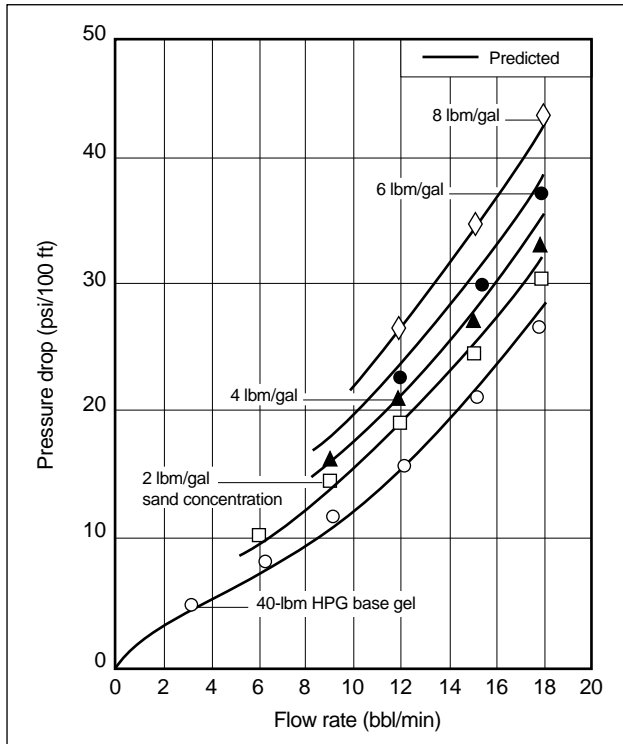


**Figure 8-29.** Comparison of actual friction pressures at various flow rates for 40 lbm HPG/1000 gal and sand-laden 40 lbm HPG/1000 gal fluids in 2 $\frac{7}{8}$ -in. tubing (Shah and Lee, 1986).

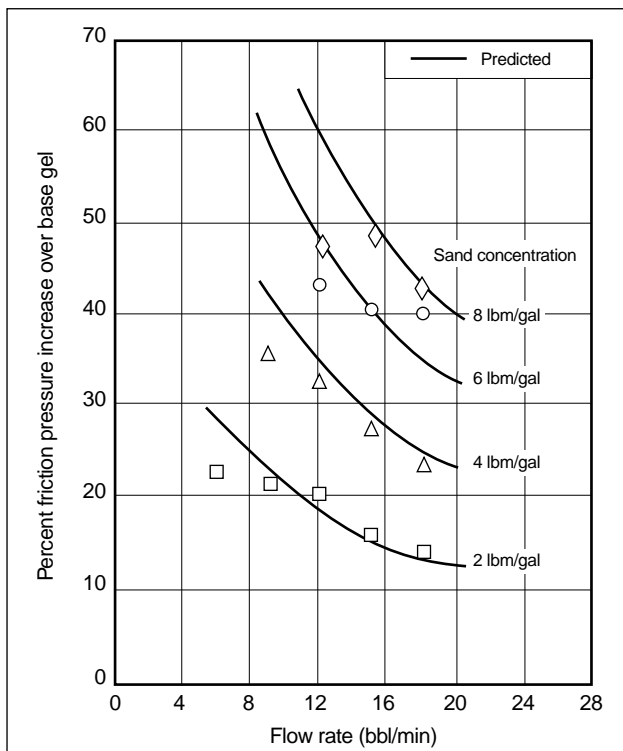


**Figure 8-30.** Effect of sand concentration on friction pressures of 40 lbm HPG/1000 gal fluid in 2 $\frac{7}{8}$ -in. tubing at various flow rates (Shah and Lee, 1986).

## 8-7. Proppant effects

In addition to the change in apparent viscosity with the addition of proppant to the fluid, an equally important factor to determine is the possibility of interaction of the fluid chemistry with the proppant to change the stability or maximum viscosity that the system can generate. This is particularly the case with resin-coated proppants. Methods for evaluating fluid and proppant interactions were described by Norman *et al.* (1990) and Nimerick *et al.* (1992).

### 8-7.1. Characterization of proppant transport properties

Measuring the ability of a fluid to transport proppant is one of the more difficult tasks in fracturing fluid characterization. Many factors, such as fluid rheology, fluid velocity and proppant concentration and density, affect proppant settling rates.

Most of the experimental studies to characterize proppant transport properties use one or more of the following three approaches:

- measuring the rheological properties of clean fluid and using these as the basis for predicting the transport properties
- measuring proppant settling velocities in stagnant fluids
- observing proppant transport in slot-flow devices, flow loops or concentric cylinder devices.

Particle settling velocities have been measured in a variety of experimental devices. Kern *et al.* (1959) and Babcock *et al.* (1967) studied the flow and deposition of sand slurries in a vertical slot-flow model. Schols and Visser (1974) and Sievert *et al.* (1981) also used a vertical slot-flow model to develop equations for both the height and length of deposition beds. Clark *et al.* (1977, 1981) and Sievert *et al.* (1981) used a large vertical slot-flow model to study the settling of particle clusters in non-Newtonian fluids.

Novotny (1977), Hannah *et al.* (1978), Harrington *et al.* (1979) and Clark and Guler (1983) used a concentric cylinder device to study proppant settling velocities. Novotny's study included wall effects, concentration effects and shear effects on a series of Newtonian and non-Newtonian fluids. Hannah *et al.* and Harrington *et al.* used two different concentric cylinder devices to study noncrosslinked and cross-



linked fluids. The results of both studies indicate that the settling of particles in the fluids deviated from Stokes law settling velocities. Clark *et al.* (1981) and Quadir (1981) reported results from a study using both a parallel-plate device and a concentric cylinder device. They also reported significant deviations from Stokes law settling velocities.

Flow loops with particles suspended in a vertical section were used by Shah (1986).

More recently, proppant transport has been evaluated in large slot-flow devices at commercial testing laboratories (Barree and Conway, 1994; Zhao *et al.*, 1995) and universities (Clark and Zhu, 1995a; Shah and Subramanian, 1997; Goel *et al.*, 1997; Hejjo *et al.*, 1997; Shah *et al.*, 1998; Shah and Asadi, 1998). The transport efficiency in these tests is usually determined by visual observation of proppant fall, and comparisons are made to the performance of other fracturing fluids under similar test conditions.

When the results of the experimental measurements are translated to predictive models, Stokes settling law for a Newtonian fluid (see Eq. 6-106) is most frequently used as an initial frame of reference.

Most fracturing fluids are non-Newtonian, with fluid viscosity decreasing as shear increases. Novotny (1977) determined that the most important variables affecting proppant settling are the non-Newtonian characteristics of the fluid, wall effects and proppant concentration. For a non-Newtonian transporting fluid, Novotny found that the shear rate within a fluid had a significant effect caused by its reduction in the apparent viscosity affecting particle settling.

A modified version of Stokes law for the terminal settling velocity  $u_t$  of a single particle in a quiescent power law fluid is

$$u_t = K \left[ \frac{(\rho_p - \rho_f) g d_{prop}^{(n+1)}}{18K(3)^{(n-1)}} \right]^{1/n}, \quad (8-19)$$

where  $\rho_p$  and  $\rho_f$  are the densities of the particle and the fluid, respectively,  $g$  is the gravitational acceleration, and  $d_{prop}$  is the particle diameter. This equation and other forms of Stokes equations in this section assume that the particle Reynold's numbers are less than 2.

With Eq. 8-19, the particle settling velocity becomes a function of the fluid parameters  $n$  and  $K$ . The settling velocity in power law fluids is proportional to

$$u_t \propto d_{prop}^{(1+n)/n}. \quad (8-20)$$

For Newtonian fluids, the relation is

$$u_t \propto d_{prop}^2. \quad (8-21)$$

Equation 8-19 can be used to determine only single-particle fall rates over shear ranges in which the fluid follows power law behavior. As shear rates approach very low or very high values, limiting values of the apparent viscosity are reached. In actual treatments, values of high-shear-limiting viscosity  $\mu_\infty$  are not approached in the fracture. However, at the center of the fracture channel the shear rate is zero and the fluid viscosity approaches the value for zero-shear viscosity  $\mu_0$  (Fig. 8-10). Roodhart (1985b) and other investigators determined that low-shear viscosity plays a considerable role in proppant transport during flow conditions (Kirkby and Rockefeller, 1985). To correct the limitation of the power law model to describe flow fields where the shear rates approach zero, Slattery and Bird (1961), Turian (1967), Dunand *et al.* (1984) and Roodhart (1985b) studied the Ellis fluid model, which incorporates a  $\mu_0$  term (Eq. 8-9).

Combining Eq. 8-9 with Stokes law leads to a settling velocity equation of the form

$$u_t = \frac{g\Delta\rho d_{prop}^2}{18\mu_0} + \frac{g\Delta\rho d_{prop}^2}{18K'} \left( \frac{u_t}{d_{prop}} \right)^{1-n'}, \quad (8-22)$$

where  $\Delta\rho = \rho_p - \rho_f$  and the shear rate induced by particle settling is assumed to be (Novotny, 1977)

$$\gamma = \frac{u_t}{d_{prop}} \quad (8-23)$$

(versus 3 times this value in Eq. 8-19).

Roodhart (1985b) tested the validity of Eqs. 8-9 and 8-22 under static and flowing conditions. He found excellent correlation with experimental data for the apparent viscosity versus shear rate (Fig. 8-31) and static settling velocities for glass and steel particles (Fig. 8-32). Roodhart also found that the shear from the horizontal fluid flow could be ignored for fracture shear conditions from 0 to approximately  $25 \text{ s}^{-1}$  and that an extended power law model that includes a term for zero-shear viscosity was applicable for determining proppant settling rates within the fracture for pump rates for these wall shear conditions.

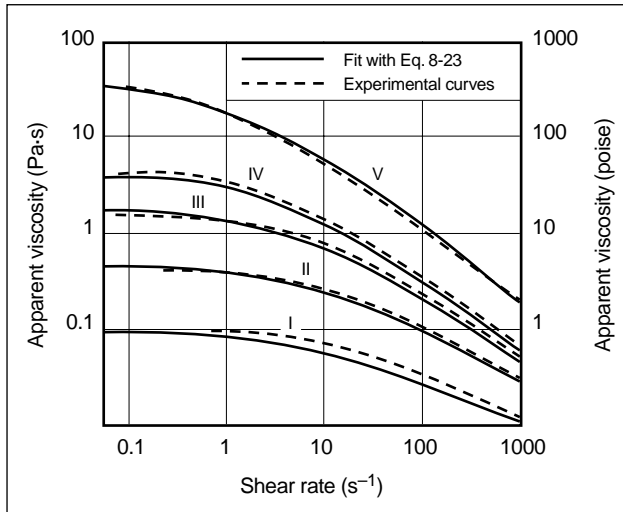


**Figure 8-31.** Comparison of experimental data (Table 8-8) with values predicted from the extended power law (Eq. 8-9) (Roodhart, 1985b).

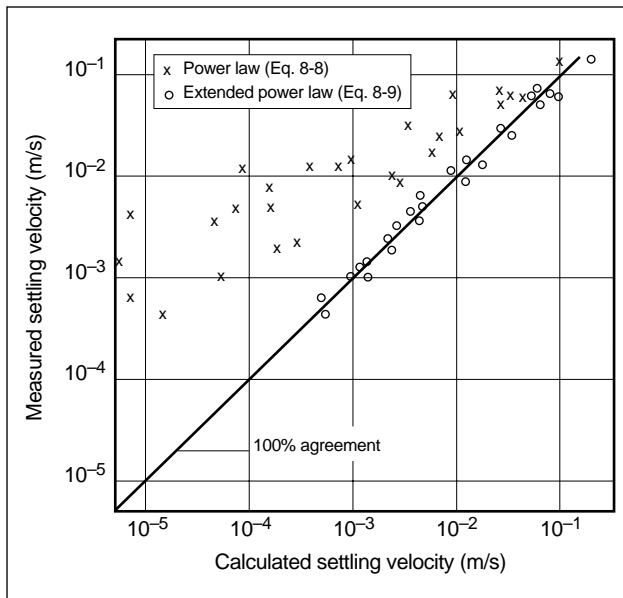


**Figure 8-32.** Experimental versus calculated settling velocities in viscous fluids ( $N_{Re} < 2$ ) (Roodhart, 1985b).

Another approach for predicting proppant settling rates from rheological measurements was reported by Acharya (1986), Shah (1986) and Meyer (1986b). This approach correlates a generalized drag coefficient defined as

$$C_{drag} = \frac{4}{3} \frac{g d_{prop}}{u_t^2} \left[ \frac{\rho_p - \rho_f}{\rho} \right] \quad (8-24)$$

and a generalized particle Reynold's number  $N_{Re}$ :

$$N_{Re} = \frac{d_{prop} u_t \rho_f}{\mu}, \quad (8-25)$$

where  $\mu$  is equal to  $K(\gamma)^{n-1}$  for power law fluids in laminar and turbulent flow. Using the definitions for  $C_{drag}$  and  $N_{Re}$ , a correlation of particle settling velocities and fluid properties was made by a generalized plot of  $\sqrt{C_{drag}^{2-n} N_{Re}^2}$  versus  $N_{Re}$ . This relation results in a family of curves that are functions of the behavior index  $n$  (Fig. 8-33). The significance of representing data in this fashion is that they can be used to predict particle settling velocities in other fluid systems if the particle density and size and the fluid properties  $n$  and  $K$  are known (Shah, 1986). This method has been reported to predict experimentally determined settling velocities to within  $\pm 20\%$  for a quiescent fluid (Meyer, 1986b).

### 8-7.2. Particle migration and concentration

One of the factors that can influence proppant transport is the tendency of particles to migrate and concentrate in preferred areas of the flow field. Under shear gradient conditions in a pipe or fracture slot, proppant particles can move to the center of the fluid for viscoelastic fluids or toward the wall for non-Newtonian fluids that are not viscoelastic. Central migration of the particles results in proppant settling rates that are greater than expected (Nolte, 1988b).

**Table 8-8.** Data plotted in Fig. 8-31 (Roodhart, 1985b).

Fluid	Type	Gelling Agent Concentration (kg/m <sup>3</sup> )	Power Law Indices $n$	$K$ (Pa·s <sup><math>n</math></sup> )	Zero-Shear Viscosity (Pa·s)
I	Guar gum	3.6	0.52	0.33	0.1
II	HEC	4.8	0.45	1.40	0.54
III	HEC	7.2	0.37	4.0	2.0
IV	Guar gum	9.6	0.29	8.5	4.2
V	HEC	12.0	0.22	40.0	32.0

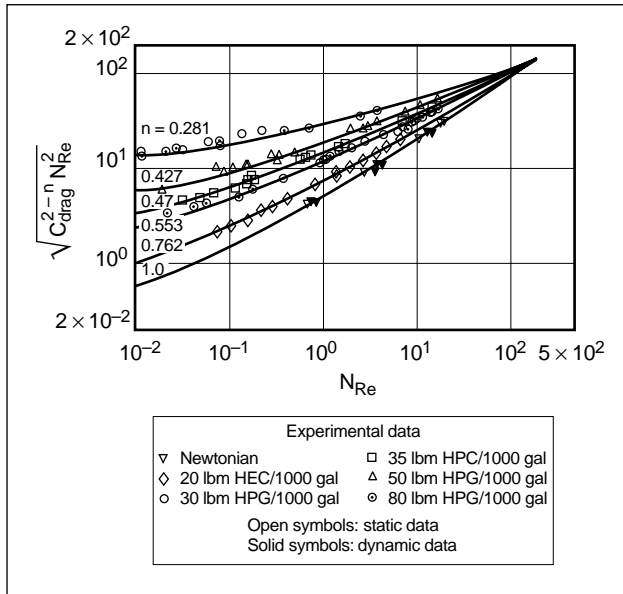


**Figure 8-33.** Relationship of  $\sqrt{C_{\text{drag}} N_{\text{Re}}^n}$  to  $n$  (Shah, 1986).

There are different techniques for measuring particle migration in fracturing fluids of varying rheological properties under different flows. The effect of rheological properties of fracturing fluids on proppant migration has been studied in large slot-flow models by videotaping the particle positions in the gap of the slot. The slot width was divided into thin slices, and the number of particles traveling in each slice during a certain interval of time was counted from individual videotape frames.

Tehrani (1996) reported particle migration experiments in pipe flow. The slurry consisted of nearly spherical, transparent acrylic particles with a density of  $1.180 \text{ g/cm}^3$  dispersed in borate-crosslinked HPG fluids. A video camera with a variable shutter speed was used to record images of the flow field in the pipe. A vertical sheet of laser light illuminated the flow field. The rheological properties of the fluids were measured, including shear viscosity and normal stress as functions of the shear rate and  $G'$  and  $G''$  as functions of the frequency. Particle migration was found to be controlled by the elastic properties of the suspending fluid and the shear rate gradient.

Particle concentration has the effect of increasing the frequency of interparticle interactions. The bulk viscous stresses that drive particles together are a strong function of the suspension viscosity, which is a function of the particle volume fraction. The lubrication forces that resist interparticle interactions

are a function of only the fluid viscosity, and they act in the narrow spaces between particles. The net effect is that the resistance encountered by a particle to movement in the suspension increases with the particle volume fraction.

On the average, particles migrate away from high-concentration zones, where the frequency of the interactions is higher, to low-concentration zones, where the frequency of the interactions is lower. This type of particle migration mechanism is referred to as shear-induced self-diffusion, as observed by Gadala-Maria and Acrivos (1980) and explained by Leighton and Acrivos (1987).

If there is a concentration gradient in the suspension caused by the migration of particles resulting from non-Newtonian or inertial effects, a net diffusional flux will oppose the migration. Unwin and Hammond (1995) used a phenomenological model that considers all these effects simultaneously to solve for the particle concentration profiles in concentric cylinder and slot-flow geometries.

## 8-8. Fluid loss

Fluid loss to the formation during a fracturing treatment is a filtration process that is controlled by a number of parameters, including fluid composition, flow rate and pressure, and reservoir properties such as permeability, pressure, fluid saturation, pore size and the presence of microfractures.

Several controlling mechanisms can be involved in limiting fluid loss, as discussed in Section 6-4. Filtrate viscosity and relative permeability can control fluid loss when their ratio is greater than that for the reservoir fluid. The filtrate- (or viscosity-) controlled fluid-loss coefficient in  $\text{ft/min}^{1/2}$  is described by

$$C_v = 0.0469 \sqrt{\frac{k_{fil} \Delta p_T \phi}{\mu_{fil}}}, \quad (8-26)$$

where  $k_{fil}$  is the filtrate permeability in millidarcies into the saturated reservoir,  $\Delta p_T$  is the total differential pressure between the fluid in the fracture and the initial reservoir pressure in psi,  $\phi$  is the formation porosity (fraction), and  $\mu_{fil}$  is the apparent viscosity in cp of the filtrate flowing into the formation.

The filtrate control mechanism is most likely in effect when a gas reservoir is fractured with a non-wall-building, high-viscosity fluid or for a formation at irreducible water saturation. Also for non-wall-building polymers, the apparent viscosity of the fil-

trate is lower than that in the fracture because of higher shear rates for the filtrate. The viscosity of the filtrate from a wall-building fluid is generally much lower than the viscosity of the fracturing fluid.

The viscosity and compressibility of the reservoir fluid also help to control leakoff into the formation. This control mechanism is most effective when the reservoir fluids have high viscosities and are not greatly compressible (e.g., heavy oil). The reservoir- (or compressibility-) controlled fluid-loss coefficient is calculated as follows:

$$C_c = 0.00118 \Delta p_T \sqrt{\frac{k_r \phi c_t}{\mu_r}}, \quad (8-27)$$

where  $k_r$  is the reservoir permeability,  $c_t$  is the compressibility of the reservoir in  $\text{psi}^{-1}$ , and  $\mu_r$  is the viscosity of the reservoir fluid in cp. These equations for  $C_v$  and  $C_c$  differ from Eqs. 6-88 and 6-99, respectively, because they are expressed in common reference to the total differential pressure.

Because it is possible for both filtrate and reservoir effects to be factors in controlling fluid loss, it is common practice to combine the two coefficients (see Eq. 6-96):

$$C_{cv} = \frac{2C_v C_c}{C_v + (C_v^2 + 4C_c^2)^{1/2}}. \quad (8-28)$$

A third fluid-loss control mechanism is in operation with wall-building fluids. When a wall-building fluid is forced onto a rock, a thin film of material (i.e., polymer, fluid-loss additives or both) is filtered out and deposited on, or within the surface region of, the formation face surface. This thin film of material, known as the filter cake, is less permeable than the rock. Fluid loss can then become controlled by the filter cake rather than by the rock (i.e.,  $C_v$  or  $C_c$ ).

Depending on the pore size of the formation, polymers and fluid-loss additives in the fracturing fluid may be filtered out on the formation surface or may invade into the matrix and deposit by bridging and adsorption mechanisms in the pore space. The depth of invasion of the polymers and fluid-loss additives is a function of their size, degree of entanglement and ionic character. High deformation gradients resulting from pressure differentials can cause polymer molecules to transform from coiled conformations to a stretched state, which enables them to flow into pore sizes smaller than their largest dimension. If adsorption or plugging occurs in the pore throats, the polymer chains form bridges in the pore throats (Pacelli

Zitha, 1995), resulting in lower leakoff rates. This mechanism is called internal filter-cake formation.

The rate of filtrate leakoff is specific to the particular fluid composition and formation properties and must be determined experimentally, either in the laboratory or by in-situ calibration treatments, as discussed in Section 9-5. The following provides an introduction to the laboratory tests.

### 8-8.1. Fluid loss under static conditions

Static fluid-loss tests for fracturing fluids have been used for many years (Howard and Fast, 1970; *Recommended Practice for Standard Procedures for Evaluation of Hydraulic Fracturing Fluids* [RP 39], 1983). A simple schematic of a static fluid-loss test is shown in Fig. 8-34.

In static fluid-loss tests, fluid is heated to the test temperature, a differential pressure is applied across

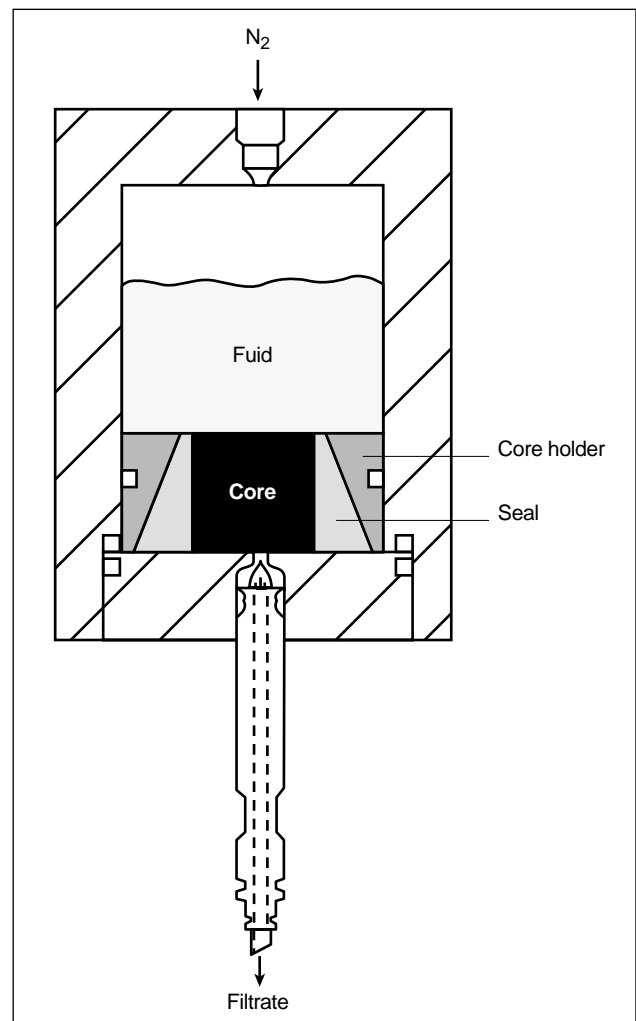


**Figure 8-34.** Schematic of a static fluid-loss cell.

the core (usually 1000 psi), and the rate of filtrate volume forced through the core is measured versus time. For wall-building fluids, the filter cake continues to grow with time and the fluid-loss rate decreases. For an ideal wall-building fluid, a plot of the filtrate volume versus the square root of time results in a straight line (see Sidebar 5A). The slope of the straight line is used to calculate the wall-building coefficient  $C_w$  and the intercept is used to calculate the spurt loss  $S_p$ . The value of  $C_w$  is directly proportional to the leakoff velocity through the established filter cake. The spurt value represents the fluid that leaks off during the formation of an effective filter cake. By using the intercept to calculate spurt, the assumption is made that the filter cake is instantaneously established. However, because a finite time or volume is required for an effective filter cake to form, calculated values of spurt only approximate the fluid-loss behavior during filter-cake formation.

$C_w$  is calculated in  $\text{ft}\cdot\text{min}^{1/2}$  as

$$C_w = \frac{0.0164m}{A}, \quad (8-29)$$

where  $m$  is the slope of the leakoff plot in  $\text{mL}/\text{min}^{1/2}$  and  $A$  is the area in  $\text{cm}^2$  of core exposed to fluid.

From the y-axis intercept  $b$ , the spurt value is determined in  $\text{gal}/100 \text{ ft}^2$ :

$$S_p = \frac{24.4b}{A}. \quad (8-30)$$

Most fluid-loss data are generated in static conditions, and these data may be misleading because the filter cake is allowed to grow without being subjected to erosion of the flowing fluid along the fracture surface.

## 8-8.2. Fluid loss under dynamic conditions

Filter-cake erosion and fluid degradation under conditions of shear and temperature have been the subject of considerable study. Studies through the mid-1980s include Hall and Dollarhide (1964, 1968), Sinha (1976), McDaniel *et al.* (1985), Gulbis (1982, 1983), Penny *et al.* (1985) and Roodhart (1985a). The results from these studies show that dynamic filtration tends to increase as the shear rate and temperature increase (Fig. 8-35). Penny *et al.* found that dynamic fluid-loss tests conducted at  $40 \text{ s}^{-1}$  produced data similar to static test results. Gulbis (1982) found

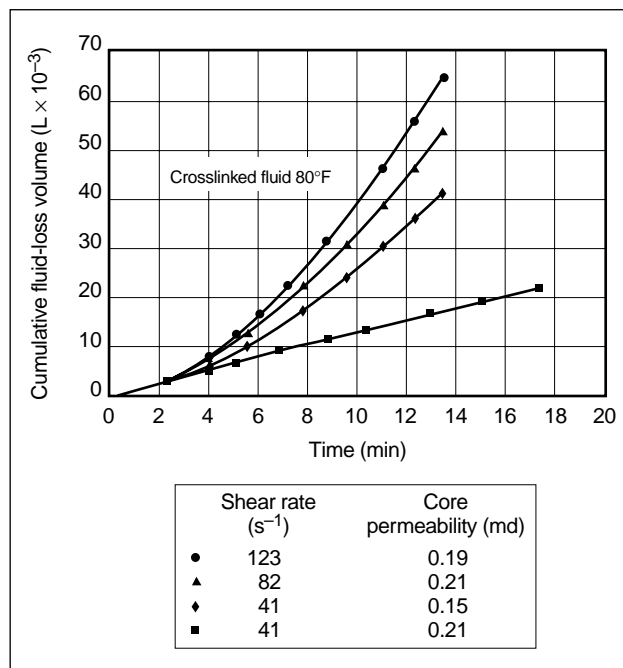


**Figure 8-35.** Cumulative fluid-loss data for different shear rates (McDaniel *et al.*, 1985).  $\Delta p = 300 \text{ psi}$ , core length =  $0.02 \text{ m}$ .

similar results for noncrosslinked HPG and for borate- and transition-metal-crosslinked HPG (Gulbis, 1983), if the test times were less than approximately 30 min. Gulbis (1983) also observed that shear rates greater than  $80 \text{ s}^{-1}$  in dynamic tests caused transition-metal-crosslinked fluids to have higher leakoff rates than noncrosslinked or borate-crosslinked fluids (Fig. 8-36). The shear rate at the fracture surface changes significantly (i.e., decreases) with

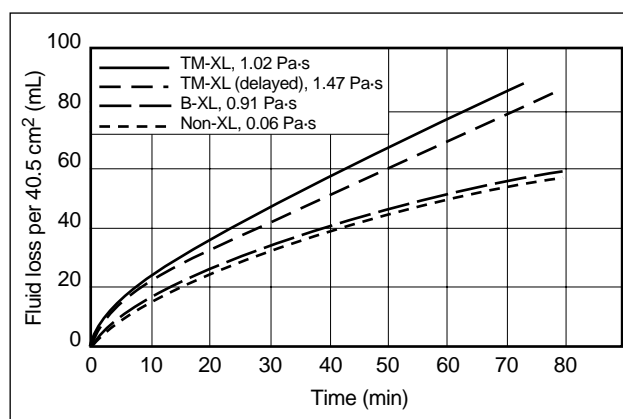


**Figure 8-36.** Effect of fluid composition on fluid loss (Gulbis, 1983). The borate-crosslinked (B-XL) system is in equilibrium. These systems approach the noncrosslinked (Non-XL) system when subjected to shear. TM-XL = transition metal crosslinked.

time for a specific element of the fracture surface. These considerations are addressed in the next section.

### 8-8.3. Shear rate in the fracture and its influence on fluid loss

During a fracturing treatment, fluid loss occurs under dynamic conditions. Prud'homme and Wang (1993) proposed that the extent to which the filter cake grows in thickness is controlled by the shear stress exerted by the fluid at the wall of the cake and the yield stress of the cake.

The cake stops growing when the fluid stress becomes equal to the yield stress of the cake. It starts to erode when the fluid stress is larger than the yield stress of the cake. The yield stress of the cake depends on the concentration and pressure gradient in the cake, whereas the shear stress of the fluid is determined by its rheological properties and the shear rate to which it is subjected.

Navarrete *et al.* (1996) compared dynamic and static fluid loss using crosslinked guar gels. The data show that the effect of shear increased leakoff by increasing spurt and after-spurt leakoff. The extent to which the gel was able to invade the core was controlled by the degree to which the crosslinked structure was broken by the shear. Also, the magnitude of the shear rate determined the rate of leakoff after spurt by limiting the extent of filter-cake growth.

The shear rate that the fluid experiences during a fracturing treatment varies with distance from the tip of the fracture and time, as shown in Fig. 8-37 for the test case in Table 8-5 at a pump time of 145 min. The

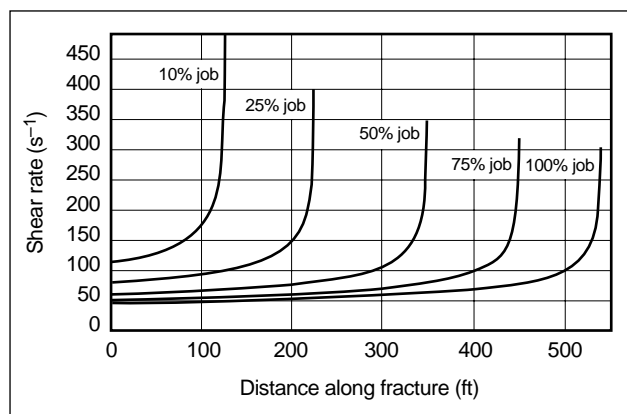


**Figure 8-37.** Shear rate profiles during a fracturing job (fracture height = 300 ft, pump rate = 40 bbl/min, pump time = 145 min) (Navarrete *et al.*, 1996).

shear rate that a rock segment sees at a fixed position from the wellbore decreases with time as a result of the widening of the fracture width (Fig. 8-38).

The effect that a decreasing shear rate history has on the rate of leakoff and filter-cake formation is illustrated in Fig. 8-39. The leakoff volume is plotted versus time for three different cores with permeabilities of 1, 10 and 62 md. The initial spurt-loss volumes increase with core permeability. The after-spurt data show that once the shear rate falls below about  $140 \text{ s}^{-1}$ , the slope of the fluid-loss curves (i.e., the leakoff rate) drops, denoting a change in the leakoff behavior.

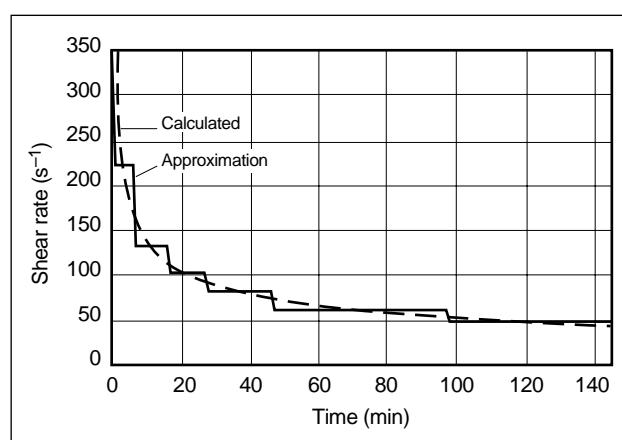


**Figure 8-38.** Shear rate history over a rock segment from Fig. 8-37 at 50 ft from the wellbore (Navarrete *et al.*, 1996).

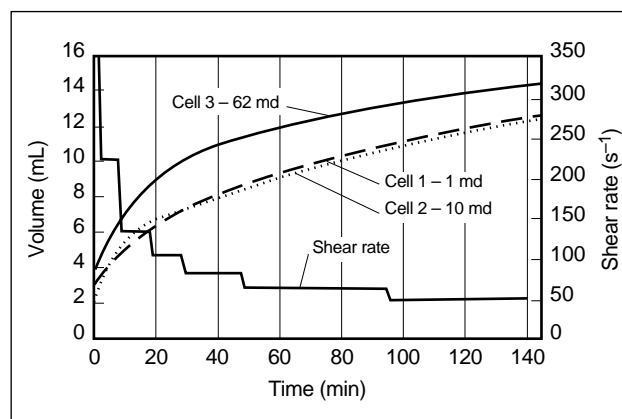


**Figure 8-39.** Comparison of fluid loss for a 40 lbm/1000 gal borate-crosslinked guar gel under static and dynamic conditions (permeability = 0.5 md, pressure drop = 1000 psi, temperature =  $150^{\circ}\text{F}$ ) (Navarrete *et al.*, 1996).

#### 8-8.4. Influence of permeability and core length

Permeability and core length are important variables in fluid-loss tests on high-permeability cores, where the polymer and fluid-loss additives can invade the rock and plug pore throats deeper into the formation.

The length of high-permeability cores used in fluid-loss tests must be longer than the invasion zone length of the polymer. Otherwise, polymer may penetrate the entire core length, and the measured spurt values will be unrealistically high. Parlar *et al.* (1995) used 1000-md cores under static conditions to determine that spurt loss became insensitive at core lengths of 5 in. and larger. For 500-md cores under dynamic conditions, Navarrete and Mitchell (1995) determined that most of the polymer accumulation occurred in less than about 1 in.

#### 8-8.5. Differential pressure effects

The effect of the pressure drop is significant on spurt in high-permeability cores. Parlar *et al.* (1995) reported a linear dependency of spurt with the pressure drop under static conditions in 1000-md, 5-in. long cores at pressure drops of 500 to 1500 psi. The effect of the pressure drop on  $C_w$  in high-permeability cores was found to scale with  $\Delta p^{0.5}$  or follow the pressure dependency of an incompressible filter cake (see Eq. 6-82). This implies that the internal filter cake, which dominates the resistance to fluid loss in high-permeability cores, behaves incompressibly.

The effect of the pressure drop on  $C_w$  under static conditions in low-permeability cores (i.e., where the filter cake is external) was found to scale with  $\Delta p^{0.6}$  for borate-crosslinked fluids and  $\Delta p^{0.56}$  for zirconium-crosslinked fluids at low pressure drops (100 psi <  $\Delta p$  < 500 psi). At higher pressure drops (600 psi <  $\Delta p$  < 1400 psi),  $C_w \sim \Delta p^{0.1}$  (Mayerhofer *et al.*, 1991). If the classic models for filter cake are considered in the interpretation of these results, the resulting conclusions are that as the pressure drop increases, the filter cake becomes less permeable and  $C_w$  becomes insensitive to the pressure drop. This indicates that the filter cake is compressible at those differential pressures. Similar results were found by Nolte (1982, 1998a) and Penny *et al.* (1985).

# Fracture Evaluation Using Pressure Diagnostics

*Sunil N. Gulrajani and K. G. Nolte, Schlumberger Dowell*

## 9-1. Introduction

The hydraulic fracture design process requires substantial information about the reservoir and the fracturing fluid. The effectiveness of a design is also dependent on the quality of the required data. The fracture design parameters can be inferred from wireline logs and through laboratory fluid and core testing procedures. The reliability of the data inferred from these methods is reduced by factors such as the scale of measurement, variability in the geologic environment, assumption of an overly simplified fracture response and significant deviations of the test environment from in-situ reservoir conditions. Fracture parameter uncertainties can result in a suboptimal fracture, at best, or in a complete failure of the stimulation procedure under the worst-case scenario.

An on-site procedure for predicting fracture dimensions is desirable but extremely difficult to obtain. Numerous fracture-mapping techniques, such as radioactive tracers, surface and bottomhole tiltmeters and various electromagnetic measurements, have been applied to infer fracture dimensions (see Section 12-1.1). The techniques, however, provide only a limited amount of information (e.g., fracture azimuth or wellbore height) that is available generally only after completion of the fracture treatment. Although sophisticated microseismic measurements have been developed to infer the created fracture dimensions, their restricted spatial range of observation and expensive instrumentation currently limit widespread application.

In contrast, pressure analysis during and after a fracture treatment is recognized as a powerful technique for developing a comprehensive understanding of the fracturing process. A recording of the wellbore pressures provides an inexpensive measurement for fracture diagnostics. The specialized analysis of pressure provides a qualitative indicator of the fracture growth, as well as estimates of the primary fracture parameters. An analysis of the reservoir

response after fracturing characterizes its hydrocarbon production potential. Finally, the versatility and ease of use of these techniques lend their application to most field situations, enabling an assessment of the fracturing process, either on site and in real time or after completion of the treatment for the improvement of future designs.

Figure 9-1 shows a recording of the bottomhole pressure measured during a fracture stimulation. Fluid and proppant were injected for approximately 3 hr, followed by an extended period of shut-in that lasted for more than 18 hr. The pressure response was recorded for all facets of the fracture and reservoir response—the pumping period, pressure decline as the fracture closes, time at which the fracture closes on the proppant and finally the asymptotic approach to the reservoir pressure. Of particular interest to the fracture design process is the analysis of pressure measured during a calibration treatment. A calibration treatment, or a mini-fracture treatment, precedes the main fracture treatment and is performed without the addition of proppant under conditions that mimic the main treatment. The pressure response for this test follows the sequence in Fig. 9-1. Fracturing pressures during each stage of fracture evolution (i.e., growth, closing phase and after-closure period) provide complementary information pertinent to the fracture design process. The frame-

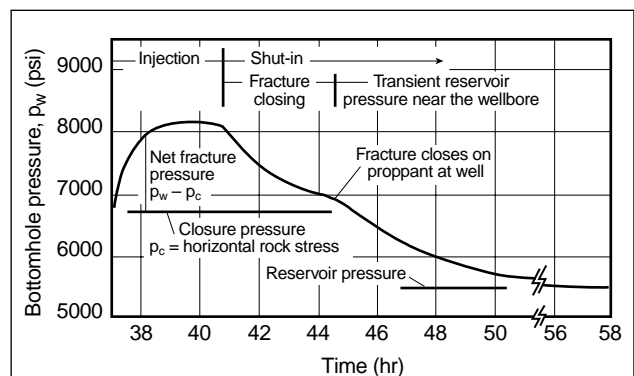


**Figure 9-1.** Bottomhole fracture pressure history (Nolte, 1982, 1988c).



work for analyzing fracturing pressure and its variation during a calibration test, along with example applications, is the focus of this chapter.

Pressure analysis is based on the simultaneous consideration of three principles that are central to the fracturing process: material balance, fracturing fluid flow and solid mechanics or the resulting rock deformation. Section 9-3 describes these principles. Material balance, or the conservation of mass, is important for analyzing the pumping and closing phases of fracturing. It also provides a framework for determining the fluid volumes and proppant schedule for a basic fracture design. Fluid flow and solid mechanics define the interaction between the fluid pressure and the formation. The fracture width and pressure relations are derived by combining these two principles. In addition, solid mechanics also introduces the concept of closure pressure, which is the reference pressure for fracture behavior. Closure pressure is the most important parameter for fracturing pressure evaluation.

The pressure measured during pumping provides an indication of the fracture growth process. The primary diagnostic tool for this period is the slope of the log-log plot of net pressure (i.e., the fracturing pressure above the reference closure pressure) versus pumping time. The slope of the log-log plot is used to characterize the fracture geometry by combining the fundamental relations, as outlined in Section 9-4. The log-log plot is complemented by the pressure derivative to identify complex fracture growth patterns and the effects of proppant injection. The pumping phase additionally characterizes the formation pressure capacity, which is the fracture pressure above which only limited fracture propagation occurs.

The pressure response during fracture closure is governed largely by the rate of fluid loss. The analysis of pressure during this period estimates the fluid efficiency and the leakoff coefficient. These parameters are determined from a plot of the pressure decline versus a specialized function of time, commonly referred to as the *G*-plot. This specialized plot provides the fracturing analog to the Horner plot (see Section 2-1) for well testing. Theoretical principles and example applications of *G*-function analysis are outlined in Section 9-5. This section also describes simple analytical corrections that extend the basic pressure decline analysis to nonideal fracture behavior.

The final fracturing pressure analysis pertains to the evaluation of pressure following fracture closure. The

pressure response during this period loses its dependency on the mechanical response of an open fracture and is governed by the transient pressure response within the reservoir. This transient results from fluid loss during fracturing and can exhibit either linear flow or a long-term radial response. Each of these flow patterns can be addressed in a manner analogous to conventional well test analysis for a fixed-length conductive fracture, as discussed in Chapter 12. The after-closure period characterizes the reservoir's production potential. Its analysis enhances the objectivity of otherwise uncertain preclosure pressure interpretation. The theoretical, operational and application aspects for describing the pressure following fracture closure are outlined in Section 9-6.

Each fracturing phase, from fracture creation through the after-closure period, provides a sequence of complementary information pertinent to the fracturing process. A comprehensive assessment thus requires an integrated procedure that combines the information provided by each phase. Sections 9-7 and 9-8 present a generalized pressure analysis methodology that unifies the various interpretative, analytical and numerical analysis techniques discussed in this chapter.

## 9-2. Background

Injection pressure has been measured for safety considerations since the inception of hydraulic fracturing. Its importance for characterizing a fracture was recognized as early as 1954 by Harrison *et al.*, who developed a relation between pressure and the fracture volume. The potential importance of understanding the fracturing pressure response was noted by Godbey and Hodges (1958). They concluded, "by obtaining the actual pressure on the formation during a fracture treatment, and if the inherent tectonic stresses are known, it should be possible to determine the type of fracture induced." Furthermore, they stated, "the observation of both wellhead and bottom-hole pressures is necessary to a complete understanding and possible improvement of this process."

Development of two-dimensional (2D) fracture models by Khristianovich and Zheltov (1955), Perkins and Kern (1961) and Geertsma and de Klerk (1969) provided a theoretical means for estimating the fracture width and its dependence on the net pressure. The early 1970s were characterized by regulated

gas prices in the United States and significant oil discoveries in the Middle East, which caused a lull in fracturing activity and hence a reduced interest in fracturing research. Renewed activity was fostered during the mid-1970s when massive hydraulic fracturing led to an emphasis on improved fracturing economics. The fluid and proppant volumes utilized for these fracturing operations significantly increased, which increased execution costs. Successful fracture execution was recognized as critical for economic field development. These developments spurred a renewed interest in understanding fracture pressure behavior for the effective design and analysis of fracture treatments. The Appendix to Chapter 5 provides a detailed discussion of these activities.

A numerical simulation describing the pressure decline response during fracture closure was presented by Novotny (1977). Nolte (1979) presented a fundamental analysis to estimate the fluid-loss parameters and the fracture length for the PKN fracture geometry. This analysis was subsequently extended to the other 2D fracture geometry models (Nolte, 1986a). Simonson *et al.* (1978) characterized height growth into stress barriers. Nolte and Smith (1981) related trends on the log-log net pressure plot to the evolution of the fracture geometry, and Clifton and Abou-Sayed (1981) generalized fracture modeling and the related pressure response to three-dimensional (3D) hydraulic fracture models.

Later developments attempted to address the non-ideal conditions that commonly occur during field practice but had been excluded in these early studies. Soliman (1986a) developed an analysis to consider the effects caused by fluid compressibility and temperature change during shut-in. A correction to incorporate pressure-dependent fluid-loss behavior was proposed by Castillo (1987). Nolte (1991) addressed several nonideal conditions during injection as well as shut-in and provided techniques to diagnose the related pressure responses. A semianalytical approach to account for variation of the fluid-leakoff coefficient following the end of treatment as well as the effects resulting from fluid flowback was developed by Meyer (1986a). A decline analysis methodology that addresses a comprehensive list of nonideal factors during fracture closure was proposed by Nolte *et al.* (1993).

Pressure analysis has been applied since the early 1980s to improve fracture performance in a variety of applications, including routine fracture design (e.g.,

Schlottman *et al.*, 1981; Elbel *et al.*, 1984; Morris and Sinclair, 1984; Cleary *et al.*, 1993) and fracturing for specialized applications (e.g., Smith, 1985; Bale *et al.*, 1992). It is most effective when used to characterize fracture growth behavior during the early stages of field development. Variations of the traditional calibration test have also been proposed for specialized purposes, such as the step rate/flowback test to determine closure pressure (e.g., Felsenthal, 1974; Nolte, 1982; Singh *et al.*, 1985; Plahn *et al.*, 1997), step-down test to identify near-wellbore effects (e.g., Cleary *et al.*, 1993) and short impulse injection test to obtain reservoir permeability (e.g., Gu *et al.*, 1993; Abousleiman *et al.*, 1994). Additional studies (Mayerhofer *et al.*, 1993; Nolte *et al.*, 1997) extend fracture pressure analysis to the realm of well testing, wherein reservoir information typically obtained from conventional well tests can be inferred from calibration treatments.

## 9-3. Fundamental principles of hydraulic fracturing

Three basic relations govern the hydraulic fracturing process: fluid flow in the fracture, material balance or conservation of mass, and rock elastic deformation. These relations are reviewed in Chapter 5, presented in the context of fracture modeling in Chapter 6 and reformulated in this section to facilitate the development of pressure analysis techniques.

### 9-3.1. Fluid flow in the fracture

The fracture essentially is a channel of varying width over its length and height. The local pressure gradient within the fracture is determined by the fracturing fluid rheology, fluid velocity and fracture width. Equations governing fluid flow within the fracture can be derived using the principle of conservation of momentum and lubrication theory applied to a fluid traveling in a narrow conduit. The rheology of fracturing fluids is generally represented by a power law model (see Chapter 8) that incorporates the parameters  $K$  and  $n$ . In recognition that fluid flow within a fracture is laminar for most fracturing applications (Perkins and Kern, 1961), the global pressure gradient along the length of a fracture can be expressed as

$$\frac{dp}{dx} \propto \frac{Kv_x^n}{w^{1+n}}, \quad (9-1)$$

where  $v_x$  is the average fluid velocity along the length of the fracture and is defined in terms of the volumetric injection rate  $q_i$ , fracture height  $h_f$  and height-averaged fracture width  $\bar{w}$ . Material balance or conservation of mass suggests that  $v_x$  is proportional to  $q_i/\bar{w}h_f$ . Equation 9-1 then becomes

$$\frac{dp}{dx} \propto \frac{K}{\bar{w}^{1+2n}} \left( \frac{q_i}{h_f} \right)^n. \quad (9-2)$$

In the special case of a Newtonian fluid ( $n = 1$  and  $K = \mu$ , where  $\mu$  is the fracturing fluid viscosity), Eq. 9-2 reduces to

$$\frac{dp}{dx} \propto \frac{\mu}{\bar{w}^2} \left( \frac{q_i}{\bar{w}h_f} \right), \quad (9-3)$$

where the term  $\bar{w}h_f$  is readily recognized as the average fracture cross-sectional area. Equation 9-3 is essentially Darcy's law with the permeability proportional to  $\bar{w}^2$ .

Equations 9-1 and 9-2 are formulated in terms of the average velocity and implicitly ignore change in the fracture width over its height. The varying width profile has an effect on the flow resistance relative to the case of a constant-width channel, as discussed in Chapter 6. The increase in the flow resistance is accentuated during periods of fracture height growth into barriers at higher stress. The varying width profile affects other physical phenomena that are highly sensitive to the velocity (e.g., temperature profile and proppant distribution).

### 9-3.2. Material balance or conservation of mass

Fluid compressibility is neglected in this chapter for the purposes of simplicity and clarity. For water- and oil-base fracturing fluids, fluid volume changes are of secondary importance to the elastic deformation of the fracture. The physical effects of pressure and temperature changes on the fracturing fluid in the wellbore could be significant for foamed fracturing fluids. In this case, using a direct measurement of the bottomhole pressure and incorporating changes in the wellbore volume during shut-in significantly reduce errors that may be introduced by the assumption of an incompressible fluid. The generally applicable assumption of an incompressible fracturing fluid therefore enables using simple expressions of volume

conservation, or volume balance, to replace those of mass conservation.

Pressure analysis, irrespective of the propagation model, is based on three expressions of material or volume balance. The first defines the treatment efficiency  $\eta$  as the ratio of the volume of the fracture created at the end of pumping  $V_{fp}$  and the cumulative injected volume  $V_i$ :

$$\eta = \frac{V_{fp}}{V_i}. \quad (9-4)$$

The second expression states that at the end of pumping,  $V_i$  is equal to  $V_{fp}$  plus the cumulative volume of fluid lost to the formation during pumping  $V_{Lp}$ :

$$V_i = V_{fp} + V_{Lp}. \quad (9-5)$$

It follows from Eqs. 9-4 and 9-5 that

$$V_{Lp} = (1 - \eta)V_i. \quad (9-6)$$

Finally, during any shut-in period  $\Delta t$ , the volume of the fracture is

$$V_f(\Delta t) = V_{fp} - V_{Ls}(\Delta t), \quad (9-7)$$

where  $V_{Ls}(\Delta t)$  is the volume of fluid lost to the formation between the shut-in time and any time  $\Delta t$  thereafter.

At closure (i.e.,  $\Delta t = \Delta t_c$ ) the volume of the fracture is equal to the bulk volume of proppant  $V_{prop}$  that was injected during pumping. At closure, Eq. 9-7 becomes

$$V_{fp} = V_{Ls}(\Delta t_c) + V_{prop}. \quad (9-8)$$

Eliminating  $V_{fp}$  from Eqs. 9-5 and 9-8 gives

$$V_i - V_{prop} = V_{Lp} + V_{Ls}(\Delta t_c). \quad (9-9)$$

These material-balance relations are illustrated in Fig. 9-2. Equation 9-9 simply states that for a calibration treatment in which no proppant is added (i.e.,  $V_{prop} = 0$ ), all injected volume is lost at closure. "Mathematical relations for fluid loss" in the Appendix to this chapter provides expressions for  $V_{Lp}$  and  $V_{Ls}(\Delta t)$  that are based on the derivations presented by Nolte (1979, 1986a).

### 9-3.3. Rock elastic deformation

The principles of fluid flow and material balance are coupled using the relation between the fracture width and fluid pressure. The relation defines the fracture

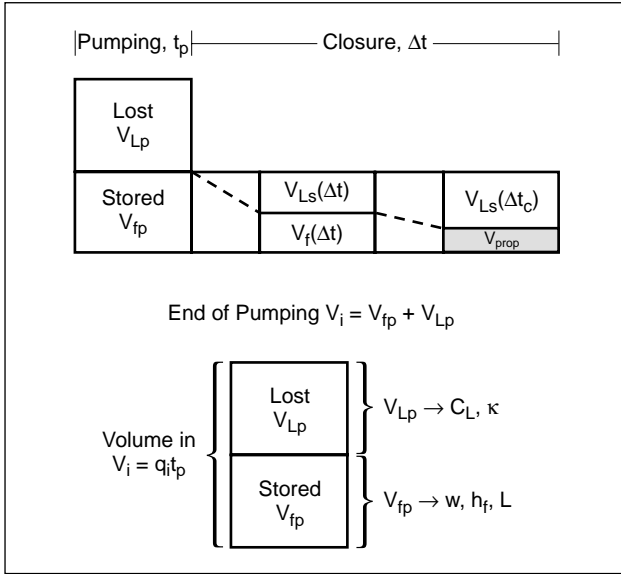


**Figure 9-2.** Fracture volume-balance relations.

compliance. Linear elastic deformation of the reservoir rock is assumed for the fracturing process. The linear elasticity assumption is justified because field-scale fractures produce relatively small additional stresses superimposed on the much larger in-situ stresses, excluding possibly the more complex deformation occurring in the fracture tip region (see Section 6-7.2). The rock deformation, or fracture width, can be predicted using two classic relations for cracks in an elastic material of infinite extent that are subjected to a constant internal pressure  $\bar{p}_f$ , with an external far-field confining stress  $\sigma_{min}$  applied perpendicular to the plane of the crack, as shown in Fig. 9-3.

The first relation predicts the width for a planar 2D crack (Sneddon and Elliot, 1946), with one dimension infinite and the other dimension with a finite extent  $d$ . The second relation provides a similar expression for a radial, or circular (also called penny-shaped), crack in an infinite elastic body (Sneddon, 1946). In both cases, the fracture width has an elliptical shape. The maximum width is proportional to the product of the characteristic dimension ( $d$  for 2D cracks and  $R$  for radial cracks) and the net pressure ( $\bar{p}_f - \sigma_{min}$ ) and inversely proportional to the plane strain modulus  $E' = E/(1 - \nu^2)$ . The formation Poisson's ratio  $\nu$  and Young's modulus  $E$  are typically estimated from laboratory experiments using cored samples of the reservoir rock (see Chapter 3) or sonic logs (see Chapter 4), and  $E'$  is preferably calibrated from pressure data (see Section 9-7.2). The average width  $\bar{w}$  and maximum width  $w_{max}$  for the 2D crack (i.e., fracture) are, respectively,

$$\bar{w} = \frac{\pi(\bar{p}_f - \sigma_{min})d}{2E'} \quad (9-10)$$

$$w_{max} = \frac{4}{\pi} \bar{w} \quad (9-11)$$

and for a radial fracture:

$$\bar{w} = \frac{16(\bar{p}_f - \sigma_{min})R}{3\pi E'} \quad (9-12)$$

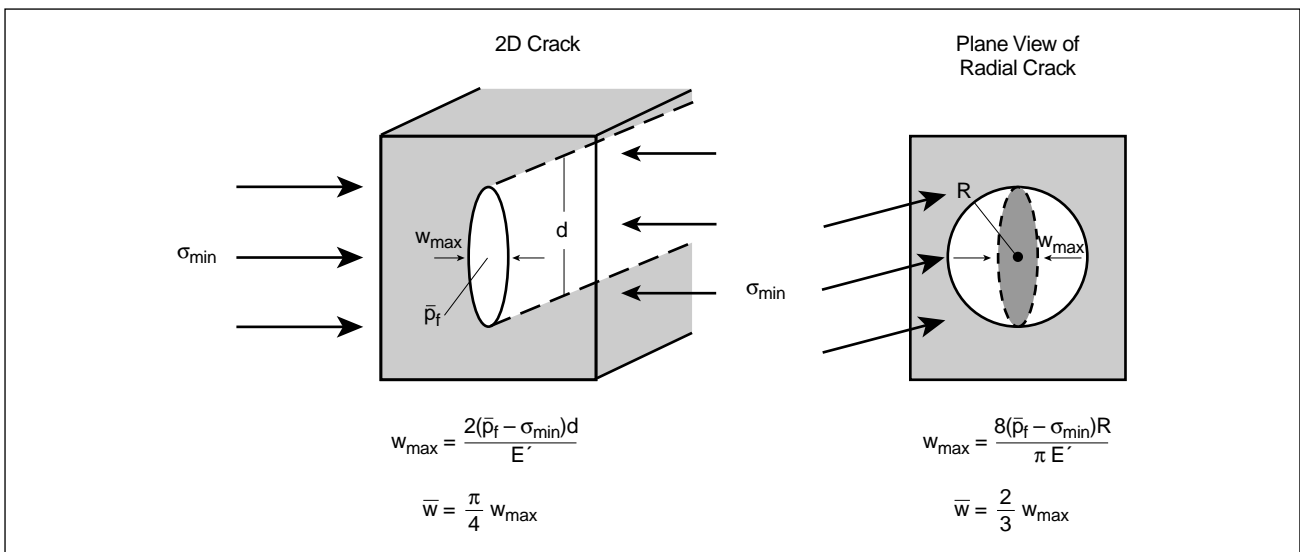


**Figure 9-3.** Sneddon cracks for 2D and radial fractures.

$$w_{max} = \frac{3}{2} \bar{w}. \quad (9-13)$$

These relations indicate that the fracture has a width greater than zero only if  $\bar{p}_f > \sigma_{min}$ . The fluid pressure at which an idealized unproped fracture effectively closes is

$$p_c = \sigma_{min} \quad (9-14)$$

and is termed the fracture closure pressure. For commercial fracturing applications,  $p_c$  is distinguished from  $\sigma_{min}$ , which is a local, directional quantity. The closure pressure approximates the average stress over the scale and orientation of the initial fracture height. It represents the stress that governs the propagation of a fracture over this scale of interest, as discussed in Sidebar 9A. Field practices for estimating  $p_c$  are described in “Estimating closure pressure” in the Appendix to this chapter.

- Basic fracture geometry models

The elastic relation for the 2D fracture (Eq. 9-10) is used in two fundamentally different ways to model a fracture. Using a more general form of this relation, the characteristic dimension  $d$  was assumed to be the total fracture length  $2L$  by Khristianovich and Zheltov (1955) and Geertsma and de Klerk (1969). The latter study also included the effect of fluid loss. This model of a fracture, denoted the KGD model, implicitly assumes that the fracture height is relatively large compared with its length. The other way to use this relation is to assume that the characteristic dimension  $d$  is the fracture height  $h_f$ , as assumed by Perkins and Kern (1961) and Nordgren (1972). Their approach, denoted the PKN model, implicitly assumes that the fracture length is the infinite dimension.

Each of these two basic, idealized models assumes that one of the fracture dimensions, the fracture length or its height, is relatively large in comparison with the other. Elastic coupling is generally ignored along the direction of the larger dimension. Which 2D model is pertinent depends on which physical dimension of the fracture more closely replicates the assumptions of the corresponding 2D fracture, as shown on Fig. 9-3. As indicated by Perkins (1973) and Geertsma and Haafkens (1979), the KGD model is more appropriate when the fracture length is smaller than the height, whereas the PKN model is more appropriate when the fracture length is much larger than

## 9A. What is closure pressure?

The fracture closure pressure  $p_c$  is defined as the fluid pressure at which an existing fracture globally closes. Mathematically, for a linear relation between the fracture width and pressure (i.e., Eq. 9-21),  $p_c$  equals  $\sigma_{min}$ , the minimum principal in-situ stress in the reservoir. Ideally, the value of  $\sigma_{min}$  is globally invariant in homogeneous formations. Reservoirs, however, are commonly characterized by lithology variations and natural fissures. These cause  $\sigma_{min}$  to become a local, directional quantity. In this case, the choice of  $p_c$  depends on the scale and orientation of the representative fracture geometry.

Closure pressure thus is a fracture-geometry-dependent quantity. For example, a micro-hydraulic fracture treatment creates a fracture with a limited height ( $\approx 5$  ft) and hence provides an estimate of  $\sigma_{min}$  only at that scale. Fracture propagation over this limited dimension is described by a value of  $p_c$  that equals the measured  $\sigma_{min}$ . A large-scale, “commercial” fracture that initiates from the same small interval, however, will grow well beyond the limited height dimension. During this process, it certainly will cross various heterogeneities prior to establishing coverage over the primary or gross interval, which is defined by meaningful stress barrier layers. Its closure pressure is not represented by the measured  $\sigma_{min}$  but by a value averaged over the gross interval. For large-scale fracturing,  $p_c$  is equal to  $\sigma_{min}$  only in the unlikely event that the gross reservoir height is devoid of any variations in the magnitude or direction of the minimum stress.

Direct measurement of the fracture width cannot be achieved during routine field fracturing operations. The inference of  $p_c$  based on the pressure-width relation outlined in Fig. 9A-1 is limited in field practice. An indirect approach that estimates  $p_c$  is based on formation tests that create fractures over the scale of interest. Such large-scale fractures are commonly achieved by the high injection rates used during step rate and calibration tests. However, conventional shut-in diagnostic plots based on these tests (see “Estimating closure pressure” in the Appendix to this chapter) may contain multiple inflection points caused by fracture length change and height recession across the reservoir layers. Pressure inflections are also introduced by the after-closure reservoir response, as discussed in Section 9-6. These additional physical phenomena introduce uncertainty in identifying  $p_c$ .

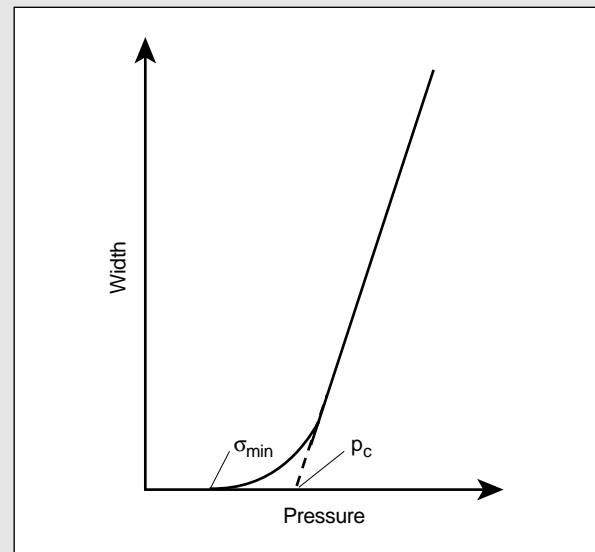


**Figure 9A-1.** Mathematical definition of closure pressure.

## 9A. What is closure pressure? (continued)

from a calibration treatment. In contrast, the step rate and flowback tests discussed in "Estimating closure pressure" in the Appendix avoid the interpretation uncertainty that is introduced by such phenomena. They provide a more objective diagnostic procedure and should be the preferred field technique for estimating  $p_c$ .

The relationship between  $p_c$  and  $\sigma_{min}$  is best illustrated with a field example adapted from the M-Site fracture experiments (Branagan *et al.*, 1996). The reservoir is characterized by a thin, clean layer ( $\approx 6$  ft) near the top of a larger sandstone interval ( $\approx 30$  ft), as shown on the well log plotted in Fig. 9A-2. From a micro-fracture test conducted within this small interval,  $\sigma_{min}$  was potentially obtained for the thin layer as 3030 psi (Branagan *et al.*, 1996). A step rate test created a fracture that, because of the higher injection rates, quickly grew within the entire 30-ft interval and indicated that  $p_c$  was 3440 psi (Fig. 9A-3). The calibration injection used downhole inclinometers (Branagan *et al.*, 1996) to quantify the fracture width, and its normalized measurement plotted as a function of the bottomhole pressure on Fig. 9A-4 shows a trend similar to that in Fig. 9A-1. Fracture opening is seen to occur at about 3030 psi, which equals approximately the measured  $\sigma_{min}$ . The linear portion of the curve, however, has an intercept of 3470 psi, which is near the value suggested by the step rate test. A  $p_c$  value of 3030 psi characterizes the micro-fracture test, where the fracture is limited to the thin sandstone interval. A  $p_c$  value of 3470 psi is more appropriate for analyzing the calibration and proppant injection treatments.

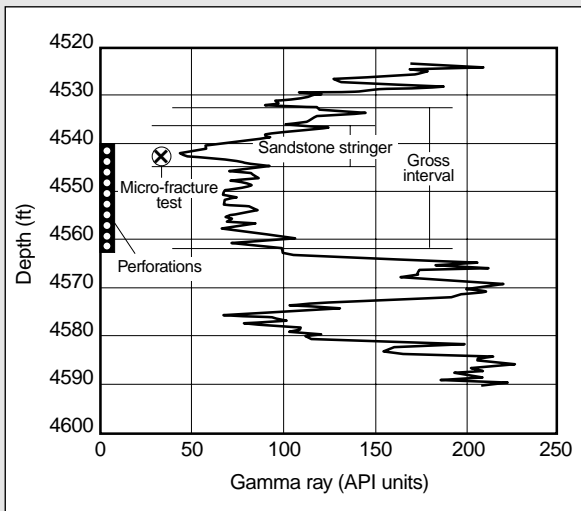


**Figure 9A-2.** Gamma ray log showing the micro-fracture test location and perforated interval.

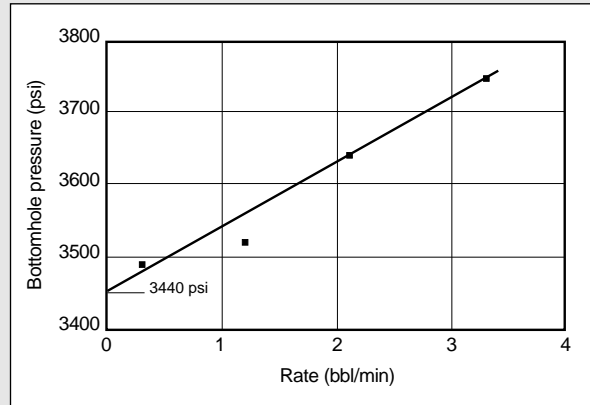


**Figure 9A-3.** Step rate test analysis.

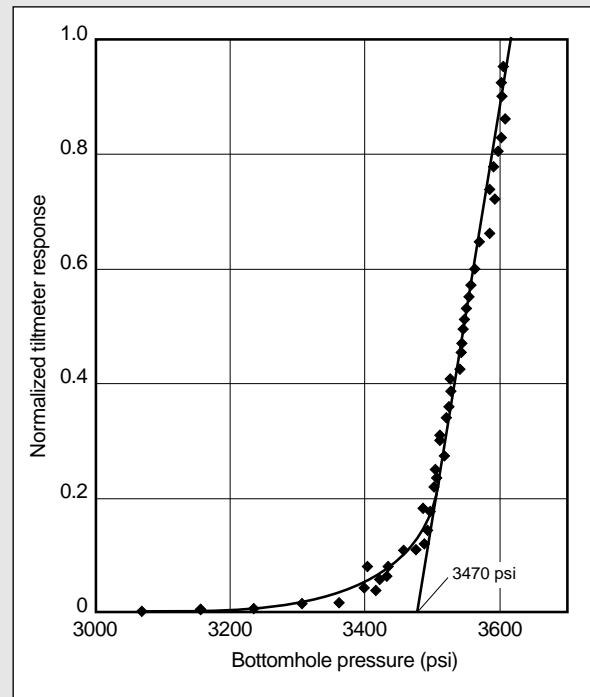


**Figure 9A-4.** Normalized inclinometer response versus bottomhole pressure.

the height. Consequently, the 2D model is valid in cases where the fracture length is either relatively small or large in comparison with the height. In practice, these models are applicable when the dimensions differ by a factor of about 3 or more.

The radial model is most appropriate when the total length  $2L$  ( $2R$  in Fig. 9-3) is approximately equal to the height. This condition occurs for fracture propagation from a point source of injection,

as is the case for a horizontal fracture in a vertical wellbore, or as an intermediate condition between the two limiting cases of the 2D models.

- Correction for fluid pressure gradient

The fundamental elastic relations (Eqs. 9-10 through 9-13) assume that the pressure in the fracture is constant. The fluid flow relation (Eq. 9-2), however, indicates that a pressure gradient exists

within a fracture. The fluid pressure varies from its maximum value  $p_w$  at the wellbore to the formation closure pressure  $p_c$  at a short distance behind the fracture tip. As discussed in Section 5.4-5, the fracturing fluid never quite penetrates the near-tip region, referred to as the fluid lag zone (see also Appendix Fig. 4 of the Appendix to Chapter 5). The fluid lag zone is characterized by a pressure that rapidly decreases from  $p_c$  at the fluid front to a value at the fracture tip that is approximately equal to the reservoir pore pressure for permeable rock or the vapor pressure for relatively impermeable rock.

The effect of the pressure gradient can be incorporated into the pressure-width relations of Eqs. 9-10 through 9-13 by introducing the factor  $\beta$  (Nolte, 1979).  $\beta$  is defined as the ratio of the average net pressure in the fracture  $\Delta\bar{p}_f$  to the net pressure at the wellbore  $p_{net}$ :

$$\beta = \frac{\Delta\bar{p}_f}{p_{net}}, \quad (9-15)$$

where

$$p_{net} = p_w - p_c. \quad (9-16)$$

The term  $\Delta\bar{p}_f$  is defined as the net pressure corresponding to a constant internal pressure  $\bar{p}_f$  that would produce the same average width as where a pressure gradient exists along the fracture length. Thus,

$$\Delta\bar{p}_f = \bar{p}_f - p_c. \quad (9-17)$$

Equation 9-15 can then be expressed as

$$\bar{p}_f - p_c = \beta p_{net} = \beta(p_w - p_c). \quad (9-18)$$

Equation 9-18 includes the pressure gradient effect from flow and fluid rheology along the fracture. In combination with Eqs. 9-10 through 9-14, it also relates the average fracture width to the bottomhole wellbore pressure  $p_w$ , which is a commonly available field measurement.

The factor  $\beta$  incorporates the effects of fluid pressure gradients in a fracture. Tip-dominated fracturing behavior (see Sidebar 9B) is characterized by a relatively constant pressure profile, and the fractures exhibit a value of  $\beta$  that approaches unity. For injection from a limited number of perforations, such as a horizontal fracture from a vertical well or a transverse vertical fracture from a

horizontal well, large pressure gradients may occur near the wellbore. In such cases, the value of  $\beta$  is relatively small. Following shut-in, the fluid pressure is relatively constant near the wellbore, and a value of  $\beta$  nearer to unity can be expected.

It is clear from the preceding discussion that the pressure gradients and hence the values of  $\beta$  during injection and shut-in differ. During injection,  $\beta$  is selected as the value at the end of pumping  $\beta_p$ . Its value for a PKN fracture can be obtained from Nolte (1979, 1991) as

$$\beta_p = (n+2)/(n+3+a). \quad (9-19)$$

The parameter  $a$  defines the degree of reduction in viscosity from the well to the fracture tip resulting from thermal and shear degradation. For a constant-viscosity profile,  $a = 0$ ; for a linearly varying profile,  $a = 1$  (i.e., effectively zero viscosity at the tip).

No expressions similar to Eq. 9-19 have been reported in literature for the KGD and radial models. An estimate of  $\beta_p = 0.85$  can be inferred from Daneshy (1973) for the KGD model. For the radial model where fluid enters from within a limited set of perforations,  $\beta_p$  can be much smaller than unity because of the high entrance flow rate and the consequently enhanced pressure gradient.

During the fracture closing phase,  $\beta$  is selected as its value after shut-in  $\beta_s$ , and Nolte (1979, 1986a) showed that

$$\beta_s \approx \begin{cases} (2n+2)/(2n+3+a) & \text{PKN} \\ 0.9 & \text{KGD} \\ (3\pi^2/32) & \text{Radial.} \end{cases} \quad (9-20)$$

The expressions for the KGD and radial fractures are approximate and based on the observation that the pressure gradient is concentrated near the fracture tip for these models. In particular, the value of  $3\pi^2/32 = 0.925$  was selected for the radial model to enable subsequent cancellation with its inverse in Eq. 9-22.

Figure 9-4 is an example of pressure and flow profiles during pumping and after shut-in based on a numerical simulation using the PKN model. In addition to the associated values of  $\beta$ , the figure shows that flow in the fracture continues until the fracture closes because of the redistribution of the stored volume from the larger width near the well to the higher rate of fluid loss near the tip. This

## 9B. Pressure response of toughness-dominated fractures

M. B. Smith, NSI Technologies, Inc.

In its broadest terms, the fracture net pressure that is measured at the wellbore represents the contribution from fluid viscosity and the rock resistance to fracture propagation (Shlyapobersky, 1985). The net pressure associated with fluid viscosity results from the flow of the fracturing fluid within the narrow fracture. The dependency of the viscous fracturing pressure on the rock mechanical and fracture geometry parameters is provided by Eq. 9-24, which is derived by assuming that the net pressure is negligible at the fracture tip.

Various mechanisms at the fracture tip have been postulated to explain the contribution from the rock resistance to the fracturing pressure, and these are discussed in Section 6-7. From the perspective of fracture pressure analysis, their contribution can be cumulatively represented as the tip-extension pressure  $p_{tip}$ . The tip-extension pressure can be expressed in terms of the apparent fracture toughness  $K_{lc-apparent}$ , which is better rationalized from the basis of fracture mechanics. The relationship between these two quantities generally depends on the fracture geometry, and for the assumption of a semi-circular fracture tip is (Shlyapobersky, 1985)

$$K_{lc-apparent} = \frac{2}{\sqrt{\pi}} p_{tip} \sqrt{h/2}, \quad (9B-1)$$

where  $h$  is the fracture height in the tip region.

Using the PKN fracture geometry model for the viscous pressure contribution  $\Delta p_{\mu}$  beyond the tip region, the wellbore net pressure can be given as (Nolte, 1991)

$$p_{net} = \Delta p_{\mu} \left( \left[ \frac{p_{tip}}{\Delta p_{\mu}} \right]^{2n+2} + 1 \right)^{1/(2n+2)}, \quad (9B-2)$$

where the fracture half-length  $L > h/2$  and  $\Delta p_{\mu}$  is the PKN pressure contribution from the tip to the wellbore but without the rock resistance to propagation. An analytical relation for  $\Delta p_{\mu}$  for the PKN fracture model beyond the tip region is derived as

$$\Delta p_{\mu} \equiv p_{net,PKN} \equiv 1.5 \frac{E'}{h} \left[ \frac{Kh}{E'} \left( \frac{q_i}{h} \right)^n (L - L_t) \right]^{1/(2n+2)}, \quad (9B-3)$$

where  $E'$  is the plane strain modulus,  $K$  is the fluid consistency coefficient,  $q_i$  is the fluid injection rate, and  $L_t$  is the length of the tip region. Equation 5-19 provides a more specific relationship for  $p_{net}$  with a Newtonian fluid.

The relative contributions of  $\Delta p_{\mu}$  and  $p_{tip}$  determine whether the fracture growth is viscosity dominated or tip dominated, respectively. Usually one phenomena dominates; a nearly equal contribution from both mechanisms is only rarely observed. Although  $p_{tip}$  generally shows little variation during a treatment, Eq. 9B-3 shows that  $\Delta p_{\mu}$  gradually increases with continued extension. This indicates that a tip-toughness-dominated fracture response is most likely manifested during the early stage of the fracture treatment. The pressure response could continue to be toughness dominated if the pressure contribution from  $\Delta p_{\mu}$  remains modest, as is the case for low injection rates, low fluid viscosity (i.e., low  $K$ ), short fracture lengths or soft rocks (i.e., low  $E'$ ). Most of these conditions are likely during micro-fracture stress tests (see Chapter 3) and tip-screenout treatments in unconsolidated formations.

The exponents for Eq. 9B-2 suggest that usually one mechanism effectively dominates the wellbore net pressure

response and thus dominates the fracture width and fracturing process. For example, for assumed values of  $n = 0.7$  and  $p_{tip} = \frac{1}{2}\Delta p_{\mu}$ , the final wellbore pressure is increased by only 3% from the case where  $p_{tip}$  is negligible. Alternatively, if  $p_{tip}$  is 50% greater than  $\Delta p_{\mu}$ , then the final wellbore net pressure is just 6% greater than for the case where  $\Delta p_{\mu}$  is ignored.

The higher injection rates used with very viscous fracturing fluids during large-scale, high-volume fracture treatments result in both a relatively large and increasing magnitude of  $\Delta p_{\mu}$ , which changes the pressure response from its early-time tip-dominated behavior to one that is viscous dominated. This change in the relative contribution of  $\Delta p_{\mu}$  compared with that of  $p_{tip}$  leads to a corresponding change in the net pressure behavior on a log-log plot.

An example is exhibited in Fig. 9B-1 by the pressure response monitored during a calibration injection into a reservoir with a relatively low Young's modulus  $E$ . The value of  $p_{net}$  is initially constant, signifying toughness-dominated behavior. At approximately 2.5 min, the pressure response gradually increases and eventually approaches a slope of 0.18 on the log-log plot, as expected for a PKN-type fracture with a negligible tip pressure (Eq. 9-24). The transition from tip-dominated to viscous-dominated behavior is identified from this positive slope on the net pressure plot. In contrast, tip-dominated fracture behavior would continue to exhibit a relatively constant net pressure response throughout the treatment.

The nearly constant pressure response during the initial stage of the treatment provides an estimate of  $p_{tip}$ , which in conjunction with Eq. 9B-1 enables the inference of  $K_{lc-apparent}$ . For the example in Fig. 9B-1,  $p_{tip}$  is obtained as 260 psi. Substituting this value in Eq. 9B-1 with a fracture height of 38 ft suggested by well logs obtains

$$K_{lc-apparent} = \frac{2}{\sqrt{\pi}} 260 \text{ psi} \sqrt{\frac{(38 \text{ ft} \times 12 \text{ ft/in.})}{2}} = 4430 \text{ psi/in.}^{1/2}.$$

This estimate for  $K_{lc-apparent}$  is higher than the critical stress intensity factor  $K_{lc}$  commonly measured with laboratory tests (see Section 3-4.6). The larger value can be attributed to any of the tip mechanisms described in Section 6-7 and results in a correspondingly higher resistance to fracture propagation.

This discussion applies exclusively to an elongated fracture geometry, as approximated by the PKN fracture model. In contrast, both  $p_{tip}$  and  $\Delta p_{\mu}$  decrease with continued injection for the radial fracture model. As a result, it is less clear which mechanism dominates the pressure response for radial fractures.

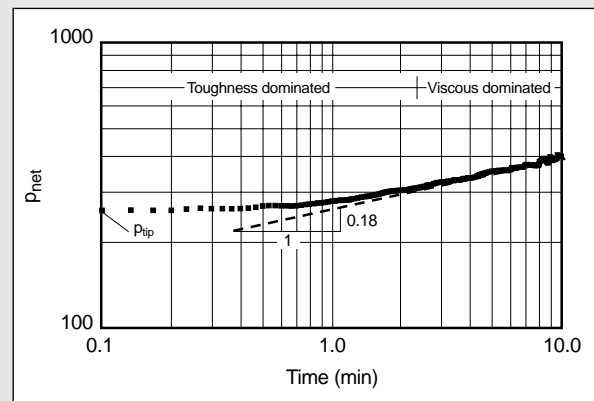


**Figure 9B-1.** Net pressure response for the transition from toughness-dominated to viscous-dominated fracture growth.



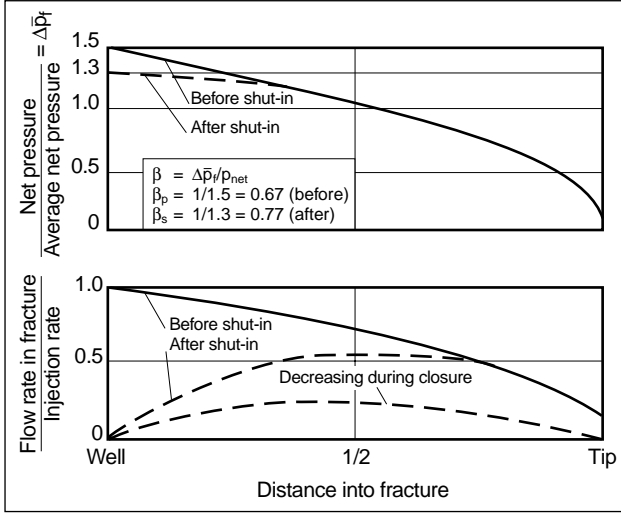


**Figure 9-4.** Pressure and flow rate in a fracture before and after shut-in (Nolte, 1986a).

afterflow causes additional extension during shut-in (Perkins and Kern, 1961), which can be significant for high fluid efficiencies and in reservoirs that show a moderate to low resistance to fracture propagation. Furthermore, shortly after shut-in, the pressure gradient equilibrates in the near-wellbore region. The redistribution of pressure is accompanied by a change in the wellbore width. The change in the value of  $\beta$  from injection to the shut-in period reflects the fact that the average width should remain relatively constant during this period.

- Fracture compliance

The net pressure within the fracture compresses the formation and results in the fracture width. The relation between the net pressure and the fracture width averaged over its length and height  $\langle \bar{w} \rangle$  can be expressed by combining Eqs. 9-10 through 9-13 with Eq. 9-18:

$$\langle \bar{w} \rangle = c_f p_{net}. \quad (9-21)$$

Equation 9-21 indicates that the average fracture width is linearly proportional to the wellbore net pressure. The constant of proportionality  $c_f$  is referred to as the fracture compliance. The use of compliance to describe the deformation of solid materials under externally applied loads is analogous to the compressibility of fluid systems during reservoir analysis. The fracture compliance depends on the formation plane strain modulus  $E'$ ,  $\beta$  coefficient and pertinent 2D fracture geometry model:

$$c_f = \frac{\pi\beta}{2E'} \begin{cases} h_f & \text{PKN} \\ 2L & \text{KGD} \\ (32/3\pi^2)R & \text{Radial,} \end{cases} \quad (9-22)$$

where  $L$  is the fracture half-length.

Martins and Harper (1985) derived the compliance for a fracture that grows as a series of confocal ellipses. In this case, the fracture width depends on the elliptic integral of the fracture aspect ratio. This analysis is applicable during fracture growth in an unbounded fashion following initiation from a perforated interval that is shorter than the fracture height.

## 9-4. Pressure during pumping

Equations for interpreting pressure during pumping are developed by combining the basic relations of material balance, fluid flow and rock elastic deformation. The relation between the fracture geometry and pressure during pumping was initially proposed by Nolte and Smith (1981), with application to the PKN-type fracture geometry. This analysis was subsequently generalized for application to each of the basic fracture geometry models (Nolte, 1986b). Extensions were also proposed by Nolte (1991) to consider deviations in the fracture geometry from the idealized 2D fracture geometry conditions.

The fundamental relation that defines fracture behavior during pumping at conditions of nearly constant injection rate and rheology can be obtained by combining the fluid flow relation (Eq. 9-2) with that of the fracture width and compliance (Eq. 9-21):

$$\frac{dp}{dx} \propto \frac{K}{(c_f p_{net})^{1+2n}} \left( \frac{q_i}{h_f} \right)^n. \quad (9-23)$$

Integration over the length with the assumption that  $p_c$  is a constant and that  $p_{net}$  is negligible at the fracture tip gives

$$p_{net} \propto \left[ \frac{K}{c_f^{1+2n}} \left( \frac{q_i}{h_f} \right)^n L \right]^{1/(2n+2)}. \quad (9-24)$$

The integration implicitly assumes that the flow profile along the fracture length has a constant shape. This is essentially the case for the three fracture models; e.g., the velocity is essentially constant for the PKN model (Nolte, 1991).

Equation 9-24 and the following equations assume that  $p_{net}$  is dominated by the frictional effects from flow of a viscous fluid within the fracture. This assumption may not be valid under specific conditions, as discussed in Section 5-4.5. Sidebar 9B outlines a diagnostic procedure for comparing the net pressure contribution from the fracture tip to the net pressure from fluid flow (or the viscous net pressure) predicted by Eq. 9-24.

Introducing the appropriate compliance relation in Eq. 9-24 for the three models and using  $L = h_f/2 = R$  for the radial model:

$$\begin{aligned} \text{PKN} \quad p_{net} &\propto (E'^{2n+1} K q_i^n)^e \left[ \frac{L}{h_f^{3n+1}} \right]^e \\ \text{KGD} \quad p_{net} &\propto (E'^{2n+1} K q_i^n)^e \left[ \frac{1}{h_f^n L^{2n}} \right]^e \\ \text{Radial} \quad p_{net} &\propto (E'^{2n+1} K q_i^n)^e \left[ \frac{1}{R^{3n}} \right]^e \end{aligned} \quad (9-25)$$

where the exponent  $e$  represents

$$e = 1/(2n + 2). \quad (9-26)$$

On the basis of Eq. 9-21, the fracture width  $w$  at the wellbore is proportional to  $c_f p_{net}$  for the three fracture geometry models. Multiplying each side of Eq. 9-25 by the appropriate definition of  $c_f$  from Eq. 9-22 results in

$$\begin{aligned} \text{PKN} \quad w &\propto \left( \frac{K q_i^n}{E'} \right)^e \left[ h_f^{1-n} L \right]^e \\ \text{KGD} \quad w &\propto \left( \frac{K q_i^n}{E'} \right)^e \left[ \frac{L^2}{h_f^n} \right]^e \\ \text{Radial} \quad w &\propto \left( \frac{K q_i^n}{E'} \right)^e \left[ R^{2-n} \right]^e. \end{aligned} \quad (9-27)$$

These fracturing pressure and width relations indicate that their dependence on the fluid rheology parameters  $K$  and  $n$ , wellbore injection rate  $q_i$  and plane strain modulus  $E'$  is the same for all the models. Their dependence on the fracture extension  $L$  or  $R$  and height  $h_f$  differs. In addition, Eqs. 9-25 and 9-27 also show that  $p_{net}$  and  $w$ , respectively, have a weak dependence on  $q_i$  and that for increasing penetration  $L$  or  $R$ ,  $p_{net}$  increases for the PKN model but decreases for the KGD and radial models.

The time dependence of the fracture width and pressure is developed using the definition of  $\eta$  from Eq. 9-4 at a constant injection rate  $q_i$  (i.e.,  $V_i = q_i t$ ):

$$A_f = \frac{q_i \eta t}{\langle \bar{w} \rangle} = \frac{q_i t^*}{\langle \bar{w} \rangle}, \quad (9-28)$$

where  $t^*$  is referred to as the reduced time (Nolte, 1991). The fracture surface area  $A_f$  for the basic fracture geometry models is

$$A_f = \begin{cases} 2Lh & \text{PKN} \\ 2Lh & \text{KGD} \\ \pi R^2 & \text{Radial.} \end{cases} \quad (9-29)$$

Combining Eqs. 9-27 through 9-29, an expression for the fracture width as a function of reduced time for the three basic models can be obtained:

$$\begin{aligned} \text{PKN} \quad w &\propto \left( \frac{K q_i^{n+1}}{E' h_f^n} \right)^{1/(2n+3)} (t^*)^{1/(2n+3)} \\ \text{KGD} \quad w &\propto \left( \frac{K q_i^{n+2}}{E' h_f^{n+2}} \right)^{1/(2n+4)} (t^*)^{1/(n+2)} \\ \text{Radial} \quad w &\propto \left( \frac{K^2 q_i^{n+2}}{E'^2} \right)^{1/(3n+6)} (t^*)^{(2-n)/(3n+6)}. \end{aligned} \quad (9-30)$$

Substituting the relation between width and net pressure in Eq. 9-21 into Eq. 9-30 gives the following expressions for  $p_{net}$  in terms of the reduced time:

$$\begin{aligned} \text{PKN} \quad p_{net} &\propto \left( \frac{K E'^{3n+1} q_i^{n+1}}{h_f^{3n+3}} \right)^{1/(2n+3)} (t^*)^{1/(2n+3)} \\ \text{KGD} \quad p_{net} &\propto (K E'^{n+1})^{1/(n+2)} (t^*)^{-n/(n+2)} \\ \text{Radial} \quad p_{net} &\propto (K E'^{n+1})^{1/(n+2)} (t^*)^{-n/(n+2)}. \end{aligned} \quad (9-31)$$

Equation 9-31 indicates that for typical fracturing fluids (i.e.,  $n \approx 0.4$ – $1.0$ ), the fracture pressure during injection is only nominally sensitive to the reduced time  $t^*$  or fluid efficiency  $\eta$ . Consequently, the efficiency, or alternatively the fluid-leakoff coefficient, cannot be determined by analyzing pressure during fluid injection exclusively.

Equations 9-30 and 9-31 also show that the net pressure and fracture width for any efficiency  $\eta$  can be approximated by their values for the case of no fluid loss, if the time is scaled by  $\eta t$ . This time scaling is illustrated for the PKN fracture model in Fig. 9-5, which shows the net pressure corresponding to no fluid loss (i.e.,  $\eta = 1$ ) and to an efficiency  $\eta = 0.2$  at a time of 50 min. The latter case corresponds to a reduced time of  $t^* = \eta t = 50 \times 0.2 = 10$  min. Figure 9-5 illustrates that the net pressure at a time of 50 min for the fluid-loss case is equal to the net pres-

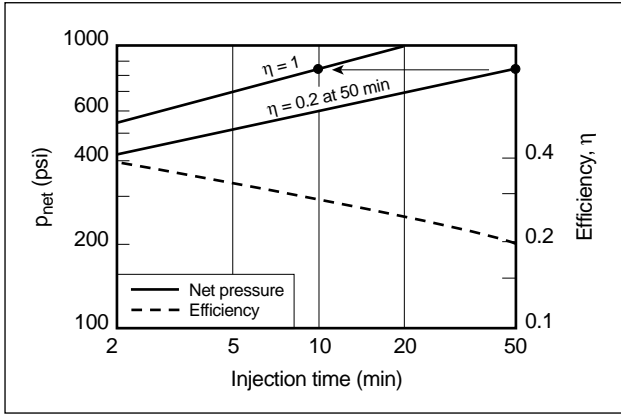


**Figure 9-5.** Reduced time illustrated for PKN fracture geometry (Nolte, 1991).

sure derived for the particular case of no fluid loss at a time of 10 min.

This observation is significant because simple analytical expressions for the three basic models are readily available when  $\eta \rightarrow 1$ . The various fracture parameters for any generalized value of  $\eta$  can then be obtained from this limiting conditions merely by scaling the time by a factor of  $1/\eta$ .

#### 9-4.1. Time variation for limiting fluid efficiencies

Approximations for the time dependency of the fracture penetration and pressure can be derived from the equations presented in the previous section for the two extreme values of the fluid efficiency  $\eta$ . These limiting cases are for very high and low fluid efficiencies, approaching 1 and 0, respectively. This simplification provides bounding expressions for the fracture penetration and related pressure. A similar approach is used in Section 9-5 to derive relations for analyzing pressure decline during the shut-in period.

Following the mathematical derivations outlined in “Mathematical relations for fluid loss” in the Appendix to this chapter, it can be shown that the fracture penetration is bounded in the following fashion:

$$\begin{aligned} \text{PKN} \quad L &\propto t^{1/2} & \eta \rightarrow 0 \\ L &\propto t^{(2n+2)/(2n+3)} & \eta \rightarrow 1 \end{aligned} \quad (9-32)$$

$$\begin{aligned} \text{KGD} \quad L &\propto t^{1/2} & \eta \rightarrow 0 \\ L &\propto t^{(n+1)/(n+2)} & \eta \rightarrow 1 \end{aligned} \quad (9-33)$$

$$\begin{aligned} \text{Radial} \quad R &\propto t^{1/4} & \eta \rightarrow 0 \\ R &\propto t^{(2n+2)/(3n+6)} & \eta \rightarrow 1. \end{aligned} \quad (9-34)$$

Limiting expressions for the fracture net pressure are similarly outlined in the Appendix:

$$\begin{aligned} \text{PKN} \quad p_{\text{net}} &\propto t^{1/4(n+1)} & \eta \rightarrow 0 \\ p_{\text{net}} &\propto t^{1/(2n+3)} & \eta \rightarrow 1 \end{aligned} \quad (9-35)$$

$$\begin{aligned} \text{KGD} \quad p_{\text{net}} &\propto t^{-n/2(n+1)} & \eta \rightarrow 0 \\ p_{\text{net}} &\propto t^{-n/(n+2)} & \eta \rightarrow 1 \end{aligned} \quad (9-36)$$

$$\begin{aligned} \text{Radial} \quad p_{\text{net}} &\propto t^{-3n/8(n+1)} & \eta \rightarrow 0 \\ p_{\text{net}} &\propto t^{-n/(n+2)} & \eta \rightarrow 1. \end{aligned} \quad (9-37)$$

Each of these bounding expressions for the net pressure is a power law relation. Consequently, the log-log graph of net pressure versus time should yield a straight line with a slope equal to the respective exponent: positive for PKN behavior and negative for KGD and radial behavior. In particular for PKN behavior, the log-log slope for commonly used fracturing fluids (i.e.,  $n \cong 0.5$ ) is typically less than  $1/4$  and decreases as the efficiency decreases. The log-log plot of the net pressure versus time during injection, commonly known as the Nolte-Smith plot, forms the fundamental basis for the interpretation of pressure profiles during fracturing and is analogous to the log-log diagnostic plot for reservoir flow, as discussed in Chapter 2.

#### 9-4.2. Inference of fracture geometry from pressure

The primary reservoir interval is bounded on both sides by shale formations in the majority of fracturing applications. Shale zones are generally at higher stress and provide the primary barrier to fracture height growth, particularly during the initial stage of fracture propagation. The restriction of fracture height growth is important in low- to moderate-permeability formations, where relatively long fractures are required for effective stimulation. Figure 9-6 shows the evolution of the fracture geometry and the corresponding wellbore pressure for fracture propagation under these conditions.

The initial character of fracture propagation, labeled as stage 1 on the figure, depends on the length of the perforation interval providing fluid entry into the fracture relative to the reservoir thickness. Two limiting

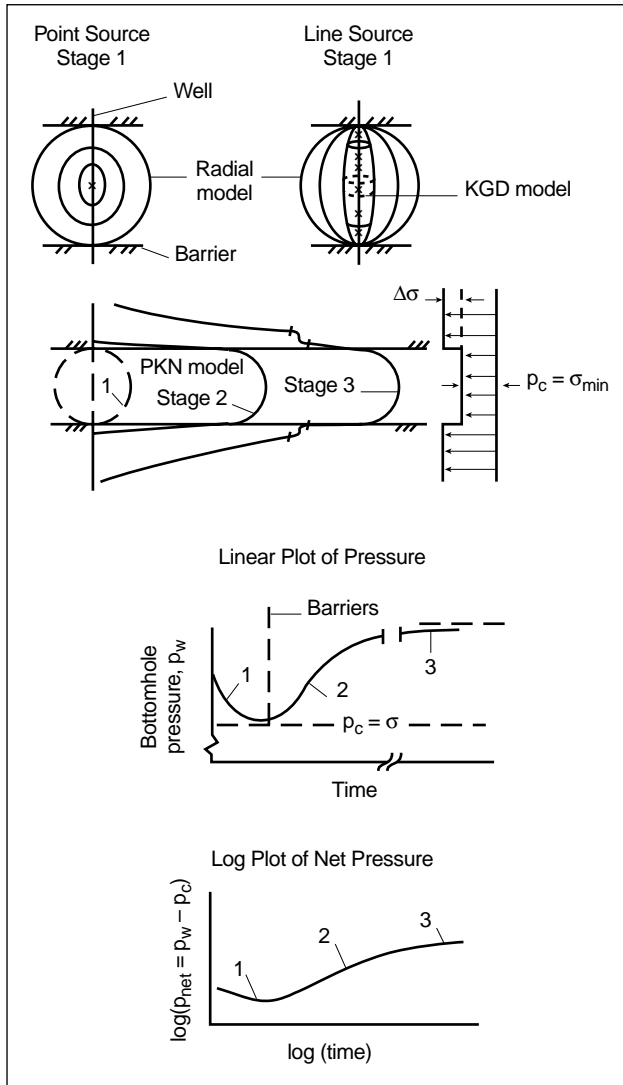


**Figure 9-6.** Evolution of fracture geometry and pressure during pumping.

cases are described: a limited fluid entry interval and one where fluid entry occurs over the complete reservoir thickness. Short fluid entry intervals (i.e., limited perforation intervals) may be desired in vertical wellbores to mitigate the occurrence of near-wellbore problems (see Section 11-3.2). They also occur in horizontally oriented fractures, during the placement of transverse hydraulic fractures in a horizontal well or in wellbores that are inclined with respect to the plane of  $\sigma_{min}$ . The limited fluid entry into the fracture is approximated by a point source. As shown in Fig. 9-6, the fracture area increases in a circular shape for a point-source fluid entry and hence is best described by the radial geometry model. Fluid entry over the complete reservoir thickness is approximated by a line

source, and the fracture area evolves in an elliptical shape. The KGD geometry model best describes the early phase of this fracture growth (Martins and Harper, 1985).

For either the radial or elliptical propagation mode during stage 1, the net pressure decreases with continued injection. It also exhibits a log-log slope between  $-1/8$  and  $-1/4$  depending on the fluid rheology exponent  $n$  and the efficiency  $\eta$ , as in Eqs. 9-36 and 9-37. The decreasing pressure reflects the fracture's preference to grow with decreasing resistance and in an unrestrained fashion as it gets larger. Stage 1 may occur for only a short time for fracture initiation within a relatively small interval or for the entire treatment in a massive zone (Smith *et al.*, 1987).

When barriers at higher stress exist above and below the reservoir pay zone, fracture height growth could be confined following stage 1. Under these conditions, the fracture is prevented from expanding in its preferred circular shape and fracture length extension is promoted. This mode of propagation is denoted as stage 2 in Fig. 9-6 and results in increasing pressure as the fracture becomes long relative to its vertical height. This type of fracture propagates in a manner similar to the PKN model. For this stage, the log-log slope of the fracturing pressure is between  $1/4$  and  $1/8$ , once again depending on  $n$  and  $\eta$  (Eq. 9-35).

Confined fracture height with its characteristic positive log-log slope can be expected until the fracturing net pressure approaches a value that is approximately one-half of the stress difference  $\Delta\sigma$  to which-ever stress barrier bounding the fracture has the lower stress value. At this magnitude of the net pressure, the fracture begins to penetrate in a restricted, or controlled, fashion into the adjacent barrier layer with the lower stress value. The fracturing pressure continues to increase with penetration, although at a rate that is progressively less than for the PKN model. This condition of fracture propagation is indicated as stage 3 in Fig. 9-6.

If one of the formation barriers is absent (i.e.,  $\Delta\sigma = 0$ ), height growth into the higher stress barrier is arrested. The fracture height, however, continues to grow essentially in a radial-like fashion along the direction where the barrier is absent and exhibits a continuously decreasing pressure (stage 1). This fracture height growth pattern could also occur when fractures are deliberately initiated from zones at higher stress and propagated into bounding layers at lower stress, as during an indirect vertical fracture completion (IVFC; see Section 5-1.2).

The magnitude of the net pressure during stage 2 (i.e., PKN-type fracture growth) can be used to infer the magnitude of the fracture compliance based on Eq. 9-31 and therefore the average width using Eq. 9-30. The net pressure exhibits a relatively small and decreasing value during stage 1, and it cannot be effectively used to estimate fracture dimensions. In such cases, significant errors could be introduced owing to uncertainties in the closure pressure and its change resulting from poroelastic effects (see Section 3-5.4).

Decreasing net pressure during the initial growth period indicates a radially evolving fracture in either the horizontal or vertical plane. Alternatively, an increasing net pressure with a small log-log slope (i.e., between  $\frac{1}{8}$  and  $\frac{1}{4}$ ) after the initial growth period is indicative of a vertical fracture extending primarily in length with restricted height growth. Following this period, if a reduction in the rate of pressure increase is observed, fracture height growth into a barrier zone should be expected. The net pressure during the period of height growth is governed primarily by the difference in stress between the primary reservoir and penetrated zones. Consequently, the pressure response during the height growth period can be used to estimate the stress difference, as discussed in the next section. The stress of the bounding formation is an important parameter for fracturing design, and it can also be used to calibrate log-inferred values of stress (see Chapter 4).

In conclusion, this discussion indicates how the pressure response during pumping can provide information on the state of stress, type of fracture created and fracture geometry, or more generally the fracture volume term for the material-balance relation in Eq. 9-5.

### 9-4.3. Diagnosis of periods of controlled fracture height growth

Fracture height growth into bounding barrier zones at higher stress requires an increasing pressure response prior to the height growth period into the barriers. Height growth into a higher stress barrier thus cannot occur during stage 1, where the decreasing pressure characteristic of the KGD and radial models occurs. Height growth into higher stress barriers (stage 3 in Fig. 9-6), however, is a commonly occurring deviation from the constant-height assumption of a PKN-type fracture.

Higher stress barriers normally have only a limited extent. Growth through barriers could eventually be followed by uncontrolled height growth, resulting in adverse effects during fracturing (see Section 9-4.5). It thus is necessary to estimate the primary parameters that govern fracture height growth: the magnitude of the stress difference  $\Delta\sigma$  between the reservoir and barrier and the bounding zone thickness. Figure 9-7, for idealized conditions such as Eq. 6-49, addresses these requirements. The figure assumes that the upper and lower barriers have the same stress value and an infinite extent. It also approximates height growth into bounding zones with unequal stress magnitudes. As shown, controlled height growth depends on the ratio of  $p_{net}$  and  $\Delta\sigma$ . For a ratio of about 0.4, negligible height growth occurs; for a ratio of about 0.65, the total fracture height is twice the initial fracture height  $h_i$  and each barrier thickness must be at least one-half of the height of the reservoir to ensure continued controlled height growth. Figure 9-7 implies that this condition requires a barrier thickness that is at least equal to the height of the reservoir for a ratio of about 0.8.

It follows from the previous discussion that the amount of height growth into the bounding zones depends on the thickness of the reservoir and the ratio  $p_{net}/\Delta\sigma$ . The reservoir thickness is defined using standard well logs whereas the magnitude of the net pressure is estimated from a fracture simulator. The appropriate fracture model for assessing net pressure and growth into barriers is based on the PKN model

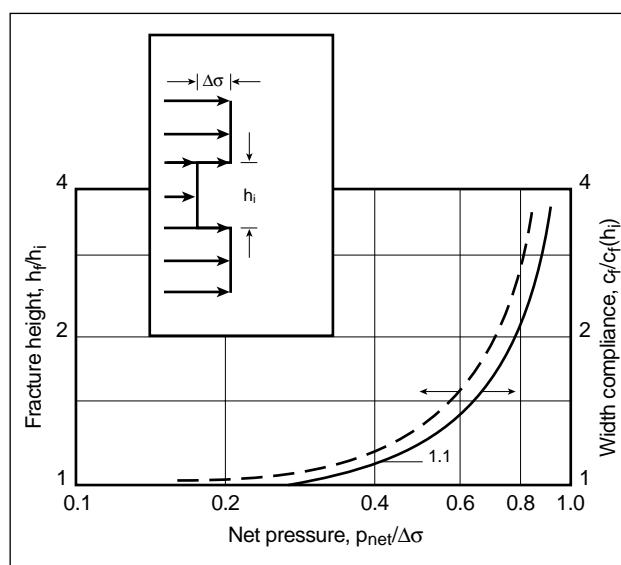


**Figure 9-7.** Net pressure and compliance for idealized fracture height growth (Nolte, 1986a).

(Fig. 9-6). Equation 9-25 provides this relation and indicates the importance of the initial fracture height (i.e., height of the reservoir) on the magnitude of the net pressure and hence the tendency for growth into barriers. The net pressure is approximately inversely proportional to the height. Therefore, the net pressure approximately doubles when the initially fractured zone height is halved. The general conclusion is that a smaller zone is more likely to experience height growth and will require both higher stress differences and thicker barrier zones for controlled fracture height growth.

Following fracture height growth into a barrier, the efficiency is relatively constant because no fluid loss is expected to occur in the barrier zone. The pressure response during this period deviates from its otherwise straight-line response on the log-log plot and is characterized predominantly by height growth behavior. It thus can be used to identify the onset of barrier penetration and to estimate the magnitude of the stress difference (Nolte, 1991; Ayoub *et al.*, 1992a). It relies on the use of a characteristic signature of the pressure derivative of the fracturing pressure during controlled height growth. Because of its increased sensitivity, the pressure derivative magnifies the deviation in the fracturing pressure from its expected response and therefore enhances the identification of fracture height growth, as discussed in the following section.

The specialized pressure derivative diagnostic has several applications in addition to quantifying fracture height growth, as discussed in Sidebar 9C: to validate the fracture geometry inferred from the log-log plot and to objectively confirm fracture closure pressure, as well as its capacity to identify the onset of a screenout.

#### 9-4.4. Examples of injection pressure analysis

Two field examples are presented here. The first example describes log-log analysis for a reservoir bounded by shale barriers. The second example discusses the pressure response for a radial fracture geometry in a reservoir where higher stress barriers are absent.

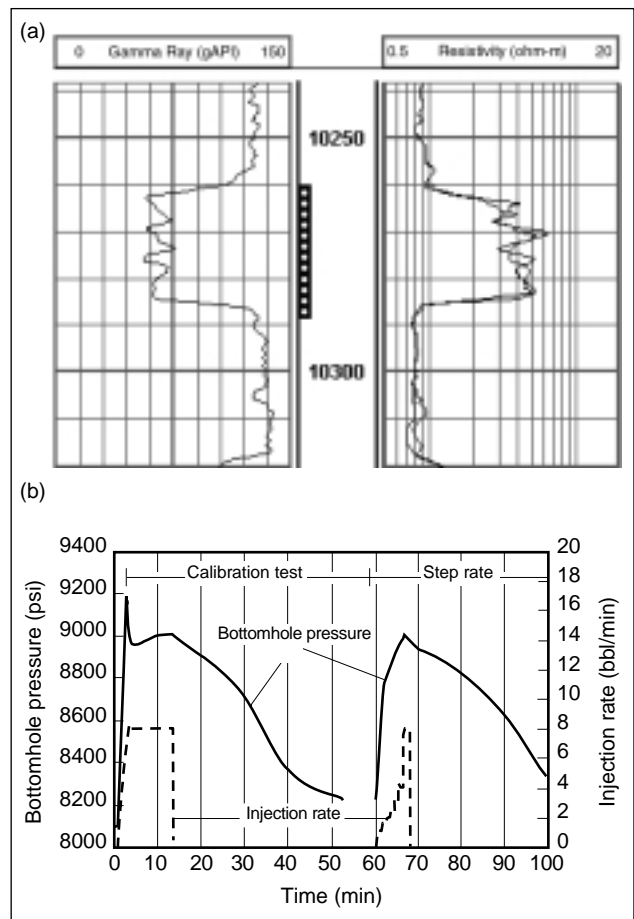
- Example of controlled fracture height growth

Table 9-1 lists the parameters relevant to the analysis of a calibration test in a gas-bearing sandstone reservoir. The producing interval has a permeable

**Table 9-1. Treatment parameters and rock mechanical properties for controlled fracture height growth example.**

$E$	$5.3 \times 10^5$ psi	$n$	0.44
$\nu$	0.22	$K$	0.248 lbf-s <sup>n</sup> /ft <sup>2</sup>
$h_L$	24 ft	$a$	0 (constant viscosity)
Calibration test			
$V_i$	95 bbl	$t_p$	12 min

height  $h_L$  of 24 ft and is bounded by higher stress shale barriers on both sides (Fig. 9-8a). As shown in Fig. 9-8b, the calibration injection lasted for 12 min and was followed by an extended shut-in period of approximately 40 min. The shut-in pressure approached the far-field reservoir pressure ( $\approx 8100$  psi) within a relatively short shut-in period because of the high formation permeability ( $\approx 250$  md). The closure pressure  $p_c$  for the formation was



**Figure 9-8.** Calibration test analysis for controlled height growth. (a) Well logs. (b) Bottomhole pressure and rate record.

## 9C. Pressure derivative analysis for diagnosing pumping pressure

Joseph Ayoub, Schlumberger Dowell

The fracture net pressure exhibits a power law variation with respect to time, as demonstrated in Section 9-4. This can be generalized as

$$p_{net} = p_w - p_c = At^b, \quad (9C-1)$$

where  $A$  is a constant and the exponent  $b$  is the slope of the log-log plot of the net pressure versus time  $t$ . The slope  $b$  depends on the fracture geometry and the fluid rheology and efficiency.

For pressure data measured during a fracturing treatment, the slope depends on the choice of the fracture initiation time and closure pressure. The fracture initiation time is selected by examining the pressure record during pumping, and it often coincides with the time when the fracturing fluid first reaches the perforations. The closure pressure is independently estimated using one of the techniques discussed in "Estimating closure pressure" in the Appendix to this chapter. Significant uncertainty is often associated with its determination, which could result in an incorrect interpretation; e.g., treatments for which the pressure data exhibit a small increase in pressure tend to exhibit a relatively constant net pressure response if a lower closure pressure estimate is used.

This sidebar introduces the pressure derivative to enhance the fracturing injection pressure diagnosis and analysis (Ayoub *et al.*, 1992a). The pressure derivative was initially introduced in well testing, for which it quickly became standard practice because it significantly enhances the identification of various flow regimes during the analysis of transient well test data (Bourdet *et al.*, 1989). Similarly, when applied to the fracturing injection pressure, the derivative "magnifies" and detects fracturing events earlier in time. It also assists in the determination of closure pressure. Differentiating Eq. 9C-1 with respect to time gives

$$\frac{d(p_w - p_c)}{dt} = \frac{dp_w}{dt} = Abt^{b-1}, \quad (9C-2)$$

and multiplying both sides of Eq. 9C-2 by  $t$  gives

$$t \frac{dp_w}{dt} = Abt^b. \quad (9C-3)$$

Defining the left side of Eq. 9C-3 as the pressure derivative, it follows that

- Pressure derivative versus time exhibits the same log-log slope as the net pressure.
- Net pressure and pressure derivative are separated by a factor of  $1/b$  on a log-log plot.

The pressure derivative is independent of the particular choice of closure pressure and is thus unaffected by errors in its determination. For typical PKN, KGD and radial fracture behavior, the closure pressure can thus be inferred from the injection pressure by selecting a value that makes the net pressure response parallel to the pressure derivative on a log-log plot (Fig. 9C-1). This feature of pressure derivative analysis was applied to the calibration test in Fig. 9-8 to confirm the closure pressure magnitude (Fig. 9-9).

The pressure derivative magnifies fracturing events because of its enhanced sensitivity. This characteristic of the pressure derivative is used to quantify fracture height growth into higher stress bounding zones, as for the examples in Section 9-4.4. The occurrence of a tip screenout (TSO) is also magnified and can be detected earlier in time. This is noted on

the net pressure response for the simulated treatment in Fig. 9C-2. The pressure derivative registers a rapid increase at 50 min, identifying the occurrence of a TSO, whereas no significant change in the net pressure response is visible until later.

Another observation from Fig. 9C-2 pertains to the long-term pressure derivative response after a TSO. The log-log slope becomes greater than 1 with continued injection. The ratio of the pressure derivative and the net pressure eventually becomes larger than 1. Consequently, after a TSO the pressure derivative eventually becomes larger than the net pressure, as shown on the figure.

Figure 9C-2 also shows an increase in the pressure derivative at 25 min. This response is attributed to increased viscosity caused by the introduction of proppant. The pressure derivative can be used to assess the importance of the apparent rock toughness relative to the viscous pressure (Nolte, 1991).

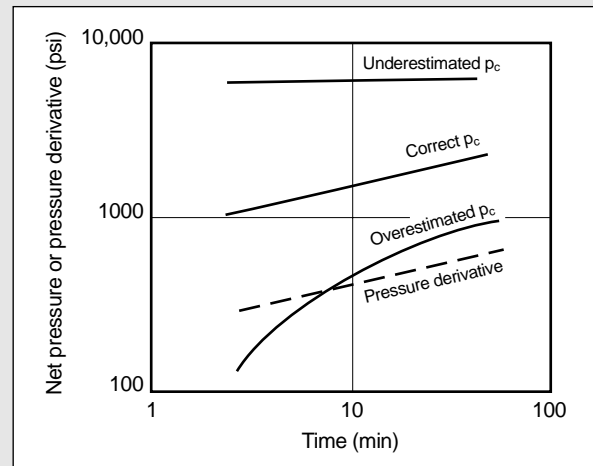


**Figure 9C-1.** Closure estimation using pressure derivative analysis.

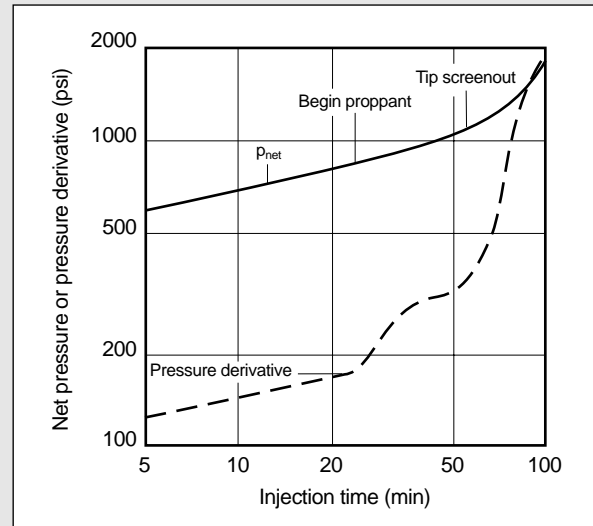


**Figure 9C-2.** Pressure derivative analysis for a TSO response (Nolte, 1991).

inferred to be 8910 psi from the step rate test (see “Estimating closure pressure” in the Appendix to this chapter) that followed the calibration treatment.

The log-log plot of the injection pressure in Fig. 9-9 is similar to the idealized example shown in Fig. 9-6 and can be interpreted in the same manner. The initially decreasing pressure response is representative of either a KGD or radial mode of fracture propagation. The initial log-log slope of  $-0.18$  is between the bounds suggested by Eqs. 9-36 and 9-37 for the KGD and radial models, respectively, for the value of  $n$  in Table 9-1. The subsequent log-log slope of  $0.16$  indicates a period of fracture extension in the PKN mode and a low fluid efficiency.

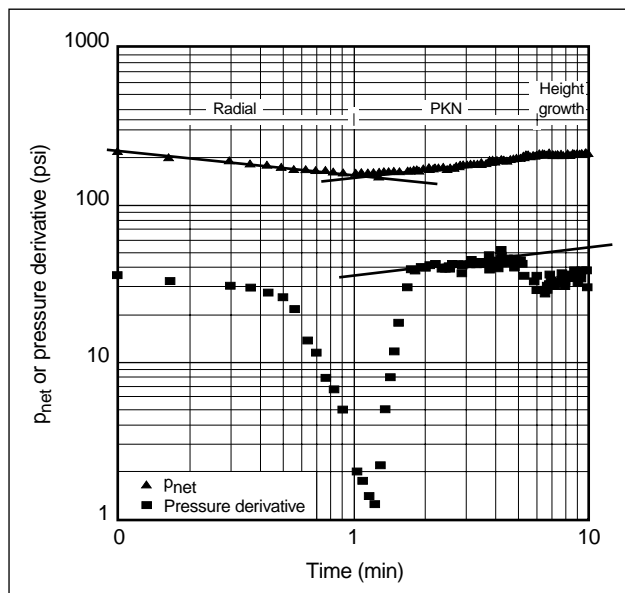


**Figure 9-9.** Log-log net pressure and pressure derivative analysis for the calibration treatment in Fig. 9-8.

The reduced rate of pressure increase during the last 3.5 min of injection is attributed to fracture growth into the higher stress bounding shales. This diagnostic is supported by the constant 36-psi value of the pressure derivative during this period. The magnitude of the stress difference is approximately 10 times the constant pressure derivative value during this period (Nolte, 1991):

$$\frac{1}{\Delta\sigma} \left( t \frac{d(p_{net})}{dt} \right) \approx 0.1 \quad (9-38)$$

$$\Delta\sigma = t \left( \frac{d(p_{net})}{dt} \right) / 0.1 = 36 / 0.1 = 360 \text{ psi.} \quad (9-39)$$

Thus, the stress difference between the lower stressed bounding zones and the perforated interval is approximately 360 psi.

#### • Example of radial fracture growth

The example of a radially propagating fracture was inferred during a calibration treatment performed in a high-permeability, heavy-oil-bearing sandstone reservoir (Fig. 9-10 and Table 9-2). The calibration treatment was preceded by a short injection using completion fluids (also called a mini-falloff injection) and a step rate test. The mini-falloff test is used to characterize the reservoir producing parameters and is discussed in Section 9-6. The formation closure pressure was estimated to be 4375 psi from the step rate test (see “Estimating

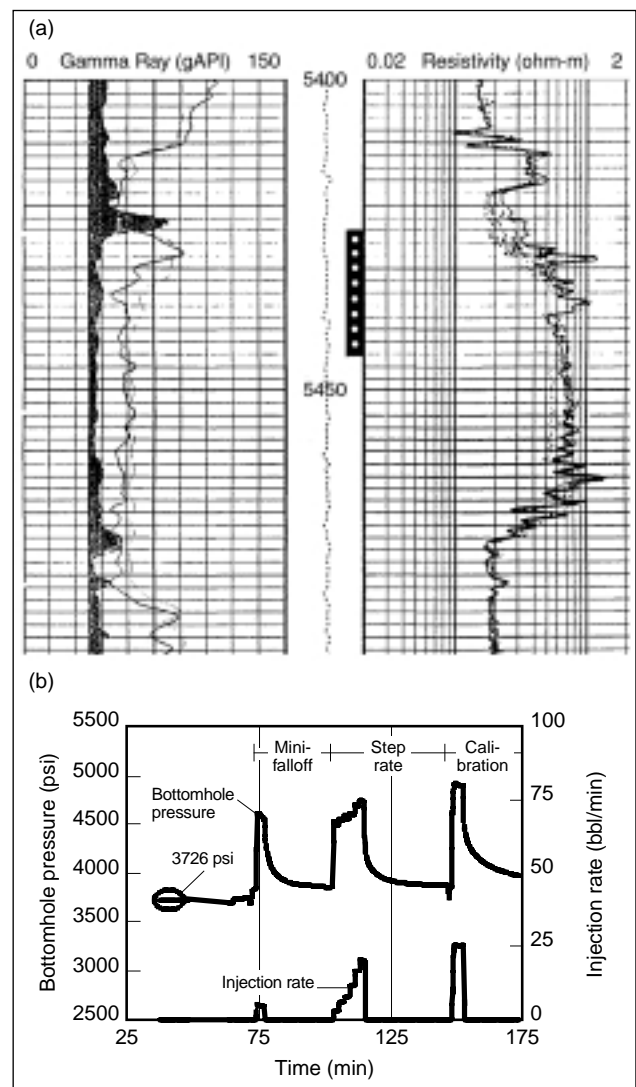


**Figure 9-10.** Calibration test analysis for radial fracture growth. (a) Well logs. (b) Bottomhole pressure and rate record.



**Table 9-2. Treatment parameters and rock mechanical properties for radial fracture growth example.**

$E$	$4.5 \times 10^5$ psi	$n$	0.40
$\nu$	0.25	$K$	0.084 lbf-s <sup><i>n</i></sup> /ft <sup>2</sup>
$a$	0 (constant viscosity)		
Mini-falloff test			
$V_i$	14.75 bbl	$t_p$	3 min
Calibration test			
$V_i$	107 bbl [600 ft <sup>3</sup> ]	$t_p$	4.6 min

closure pressure” in the Appendix to this chapter) and an after-closure linear flow analysis (see Section 9-6).

The log-log net pressure plot for the calibration injection (Fig. 9-11) indicates a slope of  $-0.11$ . This slope is within the bounds of a radial fracture suggested by Eq. 9-37 for the value of the fluid rheology exponent  $n$  in Table 2. A radially growing fracture should also be expected in this case because the reservoir lacks significant shale zones (Fig. 9-10a) that potentially could have constrained the fracture height.

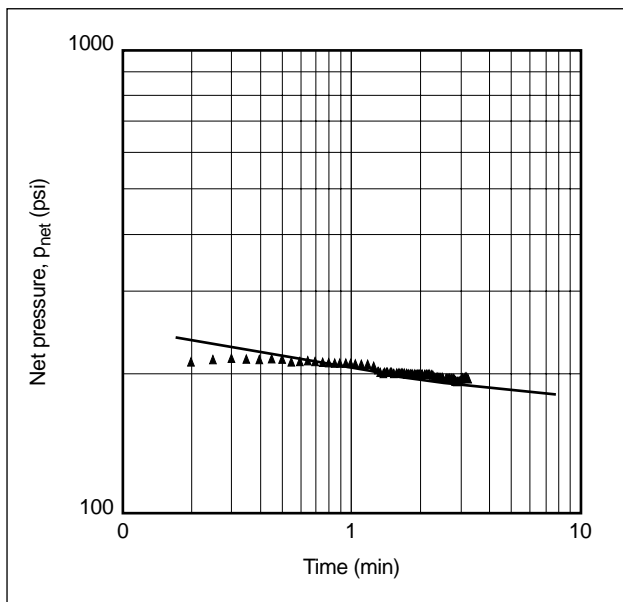


**Figure 9-11.** Log-log net pressure analysis for the calibration treatment in Fig. 9-10.

#### 9-4.5. Diagnostics for nonideal fracture propagation

The log-log diagnostic for injection pressure, presented in the previous sections, is based on idealized behaviors for fracture height growth and fluid leakoff. This section discusses common conditions that cause deviation from the idealized behaviors and could result in treatment failure from a premature near-wellbore screenout during the proppant treatment.

- Rapid growth through a barrier—uncontrolled fracture height growth

Moderate or controlled fracture height growth into higher stress zones following a period of confined fracture extension is described in Section 9-4.3. Uncontrolled or runaway fracture height growth occurs when the higher stress zone is traversed and the fracture extends into a lower stress zone. This is shown on Fig. 9-12, where fracture growth during stages a and b is the same as that in stages 2 and 3, respectively, on Fig. 9-6 (The initial stage 1 period on Fig. 9-6 of radial- or KGD-type fracture growth is not shown on Fig. 9-12.) Stage b ends when the fracture enters a lower stress zone. When this occurs, the fluid pressure is greater than the stress of the zone, initiating an accelerated rate of growth that leads to stage c. This uncontrolled growth begins at the well, where the pressure is

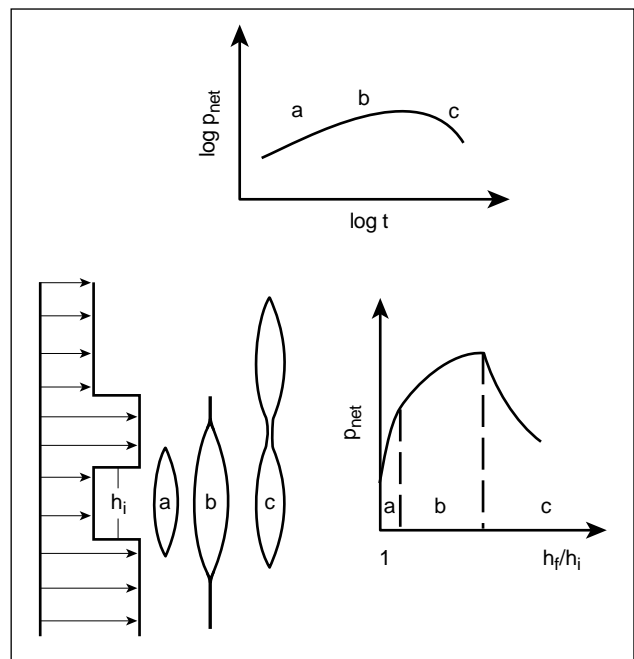


**Figure 9-12.** Pressure and width for height growth through a pinch point.

greatest, and progresses farther along the fracture as pumping continues. In a similar manner, uncontrolled height growth ceases progressively from the fracture tip to the wellbore when another higher stress barrier is reached. The fracturing pressure then increases again, indicating either height confinement or a controlled rate of barrier penetration.

Figure 9-12 also indicates that the pressure between stage b and stage c is relatively constant and is regulated by a pinch point. During the initial penetration into the lower stress zone, the pinch caused by the higher stress barrier layer results in a fracture width of nearly zero that closes if the pressure decreases. The reduced fracture width also causes additional pressure loss in the vertical direction, which limits fluid flow vertically into the lower stress zone. This pinching mechanism regulates the pressure to a nearly constant value until the penetration becomes sufficiently large to maintain a reasonable open width within the barrier layer. After the pinch point is overcome for stage c, the rate and extent of vertical growth increase significantly, accompanied by decreasing pressure and width in the primary reservoir.

Uncontrolled fracture height growth is characterized by declining pressure, as indicated on Fig. 9-12. Figure 9-12 also shows that during the phase of uncontrolled fracture growth (stage c), a rapid increase in the fracture height  $h_f$  is accompanied by a corresponding decrease in the fracturing net pressure  $p_{net}$ . In contrast, the onset of controlled fracture height growth results in a nominal change in the rate of the net pressure increase, as discussed in Section 9-4.3. Controlled height growth, therefore, is relatively difficult to identify on a net pressure log-log plot, particularly during its early stage.

The net pressure response for uncontrolled height growth is shown by the field example in Fig. 9-13. A pinch point above the perforated interval was identified on the stress log developed using sonic measurements (see Chapter 4). Fracture height growth into the lower stress sandstone above the pinch point commenced after approximately 150 min of injection and was accompanied by a steady decrease in the fracture pressure. Uncontrolled fracture height growth was also confirmed using radioactive isotopes that were injected during the treatment. The time evolution

of the fracture geometry was inferred following a consistent evaluation of the propped treatment using a pseudo-three-dimensional (P3D) fracture simulator (see Section 6-3) and the methodology outlined in Section 9-8.

As in the case of a radial fracture, decreasing net pressure generally indicates uncontrolled height growth. The pinch point resulting from height growth to a lower stress zone can cause proppant to bridge at its location during the proppant treatment but will allow fluid to pass through freely. Consequently, excessive dehydration of the slurry and decreasing width in the primary reservoir zone can result in a rapid screenout, even at low proppant concentrations.

- Horizontal fracture components—pressure greater than overburden

For the normal state of rock stress in moderate to deep reservoir depths, the horizontal stress is less than the overburden or the vertical stress, as discussed in Section 3-5. When the bottomhole treating pressure is less than the overburden stress, a fracture can propagate only in the vertical plane. A vertical fracture can also contain a horizontal component when the pressure exceeds the overburden or vertical stress component. This condition may occur

- at shallow depths where erosion has removed some of the overburden to reduce the vertical stress
- in reservoirs in tectonically active thrusting environments or in geopressed reservoirs. Both conditions increase the horizontal stress.
- in formations with low in-situ shear strength that undergo stress relaxation resulting in an increase of the horizontal stress.

The fracture geometry under these conditions could have both a vertical component and a horizontal component. This geometry is called a T-shaped fracture. Examples where T-shaped fractures resulted were reported for the fracturing of a shallow coal bed (Mahoney *et al.*, 1981), shallow limestone formation (Wood *et al.*, 1983) and laminated sandstones (Fragachan *et al.*, 1993). The corresponding pressure response and vertical cross sections of the width profile are illustrated in Fig. 9-14. The figure indicates that stage c has a nearly constant pressure response. Growth into the higher stress horizontal plane is similar to uncon-

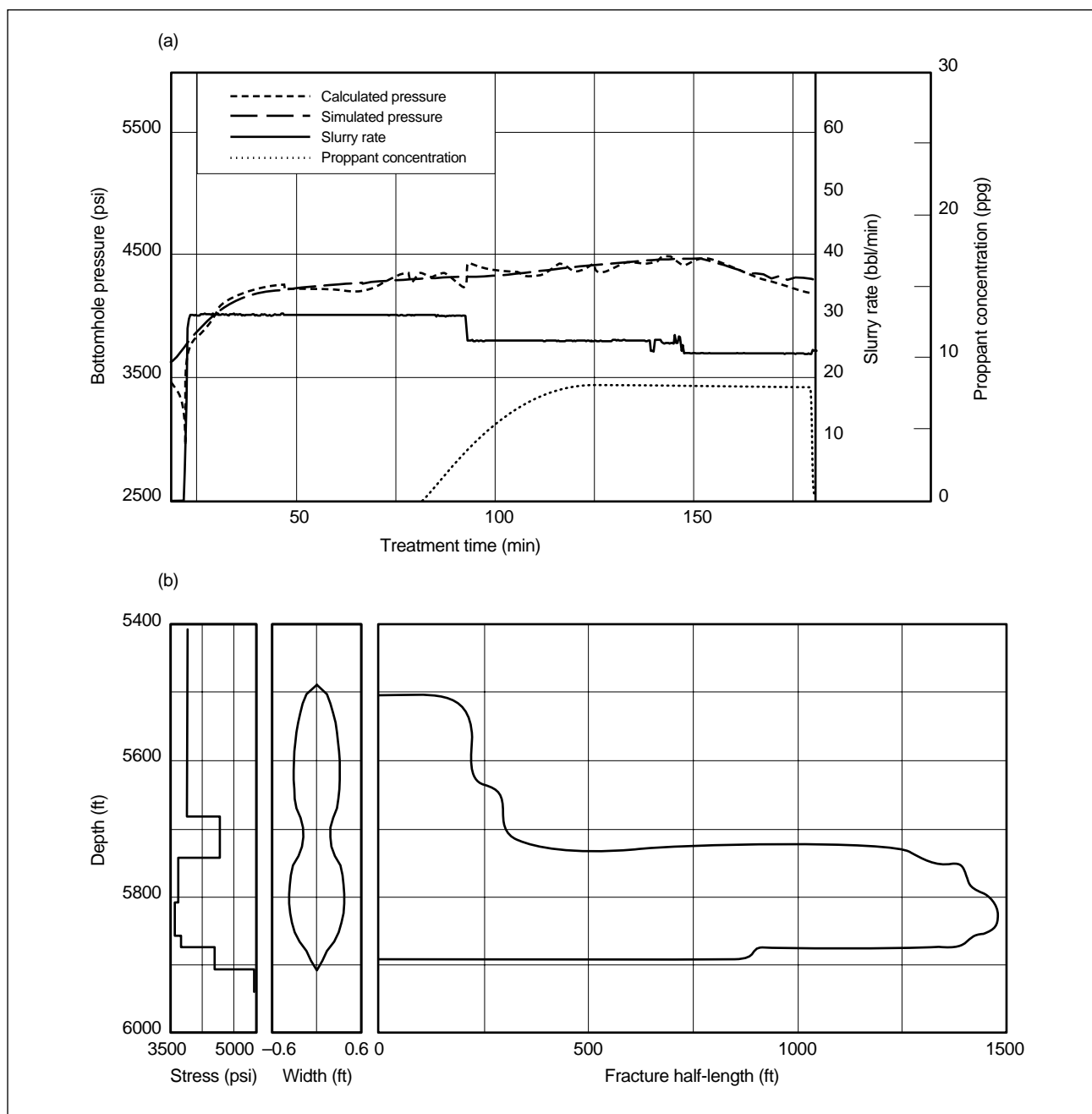


**Figure 9-13.** Pressure response for accelerated height growth. (a) Bottomhole pressure match plot. Calculated pressure is from surface pressure. (b) Fracture profile at the end of injection.

trolled vertical growth beyond a pinch point, as in Fig. 9-12. Although uncontrolled vertical growth commences at a pressure less than that of the stress barrier, T-shaped fracture growth occurs at a pressure slightly larger than the vertical stress.

The width of the horizontal fracture component is narrow and has twin pinch points at the juncture with the vertical component because of the elastic interaction of the two components (Vandamme *et*

*al.*, 1988). The horizontal fracture component increases the area available for fluid loss and decreases the treatment efficiency. In addition, the horizontal component readily accepts fluid but prevents proppant from entering because of its limited width. Both effects can excessively dehydrate the slurry in the vertical component, which could lead to premature screenout.

The pressure magnitude provides a diagnostic basis for determining whether the fracture plane is entirely vertical or has a horizontal component as well. The horizontal component occurs when the fracture pressure is nearly constant and approximately equal to the overburden stress of the formation, as illustrated in Fig. 9-14. The magnitude of the overburden stress can generally be estimated (see Section 3-5.1) and should always be compared with the magnitude of the bottomhole fracturing pressure as part of fracture pressure analysis.

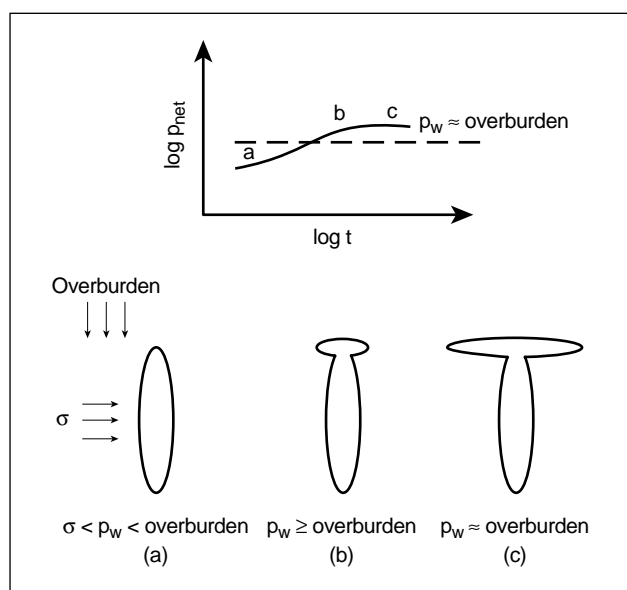


**Figure 9-14.** Pressure response for T-shaped fractures.

This pressure diagnostic was used to infer the occurrence of a T-shaped fracture during a calibration treatment performed in a tectonically active reservoir at a depth of 9750 ft. The log-log net pressure plot (Fig. 9-15) shows a positive slope lasting approximately 75 min, which indicates a confined mode of fracture extension. The pressure subsequently stabilized at approximately 10,145 psi. This constant pressure value is the magnitude of the vertical stress component for an overburden gradient of 1.04 psi/ft. During the remaining part of the treatment, the penetration of the vertical fracture component becomes less efficient because of the propagating horizontal fracture component.

- **Natural fissure opening—enhanced fluid loss**  
Natural fissures can be important for hydrocarbon production in the majority of low-permeability reservoirs, particularly where the permeability

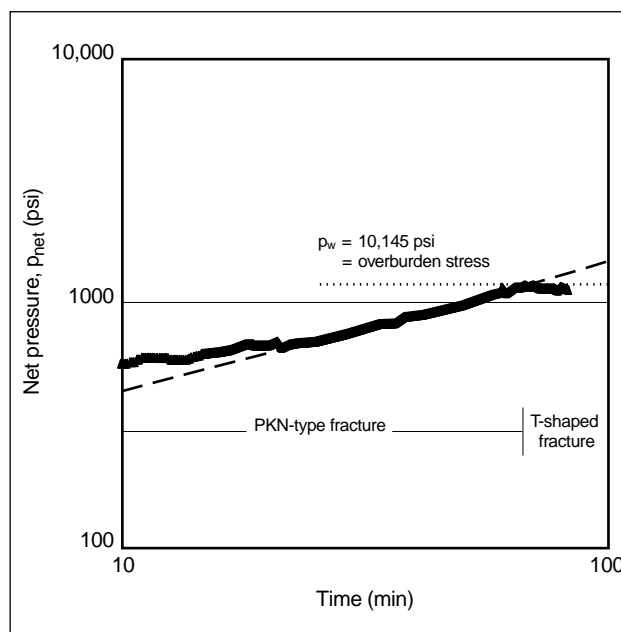


**Figure 9-15.** Calibration treatment pressure response for a T-shaped fracture.

of the rock matrix is negligible. Natural fissure systems are highly directional and show a preferential orientation along a single axis (Warpinski, 1991). The fissures can produce a complicated fracture behavior because of fracture offsets, enhanced fluid friction along the fracture length and the creation of secondary fracture strands. An important effect of natural fissures is enhanced leakoff, which can lead to a premature screenout during proppant injection.

Natural fissures have a negligible effect on the fluid leakoff process if the reservoir matrix permeability is high. In low-matrix-permeability conditions, however, the transmissibility of natural fissures can be significantly higher than that of the reservoir matrix. The fracturing fluid can readily penetrate into natural fissures during the fracturing process and maintain a pressure nearly equal to the pressure in the primary fracture. This process is illustrated in Fig. 9-16 in terms of the pressure response and a horizontal cross section of the width profile. Stage a represents the normal fracturing response in which the fluid pressure is lower than the normal stress on the fissure  $\sigma_f$ , and hence there is a relatively small increase in the fissure transmissibility. A continued increase in the fluid pressure, however, reduces the effective stress acting to close the fissure. This effect is

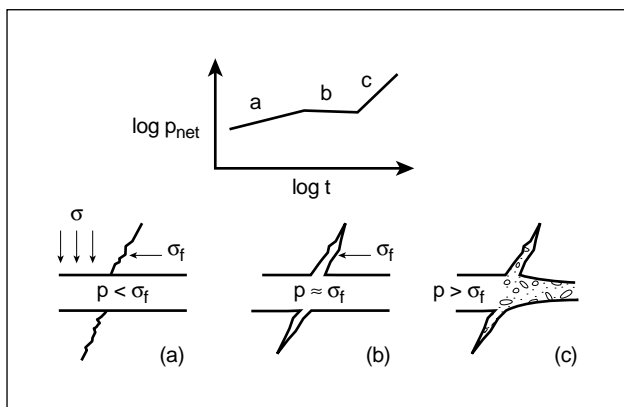


**Figure 9-16.** Pressure and width for opening natural fissures.

partially compensated for by an increase in the normal stress across the fissure  $\sigma_f$  resulting from the effect of Poisson's ratio from the main hydraulic fracture. The overall effect, however, is a decrease in the effective stress on the fissure.

When the fluid pressure eventually exceeds  $\sigma_f$ , the effective stress on the fissure becomes negative. The fissure mechanically opens at this stage, labeled stage b in Fig. 9-16. A significant portion of the injected fluid can be lost during this process because of the large number of fissures that can open at this critical pressure. The conductivity of fissures is increased by orders of magnitude when the threshold value is exceeded. The corresponding increase in fluid loss at an essentially constant net pressure greatly reduces treatment efficiency and can lead to excessive slurry dehydration in the main body of the fracture and premature screenout (stage c).

Optimized fracturing of a fissured formation requires a model to predict the effect of the fissures on fluid loss. Two fissure models have been reported in literature. The first was proposed by Nolte and Smith (1981). Their assessment pertains to fissured formations with only a slight fluid-loss enhancement unless the threshold fluid pressure required for fissure opening is exceeded. The fissures enlarge when the fluid pressure within the fracture—and the pressure inside the fissures—becomes greater than the normal stress acting to close them. When this occurs, fluid loss becomes significant and represents the worst-case situation for fissure-related leakoff behavior.

Nolte and Smith showed that the wellbore net pressure required for fissure opening is

$$P_{net,fo} = \frac{\sigma_{H,max} - \sigma_{h,min}}{(1 - 2\nu)}, \quad (9-40)$$

where  $\sigma_{H,max}$  and  $\sigma_{h,min}$  are the maximum and minimum far-field principal horizontal stresses, respectively. Equation 9-40 applies to PKN-type fractures, and the fissure can have any orientation with respect to the main fracture. An important observation is that a significant difference between the two principal stresses in a horizontal plane is required to ensure effective fracturing in fissured reservoirs.

The second model, presented by Warpinski (1991), is applicable to reservoirs where natural fissures are the primary source of permeability. This model provides a more detailed description of the effects resulting from natural fissures. It predicts an enhanced rate of fluid loss throughout the treatment, with an accelerating effect as the fracturing pressure increases (stage a of Fig. 9-16). The increase in fracture pressure reduces the effective normal stress acting to close the fissures and hence increases their permeability, as described in Sidebar 9D. For hydraulic fracturing purposes, the effect of the magnified permeability is reflected as an increase in the fluid-leakoff coefficient. As discussed in Sidebar 9D, the fluid-leakoff coefficient in the presence of natural fissures could be as high as 2 to 3 times that for normally occurring pressure-dependent leakoff behavior, even under the net pressure conditions for stage a.

Injection pressure during fracturing for these conditions exhibits a continuously decreasing slope on a log-log plot, indicating a progressively increasing rate of fluid loss. Under continued fluid injection, the negative effective stress condition described by the Nolte and Smith model can occur to open fissures and regulate the pressure to a constant threshold value (stage b of Fig. 9-16). Fracturing pressure during pumping in the presence of fissures, therefore, behaves in a manner similar to the pressure response during periods of controlled fracture height growth. Because of this similarity, the primary diagnostic for distinguishing between height growth and natural fissures is pressure decline data, as discussed subsequently in Sidebar 9F.

## 9D. Fluid leakoff in natural fissures

**Norman R. Warpinski, Sandia National Laboratories**

Control of fluid leakoff is one of the critical elements for optimizing hydraulic fracture treatments. The primary reasons for leakoff control are to ensure that the fracture acquires the desired penetration, to keep the sand slurry sufficiently hydrated to flow readily and to limit the invasion of potentially damaging fluids into the formation. In most fracture treatments, it is assumed that the leakoff coefficient is constant. However, in naturally fissured formations the assumption of a constant leakoff coefficient may cause considerable problems during the execution of the treatment and seriously hinder productivity.

The concept that natural fissures, or fractures, could alter leakoff has been examined or accounted for in some studies (Nolte and Smith, 1981; Castillo, 1987; Nolte, 1991; Warpinski, 1991; Barree and Mukherjee, 1996) through the use of fissure-opening conditions or pressure-sensitive leakoff equations. Figure 9D-1 shows conceptually the ways that elevated pressure could affect natural fissures. Fissures with rough surfaces and minimal mineralization are most likely highly sensitive to the net stress pushing on them. Under virgin reservoir conditions (i.e., the pressure  $p$  within the fissure equals the initial reservoir pressure  $p_i$ ), the effective stress is fairly high and the open slot pores are most likely deformed and closed. As the pressure in the fissure increases because of leakoff of the high-pressure fracturing fluid ( $p > p_i$ ), the net closure stress is reduced and the fissure porosity opens. In this regime, the leakoff coefficient is highly pressure dependent. As the pressure exceeds the closure stress on the fissure ( $p > p_{fo}$ ), the entire fissure opens, yielding an accelerated leakoff condition. Vuggy porosity, on the other hand, is generally insensitive to stress and remain unchanged until the pressure exceeds the closure stress and opens the entire fissure (i.e., accelerated leakoff).

The case of fissure opening when the pressure exceeds that closing the fissure is the simplest case to consider. Nolte and Smith (1981) derived a relation for the critical pressure in the hydraulic fracture for fissure opening to occur:

$$p_{net,fo} = \frac{\sigma_{H,max} - \sigma_{H,min}}{1 - 2\nu}, \quad (9D-1)$$

where  $p_{net,fo}$  is the wellbore net pressure for fissure opening,  $\sigma_{H,max}$  and  $\sigma_{H,min}$  are the maximum and minimum horizontal stresses, respectively, and  $\nu$  is Poisson's ratio. Equation 9D-1 applies to vertical fissures at any orientation and shows that fissure opening is a likely possibility in formations where the difference in the horizontal stresses is low. When the fissure opens, it behaves much like a hydraulic fracture, accepting large amounts of fluid and resulting in leakoff coefficients that increase by orders of magnitude (thus the term accelerated leakoff).

For slightly elevated pressures, the conceptual model is more complicated. The fissure porosity begins to open as the pore pressure increases because the elevated pressure relieves some of the net stress on the asperity contacts. Several models of this process have been developed, the most well known of which is by Walsh (1981). In his model, the change in permeability of the fissure resulting from changes in stress and pressure is

$$k = k_o \left\{ C \ln \left[ \frac{\sigma_{ref}}{\sigma - p} \right] \right\}^3, \quad (9D-2)$$

where  $C$  and  $\sigma_{ref}$  are constants determined from empirical data,  $k_o$  is the initial fissure permeability,  $\sigma$  is the stress on the fissure, and  $p$  is the pore pressure in the fissure.

The Walsh model has been shown to reasonably represent data from a fissured reservoir in the Mesaverde formation in the Piceance basin of Colorado, USA (Warpinski, 1991). Figure 9D-2 shows a fit of the Walsh model to data measured during injection and drawdown conditions. The reservoir is overpressured, giving a relatively high initial pressure (5400 psi) relative to the initial in-situ stress (~7000 psi). The initial reservoir permeability was measured using drawdown and buildup tests when the interval was first completed. The permeability during injection conditions was measured using both injection and falloff behavior during nitrogen tracer testing to assess the interconnectability of the fissure system among nearby wells. The permeability collapse that occurred during full drawdown was a common phenomenon in all intervals at the site. Inevitably, a hard drawdown would produce a reasonable rate of gas flow until the pressure reached a critical level at which the production would drop to an immeasurable level (but production would be restored when the pressure built back up). On the basis of the flow rates at the initial conditions, the permeability was estimated to have dropped 2–3 orders of magnitude to achieve the observed decrease.

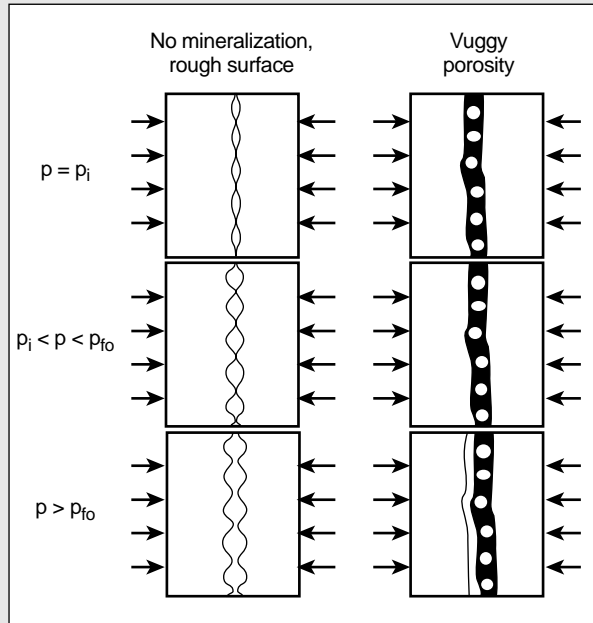


**Figure 9D-1.** The effects of pressure on fissure opening and porosity.

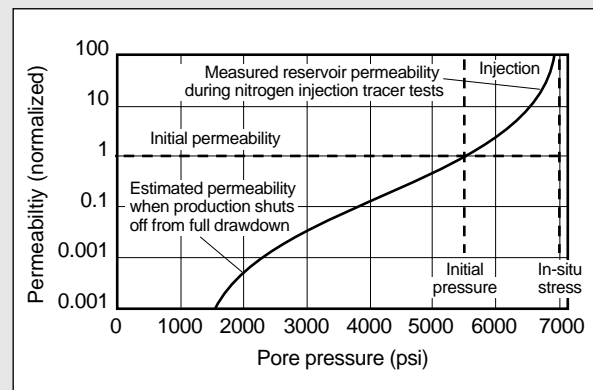


**Figure 9D-2.** Measured permeability variations of the Mesaverde natural fissure system at the M-Site (Warpinski, 1991).

## 9D. Fluid leakoff in natural fissures (continued)

The importance of Fig. 9D-2 is that it provides a mechanistic model of understanding the behavior of fissured reservoirs during and after stimulation. When the fracturing pressure is low, the fissure permeability is near the initial value and the leakoff coefficient is relatively low. As the fracturing pressure increases, the leakoff coefficient increases rapidly, causing problems with fracture size, slurry dehydration and screenout. However, the situation during cleanup reverses because the well is drawn down to extract stimulation fluids and the natural fissure permeability decreases. Thus, stimulation fluids are injected under wide-open fissure conditions but produced under clamped fissure conditions, making it difficult to clean up the reservoir.

The Walsh and other models can be incorporated into a fluid-loss equation to represent changing leakoff conditions (Warpinski, 1991). Figure 9D-3 shows the calculated pressure-sensitive leakoff of a Mesaverde fissure system compared with the normal pressure sensitivity of a conventional pore space (recall that the filtrate leakoff coefficient is proportional to the square root of the fracturing pressure minus the reservoir pressure). Generally, the pressure sensitivity of conventional reservoirs is ignored because the changes are small; in this case, it varied from 1.0 to 1.4. However, the pressure sensitivity of the fissures greatly exceeded this change, and the leakoff of the fissures reached about 3 times the conventional leakoff. Even at low fracturing pressures, the leakoff of the fissures was greater than conventional leakoff because the fracturing pressure was large relative to the reservoir pressure and the fissure pores had much less stress closing them. This example is based on a tight Mesaverde coastal zone reservoir with a base leakoff coefficient  $C_{L, \text{fissure}}$  of 0.0004–0.0006 ft/min<sup>1/2</sup> (measured during pressure declines) and a fracture-calibrated leakoff coefficient  $C_{L, \text{fissure}}$  of 0.0015–0.0019 ft/min<sup>1/2</sup> during injections.

Pressure-sensitive fissure behavior is best recognized in the pressure decline where the G-plot shows a continuously

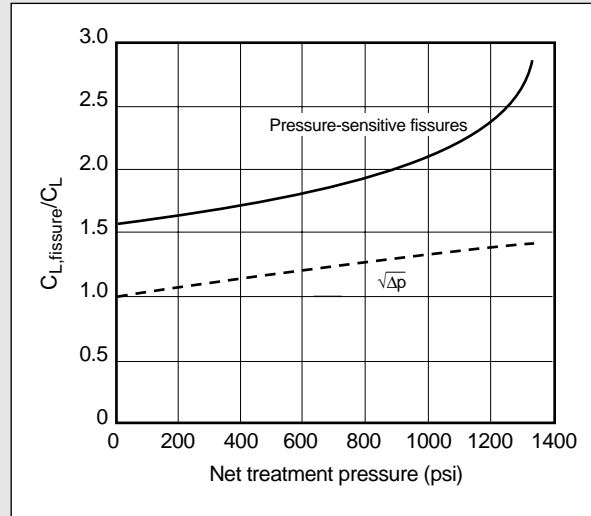


**Figure 9D-3.** Pressure-sensitive leakoff of a Mesaverde fissure system.

decreasing slope with decreasing pressure. Fissure-sensitive fluid loss can be recognized in the injection pressure behavior, but it is difficult to identify because it looks much like height growth during the injection (i.e., a nearly constant pressure derivative). Fissure dilation is usually followed by flattening of the fracturing pressure, and screenout most likely occurs relatively fast, depending on the injected proppant concentration (Fig. 9-16).

### 9-4.6. Formation pressure capacity

As discussed previously, for a PKN-type fracture, a constant pressure response can occur after a period of normal pressure increase resulting from controlled fracture height because the pressure

- approaches the stress of a barrier and causes significant height growth into a lower stress zone (determined by the horizontal stress difference between the reservoir and adjacent barrier; Fig. 9-12)
- exceeds the overburden, and the initiation of a T-shaped fracture begins at a pressure slightly greater than the overburden (determined by the horizontal and vertical stress differences in the reservoir; Fig. 9-14)
- exceeds the normal stress acting on natural fissures and causes them to open (determined by the stress difference between the two horizontal stresses in the reservoir; Fig. 9-16).

These three complicating mechanisms produce excessive fluid loss from the main body of the fracture and potential treatment problems. They depend on the stress differences along the three principal directions in the formation. The formation acts like a pressure vessel with a pressure capacity governed by the pressure-limiting mechanism and the corresponding in-situ stress difference.

When the net pressure reaches the formation pressure capacity, the fracturing process may exhibit one of the three growth patterns discussed in Section 9-4.5. Each growth pattern makes additional fracture propagation relatively inefficient. Under these conditions, an inaccurate diagnostic could lead to a design change that either compromises the effectiveness of the fracture treatment or further aggravates the problem. For example, the pad volume or the fracturing fluid viscosity may be increased to alleviate recurring screenouts. These approaches, however, could be ineffective if the screenouts are not due to excessive fluid dehy-

dration or insufficient fracture width, respectively. An important function of calibration tests is to identify the formation pressure capacity and the associated complicating mechanism. The propped treatment can then be planned to attain the desired fracture characteristics in a cost-effective manner.

Numerous alternatives have been proposed to modify fracture treatments that are constrained by the formation pressure capacity. They range from the application of unconventional designs to reduce the fracturing pressure (e.g., Veatch and Crowell, 1982; Britt *et al.*, 1994) and the use of specialized additives (e.g., Nolte, 1982; Nguyen and Larson, 1983; Warpinski, 1990) to even altering the reservoir stress state through changes of either the reservoir pressure or temperature (Cleary, 1980a). The particular choice of an alternative is driven primarily by the nature of the problem and how quickly the formation pressure capacity is reached during the propped treatment, as discussed in the following.

- Pressure capacity approached during the late stage of the treatment

The recommended approach when any of the three complicating mechanisms occurs is to engineer the propped treatment so that the fracturing pressure remains below the formation pressure capacity. Limiting the fracturing pressure may require reducing the treatment volume, injection rate or fluid viscosity. The pressure relation for the PKN fracture geometry in Eq. 9-25 provides an assessment for determining which of these changes is most effective at reducing the fracturing pressure. For example, using the typical fluid rheology exponent  $n = 0.5$  in Eq. 9-25 shows that a twofold reduction in the injection rate reduces the net pressure by only 11%. A twofold reduction in the fluid viscosity (or the fluid rheology coefficient  $K$ ), however, provides a 22% reduction in the net pressure. A reduction in the fluid viscosity thus will be more effective in controlling the fracturing pressure. Reducing the fluid viscosity, however, requires additional considerations of the potentially increased fluid loss, modifications to the breaker and proppant scheduling, fluid degradation from exposure to the reservoir temperature and near-wellbore effects (Nolte, 1982, 1988a).

Viscosity requirements for efficient proppant transport are often overestimated because the effect

of proppant convection and settling is not a limitation with the commonly used polymer fluids (Nolte, 1988a; Warpinski *et al.*, 1998a; Shah and Asadi, 1998). In addition, a reduction in the fluid viscosity only nominally affects the treatment efficiency. Therefore, a moderate decrease in the fluid viscosity should not significantly alter the propped fracture characteristics. Fracturing equipment is capable of delivering a continuous decrease in fluid viscosity throughout the treatment (see Chapter 11). All fracture treatments benefit from a reduction in the polymer mass used during the treatment. This approach limits the gel residue in the proppant pack to prevent an excessive loss of fracture conductivity (see Chapter 8).

Figure 9-17a shows a pressure record during a fracture treatment in a gas reservoir with micro-darcy permeability. The formation net pressure capacity identified as 1180 psi is attributed to uncontrolled height growth that occurred after approximately 75% of the propped treatment had been injected. Fracture treatments on offset wells were successfully designed to maintain the pressure below the formation pressure capacity by continuously reducing the fluid viscosity during the proppant treatment (Fig. 9-17b). The initially increasing fluid viscosity was required to overcome enhanced degradation of the early treatment stage from longer exposure to the reservoir temperature (Nolte, 1982, 1988a).

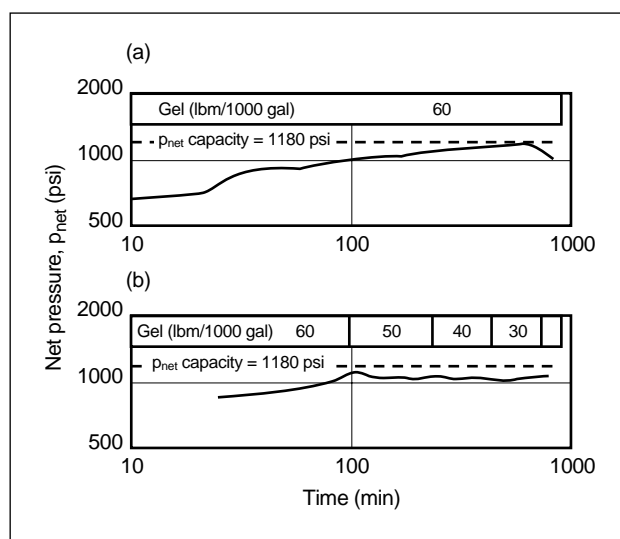


**Figure 9-17.** Control of fracture height growth through viscosity reduction (Nolte, 1982, 1988a).



- Pressure capacity approached during the intermediate stage of the treatment

The mitigating design for reaching the pressure capacity during the intermediate stage of the treatment depends on the specific mechanism associated with the formation pressure capacity. Relatively fine solids such as silica flour or platelet-based additives (Vinod *et al.*, 1997) can control accelerated fluid loss in formations where fissures provide a meaningful increase in the overall permeability, even before they are open. The fine-size additive (e.g., 300-mesh particles) should be used throughout the pad so that fluid leakoff into fissures, and hence the fluid pressure within them, is reduced from the onset of the treatment.

Controlling accelerated leakoff can significantly delay or even prevent the mechanical opening of fissures during the propped treatment. The additive will not bridge at the fracture tip because the farthest it can travel is the boundary of the fracturing fluid and the fluid lag region (see Fig. 5-16). The fracture width in this region is generally much larger than the extremely small diameter of the fine-size additive.

A larger size solid additive (e.g., 100-mesh sand) should be used to control accelerated leakoff resulting from mechanically opened fissures. This additive should be scheduled immediately prior to proppant addition. It will either bridge in the open fissure or block its opening, thereby impeding fluid entry and the associated increase in the rate of fluid loss. The additive alone may be sufficient if the fissures exhibit negligible permeability before they are mechanically opened. It can be used in conjunction with the previously discussed finer 300-mesh particles within the pad when fissures are responsible for increased fluid loss before they are mechanically opened.

The effectiveness of 100-mesh sand in controlling fluid loss is demonstrated by the calibration test shown in the field example in Fig. 9-18. Fissure opening occurred at a net pressure of 1000 psi, defining the pressure capacity of the formation. The accelerated fluid loss was mitigated by the introduction of 100-mesh sand on a subsequent calibration test, which exhibited a net pressure well in excess of the previous net pressure capacity of 1000 psi.

A 100-mesh sand or specialized proppant systems should be used to control excessive height

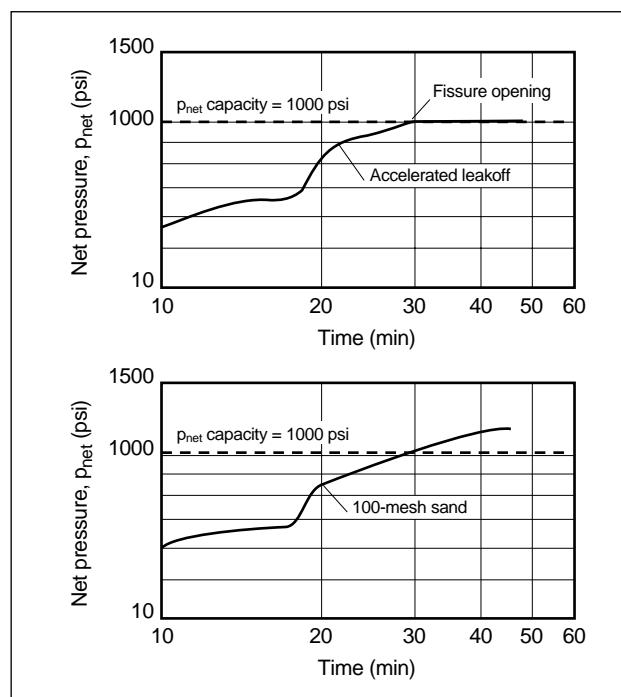


**Figure 9-18.** Control of accelerated leakoff into natural fissures using particulate-based additives (Warpinski, 1990).

growth (Mukherjee *et al.*, 1994; Nolte, 1988a) or the occurrence of T-shaped fractures. The additives bridge in the narrow pinch points associated with both of these mechanisms and arrest the further growth of secondary features. The benefit of the particle-size mixture described by Nolte (1988a) is exhibited in the field example in Fig. 9-19. The calibration treatment shows that the critical net pressure of 800 psi was reached after approximately 20 min of fluid injection (Fig. 9-19a). The pressure subsequently declined, exhibiting a signature for uncontrolled height growth similar to that in Fig. 9-12. Rapid height growth led to a premature screenout soon after the introduction of proppant. A subsequent successfully placed propped treatment exhibited a higher net pressure once height growth activity was controlled after the addition of a proppant mixture (Fig. 9-19b).

The use of solid-based additives requires caution and proper design procedures. Elbel *et al.* (1984) showed that incorrect scheduling of the larger size additives (e.g., 100-mesh sand) within the pad could result in a premature screenout. Particulate-based additives should not be scheduled in conjunction with proppant stages because their combination reduces proppant pack permeability. In

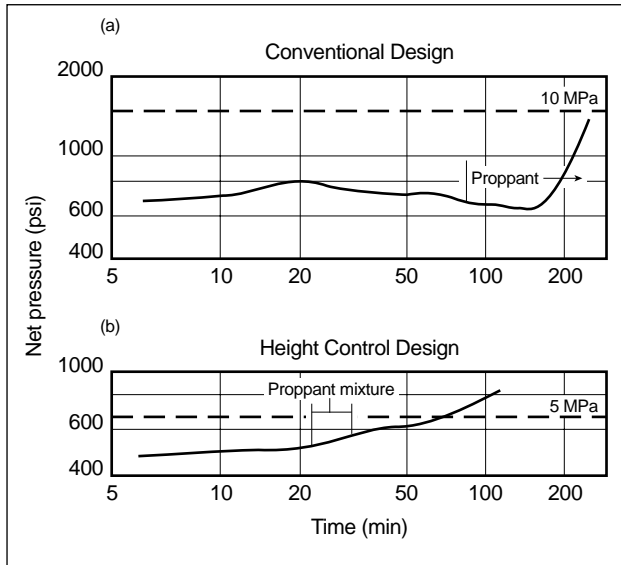


**Figure 9-19.** Control of height growth using a mixture of particle sizes (Nolte, 1982, 1988a).

general, only small concentrations of the additive are sufficient to mitigate any of the complicating mechanisms. Furthermore, even a moderate loss of fracture conductivity has a nominal effect on poststimulation production in low-permeability reservoirs, where additive use is more likely. Fissured formations may benefit from the use of particulate additives because they effectively prop the natural fissures and increase their permeability (Miller and Warembourg, 1975).

- Pressure capacity approached during the early stage of the treatment

The approach of pressure capacity during the early stage of treatment presents the worst-case scenario for effective fracture stimulation. None of the measures discussed previously may be effective in controlling the complicating mechanisms and their damaging consequences. Mitigating strategies under these conditions should focus on altering the stress state of the reservoir. Section 3-5.4 indicates that any change in the reservoir pore pressure could change the horizontal stresses by 46% to 80% of the pore pressure change. The stress state, therefore, is most practically reduced through an extended period of hydrocarbon production prior to the fracture treatment.

The best approach is to initially produce the reservoir for an extended period, possibly with a much smaller fracture. The corresponding reduction in the reservoir pore pressure will reduce the

horizontal stresses in the reservoir. Under the altered state of stress, undesirable fracture growth patterns will occur at much higher net pressure values. A subsequent, larger size fracture treatment can then be designed to obtain the desired fracture geometry with a fluid pressure that remains below the magnitude triggering complex fracture growth.

#### 9-4.7. Pressure response after a screenout

The pressure response in Fig. 9-1 is for a fracture that is free to extend until shut-in. A common occurrence during proppant injection is a screenout. Screenouts can occur in the vicinity of the wellbore when the formation pressure capacity is reached (see Section 9-4.6) or at the fracture tip and around the complete circumference of the fracture area (i.e., a tip screenout, or TSO) when the proppant slurry bridges because of insufficient width or dehydrates as a result of fluid loss. In addition to resulting from proppant bridging, screenouts can also be caused by the excessive buildup of polymer filter cake at the tip or by incorrect scheduling of particulate-based fluid-loss control additives (Elbel *et al.*, 1984). Either of these circumferential flow restrictions effectively stops fracture propagation, and subsequent injection is stored primarily by increasing the width. A screenout may be undesirable in a low-permeability reservoir where increasing the fracture length is the primary objective, or it can be deliberately designed to occur to increase production in high-permeability environments (see Chapter 5).

As the fracture pressure and width increase during the restricted growth period, the pressure gradient from fluid flow decreases. The value of  $\Delta\bar{p}_f$  approaches that of  $p_{net}$ . The value of  $\beta$  approaches 1, as discussed in Section 9-3.3 and illustrated on the log-log plot in Fig. 9-20. Figure 9-20a shows the variation of  $p_{net}$  and  $\Delta\bar{p}_f$ , which defines the average width. Post-screenout behavior is depicted in Fig. 9-20b. The time when the wellbore pressure apparently responds to the restriction is  $t_{so}/\beta_p$ , where  $t_{so}$  is the time when the screenout occurs. From the values of  $\beta_p$  determined with Eq. 9-19,  $t_{so}/\beta_p$  is on the order of  $1.5t_{so}$  or about 50% greater than at the time of injection before the restriction occurred. In contrast, Sidebar 9C shows that the pressure derivative is much more sensitive, with its change perceptible shortly after a screenout.

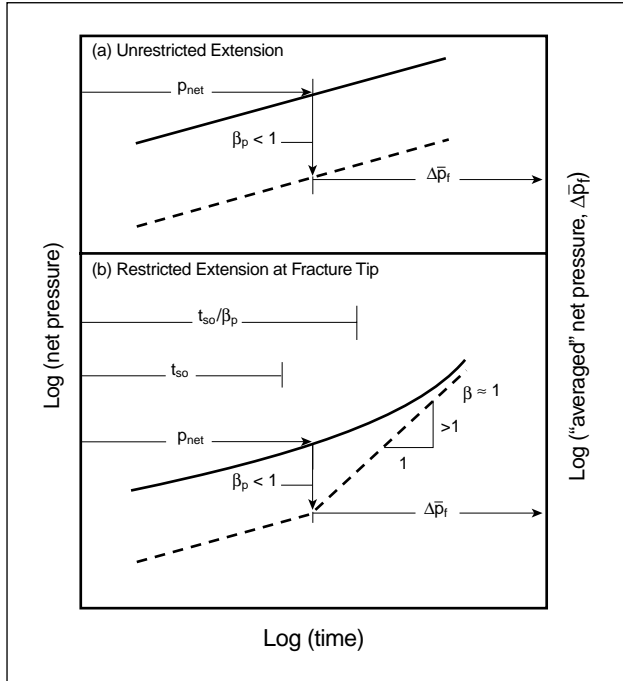


**Figure 9-20.** Log-log relations of net pressure versus time for restricted and unrestricted extension.

The pressure response and fracture width relation after the screenout can be derived using the material-balance relations from Section 9-3. For the assumption of an ideal screenout occurring around the fracture circumference, the fracture area remains constant and equal to the area immediately before the screenout. The material-balance relations following a screenout therefore are the same as those applied to describe the pressure behavior following the end of pumping, as discussed in Section 9-5. The only difference, however, is that although no additional fluid volume is introduced during the decline, slurry injection continues after the onset of the screenout and should be included in the fundamental relations presented in Section 9-3.

Applying these modifications to the material-balance relations, it can be shown (see Appendix Eq. 51) for the commonly used polymer fracturing fluids that the log-log slope of the net pressure plot after a screenout and in the absence of spurt as  $\beta$  approaches 1 is

$$\frac{t}{p_{net}} \frac{dp_{net}}{dt} = \begin{cases} \frac{\frac{\pi}{2} - \sin^{-1}(1 + \Delta t_{Dso})^{-1/2}}{\frac{\pi}{2} - \sin^{-1}(1 + \Delta t_{Dso})^{-1/2} - \sqrt{\Delta t_{Dso}}/(1 + \Delta t_{Dso})} & \eta_{so} \rightarrow 0 \\ 1.0 & \eta_{so} \rightarrow 1, \end{cases} \quad (9-41)$$

where  $\Delta t_{Dso}$  is the dimensionless time after a screenout, defined as the ratio of the incremental time after the screenout and the screenout time, and  $\eta_{so}$  is the efficiency when the screenout occurs.

Figure 9-20 shows that the log-log slope of the net pressure generally changes after a screenout. Its particular value at  $\Delta t_{Dso} = 2$  is shown in Fig. 9-21. An important conclusion based on this figure is that the postscreenout log-log slope approaches unity only for a high treatment efficiency before the TSO. An example showing the net pressure response in a low-permeability oil-bearing reservoir characterized by a high fluid efficiency is presented in Fig. 9-22a. A unit slope follows the TSO. In lower efficiency situations, however, the fracture pressure exhibits a log-log behavior with a slope that can be larger than 1.0. This case is shown in Fig. 9-22b, where the TSO is characterized by a log-log slope of 1.7. The pressure data are from a frac and pack treatment in a 1.5-darcy, oil-bearing, unconsolidated reservoir that exhibited a low treatment fluid efficiency.

Proppant bridging between the wellbore and the tip increases the rate of the pressure increase over that described by Eq. 9-41. Successive packing of the fracture toward the wellbore also results in a progressively increasing log-log slope with continued slurry injection (Martins *et al.*, 1992c).

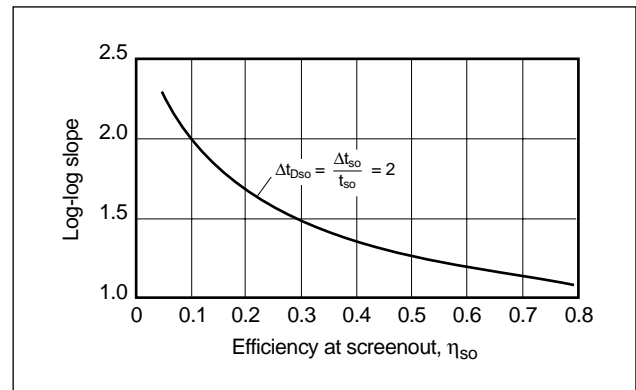


**Figure 9-21.** Log-log slope after a TSO for  $\Delta t_{Dso} = 2$ .

#### 9-4.8. Fracture diagnostics from log-log plot slopes

The previous sections provide conceptual analyses of the different types of log-log slopes of net pressure versus time. The slopes are characteristic of various types of fracture geometries and modes of propagation. Therefore, the log-log plot, its associated slopes

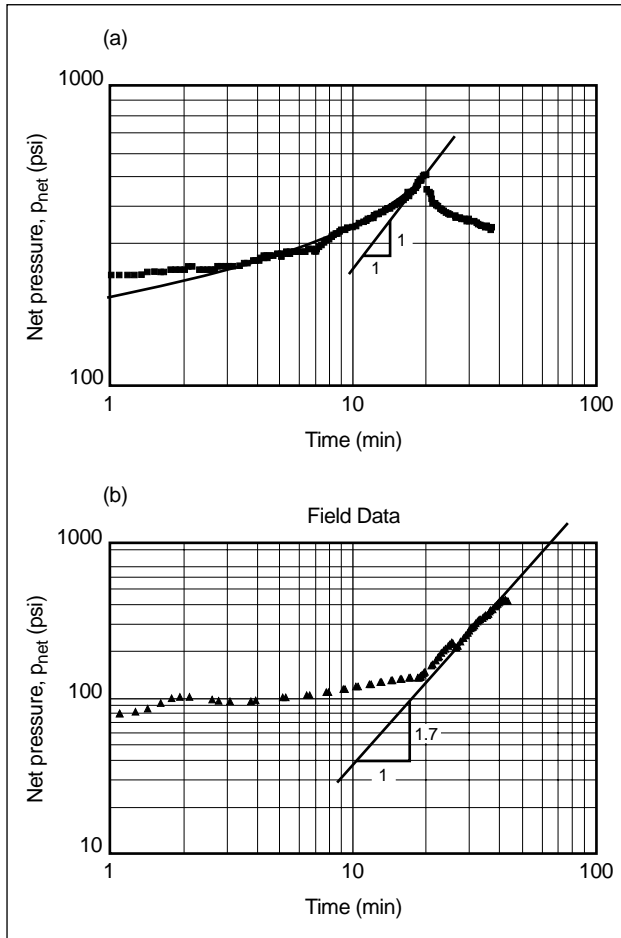


**Figure 9-22.** Log-log plot of the postscreenout pressure response for (a) low-permeability long fracture and (b) high-permeability short fracture.

and the pressure derivative provide a diagnostic tool for interpreting the fracturing process. The analyses presume that the pressure measurement represents the actual fracturing behavior, corrected for near-wellbore effects (see Section 9-4.9). Also, the pump rate and fluid properties are assumed to be relatively constant during the treatment. Therefore, for a correct interpretation of the fracturing pressure, it is important to note variations in the pressure response that occur when proppant is first injected into the formation or with significant changes in the pump rate or fluid rheology (e.g., at about 17 min on Fig. 9-18).

The basic net pressure interpretation includes the initially decreasing pressure before the fracture is influenced by barriers (Fig. 9-6). This time is generally short, particularly for zones of relatively small height. For this initial behavior, the theoretical range of the slope is given by the exponents in Eqs. 9-36 and 9-37.

After the fracture is confined by barriers, the pressure increases as predicted by the PKN model, with the range of the slope as given by Eq. 9-34. This range is from about  $\frac{1}{6}$  for low efficiency to about  $\frac{1}{4}$  for high efficiency.

As the fracture pressure increases, it can reach the pressure capacity of the formation. This leads to a regulator effect, resulting in nearly constant pressure because of accelerated fluid loss primarily near the wellbore (see Section 9-4.5). A nearly constant pressure measurement that is equal to the overburden stress indicates a T-shaped fracture. Controlled fracture height growth into a barrier is characterized by a gradually decreasing log-log net pressure slope and a constant pressure derivative. Net pressures steadily decrease if uncontrolled fracture height growth beyond a pinch point occurs. Fissure-dominated fluid-loss behavior regulates the pressure to a constant value when the fissures are mechanically opened. If the fissure permeability increases before the mechanical opening occurs, this response will be preceded by a gradually decreasing log-log slope. A significant pressure increase (i.e., log-log slope between those suggested by Eq. 9-41) indicates restricted extension or a screenout near the fracture tip, whereas a significantly higher slope should be expected for a restriction nearer the wellbore than the fracture tip (Nolte and Smith, 1981).

The types of slopes and associated interpretations for vertical fractures are listed in Table 9-3. This table, in conjunction with the interpretation plot

**Table 9-3. Interpretation of log-log plot fracture pressure slopes.**

Propagation Type	Log-Log Slope	Interpretation
Ia	$-\frac{1}{6}$ to $-\frac{1}{2}$	KGD (Eq. 9-36)
Ib	$-\frac{1}{6}$ to $-\frac{1}{2}$	Radial (Eq. 9-37)
II	$\frac{1}{6}$ to $\frac{1}{4}$	PKN (Eq. 9-35)
III	Reduced from II	Controlled height growth Stress-sensitive fissure
IV	0	Height growth through pinch point Fissure dilation T-shaped fracture
V	$\geq 1$	Restricted extension
VI	Negative following IV	Uncontrolled height growth
Note: $n = 0.5$		

in Fig. 9-23, shows that the log-log plot with its characteristic slopes provides a diagnostic tool analogous to the log-log plot for identifying flow regimes within a reservoir.

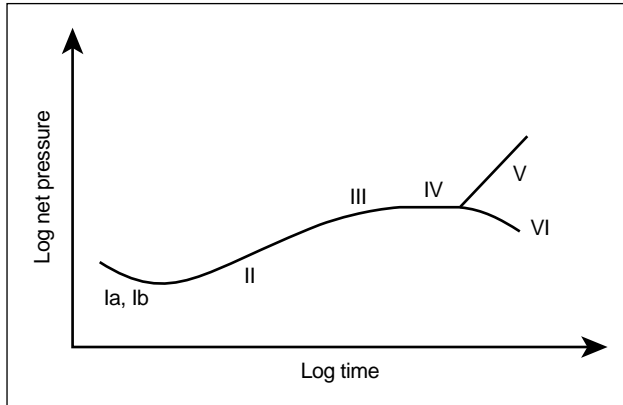


**Figure 9-23.** Log-log interpretation plot for various fracture propagation modes.

#### 9-4.9. Near-wellbore effects

The previous discussion of log-log plot diagnostics assumes that the bottomhole pressure measurement reflects the actual fracture response. The injected fluid may experience pressure loss prior to entering the main body of the fracture. Near-wellbore pressure loss could occur as a result of restrictions arising from the well completion (e.g., perforations; see Section 11-3) or the near-wellbore fracture geometry (e.g., a convoluted fracture pathway; Cleary *et al.*, 1993). The latter cause can be particularly damaging, because it reduces the fracture width close to the wellbore and increases the likelihood of a premature screenout. Near-wellbore pressure loss is rate dependent and affects the pressure response exclusively during the fluid injection. The occurrence of near-wellbore problems thus masks the actual fracture response and complicates the interpretation of injection pressure.

Chapters 6 and 11 identify three mechanisms to explain near-wellbore pressure loss: insufficient perforations, a convoluted fracture pathway in the vicinity of the wellbore (or fracture tortuosity) and a hydraulic annulus between the cement and the rock that connects the perforations with the main body of the fracture. The evolving fracture geometry, away from the wellbore, is completely independent of the near-wellbore effects. It is assumed that their pressure

contribution and the fracturing-related pressure response are additive:

$$p_{meas} = p_c + p_{net} + \Delta p_{near\ wellbore}, \quad (9-42)$$

where  $p_{meas}$  is the measured bottomhole pressure and  $\Delta p_{near\ wellbore}$  is the cumulative near-wellbore pressure loss. The result of the near-wellbore effects is an elevated pressure measurement during fluid injection and potential misinterpretation when the techniques described in the previous sections are used.

Insufficient perforations could result from improper perforating practices, poor perforation cleanup or ineffective formation breakdown procedures. It has been experimentally shown (Crump and Conway, 1988) that the perforation diameter changes only when proppant-laden slurry enters the perforation. For a constant injection rate, perforation friction is reflected as a constant increase in the treatment pressure during a calibration test and the pad stage of the main fracture treatment. The introduction of proppant erodes the perforations, increasing their diameter. This results in a progressive decrease in the measured treatment pressure during proppant injection until the pressure drop across the perforations is negligible, as shown from 25 to 35 min on Fig. 9-24.

An apparently higher net pressure with a reduced log-log slope is indicated on net pressure plots that are not corrected for the presence of perforation friction. The bottomhole pressure measurement, however, will exhibit an instantaneous change during shut-in if significant perforation friction is encountered. The instantaneous pressure change provides a measure of the excess pressure associated with perforation friction and, in conjunction with Eq. 6-120, is used to estimate the number of perforations accepting fluid.

Fracture tortuosity, or the existence of a convoluted pathway from the perforations to the main fracture body, causes the fracture to open against a normal stress that is higher than the formation closure pressure. Consequently, the fracture width is narrower in the near-wellbore region, which restricts fluid flow and increases the bottomhole pressure. The associated pressure drop in the tortuous region can be approximated using the methodology outlined in Section 6-8.4. Because the fracture width is smallest at the beginning of a treatment, the fracture reorientation pressure loss is largest during the early stage of the treatment. As fluid injection proceeds, the pressure drop associated with fracture reorientation progres-

sively decreases. Figure 9-25, developed using numerical simulation, illustrates this response for various degrees of fracture turning.

If the orientation of the perforation with the plane of the hydraulic fracture is large (typically greater

than  $10^\circ$ ; Behrmann and Elbel, 1991), the fracture may not initiate at the perforations. Rather, the fluid communicates with the fracture through a narrow annulus around the casing (Fig. 9-26) (see Section 11-3 and Sidebar 11C). As discussed in Section 6-8,

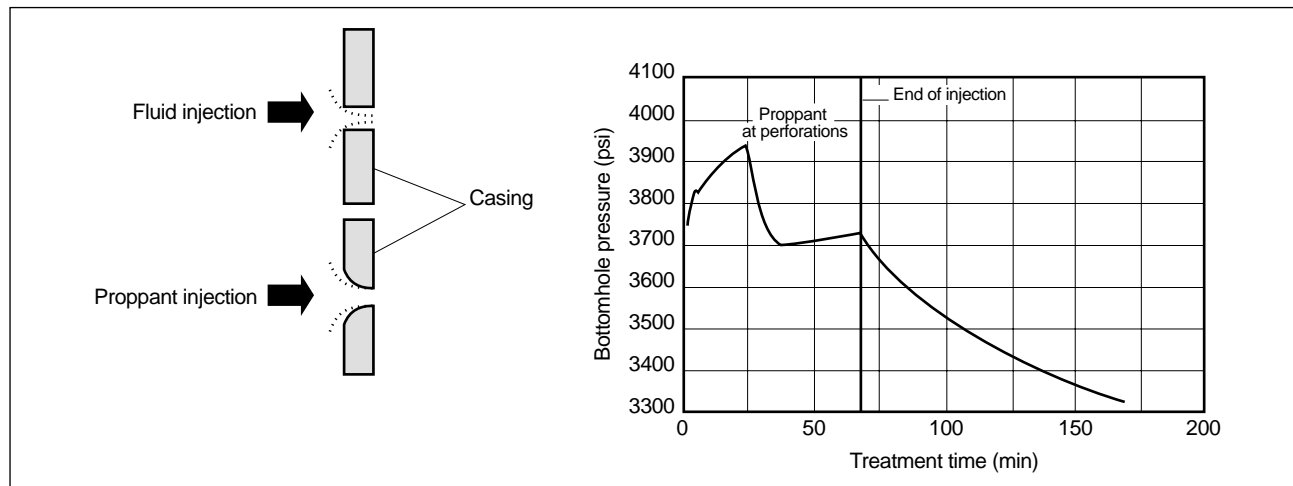


**Figure 9-24.** Perforation friction pressure response.

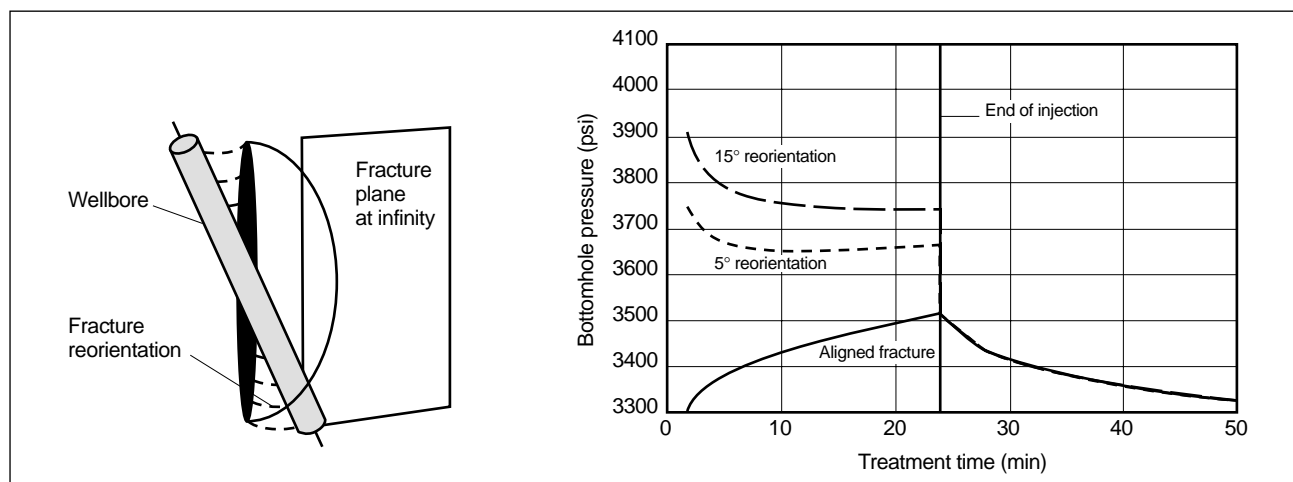


**Figure 9-25.** Fracture reorientation pressure response.

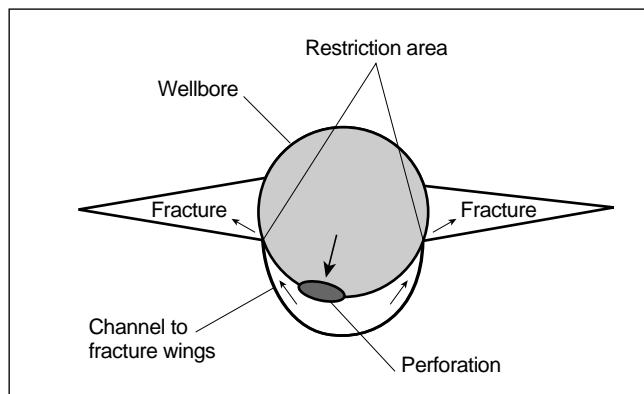


**Figure 9-26.** Pinch point caused by the rock-casing annulus.

the formation elastic response (i.e., Poisson's ratio effect) results in a pinch point at the intersection of the channel with the fracture body. This annulus can cause higher treating pressure because of the width restriction, as in the case of fracture reorientation. However, unlike for fracture reorientation, the effect of the annulus can increase with increasing fracture width because of the Poisson's ratio effect (see Fig. 6-19). The annulus effect decreases with erosion of the pinch point by fluid in soft rocks or following the injection of proppant in hard rocks. Section 6-8.5 discusses the near-wellbore pressure loss associated with perforation phasing misalignment.

Fracture pinch effects resulting from fracture reorientation or a hydraulic annulus can be surmounted during fluid injection. Consequently, an instantaneous pressure drop at shut-in, as seen for perforation friction, may not be observed when either of these effects is present. An additional contrast to perforation friction is that the associated pressure loss depends on the fracture width and hence exhibits continuous variation during injection, rather than being a discrete, time-related event. The step-down test, as discussed in Sidebar 9E, can be applied to develop a more objective prediction of the magnitude of and the mechanism governing near-wellbore pressure loss.

## 9E. Rate step-down test analysis—a diagnostic for fracture entry

Chris Wright, Pinnacle Technologies

The step-down test identifies and quantifies near-wellbore tortuosity. It also quantifies perforation effectiveness and can provide a rough estimate of the number of perforations accepting fluid. With the step-down test, on-site evaluation can be made of potential problems resulting from near-wellbore fracture tortuosity and perforating. Careful analysis of near-wellbore pressure losses, or the fracture entry friction, enables identifying the problem for resolution and subsequently evaluating the effectiveness of the remedial measures employed.

### Rate step-down test concept

Fracture entry friction (Fig. 9E-1) typically is the combination of the perforation friction  $\Delta p_{pf}$  and the tortuosity or near-wellbore friction  $\Delta p_{near\ wellbore}$ . Perforation friction is simply dissipation of the kinetic energy imparted on the fluid as it flows through a small orifice at high velocity. Perforation friction, therefore, is proportional to the injection rate  $q_i$  squared times a proportionality constant:

$$\Delta p_{pf} \equiv k_{pf} q_i^2, \quad (9E-1)$$

where the proportionality constant  $k_{pf}$  is determined in oilfield units by the fluid density  $\rho$ , perforation diameter  $D_p$ , number of perforations  $N$  and discharge coefficient  $C$ :

$$k_{pf} = 0.237 \frac{\rho}{N^2 D_p^4 C^2}. \quad (9E-2)$$

In contrast,  $\Delta p_{near\ wellbore}$  is roughly proportional to the injection rate raised to an exponent that is less than unity because it is due to laminar flow through a narrow channel in the pressure-sensitive near-wellbore region:

$$\Delta p_{near\ wellbore} \equiv k_{near\ wellbore} q_i^\beta, \quad (9E-3)$$

where  $k_{near\ wellbore}$  is a proportionality constant and the power law exponent  $\beta$  is between 0.25 and 1.0, with a value of 0.5 appropriate for most engineering applications. This marked difference in the injection rate dependence of the two components of fracture entry friction clearly distinguishes them in a rate step-down test.

### Test procedure and analysis

1. Measure the surface pressure and slurry rate at a sampling rate of every 1–3 s. In general, the measurement of the bottomhole pressure assists the analysis by avoiding uncertainties regarding the hydrostatic head (e.g., in foam treatments) or large values of wellbore friction (e.g., high-rate tubing treatments).
2. After a breakdown injection or calibration treatment, reduce the injection rate in steps of  $\frac{1}{2}$  to  $\frac{1}{3}$  of the full rate until the rate becomes zero. Hold the rate constant at each step to obtain a stabilized pressure measurement for about 15 to 20 s. The exact rate at each step is not important; rather, the goal is rapid change between the constant rates. The easiest way to achieve this is to take one or two pumps off line at a time. Record the stabilized surface pressure at each rate step for input to the step-down test analysis.
3. Determine the change in the bottomhole pressure for each change in the injection rate. Then plot the fracture entry friction  $\Delta p_{entry}$  versus the injection rate. Fit the points obtained from the rate step-down test with two functions using

$$\Delta p_{entry}(q_i) = (k_{pf} \times q_i^2) + (k_{near\ wellbore} \times q_i^{1/2}). \quad (9E-4)$$

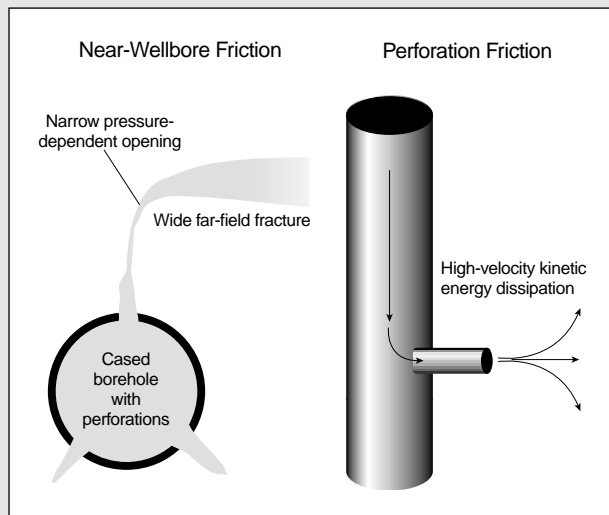


**Figure 9E-1.** Near-wellbore friction and perforation friction exhibit different dependencies on the injection rate.

## 9E. Rate step-down test analysis—a diagnostic for fracture entry (continued)

A dual-curve-fit algorithm can be used to determine the best-fit values of  $k_{pf}$  and  $k_{near\ wellbore}$ , thus defining the respective values of  $\Delta p_{pf}$  and  $\Delta p_{near\ wellbore}$  for any given rate (Fig. 9E-2).

### Limitations using surface pressure measurements

Rate step-down analysis using the surface treating pressure can be difficult if the tubular friction is large compared with  $\Delta p_{entry}$  because the wellbore friction can vary unpredictably from published or expected values. The friction of water can be significantly reduced by small amounts of gel contamination in the wellbore fluids or from a gel hydration unit. Fluid friction with crosslinked gel may vary with small variations in the fluid composition. Foam friction behavior is extremely unpredictable and variable, and the analysis is further complicated by changes in hydrostatic pressure. With turbulent flow (i.e., essentially all water injections), the friction is functionally closer to  $\Delta p_{pf}$ ; with laminar flow (i.e., low injection rates with viscosified fluids), the friction is functionally closer to  $\Delta p_{near\ wellbore}$ .

### Field example

The following example illustrates the usefulness of rate step-down test analysis resulting from the ability to understand and apply the information contained in fracture pressure behavior.

- Severe near-wellbore fracture tortuosity

The rate step-down test following a second injection of potassium chloride (KCl) water showed that the near-wellbore fracture tortuosity in a naturally fractured dolomite formation was extremely high, at 1900 psi (Fig. 9E-3). As a

result, several proppant slugs were planned for as early as possible during the pad period of the propped treatment. Before the slugs reached the perforations, the tortuosity continued to increase, which limited the injection rate so that the surface pressure could be maintained below the acceptable value of 6000 psi. However, when the proppant slugs arrived at the perforations, the tortuosity was significantly reduced, which enabled increasing the injection rate. The propped fracture treatment was successfully placed with 6-ppg maximum proppant loading.

- Poor perforation effectiveness and excessive pad volume

The rate step-down test in Fig. 9E-4 was performed after the first KCl injection. The test clearly shows the dominance of  $\Delta p_{pf}$  (i.e., near-wellbore pressure losses that relate to the injection rate to the 1.94 exponent). The estimated value of  $\Delta p_{pf}$  was about 4500 psi at 18 bbl/min, the equivalent of only 4 of 60 holes open. This condition would not allow fluid injection at the planned rate of 30 bbl/min. The near-wellbore fracture tortuosity was low, at about 50 psi at 18 bbl/min. Additional KCl breakdown injections and surging did not improve the low injectivity.

The well was reperforated with larger holes, which reduced  $\Delta p_{pf}$  to 1500 psi at 18 bbl/min. Following a crosslinked gel calibration treatment (including a 20-bbl, 4-ppg proppant slug), the equivalent of 20 holes was open, which provided an acceptable value of  $\Delta p_{pf}$  of 500 psi at 30 bbl/min. The value of  $\Delta p_{near\ wellbore}$  remained at less than 50 psi, with  $C$  equal to approximately 0.6 for fluid injection.

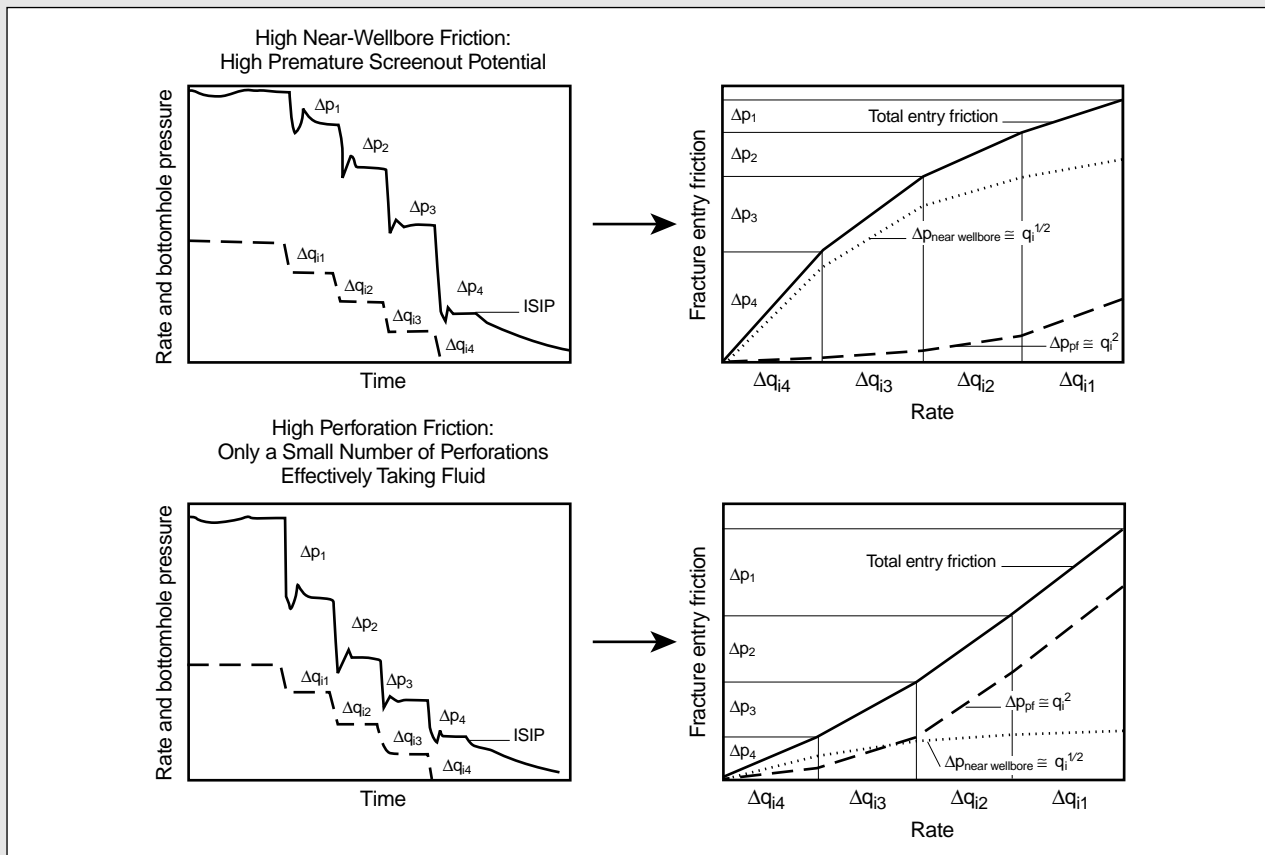


**Figure 9E-2.** The step-down test is conducted to measure  $\Delta p_{pf}$  and  $\Delta p_{near\ wellbore}$ . ISIP = instantaneous shut-in pressure.



## 9E. Rate step-down test analysis—a diagnostic for fracture entry (continued)

### Conclusions

Rate step-down tests are simple to implement and can provide key insights into the nature of the near-wellbore connection between the wellbore and the far-field hydraulic fracture. Although rate step-down tests have limitations, they can provide the rare combination of critical information at minimal additional cost.

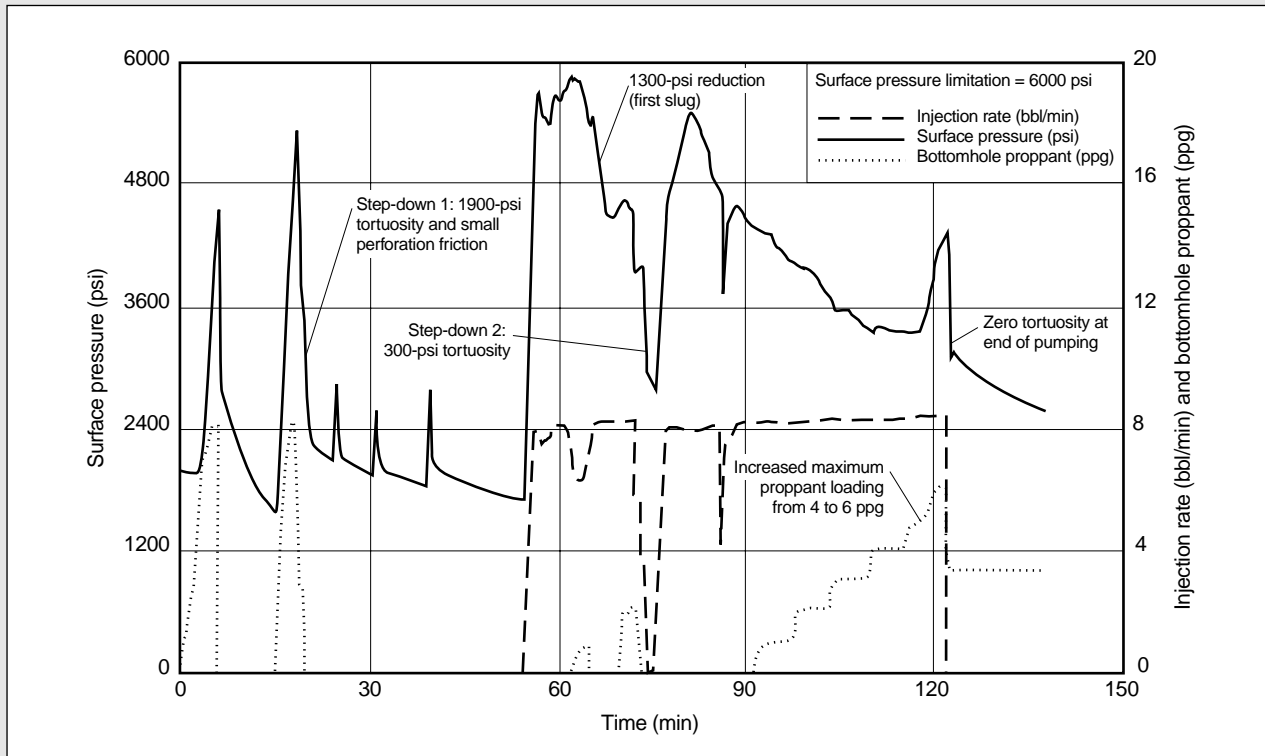


**Figure 9E-3.** Propped treatment example with severe near-wellbore friction (i.e., fracture tortuosity) that was mitigated by pumping two proppant slugs.

## 9-5. Analysis during fracture closure

Fracture behavior during shut-in and prior to closure is governed by the fluid-loss characteristics and the material-balance relation (Fig. 9-2). A mathematical description of the pressure during the fracture closing period can be developed by also incorporating the fracture compliance relation (Eq. 9-21). These two relations and that describing fluid loss are combined to develop the specialized  $G$ -plot, which describes the pressure response during shut-in. Application of the  $G$ -plot is analogous to the Horner analysis used for conventional well tests. The selection of an applicable slope for the  $G$ -plot also has the same uncertain-

ties as those observed with the interpretation of conventional well test data.

Basic decline analysis, outlined initially in this section, follows derivations presented by Nolte (1979, 1986b). A generalization of the technique using analytical extensions to address nonideal conditions (Nolte *et al.*, 1993) is also presented.

### 9-5.1. Fluid efficiency

“Mathematical relations for fluid loss” in the Appendix to this chapter derives the fundamental relations for fluid loss at the end of pumping  $V_{Lp}$  (Appendix Eq. 23) and during the subsequent shut-in

## 9E. Rate step-down test analysis—a diagnostic for fracture entry (continued)

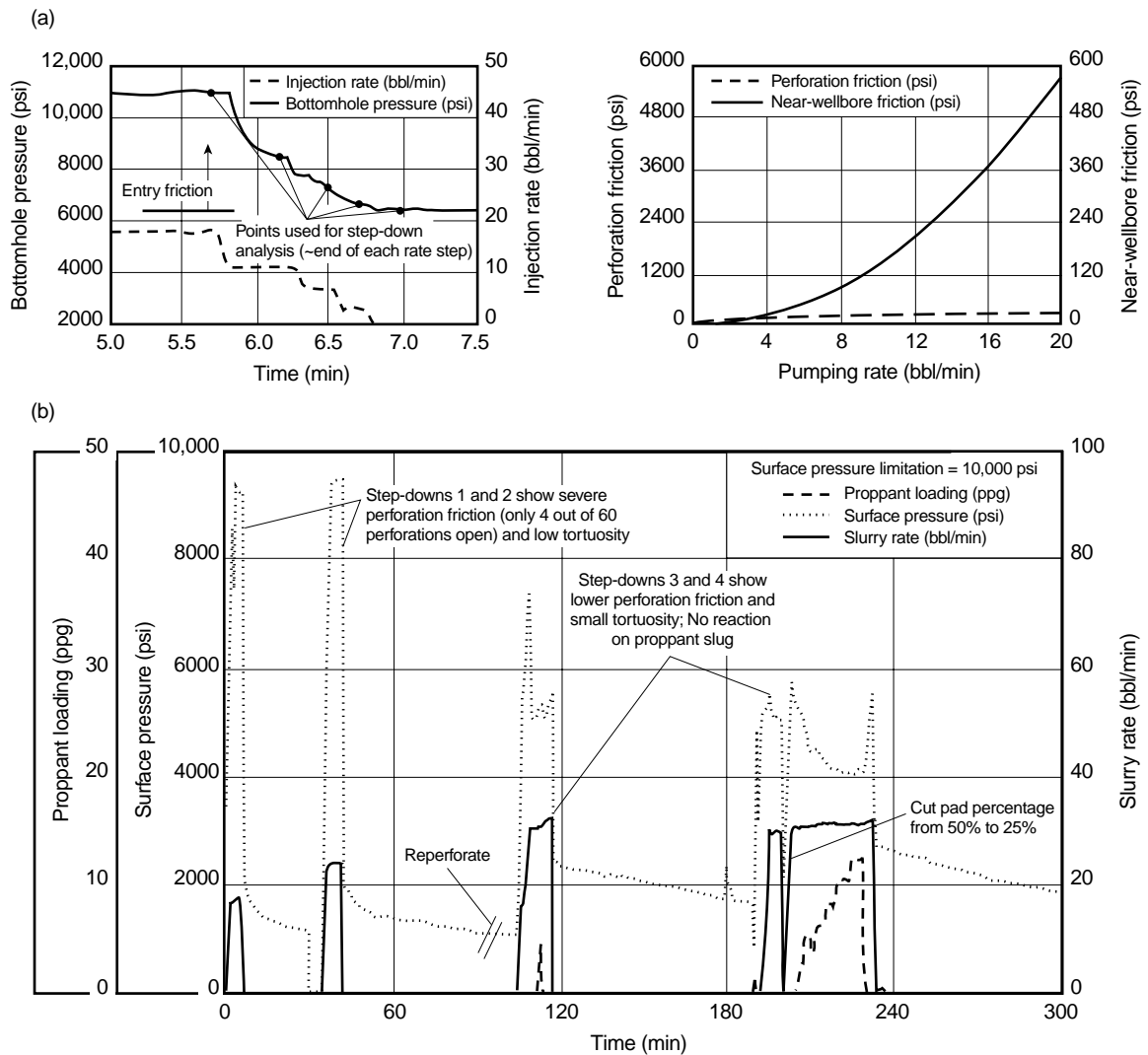


**Figure 9E-4.** The step-down test (a) diagnosed high  $\Delta p_{pf}$  that was remedied by reperforating (b).

period  $V_L$  (Appendix Eq. 27). These equations are in terms of the dimensionless volume-loss function  $g(\Delta t_D)$  and its value at shut-in  $g_0$ . In this context,  $\Delta t_D$  is referred to as the dimensionless time and is defined in Appendix Eq. 15 as the ratio of the shut-in time  $\Delta t$  to the injection (or pumping) time  $t_p$ .

The general expressions for  $g(\Delta t_D)$  and  $g_0$  in Appendix Eqs. 17 and 20, respectively, are based on the assumption of a monotonically increasing fracture area that is defined by a power law expression with an exponent  $\alpha$  (Appendix Eq. 2). The generalized expressions are relatively complicated and therefore

are not routinely used during field practice. Simple analytical approximations, however, can be derived for certain values of  $\alpha$ . These values of  $\alpha$  are valid for the commonly used crosslinked fluids that develop a polymer filter cake along the fracture walls. These fluids are the focus of the remainder of this section. Corresponding relations for the non-wall-building fluids, such as linear gels or viscoelastic surfactant-based fluids, are also discussed in "Mathematical relations for fluid loss" in the Appendix to this chapter.

The value of the area exponent  $\alpha$  can be explicitly determined for two limiting cases of fracture growth.

The lower bound  $\alpha_0$  is for the case in which fracture behavior is dominated by fluid leakoff ( $\eta \rightarrow 0$ ) and the fracture area grows as the square root of time. Treatments in which fluid leakoff is negligible ( $\eta \rightarrow 1$ ) represent the upper bound of the area exponent  $\alpha_1$ , and in this case the area increases approximately linearly with time.

“Mathematical relations for fluid loss” in the Appendix to this chapter provides expressions for  $\alpha_0$  and  $\alpha_1$ . The upper bound  $\alpha_1$  is less than 1. It depends on the fluid rheology exponent  $n$  and is given by Appendix Eq. 40 for the three fracture geometry models. The lower bound  $\alpha_0$  is independent of the fracture geometry and is defined by the fluid filtrate rheology (Appendix Eq. 41). For wall-building fluids, the following bounding values are used to provide simple analytical expressions:

$$\frac{1}{2} < \alpha < 1. \quad (9-43)$$

Generally the fluid efficiency varies throughout the treatment. The efficiency is at its maximum value during the early stage of fracture propagation, and it gradually reduces with fracture propagation because of the increasing surface area available for fluid leakoff. As a result, the fracture area extends with a decreasing exponent. The time variation of the exponent affects the fluid loss because the rate of fluid loss at any time depends on the prior history of the area evolution. However, the effect is small, and to maintain tractable fluid-loss expressions, it is assumed that the exponent remains essentially constant and is defined by the value of efficiency at the end of injection. This value of the exponent can be found by interpolation between its lower bound  $\alpha_0$  of  $1/2$  and upper bound  $\alpha_1$ :

$$\alpha = \alpha_0 + \eta(\alpha_1 - \alpha_0) = \frac{1}{2} + \eta\left(\alpha_1 - \frac{1}{2}\right), \quad (9-44)$$

where  $\alpha_1$  is from Appendix Eq. 40. For typical efficiency values of  $0.3 < \eta < 0.6$ ,  $\alpha$  is equal to approximately 0.6.

A much simplified expression for the fluid-loss volume function  $g(\Delta t_D)$  and its initial value  $g_0$  can then be developed by using the bounding values of  $\alpha$  (Eq. 9-43). These are given by Appendix Eqs. 29 and 30, respectively, and graphically presented in Fig. 9-27. Throughout this development, the difference between the upper and lower bounds of  $g(\Delta t_D)$  is nominal, as illustrated on the figure. This observation

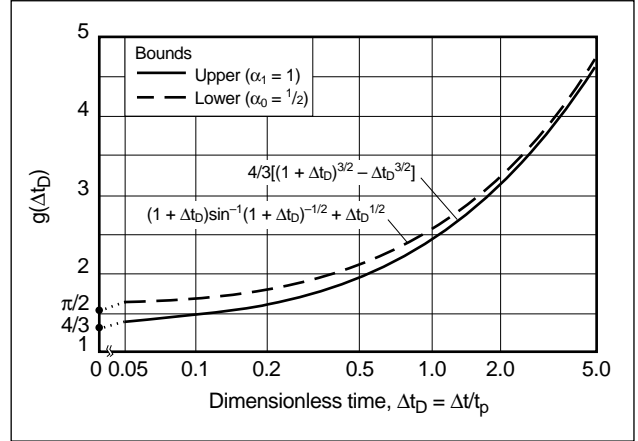


**Figure 9-27.** Bounding values of the dimensionless volume function  $g(\Delta t_D)$  for fracture closure (Nolte, 1986a).

implies that an approximation of  $g(\Delta t_D)$  based on a suitable value for  $\alpha$ , such as that suggested by Eq. 9-44, should be sufficient for field applications. The approximation is best developed by interpolation using its bounding values and a particular value of  $\alpha$ :

$$g(\Delta t_D, \alpha) = g\left(\Delta t_D, \alpha = \frac{1}{2}\right) + \eta(2\alpha_1 - 1) \times \left\{ g(\Delta t_D, \alpha = 1) - g\left(\Delta t_D, \alpha = \frac{1}{2}\right) \right\}, \quad (9-45)$$

where the values of  $g(\Delta t_D)$  at  $\alpha = 1/2$  and  $\alpha = 1$  are from Appendix Eq. 29.

The efficiency of a calibration treatment can be derived from the relation that the fracture volume at the end of injection equals the total volume of fluid lost during shut-in (Eq. 9-8):

$$\eta = \frac{V_{fp}}{V_i} = \frac{V_{Ls}(\Delta t_{cD})}{V_{Lp} + V_{Ls}(\Delta t_{cD})}. \quad (9-46)$$

Substituting Appendix Eqs. 22 and 26 into Eq. 9-46 produces the following expression for the efficiency:

$$\eta = \frac{g(\Delta t_{cD}) - g_0}{g(\Delta t_{cD}) + (\kappa - 1)g_0}, \quad (9-47)$$

where the spurt factor  $\kappa$  is defined in Appendix Eq. 24.  $\kappa$  denotes the ratio of fluid loss for a case with spurt to that without spurt. For the propagation period,  $\kappa = 1$  for no spurt; more generally,

$$\frac{\kappa - 1}{\kappa} = \frac{\text{spurt volume loss}}{\text{total leakoff volume loss}}. \quad (9-48)$$

Figure 9-28 shows the relation between the treatment efficiency  $\eta$  and the dimensionless shut-in time when the fracture closes  $\Delta t_{cD}$  for no spurt (i.e.,  $\kappa = 1$ ). The plot was generated in terms of the two bounding values of  $\alpha$  from Eq. 9-43. The equation and figure are independent of the geometry model and enable defining the efficiency for proppant scheduling (see Sidebar 6L).

The fracture penetration is determined using the following equation, which is obtained by combining Eq. 9-6 and Appendix Eq. 22:

$$A_f = \frac{(1-\eta)V_i}{2r_p \kappa C_L \sqrt{t_p} g_0}, \quad (9-49)$$

where the fracture surface area  $A_f$  for the three basic models is from Eq. 9-29,  $r_p$  is the ratio of permeable (or fluid-loss) area to fracture area, and  $C_L$  is the fluid-loss coefficient. The average fracture width is then obtained by using Eqs. 9-4 and 9-49:

$$\langle \bar{w} \rangle = \frac{V_{fp}}{A_f} = \frac{2\eta r_p \kappa C_L \sqrt{t_p} g_0}{1-\eta}. \quad (9-50)$$

Finally, the maximum fracture width immediately after shut-in for the three basic models is obtained as

$$w_{max,si} = \langle \bar{w} \rangle \begin{cases} 4/(\pi\beta_s) & \text{PKN} \\ 4/\pi & \text{KGD} \\ 3/2 & \text{Radial,} \end{cases} \quad (9-51)$$

where  $\langle \bar{w} \rangle$  is from Eq. 9-50 and  $\beta_s$  is from Eq. 9-20. The maximum width at the end of pumping is obtained similarly:

$$w_{max,p} = w_{max,si} \begin{cases} \beta_s/\beta_p & \text{PKN} \\ \approx 1 & \text{KGD} \\ \approx 1 & \text{Radial.} \end{cases} \quad (9-52)$$

The values for the PKN fracture geometry model are from Nolte (1979), whereas those for the KGD and radial models assume an elliptical width profile (Eqs. 9-11 and 9-13, respectively) and no change in the fracture volume immediately before and after shut-in. The value of  $w_{max,p}$  for the radial model from Eq. 9-52 is valid only for a line-source fluid entry condition (Fig. 9-6). The high entry velocity and pressure gradient during pumping for the point-source case produce a nonelliptical width profile (Geertsma and de Klerk, 1969).

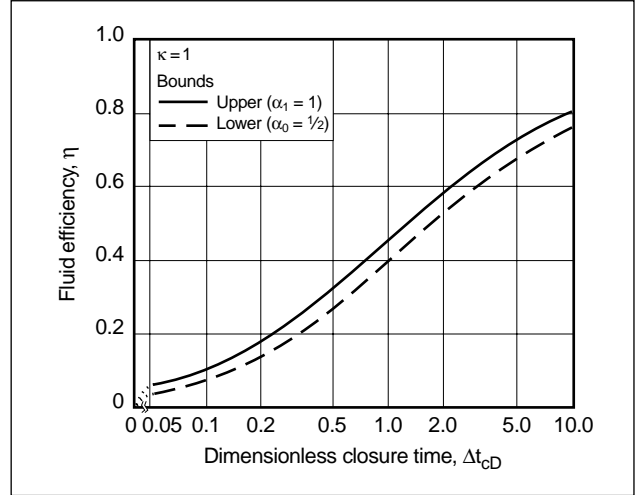


**Figure 9-28.** Relationship between efficiency and closure time (Nolte, 1986a).

### 9-5.2. Basic pressure decline analysis

The previous section presents relations for the fracture geometry parameters from simple considerations of material balance and the assumption of power-law-based fracture area growth. The basic decline analysis assumes that the end of injection marks the termination of additional fracture extension and that the change in the fracture volume during shut-in is attributed entirely to the change in the average fracture width during this period. The latter assumption also implies that the fracture area is invariant throughout the shut-in period. The fracture geometry models relate the fracture width to the net pressure through their compliance. Consequently, the combination of the compliance and fracture geometry equations enables determination of the fluid-leakoff coefficient on the basis of the rate of pressure decline during shut-in.

Using the material-balance relation during shut-in from Eq. 9-7, it follows for a constant area that

$$-\frac{dV_f(\Delta t)}{d\Delta t} = -A_f \frac{d\langle \bar{w} \rangle}{d\Delta t} = q_L. \quad (9-53)$$

For an assumed constant fracture compliance that is ensured by a constant area, differentiation of Eq. 9-21 and substitution in Eq. 9-53, with the expression for the fluid leakoff rate  $q_L$  from Appendix Eq. 11, results in

$$-A_f c_f \frac{dp_{net}}{d\Delta t} = \frac{2r_p C_L A_f}{\sqrt{t_p}} f(\Delta t_D), \quad (9-54)$$

where the fluid-loss rate function  $f(\Delta t_D)$  is from Appendix Eq. 16 and equals the derivative of  $g(\Delta t_D)$ . Equation 9-54 can be integrated between  $\Delta t_D = 0$  and  $\Delta t_D$  (assuming a constant value of  $p_c$ ):

$$p_{ws} - p_w(\Delta t_D) = \frac{\pi r_p C_L \sqrt{t_p}}{2c_f} G(\Delta t_D), \quad (9-55)$$

where  $p_{ws}$  is the bottomhole pressure at shut-in. The function  $G(\Delta t_D)$  was introduced by Nolte (1979):

$$G(\Delta t_D) = \frac{4}{\pi} [g(\Delta t_D) - g_0]. \quad (9-56)$$

This function shares the same bounds for  $\alpha$  as  $g$  (Eq. 9-45).

Castillo (1987) recognized that under ideal conditions, Eq. 9-55 linearly relates the pressure versus the  $G$ -function defined in Eq. 9-56 (Fig. 9-29) with a negative slope  $p^*$ :

$$p^* = \frac{\pi r_p C_L \sqrt{t_p}}{2c_f}. \quad (9-57)$$

Combining Eq. 9-57 with expressions for the fracture compliance  $c_f$  from Eq. 9-22 yields the following equation for determining the fluid-leakoff coefficient:

$$C_L = \frac{p^* \beta_s}{r_p \sqrt{t_p} E'} \begin{cases} h_f & \text{PKN} \\ 2L & \text{KGD} \\ (32/3\pi^2)R & \text{Radial.} \end{cases} \quad (9-58)$$

This relation provides a direct solution for the PKN model (assuming that  $h_f$  is known). For the other models, the penetration is required and must be determined first. This is achieved by substituting  $C_L$  from Eq. 9-58 into Eq. 9-49:

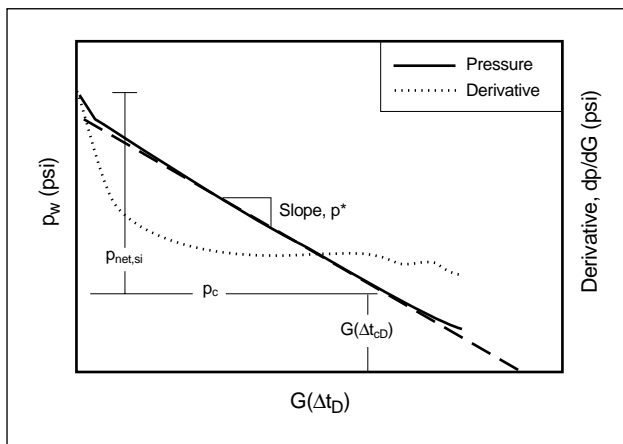


**Figure 9-29.** G-plot of the G-function response approximating idealized fracture propagation conditions.

$$\left. \begin{matrix} L \\ L^2 \\ R^3 \end{matrix} \right\} = \frac{(1-\eta)V_i E'}{2g_0 \kappa \beta_s p^*} \begin{cases} 1/(2h_f^2) & \text{PKN} \\ 1/(4h_f) & \text{KGD} \\ 32/3\pi^3 & \text{Radial.} \end{cases} \quad (9-59)$$

This equation provides the appropriate value of penetration for determining  $C_L$  from Eq. 9-58.

The fluid efficiency can be obtained by substituting the definition of the  $G$ -function from Eq. 9-56 into Eq. 9-47 with the approximation  $g_0 = \pi/2$  for  $\alpha = 1/2$ :

$$\eta \approx \frac{G_c}{2\kappa + G_c}, \quad (9-60)$$

where  $G_c$  is the value of  $G(\Delta t_D)$  at closure (i.e.,  $\Delta t_D = \Delta t_{cD}$ ). The approximation provided by Eq. 9-60 is exact at  $\eta \rightarrow 0$ .

Martins and Harper (1985) extended the application of pressure decline analysis to the case of expanding confocal ellipses. This propagation model is relevant to the early stage of propagation, before the radial model is applicable, and includes the KGD and radial models as limiting cases. Its consideration requires including the appropriate definition of the fracture compliance  $c_f$  in Eq. 9-57.

### 9-5.3. Decline analysis during nonideal conditions

The basic pressure decline analysis (see Section 9-5.2) implicitly assumes that

- Fluid loss is based on Carter's (1957) formulation of the square root of exposure time (see "Mathematical relations for fluid loss" in the Appendix to this chapter) and is characterized by a constant leakoff coefficient that is independent of pressure.
- Fracture area evolution with time is described by a power law area relation during injection.
- Fracture area and compliance are constant during the closing phase.
- Fracturing fluid is incompressible.
- Formation closure pressure is constant.

All these assumptions are seldom met in routine field practice. A departure from any of them produces a  $G$ -plot with a continuous curve (i.e., not a straight line with a constant slope). In such cases, the application of basic pressure decline analysis generally predicts optimistic estimates of the fluid-leakoff coefficient and treatment efficiency. However, a rigorous

characterization of the deviations introduced to the analysis when its assumptions are violated results in an overly complex analysis. Fortunately, most of the deviations from nonideal conditions are amenable to relatively straightforward analytical modifications.

Corrections to the basic pressure decline analysis are presented in this section. Change in the fracture area during shut-in and a pressure-dependent fluid-loss coefficient are discussed because of their common occurrence. Considerations for fluid compressibility, thermal effects and varying formation closure stress (i.e., poroelasticity) were presented by Nolte *et al.* (1993) and are not repeated here. Their effects were found to be minimal when the procedure outlined in Section 9-5.4 was applied for the decline analysis.

- Fracture geometry change during shut-in

Both the fracture length and height can change during the shut-in period. The fracture penetration initially increases before eventually receding back toward the wellbore. Continued fracture extension occurs because of the redistribution of stored volume from the larger width region near the wellbore to the fracture tip region. Simultaneously, the height recedes from any higher stress barriers because of the reducing fluid pressure (Fig. 9-30). This variation in fracture geometry changes the character of the otherwise straight-line  $G$ -plot and calls for additional considerations in using basic pressure decline analysis to estimate the fluid-loss parameters.

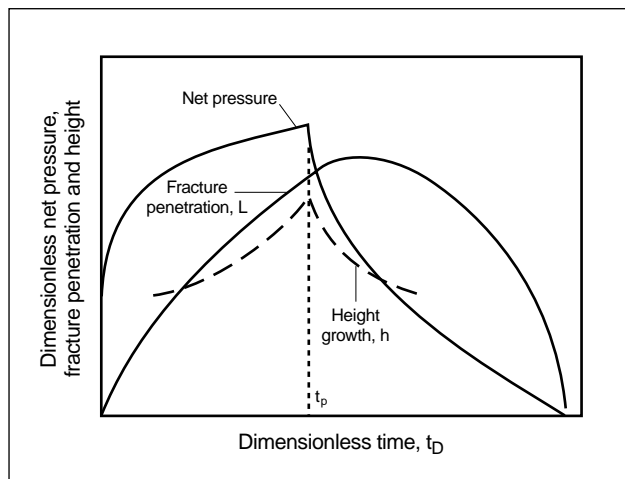


**Figure 9-30.** Time variation of the net pressure and fracture geometry for the PKN fracture geometry.

- Change in fracture penetration

Following shut-in, the initial extension of the fracture penetration increases the area exposed to fluid loss. The correspondingly increased fluid-loss rate relative to the case of constant area results in a correspondingly steeper initial slope of the  $G$ -plot. The subsequently reduced rate of pressure decline during recession results from a decrease in the fracture area and elimination of the region of relatively higher fluid loss near the fracture tip. The consequences of fracture penetration change during shut-in are a concave-upward profile on the  $G$ -plot (Fig. 9-31a) and a continuous change in its slope  $m_G$ .

The corrected slope  $p^*$  that defines the fluid-loss coefficient based on Eqs. 9-54 and 9-58 represents an instantaneously unchanged product of compliance (e.g., dependent on  $\beta_s$ ) and area (i.e.,  $d(c_f A_f)/dt = 0$ ). For the three fracture geometry models, this condition occurs near the transition between extension and recession (Fig. 9-30). Extensive numerical simulation shows that this condition occurs when the wellbore net pressure reaches about three-quarters of its value at the shut-in net pressure  $p_{net,si}$ :

$$\frac{p_{net}}{p_{net,si}} = \frac{3}{4}. \quad (9-61)$$

Thus, the slope of the  $G$ -plot can be designated as  $m_{3/4}$  and is evaluated at the  $3/4$  point. This slope is used in conjunction with Eq. 9-58 to eliminate the effect of fracture penetration changes during shut-in. The validity of selecting the slope at the  $3/4$  point has been experimentally established by de Pater *et al.* (1996).

- Fracture height recession

Fracture height growth into higher stress bounding zones results in an increase in the fracture compliance, as shown in Fig. 9-7. Equation 9-57 also indicates that the rate of pressure decline is inversely proportional to the average fracture compliance. Therefore, substantial height growth during injection leads to a decreased compliance during the initial shut-in period and reduces the rate of pressure decline until the height recedes from the bounding zones. Figure 9-31b depicts this initial period of reduced slope on the  $G$ -plot.

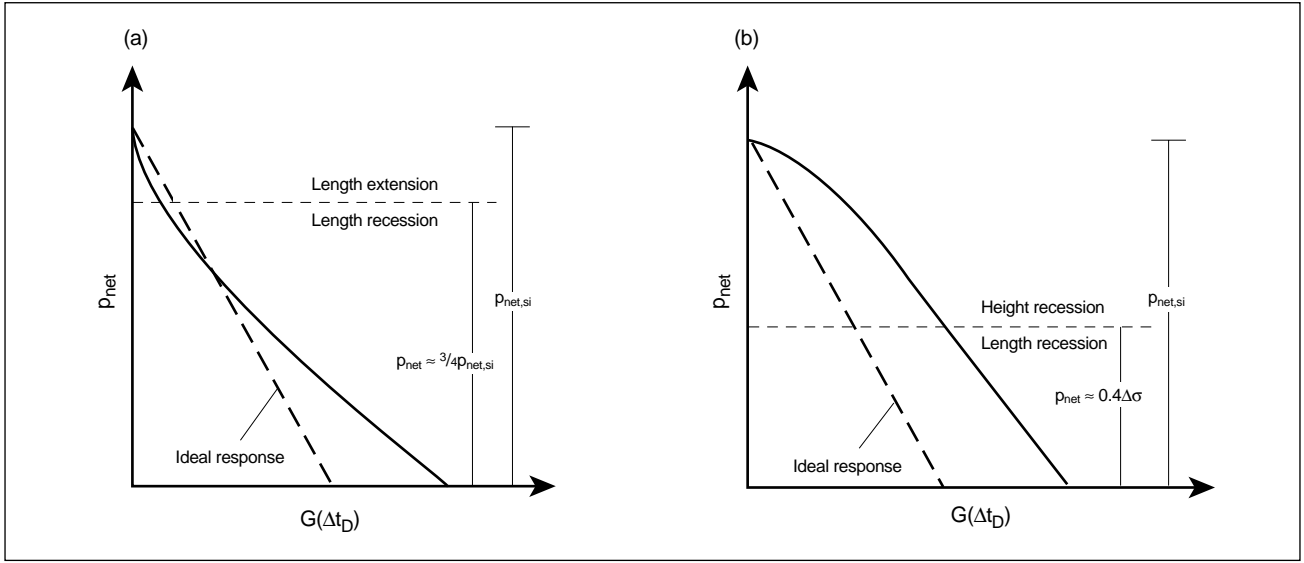


**Figure 9-31.** Conceptual  $G$ -plot response for nonideal fracture behavior during shut-in for (a) fracture extension and (b) height growth.

Complete height recession from the bounding zones occurs when the wellbore net pressure equals about 0.4 times the stress difference  $\Delta\sigma$ . Also from Fig. 9-7, the net pressure at shut-in is about  $0.8\Delta\sigma$  when significant height growth occurs. Therefore, complete height recession from the bounding zones occurs when the wellbore net pressure reduces to a value that is approximately one-half of that at shut-in. Following fracture withdrawal into the primary reservoir zone, the pressure subsequently declines faster than the initially reduced rate and as for a fracture geometry where no height growth occurs. Thus, fracture height growth into the bounding zones changes the otherwise straight-line  $G$ -plot into a convex-upward curve (Fig. 9-31b).

From this discussion, it is clear that when height growth occurs, the fracture is still receding from its bounding zones when without height recession the fracture area is momentarily stationary (i.e.,  $p_{net}/p_{net,si} = 3/4$ ). Therefore, the fluid-leakoff coefficient is underestimated by using the slope at the  $3/4$  point in Eq. 9-58. The equation also assumes constant compliance and hence is valid only after complete height recession into the primary reservoir zone. Consequently, the decline analysis requires that the  $G$ -function slope be evaluated after the period of height recession.

Height growth into a higher stress barrier requires a previously increasing net pressure response. It therefore is not consistent with the basic requirements of the radial and KGD models, both of which exhibit decreasing net pressures. Height growth should be anticipated only for PKN-type behavior, with an increasing and relatively large net pressure during injection. As a result, for the PKN model with significant height growth, the correction  $m_{Gc}$  is required to the slope of the  $G$ -plot following the termination of height recession and prior to fracture closure. The corrected slope  $m'_G$  that accounts for length recession during this latter phase can be inferred from numerical simulations and the material-balance relation during shut-in (Nolte, 1991):

$$m'_G \approx m_{Gc} \frac{1}{\beta_s} \sqrt{(1 + \Delta t_{cd})} f_D(\Delta t_{cd}), \quad (9-62)$$

where  $f_D(\Delta t_D)$  is the dimensionless fluid-loss rate function and is given in Appendix Eq. 28. The correction in Eq. 9-62 for fracture height recession complements Eq. 9-61 for length change to account for PKN-type behavior during the shut-in process.

- Variable fluid-loss coefficient

Basic pressure decline analysis assumes that the fluid-loss volume is defined by a constant leakoff coefficient. This assumption has been shown to

be generally true (Mayerhofer *et al.*, 1991; see Chapter 8) for fluid leakoff governed by a polymer wall cake (i.e.,  $C_L \approx C_w$ ). Fluid loss, however, is pressure dependent when it is controlled by either the invasion of fracturing fluid filtrate into the reservoir (i.e., filtrate-controlled fluid-loss coefficient  $C_v$ ) or reservoir properties (i.e., compressibility control leakoff coefficient  $C_c$ ), as discussed in Section 6-4.

#### – Reservoir-controlled leakoff

Reservoir-controlled leakoff commonly occurs when reservoirs with highly viscous oil are fractured. It can also occur in low-permeability reservoirs that exhibit a high water saturation. In the case of reservoir-controlled leakoff, the slope of the  $G$ -plot at the  $\frac{3}{4}$  point can be modified to include the pressure dependency on fluid leakoff (Nolte *et al.*, 1993):

$$m'_G = \gamma K_c m_{3/4}, \quad (9-63)$$

where the product  $\gamma K_c$  is applied in the same manner as the correction for mitigating height recession (i.e., Eq. 9-62) and

$$\gamma = 1 + \beta_s p_{DLs}, \quad (9-64)$$

where the dimensionless pressure difference  $p_{DLs}$  for pressure-dependent leakoff is defined as

$$p_{DLs} = \frac{p_{ws} - p_c}{p_c - p_i}, \quad (9-65)$$

where  $p_i$  is the reservoir pressure.

The correction factor  $K_c$  in Eq. 9-63 is defined in Fig. 9-32 for various values of  $\eta$  and  $p_{DLs}$ . This correction factor enables evaluation of the slope of the  $G$ -plot at a common reference point (i.e., when  $p_{net}/p_{net,si} = \frac{3}{4}$ ) for the decline analysis. For typical values of efficiency  $\eta < 0.5$  and  $p_{DLs} < 0.5$ , the figure indicates that  $K_c$  is equal essentially to 1.

The corrected  $G$ -function slope from Eq. 9-63 can be used with Eq. 9-58 for estimating the effective fluid-leakoff coefficient  $C_{ce}$  during injection.  $C_{ce}$  is related to the reservoir-controlled fluid-loss coefficient  $C_c$  (see Section 6-4.3) evaluated at the pressure difference  $\Delta p = p_c - p_i$ :

$$C_{ce} = \gamma C_c. \quad (9-66)$$

$C_{ce}$  is equivalent to the conventional pressure-independent fluid-leakoff coefficient  $C_L$  and can

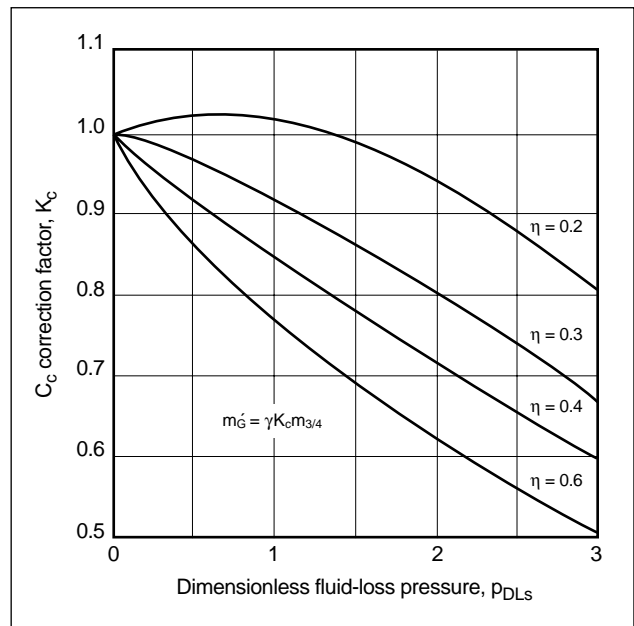


**Figure 9-32.**  $G$ -plot slope correction factor  $K_c$  for reservoir-controlled leakoff (Nolte *et al.*, 1993).

be substituted into Eqs. 9-49 and 9-50 for calculating the fracture area and width, respectively.

#### – Fracturing-fluid-filtrate-controlled leakoff

Filtrate-dominated leakoff is more characteristic of high-permeability reservoirs where the fracturing fluid itself (e.g., viscoelastic surfactant or crosslinked polymer) invades the reservoir. It can also dominate in low-permeability formations at irreducible water saturation, with small values of relative permeability to the fracturing fluid filtrate. This fluid-loss mechanism depends on the square root of the pressure difference between the fracture and the reservoir (see Section 6-4.2). The nonlinear dependence precludes a derivation similar to that for reservoir-controlled leakoff (Nolte *et al.*, 1993). However, Eqs. 9-63 and 9-66 provide an acceptable approximation if they are modified to reflect the square-root pressure behavior. The corrected  $\frac{3}{4}$  slope can be obtained in a manner analogous to Eq. 9-63:

$$m'_G = (\gamma K_c)^{1/2} m_{3/4}. \quad (9-67)$$

The equivalent filtrate-controlled leakoff coefficient  $C_{ve}$  can be defined similarly to Eq. 9-66:

$$C_{ve} = \gamma^{1/2} C_v, \quad (9-68)$$



where  $\gamma$  is defined by Eq. 9-64 and  $C_v$  is the viscosity control leakoff coefficient (see Section 6-4.3) evaluated at  $\Delta p = p_c - p_i$ . Like for Eq. 9-63, the correction factor  $K_c$  is obtained from Fig. 9-32.

In summary, for fluid loss governed by a polymer filter cake, the fluid-loss behavior is independent of pressure, and the analysis presented for Eq. 9-61 or 9-62 is used. Closed-form corrections of the type presented in Eq. 9-63 extend the basic decline analysis for the reservoir-controlled fluid-loss mechanism, such as for heavy-oil-bearing reservoirs. Filtrate-controlled behavior, which is more common in the stimulation of high-permeability reservoirs, shows a nonlinear dependence on pressure. The corrections developed for the reservoir-controlled leakoff case can be adapted to quantify these effects.

#### 9-5.4. Generalized pressure decline analysis

As discussed in the preceding section, commonly occurring nonideal conditions modify the otherwise straight-line behavior of the  $G$ -plot. The  $3/4$  point (i.e.,  $p_{net}/p_{net,si} = 3/4$ ) provides a reference to extend basic pressure decline analysis for effects resulting from change in the fracture length. In addition, the correction for recession following fracture height closure or pressure-dependent leakoff complements the  $3/4$ -point slope with the following unified methodology for the analysis of shut-in pressure decline before fracture closure:

1. For all geometry models, find the slope at  $p_{net}/p_{net,si} = 3/4$  (i.e.,  $m_{3/4}$ ).
2. If the PKN model is applicable (determined by the analysis of pumping pressure) and pressure-dependent leakoff is not expected, determine the slope at closure  $m_{Gc}$ . Obtain the corrected slope at closure  $m_G'$  using Eq. 9-62.
3. The value of  $p^*$  is selected from the following equation on the basis of the applicable fracture geometry model:

$$p^* = \begin{cases} \max(m_{3/4}, m_G') & \text{PKN} \\ m_{3/4} & \text{KGD} \\ m_{3/4} & \text{Radial.} \end{cases} \quad (9-69)$$

4.  $G_c$  is corrected to include effects resulting from nonideal conditions on the  $G$ -plot by defining a corrected value of  $G$  at closure:

$$G^* = \frac{p_{net,si}}{p^*}, \quad (9-70)$$

where  $p_{net,si}$  is the net pressure at shut-in.

5. The fluid efficiency is determined by modifying Eq. 9-60:

$$\eta = \frac{G^*}{2\kappa + G^*}. \quad (9-71)$$

6. Finally,  $C_L$  is estimated by applying Eq. 9-58 with  $p^*$  determined using Eq. 9-69.

In the absence of height growth and pressure-dependent fluid loss,  $m_{3/4}$  and  $m_G'$  are expected to be equal. With height growth but no pressure-dependent fluid loss,  $m_G'$  is expected to be greater than  $m_{3/4}$  and provide a better estimate for  $p^*$ . Alternatively, for no significant height growth but with pressure-dependent fluid loss,  $m_{3/4}$  is expected to be greater than  $m_G'$  (Eq. 9-62) and provide a better estimate for  $p^*$ .

The relative magnitudes for  $m_{3/4}$  and  $m_G'$  provide a diagnostic to infer the occurrence of pressure-dependent leakoff. An alternative diagnostic is the  $G$ -function semilog derivative, discussed in Sidebar 9F. If pressure-dependent leakoff conditions occur, Eqs. 9-63 through 9-68 should be used to determine the effective fluid-leakoff coefficient. The primary deficiency of this method is the selection of an appropriate slope when both significant height growth and pressure-dependent fluid loss occur.

The  $3/4$  point provides a common reference point, where the slope of the  $G$ -plot can be used to account for nonideal effects. Accordingly, this generalized evaluation methodology is commonly referred to as the  $3/4$  rule for pressure decline analysis.

- Example field application of PKN fracture decline analysis

Shut-in pressures monitored during the calibration treatment described in Section 9-4.4 are analyzed in this example to illustrate the application of decline analysis to a PKN-type fracture (Fig. 9-8). The relevant formation mechanical parameters are listed in Table 9-1.

The plane strain modulus  $E'$  is derived from  $E$  and  $\nu$ :

## 9F. G-function derivative analysis

R. D. Barree, Marathon Oil Company

Ideal fracture closing behavior is characterized by a straight-line pressure response on the  $G$ -plot, as described in Section 9-5.2. Extensions of this analysis use the derivative of pressure with respect to the  $G$ -function ( $dp/dG$ ; Castillo, 1987) and the semilog or superposition derivative ( $Gdp/dG$ ; Barree and Mukherjee, 1996). The characteristics of these added diagnostic curves provide a qualitative indication of the change in fracture geometry during shut-in. They also describe the dominant leakoff mechanisms. This information can be reconciled with the observed pressure behavior during pumping, knowledge of in-situ stresses and rock properties, and postfracturing measurements (e.g., tracer and temperature logs) for an improved understanding of the fracturing process.

The diagnostics and analysis can be performed on site in a simple and straightforward manner using the measured pressure during shut-in. Values of the pressure  $p$  and the derivatives  $dp/dG$  and  $Gdp/dG$  are plotted on Cartesian axes against the  $G$ -function. The plot is interpreted primarily by inspection. As with a type-curve analysis, characteristic shapes in the curves are identified. Once the general nature of the falloff behavior is developed, specific numerical values (e.g., closure pressure and fissure dilation pressure) can be determined.

The following field examples illustrate the application of these diagnostics to characterize nonideal fracture and fluid-loss behavior and the associated characteristic curve shapes.

### Fracture height recession

Height recession during shut-in from high-stress bounding layers results in changes in the fracture compliance and total fracture surface area relative to the leakoff (i.e., permeable) area (Figs. 9-7 and 9-36). This behavior causes several obvious signatures on the pressure and derivative plots (Fig. 9F-1). The pressure versus  $G$ -function curve shows a distinct downward bend as height recession progresses, as discussed in Section 9-5.3. This behavior results in an increasing magnitude of the  $dp/dG$  curve and the superposition  $Gdp/dG$  curve.

Figure 9F-1 elaborates this diagnostic using shut-in pressure measurements acquired during a water injection test in a carbonate formation. Injection was confined to a relatively small perforated interval surrounded by several hundred feet of similar lithology. The continuously increasing values of  $dp/dG$  and  $Gdp/dG$  indicate continuous height recession during closure. The figure also suggests that complete fracture closure has not occurred by the end of the shut-in period.

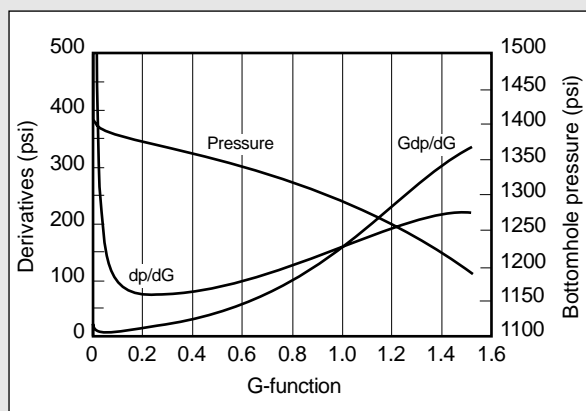


**Figure 9F-1.** Pressure derivative analysis for fracture height growth.

### Fissure-dominated leakoff

Fissure-dominated leakoff is illustrated by the analysis of a prefracture injection test (Fig. 9F-2) conducted in a low-permeability sandstone formation. The data were acquired using a surface pressure gauge and show pressure-dependent leakoff. The end of pressure-dependent leakoff is clearly indicated by the derivative becoming constant. This point corresponds to the end of a hump on the superposition  $Gdp/dG$  curve, following which the curve becomes linear. This early-time hump above the extrapolated straight line on the superposition curve, along with the sharply curving derivative, is a signature of pressure-dependent leakoff resulting from fissures. Fissure-dominated leakoff persists up to a  $G$ -function value of about 0.75, as shown by the onset of the straight-line section of the superposition derivative. After fissure closure the derivative is constant and the superposition curve is linear (i.e., constant slope), both indicating a constant leakoff coefficient. The pressure data alone provide a less clear indication of the end of pressure-dependent leakoff. Closure of the primary hydraulic fracture is apparent on the derivative and superposition curves at a  $G$ -function value of about 2.3, corresponding to a pressure of approximately 5100 psi. The instantaneous shut-in pressure (ISIP) is nearly 1500 psi higher than the closure pressure.

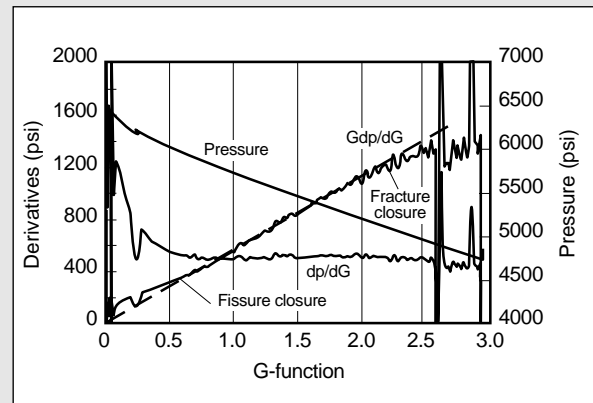


**Figure 9F-2.** Pressure derivative analysis for fissure-dominated leakoff.

### Pressure-dependent leakoff

As discussed in Section 9-5.3, the value of  $dp/dG$  can continuously decrease during the preclosure shut-in period. This behavior results because of change in the fracture penetration during shut-in, and it may occur in spite of a constant value of the fluid-loss coefficient  $C_L$ . The diminishing rate of change on the  $G$ -plot is magnified if the fluid leakoff is predominantly pressure dependent (i.e., filtrate or reservoir controlled). In this case, the superposition analysis provides a distinct signature that identifies the occurrence of pressure-dependent fluid loss, despite its similarity to fracture length change during the shut-in period.

Figure 9F-3 shows that pressure-dependent fluid loss is characterized by a superposition derivative that approaches a straight line after a short shut-in period. The straight-line period is unaffected by change in the fracture penetration during shut-in, and its slope is proportional to the total fluid leak-off. The early-time  $Gdp/dG$  curve has a much steeper slope, and it falls below the straight-line extrapolation (i.e., the hump is below the extrapolated  $Gdp/dG$  curve). This pattern differentiates fracture extension or recession from true pressure-

## 9F. G-function derivative analysis (continued)

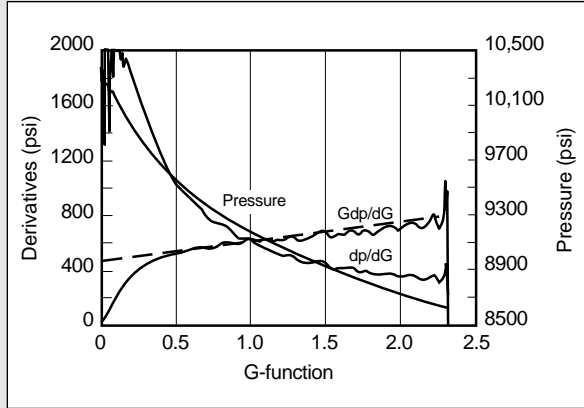


**Figure 9F-3.** Pressure derivative analysis for filtrate- or reservoir-controlled leakoff.

dependent leakoff. One ambiguity exists, however. The same pattern can be generated by extension of a preexisting natural fissure set oriented nearly parallel to the hydraulic fracture or leakoff into a swarm of parallel fractures created by the fracturing process.

$$E' = \frac{E}{1 - \nu^2} = \frac{5.3 \times 10^5}{1 - 0.22^2} = 5.6 \times 10^5 \text{ psi.} \quad (9-72)$$

Similarly,  $\beta_s$  is determined from Eq. 9-20 using the fluid rheology exponent  $n = 0.44$  and viscosity profile parameter  $a = 0$ :

$$\beta_s = \frac{(2)(0.44) + 2}{(2)(0.44) + 3 + 0} = 0.74.$$

The fracture height  $h_f$  selected as the zone of primary initial confinement is determined from well logs (Fig. 9-8a) to be 24 ft. Because separation occurs between the resistivity curves throughout this pay interval, fluid leakoff is inferred to occur over the entire initial fracture height. Thus, the ratio  $r_p$  of the leakoff height to the initial fracture height is unity.

The fracture closure pressure is determined from a step rate test (see “Estimating closure pressure” in the Appendix to this chapter) and pressure derivative analysis (Fig. 9-9) to be 8910 psi. The dimensionless time at closure is

$$\Delta t_{cD} = \frac{\Delta t_c}{t_p} = \frac{7.0}{12.0} = 0.58. \quad (9-73)$$

The steps outlined previously in this section are then applied to determine the efficiency and fluid-leakoff coefficient.

The  $3/4$ -point pressure  $p_{3/4}$  is derived from an instantaneous shut-in pressure  $p_{ISI}$  of 9012 psi and the estimated 8910-psi  $p_c$ :

$$\begin{aligned} p_{3/4} &= p_c + \frac{3}{4}(p_{ISI} - p_c) = p_c + \frac{3}{4}p_{net,si} \\ &= 8910 + \frac{3}{4}(9012 - 8910) = 8987 \text{ psi.} \quad (9-74) \end{aligned}$$

The  $G$ -function slope  $m_{3/4}$  at this  $3/4$  point is estimated to be 136 psi in Fig. 9-33. For the PKN fracture geometry model, the slope prior to closure  $m_{Gc}$  is inferred to be 123 psi. This slope is corrected for the length recession following the termination of height growth using Eq. 9-62:

$$m'_G = 123 \frac{1}{0.74} \sqrt{1 + 0.58} \times 0.93 = 194.$$

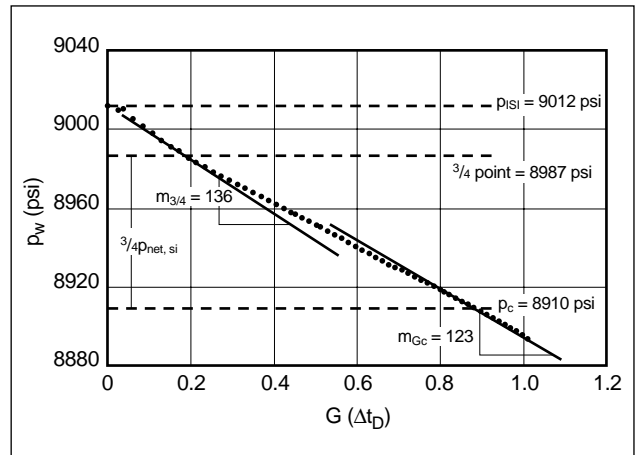


**Figure 9-33.** Pressure decline analysis for a PKN fracture.

The value of  $m'_G$  greater than that of  $m_{3/4}$  signifies fracture height growth, which agrees with the pressure derivative analysis for the injection pressure in Section 9-4.4.

The value of  $p^*$  is determined using Eq. 9-69 to be 194 psi, and  $G^*$  is determined from Eq. 9-70:

$$G^* = \frac{9012 - 8910}{194} = 0.53.$$

Assuming negligible spurt (i.e.,  $\kappa = 1$ ), the efficiency is determined from Eq. 9-71:

$$\eta = \frac{0.53}{2 + 0.53} = 0.21.$$

Equation 9-58 is then applied to obtain the fluid-loss coefficient:

$$C_L = \frac{194 \times 0.74 \times 24}{1 \times \sqrt{12} \times 5.6 \times 10^5} = 1.77 \times 10^{-3} \text{ ft/min}^{1/2}.$$

- Example field application of radial fracture decline analysis

Application of the generalized pressure decline analysis to a radial fracture is illustrated by analyzing the shut-in period during the calibration treatment depicted in Fig. 9-10b. The value of  $r_p$  is equal to approximately unity on the basis of open-hole well logs. The plane strain modulus is determined using Eq. 9-72 with the mechanical parameters listed in Table 9-2:

$$E' = \frac{4.5 \times 10^5}{1 - 0.25^2} = 4.8 \times 10^5 \text{ psi}.$$

The value of  $\beta_s$  for the radial model is 0.925 from Eq. 9-20.

As in the previous example for PKN fracture decline analysis, the steps outlined in this section are applied to determine the fluid-loss parameters.

The  $3/4$  point is calculated as

$$p_{3/4} = 4375 + \frac{3}{4}(4555 - 4375) = 4510 \text{ psi},$$

and  $m_{3/4}$  is obtained as 450 psi, as shown on Fig. 9-34.

The fracture is inferred to propagate in a radial fashion, so the correction for height growth suggested by Eq. 9-62 is not required. For the radial model,  $p^* = m_{3/4} = 450$  psi.

The corrected value of  $G$  at closure is derived from Eq. 9-70 as

$$G^* = \frac{4555 - 4375}{450} = 0.4.$$

As subsequently discussed in Section 9-6.8, a nominal spurt with a spurt factor  $\kappa = 1.02$  is estimated for this example. From Eq. 9-71 the efficiency is predicted:

$$\eta = \frac{0.4}{(2 \times 1.02) + 0.4} = 0.16.$$

The fracture radius  $R$  is determined from Eq. 9-59:

$$R = \sqrt[3]{\frac{(1 - 0.16) \times 600 \times 4.8 \times 10^5}{2 \times (\pi/2) \times 1.02 \times (32/3\pi^2) \times 450} \frac{32}{3\pi^3}} = 37 \text{ ft}.$$

Finally,  $C_L$  is determined by applying Eq. 9-58:

$$C_L = \frac{450(3\pi^2/32)}{1 \times \sqrt{4.6 \times 4.8 \times 10^5} \frac{32}{3\pi^2}} \times 37 = 1.62 \times 10^{-2} \text{ ft/min}^{1/2}.$$

## 9-6. Pressure interpretation after fracture closure

Another application of pressure evaluation pertains to the pressure response following fracture closure. The pressure during this period reflects the transient reservoir response to fracturing and is independent of the mechanisms governing fracture propagation. Its character is determined entirely by the response of a reservoir disturbed by the fluid-leakoff process. During this period, the reservoir may initially exhibit formation linear flow followed by transitional behavior and finally long-term pseudoradial flow (see Section 12-2). Formation linear flow and pseudoradial flow are hereafter referred to simply as linear and radial flow, respectively.

The after-closure response is similar to the behavior observed during a conventional well test of a propped fracture. It therefore supports an evaluation methodology analogous to the established principles of pressure transient evaluation. However, one important aspect differentiates after-closure evaluation. A propagating or receding fracture exposes the reservoir to an unequal distribution of fluid-loss flux over its length. For example, fluid loss dominated by the leakoff coefficient exhibits an elliptical profile of the specific volume (i.e., volume lost per unit area) (Fig. 9-35a). The

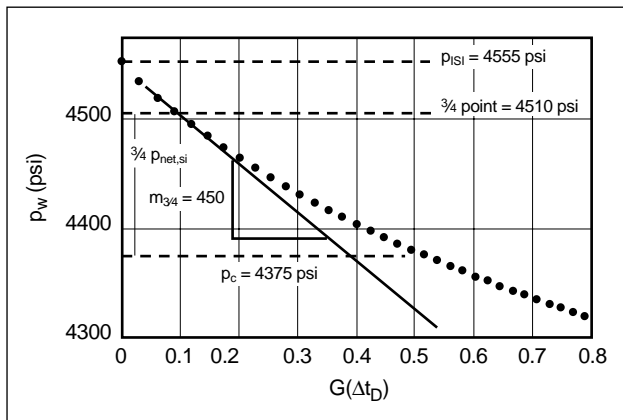


**Figure 9-34.** Pressure decline analysis for a radial fracture.

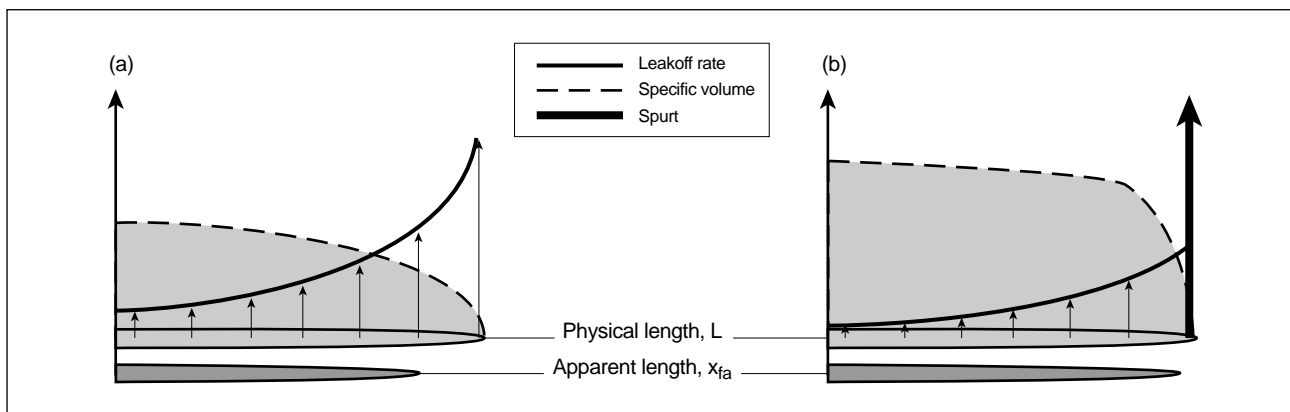


**Figure 9-35.** Fluid-loss volume and rate distribution (a) in the absence of spurt and (b) for a spurt-dominated treatment.

after-closure response can then be characterized in terms of an equivalent and spatially uniform fluid-loss flux over an apparent half-length  $x_{fa}$  that is generally less than  $L$ , the physical half-length of a propagating fracture. Consequently, the value of dimensionless time  $T$  that is expressed in terms of  $L$  for after-closure analysis can be different from that of  $t_D$ , the standard dimensionless time (see Chapter 12) based on the apparent stationary fracture half-length  $x_{fa}$  inferred from the reservoir response. This distinction between  $T$  and  $t_D$  is consistent with the notation for the fracture lengths  $L$  and  $x_f$  employed in this volume.

The after-closure period provides information that is traditionally determined by a standard well test (i.e., transmissibility and reservoir pressure). It completes a chain of fracture pressure analysis that provides a continuum of increasing data for developing a unique characterization of the fracturing process. At optimum conditions, it objectively determines parameters that either cannot be otherwise obtained (e.g., spurt) or exhibit considerable uncertainty when estimated with conventional pressure decline analyses (e.g., closure pressure).

Special attention is also required to address the interpretation aspects for application of the after-closure reservoir response. These considerations, along with an overview of related theoretical framework, are discussed in this section. A physical description of the reservoir response to fluid loss is presented initially to enhance understanding of the after-closure interpretation methodology. The synergy attained by combining the after-closure analysis with information derived from the fracture injection and preclosure periods is also discussed.

### 9-6.1. Why linear and radial flow after fracture closure?

A reservoir is disturbed by fluid-loss invasion during fracture propagation and closing. The fluid-loss rate changes with time as well as over the fracture length (i.e., has temporal and spatial components). This concept is further explained on Fig. 9-36, which illustrates the change in fracture length during a calibration test. At a time  $t = 0$ , the fracture length is zero. The fracture length increases over the injection time  $t_p$ , and it finally reaches a maximum value shortly after the end of injection. Fluid leakoff at a hypothetical location in the reservoir (labeled point a) is initiated at the time  $t_a$  when the fracture arrives at this

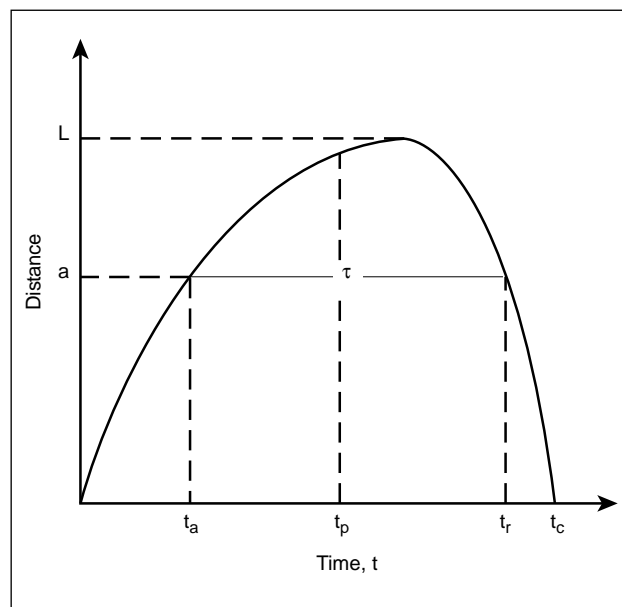


**Figure 9-36.** Rock exposure to fluid loss during fracture propagation.

location. The fluid-loss behavior can be interpreted as an injection source at point  $a$  with a strength (or intensity) equal to the rate of fluid loss that perturbs the reservoir from its initially undisturbed state. Fluid leakoff continues while the fracture remains open for the time interval  $\tau$  and ends when the fracture recedes to close at the reference point time  $t_r$ .

The calibration test creates a fracture that has negligible conductivity upon its closure at time  $t = t_c$ , following which additional fluid loss is terminated. Furthermore, following closure, the reservoir loses all recollection of the mechanical aspects (e.g., elastic deformation) of fracturing. The pressure disturbances created by leakoff, however, are preserved and dissipate with time. The wellbore pressure measurements following fracture closure reflect the dissipation process. The after-closure reservoir response is the cumulative effect (i.e., superposition) from injection sources distributed along the mechanical length of the fracture and over a time interval representing their exposure to fluid loss.

The pressure disturbances induced by fluid loss disperse or diffuse into the reservoir at a rate governed by the ratio of the mobility  $k/\mu$  and storage  $\phi c_i$  (i.e., the reservoir diffusivity  $k/\phi\mu c_i$ ) expressed in terms of the permeability  $k$ , porosity  $\phi$ , viscosity  $\mu$  and total compressibility  $c_t$ . The resulting pressure patterns created by the disturbances depend also on the rate of

fracture propagation, which is equivalent to a diffusional rate of  $L^2/t$ . The relative magnitude or ratio of the diffusional rates determines the shape of the pressure patterns and defines the dimensionless time  $T$ :

$$T = \frac{\text{pressure diffusional rate}}{\text{fracture growth diffusional rate}} = \frac{(k/\phi\mu c_i)}{(L^2/t)} = \frac{kt}{\phi\mu c_i L^2} \quad (9-75)$$

Several pressure propagation patterns are possible depending on the value of  $T$ . Figure 9-37a, based on a reservoir simulation for a low value of  $T$ , illustrates the pressure profile shortly after fracture closure in a reservoir characterized by low diffusivity and rapid fracture extension, or a low-permeability reservoir. The pressure disturbances near the wellbore have traveled a small distance into the reservoir. They are generally transmitted perpendicular to the previously fractured surface, indicating a one-dimensional (1D) pattern or linear flow. The pressure profile also reflects the fracture length attained during fluid injection.

A similar, and potentially unanticipated, pressure profile is depicted in Fig. 9-37b for the same fracture propagation rate as in Fig. 9-37a but for a reservoir with a much larger diffusional speed and therefore a relatively large dimensionless time. These conditions can be anticipated in a high-permeability reservoir

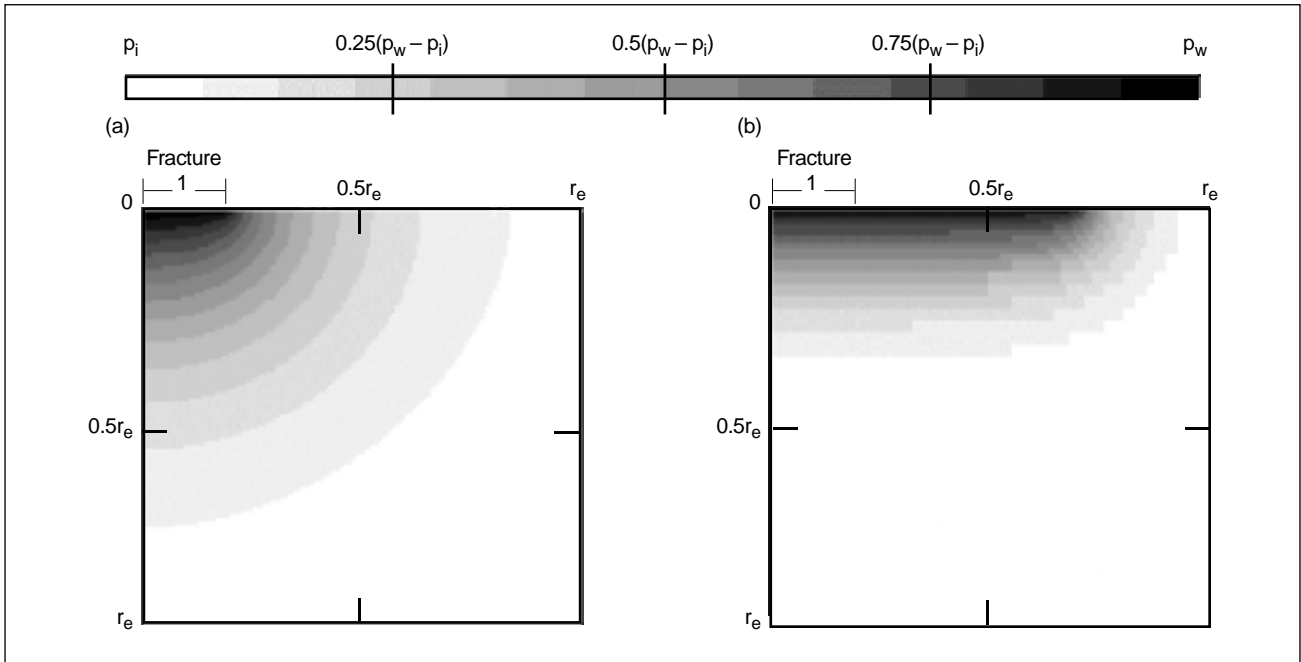


**Figure 9-37.** Pressure distribution in the reservoir shortly after closure for (a) small and (b) large values of dimensionless time.  $r_e$  = reservoir radius.

where the pressure disturbance caused by fluid leakoff travels much faster than the rate of fracture growth. Figure 9-37b clearly shows that the pressure distribution is completely devoid of any linear flow character and is represented largely as a radial flow pattern. The pressure distribution also does not reflect the fracture length. Its magnitude at the wellbore is independent of the nature of fluid injection into the reservoir but is characterized by the reservoir mobility and injected volume.

A final aspect of the volume distribution pertinent to the after-closure response must be described. In contrast to the elliptical profile in the absence of spurt (Fig. 9-35a), spurt loss acts as a moving injection source and tends to distribute the fluid-loss volume equally over the fracture length (Fig. 9-35b). As indicated previously, radial flow behavior depends primarily on the volume of fluid injection and is unaffected by the leakoff profile. However, during linear flow, the reservoir remembers this difference in the fluid-loss behavior because it affects the reservoir pressure distribution shortly after closure. Spurt-dominated fluid-loss behavior thus is manifested as a change in the attributes of after-closure linear flow.

Several conclusions can be derived from the preceding qualitative descriptions of the reservoir response:

- Fluid injection tests that achieve efficient fracture extension (as in most calibration treatments) are likely to achieve a low dimensionless time at the end of pumping. Therefore, they could display well-defined periods only of linear flow and long-term radial flow after fracture closure.
- The pressure distribution during linear flow reflects the fracture geometry attained during injection. The related analysis can provide an estimate of the fracture length.
- Linear flow is also affected by the relative contribution of spurt, which can be distinguished by evaluating the pressure data from this period.
- Fluid injection tests characterized by a low efficiency can be devoid of linear flow in spite of the creation of a fracture.
- Radial flow is independent of the nature of fluid leakoff. This period is, however, governed by the reservoir mobility and can be used to estimate the reservoir transmissibility.

## 9-6.2. Linear, transitional and radial flow pressure responses

The characteristic pressure response at the wellbore and beyond the filtrate region following the closure of an unpropagated fracture is illustrated in Fig. 9-38. The pressure difference  $\Delta p = p(t) - p_i$ , normalized with respect to its value at closure  $p(t_c) - p_i$ , was simulated for a dimensionless time  $T = 0.0001$  at fracture closure, or for a fracture that propagated much faster than the pressure disturbance in the reservoir. Figure 9-38 also shows the pressure derivative and variation of the characteristic log-log slope defined as  $d(\ln \Delta p)/d(\ln t)$ , where  $\Delta p$  is the pressure above the initial reservoir pressure  $p_i$ . This slope is used to identify the time intervals over which the various flow regimes prevail. The pressure response is illustrated for time intervals that extend beyond 10 times the closure period. For this limiting situation, known as the impulse condition (see Sidebar 9G), the pressure variation is described by the ratio of the closure time to the current time (Gu *et al.*, 1993; Abousleiman *et al.*, 1994).

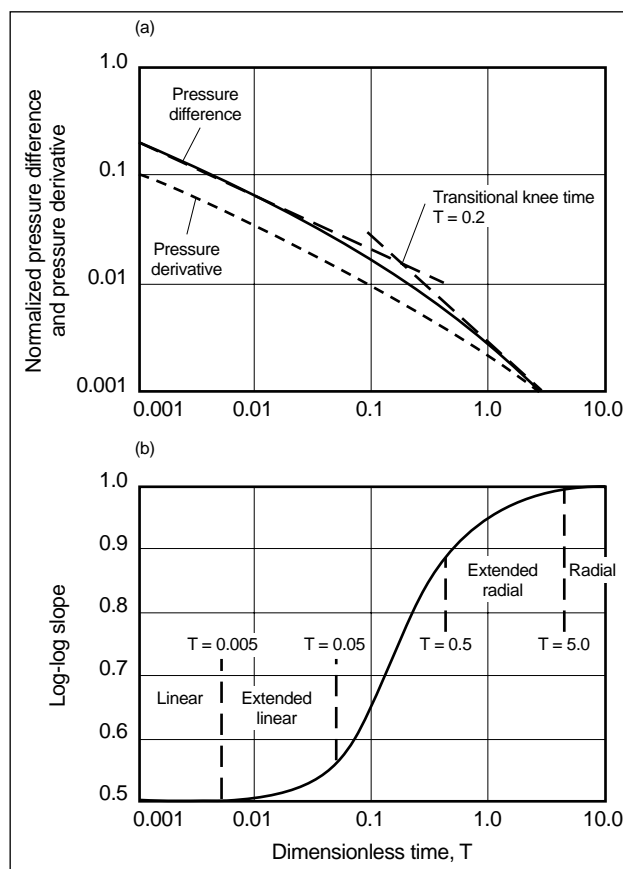


**Figure 9-38.** After-closure pressure difference and derivative (a) and log-log slope (b) plots for an impulse injection.

## 9G. Impulse testing

Joseph Ayoub, Schlumberger Dowell

The impulse test is a specialized well testing procedure that enables analysis of the reservoir response following a relatively short duration of fluid injection or production (Ayoub *et al.*, 1988). The pressure response to an ideal-rate impulse (i.e., to an instantaneous source) is given by the derivative of the pressure response to a step rate change. The impulse procedure can also be applied to a short injection that creates a hydraulic fracture within the reservoir (Abousleiman *et al.*, 1994).

The dimensionless wellbore pressure response  $p_{wD}$  following fracture closure resulting from a constant injection rate can be expressed by the principle of superposition as

$$p_{wD}(t_D > t_{cD}) = p_{wD}(t_{cD} + \Delta t_D) - p_{wD}(\Delta t_D), \quad (9G-1)$$

where  $t_D$  is the conventional dimensionless time from Eq. 12-1 and  $t_{cD}$  and  $\Delta t_D$  represent the dimensionless times for fracture closure and any subsequent interval, respectively (Fig. 9G-1).

Equation 9G-1 can be reformulated using the standard Taylor series expansion:

$$p_{wD}(t_D > t_{cD}) = t_{cD} \frac{dp_{wD}}{d\Delta t_D} + t_{cD}^2 \frac{1}{2} \frac{d^2 p_{wD}}{d\Delta t_D^2} + \text{higher order terms}. \quad (9G-2)$$

Neglecting the higher order terms in Eq. 9G-2 and substituting for  $p_{wD}$  with its expression during pseudoradial flow from Eq. 12-15 gives

$$p_w(\Delta t) - p_i = \frac{\bar{q}\mu}{2\pi kh} \frac{t_c}{2\Delta t} \left(1 - \frac{1}{2} \frac{t_c}{\Delta t}\right), \quad (9G-3)$$

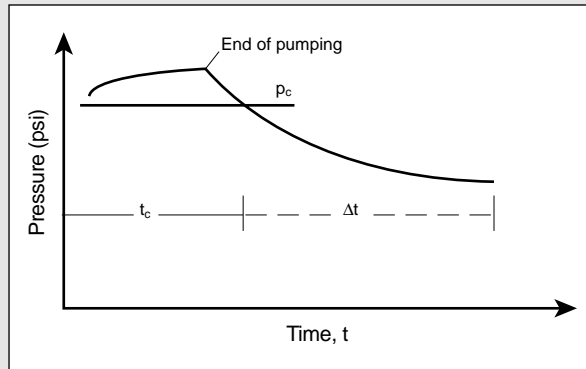


**Figure 9G-1.** Reference times for the impulse injection.  $p_c$  = closure pressure.

As shown on Fig. 9-38b, linear flow appears initially and lasts until  $T$  exceeds 0.005 and exhibits the anticipated half-slope for the pressure difference and derivative. Reservoir radial flow, characterized by a unit log-log slope, is the terminal flow regime that occurs only for  $T > 5$ . The intermediate transitional period lasts over a time period spanning a factor of approximately 1000 times beyond the end of linear flow. The plot of the pressure difference in Fig. 9-38a

where  $p_i$  is the reservoir pressure,  $\mu$  is the reservoir fluid viscosity,  $k$  is the reservoir permeability, and  $h$  is the reservoir height. The term  $\bar{q}$  defines the average injection rate into the reservoir. Equation 9G-3 can be reformulated on the basis that the injected fluid volume is the product of the average injection rate and closure time (i.e.,  $V_i = \bar{q}t_c$ ):

$$\begin{aligned} p_w(\Delta t) - p_i &= \frac{V_i \mu}{4\pi kh} \frac{1}{\Delta t} \left(1 - \frac{1}{2} \frac{t_c}{\Delta t}\right) \\ &= \frac{V_i \mu}{4\pi kh} \frac{1}{\Delta t} \left(1 - \frac{1}{2} \varepsilon\right), \end{aligned} \quad (9G-4)$$

where  $\varepsilon = t_c/\Delta t$ . It follows that for  $\Delta t \geq 10t_c$ ,  $p_w(\Delta t) - p_i$  is proportional to  $1/\Delta t$  within an error of less than 5%.

The pressure derivative  $\Delta t dp_w/d\Delta t$  can be obtained from Eq. 9G-4:

$$\Delta t \frac{dp_w(\Delta t)}{d\Delta t} = -\frac{V_i \mu}{4\pi kh} \frac{1}{\Delta t} [1 - \varepsilon]. \quad (9G-5)$$

The term  $\varepsilon$  can be neglected when the shut-in period is relatively long compared with the closure time. For  $\Delta t \geq 10t_c$ , Eqs. 9G-2 and 9G-5 become equal and proportional to  $1/\Delta t$  within a 10% error. It follows that

$$p_w(\Delta t) - p_i = \left| \Delta t \frac{dp_w(\Delta t)}{d\Delta t} \right| = \frac{V_i \mu}{4\pi kh} \frac{1}{\Delta t}, \quad (9G-6)$$

where  $\Delta t \gg t_c$ .

### Practical considerations

In theory, impulse analysis is applicable only for an instantaneous fluid injection. In practice, however, a finite injection time is required to create a pressure disturbance that is measurable for a long shut-in duration. Consequently, the analysis is valid only if the shut-in time is long in comparison with the finite injection time, as previously discussed.

Equation 9G-6 shows that during reservoir radial flow, a log-log plot of the pressure difference and pressure derivative versus  $1/\Delta t$  exhibits a unit slope. Multiplying the pressure difference and pressure derivative by  $\Delta t$  provides a horizontal line (i.e., zero slope) similar to the classic pressure response for transient radial flow. The two lines also overlie each other. This behavior provides a diagnostic method not only for identifying reservoir pseudoradial flow but also for determining the initial pressure of the reservoir. In addition, the pressure response during this period can be used in conjunction with Eq. 9G-6 to estimate the reservoir transmissibility  $kh/\mu$ . This provides the basic parameters required for evaluating the reservoir production performance.

also emphasizes the “knee” formed by the intersection of the slopes for the linear and radial flow periods. This intersection defines a unique dimensionless time that can be used to infer the fracture length achieved during propagation, as subsequently discussed in Section 9-6.7.

Figure 9-38 also illustrates a significant shortcoming for extracting the reservoir transmissibility from the after-closure response in low-permeability reser-



voirs that have extensive, efficient fracture propagation. Such conditions are characterized by a small value of  $T_p$  and require a long after-closure period to attain radial flow. For the example in Fig. 9-38, a prohibitively long shut-in period that equals 50,000 times the injection time would be required prior to obtaining radial flow. However, from an engineering perspective (i.e., an allowable error of 10%), the transitional period can be shortened by extending the linear and radial flow periods, as shown in Fig. 9-38b. This approximation considerably reduces the transitional period from a factor of 1000 to 10, which greatly increases the likelihood of obtaining a linear or radial flow analysis with an acceptable accuracy and under the normal constraints of field operations.

### 9-6.3. Mini-falloff test

A robust strategy for estimating the reservoir parameters from radial flow as well as for characterizing fracture behavior and obtaining linear flow is to apply two separate tests, with the first test a short injection test that may or may not create a fracture. This specialized calibration test is referred to as the mini-falloff test. The mini-falloff test should be performed in an undisturbed reservoir. Except in very tight formations, the test can be engineered using inefficient fluids and a low injection rate such that radial flow occurs during injection or shortly after closure (i.e., early radial flow). The subsequent fracture calibration test is performed with much higher injection rates and a more efficient fracturing fluid to characterize the fracture behavior as well as attain after-closure linear flow. The long-term radial flow behavior that normally occurs only after a prohibitively long shut-in period can be anticipated from the reservoir information derived with the mini-falloff test. The mini-falloff test, therefore, also facilitates the integration of pre- and after-closure analyses for a calibration test, as discussed in Section 9-6.4, under the time constraints of normal field fracturing operations.

A nonpolymer fluid (e.g., well completion fluid) must be injected during the mini-falloff test for two reasons. First, this type of fluid generally exhibits a larger fluid-loss rate than that of conventional polymer fracturing fluids. Consequently, it promotes a larger dimensionless time and the earlier emergence of radial flow during the shut-in period. Second, physical effects resulting from the viscoelastic nature of polymer fluids can potentially corrupt an extended

period of after-closure pressure data (Nolte *et al.*, 1997). As discussed in Chapter 8, polymer fluid invasion into a moderate- to high-permeability reservoir can result in an internal cake of a highly concentrated polymer gel. This internal cake experiences a sustained period of creeping afterflow following fracture closure. It supports a fraction of the total pressure drop between the fracture and the reservoir, masking the reservoir response. After a time that equals approximately the time before closure, the internal cake begins to flow more freely. The pressure then quickly drops to a value that reflects the pressure difference in the reservoir beyond the polymer material. Finally, the increasing effective stress during the after-closure period continues to consolidate the filter cake and fracture faces and further reduce the near-wellbore permeability. This can eventually result in a loss of communication between the wellbore and the reservoir that limits the availability of valid long-term pressure data.

“Guidelines for the field application of after-closure analysis” in the Appendix to this chapter discusses operational considerations for the mini-falloff test. Appendix Eq. 1 provides a guideline for determining the injection rate during the test. It follows from this equation that early radial flow can be achieved in a low-permeability gas reservoir (i.e., in tenths of a millidarcy) with an operationally permissible injection rate ( $\approx 1$  bbl/min). Lower injection rates are required to attain radial flow within the shut-in period in a reservoir with microdarcy permeability. Under these extreme reservoir conditions, only linear or transitional flow may occur because of field operational constraints. However, transitional flow can also be analyzed to estimate the reservoir properties, as discussed in “Comparison of fixed-length and propagating fractures” in the Appendix to this chapter.

### 9-6.4. Integration of after-closure and preclosure analyses

The after-closure analysis complements the preclosure analysis by providing parameter estimates that cannot otherwise be derived from pretreatment calibration tests. After-closure reservoir radial flow determines the formation transmissibility and initial pore pressure. These parameters are of paramount importance for optimizing a fracture stimulation (see Chapters 5 and 10). In addition, spurt can be a significant consideration for wall-building fluids in high-permeability

fracturing. However, it cannot be estimated from the standard pressure decline analysis described in Section 9-5. As previously mentioned, spurt influences the linear flow response. Consequently, after-closure linear flow analysis can be used to obtain an improved on-site assessment of spurt over conventional core-based laboratory tests.

A significant enhancement provided by after-closure analysis is its potential to validate preclosure analysis. The reservoir linear flow regime retains two critical pieces of information concerning the fracturing process: the time when fluid loss terminated (i.e., fracture closure time) and the fracture length. Cessation of fluid loss provides the linear flow period with a more distinct marker for fracture closure than that obtained from conventional shut-in procedures (see “Estimating closure pressure” in the Appendix to this chapter) that may exhibit multiple inflection points or a continuous, gradual pressure variation during closing. Fluid-loss discontinuity provides the fundamental basis for using after-closure analysis to determine the fracture closure pressure (see Section 9-6.8).

The transitional period exhibits a unique dimensionless knee time (see Fig. 9-38a) that provides information related to the fracture length through Eq. 9-75. The fracture length can also be estimated from the preclosure pressure decline analysis (see Section 9-5.2). The after-closure linear flow characteristics are derived from the principles of transient reservoir flow, which are fundamentally different from the principles of linear elasticity and material balance for a fracture that govern the preclosure pressure analyses. A consistent calibration evaluation is indicated by agreement between the fracture lengths estimated by these divergent analyses.

The preceding discussion introduces the interrelation between the pre- and after-closure flow periods, which is summarized in Fig. 9-39. The four inputs of  $c_f$ ,  $G^*$ ,  $p^*$  and  $\kappa$  are required to determine the fluid leakoff coefficient (Eq. 9-57) and the fluid efficiency (Eq. 9-71). The value of  $c_f$  is provided by the pressure response during injection (see Section 9-7). The preclosure shut-in period (see Section 9-5) estimates of  $G^*$  and  $p^*$  and the previously discussed after-closure analysis can be used to predict the spurt factor  $\kappa$ . The fracture length is independently obtained by these two approaches, and a consistent fracture analysis is indicated by agreement of the two length estimates. Finally, either the after-closure transitional or radial flow period is also used to assess the reservoir pro-

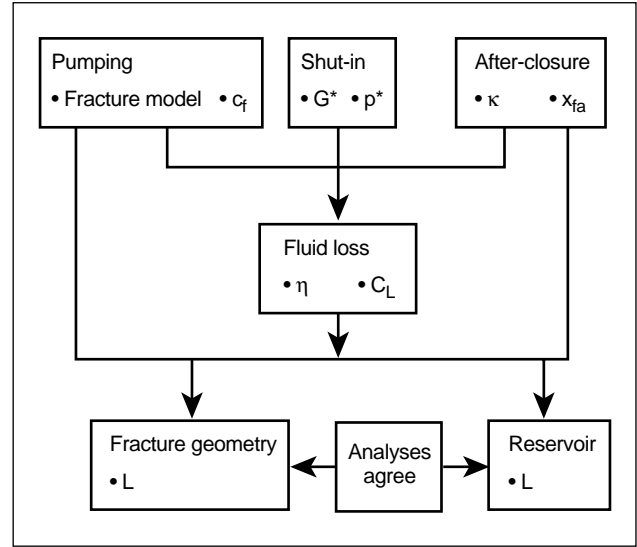


**Figure 9-39.** Interrelation of pre- and after-closure pressure analyses.

duction parameters. The synergistic, complementary character of the pre- and after-closure pressure analyses provides a comprehensive suite of crossvalidated fracture parameters for the optimized design of fracture treatments based on the economic guidelines provided in Chapter 10.

### 9-6.5. Physical and mathematical descriptions

The total pressure difference between the fracture and the reservoir  $\Delta p_T$  can be divided into three components, as shown in Fig. 5-17. Of relevance to after-closure analysis is the pressure difference  $\Delta p_R$  in the reservoir beyond the filter cake and filtrate regions. This pressure difference represents the added contributions of the two sources of fluid leakoff: a contribution from the Carter-based leakoff loss (i.e., the  $C_L$  component of fluid loss)  $\Delta p_{RC}$  and that resulting from spurt  $\Delta p_{RS}$ :

$$\Delta p_R = \Delta p_{RC} + \Delta p_{RS} \quad (9-76)$$

As discussed in Section 9-6.3, the pressure changes across the filter cake and filtrate disappear within a short time after fracture closure. The subsequent bottomhole pressure measurements  $p(t)$  then reflect the reservoir response to the pressure changes and fluid-loss distribution induced during the propagation and closing periods:

$$\Delta p(t) = \Delta p_R(t) = p(t) - p_i \quad t > t_c \quad (9-77)$$

A physical and mathematical description for the after-closure period is in this section. The focus is on  $\Delta p_{RC}$ , the reservoir response to Carter-based leakoff. The effects resulting from spurt loss are addressed separately in Section 9-6.6.

The two primary changes that the reservoir experiences following fracture closure are change in its boundary condition and change in its representation in reference to the response during production of a fixed-length fracture. First, as discussed in “Pressure characterization for a propagating fracture” in the Appendix to this chapter, the pressure difference  $\Delta p_{RC}$  in the reservoir is constant during fracture propagation. In contrast, the after-closure period is characterized by cessation of the fluid-loss flux. Consequently, the boundary condition along the closed fracture changes from one of constant, uniform pressure to zero or constant flux. The change in the boundary condition is referred to as a mixed-boundary condition.

The second difference between the preclosure and after-closure periods pertains to the representation of the after-closure period, which is analogous to the problem of a fixed-length fracture used in pressure transient analysis. The leakoff distribution following fracture closure is shown in Fig. 9-35. The illustrated volume profile closely reflects the distribution expected for a fixed-length, uniform-flux fracture and can be used to represent the after-closure pressure response. This observation contrasts with the preclosure conditions of a propagating fracture, for which the fluid-loss flux distribution is better represented by a fixed-length, uniform-pressure fracture. This distinction is elaborated in “Comparison of fixed-length and propagating fractures” in the Appendix to this chapter.

- Apparent fracture length

The previous discussion indicates that the after-closure reservoir response can be analyzed by considering the leakoff flux to be uniformly distributed over an equivalent fixed-length fracture. The apparent length of the equivalent fracture  $x_{fa}$  is generally smaller than the physical length  $L$  attained by the fracture during propagation. Its ratio with respect to the physical length is defined as the apparent length fraction:

$$f_{aL} = \frac{x_{fa}}{L}. \quad (9-78)$$

It follows from Eqs. 9-75, 9-78 and 12-1 that the dimensionless time  $t_D$ , which corresponds to the apparent length  $x_{fa}$ , is related to  $T$  as

$$T = f_{aL}^2 t_D. \quad (9-79)$$

A general expression for  $f_{aL}$  in terms of the fluid-loss parameters was given by Nolte *et al.* (1997):

$$f_{aL} = \frac{g_0}{(1-\eta)} \left[ \frac{\kappa}{g_0(\kappa-1) + 2\sqrt{t_c/t_p}} \right]. \quad (9-80)$$

For the case of inefficient fracture propagation ( $\eta \rightarrow 0$ ) and negligible spurt ( $\kappa \rightarrow 1$ ),  $g_0 = \pi/2$  and  $t_c \rightarrow t_p$ . Equation 9-80 then indicates that  $f_{aL} = \pi/4$  (Fig. 9-35a). For spurt-dominated treatments ( $\kappa \gg 1$ ), the specific volume-loss distribution over the fracture length is approximately constant, as illustrated in Fig. 9-35b. As expected for this case, Eq. 9-80 indicates that  $f_{aL}$  approaches unity.

- Linear flow

The similarity between reservoir transient flow and heat transfer arises because of the underlying “diffusional” process that governs these two physical phenomena. The physical concept of heat conductivity is similar to that of reservoir mobility, whereas the heat capacity of a solid body is equivalent to the reservoir storage. An expression for  $\Delta p_{RC}$  during the after-closure linear flow period for the mixed-boundary condition can be adapted from a similar condition presented by Carslaw and Jaeger (1959) for heat transfer (Nolte *et al.*, 1997):

$$\begin{aligned} \Delta p_{RC}(t) &= C_L \sqrt{\frac{\pi\mu}{k\phi c_t}} & t = t_c \\ &= C_L \sqrt{\frac{\pi\mu}{k\phi c_t}} \left\{ \frac{2}{\pi} \sin^{-1} \left( \sqrt{\frac{t_c}{t}} \right) \right\} & t > t_c \\ &\approx C_L \sqrt{\frac{\pi\mu}{k\phi c_t}} \left( \frac{2}{\pi} \sqrt{\frac{t_c}{t}} \right) & t > 3t_c, \end{aligned} \quad (9-81)$$

where  $t$  is the time since fracture initiation.

Equation 9-81 is based on 1D heat transfer through the surface for an infinitely long fracture. It also applies to the wellbore pressure of a finite-length fracture in linear flow because the reservoir surrounding the wellbore is experiencing 1D reservoir flow (Fig. 9-37a).

- Radial flow

No relation analogous to Eq. 9-81 for a finite-length fracture with a mixed-boundary condition applicable to radial flow has been presented in the literature. This reservoir response can alternatively be described by a superposition relation with the logarithmic time function that is commonly used to describe the radial flow response for a fixed-length fracture (Eq. 12-15):

$$\Delta p(t) = \frac{\mu}{2\pi kh} \frac{V_i}{t_c} \left\{ \frac{1}{2\lambda} \ln \left( \frac{\lambda t_c + (t - t_c)}{t - t_c} \right) \right\} \approx \frac{\mu}{4\pi kh} \frac{V_i}{t - t_c} \quad t - t_c \gg \lambda t_c. \quad (9-82)$$

The terms preceding the brackets on the right-hand side of Eq. 9-82 are incorporated to ensure that its long-term asymptotic behavior provides the well-known response for an impulse test (see Sidebar 9G).

Equation 9-82 also incorporates the apparent closure time  $\lambda t_c$ . The apparent production time used for the mixed-boundary condition in standard pressure transient analysis (Horner, 1951) is defined as the ratio of the cumulative volume and the final production rate. This definition of apparent time is not applicable for a propagating fracture. Rather, the multiplier  $\lambda$  was selected from numerical simulations as the value that provides the shortest after-closure time for the application of Eq. 9-82. For the mini-falloff test and its related conditions of negligible efficiency and spurt, the optimized value of  $\lambda$  can be characterized as

$$\lambda = 1 + \frac{0.14}{T_p} \quad \eta \rightarrow 0, \quad \kappa \rightarrow 1. \quad (9-83)$$

Equations 9-82 and 9-83 provide the reservoir transmissibility with acceptable accuracy significantly before the actual occurrence of radial flow. For example, for a dimensionless pumping time  $T_p = 0.1$ , the optimized multiplier expression enables the application of Eq. 9-82 at a dimensionless time  $T = 0.5$  as opposed to  $T = 2$  required for a standard radial flow analysis. Furthermore, Eq. 9-83 shows that  $\lambda$  is equal essentially to unity for well-developed radial flow (i.e.,  $T_p > 5$ ). For these conditions, the effect of the mixed-boundary condition diminishes. The time function in Eq. 9-82 then is equivalent

to the standard Horner function used during pressure transient testing.

### 9-6.6. Influence of spurt loss

The preceding discussion of the reservoir response does not consider the effect of spurt. Its consideration, however, is important because spurt can dominate the wall-building fluid-loss behavior of moderate- to high-permeability formations.

The role of spurt during either the pre- or after-closure period is difficult to describe with simple analytical concepts. However, characterizing its contribution to the reservoir pressure difference  $\Delta p_{RS}$  was found to be relatively simple, based on the results of numerical simulations (Nolte *et al.*, 1997). These indicate that during the linear flow period spurt causes a time-dependent increase in the pressure. Its pressure response  $\Delta p_{RS}$  is added to the pressure contribution from Carter-based leakoff behavior (Eq. 9-81). The total reservoir pressure difference  $\Delta p$  during the after-closure linear flow period that includes the spurt contribution can be expressed in terms of  $\Delta p_{RC}$  and the spurt factor  $\kappa$  as

$$\Delta p(t) = \Delta p_{RC}(t_c) \left( \frac{2}{\pi} \sin^{-1} \left( \sqrt{\frac{t_c}{t}} \right) + \frac{\kappa - 1}{2} \sqrt{\frac{t_p}{t}} \right) \quad t \geq t_c. \quad (9-84)$$

In particular, the pressure difference during an extended period of linear flow can be approximated from Eqs. 9-81 and 9-84 as

$$\Delta p(t) \approx C_L (1 + f_\kappa) \sqrt{\frac{\pi \mu}{k \phi c_i}} \left( \frac{2}{\pi} \sqrt{\frac{t_c}{t}} \right) \quad t > 3t_c, \quad (9-85)$$

where the spurt fraction  $f_\kappa$  is defined as

$$f_\kappa = \frac{\pi}{4} \sqrt{\frac{t_p}{t_c}} (\kappa - 1). \quad (9-86)$$

The distinctive time behavior exhibited by spurt during the after-closure period is illustrated in Fig. 9-40, which is based on the linear flow time function  $F_L(t/t_c)$  that is subsequently defined in Eq. 9-88. As discussed in Section 9-6.8, this presentation is consistent with the diagnostic log-log plot for flow regime identification. The reservoir pressure difference is normalized with respect to  $\Delta p_{RC}(t_c)$  and is compared for the conditions of negligible spurt ( $\kappa =$

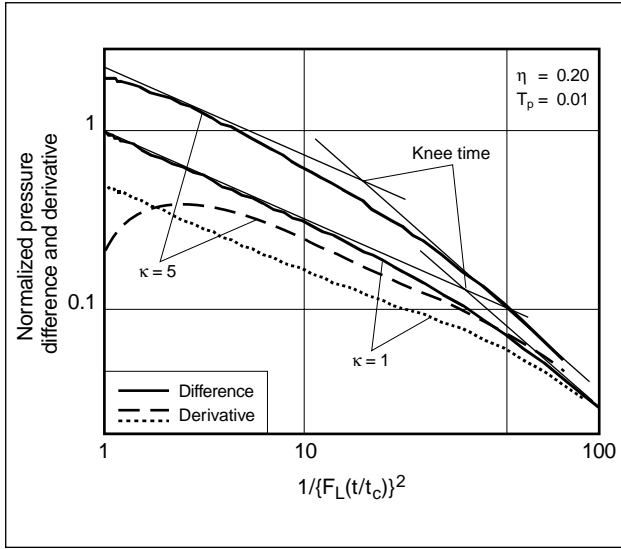


**Figure 9-40.** Simulated pressure for spurt and nonspurt cases (Nolte et al., 1997).

1) and dominant spurt ( $\kappa = 5$ ). An efficiency of 0.2 is prescribed for both cases. Under these conditions, Eq. 9-48 implies that 5 times more fluid is lost during propagation for this particular value of  $\kappa$  than for the condition of negligible spurt.

Figure 9-40 shows that spurt results in a pressure difference  $\Delta p$  and derivative that fall below the characteristic half-slope for linear flow over a time period of about  $t < 3t_c$  (Eq. 9-85). The figure also indicates that spurt apparently decreases the knee time, which is the time defined by the intersection of the asymptotic pressure responses during linear and radial flow. The apparently earlier time of the knee in the presence of spurt occurs because the time function used in Fig. 9-40 is referenced to the closure time. Spurt, however, has a significant impact on the closure time itself for a given value of efficiency (Eq. 9-60). For the spurt parameters used to develop Fig. 9-40, the closure time for spurt is 7.5 times larger than its value in the absence of spurt. In reality, the dimensional knee time for the spurt case occurs later than for the nonspurt case (i.e., by a factor of 1.4 relative to the beginning of pumping for these spurt parameters). The later knee time for the spurt case results because of its larger apparent fracture length, as indicated by Eq. 9-80. The relation between the apparent length and knee time is further discussed in Section 9-6.7.

In summary, spurt results in

- an added component to the reservoir pressure difference during the pre- and after-closure periods

- increase in the apparent length that delays the knee time
- deviation from the expected pressure response during linear flow that lasts over a shut-in time period equal to approximately  $3t_c$ .

### 9-6.7. Consistent after-closure diagnostic framework

The theoretical relations outlined in the previous sections can be readily distilled into an elementary set of equations. These simplified relations provide a consistent framework for analyzing after-closure behavior and are summarized in this section.

- Linear flow

The relation in Eq. 9-84 is used to describe the linear flow behavior because it provides a general mathematical representation for this flow regime. The equation can be reformulated as

$$\Delta p_R(t) = m_{lf} F_L(t/t_c), \quad (9-87)$$

where  $F_L(t/t_c)$  is the linear flow time function and  $m_{lf}$  is the corresponding slope on a Cartesian plot:

$$F_L(t/t_c) = \frac{2}{\pi} \sin^{-1} \left( \sqrt{\frac{t_c}{t}} \right) \quad (9-88)$$

$$\begin{aligned} m_{lf} &= C_L (1 + f_\kappa) \sqrt{\frac{\pi \mu}{k \phi c_i}} \quad \kappa > 1, \quad t > 3t_c \\ &= C_L \sqrt{\frac{\pi \mu}{k \phi c_i}} \quad \kappa = 1, \quad t > t_c, \end{aligned} \quad (9-89)$$

where the spurt fraction  $f_\kappa$  is as defined in Eq. 9-86. The dependency of  $f_\kappa$  on the spurt factor  $\kappa$ , as well as the closure time  $t_c$ , implies that both parameters cannot be simultaneously determined from the reservoir linear flow response. An accurate value of  $t_c$  is therefore required to properly characterize  $\kappa$  for spurt-dominated conditions.

In the absence of spurt,  $\kappa = 1, f_\kappa = 0$ , and the last relation in Eq. 9-89 provides an expression analogous to Eq. 2-50 for estimating the reservoir permeability from the linear flow response, as suggested by Mayerhofer *et al.* (1993). The square-root dependence of Eq. 9-89, however, makes this procedure sensitive to the general uncertainty in the parameters that define the fluid-loss coefficient

and reservoir storage. Consequently, the technique could introduce significant uncertainty in the inferred permeability (Ispas *et al.*, 1998).

- Radial flow

Equation 9-82 provides the general expression of the logarithmic time function that describes the reservoir pressure difference during radial flow. This function can be approximated by the square of its linear flow counterpart (Eq. 9-88) by introducing a coefficient of  $\pi^2/8$ :

$$\frac{1}{2\lambda} \ln \left( 1 + \frac{\lambda t_c}{t - t_c} \right) \approx \frac{\pi^2}{8} \left\{ \frac{2}{\pi} \sin^{-1} \left( \sqrt{\frac{t_c}{t}} \right) \right\}^2 (1 + \varepsilon), \quad (9-90)$$

where  $\varepsilon$  is the error introduced by the approximation. The relative error can be based on the pressure derivative because it is the primary measure for after-closure analysis. Thus,

$$\varepsilon = \left( \lambda - \frac{4}{3} \right) \left( \frac{t_c}{\Delta t} \right) \quad \Delta t > 3t_c. \quad (9-91)$$

It follows from Eq. 9-91 that the error introduced by the approximation in Eq. 9-90 is at a minimum when the apparent time multiplier  $\lambda = 4/3$ . As indicated by Eq. 9-83, this value of  $\lambda$  corresponds to a dimensionless injection time  $T_p = 0.4$ , which meets the desired condition of a mini-falloff test for early radial flow analysis. The approximation, therefore, is well suited for application to the mini-falloff test. More generally, the relative error  $\varepsilon$  can be shown to be less than 5% for the after-closure period recommended in “Guidelines for the field application of after-closure analysis” in the Appendix to this chapter and using the expression for  $\lambda$  provided by Eq. 9-83.

The radial flow period can then be represented by substituting the approximation provided by Eq. 9-90 into Eq. 9-82:

$$\Delta p(t) = m_{rf} \left\{ F_L(t/t_c) \right\}^2, \quad (9-92)$$

where the function  $F_L(t/t_c)$  is defined in Eq. 9-88 and  $m_{rf}$  is the corresponding slope on a Cartesian plot:

$$m_{rf} = \frac{\pi}{16} \frac{V_i \mu}{k h t_c}. \quad (9-93)$$

Equations 9-87 and 9-92 suggest that a log-log diagnostic plot of the pressure difference and pressure derivative based on  $\{F_L(t/t_c)\}^2$  would provide a consistent basis for diagnosing both linear and radial flow. The plot also would provide the half-slope and unit slope behavior during linear flow and radial flow, respectively, as is expected for after-closure pressure analysis.

- Spurt

Spurt is estimated from the linear flow slope  $m_{lf}$  using Eqs. 9-86 and 9-89:

$$\kappa = 1 + \frac{4}{\pi} \left[ \frac{m_{lf}}{C_L} \sqrt{\frac{k \phi C_t}{\pi \mu}} - 1 \right] \sqrt{\frac{t_c}{t_p}}. \quad (9-94)$$

The spurt factor  $\kappa$  can be related to the spurt coefficient  $S_p$  with Appendix Eq. 24.

- Fracture length

The fracture length is obtained from the dimensionless time corresponding to the knee formed by the intersection of the asymptotic log-log slopes during linear and radial flow, in a plot similar to Fig. 9-38a. A general relation for the fracture length can be derived from the pressure response for a fixed-length fracture and relating its behavior to that of the propagating fracture using the apparent length fraction  $f_{aL}$ , as discussed in Section 9-6.5.

The fracture length is required to verify the pre-closure analysis for a calibration test, where the use of a more efficient fracturing fluid generally leads to a well-defined linear flow response. The knee subsequently occurs only after a significantly longer after-closure shut-in period (Fig. 9-38). Under this extended shut-in condition, the after-closure response can be approximated by the impulse assumption (see Sidebar 9G). The asymptotic expressions for a fixed-length fracture for linear and radial flow, in terms of the classic dimensionless time  $t_D$ , follow from Eqs. 12-12 and 12-15, respectively. The derivatives during these periods are

$$\frac{dp_D}{dt_D} = \begin{cases} \frac{\sqrt{\pi}}{2\sqrt{t_D}} & \text{Linear flow} \\ \frac{1}{2t_D} & \text{Radial flow,} \end{cases} \quad (9-95)$$

where  $p_D$  is the standard dimensionless pressure, defined in Eq. 12-2. The knee time  $t_{D,knee}$ , or the dimensionless time for the crossing of the two

derivatives, is determined by equating the two expressions:

$$t_{D,knee} = \frac{1}{\pi}. \quad (9-96)$$

Equation 9-96 can be expressed in terms of the dimensionless time  $T$  for a propagating fracture by substituting Eq. 9-79:

$$T_{knee} = f_{aL}^2 t_{D,knee} = \frac{f_{aL}^2}{\pi}. \quad (9-97)$$

As discussed in Section 9-6.5, for negligible efficiency and spurt,  $f_{aL} = \pi/4$ . It follows from Eq. 9-97 that  $T_{knee} = 0.2$ , as shown for these conditions assumed by Fig. 9-38. An estimate of the actual fracture length  $L$  can be obtained in terms of the dimensional knee time  $t_{knee}$  by combining Eqs. 9-75 and 9-97:

$$L = \frac{1}{f_{aL}} \sqrt{\frac{\pi k t_{knee}}{\phi \mu c_t}}. \quad (9-98)$$

The value of  $t_{knee}$  can be defined by  $m_{lf}$  and  $m_{rf}$ , which are more readily estimated during field practice. This definition of  $t_{knee}$  also uses the extended time approximation for  $F_L$  (Eq. 9-81):

$$t_{knee} = \frac{4t_c}{\pi^2} \left( \frac{m_{rf}}{m_{lf}} \right)^2. \quad (9-99)$$

Combining this expression with Eq. 9-98 gives the fracture length as

$$L = \frac{1}{f_{aL}} \sqrt{\frac{4}{\pi} \frac{k t_c}{\phi \mu c_t} \frac{m_{rf}}{m_{lf}}}, \quad (9-100)$$

where the apparent length fraction  $f_{aL}$  is from Eq. 9-80.

It is unlikely that both linear and radial flow will occur during the same shut-in period. Consequently, applying the length relation in Eq. 9-100 for a calibration test requires a combination of its linear flow response and the radial flow analysis from a preceding mini-falloff test. Equation 9-93 can be used to anticipate  $m_{rf}$  for the calibration test from the injected volume and fracture closure time of the calibration test and transmissibility estimate obtained from a preceding mini-falloff test.

- Validation of pre- and after-closure analyses

As a final step, the fracture length estimated by decline analysis in Eq. 9-59 is compared with the

reservoir's perspective of the fracture length, as derived from the knee time concept of Eq. 9-100:

$$\frac{\kappa C_L \sqrt{t_p}}{(1-\eta)} = \frac{4 f_{aL} m_{lf} \sqrt{t_c}}{\pi} \sqrt{\frac{k}{\mu} \frac{\phi c_t}{\pi}}. \quad (9-101)$$

The derivation of Eq. 9-101 also uses the definition of  $m_{rf}$  from Eq. 9-93. The application of Eq. 9-101 to a calibration test serves as a validation check for its evaluation and provides the fundamental relation to verify the parameters predicted by the pre- and after-closure analyses.

## 9-6.8. Application of after-closure analysis

A systematic procedure for the application of after-closure analysis is presented in this section. "Guidelines for the field application of after-closure analysis" in the Appendix to this chapter discusses the operational considerations required to engineer an injection testing sequence that provides the pressure data required for an objective, comprehensive application of the after-closure analysis.

- Background information

A reliable estimate of the reservoir pressure should be established prior to the evaluation process. This can be achieved from previous analyses (e.g., well tests or production evaluation) or data measured prior to fluid injection. The estimate suitably constrains the pressure difference within the flow regime identification process, which ensures objectivity in the after-closure analysis. The fluid leak-off can be determined using the shut-in analysis described in Section 9-5. The formation storage  $\phi c_t$  is established using standard well logs and pressure-volume-temperature (PVT) data or correlations.

- Flow regime identification

The occurrence of after-closure linear or radial flow is identified using the diagnostic log-log plot of the pressure difference and pressure derivative based on  $\{F_L(t/t_c)\}^2$ , as discussed in Section 9-6.7. The two quantities are plotted as a function of  $1/\{F_L(t/t_c)\}^2$  so that the shut-in time conventionally increases from left to right along the x-axis (Fig. 9-41).

During linear flow, the curves for the two quantities show straight-line behavior separated by a

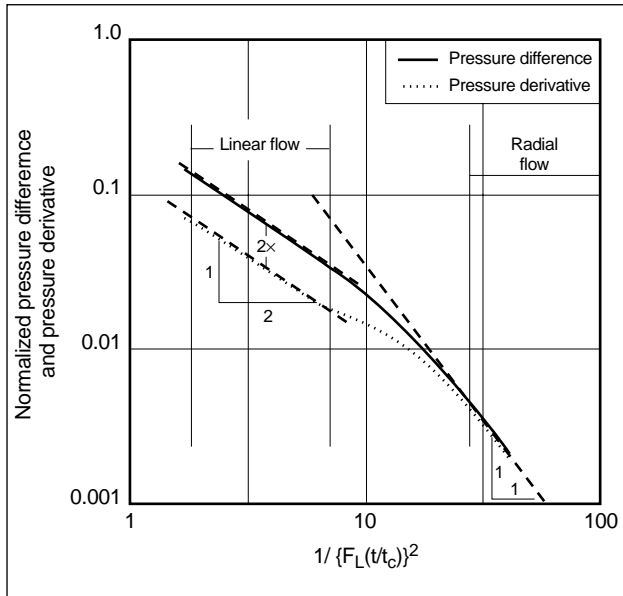


**Figure 9-41.** Identification of linear and radial flow using the diagnostic log-log plot.

factor of 2 and each has a half-slope. Radial flow is characterized by a log-log slope that approaches unity as well as an approximate overlying of both the pressure difference and pressure derivative curves.

- Reservoir parameters determination

The testing sequence should preferentially include a mini-falloff test to characterize the reservoir parameters. Shut-in pressures monitored during the mini-falloff test should initially be investigated for radial flow using the log-log diagnostic described in the preceding step. If radial flow can be identified, a Cartesian plot of the pressure response during radial flow versus  $\{F_L(t/t_c)\}^2$  is constructed. The slope of the straight-line portion on this graph, or  $m_{rf}$ , can be used with Eq. 9-93 to estimate the reservoir transmissibility. The pressure intercept of the straight-line portion is an estimate of the initial reservoir pressure. This procedure is analogous to the conventional Horner analysis used for well testing.

In the absence of radial flow, the transitional flow-based analysis described in “Comparison of fixed-length and propagating fractures” in the Appendix to this chapter should be applied to the mini-falloff test. This type-curve matching procedure estimates the initial reservoir pressure and its transmissibility based on the transitional flow period.

- Linear flow analysis

Generally, linear flow analysis is applicable only to a calibration test (i.e., because a mini-falloff test is designed to achieve early radial flow). During the calibration test, the linear flow period is identified from the diagnostic log-log plot (Fig. 9-41) for estimating either the closure time or spurt. Obtaining representative values of these parameters generally requires a good prior estimate of the initial, undisturbed reservoir pressure.

In the absence of spurt, the closure time can be estimated as the smallest value of  $t_c$  that, when used with the independently derived reservoir pressure estimate, provides the linear flow diagnostic discussed in the preceding “Flow regime identification” step. If spurt is expected, the value of  $t_c$  should be independently determined using the procedures outlined in “Estimating closure pressure” in the Appendix to this chapter. The after-closure linear flow analysis can then be used to estimate the spurt, with the linear flow period initially identified from the diagnostic log-log plot. If linear flow is identified, a Cartesian plot of the pressure versus  $F_L(t/t_c)$  is constructed to determine the slope  $m_{lf}$ . Equation 9-94 is used to obtain the spurt factor  $\kappa$ . The reservoir mobility  $k/\mu$  required by this equation is derived from transitional or radial flow analysis and  $C_L$  from the decline analysis. The spurt coefficient  $S_p$  can then be obtained from Appendix Eq. 24.

- Crossvalidation

Equation 9-101 is applied to compare the fracture length predicted by the reservoir response to that derived from decline analysis (see Section 9-5) for the calibration test. The radial flow slope  $m_{rf}$  is anticipated from Eq. 9-93, with the reservoir transmissibility as previously determined from the mini-falloff test and  $V_i$  and  $t_c$  defined as the volume injected and closure time for the calibration test, respectively. Agreement between the two independently inferred fracture lengths indicates correct evaluation of the calibration treatment.

### 9-6.9. Field example

Application of the after-closure analysis methodology is illustrated by analyzing the pressure monitored during the field calibration tests in Fig. 9-10. Analysis of the injection pressure for the calibration test



described in “Example of radial fracture growth” in Section 9-4.4 determined that the fracture is best described by the radial fracture geometry model. The fracture is approximated as having a rectangular shape of equal area to facilitate the after-closure analysis. The shut-in pressure is analyzed in “Example field application of radial fracture decline analysis” in Section 9-5.4, from which the leakoff coefficient  $C_L$  is calculated to be  $1.62 \times 10^{-2}$  ft/min<sup>1/2</sup>. A closure pressure of 4375 psi was inferred from the step rate test (see “Estimating closure pressure” in the Appendix to this chapter).

- Background information

The stabilized pressure on the bottomhole gauge is 3726 psi in Fig. 9-10. The stabilized pressure measurement provides an independent, objective assessment of the reservoir pressure. A log-determined porosity of 19% and a saturation-weighted formation compressibility of  $8.0 \times 10^{-5}$  psi<sup>-1</sup> were also obtained. PVT analysis indicated a relatively high oil viscosity of 4 cp.

- Radial flow identification

After-closure pseudoradial flow is observed in the reservoir for the initial mini-falloff test (Fig. 9-10), as shown by the diagnostic log-log plot in Fig. 9-42. A Cartesian plot of the pressure versus  $\{F_L(t/t_c)\}^2$  during the after-closure period is in Fig. 9-43. An initial reservoir pressure estimate of 3736 psi is obtained as the y-axis intercept of the straight-line period on the plot in Fig. 9-43. This value indicates consistency with the previously inferred estimate of 3726 psi from the bottomhole gauge. The slope  $m_{rf}$  of the straight line is 660 psi and the closure time  $t_c$  is 3.75 min, based on a closure pressure of 4375 psi (see “Estimating closure pressure” in the Appendix to this chapter). A total volume of 14.75 bbl was injected during the test. The transmissibility is obtained by using this information with Eq. 9-93 reformulated in dimensional form:

$$\begin{aligned} \frac{kh}{\mu} &= 2.5 \times 10^5 \frac{V_i}{t_c} \frac{1}{m_{rf}} \\ &= 2.5 \times 10^5 \frac{14.75}{3.75} \frac{1}{(660)} \quad (9-102) \\ &= 1490 \text{ md} \cdot \text{ft} / \text{cp}. \end{aligned}$$

The transmissibility estimate implies a reservoir permeability of 80 md based on the reservoir parameters.

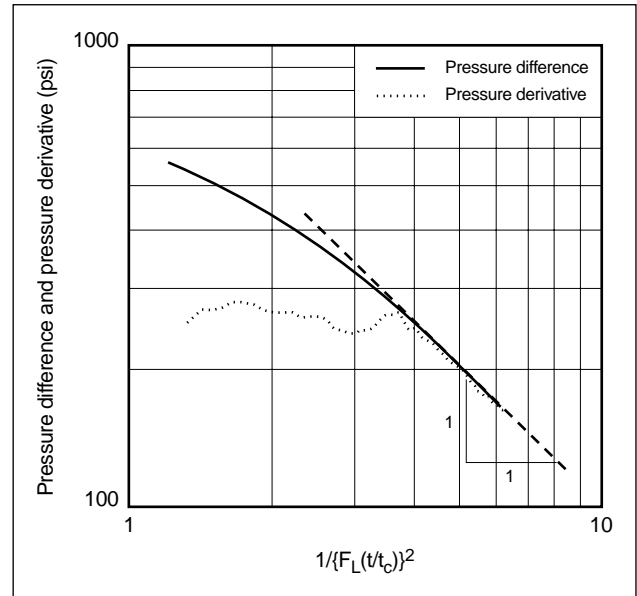


**Figure 9-42.** Identification of after-closure radial flow.

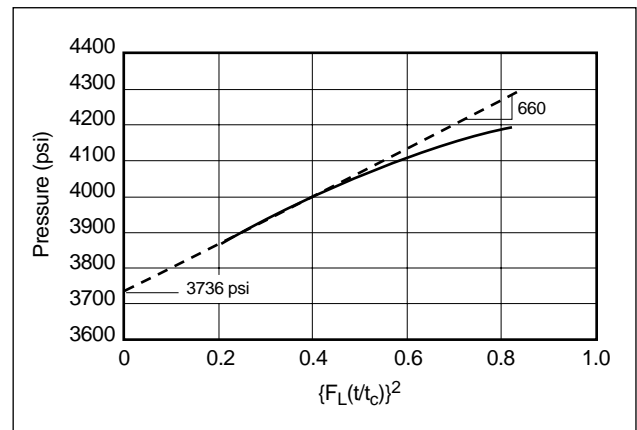


**Figure 9-43.** After-closure radial flow analysis.

- After-closure linear flow determination

The shut-in pressure measured following the calibration test is investigated for after-closure linear flow behavior. The observed potential period of linear flow is confirmed by pressure derivative analysis (Fig. 9-44). The initial pressure  $p_i$  of 3724 psi required for the analysis is in excellent agreement with the 3736-psi reservoir pressure derived from the radial flow analysis and its value of 3726 psi inferred as the stabilized pressure measurement on the bottomhole gauge prior to injection (Fig. 9-10). The linear flow slope  $m_{lf}$  is deduced to be 815 psi from the corresponding Cartesian plot.

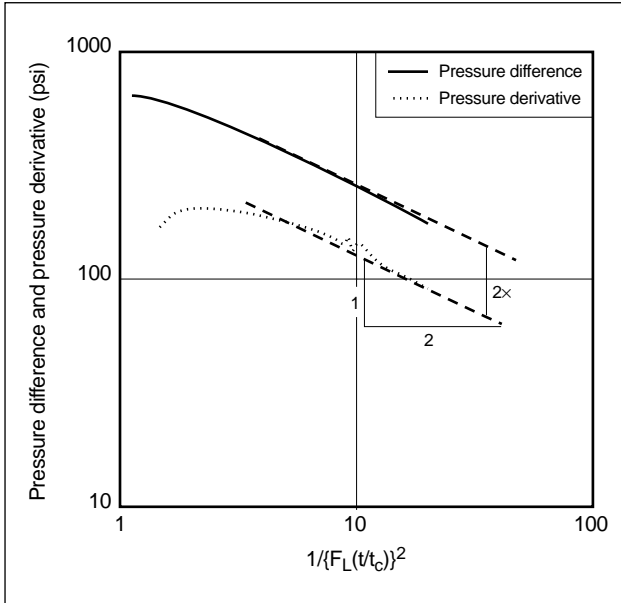


**Figure 9-44.** Identification of after-closure linear flow.

- Spurt estimation

The previously determined linear and radial flow slopes are used with the estimates of formation porosity and compressibility to estimate spurt with Eq. 9-94, which is reformulated in oilfield units as

$$\kappa = 1 + \frac{4}{\pi} \left[ 1.18 \times 10^{-3} \frac{m_{lf}}{C_L} \sqrt{\frac{k\phi c_t}{\mu}} - 1 \right] \sqrt{\frac{t_c}{t_p}}$$

$$= 1 + \frac{4}{\pi} \left[ 1.18 \times 10^{-3} \frac{815}{1.62 \times 10^{-2}} \times \sqrt{\frac{80 \times 0.19 \times 8 \times 10^{-5}}{4}} - 1 \right] \sqrt{\frac{5.6}{4.6}}$$

$$= 1.02,$$

where the closure time of 5.6 min was based on the closure pressure of 4375 psi determined with the step rate test (see “Estimating closure pressure” in the Appendix to this chapter).

The spurt coefficient  $S_p$  is determined with Appendix Eq. 24:

$$S_p = 7.48 \times 10^2 g_o C_L \sqrt{t_p} (\kappa - 1)$$

$$= 7.48 \times 10^2 \times (\pi/2) \times 1.62 \times 10^{-2} \sqrt{4.6} \times (1.02 - 1)$$

$$= 0.8 \text{ gal} / 100 \text{ ft}^2.$$

The nominal value of  $S_p$ , in spite of the high formation permeability, reflects that the fluid leakoff is governed by the reservoir. This can occur for

the conditions of high viscosity and low compressibility, as in this example.

- Reconciliation

Equation 9-80 is used to obtain the apparent fracture length  $f_{aL}$ :

$$f_{aL} = \frac{\pi/2}{(1 - 0.16)} \left[ \frac{1.02}{\pi/2 \times (1.02 - 1) + 2\sqrt{5.6/4.6}} \right] = 0.86.$$

The slope  $m_{rf}$  for the calibration injection is predicted using Eq. 9-102, the dimensional form of Eq. 9-93:

$$m_{rf} = 2.5 \times 10^5 \times \frac{V_i}{t_c} \left( \frac{\mu}{kh} \right)$$

$$= 2.5 \times 10^5 \times \frac{107}{5.6} \left( \frac{1}{1490} \right)$$

$$= 3205 \text{ psi}.$$

The fracture length is estimated using the dimensional form of Eq. 9-100:

$$L = 2.37 \times 10^{-3} \frac{1}{f_{aL}} \sqrt{\frac{kt_c}{\phi\mu c_t}} \frac{m_{rf}}{m_{lf}}$$

$$= 2.37 \times 10^{-3} \frac{1}{0.86} \sqrt{\frac{80 \times 5.6}{0.19 \times 4 \times 8.0 \times 10^{-5}}} \frac{3205}{815}$$

$$= 33 \text{ ft}.$$

The length estimate is in good agreement with the 37-ft fracture radius determined from the shut-in analysis, as described in Section 9-5.4.

## 9-7. Numerical simulation of pressure: combined analysis of pumping and closing

The pressure analysis techniques presented in this chapter are based on analytical derivations. They assume primarily a simplified fracture behavior to provide an engineering approximation of the fracture parameters. A more comprehensive analysis is required to determine rational changes in the propped treatment design (e.g., fluid viscosity, leakoff coefficient changes because of additives) without the negative impact of trial and error adjustments during commercial field development. This understanding is particularly important for reservoirs where formation pressure capacity considerations (see Section 9-4.6) require unconventional designs (Nolte, 1982, 1988a;

Warpinski and Branagan, 1988) to produce the desired fracture geometry.

These objectives are best achieved with an appropriately calibrated numerical simulator that adequately replicates the important processes that occur during a fracturing application. The simulator that best meets these objectives is most likely not one of the comprehensive, computationally intensive simulators that are better suited to research environments (e.g., Plahn *et al.*, 1997). The description of the overall fracture behavior required for routine engineering applications can generally be satisfied by P3D fracture geometry models (see Section 6-3).

### 9-7.1. Pressure matching

A typical approach for calibrating a numerical fracture simulator is through iterative pressure matching. The fracture simulator is executed with varying parameter inputs to visually match the simulated pressure with the field measurements. The quality of the pressure match is assessed by balancing objectivity, physical insight and constraints from other data sources. However, given the limited number of formation parameters that can be accurately characterized using wireline logs or laboratory tests, the procedure can require significant effort when several parameters are not known. A large number of unknown parameters may also compromise the objectivity of the matching procedure.

An alternative approach for pressure matching relies on an algorithm that repeatedly executes the fracture simulator to improve the estimates of the fracture parameters within specified bounds until the best match to the field-measured response is obtained. This semiautomated approach, discussed in Section 6-12, is based on conventional principles of nonlinear regression analysis for system identification. The technique, initially introduced by Gringarten *et al.* (1979) for well test analysis, has also been applied to log interpretation and reservoir characterization.

### 9-7.2. Nonuniqueness

Pressure matching is an inverse problem for which the input (i.e., fracture treatment schedule) and output (i.e., fracture pressure) are known and are used to determine the unknown model parameters (e.g., zone stresses, leakoff coefficient). An inherent limitation

with any inverse problem is the occurrence of nonunique solutions. With respect to hydraulic fracturing, nonuniqueness arises when more than one combination of the unknown parameters can be used to approximate the observed pressure.

A multitude of parameters govern fracture behavior in a nonlinear and coupled fashion. Uncertainty in some of the parameters leads to erroneous prediction of the unknown parameters inferred by the pressure-matching process. A nonunique parameter set that produces an incorrect prediction of the fracture geometry results in an inappropriate redesign of the propped treatment. This effect is readily apparent in Eq. 9-24, in which the pressure response during pumping exhibits an approximately first-order inverse dependency on the fracture compliance  $c_f$ . For the commonly occurring PKN-type fracture,  $c_f \approx h_f/E'$  (Eq. 9-22). Consequently, an inaccuracy in the value of the plane strain modulus  $E'$  produces a corresponding error in the predicted fracture height  $h_f$  and therefore the fracture penetration, without affecting the quality of the pressure match.

Nonuniqueness in pressure matching may also occur during periods of controlled and uncontrolled height growth. During both these conditions, the net pressure response is determined largely by the stress difference between the bounding zones and the primary interval. The pressure response exhibits a much reduced sensitivity to other fracture parameters, such as  $E'$  or  $C_L$ . Consequently, a reasonable pressure match during these periods may be attained in spite of errors in the other fracture parameters.

Nonuniqueness is avoided by preventing arbitrariness during the pressure-matching process. This is best achieved by initially applying the diagnostic procedures outlined in this chapter to obtain a first-order estimate of the unknown parameters and an approximate understanding of the nature of the fracture growth. Only moderate variation of the unknown parameters from these initial estimates should be allowed during the pressure-matching process. In addition, the numerical simulator must be adequately constrained so that the simulated fracture geometry conforms to the growth patterns inferred by the pressure diagnostics; e.g., the simulator must predict controlled height growth if this behavior was concluded from pressure derivative analysis.

The pressure-matching process should also include all independently derived information. For example, nonuniqueness resulting from  $c_f$  could be overcome

by a rational selection of the primary zone height using well logs. Young's modulus  $E$  can then be calibrated by matching pressures during the stage of the treatment that exhibits PKN behavior, before penetration of the bounding layers occurs. Alternatively, the value of  $E$  could conform to core tests or sonic logs of the reservoir (see Chapter 4), and the primary zone thickness could be calibrated with the pressure match and verified against well logs. Similarly, variation in the zone stresses must be based on their trends as predicted by stress logs. In the absence of stress logs, lithology logs can be used to develop an approximation for particular geologic environments (Smith *et al.*, 1989). Furthermore, the simulated fracture dimensions could be compared against independent measurements, such as radioactive tracers or microseismic measurements, to validate the outcome of the pressure-matching exercise (Gulrajani *et al.*, 1998).

The inversion solution is confirmed by applying the numerical simulator based on these calibrated fracture parameters to predict the fracture behavior during the propped treatment or for offset wells. An objective pressure evaluation is indicated by agreement between the simulated pressure response and actual field measurements. Conformity also establishes the ability of the calibrated numerical simulator to develop improved designs for future fracture treatments.

## 9-8. Comprehensive calibration test sequence

An optimized hydraulic fracturing program integrates the analyses and diagnostic methods discussed in this chapter with the proper design process (see Chapters 5 and 10) and execution aspects (see Chapter 11) of the stimulation procedure. These considerations include identifying candidate wells that will benefit from the stimulation treatment, determining the appropriate injection rate and proppant addition sequence as well as assessing the risks involved with treatment execution. The techniques described in the previous sections provide a basis for estimating the fracture and reservoir parameters required during the optimization process. To ensure completeness and consistency in the evaluation process, fracturing pressure data should be obtained through a planned sequence of calibration tests, as shown in Fig. 9-45. The following steps describe the fracture evaluation

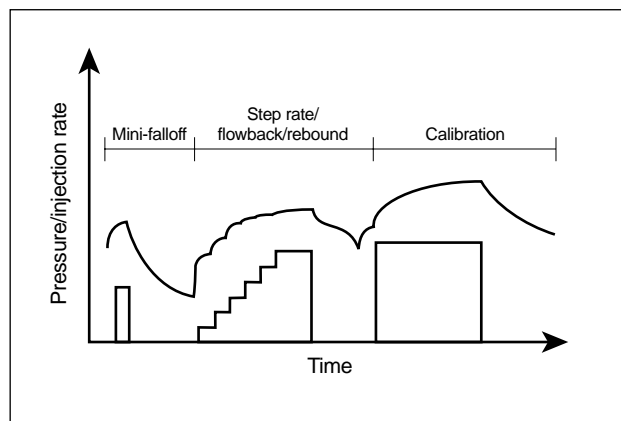


**Figure 9-45.** Formation calibration testing sequence.

process based on these tests.

### 1. Review existing information pertinent to fracturing

A properly calibrated sonic log (see Chapter 4) provides an excellent basis for assessing the formation stress profile. It can also be used to identify lithologic aggregates for developing an understanding of the zone layers. In its absence, a standard gamma ray or spontaneous potential log should be applied to define the depth and thickness of the layers. The permeable zone thickness (i.e., the thickness over which fluid loss occurs) can be identified using specialized magnetic resonance logs that directly measure permeability. This information can also be obtained from the separation of various resistivity measurements, which indicates drilling fluid invasion and therefore a finite permeability.

An estimate of the formation stresses can be derived by history matching prior fracture treatments in offset wells. This information can be used to characterize the fluid leakoff behavior as well as calibrate either sonic or gamma ray logs (Smith *et al.*, 1989) to obtain the stress variation over the depth of interest. Where available, laboratory core tests should be used to obtain related information (e.g., mechanical properties, existence of natural fissures, fluid-loss behavior).

### 2. Determine reservoir production parameters

The reservoir pressure and permeability are best determined from a well test. In its absence, the information can be obtained using the mini-falloff test. The mini-falloff test attempts to propagate a short, inefficient fracture to attain the required

reservoir transitional or pseudoradial flow (see Section 9-6) within an acceptable data-recording period. This objective is best achieved by applying the operational guidelines provided in “Guidelines for the field application of after-closure analysis” in the Appendix to this chapter. Using an a priori estimate of the reservoir pressure reduces uncertainty in the after-closure analysis.

Pore pressure and permeability are the bases of the reservoir’s producing potential and are required for an economics-based design (see Chapters 5 and 10).

### 3. Define closure pressure

The preferred method for objectively determining the fracture closure pressure is a step rate/flowback test (see “Estimating closure pressure” in the Appendix to this chapter). For low to moderate permeabilities, the step rate test typically follows the mini-falloff test (Fig. 9-45). In higher permeability formations, it follows the calibration test because the subsequent loss of completion fluid with which the step rate test is performed is significantly reduced relative to fluid loss before the calibration test.

### 4. Characterize fracture geometry

The character of fracture growth is identified during a calibration test by the analysis of pressure during pumping (see Section 9-4). The analysis also defines the formation pressure capacity (see Section 9-4.6) and can be used to calibrate the fracture compliance through pressure matching. The injection pressure is used to determine the bounding stresses (Eq. 9-39). This additional stress measure, in conjunction with an estimate of the closure pressure, provides the basis for a linear calibration for correcting a sonic-based stress log for the particular lithologic setting (Nolte and Smith, 1981; Nolte, 1988a).

### 5. Identify near-wellbore problems

A short step-down test (see Sidebar 9E) at the end of the injection period can be used to identify the magnitude and severity of near-wellbore problems. Net pressure analyses (e.g., log-log plots) should be based on the bottomhole pressure corrected to reflect measurements of near-wellbore pressure that is not associated with the fracture behavior.

### 6. Characterize fluid leakoff

A pressure decline analysis performed during the calibration test closing period and the previously calibrated fracture compliance produce the most reliable estimate of the fluid-leakoff parameters (see Section 9-5). They also determine the treatment efficiency, using an estimate of spurt from the after-closure linear flow analysis. The fluid-loss parameters are used to provide a measure of the fracture length (see Section 9-5.2).

The shut-in pressure during the closing of a calibration test can also be used to infer the closure pressure (see “Estimating closure pressure” in the Appendix to this chapter). This analysis, however, is highly subjective, and caution should be exercised during its application.

### 7. Assess after-closure response

Calibration test shut-in pressure should be monitored for a duration that is at least twice that of the closure time  $t_c$ . This enhances the prospect that a majority of the recorded after-closure response period is not masked by complications arising from polymer injection and that a well-established linear flow response is obtained. The pressure during the linear flow period is used to estimate spurt (see Section 9-6.8), which in conjunction with the shut-in analysis provides the treatment efficiency. Linear flow may be completely absent in a high-mobility reservoir.

The operational guidelines outlined in “Guidelines for the field application of after-closure analysis” in the Appendix to this chapter should be applied to prevent additional contaminating effects on the after-closure pressure data, which could lead to an inconclusive linear flow analysis.

### 8. Crossvalidate evaluation results

Information derived from the after-closure linear flow response, in combination with the previous estimate of reservoir transmissibility, provides an independent perspective for the fracture length (see Section 9-6.8). Agreement between this length estimate and that determined from the preclosure analysis indicates consistency in the pressure analysis.

#### 9. Conduct pressure history matching

The previously obtained fracture parameter estimates (i.e., zone mechanical parameters and fluid properties) can be refined through history matching the simulated pressure with the pressure measured during the calibration test. Care should be taken, however, to prevent the occurrence of nonuniqueness, an inherent limitation in pressure matching (see Section 9-7.2). This shortcoming can be prevented by performing a comprehensive evaluation and testing procedure to limit the number of unknowns as well as eliminate unrealistic solutions.

#### 10. Verify against propped treatment pressure response

The evaluation can be further refined for future treatments by matching pressures during the propped treatment and comparing the required parameter set for this treatment with that obtained from the calibration treatment. Conformity between these two parameter sets provides confidence in the fracture parameters. In the case of disagreement, a reanalysis should be conducted with emphasis on deviations from ideal behavior. A more authoritative measure of the correctness of the predicted parameters is agreement among parameter sets obtained in offset wells, with suitable corrections made to account for differences in the formation thicknesses, well completions, fracturing schedules or fracturing fluid systems.

# Appendix: Background for Hydraulic Fracturing Pressure Analysis Techniques

Sunil N. Gulrajani and K. G. Nolte, Schlumberger Dowell

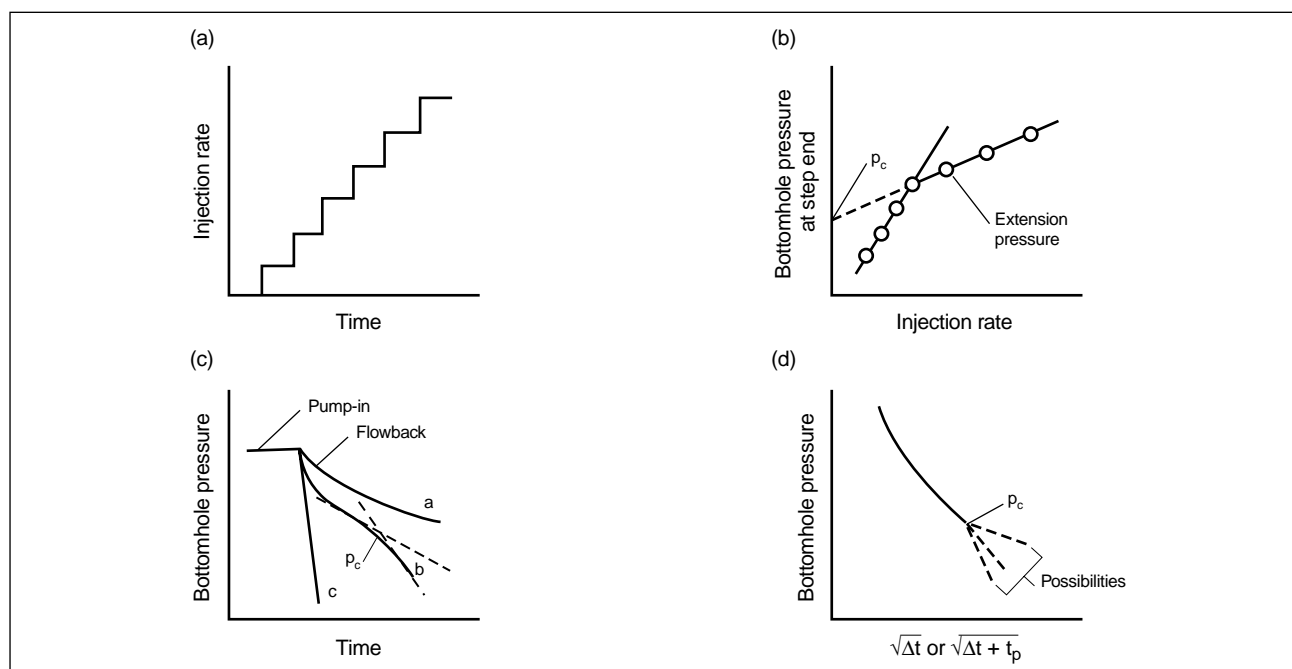
## Estimating closure pressure

The distinction between the formation closure pressure and the local stress is discussed in Sidebar 9A. The closure pressure  $p_c$  is distinguished from the minimum stress  $\sigma_{min}$  because  $\sigma_{min}$  generally varies in magnitude and direction over the gross pay interval (i.e., the zone between meaningful stress barriers) whereas  $p_c$  provides a global average for the interval.

Field procedures for estimating these two stress measures differ in two primary ways. First, estimating the magnitude of the local stress requires the creation of a small fracture by using a relatively small fluid injection rate and volume. Determining  $p_c$  requires the creation of a fracture over the entire thickness of the gross pay interval, which requires a much larger injection rate and volume. Second, a smaller net pressure occurs when a smaller fracture

is created, and the shut-in pressure is commonly used as a first-order approximation of the stress. Significantly higher net pressure, however, occurs with the procedures employed to determine  $p_c$ . Thus,  $p_c$  can be considerably different from the instantaneous shut-in pressure (ISIP), and it must be estimated with alternative procedures.

Techniques commonly used to determine  $p_c$  are the step rate, shut-in decline and flowback tests (Appendix Fig. 1) (see Section 3.6-2). Step rate and flowback tests are conducted exclusively to determine  $p_c$ . The shut-in decline test is used in conjunction with a calibration test, which is usually conducted to quantify fluid-loss behavior (see Section 9-5). The value of  $p_c$  can also be estimated from injection pressure derivative analysis (see Sidebar 9C) or after-closure linear flow analysis (see Section 9-6).



**Appendix Figure 1.** Tests to determine closure pressure (after Nolte, 1982): (a) step rate test, (b) bottomhole pressure plotted versus injection rate to infer the values of  $p_c$  and the fracture extension pressure, (c) combined step rate and flowback tests (a = rate too low, b = correct rate for  $p_c$  at curvature reversal and c = rate too high) and (d) shut-in decline test displayed on a square-root plot ( $\Delta t$  = shut-in time and  $t_p$  = injection time into the fracture).

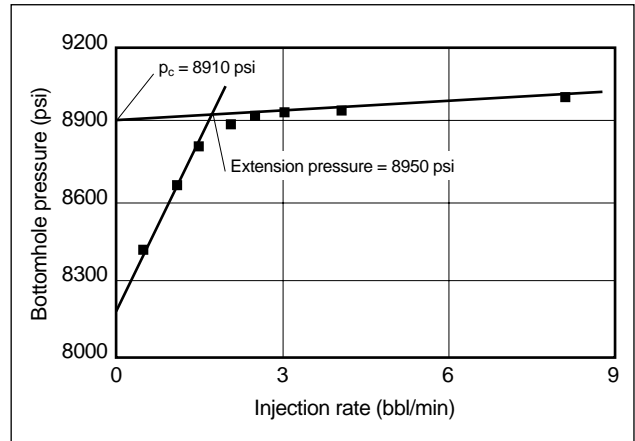
## Step rate test

The step rate test is conducted solely to determine  $p_c$ . In low-permeability reservoirs, the test generally is performed with completion fluids (e.g., treated water). The use of polymer fluids may be required in high-permeability reservoirs (Smith, 1985) to control potential fluid loss and ensure fracture creation at lower injection rates.

The step rate test can be conducted as the pumping phase of either the flowback or shut-in decline test. The time duration of the individual injection steps should be equal (Appendix Fig. 1a) and can be relatively small (i.e., the time required for the pumps to change and maintain a constant rate and the pressure to be recorded, typically 1 or 2 min). The injection rate increments over the successive steps should also be approximately the same. When the step rate test is conducted as part of a flowback or decline test, the last step is maintained for a longer duration (i.e., 5 to 10 min) to ensure the creation of a sufficient-size fracture. Injection rates typically vary from 1 to 10 bbl/min in moderate-permeability formations, and the rates in low-permeability formations are about one-half of these values. Ideally, the injection rates for three of the steps should fall below the extension pressure to define matrix injection prior to fracturing, and a similar set of values should be obtained above the extension pressure.

The fracture closure and extension pressure are inferred from a crossplot of the bottomhole pressure at the end of each injection step and the injection rate (Appendix Fig. 1b). The plot is characterized by two straight lines, with matrix injection represented by the line with the steeper slope and fracture extension characterized by the shallower sloping line. The intersection of the two lines provides an estimate of the fracture extension pressure, which is the upper bound for  $p_c$ . Typically, the extension pressure is 50 to 200 psi greater than  $p_c$ , as shown on the pressure versus rate plot in Appendix Fig. 2 for the step rate test in Fig. 9-8b. This larger value represents effects from fluid friction pressure within the fracture and resistance to fracture extension (i.e., toughness).

Laboratory tests (Rutqvist and Stephansson, 1996) also indicate that the y-axis intercept of the shallower sloped line that represents fracture extension on the crossplot provides a first-order approximation for  $p_c$ , even when the steeper line that represents matrix injection is absent. This interpretation, however,

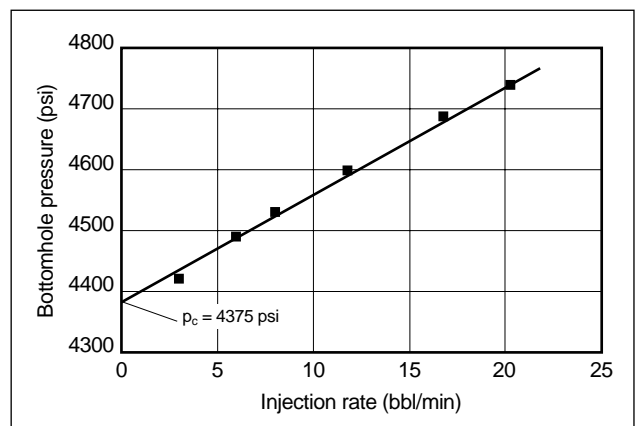


**Appendix Figure 2.** Pressure versus rate analysis for the step rate test in Fig. 9-8.

should not be used in preference to also obtaining a well-defined straight line for matrix injection, which is the only means to ensure that fracture extension occurred during the test.

The y-axis intercept interpretation was used to analyze the step rate test illustrated in Fig. 9-10b. The pressure versus rate plot is entirely characterized by the fracture extension line (Appendix Fig. 3), which has a y-axis intercept of 4375 psi for the estimated value of  $p_c$ .

An indication of a valid step rate test is that the extrapolated pressure for the zero rate of the line representing matrix injection should equal approximately the bottomhole pressure preceding the test. The zero-rate pressure is the reservoir pressure, if significant amounts of fluids were not previously injected. This quality control check can also be used while conducting the test when no apparent slope change is observed for the pressure versus injection rate plot.



**Appendix Figure 3.** Pressure versus rate analysis for the step rate test in Fig. 9-10.



## Shut-in decline test

The shut-in decline test can be used with either a step rate or calibration test. The decline data are displayed on a square-root plot (Appendix Fig. 1d) or a  $G$ -plot (Fig. 9-29) that assumes square-root exposure time for the fluid-loss behavior. The closure pressure is inferred where the slope changes on either plot. The derivative should be used to magnify the change of slope and enhance its identification.

Either of the specialized plots, however, may be completely devoid of a significant slope change or may exhibit multiple slope changes. In general, up to six events could be associated with a slope change:

- height recession from the bounding layers
- transition between fracture extension and recession
- fracture closure
- postclosure consolidation of the polymer filter cake and fracture face irregularities
- reservoir linear flow
- reservoir radial flow.

Consequently, the shut-in test commonly fails to provide an objective indication of  $p_c$  and should not be used as the primary procedure for determining it.

Experience indicates that the square-root plot may provide a better indication of closure for fluids that do not have effective fluid-loss control from wall-building behavior, whereas the  $G$ -plot may provide a better indication for fluids with wall-building behavior. The analysis of decline data typically uses both plots to determine the value of  $p_c$ .

Other specialized plots have been used, although less frequently, to identify  $p_c$ . These include the log-log shut-in plot (Elbel *et al.*, 1984) and multidimensional derivative analysis. In contrast to the square-root and  $G$ -function plots, the interpretation philosophy of these plots is based on identifying reservoir flow regime changes to obtain bounding values of  $p_c$ .

## Flowback test

The preferred method for determining  $p_c$  is a combination of the step rate test (with an extended last step) and flowback test (Appendix Fig. 1c). The essential element of the flowback test involves a flowback period at a constant rate that is between  $\frac{1}{2}$  and  $\frac{3}{4}$  of the last injection rate (i.e., at a rate that is a meaning-

ful fraction of the in-situ leakoff rate). With the assumption that a fracture has been created, the pressure response during flowback has two distinctly different profiles while the fracture is closing and after the fracture closes. Comprehensive simulations (Plahn *et al.*, 1997) indicate that the fracture  $p_c$  is identified by the intersection of the two straight lines that define these two periods. The increasing rate of pressure decline for the postclosure period results from fluid flow through the pinched fracture width (i.e., induced fluid choking) in the near-wellbore region induced by fluid flowback. The characteristic “lazy-S” signature exhibited by the pressure during the flowback period is in contrast to the multiple inflections commonly observed with the shut-in decline test. Therefore, the flowback test provides a more objective indication of closure relative to the decline test.

Maintaining a constant flowback rate as the pressure decreases is critical for a flowback test. This objective requires a field-rugged, debris-resistant flow regulator that both measures and controls the flowback rate. The flow regulator should be preset for the desired rate at the pressure expected following the end of injection, and it should be isolated by a closed valve during pumping. Presetting the flow regulator is best achieved by opening it during the last period of the step rate test to establish the desired flowback rate prior to the actual test. The effect of the additional fluid loss can be compensated for by increasing the injection rate. Fluid injection is terminated once the desired constant flowback rate has been attained, and this rate is then maintained throughout the flowback period.

Experience shows that an adjustable choke often plugs because of pipe dope and other debris loosened into the wellbore during the injection period. A gate valve is preferable for controlling the flowback rate. In addition, a pressure sensor and fixed choke at the end of the flowback line can be substituted for a flow meter to reliably measure the flow rate, particularly when the rate is low (i.e., 3 bbl/min or less). Tabulated values for the pressure drop versus the flow rate through standard choke sizes are used to select the choke size that will provide the pressure change necessary for a reliable pressure measurement at the anticipated flowback rate.

The flowback test is frequently repeated for verification and selection of a more optimum flowback rate. The first flowback period should be of sufficient duration to ensure that fracture closure in the primary

zone is recorded. Pressure during this test, however, should be controlled to prevent the production of reservoir fluids into the wellbore. The second flowback test may be preceded by either a step rate test or a constant injection rate and should end after the indication of a curvature reversal that clearly confirms the  $p_c$  estimate from the first test.

The pressure decline for the second test is limited to obtain an optimum rebound pressure. The rebound pressure is the nearly constant pressure that occurs following a short period of increasing pressure after shut-in of the flowback test (see Fig. 3-26b). This stabilized pressure is generally near to or smaller than  $p_c$  and provides its lower bound estimate. The rebound pressure is also an effective tool for estimating  $p_c$  when near-wellbore flow restrictions, as discussed in Section 9-4.9, are large. During the flowback period, these near-wellbore effects cause prediction of a lower estimate of  $p_c$  because of the additional flow restriction in the near-wellbore region. The wellbore rebound pressure, however, is unaffected by the restriction and should provide an accurate lower bound estimate of  $p_c$  (Plahn *et al.*, 1997).

In conclusion, the combination of the upper bound estimate of  $p_c$  from the intersection of the matrix and fracture extension lines on a step rate test, the lower bound of  $p_c$  determined from the rebound pressure and the estimate of  $p_c$  from the y-axis intercept of the fracture extension line as well as the intersection of the two lines during flowback provides multiple, independent values that establish a firm basis for defining  $p_c$ .

## Test sequence

Because the mini-falloff test (see Section 9-6.2) that characterizes the production potential should be conducted in an initially undisturbed reservoir, it should always be the first injection within the calibration testing sequence (Fig. 9-45). The subsequent application sequence of the step rate/flowback and calibration/shut-in tests generally depends on the formation fluid-loss characteristics.

For low fluid-loss conditions, the step rate/flowback test to establish  $p_c$  should precede the fracture calibration test where the closure time could be long (e.g., up to 3 times the injection time). This prior estimate of  $p_c$  can be used to ensure that the shut-in pressure during the subsequent calibration test is monitored during the complete time of fracture closure.

For moderate to high fluid-loss conditions, the calibration test generally exhibits a closing period that is less than the injection time, and prior estimate of  $p_c$  is not required for a shut-in period that approximates the injection period. Conducting the step rate/flowback test after the fracture calibration test reaps the following advantages from the prior fluid injection:

- Breakdown of the complete gross pay interval is ensured.
- Residual fluid-loss control from unbroken polymer or additives in the fracturing fluid enables fracturing using moderate injection rates with the completion fluid.
- Because the poroelastic effects have stabilized, the step rate/flowback test better replicates the stress conditions that occurred during the preceding calibration treatment.

## Guidelines for the field application of after-closure analysis

The reservoir response during linear flow and either radial or transitional flow is required to conduct a comprehensive analysis of the after-closure period. Several factors, however, can prevent obtaining information for one or more of the flow regimes. For example, radial flow may not be attained within a reasonable time period for the high injection rates and leakoff-resistant fracture fluids used during conventional fracturing operations. In addition, the after-closure pressure data may be compromised because of several undesirable communication effects between the wellbore and formation. Therefore, the calibration testing sequence must be engineered to provide the requisite pressure data (Talley *et al.*, 1999). The following guidelines increase the likelihood of obtaining a comprehensive, objective after-closure analysis.

- Unless a bottomhole shut-off valve is employed, the reservoir pressure should ideally be equal to or greater than the hydrostatic pressure of the wellbore fluid. Vacuum-induced fluid injection violates the no-flow assumption of the analysis for the after-closure period.
- The wellbore must be free of gas to ensure that correct values of the hydrostatic pressure and injected volume are used in the analysis and to

minimize wellbore expansion effects during pressure falloff. For gas reservoirs, this can be achieved by conducting the injection test before a production period. Alternatively, the gas should be circulated from the wellbore or bullheaded into the formation. An extended shut-in period can be required after bullheading to allow the pressure transient to dissipate before liquid injection resumes. A relatively small volume of gas injection ahead of the fluid is acceptable—e.g., gas is circulated from the intermediate casing but remains in the shorter liner.

- Circulating or bullheading (potentially with a long shut-in period) may be similarly required to spot the fracturing fluid at the perforations for the fracture calibration test. The residual reservoir response from injection of a significant volume of low-efficiency wellbore fluid causes the linear flow analysis to indicate an unrealistically high spurt loss (Talley *et al.*, 1999).
- Like preclosure analysis, after-closure analysis is an inverse problem that is inherently nonunique (see Section 9-7.2). The objectivity of after-closure analysis can be improved by obtaining an a priori estimate of the reservoir pressure, particularly if the after-closure period is abbreviated (e.g., before wellbore vacuum) and either the closure time (Nolte *et al.*, 1997) or spurt loss is inferred. The reservoir pressure estimate can be obtained
  - as the stabilized bottomhole pressure measured prior to fluid injection into the reservoir
  - as the stabilized surface pressure measured prior to fluid injection into an overpressured reservoir
  - from the surface pressure and hydrostatic column estimated through an accurate measurement of the fluid injected to completely fill the wellbore for an underpressured reservoir
  - from an accurate reservoir pressure gradient established for the field.
- In deep or hot reservoirs, bottomhole gauges are necessary because wellbore fluid expansion from the decreasing pressure and increasing temperature during shut-in decrease the hydrostatic pressure. Excessive expansion of the fluid may eventually violate the no-flow condition to the degree that the longer term data are corrupted, particularly for residual gas in the wellbore. Mitigation of these effects, like for a wellbore vacuum, requires a downhole shut-in device.

- It is unlikely that both linear and radial flow will occur during a decline period (see Section 9-6.2). The testing sequence illustrated in Fig. 9-45 is suggested to increase the likelihood of obtaining information pertinent to both the linear and radial flow periods. The mini-falloff test should be applied to determine the radial flow parameters. The subsequent calibration test is more likely to attain linear flow. The radial flow response for the calibration test can be anticipated from the reservoir information derived from the mini-falloff test (see “Fracture length” in Section 9-6.7).
- To attain radial flow within a reasonable time frame, the mini-falloff test should adhere to the following injection rate criterion, presented in conventional oilfield units:

$$\frac{q_i(\text{bbl / min})}{h_f(\text{ft})} \leq 4 \times 10^{-6} \frac{k(\text{md})}{\mu(\text{cp})} \frac{C_L}{C_R} (p_c - p_i(\text{psi})). \quad (1)$$

If the fluid loss is controlled by the reservoir, as desired for the test, the ratio of the fluid-loss coefficients  $C_L$  and  $C_R$  becomes unity and a higher injection rate is possible. The equation provides an equality for a dimensionless time of 1.0 (i.e., the beginning of radial flow during the injection period on Fig. 9-38). The guideline requires using estimates of the reservoir parameters and fluid-loss characteristics to design the mini-falloff test. In general, Appendix Eq. 1 provides an operationally reasonable rate for radial flow with a short monitoring period in a reservoir with a mobility greater than about 5 md/cp. For reservoirs with lower values of mobility, transitional flow resulting from injection rates greater than guideline can be used to determine the reservoir parameters with a type-curve-based analysis.

- Volume has a minimal effect on dimensionless time and hence the time for development of radial flow because of the quasistationary value of dimensionless time for a constant injection rate. However, a minimum volume must be pumped to ensure an accurate measure of the volume injected through the perforations because the transmissibility is proportional to the injected volume (Eq. 9-93).
- If polymer fluids are used (see Section 9-6.3) the pressure data obtained after fracture closure can be corrupted by continued consolidation (i.e., squeez-

ing) of the fracture faces and filter cake. The consolidation period lasts for a time approximating the combined injection and closing times. The calibration test shut-in pressure should therefore be monitored for a time interval that is at least 2 to 3 times the total closure time  $t_c$ . Similarly, the shut-in period for a mini-falloff test should be at least 4 to 5 times the total closure time. These guidelines for the shut-in time increase the likelihood that adequate, representative pressure data are obtained for a valid after-closure analysis.

## Mathematical relations for fluid loss

Derived in this section of the Appendix to Chapter 9 are the relations used for pressure evaluation prior to fracture closure.

### Fluid-loss relations

Two fundamental relations are required to derive the expressions for fluid loss. The first relation describes the nature of fracture growth with respect to time. The second relation is based on the expression for fluid loss introduced by Carter (1957).

The evolution of the fracture area is assumed to follow a power law relation with time in which the area monotonically increases with time. The properties of the injected fluid and the pump rate are assumed to be relatively constant. The power law expression relates any intermediate fracture area  $a$  created at a time  $\tau$  to the total fracture area  $A$  at the current time  $t$ :

$$\frac{a}{A} = \left( \frac{\tau}{t} \right)^\alpha \quad (2)$$

$$\frac{\tau}{t} = \left( \frac{a}{A} \right)^{1/\alpha}, \quad (3)$$

where  $\alpha$  is referred to as the area exponent. The exponent  $\alpha$  is also the log-log slope of  $A$  versus  $t$ , as shown by differentiating Appendix Eq. 3 with respect to time:

$$\alpha = \frac{t}{A} \frac{dA}{dt}. \quad (4)$$

The value of  $\alpha$  depends on the fluid efficiency. Bounding values for  $\alpha$  corresponding to low and high

treatment efficiencies are derived subsequently in this Appendix. The exponent generally decreases throughout the injection time, but the change is relatively small and can be ignored. For the commonly used crosslinked polymer fluids, the exponent is typically 0.6.

Three mechanisms govern the fluid filtration process during fracturing, as discussed in Section 6-4. The square root of exposure time relation, introduced by Carter (1957), is applied to predict the cumulative effect of these mechanisms on the rate of fluid loss. A more general expression used in this Appendix includes fluid-loss behavior dominated by a non-Newtonian filtrate. Consequently, in contrast to Eq. 5-1, the flux  $u_L$ , defined as the rate of fluid loss per unit leakoff area, is expressed as

$$u_L = \frac{2C_L}{(t - \tau)^{1-\theta}}, \quad (5)$$

where  $t$  is the time since the beginning of pumping,  $C_L$  is the fluid-loss coefficient, and  $\theta$  is the fluid-loss exponent. The coefficient 2 in Appendix Eq. 5 accounts for leakoff over the two walls of the fracture.

The specific fluid-loss volume  $v_L$ , defined as the fluid-loss volume  $V_L$  per unit leakoff area, is obtained by the time integration of Appendix Eq. 5:

$$v_L = \int_0^t u_L dt = \frac{2C_L}{\theta} (t - \tau(a))^\theta. \quad (6)$$

Parlar *et al.* (1995) showed that  $\theta$  is related to the power law exponent  $n_f$  of the filtrate that invades the reservoir during the leakoff process:

$$\theta = \frac{n_f}{1 + n_f}. \quad (7)$$

As discussed in Chapter 8, a filter cake is deposited by a wall-building fluid along the fracture in low-permeability reservoirs and within the formation in high-permeability reservoirs. A Newtonian filtrate (i.e., water) is created during the process. Under these conditions,  $n_f = 1$  and Appendix Eq. 5 reduces to Eq. 5-1, which is Carter's square root of exposure time relation for the fluid-loss rate (i.e.,  $\theta = 1/2$ ). Non-wall-building fracturing fluids invade high-permeability reservoirs. The resulting filtrate fluid is typically non-Newtonian, with  $n_f < 1$  and  $\theta < 1/2$ . In addition, the extensional viscosity behavior of viscoelastic filtrates above a threshold filtration rate can exhibit relatively large values of  $n_f$  (Chauveteau *et al.*, 1986). The value of  $\theta$  in this case is greater than  $1/2$  and can

approach unity. A value of  $\theta$  that is different from  $\frac{1}{2}$  has also been proposed to model the effect of natural fissures (Soliman *et al.*, 1990).

## Fluid-loss volume with the Carter-based leakoff model

The rate of fluid loss associated with Carter-based leakoff behavior (i.e., the contribution of  $C_L$  over an elemental leakoff area  $da$ ) can be obtained by substituting Appendix Eq. 3 into Appendix Eq. 5:

$$q_L(da, t) = \frac{2r_p C_L}{t_p^{1-\theta}} \frac{da}{(t_{\alpha D} - \xi^{1/\alpha})^{1-\theta}}, \quad (8)$$

where  $r_p$  is the ratio of the fracture surface area available for fluid loss to the gross fracture area and  $t_p$  is the injection or pumping time. The dimensionless parameters  $t_{\alpha D}$  and  $\xi$  are defined as

$$t_{\alpha D} = \frac{t}{t_p} \quad (9)$$

$$\xi = \frac{a}{A_f}, \quad (10)$$

where  $A_f$  is the fracture surface area at the end of pumping.

The total rate of fluid loss is obtained by the integration of Appendix Eq. 8 over the fracture area:

$$q_L(A_f, t) = \frac{2r_p C_L A_f}{t_p^{1-\theta}} f(t_{\alpha D}, \alpha, \theta), \quad (11)$$

where the function  $f(t_{\alpha D}, \alpha, \theta)$  is defined as

$$f(t_{\alpha D}, \alpha, \theta) = \int_0^1 \frac{d\xi}{(t_{\alpha D} - \xi^{1/\alpha})^{1-\theta}} \quad t_{\alpha D} \geq 1. \quad (12)$$

An expression for the  $C_L$  component of the fluid-loss volume  $V_{L,C}$  is similarly obtained by substituting Appendix Eqs. 9 and 10 into Appendix Eq. 6 and integrating over the area:

$$V_{L,C} = 2r_p C_L t_p^\theta A_f g(t_{\alpha D}, \alpha, \theta), \quad (13)$$

where the function  $g(t_{\alpha D}, \alpha, \theta)$  is defined as

$$g(t_{\alpha D}, \alpha, \theta) = \frac{1}{\theta} \int_0^1 (t_{\alpha D} - \xi^{1/\alpha})^\theta d\xi \quad t_{\alpha D} \geq 1. \quad (14)$$

The functions  $f(t_{\alpha D}, \alpha, \theta)$  and  $g(t_{\alpha D}, \alpha, \theta)$  are usually presented in terms of the dimensionless shut-in time

$\Delta t_D$ , which is defined as the ratio of the shut-in time  $\Delta t$  to the pumping time  $t_p$ :

$$\Delta t_D = \frac{t - t_p}{t_p} = \frac{\Delta t}{t_p} = t_{\alpha D} - 1. \quad (15)$$

The time functions  $f(t_{\alpha D}, \alpha, \theta)$  and  $g(t_{\alpha D}, \alpha, \theta)$  can be expressed in terms of  $\Delta t_D$ :

$$f(\Delta t_D, \alpha, \theta) = \int_0^1 \frac{d\xi}{(1 + \Delta t_D - \xi^{1/\alpha})^{1-\theta}} \quad \Delta t_D \geq 0 \quad (16)$$

$$g(\Delta t_D, \alpha, \theta) = \frac{1}{\theta} \int_0^1 (1 + \Delta t_D - \xi^{1/\alpha})^\theta d\xi \quad \Delta t_D \geq 0. \quad (17)$$

Valkó and Economides (1993b) showed that the functions  $f(t_{\alpha D}, \alpha, \theta)$  and  $g(t_{\alpha D}, \alpha, \theta)$  are part of the hypergeometric family of functions or their subset of incomplete beta functions (Meyer and Hagel, 1989). Either of these function families is relatively complicated, but simple analytical expressions can be obtained for a limited set of values, as discussed subsequently.

## Cumulative fluid-loss volume

The total fluid-loss volume at the end of pumping  $V_{Lp}$  comprises the cumulative contributions of its  $C_L$  fluid-loss component  $V_{Lp,C}$  and spurt  $V_{L,S}$ :

$$V_{Lp} = V_{Lp,C} + V_{L,S}. \quad (18)$$

An expression for  $V_{Lp,C}$  can be obtained by substituting  $\Delta t_D = 0$  into Appendix Eq. 13:

$$V_{Lp,C} = V_{L,C}(\Delta t_D = 0) = 2r_p C_L t_p^\theta A_f g_0(\alpha, \theta), \quad (19)$$

where the function  $g_0(\alpha, \theta)$  represents the value of the  $g$ -function in Appendix Eq. 17 when  $\Delta t_D = 0$ :

$$g_0(\alpha, \theta) = g(\Delta t_D = 0, \alpha, \theta) = \frac{1}{\theta} \int_0^1 (1 - \xi^{1/\alpha})^\theta d\xi. \quad (20)$$

Spurt occurs only for wall-building fluids. It accounts for the fluid-loss volume prior to the creation of a filter cake and is applicable only during the fracture propagation period. Following the spurt period, wall-building fluids exhibit a Newtonian filtrate during the fluid-loss process (i.e.,  $n_f = 1$  or  $\theta = \frac{1}{2}$ ). The total volume of fluid lost to spurt follows from definition of the spurt coefficient  $S_p$ :

$$V_{L,s} = 2r_p S_p A_f. \quad (21)$$

The cumulative fluid-loss volume during injection is obtained by substituting Appendix Eqs. 19 and 21 into Appendix Eq. 18:

$$V_{Lp} = 2r_p \kappa C_L \sqrt{t_p} A_f g_0 \left( \alpha, \theta = \frac{1}{2} \right) \quad \theta = \frac{1}{2} \quad (22)$$

$$V_{Lp} = 2r_p C_L t_p^\theta A_f g_0(\alpha, \theta) \quad \theta \neq \frac{1}{2}. \quad (23)$$

Appendix Eq. 22 is expressed in terms of the spurt factor  $\kappa$ , which provides for the increase in fluid loss over the no-spurt condition:

$$\kappa = 1 + \frac{S_p}{g_0 \left( \alpha, \theta = \frac{1}{2} \right) C_L \sqrt{t_p}}. \quad (24)$$

The rate of increase in the fracture area decreases significantly at the end of pumping. Spurt-dependent fluid loss therefore also reduces relatively quickly following the cessation of fluid injection and is assumed to terminate at the time  $t = t_p$ . The total fluid-loss volume during a shut-in period is represented entirely by its  $C_L$  component  $V_{Ls,C}(\Delta t)$ :

$$V_{Ls}(\Delta t) = V_{Ls,C}(\Delta t). \quad (25)$$

An expression for  $V_{Ls}(\Delta t)$  results from subtracting Appendix Eq. 19 from Appendix Eq. 13:

$$V_{Ls}(\Delta t) = 2r_p C_L \sqrt{t} A_f \times \left( g \left( \Delta t_D, \alpha, \theta = \frac{1}{2} \right) - g_0 \left( \alpha, \theta = \frac{1}{2} \right) \right) \quad \theta = \frac{1}{2} \quad (26)$$

$$V_{Ls}(\Delta t) = 2r_p C_L t^\theta A_f \left( g(\Delta t_D, \alpha, \theta) - g_0(\alpha, \theta) \right) \quad \theta \neq \frac{1}{2}. \quad (27)$$

## Newtonian filtrate control

Fracturing fluids produce a Newtonian filtrate following the deposition of a filter cake. For this case,  $n_f = 1$ , and Appendix Eq. 7 indicates that  $\theta = \frac{1}{2}$ . Analytical expressions for fluid loss can be derived for bounding values of  $\alpha$ . The lower bound value corresponds to negligible efficiency and is obtained by substituting

$\theta = \frac{1}{2}$  in Appendix Eq. 41, whereas Appendix Eq. 40 provides the upper bound. An upper bound of unity is assumed because it provides simple, closed-form expressions. The bounding values of  $\alpha$  for a wall-building fluid are therefore as in Eq. 9-43:

$$\frac{1}{2} < \alpha < 1.$$

Analytical equations for  $f(\Delta t_D, \alpha, \theta)$ ,  $g(\Delta t_D, \alpha, \theta)$  and  $g_0(\alpha, \theta)$  are obtained by substituting the bounding values of  $\alpha$  into Appendix Eqs. 16, 17 and 20, respectively, and integrating the resulting expressions (Nolte, 1979; Smith, 1985):

$$f(\Delta t_D) \Big|_{\theta=\frac{1}{2}} = \begin{cases} \sin^{-1}(1 + \Delta t_D)^{-1/2} & \alpha = \frac{1}{2} \\ 2 \left( (1 + \Delta t_D)^{1/2} - \Delta t_D^{1/2} \right) & \alpha = 1 \end{cases} \quad (28)$$

$$g(\Delta t_D) \Big|_{\theta=\frac{1}{2}} = \begin{cases} (1 + \Delta t_D) \sin^{-1}(1 + \Delta t_D)^{-1/2} + \Delta t_D^{1/2} & \alpha = \frac{1}{2} \\ \frac{4}{3} \left( (1 + \Delta t_D)^{3/2} - \Delta t_D^{3/2} \right) & \alpha = 1 \end{cases} \quad (29)$$

$$g_0 \Big|_{\theta=\frac{1}{2}} = \begin{cases} \pi/2 & \alpha = \frac{1}{2} \\ 4/3 & \alpha = 1. \end{cases} \quad (30)$$

All these functions are well behaved. Their values at any other value of  $\alpha$  can be obtained through simple interpolation between bounding values.

## Non-Newtonian filtrate control

A non-Newtonian filtrate occurs with fracturing fluids that exhibit a power-law-based rheology and do not develop an effective filter cake. In this case,  $n_f \neq 1$  and if the filtrate controls fluid loss,  $\theta$  deviates from its commonly assumed value of  $\frac{1}{2}$ . These conditions limit the general analytical expressions to  $g_0$  only. Explicit integration of Appendix Eq. 20 gives

$$g_0(\alpha, \theta) = \frac{\Gamma(1 + \theta) \Gamma(1 + \alpha)}{\theta \Gamma(1 + \alpha + \theta)}, \quad (31)$$

where  $\Gamma(x)$  is the gamma function.

Analytical expressions for the fluid-loss rate and volume functions (i.e., Appendix Eqs. 16 and 17,

respectively) can be obtained for only select values of their arguments that are applicable to specific field applications. The upper bound of  $\alpha = 1$  applies also for  $\theta \neq 1/2$ , and the corresponding functions are

$$f(\Delta t_D, \alpha = 1, \theta) = \frac{1}{\theta} \left[ (1 + \Delta t_D)^\theta - \Delta t_D^\theta \right] \quad (32)$$

$$g(\Delta t_D, \alpha = 1, \theta) = \frac{1}{\theta(1+\theta)} \left[ (1 + \Delta t_D)^{1+\theta} - \Delta t_D^{1+\theta} \right]. \quad (33)$$

Simple analytical expressions for these functions also result for the value of  $\theta$  approaching unity, which is applicable for time-independent fluid-loss conditions. This fluid-loss behavior can be exhibited by viscoelastic fluids with a rapidly increasing extensional viscosity above a threshold filtration rate:

$$f(\Delta t_D, \alpha, \theta = 1) = 1 \quad (34)$$

$$g(\Delta t_D, \alpha, \theta = 1) = \frac{1}{1+\alpha} + \Delta t_D. \quad (35)$$

The integral forms for both functions are well behaved and therefore can be evaluated by numerical integration for other values of their arguments.

## Bounding values for fluid efficiencies

The fracture penetration and net pressure can be represented for the bounding values of high and low fluid efficiencies. When the efficiency  $\eta \rightarrow 0$ , all the injected volume can be assumed to have leaked off. It follows from Eq. 9-5 that

$$V_i \approx V_{Lp}. \quad (36)$$

From the relation  $V_i = q_i t$  and combining Appendix Eq. 36 with the generalized expression for fluid loss during pumping in Appendix Eq. 23:

$$A_f = \frac{q_i t}{2r_p C_L t^\theta g_0} \quad \eta \rightarrow 0 \quad (37)$$

$$\propto t^{1-\theta}.$$

For the alternative situation of extremely high fluid efficiencies ( $\eta \rightarrow 1$ ), the fluid-loss volume can be ignored. In this case, Eq. 9-5 reduces to

$$V_i \approx V_{fp}. \quad (38)$$

The evolution of the fracture area for high fluid efficiencies is obtained from this expression as

$$A_f = \frac{q_i t}{\langle \bar{w} \rangle} \quad \eta \rightarrow 1, \quad (39)$$

where  $\langle \bar{w} \rangle$  is the fracture width averaged over the fracture area. The bounding expressions for fracture penetration in Eqs. 9-32 through 9-34 are derived by combining Appendix Eqs. 37 and 39 with the fracture width relations in Eq. 9-27, for which the fracture area  $A_f$  is proportional to the half-length  $L$  for the PKN and KGD models and to  $R^2$  for the radial model. For the common occurrence of Newtonian fracturing fluid filtrate (i.e.,  $\theta = 1/2$ ):

PKN	$L \propto t^{1/2}$	$\eta \rightarrow 0$
	$L \propto t^{(2n+2)/(2n+3)}$	$\eta \rightarrow 1$
KGD	$L \propto t^{1/2}$	$\eta \rightarrow 0$
	$L \propto t^{(n+1)/(n+2)}$	$\eta \rightarrow 1$
Radial	$R \propto t^{1/4}$	$\eta \rightarrow 0$
	$R \propto t^{(2n+2)/(3n+6)}$	$\eta \rightarrow 1$

The time dependency of the net pressure  $p_{net}$  for the bounding values of  $\eta$  is obtained by combining its dependency on the fracture penetration for the three fracture geometry models in Eq. 9-25 with the three preceding equations to produce Eqs. 9-35 through 9-37:

PKN	$p_{net} \propto t^{1/4(n+1)}$	$\eta \rightarrow 0$
	$p_{net} \propto t^{1/(2n+3)}$	$\eta \rightarrow 1$
KGD	$p_{net} \propto t^{-n/2(n+1)}$	$\eta \rightarrow 0$
	$p_{net} \propto t^{-n/(n+2)}$	$\eta \rightarrow 1$
Radial	$p_{net} \propto t^{-3n/8(n+1)}$	$\eta \rightarrow 0$
	$p_{net} \propto t^{-n/(n+2)}$	$\eta \rightarrow 1$

## Bounding values for the area exponent

The bounding values for the area exponent  $\alpha$  correspond to negligible ( $\eta \rightarrow 1$ ) and dominant ( $\eta \rightarrow 0$ ) fluid loss to the formation. The upper bound  $\alpha_1$  in Eq. 9-43 assumes not only negligible fluid loss but also a constant fracture width. Because the width generally increases during injection, the upper bound

for the area growth is less than unity and independent of the loss exponent  $\theta$ . It is derived from the condition of  $\eta \rightarrow 1$  in Eqs. 9-32 through 9-34:

$$\alpha_1 = \begin{cases} (2n+2)/(2n+3) & \text{PKN} \\ (n+1)/(n+2) & \text{KGD} \\ (4n+4)/(3n+6) & \text{Radial} \end{cases} \quad \eta \rightarrow 1. \quad (40)$$

The lower bound  $\alpha_0$  follows from Appendix Eq. 37:

$$\alpha_0 = 1 - \theta \quad \eta \rightarrow 0. \quad (41)$$

For the typical value of  $\theta = 1/2$ , Appendix Eq. 41 shows that  $\alpha_0 = 1/2$ , which is the value used in Eq. 9-43.

## Postscreenout pressure relations

The material-balance relations following a peripheral screenout (i.e., constant fracture area following a screenout) can be written in a manner similar to Eq. 9-5 (Nolte, 1990). At any additional time following a screenout  $\Delta t_{so}$ , the change in fracture volume is equal to the additional injected slurry volume minus the volume of fluid lost to the formation through leakoff:

$$\Delta \langle \bar{w} \rangle A_{fso} = q_i \Delta t_{so} - V_{Lp}(\Delta t_{so}), \quad (42)$$

where the subscript *so* identifies the corresponding parameter value at screenout. Similarly, an expression for the fracture volume at screenout  $V_{fso}$  can be written as

$$V_{fso} = \eta_{so} V_{iso}, \quad (43)$$

where  $\eta_{so}$  is the fluid efficiency at screenout and  $V_{iso}$  is the volume injected prior to the screenout.

For an assumed constant injection rate  $V_{iso} = q_i t_{so}$ , Eq. 9-6 and Appendix Eq. 43 can be combined:

$$(\langle \bar{w} \rangle A_f)_{so} = \eta_{so} q_i t_{so} = \eta_{so} V_{Lp}(t_{so}) / (1 - \eta_{so}), \quad (44)$$

where  $V_{Lp}(t_{so})$  represents the cumulative volume of fluid lost prior to screenout and can be expressed in a manner similar to Appendix Eq. 22 for a wall-building fluid:

$$V_{Lp}(t_{so}) = 2r_p \kappa_{so} C_L \sqrt{t_{so}} A_f g_0(\alpha), \quad (45)$$

where  $\kappa_{so}$  is the spurt factor evaluated at  $t_{so}$ .

Because the same set of conditions as that following the end of injection is assumed to exist following a screenout, the expression for  $V_{Lp}(\Delta t_{so})$  is similar to that in Appendix Eq. 26:

$$V_{Lp}(\Delta t_{so}) = 2r_p A_f C_L \sqrt{t_p} (g(\Delta t_{Dso}) - g_0), \quad (46)$$

where the dimensionless time  $\Delta t_{Dso}$  is defined as the ratio of the time after screenout  $\Delta t_{so}$  to that at the onset of screenout  $t_{so}$ .

The change in the area-averaged fracture width following a screenout is obtained by dividing the terms in Appendix Eq. 42 with those in Appendix Eq. 44 and substituting the fluid-loss expressions from Appendix Eqs. 45 and 46:

$$\frac{\Delta \langle \bar{w} \rangle}{\langle \bar{w}_{so} \rangle} = \frac{1}{\eta_{so}} \left\{ \Delta t_{Dso} - [1 - \eta_{so}] \left[ \frac{g(\Delta t_{Dso}) - g_0}{\kappa_{so} g_0} \right] \right\}. \quad (47)$$

An expression for the treatment efficiency at any time after a screenout  $\eta(\Delta t_{Dso})$  can be obtained by combining the definition of  $\eta$  from Eq. 9-4 with the width multiplier expression in Appendix Eq. 47:

$$\eta(\Delta t_{Dso}) = 1 - \frac{(1 - \eta_{so})}{(1 + \Delta t_{Dso})} \left[ 1 + \frac{g(\Delta t_{Dso}) - g_0}{\kappa_{so} g_0} \right]. \quad (48)$$

Appendix Eqs. 47 and 48 are equivalent to Eqs. 6L-6 and 6L-7.

Based on the proportionality between net pressure and width, differentiating Appendix Eq. 47 obtains the following expression:

$$\begin{aligned} \frac{1}{\langle \bar{w}_{so} \rangle} \frac{d \langle \bar{w} \rangle}{dt} &= \frac{1}{p_{net,so}} \frac{dp_{net}(\Delta t_{so})}{dt} \\ &= \frac{1}{t_{so} \eta_{so}} \left\{ 1 - [1 - \eta_{so}] \frac{f(\Delta t_{Dso})}{\kappa_{so} g_0} \right\}, \end{aligned} \quad (49)$$

where  $p_{net,so}$  is the net pressure at the screenout and  $\beta$  is assumed to be unity (Fig. 9-20). From the definition of efficiency, it can be readily shown that

$$\frac{t_{so} \eta_{so}}{p_{net,so}} = \frac{t \eta(\Delta t_{so})}{p_{net}(\Delta t_{so})}. \quad (50)$$

Combining Appendix Eqs. 49 and 50 produces the following relation for the log-log slope of the net pressure after a screenout (Nolte, 1990):

$$\begin{aligned} \frac{t}{p_{net,so}} \frac{dp_{net,so}}{dt} &= \\ &= \frac{1 - [1 - \eta_{so}] \left( f(\Delta t_{Dso}) / (\kappa_{so} g_0) \right)}{1 - [1 - \eta_{so}] / [1 + \Delta t_{Dso}] \left( 1 + (g(\Delta t_{Dso}) - g_0) / (\kappa_{so} g_0) \right)}. \end{aligned} \quad (51)$$



The bounding values of the log-log slope are obtained by substituting the appropriate values for  $\eta$  and the corresponding relations for  $f(\Delta t_{Dso})$ ,  $g(\Delta t_{Dso})$  and  $g_0$  that can be obtained from Appendix Eqs. 28, 29 and 30, respectively.

## Comparison of fixed-length and propagating fractures<sup>†</sup>

Fracture propagation and closure lead to characteristic pressure and fluid-loss distributions along the interface between the fracture and the reservoir. The time history of these distributions establishes the boundary conditions for the reservoir response before and after fracture closure. These conditions are generally different from those experienced by fixed-length fractures; however, there are also similar conditions that are shared by these two types of fractures. The similar conditions enable applying established fixed-length relations to a propagating fracture. The background for identifying these differences and similarities is reviewed in this section of the Appendix to Chapter 9 along with the fixed-length relations that are applicable to the propagating case.

Specifically, this section of the Appendix provides

- conditions that enable adapting fixed-length relations to a propagating fracture
- definition of a generalized reservoir leakoff coefficient that is applicable to fracture propagation within all flow regimes
- framework for type-curve analysis of the after-closure period.

Throughout this section, the propagating fracture is assumed to have a rectangular shape (i.e.,  $A_f = 2h_f L$ ) and a square root of time dependency of the fluid loss (i.e.,  $\theta = 1/2$  in Appendix Eq. 5).

### Pressure characterization for a propagating fracture

The total pressure difference  $\Delta p_T$  between the fluid pressure in the propagating fracture  $p_f$  and the initial reservoir pressure  $p_i$  can be divided into three components, as proposed by Howard and Fast (1957) and illustrated in Fig. 5-17. The components of interest

for describing the pressure in the reservoir are the pressure drop caused by the near-face leakoff effects (i.e., filter cake and filtrate)  $\Delta p_{nf}$  and the pressure difference in the reservoir  $\Delta p_R$ :

$$\Delta p_T = p_f - p_i = \Delta p_{nf} + \Delta p_R \quad t < t_c \quad (52)$$

$$\Delta p_T = \Delta p_R; \quad \Delta p_{nf} = 0 \quad t > t_c. \quad (53)$$

In general, each of the pressure differences depends on time and position as the fracture propagates and closes.

As shown in Eq. 9-76,  $\Delta p_R$  is represented by the added contributions from the two sources of fluid loss: the pressure difference associated with the  $C_L$  component of fluid loss  $\Delta p_{RC}$  and the component associated with spurt loss  $\Delta p_{RS}$ . Nolte *et al.* (1997) provided the linear flow expression for  $\Delta p_R$  that includes the time dependence for  $\Delta p_{RS}$  in Eq. 9-84, which is applicable both before and after closure. The remainder of this section of the Appendix assumes that near-face effects and spurt loss are negligible and focuses on the  $C_L$  component of the pressure difference:

$$\Delta p_{RC} = \Delta p_T; \quad \Delta p_{RS} = \Delta p_{nf} = 0. \quad (54)$$

Abousleiman *et al.* (1994) expressed the general relation for  $\Delta p_{RC}$  in terms of an integral equation using a Green's function approach and requiring specification of the fluid-loss history. Another approach for describing  $\Delta p_{RC}$  is to identify several simplifying features for a propagating fracture. These are the conditions of approximately constant pressure and dimensionless time during fracture propagation.

Equations 9-23 and 9-24 characterize the pressure profile within the fracture and its magnitude at the wellbore in terms of net pressure. These equations indicate that the pressure is only weakly dependent on fracture length and the position in the fracture, with the potential exception of the region near its tip. It can, therefore, be concluded that the overall spatial and temporal pressure variations within a fracture are relatively small in comparison with the total pressure drop between the fracturing fluid and the undisturbed reservoir pressure. An approximately constant and uniform pressure is a primary assumption for deriving the individual leakoff coefficients (see Section 6-4) and the primary reason for their successful application as invariant parameters. This pressure condition is also reflected in the approximately constant injec-

<sup>†</sup>This section by K. G. Nolte, Schlumberger Dowell.

tion pressure during propagation at a constant injection rate. The simultaneous condition of constant pressure and constant rate provides one of the primary distinctions between a propagating and a fixed-length fracture. The fixed-length fracture requires an increasing pressure difference to maintain a constant production rate or a decreasing rate for a constant-pressure condition. From the reservoir perspective, this difference occurs because a propagating fracture has an approximately constant or stationary value of dimensionless time with its associated condition of time invariance for pressure and flow rate.

### Propagation with a stationary dimensionless time

The dimensionless time  $T$  (Eq. 9-75) can be combined with the power law relation for fracture area versus time (Appendix Eq. 2) and an efficiency-based approximation for the area exponent  $\alpha$  (Eq. 9-44) to obtain

$$\frac{T}{T_p} = \left( \frac{t_p}{t} \right)^{0.5\eta}, \quad (55)$$

where  $T_p$  is the dimensionless time at the end of pumping and the approximation used is  $\alpha \approx 0.5 + 0.25\eta$ , which covers the values given by Appendix Eqs. 40 and 41 for typical fracturing conditions. Appendix Eq. 55 shows that  $T$  is stationary and equal to its value at the end of pumping for a fracture with vanishing efficiency (i.e.,  $\eta \rightarrow 0$ ). The equation also shows that  $T$  retains only a weak dependence on time for moderate values of efficiency. For example, for  $\eta = 0.5$ ,  $T$  decreases only 19% during the second half of a treatment. Furthermore, Fig. 9-38 shows that a 10-fold change in the dimensionless time is required before any meaningful change occurs in the reservoir flow regime. The reservoir flow regime, therefore, is even more weakly dependent on dimensional time than the case for dimensionless time. It can be concluded that typical conditions for fracture propagation result in essentially a stationary dimensionless time and reservoir flow regime.

The approximately stationary value of  $T$  provides another primary difference between a propagating fracture and a fixed-length fracture for which dimensionless time increases with increasing dimensional time. An additional difference for a calibration treatment is that it does not retain fracture conductivity,

whereas the fixed-length case is generally associated with a conductive fracture.

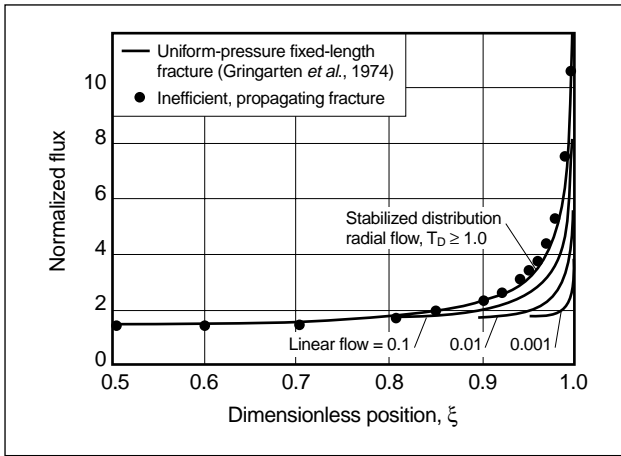
### Fluid-loss characterization for a propagating fracture

Figure 9-35 illustrates the spatial distributions of the fluid-loss rate during propagation and the specific loss volume after propagation. The discussion of this figure in Section 9-6 observes that the specific volume distribution is similar to that expected from a uniform-flux fixed-length fracture. This similarity provides the basis for the apparent fracture length relation given by Eq. 9-78. A second type of fixed-length fracture assumes uniform pressure, or equivalently infinite conductivity. Both of these fixed-length fractures were discussed and characterized by Gringarten *et al.* (1974).

The two types of fixed-length fractures can be compared to the after-closure behavior of the impulse injection shown in Fig. 9-38 for a propagating fracture. Sidebar 9G summarizes the impulse description of after-closure radial flow behavior by the time derivative of dimensionless pressure. The impulse description can also be applied to linear and transitional flow. For a propagating fracture, this application requires the apparent length relation to transform the dimensionless time (Eq. 9-79) for defining the dimensionless pressure of a fixed-length fracture. The derivative of dimensionless pressure is the same for the two fixed-length fractures in linear and radial flow (Eq. 9-95) and accurately represents the impulse behavior in Fig. 9-38 for these flow regimes.

However, the fixed-length fractures have different transitional flow behaviors (e.g., Gringarten *et al.*, 1974) and represent the transitional behavior in Fig. 9-38 with differing degrees of accuracy. The uniform-flux fracture has a deviation of less than 5% from the propagating case for the complete time range shown in the figure (i.e., that applicable to the impulse representation). The transitional behavior for the uniform-pressure case deviates by almost 25% from that for the propagating fracture. The maximum deviation in both cases occurs slightly before the knee time. These quantitative results confirm the cited qualitative inferences from Fig. 9-35, that the after-closure behavior of a propagating fracture can be represented by a uniform-flux fixed-length fracture.

In contrast to this after-closure comparison, the uniform-pressure fracture provides essentially the same flux distribution in radial flow as that for the fluid loss from an inefficient propagating fracture. This comparison is shown on Appendix Fig. 4. The fixed-length distribution from Gringarten *et al.* (1974) was described as the stabilized flux distribution. The spatial variation of the fluid loss during propagation was obtained by combining the fracture growth power law relation (Appendix Eq. 2) for vanishing efficiency (i.e., area exponent  $\alpha = 1/2$ ) and the square root of time leakoff behavior (Appendix Eq. 8).



**Appendix Figure 4.** Comparison of flux distribution for a uniform-pressure fixed-length fracture and a fluid-loss-dominated propagating fracture.

Gringarten *et al.* also noted that the stabilized distribution is independent of its prior history. Furthermore, it is spatially the same as that for a propagating fracture with vanishing efficiency and spurt. It follows that the dimensionless pressure response  $p_{D,up}$  for the uniform-pressure fixed-length fracture applies to a propagating fracture when the pressure is evaluated at its stationary value of the dimensionless time  $T_p$  (i.e.,  $p_{D,up}(T_p)$ ). This dimensionless pressure value applies for radial flow with vanishing efficiency and spurt and therefore provides the basis for subsequently defining the reservoir leakoff coefficient  $C_R$  for these conditions.

Before defining this coefficient, the conventional definition of the reservoir leakoff coefficient must be considered:

$$C_c = \sqrt{\frac{k \phi c_t}{\pi \mu}} \Delta p_T, \quad (56)$$

where reservoir linear flow is assumed (Howard and Fast, 1957) and the definition is in terms of the total pressure difference between the fracture and the initial reservoir pressure. A definition in Eq. 6-91 is in terms of the pressure difference  $\Delta p_{RC}$  between the filtrate/reservoir interface and the initial reservoir pressure. This pressure difference is defined in Appendix Eq. 54 and denoted as  $\Delta p_c$  in Eq. 6-91. Combining Appendix Eq. 56 and Eq. 6-92 gives the following ratio between the pressure differences and fluid-loss coefficients:

$$\frac{\Delta p_{RC}}{\Delta p_T} = \frac{C_L}{C_c}. \quad (57)$$

When the near-face effects and spurt are negligible, the two pressure differences are equal (i.e., Appendix Eq. 54) and Appendix Eq. 57 then indicates the expected result that the combined and reservoir coefficients are also equal. This result reflects the expected reservoir behavior based on a linear relation between the pressure difference and flux. This behavior is also required for the radial flow reservoir coefficient:

$$\frac{\Delta p_{RC}}{\Delta p_T} = \frac{C_L}{C_R}. \quad (58)$$

The previously cited application of  $p_{D,up}$  for defining  $C_R$  requires expression of the dimensionless pressure (Eq. 12-2) in terms of the quantities for the  $C_L$  component of fluid loss:

$$p_{D,up}(T_p) = \frac{2\pi k h_L \Delta p_{RC}(t_p)}{\mu q_{L,C}}, \quad (59)$$

where the fluid-loss height  $h_L = r_p h_f$  and  $q_{L,C}$  is the leakoff rate associated with Carter-based fluid loss. Substituting for the expression for  $q_{L,C}$  with vanishing efficiency and spurt from Appendix Eq. 11 and the dimensionless rate function  $f = \pi/2$  for the specified conditions (Nolte, 1986a):

$$p_{D,up}(T_p) = \frac{k}{\mu} \frac{\sqrt{t_p}}{C_L L} \Delta p_{RC}(t_p) \quad \eta \rightarrow 0, \quad \kappa \rightarrow 1. \quad (60)$$

An expression for the radial coefficient  $C_R$  can then be obtained by combining Appendix Eq. 59 with the definitions of dimensionless time (Eq. 9-75),  $C_c$  (Appendix Eq. 56) and the pressure ratio (Appendix Eq. 58):

$$C_R = \frac{C_c}{p_{D,up}(T_p)} \sqrt{\pi T_p} \quad \eta \rightarrow 0, \quad \kappa \rightarrow 1. \quad (61)$$

Limiting values for  $p_{D,up}(T_p)$  were given by Gringarten *et al.* (1974):

$$\begin{aligned} \text{Linear flow} \quad p_{D,up}(T_p) &= \sqrt{\pi T_p} & T_p < 0.01 \\ \text{Radial flow} \quad p_{D,up}(T_p) &= \frac{1}{2} [\ln T_p + 2.2] & T_p > 3. \end{aligned} \quad (62)$$

They also provided a general relation for  $p_{D,up}(T_p)$  in terms of special functions. This relation can be approximated with an error of less than 2% by

$$p_{D,up}(T_p) \cong \begin{cases} \sqrt{\pi T_p} - 0.58 T_p & T_p < 0.16 \\ \frac{1}{2} (\ln [T_p + 0.22] + 2.2) & T_p > 0.16. \end{cases} \quad (63)$$

Comparison of Appendix Eqs. 62 and 63 shows that the approximations provided by the latter equation are defined by adding a term to each of the limiting cases. The second approximation in Appendix Eq. 63 can be obtained by applying the apparent time multiplier  $(1 + 0.22/T_p)$  to the dimensionless time. Its inclusion extends the applicability of the logarithmic-based radial flow relation to a dimensionless time that is about  $1/20$  of the value normally required for radial flow (i.e.,  $T_p = 0.16$  in Appendix Eq. 63 versus  $T_p = 3$  in Appendix Eq. 62). The apparent time multiplier for application with Appendix Eq. 63 has the same form as that for a similar development introduced in Eq. 9-83 for the after-closure behavior of a propagating fracture. These two relations are seemingly different because the relation for a propagating fracture contains a different constant (i.e., 0.14 instead of 0.22). However, this difference occurs because the dimensionless times corresponding to the two cases differ by the square of the apparent length fraction  $f_{aL}$  from Eq. 9-79. For the assumed conditions of vanishing efficiency and spurt, Eq. 9-80 indicates that  $f_{aL} = \pi/4$ . Applying this value to the dimensionless time for the fixed-length case indicates that the constants for the two apparent time relations are actually equivalent.

For reservoir linear flow, Appendix Eq. 62 shows that  $p_{D,up}(T_p) \approx \sqrt{\pi T_p}$ . It follows from Appendix Eq. 61 that

$$C_R = \begin{cases} C_c & \text{Linear flow} \\ \frac{\sqrt{\pi T_p}}{p_{D,up}(T_p)} C_c & \text{Transitional and radial flow.} \end{cases} \quad (64)$$

The second relation in Appendix Eq. 64 indicates an expanded range of application relative to that assumed for the derivation of Appendix Eq. 61. The expanded range results from numerical simulations (Abousleiman *et al.*, 1994; Nolte, 1998) that indicate that Appendix Eq. 64 approximates (i.e., within a 5% error) the reservoir coefficient for transitional flow. More generally, the simulations indicate that Appendix Eq. 64 is approximately valid (i.e., within a 10% error) for moderate values of efficiency ( $\eta < 0.5$ ) and with any reservoir flow regime. Therefore,  $C_R$ , as defined by Appendix Eq. 61, represents the “general reservoir” leakoff coefficient within the accuracy required for fracture design and evaluation purposes.

Appendix Eq. 63 can be used to show that during transitional and radial flow,  $p_{D,up}(T_p) \leq \sqrt{\pi T_p}$ . Appendix Eq. 64 therefore implies that the general coefficient  $C_R$  is larger than the linear flow coefficient  $C_c$  for fracture propagation under these flow conditions. This result has been reported by Hagoort (1980) and Valkó and Economides (1997). For example, for a dimensionless time  $T_p = 1$ , the dimensionless pressure  $p_{D,up} = 1.21$  and  $\sqrt{\pi T_p} = 1.78$ . For these values, Appendix Eq. 64 indicates that the general coefficient  $C_R$  is about 1.5 times larger than  $C_c$  under these late transitional flow conditions. For a larger dimensionless time  $T_p = 10$ ,  $C_R$  becomes larger by a factor of 2.5.

This observation of a larger leakoff coefficient generally applies to the mini-falloff test because the test design should be based on  $T_p > 1$  and the achievement of reservoir-controlled fluid-loss conditions (Appendix Eq. 1). Larger values of the reservoir coefficient do not affect the fluid loss for most proppant treatments where near-face effects are designed into the fluid system to control the fluid-loss behavior.

Combining Appendix Eqs. 58 and 61 provides the general relation for the  $C_L$  component of the pressure difference  $\Delta p_{RC}$  for all flow regimes and in terms of the total pressure difference and combined fluid-loss coefficient.

## Type-curve-based analysis

The dimensionless pressure  $p_{D,up}$  can also be used to develop type-curve analyses for general after-closure conditions. The normalized pressure difference and pressure derivative variables and the log-log slope in Fig. 9-38 illustrate several characteristics of the after-

closure pressure response that motivate its analysis within a type-curve framework. For example, the character, or shape, of the curves depends on the dimensionless time  $T_p$ . Also, a suitable match pressure for the analysis can be defined as the ratio of the dimensional pressure variables and the normalized pressure variables shown on the figure.

The development of type curves applicable to generalized fluid-loss conditions requires a relation among the average value of the fluid-loss rate  $\bar{q}_L$ ,  $C_L$  component of the fluid-loss rate  $q_{L,C}$ , injection rate  $q_i$ , fluid efficiency  $\eta$  and spurt factor  $\kappa$ . This relation can be obtained by combining the rate versions of Eq. 9-6 and Appendix Eq. 22:

$$\bar{q}_L = \kappa q_{L,C} = (1 - \eta) q_i. \quad (65)$$

For general values of efficiency and spurt, the reservoir pressure difference at the end of pumping  $\Delta p_R(t_p)$  provides a convenient quantity to use as the match pressure (i.e., the multiplying factor for the type curves). The relation between  $\Delta p_R(t_p)$  and  $\Delta p_{RC}$  at the end of injection can be obtained from Eqs. 9-76 and 9-84 and Appendix Eq. 58:

$$\Delta p_R(t_p) = \left( \frac{\kappa + 1}{2} \right) \Delta p_{RC}(t_p) = \left( \frac{\kappa + 1}{2} \right) \frac{C_L}{C_R} \Delta p_T(t_p). \quad (66)$$

Rearranging Appendix Eqs. 65 and 66 and substituting them into Appendix Eq. 59 provides a more general form of the dimensionless pressure:

$$p_{D,up}(T_p) = \left[ \frac{2\kappa}{(1 - \eta)(1 + \kappa)} \right] \frac{2\pi kh}{\mu q_i} m_p \quad \Delta p_R(t_p) \rightarrow m_p, \quad (67)$$

where the fluid-loss height  $h_L = h$  and the role of  $\Delta p_R(t_p)$  is introduced as the match pressure  $m_p$ . The transmissibility can be determined from this dimensionless relation:

$$\frac{kh}{\mu} = \left[ \frac{(1 - \eta)(1 + \kappa)}{2\kappa} \right] \frac{q_i p_{D,up}(T_p)}{2\pi m_p}. \quad (68)$$

In addition to determination of the match pressure for the type-curve analysis, the dimensionless time at the end of pumping  $T_p$  is required to define  $p_{D,up}$  for Appendix Eq. 68. The value of  $T_p$  can be obtained by matching the character, or shape, of the data to that of the type curves. Once a value of  $T_p$  has been estab-

lished by the matching procedure, the dimensionless pressure  $p_{D,up}(T_p)$  can be obtained using Appendix Eq. 63.

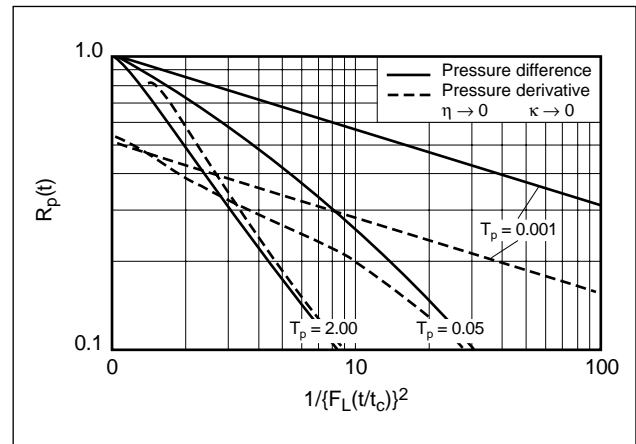
This type-curve analysis has the following relation between the after-closure pressure and the pressure-difference curve  $R_p$ :

$$\Delta p_R(t) = p(t) - p_i = m_p R_p \left[ T_p, (t - t_c)/t_c, \eta, \kappa \right]. \quad (69)$$

For fracture propagation in flow regimes other than well-established linear and radial flow,  $R_p$  must be defined by numerical simulation.

The matching procedure uses a pair of type curves: one for the pressure difference and one for the pressure derivative. Each quantity can be defined using an appropriate time function. The square of the linear flow time function  $F_L(t/t_c)$  given by Eq. 9-88 is preferred because it provides a consistent representation of the after-closure period for the reservoir response in any flow regime, as discussed in Section 9-6.7. Furthermore, the pressure difference and the pressure derivative are presented in terms of the inverse of  $F_L^2$  because this presentation provides the conventional representation of increasing time from left to right along the x-axis. Appendix Fig. 5 illustrates these curves for the case of vanishing efficiency and spurt (e.g., applicable to a mini-falloff test).

The type-curve analysis begins by matching the character (i.e., shape) of the pressure derivative for the data to the character of one of a collection of type curves based on different values of  $T_p$ . This character matching defines  $T_p$ . The selected curve for  $T_p$  is then vertically translated to match the pressure derivative of the data, and the resulting form of the pressure derivative defines the match pressure  $m_p$ :



**Appendix Figure 5.** Example type curves for negligible efficiency and spurt.

$$\left\{F_L(t/t_c)\right\}^2 \frac{dp(t)}{d\left\{F_L(t/t_c)\right\}^2} = m_p \left[ \left\{F_L(t/t_c)\right\}^2 \frac{dR_p}{d\left\{F_L(t/t_c)\right\}^2} \right] \quad (70)$$

The transmissibility is then estimated from Appendix Eq. 68 using the two type-curve parameters  $T_p$  and  $m_p$ . The initial reservoir pressure is extracted by applying Appendix Eq. 69 over the time range of the match.

Additional information concerning the nature of the fluid loss can be obtained from the value of  $m_p$

(i.e.,  $\Delta p_R(t_p)$  inferred from the after-closure data). Relative to Appendix Eq. 66,  $\Delta p_T(t_p) = p(t_p) - p_i$ , with  $p(t_p)$  defined by the ISIP, and when  $\Delta p_R(t_p) \approx \Delta p_T(t_p)$  in the absence of spurt, the reservoir and total leakoff coefficients are approximately equal. Under these conditions, essentially the entire pressure difference  $\Delta p_T$  is within the reservoir and the reservoir controls the fluid-loss behavior. Conversely, when  $\Delta p_R(t_p) \ll \Delta p_T(t_p)$ , a negligible fraction of the total pressure drop occurs in the reservoir, and the reservoir does not have a meaningful role in controlling fluid leakoff.

# Fracture Treatment Design

*Jack Elbel, Schlumberger Dowell*

*Larry Britt, NSI Technologies, Inc.*

## 10-1. Introduction

Fracture stimulation is used to overcome the adverse effects of formation damage and low permeability, accelerate production, increase reserves and control the production of water and formation solids. These fracturing applications require different fracture stimulation designs to achieve their objectives; therefore a means of evaluating treatment designs is important to determine which is the optimum approach. Fracture economic optimization techniques can be used to conduct this evaluation (Veatch, 1983; Meng and Brown, 1987). These references also provide the calculation procedures for economic analysis. The fracture optimization process requires the ability to predict fracture geometry and cost, reservoir performance and revenue and then to couple these cost and revenue streams with an economic evaluation. The following sections discuss some considerations for fracture optimization.

Economic analysis is used routinely to evaluate investment decisions in the petroleum industry. Because both the magnitude and timing of project cash flow are important yardsticks by which project performance is evaluated, it is important to understand the general economic criteria used by the industry to evaluate any investment decision, including hydraulic fracturing.

- Discount rate is analogous to an interest rate that reflects the “time value” of money and is selected to balance the targeted investment reward relative to the inherent risks for the investment.
- Present value is the sum of all future cash flows (income and expenses) discounted to the present time at a stated discount rate. Another way to think about the present value concept is that the present value is the current dollars required to be indifferent to receiving that amount of the future worth.
- Net present value (NPV) is the difference between the project’s present value of future cash flows and the present value of the investment.

- Discounted return on investment (DROI) is the ratio of the project’s NPV to the present value of the total investment discounted at a stated rate. DROI is a measure of capital efficiency, and in the simplest terms it is the expected dollars of profit per dollar invested from a discounted viewpoint.
- Return on investment (ROI) is the ratio of the project’s undiscounted cash flow to the undiscounted total investment. This economic parameter does not consider the time value of money and, therefore, artificially favors long-term projects.
- Payout is the time for the cumulative undiscounted cash flow of a project to reach zero. Payout does not consider the time value of money or the cash flow recovered after the project reaches payout. However, it does provide an indication of how long investment capital is at risk and reflects the time period for a project to reach the break-even point.
- Rate of return, or profitability index, is the compounded interest rate that has a discount effect that makes the present value of the net cash flows equal to zero. This rate is analogous to the interest rate received if the investment were considered a loan to be paid back at this interest rate.

Each of these criteria should be reviewed within the current economic environment to ensure that business objectives are achieved. If, for example, the business objective is to maximize profitability, it is necessary to recognize that in an economic environment where access to capital is constrained and fracturing candidates are unlimited, optimizing the DROI of each treatment maximizes overall profitability. If, on the other hand, the economic environment is such that capital and stimulation candidates are unlimited, the NPV of each treatment should be maximized. The design consequences for the two criteria can be substantial, with maximizing the DROI of the treatment resulting in a smaller treatment and investment. Sidebar 10A provides an example.

## 10A. NPV for fixed costs or designated proppant mass

If it is assumed that the fracturing fluid and injection rate have been selected, the other major design considerations are the treatment size, type of proppant and proppant scheduling. The size of the treatment should ideally be based on the optimum fracture penetration determined by economic considerations (see Section 10-1.1) and made after ideal model assumptions are considered (see Section 10-3.1). However, it is not uncommon for a fixed expenditure to be used in determining the size of a treatment. There may be other constraints, such as proppant mass and fluid volume, resulting from the availability of materials or logistics, which may also limit the size of a treatment. Even then, the treatment design providing the best NPV or other economic criteria within these constraints can be made by conducting a number of economic evaluations with different proppants and various maximum concentrations.

NPVs for various treatment volumes and proppant concentrations for a range of fixed costs are shown in Fig. 10A-1. In Fig. 10A-1a the NPV after 1 year is plotted versus cost of treatment with sand and a higher cost, higher strength, premium intermediate-strength proppant (ISP). The final proppant concentrations in the simulations are 10, 14 and 16 ppg. If the treatment cost is limited to \$200,000, the maximum NPV after 1 year is \$2,080,000 using sand at a final concentration of 16 ppg. This NPV is \$200,000 higher than that for a treatment at the same cost with a premium proppant at 10-ppg final concentration and \$310,000 greater than premium proppant at 16 ppg. If the treatment cost is increased to \$300,000, the maximum NPV is increased only \$20,000 and can also be achieved with premium proppant at 16- and 14-ppg final concentrations.

A maximum NPV can also be determined for cases where the proppant volume or mass is limited because of availability, location, size or an arbitrary decision. For this criterion, the curves in Fig. 10A-1b show that the premium proppant is always optimal. The plots also show that for less than 130,000-lbm proppant, 10-ppg maximum concentration is optimal. For more than 130,000 lbm, a greater economic benefit is obtained at a concentration of 14 ppg, increasing to 16 ppg with additional increases in proppant mass or treatment cost that achieve more fracture length and benefit from increased concentration for improved conductivity.

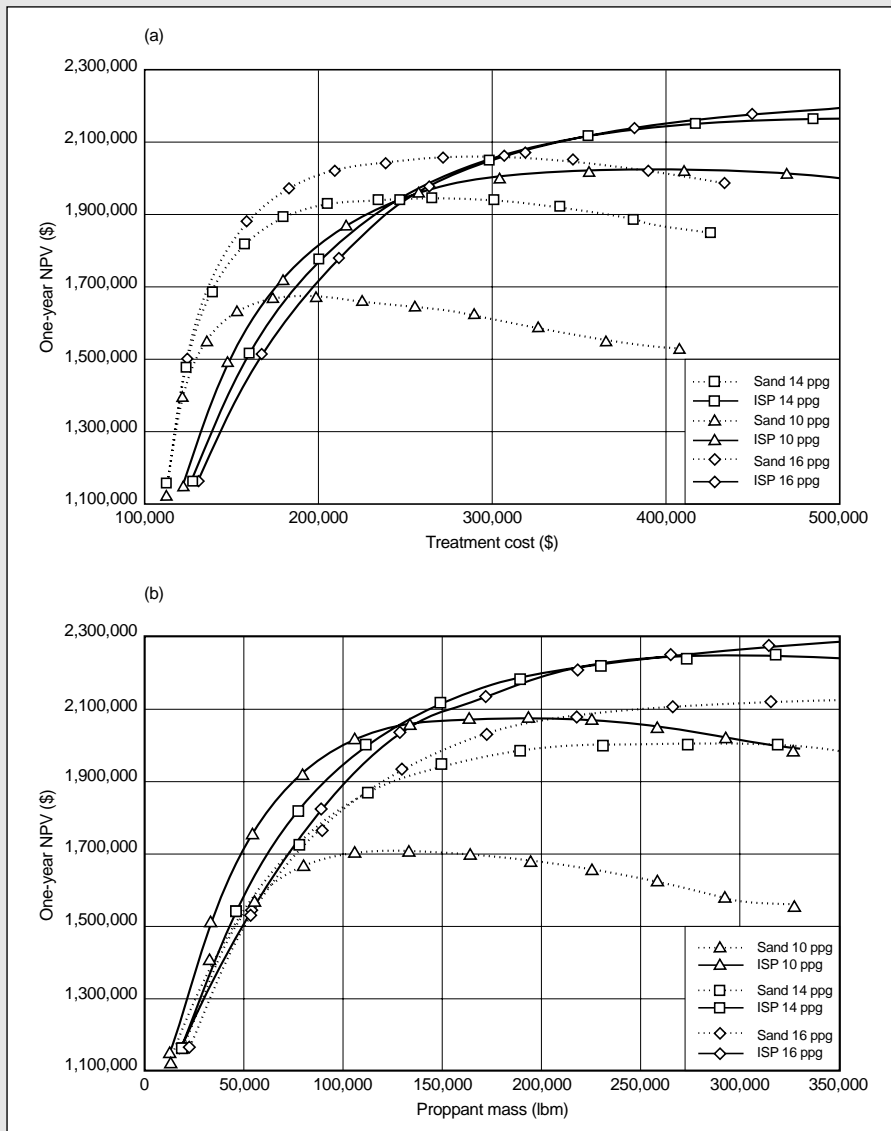


**Figure 10A-1.** Net present value versus (a) treatment cost and (b) proppant type and mass. The curves are scaled at increments of 100-ft proppant penetration, beginning at 100 ft.



## 10-2. Design considerations

### 10-2.1. Economic optimization

Economic optimization of hydraulic fracture treatments allows the production engineer to design a fracture treatment that optimizes the production rate and reserve recovery from a well to maximize well profitability. In addition, a good understanding of the key parameters for the fracture treatment can be developed from the optimization study. For example, Fig. 10-1 is a plot of 1-year NPV versus the productive fracture half-length  $x_f$  in a 0.01-md formation. This figure shows the relationship among length, conductivity and profitability. For penetrations from 200 to 600 ft, about the same NPV is produced by proppant concentrations of 6 to 14 ppg. However, the net production—and therefore cash flow—will be higher with the higher concentrations. At 1000-ft penetration, concentrations from 10 to 14 ppg yield about the same NPV and are significantly greater than when using 6 ppg. Increasing the fracture length improves the profitability of a well in this reservoir but also requires increasing fracture conductivity for most penetrations.

To estimate the cost of a fracturing treatment, the variable costs can be added to some fixed cost not directly associated with treatment size:

- variable fluid cost =  $\$/\text{unit} \times \text{units of fluid}$   
The unit cost includes
  - fracturing fluid plus additives
  - mixing and blending charges
  - transportation, storage and disposal charges (commonly included in other fixed costs).

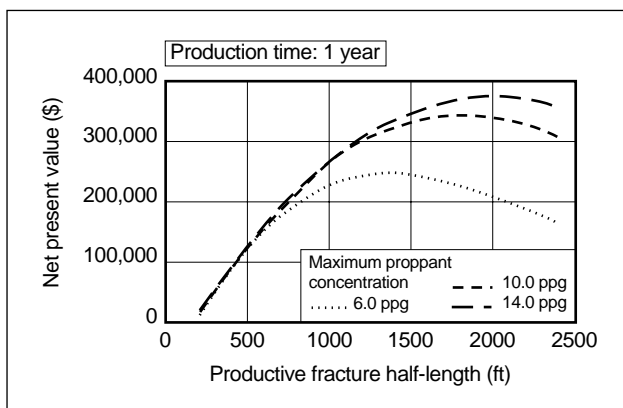


**Figure 10-1.** Net present value versus productive fracture half-length for a 0.01-md formation.

- variable proppant cost =  $\$/\text{unit} \times \text{units of proppant}$   
The unit cost includes
  - proppant
  - proppant transportation to location and storage
  - proppant pumping charges.
- variable hydraulic horsepower (hhp) cost =  $\$/\text{hhp} \times \text{injection rate} \times \text{surface treating pressure}/40.8 \times \text{standby hhp factor}$
- other fixed costs
  - mobilization
  - personnel
  - well preparation (workover rig, etc.)
  - cleanup costs (coiled tubing, disposal if not included as a fluid unit cost, etc.).

### 10-2.2. Treatment optimization design procedure

Optimization procedures require methods to determine fracture geometry and production from the propped fracture. They may be in the form of a nomograph, analytical solutions, two- or three-dimensional (2D or 3D) models for geometry and productivity index (PI) calculations, type curves, or analytical or numerical reservoir models for production simulation. The accuracy of the optimization should increase with increasing sophistication of the models and the accuracy of the input parameters. Sensitivity studies of input parameters with uncertain values are warranted.

A basic procedure for economic optimization is as follows:

1. Select the fluid systems applicable to the formation to be fractured.
2. Select the proppant on the basis of stress and conductivity requirements.
3. Determine the maximum allowable pump rate on the basis of the pressure limitations of the wellhead and tubulars. The optimum injection rate is a balance of decreased fluid loss and increased horsepower as the rate is increased. Shear degradation, for some fracturing fluid systems, should also be considered (see Chapters 7 and 8).
4. Select an appropriate fracture propagation model (e.g., pseudo-3D, or P3D) for the formation characteristics and pressure behavior on the basis of in-situ stress and laboratory tests, calibration treat-

ments and log analysis (e.g., stress profile, gamma ray) (see Chapters 3, 4 and 9).

5. Develop the input data required for the selected geometry model(s).
6. Determine fracture penetration and fracture conductivity for a selected treatment size and proppant concentration by forward simulation or determine fluid and proppant volumes required and fracture conductivity obtained for a selected penetration using inverse simulation (see Chapter 6). Determine the optimum pad fraction (see Chapters 5 and 6). If the model does not account for polymer conductivity damage, an estimated damaged conductivity should be used (see Chapters 7 and 8).
7. Determine the production rate and cumulative recovery over a selected time period for a specific propped penetration and its corresponding conductivity.
8. Calculate the present value of the net revenue of the production based on a discount rate (i.e., the sum of the present values for each year of the selected period).
9. Calculate the total treatment cost including the costs associated with fluids, proppants and hydraulic horsepower.
10. Calculate the NPV for the fracture by subtracting the treatment cost from the well's discounted net revenue (step 9 minus step 8).
11. Repeat the preceding computational cycle for incremental increases in length until the NPV decreases or a maximum length is reached.
12. Construct curves showing the fracture NPV or other appropriate economic criteria versus fracture penetration. When the NPV starts to decline with increasing fracture lengths, the cumulative production for the specific lengths will still be increasing.

The cycle can be repeated for other materials or conditions such as other fluids and additive concentrations, injection rates, proppant types and maximum proppant concentrations or even with other geometry models. The process can easily become time consuming, and the number of iterations should be governed by the accuracy required as well as the accuracy of the input parameters. The cycles can be repeated for sensitivity to parameters to determine bounds. The most important input parameters and

those with the greatest potential for error are formation permeability and fracture conductivity. Fortunately, a number of economic models combine geometry and reservoir models to allow making detailed studies in a reasonable amount of time.

Economic optimization among different fracturing fluids such as oil-base, water-base and foam fluids is difficult. These fluids are usually chosen for compatibility with formation fluids or cleanup properties, and their economic benefit cannot be quantified unless features such as formation damage, polymer damage to proppant pack and cleanup time can be determined by the production models or included by some other means in the analysis. As an example, if it is known that a foam fracturing fluid will reduce the cleanup time, the cost of cleanup can be reduced for the foam fluid relative to that for a nonfoam fluid. Some risk factor and uncertainty can also be associated with various input parameters and behavioral assumptions (Nolte and Economides, 1991).

### 10-2.3. Fracture conductivity

Placing the appropriate amount and type of proppant in the fracture is critical to the success of a hydraulic fracturing treatment. Independent of fluid residue damage, proppant concentration in the fracture and resistance to crushing determine the fracture conductivity over the producing life of the well. Proppant selection is optimized by balancing the potential to create fracture conductivity against the additional cost or risk of placement. Factors such as proppant properties (strength, particle size, roundness and fines content), closure stress, polymer damage, drawdown rate, embedment and the resultant propped fracture width affect the fracture conductivity. Several of these factors are discussed in more detail in Chapters 7 and 8.

For simplicity, the fracture conductivity used for production simulation is usually considered to be homogeneous. Advances in geometry and production modeling (see Chapter 12) enable simulation with spatial variations in horizontal (Bennett *et al.*, 1983) as well as vertical conductivity (Poe *et al.*, 1992).

Two regions over the vertical profile are affected by different criteria for conductivity. The first is a bank buildup region created at the bottom during placement where the pack width is equal to the hydraulic width for the region. The second is the overlying slurried height region at closure where the

propped width and height are affected by the proppant slurry concentration and closure time. Ignoring the effect of proppant redistribution during closure, Fig. 5-21 gives the percent of “fill” of the propped width relative to the width when pumping stops.

- Stress on proppant

When a hydraulic fracture is created, the minimum in-situ stress must be overcome to open and propagate the fracture. When the fracture closes on the proppant after the treatment, the effective closure stress (hereafter termed simply closure stress) on the proppant is equal to the minimum in-situ stress plus the additional stress induced by the pack width minus the pore pressure in the proppant pack. The additional stress caused by the width can be estimated from an appropriate width model (see Chapter 6) using the propped width and the resulting net pressure as the increased stress. To bring the well on production, the pressure in the pack at the wellbore must be reduced below that of the reservoir, increasing the stress on the proppant at this time.

The stress on the proppant changes during the life of the well. If initiating production requires that the well be swabbed, high stresses on the proppant near the wellbore may occur. If the well is swabbed off the bottom, the bottomhole producing pressure is essentially zero, creating the maximum stress on the proppant. Cyclic loading tests (Kim and Willingham, 1987; Holditch and Blakely, 1992) show that the conductivity is irreversibly reduced. Therefore, as the reservoir pressure is reduced because of depletion and the closure stress is decreased proportionally (by a ratio of about  $\frac{1}{2}$ ; see Chapter 3), the permeability of the proppant is not restored to greater than what it was when the maximum stress was applied.

Figure 7-13 shows the effect of closure stress on the permeability of various propping agents. When the stress on the proppant exceeds 10,000 psi, high-strength proppants (such as sintered bauxite) are required. In the range of 5,000 to 10,000 psi, the use of higher strength, manufactured ceramic proppant—commonly called intermediate-strength proppant (ISP)—should be considered. These premium proppants provide greater conductivity at higher closure stresses, but their cost makes them economically unattractive at lower closure stresses. Sand is the most common proppant, and its use is

considered for fracturing formations where stresses on the proppant are less than 6000 psi. The permeability of precured resin-coated proppants is between that of sand and ISP.

If a well is produced at a constant bottomhole producing pressure, the minimum stress, and hence the closure stress on the proppant, decreases during production as the effective reservoir pressure decreases. If the well is produced at a constant rate such that the bottomhole producing pressure must be decreased faster than the effective reservoir pressure decreases, the stress on the proppant may increase. When the minimum surface producing pressure is reached and the well is produced at a constant pressure, the stress will decrease.

Formations with a high stress (usually associated with abnormally high pore pressures) may not always require high-strength proppants as would be expected. This is the case where the desired production rate can be maintained at a low drawdown pressure during early production time, minimizing the effective stress on the proppant. Later, because the pore pressure has decreased as a result of production, the in-situ stress may have decreased to a point where subsequent increased drawdown will not cause the stress on the sand to become excessive. From a practical standpoint (i.e., to enable economic production during the period of low drawdown), this condition requires relatively high values of the permeability-thickness product  $kh$  for the formation and effective fracture characteristics. The incongruity of this scenario for relatively shallow reservoirs is that if the formation permeability is low, high-strength proppants may be required, and if it is high, sand may be sufficient.

- Propped width

Figure 10-2 illustrates the typical relationship of fracture conductivity to proppant concentration. Increasing the proppant concentration results in multiple layers of proppant and an increase in the fracture conductivity. Although maximum conductivity can be obtained by placing proppant in a partial monolayer (a technique developed for horizontal fractures), placement of a partial monolayer in a vertical fracture is virtually impossible to achieve. Therefore, fracture treatments are designed for multiple proppant layers. With multiple layers of proppant, the outer layer may embed in softer formations, allowing only the inner layers to

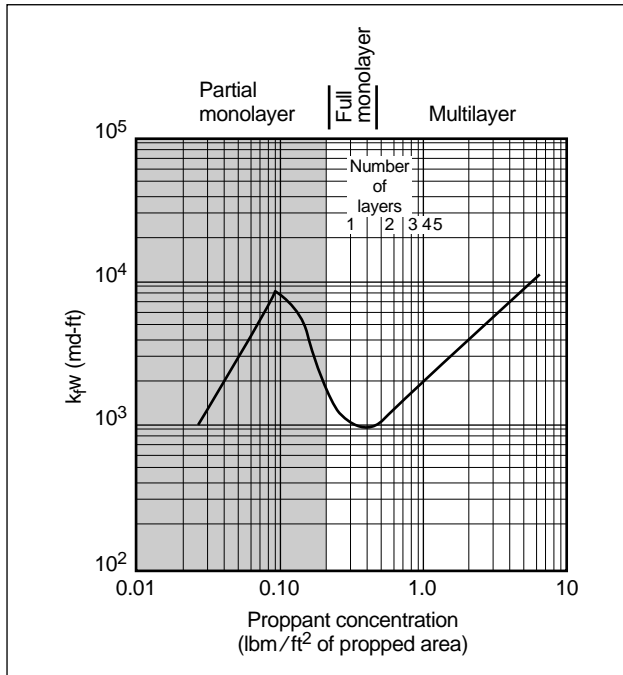


**Figure 10-2.** Relationship of fracture conductivity to fracture proppant concentration for 20/40-mesh sand, no fluid damage and relatively small stress.

remain open to flow (Strickland, 1985; Smith *et al.*, 1987; Martins *et al.*, 1992c).

Figure 10-3 is a graph of proppant concentration in the fracture versus propped fracture width for 20/40-mesh sand. The graph illustrates that once multilayer packing is achieved, the fracture width increases proportionally to the increase in proppant concentration. In Figs. 10-2 and 10-3, 2 lbm/ft² corresponds to about 0.25-in. propped width and has about 10 layers for 20/40-mesh proppant. The significance of more than five layers is discussed concerning proppant flowback in Section 11-6. Proppant packs with more than five layers of proppant were found to become unstable and produce proppant when subjected to the forces from fluid flow (Asgian *et al.*, 1995). Thus, proppant consolidation techniques are indicated.

Other factors influencing the final conductivity, particularly the gel residue in the fracture, are discussed in Chapter 8. Influences that are more difficult to define are the creation of formation fines because of stress cycling (Morita *et al.*, 1988; Ramakrishnan *et al.*, 1991), movement of formation fines into the fracture, long-term proppant degradation from dissolution and stress corrosion, and permeability loss from precipitate buildup.

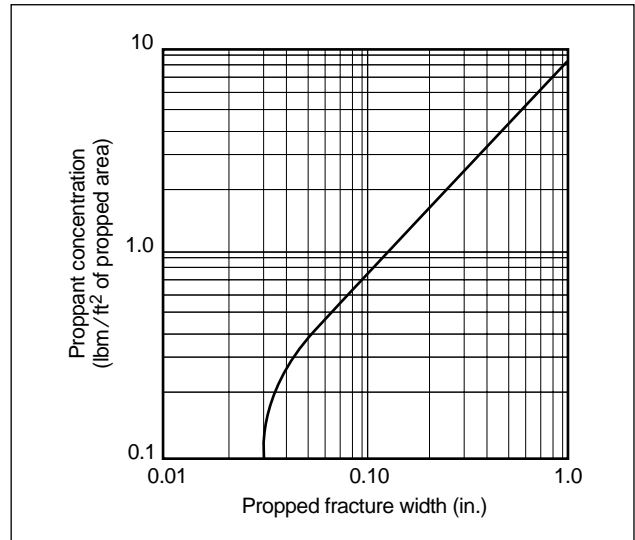


**Figure 10-3.** Fracture proppant (sand) concentration versus propped fracture width.

Therefore, treatments are generally designed with higher proppant concentrations to compensate for these unknown, negative factors.

#### 10-2.4. Dimensionless fracture conductivity

Comparison of the effect of fracture conductivity on production can be made easily if conductivity is cast in dimensionless terms and plotted against dimensionless time and rate, as shown by the constant-pressure, finite-conductivity type curves in Fig. 10-4. These type curves give the wellbore production response as the reciprocal dimensionless rate  $1/q_D$  for a range of dimensionless fracture conductivity  $C_{fD}$ .

In Fig. 10-4, a design with a calculated  $C_{fD}$  of 1.0 and a selected dimensionless time  $t_D$  of 0.01 is plotted as point A. This corresponds to production represented by  $1/q_D$  equal to 0.8. Doubling the fracture length with the same conductivity reduces  $C_{fD}$  by 50% and decreases  $t_D$  by 25% (point B). The value of  $1/q_D$  for point B has essentially not changed, indicating that the production at this time is not different from that at point A. However, if the penetration is doubled and the proppant volume is increased by a factor of 4 over that of the design for point A, the conductivity doubles but  $C_{fD}$  remains equal to 1. This is shown as point C, with a corresponding  $1/q_D$  of 0.55, which indicates a 45% increase in the production rate. However, a more significant increase in production over that for the point A design can be achieved by

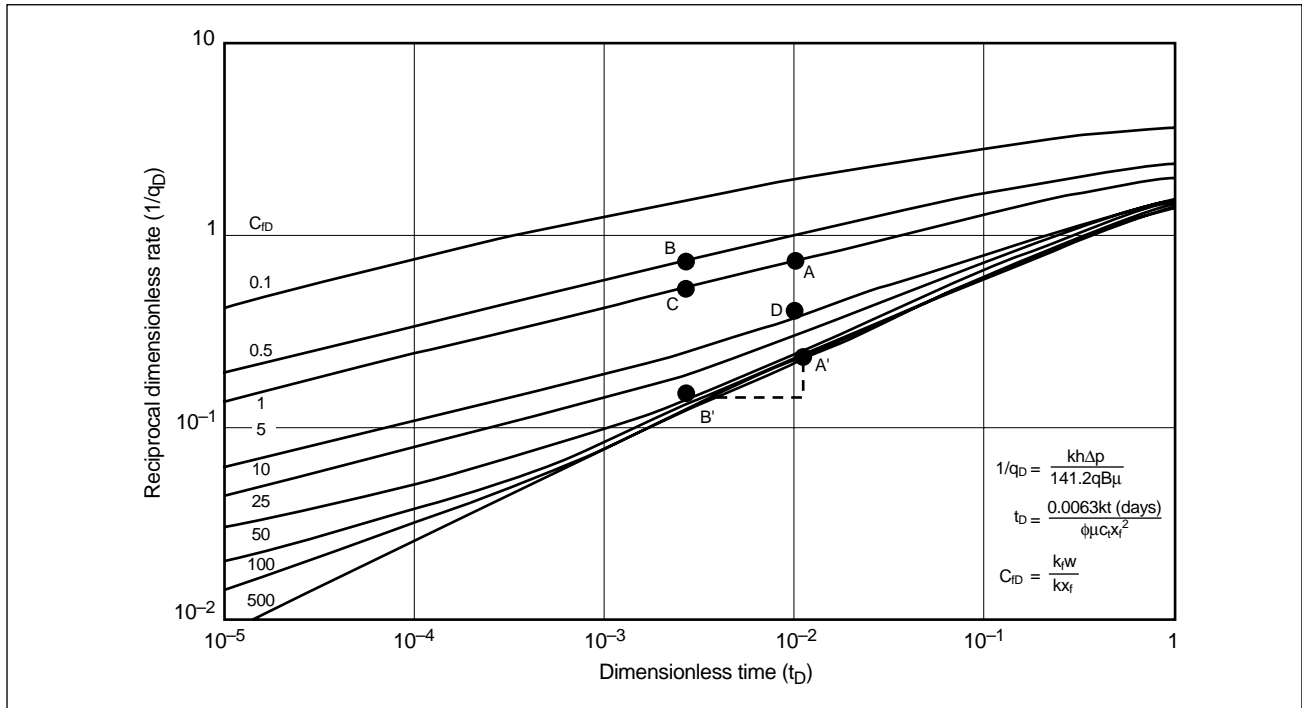


**Figure 10-4.** Finite-conductivity type curve comparisons of production for various fracture designs located as points.

increasing the proppant volume or conductivity by a factor of 4 for the same length, as shown by point D.

Increasing the conductivity for the point A design by a factor of 50 results in a  $C_{fD}$  of 50, as shown as point A'. This design corresponds to a  $1/q_D$  of 0.25. Doubling the length with the same conductivity now results in a  $1/q_D$  of approximately 0.15, or a 66% increase in production rate at that particular time (point B'). A design with twice the length, but with the same proppant volume as point A', yields a  $C_{fD}$  of 12.5, and it still results in a higher production rate than that of point A'. This requires the same proppant volume as doubling the length and maintaining the same  $C_{fD}$ .

Exercises such as this show the insight gained by using type curves in fracture design, and they have led to guidelines regarding the use of  $C_{fD}$  for design evaluation. Designs with  $C_{fD}$  equal to 3 or less cannot be improved significantly by increasing the fracture length with the same conductivity. A redesign for significantly more production requires an increase in  $C_{fD}$ . If  $C_{fD}$  is 30 or greater, increasing the length is more beneficial than increasing conductivity. The optimum conductivity should be defined by an economic analysis; however, insight into the role of conductivity is provided by considering the special cases addressed in the following.

- Constant proppant volume, optimum  $C_{fD}$

Prats (1961) showed that for a given fracture volume (proppant volume) there is a fracture width to fracture length relation for achieving maximum productivity. This relation can be expressed as  $C_{fD}$  equal to 1.26, and it is valid when the well is at pseudosteady state for the majority of its productive life. However, Morse and Von Gonten (1972) showed that because of transient production in low-permeability formations, the higher rates obtained prior to reaching pseudosteady-state conditions can significantly affect the economics of hydraulic fracturing treatments. A study by Elbel (1988) using a reservoir simulator showed that for constant proppant volume in formations with permeabilities greater than 1 md, a  $C_{fD}$  of 1.26 is optimum. For maximum production in formations with less than 0.1-md permeability, a  $C_{fD}$  of 3 is optimum. However, these evaluations, for proppant alone, ignore the cost of fluids and other associated treatment costs required to place a fracture.

- Constant length, optimum  $C_{fD}$

For a constant fracture length, a  $C_{fD}$  between 10 and 30 has generally been accepted as an optimum range (Holditch, 1979a). Because a  $C_{fD}$  of 30 for a given fracture length requires 3 times the

specific proppant volume required for a  $C_{fD}$  of 10, further refinements should be made by inspection of the constant-pressure type curve (Fig. 10-4). The effect of various values of  $C_{fD}$  can be seen by calculating dimensionless time for 36 days to observe differences in the corresponding values of  $1/q_D$  on the constant-pressure type curve. If the calculated  $t_D$  at 36 days for the fracture length is 0.1, theoretically there is little benefit from a  $C_{fD}$  greater than 10. However, if  $t_D$  is  $10^{-4}$ , a  $C_{fD}$  of 100 would be of considerably greater benefit.

- Constant length, varying conductivity  
To increase productivity, the later part of a treatment may contain a higher permeability proppant, such as bauxite or an ISP. Initially these types of treatments were made in areas where high closure stress would severely crush the sand, and the cost of using an expensive, stronger proppant throughout the treatment was considered prohibitive. Bennett *et al.* (1983), Britt and Bennett (1985) and Elbel (1988) investigated the effect of varying fracture conductivity and high-conductivity tail-in treatments and showed that this design strategy may be beneficial.

Relating real time to  $t_D$  (as in the previous section) helps determine if a fracture of varying conductivity could be of significant benefit over a fracture of uniform conductivity. Figure 10-4 shows that for  $C_{fD}$  of about 10 and a 36-day  $t_D$  greater than 0.1, varying the conductivity or tailing in with a high-strength proppant would have minimum effect except potentially for some improvement in the fracture fluid cleanup, cases with catastrophic near-wellbore proppant failure and cases with non-Darcy flow effects.

### 10-2.5. Non-Darcy effects

The previous discussion of conductivity is based on Darcy's law, for which the pressure drop for fluid flow is directly proportional to velocity. Cooke (1973) and Holditch and Morse (1976) demonstrated the role of conductivity with a non-Darcy flow effect that adds an additional pressure drop that is proportional to the product of a turbulence factor and the velocity squared. They showed that the pressure drop for this component can exceed that of Darcy flow with high-velocity production. Problems in design optimization of proppant conductivity are that the velocity varies down the fracture and the turbulence factors vary with the proppant type as well as the proppant's change in permeability

during crushing and with fluid residue (Cooke, 1973). The effects of saturation and multiphase flow can increase the non-Darcy effects (Maloney *et al.*, 1987; Martins *et al.*, 1990). Methods to correct the dimensionless conductivity term used in fracture design and well test analysis have been developed by Holditch and Morse (1976), Guppy *et al.* (1982b) and Gidley (1991). However, numerical simulation is usually required for accurate prediction and evaluation. Non-Darcy flow effects are further discussed in Section 12-3.1.

Concern for possible non-Darcy effects is another reason for the overdesign of conductivity. Because the velocity is affected by the width, doubling the propped width reduces the non-Darcy effects by a factor of 4, which may be more economical than using a higher priced proppant that has higher permeability and requires less width. This depends on the portion of the total pressure that results from the non-Darcy effects. However, it may not be good practice to use a lower permeability proppant at higher concentrations to achieve more width to try to overcome non-Darcy effects. The production velocity for fractures in low-permeability formations is usually low enough to not have significant non-Darcy effects. Again, numerical simulation is generally required to assess non-Darcy effects and achieve an optimum design.

### 10-2.6. Proppant selection

A major consideration in proppant selection is optimizing permeability or conductivity versus the associated cost and benefit. The permeability of various proppants versus stress is shown in Fig. 7-14. The proppant with the highest permeability is not always the optimum choice. The volume and cost required to obtain an optimum or desired conductivity should be considered. Figure 10-5 is a plot of relative proppant volume versus closure stress for different proppant types (Elbel and Sookprasong, 1987). The relative proppant volume  $V_{rp}$  in lbm/md-ft<sup>3</sup> reflects the amount of proppant required to achieve a specific conductivity:

$$V_{rp} = \rho_p (1 - \phi_p) / k_f, \quad (10-1)$$

where  $\rho_p$  is the proppant density in lbm/ft<sup>3</sup>,  $\phi_p$  is the porosity of the propped fracture, and  $k_f$  is the fracture permeability (i.e., the permeability of the proppant in the fracture). As stress increases, the relative proppant volume (RPV) increases but more significantly for

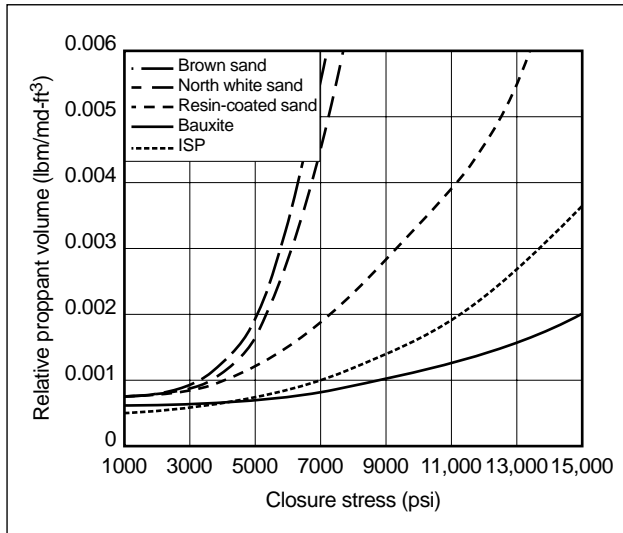


**Figure 10-5.** Relative proppant volume versus closure stress for different proppant types (Elbel and Sookprasong, 1987).

low-strength proppants because of their loss of both permeability and porosity. The product of the RPV and cost of each proppant plotted versus closure stress in Fig. 10-6 reflects the cost effectiveness to achieve conductivity. These plots should be used within the bounds of practical proppant widths in lbm/ft<sup>2</sup> of propped area (i.e., 1 to 3 lbm/ft<sup>2</sup>) and maximum slurry concentrations to achieve these widths, usually 16 ppg for low-permeability reservoirs.

### 10-2.7. Treatment size

If it is assumed that the fracturing fluid and injection rate were selected by considering proppant transport, fluid loss, and horsepower and pressure limits, the other major design considerations are treatment size, type of proppant and proppant scheduling. A general statement can be made that the greater the propped fracture length and the greater the proppant volume, the greater the production. Limiting effects are imposed by factors such as the size of the production string, limit of achievable fracture conductivity and fracture height growth, in addition to well spacing. Within these constraints the size of the treatment should ideally be based on the optimum fracture penetration determined by the economic considerations discussed earlier. A plot of NPV versus propped penetration is shown in Fig. 10-7 for a premium ISP and sand at concentrations of 10, 14 and 16 ppg. The NPV

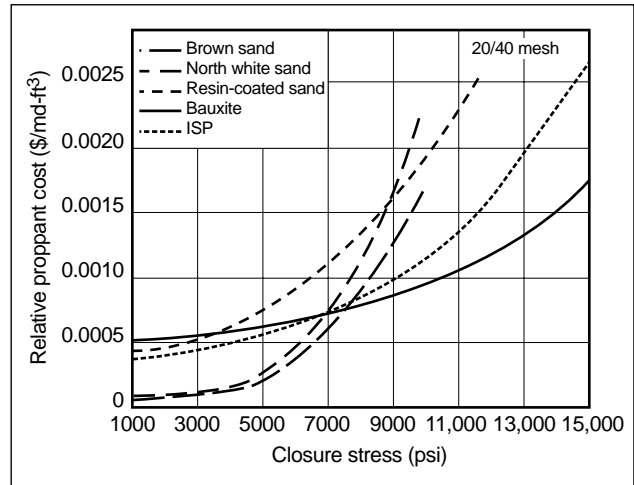


**Figure 10-6.** Relative proppant cost versus closure stress.

is less for sand at 10 ppg and the 1-year optimum is achieved at 500- to 600-ft penetration. The more permeable premium proppant at 16 ppg with a penetration of 900 ft increases the NPV by 35%. Although the maximum NPV is achieved for a specific penetration, additional penetration results in more production—but at a higher cost.

The role of fracturing fluid viscosity and leakoff characteristics is generally well known for fracture propagation and the placement of the propping agents; however, other properties must also be considered. The selected fracturing fluid should correctly balance the following, usually conflicting, properties and features:

- adequate fluid-loss control
- viscosity stability during placement for adequate proppant transport
- compatibility with the formation rock and reservoir fluids
- low friction loss in the pipe
- minimal damaging effects on proppant permeability
- controlled breaking and cleanup properties
- ease in mixing
- minimum disposal problems
- operational safety
- environmental safety
- economical price.

The last three considerations may eliminate systems that may otherwise be applicable. The first seven con-

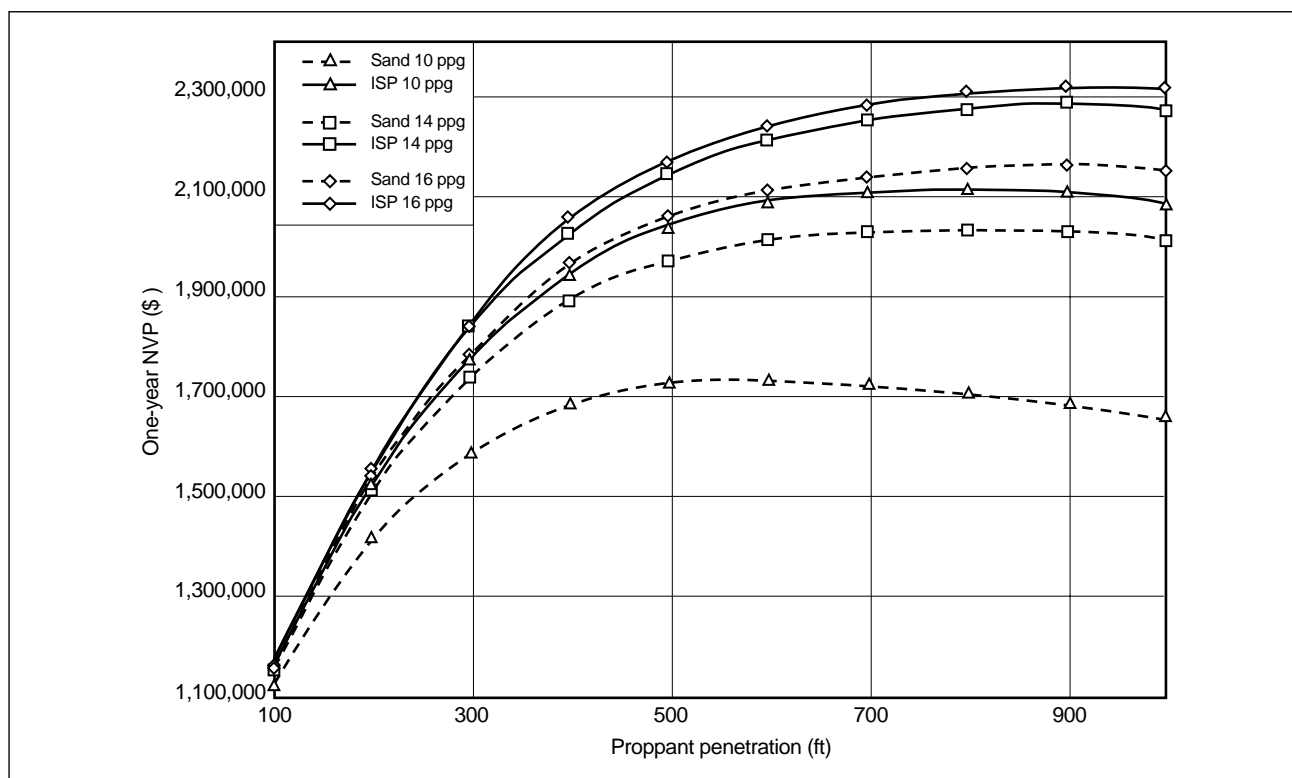


**Figure 10-7.** Net present value versus penetration for various proppant concentrations and types.

siderations are controlled to various degrees by additives, as discussed in Chapter 7. Experience in an area also influences the selection of a fluid. Experience can be either positive from “fluid proof testing” or negative, impeding the consideration of potentially more effective fluid systems. Figure 10-8 provides a general guideline for fluid selection with a distinction between oil and gas wells. Experience has shown that both water- and oil-base fluids have been used successfully in oil and gas wells. The greatest concern is the use of oil-base fluids in dry gas wells; however, they have been used in gas condensate wells.

After the fluid considerations have been balanced for the important properties of fluid loss and viscosity, the related additive concentrations remain for consideration.

### 10-2.8. Fluid loss

Fluid loss affects penetration and closure time. The mechanisms that control fluid loss are discussed in Chapters 6 and 8. There is some degree of dependence on formation permeability, but the fluid-loss control for almost any fracturing fluid system can be

improved by using additives such as solids, surfactants, liquid hydrocarbons and gases (see Chapter 8).

The time for a fracture to close after a large fracturing treatment can be hours. During this time, a significant amount of the proppant can migrate to the bottom of the fracture without connecting to the perforated interval (Cleary and Fonseca, 1992). Closure times increase in cases with fracture height growth, particularly into nonleakoff barriers and when low proppant concentrations are used. Schlottman *et al.* (1981) attributed poor apparent fracture conductivity in the early stages of the development of fracturing the Cotton Valley formation in East Texas to a treatment proppant concentration of only 4 lbm/gal. At this concentration, only 25% of the fracture height was filled if the proppant settled completely before closure. Furthermore, during closure, the fill fraction increases because of fluid loss (see Fig. 5-21). Increasing the proppant concentration in the fluid improved results on subsequent treatments. For this case, at least 50% of the fracture was filled if the proppant concentration in the fluid was 10 lbm/gal.

Fluid-loss control is also desired to minimize the extent of damage to the matrix. The damage may be



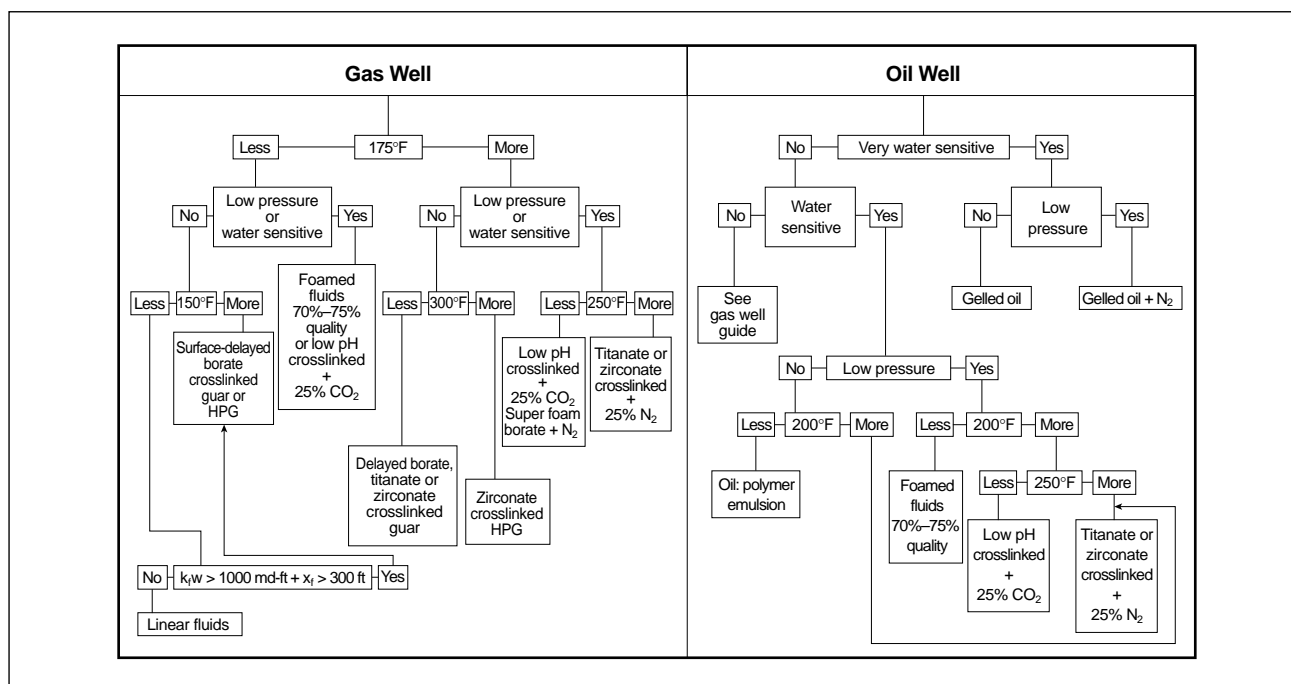


**Figure 10-8.** General guideline for fracturing fluid selection in oil and gas wells.

due to physical or chemical alterations to the matrix that result in a decrease in matrix permeability. It can also be associated with gel residue causing a reduction in fluid mobility, particularly in formations with high permeability. Holditch (1979b) and Pope *et al.* (1996) showed that for typical invasion depths of a few inches and degrees of mobility reduction as high as 90%, the damage has a negligible effect on production, but Montgomery and Berthelot (1990) and Mathur *et al.* (1995) showed that for high-permeability reservoirs fracture face damage can have a significant impact on well performance and can affect the postfracturing evaluation if not taken into account.

In fracturing highly permeable formations, the depth of fluid-loss penetration of a highly viscous fluid may be tens of inches. In the absence of an effective breaker for the fluid, a pressure drop of several hundred psi can be required to regain sufficient permeability to not affect production significantly. Damage to the proppant pack is usually of more significance than damage to the matrix, particularly in high-permeability formations that require highly conductive fractures; however, both types of damage should be considered in fracturing high-permeability formations.

### 10-2.9. Viscosity effects

The ability of fracturing fluids to transport proppants over long distances can be the limiting factor in fracture length optimization. Because of the problem of viscosity degradation with time and temperature, treatments usually start with a higher viscosity than that required in the later stages. This has resulted in the development of highly viscous, crosslinked fracturing fluids. Technology in fracture fluid chemistry continues to evolve to minimize the role of temperature on viscosity degradation.

Proppant transport concerns typically result in designing the treatment with a fluid viscosity higher than necessary. Nolte (1982) showed that without complete consideration of the effects of the fluid's behavior on the proppant settling rate, the design viscosity may be up to 50 times greater than required. The polymer concentration in water-base fracturing fluids should be minimized because of the adverse effects of residues on proppant conductivity and higher pressures on fracture geometry (Nolte, 1982, 1988c).

Schlottman *et al.* (1981), White and Daniels (1981) and Nolte (1982, 1988a) showed the benefits of tapered

polymer loading during a treatment. The polymer concentration is based on maximum exposure to time and temperature for different segments of the fracturing fluid during injection. Fluid exposure time is discussed in Sidebar 10B. An example of the time that the fracturing fluid is at the maximum temperature in the fracture and a resulting tapered polymer schedule for a treatment are shown in Fig. 10-9. Not only is there a savings in polymer cost, but there is also less potential polymer damage to the proppant pack permeability and less potential of exceeding a critical net pressure for efficient fracture extension. Experience

indicates that a viscosity as low as 50 cp at  $170 \text{ s}^{-1}$  is sufficient for proppant transport in a crosslinked fluid. Concerns about polymer damage to the proppant pack and improvements in fluid systems and mixing have resulted in treatments using low-guar fluids and polymer-free, water-base fluids (see Chapter 7).

Higher polymer concentrations can result in higher fluid efficiency because of the effect of the lower fluid-loss rate through the wall filter cake  $C_w$  and the viscosity control leakoff effect  $C_v$  (see Chapter 6), greater fracture width from the higher net pressure or both cases.

## 10B. Fluid exposure time

Polymer concentration can be excessive because of conservative laboratory test procedures. The tests are usually run at the bottom-hole temperature for a time equal to the job time, but in fact the maximum exposure of any increment of fluid at the bottomhole temperature will be less. The selected polymer concentration will maintain a greater viscosity than that required for the actual exposure conditions. A fracture design model should determine the exposure times of designated fluid stages that can be matched to laboratory data for determining more realistic conditions, thereby preventing the use of excessive polymer. A preferred case is for the laboratory data to reflect the actual heat-up condition experienced by the fluid.

Figure 10B-1 shows the maximum time in the fracture for different increments of fluid before shut-in and exposure time in the fracture before reaching various temperatures. The time that an increment of fluid is in the fracture can be approximated by a triangle with the base (x-axis) scaled to the pumping time or treatment volume (pumping time  $\times$  constant injection rate). The y-axis is the time in the fracture. Although the total pumping time in this example is 280 min, the maximum time that any increment of fluid is in the fracture is 120 min before it is either depleted early because of fluid loss or pumped later during the treatment. On the figure this condition occurs at the apex of the triangle.

For continuous polymer mixing, relatively small increments of various polymer concentrations can be considered. For batch mixing in tanks, the tank size is the obvious increment. For example, fluid from tank 1 is in the fracture for a maximum of about 37 min. The increment of fluid corresponding to the apex of the triangle (tanks 7 and 8) has the maximum time in the fracture. This corresponds to the last of the pad fluid required to get the proppant to the tip of the fracture. The fluid reaches the maximum temperature of  $360^\circ\text{F}$  [ $180^\circ\text{C}$ ] about 60 min after its injection, and tanks 7 and 8 span an exposure time of about another 60 min at that temperature. The additives for tanks 7 and 8 should be based on this time of exposure and the laboratory test selected and performed accordingly. Fluid pumped prior to this time is lost into the formation before the end of pumping (pad depletion), and fluid injected later has some portion of it left in the fracture for a time equal to the job time minus the time of injection. For these fluids, the test data should also be selected and performed accordingly. The closure time, which depends on the local proppant slurry concentration, can be added to the test time for the later fluids to reduce proppant fall during closing. An exception to reducing the duration requirement for the pad fluids would be cases where fluid leakoff into the matrix is viscosity controlled.

If the proppant slurry should not be exposed to temperatures higher than  $360^\circ\text{F}$  during injection, proppant addition should be delayed until tank 9 for this 12-tank treatment. With this planned delay, proppant will not reach the hydraulic tip of the fracture because of the

excessive pad, referred to as the cool-down pad. Higher proppant concentrations should be considered to account for the redistribution of proppant during closure and to reduce the time for closure on the proppant.

From this example, and by considering the other temperatures plotted on the figure, an effective strategy can be developed for adding fluid breaker concentrations and potentially different types that are more effective for various temperature ranges

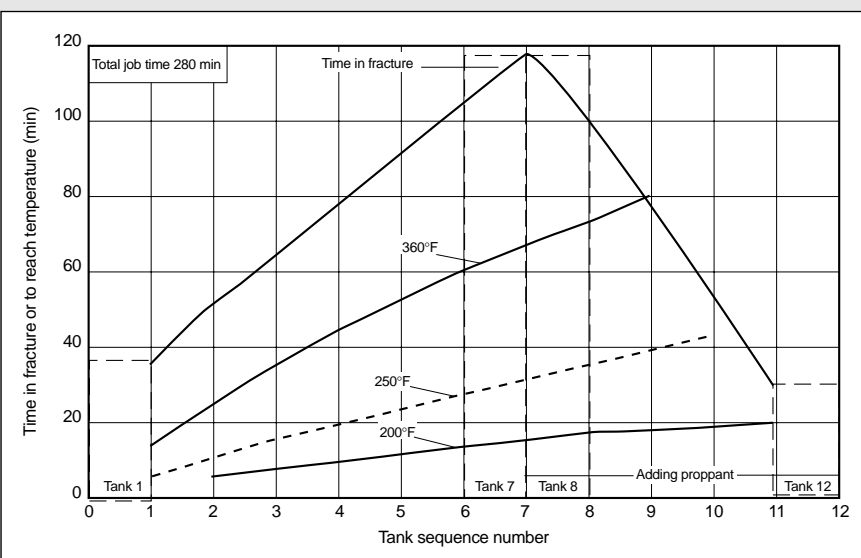


**Figure 10B-1.** Time and temperature exposure in a fracture per tank of treating fluid.

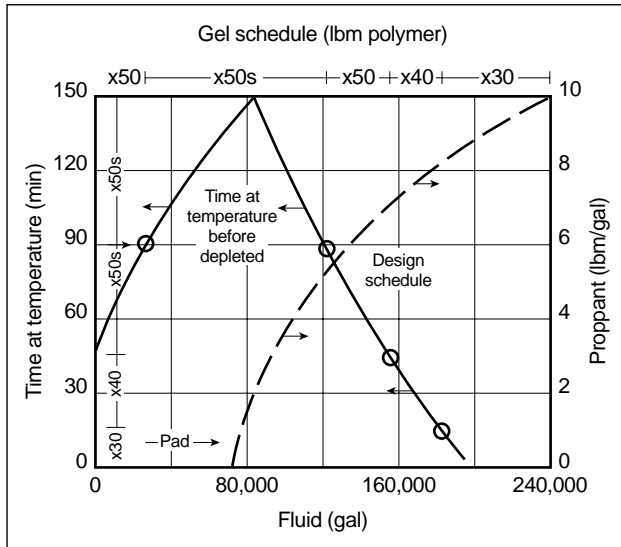


**Figure 10-9.** Fluid selection for exposure time and proppant and fluid scheduling (Nolte, 1982). An s with the polymer loading value indicates that it is stabilized.

## 10-2.10. Injection rate

Selection of the fracture treatment injection rate depends on a number of factors. Generally, high injection rates should be considered because of increased treatment efficiency resulting from decreased fluid-loss time and increased fracture width. Higher rates also directly improve proppant transport capabilities because of an increase in slurry velocity relative to proppant fall rates and a reduced pumping period, leading to less time for proppant fall and less viscosity degradation. The size of the treating tubulars and the

corresponding friction pressure typically limit the injection rates as a result of tubing or wellhead pressure ratings. The increase in surface pressure increases the horsepower requirement and cost. These factors are discussed in more detail in Chapter 11.

Height growth (see Chapter 5) is also affected by the viscosity and injection rate in some cases. Table 10-1 shows results of P3D simulations at rates of 10, 20 and 40 bbl/min. The fracture height growth is contained by a barrier below and is restricted by an upper barrier with stress 500 psi greater than that of the 100-ft pay zone. The upper barrier has no leakoff. The fluid volumes required to obtain 600-ft penetration decrease with higher rates. However, these savings are offset by the increased horsepower, and the proppant volume increases with increasing rate because of more width and height growth. The associated cost of the three variables is shown in the last column. For an upper barrier stress differential of 2000 psi with the height well contained, the comparisons are similar. These relationships are generally applicable for growth into an impermeable stress barrier only, whereas growth through a barrier and into a lower stress zone can be extremely detrimental (Nolte, 1982, 1988c). Nolte also showed that viscosity reduction is about twice as effective for height mitigation as rate reduction, on a comparable percentage reduction.

Britt *et al.* (1994) reported a 40% savings in treatment costs by reducing the polymer concentration and injection rate to limit the height growth and improve production. These examples demonstrate the result of good engineering practices for specific applications.

**Table 10-1.** Sensitivity of height to rates of 10, 20 and 40 bbl/min.

Injection Rate (bbl/min)	Wellbore Height (ft)	Slurry Volume (gal)	Surface Pressure (psi)	Hydraulic Horsepower	Proppant Mass (lbm)	Cost (\$)
Upper barrier stress + 500 psi						
10	142	42,500	3264	800	97,000	35,000
20	164	35,000	4040	1980	116,000	39,000
40	203	33,000	5537	5428	142,000	58,000
Upper barrier stress + 2000 psi						
10	104	40,700	3300	809	86,000	33,000
20	106	31,000	4075	1998	95,000	35,000
40	108	29,000	5630	5520	121,000	54,000

## 10-3. Geometry modeling

An important step in fracture design is modeling the geometry and proppant placement expected for the specific treatment conditions. The simulation allows the design engineer to

- ensure that the proppant addition schedule does not cause an undesired screenout
- determine the treatment fluid and proppant volumes required to achieve a desired fracture penetration
- ensure that the proppant concentration per unit area of the fracture face provides adequate fracture conductivity over the complete extent of the pay zone.

The various fracture geometry models are discussed in Chapters 5 and 6. The three basic types of geometry models described in Sidebar 10C can be further subdivided as follows:

- 2D
  - PKN
  - KGD
  - radial
- 3D
  - lumped P3D
  - discrete cells P3D
  - planar 3D

### 10C. Geometry models

Schematics for fracture width are shown in Fig. 10C-1 for the 2D PKN, P3D and multilayer fracture (MLF) models in a multilayer setting.

- For the 2D PKN model, the fracture height estimated by the engineer remains constant for the simulation. The fracture length grows from a line source of perforations, and all layers have the same penetration. The simulation can be approximated by the average modulus of all the layers, with the reduced width from a higher stress layer between the sands accounted for by a multiplying correction (e.g., about 2; Nolte, 1982).
- For the P3D model, the fracture initiates in the zone with the lower in-situ stress. The height growth is determined by the bounding layers' stress and other mechanical properties. Growth into the other sand layer depends on the stress and thickness of the interbedded shale layer and the distance between the two; it is independent of the wellbore and perforations in the layer. With a relatively low stress contrast, the two fractures join rapidly and behave as a single fracture. The height growth beyond the three layers depends on the stress and modulus profile of the adjoining layers. The simulated penetration is generally greater in the lower stress zone. The P3D model is a common geometry model for fracture design.  
This discussion is for the discrete cell implementation (see Section 6-3). Depending on the implementation, the lumped P3D model may not provide a variable width profile or differentiate the lengths for two zones.
- The MLF model allows simulating simultaneous fractures. The fractures (PKN) in the layers are initiated when the wellbore pressure is above the layer's stress. This model is the most applicable when separate fractures initiate and they do not coalesce, which is the expected case. After the MLF model is used to define the relative injection rates for the zones, the P3D model can be employed for a more detailed consideration of each zone (see Section 10-5.4). The fractures can have different lengths, and each fracture's geometry depends on its height, net pressure, modulus and efficiency. This model can also address the application of limited entry and determination of the stages required for adequate stimulation of a number of layers.

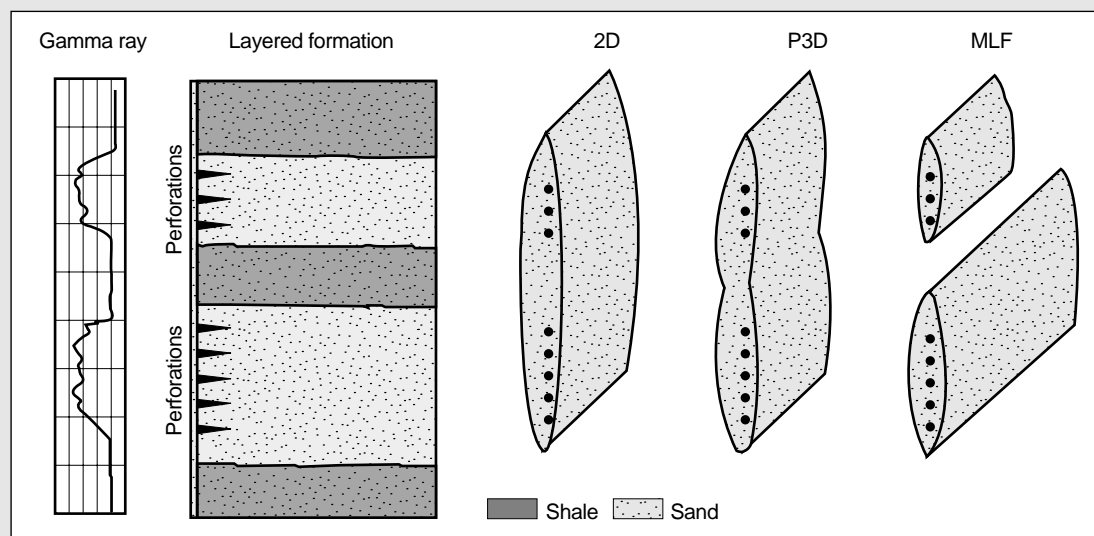


**Figure 10C-1.** Fracture geometry of 2D, P3D and MLF models.

- multilayered
  - PKN fractures
  - P3D fractures.

They can be further classified as to how they model fluid loss, postpumping behavior, tip effects, poroelasticity, various forms of fluid flow (1D and 2D), proppant transport, etc. (see Chapter 6).

### 10-3.1. Model selection

The wide range of models and features available can make selecting a model an overwhelming task. Generally, the model should be selected to match the level of complexity required for the specific application, quantity and quality of data, allocated time to perform a design and desired level of output.

Modeling hydraulic fracture propagation with a planar 3D model can be time consuming. Not as much time is required for 2D modeling, but the results can be simplistic. P3D models provide a compromise and are most often used in the industry for the evaluation of hydraulic fracturing treatments.

A diagnostic method based on the treating pressure history and analysis by history matching (Nolte, 1982, 1988c) can be used to identify various modes of propagation (see Chapter 9). Using this technique, the engineer selects the appropriate model and uses it to evaluate important fracture parameters such as treatment efficiency and net treating pressure. The concept of history matching a calibration injection test and using the parameters required for the match in the design of the propped fracture treatment forms the foundation for effective treatment design. By applying this method, the engineer becomes familiar with the advantages and limitations of the various geometry models and good engineering practices, which with experience leads to successful fracturing programs (Martinez *et al.*, 1992; Johnson *et al.*, 1993; Stadulis, 1995; Gulrajani and Romero, 1996).

When the controversy between 2D KGD and PKN models was high (e.g., Perkins, 1973), it was not uncommon to simulate the treatment design with both models, looking at each for potential problems with the final design. This practice did not ensure an optimum design but was used mainly to minimize premature screenouts by calibrating the fluid-loss coefficient on the basis of the results of prior treatments. Also, as subsequently discussed for Fig. 10-11, the proppant

schedule depends primarily on the efficiency; therefore, models that provide very different widths can predict the same schedules by calibrating a different fluid-loss coefficient for the specific width assumptions. It is still good practice and not unusual to use several models during the design phase; however, the PKN model is a more appropriate approximation for fractures where the length is considerably longer than the height, and the KGD model should be used for fractures where the fracture length is of the same order or shorter than the fracture height. An example is presented in Section 10-6.3.

Fracture design for a wildcat or high-risk well calls for the collection of a comprehensive set of design data and the use of more sophisticated models. This is also the case when treating problems or lower than expected production rates occur.

Geometry models are typically validated with well test analysis and production history matching. The evaluation of fracture treatments, however, requires sophistication in pressure transient analysis and the determination of rock properties for use in the geometry models (Elbel and Ayoub, 1992). The determination of an average permeability may not be sufficient for production history matching. Layered reservoirs with large permeability contrasts (Bennett *et al.*, 1986; Camacho-V. *et al.*, 1987) or reservoirs with horizontal permeability anisotropy (Ben Naceur and Economides, 1989) appear to have shorter fractures if the well test models used assume a single isotropic layer.

In addition to considering the effects for idealized reservoir assumptions, Nolte and Economides (1991) discussed and attempted to quantify the effects for idealized assumptions related to the design and placement of the fracture. The common assumptions about fractures and reservoirs were found to generally result in a productive length that is less than the design length. The coupling of the shorter productive length and the shorter apparent length (to compensate for the reservoir model assumptions) compounds the prospect that the actual production will be less than anticipated. An example indicated that an effective reduction of the fracture to 33% of the design length would not be an unreasonable condition.

They cast the reservoir and placement effects in terms of a design factor that has the role of a safety factor used in other engineering fields. General fracturing practice incorporates these effects in an ad hoc manner and through experience with results that fail to meet the expected ROI (e.g., increased fracture height,

fluid-loss coefficients, propped width). The design factor, equal to 33% for the cited example and analogous to the inverse of a safety factor, can be incorporated directly into the economic optimization process by effectively reducing the length axis by this factor for the expected revenue. A formal, comprehensive identification process of the various model effects is not warranted for every treatment; however, consideration of this process for each reservoir unit results in more effective treatments for the unit, particularly for the initial treatment that is early on the learning curve (Gatens *et al.*, 1991; Nolte and Economides, 1991).

### 10-3.2. Sources of formation parameters

The 3D models require more data, primarily in the form of profiles of stress and moduli. The data are obtained from log analysis, measurements on cores and interpretation of pressure from injection tests. Inverse modeling and injection pressure history matching (Bhalla and Brady, 1993; Gulrajani *et al.*, 1996; see Chapters 6 and 9) can also be used to determine unknown parameters.

Usually, log data must be averaged over intervals within the bounds of layers of higher contrasts. The height of the layers averaged should be consistent with lithology changes (Holditch and Rahim, 1994). Default values are commonly used for the lithology and porosity. If possible, data should not be accepted on a stand-alone basis but checked for consistency with other values either measured or implied. There is usually correlation among lithology, porosity and Young's modulus (Morales and Marcinew, 1993); e.g., a porous section of an otherwise dense limestone should have a lower modulus. There is also a correlation among reservoir pressure, Poisson's ratio and minimum stress as introduced by Rosepiller (1979); therefore, pressure depletion should increase the stress contrasts between the reservoir and nonpermeable barriers. In general, log-inferred stress profiles require calibration from stress tests (Nolte, 1982, 1988c) or directly from injection pressure data (Nolte and Smith, 1981; Gulrajani *et al.*, 1997a). Sidebar 10D provides a discussion of in-situ stress correlation with lithology.

### 10D. In-situ stress correlation with lithology

Correlations based on lithology can be developed from long-spaced sonic logs, core analyses and in-situ stress tests from a limited number of wellbores and subsequently used to estimate properties for similar formations in the region. A common means of correlating stress is using Poisson's ratio  $\nu$  obtained from sonic logs. Table 10D-1 provides ranges of  $\nu$  for various lithologies determined from cores or inverted from field stress tests (Holditch and Rahim, 1994). Poisson's ratio versus the minimum stress gradient for three reservoir pore pressures is shown in Fig. 10D-1.

**Table 10D-1. Poisson's ratio for various lithologies (Holditch and Rahim, 1994).**

Rock Type	Poisson's Ratio
A. Gas-bearing sandstone	0.10 to 0.25
B. Wet sandstone	0.25 to 0.30
C. Wet siltstone	0.20 to 0.30
D. Limestone	0.30 to 0.32
E. Shale	0.28 to 0.43

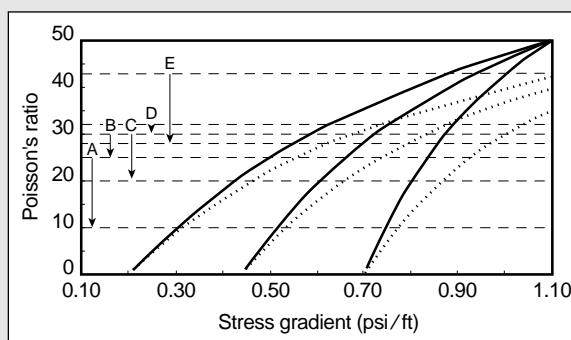


**Figure 10D-1. Poisson's ratio versus stress gradient for three reservoir pore pressures (modified from Holditch and Rahim, 1994).**

Figure 10D-1 is a modification of a Holditch and Rahim (1994) figure of the linear relation of stress versus pore pressure. The effect of tectonic stress (i.e., the ratio of maximum to minimum horizontal stress  $\sigma_{H,max}/\sigma_{H,min}$ ) was not taken into account when inverting for  $\nu$  from stress tests, as it is embedded in the Poisson's ratio correlation. The stress ratio can increase the minimum stress. The effect that a  $\sigma_{H,max}/\sigma_{H,min}$  of 1.3 has on the correlations is shown in Fig. 10D-1 by the dashed curves. If the ratio is known (from the differential strain curve, breakdown pressure or wellbore breakout analyses) and accounted for, the inverted value of  $\nu$  will be lower. For example, for a stress gradient of 1.0 psi/ft in a formation with a pore pressure gradient of 0.7, the inverted  $\nu$  is 0.43 without tectonic effect and only 0.30 for a stress ratio of 1.30.

As the pore pressure gradient increases, the effect of  $\nu$  becomes less. It can also be seen that decreases in stress resulting from pore pressure depletion are greater in cleaner sands. Consequently, depletion can increase the stress contrasts among sandstones, siltstones and shales. The pore pressure in impermeable shales does not decrease because of production, which further increases stress contrasts with the pay zone. The magnitude of the stresses obviously

## 10-4. Treatment schedule

Most fracturing treatments are performed to bring economic viability to formations with low permeability; however, as discussed in Chapter 5, the rapid growth of fracturing after its introduction was primarily for applications to bypass wellbore damage. The sensitivity of fracturing economics to formation permeability and skin effect is discussed in Sidebar 10E.

The goal of a treatment design is to provide a schedule for injecting the treating fluid and proppant. The schedule reflects the volume of fluid based on the desired penetration and viscosity profile and the mass and type of proppant based on the desired conductivity. Scheduling the proppant addition rate during the treatment is important. A major goal is to prevent

a catastrophic event such as an undesired screenout, which can be caused by insufficient width, pad depletion or slurry dehydration near the wellbore resulting from a high proppant concentration. Historically, proppant scheduling has consisted of gradual incremental increases in proppant concentration during the course of the treatment and was based on experience. The schedules were conservative to avoid screenouts. During the treatment, the slurry concentration was typically increased if the treating pressure decreased. If the pressure started to rise, the concentration was decreased under the belief that treatment pressure was greatly affected by proppant concentration at the wellbore. Nolte and Smith (1981) introduced the monitoring of net fracturing pressure and showed that there is a characteristic signature of pressure increase caused

### 10E. Fracturing economics sensitivity to formation permeability and skin effect

To illustrate some economic aspects of fracturing, consider the optimization of fracture treatments in formations with 50 ft of net pay and permeabilities ranging from 0.001 to 10 md. For this example, all the reservoir and formation properties are the same except for the permeability and wellbore skin effect  $s$ .

Three-year NPVs are used to determine the optimum penetration of the fracturing treatments for the different values of permeability and skin effect. Table 10E-1 lists the optimum penetration values, which for this example do not change with the skin effect.

The production revenues and NPVs are shown in Fig. 10E-1. The total production revenue is the greatest for the 10-md formation and decreases, as expected, with each decrease in permeability. However, the net (postfracture minus prefracture) revenue is low for the 10-md case because of the high prefracturing production. Net revenue increases for the 1.0- and 0.1-md cases and decreases for the 0.01- and 0.001-md cases. The NPVs follow the net revenue pattern.

The results of repeating the optimization with  $s = 20$  and 100 are also plotted on Fig. 10E-1. A positive skin effect has the effect of decreasing the prefracture revenues; the postfracture revenues remain the same. For  $s = 100$ , the net revenue and NPV for the 10-md case increase considerably; however, the 1-md case now has the highest net revenue and NPV. Success in fracturing high-permeability formations is attributed to overcoming the large wellbore skin effect usually associated with these formations.

Increasing the tubing size and utilizing tip screenouts for high-permeability cases and optimizing proppant and proppant concentration and increasing penetration in low-permeability cases are good engineering practices; however, they will not significantly alter the points made by this example.

**Table 10E-1. Optimum penetration for different permeabilities based on three-year net present value.**

	Formation permeability (md)				
	10	1	0.1	0.01	0.001
$x_f$ (ft)	400	1100	1300	1300	700
$C_{ID}$	0.5	2.1	19	189.2	3000
Fluid (gal)	60,000	423,000	588,000	588,000	174,000
Proppant (lbm)	37,000	136,000	170,000	170,000	76,000
Cost (\$)	47,000	205,000	275,000	275,000	120,000

Note: 12-ppg maximum concentration

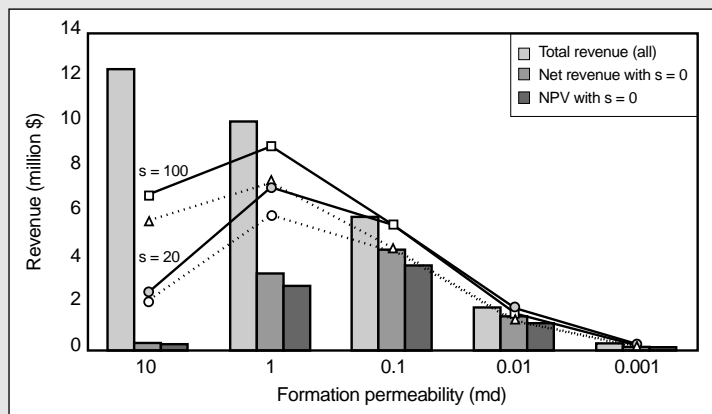


**Figure 10E-1. Economic sensitivity to formation permeability and wellbore skin effect.**

by tip screenout (TSO) and that the continued injection of high, or even higher, concentrations of proppant for a considerable time is possible. Although the fracture extension is arrested, it may be possible to get the designed final concentration of proppant into the fracture to achieve the desired conductivity.

### 10-4.1. Normal proppant scheduling

The optimum design for a conventional fracture treatment is one in which the pad volume has leaked off into the formation and the proppant has reached the tip at the end of pumping, leaving the fracture filled with the proppant-laden slurry to provide a fairly uniform propped width and sufficient conductivity to minimize the pressure drop during production.

The proppant concentration (pounds of proppant added to 1 gal of fluid, or ppg) in any segment of slurry increases because of fluid loss as the slurry moves down the fracture. The propped concentration in  $\text{lbm/ft}^2$  of fracture area depends on the rate of fluid loss from the slurry and the fracture width profile. This is illustrated in Fig. 10-10 by simulations of treatments with only one proppant concentration. All the treatments have the same pad volume: two of the simulations are for 20,000 gal of slurry at 1 and at 2 ppg, and the third is for 40,000 gal at 1 ppg with the last half of the slurry injected after a TSO. The top set of curves shows the proppant concentrations in the slurry increasing over the fracture length. The bottom set of curves shows the corresponding propped width profile decreasing slightly away from the wellbore and then starting to rise about

halfway down the length. Comparison of the simulation of the 1-ppg 40,000-gal TSO case with the same propped volume injected at 2 ppg shows about the same concentration in  $\text{lbm/ft}^2$  for the tip half of the fracture but less concentration over the wellbore half. This is because the concentration at the wellbore is only 1 ppg. Increasing the proppant concentration (ppg) during the treatment is required to obtain a fairly uniform propped width down the fracture.

The efficiency of the treatment determines the proppant addition schedule that will achieve a specific slurry concentration in the fracture at the end of pumping (Nolte, 1986b). For this approximation method, the volume and efficiency of the treatment must be known, and the efficiency can be estimated from a calibration treatment. The following discussion uses this approach; however, for general application a numerical placement simulation should also be used to define the volume, schedule and placement (see Section 6-11).

Figure 10-11 shows plots of addition schedules for a uniform concentration at shut-in and in terms of various efficiencies based on the equations in Sidebar 6L. If the efficiency is low, the ramp is almost linear; if it is high, the initial concentrations must be ramped up rapidly. However, this figure does not represent equal-penetration fractures. Small errors in the initial ramping or efficiency estimate can cause dehydration near the tip, so in practice, the early stages are usually not increased as rapidly.

Figure 10-11 or the associated equations can be used to provide a schedule to place a specific, uniform

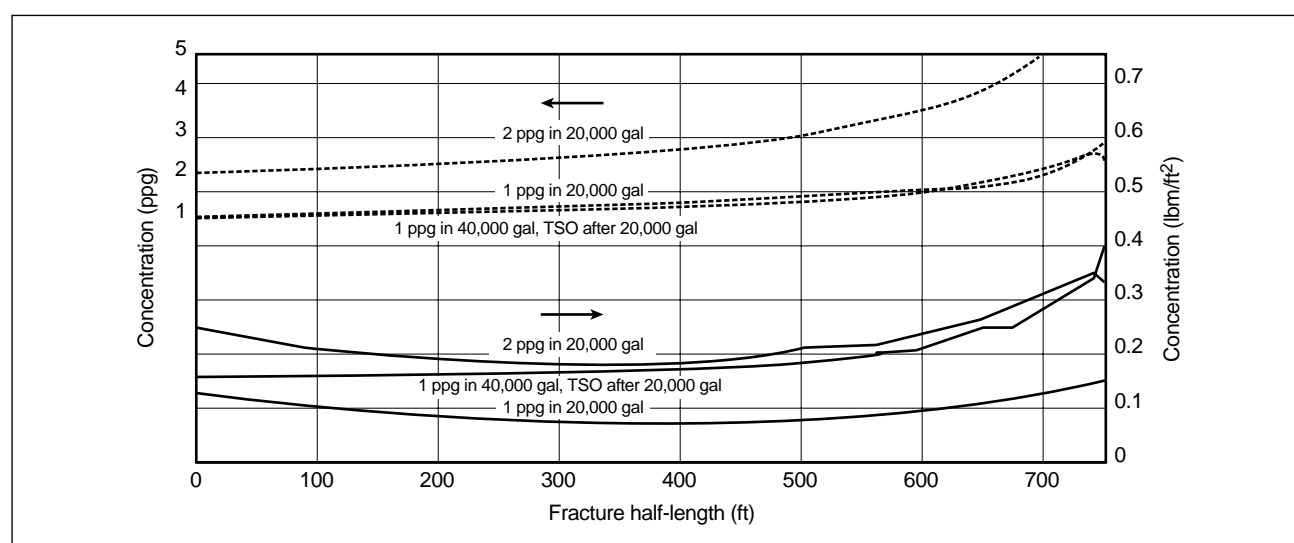


Figure 10-10. Proppant concentration profiles for slurries injected at 1 and 2 ppg.



profile of proppant concentration and also to provide a quick calculation routine. An inconvenience for this approach is that the figure is for proppant volume fractions and must be converted to ppg units for practical applications. The figure is presented in a dimensionless framework and the area under any particular curve is equal to the fluid efficiency for that treatment. The fraction of area under any segment of a curve—i.e., from the end toward the beginning pad portion—is the same fraction of the fracture volume from the wellbore toward the tip and therefore defines the placement location of that portion of the proppant. The concentration for a segment can be changed relative to the reference value by a proportional change in the value of the ordinate for the segment on the figure. Similar concepts for placement and proportional changes in concentration can be incorporated into a more accurate, automated numerical scheduling procedure presented by Nolte (1982, 1988c) for a fracture placement model to determine a specific ramping schedule and pad volume (see Chapter 6).

The proppant concentration in the slurry determines the ratio of the final propped width to hydraulic width. This relation can be inferred from the plot of fracture fill versus proppant concentration in ppg shown in Fig. 5-21. If the last injected stage is at a concentration of 8 ppg of sand, the average propped width at the wellbore cannot be greater than 40% of the hydraulic width.

The continuous curve, or ramp, schedule is typically represented as a stairstepped, incremental schedule to facilitate simulation or operational requirements.

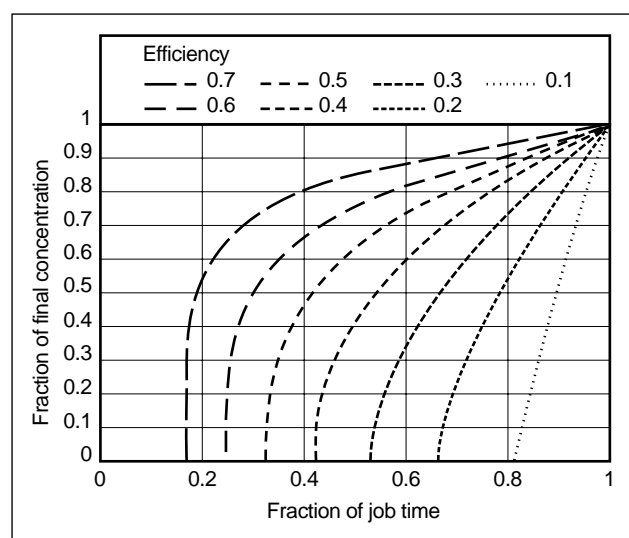


**Figure 10-11.** Proppant addition schedules for different treatment efficiencies.

Figure 10-12 shows these proppant addition schedules for a treatment with an efficiency of 0.5; the stairstepped schedule shows slightly less concentration initially compared with the ramp and reflects a common cautionary practice to avoid a screenout prior to the reaching the tip. This stairstepped schedule is used in Fig. 10-13 for a simulation illustrating proppant movement from the end of pumping to closure.

The schedule in Fig. 10-13 results in a uniform slurry concentration at the end of pumping. If there were no further movement of slurry during closure, the proppant concentration would range from 1.6 lbm/ft<sup>2</sup> at the wellbore to 1.1 lbm/ft<sup>2</sup> near the fracture tip. However, the slurry continues to move after shut-in, as shown by Nolte (1986b), and is seen here to result in a fairly uniform concentration (lbm/ft<sup>2</sup>) profile over most of the fracture with an additional penetration of about 5%. This result is the basis for a design with constant ppg at shut-in as a first target for a final schedule (e.g., Fig. 10-11).

The efficiency can also be used in Eq. 5-22 to estimate the pad fraction required for the total treatment volume. The pad fraction, in addition to creating adequate fracture width and preventing premature screenout, can also influence slurry movement during the fracture closure stage. If excess pad remains ahead of the slurry, it can continue to extend the fracture, and the position of the slurry front will continue to move forward until it dehydrates. Figure 10-14 compares the proppant concentration profile for the previous simulation with a profile that has twice the pad volume. Additional penetration from the excess pad

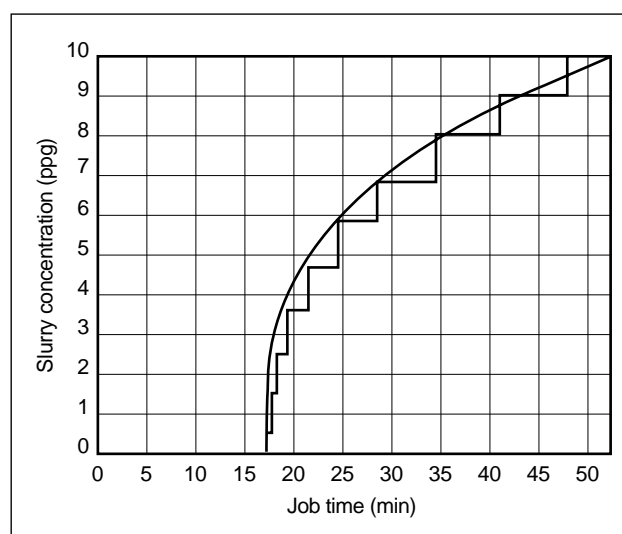


**Figure 10-12.** An optimally designed proppant addition schedule, both ramped and stairstepped.

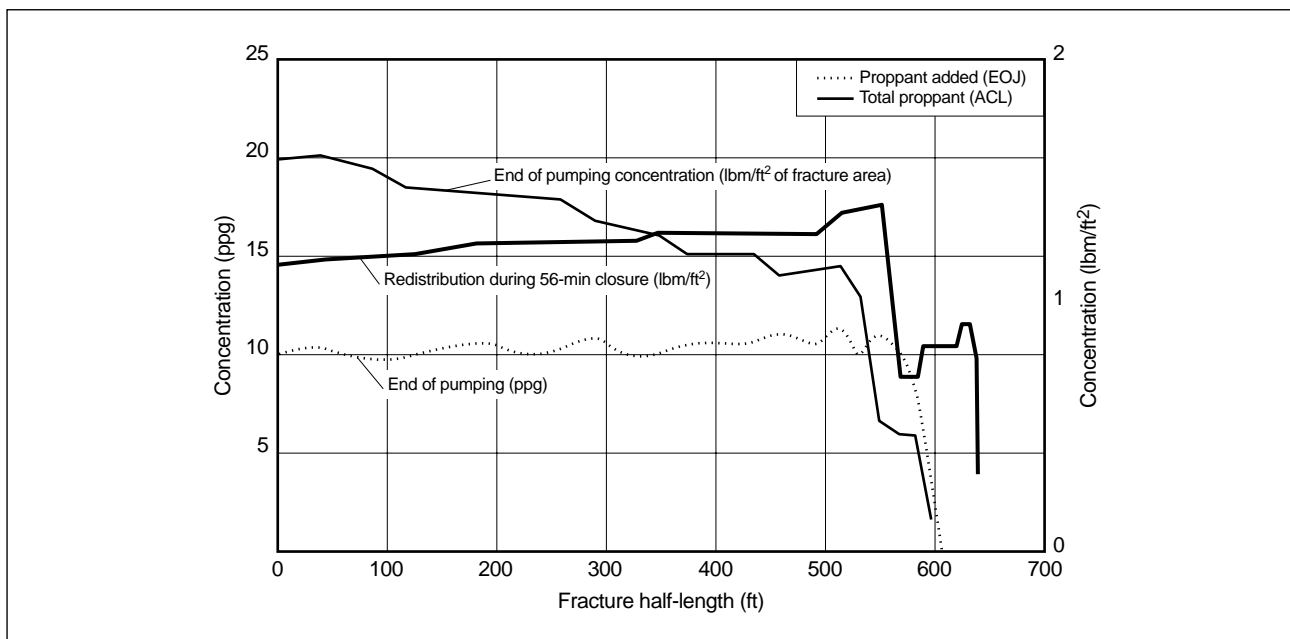


**Figure 10-13.** Change in fracture proppant concentrations from the end of pumping to closure. EOJ = end of job, ACL = after closure.

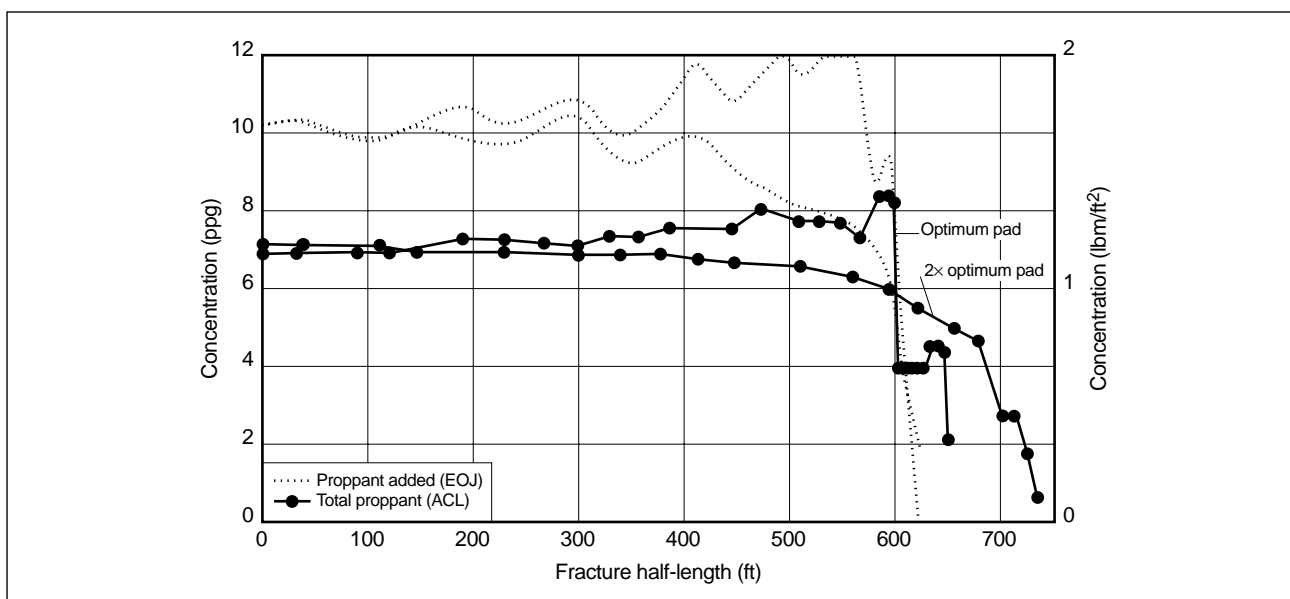


**Figure 10-14.** Proppant concentration profiles with different pad volumes.

volume is limited to about 10% because of slurry dehydration near the tip.

Excessive extension after shut-in can cause the final concentration of the proppant in lbm/ft<sup>2</sup> of fracture area to decrease as the width of the fracture decreases, creating a longer fracture with less conductivity. Both increased length and decreased conductivity work

to decrease  $C_{fD}$ . Fractures with an equal or less than optimum  $C_{fD}$  (i.e., conductivity limited) have no additional benefit from the increased length and may have lower production (see Section 10-2.2).

Insufficient pad results in less fracture penetration and possibly premature termination of the treatment. This is the case particularly with stiffer fractures that

are either short or in high-modulus formations. In the stiffer cases the pressure increase is usually relatively rapid, generally preventing placement of the design volume of proppant or in extreme cases not allowing enough time for flushing of the wellbore with only a portion of the proppant placed.

## 10-4.2. Tip screenout

Hydraulic fracturing in high-permeability reservoirs differs from conventional fracturing in that the objective is more to generate fracture conductivity than length. Techniques for increasing fracture conductivity include increasing proppant size for cases that do not produce formation fines into the proppant pack, increasing proppant concentration (all applications), using clean fluid (all applications) and using TSO design techniques. Each of these techniques has positive results on increasing fracture conductivity and the success of high-permeability fracturing; however, the application of TSO fracturing, introduced by Smith *et al.* (1984), has revolutionized the completion and stimulation of wells in higher permeability reservoirs (Smith *et al.*, 1987; Monus *et al.*, 1992; Martins *et al.*, 1992c; Hannah *et al.*, 1994).

TSO treatments can achieve proppant concentrations in excess of 20 lbm/ft<sup>2</sup> of fracture area, which can represent a 10- to 20-fold increase in fracture conductivity. Similar conductivity increases can be achieved by using synthetic proppant (relative to sand) at higher stress. The compounding effect can result in an approximately 100-fold increase in conductivity. Well productivity may be increased 4- to 7-fold if production from the well is conductivity limited (see Fig. 10-4).

A TSO is designed to deliberately cause proppant to pack at a specific location because of width restriction, pad depletion or slurry dehydration. Once packing occurs, further fracture propagation ceases at this point, usually at the tip, and generally along the restricted width over the entire perimeter. Continued injection increases the hydraulic fracture width and final conductivity. The ratio of propped to hydraulic widths at the wellbore is controlled by the final proppant concentration in the injected slurry (see Section 10-4.1), and proppant conductivity down the fracture is governed by the proppant concentration schedule, fluid-loss rate and backward packing of proppant from the fracture tip to the wellbore. Increasing the slurry concentration after the onset of a TSO is a more effi-

cient way to obtain increased conductivity than by relying on only the increase in width.

- Tip-screenout design

Smith *et al.* (1987) introduced a method of TSO design utilizing an analytical radial simulator through pad depletion and calculating the extra leakoff over a constant area after bridging. Nolte (1986b, 1990) published analytical relations based on the efficiency at screenout for the ramp schedule and width increase for the additional injected volume after a TSO (see Sidebar 6L). Martins *et al.* (1992c) modified Nolte's concepts by extending the initial low-concentration proppant stage to minimize subsequent screenout at an intermediate distance that could lead to detrimental rapid backward packing of proppant and a pressure increase, particularly for stiff fractures.

TSO treatments can be designed using either an appropriate placement simulator or analytical methods based on efficiency (see Section 6-11). The analytic technique uses the control of the TSO fracturing process by pad depletion and material-balance considerations. Because the TSO design is predicated on fracture storage and fluid loss for a fixed penetration, width increases are readily determined as a function of fluid efficiency and fracture volume increases resulting from the injected volume after screenout, as illustrated in Fig. 10-15 (K. G. Nolte, pers. comm., 1984). For example, at 50% efficiency at the time of screenout and to achieve a twofold increase in the hydraulic fracture width ratio of channel width  $w$  to the width after screenout  $w_{so}$  requires injecting a total volume that is 1.8 times that injected before the screenout.

An analytic-based proppant addition schedule for a TSO fracture stimulation can be designed in a manner similar to that for conventional treatments. First, the pad fraction is determined from the efficiency before screenout and preferably obtained from a calibration treatment. Second, the fluid efficiency and desired fracture width are used as in Fig. 10-15 to determine the additional slurry volume relative to the volume at screenout. Finally, with these parameters and the final efficiency, the proppant addition schedule can be defined as in Sidebar 6L.

As discussed previously and illustrated in Fig. 10-16, Martins *et al.* (1992c) modified the proppant scheduling method by increasing the initial low-concentra-

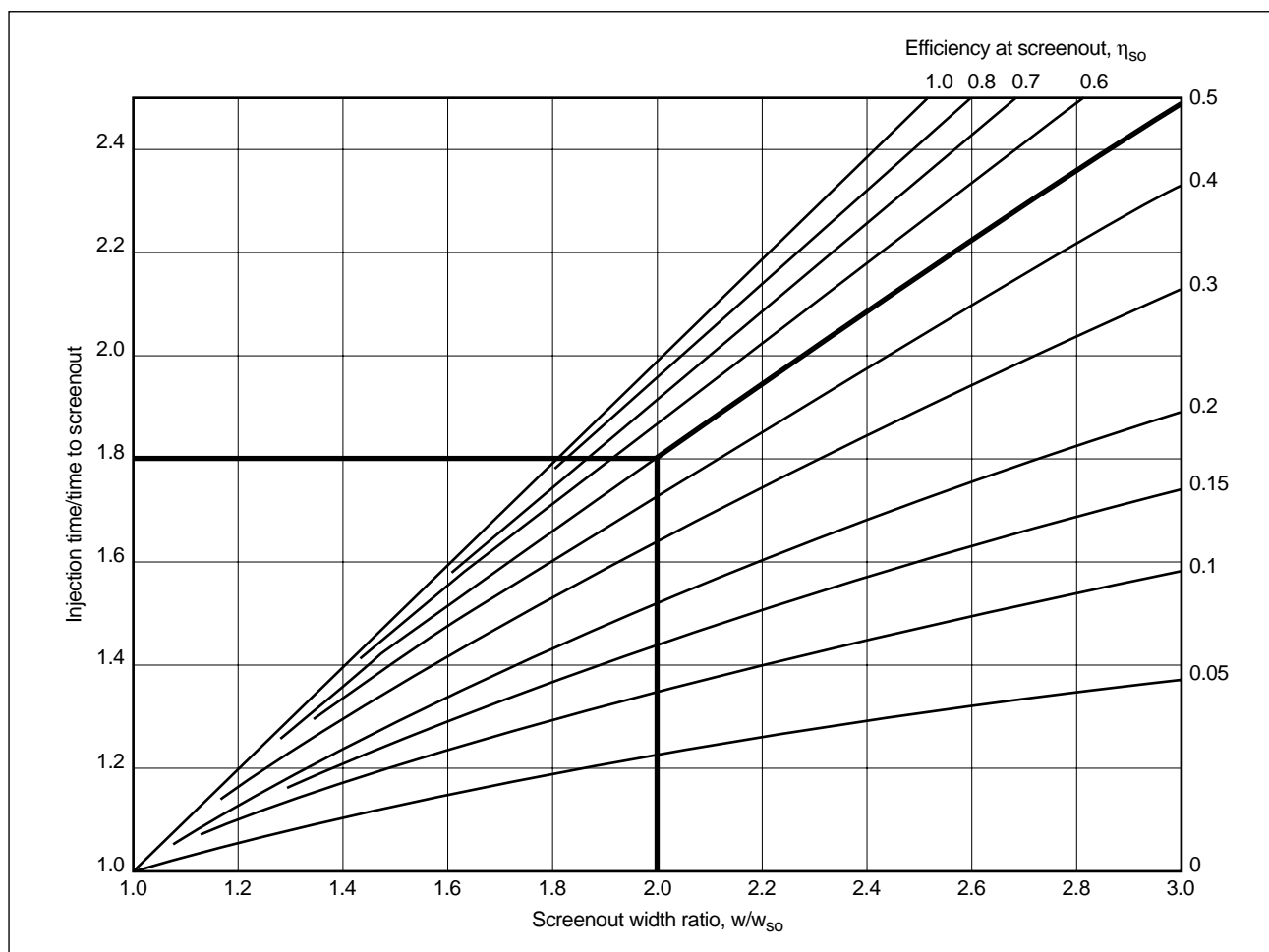


**Figure 10-15.** Width ratio increases after screenout as a function of fluid efficiency and injection time.

tion stage, which still reaches the tip and bridges at the same penetration, and designing a new schedule based on the end of job (EOJ) efficiency and a longer job time. The new schedule starting regular proppant addition at a later time is initially a more aggressive schedule because of the higher efficiency after screenout. The following discussion of Figs. 10-16 and 10-17 provides insight to these various scheduling assumptions. The figures show a normal schedule and four different TSO design assumptions.

A normal treatment design with 0.5 efficiency and final proppant concentration of 10 ppg is labeled A in Fig. 10-16. The average propped fracture width for this schedule is 1.2 lbm/ft<sup>2</sup>. From Fig. 10-15, increasing the hydraulic width by a factor of 2.5 with a TSO requires about 2.15 times more slurry (35,000 to 75,000 gal). Curve B shows the same schedule up to the TSO, after which the

final 10-ppg stage continues for the additional time. Another TSO schedule extrapolating the slurry ramping to a higher concentration of 14 ppg for the additional time is shown by curve C. These techniques are prone to creating intermediate dehydration locations and rapid pressure rises. Nolte's method (see Sidebar 6L) of modifying the ramping schedule on the basis of the estimated EOJ efficiency and using the efficiency at screenout for the pad starting time is shown as curve E. For these latter two methods, the lower initial concentrations minimize intermediate screenouts or backward packing. Martins *et al.*'s method is shown as curves D and D – *i*. The main ramping curve D is based on the EOJ efficiency, but proppant must be initiated earlier for the screenout, which is shown as curve D – *i*. For this example, with a long fracture and high efficiency, the lower concentrations in early

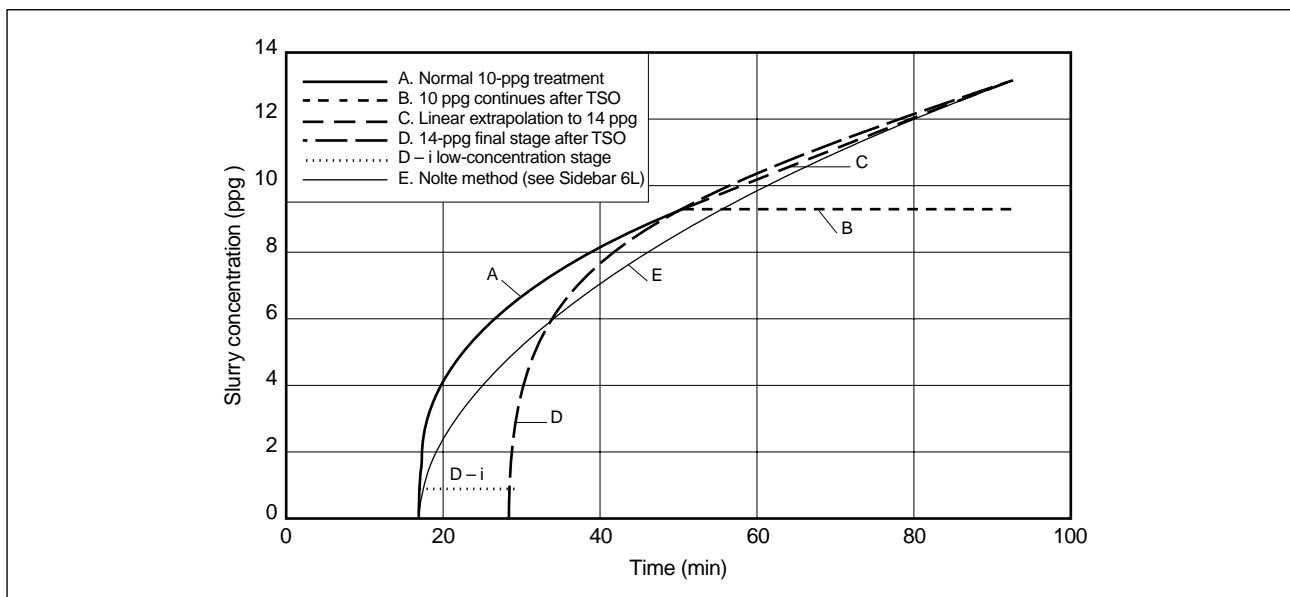


**Figure 10-16.** Various proppant scheduling practices after tip screenout.

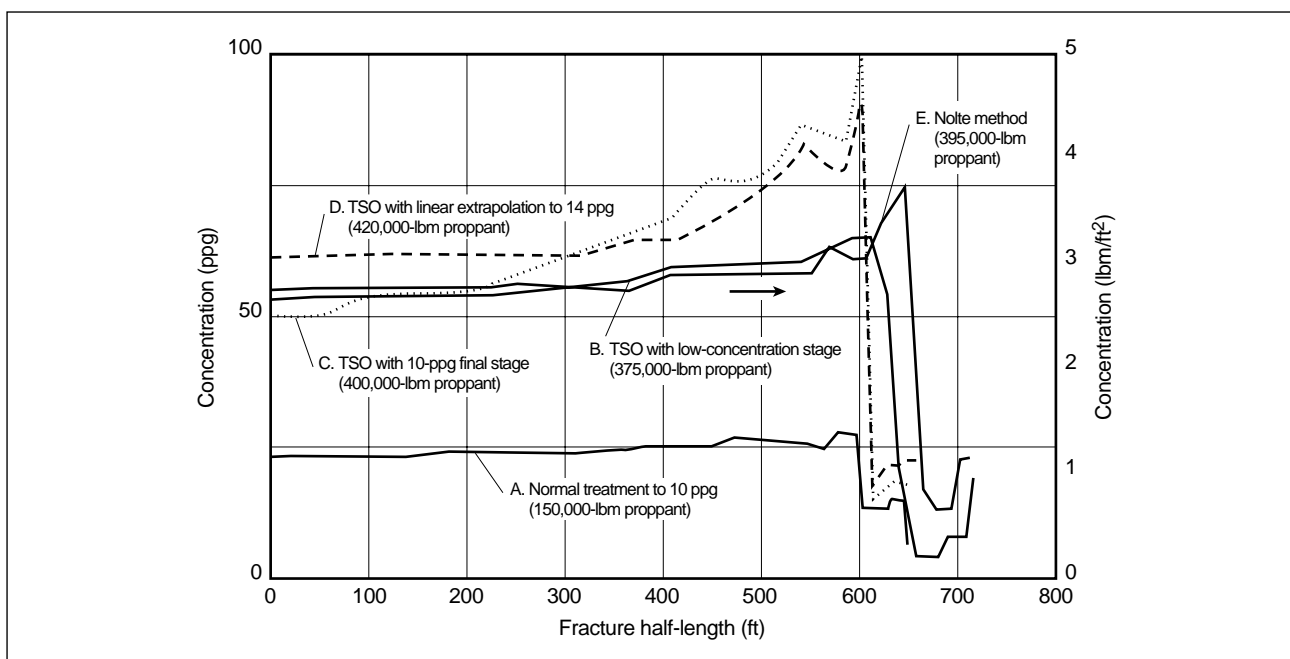


**Figure 10-17.** Proppant concentration profile comparisons for the schedules in Fig. 10-16.

ramping in curves D and D – i allow about 10% greater penetration. The corresponding proppant concentration profiles for the normal and four TSO schedules are in Fig. 10-17.

- TSO with sand control application

A large number of TSO treatments are in marginally consolidated or unconsolidated formations, and

they incorporate three basic methods to control sand production in the operations.

The first method is a four-step operation. The TSO is performed, the wellbore is cleaned up, the screen assembly is run, and the gravel-pack operation is performed (Monus *et al.*, 1992).

The second method is a one-step operation that overcomes possible damage created by the cleanup

stage of the first method. The designed fracture treatment is pumped with the screen in place, the crossover tool in the circulating position and the choke on the annulus closed. The annular choke is opened when the gravel-pack volume is pumped at a slower rate to ensure annular packing. After screenout of the casing/screen annulus, the tool is placed in reverse position and the excess slurry is reversed out of the tubing (Hannah *et al.*, 1994; Meese *et al.*, 1994).

The third method is a TSO with a proppant that is stabilized with a back-production control additive (e.g., curable resin, fibers or both). This method uses a more aggressive schedule designed to promote backward packing to an extent such that a continuous external pack is formed as a ring around the annulus on the outside of the casing created by the fracture width, which eliminates the need for an internal screen.

Executing a planned backpacking of the annulus outside the casing creates an external pack, provides maximum perforation efficiency with minimal completion skin effect and should be considered for all three completion methods.

The improved productivity of frac and pack completions over those with only gravel packs has been shown by Mullen *et al.* (1994), Monus *et al.* (1992), Fletcher *et al.* (1984), Hannah *et al.* (1994), Papinczak and Miller (1993) and Stewart *et al.* (1995). As for hard-rock applications, optimization studies of proppants, fluids and breakers result in more effective frac and pack designs. The plot of productivity ratio versus skin effect in Fig. 10-18 compares gravel-packed wells and wells completed with a frac and pack treatment in the U.S. Gulf Coast area.

## 10-5. Multilayer fracturing

Vertical wells usually penetrate a number of potential producing zones. In low-permeability formations, the zones may span hundreds of feet with no individual zone capable of economic production. For maximum reserve recovery, it is desirable to fracture each zone individually to ensure adequate penetration. To minimize fracturing costs and completion time, it is desirable to fracture all zones with one treatment or at least to minimize the number of individual fracturing treatments by efficiently grouping the layers.

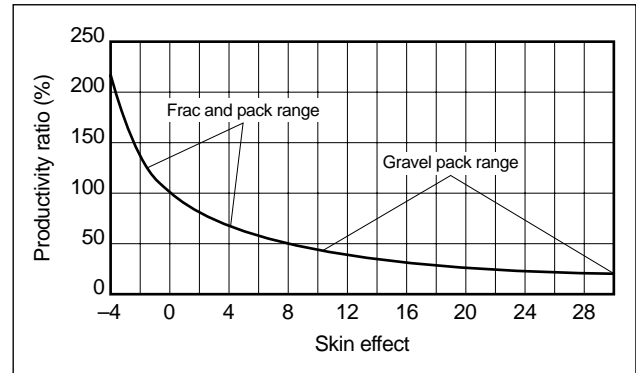


**Figure 10-18.** Typical productivity ratio and skin effect for conventional gravel-packed wells and wells completed with a frac and pack treatment in the U.S. Gulf Coast.

### 10-5.1. Limited entry

The technique of limited-entry perforating is used to achieve a large frictional pressure drop across certain perforations (e.g., in a given layer) in an attempt to ensure fluid injection through each perforation in the completed interval. By limiting the number of perforations for multiple intervals, successful application of the limited-entry technique may increase the number of intervals that can be penetrated by the fracturing fluid. During injection, the frictional backpressure offsets the stress differences between the zones to enhance injection into all the perforated zones (Lagrone and Rasmussen, 1963). The technique does not consider the distribution of the injected fluid resulting from different layer properties.

During the 1960s, the injection of perforation ball sealers was commonly used in conjunction with the limited-entry technique. The ball sealers were injected at various time intervals during one treatment to increase the wellbore pressure even more. One limited-entry method (Webster *et al.*, 1965) used the differences in stress between the individual zones. The lowest stressed zone was fractured first at an injection pressure below the stresses of the other intervals. A specific number of ball sealers was then injected to seal off the perforations for this zone to cause the next to the lowest stress zone to be fractured. This method found limited application because of the magnitude of the stress differences required to confine each stage to a single interval. Limited entry is discussed further in Chapter 11 and Section 10-6.4.

### 10-5.2. Interval grouping

The initial task in designing treatments for multilayer formations is to minimize the number of fracturing treatments by grouping the maximum number of layers that can be treated with a single fracture treatment. The simplest case is one fracture covering all layers. The one-stage treatment is effective where all productive layers have a small stress contrast relative to the adjoining nonproductive layers. Many high-rate, massive hydraulic fracturing treatments are designed for this situation.

If the layers are separated by higher stress, nonproductive intervals, the problem is more complex. For example, for an application with four separate productive zones over a large interval, eight grouping options are available.

Grouping can be made by intuitive reasoning based on the zones' thicknesses and their proximity to each other and experience gained in similar conditions. Equation 10-2 can be used to estimate injection partitioning between zones A and B (Elbel, 1993):

$$\frac{q_{iA}}{q_{iB}} = \left( \frac{p_f - \sigma_{h,minA}}{p_f - \sigma_{h,minB}} \right)^{(2n+3)/(n+1)} \left( \frac{h_{fA}}{h_{fB}} \right)^3 \left( \frac{E'_B}{E'_A} \right)^2 \left( \frac{\eta_B}{\eta_A} \right)^{1/(n+1)}, \quad (10-2)$$

where  $q_i$  is the injection rate in bbl/min,  $p_f$  is the fracture pressure in psi,  $\sigma_{h,min}$  is the minimum stress in psi,  $h_f$  is the fracture height in ft,  $E'$  is the plane strain modulus in psi, and  $\eta$  is the efficiency (ratio of the fracture volume to the injected volume).

The equation shows that the injection rate partitioning between the two zones A and B is governed by four zone parameter ratios of the gross height, net pressure, modulus and efficiency. The difference in the injection rates occurs primarily because of different fracture widths caused by a height- and modulus-dependent stiffness effect. The net pressure and efficiency are also dependent on the height and modulus; therefore, calculating the actual ratio for design requires an iterative procedure. It is evident that a zone with a small height should generally not be grouped with a much larger height zone. An exception would be where the formation is sufficiently characterized to ensure the existence of the unlikely condition that the thicker zone has a correspondingly higher

modulus or higher stress. For meaningful differences in any of the ratios, application of the limited-entry technique should be investigated, but it may not achieve the desired results.

### 10-5.3. Single fracture across multilayers

The simplest multilayer case is a zone with one fracture covering all the layers, which have relatively small heights and low stress contrasts with the adjoining nonproducing layers. If these intervals are in turn bounded by massive shales of higher stress, the height of a hydraulic fracture will be limited to the pay, and a 2D geometry model may be sufficient for the design. Nolte (1982, 1988c) showed that for height growth equal to the pay zone height into either barrier zone, the fracture penetration and net pressure are reduced only by about 10%, and a constant-height PKN model should be adequate for the design.

Design and optimization of a single fracture in a homogeneous formation were previously discussed. Production for a layered reservoir requires some adjustments relative to the case for a homogeneous formation.

If the layers penetrated by a single fracture have different permeabilities or porosities, the initial production response during transient time will be less than predicted using the average permeability over the fractured interval. This behavior has been shown by Bennett *et al.* (1986), who introduced the dimensionless reservoir conductivity term  $C_{RD}$  (see Section 12-3.5 and Eq. 12-44) and showed that the Agarwal *et al.* (1979) type curves can be used to evaluate the transient response in a layered reservoir if the  $t_D$  term is replaced by  $t_D/C_{RD}^2$ . Without this substitution, the effective fracture length is in error by a factor equal to  $C_{RD}$ , and the value of  $C_{RD}$  is always less than 1 for a layered reservoir. As a consequence, the response from the fracture treatment, based on the physical fracture length and average reservoir properties, will be less than predicted. Economic optimizations for fracture length should take this layer effect into account; e.g., if  $C_{RD}$  is 0.5, the optimization should be based on production during transient flow for a fracture penetration one-half of that predicted by the geometry simulation.

#### 10-5.4. Two fractures in a multilayer reservoir

Two perforated intervals can have different fracture geometries as illustrated by Eq. 10-2. Elbel (1993) discussed the considerations required for a design in this setting and pointed out the difficulty in achieving equal proppant penetration in each layer because of different pad volume and perforation frictional pressure drop requirements. The coalescence of two individual fractures, originating at different perforated intervals, would generally not occur unless at the unlikely condition of near-perfect alignment for the wellbore axis and preferred fracture planes. Also, for the case of the two fracture heights extending and overlapping each other, the effect of the width of each fracture would increase the surrounding stress and impede additional height growth into the overlap region.

Consider a case with two perforated intervals with the same properties except that the heights are 80 and 40 ft for the top and bottom layers, respectively; they are separated by a 40-ft interval at higher stress. Because both intervals are perforated and have the same stress, fractures will be initiated in both layers.

A common practice for this case is to design a pumping schedule for a single fracture over the three intervals. The consequences of ignoring the different stresses for the intervals, for the single-fracture assumption, are addressed in the following for a design using an injection rate of 12 bbl/min. Other design details are not critical for this purpose and are not provided. The design is to achieve a penetration of 560 ft. First, consider the single-fracture design within the constant-height multilayer fracturing model described in Chapter 6. This results in penetrations of

657 ft for the top zone and only 325 ft for the bottom zone. The injection rate in the top zone is 9.6 bbl/min and 2.4 bbl/min in the bottom zone. The bottom zone screens out at about 80% of the job time and the top layer at 95%. The simulation continues as a TSO in both zones.

The model assumes constant height of the fractures and, as previously discussed, is valid for cases with high stress contrasts that limit growth into a barrier to a distance of about the pay section. P3D simulations for the individual zones at their partitioned rates can be made to determine height growth. Figure 10-19 shows the results of this exercise and indicates that for a mid-barrier stress contrast of 1100 psi, fractures begin to overlap near the wellbore after about 80% of the treatment time. However, even if the fractures have coalesced, the mid-barrier stress should result in a pinch point for fracture width and proppant bridging would prevent vertical fluid flow communication.

An additional P3D simulation in Fig. 10-19 for a mid-zone stress contrast of only 600 psi shows fracture overlap for the two zones occurring earlier, after about 30% of the treatment time and before the first proppant stage. The similar penetrations from the idealized multilayer model and for the multiple simulations with a P3D model for each of the stress cases demonstrate the utility of the multilayer model. This model provides the generalization of Eq. 10-2 for multilayer treatment design from two to an essentially unlimited number of layers. The model enables consideration of the different penetrations that result because of different layer properties. These effects have also been demonstrated by Rahim and Holditch (1992).

The significance of different penetrations is illustrated by production forecasts made at a constant well-

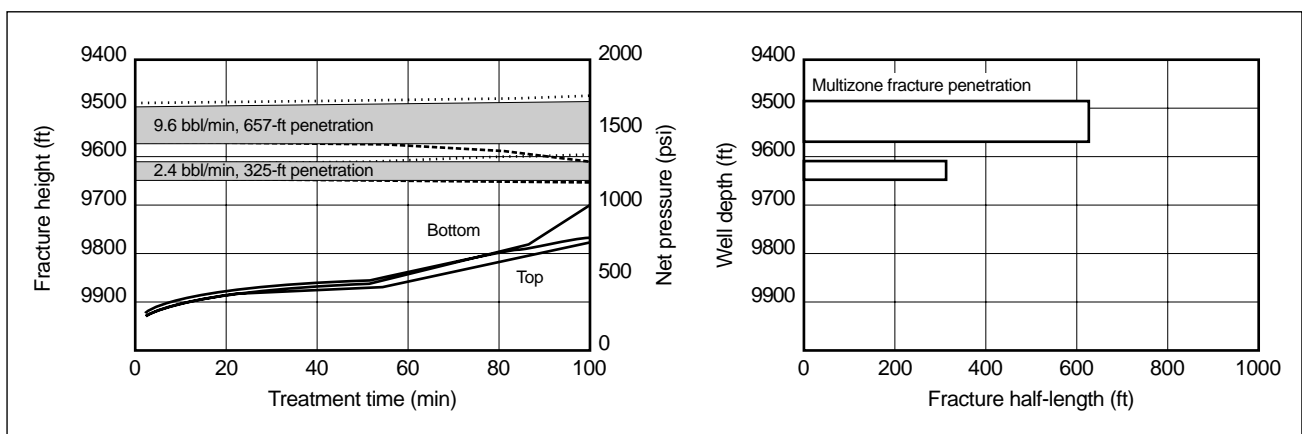


**Figure 10-19.** P3D simulations for individual zones with 2D partitioned rates.



head pressure of 300 psi for a single fracture and multifracture cases (Table 10-2). The four combinations of permeability listed all have a permeability-thickness  $kh$  of 3.6 md-ft. Cases A and B have 0.03-md permeability in both zones and cases C and D have different permeability combinations to obtain the same average permeability-thickness.

The 10-year cumulative production is listed in Table 10-2 for the individual zones and their combined production. Case A has the highest production, ~12,000 MMscf, and case C has the lowest at ~9,800 MMscf, or 82% of that for case A. Cases B and D each have about 95% percent of the production of case A. Table 10-2 also lists the percent of gas in place recovered from the individual and combined zones. The 40-ft zone in case D, which has the lower permeability of 0.01 md and a shorter fracture length, has only 7.9% recovery of the gas in place. In case C, the same zone simulated with a higher permeability of 0.07 md recovered 31% of the gas in place. These results show the role of multilayer modeling in determining the benefits for two separate treatments that can individually optimize the recovery of each zone.

The maximum recovery possible over a specific time period can be determined by the simulation of production from a fracture of infinite-acting conductivity penetrating to the drainage boundary. Production from a fracture penetrating 1500 ft, or 80% of the assumed 320-acre spacing, was simulated for all zones in cases A through D and listed as the maxi-

imum recoverable. Comparison of the 10-year cumulative production from the design with the maximum recoverable in the column labeled percent of maximum provides another perspective on design and indicates if a different completion or spacing should be considered. Smaller spacing with more wells or rectangular spacing with the long axis parallel to the fracture azimuth, if known, would improve the percent recovery (Holditch *et al.*, 1978; Elbel, 1986; Meehan *et al.*, 1988).

Application of the limited-entry technique can be considered for the two-layer cases B, C and D in Table 10-2. If the density of the open perforations is 1 shot per foot (spf) in each layer, the top 80-ft zone will take most of the fluid, and the number of perforations should be limited in that zone. Reducing the number of perforations from 80 to 14 would reduce the initial injection rate from 9.5 to 7.5 bbl/min with an initial perforation friction pressure of 100 psi in this layer. The perforation friction for the bottom interval remains negligible, and the number of perforations does not require changing. The penetration is 550 ft into each layer. The net pressure would be about 100 psi higher in the bottom interval, which could increase its fracture height growth depending on the stress in its barriers.

The previous discussions assume that the perforated zone fractures when the wellbore pressure is above its minimum stress. This generally does not occur without pretreatment injection procedures using acid, per-

**Table 10-2. Ten-year production forecasts for a single fracture (A) and multifracture cases (B–D).**

Case	$x_f$ (ft)	Net Height (ft)	Perme- ability (md)	10-yr Cumulative (MMscf)	Gas-in- Place Recovery (%)	Maximum Recoverable (MMscf)	Percent of Maximum	Difference Design – Maximum (MMscf)	Remaining Gas in Place	
									Design (MMscf)	Maximum (MMscf)
A	560	120	0.03	11,975	22.4	22,134	54.1	–10,159	41,485	31,326
B	660	80	0.03	8,596	24.1	14,819	58.0	–6,223	27,072	20,849
	330	40	0.03	<b>3,118</b>	17.5	<b>7,440</b>	41.9	<b>–4,322</b>	<b>14,720</b>	<b>10,398</b>
		Commingled		11,713	21.9	22,259	52.6	–10,546	41,795	31,249
C	660	80	0.01	4,273	12.0	8,239	51.9	–3,966	31,395	27,429
	330	40	0.07	<b>5,531</b>	31.0	<b>9,980</b>	55.4	<b>–4,449</b>	<b>12,311</b>	<b>7,862</b>
		Commingled		9,804	18.3	18,219	53.8	–8,415	43,770	35,355
D	660	80	0.04	10,409	29.2	16,718	62.3	–6,309	25,238	18,929
	330	40	0.01	<b>1,411</b>	7.9	<b>4,132</b>	34.1	<b>–2,721</b>	<b>16,450</b>	<b>13,729</b>
		Commingled		11,820	22.1	20,850	56.7	–9,030	41,664	32,634

Note: All cases have a constant wellhead pressure of 300 psi and a combined  $kh$  of 3.6 md-ft.

foration ball sealers or both to mitigate the stress concentration around the wellbore. The effect of the stress concentration is enhanced when the two horizontal stresses are similar. Plugged perforations and wellbore damage can prohibit the breakdown fluid from penetrating into the formation and beyond the stress concentration. These restrictions increase the breakdown pressure in low-permeability zones. However, unrestricted fluid penetration into high-permeability zones that allow large-scale pore pressure increases raises the breakdown pressure as a result of poroelastic-induced stress increases. Therefore, if these conditions affecting breakdown are different from zone to zone, the magnitude of the initiation pressures over that of the minimum stress will be different. Once all the initiation pressures are reached, the zonal rate partitioning discussed in this section should apply. A more detailed presentation of the stress concentration and breakdown pressure is provided in Section 3-5.7.

## 10-5.5. Field example

This section reviews a study by Morales *et al.* (1995) of multiple fractures in reservoirs with shales interbedded in soft to unconsolidated sands. The review includes some of the features of multilayer fracturing. Fracture evaluation in multilayer zones is discussed in Sidebar 10F. In one example, Morales *et al.* showed that stress contrasts as small as 200 psi can result in the simultaneous propagation of essentially independent fractures, particularly where the shales have higher moduli than the softer sands. They also showed how calibration treatment pressure decline and derivative plots can indicate more than one closure pressure (approximately 5600 and 5200 psi; Fig. 10-20); validation was conducted by matching the pressure decline with a simulation from a multilayer model (see Chapter 6).

### 10F. Fracture evaluation in multilayer zones

Bennett *et al.*'s (1986) work concerning the transient behavior of a fracture in a layered reservoir introduced the dimensionless reservoir conductivity term  $C_{RD}$  (see Eq. 12-44) to enable modeling the correct multilayer transient response with an equivalent single-layer model. Camacho-V. *et al.* (1987) expanded this work to include layers with unequal fracture lengths and conductivities. They showed that the equivalent single-layer fracture penetration  $L_{app}$  is the sum of the products of each layer's  $C_{RD}$  times the layer's fracture penetration  $L$ :

$$L_{app} = \sum_{j=1}^n C_{RD,j} L_j. \quad (10F-1)$$

An example for this relation was provided by Elbel and Ayoub (1992) for transient well tests in a well with two zones. The zones were treated separately and designed to achieve 400- and 689-ft penetrations in zones 1 and 2, respectively. After the treatment cleanup period, a well test was performed and considered by a single-zone type curve. The analysis indicated an average permeability of 0.76 md and a fracture penetration of 230 ft, considerably less than those of the design lengths.

Cores from these zones in other wells in the area have a thin high-permeability layer in most zones and a wide range of very low permeability. The interpretation was therefore modified by characterizing the two zones as having three layers with different heights, permeabilities and porosities based on the logs and cores. The zones and layer groupings are shown in Table 10F-1. The  $C_{RD}$  value for each layer was calculated using Eq. 12-44. Using the designed fracture penetrations of 400 ft in zone 1 and 689 ft in zone 2 in Eq. 10F-1 showed that the transient behavior would be similar to an apparent single-layer fracture penetration of 223 ft in a formation with an average permeability of 0.76 md. That the single-layer transient analysis gave a result of 230 ft indicates a probability that the designs were achieved, although the apparent value is considerably less than the penetration in either zone.

This example makes several important points:

- The postfracturing reservoir response is inherently nonunique in the absence of a comprehensive reservoir characterization.
- Validating fracture placement designs from well test or production data is difficult.
- The reservoir inference of fracture length  $x_f$  and the physical fracture length  $L$  should be identified by different notations, as used in this volume.

**Table 10F-1. Effect of different fracture penetrations in two multilayer zones (Elbel and Ayoub, 1992).**

	Zone 1			Zone 2			Average
Height (ft)	49.2	8.9	1.0	39.3	38.4	1.0	
Permeability (md)	0.01	0.20	80.00	0.02	0.10	20.00	0.76
Porosity	0.05	0.08	0.14	0.05	0.08	0.17	0.06
$C_{RD}$	0.04	0.04	0.11	0.04	0.11	0.06	
$x_f$ (ft)	400	400	400	689	689	689	

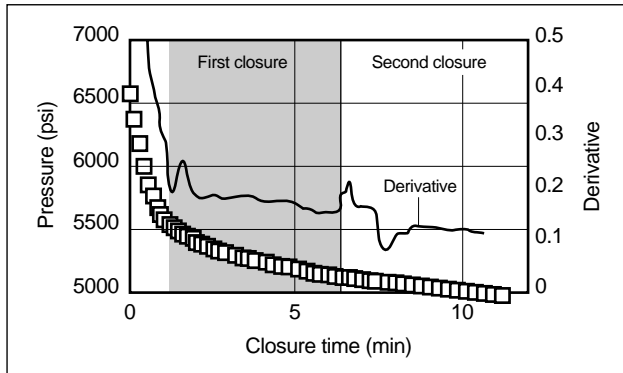


**Figure 10-20.** Treatment pressure decline and derivative showing the simulated pressure decline match (Morales et al., 1995).

For this field example, the logs in Fig. 10-21a show three distinct gas-bearing zones (layers 1, 2 and 3 are 10, 6 and 14 ft thick, respectively) separated by 22 and 20 ft of shale. Simulations of the calibration treatment using the multilayer model provide the layer rate distributions shown in Fig. 10-22. The pressure and closure time matches were made with fluid-loss coefficients of  $0.015 \text{ ft/min}^{1/2}$  for layer 3 and  $0.0006 \text{ ft/min}^{1/2}$  for layers 1 and 2. Very little fluid entered the 6-ft thick layer 2 because of the relatively higher stiffness of the

smaller zone and its lower leakoff rate. The rates of the other two layers changed during injection because of their relative fluid loss and stiffness. During closure, crossflow occurred because of the different zone properties; for the zones with dominating fractures, layer 1 gave up fluid to layer 3 until layer 3 closed at its higher stress.

The high net pressure of 1300 psi in the injection matched the multilayer model, whereas simulation of a single fracture over the entire interval estimated a net pressure of only 200 psi. The high net pressure could be matched by increasing either the modulus of the fracture by sixfold, which is an unusually large value, or the toughness by an even larger factor. (Toughness in calibration treatments is discussed in Chapter 5.) The properties used in the simulation are listed in Table 10-3.

The multilayer simulation of the rate distribution for the actual fracture treatment is shown in Fig. 10-23. For these rate distributions, the fracture lengths and heights obtained using a P3D simulator are shown in Fig. 10-21b. The barriers were assumed to have 0.1-psi/ft greater gradients than the pay zones. Because of height growth, the fracture lengths are less than those predicted by the multilayer model.

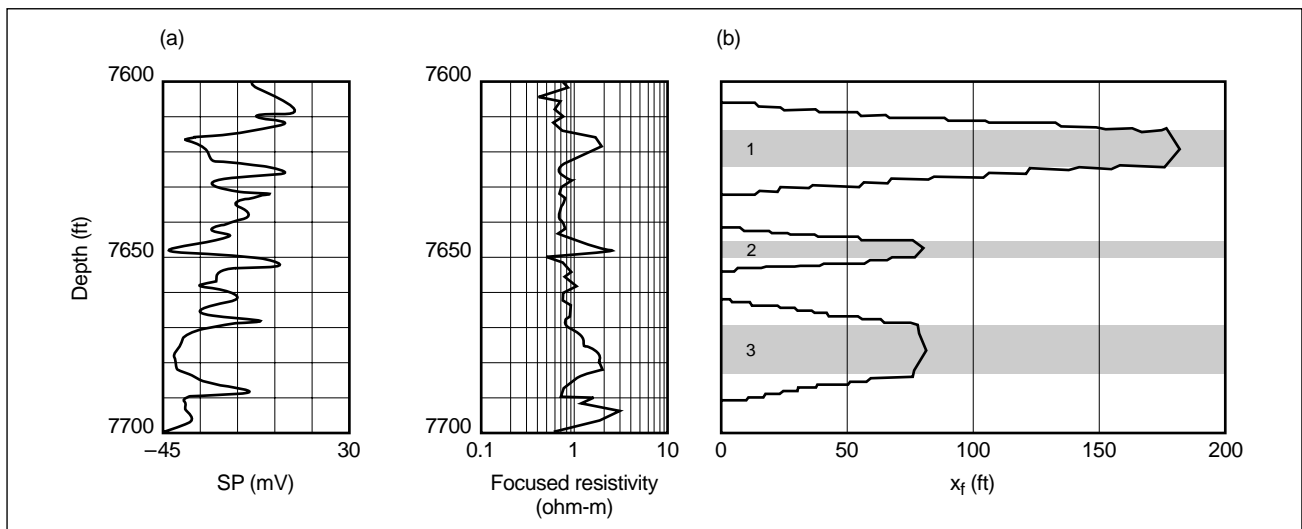


**Figure 10-21.** Logs of 10-, 6- and 14-ft gas zones and P3D simulation of the fractures (Morales et al., 1995).

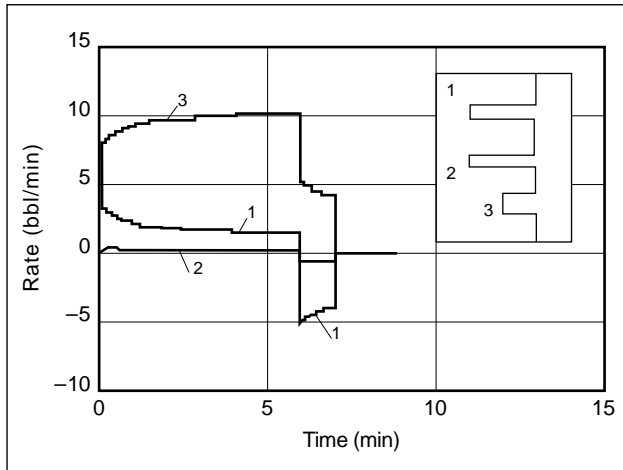


**Figure 10-22.** Multilayer fracture (MLF) PKN simulation showing the layer rate distributions during calibration injection (Morales et al., 1995).

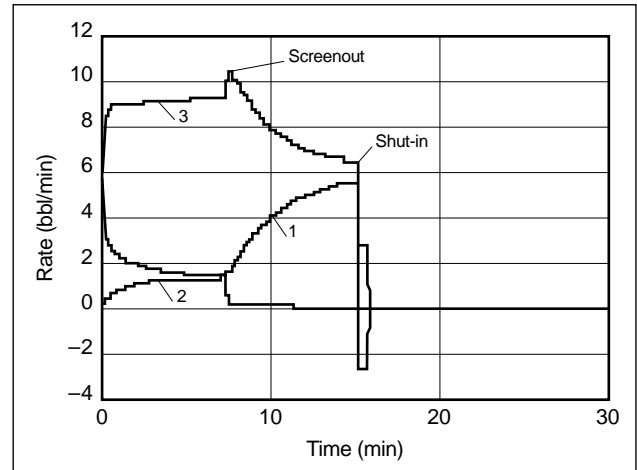


**Figure 10-23.** Simulated rate distribution and layer screen-out for the actual fracture treatment (Morales et al., 1995).

**Table 10-3. Properties for multilayer simulation example.**

Property	Value
Reservoir pressure	4700 psi
Height	
Layer 1	10 ft
Layer 2	6 ft
Layer 3	14 ft
Fluid-loss coefficient	
Layer 1	0.0006 ft <sup>2</sup> /min
Layer 2	0.0006 ft <sup>2</sup> /min
Layer 3	0.015 ft <sup>2</sup> /min
Young's modulus	2,200,000 psi
Poisson's ratio	0.25
Closure pressure	
Layer 1	5200 psi
Layer 2	5200 psi
Layer 3	5500 psi
Fracture toughness	2000 psi-in. <sup>1/2</sup>

## 10-6. Acid fracturing

Hydrochloric acid (HCl) inhibited to prevent the corrosion of wellbore tubulars was first used in 1932 by the Pure Oil Company to stimulate a limestone formation. The previously dead well responded by producing 16 BOPD. Acidizing rapidly became the preferred stimulation method for carbonate reservoirs and began to replace explosive stimulation of openhole completions. Grebe and Stoesser (1935) observed that during acid injection, the formation “lifting pressure” was sometimes obtained, indicating that the formation was also being fractured. This was the first description of hydraulic fracturing applied to petroleum reservoirs. During the late 1940s, the process of creating a fracture by the injection of oil and propping the fracture with sand was developed for stimulating sandstone formations. The primary difference between acid and propped fracturing is the means of achieving fracture conductivity after the fracture closes: an etched pattern of voids on the fracture faces and propping the faces apart, respectively.

Advances in hydraulic propped fracturing in the 1970s, particularly the ability to model the fracture geometry and proppant placement, resulted in the successful use of propped fracturing for stimulating carbonate formations. The use of acid fracturing also decreased because modeling of the etched acid geometry was more complex and less developed. However,

advances in acid fracturing modeling (Settari, 1991; Mack and Elbel, 1993) and determining reaction parameters (Li *et al.*, 1993; de Rozières, 1994) began during the 1990s. These developments support more reliable treatment designs and form a basis for choosing between acid fracturing and propped fracturing stimulation of carbonates. Section 6-9 addresses various aspects of modeling acid fracturing.

Operationally, acid fracturing is less complicated because no propping agents are used, which eliminates the risk of a screenout and subsequent problems of proppant flowback and cleanout from the wellbore. However, the effective length of an acidized fracture is limited by the distance the acid travels along the fracture before spending. At high temperatures this limit is a greater problem. Another barrier to effective acid penetration is excessive fluid loss (Nierode and Kruk, 1973). Continuous acid corrosion and erosion of the fracture faces during treatment make it difficult to deposit an effective filter-cake barrier. In addition, acid leakoff is highly nonuniform and typically results in wormholes and the enlargement of natural fractures and matrix permeability. These natural consequences of acid treatments increase the effective area and the volume of leakoff. Acid fluid loss and its control are discussed in greater detail later in this chapter.

### 10-6.1. Acid-etched fracture conductivity

The factors controlling the effectiveness of acid fracturing are the etched fracture penetration and conductivity. Laboratory measurements of acid-etched fracture conductivity are not always reproducible and may not represent actual conditions because of the small size of the laboratory samples. The normal variation of sedimentary layers, over the larger scale of the fracture face, provides local preferred paths for acid reaction and subsequent channeling of the following acid stages. This situation makes it difficult to properly model conductivity (see Chapter 6 for more discussion). In an attempt to make conductivity predictions, Nierode and Kruk (1973) used empirical laboratory data and developed a conservative method of calculating fracture conductivity (Williams *et al.*, 1979). Their predictions are based on correcting the theoretically ideal conductivity, based on the etched width cubed (Eq. 6-130), for the effect of fracture closure stress and rock embedment strength (similar to Brinnell hardness). Sidebar 10G further discusses

measuring and modeling acid-etched fracture conductivity.

Most geometry models incorporate Nierode and Kruk's correlation with various corrections for fluid loss and field-scale inhomogeneity. Beg *et al.* (1996) reported the same effect of rock embedment strength and closure stress on conductivity. Large volumes of acid and the dissolution of large volumes from the fracture faces result in negative net fracturing pressures in modeling. Laboratory tests would be more meaningful if they could be run at appropriate pre-stressed conditions.

Increased etched conductivity resulting from fracture-face heterogeneity was reported by Van Domelen (1992). Beg *et al.* (1996) reported that tests with fluid loss typically result in higher fracture conductivity than tests on similar cores without fluid loss. Fluid loss enhances surface reactions by removing the by-products of the acid reaction. They also observed, in repeated experiments, significantly higher conductivity when acid forms a deep channel.

The difficulty in accurately modeling acid fracture conductivity is apparent. Conductivity can be calibrated with well test data after a treatment for use in subsequent treatment simulations. After analyzing field production data, Aud *et al.* (1992) and Elbel (1993) suggested increasing Nierode and Kruk's correlation by 1 order of magnitude.

Fortunately, except for soft formations or extremely large closure stresses, the conductivity obtained from fracture acidizing is usually excessive because of the high reactivity of limestone and the relatively large volumes of acid required to achieve the desired penetration. Dimensionless fracture conductivity values greater than 30 are common. This makes errors in conductivity of little consequence for production forecasts. However, conductivity predictions are important for optimizing acid volume for dolomite formations and particularly for temperatures less than 120°F [50°C], for which acid reaction rates are relatively small.

A technique, described as equilibrium acidizing, was reported by Tinker (1991) to be successful for enhancing conductivity in low-temperature dolomites. With this technique, a fracture of the desired penetration is created by a volume of acid and the injection rate is reduced to maintain equilibrium with the acid leakoff rate or, more practically, to a rate that achieves a fracturing pressure between the extension and formation closure pressures. The lowered rate also minimizes vertical growth into water-producing zones

## 10G. Acid-etched conductivity

Measurements of acid-etched conductivity in the laboratory are usually not reproducible or representative of large-scale in-situ behavior because of heterogeneities in the rock and the small size of laboratory samples. This makes it difficult to calculate and validate acid-etched fracture conductivity; however, Nierode and Kruk (1973) developed an empirical equation based on closure stress and the reservoir's embedment strength from laboratory tests on formation cores (see Section 6-9.3). The amount of formation dissolved is used to calculate a uniform (ideal) etched width. The ideal conductivity for a uniform open fracture with a width of 0.1 in. is about  $4.5 \times 10^6$  md-ft. The empirical correlation for zero closure stress reduces this by almost 3 orders of magnitude to about  $6.5 \times 10^3$  md-ft. Further reductions are made as closure stress and embedment strength effects are considered. This correlation is a conservative (i.e., lower bound) estimate, and calibration with other tests was recommended by Nierode and Kruk.

Figure 10G-1a is a plot of Nierode and Kruk's conductivity calculations for average etched widths of 0.1 and 0.025 in. The undamaged conductivities of 20/40-mesh ISP and sand proppants at a concentration of  $1.5 \text{ lbm/ft}^2$  are shown for comparison. These comparisons have supported the preference of propped fracturing over acid fracturing in some areas.

The difficulty in accurately modeling acid fracture conductivity is apparent. Calculated etched conductivity has been calibrated with well test data after treatments for use in subsequent treatment simulations. After analyzing field production data, Aud *et al.* (1992) and Elbel (1993) suggested increasing the Nierode and Kruk correlation by 1 order of magnitude. Figure 10G-1b shows conductivities using this correction and a comparison with the conductivity of proppant corrected for 50% polymer damage (see Chapter 8). The comparison indicates that the correct choice between acid and propped fracturing should not be based on the assumption of low and etched conductivity; in fact, acid fracturing of competent carbonate formations should always be considered as the most prospective treatment (see Section 10-6.7).

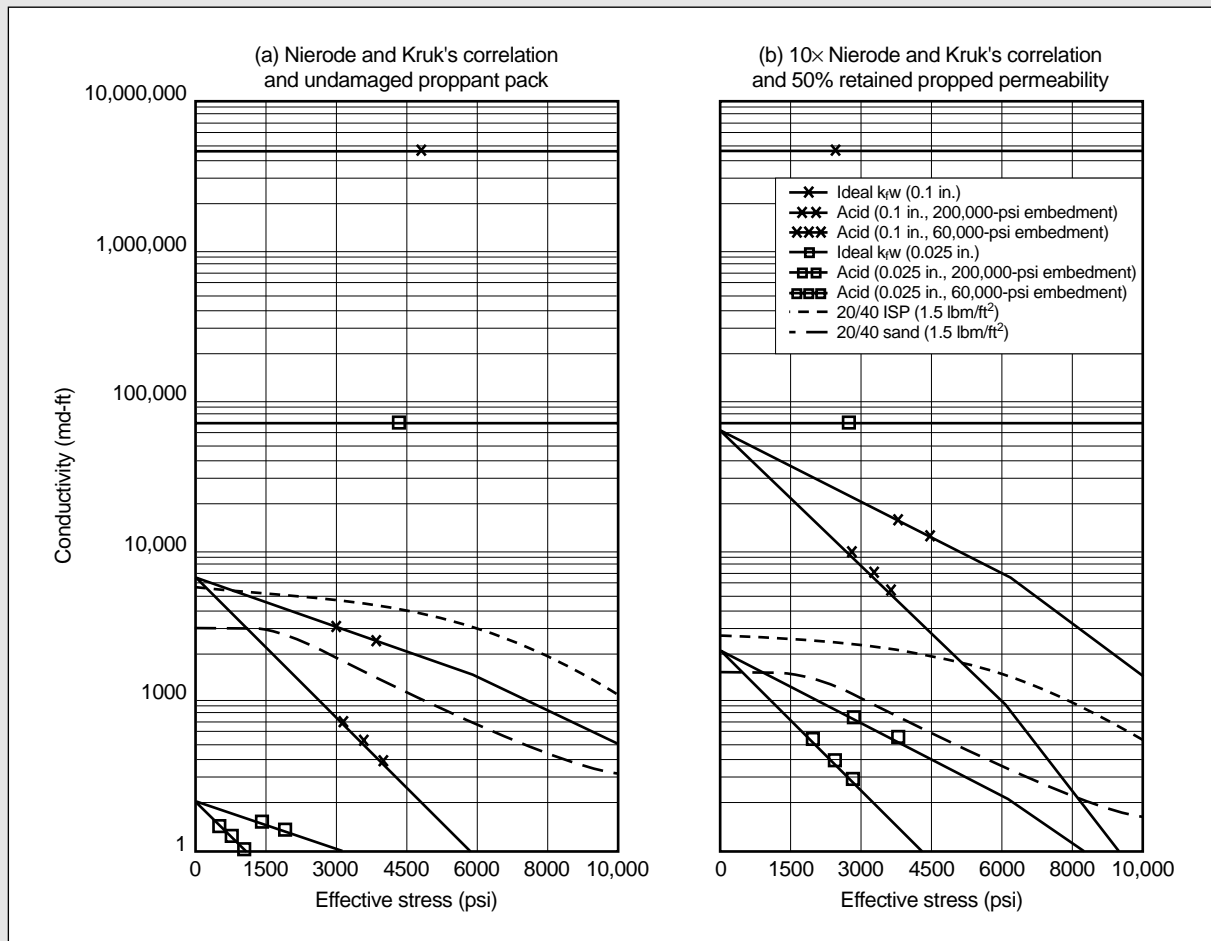


**Figure 10G-1.** Comparison of etched acid and propped fracture conductivity (Nierode and Kruk, 1973).

while creating more conductivity from additional volumes of acid.

A similar technique allows the initial etched fracture to close while injection continues at a pressure below the closure pressure. The continued injection promotes etched-channel development for increased conductivity (Sizer *et al.*, 1991). This technique most likely has limits for etched penetration (Tinker, 1991).

Using a viscous pad and limiting fluid entry points by selected perforating was reported by Davies *et al.* (1987). This technique should promote channeling of the acid through the viscous pad, localizing the acid reaction to enhance etched conductivity.

## 10-6.2. Acid fluid loss

Excessive fluid loss is generally considered to be the factor that limits fracture extension and etch penetration for acid fracturing carbonate formations. The parameters that control fluid loss are formation permeability and porosity, reservoir fluid compressibility, leakoff filtrate viscosity and the differential pressure between the fracture and reservoir (see Chapter 6). Oil reservoirs, above the bubblepoint pressure and free of gas, can have a sufficiently low compressibility to control the leakoff of fluids that would otherwise have a high fluid loss.

The role of free gas was reported by Aud *et al.* (1992) in a study of acid refracturing. The study used reservoir modeling to indicate relatively long fractures from treatments performed prior to reservoir depletion. However, they showed that the same treatments performed after the reservoir was below bubblepoint resulted in significantly less etched penetration. They concluded that the low compressibility of the reservoir fluid above the bubblepoint pressure effectively controlled fluid loss by compressibility-controlled fluid-loss behavior. Subsequent steps to control the fluid loss with viscous pads and emulsified acid, which were not required when the reservoir was above bubblepoint pressure, resulted in greater etched penetrations and increased production. The simulations from Aud *et al.* in Fig. 10-24 show the change in penetration above and below bubblepoint pressure for various injection rates and formation permeabilities.

Fluid loss occurs in a highly selective manner, which can create wormholes and enlarge natural fractures during acid treatment. This phenomenon was first described by Rowan (1957), who mathematically

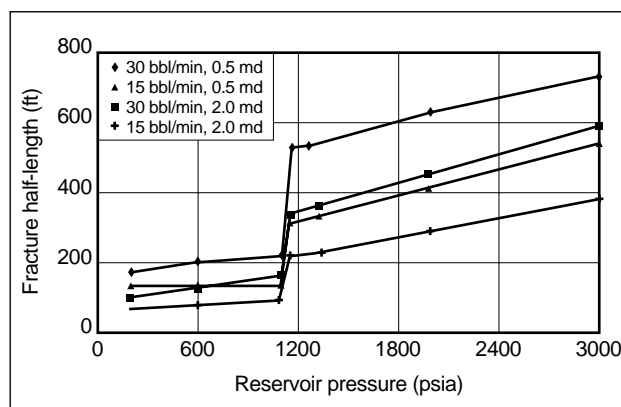


**Figure 10-24.** Effects of injection rate for permeability and reservoir pressure spanning the bubblepoint on etched fracture penetration (Aud *et al.*, 1992).

explained the selective enlargement of certain large pores present in limestone. Schechter and Gidley (1969) later addressed this same problem in greater detail. Nierode and Kruk (1973) evaluated the effect of various acid fluid-loss additives during wormhole development. Crowe *et al.* (1989) showed that wormhole depth is limited by spending of the acid along the wormhole channel (Fig. 10-25). The missing, critical parameter for effectively modeling wormholes is the areal density of the wormholes that penetrate the fracture face.

Various additives and treating techniques have been developed to control acid fluid loss. Except in the pad stages, acid fluid-loss additives with particulate material have not been used extensively because of poor performance and cost limitations. Various strategies for fluid-loss control are outlined as follows.

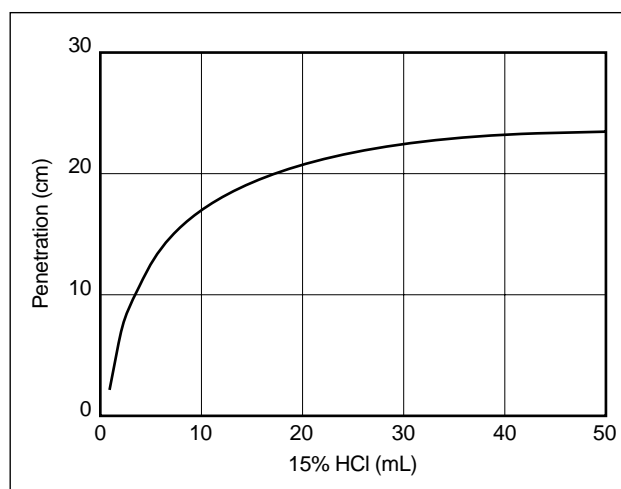


**Figure 10-25.** Wormhole growth rate during leakoff of 15% HCl at 0.065 ft/min and 150°F [65°C] (Crowe *et al.*, 1989).

- Pad stages for fluid-loss control

The use of a water-base or gelled-water viscous pad preceding the acid stage is commonly used to initiate the fracture and deposit a filter cake that can act as a barrier to acid leakoff. The actual ability of the pad fluid to control fluid loss in this manner is questionable. Studies by Nierode and Kruk (1973), Coulter *et al.* (1976) and Crowe *et al.* (1989) show that the filter cake deposited by the pad is quickly penetrated by wormholes resulting from acid leak-off. Once this occurs, acid fluid loss can be the same as if no pad were used.

Multiple stages of gelled pads have been used to control acid fluid loss (Coulter *et al.*, 1976). In this technique, the fracture is initially created by a pad, after which alternating stages of acid and pad are pumped. These additional pad stages enter and seal wormholes created by the preceding acid. The sequential pad and acid stages are effective for controlling the leakoff of acid into wormholes and enlarged natural fractures. Sidebar 10H provides additional discussion of fluid-loss control in wormholes.

The pad has other useful functions. Cooling effects decrease acid reaction within the tubulars and on the formation face, whereas the relatively large viscosity increases width, which can improve etched penetration. A wider fracture reduces the areal reaction rate by reducing the surface area relative to the transported acid volume. Viscous pads also promote acid fingering for improved conductivity.

For a treatment design, the optimum volumes for each stage of the pad and acid sequence should be determined by iterative simulations using a comprehensive acid fracturing model (see Section 6-9).

- Particulate materials for fluid-loss control

Fine particulate material is typically added to the pad stages to aid in fluid-loss control. The particulate material fills and bridges wormholes and natural fractures and improves fluid efficiency. The most common material used is 100-mesh sand (Coulter *et al.*, 1976), which is usually added at a concentration of 1 to 3 lbm/gal. Oil-soluble resins for oil reservoirs and salt of a similar particle size are also used. Although much more expensive, oil-soluble resins eliminate the possibility of conductivity impairment resulting from the 100-mesh sand in the fracture. Potential problems resulting from the return flow of sand into the wellbore also are elimi-

#### 10H. Fluid-loss control in wormholes

The creation of wormholes by acid fluid loss during acid fracturing can cause excessive leakoff and limit the etched penetration. Alternating the acid and pad stages is a technique used to minimize fluid loss in this scenario (Coulter *et al.*, 1976). The effectiveness of this technique has been demonstrated in laboratory tests (Fig. 10H-1). The core on the left illustrates the results of uncontrolled acid fluid loss in which channeling occurred completely through the core in about 15 s. The center core was first treated with a pad composed of water gelled with guar polymer and then treated with acid. Channeling occurred after only 20 s. In the core on the right, wormholes were initially created by injecting a limited amount of acid, followed by the pad fluid and then by more acid. In this test, channeling by the second acid stage was delayed for 15 to 25 min, demonstrating the effectiveness of the technique for controlling acid fluid loss. This acidizing procedure of multiple alternating stages of acid and pad is widely used in acid fracturing treatments.

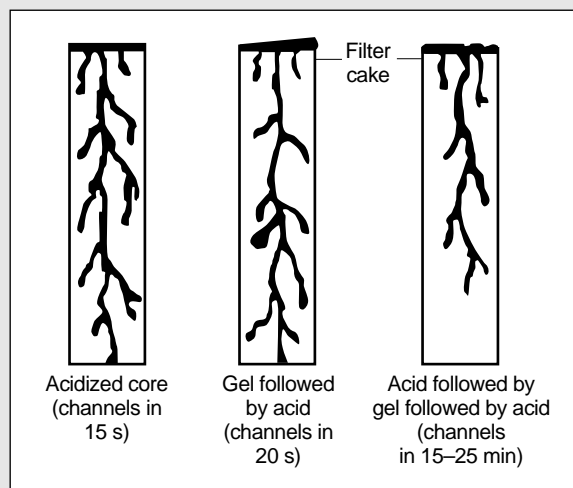


**Figure 10H-1.** Laboratory core tests show how a gel-filled channel (right) resists leakoff whereas simple filter cake has little effect (Coulter *et al.*, 1976).

nated. Fine salt can be used for acid fracturing water injection wells (Schriefer and Shaw, 1978). During such treatments, sufficient salt is added to saturate the acid solution and to provide an excess of particulate material at the bottomhole treating temperature. Following the treatment, any remaining salt is dissolved by water injection.

- Gelled acid for fluid-loss control

Acid fluid loss also can be reduced by gelling the acid. The advantages, limitations and disadvantages of this method are discussed in Section 7-4.1.

- Acid emulsion systems for fluid-loss control

Acid emulsions, both acid-external-phase and acid-internal-phase systems, have been used in acid fracturing. The leakoff is controlled by the high



viscosity of the emulsion. Excessive fluid friction pressure for emulsions limits their application. The oil-external-phase system is used because it isolates the acid and produces excellent retardation properties (see Section 10-6.3) compared with regular acid. This system is also more efficient than the acid-external phase because it increases the relative amount of acid in the fluid system.

- Foamed acid systems for fluid-loss control

The use of foamed acid is an effective method for controlling acid fluid loss (Scherubel and Crowe, 1978; Ford, 1981). Fluid-loss control is further enhanced by the use of a viscous pad preceding the foamed acid. However, foaming the acid reduces the effective amount of acid available for etching because less acid is present per unit volume injected. As a result, 28% HCl should be used in preparing the foamed acid to maximize the amount of acid available for fracture etching. The relatively unique non-Newtonian flow properties obtained by foaming or emulsifying acid can promote fingering of the fluid during fracturing to enhance channels on the fracture face.

### 10-6.3. Acid reaction rate

Acid reaction rates are defined by laboratory tests and are usually performed on pure limestone or dolomite. The effect of temperature in accelerating the reaction rate affects the depth of live acid penetration. The concentration has a similar affect. Figure 10-26 shows that 15% and 28% HCl at 100°F [40°C] produce more than twice the penetration in a dolomite than in a limestone. Increasing the temperature to 220°F [105°C] reduces the penetration distance in a limestone about 10% but reduces penetration 50% in dolomite. This is because the acid reaction rate on limestone is mass-transfer limited whereas the acid reaction rate on dolomite is limited by reaction kinetics that approaches the rate on limestone only at high temperatures. These comparisons clearly indicate the need for representative laboratory tests and model capabilities to effectively design acid treatments.

Retarded acids should always be evaluated under pressure, temperature and flow conditions simulating those existing in the formation and including the effect of fluid loss to remove by-products and transfer unreacted acid to the surface. Static reaction rates measured under atmospheric pressure are practically meaningless.

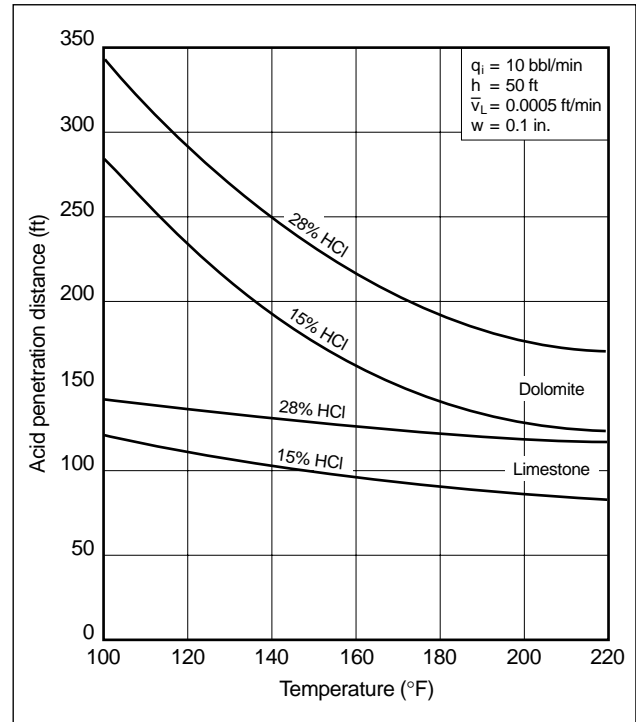


**Figure 10-26.** Penetration of 15% and 28% HCl in dolomite and limestone.  $q_i$  = injection rate,  $h$  = height,  $\bar{v}_L$  = average fluid-loss velocity,  $w$  = fracture width.

Differences in mineralogy can affect the reaction properties of HCl for different formations. Also, different acid systems, such as gelled and emulsified systems, may produce different effects even on the same formation. These effects further emphasize the role of representative and formation-specific laboratory tests.

- Effect of acid emulsion systems on reaction rate

Oil-external-phase emulsions are the most common because the external oil phase physically separates the acid from the reactive carbonate surface. The acid reaction rate can be further slowed by surfactant retarders that cause carbonate surfaces to become oil-wet. The combination of emulsification and surfactant-induced oil-wetting reduces the acid reaction rate to an extremely low level. These emulsion systems produce good retardation under static and flowing conditions (de Rozières, 1994). The effective diffusion rate of the acid spending at 150°F [65°C] is  $1.3\text{E-}5$  ft<sup>2</sup>/min for HCl and only  $3\text{E-}9$  ft<sup>2</sup>/min for emulsified acid.

- Effect of gelled acid systems on reaction rate

Gelled acids are used in acid fracturing treatments and are usually considered to be retarded because

of the role of the viscosity in reducing the mass transfer of acid at the fracture wall. However, extensive laboratory results by Crowe *et al.* (1989) indicate that this role for viscosity is most likely not significant. As discussed previously, the additional fracture width resulting from higher viscosity also increases the penetration of live acid.

The effect of retardation (i.e., diffusivity effect) on the etched conductivity, penetration and production was compared by de Rozières (1994) for neat, gelled and emulsified acids (Fig. 10-27). The same treatment was simulated with only the laboratory-determined diffusion coefficients differing for the neat, gelled and emulsified acids. The penetration, with an etched fracture greater than 1000 md-ft, is 1100 ft for the emulsified acid, 800 ft for the gelled acid and 600 ft for the neat acid system. The results also confirm the observation made in Section 10.6-1 that conductivity may be sacrificed to create additional penetration. The simulated cumulative production listed in Fig. 10-27 shows that the highest production corresponds with the greatest penetration.

#### 10-6.4. Acid fracturing models

There are various mathematical models for predicting the results of acid fracturing treatments (see Section 6-9). The models are designed to predict effective acid pene-

tration distances on the basis of considerations of surface kinetics, flow and temperature conditions in the fracture and fluid loss into the fracture faces. The models are useful in performing sensitivity studies on such parameters as rate and pad volume for various acid systems to improve the design for treatment optimization.

#### 10-6.5. Parameter sensitivity

A number of options are available for achieving deeper penetration of an etched fracture: increasing the acid volume, modifying the injection rate, modifying the acid concentration, including a pad fluid and applying retardation methods. The sensitivity of penetration to these parameters individually and in combination is shown in Figs. 10-28 through 10-31 of etched conductivity profiles for various treatment schedules. Most of the simulations are for an oil well with the reservoir pressure above the bubblepoint. As discussed in Section 10-6.2, this condition has a significant effect on controlling fluid loss. Some simulations are made with the reservoir pressure below the bubblepoint for fluid-loss comparison. The other parameters are listed in Table 10-4.

- Acid volume and concentration

Increasing the volume of acid increases the etched penetration, depending on the fluid loss and reac-

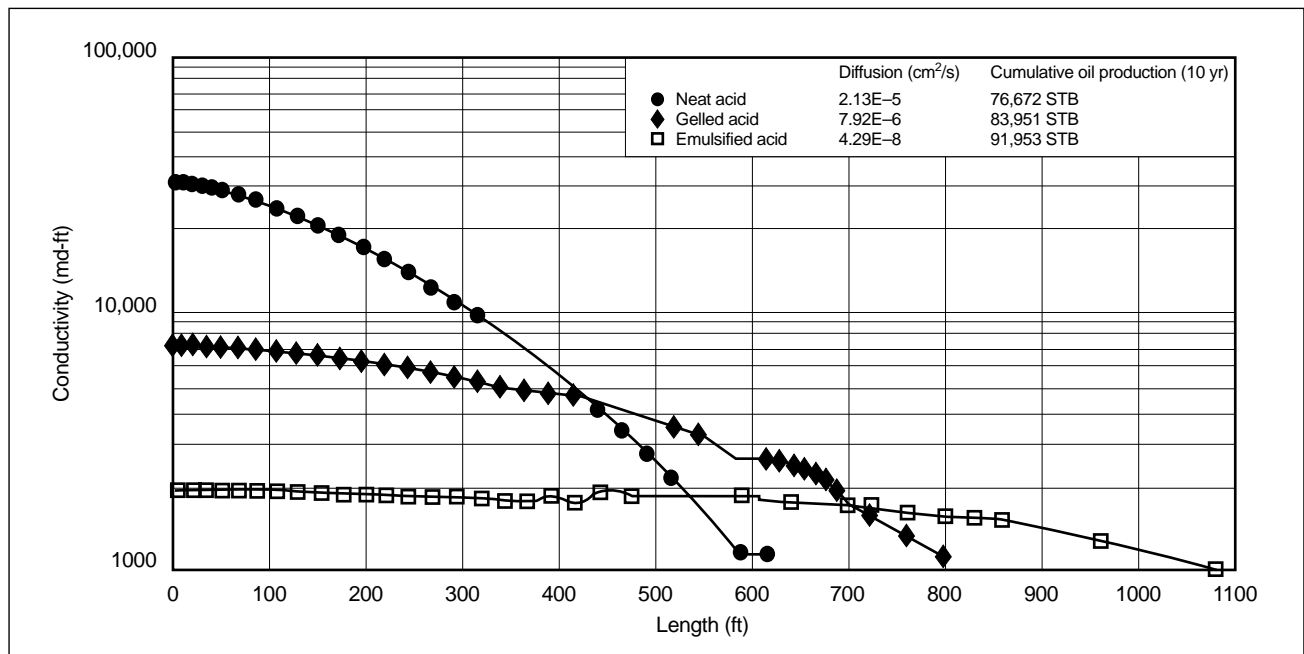


**Figure 10-27.** Effect of retardation on the etched conductivity and penetration of neat, gelled and emulsified acids (de Rozières, 1994).

**Table 10-4. Reservoir and fluid properties for acid and propped fracture simulations.**

Property	Value
Well type	Oil
Bottomhole static pressure	5000 psi
Bottomhole static temperature	150°F [65°C]
Fluid surface temperature	70°F [20°C]
Bubblepoint pressure	3000 psi
Reservoir fluid compressibility	6.8E-6 psi <sup>-1</sup>
Reservoir fluid viscosity	1.2 cp
Zone height	50 ft
Embedment strength	60,000 psi
Young's modulus	5,784,000 psi
Porosity	20%
Permeability	1 md
Fluid rheology	
Linear gel	20 cp
Crosslinked gel	200 cp
15% HCl	2 cp
28% HCl	2 cp
HCl reactivity	
Effective diffusivity	6.46E-6 ft <sup>2</sup> /min
Rate constant	5.4E-6 gmol/cm <sup>2</sup>
Rate order	0.5
Activation energy	22,600 J/gmol
Heat of reaction	40,000 J/gmol
Acid dissolving power	0.53 cm <sup>3</sup> /cm <sup>3</sup>

tion rates, and results in an increase in etched conductivity. This effect is shown in Fig. 10-28 for various volumes and concentrations of acid. The effective etched-penetration cutoffs were selected at a conductivity of 10 md-ft.

Increasing the volume of 15% HCl from 5,000 to 20,000 gal increases the etched penetration from 120 to 190 ft (53%), and the average conductivity is increased from 1,000 to 23,000 md-ft (about 2300%). For the same volume changes with 28% HCl, the penetration increases from 151 to 220 ft (46%), and the conductivity increases from 1650 to 67,000 md-ft (4100%). This demonstrates the large values of conductivity that can be obtained

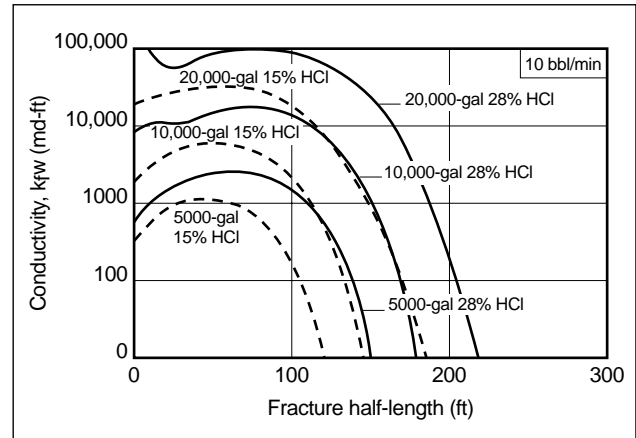


**Figure 10-28. Etched conductivity profiles for various volumes of 15% and 28% HCl.**

from fracture acidizing. Increasing the acid concentration from 15% to 28% while maintaining the same volume of acid increases the etched penetration another 20% to 25%. These simulations assume that the fluid-loss rate is not increased by the increased acid volumes.

The dissolving power of 28% HCl is about twice that of 15% HCl, and therefore 5,000 gal of 28% HCl should dissolve about the same amount of carbonate as 10,000 gal of 15% HCl. The comparison of 10,000 and 20,000 gal of 15% HCl with 5,000 and 10,000 gal of 28% HCl in Fig. 10-28 shows that the larger volumes of 15% acid achieve about the same etched penetration as the lower volumes of 28% HCl. However, the average conductivity obtained with the larger volumes of 15% HCl is about twice that of the compared 28% HCl. The difference is attributed mostly to the increased acid contact time in the fracture prior to leakoff. This will not be true for all cases, as it depends on synergy with other parameters.

These simulations were made in a formation with 1-md permeability, and  $C_{FD}$  was increased from 0.2 to 0.4 and 12 to 28, with the equivalent volume of 15% acid indicating a potential benefit from using the larger volume, lower concentration acid for this case. However, the costs and the logistics of the treatments should also be considered. The costs of various treating fluids are listed in Table 10-5.

- Injection rate sensitivity

Etched penetration can also be increased by increasing the injection rate. The 10,000- and

**Table 10-5. Costs (1997) of various treatment systems.**

	15% HCl	28% HCl	Emulsified Acid	Crosslinked Acid	Water-Base Gelled Fluid	Water-Base Crosslinked Fluid
Corrosion inhibitor (gal)	1	3	3.5	2		
Iron-reducing agent (gal)	10	28		10		
Inhibitor aid (lbm)	5	5				
Antisludge agent (gal)	4	4				
Emulsifying agent (gal)			15			
Diesel oil (gal)			300			
20% HCl (gal)			700			
Iron-reducing agent (lbm)			7			
Chelating agent (gal)			7			
Acid gelling agent (gal)				20		
Nonemulsifying agent (gal)				2		
KCl (lbm)					167	167
Slurried gelling agent (gal)					5.7	5.7
Surfactant (gal)					1	1
Crosslinker (lbm)						1.2
ph-control agent (gal)						4
Additive unit cost/1000 gal (\$)	2239	4456	2844	3403	245	279

Note: Other unit costs: Sand \$0.07/lbm, premium proppants \$0.51/lbm–\$0.89/lbm, hydraulic horsepower \$7.40/hhp

20,000-gal volumes of 28% HCl injected at a rate of 10 bbl/min have  $C_{fD}$  values from 32 to 347 and can benefit from increases in penetration at the expense of conductivity. Conductivity profiles from simulations with the rate increased to 20 bbl/min for 10,000 and 20,000 gal of 15% and 28% HCl are shown in Fig. 10-29. The penetrations are increased by about 60%.

- Pad volume sensitivity

The use of a pad stage ahead of the acid stage was first performed in the 1960s. Its purposes were to cool the formation to slow the reaction rate and to deposit a filter cake to reduce the rate of acid fluid loss, both of which should increase the penetration. The technique's results have made it almost a universal practice in acid fracturing, although the effect of the pad filter cake on the acid fluid loss and magnitude of the cooling have been disputed. Some of the benefit may result from thinner acid channeling through the more viscous pad fluid.

The simulation of acid fracturing with multiple fluids such as pads and acids has only recently been accomplished and is discussed in Section 6-9. The

effects of cooling and the pad filter cake, if there is no cake erosion, can be modeled. The results of simulations with a pad volume of 10,000 gal prior to injecting 20,000 gal of acid show an additional 20% to 25% penetration (Fig. 10-30). Acid channeling was not considered in these simulations.

Large pad volumes can cause more height growth, resulting in decreased etched penetration. Simulations of this effect must be made with a P3D acid geometry simulator, for which a stress profile is required. Maximum net pressure is usually achieved in the pad stage; the acid stage causes the pressure to decrease because of its lower viscosity and increased fluid-loss rate as well as some increase in width resulting from etching.

The optimum pad size for a given volume of acid achieves the maximum ROI, and, depending on other parameters, acid volume may be economically traded for pad fluid. The effect of the pad viscosity depends on the combination of the other parameters. Higher viscosity pads promote acid channeling, which can greatly alter penetration and etch patterns.

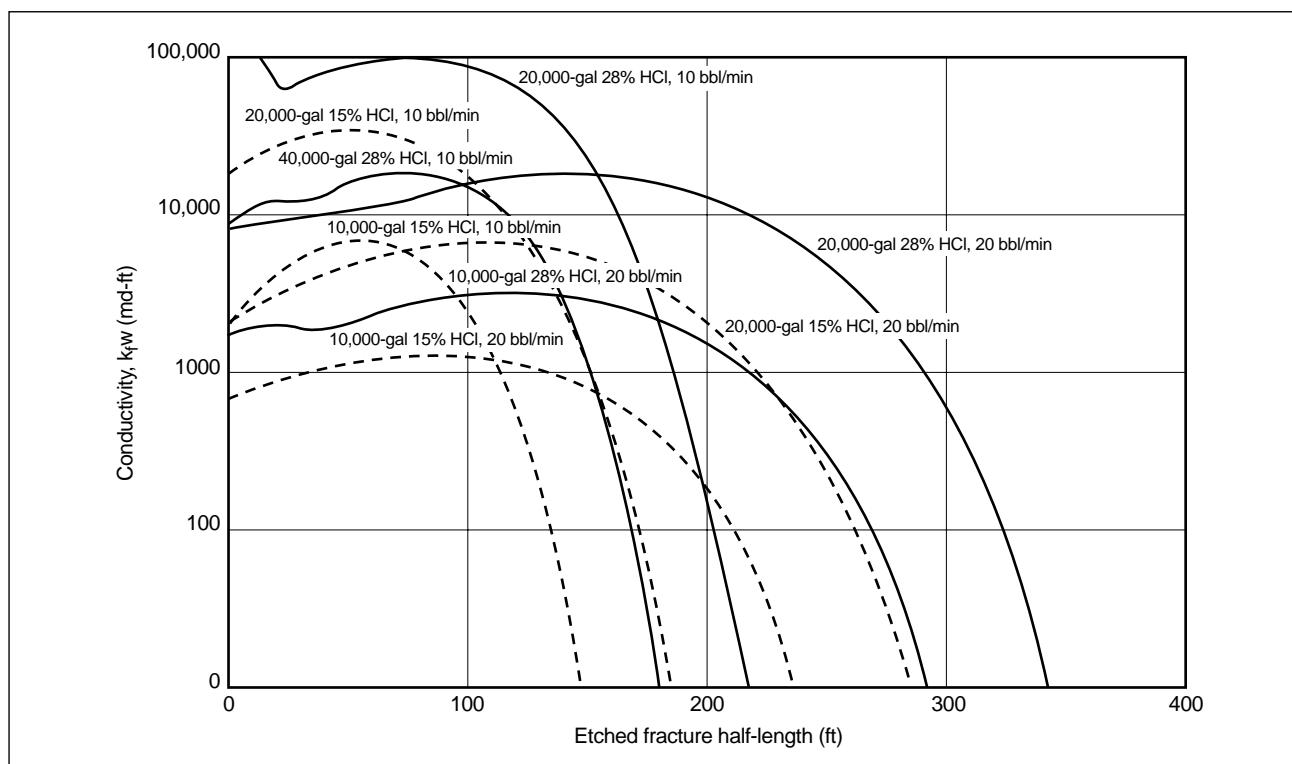


**Figure 10-29.** Conductivity profiles from simulations at a 20-bbl/min rate for 10,000 and 20,000 gal of 15% and 28% HCl.

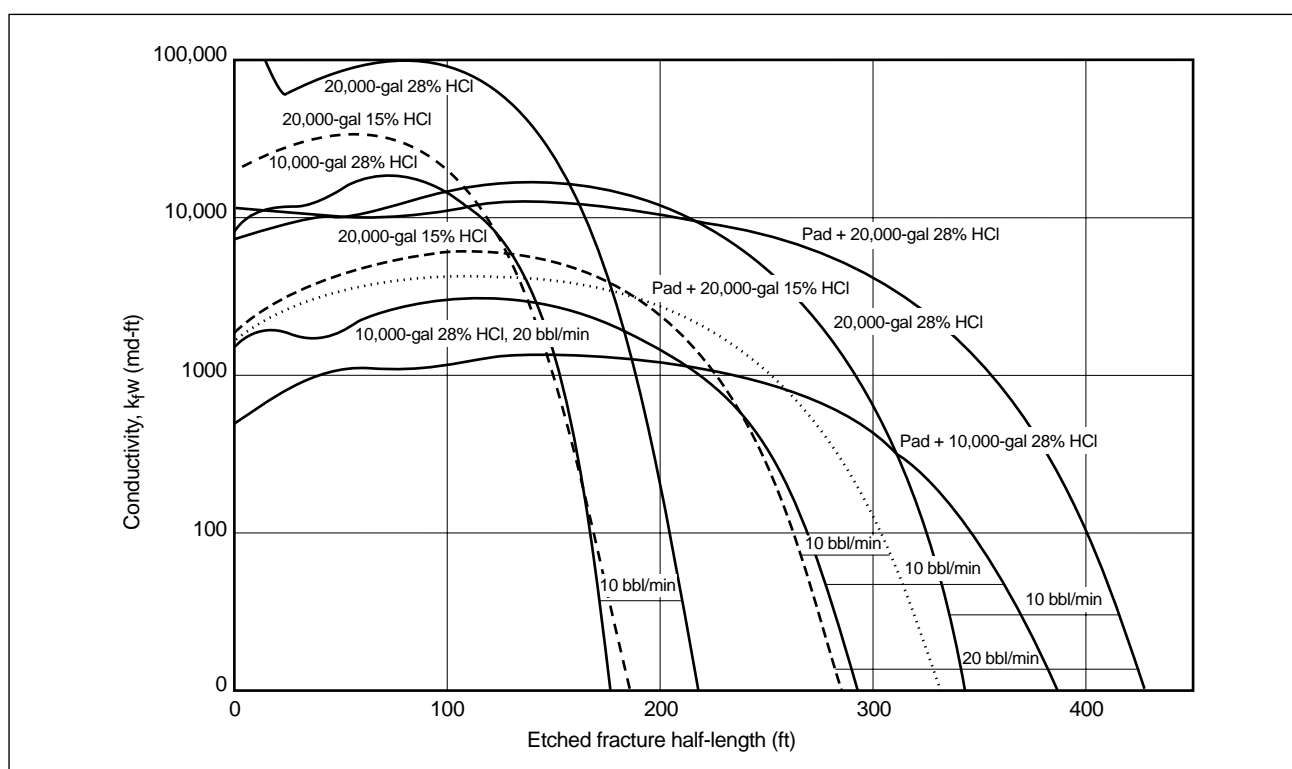


**Figure 10-30.** Effects of a 10,000-gal pad prior to injecting 20,000 gal of acid.

- Fluid-loss sensitivity

The fluid-loss rate has a significant effect on the etched penetration, not only from its effect on the total penetration of the fluid but also on the reaction rate. The previous simulations were made for an oil reservoir above the bubblepoint pressure and an equivalent fluid-loss coefficient of about 0.002 ft/min<sup>1/2</sup>. The pad fluid, which had a laboratory-measured fluid-loss coefficient through the wall filter cake  $C_w$  of 0.003 ft/min<sup>1/2</sup> for a brine-filled core, was also simulated with the reservoir-controlled leakoff coefficient because it was less than the laboratory value. Figure 10-31 compares simulations of 20,000-gal 28% HCl with and without a 10,000-gal pad injected at 20 bbl/min for leakoff above and below the bubblepoint pressure. The effective combined fluid-loss coefficient  $C_t$  of the acid below bubblepoint pressure is increased by about 1 order of magnitude, from 0.002 to 0.013 ft/min<sup>1/2</sup>, because of the effect of the increased compressibility of the reservoir fluid

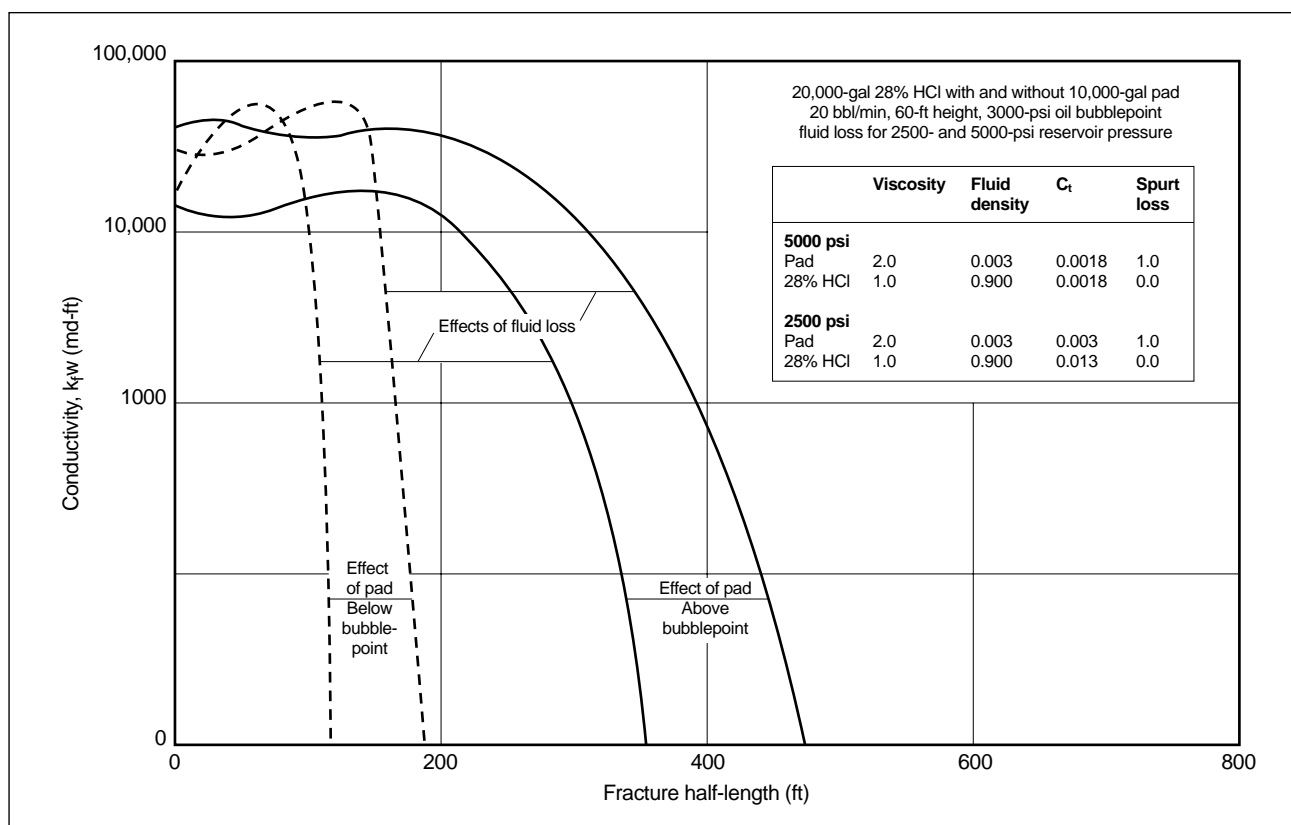
on the compressibility-controlled leakoff coefficient  $C_c$ . The pad fluid is simulated using the laboratory-measured  $C_w$  of 0.003 ft/min<sup>1/2</sup> because its filter cake controls its leakoff.

Figure 10-32 shows the stage fronts of the pad and acid stages for the simulations. Above bubblepoint pressure, the fronts advance throughout the treatment. Below bubblepoint pressure, the pad front or open fracture length starts to recede after the high-leakoff acid enters the fracture and causes the total fluid-loss rate to exceed the injection rate.

These simulations above and below bubblepoint are for equivalent acid fluid-loss coefficients of 0.002 and 0.013 ft/min<sup>1/2</sup>, respectively. Most methods of fluid-loss control discussed previously fall within this range.

- Reservoir temperature sensitivity

The reaction rate increases with temperature. Conductivity profile differences at 150° and 200°F [65° and 90°C] with and without a pad are shown in Fig. 10-33.



**Figure 10-31.** Simulation of 20,000-gal 28% HCl with and without a 10,000-gal pad and with leakoff above and below bubblepoint pressure.

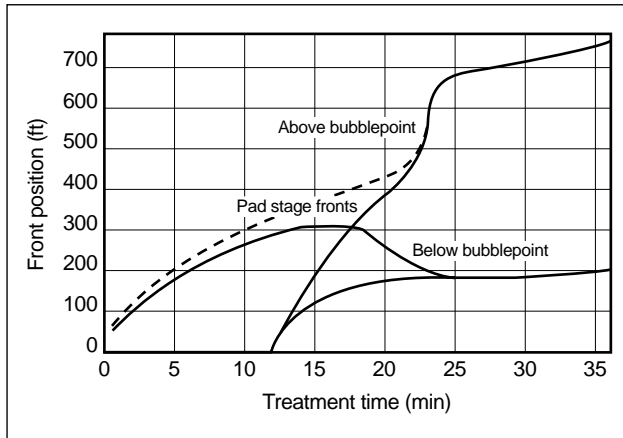


**Figure 10-32.** Simulated stage fronts of the pad and acid stages above and below bubblepoint pressure.

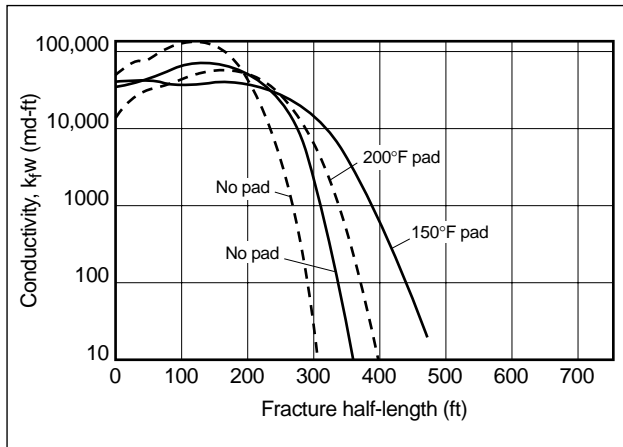


**Figure 10-33.** Conductivity profiles at 200° and 150°F with and without pad.

### 10-6.6. Formation reactivity properties

Proper simulation requires specific reaction rate parameters for the formation (see Chapter 6). Simulations of conductivity profiles with the same treatment schedule in various formations with different reaction properties are compared in Fig. 10-34.

The formation with the greatest penetration has the least conductivity. Improving its performance may require more conductivity and a different strategy than for the formations with less penetration and higher conductivity. The reaction parameters are required for generating proper predictions. Even with the same percentage of minerals in two formations, it is possible that their reaction rates may not be the same because of different grain-surface mineralogies.

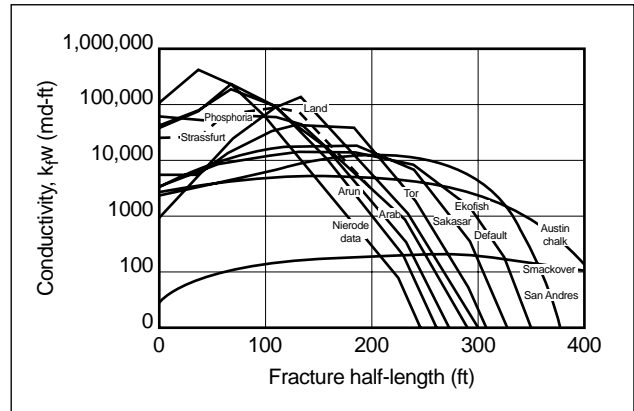


**Figure 10-34.** Simulation of conductivity profiles with the same treatment in 11 formations with different reaction properties.

Formations can have other minerals that can affect the reaction rate and therefore the penetration. Reactivity should be determined in the laboratory.

### 10-6.7. Propped or acid fracture decision

For stimulating a carbonate or dolomite formation, etched and propped fractures have both advantages and limitations in comparison to each other; however, acid fracturing should be the primary consideration. In general, acid-etched fractures are limited in penetration but can result in high conductivity whereas propped fractures usually have a deeper penetration but may be conductivity limited. The technology to overcome the limitations of both techniques continues to evolve.

The advantages of acid fracturing are

- lower net pressure, minimizing fracture height growth
- can achieve high conductivity
- no risk of screenout
- no proppant-flowback problems.

The disadvantages of acid fracturing are

- etched penetration potentially limited by higher fluid loss
- etched penetration potentially limited by the effect of temperature on the reaction rate
- potential emulsion and sludge problems in oil wells
- etched conductivity difficult to predict
- environmental considerations.

The optimization of acid treatments is more complex than that of propped hydraulic fractures. For propped fractures, there is a ratio of the pad to the total volume for a specific penetration, and the conductivity is directly related to the proppant permeability and concentration. The selection of the fracturing fluid is usually based on compatibility and stability characteristics or on field experience.

For comparison, propped fracturing treatments were considered for the reservoir described in Table 10-4 with the addition of upper and lower barriers with stress contrasts of 1000 psi and impermeable to fluid loss. An optimum fracture penetration of 750 ft using 20/40-mesh ISP as the propping agent was determined. Acid fracturing was also simulated using the same injection rates and volumes. Conductivity profiles for these treatments are shown in Fig. 10-35. For these conditions, the acid fracturing treatment provides about the same penetration and slightly more conductivity for the reactivity properties of formation A. The material costs for the proppant treatment are about twice that of the acid treatment. Performing the treatments on formation B, with only the acid reactivity on the formation differing, provides the same propped penetration, but the acid-etched penetration is only 240 ft and of significantly higher conductivity. Costs (1997) for treating fluid systems with additives are summarized in Table 10-5.

The  $C_{fD}$  for the propped fractures is 1.8 for both formations. The acid-etched fracture in formation A has a  $C_{fD}$  of 2.4. Doubling the acid volume increases the  $C_{fD}$  from 2.4 to 11.2. This approach should be consid-

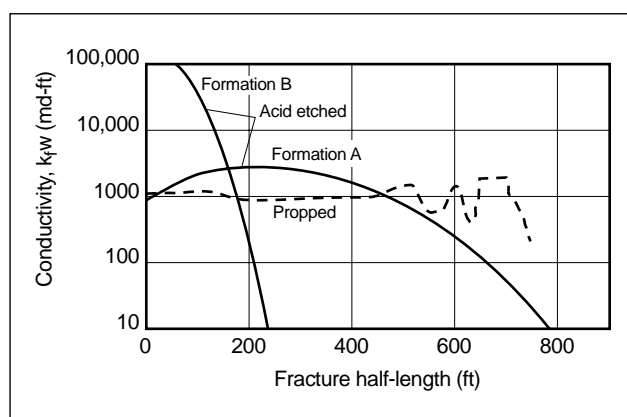


**Figure 10-35.** Conductivity profiles for propped and acid treatments. Propped treatment: 12 bbl/min, 33,000-gal 25-lbm crosslinked pad, 29,000-gal 25-lbm crosslinked fluid and 29,000-lbm 20/40-mesh ISP. Acid treatment: 12 bbl/min, 33,000-gal 25-lbm gel pad and 29,000-gal 28% HCl.

ered as a treatment option because although there is no significant change in length, the cost is still less than that of the propped treatment. The higher conductivity combined with less etched penetration of acid in formation B results in a  $C_{fD}$  of 19 but with less production because the dimensionless fracture time  $t_D$  is about 12 times higher (see explanation in Section 10-2.4). Increasing the injection rate, pad volume or both will not increase etched penetration in formation B because of the high fluid loss and fracture height growth. The wellbore height history and net pressure plots for the treatment are shown in Fig. 10-36.

If the reservoir were below bubblepoint pressure, the fluid loss would be significantly higher, and other acid systems with better fluid-loss control, albeit likely more expensive, would be required for the acid fracture treatment in formation A to compete with the propped fracture.

This comparison illustrates why there can be differences in opinion on which treatment—proppant or acid—will produce the best results. Good data are required to make the comparison.

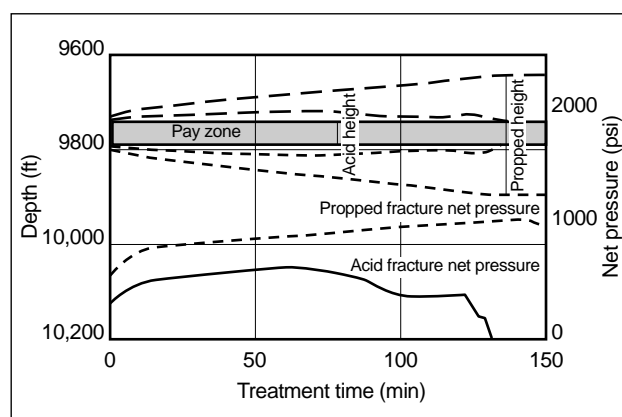


**Figure 10-36.** Wellbore height history and net pressure plots for propped and acid treatments in Fig. 10-35.

## 10-7. Deviated wellbore fracturing

Horizontal wells are often viewed as a replacement for or an alternative to hydraulically fracturing vertical wells. This view is common because in the idealized situation of a homogeneous isotropic reservoir, horizontal well performance and vertically fractured well performance are similar. Unfortunately, reservoirs are neither homogeneous nor isotropic, and as a result, the



performance of a horizontal well can differ greatly from its performance in an ideal reservoir or from the performance of a fractured vertical well.

Horizontal wells and fractured vertical wells have design considerations critical to their performance. Fracture length and conductivity are the important design parameters for a fractured vertical well, whereas in horizontal wells, the important factors are the vertical to horizontal permeability ratio, section thickness, lateral extension and wellbore damage. Insight into these critical design factors shows that coupling horizontal well and fractured vertical well technologies can maximize reserve recovery in some reservoirs.

### 10-7.1. Reservoir considerations

Comparison of horizontal well and fractured vertical well performance indicates that a fractured vertical well will outperform a horizontal well with a lateral length less than or equal to the tip-to-tip fracture length. This performance variance occurs if  $C_{fD}$  is greater than 3. The plot of cumulative recovery versus time in Fig. 10-37 compares fractured vertical wells with a 500-ft fracture half-length and varied fracture

conductivity to a horizontal well with a 1000-ft lateral extension. The fractured vertical well outperforms the horizontal well except for the low-conductivity ( $C_{fD} = 1$ ) fracture example. This indicates that for accelerating production there is little reason to utilize horizontal wells in areas where fractured vertical wells are successful, unless the horizontal lateral length can be achieved at less cost or is in excess of the achievable tip-to-tip fracture length. The comparison in Fig. 10-37 assumes that the horizontal well was placed in the middle of a homogeneous and isotropic reservoir with a vertical to horizontal permeability ratio  $k_v/k_H$  of 1. For accelerated production, vertical placement in this type of reservoir is inconsequential. However, placement of the horizontal wellbore can be important in mitigating unwanted water or gas production.

The value of  $k_v/k_H$  is critical to the success of a horizontal well's performance. This is shown in the Fig. 10-38 comparison of the PI of a fracture in a vertical well to that in a horizontal well in reservoirs with  $k_v/k_H$  values of 1, 0.5 and 0.1. A horizontal well in a reservoir with poor vertical permeability can significantly underperform in comparison with a hydraulically fractured vertical well. The extreme, but not

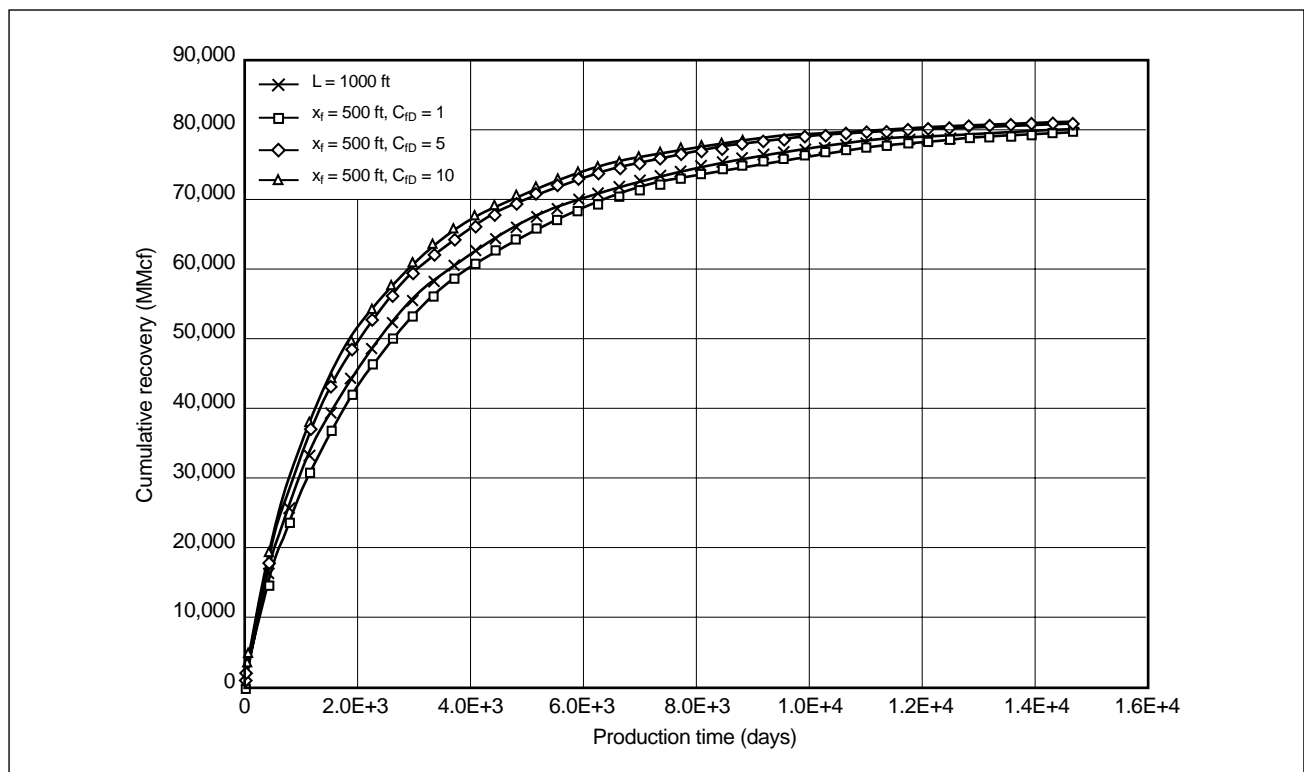


**Figure 10-37.** Comparison of vertically fractured wells with different fracture conductivity values and 500-ft penetration (1000 ft tip-to-tip) with a 1000-ft horizontal well.

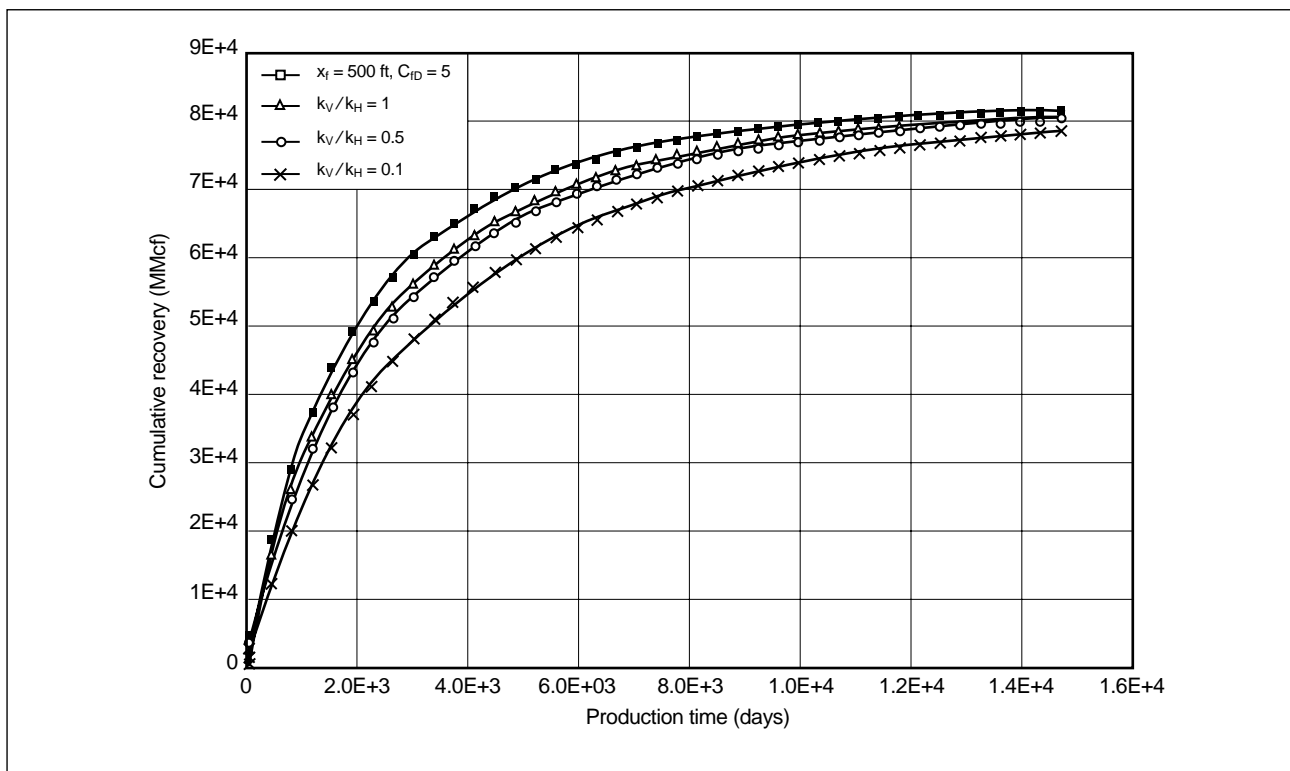


**Figure 10-38.** Production comparison of vertical and horizontal wells with vertical to horizontal permeability ratios of 1, 0.5 and 0.1.

uncommon, case is an impermeable barrier that isolates the well from a section of the reservoir.

The rule for the permeability ratio is also shown in the Fig. 10-39 production comparison of horizontal wells and fractured vertical wells with fracture conductivities of 200 and 2000 md-ft in a 100-ft thick, 160-acre reservoir with 1-md horizontal permeability. For a typical anisotropy of  $k_v/k_H = 0.33$ , the vertically fractured well outperforms the horizontal well. However, for  $k_v/k_H = 1.33$ , the horizontal well provides better performance for lengths greater than 400 ft. This result links the successful use of horizontal wells to naturally fractured formations. For this application, large values of  $k_v/k_H$  are common. For the constant-conductivity  $k_{fw}$  of 2000 md-ft,  $C_{fD}$  is 10 for a tip-to-tip length of 400 ft and decreases to 2 at a 2000-ft length. The relative performance of the vertically fractured well is greater for lower horizontal permeability and larger formation thickness. An advantage of a horizontal well is that the desired azimuth of the lateral extension can be achieved, whereas the azimuth of a vertical fracture cannot be controlled. This control can be important in complex geological settings (e.g., optimum alignment with natural fractures).

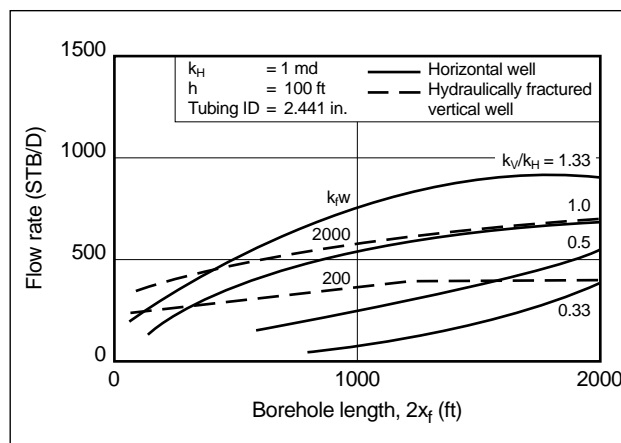


**Figure 10-39.** Anisotropy effect on the performance of a horizontal oil well and comparison with a hydraulically fractured vertical well in a thick, low-permeability formation.

The coupling of horizontal wells and hydraulic fracturing technology in reservoirs with a large pay thickness, low values of  $k_v/k_H$  or both should result in increased well performance. Drilling a long lateral and fracture stimulating with one or more orthogonal fractures provide the benefits of both technologies and

outperform the application of either individual technology. One effect of the orthogonal fractures or the role of longitudinal fractures is to introduce vertical permeability. The extended reach serves the purpose of placing the fractures at specific locations and replaces drilling vertical wells and fracturing. The azimuth of the fractures is not changed.

Because limited perforated intervals are required for a successful treatment operation (see Section 11-3.2), production from a fractured horizontal well enters the wellbore only through the fractures.

### 10-7.2. Fracture spacing

The successful application of multiple fractures in horizontal wells is dependent on the relative orientation of the wellbore with respect to the maximum principal stress (i.e., fracture orientation) as well as the number and spacing of the fractures. Longitudinal (axial) and transverse fractures are shown schematically in Fig. 10-40. In longitudinal fracturing scenarios where the horizontal wellbore is in line with the fracture direction, a fracture overcomes the adverse effects of poor vertical reservoir permeability and formation thickness. In this orientation, the wellbore area can provide a significant contribution to the effective fracture conductivity (see Section 12-5.1). Multiple longitudinal fractures originating from isolated sections may have to be created to achieve the desired geometry along the wellbore length in long horizontal

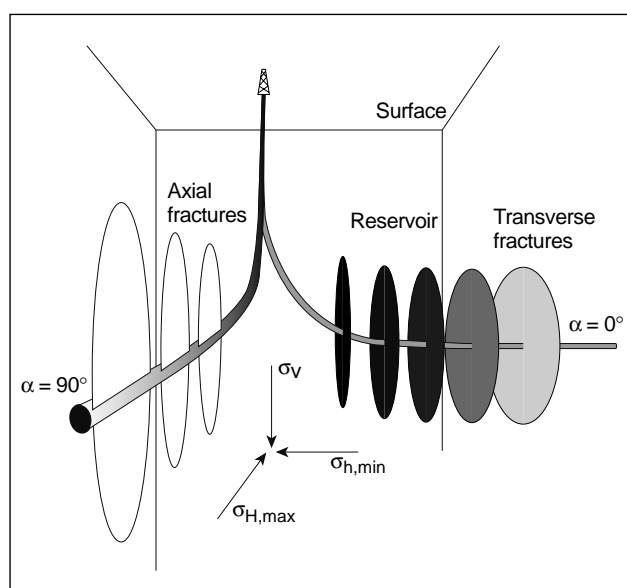


**Figure 10-40.** Longitudinal (axial) and transverse fractures.

sections. It is not necessary that axial fractures meet. If the horizontal wellbore is perpendicular to the fracture orientation, multiple transverse fractures can improve the well productivity and drainage area.

Cumulative gas recovery versus the number of transverse fractures in horizontal wells with 2000-, 3000- and 4000-ft lateral extensions is plotted in Fig. 10-41. The simulations were conducted on a gas reservoir with a permeability of 0.01 md. Production interference between the fractures is the limiting factor for the number of fractures. The spacing between the same number of fractures is greater with the increasing horizontal extension. The figure shows that for a 2000-ft horizontal well, more than three transverse fractures does not increase production significantly. This conclusion is dependent on the reservoir and fluid properties. The figure further indicates that for the 3000- and 4000-ft lateral extensions, the creation of more than three or four multiple fractures must be evaluated with the additional costs and risk associated for the operation. Three fractures in the 2000-ft lateral extension and four fractures in the 3000-ft extension will have a fracture spacing of 1000 ft.

With multiple transverse fractures, the outer fractures dominate production after some period of time. Figure 10-42 (Raghavan *et al.*, 1994) shows the normalized rate of five fractures with the same length and conductivity properties. The distance  $D$  between the outermost fractures is 10 times the fracture half-length  $x_f$ ; i.e.,  $D$  is equal to the sum of the fracture length. When production from the intermediate fractures declines significantly, perforating the section between the outermost fractures can improve production.

### 10-7.3. Convergent flow

Production into a horizontal wellbore from an orthogonal fracture or a longitudinal one with a short perforated interval will exhibit convergent flow as the flow goes from linear far from the wellbore and converges with accelerating velocity at the wellbore. The increased velocity causes an additional pressure drop and pressure loss. Under some circumstances the higher velocity may cause turbulent or non-Darcy flow that can be substantially greater than the Darcy component. Convergent flow behaves as a positive skin effect and can have an offsetting effect to the negative skin effect created by the fracture treatment. This is another instance where the fracture conductiv-

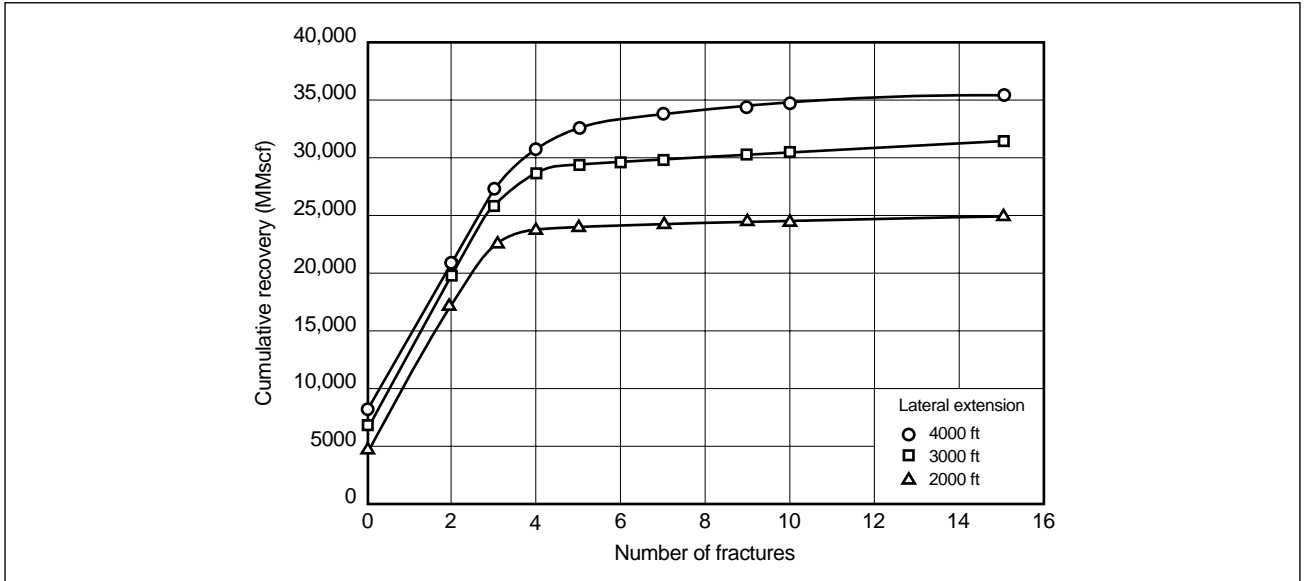


**Figure 10-41.** Cumulative gas recovery versus the number of fractures for a transverse fractured horizontal well with 2000-, 3000- and 4000-ft lateral extensions.

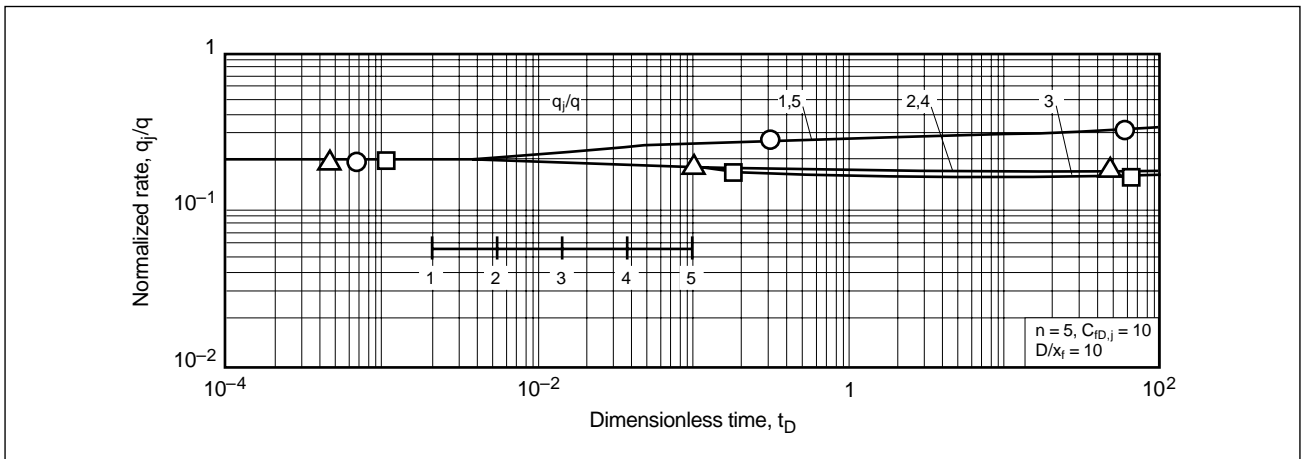


**Figure 10-42.** Normalized rate of five fractures with the same length and conductivity properties (Raghavan et al., 1994).

ity must be oversized. The effects of various parameters on the total pressure drop  $\Delta p_{ct(r_o - r_i)}$  in the fracture for a constant production rate  $q$  (Norris et al., 1996) are

$$\Delta p_{ct} = \frac{\mu q}{2\pi k_f w} \cdot \ln \left\{ \frac{r_o}{r_i} \right\} + \frac{\beta \rho q^2}{(2\pi w)^2} \cdot \left\{ \frac{1}{r_i} - \frac{1}{r_o} \right\}, \quad (10-3)$$

where  $\mu$  is the viscosity,  $\beta$  is the non-Darcy coefficient measured in the laboratory,  $\rho$  is the density,  $r_i$  is the inner radius, and  $r_o$  is the outer radius, equivalent to one-half of the fracture height. The first term on the right-hand side of the equation represents the pressure

drop because of Darcy flow, and the second term represents the additional pressure drop because of non-Darcy flow. The fracture design parameters of the fracture permeability  $k_f$  and propped width  $w$  are in the denominator of first term and the width squared in the denominator of the second term. Because the greatest part of the pressure drop is near the wellbore, a tail-in with a higher concentration could be beneficial to increasing the propped width. For the tail-in, Eq. 10-3 is used in series, and  $r_i$  could also be considered a tail-in radius if it has sufficient conductivity to be infinite acting (i.e., causing negligible pressure drop).

The relative effect of the parameters  $k_f$  and  $w$  is shown in Fig. 10-43 for all cases where the pressure drops for the Darcy and non-Darcy flows are initially equal. The parameters are constant over the converging area. The change in width affecting the non-Darcy component has a greater impact than a change in proppant permeability affecting only the Darcy component. The comparisons assume that  $\beta$  in Eq. 10-3 does not change with permeability; however,  $\beta$  usually decreases with increased permeability. If the permeability is doubled for a constant rate in Fig. 10-43, the Darcy pressure drop is reduced 50%. The total pressure drop is reduced only 25% because the non-Darcy part is not changed. Doubling the width reduces the pressure drop 63%. This example represents only the pressure drop in the region of converging flow in the fracture.

Non-Darcy flow is considered in Chapters 8 and 12. The relationship with conductivity is discussed in detail in Chapter 8, including the important role of two-phase flow.

#### 10-7.4. Fracturing execution in deviated and horizontal wells

Operational risks are magnified for placing numerous fractures in a horizontal well. These and associated costs must be considered in the planning. Horizontal wells can be completed with an uncemented liner, but this completion practice is generally unacceptable for fracture stimulation in deviated or horizontal wells. Zonal isolation is essential for successful fracture stimulation of high-angle wells and can be achieved by cementing using good cementing practices (see Chapter 11) and selective perforating. The use of external casing packers should also be considered.

Fracturing pressures can be much greater in horizontal and deviated wells in comparison with their vertical well counterparts. The excessive pressures result from restricted communication between the wellbore and the fracture (see Chapter 6). Laboratory and field evidence indicate that this poor wellbore and fracture communication is caused by poor alignment

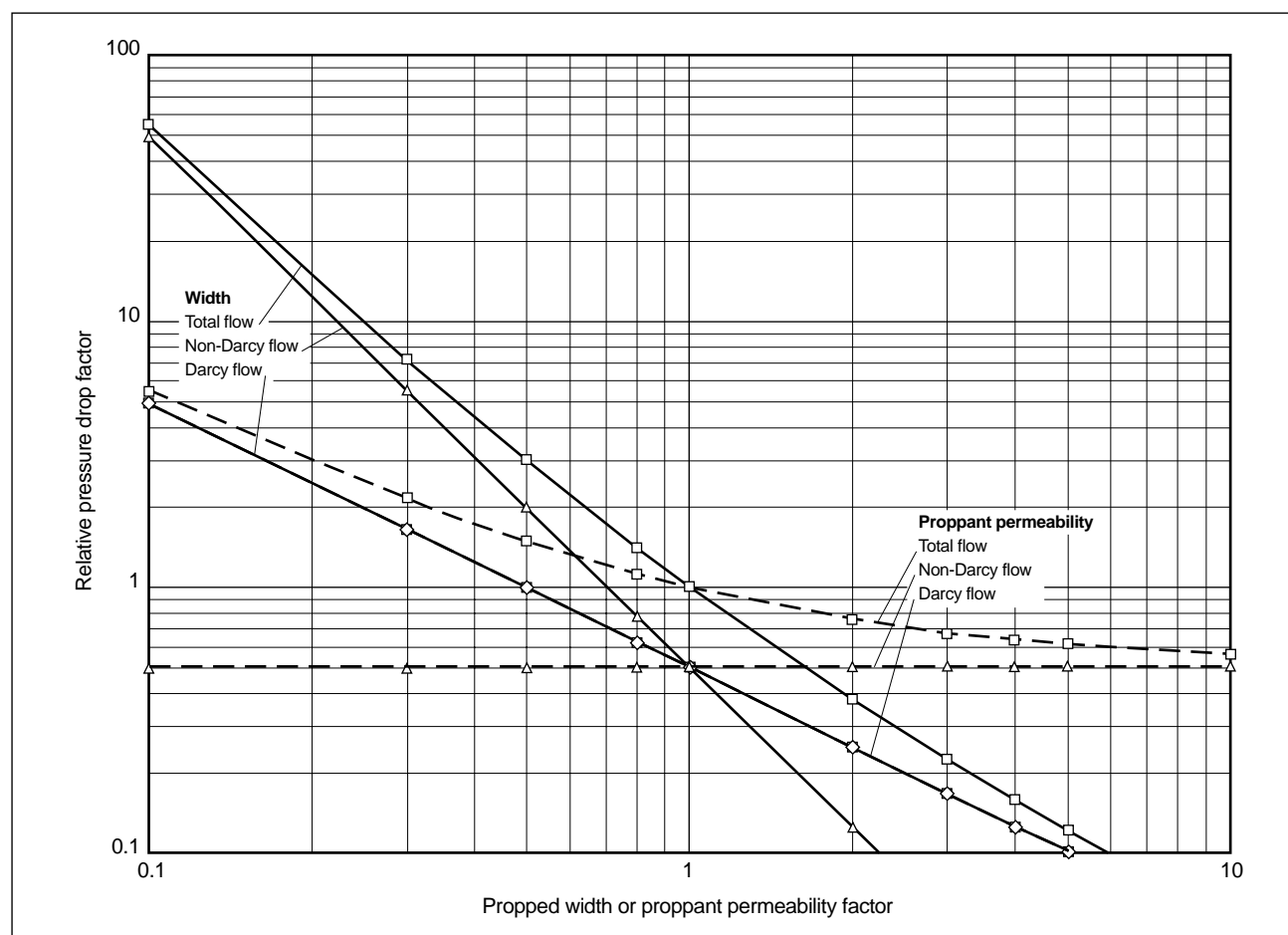


**Figure 10-43.** Effect of proppant permeability and width on the convergent pressure drop in the fracture.

among the perforations, wellbore and fracture orientation as well as by the creation and propagation of multiple fractures. In anticipation of this problem, contingency plans should be made to control excessive pressures and establish good communication between the wellbore and main fracture. Some methods are discussed in the following sections.

- Perforation strategy

Perforation plays an extremely important role in the execution of a hydraulic fracture from a horizontal or deviated well. The perforations represent the only communication channel between the wellbore (i.e., casing) and the fracture. In horizontal and deviated well fracturing, as with vertical wells, compromises can be made among the hole size, depth of penetration, shot density and perforation phasing (see Chapter 11).

Perforation alignment with respect to the far-field fracture azimuth is the most important aspect of perforation design. Because in many cases the hydraulic fractures propagate from the base of the perforation tunnel (Behrmann and Elbel, 1992; Morales *et al.*, 1993; Weijers, 1995), the depth of penetration is a much less important parameter than the diameter of the perforation (see Chapter 11).

For highly deviated wells that are not in the preferred fracture plane, minimizing the length of the perforated interval is used to minimize the creation of multiple fractures (see Chapter 11). One guideline is that the perforated interval should be limited to 4 times the wellbore diameter. Thus, for horizontal and deviated wells, it is not uncommon to perforate only a 2-ft interval in the wellbore. Extended perforation intervals can result in multiple fractures, putting the fracture stimulation and well performance at risk. In the event that a larger interval is perforated, steps should be taken to attempt to control the creation and propagation of multiple fractures as discussed in the following. Both proppant and viscous fluid slugs have been used for this purpose.

Correctly assessing excessive friction in highly deviated wells also requires consideration of the pressure drop within the radial region of the fracture. This is the injection analog of Eq. 10-3, with the channel permeability  $w^2/12$  substituted for  $k_f$  and only the laminar Darcy component applicable.

The radically diverging flow component during injection at high rates and of viscous fluids can be

substantial. Similar to the case of wellbore restrictions, this component of additional pressure drop disappears after the shut-in of pumping. An expected magnitude for the diverging-flow component can be obtained from a fracture model that considers this effect or Eq. 10-3 using the  $w^2/12$  substitution. The diverging flow component within a perfectly connected fracture can be substantial and may be misinterpreted as a restriction if this effect is not considered.

- Near-wellbore effects

Excessive friction pressure is often cited as evidence of multiple fractures, poor wellbore-fracture communication or both conditions. It is more common in horizontal or deviated wellbores, which are prone to having high tortuosity resulting from misalignment and multiple initiation fractures. Techniques used to reduce the excessive pressure are proppant slugs (Cleary *et al.*, 1993; Stadulis, 1995), viscous fluid slugs (Aud *et al.*, 1994; Hailey *et al.*, 1995), pretreatment injections and shut-ins, and an extended initial stage of low proppant concentration to erode restrictions.

Proppant slugs are small volumes of low-concentration proppant slurries that are pumped ahead of or during the main fracture stimulation treatment. The purpose of the slugs is to screen out some of the multiple fractures so they will cease accepting fluid and propagating. The successful application of proppant slugs enhances the propagation of a dominant fracture, which is of sufficient size (width) and provides the required pathway for the fracture treatment slurry. Proppant slugs are pumped at concentrations of up to 4 ppg and are typically overflushed through the perforations. Their role to reduce fracture entry restriction can also include erosion effects.

Because excessive friction is considered evidence of a near-wellbore problem or multiple fractures, the success or failure of proppant slugs is measured by the reduction of excess friction pressure. The number of proppant slugs pumped should depend on whether the excessive friction is being reduced. Therefore, the final design of this part of the fracturing operation must be performed on location and requires reliable downhole injection pressure data. As long as entry friction pressure reduction occurs, the proppant slugs should be continued. Once no additional reduction of the entry

friction pressure is observed, the main fracture stimulation can be initiated.

- Proppant transport in tubulars

Another design consideration for fracturing deviated wells is proppant transport in the horizontal or deviated section. There is a critical velocity, below which proppant is deposited at the bottom of the horizontal section; after it is deposited an even greater velocity is required to resuspend it (Shah and Lord, 1990). For normal fracturing fluids and injection rates, the velocities are generally high enough to keep the proppant in suspension. However, the velocity should be considered, particularly if low-viscosity or delayed crosslinked fluids are used and for contingency plans if the treatment is terminated early and the proppant must be cleaned out using coiled tubing or other means. These viscosity and velocity requirements also ensure that the proppant plugs reach the perforations.

### 10-7.5. Horizontal well example

The following is an example of a fracture treatment of a horizontal well in the Valhall field in the North Sea. Fracture stimulations in this chalk formation are performed in both vertical and horizontal wellbores. In addition to the normal fracture conductivity requirements, propped widths for fracture treatments are increased to offset the effects of embedment into the relatively soft reservoir rock (Smith *et al.*, 1987). To accomplish these objectives, TSO fracturing techniques are used. Creating additional fracture width beyond that to offset embedment minimizes the additional pressure drop from convergent flow to the limited perforated section.

Some of the information for this example was reported by Norris *et al.* (1996). The bottomhole treating pressure of a fracture treatment at the toe of the horizontal section is plotted in Fig. 10-44. The pressure gauge was near the heel of horizontal section, and therefore, considerable friction occurs over the horizontal distance to the fracture. Also shown on the figure are the injection periods for formation breakdown, three proppant slug stages, a calibration injection and a step rate test. Proppant slug stages were used because high injection pressures were noted during the initial formation breakdown. The difference in the maximum and final bottomhole injection pressures after these stages indicates the reduction of approxi-

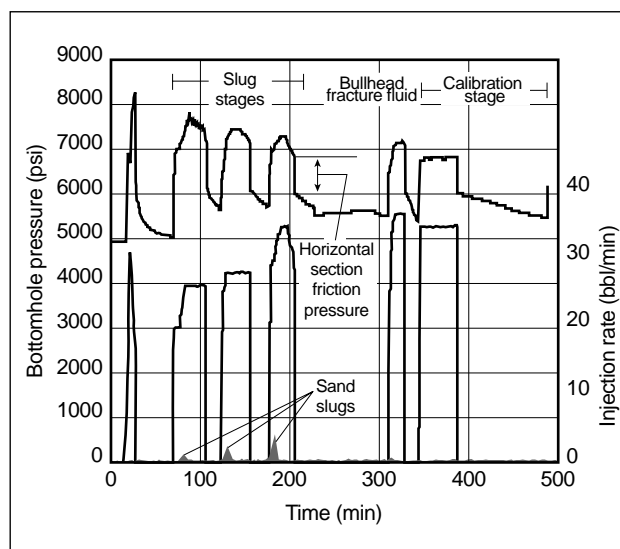


**Figure 10-44.** Bottomhole treating pressure versus time for formation breakdown, three proppant slug stages and a calibration injection.

mately 800-psi friction pressure, most of which occurred during the first stage without proppant.

The flush fluid of the last slug injection was bullheaded with fracturing fluid. The fracture was allowed to close to minimize the effect on the calibration analysis. The injection rate was reduced to 0.1 bbl/min (instead of shutting down) near the end of displacement and while the fracture was closing. This reduction provided shear on the crosslinked fluid to prevent excessive gelation. After the pressure dropped below fracture closure, a 30,000-gal calibration treatment was injected into the formation at 35 bbl/min. Figure 10-45 shows a plot of pressure versus the  $G$ -function. Analysis indicated a closure pressure of 5875 psi at a closure time of 19.9 min and a fluid efficiency of 0.4. For this efficiency, a TSO fracture treatment with a 43% pad fraction was designed and executed. An 8-min pad was pumped, and the initial proppant concentration of 2 ppg was injected. Analysis of the calibration data indicated a higher fluid-loss rate and less efficiency than anticipated by the design. Therefore, more fluid volume was required to obtain the desired TSO penetration, and a larger fraction of this volume was required as a pad. The pad was increased from 10,000 to 25,000 gal to induce the screenout at 120-ft penetration. The initial slurry stage was at 2 ppg, and the TSO occurred during the end of this stage, after which the slurry proppant concentration was increased to 3.5 ppg and then ramped up to 11 ppg during the

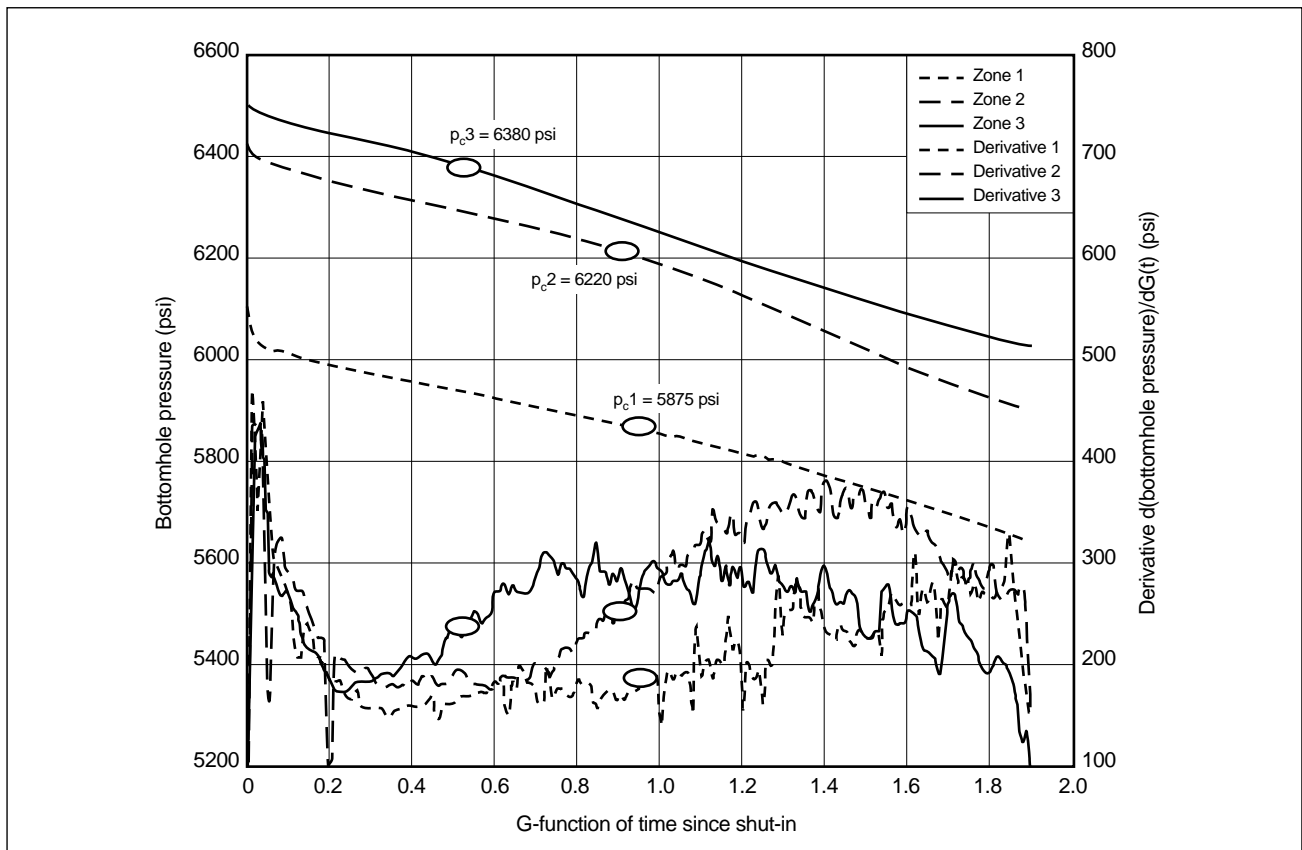


**Figure 10-45.** G-function versus time of post-mini-fracture treatment pressure decline data.

remainder of the treatment. The TSO occurred and stopped propagation at approximately 20 min; at this time the net pressure rose from 200 to more than 1000 psi during the next 70 min. The screenout and pressure were matched with a geometry simulation. The geometry simulation predicted an average propped fracture concentration of 10 lbm/ft<sup>2</sup>.

Production analysis showed a total drawdown from the reservoir to the wellbore of about 1800 psi. The convergent flow pressure drop in the fracture was calculated to be about 100 psi from Eq. 10-3, of which 60 psi was due to non-Darcy effects. This pressure drop is considered insignificant compared with the

total pressure drop of 1800 psi. The assumption of equivalent proppant embedment into the formation of 2 lbm/ft<sup>2</sup> reduced the simulated width to 8 lbm/ft<sup>2</sup> and corresponds to a width of about 1 in. For this reservoir and fracture treatment, the 1-in. propped width gives a nearly infinite-acting conductivity fracture. If the treatment had been designed for only 4 lbm/ft<sup>2</sup>, the effective width would have been 2 lbm/ft<sup>2</sup> and the pressure drop in the fracture 10 times greater (1000 versus 100 psi) at the same production rate. The PI would have been correspondingly reduced by more than 50%, with 10% of the reduction resulting from the Darcy and 40% from non-Darcy convergent flows.



# Fracturing Operations

*J. E. Brown and R. W. Thrasher, Schlumberger Dowell  
L. A. Behrmann, Schlumberger Wireline & Testing*

## 11-1. Introduction

Hydraulic fracturing is a particularly complicated enterprise. The purpose of hydraulic fracturing is the placement of an optimum fracture of a certain geometry and conductivity to allow maximum incremental production (over that of the unstimulated well) at the lowest cost. This process combines the interactions of fluid pressure, viscosity and leakoff characteristics with the elastic properties of the rock, which have been the subjects of the preceding chapters.

Accomplishing this, while taking into account all the presented technology, requires significant attention to the treatment execution involving optimized completion and perforating strategies, appropriate treatment design, control and monitoring of rate, and pressure and fluid characteristics.

## 11-2. Completions

Until recently, the majority of wellbores have been vertical and designed to produce from a single production string. Other types of completions that can be planned and performed are

- deviated wells
- horizontal wells
- multiple completions
- multiple laterals.

The choice of the type of completion should account for all considerations, ranging from drilling to production to abandonment.

### 11-2.1. Deviated and S-shaped completions

Precompletion and drilling planning should be given serious thought in cases where fracturing may be considered for highly deviated wellbores. It is important to understand the relationship between the wellbore angle, formation in-situ stress fields (dictating

fracture orientation) and potential fracture geometry under these conditions.

Fracture initiation from wellbores that are not aligned with one of the principal stress directions can be complex. In these cases, fractures may not be a simple singular planar feature. Misalignment may lead to the initiation of either multiple near-wellbore fractures or fractures that are forced to twist and change direction to ultimately reorient and align with the far-field minimum horizontal stress. Potential problems can affect the geometry and productivity of the fractures; there may be limited fracture communication with the wellbore, and the fracture width profile at or near the wellbore may be restricted. A restriction or reduced width can be sufficient to cause proppant bridging during the treatment, potentially resulting in an early screenout and restricted production after treatment.

Planning for an S-shaped completion, where the extended reach wellbore is brought back to a more vertical or 90° attitude through the formation, is generally advisable. The connectivity of a well and fracture is always important, but it is critical in high-permeability fracturing. Although tortuosity is a problem that affects all fractures during both execution and production, limited exposure is not a major issue in low-permeability reservoirs; it is in high-permeability formations. Thus, deviated wellbores with limited perforated intervals may provide attractive fracture treatments (although S-shaped wells are even better). However, for high-permeability fracturing both S-shaped wellbores and 180° phased, oriented perforations or slots cut along the well trajectory are highly advisable. This approach is intended to safeguard against further reducing a naturally small fracture conductivity (Chen and Economides, 1998). Wellbore angles of less than 20° may be necessary to achieve optimum fracture geometry and performance. In general, production engineering considerations suggest that the wellbore orientation should coincide with the fracture orientation. The

wellbore orientation can be either vertical or horizontal. In the horizontal mode, the wellbore must be placed to have either longitudinal or transverse fractures. If transverse fractures are created, multiple treatments will have to be performed that will require proper zonal isolation.

### 11-2.2. Horizontal and multilateral completions

Effective stimulation of horizontal wellbores requires specific completion procedures. In addition to the normal considerations for pressure and flow rates, horizontal completions must address the problems associated with treatment placement into or along the zone or zones of interest. In the case of executing several hydraulic fracture treatments along a single horizontal wellbore, the completion requirements can be complicated and extensive. Zonal isolation for each individual treatment must be part of the completion design. This requires cementing the entire liner, using external casing packers, placing permanently installed selective-zone mechanical tools and/or using retrievable zonal isolation tools. Coiled tubing is commonly used to place and operate zonal isolation tools in deviated and horizontal wells and multilateral completions.

The use of multilaterals can provide better reservoir drainage and management. Laterals could conceivably replace the need for fracturing in some cases. In other cases, optimum reservoir drainage may require a combination of laterals and stimulation. For these complicated completions, proper planning is essential. See Chapter 1 for an extensive discussion of appropriate well paths to match specific geological flow units.

### 11-2.3. Slimhole and monobore completions

Slimhole and monobore completions are used to lower drilling and completion costs. Slimhole completions can result in production casing sizes as small as 2 in. Tubulars, which are generally considered production tubing, become both casing and production tubulars. These small diameters can prohibit the use of special stimulation tubulars, which in turn may limit treating pressures.

The need to drill and complete wells at less cost is evident, but there may be a trade-off when stimulation must be considered. The small tubulars used in slimhole and monobore completions can limit the applica-

tion of stimulation. Because of the reduced wellbore diameters, surface treating pressures are increased owing to excessive friction pressures. This limits the rate and size of treatments that can be pumped and therefore reduces the effectiveness of the stimulation treatment. Small tubulars also limit the application of downhole tools; e.g., the stimulation of multiple zones is prevented because zonal isolation tools cannot be applied.

If it is considered essential to use slimhole completion techniques, the completion design should specify heavy-walled tubing as casing. This allows using higher pump rates for the higher treating pressure limitations.

### 11-2.4. Zonal isolation

Usually there are several potential producing zones penetrated by a wellbore that must be hydraulically fractured. To ensure that each zone is stimulated effectively, these intervals must be isolated from one another. Several isolation methods have proved to be effective. These methods can be used only when the various formations and intervals are isolated from each other behind the casing with cement.

- Importance of the cement sheath

The cement sheath must provide zonal isolation during both production and stimulation operations. For a producing well, the cement seal between the pipe and formation must be tight to prevent fluids from flowing through the annular area (see Sidebar 11A). The permeability of a set Portland cement of normal density is in the low microdarcy range. If the cement does not bond perfectly to either the pipe or the formation and a small channel remains, the effective cement permeability can be significantly increased. Large permeabilities may result from channel widths that are quite small (Nelson, 1990). For example, a channel width of only  $1.4 \times 10^{-4}$  in. is sufficient to create an effective cement permeability of 1000 md. Channel permeabilities of this order may allow significant cross-flow between zones.

During hydraulic fracturing these small channels, or microannuli, are relatively insignificant. The effective cement permeability does not create a high leakoff risk for the fracturing fluid within the annulus. A leakoff rate for a microannulus is less than 1 gal/min. If major channels within the cement

## 11A. Factors influencing cement bond integrity

### E. B. Nelson, Schlumberger Dowell

Primary cementing is the process of placing cement in the annulus between the casing and the formations exposed to the wellbore. The major objective of primary cementing is to provide zonal isolation in the wellbore. To achieve this objective, a hydraulic seal must be created at the cement/casing and cement/formation interfaces, and the cement itself must be sufficiently impermeable to prevent fluid movement through the cement matrix. Without effective zonal isolation in the wellbore, the well may never attain its full production potential.

No shortchanging the quality of the cement or the cement/casing and cement/formation bonds can ever be justified. Flow of fluids along the cement sheath is invariably an undesirable occurrence. For a producing well, this is manifested either by the loss of reservoir fluids through crossflow along the cement sheath or by the influx of underground fluids from other formations into the active layer. During hydraulic fracturing, significant escape of fluids through an imperfect cement sheath may result in either undesirable fracture height migration or screenout of the intended fracture in the targeted formation because of the fracturing fluid loss (Economides, 1990).

Many factors can influence the degree of zonal isolation provided by the cement sheath, including the removal of drilling fluid from the annulus prior to cementing, permeability of the cement matrix, dimensional stability of the cement sheath and annular fluid migration.

### Mud removal

To meet the objective of zonal isolation, the drilling fluid must be fully removed from the annulus and the annular space must be completely filled with cement. Incomplete mud displacement can result in the formation of channels (or microannuli) across producing zones and allow interzonal communication. Without complete mud removal, the benefits of all subsequent efforts to improve cement sheath integrity, and the effectiveness of stimulation treatments, are in jeopardy.

Many primary cementing techniques have been developed to maximize the probability of achieving complete mud displacement. From this work, a program of good cementing practices has evolved that is acknowledged by most operators today. Such techniques include casing centralization, mud conditioning (chemical and physical) prior to cementing, casing movement during mud displacement, preflushes and spacer fluids prior to cementing and careful optimization of the fluid flow regime by controlling the fluid rheology and pump rate (Smith, 1984).

### Cement permeability

Portland cement is used in nearly all well cementing operations. It is composed mainly of anhydrous calcium silicate and calcium aluminate compounds that, when brought in contact with water, react to form hydrated compounds. The principal reaction products are calcium hydroxide and a quasi-amorphous calcium silicate hydrate (C-S-H gel). C-S-H gel is responsible for the development and maintenance of compressive strength. The normal density of Portland cement slurries used in primary cementing operations is about 16 lbm/gal. This corresponds to a water content of about 40% by weight of cement (that is, 40-lbm water added to 100-lbm cement). Within 7 days the compressive strength is expected to reach about 4000 psi and the permeability to water will be less than 0.001 md. Depending on the wellbore environment, the optimum cement density may vary from 9 to 22 lbm/gal.

This is accomplished by adding more or less water and fillers with low or high specific gravity. Such changes in cement slurry composition can affect the compressive strength and permeability significantly (Nelson *et al.*, 1990). Although many industry and regulatory standards exist regarding the minimum compressive strength of well cements for various purposes, none pertains to cement matrix permeability. As a general rule, every effort is made to provide a cement sheath across a producing zone with at least 1000-psi compressive strength and no more than 0.1-md permeability to water.

### Volume changes

When Portland cement reacts with water, the total system undergoes a net volume diminution, usually ranging from 6% to 8% (Lea, 1971). This absolute volume decrease occurs because the absolute density of the hydrated material (calcium hydroxide and C-S-H gel) is greater than that of the initial reactants (cement and water). Despite the decrease in absolute volume, the external dimensions of the set cement, or the bulk volume, remain the same or increase slightly (Fig. 11A-1). To accomplish this, the internal porosity of the system must increase.

Cement systems that expand after setting are recognized as a means of sealing microannuli and improving primary cementing results. The improved bonding is the result of mechanical resistance or tightening of the cement against the pipe and formation, and improved bonding can be obtained even if mud is left on the casing or formation surfaces. In addition, once the cement has expanded to eliminate void spaces, further expansion is translated into a reduction of internal cement porosity. However, excessive expansion (greater than 1%) should be avoided, as buckling of casing or damage to the formation may occur.

Several cement additives are currently used to induce expansion, including sodium chloride, calcium sulfate hemihydrate and calcined magnesium oxide. All of these rely upon the crystallization or formation after the cement has set of compounds that have a lower bulk density than their precursors. For example, when magnesium oxide reacts with water to form magnesium hydroxide, the hydrated material occupies more space than the original ingredients. A comparison of unconfined linear expansion between a neat Portland cement system and a typical expansive cement system is shown in Fig. 11A-1.

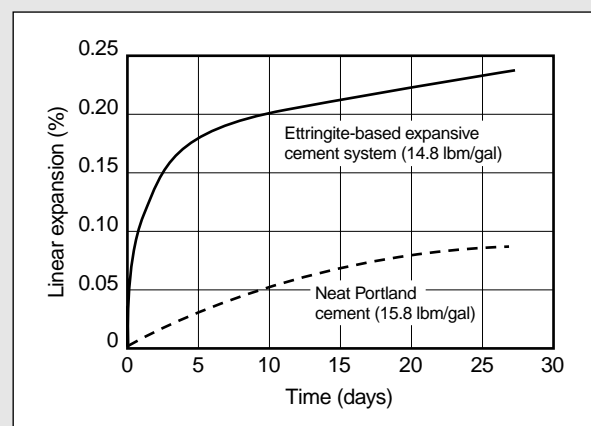


**Figure 11A-1.** Comparison of expansion between neat Portland cement and a typical expansive cement.

## 11A. Factors influencing cement bond integrity (continued)

### Annular fluid migration

During a cement job and for a short period afterward, the slurry is liquid and capable of transmitting sufficient hydrostatic pressure to prevent the invasion of formation fluids into the annulus. Before the cement slurry develops structural integrity, it undergoes a transition period. During the transition period, absolute volume reduction and gelation result in lowering of the hydrostatic pressure exerted on the formation (Fig. 11A-2). If the hydrostatic pressure falls below the formation pressure, annular fluid migration may occur. This can severely compromise zonal isolation (Parcevaux *et al.*, 1990), particularly for gas zones.

Several physical and chemical techniques have been developed that can prevent or reduce the severity of annular fluid migration. Foremost are the good cementing practices described here. Packers have been applied to seal the annular space above and below a producing zone. However, the most common methods involve the addition of chemicals to modify the behavior of the cement slurry during the transition period. Such systems include slurries with very low fluid loss, compressible cements (e.g., foams or slurries containing gas-generating agents), expanding cements, thixotropic cements, right-angle-set cements (the duration of the transition period is minimized) and "impermeable" cements (containing latices, polymers and surfactants).

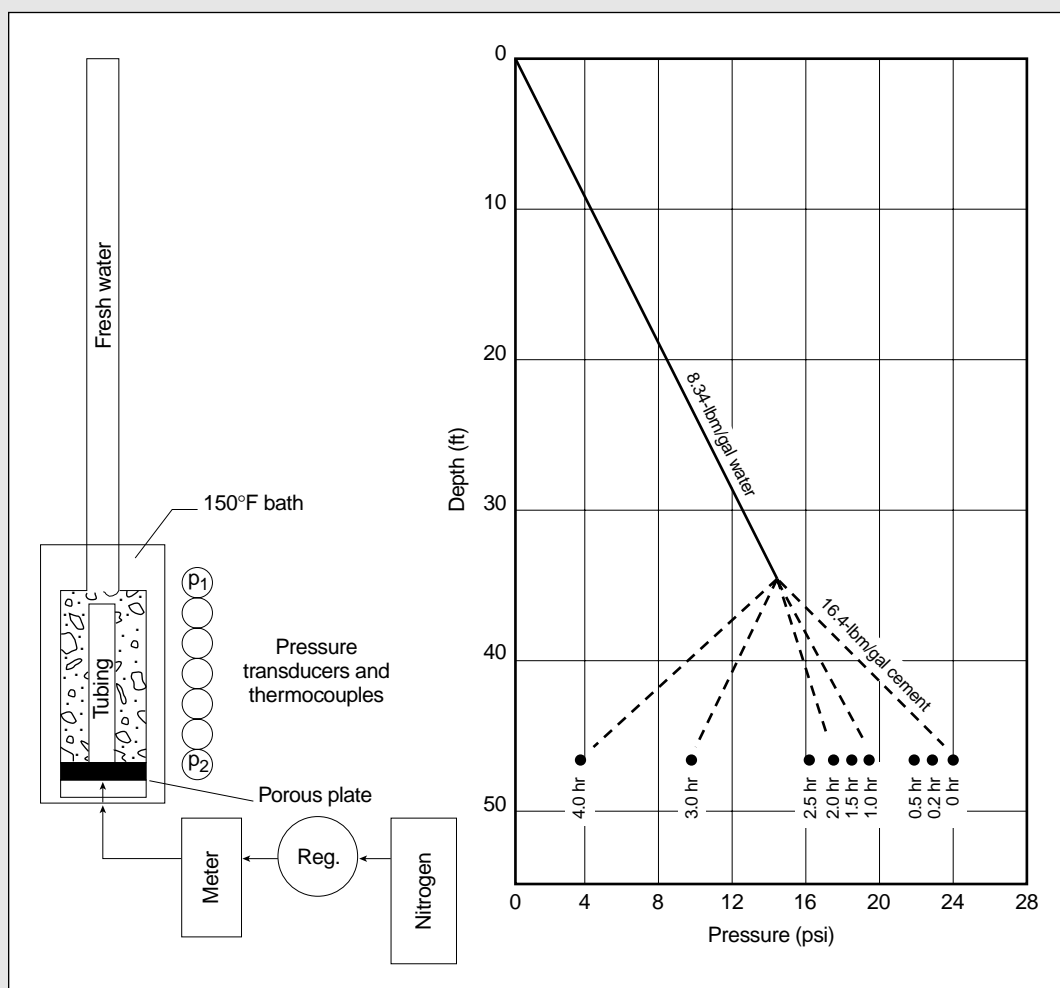


**Figure 11A-2.** Hydrostatic pressure transmission of a cement slurry versus slurry consistency (Levine *et al.*, 1979).

can be avoided, containment of the fracturing treatment should be possible.

The effects of fracturing pressures on the adhesion tension between the cement and casing or the cement and formation are not clearly understood.

Consequently, the resulting condition of the cement sheath following hydraulic fracturing is difficult to predict. Sonic logs run after fracturing treatments typically indicate that the cement bond (hydraulic seal) across the fractured interval is destroyed, but

the bond farther uphole remains intact. The loss of the cement bond across the fractured interval probably does not affect the placement or containment of the fracturing treatment. Cement of relatively low compressive strength should prevent the fracture from migrating between the casing and the formation; however, alteration of the cement bond may occur during the treatment. Any failure of the hydraulic seal may result in a microannulus that will lead to the crossflow of reservoir fluids.

- Fracture placement control

The most reliable method of controlling the placement of fracturing fluids is to limit perforations to a single zone. When several zones of a well are to be stimulated, the individual zones can be isolated from one another and stimulated individually. This can be accomplished through progressive perforation and stimulation. After a fracturing treatment has been placed in the first zone, it is isolated, and another zone of interest is perforated and treated in another single stage. Of course, this methodology works best when the deepest zone is completed first and subsequent zones are individually stimulated by working uphole.

Another effective multizone stimulation technique is coiled tubing–conveyed treatment (see Sidebar 11B). Other multilayer fracturing techniques that can be used are discussed in Chapter 10.

- Mechanical bridge plugs

Several mechanical methods are available to provide adequate isolation between perforated zones. The most reliable method is the use of mechanical bridge plugs, which can be run on tubulars or wireline. Bridge plugs that are run on tubulars are retrievable and can be moved and reset several times. Wireline bridge plugs cannot be moved once set, and their removal typically requires milling after the treatment. Wireline bridge plugs are used when several treatments are attempted in one day or when a rig is not over the hole during the treatment. They can be run in the hole quickly, and cleanout trips are not required between stages. The retrievable bridge plugs are used when zones are individually tested before another zone is opened. Any excess proppant must be circulated out of the hole before the tool is moved to prevent the proppant from sticking the tool. A typical treatment involves perforation of the bottom zone, hydraulic fracture treatment and zonal isolation by setting

a bridge plug immediately above the perforated interval. The next zone is then perforated and fractured.

- Sand plugs

A similar method of isolation can be achieved by using sand plugs after the fracturing treatment. The volume of sand necessary to cover the perforated interval is added to the casing. The sand plug is tested by applying pressure to the casing, and then the next zone is perforated and stimulated. Once all zones have been fracture stimulated, the sand can be circulated out of the wellbore by using either conventional or coiled tubing. The amount of sand required above the top perforations is generally small and can be calculated by applying Darcy's law to linear flow:

$$q_i = 7.827 \times 10^{-4} \left( \frac{Ak\Delta p}{\mu L} \right), \quad (11-1)$$

where  $q_i$  is the rate in bbl/min,  $A$  is area in ft<sup>2</sup>,  $k$  is permeability in darcies,  $\Delta p$  is the pressure drop in psi,  $\mu$  is viscosity in cp, and  $L$  is the length in ft. Using this expression, 10 ft of 20/40-mesh sand in 5½-in. casing will create a pressure drop of more than 6000 psi for a 40-cp linear gel leaking through the sand pack at 0.5 bbl/min. A mixture of sand meshes can be used if the permeability of the sand pack must be reduced to prevent flow through the pack.

- Frac baffles

Mechanical diversion can also be accomplished by using frac baffles. Frac baffles are run as part of the casing string and are placed between individual producing zones. After the lowest interval is perforated and fractured, a ball is dropped down the casing. The ball seats on the baffle and prevents fluid flow below this point. The next zone can then be perforated and fracture stimulated. When multiple zones are isolated with baffles, care must be taken to place the baffles so that the baffle openings progressively decrease in size from top to bottom; i.e., the bottom frac baffle has the smallest diameter opening. The first ball must be able to pass through the upper baffles and still seat in the bottom baffle. Similarly, the second ball must pass through the upper baffles and seat in the second baffle from the bottom, and so on.

All baffles have an inherent weakness owing to the limited area available in the casing coupling. The pressure differential across the baffle should

## 11B. Coiled tubing–conveyed fracture treatments

Sunil N. Gulrajani, Schlumberger Dowell

Wellbores typically intersect several pay intervals or zones. Usually all the pay zones require fracture stimulation for economic hydrocarbon production. A combination of economics, operational and reservoir management considerations dictates the stimulation strategy for these multizone completions. A common approach for these conditions is to stimulate as many producing intervals as possible with one fracture, either through height propagation of a single hydraulic fracture or with the limited-entry technique (see Sidebar 11C). The effectiveness of these approaches is reduced because of the uncertainty in predicting the fracture height and the inability of perforations to provide adequate diversion during slurry injection, respectively. Similarly, multistage treatments that isolate and stimulate each pay interval require additional workover operations, such as those discussed in Section 11-2.4. These operations reduce the economic benefits of the stimulation program, often to the extent that fracture stimulation can no longer be justified for marginally producing intervals. Consequently, several pay zones may remain bypassed for hydrocarbon production, either inadvertently because of the uncertainties and limitations of the fracture design process or deliberately because of economics.

The primary reason that multizone reservoirs are ineffectively stimulated is the inability of conventional fracturing operations to control the placement of a hydraulic fracture. This limitation can be overcome by using a coiled tubing work string for slurry transport within the wellbore. Its inclusion adds versatility to the fracturing operation wherein the mobility of the coiled tubing can be applied to individually fracture stimulate each producing interval within the wellbore in a single coiled tubing trip. This operational modification, however, does not limit the effectiveness of the fracture treatment. Coiled tubing deployment provides the desired fracture penetration and conductivity that would be expected with conventional multistage fracture treatments.

The economic advantages that coiled tubing fracturing brings to multistage fracture treatments can also be realized through the fracture stimulation of previously bypassed pay zones (Olejniczak *et al.*, 1999). In this application, coiled tubing fracturing prolongs the economic life of the wellbore and therefore increases the available hydrocarbon reserves.

The general operational procedure for coiled tubing fracturing treatments is illustrated in Fig. 11B-1. The application methodology is as follows:

- Perforate the pay intervals targeted for fracture stimulation 1 day before the scheduled fracturing operation.
- Run a gauge ring to ensure that there are no restrictions in the wellbore caused by scale deposition, damaged tubulars or perforation burrs.

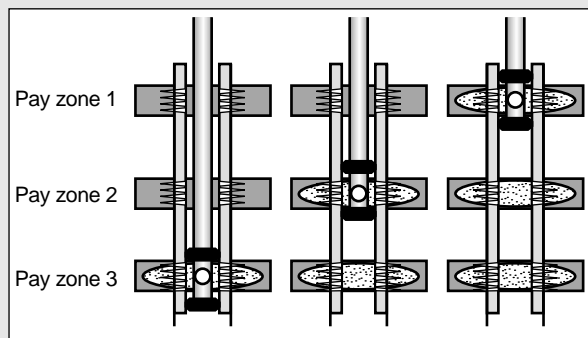


Figure 11B-1. Coiled tubing fracturing procedure.

- For multistage treatments, isolate the lowest perforated interval. For bypassed pay zones, isolate the interval of interest.
- Perform the fracture treatment as designed.
- Clean up any residual proppant in the coiled tubing work string.
- For multistage treatments, repeat the steps for isolation, fracturing and proppant cleaning for each perforated interval within the wellbore.

Coiled tubing fracturing operations rely on two technological developments:

- bottomhole assembly (BHA) that enables zonal isolation and cleanup
- fracturing fluid that reduces the friction pressure so that the injection rates required for hydraulic fracturing may be attained within the significantly smaller cross-sectional area of coiled tubing.

Zemlak *et al.* (1999) described a straddle BHA that is well-suited for the objectives of coiled tubing fracturing. The elastomer-based packers perform in a manner similar to conventional swab cups. The packers also enable injecting fluid within the annular region and flowing it back through the coiled tubing without requiring intermediate mechanical operations. This reverse circulation procedure removes any residual proppant from the coiled tubing, which can then be raised and positioned against the next perforation interval for its fracture stimulation. The effectiveness of the isolation and cleanup operations has been demonstrated by several successful fracturing operations for a range of reservoir depths, wellbore sizes and other operating conditions.

Most of the friction constraints of coiled tubing fracturing are overcome by incorporating a viscoelastic surfactant (VES) fracturing fluid. VES fluids exhibit a friction pressure that is as low as  $\frac{1}{2}$  to  $\frac{1}{3}$  that of the polymer fluid with the least friction pressure, delayed crosslinked, low-guar borate fluid (Fig. 11B-2). The nondamaging nature of VES fluids provides the additional advantage of ensuring that the desired fracture conductivity is attained at lower proppant concentrations. This capability further benefits coiled tubing fracturing because the slurry friction exponentially increases over that of the base fluid with increasing proppant concentration. The friction-reducing, nondamaging properties of VES fluids are primarily responsible for making coiled tubing fracturing a feasible operation for typical petroleum reservoir depths.

For both multistage fracturing treatments and the fracture stimulation of single-zone bypassed pay intervals, the coiled tubing work string protects the wellbore tubulars from excessive pressures encountered during fracturing. Coiled tubing deployment may achieve fracture stimulation where the compromised nature of the existing wellbore would otherwise prevent effective fracture stimulation.

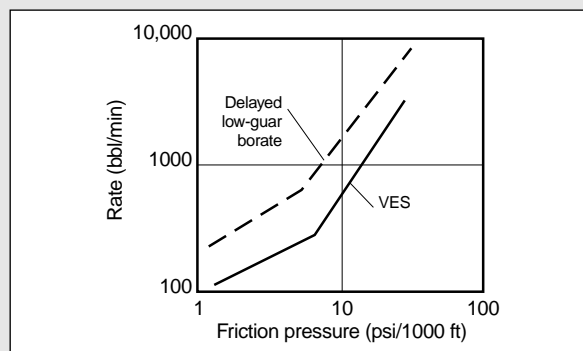


Figure 11B-2. Friction pressure of viscoelastic surfactant and delayed low-guar fracturing fluids.

be limited to the manufacturer's specification. The use of baffles in pipe sizes greater than 5½ in. is not recommended because the total force applied to the cross-sectional area of the baffle may exceed the baffle strength.

- Bridge plugs and packers

When completion practices do not allow the progressive order of fracturing to proceed from the lowest zone of interest up to higher intervals, bridge plugs must be used in conjunction with packers. Using the combination of a bridge plug and packer to straddle an interval provides an extremely reliable method of isolation. These retrievable tools can easily be moved to cover any interval, provided the unperforated casing is sufficiently long to provide a packer seat. However, caution should be taken when open perforations are present above a packer because of the possibility of proppant entering into the annular area if the fracture reaches the open perforations. Small quantities of proppant on top of a retrievable packer can stick the tool string.

- Diversion

Diverting techniques are used in some cases to control the placement of fluid and slurry into the zones of interest. A diversion treatment is advantageous over separately isolating individual zones because all the treatments can be pumped continually and are therefore more economical and time efficient. Although initially attractive, controlling placement through diversion carries many inherent risks. At a minimum, drilling damage can be bypassed; however, optimum stimulation of the formation cannot be achieved using diverting materials.

The use of bridging materials, such as rock salt and benzoic acid flakes, as the diverting medium usually results in an overflushed fracture. Some of the bridging material enters the fracture and displaces the near-wellbore proppant before diversion is achieved at the perforations. Conductivity near the wellbore may be minimized, resulting in a choked fracture with limited production capabilities.

This problem is pronounced when high-viscosity crosslinked fluids are used for fracturing. These fluids are highly efficient at proppant transport and carry the proppant away from the perforations as they are displaced by the diverter slurry. The diverter overflush may not be a significant problem if the fluids used in the treatment are of low vis-

cosity and create an equilibrium proppant bank. With this type of proppant transport, the proppant bank is not destroyed during the overflush of the diverter.

Using conventional ball sealers to divert fracturing stages has many of the same inadequacies as bridging materials. It is extremely difficult to predict the seating efficiency of ball sealers. This problem is even more pronounced after proppant has eroded the perforations. Also, the ball sealers must be introduced to the fluid while proppant is being added. The presence of proppant reduces the seating efficiencies, but it is impossible to predict by how much. If the ball sealers are introduced to a clean fluid stage immediately following the proppant stages, the clean fluid overflushes proppant away from the perforations until the balls finally seat.

Designing a schedule that ensures precise proppant placement into multiple zones by using diverter stages is almost impossible. When several zones are open to the wellbore it is extremely difficult to calculate which zone will fracture first. The zones are almost surely different in size and have slightly different rock properties. Because it is not practically possible to know which zone will fracture at a given time, most hydraulic fracturing schedules using diverters are simply divided into even stages. The uneven in-situ parameters cause slurry placement in the separate zones to create fractures of uneven geometries and conductivities.

It is also difficult to design and size the diverter stage so that all perforations in the zone being fractured become plugged and the other zones remain unaffected by the diverter. A diverter stage that is too large may plug the unfractured intervals before the fracturing slurry designed for that stage has been pumped. If the diverter stage is too small, the first zone may not be adequately plugged and the original fracture may continue to accept fluid. Portions of the pad fluid intended for the second interval will overflush the proppant pack away from the immediate wellbore. At the same time, the second zone is losing critical volumes of pad fluid, which may result in an early screenout.

- Limited entry

Limited-entry treatments are designed to place fracturing fluids into multiple zones simultaneously. The limited-entry technique uses the pressure drop created across the perforations during pumping to

divert the fracturing fluid into several different perforated intervals (see Sidebar 11C and Chapter 10). Generally, a 500- to 1000-psi pressure differential is considered necessary to provide adequate control over fluid placement.

The total flow of fluid entering a given zone is restricted by controlling the size and number of perforations in that interval. The high pressure drop at the perforations forces fluid to go to another zone. This diversion technique has proved popular because of its simplicity and economics. The diversion does not require expensive tools, and it does not require running and retrieving tools or making cleanout trips. The only cost for applying this type of diversion is the excess hydraulic horsepower required to pump the treatment at higher pressure.

If a limited-entry treatment is not applied correctly, each producing zone may not receive adequate treatment. Several factors must be considered when designing a limited-entry treatment. The number and size of perforations are calculated to divert the pad fluid. Smaller zones do not require as much fluid or proppant and therefore require fewer perforations. Some zones may require fewer than five perforations to control flow into that section. With a limited number of perforations available, the importance of the breakdown procedure becomes obvious. The loss of one or two perforations can significantly alter the flow distribution into all the zones.

Introducing sand into the fracturing fluid quickly erodes the perforations and changes the corresponding flow coefficient for each perforation. After only 10,000 lbm of proppant, the pressure drop across the perforations will be greatly reduced. Therefore, diversion of the pad fluids may be successful, but diversion of the proppant-laden stages cannot be presumed to be successful. After the perforations have been eroded, one zone is most likely to accept most of the fluid.

An accurate stress profile of the wellbore is necessary to design a successful limited-entry treatment. Each zone has a different fracture gradient and therefore they break down and fracture at different pressures. If great contrast exists among the fracture gradients of individual zones, the perforation scheme must be designed to reflect this difference.

Limited-entry designs usually do not consider the net pressure effects of the fracture. It is not uncommon for a fracturing treatment to create more than

500 psi in net pressure. An imbalance in net pressures between zones can effectively negate the perforation pressure drop. Fracture height and Young's modulus are two parameters with a major effect on net pressure. Both parameters should be closely evaluated prior to the design of a limited-entry treatment.

The net pressure in the fracture is inversely proportional to the gross fracture height. Large zones have smaller net pressures and therefore tend to accept a disproportionate amount of fracturing fluid. Very small zones most likely remain unstimulated because they rapidly build high net pressures and do not accept significant volumes of fracturing fluids. The global Young's modulus of the zone has a similar effect: the larger the Young's modulus, the narrower the fracture and the higher the net pressure.

The final parameter with significant impact on the successful placement of fractures using the limited-entry technique is fluid leakoff. The size of the zone and the rate the fluid is pumped into the zone directly impact the fluid efficiency and hence the fracture penetration. With several zones accepting fluid at one time, the total pump rate into any one interval may be quite low. Zones with the lowest pump rates generally have poor fluid efficiency, which may result in an early screenout.

Accurately placing proppant into multiple zones by using limited entry is extremely difficult. Fracture penetration and width are most likely highly irregular among zones. Smaller zones may not accept any significant amount of fluid. The increased producing capabilities of several stimulated zones resulting from isolation and separate treatments should be carefully examined and weighed against the economic advantages of a limited-entry treatment before the fracturing strategy is selected.

## 11-3. Perforating

### 11-3.1. Background

Perforating provides the means of communication between the wellbore and the reservoir, and during a stimulation treatment, the perforation is the fluid conduit between the fracture and the wellbore (see the Appendix to this chapter). Within this section, frac-



## 11C. Estimating multizone injection profiles during hydraulic fracturing

J. L. Elbel, Schlumberger Dowell

Wells completed in low-permeability formations typically have a number of layers scattered over a few hundred feet open to the wellbore. This completion is necessary to make the wells economical where no individual layer has sufficient production to warrant individual completion. These wells usually require fracturing, and obtaining the desired stimulation for each layer is difficult. The best way to ensure adequate stimulation of each layer is to isolate and treat each layer individually; however, this technique may be uneconomical considering the production potential of the individual layers. A proper economic analysis is impossible unless the injection rate and proppant penetration of each layer can be determined (see Section 10-5).

A common means of stimulating a number of layers is the limited-entry technique of perforating (Lagrone and Rasmussen, 1963). This method relies on high perforation friction, because of the limited number of perforations, to ensure that the wellbore pressure during injection is greater than the highest closure stress for all the layers. The number of perforations assigned to each layer is prorated in an attempt to distribute the injection into each layer at some desired rate. If the stress contrasts are low, it is usually assumed that the rate into each zone is governed by the number of perforations allocated to that zone. This assumption is false because other formation parameters also affect the injection rate into each zone. These parameters are the fracture height, formation modulus and current efficiency, which depends on the height, modulus, fracture fluid-loss rate and fluid-leakoff height. They affect the net pressure, which in turn must be added to the layer's closure stress when the desired perforation pressure drop is calculated. Even if one zone initially accepts all the fluid, a second zone may begin to accept a portion of the treatment later in the procedure. As net pressure in the fracture increases, so does the pressure in the wellbore. At some point the net pressure becomes sufficiently high to allow a second fracture system to accept fluid. If this scenario happens during a pad stage, proppant placement may be unsuccessful because of insufficient pad. If a second zone opens during the proppant stages, the second zone will quickly screen out. Fracture initiation in the screened-out second zone may not occur, even when a new pad fluid is started after the diverter stage.

Using diverter stages to control the placement of fracturing fluids usually results in uneven fracture geometry, poor conductivity near the wellbore and overall poor well performance. Relying on diverters to place multiple fracturing stages should be avoided unless other isolation methods are not practically feasible.

An expression for determining injection ratios during the fracturing of individually confined layers assuming PKN geometry follows. This expression is combined with previously published equations for determining fracture geometry, efficiency, pad volume and perforation friction to allow simulation of the fracture geometry for any number of layers (see Section 6-10).

### Parameter relations

The relation of the net pressure ( $p_t - \sigma_{min}$ ) to the parameters used in simulating the fracture geometry is

$$p_t - \sigma_{min} = 4.46(\mu E'^4 q_i^2 t / h_f^5)^{1/5}, \quad (11C-1)$$

where  $p_t$  is the fracture pressure,  $\sigma_{min}$  is the minimum stress,  $\mu$  is the viscosity,  $E'$  is the plane strain modulus,  $q_i$  is the injection rate,  $t$  is the time, and  $h_f$  is the fracture height.

Nolte (1991) expanded this expression to account for fluid loss and non-Newtonian fluids. It can be shown that the injection rate  $q_i$  is proportional to the formation and fracture parameters:

$$q_i \propto (p_t - \sigma_{min})^{(2n'+3)/(n'+1)} \left[ h_f^3 / (E'^2 \eta^{1/(n'+1)}) \right], \quad (11C-2)$$

where  $n'$  is the power law exponent and  $\eta$  is the efficiency. Assuming that injection into each layer begins at the same time, the ratio of  $q_{iA}/q_{iB}$  at any time can be expressed as

$$\frac{q_{iA}}{q_{iB}} = \left( \frac{p_t - \sigma_{minA}}{p_t - \sigma_{minB}} \right)^{(2n'+3)/(n'+1)} \left( \frac{h_{fA}}{h_{fB}} \right)^3 \left( \frac{E'_B}{E'_A} \right)^2 \left( \frac{\eta_B}{\eta_A} \right)^{1/(n'+1)}. \quad (11C-3)$$

The efficiency  $\eta$  can be determined by

$$\eta = \frac{F_b(p_t - \sigma_{min})h_f^2 / E'}{F_b(p_t - \sigma_{min})h_f^2 / E' + h(1.9C_L t^{1/2} + 0.0017V_s)}, \quad (11C-4)$$

which is of particular significance because it can be determined independently of the injection rate. Equation 11C-4 requires the properties used in Eq. 11C-3 plus the parameters of the ratio of the average to maximum width  $F_b$ , fluid-loss height  $h$ , fluid-leakoff coefficient  $C_L$  and spurt loss  $V_s$ .

Equation 11C-3 shows the relative importance of the various parameter ratios; the gross height ratio is the most significant. The desired injection rates for zones are commonly normalized by the zone height. For the same  $q_i/h_i$ , the relation becomes

$$\left( \frac{q_i / h_i}{q_i / h_i} \right)_A = \left( \frac{p_t - \sigma_{minA}}{p_t - \sigma_{minB}} \right)^{(2n'+3)/(n'+1)} \left( \frac{h_{fA}}{h_{fB}} \right)^2 \left( \frac{E'_B}{E'_A} \right)^2 \left( \frac{\eta_B}{\eta_A} \right)^{1/(n'+1)}, \quad (11C-5)$$

and for this condition, the net pressure ratio becomes more significant than  $h_f$ . The net pressure ratio can be controlled to some extent by changing the perforation pressure drop with the limited-entry technique. Increasing the perforation friction in one layer will increase the net pressure in the other layer.

For more than two layers, the ratio of the injection rate of an individual layer  $q_{ij}$  to the total rate  $q_{jt}$  for  $N$  layers is

$$\frac{q_{ij}}{q_{jt}} = \frac{(p_t - \sigma_{min})_i^{(2n'+3)/(n'+1)} \left[ h_{fi}^3 / (E'^2 \eta^{1/(n'+1)}) \right]_i}{\sum_{j=1}^N (p_t - \sigma_{min})_j^{(2n'+3)/(n'+1)} \left[ h_{fj}^3 / (E'^2 \eta^{1/(n'+1)}) \right]_j}, \quad (11C-6)$$

where  $p_{ti} = p_{wi} - p_{pfi}$  and  $p_{tj} = p_{wi} + \Delta p_h - p_{pfj}$  ( $p_w$  is the pressure in the cased wellbore,  $p_{pf}$  is the perforation friction pressure, and  $p_h$  is the hydrostatic pressure). The perforation friction pressure is estimated with

$$p_{pf} = \frac{q_i^2 \rho_s}{0.323 n_{per}^2 d_{pf}^4}, \quad (11C-7)$$

where  $\rho_s$  is the slurry density,  $n_{per}$  is the number of perforations, and  $d_{pf}$  is the perforation diameter. The casing friction pressure between the layers can be neglected for most cases, where it is small compared with the net pressures in the fractures.

Equations 11C-1 through 11C-6 are limited to constant-height fractures; however, it has been reported (Nolte, 1982, 1991) that if the net pressure in the fracture is less than 80% of the stress contrast of the barrier and growth into the barrier is a distance equal to the zone height, then the fracture penetration and net pressure are reduced by only about 10%. This small variation would not change the preceding equations significantly, and two-dimensional simulation would be within the required engineering accuracy in cases with moderate height growth.

turing implies using proppant; however, in general the presentation also applies to acid fracturing. The choice of the perforating parameters can have a significant effect on the quality of the subsequent fracturing or matrix-stimulated treatment (Daneshy, 1973; Warpinski, 1983). Perforating parameters are as follows:

- size and type of gun
- type of charge
- shot density
- shot phasing
- interval length
- gun orientation.

For the combination of gravel packing and fracturing (frac and pack), the perforating practices are governed by the gravel-packing considerations. These considerations are discussed at the end of this section. The objective of perforating for fracturing is to choose perforating parameters that minimize near-wellbore pressure drops during both the fracturing operation and production. Some of these near-wellbore effects are perforation friction, microannulus pinch points from gun phasing misalignment (Nolte, 1982, 1988a, 1988c), multiple competing fractures and fracture tortuosity caused by a curved fracture path (Romero *et al.*, 1995). These near-wellbore effects are discussed in Chapter 6. For any type of well treatment, there are two additional perforation-related parameters that may also affect the choice of perforating system:

- integrity of the cement/sandface hydraulic bond (microannulus) after perforating
- residual fractured sand grains in the perforation cavity, particularly for a matrix treatment.

Effective matrix treatments require communication through most of the perforations. This can be achieved by effective underbalance (see Appendix to this chapter), extreme overbalance (see Section 11-3.6) or the use of ball sealers.

If a reservoir is perforated with insufficient underbalance to remove most of the perforation sand debris, then fluid injection may cause this comminuted sand to create an external filter cake on the perforation cavity during fluid injection. This was first observed on a water injector and later on extreme overbalance tests (Behrmann and McDonald, 1996). Two unique characteristics observed in these tests are that productivity was not affected and that the “filter cake” was also a pressure barrier with an estimated pressure drop of

more than 1000 psi. The existence of comminuted sand in the perforation cavity limits injectivity and increases the fracture initiation pressure. High pump rates and high fluid viscosity enhance these effects, which are more important for extreme overbalance stimulation.

A microannulus is normally present after perforating, immediately after pumping begins or at both times. Maintaining a good bond during the breakdown phase can be problematic because a hydraulically propagated microannulus is analogous to hydraulic fracturing, as discussed in Sidebar 11D. Fracturing then proceeds as though from an openhole with some defects (perforations) that may be near the preferred hydraulic fracture plane (PFP). Most laboratory fracturing studies take extraordinary measures to avoid a microannulus by epoxying the casing to the rock, using O-rings around the perforations, etc. Thus, the generality of these laboratory findings must be viewed with caution. The magnitude of the microannulus is dependent on the wellbore fluid, wellbore size and type of perforating gun (Table 11-1).

Except when gas is the wellbore fluid, perforating debonds a portion of the cement/sandface hydraulic bond. This is a result of the loading of the wellbore fluid from the gun swell (charge/explosive coupling for capsule charges), passage of the perforating jet through the wellbore fluid and expulsion of the explosive detonation gases into the wellbore fluid. For hollow carrier guns, the debonding may be a function of the gun phasing. Figures 11-1 and 11-2 are examples of cement debonding observed in large-scale block tests (Mason *et al.*, 1994; Behrmann and Elbel, 1992).

An ideal perforation for fracture initiation would have a minimum injection pressure drop, initiate only a single bi-wing fracture and generate a fracture with minimum tortuosity (turning from the initiated frac-

**Table 11-1. Perforating parameters that affect a microannulus.**

Parameter	Promotes Microannulus
Capsule gun	Yes
Hollow carrier gun	Modestly
Small gun-to-casing clearance	Yes
Liquid in wellbore	Yes
Low shot density	No
Gas in wellbore	No

## 11D. Propagating a microannulus during formation breakdown

K. G. Nolte, Schlumberger Dowell

For normal completion practices, the creation of a microannulus should be anticipated during the breakdown process. The microannulus results from the same mechanics that govern the propagation of a hydraulic fracture, but on a smaller scale and confined to the annular circumference of the cement's interface with the well. The affected annular interface can be that of either the cement/casing or the cement/formation. The formation interface is more prospective because of the mudcake remaining between the cement and formation.

A hydraulic fracture or microannulus can propagate when fluid of sufficient pressure energizes a prospective flaw and the flaw is embedded in a deformable environment. Flaws of these types exist in the cement interfaces and around perforation tunnels, and they are in communication with the wellbore fluid. These flaws can originate in the mudcake, which can rehydrate by capillary action from the wellbore fluid, or in a region of mechanical alteration around the perforation tunnel. As the wellbore is pressurized during breakdown, the fluid in the prospective flaw is also pressurized, increasing the width of the flaw by compressing the material surrounding the flaw and allowing more fluid to enter and extend the flaw. For the microannulus, the relevant surrounding material is the rock containing the wellbore and the casing confining the cement. Increased fluid pressure in the annulus compresses the rock and enlarges the wellbore radius. Similarly, the casing radius changes as the internal pressure and the external annular pressure change. The deformation of the cement sheath is relatively small and could be considered part of the rock containing the wellbore. The annular width results from the combined radial deformation of the borehole and casing.

The evolution of the flaw's geometry is similar to that described in Chapter 9 for a hydraulic fracture originating from a point source of injected fluid.

1. The flaw opens and propagates when the energizing pressure exceeds a closure pressure equaling the stress tending to close the flaw. Sidebar 11A implies that for a typical cement composition and prior to breakdown, the stress in the cement sheath is essentially hydrostatic and about equal to the reservoir pressure of the formation. Therefore, for normally pressured conditions, the flaw's closure pressure is about the same as the hydrostatic pressure of the completion fluid within the casing, and the flaw can begin to propagate as breakdown begins.

2. The flaw initially extends in a radial geometry from the perforation tunnel. Actually, extending annular flaws would originate from most of the perforations. The mechanics describing the flaw's deformation are relatively complex during this early stage. The complexity results from the multiple regions of localized pressure acting on the curved surfaces of the casing and borehole.

3. After some period, the individual radial patterns coalesce into one microannulus around the complete circumference of the cement sheath. At this stage, the annulus is analogous to a confined-height PKN fracture (i.e., height equals the circumference of the wellbore) and can begin to extend up, down or both directions along the wellbore until breakdown of the formation by a hydraulic fracture.

For the last stage, the mechanics governing the annular width in the perforated section become relatively simple. The simplicity comes from several sources. The expressions for the change in radii of the casing and wellbore can be determined from specialized cases for the elastic deformation of a thick-walled cylinder. The multiple-connecting perforations provide fluid with minimal pressure gradients in the annulus. As a result, the pressures inside and outside of the casing become essentially equal with no radial change of the casing, and the annular width depends only on the change in radius for the borehole:

$$w = (1 + \nu)D(p_m - p_p) / 2E, \quad (11D-1)$$

where  $w$  is the microannulus width in in.,  $\nu$  is Poisson's ratio,  $D$  is the wellbore diameter in in.,  $E$  is Young's modulus in psi,  $p_m$  is the microannulus pressure in psi, and  $p_p$  is the far-field reservoir pressure in psi.

As an example, consider Eq. 11D-1 for a bottomhole pressure increase of 2000 psi over the initial hydrostatic pressure, borehole diameter of 7 in., rock modulus of  $1E+6$  psi and Poisson's ratio of 0.2. For these conditions, the hole radius and microannulus width will increase by about 0.009 in. (or the thickness of four sheets of standard writing paper). The hydraulic conductivity of such a microannulus is significant when coupled with a large pressure differential (e.g., 2000 psi) and a low-viscosity fluid (e.g., <0.4 cp for completion brine at representative bottomhole temperatures).

The conductivity microannulus created during the breakdown pressurization provides the same pressure and fracture initiation environment as an openhole, and for a vertical well it enhances the creation of a single fracture in the preferred fracture plane.

ture into the PFP) at an achievable fracture initiation pressure. The following sections provide recommendations on how best to achieve this ideal perforation. In the following sections, a vertical well is one with a deviation less than 30°.

### 11-3.2. Perforation phasing for hard-rock hydraulic fracturing

- No microannulus, vertical wellbore

For the following discussion, the PFP is assumed to be vertical and therefore can connect directly over

a significant distance for a vertical well. When the PFP is not vertical, as can occur near a significant fault, the PFP deviates from the axis of a vertical well. For this case, "Open microannulus, deviated and horizontal wellbores/vertical fractures" subsequently in this section should be consulted.

Dry gas wells, wells swabbed of liquid prior to perforating, wells shot with small hollow carrier guns and wells shot with low-shot-density (1 or 2 shots per foot [spf]) hollow carrier guns are potential candidates for maintaining good cement/sandface bonds. With a perfect cement bond, fractures are forced to initiate from the perforations,

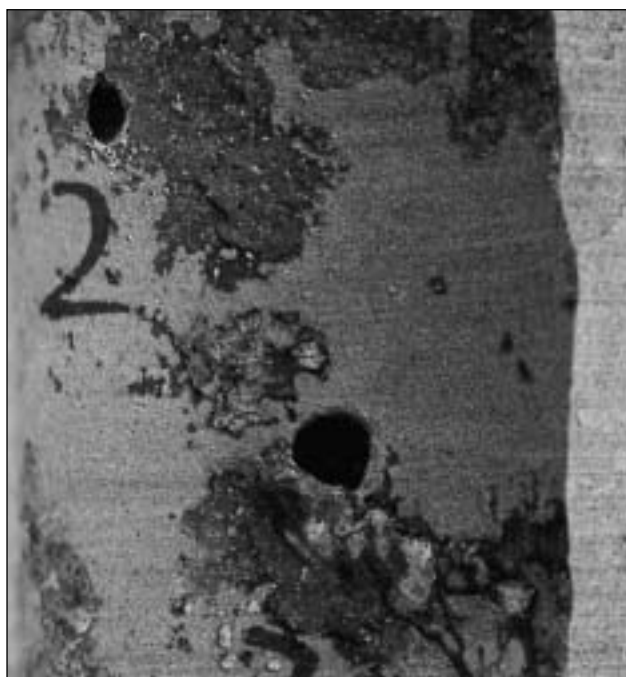


**Figure 11-1.** Disruption of the cement/sandface bond (underbalance test) (Mason et al., 1994). Intact cement sections are light gray.



**Figure 11-2.** Disruption of the cement/sandface bond (fracture test) (Behrmann and Elbel, 1992). The dark areas are fracturing fluid that flowed around the wellbore annulus.

which should eliminate additional fracture initiation sites around the sandface. Most laboratory hydraulic fracturing experiments have been conducted with a sealed annulus with the only fluid entry to the reservoir through artificial (drilled or cast) perforations. Thus, these experiments should provide insight on how to perforate wells with a good hydraulic bond, but the results must be used with caution because a microannulus is possible after perforating or during breakdown of the formation.

One of the papers describing laboratory fracture experiments (Abass *et al.*, 1994) shows that 180° phased perforations oriented within 30° of the PFP provide good communication between the perforations and the fracture. The good connection minimizes multiple fracture overlap and turning tortuosity and therefore minimizes any restriction of fracture width. As the perforation-to-PFP angle increases, the fracture initiation pressure increases as a result of the horizontal stress difference. Also, when the fracture initiates at the perforations, it must turn to eventually align with the PFP, and the near-wellbore fracture width decreases. This work suggests that if a 180° phased gun cannot be oriented within 30° of the PFP, then the use of a 60° phased gun is recommended for a good fracture connection. It is assumed that only those perforations closest to the PFP will initiate a fracture and that the shot density of the 60° phased gun must be 3 times that of a 180° phased gun to achieve the same number of holes directly linked to the fracture. These assumptions also imply that multiple parallel fractures will not initiate. However, the increased shot density of the 60° phased gun probably negates the assumption of no microannulus.

Assuming that equal perforation areas open in direct communication with the primary fracture, Table 11-2 lists the trade-offs for different non-oriented phased guns.

Selection of the optimum gun depends on assigning weighting factors to the different parameters, which becomes subjective and dependent on personal experience. For equal weighting, all guns are equivalent; however, to minimize the initiation of multiple fractures and if the possibility of higher fracture initiation pressure is acceptable, then a 180° phased gun can be used. In all cases, the casing hole diameter should be chosen to provide an

**Table 11-2. Perforating gun trade-offs for a vertical well, no microannulus and not oriented.**

Gun	Fracture Initiation Pressure	Multiple Fracture Initiation	Tortuosity	Cement Bond Destroyed
0°, 1 spf	3	1	3	1
180°, 1 spf	3	1	3	1
120°, 1.5 spf	2	2	2	2
60°, 3 spf	1	3	1	3
Note: 1 = best, 3 = worst				

acceptable injection pressure drop (see Section 11-3.3). Because injection rates are generally greater than production rates and proppant enlarges the perforations and erodes near-wellbore restrictions, the production area open to flow should generally be adequate.

The literature indicates that other perforating strategies can be applied. For example, Stadulis (1995) discussed the use of 0° phased guns at 1 spf with proppant slugs to prevent the initiation and propagation of competing multiple fractures and near-wellbore screenouts. (It is not clear if the observed success was from the use of low shot density, closed microannulus or proppant slugs.) It is not known if a dominant single- or bi-wing fracture propagates with 0° phased guns. A bi-wing fracture must initiate, but the wing opposite the perforations can have a limited flow rate and may screen out as a result of the restricted flow around the microannulus. The asymmetry for a dominant single-wing fracture offsets the drainage pattern from the well location. To minimize multiple fractures when using 0° phasing, the lower shot density helps maintain the cement/sandface integrity; whereas the use of a 60° phased gun at 6 spf (providing the same 1-ft spacing between perforations along any azimuthal plane) is more detrimental to cement debonding and increases the potential for the initiation of multiple fractures.

Because deviated (deviation greater than 30°) and horizontal wells typically have an open microannulus because of gravity (i.e., independent of the perforator), the perforating requirements for these wells are discussed in the following section.

- Open microannulus, vertical wellbore/vertical fractures

The presence of a microannulus (see Sidebar 11D) promotes fractures from the sandface, independent

of the perforations, unless the perforations are within about 10° of the PFP (Behrmann and Elbel, 1992). Fractures can also be initiated from perforations that are within about 30° of the PFP. Multiple fractures are encouraged from perforations between 10° and 30° from the PFP if sufficient fluid is allowed to move in the microannulus; however, maintaining significant flow, and hence width, in more than one fracture is inherently unstable because of the increased pressure requirement. The pressure drop across the multiple fractures increases by the square root of the number of fractures (Nolte, 1987).

When the fracture does not originate from the perforations, the flow path connects through the microannulus. The original microannulus separates further from the sandface to allow displacement continuity with the fracture width; however, geometric effects result in pinch points at the fracture entrance that can cause large pressure drops for fluid flow and near-wellbore proppant bridging. These points are subject to enhanced erosion, with their endurance depending on the rock hardness. Fracture tortuosity should not exist for a vertical wellbore in a normally stressed environment.

Table 11-3 lists the fracture trade-offs for different gun phasings for a normally stressed vertical well (deviation less than 30°). The shot densities in Table 11-3 are relative only. Determination of the required shot density is provided in Section 11-3.3.

For equal weighting, either 120° or 60° phased guns should be used. If pinch points are a greater concern than multiple fractures, a 60° phased gun should be used; however, the 60° phased gun may potentially create more multiple fractures and requires twice the shot density of a 120° phased gun because only one of three perforations will connect to the fracture.

**Table 11-3. Perforating gun trade-offs for a vertical well, with microannulus and not oriented.**

Gun	Fracture Initiation Pressure	Microannulus Pinch Points	Multiple Fracture Initiation
0°, 1 spf	3	4	1
180°, 1 spf	3	3	2
90°, 2 spf	2	3	3
120°, 1.5 spf	1	2	3
60°, 3 spf	1	1	4
Note: 1 = best, 4 = worst			

Other strategies are reported in the literature. For example, modifications of the pad with a high pump rate, use of high-viscosity fluid and use of proppant slugs (Aud, 1994; Cleary *et al.*, 1993; Stadulis, 1995) have been used to theoretically control near-wellbore screenouts by restricting fluid communication around the microannulus to reduce pinch points, tortuosity and multiple fractures.

- Open microannulus, deviated and horizontal wellbores/vertical fractures

The desired fracture geometry for an arbitrarily oriented deviated well is to initiate a single bi-wing fracture along the perforated length of the wellbore that then gradually turns into the PFP. If the wellbore is in the PFP, then the fracture will initiate from the perforations at the top and/or bottom of the casing, and thus 180° phased guns oriented up and/or down, respectively, are recommended. The use of oriented 180° phased guns has successfully been used on deviations up to 65° (Pearson *et al.*, 1992; Pospisil and Pearson, 1995; Vincent and Pearson, 1995). The guns were aligned in the plane of minimum tangential compressive stress (Yew and Li, 1988; Yew *et al.*, 1989, 1993). Recent laboratory experiments by van de Ketterij (1996) confirm these field observations. If the stress direction is not known, then a vertical, up/down, orientation is suggested. See Section 11-3.3 to ensure that the casing hole diameter on top meets the required size.

Wellbore rotation azimuthally around the PFP causes the length between the PFP and the wellbore to decrease, with a minimum occurring at a 90° rotation (i.e., the PFP and the plane through the top–bottom of the wellbore are at 90°). The perforated interval should be continually decreased as the combination of well deviation and azimuth becomes less favorable and decreases the length of this intersection. For the most extreme case,

10-ft perforated intervals would be reasonable to minimize the initiation of nonlinking multiple fractures. When the PFP approaches a 90° intersection with the wellbore for a wellbore deviation greater than about 75° (horizontal well), perforations should be clustered in a short length of less than 3 ft with maximum shot density and multiple phase angles to maximize perforation communication with the fracture (Abass *et al.*, 1992, 1994). This extremely limited interval, with sufficient zonal isolation from the cement, enhances the propagation of only one dominant fracture. Staged multiple fractures have been successful in horizontal wells drilled perpendicular to the PFP (Baumgartner *et al.*, 1993; Chambers *et al.*, 1995; Abou-Sayed *et al.*, 1995).

### 11-3.3. Other perforating considerations for fracturing

- Penetration depth

Perforation penetration beyond 4 to 6 in. into the formation is not required for fracturing because fracture initiation from a perforation generally begins near the sandface and propagates toward the preferred fracture plane (Behrmann and Elbel, 1992). Gun performance for penetration should be compromised in favor of casing hole size. Size requirements have been adopted from gravel packing (Gruesbeck and Collins, 1982) and are discussed in Chapter 5. The general requirement is that the minimum casing hole diameter exceeds 6 times the proppant diameter. A ratio of 8 to 10 times larger than the average proppant diameter should be generally used because of variance between the nominal and actual hole diameters, gun positioning and variation in proppant size. Manufactured proppant is highly biased toward larger diameters (lower

mesh range) to maximize its permeability. For manufactured proppants, the minimum casing hole diameter should be sized for the lower mesh size (e.g., 16 mesh for 16/30 mesh proppant).

- Perforated interval

Limiting the perforated interval was previously discussed for deviated wells. Even when the perforated portion of the well is nominally aligned with the PFP, consideration should be given to limiting the perforated interval, particularly for relatively thick sections that probably will be covered by the propped fracture. For example, a 6° deviation between the well and PFP over 100 ft provides a 10-ft offset and the potential for more than one dominant fracture. Multiple fractures are detrimental when they overlap and decrease their width in the overlapped region, which is usually the center of the perforated zone. Assuming vertical coverage of a zone by the propped fracture, the limiting effects for reducing the interval are achieving sufficient hole density and the resulting converging flow for the subsequent production (see Chapter 10).

Another consideration for limiting the perforated section near the center of a zone is to assist the vertical confinement of a tip-screenout (TSO) treatment. The limited section increases the vertical exposure of the slurry to fluid loss, which increases the concentration and promotes competent bridging during the increased pressure portion of the TSO.

- Large stress contrasts

Large horizontal stress contrasts favor using 60° phased guns to minimize the perforation-to-PFP alignment. Lack of alignment increases the fracture initiation pressure and enhances the microannulus-pinching effect.

- Shot density and hole diameter

Minimum shot density is determined by the diameter of the perforation casing hole, injection rate per perforation, desired perforation friction and fluid properties. The perforation friction  $\Delta p_{pf}$  in psi for noncrosslinked fluids is

$$\Delta p_{pf} = 0.237\rho \left[ q_i / (C_d \times D^2) \right]^2, \quad (11-2)$$

where  $\rho$  is fluid density in lbm/gal,  $q_i$  is injection rate in bbl/min/perforation,  $C_d$  is the dimensionless discharge coefficient, and  $D$  is the perforation casing diameter in in. Lord (1994) provided tables of  $C_d$  for different perforation sizes and fluid types

plus an additional pressure drop for crosslinked gels. See Shah *et al.* (1996) for further correlations with the viscosity for linear polymer solutions, crosslinked gels and fracturing slurries. Figure 11-3 shows the injection pressure drop versus casing hole diameter for water, where  $C_d$  is

$$C_d = \left( 1 - e^{-2.2D/\mu^{0.1}} \right)^{0.4}, \quad (11-3)$$

where  $\mu$  is the apparent viscosity in cp.

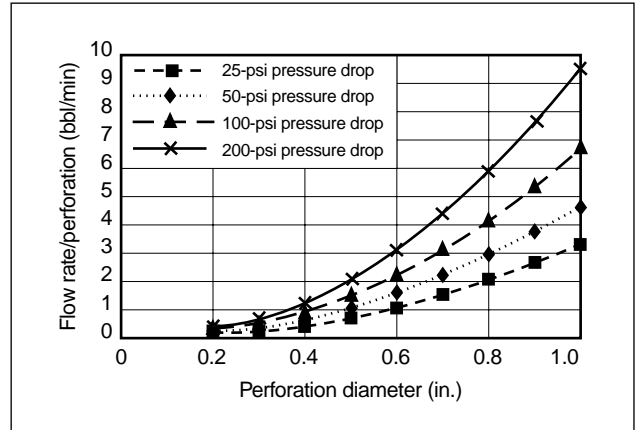


Figure 11-3. Injection rate versus perforation diameter.

Unless a perforating gun is centralized, the perforation casing hole diameter is a function of gun phasing. This means that the injection rate is different for different perforation diameters. For example, a cross-casing perforation diameter equal to 0.7 of the near-casing perforation diameter has 0.49 times the injection rate of the near-casing perforation. An average perforation diameter can be calculated using

$$\langle D \rangle = \left\{ \sum_{i=1}^{i=n} D_i^2 / n \right\}^{0.5}, \quad (11-4)$$

where  $n$  is the number of effective casing holes.

Figure 11-4 provides the typical hole size variation caused by the gun-to-casing clearance. For specific gun and casing systems, the service company should provide data on the variation in casing entrance hole size. Also, during the fracture treatment the hole entrance becomes rounded, increasing the discharge coefficient, and the hole size may also increase from erosion by the proppant. For further discussion, see Chapter 6 and Shah *et al.* (1996).

The hydraulic horsepower and surface treating pressure limit determine the maximum permissible



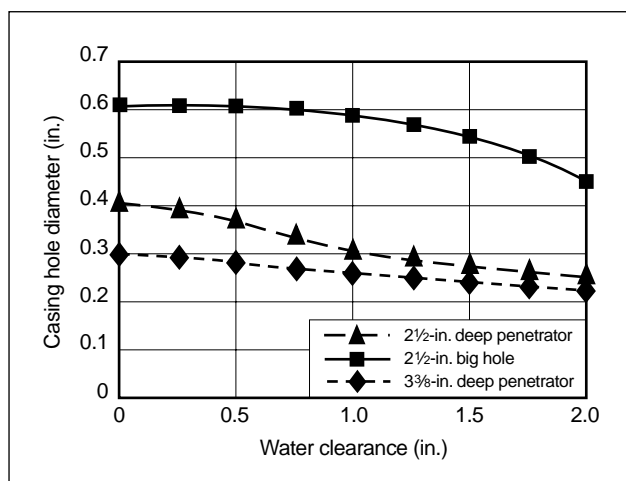


**Figure 11-4.** Casing hole diameter versus water clearance.

treating rate. The number of perforations in contact with the fracture determines the average injection rate per perforation. For 0° and 180° phased guns, all perforations should contribute to the fracture. For a 120° phased gun, only two-thirds of the perforations will probably communicate with the fracture, and for a 60° phased gun, only one-third of the perforations will likely be effective. Sidebar 11E provides an example calculation to determine the minimum required number of shots and thus shots per foot for a given pump rate and perforated interval. For an acceptable perforation friction, the casing hole diameter and shot density can be traded off for a given total injection rate. Except for limited-entry treatments (discussed in Chapter 10), perforation friction should be minimized (e.g., 25 psi) to reduce unnecessary fluid shear and proppant damage.

### 11-3.4. Frac and packs and high-rate water packs

Perforating requirements for frac and packs and high-rate water packs are the same as for an internal gravel pack (IGP). This similarity ensures a good gravel pack if the planned fracture placement is not completed successfully. Perforating requirements for gravel packs have been driven by the required minimum production pressure drop through the casing/cement tunnel that contains the packed gravel. As fines from the perforation, formation or both move into this tunnel during production, the gravel permeability is reduced and the pressure drop increases. An optimum gun for

an IGP would give the maximum area open to flow through the casing with the minimum hole diameter required for gravel placement. A gun with shots phased every 60° or 45° is desired. Depending on the expected flow rate per perforation (i.e., the required minimum pressure drop), guns using big hole charges at 12, 16 and 21 spf could be used. Because of the low modulus and strength of sand-producing formations, large fracture widths with a correspondingly large displacement of the microannulus are created to minimize pinch points.

A treatment design and execution objective should be a successful TSO fracture that packs back into the gravel pack to ensure that the large microannulus is also packed and creates an external gravel pack. The external pack provides a highly conductive path between the fracture and the perforations, which is a primary benefit of frac and pack operations. The issues of multiple fractures and tortuosity do not arise because of the erosive nature of the pumped fluid and gravel on the weak formation. To minimize the likelihood of a void within the IGP, the frac and pack interval should not exceed about 100 ft. The use of alternate path screens extends the frac and pack interval to hundreds of feet (Jones *et al.*, 1997). Consistent with the goal of achieving a competent IGP if the fracture placement is not completed successfully, standard practice is to perforate the complete gravel-packed section.

### 11-3.5. Fracturing for sand control without gravel-pack screens

Fracturing for sand control without gravel-pack screens can be accomplished by pretreating the formation or post-treating the proppant with resin, pumping curable-resin-coated proppant or pumping chopped fibers with the proppant. Except for the resin pretreatment, these techniques fix or control proppant flow-back plus provide a filter to prevent sand production.

Because no gravel is in the casing/cement tunnel to restrict flow, the perforation requirements are different than for frac and pack operations. The perforating objective, beyond the hole size for the proppant, is to eliminate any nonessential perforations that could produce formation sand. Therefore, for all well deviations a limited perforated section (e.g., 20 ft or less) and either 0° or 180° phased guns, ideally aligned with the PFP determined before the treatment, are



## 11E. Calculation of minimum shot density for fracture stimulation

The following example illustrates the process and importance of calculating the perforation friction pressure drop and using actual downhole perforation casing hole diameters.

### Problem statement

Given the maximum injection rate and length of the perforated interval, calculate the required shot density in shots per foot (spf) for two-gun systems for both 180° and 60° phasings. Calculate the pressure drop if entrance hole (EH) data from the American Petroleum Institute (API) are used instead of downhole data.

Maximum injection rate = 20 bbl/min

Perforated interval = 20 ft

Gun 1 = 2½-in. big hole (BH) with API EH = 0.61 in.

Gun 2 = 3%-in. deep penetrator (DP) with API EH = 0.40 in.

Casing size = 5½ in., 21 lbm/ft and Q125

Maximum perforation friction pressure drop  $\Delta p_{pf}$  = 25 psi

### Solution

1. Obtain the perforated casing hole diameters versus phase angle from the service company (Table 11E-1).
2. Calculate the average hole diameter for 180° and 60° phasings using Eq. 11-4. Because the effective shots are always pairs of holes at 180° phasing,  $n = 2$ . For example, the average hole diameter for the 2½-in. BH for the 0°/180° phase is

$$\langle D \rangle = [(0.58^2 + 0.36^2) / 2]^{0.5} = 0.482.$$

Table 11E-2 provides the average hole diameters.

3. For both the 180° and 60° phased guns, use the average hole diameters for the 0°/180° pairs. Because the guns are not oriented, it is not known if the preferred fracture plane will be closer to the 0°/180° or 60°/240° perforation pairs, and thus a worst-case condition is used (i.e., smaller average holes). Use Eq. 11-2 to calculate the average flow rate per perforation: 0.70 bbl/min for EH = 0.482 in. and 0.30 bbl/min for EH = 0.33 in. The flow rates for the API holes are 1.17 and 0.46 bbl/min, respectively, for EH = 0.61 and = 0.40 in. Divide these flow rates into the total injection rate of 20 bbl/min to obtain the minimum number of effective holes: 29 for the 2½-in. BH and 67 for the 3%-in. DP. To obtain the total number of holes, multiply the effective holes by the phasing deficiency, which is 1 for 180°, 1.5 for 120° and 3 for 60° phased guns, and then divide by the 20-ft perforated interval to obtain the minimum required shot density. Table 11E-3 summarizes these final numbers.
4. Check the required shot density and phasing against the available guns. Most 2½- and 3%-in. guns are built with 6 spf at 60° phasing and can be downloaded to 2 spf at 180° and 3 spf at 120°. The 10-spf 3%-in. gun at 60° phasing does not exist with the DP charge used in this example; the maximum shot density is 6 spf. This would result in a pressure drop of 70.8 psi. Other combinations of shot density and phasing would be special orders requiring lead time and planning.

Table 11E-1. Casing hole diameters.

Phase	Entrance Hole (in.)	
	2½-in. BH	3%-in. DP
API data	0.61	0.40
0°	0.58	0.38
60° and 300°	0.58	0.37
120° and 240°	0.49	0.30
180°	0.36	0.27

Table 11E-2. Average casing hole diameters.

Phase Pair	2½-in. BH (in.)	3%-in. DP (in.)
0°/180°	0.482	0.33
60°/240°	0.537	0.34

Table 11E-3. Minimum gun shot density.

Guns and Phase	Spf Using API EH	Actual Pressure Drop Using API EH (psi)	Minimum Spf Using Table 11E-2 EH and $\Delta p_{pf} = 25$ psi
2½-in. BH, 180°	0.86	70.5	1.5
2½-in. BH, 60°	2.57	70.5	4.5
3%-in. DP, 180°	2.18	58.5	3.4
3%-in. DP, 60°	6.53	58.5	10.0

recommended. As with a frac and pack, one of the design and execution objectives should be to achieve a TSO that packs back to fill the expanded microannulus with proppant. For the screenless case, the proppant is treated for flowback control to create a competent external pack that controls the formation sand. Again, as a result of the weak rock, the pumped fluids wash away any near-wellbore restrictions. Zero-degree phased guns should be used when the guns cannot be aligned with the PFP to eliminate nonessential perforations.

### 11-3.6. Extreme overbalance stimulation

Extreme overbalance (EOB) has been defined as either the application of a very high overbalance pressure during the perforating process (called extreme overbalance perforating, or EOP) or the very high pressure “surging” of existing perforations. Other names for this procedure are rapid overpressured perforation extension and high-energy stimulation. EOB utilizes pressurized gas (usually nitrogen [N<sub>2</sub>]) to inject various fluid systems into the formation at pressure gradients from 1.4 to 2.0 psi/ft. The primary objective is to create fractures either as a pre-hydraulic fracture treatment or as a dynamic fluid diversion (Handren *et al.*, 1993; Dees and Handren, 1993).

Handren *et al.*'s (1993) early publication suggests that effective multiple fractures were created from all perforations. However, additional full-scale laboratory fracture initiation experiments (Behrmann and McDonald, 1996; Willson, 1995) plus field tests (Snider, 1996) confirm that although fractures may initiate from many perforations, only a single bi-wing fracture is propagated from the perforations nearest the PFP. Furthermore, there is no evidence of the initiation of parallel multiple fractures. All fractures initiate from the perforations, with the primary fracture from the perforations nearest the PFP. It is assumed that the sudden pressurization of the wellbore casing closes any microannulus prior to hydraulic communication away from the perforations. The high fracture pressure gradients required are a result of at least four events:

- Dynamic fracture initiation is greater than static fracture initiation.
- Near-wellbore pore pressure does not increase as much as in a static injection.

- Residual “crushed” sand debris in the perforation tunnel restricts both fluid injection and pressurization of the perforation.
- Lack of a microannulus and the perforations not aligned with the PFP initiate against a larger stress.

These effects result in required pressures that are 2 to 3 times greater than those in conventional hydraulic fracturing.

Because experiments show no microannulus effect or parallel multiple fractures, only tortuosity must be considered. For a vertical well, a misaligned 0° phased gun is the least acceptable whereas 60° or 120° phased guns provide the least tortuous path (Table 11-2). However, Petitjean *et al.* (1995) reported that they mitigated tortuosity by minimizing the use of liquid to that necessary for fracture initiation and using nitrogen gas to extend the fracture and erode any near-wellbore tortuosity. This approach should be applicable for both vertical and deviated wells. Also, Snider (1996) reported the use of a proppant carrier to erode near-wellbore tortuosity and improve the near-wellbore fracture conductivity, but the fracture width is generally insufficient for proppant entry (Petitjean *et al.*, 1995).

In general, perforating considerations for EOB in vertical wells are similar to those in “No microannulus, vertical wellbore” in Section 11-3.2. Similarly, for deviated and horizontal wells, the perforating recommendations in “Open microannulus, vertical wellbore/vertical fractures” in Section 11-3.2 can be used.

A detailed discussion of extreme overbalance perforating was provided by Behrmann *et al.* (1996).

### 11-3.7. Well and fracture connectivity

The tortuosity between the initiation of a fracture from a well and the plane of its ultimate propagation has been recognized by many as an important issue during fracture execution, resulting at least in an undesirable increase in fracturing pressure or, worse, in a screen-out and even the creation of only one fracture wing.

Well deviation and unacceptable perforation phasing have already been addressed in this chapter. Well deviation can be remedied with an S-shaped well (i.e., turning a deviated well to become vertical upon entering the target formation), and problems with perforation phasing can be addressed by decreasing the phase angle among the perforation planes. To prevent

the similarly undesirable problem of multiple fracture initiation, the number of perforations can be reduced, leading to “point source” fracturing.

These solutions, although they usually prove successful in fracture execution in all types of reservoirs and will not affect well performance in low-permeability formations, may prove inadequate in high-permeability applications.

Chen and Economides (1998) demonstrated the effect of the near-well choke, resulting from inadequate fracture and well connectivity in low- and high-permeability reservoirs. Although the well performance reduction from the ideal value in low-permeability reservoirs is insignificant, the reduction in high-permeability reservoirs can be substantial (50% to 75% from the ideal) and the controlling factor in the success of the treatment. This effect suggests that for high-permeability fracturing, S-shaped wells are highly desirable and that in treating these vertical holes the indicated perforation phasing is  $180^\circ$  but with the guns oriented to align the perforation plane with the fracture plane. This assumes, of course, that the fracture is vertical. Analogous ideas may apply to horizontal wells for shallow applications where the fractures may be horizontal.

An additional idea, investigated at the time of this writing, is to forego perforating altogether for fracturing and consider the creation along the well of vertical notches parallel to the fracture plane by using a jet-cutting technique.

## 11-4. Surface equipment for fracturing operations

Assembling the surface equipment in a safe, organized and efficient manner is extremely important for the success of a fracturing treatment. Thorough pretreatment planning is essential to the organizational process of coordinating equipment hookup. An inspection of the location prior to the treatment allows making diagrams to optimize the use of available space.

Many steps of the organizational procedures are driven by common sense. Yet, small problems can easily be overlooked in the rush to get things ready. Pretreatment planning can eliminate many small problems that have the potential to develop into larger problems that may ultimately jeopardize the success of the treatment.

Figure 11-5 shows equipment positioning for a fracturing treatment. Figures 11-6 and 11-7 show fractur-

ing equipment for small and large fracturing treatments, respectively.

### 11-4.1. Wellhead isolation

Specialized isolation tools, or tree savers, can protect a Christmas tree at the wellhead from damage and the possible failure that results from exposure to high pressure, corrosive fluids or abrasive proppant-laden fluids. The pressure rating of a wellhead is usually less than the pressure required to pump a stimulation treatment. Replacing the existing tree with one that has a higher pressure rating is expensive and requires killing the well with potentially damaging fluids. Even if the existing tree has a sufficient pressure rating, exposure to high pressures and treating fluids may leave it in an unsafe condition.

The tree saver is mounted on the existing Christmas tree. A mandrel is extended through the valves on the tree and into the tubing. The mandrel has a rubber cup assembly that seals to the walls of the tubing and prevents fluid or pressure from directly reaching the tree. Once set, a tree saver can extend the working pressure of a wellhead up to 20,000 psi. Once the stimulation treatment is completed, the mandrel is pumped back out of the Christmas tree, and the wellhead valves can be closed.

### 11-4.2. Treating iron

The size of the high-pressure pipe called treating iron used on a treatment is dictated by both the anticipated rates and pressures. Smaller lines have a higher maximum treating pressure limitation than the larger sizes. The velocity of the fluid should be limited to 45 ft/s to minimize excessive erosion of the iron. Pumping above these rates for any prolonged period of time can erode the treating iron and thereby lower the effective working pressure that the iron could be exposed to before a catastrophic failure would occur. If the design treating rates exceed the rate limits of the iron's size, then either a larger iron must be used or multiple lines must be laid to the wellhead.

The treating iron should not have welded seams or exposed threaded connections. To eliminate these seams and exposed threads, the iron and associated connections should be machined from single pieces of metal. The connections between two pieces of treating iron should have nonpressure unions. This style of

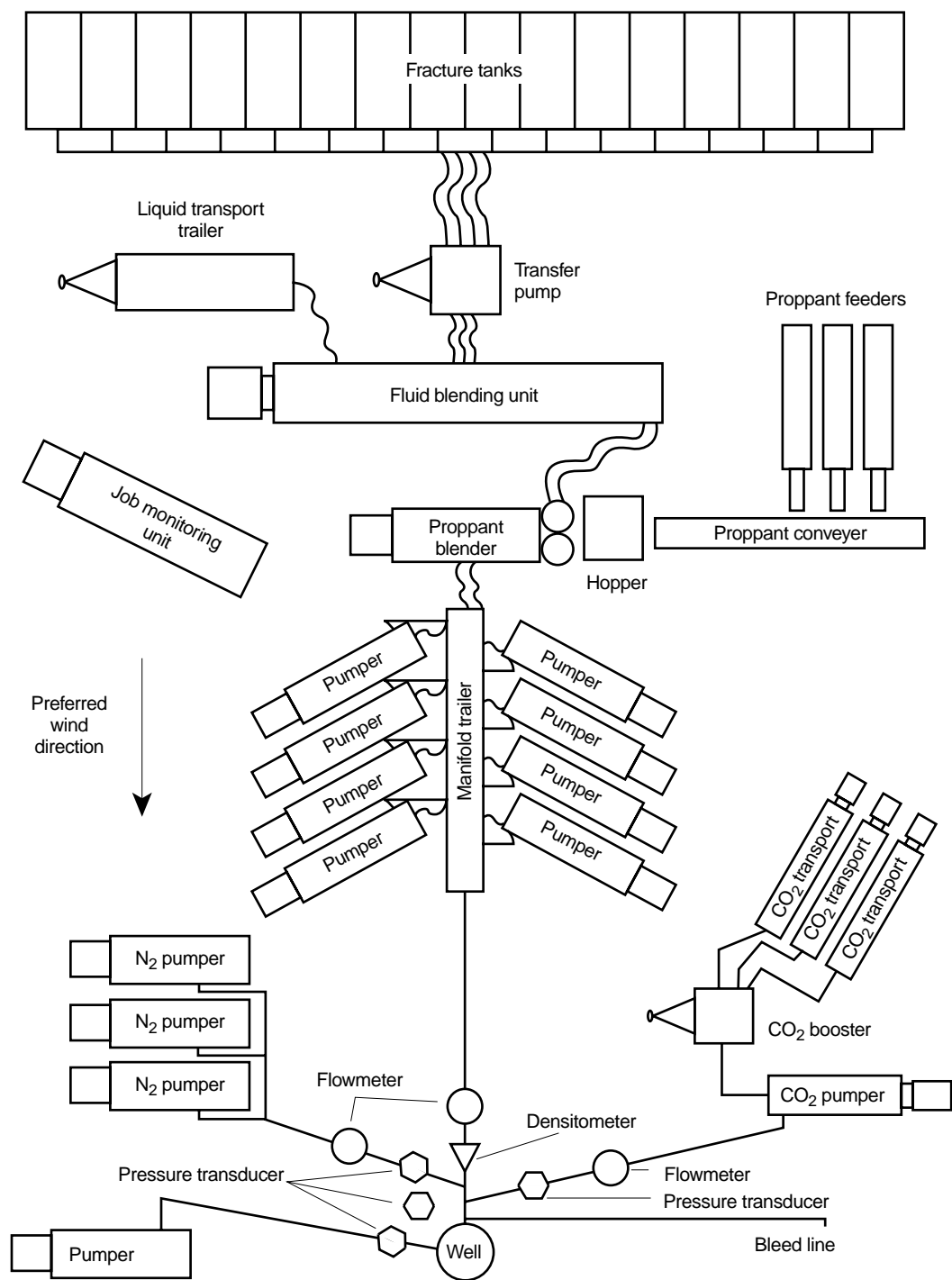


**Figure 11-5.** Equipment positions for a typical fracturing treatment.



**Figure 11-6.** Fracturing equipment on a small fracturing treatment.



**Figure 11-7.** Fracturing equipment on a large fracturing treatment.

connection prevents exposure of the threaded portion of the connection to the treating pressures.

During pumping operations the treating iron tends to move and vibrate slightly. To prevent exposure of the iron to stress from this movement, the line is laid to provide some flexibility. Swivel joints allow the iron some freedom of movement. These same connections also provide a means for the iron to make corners and change directions. To ensure that straight sections of the iron are completely free to move, it is recommended to have three swivel joints between any two fixed points in the line. A swivel joint is required at each end of a straight section, and another three-way swivel joint (i.e., the connection swivels in the center plus each end is free to rotate) is required at one of the ends.

- Check valves

A check valve should be placed in the treating line, on the ground, as close to the wellhead as practical. The valve allows flow in one direction; therefore, it can be pumped through but automatically closes once pumping stops. This isolates well pressures to the closed side of the check valve and prevents the flow of well fluids. This type of valve is essential for controlling the well when there is a sudden loss of pump pressure, such as when a treating line fails. In these emergency situations there is no time to physically close the wellhead valves, but the check valve can automatically close almost instantaneously.

Two common types of check valves are used in high-pressure treating lines. Flapper-type check valves are usually used in the main treating line. Proppants, solid diverting agents and ball sealers can all be pumped through this style of valve without fear of plugging or destroying its reliability. Dart check valves are used in nitrogen and carbon dioxide (CO<sub>2</sub>) treating lines. These valves use a spring to seat a dart and close the valve when injection stops. Because dart check valves are easily cut by proppants and plugged by diverting agents, they are not recommended for use in the main treating line.

- Bleedoff lines

A bleedoff line is used to relieve pressure from the system of high-pressure treating lines once the wellhead valves have been closed. The bleedoff line is not intended for the extended flowback of

well fluids. A permanent flowback line should be laid for the long-term flow of well fluids. This line should be placed between the check valve and the wellhead control valve. If the bleedoff arrangement is misplaced, pressure will be trapped between the wellhead and the check valve, and a pressure hazard will result when the treating line is rigged down.

A choke and double-valve arrangement should be teed off of the main treating line to start the bleedoff line. One valve serves as a master valve that is always fully open or fully closed and is opened first and closed last. The second valve is slowly opened and closed to control the flow of fluid. Swivel joints must never be used in a bleed-off line. Where a turn in the line is necessary, teed connections should be used. The bleedoff line must be restrained every 15 to 20 ft to prevent it from moving. Care should be taken when flowing back fluids that could potentially be carrying ball sealers. A ball sealer flow diverter can be included on the wellhead side of the choke to catch the balls and prevent them from interfering with the bleedoff procedure.

The bleedoff line should tee off of the main treating line and be staked. Lateral, or Y, connections should be avoided when laying the bleedoff line. A bleedoff line with a lateral is difficult to stake in place and may move when the bleed valves are opened and there is high pressure at the wellhead.

### 11-4.3. High-pressure pumps

High-pressure pumps should be spotted close enough to the blender so that the discharge pumps on the blender can easily feed slurry at a sufficiently high net-positive-suction head to the intake manifolds on the pumps. On large treatments with many pumps, a manifold trailer may be used to consolidate the hookup. The manifold trailer helps organize both the low-pressure suction hookup and the high-pressure discharge hookup.

The number of suction hoses between the blender and the pumps is determined by the pump rate. Standard 4-in. suction hoses in 25-ft lengths or less allow about 12 bbl/min of fluid flow to the pump. If higher rates are attempted through one hose, insufficient net-positive-suction head may result and cause the pump to cavitate and run roughly. If rates by one

pump are expected to exceed 12 bbl/min, another suction hose should be used to provide fluid to the intake manifold.

For low-rate treatments, the hose diameter may have to be decreased to maintain a sufficiently high fluid velocity inside the hose, especially on high-proppant-concentration treatments such as a foam fracture treatment. Alternatively, a recirculation line from the pump suction manifold to the blender can be used. If the fluid velocity in a hose drops to a point where proppant settling is severe, the hose may plug off and starve the pump for fluid.

Each pump truck should have an isolation valve where it is tied into the main treating line to facilitate making minor repairs during pumping operations. Without this valve the pump would always be exposed to the treating pressure. Behind the isolation valve a bleedoff valve should be installed so that the pressure on the pump can be safely bled off any time the pump is brought off line.

The size of the iron on the pump should be compatible with the rate and pressure capabilities of the pump. If the pump and iron are not performance matched, the effective efficiency of the pump is minimized.

Recirculation lines between the blender and the suction manifold of the high-pressure pump may be necessary when high proppant concentrations are pumped. At high concentrations the proppant may settle out of the slurry within this manifold. Settling problems are more likely to occur at low pump rates and for low-viscosity fluids. The recirculation line keeps fluid moving within the suction manifold and prevents proppant from settling out. Fracturing treatments using foamed fluids usually require a recirculation line.

#### 11-4.4. Blending equipment

Process-controlled blending equipment that meters and continuously mixes polymer slurry, concentrated potassium chloride (KCl) solution and liquid additives has made continuous-mix operations a viable alternative to batch-mix operations. There are several advantages to performing a fracture treatment in continuous-mix mode. Environmental concerns are greatly reduced because only freshwater residuals remain in the fracture tanks after a treatment. Besides eliminating the cost of gelled tank bottoms, no tank cleaning

or disposal costs are incurred. In addition, a more predictable and consistent viscosity is obtainable for large treatments, where bacteria can degrade the gel viscosity of a batch-mixed fluid before pumping begins. Personnel time and costs can also be greatly reduced. The continuous-mix process eliminates the need to have gelling crews precede fracturing operations, resulting in direct savings in time for personnel and equipment. Finally, viscosities can be easily changed throughout the treatment. This allows tapering the polymer loading so that fluid damage to proppant conductivities can be minimized or a net pressure limitation can be met.

To ensure that a continuous-mix operation goes smoothly, several requirements must be observed. The polymers should be of a liquid or slurried variety to ensure that they can be added at precise concentrations. Liquid or slurried additives can be pumped and monitored much more accurately than dry powdered materials. These polymers produce an improved, quicker hydration especially when mixed with process-controlled equipment. Specialized mixing and hydration units provide the metering capabilities, proper shear environment and sufficient residence time for proper hydration. The hydration process related to time and shear has proved to be extremely important for continuous-mix treatments. If the base fluid has not progressed sufficiently in the hydration process before the fluid is crosslinked, the fluid may experience stability problems.

Process-controlled proppant blenders use computers to meter precise proppant-to-fluid ratios throughout the treatment. This precision-blending capability is perfect for ramping proppant, which is considered the ideal for optimum proppant placement. The blenders accurately mix and meter proppant, dry additives, liquid additives and fracturing fluid together at a specified density in a preprogrammed, automatic mode. The proppant concentration can be precisely and safely controlled at concentrations higher than 22 lbm/gal added for sand or 32 lbm/gal added for high-strength proppant. The overall proppant/fluid ratio is constantly monitored and controlled in a range of  $\pm 0.5\%$ .

#### 11-4.5. Proppant storage and delivery

The total volume of proppant, rate of proppant delivery and number of different proppants to be used in the treatment must be considered when choosing the

proper vessel for storing proppant on location. Small treatments may require only dump trucks to deliver the proppant to the blender. Bobtail dumps and trailer dumps are routinely used throughout the industry. These units are spotted directly over the blender hopper and gravity feed the proppant at a controlled rate through a chute. Care should be taken to ensure that the hydraulic lift mechanism is in good working order, allowing the dump to be completely raised. If the dump is not completely raised, the proppant delivery rate may not be sufficient, especially as the dump nears empty. This can be critical at high proppant concentrations, which require the highest delivery rates. To prevent problems with the proppant delivery rate, it is a good idea to bring extra proppant if capacities allow. Bobtail units generally haul between 250 and 450 ft<sup>3</sup> of proppant, and trailer units haul up to 600 ft<sup>3</sup>. The maximum delivery rate of these units depends on the chute size and placement but is generally between 3000 and 7000 lbm/min of proppant.

Moving proppant dumps during a treatment should be minimized. Even with good operators, it takes 3 to 5 min to move a dump into place and raise it for proppant delivery. Excessive movement of the proppant dumps increases the chance of not pumping the proper proppant concentration. If a treatment is designed with large proppant volumes requiring movement of the dump trucks during pumping procedures, other proppant storage equipment should be considered.

Upright storage silos can hold up to 4000 ft<sup>3</sup> of proppant. The silos rely on gravity to feed the blender and do not require hydraulic power to operate. This type of storage eliminates moving trucks for most treatments because of the quantity of proppant it holds. However, this type of proppant storage requires considerable planning because the units are not mobile once they are spotted. Specialized cranes are required to raise these units into place and to lower them for transportation.

The conveyor-equipped sand bin is the most commonly used unit for delivering proppants to the blender. These units have several compartments for storing proppant. Each compartment has a set of hydraulically controlled doors at the bottom. When the doors are opened, proppant falls from the container onto a conveyor belt that leads to the blender. The storage capacity of these units ranges between 2500 and 4000 ft<sup>3</sup>. Hydraulically powered conveyors can unload these units at proppant delivery rates approaching 25,000 lbm/min. If extremely large vol-

umes of proppant are required for a treatment, conveyor-equipped sand bins can be positioned to offload proppant onto a second conveyor that feeds the blender. Spotting sand bins in this arrangement allows millions of pounds of proppant to be easily stored and pumped.

Regardless of the type of bulk proppant storage used, great care and planning must go into treatments in which proppant types and sizes will be changed during the treatment. The time and procedures required to make proppant changes during the treatment must be considered in the pretreatment planning.

#### 11-4.6. Vital signs from sensors

The monitoring of hydraulic fracture treatments has evolved from simple pressure strip charts to sophisticated computer recording and display. The information displayed by these instruments provides the supervising engineers with diagnostics on how the treatment is proceeding. Real-time execution decisions are made during the treatment based on this information.

Sensors acquire input data to track and account for the numerous operations taking place on location. Most of the parameters required for evaluating a fracturing treatment can be followed with sensors. Pressure, density, rate, temperature, pH value and viscosity are some of the more common parameters displayed and recorded.

- Pressure measurement

Pressure transducers measure the deformation of a sensing material to provide a pressure reading. Specially designed strain gauges are bonded to precision-machined metals that subtly deform as they are exposed to pressure. The quality of pressure transducers varies both in accuracy and resolution. The accuracy of a gauge is determined by how closely it measures pressures over an entire pressure span. The resolution indicates the size of the pressure increment required to affect the measurement.

It is imperative that treating pressures are accurately known during a treatment. The main sensor used to measure the pressure should be placed as near to the wellhead as practically possible. Care should be taken to locate the pressure sensor on the wellhead side of the check valve to ensure that an accurate pressure is available even after pumping operations have stopped. Should the transducer



inadvertently be placed on the upstream side of the check valve, pressure readings could indicate that pressures have bled off while actual wellhead pressures remain dangerously high.

Generally, several pressure sensors are available for monitoring purposes in addition to the primary transducer at the wellhead. A second transducer should be identified and calibrated to the primary sensor. Pressure measurements from this transducer should be used if the primary sensor fails during the treatment. All pump trucks should have a transducer on each high-pressure pump. However, these sensors should not be used as a backup to the primary pressure transducer because pressure measurements will be lost if the pumps are shut in and isolated during the treatment. The pump sensors can be used to indicate problems associated with each unit. A pressure that deviates significantly from the other sensors indicates that the pump should be shut in and isolated. Once the source of the abnormal pressure is located and repaired, the pump can be brought back on line.

- Density measurement

For years radioactive densitometers have been used to measure density. This technique provides a non-intrusive, continuous density measurement for any fluid flowing in a pipe. The technique is based on the absorption of gamma rays by the measured fluid.

A densitometer consists of

- radioactive source on one side of the pipe
- gamma ray detector on the other side of the pipe
- electronic panel to provide a signal reading.

As fluid passes through the pipe, gamma rays emitted by the source are attenuated in proportion to the fluid density. The detector senses the gamma rays transmitted through the fluid and converts this signal into an electrical signal. The electronic panel processes the electrical signal into a density indication. Denser materials absorb more radiation, resulting in the detection of fewer gamma rays. Thus, the signal output of the detector varies inversely with respect to density.

Most densitometers use a radioactive isotope with an extended half-life. A densitometer using <sup>137</sup>cesium can function accurately for nearly 30 years if the electronic components are maintained properly.

A good densitometer is accurate to within 0.1 lbm/gal over a density range of 8.0 to 25 lbm/gal. This remarkable accuracy can still lead to errors, especially when a densitometer is used to detect proppant totals and the treatment goes to a high proppant concentration. If the fluid and proppant densities vary by 0.1 lbm/gal and the densitometer has an accuracy level of 0.1 lbm/gal added, an error of nearly 10% can occur at proppant concentrations greater than 10 lbm/gal added because the densitometer is actually measuring radioactive adsorption, which is proportional to the density. The value of pounds per gallon must be calculated from the density reading. This calculation at higher densities is less accurate because a small change in absolute density means a larger change in pounds per gallon. As an example, the density readings comparing no proppant with 3-lbm/gal added sand are 8.43 lbm/gal and 10.06 lbm/gal, respectively (a change in density of 1.63 lbm/gal). However, a similar change in density (1.52 lbm/gal) from 13.96 to 15.48 lbm/gal corresponds to a change from 15.0- to 23.5-lbm/gal added.

- Rate measurement

Several styles of rate sensors are used for monitoring high-pressure treatments. Commonly used rate sensors include pump stroke counters, turbine flowmeters, magnetic flowmeters and venturi flowmeters for gaseous fluids. Pump stroke counters generally measure the rotational speed of the pump. Each full rotation of the pump moves the pump plunger through one complete cycle. From the volume of each pump stroke, number of pump strokes and the pump's efficiency, a rate can be easily calculated. This type of measurement is advantageous for high-pressure pumps that are pumping high volumes of solids, as is the case in pumping proppants during a fracturing treatment. The presence of solids or varying fluid rheology does not affect this type of measurement. However, if the pumps are not fully primed, the actual rate may be significantly lower than that indicated by a stroke counter.

Turbine flowmeters are designed primarily for measuring clean fluids. As fluid is pumped through the flowmeter housing, turbine blades are forced to rotate. Each of the blades on the rotor creates a small pulse as it passes beneath a magnetic pickup. Each revolution of the rotor generates a distinct

pattern of pulses equal to the number of turbine blades. The rotational speed of the rotor defines the flow rate, and each pulse defines a volume of liquid passing through the meter. Most turbine meters are calibrated with fresh water. As the viscosity of the measured fluid increases, the rotor speed decreases proportionally. Therefore, a turbine flowmeter should be calibrated with the actual fluid to be measured to ensure accuracy. These meters are useful for measuring liquid additive rates but have limited value for proppant slurries. Fracturing fluid viscosities often vary throughout a treatment, especially when proppant is introduced. The proppant also tends to erode the turbine blades, further reducing the accuracy of the flow measurement.

Magnetic flowmeters are popular for measuring treating fluid rates. These flowmeters measure the rate of fluid flow in a line, similar to a turbine flowmeter, but they do not have intruding parts that can be affected by changing viscosities or proppant addition. The electromagnetic flowmeter operates on Faraday's law of electromagnetic induction. When a conductor is moved across a magnetic field, an electromagnetic force is induced in the conductor. The electromagnetic force is orthogonal to both the direction of movement and the magnetic field itself. The electromagnetic flowmeter uses a pair of coils mounted on the outside of a nonmagnetic pipe. An electrical current flows through the coils to produce the magnetic field. The electromagnetic force is created when fluid (a conductive material) passes through the coils. The biggest limitation of the electromagnetic flowmeter is that it cannot be used with oil-base fluids.

To accurately measure  $N_2$  or  $CO_2$  rates, a venturi flowmeter should be used. The velocity of the gas through the venturi is determined by measuring the pressure drop across a reduced area. The line pressure and temperature must also be measured to compensate for changes in density.

- Data acquisition and process control

Computer monitoring systems can track and record numerous sensor inputs, making them ideal for monitoring complex treatments. These systems can also use data to create a presentation that makes interpretation easy. Real-time processing of data is essential when monitoring complex treatments.

These systems not only monitor but also control additive rates based on a predetermined schedule.

Process control of blending and pumping operations provides a major advancement in treatment execution. Proppant schedules can be ramped rather than added in stages. The viscosity of the fracturing fluids can also be changed by process control. Polymer concentrations are tailored throughout the job to deliver the desired fluid properties. The computer-controlled execution helps eliminate human-induced errors that can be detrimental to the treatment.

#### 11-4.7. Equipment placement

Several considerations must be made when planning the placement of pumping equipment. Equipment should be placed upwind and at least 50 ft from the wellhead. If a service rig is on location, equipment should be spotted out of the fall line of the rig mast. Care should also be taken to place the high-pressure pumping equipment where personnel will not be exposed to the fluid end of the pump. If the equipment on location is to be operated remotely, personnel should set up in an area protected from potential problems with high-pressure lines. If equipment for  $N_2$  or  $CO_2$  is on location, it should be spotted at least 60 ft from other equipment and the wellhead.

### 11-5. Bottomhole pressure measurement and analysis

Various modes of fracture propagation can be inferred from straight-line periods that develop on log-log plots of net pressure versus time. These modes characterize different fracture shapes. Fracture closure and fluid leakoff parameters can be determined from the analysis of fracturing pressures resulting from closure (pump-in/flowback [PI/FB]) tests. Chapter 9 provides additional fracturing analysis information.

Collection and analysis of fracturing pressures are facilitated by the monitoring vehicles provided by service companies. These vehicles are equipped with computer hardware and software that can digitize, display, analyze and record relevant data.

The successful application of any method of fracturing pressure analysis relies on the accuracy of the fracturing pressure data. For a quantitative analysis of the data, a sensitivity level on the order of 5 psi and an accuracy level on the order of 25 psi are generally

sufficient. In particular, the bottomhole fracturing pressure and magnitude of the least principal stress (fracture closure pressure) must be known before the net pressure can be calculated. An error in either of these can result in an incorrect net pressure and incorrect fracturing pressure analysis.

The sampling rate affects the amount of data that must be acquired. The fastest time is required for collecting microfracturing pressures because the pump times are typically short and closure can occur quickly. Single injection periods can be as short as 3 min; however, multiple PI/FB tests may be required. In the microfracturing case, a sampling period of 2 s is desirable; 15 to 30 s may be acceptable.

The execution and evaluation phases of a fracturing treatment tend to last for a significant period of time, and the sampling period can be longer than a microfracturing sampling period. Fracturing treatments typically last 0.5 to 12 hr. One minute per sample is acceptable; however, if adequate memory is available, the sampling period should be shorter.

Three types of pressure transducers are used in bottomhole pressure gauges:

- strain gauge
- capacitance gauge
- quartz crystal.

Each of these pressure transducers uses mechanical displacement to generate a pressure signal. When pressure is applied to the transducer or sensor, an element is elastically deformed and the displacement converted to an electrical signal. The electrical signal is measured and a pressure is inferred. All bottomhole pressure transducers are packaged with a temperature sensor to enable temperature correction of the transducer.

Several methods are used to measure bottomhole pressure: modeling from surface parameters, non-real-time downhole pressure devices (memory gauges) and real-time gauges conveyed by wireline or coiled tubing. The downhole pressure measured includes any perforation friction pressure and tortuosity effects, which must be accounted for during analysis (see Chapter 9).

Devices are available that transmit real-time data but do not require a physical connection to the surface equipment. Prior to the fracturing treatment, the transmitter is set below the perforations using wireline. Pressure data are transmitted or telemetered through the rock to a receiver at the surface. Because the trans-

mission and decoding rates are much slower than for electric line transmission, wireless telemetry is not desirable for fracturing operations.

- Computed bottomhole pressures from surface measurements

Bottomhole pressures can be estimated by extrapolating surface pressure measurements. However, these extrapolations are of little value unless the perforation friction, fluid/slurry friction, near-wellbore friction and hydrostatic pressures are known and accounted for. The degree to which computed bottomhole pressures resemble actual bottomhole pressures depends primarily on the accuracy of the fluid/slurry friction data. Fluid friction and its effect on computed bottomhole pressure increase as the pipe diameter decreases; therefore, accurate fluid friction data are especially necessary for treatments pumped down tubing.

Improved engineering estimates of closure pressure, perforation friction and fluid/slurry friction for determining the bottomhole pressure and net pressure can be computed using a methodology consisting of calibration and application phases. The calibration phase is devoted primarily to measuring the pipe friction of the fracturing fluids (fluid with and without proppant). This phase can be completed in just one fracture treatment, provided that fluid friction data are required for only one set of fluids in one pipe size. During the application phase, the results of the calibration phase are coupled with a brief on-site pump test to produce meaningful, real-time net pressure plots.

Surface pressure gauges are present at all fracturing treatments. It is standard practice to use surface measurements to infer bottomhole pressure. Pressure gauges used by service companies are accurate only to within  $\pm 50$  psi. This does not include temperature-induced errors and offsets caused by clamping forces and drift, which can be significant. If surface pressure measurements will be frequently collected for calculating bottomhole pressure data, then the pressure gauge should be of high accuracy. This is particularly true when a packerless completion is used to monitor bottomhole data (i.e., tubing or annulus used as a “dead-string”).

Significant errors can occur when inferring bottomhole pressure from surface pressure measurements of deep, hot wells. The change in fluid den-

sity as the cooler fracturing fluid heats can be significant, particularly if the fracturing treatment is pumped down tubing (faster temperature changes). Figure 11-8 shows the effect temperature has on hydrostatic pressure using water.

- Downhole memory gauges

Pressure gauges can be placed downhole to record pressure during the fracturing treatment. Placement can be in a gas-lift mandrel, in a closed-end joint at the bottom of a tubing joint with perforations above the gauge or in a packer below the zone to be fractured. After the fracturing treatment, the gauge is retrieved, and the data are downloaded and processed for analysis.

Memory gauges have several disadvantages:

- Data are stored in gauge memory, so they cannot be used immediately.
- Because the gauge is downhole, if a treatment or sensor anomaly occurs, it will not be discovered until after the treatment.
- Treatment delays can affect the recording of data, for which there is a time limit. (Pressure-triggered recorders can be used to overcome the time limit.)

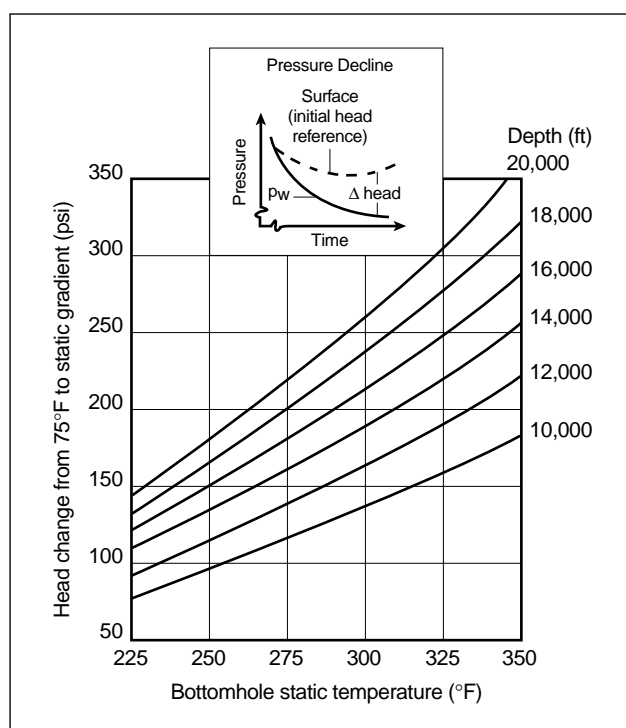


**Figure 11-8.** Hydrostatic head changes caused by temperature.  $p_w$  = wellbore pressure.

- The instrument is potentially subject to loss.
- The instrument must be retrieved using wireline or tubing after the fracture treatment.

- Wireline-conveyed gauges

Real-time bottomhole pressure data can be generated using wireline-conveyed gauges. In the case of a tubing/packer combination, the wireline is banded to the outside of the tubing (a slow process), and the gauge is on a side-port mandrel placed just above the packer. In situations where the fracture treatment is pumped down the casing/tubing annulus and the tubing is open-ended, a wireline-conveyed pressure gauge can be run in the tubing to measure the pressure near the bottom of the well. This configuration is generally not used because there are no direct advantages over surface recordings through a static fluid column in either the tubing or annulus for applications in which the density of the column remains essentially constant.

Wireline-conveyed gauges run on unprotected wireline can be used for calibration treatments without proppant if certain precautions are taken:

- Determine the increased wire tension caused by fluid drag. Equation 11-5 can be used to calculate an estimate of increased wire tension. A safety factor is used to compensate for dynamic effects and errors in the estimate of pipe friction:

$$T = T_s - T_d > 1.1 D_p D_w p_{\text{pipe friction}} \quad (11-5)$$

where  $T$  is the wire tension in lbf/ft,  $T_s$  is the wire strength in lbf/ft (for a free-end case that allows rotation and wire twist), and  $T_d$  is the dead weight in lbf. Prior to pumping,  $D_p$  is the inner diameter of the pipe in in.,  $D_w$  is the wire diameter in in., and  $p_{\text{pipe friction}}$  is the estimated pipe friction in psi (total pressure drop) for the fracturing fluid at the indicated pumping rate.

- Monitor the actual fluid friction, relative to the estimated value, to ensure a reasonable prediction.
- Protect the wire at the fluid-entry location by either mechanical isolation or equal opposing fluid streams.

The several limitations to Eq. 11-5 include the following assumptions:

- turbulent flow of a non-friction-reducing fluid (e.g., water)

- equal wire and pipe roughness
- no dynamic loading effects on the wire (no oscillations).

In situations where the fracture treatment is pumped down the casing (no tubing in the well), the wireline and gauge should never be exposed to fluid containing proppant, but should be protected for the entire length inside tubing.

- Coiled tubing–conveyed gauges  
Gauges run on the end of coiled tubing can be used to measure bottomhole pressure for real-time fracturing pressure analysis. Measurements of other parameters such as bottomhole temperature and casing collar locator data can also be made; bottomhole temperature can be used to calculate tubular stresses resulting from temperature changes. The bottomhole temperature gauge can also be used for postfracturing temperature logging.
- Measurement options  
Table 11-4 lists techniques for various well configurations for fracturing treatments.

## 11-6. Proppant flowback control

A problem with fractures in some applications is the back production of proppant (proppant flowback) with the oil or gas. Fluid drag forces dislodge and carry proppant out of the fracture. Numerical modeling indicates that arch formation in the pack is important. Places in the fracture wider than 5.5 grain diameters are inherently unstable, independent of the effective proppant stress. In these cases, fluid flow serves to sweep proppant out of the fracture. In addition to

fracture width, closure stress was shown to affect the occurrence of flowback in the modeling study and experimentally.

Proppant flowback usually occurs over a cleanup period of several weeks after the fracture treatment, but it can also occur throughout the economic life of the well. Up to 20% of the proppant placed in the fracture can return during the cleanup period. The proppant that flows back has a detrimental wear effect on the production equipment and requires the use of separators in the production line. Concern about proppant flowback can limit fluid flow rates during cleanup and production.

In most cases, proppant flowback does not reduce well production. It can therefore be concluded that the fracture does not close completely as proppant is produced. Also, the production rate can be reduced to a point where proppant is not flowed back.

Proppant flowback is more likely to occur with lower closure stress or wider fracture widths. Another possible cause is that the closure stress probably varies from point to point in the fracture between the maximum and zero as a result of uneven settling of proppant in the fracture. The resulting stress variation can allow proppant to be carried out of the fracture from regions of lower closure stress.

Several techniques have been used to control proppant flowback: forced closure, resin flush, the use of curable-resin-coated proppants and fiber technology.

Like sand control (except for wide proppant packs, as with TSO designs) the prediction of proppant flowback is specific for a site, field, formation and fracture and depends on field observations and correlations developed for an area.

**Table 11-4. Real-time measurement options.**

	Design	Execute	Evaluate
Casing	Calculation Packerless completion Electric line	Packerless completion	Packerless completion Electric line
Existing production tubing	Calculation Electric line		Electric line
New production tubing	Calculation Electric line Permanent gauge	Permanent gauge	Electric line Permanent gauge
Temporary work string	Calculation Electric line Permanent gauge	Permanent gauge	Electric line Permanent gauge

### 11-6.1. Forced closure

Forced closure is a procedure in which fluid flowback begins immediately at the end of pumping. The theorized benefits of forced closure are that a “reverse” screenout takes place at the perforations (i.e., the fracture width closes to below that required for a stable arch) and that the fracture closes before the proppant has a chance to settle in the fracture.

### 11-6.2. Resin flush

The resin flush technique involves pumping a curable resin into the fracture at the end of the job. In theory, the resin coats the proppant in the fracture near the wellbore and cures through a polymer crosslinking reaction. Additional postflushes are used to ensure that the resin does not fill the pores in the proppant pack. The disadvantages of this technology are the difficulties in covering the entire interval with resin and then pumping the postflush through the entire treated volume and the requirement to drill the excess resin out of the wellbore after it cures.

### 11-6.3. Resin-coated proppants

The use of curable phenolic resins with proppants is a popular method for controlling proppant flowback. They are used as all or some (tail-in) of the proppant placed in the fracture. Under sufficient closure stress, shut-in time and temperature, the resin coating is supposed to bind the proppant together in the fracture and form a dense aggregate around the perforations. A discussion of resin-coated proppants is in Chapter 7.

### 11-6.4. Fiber technology

Fiber technology was developed to hold the proppant in the fracture during the production of oil, gas or both and to allow more flexibility in flowback design than possible with curable-resin-coated proppants. These additives work by the physical mechanism of random fiber reinforcement; therefore, chemical curing reactions are not necessary to hold the proppant in place. No combination of temperature, pressure or shut-in time is required. Wells can be flowed back at high rates (dependent on the number of perforations). Also, flowback is possible immediately after the fracturing treatment is completed. The rapid flowback rate

enables increased polymer cleanup early in the flowback and can result in an increase in the total polymer returned. Because no curing reactions occur, wellbore cleanout is similar to that for normal proppant. Additional information on fiber technology is in Sidebar 11F.

## 11-7. Flowback strategies

Proper flowback of a fracturing treatment is designed to recover a maximum amount of the injected fluids while removing a minimum amount of proppant from the fracture. When to start the flowback and the flowback rate are the key issues. Variables such as fracture closure time, fluid break times (influenced by breaker schedule), reservoir energy available to produce the fracturing fluid, formation strength and proppant concentration in the near-wellbore area affect the flowback strategy.

The overall goal of a fracturing treatment is to achieve maximum fracture conductivity within the limits of the designed treatment. The flowback efficiency of the stimulation fluid can have a significant effect on the resultant fracture conductivity. In all cases and especially in the event that early-time proppant flowback control techniques are not used, fracturing fluid flowback efficiency should be considered during the design process.

Typically the fracture is allowed to close before flowback is initiated. Fracture closure is required to trap the proppant within the fracture and to prevent subsequent proppant movement through the application of fracture closure stress on the proppant. However, even the application of closure stress may not be sufficient to prevent some degree of proppant flowback during treatment cleanup and post-treatment production. In these cases, the application of proppant flowback control techniques may be necessary.

Some fracturing fluids contain gases to foam or energize the fluids. The gases most commonly used in energized fluids are  $N_2$  and  $CO_2$ . During flowback following a treatment, they provide an efficient source of concentrated energy to aid in rapid and more complete post-treatment cleanup, especially in low-bottomhole-pressure wells. Compared with long-term swabbing or pumping operations, energized fluids can be cost effective. Entrained gas in the fracturing fluid is also beneficial for fluid-loss control.

## 11F. Fiber technology

Simon James, Schlumberger Dowell

The inclusion of fibers in an intimate mixture with proppant is a recent innovation for controlling proppant flowback following hydraulic fracturing. The fibers stabilize the proppant pack by physical rather than chemical means. Several reinforcement mechanisms may contribute to the stabilization of the proppant arches (Card *et al.*, 1995); the relative importance of each mechanism depends on the fiber properties. Fibers at the face of the fracture may increase the force necessary to remove a proppant grain from the pack (Romero and Féraud, 1996)—the dominant mechanism for high-modulus fibers. Longer fibers also tie the proppant particles together, extending the stabilizing forces deeper into the pack—the dominant mechanism for longer, flexible fibers. Large-diameter (>50- $\mu\text{m}$ ) fibers may also stabilize proppant packs by acting as wedges between grains to prevent relative movement.

Physical reinforcement leads to the following significant advantages over curable resin-coated proppants (RCP):

- no shut-in required before flowback
- resistant to closure stress cycling
- no fluid interactions
- effective from very low to very high temperatures.

Fracturing treatments including fibers can be flowed back rapidly and immediately after the end of the job (Howard *et al.*, 1995). Rapid flowback can allow the removal of more polymer from the fracture, leading to higher productivity (Anderson *et al.*, 1996; Willberg *et al.*, 1998), earlier gas to sales and reduced flowback time compared with RCP (Howard *et al.*, 1995).

The advantages of rapid flowback cannot easily be simulated in laboratory conductivity tests, in which fibers generally provide a 20%–30% reduction in retained permeability (Card *et al.*, 1995). However, at low closure stresses ( $\leq 3000$  psi) the addition of fibers can increase retained permeabilities above 100% of the base proppant by disrupting the close packing of the proppant grains.

The stability of proppant packs containing fibers is not affected by closure stress cycling. The lack of permanent bonds between the fibers and proppant allows relative movement between the particles during closure stress cycling without

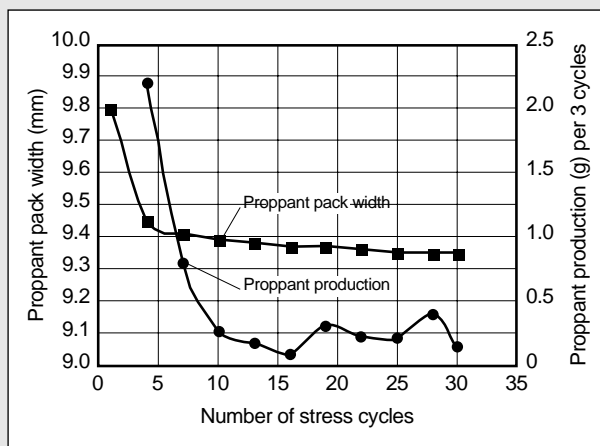


**Figure 11F-1.** Proppant production and proppant pack width as a function of closure stress cycling (Howard *et al.*, 1999). Each closure stress cycle was 4000-1000-4000 psi over 1 hr, with flow to 85 psi/ft every third cycle. After initial cleanup, the proppant pack remained stable throughout the test.

damaging the reinforcing structures (Fig. 11F-1; Howard *et al.*, 1999).

The fibers are essentially inert materials that do not interact with fluids, breakers or additives (Card *et al.*, 1995) and have been successfully applied in all fluid types—high- and low-temperature crosslinked guar, derivatized guar, gelled oil and viscoelastic surfactant. The inert nature of the fibers provides chemical stability while the physical reinforcement mechanism provides proppant pack stabilization from low to high temperatures. Fibers have been successfully applied in initially low temperature wells that were then subject to cyclic steam injection (Jones and Soler, 1999).

Fibers can also be used in conjunction with RCP to provide maximum proppant flowback control for extreme conditions. The RCP provides resistance to very high drawdowns. The fibers enable quicker cleanup times (Bartko *et al.*, 1997) and reinforce the RCP, providing resistance to failure through closure stress cycling.

An additional benefit of fibers observed in field applications is the reduction of treating pressure by as much as 8 psi/100 ft (James *et al.*, 1998). The effect is most noticeable in delayed crosslinked fluids. The presence of fibers is believed to inhibit the formation of turbulent eddies in the tubing (i.e., boundary layer effects).

Whatever type of proppant flowback material (fiber or RCP) is used, it can be effective only if it covers all the perforations attached to the fracture. If only a portion of the proppant is treated with proppant flowback control material (e.g., a tail-in treatment), there is a risk that nontreated proppant will remain in the near-wellbore region (Fig. 11F-2). Proppant placement is affected by settling, near-wellbore recirculation just above and below the perforations and post-shut-in redistribution (Smith *et al.*, 1997). The design of tail-in proppant flowback control treatments, particularly in multilayer and large intervals or where successful proppant flowback control is essential, should consider treating the entire proppant volume.

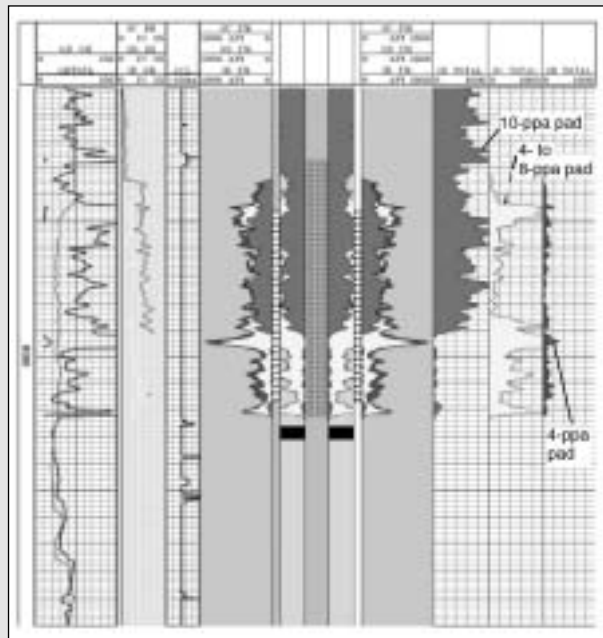


**Figure 11F-2.** Proppant placement following a fracturing treatment determined by radioactive tracers. Approximately 15 ft of the 50-ft perforated interval has proppant from the early stages close to the wellbore. If only the last stage had been treated with proppant flowback control material, proppant production might have occurred.

N<sub>2</sub> is inert and relatively immiscible in the fluid when added in small amounts and without a surfactant. CO<sub>2</sub> is soluble in water and becomes a reactive component in the fracturing fluid. CO<sub>2</sub> can be converted to carbonic acid, which lowers fluid pH values and can be incompatible with fracturing fluids.

A large percentage of CO<sub>2</sub> goes into solution at typical reservoir conditions, which can be advantageous. As a dissolved gas, CO<sub>2</sub> does not easily dissipate into the formation. During flowback, the dissolved gas evolves from the mixture and imparts a solution-gas drive to the fracturing fluid.

Energized fluids should be flowed back as soon as possible while the fluid retains high pressure; however, shut-in times of up to 4 hr can be tolerated without a great loss in the energizing medium.

## 11-8. Quality assurance and quality control

The principal factor in the successful performance of a fracturing operation is the incorporation of quality assurance and quality control (QA/QC) into all phases of the fracturing operation. This can be achieved by the implementation of a quality management system that encompasses all personnel and activities.

A significant effort is made in the design process to determine an optimum fracturing treatment. An equal effort in QA ensures that the treatment is executed as designed. Simple QA steps can greatly increase the odds of success for a hydraulic fracturing treatment.

## 11-9. Health, safety and environment

### 11-9.1. Safety considerations

At no time should the safety aspects of a treatment be compromised. Safety guidelines have been developed from experience derived from previous incidents. Many of these incidents have had great potential to seriously injure personnel or destroy valuable equipment. The inherent risk of dealing with high pressures can be greatly minimized by following simple safety procedures. Hydraulic fracturing treatments can never be considered a success if an accident results in the destruction of equipment or injury to personnel.

- **Personal safety equipment**

Each person on location should wear appropriate safety equipment to minimize the risk of personal injury. Hard hats, hard-toed shoes and safety glasses should be the minimum level of safety equipment worn on location. Other equipment such as hearing protection, goggles, fire-retardant fabrics and filter masks should be worn if exposure to the conditions they protect against is a possibility. Wearing safety equipment is a simple step that creates a positive safety atmosphere on location.

- **Safety meeting**

Holding a pretreatment safety meeting ensures that all personnel on location are aware of specific dangers and required procedures relative to the treatment. Each person on location should clearly understand his or her role during the treatment as well as individual responsibility during emergency situations. A head count must be taken to account for everyone on location. An escape route and meeting place should be agreed upon where all personnel will gather in the event of an emergency situation. Personnel who are not directly involved in the treatment should have limited location access during the actual pumping operations.

Everyone should be aware of the unique dangers of each treatment. Some locations may be in an area with hydrogen sulfide (H<sub>2</sub>S) or possibly the fluids being pumped are highly flammable. As many of the potential safety problems or concerns as possible should be brought to the attention of everyone.

Maximum pressure limits should be set at this time, and every high-pressure pump operator must be aware of these limits. Instructions for pressure testing the treating iron must also be covered. The high-pressure treating line, up to the wellhead valve, should be tested to slightly above the anticipated fracturing pressure. A properly tested line includes tests of each pump in addition to the main treating line. The pressure rating of the wellhead should be checked to make sure it exceeds the treating pressure. If the wellhead has a lower pressure rating than the anticipated treating pressure, a wellhead isolation tool will be necessary to isolate the wellhead from this pressure level.

The pretreatment safety meeting is the principal means of communication for giving final instruc-



tions to all personnel. A well-organized safety meeting helps ensure that the treatment is an operational success without being a threat to human safety.

- Well control at the wellhead

To ensure that well control is always maintained, the valve arrangement at the wellhead should consist of at least two valves. A frac or master valve should be installed above the main wellhead valve. If one valve fails to hold the pressure, the other valve can quickly be closed to control the well. It is preferable to have the main wellhead valve flanged to the casing head, rather than using a threaded connection. If a threaded connection is necessary, the condition of the threads must be thoroughly inspected for thread wear and proper taper.

- Precautions for flammable fluids

Oil-base fluids should be tested for volatility before they are accepted as a fracturing fluid. An oil is generally considered safe to pump if it has a Reid vapor pressure less than 1, API gravity less than 50° and open-cup flash point of 10°F [−12°C]. However, even if the fluid is considered safe to pump, several additional safety rules should be followed when pumping an oil.

Storage tanks for flammable fluids should be diked and spotted at least 150 ft from the wellhead. Spotting the fluids in this manner helps minimize exposing the wellhead to fire if problems occur during pumping. Also, all low-pressure hoses should be enclosed in a hose cover to prevent oil from spraying on hot engine components of the trucks, should a hose leak.

Care must be taken to ensure that there is no smoking on location. It is a good idea to have all personnel check matches and lighters when they arrive on location to prevent them from unintention-

ally lighting up. Finally, fire-fighting equipment should be on location and ready to be operated. In this way, a small fire may be contained before it has a chance to spread and become a major disaster.

- Precautions for energized fluids

N<sub>2</sub> and CO<sub>2</sub> are the gases most commonly used in foamed and energized fluids. During flowback following a treatment, they provide an efficient source of concentrated energy to aid rapid, more complete post-treatment cleanup. There are potential hazards associated with the use of N<sub>2</sub> and CO<sub>2</sub>. As the fluid exits the flowline during flowback, the gaseous phase expands rapidly. This rapid release of energy must be controlled to avoid a loss of flowback efficiency and to ensure personnel safety. Service companies have recommended procedures for the flowback of energized fluids.

Another potential hazard that is often overlooked is asphyxiation. N<sub>2</sub> and CO<sub>2</sub> can collect in low areas, displacing breathable air. Personnel should avoid these areas and remain upwind at all times. Only one person should be in the vicinity of the well during flowback operations. The use of remotely operated valves will increase the margin of safety.

## 11-9.2. Environmental considerations

Fracturing operations should be conducted using sound environmental practices to minimize the potential for contamination of air, water and soil. All operations should comply with all applicable environmental laws and regulations.

Hazardous material spills should be cleaned up quickly in accordance with a spill plan. All waste and unused materials should be handled and disposed of in an environmentally safe manner.

# Appendix: Understanding Perforator Penetration and Flow Performance

Phillip M. Halleck, Pennsylvania State University

## Introduction

The productivity of a cased, perforated well can depend to a large extent on perforation practices. Modern shaped charge perforators can penetrate for some distance into the formation, overcoming both drilling damage and restricted flow through the perforated casing. However, perforated completions frequently do not flow as predicted. Penetration differs from that in certification and quality control tests, owing to both the character of the formation rock and the in-situ overburden stress. In addition, laboratory tests (Allen and Worzel, 1957) demonstrate that perforation tunnels are commonly completely filled with debris, and even debris-free perforations may not flow as predicted from pretest permeability measurements.

Although most relevant to natural completions, the perforating procedure and the condition of the resulting perforations may affect the performance of post-perforation operations such as fracturing or gravel packing. In hydraulic fracturing, acid can be used to lower breakdown pressures, presumably because of some form of perforation damage. The orientation of perforations has also been shown to affect breakdown pressure and well performance. For fracture treatment design, the interpretation of pretreatment well tests requires knowledge of the skin resulting from penetration and perforation damage effects. During gravel-packing operations, excessive underbalance in unconsolidated formations may actually reduce flow efficiency by damaging the rock (Behrmann *et al.*, 1992).

The factors involved in perforation damage may include mechanical shock damage to the formation, deep filtration of fines from the wellbore or the formation, rock and charge debris in the perforation tunnel and multiphase flow effects. Two perforating techniques have evolved to avoid or bypass perforation damage. These are underbalance perforating and extreme overbalance perforating (EOP). For more comprehensive discussions of the field application of these techniques, the reader is referred to

Section 11-3 and the excellent monograph on perforating by Bell *et al.* (1995).

Underbalance perforating has evolved from its early purpose of preventing the infiltration of wellbore fluids to a method for removing shock-induced permeability damage. Surge flow from the reservoir into the wellbore is thought to clean loose debris from the perforation and flush the rock around the perforation to restore permeability. Although effective for certain specific applications, questions remain regarding the limits of its usefulness and the minimum underbalance and surge flow volume required to obtain maximum well performance. Answers to these questions can be sought from combined field experience, laboratory measurements and models of perforation cleanup mechanics.

The review provided by this Appendix consists of a brief discussion of penetration depth, experimental observations of the surrounding rock, models for the mechanism of underbalance surge cleanup, description of laboratory experiments that reveal the time scale and flow volume required for cleanup and a closing discussion of ancillary effects on perforation performance.

## Review of penetration depth prediction

Penetration depends on the character of the target rock formation, effective overburden stress (Saucier and Lands, 1978) and, in extreme cases, wellbore pressure (Behrmann and Halleck, 1988). In Berea sandstone, penetration can be reduced by as much as 50% with the application of 3000-psi effective overburden stress (Halleck *et al.*, 1988). More typical reductions are on the order of 20%. Little additional reduction occurs for effective stresses higher than 3000 psi. The nature of the rock affects both penetration and the extent of the stress effect. Higher strength leads to lower penetration. Conversely, stress

affects penetration less in harder rocks. Thus, penetration data obtained from a single target material under atmospheric conditions do not reflect actual hole penetration. The API standard test (Halleck, 1987, 1988; Section 2 of *Recommended Practices for Evaluation of Well Perforators*, [RP 43] 1991) in Berea sandstone at 3000-psi effective stress provides a better estimate.

Uniaxial compressive strength has long been used (Thompson, 1962) to correlate ambient-stress penetration. This approach is complicated by the lack of a comprehensive penetration theory incorporating target strength, by the change in rock strength with effective stress (Halleck and Behrmann, 1990) and by active target effects in some rocks (Aseltine, 1985), which are not explained by conventional penetration theory. An attempt was made (Ott *et al.*, 1994a) to use laboratory data to predict downhole penetration from API RP 43 Section 1 certification data. The resulting nomogram provides a simple method for estimating downhole penetration in lieu of costly tests in stressed reservoir rock. The method relies on a series of empirical correlations among compressive strength, porosity and penetration in rock and concrete targets at atmospheric pressure, combined with data in stressed rock targets. Normalization of the data at 3000 psi, combined with statistical scatter in each of the successive correlations used, may lead to substantial errors (Colle *et al.*, 1994; Ott *et al.*, 1994b), particularly at effective stresses less than 3000 psi.

An alternative for penetration estimates is acoustic log data based on direct relations between penetration and dynamic elastic moduli in stressed rock. Originally proposed by Venghiattis (1963), subsequent data (Halleck *et al.*, 1991) largely support the idea that differences in acoustic velocity resulting from rock composition and overburden stress mimic differences in shaped charge penetration.

Because of symmetry requirements, manufacturing tolerances for shaped charges are necessarily strict at all stages. Small variations in dimensions and heterogeneities in the explosive or liner density can cause disproportionate variations in penetration performance. As a result, each charge type displays a statistical variation in measured penetration depth. Sukup *et al.* (1989) reviewed quality control testing methods that can be used to ensure good reliability. King *et al.* (1986) investigated additional factors that can affect charge performance, including storage duration and environment.

## Permeability damage and flow performance

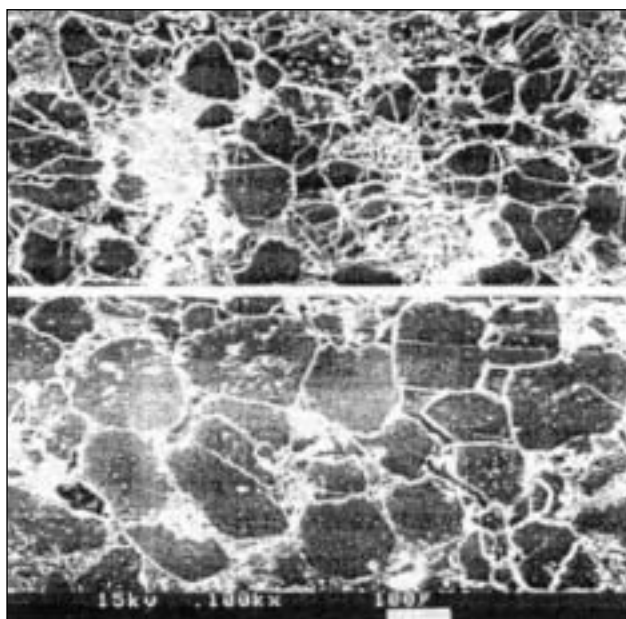
### Idealized view

Most discussions of perforation damage refer to debris in the perforation tunnel and a crushed zone surrounding the tunnel. The tunnel debris consists of broken rock, jet metal, explosive products (mostly carbon) and other charge debris. If sufficient underbalance or production flow occurs, this debris is removed, leaving a clean tunnel. In well productivity models (Locke, 1981; Tariq, 1984; Ahmed *et al.*, 1990; Behie and Settari, 1993), the perforation is usually treated as a circular cylinder surrounded by a zone of reduced permeability variously called the crushed or compacted zone. The zone is usually given (Bell *et al.*, 1972) as 0.4 to 0.5 in. thick with permeability on the order of 0.1 to 0.2 times the original rock permeability.

In reality, the diameter varies along its length, tapering toward the tip, and depends on the rock properties and charge design. The damaged zone is easily visible in perforated samples as lighter colored material around the tunnel. Microscopic examination reveals considerable grain breakage in this zone, resulting in reduced permeability as the grain-size distribution broadens and shifts to smaller diameters. Reduced porosity is also thought to play a role.

Pucknell and Behrmann (1991) confirmed earlier observations made with optical microscopes that reveal broken grains in this zone. Asadi and Preston (1991) used scanning electron microscopy (SEM) to estimate permeability damage from the size distribution of the broken grains. Appendix Fig. 1 illustrates this type of data with a comparison of SEM photos at 0.1 and 0.4 in. from the center of a perforation in Berea sandstone performed using underbalanced, liquid-saturated conditions.

Attempts to predict the extent of damage have also been made. Yew and Zhang (1993) applied the method of characteristics to obtain a solution for the amplitude of the shock waves resulting from the impact of a shaped charge jet. They assumed cylindrical radial loading and included poroelastic effects. They confirmed that stress wave amplitude falls off rapidly away from the perforation tunnel, although they did not address the specific amplitudes expected. Papamichos *et al.* (1993) used this solution to estimate the extent of grain breakage expected from such stress



**Appendix Figure 1.** Scanning electron microscope images of perforated Berea sandstone at 0.1 (top) and 0.4 in. (bottom) from the center of the perforation.

waves, taking into account the stress amplification that occurs at contacts between sand grains. They noted that grain breakage also decreases sharply away from the perforation and that this can theoretically be related to permeability. A different approach is to predict grain breakage using a smooth particle numerical model.

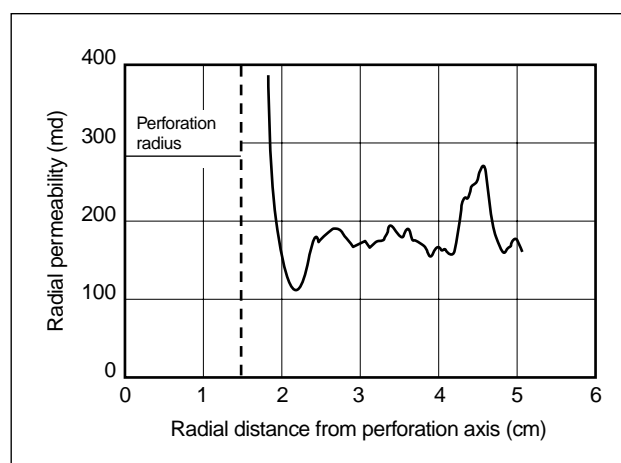
## Laboratory view

Careful laboratory examination has redefined our understanding of perforation damage. As discussed in the following, several lines of evidence show that permeability damage is not necessarily related only to the visible crushed zone adjacent to the tunnel wall. The material adjacent to an open perforation is not highly compacted, at least in liquid-saturated sandstones, and shows little consistent permeability reduction. Instead, reduced permeability is observed outside this crushed zone extending 0.1 in. or more from the tunnel. Permeability damage is not uniform along the length of the perforation but is thicker and more severe near the entrance hole. Mechanical damage patterns also reflect this observation. There is some qualitative evidence for the mobilization of clay particles, which may plug the formation as they are swept toward the perforation.

Pucknell and Behrmann (1991) measured the radial pressure profile in 2-in. long sections of perforated core during steady-state radial flow. They used five probes at one end of each 4-in. diameter core. Although the spatial resolution was limited, evidence for greatly reduced permeability near the perforation was not found consistently. They also observed no qualitative evidence of compaction in their X-ray computer-aided tomography (CT) images.

Rochon *et al.* (1995) used pressure transient analysis in a similar short section of perforated core to measure radial variations in permeability as  $k(r)$ , where  $k$  is the matrix permeability in md and  $r$  is the distance from the center of the perforation in cm. They injected light oil into the perforation and followed it with a constant-flow-rate injection of a more viscous oil. Analysis leads to an expression for  $k(r)$  in terms of the viscosities of the fluids  $\mu_1$  and  $\mu_2$ , the flow rate  $q$  and the ratio of the differential pressure to time  $\Delta p/\Delta t$ . The position of the front between the two fluids must be calculated as a function of time from the flow rate and previously measured porosity. They found that the region near the perforation tunnel had permeability reduced only 20% from the original. Permeability was reduced by about 70% in a zone from 0.2 to 1.2 in. from the perforation tunnel wall. Appendix Fig. 2 is a reproduction of one of their permeability profiles.

Ramlakhan (1994) combined this method with X-ray CT to study a complete perforation. Using X-ray CT to map the position of the interface between the two fluids eliminates the need to calculate the interface position from the volume of tracer injected. Measurements can be taken over the entire length of

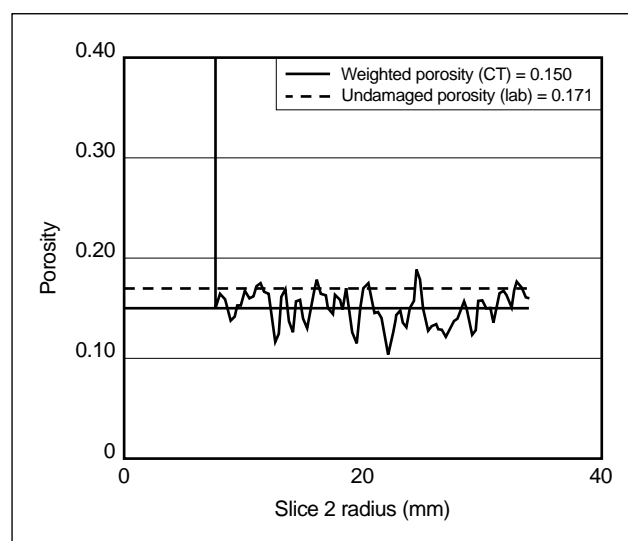


**Appendix Figure 2.** Permeability profile obtained using viscous flow transients (Rochon *et al.*, 1995).

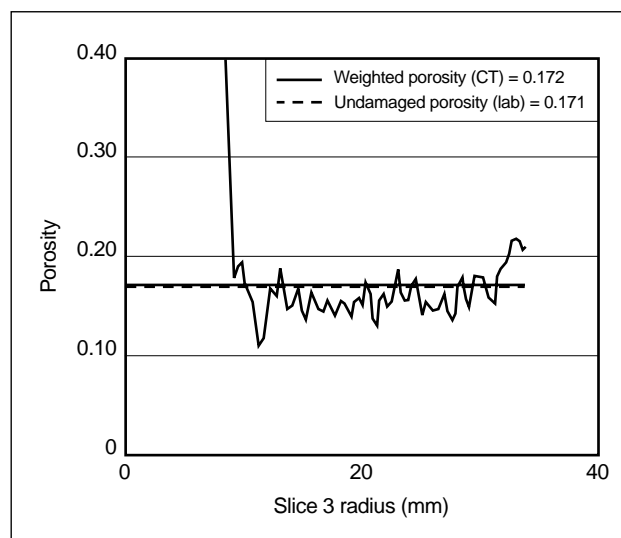
the perforation, even where permeability varies along its length. X-ray CT data were also used to determine the local porosity. This provides both a quantitative map of shock-induced compaction and data to calculate local flow rate and flow velocity. Methods similar to those described by Withjack (1987) were applied after processing the images for beam hardening caused by the pressure vessel.

Appendix Fig. 3 shows porosity results for a Berea sandstone core perforated at 1500-psi underbalance and 3000-psi effective stress with a 3.2-g charge. Although the porosity varies considerably, there is no evidence of a well-defined compacted zone near the tunnel wall. Appendix Fig. 4 shows a porosity profile at a point near the tip of the perforation. There is no open tunnel, and parts of the metal jet remain surrounded by shock-damaged rock. The radial extent of this damaged rock is consistent with the radius of the tunnel at shallower depths, and it is probable that sufficient underbalance would have loosened and removed this material to form an open tunnel. The porosity profile shows that the material is compacted, with porosity reduced from 0.18 to about 0.12. Rock beyond this is at the original porosity.

The extent of porosity reduction is a function of the pore fluid present at shot time. The vast majority of perforation flow tests have been performed in liquid-saturated rocks. As noted previously, compaction is limited to the volume of rock and charge debris that would be swept out if sufficient surge flow occurred. However, experiments by Bird and Dunmore (1995) in gas-saturated rock samples indicate that the high



**Appendix Figure 3.** Porosity profile adjacent to an open perforation tunnel was obtained from X-ray CT data.

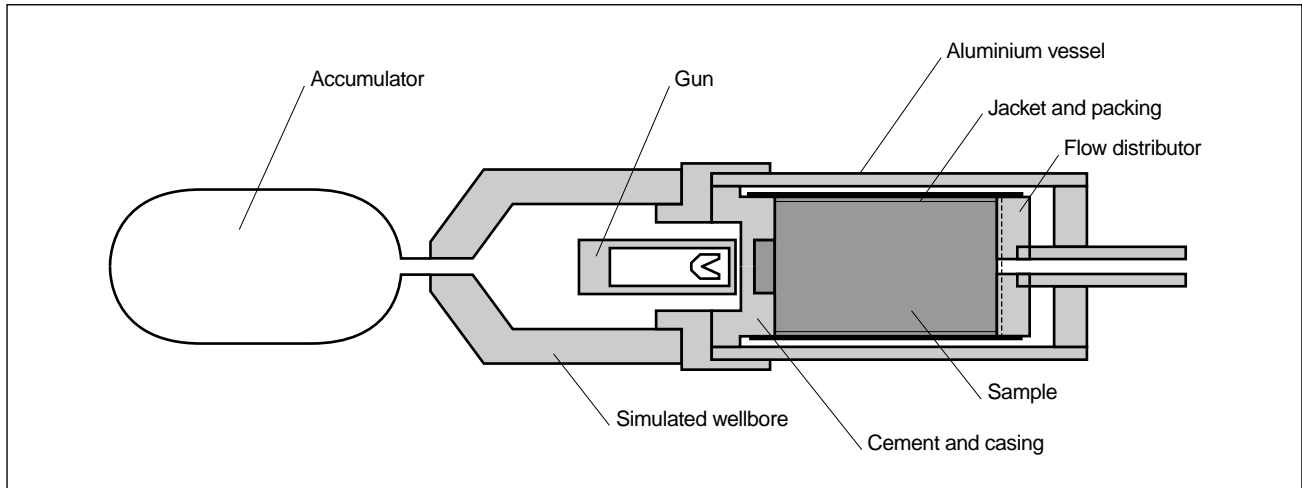


**Appendix Figure 4.** Porosity profile near the tip of a perforation containing charge and rock debris.

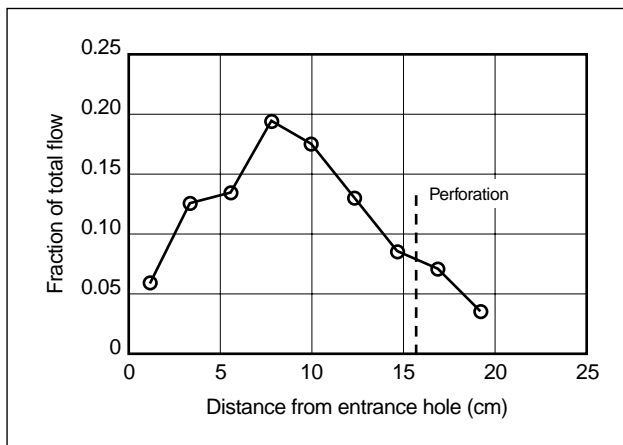
compressibility of the pore fluid in this case allows the porosity near the perforation to be largely destroyed.

X-ray CT analysis has also demonstrated that permeability damage is not distributed uniformly along the length of the perforation. Halleck *et al.* (1992) reported results of flow experiments performed in an X-ray-transparent vessel (Appendix Fig. 5). A 6.5-g charge was used to perforate a Berea sandstone core at 1500-psi effective stress and 500-psi underbalance. After flushing the perforation with 20 L of odorless mineral spirits (OMS) at 20 cm<sup>3</sup>/s, a di-iododecane tracer was substituted for the OMS. The entire sample was scanned at 0.25-in. intervals after 100 cm<sup>3</sup> of tracer and after an additional 50 cm<sup>3</sup> of tracer. The first 100 cm<sup>3</sup> of tracer saturated the porous packing around the core and started to flow into the sample. The permeability of the porous packing (20/40-mesh bauxite proppant) is on the order of 100 darcies at these confining stresses. At this low flow rate the pressure drop through the porous packing is negligible, and the fluid pressure applied to the exterior of the core is assumed to be uniform along its length.

Appendix Fig. 6 illustrates the profile of the radial advance of the flow found along the length of the core. The profile was obtained by measuring the radial advance of the flow front that took place during the second (50-cm<sup>3</sup>) tracer injection. The data have been corrected for decreasing circumference as the front moves inward to obtain an average local flow rate. Very little advance is seen near the entrance hole. The majority of flow takes place along the center of the



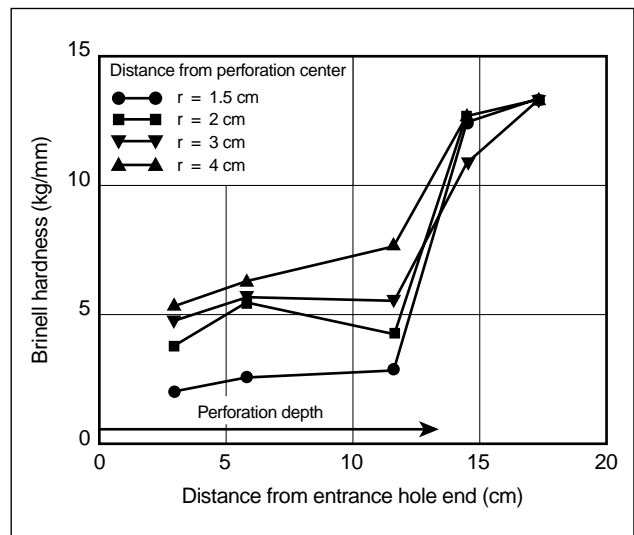
**Appendix Figure 5.** Apparatus for X-ray CT observations of perforation flow.



**Appendix Figure 6.** Profile of flow rates along the length of a perforation was obtained by X-ray CT observations.

open perforation tunnel. Little flow is observed near the perforation tip, where deformed rock and liner metal have not been removed. The permeability distribution appears to depend on specific factors such as the character of the rock and the underbalance conditions. Other (unpublished) tests show more flow near the entrance hole.

Evidence for damage at some distance from the perforation comes from indentation hardness data. Halleck *et al.* (1995) presented data based on the method of Santarelli *et al.* (1991) for mapping hardness around a perforation in a weak sandstone. Appendix Fig. 7 shows that mechanical weakening extends to the boundary of the 4-in. core. Similar unpublished data from a 15½-in. diameter core show that damage extends several inches and is not caused by boundary effects. Appendix Fig. 7 also shows that



**Appendix Figure 7.** Map of indentation hardness around a perforation in a weak sandstone.

damage is more severe near the entrance hole than near the tip. Although there is no direct evidence linking mechanical weakening and permeability damage, the pattern observed is consistent with the radial and axial permeability distributions illustrated previously.

## Role of underbalance in improved perforation flow

The flow efficiency of a perforated core has been shown to depend on the difference between the reservoir and wellbore pressures at shot time. Underbalance perforating has become a standard practice

based on the work of Bell (1984) and others. Underbalance surge flow is thought to improve perforation flow efficiency in three ways:

- Surge flow prevents the invasion of wellbore fluids and fines during the period between perforating and drawing down the well to start production.
- Surge flow removes some or all of the debris from the tunnel.
- Surge flow removes some or all of the matrix permeability damage from the rock surrounding the tunnel.

The procedure has been proved generally effective in the field. For specific applications, questions remain as to what degree of underbalance is necessary, what surge flow volume is required and whether the procedure is effective in a particular situation. Techniques to address these questions are provided in the following section.

## Laboratory and field observations

Early laboratory studies (Bell *et al.*, 1972) suggested that 200-psi underbalance was sufficient to clean a perforation in 200-md Berea sandstone, and test procedures in the fourth edition of API RP 43 (1985) were based on this number. Later, Halleck and Deo (1989) showed that the initial flow performance was only 40% of that expected until an underbalance in excess of 500 psi was applied. About 1500-psi underbalance was required to ensure a perforation with 100% of its expected flow. They also showed that production flow, even at high rates, could not completely clean the perforation if insufficient underbalance was used initially.

As part of an extensive API-sponsored project (Halleck, 1989, 1990), a different test procedure (RP 43 Section 4, 1991) was developed that better simulates in-situ conditions. This procedure provides for radial flow into the perforation and is performed under hydrostatic pressure to simulate overburden rock stress. An accumulator is attached to the wellbore chamber to simulated wellbore storage effects.

The radial flow boundary condition is based on the ambient stress tests of Regalbutto and Riggs (1988). They suggested that in-situ perforations experience this type of flow rather than that associated with the earlier (RP 43, 1985) tests, which applied pressure only to the rear of the test core. Deo *et al.* (1989) used

a finite-element simulation of wellbore flow with idealized perforations to show that the actual flow depends on shot spacing, phasing and degree of drilling and perforation damage. Typical cases lie between the radial and axial boundary condition tests. The modified test procedure thus allows for either condition and can be changed to produce intermediate conditions.

Using a form of this procedure, Hsia and Behrmann (1991) found a generally monotonic increase in core flow with increasing underbalance. They confirmed that for 200-md Berea sandstone, approximately 1500 psi was required to obtain a free-flowing perforation. This is consistent with the earlier axial boundary-condition data of Halleck and Deo (1989), suggesting that the applied pore pressure boundary conditions have little effect on surge cleanup.

King *et al.* (1986) compiled field data to correlate the effectiveness of acid stimulation in wells with formation permeability and perforating underbalance. They found a strong relationship among formation permeability, underbalance used and effectiveness of later acid treatment. It is assumed that if acid has no effect, the underbalance used was sufficient to clean the perforation. Although the cause and effect relationship is not clear, the data strongly suggest that lower permeability rock requires higher underbalance. The minimum underbalance predicted by these data is less than for laboratory tests. The laboratory tests seek conditions for zero skin whereas the field data are based on conditions for which acid did not improve the well. The latter may not actually represent ideal perforation flow.

## Models

To extend these results to a wider range of formations and to make them reliable as practical guidelines, the mechanics behind underbalance perforating must be placed in a firmer theoretical foundation. Tariq (1990) began this effort by hypothesizing that cleanup occurs when the velocity of transient flow in the rock surrounding the perforation reaches a critical value. He suggested that the Reynold's number (as defined for porous media) is the appropriate parameter. Using a finite-element model for perforation flow, he concluded that the critical Reynold's number is about 0.05.

To illustrate how the basic model functions, consider a 4-in. diameter test core with a debris-free perforation. If the pressure in the perforation is instantana-

neously lowered to simulate an underbalance surge, the pressure profile in the core can be calculated as a function of time. This is illustrated using a simple radial flow numerical model in Appendix Fig. 8 for the particular case of a 200-md sample containing 1.8-cp fluid with 1000-psi underbalance.

The pressure gradients at early times are steep and associated with equally high flow rates. However, these high rates persist briefly and are present only near the walls of the perforation. Appendix Fig. 8 shows the maximum Darcy velocity (ignoring inertial effects) as a function of radial position. Only rock within 4 cm of the perforation experiences rates above 0.005 m/s.

How do these transient flows clean a perforation? Rerunning the model with a zone of reduced permeability  $k_c$  at the tunnel wall illustrates this. For this case  $k_c$  was reduced to  $0.2k$ , as is commonly assumed. This would result in about 0.4 times the ideal flow rate if the damage were not removed. The reduced

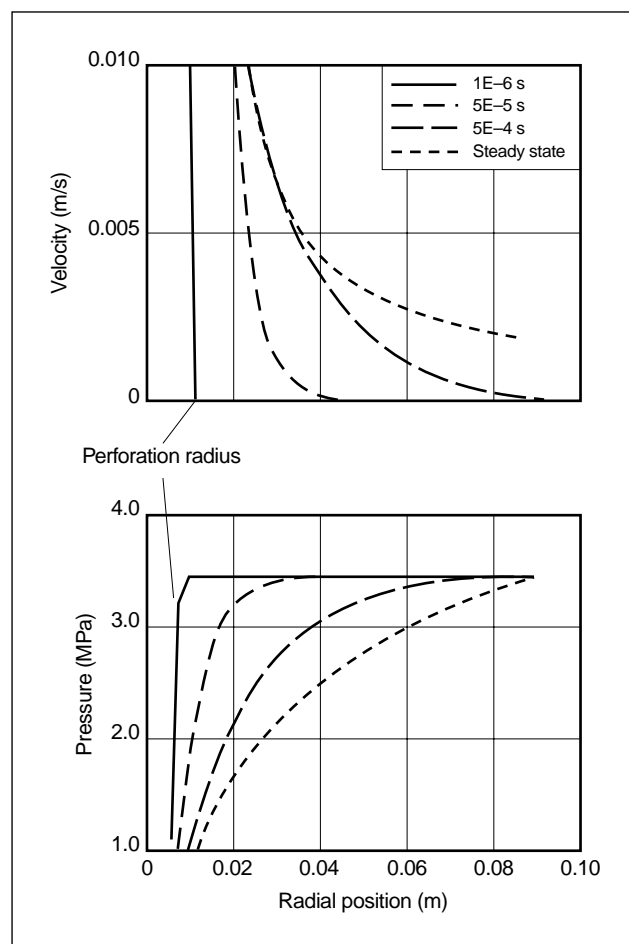
permeability lowers the transient velocity  $v_c$  from the matrix velocity  $v_m$ .

The model checks at each time step to determine whether flow in a particular element has exceeded a predetermined critical value. If so, permeability for that cell is increased back to the undamaged value. The progress of this cleanup can be followed with time. When each cell is cleaned up, the pressure gradient and flow rate in the adjacent cell are increased. If the resulting velocity is high enough, this cell may then also be cleaned up. The process stops either when all cells have been cleaned or at the radius for which velocity no longer reaches the critical value. The series of plots in Appendix Fig. 9 illustrates the progress of the cleanup with the critical flow rate based on a Reynold's number of 0.1. In this case the cleanup process terminates with some of the damage remaining. The plots show the maximum flow rate and the corresponding permeability profile with time. Higher underbalance would have resulted in cleanup of the remaining damaged zone.

The underbalance for cleanup thus depends on the required critical velocity, permeability of the damaged and undamaged rock and thickness of the damaged zone. A series of test cases for different rock permeabilities was performed using the model, varying the underbalance to find the underbalance required for complete cleanup in each case. The results are plotted in Appendix Fig. 10 with the original data of King *et al.* (1986). The trends are similar, although the model does not coincide with the field data. This may be due to a number of factors:

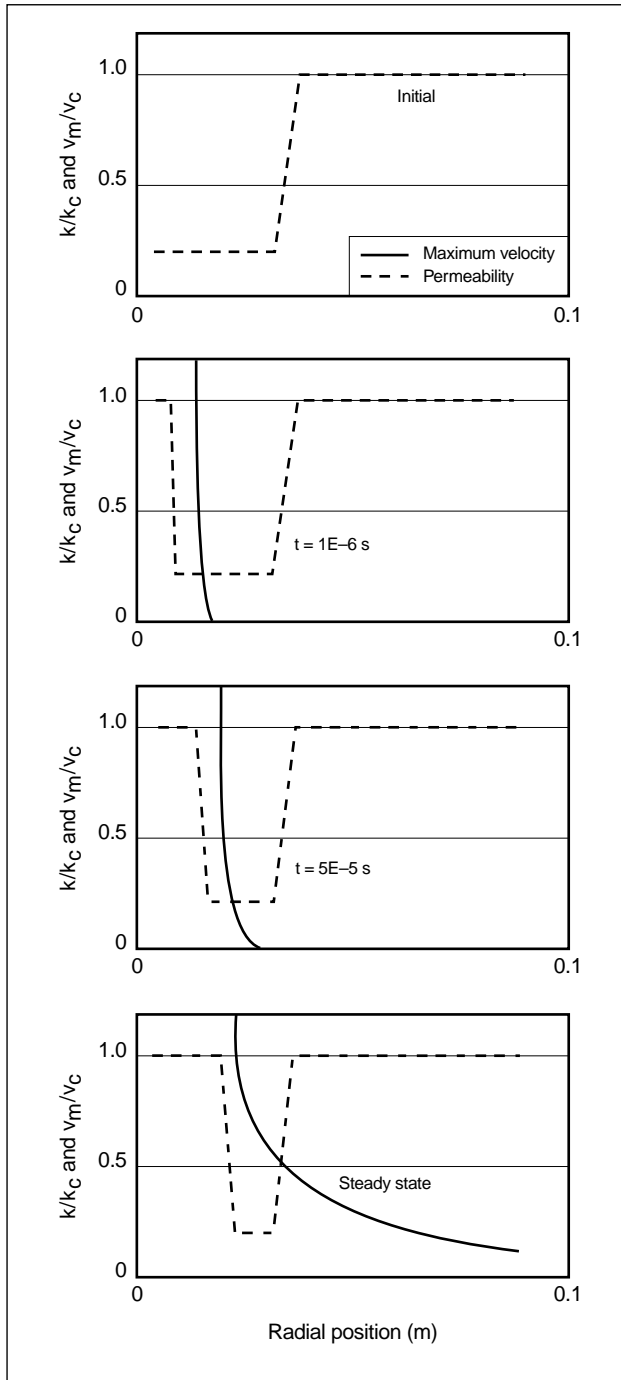
- Lack of flow improvement after acid treatment in the field may not actually indicate that perforations were clean prior to the treatment.
- Range of fluid viscosities in the field may differ from that used in laboratory experiments.
- Critical velocity was incorrectly assigned.
- Unrealistic damaged zone properties and geometry were assumed by the model.

The model assumes instantaneous pressure drop in the tunnel, implying that charge debris and damaged rock have already been removed. In reality, the time frame for reduced pressure in the perforation must be on the order of a millisecond. The penetration itself takes on the order of  $10^{-4}$  s, and flow through a debris-filled tunnel cannot lower the pressure much faster than that. An improved model must also take into



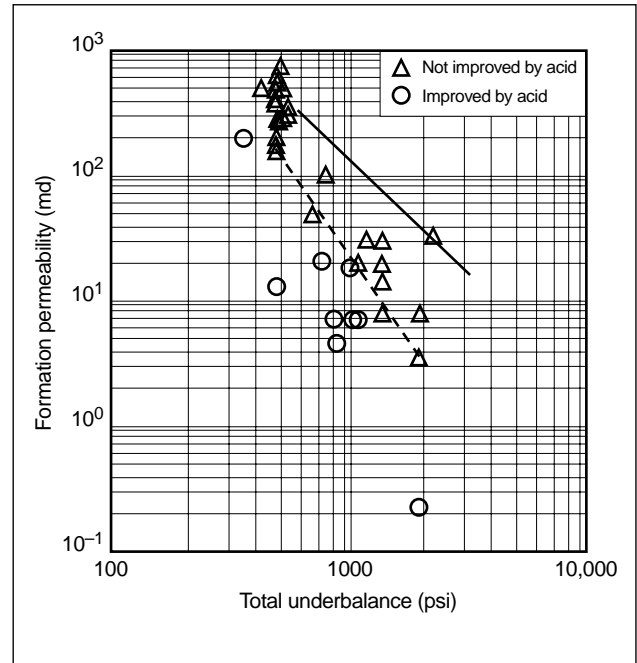
**Appendix Figure 8.** Transient flow rates and pressures for cylindrical inward flow into an ideal perforation.





**Appendix Figure 9.** Cleanup of the reduced-permeability zone around a perforation by high-velocity transient flow.

account the effects of rock remaining in the tunnel as well as its removal. Additional model runs have been made in which pressure in the tunnel is lowered during a 1-ms period (Appendix Fig. 11). Although there is some effect on cleanup, the basic results are unaffected.

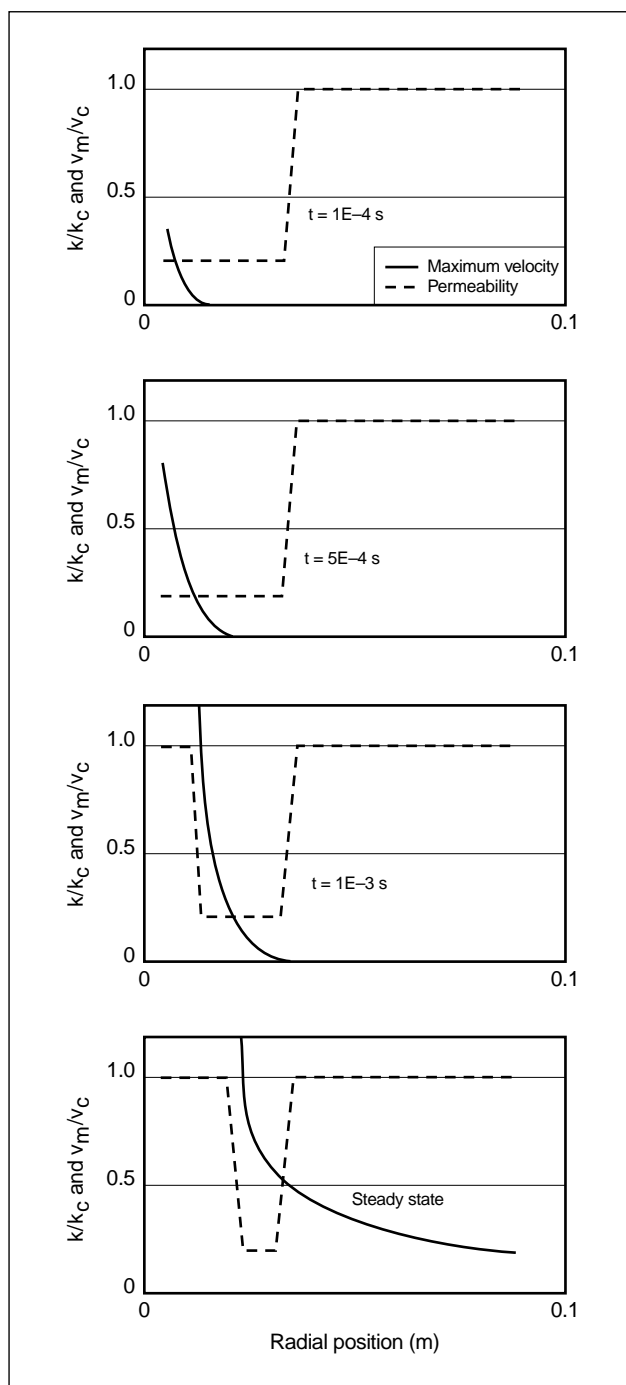


**Appendix Figure 10.** Minimum underbalance required for complete cleanup based on numerical model and Tariq's (1990) Reynold's number criterion.

There are a number of additional difficulties with this simple model. First and foremost is whether Reynold's number should be used to establish critical flow velocity. To begin with, the definition of Reynold's number is controversial. The most commonly accepted method is to use the ratio  $\beta/\alpha$  to describe the length dimension:

$$N_{Re} = \frac{\beta}{\alpha} \frac{\rho v}{\mu}, \quad (1)$$

where  $\alpha$  and  $\beta$  are the coefficients in the Forchheimer equation,  $\rho$  is the density,  $v$  is the flow velocity, and  $\mu$  is the viscosity. Using this equation requires knowledge of both  $k(1/\alpha)$  and  $\beta$  for a given rock. Because these data are seldom available, empirical correlations between  $\beta$  and  $k$  are used. Such correlations are generally of the form  $\beta$  proportional to  $k^{-m}$ . The value of  $m$  varies considerably in the literature. Tariq (1990) used a value of 1.65, but a more widely accepted value of 1.2 results in a much steeper curve in Appendix Fig. 10, which fails to reproduce the field data. In addition, these correlations are based on intact rock and may not apply to the damaged rock around the perforation. Finally, the use of Reynold's number implies that minimum underbalance should also



**Appendix Figure 11.** Cleanup while the pressure in the tunnel is lowered during a 1-ms period.

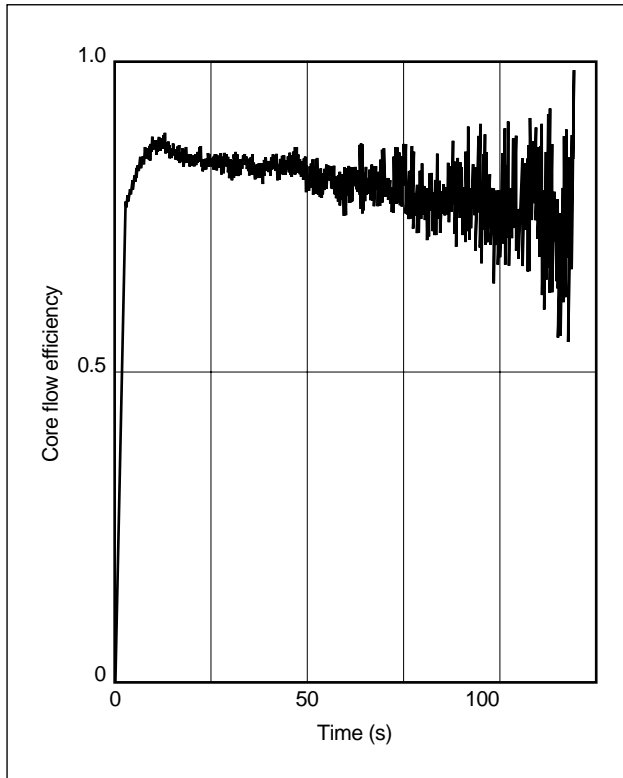
depend on fluid viscosity. Although this is true in the model, it is not supported by King *et al.*'s field data. Data from laboratory tests (L. A. Behrmann, pers. comm., 1997) also suggest that viscosity is not an important factor in determining minimum underbalance for fluids between 1.5 and 400 cp.

In an effort to resolve problems associated with the use of Reynold's number, Behrmann (1995) introduced a cleanup criterion based on the drag force on a particle in a stream of fluid. By using an adjustable shape factor, Behrmann was able to match the observed field data and eliminate the dependence on viscosity. In addition, model improvements such as fully three-dimensional finite-difference simulations (Y. Dogulu, pers. comm., 1996) allow the study of anisotropic, non-Darcy transient flow, including that through the tunnel debris, as well as comparison of different cleanup criteria to investigate the effects of nonuniform damage.

### Synergy of models and experiments

One implication from modeling is that if cleanup is to occur, it must be during the short duration of high-rate transient flow. Evidence comes from the data of Bartusiak *et al.* (1997), who used a modified RP 43 test procedure to include simulation of the fluid capacity and the impedance of the reservoir itself. In conventional testing, the surge flow volume is limited to decompression of the fluids in the pore structure of the sample and associated pore pressure plumbing. In the revised system, an accumulator attached to the sample maintains constant far-field reservoir pressure during surge flow. This pressure is applied to the sample through a series of auxiliary cores that simulate the flow impedance of the rock surrounding the well. The result is a more realistic simulation of downhole conditions during perforating.

The simulated reservoir also allows an indirect measurement of flow rate through the perforation during the surge flow process. By measuring the transient pressure drop across the simulated reservoir, the flow rate through it can be determined from its known impedance. After pseudosteady-state conditions are attained, the flow rates through the two are approximately equal. With proper calibration, this leads to a real-time measurement of the flow rate starting about 0.3 s after detonation. The measurement in turn can be converted to time-resolved values of core flow efficiency (CFE) by dividing the result by the predicted ideal flow rate. Appendix Fig. 12 illustrates the development of CFE with time for a test in Berea sandstone at 1500-psi underbalance. The CFE rises sharply in the first second to 0.8, increases to about 0.85 over the next few seconds and then remains



**Appendix Figure 12.** CFE development with time for a test in Berea sandstone at 1500-psi underbalance.

constant. This value is consistent with quasi-static flow tests performed later with conventional procedures. Another test in the series shows that reducing the total flow volume, by reducing the wellbore storage volume, had little effect on this process. These results support the idea that cleanup occurs at early times, when transient flow rates are highest. The practical result is that it should not be necessary to design the completion procedure for a minimum surge volume if sufficient underbalance is applied.

## Other phenomena

Several additional perforating phenomena are worthy of mention. These are residual stresses, damage to natural fissures or fractures, injection of detonation gases into the formation and wettability effects.

### Residual stresses

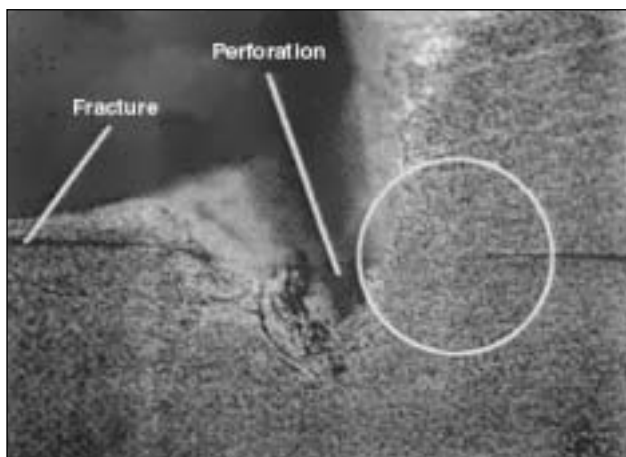
Perforations in porous rocks are left with a compressive residual stress surrounding the tunnel. This is caused by shock waves that decrease in amplitude

as they move radially away from the perforation. Rock near the perforation is stressed to failure and flows with pseudo-plasticity, whereas rock farther away remains elastic. After the shock dissipates, the failed material returns to an elastic state, although with a lower strength. The net effect of the permanent plastic displacement is a zone of rock that remains under compression even after the shock dissipates. This phenomenon has been frequently observed in the laboratory. Perforated cores encased in steel sleeves are observed to fracture when the steel sleeve is cut open. Similarly, in a pressurized core, no fractures are observed after perforating at 6000-psi overburden pressure. The core subsequently fractures when the stress is reduced to about 250 psi. Radial fractures are frequently observed in samples recovered from such pressurized tests. Although they are usually assumed to be hydrofractures, closer examination reveals that the widest part of the fracture is at the outside of the core rather than at the perforation, suggesting that the fractures grew inward when the overburden pressure was released.

The residual stress may be partly responsible for reduced flow efficiency as well as for the excessive breakdown pressures observed during some hydrofracture treatments. Warpinski (1983) found such effects in field tests in a mineback experiment in welded tuff and suggested that residual stresses may be responsible. The effects are not well understood, and further experimental and theoretical studies are needed.

## Damage to natural fractures

Ideally, if a perforation intersects a natural fracture and a connection is formed between the fracture system and the wellbore, permeability damage to the walls of the perforation would not matter because the flow would bypass any damage via the fracture system. However, laboratory data (Halleck, 1996a, 1996b; Halleck *et al.*, 1996) show that perforating can damage fracture permeability in two ways. Under some circumstances, jet metal can invade the fracture and reduce its conductivity. More generally, shock stresses deform the surrounding rock and close the fracture where it intersects the perforation. Appendix Fig. 13 is a photograph of such an intersection. The fracture was injected with epoxy after perforating. Closure of the fracture near the perforation is circled.



**Appendix Figure 13.** Fracture closure where it intersects with a perforation. The closure is a result of shock stresses.

## Injection of detonation gases

Another common laboratory observation is the production of gas from test cores that were initially liquid saturated. Flow tests performed using initial laboratory procedures had the outlet of the perforation at some elevated pressure to simulate in-situ bottomhole pressure. In a subsequently modified API test procedure, this requirement was eliminated to simplify the test. Wellbore pressure can be lowered to the ambient pressure so that outlet flow rates are simpler to measure. Early production flow in such tests contains a high gas cut. Furthermore, the CFE is observed to first decrease and then increase slowly to a final value that can be associated with the absence of further gas production. This phenomenon suggests relative permeability effects resulting from gas in the pore structure. The phenomenon was not observed in earlier tests because the applied backpressure kept the gases in solution. It is therefore recommended that the modified procedure be performed with backpressure or that the flow be sufficient to elute all the gas before the flow rates are measured.

There are two possible mechanisms for gas injection even when substantial underbalance is applied. One is that detonation gases may cause temporary overbalance in the wellbore before they cool. Laboratory tests with transient pressure gauges show short-lived wellbore pressure increases but not to the point of overbalance. The more likely explanation (Bell, 1984) is that the metallic jet has a jet of detonation gas associated with it. Early shaped charges, called Munroe jets, had no metal liners and penetrated

solely with a jet of detonation gases. Little has been published regarding the associated gas jet.

In most completions, the phenomenon may not be of importance. However, in unconsolidated rock, gas injection may lead to high transient pore pressures, causing fluidization of the sand bed. The result would be that a large zone of sand around the perforation would act temporarily like a liquid. Such a phenomenon observed in unpublished laboratory experiments resulted in the immediate production of about a kilogram of sand. There was no evidence of a perforation tunnel in the recovered sample, although charge debris was found about 20 cm deep in the sand.

## Wettability phenomena

Finally, the effect of wettability on perforation cleanup should be mentioned. The presence or absence of water has a large effect on both perforation cleanup and sand production. Halleck and Deo (1987) compared results in kerosene-saturated samples with those in samples that contained irreducible brine. They found that the brine-containing samples had higher values of CFE and cleaned up at lower underbalance conditions. Injection of brine into a previously water-free perforation resulted in rapid cleanup during subsequent kerosene flow. Halleck and Damasena (1989) observed large increases in sand production rates when simulating water breakthrough in a weak sandstone.

All these observations indicate that wettability, surface tension and capillary pressure effects are involved in the transport of solids from the perforation damage zone. These effects should not be discounted in predicting the effects of underbalance surge cleanup.

## Conclusions

Permeability damage is distributed much differently than assumed by idealized models. Permeability varies substantially with radius. Reduced permeability is not necessarily associated with the visible crushed zone. This observation suggests that permeability reduction may be more a function of fines migration than grain breakage. Mechanical damage in weaker rocks extends several inches around the perforation. The extent of the damage is not uniform along the perforation but is more severe near the entrance hole. The so-called crushed zone surrounding a clean perforation is not significantly compacted in liquid-

saturated rocks, but it may be in gas-saturated ones. Compacted material exists in the rock near the center of the perforation, but it is seen only at the perforation tip or in tests with insufficient underbalance to remove it. Perforation cleanup is related to transient flow

velocity through the rock around the perforation and occurs at early times, when transient rates are highest. Large surge flow volumes should not be necessary where sufficient underbalance is applied.

# Post-Treatment Evaluation and Fractured Well Performance

*B. D. Poe, Jr., Schlumberger Dowell*  
*Michael J. Economides, University of Houston*

## 12-1. Introduction

Evaluation of the fracture geometry, well deliverability and reservoir performance of fractured wells with post-treatment well and reservoir responses has been extensively investigated. Post-treatment measurements of the created fracture geometry have been obtained with various logging and micro-seismic fracture mapping techniques.

Pressure transient analysis has been used as a post-treatment evaluation procedure for estimating the fracture extension into the reservoir as well as for obtaining estimates of the fracture conductivity and reservoir properties. With the reservoir and fracture parameter estimates obtained with these and various other post-treatment analysis techniques, a production systems analysis can be performed to determine the post-treatment deliverability of the fractured well.

### 12-1.1. Fracture mapping techniques

The post-treatment evaluation of fracture geometry using logging techniques is usually limited to near-borehole effects, such as estimation of the created fracture height with temperature surveys, gamma ray logs and spinner surveys in cased holes. Because these are near-well measurements and the wellbore stress concentration (see Chapter 3) encourages the fracture to leave the wellbore, the measurements are lower-bound estimates of height.

Temperature surveys are useful in estimating the wellbore fracture height that results from cooling of the formations that take the fracturing fluid during the treatment. An example of prefracture static (after circulating the wellbore) and postfracture temperature surveys of a well are presented in Fig. 12-1. The survey after circulating the well, but before perforating, enables identifying thermal conductivity anomalies caused by various formation layers and variation in the cement thickness. The anomalies can be ignored or compared with the postfracture survey to identify

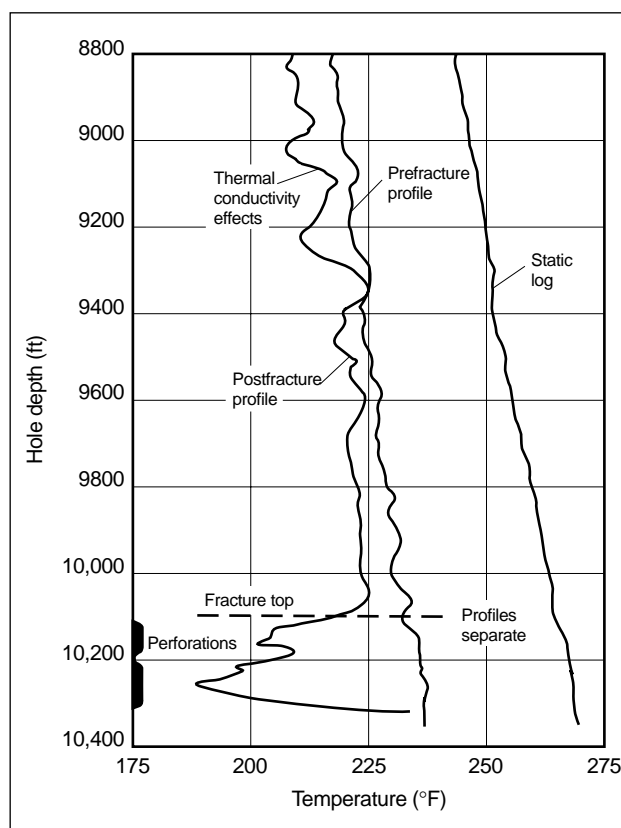


**Figure 12-1.** Pre- and postfracture temperature surveys (Dobkins, 1981).

fracturing effects. Radioactive tracers in the fracturing fluid, proppant or both can be monitored with gamma ray logs to determine which zones took fluid or proppant during the fracture treatment. Various stages may be identified by using different radioisotopes. Clearly the radioisotopes used should not naturally occur extensively. Post-treatment spinner surveys simply indicate which sets of perforations in a cased hole are producing fluid. A wellbore density log (Fig. 12-2) is used to determine what types of fluids are being produced. However, in an openhole the spinner survey may be used effectively to estimate which layers of the reservoir were stimulated.

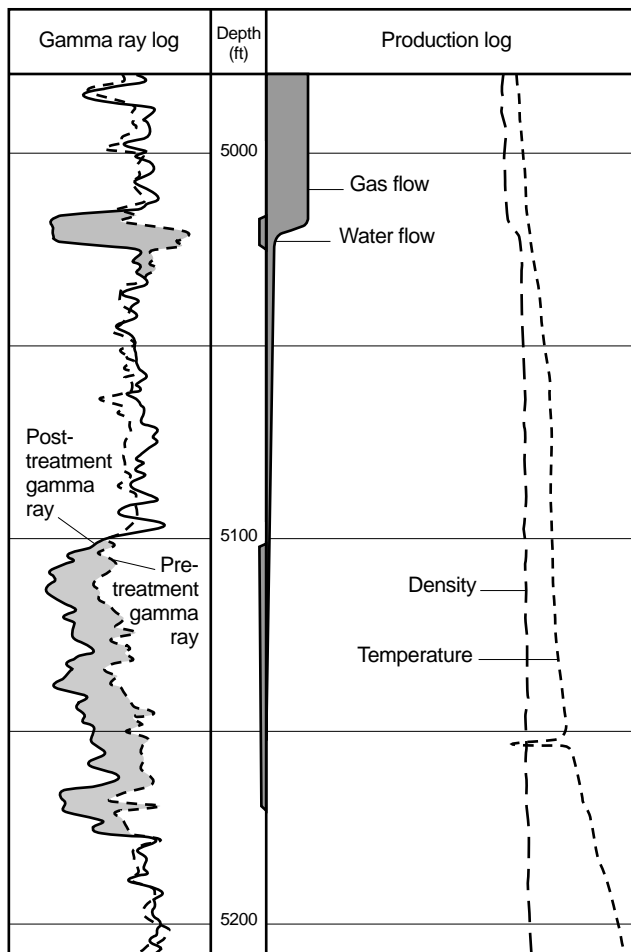


**Figure 12-2.** Production log and gamma ray log information from a fractured East Texas well.

An example of using production logs with radioactive tracers to identify fracture height and the zones that were fractured is in Fig. 12-2. The correspondence between the gamma ray log and the spinner survey indicates which intervals were fractured. The correspondence between gamma ray logging of a fractured well and temperature logging is presented in Fig. 12-3.

In openholes, the many measuring devices that can be used to estimate the wellbore fracture height include the sonic borehole televiewer, Formation MicroScanner\* tool, impression packers and downhole closed-circuit television. The direct method of measuring fracture width and height in an openhole with a downhole closed-circuit television was investigated by Smith *et al.* (1982) and may provide the most reliable estimate of fracture height at the wellbore. The results clearly show the fracture plane

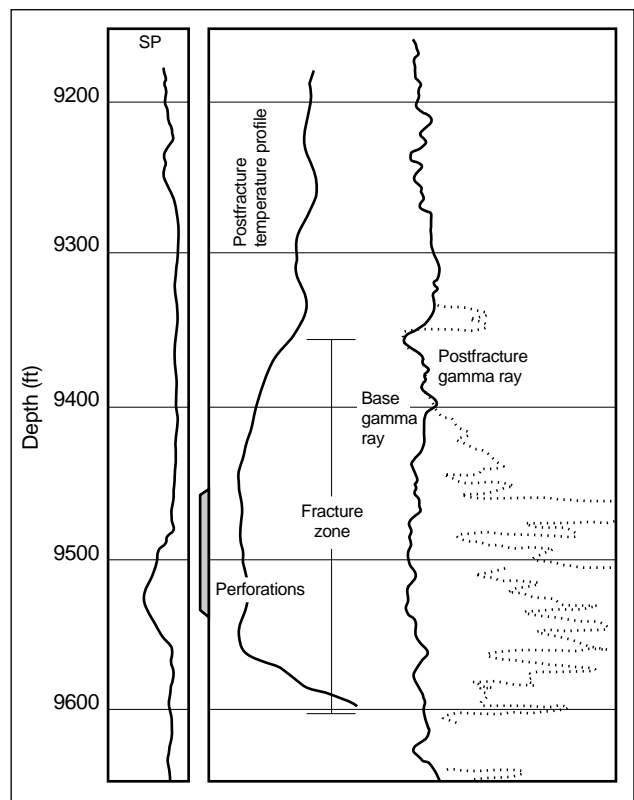


**Figure 12-3.** Gamma ray measurements match the temperature survey (Dobkins, 1981).

leaving the wellbore. In wellbores containing optically clear fluids, opening and closing of the created fracture can be visually observed to determine its height at the wellbore.

Zemanek *et al.* (1969) investigated the use of a sonic borehole televiewer to obtain estimates of the wellbore fracture height in openholes. Although the acoustic principles upon which this tool is based should result in a robust, accurate fracture identification procedure, many borehole conditions limit its reliability in practice. Some of these conditions are borehole ellipticity, wellbore deviation resulting in noncentralization of the tool and very narrow fractures that have widths at the wellbore that are significantly less than the acoustic wavelengths emitted by the tool.

The Formation MicroScanner tool is generally of comparable accuracy to the sonic borehole televiewer in an openhole. The resistivity buttons on the Formation MicroScanner tool image the inside of the wellbore wall to allow determination of the created fracture height. As for the prefracture (but postcirculating) temperature survey (Fig. 12-1), a complementary pre-

fracture survey enhances the interpretation of postfracture imaging surveys.

Impression packers are probably the oldest direct measurement devices for estimating the created fracture azimuth and orientation at the wellbore. The earliest reported investigation concerning the use of impression packers for this purpose is by Fraser and Petitt (1962). Inflatable packers with deformable rubber elements are used to take an impression of the borehole surface and record the created fracture features. Wellbore deviation surveys are commonly run in conjunction with impression packers to obtain an estimate of the fracture azimuth.

Active mapping techniques have also been used during fracture injection to estimate the growth of the fracture. Among the techniques that have proved the most useful for mapping the growth of hydraulic fractures are tiltmeter and triaxial borehole seismic analyses. In addition to the previously discussed television tool, tiltmeter arrays measure the change of the earth's surface tilt caused by the creation of hydraulic fractures at depth in the earth. Where tiltmeter analyses can be successfully employed, estimates of the fracture azimuth and potentially the extent from the wellbore can be obtained. The main limitation on the effective use of tiltmeters is generally a function of the depth of the reservoir being hydraulically fractured relative to the volume of the fracture. Volume directly increases the response, and depth attenuates the surface response. Figure 12-4

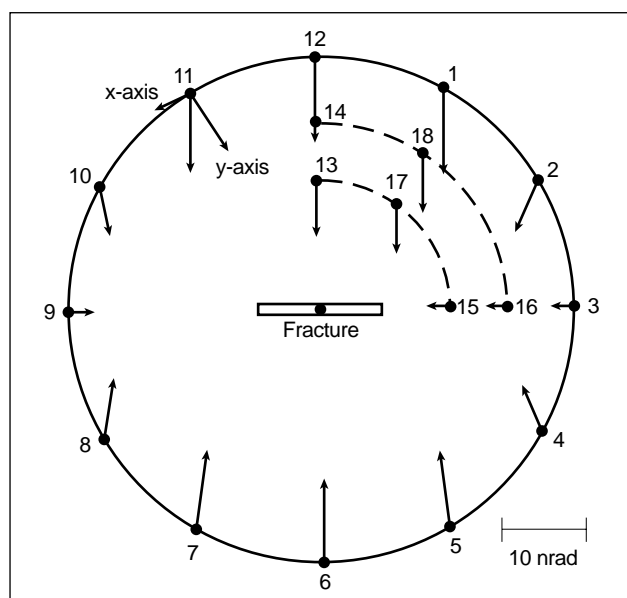


**Figure 12-4.** Vertical hydraulic fracture tiltmeter array design and computed vectors.

shows typical techniques for surface placement (a circle with a diameter equal to fracture depth) and telemetry analysis (tilt vectors toward and normal to a vertical fracture) for the use of tiltmeter arrays.

Davis (1983) reported analysis procedures for the surface displacement of horizontal and vertical fractures from tiltmeter measurements. The accuracy and reliability of tiltmeter analysis for fracture mapping purposes are limited primarily by environmental conditions. The sensitivity of the devices is such that the effects of vehicular traffic, wind, rain and any number of other environmental influences may be greater than the surface tilts caused by a subterranean hydraulic fracture.

Triaxial borehole seismics have also been used successfully to map the growth of subterranean hydraulic fractures (Albright and Pearson, 1982; Dobecki, 1983; Batchelor *et al.*, 1983). The fracture azimuth, lateral extension from the wellbore and growth into adjacent layers above and below the presumed target zone can be obtained using acoustic and seismic emissions recorded from the fracture during injection and shut-in. Subsurface acoustic telemetry is used to estimate the distance to recorded microseismic events from a variety of geophone receivers by using the difference in arrival time between the compressional and shear waves of the microseismic events. Section and plan views of basic principles for the use of borehole seismics are shown in Fig. 12-5.

- Example of microseismic imaging

Although microseismic imaging of hydraulic fractures has been used since the 1970s (Albright and Pearson, 1982; Thorne and Morris, 1987; Hart *et al.*, 1984; Vinegar *et al.*, 1992; Truby *et al.*, 1994; Warpinski *et al.*, 1995), the technique was used primarily for large-scale research experiments because of receiver limitations and processing difficulties. However, improvements in downhole receivers and the advent of high-speed portable computers have made this technology available for more general application. In addition, the technology has reached the stage where it is possible not only to image the final size and shape of the fracture but also observe the manner in which fracture growth occurs.

One large-scale research experiment where microseismic imaging was successfully used is the M-Site project in the Piceance basin of Colorado, which was jointly funded by the Gas Research



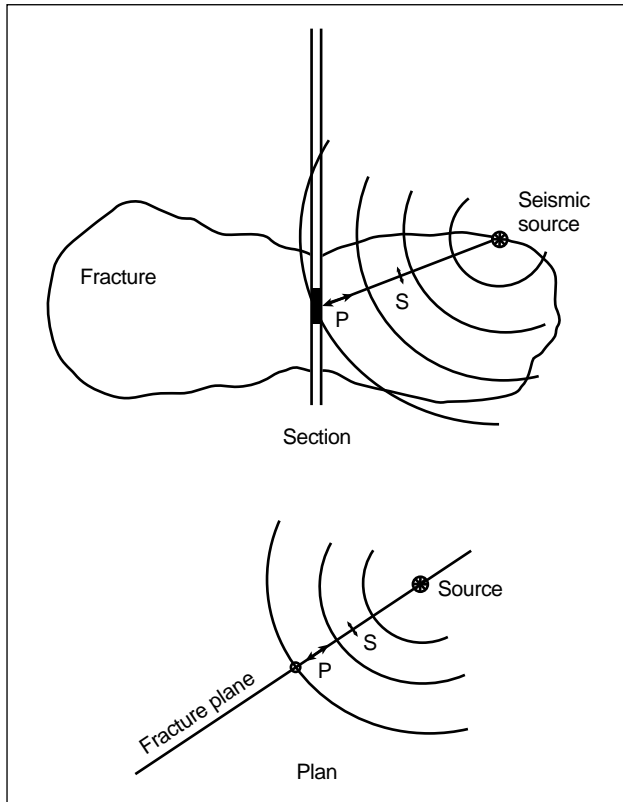


**Figure 12-5.** Section and plan views of borehole seismometer monitoring events in a fractured well (Dobecki, 1983).

Institute and the U.S. Department of Energy (Peterson *et al.*, 1996). Multilevel triaxial receiver arrays in two offset monitoring wells were used to develop time-growth images of hydraulic fractures induced in a nearby well (Warpinski *et al.*, 1996). Figure 12-6 shows treatment and formation data for one of the fractures conducted in a sandstone at this location. In this fracture, approximately 600 bbl of 40 lbm/1000 gal of crosslinked gel and 78,000 lbm of sand were injected at 20 bbl/min.

Figure 12-7 shows side-view images at three times for the microseismic locations associated with the fracturing process. In the first time period, linear gel in the wellbore and a crosslinked-gel pad have been injected, but little height growth has occurred because of the stress contrasts in the abutting shales. In the second time period, sand concentrations of up to 4 ppg have been injected, and height growth is just beginning to occur. The final microseismic image shows that as net pressure increased, fracture height growth became markedly

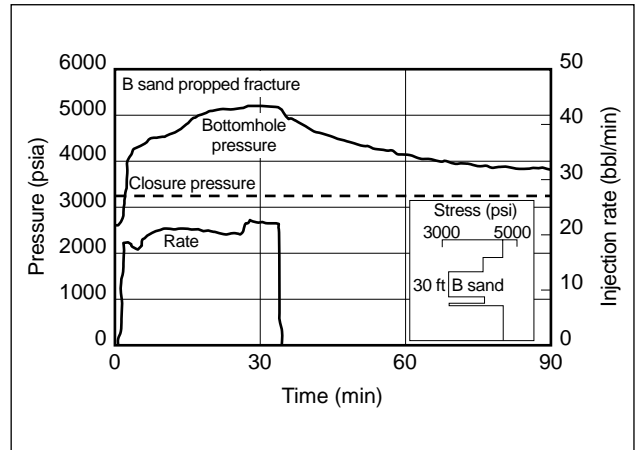


**Figure 12-6.** Treatment data and stress configuration for microseismic experiment (Warpinski *et al.*, 1996).

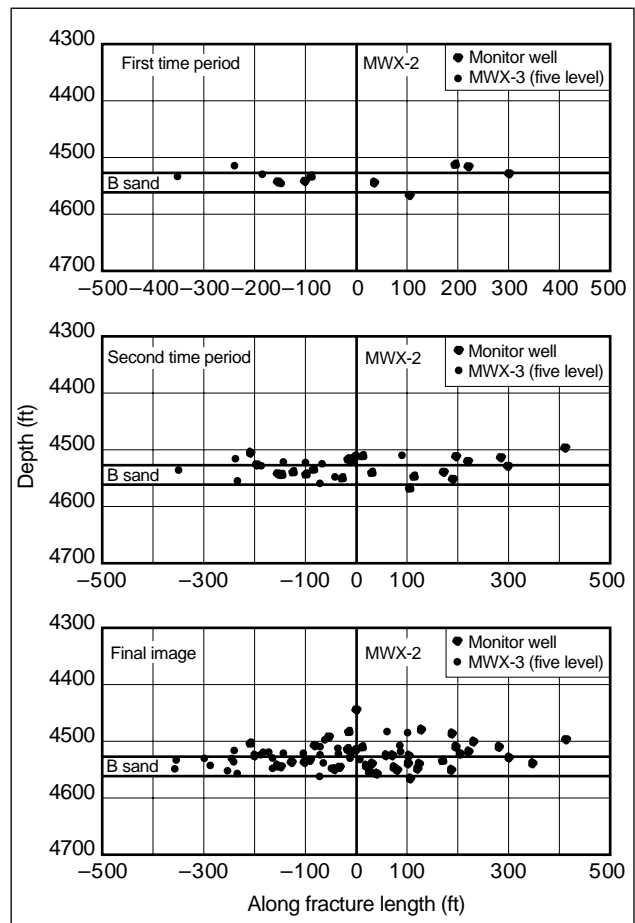


**Figure 12-7.** Side-view microseismic images for three time periods.

asymmetric, with little growth downward and upward growth on each wing. A plan view of the microseismic images in Fig. 12-8 yields an azimuth of about N75°W. As can be seen most clearly in the plan view, the microseismic image is an envelope of points in which the fracture is generally contained, as the microseisms usually occur some distance away from the actual fracture.

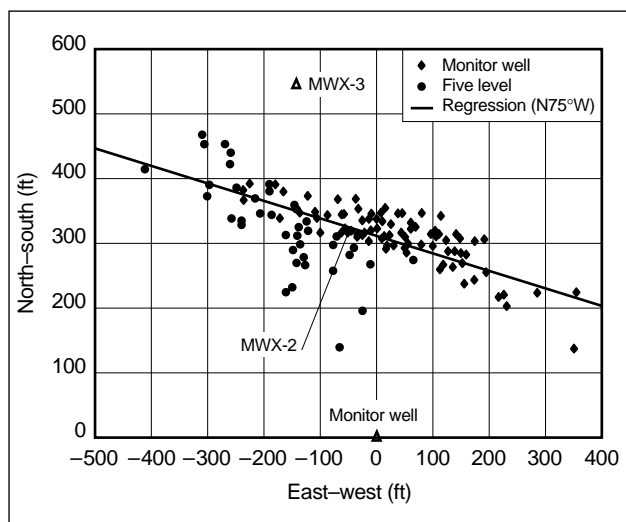


**Figure 12-8.** Plan view of a microseismic image.

- Example of downhole tiltmeter imaging

The M-Site experiments from which the microseismic images were produced is also the first site where downhole tiltmeters were employed to obtain fracture diagnostic information (Branagan *et al.*, 1996). An array of six biaxial tiltmeters was emplaced approximately 300 ft normal to the hydraulically fractured interval (Fig. 12-9). Measurement of the downhole tilt as a function of time provided data on the rotational deformation of the formation induced by the fracture opening. In the example data shown, the tiltmeter amplitudes deviate from zero as the fracture opens, with the maximum tilt occurring at shut-in. The tilt decline during shut-in can also be observed as the fracture slowly closes on the proppant.

Figure 12-10 shows the measured tilt at each tiltmeter level just prior to shut-in, as well as some modeling results for this treatment. As noted in Chapter 6, the tilts adjacent to a hydraulic fracture take on a characteristic S shape, but the lower part of the S is missing because no instruments were placed at those depths. The available data are clearly sufficient to estimate the height of the fracture and the width to produce the measured distribution. Simple homogeneous models bracket the height and give a good initial estimate but do

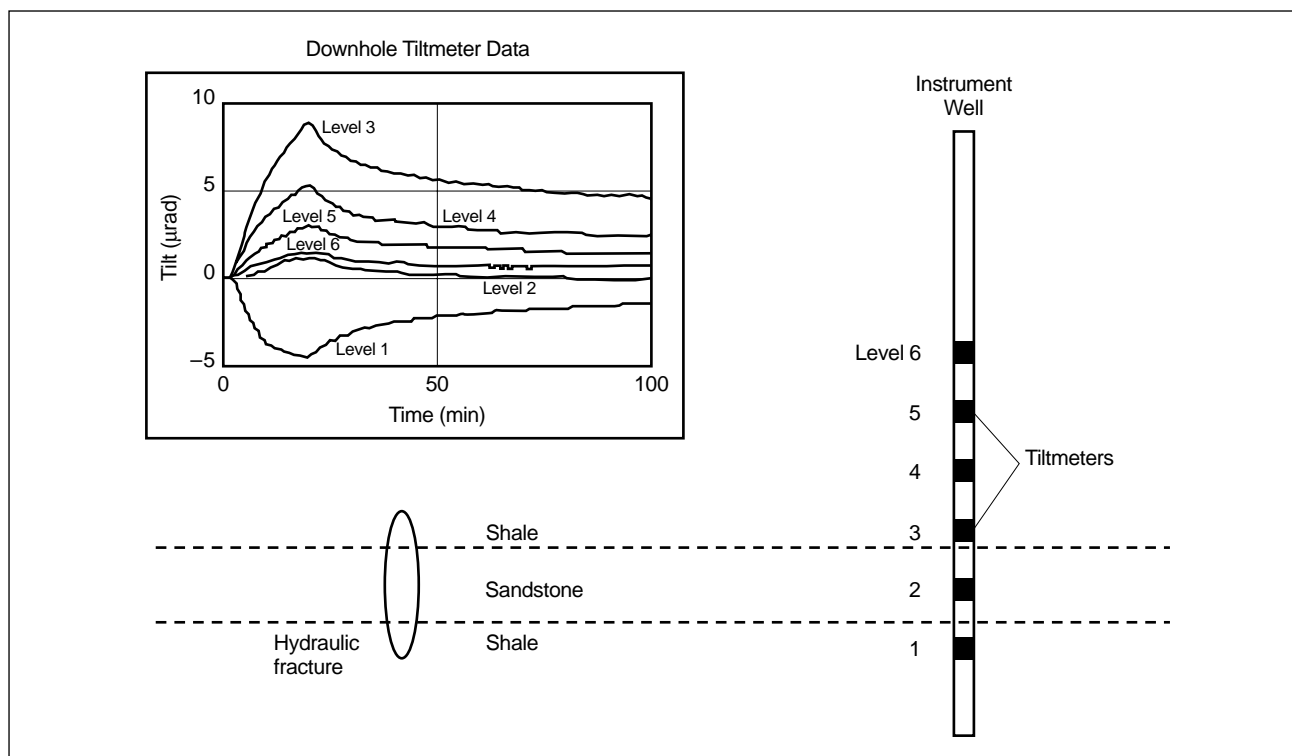


**Figure 12-9.** Tiltmeter experiment and example data.

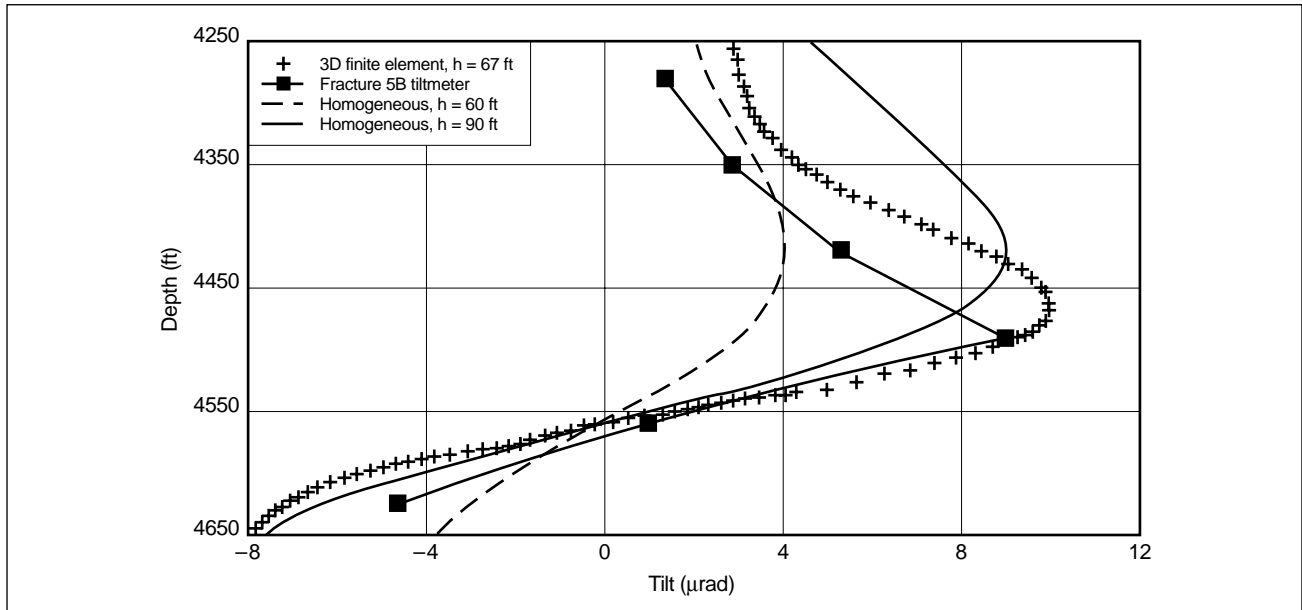


**Figure 12-10.** Tiltmeter and modeling results of a fracture treatment.

not entirely match the character of the measured data because of the effects of layering. In this example, the 60-ft fracture matches the tail-off, whereas the 90-ft fracture matches the peak amplitude. Both models, however, are offset from the measured data, most likely because of vertical asymmetric width effects. Finite-element analyses give a much better match of the character, as they can include layering effects (as well as they are known), but they are much more difficult to produce. Nevertheless, the modeled height of the fracture (67 ft) closely matches the microseismic image of the fracture and yields a width in good agreement with the elastic deformation commonly used in geometry models.

### 12-1.2. Pressure transient analysis

Pressure transient analysis has been used successfully to obtain estimates of reservoir and fracture properties. This section provides a review of developments related to fractures.

The earliest investigation reported in the literature concerning the pressure transient behavior of vertically fractured wells is by Muskat (1937). Muskat used an analytic fractured well model that assumes steady-state flow conditions to investigate the pressure distributions and fluid entry patterns in the vicinity of a vertical fracture. Other early contribu-

tions to the body of knowledge concerning the behavior of fractured wells include investigations by van Poollen *et al.* (1958) and Prats (1961). Steady-state conditions are also assumed in the van Poollen *et al.* and Prats models, which consider the response of both finite- and infinite-conductivity fractures. Prats introduced the concepts of dimensionless fracture conductivity and effective wellbore radius for vertically fractured wells, in which the effective wellbore radius is demonstrated to be a function of the fracture length and dimensionless fracture conductivity. For infinite-conductivity fractures, the effective wellbore radius is demonstrated to be equal to one-half of the fracture half-length in a fully developed flow pattern (Fig. 12-11).

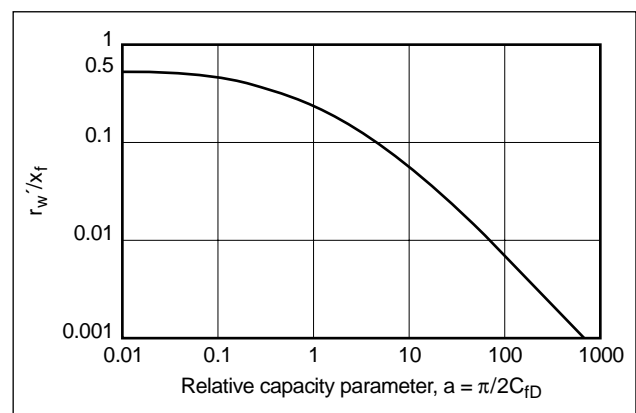


**Figure 12-11.** Concept of effective wellbore radius for vertically fractured wells (Prats, 1961).

The performance of vertically fractured wells under pseudosteady-state flow conditions was investigated by McGuire and Sikora (1960) using a potentiometric analog model. The results of that study provide the basis for evaluation of the stabilized post-treatment performance of vertically fractured wells. The stabilized productivity index ratio increase from the fracture stimulation of a well is presented in Fig. 12-12.

The earliest work reported in the literature that considers unsteady-state flow conditions on the transient behavior of vertically fractured wells is by Dyes *et al.* (1958). Prats *et al.* (1962) and Russell and Truitt (1964) also investigated the transient behavior of vertically fractured wells under transient flow conditions. Russell and Truitt used an explicit finite-difference simulator to investigate the transient behavior of an infinite-conductivity vertical fracture and found that the classic semilog analysis techniques developed for unfractured wells could be applied for the evaluation of transient behavior of vertically fractured wells during the pseudoradial flow regime. Figure 12-13 compares the results of various early studies estimating the stabilized flow efficiency improvement resulting from fracturing a well. The discrepancies observed between the results of the various studies are due primarily to the various assumptions associated with the development of the models used. Of the correlations presented in Fig. 12-13, McGuire and Sikora's (1960) results have been found to generally represent the postfracture pseudosteady-state production increase better than the other correlations.

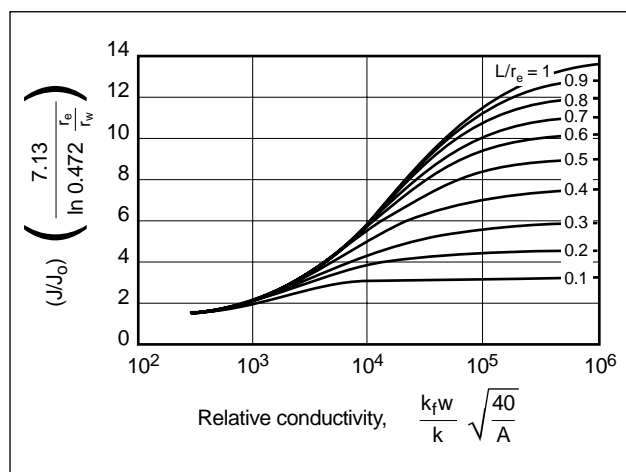


**Figure 12-12.** Productivity index ratio for vertically fractured wells (McGuire and Sikora, 1960).

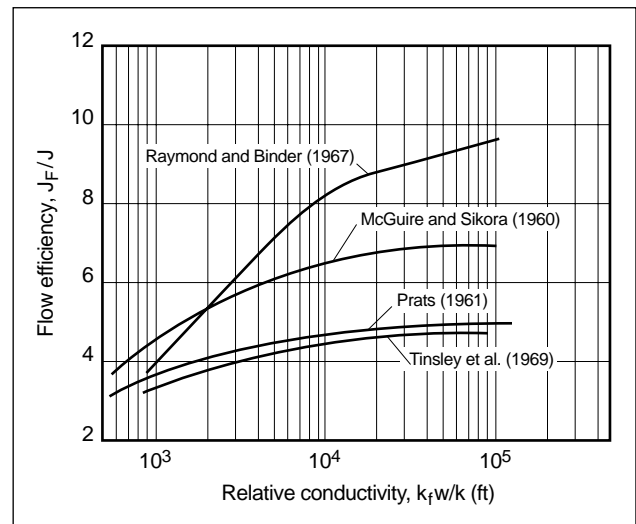


**Figure 12-13.** Flow efficiency ratios from various studies.

The investigations reported by Clark (1968) and Milheim and Cichowicz (1968) apply linear flow concepts to analysis of the pressure transient behavior of infinite-conductivity vertically fractured wells and demonstrate that a Cartesian graph of bottom-hole pressure versus the square root of time results in a linear transient behavior, thus providing an analysis procedure for the early transient formation linear flow regime.

Gringarten and Ramey (1973, 1974) first introduced application of the instantaneous Green's function and Newman's product method for the development of solutions to a wide variety of problems of fluid flow in porous media. Among the solutions developed by those authors are analytic solutions for the pressure transient behavior of uniform flux and infinite-conductivity vertical fractures and a uniform flux horizontal fracture. The instantaneous Green's function and Newman's product approach introduced by Gringarten and Ramey and Gringarten *et al.* (1974) has subsequently been used extensively to develop solutions to investigate the transient behavior of a wide variety of well types and reservoir configurations. An additional result of Gringarten *et al.*'s study is the demonstration that the infinite-conductivity vertical fracture response could be obtained with the uniform flux vertical fracture solution, in which the pressure transient behavior is evaluated at a dimensionless spatial position in the fracture from the wellbore equal to 0.732.

Using the Source and Green's function approach reported by Gringarten and Ramey and Gringarten

*et al.*, numerous studies have been reported in the literature concerning particular aspects of the performance of vertically fractured wells. Among these are Cinco-Ley *et al.*'s (1975b) study of the transient behavior of inclined wells and fractures and Raghavan's (1976) study concerning the transient behavior of partially penetrating infinite-conductivity vertical fractures, which uses the Gringarten *et al.* relationship between uniform flux and infinite-conductivity vertical fractures. A similar study on partially penetrating infinite-conductivity vertical fractures was later made by Rodriquez *et al.* (1984).

In the classic work by Cinco-Ley *et al.* (1978), the development of an analytic solution for the pressure transient behavior of a finite-conductivity vertical fracture provides a sound theoretical basis for interpretation of the transient behavior of vertically fractured wells. An idealized fracture used in that study is presented in Fig. 12-14. Cinco-Ley and Samaniego-V. (1981b) later provided a detailed analysis of the transient behavior of finite-conductivity vertical fractures and identified the various flow regimes that can be exhibited.

Cinco-Ley and Samaniego-V. (1981b) identified four flow regimes that may exist: fracture storage linear flow, bilinear flow, formation linear flow and pseudo-radial flow regimes. The reservoir and fracture fluid flow patterns of a finite-conductivity vertical fracture for the fracture linear flow (fracture storage), bilinear

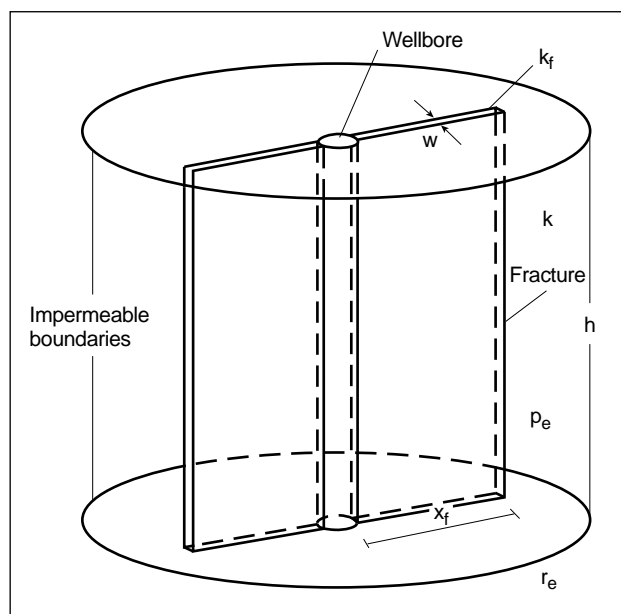


**Figure 12-14.** Geometry of an ideal vertical hydraulic fracture.

and formation linear flow regimes are in Figs. 12-15, 12-16 and 12-19, respectively. The specialized analyses developed in that study have become the theoretical basis for many of the pressure transient analysis techniques for fractured wells. Details of the procedures involved in the Cinco-Ley and Samaniego-V. analysis are presented in Section 12-2.

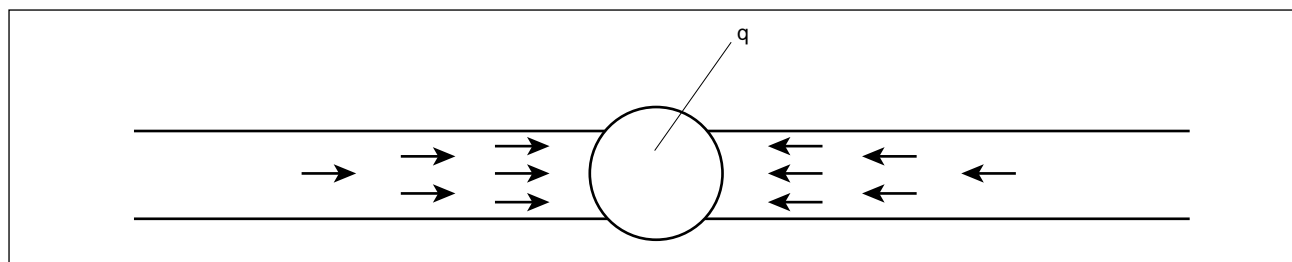


**Figure 12-15.** Fracture linear flow in a finite-conductivity vertical fracture.

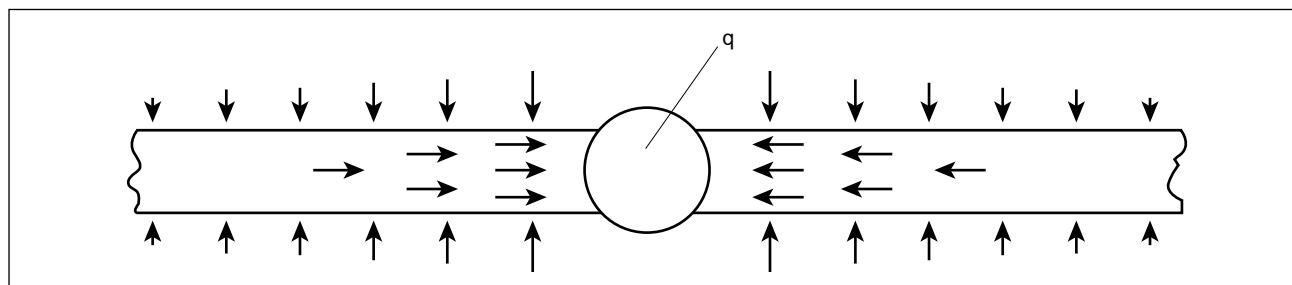


**Figure 12-16.** Bilinear flow in a finite-conductivity vertical fracture.

Agarwal *et al.* (1979) investigated the rate transient response of a finite-conductivity vertical fracture with a finite-difference reservoir simulation model. The finite-conductivity vertical fracture type curve developed by Cinco-Ley *et al.* (1978) is extended in this study so that it is more applicable for the production response of massively fractured wells in low-permeability reservoirs.

Cooke (1973) demonstrated the importance of a propped fracture and non-Darcy flow in the fracture. Guppy *et al.* (1982b) investigated the effect of inertial-turbulent (non-Darcy) flow on the pressure transient behavior of finite-conductivity vertical fractures using an analytic model. Although Wattenbarger and Ramey (1968) and Holditch and Morse (1976) provided detailed qualitative insight into the effects of non-Darcy reservoir and fracture flow, respectively, the investigation by Guppy *et al.* provided the first quantitative method for determining the reduction in apparent fracture conductivity resulting from non-Darcy fracture flow.

The application of derivative analyses to the interpretation of the transient behavior of infinite-conductivity fractures was reported by Tiab and Kumar (1980). Tiab and Puthigai (1988) developed analytic expressions for the derivative behavior of infinite-conductivity fractures and applied those relationships to analysis examples. Pressure derivative analyses for finite-conductivity vertical fractures were developed by Wong *et al.* (1984). The Wong *et al.* analysis procedure involves both pressure and pressure derivative analyses to reduce some of the uniqueness problems that commonly occur with interpretation of the behavior of finite-conductivity vertical fractures.

The transient behavior of finite-conductivity vertical fractures in multilayer reservoirs was studied by Bennett *et al.* (1985, 1986). An important contribution of the Bennett *et al.* studies is introduction of the dimensionless reservoir conductivity concept. This analysis procedure provides a means of correlating the multilayer commingled reservoir response with that of an equivalent single-layer reservoir during the early transient behavior of fractured wells, when there is essentially linear flow normal to the plane of the fracture. The dimensionless reservoir conductivity concept was extended by Camacho-V. *et al.* (1987) to include the effects of unequal fracture lengths in each of the layers of a multilayer reservoir system. A later study by Spath *et al.* (1994) presented an analysis procedure that extends the

multilayer evaluation procedure of Bennett *et al.* and Camacho-V. *et al.* for commingled systems and eliminates the requirement of linear flow to the fracture. This commingled reservoir analysis is amenable for the analysis of all flow regimes and combinations of reservoir layer completion types.

The transient behavior of vertically fractured wells in dual-porosity reservoirs was studied by Houzé *et al.* (1988), Ben Naceur and Economides (1988), Cinco-Ley and Meng (1988) and van Kruysdijk (1988). The studies of Houzé *et al.* and Ben Naceur and Economides consider infinite-conductivity vertical fractures, and the models of Cinco-Ley and Meng and van Kruysdijk were developed to study the behavior of finite-conductivity vertical fractures in dual-porosity reservoirs.

The study by van Kruysdijk also considers the effects of fracture face skin effect damage. This follows earlier work by Cinco-Ley and Samaniego-V. (1977, 1981a) in which the effects of flow restrictions in and along the face of vertical fractures are compared with the corresponding vertical fracture cases without damage.

Ozkan and Raghavan (1991) developed readily computable analytic pressure transient solutions for uniform-flux vertical fractures in a variety of reservoir configurations. A major contribution of the study by Ozkan and Raghavan, in addition to the development of the various solutions presented, is improved computational procedures for evaluating the transient response of vertically fractured wells.

A review of the limitations and uncertainties concerning the design and evaluation of hydraulic fracture treatments was presented by Nolte and Economides (1991). The uncertainty of the reservoir parameter values used in the design of hydraulic fractures is demonstrated to be of significant importance. Furthermore, analysis of the effectiveness of hydraulic fracture treatments using conventional transient analysis procedures is shown to be affected significantly by heterogeneous reservoir properties and to generally indicate a shorter fracture than the actual half-length contributing to production (i.e., why this volume distinguishes between the reservoir inferred length  $x_f$  and geometric length  $L$ ).

With the advent of fracturing horizontal wells, intensive research efforts began to develop transient analysis and well performance models for describing the behavior of horizontal wellbores that have been hydraulically fractured to improve productivity.

Transient interpretation analyses have been developed for horizontal wellbores intersected by orthogonal and colinear fractures. Soliman *et al.* (1990) studied the productivity improvement of vertically fractured horizontal wells. Models for interpretation of the performance of hydraulically fractured horizontal wells were also reported by van Kruysdijk and Dullaert (1989), Economides *et al.* (1989, 1991), Roberts *et al.* (1991) and Raghavan and Joshi (1993).

Specific interpretation principles for hydraulically fractured horizontal well behavior are not addressed in this chapter because of the length and complexity of the subject. However, most of the basic principles for the interpretation of finite-conductivity vertical fracture transient behavior discussed in this chapter are directly applicable to horizontal wells that have been vertically fractured. Section 12-5 presents a model for longitudinally fractured horizontal wells that demonstrates the important impact on fracture conductivity.

## 12-2. Post-treatment fracture evaluation

The post-treatment fracture evaluation procedures that have found the widest general use for obtaining estimates of the reservoir and propped fracture dimensions and properties are pressure transient well testing and long-term history matching. Because these techniques are essentially equivalent, the well testing method is emphasized in the following sections. Typical examples of history and dimensionless rate relations are provided by Agarwal *et al.* (1979), Lee and Holditch (1982) and Bennett *et al.* (1983).

A detailed discussion of the transient behavior of finite-conductivity vertical fractures is most readily presented using conventional definitions of the dimensionless variables that are used for the transient behavior of fractured wells and in developing appropriate analysis procedures. In the following discussion, it is assumed that the reservoir contains a slightly compressible liquid with constant viscosity and compressibility. Fluid flow in the reservoir and fracture is assumed to obey Darcy's law. The reservoir is assumed to be a homogeneous, isotropic horizontal layer with uniform thickness, porosity and permeability. Specific exceptions to these assumptions are addressed separately in Section 12-3.

Dimensionless time  $t_D$  is defined for a system with a vertically fractured well by

$$t_D = \frac{0.000264kt}{\phi\mu c_t x_f^2}. \quad (12-1)$$

Dimensionless time is related to dimensional time  $t$  in hr by the system properties (permeability  $k$  in md, porosity  $\phi$ , fluid viscosity  $\mu$  in cp and total system compressibility  $c_t$  in  $\text{psi}^{-1}$ ) and the characteristic length of the system, which is the fracture half-length  $x_f$  in ft.

Dimensionless wellbore pressure is defined by

$$p_{wD} = \frac{kh(p_i - p_{wfs})}{141.2q\mu B}, \quad (12-2)$$

where  $h$  is the net pay thickness of the reservoir in ft,  $q$  is the fluid flow rate in STB/D,  $B$  is the fluid formation volume factor in RB/STB, and the initial reservoir pressure  $p_i$  and sandface flowing pressure  $p_{wfs}$  are in psia.

The dimensionless fracture permeability  $k_{fD}$ , width  $b_{fD}$ , height  $h_{fD}$ , hydraulic diffusivity  $\eta_{fD}$  and conductivity  $C_{fD}$  are, respectively,

$$k_{fD} = \frac{k_f}{k} \quad (12-3)$$

$$b_{fD} = \frac{w}{x_f} \quad (12-4)$$

$$h_{fD} = \frac{h_f}{h} \quad (12-5)$$

$$\eta_{fD} = \frac{k_f \phi c_t}{k \phi_f c_{tf}} \quad (12-6)$$

$$C_{fD} = k_{fD} b_{fD} = \frac{k_f w}{k x_f}. \quad (12-7)$$

In Eqs. 12-3 through 12-7, the fracture permeability  $k_f$ , width  $w$ , height  $h_f$ , compressibility  $c_{tf}$  and porosity  $\phi_f$  are in consistent units.

Analysis procedures for the transient behavior of finite-conductivity vertical fractures, pioneered by Cinco-Ley and Samaniego-V. (1981b), have become the industry standard. These procedures require proper identification of the flow regimes that are exhibited in the transient response of the well. The flow regimes that can be exhibited by finite-conductivity vertical fractures are wellbore storage domi-

nated, fracture storage dominated, bilinear flow, formation linear flow, pseudoradial flow and boundary dominated flow regimes. The transient behavior also includes transition regimes that separate each of the previously identified flow regimes.

### 12-2.1. Wellbore storage dominated flow regime

A shut-in (pressure buildup or falloff), in which the well is shut in at the surface and the wellbore contains a compressible fluid, may be distorted for a significant portion of the early response by the storage effects of the wellbore. The duration of wellbore storage effects is governed primarily by the volume of the wellbore exposed to the completed reservoir and the compressibility of the fluids contained in the wellbore. Thus, downhole shut-in for pressure buildup can reduce wellbore effects considerably. Pressure drawdown or injection transients may also result in domination of a significant portion of the transient behavior by wellbore storage distortion if the well is opened for production or injected into at the surface and the wellbore contains compressible fluids.

Wellbore storage dominated flow is characterized by a unit slope for both the pressure and pressure derivative behaviors in log-log coordinates. The pressure and pressure derivative response of a system with a positive steady-state skin effect and constant wellbore storage is a single unit-slope line (see Chapter 2 for a detailed discussion of this issue). Nonideal conditions may exist in the system in which the wellbore storage cannot be characterized by a constant value. These conditions are common in wells that simultaneously produce both oil and gas and in which momentum, density and thermal effects result in afterflow and a changing liquid level in the wellbore. Changing wellbore storage effects are also referred to as wellbore phase redistribution effects (Fair, 1981).

### 12-2.2. Fracture storage linear flow regime

The initial pressure transient behavior of a finite-conductivity vertical fracture (with negligible wellbore storage effects) is dominated by the fluid storage of the fracture itself. In the case of negligible wellbore storage effects (in practice, this generally involves only wells with downhole isolation tools), the constant-rate drawdown of a well with a finite-

conductivity vertical fracture results in production at the wellbore that is due primarily to fluid expansion in the fracture.

This linear flow regime is characterized by a one-half slope on a log-log graph of the change in pressure  $\Delta p$  versus the change in time  $\Delta t$ . The fracture storage linear flow regime is generally of such short duration that an analysis of this transient behavior is usually not possible. In cases where wellbore storage effects are not negligible, they generally distort or mask the fracture storage linear behavior to an extent that it may not be readily observed in the transient data. Fluid flow patterns in a fracture for the fracture linear flow regime are illustrated in Fig. 12-15.

During the fracture linear flow regime, the behavior of dimensionless wellbore pressure  $p_{wD}$  is a function of the dimensionless fracture conductivity, hydraulic diffusivity and height, and dimensionless time:

$$p_{wD} = \frac{2}{C_{fD} h_{fD}} \sqrt{\pi \eta_{fD} t_D}. \quad (12-8)$$

The approximate dimensionless time  $t_{Defl}$  at which the fracture linear flow behavior ends is also a function of the dimensionless fracture properties:

$$t_{Defl} = \frac{0.01 (C_{fD} h_{fD})^2}{\eta_{fD}^2}. \quad (12-9)$$

### 12-2.3. Bilinear flow regime

A bilinear flow regime may be exhibited in finite-conductivity vertical fractures as a result of two linear flow patterns existing in the system simultaneously and the fracture tip effects not influencing the transient behavior of the well. The flow in the reservoir is primarily compressible linear flow to the plane of the fracture. Once the fluid crosses the fracture face into the fracture, the fluid is conducted down the fracture to the wellbore, under essentially incompressible linear flow conditions. Flow patterns in the reservoir and fracture during the bilinear flow regime are presented in Fig. 12-16. This fracture flow regime is governed by the fracture conductivity, and bilinear flow provides the optimum regime for defining conductivity.

Wellbore pressure transient behavior during the bilinear flow regime is expressed by

$$p_{wD} = \frac{2.45083}{\sqrt{C_{fD} h_{fD}}} t_D^{1/4}. \quad (12-10)$$



The transient behavior of a finite-conductivity fracture under bilinear flow is presented in Fig. 12-17 as a Cartesian graph of  $\Delta p$  versus the fourth root of time. For a finite-conductivity fracture with  $C_{fD} > 1.6$ , the tail of the transient data graph is concave upward. Similarly, for a fracture with a very low dimensionless fracture conductivity ( $C_{fD} < 1.6$ ), the transient data tails off concave downward. This quick-look diagnostic feature helps to identify the conductivity range of the fracture. Another diagnostic provided by this graphic is the nonzero  $\Delta p$  intercept: a positive value indicates near-well conductivity damage (e.g., a choked fracture from overdisplaced proppant or kill fluid damage) and a negative value indicates enhanced near-well conductivity. The slope of the graph also is used to calculate the fracture conductivity as implied by Eq. 12-10, which does not depend on fracture length. The log-log pressure and pressure derivative behavior during the bilinear flow regime are separated by a multiple  $c$  of  $\log 4$  (Fig. 12-18). The bilinear flow regime ends at the dimensionless time approximated by

$$t_{Debf} = \begin{cases} \frac{0.1}{(C_{fD} h_{fD})^2}, & C_{fD} h_{fD} \geq 3 \\ 0.0205 [(C_{fD} h_{fD}) - 1.5]^{-1.53}, & 1.6 \leq C_{fD} h_{fD} < 3 \\ \left[ \frac{4.55}{\sqrt{C_{fD} h_{fD}}} - 2.5 \right]^{-4}, & C_{fD} h_{fD} < 1.6. \end{cases} \quad (12-11)$$

Although the correlations given by Eq. 12-11 were originally developed for  $h_{fD} = 1$ , they have also been found adequate for values of  $h_{fD} \leq 2$ .

- Example calculation for the end of bilinear flow regime

Assume that  $C_{fD} = 12.5$ ,  $h = 50$  ft,  $h_f = 80$  ft,  $k = 1$  md,  $\phi = 0.15$ ,  $\mu = 1$  cp,  $c_t = 10^{-5}$  psi<sup>-1</sup> and  $x_f = 500$  ft. Calculate the time at which the bilinear flow regime will end. What is this time if  $C_{fD} = 1.25$ ?

#### Solution

From Eq. 12-5,  $h_{fD} = h_f/h = 1.6$ . Then, the product  $C_{fD} h_{fD} = 20$  and the top expression of Eq. 12-11 is in effect.

This leads to

$$t_{Debf} = \frac{0.1}{20^2} = 2.5 \times 10^{-4},$$

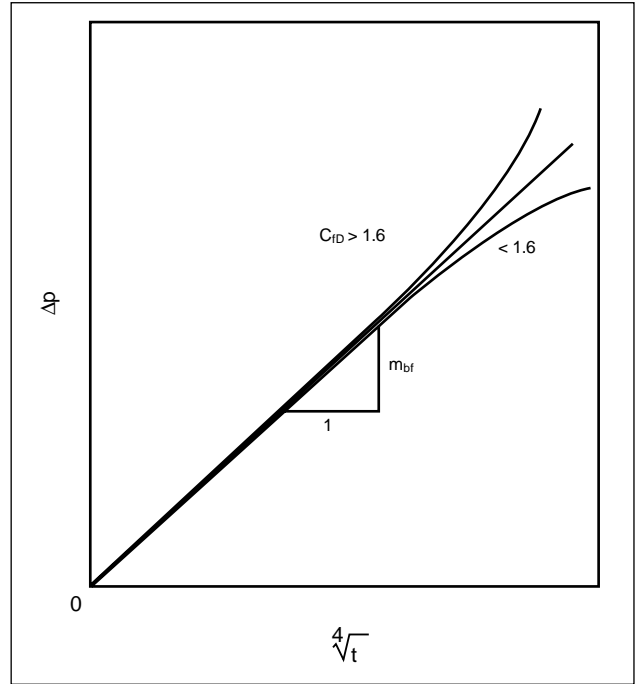


Figure 12-17. Cartesian graph of bilinear flow regime behavior.

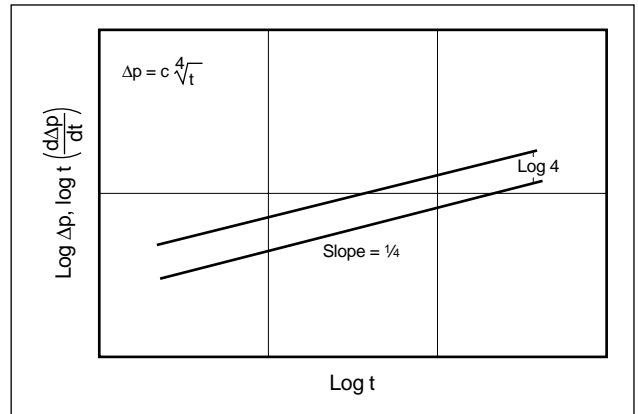


Figure 12-18. Pressure and derivative response of bilinear flow regime in log-log coordinates.

and from the definition of dimensionless time (Eq. 12-1) and rearrangement:

$$t = \frac{(2.5 \times 10^{-4})(0.15)(1)(10^{-5})(500^2)}{(0.000264)(1)} = 0.36 \text{ hr.}$$

If  $C_{fD} = 1.25$ , then  $C_{fD} h_{fD} = 2$  and the middle expression in Eq. 12-11 is indicated, leading to  $t_{Debf} = 5.9 \times 10^{-2}$  and a much larger  $t = 84$  hr.

#### 12-2.4. Formation linear flow regime

For finite-conductivity fractures with dimensionless fracture conductivity in excess of approximately 80, a second linear flow period may be exhibited in which the fracture conductivity is sufficiently high that the pressure loss caused by flow in the fracture is negligible. In this case, the pressure transient behavior at the well is governed by reservoir compressible linear flow normal to the plane of the fracture. This flow regime is commonly referred to as the formation linear flow regime. The wellbore pressure transient behavior of formation linear flow is governed by

$$p_{wD} = \sqrt{\pi t_D} \quad (12-12)$$

The start and end of the formation linear flow regime are determined, respectively, by

$$t_{Dblf} = \frac{100}{(C_{fD} h_{fD})^2} \quad (12-13)$$

$$t_{Delf} = 0.016 \quad (12-14)$$

For  $C_{fD} h_{fD} < 80$ , Eqs. 12-13 and 12-14 clearly demonstrate that a formation linear flow regime does not exist.

The flow pattern in the reservoir for a vertical fracture under formation linear flow is presented in Fig. 12-19. The transient pressure behavior illustrated in Fig. 12-20 is in log-log coordinates with the derivative offset by the multiple of log 2. The Cartesian representation of the pressure and pressure derivative behavior is in Fig. 12-21, and the slope determines  $x_f$  (see Eqs. 12-68 and 12-69). The effect of fracture conductivity on the early transient behavior of fractured wells is illustrated in Fig. 12-22.

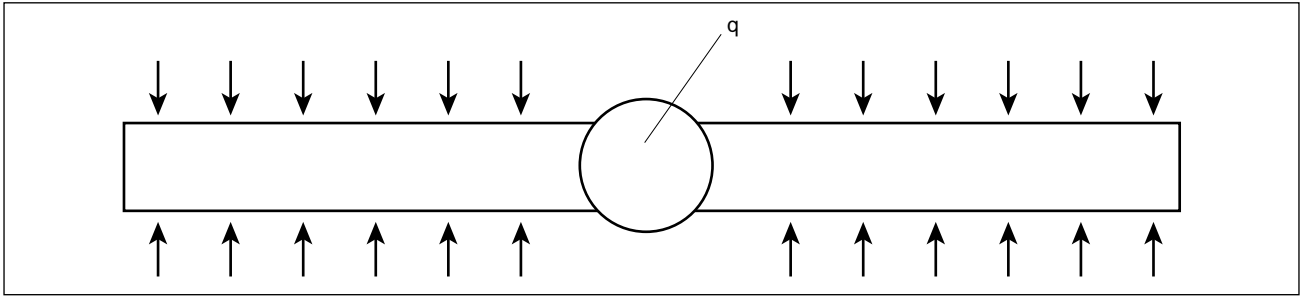


**Figure 12-19.** Formation linear flow to the plane of a finite-conductivity vertical fracture.

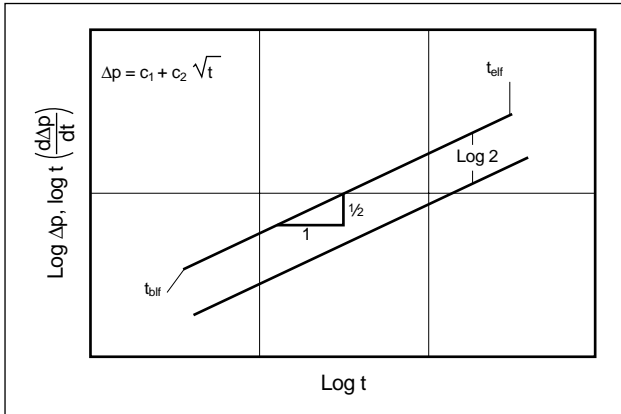


**Figure 12-20.** Pressure and derivative response of the formation linear flow regime in log-log coordinates.

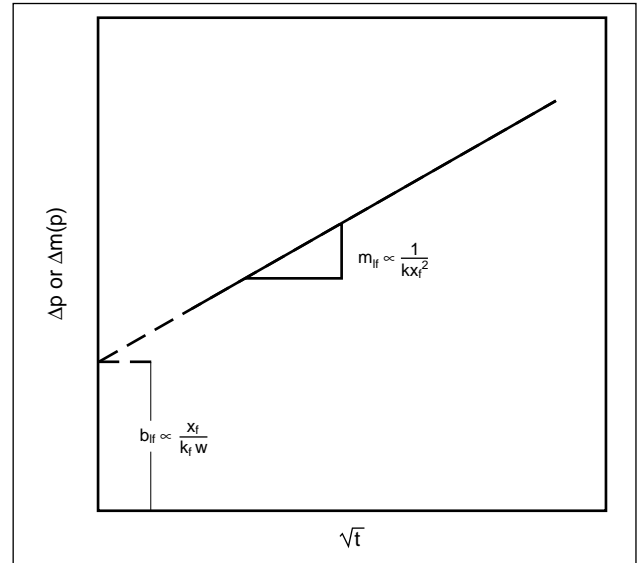


**Figure 12-21.** Cartesian graph of formation linear flow (lf) behavior.

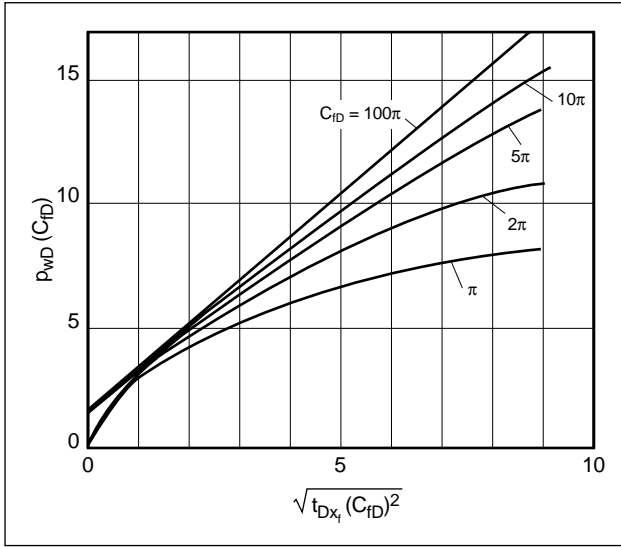


**Figure 12-22.** Effect of fracture conductivity on bilinear and formation linear flow behavior (Cinco-Ley et al., 1982).

- Example calculation for start and end of formation linear flow

A reservoir has  $h = 100$  ft,  $\phi = 10\%$ ,  $c_t = 4 \times 10^{-5}$  psi $^{-1}$ ,  $k = 0.5$  md and  $\mu = 0.02$  cp. The well is intersected by a vertical fracture with  $h_f = 150$  ft,  $k_{fw} = 12,000$  md-ft and  $x_f = 190$  ft. What would be the expected duration of the formation linear flow regime in a pressure buildup transient test?

#### Solution

The dimensionless conductivity-height product  $C_{fD}h_{fD}$  is determined with Eqs. 12-5 and 12-7:

$$C_{fD}h_{fD} = \frac{12,000}{(0.5)(190)} \frac{150}{100} = 189.$$

The dimensionless time at which the formation linear flow would start is determined with Eq. 12-13:

$$t_{Dbf} = \frac{100}{(189)^2} = 2.8 \times 10^{-3}.$$

The dimensionless times that correspond to the start and end of the formation linear flow regime are determined with Eqs. 12-1 and 12-14, respectively:

$$t_{bif} = \frac{(2.8 \times 10^{-3})(0.10)(0.02)(4 \times 10^{-5})(190^2)}{(0.000264)(0.5)} = 0.06 \text{ hr}$$

$$t_{elf} = \frac{(0.016)(0.10)(0.02)(4 \times 10^{-5})(190^2)}{(0.000264)(0.5)} = 0.35 \text{ hr.}$$

It is therefore determined that the formation linear flow regime would be exhibited in the pressure buildup transient behavior for about 17 min:

$$t_{elf} - t_{bif} = 0.35 - 0.06 = 0.29 \text{ hr} = 17.4 \text{ min.}$$

### 12-2.5. Pseudoradial flow regime

All vertically fractured wells (regardless of the  $C_{fD}$  value) may exhibit a pseudoradial flow behavior at late times before the effects of boundaries are observed. During the infinite-acting pseudoradial flow regime, the flux distribution in the fracture has stabilized and the transient behavior of the well can be equated to that of an unfractured well with an enlarged effective wellbore radius  $r_w'$ . The radial flow steady-state skin effect resulting from this flow regime is a function of  $C_{fD}$  only. Prior to the pseudoradial flow regime, an apparent radial flow steady-state skin effect resulting from a vertical fracture may also be considered. However, during the early transient behavior of a vertical fracture, the flux distribution in the fracture has not stabilized and the apparent radial flow steady-state skin effect is a function of both  $C_{fD}$  and time. A composite illustration of the various flow regimes that may be exhibited by a finite-conductivity fracture is presented in Fig. 12-23.

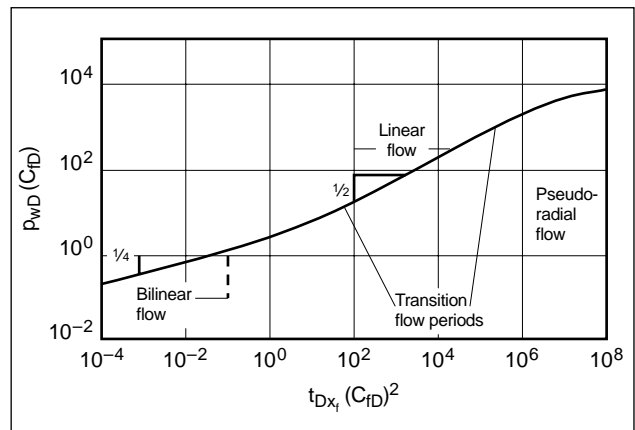


**Figure 12-23.** Log-log response of a finite-conductivity vertical fracture exhibiting various flow regimes.

The wellbore pressure transient behavior of a vertically fractured well during the pseudoradial flow regime is

$$p_{wD} = \frac{1}{2} [\ln t_{Dr'_w} + 0.8091]. \quad (12-15)$$

The corresponding dimensionless time referenced to the effective wellbore radius  $r'_w$  is

$$t_{Dr'_w} = \frac{0.000264kt}{\phi\mu c_f r_w'^2}, \quad (12-16)$$

and the effective wellbore radius is

$$r'_w = r_w e^{-s}, \quad (12-17)$$

where  $r_w$  is the wellbore radius in ft and  $s$  is the apparent steady-state skin effect caused by the fracture. The equivalent radial flow steady-state skin effect resulting from a fracture is presented in Fig. 12-24. A very high conductivity fracture ( $C_{fD} > 500$ , and for practical purposes  $C_{fD} > 50$ ) has  $r'_w = x_f/2$ , whereas the effective wellbore radius of a very low conductivity fracture ( $C_{fD} < \pi/20$ , and for practical purposes  $C_{fD} < 0.6$ ) is  $0.25x_f C_{fD} = 0.25k_f w/k$  and independent of  $x_f$ .

The onset of fully developed pseudoradial flow occurs at approximately a dimensionless time (Eq. 12-1) equal to 3. The dimensionless time at which pseudoradial flow begins is actually a function of  $C_{fD}$ , varying from a dimensionless time of 2 for  $C_{fD} = \pi/10$  to a dimensionless time of 5 for  $C_{fD} = 100\pi$ . Once fully developed pseudoradial flow behavior is exhibited, the classic semilog analysis procedures presented in Chapter 2 are applicable.

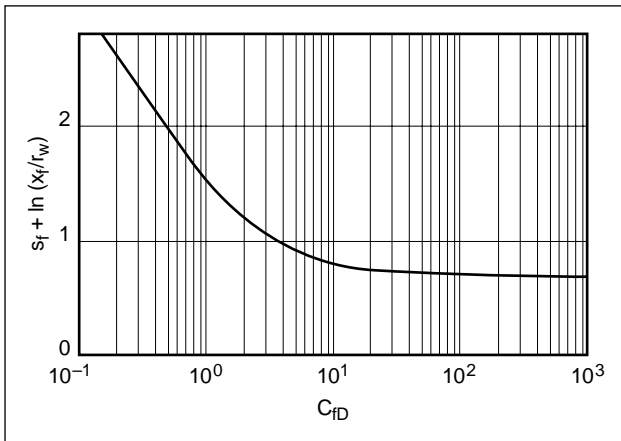


**Figure 12-24.** Equivalent radial flow steady-state skin effect resulting from a finite-conductivity vertical fracture (Cinco-Ley and Samaniego-V., 1981a).

- Example calculation of apparent pseudoradial skin effect and folds of increase

Using the variables of “Example calculation for the end of bilinear flow regime” (page 12-12) and  $C_{fD} = 1$ , calculate the folds of increase of a fractured well over an unfractured, undamaged well, with the reservoir radius  $r_e = 3000$  ft and  $r_w = 0.328$  ft.

#### Solution

With  $C_{fD} = 1$  from Fig. 12-17,  $s + \ln(x_f/r_w) = 1.5$  and thus  $s = 1.5 - \ln(500/0.328) = -5.8$ . The productivity index ratio is

$$J_F/J = \frac{\ln(r_e/r_w)}{\ln(r_e/r_w) + s} = \frac{\ln(3000/0.328)}{\ln(3000/0.328) - 5.8} \approx 2.8,$$

where  $J_F$  is the fractured well productivity index and  $J$  is the pseudosteady-state productivity index.

The effective wellbore radius is  $r'_w = 0.328 \times \exp(+5.8) = 108$  ft.

### 12-2.6. Pseudosteady-state flow regime

In finite reservoirs at late times (fully developed boundary dominated flow), the actual type of well completion does not solely govern the pressure transient behavior of the well. Rather, the dimensionless pressure in a closed system is also a function of the reservoir drainage area size and shape, well location, formation properties and time. The fully developed pseudosteady-state transient behavior (i.e., the transient has reached all boundaries) of a well is characterized by pressure and pressure derivative behavior following the same unit-slope line on a log-log graph. The dimensionless wellbore pressure  $p_{wD}$  of a vertically fractured well under fully developed pseudosteady-state flow conditions is

$$p_{wD} = 2\pi t_{DA} + \ln\left(\frac{x_e}{x_f}\right) + \frac{1}{2} \ln\left(\frac{2.25}{C_A}\right). \quad (12-18)$$

It is assumed in this relationship that the well is centrally located in a square drainage area with dimensions of  $2x_e$  on each side (Earlougher, 1977). The reservoir geometric shape factor  $C_A$  in Eq. 12-18 is a function of the reservoir drainage area shape, well location, well type and ratio of the drainage area extent to fracture half-length  $x_e/x_f$ . Table 12-1 summarizes the geometric shape factors for vertically

**Table 12-1. Geometric shape factors for pseudosteady-state flow.**

$x_e/x_f$	$C_A$
1	0.7887
2	1.6620
3	1.9607
4	2.0296
5	2.0348
6	2.0760
7	2.1665
8	2.2984
9	2.4636
10	2.6541

fractured wells that are centrally located in square drainage areas equal to  $4x_e^2$ .

The dimensionless time  $t_{DA}$  referenced to the drainage area of the reservoir is

$$t_{DA} = \frac{0.000264kt}{\phi\mu c_i A}, \quad (12-19)$$

where  $A$  is the reservoir drainage area in  $\text{ft}^2$ .

- Example calculation of time to start of pseudosteady-state flow

For a vertically fractured well centrally located in a square drainage area, the value of  $t_{DA}$  at which fully developed pseudosteady-state flow occurs is approximately equal to 0.175 (for all  $x_e/x_f$  ratios between 1 and 10). The onset of fully developed pseudosteady-state flow can be approximated for this same range of  $x_e/x_f$  values within 1% error for  $t_{DA} \approx 0.09$ . What would be the transient time required for fully developed pseudosteady-state flow behavior to occur on a constant-rate drawdown of a 160-acre reservoir with the properties in “Example calculation for start and end of formation linear flow” (page 12-14)? At what time could the pseudosteady-state approximation  $t_{DA} \approx 0.09$  be used?

#### Solution

The drainage area of the reservoir is

$$A = (43,560)(160) = 6,969,600 \text{ ft}^2.$$

The time at which fully developed pseudosteady-state flow occurs is obtained by rearranging Eq. 12-19 with  $t_{DA} = 0.175$ :

$$t = \frac{(0.175)(0.10)(0.02)(4 \times 10^{-5})(6,969,600)}{(0.000264)(0.5)} = 739 \text{ hr} \approx 31 \text{ days}.$$

Within 1% error, Eq. 12-18 would therefore be applicable for describing the dimensionless wellbore pressure transient behavior at

$$t = \frac{(0.09)(0.10)(0.02)(4 \times 10^{-5})(6,969,600)}{(0.000264)(0.5)} = 380 \text{ hr} \approx 16 \text{ days}.$$

## 12-3. Factors affecting fractured well performance

The dimensionless wellbore pressure solutions presented in the previous section are applicable for linear reservoir flow problems. Linear fluid flow problems are those in which the reservoir and fracture can be assumed to be uniform, homogeneous and isotropic. The reservoir is assumed to contain a slightly compressible liquid of constant viscosity and compressibility. The fracture is assumed to be a rectangular vertical slab of uniform width, height, length and conductivity. The fluid flow throughout the system is also assumed to obey Darcy's law.

Many nonideal conditions exist that result in a transient behavior that does not strictly follow the ideal reservoir behavior previously discussed. Some of the nonideal conditions that must be considered are non-Darcy fluid flow in the fracture and reservoir, nonlinear fluid properties, spatially varying fracture and reservoir material properties and geometry, and heterogeneous reservoir systems that include layered reservoirs and dual-porosity systems.

### 12-3.1. Non-Darcy flow behavior

High-velocity fluid flow in porous media results in pressure losses that generally cannot be described by Darcy's law. Evidence of this has been available for many years (Forchheimer, 1901). The effect of high-velocity fluid flow in a reservoir is that an additional pressure loss is exhibited that is believed to be due primarily to inertial slip effects resulting from the rapid acceleration and deceleration of the fluid particles as the fluid moves along the tortuous flow path of the interconnected pore space of the reservoir rock or fracture proppant (Geertsma, 1974). Although the additional pressure loss resulting from high-velocity fluid flow in the reservoir is often referred to as turbu-

lent flow, the proper classification for this flow behavior is inertial-turbulent, because in many cases the pore throats in the reservoir rock or fracture proppant are too small for a given production rate level to allow fully developed turbulence similar to that commonly observed in pipe flow.

Non-Darcy flow pressure losses in the fracture are of primary interest in the analysis of relatively high rate gas wells, but they can also be important for very high rate oil wells (Bale *et al.*, 1994b) and converging fracture flow because of a limited wellbore connection (e.g., orthogonal fracture in a horizontal well). Wattenbarger and Ramey (1969) investigated the effects of turbulent (or inertial) flow in both the reservoir and fracture and found that often inertial flow in the fracture is more significant than high-velocity flow effects in the reservoir.

Holditch and Morse (1976) investigated the effects of non-Darcy fluid flow in finite-conductivity fractures using a finite-difference numerical simulator. Although

Wattenbarger and Ramey and Holditch and Morse produced qualitative estimates of the effects of non-Darcy fracture flow, the study by Guppy *et al.* (1982b) was the first investigation to provide a means of quantitatively determining the effects of non-Darcy flow on the pressure transient behavior of a well intersected by a finite-conductivity vertical fracture (Fig. 12-25). The reduction in apparent fracture conductivity resulting from non-Darcy flow in a constant-rate drawdown is demonstrated in Fig. 12-26.

Guppy *et al.* (1982a) also provided a correlation for computing the apparent reduction in dimensionless fracture conductivity  $C_{fDapp}$  of a vertically fractured well that has been produced at a constant rate. The correlation resulting from non-Darcy fracture flow for a constant-rate drawdown is

$$\frac{C_{fDapp}}{C_{fDtrue}} = \frac{1}{1 + 0.31q_{DND}}, \quad (12-20)$$

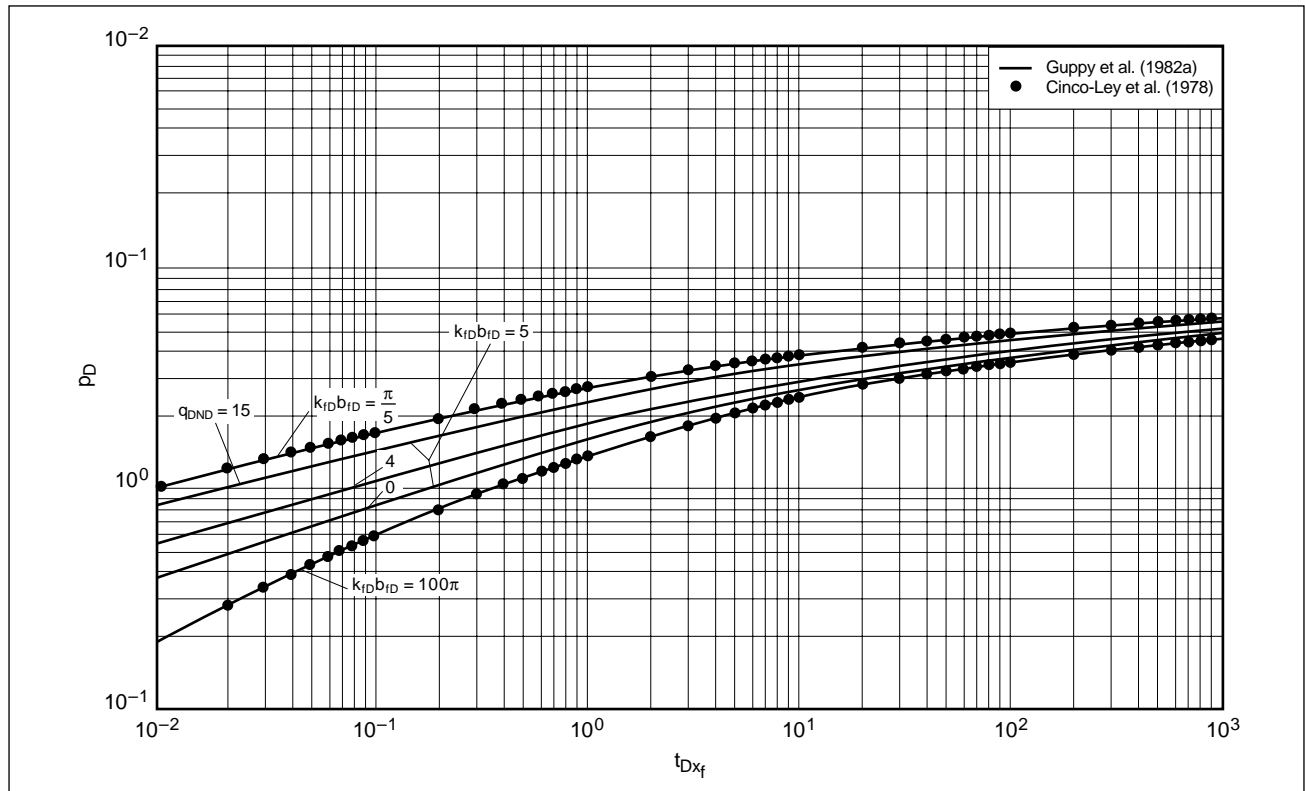


**Figure 12-25.** Effect of non-Darcy flow on the pressure transient response of finite-conductivity vertical fractures.

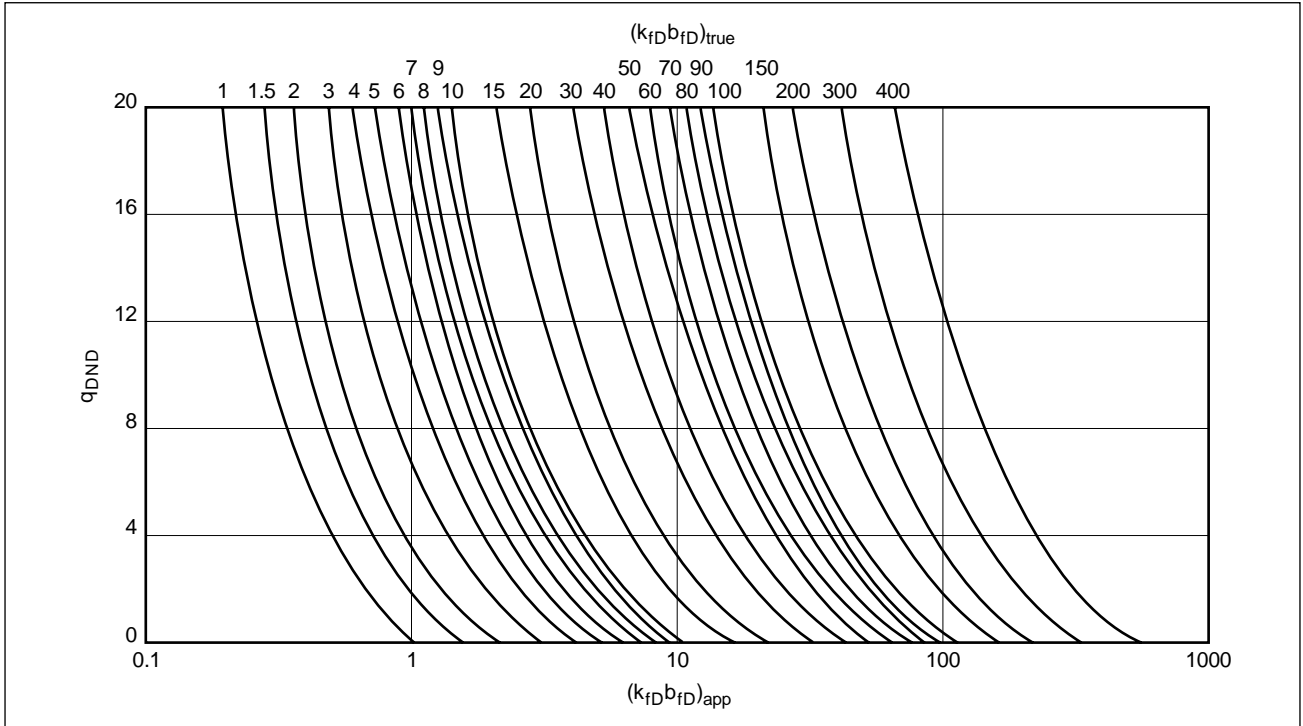


**Figure 12-26.** Apparent fracture conductivity reduction resulting from non-Darcy fracture flow.

and the dimensionless non-Darcy flow rate  $q_{DND}$  for oil and gas, respectively, is

$$q_{DND} = \frac{1.03 \times 10^{-15} k_f \rho_o \beta q_o}{w h \mu_o} \quad (12-21)$$

$$q_{DND} = \frac{4.64 \times 10^{-16} k_f \beta M W q_g}{w h \mu_{gi}}.$$

The ranges of applicability for the Eq. 12-20 correlation are

- all values of  $q_{DND}$  that yield  $C_{fDapp} > 2$ , for  $C_{fDtrue} < 10$
- for  $1 \leq q_{DND} \leq 20$  and  $10 \leq C_{fDtrue} \leq 100$
- for  $q_{DND} \leq 10$  and  $100 \leq C_{fDtrue} \leq 500$ .

The fracture permeability  $k_f$  in Eq. 12-21 is in md, fracture width  $w$  is in ft, reservoir net pay thickness  $h$  and average fracture height  $h_f$  are in ft, fluid density  $\rho_o$  is in lbm/ft<sup>3</sup>, fluid viscosities  $\mu_o$  and  $\mu_{gi}$  are in cp, oil flow rate  $q_o$  is in STB/D, gas flow rate  $q_g$  is in Mscf/D, and the gas molecular weight  $MW$  is in lbm/lbm-mol. The molecular weight of natural gas can be computed with

$$MW = 28.96 \gamma_g, \quad (12-22)$$

where  $\gamma_g$  is the gas specific gravity (relative to air) and the constant is the molecular weight of air.

The non-Darcy flow coefficient  $\beta$  in Eq. 12-21 is in ft<sup>-1</sup>. A simple expression for estimating the non-Darcy flow coefficient was specifically developed for fracture flow by Cooke (1973):

$$\beta = \frac{30.88 \times 10^6 b'}{k_f^{a'}}. \quad (12-23)$$

The coefficient  $b'$  and exponent  $a'$  in Eq. 12-23 are specific to the type and mesh size of the fracture proppant and are determined experimentally. Table 12-2 lists examples of coefficients and exponents for Hickory sand (Cooke, 1973) for which the fracture permeability  $k_f$  in Eq. 12-23 is in md.

**Table 12-2. Non-Darcy coefficients for fracture flow.**

Mesh	$a'$	$b'$
8/12	1.24	17,424
10/20	1.34	27,539
20/40	1.54	110,470
40/60	1.60	69,405

Extension of the Guppy *et al.* (1982b) correlation relating the true dimensionless fracture conductivity  $C_{fDtrue}$  and the apparent (resulting from non-Darcy flow) dimensionless fracture conductivity  $C_{fDapp}$  developed for constant-rate drawdown transients (Eq. 12-20) to other inner boundary condition transients (e.g., constant pressure drawdown or shut-in transients) is not directly possible because the non-Darcy fracture flow problem is nonlinear. However, Guppy *et al.* (1982a) also developed a similar correlation for the interpretation of pressure buildup responses of fractured wells that have been produced under non-Darcy fracture flow conditions:

$$\frac{C_{fDapp}}{C_{fDtrue}} = \frac{1}{1 + 0.55q_{DND}} \quad (12-24)$$

The dimensionless non-Darcy flow rate  $q_{DND}$  is evaluated using the production rate of the drawdown transient preceding the pressure buildup transient and Eq. 12-21. The range of applicability of Eq. 12-24 is defined as

- for  $q_{DND} \leq 2$  and  $C_{fDtrue} < 10$
- for  $1 \leq q_{DND} \leq 10$  and  $C_{fDtrue} \geq 10$ .

Gidley (1990) also developed a simple correlation procedure for estimating the reduction in  $C_{fDapp}$  resulting from non-Darcy fracture flow. This expression is correlated in terms of a fracture flow Reynold's number  $N_{Re}$ :

$$\frac{C_{fDapp}}{C_{fDtrue}} = \frac{1}{1 + N_{Re}} \quad (12-25)$$

The fracture flow Reynold's numbers for oil and gas, respectively, are

$$N_{Re} = \frac{5.53 \times 10^{-16} k_f \rho_o \beta q_o}{wh\mu_o} \quad (12-26)$$

$$N_{Re} = \frac{7.00 \times 10^{-15} k_f \gamma_g \beta q_g}{wh\mu_{gi}}$$

Additional consideration of non-Darcy fracture flow is in Chapter 10.

- Example calculation of reduction in apparent fracture conductivity resulting from non-Darcy fracture flow

A vertically fractured gas well has  $h_f = 100$  ft and  $w = 0.25$  in. The fracture is propped with

20/40-mesh Hickory fracture sand and has  $k_f = 85,000$  md at reservoir confining conditions. The well is produced at 10 MMscf/D, and  $\gamma_g = 0.6$ . Determine the percent apparent fracture conductivity reduction resulting from non-Darcy fracture flow for the reservoir described in "Example calculation for start and end of formation linear flow" (page 12-14) using both the Guppy *et al.* and Gidley evaluation procedures.

#### Solution

The molecular weight of the reservoir gas is determined with Eq. 12-22:

$$MW = 28.96(0.6) = 17.4 \text{ lbm/lbm-mol.}$$

The inertial flow coefficient is determined with Eq. 12-23 and the values in Table 12-2:

$$\beta = \frac{30.88 \times 10^6 (110,470)}{85,000^{1.54}} = 87,421 \text{ ft}^{-1}.$$

The dimensionless non-Darcy fracture flow rate  $q_{DND}$  is determined with Eq. 12-21 for gas:

$$q_{DND} = \frac{(4.64 \times 10^{-16})(85,000)(87,421)(17.4)(10,000)}{(0.25/12)(100)(0.02)} = 14.4.$$

The true dimensionless fracture conductivity  $C_{fDtrue}$  of the fracture system is determined with Eq. 12-7:

$$C_{fDtrue} = \frac{(85,000)(0.25/12)}{(0.5)(190)} = 18.6.$$

Therefore, the second condition governing the range of applicability of Eq. 12-20 is satisfied. The apparent dimensionless fracture conductivity  $C_{fDapp}$  is determined for the Guppy *et al.* analysis with Eq. 12-20:

$$C_{fDapp} = \frac{18.6}{1 + (0.31)(14.4)} = 3.4.$$

The percent reduction in apparent fracture conductivity using the Guppy *et al.* analysis procedure is thus

$$\% \text{ reduction} = \frac{(18.6 - 3.4)(100)}{18.6} = 81.7\%.$$

The vertically fractured well would therefore behave as if the fracture had a conductivity  $k_f w$  of only



$$(k_f w)_{app} = (85,000) \left( \frac{0.25}{12} \right) (1 - 0.817) = 324 \text{ md-ft},$$

when the actual conductivity of the propped fracture was 1771 md-ft.

For the Gidley analysis procedure, the fracture flow  $N_{Re}$  is determined with Eq. 12-26 for gas:

$$N_{Re} = \frac{(7.00 \times 10^{-15})(85,000)(0.6)(87,421)(10,000)}{(0.25/12)(100)(0.02)} = 7.49.$$

The apparent dimensionless fracture conductivity is determined with Eq. 12-25:

$$C_{fDapp} = \frac{18.6}{1 + 7.49} = 2.19.$$

The percent reduction in apparent fracture conductivity is therefore

$$\% \text{ reduction} = \frac{(18.6 - 2.19)(100)}{18.6} = 88.2\%.$$

Both analysis procedures demonstrate that a significant reduction in  $C_{fDapp}$  would be observed for non-Darcy fracture flow in this example and that fracture design changes are warranted, as discussed in Chapter 10.

### 12-3.2. Nonlinear fluid properties

A common factor that may complicate analysis or prediction of the transient behavior of a well is the nonlinear behavior of reservoir fluids. The variation of reservoir fluid physical properties with time and pressure must be accounted for to evaluate the transient behavior of a well and obtain reliable estimates of the fracture and reservoir properties for long-term production forecasts. All gas reservoirs and some oil solution-gas reservoirs require integral transformations to effectively linearize the resulting nonlinear reservoir flow problem.

Integral transformations are used to account for variation in reservoir fluid properties with the pressure level and time. For gas reservoirs, Al-Hussainy *et al.* (1966) introduced the real gas pseudopressure integral transformation to effectively linearize the diffusive part of the diffusivity equation governing real gas flow in the reservoir:

$$m(p) = \int_{p_o}^p \frac{p' dp'}{\mu_g Z}. \quad (12-27)$$

The gas viscosity  $\mu_g$  and the real gas law deviation factor  $Z$  in Eq. 12-27 are pressure-dependent fluid properties.

A similar integral transformation was presented by Agarwal *et al.* (1979) to effectively complete the linearization of the gas diffusivity equation. This integral transformation, to account for variation in reservoir fluid properties with respect to time, is commonly referred to as pseudotime:

$$t_a(t) = \int_0^t \frac{dt}{\mu_g C_i} = \int_{p_i}^{p_r(t)} \left( \frac{\partial t}{\partial p} \right) \frac{dp}{\mu_g C_i}. \quad (12-28)$$

Agarwal *et al.* introduced the pseudotime integral transformation on an intuitive basis. Lee and Holditch (1982) later provided theoretical justification for use of the pseudotime integral transformation in analysis of the transient behavior of gas wells. The evaluation of pseudopressure and pseudotime integral transformations for well performance prediction with analytic solutions is discussed in greater detail by Poe *et al.* (1995). Evaluation of the pseudotime integral transformation for long-term well performance prediction includes consideration of the variation in fluid properties over the entire reservoir volume with respect to time to effectively linearize the gas diffusivity equation.

The corresponding definitions of dimensionless pseudotime and pseudopressure for gas reservoir analyses, respectively, are

$$t_{aD} = \frac{0.000264 k t_a(t)}{\phi x_f^2} \quad (12-29)$$

$$p_{pWD} = \frac{khT_{sc} [m(p_i) - m(p_{wf})]}{50,300 p_{sc} T q_g}. \quad (12-30)$$

The dimensionless pseudotime and pseudopressure definitions in these equations are used in gas reservoir analyses in place of Eqs. 12-1 and 12-2, respectively.

The standard condition temperature  $T_{sc}$  and pressure  $p_{sc}$  in Eq. 12-30 are specified by the applicable governmental regulatory agency. A typical value for  $p_{sc}$  is 14.7 psia, but it may range between 14.65 and 14.73 psia. The most common  $T_{sc}$  used is 60°F [520°R].

The multiphase flow analysis procedure developed by Perrine (1957) and Martin (1959) for radial flow

has been successfully applied to the analysis of pressure buildup data for fractures. The linearization of the multiphase flow nonlinear problem using Perrine and Martin's approach assumes that the fluid saturation distributions in the reservoir are essentially uniform over the reservoir drainage area. The linearization involves replacing the single-phase mobility of the system with a comparable multiphase mobility:

$$\lambda_i = k \left( \frac{k_{ro}}{\mu_o} + \frac{k_{rw}}{\mu_w} + \frac{k_{rg}}{\mu_g} \right). \quad (12-31)$$

The products of the absolute permeability  $k$  and the relative permeabilities  $k_{ro}$ ,  $k_{rw}$  and  $k_{rg}$  of each of the fluid phases are the respective effective permeabilities  $k_o$ ,  $k_w$  and  $k_g$ . The total system compressibility is identical to that used in the single-phase flow analysis procedures:

$$c_t = S_o c_o + S_w c_w + S_g c_g + c_f, \quad (12-32)$$

where the fluid saturations  $S_o$ ,  $S_w$  and  $S_g$  of the oil, water and gas phases, respectively, are expressed as fractions of the pore volume, and the compressibilities  $c_o$ ,  $c_w$  and  $c_g$  of the fluids and pore compressibility  $c_f$  are in  $\text{psia}^{-1}$ .

The total reservoir production rate  $q_{RT}$  represents the contribution of each of the fluid phases:

$$q_{RT} = q_o B_o + q_w B_w + \left( q_g - \frac{q_o R_{so}}{1000} - \frac{q_w R_{sw}}{1000} \right) B_g, \quad (12-33)$$

where  $q_{RT}$  is in RB/D and the fluid-phase production rates  $q_o$ ,  $q_w$  and  $q_g$  are in STB/D, STB/D and Mscf/D, respectively. The fluid formation volume factors  $B_o$ ,  $B_w$  and  $B_g$  are in RB/STB, RB/STB and RB/Mscf, respectively. The solution-gas/oil ratio  $R_{so}$  and solution-gas/water ratio  $R_{sw}$  are in scf/STB.

Substitution of these relationships into Eqs. 12-1 and 12-2 results in definitions of the multiphase flow analysis dimensionless time and pressure, respectively:

$$t_D = \frac{0.000264 \lambda_i t}{\phi c_t x_f^2} \quad (12-34)$$

$$p_{wD} = \frac{\lambda_i h (p_i - p_{wf})}{141.2 q_{RT}}. \quad (12-35)$$

For wells that produce significant amounts of oil, gas and water simultaneously, a multiphase flow

analysis of the reservoir performance is usually preferable to a single-phase flow transient analysis. There are no set standards for selecting multiphase analysis over single-phase analysis. However, there are qualitative guidelines that classify which type of analysis is appropriate:

- If the producing gas/liquid ratio exceeds approximately 45,000 scf/STB, there is essentially single-phase gas flow in the reservoir and a gas reservoir analysis should be used.
- If the gas/oil ratio is less than 20,000 scf/STB and the water production rate is significantly less (1 order of magnitude or more) than the oil production rate, a single-phase oil reservoir analysis is generally appropriate.
- If the water production rate is comparable to or exceeds the oil production rate and the gas/liquid ratio is less than 45,000 scf/STB, a multiphase analysis is generally appropriate.
- Wells that cannot be classified in the preceding three steps may require both a single-phase analysis (of the principal produced-fluid phase) and a multiphase analysis. The effective permeabilities to the principal fluid phase from both analyses should be in reasonable agreement. If significant disagreement exists, the multiphase analysis estimates of effective permeabilities and steady-state skin effect are usually the more reliable of the two analyses.

### 12-3.3. Fracture damage and spatially varying fracture properties

The effects of flow impairments along the fracture face and in the fracture near the wellbore on the transient behavior of finite-conductivity vertical fractures were investigated by Cinco-Ley and Samaniego-V. (1977, 1981a). Fluid-loss flow impairment along the fracture surface in the reservoir is commonly referred to as a fracture face skin effect. Flow impairment caused by reduced conductivity in the fracture near the wellbore is commonly described as a choked fracture. Both of these types of flow impairments in fractured wells result in a lowered productivity than would be obtained if flow impairments were not present.

Fluid-loss damage in the reservoir adjacent to the fracture is illustrated in Fig. 12-27. A choked fracture with a significant fracture conductivity reduction

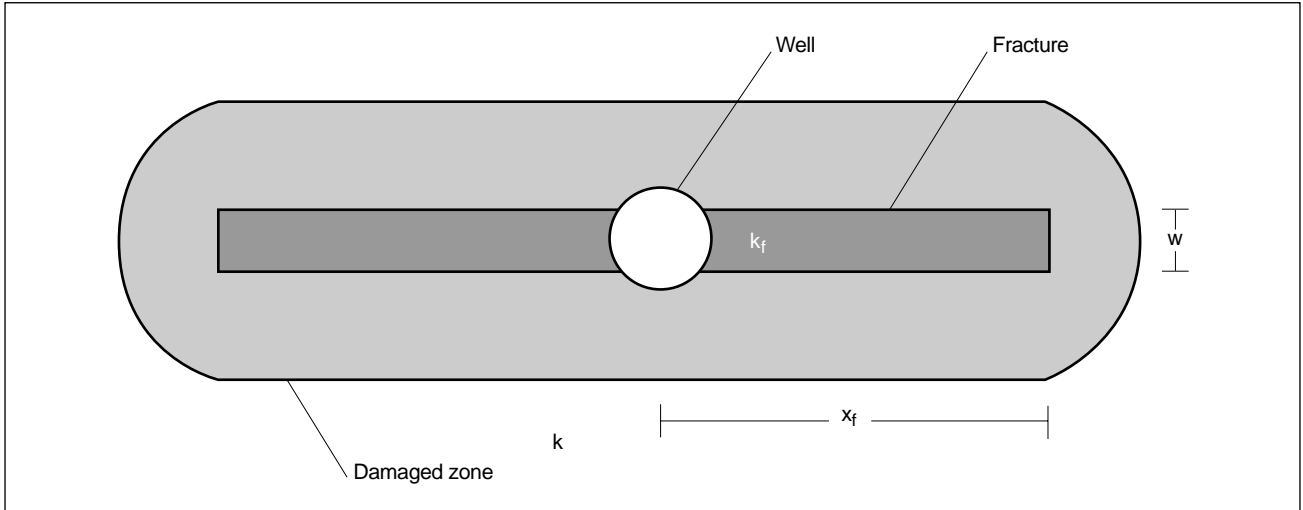


**Figure 12-27.** Fracture face skin effect damage flow impairment.

in the vicinity of the wellbore is shown in Fig. 12-28. As noted in Section 12-2.3, the bilinear flow graph of  $\Delta p$  versus the fourth root of time provides a diagnostic of a choked fracture and the  $\Delta p$  intercept quantifies the choke's pressure loss. The effect on the transient behavior of finite-conductivity fractures resulting from fracture damage skin effects is illustrated in Fig. 12-29. The effects on the effective wellbore radius of choked and damaged infinite-conductivity fractures in the pseudoradial regime are compared in Fig. 12-30.

Cinco-Ley and Samaniego-V. (1977, 1981a) introduced a relationship for quantifying fracture damage skin effects in terms of the fracture half-length  $x_f$ , extent of the damaged region into the reservoir normal to the fracture plane  $b_s$  and undamaged-to-damaged permeability ratio  $k/k_s$ :

$$s_{fs} = \frac{\pi b_s}{x_f} \left( \frac{k}{k_s} - 1 \right). \quad (12-36)$$

The fracture damage skin effect  $s_{fs}$  from Eq. 12-36 is not readily equated to a radial flow steady-state skin effect  $s$  because these two quantities are referenced to different system characteristic lengths and the different flow patterns in the reservoir are described by the two steady-state skin effects. Typical values of fracture face skin effect damage from clean-breaking fracturing fluids are generally low, on the order of 0.05 or less.

Holditch (1979b) also studied the effect of fluid-loss-induced impairment in low-permeability reservoirs. A finite-difference reservoir simulation model was used to investigate water blockage and post-treatment fracture fluid cleanup of vertical fractures, including the effects of relative permeability and capillary pressure changes in the vicinity of the fracture. The study found water blockage (i.e., relative permeability effects) in low-permeability gas reservoirs could result in significant production impairment of a fractured well.

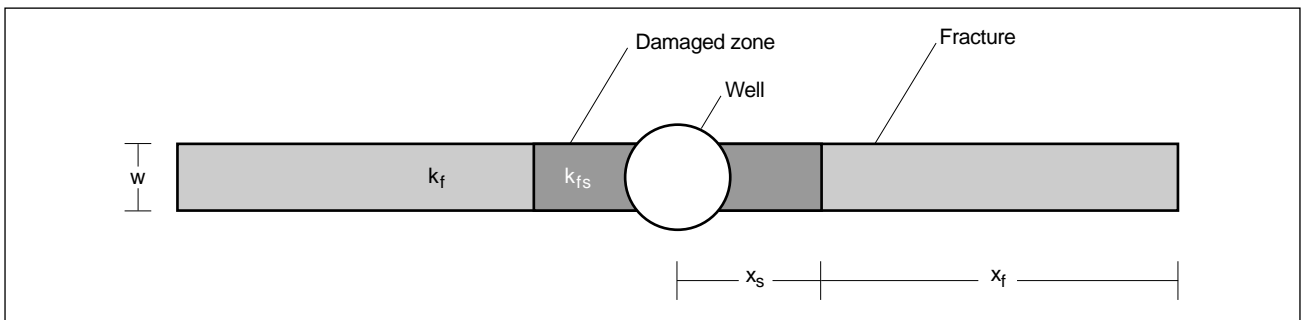


**Figure 12-28.** Choked-fracture flow impairment.  $k_{fs}$  = fracture permeability in the near-well skin effect zone,  $x_s$  = half-length of the skin effect zone.

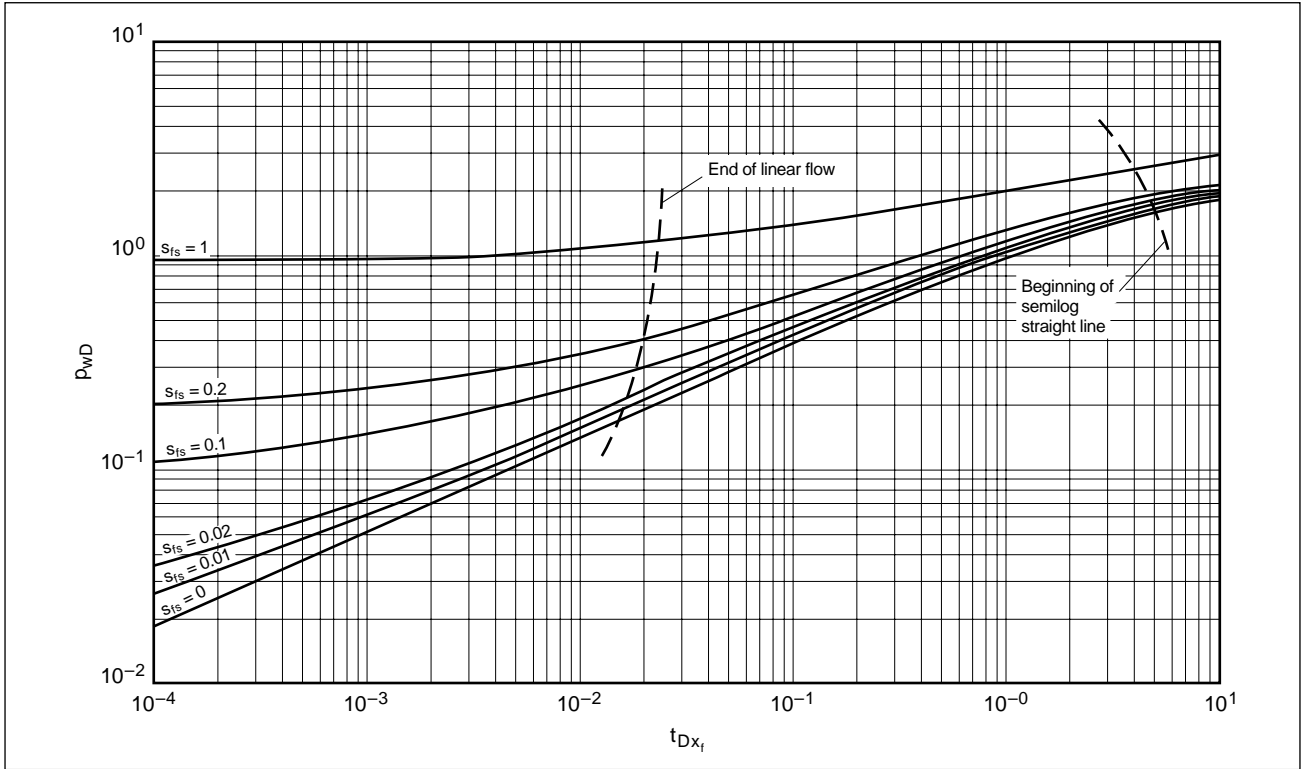


**Figure 12-29.** Damaged fracture pressure response (Cinco-Ley and Samaniego-V., 1981a).

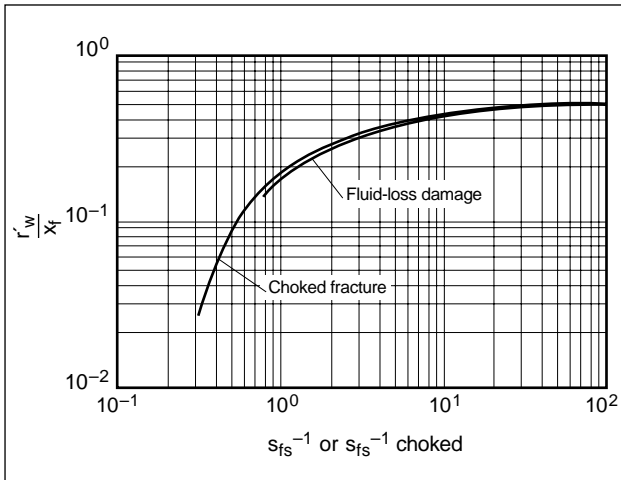


**Figure 12-30.** Effect of damaged fractures on effective wellbore radius.

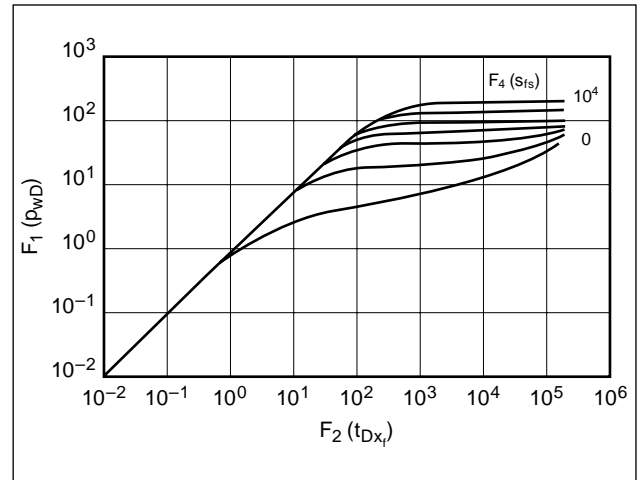


**Figure 12-31.** Pressure response of fluid-loss-damaged fractures (Wong et al., 1984).

Wong *et al.* (1984) presented a correlation technique for evaluating the pressure response of fluid-loss-damaged fractures. Figure 12-31 represents the effect of fluid-loss damage on the bilinear flow transient behavior of finite-conductivity fractures and is correlated in terms of three functional groups:

$$F_1(p_{wD}) = p_{wD} \left( \frac{C_{fD}^2}{C_D} \right)^{1/3} \quad (12-37)$$

$$F_2(t_D) = t_D \left( \frac{C_{fD}}{C_D^2} \right)^{2/3} \quad (12-38)$$

$$F_4(s_{fs}) = \frac{s_{fs}}{(C_{fd} C_D^2)^{1/3}}. \quad (12-39)$$

The dimensionless wellbore storage coefficient  $C_D$  used in these functional groups is

$$C_D = \frac{0.89C}{\phi c_f h x_f^2}, \quad (12-40)$$

where the dimensional wellbore storage  $C$  is in bbl/psi. Cinco-Ley and Samaniego-V. (1977, 1981a) investigated the transient behavior of a choked fracture with a conductivity reduction in the fracture near the wellbore. This is one subset of a more general set of problems involving evaluation of the transient behavior of vertical fractures with spatially varying conductivity.

Bennett *et al.* (1983) studied the transient behavior of a vertically fractured well with spatially varying fracture conductivity. A finite-difference reservoir simulator was used to investigate the transient performance of a fractured well with a stepwise-varying conductivity distribution. It was found that the initial transient behavior of a fractured well with this type of conductivity distribution is governed by the conductivity of the fracture nearest the wellbore. At later transient times, the transient behavior of a well with a monotonically decreasing fracture conductivity with distance from the wellbore can be correlated with the transient behavior of an equivalent uniform-conductivity fracture by using an average of the dimensionless fracture conductivity distribution:

$$\bar{C}_{fd} = \frac{1}{k x_f^2} \int_0^x k_f w dx'. \quad (12-41)$$

Soliman (1986a, 1986b) also investigated the effect of spatially varying fracture conductivity on the pressure transient behavior of a finite-conductivity fracture. The results of those studies provide a qualitative reference for the effects of spatially varying fracture conductivity on the transient behavior of vertical fractures. The analytic solutions for the pressure transient behavior of finite-conductivity vertical fractures with arbitrarily varying fracture conductivity and height were later developed by Poe *et al.* (1992). The solutions presented by Poe *et al.* for finite-conductivity vertical fractures include fracture storage effects, as well as an extension of the model by Cinco-Ley and Meng (1988) to include spatially varying fracture

conductivity, for which the fracture storage effects are assumed negligible.

- Example calculation of fracture face skin effect

A vertical well is hydraulically fractured with 300 bbl of proppant-laden slurry comprising water-base gel fracturing fluid and proppant. The fracture is created using a tip screenout procedure (i.e., proppant is distributed over the entire created hydraulic fracture length), which results in a symmetrical fracture with  $x_f = 200$  ft,  $h_f = 120$  ft (also the permeable section for fluid-loss thickness) and an average propped  $w = 0.25$  in. The reservoir initially has  $k_o = 5$  md,  $k_{ro} = 0.8$  and  $\phi = 10\%$  with an initial oil saturation  $S_{oi} = 80\%$ . The flushed zone is assumed to have an oil saturation of 25%, for which the relative permeability to oil is 0.1. What would be the steady-state fracture face skin effect observed in a single-phase pressure buildup analysis of this fractured well? For simplicity, assume that all damage is caused by fluid saturation changes only.

#### Solution

The closed fracture volume is estimated as

$$\begin{aligned} V_f &= 2x_f w h_f \\ &= 2(200) \left( \frac{0.25}{12} \right) (120) \\ &= 1000 \text{ ft}^3 \approx 178 \text{ bbl.} \end{aligned}$$

The total fracturing fluid lost into the formation is therefore

$$V_L = 300 - 178 \approx 122 \text{ bbl.}$$

The distance into the reservoir at which the fracturing fluid has penetrated through each face of the fracture is estimated volumetrically as

$$\begin{aligned} b_s &= \frac{V_L}{4\phi(S_{oi} - S_{or})h x_f} \\ &= \frac{122(5.615)}{4(0.1)(0.8 - 0.25)(120)(200)} \\ &= 0.13 \text{ ft} \approx 1.6 \text{ in.,} \end{aligned}$$

where  $S_{or}$  is the residual oil saturation.

The flushed zone effective permeability to oil is therefore

$$k_s = k_r(S_{or}) \left( \frac{k_o}{k_r(S_{oi})} \right) = (0.1) \left( \frac{5}{0.8} \right) = 0.625 \text{ md,}$$

which is an 87.5% reduction in the effective permeability to oil.

The steady-state fracture face skin effect that would be exhibited in the pressure transient analysis as a result of fracture fluid leakoff is determined with Eq. 12-36:

$$s_{fs} = \frac{\pi(0.13)}{200} = \left( \frac{5}{0.625} - 1 \right) = 0.014.$$

From Eq. 12-30,  $s_{fs}^{-1} = 1/0.014 = 70$ . This amount of fluid-loss impairment would have a negligible effect on the effective wellbore radius.

#### 12-3.4. Damage in high-permeability fracturing

Fracture face damage is most likely to have minor effects on the performance of fractured wells in low-permeability reservoirs. Long lengths, characteristic of fractures in these reservoirs, result in small values of the skin effect determined with Eq. 12-36. This is not the case in high-permeability wells, where fracture lengths are smaller, by as much as 2 orders of magnitude. Furthermore, high reservoir permeability results in considerable penetration of fluid-loss damage, unless extraordinary leakoff control measures are taken.

Mathur *et al.* (1995) studied various types of damage in high-permeability fractured wells and introduced a composite skin effect accounting for radial and fracture face permeability effects:

$$s_d = \frac{\pi}{2} \left[ \frac{b_2 k_r}{b_1 k_3 + (x_f - b_1) k_2} + \frac{(b_1 - b_2) k_r}{b_1 k_1 + (x_f - b_1) k_r} - \frac{b_1}{x_f} \right], \quad (12-42)$$

where, for convenience,  $b_1$  and  $b_2$  are the extents of the radial and fracture face damages, respectively, and  $k_r$ ,  $k_1$ ,  $k_2$  and  $k_3$  are the virgin radial, damage radial, fracture face and composite radial/fracture face permeabilities, respectively. If  $k_1 = k_r$ ,  $k_3 = k_2$  and  $b_1 = b_2$ , Eq. 12-42 reduces to Eq. 12-36.

Figure 12-32 is a graph of the composite skin effect as a function of the fracture face permeability impairment  $k_2/k_r$ , ratio of the extent of the fracture face damage to the fracture length  $b_2/x_f$  and radial skin effect. It is apparent that radial damage is largely insignificant, even in very high permeability reservoirs, except

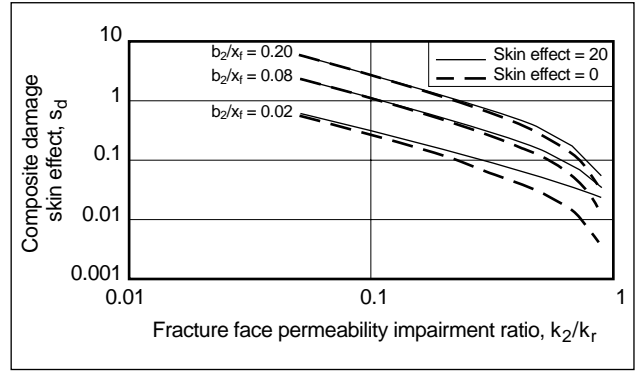


**Figure 12-32.** Variation of composite damage skin effect with the fracture face permeability impairment ratio (Mathur *et al.*, 1995).

for low fracture face permeability impairment, but in this case the composite skin effect is itself small.

The total pseudoradial skin effect ( $s_d$  plus the Cinco-Ley *et al.* [1978] fracture skin effect; Fig. 12-24) is plotted in an example calculation in Fig. 12-33 for  $C_{FD} = 1$ ,  $x_f = 25$  ft and  $k_r = 10$  md. The first conclusion is that the total skin effect  $s_t$  can be positive, as reported by several investigations of high-permeability fracturing.

A more important conclusion, however, is that the total skin effect is favorable (negative) if the extent of fracture face permeability impairment is controlled by reducing either the damage ratio  $k_2/k_r$  or the penetration ratio  $b_2/x_f$ . Impairment control for relatively short fractures in higher permeability formations has major implications in fracturing fluid selection (for damage) and the importance of leakoff control (fluid penetration).

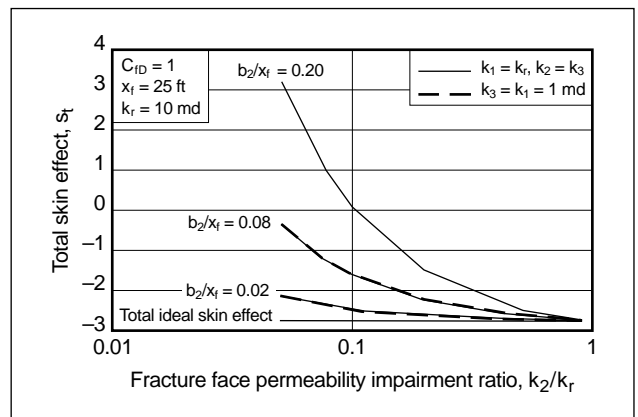


**Figure 12-33.** Variation of total skin effect with the fracture face permeability impairment ratio (Mathur *et al.*, 1995).

### 12-3.5. Heterogeneous systems

The transient behavior discussed in the preceding sections of this chapter is presented with the assumption that the reservoir is homogeneous and isotropic. Spatial variation in reservoir thickness, porosity, permeability and fluid saturations can be readily considered with finite-difference or finite-element simulation models. However, using analytic solutions to evaluate the transient behavior of vertically fractured wells, or their long-term production behavior, may require normalization procedures to properly account for spatial variation in the reservoir properties. Geostatistical techniques have been used to normalize spatial variation in reservoir properties and to correlate transient analysis and reservoir simulation results.

Reservoir permeability anisotropy is another common factor that complicates analysis of the transient behavior of finite-conductivity fractures. Directional permeability anisotropic effects on the transient behavior of finite-conductivity fractures were studied by Ben Naceur and Economides (1988). That study found that the anisotropy case believed most common is the one in which the direction of maximum permeability is perpendicular to the direction of minimum in-situ horizontal stress (i.e., parallel to the fracture plane). For this case, reservoir permeability anisotropy has an unfavorable effect on the productivity improvement obtained by fracturing the well. This unfavorable anisotropy ratio in effect results in a shorter apparent fracture half-length than that actually obtained.

For radial flow in anisotropic reservoirs, it is common practice to define an average effective horizontal permeability for the system that is the geometric mean of the directional permeabilities  $k_x$  and  $k_y$ :

$$k = \sqrt{k_x k_y}. \quad (12-43)$$

For  $k_x = 10k_y$ , the radial response from a prefracture well test yields  $k = 3.1k_y$ , whereas the fracture responds approximately as if  $k$  were only  $1.8k_x$ .

Another reservoir heterogeneity that must be considered in analysis of the transient behavior of vertically fractured wells and their future production performance is the effect of multiple reservoir layers, which may have significantly different formation properties, pore pressure levels, fracture half-lengths and drainage areal extents.

Bennett *et al.* (1986) investigated the transient response of hydraulically fractured wells in multi-

layer systems. They determined that fracture half-length is underestimated in a layered commingled reservoir if the layered nature of the formation is not properly considered. Bennett *et al.* introduced the concept of dimensionless reservoir conductivity  $C_{RD}$  to correlate single-layer and multilayer responses:

$$C_{RD} = \frac{1}{\bar{h} \sqrt{\bar{k} \phi c_i}} \sum_{j=1}^n h_j \sqrt{k_j (\phi c_i)_j}, \quad (12-44)$$

where  $C_{RD}$  is always less than or equal to unity for a multilayer system. For post-treatment analysis of fractured well transient behavior, the dimensionless time scale is  $t_D/C_{RD}^2$ , which shifts the fracture half-length scale by a factor of  $C_{RD}$ . Ignoring the layered reservoir nature may result in shorter than actual apparent fracture lengths from the analysis.

Camacho-V. *et al.* (1987) later extended the work by Bennett *et al.* on the concept of dimensionless reservoir conductivity  $C_{RD}$  to include the effects of differing fracture half-lengths in multilayer reservoir systems. The total system net pay thickness  $\bar{h}$  is

$$\bar{h} = \sum_{j=1}^n h_j, \quad (12-45)$$

average system reference permeability  $\bar{k}$  is

$$\bar{k} = \frac{1}{\bar{h}} \sum_{j=1}^n k_j h_j, \quad (12-46)$$

and average system storage  $\bar{\phi} \bar{c}_i$  is

$$\bar{\phi} \bar{c}_i = \frac{1}{\bar{h}} \sum_{j=1}^n \phi_j c_{ij} h_j. \quad (12-47)$$

The individual layer and composite system average hydraulic diffusivities are, respectively,

$$\eta_j = \frac{k_j}{\phi_j c_{ij} \mu} \quad (12-48)$$

$$\bar{\eta} = \frac{\bar{k}}{\bar{\phi} \bar{c}_i \mu}. \quad (12-49)$$

An equivalent system average fracture half-length  $\bar{x}_f$  is, therefore,

$$\bar{x}_f = \frac{\sqrt{\bar{\eta}}}{\bar{k} \bar{h}} \sum_{j=1}^n \frac{k_j h_j x_{fj}}{\sqrt{\eta_j}}. \quad (12-50)$$

An average fracture conductivity  $\bar{k}_f \bar{w}$  is

$$\bar{k}_f \bar{w} = \frac{1}{\bar{h}} \left( \sum_{j=1}^n \sqrt{k_{fj} w_j h_j C_{RDj}} \right)^2, \quad (12-51)$$

where the individual fracture layer dimensionless reservoir conductivity  $C_{RDj}$  is

$$C_{RDj} = \frac{k_j h_j}{k h} \sqrt{\frac{\eta}{\eta_j}}. \quad (12-52)$$

The dimensionless reservoir conductivity  $C_{RD}$  concept of Bennett *et al.* and Camacho-V. *et al.* is applicable only for analysis of the early transient behavior of finite-conductivity fractures (dimensionless fracture time  $t_{Dxf} < 1$ ) for which there is essentially linear flow in the reservoir normal to the plane of the fracture. This correlation technique is not applicable to pseudoradial or pseudosteady-state flow regimes.

An entirely general commingled reservoir solution developed by Spath *et al.* (1994) using Laplace transform solutions of the reservoir performance of each reservoir layer eliminates the linear flow restriction of the Bennett *et al.* and Camacho-V. *et al.* analyses.

## 12-4. Well test analysis of vertically fractured wells

Analysis of the transient behavior of a finite-conductivity fracture to obtain reliable estimates of the reservoir and fracture properties requires proper identification of the flow regimes exhibited in the transient data. The analysis procedure includes (1) log-log diagnostic analyses of both the pressure and pressure derivative responses, (2) specialized Cartesian analysis and verification of identified flow regimes, (3) simulation of the entire transient history using the determined reservoir and fracture parameter estimates and (4) a final validation check of the obtained parameter estimates in conjunction with the flow regime demarcation limits.

A prefracture estimate of the formation average permeability  $k$  is necessary for the interpretation of fracture properties in the postfracture transient analysis, unless the transient data contain at least some pseudoradial flow, for which an estimate of formation permeability can be computed directly from the transient data. Depending on the formation permeability, fracture half-length and conductivity, the pseudoradial flow regime may not be exhibited for an extensive period of time, making it impractical to obtain postfracture estimates of formation permeability with well tests. However, the synergy of history matching long-term production with well test data (e.g., Agarwal *et al.*, 1979) may overcome this limitation.

The uniqueness problem in interpretation of the transient behavior of finite-conductivity fractures is due to the fact that the transient performance of a fractured well in each of the flow regimes considered is a function of both reservoir and fracture properties. An independent estimate of formation permeability is required to quantify the fracture parameter estimates separately from the combined response of the reservoir and fracture.

Evaluation of the drawdown (or injection) transient behavior of a fractured well involves graphical analysis of the pressure drawdown  $\Delta p = p_i - p_{wf}$  or the pressure rise for injection  $\Delta p = p_{wf} - p_i$ , where  $p_i$  is the initial pressure and  $p_{wf}$  is the bottomhole flowing pressure, for liquid or multiphase flow analysis as a function of transient time  $\Delta t$ . Gas reservoir analyses are most properly evaluated for drawdown transients using the appropriate pseudopressure differences of  $\Delta m(p) = m(p_i) - m(p_{wf})$  for a drawdown and  $\Delta m(p) = m(p_{wf}) - m(p_i)$  for an injection transient and the elapsed transient pseudotime  $\Delta t_a$ . For shut-in transients, similar pressure graphing functions are used. For pressure buildup transients in oil or multiphase analyses, the pressure buildup rise is  $\Delta p = p_{ws} - p_{wf}(\Delta t = 0)$ , where  $p_{ws}$  is the bottomhole shut-in pressure. For pressure falloff transients (following an injection transient), the appropriate graph function is  $\Delta p = p_{wf}(\Delta t = 0) - p_{ws}$ . For gas reservoir analyses, the pseudopressure equivalents of these functions are used.

Shut-in transients may be analyzed using drawdown solution type curves and Agarwal *et al.*'s (1979) "effective" time correlation parameter:

$$\Delta t_e = \frac{t_p \Delta t}{t_p + \Delta t}. \quad (12-53)$$

The producing time  $t_p$  prior to the shut-in transient and shut-in transient elapsed time  $\Delta t$  correlate the shut-in transient behavior with the drawdown solution. This correlation parameter is derived directly from the superposition-in-time principle for a two-rate transient history in which the last rate step is the shut-in transient. For a multirate production history prior to the final shut-in transient, it is generally preferred to use continuous superposition of the production history in the analysis instead of Agarwal *et al.*'s effective time.

For gas reservoirs, the analysis may be performed either with dimensional time or preferably with the



pseudotime equivalent of the time-scale function. The effective pseudotime equivalent of Eq. 12-53 is

$$\Delta t_{ae} = \frac{t_a(t_p)t_a(\Delta t)}{t_a(t_p) + t_a(\Delta t)}. \quad (12-54)$$

Pressure buildup analysis of a pseudoradial flow regime using classic semilog analysis procedures may be performed with Horner's (1951) approximation:

$$t_p = \frac{Q_p}{q_{last}}, \quad (12-55)$$

where  $Q_p$  is the cumulative production of the principal fluid phase of the analysis and  $q_{last}$  is the production rate of the flowing transient immediately prior to the shut-in transient.

#### 12-4.1. Wellbore storage dominated flow analysis

The wellbore storage dominated transient behavior discussed in Section 12-2.1 (unit-slope behavior) is described mathematically by

$$p_{wD} = \frac{t_D}{C_D}. \quad (12-56)$$

In dimensional units, the log linear behavior of the  $\Delta p$  function versus transient time is

$$\Delta p = \frac{qB}{24C} \Delta t. \quad (12-57)$$

The wellbore storage coefficient  $C$  can therefore be computed directly using the coordinates of any point on the unit-slope  $\Delta p$  line ( $\Delta t_{usl}$ ,  $\Delta p_{usl}$ , where the subscript  $usl$  denotes unit-slope line) or from the derivative  $\partial \Delta p / \partial \Delta t$  with

$$C = \frac{qB}{24\Delta p_{usl}} \Delta t_{usl} = \frac{qB}{24 \left[ \Delta t \frac{\partial \Delta p}{\partial \Delta t} \right]_{usl}} \Delta t_{usl} \quad (12-58)$$

for liquid flow analyses. Either the pressure or pressure derivative responses can be used because they are identical (assuming constant wellbore storage).

A similar relationship for determining the wellbore storage coefficient for gas wells is

$$C = \frac{14.8 p_{sc} T c_i q_g}{T_{sc} \Delta m(p)_{usl}} \Delta t_{ausl} = \frac{14.8 p_{sc} T c_i q_g}{T_{sc} \left[ \Delta t_a \frac{\partial \Delta m(p)}{\partial \Delta t_a} \right]_{usl}} \Delta t_{ausl}. \quad (12-59)$$

#### 12-4.2. Fracture storage linear flow analysis

The fracture storage linear flow regime is generally exhibited clearly in the transient behavior of finite-conductivity fractures only when wellbore storage effects are minimized, typically with downhole isolation devices. When this behavior is exhibited in the transient response, an analysis can be performed that provides an estimate of the fracture diffusivity/conductivity relationship  $\sqrt{\eta_f/k_f w}$ . If only fracture storage dominated flow behavior is used, the hydraulic diffusivity and conductivity cannot be determined separately. Separation of the quantities is obtained in conjunction with analysis of the other fracture flow regimes exhibited in the data to determine fracture conductivity.

The log-log fracture storage linear flow behavior of an oil reservoir analysis can be evaluated using the pressure derivative response  $\Delta t(\partial \Delta p / \partial \Delta t)$ . The fracture hydraulic diffusivity can be determined (for a known fracture conductivity) with

$$\eta_f = \left[ \frac{k_f w h_f}{4.06 q_o \mu_o B_o} \right]^2 \frac{\left[ \Delta t \frac{\partial \Delta p}{\partial \Delta t} \right]_{fsl}^2}{\Delta t_{fsl}}, \quad (12-60)$$

where the subscript  $fsl$  denotes fracture storage linear flow. Similarly, fracture hydraulic diffusivity may be obtained in a gas reservoir analysis using pseudo-pressure and pseudotime with

$$\eta_f = \left[ \frac{k_f w h_f T_{sc}}{1448 q_g T p_{sc}} \right]^2 \frac{\left[ \Delta t_a \frac{\partial \Delta m(p)}{\partial \Delta t_a} \right]_{fsl}^2}{\Delta t_{afsl} \mu_{gi} c_t}. \quad (12-61)$$

Verification graphs can then be constructed by graphing  $\Delta p$  versus  $\Delta t^{1/2}$  (or  $\Delta m(p)$  versus  $\Delta t_a^{1/2}$  for gas) on a Cartesian scale, for which the fracture storage linear flow behavior is characterized by a straight line passing through the origin for oil and gas, respectively:

$$\Delta p = \frac{8.13 q_o \mu_o B_o}{k_f w h_f} (\eta_f \Delta t)^{1/2} \quad (12-62)$$

$$\Delta m(p) = \frac{2895 q_g T_{p_{sc}}}{k_f w h_f T_{sc}} (\eta_f \mu_{gi} c_i \Delta t_a)^{1/2}. \quad (12-63)$$

### 12-4.3. Bilinear flow analysis

The analysis of transient data that exhibits bilinear flow behavior is performed by a log-log diagnostic analysis of the pressure and pressure derivative behavior, with a Cartesian analysis and verification of the identified flow regime. On a log-log graph of  $\Delta p$  versus  $\Delta t$  (or  $\Delta m(p)$  versus  $\Delta t_a$  for gas reservoirs), the bilinear flow regime is identified as that with quarter-slope behavior on both the pressure and pressure derivative responses.

The fracture conductivity  $k_f w$  can be determined using any point on the log-log derivative quarter-slope line. The interpretation relationships for oil and gas reservoir analyses, respectively, are

$$k_f w = \left[ \frac{11.025 q_o \mu_o B_o}{\sqrt{h h_f} \left( \Delta t \frac{\partial \Delta p}{\partial \Delta t} \right)_{bf}} \right]^2 \left[ \frac{\Delta t_{bf}}{\phi \mu_o c_i k} \right]^{1/2} \quad (12-64)$$

$$k_f w = \left[ \frac{3927.3 q_g T_{p_{sc}}}{\sqrt{h h_f} T_{sc} \left( \Delta t_a \frac{\partial \Delta m(p)}{\partial \Delta t_a} \right)_{bf}} \right]^2 \left[ \frac{\Delta t_{abf}}{\phi k} \right]^{1/2}, \quad (12-65)$$

where the subscript  $bf$  denotes bilinear flow.

Verification graphs are generated on Cartesian scales using  $\Delta p$  versus  $\Delta t^{1/4}$  for oil reservoir analyses and  $\Delta m(p)$  versus  $\Delta t_a^{1/4}$  for gas reservoir analyses. The straight line is characterized by the relationships for oil and gas reservoir analyses, respectively, as

$$\Delta p = \frac{44.1 q_o \mu_o B_o}{\sqrt{h h_f} k_f w} \left( \frac{\Delta t}{\phi \mu_o c_i k} \right)^{1/4} \quad (12-66)$$

$$\Delta m(p) = \frac{15,710 q_g T_{p_{sc}}}{T_{sc} \sqrt{h h_f} k_f w} \left( \frac{\Delta t_a}{\phi k} \right)^{1/4}. \quad (12-67)$$

The Cartesian graphs for the analysis and verification of bilinear flow also provide additional information concerning the fracture conductivity. As discussed in Section 12-2.3, the deviation of the transient data from the straight-line flow of the bilinear

and near-wellbore conductivity alternations after the end of the bilinear flow regime clearly indicates whether the dimensionless fracture conductivity is less than, equal to or greater than 1.6 (Fig. 12-17). If the transient data tail off upward above the bilinear flow straight line,  $C_{fd} > 1.6$ ; if the transient data trend below the bilinear flow straight line,  $C_{fd} < 1.6$ .

### 12-4.4. Formation linear flow analysis

The formation linear flow regime is exhibited in the transient behavior of a finite-conductivity fracture only if  $C_{fd} > \sim 80$ . The fracture half-length can be determined from formation linear flow transient data using log-log pressure derivative behavior for oil and gas reservoir analyses, respectively:

$$x_f = \frac{2.03 q_o B_o}{h \left[ \Delta t \frac{\partial \Delta p}{\partial \Delta t} \right]_{lf}} \left( \frac{\mu_o \Delta t_{lf}}{\phi c_i k} \right)^{1/2} \quad (12-68)$$

$$x_f = \frac{724 q_g T_{p_{sc}}}{T_{sc} h \left[ \Delta t_a \frac{\partial \Delta m(p)}{\partial \Delta t_a} \right]_{lf}} \left( \frac{\Delta t_{alf}}{k \phi} \right)^{1/2}, \quad (12-69)$$

where the subscript  $lf$  denotes formation linear flow.

Cartesian graphs of  $\Delta p$  versus  $\Delta t^{1/2}$  for oil reservoirs or  $\Delta m(p)$  versus  $\Delta t_a^{1/2}$  for gas reservoirs are used to verify that the transient data selected in the log-log derivative analysis are exhibiting formation linear flow. The Cartesian graph relations describing the formation linear flow for oil and gas reservoirs, respectively, are

$$\Delta p = \frac{4.06 q_o B_o}{h x_f} \left( \frac{\mu_o \Delta t}{k \phi c_i} \right)^{1/2} \quad (12-70)$$

$$\Delta m(p) = \frac{1448 p_{sc} T_{p_{sc}}}{T_{sc} h x_f} \left( \frac{\Delta t_a}{k \phi} \right)^{1/2}. \quad (12-71)$$

### 12-4.5. Pseudoradial flow analysis

Analysis of the pressure transient behavior of a finite-conductivity fracture that exhibits pseudoradial flow behavior involves log-log analysis of the transient data and classic semilog analysis procedures. The transient behavior of a finite-conductivity fractured well during the pseudoradial flow regime is discussed in Section 12-2.5.

The formation permeability can be determined directly using any point on the log-log derivative curve during the pseudoradial flow regime (where the dimensionless derivative is a horizontal line equal to 0.5). The dimensional derivative is also a horizontal line, and the permeability is evaluated using the coordinates of a point on this straight line for oil and gas reservoirs, respectively:

$$k = \frac{70.6q_o\mu_o B_o}{h \left[ \Delta t \frac{\partial \Delta p}{\partial \Delta t} \right]_{pr}} \quad (12-72)$$

$$k = \frac{25,150q_g T p_{sc}}{h T_{sc} \left[ \Delta t_a \frac{\partial \Delta m(p)}{\partial \Delta t_a} \right]_{pr}}, \quad (12-73)$$

where the subscript *pr* denotes pseudoradial flow.

The apparent steady-state skin effect caused by the fracture can also be determined from log-log analysis during the pseudoradial flow regime using a point on the pressure curve ( $\Delta t_{pr}$ ,  $\Delta p_{pr}$ ) for oil reservoir analyses or a point on the pseudopressure curve ( $\Delta t_{apr}$ ,  $\Delta m(p)_{pr}$ ) for gas reservoir analyses for oil and gas reservoirs, respectively:

$$s = \frac{kh\Delta p_{pr}}{141.2q_o\mu_o B_o} - \frac{1}{2} \left[ \ln \left( \frac{0.000264k\Delta t_{pr}}{\phi\mu c_t r_w^2} \right) + 0.8091 \right] \quad (12-74)$$

$$s = \frac{khT_{sc}\Delta m(p)_{pr}}{50,300p_{sc}Tq_g} - \frac{1}{2} \left[ \ln \left( \frac{0.000264k\Delta t_{apr}}{\phi r_w^2} \right) + 0.8091 \right]. \quad (12-75)$$

Semilog analysis procedures may also be used to obtain estimates of the formation permeability and apparent steady-state skin effect of vertically fractured wells (see Chapter 2).

#### 12-4.6. Well test design considerations

Analysis of the pressure buildup behavior of a fractured well to obtain meaningful and reliable reservoir and fracture parameter estimates requires an accurate record of the well flow history. The stabilized flow period immediately prior to the pressure buildup should be of equal or greater duration than the buildup transient. Otherwise, production time effects are observed in both

the pressure and derivative responses at late times in the shut-in transient. Production time effects appear in the transient data as a steep increase in the log-log derivative response and a generally smaller (although it can be significantly greater) increase in the pressure behavior. Commonly, the derivative response caused by production time effects is greater in magnitude than the  $\Delta p$  response.

Production time effects are due to the simple physical principle that each time there is a unit step change in the well production rate, a new pressure pulse is propagated away from the well into the reservoir. The velocity at which the pressure pulse propagates in the reservoir is a function of the formation properties and time. In the case of vertically fractured wells, this also includes the effect of fracture length.

If a given reservoir feature (boundaries, reservoir heterogeneities, interference from offset wells, etc.) or fracture feature that requires the end of bilinear flow (length or conductivity near the top) is of interest, the flow period immediately prior to the shut-in transient must be of sufficient duration that the distance of investigation from the well for the flow period exceeds that required to see the same reservoir or fracture feature in the interpreted shut-in transient. The post-treatment cleanup process must also be completed, as this period can be of substantial duration in lower permeability reservoirs (Holditch, 1979).

The use of continuous superposition-in-time in the transient analysis does not remove or eliminate production time effects in the transient data. They are the actual response of the reservoir, and any interpretation that includes the identification of a reservoir or fracture feature, such as a boundary or fracture length, from data distorted by production time effects is incorrect or highly questionable at best.

To distinguish between what may actually be the effect of reservoir or fracture limits and production time effects, the duration of the flow period immediately prior to the pressure buildup transient can be easily checked. If the flow period is of greater duration than the pressure buildup, then the response observed in the transient data is actually a reservoir or fracture feature. However, if the elapsed shut-in time at which an anomalous behavior in the derivative response occurs corresponds to the duration of the stabilized flow period prior to the buildup, the transient response can be strongly suspected as resulting from production time effects.

### 12-4.7. Example well test analyses

To demonstrate the appropriate well test analysis procedures that should be used in the interpretation of post-treatment fractured well buildup behavior, examples are presented in this section for two adjacent wells in the same reservoir. Both wells were fracture treated with identical fluid volumes. The only difference between the fracture treatments of the two wells is that one treatment used bauxite for proppant and the other well was propped with conventional fracture sand.

The reservoir is relatively uniform in thickness ( $h = 100$  ft), homogeneous and isotropic, and it is assumed that all reservoir and fluid properties are initially identical for the two analyses:  $\phi = 10\%$ ,  $S_o = 90\%$  and  $S_w = 10\%$ ,  $p_w = \sim 6000$  psia,  $B_o = 1.0588$  RB/STB,  $\mu_o = 5$  cp and  $c_t = 3 \times 10^{-6}$  psi. The wellbore radius for both wells is  $r_w = 0.33$  ft. For these analyses,

assume that the effective hydraulic flowing height  $h_f$  in the fracture is equal to the net pay thickness  $h$  of the reservoir.

Table 12-3 is a summary of the recorded pressure buildup response of the well that was propped with bauxite (Well A). The corresponding pressure buildup behavior of the sand-propped fracture (Well B) is presented in Table 12-4. Both wells were produced at a relatively constant production rate of 100 STB/D using temporary production facilities for 2 months to effectively clean up the fracture treatment from the wells. The wells were then shut in for 2 months to monitor pressure buildups and evaluate the formation potential and fracturing treatment effectiveness. During this time, the wells were connected to permanent production facilities and a pipeline connection.

Analysis of the pressure buildup behavior of the bauxite-propped fracture in Well A begins with preparation of a log-log diagnostic plot of the  $\Delta p$  and pres-

**Table 12-3. Pressure buildup data for high-conductivity fracture (Well A).**

Transient time, $\Delta t$ (hr)	Bottomhole shut-in pressure, $p_{ws}$ (psia)	Transient time, $\Delta t$ (hr)	Bottomhole shut-in pressure, $p_{ws}$ (psia)
0.0216	2393.15	4.2101	3788.99
0.0280	2412.85	4.8118	3863.52
0.0365	2435.41	5.5939	3950.32
0.0474	2461.43	6.3363	4025.48
0.0616	2491.65	7.1509	4101.00
0.0801	2526.88	8.0420	4176.81
0.1041	2567.82	9.0155	4252.88
0.1354	2614.81	10.0780	4329.15
0.1760	2667.76	11.2378	4405.50
0.2288	2726.14	12.5053	4481.89
0.2975	2789.26	13.8932	4558.21
0.3867	2856.57	15.4175	4634.33
0.5027	2928.02	17.0986	4710.19
0.6535	3004.36	19.2842	4797.23
0.8199	3075.96	21.3978	4872.09
1.0363	3155.61	24.1454	4956.36
1.2632	3228.99	26.8935	5029.66
1.5583	3312.25	30.4660	5110.06
1.8529	3386.12	34.2129	5181.19
2.2358	3470.35	39.0838	5256.56
2.6141	3544.49	45.4160	5333.58
3.1057	3629.27	52.3480	5399.85
3.5859	3703.47	60.0000	5457.39

**Table 12-4. Pressure buildup data for moderate-conductivity fracture (Well B).**

Transient time, $\Delta t$ (hr)	Bottomhole shut-in pressure, $p_{ws}$ (psia)	Transient time, $\Delta t$ (hr)	Bottomhole shut-in pressure, $p_{ws}$ (psia)
0	2182.56	0.8188	3068.21
0.0001	2219.87	1.0336	3147.92
0.0002	2232.96	1.2586	3221.26
0.0003	2239.68	1.5510	3304.52
0.0004	2243.52	1.8430	3378.40
0.0005	2247.82	2.2225	3462.65
0.0007	2252.65	2.5971	3536.81
0.0009	2258.07	3.0842	3621.62
0.0012	2264.08	3.5599	3695.85
0.0016	2270.65	4.1783	3781.39
0.0020	2277.74	4.7746	3855.95
0.0026	2285.32	5.5497	3942.76
0.0034	2293.39	6.2857	4017.94
0.0045	2302.05	7.0934	4093.48
0.0058	2311.46	7.9772	4169.31
0.0076	2321.91	8.9427	4245.39
0.0098	2333.71	9.9966	4321.68
0.0128	2347.19	11.1468	4398.06
0.0166	2362.62	12.4038	4474.48
0.0216	2380.23	13.7799	4550.83
0.0280	2400.29	15.2908	4627.00
0.0365	2423.21	16.9567	4702.92
0.0474	2449.59	19.1223	4790.07
0.0616	2480.19	21.2142	4865.00
0.0801	2515.81	23.9336	4949.43
0.1041	2557.15	26.6491	5022.83
0.1354	2604.54	30.1792	5103.44
0.1760	2657.88	33.8730	5174.70
0.2288	2716.67	38.6749	5250.32
0.2975	2780.18	44.9170	5327.74
0.3867	2847.89	51.7180	5394.18
0.5027	2919.78	60.0000	5456.69
0.6535	2996.59		

sure derivative behavior versus the equivalent shut-in time (Fig. 12-34). By observation of the character and shape of pressure and derivative behavior, it is readily determined that the well is intersected by a high-conductivity fracture because a significant portion of the data exhibits linear flow (half-slope behavior) and the

transient was conducted long enough to observe some pseudoradial flow behavior.

Selecting the best-fit half-slope linear derivative behavior of the data results in a computed estimate of the formation permeability and fracture half-length squared  $kx_f^2$  by rearrangement of Eq. 12-68.

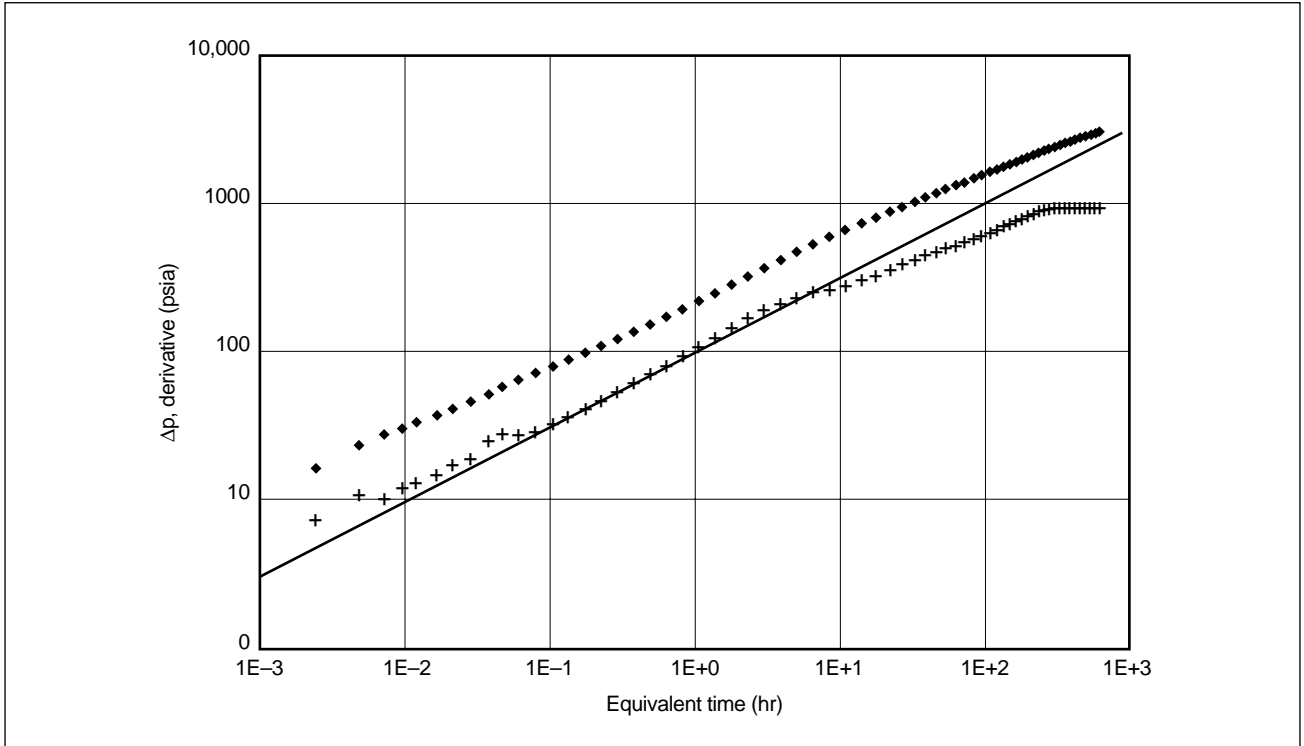


**Figure 12-34.** Diagnostic graph of a high-conductivity fracture.

Selecting a point on the linear flow portion of the derivative curve (1.14 hr, 107.5 psia):

$$\begin{aligned}
 kx_f^2 &= \frac{4.1292q_o^2\mu_o B_o^2 \Delta t_{lf}}{h^2 \left[ \Delta t \frac{\partial \Delta p}{\partial \Delta t} \right]^2 \phi c_i} \\
 &= \frac{(4.1292)(100)^2(5)(1.0588)^2(1.14)}{(100)^2(107.527)^2(0.1)(3 \times 10^{-6})} = 7607 \text{ md} \cdot \text{ft}^2.
 \end{aligned}
 \quad (12-76)$$

The verification graph of the selected linear flow regime is prepared by graphing the buildup pressure rise versus the square root of the shut-in time (Fig. 12-35). The equation of the straight line is

$$\begin{aligned}
 \Delta p &= \frac{4.06q_o B_o}{h \sqrt{kx_f^2}} \sqrt{\frac{\mu_o \Delta t}{\phi c_i}} \\
 &= \frac{(4.06)(100)(1.0588)}{(100)\sqrt{7607}} \sqrt{\frac{5}{(0.1)(3 \times 10^{-6})}} \sqrt{\Delta t} = 201.2 \sqrt{\Delta t}.
 \end{aligned}
 \quad (12-77)$$

Because the same shut-in time range of the data that lies on the best-fit derivative linear flow agrees with the data following the linear flow behavior on the verification graph, the linear flow regime of the diagnostic graph has been properly selected and  $kx_f^2$  is approximately 7600 md-ft<sup>2</sup>.

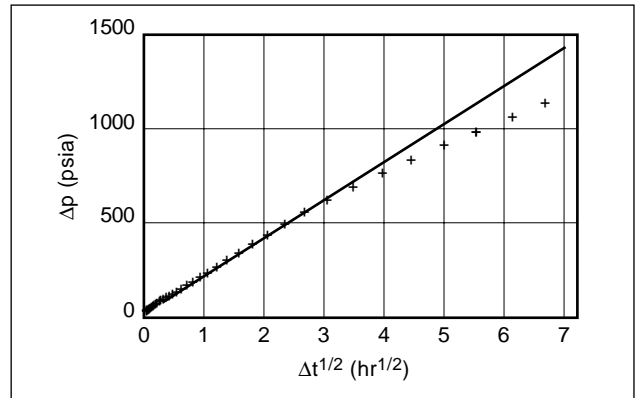


**Figure 12-35.** Formation linear flow verification graph.

The next step in the analysis of the transient behavior of Well A is to perform the log-log type-curve match of the pressure buildup behavior using a finite-conductivity type curve (such as Cinco-Ley *et al.*, 1978) or a well test analysis computer model that can generate the corresponding type-curve dimensionless solutions (Fig. 12-36). The matching parameters of this analysis indicate an effective  $k = 0.442$  md,  $x_f = 130$  ft and 10,000-md-ft fracture conductivity. A quick check of the agreement between the results of type-curve matching and the diagnostic graph analysis

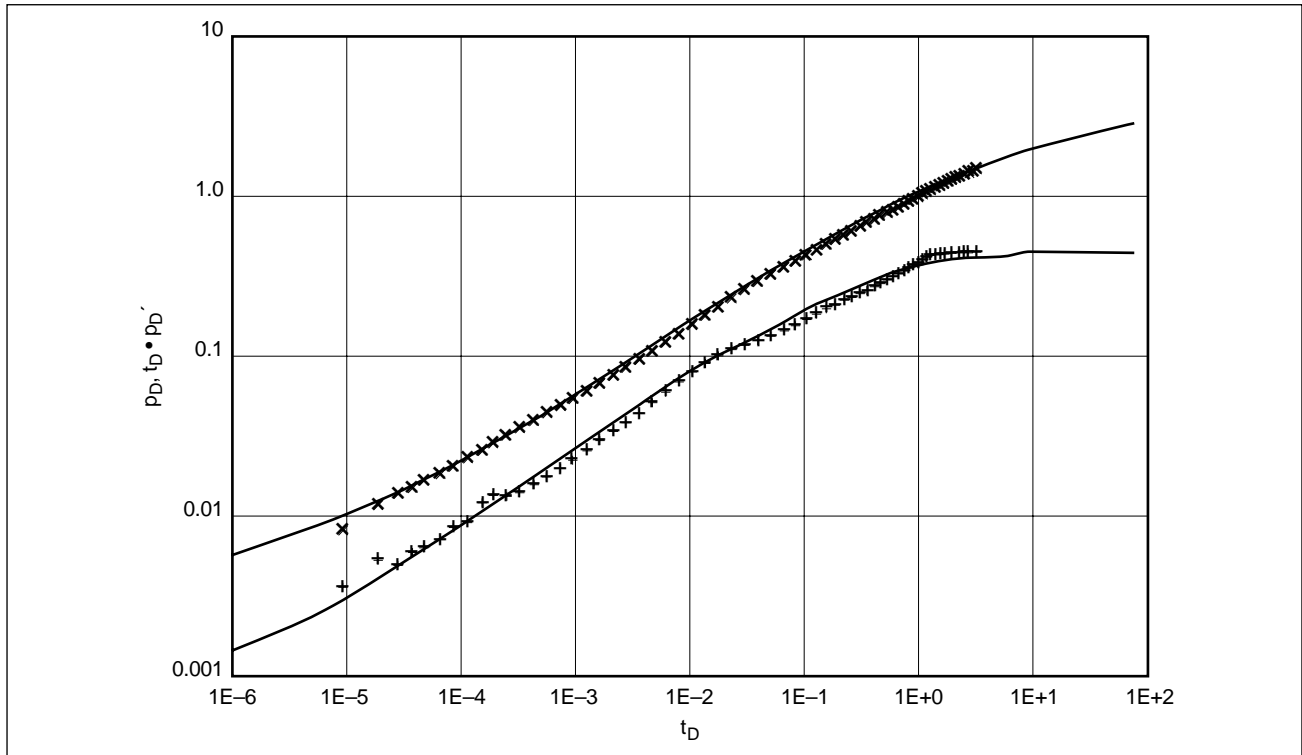


**Figure 12-36.** Type-curve match of a high-conductivity fracture.

is obtained by computing the corresponding  $kx_f^2$  value of the type-curve match:

$$kx_f^2 = (0.442)(130) = 7470 \text{ md-ft.}$$

This indicates relatively good agreement between the two analyses.

Because pseudoradial flow was indicated on the diagnostic graph (i.e., the derivative trends to one-half at the end), a classic semilog analysis is valid for this transient interpretation. The representation of the classic Horner semilog analysis of these transient data in Fig. 12-37 exhibits a semilog straight-line slope of 1880 psi/log cycle, extrapolated initial pressure estimate  $p^* = 6023$  psia, effective  $k_o = 0.458$  md and apparent radial flow steady-state skin effect of  $-5.02$  owing to the presence of the vertical fracture. The interpretation equations for the classic semilog analysis procedure are presented in Chapter 2 and are not duplicated in this example. However, an additional method for determining the effective permeability of the reservoir and the apparent radial flow steady-state skin effect of the well is provided by Eqs. 12-78 and 12-74, respectively. The effective permeability is

$$\begin{aligned} k &= \frac{70.6q_o\mu_o B_o}{h \left[ \Delta t \frac{\delta \Delta p}{\delta \Delta t} \right]_{pr}} \\ &= \frac{(70.6)(100)(5)(1.0588)}{(100)(980)} = 0.4 \text{ md.} \end{aligned} \quad (12-78)$$

The apparent radial flow steady-state skin effect the well is computed using the last pressure point (720 hr, 3222.4 psia):

$$\begin{aligned} s &= \frac{(0.4)(100)(3222.39)}{141.2(100)(5)(1.0588)} - \frac{1}{2} \left[ \ln \left( \frac{0.000264(0.4)(720)}{0.1(5)(3 \times 10^{-6})(0.33)^2} \right) + 0.8091 \right] \\ &= -5.21. \end{aligned}$$

These results are in agreement with the permeability and skin effect estimates obtained for Well A using the semilog analysis procedure. In summary, it is concluded that the interpretation indicates that the reservoir associated with Well A has  $k_o = \sim 0.45$  md, the effective propped half-length is approximately 130 ft, and the fracture conductivity is very high, about 10,000 md-ft. This corresponds to  $C_{FD} = 171$ .

As a final check on the validity of the analysis, the start and end times for the formation linear flow regime can be computed using Eqs. 12-13 and 12-14:

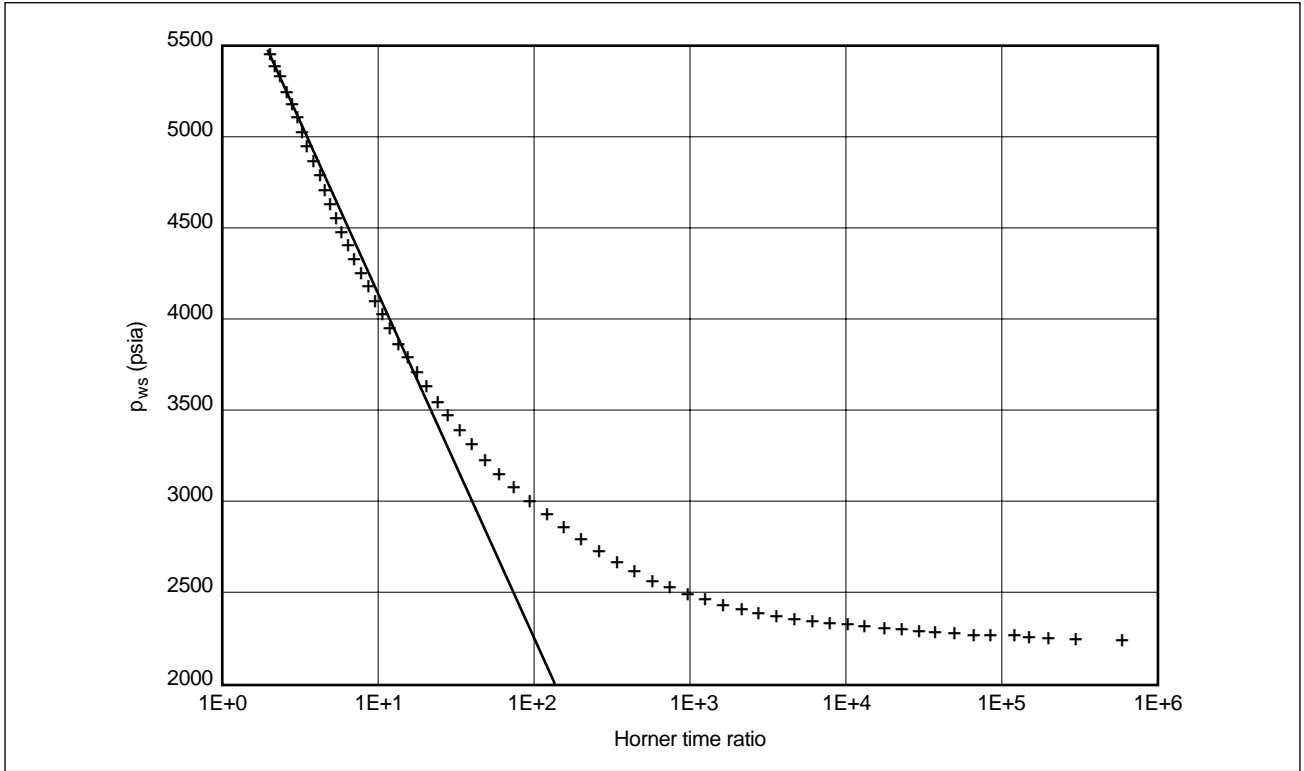


**Figure 12-37.** Semilog graph of a high-conductivity fracture.

$$t_{Dblf} = \frac{100}{(171)^2} = 0.00342$$

$$t_{Delf} = 0.016.$$

These dimensionless times correspond to dimensional times of

$$\begin{aligned} t_{blf} &= \frac{t_{Dblf} \phi \mu_o c_t x_f^2}{0.000264k} \\ &= \frac{(0.00342)(0.1)(5)(3 \times 10^{-6})(130)^2}{0.000264(0.45)} = 0.73 \text{ hr} \end{aligned}$$

$$\begin{aligned} t_{elf} &= \frac{t_{Delf} \phi \mu_o c_t x_f^2}{0.000264k} \\ &= \frac{(0.016)(0.1)(5)(3 \times 10^{-6})(130)^2}{0.000264(0.45)} = 3.41 \text{ hr}. \end{aligned}$$

These linear flow period demarcation times agree with the transient behavior exhibited on the diagnostic graph.

The interpretation of the transient behavior of Well B, which was propped with sand, is performed in a manner similar to that used for Well A. In the diag-

nostic graph of the data in Fig. 12-38, it is readily observed that bilinear flow is exhibited at early time, followed by a relatively long transition period and finally by a short pseudoradial flow regime near the end of the transient. No linear flow regime is exhibited in the pressure buildup behavior of this well.

A quarter-slope linear best-fit portion of the derivative curve is selected and an estimate of the reservoir permeability and fracture conductivity squared  $k(k_f w)^2$  is obtained by rearranging Eq. 12-64 and using a point on the best-fit derivative line (0.0012 hr, 17.3 psia):

$$\begin{aligned} k(k_f w)^2 &= \left[ \frac{11.025 q_o \mu_o B_o}{\left( \Delta t \frac{\delta \Delta p}{\delta \Delta t} \right)_{bf}} \right]^4 \frac{\Delta t_{bf}}{\phi \mu_o c_t h^2 h_f^2} \\ &= \left[ \frac{11.025(100)(5)(1.0588)}{17.3102} \right]^4 \frac{0.012}{(0.1)(5)(3 \times 10^{-6})(100)^4} \\ &= 1.034 \times 10^6 \text{ md}^3 \cdot \text{ft}^2. \end{aligned} \tag{12-79}$$

Verification of the selected bilinear flow behavior is shown in Fig. 12-39, and the equation of the straight line is



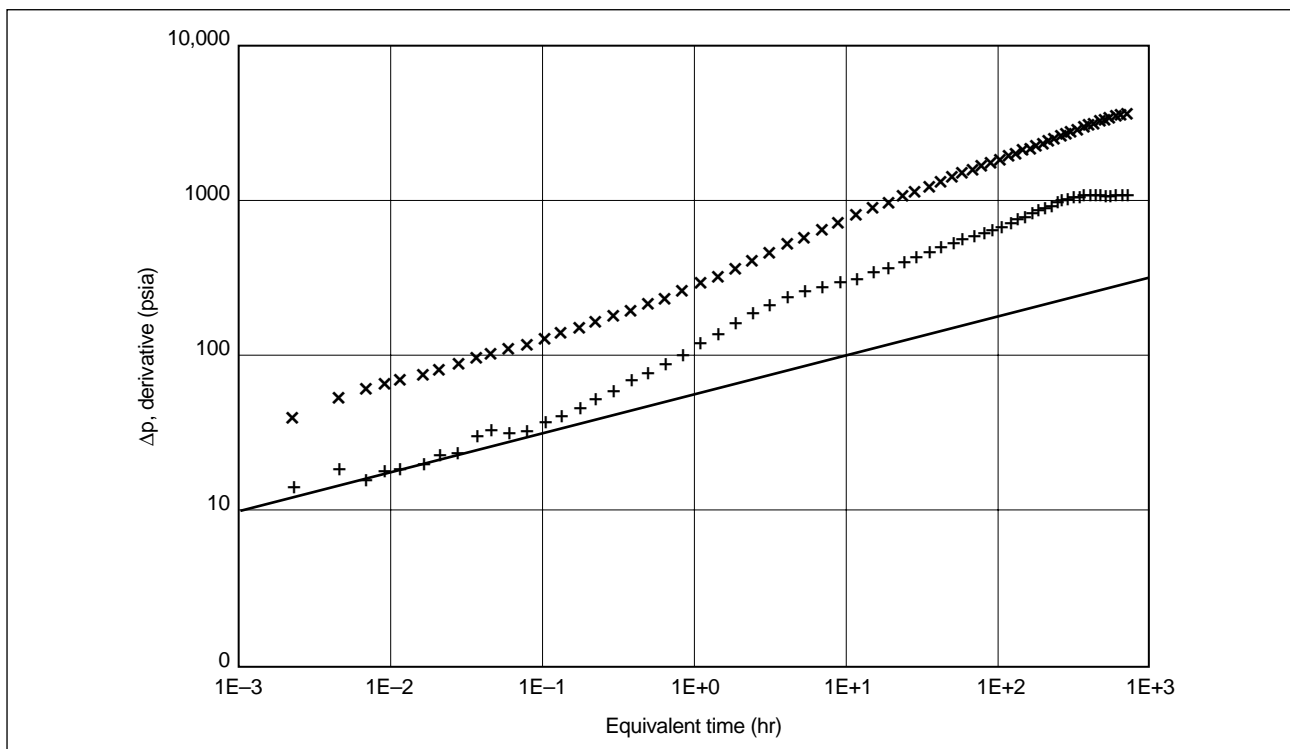


**Figure 12-38.** Diagnostic graph of a moderate-conductivity fracture.

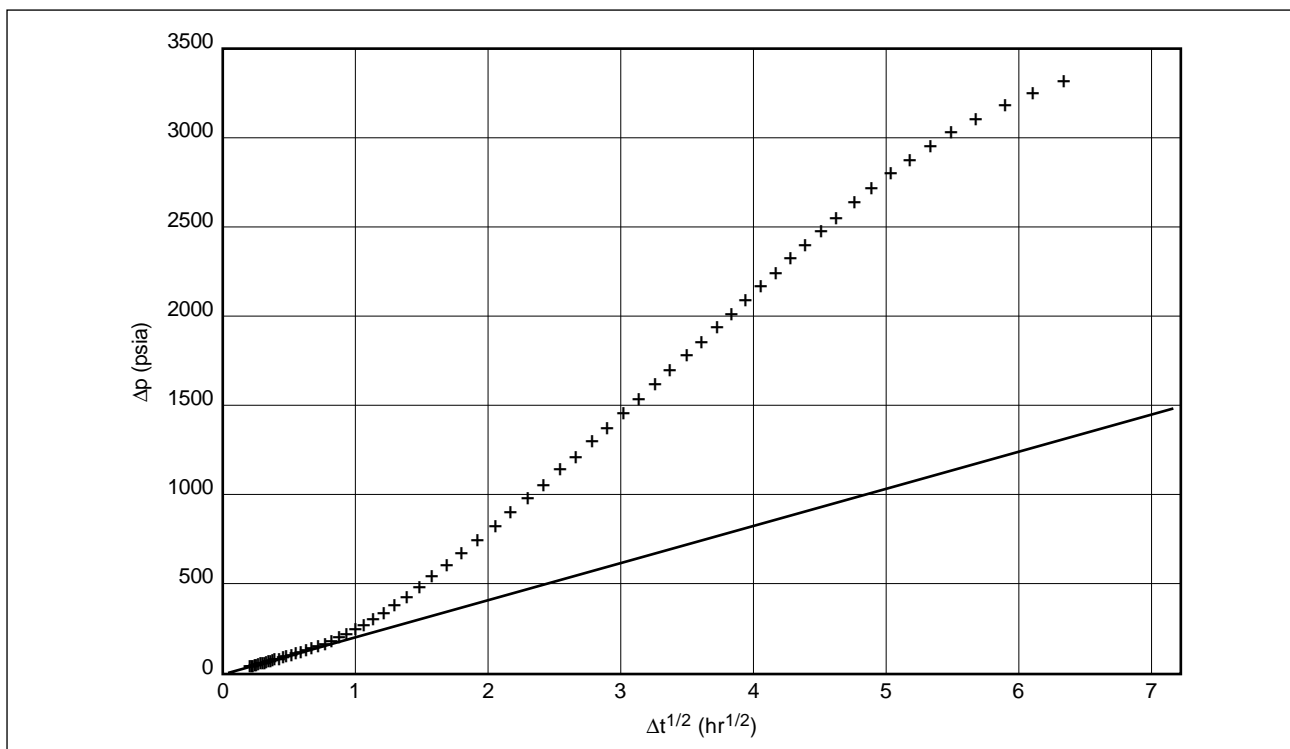


**Figure 12-39.** Bilinear flow verification graph.

$$\begin{aligned}
\Delta p &= \frac{44.1 q_o \mu_o B_o}{\sqrt{h h_f}} \left( \frac{\Delta t}{\phi \mu_o c_i k (k_f w)^2} \right)^{1/4} \\
&= \frac{44.1(100)(5)(1.0588)}{\sqrt{(100)(100)}} \left( \frac{\Delta t}{(0.1)(5)(3 \times 10^{-6})(1.034 \times 10^6)} \right)^{1/4} \\
&= 209.2(\Delta t)^{1/4}.
\end{aligned}
\tag{12-80}$$

The same pressure buildup data points that lie on the diagnostic plot quarter-slope linear behavior correspond to the data points that are on the verification graph line, indicating that the proper bilinear flow regime data were selected on the diagnostic graph.

The type-curve matching procedure is identical to that discussed for Well A, with the resulting type curve match for Well B shown in Fig. 12-40. The determined values are  $k_o = 0.409$  md and  $x_f = 124$  ft; the fracture conductivity is 1746 md-ft. The match results in  $C_{fD} = 34.4$ . By referring to the expressions for obtaining estimates for the end of the bilinear flow regime (Eq. 12-11), a check of the validity of the range of data selected for the bilinear flow regime on the diagnostic plot can also be obtained:

$$t_{Debf} = \frac{0.1}{(C_{fD} h_{fD})^2} = \frac{0.1}{(344)^2} = 8.45 \times 10^{-5}.$$

In terms of dimensional time, this becomes

$$\begin{aligned}
t_{ebf} &= \frac{t_{Debf} \phi \mu_o c_i x_f^2}{0.000264 k} \\
&= \frac{(8.45 \times 10^{-5})(0.1)(5)(3 \times 10^{-6})(124)^2}{0.000264(0.409)} \\
&= 0.0181 \text{ hr.}
\end{aligned}
\tag{12-81}$$

This result agrees with selection of the bilinear flow regime range on the diagnostic graph because the chosen data on the graph are prior to this time. Another qualitative validity check that can be made to ensure the internal consistency of the interpretation results is to compare the type-curve match estimate of the permeability and fracture conductivity squared  $k(k_f w)^2$  with the result of the diagnostic analysis:

$$k(k_f w)^2 = (0.409)(1746)^2 = 1.5 \times 10^6 \text{ md}^3\text{-ft}^2.$$

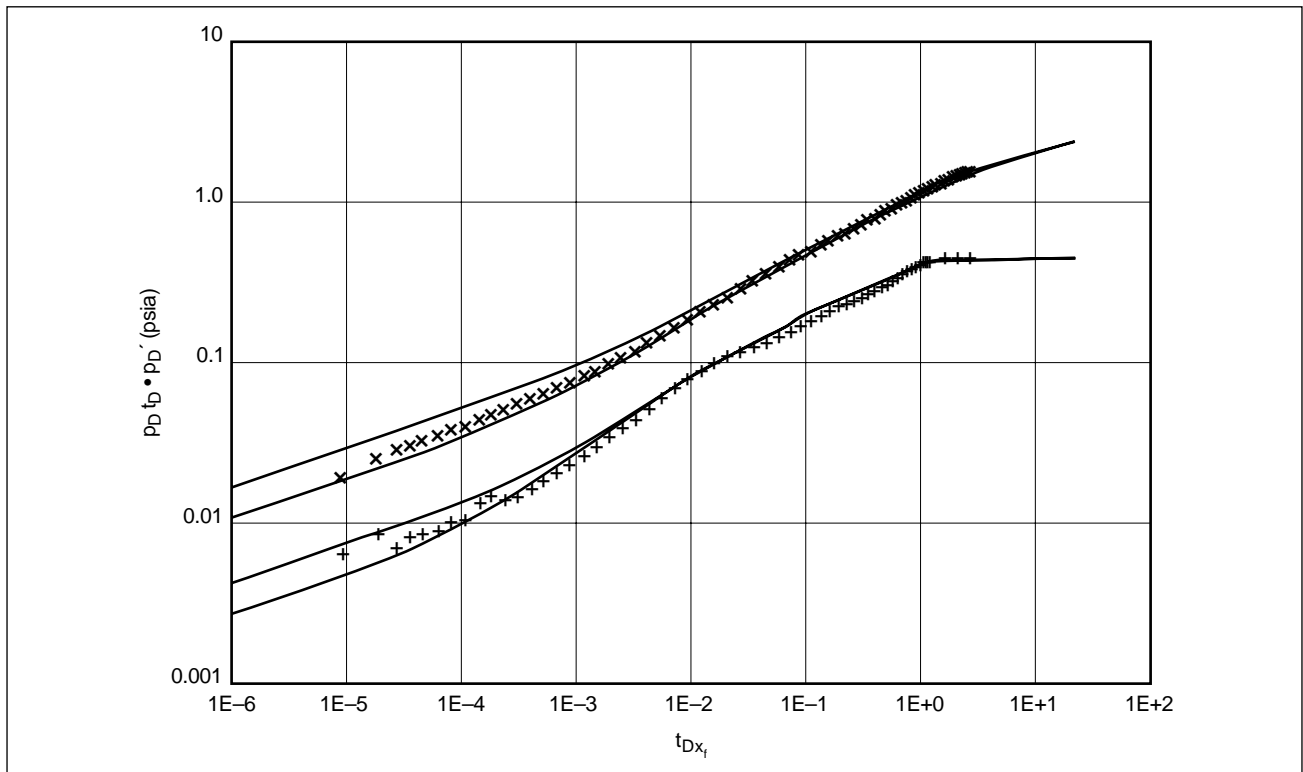


**Figure 12-40.** Type-curve match of a moderate-conductivity fracture.

Again, good agreement is obtained between the results of the two analyses.

Finally, because the pseudoradial flow regime is also exhibited in the transient behavior of Well B, a semilog analysis is valid (Fig. 12-41). The results of the semilog analysis indicate a straight-line slope of 1870 psi/log cycle, extrapolated initial pressure estimate  $p^*$  of 6019 psia, effective permeability of 0.461 md and apparent radial flow steady-state skin effect of  $-4.98$ .

By performing the analysis of the pseudoradial flow regime as discussed previously for Well A, the effective permeability is computed from the derivative value at the end of the transient (843.2 psia) and Eq. 12-72:

$$k = \frac{70.6q_o\mu_o B_o}{h \left[ \Delta t \frac{\delta \Delta p}{\delta \Delta t} \right]_{pr}} = \frac{70.6(100)(5)(1.0588)}{(100)(843.21)} = 0.44 \text{ md}.$$

The apparent radial flow steady-state skin effect of the fractured well is evaluated using Eq. 12-74:

$$\begin{aligned} s &= \frac{kh\Delta p_{pr}}{141.2q_o\mu_o B_o} - \frac{1}{2} \left[ \ln \left( \frac{0.000264k\Delta t p_r}{\phi\mu c_i r_w^2} \right) + 0.8091 \right] \\ &= \frac{(0.44)(100)(3273.69)}{141.2(100)(5)(1.0588)} \\ &\quad - \frac{1}{2} \left[ \ln \left( \frac{0.000264(0.44)(720)}{(0.1)(5)(3 \times 10^{-6})(0.33)^2} \right) + 0.8091 \right] \\ &= -5.05. \end{aligned}$$

The transient behavior of these two wells, which were stimulated using different types of proppants with different conductivities, demonstrates the various flow regimes and analysis procedures that are commonly employed in postfracture formation evaluation.

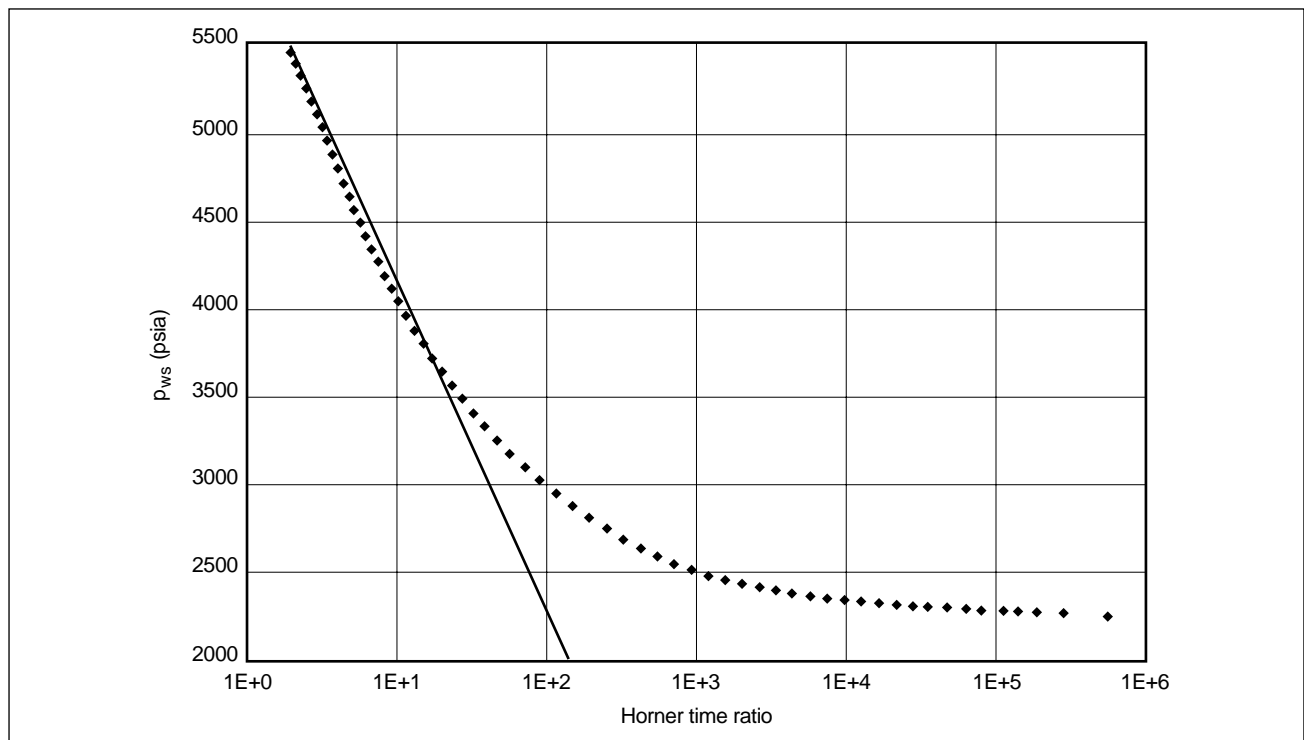


**Figure 12-41.** Semilog graph of a moderate-conductivity fracture.

## 12-5. Prediction of fractured well performance

Simulation of the future performance of a vertically fractured well can be performed with a variety of different types of reservoir models. The most general type of model for estimating the future production performance of a fractured well is a conventional finite-difference (or finite-element) reservoir simulator. Other types of predictive models for estimating the performance of vertically fractured wells are numerical models developed using analytic solutions to the diffusivity equation governing fluid flow in the system and the appropriate initial and boundary conditions.

Reservoir heterogeneities and anisotropy, boundaries, multiple wells and changing inner boundary conditions can be readily specified with finite-difference reservoir simulation models to simulate relatively realistic production scenarios. Finite-difference models are also ideally suited for solving nonlinear problems such as those associated with nonlinear fluid pressure-volume-temperature (PVT) properties, multiphase flow, non-Darcy fracture and reservoir flow, and stress-dependent fracture conductivity. These effects are important for the long-term (e.g., 20-year) economic analyses commonly used for tight gas wells.

Finite-difference reservoir simulation models are generally the preferred method for estimating the future performance of vertically fractured wells. Limitations related to the use of a finite-difference model are

- quantity and quality of reservoir and fracture information that is required as input data for the model
- generally greater computational expense associated with the use of finite-difference reservoir models over analytic techniques.

Numerical models developed using analytic solutions for the transient behavior of vertically fractured wells have been used for many years, largely because of these limitations for finite-difference simulation models.

Brown *et al.* (1984) demonstrated the utility of analytic models for future well performance prediction. Brown *et al.* introduced the use of a systems analysis approach for estimating the production behavior of a well for which the system inner boundary condition may be specified at a system location other than the sandface. An example is the constant

wellhead pressure production condition that requires simultaneous solution of the reservoir inflow performance and wellbore outflow analysis to estimate the productivity of the well.

Meng *et al.* (1982) applied the production systems analysis approach specifically to vertically fractured wells and developed a correlation technique for estimating the inflow performance of finite-conductivity fractures in gas reservoirs. This analysis procedure was utilized by Hunt (1986) to develop a systems analysis procedure for evaluating the rate-transient performance of fractured gas wells using analytic solutions.

A more general approach reported by Poe *et al.* (1995) for estimating the future performance of vertically fractured wells incorporates reservoir voiding effects in the production system analyses. The commingled reservoir evaluation procedure of Spath *et al.* (1994) was used in that study to evaluate the production performance of multilayer reservoirs using Laplace space analytic solutions for the transient behavior of finite-conductivity fractures. The commingled reservoir algorithm allows mixed reservoir completion types, such as a combination of fractured and unfractured reservoir layers, in the prediction of the future performance of the well.

In almost all cases of interest, hydraulic fractures are vertical and normal to the minimum horizontal stress direction. Horizontal wells can thus be drilled either normal or longitudinal to the fracture azimuth. The first configuration results in orthogonal fractures and has been found applicable for relatively low-permeability formations (Brown and Economides, 1992) and is discussed in Chapter 10 with multiple orthogonal fractures.

The other configuration, involving longitudinally fractured horizontal wells, was first studied by Larsen and Hegre (1991). Their work neglects the horizontal flow component and the nonuniformity of the vertical pressure distribution in the fracture. A more general approach that is free of these restrictions was introduced by Valkó and Economides (1996a). They considered the same reservoir-fracture system as the one studied by Cinco-Ley and Meng (1988), including the possibility of double porosity. In the Valkó and Economides case, the well is horizontal and located in the middle of the fracture (Fig. 12-42). The fracture is longitudinal with respect to the well, and communication between the fracture and the well is established along the total fracture length. The height of

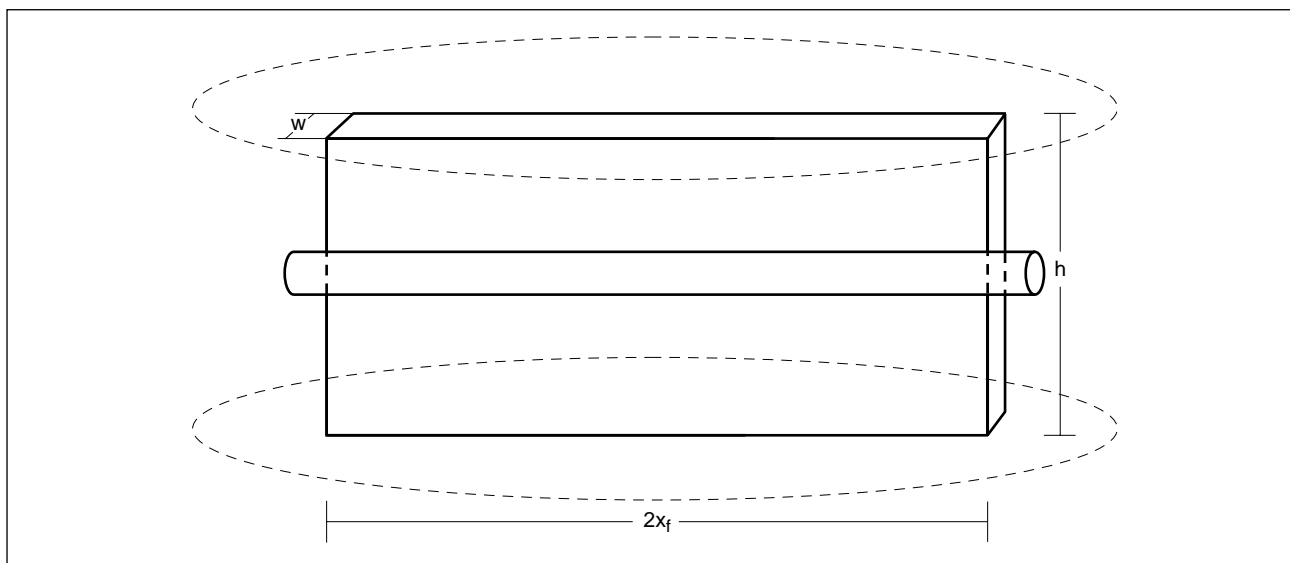


**Figure 12-42.** Horizontal well intersected by a longitudinal vertical fracture.

the fracture coincides with the thickness of the hydrocarbon-bearing stratum. The performance of the fracture depends on both the dimensionless fracture conductivity and the ratio of the height to the half-length, called the dimensionless height  $h_D$  and providing the dimensionless conductivity for vertical flow.

The results show that  $C_{fD} = 1$  is no longer necessary if the fracture is intersected by a horizontal well instead of a vertical well and the dimensionless height is small or moderate. Figure 12-43 shows the folds of increase in production from the same fracture intersected by a horizontal well instead of a vertical well with a small dimensionless height. Although at large  $C_{fD}$  values the location of the well

is irrelevant (i.e., the fracture behaves nearly as an infinite-conductivity fracture), at lower  $C_{fD}$  values the production increase is significant. At a given  $C_{fD}$  the increase is more pronounced at lower  $h_D$  values, which provide increased vertical dimensionless conductivity (Fig. 12-44). On both Figs. 12-43 and 12-44 the highest production increase is already near the theoretical maximum production increase, assuming an idealized infinite-conductivity fracture.

The reason for this effect is that the horizontal well acts as a high-conductivity streak in an otherwise limited-conductivity flow conduit. The lower the dimensionless height and fracture conductivity, the more pronounced the effect of the high-conduc-

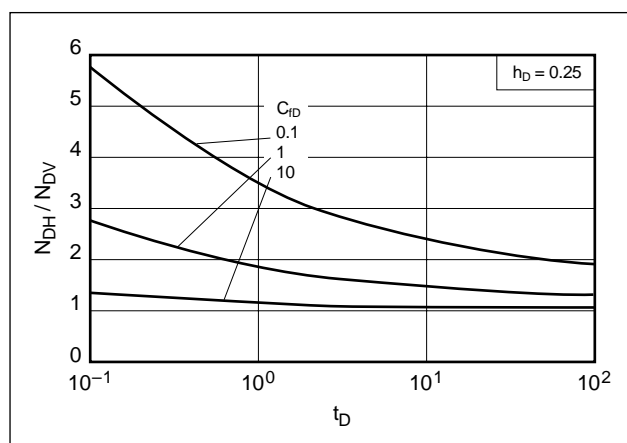


**Figure 12-43.** Ratio of dimensionless cumulative production (longitudinally fractured horizontal well to a fractured vertical well) for dimensionless height  $h_D = 0.25$  (Valkó and Economides, 1996a).

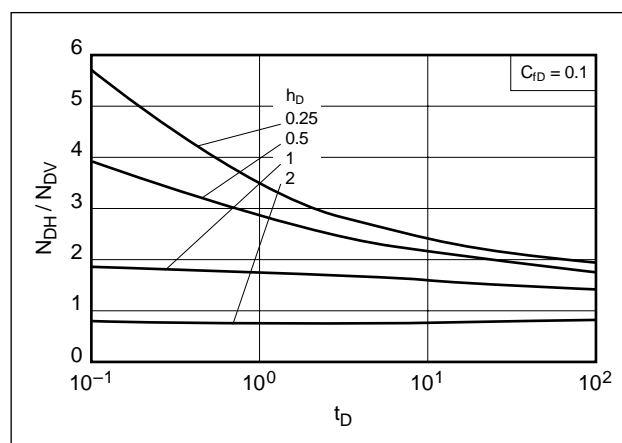


**Figure 12-44.** Ratio of dimensionless cumulative production (longitudinally fractured horizontal well to a fractured vertical well) for dimensionless fracture conductivity  $C_{fD} = 0.1$  (Valkó and Economides, 1996a).

tivity streak. The model predicts an almost infinite conductivity fracture behavior for  $C_{fd} = 0.1$  and  $h_D = 0.25$ , in contrast to the finite-conductivity behavior of a vertical well intersected by a similar fracture. For the vertical well, a  $C_{fd}$  at least 2 orders of magnitude higher is required to see the same nearly infinite conductivity behavior. In addition, a large  $C_{fd}$  value is difficult to achieve in high permeability for a long fracture from a vertical well.

The key advantages of a horizontal well combined with a longitudinal fracture is that a much smaller fracture width (than that suggested for the fractured vertical well) may be sufficient to achieve a certain production goal, reducing the necessity of very wide fractures, which are generally obtained only with the tip screen-out technique. The fracture also overcomes two limitations of a conventional horizontal well: removing drilling-induced damage and mitigating the adverse effect of the relatively low vertical permeability.

# Introduction to Matrix Treatments

*R. L. Thomas, Schlumberger Dowell*

*L. N. Morgenthaler, Shell E&P Technology Company*

This chapter is dedicated to Alfred R. (Al) Hendrickson, the father of modern-day acidizing. Al made numerous unique discoveries during his career and is best known for his work in sandstone acidizing. The knowledge he offered the industry is the cornerstone of acidizing technology today. His energetic personality and technical contributions will forever be appreciated.

## 13-1. Introduction

Matrix stimulation is a technique that has been used extensively since the 1930s to improve production from oil and gas wells and to improve injection into injection wells. Sidebar 13A discusses the history of matrix stimulation. Matrix stimulation is accomplished by injecting a fluid (e.g., acid or solvent) to dissolve and/or disperse materials that impair well production in sandstones or to create new, unimpaired flow channels between the wellbore and a carbonate formation. In matrix stimulation, fluids are injected below the fracturing pressure of the formation (McLeod, 1984). At the time of this writing, it is estimated that matrix treatments constitute 75% to 80% of all stimulation treatments (matrix and fracturing) worldwide, but the total expenditure for matrix treatments is only 20% to 25% of the total for all stimulation treatments. However, because the payout time for matrix treatments is normally days rather than months as it is for conventional fracturing treatments, engineers should master this technique. Many operators around the world have indicated that an average of 40% to 50% of their wells have significant damage, but routinely only 1% to 2% of their wells are treated every year.

Substantial production improvements can be achieved with matrix stimulation if treatments are engineered properly. A success rate greater than 90% is reasonable. The systematic approach to stimulation treatments consists of candidate selection, formation damage characterization, stimulation technique deter-

mination, treatment design, job execution and treatment evaluation. Although many matrix stimulation treatments are performed in an unsystematic manner, the success of matrix stimulation can be enhanced when each of these activities is performed properly. Proper performance of these steps requires the interaction of numerous individuals with expertise in geoscience, engineering and operations. The remaining chapters in this volume provide detailed discussions of the state of the art in matrix stimulation. The purpose of this chapter is to provide an integrated overview of the process of engineering successful matrix stimulation treatments.

Engineering a matrix treatment includes many tasks and a methodology that are accomplished on the basis of the best available data and knowledge at hand, which is usually incomplete. This does not mean a treatment will be unsuccessful. The process is a continuous cycle, starting with the diagnostic phase of the design process and progressing through the execution and evaluation phases to develop improvements. In addition, computer systems with “advisors” are available to assist the process. Advisors are expert systems with a knowledge base derived from current technology.

### 13-1.1. Candidate selection

Candidate selection for matrix stimulation is based on finding wells with impaired productivity and diagnosing the cause of the impairment. Failure of a well to obtain economic objectives alone is not evidence of impaired productivity. Failure to achieve economic objectives may be the result of limitations of the reservoir (e.g., pressure, permeability) or wellbore (e.g., artificial lift, inadequate tubing size). Matrix stimulation cannot solve these problems.

Candidate selection requires an accurate assessment of what a well can produce without impairment and the current productivity of the well. Techniques for making these assessments rely heavily on knowl-

### 13A. The history of matrix stimulation

"The results gained by the use of acid to increase oil and gas production are no longer hypothetical. Wherever production comes from essentially limestone reservoirs, its use is indicated and recommended." This quote is from "The Value of Repeated Acid Treatments" by P. E. Fitzgerald of Dowell Inc. in 1934. Fitzgerald went on to write, "It is recognized now that every well is a problem in itself, and must be analyzed individually in order to obtain the best results." It is interesting to note that the forefathers of matrix stimulation realized the importance of proper well diagnosis for treatment success, because it is a key step in the matrix stimulation engineering process used today. In addition, it is interesting that the "acidizing era" began more than 30 years following development of the concept. It took that long to develop the technology required to overcome the fundamental problem of acid corrosion of the tubing and casing. As history indicates, a chemical company with a need to stimulate brine wells developed the solution of an acid corrosion inhibitor. With this key invention the matrix stimulation era began in full force.

The history of acidizing dates back to 1895, when the Ohio Oil Company acidized both oil and gas wells with significant increases in production; however, the casing was severely corroded and the process became unpopular. One year later, a patent was issued to Herman Frasch of Standard Oil Company. His patent described the use of hydrochloric acid (HCl) in wells with limestone pay formations but did not address the corrosion problem.

Not until 1928 was the use of acid again attempted. This was when the problem of brine disposal, as well as increased production of natural brine, became important. Dr. Herbert Dow, early in his career, lowered bottles of acid into brine wells for the purpose of increasing their production. However, the results were not satisfactory, largely on account of the corrosion incurred and the expensive materials required to protect the metal equipment. Thus, the Dow Chemical Company initiated a project to develop the first acid corrosion inhibitor.

In 1931, Dr. John Grebe of Dow discovered that arsenic acid acted as a corrosion inhibitor. Later, copper salts were used with arsenic to avoid the formation of calcium arsenate precipitate, and soon organic inhibitors were found to be far superior. Soon after the discovery of the arsenic inhibitor, it was applied in the field by Dow and Pure Oil Company to successfully treat the latter's Fox No. 6 well in the Greendale Pool, Michigan, in February 1932. Five hundred gallons of HCl were siphoned into the well, resulting in a previously "dead" well flowing 16 BOPD. Thus, acidizing was reborn, and Dow formed the Dow Well Services Group that soon evolved into Dowell. Three years later, the small company Halliburton Oil Well Cementing Co. in Duncan, Oklahoma, began commercial acidizing service.

In 1935 Drs. Grebe and Stoesser of Dowell wrote, "Commercial acidization of oil and gas wells—although nonexistent four years ago, now is practiced over the entire country. Approximately 6000 oil and gas wells have been treated by Dowell Incorporated, to give an average increase in production of 412 percent. In central Michigan alone, one-sixth of the total oil production is the result of acid treatments, thus indicating a net gain of \$5,000,000 to the oil companies."

When this was published in *World Petroleum* the price of oil was \$1.00 per barrel and acidizing was directed at limestone formations. Since then acidizing technology has expanded, driven by oil and gas discoveries in a variety of formations, all with unique problems.

Sandstone acidizing with hydrofluoric acid (HF) was practiced in Texas in 1933 following the issuance of a patent to the Standard Oil Company; however, the field tests were not successful because of plugging of the formation. Commercial application of HF acidizing of sandstones occurred in the Gulf Coast of Mexico in 1940 when Dowell introduced mud acid, a mixture of HCl and HF. Dowell research indicated that the HCl helped maintain a low pH and decreased the precipitation of damaging precipitates. Following this event, the application of sandstone acidizing grew rapidly.

As the application of acidizing expanded, several chemical and mechanical problems were addressed. Numerous acid additives and systems were developed to solve the problems of acid sludging, acid-induced emulsions, spent acid cleanup, live acid penetration and fines migration. Parallel to this development was the development of methods to improve zone coverage during acidizing.

Acidizing has progressed through the following eras:

- 1950s and 1960s—Emphasis was on the development of additives to address emulsions, sludge, spent acid return and zone coverage. In addition, work on the physics of acidizing in limestones and the secondary reactions of sandstone acidizing was performed. The emphasis for clay problems shifted from clay swelling to clay migration, and numerous clay control agents were developed. Oil-soluble resins were introduced as diverting agents for improved zone coverage.
- 1970s—A need for deeper penetration of live HF acid was addressed with various systems, including alternating stages of HCl and HF, fluoboric acid and a mixture of methyformate and HF.
- 1980s—Foam diversion and coiled tubing placement were introduced to improve zone coverage. Production system analysis became a common tool of the design engineer. Computers were used to assist in all phases of the matrix process, including candidate selection, treatment design, monitoring of execution (real-time evaluation of skin effect evolution) and post-treatment evaluation.
- 1990s—Computers continued to evolve to faster and more user-friendly programs that incorporate improved production prediction capability, economics software, geochemical models and on-site evaluation techniques. Environmentally friendly additives were introduced to meet government regulations along with the development of a better understanding of sandstone acidizing chemistry. Emphasis was placed on the entire matrix process through matrix stimulation engineering.

Great advances have been made since the first acidizing treatment was performed. As wells become deeper, with higher temperatures and harsher conditions along with longer zones as in horizontal wells, matrix technology will expand to meet operators' needs. Matrix stimulation will continue to be a useful, economical tool for production enhancement in the years to come.

edge of the formation geology and reservoir properties. Methods for assessment of production system performance have been developed and are in wide use. Methods for pressure transient testing of reser-

voirs and well performance analysis have been published (Earlougher, 1977). These methods enable the engineer to quantify the extent of formation damage and the potential for productivity improvement.



### 13-1.2. Formation damage characterization

Once it has been established that a well is producing below its potential, an assessment of the cause and location of the impairment must be made (Krueger, 1986, 1988). Diagnosis can be based on a review of the well and field history, samples of plugging material recovered from the field and analyzed, knowledge of formation mineral and fluid (e.g., water and oil) properties, as well as pressure testing and logging evaluation. The process of searching and sifting through the mass of data that may provide clues to the problem of a particular well is facilitated by databases and expert systems. In the end, the ingenuity and training of the person analyzing the data and the application of engineering tools are critical to a successful diagnosis. The challenge is to recognize the cause of the well impairment from the information available. In many cases, it is not possible to characterize the formation damage completely. If the diagnosis is uncertain, it is recommended to prioritize the probable causes and design a treatment for the most probable scenarios. Thus, multiple damage types may be suspected, and all should be considered in designing the treatment.

### 13-1.3. Stimulation technique determination

Selection of the stimulation technique is based on the productivity target, lithology, operational limitations and various other considerations. Normally the productivity target dictates the stimulation technique. For example, if a 90% reduction in skin effect in a sandstone yields the target production, then matrix stimulation will probably be the most cost-effective technique. If matrix stimulation cannot be accomplished, then the feasibility of using propped fracturing should be evaluated.

In carbonates, acid fracturing, propped fracturing and matrix acidizing techniques are applicable. However, if matrix acidizing yields a final skin effect of  $-2$  to  $-3$ , it will probably be the most cost-effective technique.

### 13-1.4. Fluid and additive selection

Identification of the cause and location of the well impairment drives the treatment design process. The chemistry of the stimulation fluids is chosen either to dissolve or disperse the impairment or in the case of carbonate reservoirs to create high-permeability channels through the damage zone. The treating fluid system is selected on the basis of field experience and

laboratory testing and can be derived from an expert system.

In cases where it is impossible to remove or bypass damage chemically, a small-volume fracturing treatment may be indicated (Fletcher *et al.*, 1995). This is particularly true today, with the tip-screenout (TSO) technique applied to high-permeability reservoirs. Chemical additives, as well as pre- and postflushes, are selected to enhance the action of the main stimulation fluid, prevent acid corrosion or prevent productivity impairment from by-products of the stimulation process (see Chapter 15).

### 13-1.5. Pumping schedule generation and simulation

The volume of each material pumped is based on an assessment of the amount of damage or the required depth of treatment and must address the potential inefficiency of the placement process. The location of the damage dictates the placement technique. Both mechanical methods using tools and fluid mechanical methods (e.g., particulate suspensions and foams) can be used to ensure that the stimulation fluids contact the formation damage.

Once the volume, composition and sequence of a treatment are established, a treating schedule can be designed on the basis of the well and reservoir properties. However, the effect of acidizing on formation strength may impose an upper limit on the acid strength and volume in wells that are not gravel packed. The pumping schedule includes the treating fluid and diverter sequence and injection rate for each stage. It can be generated using empirical rules based on previous field experience. In addition, the schedule can be optimized to meet specific objectives for each fluid type by using a single-phase reservoir model (Perthuis *et al.*, 1989).

A field-validated stimulation simulator should be used for the systematic engineering of matrix stimulation treatments. A numerical simulator can be a valuable tool for predicting damage removal and evaluating skin effect evolution, flow profile and wellhead and bottomhole pressures versus injection rate for the proposed pumping schedule. The simulator should take into consideration both the chemistry and damage removal along with the placement strategy, which is another important part of the design process. This step allows the design engineer to fine tune or optimize the schedule to obtain the desired results in the most cost-

effective manner. Because many key parameters in the simulation may not be accurately assessed in the laboratory, the simulator is most useful for predicting trends. Comparison to field data is critical to fully validate the simulation model for future design work (Bartko *et al.*, 1996).

### 13-1.6. Economic evaluation

Although a preliminary economic analysis is performed during the candidate selection process, the final analysis should be conducted once the treatment design is finalized. Production performance is predicted by using a production forecast module and is based on initial and/or final skin effect calculations. Payout time, net present value (NPV), cash flow or other financial indicators may be determined to evaluate economic justifications (Bartko *et al.*, 1996).

### 13-1.7. Execution

Execution of the treatment is an often neglected step by the design engineer but is obviously critical to the process. Materials must be monitored to ensure that they meet the specifications of the design, equipment must be maintained to perform properly, and personnel on site must understand and execute their assigned roles. Quality control (QC) testing and training should be documented as standard practices (Brannon *et al.*, 1987). Modern data acquisition and communication equipment make it possible to obtain and analyze detailed data during the well treatment, on and off the wellsite.

### 13-1.8. Evaluation

Treatment evaluation consists of pretreatment, real-time and post-treatment phases. Each is an important link to treatment success and the economic impact of the stimulation treatment. In addition, technical evaluation is required to validate and calibrate the models and assumptions used in candidate selection, treatment design and execution. Treatment evaluation uses the same well evaluation tools and knowledge of potential well productivity as candidate selection. Consistently following the engineering concepts outlined here makes stimulation a learning process and drives improvement in production performance in the field.

## 13-2. Candidate selection

### 13-2.1. Identifying low-productivity wells and stimulation candidates

The process of candidate selection consists of identifying wells with low productivity relative to what they are capable of producing and then evaluating possible mechanical problems in these wells (Thomas and Milne, 1995).

Geology, petrophysics and reservoir engineering play important roles in quantifying the productive potential of a given well. Ideally, a thorough understanding of the reservoir geology and reservoir drive mechanics is required to quantify production potential. In many cases such data are incomplete, and the engineer must rely on comparison to similar wells or the field history to identify performance norms. The productivity of each well can be mapped using a three-dimensional (3D) surface graph to assist the identification of underproducers (i.e., candidates). For oil wells, the productivity index (PI), productivity index per net pay thickness  $PI/h$ , production rate in barrels of oil per day (BOPD), production rate per reservoir porosity thickness product (BOPD/porosity-ft) or skin effect can be plotted for each location. The variable selected is a function of the data available. For example, if limited data are available (e.g., permeability-height  $kh$  is unknown) BOPD/porosity-ft or  $h$  can be plotted. This process allows the engineer to pinpoint likely underproducers and determine their relationship with other wells in the field.

Once the production potential of a well is established (to the highest certainty possible with the available data), it can be compared with the actual production. This is a deceptively simple statement because it hides the difficulty in measuring actual production in some cases. A facility's engineers and operations staff can help ensure that an accurate assessment of current well performance is obtained.

Once a well is diagnosed as underperforming, the reason or reasons must be determined. Appropriate remedial action must be taken, including the determination of whether artificial lift is required or if the existing lift is adequate and functioning properly. In some cases, production is constrained by tubing size, downhole equipment restrictions or other mechanical reasons. Stimulation will not help in these cases. Once mechanical reasons are eliminated as a potential cause of poor production, the remaining wells become stimulation candidates.

Well screening should be based on the potential production increase and incremental economics. Obviously, wells with the greatest potential should be selected as candidates. This process should include determination of the maximum allowable drawdown pressure before formation or sand production occurs (i.e., critical drawdown). The critical drawdown is used to predict expected production and is important in evaluating the economic potential of the treatment (Weingarten and Perkins, 1992).

An expert system can be used to screen potential candidate wells. Its knowledge base uses a series of rules to determine the suitability of a well for matrix stimulation. The determination is based on the results of pressure transient analysis (PTA) of the well or on the ratio of actual to theoretical flow rates. Consideration of possible mechanical problems is also built into the rules. Alternatively, a systems analysis can be used to determine the production potential of a well immediately following treatment. Matrix acidizing simulators and field experience indicate that a 90% reduction in skin effect in sandstones and skin effect values of  $-2$  in carbonates are conservative assumptions for a properly designed and executed treatment unless local experience indicates otherwise.

In Fig. 13-1, the knowledge base uses a simplified method to estimate the theoretical reservoir flow (i.e.,

no systems analysis). Comparison of the actual rate to the computed theoretical rate is made. The engineer then determines whether further evaluation is warranted. One rule-of-thumb cutoff suggests that the well should be stimulated if the actual rate is less than 75% of the theoretical. This cutoff should be used as a gross indicator only because the theoretical rate does not include effects resulting from production tubulars or separation equipment. By using this process to screen several wells, the engineer can identify underproducers, followed by refinement using systems analysis.

Once the analysis has been completed, wells with low permeability or pressure can be identified. In these cases, matrix stimulation will not provide an economic improvement in performance, but fracture stimulation may be appropriate. Sidebar 13B discusses the candidate selection process applied to a highly damaged well located in the Gulf of Mexico.

A useful and quick indicator of well performance is the productivity index:

$$PI = \frac{q}{\bar{p}_r - p_{wf}}, \quad (13-1)$$

where  $q$  is the flow rate in BOPD,  $\bar{p}_r$  is the average reservoir pressure in psi, and  $p_{wf}$  is the bottomhole flowing pressure in psi.

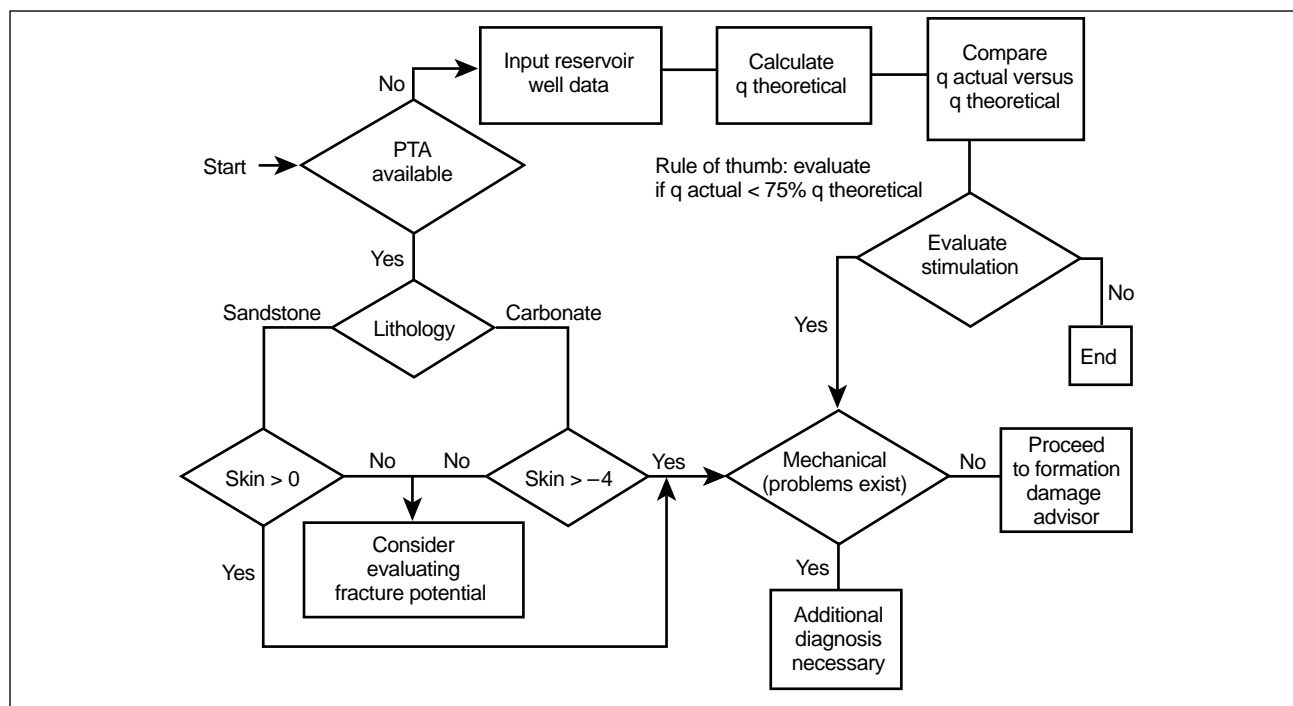


Figure 13-1. Candidate selection advisor (CSA) flowchart.

### 13B. Candidate selection field case history

Schiaie *et al.* (1986) reported the identification and successful removal of severe damage in a newly completed oil well.

Well logs and completion records documented that a uniform sandstone with 71 ft of net pay was completed using an inside-casing gravel pack. All wells on the platform were producing from a similar zone.

Mapping indicated that the wells on the platform completed in this formation had similar production with the exception of the new well. A knowledge-base expert system indicated that the well was producing at less than 5% of its theoretical flow rate and should have a skin effect of more than 200 on the basis of the following equations. Assumptions were made for  $k$  from previous well test results on offset wells, and the calculation did not consider tubing or completion pressure drops (i.e., systems analysis).

The following equations incorporate assumptions for certain variables.

For oil:

$$q = \frac{7.082 \times 10^{-3} kh(p_r - p_{wf})}{\mu(7.5 + s)}, \quad (13B-1)$$

where  $k$  is the permeability in md,  $h$  is the net pay in ft,  $p_r$  is the reservoir pressure in psi,  $p_{wf}$  is the flowing pressure in psi,  $\mu$  is the viscosity in cp,  $B_o$  is the formation volume factor for oil (default value of 1),  $\ln(r_e/r_w)$  is the ratio of the radial distance to the external reservoir boundary to the radius of the wellbore (estimated value of 7.5), and  $s$  is the skin effect.

For gas:

$$q = \frac{5.39 \times 10^{-2} kh(p_r^2 - p_{wf}^2)}{(7.5 + s)}, \quad (13B-2)$$

where the variables are as described for oil, with default values of viscosity  $\mu = 0.02$  cp, standard pressure  $p_{sc} = 14.5$  psi, standard temperature  $T_{sc} = 487.3^\circ\text{R}$  and flowing temperature  $T_f = 620^\circ\text{R}$ .

On the basis of this information, a well test was performed to determine the permeability and skin effect. As suspected, the pressure transient test indicated that the well had a significant skin effect of 209 and permeability of 526 md. The time to pseudosteady state was 9 hr. Production system analysis indicated that the well could increase from 1200 to 5000 BOPD at a skin effect of 20 and 1450-psi wellhead pressure. In addition, the well was tubing limited, and the 34,479-BOPD rate predicted by the knowledge-base expert system was not possible through the 3½-in. tubing. Because all wells completed in this zone were unconsolidated and gravel packed, a critical computer-aided analysis of drawdown was not performed. Other considerations were that the well was located in an easily accessible area with good chemical supplies, availability of service companies and no environmental hazards.

A preliminary economic evaluation based on an estimate for the entire treatment and a 90% reduction in skin effect yielded excellent economics. Assuming a net gain of 3800 BOPD at \$15 per barrel net yielded \$57,000 revenue per day. Payout for the treatment and associated costs would be less than a week, with an NPV of several million dollars in 3 to 4 months.

The variable  $PI/h$  takes into account the effect of drawdown on the production rate. The key parameters required (and not always well known) are  $\bar{p}_r$  and  $p_{wf}$ . Although  $q$  is not always accurately known, it is usually an accessible number. Pressure testing and sur-

veys are required to measure the two pressures accurately. These can also provide data on near-wellbore damage, as discussed in the following. An ideal PI can be calculated from reservoir data by using the equations described in Chapter 1. The ratio of the actual PI to the ideal PI can be used as an indicator of well performance.

Well tests are required to quantify permeability and current reservoir pressure, but usually they are not available. When this is the case, systems analysis can be performed to match current production or bottom-hole flowing pressure and calibrate the reservoir net pay, permeability, average reservoir pressure, skin effect, etc., for an underproducer. The key is to calibrate the system to forecast production on the basis of various stimulation scenarios.

### 13-2.2. Impact of formation damage on productivity

Matrix stimulation is successful because the near-wellbore region controls well productivity. Damage in this area can significantly decrease production by restricting flow in the formation (Krueger, 1986, 1988).

A knowledge of the inflow relationship and Hawkins's equation is essential to understand the effects of near-wellbore formation damage on well production. The steady-state equation for an oil well is:

$$q = \frac{kh(p_e - p_{wf})}{141.2B\mu \left( \ln \frac{r_e}{r_w} + s \right)}, \quad (13-2)$$

where  $k$  is the permeability in md,  $h$  is the reservoir thickness in ft,  $p_e$  is the constant outer reservoir pressure in psi,  $p_{wf}$  is the bottomhole flowing pressure in psi,  $B$  is the formation volume factor in RB/STB,  $\mu$  is the viscosity in cp,  $r_e$  is the drainage radius in ft,  $r_w$  is the wellbore radius in ft, and  $s$  is the skin effect.

The total skin effect  $s$  is a dimensionless term used to account for the additional pressure drop in the wellbore area that results from formation damage and other factors (e.g., inadequate perforations, partial completion). Skin effect values, determined from PTA, typically range from 0 to more than 100. Skin effect is positive if an additional pressure drop is present and negative if the actual  $p_{wf}$  is lower than the ideal  $p_{wf}$ . For example, natural fissures in a reservoir or a deviated well contribute a negative skin effect to the total skin effect.

For a given well, Eq. 13-2 can be simplified to

$$\frac{q}{q_o} = \frac{7.5 + s_o}{7.5 + s}, \quad (13-3)$$

where  $q$  and  $q_o$  are the final and initial flow rates, respectively, in BOPD, and  $s$  and  $s_o$  are the final and initial skin effects, respectively.

A realistic value for  $\ln r_e/r_w$  is 7.5 because this term is relatively insensitive to the actual values of  $r_e$  and  $r_w$  for oilfield conditions. Thus, for a well with total and damage skin effects equal to 100, a reduction to 10 can exhibit a sixfold increase in productivity. A skin effect reduction from 100 to 0 leads to a 14-fold increase in productivity. Although reduction to 0 is usually unrealistic in a sandstone, reduction to values less than 10 is a reasonable expectation. The actual value would have to be quantified using a valid systems analysis to consider tubing flow, etc. In the same well, a reduction of skin effect from 10 to 0 would yield a 2.3-fold increase in production. Chapter 1 provides the productivity equations for gas wells and horizontal wells.

Hawkin's equation relates permeability and the thickness of the damaged zone to the skin effect for vertical wells:

$$s = \left( \frac{k}{k_s} - 1 \right) \ln \frac{r_s}{r_w}, \quad (13-4)$$

where  $k_s$  is the damaged permeability in md and  $r_s$  is the damage penetration beyond the wellbore in ft, and for horizontal wells:

$$s = \left( \frac{\sqrt{k_H k_V}}{\sqrt{k_{Hs} k_{Vs}}} - 1 \right) \ln \frac{r_s}{r_w}, \quad (13-5)$$

where  $k_H$  is the horizontal permeability,  $k_V$  is the vertical permeability,  $k_{Hs}$  is the horizontal damaged permeability, and  $k_{Vs}$  is the vertical damaged permeability, with all the permeabilities in md.

Hawkin's equation can be used to determine the skin effect when assumptions are made for the damage radius and permeability. These variables cannot be absolutely quantified, but in combination with well analysis data and/or bottomhole treating pressure response they may indicate trends and define limits.

Combining Eqs. 13-2 and 13-4 yields

$$\frac{PI_s}{PI} = \frac{\frac{k_s}{k} \log \frac{r_e}{r_w}}{\log \frac{r_s}{r_w} + \frac{k_s}{k} + \log \frac{r_e}{r_s}}. \quad (13-6)$$

Figure 13-2 shows the productivity index ratio  $PI_s/PI$  versus the permeability ratio  $k_s/k$ , where the subscript  $s$  indicates damage.  $PI$  and  $k$  represent the nondamaged (ideal) well productivity and reservoir permeability, respectively (Muskat, 1949).

$PI_s/PI$  is equal to  $q_s/q$  for a constant-pressure drawdown. If all damage is removed (i.e., the natural permeability is restored), the well will produce at its natural flow capacity. A 90% permeability reduction extending radially 0.25 and 1.0 ft from the wellbore can decrease production by 35% and 50%, respectively (Fig. 13-2). However, a 90% permeability increase that extends less than 2 ft has little impact on productivity. Unlike in carbonates, in sandstones it is difficult to increase the permeability above the natural state because of reaction kinetics limitations, reaction stoichiometry and economics.

At this point in the candidate selection process, the engineer knows how the productivity of the candidate well compares with what it would be if the well were undamaged and if artificial lift, tubing restriction, etc., are not the problem. An estimate of the skin effect may be available from production system analysis, or the skin effect may have been determined directly by PTA. If the skin effect is greater than zero, there is potential benefit from matrix stimulation.

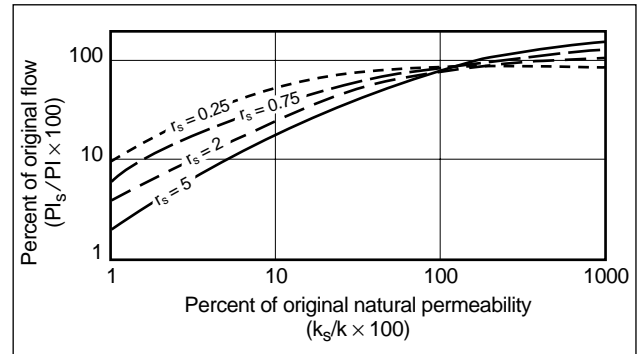


Figure 13-2. Matrix productivity improvement.

### 13-2.3. Preliminary economic evaluation

Having established the production potential of the well as a function of the skin effect and what it is actually producing, the engineer can evaluate the economic value of improved production and the required investment in well work. Economic evaluation requires a good production forecast for the current

well condition and a forecast for the stimulated well, possibly as a function of how successful the stimulation is (e.g., post-treatment skin effect). A brief discussion of the methodology follows.

The preliminary economic evaluation requires a model for production (revenue) and job cost (expense) as a function of skin effect. The engineer must determine the effect of the treatment on well economics on the basis of the net gain in cumulative oil or gas over a given period of time and the cost associated with the treatment. The production prediction model should include material balance, allow analysis under different outer boundary conditions (infinite acting, no flow and constant pressure) and forecast on the basis of constant sandface (bottomhole pressure or constant wellhead pressure). The sensitivity of economic performance to skin effect is quantified with this model. The range of skin effects input should be based on the analysis of current (presumably damaged) performance and expected post-stimulation behavior. Post-stimulation skin effect expectations and job costs can be based on field experience or analysis from a numerical stimulation simulator. The numerical stimulation simulator can be used to evaluate potential skin effect removal as a function of job design (e.g., volume pumped).

The economics portion of the model must enable the evaluation of cost versus expected revenue. Estimated costs should include treatment cost, operation costs, cost of money, applicable taxes and any auxiliary costs. Produced product price, price adjustment factors and treatment chance (risk) factors should be included to compute various financial indicators such as the rate of return (ROR), return on investment (ROI), NPV, payout (days) for investment only, payout (days) for investment plus interest and unit cost (investment divided by incremental production).

Several important decisions can be made at this point. For example, if the skin effect required to provide an acceptable return is greater than 0 in a sandstone or  $-4$  in a carbonate, then matrix stimulation is practical; i.e., fracture stimulation is not required.

In conclusion, from a knowledge of the reservoir and well history coupled with the use of diagnostic tools, the engineer should select candidate wells with low risk and significant potential for economic return. This requires the evaluation of numerous wells and is an important link to matrix stimulation success.

### 13-3. Formation damage characterization

Damage characterization is the next step in the matrix stimulation engineering process. It is an essential task prior to treating fluid selection and treatment design. Damage is characterized using laboratory tests, logging techniques and well history. Detailed study is necessary to develop a list of suspected damages from the available data. Multiple types of damage are normally suspected and are all considered when designing the treatment. Tables 14-3 through 14-5 list damage types, diagnostic clues and remedial recommendations for comparison to the condition and characteristics of the candidate well.

The following sections focus on problems that commonly occur in the field and discuss how expert systems can guide an engineer through the damage characterization process. Expert and advisor systems have proved especially useful in the damage characterization process (Krueger, 1988).

All available information on the well such as well logs and records, reservoir characteristics and information on the completion and previous workovers should be collected. Samples of produced fluids and any solid materials from the well should be analyzed. In some cases, it may be useful to conduct laboratory compatibility tests of the completion or drilling fluids and the formation fluid or rocks. Such tests can help in developing understanding of the problem in the current well and lead to corrective action.

Chemical analysis of solid and liquid samples retrieved from the well can provide valuable insights into damage mechanisms and characteristics. Field testing can quantify certain species (e.g., carbonates and oxides are soluble in hydrochloric acid [HCl], paraffins and asphaltenes float in water, an oil-external-phase emulsion disperses in diesel). Water analyses are commonly performed to assist the determination of scaling potential. The ionic composition of one or two samples can be used to calculate potential scales based on a minimum Gibb's free energy or a Stiff-Davis calculation. In addition, gamma logs can be run to complement the water analyses and detect barium and strontium sulfate scale buildups. Because of trace amounts of the naturally occurring radioactive materials (NORM) radon and radium, barium and strontium sulfate deposits may exhibit an abnormally high gamma count.

The history of the well should be evaluated in detail to assist damage characterization. All phases of well operations—including drilling, cementing, perforating, gravel packing, workover operations, stimulation operations and production or injection—are potential originators of damage (Krueger, 1986).

Expert and advisor systems have been developed to assist damage characterization (Bartko *et al.*, 1996). They provide a guide through a series of questions directed at relating the type of damage to the well behavior and available data. They can pinpoint key gaps in the available data and recommend additional required diagnostics. A brief discussion of the most common questions the engineer should ask in using an advisor are in Sidebar 13C.

Production logs can be run to quantify the flow per layer. This information is input into computer programs to determine the formation damage skin effect per layer. The use of a production log is reviewed in the field case history in Sidebar 13D.

Damage characterization is the basis of treatment design. Chemicals will be selected to remove the suspect cause or causes of damage. Treating procedures will be designed to access the suspected damage with adequate amounts of chemicals to remove enough damage to achieve the well productivity goals. Correct damage characterization is critical to matrix stimulation success.

### 13C. Formation damage characterization field case history

Schiabbe *et al.* (1986) performed a detailed laboratory and field study to characterize formation damage. Some of the questions and answers resulting from the study follow.

#### Well history

- Is the well newly completed, an old well, huff and puff, a recent workover and/or a recent stimulation treatment? This is a newly completed gravel-packed well that has been tested.
- Is it an oil, gas or water producer or injector with water or hydrogen sulfide (H<sub>2</sub>S) production? This oil well produces 29.5°API gravity crude.
- Was the well perforated under- or overbalance? The well was perforated underbalance at 12 shots per foot (spf).
- What type of completion fluid was used? Filtered calcium chloride and potassium chloride completion fluids were used to provide temporary clay control.
- Was the well produced at high drawdown rates? Although newly completed, the well was produced at high drawdown rates during the well test.
- Has the well responded to previous treatments? No previous treatments were performed on this well, but offset wells have responded to mud acid treatments.
- Did the production decline slowly or rapidly? Not applicable
- Did the well respond positively to a pump-in test? A pump-in test was not performed because of the associated cost and availability of other data (see "Laboratory and field testing" section).
- Was there excessive drilling mud loss to the pay zone? No unusual loss of drilling mud occurred when drilling through the pay zone.
- Is there fill in the wellbore, produced solids or solids in surface equipment? (Obviously, this would be a major problem indicative of gravel-pack failure.) There is no water production to create scale or solids.

#### Well logging and testing

- Are the results of a pressure transient test available? High skin effect values indicate there is severe formation damage.
- Does a production log show nonuniform production rates? Although the porosity logs indicate that the pay zone is a homogeneous sandstone, it is not damaged uniformly.
- Is there fill, a reduction of tubing inner diameter or an increase in gamma count? There is no indication of any of these.
- Is there water production from a specific zone? There is no water production.

#### Laboratory and field testing

- What is the mineralogy of the pay zone? Laboratory core testing indicates that the formation is composed of approximately 75% quartz, 10% feldspar and 10% clay with kaolinite, illite, chlorite and illite-smectite present with a 4% to 5% HCl solubility.
- Was a water analysis performed? No, because the well did not produce water.
- What is the composition of samples from the well? No samples other than cores and oil were retrieved from the well.
- Is the salinity of the completion fluid lower than that of the formation water? Not applicable
- Does the oil have an emulsion or sludging tendency? Laboratory testing indicates that the crude will not form an emulsion or sludge.
- Do core tests using the completion or stimulation fluids indicate damage? Laboratory testing indicates that the 2% KCl fluid used during gravel packing created a 62% reduction in permeability to oil (101 md damaged to 45 md).
- Do core flow tests using stimulation fluids improve the permeability? Core testing using fluoboric acid stimulation fluid indicates that the formation damage can be removed, with 280% of the initial permeability to oil obtained.

### 13D. Fluid and additive selection field case history

The well was severely damaged by the completion fluid (clay swelling in mixed-layer clays) and had possible fines migration during the well test. Production could potentially increase from 1200 to 5000 BOPD. Schiabel *et al.* (1986) reported the laboratory testing performed to quantify the fluid and additive selection.

- Mineralogy

X-ray diffraction and scanning electron microscopy of formation cores indicated that the formation contained 8% to 11% clay and 8% to 12% feldspar. The clay was composed of 7% to 31% kaolinite, 9% to 18% chlorite, 37% to 46% illite and 22% to 29% mixed-layer clays.

- Petrophysics

The 71-ft zone was not fissured and consisted of a relatively homogeneous sandstone with approximately 29% porosity and 526-md permeability.

The formation was borderline, between the first two classes of the mud acid fluid selection guide in Table 18-7. Assuming that the sandstone was less than 10% silt and less than 10% clay, a 12% HCl–3% HF system would be used, whereas a sandstone with high clay (greater than 10%) and low silt (less than 10%) would require a 12% HCl–2% HF system. Because the 12% HCl–3% HF sys-

tem had been previously used successfully in the formation, laboratory core tests were performed to determine the damage removal efficiency of the system. A 101-md core was damaged with completion fluid by flowing 20 pore volumes of water containing 2% KCl to yield 45.6-md permeability to oil. The core was then treated with a 7.5% HCl preflush followed by 12% HCl–3% HF mud acid overflushed with fluoboric acid. The fluoboric acid was used to decrease silt and clay migration. The resulting final permeability to oil was 284 md (>500% increase). On the basis of laboratory results, the mud acid–fluoboric acid system was selected to restore permeability in the damaged well.

- Treating and reservoir fluid compatibility

The 29.5°API gravity crude did not exhibit sludging or emulsion tendencies in laboratory testing.

- Damage and permeability profiles

A log recorded by the PLT\* Production Logging Tool indicated that the homogeneous sand was not damaged uniformly. The skin effect per layer based on the production per layer and completion are listed in Table 13D-1.

An oil-soluble diverter was selected to provide uniform flow per layer (i.e., uniform volume of each fluid per foot of zone). Other additives to the acids were an iron control agent, acid corrosion inhibitor and surfactant. An ammonium chloride flush with a mutual solvent ahead of the HCl preflush was recommended to remove oil from the wellbore area.

Table 13D-1. Skin effect per layer based on production per layer and completion.

Layer	Skin Effect					
	Development and Partial Completion	Perforation and Gravel Pack	Damage	Total	Production (%)	Porosity (%)
1	0	0.1	48.5	48.6	50	29
2	0	0.1	277.4	277.5	10	29
3	0	0.1	75.0	75.1	35	29
4	11.5	0.3	2534.2	2546.0	5	29

## 13-4. Stimulation technique determination

At this point, the well has been identified as an underperformer. The monetary value of improving well productivity and the possible cause or causes of formation damage have been determined. Next, the engineer must determine the remedial action.

The entire production system must be considered in making this decision. If the problem is in the well design or operation (e.g., tubing size or artificial lift), then stimulation is not indicated and the equipment should be upgraded or repaired. The target well performance must be balanced; i.e., there is no need to produce more than the tubing or lift will transport or than the facilities will process. This may affect the economics of incremental improvements in skin

effect. The impact of skin effect on the economic limit and reserve recovery must also be considered.

Figure 13-3 is a decision tree to help the process of candidate selection and stimulation technique. This type of flowchart can be incorporated into computer software. As shown in the figure, the productivity target dictates the stimulation technique.

If the productivity target can be reached with a skin effect of 10% of the original damage skin effect in sandstones and –2 to –3 in carbonates, matrix stimulation will be adequate and probably cost effective. In sandstone reservoirs the only stimulation alternative is hydraulic fracturing. In carbonate reservoirs (limestones or dolomites) acid fracturing can be a cost-effective way to increase productivity. In both cases, a hydraulic fracture is induced in the reservoir. In conventional fracturing, the conductivity of the fracture is



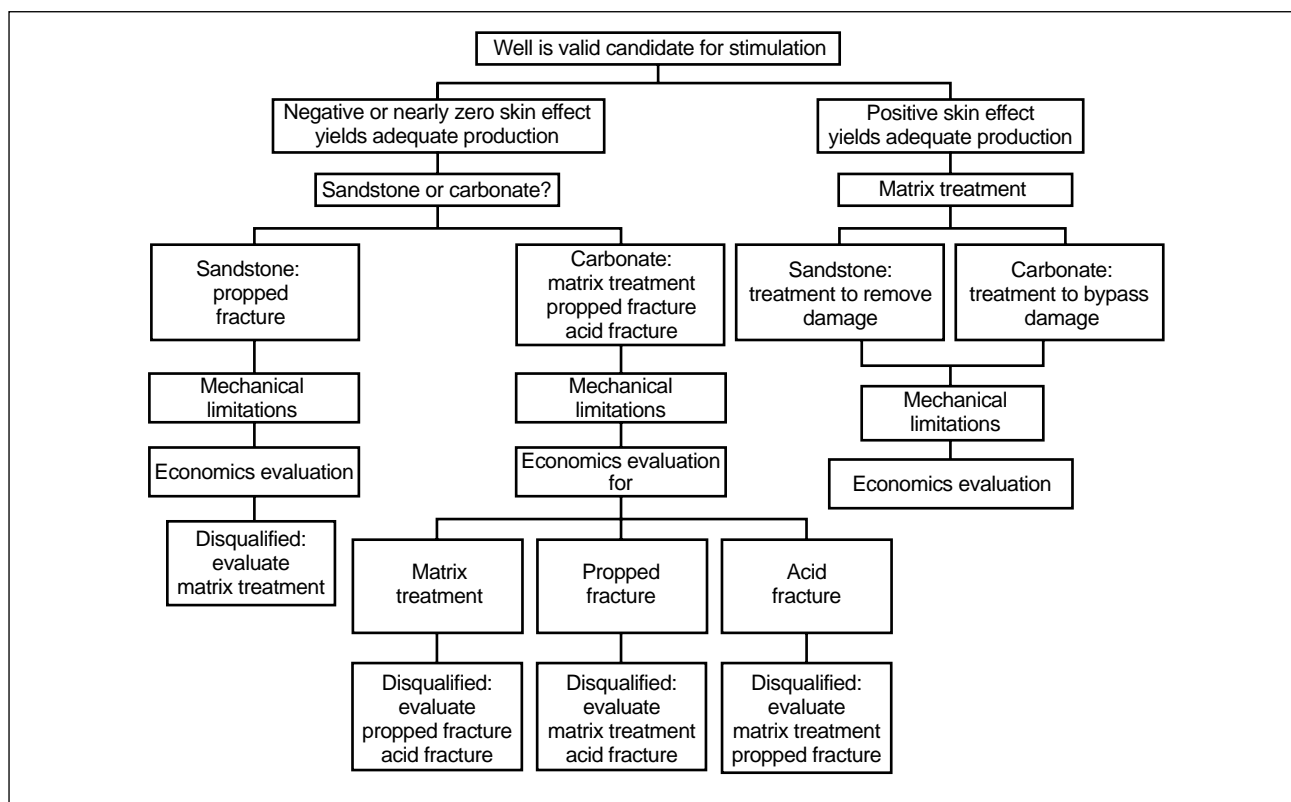


**Figure 13-3.** Stimulation decision tree.

maintained by propping it with high-permeability proppant. In acid fracturing, conductivity is created by differential (nonuniform) etching of the rock surface.

Other factors may influence selection of the stimulation technique. In unconsolidated or friable sands, it is advisable to examine the maximum pressure drawdown allowed before formation (sand) production. This drawdown limit may lead to the selection of fracture stimulation to allow obtaining target rates at a lower drawdown. On the other hand, concern about zonal isolation may preclude fracture stimulation. If vertical fracture growth into an aquifer or gas cap cannot be controlled, matrix stimulation may be indicated.

The engineer must also make some decisions about data collection before designing the treatment. As discussed in the following, many technologies are available to improve job monitoring and evaluation. Among the options to be considered are real-time data acquisition, use of downhole pressure gauges (memory or surface readout) and use of wireline surveys and tracers to determine treatment placement. For some wireline evaluations, baseline surveys must be run prior to the treatment.

## 13-5. Treatment design

### 13-5.1. Matrix stimulation techniques

Two types of nonfracture treatments are used to improve production in oil and gas wells. Wellbore cleanup uses chemical and/or mechanical methods to clean the wellbore. For matrix stimulation, fluids are injected into the formation to treat the near-wellbore region.

- Wellbore cleanup

Wellbore cleanup is commonly used to remove scale, paraffin, bacteria or other materials from the tubing, casing or gravel-pack screen. These treatments normally use acid or solvent systems that are placed in the wellbore area to soak. Key parameters in treatment design are the placement technique, chemical selection and soak time.

Mechanical assemblies such as packers, bridge plugs, spring-loaded “spot control” valves and coiled tubing can be used to ensure proper placement. This is critical in minimizing the volume of treating fluid.

Density differences between treating fluids and displacement or well control fluids must also be considered when designing a treatment that will stay in contact with the damage for the required soak time. The well cannot be assumed to remain static (no cross flow) during the soak time.

Chemicals should be selected on the basis of their effectiveness at dissolving the suspected damage. Laboratory tests at bottomhole temperature and, if possible, pressure are desirable to determine necessary soak times. Because of the small surface area of the exposed damage, the soak time can be hours to days depending on the type of damage, temperature and damage removal fluid. Agitation or jetting with coiled tubing can accelerate damage removal. In low-pressure wells, nitrogen ( $N_2$ ) is recommended to assist the removal of reacted treating fluid.

- **Matrix stimulation**

Matrix stimulation treatments injected below fracturing pressure down tubing, drillpipe or coiled tubing usually include a sequence of several fluids, referred to as stages. A minimal treatment consists of a preflush stage with a nondamaging, nonreactive fluid to establish an injection rate, a stage of the main treating fluid and an overflush stage to clear the main treatment fluid out of the tubing and displace it into the near-wellbore area. In most treatments, other auxiliary stages are included to enhance the effectiveness of the treatment. The selection of chemicals for the stages and the design of the treating sequence (pumping schedule) are reviewed in the following sections.

### 13-5.2. Treatment fluid selection

Treatment fluid selection is an important step in the engineering process. Multiple fluids (fluid systems), composed of base fluids and additives, are selected on the basis of lithology, damage mechanism and well condition. Each fluid in the treating schedule serves a special purpose. Although the process of fluid selection is complex because many parameters are involved (e.g., damage type, mineralogy), guidelines have been developed to simplify the process and improve treatment success.

- **Main treating fluid selection**

The main treating fluid is selected to dissolve or disperse the principal damage in sandstone formations

and to allow soluble products or solids to flow out of the well (Smith and Hendrickson, 1965). In the case of carbonate formations, the goal is to bypass the damage with acid or dissolve the damage with solvents (Hendrickson *et al.*, 1960). The main treating chemicals fall into the following categories:

- solvents to remove organic deposits (such as paraffin)
- oxidizers to remove damage from polymers
- scale removers to remove sulfate or oxide scales
- acids to remove carbonate and oxide scales, break polymer residues or stimulate carbonate formations
- hydrofluoric acid (HF) to remove aluminosilicate damage (primarily clays) from sandstone formations.

The main treating fluid is chosen to bypass, dissolve or remove the main damage. If multiple damages are suspected, it may be necessary to use several main fluids or to combine the listed functions into a single fluid; however, in combining fluids and functions, care must be taken to maintain the effectiveness of each and avoid incompatibilities.

Solvents are selected when organic deposits are suspected. If possible, the solvent should be evaluated in the laboratory with samples of the deposit. Various oxidizers have been reported for use in well stimulation. Because the polymer is usually introduced into the wellbore during drilling or completion operations, its identity is well known. An effective oxidizer can be evaluated in the laboratory using this knowledge. In addition, the effect of other fluid components, well materials and formation minerals on the oxidizer must be assessed. Scale removers can likewise be evaluated in the laboratory with samples of scale deposits. Soak time and chemical concentration can be optimized with these tests. One drawback to these forms of stimulation is that they are effective against a limited range of damage materials. If the damage diagnosis is uncertain, a more broad-spectrum treatment may be indicated.

Acid stimulation is performed to remove or bypass a variety of damages. When used to remove carbonate scale or polymer residues, acids act similarly to the treating chemicals discussed previously. Acids are also used to stimulate the near-wellbore region of the reservoir. In carbonates, HCl or organic acids (formic or acetic) are used to etch

conductive paths between the wellbore and the formation. In sandstones, mixtures of HCl and HF (mud acids) are used to remove drilling mud, formation fines, fines generated during drilling and perforating residue. These materials are usually more difficult to define or sample than other forms of damage.

Because acids are effective against several types of damage and are inexpensive, they are used in the vast majority of matrix stimulations. As a result, more effort has been expended in the engineering of acid treatments. In the remainder of this chapter, the focus is on engineering matrix acidizing treatments, but the concepts discussed apply to all types of matrix stimulation.

- Fluid formulation for matrix acid stimulation

Formulating fluids for matrix acid stimulation includes selection of the main acid and identification of the need for preflushes and overflushes. Figure 13-4 shows a decision tree for fluid selection in sandstones and carbonates. Fluid selection depends on the damage type, lithology, mineralogy and type of well. It is also based on field and laboratory experience and can be derived from an expert system (Perthuis *et al.*, 1989). Oil wells are more difficult to treat than gas wells because of potential emulsion,

sludging and wettability problems. To remove damage, the treating fluid must be in intimate contact with the damage. This requires a water-wet formation and oil displacement from the pore throats. Thus, preflushes used in oil wells may include an organic solvent or ammonium chloride with surfactants and/or a mutual solvent to remove heavy hydrocarbons from the wellbore area and ensure a water-wet environment.

The main acid formulation is based on the type of formation to be stimulated. Formulation guidelines are based on studies of acid-mineral reaction chemistry. A brief review of the main considerations in acid formulations follows.

- Fundamentals of acid-rock chemistry

Chapter 16 presents a detailed discussion of the chemistry and physics associated with acidizing. An appreciation of the key points in the chapter is necessary to understand the fluid selection process.

- Acid types and kinetics for carbonates

HCl is used for carbonate acidizing because it readily dissolves calcite and dolomite.

The reaction of limestone (calcium carbonate, or  $\text{CaCO}_3$ ) with HCl is

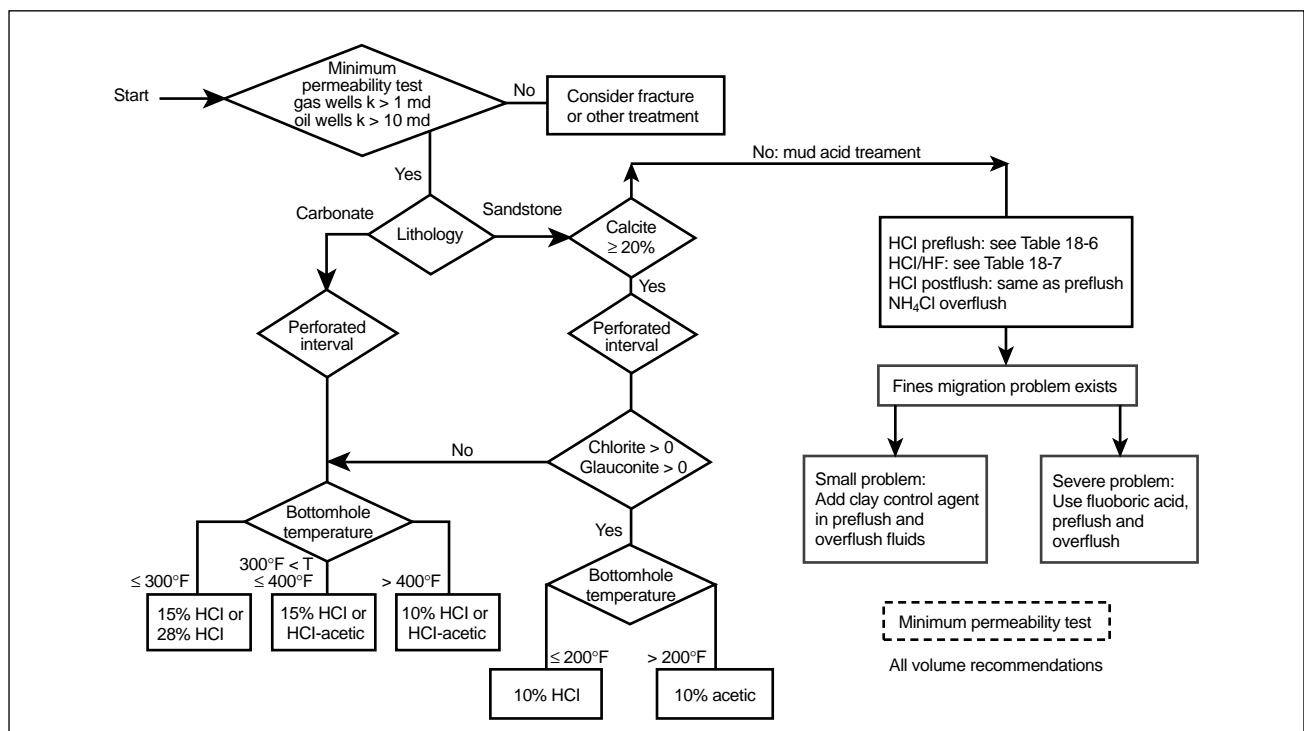
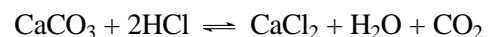
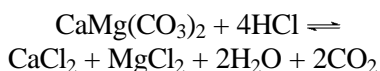


Figure 13-4. Fluid selection flowchart.

For dolomite, the reaction becomes



Normally, formation damage is not dissolved but rather bypassed to yield new flow channels (wormholes) and/or an etched surface on fissures, resulting in a reduced pressure drop (decrease in skin effect). The wormhole pattern is created because the highly reactive acid enters the largest pore throats, vugs and/or fissures and essentially enlarges them. The number of wormholes is a function of the pore-size distribution (Schechter and Gidley, 1969).

Acid reaction with carbonate reservoirs is governed by three mechanisms: wormholing, compact dissolution and radial flow. Each mode occurs under certain conditions. For example, at low injection rates, compact dissolution occurs when the formation face is dissolved to enlarge the well-bore. If the flow rate is increased to where the Peclet number (a function of injection rate, acid concentration and diffusion rate) is approximately 1, then wormholing initiates. If the rate is increased significantly, radial flow dominates in a manner similar to sandstones. Wormholing probably occurs in most treatments owing to the heterogeneous nature of carbonates; i.e., normally there are thief pores where wormholing initiates.

In cases where the temperature exceeds 400°F [205°C] (where corrosion inhibitors are ineffective in HCl), organic acids (acetic or formic acid) are used.

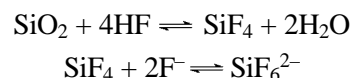
The reaction of HCl with calcite is diffusion limited (i.e., mass-transport limited). The limiting step in the dissolution reaction is the diffusion of acid (hydronium ion,  $\text{H}_3\text{O}^+$ ) to the surface of the calcite. Once the  $\text{H}_3\text{O}^+$  contacts the surface of the calcite, the reaction occurs very fast. The reaction of HCl with dolomite is diffusion limited at temperatures greater than 150°F [65°C] and limited by the surface reaction rate (i.e., diffusion is not the slowest step) below this temperature. Thus, because of the diffusion-limited kinetics of HCl on calcite, wormholes can normally be easily formed through the damaged zone (2 to 3 ft radially).

#### – Acid types and kinetics for sandstones

Mud acid mixtures of HF and HCl are used for sandstone acidizing. Unlike carbonate acidizing,

wormholes are not created in sandstones. In a typical sandstone, 80% of the radial flow can be through 20% of the pores (the larger pores). The damage is removed from the larger pores, resulting in a skin effect reduction but possibly not restoration of the natural permeability of the formation.

The primary reaction of HF with quartz grains (pure silica) is expressed in the two following equilibria:

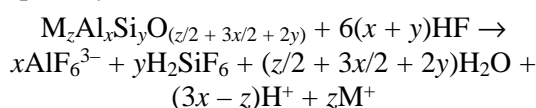


In the latter, silicon tetrafluoride combines with fluoride to produce silicon hexafluoride.

The conventional mud acid formulations (12% HCl–3% HF and 6% HCl–1% HF) used in matrix acidizing dissolve little quartz. The intent of sandstone matrix acidizing is to dissolve clays and other damaging materials, leaving the sandstone matrix undisturbed.

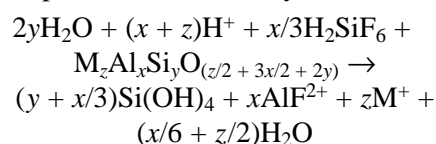
Although the primary reaction of HF with silica is simple, the reaction with silt and clay is more complex.

For aluminosilicates (clays and feldspars), the primary reaction is



where M is a metal atom (e.g., Na or K).

The reaction products  $\text{AlF}_6^{3-}$  and  $\text{H}_2\text{SiF}_6$  continue to react with the aluminosilicates to form silica gel on the surface of the clay (Crowe, 1986). An example of such a secondary reaction is



Theoretically, other secondary reactions can produce aluminum fluorosilicate solids, which may be damaging. Thus, there is a potential for the generation of damaging reaction products, although the effects are normally minimal.

Although HCl accelerates the reaction of HF with siliceous minerals (silt and clay) the reaction is far slower compared with that of HCl reacting with calcite. The reaction is reaction rate limited (i.e., numerous collisions of  $\text{F}^-$  with the surface of the mineral must occur before a reac-

tion occurs) and yet results in most of the HF reacting within the first foot of the wellbore. This occurs because of the large surface area of the silt and clay. (Five grams of smectite clay has the surface area of a basketball court.) Retarded acids have been developed to yield deeper live acid penetration (Thomas and Crowe, 1981).

- Acid and formation compatibility

- Iron hydroxide

Precipitation of iron (ferric,  $\text{Fe}^{3+}$ ) hydroxide ( $\text{Fe}(\text{OH})_3$ ) can occur during sandstone and carbonate acidizing when the pH value is greater than 2.2. Sources of iron in the formation and tubulars are chlorite, siderite, hematite and rust. Ferrous iron ( $\text{Fe}^{2+}$ ) is not a problem in sandstone acidizing because ferrous hydroxide does not precipitate until the pH value exceeds 7.7. Although fluoride complexation of iron increases the pH required for precipitation, iron control agents are recommended in all acid stages during sandstone and carbonate acidizing (Crowe, 1985).

Iron also increases the tendency of oil to form rigid films and emulsions with acids. These problems can result in formation damage and facility upsets when producing wells after acidizing.

Live acid or partially to completely spent acid occasionally forms an emulsion with crude oil or condensate, resulting in two-phase flow and a production decrease. In addition, sludging can occur because of the coagulation of asphaltenes plugging pore throats. Both emulsions and sludging can be avoided by adding the appropriate chemical determined from laboratory testing. In severe cases, organic acids replace mineral acids to decrease emulsion and sludging tendencies. Preflushes of solvents or potassium or ammonium chloride with mutual solvents are used to separate the crude oil from the acidic fluids.

- Carbonates

Formulating acids for carbonates is relatively simple because the majority of the reaction products is simply calcium chloride, water and carbon dioxide, which do not undergo further reactions. However, there are numerous minerals (silt and clay) in most carbonates that are insoluble in HCl. The insoluble material normally flows back through large wormholes or fissures and is not a problem.

In addition, acids selected for carbonate acidizing must be compatible with the formation fluids. Ensuring oil-acid compatibility is discussed later and in Chapter 15.

- Sandstones

The sensitivity of a sandstone formation to a matrix treatment fluid depends on the mineralogy of the formation, damage type, reaction products, temperature and permeability. As a rule of thumb, the more silt, feldspar and clay and the lower the permeability, the greater the sensitivity of the formation. The amount of precipitate formed is proportional to the amount of rapidly HF-soluble material present, and the impact of the precipitate on plugging is greater at lower permeability. In addition, fines migration and the formation of precipitates during a treatment create more problems in low-permeability formations. Thus, sensitivity is related to chemical and mechanical problems in sandstones.

Although sensitivity cannot be eliminated completely, the goal is to minimize it by selecting fluids with the greatest possible compatibility with the formation. The mineralogy of the formation plays a large role in formation sensitivity and fluid selection. The solubility of the minerals in a sandstone depends on their location. Authigenic clays are pore lining and come into contact with the treating fluid, whereas detrital clays were deposited with the original sand and are not completely exposed to the treating fluids. A discussion of the most important reactive minerals in a sandstone follows.

The solubility of the formation in HCl is normally considered to represent the carbonate content of the sandstone. This assumption is incorrect where other acid-soluble species are present (e.g., chlorite, zeolites, oxides and sulfides). If the acid solubility is greater than 20%, HF is not recommended. Excessive carbonate can react with the HF to precipitate calcium fluoride, and spent HF can react to form calcium hexafluosilicate. Chlorite clay and some zeolites (hydrous calcium/sodium/potassium aluminum silicates) are partially soluble in HCl and can cause severe plugging from the migration of their residue. Special precautions must be taken when treating formations with these minerals (see Chapter 18). Thus, in sandstone acidizing, an HCl (or organic acid) preflush is used ahead of the mud acid.

The silt and clay content can be determined in the laboratory by dissolving a core sample in mud acid. The difference between the mud acid and HCl solubilities is the approximate silt and clay content. Although it is important to know the amount and type of silt, feldspar and clay present, it may be equally important to know their position in the formation.

Secondary reactions can occur to form precipitates in the sandstone if precautions are not taken (see the “Design types” discussion in Section 13-5.3). Potential precipitates are as follows.

Fluosilicates ( $\text{SiF}_6^{2-}$ ) are the most detrimental precipitates produced in sandstone matrix acidizing. Sodium, potassium and calcium fluosilicates ( $\text{Na}_2\text{SiF}_6^{2-}$ ,  $\text{K}_2\text{SiF}_6^{2-}$  and  $\text{CaSiF}_6^{2-}$ , respectively) are extremely insoluble and form when formation water or any sodium/potassium/calcium brine contacts spent mud acid. They are avoided by preflushing with a compatible fluid such as ammonium chloride or HCl and then overflushing.

Calcium fluoride forms from the reaction of HF with calcite if adequate HCl (or organic acid) is not injected ahead of the mud acid. It is not necessary to dissolve all the calcite. As reported by Walsh *et al.* (1982), as much as 6% calcite can remain and not cause the precipitation of calcium fluoride or aluminum fluoride.

Precipitation of the aluminum salts aluminum fluoride ( $\text{AlF}_3$ ) and aluminum hydroxide ( $\text{Al}(\text{OH})_3$ ) (Walsh *et al.*, 1982) can be avoided by maintaining a low pH (less than 2). In addition, the tertiary reaction of aluminum bifluoride cations with silt and clay can occur very slowly at temperatures greater than 200°F [95°C] or with retarded mud acid formulations containing  $\text{AlCl}_3$ . The addition of more Al to the mud acid formulation results in Al saturation and precipitation. This process consumes acid, resulting in a pH increase and the precipitation of aluminum silicate and/or fluoride species. Citric acetic acid has been used successfully in treatments to complex aluminum and buffer the pH below 2, thus avoiding precipitation (Rogers *et al.*, 1998).

Hydrated silica precipitate forms in all mud acid treatments but is normally not a problem because it occurs during the topochemical reaction of spent mud acid with the surface of the silt and clay. The precipitate is not mobile like other

precipitates. However, adequate HCl must be present to account for this process because it consumes acid that may result in the precipitation of other species.

- Acid selection guidelines for carbonates
  - Temperature—Acid selection depends greatly on temperature because of corrosion inhibition limitations. For example, at temperatures greater than 300°F [150°C], 28% HCl cannot be used because of excessive corrosion whereas 15% HCl can be used. Above 400°F, organic acid or fluids containing ethylenediaminetetraacetic acid (EDTA, a non-acid-reactive solvent) can be used. In addition, emulsified acid or HCl with a retarder is used to increase penetration.
  - Mineralogy—Calcite and dolomite react differently with acids. Acid formulation should be optimized to achieve the desired reaction and penetration characteristics in each formation. Carbonates commonly contain insoluble minerals (silt and clay) that are released during acidizing. When this occurs, a silt-suspending agent is required along with  $\text{N}_2$  in wells where spent acid will not flow back naturally (less than 0.46 psi/ft pressure gradient).
  - Petrophysics—Acid penetration and the amount of damage depend on the type and distribution of porosity. For example, a highly vugular, high-permeability or fissured carbonate usually is damaged severely during drilling and completion because of solids. Attempts to obtain deep penetration (greater than 5 ft) may be difficult, with short but wide wormholes formed. An emulsified, retarded or foamed acid is required to achieve deep penetration. Because much of the porosity (hydrocarbons in place) is located in the vugular or fissure network, it is essential to remove the damage and restore communication with the wellbore. As stated previously, a silt-suspending agent in a gelled or nongelled acid and  $\text{N}_2$  are recommended to remove drilling mud and completion solids.
- Acid selection guidelines for sandstones
  - Temperature—Acid selection depends only slightly on temperature because lower acid concentrations are normally used (i.e., corrosion is not a major issue). The sensitivity of a sandstone formation increases with temperature because of

the rapid spending of HCl and mud acid and generation of mobile fines in the spent acid; however, the sensitivity resulting from precipitation reaction products decreases with temperature because of their increased solubility. These processes tend to counterbalance one another, resulting in little temperature dependence.

- Mineralogy—Sandstone mineralogy is the most important factor to consider in fluid selection because of the potential formation of precipitates. Because of the large surface area of silts and clays, most mud acid reacts rapidly to generate a complex mixture of compounds. Numerous guidelines have been developed from field experience and laboratory data (Fogler *et al.*, 1976; Walsh *et al.*, 1982; McLeod, 1984; Ayorinde *et al.*, 1992; Gdanski, 1996), and their use has improved field results. In addition, acid penetration is highly dependent on mineralogy because of the large surface area of silts and clays.
- Petrophysics—As in carbonates, acid penetration and the amount of damage depend on the type and distribution of porosity. Fissured sandstones are not common in most matrix candidates but can be present in basement formations and geothermal areas. A silt-suspending agent in acid and N<sub>2</sub> are recommended to remove drilling mud and completion solids. Although HCl can be used exclusively in this operation, mud acid is recommended to assist damage removal and dispersion.

The sensitivity of a sandstone depends on the permeability of the formation. Because permeability is a function of pore size, low-permeability sandstones are more sensitive than high-permeability sandstones for a given mineralogy. Thus, the permeability must be considered in fluid selection. Guidelines for mud acid selection and HCl selection are in Chapter 18 (Ayorinde *et al.*, 1992). Although they provide useful general guidance, acid formulations should be optimized on the basis of a detailed formation evaluation (Davies *et al.*, 1992; Nitters and Hagelaars, 1990).

- Preflush fluid selection

The preflush has three important functions. A preflush of a nonreactive fluid is pumped initially to ensure that injection can occur at an acceptable rate and pressure. In some oil wells, it is advisable to inject a preflush formulated to remove oil from the

near-wellbore region and leave the minerals and damage in a water-wet condition. This enhances the rate of acid attack. A solvent or solutions containing mutual solvents can be injected for this purpose. Gidley *et al.* (1996) advocated using carbon dioxide as a preflush in oil wells to remove oil and increase acid effectiveness. When acidizing with mud acid, an acid (HCl or organic acid) preflush is used to remove calcium carbonate and iron carbonate or oxide from the near-wellbore region. This helps to eliminate calcium fluoride- and iron-related impairment problems. Once injection is acceptable and the formation is in the proper condition, the main treating fluid can be injected. The main treating fluid normally contains HF and is displaced into the reservoir by an overflush fluid.

- Diverting agent selection

Nonuniform damage and permeability heterogeneity in targeted zones cause treating fluids to preferentially enter thief zones. The result is nonuniform damage removal and economic failure in most cases. Chapter 19 addresses treating fluid placement (diversion) in detail. Numerical simulators can model this process and assist treatment optimization (Bartko *et al.*, 1996). The heterogeneity of pay zones requires that the diversion and treating fluids must be compatible with the chemical systems used in the process.

Diverters are used to help control the distribution of acid in the wellbore. The four general types are bridging agents (60 mm), particulates (4 to 60 mm), viscous solutions (gels) and foams. Bridging agents are relatively large particles that are used to bridge at the face of fissures in carbonate formations; particulates are smaller particles that are used in sandstones. For particulates, size and composition are the key parameters (Crowe and Cryar, 1975). Particulates should be sized to form an external filter cake on the formation and should be soluble in the produced fluids (King and Hollingsworth, 1979). Viscosifiers should be stable enough to provide significant resistance to flow, but they must degrade fast and completely so that they do not impede production. Viscosifiers are normally used in carbonate formations. Foams are made by adding a foaming surfactant to the acid or brine and mixing it with N<sub>2</sub>. The foaming material should be stable in the fluid it is mixed in, and sufficient N<sub>2</sub> should be available to ensure a foam with a 65% to 70% (gas volume) quality downhole (Thomas *et al.*, 1998).

All types of diverters can be injected continuously with the acid or staged in discrete segments of the injection sequence. The concentration can also be varied as required. Experience can provide guidance as to which approach works best, or a numerical model can be used to optimize the diversion process.

- Postflush fluid selection

A postflush is almost always used to remove the reactive (and corrosive) fluid from the tubing and maximize the contact of main fluid with the near-wellbore area. The decision to inject a postflush fluid depends on the type of stimulation. If the dissolved or dispersed damage has the potential to damage the formation if displaced radially into the formation, injection into the reservoir must be avoided (e.g., paraffin solvent, mud/silt dispersant fluids would not be overflushed). At the other extreme is sandstone HF acidizing in which the overflush is essential to ensure that secondary precipitation occurs deep in the reservoir, where the impact on productivity is greatly reduced. Damage in the near-wellbore area can significantly decrease production by restricting flow in the formation; however, a 6-in. collar with 80% damage will reduce production by only 10% from ideal if located more than 3 ft radially from the wellbore (Fig. 13-5).

An overflush is also commonly used to displace HCl into a carbonate formation to improve the live acid penetration. Following the treatment, the well is cleaned up by flowing the reacted fluids to the surface along with the undissolved damage (i.e., drilling fluid, scale, paraffin and asphaltenes).

- Matrix treatment fluid additives

Chapter 15 provides a detailed discussion of the additives required in matrix fluids. Additives are

mixed with the treating fluid to modify a property (e.g., corrosion, precipitation, emulsification, sludging, scaling, fines migration, clay swelling tendency, surface tension, flow per layer, friction pressure). The brief discussion that follows emphasizes the optimization of treatment results. Most additives do not depend on the formation type but rather on the reservoir conditions (i.e., hydrocarbon type and temperature).

All additives should be tested for compatibility to ensure that they are chemically compatible with the other additives used in a particular fluid stage. In addition, stages that will be in contact with each other in the wellbore should be tested for compatibility. Compatible spacer stages can be used if incompatible fluids must be pumped, but eliminating incompatibilities is preferred if possible.

Additive types are as follows:

- Acid corrosion inhibitors—Different corrosion inhibitors are required for all inorganic and organic acids. In selecting an inhibitor and concentration level, it is important to realize that partially spent HF may still be highly corrosive. Recommended practices for testing acid corrosion inhibitors and methods for handling returned acid production have been published (NACE International, 1995).
- Solvents—General purpose aromatic solvents based on xylene are used widely as preflushes. In some cases, treating data show a significant reduction in injection pressure with the use of a solvent. Solvent preflushes may also help to prevent interaction with the formation oil by separating the crude oil and aqueous treating fluids.
- Iron stabilizers—Additives to control iron are required in all acid treatments. They can be grouped in three categories: buffers keep the pH value less than 2.2, and the most common buffer is acetic acid, which helps suppress oxide precipitation at temperatures less than 125°F [50°C]; chelating or complexing agents bond to the iron and suppress other reactions and are used to prevent precipitation and sludging (Crowe, 1985); and reducing agents prevent oxidation of the iron from ferrous to ferric (Crowe, 1985). Ferrous iron is less likely to precipitate and form sludges.
- Surfactants—Surfactants are used to reduce oil/water surface tension, ensure water wetness, prevent sludge and stabilize foams. They are

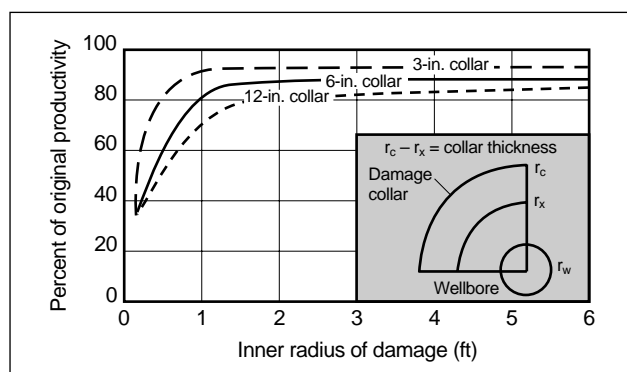


Figure 13-5. The effect of shifting an 80% damage collar.



recommended in most acid treatments to solve one or more potential problems. Small concentrations (e.g., 0.2% to 1%) of surfactants are sufficient. Surfactants are also used as dispersants to keep materials (oil or solids) dispersed in the stimulation fluid and as nonemulsifiers to help prevent emulsions from oil-acid interaction.

- Mutual solvents—Mutual solvents are used to ensure that the formation remains water-wet and to lower surface/interfacial tension. They are recommended in most acid treatments.
- Diverters—Diversion is recommended for all matrix treatments. The bridging agents benzoic acid and rock salt are used to bridge in perforations and/or fissures in carbonate formations and injection wells. Oil-soluble resins (OSRs) sized to form an external filter cake on the formation face are typically used as particulate diverters. Small benzoic acid particles can be used in injection wells completed in sandstone and nonfissured carbonate reservoirs. Water-soluble polymers used as gel diverters must be carefully chosen to have the right combination of stability during the treatment yet break sufficiently to prevent formation damage. They should not be used in sandstones. Foams are formulated with surfactants and a gas phase (usually N<sub>2</sub>). Surfactants must be compatible with other additives included in the foaming solution (Zerhoub *et al.*, 1991).
- Scale inhibitors—Scale inhibitors are materials that suppress the precipitation of inorganic scales from produced fluids. In general, they are retained on the formation and are more effective at neutral pH values. They are normally applied as an overflush to an acid treatment or mixed with a brine (with or without N<sub>2</sub>) and displaced into the reservoir when scale formation is a problem.
- Clay stabilizers—In treatments of clay-bearing sand formations, these polymeric cationic materials decrease clay migration. They are temporarily effective at low concentrations. Clay stabilizers do not prevent silt (e.g., feldspar, mica, chert) migration (Ezeukwu *et al.*, 1998). They are available in different molecular weight ranges for higher and lower permeability formations, and they must be tailored to the formation to avoid causing damage from the physical plugging of pore throats. Clay stabilizers are recommended where experience indicates that clay migration is a problem.

- Aluminum stabilizer—This class of chemicals was introduced in recognition of the role of fluoroaluminates in secondary precipitation in wells at temperatures above 200°F in sandstones (Gdanski, 1996). Although new chemicals have been introduced to address this problem, citric acid works well and is economical (Rogers *et al.*, 1998).
- Retarders—Numerous systems for delaying acid reaction in carbonates and allowing deeper penetration into the reservoir have been developed. Simulations should be performed to quantify their benefit.
- Nitrogen—N<sub>2</sub> is commonly added to treating fluids in low-pressure wells to assist in cleanup or to create a foam diverter.

Once the proper treating fluid formulations have been selected, the pumping schedule must be designed.

### 13-5.3. Pumping schedule generation and simulation

The pumping schedule includes the treating fluid and diverter sequence and the injection rate of each stage. It is generated using empirical rules based on previous field experience or computers.

A numerical simulator can be used to simulate damage removal and evaluate skin effect evolution, flow profile and wellhead or bottomhole pressure versus injection rate for the proposed pumping schedule. The simulator takes into consideration the placement strategy, an important part of the design process. The schedule can be optimized using a single-phase reservoir model to meet specific objectives for each fluid type (Bartko *et al.*, 1996). This step allows the design engineer to optimize the schedule to obtain the desired results in the most cost-effective manner. A treatment design is not systematically engineered until it is run using a field-validated simulator. Most treatments are currently based on empirical rules of thumb.

The matrix treatment design process includes several steps. The manual process that is discussed in detail in Chapters 17 through 19 should be understood before using computer-aided design programs. This section focuses on computer-generated design, with emphasis on the required input and interpretation of the output. A field case history for a sandstone is used to illustrate the utility of the procedure.

- Design types

The four levels of matrix design are photocopy design, advisor design, empirical/kinetic-based design and geochemical-based design. The first two are used for 98% of all matrix treatments. The high failure rate is partially attributed to this nonengineered approach. A discussion of each follows.

- Photocopy design

A photocopy design is based on a previous treatment pulled from the well file or an offset well file. The well name and date are changed, and the treatment is submitted for approval or simply processed and pumped.

- Advisor design

An advisor treatment design is developed on the basis of guidelines (rules of thumb) or experience. The design may be a refinement over the photocopy design, or it may be similar to it. Obviously, because a treatment design should be reservoir- and formation-damage specific, application of the advisor design is usually not optimum, as shown for the sandstone case history.

Sandstone field case history—The well was previously selected as a matrix stimulation candidate, with clay swelling and/or fines migration damage. Laboratory testing indicated that the well should be treated with mud acid and overflushed with fluoboric acid. Following the guide-

lines in Fig. 13-4, 50 gal/ft of HCl and 75 gal/ft of mud acid were recommended. Normally, the fluoboric volume is equal to the mud acid volume. Thus, the pumping schedule in Table 13-1 was developed.

Simulation of the advisor design using the kinetic-based numerical simulator described subsequently yielded a decrease in the damage skin effect from 206 to 37. Figure 13-6 shows adequate skin effect evolution in all layers except layer 4. Based on the negative slope of skin effect evolution in layers 2 and 4, it appears that more mud acid should be pumped. The total damage skin effect versus volume for the same treatment is shown in Fig. 13-7. The change in slope during the mud acid and fluoboric acid stages is attributed to retardation of the fluoboric acid and the

**Table 13-1. Advisor design for sandstone field case.**

Fluid Stage	Description	Rate (bbl/min)	Volume (gal)
Preflush	3% NH <sub>4</sub> Cl brine	1.0	1000
Preflush	7.5% HCl	1.0	2000
Main fluid	12% HCl–3% HF mud	1.0	3000
Overflush	3% NH <sub>4</sub> Cl brine	1.0	250
Main fluid	Fluoboric acid	1.0	3000

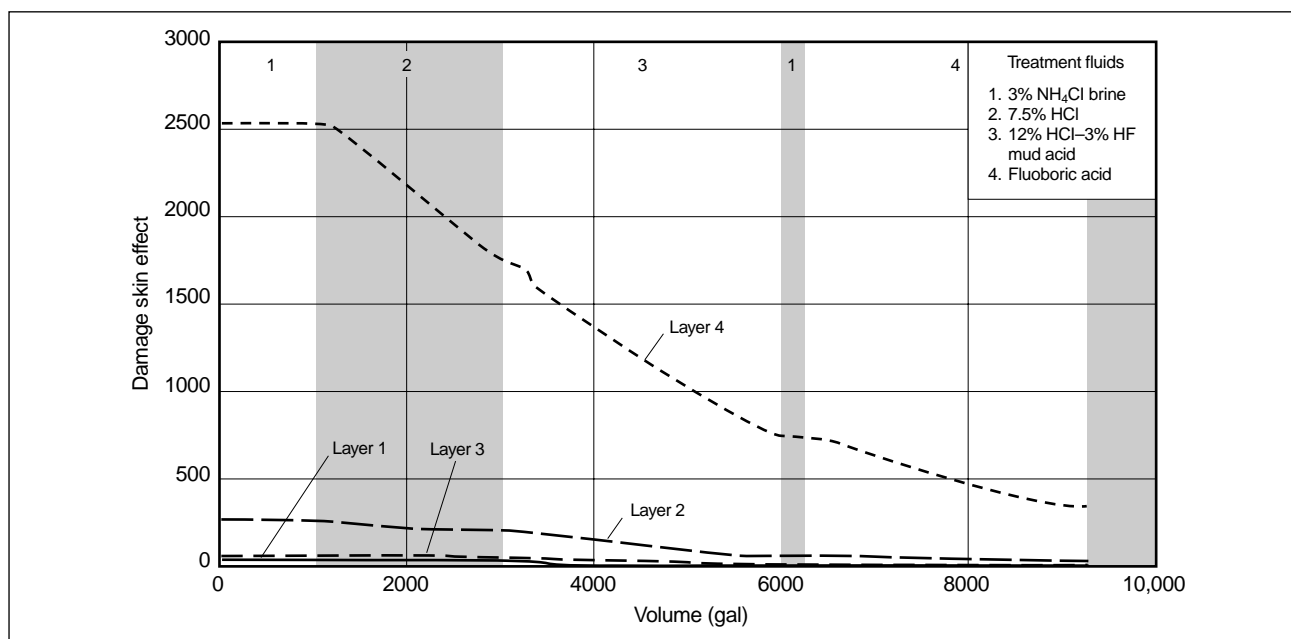


**Figure 13-6.** Acid placement: skin effect versus volume by layer (advisor design).

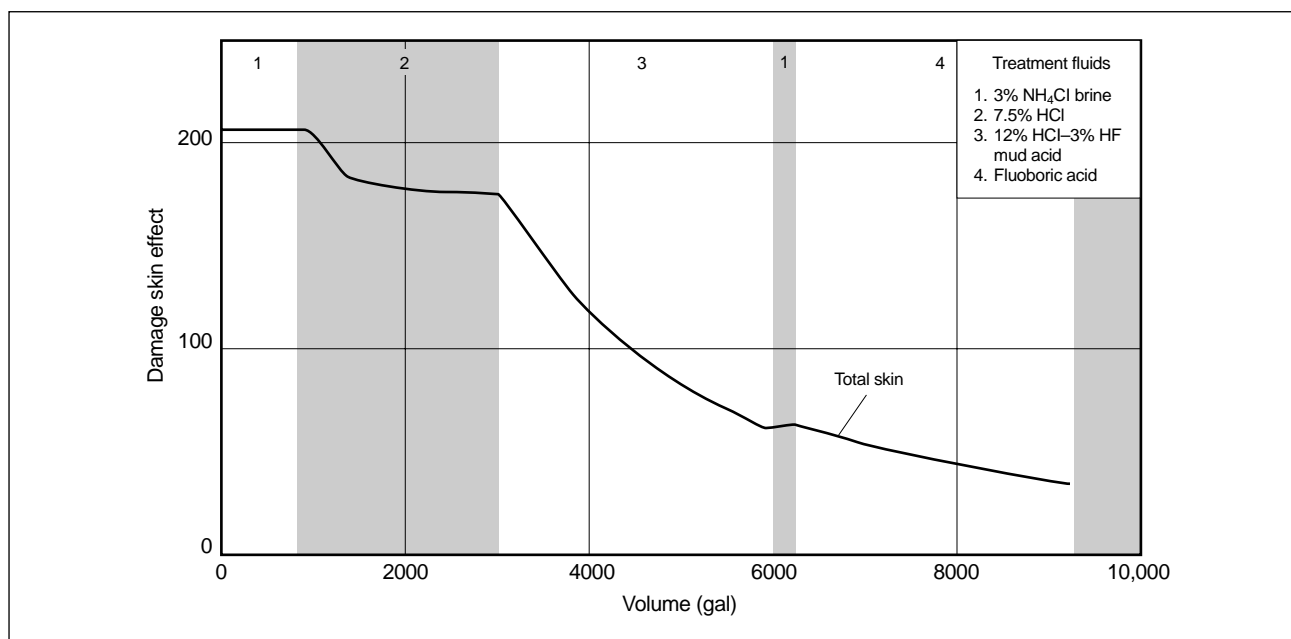


**Figure 13-7.** Acid placement: skin effect versus volume (advisor design).

change in available HF. The fluoboric acid generates 2.2% HF whereas the mud acid contains 3% free HF (Thomas and Crowe, 1981).

#### – Empirical/kinetic-based design

An empirical/kinetic-based design is produced using a numerical simulator. At a minimum, the simulator should be a two-dimensional (2D), two-phase, finite-difference simulator that allows a multilayer configuration for computing pressure and skin effect evolution during the matrix acidizing of sandstones and carbonates. Mineral dissolution should be simulated using the most common minerals and acids along with the appropriate reaction kinetics (reaction rate limited in sandstones and mass-transfer limited in carbonates with wormholing). This type of simulator correlates the local porosity change during acidizing to a local permeability modification and finally to an overall damage skin effect evolution per layer. Currently, precipitation is not considered in the empirical/kinetic-based simulator; however, if the acids are formulated properly this should not affect treatment results.

The empirical/kinetic-based simulator can model damage removal and evaluate skin effect evolution, flow profile and wellhead or bottom-hole pressure versus injection rate for the proposed pumping schedule. This step allows the

design engineer to fine tune or optimize the schedule to obtain the desired results in the most cost-effective manner. The simulator should be validated using field data to remove uncertainties in the design parameters (Bartko *et al.*, 1996; Thomas *et al.*, 1998).

Before using an empirical/kinetic-based simulator, a preliminary pumping schedule should be generated with a numerical simulator for matrix sandstone and carbonate acidizing. This advisor recommends treatment volumes based on the damage penetration. The flowchart in Fig. 13-8 is incorporated in the expert system to assist diversion selection. The pumping schedule includes the treating fluid and diverter sequence and injection rate of each stage. It is generated using empirical rules based on previous field experience or computers. The schedule can be optimized with a single-phase reservoir model to meet specific objectives for each fluid type (Perthuis *et al.*, 1989).

**Sandstone field case history**—The pumping schedule shown in Table 13-2 was generated using the numerical simulator described in this section. The objective input to the model was a target damage skin effect per layer of approximately 10% of the original for the mud acid system. This design is approximately twice the volume of the preceding advisor design.

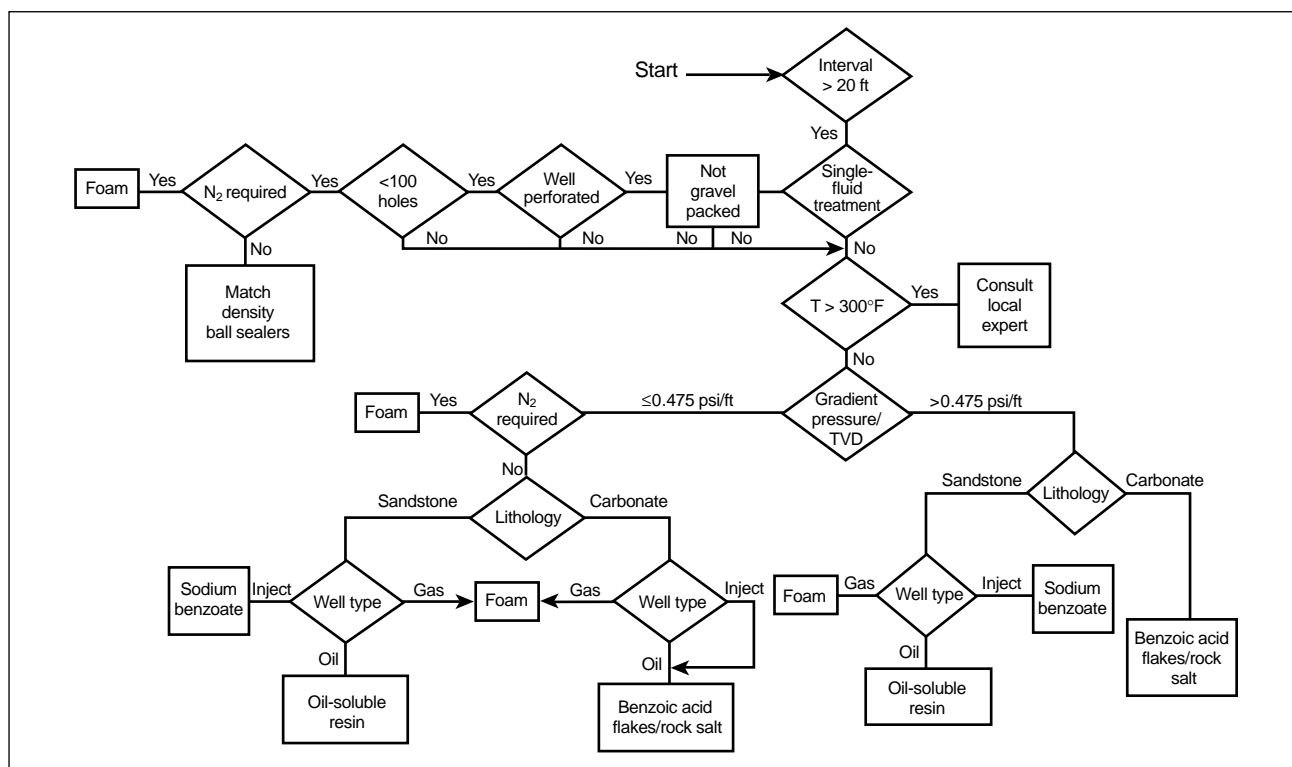


Figure 13-8. Diversion selection flowchart.

Fluid Stage	Description	Rate (bbl/min)	Volume (gal)
Preflush	3% NH <sub>4</sub> Cl brine	1.0	1500
Preflush	7.5% HCl	1.0	5350
Main fluid	12% HCl–3% HF mud	1.0	6660
Overflush	3% NH <sub>4</sub> Cl brine	0.8	840
Main fluid	Fluoboric acid	0.8	5050

The empirical/kinetic-based numerical simulation pumping schedule yields a total damage skin effect of 16.6 (8% of the original damage skin effect) with good skin effect evolution in layer 4 (Fig. 13-9).

The bottomhole pressure and pumping rate are shown in Fig. 13-10. The overall increase in pressure during the treatment results from diverter deposition. This especially dominates in the stages with the least amount of damage removal (i.e., HCl and fluoboric acid stages).

To check the validity of the simulator, the actual treatment performed on the well was simulated. The actual pumping schedule is shown in Table 13-3. The empirical/kinetic-based simulator yielded a final damage skin effect of 14.2; the actual damage skin effect was 11.4 from a post-treatment pressure transient test. Thus, the simulator predicted a 93% reduction in damage skin effect whereas the actual skin effect reduction was 94%, indicative of model validation. The good agreement of the simulated skin effect evolution of the treatment with the actual pressure transient test results is shown in Fig. 13-11. Figure 13-12 shows the excellent skin effect evolution in each layer for the actual treatment. Figure 13-13 shows the flow rate into each layer versus the volume injected. The flow rate into all layers changed during the treatment; i.e., the rate into the thief zones decreased whereas the rate into the highly damaged zones increased.

#### – Geochemical-based design

A numerical simulator similar to that discussed for the empirical/kinetic-based design is used for

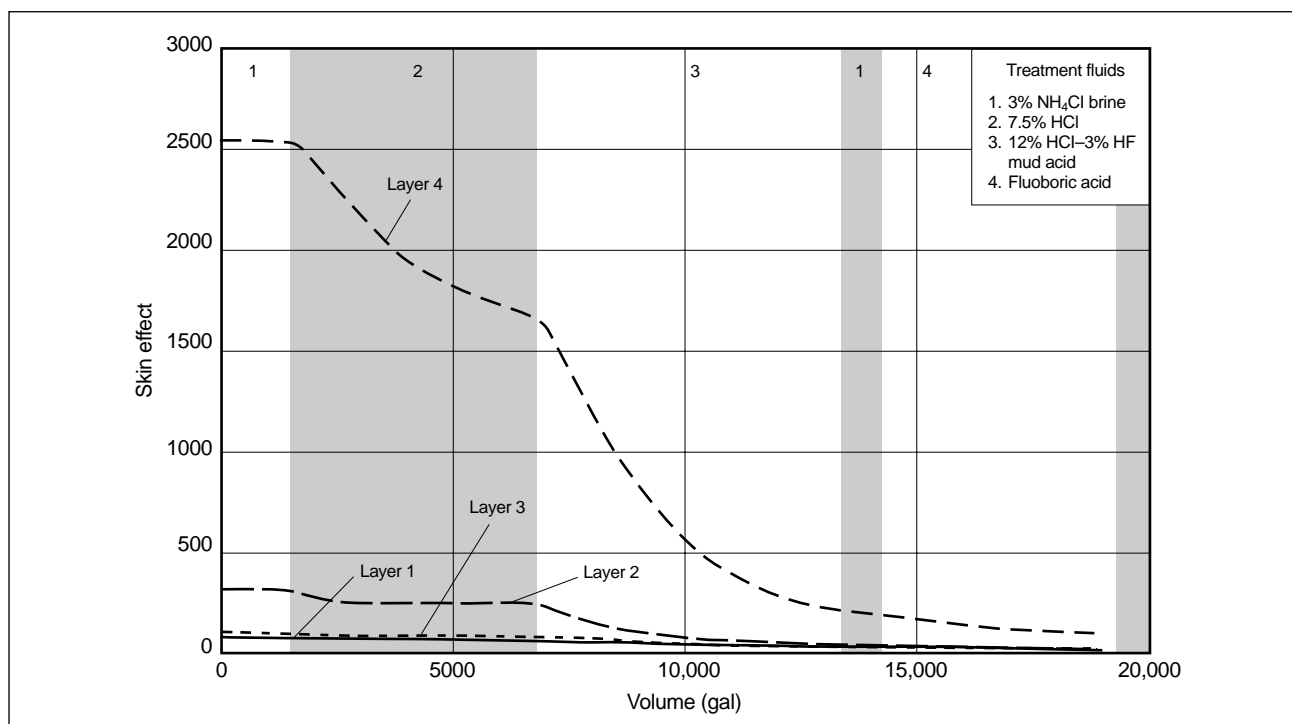


**Figure 13-9.** Acid placement: skin effect versus volume (empirical/kinetic-based design).

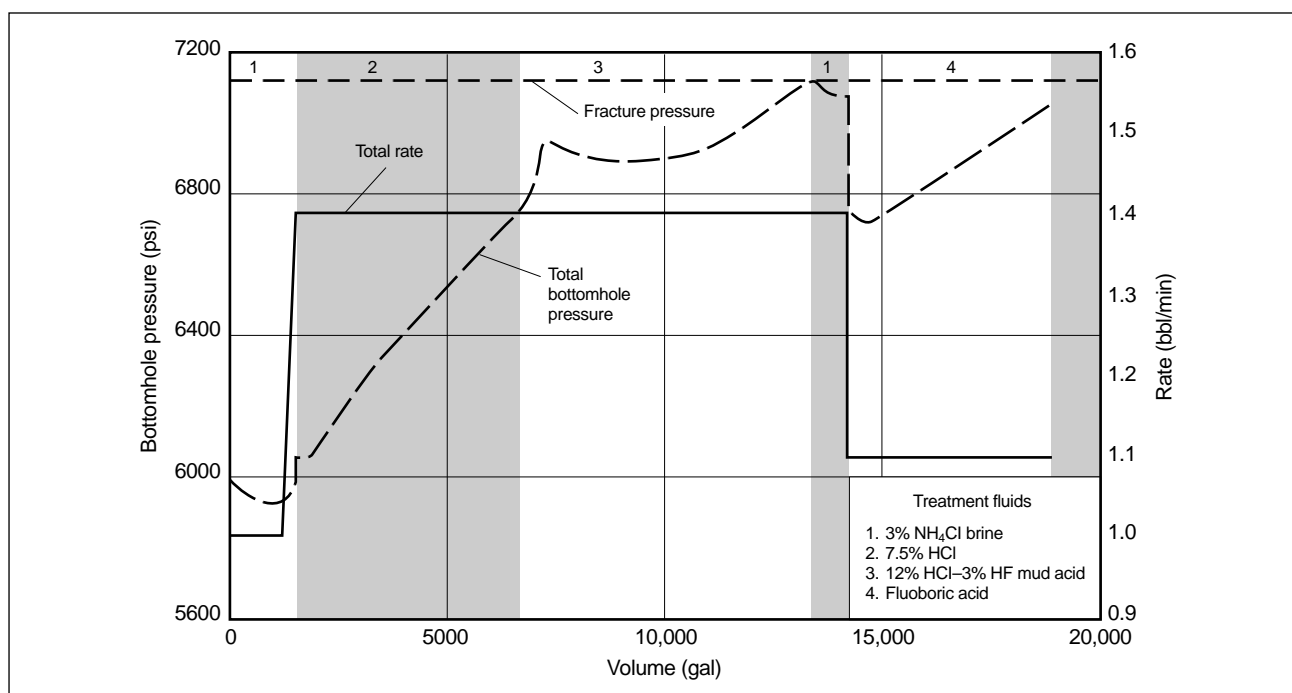


**Figure 13-10.** Bottomhole pressure and pumping rate versus volume (empirical/kinetic-based design).

<b>Fluid Stage</b>	<b>Description</b>	<b>Rate (bbl/min)</b>	<b>Volume (gal)</b>
Preflush	7.5% HCl	1.0	4000
Main fluid	12% HCl–3% HF mud	1.0	8000
Overflush	3% NH <sub>4</sub> Cl brine	1.0	500
Main fluid	Fluoboric acid	1.0	5000

the geochemical-based design; however, the precipitation of reaction products is considered and reported. This is accomplished by incorporating acidizing equilibrium chemistry for up to 14 elements and 100 reaction products.

- **Calculations**

Equations to calculate the maximum surface treating pressure and injection rate are provided in Chapter 16 for vertical and horizontal wells. The maximum injection rate in a horizontal well usually exceeds the available pumping equipment capability; however, many jobs pumped into horizontal wells employ coiled tubing, which limits the rate far below that necessary to fracture.

- **Placement strategy**

Placement strategy is an important step in the design of a matrix treatment (see Chapter 19). The goal is how to obtain uniform penetration of the treating fluid throughout the entire section and/or into each natural fracture system. If complete zone coverage is not achieved, full production potential cannot be realized.

Simulation of the actual sandstone design without a diverter indicates that layers 1 and 3 remain thief zones throughout the entire treatment (Fig. 13-14). In addition, skin effect values for the severely damaged bottom layer reduce to 75 for treatments with diverter and 1250 for treatments without diverter (Figs. 13-12 and 13-14, respectively). The poor fluid distribution can result in an excessive acid volume per foot of layer in the case without a diverter and inefficient formation damage removal. Figure 13-15 shows that the final damage skin effect is 20 in the case without a diverter. Although this represents a 90% reduction in skin effect and would yield approximately 4000 BOPD, the actual treatment with a particulate diverter yielded a 93% reduction in skin effect and more than 5000 BOPD. Thus, the small amount of

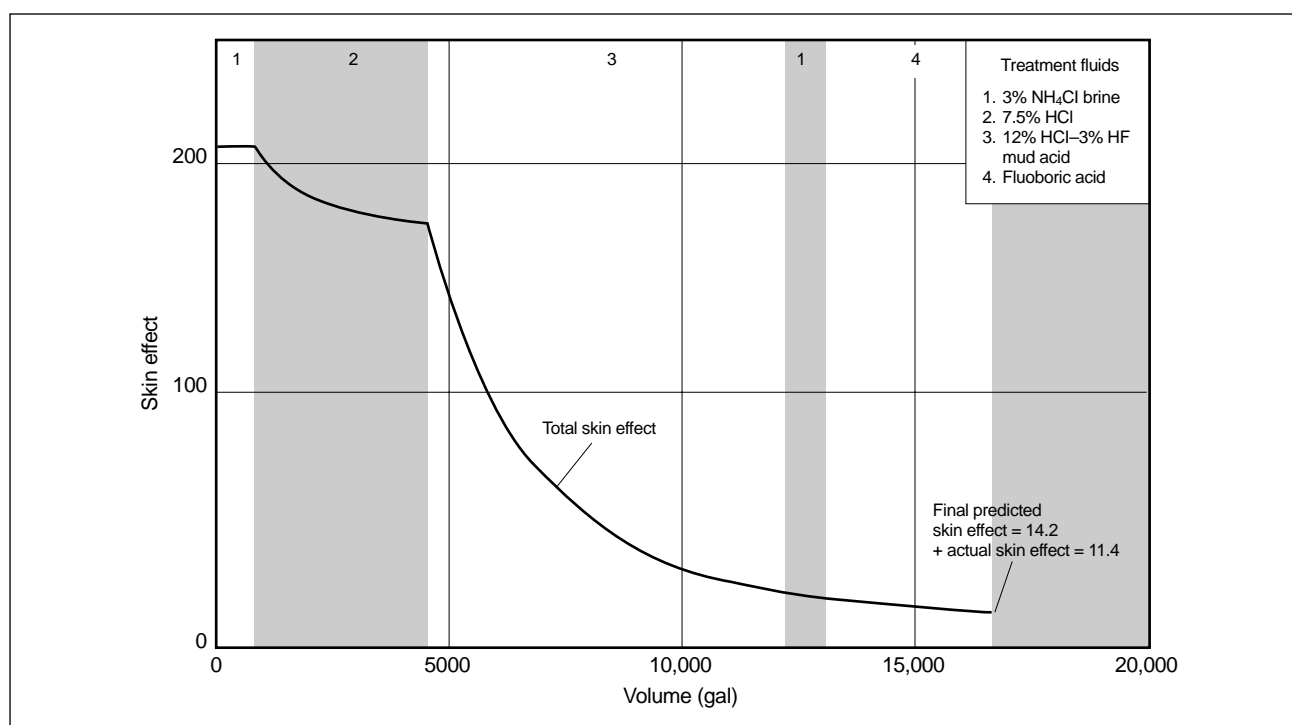


**Figure 13-11.** Skin evolution of the simulation of the actual treatment.

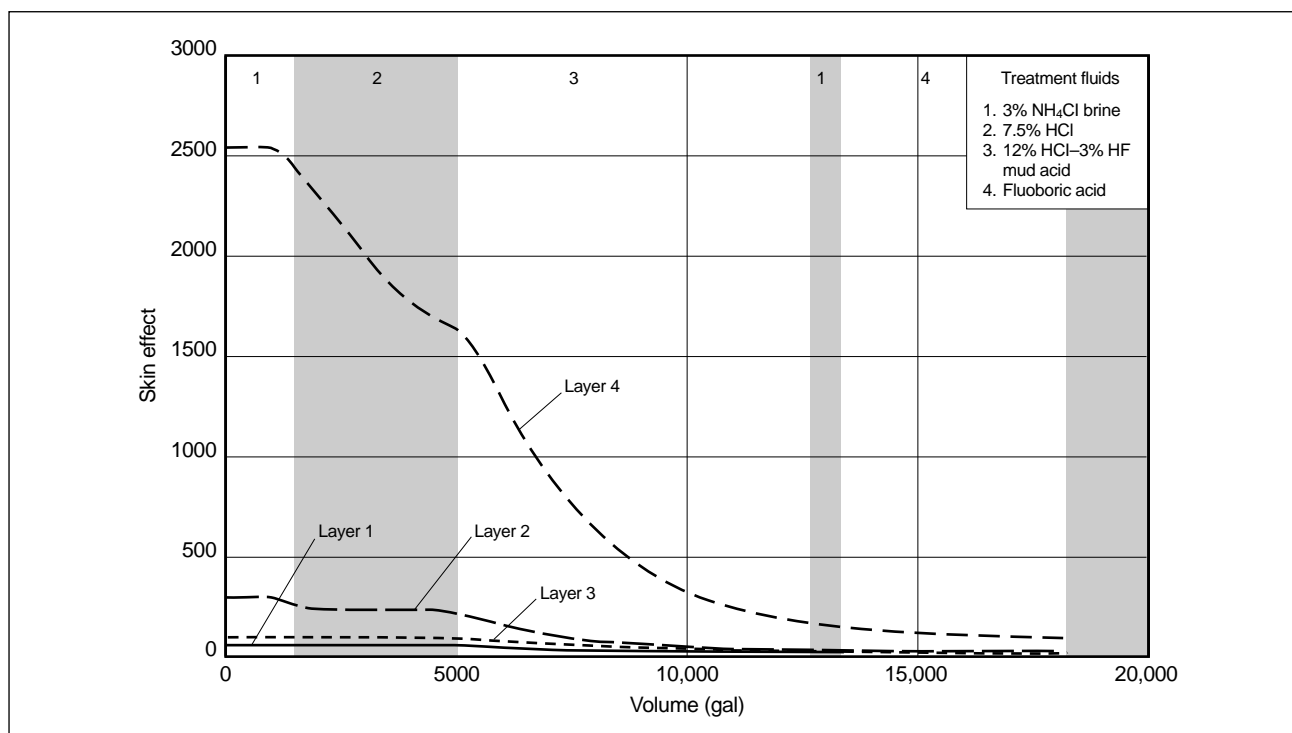


**Figure 13-12.** Skin effect evolution per layer for the actual treatment.

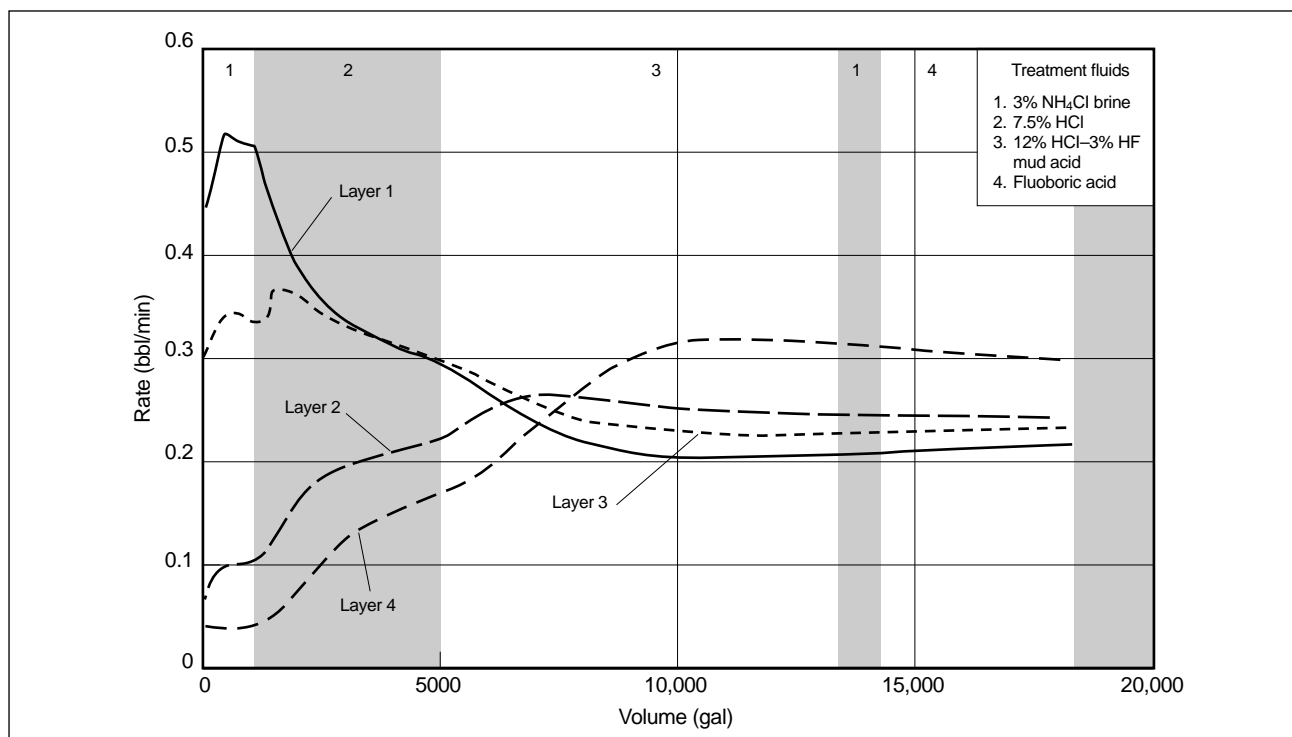


**Figure 13-13.** Flow rate into each layer versus volume injected.

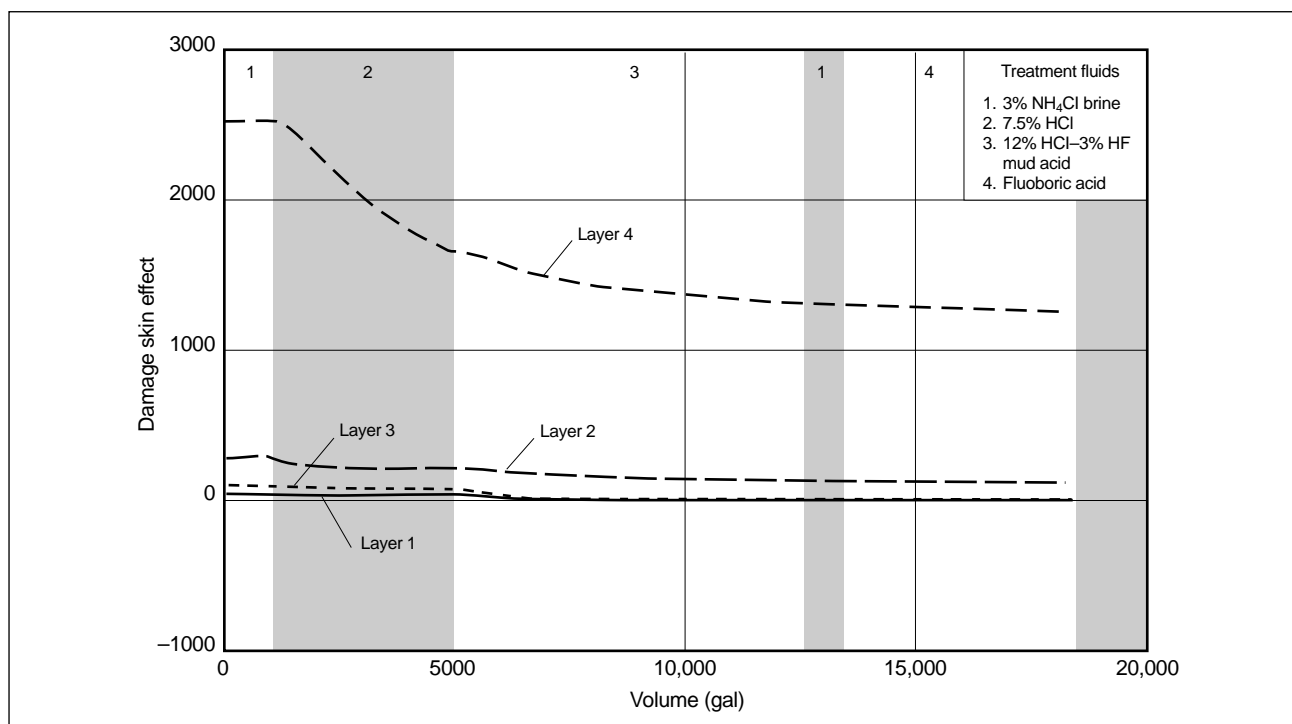


**Figure 13-14.** Damage skin effect per layer versus volume for a treatment incorporating the actual treatment volume without a diverter.

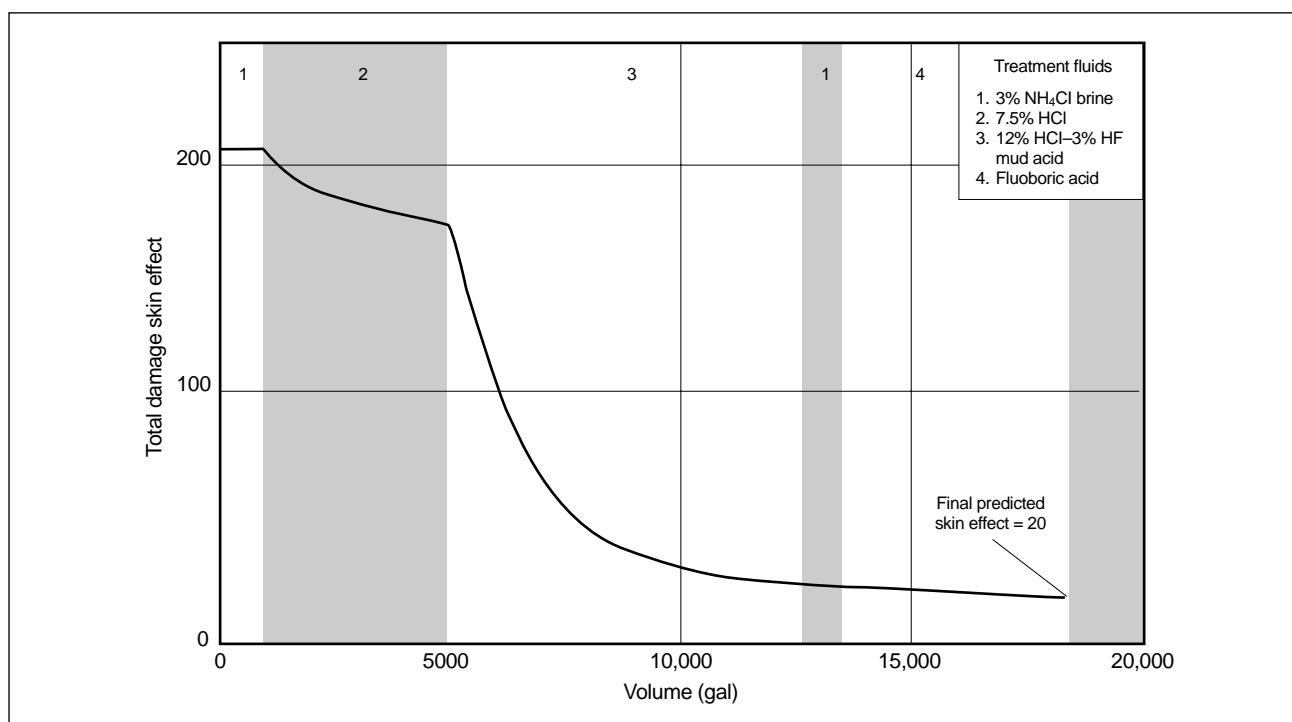


**Figure 13-15.** Total damage skin effect evolution versus volume.



diverter added to the treating fluids improved the efficiency of the acid and the resulting well performance (i.e., added approximately 1000 BOPD).

The importance of the placement strategy is magnified in a horizontal well because of the long interval. The placement strategy must address the type of tubing used to inject the fluid and diversion of the fluid from thief zones to the damaged sections. (The term zone is used here to describe longitudinal sections of a horizontal well, from the heel to the toe.) Although conventional tubing or casing can be used to place the treating fluid, this process can be time consuming or inefficient (Fig. 13-16).

Coiled tubing is generally used to overcome these problems. Unlike conventional tubing, coiled tubing can easily be run in and out of the hole, and treating fluid and diverters can be injected during movement (Thomas and Milne, 1995.) Figure 13-17 shows the good skin effect evolution obtained with this technique. Injection down the annulus of the coiled tubing and tubing may be required to optimize fluid diversion and should be modeled during simulations.

The placement technique is based on the information available for the well. For example, if a production log or spinner survey, mud logs or a log to locate fissures is available, this information can be used to aid the treatment design. If a spinner survey indicates that a thief zone exists in the center of the horizontal length, the coiled tubing can be run to that depth, followed by injection of a diverter slug. The diverter does not completely plug the thief zone but greatly decreases fluid flow into the

zone. This process can be repeated as required on the basis of information from production and fissure location logs. The coiled tubing can subsequently be run to total depth to start the treatment. Drilling breaks and mud logs can be used for the same purpose. If the data are inadequate, the entire section is normally treated by alternating acid and diverter stages as the coiled tubing is retrieved.

Diversion must be achieved to ensure that the treating fluid is continuously removing damage rather than simply being injected into a thief zone. Mechanical techniques (straddle packers or ball sealers) are not practical in many wells because they are completed openhole, with slotted liners or gravel packed. In cased hole completions, a straddle packer can be used to selectively place the treating fluid. In carbonate reservoirs, a chemical diverter (i.e., benzoic acid, rock salt, polymer systems, wax beads) can be used.

OSR or foam is normally used in sandstone formations for diversion. Solid diverting agents such as benzoic acid flakes have been used for decades but sometimes do not clean up well following the treatment. This especially occurs in carbonates, where large quantities of inefficient diverters are commonly required to create an increase in bottomhole pressure, resulting in diversion. Although OSRs perform well in sandstones, numerous operators use foam diversion techniques to avoid any chance of plugging by the diverter. A special application of foam diversion is in high-water-cut wells, where the foam preferentially plugs the water zone, allowing acid to

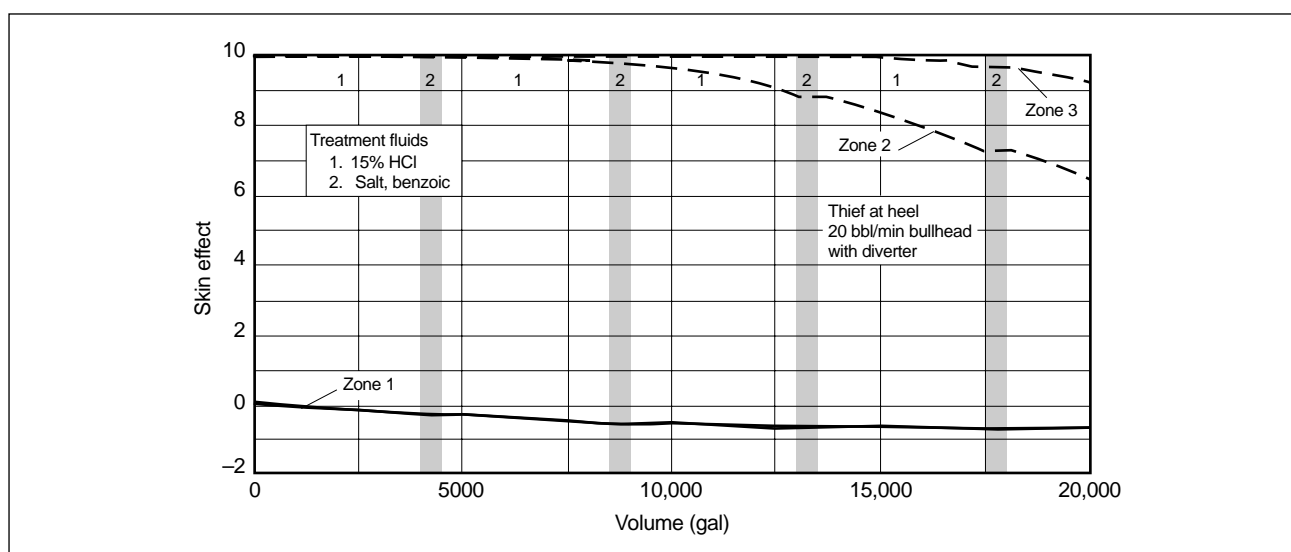


**Figure 13-16.** Skin effect evolution in a horizontal well treated using the bullhead technique.

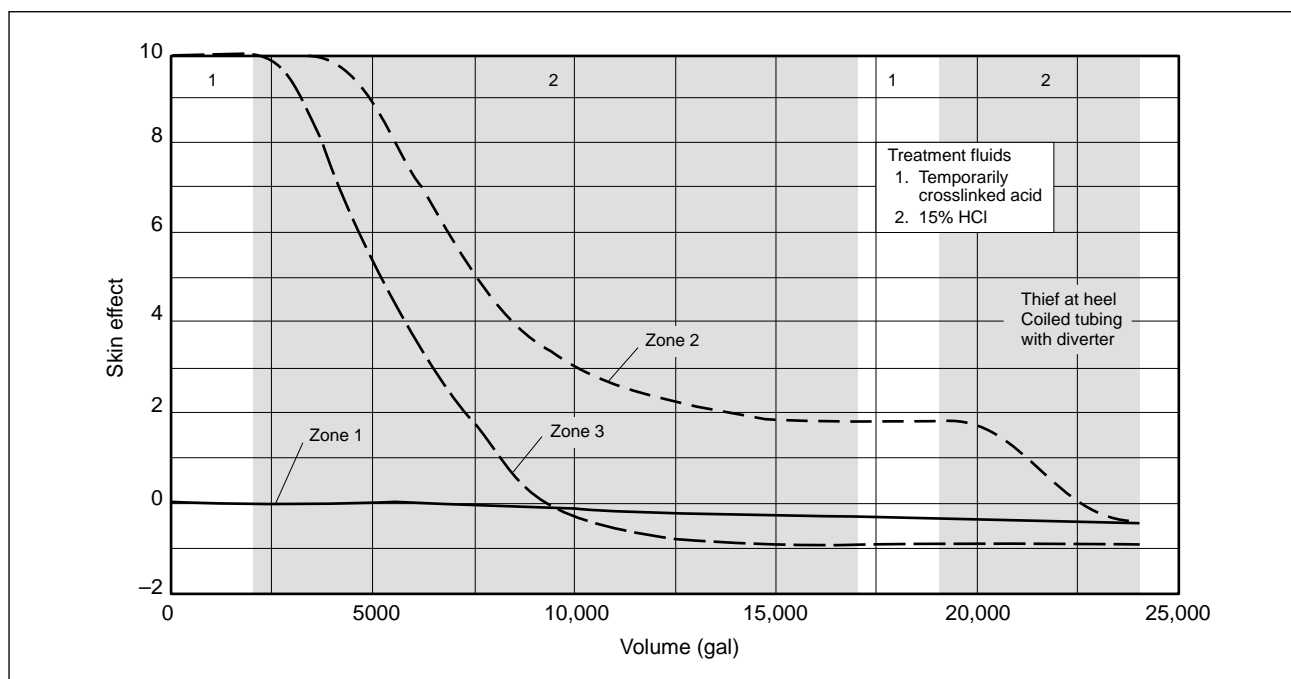


**Figure 13-17.** Skin effect evolution in a horizontal well treated using a coiled tubing placement technique with a temporarily crosslinked gelled acid diverter.

flow into the damaged oil zones (Zerhoub *et al.*, 1991). Similarly, the use of solids for diversion in carbonates has decreased in favor of foam and temporarily crosslinked polymer (Saxon *et al.*, 1997). This approach eliminates the slow cleanup experienced following conventional treatments and results in good zone coverage in vertical and horizontal wells.

Modeling of matrix acidizing of a horizontal well with the 2D simulator previously discussed (Thomas and Milne, 1995; Jones and Davies, 1996) indicates that bullhead matrix treatments in high-permeability or highly fractured limestones may be inefficient. Bullheading acid with a diverter normally results in poor coverage beyond 200 to 300 ft. Apparently the acid rapidly creates a thief zone at the entrance to the zone, and conventional chemical diversion techniques are ineffective (Fig. 13-16). If coiled tubing is used, a diverter can be placed across a known thief

zone followed by running the coiled tubing to total depth. Acid is then pumped as the coiled tubing is withdrawn, and a diverter slug is injected every 100–200 ft as required. The result is uniform penetration over the damaged sections with a small amount of acid injection into the thief zone located at the heel. Figure 13-17 shows the results of a numerical simulation, indicating diversion from the heel (i.e., the thief zone) is accomplished using coiled tubing and a diverter. Improved diversion is achieved when annular flow is optimized during the coiled tubing treatment. Figure 13-18 shows a poor distribution of acid per zone when the bullheading technique is used, whereas the treatment goal is achieved when coiled tubing placement is used (i.e., proper stimulation of damaged zones 2 and 3). The case histories reported in Sidebar 13E support the results of the simulations.

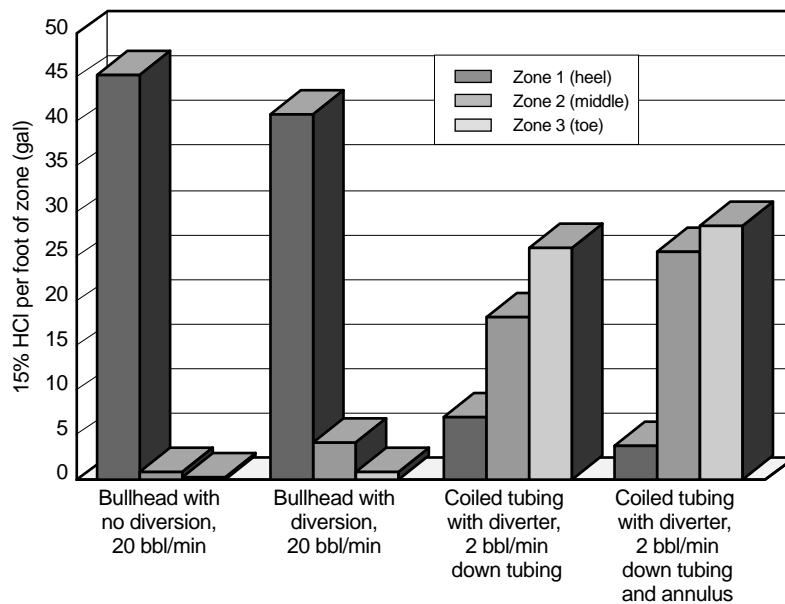


Figure 13-18. Simulation of acidizing a horizontal well with a thief zone at the heel.

### 13E. Placement study case histories

The following placement studies are the results of work reported by Thomas and Milne (1995).

#### Horizontal oil Well 1: bullhead technique

Horizontal injection Well 1 was completed in a limestone formation with 1800 ft of 5½-in. slotted liner inside an 8½-in. openhole. The well initially accepted 1000 BWPD. Because drilling mud damage was suspected, the well was acidized with 90,000 gal of 15% HCl at 25 bbl/min using the bullhead technique. Diversion was not used in the treatment. After the treatment, injection increased to 16,000 BWPD. The post-treatment PLT log indicated that 80% of the flow was into the first 100 ft below the casing shoe (Fig. 13E-1).

Although no diverter was used in this treatment, the addition of conventional benzoic acid or rock salt diverters was predicted to not improve zone coverage significantly. This was based on similar results observed in vertical wells completed in long limestone zones acidized using a bullhead technique with diverter. Thus, the acidizing treatment using the bullheading technique was not effective in obtaining zonal coverage as predicted by the modeling work.

Injectivity into Well 1 declined over the following 2-month period to 12,000 BWPD. The well was subsequently treated with 26,000 gal of HCl (15 gal/ft) using coiled tubing without a diverter, and injection was restored to 15,000 BWPD. Although injection was not restored to the original level, it was maintained for 1 year, which was indicative of a larger surface area accepting fluid.

#### Horizontal oil Well 2: coiled tubing with foam diversion

Well 2 was completed with a 4½-in. slotted liner in two sections of the Arab D limestone to yield 2378 ft of horizontal hole. The upper section was approximately 1500 ft long with a 100-ft barrier leading down to the lower Arab D limestone with approximately 780 ft of hole. The well was acidized using 25 and 20 gal/ft of 15% HCl in the upper and lower sections, respectively. The larger volume in the upper section was used because of the extended exposure time to drilling mud and suspected higher damage.

The treatment was performed by running 1½-in. coiled tubing in the hole to total depth, followed by loading the hole with diesel. HCl

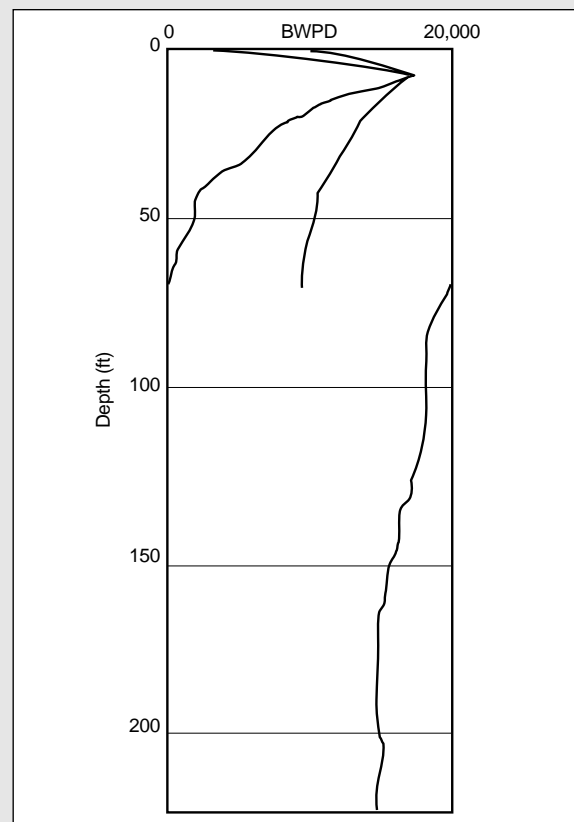


Figure 13E-1. Post-treatment injection log of a horizontal well acidized using the bullhead technique.

### 13E. Placement study case histories (continued)

was then injected at 2.5 bbl/min while the coiled tubing was withdrawn to yield the appropriate gallons per foot. A pressure of 1200 psi was maintained on the coiled tubing annulus to minimize acid flow up the backside. After it was pulled 50 ft, the coiled tubing was stopped and 65% quality foam was injected as a diverter. This sequence was repeated 15 times. Subsequently, the barrier section was loaded with 65% quality foam.

Once the coiled tubing was in the upper section of the Arab D limestone, it was acidized in 30 stages using the same process of alternating stages of acid and foam. Following the last acid stage, the coiled tubing was run to total depth and the horizontal section was displaced with diesel.

Prior to acidizing the well would not flow, yet post-treatment production was 2484 BOPD at 1318-psi flowing tubing pressure. Post-treatment production from the well is more than that from similar horizontal wells treated with up to 4 times more acid (100 gal of 15% HCl per foot of the horizontal section). The key to successful horizontal well acidizing was apparently not the volume of acid but the placement and diversion techniques.

#### Horizontal oil Well 3: coiled tubing with temporarily crosslinked acid diversion

Well 3 was completed openhole in the Arab D limestone with 1000 ft of horizontal hole. Upon initial completion a bullhead acid treatment was performed to remove drilling mud and cuttings damage. However, the results were unsatisfactory. The goal of the treatment was to provide uniform injection along the entire wellbore. Subsequently, the well was acidized using coiled tubing placement to inject 10 gal/ft of 15% HCl with silt dispersants and 4 gal/ft of temporarily crosslinked HCl (Saxon *et al.*, 1997). The treatment was performed by running coiled tubing in the hole to total depth and then injecting 6.3 gal/ft of HCl while withdrawing the coiled tubing from 10,553 to 10,353 ft. This process was repeated while running to total depth (10,553 ft). Next a temporarily crosslinked HCl diverter was injected while pulling out of the hole to 10,353 ft, which was then repeated 3 times to obtain good coverage. Once the coiled tubing reached 9753 ft, it was withdrawn while injecting HCl.

The post-treatment production log in Fig. 13E-2 shows an 800-ft section from the heel with significant flow near the toe of the well. (The production logging tool could not go beyond 800 ft.) This favorable flow profile is completely opposite that of Fig. 13E-1, showing a majority of the flow coming from near the heel of the well. Coiled tubing placement complemented by a temporarily crosslinked acid diverter apparently yielded improved coverage.

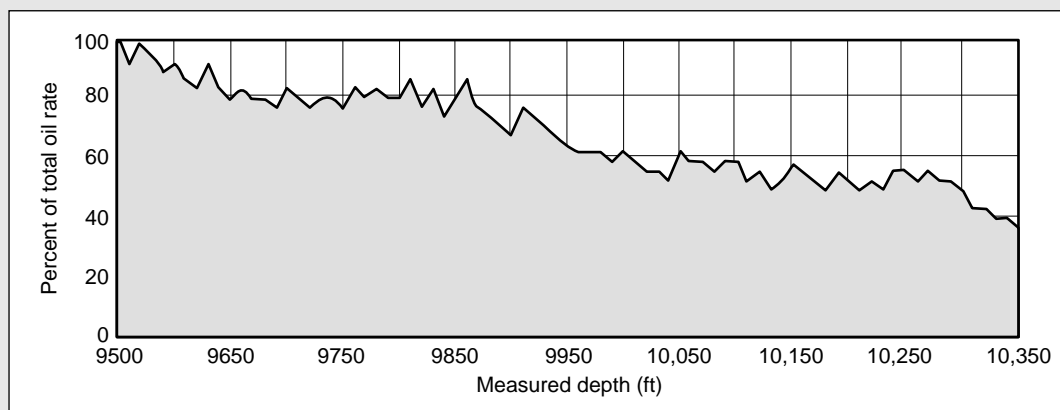


**Figure 13E-2.** Post-treatment production log of a horizontal well acidized using coiled tubing and temporarily crosslinked HCl diversion.

#### Horizontal oil Wells 4, 5 and 6: coiled tubing with temporarily crosslinked acid diversion

Wells 4, 5 and 6 were treated similarly to Well 3 with coiled tubing and a temporarily crosslinked HCl diverter. Eight to 15 gal of HCl with mud dispersants per foot of the horizontal zone was used in combination with 4 to 5 gal/ft of temporarily crosslinked HCl diverter.

The treatment was performed by running coiled tubing in the hole to total depth and subsequently reciprocating across a 100- to 500-ft section while pumping HCl. Next the coiled tubing was withdrawn while the diverter was injected. This process was repeated as required to obtain coverage over the entire horizontal section. The horizontal length, permeability and production results for the wells are summarized in Table 13E-1. In all cases, production increased significantly, with treatment payout in less than a month. The average increase in production was 1630 BOPD.

#### Vertical wells: bullhead technique

Long (150- to 200-ft) vertical openhole sections of the Arab D formation were historically treated with large volumes of HCl using the bullhead technique. Normally, 100 gal/ft of 15% HCl was injected down the tubing with diverter stages consisting of rock salt and benzoic acid flakes. As reported in the preceding horizontal well case histories, the authors observed that the acid went primarily into the high-permeability zones and the upper sections. This observation is based on the evaluation of pre- and post-treatment flow-meter injection surveys, which indicated a highly nonuniform injection profile.

Laboratory tests indicated that the diverter system was inefficient. Although a low-permeability filter cake was formed with the diverter, it was readily penetrated and destroyed by live acid. This situation explained the poor injection profile following the bullhead technique.

### 13E. Placement study case histories (continued)

**Table 13E-1. Production in horizontal oil Wells 4, 5 and 6 increased 440, 1750 and 2700 BOPD, respectively, following HCl treatment placed with coiled tubing and diverted with temporarily crosslinked HCl.**

Well	Horizontal Length (ft)	$k_H$ (md)	$k_V$ (md)	$p_e$ (psi)	Pretreatment		Post-Treatment	
					Wellhead Pressure (psi)	$q$ (STB/D)	Wellhead Pressure (psi)	$q$ (STB/D)
4	3600	6	3	2089	500	970	600	1410
5	1500	10	3	2950	750	950	875	2700
6	2000	25	12	2800	320	1000	260	3700

As indicated in Table 13E-2, the injectivity index increased although injection into the lower permeability zones in the six studied wells was not achieved. The average post-treatment injectivity index was 61 BWPD/psi.

**Table 13E-2. Pre- and post-treatment injectivity index of vertical wells acidized using the bullhead technique.**

Well	Pretreatment Injection Rate (BWPD)	Pretreatment Injection Pressure (psig)	Post-Treatment Injection Rate (BWPD)	Post-Treatment Injection Pressure (psig)	Pretreatment Injectivity Index (BWPD/psi)	Post-Treatment Injectivity Index (BWPD/psi)
A	21,200	1950	12,000	550	24	65
B	41,700	2750	55,300	2200	20	48
C	27,700	2950	52,800	2100	21	70
D	44,200	2800	44,800	1950	30	72
E	33,600	2900	25,700	1200	20	62
F	33,500	2200	41,600	1815	32	47
Average injectivity index = 61 BWPD/psi						

#### Vertical wells: coiled tubing with foam diversion

Five wells were completed in the same field and formation as the six vertical wells discussed previously. Coiled tubing and foam diverter stages were used to improve placement of the acid. The goal was to improve the injection profile by effectively acidizing both the high- and low-permeability zones in each well.

Approximately 50 gal/ft of 15% HCl was injected via coiled tubing at 1 to 1.5 bbl/min in stages. The coiled tubing was run to total depth as the foam was injected. Once at total depth, the coiled tubing was withdrawn as acid was pumped to yield 50 gal/ft. After withdrawing 20 to 50 ft, the coiled tubing was stopped and a stabilized foam was pumped. This viscous foam was designed to fill the wormholes created by the previous acid stage to yield improved zone coverage. The staging process was repeated until the top of the zone was reached.

From Table 13E-3, the average injectivity index for the studied wells was 120 BWPD/psi, nearly double that obtained with the bullhead technique. Injection surveys also show that the coiled tubing and foam diversion treatment yielded a more uniform injection profile, indicating that both the high- and low-permeability zones were acidized. This placement technique resulted in excellent overall results and cost 20% less than the conventional bullhead technique.

### 13E. Placement study case histories (continued)

**Table 13E-3. Pre- and post-treatment injectivity index of vertical wells acidized using the foam diversion technique.**

Well	Pretreatment Injection Rate (BWPD)	Pretreatment Injection Pressure (psig)	Post-Treatment Injection Rate (BWPD)	Post-Treatment Injection Pressure (psig)	Pretreatment Injectivity Index (BWPD/psi)	Post-Treatment Injectivity Index (BWPD/psi)
G	5,000	1,300	67,800	1240	4	119
H	26,200	1,550	42,400	1200	26	112
I	10,000	24,000	59,000	1100	5	139
J	0		38,500	934		65
K	5,000	2,000	73,000	1200	3	165

Average injectivity index = 120 BWPD/psi, a 97% increase over the results obtained with the bullhead technique

#### Summary

These case histories illustrate that the key to successful matrix acidizing in carbonate reservoirs is not the amount of acid injected but how it is injected. This is also true for sandstone reservoirs. Coiled tubing placement in combination with foam diversion in sandstones or carbonates appears to be an improved technique. Chapter 17 discusses the self-diverting acid system, which has been used successfully in long carbonate sections, including horizontal wells. This system is advantageous over foam diversion because it does not require nitrogen.

## 13-6. Final economic evaluation

As discussed for the preliminary economic evaluation in Section 13-2.3, an economic analysis is important. A final economic evaluation should be made on the basis of various treatment scenarios (i.e., advisor-based and empirical/kinetic-based designs). An evaluation of the sandstone field case history designs in the previous section follows.

- Sandstone field case history

The advisor-based design decreased the skin effect from 206 to 37 (Fig. 13-7), but the empirical/kinetic-based design decreased the skin effect from 206 to 16.6 (Fig. 13-9) to yield an additional 1373 BOPD (3406 versus 4779) and nearly \$1.9 million in NPV (almost \$2.7 million versus \$4.5 million). The actual treatment resulted in more than 5000 BOPD at a lower drawdown, with more than 3 million bbl of oil produced over the life of the well. Figures 3-19 and 3-20 show the economic indicators for the advisor- and empirical/kinetic-based designs, respectively.

## 13-7. Execution

The execution (pumping operation) must be performed as specified by the treatment schedule or operator on location. During this process, QC and data collection are important. The operational objective is defined by the design. QC is the process of ensuring that the materials and equipment meet specifications and are delivered in proper condition to the wellsite.

Properly trained personnel are the key to success. The wellsite personnel must understand the fundamentals of the stimulation techniques that will be used and must know how to use the equipment, software and techniques.

### 13-7.1. Quality control

Two keys to effective QC are communication and documentation. The designer must communicate the design expectations to the material suppliers. Because these expectations must be consistent with the supplier or manufacturer's specifications, the specifications

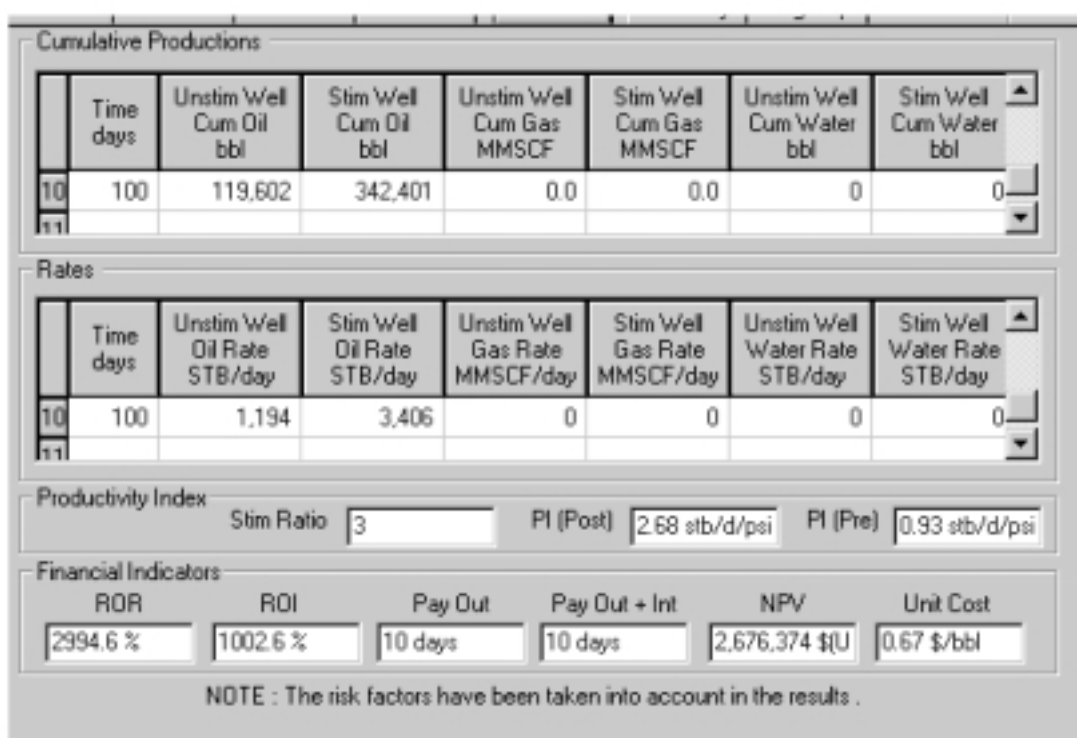


Figure 13-19. Economic indicators for the advisor design sandstone case history. Skin effect decreased from 206 to 37.

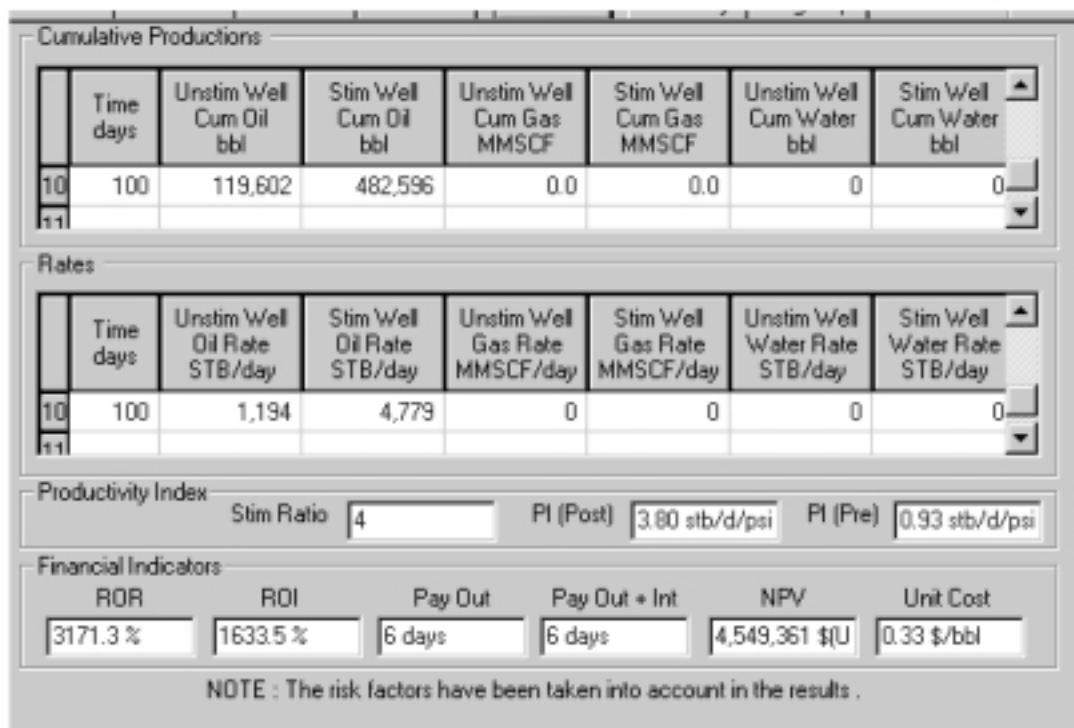


Figure 13-20. Economic indicators for the empirical/kinetic-based design sandstone case history. Skin effect decreased from 206 to 16.6.

should be available to the designer. The designer should request and receive test data on the performance of materials (e.g., corrosion inhibitors) as necessary to ensure that the materials will perform adequately. Numerous standardized test methods developed by the American Petroleum Institute (API), American Institute of Mechanical Engineers (AIME) and National Association of Corrosion Engineers (NACE) can be used to evaluate materials. Additional specialized testing may also be required in critical applications.

QC documentation should follow materials throughout their life cycle and be available if needed by the designer and operating personnel. Suppliers and vendors should ensure that materials shipped to the wellsite meet specifications. Given the time, distance and expense of delivering materials to the wellsite, nobody benefits if materials not meeting specifications arrive on location. In many cases, a material passes through several hands before being delivered to the wellsite. The QC testing routine and required documentation should be agreed on by vendors and customers as part of the commercial arrangement under which services are supplied. Testing should be sufficient to ensure that materials will perform their required functions in the field. Chronic failures in testing are a sign that a more reliable material or better handling procedures are required. Testing methods and options are discussed in Chapter 14.

The degree of attention paid to QC will vary with the critical nature of the operation. For stimulation operations, useful QC measures include

- on-site titration of acids to verify concentration
- regular QC testing of each batch or lot of corrosion inhibitors by the service company
- verification that surface-active agents are supplied in the specified concentration
- on-site testing of gel viscosity for diverters (carbonates)
- regular testing of particle size and solubility of particulate diverters
- sampling of fluids pumped during stimulation treatments, with the samples retained until the treatment has been evaluated.

The equipment must be able to execute the design required. The designer and operations personnel must

review procedures in detail to ensure that the available equipment is capable of conducting all required operations. All equipment to be used in stimulation operations should be properly maintained to perform reliably and accurately. As discussed in Section 13-5 for treatment design, adherence to the design is required to increase the chance of success.

Calibration of all measuring devices, such as transducers and flowmeters, should be a regular part of maintenance procedures. Calibration conditions should mimic operating conditions to the extent required to properly calibrate the equipment. Sufficient inventories of spare parts should be available to make maintenance repairs quickly. Calibration tests should be conducted routinely and the results documented.

### 13-7.2. Data collection

Careful recording of events during the treatment should be made, including records of unusual observations by operations personnel (McLeod and Coulter, 1969). Over the past decade, the emphasis on improved monitoring and recording equipment and QC rather than pumping and mixing equipment has resulted in better records for postjob treatment evaluation and improved matrix success.

The basic information available from a stimulation treatment minimally consists of a record of pressure and rate and a log of operations prepared by operations personnel. All pressure charts can be analyzed; however, their usefulness may be limited by their imprecision (e.g., pressure gauge accuracy may be  $\pm 150$  psi) and the difficulty and time required to put the data in a more useable form.

The modern approach is to provide continuous digital monitoring of the surface rate and pressure with either an on-site computer or digital data logger. Combined with a detailed log of operations, this information can be analyzed in real time or processed after the procedure with the same type of software. The key advantages of continuous monitoring are higher precision of the data and easier manipulation of the digital data files using computers. The chief drawback is that bottomhole treating pressure must be calculated from surface treating pressure. Reliable means for this calculation are available for Newtonian fluids (e.g., brines and acids), but the calculation for complex fluids (e.g., gels, slurries, foams) is not always reliable.



A relatively simple solution to this problem is to allow pressure communication between the injected fluid column and a static fluid column if the reservoir pressure is greater than the hydrostatic pressure resulting from a column of fluid. The surface pressure of the static fluid is measured, and the bottomhole treating pressure is obtained by subtracting the hydrostatic pressure of the static fluid column. The static column is normally an annulus, either tubing/casing or coiled tubing/tubing. Packer assemblies can be modified to allow pressure communication. The main operational drawback is that stimulation fluids may leak into the tubing casing annulus, which necessitates additional operations to remove them.

Memory gauges can also be run on treating strings to record the bottomhole temperature and pressure during treatment. They are retrieved after the treatment and analyzed directly. Their obvious drawback is that real-time analysis is not possible. In running memory gauges, it is critical to select a sufficiently long time interval to record the operation. If similar treatments using gel, foam or slurry diverters are to be performed on a series of wells, a memory gauge can be run on the first one and the data used to develop a friction pressure correlation for the diverters. Surface pressure can then be used with acceptable accuracy on subsequent treatments.

Surface-readout bottomhole pressure recording devices are also available. In general, the devices are expensive and the additional operational difficulties associated with running them further increase their cost. However, they are invaluable for stimulation evaluation and also for reservoir evaluation and management.

In addition, where coiled tubing is run, sensor packages to monitor pressure and temperature are used to determine bottomhole treating pressure for calculation of the skin effect. The temperature profile is determined prior to a treatment following injection of an inert fluid (e.g., water containing ammonium chloride) to estimate the flow profile. Another temperature profile can be run after the treatment to quantify zone coverage.

Technology exists to transmit the job data to the office from most locations. This efficient technique allows an engineer to monitor numerous jobs, participate in decision making and direct operations from off site.

## 13-8. Treatment evaluation

### 13-8.1. Pretreatment evaluation

A step-rate test can be performed prior to the stimulation treatment to quantify reservoir pressure, permeability and skin effect. The benefit to the operator is improved real-time evaluation. The test requires injection of an inert fluid into the zone of interest and bottomhole pressure calculation and recording. The first diagnostic performed determines the reservoir pressure using a plot of the bottomhole pressure versus rate. Theoretically, the y-axis intercept at zero rate is the reservoir pressure (1815 psi in Fig. 13-21).

The second diagnostic incorporates PTA of the data using the Odeh-Jones methodology. Figure 13-22 shows the analysis plot used in the process. This water injection well exhibits permeability of approximately 12.8 md and skin effect of 0.1. The permeability and reservoir pressure determined from the step rate test should be used in the subsequent real-time evaluation.

### 13-8.2. Real-time evaluation

In recent years, technology to determine real-time skin effect evolution during a treatment has been developed. Although this technology is not practiced routinely, it can be a useful diagnostic tool (see Chapter 20). For example, if the skin effect is decreasing during an HCl stage, an acid-soluble species (e.g., calcium carbonate/oxide, iron carbonate/oxide) created damage. This information should be complemented by the well history, laboratory testing, etc., to improve understanding of the present problem and assist future work.

One method available to the industry is based on the steady-state design and evaluation method developed by Paccaloni (1979b). Data can be displayed on a graph of the bottomhole pressure versus injection rate. Comparison is made with standard curves calculated for fixed values of skin effect to evaluate skin effect evolution.

More advanced programs calculate skin effect evolution in real time, taking into account transient effects (Prouvost and Economides, 1989). The reservoir pressure response during pumping is computed assuming

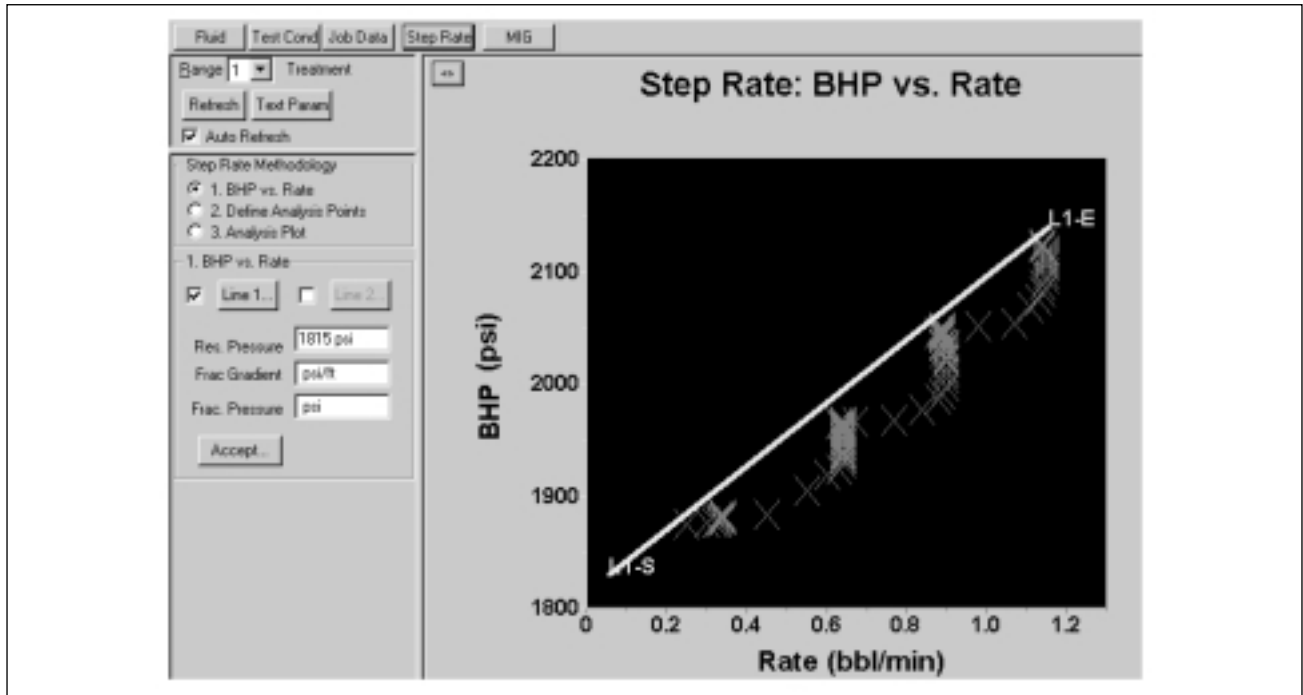


Figure 13-21. Determination of reservoir pressure from a step rate test.

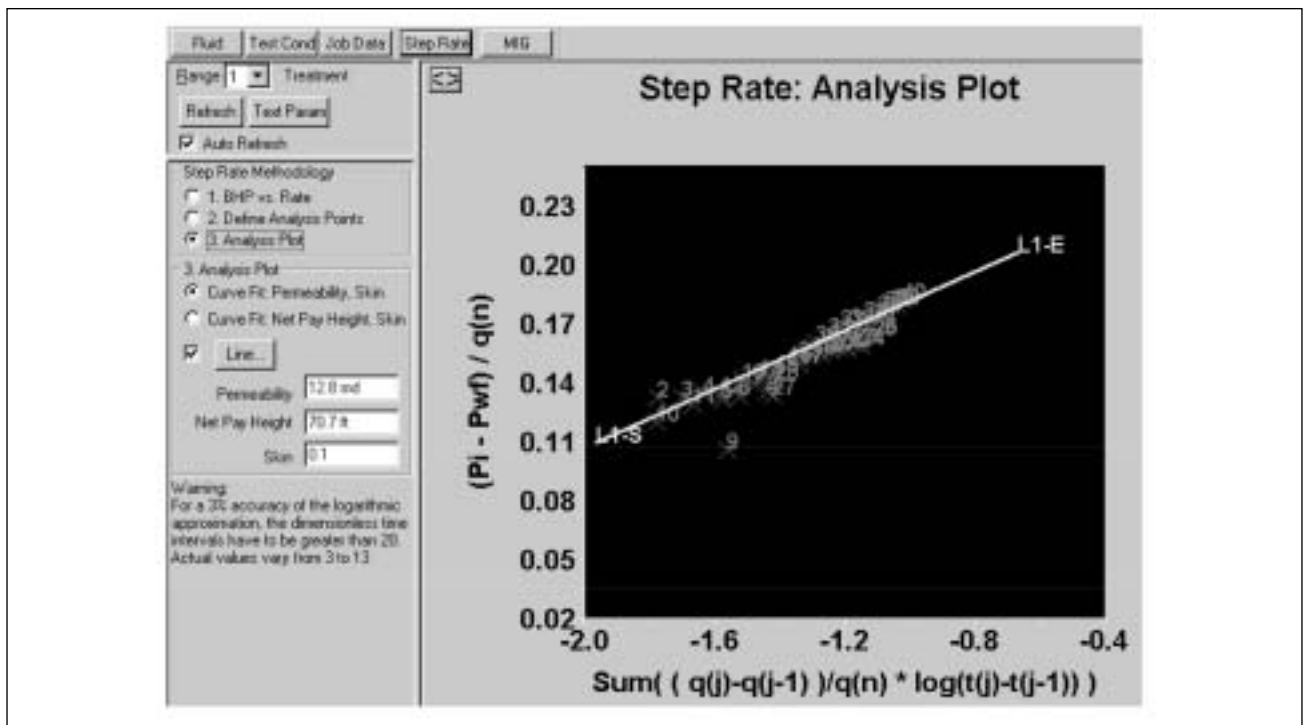


Figure 13-22. Pressure transient analysis from a step rate test.

zero constant skin effect. One value of skin effect is provided, combining the effects of damage, completion and diverters. Using these tools, a more quantitative assessment of each component of the stimulation design can be made.

Figure 13-23 shows the real-time skin effect evolution of the injection well analyzed in the step rate test. The initial skin effect observed when water containing ammonium chloride was injected is close to the skin effect obtained in the previous step rate test. The increase in skin effect when HCl was injected into the formation indicates that the HCl was incompatible with the formation or was incompatible with something that was injected in the leading portion of the acid. In this example, the latter is suspected because the tubing was not cleaned (pickled) prior to the injection of acid down the pipe. The initial acid dissolved magnetite and/or rust on the walls of the tubing and precipitated ferric oxide before the acid reached the zone. Thus, the pressure increased when the solid material (ferric oxide) filtered out on the formation face with an increase in skin effect to approximately 2. As shown in Fig. 13-23, unspent acid removed the damage and the skin effect decreased to a value of approximately 1.

### 13-8.3. Post-treatment evaluation

The evaluation of stimulation effectiveness is a process similar to well performance evaluation. In this section, the process is applied to returning wells to production following stimulation. Details on the techniques are provided elsewhere in this volume.

Careful recording should be made while bringing a well on production following stimulation. Early indications of success can be found in the ease of initiating production and higher flow rates and flowing tubing pressures. Return fluids should also be sampled. Early production problems may indicate an incompatibility between treating fluids and the produced oil. The analysis of water samples may indicate other problems with the treating fluid selection (e.g., precipitation problems with HF acidizing).

Wells should be subjected to pressure buildup and PTA following a stimulation treatment. These data are the basis for a quantitative assessment of the well and reservoir characteristics. Comparison of these results to pretreatment buildups can provide the best assessment of the success of the stimulation treatment.

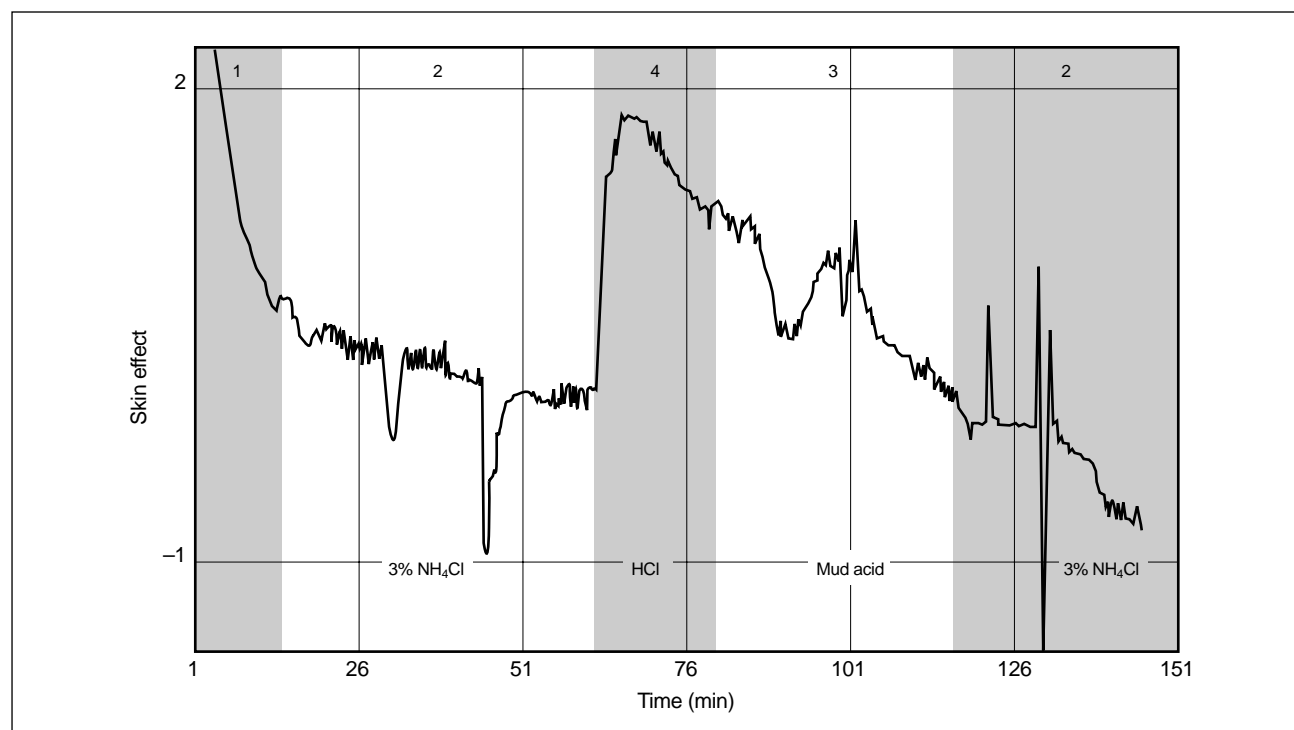


**Figure 13-23.** Real-time skin effect evolution in the injection well analyzed in the step rate test.

In the final analysis, stimulation treatments are evaluated at the sales meter. If the treatment results in sustained oil production at a higher rate than before and if the revenue generated by the increased production represents an acceptable return on the cost of the stimulation, the treatment is considered a success. The designer can learn valuable information from the evaluation of well performance, regardless of whether the stimulation is an economic success.

In addition to examining oil production response, changes in the total fluid production (oil, water and gas) in reservoir volumes, gas/oil ratio and water/oil ratio must be reviewed. Well productivity must also be examined. An increase in the productivity of total fluids may not be economic, but it may indicate that the target reservoirs were not stimulated or were watered-out in the candidate well. This can result in a change in treatment design philosophy (i.e., to sacrifice total stimulation effectiveness for the selective treatment of a limited part of the reservoir).

Correlation of the unwanted results from stimulation can provide data for improved performance in the future. They may also identify other opportunities to improve field performance, such as water or gas shut-off. In the end, the data acquired from evaluating recently stimulated wells can lead to improved reservoir management.

Ultimately, a treatment should be evaluated on the basis of the well performance and economic parameters used to justify the treatment. Factors such as rate, flowing bottomhole pressure, reservoir characterization, artificial lift performance and equipment performance have been discussed. Several weeks or even months may be required for production to stabilize and establish a representative trend. In addition, shutting

in the well for pressure buildup is less attractive—and may not be acceptable—after the well has responded.

Using field data, the engineer can evaluate differences between the design and actual treatment. If a numerical simulator can be rerun with the actual treatment parameters, the model can be calibrated by adjusting reservoir parameters such as the damage radius, permeability per layer, skin effect per layer, damage mineralogy and diverter efficiency until a match with the actual treatment profiles is obtained. If a post-treatment well test is performed and evaluated, the resulting data can be used to further calibrate the simulator.

Wireline formation logs and the combination of radioactive tracers and gamma ray or gamma ray spectroscopy surveys (where the energy and intensity of the gamma rays are measured to enable the discrimination of multiple tracers) can be used to quantify zone coverage. Of course, the decision to run tracers and baseline logs must be made while planning the stimulation. A pressure transient test (e.g., buildup, four-point) to quantify permeability and skin effect can be performed. Thus, adequate evaluation tools exist today to significantly improve matrix treatment success.

Future treatment designs for the well or field can be optimized with the calibrated model. All results should be compiled in a report with recommendations for all phases of the design, execution and evaluation (i.e., continuous improvement).

Stimulation operations present the engineer with an opportunity to significantly improve the economic performance of the assets under his or her stewardship. If properly designed, executed and evaluated, stimulation operations can teach the engineer about the current condition of the well and reservoir and identify other opportunities to improve economic performance.

# Formation Damage: Origin, Diagnosis and Treatment Strategy

Donald G. Hill, Olivier M. Liétard and Bernard M. Piot, Schlumberger Dowell  
George E. King, BP Amoco

## 14-1. Introduction

Formation damage reduces the well production or injection capacity, and the removal of damage is one of the major goals of petroleum engineers. This chapter identifies and quantifies formation damage and includes ideas on treatment strategy. It is important to note that not all types of formation damage require a removal treatment. Some types of damage will clean up during production, and others can be removed by changes in operating practices. In addition, some producible impairment is misconceived as “damage,” when it is actually poor well design that can be remedied with operational changes. Classifying damage correctly requires more than experience in the chemistry or physics of damage. A thorough knowledge of field operating conditions is essential, and correct identification is critical to successful removal.

The terms formation damage and skin effect damage have been applied to describe many well productivity impairments (Krueger, 1986; Porter, 1989). Damage can be anything that obstructs the normal flow of fluids to the surface; it may be in the formation, perforations, lift system, tubulars or restrictions along the flow path. Formation damage specifically refers to obstructions occurring in the near-wellbore region of the rock matrix. Other types of damage can be identified by location. Figure 14-1 shows some common types of damage; these production impairments can occur anywhere in the production system, from the wellbore to perforations and into the formation. Such a distinction is not usually made because seldom are most of the plugging phenomena located in only one part of the flow system. The importance of determining the causes of the observed damage cannot be understated. Only by knowing the damage mechanism, its location and how it is affecting flow can an effective treatment strategy be developed. There have been significant improvements over the past few years in recognizing and describing the various types of damage, and

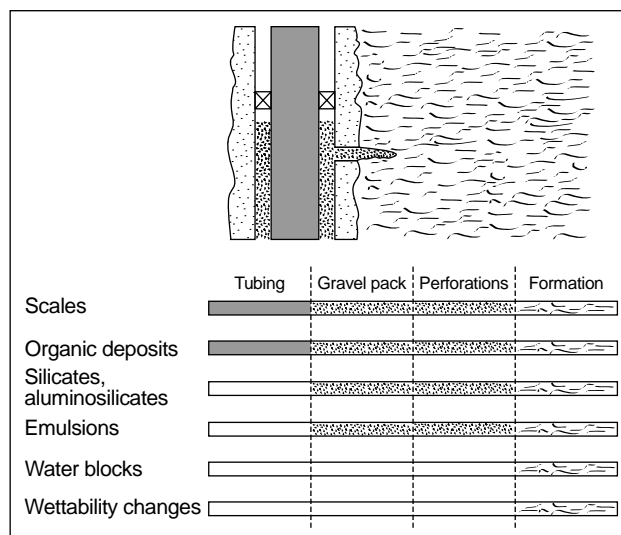


Figure 14-1. Location of various types of damage.

many publications have appeared on the subject (Allen, 1973; Hurst, 1973; Leon, 1973; Sands, 1973; Christian and Ayres, 1974; Bruist, 1974; Shaw and Rugg, 1974; Black and Rike, 1976; Maly, 1976; Sparlin and Hagen, 1983; Krueger, 1988; Amaefule *et al.*, 1998; Adair and Smith, 1994; Beadie, 1995; Reid, 1996).

The goal of this chapter is to give a broad view of formation damage. Damage characterization is the key to proper design of removal treatments. A general description of the various damage types and mechanisms is presented, followed by a discussion of the origins of damage resulting from natural causes and well operations. The testing required to determine the presence of formation damage and its characterizations are also discussed. Treatment strategies for removing formation damage are presented.

## 14-2. Damage characterization

Damage characterization is the “history” in damage removal. The search for the identity of the damage

begins in the production and development history of the well and even neighboring wells. Drilling records, completion design, offset well performance and/or operator experiences and past treatment records are all sources of information. The objective is to identify the location and types of damage that may be a problem. Although damage is usually considered a singular problem, multiple occurrences of damage are common, some with interfering removal treatments.

Formation damage identification and investigation include

- types of damage
- location of damage
- extent and screening of damage
- effect of damage on well production or injection.

### 14-2.1. Pseudodamage

Chapter 1 demonstrates the impact of skin effect reduction on well performance. Chapter 2 describes techniques for estimation of the total well skin effect, which are accomplished primarily through well testing. As discussed in Chapter 1, not all skin effect is due to damage. There are other contributions that are not related to formation damage. These pseudoskin effects are generally mechanical, resulting from obstructions to flow or because of rate- and phase-dependent effects. Their values must be subtracted from the total skin effect to estimate the skin effect associated with formation damage (Petersen *et al.*, 1984). One way to accomplish this is to use NODAL production system analysis to develop an inflow performance relationship (IPR) curve specific to the well. NODAL analysis allows optimizing production conditions for a given well and thus optimizing the well completion (Fig. 14-2).

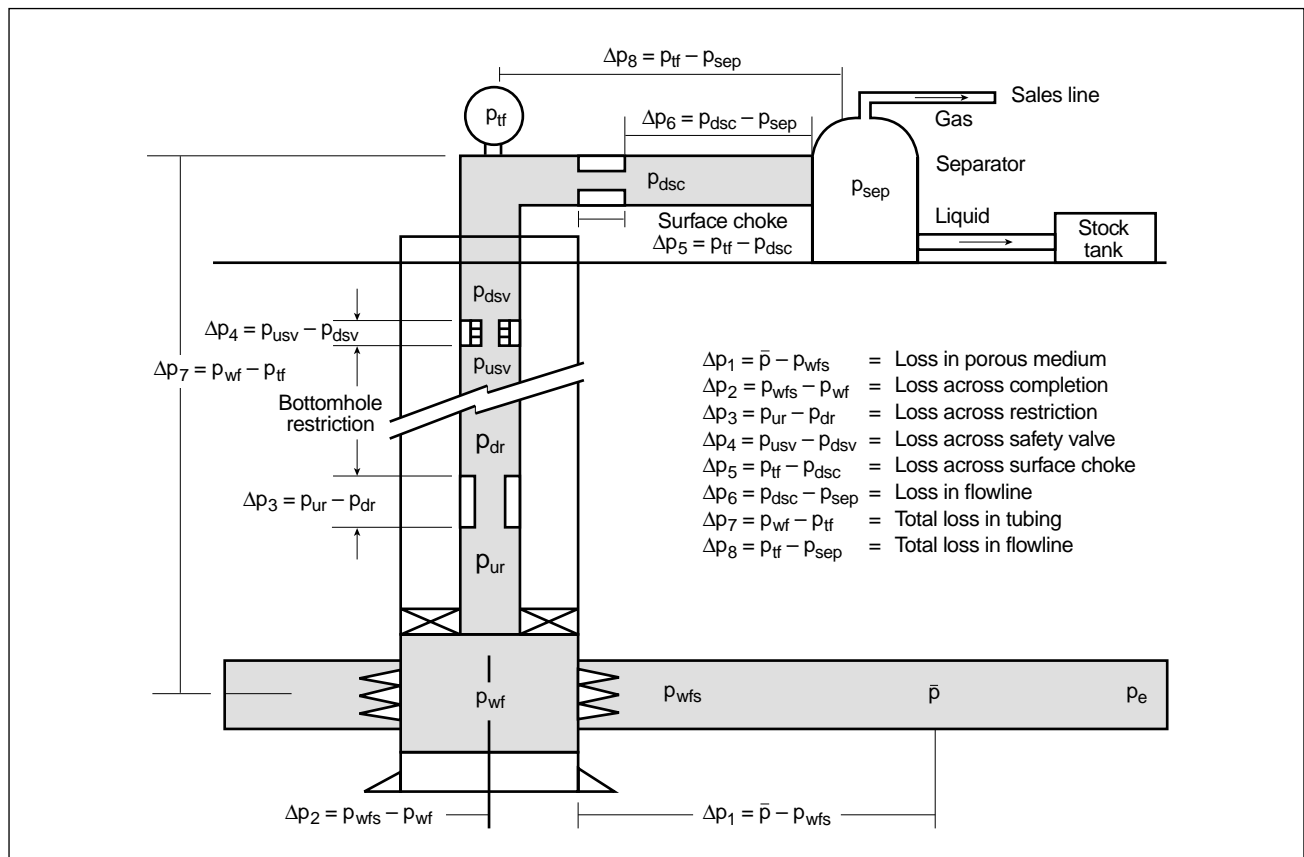


**Figure 14-2.** Pressure losses in the producing system of a flowing well.  $p_{wf}$  = bottomhole flowing pressure,  $\bar{p}$  = average pressure,  $p_e$  = reservoir pressure,  $p_{dr}$  = downstream restriction pressure,  $p_{dsc}$  = pressure downstream of the surface choke,  $p_{dsv}$  = pressure downstream of the safety valve,  $p_{sep}$  = separator pressure,  $p_{tf}$  = tubing flowing pressure,  $p_{ur}$  = upstream restriction pressure,  $p_{usv}$  = pressure upstream of the safety valve,  $p_{wfs}$  = wellbore sandface pressure.

### 14-2.2. Pseudoskin effects and well completion and configuration

Positive pseudoskin effects can result from the well completion design or well configuration. Problems include

- limited entry to flow (Odeh, 1968; Jones and Watts, 1971; Saidikowski, 1979)
- off-center wells (Denson *et al.*, 1976; Fetkovitch and Vienot, 1984)
- low perforation density, short perforations or incorrect phasing (Hong, 1975; Locke, 1981; McLeod, 1983)
- mechanical flow restrictions
- mismatched or inadequate fluid-lift systems
- laminated reservoirs (shale streaks).

A negative pseudoskin effect always exists in deviated wells; it is a function of the deviation angle and the formation thickness (Cinco-Ley *et al.*, 1975).

#### • Pseudoskin and rate-and-phase effects

Operating pressures and production conditions may induce additional pressure drops or pseudoskin effects. Producing a well at a high flow rate can cause turbulent flow in perforations and sometimes in the formation (Fig. 14-3) (Tariq, 1984; Himmatramka, 1981). The corresponding positive pseudoskin effect is proportional to the flow rate above a minimum threshold value. Below this critical value, this pseudoskin effect is suppressed (Jones *et al.*, 1976). The problem increases with gravel-packed perforations (for sand control) and for high-production-rate gas wells in general. The problem becomes particularly acute for the fracture-to-wellbore connection in deviated wells with fractures at an angle to the wellbore.

Scale precipitation in and around the perforations can progressively modify the reservoir flow conditions, increasing the pressure drop and changing the flow regime from Darcy to non-Darcy and creating a turbulence pseudoskin effect (Meehan and Schell, 1983). This is in addition to the actual damage skin effect.

Producing a well below the bubblepoint pressure may cause a positive pseudoskin effect as liquids condense around the wellbore, impeding flow (Blackmer, 1982; Hinchman and Barree, 1985; Economides *et al.*, 1989). This is a relative permeability phenomenon, with free gas concentrating

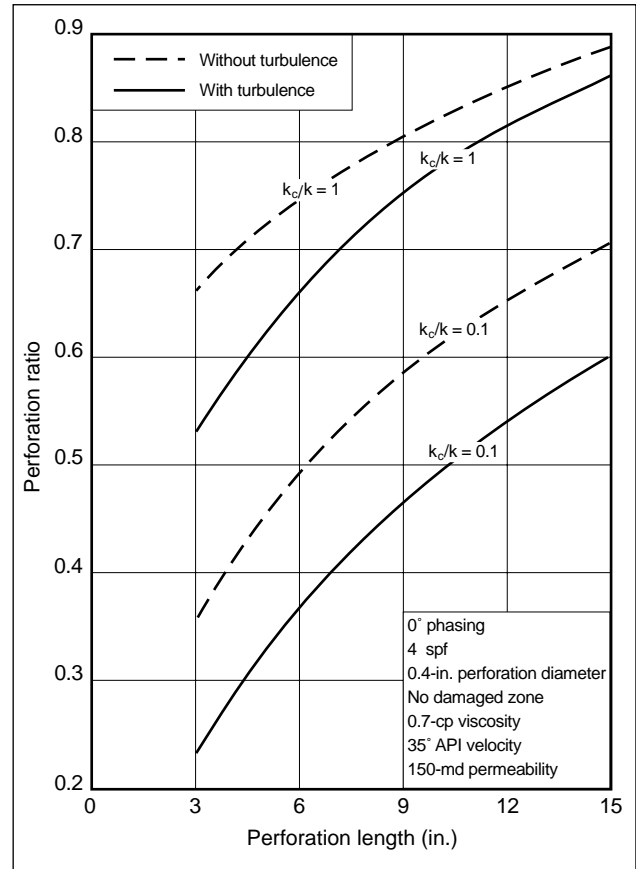


**Figure 14-3.** Effect of turbulence and a compacted zone (90% permeability reduction) on the productivity ratio (Tariq, 1984).  $k$  = permeability,  $k_c$  = damaged zone permeability.

around the wellbore causing a reduction to the relative permeability to oil. A similar but more severe problem can happen when producing gas condensate wells below the dewpoint. Both phenomena manifest as positive pseudoskin effects.

In unconsolidated sand reservoirs, a flow-rate-dependent skin effect can be caused by modifications of the sand arches around the perforations. Abrupt variations of skin effect and concomitant sand releases occur above the threshold flow rate value (Tippie and Kohlhaas, 1974).

#### • Other pseudodamages

Other mechanical causes of production impairment are

- tubing collapse or restriction by lost objects or any adhering deposit
- collapsed perforations in formations where the formation competence has been overestimated

(Antheunis *et al.*, 1976; Chenevert and Thompson, 1985)

- poor isolation between zones resulting from poor cementation of the annulus—e.g., oil invasion of a gas cap significantly reduces the relative gas permeability, mixing oils of two different zones may cause paraffin and asphaltene precipitation, or water invading an oil-bearing zone reduces the relative permeability to oil (water block), may create emulsions and may cause clay and scale problems. Stimulation treatments that do not achieve required results and that cause additional damage may have been sabotaged by bad isolation (Abdel-Mota'al, 1983).
- poor design of gas lift systems—small-diameter tubing, unadapted operating gas lift pressure (Blann and Williams, 1994), improper valve design and high surface backpressure (Jones and Brown, 1971).

## 14-3. Formation damage descriptions

Once mechanical pseudoskin effects are identified, positive skin effects can be attributed to formation damage. Formation damage is typically categorized by the mechanism of its creation as either natural or induced. Natural damages are those that occur primarily as a result of producing the reservoir fluid. Induced damages are the result of an external operation that was performed on the well such as a drilling, well completion, repair, stimulation treatment or injection operation. In addition, some completion operations, induced damages or design problems may trigger natural damage mechanisms.

Natural damages include

- fines migration
- swelling clays
- water-formed scales
- organic deposits such as paraffins or asphaltenes
- mixed organic/inorganic deposits
- emulsions.

Induced damages include

- plugging by entrained particles such as solids or polymers in injected fluids
- wettability changes caused by injected fluids or oil-base drilling fluids

- acid reactions
- acid by-products
- iron precipitation
- iron-catalyzed sludges
- bacteria
- water blocks
- incompatibility with drilling fluids.

Each of these mechanisms is addressed in detail in the following sections. Damage from iron precipitation and iron-catalyzed sludges is discussed elsewhere in this volume.

### 14-3.1. Fines migration

Formation damage can occur as a result of particle migration in the produced fluid. The particles can bridge across the pore throats in the near-wellbore region and reduce the well productivity. When the damaging particles come from the reservoir rock, they are usually referred to as fines. Migrating fines can be a variety of different materials, including clays (phyllosilicates with a typical size less than 4  $\mu\text{m}$ ) and silts (silicates or aluminosilicates with sizes ranging from 4 to 64  $\mu\text{m}$ ). Kaolinite platelets (Fig. 14-4) are thought to be some of the more common migratory clays. Table 14-1 lists the major components of various clays and fines particles. The table also lists the surface area of the clays, one of the indicators of how quickly the clay can react with a reactive fluid (Davies, 1978). Damage from fines is located in the near-wellbore area, within a 3- to 5-ft radius. Damage can also occur in a gravel pack (e.g., silicates and aluminosilicates in Fig. 14-1).

The distinction between types of clays depends more on the arrangement of the atoms in their crystalline structure rather than any major difference in

**Table 14-1. Major components of various clay and fines particles.**

Particle Mineralogy	Major Components	Surface Area ( $\text{m}^2/\text{g}$ )
Quartz	Si, O	0.000015
Kaolinite	Al, Si, O, H	22
Chlorite	Mg, Fe, Al, Si, O, H	60
Illite	K, Al, Si, O, H	113
Smectite (montmorillonite)	Na, Mg, Ca, Al, Si, O, H	82



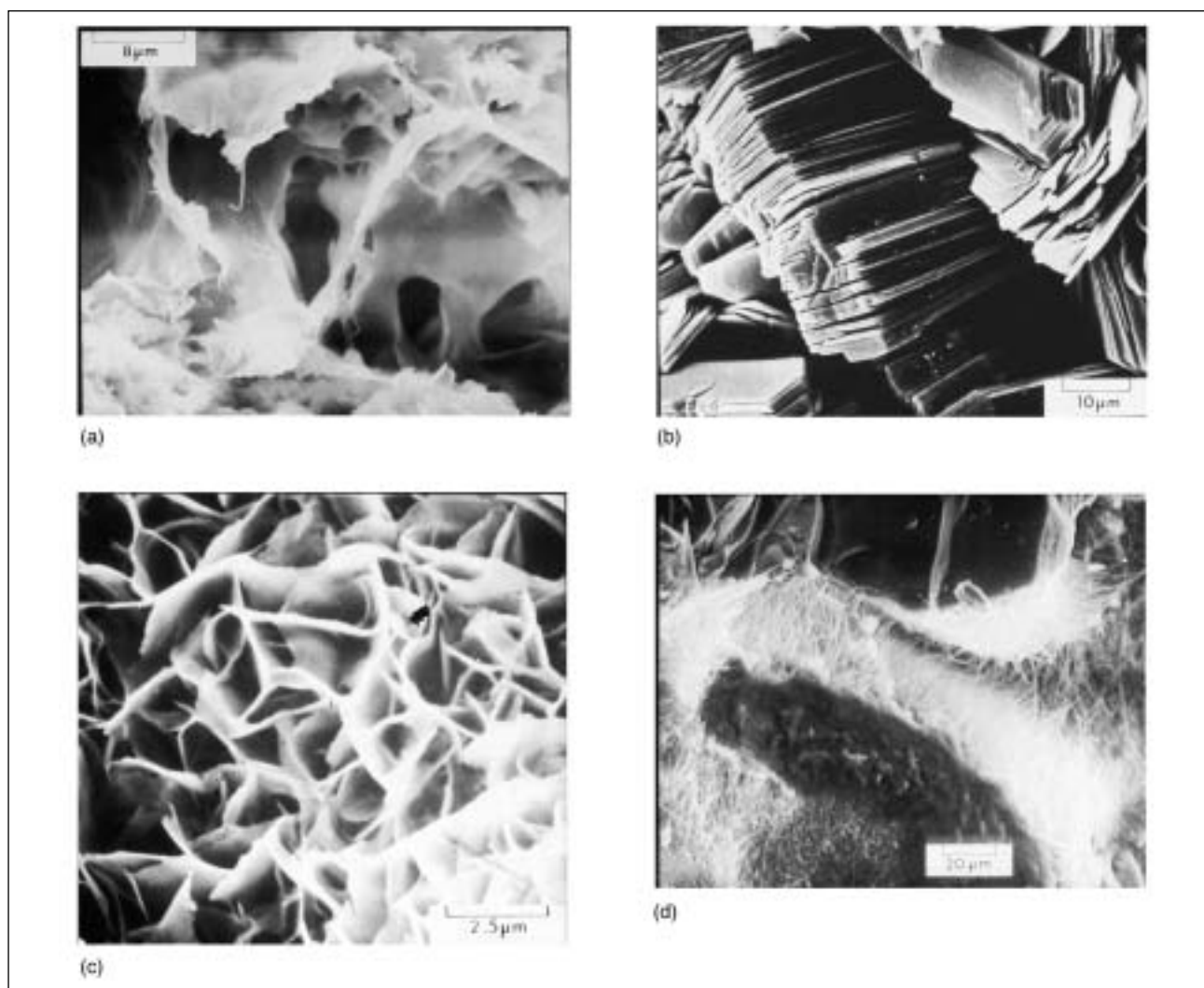


**Figure 14-4.** Photomicrographs of (a) pore-filling smectite sheets, (b) “books” of kaolinite platelets in a pore space, (c) honeycomb growth of chlorite on a sand grain and (d) hairs of illite extending from a sand grain.

chemical formula. These structural differences determine the surface area exposed to the reservoir fluids for each clay. Clay reactivity is a function of this surface area. The location of the clay is also critical to its reactivity. Authigenic clay is in a pore throat as fill or as a lining (i.e., grown in the pore from minerals in the connate water) (Wilson and Pittman, 1977). Authigenic clays have a large amount of surface area exposed in the pore and can be reactive. Detrital clay is part of the building material in the original matrix. Detrital clays are usually less reactive than authigenic clays because they have less surface area in contact with the fluids in the pore. The vast majority of detrital clays usually cannot be contacted by sufficient volumes of reactive fluids to cause problems. Clay may also act as a cement,

holding the matrix grains together. As a binder or cement, clay may react with fluids such as acid and water to disaggregate the formation. If the clay cement is shielded by a quartz overgrowth, as is common in many sandstones, the clay will not be reactive.

Only authigenic clays, unprotected clay cements and the few detrital clays on the pore boundary are worth consideration as potential damage mechanisms. Scanning electron microscopy (SEM) is generally used to determine clay type; however, recognition of the type of clay should not be staked entirely on an SEM analysis. Focused dispersive X-ray analysis is much more accurate. Even after identification of the clay, laboratory core flow tests are typically required to determine if the clays within the

flow channels are reactive with a given fluid. The common clays that account for most of the real and perceived clay problems are kaolinite, smectite (montmorillonite), illite and chlorite. The structures of kaolinite, smectite, illite and chlorite are shown in Fig. 14-4. Simply because the clay is in the rock does not mean that the clay is reactive.

### 14-3.2. Swelling clays

Clays may change volume as the salinity of the fluid flowing through the formation changes. Several authors have dealt with clay swelling in sandstones, showing either ion exchange, movement or critical salt concentration triggering clay dispersion (Azari and Leimkuhler, 1990b; Jones, 1964; Khilar and Fogler, 1983; Mungan, 1968; Sharma *et al.*, 1985; Priisholm *et al.*, 1987). Changes in formation permeability resulting from the alteration of clay are due to the amount, location and type of clay minerals within the formation. The total quantity of clay inside the formation is a misleading indication of potential changes to permeability. It is the arrangement of the clay, its chemical state at the moment of contact and the location of the clay with respect to the flowing fluids that are responsible for the changes. Predicting the response of a clay to water flow is almost impossible without testing.

The most common swelling clays are smectite and smectite mixtures. Smectite swells by taking water into its structure. It can increase its volume up to 600%, significantly reducing permeability. If smectite clay occupies only the smaller pore throats and passages, it will not be a serious problem; however, if it occupies the larger pores and especially the pore throats, then it is capable of creating an almost impermeable barrier to flow if it swells.

Clays or other solids from drilling, completion or workover fluids can invade the formation when these particles are smaller than the pore throat openings. Any subsequent increase in flow rate through the invaded zone will force a high concentration of particles into the rock matrix.

### 14-3.3. Scales

Scales are water-soluble chemicals that precipitate out of solution in response to changes in conditions or the mixing of incompatible waters. They can be

present in the tubing, perforations and formation (Fig. 14-1). The most common oilfield scales are calcium carbonate, calcium sulfate and barium sulfate. Water-formed scale deposits are among the most troublesome damage problems (Cowen and Weintritt, 1976). Scale usually consists of precipitates formed from mixing incompatible waters or upsetting the solution equilibrium of produced waters. A water that may be stable under reservoir conditions may become supersaturated with an ion when the pressure decreases, which allows carbon dioxide ( $\text{CO}_2$ ) outgassing, or the temperature changes. The supersaturated solutions react by precipitating a compound from solution. The deposition of scale is influenced by pressure drop, temperature, dissolved gases, flow viscosity, nucleation sites and metal type—in short, anything that upsets the solution equilibrium.

The following scales are among the most troublesome.

- Calcium carbonate or calcite ( $\text{CaCO}_3$ )  
 $\text{CaCO}_3$  is usually formed when the pressure is reduced on waters that are rich in calcium and bicarbonate ions. The deposition can be affected by  $\text{CO}_2$  outgassing, which raises the pH value and makes the high concentrations of calcium unstable.
- Gypsum (“gyp”)  
Gypsum may be the most common sulfate scale in the oil industry (Cowen and Weintritt, 1976). With a chemical structure of  $\text{CaSO}_4 \cdot 2\text{H}_2\text{O}$ , it shares a similar composition to the hemihydrate  $\text{CaSO}_4 \cdot \frac{1}{2}\text{H}_2\text{O}$ , commonly called plaster of paris or by its mineral name, bassonite. It is also formulaically similar to the evaporite mineral anhydrite ( $\text{CaSO}_4$ ).
- Barium sulfate ( $\text{BaSO}_4$ )  
 $\text{BaSO}_4$  is a less common form of sulfate deposit, but it causes extensive problems. Almost any combination of barium and sulfate ions causes precipitation. It is difficult to remove, as it is not significantly soluble in acids and solvents unless it is finely ground or the structure is interrupted with impurities such as carbonate scale. Like calcium sulfate, barium sulfate is usually thought to be a product of mixing incompatible waters, with precipitation accelerated by pressure drop, outgassing or turbulence. Some barium sulfate is radioactive; this is part of naturally occurring radioactive

material (NORM) scales. The radioactivity results from a concentration of uranium in the lattice of the scale. The buildup of radioactive scale can be monitored using a gamma ray logging tool. Care must be exercised when analyzing well debris to avoid mislabeling barite ( $\text{BaSO}_4$ ) from drilling mud residue as barium sulfate scale.

Strontium sulfate or celestite ( $\text{SrSO}_4$ ) is a common substitute in the barium sulfate crystal lattice. Strontium scale can be associated with radioactive scale (NORM). It may be more soluble than barium sulfate in chemical remover systems.

- Iron scales

Iron scales such as iron carbonate and iron sulfide can be extremely difficult to remove. They are usually seen in wells that have both a high background iron count and a tendency to precipitate calcium carbonate. Iron sulfide scales react according to their structure. Seven different forms of iron sulfide scale have been identified. Only two of these iron sulfide forms are readily soluble in hydrochloric acid (HCl). The remaining iron sulfide scales are either slowly soluble or not significantly soluble.

- Chloride scales

Chloride scales, such as sodium chloride precipitation from water caused by temperature decrease or evaporation of the water, are common. There is no effective way to prevent salt precipitation, and cleanup has been accomplished using water only. Salt has a limited solubility in acid ( $\frac{1}{4}$  lbm/gal in 28% HCl), so using acid is not generally considered. Redesigning the mechanical system to avoid temperature loss and water evaporation is also a possibility.

- Silica scales

Silica scales generally occur as finely crystallized deposits of chalcedony or as amorphous opal. They are associated with alkaline or steamflood projects and stem from the dissolution of siliceous formation minerals by high-pH fluids (Lieu *et al.*, 1985) or high-temperature steam condensates (Reed, 1980; McCorrison *et al.*, 1981; Amaefule *et al.*, 1984). This dissolution can cause poorly consolidated sandstones to collapse or silica to reprecipitate at a distance from the wellbore where the alkalinity, temperature or both of the floods has decreased.

### 14-3.4. Organic deposits

Organic deposits are heavy hydrocarbons (paraffins or asphaltenes) that precipitate as the pressure or temperature is reduced. This is a form of distillation. They are typically located in the tubing, perforations or formation (Fig. 14-1). Although the formation mechanisms of organic deposits are numerous and complex (Houchin and Hudson, 1986), the main mechanism is a change in temperature or pressure in the flowing system. Cooling of the wellbore or the injection of cold treating fluids has a much more pronounced effect.

Organic deposits must not be confused with another type of deposit called sludge. Sludges are viscous emulsions produced by the reactions between certain crude oils and strong inorganic acids or some brines. Sludges cannot be easily dissolved.

- Paraffins

Paraffins are the simplest of hydrocarbons. They are composed of only carbon and hydrogen atoms, and the carbons occur as an unbranched chain. Carbon chain length associated with formation of solid paraffin deposits has a minimum of 16 carbon atoms per molecule and may have up to 60 or more. The precipitation of paraffins is triggered by a loss of pressure, loss of temperature or loss of short-chain hydrocarbon compounds (i.e., the light ends). The temperature at which the first solid paraffin crystal forms from an all-liquid solution is called the cloud point. Designing the completion so that produced fluid surface temperatures are above the cloud point and modifying the cloud point using chemical methods are accepted practices to prevent paraffin deposition in the tubing.

Melting points increase as the length of the paraffin chain increases. The hardness of the solid paraffin structure also increases with molecular size. Table 14-2 lists several paraffin chain lengths and their melting points. Impurities may cause the melting point of a field sample to vary slightly.

Paraffins can form anywhere in the producing system when conditions become favorable for precipitation (Cole and Jessen, 1960; Burger *et al.*, 1981; Newberry *et al.*, 1986; Thomas, 1988; Newberry, 1981; Sutton and Roberts, 1974). Paraffins are normally found in the tubing near the surface, where the temperature and pressure drops are highest. In cases such as reservoirs that are

**Table 14-2. Melting points of paraffins.**

Carbon Atoms (no.)	Melting Point (°F)
16	64
17	72
18	82
20	100
23	122
25	129
32	158
42	181
49	196
60	211

nearly pressure depleted or formations that have experienced dry gas cycling (which removes the light hydrocarbon ends), the paraffins can form at the perforations or in the formation. Paraffins may also be precipitated by the injection of a cool fluid. Although not typically considered, this latter cause can be the reason for the slow cleanup of many wells after stimulation.

- **Asphaltenes**

Asphaltenes are organic materials consisting of condensed aromatic and naphthenic ring compounds with molecular weights of several hundred to several thousand (Leontaritis, 1989; Leontaritis and Mansoori, 1987; Tuttle, 1983; Newberry and Barker, 1985; Addison, 1989; Bunger, 1979; Thawer *et al.*, 1990). They are characterized by the nitrogen, sulfur and oxygen molecules they contain and are defined as the organic part of the oil that is not soluble in a straight-chain solvent such as pentane or heptane. Asphaltenes are generally found in one of three distinctive forms:

- hard coal-like substance
- blackened sludge or rigid-film emulsion (usually triggered by iron in solution)
- in combination with paraffins.

In “solution,” they usually exist as a colloidal suspension, forming particles 30 to 65 Å in diameter and stabilized by maltene molecules in the oil. The volume of the maltene resins is the first key to the stability of the asphaltene in suspension. The actual quantity of asphaltenes in the oil is much less important. The stability of asphaltic dispersions depends on the ratio of the quantity of resins

to the quantity of asphaltic materials. Ratios larger than 1:1 (resins to asphaltenes) are more stable, whereas ratios less than 1:1 are unstable and may precipitate during production. Ratios of more than 10:1 are known and are much less likely to cause significant problems. Although asphaltene contents up to 60% have been found, major problems occur with oils with a 1% to 3% asphaltene range.

Asphaltene precipitation can be influenced by pressure drop, shear (turbulence), acids, solution CO<sub>2</sub> (lowers the pH value), outgassing of CO<sub>2</sub> and other gases (turbulence), injected condensate, gas, commingling with other (incompatible) oils and charged metal surfaces (Danesh *et al.*, 1988; Monger and Trujillo, 1991; Kawanaka *et al.*, 1991; Monger and Fu, 1987; Pittaway *et al.*, 1987).

Anything that takes away the resins or breaks the stability of the aggregate particle can lead to a precipitation of asphaltene. Iron ions in solution (usually during an acid job) compound and favor the formation of asphaltene deposition. As noted previously, the concentration of asphaltenes is not a good indicator of potential problems. Only the treatment history and well response examination can suggest the potential for asphaltene problems.

Asphaltene deposition on pore walls may not significantly decrease the formation porosity and absolute permeability. However, through this process, the rock tends to become oil-wet, which reduces the relative permeability to oil (Clementz, 1982; Collins and Melrose, 1983) and, under certain conditions, favors the buildup of emulsion blocks if water is simultaneously produced.

- **Tar**

Tar is simply an asphaltene or other heavy-oil deposit. It cannot be removed by acid or mutual solvents. Removal requires dispersion in an aromatic solvent, and energy is typically necessary to achieve removal.

### 14-3.5. Mixed deposits

Mixed organic/inorganic deposits are a blend of organic compounds and either scales or fines and clays. When migrating, fines associated with an increase in water production in a sandstone reservoir become oil-wet, and they act as a nucleation site for organic deposits (Houchin and Hudson, 1986).

Figure 14-5 shows such a mixed deposit in which clear (white) crystals of sodium chloride are dispersed in a dark organic matrix.

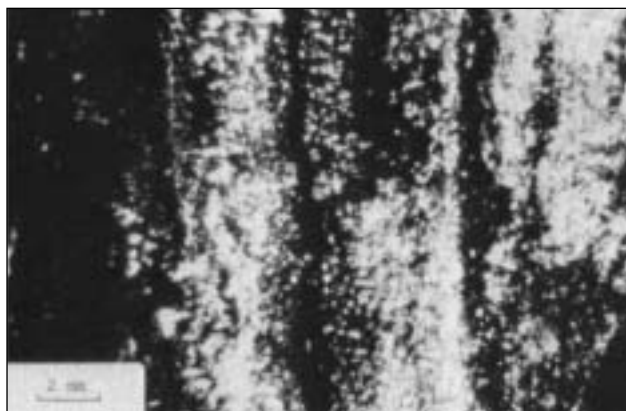


**Figure 14-5.** Thin section of a layered matrix deposit. The black layers are organic deposits, and the clear (white) layers are inorganic scales of mainly halite (NaCl).

### 14-3.6. Emulsions

Emulsions are combinations of two or more immiscible fluids (including gas) that will not disperse molecularly into each other (Hoover, 1970; Sherman, 1968; Lissant, 1974; Lissant and Mayhan, 1973; Bandbach, 1970; Hausler, 1978; Bikerman, 1964; Ogino and Onishi, 1981; Gidley and Hanson, 1973; Coppel, 1975). Emulsions are composed of an external phase (also called nondispersed or continuous) and an internal phase (also called dispersed or discontinuous). The internal phase consists of droplets suspended in the external phase. Almost all emulsions found in the field are produced by the addition of some form of energy that produces mixing. Most emulsions break rapidly when the source of energy is removed. The breaking mechanism of these unstable emulsions is by droplet contact and growth and then by fluid density separation. As the droplets draw near and touch, the surface film around the drop may thin and rupture, forming large drops in a process called coalescence. The larger droplets settle rapidly owing to density differences between the liquids forming separate layers. Only a portion of the drops that touch will coalesce. When minimum coalescence occurs, the emulsion is stable.

If separation of the emulsion does not occur, there is a stabilizing force acting to keep the fluids emulsified. The most common stabilizing forces are a modi-

fication of the surface film strength at the interface by chemical reaction, precipitation or the addition of partially wetted fine particles, electric charge, or high viscosity of the components or resultant fluid viscosity. These forces may act singly or in combination.

Natural surfactants help stabilize emulsions by stiffening the film around the droplet or by partially wetting small solid particles. Natural surfactants are present in many waters and most crude oils. They may be of several chemical formulas and may be a by-product of bacteria or originate as part of the oil-generation process. Like other surfactants, they have an oil-soluble end and a water-soluble end (usually possessing a small electric charge) and congregate at the oil/water interface.

Micron-size solids in the liquid may stabilize an emulsion by increasing the toughness of the surface film around the droplets or by acting as an emulsifier and binding droplets of the dispersed liquid with an electrical charge. Almost any solid can be a stabilizing agent if it is sufficiently small. For a solid to be effective in stabilizing an emulsion, it must be present at the interface of the drop and the continuous phase. The more common solid materials that stabilize oilfield emulsions are iron sulfide, paraffin, sand, silt, clay, asphalt, scale, metal flakes (from pipe dope), cuttings and corrosion products.

Changes in the pH value can affect emulsion stability. Most free-water knockouts and treaters operate efficiently at a pH value of 6 to 7, depending on individual well conditions. Following an acid treatment, the pH value may drop below 4 and emulsions may be created. Emulsions created in this manner are stable until the pH value rises above 6 or 7. When acid treating a well where the crude is an emulsifier or a sludge former, the wellhead may be equipped with a chemical injection port just upstream of the choke or a chemical injection valve may be placed in a gas-lift mandrel at some point in the treatment string. These ports are used to inject an emulsion breaker or de-emulsifier.

### 14-3.7. Induced particle plugging

In addition to naturally occurring migrating particles such as clays and fines, many foreign particles are introduced into the formation during normal well operations. Drilling, completion, workover, stimulation, and secondary or tertiary production operations

can cause the injection of extraneous particles into the formation.

Particle damage from injected fluids happens in the near-wellbore area, plugging formation pore throats. Problems include bridging of the pores, packing of perforations and the loss of large amounts of high-solids fluid into natural fractures or propped fracture systems. The best method of avoiding this type of damage is to use a clean fluid in a clean flow system with a controlled range of particle sizes that will stop fluid loss quickly by bridging at the wellbore.

Induced particles can be composed of a wide range of materials. Particulate materials in drilling fluids that are potentially damaging are clays, cuttings, weighting agents and loss-control materials, including polymers (Barna and Patton, 1972; Fisher *et al.*, 1973; Sloan *et al.*, 1975). These materials can be a problem independent of mud type (oil, water or polymer base). Workover and stimulation fluids can also contain suspended solids (Rike, 1980; Rike and Pledger, 1981) including bacteria and polymer residues (Tuttle and Barkman, 1974). Kill fluids in particular use various polymers as weighting agents or for fluid-loss control. Typical kill-fluid solids include salt pills with polymer, crosslinked polymers, hydroxyethylcellulose (HEC) polymers, lost-circulation pills and  $\text{CaCO}_3$  with polymer.

Particles in stimulation fluids are a result of poor water quality, tank coatings, tank residuals, and piping and tubing debris (e.g., dried mud, scale and pipe dope). The problem with stimulation fluids is that they can contain effective cleaners and acids that disperse and partially dissolve the debris inside of the tanks and piping on their way to the formation.

Particle damage after stimulation may also occur when partially dissolved parts of the formation or the damage materials come back, through either the pores or the natural fracture or propped fracture system. The release of fines from the formation is usually brought about by cleaners and mutual solvents. Acid treatments may also cause formation damage because of the precipitation of secondary acid reaction products. Precipitation products include iron hydroxide, calcium fluoride, potassium fluorsilicate and silica.

Geochemical models can predict the chemical nature of these by-products, depending on formation rock and treatment fluid compositions on one hand and pressure, temperature and contact time on the other (Walsh *et al.*, 1982; Dria *et al.*, 1988). The

models cannot predict the damaging potential of these products because they do not include any physical description of the way they are precipitated. Hydrated silica (Crowe, 1985) may precipitate on clay surfaces but is not necessarily damaging. Compounds such as borosilicates (Thomas and Crowe, 1978) and fluoborates (Bertaux, 1989) can even be beneficial, probably because they precipitate as films that bind fines to the sand grains. This phenomenon, when purposely produced, leads to efficient fines-stabilization treatments (Thomas and Crowe, 1978; Sharma and Sharma, 1994). However, gelatinous precipitates, such as ferric hydroxide, can completely plug pores and can be particularly difficult to remove (Crowe, 1985). Another class of by-products consists of species such as fluorsilicates (Bertaux, 1989), which precipitate in the form of individual crystals that can migrate toward pore throats and produce a "log jam." Iron sulfide, which precipitates even at low pH values during the acid treatment of sour wells, is another compound belonging to this category.

### 14-3.8. Wettability alteration

Formation plugging can be caused by liquid (or gas) changing the relative permeability of the formation rock. Relative permeability can reduce the effective permeability of a formation to a particular fluid by as much as 80% to 90%. The wettability and related relative permeability of a formation are determined by the flowing-phase quantity and by coatings of natural and injected surfactants and oils.

If a drop of a liquid is placed on the surface of another immiscible liquid or on the surface of a solid that it cannot dissolve, it may spread out into a thin film or it may remain in the form of a drop or a thick lens (Hausler, 1978). If the drop of liquid spreads, it wets the surface; if the drop of liquid does not spread, it does not wet the surface. The surface free energy of the two phases and the interfacial tension between them determine whether the liquid spreads or remains in a deformed drop. Wettability is measured by the contact angle that a droplet of fluid forms on a particular surface. If the angle of contact  $\theta$  is less than  $90^\circ$ , the drop spreads from the initial ball shape and the surface is said to be wetted by the liquid. The smaller the angle, the greater the water wettability. If the angle is more than  $90^\circ$ , the surface is not wetted by the liquid. Wettability can be mea-

sured with a liquid surrounded by gas or a liquid surrounded by an immiscible liquid. Simple wetting has little meaning—it is the resultant effect of wetting on fluid flow that is important.

In the natural state, formations may be water-wet, oil-wet or neutral, depending both on the surface exposed to the fluid and the natural surfactants in the fluid. There are some instances, such as the Cardium reservoir in Alberta, Canada, where both oil- and water-wetting behavior have been reported in different sections of the reservoir.

When a surface of a pore passage is oil-wet, more of the passage is occupied by the bound oil (thicker monomolecular layer), and less of the pore is open to flow than in a water-wet pore. Naturally, to get as much flow capacity as possible in a formation, it is desirable to change the wettability to water-wet (in most cases). Unfortunately, it is impossible to change most naturally oil-wet surfaces for long. Wettability can be modified by preflushing the formation with a wetting surfactant or a solvent that establishes a new coating on the face of the formation or cleans the current coating from the formation. Regardless of the altered condition of a surface, the wettability is eventually decided by the surfactants in the produced fluid. Thus, the water-wet condition of a formation following an acid job can revert to an oil-wet condition after a sufficient volume of strongly oil-wetting crude is produced.

### 14-3.9. Acid reactions and acid reaction by-products

Numerous problems that may occur during acidizing treatments include

- damaging material from the tubing entering the formation
- oil-wetting of the reservoir by surfactants, especially corrosion inhibitors, which can create emulsion blocks
- water blocks
- asphaltene or paraffin deposition when large volumes of acid are injected.

In addition to these common damaging processes, production impairment can result from poor design of an acidizing treatment. Impairments include the following:

- sludges produced by the reaction between acids and asphaltenes, especially in the presence of some additives (particularly surfactants) or dissolved iron
- by-products precipitated by the reaction of acids with formation materials. Geochemical simulators can predict the chemical nature of the by-products, depending on the formation rock and treatment fluid compositions and the pressure and temperature. Simulators cannot predict the damaging potential of the by-products. Hydrated silica may precipitate on clay surfaces and is not necessarily damaging. Compounds such as borosilicates and fluoborates can even be beneficial. Gelatinous precipitates, such as ferric oxide, can completely plug pores and be particularly difficult to remove. Another class of by-products consists of species such as fluorsilicates precipitating in the form of individual crystals that can migrate toward pore throats and then bridge in the throats. Iron sulfide that precipitates, even at very low pH values during the acidization of sour wells, is another compound belonging to this category.
- precipitates formed by the addition of certain sequestering agents to acids to prevent iron problems when the acid is spent and no iron is present
- permeability impairment by residues present in corrosion inhibitors or produced through the thermal degradation of polymers, such as friction reducers.

### 14-3.10. Bacteria

Although many microorganisms can be present in the unsterile world of the oilfield, only a handful produce widespread problems (Shuler et al., 1995; Clementz *et al.*, 1982; Crowe, 1968; Carlson *et al.*, 1961; Raleigh and Flock, 1965). Bacteria can be a serious problem in production operations because of what they consume and their by-products. Bacteria can grow in many different environments and conditions: temperatures ranging from 12°F to greater than 250°F [–11° to >120°C], pH values ranging from 1 to 11, salinities to 30% and pressures to 25,000 psi.

Bacteria are classified as follows:

- Aerobic bacteria are bacteria that require oxygen.



- Anaerobic bacteria do not need oxygen (in fact, their growth is inhibited by oxygen).
- Facultative bacteria can grow either with or without oxygen because their metabolism changes to suit the environment. They usually grow about 5 times faster in the presence of oxygen.

The bacteria most troublesome in the oilfield are sulfate-reducing bacteria, slime formers, iron-oxidizing bacteria and bacteria that attack polymers in fracturing fluids and secondary recovery fluids.

Sulfate-reducing bacteria cause the most problems in a reservoir. Sulfate-reducing bacteria reduce the sulfate or sulfite in the water to sulfide and produce hydrogen sulfide ( $H_2S$ ) as a by-product. The reduction process provides the energy for bacterial growth. Biomass accumulation can lead to pitting of the steel under large colonies. The  $H_2S$  increases the corrosivity of the water and creates the possibility of blistering of carbon steels and sulfide cracking. The by-product of an  $H_2S$  attack on steel is iron sulfide (the general form is  $FeS$ ). Sulfate-reducing bacteria are anaerobic bacteria with slow growth rates when oxygen is present. Sulfate-reducing bacteria occur naturally in surface waters, including seawater. The growth of the sulfate-reducing bacteria is controlled by temperature and limiting their access to nutrients. The primary nutrients are carbon, nitrogen, phosphorus and dissolved iron. Bactericides are also used commonly to control these bacteria.

Iron-oxidizing bacteria are aerobic and convert iron from the ferrous ( $Fe^{2+}$ ) to the ferric ( $Fe^{3+}$ ) state. They produce gelatinous ferric hydroxide, which is highly insoluble and precipitates out of water. The bacteria metabolize dissolved iron in the water. Ferrous iron is soluble only at low pH values (i.e., when the water is acidic). Therefore,  $FeOH_3$  is typically considered an acid-reaction product. The iron-oxidizing bacteria produce some corrosion, but they usually cover sulfate-reducing bacteria colonies and protect them from attack.

Slime-forming bacteria are facultative and produce mats of high-density slime that cover surfaces. Their primary detrimental effects are the protection of colonies of sulfate-reducing bacteria and pore plugging.

The bacteria that attack polymers are various aerobic types and a few of the anaerobic bacteria. Most polymers are excellent carbon sources that are readily consumed to support rapid bacterial growth rates. The resulting large quantities of biomass contribute to formation plugging. All these bacteria can be controlled by the application of various biocides.

### 14-3.11. Water blocks

Water can cause blocking in low-permeability rocks (Fig. 14-6) (Keelan and Koepf, 1977). Water blocks are a special case of relative permeability problems. In a water block, water usually occupies the flowing spaces (either pores or natural fractures) that are typically used by hydrocarbons to flow to the wellbore. Because of the mobility and viscosity differences, the hydrocarbon fluid may not be capable of displacing the water. The most severe cases of water blocks are usually observed in low-pressure, low-permeability, gas-producing formations after treatment with water that has a high surface tension.

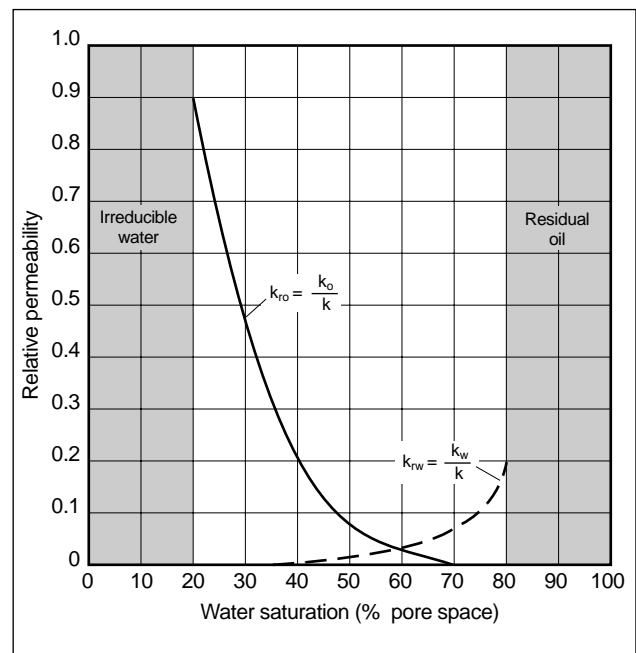


**Figure 14-6.** Water blocks: increasing the water saturation from 20% to 35% decreases the relative oil permeability from 90% to 30%, respectively (Keelan and Koepf, 1977).  $k_o$  = oil effective permeability,  $k_{ro}$  = oil relative permeability,  $k_w$  = water effective permeability,  $k_{rw}$  = water relative permeability.



### 14-3.12. Oil-base drilling fluids

Oil-base mud (OBM) is the drilling fluid of choice for the lubricity required in many highly deviated wells and for formations that are extremely sensitive to water-base mud (WBM). Most OBMs, and particularly those with densities greater than 14 lbm/gal, contain sufficient solids to create silt-stabilized emulsions when mixed with high-salinity brines or acids. These emulsions are viscous and resist breaking. Some of these emulsions have been shown to be stable for several months, both in the laboratory and in the wellbore. The level of damage caused by these emulsions can be so severe that an entire pay zone can be missed. For example, in a South Texas well the OBM emulsion created damage so severe that almost no flow from the well could be measured. When the damage was removed, the well tested at more than 12 MMscf/D.

A related problem with OBM is the relative permeability effects commonly created by the powerful wetting surfactants used for creating stable OBM. When these materials coat or adsorb onto the formation, the wettability of the formation is altered, and permeabilities may be only 10% to 20% of what they were initially. The most severe problems usually occur with muds weighing more than 14 lbm/gal. The main cause of problems is oil-wetting of the fines from weighting and viscosifying agents and from cuttings.

## 14-4. Origins of formation damage

This section describes the origins of formation damage and reviews typical well operations, including drilling, cementing, completion, gravel packing, production, stimulation and injection for enhanced oil recovery. All are potential sources of damage. Damage is also commonly categorized by its associated well operation (Tables 14-3, 14-4 and 14-5).

### 14-4.1. Drilling

- Mud solids invasion

Mud solids can progressively fill the porosity of the reservoir rock if forced into the pay zone. Subsequent attempts to start production or injection at moderate or high flow rates may cause

these materials to bridge and severely decrease the permeability of the near-wellbore area.

Such damaging processes are usually limited to the first few inches around the wellbore (an average value of 3 in. is commonly used), but the resultant permeability reduction can be as high as 90%. Invasion of formation rock by drilling fluid solids is favored by

- large pore size of the formation rock (Brownson *et al.*, 1980)
- presence of fissures and natural fractures in the reservoir
- small particle size of the solid components of the drilling fluid (the initial particle size of weighting agents and lost-circulation preventers is usually coarse but can be fragmented by the drill bit) (Abrams, 1977)
- low drilling rate resulting in mudcake destruction (mud-loss increase) and long formation-to-mud contact time
- high drilling fluid circulation rate (mudcake erosion)
- high drilling fluid density causing large overbalance pressure (Givens, 1976)
- scraping of mudcake, provoking pressure surges and increasing formation-to-mud contact time during bit trips (Records, 1976).

Using clear brines (containing no particulate materials) as drilling fluids minimizes formation invasion by fines but may create a large loss of fluids in the rock matrix.

When drilling a formation with natural fractures, some mud loss is expected in the natural fracture system. Because natural fractures are important to reservoir flow, avoiding loss of mud to the fracture system by using a high-quality fluid-loss control system is crucial. If the natural fractures are already damaged by mud, the success of the cleanout will depend on how much mud was lost and the type and condition of the mud when it was lost. If a low-solids mud was used in a system with minimal overbalance, little damage may have occurred. If a high-weight mud system with a large amount of fines was used or if the drilling overbalance was high (more than 2 lbm/gal overbalance equivalent), damage may be severe.

**Table 14-3. Initial damage during drilling or completion.**

Condition or Type of Damage	Diagnostic Clues	Remedial Operation
Unstable formation	<p>May occur in any formation that is poorly consolidated or that will fail under pressure</p> <p>May occur with onset of water production or loss of pressure from depletion</p> <p>Problems include embedment of proppant, closing of acidized channels in acid fractures, spalling of formation into perforations or wellbore, or production of solids.</p>	Gravel packing, fracture packing, plastic consolidation or production rate limits
Oil-base mud emulsion damage	<p>Common in wells drilled with OBM</p> <p>If treated with acid or brine before the sulfonate emulsifiers are washed off the cuttings by production or solvent treatments, an emulsion can lock up the well.</p> <p>The first one or two treatments may be short-lived as more mud and mud filtrate move back toward the wellbore, as is often the case in naturally fractured formations.</p>	<p>Wash with aromatic solvent followed by mutual solvent and acid</p> <p>May require several treatments</p> <p>Cuttings removal is important.</p>
Fracture plugging from mud	<p>Large whole-mud losses in naturally fractured formations</p> <p>Intermittent production at low and moderate rates</p> <p>Infrequent recovery of whole mud and mud fines</p> <p>Some emulsions, especially after acid treatments</p> <p>May also occur if the hole is poorly cleaned during drilling</p>	<p>Acid useful if damage is shallow</p> <p>Fracture if damage is deep</p> <p>Prevent by improving solids recovery</p> <p>In severe cases, a sidetrack drill of the pay may be necessary.</p>
Particle damage from drilling and completions	<p>Skin effect on buildup test</p> <p>Injection difficult</p> <p>May show emulsions in oil wells</p> <p>Poor mud conditioning before cement</p> <p>Common in openhole completions and horizontal wells</p>	<p>HCl or HCl-HF in matrix acid job and solvent wash followed with acid in wells with OBM</p> <p>Foam or jetting cleanups can be useful.</p>
Poor perforations	<p>Shows up as damage on a buildup test but cannot be cured with acid or mechanical changes in the well</p> <p>Common problems are screenouts of fracture downhole scale occurrence, unstable emulsions, and downhole paraffin and asphaltene deposits.</p>	<p>Reperforate</p> <p>Problems with a well that cannot be broken down or even pumped into should always be approached by reperforating the well.</p>
Cement in natural fractures	Poor well response following completion when possible perforation problems have been eliminated	Small fracture treatment or sidetrack drill

Table 14-4. Damage during and after stimulation.		
Condition or Type of Damage	Diagnostic Clues	Remedial Operation
Migrating fines	<p>Kaolinite or fibrous illite clay or some feldspars (nonclays)</p> <p>Brine changes may trigger fines movement.</p> <p>Sporadic reductions in flow rate</p> <p>Variable production rate tests</p> <p>Fines in produced fluids</p> <p>Emulsions rare but possible</p>	<p>Clay control for prevention</p> <p>Retarded acid for removal</p> <p>May require limiting rate in extreme case or fracture treatment to spread out draindown</p>
Particle damage after stimulation	<p>May also occur following acid or fracture stimulations or workover fluids where dirty water was used or the water was hauled or stored in a dirty tank</p>	<p>Filter treatment fluids</p> <p>Use clean tanks</p>
Particles in waterfloods	<p>Reduced injection rate</p> <p>Higher injection pressures</p> <p>Backflow shows particles and oil carryover return.</p>	<p>Better water filtering</p>
Wettability problems	<p>Commonly occurs after an acid job where the corrosion inhibitor was not mixed in the acid just before injection</p> <p>Emulsions and reduced flow are common, particularly after inhibitor loss or OBM contact. May be permanent, but usually cleans up slowly with time and flow</p> <p>Attempts to reverse natural wettability are usually short-lived.</p> <p>Natural wettability is determined by the natural surfactants in the produced fields.</p>	<p>Treat with mutual solvent wash over the pay, displace and soak</p>
Relative permeability problems	<p>May occur when oil is injected into a gas zone or gas is injected into an oil zone that is above the bubblepoint</p>	<p>Treat with a high-API-gravity solvent such as condensate or xylene (low flash point)</p> <p>Squeeze and produce back</p>
Poor load-fluid recovery	<p>Usually formation dependent</p> <p>May decrease production rate in severe cases or cause a long cleanup time</p> <p>Most common in formations with small pores and in microporous clays</p>	<p>Avoid or minimize water contact and lower the surface tension of the water to prevent</p> <p>Removal with alcohols and some surfactants</p>
Water blocks	<p>Usually in gas wells with small pore throats, untreated water and low-pressure formation</p> <p>If low pressure (less than about 0.2 psi/ft), the pore throat size has no effect</p>	<p>Matrix treat with alcohol or surface-tension-lowering surfactant</p> <p>Inject gas in gas reservoir to a distance of 10 ft</p>
Swelling clay	<p>Smectite clay, some illite and smectite interbedded clay</p> <p>Permeability is sensitive to change in water salinity or brine type.</p>	<p>Acidize with HCl-HF if damage is shallow</p> <p>Fracture if damage is deeper than 12 in.</p>
Microporosity (water trapping)	<p>Caused by some forms of clay</p> <p>May bind water and make high <math>S_w</math> readings on log without water production</p>	<p>No treatment necessary</p>

**Table 14-5. Damage during production.**

Condition or Type of Damage	Diagnostic Clues	Remedial Operation
Retrograde condensate	<p>This special case of the relative permeability effect is a condensate (liquid phase) that forms from a rich gas.</p> <p>If the condensate forms in the tubing or casing, heading may occur.</p> <p>If the condensate forms in the formation, creation of another phase will reduce permeability to gas.</p> <p>Usually occurs near the wellbore as pressure drops there</p>	<p>Control drawdowns and repressure reservoir</p> <p>Redesign tubing if forming in tubulars</p>
Paraffins in tubulars	<p>Pressure restriction in tubulars</p> <p>Soft to hard mass found at pressure drops</p> <p>Reddish brown to black in color, with white or gray also possible</p> <p>Also commonly occurs in tubing near the surface as oil cools and the cloud point is reached</p> <p>May increase as a problem as a field ages</p> <p>Most paraffin deposits melt at less than 150°F [65°C].</p>	<p>Scraping and cutting for mechanical removal</p> <p>Hot oil useful if the deposit is less than 100 ft from surface</p> <p>Solvent soaks on deeper deposits</p> <p>Inhibitors available for pipelines and some problem wells</p> <p>Some wells require continuous downhole treatment through "macaroni string."</p> <p>Special bacteria are useful.</p>
Paraffins in flowlines	<p>Soft to hard deposits (not a scale) in surface flowlines and equipment</p> <p>Paraffin melts when exposed to sufficient heat . (usually about 150°F).</p>	<p>Mechanical or solvent removal or pigging</p> <p>Inhibitors can be used</p>
Paraffins after stimulation	<p>Injection of a cool stimulation fluid may precipitate paraffin in the reservoir on contact.</p> <p>The well may be cleaned up slowly (1 to 4 weeks) after stimulation, although load fluid is recovered faster.</p> <p>May have decreasing skin if multiple buildup tests are performed</p>	<p>Allow the well to clean up on its own</p> <p>Where this problem is known to occur, prevent by using xylene preflush ahead of acid</p>
Paraffins in formation	<p>Seen as skin on test</p> <p>May disappear if well is shut in for several days</p> <p>Cloud point of oil is near the reservoir temperature.</p> <p>Pressure drop may trigger paraffin drop out.</p>	<p>Treat with downhole heat-generating processes if the well is a good producer</p> <p>Solvent soaks also used</p> <p>Some inhibitors can be used with a fracture treatment.</p>
Asphaltenes	<p>Black, soft to hard mass that may occur as flakes, sludge, marble-size balls and a sticky buildup that occurs with paraffins</p> <p>Precipitation is triggered by destabilization of maltene resins caused by acid contact, outgassing, shear in pumps, electrically charged metal surfaces, temperature reduction and CO<sub>2</sub>.</p> <p>Asphaltenes soften with increasing temperature (&gt;150°F) but do not melt.</p>	<p>Treatment with aromatic (cyclic ring) solvents such as xylene or toluene</p> <p>Some surfactants are also useful for dispersion of the asphaltic mass.</p> <p>Use antisludge additive or xylene with acid in reservoirs with more than 0.5% asphalt to prevent sludges</p>

**Table 14-5. Damage during production (continued).**

Condition or Type of Damage	Diagnostic Clues	Remedial Operation
Tar	<p>Flows slowly into perforations during production of oil</p> <p>Usually associated with the presence of a tar deposit near pay and typically highly asphaltic</p> <p>May contain some water that is tied up as droplets or "pockets" in the high-viscosity mass</p>	<p>Solvent soak as required</p> <p>Test solvent with sample of tar before job</p> <p>Heat often helps.</p>
Emulsion	<p>Unstable emulsions that break on standing</p> <p>Created in tubing at pressure drop points in the piping system from pumps to choke</p>	<p>No downhole treatment suggested</p> <p>Treat on surface if string redesign is impractical</p>
Silt-stabilized emulsion	<p>Stable emulsion with partially wetted fines at interface</p> <p>Common after drilling mud dispersal or cleanup of mud or cement fines by acid</p> <p>May also occur on polymer cleanup</p> <p>Common in production from unconsolidated formations, especially after acid or gravel-pack operations</p>	<p>Treat with mutual solvent and acid</p> <p>Remove downhole source of solids if possible</p>
Surfactant-stabilized emulsion	<p>Stable to highly stable emulsion</p> <p>Common to severe after acid treatment</p> <p>Stabilized skin may be seen at the drop interface.</p>	<p>Treat on surface if temporary</p> <p>Use mutual solvent or surfactant to prevent emulsion with next acid treatment</p>
Sludge (iron/asphaltic)	<p>Sludge is an emulsion that is nearly solid.</p> <p>May be triggered by acid, OBM, asphaltenes or iron compounds</p> <p>Disperse the sludge in xylene and analyze for components, particularly iron</p>	<p>Prevention is the best cure.</p> <p>Use nonsludging acid systems, and test at the iron content expected in the well</p>
Bacterial infestation	<p>This difficult problem to predict is more common in injection wells where surface or produced water is injected.</p> <p>If the colony is established in the water handling system, it can occur with the injection of any waters.</p> <p>Brown to black slimy masses or an H<sub>2</sub>S odor when tubing is pulled</p> <p>Bacteria may cause slow reductions in the injectivity of an entire field.</p> <p>Complete removal of bacteria is rarely possible.</p> <p>Treatment is usually on a remedial basis.</p> <p>Untreated water in treatments</p> <p>Drilling fluid or injection water can sour reservoirs with sulfate-reducing bacteria.</p>	<p>Treat with sodium hypochlorite followed by HCl (do not allow contact of sodium hypochlorite and HCl)</p> <p>More than one treatment may be necessary.</p> <p>Alternative treatments are chlorine dioxide and bactericide slugs.</p>
Calcium carbonate scale	<p>May form at any pressure drop, either in the formation or tubulars</p>	<p>HCl to remove and inhibitor to prevent</p>

**Table 14-5. Damage during production (continued).**

Condition or Type of Damage	Diagnostic Clues	Remedial Operation
Calcium carbonate scale (continued)	<p>May form quickly and can sharply limit production, especially at gravel-pack interfaces or near perforations in wells with high drawdown across the perforations</p> <p>May be more common in earlier stages in some fields when the pressure drop is more severe</p> <p>Usually has no crystal pattern</p>	<p>Inhibitor may be squeezed into the formation for longer lived protection.</p> <p>Some HCl jobs may trigger calcium carbonate scale in rare cases; inhibit acid or treat with EDTA if this is a problem.</p>
Calcium sulfate scale	<p>Usually forms at pressure drop induced by turbulence or dissolver with acid)</p> <p>More common where high-sulfate waters contact high-calcium waters and in CO<sub>2</sub> floods</p> <p>Scale is not acid soluble.</p> <p>May be found on the outside of pumps and at intakes and gas expulsion ports and valves downhole</p> <p>Crystals are characteristic for this scale.</p>	<p>Chemical converter or dissolver followed by acid (do not contact converter</p> <p>Acid is not useful alone.</p> <p>Inhibitors placed by squeeze treatments are useful for prevention.</p>
Barium sulfate scale	<p>Nonreactive scale that forms at pressure draw-downs or where outgassing occurs</p> <p>No readily apparent crystal pattern in many deposits</p> <p>May occur as NORM scale in areas where radioactive isotopes form in the lattice</p> <p>NORM scales are detectable with gamma ray logging tools.</p>	<p>Scraping, water blasting or other mechanical removal</p> <p>Chemical treatment is usually not possible if scale occurs as a nearly pure (greater than 90%) deposit or as thick (greater than ¼ in.) deposits in pipe.</p> <p>Can be prevented by inhibitors</p>
Iron carbonate scale	<p>Carbonate scale tendencies with large iron content</p> <p>Molar acid reactivity on the scale</p> <p>Brownish colored scale (cleaned of oil)</p>	<p>HCl for thin deposits or mechanical removal where possible</p>
Iron sulfide scale	<p>Hard scale, dense and heavy</p> <p>Many forms are not acid soluble.</p> <p>Some forms are mildly magnetic.</p>	<p>Mechanical removal with mills or cutters</p> <p>Water jets may not work.</p>
Salt	<p>Precipitates as a white mass in the tubulars or in the formation</p> <p>Usually associated with a cooling of super-saturated water, but can also be triggered by a pressure drop</p> <p>May be seen early in some wells but becomes less of a problem as the water cut increases</p> <p>Problems in formations with produced water salinity that is near saturation</p>	<p>Freshwater or weak brine wash</p>
Hydrates (ice) in gas wells	<p>Gas well with intermittent flow to nearly total shutoff, followed by return to flow in a few minutes</p> <p>Produces a small amount of water</p>	<p>Glycol or alcohol injection below the hydrate formation point</p> <p>Insulated risers or tubing</p>

**Table 14-5. Damage during production (continued).**

Condition or Type of Damage	Diagnostic Clues	Remedial Operation
Hydrates (ice) in oil wells	In oil wells, usually forms only near the mudline in Arctic regions  May also form in drilling fluid	Insulated risers
Fill in perforations	High skin effect  Well can be injected into at low rates.  Reperforating may show sharp increases.	Clean out or reperforate
Fill in casing	High skin effect  Difficult or impossible to inject into well  Partial fill shows skin effect on a buildup test, but injection is possible at a reduced rate.  Confirm with a sinker bar on wireline	Reverse circulation or regular circulation
Water coning	Onset of water production after extended production  Formation has no vertical permeability barriers and sufficient vertical permeability to allow water to move toward drawdown.	Limit rate  Some treatments may be temporarily useful.  Most water control products are not useful without natural reservoir barriers
Waterflood breakthrough through high-permeability zone	Examine produced water analysis and compare with flood water for identification  Watch for scale	High-permeability zones should be plugged deep (depth greater than 100 ft) from producer and injector when oil recovery from the zone is complete.
Commingled water production	Initial production of water with oil in primary, with breakthrough in flood  Water cut increases in flood.	Temporary or no treatment
Collapsed pipe	May show up as reduced rate or destruction of lift equipment  Check with a gauge ring on wireline or tubing  Most common causes are earth-shift loads caused by subsidence of producing formations with fluid and sand withdrawals, active faults and formation movement near salt zones.  Other causes include severe corrosion, malfunctioning perforating guns, pipe flaws and wear of tubulars from drilling or lift system.	If caused by earth-shift forces, use heavier pipe or multiple strings  Liners, cement and patches are used for repair.
Tubing problem	Well refuses to flow although pressure is sufficient with the expected assistance from dissolved gas.  Well may load up and die, or liquid slugs may be produced if the string is too large.  Rate is restricted by friction backpressure if tubing is too small.	Redesign string  A velocity string that fits inside the existing tubing may help if tubing is too large.
Leaks	Sudden changes in gas/oil ratio, water/oil ratio, pressure or chemical analysis of water	Repair  Consider corrosion control program

- Drilling fluid filtrate invasion

For economic reasons, wells have to be drilled as fast as possible. To increase the penetration rate, it is tempting to reduce the fluid-loss control of the mud (Black *et al.*, 1985; Simpson, 1985a, 1985b; Montgomery, 1985). About 600 bbl of fluid can be lost into a typical formation (Kutasov and Bizanti, 1985) during the drilling of a 10,000-ft well. Higher values of filtrate invasion may result from the deliberate choice of high penetration rates. Before this decision is made, the effect of the filtrate and any associated solids should be known.

The liquid phase of a drilling fluid also contains many potentially damaging compounds. Because filtrate invasion can be deep, as shown in Table 14-6 (Simpson, 1974; Hassen, 1980), drilling filtrate damage can be one of the most important causes of production impairment. The severity of this damage depends on the sensitivity of the formation to the filtrate. High-permeability clean sandstones undergo more invasion than low-permeability reservoirs (Phelps *et al.*, 1984) but are more likely to be less affected when their connate water is chemically compatible with the filtrate. An average permeability reduction of 40% has been suggested; however, any value between 0% and 100% is possible, depending on the nature of the formation rock and fluids.

Sensitive formations contain clays that can be dispersed or swollen, are low-permeability rocks in which saturation problems dominate or are reservoirs producing almost saturated brines or high-content asphaltene or paraffin oils.

Problems with clays are not detailed here.

However, any change in the salinity of the pore fluids may affect the stability of clay particles in the porous medium. In particular, reducing the salinity or increasing the pH value of the water surrounding clay particles can promote dispersion of these materials. Destabilized formation fines act similarly to mud particles forced into formation rocks. As production or injection starts, fines migrate toward pore throats and either block them or bridge over them, depending on the particle size. The severity of the resulting permeability impairment varies with the fines concentration in the reservoir rock (Krueger *et al.*, 1967; Drodgy *et al.*, 1988; Jiao and Sharma, 1992).

Factors that increase the probability of drilling fluid invasion include

- high permeability of the mud filter cake (a result of either poor design of the drilling fluid or detrimental drilling procedures)
- high overbalance
- long formation-to-drilling-fluid contact time.

WBM filtrates may have a low salinity and a high pH value and may contain dispersants and polymers. Water is a cause of in-situ clay disturbance and water blocking in low-permeability rocks (Keelan and Koepf, 1977). The numerous drawbacks of water-base drilling fluids led to the development of OBM for drilling through sandstones containing clay (Methven and Kemick, 1969). The initial conclusion was that this new mud was a safe, all-purpose drilling fluid. It is now recognized, however, that although the problems of OBM are less numerous than those of WBM, they are commonly much more severe (Goode *et al.*, 1984). OBM filtrates contain additives that cause emulsion and wettability problems (Ballard and Dawe, 1988; McKinney and Azar, 1988; Sanner and Azar, 1994; Ventresca *et al.*, 1995). Polymer filtrates that are stable at circulating temperatures, but already potentially damaging, can decompose and form residues when exposed to static reservoir temperatures for long periods of time (Tuttle and Barkman, 1974), as previously discussed.

**Table 14-6. Depth of filtrate invasion (Simpson, 1974).**

Time (D)	Depth of Invasion (in.)		
	Oil-Base Mud	Low-Colloid Oil-Base Mud	Water-Base Mud
1	1.2	3.3	7.7
5	4.6	11	12
10	7.7	17	18
15	10	21	23
20	12	23	27
25	14	29	31
30	16	32	34



## 14-4.2. Cementing

- Washes and spacers

The removal of drilling mud, while necessary for improving cement bonding, typically exacerbates formation damage through either increased fluid loss or incompatibility problems with cement washes and spacers.

The duration of a cementing job is short compared with the duration of drilling through a pay zone. The maximum depth of invasion by the filtrate from either spacers or cement slurries is a few inches, which is negligible compared to the few feet of drilling mud filtrate invasion. This does not mean that cement or spacer fluid loss should be neglected. Poor fluid-loss control can result in premature job failure by either complete loss of the preflush fluids (insufficient volumes) and subsequent contamination (and strong gelling) of the cement slurry by the drilling fluid or dehydration of the cement slurry itself.

- Cement slurries

The broad particle-size distribution of cement grains, together with the use of high-efficiency fluid-loss agents, results in limited particle and filtrate invasion of cement slurries (Jones *et al.*, 1991b). However, there are four cases where large permeability impairments can occur:

- The relatively high pH value of cement slurry filtrates is particularly detrimental to formation clay minerals. Calcium ions liberated by cement particles are quickly exchanged on clays near the wellbore, and the resulting modification of the filtrate composition makes it a perfect destabilizing fluid in terms of dispersing ability (Cunningham and Smith, 1968).
- Cement filtrate that comes into contact with carbonate brines that contain high concentrations of calcium can provoke the precipitation of calcium carbonate, lime (Records and Ritter, 1978) or calcium silicate hydrate (Krueger, 1986).
- Overdispersed slurries (with no yield value) promote the rapid separation of cement particles at the bottom and water at the top of the cement column. A large invasion of free water will most likely take place, and the resulting water blockage may be significant.

- Loss of cement to the natural fracture system is a catastrophic problem when using a cased and perforated completion through formations with natural fracture systems. In side-by-side well comparisons, cement loss in natural fractures in the pay zone has been shown to decrease production to the point where the zone cannot flow effectively. Once cement is lost into the fracture system, hydraulic fracturing or sidetracking and redrilling the well are the best alternatives. In some carbonate formations, acid fracturing may be beneficial.

## 14-4.3. Perforating

Perforations are the entry point from the formation to the wellbore, and all flow in a cased, perforated completion must pass through these tunnels. Although perforation job quality is at times overlooked in the search for reasons why a well does not produce as expected, any time that formation damage is suspected the perforations should be examined first. Perforating is always a cause of additional damage (Suman, 1972). Extreme overbalance (EOB) perforating has been used expressly to reduce damage to the perforation tunnels (see Chapter 11).

- Perforating mildly overbalance always forces formation and gun debris into perforation walls and decreases the permeability near the perforations (Keese and Oden, 1976).
- Perforating mildly overbalance in fluids that contain particles produces a similar effect (Paul and Plonka, 1973; Wendorff, 1974) and also builds a dense, impermeable cake on the perforation walls.
- Insufficient perforation penetration does not bypass drilling damage (Klotz *et al.*, 1974; Weeks, 1974). Penetration also decreases with formation effective stress (Saucier and Lands, 1978), a definite concern in deep wells.
- If the underbalance pressure required to achieve damage-free perforations is incorrectly estimated, the insufficient pressure difference will limit damage removal (Hsia and Behrmann, 1991; Behrmann, 1995; Bird and Dunmore, 1995), whereas excessive pressure differences lead to sand influx in the wellbore (King *et al.*, 1985; Seanard, 1986).

- Low perforation density restricts flow.

The perforating guns and processes should leave adequate entrance holes for the amount of fluid flowing into the wellbore. This can range from one shot every other foot in low-rate, homogenous formations (high vertical permeability) to as many as 12 to 16 shots per foot (spf). Most formations differ in vertical to horizontal permeability, with horizontal permeability from 3 to more than 10 times the vertical permeability. This property makes perforation density critical, especially if there are shale laminations in the pay zone. If too few perforations are used in a laminated or highly structured zone (many vertical permeability barriers), then flow from the zone will be only a fraction of what an openhole completion could be.

#### 14-4.4. Gravel packing

Formation damage mechanisms can affect gravel packs. Gravel packs are sand-exclusion techniques, essentially filters, in front of which formation fines are expected to bridge. It is almost universally true that gravel packs deteriorate with time, causing a progressive reduction of well performance. This is in contrast to current methods of sand production control and high-permeability fracturing (called frac and pack), in which well performance improves with time.

Major sources of damage in gravel packs are

- improper placement of the gravel pack (perforations remain empty or the annulus between casing and screen is incompletely filled), allowing perforation filling by formation sand, pack fluidization and subsequent intermixing of sand and gravel in the case of pressure surges (Stadlman *et al.*, 1985; Jones *et al.*, 1991a; Chuah *et al.*, 1994)
- damage by unbroken gels or formation particles during placement as a result of incomplete perforation cleaning (Sparlin, 1974)
- invasion by loss-control materials (LCM) (Blanton, 1992; McLeod and Minarovic, 1994; Hodge *et al.*, 1995)
- thread dope, paint, rust and polymer residues forced between formation sand and the gravel pack during placement
- inadequate gravel size, leading to gravel-pack invasion by formation fines during production (Gulati and Maly, 1975)

- screens with slots too large (do not retain gravel) (Flanigan, 1980) or with slots too narrow that become plugged and reduce production.

#### 14-4.5. Workovers

The various types of damage from completion and workover fluids are similar to the damage created by drilling fluids (Eaton and Smithey, 1971; Patton and Phelan, 1985):

- permeability impairment of formation rocks and productivity impairment of perforations by suspended solids (Rike, 1980; Rike and Pledger, 1981) including bacteria and polymer residues (Lissant, 1974)
- common problems resulting from filtrate invasion: clay swelling and dispersion (Azari and Leimkuhler, 1990a, 1990b), water blocks (Oudeman *et al.*, 1994) and emulsion blocks, and scale precipitation.

The necessity of using clean, filtered workover fluids has long been recognized (Fig. 14-7). Techniques to place these fluids adequately without contamin-

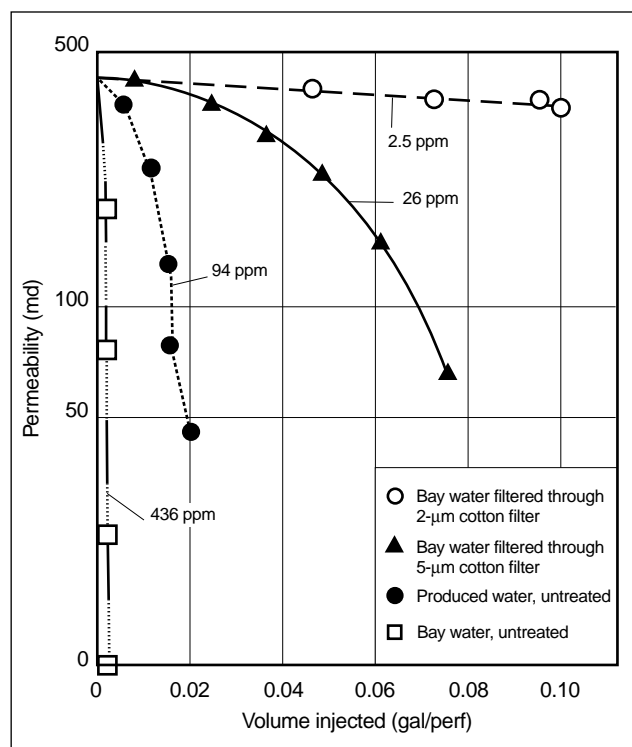


**Figure 14-7.** Apparent permeability reduction in Cypress sandstone cores with the injection of various filtered and unfiltered waters (Tuttle and Barkman, 1974).

ating them with the various particulate or gumlike materials in the wellbore (including thread dope) have also been proposed (Krause, 1986).

There is a strong requirement for fluid-loss control, especially in depleted reservoirs, and additives have been developed for this purpose (Crowe and Cryar, 1975; Mahajan and Barron, 1980). Another approach is to use foams, gases (Dahlgaard, 1983) or mists as completion fluids (Millhone, 1983). Instead of physically reducing the extent of filtrate invasion, the fluid-loss agents can deliberately be removed from workover fluids. In this approach, the compatibility of the fluid with formation minerals and brine must be carefully studied (Morgenthaler, 1986).

Workover brines (especially high-density brines) usually require inhibitors to control corrosion. These products can contribute to emulsion-block problems through the wettability modification of formation minerals and sometimes promote iron precipitation in the reservoir (Potter, 1984).

#### 14-4.6. Stimulation and remedial treatments

- Wellbore cleanup

When wells are cleaned to remove deposits or corrosion products from the tubing, high concentrations of damaging materials may invade the pay zone. Extreme care should be devoted to preventing these suspensions from being forced into the porous medium. Particularly dangerous are compounds that are soluble in the cleaning fluid because they cannot form impermeable cakes that prevent formation invasion. Rust in acid (Gougler *et al.*, 1985) or paraffins in hot oil (Newberry and Barker, 1985) are the two most typical redissolved wellbore compounds. They reprecipitate in the formation and cause extensive, severe and usually permanent damage.

- Acid treatments

Problems already encountered in other phases of the life of a well may also occur during acidizing treatments, especially in cases of inappropriate design. These include

- damaging materials from the tubing entering the formation rock

- oil-wetting of the reservoir by surfactants, especially corrosion inhibitors (Crowe and Minor, 1982), which can create emulsion blocks
- water blocks
- asphaltene/paraffin deposition when large volumes of acid are injected.

In addition to these common damaging processes, specific production impairment can result from poor design of acidizing treatments. These impairments include the following:

- sludges produced by reaction between acids and asphaltenes (Moore *et al.*, 1965; Houchin *et al.*, 1990), especially in the presence of some additives (particularly surfactants) (Knobloch *et al.*, 1978) or dissolved iron (Jacobs and Thorne, 1986)
- deconsolidation of the formation rock caused by excessive dissolution of the cementing materials by acids
- precipitation of by-products from the reaction of acids with formation minerals (Boyer and Wu, 1983; Gadiyar and Civan, 1994)
- precipitation caused by some sequestering agents added to acids to prevent iron problems if iron is suspected present (Smith *et al.*, 1969)
- permeability impairment by residues from corrosion inhibitors (Crowe and Minor, 1985) or produced through the thermal degradation of polymers, such as friction reducers (Woodroof and Anderson, 1977)
- dissolution of pack sands, to a limited extent, in hydraulically fractured and gravel-packed wells (Cheung, 1988; Yeager, 1990).

- Fracture treatments

Damage resulting from hydraulic fracturing takes two distinct forms: damage inside the fracture itself (proppant-pack damage) and damage normal to the fracture intruding into the reservoir (fracture-face damage). The first generally occurs because of inadequate breaking of the fracturing fluid polymer; the second occurs because of excessive leakoff. Depending on the reservoir permeability, the impact of these two damages varies.

For low reservoir permeability, neither one is much of a factor. As the permeability increases, proppant-pack damage (and its avoidance) becomes increasingly important, whereas damage to the reservoir face is relatively unimportant. At high permeabilities, both are important, with fracture-face damage dominating at very high permeabilities.

The selection of fracturing fluids, polymer concentrations and breakers is critical in addressing these issues. Incomplete breaking of the polymers in fracturing fluid is the most obvious cause of damage within hydraulic fractures (Gidley *et al.*, 1992), as well as the poor selection of proppant fracturing fluids (Brannon and Pulsinelli, 1990) and formation rock spalling or creeping into the proppant pack (Strickland, 1985). True damage in the formation rock is the consequence of excessive leakoff in high-permeability reservoirs when polymer-base gels are used in combination with inefficient fluid-loss agents (Elbel *et al.*, 1995; Parlar *et al.*, 1995). These damages are usually severe and usually cannot be improved with matrix treatments. To alleviate this problem, polymer-free, surfactant-base fluids have been proposed (Stewart *et al.*, 1995); however, they cannot be used in the absence of crude oil, which is required for breaking the surfactant micelles.

- Poor load-fluid recovery

Typical load-fluid recovery on a stimulation treatment or remedial treatment may range from as little as 20% to 100%. Load fluids can invade and become trapped in the formation by entering the smaller capillary pores during higher injection pressures, or they may coat clays with high micro-porosity (a condition in which a large surface area exists for water coating or trapping). Once the injection pressure is released, capillary pressure effects will hold significant volumes of the fluid in the formation. In some formations, more than 50% of the load fluid can be trapped after a treatment, and yet the formation may not appear damaged. Most of the flow is through the larger pore system and natural fractures, and these passages usually clean out quickly. The smaller pore passages can trap fluid by imbibing or absorbing it, but they have no real effect on the flow through the formation.

#### 14-4.7. Normal production or injection operations

- Unconsolidated formations

Formations that are capable of releasing parts of the matrix during production or after stimulation pose special treating problems. Although these situations are commonly thought of as sand-control problems rather than formation damage, the effect of mobile sand and the pressure drop caused by collapsed formation tunnels closely resemble the effect of formation damage. Some reservoirs cannot be produced at high flow rates or large draw-downs without being affected adversely. Permanent damage, which cannot be removed simply by the reducing production rate, may be created.

A major problem is the movement of fines in the formation in response to either flow velocity or changes in the salinity of the flowing fluid. Although this subject was addressed in Section 14-3.1, it is worth mentioning again, because it is usually a significant factor in the behavior of unstable formations. Native silts and clays loosely attached to pore walls can be put into motion by high flow rates (Hower, 1974; Holub *et al.*, 1974), especially when two or more immiscible fluids are produced at the same time (Muecke, 1979; Sengupta *et al.*, 1982). Depending on their particle size, they can either block pore throats in the vicinity of their initial location or migrate toward the wellbore.

Whether migrating particles reach the wellbore or bridge over pore throat entrances depends on their original concentration in the formation, their size, the extent of the increase of their concentration near the wellbore (because of radial flow) and the maximum flow rate (Vaidya and Fogler, 1990; Gunter *et al.*, 1992; Oyeninin *et al.*, 1995). Bridging is promoted when one or more of these parameters are increased. Bridging is less detrimental than blocking because a short period of reverse flow, followed by production at a flow rate lower than that at which bridging occurred, may mechanically disperse bridges (Fig. 14-8). However, this cannot be achieved when the bridging agglomerates were previously cemented by precipitates (asphaltenes or scales) or chemically stabilized through the injection of flocculants (such as clay stabilizers).

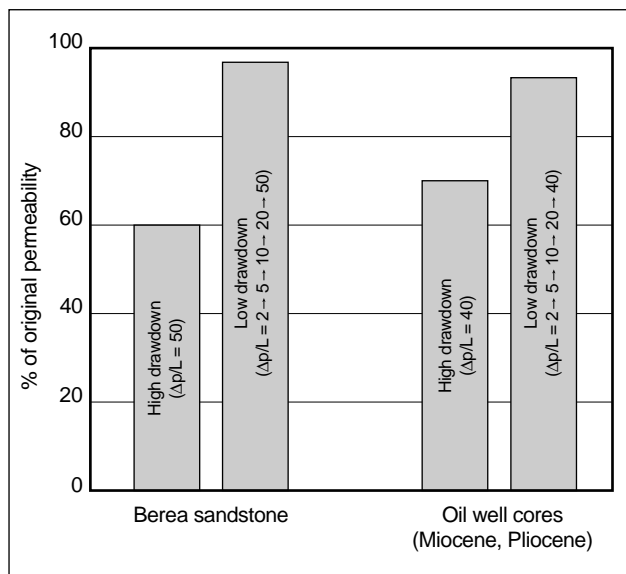


**Figure 14-8.** Effect of drawdown pressure during cleanup on the permeability regained by damaged sandstones (Krueger et al., 1967).  $\Delta p$  = pressure difference,  $L$  = length.

Excessive drawdown can also decrease pore pressure near the wellbore to such an extent that the effective stress exceeds the formation rock compressive strength. This phenomenon is obvious in poorly cemented sandstones, where wellbore filling by formation sand is progressive (Stein and Hilchie, 1972; Stein *et al.*, 1974; Anthunis *et al.*, 1979). It is less apparent in chalks, where formation compaction and significant porosity reduction affect the near-wellbore region without any occurrence of formation debris in the produced fluids (Morita *et al.*, 1984; Blanton, 1978; Ben Marek, 1979; Van Ditzhuijzen and de Waal, 1984). Chalk compaction is four- to eightfold greater when soft waters are injected during completion (Newman, 1983). Formation breakage is particularly damaging in hydraulically fractured wells, where creeping inside the proppant pack results in large-scale drops in production (Strickland, 1985). It has to be emphasized that once created, this type of damage cannot be removed by matrix treatments.

Reduction in the pore pressure during production (Fig. 14-9) (Fulford, 1968), and sometimes cooling resulting from gas expansion, results in the precipitation of organic (Hirschberg *et al.*, 1984; McClafin and Whitfill, 1983; Schantz and Stephenson, 1991; Singhal *et al.*, 1991; Leontaritis *et al.*, 1992; Takhar *et al.*, 1995; Piro *et al.*, 1995) or inorganic materials. Generally, these deposits

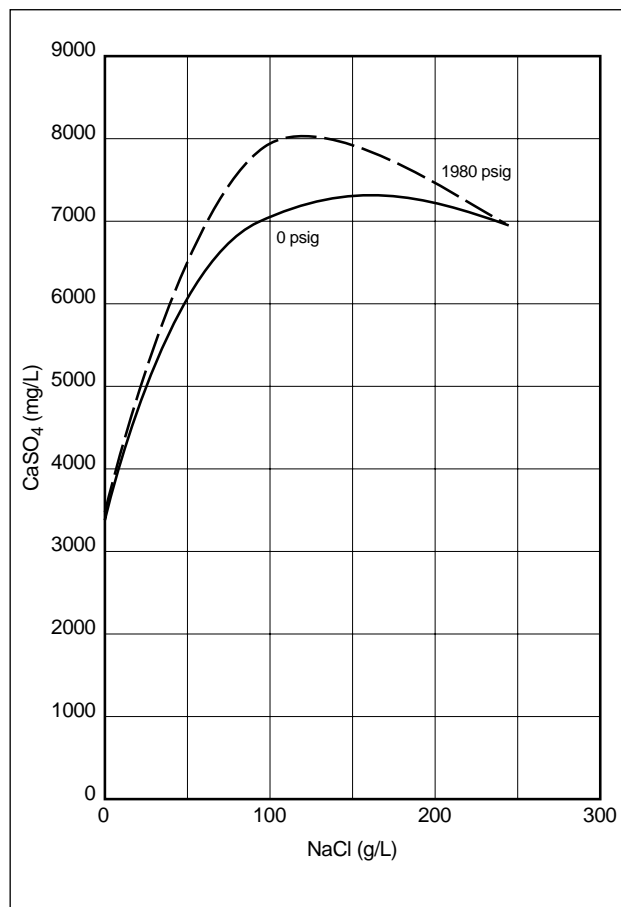


**Figure 14-9.** Pressure effect on gypsum scale solubility at 95°F [35°C] (Fulford, 1968).

affect only the production string and surface equipment. However, they can reduce formation permeability. Seeds, such as high-surface-area clays, promote the deposition of organic materials (especially asphaltenes) (Rogers, 1976) or the precipitation of supersaturated salt solutions.

Common scales are calcium carbonate (Vetter and Kandarpa, 1980; Nancollas and Sawada, 1982; Gudmundson and Oritz-R., 1984) and calcium sulfate (Vetter and Phillips, 1970; Oddo *et al.*, 1991; Lejon *et al.*, 1995). Problems associated with the deposition of elemental sulfur (Kuo, 1972), sodium chloride (Place and Smith, 1984) and barium sulfate (Wat *et al.*, 1992) have also been described. Commingled precipitation of asphaltene and calcium carbonate is common (Efthim *et al.*, 1990).

Special cases of spalling or sloughing of particles from brittle formations are also problems. These particles are derived from tensile failure created during flow that results in chips of the forma-

tion spalling into the perforations or the wellbore. Brittle formation behavior is seen typically in hard dolomites, brittle shales and a few shaly sandstones. Brittle formation failure is generally created by stresses in the formation and confining stresses caused by depletion. Prevention of these stresses is difficult without repressuring the reservoir.

- Retrograde condensation and two-phase flow  
Retrograde condensation and bubblepoint problems are relative permeability blocking problems. Retrograde condensation is the condensation of a liquid from gas. When this happens, the relative permeability to gas can be reduced substantially. In oil reservoirs produced below the bubblepoint pressure, free gas is formed, which reduces the relative permeability to oil.

## 14-5. Laboratory identification and treatment selection

The objectives of laboratory experiments are to identify potential damage and aid selection of the optimum treatment fluid and design. To achieve these objectives, the formation material (cores), produced fluids and damaged material must be analyzed. Definitive core flow studies and solubility tests are usually required to identify the source of damage and to help determine the best procedure for damage removal.

### 14-5.1. Damage identification

- Core analysis  
The detailed analysis of formation cores is required to design the damage removal treatment. It is difficult to determine formation mineralogy without the use of cores (sidewall or conventional). Conventional cores are recommended to complete the analysis because sidewall cores can be contaminated with drilling fluids and may not be representative of the formation. If sidewall cores are used, the analysis should be conducted on duplicate cores.
- Formation mineralogy  
The formation mineralogy is an important parameter affecting stimulation success. Knowledge of the petrography of the formation is essential to

understanding what the response of the rock (formation material) will be to any fluid. The relation between the rock and the treating fluid depends on the minerals present and the position of the minerals within the rock matrix. The analytical techniques used to characterize the mineralogy are X-ray diffraction (XRD), SEM and thin-section analysis.

XRD analysis provides rapid and accurate identification of the crystalline material of the rock matrix. Each crystalline material has a specific XRD pattern. The types and quantities of clays and feldspars can be qualitatively determined using XRD. Crystalline scale deposits can also be identified using XRD.

SEM provides information on mineralogy and morphology and the size of pore-lining materials. Quantitative elemental analysis and mineral identification can be achieved by using this technique in conjunction with energy-dispersive spectrophotometry (EDS). The primary advantages of SEM-EDS analysis over light microscopy are the depth of focus and magnification. The techniques are useful for observing clay platelet structure and analyses. The structures of smectite, kaolinite, chlorite and illite are shown in Fig. 14-4.

Thin-section analysis is used widely to study rock structure and quantify minerals. In addition, cementing minerals and the types and location of pores can be identified. The rock is impregnated with a blue-colored resin to fill the interconnected porosity. A thin (approximately 30  $\mu\text{m}$  in thickness) slice is cut perpendicular to the bedding plane, and the surfaces are polished. Using a polarized microscope, the minerals can be observed by transmitted light because they have characteristic optical properties. The pore structure is easily identified by the blue resin.

- Formation wettability  
Most formations (sandstone or carbonates) are water-wet. Occasionally, oil-wet formations are encountered, especially when the produced oil is a low-gravity oil. In some situations, the formation appears to be oil-wet because of the produced oil and the natural surfactants present in the oil; however, when the oil is removed using appropriate solvents, the formation may be water-wet. When the oil adheres to the rock matrix strongly, it must be removed prior to mineralogy or reactivity test-

ing. If the formation material is coated with oil, it should be cleaned with an aromatic solvent such as xylene until all traces of oil have been removed and followed with a xylene- and water-miscible solvent such as methanol.

The simplest test to determine formation wettability is to take approximately 10 cm<sup>3</sup> of formation material and place it in the produced brine to equilibrate for approximately 30 min. The formation material is then placed in an oil (such as kerosene) and observed. To accentuate the test results, red dye can be added to the clear oil to aid identification of the oil adhering to the formation material. After it is allowed to equilibrate for an additional 30 min, the formation material is added to a fresh aqueous solution. Strongly water-wet formations or other fines disperse readily in aqueous fluids but agglomerate or clump together in the clear oil-base fluids. Conversely, oil-wet particles disperse in oil but agglomerate in water-base fluids. The surface is water-wet if the contact angle of the fluid with the formation material is less than 90°; the surface is oil-wet if the contact angle is greater than or equal to 90°. Wettability can exist in various degrees between extremely water-wet and extremely oil-wet. Intermediate wettability is difficult to identify and describe, with contact angles greater than 80° but less than 100°.

The wettability test can also be used to determine if the desired treatment fluid is water-wetting or oil-wetting and how the treatment fluid may affect the desired natural wettability. The cleaned formation material is treated as described previously except the formation material is placed in the desired treatment fluid instead of naturally produced brine. Changes in wettability resulting from the selected treatment fluid can be detected using this method.

- **Petrophysical characterization**

Core porosity and permeability should be measured before performing a core flow evaluation.

- **Porosity**

Porosity is the ratio of the void space volume to the bulk volume of the rock material. It is a measure of the volume occupied by oil, gas and other fluids in the reservoir. Total, effective and residual porosities are defined in Chapter 1.

The porosity of the rock sample can be determined using one of several techniques. The simplest technique for the determination of effective porosity uses Boyle's law; the pressure of nitrogen is determined in a constant-volume cell, with and without the core. The total porosity is derived by bulk and matrix density measurements with a helium pycnometer. When required, the pore-size distribution can also be measured using a mercury intrusion porosimeter. The size and number of pores can be calculated and the microporosity can be estimated. The microporosity can be more accurately determined using the Brunauer, Emmett, Teller (BET) gas adsorption technique if required.

- **Permeability**

Permeability, an intrinsic characteristic of the rock, is a measure of the rock's capacity to transmit fluids. The measurement is usually made with gas (e.g., nitrogen [N<sub>2</sub>]) or liquids (e.g., brines and oils).

Permeabilities must be determined using simulated downhole temperature and stress conditions. In certain stress-sensitive formations, permeability determined under 1,000-psi confining stress may be 1 order of magnitude higher than the permeability determined at 10,000-psi stress.

- **Formation fluid analysis**

Analysis of the formation brine and oil can aid in determining the types of damage that may be present.

- **Brine**

Analysis of the formation brine can be used to predict scale formation. Common ions are listed in Table 14-7. Their presence can be determined using standard laboratory wet-chemical or instrumentation techniques.

**Table 14-7. Common ions in formation brines.**

Cations	Anions
Sodium (Na <sup>+</sup> )	Chloride (Cl <sup>-</sup> )
Potassium (K <sup>+</sup> )	Bicarbonate (HCO <sub>3</sub> <sup>-</sup> )
Calcium (Ca <sup>2+</sup> )	Carbonate (CO <sub>3</sub> <sup>2-</sup> )
Magnesium (Mg <sup>2+</sup> )	Sulfate (SO <sub>4</sub> <sup>2-</sup> )
Barium (Ba <sup>2+</sup> )	
Strontium (Sr <sup>2+</sup> )	
Iron (Fe <sup>2+</sup> and Fe <sup>3+</sup> )	

Calculations are available to predict scaling tendencies. The intermixing of produced brines with spent acid can result in the formation of insoluble precipitates. Analysis of these brine data aids in selecting the treatment fluids and their sequence.

– Oil

Analysis and testing of the produced oil can also help stimulation treatment design. The use of treating fluids that are incompatible with the produced oil can result in the formation of emulsions and sludge that will subsequently result in an unacceptable response to the stimulation treatment. The oil may contain paraffins and asphaltenes that can interact with the treatment fluid. The quantity of various fractions of asphaltenes and paraffins and their ratio to each other are used to assess the possibility of organic precipitation damage. It is also imperative that the identity of deposits recovered from a well be determined. This is particularly true of organic deposits because treatments for paraffin and asphaltene removal are different.

A test of the API gravity is performed on the produced oil to evaluate sludging tendencies. Certified hydrometers are used to measure the specific gravity as a function of temperature.

For analysis of the asphaltene content, the produced oil is centrifuged to separate out emulsified aqueous fluids. Mixing the crude oil with pentane and centrifuging the sample enables preferential separation of asphaltenes from the produced fluid. Repeated extraction is performed until all oil has been removed. The precipitated asphaltene material is collected, and standard laboratory techniques are used to obtain the content by weight. The oil pentane fraction is saved and the pentane solvent is evaporated. The residual oil is then used to complete the analysis for the paraffin content.

For analysis of the paraffin content, a sample of vigorously mixed crude oil and acetone is centrifuged to enable preferential extraction of the paraffin material into acetone. Repeated extraction and holding at temperatures less than 32°F [0°C] result in precipitation of the paraffins. The acetone mixture is filtered to remove the paraffins, which are dried to remove residual acetone. On the basis of the total composition of the pro-

duced oil used for the analysis, the percentage of paraffin is determined.

## 14-5.2. Treatment selection

The solubility of the formation or damage material, treating fluid compatibility and core flow studies should be conducted to aid designing the best treatment for damage removal and to select the chemical products that are the most compatible.

- Solubility tests

- Formation material

Calcite, dolomite and ankerite are soluble in HCl and mud acid systems. Clay and silt are soluble only in mud acid systems. Because of their high surface area, clays and other fines are much more reactive with mud acid than sand grains are. The total solubility of the formation material is the sum of the solubility of each mineral in the formation sample. Minerals other than carbonates are also soluble in HCl; therefore, solubilities should be used with caution. These minerals include sulfates (e.g., anhydrite), iron oxides and halite. The solubilities of common minerals are shown in Table 14-8.

Solubility tests are performed under ideal laboratory conditions and therefore exhibit the maximum formation solubility. The structure of the rock and the position of each mineral in relation to the flow paths in the rock matrix may result in different solubilities during actual acidizing operations. Solubility determined in the laboratory is not a definitive value for the maximum solubility that may result during the acidizing process, but it provides guidelines as to which treating fluids are most applicable.

A combination of solubility test results and XRD is commonly used to estimate the carbonate, silt and clay minerals and other mineral contents in the rock matrix. Determination of the acid solubilities of the various materials in HCl and mud acid determines the total solubility. When the results are used in conjunction with XRD analysis, the composition can be determined by the following procedure.

1. The total solubility in HCl is typically used as an estimate of the total carbonate content.



**Table 14-8. Solubility of common minerals in acids.**

Mineral	Chemical Composition	Solubility	
		HCl	HF
Quartz	SiO <sub>2</sub>	None	Low
Feldspar			
Microcline	KAlSi <sub>3</sub> O <sub>8</sub>	None	Moderate
Orthoclase	KAlSi <sub>3</sub> O <sub>8</sub>	None	Moderate
Albite	NaAlSi <sub>3</sub> O <sub>8</sub>	Very low	Moderate
Plagioclase	(Na,Ca)Al(Si,Al)Si <sub>2</sub> O <sub>8</sub>	Very low	Moderate
Mica			
Biotite	K(Mg,Fe <sup>2+</sup> ) <sub>3</sub> (Al,Fe <sup>3+</sup> )Si <sub>3</sub> O <sub>10</sub> (OH) <sub>2</sub>	Low	Moderate
Muscovite	KAl <sub>2</sub> (AlSi <sub>3</sub> )O <sub>10</sub> (OH) <sub>2</sub>	Low	Moderate
Clay			
Kaolinite	Al <sub>2</sub> Si <sub>2</sub> O <sub>5</sub> (OH) <sub>4</sub>	Low	High
Illite	(H <sub>3</sub> O,K) <sub>y</sub> (Al <sub>4</sub> · Fe <sub>4</sub> · Mg <sub>4</sub> · Mg <sub>6</sub> )(Si <sub>8-y</sub> · Al <sub>y</sub> )O <sub>20</sub> (OH) <sub>4</sub>	Low	High
Chlorite	(Mg,Fe <sup>2+</sup> ,Fe <sup>3+</sup> )AlSi <sub>3</sub> O <sub>10</sub> (OH) <sub>8</sub>	Moderate	High
Smectite	(Ca <sub>0.5</sub> Na) <sub>0.7</sub> (Al,Mg,Fe) <sub>4</sub> (Si,Al) <sub>8</sub> O <sub>20</sub> (OH) <sub>4</sub> · nH <sub>2</sub> O	Low	High
Mixed layers	Kaolinite, illite or chlorite layered with smectite		
Carbonate			
Calcite	CaCO <sub>3</sub>	High	High <sup>†</sup>
Dolomite	CaMg(CO <sub>3</sub> ) <sub>2</sub>	High	High <sup>†</sup>
Ankerite	Ca(Fe,Mg,Mn)(CO <sub>3</sub> ) <sub>2</sub>	High	High <sup>†</sup>
Sulfate			
Gypsum	CaSO <sub>4</sub> · 2H <sub>2</sub> O	Moderate	High
Anhydrite	CaSO <sub>4</sub>	Moderate	High
Other			
Halite	NaCl	High	High
Iron oxide	Hematite (Fe <sub>2</sub> O <sub>3</sub> ), goethite (α-FeO(OH)), magnetite (Fe <sub>3</sub> O <sub>4</sub> ), siderite (FeCO <sub>3</sub> )	High	High
<sup>†</sup> Precipitation of CaF <sub>2</sub>			

- The solubility of the formation material in mud acid is used to determine the silt and clay content (total fines) and the carbonate content.
- The difference between the solubilities in mud acid and HCl is considered the approximate content of clay and fines.
- The total reactive silt content is calculated as the difference between the silt and clay content determined by solubility and the total clay content determined by XRD.

- Other minerals that are soluble in the acid should also be determined and confirmed by XRD.

#### – Scales

The solubility of scale deposits depends on the mineralogy of the rock. Tests similar to the tests performed to determine formation solubility can be performed to determine the best solvent for scale removal. Identification of the deposit by XRD prior to the solubility evaluation is recommended to aid selecting the most active solvent.

Typically, acids, chelating agents or mechanical systems are used for removal. These tests should be performed under simulated well conditions to determine the optimum treatment.

– Organic deposits

Solubility tests at temperature and pressure can be performed to evaluate the most effective solvent to remove the plugging deposit. Typically, paraffin, asphaltene and tar deposits are soluble in aromatic solvents such as xylene or toluene; however, most deposits are a combined deposit and may require a combined treatment of an organic solvent with acid and other surface-active agents to improve the wettability of the deposit and enhance the dissolving capacity of the selected treatment fluid. Other solvents, such as mutual solvents and alcohols, may also aid the removal of an organic deposit.

– Bacterial slime

Bacterial slime is also removed by treating with solvents. These deposits are soluble in water containing oxidizing agents such as sodium hypochlorite. If required, solubility tests can be performed to evaluate the efficiency of the oxidizing agent. Tests should be performed using simulated downhole conditions, if possible.

• Treating fluid–formation compatibility

Preventing emulsion and sludge formation following a damage-removal treatment requires an optimum fluid design to minimize or eliminate the formation of precipitates. The potential for the formation of acid and produced crude oil emulsions and optimization of the de-emulsifier treatment are currently evaluated using American Petroleum Institute (API) *Recommended Practices for Laboratory Testing of Surface Active Agents for Well Stimulation* (RP 42) (1977).

– Emulsion prevention testing

Prior to a stimulation treatment, the compatibility of the treatment fluid with the produced oil must be determined. Fine siliceous materials, ferric iron or both can be added to evaluate emulsion stability mechanisms. These fluid interactions can produce downhole emulsion problems. The quantity of additives used to control emulsion stability and sludge formation

must be established. Additives such as corrosion inhibitors, surfactants and mutual solvents must also be included in the desired acid formulation for compatibility testing. The concentrations of these additives are established by core flow tests, metallurgy and the well conditions that occur during treatment.

Acid, or another aqueous treating fluid, is mixed with fresh crude oil (at low energy to simulate downhole mixing) in a glass container and observed at bottomhole temperature, if possible. The characteristics and time for emulsion breakout are determined. The quantity of aqueous fluid breakout is determined at set time intervals. The sample that provides the most rapid emulsion breakout is desired. The acid system is modified, including the type and quantity of nonemulsifier, until the minimum aqueous breakout time is achieved. A clean oil/water interface and rapid emulsion break (less than 10 min) are desired. The oil phase must also be clear, with no emulsified water draining freely from the glass surface (signifying a water-wet surface).

Differences in emulsion stability are attributed to more dominant factors such as stabilization by solids precipitation (organic and inorganic), ferric ion interaction with the asphaltene component of crude oil and viscosity increase at the interface. Results presented by Coppel (1975) show that partially spent acids contain potentially precipitable materials in solution. As the pH value of the spent acid increases during flowback and mixes with other produced fluids, materials precipitate that can stabilize emulsions. Dunlap and Houchin (1990) recommended using polarized microscopy to evaluate return fluids to establish the cause for a stabilized emulsion. Specific damage mechanisms such as emulsion stabilization by organic deposits, solids and iron may be detected and identified. Stabilization by solids can be evaluated by the use of fine silica or clay in the emulsion test described previously.

Downhole emulsions can be attributed to inadequate prejob compatibility testing because the additives used in the acid system may preferentially adsorb onto the rock matrix or partition to the oil phase during production. Alternate testing procedures have been recommended to simulate reservoir conditions more accurately.

Ali *et al.* (1994) recommended using an alternate procedure that better simulates downhole intermixing of the stimulation fluids and the produced crude. The formulated acid containing inhibitor, surfactants, mutual solvents and non-emulsifiers is filtered through a sand pack containing 10% silica flour, 10% clays (such as montmorillonite) and 80% 100-mesh sand prior to completion of the emulsion test. This procedure simulates the filtration of the acid system within the rock matrix. Surfactants, such as those used in nonemulsifiers, are adsorbed onto the mineral surfaces. This adsorption minimizes the availability of the surfactants in solution to prevent emulsions.

#### – Sludge prevention testing

Prior to the stimulation treatment, the compatibility of the treating fluid with the produced oil must be determined for sludging tendencies. Interaction of the acid with crude oil can generate the formation of solid precipitates, although the system does not form stable emulsions. These precipitates are sludge and are insoluble in the hot formation oil or brine. The sludging tendencies are aggravated by intermixing with ferric iron. If not prevented, precipitated solids can result in decreased production following an acid treatment.

The sludging evaluation is similar to the emulsion test previously described. The oil should be free of solids and emulsified water. Following completion of the emulsion test, the acid and oil mixture is maintained at the bottomhole temperature for 1 to 4 hr. The mixture is then filtered through a 100-mesh screen, and the precipitated sludge on the filter is identified.

To eliminate the formation of sludge, the acid system must contain an antisludge additive. The concentration of antisludge additive is increased in the acid system until formation of the sludge precipitate is eliminated.

#### • Core flow tests

Core flow tests are used to determine the effects of treatment fluids on formation samples at simulated well treating conditions. The structure of the rock and the position of each mineral in relation to the flow channels in the rock matrix may result in different solubilities during actual acidizing opera-

tions. Therefore, the permeability changes depend on the dissolution and precipitation reactions that occur. Observations that indicate what dissolves and what precipitates are extremely useful in selecting the best treatment fluid.

The effects of sequential injection of the different treatment fluids can also be observed. Fluid injection rates range from 0.2 to 10 mL/min and pressures range up to 1500 psi. Flow rates should be selected to ensure that the fluid movement has minimal effect on the movement of fines contained within the pore structure. The 1-in. diameter, 12-in. long cores are placed in a core holder and confined under pressure to simulate reservoir stresses. To ensure fluid flow through the core, the confinement pressure should be greater than the pressure required to initiate flow through the core. Tests should also be performed with backpressure. For core flow studies of acids, a backpressure of at least 1000 psi is required to maintain the CO<sub>2</sub> produced by acid dissolution of carbonate deposits in solution. For scale and deposit removal, sufficient backpressure is required to prevent vaporization of the treating fluid. The diagram of the core flow apparatus is shown in Fig. 14-10.

The results of these tests are shown by an acid response curve (ARC), as illustrated in Fig. 14-11. The evolution of permeability versus the volume of treating fluids is determined and the effect of each fluid on the core permeability is calculated and displayed. Core holders utilizing multiple pressure taps can be used to examine the effect of each fluid as it penetrates deeper into the formation.

Permeability changes depend on dissolution and precipitation reactions. Tests to determine what dissolves and what precipitates are not used to determine treatment volumes, which depend on the type and extent of damage. If formation cores are used for the study, they should be cleaned with aqueous alcohol or ethylene glycol monobutyl ether solutions to remove traces of oil and ensure that the cores are water-wet.

## 14-6. Treatment strategies and concerns

Once the damage and its origin have been characterized, the correct remedial action can be taken. Various types of damage can coexist because almost

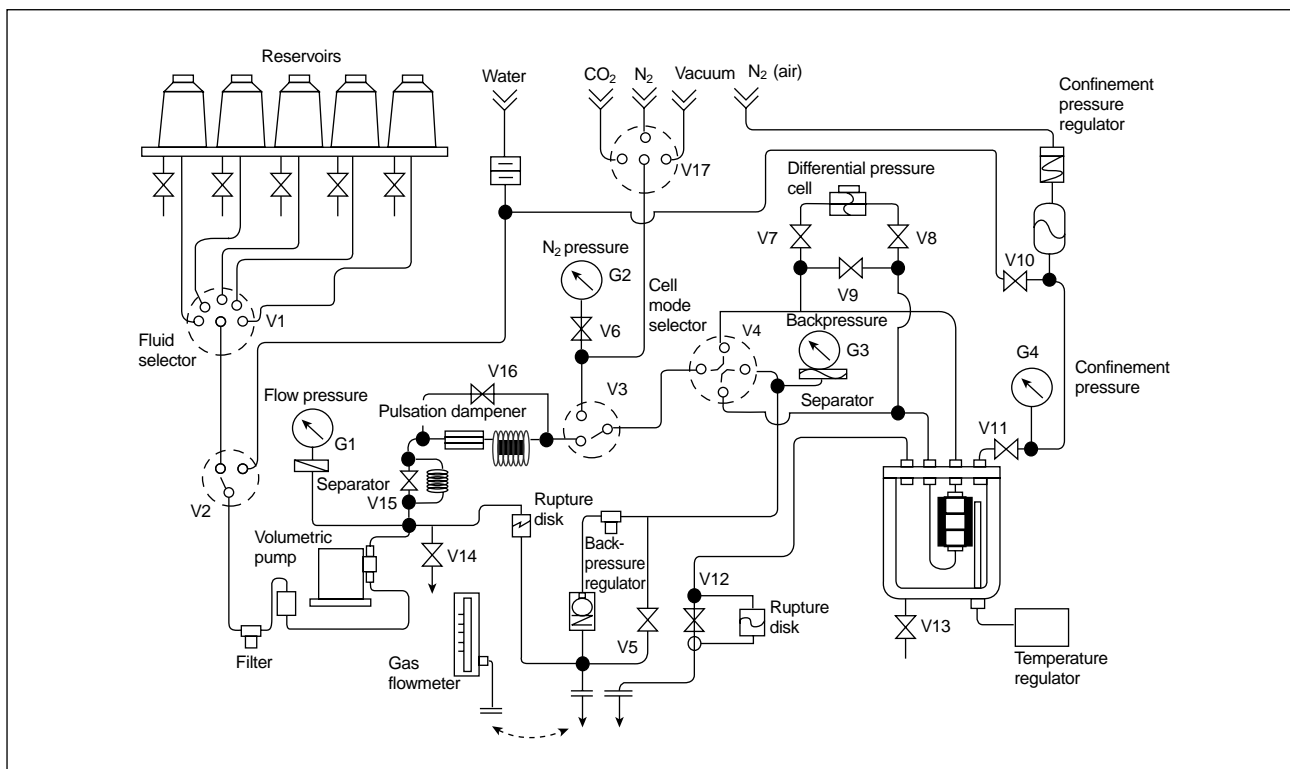


**Figure 14-10.** ARC core flow test apparatus.

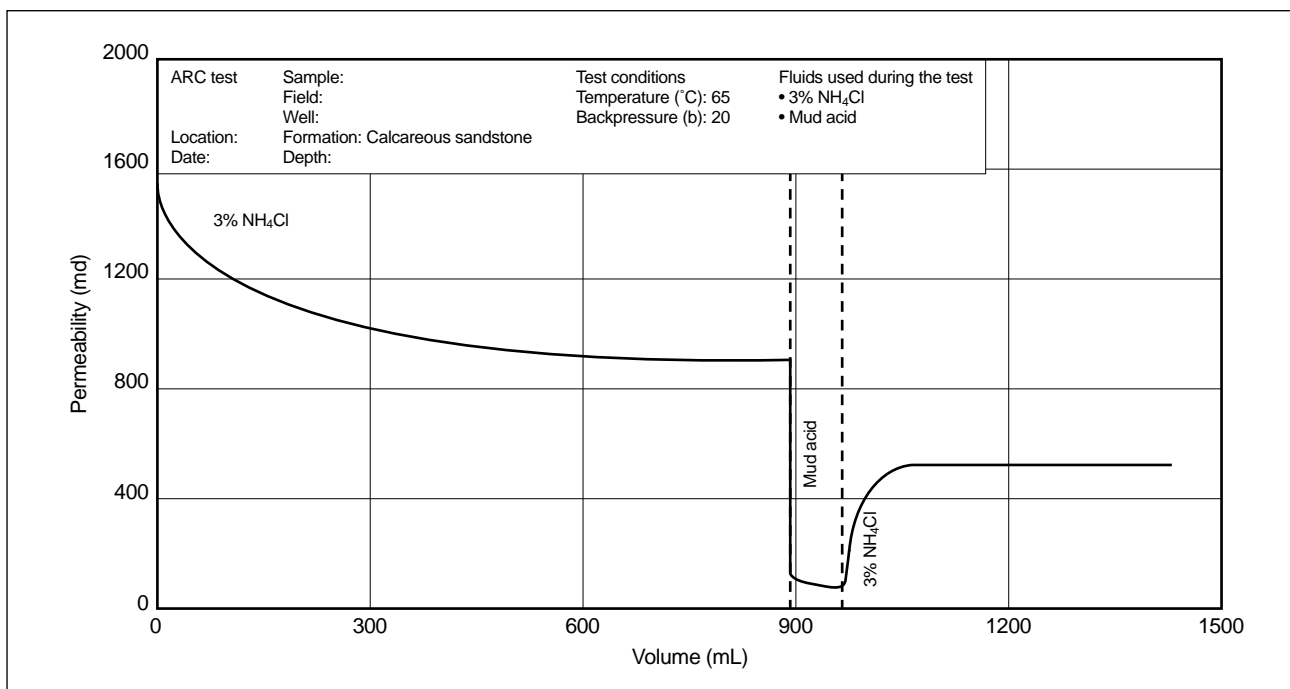


**Figure 14-11.** ARC of a carbonate-cemented sandstone to mud acid.

every operation performed on the well (drilling, completion, workover, production and stimulation) is a potential source of damage (Krueger, 1986).

The efficiency of a matrix treatment in sandstones depends primarily on removing the damage affecting productivity or injectivity (Williams *et al.*, 1979). This restriction is usually shown by an overall lower level of or sharper than expected decline in production. The extent of damage is typically estimated using pressure transient analysis.

The physical characteristics, not the origin, of the damage determine the treating fluid. A fluid can be used to treat occurrences of the same type of damage, regardless of what caused the damage. Seven basic types of damage are shown in Fig. 14-12.

When formation damage has reduced the productivity of a well, matrix acidizing is usually the appropriate treatment, though reperforating with deeper penetrating holes may be a ready alternative for shallow damage. Typically, formation damage is associated with partial plugging of the rock matrix around the wellbore. The objective of matrix acidizing is to remove the damage or bypass it by creating channels, such as wormholes. When matrix acidizing or reperforating is not possible, a short proppant fracturing treatment can be an alternative.

Matrix acidizing treatments remove damage by injecting reactive fluids into the natural porosity of

the reservoir at “matrix” (subfracturing) rates and pressures. These relatively low rates and pressures are necessary to remove the damage located in the near-wellbore area. The flow rate is also limited to prevent fracturing of the formation, which would result in the loss of treatment fluid behind the damaged zone.

Inexpensive and readily available inorganic acids, such as HCl or hydrofluoric acid (HF), are used to dissolve some of the damaging materials, rock constituents or both. A certain volume of acid is pumped into the formation to restore near-well permeability (sandstones) or to increase rock permeability (carbonates).

Treatment strategies for the various formation damages discussed previously are reviewed in the following sections. In addition, strategies for some common types of wellbore damage are discussed.

### 14-6.1. Fines and clays

#### • Migrating fines

The treatment of moveable fines can be accomplished by either prevention (using a clay-control process) or removal. Removal of migrating fines in sandstone formations is best accomplished by treatment with a fluid containing HF and HCl mix-

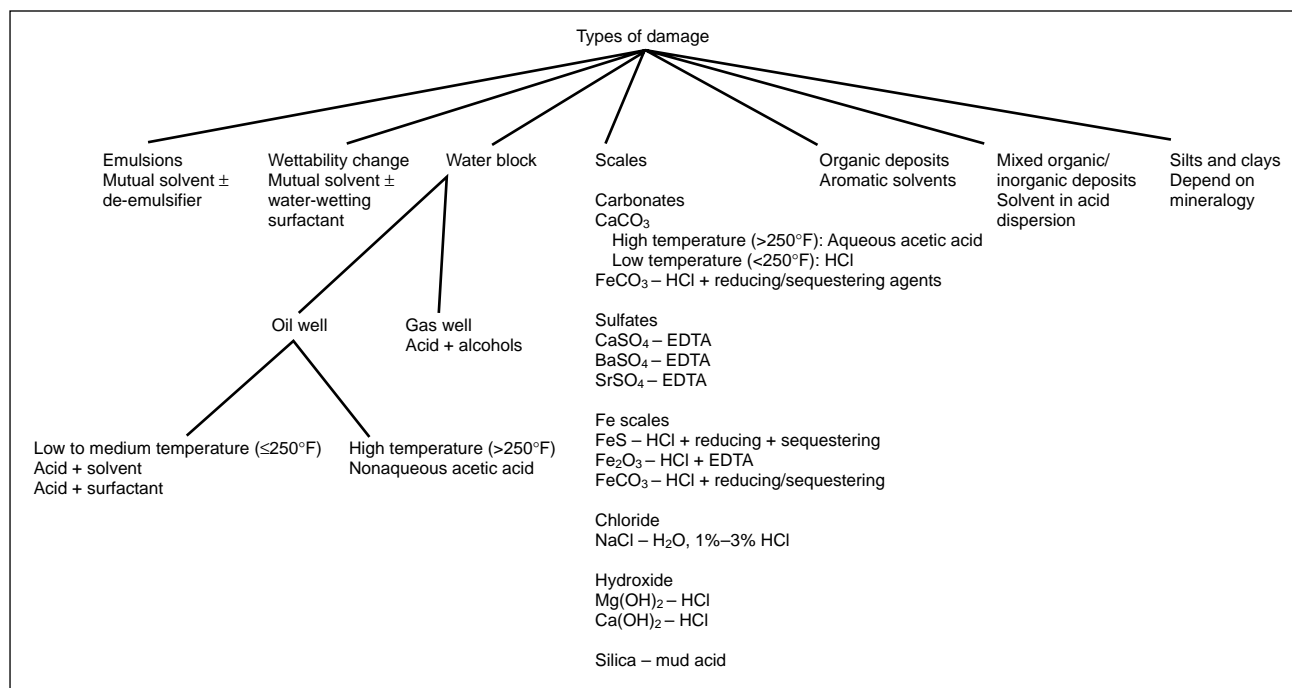


Figure 14-12. Treatment selection and the nature of damage.

tures—these are the commonly used mud acids. Deeply penetrating acid systems, containing fluoboric acid, show a good possibility for particle destruction and extend some potential for clay stabilization. Fracturing the formation is also a treatment possibility because the effect from linear flow in the walls of the fracture has a less detrimental effect on production than inward radial flow in an unfractured well. The success of both clay control and fines removal depends on the depth extent of the fines movement problem. In many cases, tip-screenout (TSO) fracture design using a short fracture for damage bypass is a better alternative.

HCl systems are typically used to remove fines damage in a carbonate formation. Because the fines are not dissolved, but are dispersed in natural fractures or the wormholes that are created, N<sub>2</sub> is usually recommended to aid fines removal when the well has a low bottomhole pressure.

- Swelling clays

The removal of smectite is usually accomplished with HF or fluoboric acid, depending on the depth of penetration. In the event of deep clay-swelling problems (more than 2 ft), the best treatment is usually a fracture to bypass the damage.

- Unconsolidated formations

Two basic problems determine the method of treatment for unconsolidated formations. If the formation moves as discrete large particles (i.e., the building blocks of the formation are moving), then the problem is a lack of cementation between the grains for the applied production forces, and the formation is classified as a low-strength formation. Treating low-strength formations can be difficult if the cementing materials are reactive with the fluid that is injected to remove formation damage or to improve permeability. Fortunately, the cementing materials in most formations have a small surface area and are less reactive with acids than with fines or clay particles in the pores of the rock.

When formations expel large grains into the wellbore, it may be beneficial to add additional perforations to reduce the velocity across the sandface or to design a fracture to reduce the drawdown. (It is common to fracture formations with permeabilities higher than 100 md.) These fractures are usually TSO designs that provide short, highly conductive fractures that can reduce the

drawdown and control sand movement by both pressure reduction and use of the proppant at the interface contacts of a gravel pack as an “in-formation” gravel pack.

The treatment of spalling problems is extremely difficult. Propped fractures may help contain the formation and spread out the drawdown to reduce the spalling force, although totally halting spalling may be impossible. One of the keys to treatment selection is whether the spalling is caused by high initial pressures that will quickly deplete or by cyclic mechanical loads that will recur. If high initial pressure is the problem, a cleanout may suffice. If cycling is the problem, a permanent control method is the best solution. Control methods include gravel packing, fracture packing, selective perforating (along the fracture axis) and some plastic-bonding methods.

## 14-6.2. Scales

Various solvents dissolve scales, depending on their mineralogy. The most common treatments for the scales in a well are as follows:

- Carbonate scale (CaCO<sub>3</sub> and FeCO<sub>3</sub>)—HCl will readily dissolve all carbonate scales if the acid can penetrate to the scale location (Tyler *et al.*, 1985).
- Gypsum (CaSO<sub>4</sub> · 2H<sub>2</sub>O) or anhydrite (CaSO<sub>4</sub>)—These calcium sulfate scales are removed with compounds that convert the sulfate to a hydroxide or other ion form followed by acid or by direct dissolvers such as ethylenediaminetetraacetic acid (EDTA) or other types of agents. Following a calcium sulfate dissolver with acid may double the amount of scale dissolved because most scales are mixtures of materials and HCl has some ability to dissolve the finest particles of calcium sulfate. The tetrasodium salt of EDTA is preferred because its dissolution rate is greater at a slightly alkaline pH value; the more acidic disodium salt has also been used, as well as other strong sequestrants of the same family, although they do not show a marked difference from the EDTA performance. Care must be used not to over-run the spent scale dissolver or converter solutions with acid because massive reprecipitation of the scale will occur.
- Barite (BaSO<sub>4</sub>) or celestite (SrSO<sub>4</sub>)—These sulfate scales are much more difficult to remove, but their occurrence is more predictable. Barium and stron-

tium sulfates can also be dissolved with EDTA if the temperature is high enough and contact times are sufficient (typically a 24-hr minimum soaking time for a 12,000-ft well with a bottomhole temperature of about 212°F [100°C]; Clemmit *et al.*, 1985). Barium and strontium sulfate removal methods are usually mechanical. Most chemical removers are only slightly reactive, especially in thick deposits, but mixtures of barium sulfate and other scales can usually be removed by properly formulated dissolvers with sufficient soak times. Thick deposits should be removed by mechanical or abrasive methods. Care must be exercised when analyzing well debris to avoid mislabeling barite from drilling mud residue as barium sulfate scale.

- Sodium chloride (NaCl)—Sodium chloride scale is readily dissolved with fresh water or weak acidic (HCl, acetic) solutions. Redesigning the mechanical system to avoid heat loss and water drop-out are also treatment possibilities.
- Iron scales, such as iron sulfide (FeS) or iron oxide (Fe<sub>2</sub>O<sub>3</sub>)—HCl with reducing and sequestering (EDTA) agents dissolves these scales and prevents the reprecipitation of by-products, such as iron hydroxides and elemental sulfur (Crowe, 1985). Soak times of 30 min to 4 hr are usually beneficial in removing these scales when using acid. Where iron sulfide is a thick deposit, mechanical action such as milling is suggested. Water jetting typically will not cut an iron sulfide scale except where it is dispersed with other scales or exists as a thin coating.
- Silica scales—Silica scales generally occur as finely crystallized deposits of chalcedony or as amorphous opal and are readily dissolved by HF.
- Hydroxide scales: magnesium (Mg(OH)<sub>2</sub>) or calcium (Ca(OH)<sub>2</sub>) hydroxides—HCl or any acid that can sufficiently lower the pH value and not precipitate calcium or magnesium salts can be used to remove these deposits.

Contact time is an important factor in the design of a scale removal treatment. The major concern in treating scale deposits is allowing sufficient time for the treating fluid to reach and effectively dissolve the bulk of the scale material. The treating fluid must dissolve most of the scale for the treatment to be successful.

### 14-6.3. Organic deposits

Organic deposits are usually resolubilized by organic solvents. Blends of solvents can be tailored to a particular problem, but an aromatic solvent is an efficient, general-purpose fluid. Environmental concerns have led to the development of alternative solvents (Samuelson, 1992).

Paraffin removal can be accomplished using heat, mechanical scraping or solvents. Heating the tubing with a hot oiler may be the most common type of treatment. It may also be the most damaging and least effective in some cases. Injection of hot oil from the surface will melt the paraffin from the walls of the pipe, but the depth to which the injected fluid stays hot is a function of the well configuration. If the well is allowed to circulate up the annulus while the hot oil is injected down the tubing, the heat will not penetrate more than a few joints of tubing from the surface. The heat is quickly transferred through the steel tubing to the fluids rising in the annulus and little, if any, heat reaches deep in the well. As the hot oil cools, the paraffin picked up in the upper part of the well can precipitate. If hot oiling is required at depths greater than 150 ft, an alternate method of placement must be used. Deeper application of heat is available with other processes that feature heat generation as part of an exothermic chemical reaction. The processes require close control and are generally expensive.

Mechanical scraping can be useful in cases where extensive deposits of paraffin must be removed routinely. Scraping is usually accomplished with slick-line and a cutter. In wells that utilize a rod string, placing scrapers on the string may automatically scrape the tubing walls.

Solvent treating to remove paraffin may be based around a straight- or aromatic-chain solvent. The most appropriate solvent depends on the specific paraffin and the location of the deposit. Heat (at least to 130°F [55°C]) and agitation significantly increase the rate of removal.

Removal treatments for asphaltenes use aromatic solvents such as xylene and toluene or solvents containing high percentages of aromatics. Naphtha is usually not effective as a solvent. Some materials being tested provide dispersant benefits without stabilizing the entire mass of the asphaltene. Solvent soak time, heat and agitation are important considerations for treatment.

#### 14-6.4. Mixed deposits

Combined deposits require a dual-solvent system, such as dispersion of a hydrocarbon solvent (usually aromatic) into an acid.

#### 14-6.5. Emulsions

Emulsions are stabilized by surface-active materials (surfactants) and by foreign or native fines. Generally, mutual solvents, with or without de-emulsifiers, are used for treating emulsion problems. De-emulsifiers, which may work well in a laboratory or in a separator or tank because of the large number of droplets in contact per unit volume, may not work by themselves in a porous medium because of mass-transport phenomena in getting the product to where it should work. Another reason they may not work alone is the mechanism involved in breaking emulsions, which should provoke the coalescence of droplets and then phase separation.

Asphaltic iron-catalyzed sludges are the most difficult emulsions to break. These emulsions are catalyzed by dissolved iron in the acid or water and resemble a crosslinked oil polymer in some instances. Prevention is the best treatment. An effective antisludge treatment for the area and an iron-reducing agent in the acid are the best methods. Removal of an existing asphaltene sludge is usually accomplished by dispersing it in a solvent and attacking the components of the sludge with additives designed for cleanup and removal.

#### 14-6.6. Bacteria

Prevention of polymer destruction by bacteria is usually handled with biocides and tank monitoring. Control of bacteria downhole is more difficult and involves scraping or treatments with sodium hypochlorite or other oxidizers followed by acidizing and then treatment with an effective biocide at a level at least 1.2 times the minimum kill level. Frequent rotation of the type of biocide is also necessary to prevent the development of biocide-resistant strains of bacteria.

#### 14-6.7. Induced particle plugging

- Mud solids

To remove shallow mud damage in natural fractures, a solvent or cleaner that will disperse the mud should be selected on the basis of tests of a field sample of the mud. Energizing the fluid with N<sub>2</sub> can assist in removing large masses of drilling mud from a fracture system. Experience with drilling mud cleanup from natural fracture systems shows that slugs of drilling mud may flow back on initial treatment, and damage can often reassert itself as mud moves from the outer reaches of the fracture system into the wellbore. This condition can require repeated treatments of the same high-efficiency cleaner, plus N<sub>2</sub>, to get good cleanup of the well. Acid may help, but tests of the acid's effect on the field mud sample are required.

When extremely large volumes of heavyweight mud are lost, it may be beneficial to sidetrack the well and redrill the pay zone. Whenever possible, the drilling mud overbalance should be minimized, and the mud should be conditioned to reduce solids before the pay zone is drilled. Experience with drilling highly fractured formations has led to experimentation with underbalance drilling in some zones. Underbalance drilling can result in only minimal damage in producing wells in comparison with the damage created by traditional drilling methods. There are dangers, however, in underbalance drilling, and the risk versus benefit must be evaluated carefully.

Mudcakes are usually damaging only in open-hole completions without significant fractures (Burton, 1995). In vertical wells, they are usually easily mechanically removed to a great extent by pressure drawdown. In long horizontal wellbores, the necessary drawdown is almost impossible to impose on any section other than the heel, particularly when a compressible fluid is in the hole. Circulations for mudcake removal should be conducted with minimum clearance between the wash pipe and the borehole to promote turbulence. Residual mudcake in prepacked screens or slotted liners completions is particularly problematic because it can plug the screen (Browne *et al.*, 1995; Ryan *et al.*, 1995).



- **Dirty fluids**

When particle damage is known to have occurred because of the use of unfiltered or poor-quality fluids, cleanup depends on finding a solvent or acid that can either remove the particles or break the structure of the bridges formed in the formation or fracture system. Surfactants, acids and mutual solvents are usually the most beneficial materials. The addition of  $N_2$  to provide a high-energy boost may also be beneficial.

The decision of which surfactant or mutual solvent to use should be based on core tests or field response. Including a gas such as  $N_2$  or  $CO_2$  is based on fluid and solids recovery requirements and wellbore unloading ability. For designing cleanup operations for particulate damage, flowing the well back quickly after the treatment helps in the removal of the particles. Lower pressure formations may require a gas boost. In higher pressure formations, natural flow is usually adequate to unload these solids, especially when a properly designed fluid has been used and the solids are no deeper than the surface of the wellbore face. Mechanical scraping and cleaning can exert influence only as far as the wellbore wall.

- **Acidizing**

The leading edge of an otherwise effective mutual solvent and acid system can be loaded with debris cleaned off the walls of the tanks and tubing. For this reason, the leading edge of the acid job is usually circulated out of the well using a process called pickling the tubing. In this treatment, acid and solvents are injected down the tubing to disperse and dissolve iron, pipe dope, mud and other debris from the tubing and are then circulated or reversed out of the well without being injected into the formation. These jobs are extremely effective when the tubing has not been cleaned or its condition is unknown. Volumes of both acids and additive treatments range from 1 to 2½ tubing volumes depending on the condition of the tubulars. Minimum acid and solvent volumes typically range from 250 to 500 gal. Coated tubing can reduce iron scale significantly, but other contaminants, such as scale and pipe dope, may still be present.

If load-fluid recovery influences well production, surfactants or mutual solvents that reduce surface and interfacial tension are usually benefi-

cial. The treatment volumes depend on the fluid, formation and amount of load fluid lost.

- **Waterfloods**

The removal of particles injected during waterflood operations depends on the identity of the material and use of a cleaner and an acid to disperse the material. One of the best techniques for cleaning up injection wells or disposal wells is to backflow the well as hard as possible prior to the treatment. This usually removes enough mass from the wellbore to eliminate the need for stimulation. However, if backflowing does not adequately clean the wellbore, acid and a mutual solvent in volumes ranging from 50 to 100 gal/ft are usually necessary. When large amounts of solids are expected, the well should be backflowed after acidizing. If oil carryover and emulsions are the problem, acid and a mutual solvent can be injected and displaced permanently with injection water behind the acidizing job.

#### 14-6.8. Oil-base drilling fluids

The prevention of OBM emulsions is relatively easy. Either a surfactant-base cleaner that is mixed after specific OBM testing or a more general xylene wash of the zone must be done before contact with either high-salinity brine or acid. After the cuttings and mud fines have been cleaned and totally water-wetted, the remaining damage problems of wettability can be reversed with a formation cleaner or mutual solvent. Acid is usually used as a following stage after cleaning to remove mud particles and clean up formation debris. Removal of known OBM emulsions resulting from mixing with high-salinity brine or acid usually requires an aromatic solvent wash or a specialized surfactant treatment that targets the silt-stabilized emulsion. Evaluation of any cleanup mechanism or treatment using laboratory samples of OBM should be avoided. Only field samples of the mud are appropriate for designing the removal treatment. Treatment fluid volumes range from 15 to 50 gal/ft of aromatic solvent or surfactant mixture, and the agitation and soak times are critical to the success of the treatment. Application difficulties include trapping the treating fluids across the pay in a column of heavyweight fluids where density segregation may be rapid. Packers and gelled plugs are the first line of isolation.

### 14-6.9. Water blocks

Removal of a water block can be accomplished using a surfactant or alcohol applied as a preflush to reduce surface tension, followed by a postflush of N<sub>2</sub> or CO<sub>2</sub> to remove the water from the near-wellbore area and reestablish gas saturation. Once the water has been mixed with the surface-tension-lowering materials, removal is easier. The difficulties in this type of operation are placement of the fluid and getting an even distribution of the fluid around the wellbore. Repeated treatments are usually necessary, and selective injection devices are beneficial.

### 14-6.10. Wettability alteration

Wettability alteration damage is removed by injecting (mutual) solvents to remove the oil-wetting hydrocarbon phase and then injecting strongly water-wetting surfactants. Again, a surfactant by itself will not work. The oil phase, which is usually precipitated asphaltenes or paraffins, must first be removed with a solvent. (The same applies to an adsorbed oleophilic surfactant.) Then, a strongly water-wetting surfactant can be injected and adsorbed onto the rock minerals. This reduces the tendency for new hydrocarbon precipitates to stick to the mineral surfaces and oil-wet them again.

For retrograde condensation problems, the most appropriate treatment technique is the injection of neat natural gas in a periodic “huff and puff” operation. Condensate is picked up by the gas and transported into the reservoir. Reprecipitation requires the retrograde of the process after several months of production.

### 14-6.11. Wellbore damage

- Mechanical damage from drilling

The drilling process itself modifies the local stresses around the wellbore, generating a zone of reduced permeability in the near-wellbore area (Dusseault and Gray, 1992). It has been shown that such damage affects primarily soft formations where the difference between the minimum and maximum stresses orthogonal to the wellbore is large. In the worst cases, the extent of the permeability decrease can be as large as 2½ wellbore diameters (Morales *et al.*, 1995), and perforations do not bypass the damaged zone. Because perme-

ability impairment in this case is the result of rock compaction, acidizing is ineffective. Short proppant fracturing treatments are apparently the only cure, though extreme overbalance perforating may give positive results in some cases (Petitjean *et al.*, 1995).

- Pipe problems

Whenever well production is reduced, the first determination should be to establish that the tubing is open and the lift system is working. Numerous pipe problems from leaks to collapsed pipe can occur, and fill in the tubing is also a possibility. Well conditions change over time, and an effective completion at the start of the well's life may not be effective after several years of production as the reservoir pressure declines.

- Poor perforations

The usual treatment for poor perforations is to add additional perforations. In zones that are extremely laminated, such as the shaly sands of the U.S. Gulf Coast and other areas, 8 to 12 spf is considered adequate, but perforation breakdowns (i.e., small fractures) may be required for complete linking. Lower perforation density is possible if the well will be fractured. Fracturing will cross the barriers of laminations, and in many field cases has provided extensive productivity increases.

Adding perforations is easy, but the typical 0° phased, small through-tubing guns deliver only small holes and short penetrations. The newer downhole-deployable guns that provide minimum clearance and phasing are preferred, especially when hydraulic fracturing will be performed.

- Hydrates

Hydrates are mixtures of ice and other elements, principally natural gas, that may resemble a dirty ice deposit. Unlike ice, they can form at temperatures greater than 32°F. The formation of hydrates is usually associated with a drop in temperature or a reduction in pressure that may accompany the production of fluids. Hydrates may also form in gas-cut drilling mud, particularly when the mud is circulated near the seafloor in cold locations. Hydrate plugging of chokes and valves can be a serious problem. Hydrate particle abrasion of equipment is also possible.

The most common occurrence of hydrates is in gas wells with a small amount of water produc-

tion. The quantity of water relative to the quantity of gas production is critical. As the water cut increases, many hydrate problems disappear. Hydrates are prevented by adding a freezing-point depressant such as alcohol or glycol below the hydrate formation point. They may also be controlled by temperature preservation in the produced fluid or the elimination of severe pressure drops that allow expanding gas to chill the liquids to their freezing points.

- Fill

Debris from formation spalling into the perforation or wellbore can be one of the most serious detriments to production. Fill in the wellbore is easily identified with a sinker bar on the wireline and is usually easily removed using tubing or coiled tubing and N<sub>2</sub> or foam unloading practices. Fill in the perforations is more difficult to identify and much more difficult to remove. When fill in the perforations is suspected, reperforating the well is generally the most direct method of testing the theory and restoring the well to productivity. Where the fill is acid soluble, acid injection may be useful; however, injecting acid into a perforation that is filled with small debris is usually difficult.

- Water problems

Water production is not only a major economic problem in surface separation, but it also causes a major reduction in the relative permeability of oil and gas. Water production from the well can lead to significant problems such as corrosion, back-pressure, emulsions and movement of the formation or fines. Water may flow from the bottom (coning), rise through fractures or flow from the edge in fractures through the matrix or in high-permeability streaks. Because of its low viscosity, water flows much easier than oil, and once in the

pores of the rock it is difficult to displace with low-viscosity fluids such as gas. Shutting off water (water control) is a special technique and is discussed elsewhere in the literature.

- Microporosity

Microporosity is created by a number of clays and a few minerals. It is simply a condition where a large surface area exists for water coating or trapping. Microporosity rarely presents a problem except when it occupies the pore throat area of the formation. In these cases, it may trap either debris or water and obstruct flow. The removal of microporosity can generally be accomplished with HF, or deep problems can be bypassed by fracturing.

## 14-7. Conclusions

To maximize well performance, the paths from the formation to the pipeline must present the lowest pressure impedance possible. Achieving this condition requires both a well-designed completion and the elimination of formation damage. The tools are an array of stimulation and damage removal techniques and chemicals that are readily available. Still, although formation damage removal seems easily achievable, the goal of a damage-free completion can be elusive. The problem is not so much one of finding a tool, but one of finding the right tool. A little experience shows that the right tool can be selected only when the problem has been identified. The effort and expense to understand the nature and identity of the problem can be the wisest investments.

The most common damage mechanisms and suggested methods of removal are listed in Tables 14-3, 14-4 and 14-5. It bears repeating that many damage conditions have similar symptoms and that there are no universal treatments.

# Additives in Acidizing Fluids

Syed A. Ali, Chevron U.S.A. Production Co.

Jerald J. Hinkel, Schlumberger Dowell

## 15-1. Introduction

Proper fluid selection is critical to the success of a matrix treatment. Figure 15-1 shows the types of damage that may occur and what types of treatment would be required. The treatment may be a failure if the proper additives are not used. The treating fluid is designed to effectively remove or bypass the damage, whereas additives are used to prevent excessive corrosion, prevent sludging and emulsions, prevent iron precipitation, improve cleanup, improve coverage of the zone and prevent precipitation of reaction products. Additives are also used in preflushes and overflushes to stabilize clays and disperse paraffins and asphaltenes. The functions of some of the additives are discussed briefly in this chapter.

Throughout this chapter references are made to the interactions of additives with the formation. Schechter (1992) provided an excellent discussion of the chemical properties of formation materials

and their interactions with fluids. Clay minerals are important because of their large surface area and because the surface carries an electrical charge. Although relatively minor, some surface charge results from ionic substitution and structural imperfections. For instance, the substitution of  $\text{Al}^{3+}$  for  $\text{Si}^{4+}$  in tetrahedral sheets or  $\text{Mg}^{2+}$  or  $\text{Fe}^{2+}$  for  $\text{Al}^{3+}$  in octahedral sheets is the origin of negative charges in the lattice of smectites. These are unaltered by changes in the solutions that contact them.

Silicon and aluminum oxides, the principle ingredients of sandstone and clays, exhibit amphoteric behavior. Therefore, the surface charges of these minerals depend on the pH of the solutions in contact with them. The surface charge changes from positive to negative as the pH increases. The point at which the surface charge is neutral is known as the point of zero charge (pzc). Table 15-1 provides the approximate values of the pzc for several common minerals.

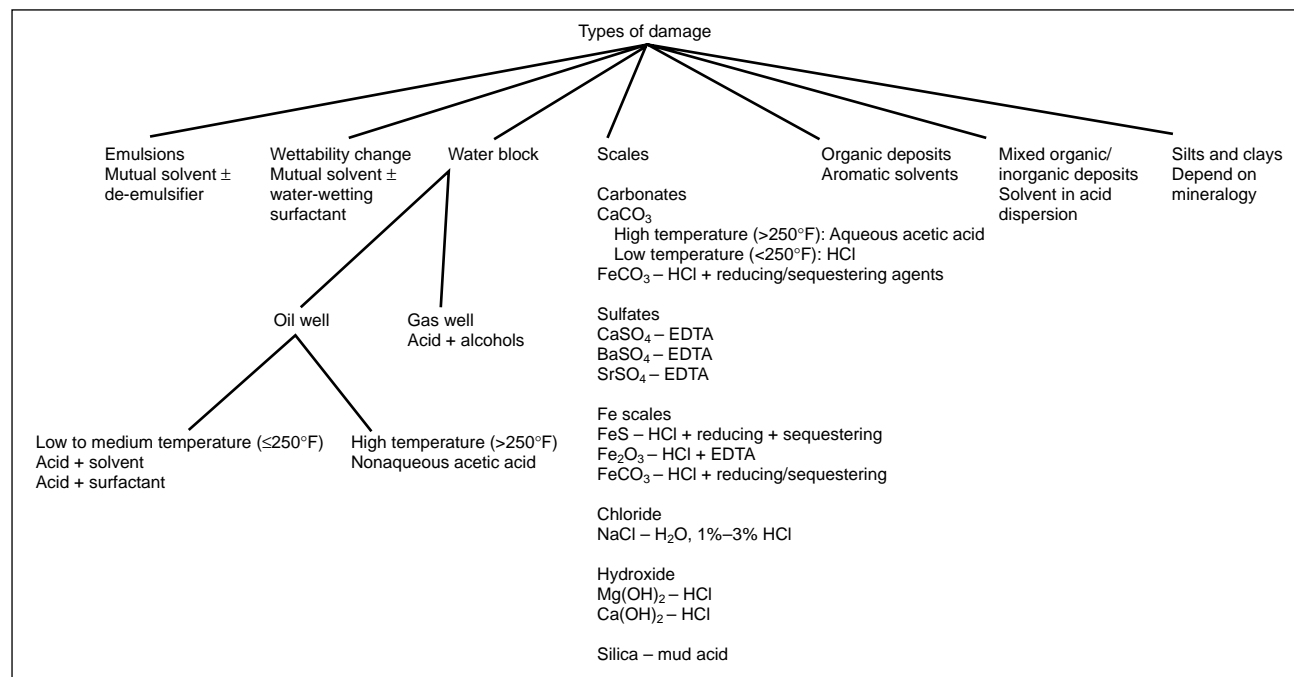


Figure 15-1. Types of damage.

Table 15-1. Point of zero charge of some representative reservoir materials.	
Material	Point of Zero Charge
Quartz (SiO <sub>2</sub> )	2.7
Corundum (Al <sub>2</sub> O <sub>3</sub> )	9.0
Hematite (Fe <sub>2</sub> O <sub>3</sub> )	5.0
Calcite (CaCO <sub>3</sub> )	9.5
Kaolinite (Al <sub>4</sub> Si <sub>4</sub> O <sub>10</sub> (OH) <sub>8</sub> )	4.6
Montmorillonite (Al,Mg,Fe) <sub>4</sub> (Al, Si) <sub>8</sub> O <sub>20</sub> (OH) <sub>4</sub> · nH <sub>2</sub> O	2.0
Albite (NaAlSi <sub>3</sub> O <sub>8</sub> )	2.0

Thus, the way in which additives interact with the reservoir actually depends on the pH. Under the conditions normally associated with the matrix acidization of sandstones, the pH of the acid is less than the pzc of the reservoir constituents, which causes the formation materials to behave as positively charged. It is important to keep this concept in mind.

## 15-2. Corrosion inhibitors

The most important acid additives are corrosion inhibitors. A corrosion inhibitor is a chemical that slows the attack of acid corrosion on drillpipe, tubing or any other metal that the acid contacts during treatment. Brief explanations of corrosion mechanisms, corrosion inhibition and techniques for evaluating inhibitor performance are presented in this section.

### 15-2.1. Corrosion of metals

Any metal surface is a composite of electrodes electrically short-circuited through the body of the metal itself (Fig. 15-2). As long as the metal remains dry, local currents and corrosion are not observed. However, on exposure of the metal to aqueous salt, alkali or acid solutions, local action cells are able to function, leading to chemical conversion of the metal to corrosion products.

### 15-2.2. Acid corrosion on steel

All uninhibited acid solutions corrode steel. The attack of acid on steel occurs through the dissociated hydrogen ions in the acid solution. This results in the oxidation and dissolution of iron at the anodic sites

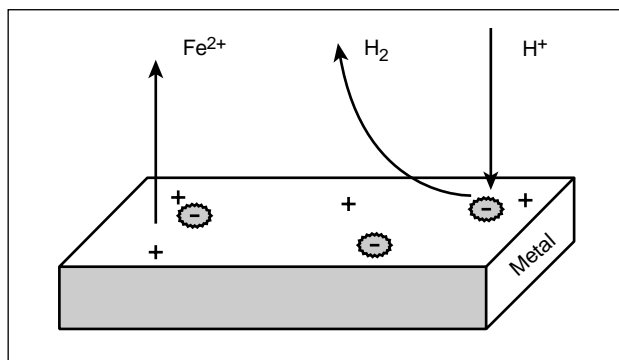
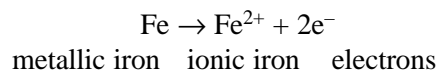


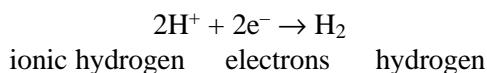
**Figure 15-2.** A metal surface composed of both anodic and cathodic sites (Schechter, 1992).

on the metal surfaces, along with the reduction of hydrogen ions and formation of hydrogen at the cathodic sites.

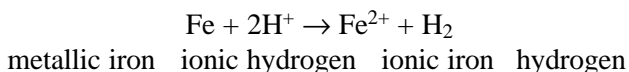
The equations for an anodic reaction (oxidation):



and a cathodic reaction (reduction):



can be combined to show the overall reaction:



The unit of measurement used to determine the amount of corrosion is lbm/ft<sup>2</sup>. Acceptable corrosion limits for low-alloy steel are shown in Table 15-2. The acceptable range is from 0.02 to 0.09 lbm/ft<sup>2</sup> of metal surface, depending on the temperature and exposure time. Acids corrode more evenly, with less pitting, at higher temperatures. At elevated temperatures, more corrosion may occur, but the chance of forming a hole in the drillpipe or tubing string is actually less.

The effectiveness of a given corrosion inhibitor depends on the metal. McDougall (1969) reported tests of five different commercial corrosion inhibitors on N80, J55 and P105 tubulars. These results clearly

Table 15-2. Corrosion limits for low-alloy steel.	
Temperature	Corrosion Limit (lbm/ft <sup>2</sup> )
200°F [95°C]	0.02
200° to 275°F [95° to 135°C]	0.05
275° to 350°F [135° to 175°C]	0.09

show the necessity of matching the inhibitor to the steel, because a wide range of responses was obtained for a given inhibitor. Smith *et al.* (1978) pointed out that American Petroleum Institute (API) designations for steels are inadequate to distinguish corrosion rates because they identify yield strength, whereas corrosion characteristics are determined primarily by chemical composition. Because yield strength may be achieved either by physical or chemical modifications in manufacturing, it is essential that the metal coupons tested are representative of the tubulars to be protected.

### 15-2.3. Pitting types of acid corrosion

In uninhibited acid solutions, the corrosion of steel is usually uniform. The constant shifting of anodic and cathodic areas spreads corrosion fairly evenly over the entire surface of the metal. In inhibited acids, pitting of the surface occurs in some situations as a result of inhibitor breakdown, insufficient inhibitor or metal impurities.

- Inhibitor breakdown

Pitting-type corrosion is not uncommon on steel containing an inferior corrosion inhibitor that is exposed to acid solutions. All corrosion inhibitors eventually break down after some period of time, depending on various factors including temperature, acid strength and metal type. When this point is reached, an inferior inhibitor may actually promote pitting by desorbing from the metal surface in localized areas.

- Insufficient inhibitor

Regardless of the quality of the corrosion inhibitor, pitting may also occur if there is an insufficient amount of inhibitor to effectively coat the steel surfaces. Unprotected steel surfaces are rapidly attacked by the acid solution and pitting occurs.

- Metal impurities

Another condition that promotes pitting is the presence of impurities or inclusions within the steel. For example, small pieces of slag may become trapped during the forming of the steel, or improper heat treating or quenching of the steel may produce discontinuities in its grain structure. These imperfections may, in turn, become anodic

relative to the surrounding steel structure and thus promote acid attack.

### 15-2.4. Hydrogen embrittlement

Hydrogen embrittlement results from the cathodic reaction described previously in which hydrogen ions are reduced to elemental hydrogen. Elemental hydrogen results from acidizing operations. Elemental hydrogen adsorbed by a metal can lower ductility to the point that the metal becomes brittle. Figure 15-3 shows the effect of hydrogen content and tensile strength on the loss of ductility of steel. The N80, P110 and Q125 grades of tubing and casing are prone to embrittlement as a result of acidizing. Consequently, inhibitor selection must take this into account.

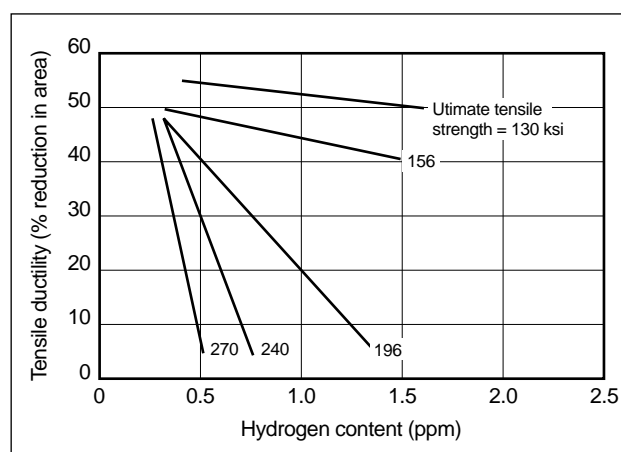


**Figure 15-3.** Reduction in ductility with increasing hydrogen content and strength (Tetelman, 1973). 1 ksi = 100 lbf/in.<sup>2</sup>.

### 15-2.5. Corrosion by different acid types

The degree of dissociation of hydrogen ions from the acid molecule, along with the acid concentration, determines the hydrogen ion activity, which is directly proportional to its corrosivity on steel. The relative degree of dissociation for some common acids is hydrochloric > formic > acetic. Therefore, hydrochloric acid (HCl) is more corrosive on steel than formic acid, which is more corrosive than acetic acid. Quite logically, the more aggressive an acid is in its attack on steel, the more difficult it is to inhibit. However, the mechanism of attack is the same for all acid types.

## 15-2.6. Inhibitor types

Inhibitors function by interfering with the chemical reactions that occur at the anode or cathode of the corrosion cell. The two basic types of corrosion inhibitors are inorganic and organic. There are also inhibitor aids.

- Inorganic corrosion inhibitors

This class of inhibitors includes the salts of zinc, nickel, copper, arsenic, antimony and various other metals. Of these, the most widely used are the arsenic compounds. When these arsenic compounds are added to an acid solution, they “plate out” at cathodic sites of exposed steel surfaces. The plating decreases the rate of hydrogen ion exchange, because the iron sulfide that forms between the steel and the acid acts as a barrier. It is a dynamic process in which the acid reacts with iron sulfide, rather than the metal.

Some advantages of inorganic inhibitors are that they

- work effectively at high temperatures for long contact times
- cost less than organic inhibitors.

Disadvantages of inorganic inhibitors are that they

- tend to lose their effectiveness in acid solutions stronger than about 17% HCl
- react with hydrogen sulfide ( $H_2S$ ) through the iron sulfide that may be present to form an insoluble precipitate such as arsenic sulfide
- poison refinery catalysts (such as platinum)
- may liberate toxic arsine gas as a corrosion by-product
- are difficult to mix and unsafe to handle.

- Organic corrosion inhibitors

Organic corrosion inhibitors are composed of polar organic compounds capable of adsorbing onto the metal surface, thereby establishing a protective film that acts as a barrier between the metal and the acid solution. They usually serve as a cathodic polarizer by limiting hydrogen ion mobility at cathodic sites. Organic inhibitors are composed of rather complex compounds, with one or more polar groups made of sulfur, oxygen or nitrogen.

Some advantages of organic inhibitors are that they

- can be used in the presence of  $H_2S$  without the precipitation of salts such as arsenic sulfide (which can plug the wellbore)
- do not poison refinery catalysts
- work effectively in all acid concentrations.

Disadvantages of organic inhibitors are that they

- chemically degrade with time in the presence of acid and thus do not readily provide long-term protection at temperatures above 200°F [95°C] (Table 15-3)
- cost more than the inorganic corrosion inhibitors.

- Inhibitor aids

Although these additives do not function as inhibitors, they increase the effectiveness of organic inhibitors. The common inhibitor aids are potassium iodide, cuprous iodide, cuprous chloride and formic acid. The addition of these materials to existing organic inhibitor formulations greatly extends the range of their effectiveness, particularly in higher temperature applications.

**Table 15-3. Effectiveness of corrosion inhibitors at high temperatures in 15% HCl.**

Inhibitor	Inhibitor Concentration (%)	Temperature (°F)	Protection Time <sup>†</sup> (hr)
Organic	0.6	200	24
	1.0	250	10
	2.0	300	2
Inorganic	0.4	200	24
	1.2	250	24
	2.0	300	12

<sup>†</sup> Time required for 15% HCl to remove 0.05 lbm/ft<sup>2</sup> of exposed metal area

## 15-2.7. Compatibility with other additives

Any additive that alters the tendency of the corrosion inhibitor to adsorb will also change its effectiveness. For example, surfactants added to acid for various purposes may form micelles that solubilize the inhibitor, thereby decreasing the tendency for the inhibitor to adsorb on the metal surface. Inorganic salts and mutual solvents can also interfere with inhibitor adsorption. If possible, additives that reduce

the effectiveness of inhibitors should be included in a preflush or overflush rather than in the acid solution.

### 15-2.8. Laboratory evaluation of inhibitors

The laboratory evaluation of a corrosion inhibitor involves subjecting a coupon of the metal to be protected to the acid to be used. The coupon is normally inserted into a mixture of the acid and corrosion inhibitor to be evaluated and placed in a heated pressure vessel. The replication of downhole conditions is important. The amount of corrosion is determined by weighing the coupon before and after the test. Inhibitor effectiveness is expressed in terms of metal loss per unit area of metal exposed per unit of time. The typical unit is  $\text{lbm/ft}^2/\text{day}$ .

Also to be noted is pitting, which is a localized attack. If appreciable attack is confined to a relatively small area of the metal acting as an anode, then the resultant pits may be deep. A pitting factor, defined as the ratio of the deepest metal penetration to the average penetration, as determined by the weight loss of the specimen, is sometimes reported. A pitting factor of unity represents uniform attack. Many factors influence the corrosion rate measured in such tests. Of major importance are

- degree of agitation
- metal type
- exposure time
- temperature
- acid type and concentration
- inhibitor type and concentration
- metal-to-acid volume ratio
- gas composition (if an interface is present)
- pressure
- presence of other additives such as surfactants.

### 15-2.9. Suggestions for inhibitor selection

Some metal loss from wellbore tubular goods must be expected when acidizing, and the primary issue is what level can be tolerated. Most service company information is based on the assumption that a metal loss of  $0.02 \text{ lbm/ft}^2$  can be tolerated during the treat-

ment if no pitting occurs. For some cases an amount as high as  $0.095 \text{ lbm/ft}^2$  is allowable. If these metal losses cannot be sustained without adverse effects, a more effective inhibitor must be found.

If inhibitor cost becomes prohibitive, it may be possible to reduce the cost by careful treatment design. Precooling the tubing by injecting a large water preflush will be helpful. Using formic acid rather than HCl helps reduce the corrosion problem. Also, minimizing the contact time reduces inhibitor requirements.

The most important aspect is the proper testing of representative metal samples using the precise acid formulation to be applied at the most adverse conditions of temperature and pressure. The test should be conducted in an oxygen-free environment. Only under these conditions can a decision about the adequacy of the corrosion inhibitor be made.

## 15-3. Surfactants

Surfactants, or surface-active agents, are used in acidizing to break undesirable emulsions, reduce surface and/or interfacial tension, alter wettability, speed cleanup, disperse additives and prevent sludge formation. The use of surfactants requires careful selection of an appropriate molecule. Remarkably, in the design of most well treatments, surfactants are selected with little or no laboratory data to support the choice and sometimes without full knowledge of their properties at the conditions in which they will be applied. Improper surfactant selection can lead to results contrary to those intended and may be detrimental to the success of the treatment.

Surfactants owe their properties to their “dipolar” composition (Fig. 15-4). The surfactant molecule consists of a water-soluble (hydrophilic) group and

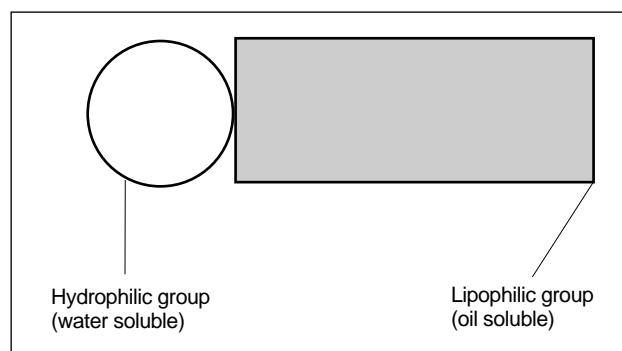


**Figure 15-4.** Dipolar surfactant composition.



an oil-soluble (lipophilic) group, which are separated from each other although linked by a strong covalent chemical bond. The molecules are classified into five groups according to the ionic charge carried by the water-soluble group:

- anionic
- cationic
- nonionic
- amphoteric
- fluorocarbons.

The hydrophilic-lipophilic balance (HLB) depends on the composition of the organic chain, which can be 100% oleophilic (e.g., an alkane chain) or contain some oxygen atoms (e.g., an ethylene oxide chain) and become more hydrophilic. The HLB value of a surfactant indicates how much its chains can oil wet a mineral.

### 15-3.1. Anionic surfactants

Anionic surfactants are commonly added to well treatment fluids. These surfactants carry a negative charge when they ionize in an aqueous solution. Because most reservoir minerals are also negatively charged at nearly neutral and higher pH values, anionic surfactants exhibit minimal adsorption. Some examples of anionic surfactants are

Sulfates	$R-O-SO_3^-$
Sulfonates	$R-SO_3^-$
Phosphates	$R-O-PO_3^-$
Phosphonates	$R-PO_3^-$

where R is an oil-soluble organic group.

Of these, the most common anionic surfactants are sulfates and sulfonates. Anionic surfactants are sensitive to multivalent ions such as  $Ca^{2+}$  and  $Mg^{2+}$ . These tend to precipitate anionic surfactants, although this tendency can be overcome to some extent by increasing the surfactant concentration. Anionic surfactants are used primarily as nonemulsifying agents, retarding agents and cleaning agents.

### 15-3.2. Cationic surfactants

Cationic surfactants carry a positive charge when they ionize in aqueous solutions. There are two general categories of cationic surfactants. The first category consists of long-chain primary, secondary and tertiary amines. These are soluble only in acidic solutions, where they ionize to form a long-chain cation and simple anion salt. Figure 15-5 shows various molecular cationic structures.

The second important category of cationic surfactants is the quaternary ammonium compounds. These ionize to form long-chain cations over a wide range of solution pH. Cationic surfactants experience the same sensitivity to multivalent ions or increased concentrations of dissolved solids as anionic surfactants; therefore, the same care must be exercised in their application as with anionic surfactants.

Cationic and anionic surfactants are generally incompatible. When mixed, they tend to precipitate in aqueous solutions.

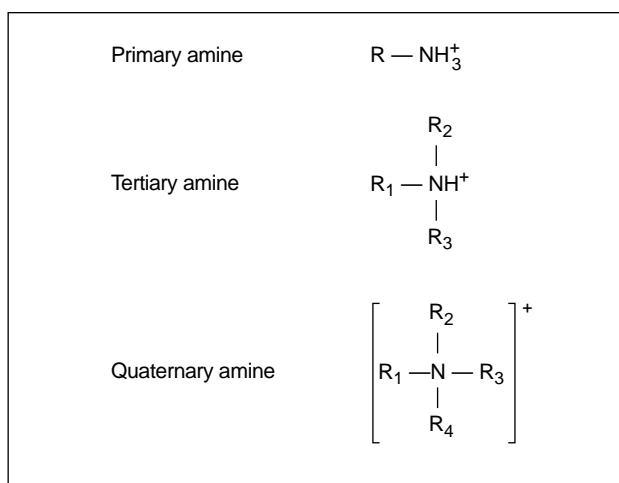


Figure 15-5. Various types of cationic surfactants.

### 15-3.3. Nonionic surfactants

Nonionic surfactants have no charge at all in the hydrophilic group and a long-chain organic (R) for the lipophilic group. The water-soluble group is a polymer made from either ethylene oxide or propylene oxide. Other types include alkanol amine condensates and amine oxides. The general formulas for these products are as follows:

Ethylene oxide polymer  $R-O-(CH_2CH_2O)_xH$

Propylene oxide polymer  $R-O-\underset{\begin{array}{c} | \\ CH_3 \end{array}}{(CHCH_2O)_y}H$

Alkanol amine condensate  $R-C-N-\underset{\begin{array}{c} | \\ O \end{array}}{(CH_2CH_2OH)_2}$

Amine oxides  $\begin{array}{c} CH_2CH_2OH \\ | \\ COCO-N-O \\ | \\ CH_2CH_2OH \end{array}$

Nonionic surfactants obtain their water solubility by attaching the long hydrocarbon chain to a highly soluble molecule such as polyhydric alcohol or by reacting it with ethylene oxide. Most of the compounds in this classification are esters, ethers and ether-esters. The lipophilic group may be derived from natural oils and fats, petroleum oils or synthesized hydrocarbons. The hydrophilic group is usually a polyhydric alcohol or an alkyd oxide polymer. These surfactants are used as nonemulsifiers and foaming agents.

### 15-3.4. Amphoteric surfactants

Amphoteric surfactants have a hydrophilic group that changes from cationic to nonionic to anionic with increasing pH. In other words, if the solution is acidic, the amphoteric surfactant acts like a cationic surfactant; if the solution is neutral, it acts like a nonionic surfactant; and if the solution is basic, it acts like an anionic surfactant. These properties are derived from the two groups of opposite charge on the surfactant head. The amphoteric surfactants are usually either amine sulfonates or amine phosphates. The general formulas are as follows:

Amine sulfonates  $RNH-(CH_2)_xSO_3H$

Amine phosphates  $RNH-(CH_2)_yOPO_3H$

### 15-3.5. Fluorocarbon surfactants

Fluorocarbons form surfaces of lower free energy than hydrocarbon surfaces. Consequently, fluorocarbon surfactants lower the surface tension of solutions

to a greater extent than hydrocarbon surfactants. Surface tensions as low as 30 dynes/cm can be obtained using surfactants with a hydrocarbon tail. Values as low as 17 dynes/cm have been reported using fluorocarbon surfactants. Fluorocarbons are commercially available in anionic, cationic and non-ionic forms.

### 15-3.6. Properties affected by surfactants

The main properties of a fluid or a mineral affected by surfactants are the surface and interfacial tensions, emulsification tendency, wettability, micelle formation and dispersibility.

#### • Surface and interfacial tensions

Rosen (1989) presented a good discussion of how surface and interfacial tensions are reduced by surfactants. Figure 15-6 is a simplified diagram of the interface between two condensed phases. A molecule in the bulk of a liquid is surrounded by molecules like itself and the forces are balanced. At the interface, however, the forces acting on the molecules in the two liquids are different from the forces acting on the molecules in the bulk liquids. The terms  $A_{aa}$  and  $A_{bb}$  in Fig. 15-6 represent the interaction energy between molecules at the interface and similar molecules in the bulk of the liquid whereas  $A_{ab}$  represents the interaction energy between dissimilar molecules at the interface.

The increase in potential energy of the molecules at the interface compared with that of the molecules in the bulk liquid is simply  $A_{aa} - A_{ab}$  and  $A_{bb} - A_{ab}$ . Therefore, the total increase in

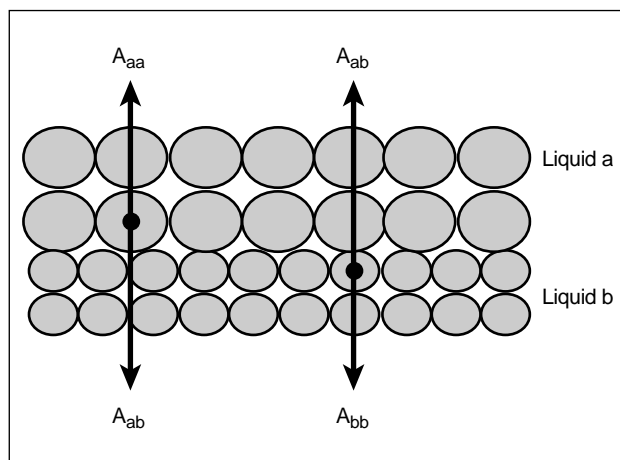


**Figure 15-6.** The interface between two liquids (Rosen, 1989).

potential energy at the interface becomes  $A_{aa} + A_{bb} - 2A_{ab}$ . The interfacial free energy per unit of surface area, which is also known as the interfacial tension  $\gamma_I$ , becomes

$$\gamma_I = \gamma_a + \gamma_b - 2\gamma_{ab} , \quad (15-1)$$

where  $\gamma_a$  and  $\gamma_b$  are the surface tensions of pure liquid a and liquid b, respectively, and  $\gamma_{ab}$  is the interaction energy per unit of surface area between liquids a and b.

The value of  $\gamma_{ab}$  tends to be large when similar liquids are in contact; this causes  $\gamma_I$  to be small. Conversely, if liquid a is quite different from liquid b, then the interaction energy is small and the interfacial tension between the two liquids is large. Surface tensions of some liquids are listed in Table 15-4.

Table 15-4. Surface tension of some liquids.	
Liquid	Surface Tension (dynes/cm)
Water	72.0
15% HCl	72.0
Spent 15% HCl	76.9
Octane	21.8

Figure 15-7 illustrates the interaction between a liquid and a gas. In this case the interface is the surface of the liquid. The interaction between a gas molecule and other gas molecules is negligible, as is the interaction between gas molecules and the liquid. Therefore,  $\gamma_I = \gamma_b$ ; in other words, the interfacial tension is simply the surface tension of the liquid.

A surfactant, when added to two immiscible phases, adsorbs at the interface. If one of the liquids is water and the other is a hydrocarbon, the hydrophobic end of the surfactant will be oriented toward the hydrocarbon, and the hydrophilic group will be oriented toward the water phase. This causes a change in the interface. Now the interaction is between the hydrophilic group of the surfactant and the water phase and the hydrophobic group of the surfactant and the hydrocarbon phase. These interactions are much stronger than the original interaction between the water and hydrocarbon, which effectively leads to an increase in  $\gamma_{ab}$  and a concomitant decrease in  $\gamma_I$ .

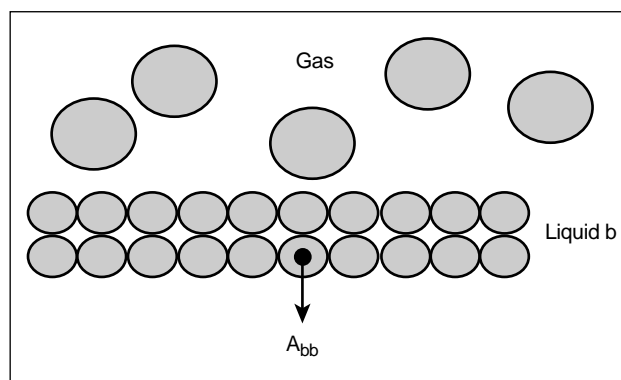


Figure 15-7. The interface between a liquid and a gas.

- Emulsification tendency

An emulsion is a mixture of two fluids in which fine droplets of one fluid are suspended in the other. Emulsions may be oil external or water external. In the first instance, oil is the continuous phase with the water droplets dispersed throughout. This is the most common emulsion found in wellbores. A water-external emulsion has an aqueous external phase with oil droplets distributed throughout.

Many crudes contain naturally occurring surfactants that reduce the surface tension between oil and formation water and thus promote the development of emulsions. Treatment of the formation with certain surfactants can also lead to the development of emulsions. However, appropriate surfactants can be used to treat wells with emulsion problems. Laboratory testing is required to determine the appropriate surfactant.

- Wettability

Oil and water are immiscible liquids that compete for space on the formation surface. Which liquid preferentially wets the rock surface is an important factor in acidizing. When the formation surface is completely covered by a film of oil, the formation is termed oil-wet. Conversely, when covered by water, the formation is water-wet.

An electrochemical approach helps to explain the ability of a surfactant to adsorb at interfaces between liquids and solids and alter the wettability of solids. Sand usually has a negative surface charge. When a cationic surfactant is present and the pH rises above the pzc, the positive water-soluble group is adsorbed by the negative silica particle. This leaves the oil-soluble group to influence

wettability. As a result, cationic surfactants generally create an oil-wet sand, although cationic surfactants can be chemically modified to yield a water-wet sand. When anionic surfactants are used, the sand and silicate minerals are generally left in their natural water-wet state. Wettability characteristics exhibited by anionic and cationic surfactants on a silicate particle are shown in Fig. 15-8. Carbonates have a pzc at a pH of 9–10 and thus are normally oil-wet by cationic surfactants above a pH of 9 whereas anionic surfactants oil wet the rock below a pH of 9.

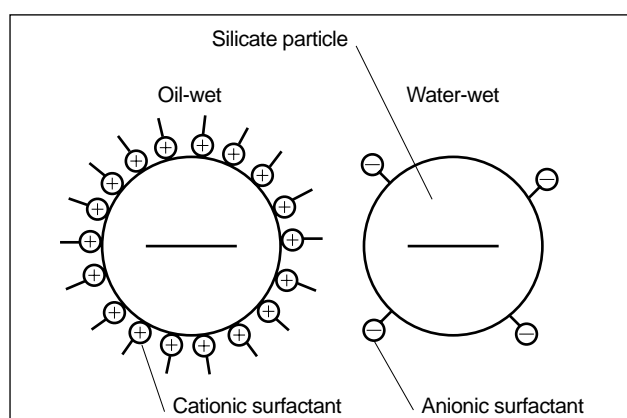


**Figure 15-8.** Silicate particle wettability characteristics (Hall, 1986).

- Micelle formation

Surfactants can form micelles in liquids when present above a specific concentration for each molecule, solvent and temperature. This concentration is referred to as the critical micelle concentration (CMC). Below the CMC, many properties of the system are concentration dependent. Some of these properties are surface tension, interfacial tension, foam stability and emulsion tendencies. Figure 15-9 shows examples of surfactant micelles.

- Dispersibility

To separate a highly associated structure (e.g., a sludge) into its particulate elements usually requires energy. If the dispersed phase is not in intimate contact with the continuous liquid phase, then the energy transfer will not be very efficient. A wetting surfactant that wets the dispersed phase with the liquid phase greatly improves the dispersibility. This is one aspect of aiding dispersion.

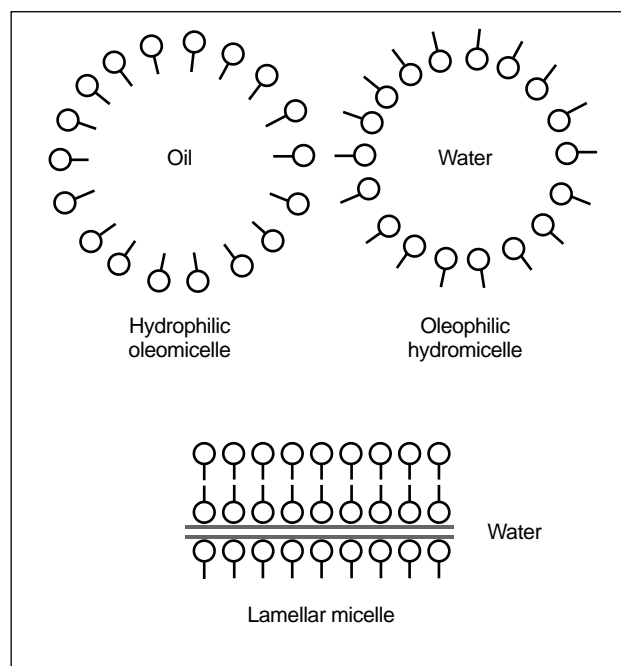


**Figure 15-9.** Examples of surfactant micelles that can form in liquids above a specific surfactant concentration (Hall, 1986).

Once the aggregate has been dispersed, a different surfactant may be required to prevent the dispersed particles from rejoining.

### 15-3.7. Applications and types of surfactants

In recent years, the uses of surfactants have grown quickly. This unique class of chemicals has found application in almost all phases of acidizing. A comprehensive review is beyond the scope of this chapter. However, a brief review follows.

- De-emulsifiers

A de-emulsifier is used to break oil-water emulsions, which occur commonly. The action of a de-emulsifier depends on how quickly it can concentrate at the oil/water interface. The faster the concentration at the interface, the more rapid will be the rate of emulsion breaking. These surfactants are usually oil-soluble chemicals that are blended with other de-emulsifying surfactants to achieve a synergistic response.

- Nonemulsifiers

These surfactants are added to well treating or workover fluids to prevent emulsions. Chemical

suppliers and service companies have many different surfactants that are classified as nonemulsifiers. The chemicals are usually mixtures of surfactants and solvents that are blended to obtain a final composition with broader applications. Normally, the surfactants are chosen so that they will water wet the formation. They should also mix easily with treating or workover fluids and prevent the formation of emulsions with the reservoir fluids.

- Emulsifiers

Specialized emulsions are often used as treating fluids. Many solvent systems concurrently use aqueous and hydrocarbon phases. Such emulsions may exhibit higher viscosity than either base fluid. Emulsions also have the ability to isolate the internal phase so that it is not as reactive. A common example of this technology is the use of emulsified acid.

With these properties, emulsions are efficient scale removal systems. When an inorganic scale is deposited in combination with a hydrocarbon scale (paraffin or asphaltene), an efficient scale removal system can be formulated by emulsifying a solvent for the inorganic scale—usually HCl—with the hydrocarbon. Usually, the emulsion has a low viscosity with a stability of up to several hours at bottomhole conditions. The stability of the emulsion is low to minimize the potential for damaging the well with the emulsion during workover. The hydrocarbon phase ranges from 10% to 30% by volume with a water-base fluid as the external phase. Most emulsifiers used in this application are nonionic.

- Silt-suspending agents

Surfactants can also be used to remove acid-insoluble clay and silt during an acidizing treatment. A surfactant is added that adsorbs onto the clay or silicate particles and keeps them suspended by electrostatic repulsion. With this surfactant present, damaging insoluble residues can be removed with the spent acid. These particles, if not removed, can stabilize emulsions or settle out and block the pore throats of the producing formation.

The mechanism for suspending silt with a surfactant can also be best understood by an electrochemical approach. Silt particles are minerals, such as quartz, feldspars and clays, that, assuming the treating fluid has a pH above the pzc, carry a negative surface charge. Silt-suspending surfactants are cationic, and the positively charged end of the molecule adsorbs onto the surface of these minerals.

This normally renders the particles oil-wet and causes them to act more like droplets of oil than solid particles. As long as they remain oil-wet, they tend to remain suspended in the spent acid.

Another force working to suspend the silt particles is electrostatic repulsion. Because all the particles carry the same charge, the particles repel each other and tend to not agglomerate. This combination of oil-wetting and electrostatic repulsion makes an effective silt-suspending system.

- Antisludge agents

When acid contacts some crude oils, a sludge can form at the acid/oil interface. This is most severe with high-strength acid systems (20% or higher). Once formed, the sludge is difficult to redissolve into the oil. As a result, the sludge accumulates in the formation and decreases permeability.

To combat the formation of sludge, cationic and anionic surfactants are used to adsorb and provide a continuous layer of protection at the acid/oil interface. Sludge development can often be prevented by lowering the acid strength.

- Surface tension reducers

Surfactants are commonly used in treating tight gas wells and in scale removal treatments. Their main function is to lower the surface and interfacial tensions of the treating fluid. This reduces the capillary pressure, which makes it easier to recover fluid from the capillary pore channels and to prevent oil-wetting films. Lowering the capillary pressure aids in cleaning up the well because less differential pressure is required to move the fluid through the capillary channels. The maximum differential pressure available to clean up a well is the reservoir pressure less the lowest drawdown that can be achieved at the perforations. If this maximum differential pressure is not high enough to move the liquid out of a pore channel, a block exists and its removal may require a surfactant that provides a lower surface tension (i.e., lower capillary pressure).

- Corrosion inhibitors

Corrosion inhibitors function by adsorbing onto the steel and providing a protective barrier between it and the acid. Surfactants that are effective as corrosion inhibitors include certain quaternary amines and acetylenic nonionics. Generally, these materials contain some cationic species.

- Bactericides

When treating a formation, it is usually desirable to leave it water-wet to aid the production of oil. This is done with an appropriate surfactant. It is also desirable to leave the formation free of contaminating bacteria that may have been inadvertently pumped into the well with the treating fluid. Many cationic surfactants possess this biocidal property and are commonly used in conjunction with other wetting surfactants.

- Clay treaters

Drilling muds commonly contain the highly water swelling clay smectite (bentonite). While a well is being drilled and completed, some of the clay may invade the producing zone and decrease formation productivity. Several chemical solutions are used for the removal of this invading clay.

The swelling properties of smectite may be changed by chemical reactions, because all clays are negatively charged at pH values above their pzc values. Thus, positively charged cations (calcium, sodium, potassium and hydrogen) may be attracted to the clay and are known as exchangeable cations. The particular cation and the quantity present in a clay system govern the degree of water swelling or clay expansion. For example, hydrogen smectite swells less in water than sodium smectite. By reacting sodium smectite (bentonite) with acid, hydrogen ions will replace the sodium ions by the cation-exchange process. Because hydrogen clay retains less water than sodium clay, the treatment of drilling mud with acid can shrink smectite and clean up mud filter cake. However, acid may also cause clay particles to flocculate. This flocculation results in larger clay particles that may be more difficult to remove from the well.

Surfactants have been developed to inhibit the flocculation of clays, even in solutions of high ionic strength. This is accomplished by using a surfactant that effectively disperses clay particles and minimizes the formation of aggregates. In addition, smaller particles are easier to suspend, resulting in more efficient removal from the well.

- Foaming agents

Surfactants are used to generate a stable foam. The following guidelines are usually applicable for surfactant application:

- nonionic—stable foam with acid or brine; because of cloud point problems, nonionics normally cannot be used above 200° to 250°F [95° to 120°C]
- anionic—stable foam with brine; can be used up to 300°F [150°C]
- cationic—stable foam with acid or brine; can be used up to 300°F
- amphoteric—stable foam with acid or brine; can be used up to 350°F [175°C].

Foam stability usually can be improved by gelling the liquid.

## 15-4. Clay stabilizers

Chemicals used to stabilize clays and fines function by being adsorbed, usually by electrostatic attraction or ion exchange, on the minerals to be stabilized. Because silicates above their pzc values have a negative charge, the most effective stabilizer has a positive charge (cationic). Common clay stabilizers are highly charged cations, quaternary surfactants, polyamines, polyquaternary amines and organosilane.

### 15-4.1. Highly charged cations

Two highly charged cations that were once widely used as clay stabilizers are hydroxyaluminum ( $\text{Al}_6(\text{OH})_{12}(\text{H}_2\text{O})_{12}^{6+}$ ) and zirconium ( $\text{Zr}^{4+}$ ) added as zirconium oxychloride ( $\text{ZrOCl}_2$ ). Solutions containing either stabilizer are usually pumped after various preflushes. The stabilizer solution is then overflushed with a compatible fluid to remove excess clay stabilizer from the near-wellbore region, and the well is shut in. These systems do not appreciably affect formation wettability.

The primary advantages of these systems are

- inexpensive
- treat for both migration and swelling damage
- can treat a large area of rock.

The disadvantages are

- hydroxyaluminum is not acid resistant
- require shut-in to polymerize
- can cause plugging

- difficult to use in fracturing
- require proper preflushes and overflushes.

Systems such as hydroxyaluminum can also be used in treating water injection and disposal wells to stabilize silicates and minimize future plugging from colloidal fines in the injection water.

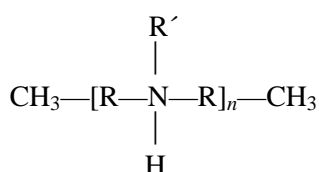
### 15-4.2. Quaternary surfactants

Quaternary surfactants have been used as clay stabilizers for dry gas wells. At conditions above the pzc, these surfactants are readily adsorbed by silicates owing to electrostatic attraction between the positively charged surfactant and negatively charged clay. The resulting charge neutralization reduces the ion-exchange capacity of the clay. Therefore, the clay is not as susceptible to swelling resulting from the adsorption of hydrated cations.

Quaternary surfactants promote oil-wetting of the silicate, which tends to minimize the adsorption of water by the silicate. However, if any liquid hydrocarbons are present, the silicate can readily become oil-wet. This, of course, reduces the relative permeability of the rock to hydrocarbons. Also, clays swell by imbibing fluids into their lattice structure.

### 15-4.3. Polyamines

Polyamines are organic polymers that contain more than one amine group. For the purpose of this discussion, only primary, secondary and tertiary amines are considered polyamines. Polyamines are positively charged in acidic fluids. The general structure of a polyamine is as follows:



where R is a repeating hydrocarbon unit, R' can be either a hydrocarbon unit or a hydrogen, and  $n$  is the number of amine units in the polymer.

Because the polymer has many amine units, it can adsorb strongly on the silicate with many points of attachment. The polymers can effectively neutralize the negative charge of the silicate. By carefully controlling the carbon:nitrogen ratio, usually 8:1 or less,

the polymers also promote water-wetting of the silicate. In addition, polymers of sufficient length can promote polymeric bridging between silicate particles.

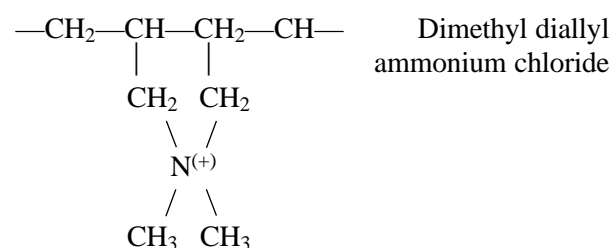
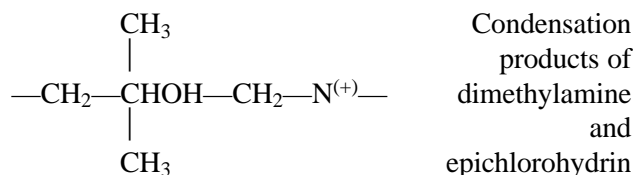
If a treated silicate is contacted by brines, the polyamine can lose its positive charge and be washed off the silicate. When this occurs, that silicate is no longer stabilized.

The disadvantages of polyamines are that

- treatment may not be permanent
- they are expensive.

### 15-4.4. Polyquaternary amines

Polyquaternary amines can be used in any water-base fluid, including acids and bases. The chemical structure of the two polyquaternary amines that have been widely used is as follows:

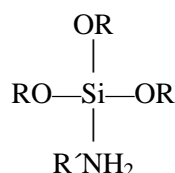


Clays and fines are stabilized by charge neutralization, water-wetting and polymeric bridging. Silica fines have a lower charge density than clays. Therefore, polyquaternary amines preferentially adsorb on clays as opposed to silica. When acidizing a water-sensitive formation with hydrofluoric acid (HF), clay stabilizer should be used if possible. If it is not possible to put clay stabilizer in all fluids, it should be used in the overflush, which should be overdisplaced with fluid that contains no clay stabilizer to ensure that no unadsorbed clay stabilizer is left at the wellbore. A normal concentration of polyquaternary amine for applications in HF treatments is 5 gal/1000 gal of active polymer in all fluids or 7½ gal/1000 gal of clay stabilizer in 200 gal of overflush.

There has been concern regarding the distinction between fines migration and clay migration. Fines consist predominantly of silt-sized particles of quartz and feldspars. Laboratory data indicate that the polyquaternary amines are not as effective in controlling fines migration as compared with clays (Hall, 1986; Ayorinde *et al.*, 1992).

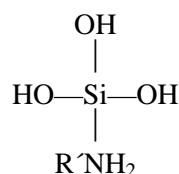
### 15-4.5. Organosilane

Kalfayan and Watkins (1990) proposed that an organosilane compound can be used as an additive to HCl-HF mixtures to prevent poststimulation fines migration. Organosilane has the following general structure:



where R and R' are hydrolyzable organic groups.

As an additive to acid, organosilane hydrolyzes to form silanols, which have the following structure:



The silanols react with each other and with silanol (Si—OH) sites present on siliceous mineral surfaces to form covalent siloxane (Si—O—Si) bonds by a condensation/polymerization reaction mechanism. The reaction of the silanols with one another and with the silanol sites on siliceous mineral surfaces forms a non-oil-wetting polysiloxane coating on siliceous mineral surfaces. The length of the polysiloxane chain formed by the hydrolysis of the organosilane, and the subsequent condensation/polymerization of silanols, is not known but is believed to be short. Acid, which catalyzes the initial hydrolysis of the organosilane, also retards the growth of polymer chains.

The mechanism by which the polysiloxane coating stabilizes fines is different from the ion-exchange mechanism by which other clay stabilizers work. However, it is similar to the coating process proposed for fluoboric acid (Boyer and Wu, 1983). The polysiloxane coating binds clay and other siliceous fines in place through covalent siloxane bonds. The

polysiloxane coating stabilizes fines by blocking ion-exchange sites and increasing interparticle attractive forces. Interparticle attractive forces can include van der Waal forces and hydrogen bonding. These forces, in addition to the electrostatic forces, help maintain the fines in their aggregated state along the pore wall. By blocking the ion-exchange sites, the polysiloxane coating decreases the magnitude of double-layer repulsion.

The polysiloxane formed can bind to minerals that have low-cation-exchange capacities (quartz), as well as to clays that have high-cation-exchange capacities. Therefore, the organosilane additive is well suited for formations that contain nonclay fines as well as clay fines.

### 15-5. Mutual solvents

Mutual solvents, as the name implies, are chemicals that are mutually soluble in both hydrocarbons and water. The most efficient mutual solvents are glycol ethers, a reaction product of alcohols and ethylene oxide. These chemicals are relatively safe and easy to use in the field. The preferred glycol ethers contain at least a butyl or higher molecular weight group.

The use of mutual solvents in the acid stimulation of a sandstone reservoir is a common practice. Mutual solvents are used in acid solutions and over-flushes to

- aid in reducing water saturation around the well-bore by lowering the surface tension of the water to prevent water blocks
- solubilize a portion of the water into a hydrocarbon phase to reduce the water saturation
- aid in providing a water-wet formation to maintain the best relative permeability to oil
- help to prevent insoluble fines from becoming oil-wet and stabilizing emulsions
- help to maintain the required concentration of surfactants and inhibitors in solution by reducing adsorption of these materials
- help to dissolve both the adsorbed inhibitor and acid-insoluble residue (certain acid corrosion inhibitors contain acid-insoluble residues that can cause formation plugging and inhibitor adsorption on formation minerals and change the wettability)
- dissolve any oil on the formation pore surface



- serve as a de-emulsifier
- improve the cleanup of spent acid following treatment.

Commonly used mutual solvents and their normal concentrations are

- ethylene glycol monobutyl ether (EGMBE): 10% by volume
- ether/surfactant/alcohol blends: 5% by volume.

### 15-5.1. Adsorption of mutual solvents

King and Lee (1988) studied the adsorption properties of an alcohol-mixture mutual solvent, such as a blend of isopropyl alcohol and isooctyl alcohol, and EGMBE. They found that adsorption of the mutual solvent can be severe depending on the type of mutual solvent. For deep damage removal, products that are lost during injection through the formation are not acceptable because the mutual solvent is removed from the leading edge of the acid. Although there appears to be no direct damage caused by adsorption of the mutual solvent, the acid is left after the loss without any material to lower surface tension or to break emulsions. Paktinat (1991) recommended the use of ethoxylated alcohol with EGMBE to minimize adsorption, thus resulting in deeper penetration of the mutual solvent and reduced emulsion tendencies.

### 15-5.2. Chlorination of mutual solvents

King and Lee (1988) presented data on the chlorination of mutual solvents with 15% and 28% HCl at temperatures from 70° to 250°F [20° to 120°C]. The chlorination issue has long been of interest because chlorinated hydrocarbons poison refinery catalysts. Their data show that the chlorination of mutual solvents is a function of

- type of mutual solvent
- temperature
- concentration of HCl (i.e., spending of HCl reduces the possibility).

At temperatures exceeding 200°F, especially with 28% HCl, the chlorination of most mutual solvents was severe, if there were no carbonates with which the acid could react. The presence of carbonates resulted in very low production of chlorinated hydrocarbons.

## 15-6. Iron control additives

### 15-6.1. Sources of iron

When appreciable quantities of iron in the form of  $\text{Fe}^{3+}$  (ferric ions), rather than the usual  $\text{Fe}^{2+}$  (ferrous ions), are dissolved by the acid, iron precipitation and permeability reductions can occur after acidizing. The oxidation state of the iron governs precipitation. Ferric iron precipitates at a pH of about 2, whereas ferrous iron precipitates at a pH of about 7—the actual values depend on the concentrations of the ferrous and ferric ions. Because spent acid solutions seldom rise to a pH above 6, precipitation of ferrous iron is seldom a problem. Sources of iron include

- corrosion products found on the walls of the tubulars
- mill scale
- iron-bearing minerals.

Iron occurs naturally in formation waters or in formation minerals (Table 15-5). However, the tubulars in the well are one of the most prominent sources of iron. Before the acid reaches the formation, it flows for a relatively long time through the tubing. Tubing usually contains rust, which is dissolved by acid. Newly manufactured tubing has a crust of mill scale.

The thickness of the mill scale on oilfield tubulars varies considerably depending on the cooling rate and how much the pipe was manipulated during the straightening procedure. Mill scale is composed of two distinct layers—a hard, dense layer next to the pipe that is approximately 0.003 in. thick; on top of the dense mill scale is a layer of softer, flaky mill scale that is approximately 0.007 in. thick. Most of the softer scale pops off the pipe during the straightening procedure.

**Table 15-5. Oxidation state of iron in formation minerals.**

Mineral	Chemical Formula	Oxidation State
Hematite	$\text{Fe}_2\text{O}_3$	$\text{Fe}^{2+}$
Magnetite	$\text{FeO}-\text{Fe}_2\text{O}_3$	$\text{Fe}^{2+}-\text{Fe}^{3+}$
Pyrite	$\text{FeS}$	$\text{Fe}^{2+}$
Siderite	$\text{FeCO}_3$	$\text{Fe}^{2+}$
Chlorite clay	—	$\text{Fe}^{2+}$
Mixed-layer clay	—	$\text{Fe}^{2+}$

The theoretical quantity of 15% HCl required to remove 0.073 lbm of mill scale from 2 $\frac{7}{8}$ -in. tubing is 69 gal/1000 ft of tubing. If a 10,000-ft well is acidized for damage removal, approximately 690 gal of 15% HCl could be neutralized by the mill scale. Of course, the acid contact time and temperature control the quantity of mill scale removed. If acid is spent on mill scale, it will contain 85,900 ppm of total iron. Of this, 57,300 ppm will be ferric iron (Fe<sup>3+</sup>). Thus, the leading edge of the treating fluid may be partially spent acid that contains a high concentration of iron. The ferric iron can be precipitated as ferric hydroxide (Fe(OH)<sub>3</sub>), a dark brown gelatinous precipitate that can be damaging to the formation.

It should be emphasized that acid dissolves iron compounds regardless of the presence of any type of inhibitor used to protect the elemental iron in the steel. Iron control additives help prevent the precipitation of iron hydroxide.

Concern is often expressed about the dissolution of iron-containing minerals (siderite, hematite and chlorite) from the formation and subsequent precipitation of the dissolved iron. Previous studies indicate that most of the iron contained in these minerals occurs in the Fe<sup>2+</sup> oxidation state (Table 15-5) and does not present a precipitation problem. However, numerous exceptions to this rule exist. Streaks of pure hematite (Fe<sub>2</sub>O<sub>3</sub>) occur in some sandstones, whereas others contain Fe<sup>3+</sup>-type minerals uniformly distributed within the matrix of rock. Where these conditions are present, greater amounts of an iron control additive are required to control ferric hydroxide precipitation.

## 15-6.2. Methods of iron control

The three methods currently used to help keep iron in solution are pH control, sequestering agents and reducing agents (also effective as oxygen scavengers). These may be used individually or in combination, depending on the source and amount of iron dissolution expected.

- pH control

pH control is accomplished by the addition of a weak acid that is very slow to react so that a low pH is maintained after the HCl has spent. Acetic acid is typically used for this purpose. A low pH aids in preventing the secondary precipitation of iron.

- Sequestering agents

Sequestering agents bond to the iron and hold it in solution so that it cannot precipitate. Citric acid, ethylenediaminetetraacetic acid (EDTA) and nitrilotriacetic acid (NTA) are some of the more commonly used sequestering agents.

- Reducing agents

Reducing agents convert ferric (Fe<sup>3+</sup>) to ferrous (Fe<sup>2+</sup>) iron. Secondary precipitation of ferric iron occurs at a pH of about 2.0. The secondary precipitation of ferrous iron hydroxides does not occur until the pH is above 7.0. Returned spent acids never have a pH this high. Erythorbic acid and sodium erythorbate are commonly used as reducing agents. Erythorbic acid is preferred over sodium erythorbate in sandstone acidizing because the addition of sodium salts of either sequestering or reducing agents to mud acid can lead to the precipitation of insoluble hexafluorosilicate. Hall and Dill (1988) reported that erythorbic acid is unstable in hot HCl and decomposes to form an insoluble precipitate. Although this is true, the decomposition process is slow and the acid normally spends long before precipitation can occur (Crowe, 1985).

Most reducing agents also act as oxygen scavengers that remove dissolved oxygen from the fluid. The scavengers prevent the oxidization of ferrous iron to ferric iron. This maintains iron in solution by preventing the precipitation of ferric iron. The amount of iron that can be reduced depends on the quantity of chemical added. Aeration of the solution can introduce additional oxygen.

Table 15-6 compares iron control additives, showing their advantages and disadvantages and the amount of each required in 1000 gal of 15% HCl to sequester 5000 ppm of ferric iron at 150°F [65°C] for a minimum of 2 days.

The safest way to prevent damage to the reservoir from precipitated iron hydroxide is to clean or pickle the pipe with acid before acidizing the formation. The acid should contain large quantities of iron control additives and should be circulated out of the well, not pumped into the formation. In conjunction with this treatment, a dispersed hydrocarbon phase should be incorporated or used as a pre-flush to remove pipe dope that could plug the perforations.

Table 15-6. Comparison of various iron control agents.			
Control Agent	Advantages	Disadvantages	Amount (lbm)
Citric acid	Effective at temperatures up to 400°F [205°C]	Precipitates as calcium citrate if excess uncomplexed quantities are used (more than 10 lbm/1000 gal)	175
Citric acid–acetic acid mixture	Very effective at lower temperatures	Even for the indicated amount, calcium citrate precipitates unless at least 2000-ppm Fe <sup>3+</sup> is present in spent acid.  Efficiency decreases rapidly at temperatures above 150°F [65°C]	Citric: 50 Acetic: 87
Lactic acid	Little chance of calcium lactate precipitation if excessive quantities are used	Not very effective at temperatures above 100°F [40°C]	190 (at 75°F [25°C])
Acetic acid	No problem from possible precipitation as calcium acetate	Effective only at temperatures at about 150°F	435
Gluconic acid	Little chance of calcium gluconate precipitation	Effective only at temperatures up to 150°F  Expensive on a cost-performance basis	350
Tetrasodium salt of EDTA	Large quantities may be used without precipitation of calcium salt.  Effective at temperatures up to 400°F	More expensive to use than many other agents	296
Nitrilotriacetic acid	Effective at temperatures up to 400°F  More soluble in acid than EDTA—higher concentrations can be used  Less expensive than EDTA		150
Sodium erythorbate	Smaller quantities required  Effective at temperatures up to 400°F	Increased corrosion inhibitor concentration required for certain applications  Should not be used in HF—use erythorbic acid	23

The treatment of sour wells presents an entirely different type of precipitation problem. In addition to free sulfur precipitation, by the reaction of Fe<sup>3+</sup> with H<sub>2</sub>S, the dissolved Fe<sup>2+</sup> also precipitates as ferrous sulfide (FeS) on spending of the acid. FeS precipitates at a pH of about 2. Laboratory and field data presented by Hall and Dill (1988) show that a combination of NTA, EGMBE and a sulfide modifier is an effective system for controlling the precipitation of FeS and free sulfur when acidizing sour wells. Crowe (1985) previously proposed a two-component system to address sour well problems. The system incorporates erythorbic acid to reduce ferric iron to ferrous iron and EDTA to chelate ferrous iron and eliminate the precipitation of FeS.

## 15-7. Alcohols

Alcohols are used in acidizing fluids to remove water blocks, enhance fluid recovery, retard acid reactivity and decrease water content. The most common alcohols used in acidizing are isopropanol and methanol. Their physical and chemical properties are listed in Table 15-7.

Table 15-7. Physical and chemical properties of isopropanol and methanol.		
Property	Isopropanol	Methanol
Density at 68°F [20°C]	0.785	0.792
Weight (lbm/1000 gal)	6.54	6.60
Flash point (closed up, °F [°C])	54 [12]	54
Solubility in water	Complete	Complete

Isopropanol is normally used at a maximum of 20% by volume. Methanol is used at various concentrations, but a typical concentration may be 25% by volume. Alcohol is used in acidizing fluids for the following reasons.

- Removal of water blocks

One problem that can severely decrease production is blockage of the pore spaces by water; this is commonly known as a water block. Water blocks may form where high capillary forces are present in porous rocks. The most severe water block problems occur in formations with gas permeabilities less than 120 md. The alcohol in the treating fluid reduces the capillary forces within the reservoir, thus enabling easier removal of the liquid phases.

- Enhancement of fluid recovery

Another problem that occurs in treating oil or gas wells is the recovery of treating fluids, especially in gas reservoirs. The high surface tension of water or acid solutions hinders their penetration and recovery. Conventional surfactants help, although they lose much of their activity by adsorption. The addition of alcohol to acid solutions reduces their surface tension. The concentration of alcohol normally used for this purpose is sufficient so that loss by adsorption is not a problem.

- Retardation of acid reactivity

Alcohol has a retarding effect on acid reactivity. The retardation rate is related to the type and percentage of alcohol added.

- Decrease of water in acids

Some formations contain a large amount of water-sensitive clays. To minimize the amount of water contained in acidizing solutions, alcohols are used in place of the dilution water.

The major disadvantages of using alcohol in acidizing fluids are as follows:

- Effective concentration

It takes a large amount of alcohol, 20% or more, to provide beneficial effects.

- Cost

Replacing water with alcohol in the acidizing solution makes the treatment more expensive.

- Low flash point

Both isopropanol and methanol, and even acid solutions containing 20% or more by volume of either, have low flash points.

- Increase in corrosiveness

Corrosion tests have shown that alcohol-acid mixtures require a higher concentration of inhibitor than equivalent acid mixtures without alcohol.

- Adverse reactions

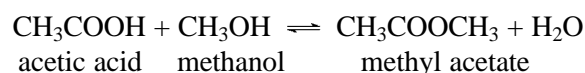
Formation brines with a high concentration of dissolved salts can “salt out” in the presence of alcohols. To help prevent the occurrence of salt precipitation, treating solutions should not exceed 20% by volume of isopropanol or 40% by volume of methanol.

- Incompatibility

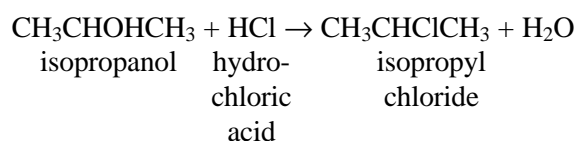
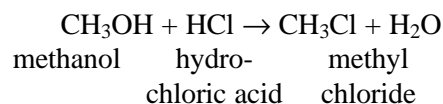
Some crude oils are incompatible with both methanol and isopropanol. Compatibility tests should be conducted before acidizing a well with a fluid containing alcohol. Some formation types may even be extremely sensitive to aqueous solutions that contain high concentrations of alcohols.

- Side reactions

There are undesirable side reactions when alcohols are used in acidizing. Even under moderate temperature conditions, alcohols react readily with acid. In the case of organic acids (e.g., acetic or formic acid), these reactions result in ester formation, with the only resulting problem being a possible loss of available acid for the stimulation reaction. Even this may be of small consequence, because the esterification reaction is reversible and regeneration of the organic acid for the desired stimulation reaction is possible (Keeney and Frost, 1975):



However, in an alcoholic solution of HCl, a reaction takes place that results in the formation of the following organic chlorides:



This poses a genuine problem in gas well stimulation because the second and third of these reactions are irreversible, and any HCl lost to this process cannot be regenerated, as is possible with organic acids in the first equation. Thus, these reactions reduce the HCl content. A second problem concerns the reaction products themselves. Although the presence of organic chlorides in natural gas might not present any special problems, their presence in produced crudes or distillates is considered serious contamination, because of the detrimental effect of chlorinated hydrocarbons on refinery catalysts.

Figure 15-10 shows the effects of increasing temperature on the reduction of acid strength for four concentrations of methanol. The data show that there is no significant loss of acid strength with methanol concentrations up to 32% by volume until the temperature exceeds 175°F [80°C].

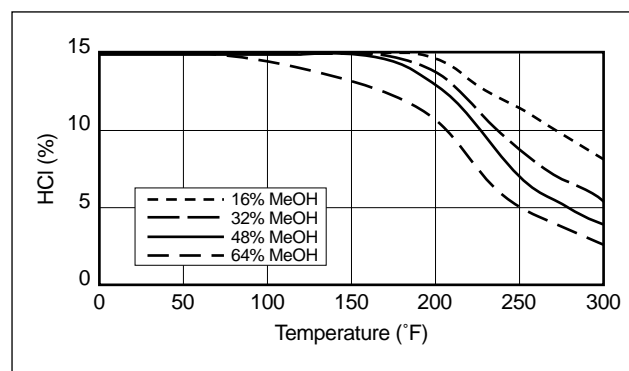


**Figure 15-10.** Effect of various concentrations of methanol on acid strength at increasing temperatures (courtesy of Halliburton Services).

## 15-8. Acetic acid

A common problem in HF acidizing is the precipitation of reaction products. Many of the precipitation reactions occur almost immediately on spending the acid solution. Most of these precipitation problems can be overcome by the use of an adequate acid pre-flush and ammonium chloride ( $\text{NH}_4\text{Cl}$ ) overflush. However, precipitation can also occur days, months or even years after an HF acidizing treatment. This precipitation is often called aluminosilicate scaling. Scales of this type are believed to form when the spent HF mixes with formation fluid to slightly raise the pH, thus causing precipitation.

Recent field trials by Shuchart and Ali (1992) show that the use of 3% acetic acid in HF acidizing sequences decreases the occurrence of scaling. The use of acetic acid delays the precipitation of aluminosilicate scale by two mechanisms—a buffering effect and a chelating effect.

## 15-9. Organic dispersants

A relatively new method of removing organic deposits is the use of a dispersant surfactant with xylene. These surfactants can penetrate and loosen organic deposits so that the xylene can effectively dissolve or remove the deposit. Concentrations of 1% to 10% volume/volume are used depending on the deposit type, hardness and adhesion and the bottomhole temperature. For matrix, wellbore and tubing cleanup treatments, a soaking period of several hours is recommended.

## 15-10. Organic solvents

As Fig. 15-1 shows, organic solvents used alone or in combination with acid and other materials are useful for removing water blocks and solids. King (1986) provided a good discussion of the uses of these solvents alone and in combination with acid for damage removal. Organic solvents include alcohols in addition to more traditional solvents such as xylene, toluene and diesel.

Organic solvents are particularly useful for the removal of organic deposits. An organic solvent can be combined with acid when the inorganic scales are mixed with or coated by asphaltenes and paraffins. An oil-external emulsion with the appropriate acid as the internal phase is useful for treating mixed deposits. The emulsion provides a further benefit of retarding the acid, thus allowing the deeper penetration of live acid.

## 15-11. Diversion

Diversion is often required to ensure that the treating fluid works effectively. Diverters function simply by equalizing the flow so that zones of differing permeabilities can be treated. Schechter (1992) provided a good discussion of diversion principles. The emphasis in this section is on diversion through the use of

particulates added to the treating fluid and foams rather than the use of packers or ball sealers.

Ideally the diverter should

- be insoluble in the treating fluid
- form an essentially impermeable layer on the formation face without penetrating deeply into the formation
- be easily removed following the treatment.

Generally all, or at least most, of these criteria can be met using materials such as oil-soluble resins, benzoic acid flakes and other particulates. Particulate diverters may cause damage and can be difficult to clean up as a result.

Foams may also provide effective diversion (Zerhoub *et al.*, 1991). Foamed fluids have the additional advantage of good cleanup with little or no potential for damaging the formation. The ratio of nitrogen to fluid depends on the bottomhole conditions during the treatment. Diversion and fluid placement strategy are addressed in Chapter 19.

## 15-12. Additive compatibility

All additives should be tested in the laboratory. Compatibility of additives with formation fluids should be tested using a sandpack method developed by Ali *et al.* (1994). This procedure is more representative of downhole conditions and uses more sand than the test in *API Recommended Practices for Laboratory Testing of Surface Active Agents for Well Stimulation* (RP 42) (1977). The acid system with additives is drawn through a pack of formation core material or a mixture consisting of 10-wt% illite-bentonite, 10-wt% silica flour and 80-wt% 100-mesh sand. There are no universal additives for all formation problems. Any potential incompatibilities between additives and formation fluids must be identified and corrected before acidizing.

## 15-13. Facility upsets following acid stimulation

### 15-13.1. Discharge requirements

The chemicals used in acidizing treatments have been linked with oil and water separation facility upsets, causing noncompliance with environmental

discharge regulations. On flowback, emulsion and oil/water separation problems that occur can potentially result in excess oil solubilized in the water by the formation of microemulsions. Emulsion problems under such circumstances can result in thousands of gallons of non-pipeline-quality oil and could shut down the separation unit and minimize production from these wells. Dehydrated oil and clean discharge water are required to maintain normal uninterrupted production.

Regulations for the disposal of produced water in offshore operations are becoming increasingly stringent. The U.S. National Pollutant Discharge Elimination System (NPDES) has established discharge levels for oil and grease at a 29-mg/L monthly average with a grab sample maximum of 42 mg/L. This is a reduction in the allowable levels from 48 to 29 mg/L. The penalty for noncompliance by the operator can be severe. These discharge levels are causing the reevaluation of acidizing treatments.

During the flowback immediately following an acid treatment, significantly higher levels of oil and grease than those permitted for discharge have also been recorded. During flowback, spikes in the basic sediment and water (BS&W) values occur immediately after an acid treatment. Microemulsions are suspected of occurring during flowback. The produced oil is solubilized in the returned spent acid, and this results in significantly higher levels of oil and grease. The use of matrix additives is believed to contribute to the solubilization of the oil and additives. These additives should be optimized to minimize emulsion upsets and the levels of oil and grease.

Verification and optimization of the additives used in acid stimulation treatments have been requested by operators. Obtaining an answer to treatment facility upsets by additive optimization in matrix treatments can have a tremendous impact on acidizing workover operations. Research by Bansal (1993) determined the following maximum concentrations of inhibitors, surfactants and mutual solvents that may be present in the returned fluids to maintain oil and grease levels below 48 mg/L:

- inhibitors: 80 ppm
- surfactants: 10 ppm
- mutual solvents: 100 ppm.

The common denominator for each of these additives is surface-active compounds (i.e., surfactants).

The surfactants provide acceptable fluid performance, such as corrosion inhibition, dispersion and wetting properties, as they were initially designed for the acid treatment. However, if the additives are used in excessive concentrations, they may exacerbate the emulsification tendencies of fluids during flowback.

The difference in emulsion stability is attributed to other, more dominant factors (e.g., stabilization by solids precipitation [organic and inorganic], ferric ion interaction with the crude oil and viscosity increase at the interface). Results presented by Coppel (1975) show that acids partially spent on formations contain potentially precipitable materials in solution. As the pH of the produced acid increases during flowback and mixes with other produced fluids, precipitates form that can stabilize emulsions. Dunlap and Houchin (1990) recommended polarized microscopy to evaluate return fluids to establish the cause for a stabilized emulsion. Specific damage mechanisms, such as emulsion stabilization by organic deposits, solids and iron, could be detected and identified.

### 15-13.2. Prevention of facility upsets

Preventing upsets requires optimizing the fluid design to minimize or eliminate the formation of precipitates and using the optimum de-emulsifier. The potential for the formation of emulsions of acid and produced crude oil while still providing the required downhole function optimization of the de-emulsifier treatment is evaluated currently by the procedures recommended in API RP 42 (1977). Vigorous mixing of acid with fresh crude oil in a glass container is observed under bottomhole temperatures (hot-water bath) to determine the characteristics and time for emulsion breakout. Fine siliceous materials, ferric iron or both can be added to evaluate emulsion stability.

These fluid interactions can simulate the downhole emulsion problems encountered; however, these tests fail to accurately predict the interaction of the treating fluids with the acid-sensitive crudes during flowback. As a result, marginal treatment response is observed. Downhole emulsions and facility upsets may be attributed to inadequate prejob compatibility testing, because the additives employed in the acid system may preferentially adsorb out onto the rock matrix or partition to the oil phase during production.

Alternate testing procedures have been developed to more accurately simulate reservoir conditions. Ali

*et al.* (1994) recommended an alternate procedure that better simulates downhole intermixing of the stimulation fluids and the produced crude. The procedure involves filtering formulated acid, containing inhibitor, surfactants, mutual solvents and nonemulsifiers, through a sandpack containing 10-wt% silica flour, 10-wt% clays (such as montmorillonite) and 80-wt% 100-mesh sand prior to completion of the emulsion test. This procedure simulates the filtration of the acid system within the rock matrix. Surfactants, such as those used in nonemulsifiers, are adsorbed onto mineral surfaces. The adsorption minimizes the availability of the surfactants in solution to prevent emulsions.

Durham *et al.* (1995) reported that oil and water emulsion upsets could be minimized by proper selection of the acidizing additives and surface treating chemicals. When acid flowbacks are introduced into a production system, the control of emulsions by chemical treatment can significantly change in comparison with control during production of the well prior to treatment. These authors completed extensive emulsion breaker and water clarification tests with the desired acid/additive systems and fresh crude oil to duplicate the commingling of the acid with the oil during flowback. The low pH of the water in the emulsion rendered the current treating program ineffective until the acid flowback was completed. Nonionic de-emulsifiers were found to be more effective than sulfonate-type additives for treating these emulsions. On-site testing is recommended to select an effective chemical treatment.

Ali *et al.* (1997) reported the optimization of acidizing additives to reduce production facility upsets. The authors combined additive treatment optimization with a new absorption/filtration process. The optimized treatments involved the evaluation of surfactants and mutual solvents, which are considered to be the additives primarily responsible for emulsion problems during acid flowback. Elimination of some additives, minimizing the concentrations of other additives and using a dual-purpose mutual breakout solvent reduced facility upsets. All recommendations were based on laboratory testing using the sandpack method and on-site testing with a laboratory unit. The filtration process used a specialized absorption medium to aid in lowering oil and grease levels. This combination of treatment optimization with filtration/absorption reduced facility upsets while not interfering with the efficacy of the treatment.

# Fundamentals of Acid Stimulation

*A. Daniel Hill and Robert S. Schechter, University of Texas at Austin*

## 16-1. Introduction

Matrix stimulation is a technique in which a solvent is injected into the formation to dissolve some of the materials present and hence recover or increase the permeability in the near-wellbore region. Such treatments are called “matrix” treatments because the solvent is injected at pressures below the parting pressure of the formation so that fractures are not created. The objective is to greatly enhance or recover the permeability near the wellbore, rather than affect a large portion of the reservoir.

The most common matrix stimulation treatment is acidizing, in which an acidic solution is injected to dissolve minerals in the formation. However, other solvents are also used. The next most common fluids are organic solvents aimed at dissolving waxes, paraffins, asphaltenes or other organic damaging materials. Nonacid matrix stimulation is addressed in Chapter 14. This chapter focuses on matrix acidizing; however, the reader should keep in mind that many of the theories and calculation procedures presented here can also be applied to nonacid solvent treatments.

The most common acids are hydrochloric acid (HCl), used primarily to dissolve carbonate minerals, and mixtures of HCl and hydrofluoric acid (HF), used to attack silicate minerals such as clays and feldspars. Other acids, particularly some weak organic acids, are used in special applications, such as high-temperature wells. Matrix acidizing is a near-wellbore treatment, with all the acid reacting within about 1 ft of the wellbore in sandstone formations and within a few inches to perhaps as much as 10 ft from the wellbore in carbonates.

Matrix acidizing can significantly enhance the productivity of a well when near-wellbore formation damage is present and, conversely, is of limited benefit in an undamaged well, as shown in Chapter 1. Thus, matrix acidizing generally should be applied only when a well has a high skin factor that cannot be attributed to partial penetration, perforation efficiency

or other mechanical aspects of the completion. Two exceptions to this rule may occur. First, in highly productive wells, the productivity improvement of about 20% that is possible with matrix stimulation of an undamaged well may be economic. Second, in naturally fractured or highly vugular carbonate reservoirs, live acid may penetrate to a sufficient distance to yield a productivity enhancement greater than that normally expected from a true matrix treatment.

An ideal matrix treatment restores the permeability in the near-wellbore region to a value at least as high as the original undamaged permeability; it accomplishes this over the entire completed interval and it leaves the formation in the treated region with high relative permeability to the oil and/or gas phase. Designing a treatment should strive to achieve this ideal at the lowest possible cost, which requires consideration of the many physical and chemical interactions taking place between the injected fluids and the reservoir minerals and fluids. The most important of these phenomena are the following:

- mass transfer of acid molecules to the mineral surface and subsequent reaction at the surface—This fundamental process of acidizing is illustrated in Fig. 16-1. Acid reactions with minerals are termed heterogeneous reactions because they occur at a boundary between the solid and the liquid rather than in the bulk phases. Before the reaction can occur, acid must be transported to the mineral surface by convection or diffusion. The overall reaction rate (i.e., the rate of change of the concentration of one component in the bulk liquid phase) may depend on both the rate of mass transfer and the rate of surface reaction. Many times, however, one of these processes is much slower than the other and controls the overall rate, in which case the faster process can be ignored.
- changing pore structure—The physical change in the pore structure caused by dissolution of some of the minerals by acid is the mechanism by which



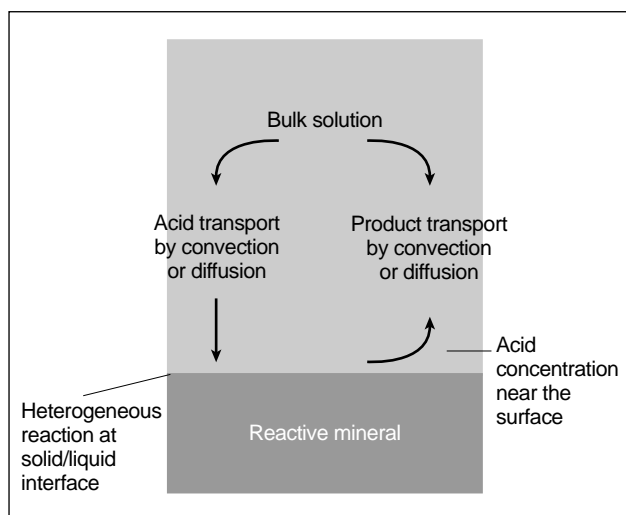


**Figure 16-1.** Acid reaction occurring in a system.

matrix acidizing increases permeability. The manner in which the pore structure changes is fundamentally different in sandstones and carbonates, which leads to radically different approaches to modeling the acidizing process in these two mineralogies.

- precipitation of reaction products—Secondary reactions occur in acidizing, particularly in sandstones, that can result in the precipitation of reaction products from the bulk liquid phase. Obviously, precipitated solids may block pore spaces and work against the goal of matrix acidizing.
- acid fluid–reservoir fluid interactions—The acid solution injected in matrix acidizing may interact physically and/or chemically with the reservoir fluids as well as with the minerals. These interactions can result in changes in wettability, phase saturation distribution, precipitation of solids or emulsification.
- variations in reservoir permeability or the distribution of damage—A successful acidizing treatment requires contacting all damaged regions around the well with acid. This is usually complicated by variations in the injectivity to acid along the wellbore, which leads to the use of techniques to affect good acid coverage (acid diversion).

In considering the many aspects of the matrix acidizing process, the focus is on the key design variables; to be useful, any model of the process must aid in optimizing the design. The primary design considerations are

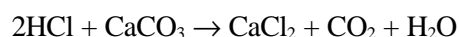
- fluid selection—acid type, concentration and volume
- injection schedule—planned rate schedule and sequence of injected fluids
- acid coverage and diversion—special steps taken to improve acid contact with the formation
- real-time monitoring—methods to evaluate the acidizing process as it occurs
- additives—other chemicals included in the acid solution to enhance the process or to protect tubular goods.

Treatment design is considered in detail in other chapters. This chapter lays the foundation for the design methods aimed at optimizing a matrix acidizing treatment by reviewing the underlying chemistry and physics of the acidizing process and introducing the latest models of the processes involved. First, the interaction of acids with reservoir minerals is addressed. Then, current models of the matrix acidizing process in sandstones and in carbonates are presented.

## 16-2. Acid-mineral interactions

### 16-2.1. Acid-mineral reaction stoichiometry

The amount of acid required to dissolve a given amount of mineral is determined by the stoichiometry of the chemical reaction, which describes the number of moles of each species involved in the reaction. For example, the simple reaction between HCl and calcite ( $\text{CaCO}_3$ ) can be written as

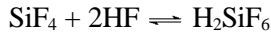


which shows that 2 moles of HCl are required to dissolve 1 mole of  $\text{CaCO}_3$ . The numerals 2 and 1 multiplying the species HCl and  $\text{CaCO}_3$  are the stoichiometric coefficients  $\nu_{\text{HCl}}$  and  $\nu_{\text{CaCO}_3}$  for HCl and  $\text{CaCO}_3$ , respectively.

When HF reacts with silicate minerals, numerous secondary reactions may occur that influence the overall stoichiometry of the reaction. For example, when HF reacts with quartz ( $\text{SiO}_2$ ), the primary reaction is



producing silicon tetrafluoride ( $\text{SiF}_4$ ) and water. The stoichiometry of this reaction shows that 4 moles of HF are required to consume 1 mole of  $\text{SiO}_2$ . However, the  $\text{SiF}_4$  produced may also react with HF to form fluosilicic acid ( $\text{H}_2\text{SiF}_6$ ) according to



If this secondary reaction goes to completion, 6 moles of HF, rather than 4 moles, will be consumed to dissolve 1 mole of quartz. A complication is that the fluosilicates may exist in various forms, so that the total amount of HF required to dissolve a given amount of quartz depends on the solution concentration.

Typical reactions involved in HF acidizing are summarized in Table 16-1. Only the primary reaction products,  $\text{AlF}_2^+$  and  $\text{SiF}_4$ , are shown although many other products are possible (Labrid, 1975; Hekim and Fogler, 1982; Walsh *et al.*, 1982; Sevougian *et al.*, 1992; Shuchart and Gdanski, 1996). How many moles of mineral are dissolved by a mole of acid is an important consideration in the selection of an acid treatment volume that may differ substantially from the values shown in Table 16-1. As an example of the uncertainty, Schechter (1992) suggested that for conservative design purposes, about 20 moles of acid are required to dissolve 1 mole of feldspar rather than the 14 moles shown in Table 16-1. Depending on the composition of the acid solution, the actual value may be substantially less. This is especially the case if the silicon extracted from the feldspar crystals appears finally as the precipitate  $\text{Si}(\text{OH})_4$  rather than as soluble  $\text{SiF}_4$  as shown in Table 16-1. If the final silicon product is, in fact,  $\text{Si}(\text{OH})_4$ , then only 1 mole of HF would be required to dissolve a single mole of albite.

**Table 16-1. Primary chemical reactions in acidizing.**

<b>HCl</b>	
Calcite	$2\text{HCl} + \text{CaCO}_3 \rightarrow \text{CaCl}_2 + \text{CO}_2 + \text{H}_2\text{O}$
Dolomite	$4\text{HCl} + \text{CaMg}(\text{CO}_3)_2 \rightarrow \text{CaCl}_2 + \text{MgCl}_2 + 2\text{CO}_2 + 2\text{H}_2\text{O}$
Siderite	$2\text{HCl} + \text{FeCO}_3 \rightarrow \text{FeCl}_2 + \text{CO}_2 + \text{H}_2\text{O}$
<b>HCl-HF</b>	
Quartz	$4\text{HF} + \text{SiO}_2 \rightleftharpoons \text{SiF}_4 \text{ (silicon tetrafluoride)} + 2\text{H}_2\text{O}$ $\text{SiF}_4 + 2\text{HF} \rightleftharpoons \text{H}_2\text{SiF}_6 \text{ (fluosilicic acid)}$
Albite (sodium feldspar)	$\text{NaAlSi}_3\text{O}_8 + 14\text{HF} + 2\text{H}^+ \rightleftharpoons \text{Na}^+ + \text{AlF}_2^+ + 3\text{SiF}_4 + 8\text{H}_2\text{O}$
Orthoclase (potassium feldspar)	$\text{KAlSi}_3\text{O}_8 + 14\text{HF} + 2\text{H}^+ \rightleftharpoons \text{K}^+ + \text{AlF}_2^+ + 3\text{SiF}_4 + 8\text{H}_2\text{O}$
Kaolinite	$\text{Al}_2\text{Si}_2\text{O}_5(\text{OH})_4 + 24\text{HF} + 4\text{H}^+ \rightleftharpoons 4\text{AlF}_2^+ + 4\text{SiF}_4 + 18\text{H}_2\text{O}$
Montmorillonite	$\text{Al}_2\text{Si}_4\text{O}_{20}(\text{OH})_4 + 40\text{HF} + 4\text{H}^+ \rightleftharpoons 4\text{AlF}_2^+ + 8\text{SiF}_4 + 24\text{H}_2\text{O}$

In modeling the acidizing process, it is therefore crucial to determine the local solution composition as the process progresses. To satisfy this requirement, Sevougian *et al.* (1992) developed a geochemical model that considers a local partial equilibrium among certain reactions involved in the acidizing process. This is an important modeling capability; for example, Shuchart and Gdanski (1996) observed that the  $\text{AlF}_2^+/\text{AlF}^{2+}$  ratio obeys a pseudoequilibrium relation over a range of reaction conditions. This implies local equilibrium among the various aluminum fluoride species in the aqueous phase. To utilize the full capability of the Sevougian *et al.* model, the rates of both the homogeneous and heterogeneous reactions that are not fully at equilibrium are required. Not all the important reaction rates are known.

Thus, the chemistry of the reactions of HF with the minerals found in sandstone formations is complex and difficult to model. An additional complexity is the tendency for some of the reaction products to precipitate as the acid reactions go to completion (see Section 16-2.3). For practical purposes, it is convenient to express the stoichiometry in terms of the approximate “dissolving power,” as introduced by Williams *et al.* (1979).

The dissolving power expresses the amount of mineral that can be consumed by a given amount of acid on a mass or volume basis. First, the gravimetric dissolving power  $\beta$ , which is the mass of mineral consumed by a given mass of acid, is defined as

$$\beta = \frac{v_{\text{mineral}} MW_{\text{mineral}}}{v_{\text{acid}} MW_{\text{acid}}}, \quad (16-1)$$

where the  $v$  terms are the stoichiometric coefficients and  $MW_{\text{mineral}}$  and  $MW_{\text{acid}}$  are the molecular weights of the mineral and the acid, respectively. Thus, for the reaction between 100% HCl and  $\text{CaCO}_3$ ,

$$\beta_{100} = \frac{(1)(100.1)}{(2)(36.5)} = 1.37 \text{ lbm CaCO}_3/\text{lbm HCl}, \quad (16-2)$$

where the subscript 100 denotes 100% HCl. The dissolving power of any other concentration of acid is  $\beta_{100}$  times the weight fraction of acid in the acid solution. For the commonly used 15% HCl,  $\beta_{15} = 0.15 \times \beta_{100} = 0.21 \text{ lbm CaCO}_3/\text{lbm HCl}$ . The stoichiometric coefficients for common acidizing reactions are found from the reaction equations in Table 16-1.

The volumetric dissolving power  $X$ , which is similarly defined as the volume of mineral dissolved by a given volume of acid, is related to the gravimetric dissolving power by

$$X = \beta \frac{\rho_{\text{acid solution}}}{\rho_{\text{mineral}}} \quad (16-3)$$

A 15% HCl solution has a specific gravity of about 1.07 and CaCO<sub>3</sub> has a density  $\rho$  of 169 lbm/ft<sup>3</sup>. For the reaction of these species, the volumetric dissolving power is

$$X_{15} = 0.21 \left( \frac{\text{lbm CaCO}_3}{\text{lbm 15\% HCl}} \right) \left( \frac{(1.07)(62.4) \frac{\text{lbm 15\% HCl}}{\text{ft}^3}}{169 \frac{\text{lbm 15\% CaCO}_3}{\text{ft}^3}} \right) = 0.082 \frac{\text{ft}^3 \text{ CaCO}_3}{\text{ft}^3 \text{ 15\% HCl}} \quad (16-4)$$

The dissolving powers of various acids with limestone and dolomite and of HF with quartz and albite are given in Tables 16-2 and 16-3, respectively (Schechter, 1992). Sidebar 16A is an example calculation using dissolving power.

## 16-2.2. Acid-mineral reaction kinetics

The reaction between an acid and a mineral occurs when acid reaches the surface of the mineral by diffusion or convection from the bulk solution. The overall rate of acid consumption or mineral dissolution depends on two distinct phenomena—the rate of transport of acid to the mineral surface by diffusion or convection and the actual reaction rate on the mineral surface. Usually, one of these processes is much slower than the other. In this case, the fast process can be ignored, because it can be thought of as occurring in an insignificant amount of time compared with the slow process.

For example, the HCl-CaCO<sub>3</sub> reaction rate is extremely high, so the overall rate of this reaction is usually controlled by the rate of acid transport to the surface, the slower of the two processes. On the other hand, the surface reaction rates for many HF-mineral reactions are slow compared with the acid transport rate, and the overall rate of acid consumption or mineral dissolution is reaction-rate controlled. The “kinetics”

**Table 16-2. Dissolving power of various acids (Schechter, 1992).**

Formation	Acid	X (%)				
		$\beta_{100}$	5	10	15	30
Limestone (CaCO <sub>3</sub> )	Hydrochloric (HCl)	1.37	0.026	0.053	0.082	0.175
	Formic (HCOOH)	1.09	0.020	0.041	0.062	0.129
	Acetic (CH <sub>3</sub> COOH)	0.83	0.016	0.031	0.047	0.096
Dolomite (CaMg(CO <sub>3</sub> ) <sub>2</sub> )	Hydrochloric	1.27	0.023	0.046	0.071	0.152
	Formic	1.00	0.018	0.036	0.054	0.112
	Acetic	0.77	0.014	0.027	0.041	0.083

Notes:  $\rho_{\text{CaCO}_3} = 2.71 \text{ g/cm}^3$ ,  $\rho_{\text{CaMg(CO}_3)_2} = 2.87 \text{ g/cm}^3$

**Table 16-3. Dissolving power of hydrofluoric acid (Schechter, 1992).**

Acid concentration (wt%)	Quartz (SiO <sub>2</sub> )		Albite (NaAlSi <sub>3</sub> O <sub>8</sub> )	
	$\beta$	X	$\beta$	X
2	0.015	0.006	0.019	0.008
3	0.023	0.010	0.028	0.011
4	0.030	0.018	0.037	0.015
6	0.045	0.019	0.056	0.023
8	0.060	0.025	0.075	0.030

Notes:  $\beta$  = mass of rock dissolved/mass of acid reacted, X = volume of rock dissolved/volume of acid reacted

## 16A. Calculating minimum acid volume using dissolving power

The volume of acid required for a matrix acidizing treatment can be estimated using the concept of dissolving power. Because the volumetric dissolving power  $X$  is the volume of a particular mineral that is dissolved by a given volume of a particular acid solution, the minimum acid requirement to remove that mineral can be calculated with little information other than the dissolving power. Consider the following problem:

A sandstone formation with a porosity of 0.2 contains 5-vol% albite (sodium feldspar). What is the minimum volume of 3% HF solution required to dissolve all the albite a distance of 6 in. beyond a 6-in. diameter wellbore?

### Solution

The minimum acid volume is the amount  $V_{HF}$  required to dissolve all the feldspar plus the amount  $V_p$  required to fill the pore space in the region of feldspar dissolution. These volumes are

$$V_{feldspar} = \pi(r_{HF}^2 - r_w^2)(1 - \phi)x_{feldspar} = \pi(0.75^2 - 0.25^2)(1 - 0.2)(0.05) = 0.063 \frac{\text{ft}^3}{\text{ft}} \text{feldspar} \quad (16A-1)$$

$$V_{HF} = \frac{V_{feldspar}}{X_3} = \frac{0.063}{0.011} = 5.7 \frac{\text{ft}^3 \text{HF}}{\text{ft}}. \quad (16A-2)$$

In these equations,  $r_{HF}$  is the radial penetration distance of HF,  $r_w$  is the wellbore radius,  $\phi$  is the porosity, and  $x_{feldspar}$  is the volume fraction of the sandstone that is feldspar. The volume of pore space within 6 in. of the wellbore after removal of the feldspar is

$$V_p = \pi(r_{HF}^2 - r_w^2)(\phi + x_{feldspar}(1 - \phi)) = \pi(0.75^2 - 0.25^2)(0.2 + 0.05(1 - 0.2)) = 0.38 \frac{\text{ft}^3}{\text{ft}}, \quad (16A-3)$$

so the total volume of HF required is

$$V_{HF,T} = V_{HF} + V_p = (5.7 + 0.38) \frac{\text{ft}^3}{\text{ft}} \left( \frac{7.48 \text{ gal}}{\text{ft}^3} \right) = 46 \frac{\text{gal}}{\text{ft}}. \quad (16A-4)$$

Thus, the minimum volume of 3% HF solution required to remove all feldspar in a radial region extending 6 in. beyond the wellbore is 46 gal/ft of reservoir thickness. In an actual acidizing treatment, the injected acid does not react with feldspar only, and as shown by examining models of the acidizing process, the acid is not spent uniformly, as tacitly assumed in this calculation. Nevertheless, this simple calculation provides a ballpark figure for acid requirements and is a handy check of more complex models of the process.

of a reaction is a description of the rate at which the chemical reaction takes place, once the reacting species have been brought into contact.

A reaction rate is generally defined as the rate of appearance in the solution of the species of interest in units of moles per second (mol/s). A surface reaction rate depends on the amount of surface exposed to reaction, so these reactions are expressed per unit of surface area. In general, the surface reaction rate of an aqueous species of acid A reacting with mineral B is

$$R_A = r_A S_B, \quad (16-5)$$

where  $R_A$  is the rate of appearance of acid A in mol/s,  $r_A$  is the surface area-specific reaction rate of A in mol/s-m<sup>2</sup>, and  $S_B$  is the surface area of mineral B. When A is being consumed, the reaction rates  $r_A$  and  $R_A$  are negative. Acid-mineral reaction rates are typically expressed as the rate of dissolution of the min-

eral  $R_B$ , which is related to the acid consumption rate through the stoichiometry of the reaction

$$R_A = \frac{v_A}{v_B} R_B, \quad (16-6)$$

where  $v_A$  and  $v_B$  are the stoichiometric coefficients for acid A and mineral B.

The reaction rate  $r_A$  generally depends on the concentrations of the reacting species. However, in the reaction between an aqueous species and a solid, the concentration of the solid can be ignored, because it remains essentially constant. For example, a grain of quartz has a fixed number of moles of quartz per unit volume of quartz, irrespective of reactions that may be occurring on the surface of the grain. Incorporating concentration dependence into the rate expression yields

$$-R_A = E_f C_A^\alpha S_B, \quad (16-7)$$

where  $E_f$  is a reaction rate constant in mol A/[m<sup>2</sup>-s-(mol A/m<sup>3</sup>)<sup>α</sup>],  $C_A$  is the concentration of species A at the reactive surface, and  $\alpha$  is the order of the reaction (i.e., a measure of how strongly the reaction rate depends on the concentration of A). The reaction rate constant depends on temperature and sometimes on the concentration of chemical species other than A. Finally, Eq. 16-7 is written in the conventional manner for a species of acid that is being consumed from solution, by placing a minus sign with  $R_A$  so that  $E_f$  is a positive number.

- Laboratory measurement of reaction kinetics

To measure the surface reaction rate of acid-mineral reactions, it is necessary to maintain a constant mineral surface area or measure its change during reaction and to ensure that the rate of acid transport to the mineral surface is fast relative to the reaction rate. The two most common methods of obtaining these conditions are with a well-stirred slurry of mineral particles suspended in an acid solution (a stirred reactor) or with a rotating disk apparatus (Fogler *et al.*, 1976.) In the rotating disk apparatus, a disk of the mineral is placed in a large container holding the acid solution. The disk is rotated rapidly, so that the acid mass-transfer rate is high relative to the surface reaction rate. A third, more indirect method is by matching the coreflood response to acidizing with a model of the process of flow with reaction.

Lund *et al.* (1975, 1973) measured the kinetics of the HCl-calcite and HCl-dolomite reactions, respectively. Their results may be summarized as

$$-r_{HCl} = E_f C_{HCl}^\alpha \quad (16-8)$$

$$E_f = E_f^o \exp\left(-\frac{\Delta E}{RT}\right). \quad (16-9)$$

The constants  $\alpha$ ,  $E_f^o$  and  $\Delta E/R$  are listed in Table 16-4. SI units are used in these expressions, so  $C_{HCl}$  is in kg-mol/m<sup>3</sup> and temperature  $T$  is in degrees Kelvin. The reaction rate  $r_{HCl}$  is expressed as kg-mol HCl reacted/m<sup>2</sup>-s.

- Reactions of hydrochloric and weak acids with carbonates

HCl is a strong acid, meaning that when HCl is dissolved in water, the acid molecules almost completely dissociate to form hydrogen ions (H<sup>+</sup>) and chloride ions (Cl<sup>-</sup>). The reaction between HCl and carbonate minerals is actually a reaction of the H<sup>+</sup> with the mineral. With weak acids, such as acetic or formic acid, the reaction is also between H<sup>+</sup> and the mineral, with the added complication that the acid is not completely dissociated, thus limiting the supply of H<sup>+</sup> available for reaction. Because H<sup>+</sup> is the reactive species, the kinetics of the HCl reaction can also be used for weak acids by considering the acid dissociation equilibrium.

The kinetics of a weak acid-carbonate mineral reaction may therefore be obtained from Eq. 16-8 as follows (Schechter, 1992):

$$-r_{weak\ acid} = E_f K_d^{\alpha/2} C_{weak\ acid}^{\alpha/2}, \quad (16-10)$$

where  $K_d$  is the dissociation constant of the weak acid and  $E_f$  is the reaction rate constant for the HCl-mineral reaction.

- Reactions of hydrofluoric acid with sandstone minerals

HF reacts with virtually all of the many mineral constituents of sandstone. Reaction kinetics have been reported for the reactions of HF with quartz (Bergman, 1963; Hill *et al.*, 1977), feldspars (Fogler *et al.*, 1975) and clays (Kline and Fogler,

Table 16-4. Constants in HCl-mineral reaction kinetics models.

Mineral	$\alpha$	$E_f^o$ $\left( \frac{\text{kg-mol HCl}}{\text{m}^2\text{-s} \left( \frac{\text{kg-mol HCl}}{\text{m}^3 \text{ acid solution}} \right)^\alpha} \right)$	$\frac{\Delta E}{R}$ (K)
Calcite (CaCO <sub>3</sub> )	0.63	$7.291 \times 10^7$	$7.55 \times 10^3$
Dolomite (CaMg(CO <sub>3</sub> ) <sub>2</sub> )	$\frac{6.18 \times 10^{-4} T}{1 - 2 \times 10^{-3} T}$	$\frac{9.4 \times 10^{11}}{1000^a}$	$11.32 \times 10^3$

1981a). These kinetic expressions can all be represented by

$$-r_{\text{mineral}} = E_f \left[ 1 + K(C_{\text{HCl}})^\beta \right] C_{\text{HF}}^\alpha, \quad (16-11)$$

for which the parameters  $\alpha$ ,  $\beta$ ,  $E_f$  and the empirical kinetic constant  $K$  are listed in Table 16-5.

These expressions show that the dependence on HF concentration is approximately first order ( $\alpha = 1$ ). For feldspar reactions, the reaction rate increases with increasing HCl concentration, although HCl is not consumed in the reaction. Thus, HCl catalyzes HF-feldspar reactions. Kline and Fogler (1981a) showed that the reactive area depends on the crystalline structure of the clay reacting with an HCl-HF mixture and is generally only a small fraction of the total surface area of clays as determined by traditional methods of measurement. Thus, the surface area of montmorillonite as determined by nitrogen ( $\text{N}_2$ ) adsorption may be as high as  $5 \times 10^5 \text{ m}^2/\text{kg}$ , whereas the reactive surface area is approximately  $10^4 \text{ m}^2/\text{kg}$ . The surface areas in Eq. 16-8 must be the reactive areas that are actually in con-

tact with the acidic solution. Therefore, the morphology of the mineral assemblage becomes an important issue.

Comparison of the reaction rates of various minerals requires placing the rates on the basis of a unit of reactive area. On this basis, montmorillonites and kaolinites react about 2 orders of magnitude slower than feldspars, and illites react at least 1 order of magnitude slower than kaolinite. Viewing thin sections of rocks following acid treatment with HCl-HF mixtures shows that the feldspars are usually removed because of their high specific reaction rates. Authogenic clays also appear to react rapidly because of their intimate exposure to the acidic solution. On the other hand, clastic clays are commonly found in thin sections following acid treatment (Hill *et al.*, 1977). Thus, it is not only the specific reaction rate but also the area in contact with the acid that determines the rate of removal of a specific mineral. An example calculation of relative reaction rates of sandstone minerals is in Sidebar 16B.

**Table 16-5. Reaction rate constants for Eq. 16-11.**

Mineral	$E_f$ $\left( \frac{\text{kg-mol mineral}}{\text{m}^2\text{-s} \left( \frac{\text{kg-mol HF}}{\text{m}^3} \right)^\alpha} \right)$	$K$ $\left( \left( \frac{\text{kg-mol HF}}{\text{m}^3} \right)^{-\beta} \right)$	$\beta$	$\alpha$
Potassium feldspar <sup>†</sup> (orthoclase)	$0.127 \exp \left( -\frac{4680}{T} \right)$	$5.66 \times 10^{-2} \exp \left( \frac{956}{T} \right)$	0.4	1.2
Sodium feldspar <sup>†</sup> (albite)	$9.50 \times 10^{-3} \exp \left( -\frac{3930}{T} \right)$	$6.24 \times 10^{-2} \exp \left( \frac{554}{T} \right)$	1.0	1.0
$\alpha$ -quartz <sup>‡</sup>	$1.39 \times 10^{-7} \exp \left( -\frac{1150}{T} \right)$	0	—	—
Montmorillonite <sup>§</sup>	$1.1 \times 10^{-2} \exp \left( -\frac{5200}{T} \right)$	0	—	1.0
Kaolinite <sup>§</sup>	$0.86 \exp \left( -\frac{6800}{T} \right)$	0	—	1.0
<sup>†</sup> Fogler <i>et al.</i> (1973) <sup>‡</sup> Adapted from Hill <i>et al.</i> (1977) <sup>§</sup> Adapted from Kline and Fogler (1981)				

## 16B. Relative reaction rates of sandstone minerals

A matrix acidizing treatment is aimed at overcoming the effects of near-wellbore formation damage. Ideally, the injected acid attacks only the material causing the damage, which in most instances is clay particles or other fines. How efficiently the acid is being used can be determined by calculating the reaction rates of all major mineral species present with the injected acid.

Consider a sandstone formation that has been damaged by the invasion of bentonite (montmorillonite) particles from drilling mud. After the carbonate minerals have been removed by an HCl preflush, this clean sandstone contains 90% quartz, 5% albite (sodium feldspar) and 5% montmorillonite by weight. The reactive surface areas of the minerals are 10 m<sup>2</sup>/kg for the quartz and albite and 8000 m<sup>2</sup>/kg for the montmorillonite. (A cube of quartz with a side of 1 mm has a surface area of 2.2 m<sup>2</sup>/kg; if it is 0.1 mm on a side, its surface area is 22 m<sup>2</sup>/kg. Clays have a much larger surface area than detrital grains of quartz or feldspar.) Assume stoichiometric ratios of 6 moles HF/mole quartz, 20 moles HF/mole feldspar and 40 moles HF/mole montmorillonite.

If this rock is contacted with a 12% HCl–3% HF solution at 125°F [50°C], what proportion of the HF will initially be consumed by each of the three minerals? What are the mineral proportions of the rock dissolved?

### Solution

Per unit mass of rock, the surface area of each mineral is its reactive surface area times the mass fraction of the mineral present in the sandstone. For example, the reactive surface area of quartz per mass of sandstone  $S_q$  is (10 m<sup>2</sup>/kg)(0.9) = 9 m<sup>2</sup>/kg rock. Similarly, the surface areas of feldspar and montmorillonite are 0.5 and 400 m<sup>2</sup>/kg rock, respectively. The acid concentrations in Eq. 16-11 are in units of kg-mol/m<sup>3</sup> solution (equivalent to gmol/L); the concentrations given as mass fractions are converted to these units by multiplying by the solution density and the acid molecular weight, yielding 1.61 kg-mol HF/m<sup>3</sup> solution and 3.53 kg-mol HCl/m<sup>3</sup> solution. Quartz is used to illustrate the calculation sequence to determine the reaction rates for each mineral.

First, the rate constant is calculated with the data from Table 16-5:

$$E_i = 1.39 \times 10^{-7} \exp\left(-\frac{1150}{273 + 50}\right) = 3.95 \times 10^{-9} \frac{\text{kg-mol quartz}}{\text{m}^2\text{-s} \left(\frac{\text{kg-mol HF}}{\text{m}^3 \text{ solution}}\right)} \quad (16B-1)$$

Then, the specific reaction rate for quartz from Eq. 16-11 is

$$-r_q = 6.59 \times 10^{-10} (1.61) = 1.06 \times 10^{-9} \frac{\text{kg-mol quartz}}{\text{m}^2\text{-s}} \quad (16B-2)$$

The overall reaction rate for quartz is the specific reaction rate multiplied by the reactive surface area:

$$-R_q = 1.06 \times 10^{-9} (9) = 9.54 \times 10^{-9} \frac{\text{kg-mol quartz}}{\text{kg rock-s}}, \quad (16B-3)$$

which is multiplied by the molecular weight of quartz to put it on a mass basis:

$$-R_q = 9.54 \times 10^{-9} (60.1) = 5.73 \times 10^{-7} \frac{\text{kg quartz}}{\text{kg rock-s}} \quad (16B-4)$$

Finally, the rate of consumption of HF by the quartz reaction is obtained with Eq. 16-9, assuming 6 moles of HF are consumed for each mole of quartz dissolved:

$$-R_{HF,q} = 9.54 \times 10^{-9} (6) = 3.44 \times 10^{-7} \frac{\text{kg-mol HF}}{\text{kg rock-s}} \quad (16B-5)$$

The results of these calculations for all three minerals are summarized in Table 16B-1.

The fraction of HF expended in a particular reaction is the overall reaction rate for the mineral divided by the sum of the reaction rates, which shows that 1.1% of the HF is reacting with quartz, 5.7% is reacting with feldspar and 93.2% is reacting with montmorillonite. On the basis of the mass of mineral being dissolved, 95.1% of the rock dissolved is clay, 4.3% is feldspar, and less than 0.6% is quartz. This is because of the high surface area of the authogenic clays (including, however, clay particles from drilling muds) and the low reactivity of the quartz. Because clay and feldspar have relatively high reaction rates and generally form a small portion of the total rock mass, they are dissolved first in sandstone acidizing. The quartz reaction becomes important in regions where most of the clay, except clastic clays, and feldspar have already been removed.

**Table 16B-1. Relative reaction rates of sandstone minerals.**

Mineral	$-r_i$ (kg-mol $i$ /m <sup>2</sup> -s)	$S_i$ (m <sup>2</sup> /kg rock)	$-R_i$ (kg $i$ /kg rock-s)	$-R_{HF,i}$ (kg-mol HF/kg rock-s)
Quartz	$5.73 \times 10^{-8}$	9	$3.44 \times 10^{-6}$	$3.44 \times 10^{-7}$
Feldspar	$1.77 \times 10^{-7}$	0.5	$2.32 \times 10^{-5}$	$1.77 \times 10^{-6}$
Clay	$1.81 \times 10^{-9}$	400	$5.19 \times 10^{-4}$	$2.89 \times 10^{-5}$
Note: The subscript $i$ denotes the mineral.				

## 16B. Relative reaction rates of sandstone minerals (continued)

### Notes for Sidebar 16B

Given 90% quartz, 5% albite and 5% montmorillonite by weight, the surface areas are 10 m<sup>2</sup>/kg quartz, 10 m<sup>2</sup>/kg albite and 8000 m<sup>2</sup>/kg montmorillonite. The reaction rates used are from Table 16-5.

- Quartz ( $MW = 60.1$ )

Because 1 kg rock has 0.9-kg quartz, the quartz area is  $(0.9)(10)90$  m<sup>2</sup>/kg rock.

$$E_i = 1.39 \times 10^{-7} \exp\left(-\frac{1150}{273+50}\right) = 3.95 \times 10^{-9}$$

$$-r_q = E_i C_{HF} = 6.36 \times 10^{-9} \frac{\text{kg-mol quartz}}{\text{m}^2\text{-s}}$$

$$-R_q = (6.36 \times 10^{-9})(9) = 5.72 \times 10^{-8} \frac{\text{kg-mol quartz}}{\text{kg rock-s}}$$

$$-R_q = (5.72 \times 10^{-8})(60.1) = 3.44 \times 10^{-6} \frac{\text{kg quartz}}{\text{kg rock-s}}$$

$$R_{HF} = \left(\frac{5.72 \times 10^{-8} \text{kg-mol quartz}}{\text{kg rock-s}}\right)(6) = 3.43 \times 10^{-7} \frac{\text{mol HF}}{\text{kg rock-s}}$$

- Albite ( $MW = 262$ ,  $\beta = 1.0$ ,  $\alpha = 1.0$ )

$$K = 6.24 \times 10^{-2} \exp\left(\frac{554}{323}\right) = 0.3468$$

$$C_{HCl} = 3.53 \text{ kg mol/m}^3$$

$$E_i = 9.5 \times 10^{-3} \exp\left(-\frac{3930}{323}\right) = 4.938 \times 10^{-8}$$

$$R_A = \left(\frac{10^3 \text{ m}^3}{\text{kg albite}}\right) \left(\frac{0.05 \text{ kg albite}}{\text{kg rock}}\right) \left(1.77 \times 10^{-7} \frac{\text{kg-mol albite}}{\text{m}^2\text{-s}}\right) = 8.84 \times 10^{-8} \frac{\text{kg-mol albite}}{\text{kg rock-s}}$$

$$R_A = 8.84 \times 10^{-8} (262) = 2.32 \times 10^{-5} \frac{\text{kg albite}}{\text{kg rock-s}}$$

$$R_A = 8.84 \times 10^{-8} \frac{\text{kg-mol albite}}{\text{kg rock-s}} \left(20 \frac{\text{kg-mol HF}}{\text{kg-mol albite}}\right) = 1.77 \times 10^{-6} \frac{\text{kg-mol albite}}{\text{kg rock-s}}$$

- Montmorillonite ( $MW = 720$ )

$$E_i = 1.1 \times 10^{-2} \exp\left(-\frac{5200}{323}\right) = 1.12 \times 10^{-9}$$

$$-r_{\text{montmorillonite}} = (1.12 \times 10^{-9})(1.61) = 1.81 \times 10^{-9} \frac{\text{kg-mol montmorillonite}}{\text{m}^2\text{-s}}$$

$$\text{surface area} = \left(8000 \frac{\text{m}^2}{\text{kg montmorillonite}}\right) \left(\frac{0.05 \text{ kg montmorillonite}}{\text{kg rock}}\right) = 400 \frac{\text{m}^2}{\text{kg rock}}$$

$$R_{\text{montmorillonite}} = 7.22 \times 10^{-7} \frac{\text{kg-mol montorillonite}}{\text{kg rock-s}}$$

$$R_{\text{montmorillonite}} = 5.20 \times 10^{-4} \frac{\text{kg montorillonite}}{\text{kg rock-s}}$$

$$R_{\text{montmorillonite}} = 7.22 \times 10^{-7} (40) = 2.89 \times 10^{-5} \frac{\text{kg montorillonite}}{\text{kg rock-s}}$$



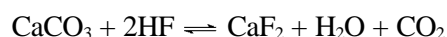
- Reactions of fluosilicic acid with sandstone minerals

As discussed in Section 16-2.1, fluosilicic acid is produced when HF dissolves silicate minerals, and the fluosilicic acid itself may then react with aluminosilicates. From models of coreflood experiments, Bryant (1991) and da Motta *et al.* (1992a, 1992b) suggested that the reaction between fluosilicic acid and clays and feldspars is slow at room temperature, but that it is of the same order of magnitude as the HF reactions with these minerals at temperatures above 125°F [50°C]. These conclusions have been substantiated by more direct experimentation (see Shuchart and Gdanski, 1996).

### 16-2.3. Precipitation of reaction products

A major concern in acidizing, particularly the acidizing of sandstones, is damage caused by the precipitation of acid-mineral reaction products. In acidizing sandstones with HF, the formation of some precipitates is probably unavoidable. However, the amount of damage they cause to the well productivity depends on the amount and location of the precipitates. These factors can be controlled to some extent with proper job design.

The most common damaging precipitates that may occur in sandstone acidizing are calcium fluoride (CaF<sub>2</sub>), colloidal silica (Si(OH)<sub>4</sub>), ferric hydroxide (Fe(OH)<sub>3</sub>) and asphaltene sludges. Calcium fluoride is usually the result of the reaction of calcite with HF, according to



Calcium fluoride is highly insoluble, so the precipitation of CaF<sub>2</sub> is likely if any calcite is available to react with the HF. Inclusion of an adequate HCl pre-flush ahead of the HCl-HF stage prevents the formation of CaF<sub>2</sub>.

Production of some colloidal silica precipitate is probably unavoidable in sandstone acidizing. The equilibrium calculations of Walsh *et al.* (1982) show that there are virtually always regions where the spent acid solution has the tendency to precipitate colloidal silica. However, laboratory corefloods suggest that the precipitation is not instantaneous and in fact may occur at a fairly slow rate (Shaughnessy and Kunze, 1981) that, however, increases with temperature. To minimize the damage caused by colloidal silica, it is probably advantageous to inject at relatively high

rates, so that the potential precipitation zone is rapidly displaced away from the wellbore. Also, spent acid should be produced back immediately after the completion of injection, because shutting in the well for even a relatively short time may allow significant silica precipitation to occur in the near-well vicinity.

When ferric ions (Fe<sup>3+</sup>) are present, they can precipitate from spent acid solutions as Fe(OH)<sub>3</sub> when the pH is greater than about 2. Ferric ions may result from the dissolution of iron-bearing minerals in an oxidative environment or may derive from the dissolution of rust in the tubing by the acid solution. When a high level of ferric ions is likely in the spent acid solution, sequestering agents can be added to the acid solution to prevent the precipitation of Fe(OH)<sub>3</sub>. However, Smith *et al.* (1969) suggested using these sequestrants with caution, as they may cause more damage through their own precipitation than would have been caused by the iron.

Finally, in some reservoirs, contact of the crude oil by acid can cause the formation of asphaltenic sludges. Simple bottle tests in which a sample of crude oil is mixed with the acid can indicate whether the crude has a tendency for sludge formation when contacted by acid. When sludge formation is a problem, emulsions of acid in aromatic solvents or surface-active additives have been used to prevent asphaltene precipitation (Moore *et al.*, 1965).

The tendency for precipitation reactions to occur in acidizing is predicted with comprehensive geochemical models of the chemical reactions between aqueous species and the host of minerals present. The most common type of geochemical model used to study sandstone acidizing is the local equilibrium model, such as described by Walsh *et al.* (1982) and Faber *et al.* (1994). This type of model assumes that all reactions are in local equilibrium; i.e., all reaction rates are infinitely fast. A typical result from this model is shown in Fig. 16-2, a time-distance diagram for the injection of 11% HCl–4% HF into a formation containing calcite, kaolinite and quartz. This plot shows regions where amorphous silica and aluminum fluoride will tend to precipitate. A vertical line on the plot represents the mineral species present as a function of distance if all reactions are in local equilibrium. By coupling this model with a model of the formation permeability response to both dissolution and precipitation, predictions of the productivity improvement expected from particular acid formulations may be obtained, as illustrated in Fig. 16-3 (Faber *et al.*, 1994).

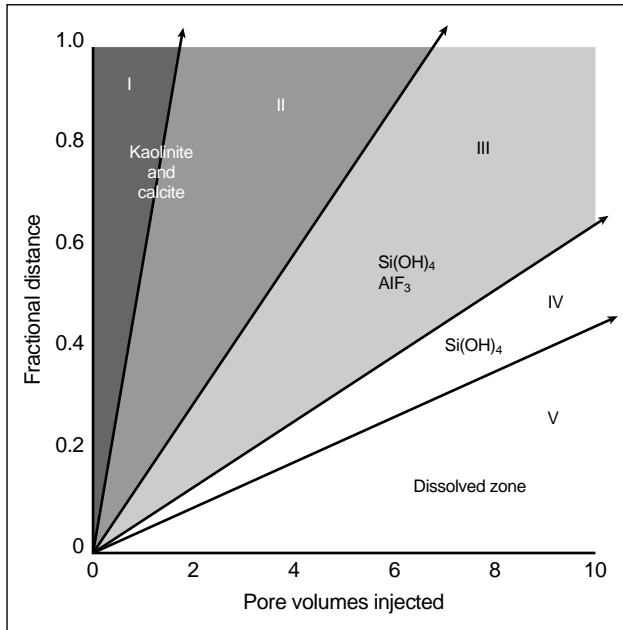


**Figure 16-2.** Time-distance diagram showing regions of possible precipitation (Schechter, 1992).

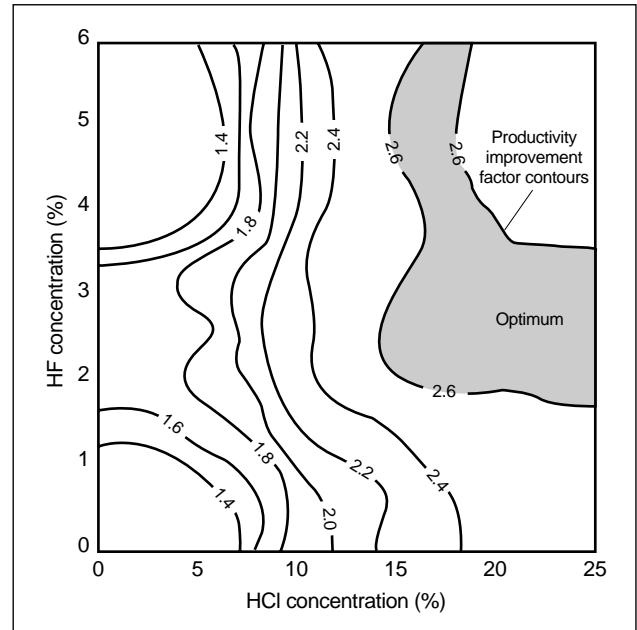


**Figure 16-3.** Productivity improvement plot (Faber et al., 1994).

Recently, Sevougian *et al.* (1992) and Quinn (1994) presented a geochemical model that includes kinetics for both dissolution and precipitation reactions (see Sidebar 16C). This model predicts less permeability

damage than a local equilibrium model because the finite rate of the reactions allows displacing the precipitate farther from the wellbore.

### 16C. Geochemical model predictions

An example presented by Quinn (1994) illustrates how acid formulation can be evaluated with a comprehensive geochemical model. A high-quartz-content sandstone will be acidized with 100 gal/ft of 12% HCl–3% HF solution (commonly referred to as full-strength mud acid). The mineralogy is illustrated in Fig. 16C-1. The region to be studied includes a damaged zone extending 6 in. beyond the wellbore.

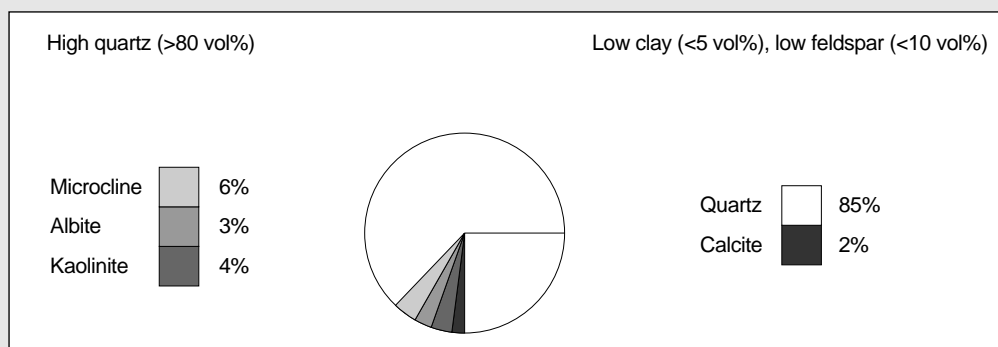


**Figure 16C-1.** A representative sandstone used in acidizing simulation.

The geochemical model predicts the distribution of acid and minerals after injection of the acid, as shown in Fig. 16C-2. All the HF is consumed near the wellbore; some precipitation occurs, but the amorphous silica precipitation occurs beyond the damage zone, where its effect is small. From these results, the porosity distribution around the wellbore is determined. Then, a model of the permeability response generates a prediction of the productivity improvement expected for this treatment.

## 16C. Geochemical model predictions (continued)

By repeating this modeling procedure for many different acid concentrations, the optimal acid formulation can be determined (Fig. 16C-3). For this formation, 3% HF and high HCl concentrations are optimal.

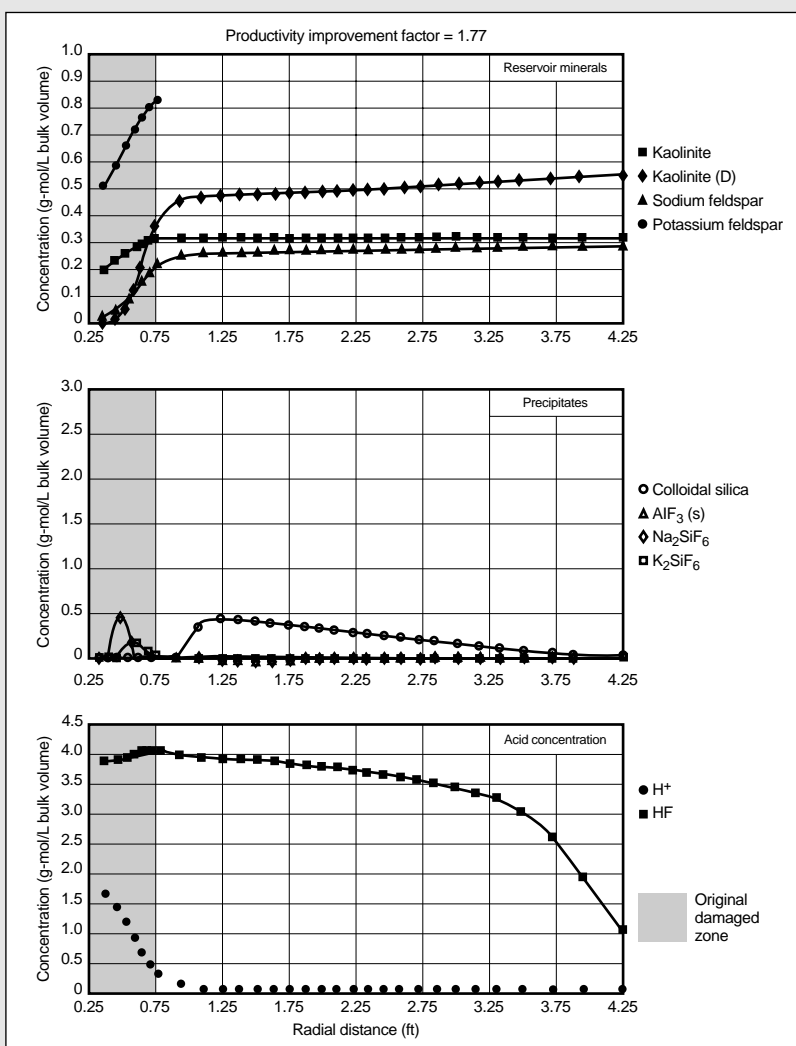


**Figure 16-C-2.** Partial local equilibrium assumption (PLEA) model mineral profile of a high-quartz sandstone after acidization with 100 gal/ft of 12% HCl–3% HF injected at 0.1 bbl/min/ft at 125°F [50°C].

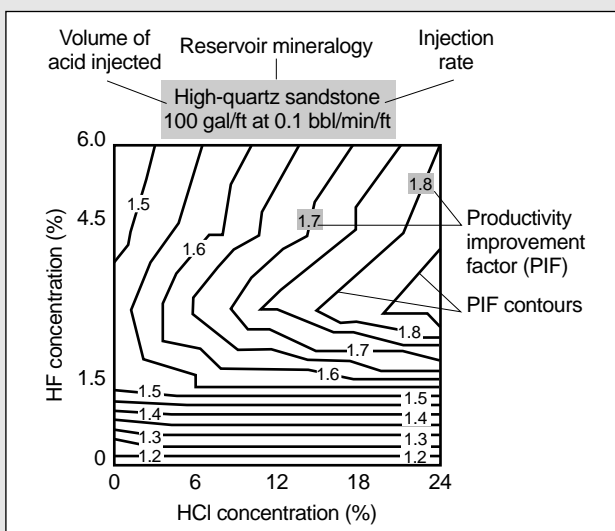


**Figure 16C-3.** Productivity improvement plot.

## 16-3. Sandstone acidizing

### 16-3.1. Introduction

A typical acid treatment in sandstones consists of the injection of an HCl preflush, with 50 gal/ft of formation a common preflush volume, followed by the injection of 50 to 200 gal/ft of HCl-HF mixture. A postflush of diesel, brine or HCl then displaces the HCl-HF from the tubing or wellbore. Once the treatment is completed, the spent acid should be immediately produced back to minimize damage by the precipitation of reaction products.

A sandstone acidizing treatment design begins with the selection of the type and concentration of acid to be used. The volumes of preflush, HCl-HF mixture and postflush required and the desired injection rate(s) are considered next. In virtually all acid treatments, the placement of the acid is an important issue—a strategy to ensure that sufficient volumes of acid contact all productive parts of the formation should be carefully planned. Proper execution of the treatment is critical to acidizing success, so the conduct of the treatment, including the mechanical arrangements for introducing the acid to the formation and the methods of treatment monitoring, should be planned in detail. Finally, numerous additives are incorporated with acid solutions for various purposes. The types and amounts of additives to be used in the treatment must be determined on the basis of the completion, formation and reservoir fluids. These design factors are considered in detail in other chapters: acid selection in Chapters 13 and 18, treatment design (rate and volume) in Chapter 18, fluid placement and diversion in Chapter 19, treatment monitoring and evaluation in Chapter 20 and acid additives in Chapter 15. This section presents models of the sandstone acidizing process that provide a foundation for the design methods used for field application.

### 16-3.2. Acid selection

The type and strength (i.e., concentration) of acid used in sandstones are selected primarily on the basis of field experience with particular formations. For years, the standard sandstone acidizing formulation consisted of a 12% HCl–3% HF mixture, preceded by a 15% HCl preflush. In fact, the 12% HCl–3% HF mixture has been so common that it is referred to generically as mud acid. In recent years, however, the trend has been toward the use of lower strength HF solutions

(Brannon *et al.*, 1987). The benefits of lower concentration HF solutions are a reduction in damaging precipitates from the spent acid and lessened risk of unconsolidation of the formation around the wellbore. The selection of acidizing fluids should always begin with an assessment of the formation damage present—in general, the damaging material must be soluble in the treating fluids. Geochemical models can be used to guide acid selection, once the composition of the damaged formation is determined, as described in Section 16-2.3. Chapters 17 and 18 provide a comprehensive treatment of acid selection for sandstone and carbonate reservoirs, respectively.

### 16-3.3. Sandstone acidizing models

#### • Two-mineral model

Numerous efforts have been made over the years to develop a comprehensive model of the sandstone acidizing process that could then be used as a design aid. The most common model in use today is the two-mineral model (Hill *et al.*, 1977; Hekim *et al.*, 1982; Taha *et al.*, 1989) that divides all minerals into two categories—fast-reacting and slow-reacting species. Schechter (1992) categorizes feldspars, authogenic clays and amorphous silica as fast reacting, and detrital clay particles and quartz grains are the primary slow-reacting minerals. The model consists of material balances applied to the HF acid and reactive minerals, which for linear flow, such as in a coreflood, are

$$\frac{\delta(\phi C_{HF})}{\delta t} + u \frac{\delta C_{HF}}{\delta x} = -\{S_F^* V_F E_{f,F} + S_S^* V_S E_{f,S}\}(1-\phi)C_{HF} \quad (16-12)$$

$$\frac{\delta}{\delta t}[(1-\phi)V_F] = \frac{-MW_{HF}S_F^*V_F\beta_F E_{f,F}C_{HF}}{\rho_F} \quad (16-13)$$

$$\frac{\delta}{\delta t}[(1-\phi)V_S] = \frac{-MW_{HF}S_S^*V_S\beta_S E_{f,S}C_{HF}}{\rho_S} \quad (16-14)$$

In these equations,  $C_{HF}$  is the concentration of HF in solution and  $MW_{HF}$  is its molecular weight,  $u$  is the acid flux,  $s$  is the distance,  $S_F^*$  and  $S_S^*$  are the specific surface areas per unit volume of solids,  $V_F$  and  $V_S$  are the volume fractions,  $E_{f,F}$  and  $E_{f,S}$  are the reaction rate constants (based on the rate of consumption of HF),  $MW_F$  and  $MW_S$  are the molec-

ular weights,  $\beta_F$  and  $\beta_S$  are the dissolving powers of 100% HF, and  $\rho_F$  and  $\rho_S$  are the densities of the fast- and slow-reacting minerals, respectively, denoted by the subscripts  $F$  and  $S$ . When made dimensionless, assuming porosity remains constant, these equations become

$$\frac{\delta\psi}{\delta\theta} + \frac{\delta\psi}{\delta\epsilon} + \{Da^{(F)}\Lambda_F + Da^{(S)}\Lambda_S\}\psi = 0 \quad (16-15)$$

$$\frac{\delta\Lambda_F}{\delta\theta} = -Da^{(F)}A_c^{(F)}\psi\Lambda_F \quad (16-16)$$

$$\frac{\delta\Lambda_S}{\delta\theta} = -Da^{(S)}A_c^{(S)}\psi\Lambda_S, \quad (16-17)$$

where the dimensionless variables are defined as

$$\psi = \frac{C_{HF}}{C_{HF}^o} \quad (16-18)$$

$$\Lambda_F = \frac{V_F}{V_F^o} \quad (16-19)$$

$$\Lambda_S = \frac{V_S}{V_S^o} \quad (16-20)$$

$$\epsilon = \frac{x}{L} \quad (16-21)$$

$$\theta = \frac{ut}{\phi_o L}, \quad (16-22)$$

where  $\psi$  is the dimensionless HF concentration,  $\Lambda$  is the dimensionless mineral composition,  $\epsilon$  is dimensionless distance,  $\theta$  is dimensionless time (pore volumes), and  $\phi$  is the porosity. The superscript  $o$  denotes initial values prior to acid treatment. For a coreflood,  $L$  is the core length. In Eqs. 16-15 through 16-17, two dimensionless groups appear for each mineral: the Damköhler number  $Da$  and the acid capacity number  $A_c$ . These two groups describe the kinetics and the stoichiometry of the HF-mineral reactions. The Damköhler number is the ratio of the rate of acid consumption to the rate of acid convection, which for the fast-reacting mineral is

$$Da^{(F)} = \frac{(1 - \phi_o)V_F^o E_f^{(F)} S_F^* L}{u} \quad (16-23)$$

The acid capacity number is the ratio of the amount of mineral dissolved by the acid occupying

a unit volume of rock pore space to the amount of mineral present in the unit volume of rock, which for the fast-reacting mineral is

$$A_c^{(F)} = \frac{\phi_o \beta_F C_{HF}^o MW_{HF}}{(1 - \phi_o)V_F^o \rho_F}. \quad (16-24)$$

The Damköhler and acid capacity numbers for the slow-reacting minerals are similarly defined.

As acid is injected into a sandstone, a reaction front is established by the reaction between the HF and the fast-reacting minerals. The shape of this front depends on  $Da^{(F)}$ . For low values of  $Da$ , the convection rate is high relative to the reaction rate and the front is diffuse. With a high  $Da$ , the reaction front is relatively sharp because the reaction rate is high compared with the convection rate. Figure 16-4 (da Motta *et al.*, 1992a) shows typical concentration profiles for high and low values of  $Da^{(F)}$ .

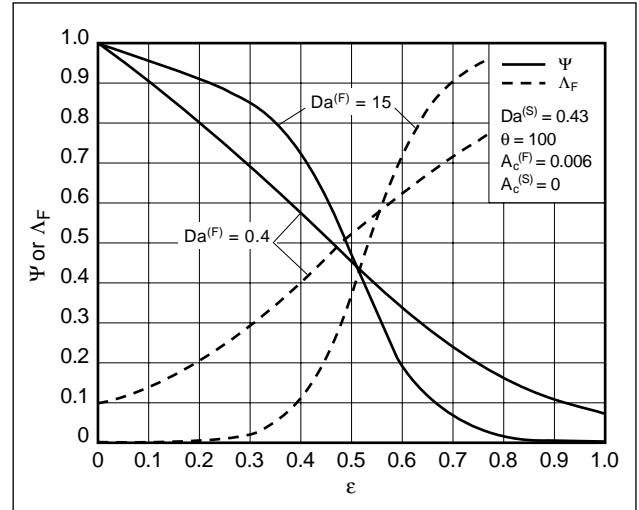


**Figure 16-4.** Acid and fast-reacting mineral concentration profiles (da Motta *et al.*, 1992a).

Equations 16-15 through 16-17 can be solved only numerically in their general form. Numerical models providing solutions to these equations, such as that presented by Taha *et al.* (1989), are frequently used for acidizing design. However, analytical solutions are possible for certain simplified situations. Schechter (1992) presented an approximate solution that is valid for relatively a high  $Da$  ( $Da^{(F)} > 10$ ). This solution approximates the HF/fast-reacting-mineral front as a sharp front, behind which all the fast-reacting minerals have been removed. Conversely, ahead of the front, no dissolution has occurred. The reaction between slow-reacting minerals and HF

behind the front serves to diminish the HF concentration reaching the front. The location of the front is

$$\theta = \frac{\exp(Da^{(S)}\epsilon_f) - 1}{A_c^{(F)} Da^{(S)}} + \epsilon_f, \quad (16-25)$$

which relates dimensionless time (or equivalently acid volume) to the dimensionless position of the front  $\epsilon_f$ , defined as the position of the front divided by the core length for linear flow. The dimensionless acid concentration behind the front is

$$\psi = \exp(-Da^{(S)}\epsilon). \quad (16-26)$$

A particularly convenient feature of this approximation is that it is applicable to linear, radial and ellipsoidal flow fields with the appropriate definition of dimensionless variables and groups. Radial flow represents the flow of acid from an openhole, gravel-pack or slotted liner completion and may also be a reasonable approximation of the flow from a perforated well with sufficient perforation density. The ellipsoidal flow geometry approximates the flow around a perforation (Fig. 16-5). The proper dimensionless variables and groups for these three flow fields are given in Table 16-6. For the perforation geometry, the position of the front  $\epsilon_f$  depends on position along the perforation. In Table 16-6, expressions are given for the front position of the acid extending directly from the tip of the perforation and for acid penetration along the wellbore wall.

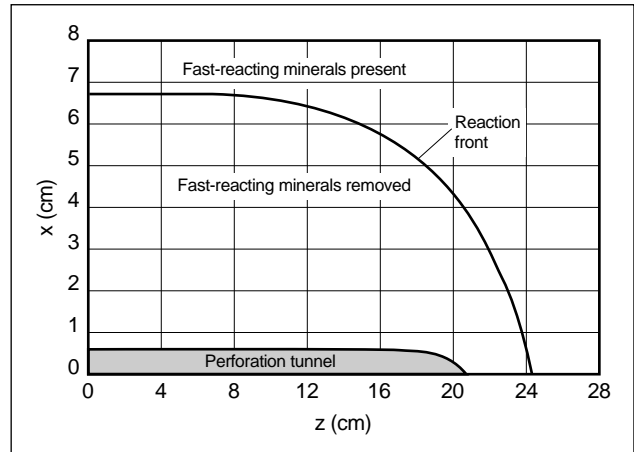


**Figure 16-5.** Ellipsoidal flow around a perforation (Schechter, 1992).

These two positions should be sufficient for design purposes; the reader is referred to Schechter (1992) for methods to calculate the complete acid penetration profile in this geometry (see Sidebar 16D).

The characteristic lengths referred to in Table 16-6 are the length of a core  $L$ , wellbore radius  $r_w$  and length of the perforation  $l_p$ . Different measures of acid flow are used in which  $u$  is the linear flux in a core,  $q_i/h$  is the volumetric rate of acid injection per foot into an openhole, and  $q_{perf}$  is the volume of acid per time entering a perforation. The definition of  $Da$  must correspond to the geometry considered, but  $\Psi$ ,  $\Lambda_F$  and  $A_c^{(F)}$  as defined by Eqs. 16-18, 16-19 and 16-24, respectively, apply to all geometries.

**Table 16-6. Dimensionless groups in sandstone acidizing models.**

Flow geometry	$\epsilon$	$\theta$	$Da^{(S)}$
Linear	$\frac{x}{L}$	$\frac{ut}{\phi_o L}$	$\frac{(1-\phi_o)V_s E_t^{(S)} S'_s L}{u}$
Radial	$\frac{r^2}{r_w^2} - 1$	$\frac{q_i t}{\pi r_w^2 h \phi_o}$	$\frac{(1-\phi_o)V_s E_t^{(S)} S'_s \pi r_w^2 h}{q_i}$
Ellipsoidal			
Penetration from the tip of the perforation	$\frac{1}{3}\bar{z}^3 - \bar{z} + \frac{2}{3}; \bar{z} = \frac{z}{l_p}$	$\frac{q_{perf} t}{2\pi l_p^3 \phi_o}$	$\frac{2\pi(1-\phi_o)l_p^3 S'_s V_s E_t^{(S)}}{q_{perf}}$
Penetration adjacent to the wellbore	$\frac{1}{3}\left(\bar{x} + \frac{1}{\bar{x} + \sqrt{\bar{x}^2 + 1}}\right)^3 - \frac{1}{3}; \bar{x} = \frac{x}{l_p}$		

## 16D. Comparison of acid volumes for radial and perforation flow

The amount of acid required to remove damage beyond the tip of a perforation is typically larger than the amount required to remove damage to the same distance in radial flow. This is illustrated by using Schechter's (1992) model to find the volume of acid required to penetrate a given distance for these two geometries.

Consider a formation with 20% porosity containing 10% fast-reacting minerals (feldspar, clay or both), 5% calcium carbonate and 85% quartz. A damage region extends 6 in. into the formation (a radial region or 6 in. beyond the tip of a perforation), and the initial skin effect resulting from the damage is 10. The wellbore radius is 0.328 ft. In the perforated well case, there are 4 shots per foot (spf) and the perforations are 6 in. long with a diameter at the wellbore of 0.5 in. A 12% HCl–3% HF solution is injected at 0.1 bbl/min/ft after the injection of sufficient preflush of 15% HCl to remove the carbonates from the region to be contacted with live HF. Determine the acid volume required as a function of the penetration distance of the acid and the skin effect evolution for radial and perforation geometries. The downhole treating temperature is 125°F [50°C]. For these conditions, the Damköhler number  $Da$  for the slow-reacting mineral in radial flow is 0.013.

### Solution

Equation 16-25 can be used with the appropriate definitions of the dimensionless variables and groups for the two geometries from Table 16-6. The acid capacity number  $A_c$  is the same for either geometry; the ratio of the Damköhler numbers is

$$\frac{Da_{\text{perf}}}{Da_{\text{rad}}} = \frac{21_{\text{perf}}^3 (SPF)}{r_w^2} = \frac{(2) \left(\frac{6}{12}\right)^3}{(0.328)^2} = 93, \quad (16D-1)$$

where  $SPF$  is the perforation density in spf.  $Da$  for the slow-mineral reaction is calculated as 0.12 for perforation flow.  $A_c$  for the fast-mineral reaction is 0.021. (The values of  $Da$  and  $A_c$  used in this example were obtained from laboratory core-flood tests as described by Economides *et al.*, 1994).

Using these values in Eq. 16-25 for acid penetration ranging from 0 to 6 in. obtains the results shown in Figs. 16D-1 and 16D-2. For acid penetrations beyond 2 in., more acid is required for the perforation geometry than for radial flow. The skin effect evolution reflects the larger volumes of acid required to penetrate through the damaged region for the perforation geometry compared with the radial geometry.

It is interesting to note that the slow-reacting mineral  $Da$  and the fast-reacting mineral  $A_c$  are the only dimensionless groups that appear in this solution.  $Da^{(S)}$  regulates how much live HF reaches the front; if the slow mineral reacts fast relative to the convection rate, little acid is available to propagate the fast-mineral front.  $A_c$  for the slow-reacting mineral is not important because the supply of slow-reacting mineral is almost constant behind the front.  $A_c^{(F)}$  directly affects the frontal propagation rate—the more fast-reacting mineral present, the slower the front will move.  $Da^{(F)}$  does not appear because a sharp front

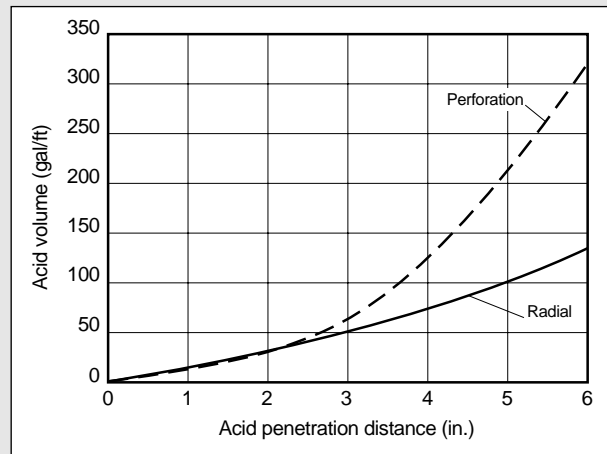


Figure 16D-1. Acid penetration for radial and perforation flow.

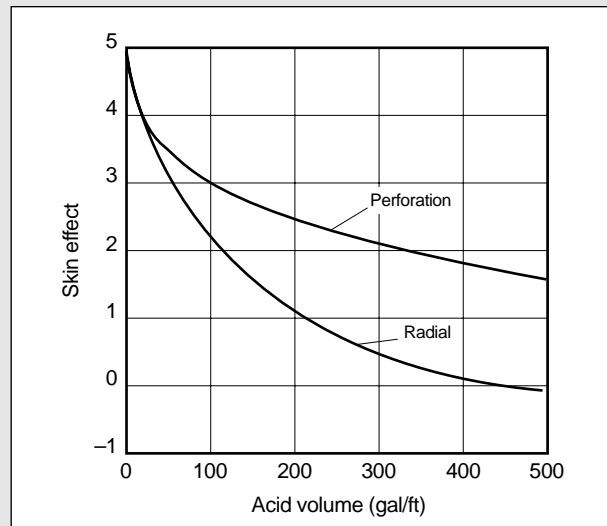


Figure 16D-2. Reduction in skin effect value for radial and perforation flow.

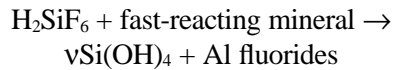
is assumed, implying that  $Da^{(F)}$  is infinite. This solution can be used to estimate the volume of acid required to remove the fast-reacting minerals from a given region around a wellbore or perforation.

The dimensionless groups  $Da^{(S)}$  and  $A_c^{(F)}$  can be calculated with Eqs. 16-23 and 16-24, respectively, and Table 16-6 on the basis of the rock mineralogy or can be obtained from experiments.

- Two-acid, three-mineral model

Recently, Bryant (1991) and da Motta *et al.* (1992b) presented evidence that the sandstone acidizing

process is not well described by the two-mineral model, particularly at elevated temperatures. These studies suggest that the reaction of fluosilicic acid with aluminosilicate (fast-reacting) minerals may be significant. Thus, an additional acid and mineral must be considered to accommodate the following reaction, which is added to the two-mineral model:



The practical implications of the significance of this reaction are that less HF is required to consume

the fast-reacting minerals with a given volume of acid because the fluosilicic acid also reacts with these minerals and the reaction product of silica gel ( $\text{Si(OH)}_4$ ) precipitates. This reaction allows live HF to penetrate farther into the formation; however, there is an added risk of a possibly damaging precipitate forming.

Sumotarto (1995) presented an example that illustrates the improved performance predicted with the two-acid, three-mineral model compared with the one-acid, two-mineral model. Figure 16-6 compares the mineral concentration profiles predicted by these

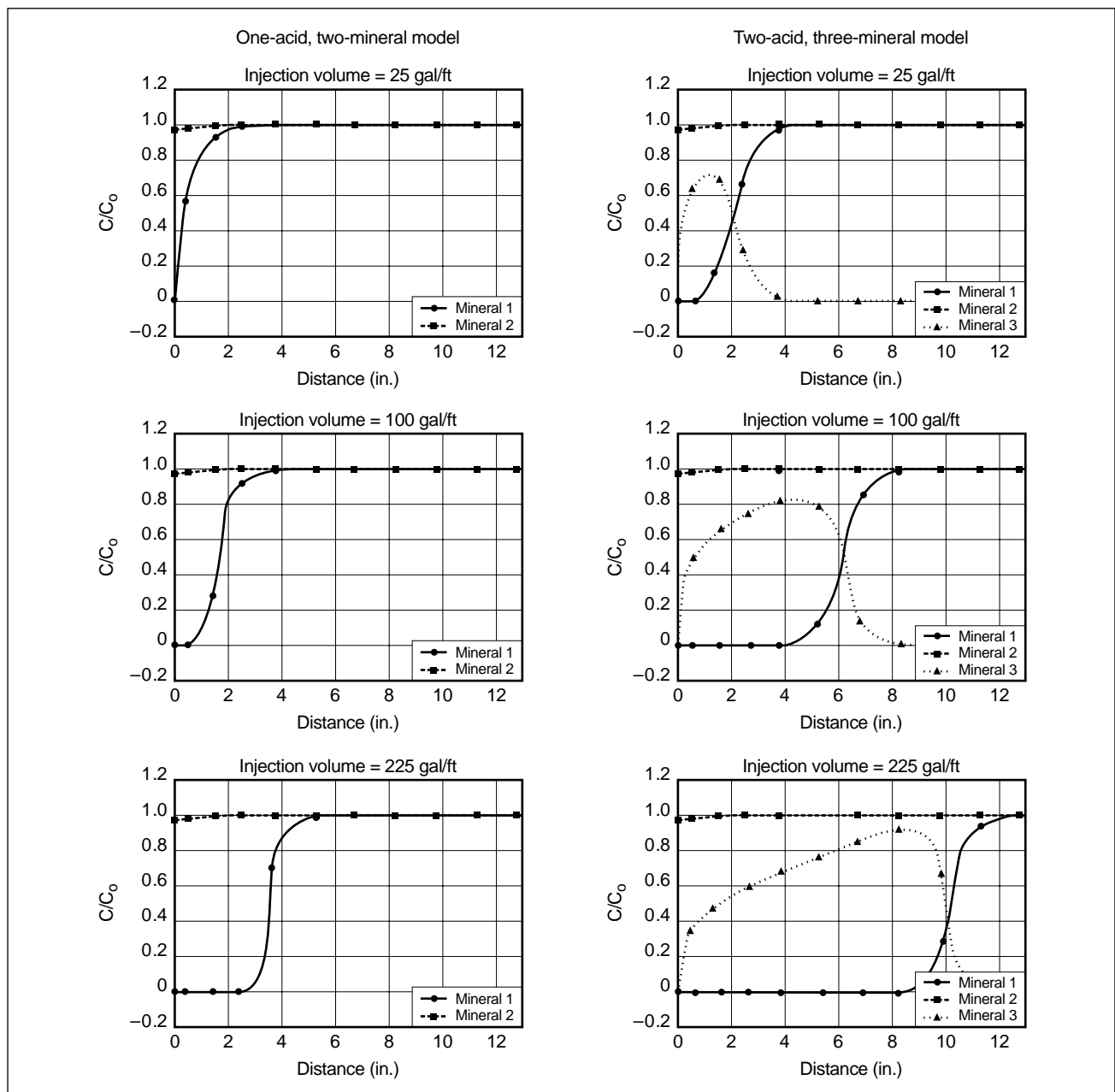


**Figure 16-6.** Dimensionless mineral concentrations at various injection volumes.



two models for the injection of 12% HCl–3% HF into a damaged formation composed initially of 17% clays and feldspars (fast reacting) and 83% quartz (slow reacting). In this figure, mineral 1 is clay and feldspar, mineral 2 is quartz, and mineral 3 is silica gel. After 100 gal/ft of injection, the feldspars and clays have been dissolved in a region extending about 6 in. beyond the wellbore according to the two-acid, three-mineral model, whereas only 2 in. of dissolution is predicted by the one-acid, two-mineral model. In addition, a significant zone of silica

precipitation is predicted by the two-acid, three-mineral model. Using a model of the permeability response to both mineral dissolution and precipitation, the permeability and skin effect response are predicted for each model and compared in Figs. 16-7 and 16-8. Although some precipitation is indicated by the two-acid, three-mineral model, improved performance because of the fluosilicic acid reactions is predicted compared with the one-acid, two-mineral model.

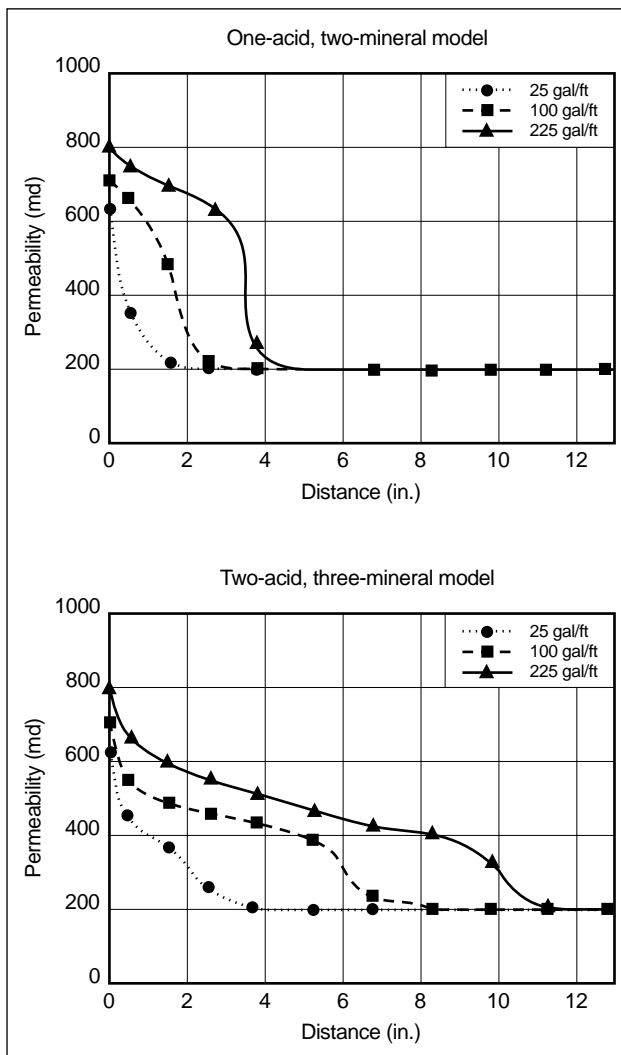


**Figure 16-7.** Permeability at various injection volumes.

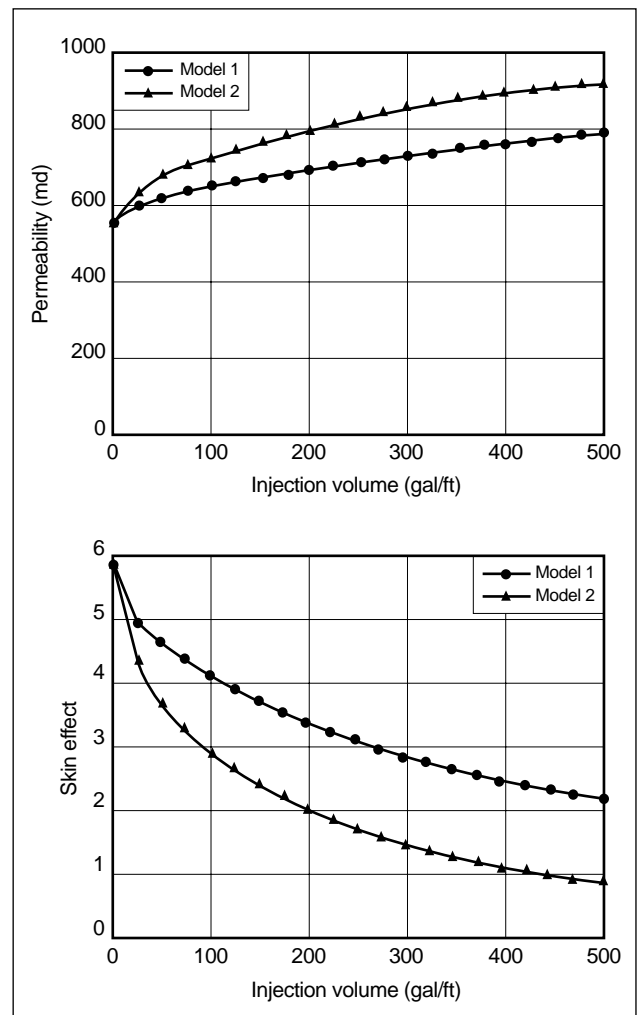


**Figure 16-8.** Top: Average permeability versus injection volume obtained from running the simulator with models 1 (one-acid, two-mineral model) and 2 (two-acid, three-mineral model). Bottom: Skin effect calculated using models 1 and 2 as a function of injection volume (time).

### 16-3.4. Permeability response

To predict the response of a formation to acidizing, it is necessary to predict the change in permeability as acid dissolves some of the formation minerals and other minerals precipitate. The permeability change as a result of acidizing is an extremely complicated process because it is affected by several different, sometimes competing phenomena in the porous media. The permeability increases as the pores and pore throats are enlarged by mineral dissolution. At the same time, small particles are released as cementing material is dissolved, and some of these particles lodge (perhaps temporarily) in pore throats, reducing the permeability. Any precipitates formed also tend to decrease the permeability. The formation of carbon dioxide (CO<sub>2</sub>) as carbonate minerals are dissolved may also cause a temporary reduction in the relative permeability to liquids. The result of these competing effects is that the permeability in corefloods usually decreases initially; with continued acid injection, the permeability eventually increases to values significantly higher than the original permeability.

The complex nature of the permeability response has made its theoretical prediction for real sandstones impractical, though some success has been achieved for more ideal systems such as sintered disks (Guin *et al.*, 1971). As a result, empirical correlations relating the permeability increase to the porosity change during acidizing are used. The most common correlations are those of Labrid (1975), Lund and Fogler (1976) and Lambert (1981). The Labrid correlation is

$$\frac{k}{k_o} = M \left( \frac{\phi}{\phi_o} \right)^n, \quad (16-27)$$

where  $k_o$  and  $\phi_o$  are the initial permeability and porosity and  $k$  and  $\phi$  are the permeability and porosity after acidizing, respectively.  $M$  and  $n$  are empirical constants, reported to be 1 and 3, respectively, for Fontainebleau sandstone.

The Lund and Fogler correlation is

$$\frac{k}{k_o} = \exp \left[ M \left( \frac{\phi - \phi_o}{\Delta\phi_{max}} \right) \right], \quad (16-28)$$

where  $M = 7.5$  and the difference in maximum porosity is  $\Delta\phi_{max} = 0.08$  from best-fit data for Phacoides sandstone.

The Lambert correlation is

$$\frac{k}{k_o} = \exp[45.7(\phi - \phi_o)]. \quad (16-29)$$

The Lambert expression is identical to that of Lund and Fogler when  $M/\Delta\phi_{max} = 45.7$ .

Using the values of the constants suggested, the Labrid correlation predicts the smallest permeability increase, followed by the Lambert and then the Lund and Fogler correlations. The best approach in using these correlations is to select the empirical constants on the basis of coreflood responses, if available. If data are lacking for a particular formation, the Labrid equation will yield the most conservative design.

## 16-4. Carbonate acidizing

### 16-4.1. Distinctive features

In this chapter, sandstone acidizing is distinguished from carbonate acidizing although sedimentary rocks exhibit a spectrum of compositions ranging from almost pure calcite or dolomite to very clean sands. The fundamental distinguishing feature is the HCl-soluble fraction. If the HCl solubility of a rock is less than 20%, a sandstone treatment using an HCl-HF mixture (for a discussion of such rules of thumb, see McLeod, 1984) would most likely be applied. Formations composed largely of calcite or dolomite, including chalks and marls, are largely soluble in HCl and are candidates for carbonate acidizing using HCl without HF.

Carbonate acidizing with HCl is not complicated by a tendency for precipitates to form, as is the case for sandstone acidization. As shown by the typical reactions in Table 16-1, the reaction products CO<sub>2</sub> and CaCl<sub>2</sub> are both quite water soluble (for a discussion of their solubilities, see Shaughnessy and Kunze, 1981; Schechter, 1992). Therefore, the formation of a precipitate or a separate CO<sub>2</sub>-rich phase is generally not a problem. Even if CaCl<sub>2</sub> precipitates or a CO<sub>2</sub> phase separates, these phases are readily dissolved when oil (or gas) and water production is resumed. Despite the simplified chemistry, HCl acidizing is a difficult process to model. The origin of the difficulty is the rate at which the reactions take place as compared with those of HF with the various minerals prevalent in sandstones. Reaction rates are discussed in Section 16-2.2, and it is instructive to compare some of them. HCl reactions with carbonates are orders of magnitude faster than HF reactions with sand (quartz), clays, etc.

Because of the high reaction rate, HCl tends to etch preferred pathways in carbonate rocks, apparently following local high-permeability streaks (Wang, 1993),

rather than progressing through the formation as a uniform front, as is the case in sandstone acidizing. These pathways are soon enlarged by acid reaction at the walls into sizable holes that have a diameter much larger than that of naturally occurring pores. The process continues until a few large holes become so dominant that essentially all the injected acid flows through these pathways, both enlarging and extending them.

It is this tendency for macroscopic pathways to form that makes HCl acidizing difficult to model. Because the holes that form are large, they become the most important feature of the process. To model carbonate acidizing, the formation of these holes must be taken into account. In fact, it is believed that the success of acid stimulation of carbonate formations is due to the formation of these preferred flow paths extending outward from the wellbore or perforation. If the pathways extend through the damaged zone, the produced fluids can flow into the wellbore through these flow paths with relatively little pressure drop because the holes are much larger than the natural pores.

Thus, the fundamental physics of carbonate acidizing is embodied in three topics discussed in this section. The first concern is the characterization of the holes or flow paths created by the acid. Second, the conditions under which they form must be defined. And third, the rate at which they are extended is an issue of considerable practical significance.

### 16-4.2. Wormholes

It is not known who first described the acid-etched pathway as a “wormhole,” but this appellation is commonly accepted by those familiar with the complex etch pattern produced by acidizing carbonate cores in the laboratory. Perhaps it was A. R. Hendrickson of Dowell. Figure 16-9 shows that the terminology is apt. This is a photograph of a metal casting of a wormhole created by forcing molten metal into a wormhole, allowing the metal to solidify and then dissolving the remaining rock with HCl. The casting illustrates the complex morphology of the etch pattern. This is typical of many castings, which have been produced under a variety of experimental conditions. The chaotic nature of the pattern seemingly discourages any attempt to characterize its structure. However, it has been suggested that there is an underlying regularity that may be useful for modeling.

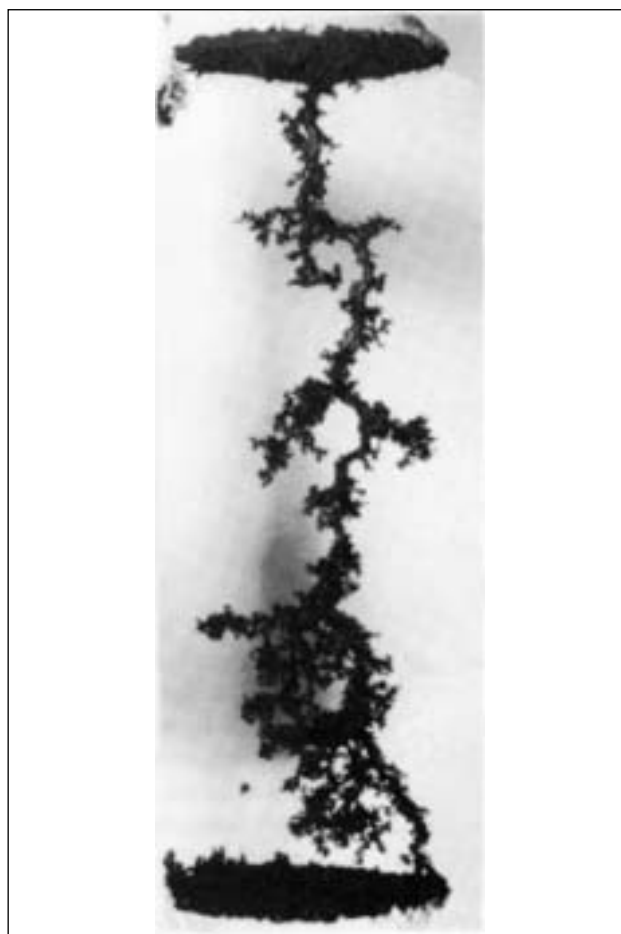


**Figure 16-9.** Wormholes created by acid dissolution of limestone (Hoefner and Fogler, 1988; reproduced with permission of the American Institute of Chemical Engineers. Copyright 1998 AIChE. All rights reserved.).

Daccord and Lenormand (1987) considered the characterization of a wormhole in terms of its fractal dimension. A fractal is a self-similar geometric pattern. This implies that under increasing magnification the same pattern will continue to reappear. Thus, according to this notion the structure of a large wormhole is repeated with branches from the main trunk that are smaller replicas of the larger one. This replication is repeated as the magnification is increased until the pores of the native rock come into view. These do not resemble acid etch patterns because they were created by different processes. The discovery by Daccord and Lenormand that wormholes are fractals is a significant contribution.

One manifestation of the repeating, or self-similar, character is that the perimeter or the length of a wormhole increases as the degree of magnification used in

its measurement increases. This is because at higher magnification, more of the detailed structure becomes evident and is, therefore, susceptible to measurement. For self-similar systems, the length of a wormhole plotted against the length of a ruler used to measure the length is a straight line on a log-log plot. The slope of this line is related to the fractal dimension. In the case of wormholes, Daccord and Lenormand reported that the fractal dimension is 1.6. This implies that the length of a wormhole is proportional to  $L^{1.6}$  rather than  $L$ , where  $L$  is the macroscopic length. Daccord *et al.* (1989) utilized this fractal dimension in developing a field design method for carbonate acidizing. In their approach, the complexity of the wormhole is portrayed by its fractal dimension. This is only a partial characterization, because it is not possible to describe the minute details of wormhole geometry.

Although a precise description of a wormhole is not attainable, it is desirable to have a model that provides guidance in determining the best treatment parameters. What should be the injection rate? Should the injection rate be constant during the entire course of the treatment? What acid type and concentration are best? What additives should be included in the acidic solution? These questions relate to controllable variables and, therefore, must be addressed each time an acid treatment is designed. Rather than depending solely on past experience, some theoretical help is welcome for developing the best strategy possible based on the information available.

The problem is approached in the following sections by addressing two separate issues, both of which are relevant to the questions posed. The first concerns the conditions requisite for the initiation of wormholes, and the second deals with their growth or propagation. Both of these studies provide information required for the design of carbonate acid treatments. The Appendix to this chapter discusses advances in understanding and predicting wormhole formation.

### 16-4.3. Initiation of wormholes

The fractal, or self-similar, topology of a wormhole structure implies that the mechanism for the initiation of wormholes is a “local” phenomenon that occurs continuously along its bounding surfaces as well as at its tip. Thus, tiny wormholes may be initiated whenever live acid enters the pores of the virgin rock irrespective of the etch pattern already in existence. Experiments have shown that in cases where the acid

flux entering the matrix is quite small, wormhole initiation is not prolific, thereby indicating a flow-rate dependence of the initiation process. The proof of this assertion is based primarily on metal casts of wormholes, such as that shown by Fig. 16-9. However, adopting the notion of a flow-rate-dependent initiation process allows interpreting the results of laboratory acidizing experiments and understanding the origin of the fractals. Furthermore, this approach leads to prediction of the optimum injection rate in linear core experiments that has been experimentally observed. Thus, the analysis presented here represents a foundation upon which the design of acid treatments can be based, but further work is required to achieve the desired goal, namely, the ability to predict the stimulation resulting from an acid treatment given the essential parameters of acid composition, injection rate, formation temperature and rock properties.

The initiation of wormholes occurs when live acid penetrates into pores present in the native rock. These pores are distributed in size and shape; therefore, the amount of acid flowing through each of the pores differs. The rate at which a given pore is enlarged by the acid depends, of course, on the amount of acid entering that pore and the fraction of the acid reacted at the walls of the pore before the acid exits and then enters other pores located downstream. Thus, even at the pore level, the processes that contribute to the creation of an etch pattern are complex, involving convection, diffusion and chemical reactions within each of the invaded pores. It has not been proved practical to consider these processes in a single pore and then attempt to consider the collective behavior to derive a macroscopic etch pattern. Schechter and Gidley (1969) used this approach, but to make progress using their results requires knowing in advance the entire distribution of pore sizes, permeability and porosity of the native rock to be acidized. Even armed with this knowledge, which is seldom available, prediction of the etch pattern is not routine.

The prediction of wormhole initiation is, however, based on a result that emerged from considering the behavior of each pore in the medium. If a pore is represented as a cylindrical hole with a radius  $R$  and a length  $l$ , then the rate at which the pore cross-sectional area  $A$  increases as a result of acid reaction at the pore walls may, in general, be written in the form

$$\frac{dA}{dt} = \psi A^n, \quad (16-30)$$

where  $\psi$  is a function of the fluid velocity in the pore, reaction rate and other parameters that determine the rate at which rock is dissolved. The exponent  $n$  is also a function of the many parameters that contribute to  $\psi$ . The advantage of representing the rate of acid reaction within a pore in this form is that the stability of the enlargement process depends on the value of the exponent  $n$  (see Schechter, 1992). If  $n > 1$  for a certain few pores in the native rock, then these pores become larger faster than all the other pores that have growth characterized by exponents smaller than unity. This criterion for uncontrolled growth determines whether a wormhole is initiated. The growth of each individual pore is characterized by the value of the exponent  $n$ . Wormholes form whenever one or more of the pores grow at a rate determined by  $n > 1$ .

Thus, this criterion for wormhole initiation hinges on the value on the exponent  $n$ . To investigate the factors determining  $n$ , recall that the rate of acid reaction at a pore wall is given by the empirical expression

$$\text{reaction rate} = -E_f C_w^m. \quad (16-31)$$

The acid concentration  $C_w$  in this equation is the concentration near the solid/liquid interface. The acid that reacts at the pore surface must be replenished by acid diffusing from the bulk solution to the pore wall. If this diffusion rate is slow, the rate of pore area enlargement may be limited by diffusion. However, the native pores are generally small enough so that diffusion is relatively fast, and the average velocity within a pore  $\bar{v}$  is sufficient to maintain a rate of mass transfer to the surface so that the acid reaction at the wall is the controlling factor. The rate at which a pore is enlarged is, therefore, (see Schechter, 1992)

$$l \frac{dA}{dt} = \bar{v} A X C_0 \left[ 1 - \exp \left( - \frac{2\sqrt{\pi} E_f C_0^{m-1} l}{\sqrt{A} \bar{v}} \right) \right], \quad (16-32)$$

where  $l$  is the length of a pore defined as the distance the acid in a pore travels before mixing with acid emerging from other pores. The acid concentration  $C_0$  is the concentration at the pore entrance.

The average velocity in a pore  $\bar{v}$  depends on the local Darcy flux  $u$  and the pore cross-sectional area. The flow within a single pore is laminar, so that

$$\bar{v} = \frac{dp}{dt} \frac{A}{8\pi\mu} = \frac{uA}{8\pi k}, \quad (16-33)$$

where  $k$  is the permeability of the rock matrix.

Equation 16-32 looks formidable, but the goal is to reduce this expression to a form that reveals the exponent  $n$ . To accomplish this goal, two extreme conditions are considered. First, examine the limit

$$\frac{2\sqrt{\pi} E_f C_0^{m-1} l}{\sqrt{A} \bar{v}} \ll 1, \quad (16-34)$$

which implies that only a small fraction of the acid reacts within the pore. In this limit, which applies for large  $\bar{v}$ , the rate of pore enlargement reduces to

$$\frac{dA}{dt} \rightarrow 2\sqrt{\pi} E_f C_0^{m-1} X A^{1/2} = \psi_1 A^{1/2}. \quad (16-35)$$

Thus, in this limit the exponent  $n$  is  $1/2$  ( $n < 1$ ) and pores with a cross-sectional area such that the inequality of Eq. 16-34 is satisfied do not form wormholes. The pores will enlarge rather uniformly, and the acid front will remain sharp, progressing through the porous matrix also rather uniformly. Not all pores, however, satisfy the inequality. A second limit for some of the pores may be possible. This second limit occurs when the pores are of such a size that the inequality of Eq. 16-34 is reversed, implying almost complete acid reaction within these pores. In this second limit, which applies for small  $\bar{v}$ , can be found

$$\frac{dA}{dt} \rightarrow \frac{\bar{v} X C_0}{8\pi l} A^2 = \psi_2 A^2. \quad (16-36)$$

Thus, pore areas satisfying the second limit are unstable ( $n > 1$ ). They grow more rapidly than the neighboring pores. They become small wormholes and continue to evolve into the macroscopic etch patterns shown by the metal casts.

For a given reaction rate and acid flux, there are pores that are essentially too small to become wormholes and perhaps others that are of sufficient size to exhibit uncontrolled growth and eventually become macroscopic. Thus, for a given acid flux, the native pores may fall into two different categories: candidates for incipient wormhole formation and noncandidates. There is, therefore, a critical (or transitional) pore size  $A_T$  that may be estimated as the value where the two limiting growth rates become equal:

$$\psi_1 A_T^{1/2} = \psi_2 A_T^2. \quad (16-37)$$

Solving this expression for  $A_T$  yields

$$A_T \cong 20 Da^{2/3} (kl)^{2/3}, \quad (16-38)$$

where  $Da = EfC_0^{m-1}/u$  and  $k$  is the formation permeability (Wang, 1993; Wang *et al.*, 1993). Thus, if all the pores in the native rock have cross-sectional areas less than  $A_T$ , wormhole initiation cannot occur until at least one of the pores has been enlarged by acid reaction to a size sufficient to allow wormhole development. The critical, or transitional, area depends on both the reaction rate and the acid flux. This condition has, as discussed subsequently in this chapter, considerable practical relevance.

The average length of a pore is a rather nebulous quantity that, on the basis of a number of laboratory experiments using two different limestones and a dolomite, appears to be about 0.1 mm. If we use this value, the criterion for the critical pore dimension becomes

$$A_T = 0.93[Da k]^{2/3}, \quad (16-39)$$

where both  $k$  and  $A_T$  must be expressed as  $\text{cm}^2$ .<sup>†</sup>

This equation is quite simple in appearance, but its implications are profound and these may be tested experimentally. Laboratory results that are seemingly counterintuitive may be satisfactorily explained by invoking the concept embodied by Eq. 16-39.

#### 16-4.4. Acidizing experiments

Essentially two different types of results are found on the basis of acidizing carbonate cores in the laboratory. One is the metal cast of a wormhole and the other is the pressure drop measured while acidizing at a constant injection rate. Both types of experiments have proved instructive. The transition area defined by Eq. 16-39 depends on the acid flux and reaction rate, which in turn is a function of the acid concentration, reaction temperature and rock composition. The acid flux is the easiest to control and is the most widely studied variable.

- Acid flux

The flow rate is expected to influence the acid etch pattern for reasons that may be best understood by considering the idealized depiction of a wormhole shown by Fig. 16-10. It is a cylinder with fluid loss about the perimeter as well as at the tip. Depending on the external pressure field surrounding the wormhole, the fluid-loss flux may vary from point to point about the surface of the cylinder. If the flux into the rock is small at some points,  $A_T$  as determined by Eq. 16-38 may exceed the cross-sectional area of all

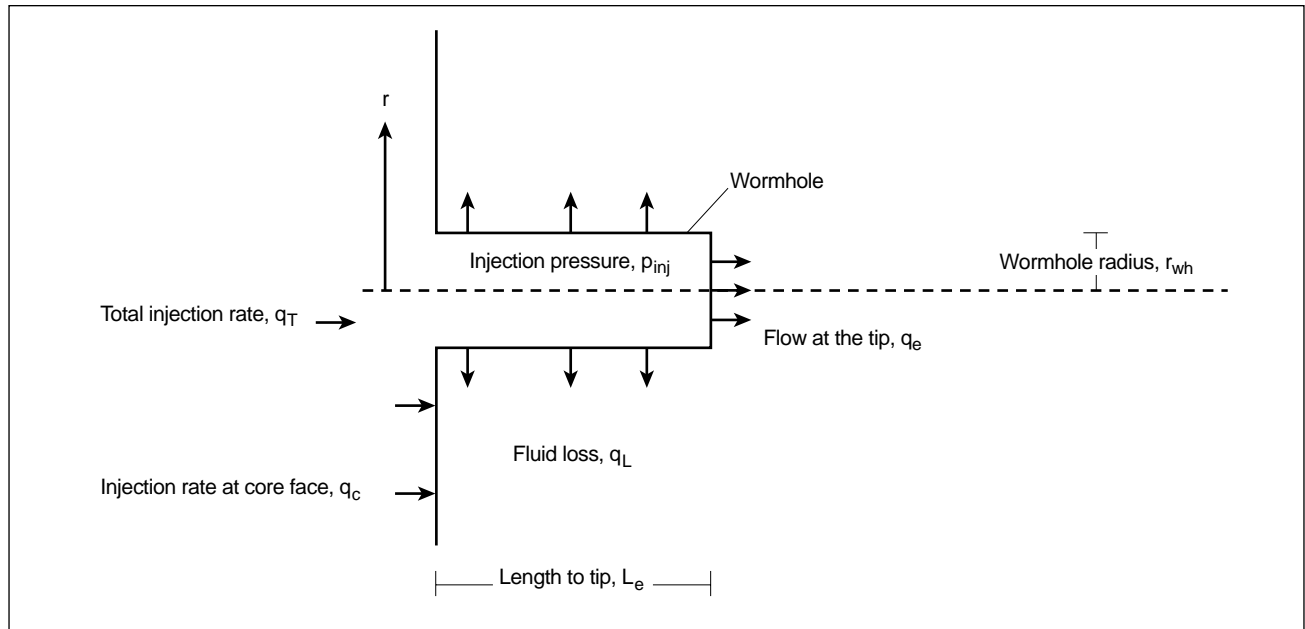


**Figure 16-10.** Single-wormhole model.

<sup>†</sup> Given a permeability in md, multiply by  $9.869 \times 10^{-12}$  to obtain the dimensions in  $\text{cm}^2$ .

the native pores, and wormholes will not form at that point. The walls of the wormhole will then be eroded in a generally uniform manner. If, however, the flux at the tip is large enough to initiate wormholes, a network of small wormholes will continuously form at the tip, rapidly extending its length.

In summary, it is expected that for injection rates that are very slow, wormholes will not form and the face of the core will dissolve rather uniformly. At modest injection rates, large enough to initiate wormholes at the tip of the primary wormhole, an etch pattern is expected to develop that shows little branching from the primary wormhole. Most of the acid is then expended in extending the primary wormhole. If the rate of acid injection is then increased, the acid fluid-loss flux into the rock matrix may be large enough everywhere—or at least at many points—to allow the initiation of wormholes along the boundary of the primary one. A highly ramified wormhole structure is expected at the higher injection rates.

Hoefner and Fogler (1988) prepared metal casts of wormholes that developed in calcite cores at various rates of injection (Fig. 16-11). The casts are arrayed from left to right to correspond to increasing flow

rate. The left-hand core at the lowest flow rate is an example of a nearly uniform dissolution front, where the inlet face of the core has essentially been dissolved. The flow rate was evidently less everywhere than the critical one. As predicted, the wormholes that developed at the higher flow rates show substantial branching, displaying the fractal structure postulated by Daccord and Lenormand (1987). At higher rates, much of the acid is expended in the creation of the highly ramified structure shown by the casts.

Of primary practical interest are the wormholes created at intermediate injection rates. They develop a minimum of side branches extending from the perimeter of the main channel, in agreement with the etch pattern anticipated by consideration of a critical pore area. Indeed, the series of casts in Fig. 16-11 confirms the existence of a transitional area. Although the casts provide strong evidence supporting the hypothesis set forth in the preceding section, they also suggest a means for further verification. It seems evident in considering the series of casts that a wormhole formed with a minimum of side branching will penetrate through the core using a smaller quantity of acid than would be required otherwise.

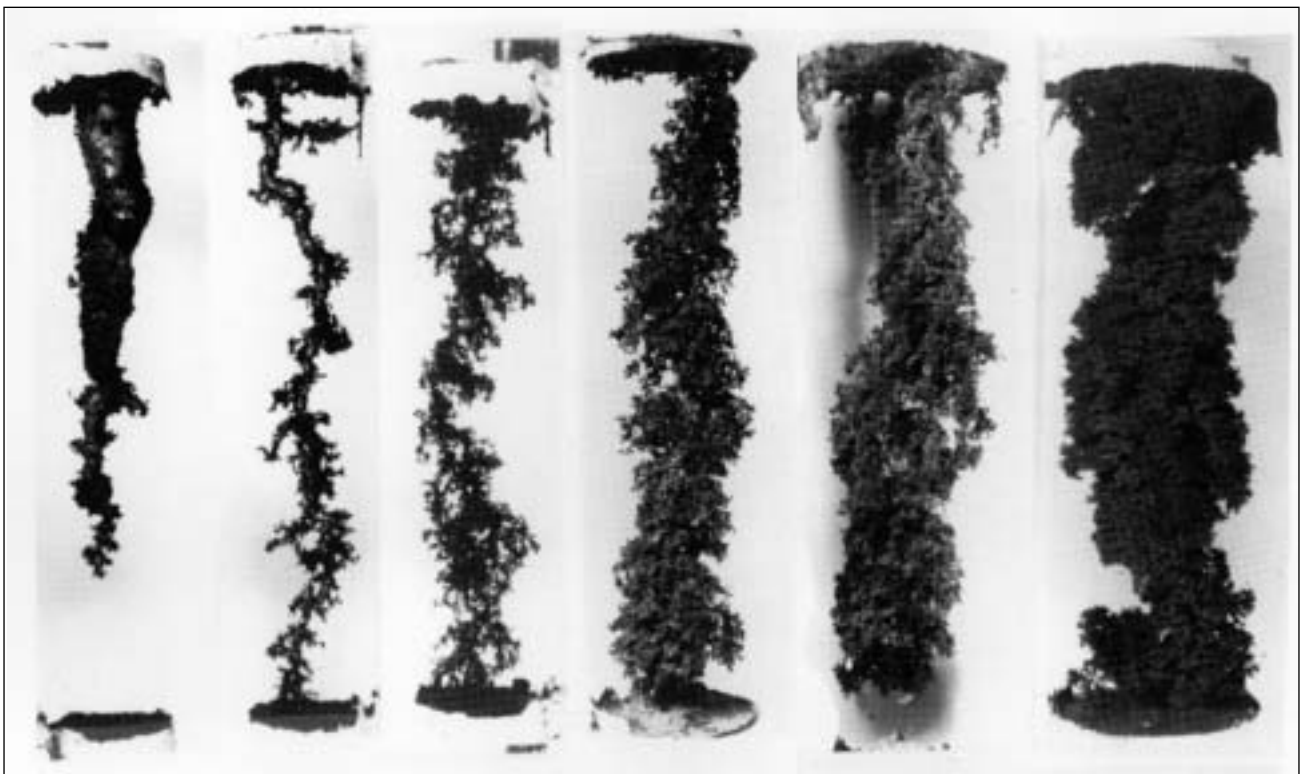


**Figure 16-11.** Metal casts of wormholes that developed in calcite cores at various rates of injection are arrayed from left to right to correspond to increasing flow rate (Hoefner and Fogler, 1988).

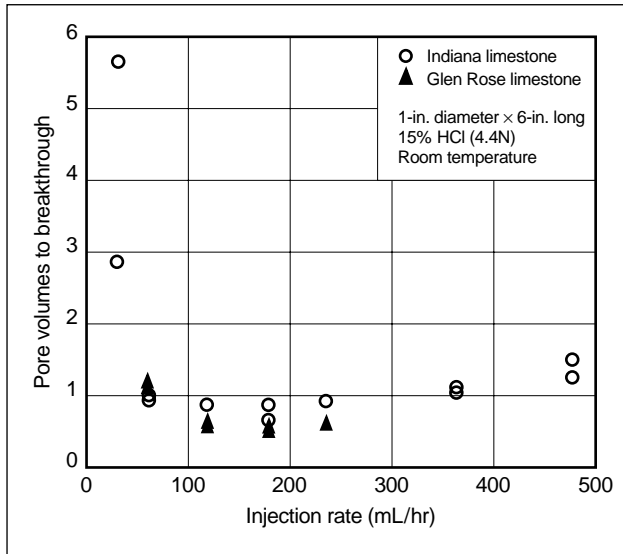


**Figure 16-12.** Coreflood results for Indiana and Glen Rose limestones.

Wang *et al.* (1993) measured the volume of acid required to achieve wormhole penetration through a core (breakthrough). Figure 16-12 is a plot of the acid pore volumes to breakthrough as a function of the injection rate. As anticipated, an optimum injection rate exists. Wang *et al.* calculated the acid fluxes about the wormhole that develop during the experiment to find the flux at the tip as well as along the sides of the wormhole. They calculated for the optimum case (i.e., the experiment requiring the least volume of acid) that the flux at the tip is well predicted by Eq. 16-39. The critical size  $A_T$  was determined by the capillary entry pressure and the reaction rate was determined by Eq. 16-8.

A subsequent study by Bazin *et al.* (1995) using two other limestones (Lavoux and Savonnieres) shows the importance of core length in laboratory studies. As the length of the dominant wormhole increases, the amount of acid lost through the lateral boundaries increases, thereby reducing the volume of acid reaching the tip and ultimately resulting in an acid flux at the tip that is too small to initiate wormholes there. In such a case, the wormhole can extend only slowly while it is also being enlarged. Wormhole growth is slowed, as observed by Bazin *et al.* T. Huang (pers. comm., 1996) studied the rates of wormhole propagation reported by Bazin *et al.* and found them predictable on the basis of Eq. 16-39 when fluid loss is properly taken into account.

Thus, Eq. 16-39 appears to be the key to the determination of the effect of acid injection rates in field operations. Ideally, a few dominant wormholes should be initiated extending from the wellbore in openhole completions or from the perforations in cased holes. This would initially entail a modest acid injection rate (calculated by Eq. 16-39). As the acid treatment progresses and the lengths of the few dominant wormholes increase, higher injection rates are then desirable to continue to extend the dominant wormholes, if possible. Nierode and Williams (1971) were apparently the first to emphasize the primary importance of fluid loss from wormholes as a limiting factor in extending them. Their hypothesis is in no way weakened by the experiments and analysis presented here. Acid fluid loss from a wormhole remains a limiting factor in the propagation of wormholes.

- Reaction temperature

Increasing the reaction temperature increases  $E_f$  exponentially (see Eq. 16-9). In accordance with Eq. 16-39, this should result in a corresponding increase in  $A_T$ . Therefore, the optimum injection rate must correspondingly be increased (see Sidebar 6E). This predicted trend is shown by Fig. 16-13. The optimum injection rate at a temperature of 125°F is almost twice as large as the optimum at room temperature. According to Wang *et al.* (1993), the increased rate is predicted by Eq. 16-39. An implication of this result is that, if possible, deep wells should be acidized at higher rates than shallow ones; but in either case, increasing the rate during the course of the treatment is apt to be beneficial in extending the wormholes. Initially, however, the acid flux should be restricted by the value determined with Eq. 16-39 if this rate is possible without fracturing the formation. As shown by Figs. 16-12 and 16-13, the volume of acid required to achieve breakthrough does not increase rapidly for injection rates in excess of the optimum, so maintaining the optimum injection rate is not thought to be critical. Stimulations conducted at rates somewhat in excess of those demanded by Eq. 16-39 may not differ greatly from those achieved at optimum. On the other hand, the amount of acid to achieve breakthrough does increase substantially for rates less than the optimum, so maintaining a sufficient rate if possible is recommended.



### 16E. Optimum injection rate for initiating carbonate treatment

Consider an acid treatment of a well in a carbonate formation known to be composed of calcite with little dolomite and to have a permeability of 5 md. The treatment will be conducted using 15% HCl injected initially, if possible, at a rate nearly corresponding to the optimum one. The reservoir temperature is 125°F [50°C]. The thickness of the formation to be treated is 30 ft. The well is completed openhole with a wellbore diameter of 6 in.

To determine the optimum injection rate, the cross-sectional area of the largest native pores must be estimated. Generally, this cross-sectional area is determined from the capillary entry pressure measured by mercury porosimetry, if an adequate core sample is available. For the present example, use  $A_T = 1.45 \times 10^{-7} \text{ cm}^2$ . If a sample of the formation is not available, then  $A_T$  may be estimated as a multiple of the formation permeability (Dullien, 1979). What is the optimum acid injection rate?

#### Solution

Based on the data provided in Table 16-4,

$$E_i = 7.291 \times 10^7 \exp \left[ -\frac{7.55 \times 10^3}{(50 + 273)} \right] = 5.14 \times 10^{-3}, \quad (16E-1)$$

and because the acid is 15%,  $C_0 = 4.4 \text{ kg-mol/m}^3$  (= 4.4 mol/L). Therefore,

$$E_i C_0^{m-1} = \frac{(5.14 \times 10^{-3})(4.4)^{0.63}}{4.4} = 2.97 \times 10^{-3} \text{ m/s}. \quad (16E-2)$$

In an appropriate set of units,  $k = (5 \text{ md})9.869 \times 10^{-12} \text{ cm}^2/\text{md} = 4.9345 \times 10^{-11} \text{ cm}^2$ . Therefore, the optimum flux from Eq. 16-39 is  $u = 2.38 \times 10^{-3} \text{ m/s} = 0.0078 \text{ ft/s}$ . This corresponds to an initial acid injection rate of 3.9 bbl/min (0.13 bbl/min/ft). If this injection rate exceeds the formation parting pressure, injection would be at the highest possible matrix rate during the entire treatment.

The optimum rate decreases with formation temperature. Consider the same treatment when the temperature is 85°F [30°C] rather than 125°F. Then,  $E_i = 1.1 \times 10^{-3}$ . This leads to an optimum flux  $u = 5.09 \times 10^{-4} \text{ m/s}$  corresponding to an injection rate of 0.8 bbl/min. This rate is usually sustainable without fracturing the matrix.

Thus, most calcite formations are treated using rates near the maximum that the matrix will accept, except perhaps in cool, shallow formations. Once the treatment has been initiated, it may be beneficial to increase the rate to propagate the wormholes created by the initial acid contact.

- Formation composition

The reaction rate of HCl with dolomite is much slower than that with calcite (see Table 16-4). This being the case, Eq. 16-39 indicates that unless the acid flux is greatly reduced, many of the native pores are likely to exceed  $A_T$  in size and be candidates for wormhole initiation. Thus, closely spaced multiple wormholes are likely to form, producing a highly

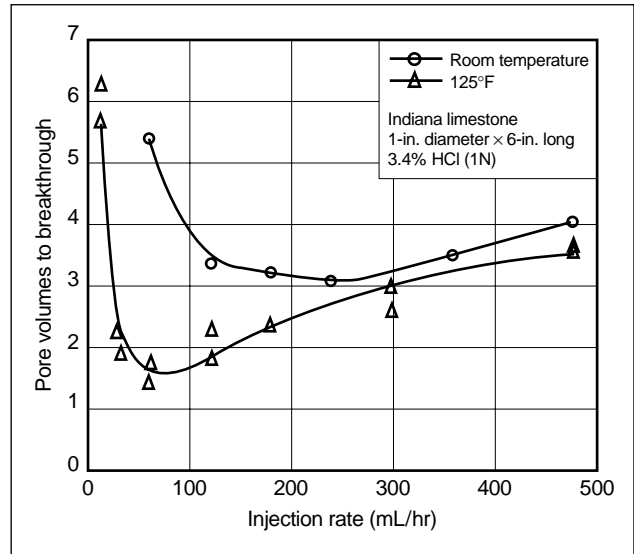
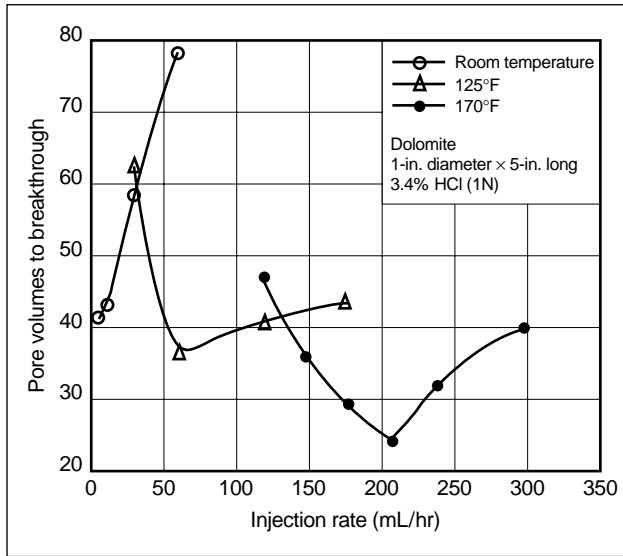


Figure 16-13. Indiana limestone coreflood results at different temperatures.

ramified structure that is inefficient in developing an etch pattern consisting of a few dominant wormholes. It is, therefore, expected that corresponding to a substantial decrease in the reaction rate, there must be an associated decrease in the acid injection rate to remain at optimum. Figure 16-14 shows the acid pore volumes to breakthrough as a function of the injection rate for dolomite cores. The optimum rate at room temperature is not readily discernible, but it is evident that slow rates are preferred to higher ones. Hoefner and Fogler (1988) also studied the acidization of dolomite cores and found results similar to those shown by Fig. 16-14. The results for dolomite represent a striking confirmation of predictions based on Eq. 16-39.

The field implication is that acidizing in shallow dolomite formations should be conducted at low rates. High rates result in a multiple wormhole pattern that does not penetrate far into the formation and appears as uniform acid invasion dissolving the face of the wellbore, which is inefficient for removal of skin effect damage compared with producing a few dominant wormholes that penetrate into the formation. In deeper dolomite formations, the rate may be increased to some extent because the reaction temperature increases with depth. The increased optimum rate with increasing temperature shown in Fig. 16-14 confirms predictions based on Eq. 16-39.



**Figure 16-14.** Effect of temperature on the variation of volumes to breakthrough with the injection rate for dolomite.

#### 16-4.5. Propagation of wormholes

Once wormholes are initiated in the rock surrounding the face of the wellbore or perforation, it is desirable to extend them into the formation as far as possible with a given volume of acid. The skin effect should be reduced within the regions penetrated by wormholes. To promote understanding of the factors governing the rate of extension of a wormhole, Hung *et al.* (1989) modeled wormhole growth by considering it to be a cylinder with fluid loss as depicted by Fig. 16-10. Hung *et al.* took into account a number of factors, including the contributions of both acid diffusion and convection resulting from fluid loss to the walls of the wormhole where the acid reacts. These are important factors because the acid reactions in a wormhole are, in general, limited by mass transfer as contrasted to those in natural pores, which are controlled by the reaction rate.

The rate of wormhole extension is determined by the amount of the acid arriving at the tip:

$$\frac{dL}{dt} = \frac{u_e C_e \beta_{100}}{(1 - \phi) \rho_{rock}} = \frac{u_e C_e}{\phi C_0} A_c, \quad (16-40)$$

where the subscript *e* refers to conditions evaluated at the end or tip of the wormhole,  $\rho_{rock}$  is the density of the rock, and *L* is the length of the wormhole. This equation shows the importance of diffusion, acid convection and fluid loss on wormhole propagation. The

greater the rate of acid diffusion toward the wall, the lower the concentration of acid at the tip of the wormhole and the slower its rate of propagation. Increased fluid-loss rates serve to convect acid to the wall and at the same time reduce the acid flux reaching the tip, thereby decreasing the rate of propagation. Taking into account both fluid loss and diffusion, Hung (1987) found that for a constant injection rate, the rate of extension of a wormhole begins to decrease as the wormhole length increases. The length appears to ultimately reach a plateau, as shown by Fig. 16-15 (Hung, 1987) but never actually ceases to grow. Hung attributed the diminishing growth rate entirely to fluid loss. Thus, it is anticipated that wormhole penetration will essentially cease after a certain length has been attained as long as the injection rate is fixed. In long-core experiments, an ultimate length was observed by Bazin *et al.* (1995).

Hung calculated that the wormhole evolves in shape depending on the local rate of acid reaction and fluid loss and the rate of fluid injection. Once the wormhole length stabilizes, the acid that is injected serves primarily to increase the diameter. Because Hung's model does not account for the meandering nature of wormholes caused by small-scale heterogeneities in the rock or the creation of side branches, it tends to overpredict wormhole length.

Daccord *et al.* (1989) recognized the importance of propagating the wormhole to the fullest extent possible and proposed a model based on laboratory experiments

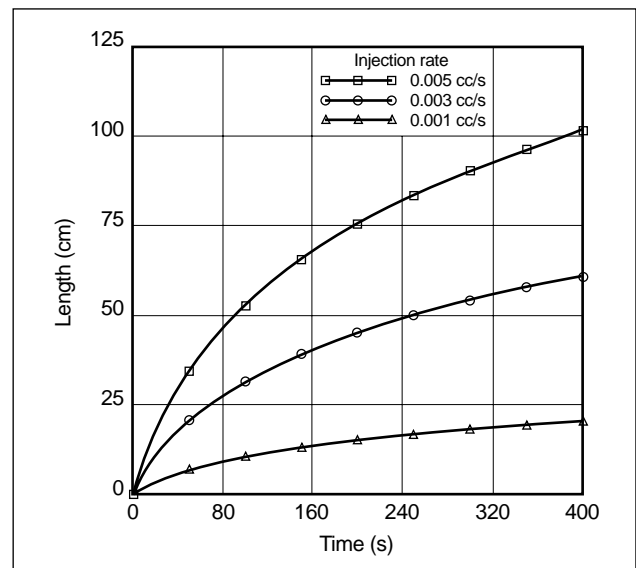


**Figure 16-15.** Predicted wormhole length (Hung, 1987).

that differs from that proposed by Hung. Daccord *et al.*'s expression for the rate of wormhole propagation in linear systems is

$$\frac{dL}{dt} = \frac{aA_c}{A\phi} \left( \frac{q}{D} \right)^{2/3}, \quad (16-41)$$

where  $a$  is a constant determined experimentally,  $D$  is the molecular diffusion coefficient, and  $A$  is the cross-sectional area of the wormhole. Daccord *et al.*'s model considers the influence of acid diffusion but does not take into account fluid loss; therefore, this equation

does not indicate a plateau value as the wormhole lengthens. Thus, the equation is applicable to short wormholes where fluid loss is not a factor, but it should not be used for the prediction of wormhole penetration length.

Thus, none of the existing models for the rate of wormhole propagation is strictly correct. Because wormhole length is thought to be a crucial factor in determining stimulation, better models incorporating the important features of the ones that have been proposed are required.

# Appendix: Advances in Understanding and Predicting Wormhole Formation

*Christopher N. Fredd, Schlumberger Dowell*

## Introduction

The transport and reaction of reactive fluids in carbonate porous media results in the formation of highly conductive flow channels, or wormholes. Wormholes significantly influence the flow of reservoir fluids because their conductivity is several orders of magnitude larger than that of the porous medium. Therefore, the success of carbonate stimulation treatments is highly dependent on wormhole formation (i.e., wormhole formation during matrix acidizing treatments and lack thereof during fracture acidizing treatments). Wormhole formation is desirable during matrix acidizing treatments because the wormholes are capable of bypassing near-wellbore damage. In contrast, wormhole formation increases fluid leakoff during fracture acidizing and, consequently, limits the depth of acid penetration. The structure of the wormhole channel varies significantly with the flow conditions and the properties of the fluid-mineral system. Because the structure ultimately controls the effectiveness of the stimulation treatment, a fundamental understanding of the dissolution phenomenon is required to design effective treatments.

Wormhole formation occurs because carbonate dissolution is influenced by mass-transfer processes. Many investigators have recognized the importance of mass transfer to the phenomenon of wormhole formation in the hydrochloric acid (HCl)-limestone system (Barron *et al.*, 1962; Williams *et al.*, 1970; Nierode and Williams, 1971; Hoefner and Fogler, 1988; Daccord *et al.*, 1993; Wang *et al.*, 1993; Frick *et al.*, 1994b; Mostofizadeh and Economides, 1994; Bazin *et al.*, 1995; Huang *et al.*, 1997; Fredd and Fogler, 1998a). Recent studies demonstrate that in the presence of weak acids and chelating agents wormhole formation is influenced by a variety of transport and reaction processes (Fredd and Fogler, 1998b). Thus, to provide the reader with a full understanding of the dissolution phenomenon, this Appendix to Chapter

16 discusses the various transport and reaction processes that influence carbonate dissolution in a variety of fluid systems including strong acids, weak acids and chelating agents. A brief review of the theories of wormhole formation is provided, and wormhole formation is discussed in terms of the Damköhler number for flow and reaction. The existence of an optimum Damköhler number for effective wormhole formation is demonstrated by laboratory experiments, and a new extension of the theory is introduced to predict optimum injection strategies for matrix acidizing treatments in the field.

## Carbonate dissolution

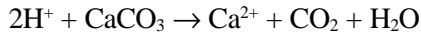
### Influence of transport and reaction

The dissolution of carbonate minerals involves a heterogeneous reaction that may be influenced by a variety of transport and reaction processes. These processes include the transport of reactants to the surface, the reversible surface reaction and the transport of products away from the surface. The rate-limiting process depends on the fluid-mineral system and may vary significantly in the presence of strong acids, weak acids and chelating agents.

This section demonstrates the interplay between the various transport and reaction processes and summarizes results from kinetic studies for a variety of fluid-mineral systems. The results are based on experimental studies conducted using a rotating disk apparatus, which allows the differentiation of the surface reaction kinetics from the transport processes because of the well-defined hydrodynamics. From an understanding of the processes that influence the dissolution, as well as appropriate expressions for the kinetics of the surface reaction and rate of mass transfer, the overall rate of carbonate dissolution can be determined as discussed in “Generalized description of carbonate dissolution.”

- Strong acids

The rate of calcite dissolution has been shown to be mass-transfer limited in a variety of acidic media (pH less than about 4) ranging from HCl to pseudoseawater (Williams *et al.*, 1970; Lund *et al.*, 1975; Plummer *et al.*, 1978; Sjöberg and Rickard, 1984; de Rozières *et al.*, 1994). In strong acids such as HCl, calcite is readily dissolved and the reaction may be considered irreversible:

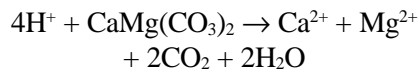


Because the reaction is essentially irreversible, the products do not influence the rate of dissolution, and the observed mass-transfer limitations are due to the transport of hydrogen ions to the calcite surface. The mass-transfer limitations are more significant when HCl is emulsified or gelled because of a reduction in the effective diffusivity (Hoefner and Fogler, 1985; de Rozières *et al.*, 1994). The dissolution of calcite by HCl becomes influenced by the kinetics of the surface reaction at temperatures below about 32°F [0°C] (Lund *et al.*, 1975). The following rate expression was found to describe the rate of the surface reaction:

$$r_D = k_r C_i^n, \quad (1)$$

where  $C_i$  is the concentration at the solid/liquid interface,  $k_r$  is the surface reaction rate constant, and  $n$  is the reaction order. The kinetic parameters are summarized in Table 16-4 (Lund *et al.*, 1975).

The dissolution of dolomite by HCl is mass-transfer limited at temperatures greater than about 200°F [95°C] (Lund *et al.*, 1973) and reaction rate limited at temperatures less than about 125°F [50°C]. Between these two temperatures, the dissolution is influenced by both the rate of mass transfer and the kinetics of the surface reaction. Like for calcite, the reaction can be considered irreversible, so the influence of mass transfer is due to the transport of hydrogen ions to the dolomite surface.



The kinetics of the surface reaction is also described by Appendix Eq. 1, using the kinetic parameters summarized in Table 16-4 (Lund *et al.*, 1973).

- Weak acids

In weak acids (i.e., partially dissociating acids), carbonate dissolution still occurs through hydrogen

ion attack (see the two preceding chemical reactions). However, dissolution is complicated by the reversible surface reaction (Chatelain *et al.*, 1976) and the additional influence of the mass transfer of products away from the surface. The dissolution of calcite by acetic acid was found to be influenced by the rate of transport of reactants to the surface and the rate of transport of products away from the surface at ambient temperature (Fredd and Fogler, 1998d). The interplay between the two transport processes causes transport limitations that are much more significant than either limitation independently. This interplay results in an apparent effective diffusion coefficient that is over an order of magnitude lower than that of acetic acid. Similar results were observed during the dissolution of calcite by formic and maleic acids (Takulpakdee, 1998).

The kinetics of the surface reaction for the dissolution of calcite by acetic acid was shown to be a significant limitation at pH values greater than about 3.7 (Fredd and Fogler, 1998d). The rate of the surface reaction can be expressed as

$$r_D = k_r (C_i - C_{pi} / K_{eq}), \quad (2)$$

where  $C_i$  and  $C_{pi}$  are the reactants and products concentrations at the solid/liquid interface, respectively, and  $K_{eq} = K_c / C_{COi}$  is the effective equilibrium constant. The reactants concentration is the total concentration of associated and dissociated hydrogen ions (i.e., acetic acid and  $\text{H}^+$ ), whereas the products concentration represents the total concentration of calcium-containing species. The total interface concentration of carbonate species  $C_{COi}$  was found to be independent of the rate of mass transfer (Fredd, 1998) and was, therefore, lumped into the effective equilibrium constant. The effective equilibrium constant also includes the conditional equilibrium constant  $K_c$ , which is a complex function of the equilibrium constants for the various equilibrium reactions occurring near the interface.

Kinetic parameters evaluated at 72°F [22°C] using a rotating disk (Fredd and Fogler, 1998d) are listed in Appendix Table 1. Additional data for various acid concentrations and higher temperatures (125°F) are in the literature (Fredd and Fogler, 1998d). These kinetic parameters are influenced by a variety of adsorption processes and equilibrium reactions. Therefore, extrapolation of the parameters to significantly higher temperatures requires careful evaluation of the surface chemistry

**Appendix Table 1. Parameters used to calculate the overall dissolution rate constant at 72°F.**

	$D_e$ (cm <sup>2</sup> /s)	$D_{pe}$ (cm <sup>2</sup> /s)	$k_r$ ( $\Delta E$ [kcal/mol])	$K_{eq}$
0.25M CDTA (pH = 4.4)	$4.5 \times 10^{-6}\dagger$	$3 \times 10^{-6}\dagger$	$2.3 \times 10^{-4}\S$	$1 \times 10^{10}\ddagger$
0.25M DTPA (pH = 3.3)	$4 \times 10^{-6}\dagger$	$3 \times 10^{-6}\dagger$	$7.8 \times 10^{-5}\S$	$1 \times 10^{10}\ddagger$
0.25M DTPA (pH = 4.3)	$4 \times 10^{-6}\dagger$	$3 \times 10^{-6}\dagger$	$4.8 \times 10^{-5}\S$	$1 \times 10^{10}\ddagger$
0.25M DTPA (pH = 12.5)	$4 \times 10^{-6}\dagger$	$3 \times 10^{-6}\dagger$	$2.6 \times 10^{-5}\S$	$1 \times 10^{10}\ddagger$
0.25M EDTA (pH = 4)	$6 \times 10^{-6}\dagger\dagger$	$4 \times 10^{-6}\S\S$	$1.4 \times 10^{-4}\S$ (12) <sup>§</sup>	$1 \times 10^{10}\ddagger$
0.25M EDTA (pH = 8 to 13)	$6 \times 10^{-6}\S$	$4 \times 10^{-6}\S\S$	$5.3 \times 10^{-5}\S$	$1 \times 10^{10}\ddagger$
0.5M acetic acid (pH = 2.5)	$1.1 \times 10^{-5}\dagger\dagger\dagger$	$8 \times 10^{-6}\dagger\dagger\dagger$	$5 \times 10^{-3}\S\S\S$	$1.6 \times 10^{-1}\S\S\S$
0.5M acetic acid (pH = 4.6)	$1.1 \times 10^{-5}\dagger\dagger\dagger$	$8 \times 10^{-6}\dagger\dagger\dagger$	$2.1 \times 10^{-4}\S\S\S$	$2.7 \times 10^{-1}\S\S\S$
0.5M HCl	$3.6 \times 10^{-5}\dagger\dagger\dagger\dagger$	$2 \times 10^{-5}\dagger\dagger\dagger$	$2 \times 10^{-1}\dagger\dagger\dagger\dagger$ (15) <sup>††††</sup>	$1 \times 10^{10}\ddagger$
<p>Note: <math>D_e</math> = effective diffusion coefficient, <math>D_{pe}</math> = effective diffusion coefficient for reaction products, <math>k_r</math> = effective surface reaction rate constant, <math>\Delta E</math> = activation energy, <math>K_{eq}</math> = effective equilibrium constant</p> <p>† Estimated from the Stokes-Einstein equation</p> <p>‡ Assumed on the basis of <math>D_e</math> and value for Ca-EDTA</p> <p>§ Fredd and Fogler (1998c)</p> <p>†† Assumed on the basis of the irreversibility of surface reactions</p> <p>†† Assumed equal to the diffusion coefficient of EDTA at pH = 13</p> <p>§§ Assumed on the basis of the value for Ru-EDTA (Jiang and Anson, 1992)</p> <p>††† Vitagliano and Lyons (1956)</p> <p>††† Estimated from ionic diffusion coefficients (Cussler, 1984)</p> <p>§§§ Fredd and Fogler (1998d)</p> <p>†††† Lund <i>et al.</i> (1975)</p>				

involved in the dissolution. The method of approximating the surface reaction rate reported by Schechter (1992) (see Eq. 16-10) provides an order-of-magnitude estimate of the reaction rate constant but does not account for the significant contribution of the reverse reaction.

The rate of dolomite dissolution by weak acids is currently not available in the literature. Because the dissolution occurs through hydrogen ion attack, the rate of the surface reaction can be estimated from Appendix Eq. 2 by scaling the surface reaction rate constant by the ratio of the surface reaction rate constants of dolomite to calcite for HCl. This scaling should provide a reasonable order-of-magnitude estimate from which the relative influences of transport and reaction can be determined.

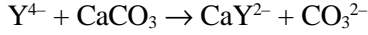
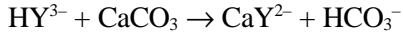
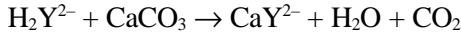
- Chelating agents

In the presence of calcium chelating agents such as ethylenediaminetetraacetic acid (EDTA), the rate of calcite dissolution is influenced predominantly by

the rate of transport of reactants to the surface and the kinetics of the surface reactions at ambient temperature (Fredd and Fogler, 1998c). Although the reactions are essentially irreversible because of the formation of a stable calcium complex, the reactions are influenced by the transport of products away from the surface. This influence is due to the blocking of surface sites involved in the dissolution. The dissolution mechanism is different from conventional acids in that hydrogen ions are not required. However, the rate of dissolution is enhanced at low pH as a result of the combined influence of hydrogen ion attack and chelation.

The rate of calcite dissolution varies considerably with pH and the type of chelating agent because of changes in the ionic form of the chelating agent and the influence of hydrogen ion attack. In general, the rate of calcite dissolution increases as the number of hydrogen ions associated with the chelating agent increases. As the pH is increased from about 4.5 to 8.5 to 13, EDTA successively

deprotonates from  $\text{H}_2\text{Y}^{2-}$  to  $\text{HY}^{3-}$  to  $\text{Y}^{4-}$ . The corresponding overall surface reactions are



The rate of calcite dissolution by chelating agents can be described by Appendix Eq. 2. The appropriate kinetic parameters are listed in Appendix Table 1 for EDTA, 1,2-cyclo-hexanediaminetetraacetic acid (CDTA) and diethylenetriaminepentaacetic acid (DTPA) (Fredd and Fogler, 1998c). Calcite dissolution requires the formation of stable calcium chelates. For example, nitrilotriacetic acid (NTA), which forms a relatively weak calcium chelate, is ineffective for calcite dissolution (Fredd, 1998).

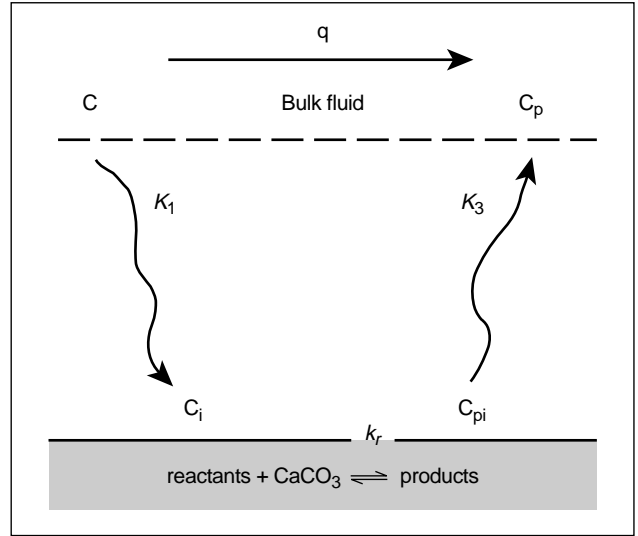
The dissolution of dolomite by chelating agents has not been thoroughly investigated. Preliminary experiments with EDTA at ambient temperature reveal no significant dolomite dissolution. The dissolution mechanism is probably inhibited by the low stability of the magnesium chelate at that temperature.

## Generalized description of carbonate dissolution

A generalized description of carbonate dissolution is required to account for the various transport and reaction processes that may influence the rate of dissolution. This description is provided by modeling the overall carbonate dissolution mechanism as three sequential processes (Fredd and Fogler, 1998b) of the mass transfer of reactants to the surface, reversible surface reactions and mass transfer of products away from the surface (Appendix Fig. 1). At steady state, the rates of the three sequential processes are equal and the rate of reactant consumption  $r_A$  is

$$\begin{aligned} r_A &= \nu r_D \\ &= K_1(C - C_i) \\ &= \nu k_r(C_i - C_{pi}/K_{eq}) \\ &= \nu K_3(C_{pi} - C_p), \end{aligned} \quad (3)$$

where  $\nu$  is the stoichiometric ratio of reactants consumed to products produced and  $K_1$  and  $K_3$  are the mass-transfer coefficients for the reactants and products, respectively. Appendix Eq. 3 assumes that the surface reaction can be expressed as a first-order heterogeneous reaction. This expression is valid for



**Appendix Figure 1.** Carbonate dissolution involves reactants transport, reversible surface reaction and products transport.

weak acids and chelating agents. It is a reasonable approximation for strong acids when the concentration dependence is lumped into the reaction rate constant (i.e.,  $k_r = k'_r C_i^{n-1}$ ). This approximation does not significantly affect the interplay between transport and reaction for systems that are mass-transfer limited.

The expressions in Appendix Eq. 3 were solved simultaneously for the interface concentrations, which were then substituted back into the equation. Making an additional substitution for  $C_p$  based on the stoichiometry of the reaction, the rate of reactant consumption can then be expressed as

$$r_A = \kappa \left[ C - \frac{C_o}{1 + \nu K_{eq}} \right], \quad (4)$$

where  $\kappa$  is the overall dissolution rate constant and  $C_o$  is the initial reactant concentration. The overall dissolution rate constant depends on the sum of resistances in series:

$$\kappa = \frac{1 + \frac{1}{\nu K_{eq}}}{\frac{1}{K_1} + \frac{1}{\nu k_r} + \frac{1}{\nu K_{eq} K_3}}. \quad (5)$$

Appendix Eqs. 4 and 5 have been used to describe the rate of dissolution observed during rotating disk experiments (Fredd and Fogler, 1998c, 1998d) and during flow and reaction within carbonate porous media (Fredd and Fogler, 1998b). These equations can

be used to determine the rate of carbonate dissolution in any flow geometry, provided that an appropriate expression for the rate of mass transfer is available.

## Wormhole formation

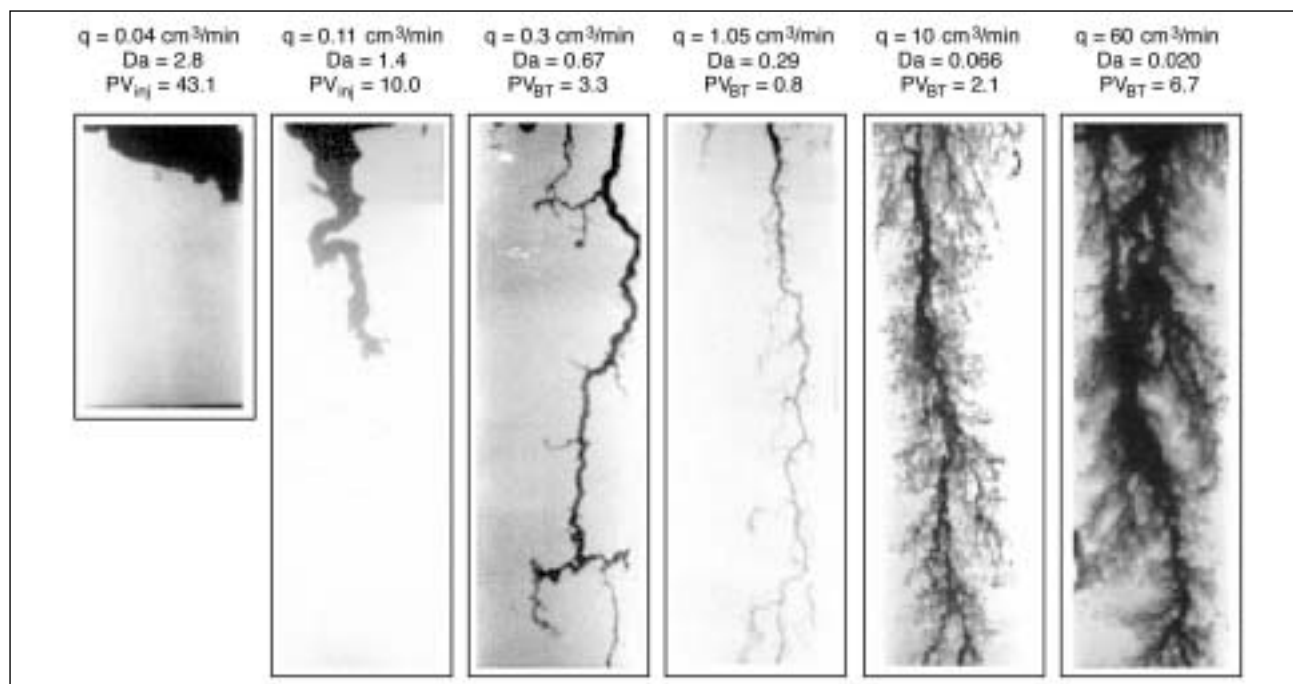
The transport and reaction of reactive fluids in carbonate porous media results in the formation of highly conductive flow channels, or wormholes. Wormholes form because of the natural heterogeneity of the porous medium and the rapid and almost complete dissolution of the mineral in the reactant fluid. During stimulation, the fluid preferentially flows to the regions of highest permeability (i.e., the largest pores, vugs or natural fractures). The initial flow paths are enlarged by rapid dissolution of the matrix material, causing these regions to receive even more of the flow. A dominant channel quickly forms and continues to propagate while diverting flow from other regions. Once formed, the wormhole channels provide negligible resistance to flow and carry essentially all the injected fluid.

## Dissolution structures

The structure of the dissolution channel is highly dependent on the injection rate and fluid-mineral

properties. The typical dependence on the injection rate is demonstrated in Appendix Fig. 2 by neutron radiographs of dissolution structures formed during the dissolution of limestone by 0.5M [1.7%] HCl at 72°F. At low injection rates (far left structure), the reactant is consumed on the inlet flow face of the core, resulting in complete dissolution of the core starting from the inlet flow face. This face dissolution (also referred to as compact dissolution) consumes large volumes of reactant and provides negligible increases in permeability. At slightly higher injection rates, the reactant can penetrate into the porous matrix and enlarge flow channels. However, a significant amount of reactant is consumed on the walls of the flow channels. This consumption results in the formation of a conical-shaped dissolution channel and requires the injection of several pore volumes of fluid for the channel to break through the porous medium.

At intermediate injection rates, unconsumed reactant reaches the tip of the evolving flow channels. Subsequent consumption at the tip propagates the dissolution channels and eventually leads to the formation of a dominant wormhole. The wormhole provides significant permeability increases and requires a minimum pore volume of fluid to break through the rock matrix. At high injection rates, the flow channels become more highly branched or ramified (far right structure) as fluid is forced into smaller pores. Dissolution occurs



**Appendix Figure 2.** Neutron radiographs of dissolution structures formed during the dissolution of limestone by 0.5M HCl at 72°F (Fredd and Fogler, 1998a).  $PV_{inj}$  = number of pore volumes injected,  $PV_{BT}$  = number of pore volumes to breakthrough.



over a high surface area, which results in an increase in the number of pore volumes to breakthrough. At extremely high injection rates, all the pores are dissolved uniformly as unconsumed reactant penetrates deep into the porous medium. This uniform dissolution is typically observed when dolomite is dissolved by HCl at ambient temperature (Hoefner and Fogler, 1988).

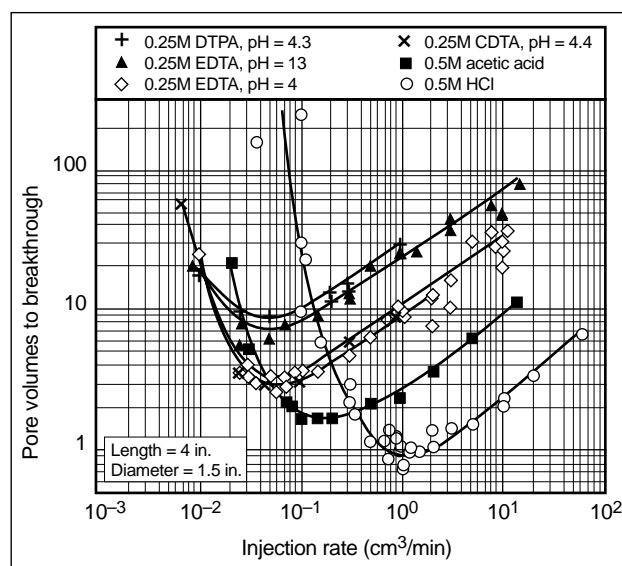
The flow rate at which the various dissolution structures are formed is influenced by mass-transfer and reaction processes. Therefore, the structures depend on the temperature and fluid-mineral system. For example, the same trend of decreasing channel branching observed when the injection rate is decreased is also observed when the temperature is increased (Fredd, 1998). Increasing the temperature results in an increase in the mass-transfer limitations (because the activation energy for diffusion is less than the activation energy for reaction) and causes more reactant to be consumed on the walls of the dissolution channel. The result is an increase in the number of pore volumes to breakthrough and an increase in the injection rate required to form the dominant wormhole channels (Wang *et al.*, 1993; Fredd, 1998). Thus, although the dissolution must be influenced by mass transfer (i.e., the surface reaction rate must be rapid) for wormhole formation to occur, ineffective wormhole formation will occur if the system is too mass-transfer limited. Hence, there is an optimum degree of transport and reaction limitations for effective wormhole formation (Fredd, 1998).

## Optimum injection rate

Several investigators have studied the phenomenon of wormhole formation in a variety of fluid-mineral systems and reported the existence of an optimum injection rate (Hoefner and Fogler, 1988; Daccord *et al.*, 1989, 1993; Wang *et al.*, 1993; Frick *et al.*, 1994b; Mostofizadeh and Economides, 1994; Bazin *et al.*, 1995; Huang *et al.*, 1997; Fredd and Fogler, 1998a, 1998b). The optimum injection rate represents the conditions at which a minimum volume of fluid is required to obtain a given depth of wormhole penetration. The optimum injection rate corresponds to the formation of dominant wormhole channels. Because no significant difference in the conductivity of the various dissolution structures is observed for the same depth of penetration (C. N. Fredd, unpubl. data, 1998), the injection rate at which the volume of fluid is minimized represents the most effective condition for matrix stimulation.

The existence of an optimum injection rate is demonstrated in Appendix Fig. 3, which shows the dependence of the number of pore volumes to breakthrough on the injection rate for a variety of fluid-limestone systems (Fredd and Fogler, 1998b). The figure includes data from linear coreflood experiments with 0.25M CDTA (pH = 4.4), 0.25M DTPA (pH = 4.3), 0.25M EDTA (pH = 4 and 13), 0.5M acetic acid and 0.5M HCl. All the fluids exhibit an optimum injection rate at which the number of pore volumes to breakthrough is minimized and dominant wormhole channels are formed. The number of pore volumes to breakthrough increases to the left and right of the minimum owing to the formation of conical dissolution channels and ramified wormholes, respectively.

The importance of mass transfer on the dissolution phenomenon is demonstrated by the influence of the diffusion coefficient on the optimum injection rate. As the fluid type was varied, the optimum injection rate decreased with decreasing diffusion coefficient in the order of HCl > acetic acid > chelating agents. (The diffusion coefficients are listed in Appendix Table 1.) Because of this influence of diffusion, alternative fluid systems such as chelating agents and weak acids are more effective than HCl when injected at rates below about 0.2 cm<sup>3</sup>/min in linear coreflood experiments. Therefore, in shallow or tight formations where low injection rates are required to prevent fracturing the formation or when injection rates are limited because of frictional pressures, alternative fluids may be more effective than HCl for matrix stimulation.



**Appendix Figure 3.** Optimum injection rates for the dissolution of limestone by various stimulation fluids at 72°F (Fredd and Fogler, 1998b).

# Fundamentals of wormhole formation

## Influence of transport and reaction

The obvious importance of wormhole formation on carbonate acidizing has led many investigators to study the dissolution phenomenon. Early investigators recognized the significant influence of mass transfer on the dissolution of limestone by HCl (Barron *et al.*, 1962; Williams *et al.*, 1970; Nierode and Williams, 1971). This influence has served as a basis for many of the theories describing wormhole formation.

Daccord *et al.* (1989) investigated a water–plaster of paris system and reported wormhole formation to depend on the Peclet number  $Pe$ .  $Pe$  is defined as the ratio of transport by convection to transport by diffusion (see Chapter 17). A similar dependence on  $Pe$  was observed for the HCl–limestone system (Daccord *et al.*, 1993; Mostofizadeh and Economides, 1994; Buijse, 1997). Daccord *et al.* (1993) and Frick *et al.* (1994b) combined the concepts of fractal geometry with the dependence on  $Pe$  to describe wormhole formation in the HCl–limestone system. Bazin *et al.* (1995) studied the HCl–limestone system and reported efficient wormhole formation to occur at the transition between convection-limited and mass-transfer-limited regimes. In contrast, Wang *et al.* (1993) and Huang *et al.* (1997) investigated HCl–carbonate systems and proposed that the optimum injection rate occurred at a transition between reaction-rate-limited and fluid-loss-limited regimes (see Chapter 16). Despite the major influence of mass transfer on wormhole formation, diffusion plays only a minor role in their theory.

Hoefner and Fogler (1988) investigated HCl–carbonate systems and found that the phenomenon of wormhole formation is governed by the Damköhler number  $Da$  for flow and reaction.  $Da$  is defined as the ratio of the overall rate of dissolution to the rate of transport by convection. When the overall rate of dissolution is mass-transfer limited,

$$Da_{mt} = aD_e^{2/3}l/q, \quad (6)$$

where  $D_e$  is the effective diffusion coefficient,  $q$  is the flow rate,  $l$  is the pore length, and  $a$  is a constant that depends on the carbonate core. On the other hand, when the net rate of dissolution is reaction rate limited,

$$Da_{rxn} = ak_r dl/q, \quad (7)$$

where  $d$  is the pore diameter. The units of  $a$  vary from Appendix Eq. 6 to 7 such that  $Da$  is dimensionless. Hoefner and Fogler observed that a minimum volume of fluid was required for channel breakthrough (i.e., optimum conditions for wormhole formation) when  $Da$  was varied over several orders of magnitude. This observation is consistent with the existence of an optimum injection rate for constant fluid–mineral properties because the value of  $Da$  is inversely proportional to the injection rate.

Recently, a similar dependence on  $Da$  was demonstrated for the flow and reaction of chelating agents and weak acids in carbonate porous media (Fredd and Fogler, 1998a, 1998b). These alternative fluid systems are influenced by both transport and reaction processes (as described previously in “Carbonate dissolution”) and therefore cannot be described by theories developed in previous studies. To describe wormhole formation with these fluid systems, the various transport and reaction processes were included in a generalized description of the dissolution phenomenon. A common dependence on  $Da$  was observed when the combined effects of transport and reaction were taken into account. This common dependence on  $Da$  is described in detail in the sections that follow.

## Dependence on the Damköhler number

To simulate transport and reaction within a wormhole channel, the dissolution of a porous medium was modeled as the dissolution of a representative cylindrical tube (Fredd and Fogler, 1998b). The cylindrical tube represents the dominant flow channels within the porous medium (i.e., the wormholes). Convection and reaction in the tube were included in a reactant mass balance, where Appendix Eq. 4 was used for the rate of reactant consumption. Solution of the reactant mass-balance equation resulted in an expression for the concentration profile along the length of the channel that is dependent on  $Da$ :

$$\frac{C}{C_o} = \frac{1 + vK_{eq}e^{-Da}}{1 + vK_{eq}}, \quad (8)$$

where  $Da$  is defined as

$$Da = \frac{\pi dl\kappa}{q}, \quad (9)$$

where  $d$  and  $l$  are the diameter and length of the capillary tube, respectively. Because of the dependence on

the overall dissolution rate constant, this  $Da$  includes the effects of reactants transport, reversible surface reactions and products transport. This  $Da$  reduces to those defined in Appendix Eqs. 6 and 7 for reactants-transport-limited ( $\kappa = K_1$ ) and reaction-rate-limited ( $\kappa = k_r$ ) dissolution, respectively. Physically,  $Da$  provides a measure of the amount of reactant being consumed on the walls of the wormhole, as opposed to being transported to the tip of the wormhole, where it can be consumed efficiently. Unlike previous parameters that assume either mass-transfer-limited or reaction-rate-limited dissolution, this  $Da$  accounts for a variety of transport and reaction processes and is, therefore, able to describe alternative fluid systems such as chelating agents and weak acids.

To determine the overall dissolution rate constant, the mass-transfer coefficients were obtained from Levich's (1962) solution of the convective diffusion equation for laminar flow in a cylindrical tube. The average mass-transfer coefficient  $K_{mt}$  along the length of a tube is

$$K_{mt} = 1.86 D_e^{2/3} \left( \frac{u}{dl} \right)^{1/3}, \quad (10)$$

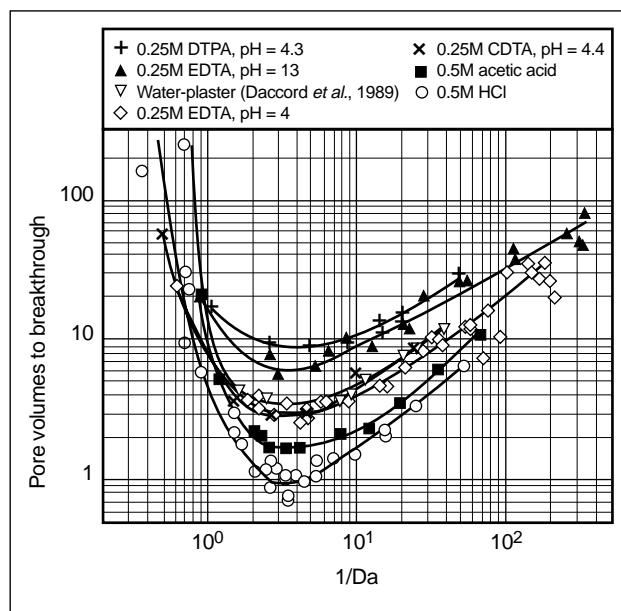
where  $K_{mt}$  is for either reactants or products ( $K_1$  or  $K_3$ ), depending on the value of the diffusion coefficient, and  $u$  is the superficial velocity in the capillary tube. Because the diameter and length of the capillary tube, or wormhole channel, change with time, the mass-transfer coefficients and  $Da$  were evaluated on the basis of the final wormhole dimensions. The diameter was measured from neutron radiographs. Typical diameters were of the order of 0.02 in. The length was assigned a representative length of the wormhole (one-half the core length). The effective surface reaction rate constant and effective equilibrium constant were obtained from independent kinetic studies using a rotating disk. The effective constants are listed in Appendix Table 1 with values for the diffusion coefficients for reactants and products. For the case of HCl and the chelating agents,  $K_{eq}$  is relatively high, so the products transport and reverse reaction terms become negligible.

## Optimum Damköhler number

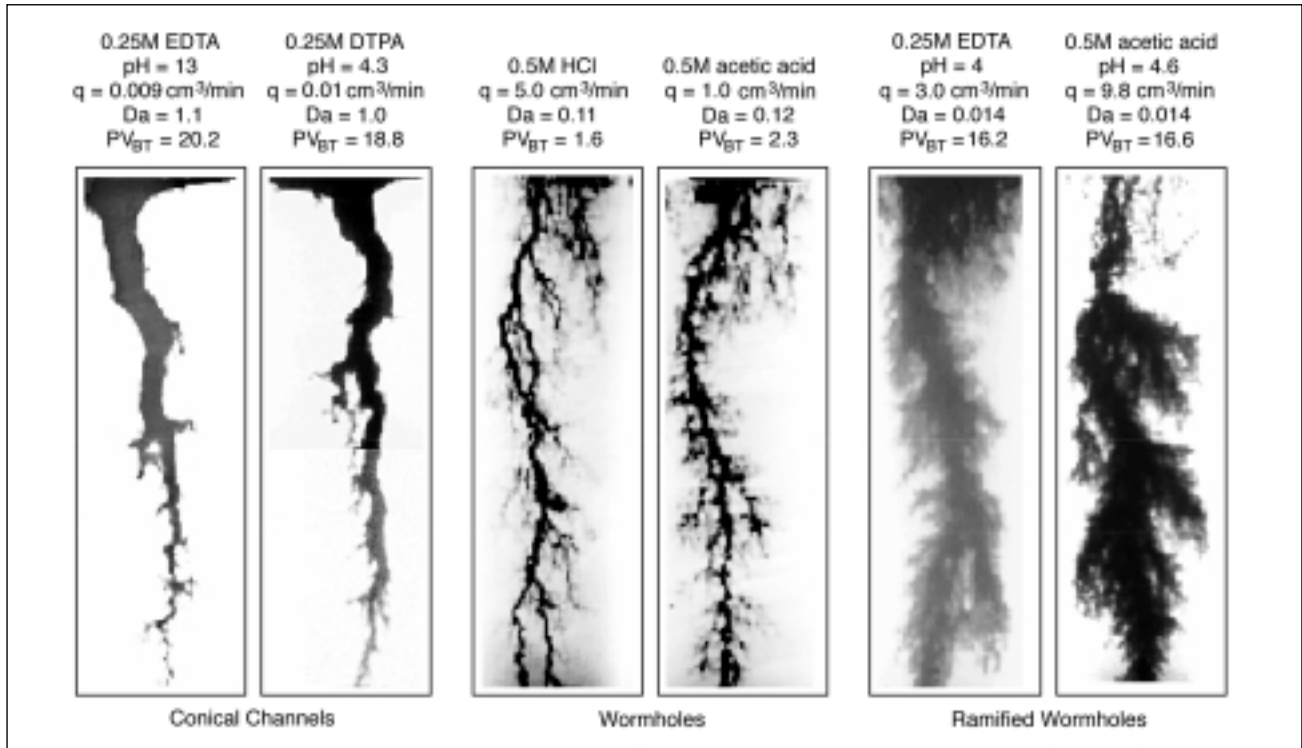
$Da$  has been shown to describe the phenomenon of wormhole formation for a wide range of fluid-mineral systems (Fredd and Fogler, 1998b). A common depen-

dence of wormhole formation on  $Da$  is observed when the various transport and reaction processes are taken into account. This dependence is shown in Appendix Fig. 4, where the number of pore volumes to breakthrough is plotted as a function of the inverse of  $Da$  (as defined in Appendix Eq. 9). The curves for the chelating agents and acetic acid are shifted to the right in comparison with Appendix Fig. 3 such that the minimum number of pore volumes to breakthrough occurs at about the same value of  $Da$  for all the fluids. Thus, these fluids are all characterized by the same optimum  $Da$ . This optimum is observed for fluid-limestone systems that range from reactants transport limited (HCl) to reactants transport and surface reaction influenced (chelating agents) to reactants and products transport limited (acetic acid). Also included in Appendix Fig. 4 are data from Daccord *et al.* (1989) for the dissolution of plaster of paris by water. This system, which is limited by the transport of products away from the surface (Christofferson and Christofferson, 1976), also exhibits the same optimum  $Da$ . For this wide range of fluid-mineral systems, the optimum  $Da$  occurs at a value of approximately 0.29.

The dependence of the wormhole structure on  $Da$  is shown in Appendix Fig. 5 for a variety of fluid-limestone systems. The pairs of neutron radiographs are at similar values of  $Da$  and represent a wide range of transport and reaction limitations. The neutron radio-



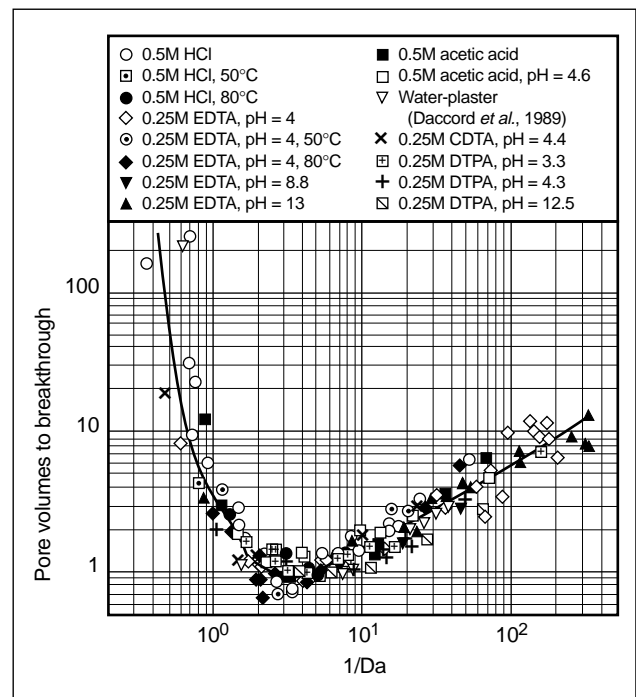
**Appendix Figure 4.** The optimum  $Da$  for the dissolution of limestone by various stimulation fluids (Fredd and Fogler, 1998b).



**Appendix Figure 5.** Comparison of wormhole structures formed at similar  $Da$  values by a variety of fluid systems (Fredd, 1998).

graphs show wormhole structures formed at  $Da$  values of approximately 1.1, 0.11 and 0.014. The wormhole structures exhibit similarities in the amount and type of channel branching at each of these values. As  $Da$  is decreased, the dissolution structures change from conical-shaped channels to dominant wormholes to highly ramified wormholes. These similarities demonstrate that  $Da$  dictates the structure of the dissolution channels formed by systems with a wide range of mass-transfer and reaction limitations.

A variety of fluid systems exhibit similar trends in the number of pore volumes to breakthrough and the corresponding wormhole structures. Because these trends are a result of a common dependence on  $Da$  and, therefore, the transport and reaction processes, a single description of the dissolution phenomenon is possible. This single description is obtained by normalizing the number of pore volumes to breakthrough by the minimum number of pore volumes to breakthrough for the respective fluids (Fredd, 1998). The normalized number of pore volumes to breakthrough is plotted versus the inverse of  $Da$  in Appendix Fig. 6. The results reveal a single curve for a wide range of fluid-mineral systems, including different fluid types, pH values and temperatures. (Unless otherwise stated,



**Appendix Figure 6.** Normalized number of pore volumes to breakthrough versus  $Da$  (Fredd, 1998).

the data are for the dissolution of limestone at ambient temperature.) This single curve provides a means of estimating the entire curve for the number of pore volumes to breakthrough and the wormhole structures from a single coreflood experiment near the optimum  $Da$ . Thus, the need for exhaustive coreflood studies to determine the effectiveness of a fluid under particular reservoir conditions is eliminated.

## Wormhole formation modeling

In addition to involving a variety of transport and reaction processes, the dissolution of porous media is complicated by the stochastic nature in which the flow channels evolve. The difficulties associated with accounting for all the complexities of wormhole formation have led to many simplifications of the dissolution phenomenon. These simplifications typically limit the models to either mass-transfer-limited or reaction-rate-limited dissolution and include an ideal representation of the porous medium. Early investigators simulated mass-transfer-limited dissolution using models of the porous medium that were based on bundles of capillary tubes (Nougaro and Labbé, 1955; Rowan, 1959). These simple models were extended by Schechter and Gidley (1969) to include the effects of pore merging and either mass-transfer-limited or reaction-rate-limited dissolution. Although the dominant pores were observed to grow more rapidly, these models were unable to capture the branching characteristics of the dissolution phenomenon.

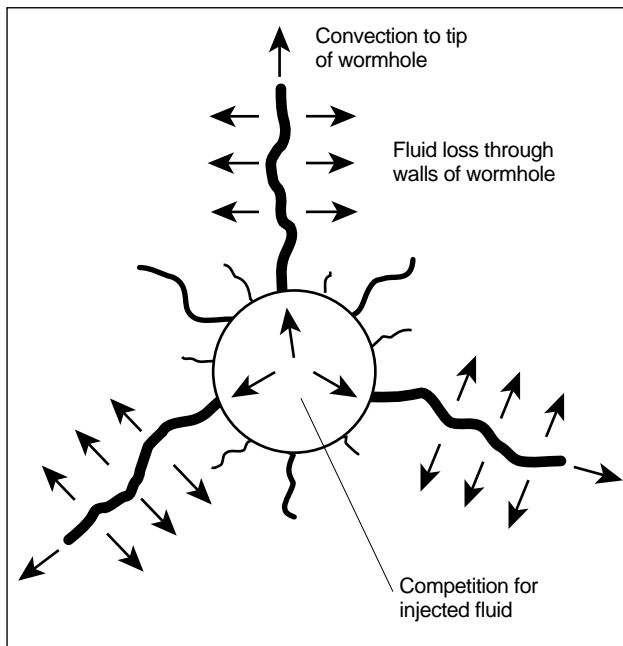
More recently, Hoefner and Fogler (1988) successfully modeled the phenomenon of wormhole formation using a network model. They simulated pore-scale flow and reaction by representing the porous medium as a two-dimensional network of nodes connected by cylindrical bonds. The model provided qualitative predictions of the dissolution structure (see Fig. 17-1) and corresponding permeability response for both mass-transfer-limited and reaction-rate-limited dissolution. Similar results were observed by Daccord *et al.* (1989), who utilized a network model to simulate the mass-transfer-limited dissolution of plaster of paris by water. Although these network models do not include pore merging, they were able to predict the experimentally observed trends in wormhole formation because they capture the effects of pore-level heterogeneity on the macroscopic dissolution phenomenon.

The combined effects of transport and reaction have been included in a three-dimensional physically representative network (PRN) model for flow and reaction in porous media (Fredd and Fogler, 1998b). The PRN model is based on a packed-bed description of the porous medium (Bryant *et al.*, 1993; Thompson and Fogler, 1997). Although the use of a packed-bed description of the medium limits the ability of the model to represent consolidated carbonate porous media, it is a major advancement over the capillary tube representations typically used. The model provides a complete topological description of the medium and a fundamental description of the pore-scale hydrodynamics. These descriptions serve as a physical basis for determining macroscopic parameters, such as the permeability. Dissolution is simulated by allowing the spherical particles that compose the bed to shrink as reactant is consumed. The pores naturally merge as the spherical particles are dissolved. The simulations are in qualitative agreement with experimental observations and demonstrate the common dependence of wormhole formation on  $Da$ . More importantly, the existence of an optimum  $Da$  is substantiated by PRN model simulations.

## Prediction of optimum field conditions

The ultimate goal of all laboratory studies is to aid the design of effective field treatments. Two main design requirements are predicting the optimum injection rate and selecting the most appropriate stimulation fluid. Unfortunately, the direct application of laboratory data to the field is not straightforward, as noted by several investigators (Daccord *et al.*, 1989; Frick *et al.*, 1994b; Bazin, 1995; Buijse, 1997). Wormhole formation in the field is complicated by the effects of fluid loss through the walls of the wormhole in the radial geometry and by competition among wormholes for the injected fluid (Appendix Fig. 7). The importance of these processes has been demonstrated theoretically (Nierode and Williams, 1971; Hung *et al.*, 1989; Buijse, 1997). However, these studies were limited in their ability to predict optimum injection conditions in the field because of a lack of consideration of the critical parameters required for effective wormhole formation.

To account for the influence of fluid loss and wormhole competition on wormhole formation, two approaches are the most obvious:



**Appendix Figure 7.** Idealized representation of fluid loss from the walls of wormholes and competition among wormholes for injected fluid.

- simulate wormhole formation using large network models that account for the effects of pore-scale transport and reaction
- account for the added complications in macroscopic theories such as the existence of an optimum  $Da$ .

Network models inherently include the effects of fluid loss and wormhole competition because the pressure profile and flow rates through all pores in the network are continually updated during the simulation. Although the use of network models would eliminate the need for macroscopic correlations, the ability to simulate wormhole formation at the field scale is limited by the excessive memory and computational time required for such simulations. Thus, the most tractable approach at this time is to extend macroscopic theories. This section introduces an extension of the optimum  $Da$  to predict optimum injection strategies for matrix stimulation treatments in the field.

## Significance of the Damköhler number

The existence of an optimum  $Da$  was observed in laboratory experiments conducted in linear cores. In these experiments, only one wormhole was typically observed because of the limited cross-sectional area available for flow. In addition, essentially all the flow

is through that single wormhole because the conductivity of the wormhole is several orders of magnitude higher than that of the porous medium and fluid loss through the walls of the wormhole is insignificant in the linear geometry. Therefore, these experiments demonstrate the optimum  $Da$  within a single wormhole with negligible fluid loss. Applying the concept of the optimum  $Da$  to the field requires knowledge of both the relative amount of reactant lost from the wormhole because of fluid loss and the number of wormholes that will form per unit surface area of the formation (i.e., wormhole density). To account for the effects of fluid loss and wormhole competition on wormhole formation, it is first necessary to understand the conditions at which the dependence on  $Da$  is affected most significantly by these processes.

### • Fluid loss

Fluid loss through the walls of a wormhole has three main effects on transport and reaction within the wormhole. These effects are decreasing the flow rate along the length of the wormhole, affecting the rates of mass transfer within the wormhole (because of the combined influence of convection and diffusion normal to the walls of the wormhole) and increasing the amount of reactant lost through the walls of the main wormhole channel (because of reactant leakoff). Each of these effects reduces the amount of reactant that is transported to the tip of the wormhole (because of either increased consumption or leakoff) and, consequently, reduces the rate of wormhole propagation.

The significance of these effects depends on the rate of fluid loss and, therefore, depends on the permeability of the medium that is being stimulated. Fluid-loss velocities reported in the literature range from about  $1 \times 10^{-4}$  to  $1 \times 10^{-2}$  cm/s at a permeability of about 1 md (Hung *et al.*, 1989; Wang *et al.*, 1993; Settari, 1993). This range provides a conservative estimate of fluid-loss velocities expected in typical matrix stimulation treatments, which are usually conducted in damaged formations with near-wellbore permeabilities of less than 1 md. This range of fluid-loss velocities serves as the basis for the discussion that follows. Although there is a complex interplay between the three fluid-loss effects, they are discussed independently.

#### – Flow rate

Fluid loss results in a decrease in the flow rate along the length of the wormhole and, hence,

leads to an increase in the value of  $Da$ . As  $Da$  increases, an increasing amount of reactant is consumed on the walls of the wormhole. Thus, fluid loss reduces the amount of reactant being transported to the tip of the wormhole and leads to ineffective wormhole propagation. Ineffective propagation can be overcome by changing the injection conditions (i.e., increasing the flow rate or decreasing the overall rate of dissolution) to maintain the optimum  $Da$ . Increasing the injection rate to maintain efficient wormhole formation is consistent with investigators reporting a higher optimum injection rate in radial experiments than in linear experiments (Frick *et al.*, 1994b; Mostofizadeh and Economides, 1994).

#### – Mass transfer

Fluid loss affects the rates of mass transfer (and, consequently, the overall rate of dissolution) within the wormhole as a result of the combined influence of convection and diffusion normal to the walls of the wormhole. Fluid loss increases the rate of reactants transport to the walls of the wormhole, because mass transfer and fluid loss act in the same direction. Conversely, fluid loss decreases the rate of products transport away from the walls of the wormhole to the bulk fluid. The overall rate of products transport increases because of the added effect of products leaking off into the formation. These changes lead to an increase in the amount of reactants consumed on the walls of the wormhole and a decrease in the effectiveness of wormhole formation.

The effect of fluid loss on the rates of mass transfer can be taken into account by correcting the mass-transfer coefficient  $K_{mt}$  used in the absence of fluid loss. In considering rapid mass transfer resulting from both diffusion and convection, the corrected mass-transfer coefficient  $K$  is (Cussler, 1984)

$$K = \frac{v_L}{e^{(v_L/K_{mt})} - 1}, \quad (11)$$

where  $v_L$  is the fluid-loss velocity. The value of  $v_L$  is negative for flow in the direction of diffusion (i.e., for the transport of reactants to the surface). At typical reservoir conditions, the corrected and uncorrected mass-transfer coefficients differ by less than an order of magnitude, a difference that becomes less significant as  $v_L/K_{mt}$

decreases. For high  $v_L$  values at 200°F, the mass-transfer coefficients for HCl and EDTA are increased by factors of about 2 and 5, respectively. The mass-transfer coefficients for the products are decreased more significantly. However, the decrease is more than offset by products leaking off into the formation and, hence, reducing their concentration near the interface. As a result of these corrections,  $Da$  is increased by a factor of only about 2 if the flow rate is increased to offset the effects of fluid loss.

#### – Reactant leakoff

Fluid loss decreases the amount of reactants transported to the tip of the main wormhole channel because of reactants leaking off into the formation. Although reactant leakoff leads to dissolution of the rock matrix surrounding the wormhole, the dissolution is ineffective because it contributes to propagation of the dominant flow channel. To quantify the effects of fluid loss on the concentration of reactants transported along the wormhole, fluid loss was added to the model for the dissolution of a representative cylindrical tube discussed in “Dependence on the Damköhler number.” Fluid loss (i.e., convection in the radial direction) was included in the reactant mass balance within the cylindrical tube. To obtain an analytical solution, the concentration of reactants leaking off into the formation was assumed to equal the concentration at the solid/liquid interface. This assumption is valid for three cases: zero fluid-loss velocity, reaction-rate-limited dissolution and mass-transfer-limited dissolution. This assumption is commonly used to model fracture acidizing and has been described in more detail in the literature (Settari, 1993). The resulting expression for the concentration profile along the length of the flow channel is similar to that in Appendix Eq. 8:

$$\frac{C}{C_o} = (1 - B)e^{-(Da+\xi)} + B, \quad (12)$$

where

$$B = \frac{Da}{(Da + \xi)} \frac{\left(1 - \frac{v_L}{K_1}\right)}{(1 + vK_{eq})}. \quad (13)$$

The exponent in Appendix Eq. 12 includes  $Da$  as defined in Appendix Eq. 9 (with  $\kappa$  based on

the corrected mass-transfer coefficients, as defined in Appendix Eq. 11) and an additional dimensionless fluid-loss term:

$$\xi = \frac{\pi d l v_L}{q} \left( 1 - \frac{\kappa}{K_1} \right). \quad (14)$$

The obvious importance of  $v_L$  is demonstrated by the fluid-loss term  $\xi$ . As  $v_L$  decreases, the influence of  $\xi$  decreases and  $Da$  eventually dominates the dissolution. Such is the case in linear coreflood experiments in the laboratory. Not so obvious is the dependence of  $\xi$  on the degree of mass-transfer limitations. When dissolution is limited by the transport of reactants to the surface ( $\kappa = K_1$ ),  $\xi$  becomes zero. Physically, this trend is due to the interface concentration of reactants (and, consequently, the concentration of reactants leaking off into the formation) becoming negligible. The leakoff concentration can become negligible even at high rates of fluid loss when the rate of surface reaction is much more rapid than the rate of mass transfer and the rate of fluid loss—i.e., when the dissolution is mass-transfer limited. Thus, for a reactants-transport-limited system such as HCl-limestone, dissolution is dependent on transport and reaction within the wormhole and, hence,  $Da$  dictates the reactant consumption (e.g.,  $Da/(Da + \xi) = 0.999$  for the HCl-limestone system at 200°F with a high  $v_L$ ). On the other hand, for fluid-mineral systems that are influenced by the kinetics of the surface reaction (e.g., HCl-dolomite and EDTA-limestone at ambient temperature),  $\xi$  and  $Da$  are both significant. Under these conditions, an optimum  $Da + \xi$  may exist. Hence, the dependence of wormhole formation on only  $Da$  is valid for wormhole formation in all fluid-mineral systems when the value of  $\xi$  is low (i.e., in damaged formations with low permeability, when fluid-loss additives are present or when the wormholes are relatively short) or the dissolution is limited by the transport of reactants to the surface. These conditions are consistent with the assumption used in deriving the analytical solution to this problem.

- Wormhole competition

During field treatments, many wormholes form and compete for the injected fluid. The longer wormholes, which typically have larger diameters, accept

more fluid than the shorter wormholes. As a result, the longer wormholes propagate more rapidly, while the shorter wormholes eventually stop growing as they receive an insufficient amount of reactant (Hoefner and Fogler, 1988; Hung *et al.*, 1989). The number of wormholes that are capable of penetrating to a given depth depends on the length of the competing wormholes and the distance between them. For example, results from simulations in linear geometry have shown that wormhole interactions significantly reduce the flow rate in a wormhole when the distance between neighboring wormholes is less than the wormhole length (Hoefner and Fogler, 1988; Buijse, 1997). In general, the number of dominant wormholes decreases as the depth of penetration increases. In addition, the number of dominant wormholes depends on  $Da$  within each wormhole. At the extremes of high and low  $Da$  values, face dissolution and uniform dissolution result in a single dissolution structure and an infinite number of dissolution channels, respectively. Between these extremes, a gradual increase in the wormhole density is expected as  $Da$  is decreased.

To maintain efficient wormhole formation, the optimum  $Da$  must be maintained in each of the competing wormholes. Therefore, the optimum injection rate required for efficient wormhole formation in laboratory experiments must be scaled by the number of wormholes that will form in the formation. Some investigators have proposed scaling laboratory data by the relative surface areas (i.e., maintaining the same superficial injection velocity) (Buijse, 1997; Frick *et al.*, 1994b). However, this scaling inherently assumes that the same number of wormholes will form per unit surface area in the field as in the laboratory. In general, this assumption overestimates the number of wormholes that will form and, correspondingly, overpredicts the effect of wormhole competition on the optimum injection rate. The importance of maintaining an optimum injection rate per wormhole (i.e., the optimum  $Da$  in each wormhole) is demonstrated by results from laboratory studies. Different wormhole structures were observed during linear coreflood experiments when the cross-sectional area for flow was varied and the superficial velocity was held constant (Buijse, 1997). In contrast, similar wormhole structures were observed when the cross-sectional area was changed and the injection rate was held constant (C. N. Fredd, unpubl. data, 1989).



## Application of the optimum Damköhler number

The previous section demonstrates the conditions at which wormhole formation is dominated by the dependence on  $Da$ . Because those conditions are typical of conditions often experienced during field treatments, it is reasonable to assume that effective wormhole formation will occur if  $Da$  is maintained near its optimum value. Therefore, an optimum  $Da$  of 0.29 was used as the basis for predicting optimum injection conditions during field treatments. To scale the laboratory observations to the field, additional information about the fluid loss and wormhole competition is required. Although the effects of fluid loss and wormhole competition have not been rigorously investigated, this information can be estimated from the literature. These estimates, along with the method of calculating the optimum injection conditions, are discussed here.

The predictions of the optimum injection conditions are based on determining the injection rate required to maintain an optimum  $Da$  of 0.29. It was assumed necessary to maintain the optimum  $Da$  in only the dominant wormhole channels (i.e., the longer wormholes that carry most of the injected fluid, as shown in Appendix Fig. 7). Therefore, the calculations depend on the number of dominant wormholes that can penetrate to a depth  $l$ . Because the number of wormholes, diameter of the wormholes, growth rate and fluid-loss rate change as the depth of penetration increases, the wormhole properties are evaluated for discrete increases in the depth of penetration. The fluid-mineral system and temperature are specified, and the relevant parameters are evaluated (i.e., diffusion coefficients, surface reaction rates and effective equilibrium constants). The optimum injection rate in a single wormhole of length  $l$  is then determined from Appendix Eq. 9. The change in wormhole diameter is determined from the volume of reactant consumed within the wormhole channel, which is a function of  $Da$  and the wormhole growth rate. The growth rate is calculated by assuming all reactant transported to the tip of the wormhole propagates the wormhole channel by dissolving the tip over the same cross-sectional area as the existing wormhole. The growth rate is

$$\frac{dl}{dt} = r_{At} \frac{MW_A}{\rho_A} X_t, \quad (15)$$

where  $r_{At}$  is the rate of reactant consumption at the tip,  $MW_A$  and  $\rho_A$  are the molecular weight and density of the reactant, respectively, and  $X_t$  is the volumetric dissolving power (i.e., volume of mineral dissolved by a given volume of reactant) at the tip. The rate of reactant consumption at the tip is given by Appendix Eqs. 4 and 5 with the mass-transfer coefficients replaced by the superficial velocity in the wormhole at the tip, which is a function of the wormhole diameter. Appendix Eq. 15 is similar to the growth rate expression introduced by Hung *et al.* (1989). These calculations require an iterative solution because  $Da$  and the growth rate are functions of the wormhole diameter. (If the system is mass-transfer limited,  $Da$  is independent of the wormhole diameter.) The injection rate determined in this manner represents an average injection rate along the length of the dominant wormhole that is required to maintain the optimum  $Da$  in that wormhole. To achieve that average injection rate, the injection rate into the wormhole must be larger to compensate for fluid loss from the walls of the wormhole. The required injection rate  $q_i$  is approximated as

$$q_i = q + q_L, \quad (16)$$

where  $q$  is the average optimum flow rate within the wormhole (such that the optimum  $Da$  is maintained) and  $q_L$  is the rate of fluid loss. The rate of fluid loss was estimated from predictions for fluid loss from a single wormhole (Wang *et al.*, 1993).

Once the optimum flow rate in a single wormhole has been calculated, the optimum injection rate in the field is calculated by scaling by the number of dominant wormholes that will penetrate to the given depth. Although no study has reported wormhole density as a function of injection conditions, two studies have provided a basis for estimating the parameter. The results of network model simulations indicate that the number of wormholes should scale roughly with the ratio of the inlet area to the depth of penetration (Hoefner and Fogler, 1988). A similar observation was made from a capillary tube model (Buijse, 1997). Both of these studies are based on wormhole structures consistent with the dominant wormhole channels. Because the goal of this extension is to predict the growth and competition of dominant wormhole channels, the wormhole density was estimated on the basis of the scaling observed by Hoefner and Fogler (1988).

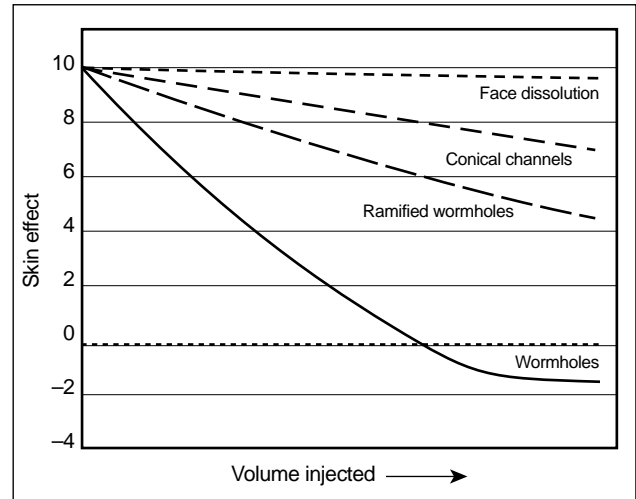
## Optimum injection strategies

Optimum injection strategies for field treatments were predicted for an optimum  $Da$  of 0.29. The predictions are based on three main assumptions: the value of the optimum  $Da$  is not affected by fluid loss or wormhole competition, the rate of fluid loss is consistent with that predicted for a single wormhole, and wormhole density in the near-wellbore region is consistent with that predicted by network models. Because these assumptions must be verified experimentally, the optimum injection strategies presented in this section are considered qualitative trends.

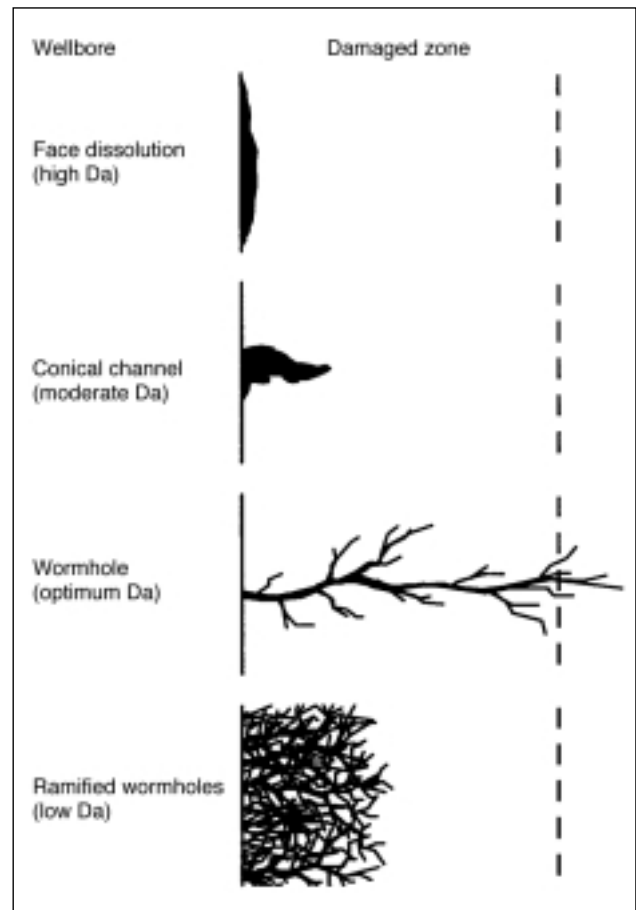
Before optimum injection strategies for field treatments can be presented, it is first necessary to understand how the various dissolution structures, and hence  $Da$ , influence the effectiveness of matrix stimulation treatments. Typical skin effect evolution curves are shown in Appendix Fig. 8 for various dissolution structures. The skin effect was calculated using the three-zone model described by Frick *et al.* (1994a) and the depth of stimulation as determined from the dependence on  $Da$ . The results demonstrate that no significant skin effect evolution is observed when face dissolution occurs. As the value of  $Da$  decreases, the dissolution structure changes to conical channels and a slight decrease in skin effect is observed. Near the optimum  $Da$ , wormhole formation results in effective stimulation as evidenced by the negative skin effect. Additional decreases in  $Da$  result in more ramified wormholes and a less effective evolution of skin effect. This later trend of decreasing effectiveness with decreasing  $Da$  (below the optimum value) is consistent with that predicted by Frick *et al.* for an increasing injection rate.

Appendix Fig. 8 demonstrates that the formation of dominant wormhole channels represents the most effective mode of stimulation for a given volume of fluid injected. This effectiveness is due to the dominant wormhole channels providing the greatest depth of penetration, as shown in Appendix Fig. 9. Obviously the other types of dissolution structures are also capable of stimulation beyond the damaged zone if a sufficient volume of fluid is injected. The trade-off is the cost of the additional fluid injected and possible loss of integrity of the near-wellbore matrix as a result of excessive dissolution.

The influence of the dissolution structure on the effectiveness of the matrix stimulation treatment demonstrates the importance of maintaining the opti-



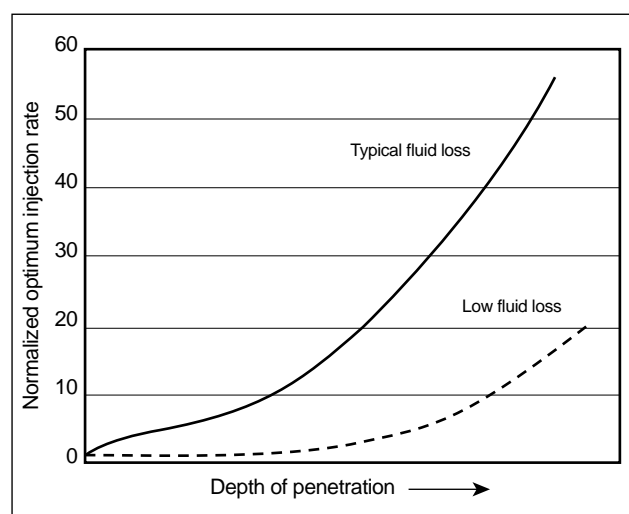
**Appendix Figure 8.** Dependence of skin effect evolution on the dissolution structure.



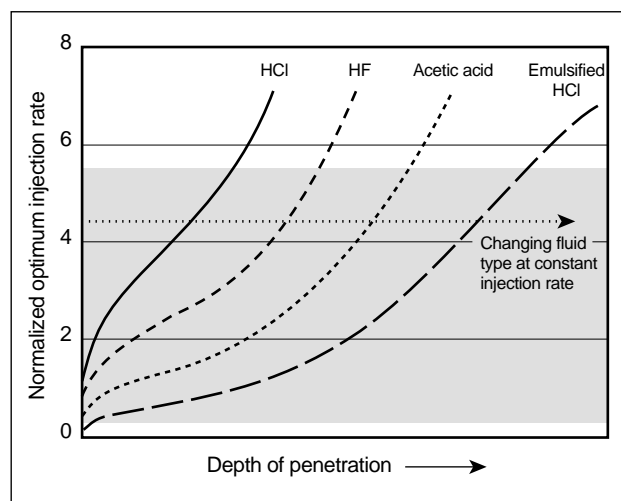
**Appendix Figure 9.** Schematic of dissolution structures and relative depth of penetration obtained by injecting the same volume of fluid at different  $Da$  values.

imum  $Da$ . The question that now must be addressed is how to maintain that optimum injection condition when dissolution is influenced by fluid loss and wormhole competition. The optimum condition can be maintained by increasing the injection rate as the depth of penetration increases. This approach is demonstrated in Appendix Fig. 10, which shows the normalized optimum injection rate required to maintain the optimum  $Da$  as a function of the depth of penetration. The optimum injection rate is normalized by the optimum injection rate for HCl at 200°F with zero fluid loss. The curve represents injection rates at which efficient wormhole formation occurs. At injection rates above and below the optimum curve, ramified wormholes and face dissolution form, respectively. The curves reveal that the injection rate must be increased significantly as the depth of penetration increases. This increase in injection rate is necessary to offset the effects of fluid loss from the wormhole channels. The amount of fluid diverted to the dominant wormholes as a result of wormhole competition is not sufficient to overcome the effects of fluid loss. When  $v_L$  is low (such as in low-permeability damaged zones), the rate at which the injection rate must be increased is less significant. This effect of fluid loss is consistent with experimental data that demonstrate a decrease in stimulation efficiency when the permeability is increased and the injection rate held constant (Frick *et al.*, 1994b; Mostofizadeh and Economides, 1994).

The effect of fluid type on the injection strategy in limestone formations at 200°F is shown in Appendix Fig. 11. The shaded area represents typical injection



**Appendix Figure 10.** Effect of fluid loss on optimum injection strategies for effective wormhole formation with HCl at 200°F.

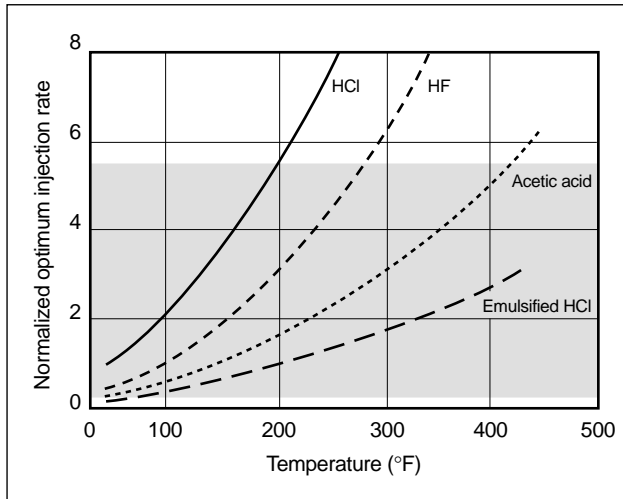


**Appendix Figure 11.** Optimum injection strategies for various acid systems at 200°F. The shaded area (Paccaloni, 1995) represents typical injection rates used in matrix acidizing treatments.

rates used in conventional matrix stimulation treatments (Paccaloni, 1995). The results show that HCl is unable to achieve significant penetration without requiring excessive injection rates that would fracture the formation. In contrast, alternative fluids such as weak acids and emulsified HCl can stimulate to increasingly deeper depths without exceeding the same maximum injection rate. Under these conditions, emulsified HCl would be the most effective stimulation fluid. Results for EDTA are similar to those of emulsified HCl. The data also demonstrate that weak acids and emulsified HCl are more effective than aqueous HCl when the treatments are limited to low injection rates. This effectiveness at low injection rates is consistent with results reported by previous investigators (Hoefner and Fogler, 1985; Fredd and Fogler, 1998a; Takulpakdee, 1998).

Appendix Fig. 11 reveals an alternative injection strategy, as indicated by the dashed arrow. This strategy involves maintaining a constant injection rate and gradually changing the reactant type (thereby changing the overall rate of dissolution). For example, a more effective stimulation could be achieved by injecting an HCl–acetic acid blend that is gradually changed from HCl to acetic acid as the depth of penetration increases.

The optimum injection rate is a strong function of temperature, as shown in Appendix Fig. 12. To obtain a particular depth of penetration, the optimum injection rate must be increased as the temperature increases.



**Appendix Figure 12.** Effect of temperature on the optimum injection rate required to achieve a given depth of penetration with various acid systems. The shaded area represents typical injection rates used in matrix acidizing treatments.

This trend is consistent with experimental results with HCl where increasing the temperature resulted in an increase in the optimum injection rate (Wang *et al.*, 1993; Fredd, 1998). A much more significant dependence of the optimum injection rate on temperature was predicted by Huang *et al.* (1997) because of the emphasis they placed on the kinetics of the surface reaction. Appendix Fig. 12 demonstrates that optimal stimulation with HCl is limited to low temperatures if excessive injection rates and, consequently, fracturing the formation are to be avoided. The figure also reveals that weak acids and emulsified HCl are more effective than aqueous HCl for stimulating high-temperature limestone formations.

This section has provided a means of predicting optimum injection strategies based on laboratory data. With the effective strategies demonstrated, it must be emphasized that the effectiveness of a matrix stimulation treatment depends significantly on the depth of penetration, as shown in Appendix Fig. 8. The depth of penetration is typically limited by fluid loss from the wormholes (Nierode and Williams, 1971; Hung *et al.*, 1989). Therefore, limiting fluid loss is critical to obtaining effective penetration depths, whereas maintaining an optimum  $Da$  is critical to maintaining effective wormhole growth. (Fluid loss from wormholes is inhibited when foamed acids are used for matrix acidization; Bernadiner *et al.*, 1992.) These influences are not independent because fluid loss from the main

wormhole channel increases with increasing wormhole branching. Fortunately, effective wormhole formation tends to minimize fluid loss by minimizing wormhole branching. Therefore, effective wormhole formation provides the combined benefits of reducing fluid loss from the dominant channels and reducing the volume of fluid required to achieve a given depth of penetration. Thus, maintaining the optimum  $Da$  can result in significant improvements in the effectiveness of matrix stimulation treatments.

## Conclusions

Wormhole formation in carbonate porous media involves complex interplay between a variety of transport and reaction processes. Stimulation fluids, such as strong acids, weak acids and chelating agents, are influenced by the effects of convection, reactants transport, reversible surface reactions and products transport. Thus, to adequately describe the dissolution phenomenon, a generalized description of carbonate dissolution is required. When the combined effects of transport and reaction are accounted for, a common dependence on  $Da$  for flow and reaction is observed. The value of  $Da$  dictates the type of wormhole structures that is formed by systems with various degrees of transport and reaction limitations. In addition, there exists an optimum  $Da$  at which dominant wormhole channels are formed and the number of pore volumes to breakthrough is minimized. This optimum  $Da$  occurs at approximately 0.29 for a wide range of fluid-mineral systems. The existence of an optimum  $Da$  was substantiated by network model simulations.

The use of laboratory data to predict the optimum injection conditions in the field, such as fluid type and injection strategy, is complicated by the effects of fluid loss and wormhole competition. From estimates of the effects of these processes on wormhole formation, the theory for the optimum  $Da$  has been extended to predict optimum field conditions. Direct extension of the optimum  $Da$  to the field is valid for three cases: low fluid-loss velocity, reaction-rate-limited dissolution and mass-transfer-limited dissolution. Because these conditions often exist in the field, injection strategies required to maintain the optimum  $Da$  can be used to determine optimum injection conditions in the field. Results predict that to maintain efficient wormhole formation, either the injection rate should be increased or the overall dissolution rate decreased (by changing the fluid

type) as the depth of penetration increases. At the injection rates commonly used for matrix acidizing, conventional treatments with HCl are optimal only in low-temperature formations. Fluids such as weak acids and emulsified HCl provide effective alternatives to HCl at high temperatures and low injection rates. The results discussed in this Appendix to Chapter 16 provide qualitative predictions of optimum injection strategies that are in agreement with experimental observations. A rigorous investigation of the effects of fluid loss and wormhole competition on wormhole formation will enable more quantitative predictions of the optimum injection conditions.

# Carbonate Acidizing Design

*J. A. Robert and C. W. Crowe, Schlumberger Dowell*

## 17-1. Introduction

Carbonate rocks, by definition, contain more than 50% carbonate minerals. The most common carbonate minerals are calcite (calcium carbonate,  $\text{CaCO}_3$ ) and dolomite, a single mineral associating 1 mole of  $\text{CaCO}_3$  with 1 mole of  $\text{MgCO}_3$ . Carbonate rocks are typically classified by the calcite:dolomite ratio, and those with a ratio higher than 50% are generally called limestones. Carbonate rocks present singular physical characteristics, such as double porosity or high permeability contrasts, which are inherited from their process of formation.

Hydrochloric acid (HCl) is usually selected for carbonate acidizing. It reacts readily with carbonate minerals and is available in large quantities at a relatively low price. Whereas the purpose of sandstone acidizing is to dissolve the damage, acid is used in carbonate formations to dissolve the matrix and bypass the damage. For this reason, both damage and rock characteristics must be taken into account when designing the treatment.

## 17-2. Rock and damage characteristics in carbonate formations

### 17-2.1. Rock characteristics

Carbonate rocks are sedimentary rocks resulting mostly from organic activity. The vast majority of these sediments is composed of skeletons of marine organisms that vary in size from a few microns to several centimeters. Some carbonate sediments are formed by the chemical precipitation of  $\text{CaCO}_3$ .

Because they consist of noneroded, homogeneous materials, carbonate sediments usually have a high initial porosity. Conversely, because the permeability of sediments depends mainly on grain size, carbonate rocks present a wide range of permeabilities. For example, chalks formed from sediments of

microscopic fossils have low permeabilities in comparison with those of oolitic limestones, although they can have similar porosities.

After deposition, carbonate sediments are subject to chemical and physical transformation (diagenesis). Chemical modifications consist primarily of the evolution of the sediments to stable forms such as calcite and dolomite. This process is called neomorphism. Dolomites result from evolution under long-term contact with fluids with a high magnesium content. Dolomitization usually increases porosity but impairs permeability by precipitating dolomite crystals. When dolomites are in contact with rainwater, the inverse process of dedolomitization can occur.

Modifications of permeability and porosity can also result from other chemical transformations such as dissolution, reprecipitation and cementation while in contact with subterranean water or molecular diffusion during severe subsurface conditions. Stress and pressure modifications occurring upon burial of the sediments may also entail a lithologic change, with porosity and permeability reductions. High in-situ pressures result in grain compaction, with loss of most of the interstitial water. Higher pressures trigger physical dissolution with immediate reprecipitation causing pore lining. If the interstitial water can be expelled, grain joints are also dissolved and reprecipitated, decreasing the rock porosity to nearly zero and creating fissures of residual circulation. Carbonate sediments are much more sensitive to these phenomena than sandstones are. For example, a chalky mud becomes a compact calcitic rock at depths greater than 6500 ft if all the interstitial water escapes. Mechanical stress modifications also induce fractures, which are important for the economic viability of carbonate reservoirs.

Carbonate reservoirs present a wide range of porosities and permeabilities, depending on the degree of reprecipitation and cementation. Many carbonate reservoirs are fissured under the action of tectonic stresses and behave like homogeneous, pri-

mary porosity reservoirs, with an apparent permeability several orders of magnitude higher than the rock permeability.

### 17-2.2. Damage characteristics

Damage identification is a prerequisite to the proper design of a carbonate acidizing treatment. In formations that are highly sensitive to acid, nonacidic formulations should be used, and the choice of the treating fluid is usually determined by the type of damage. Furthermore, the volume of treating fluid depends on the extent and location of the damage.

All the types of damage that occur in sandstone formations (see Chapter 14) can occur in carbonate formations, except those related to the presence of clay particles in the matrix. In addition, poorly cemented chalks can be permanently impaired by acidic water-base fluids, which can easily dissolve the calcitic cement material, resulting in formation compaction from a loss of mechanical strength.

Problems related to fluid surface tension (i.e., water blocks) are not expected in fissured reservoirs with low matrix permeabilities. In this type of formation, induced damage is concentrated in the fissures, and a greater invasion depth is expected than in a homogeneous reservoir. Pressure variation in the fissures can also result in the precipitation of mineral (scales) and hydrocarbon (asphaltenes) deposits.

## 17-3. Carbonate acidizing with hydrochloric acid

### 17-3.1. Introduction

HCl is generally selected for carbonate acidizing. It can be replaced by organic acids, mainly to minimize corrosion problems at temperatures greater than 400°F [205°C]. The purpose of acidizing with HCl is either to bypass the damage by creating high-conductivity channels (also called wormholes) or to etch partially plugged fissures in low-permeability fissured formations. Although mere permeability restoration is usually targeted for sandstone formations (zero damage skin effect), carbonate acidizing commonly results in negative skin effects. This is due to the reopening of natural fissures and creation of high-permeability wormholes in the near-wellbore area.

HCl can be retarded through the use of emulsions or microemulsions to prevent rock deconsolidation. In this case the wormholes are replaced by a more uniform increase of pore size throughout the stimulated zone. Deep penetration of live acid is obtained by reducing the contact area between the acid and the rock.

### 17-3.2. Historical background

Acidizing was one of the earliest methods developed for increasing well productivity, along with nitro shooting. The technique was first used in 1895, with patents issued in 1896. The original Frasch (1896) patent describes a technique in which HCl is injected into a limestone formation, where it reacts to create channels within the rock. Frasch did not envision the use of corrosion inhibitors, and his process required pipe lined with rubber or some other corrosion-resistant coating.

Although the early acidizing treatments produced some impressive results, their actual use declined within a few years, possibly because of corrosion problems resulting from the uninhibited acid. About 30 years later, the Gypsy Oil Company performed a number of well treatments in sandstone formations in which inhibited HCl was used in an attempt to remove “gyp” deposits (calcium sulfate). The inhibitor used had been developed earlier in the steel industry for the acid pickling of metals. The treatment results were mostly unimpressive, and no patents were filed on the process.

The modern era of acidizing began on February 11, 1932, when the Dow Chemical Company siphoned 500 gal of HCl containing 2 gal of an arsenic inhibitor into a well owned by the Pure Oil Company and displaced it with an oil flush. This was the first use of an inhibited acid on a limestone formation. The previously dead well responded by producing 16 BOPD.

The first treatments were apparently done in an attempt to dispose of surplus HCl. However, it was soon noted that these acid disposal wells accepted fluid at an increasing rate. Treatments performed later on brine-producing wells at the Dow plant in Midland, Michigan, resulted in increased brine flow, prompting the idea that the process might also have application for oil wells.

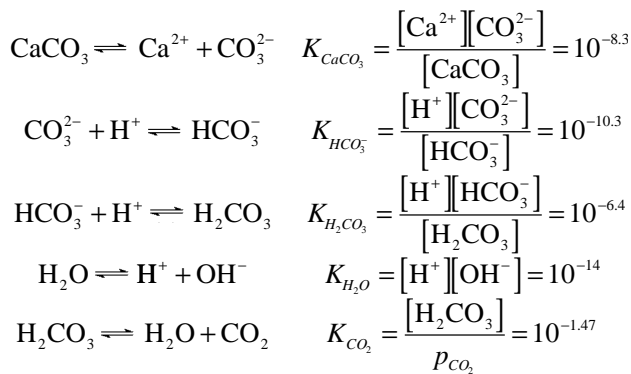
The use of inhibited acid to treat oil wells spread quickly, and the Dow Well Service Group was

formed to exploit this new process. The first two words of the company's name were combined, becoming Dowell, Inc., in November 1932. Other service companies soon followed. Within 3 years, acidizing was practiced widely.

The first hydraulic fracturing treatments were probably performed with acid, although they were not recognized at the time. Wells in tight carbonate formations would usually not accept acid until a critical pressure was reached. However, after this pressure was reached, acid could be easily injected at high rates. It was later recognized that these wells had been hydraulically fractured. For this reason, later hydraulic fracturing patents were never enforced against acid fracturing treatments.

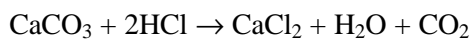
### 17-3.3. Reactivity of carbonate minerals with hydrochloric acid

Calcium carbonate reacts with HCl to produce carbon dioxide, water and calcium chloride. This system is governed by several chemical reactions (Garrels and Christ, 1965), listed as follows with their values of the equilibrium constant  $K$ :

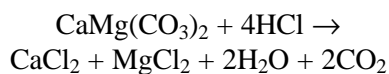


where the use of square brackets indicates the concentration in mol/L and  $p_{\text{CO}_2}$  is the pressure of carbon dioxide.

Because  $\text{H}_2\text{CO}_3$  is a weak acid, and the concentrations of  $\text{HCO}_3^-$  and  $\text{CO}_3^{2-}$  are negligible in presence of HCl, the reaction of  $\text{CaCO}_3$  with HCl can be written as



For dolomite, the reaction equation becomes



This solid-liquid reaction takes place at the rock surface. In excess of HCl, it is complete and irreversible. Table 17-1 lists the quantities of different by-products of the reaction of 15% HCl with calcite. Calcium chloride ( $\text{CaCl}_2$ ) and magnesium chloride ( $\text{MgCl}_2$ ) are highly soluble in spent acid and present no risk of reprecipitation.

**Table 17-1. Quantities of by-products created by the reaction of 15% HCl and limestone.**

HCl	CaCO <sub>3</sub>	CO <sub>2</sub>	H <sub>2</sub> O	CaCl <sub>2</sub>
1000 gal	1846 lbm	6616 scf	343 lbm [41 gal]	2121 lbm

The reaction rate  $K_r$ , expressing the moles of acid reacting per square meter of wetted surface area per second, depends primarily on the temperature and acid concentration:

$$K_r = k_r C^n, \quad (17-1)$$

where  $k_r$  is the reaction rate constant,  $C$  is the HCl concentration in mol/m<sup>3</sup>, and  $n$  is the reaction order. The terms  $k_r$  and  $n$  have been determined experimentally (Lund *et al.*, 1973, 1975; Li *et al.*, 1993). The constant  $k_r$  varies with temperature according to Arrhenius' law, and the coefficient  $n$  varies with temperature for dolomite. The reaction of limestone with HCl is fast and cannot be measured at room temperature. Lund *et al.* (1975) measured limestone reactivity with a rotating disk apparatus at a maximum temperature of 28.4°F [-12°C]. Dolomite is less reactive, and reaction rates can be measured at much higher temperatures (212°F [100°C]).

The reaction rates obtained by Lund *et al.* are given in Chapter 16. The following example provides the order of magnitude of the reactivity of limestone and dolomite: assuming a reaction-rate-limited process (see Section 17-3.4) and using data from Lund *et al.* (1973, 1975), it can be calculated that at 75°F [25°C], the thickness of a rotating disk of calcite reacting with excess 5% HCl decreases by 1.2 mm/min. This value drops to 1.4 μm/min for dolomite at the same conditions.

Weak acids such as formic acid or acetic acid also react with carbonate rocks. However, the high concentration of  $\text{CO}_2$  produced by the reaction prevents it from going to completion, even in the presence of excess fresh acid.



### 17-3.4. Acidizing physics

- Reaction process

A solid-liquid reaction such as HCl with carbonate minerals involves the transport of hydronium ions ( $\text{H}_3\text{O}^+$ ) to the rock surface, reaction of the ions with the rock and transport of the reaction products from the surface to solution. When one of the steps is much slower than the others, it imposes itself on the reaction rate and is said to be the limiting step. Lund *et al.* (1973, 1975) studied the reaction rate of calcite and dolomite with HCl using the rotating disk technique. Theory predicts that for a diffusion-limited process, the rate of dissolution is proportional to the square root of the rotation speed and to the bulk concentration. Lund *et al.* found that the reaction with calcite at room temperature and higher is transport limited, whereas dolomite switches from reaction rate limited to diffusion rate limited between 125° and 212°F [50° and 100°C]. These results were confirmed by de Rozières *et al.* (1994). On the other hand, Wang *et al.* (1993) argued that at the pore level the reaction rate determines the overall rate of acid consumption, thereby implying that the process is reaction rate limited.

Reaction rate limited and diffusion rate limited represent extreme cases in which one phenomenon is much slower than the others. There is also an intermediate case in which different processes have kinetics of the same order of magnitude and influence each other. Both the diffusion rate and the reaction rate depend on ion concentrations at the surface. Therefore, for surface concentrations of the same range as the bulk concentration, transport by diffusion and the reaction rate are interdependent phenomena. This is the case for dolomite and HCl at intermediate temperatures and for calcite and ethylenediaminetetraacetic acid (EDTA) at room temperature (Fredd *et al.*, 1997).

- Wormholing phenomenon

Limestone cores acidized with HCl show the formation of macroscopic channels, called wormholes. Most of the published experiments were performed with linear cores (radial section, flow parallel to the longitudinal axis). They show that the acid injection rate affects the geometry of the channels and the amount of acid required for breakthrough. Daccord *et al.* (1989) found that wormholing occurs in limestone cores above a

critical flow rate and that within the wormholing region the volume required for breakthrough increases with the rate at a power of  $\frac{1}{3}$ . These results were confirmed by Wang (1993) for calcite and dolomite at high temperatures.

Wormholing can be explained by the instability of the acidizing phenomenon: bigger pores tend to receive more acid, which increases both their area and length. This eventually creates a macroscopic channel, or wormhole, that accepts more acid than the surrounding pores and propagates through the core. Wormhole branching depends on the injection rate. Near the wormholing threshold, a single, thick wormhole is formed. As the injection rate is increased, a denser network of thinner channels is created.

Computer network simulations have been used to replicate the wormholing phenomenon (Hoefner and Fogler, 1988; Pichler *et al.*, 1992; Lauritzen *et al.*, 1992). The porous medium is represented by a two-dimensional (2D) network of capillaries. In each pore, the flow obeys Kirchhoff's laws, and the growth of each pore is assumed to follow a given function. These 2D models are extensions of the one-dimensional analytical model of Schechter and Gidley (1969) and Guin and Schechter (1971). Similar results are obtained with regard to the development of unstable patterns. The main advantage of the models is that the dissolution function and flow parameters can be changed in a much wider range than experimentally possible. In these simulations, the occurrence of fractal behavior is bounded by two extreme cases (Fig. 17-1):

- At low velocity, molecular diffusion is predominant, and the solution becomes saturated before any appreciable volume can enter the pore.
- At high velocity, the thickness of the boundary layer becomes so small that the kinetics crosses over to surface reaction rate limited. The velocity is sufficiently high compared with the dissolution rate to allow the invasion of all pores by fresh solution. Uniform etching occurs.

Daccord *et al.* (1993) presented a dimensionless analysis in which the rate of acid diffusion toward the pore walls is compared with the rate of acid convection into the pore. For a wormhole to form, the initial pore radius must be large enough to allow acid transport beyond the pore inlet (see Sidebar 17A).

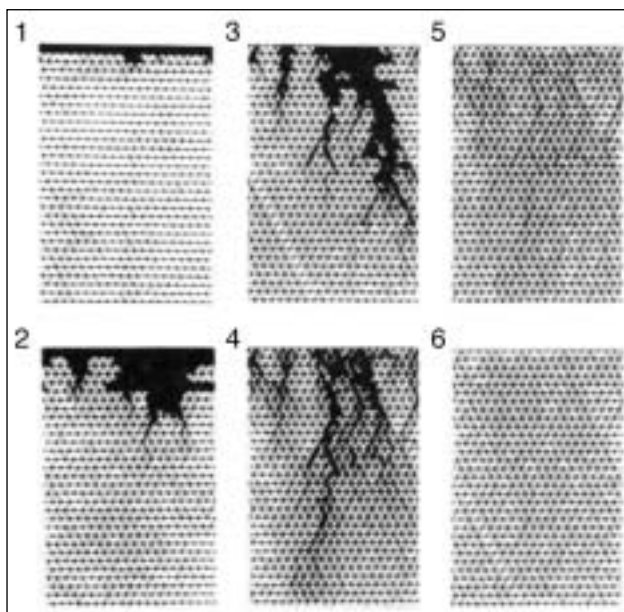


**Figure 17-1.** Dissolution patterns observed with a network model (Hoefner and Fogler, 1988). The width of the bonds is proportional to the amount of material removed for 6 orders of magnitude of the Peclet number (1 = lowest, 6 = highest). Flow is from top to bottom.

Wang *et al.* (1993) presented a different analysis but came also to the conclusion that a critical initial pore size is required to initiate a wormhole.

According to Daccord *et al.* (1989, 1993), the Peclet number  $Pe$ , which represents the ratio of axial flow to radial transport in the pores, is the dimensionless variable governing the transition between compact dissolution at low rates and wormholing at higher rates for a transport-limited reaction (i.e., calcite and high-temperature dolomite). The Peclet number is

$$Pe = \frac{mq\sqrt{k}}{\phi AD}, \quad (17-2)$$

where  $m$  is a coefficient introduced for consistency with earlier publications,  $q$  is the total injection rate,  $k$  is the matrix permeability,  $\phi$  is the porosity,  $A$  is the area perpendicular to flow, and  $D$  is the diffusion constant. The coefficient  $m$  is equal to 1 for a linear geometry and 2 for radial flow.

Table 17-2 shows the results of linear core tests with various values of acid concentration,  $Pe$  and temperature. The dimensionless volume to breakthrough is the ratio of the pore volumes to breakthrough to the volume required for complete dissolution of the core. The limit for wormholing is between  $Pe = 10^{-3}$  and  $Pe = 10^{-2}$ . The tendency for the critical Peclet number to increase with acid concentration has been explained by the onset of gravity phenomena caused by the difference between the fresh and spent acid densities, which creates additional currents near the pore walls that modify the effective acid diffusivity (Daccord *et al.*, 1989).

Fredd *et al.* (1997) used the generalized Damköhler number  $Da$  instead of  $Pe$ :

$$Da = \frac{2\pi rLK}{q_c}, \quad (17-3)$$

where  $r$  is the capillary radius,  $L$  is the capillary length,  $K$  the overall reaction rate taking into account transport by diffusion and reaction, and  $q_c$  is the rate in the capillary. This method enables extending the analysis to systems that are not purely transport limited. Fredd *et al.* reported a series of tests with linear calcite cores and different solvents (EDTA, acetic acid and 1.7% HCl [0.5N]). For all systems the critical Damköhler number is equal to 0.29.

**Table 17-2. Acidizing results for Indiana limestone cores.**

Acid Concentration (N)	Temperature	$Pe$	Dimensionless Volume to Breakthrough	Reference
0.147	75°F [25°C]	5.5E-3	3.2E-3	Wang (1993) <sup>†</sup>
0.235	125°F [50°C]	8.9E-3	7.5E-3	G. Daccord (pers. comm., 1988)
0.47	75°F	4.6E-3	1.0E-2	G. Daccord (pers. comm., 1988)
0.47	175°F [80°C]	6.7E-3	1.1E-2	G. Daccord (pers. comm., 1988)
1	75°F	9.6E-3	3.11E-3	Wang (1993) <sup>†</sup>
1	125°F	2.2E-2	9.75E-3	Wang (1993) <sup>†</sup>
4.4	75°F	4.9E-2	6.47E-3	Wang (1993) <sup>†</sup>

<sup>†</sup> Data for the near-critical Peclet number

## 17A. Wormhole initiation and propagation

Acid transport inside a pore can be schematically represented by two perpendicular fluxes: axial transport by convection and transport to the pore walls by diffusion.

The diffusion constant  $D$  expresses the ability of ions to migrate when submitted to a concentration gradient:

$$J = D \frac{dC}{dx}, \quad (17A-1)$$

where  $J$  is the acid flux (i.e., the number of moles passing through a unit surface per unit time) and  $dC/dx$  is the concentration gradient. In a pore, because of acid reaction with the rock, the acid concentration at the walls is lower than the bulk concentration. Levich (1962) used boundary layer theory to calculate the rate of diffusion in a capillary:

$$I = 2\pi C_0 D \left( \frac{q_c r^2}{\pi D} \right)^{1/3}, \quad (17A-2)$$

where  $I$  is the diffusion flux in the capillary in mol/s,  $C_0$  is the acid concentration at the capillary inlet,  $q_c$  is the rate in the capillary, and  $I$  is the capillary length.

Under laminar flow conditions, the rate in the capillary  $q_c$  is

$$q_c = \frac{\pi r^4}{8\mu} \frac{\Delta p}{l}, \quad (17A-3)$$

where  $r$  is the capillary radius,  $\Delta p$  is the pressure drop in the capillary, and  $\mu$  is the dynamic viscosity.

Wormholing results from the instability of acid propagation: the rate in a wormhole (or a pore) is proportional to  $r$  to the 4th power (Eq. 17A-3), whereas the rate of acid consumption, equal to the diffusion flux for transport-limited reactions, is proportional to the flow rate to the  $1/3$  power (i.e.,  $r^{4/3}$ , Eq. 17A-2). Therefore, bigger pores accept more and more acid, compared with smaller pores, and the acid is used to increase the

pore length and diameter, which promotes wormhole propagation. Once a wormhole is formed, it tends to capture the whole flow because the pressure drop  $\Delta p$  in a wormhole is negligible compared with  $\Delta p$  in the matrix.

Assuming that a pore is a site for wormhole initiation if only one-half of the fresh acid is spent within a length equal to the pore radius:

$$\frac{q_c C_0}{2} = 2\pi C_0 D \left( \frac{q_c r^2}{\pi D} \right)^{1/3}. \quad (17A-4)$$

Equation 17A-4 leads to

$$\frac{q}{Dr\pi} = \frac{ur}{D} = 8, \quad (17A-5)$$

where  $u$  is the axial velocity in the capillary.

The limit between a transport-limited and a convection-limited regime is therefore defined by the Peclet number  $Pe$  from Eq. 17A-6. For a low value of  $Pe$  (low rate or small radius), all the acid is spent at the pore inlet. For a high value of  $Pe$ , fresh acid is transported beyond the pore inlet and a wormhole is created:

$$Pe = \frac{ur}{D}. \quad (17A-6)$$

If a low injection rate is applied, all pores are below the critical rate for wormhole initiation and all the acid is consumed at the wellbore face. This is compact dissolution. Compact dissolution produces poor stimulation and should be avoided. As the rate increases, the fraction of pores able to initiate wormholing increases, which leads to a denser network of wormholes.

A similar analysis can be performed for a reaction-limited process. In that case, the dimensionless number derived is the Damköhler number  $Da$ , expressing the ratio of axial flow to the rate of consumption at the pore walls (Daccord *et al.*, 1993).

Limestone cores acidized with acetic acid exhibit wormholes with more branching than acidizing with HCl at the same injection rate, and lower live acid penetration is obtained (Hendrickson, 1972; Fredd and Fogler, 1996). Rotating disk measurements indicate that the dissolution of limestone by acetic acid is mass-transport limited (G. Daccord, pers. comm., 1988; Fredd *et al.*, 1997), and the effective diffusivity of acetic acid is lower than that of HCl (Table 17-3). The lower overall reac-

tivity of systems such as EDTA and acetic acid allows fresh acid to penetrate into more pores and causes the more homogeneous dissolution pattern. It also lowers the transition rate between compact dissolution and the wormholing regime (Fredd and Fogler, 1996).

- Radial geometry

Very few results have been published for acidizing tests using radial geometries. Daccord *et al.* (1989)

**Table 17-3. Effective diffusivity coefficients (m<sup>2</sup>/s) for 0.5N acetic acid at different temperatures.**

73°F [23°C]	165°F [75°C]	230°F [110°C]	Reference
1.14 × 10 <sup>-9†</sup>	2.7 × 10 <sup>-9‡</sup>	4.0 × 10 <sup>-9</sup>	Dunn and Stokes (1965)
0.21 × 10 <sup>-9</sup>	0.51 × 10 <sup>-9</sup>	0.74 × 10 <sup>-9</sup>	Nierode and Williams (1970) <sup>§</sup>
0.08 × 10 <sup>-9</sup>	0.40 × 10 <sup>-9</sup>	0.57 × 10 <sup>-9</sup>	G. Daccord (pers. comm., 1988)
Note: For comparison, the diffusivity for 0.5N HCl at 73°F is 2.4 × 10 <sup>-9</sup> m <sup>2</sup> /s.			
† Value at 75°F [25°C]			
‡ Extrapolated from data at 75°F			
§ Extrapolated from data for 2N acetic acid at 199°F [93°C]			

used a plaster and water system to obtain casts of wormhole patterns (Fig. 17-2). From the experimental data, they derived a formula in Eq. 17-4 linking the apparent stimulation radius  $r_{ac}$  with the injected acid volume  $V_{ac}$ . The apparent stimulation radius is calculated from the pressure differential across the core, assuming that the pressure differential in the wormholes is null:

$$V_{ac} = \frac{ar_w^2 h Pe^{1/3}}{A_c} \left[ \left( \frac{r_{ac}}{r_w} \right)^d - 1 \right], \quad (17-4)$$

where  $r_w$  is the wellbore radius,  $h$  is the core height,  $Pe$  is the Peclet number as defined in Eq. 17-2, and  $A_c$  is the acid capacity number:



**Figure 17-2.** Cast of a wormhole pattern in radial geometry (Daccord and Lenormand, 1987).

$$A_c = \frac{CV_M}{\Omega(1-\phi)}, \quad (17-5)$$

where  $C$  is the acid concentration,  $V_M$  is the molar volume, and  $\Omega$  is the stoichiometric coefficient (2 for calcite, 4 for dolomite).

Wormholes in radial geometry exhibit a fractal pattern with a fractal dimension  $d$  equal to 1.7. The constant  $a$  is introduced to fit experiments with the model. Other experiments (Frick *et al.*, 1994b) on low-permeability (0.2-md) limestone cores with various acid concentrations and temperatures confirm the trends expressed by Eq. 17-4:

- Rate of wormhole propagation increases with acid strength.
- Rate of wormhole propagation increases as the temperature is increased (acid diffusion increases).
- Within the wormholing regime, the volume for breakthrough increases with the injection rate at  $\frac{1}{3}$  power.

However, the constant  $a$  varies with the system considered. Daccord *et al.* (1993) found that  $a = \frac{1}{84}$  for the plaster and water system. Frick *et al.*'s (1994b) data indicate that the constant  $a$  is approximately  $\frac{1}{18}$  for low-concentration acid (4% HCl) and  $\frac{1}{4}$  for high-strength acid (30% HCl). These different values could be explained by gravity effects or differences in the pores structures of the systems studied. Discrepancies may also be due to different test conditions; i.e., data from Frick *et al.* were obtained with low-permeability rock and low rates (maximum  $Pe$  of 6E–2), near the compact dissolution/wormholing transition, whereas Daccord *et al.* studied higher  $Pe$  values for which the wormholing regime was fully established.

### 17-3.5. Application to field design

- Injection rate

To ensure wormhole propagation and successful treatment, the acid velocity near the wellbore should be sufficiently high to reach the wormholing regime. Examples of the rates required to exceed the critical velocity at the wellbore are in Table 17-4. The critical rate is calculated from Eq. 17-2, with the critical  $Pe$  taken as 5E–2.

Table 17-4 shows that pump rates applied for matrix acidizing are usually well above the critical rate for wormholing. Field data generally confirm these results and show that good stimulation can be obtained even with moderate pumping rates over large intervals (see the case study in Sidebar 17B).

It is common practice to increase pumping rates as injectivity increases during a treatment. Applying high rates ensures that all portions of the reservoir reach the wormholing regime, even in case of injectivity contrasts between different zones. It also allows sustaining wormhole growth as the stimulation radius increases and the velocity at the acid front decreases. Furthermore, in fissured reservoirs where the purpose of the treatment is to clean up fissures, applying high rates increases the live acid penetration.

- Acid volumes

The results listed in Table 17-2 indicate that at optimum conditions (i.e., the near-critical rate), breakthrough is obtained when less than 1% of the total core has been dissolved. This indicates that designing fluid volumes for 5% to 10% rock dissolution over the stimulated area should provide a conservative design. For a radial geometry, the volume of acid required for a given porosity increase varies with the square of the treatment radius, assuming homogeneous dissolution. Figure 17-3 shows the volume of HCl required to increase porosity by 10% for different values of the treatment radius. For example, 50 gal/ft of 15% HCl is required to increase the porosity by 10% up to 2 ft from the wellbore.

For a more accurate design, use of a numerical simulator is required (Bartko *et al.*, 1997). Using a finite-difference simulator enables tracking acid velocity and mineralogy evolution. The amount of rock dissolved as a function of time and acid location can then be calculated in each grid block

## 17B. Acidizing case study

The well was acidized with 60 gal/ft of 20% HCl pumped through coiled tubing over a 135-ft interval. The pumping rate was limited to 2 bbl/min. Permeability varied from 15 to 150 md. Foamed diesel was pumped between the acid stages for diversion.

Figure 17B-1 compares the production profiles before and after stimulation. The new open interval between 31 and 37 ft corresponds to a high-permeability zone. The poorly producing zone between 37 and 79 ft corresponds to a zone of low porosity, according to the results of a log survey. The stimulation increased the well productivity index from 1.1 to 23.9 STB/D/psi. These results indicate that successful stimulation can be achieved at moderate injection rates, provided that coverage of the whole producing interval is ensured.

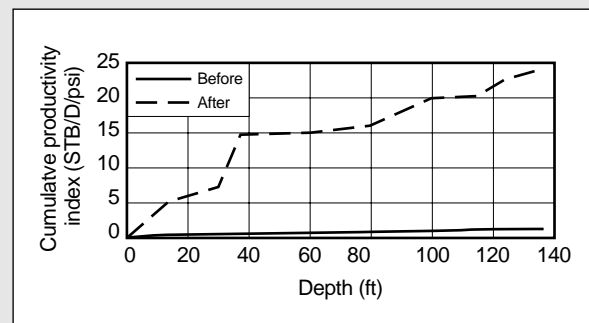


Figure 17B-1. Flow profiles before and after treatment.

using local conditions of mineralogy and acid concentration and velocity. Reaction parameters and the rate of wormhole growth are correlated from experimental data obtained with linear cores for a broad range of flow and acid conditions. Tracking the wormhole propagation front allows calculating a skin effect factor  $s$ , assuming an infinite permeability in the stimulated area:

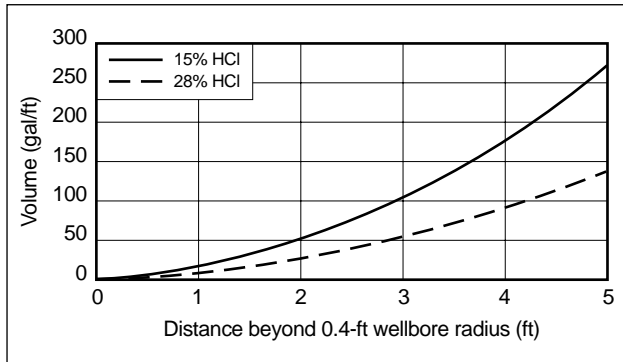
$$s = -\ln\left(\frac{r_{ac}}{r_w}\right). \quad (17-6)$$

Table 17-5 lists examples of stimulation radii required for different values of skin effect. The completion skin effect resulting from partial com-

Table 17-4. Critical flow rates (bbl/min/10 ft) for transport-limited regimes.

Critical Flow Rate, at Sandface	15% HCl		28% HCl	
	$k = 5$ md	$k = 100$ md	$k = 5$ md	$k = 100$ md
Cased completion	0.015	0.003	0.031	0.006
Openhole, 0.8-ft diameter wellbore	0.14	0.03	0.3	0.063

Notes: Diffusivities were computed at 150°F [65°C]. For the perforated case, a density of 4 shots per foot (spf) was assumed, with an 8-in. perforation length and 0.4-in. perforation diameter. Porosity = 15%. These are the critical rates at the wellbore. Higher rates are required to sustain wormhole growth in the matrix.



**Figure 17-3.** Acid volume required to increase porosity 10% (absolute) as a function of the depth of live acid reaction.

**Table 17-5. Stimulation radii for different values of skin effect.**

Skin Effect	Stimulation Radius (ft)
-1	1.1
-2	3
-3	8

Note: Calculated using Eq. 17-6 for a 0.4-ft wellbore radius

pletion or well deviation must be added to the stimulation skin effect to obtain the total formation skin effect.

Using a simulator provides a more accurate calculation of skin effect evolution than Eq. 17-6 because factors such as the decrease of velocity as the acid front progresses into the formation and heterogeneities in the reservoir can be taken into account.

## 17-4. Other formulations

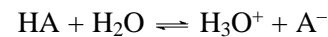
### 17-4.1. Organic acids

Organic acids are used instead of HCl when high bottomhole temperatures prevent efficient protection against corrosion (above 400°F). The two main types of organic acids used are acetic acid and formic acid. Acetic acid is easier to inhibit than formic acid and is used more often. Table 17-6 lists examples of corrosion inhibition with organic acid and HCl.

Organic acids are weak acids, which do not totally dissociate in water. The equilibrium reaction is written as

**Table 17-6. Maximum protection times for different acids and temperatures.**

Acid	Temperature	Maximum Protection Time (hr)
15% HCl	375°F [190°C]	8
	400°F [205°C]	4
28% HCl	350°F [175°C]	4
10% acetic acid	400°F	24
	500°F [260°C]	16

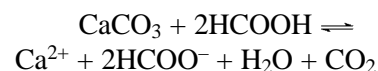
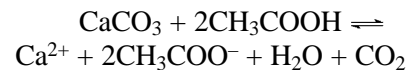


The equilibrium is characterized by the dissociation constant  $k_d$ :

$$k_d = \frac{[\text{H}_3\text{O}^+][\text{A}^-]}{[\text{HA}]} \quad (17-7)$$

The dissociation constant  $k_d$  depends on the type of acid and varies with temperature. At 75°F, acetic acid has a dissociation constant of  $1.76 \times 10^{-5}$  mol/L and formic acid has a dissociation constant of  $1.77 \times 10^{-4}$  mol/L. The value of  $k_d$  increases slightly with temperature up to 175°F [80°C] and then decreases as the temperature increases further. This implies that at usual reservoir conditions, organic acids are less reactive than at surface conditions.

Acetic and formic acids react with  $\text{CaCO}_3$  to form calcium acetate and formate, respectively:



Calcium acetate is highly soluble in spent acid (374 g/L at 75°F). High concentrations of acid, up to 20% to 25%, can be used without any precipitation problem, although concentrations above 10% are generally not used (Table 17-7). Calcium formate and magnesium formate are much less soluble (162 and 140 g/L at 75°F, respectively). Formic acid strength should be limited to 9% to 10% to avoid calcium formate reprecipitation.

**Table 17-7. Quantities of calcite and dolomite dissolved per volume of acid, assuming complete spending.**

	Acid	Calcite	Dolomite
10% formic	1000 gal	920 lbm [5.4 ft <sup>3</sup> ]	854 lbm [4.8 ft <sup>3</sup> ]
10% acetic	1000 gal	720 lbm [4.3 ft <sup>3</sup> ]	663 lbm [3.7 ft <sup>3</sup> ]

When weak acids attack  $\text{CaCO}_3$ , an equilibrium is established between the chemical species produced by the reaction (see the first five reactions in Section 17-3.3) and the acid species ( $\text{HA} + \text{H}_2\text{O} \rightleftharpoons \text{H}_3\text{O}^+ + \text{A}^-$ ). In static conditions, the degree of completion of the reaction depends on the concentration of  $\text{CO}_2$  in solution. For instance, at high-pressure conditions (typically above 1000 psi), only one-half of 10% acetic acid reacts with limestone at 150°F [65°C]). In similar conditions, 80% of 10% formic acid reacts. Although some live acid remains once the reaction reaches equilibrium, a low pH is not maintained because of buffering by the reaction products. Acetic acid is also beneficial for preventing ferric hydroxide precipitates, because it creates a weak complex with the iron in solution and thus increases the pH at which hydroxide precipitation occurs (Crowe, 1985). This effect is particularly significant at low temperatures (i.e., below 125°F). At higher temperatures, some delay of ferric hydroxide precipitation is expected.

Formic and acetic acids can be pumped together, but usually only one acid is selected. Mixtures of organic acid and HCl are also used. The design volume depends on the suspected damage extent around the wellbore. Because organic acids react more homogeneously than HCl, larger volumes are required. Good results have been reported with volumes of the order of 100 gal/ft of 20% acid mixture if proper placement is ensured (Ridwan and Cannan, 1990). Organic acids are much more expensive than HCl per unit volume of rock dissolved. The economics of the treatment must be taken into account for the design.

Acetic acid has other specific applications. Combined either with an aromatic solvent and a mutual solvent to obtain a clear solution or with methanol, it is used to remove water blocks and break emulsions. Combined with a highly concentrated corrosion inhibitor, it can be used as completion fluid to keep the pH low near the wellbore and prevent clay swelling or as a perforating fluid. In the latter case, organic acids are preferred to HCl at temperatures above 200°F [95°C] because their reduced reactivity at higher temperatures enables good corrosion protection for several days.

## 17-4.2. Gelled acids

Gelled acids were developed primarily for fracturing but have found some applications in matrix acidizing. They are used in acid fracturing to increase the viscosity and decrease the leakoff rate. The same principle applies to matrix acidizing conditions in fissured or vugular formations with low primary porosity. In this case, gelled acids are used mainly to clean up the high-permeability channels and minimize fluid loss in the lower permeability matrix. Gelled acids can also be used as a carrier fluid for ball sealers or particulate diverters (flakes).

In the design of gelled acid treatments, the stability of the gelling agent at bottomhole temperatures must be checked carefully. Several types of gelling agents are used. Xantham gums are adequate for moderate conditions (i.e., temperatures up to 230°F [110°C]), with the acid strength limited to 15% (Crowe *et al.*, 1981). Under more severe conditions, synthetic polymers are more appropriate for use up to 400° to 450°F [205° to 230°C].

Crowe *et al.* (1990) showed that under dynamic conditions gelled HCl exhibits the same reaction rate with limestones as ungelled acid. In some cases, reaction rates are accelerated. The reaction rate measured is the rate of calcite consumption. It is the overall reaction rate, determined by the limiting step, which is acid transport by diffusion. It is generally agreed (Muhr and Blanshard, 1982) that the rate of diffusion depends on the solvent viscosity and is not modified by the presence of polymers, at least as long as the distance between the polymer chains is large compared with the size of the ions in solution.

The interaction between polymer chains and the rock surface can affect the overall reaction rate and live acid penetration. If the gel exhibits a non-Newtonian behavior, the shear rate at the rock surface can be modified, which may increase the mass transfer and result in a higher reaction rate. Aside from this effect, the polymer can plug the smaller pores, acting as a fluid-loss agent. This effect was studied by Nierode and Kruk (1973), who found that the growth rate of wormholes is maximum for a small concentration of fluid-loss agent.

HCl is usually the acid component of gelled mixtures. Acid strength varies typically from 5% to



28%. The volume of acid depends on the suspected depth of damage in the fissures and vugs and on fluid placement efficiency.

### 17-4.3. Emulsions

Emulsions are obtained by mixing acid with a refined-oil-base fluid in the presence of a surfactant. The stability of the emulsion depends on the temperature and the ionic strength of the aqueous phase. Some emulsifying agents provide stable emulsions in temperatures up to 300°F [150°C]. Depending on the type of surfactant, a water-in-oil or an oil-in-water emulsion can be obtained (see Chapter 15).

In static conditions, emulsions have been found to lower the overall reaction rate of the acid. Acid-in-oil emulsions are more effective for reaction retardation. It is generally agreed that these emulsions build an oil barrier at the rock surface, preventing the acid from reacting readily with the substrate. Acid-external emulsions also provide some retardation, which is generally attributed to physical interaction of the oil with the path of acid transport to the rock surface. Few results have been published on core acidizing with emulsions under dynamic conditions. The initial studies show that oil-external emulsions can treat low-permeability cores more efficiently than plain acid (Horton *et al.*, 1965).

Limestone cores acidized with emulsions display a highly permeable network of microwormholes that reflect significant modification of the process of acid transport and reaction. Emulsions tend to stabilize the acidizing process by reducing the contact area of the acid with the matrix, thereby decreasing the apparent reaction rate. Measurement of diffusion coefficients in acid-in-oil emulsions by de Rozières *et al.* (1994) using the rotating disk technique found that effective diffusion coefficients in these systems are as much as 3 orders of magnitude lower than diffusion coefficients in plain acid at the same temperature conditions. Therefore, good stimulation can be obtained with emulsions at low rates corresponding to the compact dissolution regime with plain acid.

Like gelled acids, emulsions are usually prepared with HCl. Various acid strengths and volumes can be selected for the fractions, with 70:30 acid-in-oil emulsion a commonly used system. The viscosity of the emulsion is an important parameter because the high viscosity of some mixtures used for fracturing limits their application to matrix acidizing.

A recent trend involves adding nitrogen (N<sub>2</sub>) to the emulsion to obtain a triphase system. Static tests show that this further reduces the reactivity of the acid (Guidry *et al.*, 1989). The exact mechanism of the retardation has not been fully studied. It is generally admitted that N<sub>2</sub> reduces the contact area of acid with the rock. With this type of system, the dissolution pattern is expected to be more homogeneous (in comparison with plain HCl at same pump rate), and relatively large volumes are pumped to obtain large stimulation radii. Liquid volumes as large as 500 gal/ft are usually pumped. This type of treatment is economically advantageous because as much as 50% of the volume pumped consists of nonacid fluids. To increase the matrix injectivity prior to pumping the emulsion, a pretreatment with plain acid is usually performed. Furthermore, to allow injection at higher rates than normally prescribed by the fracturing limit, the wells are generally drawn down as much as possible, and the shut-in time prior to the treatment is reduced to the minimum technically possible. Under these conditions, the near-wellbore pressure is much lower than the average reservoir pressure, and higher matrix rates can be applied. Two- and triphase emulsions are recommended for the treatment of deep damage or if the purpose of the treatment is to stimulate the formation to obtain a highly negative skin effect.

### 17-4.4. Microemulsions

Microemulsions consist of a fine dispersion of oil and acid, stabilized by proper surfactant and cosurfactant additives. Depending on the concentration of the different components, an oil-in-acid or acid-in-oil emulsion can be obtained. The main difference from macroemulsions is the size of the droplets, which are reported to be in the range of 0.005 to 0.2 μm.

Oil-external microemulsions may behave as a single-phase fluid in porous media and sweep oil more easily than plain acid, facilitating acid injection and flow-back. Acid diffusivity in acid-in-oil microemulsions is also greatly reduced compared with plain acid, by at least 2 orders of magnitude (Hoefner and Fogler, 1985). This results in a more homogeneous attack of the rock, as observed in core experiments (Hoefner *et al.*, 1987), which presents two advantages. First, it should enable acidizing tight carbonate rocks at low rates that correspond to compact dissolution conditions with plain acid. Second, at higher rates it avoids



the formation of large wormholes, which can be detrimental to the mechanical properties of soft formations such as chalks.

Despite their advantages, microemulsions are not commonly used in field operations. Because of the high surfactant concentration required, these systems are more expensive and difficult to inhibit. Furthermore, stability problems have been encountered. In most cases similar results can be achieved with macroemulsions. The additional cost of microemulsions is justified only for sensitive formations where mechanical stability is a concern.

### 17-4.5. Special treatments

HCl can be used in combination with other chemicals for specific treatments. This section briefly reviews the main formulations using HCl. More detailed description is in Chapter 15.

Blends of alcohol (mainly methanol) and HCl are used for gas well treatments. Alcohol lowers the surface tension, but not as much as surfactants. However, because it does not adsorb on the rock, it penetrates into the formation as deeply as the acid. It also increases the vapor pressure of the spent acid. This facilitates cleanup of the spent acid and improves gas permeability by reducing the residual water saturation. The addition of alcohol slightly slows the reaction of acid with the rock and slightly accelerates the corrosion rate. The volume fraction of alcohol can vary widely depending on the application, from 20% to 67%. Mixtures with 67% methanol are stable up to 250°F [120°C].

Mixed with an aromatic solvent and a stabilizer, HCl forms a solvent-in-acid emulsion. The volume fraction of the acid varies typically from 50% to 90%. The emulsion stability depends on the solvent concentration and temperature. This formulation is used to remove paraffin and mixed deposits. It is also recommended for removing scale and treating wells being converted from producers to injectors.

HCl can also be used in combination with a surfactant and a chelating agent to remove mud damage in carbonate formations. The combined action of the additives has been found to successfully disperse and remove clays and mud damage. In formations presenting a risk of deconsolidation, HCl can be replaced by a brine or calcium chelant solution such as EDTA. This type of formulation is recommended

particularly for naturally fissured reservoirs where completion materials have invaded the fissures (see Sidebar 17C).

For shallow damage caused by cake deposition in natural fissures, such formulations are highly efficient when acid is spotted through coiled tubing and flowed back, possibly several times (Liétard *et al.*, 1995). If an oil-base mud was used, or if damage material has been in contact with oil downhole, the use of a surfactant and mutual solvent is required to water wet the cake surface and facilitate acid flow in the fissures.

### 17-4.6. Self-diverting acid

Self-diverting acid, originally developed for fracturing, has also been used to improve placement during carbonate acidizing. It consists of HCl mixed with a gelling agent and a pH-sensitive crosslinker. Cross-linking occurs at intermediate values of pH (typically from 1 to 3.5) corresponding to partially spent acid. The lower fresh acid viscosity allows penetration in wormholes and fractures until acid reaction increases the pH and causes crosslinking, thereby diverting the following acid stages to other portions of the reservoir (Fig. 17-4). Because the gel breaks at a pH above 3.5, flowback presents no problem once fresh acid injection is stopped and the acid is allowed to spend completely. Like particulate diverters or foams, self-diverting acids are pumped in several stages, alternating with regular acid stages. Good results are reported in fractured formations and in long, open intervals where benzoic flakes or gelled acid has failed to provide fluid diversion (see Sidebar 17D).

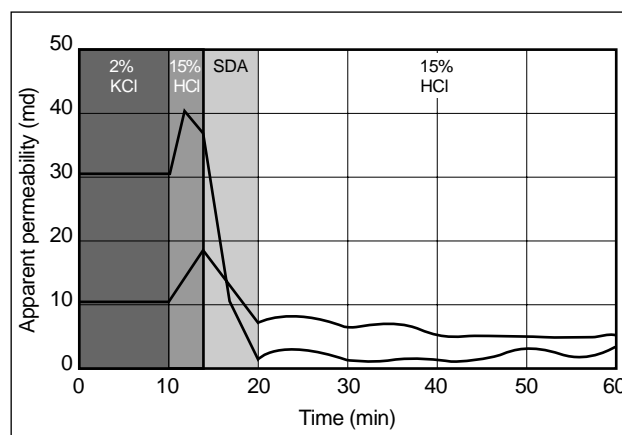


**Figure 17-4.** Effect of self-diverting acid (SDA) on fluid placement.

## 17C. Examples of special treatments

### Well A

Well A was an oil producer from a fissured dolomitic reservoir with an average matrix permeability of 10 md and a porosity of 3%. Damage by mixed silts and organic deposits was suspected. The well was treated with 130 gal/ft of solvent-in-acid emulsion, with a 90 gal/ft preflush of a mixture of 80% solvent with acetic acid and mutual solvent. The pumping schedule was as follows:

1. Preflush: solvent + acetic acid (42 bbl)
2. Main fluid: solvent-in-acid emulsion (63 bbl)
3. Diverter: benzoic acid flakes (31 bbl)
4. Repeat steps 1, 2 and 3
5. Repeat steps 1 and 2
6. Displacement: nitrogen

Production before the treatment had dropped to 1172 STB/D at a wellhead pressure 455 psi. Postjob production increased to 3580 STB/D at a wellhead pressure of 1179 psi.

### Well B

Well B was an oil producer from a calcitic reservoir containing 5% clays. Reservoir porosity was 2% and the average matrix permeability did not exceed a few millidarcies. The production rate prior to the treatment indicated a damage skin effect of approximately 40. The treatment was executed with 75 gal/ft of 15% HCl laden with suspending and sequestering agents, preceded by a preflush of suspending agent-laden brine. The schedule was as follows:

1. Preflush: suspending agent-laden brine (63 bbl)
2. Main fluid: 15% HCl with suspending agent + nitrogen (107 bbl)
3. Diverter: benzoic acid flakes in gelled acid (31 bbl)
4. Repeat steps 1 and 2
5. Displacement: nitrogen

Production increased from 500 STB/D before the job to 3700 STB/D after the treatment at a wellhead pressure of 5900 psi (i.e., 500 psi below the wellhead shut-in pressure). Striking evidence of the acid effect is provided by the pressure record during the treatment, which shows that the well

head pressure decreased by 1200 psi while the first acid stage was injected into the formation. According to Eq. 17C-1, this pressure falloff is equivalent to a skin effect decrease of more than 40:

$$\Delta s = \frac{2\pi kh\Delta p}{\mu q} \quad (17C-1)$$

### Well C

Well C was converted from an oil producer to a water injector. A well test indicated near-wellbore damage, presumably from the presence of workover material. The average reservoir porosity was 16%, and permeability deduced from a porosity log varied from 5 to 500 md across the 200-ft open interval. The well was treated with 30 gal/ft of 15% HCl laden with suspending agents. The acid was pumped through coiled tubing, and four foam stages were used for diversion. The injection profiles before and after the treatment are shown in Fig. 17C-1. The acid significantly improved injectivity in the middle interval, corresponding to a lower permeability region (less than 25 md). The porosity log indicated that the bottom part of the interval (below 170 ft) corresponded to a very low permeability zone. The total injectivity increased from 30,000 BWPD at a wellhead pressure of 1640 psi to 54,000 BWPD at 1420 psi at the wellhead.

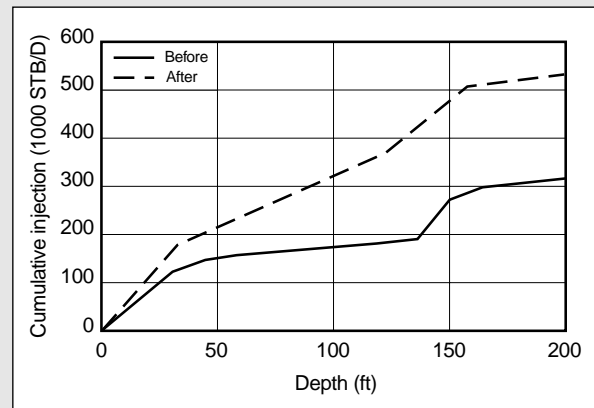


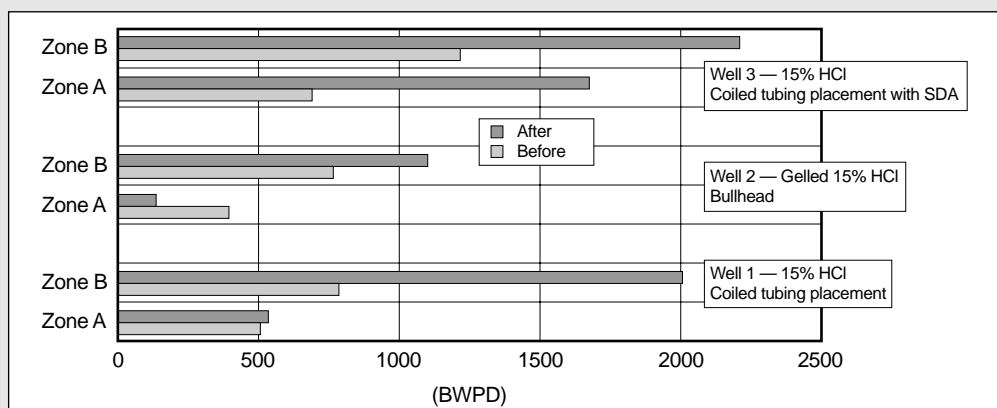
Figure 17C-1. Comparison of injection profiles before and after treatment.

## 17D. Placement using self-diverting acid

Three similar injector wells were treated with different placement techniques. The average reservoir permeability varied from 4 to 10 md. The formation comprised two zones of different injectivities. Treatment for the first well consisted of pumping 15% HCl through coiled tubing. The second well was acidized with gelled acid pumped through tubing. For the third well, three stages of a blend of HCl and suspending agents were pumped through coiled tubing. Two stages of self-diverting acid were used to separate the main stages.

Figure 17D-1 compares the injectivities of the three wells before and after acidizing. Zone A was treated successfully only in the third well with the use of self-diverting acid.

Figure 17D-1. Comparison of acidizing results of three placement techniques.



## 17-5. Treatment design

### 17-5.1. Candidate selection

As explained in Chapter 13, candidate recognition utilizing a systems analysis approach is the first step for the design of carbonate acidizing. Whereas sandstone acidizing is usually limited to damage removal, carbonate acidizing is typically oriented toward reservoir stimulation. Wells exhibiting a slightly negative skin effect prior to the treatment are usually still considered good candidates.

Because of the ability of HCl to create channels, it ensures excellent communication with the reservoir. In higher permeability formations, acidizing can also be used as an alternative to dense perforating. Field experience shows that cased completions with small perforation densities (as low as one perforation every 3 or 5 ft) can exhibit a negative skin effect after stimulation with HCl.

### 17-5.2. Pumping schedule

The second step in the design consists of choosing the right acid formulation, depending on the damage and formation characteristics. Examples of pumping schedules are given in the sidebars to this chapter. Generally, carbonate treatments consist of alternating stages of the main fluid and diverter. A solvent pre-flush can be used ahead of the main fluid to clean up the formation and increase its receptivity to acid. An overflush of brine or seawater can be used to displace the acid into the formation and ensure complete spending away from the wellbore. N<sub>2</sub> can be used for displacement at the end of the job or added to the treatment fluids to assist the flowback of spent acid that may contain insoluble material or high-viscosity gel residuals remaining in the formation. Generally, N<sub>2</sub> is recommended for low-pressure wells with a pressure gradient below 0.46 psi/ft.

The pumping rate is limited by the fracturing pressure. In tight formations, the rate must be sufficiently high to prevent compact dissolution near the wellbore if plain HCl is used. In naturally fractured formations, good results have been obtained with high flow rates. Such pump rates and high pressures do not correspond to usual matrix conditions and are likely to mechanically enlarge natural fractures and increase their conductivity during the treatment.

### 17-5.3. Additives

Additives must be added to the different stages to protect tubulars and ensure successful treatment of the formation. This topic is fully covered in Chapter 15.

For oil wells, adding a mutual solvent to the pre-flush or acid stages helps to water wet the formation and provides good contact of the treating fluids with the rock surface.

Acid corrosion inhibitors and inhibitor aids are required to protect tubulars. Organic acids are easier to inhibit than HCl. Stable emulsions are also relatively easy to inhibit. However, in most corrosion tests, emulsion breakage occurs, and the corrosion rate is similar to or greater than that of the nonemulsified acid.

The addition of surfactant and demulsifiers may also be necessary to lower the interfacial tension between treating fluids and the reservoir fluid and to prevent emulsions. Finally, antisludging agents, scale inhibitors and iron control agents can be used to prevent specific problems. When mixing additives, the compatibility of the different components with each other and with the downhole conditions must be checked thoroughly.

### 17-5.4. Placement

Proper placement of acid over the whole pay zone is required for successful treatment. In thick formations or multilayer reservoirs with different values of permeability or damage severity, acid tends to penetrate the more permeable zones and create high-injectivity streaks that prevent injection into the whole interval.

Five main diversion techniques can be used to improve fluid placement in carbonate acidizing: packers, ball sealers, particulate diverters, foam diversion and self-diverting acid. The first four methods are discussed in Chapter 19. The use of self-diverting acid has increased recently (see Section 17-4.6). In large intervals (e.g., horizontal wells) some of these techniques can be combined with the use of coiled tubing (Thomas and Milne, 1995).

## 17-6. Conclusions

Limestone and dolomite formations can easily be stimulated with acid formulations. Unlike sandstone acidizing, the goal of carbonate acidizing is usually

to bypass the damage rather than dissolve it. HCl is typically used for carbonate acidizing. In case of incompatibility with the formation or the completion (i.e., risk of corrosion), other formulations are used, such as emulsions or organic acids. Suspending agents or solvents can also be used if required by the type of damage.

The high reactivity of acid with limestones and high-temperature dolomites results in the creation of wormholes, which considerably increase the apparent permeability around the wellbore. When wormholes extend beyond the damaged zone or connect with natural fissures in the formation, a negative skin effect is obtained.

An engineering approach should be adopted to design effective carbonate treatments. As in sand-

stone acidizing, proper placement of the acid over the whole interval is necessary for successful treatment and usually requires employing placement techniques. Foam diversion and self-diverting acid are two methods that are increasingly used, with good results.

## Acknowledgments

Some of the material in this chapter was previously authored by G. Daccord and published in the second edition of this volume. The authors also thank G. Daccord, C. Fredd, R. Marcinew, A. Saxon and R. Thomas for reviewing this chapter.

# Sandstone Acidizing

*Harry O. McLeod, Conoco, USA*

*William David Norman, Schlumberger Dowell*

## 18-1. Introduction

Sandstone matrix acidizing is distinguished from carbonate acidizing in that it involves the dissolution of damage that is blocking or bridging the pore throats in the formation matrix, thus ideally recovering the original reservoir permeability. Carbonate acidizing dissolves the formation minerals around the damage, creating new permeability. The mineral acids required to dissolve the damage are usually highly reactive with the numerous formation minerals. The resulting chemical complexes can become insoluble in the environment created and can precipitate, yielding gelatinous or solid particles. Because the formation and the damage can have complicated crystalline structures that can yield a variety of reaction products, sandstone acidizing success requires a significantly better understanding of chemistry than does carbonate acidizing. As discussed in Chapter 13, 75% of well-engineered sandstone acid treatments should be successful, resulting in significant production enhancement.

The descriptor “sandstone” is derived from the geologic classification of rocks with a high quartz silica content. Besides the obvious quartz component, they contain other minerals such as aluminosilicates, metallic oxides, sulfates, chlorides, carbonates and noncrystalline (amorphous) siliceous material. The minerals deposited in the original sediment are called detrital species. Most have a high degree of associated water. As fluids are produced through the matrix of the rock, the drag forces can move some of these minerals, clogging the pore throats.

Connate water in a sandstone contains many of the dissolved native mineral species. This is due to equilibrium and partial pressures of gaseous solvents (such as carbon dioxide [CO<sub>2</sub>]) and the presence of other ionic species. As fluids are produced, the associated pressure drop can disturb this equilibrium and the normal ionic content of the formation brines, resulting in precipitation and possible pore-throat restriction. This type of diagenesis yields authigenic

species (e.g., scales such as calcium carbonates as well as some clay species such as zeolites, illites, kaolinites and smectites).

Various well operations can result in formation damage (see Chapter 14). For example, drilling mud and completion fluid usually penetrate sandstone formations. This invasion of filtrate can introduce an entirely different chemical environment, which the acid treatment must address. Additional formation damage may occur during perforating, gravel packing, and normal production or injection operations. Acid dissolves a variety of damaging materials along with most formation minerals. An understanding of the chemistry is basic to the selection of the acid type and concentration.

This chapter includes the reaction chemistry of the primary solvent used in sandstone acidizing, hydrofluoric acid (HF). Acid systems that contain mixtures of hydrofluoric and hydrochloric acid (HCl) are commonly called mud acids because they were first used to remove mud damage.

## 18-2. Treating fluids

### 18-2.1. Hydrochloric acid chemistry

HCl reactions are discussed in Chapter 17, and details of the reaction and by-products are omitted in this chapter except for how they relate to sandstone minerals. The compatibility of the HF blends used in this process is twofold; these mixtures must meet both compatibility standards for the formation mineralogy and dissolution of the damage mineralogy. HF mixtures are preceded by HCl to avoid precipitation of the slightly soluble and insoluble reaction products of HF with certain chemical species. The chemistry of HCl with carbonate minerals is discussed in a previous chapter, so the focus here is on the chemistry of the HF systems. Although the chemistry of the reaction of HCl with carbonate or calcite is simple, the chemistry of the reaction of HF and siliceous minerals is complex.

Some complex reactions that occur with certain siliceous minerals have only recently been included in the reactions reported in mineralogy breakdowns. These reactions involve HCl and the mineral family known as zeolites. Zeolite minerals are crystalline, but hydrated with active, porous channels in the crystalline lattice. Zeolites are known in other industries as “molecular sieves” because their porosity allows the chemical extraction and filtering of selective materials. Zeolite minerals occur in nature as a by-product of volcanic activity and precipitate from water that is rich in silica. It is theorized that as zeolites are exposed to progressively higher pressures and temperatures they metamorphose from extremely loose, hydrated crystalline structures to more dense and compact structures. The results of this process have different mineral names. The hierarchy of their structure and crystalline nature is provided in Table 18-1. Because these minerals are precipitates, they are always authigenic and located in pore spaces.

Zeolite minerals are sensitive to HCl and strong mineral acids. Several core studies have shown that the use of HCl alone causes significant damage, whereas weak organic acid reduces the damage. The problem is that the weak organic acid does not necessarily remove the damaging mineralogy to restore permeability. The solution to the problems associated

with zeolites is to recognize the presence of these minerals before a treatment is performed. The use of an organic acid as one of two preflush stages and following the preflushes with a low-concentration HF mixture that conforms with the remaining minerals in the formation has proved to be highly effective in restoring permeability and removing damage. All fluids that are injected should have an organic acid included to maintain a low-pH environment. Some operators have found the use of an all-organic-acid system followed by an organic acid–HF formulation to be effective in high-temperature environments.

## 18-2.2. Chemistry of hydrofluoric acid systems

HF is the only common, inexpensive mineral acid able to dissolve siliceous minerals. For any acid system to be capable of damage removal, it should contain HF in some form. The most common formulation is simply ammonium bifluoride dissolved in HCl; another is by diluting concentrated HCl–HF formulations. The HCl:HF ratio is varied to accommodate the solubility of the dissolved mineral species present in the formation. This can be augmented by both preflush and overflush acid formulations. Several potential precipitates can be addressed simply by the use of appropriate HCl:HF ratios in the formulations. Numerous mineral species react with HF, and they all generate aluminum silica fluoride complexes (Table 18-2).

- Reactions of hydrofluoric acid with formation minerals

Details of HF reactions with formation minerals have, for more than 60 years, been known and studied. As early as 1965, it was quantified that 1000 gal of 2% HF can dissolve as much as 350 lbm of clay (Smith *et al.*, 1965).

An HCl preflush is always injected in sandstones prior to the HF. This is done to avoid the possible precipitation of insoluble or slightly soluble reaction products. Typically, the insoluble species are calcium fluoride ( $\text{CaF}_2$ ), which forms on reaction of HF with calcium carbonate ( $\text{CaCO}_3$ ), or sodium or potassium hexafluorosilicates ( $\text{M}_2\text{SiF}_6$ , where  $\text{M} = \text{Na}$  or  $\text{K}$ ), which result from the reaction of cations in formation brines with solubilized species. The dissolution of calcium carbonate or magnesium carbonate by reaction with HCl is discussed in detail in Chapter 17.

**Table 18-1. The zeolite family.**

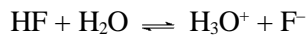
Mineral	Description
Stilbite	Hydrous calcium aluminum silicate Dissolves in contact with HCl; no gelatin formed Occurs in shallow environments and may occur inside tubulars in silica-rich connate water formations with high pressure drops
Heulandite	Hydrous calcium/sodium/potassium aluminum silicate Dissolves in contact with HCl; no gelatin formed Occurs in shallow environments
Chabazite	Hydrous calcium/sodium/potassium aluminum silicate Dissolves in contact with HCl; no gelatin formed Occurs in medium-depth environments
Natrolite	Hydrous sodium/potassium aluminum silicate Dissolves in contact with HCl; gelatin formed Occurs in deeper environments
Analcime	Hydrous sodium aluminum silicate Dissolves in contact with HCl; gelatin formed Occurs in deeper environments

**Table 18-2. Chemical composition of typical sandstone minerals.**

Classification	Mineral	Chemical Composition
Quartz		SiO <sub>2</sub>
Feldspar	Microcline	KAlSi <sub>3</sub> O <sub>8</sub>
	Orthoclase	KAlSi <sub>3</sub> O <sub>8</sub>
	Albite	NaAlSi <sub>3</sub> O <sub>8</sub>
	Plagioclase	(Na,Ca)Al(Si,Al)Si <sub>2</sub> O <sub>8</sub>
Mica	Biotite	K(Mg,Fe <sup>2+</sup> ) <sub>3</sub> (Al,Fe <sup>3+</sup> )Si <sub>3</sub> O <sub>10</sub> (OH) <sub>2</sub>
	Muscovite	KAl <sub>2</sub> (AlSi <sub>3</sub> )O <sub>10</sub> (OH) <sub>2</sub>
	Chlorite	(Mg,Fe <sup>2+</sup> ,Fe <sup>3+</sup> )AlSi <sub>3</sub> O <sub>10</sub> (OH) <sub>8</sub>
Clay	Kaolinite	Al <sub>2</sub> Si <sub>2</sub> O <sub>5</sub> (OH) <sub>4</sub>
	Illite	(H <sub>3</sub> O,K) <sub>y</sub> (Al <sub>4</sub> · Fe <sub>4</sub> · Mg <sub>4</sub> · Mg <sub>6</sub> )(Si <sub>8-y</sub> · Al <sub>y</sub> )O <sub>20</sub> (OH) <sub>4</sub>
	Smectite	(Ca <sub>0.5</sub> Na) <sub>0.7</sub> (Al,Mg,Fe) <sub>4</sub> (Si,Al) <sub>8</sub> O <sub>20</sub> (OH) <sub>4</sub> · nH <sub>2</sub> O
	Chlorite	(Mg,Fe <sup>2+</sup> ,Fe <sup>3+</sup> )AlSi <sub>3</sub> O <sub>10</sub> (OH) <sub>8</sub>
Carbonate	Calcite	CaCO <sub>3</sub>
	Dolomite	CaMg(CO <sub>3</sub> ) <sub>2</sub>
	Ankerite	Ca(Fe,Mg,Mn)(CO <sub>3</sub> ) <sub>2</sub>
	Siderite	FeCO <sub>3</sub>
Sulfate	Gypsum	CaSO <sub>4</sub> · 2H <sub>2</sub> O
	Anhydrite	CaSO <sub>4</sub>
Chloride	Halite	NaCl
Metallic oxide	Iron oxides	FeO, Fe <sub>2</sub> O <sub>3</sub> , Fe <sub>3</sub> O <sub>4</sub>

- Stoichiometric equations

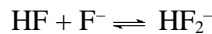
Reactions of mud acid with the aluminosilicate components of sandstones are those of HF; however, HF is a weak acid and, because of the equilibrated reaction, is only slightly dissociated when mixed with HCl:



$$K_a = 10^{-3.2} \text{ at } 75^\circ\text{F} [25^\circ\text{C}]$$

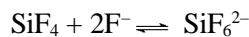
where  $K_a$  is the acid equilibrium constant.

HF can also combine and form complexes, but this reaction must be taken into account (Fogler *et al.*, 1976) only when the HF concentration is sufficiently high (less than 10M) to allow numerous collisions to occur between the fluoride species. This occurs only in the case of ultra mud acid (25% HCl–20% HF) formulations:



$$K = 3.86 \text{ at } 75^\circ\text{F}$$

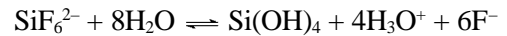
The reaction of HF with quartz grains (pure silica) is expressed in the following two equilibria:



The intermediate silicon complex,  $\text{SiF}_5^-$ , which is not stable in aqueous solution, is not considered. The first step of silica dissolution consists of the chemisorption of the fluoride anion at the silica surface (Iler, 1979). Kline and Fogler (1981b), on the contrary, showed that it is the molecular HF rather than the fluoride anion that adsorbs (see Section 18-4).

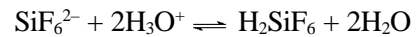
Gaseous silicon tetrafluoride usually remains dissolved in the liquid phase at bottomhole pressure, as CO<sub>2</sub> does in the case of carbonate acidization, so the equilibrium is shifted toward the formation of silicon hexafluoride anions and the remaining SiF<sub>4</sub> does not represent more than 1% of the total dissolved silicon (Labrid, 1971).

Silicon hexafluoride anions can be hydrolyzed further into monosilicic acid with the evolution of heat:



$$K = 1.2 \times 10^{-27} \text{ at } 75^\circ\text{F}$$

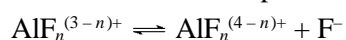
When the silicon concentration increases in the aqueous phase, part of the hexafluorosilicate anions are also transformed into the acidic form of fluosilicic acid according to the reaction



$$K = 6.7 \times 10^{-4} \text{ at } 75^\circ\text{F}$$

This transformation is usually limited, because fluosilicic acid is a strong acid. Aluminosilicate minerals generally have complex chemical compositions, such as those listed in Table 18-2. Their overall dissolution reactions thus involve many simple equilibria.

The disintegration of aluminosilicate minerals by HF can be considered stoichiometric as a first step; i.e., the Al:Si ratio is the same in the solution as in the mineral. Silicon is solubilized by the same process mentioned for quartz, whereas aluminum is involved in several fluorinated complexes:



where  $0 \leq n \leq 6$ .

The prominent form of aluminum complexed varies as a function of the free fluoride ion concentration: the average ratio of fluorine to aluminum decreases as the dissolution reaction progresses (fewer fluoride anions are available), as shown in Fig. 18-1 (Labrid, 1971).

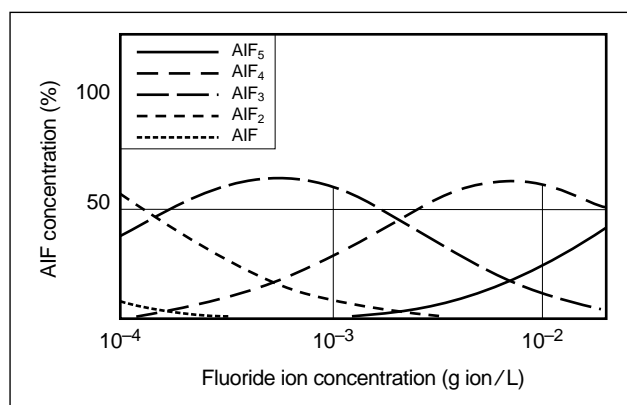
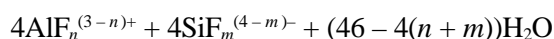
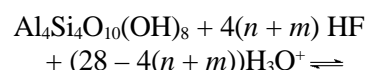


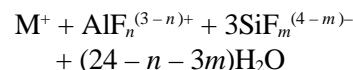
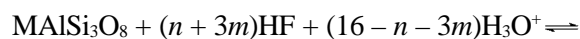
**Figure 18-1.** Domains of existence of aluminum-fluorine complexes (Labrid, 1971).

The dissolution reaction of all aluminosilicate minerals in sandstones follows the previous equations for the basic lattice atoms (Si, Al) concerned. Other metallic ions, such as Na, K, Mg, Ca and Fe, which are in the minerals constituting the rock as substitution cations in the lattice or as exchangeable (adsorbed) cations, come into solution as free ions during the reaction. In the case of iron, fluorinated complexes ( $\text{FeF}_z^{(3-z)+}$ , where  $1 < z < 3$ ) also are formed through reactions similar to those for aluminum. Thus, different global reactions can be written as a function of the considered mineral:

– Kaolinite clay



– Sodic or potassic feldspar



where  $0 \leq n < 6$  and  $m = 4$  or  $6$ .

### 18-3. Solubility of by-products

When minerals are dissolved by HF, numerous by-products can form. Some potential precipitates are listed in Table 18-3. In many cases, the increase in the liquid-phase pH value resulting from acid mixture spending constitutes the driving force for precipitate formation; therefore, precipitation can be predicted from consideration of the sole liquid phase. The extent of precipitation should always be limited. If this is not possible, the potential precipitation zone that would cause a decrease in permeability should be diluted and displaced from the wellbore (Walsh *et al.*, 1982).

Should precipitation occur, most of the calcium and sodium complexes that precipitate in the field can be redissolved by using boric acid. This is not true, however, for potassium and some of the magnesium complexes. The very low solubility of potassium complexes has been shown both in the laboratory and in the field.

Colloidal silica precipitation cannot be avoided, as it results partly from the greater affinity of fluorine for

**Table 18-3. Solubility in water at room temperature of HF reaction by-products.**

Secondary Product	Solubility (g/100 cm <sup>3</sup> )
Orthosilicic acid ( $\text{H}_4\text{SiO}_4$ )	0.015
Calcium fluoride ( $\text{CaF}_2$ )	0.0016
Sodium fluosilicate ( $\text{Na}_2\text{SiF}_6$ )	0.65
Sodium fluoaluminate ( $\text{Na}_3\text{AlF}_6$ )	Slightly soluble
Potassium fluosilicate ( $\text{K}_2\text{SiF}_6$ )	0.12
Ammonium fluosilicate ( $(\text{NH}_4)_2\text{SiF}_6$ )	18.6
Calcium fluosilicate ( $\text{CaSiF}_6$ )	Slightly soluble
Aluminum fluoride ( $\text{AlF}_3$ )	0.559
Aluminum hydroxide ( $\text{Al}(\text{OH})_3$ )	Insoluble
Ferrous sulfide ( $\text{FeS}$ )	0.00062



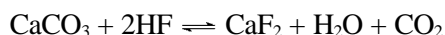
aluminum than for silicon. This process accelerates the hydrolysis of  $\text{SiF}_6$  because the released  $\text{F}^-$  anions are further involved in aluminum complexes and more monosilicic acid ( $\text{Si}(\text{OH})_4$ ) is generated. Certain authors (Labrid, 1971; Shaughnessy and Kunze, 1981; Walsh *et al.*, 1982) have emphasized the highly damaging potential of the precipitation of colloidal silica in a porous medium; however, this damaging action has never been demonstrated clearly and satisfactorily.

On the contrary, other authors (Crowe, 1986) showed that such “precipitation” is actually the result of a topochemical reaction (exchange of fluoride from the hexafluorosilicate anion occurs with aluminum on the surface of the silt and clay), and it does not induce damage.

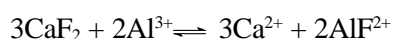
Precipitation begins earlier in the dissolution process at higher temperatures (within 10 min at 200°F [95°C]) because of the increased thermal agitation. It also occurs more quickly in montmorillonite-type clays than in kaolinite clays because of the different initial Al:Si ratios in these minerals (molar ratio of 1 for kaolinite and less than 0.5, depending on the substitution extent, for montmorillonite). Finally, aluminum can be totally removed from clays, with a correlated silica deposition at the surface (topochemical reaction).

### 18-3.1. Calcium fluoride

Some carbonates may remain after preflushing, either because of the initial amount of carbonate cementing material in the sandstone or as a result of the carbonates' initial protective siliceous coating. Also, slightly soluble, fine crystalline  $\text{CaF}_2$  readily forms when calcite contacts HF. This can lead to substantial damage:



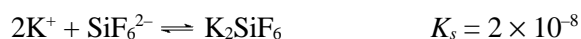
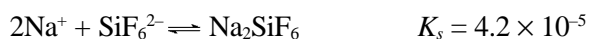
Where this precipitate has formed but has not completely blocked the porosity of the formation, it may partially redissolve when HF is near complete spending toward the end of the job. At this time, the concentration of fluoride anions in solution is so low that aluminum is hardly complexed and appears mainly as free  $\text{Al}^{3+}$  ions (Labrid, 1971). These aluminum ions are then able to extract fluorine from the  $\text{CaF}_2$  precipitates, as they did for silicofluorides, and partly redissolve the  $\text{CaF}_2$  according to the reaction



This reaction may be followed by subsequent equilibria between the different aluminum and fluorine complexes.

### 18-3.2. Alkali fluosilicates and fluoaluminates

The aluminum or silicon fluorine complexes can react with alkali ions released in the solution from highly substituted clays or alkali feldspars as soon as their concentration becomes sufficiently high to form insoluble alkali fluosilicates and, probably, fluoaluminates:

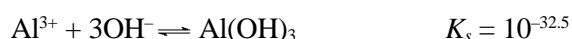


where  $K_s$  is the solubility constant.

Alkali fluosilicate precipitation is favored by a high level of HF. Fluosilicate precipitates, which form from the attack of mud acid on alkali feldspars or clays, are well crystallized and very damaging (Bertaux, 1989). These damaging precipitates also form when the volume of preflush is insufficient and HF contacts formation brine containing alkali ions.

### 18-3.3. Aluminum fluoride and hydroxide

Aluminum fluoride ( $\text{AlF}_3$ ) or aluminum hydroxide ( $\text{Al}(\text{OH})_3$ ) in the gibbsite form can precipitate upon spending of the acid. The precipitation of  $\text{AlF}_3$  can be reduced by maintaining a high proportion of HCl to HF (Walsh *et al.*, 1982). These precipitates form according to the reactions



### 18-3.4. Ferric complexes

This mechanism of forming iron fluorine complexes applies only to relatively clean sandstones. In the presence of clays, the dissolved aluminum ions have a greater affinity for fluorine than iron does. Therefore, the iron fluorine complexes do not form and iron hydroxide still precipitates at pH levels greater than 2.2.

The nature of the precipitate (crystalline or amorphous) varies as a function of the anions present (Smith *et al.*, 1969). Ferric hydroxide can be strongly bound to the quartz surface by electrostatic interactions because its point of isoelectric charge is above a pH value of 7. In the presence of excess calcite, the

dissolved CO<sub>2</sub> can also lead to the precipitation of insoluble ferric carbonates (siderite or ankerite). Chapter 15 provides additional information about iron control and solutions for problems.

## 18-4. Kinetics: factors affecting reaction rates

This section summarizes qualitatively the results described in detail in Chapter 16. Because theoretical aspects are covered in Chapter 16, only the practical implications are discussed here.

Kinetically controlled reactions (surface reaction limited) are effective during the acidization process of sandstones, and factors affecting reaction rates are discussed to complete previous thermodynamic considerations.

### 18-4.1. Hydrofluoric acid concentration

Dissolution reaction rates are proportional to the HF concentration (Fogler *et al.*, 1976; Kline and Fogler, 1981b) for most sandstone minerals, except smectite. This explains why formations with low competence (i.e., weak cementation, potentially mobile fine particles) should be treated with a reduced-strength mud acid (1.5% HF) to avoid crumbling, especially at bottomhole temperatures greater than 200°F. Fluoboric acid performs similarly because of the low concentration of HF present at any time.

### 18-4.2. Hydrochloric acid concentration

Dissolution reaction rates generally increase in a more acidic medium because the leaching of constitutive surface cations involves their replacement by protons, but the dependence on HCl concentration is not straightforward (Gdanski and Peavy, 1986). The principal role of HCl is to prevent secondary precipitation by maintaining a low pH value. The other main effect of HCl is to catalyze the attack of sandstone minerals by HF. The mechanism and degree of catalysis depend on the type of mineral, as shown in the following.

For example, the reaction rate measured at 95°F [35°C] for pure quartz has the following expression (Fogler *et al.*, 1976):

$$r_{\text{quartz}} = 9.2 \times 10^{-9} (1 + 0.8[H^+])[HF] \quad (18-1)$$

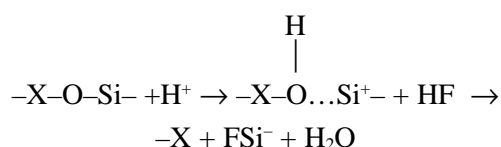
in mol quartz/cm<sup>2</sup>/s.

In the case of a feldspar with the overall formula Na<sub>0.72</sub>K<sub>0.08</sub>Ca<sub>0.2</sub>Al<sub>1.2</sub>Si<sub>2.8</sub>O<sub>8</sub>, the following expression has been determined (at 75°F under 275-kPa pressure) as the reaction rate (Fogler *et al.*, 1976):

$$r_{\text{feldspar}} = 1.3 \times 10^{-9} (1 + 0.4[H^+])[HF] \quad (18-2)$$

in mol feldspar/cm<sup>2</sup>/s.

An elemental mechanism proposed to explain the previous variation involves the adsorption of protons on the surface that weakens the siloxane bondings, which is followed by the reaction of HF molecules that creates unstable silicon-fluorine bonds at the surface, according to the scheme



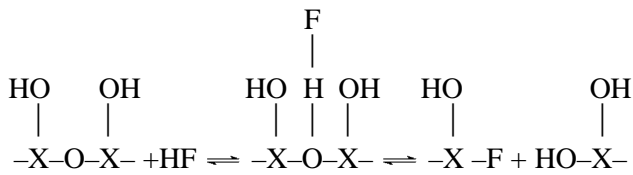
where X = Al or Si.

This is the acid (proton) catalysis mechanism proposed by Kline (1980) for feldspar.

The dissolution reaction is a first-order reaction with respect to the HF concentration for most aluminosilicate minerals. Nevertheless, dissolution kinetics is better represented by a Langmuir-Hinshelwood-type law in the case of sodium montmorillonite (Kline and Fogler, 1981):

$$R = \frac{KK_{\text{ads}}[HF]}{1 + K_{\text{ads}}[HF]}, \quad (18-3)$$

where  $K_{\text{ads}}$  is the equilibrium constant of the exothermic adsorption of HF molecules at surface-reactive sites. This adsorption constant is independent of the total acidity, whereas  $K$  increases with proton concentration (acid catalysis).  $K_{\text{ads}}$  is especially high for a mineral with a high cation exchange capacity (CEC), such as sodium montmorillonite. For most other clay minerals, the value of this adsorption constant is small. Therefore, when  $1 \gg K_{\text{ads}}[HF]$  the expression can be simplified to the experimentally determined first-order kinetics law. An elemental mechanism different from that mentioned for feldspars can be proposed to explain the kinetics and to take into account solely the HF adsorption:



### 18-4.3. Temperature

The dissolution of minerals is a thermally activated phenomenon; thus, the rates increase greatly as a function of temperature (approximately multiplied by 2 for quartz for a 25°C increment), and the penetration depths of live acid diminish accordingly. In the case of quartz, the activation energy is about 5.2 kcal/mol, and in the case of the previous feldspar, it is about 8 kcal/mol (Fogler *et al.*, 1976).

Figure 18-2 shows the variation of the reaction rate of mud acid with vitreous silica (more reactive than quartz) as a function of both HF concentration and temperature (Smith and Hendrickson, 1965). Aluminum and iron solubilities also increase slightly with a rise in temperature.

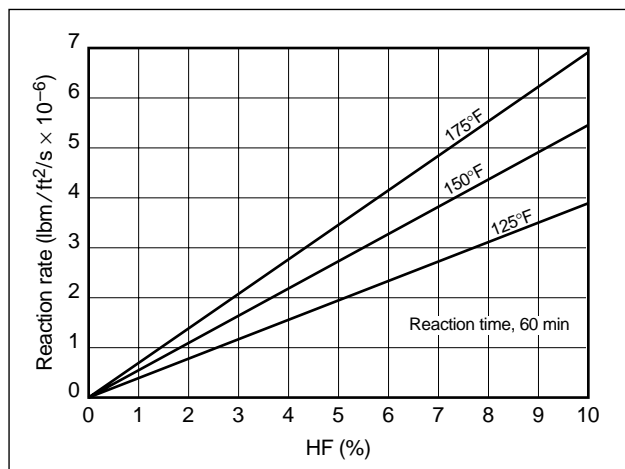


**Figure 18-2.** Reaction rate of HCl-HF on silicate glass (Smith and Hendrickson, 1965).

### 18-4.4. Mineralogical composition and accessible surface area

The relatively high total specific surface area of sandstone rocks is the primary parameter determining mud acid spending because of the heterogeneous nature of the dissolution reaction. However, if the contribution

of each mineral to the total accessible surface area is considered, great discrepancies between the reaction rates of pure phases can be predicted and observed (Table 18-4).

Table 18-4. Relative surface areas of sandstone minerals.	
Mineral	Surface Area
Quartz	<0.1 cm <sup>2</sup> /g
Feldspar	Few m <sup>2</sup> /g
Kaolinite	15–30 m <sup>2</sup> /g
Illite	113 m <sup>2</sup> /g
Smectite	82 m <sup>2</sup> /g

Clays react much faster than feldspars, which react much faster than quartz, especially in the presence of high proton (H<sup>+</sup>) concentrations. Thus, most of the quartz matrix (about 95%) can be considered inert with respect to the dissolution reaction, and the mineralogical nature of the accessible rock components determines the overall reaction rate. This situation also emphasizes the necessity of HCl preflushes and excess HCl in the HCl-HF mixture. Calcite reacts at the highest rate of all the minerals that can be present in a sandstone, leading to HF microchanneling, but the mechanism of attack is not comparable because protons coming from either HCl or HF can provoke the dissolution.

### 18-4.5. Pressure

An increase in pressure speeds up the overall dissolution reaction slightly, because dissolved silicon tetrafluoride can be transformed partially into an acidic species (H<sub>2</sub>SiF<sub>6</sub>) and can quickly initiate further reactions. For quartz, a 24% rise in the reaction rate was noticed between the two extreme conditions (Smith *et al.*, 1965).

In a radial injection situation, the mineral pore-space texture that determines flow partition around the wellbore (most live acid flows through the large pores) is also a relevant parameter; clay clasts can be bypassed by the acid flow (Williams, 1975).

## 18-5. Hydrofluoric acid reaction modeling

The parameters that affect the reaction rate of HF on sandstone minerals are incorporated in a model that

predicts the evolution of formation parameters when acid is injected.

In terms of surface reaction rates, sandstones are typically considered a two-component system:

- slow-reacting pseudocomponent, forming the crystalline quartz fraction
- fast-reacting pseudocomponent, comprising all other species (e.g., clays, feldspars and poorly crystallized silica).

For both pseudocomponents, the overall kinetics, which includes the diffusion of HF-reactant species to the surface, surface reactions and the diffusion of reacted products back to the bulk solution, is governed by the surface reactions because they are the slowest step. Therefore, matrix acidizing of sandstones with HF is called surface reaction limited.

This is the major difference from the matrix acidizing of limestone, where the process is diffusion controlled. In sandstones, the increase in permeability results from damage removal and is correlated with a small increase in rock porosity. Quartz reacts very slowly with HF; reactions with most aluminosilicates provoke a rapid spending of the acid. A pseudo-stationary state reflects the much faster variation in species concentration (chemical modifications) than the one within the rock porosity (resulting in physical modification). The HF progresses and homogeneously dissolves every pore and never forms conductive channels or wormholes. The flow is stable, and sharp fronts are formed in response to the dissolution of different mineral species as acid injection progresses radially (McCune *et al.*, 1975).

Several authors have tried to model this process. Taha *et al.* (1986) used the reaction model developed by Fogler and various coworkers (see particularly Hekim *et al.*, 1982). Such a simplified, two-pseudocomponent model and macroscopic description can be used because Fogler *et al.* (1976) showed that the order of reaction of HF with each pseudocomponent is equal to unity relative to the concentrations of HF and of the pseudocomponent. The flow is considered stable.

In this model the mineral dissolution fronts can be computed and the concentration of remaining clays (or fast-reacting materials) can be calculated. Then, the permeability increase can be estimated from the change in porosity (or amount of material dissolved). The velocity of the mineral dissolution front depends on the acid capacity number  $A_c$ , which is a function of

the volume of clays (or fast-reacting dissolvable material) and of the acid concentration.

The acid concentration (or spending) front can be modeled similarly. The thickness of the front depends on the Damköhler number  $Da$ , which is a function of the reaction rate and the acid velocity. These simulations show why HF does not penetrate deeply into the reservoir before spending unless unrealistically large volumes are used. (These large volumes would almost dissolve everything around the wellbore and thus leave the reacted formation totally unconsolidated.)

## 18-6. Other acidizing formulations

Problems related to the use of mud acid to remove damage in sandstone formations include the following:

- Rapid spending provides only a short penetration, especially at high temperatures (maximum depth about 12 in.).
- Fines, composed of either mostly quartz or mostly clay minerals, can be generated during the acid reaction and can migrate with the fluid flow. The destabilization of fines can lead to a quick production decline after treatment. Gravel-packed gas wells can exhibit a 50% productivity reduction.
- The high dissolving power of mud acid destroys rock integrity at the formation face.

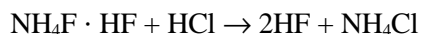
New sandstone acidizing systems are designed to alleviate these shortcomings.

### 18-6.1. Fluoboric acid

Fluoboric acid is recommended by Thomas and Crowe (1981) as an alternative to mud acids. It does not contain large amounts of HF at any given time and thus has a lower reactivity. However, it generates more HF, as HF is consumed, by its own hydrolysis. Therefore, its total dissolving power is comparable to a 2% mud acid solution. Fluoboric acid solutions are used as a preflush before treating formations sensitive to mud acid; this avoids fines destabilization and subsequent pore clogging. They are also used as a sole treatment to remove damage in a sandstone matrix with carbonate cement or in fissures that contain many clay particles. Another use is as an overflush after a mud acid treatment that has removed near-wellbore damage (up to 0.5 ft) to allow easier penetration of the

fluoboric acid solution (a few feet). Fluoboric acid is recommended when the sandstone contains potassic minerals to avoid damaging precipitates and in the case of fines migration owing to its fines stabilization properties.

In the field, fluoboric acid is easily prepared by mixing boric acid ( $H_3BO_3$ ), ammonium bifluoride ( $NH_4F \cdot HF$ ) and HCl. Ammonium bifluoride, an acidic salt of HF, reacts first with HCl to generate HF:

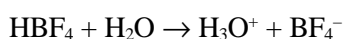


Tetrafluoboric acid is formed as a reaction product of boric acid with HF, according to



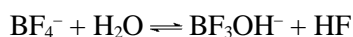
Hydroxyfluoboric acid ( $HBF_3OH$ ) probably does not exist in aqueous solutions unless it is in equilibrium with fluoboric acid (Wamser, 1948). The preceding slow reaction is of an order equal to unity with respect to both HF and  $HBF_3OH$ . For this reaction, equilibrium is attained at room temperature after nearly 40 min for a resulting 1M  $HBF_4$  solution. Because the equilibrium constant at 75°F is  $K = 2.3 \times 10^{-3}$  (Wamser, 1948), about 6% (molar)  $HBF_4$  is converted into  $HBF_3OH$  at equilibrium for a 1M  $HBF_4$  solution. These equilibrium considerations mean that at any given time and place there is only between 0.1% and 0.2% (weight) of free HF at ambient temperature and 212°F [100°C], respectively.

Fluoboric acid is a strong acid with strength comparable to that of HCl (Maya, 1977); thus, the following reaction occurs in solution:



In the following text, reactions are written using  $BF_4^-$  instead of  $HBF_4$ . Acid strength diminishes in the following order: fluoboric, hydroxyfluoboric (the strength of which can be compared to that of trichloroacetic acid; Maya, 1977) and boric acid ( $K_{H_3BO_3} = 9.2$  at 75°F).

The dissolving power of fluoboric acid results from the generation of HF through its hydrolysis:



The  $BF_3OH^-$  anions can be further hydrolyzed successively into  $BF_2(OH)_2^-$ ,  $BF(OH)_3^-$  and  $H_3BO_3$  with correlated HF formation, but these reactions must be taken into account only when the  $BF_3OH^-$  concentration is lower than  $3 \times 10^{-3}$  at 75°F (Wamser, 1948). In

the following text,  $BF_3OH^-$  hydrolysis is neglected at the usual acid concentrations.

The hydrolysis reaction kinetics of fluoborate ions is affected by

- concentration of the fluoborate ions
- medium acidity, which has a catalyzing effect (reaction is proportional to the proton concentration)
- temperature, through the usual activation energy effect.

Thus, the reaction rate, assuming the reverse reaction is negligible, can be expressed after Kunze and Shaughnessy (1983) as

$$r = \frac{d[BF_4^-]}{dt} = K[H_3O^+][BF_4^-], \quad (18-4)$$

where

$$K = 1.44 \times 10^{17} \exp\left[-\frac{26,183}{1.987T}\right]$$

in  $(\text{mol/L})^{-1}\text{min}^{-1}$  and  $T$  is the temperature in kelvin.

Thus, the reaction rate is increased 300-fold when the mixture is heated from 75° to 150°F [25° to 65°C] and is increased 12,000-fold when heated from 75° to 220°F [105°C]. Because the hydrolysis reaction kinetics is not affected by clays, fluoboric acid can be considered a retarded acid in normal use (i.e., less than 200°F). In the presence of excess bentonite, pure 0.1M fluoboric acid is spent within 30 min at 150°F (Kunze and Shaughnessy, 1983). In a slurry test, which has an infinite surface area (1 L of acid with 20 g of bentonite or 1600 m<sup>2</sup> of surface area, which is equivalent to several football fields of exposed area), the reaction rate is a function of the rate of hydrolysis. However, in the matrix, where there is a finite amount of clay surface, the reaction rate is a function of the amount of HF present, which in the case of fluoboric acid is low.

The reaction of fluoboric acid in sandstones involves at the same time the hydrolysis reaction of fluoboric acid, standard reactions of the generated HF with minerals and additional slow reactions related to the fluoborate ions in the liquid phase. As expected, the dissolution reaction of clays with fluoboric acid is a first-order reaction with respect to the fluoborate concentration, similar to the relation of the reaction of mud acid to the HF concentration.

The spending rate of fluoboric acid on glass slides at 150°F is one-tenth that of a mud acid with the same total HF content (Thomas and Crowe, 1981). Amor-

phous silica reacts faster than quartz, which limits the destruction of cores near the injection face during flow tests with fluoboric acid. Significantly less destruction is noted than during mud acid flow testing. The reduced destruction with fluoboric acid results in 30% to 50% higher compressive strengths than observed for mud acid.

The unique advantage of fluoboric acid is that it provides efficient stabilization of clays and fines through reactions related to borate and fluoborate ions. Swelling clays are desensitized by fluoboric acid, and there is a large decrease in the CEC (e.g., a 93% decrease after 18 hr in fluoboric acid at 150°F for a Wyoming bentonite was observed by Thomas and Crowe).

After a fluoboric acid treatment, migrating clays and other fines stabilize as a result of the rock's exposure to acid. This is why a long shut-in time is recommended in fluoboric acid treatments. During injection, while the acid spends normally, cores treated only with fluoboric acid exhibit a normal increase in permeability. However, no long-term stabilization occurs after treatment because only a portion of the clay was dissolved; the remainder did not have time to stabilize. Additional shut-in time allows this stabilization.

When treated by fluoboric acid, montmorillonite progressively decreases in aluminum content and then progressively incorporates boron atoms; silicon precipitates from the solution. Cores originally containing 30% silicoaluminates at 150°F attain maximum static solubilities after only 24 hr in the presence of 1M  $\text{HBF}_4$  (4 hr for mud acid), whereas the maximum increase in permeability is obtained after only 4 hr under dynamic conditions (Thomas and Crowe, 1981). These results prove the dissociated effects of mineral dissolution by the generated HF (essentially kinetically controlled) and of particle stabilization resulting from the slow complex dissolution/precipitation mechanisms (toward thermodynamic equilibrium) during the shut-in period.

Examination under a scanning electron microscope (SEM) shows that the original kaolinite clay platelets—pure aluminosilicates—that are not dissolved by fluoboric acid appear welded together and to the quartz grains. A type of chemical fusion of any fines seems to take place slowly onto the silica surface. The formation of borosilicate “glass” has been assumed to account for this reaction.

Bertaux (1989) observed that in silicoaluminates containing potassium, such as illite, potassium fluoborate forms after treatment with fluoboric acid as a nondamaging coating on the clay; potassium hexafluosilicate

forms after treatment with mud acid. This shows that nondamaging by-products are formed by fluoboric acid, whereas formation plugging by alkali fluosilicates can occur with mud acid. This is another advantage of using fluoboric acid in some “acid-sensitive” formations.

During the injection period, fluoboric acid behaves like a weak HF solution, but one in which the HF is constantly replenished. The small amount of fluoride ions available at any time limits the danger of precipitating aluminum species. Only the first acidity is used during this step. Hydroxytrifluoroboric acid ( $\text{HBF}_3\text{OH}$ ) buffers the solution and prevents other undesirable precipitations.

During shut-in,  $\text{HBF}_4$  and  $\text{HBF}_3\text{OH}$  continue to react, but at a slow pace because the hydrolysis is minimal. The liberated HF reacts further with mineral species. It also reacts by topochemical reactions, in which the aluminum from the undissolved clay structure is put into solution by forming one of the fluoaluminate complex ions (depending on  $\text{F}^-$ ), and the surface of the mineral is therefore enriched in silicon and boron. An amorphous coating of silica and borosilicate glass is then formed over the remaining silicate and fine silica grains, welding them to the framework and thus preventing their migration.

This effect is clearly seen in Figs. 18-3 and 18-4, where the same pore, containing two different clays (kaolinite and illite), is shown before and after reaction with a fluoboric acid solution. The quartz is barely etched, whereas the high-surface-area, fast-reacting illite is completely dissolved. The kaolinite platelets are about half-dissolved, and an amorphous material is coating the undissolved kaolinite, welding them together and to the underlying quartz grain.

## 18-6.2. Sequential mud acid

The sequential mud acid system involves the in-situ generation of HF, occurring from the alternate injection of HF and ammonium fluoride (Hall *et al.*, 1981). The reactions of HF are thought by some to take place at the rock surface by adsorption followed by ion exchange, but the yield of this heterogeneous process seems highly doubtful for several reasons:

- If HF were generated through such a process, it would be a small quantity, hardly enough to etch the surface of the clay material.
- Because this process is based on the CEC of the clays, migrating kaolinite would hardly be touched.

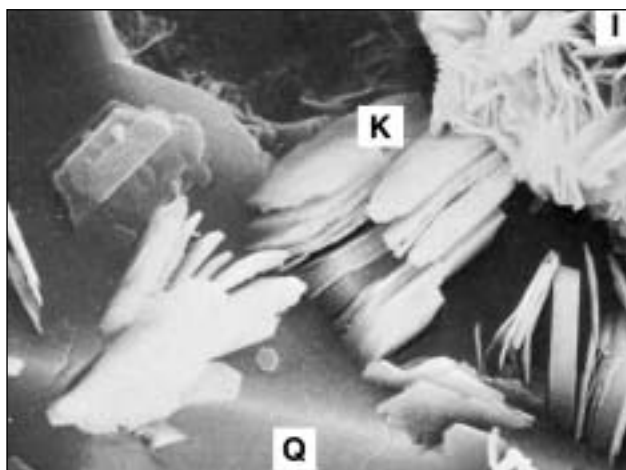


Figure 18-3. SEM photograph of kaolinite (K) and illite (I) clays in a pore (Q = quartz), before attack.

- This process supposes the initial adsorption of the hydronium ( $\text{H}_3\text{O}^+$ ) ions on the clay surface, followed by their exchange with  $\text{NH}_4^+$ , to generate HF in situ. Exchange and replacement of  $\text{H}_3\text{O}^+$  by  $\text{NH}_4^+$  depends on many parameters and cannot be ascertained. Therefore, even the generation of HF is dubious.

### 18-6.3. Alcoholic mud acid

Alcoholic mud acid formulations are a mixture of mud acid and isopropanol or methanol (up to 50%). The main application is in low-permeability dry gas zones. Dilution with alcohol lowers the acid-mineral reaction rate and provides a retarding effect.

Cleanup is facilitated; acid surface tension is decreased by the alcohols while the vapor pressure of the mixture is increased, which improves gas permeability by reducing water saturation.

### 18-6.4. Mud acid plus aluminum chloride for retardation

An acidizing system to retard HF-mineral reactions has been proposed in which aluminum chloride ( $\text{AlCl}_3$ ) is added to mud acid formulations to complex some of the fluoride ions in the injected mixture, according to the reactions (Gdanski, 1985)

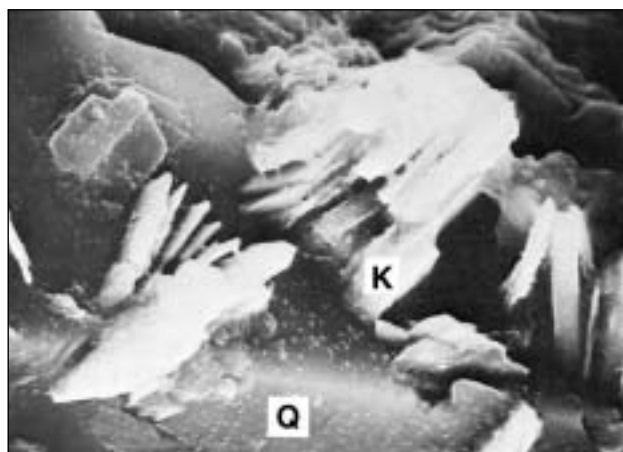
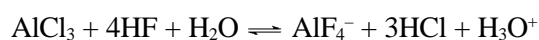


Figure 18-4. SEM photograph of the same pore after an 8%  $\text{HBF}_4$  treatment.

This procedure is tantamount to adding dissolution reaction products to the mixture before the reactions occur (i.e., the injection of spent acid). In theory this should slow the rates. However, the retardation of clay dissolution has not been proved experimentally because of the prime importance of the high surface area on clay reactivity, which is much more important than a slight depletion of acid at high temperatures. The risk of early precipitation of damaging products, such as  $\text{AlF}_3$  or fluoaluminates, is probably increased by the use of an acid that already contains aluminum ions before reaction. Flow tests have shown a smaller effective live acid penetration than in the case of mud acid. In addition, field experience has shown that the addition of aluminum to the system increases the precipitation of amorphous aluminosilicate scale. This white material plugs near-wellbore perforations and gravel packs.

### 18-6.5. Organic mud acid

Because total acidity speeds mineral dissolution with mud acid, organic mud acid involves replacement of the 12% HCl component with organic acids (9% formic acid, a weak acid that only partially dissociates), mixed with 3% HF, to retard HF spending. This system is particularly suited for high-temperature wells ( $200^\circ$  to  $300^\circ\text{F}$  [ $90^\circ$  to  $150^\circ\text{C}$ ]), for which pipe corrosion rates are diminished accordingly. This system also reduces the tendency to form sludge.

### 18-6.6. Self-generating mud acid systems

Self-generating acidizing systems were originally developed by Templeton *et al.* (1975), and their application was widened by Abrams *et al.* (1983). They involve the hydrolysis of organic esters into the corresponding carboxylic acids, followed by the reaction of these acids with ammonium fluoride to yield HF.

Because the hydrolysis reaction is activated by temperature and the acidity obtained is not as strong as with mud acid, a low corrosion rate of tubular goods and delayed reaction of the progressively generated HF are expected. The latter would allow deep penetration of live HF.

Depending on the bottomhole temperature, different organic esters are used:

- methyl formate between 130° and 180°F [55° and 80°C] with the reactions



(the latter is the slow, rate-controlling reaction).

- ammonium salt of monochloroacetic acid between 180°F and 215°F [102°C]:



- methyl acetate between 190° and 280°F [90° and 140°C].

The reagent choice is intended to limit at 30% (maximum) the generation of HF during pumping of the mixture in the tubing; thus, a minimum of 40 min of spending time seems necessary. However, field tests of these systems have not been conclusive. Many precipitates form in these low acidic systems, such as ralstonite ( $\text{NH}_4\text{MgAlF}_6$ ) and other fluoaluminates (silicates) upon spending of these mixtures on clays; thus, the use of complexing agents or acids, such as citric acid, is suggested. Furthermore, formation sensitivity after treatment has not been tested, and handling problems arise from the high flammability of methyl formate.

Overall, these systems have many drawbacks. Based on the hydrolysis of various organic esters, they are temperature activated. Unlike fluoboric acid, which generates new HF only upon spending, no equilibrium is reached. This means that more HF is generated as the temperature increases, and the ester can eventually be completely hydrolyzed long before reaching the final

depth of damage. The true degree of retardation depends on the temperature and pumping time. These esters are more expensive and more dangerous to handle because of their flammability than HCl or inorganic salts. More precipitates are formed as a result of the poor solubility of the organic by-products. The only advantage over reduced-strength HF is lower corrosion rates.

### 18-6.7. Buffer-regulated hydrofluoric acid systems

Other high-pH acidizing systems proposed for use up to 360°F [180°C] involve the buffering effect of an organic acid and its ammonium salt, mixed with ammonium fluoride, as an HF precursor (Abrams *et al.*, 1983). To minimize corrosion, the use of the same uninhibited buffer without ammonium fluoride as a preflush has been recommended up to 350°F [175°C]. The ammonium salt of the organic acid is generated from the partial neutralization of the acid with ammonium hydroxide. The proposed buffered systems are

- formic acid/ammonium formate with pH = 3.5 to 4
- acetic acid/ammonium acetate and citric acid/ammonium citrate with pH = 4.5 to 5.

To extend the application to higher temperatures (up to 550°F [290°C]), an excess of ammonium salt is formed by using a higher ratio of ammonium hydroxide to organic acid. Because the kinetics of clay dissolution increases with the fluoride ion concentration, more ammonium fluoride is added to compensate for the pH increase (Scheuerman, 1988). Successful in-depth stimulation has been observed with this system only for bottomhole temperatures lower than 129°F [54°C]. In most cases using this system, many damaging precipitates are noticed (e.g., fluosilicates, fluoaluminate usually involving ammonium), the formation of which is related to the weak acidity in the near-wellbore area. These systems suffer from the same drawbacks as the self-generated mud acid system.

## 18-7. Damage removal mechanisms

Selection of a chemical as a treatment fluid for any application depends on the contaminants plugging the formation. HCl does not dissolve pipe dope, paraffin or asphaltenes. These solids or plugging agents are organic in nature, and their treatment requires an effective organic solvent (usually an aromatic solvent



such as toluene, xylene or orthonitrotoluene). Because different plugging solids require a variety of solvents for their removal, there is no universal solvent for wellbore damage. The proper evaluation of damage and treatment design are illustrated by Clementz *et al.* (1982) for the successful removal of bacterial damage in water injection wells. Solvent or acid should never be pumped into a well until the probable causes of damage and the best chemical to remove the damage have been defined.

Compatibility with formation fluids and mineralogy is extremely important in sandstone acidizing. Thus, determination of the precipitation potential of mud acid mixtures requires close scrutiny of the mineralogy and connate water present. Acid reaction products are not necessarily soluble in the spent solution or in certain ionic environments.

Formation damage is fully discussed in Chapter 14.

### 18-7.1. Formation response to acid

Incompatibilities may occur even if the damage is identified, an appropriate removal fluid system is available and the probable response of the formation fluids and minerals to the acid and spent acid solution has been determined. These incompatibilities can result in solid or gelatinous precipitates, which can plug pores and offset the improvement the acid was intended to create. Results can range from no harmful effects and complete cleanup of the damage to less than optimum improvement or plugging of the formation with acid-generated precipitates.

When detailed petrographic core analyses are available, geochemical simulators can be used to estimate potential problems. This type of simulation requires detailed definition of the chemistry of the treating fluid, formation damage and matrix mineralogy. The release of fines and undefined spent-acid precipitates still have the potential to damage the formation and are not identified by core testing.

### 18-7.2. Formation properties

Damage prevention and dealing with formation response before acidizing are the goals of proper design. Although it may be easy to dissolve formation damage, success is dependent on dissolving this material without damaging the formation. This is possible, yet it is paramount to define the chemistry of the formation minerals and treat-

ing fluids to predict how the spent acid will react as it penetrates the formation. Potential incompatibilities can be prevented by proper log and core evaluation. Because the secondary reactions can be just as damaging, defining the potential problems generated by long-term exposure should also be evaluated.

Two key formation characteristics for fluid selection are mineralogy and permeability. Defining formation mineralogy helps to confirm the types of acid systems and acid concentrations to use. Defining formation permeability provides the information required to estimate the matrix injection rate and the maximum bottomhole pressure allowed before hydraulically fracturing the formation.

Pore pressure, temperature and the mechanical condition of the formation are influential in the design. High-pore-pressure formations fracture at much lower pressure differentials than depleted formations. Depleted formations have a lower fracture pressure than that originally observed. Temperature significantly affects the selected fluid's reaction rate with different mineral types. Acid concentrations are usually lower for higher temperatures. The mechanical integrity of the formation biases the fluid selection in that the acid concentrations are usually reduced in less consolidated formations.

### 18-7.3. Formation brine compatibility

Compatibility with formation brines must be considered when treating with mud acid. Mud acid mixtures can form  $\text{CaF}_2$  (a solid) when excess  $\text{Ca}^{2+}$  ions are present. Similar solid materials are also created with  $\text{K}^+$  and  $\text{Na}^+$  ions. The use of clear brines as completion and work-over fluids has increased the necessity of checking the formation waters for compatibility. This brine usage has also increased the necessity of ensuring that sufficient compatible preflush is used to dilute and remove these ionic species prior to injection of the mud acid system. Several available methods have been tested. The salinity of the connate brine is in equilibrium with the native minerals and their CEC. When possible, the salinity of the preflush and overflush fluids should closely approximate that of the connate brine. Historically, the use of low-salinity brines has rarely presented catastrophic problems when used in conjunction with acid treatments.

Several additives have been demonstrated to positively affect the formation's sensitivity to changes in salinity. Other species in connate water have equal, if not more, influence on the success of the treatments.

Each of these species has specialty chemical additives that address them individually. While there is documentation on the benefits of certain types of additives (Gidley, 1971; Hall, 1975), other authors have reported damage caused by a similar system in multiphase-flow environments (Muecke, 1979; Davies *et al.*, 1988). Shaughnessy and Kline (1983) showed the difficulties with high bicarbonate ion content in formation waters. The use of HCl was not sufficient to keep the well from redamaging itself quickly. They used an ingenious treatment with a form of ethylenediaminetetraacetic acid (EDTA) to both remove the calcium carbonate scale that had damaged productivity and prevent recurrence of the scale for long periods of time.

High sulfate ion contents (>1000 ppm) exist in some formation waters. Spending HCl on calcium carbonates generates a high concentration of calcium ions that will precipitate calcium sulfate when the spent acid mixes with formation water. This can be prevented by pre-flushing the formation water away from the wellbore. In sandstone formations, water containing ammonium chloride (NH<sub>4</sub>Cl) should be used as a preflush fluid.

#### 18-7.4. Crude oil compatibility

Another serious problem with formation fluids is the reaction of crude oil with acid. Removal of the residual hydrocarbon phase improves the effectiveness of aqueous acid systems. Some oils, particularly black heavy oils (less than 30° API gravity), react with acid to form either damaging sludge (precipitated asphaltenes) or a stable emulsion. Moore *et al.* (1965) reported this problem and gave the treatment to prevent it. Sometimes sludge preventers and emulsion breakers cannot prevent the formation of stable emulsions. Houchin and Hudson (1986) discussed similar problems with organic deposits. Recent work shows how dissolved iron creates more stable sludges and emulsions with these crude oils. Some “difficult” crude oils require a hydrocarbon solvent buffer between the crude oil and the acid that is mutually compatible with both the crude oil and the acid. The buffer reduces contact between the acid and the problem oil and prevents or reduces the problems with sludge and emulsion. Using this technique in one Wyoming oil field increased the success rate from 25% to 75%.

Asphaltene particles can precipitate during production as a result of a pressure drop. Solvents can be used to loosen and partially or completely disperse them. This action helps the acid do a better job of dissolving acid-soluble solids. When a well has been

completed with oil-base muds, presoaks with an aromatic solvent and producing back before acidizing are helpful. Solvent formulations and surfactant solutions are available as a pretreatment to clean up oil-base mud filtrates and restore the formation to a water-wet condition.

Gidley (1985) reported that the use of CO<sub>2</sub> as a pre-flush to acid treatments has many benefits, including reducing the volumes of acid required to generate successful production increases. This type of preflush has worked well in core studies to enhance crude oil displacement and improve mobility.

#### 18-7.5. Formation mineral compatibility with fluid systems

An analysis of the formation minerals is important for designing the HCl preflush, mud acid treatment and overflush in sandstone formations. Basic questions that must be answered are listed here.

##### 1. How much of the formation will dissolve in HCl?

Where a high HCl solubility exists (20% or more), mud acid should not be used. This statement is based on the assumption that HCl-soluble compounds are carbonate-base minerals. These minerals are the common cementing material of sandstone formations. Dissolution of this cementing material releases particles that can decrease the permeability. In addition, precipitants exist as small discrete particles that cannot be produced back through the perforations and out of the well. The use of mud acid in sandstones with a high carbonate content produces numerous precipitates.

Calcium carbonate, magnesium carbonate and iron compounds are soluble in HCl. Even feldspars and chlorite clay are slightly soluble (Gdanski and Peavy, 1986). Recent investigations of HCl involvement in the HF reaction with clays show that the HCl is consumed on the clay surfaces, and this should also be accounted for in the preflush volumes and in the HCl:HF ratio of the main fluid stage (Gdanski and Peavy, 1986). Zeolite minerals can produce gelatinous precipitates when exposed to HCl. This can be avoided by the use of organic acid mixtures, as discussed later in this chapter. Sufficient volumes of HCl must be injected ahead of the mud acid to dissolve enough of the HCl-soluble materials before the mud acid or spent mud acid reaches them.

2. How much of the formation will dissolve in mud acid? Will acid reaction by-products precipitate?

The volume of mud acid used depends on the concentration of the acid and the amount of damage. Optimizing this volume can be done only by detailing the damage in a valid numerical simulator (Perthuis *et al.*, 1989). The HCl:HF ratio and concentration are selected to prevent or reduce the formation of damaging precipitates (Table 18-5).

Some minerals automatically precipitate fluoride compounds when high concentrations of HF are used, particularly 6% HF. Even 3% HF will precipitate potassium fluosilicate when mud acid reacts with potassium feldspar. HF-dissolved sodium feldspars do not usually precipitate sodium silicate with 3% or less HF.

When HF is used in a formation containing clay, feldspar and micas, hydrous silica always precipitates. Hydrated silica has been reported in a sticky, gelatinous form that if left stagnant can attach to the mineral surfaces. However, Crowe's (1986) work on sandstone cores demonstrates that hydrated silica does not precipitate as a sticky, gelatinous mass. The reaction between the spent mud acid and formation fines is a topochemical reaction, with hydrated silica deposited on the surface of the fines.

It is important to design the overflush to dilute and displace the hydrous silica at least 3 to 5 ft away from the wellbore to reduce the effect of the damage. To avoid silica-creating damage, it is important to limit any static time while the mud

acid stage is in the near-wellbore area. If the precipitates are diluted and flushed, the likelihood of permanent damage is reduced. The by-products can be flushed away and sometimes even stabilize formation fines in the process. If the well is then returned to flow quickly, some of the precipitate may be produced back. "Quickly" refers to non-producing time, not the rate at which flowback is accomplished. The quick return of fluids can help improve cleanup of the formation after acid treatment, regardless of the flow rate. If an inadequate amount of HCl preflush is used in formations with 5% to 15% carbonate, residual carbonate near the wellbore reacts with spent HF (fluosilicic acid or  $\text{AlF}_3$ ), and voluminous precipitates form. The hydrated precipitates occupy a much larger volume than that of the original clays and carbonate dissolved.

3. Will iron be a problem?

Where a lot of iron-rich minerals are in the formation, dissolved iron can precipitate in the formation. It is well known that ferric iron precipitates as acid spends to a pH of 2 to 4. The precipitation of iron hydroxide, where concentrations as high as 10,000-ppm iron are present in solution, can be prevented by adequate treatment with a sequestering agent such as nitrilotriacetic acid (NTA), EDTA, citric acid or combinations of acetic and citric acid (Shaughnessy and Kunze, 1981; McLeod *et al.*, 1983; Paccaloni, 1979a, 1979b) (see Chapter 15). Crude oil with a high asphaltene content should be tested for sensitivity to different iron concentrations. Sludge and ridged-film emulsions are common problems for these crude oils.

Damage with iron hydroxides can be compounded by the high iron concentration that comes off the surface of the tubing during acid injection (De Ghetto, 1982). Injecting acid through new tubing can be highly damaging in this respect (Fogler and Crain, 1980; Lybarger and Gates, 1978a, 1978b). Newly manufactured tubing has a crust of mill scale, or magnetite, which is a form of ferric and/or ferrous oxide. The mill scale is dissolved and loosened by the acidic fluid, and in the early stages, partially spent, iron-rich weak acid is injected. Particles of mill scale can then be injected into the perforations and trapped there. Injected acid will continue to dissolve the mill scale, creating ferric chloride that enters the formation. If the ferric chloride combines with iron leached out of iron-rich chlorite clay or

**Table 18-5. Acid use guidelines for sandstone acidizing (McLeod, 1984).**

Condition or Mineralogy	Acid Strength (blend)
HCl solubility > 20%	HCl only
High permeability (>50 md)	
High quartz (>80%), low clay (<5%)	12% HCl–3% HF <sup>†</sup>
High feldspar (>20%)	13.5% HCl–1.5% HF <sup>†</sup>
High clay (>10%)	10% HCl–1% HF <sup>‡</sup>
High iron/chlorite clay (>15%)	10% acetic acid–1% HF <sup>§</sup>
Low permeability (≤10 md)	
Clay (<10%)	6% HCl–1% HF
Clay (>10%)	6% HCl–0.5% HF
<sup>†</sup> Preflush with 15% HCl <sup>‡</sup> Preflush with 10% HCl <sup>§</sup> Preflush with 10% acetic acid	

other iron compounds, a large amount of iron hydroxide precipitates is possible, which can severely damage the formation. This aggravated iron damage can be prevented by pickling (cleaning) new tubing to remove mill scale and then circulating the pickling acid back out of the well, as discussed later.

4. Do the sidewall core samples contain drilling mudcake?

Testing results from samples of sidewall cores with excessive mudcake should be reviewed closely and compared to the log response and other data sources such as a produced water sample analysis. High concentrations of drilling mud solids (e.g., barite, smectite, mica, bentonite or illite minerals) should not be present in clean, high-porosity sandstone formations. The solubility of the samples in mud acid mixtures may be exaggerated.

## 18-7.6. Acid type and concentration

Permeability and mineralogy determine the compatible concentration of HCl or acetic acid in the preflush stage and HF and HCl in the mud acid stage. Concentration recommendations are provided in Table 18-6 for preflush fluids and Table 18-7 for mud acid fluids. The previously presented acid use guidelines in Table 18-5 were published in 1984 (McLeod, 1984). Lower mud acid concentrations were first recommended in 1970 by Farley *et al.* (1970) to prevent unconsolidation in California sandstones. U.S. West Coast sandstones are generally rich in potassium feldspars. Holcomb (1975) published work on the first successful acid stimulation of the Morrow formation in West Texas–New Mexico with weak acid (6% HCl–1.0% HF and 3% HCl–0.5% HF). Lybarger and Gates (1978b) subsequently developed the slow-rate, low-

**Table 18-6. Fluid selection guidelines for preflush fluids.**

Mineralogy	Permeability		
	>100 md	20 to 100 md	<20 md
<10% silt and <10% clay	15% HCl	10% HCl	7.5% HCl
>10% silt and >10% clay	10% HCl	7.5% HCl	5% HCl
>10% silt and <10% clay	10% HCl	7.5% HCl	5% HCl
<10% silt and >10% clay	10% HCl	7.5% HCl	5% HCl
Note: Selection guidelines for all temperatures For 4% to 6% chlorite/glaucanite, use <20-md guidelines with 5% acetic acid. For >6% to 8% chlorite/glaucanite, do not use HCl; use 10% acetic acid preflush to mud acid plus 5% acetic acid. For >8% chlorite/glaucanite, do not use HCl; use 10% acetic acid and organic mud acid. For <2% zeolite, use 5% acetic acid in all fluids containing HCl and preflush with 10% acetic acid. For >2% to 5% zeolite, do not use HCl preflush; use 10% acetic acid preflush and overflush to mud acid containing 10% acetic acid. For >5% zeolite, do not use HCl in any system; use 10% acetic acid preflush and overflush to organic acid prepared from 10% citric acid/HF.			

**Table 18-7. Fluid selection guidelines for mud acid fluids.**

Mineralogy	Permeability		
	>100 md	20 to 100 md	<20 md
<10% silt and <10% clay	12% HCl–3% HF	8% HCl–2% HF	6% HCl–1.5% HF
>10% silt and >10% clay	13.5% HCl–1.5% HF	9% HCl–1% HF	4.5% HCl–0.5% HF
>10% silt and <10% clay	12% HCl–2% HF	9% HCl–1.5% HF	6% HCl–1% HF
<10% silt and >10% clay	12% HCl–2% HF	9% HCl–1.5% HF	6% HCl–1% HF
Notes: Selection guidelines for all temperatures For 4% to 6% chlorite/glaucanite, use <20-md guidelines with 5% acetic acid. For >6% to 8% chlorite/glaucanite, use 10% acetic acid preflush to mud acid plus 5% acetic acid. For >8% chlorite/glaucanite, use 10% acetic acid and organic mud acid. For <2% zeolite, use 5% acetic acid in all fluids containing HCl. For >2% to 5% zeolite, use 10% acetic acid preflush and overflush to mud acid containing 10% acetic acid. For >5% zeolite, use 10% acetic acid preflush and overflush to 10% citric acid/HF.			

pressure injection technique, in which they used 7.5% HCl–1.5% HF for Gulf Coast sandstones.

The guidelines are based on industry practices and the chemistry of sandstone acidizing from limited research studies; however, many case histories have corroborated them with high levels of success.

From 1975 through 1980, poor success in acidizing several formations such as the Frio and Wilcox in Texas led to the concern that spent acid generated damaging precipitates. Quick, qualitative laboratory bench tests confirmed that precipitates occur depending on the solubility of the acid reaction products. These same observations were first pointed out by Smith and Hendrickson (1965), in particular the problem with sodium fluosilicate. Labrid (1971) discussed the precipitation of hydrous silica, which caused some plugging in cores. This damage was later demonstrated by Shaughnessy and Kunze (1981) by leaving spent acid in the core for several hours, a condition that occurs in an actual acid job. This allows the slow reaction rate between the spent mud acid and the clay minerals and feldspars (aluminosilicates) to produce hydrous silica that decreases the permeability.

Crowe (1986) showed that there was little or no plugging during the injection of spent acid (fluosilicic acid) in a Berea core. This reassuring result matches the behavior seen during acid injection; however, plugging conditions are worse during the static conditions of shut-in examined by Shaughnessy and Kunze (1981). Crowe's work does not address shut-in conditions or conditions of inadequate preflush with HCl. Walsh *et al.* (1982) presented theoretical work on the equilibrium of spent acid and showed that plugging precipitates are possible with various acid concentrations and mineral compositions in sandstones.

Research by Bertaux (1986) addresses reprecipitation and plugging problems in acidizing sandstones containing potassium feldspars. The solubility of potassium fluosilicate is less than one-half of the solubility of sodium fluosilicate, which is why lower mud acid concentrations are recommended in the presence of potassic feldspars such as orthoclase or microcline ( $\text{KAlSi}_3\text{O}_8$ ). The amount of potassium in the mineral orthoclase (potassium feldspar) is enough that the solubility of potassium fluosilicate is exceeded at normal reservoir temperatures (less than 200°F) by dissolving pure orthoclase in regular mud acid (12% HCl–3% HF). Bryant and Buller (1990) observed the generation of fines by the reaction of HCl with feldspars.

The early work of Smith *et al.* (1965) in acidizing various cores with different permeabilities shows different responses to mud acid. C. F. Smith (pers. comm., 1979) found it more difficult to stimulate wells producing from sandstones with permeabilities of 10 to 60 md, which are much lower than the usual Berea sandstone permeability (100 to 300 md) in mud acid experiments. Smith attributed much of the difficulty to the release of fines by the acid.

Long-core tests performed by R. D. Gdanski (pers. comm., 1985) in low-permeability sandstone at high temperatures demonstrate increased permeability with mud acid in the first two 4-in. cores in series and decreased permeability in the third 4-in. core in a total core length of 16 in. Gdanski and Peavy (1986) also discussed the depletion of the preflush HCl in sandstone acidizing by ion exchange of  $\text{H}^+$  with  $\text{K}^+$  or  $\text{Na}^+$  ions on the formation clay minerals. This gives new insights into potential problems with sandstones rich in clay minerals with high CECs (smectite and illite).

Simon *et al.* (1979) showed that HCl attacks chlorite clay, extracting the iron and magnesium and leaving an amorphous aluminosilicate residue. J. M. Kullman (pers. comm., 1988) observed plugging problems with these residues as well as with rim coatings of chlorite liberated by HCl in core flow tests. Chlorite is prevalent in the Morrow formation in the same areas where Holcomb (1975) worked and could be the reason why weaker acids worked better in that environment (i.e., they were easier on the chlorite). Thus, weaker acids are recommended for use in sandstones with significant chlorite content and acetic acid is recommended to dissolve the carbonate and not attack chlorite ahead of the mud acid.

A common misunderstanding about the recommended acid concentrations is that they are not absolute. The guidelines are a conservative approach to avoid problems with spent acid precipitates when no previous experience exists in acidizing a particular formation. Significant deviation from these guidelines should not be necessary. Unless evaluated experience exists, the guidelines are the most reliable source of information. Also, acid flow tests with cores are reliable if long cores are used and if the spent acid is left in a portion of the unacidized core for the same period of time and at the same temperature that will occur in the downhole treatment. These tests are expensive and therefore seldom performed.

## 18-8. Methods of controlling precipitates

The methods used to control the precipitates caused by acidizing are proper acid staging, lower acid concentrations, correct usage of preflushes and sufficient overflushing, as illustrated in the following guidelines.

### 18-8.1. Preflush

Preflush with

1. 5% to 15% HCl
2. acetic acid (see Section 18-3).

The preflush displaces formation brine away from the wellbore to prevent it from mixing with reacted mud acid and causing a damaging precipitate. If the formation contains more than 1% to 2% carbonate, an HCl preflush is necessary to dissolve the carbonate, prevent the waste of mud acid and prevent formation of the insoluble precipitate  $\text{CaF}_2$ .

If completion brines such as seawater, potassium chloride (KCl), calcium chloride ( $\text{CaCl}_2$ ) or calcium bromide (CaBr) have been used in the well prior to acidizing, the brines will mix with the mud acid in the formation. Preflushing the mud acid with HCl or brine containing ammonium chloride to dilute the brines and remove them away from the wellbore helps avoid this problem.

Preflushes can also be used to displace and isolate incompatible formation fluids (either brine or crude oil), as previously discussed.

### 18-8.2. Mud acid volume and concentration

- Volume

Gidley (1985) reported that for the most successful mud acid treatment, more than 125 gal/ft of mud acid is required. Less may be used where only shallow damage exists around new perforations (e.g., 25 to 75 gal/ft is used to remove mud damage or in a spearhead treatment as an aid to perforation breakdown prior to hydraulic fracturing).

When the damage is quantified, a simulator can be used to optimize the volumes of mud acid mixtures to be used. Simulators can be used to aid the modification of volumes if several job stages are used (see Chapter 14).

- Concentration

Regular mud acid (12% HCl–3% HF) is the normal concentration to use to remove damage in clean quartzose sands. Field experience has shown that weaker concentrations (0.5% to 1.5% HF) can be effective for other sands. Mineral composition from a laboratory analysis can also dictate when less than 3% HF should be used. If the combined percentage of clay and feldspar is more than 30%, 1.5% HF or less should be used. Field experience with some tight sandstones has shown that concentrations as low as 0.6% HF may be used (e.g., the Morrow formation in Texas and New Mexico; Holcomb, 1975). If the appropriate concentration is in doubt, an acid response test on a typical core should be performed if a core sample is available.

### 18-8.3. Postflush or overflush

The overflush is an important part of a successful sandstone acidizing treatment. An overflush has several purposes:

- to displace nonreacted mud acid into the formation
- to displace mud acid reaction products away from the wellbore
- to remove oil-wet relative permeability problems caused by some corrosion inhibitors.

When overflushing the acid treatment, it is important to remember that miscible fluids are required to perform these listed functions. Aqueous-base liquids should therefore be considered as the first displacing and flushing fluid. Another fluid system can then be used for addressing the other concerns as the conditions dictate. This suggests that multiple fluid types should be used as overflush stages for a given set of circumstances.

Typical overflushes for mud acid treatments are

- water containing 3% to 8% ammonium chloride
- weak acid (3% to 10% HCl)
- diesel oil (oil wells only and only following a water or weak acid overflush)
- nitrogen (gas wells only and only following a water or weak acid overflush).

Studies of displacement fronts indicate that the reactivity and fluid character of the overflush have a major influence on the volume required to displace the

spent mud acid. For most overflush fluids (weak HCl and water containing ammonium chloride), volumes less than twice the mud acid stage should be considered inappropriate. The volume of overflush should never provide less than 3 ft of radial penetration. This means that for most situations, the overflush should be at least 200 gal/ft of perforations to push all the spent acid past the critical flow radius of 3 to 5 ft. A large overflush is necessary to prevent the near-wellbore precipitation of amorphous silica, which occurs after spent HF contacts the clay in the formation. At formation temperatures of 200°F or higher, amorphous silica precipitation occurs while the mud acid is being pumped into the formation. The precipitate is somewhat mobile at first but may set up as a gel after flow stops. If it is kept moving by overflushing with water containing ammonium chloride or weak acid, it is diluted and dispersed far enough away from the wellbore to where it has a less harmful influence.

Recent experience indicates the advantage of including HCl or acetic acid in the first part of the overflush to maintain a low-pH environment for the displaced spent mud acid stage. This supports the original recommendations of Smith and Hendrickson (1965). As the hydrogen ions adsorb on nonreacted clay deeper in the formation, the pH rises unless it is replaced by fresh acid in the first part of the overflush. Although the most economic overflush of a mud acid treatment is water containing 3% to 8% ammonium chloride with 10% ethylene glycol monobutyl ether (EGMBE) and a polyquaternary amine clay stabilizer, it does not address the pH problem without acetic acid addition. Also, certain chemicals can be added to acids to prevent or reduce the precipitation of some compounds (e.g., iron complexing agents, sulfate scale inhibitors and antisludge agents).

An example of the role of reservoir mineralogy was presented by Boyer and Wu (1983) in evaluating acid treatments in the Kuparuk River formation in Alaska. Their results indicate that fluoboric acid significantly reduces the amount of hydrated silica formed in comparison with conventional HCl-HF systems.

## 18-9. Acid treatment design considerations

Once a well is determined to be a candidate for a matrix acid treatment, the design should account for many different issues. A systematic approach to the

estimation and calculation of critical parameters is required. Pressures, rates and volumes must conform to the constraints of the mechanical conditions of the well equipment and the available space for surface and pumping equipment, along with logistical time constraints. The following discussion includes the different types of acid sequences, how and why attempts are made to retard the acid reaction rate, potential contamination from various sources and the resultant damaging precipitation. The basic quality assurance and quality control (QA/QC) checks and the design of treatments from both a formation compatibility and operational standpoint are included.

An acid design technique based on the work of Williams *et al.* (1979) for mud acid injection is in the SPE Monograph *Acidizing Fundamentals*. Although the technique is based on studies of one sandstone, it does show the important effects of temperature and injection rate on live mud acid penetration. Well illustrated is the small depth of invasion of mud acid in sandstone, particularly when formation temperatures are greater than 200°F. Live mud acid usually penetrates only about 6 to 12 in. into the sandstone before spending. This work was extended by Hill *et al.* (1977), who incorporated the effect of specific mineralogy and added the reaction kinetics of HF to the slower but finite quartz reaction rate. They also discussed the different reactivities of clay minerals and the importance of their morphology in the pore network. McElhiney *et al.* (1979) also reviewed the progress in methods of predicting live mud acid penetration and permeability increases in sandstone. These are worthwhile developments, but a simple guideline of wellbore contact time offers a practical solution to determining acid volumes to remove near-wellbore damage.

### 18-9.1. Selection of fluid sequence stages

The damage type dictates the sequence of acid systems used for each treatment. The preflushes, main stage and overflush should be matched to the type of damage. Diversion should be matched to formation characteristics and the type of treating fluid. Diversion guidelines are provided in Chapter 19. Each type of diversion technique is addressed as it pertains to sandstone treatments in this section. The sequence of fluids that compose an acid treatment can be the key to making a treatment successful.

### 18-9.2. Typical sandstone acid job stages

A preflush stage should be used ahead of the HCl especially when high sulfate ion or high bicarbonate ion concentrations exist in the formation connate water or seawater or when  $\text{CaCl}_2$ , KCl or CaBr completion fluids have been used and calcium carbonate is a formation mineral. HCl dissolution of the calcite generates high calcium ion concentrations that mix with the incompatible formation water and generate scale (calcium sulfate or calcium carbonate).

### 18-9.3. Tubing pickle

One of the first items to be addressed when matrix treatments are considered should always be a tubing pickle (cleaning). This one step can have a significant impact on the success of treatments. Tubulars, regardless of how new, have scale, rust and other debris that result from handling, installation and production and that can be loosened by the solvents and acid injected into the well. The pickling process may be multiple staged and may involve expensive solvent packages. Typically, a small treatment containing solvent and acid stages will greatly improve, if not completely eliminate, the problems associated with tubular debris. The pickling process should be included in the procedure and time allotted for job execution. The purpose of the pickling process is to

- remove rust, iron oxides and scale
- dissolve oily films and pipe dope that could plug the downhole equipment and perforations
- limit the amount of iron that gets into the formation and contacts the crude oil.

### 18-9.4. Preflushes

The sequence of fluids in sandstone treatments is dependent largely on the damage type or types. The use of multiple-stage preflushes should functionally address the different types of damage and thereby prepare the surfaces for the main treatment fluids. Hydrocarbon solvents are used to remove oil films and paraffin deposits so the aqueous acid systems can contact the mineral surfaces. These types of preflushes affect treatment success and should not be overlooked or demoted in importance. Acid-compatible brines (e.g., brine containing ammonium chloride) can be used as an excellent

preparatory flush to help remove and dilute acid-incompatible species (e.g., potassium or calcium). An example of a preflush sequence is preceding the HCl portion of the preflush with a large quantity of brine containing ammonium chloride followed by a hydrocarbon-base surfactant mixture. The purpose of the brine preflush is to dilute the incompatible species to soluble levels. The hydrocarbon mixture has the same purpose as mentioned previously.

The next consideration for preflushes is compatibility with formation fluids. Certain crude oils have a high sensitivity to acidic mixtures. These situations may require dilution with hydrocarbons or other isolating or buffering fluid systems (e.g., foams). Further compatibility consideration should be given to the iron content of the initial injection fluids that contact the crude or condensate, because even low iron concentrations can cause sludge formation. Displacement of the fluids away from the near-wellbore region reduces the potential of problems that can reduce production success and limit or halt the injection process.

HCl preflushes in sandstone acidizing are extremely important. Their function is to remove as much of the calcareous material as possible prior to injection of the mud acid. Strength and volume guidelines are based on the criteria set in work by Labrid (1971), Fogler *et al.* (1976), Kline (1980), Kline and Fogler (1981) and Walsh *et al.* (1982). Their theoretical work was further investigated and confirmed by field work by Gidley (1985), McLeod (1984), Thomas and Crowe (1981) and others. Table 18-6 provides selection guidelines for the appropriate strength of the HCl preflush. The table is based on the solubility of the formation in HCl and the requirement of minimizing the remaining carbonate or calcite prior to introducing the mud acid.

Figure 18-5 summarizes Walsh *et al.*'s (1982) work on the selection of HCl-HF formulations based on the amount of calcite remaining after the preflush. The figure illustrates the importance of HCl preflushes. The HCl preflush step should never be neglected when using mud acid mixtures. A few systems containing HF can be injected without an HCl preflush, but these are systems with extremely low HF concentrations, such as fluoboric acid. These systems can be used without an HCl preflush because the HF concentration in fluoboric acid is low enough not to present a precipitation potential.



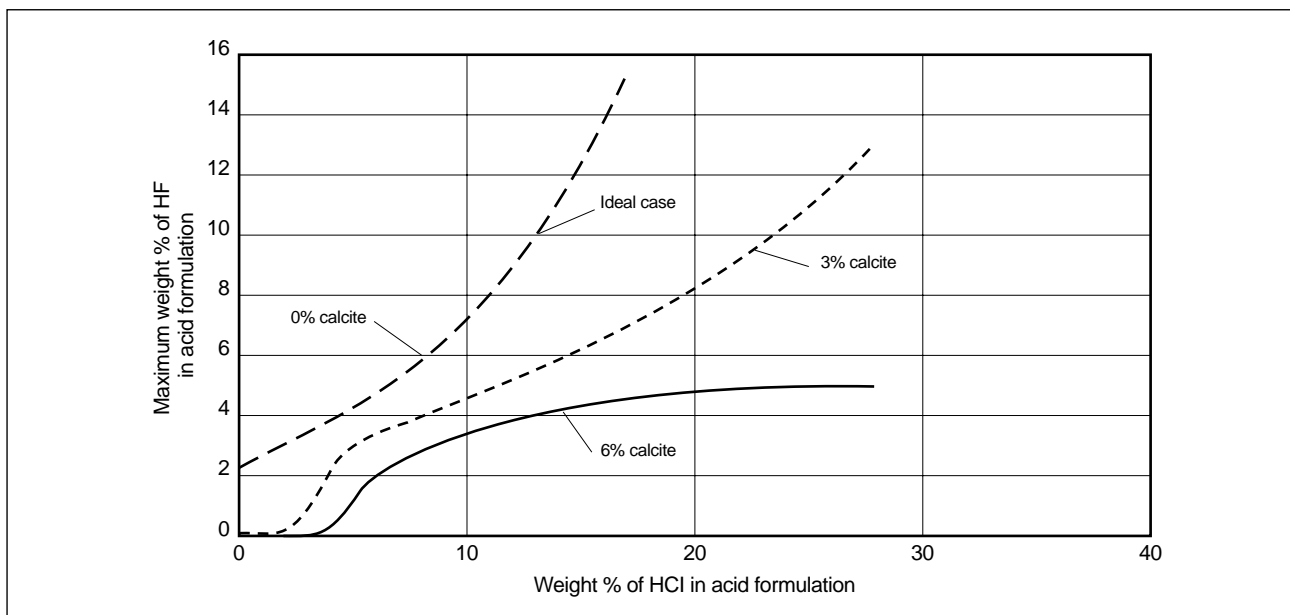


**Figure 18-5.** HCl-HF treatment fluid selection based on  $AlF_3$  or  $CaF_2$  precipitation (Walsh et al., 1982).

### 18-9.5. Main fluid stage

The HCl-HF mixture used in each treatment should conform to the guidelines in Table 18-7. Work by Walsh *et al.* (1982) demonstrates that low HF concentrations should be used to avoid the precipitation of  $AlF_3$  or  $CaF_2$  if the remaining calcite cannot be quantified. Their work also suggests that 12% HCl–3% HF can be used even in low-calcite environments without a precipitation problem. Some significant problems that may occur in high-clay-content formations include compromised formation integrity and excessive fines generation. These conditions can be the result of too high HF concentrations. The volumes should be determined using a field-validated simulator to sensitize the severity of the damage. Gidley (1985) reported that the percentage of acidizing successes increases as the volume of mud acid increases for gas wells, whereas a maximum of 100 to 125 gal/ft of perforations is required to maximize success for oil wells. This study did not take into account the preflush used or the quantity of overflush. If diversion is maximized and the damage is known or perceived to be shallow, then smaller quantities per foot can be used. The acid strength is important, because precipitation potential and formation matrix collapse are problems that can be irreversible. Table 18-5 provides the original guidelines for HCl-HF mixtures to obtain the appropriate HCl:HF ratio to avoid precipitation and formation col-

lapse. Table 18-7 is derived from this guideline on the basis of further laboratory testing and extensive field experience.

### 18-9.6. Overflush stage

The purpose of the overflush is twofold. First, it should displace the main fluid stage more than 3 to 4 ft away from the wellbore, which is the critical matrix area for radial flow. Second, the portion of the main stage that is not displaced should be diluted. Both of these factors help to eliminate damage in the near-wellbore area caused by the precipitation potential of the spent main fluid stage. Overflush fluids must be chosen carefully to avoid creating damage during the treatment flowback.

Overflush systems should meet the following criteria. The portion of the overflush immediately following the main fluid stage should be aqueous based, have a low pH value and have dilution potential for the spent mud acid. Smith *et al.* (1965) recommended an HCl overflush to maintain a low-pH environment and match the fluid density of the previous stages. The remainder of the overflush should be miscible and compatible with the previous stages. The total minimum overflush volume must completely displace the main fluid stage at least 4 ft away from the wellbore. Any anisotropy of the formation permeability can warrant doubling or tripling the overflush volume

if the energy in the reservoir is sufficient to unload the injected fluid. Although not previously reported, one of the authors of this chapter has achieved notable improvement where larger overflushes were used. This is especially true for wells where heavy bromide brines are used during the completion phase.

### 18-9.7. Diversion techniques

Common practice in sandstone acidizing is for the diverter stage to be applied as merely another stage. This is an excellent way to ensure that the main fluid stages are properly isolated by the preflush and overflush fluids. Some methods described in other chapters (e.g., ball sealers, rock salt) are not suitable for use in sandstone acidizing. The compatibility of the diverting agent with the live and spent acid species requires knowledge of the chemicals. Some forms of benzoic acid solids should not be used because the sodium content in some environments causes precipitation. Rock salt should never, under any circumstances, be used as a diverter with HF mixtures. Other materials can be incompatible with the solvents and surfactants used in the acid systems.

Operational considerations should always be taken into account when designing diversion stage sequences. The use of oil-soluble resins (OSRs) dictates that the method should be slug application. The last stage of preflush can contain a solvent to help dissolve the OSR material, creating uniform injectivity of the last sequence throughout the interval. A few exceptions apply to using certain acid systems. For example, when using fluoboric acid as the overflush to a mud acid treatment for silt and clay control, the fluids should be staged as in Table 18-8.

Other sequences could include brine flushes separating the hydrocarbon preflush from the HCl preflush before the main fluid stage; brine or weaker acid stages could be used to increase the volume of the overflush stage.

### 18-9.8. Typical sandstone acid job stages

The key to successful staging is to address all damage types present and maintain compatibility with formation fluids and formation mineralogy while minimizing the quantities of fluids injected. Table 18-9 provides a listing of typical stage sequences for a sandstone acidizing treatment.

**Table 18-8. Acid treatment sequence and fluid options.**

Stage	Fluid System
1. Preflush	Brine Hydrocarbons HCl
2. Main fluid	HCl-HF formulation
3. Overflush	HCl or $\text{NH}_4\text{Cl}$
4. Diverter	Foam or slug OSR
5. Repeat stages 1–4 as necessary with 1–3 as the last fluid sequence	
6. Fluoboric acid	With diverter solvent for OSR or foam-weakening agent (mutual solvent)
7. Fluoboric acid diverter	Fluoboric acid-based fluid system, either foamed or slug OSR
8. Fluoboric acid	Fluid left at the perforations

**Table 18-9. Typical stage sequence for a sandstone acidizing treatment.**

Table 18-9. Typical stage sequence for a sandstone acidizing treatment.						
Stage Number	Stage	Reason for Stage	Information Source	Stage Composition	Stage Volume	
1	Crude oil displacement	To prevent oil sludge formation by the acid	Acid–crude oil sludge test	Aromatic solvent	To achieve 3-ft radial displacement	
2	Formation water displacement	To prevent scale deposition	HCO <sub>3</sub> and SO <sub>4</sub> contents from formation water analysis	Ammonium chloride (NH <sub>4</sub> Cl) at 3%–8% depending on the salinity of the formation water	To achieve 3-ft radial displacement	
3	Acetic acid	Iron compounds in formation (pyrite, siderite, hematite), chlorite, clay, zeolites	X-ray-diffraction (XRD) analysis	3%–10% acetic acid	CaCO <sub>3</sub> (%)	Volume (gal/ft)
					0–5	25
					5–10	50
					10–15	75
					15–20	100
4	Hydrochloric acid	CaCO <sub>3</sub> or other HCl-soluble minerals	HCl solubility test and/or XRD analysis	According to core mineralogy: 3%–15% HCl	Calculated on the basis of HCl solubility and porosity (see Table 18-5) or this schedule:	
					HCl Solubility of HF (%)	Stage Volume (gal/ft)
					<5	50
					5–10	100
					10–20	200
5	Hydrofluoric acid (not used for carbonates and sandstones where HCl solubility > 20%)	To remove clay, other formation fines and mud damage	XRD analysis, SEM analysis, HCl:HF solubilities	According to formation mineralogy: 3%–13.5% HCl with 0.5%–3% HF	75–100 gal/ft	
6	Overflush	To spend acid and flush spent acid away from the near-wellbore area	Always used	3%–8% NH <sub>4</sub> Cl or 3%–5% HCl in all wells followed by nitrogen (gas wells), kerosene (oil wells) or 5% HCl (water injection wells)	One to two volumes of the HCl:HF volume or to achieve 5-ft radial displacement	
7	Diversion	To improve injection throughout the interval	Used as required for heterogeneous formation permeability	OSR for oil or low gas/oil ratio wells, foam for either oil or gas wells and water-soluble resins for water injector wells		

## 18-10. Matrix acidizing design guidelines

Matrix acidizing is the process of injecting acid into the formation in radial flow below fracturing pressure to remove damage and restore the permeability to the original reservoir permeability or higher. More detailed procedures are available from McLeod *et al.* (1983), who recommended the following steps for treatment design:

1. Estimate safe injection pressures:
  - a. determine present fracturing gradient
  - b. determine present bottomhole fracturing pressure
  - c. determine allowable safe injection pressure at both the wellbore and at the surface.
2. Estimate safe injection rate into the damage-free formation.
3. Estimate safe injection rate into the damaged formation.
4. Select stages required for fluid compatibility.

5. Calculate volume of each stage required:
  - a. crude oil displacement
  - b. formation brine displacement
  - c. HCl stage or acetic acid stage
  - d. mud acid stage
  - e. overflush stage.
6. Select acid concentrations according to formation mineralogy.

### 18-10.1. Calculations

- Fracturing pressure

Matrix treatments are defined as fluid injection occurring below fracturing pressure. If the fluid is injected above fracturing pressure, the acid may bypass the damage. It is important to perform some basic calculations to ensure that this pressure is not exceeded, and the exercise also provides the pressure and rates that may occur. Thorough discussions of fracturing pressure and bottomhole injection pressure and how these aspects are derived are provided in Chapters 3 and 20, respectively.

An important item to keep in mind with matrix treatments is that fracturing pressure is related to the pore pressure but is not directly proportional. As the pore pressure declines, so does the fracturing pressure. Although this is not a one-to-one relationship, it can be important when treating low-bottomhole-pressure wells. The hydrostatic pressure exerted by the column of fluid in the tubulars can be sufficient to fracture the formation.

- Injection rates

The injection rate can be as significant as the injection pressure. The maximum injection rate that does not fracture the formation can be estimated by

$$q_{i,max} = \frac{4.917 \times 10^{-6} kh \left[ (g_f \times H) - \Delta p_{safe} - p \right]}{\mu B \left( \ln \frac{r_e}{r_w} + s \right)}, \quad (18-5)$$

where  $q_{i,max}$  is the injection rate in bbl/min,  $k$  is the effective permeability of the undamaged formation in md,  $h$  is the net thickness in ft,  $g_f$  is the fracture gradient in psi/ft,  $H$  is the depth in ft,  $\Delta p_{safe}$  is the safety margin for the pressure in psi (usually 200 to 500 psi),  $p$  is the reservoir pressure in psi,  $\mu$  is the viscosity of the injected fluid in cp,  $r_e$  is the drainage

radius in ft,  $r_w$  is the wellbore radius in ft, and  $s$  is the skin effect factor.  $B$  is the formation volume factor and has a value of 1 for noncompressible fluids.

Equation 18-5 is a simple way of estimating the injection rate. However, Eq. 18-5 does not account for several factors, which are detailed in Chapter 20 for accurately modeling the injection rate. Equation 18-5 with zero skin effect and with the estimated value of the skin effect provides respective values for the minimum and a maximum pump rate during the job. These values enable allocating appropriate equipment for the treatment. True transient injection monitoring can be done in real time on location to monitor the progress of the job.

- Friction pressure estimation

Accurate fluid friction pressure is a difficult parameter to obtain. Because the tubular arrangement can be different in each case, a fairly accurate number is important. The following limited-range equation has been used with relatively good accuracy for estimating friction pressures for Newtonian fluids at rates less than 9 bbl/min:

$$p_{pipe\ friction} = \frac{518 \rho^{0.79} q^{1.79} \mu^{0.207}}{D^{4.79}}, \quad (18-6)$$

where  $p_{pipe\ friction}$  is the friction pressure in psi/1000 ft,  $\rho$  is the density of the fluid (specific gravity) in g/cm<sup>3</sup>,  $q$  is the pump rate in bbl/min, and  $D$  is the diameter of the pipe in in. Coiled tubing friction pressures can also be calculated using Eq. 18-6.

- Fluid volumes

If it is assumed that acid flows through porous media with a front that is uniform and stable, then the injection is piston-like and the first fluid in should be the last fluid out. To calculate fluid volume, the following equation should be sufficient:

$$V_p = 7.48 \left[ \phi (r_s^2 - r_w^2) \pi \right], \quad (18-7)$$

where  $V_p$  is the pore volume for the distance  $s$  in gal/ft,  $\phi$  is the fractional porosity, and  $r_s$  is the distance it is necessary to penetrate the damaged or displaced section in ft.

Mud acid treatments do not dissolve much of the formation minerals but rather dissolve the materials clogging the pore throats. This means that significant changes in the flow distribution of the injected fluids occur during the treatment as the pore-plugging materials are dissolved (see Chapter 19 on diver-

sion). Because the acid does not follow the ideal mode, adjustments to the injection volumes must be made. Significant changes in the fluid can also occur in the tubulars, before the fluid reaches the formation. The dilution of stage composition and spending are just some of the complications that must be addressed by the designer. The use of smaller tubulars, such as coiled tubing, during acid treatments can contribute to a better acid job by facilitating the maintenance of stage integrity and reducing displacement volumes. Mechanical limitations associated with artificial lift (e.g., gas lift) are more easily overcome by the use of coiled tubing. The risks of leaking valves, undiluted acid remaining in the mandrels and acid leaking into the tubing/casing annulus are avoided. The limited injection rate coincidentally controls the contact time. The pump rate and extraction out of the tanks holding the acid can create a bottleneck during execution. A complete understanding of the operational aspects is necessary for proper execution.

One of the considerations in selecting the stage volumes is the tubulars. The volumes of diverter and their location in the tubulars while injecting must be considered, especially for the use of foam diverters. When using foam diversion techniques, brief shut-downs or momentum changes are called for to maximize diversion. If the foam is in the tubulars when the shutdown occurs, phase separation of the foam can occur, affecting the foam diverter performance.

Another consideration is the preflush activity. If formations do not have much solubility in HCl, operators have tended to lower the volume of acid preflush and use brine. However, Gdanski and Peavy (1986) reported that this is not a good idea because the HCl preflush performs the vital function of cation exchange, which prepares the mineral surfaces for the HF mixture. The cation exchange must otherwise be done by the HCl portion of the HF mixture, which raises the pH of the acid system and induces the precipitation of silicate complexes. As a minimum, the preflush should penetrate the same distance as the HF mixture (e.g., if the HF blend volume penetrates 2 ft, then the preflush should penetrate a minimum of 2 ft).

Where the HCl solubility is moderate to high, more HCl is necessary. The following equation is used to calculate this volume and address the HCl-soluble materials:

$$V_{HCl} = 7.48 \frac{\pi(1-\phi)X_{HCl}[r_s^2 - r_w^2]}{\beta}, \quad (18-8)$$

where  $V_{HCl}$  is the volume of HCl required in gal/ft,  $X_{HCl}$  is the fraction of the bulk rock dissolved by HCl, and  $\beta$  is the dissolving coefficient expressed as the amount of rock dissolved per gallon of acid and is related to the acid strength.

## 18-10.2. Flowback and cleanup techniques

Selection of the correct flowback procedure is critical. The flowback during multiphase transition periods can cause irreversible damage. The fines loosened during the acid job are invariably produced back into the near-wellbore area. These fines can be removed in diluted concentrations that pass through the completion if small, gradual pressure drops are created. This was demonstrated by Krueger (1986).

The following are key factors to consider for flowback in sandstone formations:

- The fluids flowing back are more viscous than those injected. They are capable of carrying natural formation fines and other partially dissolved solids at lower velocities, which can cause plugging before the well cleans up completely.
- The spent acid usually has a higher density than the formation water. The tubing pressure should be lower than when connate water is produced, owing to the higher hydrostatic pressure of the spent acid.
- Spent acid has an equilibrium established of potential precipitants, held in place by dissolved gases and dissolved salts. Should these gases (e.g.,  $\text{CO}_2$ ) be removed from the spent fluid as a result of creating an excessive pressure drop, precipitation will occur.
- A minimum velocity is necessary for liquid to be voided from the tubing without slippage occurring. The minimum velocity to the unload tubing can be calculated. The flow rate and tubing pressure in this calculation should include the heavier liquid density. The flow rate should be achieved gradually but sufficiently soon to avoid precipitation in the formation. The rate should then be maintained until all injected fluids are returned and both the tubing pressure and production rate are steady. Plotting the gradual incremental choke changes as pressure and rate stabilize provides insight to the affect of the acid treatments on the formation and completion.

- HF systems should be flowed back immediately after injection of the overflush. The potential damaging precipitates that are generated form when the pH increases as the HCl is spent. If the acid is returned quickly, then the pH change may not reach the range for precipitation. Many iron precipitates also drop out when the pH increases. The exception is fluoboric acid treatments. The shut-in time required for complete HF generation and fines stabilization varies on the basis of temperature.
- The majority of the additives that are injected are produced back. Because the acidizing additives are by design water soluble, they are partitioned into the water phase. This can cause separation and floatation equipment problems. The return fluids are also acidic, which creates problems for chemical-electric detection devices in the separation equipment. Local environmental regulations may dictate water quality standards that are difficult to achieve, and disposal of the returned fluids can be cost prohibitive. Alternatives to disposal of the returns as hazardous waste have been developed, including filtration through inexpensive media (Hebert *et al.*, 1996).
- Did any of the treatment fluids or stages create problems during the execution? During the treatment were there mixing or handling problems associated with any of the additives or the fluid system?
- What are the properties of the formation fluids (i.e., hydrocarbons and brine) and are these compatible with the treating fluids? Post-treatment flowback inspection and analysis of fluids identifies emulsions (treating fluid additive formulation), solid debris (proper acid strength) and other telltale signs of precipitation caused by incompatibilities.
- What is the type of completion injected into and was this a consideration during the treatment? When injecting into gravel packs or frac and pack completions, injection rates should be limited if the injected height is limited. Too high an injection rate through the perforations can evacuate them of gravel and create an unstable and unsatisfactory environment where the potential exists for formation sand production. This is especially true for high-solubility zones where a small percentage of the perforations is taking fluid.
- Was the proper diversion technique or sequence chosen and applied? Most acid treatments require diversion. The application of proper diversion techniques with the selected acid system is vital to the ultimate success of the treatment.
- Was the well appropriately prepared before acidizing? When key steps of preparing the wellbore for the acidizing process are left out (e.g., not pickling the tubing, not removing the gas lift valves, not removing the rods or an electrical submersible pump), the prospects for ultimate success are reduced. Wellbore preparation is especially critical for acid treatments. Injection of tubular debris into the formation can be disastrous, and acid in the annulus of a gas lift completion string is corrosive.
- Were the injected fluids checked using quality control steps? Acid strength and certain additives must meet at least threshold ranges for activity and compatibility limits.
- Was the tubing acid cleaned (pickled)? Rust and mill scale must be removed, even with new pipe.
- Were the pumped fluids sampled and checked for cleanliness and concentration? Although samples are routinely taken and checked before the job starts, samples should be taken during the pumping of each stage. Many changes in injection behavior

## 18-11. Acid treatment evaluation

Matrix treatment evaluation is the subject of Chapter 20. The following is a partial list of the basic questions that should be answered during the evaluation of an acid treatment to help determine the success or failure of the treatment.

- Was the well damaged? Was there an improvement in the injectivity or transient skin during the treatment? Is there evidence that the well was damaged?
- Which fluid system or stage accomplished the most damage removal? Injectivity values or transient skin values for each of the fluid stages must be evaluated to help identify what damage was causing the most significant production impairment.
- Were emulsions observed during cleanup? During the cleanup of the treatment is when the effectiveness of additives and treatment fluid packages demonstrates value. Cleanup time, emulsion problems and facility upset have an economic impact and can be cause for considering different methods of handling the problems.

can be explained when these samples are analyzed. Fluctuations in injectivity may be due to a process problem that was innocently incorporated for operational expedience or safety compliance.

- Was an injection test with the appropriate fluid made before pumping acid to establish a base injectivity before acidizing? Injection testing conducted with platform or field equipment not intended for this purpose can produce misleading results. Contaminated fluids or poorly equipped monitoring can result in bad data.
- Did the acid response during the injection validate the damaging substance identified? HCl-soluble scale may be revealed as the obvious contributor to the injectivity problem when large pressure drops occur when the HCl reaches the formation. If the injection rate is increased, similar pressure drops could also be noted when the HCl-HF mixture reaches the formation.
- Did the pressure response indicate good diversion? Pressure increases may be interpreted as diverter action, but this is not always the case. Diverter response should coincide with the use of a diverter; if not, other parts of the process should be investigated.
- How long was the spent acid left in the well before flowback? Some secondary and tertiary reactions require time to produce precipitates. Quick turn-around for flowback, not high production rates, lessens the potential for these reactions to create damage. Most of these reactions result in damage that is detected only after production is initiated.
- Were spent acid samples recovered and analyzed? Flowback fluid samples should be acquired regardless of the volume of the treatment. These samples should be marked, with the date and time, total volume recovered to that point and other pertinent data, such as choke size, flowing tubing pressure, water cut and produced quantities.
- Were the production results consistent with the acid injection pressure response? If the injection pressure declines too quickly, the acid treatment causes the well to develop a vacuum. Once the well is

brought back on line, the production does not improve because of limitations associated with the wellbore construction or production facilities.

- Was a pressure buildup test performed and interpreted? A pressure test analysis is the definitive method to answer whether the treatment is a success or failure.

## 18-12. Conclusions

Acidizing sandstone formations is not an impossible task, but it is not simple either. Success requires a methodical, systematic approach. It can be accomplished without any detrimental effects by analyzing vital information. The flow chart in Fig. 18-6 shows the steps the process encompasses.

The following conclusions can be made about sandstone acidizing:

- Damage identification determines the types of acids and other solvents to use in a sandstone acidizing treatment.
- A knowledge of the chemical reactions involved among acids and formation minerals and connate fluids provides some guidelines for acid types, concentrations and the sequence to prevent or reduce the precipitation of insoluble reaction products.
- The selection of appropriate types and volumes of preflushes and overflushes also helps prevent incompatibilities between formation fluids and acid systems.
- A numerical simulator should be used to quantify acid volumes, although simple guidelines are provided to assist in the selection of treatment volumes. The most important factor in successful acid stimulation is to provide clean, filtered acids at the perforations by filtering all fluids and cleaning (pickling) the tubing before the acid treatment is injected into the formation.
- Evaluating the executed acid treatment provides information to improve subsequent acid treatments in the same or similar formations.

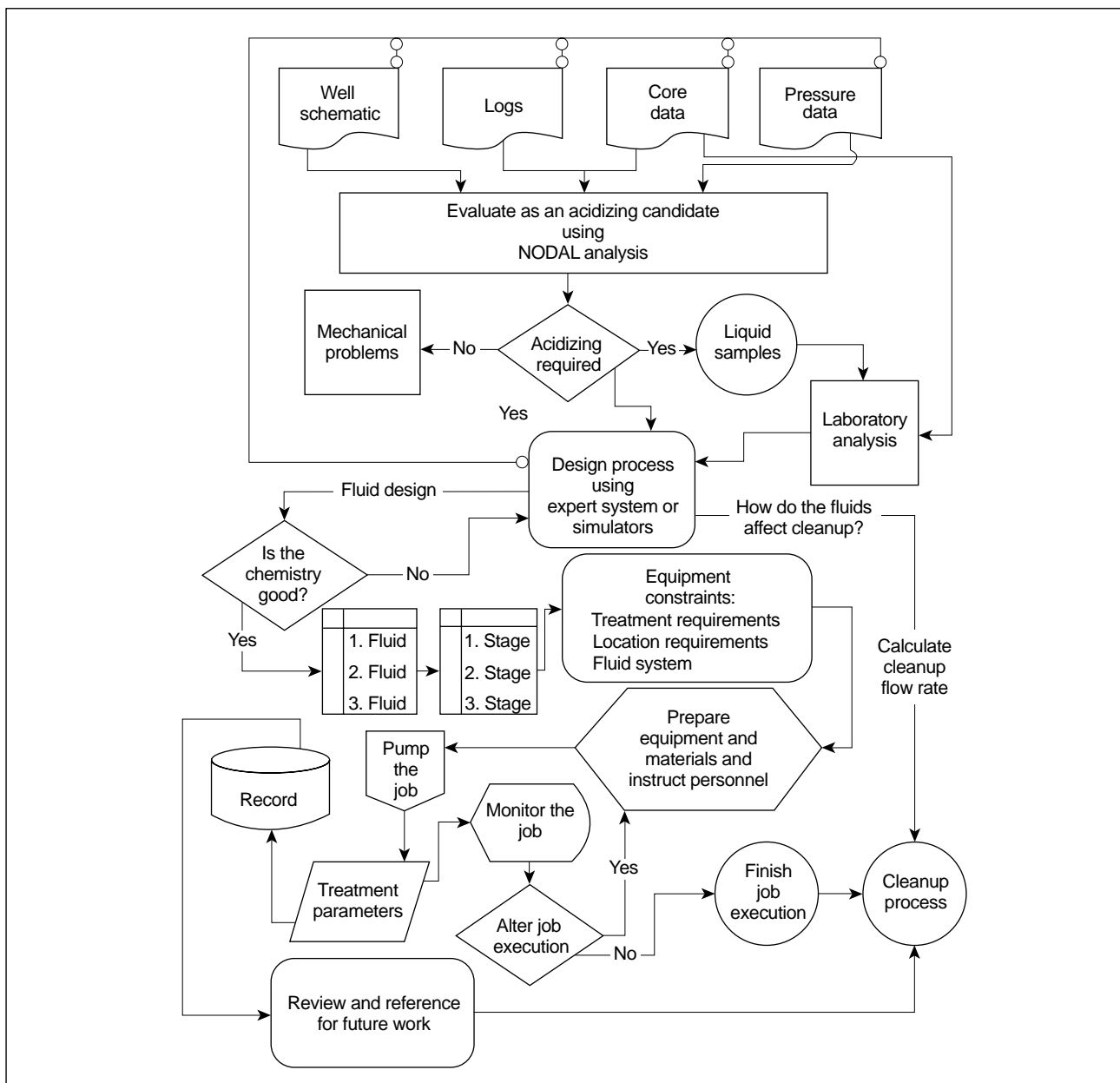


**Figure 18-6.** Sandstone acidizing treatment design process.



# Fluid Placement and Pumping Strategy

*J. A. Robert, Schlumberger Dowell*  
*W. R. Rossen, University of Texas at Austin*

## 19-1. Introduction

Fluid placement is critical to the success of a matrix stimulation treatment (Pye *et al.*, 1970; Cooper and Bolland, 1984). Damage, depending often on fluid-rock interactions, may be unevenly distributed along the net thickness. Also, the natural reservoir permeability may vary considerably, with substantial contrasts. In this environment, matrix stimulation tends to remove or bypass the damage that is easier to reach (i.e., a lower degree of damage or higher permeability) and becomes self-defeating. Each additional volume of stimulation fluid follows the path of least resistance, and more of it invades the layer where it is least required.

Several methods have been developed to improve fluid placement during matrix acidizing. Nonmechanical methods include the use of particles accumulating at the sandface to form a low-permeability cake (i.e., particulate diverters). The size of the particles varies from a few tens of micrometers to a few millimeters. Other methods involve the use of viscous fluid slugs or the use of foam either as staged slugs or combined with the acid stages (i.e., foamed acid). Each of these methods is based on the temporary impairment of the high-injectivity zones accepting most of the diverting material, which results in an increase of the proportion of fluid going into the low-injectivity zones. It is essential, of course, to avoid permanently damaging the higher injectivity zones.

Mechanical techniques consist of ball sealers, which are rubber-lined balls added to treating fluids to plug fluid-taking perforations, and packers, which enable isolating a given zone during a treatment. Mechanical techniques differ from the other diversion methods in that they completely shut off a part of the reservoir to direct all the stimulation fluid to a subsection of the open zone. Another technique is coiled tubing placement in which acid is spotted or injected across the zone of interest. This is especially important in horizontal wells or vertical wells with long producing zones (Thomas and Milne, 1995).

The last method is specific to carbonate formations. It involves pumping gelled acid, with the viscosity varying with the degree of spending. Injectivity is reduced in zones containing large volumes of spent acid, and fresh acid is directed to lower injectivity zones. This method has been increasingly used recently and has produced good results in terms of placement. It is described in more detail in Chapter 17.

The choice of the pumping strategy must take into account several parameters, such as producing-interval thickness, lithology and permeability profile, damage distribution and the economics of the treatment.

## 19-2. Choice of pumping strategy

### 19-2.1. Importance of proper placement

Matrix stimulation is almost always performed in multilayer reservoirs containing zones with, at times, wide injectivity contrasts caused either by different permeabilities or by uneven severity of damage. Other phenomena causing vertical heterogeneities within a completion interval include permeability gradients in thick reservoirs and selective damage in some perforations. The natural trend of stimulation fluids is to follow the path of least resistance (i.e., to invade the most permeable or least damaged zones). To optimize treatment results, most of the open interval must be treated, and thus, treating fluids must also be injected in significant volumes into the least permeable and most damaged zones.

In many cases, the use of diverting techniques has proved successful in improving fluid placement and treatment results, especially in cases with large variations of initial injectivity throughout the open interval (Brannon *et al.*, 1987).

As an example, consider the three-layer reservoir described in Table 19-1. Middle layer 2 is a high-injectivity zone of limited thickness (10% of the total pay zone) with high permeability and a lower skin effect. A simple calculation, using a steady-state

**Table 19-1. Example three-layer reservoir.**

Layer	Permeability (md)	Net Thickness (ft)	Skin Effect
1	50	50	10
2	500	10	5
3	100	40	10

injection relationship, suggests that the high-permeability layer would initially take 51% of the total flow. Assuming that 150 gal/ft of perforated interval is required in each zone to remove the damage, the total volume required to place at least this amount in each zone depends on the placement strategy:

- Total volume is equal to 150 gal/ft  $\times$  100 ft = 15,000 gal in the case of “perfect” placement (i.e., the same injectivity in the three layers).
- With no diversion, a volume of about 39,500 gal is necessary to treat the entire interval, including the layer with the lowest injectivity. In this calculation it is assumed that the ratio of the flow rate into each layer remains constant throughout the treatment, but because damage is removed more rapidly in the highest injectivity zone, an even larger volume would be actually required (see also Chapter 13 for numerical simulations).

### 19-2.2. Comparison of diversion methods

A good early review of the development and use of diverting techniques, including mechanical techniques (packers and plugs) and various diverting agents, was presented by Harrison (1972).

Hill and Rossen (1994) presented a comparative study of the efficiency of the existing nonmechanical placement techniques, including the maximum pressure differential and injection rates (MAPDIR) technique introduced by Paccaloni and coworkers (Paccaloni and Tambini, 1990; Paccaloni, 1992). The MAPDIR technique involves pumping at the highest possible rate without fracturing. Hill and Rossen also considered particulate diverters, foams and viscous fluids. In their paper, they compared the evolution of skin effect for a hypothetical two-layer case. For an assumed initial skin effect of 10, the skin effect decrease is proportional to the acid volume injected per layer, and total damage removal is achieved with 50 gal/ft of acid. The permeability and thickness are, respectively, 100 md and 1 ft

for the first layer and 10 md and 10 ft for the second layer. Simulation results show that the MAPDIR technique allows the fastest total skin effect reduction in terms of pumping time but at the expense of large acid volumes injected into the layer with lower damage. Furthermore, it does not allow treating the low-permeability layer fully.

In terms of the total pumped volume, the continuous injection of particulate diverter appears to be the most efficient technique (Fig. 19-1). The viscous fluid method appears to be far less efficient than the other diversion methods. Moreover, because of the implied reduction in the injection rate, this last technique requires the largest pumping time for treatment completion. However, the study assumed Newtonian fluids. Power law gels may be more effective. Another simulation with the same permeabilities in each layer, but different initial values of skin effect, led to similar conclusions.

The choice of the best diversion technique depends also on a variety of other parameters. Particulate diversion can be used in most cases, with some restrictions in the case of gravel-pack completions. Materials have been developed for a wide range of reservoir properties, the most important of which are the reservoir permeability and the pore-throat size and distribution. Proper design of particulate diverters requires consideration of the compatibility of the diverting agent with the well-bore and reservoir conditions (e.g., temperature, reservoir fluid) and with other treating fluids (e.g., solubility and flocculation in the carrying fluid or adjacent stages can impair particulate diverter efficiency).

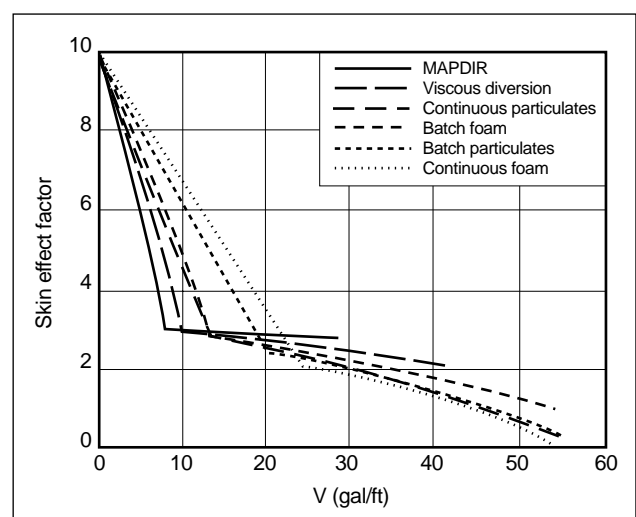


**Figure 19-1.** Total skin effect evolution versus volume for different placement techniques (Hill and Rossen, 1994).

In the case of gravel-pack completions, large-particle-size chemical diverters are not used. Oil-soluble resin (OSR) may be used, but it must be mixed well and injected continuously with the acid to avoid the risk of plugging the screen or gravel pack (McLeod, 1984). Foam diversion is also common for gravel-pack completions and where particulate diverters are not appropriate.

In the case of oil wells with a well-defined water zone, foam has been found to plug the water zone successfully and direct acid to the oil-bearing interval. This is due to the detrimental effect of oil on foam formed by certain surfactants. Acidizing with foam diversion has been reported to improve overall production in some cases without increasing the water cut, but instead reducing it (Zerhoub *et al.*, 1994).

For cemented and perforated completions, buoyant ball sealers have been shown to give good results (Erbstoesser, 1980; Bale, 1983). Conventional ball sealers are generally not recommended for long intervals or high-shot-density completions, as they require a minimum injection rate per perforation to prevent settling in the rat hole (McLeod, 1984).

Packers are the most effective means of selective fluid placement. However, they require the use of coiled tubing or rig operations. They can be used after completion or workover, if a rig is already on site.

Coiled tubing has been increasingly used for matrix acidizing over the past few years. Treatment analysis shows that coiled tubing is especially helpful for acidizing long intervals by allowing spotting successive diverter and acid stages throughout the open interval, thereby ensuring good coverage of the entire producing zone (Economides *et al.*, 1991; Thomas and Milne, 1995).

### 19-2.3. Fluid placement versus injection rate

Selection of the treatment strategy must be based on the trade-off between pump rate and fluid placement. Except for the MAPDIR technique, placement methods result in a reduction in the injection rate, even in low-injectivity zones, with possible loss of treatment efficiency and creation of precipitation damage. Williams *et al.* (1979) mentioned that sandstone acidizing is more efficient at higher rates, both avoiding the creation of precipitates near the wellbore and extending the radius of live-acid penetration. McLeod

(1984) and Schechter (1992), however, argued that there exists an optimum rate for sandstone acidizing, based on the reaction rate with damage and acid and/or damage contact time. For carbonate acidizing, it has been shown that the injection rate must be high enough to allow wormholes to form and propagate. Pumping below this rate can cause a considerable reduction in treatment effectiveness.

### 19-2.4. MAPDIR method

The MAPDIR method suggests pumping treating fluids as fast as possible below the fracturing limit without using any diversion technique. It allows a decrease of pumping time and minimizes the risk of treatment failure caused by low pumping rates. However, MAPDIR is not a true diversion technique, as it does not modify the natural flow profile, nor does it necessarily distribute stimulation fluids or remove all damage.

Paccaloni and coworkers analyzed a large series of matrix-acidizing treatments to identify the factors leading to success or failure, including pump rate and the use of diversion (Paccaloni *et al.*, 1988; Paccaloni and Tambini, 1990). Criteria for success or failure were specific to the authors. With development wells, job success involved treating the entire interval. On the basis of the analysis of more than 170 jobs, the authors claimed that the MAPDIR technique is sufficient to obtain full coverage of the pay zone if the permeability contrast is less than 300 md and the pay zone does not exceed 200 ft. They concluded that the method actually gives better results than diverting agents.

In the case of carbonate formations, they reported that relatively small volumes of concentrated acid (5 to 10 gal/ft) led to a substantial skin effect reduction, allowing for reasonable injectivity of the zone for further reduction. This could explain why the MAPDIR method can eventually provide full zone coverage: if the treatment is maintained long enough to inject the few gallons required to improve injectivity in the highly damaged zones, then injectivity contrasts are reduced and the entire interval can be treated. However, this method can be applied only for intervals with limited contrasts of permeability, and it does not optimize fluid placement.

For better efficiency, the authors recommended the use of coiled tubing for preacidizing operations such as wellbore cleanup, acid circulation for completion string cleaning and acid spotting in front of the pay

zone. Then a T connection can be used to pump acid through both the coiled tubing and tubing string to maximize the pump rate during matrix injection.

## 19-3. Chemical diverter techniques

Chemical diverters, which are materials insoluble in acid but highly soluble in water or hydrocarbons, have been used either to form a low-permeability filter cake at the sandface or to reduce the injectivity of high-permeability zones with the injection of a viscous polymer slug. The first technique has been found to be more effective and can provide faster cleanup. It has prevailed over the viscous slug technique.

### 19-3.1. Historical background

The first attempts at fluid placement made use of chemical additives. Harrison (1972) reported the injection, as early as 1936, of soap solutions that could react with calcium chloride ( $\text{CaCl}_2$ ) to form water-insoluble, but oil-soluble, calcium soaps. The precipitate acted as a diverting agent for hydrochloric acid (HCl). The generation of solid precipitates in the formation was not, of course, desirable, because they could cause permanent damage. Thus, in the late 1930s, more sophisticated systems were used, such as heavy  $\text{CaCl}_2$  solutions. Diversion effects were possible by impairing injectivity in the zones accepting most of the high-viscosity solution. Other systems utilized cellophane flakes suspended in a water gel with a bacterial breaker. Later, gels were replaced by oil-external emulsions.

In 1954, naphthalenes were first used as a blocking material. Oil-soluble naphthalenes were thought to be ideal diverters because they sublime above  $175^\circ\text{F}$  [ $80^\circ\text{C}$ ]. Also, crushed limestone, sodium tetraborate, oyster shells, gilsonite, perillite, paraformaldehyde and “chicken feed” were used as diverters with mixed success. These compounds were replaced progressively by rock salt, which is partly soluble in the acid but inexpensive and easy to handle.

A major improvement in diversion techniques was brought about by completely soluble materials, including wax-polymer blends and hydrocarbon resins in production wells and rock salt and benzoic acid in water-injection wells.

### 19-3.2. Diverting agent properties

An effective diverting agent must meet both physical and chemical requirements.

- Physical requirements

**Cake permeability**—Cakes created on the reservoir walls by agents must be as impermeable as possible to the acid for the maximum diverting effect. If the permeability of the diverter cake is greater than or equal to the permeability of the tightest zone, little or no diversion occurs.

**Invasion**—Deep invasion of the reservoir rock by the diverter particles must be prevented, regardless of the nature of the rock, for maximum diverter effectiveness and minimum problems in cleanup. This and the previous requirement suggest that an optimum particle size must be determined.

**Dispersion**—Diverting agent particles must be properly dispersed in the carrying fluid. If flocculation occurs, the cake will be thicker but with high porosity and permeability.

- Chemical requirements

**Compatibility**—Diverting agents must be compatible with the bulk treatment fluid and with other additives, such as corrosion inhibitors, surfactants and antifoaming agents. They must be inert toward the carrying fluid at the well treating conditions.

**Cleanup**—Diverting agents must be soluble in either the production or injection fluids. Having acted as diverters, they should undergo a rapid and complete cleanup.

### 19-3.3. Classification of diverting agents

Diverting agents can be classified, according to their particle size, as bridging agents or particulate diverters.

- Bridging and plugging agents

These diverting agents consist of large-size particles, from 10/20 to 100 mesh. They are used as diverters in carbonate formations, where natural fractures are common. However, their efficiency is limited by the high permeability of the cakes they create. As an example, a cake formed with 10-mesh particles has a permeability between 20,000 and 40,000 md, whereas a cake created with 100-mesh particles has a permeability between 1,000 and 3,000 md.

When effective diversion is required in fractured zones, a slug of bridging agent is injected first, followed by the treating fluid containing a diverting agent. The bridging agent fills the fractures, creates a coating in front of high-permeability formations or both. If the plugging agent consists of particles small enough (e.g., 100 mesh), the diverting agent does not penetrate the coating and allows effective diversion through the development of low-permeability cakes.

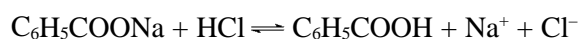
Bridging agents with various chemical compositions are available:

- inert materials, such as silica sand or a mixture of silica, nonswelling clay and starch (Soluble materials reduce the risk of permanently plugging the formation.)
- water-soluble bridging agents, including rock salt and benzoic acid
- oil-soluble bridging agents, including graded oil-soluble resins, naphthalenes flakes and beads made of wax-polymer blends that are soluble in oil, deformable and temperature degradable. (Their composition can be selected according to the bottomhole temperature.)

- Particulate diverters

Particulate diverters are characterized by very small particle sizes, well below 0.004 in. in diameter. Both water- and oil-soluble particulate diverters are available.

- Water-soluble, for injection wells—A fine grade of benzoic acid is typically used as a water-soluble diverting agent. Because this product agglomerates during storage, it is difficult to achieve a constant particle-size distribution before injection. For this reason, salts (i.e., ammonium or sodium benzoate) can be used instead. In HCl, the salts are converted to benzoic acid. For instance, sodium benzoate reacts according to



Benzoic acid is only slightly soluble in HCl but highly soluble in water or alkaline solutions. After acting as a diverter, this compound dissolves in the injection water. Because benzoic acid particles are hydrophobic, surfactants are required to properly disperse the agent in the treating fluid.

- Oil-soluble, for production wells—Oil-soluble agents are blends of hydrocarbon resins. They are totally inert in an acidic medium, yet quickly and completely dissolve in the produced oil after treatment. It is often difficult to disperse these resins in the acid. They are usually injected as dispersions in aqueous solutions.

### 19-3.4. Potential problems during diversion treatment

During a diversion treatment several major problems may occur.

- Decantation

Bridging agents are subject to gravity effects during injection. They tend to settle in the fluid that fills the well, and the best results are therefore obtained when the solid additives are placed in a water-base gel. Decantation problems rarely occur with diverting agents because of their small particle size and the low density of their constituent materials (1.1 g/cm<sup>3</sup> for resin, 1.3 g/cm<sup>3</sup> for benzoic acid).

- Solubility

Water-soluble agents are also slightly soluble in acid. Therefore, a portion of these additives dissolves during mixing with the acid. Another portion dissolves during injection because of intermixing with wellbore fluids and heating. If the plugging agent is injected in slugs, after it is deposited in the fractures or on the formation walls it undergoes additional dissolution. Thus, the effectiveness of water-soluble products is always low, and large initial concentrations are required. The dissolution rate during the different stages of injection must be considered in the job design.

- Particle-size distribution

The particle size of the diverting agent must correspond to the petrophysical properties of the treated zones, such as permeability and pore-size distribution. If bridging agents are used in a reservoir with permeability from 100 to 1000 md, the resistance of the diverter cake may not be high enough to avoid fluid penetration in the high-permeability zones. On the other hand, if too fine a diverting agent is used, the solid particles migrate through

the porous medium with the treating fluid and diversion will not occur. Where the rock pores have a slightly larger diameter than the diverter particles, an internal cake can be created, and although the diverter will be efficient, cleanup can be difficult.

- Flocculation

Incompatibility of diverting agents with additives used in the same stage or in adjacent stages can cause diverter flocculation. Carrier fluid composition should follow technical memoranda recommendations or be tested in the laboratory.

- Compatibility

Rock salt should never be used as a bridging agent in hydrofluoric acid (HF) treatments or before HF treatments because it may increase the risk of sodium fluosilicate precipitation. Such a problem is not anticipated when using sodium benzoate, because this compound is readily converted into benzoic acid in HCl, and the released sodium ions do not contact the subsequent HF flush.

### 19-3.5. Laboratory characterization

Crowe (1971) designed equipment that injects slugs of diverting agent under constant pressure into parallel cores of different permeabilities. By measuring the time required to equalize the flow rates entering each core, he compared the efficiency of different diverters. The best results were obtained using OSRs.

Other investigators (Hill and Galloway, 1984; Houchin *et al.*, 1986) attempted to use a slightly different experimental setup consisting of a well model with three cores of various permeabilities to predict flow distribution at presumed reservoir conditions. This approach, because of differing pressure-drop ratios and slug-volume ratios between laboratory and reservoir conditions, cannot always be extrapolated to field conditions (Doerler and Prouvost, 1987).

Hill and Galloway's original attempt to measure the pressure drop across a diverter cake included the experimental data in a simple numerical reservoir model. However, they assumed the pressure drop to be a linear function of the cumulative volume of diverter and neglected the effect of flow rate and other important parameters, such as diverter concentration and temperature.

Doerler and Prouvost investigated separately the intrinsic properties of the cakes created by diverters and their effects on the flow distribution in heteroge-

neous reservoirs. Pressure drops through cakes of diverting agents were measured under various well-bore and fluid conditions, such as temperature, flow rate, concentration of diverting agent and nature of the carrying fluid. Filtration theory was used to express the experimental results in a more general form:

$$R_{cake} = \frac{\Delta p}{\mu u}, \quad (19-1)$$

where  $R_{cake}$  is the cake resistance in  $m^{-1}$ ,  $\Delta p$  is the pressure drop across the diverter cake,  $\mu$  is the carrying fluid viscosity, and  $u$  is the superficial velocity across the cake. By analogy with the pressure drop in a porous medium, the cake resistance can be defined as the inverse of the cake permeability divided by the cake thickness. Laboratory testing allows correlation between the cake resistance and the volume of diverter deposited at the sandface per unit area, which can then be used to simulate the diverter effect at reservoir conditions.

Taha *et al.* (1989) and Economides *et al.* (1994) extended the model introduced by Hill and Galloway. They defined a specific cake resistance  $\alpha$  in  $m/kg$ :

$$\alpha = \frac{1}{\rho_{div}(1 - \phi_{cake})k_{cake}}, \quad (19-2)$$

which then leads to the pressure drop  $\Delta p$  across the cake:

$$\Delta p = \frac{\alpha \mu u C_{div} \rho_{div} V}{A}. \quad (19-3)$$

In Eqs. 19-2 and 19-3,  $\rho_{div}$  is the density of diverter particles in  $kg/m^3$ ,  $\phi_{cake}$  is the cake porosity,  $k_{cake}$  is the cake permeability,  $C_{div}$  is the concentration of diverter particles in  $m^3$  of particles per  $m^3$  of solution,  $V$  is the total volume of diverter solution injected, and  $A$  is the surface of cake deposition.

Equation 19-3 is obtained by writing Darcy's law across the cake:

$$\Delta p = \frac{\mu l u}{k_{cake}}. \quad (19-4)$$

The cake thickness  $l$  varies with the diverter volume as

$$l = \frac{C_{div} V}{(1 - \phi_{cake}) A}. \quad (19-5)$$

Combining Eqs. 19-4 and 19-5 and using  $\alpha$  as defined in Eq. 19-2 yields the expression of the pressure drop across the cake as in Eq. 19-3.

The cake resistance  $R_{cake}$  and the specific cake resistance  $\alpha$  are related by

$$R_{cake} = \frac{\alpha C_{div} \rho_{div} V}{A} \quad (19-6)$$

Either characterization of the diverter cake can be used. However, Doerler and Prouvost took into account the cake compressibility in their correlations for  $R_{cake}$ , whereas the other authors neglected the cake compressibility and assumed  $\alpha$  to be constant.

### 19-3.6. Modeling diverter effects

Presented in this section is a methodology using cake resistance data obtained in the laboratory to predict the efficiency of the treatment in terms of flow distribution between the different layers. The concept of diverter cake pseudoskin effect is introduced.

The diverter cake created at the sandface of a layer induces a pressure drop across a zone of negligible thickness. Figure 19-2 depicts the radial pressure profiles in a formation layer during injection for two different situations:

- fluid injection without a diverter (dashed line)
- injection after a diverter cake has been deposited at the sandface (solid line).

The injection and reservoir pressures are identical in both cases, but the injection rates are different. The cake acts as a temporary skin effect. Consequently, a pseudoskin effect factor can be defined by the standard (van Everdingen and Hurst, 1949) with an injection rate  $q_i$ :

$$s_{cake} = \frac{2\pi kh}{\mu q_i} \Delta p, \quad (19-7)$$

where  $k$  is the permeability and  $h$  is the thickness.

Use of particulate diverters in a perforated completion requires special attention because they can modify the flow pattern in the perforation tunnel itself. Lea *et al.* (1993) showed that a diverting agent tends to equalize the flux entering the formation at the perforation walls. However, the flow profile in the formation is determined mostly by the damage distribution, as acid tends to migrate toward the higher permeability zone. Figure 19-3 shows the acid concentration contours obtained by numerical simulation of a perforation affected by both a crushed zone and shallow

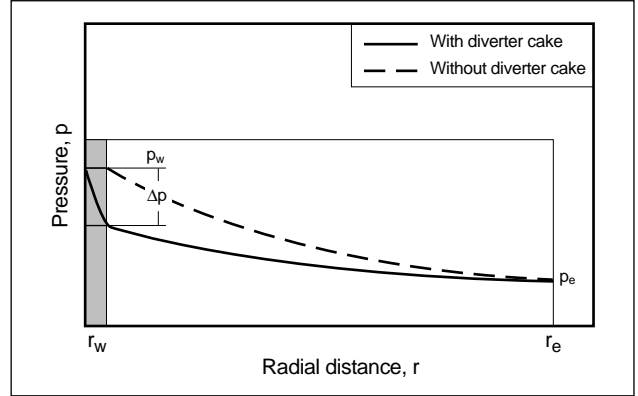


**Figure 19-2.** Radial pressure profile in the reservoir with and without a diverter cake.

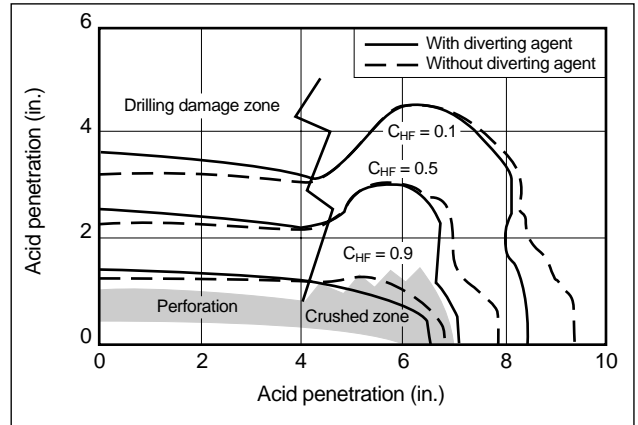


**Figure 19-3.** Hydrofluoric acid concentration  $C_{HF}$  contours around a perforation (Lea *et al.*, 1993).

drilling mud damage (4 in. depth). The figure shows that the diverting agents do not significantly modify the flow patterns around the perforation, and therefore they have little impact on the rate of skin effect reduction for a single perforation (Fig. 19-4). These results indicate that particulate diverters do not provide diversion within the perforations. They provide diversion from one perforated zone to another. The model presented in this section is thus applicable also to a perforated completion.

Using the definition of cake resistance (Eq. 19-1) and expressing the fluid superficial velocity  $u$  through the cake as  $q_i/A$  in Eq. 19-7, then

$$s_{cake} = \frac{2\pi kh}{A} R_{cake}, \quad (19-8)$$

where  $A$  is the sandface area exposed to flow and available for cake deposition.

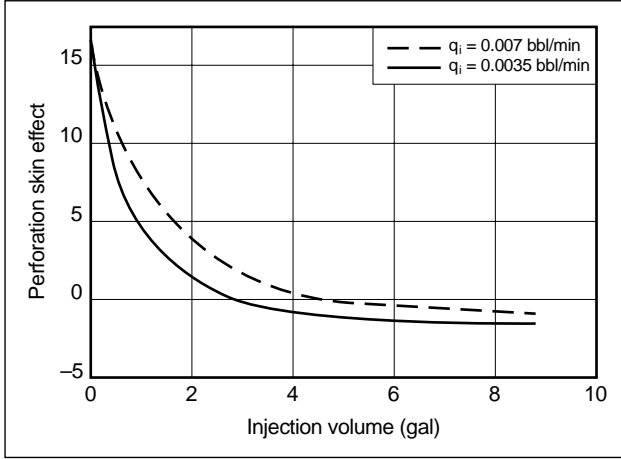


**Figure 19-4.** Skin effect evolution for different injection rates and diverting agents (Lea et al., 1993).

- For an openhole:  $A = 2\pi r_w h$ , where  $r_w$  is the wellbore radius.
- For a cased hole:  $A = n_{perf} 2\pi r_{perf} l_p$ , where  $n_{perf}$  is the number of perforations in the layer,  $r_{perf}$  is the radius of a perforation, and  $l_p$  is the length of the perforation tunnel.

For the assumptions that the cake thickness is negligible and the fluid velocity across the cake does not vary, the cake resistance obtained under linear flow conditions in the laboratory can be used.

The growth rate of the diverter cake can be related to the injection rate. If  $\rho_a$  is denoted as the mass of cake per unit area of sandface available for deposition, its derivative with respect to time can be expressed for any layer by

$$\frac{d\rho_a}{dt} = \frac{C'_{div} q_i}{A}, \quad (19-9)$$

where  $t$  is the time and  $C'_{div}$  is the net diverter concentration in  $\text{kg/m}^3$  after dissolution effects are considered. In Eq. 19-9, it is assumed that the injected fluid is evenly distributed on the sandface. If this were not the case, as along a perforation tunnel, a finer modeling involving infinitesimal elements of the surface  $dA$  would be required.

To calculate the evolution of flow and pressure during diverter injection requires expressing the inflow performance relationship (IPR) for a multilayered reservoir and linking the diverter pseudoskin effect to the flow rate entering each layer. Figure 19-5 depicts a cylindrical reservoir made of  $n$  horizontal layers, at the center of which is a vertical well.

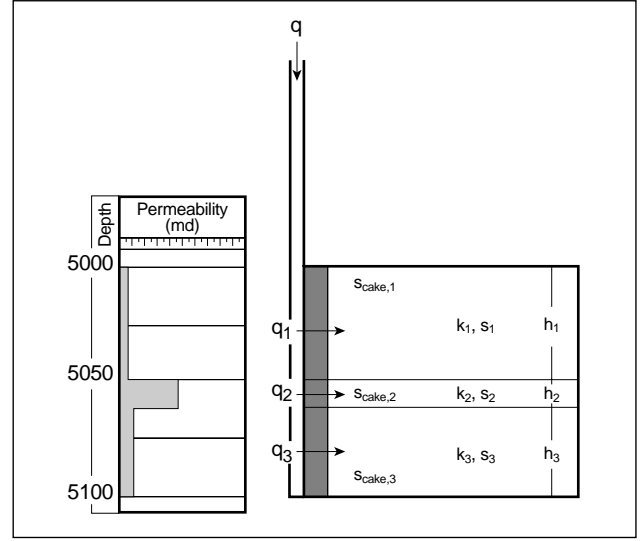


**Figure 19-5.** Flow distribution in a multilayered reservoir: on the left, without a diverter; on the right, with a diverter.

equations, the wellbore radius is  $r_w$  and the reservoir radius is  $r_e$ . Each layer is characterized by its net thickness  $h_j$ , undamaged permeability  $k_j$  and skin effect  $s_j$ . The subscript  $j$  denotes the layer number. For simplicity, a single-phase, radial and horizontal steady-state flow is assumed to prevail. Whenever more complicated geometries exist, such as commingled layers and crossflow, a more sophisticated inflow performance relationship may be used. This would require the results of layered reservoir testing, such as described by Ehlig-Economides and Joseph (1985).

With the simplified assumptions, and assuming steady state, the injection rate entering layer  $j$  is

$$q_j = \frac{2\pi k_j h_j \Delta p}{\mu \left( \ln \left( \frac{r_e}{r_w} \right) + s_j + s_{cake,j} \right)}, \quad (19-10)$$

where  $s$  is the skin effect from damage and  $\Delta p$  is the pressure differential of the wellbore pressure  $p_{w,j}$  minus the outer reservoir pressure  $p_e$ . The skin effect  $s_{cake,j}$  is time dependent because of cake buildup, and  $s_j$  varies with time if the effect of damage removal by acid is considered.

Equations 19-8, 19-9 and 19-10 are coupled because the cake resistance and pseudoskin effect depend on  $\rho_a$ , which is itself dependent on the injection rate. Eliminating  $q_j$  between Eqs. 19-9 and 19-10 and using Eq. 19-8 to replace  $s_{cake,j}$ , an equation governing the rate of growth of the cake in layer  $j$  is obtained:



$$\frac{d\rho_{a,j}}{dt} = \frac{2\pi k_j h_j \Delta p}{\mu \left( \ln \left( \frac{r_e}{r_w} \right) + s_j + 2\pi k_j h_j R_{cake,j} / A_j \right)} \frac{C'_{div,j}}{A_j}, \quad (19-11)$$

where  $\rho_{a,j}$  is the mass of diverter per unit area in front of layer  $j$ . Equation 19-11 is readily solved for two cases:

- If the injection is performed at constant excess pressure  $\Delta p$ , each differential equation can be solved independently. If the cake resistance varies linearly with the mass of diverter deposited, the system of equations can be solved analytically (Economides *et al.*, 1994; Hill and Rossen, 1994).
- If the injection is performed at a constant total rate  $q_{tot}$ , the differential equations are coupled through the expression of total rate for  $n$  layers:

$$q_{tot} = \sum_j q_j. \quad (19-12)$$

The term  $\Delta p$  derived from Eqs. 19-10 and 19-12 is substituted into Eq. 19-11, which is then solved for each layer. A numerical method is required in this case (Doerler and Prouvost, 1987). Hill and Rossen (1994) presented a simplified numerical method that applies in some cases.

Once Eq. 19-11 is solved for  $\rho_{a,j}(t)$ , the other parameters of interest, such as  $q_j(t)$  or  $\Delta p(t)$  can be derived. The solution shows that the system tends toward equalization of the layer injectivities. Figure 19-6 illustrates the evolution of the fractional flow rate under diverter injection in a three-layer case. At the end of the diverter stage, the rate per layer is roughly proportional to the layer thickness. Table 19-2 details the reservoir geometry corresponding to this case.

For a more accurate calculation of the diverter effect, this model can be included in a finite-difference matrix acidizing simulator. This enables due accounting of other factors such as the effect of damage removal on injectivity and transient effects and the use of more realistic and complicated relations for the cake resistance versus deposited diverter mass.

### 19-3.7. Field design

To ensure proper coverage of the zones to be stimulated, the diverter placement design must include the following several steps.

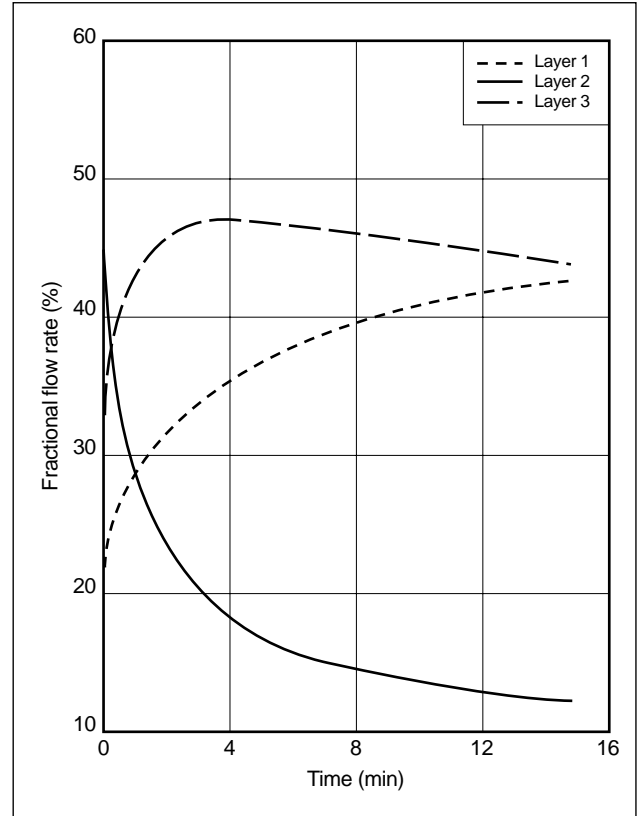


Figure 19-6. Flow redistribution caused by a diverter slug.

Table 19-2. Reservoir data for the example in Fig. 19-6.

Wellbore radius	0.35 ft		
Reservoir radius	2000 ft		
Carrying fluid viscosity	1 cp		
Diverter concentration	150 lbm/1000 gal		
Temperature	150°F [65°C]		
Cake resistance function at 150°F	$R_{cake} = 5 \times 10^{12} \rho_a$		
Total injection rate	2 bbl/min		
	Layer 1	Layer 2	Layer 3
Layer permeability	50 md	100 md	500 md
Layer thickness	15 m	3 m	12 m
Initial skin effect	10	5	10

- The chemical nature of the diverter must be selected considering the type of well (injector or producer), formation type (sandstone or carbonate), bottomhole temperature, treating fluid and cleanup procedure.

- The particle-size distribution must be adapted to the pore size of the formation upon which the cake will be deposited. This should prevent any invasion of the porous medium by diverter particles. In general, the particle size must be adapted to the formation layer with the highest permeability.
- A dispersant must be used to ensure that particles will not flocculate in the carrying fluid. Although not recommended, bridging agents must be mixed in gel pads to prevent sedimentation in some cases.
- Once the proper material has been selected, the volume, concentration and injection rate of the diverter must be determined. Generally, concentrated slugs have been found more effective than continuous injection at a lower concentration. The pumping parameters, namely bottomhole pressure and injection rate, must then be estimated to ensure their compliance with field operational constraints, such as fracturing pressure. The overall injectivity of the well should not be lowered to the point that only small injection rates are possible.

The method described in this section can be used to optimize diverter slugs if the well and reservoir data are known. Unfortunately, in many cases, critical parameters such as the exact perforation geometry, pore size near the sandface and distributions of permeability and damage are poorly characterized. In the past, this has limited the use of mathematical models for diverter design. Many practical designs are based on local experience (i.e., trial and error). With the use of coiled tubing, which greatly decreases the volume of the injection string, design can be modified on the fly and the pressure response of the well to acid and diverter slugs can help guide diversion optimization. A flat pressure response to acid indicates that a diverter is required, and the efficiency of cake buildup can be assessed from the reservoir response (pressure increase) to diverter injection. This method of design optimization based on real-time well response is more reliable than a priori estimates and is most likely to be effective if facilities are available for on-site stimulation monitoring.

## 19-4. Foam diversion

### 19-4.1. Historical background

Foams have been used for acid diversion since at least the 1960s (Smith *et al.*, 1969). The acid itself

can be foamed with the addition of gas and surfactant, or, more commonly, foam can be injected in alternating slugs with acid. Until recently, there was little published information on acid diversion with foam, in contrast to the extensive literature on foam for diverting gas flow in improved oil recovery (IOR) processes (Hirasaki, 1989a, 1989b; Schramm, 1994; Rossen, 1996). The findings of IOR foam research have exerted a strong influence on the understanding of foam acid diversion. More recent research suggests that although the basic mechanisms of the two processes are similar, differences in the flow regime between near-well and reservoir applications cause significant differences in behavior. This section summarizes the current consensus on foam behavior and process design. This is an active area of research, and this consensus may well shift within the next few years.

### 19-4.2. Foam mechanisms

Foams act fundamentally differently as they penetrate and plug the pore space of rock compared with the behavior of foams used for drilling, cementing, fracturing or well cleanout. Therefore, analogies to these other foams can be misleading. For example, foams in pipes are created and maintained by shear forces, and the resulting bubbles are much smaller than the pipe diameter. Within the tiny pores of an oil or gas reservoir, however, foam bubbles larger than the individual pores are squeezed down into elongated shapes, spanning several pores, with a liquid film or lamella between each pair of bubbles (Ettinger and Radke, 1992; Falls *et al.*, 1989). The behavior of foam is dominated by the capillary forces on the lamellae; viscous forces in the conventional sense are relatively unimportant.

Numerous IOR foam studies agree that foam does not directly alter liquid mobility in porous media (Bernard *et al.*, 1965; Friedmann *et al.*, 1991; Huh and Handy, 1989; de Vries and Wit, 1990). In other words, the aqueous-phase relative permeability  $k_{rw}$  is the same function of its saturation  $S_w$  as in the absence of foam. (For the remainder of this section, for simplicity the aqueous phase is referred to as water.) Evidently, upon entering rock most of the water leaves the foam and flows through the same network of narrow pores and pore crevices through which it would flow at that same  $S_w$  in the absence of foam. As a result, overall mobility with foam can be inferred from Darcy's law if the rela-

tive permeability function  $k_{rw}(S_w)$  without foam and the water saturation in the presence of foam are known:

$$\Delta p = \frac{(u_g + u_w)}{k\lambda_{rt}} = \frac{u_w}{(k k_{rw}/u_w)} \quad (19-13)$$

$$\lambda_{rt} = \frac{k_{rw}(S_w)}{u_w f_w} \quad (19-14)$$

$$f_w = \frac{100 - \Gamma}{100}, \quad (19-15)$$

where  $u_g$  and  $u_w$  are the volumetric fluxes of gas and water, respectively,  $\lambda_{rt}$  is the total mobility as defined by Eq. 19-14,  $\mu_w$  is the water viscosity,  $f_w$  is the water fractional flow (i.e., water volume fraction of the injected foam), and  $\Gamma$  is the foam quality (i.e., volume percentage of gas in the injected foam). Therefore, the only way to divert acid (i.e., to reduce  $k_{rw}$ ) is to reduce the water saturation  $S_w$  by increasing the gas saturation. During steady foam injection,  $S_w$  is governed by the equation for water fractional flow  $f_w$ :

$$f_w = \frac{u_w}{u_w + u_g} = \frac{1}{\left(1 + \frac{k_{rg}}{\mu_g} \frac{\mu_w}{k_{rw}(S_w)}\right)}, \quad (19-16)$$

where  $k_{rg}$  and  $\mu_g$  are the relative permeability and the viscosity of gas, respectively.

Capillary forces tend to lower the gas mobility ( $k_{rg}/\mu_g$ ) and drive down  $S_w$  (Eq. 19-16). For example, the IOR foam of Persoff *et al.* (1990, 1991) reduced gas mobility by a factor of almost 20,000, which in turn drove down the liquid saturation  $S_w$  and relative permeability  $k_{rw}$  to about 0.37 and 0.001, respectively. During the injection of surfactant solution without gas following foam,  $k_{rw}$  remained at 0.001 during several pore volumes of injection. As discussed subsequently, foams used for acid diversion are neither so strong nor so durable, probably as a result of the higher flow rates used in acid diversion.

The key to the success of foam as a diverter is low gas (and consequently liquid) mobility during foam injection and gas trapping during the subsequent injection of liquid. Foam reduces gas mobility proportionally to the number of liquid films, or lamellae, blocking the flow of gas or, viewed another way, in inverse proportion to the bubble size (Falls *et al.*, 1989; Ettinger and Radke, 1992; Kovscek and Radke, 1994). This reduction is due primarily to the capillary forces resisting movement of the lamellae separating gas bubbles.

These forces completely trap gas bubbles in from 70% to 99% of the gas-filled pore space even as injected foam flows through the remaining pores (Radke and Gillis, 1990; Friedmann *et al.*, 1991). The fraction of the pore space completely blocked by foam declines as the pressure gradient increases. Because of these same capillary forces, the effective viscosity of the gas that flows is much higher than that of gas alone.

Both gas trapping and effective viscosity are even more sensitive to bubble size than to flow rates, however. There are many processes that can spontaneously alter bubble size as foam flows through rock (Hirasaki, 1989a; Kovscek and Radke, 1994; Rossen, 1996). For example, if unfoamed gas and water with surfactant are injected into rock under appropriate conditions, foam may be created within the first inch or two of the rock face (Ettinger and Radke, 1992). Although it may be convenient to assume that foam is created instantaneously at the rock face, this entrance region of low  $\Delta p$  in which foam is created can be significant in a well treatment focused on the near-well region. Similarly, if a foam of very small bubbles is injected into rock, there may be an entrance region with  $\Delta p$  higher than that downstream. In addition, if flow rates are suddenly changed, it may take some time for foam to adjust to the changes in conditions.

The various processes that create and destroy lamellae, together with the non-Newtonian mobility of gas at a fixed bubble size, enormously complicate the prediction of foam behavior in rock. Fortunately, two regimes observed experimentally greatly simplify the description of foam mechanisms.

First, under some conditions bubble size is dominated by processes that destroy lamellae, and these processes appear to be sensitive to capillary pressure  $p_c$  in the rock (Khatib *et al.*, 1988): foam properties change greatly upon a small change in  $p_c$ . Because  $p_c$  depends on the water saturation  $S_w$ , the large changes in foam properties upon small changes in  $S_w$ , combined with Eq. 19-13, suggest that  $\Delta p$  is a simple function of the water saturation  $S_w^*$  at which this change occurs (Zhou and Rossen, 1994; Rossen and Zhou, 1995). Under some conditions common in IOR foam processes,  $S_w^*$  appears to be independent of flow rates in a given rock (Persoff *et al.*, 1990). This implies that foam in this regime can be treated simply as a Newtonian fluid of low mobility: the effect of  $p_c$  on bubble size just balances the non-Newtonian mobility of foam at fixed bubble size. The fixed- $p_c^*$  model for foam, discussed subsequently, is based on

this mechanism. In conditions where this regime applies, foams are stronger in higher permeability rock (higher  $p_c$ ; i.e., lower  $S_w^*$ ), diverting flow into lower permeability zones (Lee *et al.*, 1991; Zhou and Rossen, 1995).

The second regime in which foam behavior appears to be simplified is that in which capillary trapping of the foam bubbles controls overall mobility. In some cases discussed in the following sections,  $\Delta p$  during foam flow or subsequent liquid injection is nearly independent of the foam or liquid flow rate (Parlar *et al.*, 1995). As mentioned, the trapping of foam bubbles in much of the pore space of the rock depends on a balance of capillary forces trapping the bubbles and applied  $\Delta p$  (Rossen, 1990). Evidently, in some cases this balance is highly sensitive to  $\Delta p$ : as the flow rate increases, causing a slight rise in  $\Delta p$ , previously trapped foam bubbles are liberated and allowed to flow, accommodating the increase in flow rate without a further rise in  $\Delta p$ . Whether this conjecture is correct, and its full implications for the design of foam diversion processes, remains to be confirmed.

### 19-4.3. Foam behavior in porous media

- Mobility of injected foam

There is a wide body of experimental data on foam behavior in rock for IOR foams and a growing body of data on foams for acid diversion. It appears that there is a substantial difference between foam behavior in the two applications, probably because of the lower quality  $\Gamma$  and much higher flow rates of foams for acid diversion. Observed trends in behavior include the following.

- Foam mobility is at a minimum (i.e., foam is strongest) at qualities between about 70% and 90% (Thompson and Gdansk, 1993). Foams are weaker for qualities greater than 90%. This is probably due to the collapse of foams at high capillary pressures; the reason for weak foams at low quality is not clear.
- Foams are extremely non-Newtonian at high flow rates (Parlar *et al.*, 1995; Zerhoub *et al.*, 1994), as shown in Fig. 19-7. In this case, the pressure gradient responds nearly linearly to the flow rate at low values. At high flow rates  $\Delta p$  becomes independent of flow rate. This suggests that foam

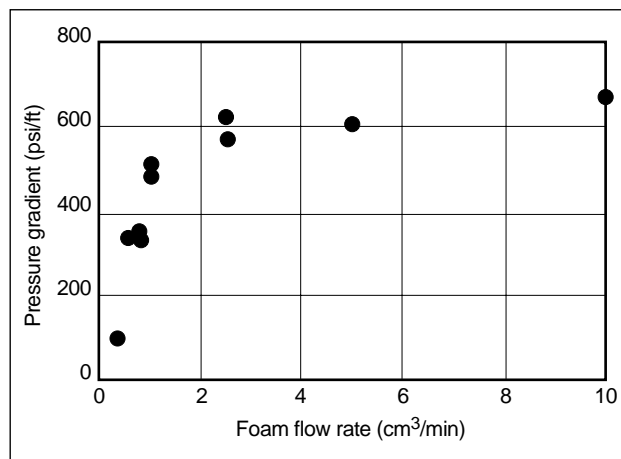


**Figure 19-7.** Example of  $\Delta p$  versus foam flow rate (Robert and Mack, 1995).

mobility is controlled by mobilization and liberation of trapped gas in this high-flow-rate regime. Parlar *et al.* reported that the threshold  $\Delta p$  at which flow becomes independent of flow rate scales roughly as the  $-\frac{1}{2}$  power of permeability values greater than 800 md.

- During foam injection, foams are stronger (i.e., higher apparent viscosity) in high-permeability rock, implying the diversion of flow from higher permeability to lower permeability or more damaged intervals (see, e.g., Kibodeaux *et al.*, 1994). Whether similar trends apply to diversion between layers differing in the extent of damage rather than permeability per se is not clear. Behenna (1995) used a thin wafer of 0.3-md sandstone to simulate a damaged zone at the face of a 1-ft sandstone core. Thompson and Gdansk (1993) used the same approach with carbonates. However, most foam studies use relatively high-permeability rock (hundreds of millidarcies). More studies are required to characterize foam behavior in lower permeabilities.
- Oil weakens or destroys most foams (Jensen and Friedmann, 1987; Schramm and Novosad, 1992; Rossen, 1996; Manlowe and Radke, 1990). Oil is extremely detrimental to foam in oil-wet rock. It is possible to tailor a foam formulation to partially withstand the adverse effects of oil, but this weakening can be an advantage, causing foam to collapse in oil-saturated layers and diverting acid to stimulate those productive layers.

- Mobility of acid injected after foam

Most laboratory studies have used an aqueous slug without acid to simulate acid injection following foam. This is a reasonable simplification if the effects of acid removal of damage and foam diversion are separable. This is clearly not the case for carbonates, as discussed subsequently. The mobility of the liquid injected following foam is the key to processes of alternating slugs of acid and foam; diversion of the foam itself is useless unless the acid following the foam is diverted as well. Observations from laboratory corefloods include the following:

- Trapping of gas by liquid injected following foam is incomplete, and the pressure gradient declines nearly simultaneously throughout the core to a lower, uniform value (Fig. 19-8) (Parlar *et al.*, 1995; Kibodeaux *et al.*, 1994). There is a later decline in  $\Delta p$  that starts near the inlet and proceeds through the core. The second decline is due to the dissolution of trapped gas in injected liquid, which is undersaturated with gas at the high pressure of the core (Robert and Mack, 1995; Zeilinger *et al.*, 1995). The second decline may be unimportant in the field, owing to the large number of pore volumes of liquid required to dissolve the gas. In any event, it can be avoided by including a small amount of gas with the acid.
- The lower, steady pressure gradient observed after liquid follows foam is nearly independent

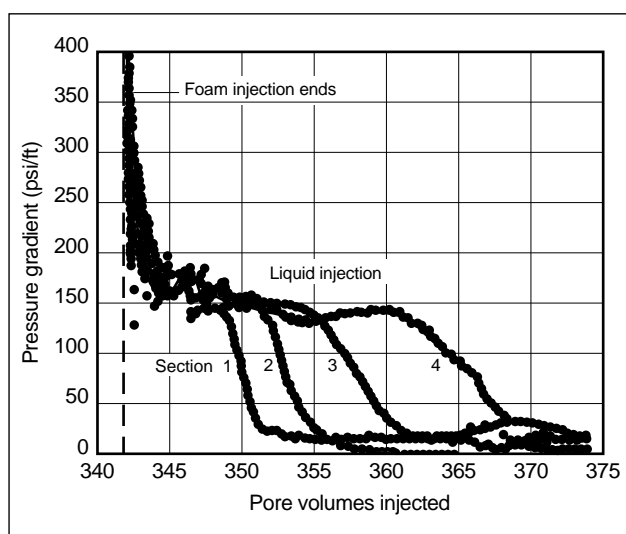


**Figure 19-8.** Pressure evolution during liquid injection following foam (Zeilinger *et al.*, 1995).

of the foam injection rate preceding liquid injection, the liquid flow rate after foam and whether there is a shut-in period preceding liquid injection (Zeilinger *et al.*, 1995; Parlar *et al.*, 1995). In other words, there is virtually unlimited liquid flow above a threshold  $\Delta p$ . Evidently,  $\Delta p$  during this period is controlled by the mobilization of trapped gas bubbles, as discussed previously (Rossen, 1990). Parlar *et al.* reported that the threshold  $\Delta p$  value scales with the  $-\frac{1}{2}$  power of permeability, which suggests that at any given  $\Delta p$ , high-permeability zones would take large amounts of fluid while low-permeability zones would receive little. This finding considerably affects strategy for foam diversion.

- In the field, however, the entire diversion process may occur within the period of decline in  $\Delta p$  to its lower, steady value. The rate of decline depends on the rate of liquid injection. In Fig. 19-8, it takes about 2½ hr for  $\Delta p$  to decline to the plateau, with a liquid velocity of about 1 m/d. Parlar and coworkers found that for a velocity of 6 m/d (equivalent to a pump rate of 0.05 bbl/min/10 ft at the wellbore), the plateau value is reached within 10 min. In field application, injection of an entire acid slug may last only 30 min. Thus the rate of decline in  $\Delta p$  may be as important as the lower, steady value. What controls this rate of decline is not yet clear.

- Foam propagation rate

Foam cannot propagate faster than the surfactant advances into the porous medium, so surfactant adsorption losses to the rock play an important part in foam propagation. The latter can lag behind surfactant propagation, however. Whether controlled by surfactant adsorption or by other factors, foam propagation is faster in high-permeability rock than lower permeability rock and faster with a surfactant preflush than without (Friedmann and Jensen, 1986; Kibodeaux *et al.*, 1994; Parlar *et al.*, 1995). Both effects help the diversion process. Because most preflush enters the higher permeability or less damaged intervals that are to be blocked with foam, a preflush helps to place more foam in the layer to be blocked (Zerhoub *et al.*, 1994; Zhou and Rossen, 1994).

- Interactions between foam and acid

As noted, most studies of foam diversion do not include acid, on the assumption that the effects of acid and foam are separable. For carbonate rocks,

however, acid dissolves the rock matrix in which foam resides, forming channels or wormholes through the rock (see Chapters 16 and 17). Two effects of foam on the formation of wormholes are crucial to the acid stimulation of carbonates. First, foam causes the formation of longer wormholes with fewer branches, leading to more efficient stimulation of a formation with less acid required (Bernardiner *et al.*, 1992). Second, foam evidently fills and plugs wormholes, diverting acid to layers with fewer or shorter wormholes. This leads to a more even distribution of acid between intervals (Thompson and Gdanski, 1993).

#### 19-4.4. Foam diversion experiments

The first published foam diversion tests in connection with acidizing used high-permeability sandpacks (20/40 and 40/60 mesh) with a permeability ratio of 20 and alternate injection of foaming solution and gas. Smith *et al.* (1969) reported successful plugging of the high-permeability pack, even during the liquid stages following the gas stages. Later, Burman and Hall (1986) used lower permeability cores with permeability ratios between 1.6 and 3.8. They observed durable diversion with core permeabilities of 100 md and higher: equal flow in both cores was eventually obtained after several foam stages, and diversion was maintained during the liquid stage. For experiments conducted with lower permeability cores (10 to 66 md), little or no improvement was achieved in the flow profile during liquid stages. However, some diversion was obtained during the foam stages, with better efficiency obtained with lower quality foam.

Zerhboub *et al.* (1994) and Parlar *et al.* (1995) used small preflush volumes of surfactant solution ahead of the foam stage and limited the size of the foam slug to a fraction of the pore volume. They obtained successful diversion, which was maintained during the liquid stages following the foam slugs. Zerhboub *et al.* tested sandpacks from 300 md to 20 d and reported better efficiency with higher permeability cores. Applying a shut-in after the foam stage and increasing the foam-stage volume resulted in better diversion. A test performed with two cores of the same permeability, one saturated with brine and the other containing residual oil, showed that foam was able to impair temporarily the brine-saturated core and redirect flow into the oil-bearing core. Parlar *et al.* obtained diversion with the slug technique

in cores with permeabilities between 100 and 1200 md. Behenna (1995) also reported diversion with this technique in two cores with permeabilities of 18 and 126 md. However, when strong foam was generated in both cores by the injection of larger foam slugs, no diversion or even reverse effects were obtained.

Behenna (1995) also tested the effect of acid on foam diversion. A 5-mm thick wafer of Ohio sandstone was placed at the face of the high-permeability core (322-md Berea sandstone) to simulate a thin layer of near-wellbore damage. Injection of a small foam slug slightly increased the fraction of flow entering the “damaged” core. The subsequent acid stage, however, directed most of the flow to the damaged core by increasing substantially the permeability of the wafer while the permeability of the foamed undamaged core remained fairly constant. In this case diversion resulted from the combined effect of both foam and acid.

Laboratory experiments show that the keys to foam diversion are placing more foam and (if possible) stronger foam in the higher permeability or less damaged intervals and keeping the gas trapped during subsequent liquid injection. As discussed previously, foam itself is stronger in higher permeability rock, but inefficient trapping of gas during the stages following foam negates some of this effect. Other factors such as slower foam propagation caused by surfactant adsorption in lower permeability zones can help achieve foam diversion during the liquid stages following foam. Furthermore, if partial temporary diversion is achieved, the effect of acid on damaged zones can combine with the foam effect to complete the reversal in flow distribution between the damaged and undamaged zones after the first exposure to a foam slug–acid sequence.

Zeilinger *et al.* (1995) showed, however, that a process that relies primarily on faster foam propagation in higher permeability or undamaged rock may work better in the linear flow geometry of laboratory corefloods than in radial flow in reservoirs. In essence, in radial flow, faster propagation helps only if the slugs are small, because otherwise foam fills the crucial near-well region in all layers.

In carbonate cores, foam diversion is coupled to the formation of wormholes. Thompson and Gdanski (1993) showed that foam can help equalize flow between two cores with wormholes of different lengths; evidently bulk foam fills and blocks the wormhole, diverting acid to the core with shorter or no wormholes.

### 19-4.5. Modeling and predicting foam diversion

IOR foam researchers use a variety of mathematical models to describe foams (Kular *et al.*, 1989; Fisher *et al.*, 1990). In principle, the most complete, but also highly complex, population balance model (Friedmann *et al.*, 1991; Falls *et al.*, 1989; Kovscek and Radke, 1994) attempts to represent all mechanisms of non-Newtonian mobility and processes altering bubble size. There is no published application of this model to foams for diverting acid.

The much simpler approach of the fixed- $p_c^*$  model (Rossen and Zhou, 1995; Zhou and Rossen, 1994, 1995), focuses on the coalescence of foam as a function of capillary pressure  $p_c$  or water saturation  $S_w$ . Combined with fractional-flow modeling, this foam model predicts some important aspects of foam behavior: the benefits of a surfactant preflush, the importance of compatibility of acid and foam slugs, foam diversion between layers differing in permeability and differences between diversion processes in linear and radial flow. In this approach, laboratory corefloods are used to determine the rates of advance and mobility of foam during the injection of foam and subsequent injection of liquid (Kibodeaux *et al.*, 1994). Mobilities are assumed independent of flow rates. These parameters are then used with equations for radial flow such as Eq. 19-10 to predict diversion in a field application. The model identifies the keys to effective foam diversion as the rate of foam propagation, foam mobility during injection and foam mobility during liquid injection in each layer.

Hill and Rossen (1994) presented an even simpler version that gives essentially equivalent results for many applications. In this model, the foam skin

effect  $s_{foam,j}$  replaces  $s_{cake,j}$  in Eq. 19-10. The foam skin effect is

$$s_{foam,j} = \left( \frac{k_j}{k_{foam,j}} - 1 \right) \ln \left( \frac{r_{f,j}}{r_w} \right), \quad (19-17)$$

where  $k_j/k_{foam,j}$  is the mobility reduction resulting from foam (assumed for simplicity to affect only permeability) in layer  $j$  and  $r_{f,j}$  is the radial extent of the foam bank in that layer. Foam advances in each layer at a constant volumetric rate that reflects permeability and the volume of preflush in that layer. Upon switching from foam to acid injection in a slug process, the mobility reduction factor  $k_j/k_{foam,j}$  suddenly takes a new, usually higher, constant value, and  $r_{f,j}$  stays constant during acid injection. An analytical solution is obtained for constant-pressure injection, and other cases, such as injection at a fixed overall injection rate, can be derived easily.

This approach uses many simplifying assumptions, of which two now appear to distort predictions of foam performance in the field: assuming mobility is independent of flow rates and assuming instantaneous attainment of steady-state mobilities upon a change in injection conditions. As noted previously, foams are strongly non-Newtonian in the flow regime relevant to acid diversion, and the period of transition between high  $\Delta p$  with foam and lower  $\Delta p$  during liquid injection (Fig. 19-8) may be crucial to the diversion process. Work to extend this model to account for these effects is ongoing.

The simulator described by Robert and Mack (1995) and Bartko *et al.* (1996) does not make these assumptions and fits their laboratory corefloods well (Fig. 19-9). This approach is closer to full reservoir simulation: the computer solves a partial differential equation for pressure and flow rates as functions of

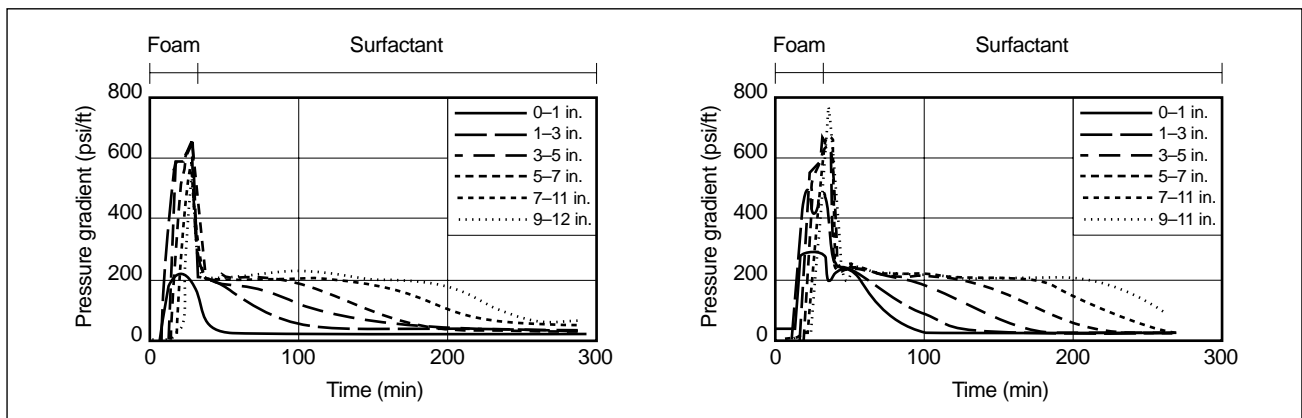


**Figure 19-9.** Comparison of simulation (right) with laboratory coreflood (actual data, left) (Robert and Mack, 1995).

position and time, interpolating mobilities from tables of laboratory data. Local gas and liquid saturations are computed from mobilities and local foam flow conditions using Eqs. 19-14 and 19-15. A mass balance is then used to compute the local flow rates for each phase from the variations of saturation. Both regimes shown in Fig. 19-7—the low-flow-rate regime, in which mobilities are roughly Newtonian at constant quality and the constant-pressure-gradient regime at high flow rates—are included in the simulator foam-mobility model. For liquid injection after a foam stage (i.e., the reimbibition stage), the simulator assumes a sharp transition in gas mobility from complete plugging to high mobility at the threshold pressure gradient. This tends to maintain the actual pressure gradient at the threshold value during liquid injection, as observed experimentally. An empirical correlation is used to account for the delay of gas removal (and the corresponding delay of pressure decrease) observed at low liquid rates. This is the most difficult part of the corefloods to model accurately, and in some cases the simulator tends to overestimate this delay slightly, especially in the downstream section of the cores. Effects of surfactant adsorption, gas compressibility and gas solubility are also included. In principle, there is no limit to the complexity of mobility behavior that can be incorporated in this approach.

#### 19-4.6. Application to field design

Recent laboratory results have led to the development of guidelines for foam diversion (Gdanski, 1993; Zerhoub *et al.*, 1994). Foam diversion has been used increasingly in recent years, particularly in cases where other diversion techniques are impractical or less efficient such as the application of particulate diverters and ball sealers over large intervals. Foams also help in cleanup and back-production of treating fluids.

- Choice of surfactant

Traditionally, half-life measurements have been used to rank the foaming performance of surfactants. In these static tests, foam is generated and allowed to decay slowly in a beaker under the action of liquid drainage and gas migration. The time for one-half of the liquid to drain out of the foam is called the foam half-life. These tests are useful for determining chemical compatibility and identifying ineffective foams but not for optimizing surfactant formulation (Rossen, 1996). Foam

formation in porous media is a dynamic process in which bubbles (or lamellae) are constantly created and broken. Surfactant adsorption on the rock surface, elasticity of lamellae and kinetics of foam formation are important properties that cannot be measured by static half-life tests. Therefore, only core flow tests can be used to select the most appropriate surfactant formulation for diversion.

Laboratory experiments indicate that diversion requires rapid formation and propagation of strong foam in higher permeability cores, with delayed foam formation in the lower permeability zones. This suggests that surfactant adsorption is a critical parameter for diversion. Oil present in the formation is another parameter to take into account for surfactant selection: the presence of oil can impair significantly the foam strength or delay the onset of effective foam banks, especially in oil-wet formations.

- Pumping strategy

On the basis of laboratory experiments, Zerhoub *et al.* (1994) proposed a set of guidelines for foam diversion. The principle of the method consists of pretreating the matrix to facilitate the formation of strong foam with a minimum foam volume and adding surfactant to acid stages to preserve the foam bank stability. Experiments on sandstones and carbonates show that effective and durable diversion can be obtained with repetitive slugs of foam and acid. Indeed, once a damaged zone has been acidized, it must be plugged by foam to redirect acid to zones that have not been treated. Furthermore, foam in place tends to undergo slow decay (presumably because of gas dissolution), and periodic regeneration of the foam bank is required.

Use of a mutual solvent is recommended ahead of the treatment to reduce interfacial tension and to help sweep oil from the near-wellbore region. For a well-defined water zone, treatment can be started with a foam slug aimed at selectively plugging the water zone, while the oil prevents strong foam formation in the hydrocarbon-bearing zone. In that case, a mutual-solvent preflush is not beneficial. A gel-based water- or oil-specific diverter can be also used in addition to foam to help plug water zones (Kennedy *et al.*, 1992).

The size of foam slugs can be extrapolated from laboratory studies. As with particulate diverters, the design consists of pumping enough foam to plug



higher injectivity zones while keeping the overall injectivity high enough to perform the treatment in a reasonable time and ensure effective acid action. Generally, the volume of the foam stages is gradually increased throughout the treatment to provide diversion over increasing interval lengths and replenish the degenerating foam pumped during prior stages. For carbonate acidizing, increasing the volume of the foam stages accommodates the void space created by rock dissolution during the previous acid stages. Gdanski (1993) recommended also that the volume of the foam slugs be sufficiently large to allow transport in the tubing without excessive mixing with other stages.

Zerhoub *et al.* (1994) found that better diversion is obtained on parallel sandpack cores if moderate acid rates are used. This phenomenon can be explained by the behavior of foam during subsequent liquid injection: mobility in the foam bank appears to be governed by a threshold  $\Delta p$  for foam mobilization and therefore increases strongly with increasing pump rate (Parlar *et al.*, 1995). At high flow rates, foam directs a greater fraction of flow into foam-filled high-permeability intervals. Simulation of field application shows that under certain conditions diversion can depend strongly on the pumping rate (Fig. 19-10).

Foam quality in diverter slugs varies generally from 60% to 80%. Experiments on low-permeability carbonate samples showed better diversion efficiency if higher quality foams (70% to 80%) were used (Thompson and Gdanski, 1993). Single-core tests on Berea sandstones showed that increasing foam quality from 65% to 80% at a constant liquid rate resulted in a slight increase of the pressure gra-

dient in the foam bank (Parlar *et al.*, 1995). However, little variation of foam behavior was observed during the following liquid stage; therefore, diversion efficiency is not expected to vary.

For long intervals, especially in horizontal wells, coiled tubing is often used to help place treating fluid throughout the interval. Treatment is started at the bottom of the interval, and the coiled tubing is pulled out while pumping. Foam stages are pumped at regular intervals, usually of 30 to 50 ft. This method has been shown to yield better results than simple bullheading (i.e., injection at the top of the interval). Analysis of stimulation results for water injection wells with long open-hole intervals (e.g., 300 ft) in a carbonate formation showed that replacing the conventional bullheading technique (with or without a particulate diverter) with the use of coiled tubing and foam diversion doubled the average post-treatment injectivity index while reducing the required acid volume from 100 to 50 gal/ft (Ginest *et al.*, 1993). Figure 19-11 is an example of a post-treatment flow profile after acidizing with coiled tubing and foam diversion. It shows that acidizing opened the entire interval to flow, which indicates successful damage removal over the entire zone.

Coiled tubing can also help in designing diversion stages on the fly. It allows using downhole sensors to measure pressure or to get an estimate of the bottom-hole pressure from the pressure at the wellhead in the annulus between the production tubing and the coiled tubing. An increase of bottomhole pressure when foam is at bottomhole indicates that foam is entering the formation, but this is not a sufficient indication to prove that diversion is taking place. A significant

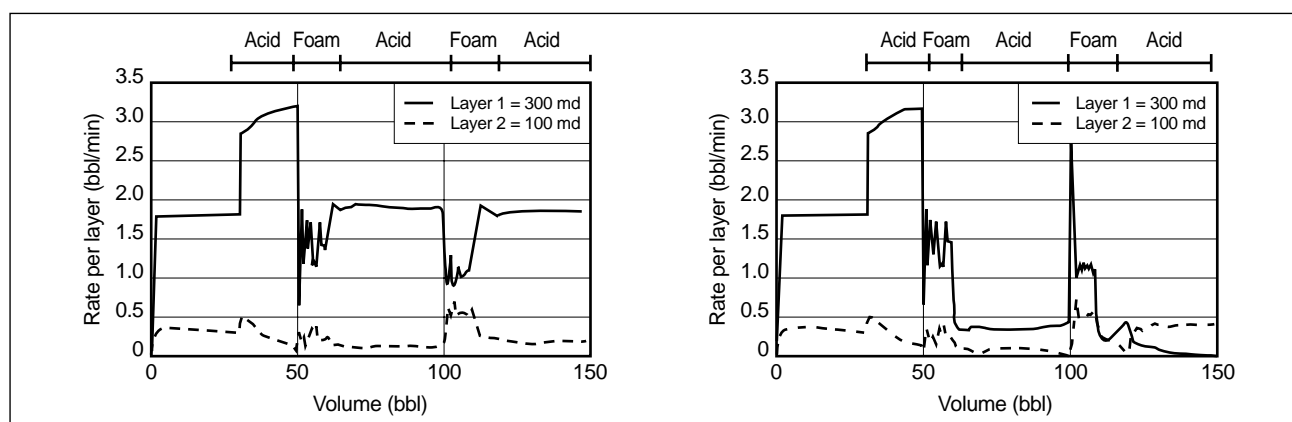


**Figure 19-10.** Effect of acid injection rate on diversion efficiency (Robert and Mack, 1995). Left: high injection rate (no diversion). Right: low injection rate (diversion).

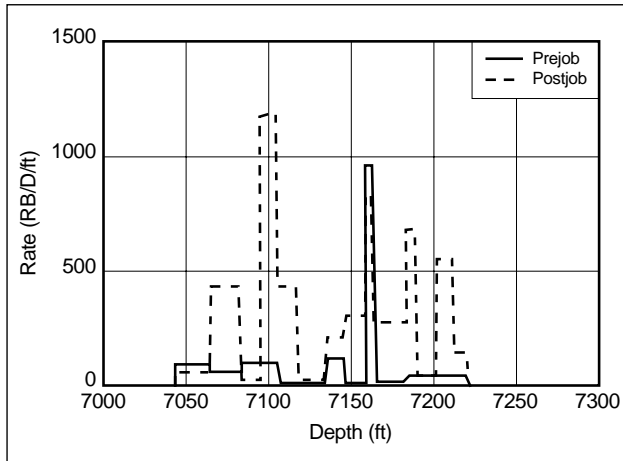


**Figure 19-11.** Flow profile after acidizing with foam diversion (Ginest et al., 1993). Prejob = 102,000 BWPD at 1500 psig; postjob = 608,000 BWPD at 1180 psig.

reduction of pressure during the following acid stage can indicate that a new zone is acidized and that diversion was obtained. However, laboratory experiments show that a drop in injection pressure during the acid stage may also reflect foam displacement and decay (Parlar *et al.*, 1995; Kibodeaux *et al.*, 1994). Therefore, pressure evolution is more difficult to interpret for foam than for particulate diverters.

Foam may be mixed with acid throughout the treatment. Generally, lower qualities are used for foamed acid than for foam slugs. This method was first tried for acidizing gravel-pack formations (Burman and Hall, 1986). Laboratory data indicate that foamed acid provides better coverage than straight acid, even if inversion of the flow profile (i.e., more flow into the damaged or low-permeability zones) cannot be attained. However, this technique requires higher gas volumes and pumping times than the slug method. Thompson and Gdanski (1993) reported that foamed acid does not provide sufficient diversion in high-porosity carbonates.

## 19-5. Ball sealers

Originally introduced in 1956, ball sealers are small spheres intended to seal perforations on the inside of the casing. Added to treating fluids during stimulation, they are carried downhole and seal the perforations accepting the largest quantities of fluid. Although they are widely used, conventional ball sealers often fail to provide diversion. A sufficient rate must be available to maintain a differential pressure across the perfora-

tions to keep the balls in place. Their effectiveness is also limited by the roundness and smoothness of the perforation holes. Moreover, ball sealers are not effective in wells with a large number of perforations.

Better efficiency can be gained by using buoyant ball sealers instead of conventional nonbuoyant ones (Erbstoesser, 1980; Gabriel and Erbstoesser, 1984). As shown in Fig. 19-12, when a buoyant ball sealer is transported to the perforations, it either seals an upper perforation or is carried to the lowest one that is accepting fluid. However, because of its buoyancy, it does not remain in the quiescent fluid in the Rathole.

Contrary to chemical diverters, ball sealers seated on the perforations facing a high-permeability interval effectively stop fluid entry and direct the entire flow to areas with lower injectivity. Figure 19-13 shows the injected flow distribution resulting from this diversion technique.

The density of buoyant ball sealers must be compatible with the density of the carrying fluid to allow transport downhole while prohibiting settling in the Rathole. Ball sealers are transported downhole as long as the rising velocity does not exceed the fluid velocity in the wellbore. The rising velocity  $u_r$  of spherical particles in a fluid is

$$u_r = \sqrt{\frac{4}{3} \frac{\Delta \rho g d}{\rho_f f_d}}, \quad (19-18)$$

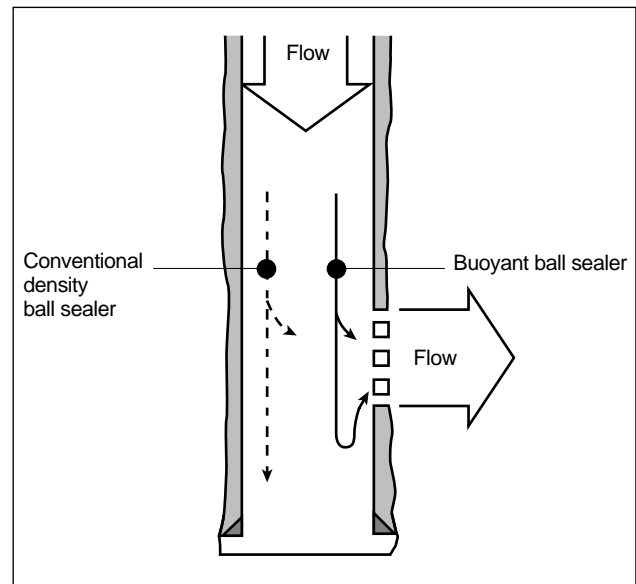


**Figure 19-12.** Two ball sealer seating processes (Erbstoesser, 1980). The dashed trajectory shows the conventional density (nonbuoyant) ball sealer, and the solid trajectory shows the 100%-efficient buoyant ball sealer.

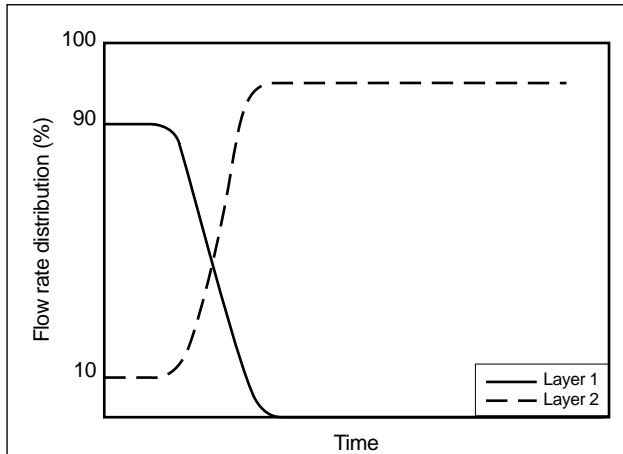


**Figure 19-13.** Flow distribution using ball sealers in a two-layer reservoir ( $h_1/h_2 = 1$ ,  $k_1/k_2 = 9$ ).

where  $\Delta p$  is the difference between the fluid and ball densities,  $d$  is the ball diameter,  $g$  is the acceleration of gravity,  $r_f$  is the fluid density, and  $f_d$  is the drag coefficient. The drag coefficient depends on the Reynold's number  $N_{Re}$  and can be obtained from the well-known Moody diagram or from empirical expressions:

$$N_{Re} = \frac{u_r d \rho_f}{\mu}, \quad (19-19)$$

where  $\mu$  is the dynamic viscosity. A trial and error technique is required to solve Eq. 19-18 rigorously (Brown *et al.*, 1963), because  $N_{Re}$  depends on the calculated velocity. However, in high-flow regimes, and thus at large values of  $N_{Re}$  (between 2,000 and 100,000),  $f_d$  varies slightly about an average value of 0.44. If  $f_d$  is assumed constant over this interval, then the rising velocity can be estimated readily (Gabriel and Erbstoesser, 1984).

## 19-6. Mechanical tools

During the mid-1940s, downhole tools were used to locate the contact between a conductive fluid (acid) and a nonconductive fluid (oil). Both fluids were pumped simultaneously to maintain the interface at a constant level. This allowed treatment of a selected portion of the reservoir. A schematic of this procedure is given in Fig. 19-14. In 1950, the development of hydraulically operated inflatable packers led to improved diverting techniques. When these packers are used as a straddle tool, it is possible to treat three intervals (below, between and above the packers)

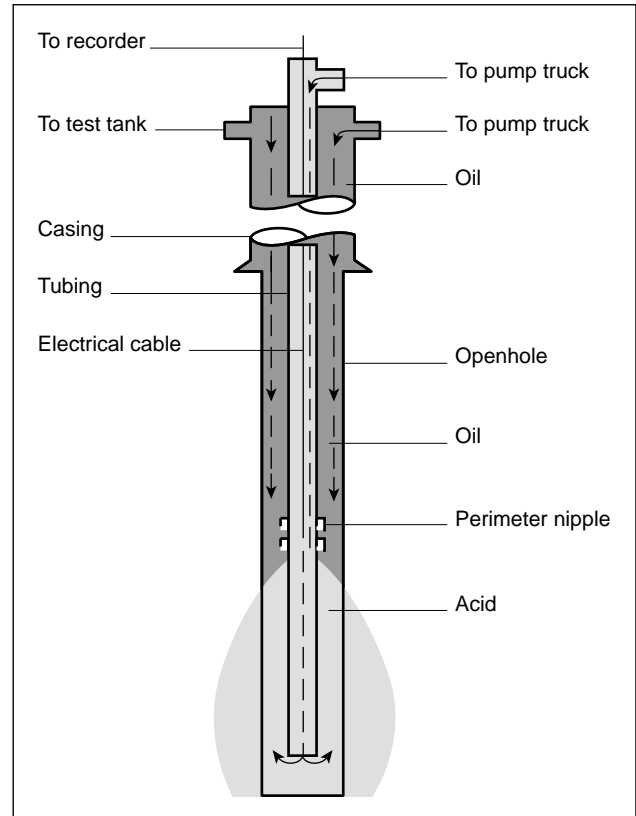


**Figure 19-14.** Diversion in openhole using an "interface locator" tool (Harrison, 1972).

without moving the completion. Although this is an effective means of obtaining excellent control on coverage, it is expensive and time consuming.

Frac baffles were invented in 1965 to provide economically attractive completions in multilayered reservoirs. In this method, shown in Fig. 19-15, one or more concentric baffle rings of different diameters are designed to accept a "bomb." Bombs of different diameters are dropped to sit on the correct-diameter baffle and thus isolate the zone of treatment. However, this technique limits the treatment to downcasing and requires accurate placement of the baffles when running the casing.

Retrievable packers have also been developed that use various techniques for setting and retrieving. Tension-set packers are particularly suitable for matrix acidizing operations. They are initially set by pulling tension on the tubing and held in place by the pressure differential between the tubing and the annulus above the packer.

Conventional mechanical techniques are efficient at controlling the placement of acid. However, they

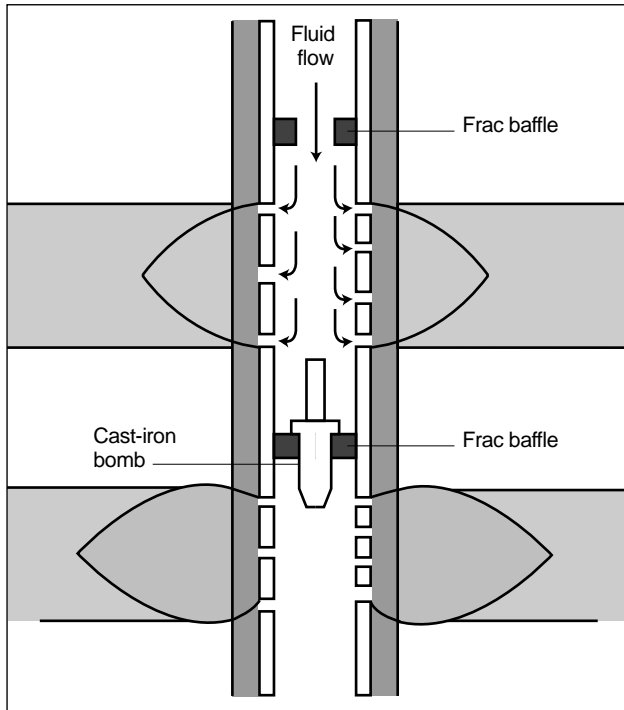


**Figure 19-15.** Frac baffle diverting technique (Harrison, 1972).

are cumbersome and generally require a rig on site. They are also expensive and time consuming.

New techniques have been developed to convey packers with coiled tubing. Inflatable straddle packers can provide zonal isolation during matrix treatment. Before packer setting, the treating fluid can be circulated down the coiled tubing above the packers. Setting is obtained by picking up on the coiled tubing and applying pump pressure to inflate the packer elements. Treating fluid can then be directed to the interval between the packers by slacking off weight on the tool string (Fig. 19-16). Picking up over the string weight and then slacking off closes the injection port and reopens the circulating port above the packers. Finally, sustained overpull allows the packer elements to deflate, and the packer can be moved to another zone (Milne, 1991).

## 19-7. Horizontal wells

### 19-7.1. Optimal treatment

Producing sections in horizontal wells are typically between 1 and 2 orders of magnitude longer than in vertical wells. Therefore, even distribution of treating

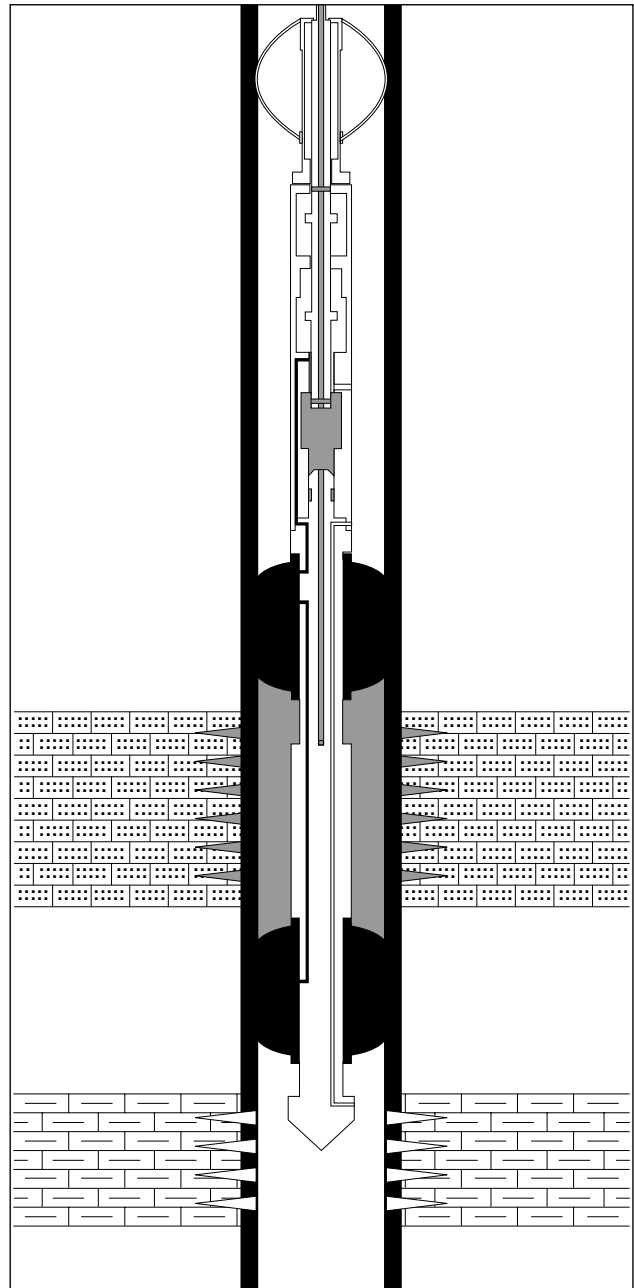


**Figure 19-16.** Treating between the packers (Milne, 1991).

fluid over the entire open interval is more difficult to achieve. Furthermore, the limits of corrosion-inhibitor efficiency, as well as other practical considerations, restrict the treatment duration and therefore require pumping smaller volumes per length of open interval, which makes the issue of placement control even more critical. Better results are generally reported when a diversion technique is used than when acid is simply bullheaded via the production tubing. In sever-

al cases, production logs performed after acidizing without the use of any diversion technique show that only a small portion of the well was open to flow, generally the area nearest to the vertical section (Frick and Economides, 1991; Thomas and Milne, 1995).

Efforts have been made to determine the optimum treatment design, taking into account the limitation of the total volume that can be pumped. Economides and Frick (1992) recommended adjusting the injection volumes according to the severity of damage. For instance, in the case of completion-induced damage, cone-shaped damage invasion is expected as damage severity increases with the time of exposure to drilling mud, which decreases with increasing measured depth (Fig. 19-17). In that case, a “tapered” injection would be optimal, with more acid pumped near the vertical section of the well. If complete damage removal requires impractical acid volumes, partial damage removal throughout the open interval should be targeted, leaving a uniform damage collar around the wellbore.

Da Motta *et al.* (1994) suggested that in some cases treatment efficiency can be improved by selective acidizing, where some intervals in the horizontal section of the well are intentionally left unperforated or untreated. For example, Fig. 19-18 shows the normalized productivity index (ratio of the productivity index to undamaged productivity index) for three different

treatment configurations. Simulations were performed with a 2000-ft well with 12-in. damage penetration and a permeability reduction of 90% in the damaged zone. The original vertical and horizontal permeabilities were 90 and 10 md, respectively. A total volume of 100,000 gal was pumped, corresponding to 50 gal/ft for full coverage and 125 gal/ft for 40% coverage. For partial coverage, the treated area was divided into five equally spaced intervals. In the particular case shown in Fig. 19-18, optimum treatment would be achieved with partial coverage. However, these simulation results must be interpreted with caution, as they depend on the total volume required for total damage removal. For example, if only 50 gal/ft were required to achieve zero skin effect, then full coverage would obviously become the optimal configuration.

The total volume used in horizontal well treatments is usually limited by practical constraints not directly linked to the acidizing itself, such as pumping time (especially if coiled tubing is used). However, because of the relatively low cost of matrix acidizing compared with the return in terms of a production increase, the highest net present value (NPV, or the difference between revenue from additional production and the treatment cost) is usually obtained when the entire interval is treated, even if this entails large acid volumes (Economides and Frick, 1992).

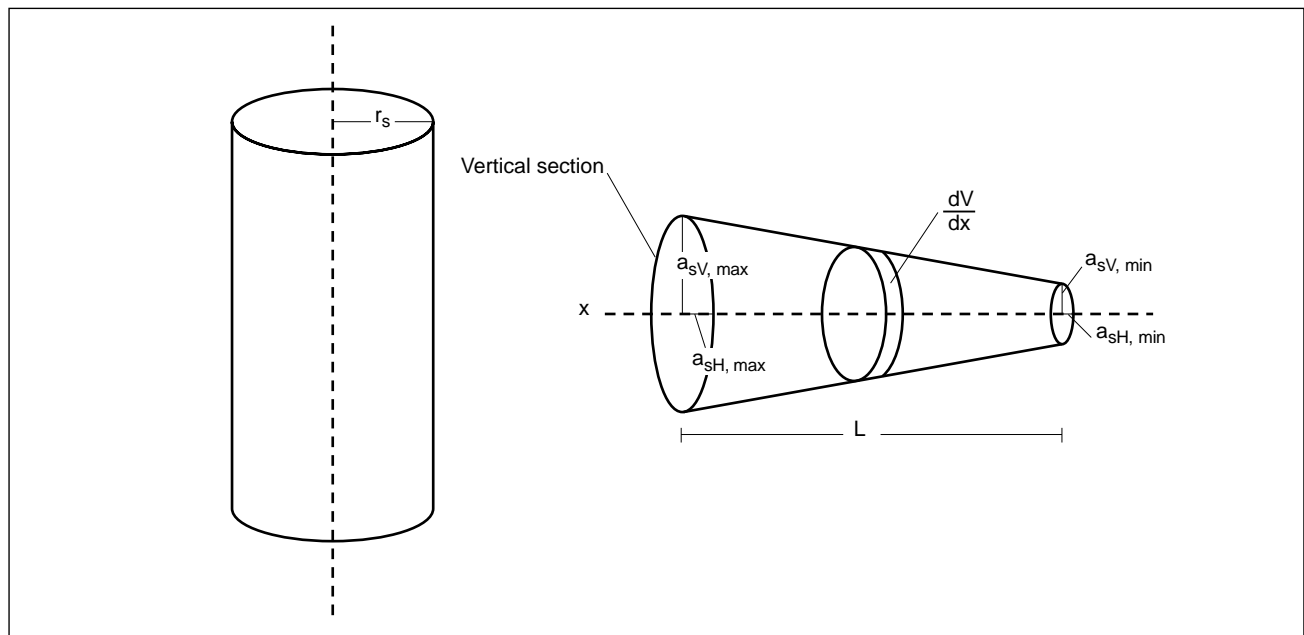


**Figure 19-17.** Cone-shaped damage (Frick and Economides, 1991).  $r_s$  = radius of the damaged section,  $L$  = length,  $a_s$  = axis of the damaged ellipse with the subscripts V and H denoting vertical and horizontal dimensions and min and max denoting minimum and maximum values, respectively.

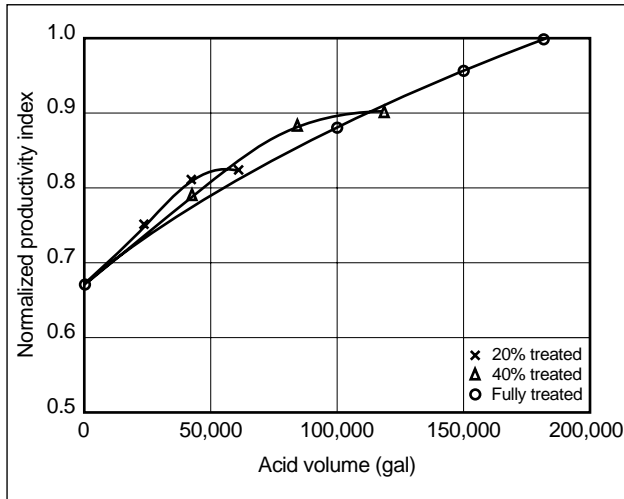


**Figure 19-18.** Normalized productivity index for different fractions of the treated interval (da Motta et al., 1994).

### 19-7.2. Placement techniques

Different placement techniques can be used to treat horizontal wells. As most completions are openhole or with slotted liner, ball sealers are generally not applicable. Furthermore, conventional ball sealers are not recommended in horizontal wells, as seating requires a minimum velocity per perforation.

Most recommended techniques include the use of coiled tubing. A standard practice consists of starting the treatment with coiled tubing at bottomhole, then slowly pulling the coiled tubing out while acid is injected, with the rate of coiled tubing retrieval set according to the desired volumetric coverage (Fig. 19-19). This technique provides contact of the entire interval with the treating fluid. A diverter stage in the form of foam or particulate agents is usually pumped at regular intervals to avoid the formation of thief zones.

Figure 19-20 shows the rate of skin effect reduction with and without the use of coiled tubing as determined by simulation, assuming a 2000-ft horizontal section with an initial skin effect of 6, damage penetration of 1.5 ft and damage consisting solely of clays. Clay dissolution with 12% HCl–3% HF was simulated, and the evolution of skin effect with time calculated from the permeability profile around the wellbore. The injection rate was equal to 1.5 bbl/min, corresponding to a total volume of 100 gal/ft over 52 hr. Without coiled tubing, it was found that only the first half of the interval could be stimulated, whereas coiled tubing provided good coverage accompanied with better skin effect reduction.

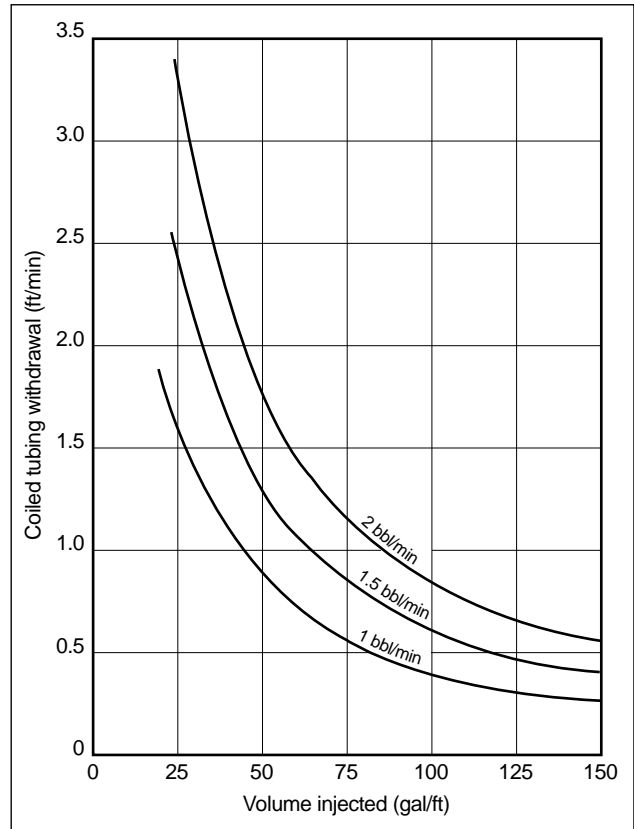


**Figure 19-19.** Coiled tubing withdrawal rate (Economides et al., 1991).

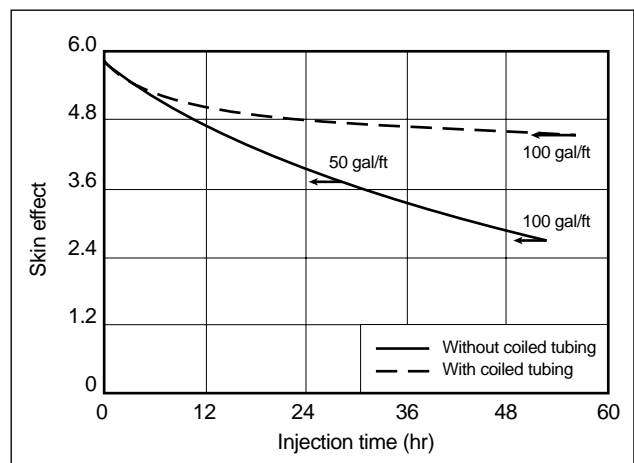


**Figure 19-20.** Skin effect evolution versus time with and without coiled tubing (Economides et al., 1991).

Economides *et al.* (1991) recommended pumping a nonreactive fluid through the annulus between the production tubing and coiled tubing to provide back-pressure and force the treating fluid to enter the reservoir next to or below the coiled tubing end. For a

tapered treatment, the rate of coiled tubing retrieval should be progressively decreased to follow the pattern of damage severity and gradually increase the volumetric coverage.

Tambini (1992) showed that the method developed by Paccaloni for vertical wells can be adapted to horizontal completions, mainly by adding a friction reducer to allow pumping at the maximum rate under fracturing pressure. The technique consists of spotting acid (one-third of the total volume) throughout the entire interval by pumping through coiled tubing only (still starting at total depth and pumping while the coiled tubing is retrieved). Then acid is pumped through both the annulus and coiled tubing at the maximum rate allowed by the surface equipment and reservoir. Good results are reported with this technique for production interval lengths up to 1500 ft. Pressure analysis during the treatment and production logs run on cemented completions indicate that treatment efficiency depends heavily on the injection rate during the bullheading phase, with the best results reported for rates as high as 5 to 6 bbl/min/100 ft in 15-md formations (Fig. 19-21). However, this technique requires additional pumping equipment and therefore can be more costly than other methods. Moreover, in some cases the required rates cannot be achieved because of well and surface equipment limitations. Finally, as mentioned earlier, the method does not provide fluid placement optimization, which is critical for long intervals.

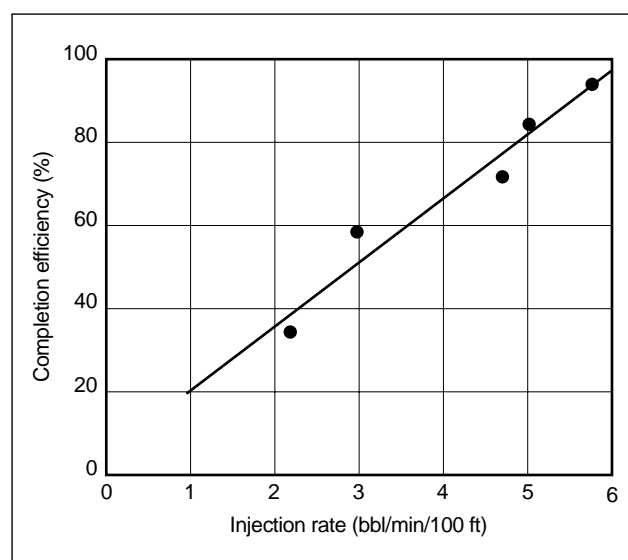


**Figure 19-21.** Completion efficiency versus injection rate (Tambini, 1992).

Coiled tubing can also be used to convey inflatable straddle packers in cased completions or completions including external casing packers. The drawback of this technique is that the interval between packers is limited to 30 ft, which entails many setting and unsetting operations. When zonal segmentation is provided by slotted liner with external packers, each segment (500 ft long on average) must be treated with retrievable packers set opposite to the casing packers to prevent treating fluid migration along the wellbore behind the slotted liner (Milne, 1991).

## 19-8. Conclusions

Pumping strategy is one of the major issues for the success of matrix acidizing. Improving the placement of treating fluids also addresses increasing concerns for environmental protection and cost control.

Four placement techniques are discussed in this chapter: particulate diverter, foam, mechanical tools and ball sealers. The design of particulate diverter or bridging agents requires checking compatibility with the formation and carrying fluids. Particle size must be adapted to the pore-throat distribution of the formation, and the diverter must be soluble in the reservoir fluid to help flowback. Compatibility with the carrying fluid is required to ensure proper dispersion of the particles and prevent dissolution or reaction with other additives.

Foam diversion has been used with success in long intervals. Qualities from 65% to 70% are commonly used. Current practice involves pumping surfactant-laden preflush to saturate high-permeability zones and ensure foam stability in these zones. Better foam durability is obtained if surfactant is added to all stages, even at moderate concentrations. Laboratory tests and computer simulations indicate that better diversion is obtained if moderate pump rates are applied.

Contrary to the other techniques, mechanical tools and ball sealers allow complete shut-off of a portion of the wellbore. Mechanical tools provide the best placement control but require additional equipment and costly operations. Ball sealers are normally limited to a single stage in cased completions and cannot be used for long intervals.

One other technique has emerged for carbonate acidizing: self-diverting acid. This technique is presented in Chapter 17. Field and laboratory data indicate that it is highly effective for plugging high-injectivity streaks created by acid.

The application of coiled tubing in matrix stimulation has improved results, especially for the stimulation of long intervals. Combining most of the placement techniques (i.e., particulate diverter, foam, packers) with the use of coiled tubing increases their efficiency. In long intervals, as in horizontal wells, coiled tubing is run to the well bottom and then withdrawn while pumping acid. Diverter stages are pumped between acid stages. This technique allows spotting acid across the entire interval and minimizes the effect of thief zones.

## Acknowledgments

Some of the material in this chapter was written by L. P. Prouvost and N. Doerler and previously published in second edition of this volume. The authors also thank O. Liétard and R. Thomas for reviewing this chapter.



# Matrix Stimulation Treatment Evaluation

*Carl T. Montgomery, ARCO Exploration and Production Technology*

*Michael J. Economides, University of Houston*

## 20-1. Introduction

As for any stimulation operation, it is important to evaluate the effectiveness of a matrix treatment. In Chapter 12, the methodology of evaluating hydraulic fracturing through pretreatment and post-treatment well tests is outlined. For matrix stimulation, such a comprehensive approach is rarely justified economically. Usually, the effectiveness is gauged by apparent increases in the productivity index, without the benefits of a post-treatment test. Clearly, increases in the productivity (or injectivity) index, although desirable, may not provide an adequate picture of optimum well conditions.

Estimation of the well skin effect and identification of its individual components are covered in Chapter 1. The total skin effect can be determined from a well test, and test analysis is outlined in Chapter 2. Mechanical skin effects (such as from partial completion and inadequate perforations) may often overwhelm the damage skin component. An appropriate production engineering analysis should enable the identification and separation of these skin effects. Only the portion of the skin effect resulting from damage can be removed by a matrix treatment, which should reduce the total skin effect by that amount. Furthermore, to be cost effective, the injected volume and the pumping time should be minimized.

Several attempts have been made to evaluate the effectiveness of a remedial matrix treatment by monitoring evolution of the skin effect in real time. Monitoring to evaluate whether an adequate fluid volume has been injected indicates whether the treatment requires modification and helps to improve future designs in similar situations.

Techniques for real-time monitoring have been introduced by McLeod and Coulter (1969) and Pacaloni (1979a, 1979b) and further augmented by Prouvost and Economides (1987, 1989), Behenna (1994) and Hill and Zhu (1994). They are described in this chapter.

## 20-2. Derivation of bottomhole parameters from wellhead measurements

In many matrix stimulation treatments, wellhead pressures and injection rates are recorded. Ideally, these variables should be measured bottomhole. However, the hostile nature of the stimulation fluids prevents the use of downhole pressure gauges and flowmeters. Thus, bottomhole parameters are often extrapolated from measurements made at the surface by simple mechanical energy balance applications and estimates of the hydrostatic and friction pressure losses. When stimulation fluids are injected through a conduit such as coiled tubing or rigid tubing, measurement of the bottomhole injection pressure can be done in the “backside” (i.e., at the annulus formed between the injection tubing and other well tubulars). Echometers have also been employed to measure the level of backside fluids if the wellhead pressure is below hydrostatic.

## 20-3. Monitoring skin effect evolution during treatment

Different attempts have been made to interpret recorded wellhead pressures (or derived bottomhole pressures) and injection rates in terms of progress of the remedial treatment. Several techniques have been used to derive the evolution of the skin effect from these records.

### 20-3.1. McLeod and Coulter technique

Each stage of injection or shut-in during the treatment is considered a short, individual well test (McLeod and Coulter, 1969). The transient reservoir pressure response to the injection of fluids is analyzed and interpreted to determine the skin effect and the for-

mation transmissibility. This is accomplished using conventional pressure transient analysis methods, namely the solution to the diffusivity equation and the superposition principle (see Chapters 1 and 2.)

Although the results are presented not in terms of skin effect but in terms of the permeability and the radius of the damaged zone (i.e., the short-term nature of the test has a limited radius of investigation), the objective is essentially the same: the skin effect can be related to the properties of the damaged zone. For example, if the well is initially injected at a constant rate, a graph of the pressure response plotted against the logarithm of elapsed time since injection started yields the permeability in both the damaged and undamaged zones and the radial extent of the damaged zone. With a little modification, the same information can be obtained from pressure falloffs when injection stops.

The technique has several drawbacks:

- The analysis of pressure transients is valid only if the skin effect factor does not change while a set of pressure data for one particular interpretation is collected. This is not the case when reactive fluids are injected into the formation to remove damage. Hence, to be correct, this method requires the injection of a slug of inert fluid each time the damage removal is assessed. This is not usually practical.
- No continuous assessment of the evolution of the treatment is possible. Skin effect measurements are allowed only at discrete times during the course of the treatment, usually before and after the treatment. Thus, real-time analysis is not feasible.

### 20-3.2. Paccaloni technique

A second method, presented by Paccaloni (1979a, 1979b), uses instantaneous pressure and rate values to compute the skin effect at any given time during the treatment. This method is based on the equation for steady-state, single-phase, radial and horizontal flow in the reservoir:

$$p_{iw} - p_e = \frac{141.2q_i B \mu}{kh} \left( \ln \frac{r_e}{r_w} + s \right), \quad (20-1)$$

where  $p_{iw}$  is the bottomhole injection pressure,  $p_e$  is the reservoir pressure,  $q_i$  is the injection rate,  $B$  is the formation volume factor,  $\mu$  is the viscosity,  $k$  is the permeability,  $h$  is the reservoir thickness,  $r_e$  is the reservoir radius,  $r_w$  is the wellbore radius, and  $s$  is the skin effect.

Paccaloni (1979a) used an arbitrary constant value for an acid bank radius  $r_b$  and the concept of the effective wellbore radius  $r_w' = r_w e^{-s}$  to transform Eq. 20-1 into

$$p_{iw} - p_e = \frac{141.2q_i B \mu}{kh} \left( \ln \frac{r_b}{r_w'} \right). \quad (20-2)$$

Assuming that the permeability-thickness product  $kh$  of the reservoir is known, the bottomhole pressures, corresponding to the injection rate, can be predicted for any value of the skin effect. The wellhead injection pressures are then derived from the bottomhole pressures, and at any time, a match of the measured wellhead pressures with the ones corresponding to different values of the skin effect yields the actual skin effect at that time.

Paccaloni used the concept of a damage ratio  $DR$ , which is simply the rewriting of Eq. 20-1 under ideal ( $s = 0$ ) and real ( $s \neq 0$ ) conditions, and obtained the ratio of the productivity indices:

$$DR = \frac{J_{ideal}}{J_{real}} = \frac{\ln(r_e/r_w) + s}{\ln(r_e/r_w)}. \quad (20-3)$$

- Example application of the Paccaloni method

Figure 20-1 depicts a series of damage ratio curves for a range of injection rates and calculated wellhead pressures. Table 20-1 lists the well and reservoir variables used for this construction.

The Paccaloni method (1979a, 1979b) implies that as acid is injected, superimposition of the measured wellhead pressure on the graph indicates the progress of the stimulation. This is shown by the dashed line on the figure.

Among the assumptions listed in the Paccaloni method, the “steady-state” assumption is one that may cause problems and, potentially, errors.

Although a steady-state relationship is assumed, transient behavior is in effect for a time duration far exceeding the injection test. For a radial reservoir, for example, the time to a pseudosteady-state condition is

$$t_{pss} \approx \frac{1000 \phi \mu c_t r_e^2}{k}, \quad (20-4)$$

where  $c_t$  is the total compressibility. For a typical oil reservoir (e.g.,  $\phi = 0.25$ ,  $\mu = 1$  cp,  $c_t = 5$  psi<sup>-1</sup>,  $k = 50$  md and 80-acre spacing or  $r_e \approx 1000$  ft), the time to pseudosteady state (which may be perceived as a succession of steady states) is more than 50 hr, which is significantly longer than the normal pumping times for a typical matrix acidizing job.

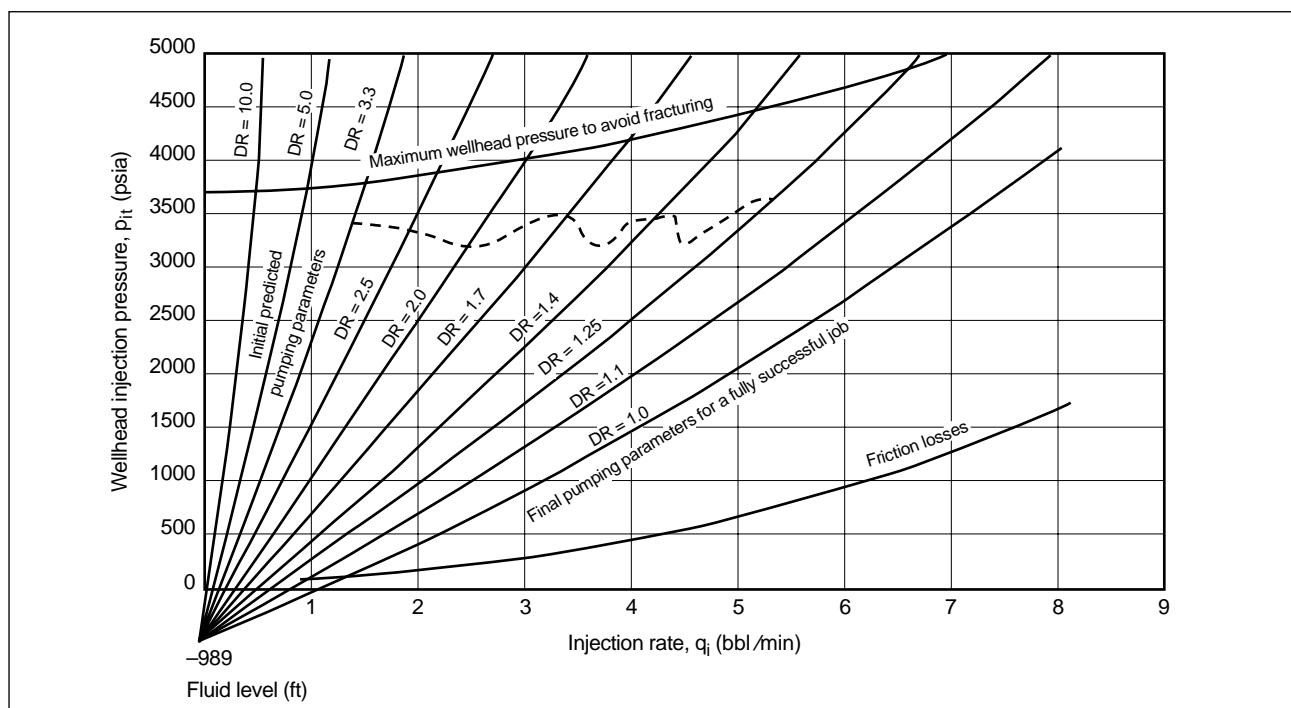


**Figure 20-1.** Job control chart with the damage ratio DR plotted as a parameter. The measured injection rates and injection pressures are recorded on the chart (Pacaloni, 1979b).

**Table 20-1. Well and fluid data used for Fig. 20-1 (Pacaloni, 1979a).**

Depth, $H$	13,540 ft
Density, $\rho$	8.9 lbm/gal [66.6 lbm/ft <sup>3</sup> ]
Viscosity, $\mu$	0.7 cp
Reservoir pressure, $p_e$	5805 psi
Hydrostatic pressure drop, $\Delta p_h$	6262 psi
Reservoir thickness, $h$	30 ft
Permeability, $k$	35 md
Wellbore radius, $r_w$	0.25 ft
Reservoir radius, $r_e$	800 ft
Tubing 1 ID	2.992 in.
Tubing 1 length	12,750 ft
Tubing 2 ID	2.441 in.
Tubing 2 length	750 ft
Acid bank radius, $r_b$	4 ft

Figure 20-2 is a graph comparing bottomhole pressure evolution using steady-state and transient models. The simulations were generated for  $q_i = 0.5$  bbl/min,  $kh = 1000$  md-ft,  $\phi = 0.2$ ,  $c_t = 1.5 \times 10^{-5}$  psi<sup>-1</sup> and  $r_w = 0.35$  ft. The initial skin effect is equal to 10. For the Pacaloni (1979b) method,  $r_b = 3$  ft

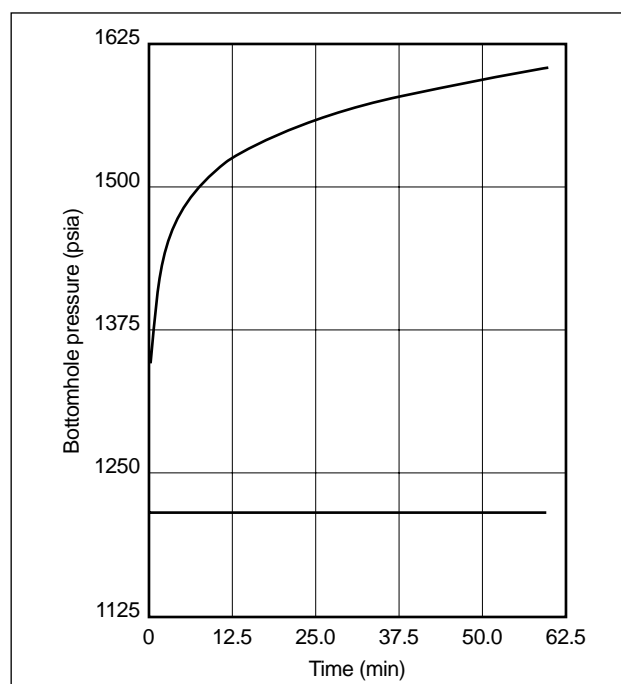


**Figure 20-2.** Comparison of calculated steady-state and transient bottomhole pressure responses.

was used. It is obvious that the bottomhole transient pressure evolution could lead to errors. The pressure departure between the two curves in Fig. 20-2 could

be identified as the result of an additional skin effect where such a skin effect does not exist. For the example in Fig. 20-2, after about 1 hr of injection and a pressure departure  $\Delta p_{\text{departure}}$  equal to 400 psi, this additional false skin effect is equal to

$$\Delta s = \frac{kh\Delta p_{\text{departure}}}{141.2q_i B \mu}, \quad (20-5)$$

a value equal to approximately 4. The practical implication is that more acid may be employed to eradicate this seemingly present skin effect when, in fact, the pressure difference is due to easily explainable transient phenomena.

## 20-4. Prouvost and Economides method

A technique presented by Prouvost and Economides (1987, 1989) enables continuous calculation of the skin effect factor during the course of the treatment and accounts for transient response. The technique is based on a continuous comparison of measured and simulated pressures. The diminishing difference is attributed to the diminishing skin effect. A good reservoir description is presumed, including the type of model and well and reservoir variables. Section 20-4.2 presents an associated methodology to obtain unknown variables just prior to the treatment.

### 20-4.1. Deriving skin effect during treatment

The Prouvost and Economides (1987, 1989) method simulates the reservoir pressure response to the injection of fluids using the sequence of flow rates measured during job execution. Each simulation is performed with a constant skin effect  $s_o$ .

At any time, the difference between the simulated pressure response  $p_{\text{sim}}(t, s_o)$  and the measured value  $p_{\text{meas}}(t)$  is interpreted as the result of the difference between the actual skin effect value and the value used for the simulation ( $s_o$ ). The latter can be zero or some other finite value for a known nondamage skin effect.

Because all other effects that influence the pressure response are accounted for in the simulation, the difference between the simulated and actual pressure responses is attributed to the changing skin effect:

$$s(t) = s_o + \frac{kh}{141.2q(t)B(t)\mu(t)} [p_{\text{meas}}(t) - p_{\text{sim}}(t, s_o)], \quad (20-6)$$

where  $s(t)$  is the skin effect at time  $t$ , and  $q(t)$ ,  $B(t)$  and  $\mu(t)$  are the injection rate, formation volume factor and viscosity of each slug at time  $t$ , respectively.

The method can be executed in real time. The “measured” bottomhole pressure can be calculated from measured wellhead values as shown earlier. Hence, a skin effect evolution with time can be obtained using Eq. 20-6.

### 20-4.2. Determining reservoir characteristics before treatment

Simulation of the pressure response, described in the previous section, requires a good knowledge of the reservoir and the initial value of the skin effect. Even if a well test was performed on the well earlier, the following procedures are recommended to alleviate any changes brought about by time. They apply mainly to oil producers and water injectors and are based on an injection/falloff test, in which native reservoir fluids in the wellbore are displaced and injected into the formation. There are three steps:

1. The reservoir fluid contained in the tubular string before treatment is partly or totally displaced into the reservoir at a matrix rate (i.e., at a rate that no fracture is initiated in the reservoir). To save pumping time, this fluid can be displaced by the first treating fluid.
2. The injection is stopped before any foreign fluid is injected into the formation. The evolution of pressure with time during this period is recorded typically for a duration of 1 hr, depending on the reservoir parameters, until valuable information on the reservoir can be obtained using the appropriate pressure testing methods extensively described in the literature and Chapter 2.
3. Analysis of the pressure falloff data yields a model of reservoir behavior and the associated well and reservoir variables, such as the permeability-thickness product and especially the initial value of the skin effect.

In the case of layered reservoirs and the absence of more detailed downhole measurements, this technique results only in an averaged skin effect factor. Nevertheless, this remains a valuable piece of information, because variation in the average skin effect during treatment can be interpreted as the progress of damage removal by the stimulation fluid. For example, flat-

tening of the  $s$  versus  $t$  curve at a nonzero level could indicate poor fluid placement (or, of course, complete damage removal in a single zone). Knowledge of the type of behavior and parameters enables computing the pressure response at the wellbore to any injection history, as described in Section 20-4.1.

The technique can be generalized by varying the injection rate instead of just stopping the injection, as described in the second step of the procedure. Although it can introduce some error from computation of the friction pressure drop, this modified procedure is of interest for depleted reservoirs (i.e., when reservoir pressure is not sufficient to balance the head of a column of fluid up to the surface).

An example calculation of the Prouvost and Economides method is presented in Sidebar 20A.

## 20-5. Behenna method

A technique that extends the Prouvost and Economides (1987, 1989) approach was provided by Behenna (1994). He accounted for the effects of diverting agents by subtracting the pressure drop created by the diverting agent from the bottomhole pressure used in the skin effect calculation. The pseudoskin effect caused by the placement of diverting agent slugs corrects the observed pressure response by an amount equal to the pressure increase caused by the diverter placement. Figure 20-3 from Behenna's paper shows an example application. An assumption made with this technique is that all subsequent response is due to removal of damage and not inadvertent removal of diverter.

A second extension that the Behenna method offers is use of the derivative of the skin effect with time as a diagnostic aid. The derivative plot accentuates peri-

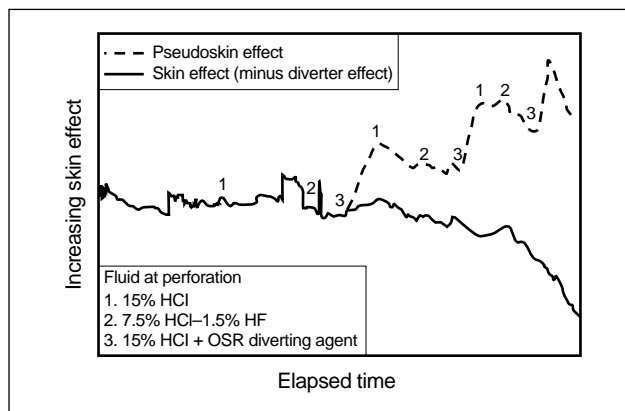


**Figure 20-3.** Skin effect evolution with diverters (Behenna, 1994). OSR = oil-soluble resin.

ods of rapidly changing skin effect and has the effect of smoothing the effects of noisy data. The slope of the derivative is useful in quantifying the rate at which formation damage is removed. The steeper the slope, the faster the rate of change.

## 20-6. Inverse injectivity diagnostic plot

Hill and Zhu (1994) proposed a technique that is as simple to use as the Paccaloni (1979a, 1979b) method and also takes into account the effects of transient flow as suggested by Prouvost and Economides (1987, 1989). The method utilizes an expression derived from transient analysis methods extensively described in the literature (Earlougher, 1977):

$$\frac{p_i - p_{wf}}{q_N} = m' \sum_{j=1}^N \left[ \frac{(q_j - q_{j-1})}{q_N} \log(t - t_{j-1}) \right] + b', \quad (20-7)$$

where  $p_i$  is the initial reservoir pressure,  $p_{wf}$  is the bottomhole flowing pressure, and

$$m' = \frac{162.6 B \mu}{k h} \quad (20-8)$$

$$b' = m' \left[ \log \left( \frac{k}{\phi \mu c_i r_w^2} \right) - 3.23 + 0.87 s \right]. \quad (20-9)$$

From Eq. 20-7, a plot is made of inverse injectivity versus the superposition time function  $\Delta t_{sup}$ , which is defined as

$$\Delta t_{sup} = \sum_{j=1}^N \frac{(q_j - q_{j-1})}{q_N} \log(t - t_{j-1}). \quad (20-10)$$

With all parameters remaining constant, a straight line with a slope  $m'$  and intercept  $b'$  can be produced. To utilize the technique, a series of straight lines with different skin effects at varying rates and times is produced before treatment.

An example application of the Hill and Zhu method is presented in Sidebar 20B.

## 20-7. Limitations of matrix treatment evaluation techniques

Coupling the calculated bottomhole pressure (based on measured variables) and the anticipated reservoir response leads to calculation of the reservoir response.

## 20A. Example calculation of the Prouvost and Economides method

In the injection profile in Fig. 20A-1 the rate was maintained at approximately 1 bbl/min and then dropped to 0.25 bbl/min after approximately 1.5 hr of injection. The “measured” bottomhole pressure that appears as the top curve in Fig. 20A-2 is based on the recorded wellhead pressures and the calculated bottomhole pressures using the procedure outlined in Section 20-2.

Underneath this curve is the simulated expected pressure response, using the injection profile of Fig. 20A-1 as an input and a skin effect equal to zero. For this well, the permeability-thickness product  $kh = -5000$  md-ft, the wellbore storage constant  $C = 2.6 \times 10^{-3}$  bbl/psi, and the porosity  $\phi = 0.22$ . As usual, both the formation volume factor  $B$  and the viscosity  $\mu$  are taken as equal to unity (water). As outlined earlier, the Prouvost and Economides (1987, 1989) method attributes the departure between the two curves in Fig. 20A-2 to the skin effect. As can be seen, the departure diminishes as injection progresses, and in spite of the reduced rate, after 1.5 hr the two curves coincide and show the effectiveness of the job.

The associated skin effect evolution is shown in Fig. 20A-3. The bottom curve is the predicted skin effect using the Prouvost and Economides technique. The initial value is provided by the injection/falloff test described in Section 20-4.2. The skin effect reduces smoothly during the acid injection and approaches a zero value after approximately 2 hr of operation. Above this curve is the skin effect calculated by the Paccaloni (1979a, 1979b) technique. A continuous overestimation is shown, as explained earlier. This is due to the misidentification of a certain amount of pressure transients as caused by an additional skin effect.

An interesting observation is what happens when the flow rate is reduced. The steady-state relationship of the Paccaloni method requires an analogous reduction in the pressure drop. Because this effect is not forthcoming, a substantial increase (usually unrealistic) in the calculated skin effect is obtained. Such an increase is easy to surmise from Eq. 20-5 and is shown graphically in Fig. 20A-3.

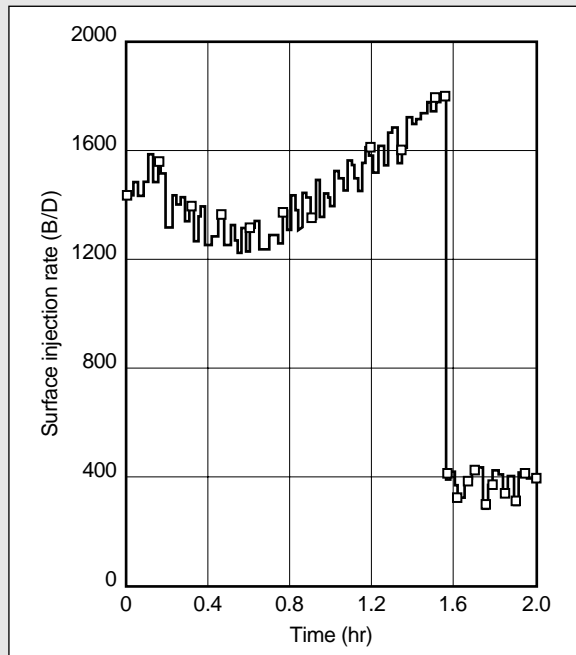


Figure 20A-1. Example injection rate profile.

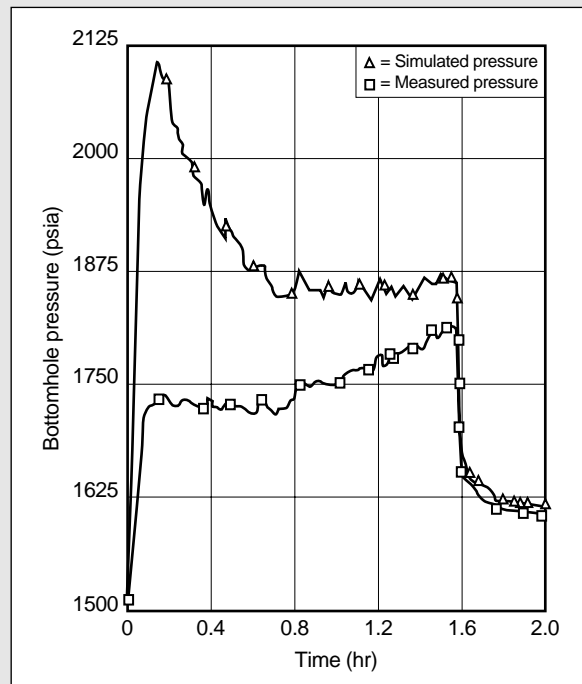


Figure 20A-2. Calculated bottomhole pressure (based on measured well pressure) and simulated pressure response with zero skin effect.

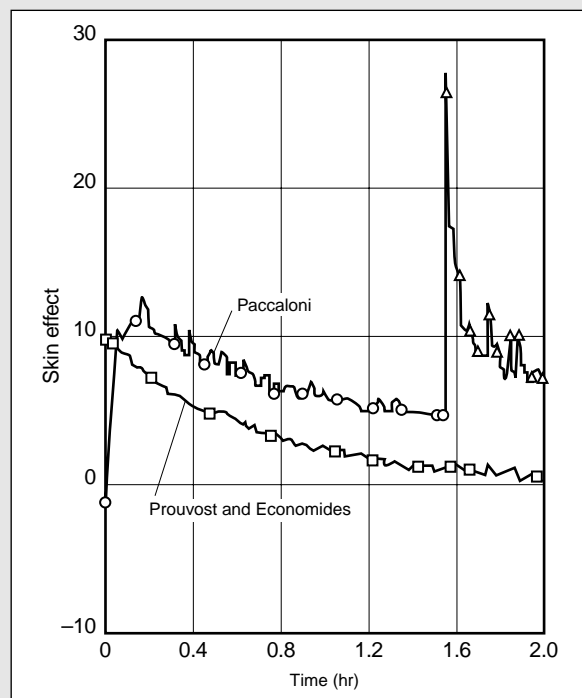
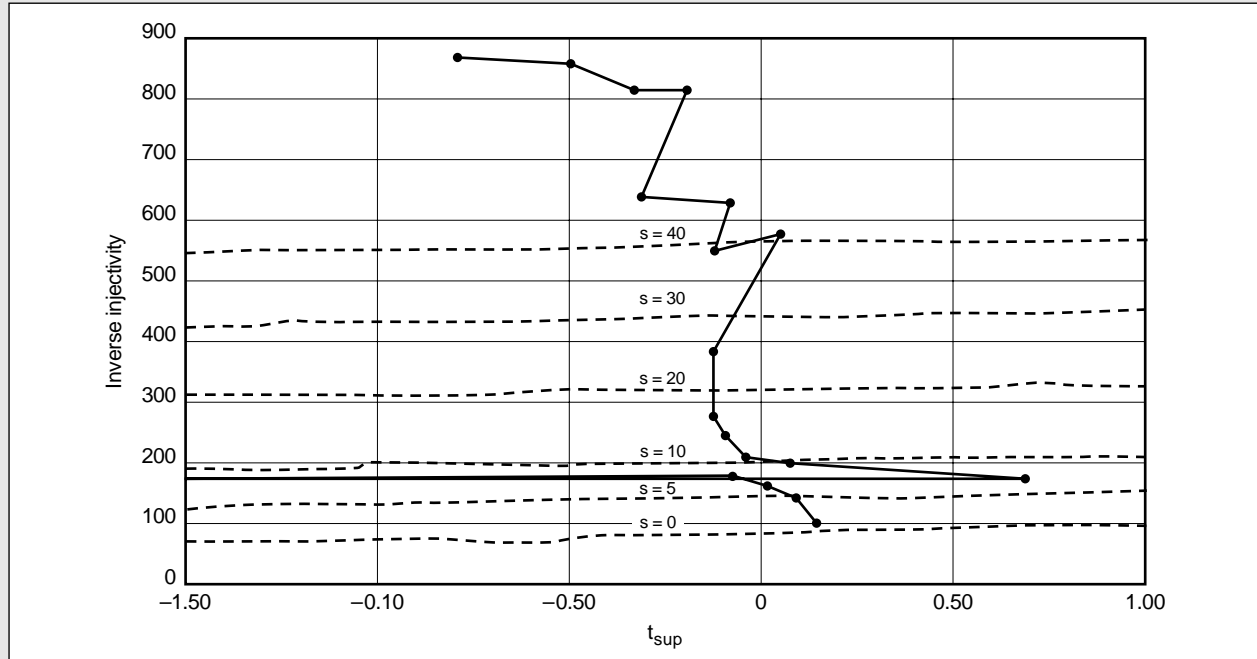


Figure 20A-3. Example skin effect evolution calculation.

## 20B. Example application of the Hill and Zhu method

An example of the Hill and Zhu (1994) method is shown in Fig. 20B-1 from the data in Tables 20B-1 and 20B-2 (Prouvost and Economides, 1989). As the skin effect changes during an acid treatment,  $\Delta p/q_i$  shifts from one line to another. The changing skin effect is monitored by comparing  $\Delta p/q_i$  versus the  $\Delta t_{sup}$  response. As with the Paccaloni (1979a, 1979b) technique, this job control graph is used in the field to monitor job performance. The advantage of this technique in comparison with the Paccaloni technique is that it includes transient effects caused by injection rate changes.



**Figure 20B-1.** Inverse injectivity plot using the Hill and Zhu (1994) technique and data from Tables 20B-1 and 20B-2.

**Table 20B-1. Well parameters used in example application of the Hill and Zhu (1994) method (Prouvost and Economides, 1989).**

Parameter	Value
$k$	80 md
$h$	253 ft
$\mu$	1 cp
$r_w$	0.51 ft
$\phi$	0.2
$B$	1.2 RB/STB
$c_t$	$10^{-5}$ psi $^{-1}$
$p_i$	2750 psi
$q_i$	2 bbl/min
$s_o$	40

**Table 20B-2. Injection data for example application of the Hill and Zhu (1994) method (Prouvost and Economides, 1989).**

Stage	Fluid	Time (hr)	Time (min)	$q_i$ (bbl/min)	$p_{it}$ (psi)
1	Water	0.15	9	2	4500
2	Water	0.3	18	2	4480
3	Water	0.45	27	2	4400
4	Xylene	0.6	36	2	4390
5	Xylene	0.75	45	2.5	4350
6	Xylene	0.9	54	2.4	4270
7	Xylene	1.05	63	2.7	4250
8	15% HCl	1.2	72	2.5	4200
9	15% HCl	1.35	81	3.2	3970
10	3% HCl-12% HF	1.5	90	3.7	3800
11	3% HCl-12% HF	1.65	99	4.1	3750
12	3% HCl-12% HF	1.8	108	4.4	3670
13	3% HCl-12% HF	1.9	114	4.2	3600
14	3% HCl-12% HF	2.1	126	0.9	2900
15	3% HCl-12% HF	2.25	135	5.6	3730
16	3% HCl-12% HF	2.4	144	5.6	3750
17	3% HCl-12% HF	2.55	153	5.6	3650
18	3% HCl-12% HF	2.7	162	5.7	3600
19	3% HCl-12% HF	2.85	171	5.8	3400

However, removal of damage by the stimulation fluid is not the only reason why the bottomhole pressure evolves during the course of a matrix stimulation treatment. It is important that the engineer is aware of the different components that can affect the reservoir pressure response.

- Reservoir response to changing injection rate

When fluid is injected at a constant rate into the reservoir, a pressure transient response develops that at early injection times is dominated by well-bore storage and skin effects. Later, the infinite-acting radial flow regime prevails, and usually for long injection times the effects of the outer reservoir boundaries are not felt. The same series of flow patterns develops when the rate is varied, and the overall response is obtained through the superposition principle. This is described in detail by Earlougher (1977).

- Different viscosities of the various treating fluids

During a typical stimulation treatment, several different fluids are pumped in sequence. Because these fluids have different rheologies and viscosities at reservoir conditions, the pressure response is affected.

- Temporary skin effects created by diverters or ball sealers

When a diversion technique is used, with either chemical diverters or ball sealers, a temporary skin effect is created that reduces the well injectivity and then affects the pressure evolution. Computation of the pseudoskin effect created by diverter cakes is detailed in Section 20-5.

- Other effects

Other effects can obscure the pressure response:

- Two-phase flow can occur when water-base fluid is injected into an oil or gas reservoir. The reduced mobility of the injected foreign fluid can complicate the pressure response.
- The reservoir can be multilayered with commingled flow, or it can be fissured. In the latter case, the fissures may be opened by injection.
- In carbonate reservoirs, the pressure response may be related to reaction kinetics.

- Removal of damage by reactive fluids

As a result of the stimulation and damage removal, the skin effect from damage should decrease during the course of the treatment. This is the component

of the pressure response that should be isolated for a proper evaluation of the stimulation treatment.

Compared with this physical analysis, some of the techniques presented in this chapter pose additional limitations:

- The McLeod and Coulter (1969) method properly acknowledges the importance of transient reservoir pressure response, but it fails to provide a continuous, real-time measurement of the skin effect. It implicitly assumes that while one measurement is taken the evolution of the skin effect is frozen.
- Although the Paccaloni (1979a, 1979b) method enables continuous, real-time measurement of the skin effect for the duration of the treatment, it is limited by not properly accounting for transient phenomena. As a result, all transient phenomena occurring in the reservoir are interpreted as changes in the skin effect.

## 20-8. Treatment response diagnosis

Montgomery *et al.* (1995) described techniques that can be used during a treatment to provide several levels of diagnostics and interpretation. Figure 20-4 provides an overall schematic of how these diagnostics can be used. An example determination of a well stimulation candidate is provided in Sidebar 20C.

- Well diagnostics

To determine if a well is a candidate for stimulation, a step rate or injectivity test is performed. A nonreactive fluid that is compatible with the formation is injected at various subfracturing rates, with the rate and pressure response carefully monitored. At a constant rate and pressure, a skin effect value can be calculated. When a new constant rate and pressure are achieved, a new skin effect is calculated. At the various rates and pressures the calculated skin effect value should be constant. If a shift is noted in the skin effect value, a new assumption for  $kh$  should be used until a constant value of skin effect is achieved. Although the calculated skin effect is an apparent skin effect, the test gives an indication of  $kh$  and the skin effect. If the value of the skin effect is zero or less, the need for stimulation should be questioned. An analytical technique for the analysis of this type of step rate test is provided in Earlougher (1977).



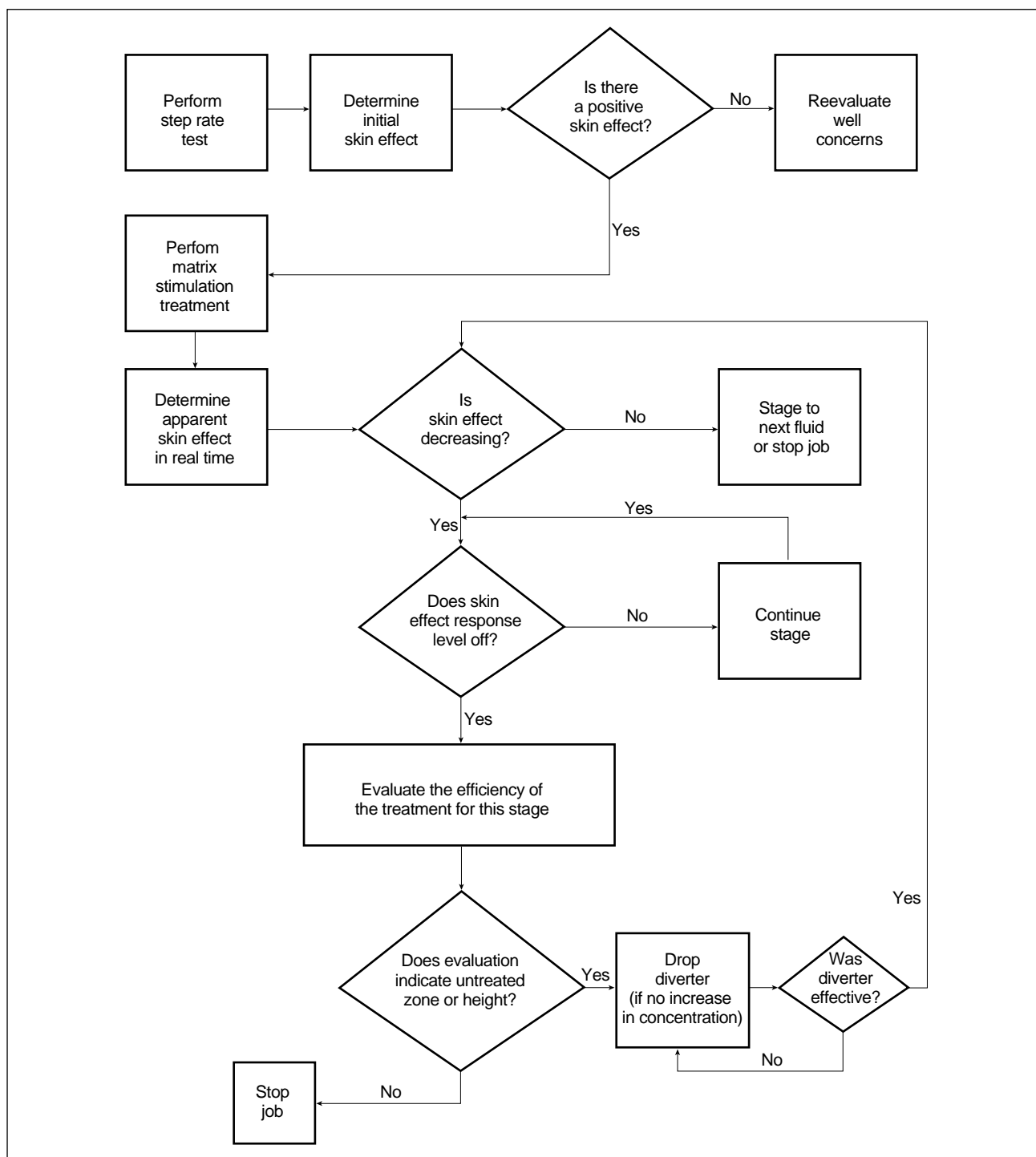


**Figure 20-4.** Job treatment diagnosis.

## 20C. Production indications for matrix stimulation requirements

For this example, the well is in a two-phase reservoir with  $k = 50$  md,  $h = 70$  ft,  $B = 1.1$  RB/STB,  $\mu = 0.8$  cp,  $r_w = 0.328$  ft and  $\bar{p} = 4700$  psi. The drainage radius  $r_e$  is unknown but presumed to be at least 750 ft. A well test 6 months ago suggested zero skin effect. The original inflow performance relationship (IPR) curve (using Eq. 1-17) and the vertical lift performance (VLP) curve are drawn with solid lines on Fig. 20C-1. The original production rate was more than 6600 STB/D, but 6 months later dropped to less than 5150 STB/D. The question is whether this well is a stimulation candidate.

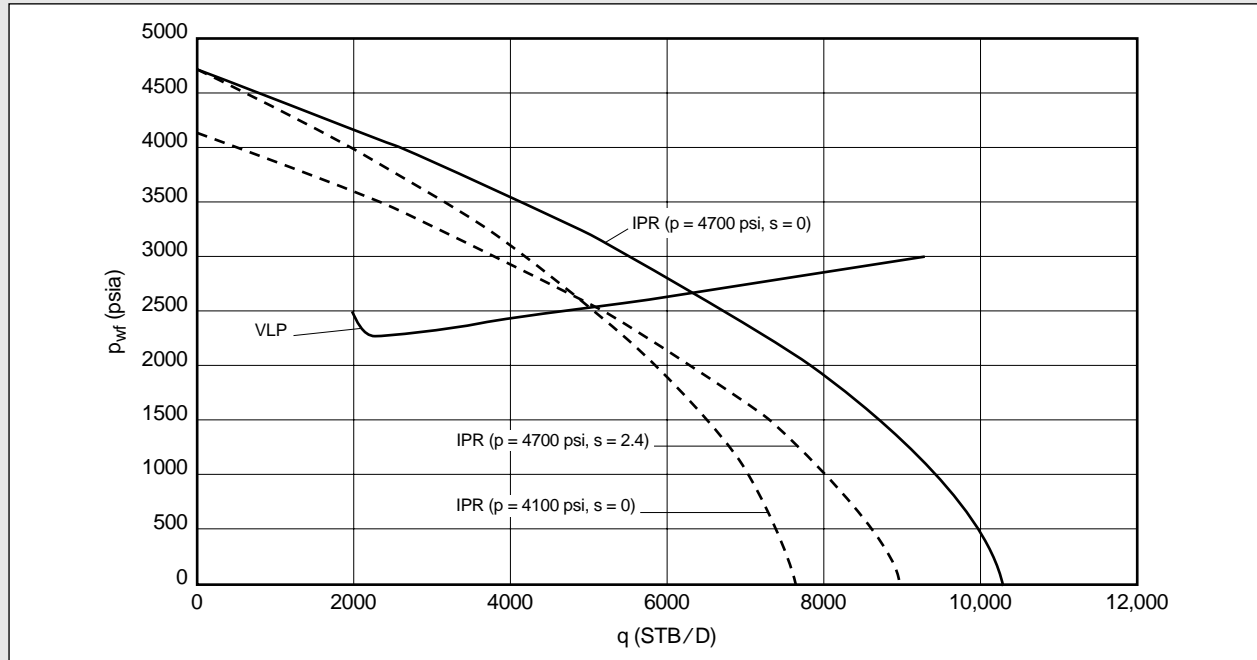


Figure 20C-1. Deliverability of the producing system.

### Solution

From the VLP curve, the flowing bottomhole pressure should be about 2550 psi (for  $q = 5150$  STB/D). Assuming that the average reservoir pressure remains approximately equal to 4700 psi, then from Eq. 1-17 a skin effect equal to 2.4, represented by one of the dashed IPR curves on Fig. 20C-1, would result in this production performance. However, the same performance can be observed with zero skin effect but with the reservoir pressure declining to about 4100 psi. This is shown by the second dashed IPR curve in Fig. 20C-1. Clearly, this example shows the necessity of well management and testing for the appropriate production engineering decision (i.e., deciding whether the well is damaged and requires stimulation or whether the well drainage area is limited).

### • Treatment optimization

The shape and period of the treatment response curve provide a number of clues about the treatment. Figure 20-5 is an acidizing response curve from a water injection well (Montgomery *et al.*, 1995). The relevant parameters used to interpret this curve are  $\phi = 22\%$ ,  $h = 33$  ft (from a step rate interpretation), average flow rate  $q_{ave} = 1.2$  bbl/min and  $r_w = 0.178$  ft.

From this plot the following conclusions can be drawn:

- Damage mechanism—The damage is clearly removable by hydrochloric acid (HCl). Mud acid does not have an effect. Carbonate scale or iron oxide damage are the most plausible.

- Treatment volume—Most of the damage was removed by the first one-third of the HCl pumped. This is in the time period from 27 to 60 min. The volume used to remove this damage is  $33 \text{ min} \times 1.2 \text{ bbl/min} \approx 40 \text{ bbl}$ . Using the 33-ft height determined from a step rate test, the damage was removed by a treatment of approximately 50 gal/ft.
- Damage radius—Using a porosity equal to 0.22, the radius of formation damage  $r_s$  is 3.26 ft. This ignores residual water saturation and assumes that 100% of the pore volume is displaced.
- Treatment improvement—On the basis of post-treatment spinner surveys, it was determined that only about one-third of the 100-ft perforated interval was treated. To improve effectiveness,

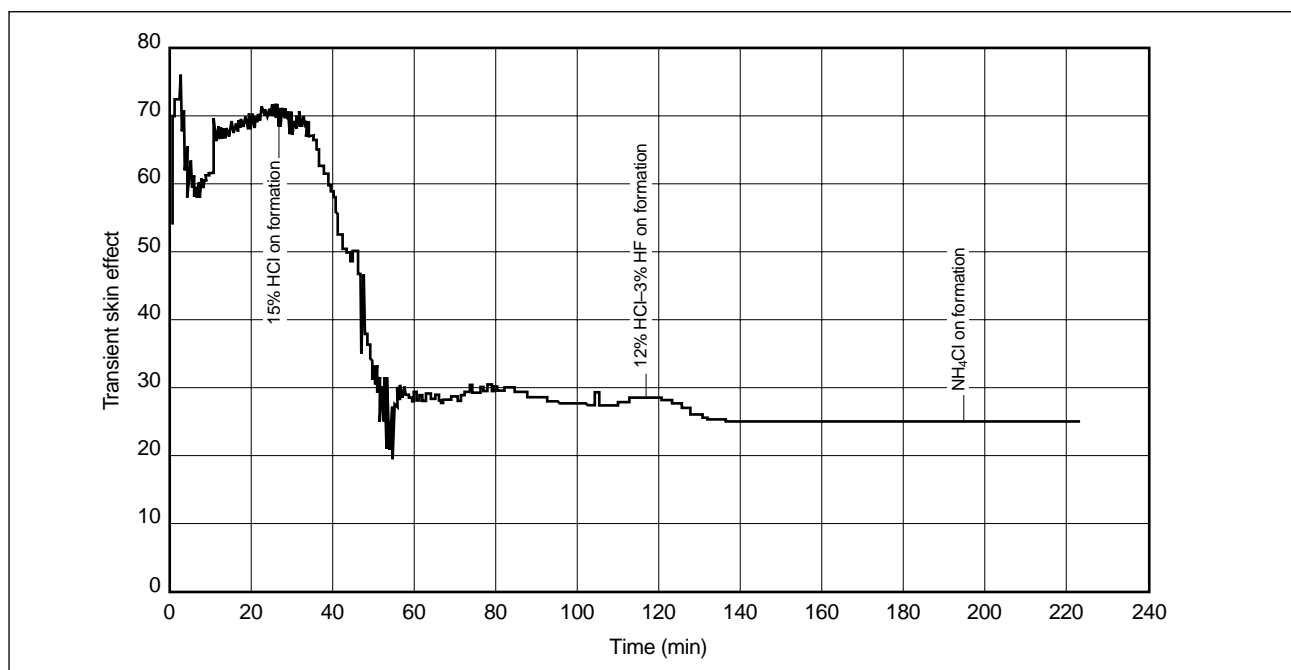


**Figure 20-5.** Example matrix acid treatment response curve (Montgomery et al., 1995).

the use of a diverter is warranted. In addition, the use of hydrofluoric acid (HF) in this well only increases the cost of the treatment, without any measurable stimulation benefit.

## 20-9. Post-treatment evaluation

Several other techniques are available to evaluate the effectiveness of matrix stimulation treatments. In addition to the techniques described in this section, pre- and postbuildup tests and production logging techniques as described in Chapters 1 and 2 can be used to evaluate acid treatments. It should always be remembered that the primary criterion for a treatment is the economic rather than the technical success.

### 20-9.1. Return fluid analysis

Almond *et al.* (1990) showed that monitoring the ionic content of returned fluids following acidizing treatments can provide insight into the actual chemical acid-spending processes downhole. The mass balance of the injected and returned fluids and the relative percent of silicate reprecipitation allow the determination of relative spending levels of various acids on the formation and well scale. Table 20-2 is an example of the results

that can be extracted from this type of analysis. The table shows the concentration of aluminum and silicon contained in the returned fluids from two wells in the same formation. Comparison of the actual Si and Al concentrations with the theoretical Si and Al concentrations expected from the volume percent of HF indicates that severe secondary clay reaction precipitation occurred. Much less Si and Al were observed in the return samples than expected from the mass-balance equations. On the basis of the tertiary reaction kinetic work of Gdanski (1996) as described in Chapter 15, future jobs should be conducted with higher HCl to HF ratios than the 6.5–0.5 used for these treatments to minimize secondary precipitation problems.

### 20-9.2. Tracer surveys

The use of various radioactive tracers placed strategically in the fluid or with the diverter can provide insight on the effectiveness of matrix treatments. Figure 20-6 shows a log for two treatments placed in the same well. The treatments were into a limestone formation perforated at 4 shots per foot (spf) at a depth of 6902 to 6982 ft. The first treatment was a 6000-gal, three-stage treatment (2000 gal/stage) diverted with rock salt and pumped at a rate of 7 bbl/min. The acid was traced with liquid <sup>46</sup>scandium. The first 1000-lbm rock salt diverter

**Table 20-2. Example acid flowback analysis showing aluminum and silicon concentrations in returned fluids (from Almond *et al.*, 1990).**

Well	HF (%)	Flowback Concentration (mg/L)		Theoretical Concentration (mg/L)		Si:Al
		Si	Al	Si	Al	
1	16.5	216	2560	1311	15,543	0.08:1
1	12.1	190	1700	1573	14,070	0.11:1
1	7.5	142	990	1903	13,270	0.14:1
1	3.7	112	312	3060	8,525	0.35:1
1	2.5	102	117	4064	4,661	0.84:1
1	0.4	39	6	9512	1,415	6.5:1
2	7.1	162	675	2270	9,450	0.23:1
2	18.5	60	3810	325	20,630	0.015:1

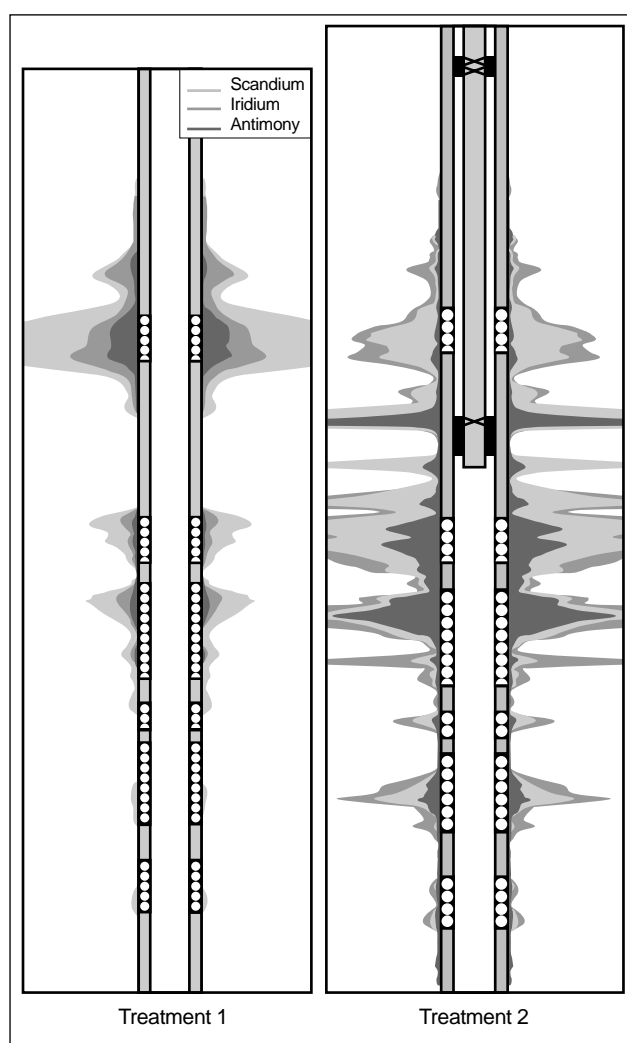


**Figure 20-6.** Tracer scan comparison of two matrix acid treatments on the same well treatment (courtesy of ProTechnic International, Inc.).

stage was tagged with  $^{192}\text{Ir}$ , and the second 1000 lbm of rock salt was tagged with  $^{124}\text{Sb}$ . The log indicates that the diverter stages were ineffective and that the thief zone at the top took the majority of the treatment.

A second three-stage treatment was attempted in which 4500 gal of acid was staged (1000, 1000 and 1500 gal/stage) by placing rock salt between the stages. In the second treatment the upper thief zone was isolated mechanically by placing tubing and a packer at 6886 ft. The first 1000 gal of acid was traced with  $^{192}\text{Ir}$ , the second 1000 gal with  $^{46}\text{Sc}$  and the third 1500 gal with  $^{124}\text{Sb}$ . In this case, much better placement of the acid was achieved, indicating that mechanical isolation was much more effective than chemical diversion. The scan also indicates that the rock salt dropped at the end of the second stage was effective in diverting into a lower zone. It would also appear that there was some transfer of acid around the packer into the upper zone. Explanations for this are a poor cement job, poor packer efficiency or a fractured formation. The postproduction curves for the second treatment are shown in Fig. 20-7.

## 20-10. Conclusions

Methods to assess the effectiveness of matrix stimulation treatments have been sought over the years. The low overall cost and “low technology” of these treatments usually preclude the justification of comprehensive pretreatment and post-treatment well tests.

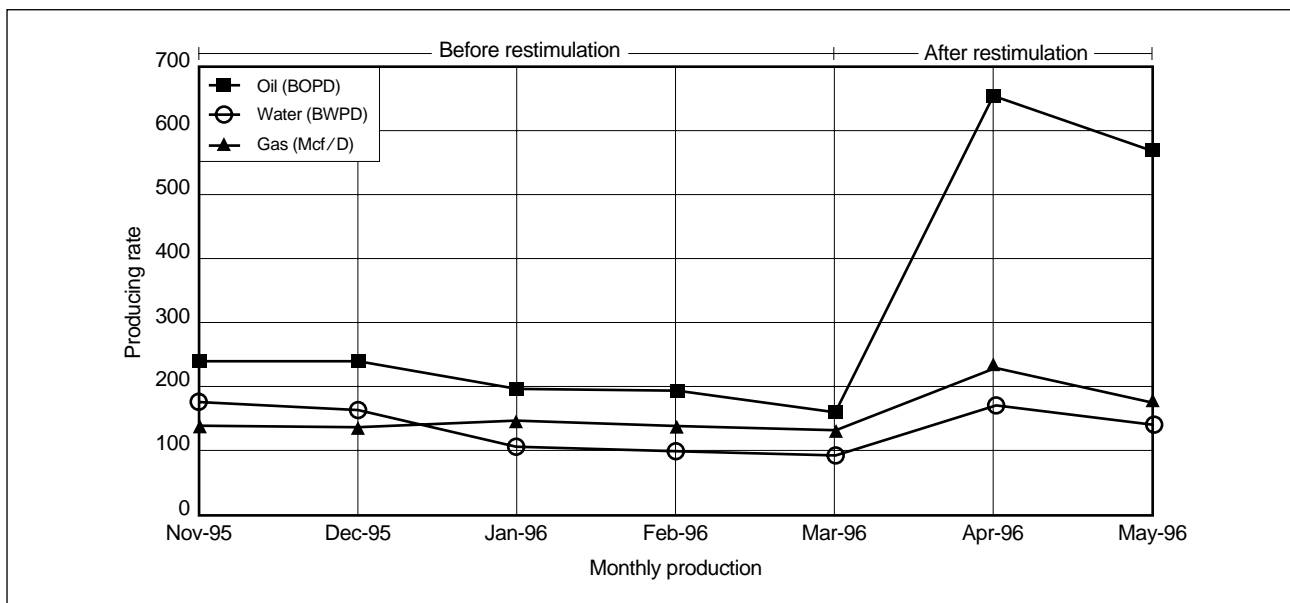


**Figure 20-7.** Results of the second treatment based on use of tracers to evaluate the effectiveness of the primary acid treatment (courtesy of ProTechnic International, Inc.).

Several real-time skin effect evolution techniques are presented in this chapter. The recent ones enable definitive calculation of the initial value of the skin effect and its evolution during injection, taking into account pressure transients and appropriate reservoir models. The efficiency of the stimulation treatment may then be assessed in real time. Changes in the design and optimum termination of the injection are therefore possible.

Several techniques for evaluating the effectiveness of matrix stimulation treatments are also presented. These include the use of pre- and postbuildup tests, production logging, tracer scans, fluid flowback analysis and comparison of inflow performance relationship (IPR) curves.

# References

## Chapters 1–12

Abass, H., Meadows, D., Brumley, J. and Venditto, J.: “Oriented Perforations—A Rock Mechanics View,” paper SPE 28555, presented at the SPE Annual Technical Conference and Exhibition, New Orleans, Louisiana, USA (September 25–28, 1994).

Abass, H.H., Saeed, H. and Meadows, D.L.: “Non-planar Fracture Propagation from a Horizontal Wellbore: Experimental Study,” paper SPE 24823, presented at the SPE Annual Technical Conference and Exhibition, Washington, D.C., USA (October 4–7, 1992).

Abdulraheem, A., Roegiers, J.-C. and Zaman, M.: “Mechanics of Pore Collapse and Compaction in Weak Porous Rocks,” *Proc.*, 33rd U.S. Symposium on Rock Mechanics, Santa Fe, New Mexico, USA (1992), 233–242.

Abou-Sayed, A.S. and Dougherty, R.L.: “Evaluation of the Influence of In Situ Reservoir Conditions on the Geometry of Hydraulic Fractures Using a 3D Simulator,” paper SPE 13275, presented at the SPE Annual Technical Conference and Exhibition, Houston, Texas, USA (September 16–19, 1984).

Abou-Sayed, I.S., Schueler, S., Ehrl, E. and Hendricks, W.: “Multiple Hydraulic Fracture Stimulation in a Deep Horizontal Tight Gas Well,” paper SPE 30532, presented at the SPE Annual Technical Conference and Exhibition, Dallas, Texas, USA (October 22–25, 1995).

Abousleiman, Y., Cheng, A.H.-D. and Gu, H.: “Formation Permeability Determination by Micro or Mini-Hydraulic Fracturing,” *J. Ener. Res. Tech.* (June 1994) 116, No. 2, 104–114.

Abramowitz, M. and Stegun, I.A. (eds.): *Handbook of Mathematical Functions*, ninth edition, New York, New York, USA, Dover (1989).

Acharya, A.R.: “Particle Transport in Viscous and Viscoelastic Fracturing Fluids,” paper SPE 13179, *SPE Production Engineering* (1986), 104.

Acharya, A.R.: “Viscoelasticity of Crosslinked Fracturing Fluids and Proppant Transport,” paper SPE 16221, presented at the SPE Production Operations Symposium, Oklahoma City, Oklahoma, USA (March 8–10, 1987); also paper SPE 15937, *SPE Production Engineering* (November 1988), 483.

Acharya, A.R. and Deysarkar, A.K.: “Rheology of Fracturing Fluids at Low-Shear Conditions,” paper SPE 16917, presented at the SPE Annual Technical Conference and Exhibition, Dallas, Texas, USA (September 27–30, 1987).

Advani, S.H., Lee, T.S. and Dean, R.H.: “Variational Principles for Hydraulic Fracturing,” *Journal of Applied Mechanics* (December 1992) 59, No. 4, 819–826.

Advani, S.H., Lee, T.S., Dean, R.H., Pak, C.K. and Avasthi, J.M.: “Consequences of Fracturing Fluid Lag in Three-Dimensional Hydraulic Fractures,” paper SPE 25888, presented at the SPE Rocky Mountain Regional/Low Permeability Reservoirs Symposium, Denver, Colorado, USA (April 12–14, 1993).

Agarwal, R.G., Al-Hussainy, R. and Ramey, H.J. Jr.: “An Investigation of Wellbore Storage and Skin Effect in Unsteady Liquid Flow: I. Analytical Treatment,” paper SPE 2466, *SPE Journal* (September 1970) 10, No. 3, 279–290.

Agarwal, R.G., Carter, R.D. and Pollock, C.B.: “Evaluation and Performance Prediction of Low Permeability Gas Wells Stimulated by Massive Hydraulic Fracturing,” paper SPE 6838, *Journal of Petroleum Technology* (March 1979) 31, No. 3, 362–372; also in *Trans.*, *AIME* (1979) 267.

- Ahmed, G., Horne, R.N. and Brigham, W.E.: "Theoretical Development of Flow into a Well Through Perforations," report DE90000251, U.S. DOE (August 1990).
- Ahmed, U., Newberry, B.M. and Cannon, D.E.: "Hydraulic Fracture Treatment Design of Wells with Multiple Zones," paper SPE 13857, presented at the SPE Low Permeability Gas Reservoir Symposium, Denver, Colorado, USA (May 19–22, 1985).
- Ainley, B.R.: "Development of Foam Fracturing and Cementing Fluids for Use in Tight Gas Sands," presented at the 1983 AIChE National Meeting, Denver, Colorado, USA (August 28–31, 1983).
- Akram, A.H., Fitzpatrick, A.J. and Halford, F.R.: "A Model to Predict Wireline Formation Tester Sample Contamination," paper SPE 48959, presented at the SPE Annual Technical Conference and Exhibition, New Orleans, Louisiana, USA (September 27–30, 1998).
- Albright, J.N. and Pearson, C.F.: "Acoustic Emissions as a Tool for Hydraulic Fracture Location: Experience at the Fenton Hill Hot Dry Rock Site," paper SPE 9509, *SPE Journal* (August 1982) 22, No. 4, 523–530.
- Aleksandrowksi, P., Inderhaug, O.H. and Knapstad, B.: "Tectonic Structures and Wellbore Breakout Orientation," *Proc.*, 33rd U.S. Symposium on Rock Mechanics, Santa Fe, New Mexico, USA (June 3–5, 1992).
- Al-Hussainy, R. and Ramey, H.J. Jr.: "Application of Real Gas Theory to Well Testing and Deliverability Forecasting," paper SPE 1243-B, *Journal of Petroleum Technology* (May 1966) 18, 637–642.
- Al-Hussainy, R., Ramey, H.J. Jr. and Crawford, P.B.: "The Flow of Real Gases Through Porous Media," paper SPE 1243-A, *Journal of Petroleum Technology* (May 1966) 18, 624–636.
- Allen, L.S., Tittle, C.W., Mills, W.R. and Caldwell, R.L.: "Dual Spaced Neutron Logging for Porosity," *Geophysics* (1967), 32, No. 1.
- Allen, T.O. and Worzel, H.C.: "Productivity Method of Evaluating Gun Perforating," *Drilling and Production Practice 1956*, New York, New York, USA, American Petroleum Institute (1957), 112–125.
- Almond, S.W., Bland, W.E. and Ripley, H.E.: "The Effect of Break Mechanisms on Gelling Agent Residue and Flow Impairment in 20/40 Mesh Sand," paper CIM 84-35-30, presented at the 35th Annual Technical Meeting of Petroleum Society of CIM and Canadian Association of Drilling Engineers, Calgary, Alberta, Canada (June 10–13, 1984).
- Almond, S.W. and Garvin, T.R.: "High Efficiency Fracturing Fluids for Low Temperature Reservoirs," *Proc.*, 31st Annual Southwestern Petroleum Short Course, Lubbock, Texas, USA (1984), 76–88.
- Amadei, B., Swolfs, H.S. and Savage, W.S.: "Gravity Induced Stresses in Stratified Rock Masses," *Rock Mechanics and Rock Engineering* (January 1988) 21, No. 1, 1–20.
- Amyx, B., *et al.*: *Petroleum Reservoir Engineering Physical Properties*, McGraw Hill (1960).
- Anderson, A.J., Ashton, P.J.N., Lang, J. and Samuelson, M.L.: "Production Enhancement Through Aggressive Flowback Procedures in the Codell Formation," paper SPE 36468, presented at the SPE Annual Technical Conference and Exhibition, Denver, Colorado, USA (October 6–9, 1996).
- Anderson, B., Barber, T., Druskin, V., Lee, P., Dussan, V.E., Knizhnerman, L. and Davydycheva, S.: "The Response of Multiarray Induction Tools in Highly Dipping Formations with Invasion and in Arbitrary 3D Geometries," *Transactions of the SPWLA 37th Annual Logging Symposium* (June 16–19, 1996), paper A.
- Anderson, E.M.: *The Dynamics of Faulting and Dyke Formation with Application to Britain*, second edition, Edinburgh, Scotland, Oliver and Boyd (1951).
- Archie, G.E.: "The Electrical Resistivity Log as an Aid in Determining Some Reservoir Characteristics," *Journal of Petroleum Technology* (January 1942) 5.
- Asadi, M. and Preston, F.W.: "Characterization of the Crushed-Zone Formed During Jet Perforation by Qualitative Scanning Electron Microscopy and Quantitative Image Analysis," paper SPE 22812, presented at the SPE Annual Technical Conference and Exhibition, Dallas, Texas, USA (October 6–9, 1991).
- Aseltine, C.: "Flash X-Ray Analysis of the Interaction of Perforators with Different Target Materials," paper SPE 14322, presented at the SPE Annual Technical Conference and Exhibition, Las Vegas, Nevada, USA (September 22–25, 1985).

- Asgian, M.I., Cundall, P.A. and Brady, B.H.: "Mechanical Stability of Propped Hydraulic Fractures: A Numerical Study," paper SPE 28510, *Journal of Petroleum Technology* (March 1995) 47, No. 3, 203–208.
- Atkinson, B.K. (ed.): *Fracture Mechanics of Rock*, London, UK, Academic Press (1987).
- Atkinson, B.K. and Meredith, P.G.: "Experimental Fracture Mechanics Data for Rocks and Minerals," B.K. Atkinson (ed.): *Fracture Mechanics of Rock*, London, UK, Academic Press (1987), 477–525.
- Aud, W.W., Sullivan, R.B., Coalson, E.B., Poulson, T.D. and Warembourg, P.A.: "Acid Refracting Program Increases Reserves, Cottonwood Creek Unit, Washakie County, Wyoming," paper SPE 21821, *Journal of Petroleum Technology* (January 1992), 11; also presented at the Rocky Mountain Regional Meeting and Low-Permeability Reservoirs Symposium, Denver, Colorado, USA (April 15–17, 1992).
- Aud, W.W., Wright, T.B., Cipolla, C.L., Harkrider, J.D. and Hansen, J.T.: "The Effect of Viscosity on Near-Wellbore Tortuosity and Premature Screenouts," paper SPE 28492, presented at the SPE Annual Technical Conference and Exhibition, New Orleans, Louisiana, USA (September 25–28, 1994).
- Ayoub, J.A., Bourdet, D.P. and Chauvel, Y.L.: "Impulse Testing," paper SPE 15911, *SPE Formation Evaluation* (September 1988), 534.
- Ayoub, J.A., Brown, J.E., Barree, R.D. and Elphick, J.J.: "Diagnosis and Evaluation of Fracturing Treatments," *SPE Production Engineering* (February 1992a), 39.
- Ayoub, J.A., Kirksey, J.M., Malone, B.P. and Norman, W.D.: "Hydraulic Fracturing of Soft Formations in the Gulf Coast," paper SPE 23805, presented at the SPE Formation Damage Control Symposium, Lafayette, Louisiana, USA (February 26–27, 1992b).
- Babcock, R.E., Prokop, C.L. and Kehle, R.O.: "Distribution of Propping Agents in Vertical Fractures," *Production Monthly* (November 1967), 11.
- Badon Ghyben, W.: "Nota in Verband Met de Voorgenomen Putboring Nabij Amsterdam," *Tijdschr. Kon. Inst. Ing.* (1888–1889), 1988, 8–22.
- Baker, H.R., Bolster, R.N., Leach, P.B. and Little, R.C.: "Association Colloids in Nonaqueous Fluids," *Ind. Eng. Chem., Prod. Res. Develop.* (1970) 9, No. 4, 541–547.
- Bale, A., Owren, K. and Smith, M.B.: "Propped Fracturing as a Tool for Sand Control and Reservoir Management," paper SPE 24992, presented at the SPE European Petroleum Conference, Cannes, France (November 16–18, 1992); also in *SPE Production & Facilities* (February 1994a) 9, No. 1, 19–28.
- Bale, A., Smith, M.B. and Settari, A.: "Post-Frac Productivity Calculation for Complex Reservoir/Fracture Geometry," paper SPE 28919, presented at the European Petroleum Conference, London, UK (October 24–27, 1994b).
- Baranet, S.E. and Ainley, B.R.: "Delayed Crosslinking Improves Performance of Fracturing Fluids in Deep Formations," paper CIM 85-36-39, presented at the 36th Annual Technical Meeting of the Petroleum Society of CIM, Edmonton, Alberta, Canada (June 2–5, 1985).
- Barenblatt, G.I.: "Mathematical Theory of Equilibrium Cracks," *Advances in Applied Mech.* (1962) 7, 56–131.
- Barree, R.D.: "A Practical Numerical Simulator for Three-Dimensional Fracture Propagation in Heterogeneous Media," paper SPE 12273, presented at the SPE Reservoir Simulation Symposium, San Francisco, California, USA (November 15–18, 1983).
- Barree, R.D.: "A New Look at Fracture-Tip Screen-out Behavior," paper SPE 18955, *Journal of Petroleum Technology* (February 1991) 43, No. 2, 138–143.
- Barree, R.D. and Conway, M.W.: "Experimental and Numerical Modeling of Convective Proppant Transport," paper SPE 28564, presented at the SPE Annual Technical Conference and Exhibition, New Orleans, Louisiana, USA (September 25–28, 1994); also in *Journal of Petroleum Technology* (March 1995) 47, No. 3, 216–222.
- Barree, R.D. and Mukherjee, H.: "Determination of Pressure Dependent Leakoff and Its Effect on Fracture Geometry," paper SPE 36424, presented at the SPE Annual Technical Conference and Exhibition, Denver, Colorado, USA (October 6–9, 1996).



- Bartko, K.M., Robertson, B. and Wann, D.: "Implementing Fracturing Technology to the UKCS Carboniferous Formation," paper SPE 38609, presented at the SPE Annual Technical Conference and Exhibition, San Antonio, Texas, USA (October 5–8, 1997).
- Barton, C. and Zoback, M.: "Stress Perturbations Associated with Active Faults Penetrated by Boreholes: Evidence for Near Complete Stress Drop and a New Technique for Stress Magnitude Measurement," *Journal of Geophysical Research* (1994) 99, 9373–9390.
- Bartusiak, R., Behrmann, L.A. and Halleck, P.M.: "Experimental Investigation of Surge Flow Velocity and Volume Needed to Obtain Perforation Cleanup," *Journal of Petroleum Science & Engineering* (February 1997) 13, Nos. 1–2, 19–28.
- Batchelor, A.S., Baria, R. and Hearn, K.: "Monitoring the Effects of Hydraulic Stimulation by Microseismic Event Location: A Case Study," paper SPE 12109, presented at the SPE Annual Technical Conference and Exhibition, San Francisco, California, USA (October 5–8, 1983).
- Baumgartner, W.E., Shlyapobersky, J., Abou-Sayed, I.S. and Jacquier, R.C.: "Fracture Stimulation of a Horizontal Well in a Deep, Tight Gas Reservoir: A Case History from Offshore The Netherlands," paper SPE 26795, presented at the Offshore European Conference, Aberdeen, Scotland (September 7–10, 1993).
- Beg, M.S., Kunak, A., Oguz, G., Ming, Z.D. and Hill, A.D.: "A Systematic Experimental Study of Acid Fracture Conductivity," paper SPE 31098, presented at the SPE International Symposium on Formation Damage Control, Lafayette, Louisiana, USA (February 14–15, 1996).
- Beggs, H.D. and Brill, J.P.: "A Study of Two-Phase Flow in Inclined Pipes," paper SPE 4007, *Journal of Petroleum Technology* (May 1973) 25, No. 5, 607–617.
- Behie, A. and Settari, A.: "Perforation Design Models for Heterogeneous, Multiphase Flow," paper SPE 25901, presented at the SPE Rocky Mountain Regional/Low Permeability Reservoirs Symposium, Denver, Colorado, USA (April 12–14, 1993).
- Behrmann, L. and Elbel, J.: "Effect of Perforations on Fracture Initiation," paper SPE 20661, *Journal of Petroleum Technology* (May 1991) 43, No. 5, 608–615; also presented at the SPE Annual Technical Conference and Exhibition, New Orleans, Louisiana, USA (September 23–26, 1992).
- Behrmann, L., *et al.*: "Quo Vadis, Extreme Overbalance?" *Oilfield Review* (Autumn 1996) 8, No. 3, 18–33.
- Behrmann, L.A.: "Underbalance Criteria for Minimum Perforation Damage," paper SPE 30081, presented at the SPE Formation Damage Symposium, The Hague, Netherlands (May 15–16, 1995).
- Behrmann, L.A. and Halleck, P.M.: "Effects of Wellbore Pressure on Perforator Penetration Depth," paper SPE 18243, presented at the SPE Annual Technical Conference and Exhibition, Houston, Texas, USA (October 2–5, 1988).
- Behrmann, L.A. and McDonald, B.: "Underbalance or Extreme Overbalance," paper SPE 31083, presented at the SPE International Symposium on Formation Damage Control, Lafayette, Louisiana, USA (February 14–15, 1996).
- Behrmann, L.A., Pucknell, J.K. and Bishop, S.R.: "Effects of Underbalance and Effective Stress on Perforation Damage in Weak Sandstone: Initial Results," paper SPE 24770, presented at the SPE Annual Technical Conference and Exhibition, Washington, D.C., USA (October 4–7, 1992).
- Bell, W.T.: "Perforating Underbalanced—Evolving Techniques," paper SPE 13413, *Journal of Petroleum Technology* (October 1984) 36, No. 11, 1653–1662.
- Bell, W.T., Brieger, E.F. and Harrigan, J.W. Jr.: "Laboratory Flow Characteristics of Gun Perforations," paper SPE 3444, *Journal of Petroleum Technology* (September 1972) 36, No. 11, 1095–1103.
- Bell, W.T., Sukup, R.A. and Tariq, S.M.: *Perforating*, Henry L. Doherty Monograph Series, Richardson, Texas, USA, Society of Petroleum Engineers (1995) 16.
- Ben Naceur, K. and Economides, M.J.: "Production from Naturally Fissured Reservoirs Intercepted by a Vertical Hydraulic Fracture," paper SPE 17425, presented at the SPE California Regional Meeting, Long Beach, California, USA (March 23–25, 1988); also in

*SPE Formation Evaluation* (December 1989) 4, No. 4, 550–558.

Ben Naceur, K. and Roegiers, J.-C.: “Design of Fracturing Treatments in Multilayered Formations,” paper SPE 17712, presented at the SPE Gas Technology Symposium, Dallas, Texas, USA (June 13–15, 1988); also in *SPE Production Engineering* (February 1990) 5, No. 1, 21–26.

Bennett, C.O., Reynolds, A.C. and Raghavan, R.: “Analysis of Finite-Conductivity Fractures Intercepting Multilayer Commingled Reservoirs,” paper SPE 11030, *SPE Formation Evaluation* (June 1986) 1, 259–274.

Bennett, C.O., Rodolpho, C.-V., Reynolds, A.C. and Raghavan, R.: “Approximate Solutions for Fractured Wells Producing Layered Reservoirs,” paper SPE 11599, *SPE Journal* (October 1985) 25, 729–742.

Bennett, C.O., Rosato, N.D., Reynolds, A.C. and Raghavan, R.: “Influence of Fracture Heterogeneity and Wing Length on the Response of Vertically Fractured Wells,” paper SPE 9886, *SPE Journal* (April 1983) 23, 219–230.

Besson, J.: “Performance of Slanted and Horizontal Wells on an Anisotropic Medium,” paper SPE 20965, presented at Europec 90, The Hague, Netherlands (October 22–24, 1990).

Bhalla, K. and Brady, B.H.: “Formation and Fracture Characterization by Inversion of Fracture Treatment Records,” paper SPE 26526, presented at the SPE Annual Technical Conference and Exhibition, Houston, Texas, USA (October 3–6, 1993).

Bilhartz, H.L. and Ramey, H.J. Jr.: “The Combined Effects of Storage, Skin, and Partial Penetration on Well Test Analysis,” paper SPE 6753, presented at the SPE Annual Technical Conference and Exhibition, Denver, Colorado, USA (October 9–12, 1977).

Biot, M.A.: “General Theory of Three-Dimensional Consolidation,” *Journal of Applied Physics* (February 1941) 12, 155–164.

Biot, M.A.: “General Solutions of the Equations of Elasticity and Consolidation for a Porous Material,” *Journal of Applied Mechanics* (March 1956a) 23, No. 1, 91–96.

Biot, M.A.: “Theory of Propagation of Elastic Waves in a Fluid-Saturated Porous Solid. I. Low Frequency Range,” *J. Acoust. Soc. Am.* (1956b) 28, 168–178.

Biot, M.A.: “Theory of Propagation of Elastic Waves in a Fluid-Saturated Porous Solid. II. High Frequency,” *J. Acoust. Soc. Am.* (1956c) 28, 179–191.

Bird, K. and Dunmore, S.: “Optimising Perforation Performance for the Armada Gas Condensate Development,” paper SPE 30083, presented at the 1995 European Formation Damage Conference, The Hague, Netherlands (May 15–16, 1995).

Boone, T.J., Kry, P.R., Bharatha, S. and Gronseth, J.M.: “Poroelastic Effects Related to Stress Determination by Micro-Frac Tests in Permeable Rock,” *Proc.*, 32nd U.S. Symposium on Rock Mechanics, Norman, Oklahoma, USA (1991), 25–34.

Boone, T.J., Wawryznek, P.A. and Ingraffea, A.R.: “Simulation of the Fracture Process in Rock with Application to Hydrofracturing,” *International Journal of Rock Mechanics and Mining Sciences & Geomechanics Abstracts* (June 1986) 23, No. 3, 255–265.

Bourdet, D.: “Pressure Behavior of Layered Reservoirs with Crossflow,” paper SPE 13628, presented at the SPE California Regional Meeting, Bakersfield, California, USA (March 27–29, 1985).

Bourdet, D., Alagoa, A., Ayoub, J.A. and Pirard, Y.M.: “New Type Curves Aid Analysis of Fissured Zone Well Tests,” *World Oil* (April 1984) 198, No. 5, 111–124.

Bourdet, D., Ayoub, J.A. and Pirard, Y.M.: “Use of Pressure Derivative in Well-Test-Interpretation,” paper SPE 12777, *SPE Facilities & Engineering* (June 1989), 293–302; also in *Trans.*, AIME 287.

Bourdet, D., Whittle, T.M., Douglas, A.A. and Pirard, Y.M.: “A New Set of Type Curves Simplifies Well Test Analysis,” *World Oil* (May 1983) 196, No. 6, 95–106.

Boutéca, M.J., Bary, D., Piau, J.M., Kessler, N., Boisson, M. and Fourmaintraux, D.: “Contribution of Poroelasticity to Reservoir Engineering: Lab Experiments, Application to Core Decompression and Implication in HP-HT Reservoirs Depletion,” *Proc.*, Eurock '94 Symposium, Delft, Netherlands (1994), 525–533.

Bradley, W.B.: “Failure of Inclined Boreholes,” *Journal of Energy Research Technology* (December 1979) 101, 232–239.

- Brady, B.H., Ingraffea, A.R. and Morales, R.H.: "Three-Dimensional Analysis and Visualization of the Wellbore and the Fracturing Process in Inclined Wells," paper SPE 25889, presented at the SPE Rocky Mountain Regional/Low Permeability Reservoirs Symposium, Denver, Colorado, USA (April 12–14, 1993).
- Branagan, P.T., Warpinski, N.R., Engler, B.P. and Wilmer, R.: "Measuring the Hydraulic Fracture-Induced Deformation of Reservoirs and Adjacent Rocks Employing a Deeply Buried Inclinator Array: GRI/DOE Multi-Site Project," paper SPE 36451, presented at the SPE Annual Technical Conference and Exhibition, Denver, Colorado, USA (October 6–9, 1996).
- Brannon, H.D. and Pulsinelli, R.J.: "Breaker Concentrations Required to Improve the Permeability of Proppant Packs Damaged by Concentrated Linear and Borate-Crosslinked Fracturing Fluids," paper SPE 21583, *SPE Production Engineering* (November 1992) 7, No. 4, 338–342.
- Brannon, H.D. and Tjon-Jo-Pin, R.M.: "Biotechnological Breakthrough Improves Performance of Moderate to High-Temperature Fracturing Applications," paper SPE 28513, presented at the SPE Annual Technical Conference and Exhibition, New Orleans, Louisiana, USA (September 25–28, 1994).
- Bratli, R.K. and Risnes, R.: "Stability and Failure of Sand Arches," paper SPE 8427, *SPE Journal* (April 1981) 21, No. 2, 236–248.
- Bratton, T., Bornemann, T., Li, Q., Plumb, R. and Rasmus, J.: "Logging-While-Drilling Images for Geomechanical, Geological and Petrophysical Interpretations," *Transactions of the SPWLA 40th Annual Logging Symposium*, Oslo, Norway (June 8–10, 1999).
- Breckels, I.M. and van Eekelen, H.A.M.: "Relationship Between Horizontal Stress and Depth in Sedimentary Basins," paper SPE 10336, *Journal of Petroleum Technology* (September 1982) 34, No. 9, 2191–2199.
- Brie, A., Endo, T., Johnson, D.L. and Pampuri, F.: "Quantitative Formation Permeability Evaluation from Stoneley Waves," presented at the SPE Annual Technical Conference and Exhibition, New Orleans, Louisiana, USA (September 27–30, 1998).
- Britt, L.K. and Bennett, C.O.: "Determination of Fracture Conductivity in Moderate-Permeability Reservoirs Using Bilinear Flow Concepts," paper SPE 14165, presented at the SPE Annual Technical Conference and Exhibition, Las Vegas, Nevada, USA (September 22–25, 1985).
- Britt, L.K., Hager, C.J. and Thompson, J.W.: "Hydraulic Fracturing in a Naturally Fractured Reservoir," paper SPE 28717, presented at the SPE International Petroleum Conference and Exhibition of Mexico, Veracruz, Mexico (October 10–13, 1994).
- Brown, E.T. (ed.): *Rock Characterization Testing and Monitoring*, International Society for Rock Mechanics, Commission on Testing Methods, Oxford, UK, Pergamon Press (1981).
- Brown, J.E. and Economides, M.J.: "An Analysis of Horizontally Fractured Horizontal Wells," paper SPE 24322, presented at the SPE Rocky Mountain Regional Meeting, Casper, Wyoming, USA (May 18–22, 1992).
- Brown, J.E., King, L.R., Nelson, E.B. and Ali, S.A.: "Use of a Viscoelastic Carrier Fluid in Frac-Pack Applications," paper SPE 31114, presented at the SPE International Symposium on Formation Damage Control, Lafayette, Louisiana, USA (February 14–15, 1996).
- Brown, K.E., *et al.*: *The Technology of Artificial Lift Methods*, Tulsa, Oklahoma, USA, PennWell Publishing Co. (1984).
- Bui, H.D.: "An Integral Equations Method for Solving the Problem of a Plane Crack of Arbitrary Shape," *J. Mech. Phys. Solids* (February 1977) 25, No. 1, 29–39.
- Burnham, J.W., Harris, L.E. and McDaniel, B.W.: "Developments in Hydrocarbon Fluids for High-Temperature Fracturing," paper SPE 7564, presented at the SPE Annual Technical Conference and Exhibition, Houston, Texas, USA (October 1–3, 1978); also in *Journal of Petroleum Technology* (February 1980) 32, No. 2, 217–220.
- Camacho-V., R.G., Raghavan, R. and Reynolds, A.C.: "Response of Wells Producing Layered Reservoirs: Unequal Fracture Length," paper SPE 12844, *SPE Formation Evaluation* (March 1987) 2, 9–28.

- Cameron, J.R.: "Rheological Modeling and Scale-Up of a Delayed-Crosslinked Gel in Nonhomogeneous Flow," paper SPE 21858, presented at the SPE Rocky Mountain Regional Meeting and Low-Permeability Reservoirs Symposium, Denver, Colorado, USA (April 15–17, 1991); also in *SPE Production & Facilities* (February 1993), 23.
- Cameron, J.R., Joha, R.J. and Veatch, R.W. Jr.: "The Nonhomogeneous Flow Character of a Delayed Crosslinked Gel," paper SPE 20638, presented at the SPE Annual Technical Conference and Exhibition, New Orleans, Louisiana, USA (September 23–26, 1990).
- Cameron, J.R. and Prud'homme, R.K.: "Fracturing-Fluid Flow Behavior," *Recent Advances in Hydraulic Fracturing*, J.L. Gidley, S.A. Holditch, D.E. Nierode and R.W. Veatch Jr. (eds.), Monograph Series, Richardson, Texas, USA, Society of Petroleum Engineers (1989), 177–209.
- Cantu, L.A. and Boyd, P.A.: "Laboratory and Field Evaluation of a Combined Fluid-Loss Control Additive and Gel Breaker for Fracturing Fluids," paper SPE 18211, presented at the SPE Annual Technical Conference and Exhibition, Houston, Texas, USA (October 2–5, 1988).
- Card, R.J., Howard, P.R. and Féraud, J.-P.: "Control of Particulate Flowback in Subterranean Wells," U.S. Patent No. 5,330,005 (July 19, 1994).
- Card, R.J., Howard, P.R. and Féraud, J.-P.: "A Novel Technology to Control Proppant Back Production," paper SPE 31007, *SPE Production & Facilities* (November 1995), 271.
- Carico, R.D. and Bagshaw, F.R.: "Description and Use of Polymers Used in Drilling, Workovers, and Completions," paper SPE 7747, presented at the SPE Production Technology Symposium, Hobbs, New Mexico, USA (October 30–31, 1978).
- Carmen, P.C.: "Fundamental Principles of Industrial Filtration," *Trans. Inst. Chem. Eng.* (1938) 16, 168–188.
- Carnahan, B., Luther, H.A. and Wilkes, J.O.: *Applied Numerical Methods*, New York, New York, USA, John Wiley (1969).
- Carslaw, H.S. and Jaeger, J.C.: *Conduction of Heat in Solids*, second edition, Oxford, UK, Clarendon Press (1959).
- Carter, R.D.: "Derivation of the General Equation for Estimating the Extent of the Fractured Area," Appendix I of "Optimum Fluid Characteristics for Fracture Extension," *Drilling and Production Practice*, G.C. Howard and C.R. Fast, New York, New York, USA, American Petroleum Institute (1957), 261–269.
- Castillo, J.L.: "Modified Fracture Pressure Decline Analysis Including Pressure-Dependent Leakoff," paper SPE 16417, presented at the SPE/DOE Low Permeability Reservoirs Symposium, Denver, Colorado, USA (May 18–19, 1987).
- Cawiezel, K.E. and Elbel, J.L.: "A New System for Controlling the Crosslinking Rate of Borate Fracturing Fluids," paper SPE 20077, presented at the SPE California Regional Meeting, Ventura, California, USA (April 4–6, 1990).
- Cawiezel, K.E. and Niles, T.D.: "Rheological Properties of Foam Fracturing Fluids Under Downhole Conditions," paper SPE 16191, presented at the SPE Hydrocarbon Economics and Evaluation Symposium, Dallas, Texas, USA (March 2–3, 1987).
- Cesaro, M., Cheung, P., Etchecopar, A. and Gonfalini, M.: "Shaping Up to Stress in the Appenines," *Italy 2000: Value Added Reservoir Characterization* (Well Evaluation Conference, Italy), Schlumberger (1997).
- Chambers, M.R., Mueller, M.M. and Grossmann, A.: "Well Completion Design and Operations for a Deep Horizontal Well with Multiple Fractures," paper SPE 30417, presented at the Offshore Europe Conference, Aberdeen, Scotland (September 5–8, 1995).
- Chaveteau, G.: "Fundamental Criteria in Polymer Flow Through Porous Media and Their Relative Importance in the Performance Differences of Mobility Control Buffers," *Water Soluble Polymers*, J.E. Glass (ed.), Advances in Chemistry Series (1986), 213.
- Cheatham, J.B. Jr. and McEver, J.W.: "Behavior of Casing Subjected to Salt Loading," paper SPE 828, *Journal of Petroleum Technology* (September 1964) 16, 1069–1075.
- Chen, W.F. and Han, D.J.: *Plasticity for Structural Engineers*, New York, New York, USA, Springer-Verlag (1988).
- Chen, Z. and Economides, M.J.: "The Effect of Near-Wellbore Fracture Geometry on Fracture Execution

and Post-Treatment Production of Deviated and Horizontal Wells,” paper SPE 39425, presented at the SPE International Formation Damage Control Conference, Lafayette, Louisiana, USA (February 18–19, 1998).

Cheng, C.H. and Johnston, D.H.: “Dynamic and Static Moduli,” *Geophys. Res. Letters* (January 1981) 8, No. 1, 39–42.

Cherepanov, G.P.: *Mechanics of Brittle Fracture*, New York, New York, USA, McGraw-Hill (1979).

Chrisp, J.: U.S. Patent No. 3,301,723 (1967).

Cinco-Ley, H. and Meng, H.Z.: “Pressure Transient Analysis of Wells with Finite Conductivity Vertical Fractures in Double Porosity Reservoirs,” paper SPE 18172, presented at the SPE Annual Technical Conference and Exhibition, Houston, Texas, USA (October 2–5, 1988).

Cinco-Ley, H., Ramey, H.J. Jr. and Miller, F.G.: “Pseudoskin Factors for Partially Penetrating Directionally Drilled Wells,” paper SPE 5589, presented at the SPE Annual Technical Conference and Exhibition, Dallas, Texas, USA (September 28–October 1, 1975a).

Cinco-Ley, H., Ramey, H.J. Jr. and Miller, F.G.: “Unsteady-State Pressure Distribution Created by a Well with an Inclined Fracture,” paper SPE 5591, presented at the SPE Annual Technical Conference and Exhibition, Dallas, Texas, USA (September 28–October 1, 1975b).

Cinco-Ley, H. and Samaniego-V., F.: “Effect of Wellbore Storage and Damage on the Transient Pressure Behavior of Vertically Fractured Wells,” paper SPE 6752, presented at the SPE Annual Technical Conference and Exhibition, Denver, Colorado, USA (October 9–12, 1977).

Cinco-Ley, H. and Samaniego-V., F.: “Transient Pressure Analysis: Finite Conductivity Fracture Case Versus Damaged Fracture Case,” paper SPE 10179, presented at the SPE Annual Technical Conference and Exhibition, San Antonio, Texas, USA (October 5–7, 1981a).

Cinco-Ley, H. and Samaniego-V., F.: “Transient Pressure Analysis for Fractured Wells,” paper SPE 7490, *Journal of Petroleum Technology* (September 1981b) 33, 1749–1766.

Cinco-Ley, H., Samaniego-V., F. and Dominguez, N.: “Transient Pressure Behavior for a Well with a Finite-Conductivity Vertical Fracture,” paper SPE 6014, presented at the SPE Annual Technical Conference and Exhibition, New Orleans, Louisiana, USA (October 3–6, 1976); also in *SPE Journal* (August 1978) 18, 253–264.

Clark, J.B.: “A Hydraulic Process for Increasing the Productivity of Wells,” *Petroleum Trans., AIME* (January 1949) 186, 1–8.

Clark, K.K.: “Transient Pressure Testing of Fractured Water Injection Wells,” paper SPE 1821, *Journal of Petroleum Technology* (June 1968) 20, 639–643.

Clark, P.E.: “Stimulation Fluid Rheology—A New Approach,” paper SPE 8300, presented at the SPE Annual Technical Conference and Exhibition, Las Vegas, Nevada, USA (September 23–26, 1979).

Clark, P.E., Balakrishnan, M. and Sundram, L.: “Crosslinking of Hydroxypropyl Guar with Metal Ions,” paper SPE 25208, presented at the SPE International Symposium on Oilfield Chemistry, New Orleans, Louisiana, USA (March 2–5, 1993).

Clark, P.E. and Barkat, O.: “Hydraulic Fracturing Fluids: The Crosslinking of Hydroxypropyl Guar with Titanium Chelates,” paper SPE 19331, presented at the SPE Eastern Regional Meeting, Morgantown, West Virginia, USA (October 24–27, 1989).

Clark, P.E. and Courington, T.J.: “Visualization of Flow Into a Vertical Fracture,” paper SPE 27692, presented at the SPE Permian Basin Oil and Gas Recovery Conference, Midland, Texas, USA (March 16–18, 1994).

Clark, P.E. and Guler, N.: “Prop Transport in Vertical Fractures: Settling Velocity Correlations,” paper SPE 11636, presented at the SPE/DOE Symposium on Low Permeability, Denver, Colorado, USA (March 14–16, 1983).

Clark, P.E., Halvaci, M., Ghaeli, H. and Parks, C.F.: “Proppant Transport by Xanthan and Xanthan-Hydroxypropylguar Solutions: Alternatives to Cross-linked Fluids,” paper SPE/DOE 13907, presented at the SPE/DOE Low Permeability Gas Reservoirs Conference, Denver, Colorado, USA, (May 19–22, 1985).

- Clark, P.E., Harkin, M.W., Wahl, H.A. and Sievert, J.A.: "Design of a Large Vertical Prop Transport Model," paper SPE 6814, presented at the SPE Annual Technical Conference and Exhibition, Denver, Colorado, USA (October 9–12, 1977).
- Clark, P.E., Manning, F.S., Quadir, J.A. and Guler, N.: "Prop Transport in Vertical Fractures," paper SPE 10261, presented at the SPE Annual Technical Conference and Exhibition, San Antonio, Texas, USA (October 5–7, 1981).
- Clark, P.E. and Zhu, Q.: "Flow Visualization of Flow Into 8 Point-Source Fractures II: The Effect of Fracture Non-Uniformity and Fluid Crosslinking," paper SPE 29503, presented at the SPE Production Operations Symposium, Oklahoma City, OK, USA (April 2–4, 1995a).
- Clark, P.E. and Zhu, Q.: "Fluid Flow in Vertical Fractures from a Point Source," paper SPE 28509, presented at the SPE Annual Technical Conference and Exhibition, New Orleans, Louisiana, USA (September 25–28, 1994); also in *Journal of Petroleum Technology* (March 1995b) 47, No. 3, 209–215.
- Cleary, M., Johnson, D., Kogsboll, H., Owens, K., Perry, K., de Pater, C., Stachel, A., Schmidt, H. and Tambini, M.: "Field Implementation of Proppant Slugs to Avoid Premature Screen-Out of Hydraulic Fractures with Adequate Proppant Concentration," paper SPE 25892, presented at the SPE Rocky Mountain Regional/Low Permeability Reservoirs Symposium, Denver, Colorado, USA (April 12–14, 1993).
- Cleary, M.P.: "Analysis of Mechanisms and Procedures for Producing Favourable Shapes of Hydraulic Fractures," paper SPE 9260, presented at the SPE Annual Technical Conference and Exhibition, Dallas, Texas, USA (September 21–24, 1980a).
- Cleary, M.P.: "Comprehensive Design Formulae for Hydraulic Fracturing," paper SPE 9259, presented at the SPE Annual Technical Conference and Exhibition, Dallas, Texas, USA (September 21–24, 1980b).
- Cleary, M.P., Doyle, R.S., Teng, E.Y., Cipolla, C.L., Meehan, D.N., Massaras, L.V. and Wright, T.B.: "Major New Developments in Hydraulic Fracturing, with Documented Reductions in Job Costs and Increases in Normalized Production," paper SPE 28565, presented at the SPE Annual Technical Conference and Exhibition, New Orleans, Louisiana, USA (September 25–28, 1994).
- Cleary, M.P. and Fonseca, A.: "Proppant Convection and Encapsulation in Hydraulic Fracturing: Practical Implications of Computer Laboratory Simulations," paper SPE 24825, presented at the SPE Annual Technical Conference and Exhibition, Washington, D.C., USA (October 4–7, 1992).
- Cleary, M.P., Keck, R.G. and Mear, M.E.: "Micro-computer Models for the Design of Hydraulic Fractures," paper SPE 11628, presented at the SPE/DOE Symposium on Low Permeability, Denver, Colorado, USA (March 14–16, 1983).
- Cleary, M.P., Wright, C.A. and Wright, T.B.: "Experimental and Modeling Evidence for Major Changes in Hydraulic Fracturing Design and Field Procedures," paper SPE 21494, *Proc., SPE Gas Technology Symposium*, Houston, Texas, USA (1991), 131–146.
- Clifton, R.J. and Abou-Sayed, A.S.: "On the Computation of the Three-Dimensional Geometry of Hydraulic Fractures," paper SPE 7943, presented at the SPE/DOE Low Permeability Gas Reservoirs Symposium, Denver, Colorado, USA (May 20–22, 1979).
- Clifton, R.J. and Abou-Sayed, A.S.: "A Variational Approach to the Prediction of the Three-Dimensional Geometry of Hydraulic Fractures," paper SPE 9879, presented at the SPE Low Permeability Symposium, Denver, Colorado, USA (May 27–29, 1981).
- Clifton, R.J. and Wang, J.-J.: "Multiple Fluids, Proppant Transport, and Thermal Effects in Three-Dimensional Simulation of Hydraulic Fracturing," paper SPE 18198, presented at the SPE Annual Technical Conference and Exhibition, Houston, Texas, USA (October 2–5, 1988).
- Colle, E.A., Halleck, P.M., Saucier, R.J. and Wesson, D.S.: "Discussion of Simple Method Predicts Downhole Shaped-Charge Gun Performance," *SPE Production & Facilities* (November 1994) 9, No. 4, 292–293.
- Collins, R.E.: *Flow of Fluids Through Porous Materials*, New York, New York, USA, Van Nostrand Reinhold (1961).
- Constien, V.G., Brannon, H.D. and Bannister, C.E.: "Continuous Mix Technology Adds New Flexibility

to Frac Jobs,” *Oil & Gas Journal* (June 6, 1988) 86, No. 23, 49–54.

Constien, V.G., Fellin, E.L. and King, M.T.: “Automated Rheology Laboratory—Part 1,” *ACS Symp. Ser.* (1986) 313, 105.

Conway, M.W., Almond, S.W., Briscoe, J.E. and Harris, L.E.: “Chemical Model for the Rheological Behavior of Crosslinked Fluid Systems,” paper SPE 9334, presented at the SPE Annual Technical Conference and Exhibition, Dallas, Texas, USA (September 21–24, 1980).

Cook, J.M., Bradford, I.D.R. and Plumb, R.A.: “A Study of the Physical Mechanisms of Sanding and Application to Sand Production Prediction,” paper SPE 28852, *Proc.*, European Petroleum Conference, London, UK (1994), 473–480.

Cook, N.G.W.: “The Design of Underground Excavations,” *Proc.*, 8th Symposium on Rock Mechanics, Minneapolis, Minnesota, USA (1967), 167–193.

Cooke, C.E. Jr.: “Conductivity of Fracture Proppants in Multiple Layers,” paper SPE 4117, *Journal of Petroleum Technology* (September 1973) 25, 1101–1107; also in *Trans.*, *AIME* (1973) 255.

Cooke, C.E. Jr.: “Effect of Fracturing Fluids on Fracture Conductivity,” paper SPE 5114, *Journal of Petroleum Technology* (October 1975) 27, 1273–1282; also in *Trans.*, *AIME* (1975) 259.

Coon, R.: “Correlation of Engineering Behaviour with the Classification of In Situ Rock,” PhD dissertation, University of Illinois, Illinois, USA (1968).

Cotton, F.A. and Wilkinson, G.: *Advanced Inorganic Chemistry*, New York, New York, USA, Interscience Publishers (1972).

Coulter, A.W., Crowe, C.W., Barrett, N.D. and Miller, B.D.: “Alternate Stages of Pad Fluid and Acid Provide Improved Leakoff Control for Fracture Acidizing,” paper SPE 6124, presented at the SPE Annual Technical Conference and Exhibition, New Orleans, Louisiana, USA (October 3–6, 1976).

Craft, B.C., Kemp, C.E. and Caulde, B.H.: *Well Design: Drilling and Production*, Englewood Cliffs, New Jersey, USA, Prentice Hall (1962), 494.

Craigie, L.J.: “A New Method for Determining the Rheology of Crosslinked Fracturing Fluids Using

Shear History Simulation,” paper SPE/DOE 11635, presented at the SPE/DOE Symposium on Low Permeability, Denver, Colorado, USA (March 14–16, 1983).

Cramer, D.: “Limited Entry Extended to Massive Hydraulic Fracturing,” *Oil & Gas Journal* (December 14, 1987) 85, No. 50, 40–50.

Cramer, D.D., Dawson, J. and Ouabdesselam, M.: “An Improved Gelled Oil System for High-Temperature Fracturing Applications,” paper SPE 21859, presented at the Rocky Mountain Regional Meeting and Low Permeability Reservoirs Symposium, Denver, Colorado, USA.

Crawford, D.L., Earl, R.B. and Monroe, R.F.: “Friction Reducing and Gelling Agent for Organic Liquids,” U.S. Patent No. 3,757,864 (September 11, 1973).

Crockett, A.R., Willis, R.M. and Cleary, M.P.: “Improvement of Hydraulic Fracture Predictions by Real-Time History Matching on Observed Pressures,” *SPE Production Engineering* (November 1989) 4, No. 4, 408–416.

Crouch, S.L. and Starfield, A.M.: *Boundary Element Methods in Solid Mechanics*, London, UK, Allen and Unwin (1983).

Crowe, C.W.: “Clay Stabilization Ups Productivity,” *Oil and Gas Suppliers’ Digest* (1979) 1, No. 6.

Crowe, C.W., Hutchinson, B.H. and Trittipio, B.L.: “Fluid-Loss Control: The Key to Successful Acid Fracturing,” *SPE Production Engineering* (August 1989) 4, No. 3, 215–220.

Crowe, C.W., Martin, R.C. and Michaelis, A.M.: “Evaluation of Acid-Gelling Agents for Use in Well Stimulation,” paper SPE 9384, *SPE Journal* (August 1981), 415.

Crowe, C.W., McGowan, G.R. and Baranet, S.E.: “Investigation of Retarded Acids Provides Better Understanding of Their Effectiveness and Potential Benefits,” paper SPE 1822, *SPE Production Engineering* (May 1990), 166.

Crump, J. and Conway, M.: “Effects of Perforation-Entry Friction on Bottomhole Treating Analysis,” paper SPE 15474, *Journal of Petroleum Technology* (August 1988) 40, No. 8, 1041–1048.



- Daccord, G., Lamanczyk, R. and Vercaemer, C.: "Method for Obtaining Gelled Hydrocarbon Compositions According to Said Method and Their Application the Hydraulic Fracturing of Underground Formations," U.S. Patent No. 4,507,213 (March 26, 1985).
- Dake, L.: *Fundamentals of Reservoir Engineering*, Developments in Petroleum Science, Amsterdam, Netherlands, Elsevier Scientific Publishing Company (1982) 8.
- Daneshy, A.A.: "Experimental Investigation of Hydraulic Fracturing Through Perforations," paper SPE 4333, *Journal of Petroleum Technology* (October 1973) 25, No. 10, 1201–1206.
- Darcy, H.: *Les Fontaines Publiques de la Ville de Dijon*, Paris, France, Victor Dalmont (1856).
- Davidson, B.M., Saunders, B.F. and Holditch, S.A.: "Field Measurement of Hydraulic Fracture Fluids: Case Study," paper SPE 27694, presented at the SPE Permian Basin Oil and Gas Recovery Conference, Midland, Texas, USA (March 16–18, 1994).
- Davies, D.R., Bosma, M.G.R. and de Vries, W.: "Development of Field Design Rules for Viscous Fingering in Acid Fracturing Treatments: A Large-Scale Model Study," paper SPE 15772, presented at the SPE Middle East Oil Show, Manama, Bahrain (March 7–10, 1987).
- Davies, D.R., Lau, H.C., Kamphuis, H. and Roodhart, L.P.: "Development and Field Testing of a Novel Fracturing Fluid," paper SPE 23109, presented at the SPE Offshore Petroleum Conference, Aberdeen, Scotland (September 3–6, 1991).
- Davis, P.M.: "Surface Deformation Associated with Dipping Hydrofracture," *Journal of Geophysical Research* (July 10, 1983) 88, No. B7, 5826–5834.
- Dawson, J.: "Method and Composition for Delaying the Gellation of Borated Galactomannons," U.S. Patent No. 5,082,579 (1992).
- Dawson, J.C.: "A Thermodynamic Study of Borate Complexation with Guar and Guar Derivatives," paper SPE 22837, presented at the SPE Annual Technical Conference and Exhibition, Dallas, Texas, USA (October 6–9, 1991).
- Dees, J.M. and Handren, P.J.: "A New Method of Overbalance Perforating and Surging of Resin for Sand Control," paper SPE 26545, presented at the SPE Annual Technical Conference and Exhibition, Houston, Texas, USA (October 3–6, 1993).
- de Kruijf, A., Roodhart, L.P. and Davies, D.R.: "The Relation Between Chemistry and Flow Mechanics of Borate Crosslinked Fracturing Fluids," paper SPE 25206, presented at the SPE International Symposium on Oilfield Chemistry in New Orleans, Louisiana, USA (March 2–5, 1993); also in *SPE Production & Facilities* (August 1993), 165.
- de Pater, C.J., Desroches, J., Gronenbroom, J. and Weijers, L.: "Physical and Numerical Modelling of Hydraulic Fracture Closure," paper SPE 28561, presented at the SPE Annual Technical Conference and Exhibition, New Orleans, Louisiana, USA (September 25–28, 1994); also in *SPE Production & Facilities* (May 1996), 122.
- de Pater, C.J., Weijers, L., Savic, M., Wolf, K.H.A.A., van den Hoek, P.J. and Barr, D.T.: "Experimental Study of Nonlinear Effects in Hydraulic Fracture Propagation," paper SPE 25893, presented at the SPE Joint Rocky Mountain Regional Meeting/Low Permeability Reservoirs Symposium, Denver, Colorado, USA (April 12–14, 1993); also in *SPE Production Engineering* (November 1994) 9, No. 4, 239–246.
- Deo, M., Tariq, S.M. and Halleck, P.M.: "Linear and Radial Flow Targets for Characterizing Downhole Flow in Perforations," paper SPE 16896, *SPE Production Engineering* (August 1989) 4, No. 3, 295–300.
- de Rozières, J.: "Measuring Diffusion Coefficients in Acid Fracturing Fluids and Their Application to Gelled and Emulsified Acids," paper SPE 28552, presented at the SPE Annual Technical Conference and Exhibition, New Orleans, Louisiana, USA (September 25–28, 1994).
- Desbrandes, R. and Gualdrón, J.: "In Situ Rock Wettability Determination with Wireline Formation Tester Data," *The Log Analyst* (July–August 1988) 29, No. 4, 244–252.
- Desroches, J. and Kurkjian, A.: "Applications of Wireline Stress Measurements," paper SPE 58086, *SPE Reservoir Evaluation* (October 1999).
- Desroches, J., Lenoach, B., Papanastasiou, P. and Thiercelin, M.: "On the Modelling of Near Tip



- Processes in Hydraulic Fracturing,” *International Journal of Rock Mechanics and Mining Sciences & Geomechanics Abstracts* (1993) 30, No. 7, 1127–1134.
- Desroches, J. and Thiercelin, M.: “Modelling the Propagation and Closure of Micro-Hydraulic Fractures,” *International Journal of Rock Mechanics and Mining Sciences & Geomechanics Abstracts* (1993) 30, No. 7, 1231–1234.
- Desroches, J. and Woods, T.E.: “Stress Measurements for Sand Control,” paper SPE 47247, presented at the SPE/ISRM Eurock ‘98, Trondheim, Norway (July 8–10, 1998).
- Detournay, E. and Carbonell, R.: “Fracture Mechanics Analysis of the Breakdown Process in Minifrac or Leak-Off Tests,” paper SPE 28076, presented at the SPE/ISRM Rock Mechanics in Petroleum Engineering Conference, Delft, Netherlands (August 29–31, 1994).
- Detournay, E. and Cheng, A.: “Poroelastic Response of a Borehole in a Non-Hydrostatic Stress Field,” *International Journal of Rock Mechanics and Mining Sciences & Geomechanics Abstracts* (June 1988) 25, No. 3, 171–182.
- Detournay, E. and Cheng, A.: “Plane Strain Analysis of a Stationary Hydraulic Fracture in a Poroelastic Medium,” *Int. J. Solids & Structures* (March 1991) 27, No. 13, 1645–1662.
- Detournay, E. and Cheng, A.: “Influence of Pressurization Rate on the Magnitude of the Breakdown Pressure,” *Proc.*, 33rd Symposium on Rock Mechanics, Santa Fe, New Mexico, USA (1992), 325–333.
- Detournay, E. and Cheng, A.: “Fundamentals of Poroelasticity,” *Comprehensive Rock Engineering*, J.A. Hudson (ed.), Oxford, UK, Pergamon Press (1993) 2, 113–171.
- Deuel, H. and Neukorn, H.: “Über die Reaktion von Borsäure und Borax mit Polysacchariden und Anderen Hochmolekularen Polyoxy-Verbindungen,” *Makromol. Chem.* (1949) 13.
- Dewprashad, B., Abass, H.H., Meadows, D.L., Weaver, J.D. and Bennett, B.J.: “A Method to Select Resin-Coated Proppants,” paper SPE 26523, presented at the SPE Annual Technical Conference and Exhibition, Houston, Texas, USA (October 3–6, 1993).
- Dietz, D.N.: “Determination of Average Reservoir Pressure from Build-Up Surveys,” paper SPE 1156, *Journal of Petroleum Technology* (August 1965) 17, No. 8, 955–959.
- Dobecki, T.L.: “Hydraulic Fracture Orientation Using Passive Borehole Seismics,” paper SPE 12110, presented at the SPE Annual Technical Conference and Exhibition, San Francisco, California, USA (October 5–8, 1983).
- Dobkins, T.A.: “Improved Methods to Determine Hydraulic Fracture Height,” paper SPE 8403, *Journal of Petroleum Technology* (April 1981) 33, No. 4, 719–726.
- Dovan, H.T. and Hutchins, R.D.: “Crosslinked Hydroxyethylcellulose and Its Uses,” U.S. Patent No. 5,207,934 (May 4, 1993).
- Dunand, A., Guillot, D. and Soucemarianadin, A.: “Viscous Properties of Glass-Bead Suspensions and Falling Sphere Experiments in Hydroxypropyl Guar Solutions,” *Proc.*, Ninth International Congress on Rheology, Mexico City, Mexico (1984).
- Dunning, J.D.: “Surfactants,” *Chemtech* (June 1980) 10, No. 6, 356–359.
- Dyes, A.B., Kemp, C.E. and Caudle, B.H.: “Effect of Fractures on Sweep-Out Pattern,” *Trans., AIME* (1958) 213, 245–249.
- Earlougher, R.C. Jr.: *Advances in Well Test Analysis*, Dallas, Texas, USA, Society of Petroleum Engineers (1977).
- Economides, M.J.: “Implications of Cementing on Well Performance,” *Well Cementing*, E.B. Nelson (ed.), Sugar Land, Texas, USA, Schlumberger (1990), 1-1–1-6.
- Economides, M.J., Brand, C.W. and Frick, T.P.: “Well Configurations in Anisotropic Reservoirs,” *SPE Formation Evaluation* (December 1996) 11, No. 4, 257–262.
- Economides, M.J., Deimbacher, F.X., Brand, C.W. and Heinemann, Z.E.: “Comprehensive Simulation of Horizontal Well Performance,” *SPE Formation Evaluation* (December 1991) 6, No. 4, 418–426.

- Economides, M.J., Hill, A.D. and Ehlig-Economides, C.A.: *Petroleum Production Systems*, Englewood Cliffs, New Jersey, USA, Prentice-Hall (1994).
- Economides, M.J., McLennan, J.D., Brown, E. and Roegiers, J.-C.: "Performance and Stimulation of Horizontal Wells," *World Oil* (June–July 1989) 208, No. 6, 41–45, and 209, No. 1, 69–72 and 76–77.
- Edimann, K., Somerville, J.M., Smart, B.G.D., Hamilton, S.A. and Crawford, B.R.: "Predicting Rock Mechanical Properties from Wireline Porosities," paper SPE 47344, presented at the SPE/ISRM Eurock '98, Trondheim, Norway (July 8–10, 1998).
- Ehlig-Economides, C.A.: "Implications of the Test Area of Investigation in Nonradial Geometries," *SPE Memorial Series*, Richardson, Texas, USA, Society of Petroleum Engineers (1995) 1, 103–112.
- Ehlig-Economides, C.A., Chan, K.S. and Spath, J.B.: "Production Enhancement Strategies for Strong Bottomwater Drive Reservoirs," paper SPE 36613, presented at the SPE Annual Technical Conference and Exhibition, Denver, Colorado, USA (October 6–9, 1996).
- Ehlig-Economides, C.A. and Economides, M.J.: "Pressure Transient Analysis in an Elongated Linear Flow System," *SPE Journal* (December 1985) 25, No. 6, 347–360.
- Ehlig-Economides, C.A., Joseph, J., Erba, M. and Vik, S.A.: "Evaluation of Single-Layer Transients in a Multilayered System," paper SPE 15860, presented at the European Petroleum Conference, London, UK (October 20–22, 1986).
- Elbel, J.L.: "Designing Hydraulic Fractures for Efficient Reserve Recovery," paper SPE 15231, presented at the SPE Unconventional Gas Technology Symposium, Louisville, Kentucky, USA (May 18–21, 1986).
- Elbel, J.L.: "Considerations for Optimum Fracture Geometry Design," *SPE Production Engineering* (August 1988) 3, No. 3, 323–327.
- Elbel, J.L.: "A Method To Estimate Multizone Injection Profiles During Hydraulic Fracturing," paper SPE 21869, presented at the Rocky Mountain Regional Meeting and Low-Permeability Reservoirs Symposium, Denver, Colorado, USA (April 15–17, 1993).
- Elbel, J.L. and Ayoub, J.A.: "Evaluation of Apparent Fracture Lens Tip Indicated from Transient Tests," paper 91-44, presented at the CIM-AOSTRA Technical Conference, Banff, Alberta, Canada (April 21–24, 1991); also in *Journal of Canadian Petroleum Technology* (December 1992) 31, No. 10, 41–46.
- Elbel, J.L., Howard, R.L., Talley, G.R. and McLaughlin, B.H.: "Stimulation Study of Cottage Grove Formation," paper SPE 11564, *Journal of Petroleum Technology* (July 1984), 1199–1205.
- Elbel, J.L., Piggott, A.R. and Mack, M.G.: "Numerical Modeling of Multilayer Fracture Treatments," paper SPE 23982, presented at the SPE Permian Basin Oil and Gas Recovery Conference, Midland, Texas, USA (March 18–20, 1992).
- Elbel, J.L. and Sookprasong, P.A.: "Use of Cumulative-Production Type Curves in Fracture Design," *SPE Production Engineering* (August 1987) 2, No. 3, 191–198.
- El Rabaa, W.: "Experimental Study of Hydraulic Fracture Geometry Initiated from Horizontal Wells," paper SPE 19720, presented at the SPE Annual Technical Conference and Exhibition, San Antonio, Texas, USA (October 8–11, 1989).
- Ely, J.W.: *Stimulation Treatment Handbook*, Tulsa, Oklahoma, USA, PennWell Publishing Co. (1985).
- Ely, J.W.: "GRI's Fracture Fluid Rheology Unit—Portable Equipment for Measuring Fluid Behavior Under Simulated Downhole Conditions," *In Focus—Tight Gas Sands*, Gas Research Institute (September 1987) 4, No. 2.
- Endo, T., Brie, A. and Badri, M.: "Fracture Evaluation from Dipole Shear Anisotropy and Borehole Stoneley Waves," *Transactions of the SPWLA 2nd Annual Logging Symposium of Japan* (1996), paper U.
- Engelder, T.: *Stress Regimes in the Lithosphere*, Princeton, New Jersey, USA, Princeton University Press (1993).
- Enzendorfer, C., Harris, R.A., Valkó, P., Economides, M.J., Fokker, P.A. and Davies, D.D.: "Pipe Viscometry of Foams," *J. Rheol.* (March–April 1995) 39, No. 2, 345–358.
- Esmeroy, C., Koster, K., Williams, M., Boyd, A. and Kane, M.: "Dipole Shear Anisotropy Logging,"

*Proc.*, 64th International Meeting of the Society of Exploration Geophysicists (1994), 1139–1142.

Evans, K.F., Engelder, T. and Plumb, R.A.: “Appalachian Stress Study: 1. A Detailed Description of In-Situ Stress Variations in Devonian Shales of the Appalachian Plateau,” *Journal of Geophysical Research* (1989) 94, No. B6, 7129–7154.

Fair, W.B. Jr.: “Pressure Buildup Analysis with Wellbore Phase Distribution Effects,” *SPE Journal* (April 1981) 21, 259–270.

Fan, Y.: “Measurements of Viscous and Degradation Properties of Fracturing Fluids at Insitu Conditions of Shear Rate and Temperature Using FANN 50C Viscometer,” PhD dissertation, Texas A&M University, College Station, Texas, USA (1992).

Fan, Y. and Holditch, S.A.: “Testing Crosslinked Fluids on the Fann 50 Viscometer Using the Volumetric Average Shear Rate,” paper SPE 26895, presented at the SPE Eastern Regional Conference and Exhibition, Pittsburgh, Pennsylvania, USA (November 2–4, 1993).

Farris, R.F.: “Fracturing Formations in Wells,” reissue No. 23,733 of U.S. Patent No. 2,596,843 (November 1953).

Fast, C.R., Holman, G.B. and Colvin, R.J.: “The Application of Massive Hydraulic Fracturing to the Tight Muddy ‘J’ Formation, Wattenberg Field, Colorado,” paper SPE 5624, *Journal of Petroleum Technology* (January 1977) 29, 10–17.

Felsenthal, M.: “Step Rate Tests to Determine Safe Injection Pressures in Floods,” *Oil & Gas Journal* (October 1994), 49–54.

Fenner, R.: “Untersuchen zur Erkenntnis des Gebirgsdrucks,” *Glukauf* (1938) 74.

Fletcher, P.A., Montgomery, C.T., Ramos, G.G., Miller, M.E. and Rich, D.A.: “Using Fracturing as a Technique for Controlling Formation Failure,” paper SPE 27899, presented at the Western Regional Meeting, Long Beach, California, USA (March 23–25, 1984).

Forchheimer, P.: “Wasserbewegung Durch Boden,” *ZVDI* (1901) 45, 1781.

Ford, T.F.: “Viscosity Concentration and Fluidity-Concentration Relationships for Suspensions of

Spherical Particles in Newtonian Liquids,” *J. Phys. Chem.* (1960), 1168–1174.

Ford, W.G.F.: “Foamed Acid—An Effective Stimulation Fluid,” paper SPE 9385, *Journal of Petroleum Technology* (July 1981) 33, 1203–1210.

Fragachan, F.E., Mack, M.G., Nolte, K.G. and Teggins, D.E.: “Fracture Characterization from Measured and Simulated Bottomhole Pressures,” paper SPE 25848, presented at the SPE Rocky Mountain Regional/Low Permeability Reservoirs Symposium, Denver, Colorado, USA (April 12–14, 1993).

Franquet, J.A. and Economides, M.J.: “Effect of Stress and Stress Path on Young’s Modulus and Poisson Ratio of Unconsolidated Rocks: A New Idea for Hydraulic Fracturing,” paper SPE 54012, presented at the SPE Latin America and Caribbean Petroleum Engineering Conference, Caracas, Venezuela (April 21–23, 1999).

Fraser, C.D. and Pettitt, B.E.: “Results of a Field Test to Determine the Type and Orientation of a Hydraulically Induced Formation Fracture,” paper SPE 180, *Journal of Petroleum Technology* (May 1962) 14, 463–466.

Frick, T.P. and Economides, M.J.: “Horizontal Well Damage Characterization and Removal,” *SPE Production & Facilities* (February 1993) 8, No. 1, 15–22.

Friedman, G.M. and Sanders, J.E.: *Principles of Sedimentology*, John Wiley & Sons, New York, New York, USA (1978).

Friedman, M., Handin, J. and Alani, G.: “Fracture-Surface Energy of Rocks,” *International Journal of Rock Mechanics and Mining Sciences & Geomechanics Abstracts* (November 1972) 9, No. 6, 757–766.

Frimann-Dahl, C., Irvine-Fortescue, J., Rokke, E., Vik, S. and Wahl, O.: “Formation Testers Vs. DST—The Cost Effective Use of Transient Analysis to Get Reservoir Parameters,” paper SPE 48962, presented at the SPE Annual Technical Conference and Exhibition, New Orleans, Louisiana, USA (September 27–30, 1998).

Fung, R.L., Vilajakumar, S. and Cormack, D.E.: “Calculation of Vertical Fracture Containment in Layered Formations,” paper SPE 14707, *SPE Formation Evaluation* (December 1987) 2, No. 4, 518–523.

- Gadala-Maria, F. and Acrivos, A.: "Shear-Induced Structure in a Concentrated Suspension of Solid Spheres," *J. Rheol.* (1980) 24, No. 6, 799–814.
- Gall, B.L. and Raible, C.J.: "A Method to Study Fracturing Fluid Polymer Degradation Using Size Exclusion Chromatography," DOE/BETC/RI-83/10 (1984).
- Gall, B.L. and Raible, C.J.: "Molecular Size Studies of Degraded Fracturing Fluid Polymers," paper SPE 13566, presented at the SPE Oilfield and Geothermal Chemistry Symposium, Phoenix, Arizona, USA (April 9–11, 1985).
- Gardner, D.C.: "High Fracturing Pressures for Shales and Which Tip Effects May Be Responsible," paper SPE 24852, presented at the SPE Annual Technical Conference and Exhibition, Washington, D.C., USA (October 4–7, 1992).
- Gardner, D.C. and Eikerts, J.V.: "The Effects of Shear and Proppant on the Viscosity of Cross-Linked Fracturing Fluids," paper SPE 11066, presented at the SPE Annual Technical Conference and Exhibition, New Orleans, Louisiana, USA (September 26–29, 1982).
- Gatens, J.M., Lee, W.J., Hopkins, C.W. and Lancaster, D.E.: "The Effect of Permeability Anisotropy on the Evaluation and Design of Hydraulic Fracture Treatments and Well Performance," paper SPE 21501, presented at the SPE Gas Technology Symposium, Houston, Texas, USA (January 23–25, 1991).
- Gauthier, F., Goldsmith, H.L. and Mason, S.G.: "Particle Motions in Non-Newtonian Media," *Rheol. Acta* (September 1971) 10, No. 3, 344–364.
- Gdanski, R.D. and Norman, L.R.: "Using the Hollow-Core Test to Determine Acid Reaction Rates," paper SPE 12151, *SPE Production Engineering* (March 1986), 111.
- Geertsma, J.: "Estimating the Coefficient of Inertial Resistance in Fluid Flow Through Porous Media," *SPE Journal* (October 1974) 14, No. 5, 445–450.
- Geertsma, J.: "Some Rock-Mechanical Aspects of Oil and Gas Well Completions," paper SPE 8073, *SPE Journal* (December 1985) 25, No. 6, 848–856.
- Geertsma, J. and de Klerk, F.: "A Rapid Method of Predicting Width and Extent of Hydraulic Induced Fractures," paper SPE 2458, *Journal of Petroleum Technology* (December 1969) 21, 1571–1581.
- Geertsma, J. and Haafkens, R.: "A Comparison of the Theories to Predict Width and Extent of Vertical, Hydraulically Induced Fractures," *Trans., AIME* (March 1979) 101, 8.
- Geilikman, M.B., Dusseault, M.B. and Dullien, F.A.: "Sand Production as a Viscoplastic Granular Flow," paper SPE 27343, *Proc., SPE International Symposium on Formation Damage Control*, Lafayette, Louisiana, USA (1994), 41–50.
- Germanovich, L.N., Salganik, R.L., Dyskin, A.V. and Lee, K.K.: "Mechanisms of Brittle Fracture of Rock with Pre-Existing Cracks in Compression," *Pure and Applied Geophysics* (1994) 143, Nos. 1–3, 117–149.
- Gidley, J.L.: "A Method for Correcting Dimensionless Fracture Conductivity for Non-Darcy Flow Effects," paper SPE 20710, presented at the SPE Annual Technical Conference and Exhibition, New Orleans, Louisiana, USA (September 23–26, 1990); also in *SPE Production Engineering* (November 1991) 6, No. 4, 391–394.
- Gidley, J.L., Holditch, S.A., Nierode, D.E. and Veatch, R.W. Jr.: *Recent Advances in Hydraulic Fracturing*, Monograph Series, Richardson, Texas, USA, Society of Petroleum Engineers (1989).
- Gnirk, P.F.: "The Mechanical Behavior of Uncased Wellbores Situated in Elastic/Plastic Media Under Hydrostatic Stress," paper SPE 3224, *SPE Journal* (February 1972) 12, No. 1, 49–59.
- Godbey, J.K. and Hodges, H.D.: "Pressure Measurements During Formation Fracturing Operations," *Trans., AIME* (1958) 213, 65–69.
- Goel, N., Willingham, J.D., Shah, S.N. and Lord, D.L.: "A Comparative Study of Borate-Crosslinked Gel Rheology Using Laboratory and Field Scale Fracturing Simulations," paper SPE 38618, presented at the SPE Annual Technical Conference and Exhibition, San Antonio, Texas, USA (October 5–8, 1997).
- Goode, P.A., Pop, J.J. and Murphy, W.F. III: "Multiple-Probe Formation Testing and Vertical Reservoir Continuity," paper SPE 22738, presented at the SPE Annual Technical Conference and Exhibition, Dallas, Texas, USA (October 6–9, 1991).

- Goodman, R.E.: *Methods of Geological Engineering in Discontinuous Rocks*, St. Paul, Minnesota, USA, West Publishing (1976).
- Graham, J.W., Kiel, O.M., Terry, W.M. and Sinclair, A.R.: "Hydraulic Fracturing Using Petroleum Coke," U.S. Patent No. 3,664,420 (May 23, 1972).
- Grebe, J.J. and Stoesser, M.: "Increasing Crude Production 20,000,000 Bbl. from Established Fields," *World Petroleum* (August 1935), 473–482.
- Griffith, A.A.: "The Phenomena of Rupture and Flow in Solids," *Phil. Trans. Roy. Soc.* (1921) 221, 163–198.
- Griffith, A.A.: "The Theory of Rupture," *Proc.*, 1st International Congress for Applied Mechanics, Delft, Netherlands (1924), 55–63.
- Gringarten, A.C., Bourdet, D.P., Landel, P.A. and Kniazeff, V.: "A Comparison Between Different Skin and Wellbore Storage Type-Curves for Early-Time Transient Analysis," paper SPE 8205, presented at the SPE Annual Technical Conference and Exhibition, Las Vegas, Nevada, USA (September 23–26, 1979).
- Gringarten, A.C. and Ramey, H.J. Jr.: "The Use of Source and Green's Functions in Solving Unsteady Flow Problems in Reservoirs," *SPE Journal* (October 1973) 13, No. 5, 285–296.
- Gringarten, A.C. and Ramey, H.J. Jr.: "Unsteady-State Pressure Distributions Created by a Well with a Single Horizontal Fracture, Partial Penetration, or Restricted Entry," paper SPE 3819, *SPE Journal* (August 1974) 14, No. 4, 413–426.
- Gringarten, A.C., Ramey, H.J. Jr. and Raghavan, R.: "Unsteady State Pressure Distributions Created by a Well with a Single Infinite-Conductivity Vertical Fracture," paper SPE 4051, *SPE Journal* (August 1974) 14, No. 4, 347–360.
- Gross, J.M.: "Gelling Organic Liquids," U.S. Patent No. 5,190,675 (March 2, 1993).
- Gruesbeck, C. and Collins, R.E.: "Particle Transport Through Perforations," paper SPE 7006, presented at the SPE Symposium on Formation Damage Control, Lafayette, Louisiana, USA (February 15–16, 1978).
- Gu, H., Elbel, J.L., Nolte, K.G., Cheng, A.H.-D. and Abousleiman, Y.: "Formation Permeability Determination Using Impulse Fracture Injection," paper SPE 25425, presented at the Production Operations Symposium, Oklahoma City, Oklahoma, USA (March 21–23, 1993).
- Guar and Derivatives*, Henkel Corporation (1986).
- Guenot, A.: "Instability Problems at Great Depth Drilling Boreholes and Wells," *Proc.*, Rock at Great Depth, International Symposium of Rock Mechanics, Pau, France (1989), 1199–1208.
- Guillot, D. and Dunand, A.: "Rheological Characterization of Fracturing Fluids by Using Laser Anemometry," paper SPE 12030, *SPE Journal* (February 1985), 39.
- Gulbis, J.: "Dynamic Fluid Loss Study of Fracturing Fluid," paper CIM 82-33-18, presented at the 33rd Annual Technical Meeting of Petroleum Society of CIM (1982).
- Gulbis, J.: "Dynamic Fluid Loss of Fracturing Fluids," paper SPE 12154, presented at the SPE Annual Technical Conference and Exhibition, San Francisco, California, USA (October 5–8, 1983).
- Gulbis, J., King, M.T., Hawkins, G.W. and Brannon, H.D.: "Encapsulated Breaker for Aqueous Polymeric Fluids," *SPE Production Engineering* (February 1992) 7, No. 1, 9–14.
- Gulrajani, S.N., Mack, M.G. and Elbel, J.L.: "Pressure History Inversion for Interpretation of Fracture Treatments," paper SPE 36439, presented at the SPE Annual Technical Conference and Exhibition, Denver, Colorado, USA (October 6–9, 1996); also in *SPE Production & Facilities* (November 1998) 13, No. 4, 258–266.
- Gulrajani, S.N., Nolte, K.G. and Romero, J.: "Evaluation of the M-Site B-Sand Experiments: The Evolution of a Pressure Analysis Methodology," paper SPE 38575, presented at the SPE Annual Technical Conference and Exhibition, San Antonio, Texas, USA (October 5–8, 1997a).
- Gulrajani, S.N. and Romero, J.: "Evaluation and Modification of Fracture Treatments Showing Near-Wellbore Effects," paper SPE 36901, presented at the SPE European Petroleum Conference, Milan, Italy (October 22–24, 1996).
- Gulrajani, S.N., Tibbles, R.J. and Nolte, K.G.: "Evaluation of Calibration Treatments, for Frac-Pack Completions, in Offshore West Africa," paper SPE

38192, presented at the SPE European Formation Damage Symposium, The Hague, Netherlands (June 2–3, 1997b).

Guo, F., Morgenstern, N.R. and Scott, J.D.: “Interpretation of Hydraulic Fracturing Breakdown Pressure,” *International Journal of Rock Mechanics and Mining Sciences & Geomechanics Abstracts* (1993) 30, No. 6, 617–626.

Guppy, K.H., Cinco-Ley, H. and Ramey, H.J. Jr.: “Pressure Buildup Analysis of Fractured Wells Producing at High Flow Rates,” paper SPE 10178, *Journal of Petroleum Technology* (November 1982a) 34, 2656–2666.

Guppy, K.H., Cinco-Ley, H., Ramey, H.J. Jr. and Samaniego-V., F.: “Non-Darcy Flow in Wells with Finite-Conductivity Vertical Fractures,” paper SPE 8281, *SPE Journal* (October 1982b) 22, No. 5, 681–698.

Gupta, D.V.S. and Cooney, A.P.: “Encapsulations for Treating Subterranean Formations and Methods for the Use Thereof,” U.S. Patent No. 5,164,099 (November 17, 1992).

Hagedorn, A.R. and Brown, K.E.: “Experimental Study of Pressure Gradients Occurring During Continuous Two-Phase Flow in Small-Diameter Vertical Conduits,” paper SPE 940, *Journal of Petroleum Technology* (April 1965) 17, 475–484.

Hagoort, J.: “Waterflood Induced Hydraulic Fracturing,” PhD thesis, Delft University of Technology, Delft, Netherlands (1980).

Haimson, B. and Fairhurst, C.: “Hydraulic Fracturing in Porous-Permeable Materials,” paper SPE 2354, *Journal of Petroleum Technology* (July 1969) 21, 811–817.

Haimson, B.C.: “The Hydraulic Fracturing Method of Stress Measurement: Theory and Practice,” *Comprehensive Rock Engineering*, J. Hudson (ed.), Oxford, UK, Pergamon Press (1993), 3, 297–328.

Haimson, B.C. and Huang, X.: “Hydraulic Fracturing Breakdown Pressure and In-Situ Stress at Great Depth,” *Rock at Great Depth*, V. Fourmaintraux and D. Maury (eds.), Rotterdam, Netherlands, Balkema (1989), 939–946.

Haimson, B.C. and Zhongliang, Z.: “Effect of Borehole Size and Pressurization Rate on Hydraulic

Fracturing Breakdown Pressure,” *Proc.*, 32nd U.S. Symposium on Rock Mechanics, Norman, Oklahoma, USA (1991), 191–199.

Hainey, B.W., Weng, X. and Stoitsits, R.F.: “Mitigation of Multiple Fractures from Deviated Wellbores,” paper SPE 30482, presented at the SPE Annual Technical Conference and Exhibition, Dallas, Texas, USA (October 22–25, 1995).

Hall, B.E. and Houk, S.G.: “Fluid-Loss Control in the Naturally Fractured Buda Formation,” paper SPE 12152, presented at the SPE Annual Technical Conference and Exhibition, San Francisco, California, USA (October 5–8, 1983).

Hall, C.D. Jr. and Dollarhide, F.E.: “Effects of Fracturing Fluid Velocity on Fluid Loss Agent Performance,” paper SPE 736, *Journal of Petroleum Technology* (May 1964), 555–560; also in *Trans., AIME* (1964) 231.

Hall, C.D. Jr. and Dollarhide, F.E.: “Performance of Fracturing Fluid Loss Agents Under Dynamic Conditions,” paper SPE 1904, *Journal of Petroleum Technology* (July 1968), 763–769.

Halleck, P.M.: “The Effects of Stress and Pore Pressure on Penetration of Jet Perforators in Berea Sandstone,” final report, API Project 86-36, American Petroleum Institute (1987).

Halleck, P.M.: “Further Effects of Stress on Penetration Flow Performance of Jet Perforations,” final report, API Project 87-36, American Petroleum Institute (1988).

Halleck, P.M.: “Minimum Size and Stress Requirements for a Possible API Standard Test Target for Performance Evaluation of Shaped Charge Oil Well Perforators in Stressed Rock,” final report, API Project 88-36, American Petroleum Institute (1989).

Halleck, P.M.: “The Application of Prototype Penetration and Flow Tests in Stressed Targets to Several Perforator Charges and Rocks,” final report, API Project 89-36, American Petroleum Institute (1990).

Halleck, P.M.: “Minimizing Skin in Fractured Reservoirs,” final report GRI-95/0472, Contract 5094-210-2901, Gas Research Institute (March 1996a).

Halleck, P.M.: "Studies Reveal Fractured Reservoir Perforating Damage," *Petroleum Engineering International* (April 1996b) 69, No. 4, 35–44.

Halleck, P.M., Atwood, D.C. and Black, A.D.: "X-Ray CT Observations of Flow Distribution in a Shaped-Charge Perforation," paper SPE 24771, presented at the SPE Annual Technical Conference and Exhibition, Washington, D.C., USA (October 4–7, 1992).

Halleck, P.M. and Behrmann, L.A.: "Penetration of Shaped Charges in Stressed Rock," *Rock Mechanics Contributions and Challenges*, Rotterdam, Netherlands, Balkema (1990), 629–636; also presented at the 31st U.S. Symposium on Rock Mechanics (1990).

Halleck, P.M. and Damasena, E.: "Sand Production Tests Under Simulated Down Hole Pressure Conditions Using Shaped-Charge Perforated Well Cores," paper SPE 19748, presented at the SPE Annual Technical Conference and Exhibition, San Antonio, Texas, USA (October 8–11, 1989).

Halleck, P.M. and Deo, M.: "The Effect of Underbalance on Perforation Flow," paper SPE 16895, presented at the SPE Annual Technical Conference and Exhibition, Dallas, Texas, USA (September 27–30, 1987); also in *Journal of Production Engineering* (May 1989) 4, No. 2, 113–116.

Halleck, P.M., Poyol E. and Santarelli, F.J.: "Estimating Perforation Flow Performance from Variation in Indentation Hardness," paper SPE 24769, presented at the SPE Annual Technical Conference and Exhibition, Washington, D.C., USA (October 4–7, 1992); also in *SPE Drilling and Completion* (December 1995) 10, No. 4, 271–275.

Halleck, P.M., Safargar, M.S. and Dogulu, Y.S.: "Perforating Naturally Fractured Formations: Fracture Plugging by Jet Metal and Rock Deformation," *Turkish Journal of Oil and Gas* (1996) 2, 20–38.

Halleck, P.M., Saucier, R.J., Behrmann, L.A. and Ahrens, T.J.: "Reduction of Jet Perforator Penetration in Rock Under Stress," paper SPE 18245, presented at the SPE Annual Technical Conference and Exhibition, Houston, Texas, USA (October 2–5, 1988).

Halleck, P.M., Wesson, D.S., Snider, P.M. and Navarrete, M.: "Prediction of In-Situ Shaped Charge Penetration Using Acoustic and Density Logs," paper

SPE 22808, presented at the SPE Annual Technical Conference and Exhibition, Dallas, Texas, USA (October 6–9, 1991).

Handren, P.J., Jupp, T.B. and Dees, J.M.: "Overbalance Perforating and Stimulation Method for Wells," paper SPE 26515, presented at the SPE Annual Technical Conference and Exhibition, Houston, Texas, USA (October 3–6, 1993).

Hannah, R.R., Harrington, L.J. and Anderson, R.W.: "Measurement of Dynamic Proppant Fall Rates in Fracturing Gels Using a Concentric Cylinder Tester," paper SPE 7571, presented at the SPE Annual Technical Conference and Exhibition, Houston, Texas, USA (October 1–3, 1978).

Hannah, R.R., Harrington, L.J. and Lance, L.C.: "The Real Time Calculation of Accurate Bottomhole Fracturing Pressure from Surface Measurements with Measured Pressure as a Base," paper SPE 12062, presented at the SPE Annual Technical Conference and Exhibition, San Francisco, California, USA (October 5–8, 1983).

Hannah, R.R., Park, E.I., Porter, D.A. and Black, J.W.: "Combination Fracturing/Gravel Packing Completion Technique on the Amberjack, Mississippi Canyon 109 Field," paper SPE 26562, *SPE Production & Facilities* (November 1994) 9, No. 4, 262–267.

Hannah, R.R. and Walker, E.J.: "Fracturing a High-Permeability Oil Well at Prudhoe Bay, Alaska," paper SPE 14372, presented at the SPE Annual Technical Conference and Exhibition, Las Vegas, Nevada, USA (September 22–25, 1985).

Harrington, L. and Hannah, R.R.: "Fracturing Design Using Perfect Support Fluids for Selected Fracture Proppant Concentrations in Vertical Fractures," paper SPE 5642, presented at the SPE Annual Meeting, Dallas, Texas, USA (September 28–October 1, 1975).

Harrington, L.J., Hannah, R.R. and Williams, D.: "Dynamic Experiments on Proppant Settling in Crosslinked Fracturing Fluids," paper SPE 8342, presented at the SPE Annual Technical Conference and Exhibition, Las Vegas, Nevada, USA (September 23–26, 1979).

Harrington, L.J., Whitsitt, N.F. and Hannah, R.R.: "Prediction of the Location and Movement of Fluid Interfaces in the Fracture," *Southwestern Petroleum*

Short Course, Texas Tech University, Lubbock, Texas, USA (April 1973).

Harris, L.E., Holtmyer, M.D. and Pauls, R.W.: "Method for Fracturing Subterranean Formations," U.S. Patent No. 4,622,155 (November 11, 1986).

Harris, M.H.: "The Effect of Perforating on Well Productivity," paper SPE 1236, *Journal of Petroleum Technology* (April 1966) 18, 518–528.

Harris, P.C.: "Dynamic Fluid-Loss Characteristics of Nitrogen Foam Fracturing Fluids," *Journal of Petroleum Technology* (October 1985) 18, No. 10, 1847–1852.

Harris, P.C.: "Chemistry and Rheology of Borate Crosslinked Fluids at Temperatures Up to 300°F," paper SPE 24339, presented at the SPE Rocky Mountain Regional Meeting, Casper, Wyoming, USA (May 18–21, 1993).

Harris, P.C. and Heath, S.J.: "Rheology of Cross-linked Foams," paper SPE 28512-P, *SPE Production & Facilities* (May 1996) 11, No. 2, 113–116.

Harris, P.C. and Heath, S.J.: "Rheological Properties of Low-Gel-Loading Borate Fracture Gels," paper SPE 52399, *SPE Production & Facilities* (1998).

Harrison, E., Kieschnick, W.F. Jr. and McGuire, W.J.: "The Mechanics of Fracture Induction and Extension," *Trans., AIME* (1954) 201, 252–263.

Hart, C.M., Engi, D., Fleming, R.P. and Morris, H.E.: "Fracture Diagnostics Results for the Multiwell Experiment's Paludal Zone Stimulation," paper SPE 12852, presented at the SPE/DOW/GRI Unconventional Gas Recovery Symposium, Pittsburgh, Pennsylvania, USA (May 13–15, 1984).

Hashem, M.N., Thomas, E.C., McNeil, R.I. and Mullins, O.C.: "Determination of Producing Hydrocarbon Type and Oil Quality in Wells Drilled with Synthetic Oil-Based Muds," paper SPE 39093, presented at the SPE Annual Technical Conference and Exhibition, San Antonio, Texas, USA (October 5–8, 1997).

Haskin, C.A.: "A Review of Hydroxy Aluminum Treatments," paper SPE 5692, presented at the SPE Symposium on Formation Damage Control, Houston, Texas, USA (January 29–30, 1976).

Havlena, D. and Odeh, A.S.: "The Material Balance as an Equation of a Straight Line," paper SPE 559,

*Journal of Petroleum Technology* (August 1963) 15, 896–900.

Hawkins, G.W.: "Molecular Weight Reduction and Physical Consequences of Chemical Degradation of Hydroxypropylguar in Aqueous Brine Solutions," *Proc.*, ACS Division of Polymeric Materials: Science and Engineering (1986) 55.

Hawkins, G.W.: "Laboratory Study of Proppant-Pack Permeability Reduction Caused by Fracturing Fluids Concentrated During Closure," paper SPE 18261, presented at the SPE Annual Technical Conference and Exhibition, Houston, Texas, USA (October 2–5, 1988).

Hawkins, M.F.: "A Note on the Skin Effect," *Journal of Petroleum Technology* (December 1956) 8, 356–357.

Hejjo, H., Fagan, J.E. and Shah, S.N.: "Flow Visualization Technique for Investigation of Hydraulic Fracturing," paper SPE 38579, presented at the SPE Annual Technical Conference and Exhibition, San Antonio, Texas, USA (October 5–8, 1997).

Herron, M.M., Johnson, D.L. and Schwartz, L.M.: "A Robust Permeability Estimator for Siliclastics," presented at the SPE Annual Technical Conference and Exhibition, New Orleans, Louisiana, USA (September 27–30, 1998).

Herzberg, A.: "Die Wasserversorgung einiger Nordseebaden," *Z. Gasbeleucht. Wasserversorg.* (1901) 44, 815–819, 824–844.

Hilbert, L.B., Hwong, T.K., Cook, N.G.W., Nihei, K.T. and Myer, L.R.: "Effects of Strain Amplitude on the Static and Dynamic Nonlinear Deformation of Berea Sandstone," *Proc.*, 1st North American Symposium on Rock Mechanics, Austin, Texas, USA (1994), 497–504.

Hill, R.: *The Mathematical Theory of Plasticity*, Oxford, UK, Clarendon Press (1951).

Himes, R.E. and Vinson, E.F.: "Environmentally Safe Salt Replacement for Fracturing Fluids," paper SPE 23438, presented at the SPE Eastern Regional Meeting, Lexington, Kentucky, USA (October 2–5, 1991).

Hinkel, J.J.: "Breaker System for High Viscosity Fluids," U.S. Patent No. 4,250,044 (February 10, 1981).



- Hirth, J.P. and Lothe, J.: *Theory of Dislocations*, New York, New York, USA, McGraw-Hill (1968).
- Hodge, R.M.: "Hydraulic Fracturing Method Using Delayed Crosslinker Composition," U.S. Patent No. 4,749,041 (June 7, 1988a).
- Hodge, R.M.: "Method of Fracturing a Subterranean Formation Using Delayed Crosslinker Compositions Containing Organic Titanium Complexes," U.S. Patent No. 4,749,040 (June 7, 1988b).
- Hodge, R.M. and Baranet, S.E.: "Evaluation of Field Methods to Determine Crosslink Times of Fracturing Fluids," paper SPE 16249, presented at the SPE International Symposium on Oilfield Chemistry, San Antonio, Texas, USA (February 4–6, 1987).
- Hodgson, K. and Joughin, N.C.: "The Relationship Between Energy Release Rate, Damage and Seismicity in Deep Mines," *Failure and Breakage of Rock*, C. Fairhurst (ed.), Minneapolis, Minnesota, USA, University of Minnesota Press (1967), 194–203.
- Holder, J., Morita, N., Kenrick, A.J., Thallak, S. and Gray, K.E.: "Measurements of Effective Fracture Toughness Values for Hydraulic Fracture: Dependence on Pressure and Fluid Rheology," paper SPE 25491, presented at the SPE Production Operations Symposium, Oklahoma City, Oklahoma, USA (March 21–23, 1993).
- Holditch, S.A.: "Criteria of Propping Agent Selection," prepared for the Norton Company (1979a).
- Holditch, S.A.: "Factors Affecting Water Blocking and Gas Flow from Hydraulically Fractured Gas Wells," *Journal of Petroleum Technology* (December 1979b) 31, No. 12, 1515–1524.
- Holditch, S.A. and Blakeley, D.M.: "Flow Characteristics of Hydraulic Fracture Proppants Subjected to Repeated Production Cycles," paper SPE 19091, *SPE Production Engineering* (February 1992) 7, No. 1, 15–20.
- Holditch, S.A., Jennings, J.W., Neuse, S.H. and Wyman, R.E.: "The Optimization of Well Spacing and Fracture Length in Low Permeability Gas Reservoirs," paper SPE 7496, presented at the SPE Annual Technical Conference and Exhibition, Houston, Texas, USA (October 1–3, 1978).
- Holditch, S.A. and Morse, R.A.: "The Effects of Non-Darcy Flow on the Behavior of Hydraulically Fractured Gas Wells," paper SPE 5586, *Journal of Petroleum Technology* (October 1976) 28, 1169–1178.
- Holditch, S.A. and Rahim, Z.: "Developing Data Sets for 3D Fracture Propagation Models," paper SPE 26155, *SPE Production & Facilities* (November 1994) 9, No. 4, 257–261.
- Hornby, B.E.: "Tomographic Reconstruction of Near-Borehole Slowness Using Refracted Borehole Sonic Arrivals," *Geophysics* (December 1993) 58, No. 12, 1726–1738.
- Horne, R.N.: *Modern Well Test Analysis: Computer-Aided Approach*, Palo Alto, California, USA, Petroway (1990).
- Horner, D.R.: "Pressure Buildup in Wells," *Proc.*, Third World Petroleum Congress, The Hague, Netherlands (1951) Sec. II, 503–523; also in *Pressure Analysis Methods*, SPE Reprint Series, Richardson, Texas, USA, Society of Petroleum Engineers (1967) 9, 25–43.
- Houzé, O.P., Horne, R.N. and Ramey, H.J. Jr.: "Pressure-Transient Response of an Infinite-Conductivity Vertical Fracture in a Reservoir with Double-Porosity Behavior," paper SPE 16778, *SPE Formation Evaluation* (September 1988) 3, No. 3, 510–518.
- Howard, G.C. and Fast, C.R.: "Optimum Fluid Characteristics for Fracture Extension," *Drilling and Production Practice*, New York, New York, USA, American Petroleum Institute (1957) 24, 261–270. (Appendix by E.D. Carter)
- Howard, G.C. and Fast, C.R.: *Hydraulic Fracturing*, Monograph Series, Richardson, Texas, USA, Society of Petroleum Engineers (1970) 2.
- Howard, P.R., James, S.G. and Milton-Taylor, D.: "High Permeability Channels in Proppant Packs Containing Random Fibers," *SPE Production & Facilities* (August 1999) 14, No. 3, 197.
- Howard, P.R., King, M.T., Morris, M., Féraud, J.-P., Slusher, G. and Lipari, S.: "Fiber/Proppant Mixtures Control Proppant Flowback in South Texas," paper SPE 30495, presented at the SPE Annual Technical Conference and Exhibition, Dallas, Texas, USA (October 22–25, 1995).

- Hsia, T.-Y. and Behrmann, L.A.: "Perforating Skins as a Function of Rock Permeability and Under-balance," paper SPE 22810, presented at the SPE Annual Technical Conference and Exhibition, Dallas, Texas, USA (October 6–9, 1991).
- Hubbert, M.K. and Willis, D.G.: "Mechanics of Hydraulic Fracturing," paper 686-G, presented at the SPE Annual Meeting, Los Angeles, California, USA (October 14–17, 1956); also in *Journal of Petroleum Technology* (September 1957) 9, No. 6, 153–168 and *Trans., AIME* (1957) 210.
- Huddleston, D.A.: "Liquid Aluminum Phosphate Salt Gelling Agent," U.S. Patent No. 5,110,485 (May 5, 1992).
- Hunt, J.L.: "Production Systems Analysis for Fractured Wells," paper SPE 15931, presented at the SPE Eastern Regional Meeting, Columbus, Ohio, USA (November 12–14, 1986).
- Hunter, J. and Walker, R.N. Jr.: "Clean Frac Fluids Improve Load Recovery, Tight-Gas Production," *World Oil* (October 1991) 212, No. 10, 76–78.
- International Society for Rock Mechanics Commission on Testing Methods: *Suggested Methods for Determining the Fracture Toughness of Rocks*, Lisbon, Portugal, ISRM (1988).
- Irwin, G.R.: "Analysis of Stresses and Strains Near the End of a Crack Traversing a Plate," *Journal of Applied Mechanics* (September 1957) 24, 361–364.
- Ispas, I.N., Britt, L.K., Tiab, D., Valkó, P. and Economides, M.J.: "Methodology of Fluid Leakoff Analysis in High Permeability Fracturing," paper SPE 39476, presented at the SPE Formation Damage Conference, Lafayette, Louisiana, USA (February 18–19, 1998).
- ISRM Commission on Testing Methods: "Suggested Methods for Determining Mode I Fracture Toughness Using Cracked Chevron Notched Brazilian Disc (CCNBD) Specimens," *International Journal of Rock Mechanics and Mining Sciences & Geomechanics Abstracts* (1995) 32, No. 1, 59–64.
- Ito, T. and Hayashi, K.: "Physical Background to the Breakdown Pressure in Hydraulic Fracturing Tectonic Stress Measurements," *International Journal of Rock Mechanics and Mining Sciences & Geomechanics Abstracts* (1991) 28, No. 4, 285–293.
- James, S.G., Samuelson, M.L., Reed, G.W. and Sullivan, S.C.: "Proppant Flowback Control in High Temperature Wells," paper SPE 39960, presented at the SPE Rocky Mountain Regional/Low Permeability Reservoirs Symposium and Exhibition, Denver, Colorado, USA (April 5–8, 1998).
- Jasinski, R., Redwine, D. and Rose, G.: "Boron Equilibria with High Molecular Weight Guar: An NMR Study," *J. Polymer Science: Part B: Polymer Physics* (1996) 34, 1477–1488.
- Jeffrey, R.G.: "The Combined Effect of Fluid Lag and Fracture Toughness on Hydraulic Fracture Propagation," paper SPE 18957, presented at the SPE Joint Rocky Mountain Regional/Low Permeability Reservoirs Symposium, Denver, Colorado, USA (March 6–8, 1989).
- Jennings, A.R.: "Fracturing Fluids—Then and Now," paper SPE 36166-P, *Journal of Petroleum Technology* (July 1996) 48, No. 7, 604–611.
- Jizba, D. and Nur, A.: "Static and Dynamic Moduli of Tight Gas Sandstones and Their Relation to Formation Properties," *Transactions of the SPWLA 31st Annual Logging Symposium*, Lafayette, Louisiana, USA (June 24–27, 1990), paper BB.
- Johnson, D.E., Wright, T.B., Tambini, M., Moroli, R. and Cleary, M.P.: "Real-Data On-Site Analysis of Hydraulic Fracturing Generates Optimum Procedures for Job Design and Execution," paper SPE 25920, presented at the SPE Rocky Mountain Regional Meeting, Denver, Colorado, USA (April 12–14, 1993).
- Johnson, E. and Cleary, M.P.: "Implications of Recent Laboratory Experimental Results for Hydraulic Fractures," paper SPE 21846, *Proc.*, Rocky Mountain Regional/Low-Permeability Reservoirs Symposium, Denver, Colorado, USA (1991), 413–428.
- Jones, J. and Soler, D.: "Fracture Stimulation of Shallow, Unconsolidated Kern River Sands," paper SPE 54102 (in press).
- Jones, L.G., Tibbles, R.J., Myers, L., Bryant, D., Hardin, J. and Hurst, G.: "Gravel Packing Horizontal Wellbores with Leak-Off Using Shunts," paper SPE 38640, presented at the SPE Annual Technical Conference and Exhibition, San Antonio, Texas, USA (October 5–8, 1997).

- Joshi, S.D.: "Augmentation of Well Productivity with Slant and Horizontal Wells," paper SPE 15375, *Journal of Petroleum Technology* (June 1988) 40, No. 6, 729–739.
- Kamphuis, H., Davies, D.R. and Roodhart, L.P.: "A New Simulator for the Calculation of the In-Situ Temperature Profile During Well Stimulation Fracturing Treatments," paper CIM/SPE 90-46, *Journal of Canadian Petroleum Technology* (May 1993) 30, No. 5, 38–47.
- Kanninen, M.F. and Popelar, C.H.: *Advanced Fracture Mechanics*, New York, New York, USA, Oxford University Press (1985).
- Karakas, M. and Tariq, S.: "Semi-Analytical Productivity Models for Perforated Completions," paper SPE 18247, presented at the SPE Annual Technical Conference and Exhibition, Houston, Texas, USA (October 2–5, 1988).
- Karakas, M., Yokoyama, Y. and Arima, E.: "Well Test Analysis of a Well with Multiple Horizontal Drainholes," paper SPE 21424, presented at the Middle East Oil Show, Bahrain (November 16–19, 1991).
- Kaufman, H. and Falcetta, J.: *Introduction to Polymer Science and Technology*, John Wiley and Sons, New York, New York, USA (1977), 153.
- Kern, L.R., Perkins, T.K. and Wyant, R.E.: "The Mechanics of Sand Movement in Fracturing," *Journal of Petroleum Technology* (July 1959), 55; also in *Trans., AIME* (1959) 216, 403–405.
- Kesavan, S., Prud'homme, R.K. and Parris, M.D.: "Crosslinked Borate HPG Equilibria and Rheological Characterization," paper SPE 25205, presented at the SPE International Symposium on Oilfield Chemistry, New Orleans, Louisiana, USA (March 2–5, 1993).
- Khristianovich, S.A. and Zheltov, Y.P.: "Formation of Vertical Fractures by Means of Highly Viscous Liquid," *Proc., Fourth World Pet. Congress, Rome* (1955) 2, 579–586.
- Khristianovich, S.A., Zheltov, Y.P., Barenblatt, G.I. and Maximovich, G.K.: "Theoretical Principles of Hydraulic Fracturing of Oil Strata," *Proc., Fifth World Petroleum Congress, New York* (1959).
- Kiel, O.M.: "Process of Hydraulic Fracturing with Viscous Oil-in-Water Emulsion," U.S. Patent No. 3,552,494 (January 5, 1971).
- Kim, C.M. and Willingham, J.R.: "Flow Response of Propped Fracture to Repeated Production Cycles," paper SPE 16912, presented at the SPE Annual Technical Conference and Exhibition, Dallas, Texas, USA (September 27–30, 1987).
- King, G.E.: "Foam Stimulation Fluids: What They Are, Where They Work," *Pet. Eng. Int.* (July 1982) 54, No. 8, 52–60.
- King, G.E., Bingham, M.D. and Kidder, R.W.: "Factors Affecting Perforating Charge Performance and Relationship to Port Plug Condition," paper SPE 13128, *SPE Production Engineering* (September 1986) 1, No. 5, 379–387.
- King, M.S.: "Static and Dynamic Elastic Properties of Rock from the Canadian Shield," *International Journal of Rock Mechanics and Mining Sciences & Geomechanics Abstracts* (October 1983) 20, No. 5, 237–241.
- Kirkby, L.L. and Rockefeller, H.A.: "Proppant Settling Velocities in Nonflowing Slurries," paper SPE/DOE 13906, presented at the SPE/DOE Low Permeability Gas Reservoirs Symposium, Denver, Colorado, USA (May 19–22, 1985).
- Knoll, S.K.: "Wall Slip Evaluation in Steady Shear Viscosity Measurements of Hydraulic Fracturing Fluids," paper SPE/DOE 13904, presented at the SPE/DOE Low Permeability Gas Reservoirs Symposium, Denver, Colorado, USA (May 19–22, 1985).
- Kooijman, A.P., Halleck, P.M., de Bree, P. and Kenter, C.J.: "Large Scale Laboratory Sand Production Test," paper SPE 24798, presented at the SPE Annual Technical Conference and Exhibition, Washington, D.C., USA (October 4–7, 1992).
- Kowalski, J.: "Formation Strength Parameter from Well Logs," *Transactions of the SPWLA 16th Annual Logging Symposium* (June 4–7, 1975), paper N.
- Kuchuk, F.J., Goode, P.A., Brice, B.W., Sherrard, D.W. and Thambynayagam, R.K.M.: "Pressure Transient Analysis and Inflow Performance for Horizontal Wells," paper SPE 18300, presented at the SPE Annual Technical Conference and Exhibition, Houston, Texas, USA (October 2–5, 1988).
- Kulhman, R.D., Heemstra, T.R., Ray, T.G., Lin, P. and Charlez, P.A.: "Field Tests of Downhole Extensometer Used to Obtain Formation In-Situ Stress Data," paper SPE 25905, *Proc., Rocky Mountain/*

- Low Permeability Reservoirs Symposium, Denver, Colorado, USA (1993), 625–634.
- Labrid, J.C.: “Thermodynamic and Kinetic Aspects of Argillaceous Sandstone Acidizing,” paper SPE 5165, *SPE Journal* (April 1975), 117–128.
- Labuz, J.F., Shah, S.P. and Dowding, C.H.: “Experimental Analysis of Crack Propagation in Granite,” *International Journal of Rock Mechanics and Mining Sciences & Geomechanics Abstracts* (April 1985) 22, No. 2, 85–98.
- Lagrone, K.W. and Rasmussen, J.W.: “A New Development in Completion Methods—The Limited Entry Technique,” paper SPE 530, *Journal of Petroleum Technology* (July 1963) 15, 695–702.
- Lamb, H.: *Hydrodynamics*, sixth edition, New York, New York, USA, Dover Publications (1932), 581–587.
- Lambert, M.E.: “A Statistical Study of Reservoir Heterogeneity,” MS thesis, The University of Texas at Austin, Austin, Texas, USA (1981).
- Lane, H.S.: “Numerical Simulation of Mud Filtrate Invasion and Dissipation,” *Transactions of the SPWLA 34th Annual Logging Symposium* (June 13–16, 1993), paper D.
- Larsen, L. and Hegre, T.M.: “Pressure-Transient Behavior of Horizontal Wells with Finite-Conductivity Vertical Fractures,” paper SPE 22076, presented at the International Arctic Technology Conference, Anchorage, Alaska, USA (May 29–31, 1991).
- Last, N., Plumb, R., Harkness, R., Charlez, P., Alsen, J. and McLean, M.: “An Integrated Approach to Evaluating and Managing Wellbore Instability in the Cusiana Field, Colombia, South America,” paper SPE 30464, presented at the SPE Annual Technical Conference and Exhibition, Dallas, Texas, USA (October 22–25, 1995).
- Lea, F.M.: *The Chemistry of Cement and Concrete*, third edition, New York, New York, USA, Chemical Publishing Co. (1971).
- Lear, T.A.: “Near-Wall Velocity Measurements Using Laser Doppler Velocimetry in the FFCF Simulator,” MS thesis, University of Oklahoma, Oklahoma, USA (1996).
- Lee, M.H. and Roberts, L.D.: “Effect of Heat of Reaction on Temperature Distribution in a Fracture,” paper SPE 7893, *SPE Journal* (December 1980) 20, No. 12, 501–507.
- Lee, M.Y. and Haimson, B.C.: “Statistical Evaluation of Hydraulic Fracturing Stress Measurement Parameters,” *International Journal of Rock Mechanics and Mining Sciences & Geomechanics Abstracts* (December 1989) 26, No. 6, 447–456.
- Lee, W.J. and Holditch, S.A.: “Application of Pseudotime to Buildup Test Analysis of Low-Permeability Gas Wells with Long-Duration Wellbore Storage Distortion,” paper SPE 9888, *Journal of Petroleum Technology* (December 1982) 34, No. 12, 2877–2887.
- Leighton, D. and Acrivos, A.: “The Shear-Induced Migration of Particles in Concentrated Suspensions,” *J. Fluid Mech.* (1987) 181, 415–439.
- Lenoach, B.: “Hydraulic Fracture Model Based on Analytical Near-Tip Solutions,” *Computer Methods and Advances in Geomechanics* (1994), 1597–1602.
- Lenoach, B.: “The Crack Tip Solution for Hydraulic Fracturing in a Permeable Solid,” *J. Mech. Phys. Solids* (1995) 43, No. 7, 1025.
- Levine, D.C., Thomas, E.W., Bezner, H.P. and Talle, G.C.: “Annular Gas Flow After Cementing: A Look at Practical Solutions,” paper SPE 8255, presented at the SPE Annual Technical Conference and Exhibition, Las Vegas, Nevada, USA (September 23–26, 1979).
- Li, Y., Sullivan, R.B., de Rozières, J., Gaz, G.L. and Hinkel, J.J.: “An Overview of Current Acid Fracturing Technology with Recent Implications for Emulsified Acids,” paper SPE 26581, presented at the SPE Annual Technical Conference and Exhibition, Houston, Texas, USA (October 3–6, 1993).
- Lipton, D. and Burnett, D.B.: “Comparisons of Polymers Used in Workover and Completion Fluids,” paper SPE 5872, presented at the Improved Oil Recovery Symposium, Tulsa, Oklahoma, USA (March 22–24, 1976).
- Locke, S.: “An Advanced Method for Predicting the Productivity Ratio of a Perforated Well,” paper SPE 8804, *Journal of Petroleum Technology* (December 1981) 33, 2481–2488.

- Lord, D.L., Shah, S.N., Rein, R.G. and Lawson, J.T. III: "Study of Perforation Friction Pressure Employing a Large-Scale Fracturing Flow Simulator," paper SPE 28508, presented at the SPE Annual Technical Conference and Exhibition, New Orleans, Louisiana, USA (September 25–28, 1994).
- Love, A.E.H.: *A Treatise on the Mathematical Theory of Elasticity*, fourth edition, New York, New York, USA, Dover Publications (1927).
- Lubinski, A.: "The Theory of Elasticity for Porous Bodies Displaying a Strong Pore Structure," *Proc.*, 2nd U.S. National Congress of Applied Mechanics (1954), 247.
- Lund, K. and Fogler, H.S.: "Acidization V. The Prediction of the Movement of Acid and Permeability Fronts in Sandstone," *Chemical Engineering Science* (1976) 31, No. 5, 381–392.
- Mack, M.G. and Elbel, J.L.: "A Simulator for Modeling Acid Fracturing Treatments," *Proc.*, 8th International Conference on Computer Methods and Advances in Geomechanics, Morgantown, West Virginia, USA (1994).
- Mack, M.G., Piggott, A.R. and Elbel, J.L.: "Numerical Representation of Multilayer Hydraulic Fracturing," *Proc.*, 33rd U.S. Symposium on Rock Mechanics, Santa Fe, New Mexico, USA (1992), 335–344.
- Mahoney, J.V., Stubbs, P.B., Schwerer, F.C. III and Dobscha, F.X.: "Effects of a No-Proppant Foam Stimulation Treatment on a Coal-Seam Degasification Borehole," *Journal of Petroleum Technology* (November 1981), 2227.
- Malone, B.P., Moran, J.H., Nasution, R.D., Putra, P.H. and Thurston, F.K.: "Start-Up of a TSO Fracturing Campaign in Shallow, Heavy Oil Steamflood," paper SPE 38096, presented at the Asia Pacific Oil and Gas Conference, Kuala Lumpur, Malaysia (April 14–16, 1997).
- Maloney, D.R., Gall, B.L. and Raible, C.J.: "Non-Darcy Flow Through Propped Fractures: Effect of Partial Saturation, Gel Damage, and Stress," paper SPE 16899, presented at the SPE Annual Technical Conference and Exhibition, Dallas, Texas, USA (September 27–30, 1987).
- Martin, J.C.: "Simplified Equations of Flow in Gas Drive Reservoirs and the Theoretical Foundation of Multiphase Pressure Buildup Analyses," paper SPE 1235-G, *Journal of Petroleum Technology* (October 1959) 11, 321–323; also in *Trans., AIME* (1959) 216.
- Martinez, A.D., Pardo, C.W., Ellis, P.D. and Pittman, R.W.: "Determination of Fracture Geometry Using Field Data Coupled with a Fracture Simulator," paper SPE 24826, presented at the SPE Annual Technical Conference and Exhibition, Washington, D.C., USA (October 4–7, 1992).
- Martins, J.P., Abel, J.C., Dyke, C.G., Michel, C.M. and Stewart, G.: "Deviated Well Fracturing and Proppant Production Control in the Prudhoe Bay Field," paper SPE 24858, presented at the SPE Annual Technical Conference and Exhibition, Washington, D.C., USA (October 4–7, 1992a).
- Martins, J.P., Collins, P.J., Rylance, M., Ibe, O.E., Kelly, R.T. and Bartel, P.A.: "Small, Highly Conductive Fractures Near Reservoir Fluid Contacts: Application to Prudhoe Bay," paper SPE 24856, presented at the SPE Annual Technical Conference and Exhibition, Washington, D.C., USA (October 4–7, 1992b).
- Martins, J.P. and Harper, T.R.: "Mini-Frac Pressure Decline Analysis for Fractures Evolving from Long Perforated Intervals and Unaffected by Confining Strata," paper SPE 13869, presented at the SPE/DOE Low Permeability Gas Reservoirs Symposium, Denver, Colorado, USA (May 19–22, 1985).
- Martins, J.P., Leung, K.H., Jackson, M.R., Stewart, D.R. and Carr, A.H.: "Tip Screen-Out Fracturing Applied to the Ravenspurn South Gas Field Development," paper SPE 19766, presented at the SPE Annual Technical Conference and Exhibition, San Antonio, Texas, USA (October 8–11, 1989; also in *SPE Production Engineering* (August 1992c) 7, No. 3, 252–258).
- Martins, J.P., Milton-Taylor, D. and Leung, H.K.: "The Effects of Non-Darcy Flow in Propped Hydraulic Fractures," paper SPE 20709, presented at the SPE Annual Technical Conference and Exhibition, New Orleans, Louisiana, USA (September 23–26, 1990).
- Mason, J.N., Dees, J.M. and Kessler, N.: "Block Tests Model the Near-Wellbore in a Perforated Sandstone," paper SPE 28554, presented at the SPE Annual Technical Conference and Exhibition, New Orleans, Louisiana, USA (September 25–28, 1994).

Mathur, A.K., Ning, X., Marcinew, R.B., Ehlig-Economides, C.A. and Economides, M.J.: "Hydraulic Fracture Stimulation of Highly Permeable Formations: The Effect of Critical Fracture Parameters on Oilwell Production and Pressure," paper SPE 30652, presented at the SPE Annual Technical Conference and Exhibition, Dallas, Texas, USA (October 22–25, 1995).

Maury, V.: "Rock Failure Mechanisms Identification: A Key for Wellbore Stability and Reservoir Behaviour Problems," *Proc.*, Eurock '94, Rock Mechanics in Petroleum Engineering, Delft, Netherlands (1994), 175–182.

Maury, V., Etchecopar, A. and Pezard, P.A.: "New Borehole Imagery Techniques: An Aid for Failure Modes and In Situ Stress Analysis and for Minimizing Drilling Incidents," *Transactions of the SPWLA 40th Annual Logging Symposium*, Oslo, Norway (June 8–10, 1999).

Mayerhofer, M.J., Economides, M.J. and Ehlig-Economides, C.A.: "Pressure Transient Analysis of Fracture Calibration Tests," paper SPE 26527, presented at the SPE Annual Technical Meeting and Exhibition, Houston, Texas, USA (October 3–6, 1993).

Mayerhofer, M.J., Economides, M.J. and Nolte, K.G.: "An Experimental and Fundamental Interpretation of Fracturing Filter-Cake Fluid Loss," paper SPE 22873, presented at the SPE Annual Technical Conference and Exhibition, Dallas, Texas, USA (October 6–9, 1991).

McCabe, M.A., Terracina, J.M. and Kunzl, R.A.: "Continuously Gelled Diesel Systems for Fracturing Applications," paper CIM/SPE 90-93, presented at the Petroleum Society of CIM/SPE International Technical Meeting, Calgary, Alberta, Canada (June 10–13, 1990).

McClain, C.: *Fluid Flow in Pipes*, New York, New York, USA, The Industrial Press (1963), 117–128.

McConnell, B.: "Fracturing Fluid High-Temperature Breaker for Improving Well Performance," paper SPE 28219, *Journal of Petroleum Technology* (May 1994) 46, No. 5, 382.

McDaniel, R.R., Deysarkar, A.K., Callanan, M.J. and Kohlhaas, C.A.: "An Improved Method for Measuring Fluid Loss at Simulated Fracture Conditions," paper SPE 10259, *SPE Journal* (August 1985), 482.

McGuire, W.J. and Sikora, V.T.: "The Effect of Vertical Fractures on Well Productivity," paper SPE 1618-G, *Journal of Petroleum Technology* (October 1960) 12, 72–74; also in *Trans.*, *AIME* (1960) 219, 401–403.

McKenzie, L.F. and Hughes, B.J.: "Hydrocarbon Gels of Alumino Alkyl Acid Orthophosphates," paper SPE 9007, presented at the 5th International Symposium on Oilfield and Geothermal Chemistry, Stanford, California, USA (May 28–30, 1980).

Meehan, D.N., Horne, R.N. and Aziz, K.: "Effects of Reservoir Heterogeneity and Fracture Azimuth on Optimization of Fracture Length and Well Spacing," paper SPE 17606, presented at the SPE International Meeting on Petroleum Engineering, Tianjin, China (November 1–4, 1988).

Meese, C.A., Mullen, M.E. and Barree, R.D.: "Offshore Hydraulic Fracturing Technique," paper SPE 28159, *Journal of Petroleum Technology* (March 1994) 46, No. 3, 226–229.

Meng, H.Z. and Brown, K.E.: "Coupling of Production Forecasting, Fracture Geometry Requirements and Treatment Scheduling in the Optimum Hydraulic Fracture Design," paper SPE 16435, presented at the SPE/DOE Low Permeability Reservoirs Symposium, Denver, Colorado, USA (May 18–19, 1987).

Meng, H.Z., Proano, E.A., Buhidma, I.M. and Mach, J.M.: "Production Systems Analysis of Vertically Fractured Wells," paper SPE/DOE 10842, presented at the SPE/DOE Unconventional Gas Recovery Symposium, Pittsburgh, Pennsylvania, USA (May 16–18, 1982).

Menjivar, J.: "On the Use of Gelation Theory to Characterize Metal Crosslinked Polymer Gels," *Proc.*, ACS Division of Polymer Materials: Science and Engineering, Washington, D.C., USA, American Chemical Society (1984), 88–95.

Meyer, B.R.: "Design Formulae for 2-D and 3-D Vertical Hydraulic Fractures: Model Comparison and Parametric Studies," paper SPE 15240, presented at the SPE Unconventional Gas Technology Symposium, Louisville, Kentucky, USA (May 18–21, 1986a).

Meyer, B.R.: "Generalized Drag Coefficient Applicable for All Flow Regimes," *Oil & Gas Journal* (May 1986b), 71–77.

- Meyer, B.R.: "Heat Transfer in Hydraulic Fracturing," paper SPE 17041, presented at the SPE Eastern Regional Meeting, Pittsburgh, Pennsylvania, USA (October 21–23, 1987).
- Meyer, B.R. and Hagel, M.W.: "Simulated Mini-Frac Analysis," *Journal of Canadian Petroleum Engineering* (September–October 1989) 28, No. 5, 63–73.
- Michels, P.C. and Clark, D.S.: "Pressure Dependence of Enzyme Catalysis," *Biocatalysis at Extreme Temperatures*, M.W.W. Adams and R.M. Kelly (eds.), Symposium Series, Washington, D.C., USA, American Chemical Society (1992), 498, 108–121.
- Miller, B.D. and Warembourg, P.A.: "Prepack Technique Using Fine Sand Improves Results of Fracturing and Fracture Acidizing Treatments," paper SPE 5643, presented at the SPE Annual Technical Conference and Exhibition, Dallas, Texas, USA (September 28–October 1, 1975).
- Miller, W.K. II and Smith, M.B.: "Reanalysis of the MWX Fracture Stimulation Data from the Paludal Zone of the Mesaverde Formation," paper SPE 19772, SPE Annual Technical Conference and Exhibition, San Antonio, Texas, USA (October 8–11, 1989).
- Millheim, K.K. and Cichowicz, L.: "Testing and Analyzing Low-Permeability Fractured Gas Wells," paper SPE 1768, *Journal of Petroleum Technology* (February 1968) 20, 193–198; also in *Trans., AIME* (1968) 243.
- Minh, C.C., Freedman, R., Crary, S. and Cannon, D.: "Integration of NMR with Other Openhole Logs for Improved Formation Evaluation," paper SPE 49012, presented at the SPE Annual Technical Conference and Exhibition, New Orleans, Louisiana, USA (September 27–30, 1998).
- Misak, M.D.: "Temperature-Stable Aqueous Gels," U.S. Patent No. 3,922,173 (November 25, 1975).
- Mitchell, B.J.: "Viscosity of Foam," PhD dissertation, Oklahoma University, Norman, Oklahoma, USA (1969).
- Mitchell, B.J.: "Test Data Fill Theory Gap on Using Foam as a Drilling Fluid," *Oil & Gas Journal* (September 6, 1971), 96–100.
- Mondshine, T.C.: "Crosslinked Fracturing Fluids," U.S. Patent No. 4,619,776 (October 28, 1986).
- Mondshine, T.C.: "Process for Decomposing Polysaccharides in Alkaline Aqueous Systems," U.S. Patent No. 5,253,711 (October 19, 1993).
- Montgomery, K.T. and Berthelot, J.M.: "Effects of Fracture Fluid Invasion on Cleanup Behavior and Pressure Buildup Analysis," paper SPE 20643, presented at the SPE Annual Technical Conference and Exhibition, New Orleans, Louisiana, USA (September 23–26, 1990).
- Monus, F.L., Broussard, F.W., Ayoub, J.A. and Norman, W.D.: "Fracturing Unconsolidated Sand Formations Offshore Gulf of Mexico," paper SPE 24844, presented at the SPE Annual Technical Conference and Exhibition, Washington, D.C., USA (October 4–7, 1992).
- Moore, J.E.: "Clay Mineralogy Problems in Oil Recovery," *Petroleum Engineering* (1960) B40.
- Morales, R.H., Brady, B.H. and Ingraffea, A.R.: "Three-Dimensional Analysis and Visualization of the Wellbore and the Fracturing Process in Inclined Wells," paper SPE 25889, presented at the SPE Rocky Mountain Regional/Low Permeability Reservoirs Symposium, Denver, Colorado, USA (April 12–14, 1993).
- Morales, R.H., Brown, J.E., Norman, W.D., DeBonis, V., Mathews, M., Park, E.I. and Brown, D.: "Mechanical Skin Damage on Wells," paper SPE 30459, presented at the SPE Annual Technical Conference and Exhibition, Dallas, Texas, USA (October 22–25, 1995).
- Morales, R.H. and Marcinew, R.P.: "Fracturing of High-Permeability Formations: Mechanical Properties Correlations," paper SPE 26561, presented at the SPE Annual Technical Conference and Exhibition, Houston, Texas, USA (October 3–6, 1993).
- Moricca, G., Ripa, G., Sanfilippo, F. and Santarelli, F.J.: "Basin Scale Rock Mechanics: Field Observation of Sand Production," *Proc., Eurock '94, Rock Mechanics in Petroleum Engineering*, Delft, Netherlands (1994), 317–328.
- Morita, N., Burton, R.C. and Davis, E.: "Fracturing, Frac Packing and Formation Control: Can Screenless Completions Prevent Sand Production," *SPE Drilling and Completion* (September 1998), 157–162.



- Morita, N., Whitfill, D.L., Fedde, O.P. and Levik, T.H.: "Parametric Study of Sand Production Prediction: Analytical Approach," paper SPE 16990, *SPE Production Engineering* (February 1989) 4, No. 1, 25–33.
- Morita, N., Whitfill, D.L. and Wahl, H.A.: "Stress-Intensity Factor and Fracture Cross-Sectional Shape Predictions from a Three-Dimensional Model for Hydraulically Induced Fractures," paper SPE 14262, *Journal of Petroleum Technology* (October 1988) 40, No. 10, 1329–1342.
- Morris, C.W. and Sinclair, A.R.: "Evaluation of Bottomhole Treatment Pressure for Geothermal Well Hydraulic Fracture Stimulation," paper SPE 11157, *Journal of Petroleum Technology* (May 1984), 829.
- Morse, R.A. and Von Gonten, W.D.: "Productivity of Vertically Fractured Wells Prior to Stabilized Flow," paper SPE 3631, *Journal of Petroleum Technology* (July 1972) 24, 807–812.
- Mukherjee, H., Paoli, B.F., McDonald, T., Cartaya, H. and Anderson, J.A.: "Successful Control of Fracture Height Growth by Placement of Artificial Barrier," paper SPE 25917, presented at the SPE Rocky Mountain Regional/Low Permeability Reservoirs Symposium, Denver, Colorado, USA (April 12–14, 1994); also in *SPE Production & Facilities* (May 1995), 89.
- Mullen, M.E., Norman, W.D. and Granger, J.C.: "Productivity Comparison of Sand Control Techniques Used for Completions in the Vermilion 331 Field," paper SPE 27361, presented at the SPE International Symposium on Formation Damage Control, Lafayette, Louisiana, USA (February 7–10, 1994).
- Muskat, M.: *The Flow of Homogeneous Fluids Through Porous Media*, New York, New York, USA, McGraw-Hill Book Co. (1937).
- Muskhelishvili, N.I.: *Some Basic Problems of the Theory of Elasticity*, fourth edition, J.R. Radok (trans.), Groningen, Netherlands, P. Noordhoff (1953).
- Navarrete, R.C., Cawiezel, K.E. and Constien, V.G.: "Dynamic Fluid Loss in Hydraulic Fracturing Under Realistic Shear Conditions in High-Permeability Rocks," paper SPE 28529, presented at the SPE Annual Technical Conference and Exhibition, New Orleans, Louisiana, USA (September 25–28, 1994); also paper SPE 28529-P, *SPE Production & Facilities* (August 1996), 138.
- Navarrete, R.C. and Mitchell, J.P.: "Fluid-Loss Control for High-Permeability Rocks in Hydraulic Fracturing Under Realistic Shear Conditions," paper SPE 29504, presented at the SPE Production Operations Symposium, Oklahoma City, Oklahoma, USA (April 2–4, 1995).
- Nelson, E.B.: "Introduction," *Well Cementing*, E.B. Nelson (ed.), Houston, Texas, USA, Schlumberger (1990), I-1–I-3.
- Nelson, E.B., Baret, J.-F. and Michaux, M.: "Cement Additives and Mechanisms of Action," *Well Cementing*, E.B. Nelson (ed.), Houston, Texas, USA, Schlumberger (1990), 3-1–3-37.
- Nelson, E.B., Constien, V.G. and Cawiezel, K.E.: "Delayed Borate Crosslinked Fracturing Fluid Having Increased Temperature Range," U.S. Patent No. 5,658,861 (1997).
- Nester, J.H., Jenkins, D.R. and Simon, R.: "Resistances to Failure of Oil-Well Casing Subjected to Non-Uniform Transverse Loading," *Drilling and Production Practice*, New York, New York, USA, American Petroleum Institute (1956), 374–378.
- Nguyen, H.X. and Larson, D.B.: "Fracture Height Containment by Creating an Artificial Barrier with a New Additive," paper SPE 12061, presented at the SPE Annual Technical Conference and Exhibition, San Francisco, California, USA (October 5–8, 1983).
- Nierode, D.E. and Kruk, K.F.: "An Evaluation of Acid Fluid Loss Additives, Retarded Acids, and Acidized Fracture Conductivity," paper SPE 4549, presented at the SPE Annual Meeting, Las Vegas, Nevada, USA (September 30–October 3, 1973).
- Nikolaevskiy, V.N. and Economides, M.J.: "The Near-Well State of Stress and Induced Rock Damage," paper SPE 58716, presented at the SPE International Symposium on Formation Damage, Lafayette, Louisiana, USA (February 23–24, 2000).
- Nimerick, K.H., McConnell, S.B. and Samuelson, M.L.: "Compatibility of Resin-Coated Proppants with Crosslinked Fracturing Fluids," paper SPE 20639, presented at the SPE Annual Technical Conference and Exhibition, New Orleans, Louisiana, USA (September 23–26, 1990); also in *SPE Production Engineering* (February 1992), 29.



- Nolte, K.G.: "Determination of Fracture Parameters from Fracturing Pressure Decline," paper SPE 8341, presented at the SPE Annual Technical Conference and Exhibition, Las Vegas, Nevada, USA (September 23–26, 1979).
- Nolte, K.G.: "Fracture Design Considerations Based on Pressure Analysis," paper SPE 10911, presented at the SPE Cotton Valley Symposium, Tyler, Texas, USA (May 20, 1982).
- Nolte, K.G.: "Fracturing Fluid Breaker System Which Is Activated by Fracture Closure," U.S. Patent No. 4,506,734 (March 26, 1985).
- Nolte, K.G.: "A General Analysis of Fracturing Pressure Decline Analysis with Application to Three Models," paper SPE 12941, *SPE Formation Evaluation* (December 1986a) 1, No. 6, 571–583.
- Nolte, K.G.: "Determination of Proppant and Fluid Schedules from Fracturing Pressure Decline," paper SPE 13278, *SPE Production Engineering* (July 1986b) 1, No. 4, 255–265.
- Nolte, K.G.: "Discussion of Influence of Geologic Discontinuities on Hydraulic Fracture Propagation," paper SPE 17011, *Journal of Petroleum Technology* (August 1987) 39, No. 8, 998.
- Nolte, K.G.: "Application of Fracture Design Based on Pressure Analysis," paper SPE 13393, *SPE Production Engineering* (February 1988a) 3, No. 1, 31–42.
- Nolte, K.G.: "Fluid Flow Considerations in Hydraulic Fracturing," paper SPE 18537, *Proc.*, SPE Eastern Regional Meeting, Charleston, West Virginia, USA (1988b), 145–156.
- Nolte, K.G.: "Principles for Fracture Design Based on Pressure Analysis," paper SPE 10911, *SPE Production Engineering* (February 1988c) 3, No. 1, 22–30.
- Nolte, K.G.: "Derivations and Considerations for Pressure Decline Analysis," Appendix J of *Recent Advances in Hydraulic Fracturing*, J.L. Gidley, S.A. Holditch, D.E. Nierode and R.W. Veatch Jr. (eds.), Monograph Series, Richardson, Texas, USA, Society of Petroleum Engineers (1989), 410–415.
- Nolte, K.G.: "Fracturing Pressure Analysis for Non-Ideal Behavior," paper SPE 20704, presented at the SPE Annual Technical Conference and Exhibition, New Orleans, Louisiana, USA (September 23–26, 1990); also in *Journal of Petroleum Technology* (February 1991) 43, No. 2, 210–218.
- Nolte, K.G.: "Background for After-Closure Analysis of Calibration Treatments," paper SPE 39407 (1998).
- Nolte, K.G. and Economides, M.J.: "Fracture Design and Validation with Uncertainty and Model Limitations," paper SPE 18979, *Journal of Petroleum Technology* (September 1991) 43, No. 9, 1147–1155.
- Nolte, K.G., Mack, M.G. and Lie, W.L.: "A Systematic Method for Applying Fracturing Pressure Decline: Part 1," paper SPE 25845, presented at the SPE Rocky Mountain Regional Meeting and Low Permeability Reservoirs Symposium, Denver, Colorado, USA (April 12–14, 1993).
- Nolte, K.G., Maniere, J.L. and Owens, K.A.: "After-Closure Analysis of Fracture Calibration Tests," paper SPE 38676, presented at the SPE Annual Technical Conference and Exhibition, San Antonio, Texas, USA (October 5–8, 1997).
- Nolte, K.G. and Smith, M.B.: "Interpretation of Fracturing Pressures," paper SPE 8297, presented at the SPE Annual Technical Conference and Exhibition, Las Vegas, Nevada, USA (September 23–26, 1979); also in *Journal of Petroleum Technology* (September 1981) 33, No. 9, 1767–1775.
- Nordgren, R.P.: "Propagation of a Vertical Hydraulic Fracture," paper SPE 7834, *SPE Journal* (August 1972) 12, No. 8, 306–314.
- Norman, L.R.: "Properties and Early Field Results of a Liquid Gelling Agent for Acid," paper SPE 7834, presented at the SPE Production Technology Symposium, Hobbs, New Mexico, USA (October 30–31, 1978).
- Norman, L.R., Hollenbeak, K.H. and Harris, P.C.: "Fracture Conductivity Impairment Removal," paper SPE 19732, presented at the SPE Annual Technical Conference and Exhibition, San Antonio, Texas, USA (October 8–11, 1989).
- Norman, L.R., Terracina, J.M., McCabe, M.A. and Nguyen, P.D.: "Application of Curable Resin-Coated Proppants," paper SPE 20640, presented at the SPE Annual Technical Conference and Exhibition, New Orleans, Louisiana, USA (September 23–26, 1990); also in *SPE Production Engineering* (November 1992), 343.

- Norman, R.O.C.: *Principles of Organic Synthesis*, London, UK, Methuen & Co., Ltd. (1968).
- Norris, M.R., Berntsen, B.A., Myhre, P. and Winters, W.J.: "Multiple Proppant Fracturing of a Horizontal Wellbore: An Integration of Two Technologies," paper SPE 36899, presented at the SPE European Petroleum Conference, Milan, Italy (October 22–24, 1996).
- Novotny, E.J.: "Proppant Transport," paper SPE 6813, presented at the SPE Annual Technical Conference and Exhibition, Denver, Colorado, USA (October 9–12, 1977).
- Olejniczak, S.J., Swaren, J.A., Gulrajani, S.N. and Olmstead, C.C.: "Fracturing Bypassed Pay in Tubingless Completions," paper SPE 56467, presented at the SPE Annual Technical Conference and Exhibition, Houston, Texas, USA (October 3–6, 1999).
- Ong, S.H. and Roegiers, J.-C.: "Influence of Anisotropies in Borehole Stability," *International Journal of Rock Mechanics and Mining Sciences & Geomechanics Abstracts* (June 1993) 30, No. 7, 1069–1075.
- Ott, R.E., Bell, W.T., Golian, T.G. and Harrigan, J.W. Jr.: "Simple Method Predicts Downhole Shaped Charge Gun Performance," paper SPE 27424, *SPE Production & Facilities* (August 1994a) 9, No. 3, 171–178.
- Ott, R.E., Bell, W.T., Golian, T.G. and Harrigan, J.W. Jr.: "Authors' Reply to Discussion of Simple Method Predicts Downhole Shaped Charge Gun Performance," paper SPE 30069, *SPE Production & Facilities* (November 1994b) 9, No. 4, 294–295.
- Ouchterlony, F.: "Review of Fracture Toughness in Rock," *Solid Mechanics Archives* (1982) 7, No. 2, 131–211.
- Ozkan, E. and Raghavan, R.: "New Solutions for Well Test Analysis Problems: Part I—Analytical Considerations," paper SPE 18615, *SPE Formation Evaluation* (September 1991) 6, No. 3, 359–368.
- Pacelli Zitha: "Effects of Bridging-Adsorption of Macromolecules on the Flow of Linear Flexible Polymer Solutions in Porous Media," *C.R. Acad. Sci. Paris, Serie Iib* (1995), 320, 447–453.
- Paillet, F.L. and Chang, C.H.: *Acoustic Waves in Boreholes*: CRC Press, Inc., Boca Raton, Florida, USA (1991).
- Palmer, I.D.: "Induced Stresses due to Propped Hydraulic Fracture in Coalbed Methane Wells," paper SPE 25861, *Proc.*, Rocky Mountain Regional/Low Permeability Reservoirs Symposium, Denver, Colorado, USA (1993), 221–232.
- Palmer, I.D. and Veatch, R.W. Jr.: "Abnormally High Fracturing Pressures in Step-Rate Tests," paper SPE 16902, presented at the SPE Annual Technical Conference and Exhibition, Dallas, Texas, USA (September 27–30, 1987).
- Papamichos, E., Vardoulakis, I. and Ouadfel, H.: "Permeability Reduction due to Grain Crushing Around a Perforation," *International Journal of Rock Mechanics and Mining Sciences & Geomechanics Abstracts* (December 1993), 30, No. 7, 1223–1229.
- Papanastasiou, P.: "A Coupled Elasto-Plastic Hydraulic Fracturing Model," *International Journal of Rock Mechanics and Mining Sciences & Geomechanics Abstracts* (1997) 34, 240.
- Papanastasiou, P. and Thiercelin, M.: "Influence of Inelastic Rock Behavior in Hydraulic Fracturing," *International Journal of Rock Mechanics and Mining Sciences & Geomechanics Abstracts* (June 1993) 30, No. 7, 1241–1247.
- Papanastasiou, P., Thiercelin, M., Cook, J. and Durban, D.: "The Influence of Plastic Yielding on Breakdown Pressure in Hydraulic Fracturing," *Proc.*, 35th U.S. Symposium on Rock Mechanics, Reno, Nevada, USA (1995), 281–286.
- Papinczak, A. and Miller, W.K. II: "Fracture Treatment Design to Overcome Severe Near-Wellbore Damage in a Moderate Permeability Reservoir, Mereenie Field, Australia," paper SPE 25379, presented at the Asia Pacific Oil and Gas Conference and Exhibition, Singapore (February 8–10, 1993).
- Parcevaux, P., Rae, P. and Drecq, P.: "Prevention of Annular Gas Migration," *Well Cementing*, E.B. Nelson (ed.), Houston, Texas, USA, Schlumberger (1990), 8-1–8-22.
- Parlar, M., Nelson, E.B., Walton, I.C., Park, E. and Debonis, V.: "An Experimental Study on Fluid-Loss Behavior of Fracturing Fluids and Formation Damage in High-Permeability Porous Media," paper SPE 30458, presented at the SPE Annual Technical Conference and Exhibition, Dallas, Texas, USA (October 22–25, 1995).

- Pattillo, P.D. and Smith, M.B.: "The Effect of Formation Flow on the Integrity of Perforated Casing," paper SPE 11123, *SPE Journal* (October 1985) 25, No. 5, 637–646.
- Payne, K.L. and Harms, S.D.: "Chemical Processes for Controlling Crosslinking Reaction Rates," presented at the AIChE National Spring Meeting, Anaheim, California, USA (May 20, 1984).
- Pearson, C.M., Bond, A.J., Eck, M.E. and Schmidt, J.H.: "Results of Stress Oriented and Aligned Perforating in Fracturing Deviated Wells," paper SPE 22836, *Journal of Petroleum Technology* (January 1992) 44, 10–18.
- Penny, G.S.: "An Evaluation of the Effects of Environmental Conditions and Fracturing Fluids upon the Long-Term Conductivity of Proppants," paper SPE 16900, presented at the SPE Annual Technical Conference and Exhibition, Dallas, Texas, USA (September 27–30, 1987).
- Penny, G.S., Conway, M.W. and Lee, W.: "Control and Modeling of Fluid Leakoff During Hydraulic Fracturing," paper SPE 12486, *Journal of Petroleum Technology* (June 1985) 37, No. 6, 1071–1081.
- Penny, G.S. and Jin, L.: "The Development of Laboratory Correlations Showing the Impact of Multiphase Flow, Fluid, and Proppant Selection upon Gas Well Productivity," paper SPE 30494, presented at the SPE Annual Technical Conference and Exhibition, Dallas, Texas, USA (October 22–25, 1995).
- Penny, G.S., Soliman, M.Y., Conway, M.W. and Briscoe, J.E.: "Enhanced Load Water-Recovery Technique Improves Stimulation Results," paper SPE 12149, presented at the SPE Annual Technical Conference and Exhibition, San Francisco, California, USA (October 5–8, 1983).
- Perkins, T.K.: "Discussion of 'On the Design of Vertical Hydraulic Fractures,'" *Journal of Petroleum Technology* (January 1973) 25, No. 1, 80–81; also in *Trans., AIME* (1973) 255, 93–95.
- Perkins, T.K. and Gonzalez, J.A.: "Changes in Earth Stresses Around a Wellbore Caused by Radially Symmetrical Pressure and Temperature Gradients," paper SPE 10080, *SPE Journal* (April 1984), 129–140.
- Perkins, T.K. and Kern, L.R.: "Widths of Hydraulic Fractures," paper SPE 89, *Journal of Petroleum Technology* (September 1961) 13, No. 9, 937–949.
- Perkins, T.K. and Krech, W.W.: "The Energy Balance Concept of Hydraulic Fracturing," paper SPE 1901, *SPE Journal* (March 1968) 8, No. 1, 1–12.
- Perkins, T.K. and Weingarten, J.S.: "Stability and Failure of Spherical Cavities in Unconsolidated Sand and Weakly Consolidated Rock," paper SPE 18244, presented at the SPE Annual Technical Conference and Exhibition, Houston, Texas, USA (October 2–5, 1988).
- Perrine, R.L.: "Analysis of Pressure-Buildup Curves," *Drilling and Production Practice* 1956, New York, New York, USA, American Petroleum Institute (1957), 482–509.
- Peterson, R.E., Wolhart, S.L., Frohne, K.-H., Warpinski, N.R., Branagan, P.T. and Wright, T.B.: "Fracture Diagnostics Research at the GRI/DOE Multi-Site Project: Overview of the Concept and Results," paper SPE 36449, presented at the SPE Annual Technical Conference and Exhibition, Denver, Colorado, USA (October 6–9, 1996).
- Petitjean, L., Couet, B., Abel, J.C., Schmidt, J.H. and Ferguson, K.R.: "Well Productivity Improvement Using Extreme Overbalanced Perforating and Surging—Case History," paper SPE 30527, presented at the SPE Annual Technical Conference and Exhibition, Dallas, Texas, USA (October 22–25, 1995).
- Pezron, E., Leibler, L., Ricard, A. and Audebert, R.: "Glactomannan-Borate Systems: A Complexation Study," *Giol. Synt. Polym. Network*, O. Kramer (ed.) (1988a), 113–126.
- Pezron, E., Ricard, A., Lafuma, F. and Audebert, R.: "Reversible Gel Formations Induced by Ion Complexation," *Macromolecules* (1988b) 21, No. 4, 1121–1125.
- Phelps, G.D., Stewart, G., Peden, J.M. and Heriot-Watt, U.: "The Analysis of the Invaded Zone Characteristics and Their Influence on Wireline Log and Well-Test Interpretation," paper SPE 13287, presented at the SPE Annual Technical Conference and Exhibition, Houston, Texas, USA (September 16–19, 1984).

- Piggott, A.R., Brady, B.H. and Gu, H.: "Reservoir Formation Characterization from Hydraulic Fracturing Records," *Proc.*, Eurock '92 Symposium, London, UK (1992), 360–365.
- Plahn, S.V., Nolte, K.G., Thompson, L.G. and Miska, S.: "A Quantitative Investigation of the Fracture Pump-In/Flowback Test," paper SPE 30504, presented at the SPE Annual Technical Conference and Exhibition, Dallas, Texas, USA (October 22–25, 1995); also in *SPE Production & Facilities* (February 1997) 12, No. 1, 20–27.
- Plona, T.J. and Cook, J.M.: "Effects of Stress Cycles on Static and Dynamic Young's Moduli in Castlegate Sandstones," *Proc.*, 35th U.S. Symposium on Rock Mechanics, Reno, Nevada, USA (1995), 155–160.
- Plumb, R.A.: "Influence of Composition and Texture on the Failure Properties of Clastic Rocks," paper SPE 28022, presented at the SPE/ISRM Rock Mechanics in Petroleum Engineering Conference, Delft, Netherlands (August 29–31, 1994a).
- Plumb, R.A.: "Variations of the Least Horizontal Stress Magnitude in Sedimentary Rocks," *Proc.*, 1st North American Symposium on Rock Mechanics, Austin, Texas, USA (1994b), 71–78.
- Plumb, R.A. and Cox, J.W.: "Stress Directions in Eastern North American Determined to 4.5 Km from Borehole Elongation Measurements," *Journal of Geophysical Research* (1987) 92, No. B6, 4805–4816.
- Plumb, R.A., Evans, K.F. and Engelder, T.: "Geophysical Log Responses and Their Correlation with Bed-to-Bed Stress Contrasts in Paleozoic Rocks, Appalachian Plateau, New York," *Journal of Geophysical Research* (August 1991) 96, No. B9, 14509–14528.
- Plumb, R.A. and Hickman, S.H.: "Stress Induced Borehole Elongation: A Comparison Between Four-Arm Dipmeter and the Borehole Televiewer in the Auburn Geothermal Well," *Journal of Geophysical Research* (1985), 90, No. B7, 5513–5521.
- Poe, B.D. Jr., Elbel, J.L., Spath, J.B. and Wiggins, M.L.: "Prediction of Future Well Performance, Including Reservoir Depletion Effects," paper SPE 29465, presented at the SPE Operations Symposium, Denver, Colorado, USA (April 2–4, 1995).
- Poe, B.D. Jr., Shah, P.C. and Elbel, J.L.: "Pressure Transient Behavior of a Finite-Conductivity Fractured Well with Spatially Varying Fracture Properties," paper SPE 24707, presented at the SPE Annual Technical Conference and Exhibition, Washington, D.C., USA (October 4–7, 1992).
- Pop, J.J., Badry, R.A., Morris, C.W., Wilkinson, D.J., Tottrup, P. and Jonas, J.K.: "Vertical Interference Testing with a Wireline-Conveyed Straddle-Packer Tool," paper SPE 26481, presented at the SPE Annual Technical Conference and Exhibition, Houston, Texas, USA (October 3–6, 1993).
- Pope, D., Britt, L., Constien, V., Anderson, A. and Leung, L.: "Field Study of Guar Removal from Hydraulic Fractures," paper SPE 31094, presented at the SPE International Symposium on Formation Damage Control, Lafayette, Louisiana, USA (February 14–15, 1996).
- Pope, D.S., Leung, L.K.-W., Gulbis, J. and Constien, V.G.: "Effects of Viscous Fingering on Fracture Conductivity," paper SPE 28511, presented at the SPE Annual Technical Conference and Exhibition, New Orleans, Louisiana, USA (September 25–28, 1994).
- Pospisil, G., Carpenter, C.C. and Pearson, C.M.: "Impacts of Oriented Perforating on Fracture Stimulation Treatments: Kuparuk River Field, Alaska," paper SPE 29645, presented at the SPE Western Regional Meeting, Bakersfield, California, USA (March 8–10, 1995).
- Poupon, A., Clavier, C., Dumanoir, J., Gaynard, R. and Misk, A.: "Log Analysis of Sand-Shale Sequences: A Systematic Approach," *Journal of Petroleum Technology* (July 1970), 867–881.
- Power, D.J., Paterson, L. and Boger, D.V.: "The Influence of Fluid Properties on the Success of Hydraulic Fracturing Operations," paper SPE 28804, presented at the SPE Asia Pacific Oil & Gas Conference, Melbourne, Australia (November 7–10, 1994).
- Prats, M.: "Effect of Vertical Fractures on Reservoir Behavior—Incompressible Fluid Case," paper SPE 1575-G, *SPE Journal* (June 1961) 1, No. 1, 105–118; also in *Trans., AIME* (1961) 222.
- Prats, M.: "Effect of Burial History on the Subsurface Horizontal Stresses of Formations Having Different

Material Properties,” paper SPE 9017, *SPE Journal* (December 1981) 21, No. 6, 658–662.

Prats, M., Hazebroek, P. and Strickler, W.R.: “Effect of Vertical Fractures on Reservoir Behavior—Compressible Fluid Case,” paper SPE 98, *SPE Journal* (June 1962) 2, No. 2, 87–94.

Press, W.H., Flannery, B.P., Teukolsky, S.A. and Vetterling, W.T.: *Numerical Recipes—The Art of Scientific Computing*, New York, New York, USA, Cambridge University Press (1986).

Proano, E.A. and Lilley, I.J.: “Derivative of Pressure: Application to Bounded Reservoir Interpretation,” paper SPE 15861, presented at the SPE European Petroleum Conference, London, UK (October 20–22, 1986).

Prud’homme, R.K.: “Rheological Characterization of Fracturing Fluids,” final report, API Practices Projects 84-45, 85-45 and 86-45, American Petroleum Institute (1984–1986).

Prud’homme, R.K.: “Laboratory Preparation and Rheological Characterization of Crosslinked Fracturing Fluids,” paper SPE 20637 (1990).

Prud’homme, R.K.: “Rheology of Fracturing Fluid Gels and Slurries,” *GRI/API Quarterly Progress Report* (April 1991).

Prud’homme, R.K., Constien, V.G. and Knoll, S.: “The Effects of Shear History on the Rheology of Hydroxypropyl Guar Gels,” *Polymers in Aqueous Media*, J.E. Glass (ed.), Advances in Chemistry Series, Washington, D.C., USA, American Chemical Society (1989), 223.

Prud’homme, R.K., Ellis, S., Constien, V.G. and Knoll, S.: “Reproducible Rheological Measurements on Crosslinked Fracturing Fluids,” paper SPE 18210, presented at the SPE Annual Technical Conference and Exhibition, Houston, Texas, USA (October 2–5, 1988).

Prud’homme, R.K. and Khan, S.A. (eds.): *Foams: Theory, Measurements, and Applications*, Marcel Dekker, Inc. (1996).

Prud’homme, R.K. and Wang, J.K.: “Filter-Cake Formation of Fracturing Fluids,” paper SPE 25207, presented at the SPE International Symposium on Oilfield Chemistry, New Orleans, Louisiana, USA (March 2–5, 1993).

Pucknell, J.K. and Behrmann, L.A.: “An Investigation of the Damaged Zone Created by Perforating,” paper SPE 22811, presented at the SPE Annual Technical Conference and Exhibition, Dallas, Texas, USA (October 6–9, 1991).

Quadir, J.A.: “Particle Transport by Non-Newtonian Fluids in Vertical Slots,” MS thesis, The University of Tulsa, Tulsa, Oklahoma, USA (1981).

Quirein, J., Kimminau, S., LaVigne, J., Singer, J. and Wendel, F.: “A Coherent Framework for Developing and Applying Multiple Formation Evaluation Models,” Transactions of the SPWLA 27th Annual Logging Symposium (June 9–13, 1986), paper DD.

Raghavan, R.: “Some Practical Considerations in the Analysis of Pressure Data,” paper SPE 5876, *Journal of Petroleum Technology* (October 1976) 28, 1256–1268.

Raghavan, R., Chen, C. and Agarwal, B.: “An Analysis of Horizontal Wells Intercepted by Multiple Fractures,” paper SPE 27652, presented at the SPE Permian Basin Oil and Gas Recovery Conference, Midland, Texas, USA (March 16–18, 1994).

Raghavan, R. and Joshi, S.D.: “Productivity of Multiple Drainholes or Fractured Horizontal Wells,” paper SPE 21263, *SPE Formation Evaluation* (March 1993) 8, No. 1, 11–16.

Rahim, Z. and Holditch, S.A.: “The Effects of Mechanical Properties and Selection of Completion Interval upon the Created and Propped Fracture Dimensions in Layered Reservoirs,” paper SPE 24349, presented at the SPE Rocky Mountain Regional Meeting, Casper, Wyoming, USA (May 18–21, 1992).

Ramakrishnan, T.S., Dave, Y. and Cappiello, A.: “A Laboratory Investigation of Permeability in Hemispherical Flow with Application to Formation Testers,” paper SPE 22689, presented at the SPE Annual Technical Conference and Exhibition, Dallas, Texas, USA (October 6–9, 1991).

Ramlakhan, T.: “Characterization of the Altered Zone Around a Shaped-Charge Perforation Using X-Ray Computerized Tomography,” thesis, Pennsylvania State University, Pennsylvania, USA (1994).

Ramos, G.G., Katahara, K.W., Gray, J.D. and Knox, D.J.W.: “Sand Production in Vertical and Horizontal

Wells in a Friable Sandstone Formation, North Sea," *Proc.*, Eurock '94, Rock Mechanics in Petroleum Engineering, Delft, Netherlands (1994), 309–315

Raymond, L.R. and Binder, G.G.: "Productivity of Wells in Vertically Fractured, Damaged Formations," paper SPE 1454, *Journal of Petroleum Technology* (January 1967) 19, 120–130.

*Recommended Practice for Standard Procedures for Evaluation of Hydraulic Fracturing Fluids (RP 39)*, second edition, Dallas, Texas, USA, American Petroleum Institute (1983).

*Recommended Practices for Evaluation of Well Perforators (RP 43)*, fourth edition, New York, New York, USA, American Petroleum Institute (August 1985).

*Recommended Practices for Testing Sand Used in Hydraulic Fracturing Operations (RP 56)*, first edition, Dallas, Texas, USA, American Petroleum Institute (1983).

Regalbuto, J.A. and Riggs, R.S.: "Underbalanced Perforation Characteristics as Affected by Differential Pressure," paper SPE 15816, *SPE Production Engineering* (February 1988) 3, No. 1, 83–88.

Reidenbach, V.G., Harris, P.C., Lee, Y.N. and Lord, D.L.: "Rheological Study of Foam Fracturing Fluids Using Nitrogen and Carbon Dioxide," paper SPE 12026, *SPE Production Engineering* (January 1986) 1, No. 1, 31–41.

Reimers, D.R. and Clausen, R.A.: "High-Permeability Fracturing at Prudhoe Bay, Alaska," paper SPE 22835, presented at the SPE Annual Technical Conference and Exhibition, Dallas, Texas, USA (October 22–25, 1991).

Rice, J.R.: "Mathematical Analysis in the Mechanics of Fracture," *Fracture, An Advanced Treatise*, New York, New York, USA, Academic Press (1968), 2.

Rice, J.R.: "Pore Pressure Effects in Inelastic Constitutive Formulations for Fissured Rock Masses," *Advances in Civil Engineering Through Engineering Mechanics*, New York, New York, USA, American Society of Civil Engineers (1977), 295–297.

Risnes, R., Bratli, R.K. and Horsrud, P.: "Sand Stresses Around a Wellbore," paper SPE 9650, *SPE Journal* (December 1982) 22, No. 6, 893–898.

Roberts, B.E., van Engen, H. and van Kruysdijk, C.P.J.W.: "Productivity of Multiply Fractured Horizontal Wells in Tight Gas Reservoirs," paper SPE 23113, presented at the SPE Offshore Europe Conference, Aberdeen, Scotland (September 3–6, 1991).

Roberts, C.N.: "Fracture Optimization in a Tight Gas Play: Muddy-J Formation, Wattenberg Field, Colorado," paper SPE 9851, presented at the SPE Low Permeability Symposium, Denver, Colorado, USA (May 27–29, 1981).

Robinson, B.M., Holditch, S.A. and Peterson, R.E.: "The Gas Research Institute's Second Staged Field Experiment: A Study of Hydraulic Fracturing," paper SPE 21495, presented at the SPE Gas Technology Symposium, Houston, Texas, USA (January 23–25, 1991).

Robinson, G., Ross-Murphy, S.B. and Morris, E.R.: "Viscosity-Molecular Weight Relationships, Intrinsic Chain Flexibility, and Dynamic Solution Properties of Guar Galactomannan," *Carbohydrate Research* (1982) 107, 17–32.

Rochon, J., Creusot, M.R., Feugas, D., Thibeau, S. and Bergerot, J-L.: "Viscous Fluids Characterize the Crushed Zone," paper SPE 27383, *SPE Drilling and Completion* (September 1995) 10, No. 3, 198–203.

Rodriguez, F., Horne, R.N. and Cinco-Ley, H.: "Partially Penetrating Vertical Fractures: Pressure Transient Behavior of a Finite-Conductivity Fracure," paper SPE 13057, presented at the SPE Annual Technical Conference and Exhibition, Houston, Texas, USA (September 16–19, 1984).

Romero, J. and Féraud, J.P.: "Stability of Proppant Packs Reinforced with Fiber for Proppant Flowback Control," paper SPE 31093, presented at the SPE International Symposium on Formation Damage Control, Lafayette, Louisiana, USA (February 14–15, 1996).

Romero, J., Mack, M.G. and Elbel, J.L.: "Theoretical Model and Numerical Investigation of Near-Wellbore Effects in Hydraulic Fracturing," paper SPE 30506, presented at the SPE Annual Technical Conference and Exhibition, Dallas, Texas, USA (October 22–25, 1995).

Roodhart, L.P.: "Fracturing Fluids: Fluid-Loss Measurements Under Dynamic Conditions," paper SPE 11900, *SPE Journal* (October 1985a), 629–636.

- Roodhart, L.P.: "Proppant Settling in Non-Newtonian Fracturing Fluids," paper SPE/DOE 13905, presented at the SPE/DOE 1985 Low Permeability Gas Reservoirs Symposium, Denver, Colorado, USA (May 19–22, 1985b).
- Roodhart, L.P., Kamphuis, H. and Davies, D.R.: "Improved Acid-Fracturing Treatment Designs Based on In-Situ Temperature Calculations," paper SPE 26185, presented at the SPE Gas Technology Symposium, Calgary, Alberta, Canada (June 28–30, 1993).
- Roodhart, L., Kulper, T.O.H. and Davies, D.R.: "Proppant Pack and Formation Impairment During Gas-Well Hydraulic Fracturing," paper SPE 15629, presented at the SPE Annual Technical Conference and Exhibition, New Orleans, Louisiana, USA (October 5–8, 1986).
- Rosen, M.J.: "Relation of Structure to Properties in Surfactants," *J. Amer. Oil Chem. Soc.* (1972) 49, No. 5, 293–297.
- Rosepiller, M.J.: "Determination of Principal Stresses and Confinement of Hydraulic Fractures in Cotton Valley," paper SPE 8405, presented at the SPE Annual Technical Conference and Exhibition, Las Vegas, Nevada, USA (September 23–26, 1979).
- Rowan, G.: "Theory of Acid Treatment of Limestone Formations," *International Institute Petroleum* (1957) 45, No. 431.
- Royce, T.N., Beck, L.M. and Rickards, A.R.: "Rheological Characteristics of Adjustable Crosslinked Fracturing Fluids," paper SPE 13178, presented at the SPE Annual Technical Conference and Exhibition, Houston, Texas, USA (September 16–19, 1984).
- Rudnicki, J.W.: "Effect of Pore Fluid Diffusion on Deformation and Failure of Rock," *Mechanics of Geomaterials, Proc.*, IUTAM William Prager Symposium on Mechanics of Geomaterials: Rocks, Concrete, Soils, Chichester, UK, Wiley (1985), 315–347.
- Rummo, G.J.: "Crosslinking Delay Achieved with Gel Additive," *Oil & Gas Journal* (September 13, 1982) 80, No. 37, 84–89.
- Ruseska, I., Robbins, J. and Costerton, J.W.: "Biocide Testing Against Corrosion-Causing Oil-Field Bacteria Helps Control Plugging," *Oil & Gas Journal* (March 8, 1982) 80, No. 10, 253–264.
- Russell, D.G. and Truitt, N.E.: "Transient Pressure Behavior in Vertically Fractured Reservoirs," paper SPE 967, *Journal of Petroleum Technology* (October 1964) 16, 1159–1170.
- Rutqvist, J. and Stephansson, O.: "A Cyclic Hydraulic Jacking Test to Determine the In Situ Stress Normal to a Fracture," *International Journal of Rock Mechanics and Mining Sciences & Geomechanics Abstracts* (1996) 33, No. 7, 695.
- Sack, R.A.: "Extension of Griffith's Theory of Rupture to Three Dimensions," *Proc. Phys. Soc. of London* (1946) 58, 729–736.
- Salz, L.B.: "Relationship Between Fracture Propagation Pressure and Pore Pressure," paper SPE 6870, presented at the SPE Annual Technical Conference and Exhibition, Denver, Colorado, USA (October 9–12, 1977).
- Samuel, M., Card, R.J., Nelson, E.B., Brown, J.E., Vinod, P.S., Temple, H.L., Qu, Q. and Fu, D.K.: "Polymer-Free Fluid for Hydraulic Fracturing," paper SPE 38622, presented at the SPE Annual Technical Conference and Exhibition, San Antonio, Texas, USA (October 5–8, 1997).
- Santarelli, F.J., Dahren, D., Baroudi, H. and Sliman, K.B.: "Mechanisms of Borehole Instability in Heavily Fractured Rock Media," *International Journal of Rock Mechanics and Mining Sciences & Geomechanics Abstracts* (October 1992) 29, No. 5, 457–467.
- Santarelli, F.J., Ouadfel, H. and Zundel, J.P.: "Optimizing the Completion Procedure to Minimize Sand Production Risk," paper SPE 22797, presented at the SPE Annual Technical Conference and Exhibition, Dallas, Texas, USA (October 6–9, 1991).
- Sattler, A.R., Raible, C.J. and Gall, B.R.: "Integration of Laboratory and Field Data for Insight on the Multiwell Experiment Paludal Stimulation," paper SPE 13891, presented at the SPE/DOE 1985 Low Permeability Gas Reservoirs Symposium, Denver, Colorado, USA (May 19–22, 1985).
- Saucier, R.J. and Lands, J.F.: "A Laboratory Study of Perforations in Stressed Formations," paper SPE 6758, *Journal of Petroleum Technology* (September 1978) 30, 1447–1353.
- Savage, W.Z., Swolfs, H.S. and Powers, P.S.: "Gravitational Stresses in Long Symmetric Ridges and



Valleys,” *International Journal of Rock Mechanics and Mining Sciences & Geomechanics Abstracts* (October 1985) 22, No. 5, 291–302.

Savins, J.G.: “Generalized Newtonian (Pseudoplastic) Flow and Stationary Pipes and Annuli,” *Trans., AIME* (1958) 213, 325.

Schatz, J.F., Olszewski, A.J. and Schraufnagel, R.A.: “Scale Dependence of Mechanical Properties: Application to the Oil and Gas Industry,” paper SPE 25904, *Proc., Rocky Mountain Regional/Low Permeability Reservoirs Symposium and Exhibition*, Denver, Colorado, USA (1993), 615–624.

Schechter, R.S. and Gidley, J.L.: “The Change in Pore Size Distribution from Surface Reactions in Porous Media,” *AICHE J.* (May 1969) 15, 339–350.

Scherubel, G.A. and Crowe, C.W.: “Foamed Acid: A New Concept in Fracture Acidizing,” paper SPE 7568, presented at the SPE Annual Technical Conference and Exhibition, Houston, Texas, USA (October 1–3, 1978).

Schiuma, M., Claverie, M. and Brie, A.: “Hydrocarbon Identification from Shear Sonic Logs in the Newquen Basin, Argentina,” *Transactions of the SPWLA 38th Annual Logging Symposium* (1997), paper EEE.

Schlottman, B.W., Miller, W.K. II and Lueders, R.K.: “Massive Hydraulic Fracture Design for the East Texas Cotton Valley Sands,” paper SPE 10133, presented at the SPE Annual Technical Conference and Exhibition, San Antonio, Texas, USA (October 5–7, 1981).

Schmidt, R.A.: “Fracture Toughness Testing of Limestone,” *Exp. Mech.* (May 1976) 16, No. 5, 161–167.

Schmidt, R.A. and Huddle, C.W.: “Effect of Confining Pressure on Fracture Toughness of Indiana Limestone,” *International Journal of Rock Mechanics and Mining Sciences & Geomechanics Abstracts* (November 1977) 14, Nos. 5–6, 289–293.

Schmidt, R.A. and Lutz, T.J.: “ $K_{Ic}$  and  $J_{Ic}$  of Westerly Granite—Effects of Thickness and In-Plane Dimensions,” *Fracture Mechanics Applied to Brittle Materials*, S.W. Freidman (ed.), Philadelphia, Pennsylvania, USA, ASTM STP (1979), 166–182.

Schols, R.S. and Visser, W.: “Proppant Bank Buildup in a Vertical Fracture Without Fluid Loss,” paper SPE

4834, presented at the SPE European Spring Meeting, Amsterdam, Netherlands (May 29–30, 1974).

Schriefer, F.E. and Shaw, M.S.: “Use of Fine Salt as a Fluid Loss Material in Acid Fracturing Stimulation Treatments,” paper SPE 7570, presented at the SPE Annual Technical Conference and Exhibition, Houston, Texas, USA (October 1–3, 1978).

SCR Geomechanics Group: “On the Modelling of Near Tip Processes in Hydraulic Fractures,” *International Journal of Rock Mechanics and Mining Sciences & Geomechanics Abstracts* (1993) 30, No. 7, 1127–1134.

“Section 2,” *Recommended Practices for Evaluation of Well Perforators (RP 43)*, fifth edition, Dallas, Texas, USA, American Petroleum Institute (January 1991).

“Section 4,” *Recommended Practices for Evaluation of Well Perforators (RP 43)*, fifth edition, Dallas, Texas, USA, American Petroleum Institute (January 1991).

Senseney, T.W. and Pfieffe, T.W.: “Fracture Toughness of Sandstones and Shales,” *Proc., 25th U.S. Symposium on Rock Mechanics* (1984), 390–397.

Serra, O. and Andreani, M.: *Thin Beds*, Schlumberger (1991).

Settari, A.: “A New General Model of Fluid Loss in Hydraulic Fracturing,” paper SPE 11625, *SPE Journal* (August 1985) 25, No. 4, 491–501.

Settari, A.: “Modeling of Acid-Fracturing Treatments,” paper SPE 21870, presented at the SPE Rocky Mountain Regional/Low Permeability Reservoirs Symposium, Denver, Colorado, USA (April 15–17, 1991); also in *SPE Production & Facilities* (February 1993) 8, No. 1, 30–38.

Settari, A. and Cleary, M.P.: “Three-Dimensional Simulation of Hydraulic Fracturing,” paper SPE 10504, presented at the SPE Symposium on Reservoir Simulation, New Orleans, Louisiana, USA (January 31–February 3, 1982); also in *Journal of Petroleum Technology* (July 1984) 36, No. 7, 1177–1190.

Shah, S.N.: “Proppant-Settling Correlations for Non-Newtonian Fluids,” paper SPE 13835, *SPE Production Engineering* (November 1986), 446.



- Shah, S.N. and Asadi, M.: "Convection/Encapsulation in Hydraulic Fracture," paper SPE 39961, presented at the SPE Rocky Mountain Regional/Low Permeability Reservoirs Symposium, Denver, Colorado, USA (April 5–8, 1998).
- Shah, S.N., Asadi, M. and Lord, D.L.: "Proppant Transport Characterization of Hydraulic Fracturing Fluids Using a High Pressure Simulator Integrated with a Fiber Optic/LED Vision System," paper SPE 49040, presented at the SPE Annual Technical Conference and Exhibition, New Orleans, Louisiana, USA (September 27–30, 1998).
- Shah, S.N. and Lee, Y.N.: "Friction Pressures of Proppant-Laden Hydraulic Fracturing Fluids," paper SPE 13836, *SPE Production Engineering* (November 1986), 437–445.
- Shah, S.N. and Lord, D.L.: "Hydraulic Fracturing Slurry Transport in Horizontal Pipes," paper SPE 18994, *SPE Drilling Engineering* (September 1990) 5, No. 3, 225–232.
- Shah, S.N. and Subramanian, R.: "Effects of Coiled Tubing Shear History on the Rheological and Hydraulic Properties of Fracturing Fluids," paper SPE 38421, presented at the SPE 2nd North American Coiled Tubing Roundtable, Montgomery, Texas, USA (April 1–3, 1997).
- Shah, S.N., *et al.*: *New Correlations for Perforation Pressure Loss*, GRI Technical Summary (1996) GRI-96/0208.
- Shaly Sands*, Reprint Volume, SPWLA (July 1982).
- Sharman, W.R., Richards, E.L. and Malcolm, G.N.: "Hydrodynamic Properties of Aqueous Solutions of Galactomannans," *Biopolymers* (1978) 17, 2817–2833.
- Sheppard, C.S. and Kamath, V.R.: "Azo and Peroxide Free Radical Initiators: What They Are, How They Differ, and How They Work," *Proc.*, 33rd Annual Technical Conference of Reinforced Plastics/Composites Institute, The Society of the Plastics Industry, Inc. (February 7–10, 1978), section 5-D.
- Shlyapobersky, J.: "Energy Analysis of Hydraulic Fracturing," *Proc.*, 26th U.S. Symposium on Rock Mechanics, Rapid City, South Dakota, USA (1985), 539–546.
- Shlyapobersky, J., Walhaug, W.W., Sheffield, R.E. and Huckabee, P.T.: "Field Determination of Fracturing Parameters for Overpressure Calibrated Design of Hydraulic Fracturing," paper SPE 18195, presented at the SPE Annual Technical Conference and Exhibition, Houston, Texas, USA (October 2–5, 1988a).
- Shlyapobersky, J., Wong, G.K. and Walhaug, W.W.: "Overpressure Calibrated Design of Hydraulic Fracture Simulations," paper SPE 18194, presented at the SPE Annual Technical Conference and Exhibition, Houston, Texas, USA (October 2–5, 1988b).
- Siegfried, R. and Simmons, G.: "Characterization of Oriented Cracks with Differential Strain Analysis," *Journal of Geophysical Research* (February 1978) 83, No. B3, 1269–1278.
- Sievert, J.A., Wahl, H.A., Clark, P.E. and Harkin, M.W.: "Propped Transport in a Large Vertical Model," paper SPE 9865, presented at the SPE/DOE Low Permeability Symposium, Denver, Colorado, USA (May 27–29, 1981).
- Simmons, G. and Brace, W.F.: "Comparison of Static and Dynamic Measurements of Compressibility of Rocks," *Journal of Geophysical Research* (November 1965) 70, No. 22, 5649–5656.
- Simonson, E.R., Abou-Sayed, A.S. and Clifton, R.J.: "Containment of Massive Hydraulic Fractures," paper SPE 6089, *SPE Journal* (February 1978) 18, No. 1, 27–32.
- Sinclair A.R.: "Heat Transfer Effects in Deep Well Fracturing," paper SPE 3011, *Journal of Petroleum Technology* (November 1971) 23, No. 11, 1484–1492.
- Singh, P.K., Agarwal, R.G. and Krase, L.D.: "Systematic Design and Analysis of Step-Rate Tests to Determine Formation Parting Pressure," paper SPE 16798, presented at the SPE Annual Technical Conference and Exhibition, Dallas, Texas, USA (September 27–30, 1985).
- Sinha, B.K.: "Fluid Leak-Off Under Dynamic and Static Conditions Utilizing the Same Equipment," paper SPE 6126, presented at the SPE Annual Technical Conference and Exhibition, New Orleans, Louisiana, USA (October 3–6, 1976).

- Sizer, J.P., Moullem, A.S. and Abou-Sayed, I.S.: "Evaluation of Closed Fracture Acidizing Performed in a Tight Limestone Formation," paper SPE 21440, presented at the SPE Middle East Oil Show, Bahrain (November 16–19, 1991).
- Skempton, A.W.: "Effective Stress in Soils, Concrete and Rocks," *Proc., Pore Pressure and Suction in Soils*, London, UK, Butterworth (1960), 4–16.
- Slattery, J.C. and Bird, R.B.: "Non-Newtonian Flow Past a Sphere," *Chem. Eng. Sci.* (1961) 16, 231–241.
- Smith, M.B.: "Effect of Fracture Azimuth on Production with Application to the Wattenberg Gas Field," paper SPE 8298, presented at the SPE Annual Technical Conference and Exhibition, Las Vegas, Nevada, USA (September 23–26, 1979).
- Smith, M.B.: "Stimulation Design for Short, Precise Hydraulic Fractures," paper SPE 10313, *SPE Journal* (June 1985), 371.
- Smith, M.B., Bale, A., Britt, L.K., Hainey, B.E. and Klein, H.K.: "Enhanced 2D Proppant Transport Simulation: The Key to Understanding Proppant Flowback and Post-Frac Productivity," paper SPE 38610, presented at the SPE Annual Technical Conference and Exhibition, San Antonio, Texas, USA (October 5–8, 1997).
- Smith, M.B. and Hannah, R.R.: "High Permeability Fracturing: The Evolution of a Technology," paper SPE 27984-P, *Journal of Petroleum Technology* (July 1996), 628.
- Smith, M.B. and Klein, H.H.: "Practical Applications of Coupling Fully Numerical 2-D Transport Calculation with a PC-Based Fracture Geometry Simulator," paper SPE 30505, presented at the SPE Annual Technical Conference and Exhibition, Dallas, Texas, USA (October 22–25, 1995).
- Smith, M.B., Miller, W.K. and Haga, J.: "Tip Screen-Out Fracturing: A Technique for Soft, Unstable Formations," paper SPE 13273, presented at the SPE Annual Technical Conference and Exhibition, Houston, Texas, USA (September 16–19, 1984); also in *SPE Production Engineering* (May 1987) 2, No. 2, 95–103.
- Smith, M.B., Reeves, T.L. and Miller, W.K. II: "Multiple Fracture Height Measurements: A Case History," paper SPE 19092, presented at the SPE Gas Technology Symposium, Dallas, Texas, USA (June 7–9, 1989).
- Smith, M.B., Rosenberg, R.J. and Bowen, J.F.: "Fracture Width: Design vs. Measurement," paper SPE 10965, presented at the SPE Technical Conference and Exhibition, New Orleans, Louisiana, USA (September 26–29, 1982).
- Smith, R.C.: "Successful Primary Cementing Can Be a Reality," paper SPE 13498, *Journal of Petroleum Technology* (November 1984) 36, No. 11, 1851–1858.
- Smith, V.T., Colt, J.R., Johnson, R.L. II and Sinclair, A.R.: "Proppant Effects on Zirconium Crosslinked Frac Fluids," paper SPE 27720, presented at the SPE Permian Basin Oil and Gas Recovery Conference, Midland, Texas, USA (March 16–18, 1994).
- Smits, R.M.M., de Waal, J.A. and van Kooten, J.F.C.: "Prediction of Abrupt Reservoir Compaction and Subsurface Subsidence Caused by Pore Collapse in Carbonates," paper SPE 15642, *SPE Formation Evaluation* (June 1988) 3, No. 2, 340–346.
- Sneddon, I.N.: "The Distribution of Stress in the Neighbourhood of a Crack in an Elastic Solid," *Proc., Royal Soc. London* (1946) 187, Ser. A., 229–260.
- Sneddon, I.N. and Elliot, A.A.: "The Opening of a Griffith Crack Under Internal Pressure," *Quarterly of Appl. Math.* (1946) 4, 262–267.
- Snider, P.M., Hall, F.R. and Whisonant, R.J.: "Experiences with High Energy Stimulations for Enhancing Near-Wellbore Conductivity," paper SPE 35321, presented at the SPE International Petroleum Conference and Exhibition, Villahermosa, Mexico (March 5–7, 1996).
- Soliman, M.Y.: "Design and Analysis of a Fracture with Changing Conductivity," *J. Cdn. Pet. Tech.* (September–October 1986a) 25, No. 5, 62–67.
- Soliman, M.Y.: "Fracture Conductivity Distribution Studied," *Oil & Gas Journal* (February 10, 1986b) 84, No. 6, 89–93.
- Soliman, M.Y.: "Technique for Considering Fluid Compressibility and Temperature Changes in Mini-Frac Analysis," paper SPE 15370, presented at the SPE Annual Technical Conference and Exhibition, New Orleans, Louisiana, USA (October 5–8, 1986c).

- Soliman, M.Y., Hunt, J.L. and El Rabaa, A.M.: "Fracturing Aspects of Horizontal Wells," paper SPE 18542, *Journal of Petroleum Technology* (August 1990) 42, No. 8, 966–973.
- Soliman, M.Y., Kuhlman, R.D. and Poulsen, D.K.: "Minifrac Analysis for Heterogeneous Reservoirs," paper SPE 21554, presented at the CIM/SPE International Technical Meeting, Calgary, Alberta, Canada (June 10–13, 1990).
- Souhaite, P., Misk, A. and Poupon, A.: " $R_t$  Determination in the Eastern Hemisphere," *Transactions of the SPWLA 16th Annual Logging Symposium* (June 4–7, 1975), paper LL.
- Spath, J.B., Ozkan, E. and Raghavan, R.: "An Efficient Algorithm of Well Responses in Commingled Reservoirs," paper SPE 21550, *SPE Formation Evaluation* (June 1994) 9, No. 2, 115–121.
- Stadulis, J.: "Development of a Completion Design to Control Screenouts Caused by Multiple Near-Wellbore Fractures," paper SPE 29549, presented at the SPE Rocky Mountain Regional/Low Permeability Reservoirs Symposium, Denver, Colorado, USA (March 20–22, 1995).
- Starfield, A.M., Smith, K.A. and Bleloch, A.L.: *How to Model It—Problem Solving for the Computer Age*, New York, New York, USA, McGraw-Hill (1990).
- Stewart, B.R., Mullen, M.E., Howard, W.J. and Norman, W.D.: "Use of a Solids-Free Viscous Carrying Fluid in Fracturing Applications: An Economic and Productivity Comparison in Shallow Completions," paper SPE 30114, presented at the SPE European Formation Damage Conference, The Hague, Netherlands (May 15–16, 1995).
- Stewart, G., Heriot-Watt, U. and Ayestaran, L.: "The Interpretation of Vertical Pressure Gradients Measured at Observation Wells in Developed Reservoirs," paper SPE 11132, presented at the SPE Annual Technical Conference and Exhibition, New Orleans, Louisiana, USA (September 26–29, 1982).
- Stiles, D.A.: "Compatibility of Curable Resin-Coated Proppants with Breakers in Crosslinked Fracturing Fluids," presented at the 1991 Southwestern Petroleum Short Course, Lubbock, Texas, USA (April 17–18, 1991).
- Strickland, F.G.: "Reasons for Production Decline in the Diatomite, Belridge Oil Field: A Rock Mechanics View," paper SPE 10773, *Journal of Petroleum Technology* (March 1985) 37, No. 3, 521–526.
- Strickland, F.G. and Ren, N.-K.: "Predicting the In-Situ Stress for Deep Wells Using Differential Strain Curve Analysis," paper SPE 8954, *Proc., SPE/DOE Symposium on Unconventional Gas Recovery*, Pittsburgh, Pennsylvania, USA (1980), 251–258.
- Sukup, R.A., Ott, R.E., Robson, M.K. and Bell, W.T.: "Simple Method Tracks Charge Performance," paper SPE 17172, *Journal of Petroleum Technology* (October 1989) 41, No. 10, 1026–1032.
- Swanson, P.L. and Spetzler, H.: "Ultrasonic Probing of the Fracture Process Zone in Rock Using Surface Waves," *Proc., 25th U.S. Symposium on Rock Mechanics*, Evanston, Illinois, USA (1984), 67–76.
- Talley, G.R., Swindell, T.M., Waters, G.A. and Nolte, K.G.: "Field Application of After-Closure Analysis of Fracture Calibration Tests," paper SPE 52220, presented at the SPE Mid-Continent Operations Symposium, Oklahoma City, Oklahoma, USA (March 28–31, 1999).
- Talobre, J.: *La Mécanique des Roches*, Paris, France, Dunod (1957).
- Talobre, J.: "Dix Ans de Mesures de Compression Interne des Roches: Progrès et Résultats Pratiques," *Geologie Bauwes.* (1958) 25, 148–165.
- Tan, H.C., Wesselowski, K.S. and Willingham, J.D.: "Delayed Borate Crosslinked Fluids Minimize Pipe Friction Pressure," paper SPE 24342, presented at the SPE Rocky Mountain Regional Meeting, Casper, Wyoming, USA (May 18–21, 1992).
- Tariq, S.M.: "Evaluation of Flow Characteristics of Perforations Including Nonlinear Effects Using Finite-Element Method," paper SPE 12781, presented at the SPE California Regional Meeting, Long Beach, California, USA (April 11–13, 1984).
- Tariq, S.M.: "New, Generalized Criteria for Determining the Level of Underbalance for Obtaining Clean Perforations," paper SPE 20636, presented at the SPE Annual Technical Conference and Exhibition, New Orleans, Louisiana, USA (September 23–26, 1990).
- Tehrani, M.A.: "An Experimental Study of Particle Migration in Pipe Flow of Viscoelastic Fluids," *J. Rheol.* (1996) 40, 1057–1077.

- Terzaghi, K. van: "Die Berechnung der Durchlässigkeitsziffer des Tones aus dem Verlauf der Hydrodynamischen Spannungserscheinungen," *Sitzungsber. Akad. Wiss., Wien Math. Naturwiss. Kl.* (1923) 132, 105–124.
- Teufel, L.W.: "Determination of the In-Situ Stress from Anelastic Strain Recovery Measurements of Oriented Cores," paper SPE 11649, *Proc.*, SPE/DOE Symposium on Low-Permeability Reservoirs, Denver, Colorado, USA (1983), 421–427.
- Teufel, L.W. and Farrell, H.E.: "In-Situ Stress and Natural Fracture Distribution in the Ekofisk Field, North Sea," presented at the 3rd North Sea Chalk Symposium, Copenhagen, Denmark (June 11–12, 1990).
- Teufel, L.W. and Rhett, D.W.: "Geomechanical Evidence for Shear Failure of Chalk During Production of the Ekofisk Field," paper SPE 22755, presented at the SPE Annual Technical Conference and Exhibition, Dallas, Texas, USA (October 6–9, 1991).
- The Log Analyst*, Special Issue on NMR Logging (November–December 1996) 37, No. 6.
- The Log Analyst*, Special Issue on NMR Logging (March–April 1997) 38, No. 2.
- Thiercelin, M.: "Fracture Toughness Under Confining Pressure Using the Modified Ring Test," *Proc.*, 20th U.S. Symposium on Rock Mechanics, Tucson, Arizona, USA (June 29–July 1, 1987), 149–156.
- Thiercelin, M.: "Fracture Toughness and Hydraulic Fracturing," *International Journal of Rock Mechanics and Mining Sciences & Geomechanics Abstracts* (July 1989) 26, Nos. 3–4, 177–183.
- Thiercelin, M., Desroches, J. and Kurkjian, A.: "Open Hole Stress Test in Shales," *Proc.*, Eurock '94 Symposium, Delft, Netherlands (1994), 921–928.
- Thiercelin, M., Jeffrey, R.G. and Ben Naceur, K.: "Influence of Fracture Toughness on the Geometry of Hydraulic Fractures," paper SPE 16431, *SPE Production Engineering* (November 1989) 4, No. 4, 435–442.
- Thiercelin, M. and Plumb, R.A.: "A Core-Based Prediction of Lithologic Stress Contrasts in East Texas Formations," paper SPE 21847, presented at the SPE Rocky Mountain Regional Meeting/Low Permeability Reservoirs Symposium, Denver, Colorado, USA (April 15–17, 1991); also in *SPE Formation Evaluation* (December 1994) 4, No. 4, 251–258.
- Thiercelin, M., Plumb, R.A., Desroches, J., Bixenman, B., Jonas, J.K. and Davie, W.: "A New Wireline Tool for In-Situ Stress Measurements," paper SPE 25906, *Proc.*, Rocky Mountain Regional/Low Permeability Reservoirs Symposium and Exhibition, Denver, Colorado, USA (1993), 635–646.
- Thiercelin, M. and Roegiers, J.-C.: "Toughness Determination with the Modified Ring Test," *Proc.*, 27th U.S. Symposium on Rock Mechanics, Tuscaloosa, Alabama, USA (1986), 615–622.
- Thomas, R.L., Crowe, C.W. and Simpson, B.E.: "Effect of Chemical Treatment upon Formation Clays Is Revealed by Improved SEM Technique," paper SPE 6007, presented at the SPE Annual Technical Conference and Exhibition, New Orleans, Louisiana, USA (October 3–6, 1976).
- Thomas, R.L. and Elbel, J.L.: "The Use of Viscosity Stabilizers in High-Temperature Fracturing," paper SPE 8344, presented at the SPE Annual Technical Conference and Exhibition, Las Vegas, Nevada, USA (September 23–26, 1979).
- Thompson, G.D.: Effects of Formation Compressive Strength on Perforator Performance," *Drilling and Production Practice*, 1962, New York, New York, USA, American Petroleum Institute (1963) 191–197.
- Thompson, M. and Willis, J.R.: "A Reformulation of the Equations of Anisotropic Poro-Elasticity," *Journal of Applied Mechanics* (September 1991) 58, No. 3, 612–616.
- Thorne, B.J. and Morris, H.E.: "Advances in Borehole Seismic Fracture Diagnostics," paper SPE/DOE 16405, presented at the SPE/DOE Low Permeability Reservoirs Symposium, Denver, Colorado, USA (May 18–19, 1987).
- Tiab, D. and Kumar, A.: "Application of the  $pD'$  Function of Interference Analysis," paper SPE 6053, *Journal of Petroleum Technology* (August 1980) 32, 1465–1470.
- Tiab, D. and Puthigai, S.K.: "Pressure-Derivative Type Curves for Vertically Fractured Wells," paper SPE 11028, *SPE Formation Evaluation* (March 1988) 3, No. 1, 156–158.

- Timoshenko, S.P. and Goodier, J.N.: *Theory of Elasticity*, third edition, New York, New York, USA, McGraw-Hill Book Company (1970).
- Timur, A.: "An Investigation of Permeability, Porosity and Water Saturation Relationships," *Transactions of the SPWLA 9th Annual Logging Symposium*, New Orleans, Louisiana, USA (June 23–26, 1968), paper J.
- Tinker, S.J.: "Equilibrium Acid Fracturing: A New Fracture Acidizing Technique for Carbonate Formations," paper SPE 18883, *SPE Production Engineering* (February 1991) 6, No. 1, 25–32.
- Tinsley, J.M., Williams, J.R., Tiner, R.L. and Malone, W.T.: Vertical Fracture Height—Its Effect on Steady State Production Increase," paper SPE 1900, *Journal of Petroleum Technology* (May 1969) 21, 633–638.
- Tittman, J. and Wahl, J.S.: "The Physical Foundations of Formation Density Logging (Gamma/Gamma)," *Geophysics* (1965) 30, No. 2.
- Torrest, R.S.: "Aspects of Slurry and Particle Settling and Placement for Viscous Gravel Packing (AQUA-PAC)," paper SPE 11009, presented at the SPE Annual Technical Conference and Exhibition, New Orleans, Louisiana, USA (September 26–29, 1982).
- Trouiller, J.-C., Delhomme, J.-P., Carlin, S. and Anxionnaz, H.: "Thin-Bed Reservoir Analysis from Borehole Electrical Images," paper SPE 19578, presented at the SPE Annual Technical Conference and Exhibition, San Antonio, Texas, USA (October 8–11, 1989).
- Truby, L.S., Keck, R.G. and Withers, R.J.: "Data Gathering for a Comprehensive Hydraulic Fracture Diagnostic Project: A Case Study," paper SPE 27506, presented at the IADC/SPE Drilling Conference, Dallas, Texas, USA (February 15–18, 1994).
- Turian, R.M.: "An Experimental Investigation of the Flow of Aqueous Non-Newtonian High Polymer Solutions Past a Sphere," *AIChE J.* (1967) 13, No. 5, 999–1006.
- Underdown, D.R., Das, K. and Nguyen, H.: "Gravel Packing Highly Deviated Wells with a Crosslinked Polymer System," paper SPE 12481, presented at the SPE Formation Damage Symposium, Bakersfield, California, USA (February 13–14, 1984).
- Unwin, A.T. and Hammond, P.S.: "Computer Simulations of Proppant Transport in a Hydraulic Fracture," paper SPE 29649, presented at the SPE Western Regional Meeting, Bakersfield, California, USA (March 8–10, 1995).
- Valkó, P. and Economides, M.J.: "A Continuum-Damage-Mechanics Model of Hydraulic Fracturing," paper SPE 25304, *Journal of Petroleum Technology* (March 1993a) 45, No. 3, 198–205.
- Valkó, P. and Economides, M.J.: "Fracture Height Containment with Continuum Damage Mechanics," paper SPE 26598, presented at the SPE Annual Technical Conference and Exhibition, Houston, Texas, USA (October 3–6, 1993b).
- Valkó, P. and Economides, M.J.: "Propagation of Hydraulically Induced Fractures—A Continuum Damage Mechanics Approach," *International Journal of Rock Mechanics and Mining Sciences & Geomechanics Abstracts* (June 1994) 31, No. 3, 221–229.
- Valkó, P. and Economides, M.J.: *Hydraulic Fracture Mechanics*, Chichester, UK, Wiley (1995).
- Valkó, P. and Economides, M.J.: "Performance of a Longitudinally Fractured Horizontal Well," paper SPE 31050-P, *SPE Journal* (March 1996a) 1, No. 1, 11–19.
- Valkó, P. and Economides, M.J.: "Performance of Fractured Horizontal Wells in High-Permeability Reservoirs," paper SPE 31149, presented at the SPE International Symposium on Formation Damage Control, Lafayette, Louisiana, USA (February 14–15, 1996b).
- Valkó, P. and Economides, M.J.: "Fluid Leakoff Delineation in High-Permeability Fracturing," paper SPE 37403, presented at the SPE Production Operations Symposium, Oklahoma City, Oklahoma, USA (March 9–11, 1997).
- van Dam, D.B., de Pater, C.J. and Romijn, R.: "Analysis of Fracture Closure in Laboratory Experiments," paper SPE 47380, presented at the SPE/ISRM Eurock '98, Trondheim, Norway (July 8–10, 1998).
- Vandamme, L., Jeffrey, R.G. and Curran, J.H.: "Pressure Distribution in Three-Dimensional Hydraulic Fractures," paper SPE 15265, *SPE Production Engineering* (May 1988), 181.

- van de Ketterij, R.G.: "Raw Data of Hydraulic Fracturing Model Tests—Series 5," test report, Delft University of Technology, Delft, Netherlands (April 1996).
- van der Vlis, A.C., Haafkens, R., Schipper, B.A. and Visser, W.: "Criteria for Proppant Placement and Fracture Conductivity," paper SPE 5637, presented at the SPE Annual Technical Conference and Exhibition, Dallas, Texas, USA (September 28–October 1, 1975).
- Van Domelen, M.S.: "Optimizing Fracture Acidizing Treatment Design by Integrating Core Testing, Field Testing, and Computer Simulation," paper SPE 22393, presented at the SPE International Meeting on Petroleum Engineering, Beijing, China (March 24–27, 1992).
- Van Everdingen, A.F. and Hurst, W.: "The Application of the Laplace Transformation to Flow Problems in Reservoirs," *Trans., AIME* (1949) 186, 305–324.
- van Heerden, W.L.: "General Relations Between Static and Dynamic Moduli of Rocks," *International Journal of Rock Mechanics and Mining Sciences & Geomechanics Abstracts* (1987) 24, No. 6, 381–385.
- van Kruysdijk, C.P.J.W.: "Semianalytical Modeling of Pressure Transients in Fractured Reservoirs," paper SPE 18169, presented at the SPE Annual Technical Conference and Exhibition, Houston, Texas, USA (October 2–5, 1988).
- van Kruysdijk, C.P.J.W. and Dullaert, G.M.: "A Boundary Element Solution to the Transient Pressure Response of Multiple Fractured Horizontal Wells," presented at the 2nd European Conference on the Mathematics of Oil Recovery, Cambridge, UK (July 25–27, 1989).
- van Poolen, H.K., Tinsley, J.M. and Saunders, C.D.: "Hydraulic Fracturing: Fracture Flow Capacity vs. Well Productivity," *Trans., AIME* (1958) 213, 91–95.
- Veatch, R.W. Jr.: "Overview of Current Hydraulic Fracturing Design and Treatment Technology—Part 1," paper SPE 10039, *Journal of Petroleum Technology* (April 1983) 35, No. 4, 677–687.
- Veatch, R.W. Jr.: "Economics of Fracturing: Some Methods, Examples, and Case Studies," paper SPE 15509, presented at the SPE Annual Technical Conference and Exhibition, New Orleans, Louisiana, USA (October 5–8, 1986).
- Veatch, R.W. Jr. and Crowell, R.F.: "Joint Research Operations Programs Accelerate Massive Hydraulic Fracturing Technology," paper SPE 9337, *Journal of Petroleum Technology* (December 1982) 34, No. 2, 2763–2775.
- Veeken, C.A.M., Davies, D.R., Kenter, C.J. and Kooijman, A.P.: "Sand Production Prediction Review: Developing an Integrated Approach," paper SPE 22792, presented at the SPE Annual Technical Conference and Exhibition, Dallas, Texas, USA (October 6–9, 1991).
- Veley, C.D.: "How Hydrolyzable Metal Ions React with Clays to Control Formation Water Sensitivity," paper SPE 2188, *Journal of Petroleum Technology* (September 1969) 21, No. 9, 1111–1118.
- Venghiattis, A.A.: "Prediction of the Efficiency of a Perforator Down-Hole Based on Acoustic Logging Information," paper SPE 422, *Journal of Petroleum Technology* (July 1963) 15, No. 6, 761–768.
- Vincent, M.C. and Pearson, C.M.: "The Relationship Between Fractured Well Performance and Hole Deviation," paper SPE 29569, presented at the SPE Rocky Mountain Regional Low-Permeability Reservoirs Symposium, Denver, Colorado, USA (March 20–22, 1995).
- Vinegar, H.J., Wills, P.B., DeMartini, D.C., Shlyapobersky, J., Deeg, W.F.J., Adair, R.G., Woerpel, J.C., Fix, J.E. and Sorrells, G.G.: "Active and Passive Seismic Imaging of a Hydraulic Fracture in Diatomite," paper SPE 22756, *Journal of Petroleum Technology* (January 1992) 44, 28–34, 88–90.
- Vinod, P.L., Flindt, M.L., Card, R.J. and Mitchell, J.P.: "Dynamic Fluid-Loss Studies in Low-Permeability Formations with Natural Fractures," paper SPE 37486, presented at the SPE Production Operations Symposium, Oklahoma City, Oklahoma, USA (March 9–11, 1997).
- Vliet, M.R.A. v.: "Size Effect of Concrete and Rock Under Uniaxial Tension," Delft University of Technology, Delft, Netherlands (1999).
- Vogel, J.V.: "Inflow Performance Relationships for Solution-Gas Drive Wells," paper SPE 1476, *Journal of Petroleum Technology* (January 1968) 20, 83–92.

- Voight, B.: "Determination of the Virgin State of Stress in the Vicinity of a Borehole from Measurements of a Partial Anelastic Strain Tensor in Drill Cores," *Felsmech. Ingenieur Geol.* (1968) 6, No. 4, 201–215.
- Wagoner, J.C. van, Mitchum, R.M., Campion, K.M. and Rahmanian, V.D.: *Siliclastic Sequence Stratigraphy in Well Logs, Core and Outcrops*, Tulsa, Oklahoma, USA, American Association of Petroleum Geologists (1990).
- Walker, M.L., Shuchart, C.E., Yaritz, J.G. and Norman, L.R.: "Effects of Oxygen on Fracturing Fluids," paper SPE 28978, presented at the SPE International Symposium on Oilfield Chemistry, San Antonio, Texas, USA (February 14–17, 1995).
- Wallis, W.E., Williamson, T.D. and Tomkinson, D.L.: "Method for Testing Subterranean Formations," U.S. Patent No. 4,741,401 (May 3, 1988).
- Walsh, J.B.: "Effect of Pore Pressure and Confining Pressure on Fracture Permeability," *International Journal of Rock Mechanics and Mining Sciences & Geomechanics Abstracts* (1981) 18, 429–435.
- Ward, V.L.: "Nitrogen and Carbon Dioxide in the Oil Field: Stimulation and Completion Applications," paper SPE 12594, presented at the SPE Permian Basin Oil & Gas Recovery Conference, Midland, Texas, USA (March 8–9, 1984).
- Warpinski, N.R.: "Investigation on the Accuracy and Reliability of In Situ Stress Measurements Using Hydraulic Fracturing in Perforated Cased Holes," *Rock Mechanics: Theory-Experiment-Practice, Proceedings of the 24th U.S. Symposium on Rock Mechanics* (June 1983), 773–776.
- Warpinski, N.R.: "Measurement of Width and Pressure in a Propagating Hydraulic Fracture," paper SPE 11648, *SPE Journal* (February 1985) 25, No. 1, 46–54.
- Warpinski, N.R.: "Dual Leakoff Behavior in Hydraulic Fracturing of Tight, Lenticular Gas Sands," paper SPE 18259, *SPE Production Engineering* (August 1990), 243.
- Warpinski, N.R.: "Hydraulic Fracturing in Tight, Fissured Media," paper SPE 21054, *Journal of Petroleum Technology* (February 1991) 43, No. 2, 146–152, 208–209.
- Warpinski, N.R.: "Interpretation of Hydraulic Fracture Mapping Experiments," paper SPE 27985, presented at the University of Tulsa Centennial Petroleum Engineering Symposium, Tulsa, Oklahoma, USA (August 29–31, 1994).
- Warpinski, N.R. and Branagan, P.T.: "Altered Stress Fracturing," paper SPE 17533, *Proc.*, SPE Rocky Mountain Regional Meeting, Casper, Wyoming, USA (1988), 465–476.
- Warpinski, N.R., Branagan, P.T., Peterson, R.E. and Wolhart, S.L.: "An Interpretation of M-Site Hydraulic Fracture Diagnostic Results," paper SPE 39950, presented at the SPE Rocky Mountain Regional/Low Permeability Reservoirs Symposium, Denver, Colorado, USA (April 5–8, 1998a).
- Warpinski, N.R., Branagan, P. and Wilmer, R.: "In-Situ Stress Measurements at the DOE's Multiwell Experiment Site, Mesaverde Group, Rifle, Colorado," paper SPE 12142, *Journal of Petroleum Technology* (March 1985) 37, 527–536.
- Warpinski, N.R., Engler, B.P., Young, C.J., Peterson, R.E., Branagan, P.T. and Fix, J.E.: "Microseismic Mapping of Hydraulic Fractures Using Multi-Level Wireline Receivers," paper SPE 30507, presented at the SPE Annual Technical Conference and Exhibition, Dallas, Texas, USA (October 22–25, 1995).
- Warpinski, N.R., Lorenz, J.C., Branagan, P.T., Myal, F.R. and Gall, B.L.: "Examination of a Cored Hydraulic Fracture in a Deep Gas Well," paper SPE 22876, *SPE Formation Evaluation* (September 1993) 8, No. 3, 150–158.
- Warpinski, N.R., Peterson, R.E., Branagan, P.T., Engler, B.P. and Wolhart, S.L.: "In Situ Stress and Moduli: Comparison of Values Derived from Multiple Techniques," paper SPE 49190, presented at the SPE Annual Technical Conference and Exhibition, New Orleans, Louisiana, USA (September 27–30, 1998b).
- Warpinski, N.R. and Teufel, L.W.: "In-Situ Stresses in Low-Permeability, Nonmarine Rocks," paper SPE 16402, *Journal of Petroleum Technology* (April 1989) 41, No. 4, 405–414.
- Warpinski, N.R., Wright, T.B., Uhl, J.E., Engler, B.P., Drozda, P.M., Peterson, R.E. and Branagan, P.T.: "Microseismic Monitoring of the B-Sand Hydraulic Fracture Experiment at the DOE/GRI Multi-Site Proj-

ect,” paper SPE 36450, presented at the SPE Annual Technical Conference and Exhibition, Denver, Colorado, USA (October 6–9, 1996).

Watkins, E.K., Wendorff, C.L. and Ainley, B.R.: “A New Crosslinked Foamed Fracturing Fluid,” paper SPE 12027, presented at the SPE Annual Technical Conference and Exhibition, San Francisco, California, USA (October 5–8, 1983).

Wattenbarger, R.A. and Ramey, H.J. Jr.: “Gas Well Testing with Turbulence, Damage, and Wellbore Storage,” paper SPE 1835, *Journal of Petroleum Technology* (August 1968) 20, No. 8, 877–887; also in *Trans., AIME* (1968) 243.

Wattenbarger, R.A. and Ramey, H.J. Jr.: “Well Test Interpretation in Vertically Fractured Gas Wells,” paper SPE 2155, *Journal of Petroleum Technology* (May 1969) 21, No. 5, 625–632; also in *Trans., AIME* (1969) 246.

Webster K.R., Goins, W.C. and Berry S.C. “A Continuous Multistage Fracturing Technique,” paper SPE 977, *Journal of Petroleum Technology* (June 1965) 17, No. 6, 619–625.

Weijers, L.: *The Near-Wellbore Geometry of Hydraulic Fractures Initiated from Horizontal and Deviated Wells*, Delft, Netherlands, Delft University Press (1995).

Wendorff, C.L. and Ainley, B.R.: “Massive Hydraulic Fracturing of High-Temperature Wells with Stable Frac Foams,” paper SPE 10257, presented at the SPE Annual Technical Conference and Exhibition, San Antonio, Texas, USA (October 5–7, 1981).

Weng, X.: “Incorporation of 2D Fluid Flow into a Pseudo-3D Hydraulic Fracturing Simulator,” paper SPE 21849, presented at the SPE Rocky Mountain Regional Meeting and Low-Permeability Reservoirs Symposium, Denver, Colorado, USA (April 15–17, 1991).

Whistler, R.L. (ed.): *Industrial Gums*, New York, New York, USA, Academic Press (1959).

White, J.L. and Daniel, E.F.: “Key Factors in MHF Design,” paper SPE 9065, *Journal of Petroleum Technology* (August 1981) 33, No. 8, 1501–1512.

Whitehead, W.S., Hunt, E.R. and Holditch, S.A.: “The Effects of Lithology and Reservoir Pressure on the In-Situ Stresses in the Waskom (Travis Peak)

Field,” paper SPE 16403, presented at the SPE/DOE Low Permeability Reservoirs Symposium, Denver, Colorado, USA (May 18–19, 1987).

Whitsitt, N.F. and Dysart, G.R.: “The Effect of Temperature on Stimulation Design,” paper SPE 2497, presented at the SPE Annual Meeting, Denver, Colorado, USA (September 28–October 1, 1969); also in *Journal of Petroleum Technology* (April 1970), 493–502; also in *Trans., AIME* (1970) 249.

Wilkinson, D.J. and Hammond, P.A.: “A Perturbation Theorem for Mixed Boundary Value Problems in Pressure Transient Testing,” *Transport in Porous Media* (1992) 5, 609–636.

Willberg, D.M., Steinsberger, N., Hoover, R., Card R.J. and Queen, J.: “Optimization of Fracture Clean-up Using Flowback Analysis,” paper SPE 39920, presented at the SPE Rocky Mountain Regional/Low Permeability Reservoirs Symposium and Exhibition, Denver, Colorado, USA (April 5–8, 1998).

Williams, B.B.: “Fluid Loss from Hydraulically Induced Fractures,” paper SPE 2769, *Journal of Petroleum Technology* (July 1970) 22, No. 6, 882–888.

Williams, B.B., Gidley J.L. and Schechter, R.S.: *Acidizing Fundamentals*, Richardson, Texas, USA, Society of Petroleum Engineers (1979).

Williamson, C.D. and Allenson, S.J.: “A New Non-damaging Particulate Fluid-Loss Additive,” paper SPE 18474, presented at the SPE International Symposium on Oilfield Chemistry, Houston, Texas, USA (February 8–10, 1989).

Willson, S.M.: “Maximizing Completions Efficiency Through High Overbalanced Perforating,” TerraTek (February 1995) CEA 61 Phase I.

Winkler, K.W. and Murphy, W.F. III: “Acoustic Velocity and Attenuation in Porous Rocks,” *Rock Physics and Phase Relations. A Handbook of Physical Constants*, AGU Reference Shelf, Washington, D.C., USA, American Geophysical Union (1995) 3, 20–34.

Winkler, W., Valkó, P. and Economides, M.J.: “Laminar and Drag-Reduced Polymeric Foam Flow,” *J. Rheol.* (January–February 1994) 38, No. 1, 111–127.



- Wiprut, D.J. and Zoback, M.D.: "High Horizontal Stress in the Visund Field, Norwegian North Sea: Consequences for Borehole Stability and Sand Production," paper SPE 47244, presented at the SPE/ISRM Eurock '98, Trondheim, Norway (July 8–10, 1998).
- Withjack, E.M.: "Computed Tomography for Rock-Property Determination and Fluid-Flow Visualization," paper SPE 16951, presented at the SPE Annual Technical Conference and Exhibition, Dallas, Texas, USA (September 27–30, 1987).
- Wong, D.W., Harrington, A.G. and Cinco-Ley, H.: "Application of the Pressure Derivative Function in the Pressure Transient Testing of Fractured Wells," paper SPE 13056, presented at the SPE Annual Technical Conference and Exhibition, Houston, Texas, USA (September 16–19, 1984).
- Woo, G.T. and Cramer, P.D.: "Laboratory and Field Evaluation of Fluid-Loss Additive Systems Used in the Williston Basin," paper SPE 12899, presented at the SPE Rocky Mountain Regional Meeting, Casper, Wyoming, USA (May 21–23, 1984).
- Wood, M.D., Smith, M.B., Abbot, R.L., Cox, D. and O'Shea, P.: "Fracture Proppant Mapping by Use of Surface Superconducting Magnetometers," paper SPE 11612 (1983).
- Worlow, D.W.: "Development and Testing of a Standard Procedure for Determining the Viscous Properties of Crosslinked Fracturing Fluids," MS thesis, Texas A&M University, College Station, Texas, USA (1987).
- Wright, C.A., Weijers, L., Minner, W.A. and Snow, D.M.: "Robust Technique for Real-Time Closure Stress Estimation," paper SPE 30503, presented at the SPE Annual Technical Conference and Exhibition, Dallas, Texas, USA (October 22–25, 1995).
- Wroth, C.: "In-Situ Measurement of Initial Stresses and Deformation Characteristics," *Proc.*, ACE Specialty Conference in In-Situ Measurements of Soil Properties, Raleigh, North Carolina, USA (1975), 181–230.
- Wylie, D.J. and Rose, W.D.: "Some Theoretical Considerations Related to the Quantitative Evaluation of Physical Characteristics of Reservoir Rocks from Electrical Log Data," *Trans., AIME* (1950) 189, 105–108.
- Yale, D.P., Nieto, J.A. and Austin, S.P.: "The Effect of Cementation on the Static and Dynamic Mechanical Properties of the Rotliegendes Sandstone," *Proc.*, 35th U.S. Symposium on Rock Mechanics, Reno, Nevada, USA (1995), 169–175.
- Yeager, R.R. and Bailey, D.E.: "Diesel-Based Gel Concentrate Improves Rocky Mountain Region Fracture Treatments," paper SPE 17535, presented at the SPE Rocky Mountain Regional Meeting, Casper, Wyoming, USA (May 11–13, 1988).
- Yew, C.H. and Li, Y.: "Fracturing of a Deviated Well," paper SPE 16930, *SPE Production Engineering* (November 1988) 3, No. 4, 429–437.
- Yew, C.H. and Liu, G.F.: "Fracture Tip and Critical Stress Intensity Factor of a Hydraulically Induced Fracture," paper SPE 22875, *SPE Production & Facilities* (August 1993) 8, No. 3, 171–177.
- Yew, C.H., Mear, M.E., Chang, C.C. and Zhang, X.C.: "On Perforating and Fracturing of Deviated Cased Wellbores," paper SPE 26514, presented at the SPE Annual Technical Conference and Exhibition, Houston, Texas, USA (October 3–6, 1993).
- Yew, C.H., Schmidt, J.H. and Li, Y.: "On Fracture Design of Deviated Wells," paper SPE 19722, presented at the SPE Annual Technical Conference and Exhibition, San Antonio, Texas, USA (October 8–11, 1989).
- Yew, C.H. and Zhang, X.: "A Study of the Damage Zone Created by Shaped-Charge Perforating," paper SPE 25902, presented at the Rocky Mountain Regional/Low Permeability Reservoirs Symposium, Denver, Colorado, USA (April 12–14, 1993).
- Zasadzinski, J.A.N., Kramer, J., Chu, A. and Prud'homme, R.A.: "Transmission Electron Microscopy of Aqueous Polymer Gel Network Morphology," *Chem. Eng. Comm.* (1987) 52, 283–289.
- Zemanek, J., Caldwell, R.L., Glenn, E.F., Holcomb, S.V., Norton, L.J. and Straus, A.J.D.: "The Borehole Televue—A New Logging Concept for Fracture Location and Other Types of Borehole Inspection," paper SPE 2402, *Journal of Petroleum Technology* (June 1969) 21, 762–774; also in *Trans., AIME* (1969) 246.
- Zemlak, W., Lemp, S. and McCollum, R.: "Selective Hydraulic Fracturing of Multiple Perforated Intervals with a Coiled Tubing Conduit: A Case History of the

Unique Process, Economic Impact and Related Production Improvements,” paper SPE 54474, presented at the SPE/ICOTA Coiled Tubing Roundtable, Houston, Texas, USA (May 25–26, 1999).

Zhao, X.L., Roegiers, J.-C. and Guo, M.: “The Determination of Fracture Toughness of Rocks by Chevron-Notched Brazilian Disk Specimens,” 4th Annual SCA Technical Conference, Dallas, Texas, USA (August 15–16, 1990), paper 9014.

Zhao, Z.-Y., Cui, M., Conway, M.W. and Chang, F.F.: “The Rheology of Chinese XD and ZW Borate Crosslinked Fracturing Fluids and Their Proppant Transport Capability,” paper SPE 29991, presented at the SPE International Meeting on Petroleum Engineering, Beijing, People’s Republic of China (November 14–17, 1995).

Zimmerman, R.W., Somerton, W.H. and King, M.S.: “Compressibility of Porous Rock,” *Journal of Geophysical Research* (November 1986) 91, No. B12, 12765–12777.

Zimmerman, T., MacInnis, J., Hoppe, J., Pop, J. and Long, T.: “Application of Emerging Wireline Formation Testing Technologies,” paper OSEA 90105, presented at the Offshore South East Asia Conference, Singapore (December 4–7, 1990).

Zoback, M.D., Moos, D. and Mastin, L.: “Well Bore Breakouts and In Situ Stress,” *Journal of Geophysical Research* (1985) 90, No. B7, 5523–5530.

## Chapters 13–20

Abdel-Mota’al, A.A.: “Detection and Remedy of Behind-Casing Communication During Well Completion,” paper SPE 11498, presented at the SPE Middle East Oil Technical Conference, Manama, Bahrain (March 14–17, 1983).

Abrams, A.: “Mud Design to Minimize Rock Impairment Due to Particle Invasion,” paper SPE 5713, *Journal of Petroleum Technology* (March 1977), 586–592.

Abrams, A., Scheuerman, R.F., Templeton, C.C. and Richardson, E.A.: “Higher-pH Acid Stimulation Systems,” paper SPE 7892, *Journal of Petroleum Technology* (December 1983), 2175–2184.

Adair, P. and Smith, P.S.: “The Miller Field: Appraisal and Development Formation Damage Experiences,” paper SPE 27406, presented at the SPE International Symposium on Formation Damage Control, Lafayette, Louisiana, USA (February 7–10, 1994).

Addison, G.E.: “Identification and Treating of Downhole Organic Deposits,” paper SPE 18894, presented at the SPE Production Operations Symposium, Oklahoma City, Oklahoma, USA (March 13–14, 1989).

Ali, S.A., Durham, D.K. and Elphinstone, E.A.: “Testing Identifies Acidizing Fluid/Crude Compatibility Problems,” *Oil & Gas Journal* (March 1994), 47–51.

Ali, S.A., Hill, D.G., McConnell, S.B. and Johnson, M.R.: “Process, Optimized Acidizing Reduce Production Facility Upsets,” *Oil & Gas Journal* (February 1997), 44–48.

Allen, T.O.: “Creative Task Force Attack on Profit Loss Due to Formation Damage,” paper SPE 4658, presented at the SPE Annual Meeting, Las Vegas, Nevada, USA (September 30–October 3, 1973).

Almond, S.W., Brady, J.L. and Underdown, D.R.: “Prudhoe Bay Field Study—Return Fluid Analysis,” paper SPE 18223, *Journal of Petroleum Technology* (April 1990) 42, No. 4, 466.

Amaefule, J.O., *et al.*: “Advances in Formation Damage Assessment and Control Strategies,” paper CIM 88-39-65 (1988).

Amaefule, J.O., Padilla, P.C., McCaffery, F.G. and Teal, S.L.: “Steam Condensate: Formation Damage and Chemical Treatments for Injectivity Improvement,” paper SPE 12499, presented at the SPE Formation Damage Control Symposium, Bakersfield, California, USA (February 13–14, 1984).

Antheunis, D., Luque, F.R., van der Vlis, A.C. and Vriezen, P.B.: “The Onset of Sand Influx from Gas-Producing Friable Sandstone Formations—Laboratory Investigations,” paper SPE 8031 (1979).

Antheunis, D., Vriezen, P.B., Schipper, B.A. and van der Vlis, A.C.: “Perforation Collapse: Failure of Perforated Friable Sandstones,” paper SPE 5750, presented at the SPE European Spring Meeting, Amsterdam, Netherlands (April 8–9, 1976).

- Ayorinde, A., Granger, C. and Thomas, R.L.: "The Application of Fluoboric Acid in Sandstone Matrix Acidizing: A Case Study," paper IPA92-2.3.23, presented at the 21st Annual Indonesian Petroleum Association Convention, Jakarta, Indonesia (October 1992).
- Azari, M. and Leimkuhler, J.: "Completion Fluid Invasion Simulation and Permeability Restoration by Sodium- and Potassium-Based Brines," paper SPE 19431, presented at the SPE Formation Damage Control Symposium, Lafayette, Louisiana, USA (February 22–23, 1990a).
- Azari, M. and Leimkuhler, J.: "Formation Permeability Damage Induced by Completion Brines," paper SPE 17149, *Journal of Petroleum Technology* (April 1990b), 486.
- Bale, G.E.: "Matrix Acidizing in Saudi Arabia Using Buoyant Ball Sealers," paper SPE 11500, presented at the SPE Middle East Oil Technical Conference, Manama, Bahrain (March 14–17, 1983).
- Ballard, T.J. and Dawe, R.A.: "Wettability Alteration Induced by Oil-Based Drilling Fluid," paper SPE 17160, presented at the SPE Formation Damage Control Symposium, Bakersfield, California, USA (February 8–9, 1988).
- Bandbach, P.L.: "The How and Why of Emulsions," *Oil & Gas Journal* (September 7, 1970).
- Bansal, K.M.: "Effect of Nonproduced Fluids on Produced Water Treatment Equipment Efficiency," paper SPE 25199, presented at the SPE International Symposium on Oilfield Chemistry, New Orleans, Louisiana, USA (March 2–5, 1993).
- Barna, B.A. and Patton, J.T.: "Permeability Damage from Drilling Fluid Additives," paper SPE 3830, presented at the SPE Rocky Mountain Regional Meeting, Denver, Colorado, USA (April 10–12, 1972).
- Barron, A.N., Hendrickson, A.R. and Wieland, D.R.: "The Effect of Flow on Acid Reactivity in a Carbonate Fracture," *Journal of Petroleum Technology* (April 1962), 409–415.
- Bartko, K.M., Acock, A.M., Robert, J.A. and Thomas, R.L.: "A Field Validated Matrix Acidizing Simulator for Production Enhancement in Sandstone and Carbonates," paper SPE 38170, presented at the SPE European Formation Damage Conference, The Hague, Netherlands (June 2–3, 1997).
- Bartko, K.M., Montgomery, C.T., Boney, C.L. and Ward, V.L.: "Development of a Stimulation Treatment Integrated Model," paper SPE 35991, presented at the SPE Petroleum Computer Conference, Dallas, Texas, USA (June 2–5, 1996).
- Bazin, B., Roque, C. and Bouteica, M.: "A Laboratory Evaluation of Acid Propagation in Relation to Acid Fracturing: Results and Interpretation," paper SPE 30085, presented at the SPE European Formation Damage Conference, The Hague, Netherlands (May 15–16, 1995).
- Beadie, G.: "Well Productivity Awareness School (WPAS)," paper SPE 30131, presented at the SPE European Formation Damage Conference, The Hague, Netherlands (May 15–16, 1995).
- Behenna, F.R.: "Interpretation of Matrix Acidizing Treatments Using a Continuously Monitored Skin Factor," paper SPE 27401, presented at the SPE International Symposium on Formation Damage Control, Lafayette, Louisiana, USA (February 7–10, 1994).
- Behenna, F.R.: "Acid Diversion from an Undamaged to a Damaged Core Using Multiple Foam Slugs," paper SPE 30121, presented at the SPE European Formation Damage Conference, The Hague, Netherlands (May 15–16, 1995).
- Behrmann, L.A.: "Underbalance Criteria for Minimum Perforation Damage," paper SPE 30081, presented at the SPE European Formation Damage Conference, The Hague, Netherlands (May 15–16, 1995).
- Ben Marek, F.: "Permeability Loss in Depletion of Reservoirs," paper SPE 8433, presented at the SPE Annual Technical Conference and Exhibition, Las Vegas, Nevada, USA (September 23–26, 1979).
- Bergman, I.: "Silica Powders of Respirable Sizes IV. The Long-Term Dissolution of Silica Powders in Dilute Hydrofluoric Acid: An Anisotropic Mechanism of Dissolution for the Coarser Quartz Powders," *J. Appl. Chem.* (August 1963) 3, 356–361.
- Bernadiner, M.G., Thompson, K.E. and Fogler, H.S.: "The Effect of Foams Used During Carbonate Acidizing," paper SPE 21035, *SPE Production Engineering* (November 1992), 350–356.
- Bernard, G.G., Holm, L.W. and Jacobs, W.L.: "Effect of Foam on Trapped Gas Saturation and

on Permeability of Porous Media to Water,” *SPE Journal* (December 1965), 295.

Bertaux, J.: “Treatment Fluid Selection for Sandstone Acidizing: Permeability Impairment in Potassic Mineral Sandstones,” paper SPE 15884, *SPE Production Engineering* (February 1989), 41.

Bikerman, J.J.: “Foams and Emulsions—Formation Properties and Breakdowns,” presented at the Chemistry and Physics of Interfaces—Symposium on Interfaces (June 15–16, 1964).

Bird, K. and Dunmore, S.: “Optimising Perforation Performance for the Armada Gas Condensate Development,” paper SPE 30083, presented at the SPE European Formation Damage Conference, The Hague, Netherlands (May 15–16, 1995).

Black, A.D., Dearing, H.L. and DiBona, B.G.: “Effects of Pore Pressure and Mud Filtration on Drilling Rates in a Permeable Sandstone,” paper SPE 12117, *Journal of Petroleum Technology* (September 1985), 1671.

Black, S.J. and Rike, J.L.: “The Role of the Consultant in Meeting the Formation Damage Challenge,” paper SPE 5700, presented at the SPE Symposium on Formation Damage Control, Houston, Texas, USA (January 29–30, 1976).

Blacker, L.K.: “An Analysis of Rate-Sensitive Skin in Oil Wells,” paper SPE 11187, presented at the SPE Annual Technical Conference and Exhibition, New Orleans, Louisiana, USA (September 26–29, 1982).

Blann, J.R. and Williams J.D.: “Determining the Most Profitable Gas Injection Pressure for a Gas Lift Installation,” paper SPE 12202, *Journal of Petroleum Technology* (August 1994), 1305.

Blanton, R.J.: “Formation Damage Control During Underreaming and Gravel Packing in an Overpressured Reservoir,” paper SPE 23804, presented at the SPE International Symposium on Formation Damage Control, Lafayette, Louisiana, USA (February 26–27, 1992).

Blanton, T.L. III: “Deformation of Chalk Under Confining Pressure and Pore Pressure,” paper SPE 8076, presented at the SPE European Offshore Petroleum Conference and Exhibition, London, UK (October 24–27, 1978).

Boyer, R.C. and Wu, C.-H.: “The Role of Reservoir Lithology in Design of an Acidization Program: Kuparuk River Formation, North Slope, Alaska,” paper SPE 11722, presented at the SPE California Regional Meeting, Ventura, California, USA (March 23–25, 1983).

Brannon, D.H., Netters, C.K. and Grimmer, P.J.: “Matrix Acidizing Design and Quality-Control Techniques Prove Successful in Main Pass Area Sandstone,” paper SPE 14827, *Journal of Petroleum Technology* (August 1987), 931–942.

Brannon, H.D. and Pulsinelli, R.J.: “Evaluation of the Breaker Concentrations Required to Improve the Permeability of Proppant Packs Damaged by Hydraulic Fracturing Fluids,” paper SPE 19402, presented at the SPE Formation Damage Control Symposium, Lafayette, Louisiana, USA (February 22–23, 1990).

Brown, R.W., Neill, G.H. and Loper, R.G.: “Factors Influencing Optimum Ball Sealer Performance,” *Journal of Petroleum Technology* (April 1963), 450–454.

Browne, S.V., Ryan, D.F., Chambers, B.D., Oilchrist, J.M. and Bamforth, S.A.: “Simple Approach to the Clean-Up of Horizontal Wells with Pre-Packed Screen Completions,” paper SPE 30116, presented at the SPE European Formation Damage Conference, The Hague, Netherlands (May 15–16, 1995).

Brownson, G.W., Peyden, J.M. and Heriot-Watt, U.: “A Systematic Approach to Assessing Permeability Impairment Due to Drilling Fluids,” paper SPE 9727 (November 18, 1980).

Bruist, E.H.: “Better Performance of Gulf Coast Wells,” paper SPE 4777, presented at the SPE Symposium on Formation Damage Control, New Orleans, Louisiana, USA (February 7–8, 1974).

Bryant, S.L.: “An Improved Model of Mud Acid/Sandstone Chemistry,” paper SPE 22855, presented at the SPE Annual Technical Conference and Exhibition, Dallas, Texas, USA (October 6–9, 1991).

Bryant, S.L. and Buller, D.C.: “Formation Damage from Acid Treatments,” paper SPE 17597, *SPE Production Engineering* (November 1990), 455.

Bryant, S.L., Mellor, D.W. and Cade, C.A.: “Physically Representative Network Models of Transport

in Porous Media,” *AIChE J.* (March 1993) 39, No. 3, 387.

Buijse, M.A.: “Understanding Wormholing Mechanisms Can Improve Acid Treatments in Carbonate Formations,” paper SPE 38166, presented at the SPE European Formation Damage Conference, The Hague, Netherlands (June 2–3, 1997).

Bunger, J.W.: “Chemistry of Asphaltenes—Summary of Symposium,” *Proc.*, Salt Lake City, Utah, USA (1979), 1028–1031.

Burger, E.D., Perkins, T.K. and Striegler, J.H.: “Studies of Wax Deposition in the Trans Alaska Pipeline,” paper SPE 8788, *Journal of Petroleum Technology* (June 1981), 1075–1086.

Burman, J.W. and Hall, B.E.: “Foam as a Diverting Technique for Matrix Sandstone Stimulation,” paper SPE 15575, presented at the SPE Annual Technical Conference and Exhibition, New Orleans, Louisiana, USA (October 5–8, 1986).

Burton, B.: “Estimate Formation Damage Effects on Horizontal Wells,” *Petroleum Engineer International* (August 1995), 29–34.

Carlson, V., Bennett, E.O. and Rowe, J.A. Jr.: “Microbial Flora in a Number of Oilfield Water-Injection Systems,” paper SPE 1553-G, *SPE Journal* (June 1961), 71.

Chatelain, J.C., Silberberg, I.H. and Schechter, R.S.: “Thermodynamic Limitations in Organic-Acid/Carbonate Systems,” paper SPE 5647, *SPE Journal* (August 1976), 189–195.

Chenevert, M.E. and Thompson, T.W.: “Perforation Stability in Low-Permeability Gas Reservoirs,” paper SPE 13902, presented at the SPE/DOE Low Permeability Gas Reservoirs Symposium, Denver, Colorado, USA (May 19–22, 1985).

Cheung, S.K.: “Effect of Acids on Gravels and Proppants,” paper SPE 13842, *SPE Production Engineering* (May 1988), 201.

Christian, W.W. and Ayres, H.J.: “Formation Damage Control in Sand Control and Stimulation Work,” paper SPE 4775, presented at the SPE Symposium on Formation Damage Control, New Orleans, Louisiana, USA (February 7–8, 1974).

Christofferson, J. and Christofferson, M.R.: “The Kinetics of Dissolution of Calcium Sulphate Dihydrate in Water,” *J. Crystal Growth* (1976) 35, 79–88.

Chuah, B.-S., Hasumi, A.R., Samsudin, N. and Matzain, A.: “Formation Damage in Gravel Packed and Non-Gravel Packed Completions: A Comprehensive Case Study,” paper SPE 27360, presented at the SPE International Symposium on Formation Damage Control, Lafayette, Louisiana, USA (February 7–10, 1994).

Cinco-Ley, H., Ramey, H.J. Jr. and Miller, F.G.: “Unsteady-State Pressure Distribution Created by a Well with an Inclined Fracture,” paper SPE 5591, presented at the SPE Annual Technical Conference and Exhibition, Dallas, Texas, USA (September 28–October 1, 1975).

Clementz, D.M.: “Alteration of Rock Properties by Adsorption of Petroleum Heavy Ends: Implication for Enhanced Oil Recovery,” paper SPE 10683, presented at the SPE/DOE Third Joint Symposium on Enhanced Oil Recovery, Tulsa, Oklahoma, USA (April 4–7, 1982).

Clementz, D.M., Patterson, D.E., Aseltine, R.J. and Young, R.E.: “Stimulation of Water Injection Wells in the Los Angeles Basin by Using Sodium Hypochlorite and Mineral Acids,” paper SPE 10624, *Journal of Petroleum Technology* (September 1982), 2087–2096.

Clemmit, A.F., Ballance, D.C. and Hunton, A.G.: “The Dissolution of Scales in Oilfield Systems,” paper SPE 14010, presented at the SPE Offshore Europe 85 Conference, Aberdeen, Scotland, UK (September 10–13, 1985).

Cole, R.J. and Jessen, F.W.: “Paraffin Deposition,” *Oil & Gas Journal* (September 19, 1960), 87–91.

Collins, S.H. and Melrose, J.C.: “Adsorption of Asphaltenes and Water on Reservoir Rock Minerals,” paper SPE 11800, presented at the SPE International Symposium on Oilfield and Geothermal Chemistry, Denver, Colorado, USA (June 1–3, 1983).

Cooper, R.E. and Bolland, J.A.: “Effective Diversion During Matrix Acidization of Water and Injection Wells,” paper OTC 4795, presented at the Offshore Technology Conference, Houston, Texas, USA (1984).

- Coppel, C.P.: "Factors Causing Emulsion Upsets in Surface Facilities Following Acid Stimulation," paper SPE 5154, *Journal of Petroleum Technology* (September 1975), 1060–1066.
- Cowen, J.C. and Weintritt, D.J.: *Water Formed Scale Deposits*, Houston, Texas, USA, Gulf Publishing Co. (1976).
- Crowe, C.W.: "Evaluation of Oil Soluble Resin Mixtures as Diverting Agents for Matrix Acidizing," paper SPE 3505, presented at the SPE Annual Meeting, New Orleans, Louisiana, USA (October 3–6, 1971).
- Crowe, C.W.: "Evaluation of Agents for Preventing Precipitation of Ferric Hydroxide from Spent Treating Acid," paper SPE 12497, *Journal of Petroleum Technology* (April 1985), 691–695.
- Crowe, C.W.: "Precipitation of Hydrated Silica from Spent Hydrofluoric Acid—How Much of a Problem Is It?," paper SPE 13083, *Journal of Petroleum Technology* (1986), 1234.
- Crowe, C.W. and Cryar, H.B. Jr.: "Development of Oil Soluble Resin Mixture for Control of Fluid Loss in Water Base Workover and Completion Fluids," paper SPE 5662, presented at the SPE Annual Technical Conference and Exhibition, Dallas, Texas, USA (September 28–October 1, 1975).
- Crowe, C.W., Martin, R.C. and Michaelis, A.M.: "Evaluation of Acid Gelling Agents for Use in Well Stimulation," paper SPE 9384, *SPE Journal* (August 1981), 415.
- Crowe, C.W., McGowan, G.R. and Baranet, S.E.: "Investigation of Retarded Acids Provides Better Understanding of Their Effectiveness and Potential Benefits," paper SPE 18222, *SPE Production Engineering* (May 1990), 166.
- Crowe, C.W. and Minor, S.S.: "Acid Corrosion Inhibitor Adsorption and Its Effect on Matrix Stimulation Results," paper SPE 10650, presented at the SPE Formation Damage Control Symposium, Lafayette, Louisiana, USA (March 24–25, 1982).
- Crowe, C.W. and Minor, S.S.: "Effect of Acid Corrosion Inhibitors on Matrix Stimulation Results," paper SPE 11119, *Journal of Petroleum Technology* (1985), 1853.
- Cunningham, W.C. and Smith, D.K.: "Effect of Salt Cement Filtrate on Subsurface Formations," paper SPE 1920, *Journal of Petroleum Technology* (March 1968), 259–264.
- Cussler, E.L.: *Diffusion: Mass Transfer in Fluid Systems*, New York, New York, USA, Cambridge University Press (1984).
- Daccord, G.: "Acidizing Physics," *Reservoir Stimulation*, M.J. Economides and K.G. Nolte (eds.), second edition, Englewood Cliffs, New Jersey, USA, Prentice Hall (1989), 13-1–13-13.
- Daccord, G. and Lenormand, R.: "Fractal Patterns from Chemical Dissolution," *Nature* (1987) 325, 41–43.
- Daccord, G., Lenormand, R. and Liétard, O.: "Chemical Dissolution of a Porous Medium by a Reactive Fluid," *Chemical Engineering Science* (1993) 48, No. 1, 169–186.
- Daccord, G., Touboul, E. and Lenormand, R.: "Carbonate Acidizing: Toward a Quantitative Model of the Wormholing Phenomenon," paper SPE 16887, *SPE Production Engineering* (February 1989), 63–68.
- Dahlgaard, C.C.: "Compressed Air and Foam, Cleanout Technique for Old Open Hole Completions," paper SPE 11854, presented at the SPE Rocky Mountain Regional Meeting, Salt Lake City, Utah, USA (May 23–25, 1983).
- da Motta, E.P., Hill, A.D. and Sepehrnoori, K.: "Selective Matrix Acidizing of Horizontal Wells," paper SPE 27399, presented at the SPE International Symposium on Formation Damage Control, Lafayette, Louisiana, USA (February 7–10, 1994).
- da Motta, E.P., Plavnik, B. and Schechter, R.S.: "Optimizing Sandstone Acidization," *SPE Reservoir Engineering* (February 1992a), 149–153.
- da Motta, E.P., Plavnik, B., Schechter, R.S. and Hill, A.D.: "The Relationship Between Reservoir Mineralogy and Optimum Sandstone Acid Treatment," paper SPE 23802, presented at the SPE International Symposium on Formation Damage Control, Lafayette, Louisiana, USA (February 26–27, 1992b).
- Danesh, A., *et al.*: "Asphaltene Deposition in Miscible Gas Flooding of Oil Reservoirs," *Chem. Eng. Res. Des.* (July 1988) 66, 339–344.

- Davies, D.K.: "Clay Technology and Well Stimulation," presented at Southwestern Petroleum Short Course, Lubbock, Texas, USA (April 20–21, 1978).
- Davies, D.R., Faber, R., Nitters, G. and Ruessink, B.H.: "A Novel Procedure to Increase Well Response to Matrix Acidising Treatments," paper SPE 23621, presented at the Second SPE Latin American Petroleum Engineering Conference, Caracas, Venezuela (March 8–11, 1992).
- Davies, D.R., Lievaart, L. and Nitters, G.: "The Effects of Corrosion Inhibitors and Mutual Solvents on Matrix Acidizing Treatments," paper SPE 17153, presented at the SPE Formation Damage Control Symposium, Bakersfield, California, USA (February 8–9, 1988).
- De Ghetto, G.: "Chart Eases Field Use of AGIP Matrix-Stimulation Method If Computer Program Not Available," *Oil & Gas Journal* (November 29, 1982), 76–77.
- Denson, A.H., Smith, J.T. and Cobb, W.M.: "Determining Well Drainage Pore Volume and Porosity from Pressure Buildup Tests," *SPE Journal* (August 1976), 209–216.
- de Rozières, J., Chang, F.F. and Sullivan, R.B.: "Measuring Diffusion Coefficients in Acid Fracturing Fluids and Their Application to Gelled and Emulsified Acids," paper SPE 28552, presented at the SPE Annual Technical Conference and Exhibition, New Orleans, Louisiana, USA (September 25–28, 1994).
- de Vries, A.S. and Wit, K.: "Rheology of Gas/Water Foam in the Quality Range Relevant to Steam Foam," *SPE Reservoir Engineering* (May 1990), 185–192.
- Doerler, N. and Prouvost, L.P.: "Diverting Agents: Laboratory Study and Modeling of Resultant Zone Injectivities," paper SPE 16250, presented at the SPE International Symposium on Oilfield Chemistry, San Antonio, Texas, USA (February 4–6, 1987).
- Dria, M.A., Schechter, R.S. and Lake, L.W.: "An Analysis of Reservoir Chemical Treatments," paper SPE 13551, *SPE Production Engineering* (February 1988), 52.
- Droddy, M.J., Jones, T.A. and Shaw, D.B.: "Drill Fluid and Return Permeability Tests of South Texas Wilcox Cores," paper SPE 17159, presented at the SPE Formation Damage Control Symposium, Bakersfield, California, USA (February 8–9, 1988).
- Dullien, F.A.L.: *Porous Media: Fluid Transport and Pore Structure*, New York, New York, USA, Academic Press (1979).
- Dunlap, D.D. and Houchin, L.R.: "Evaluation of Acid System Design and Formation Damage Using Polarized Microscopy," paper SPE 19425, presented at the SPE Formation Damage Control Symposium, Lafayette, Louisiana, USA (February 22–23, 1990).
- Dunn, L.A. and Stokes, R.H.: "The Diffusion of Monocarboxylic Acids in Aqueous Solution at 25°," *Aust. J. Chem.* (1965) 18, 285–296.
- Durham, D.K., Ali, S.A. and Stone, P.J.: "Causes and Solutions to Surface Facilities Upsets Following Acid Stimulation in the Gulf of Mexico," paper SPE 29528, presented at the SPE Production Operations Symposium, Oklahoma City, Oklahoma, USA (April 2–4, 1995).
- Dusseault, M.B. and Gray, K.E.: "Mechanisms of Stress-Induced Wellbore Damage," paper SPE 23825, presented at the SPE International Symposium on Formation Damage Control, Lafayette, Louisiana, USA (February 26–27, 1992).
- Earlougher, R.C. Jr.: *Advances in Well Test Analysis*, Dallas, Texas, USA, Society of Petroleum Engineers (1977).
- Eaton, B.A. and Smithey, M.: "Formation Damage from Workover and Completion Fluids," paper SPE 3707, presented at the SPE Annual California Regional Meeting, Los Angeles, California, USA, (November 4–5, 1971).
- Economides, M.J., Ben Naceur, K. and Klem, R.C.: "Matrix Stimulation Method for Horizontal Wells," paper SPE 19719, *Journal of Petroleum Technology* (July 1991), 854–861.
- Economides, M.J., Cikes, M., Pforter, H., Udick, T.H. and Uroda, P.: "The Stimulation of a Tight, Very-High-Temperature Gas-Condensate Well," paper SPE 15239, *SPE Formation Evaluation* (March 1989), 63.
- Economides, M.J. and Frick, T.P.: "Optimization of Horizontal Well Matrix Stimulation Treatments," paper SPE 22334, presented at the SPE International Meeting on Petroleum Engineering, Beijing, China (March 24–27, 1992).



- Economides, M.J., Hill, A.D. and Ehlig-Economides, C.: *Petroleum Production Systems*, Englewood Cliffs, New Jersey, USA, Prentice-Hall (1994).
- Efthim, F.P., Garner, J.J., Bilden, D.M., Kovacevich, S.T. and Pence, T.C.: "Evaluation and Treatment of Organic and Inorganic Damage in an Unconsolidated Asphaltic Crude Reservoir," paper SPE 19412, presented at the SPE Formation Damage Control Symposium, Lafayette, Louisiana, USA (February 22–23, 1990).
- Ehlig-Economides, C.A. and Joseph, J.A.: "A New Test for Determination of Individual Layer Properties in a Multilayered Reservoir," paper SPE 14167, presented at the SPE Annual Technical Conference and Exhibition, Las Vegas, Nevada, USA (September 22–25, 1985).
- Elbel, J.L., Navarrete, R.C. and Poe, B.D. Jr.: "Production Effects of Fluid Loss in Fracturing High-Permeability Formations," paper SPE 30098, presented at the SPE European Formation Damage Conference, The Hague, Netherlands (May 15–16, 1995).
- Erbstoesser, S.R.: "Improved Ball Sealer Diversion," paper SPE 8401, *Journal of Petroleum Technology* (November 1980), 1903.
- Ettinger, R.A. and Radke, C.J.: "Influence of Texture on Steady Foam Flow in Berea Sandstone," paper SPE 19688, *SPE Reservoir Engineering* (February 1992), 83.
- Ezeukwu, T., Thomas, R.L. and Gunnerød, T.: "Fines Migration Control in High-Water-Cut Nigerian Oil Wells: Problems and Solutions," paper SPE 39482, presented at the SPE International Symposium on Formation Damage Control, Lafayette, Louisiana, USA (February 18–19, 1998).
- Faber, M.J., Davies, D.R., Nitters, G. and Ruessink, B.H.: "A Novel Procedure to Increase Well Response to Matrix Acidising Treatments," paper SPE 23621, *SPE Advanced Technology Series* (1994) 2, No. 1, 5–14.
- Falls, A.H., Musters, I.J. and Ratulowski, J.: "The Apparent Viscosity of Foams in Homogeneous Bead Packs," paper SPE 16048, *SPE Reservoir Engineering* (May 1989), 1263.
- Farley, J.T., Miller, B.M. and Schoettle, V.: "Design Criteria for Matrix Stimulation with Hydrochloric-Hydrofluoric Acid," paper SPE 2621, *Journal of Petroleum Technology* (April 1970), 433–440.
- Fetkovitch, M.J. and Vienot, M.E.: "Shape Factor, CA, Expressed as Skin, sCA," paper SPE 13304, *Journal of Petroleum Technology* (February 1985), 321.
- Fischer, P.W., Gallus, J.P., Krueger, R.F., Pye, D.S., Simmons, F.J. and Talley, B.E.: "An Organic 'Clay Substitute' for Nondamaging Water Base Drilling and Completion Fluids," paper SPE 4651, presented at the SPE Annual Meeting, Las Vegas, Nevada, USA (September 30–October 3, 1973).
- Fisher, A.W., Foulser, R.W.S. and Goodyear, S.G.: "Mathematical Modeling of Foam Flooding," paper SPE 20195, presented at the SPE/DOE Symposium on Enhanced Oil Recovery, Tulsa, Oklahoma, USA (April 22–25, 1990).
- Flanigan, M.J.: "Smaller Gravel and Coated Screens Enhance 50-Year-Old Field," paper SPE 7973, *Journal of Petroleum Technology* (May 1980), 757–763.
- Fletcher, P.A., Montgomery, C.T. and Ramos, G.G.: "Optimizing Hydraulic Fracture Length to Prevent Formation Failure in Oil and Gas Reservoirs," *Proc.*, 35th U.S. Rock Mechanics Symposium, Reno, Nevada, USA (June 1995), 293–298.
- Fogler, H.S. and Crain, E.R.: "Stimulation of Gas Storage Fields to Restore Deliverability," paper SPE 8731, *Journal of Petroleum Technology* (September 1980), 1612–1620.
- Fogler, H.S., Lund, K. and McCune, C.C.: "Acidization. Part 3. The Kinetics of the Dissolution of Sodium and Potassium Feldspar in HF/HCl Acid Mixtures," *Chem. Eng. Sci.* (1975) 30, No. 11, 1325–1332.
- Fogler, H.S., Lund, K. and McCune, C.C.: "Predicting the Flow and Reaction of HCl/HF Mixtures in Porous Sandstone Cores," paper SPE 5646, *SPE Journal* (October 1976), 248–260.
- Fogler, H.S., Lund, K., McCune, C.C. and Ault, J.W.: "Dissolution of Selected Minerals in Mud Acid," paper 52C, presented at the American Institute of Chemical Engineers 74th National Meeting, New Orleans, Louisiana, USA (March 1973).



- Frasch, H.: "Increasing the Flow of Oil Wells," U.S. Patent No. 556,669 (March 17, 1896).
- Fredd, C.N.: "The Influence of Transport and Reaction on Wormhole Formation in Carbonate Porous Media: A Study of Alternative Stimulation Fluids," PhD thesis, University of Michigan, Ann Arbor, Michigan, USA (1998).
- Fredd, C.N. and Fogler, H.S.: "Alternative Stimulation Fluids and Their Impact on Carbonate Acidizing," paper SPE 31074, presented at the SPE International Symposium on Formation Damage Control, Lafayette, Louisiana, USA (February 14–15, 1996).
- Fredd, C.N. and Fogler, H.S.: "Alternative Stimulation Fluids and Their Impact on Carbonate Acidizing," *SPE Journal* (March 1998a) 13, No. 1, 34.
- Fredd, C.N. and Fogler, H.S.: "Influence of Transport and Reaction on Wormhole Formation in Porous Media," *AIChE J.* (September 1998b), 1933–1949.
- Fredd, C.N. and Fogler, H.S.: "The Influence of Chelating Agents on the Kinetics of Calcite Dissolution," *J. Colloid and Interface Science* (August 1998c) 204, No. 1, 187–197.
- Fredd, C.N. and Fogler, H.S.: "The Kinetics of Calcite Dissolution in Acetic Acid Solutions," *Chem. Eng. Sci.* (October 1998d) 53, No. 22, 3863–3894.
- Fredd, C.N., Tija, R. and Fogler, H.S.: "The Existence of an Optimum Damköhler Number for Matrix Stimulation of Carbonate Formations," paper SPE 38167, presented at the SPE European Formation Damage Control Conference, The Hague, Netherlands (June 2–3, 1997).
- Frick, T.P. and Economides, M.J.: "Horizontal Well Damage Characterization and Removal," paper SPE 21795, presented at the SPE Western Regional Meeting, Long Beach, California, USA (March 20–22, 1991).
- Frick, T.P., Kürmayr, M. and Economides, M.J.: "Modeling of Fractal Patterns in Matrix Acidizing and Their Impact on Well Performance," paper SPE 23789, presented at the SPE International Symposium on Formation Damage, Lafayette, Louisiana, USA (February 26–27, 1992); also in *SPE Production & Facilities* (February 1994a), 61–68.
- Frick, T.P., Mostofizadeh, B. and Economides, M.J.: "Analysis of Radial Core Experiments for Hydrochloric Acid Interaction with Limestones," paper SPE 27402, presented at the SPE International Symposium on Formation Damage Control, Lafayette, Louisiana, USA (February 7–10, 1994b).
- Friedmann, F., Chen, W.H. and Gauglitz, P.A.: "Experimental and Simulation Study of High-Temperature Foam Displacement in Porous Media," paper SPE 17357, *SPE Reservoir Engineering* (February 1991), 37–75.
- Friedmann, F. and Jensen, J.A.: "Some Parameters Influencing the Formation and Propagation of Foams in Porous Media," paper SPE 15087, presented at the SPE California Regional Meeting, Oakland, California, USA (April 2–4, 1986).
- Fulford, R.S.: "Effects of Brine Concentration and Pressure Drop on Gypsum Scaling in Oil Wells," paper SPE 1830, *Journal of Petroleum Technology* (June 1968), 559–564.
- Gabriel, G.A. and Erbstoesser, S.R.: "The Design of Buoyant Ball Sealer Treatments," paper SPE 13085, presented at the SPE Annual Technical Conference and Exhibition, Houston, Texas, USA (September 16–19, 1984).
- Gadiyar, B.R. and Civan, F.: "Acidization-Induced Formation Damage: Experimental and Modeling Studies," paper SPE 27400, presented at the SPE International Symposium on Formation Damage Control, Lafayette, Louisiana, USA (February 7–10, 1994).
- Garrels, R.M. and Christ, C.L.: *Solutions, Minerals and Equilibria*, New York, New York, USA, Harper & Row (1965).
- Gdanski, R.: "Kinetics of Tertiary Reaction of HF on Alumino-Silicates," paper SPE 31076, presented at the SPE International Symposium on Formation Damage Control, Lafayette, Louisiana, USA (February 14–15, 1996).
- Gdanski, R.D.: "AlCl<sub>3</sub> Retards HF Acid for More Effective Stimulation," *Oil & Gas Journal* (October 28, 1985), 111–115.
- Gdanski, R.D.: "Experience and Research Show Best Designs for Foam-Diverted Acidizing," *Oil & Gas Journal* (September 1993), 85–89.

- Gdanski, R.D. and Peavy, M.A.: "Well Return Analysis Causes Re-Evaluation of HCl Theories," paper SPE 14825, presented at the SPE Symposium on Formation Damage Control, Lafayette, Louisiana, USA (February 26–27, 1986).
- Gidley, J.L.: "Stimulation of Sandstone Formations with the Acid-Mutual Solvent Method," paper SPE 3007, *Journal of Petroleum Technology* (May 1971), 551–558.
- Gidley, J.L.: "Acidizing Sandstone Formations: A Detailed Examination of Recent Experience," paper SPE 14164, presented at the SPE Annual Technical Conference and Exhibition, Las Vegas, Nevada, USA (September 22–25, 1985).
- Gidley, J.L., Brezovec, E.J. and King, G.E.: "An Improved Method for Acidizing Oil Wells in Sandstone Formations," paper SPE 26580, *SPE Production & Facilities* (February 1996).
- Gidley, J.L. and Hanson, H.R.: "Prevention of Central Terminal Upsets Related to Stimulation and Consolidation Treatments," paper SPE 4551, presented at the SPE Annual Meeting, Las Vegas, Nevada, USA (September 30–October 3, 1973).
- Gidley, J.L., Penny, G.S. and McDaniel, R.R.: "Effect of Proppant Failure and Fines Migration on Conductivity of Propped Fractures," paper SPE 24008, presented at the SPE Permian Basin Oil and Gas Recovery Conference, Midland, Texas, USA (March 18–20, 1992); also in *SPE Production & Facilities* (February 1995), 20.
- Ginest, N.H., Phillips, J.E., Al-Gamber, A.W.A. and Wright, D.W.: "Field Evaluation of Acid Stimulation Diverter Materials and Placement Methods in Arab-D Injection Wells with Openhole Completions," paper SPE 25412, presented at the SPE Middle East Oil Technical Conference and Exhibition, Bahrain (April 3–6, 1993).
- Givens, J.C.: "Old Idea (with New Application) Increases Oil and Gas Production," paper SPE 6499 (November 1976).
- Goode, D.L., Berry, S.D. and Stacy, A.L.: "Aqueous-Based Remedial Treatments for Reservoirs Damaged by Oil-Phase Drilling Muds," paper SPE 12501, presented at the SPE Formation Damage Control Symposium, Bakersfield, California, USA (February 13–14, 1984).
- Gougler, P.D. Jr., Hendrick, J.E. and Coulter, A.W.: "Field Investigation Identifies Source and Magnitude of Iron Problems," paper SPE 13812, presented at the SPE Production Operations Symposium, Oklahoma City, Oklahoma, USA (March 10–12, 1985).
- Gudmundson, J.S. and Ortiz-R., J.: "Two-Phase Flow and Calcite Deposition," paper SPE 12741, presented at the SPE California Regional Meeting, Long Beach, California, USA (April 11–13, 1984).
- Guidry, G.S., Ruiz, G.A. and Saxon, A.: "SXE/N<sub>2</sub> Matrix Acidizing," paper SPE 17951, presented at the SPE Middle East Oil Technical Conference and Exhibition, Manama, Bahrain (March 11–14, 1989).
- Guin, J.A. and Schechter, R.S.: "Matrix Acidization with Highly Reactive Acids," *SPE Journal* (December 1971), 390–398.
- Guin, J.A., Schechter, R.S. and Silberberg, I.H.: "Chemically Induced Changes in Porous Media," *Ind. & Eng. Chem. Fund.* (February 1971) 10, No. 1, 50–54.
- Gulati, M.S. and Maly, G.P.: "Thin-Section and Permeability Studies Call for Smaller Gravels in Gravel Packing," paper SPE 4773, *Journal of Petroleum Technology* (January 1975), 107–112.
- Gunter, W.D., Zhou, Z. and Perkins, E.H.: "Modeling Formation Damage Caused by Kaolinite from 25 to 300 Degrees Centigrade in the Oil Sand Reservoirs of Alberta," paper SPE 23786, presented at the SPE International Symposium on Formation Damage Control, Lafayette, Louisiana, USA (February 26–27, 1992).
- Hall, B.E.: "The Effect of Mutual Solvents on Adsorption in Sandstone Acidizing," *Journal of Petroleum Technology* (December 1975), 1439.
- Hall, B.E.: "Workover Fluids: Parts 1–5," *World Oil* (May–July, October and December 1986), 111–114, 64–67, 65–68, 61–63 and 49–50.
- Hall, B.E. and Dill, W.R.: "Iron Control Additives for Limestone and Sandstone Acidizing of Sweet and Sour Wells," paper SPE 17159, presented at the SPE Formation Damage Control Symposium, Bakersfield, California, USA (February 8–9, 1988).
- Hall, B.E., Tinnemeyer, A.C. and Underwood, P.J.: "Stimulation of the North Coles Levee Field with a Retarded HF-Acid," paper SPE 9934, presented at

the SPE California Regional Meeting, Bakersfield, California, USA (March 25–26, 1981).

Harrison, N.W.: “Diverting Agents—History and Application,” paper SPE 3653, *Journal of Petroleum Technology* (May 1972), 593.

Hassen, B.R.: “New Technique Estimates Drilling Filtrate Invasion,” paper SPE 8791, presented at the SPE Symposium on Formation Damage Control, Bakersfield, California, USA (January 28–29, 1980).

Hausler, R.H.: “Guidelines Help Avoid, Treat Oil Field Emulsions,” *Oil & Gas Journal* (September 4, 1978).

Hebert, P.B., Khatib, Z.I., Norman, W.D., Acock, A. and Johnson, M.: “Novel Filtration Process Eliminates System Upset Following Acid Stimulation Treatment,” paper SPE 36601, presented at the SPE Annual Technical Conference and Exhibition, Denver, Colorado, USA (October 6–9, 1996).

Hekim, Y., Fogler, H.S. and McCune, C.C.: “The Radial Movement of Permeability Fronts and Multiple Reaction Zones in Porous Media,” *SPE Journal* (February 1982), 99–107.

Hendrickson, A.R.: “Stimulation of Carbonate Reservoirs,” *Oil and Gas Production from Carbonate Rocks*, G.V. Chilingar, R.W. Manson and H.H. Ricke (eds.), New York, New York, USA, Elsevier (1972), 309–339.

Hendrickson, A.R., Hurst, R.E. and Wieland, D.R.: “Engineered Guide for Planning Acidizing Treatments Based on Specific Reservoir Characteristics,” *Trans., AIME* (January 1960) 219, 16–23.

Hill, A.D. and Galloway, P.J.: “Laboratory and Theoretical Modeling of Diverting Agent Behavior,” paper SPE 11576, *Journal of Petroleum Technology* (July 1984), 1157.

Hill, A.D., Lindsay, D.M., Schechter, R.S. and Silberberg, I.H.: “Sandstone Acidizing: The Development of Design Method,” paper SPE 6607, presented at the SPE-AIME International Symposium on Oilfield and Geothermal Chemistry, La Jolla, California, USA (June 27–28, 1977).

Hill, A.D. and Rossen, W.R.: “Fluid Placement and Diversion in Matrix Acidizing,” paper SPE 27982, presented at the University of Tulsa Centennial Petroleum Engineering Symposium, Tulsa, Oklahoma, USA (August 29–31, 1994).

Hill, A.D. and Zhu, D.: “Real-Time Monitoring of Matrix Acidizing Including the Effects of Diverting Agents,” paper SPE 28548, presented at the SPE Annual Technical Conference and Exhibition, New Orleans, Louisiana, USA (September 25–28, 1994).

Himmatramka, A.K.: “Analysis of Productivity Reduction Due to Non-Darcy Flow and True Skin in Gravel-Packed Wells,” paper SPE 10084, presented at the SPE Annual Technical Conference and Exhibition, San Antonio, Texas, USA (October 5–7, 1981).

Hinchman, S.P. and Barree, R.D.: “Productivity Loss in Gas Condensate Reservoirs,” paper SPE 14203, presented at the SPE Annual Technical Conference and Exhibition, Las Vegas, Nevada, USA (September 22–25, 1985).

Hirasaki, G.J.: “A Review of Steam-Foam Process Mechanisms,” paper SPE 19518 (1989a).

Hirasaki, G.J.: “The Steam-Foam Process,” paper SPE 19505, *Journal of Petroleum Technology* (May 1989b), 449–456.

Hirschberg, A., deJong, L.N.J., Schipper, B.A. and Meijer, J.G.: “Influence of Temperature and Pressure on Asphaltenes Flocculation,” paper SPE 11202, *SPE Journal* (1984), 283.

Hodge, R.M., MacKinlay, W.M. and Landrum, W.R.: “The Selection and Application of Loss Control Materials to Minimize Formation Damage in Gravel Packed Completions for a North Sea Field,” paper SPE 30119, presented at the SPE European Formation Damage Conference, The Hague, Netherlands (May 15–16, 1995).

Hoefner, M.L. and Fogler, H.S.: “Effective Matrix Acidizing in Carbonates Using Microemulsions,” *Chem. Eng. Prog.* (May 1985), 40–44.

Hoefner, M.L. and Fogler, H.S.: “Pore Evolution and Channel Formation During Flow and Reaction in Porous Media,” *AIChE J.* (January 1988) 34, No. 1, 45–54.

Hoefner, M.L., Fogler, H.S., Stenius, P. and Sjöblom, J.: “Role of Acid Diffusion in Matrix Acidizing of Carbonates,” *Journal of Petroleum Technology* (February 1987), 203–208.

Holcomb, D.L.: “Low Surface Tension Hydrochloric-Hydrofluoric Acid Mixtures in Low Porosity, Low Permeability Sandstones,” paper SPE 5411,

presented at the SPE Oklahoma City Regional Meeting, Oklahoma City, Oklahoma, USA (March 24–25, 1975).

Holub, R.W., Maly, G.P., Noel, R.P. and Weinbrandt, R.M.: “Scanning Electron Microscope Pictures of Reservoir Rocks Reveal Ways to Increase Oil Production,” paper SPE 4787, presented at the SPE Symposium on Formation Damage Control, New Orleans, Louisiana, USA (February 7–8, 1974).

Hong, K.C.: “Productivity of Perforated Completions in Formations With or Without Damage,” paper SPE 4653, *Journal of Petroleum Technology* (August 1975), 1027–1038.

Hoover, J.E. (ed.): *Remington’s Pharmaceutical Sciences*, 14th edition, Easton, Pennsylvania, USA, Mack Publishing Co. (1970).

Horton, H.L., Hendrickson, A.R. and Crowe, C.W.: “Matrix Acidizing of Limestone Reservoirs,” paper API N906-10-F, presented at the Spring Meeting of the Southwestern District, Dallas, Texas, USA (March 10–12, 1965).

Houchin, L.R., Dunlap, D.D., Arnold, B.D. and Domke, K.M.: “The Occurrence and Control of Acid-Induced Asphaltene Sludge,” paper SPE 19410, presented at the SPE Formation Damage Control Symposium, Lafayette, Louisiana, USA (February 22–23, 1990).

Houchin, L.R., Dunlap, D.D., Hudson, L.M. and Begnaud, P.C.: “Evaluation of Oil-Soluble Resin as an Acid-Diverting Agent,” paper SPE 15574, presented at the SPE Annual Technical Conference and Exhibition, New Orleans, Louisiana, USA (October 5–8, 1986).

Houchin, L.R. and Hudson, L.M.: “The Prediction, Evaluation and Treatment of Formation Damage Caused by Organic Deposition,” paper SPE 14818, presented at the SPE Symposium on Formation Damage Control, Lafayette, Louisiana, USA (February 26–27, 1986).

Hower, W.F.: “Influence of Clays on the Production of Hydrocarbons,” paper SPE 4785, presented at the SPE Symposium on Formation Damage Control, New Orleans, Louisiana, USA (February 7–8, 1974).

Hsia, T-Y. and Behrmann, L.A.: “Perforating Skins as a Function of Rock Permeability and Underbalance,” paper SPE 22810, presented at the SPE

Annual Technical Conference and Exhibition, Dallas, Texas, USA (October 6–9, 1991).

Huang, T., Hill, A.D. and Schechter, R.S.: “Reaction Rate and Fluid Loss: The Keys to Wormhole Initiation and Propagation in Carbonate Acidizing,” paper SPE 37312, presented at the SPE International Symposium on Oilfield Chemistry, Houston, Texas, USA (February 18–21, 1997).

Huh, D.G. and Handy, L.L.: “Comparison of Steady- and Unsteady-State Flow of Gas and Foaming Solution in Porous Media,” paper SPE 15078, *SPE Reservoir Engineering* (February 1989), 77–84.

Hung, K.M.: “Modeling of Wormhole Behavior in Carbonate Acidizing,” PhD dissertation, The University of Texas at Austin, Austin, Texas, USA (1987).

Hung, K.M., Hill, A.D. and Sepehrnoori, K.: “A Mechanistic Model of Wormhole Growth in Carbonate Matrix Acidizing and Acid Fracturing,” paper SPE 16886, *Journal of Petroleum Technology* (January 1989) 41, No. 1, 59–66.

Hurst, R.E.: “Our Petroleum Reservoirs Deserve Better Care,” paper SPE 4659, presented at the SPE Annual Meeting, Las Vegas, Nevada, USA (September 30–October 3, 1973).

Iler, R.K.: *The Chemistry of Silica: Solubility, Polymerization, Colloid and Surface Properties, and Biochemistry*, New York, New York, USA, J. Wiley and Sons, Inc. (1979).

Jacobs, I.C. and Thorne, M.A.: “Asphaltene Precipitation During Acid Stimulation Treatments,” paper SPE 14823, presented at the SPE Symposium on Formation Damage Control, Lafayette, Louisiana, USA (February 26–27, 1986).

Jensen, J.A. and Friedmann, F.: “Physical and Chemical Effects of an Oil Phase on the Propagation of Foam in Porous Media,” paper SPE 16375, presented at the SPE California Regional Meeting, Ventura, California, USA (April 8–10, 1987).

Jiang, R. and Anson, F.C.: “Association of Electroactive Counterions with Polyelectrolytes. 4. Coordinative Binding of Ru (EDTA) to Poly (4-Vinylpyridine),” *J. Phys. Chem.* (1992) 96, 452.

Jiao, D. and Sharma, M.M.: “Formation Damage Due to Static and Dynamic Filtration of Water-Based Muds,” paper SPE 23823, presented at the SPE

International Symposium on Formation Damage Control, Lafayette, Louisiana, USA (February 26–27, 1992).

Jones, A.T. and Davies, D.R.: “Qualifying Acid Placement: The Key to Understanding Damage Removal in Horizontal Wells,” paper SPE 31146, presented at the SPE International Formation Control Symposium, Lafayette, Louisiana, USA (February 14–15, 1996).

Jones, D.L. and Brown, K.: “Application of Systems Analysis Can Increase Production by 200 Percent in High Volume Gas Lift Wells,” paper SPE 3547, presented at the SPE Annual Meeting, New Orleans, Louisiana, USA (October 3–6, 1971).

Jones, F.O. Jr.: “Influence of Chemical Composition of Water on Clay Blocking of Permeability,” paper SPE 631, *Journal of Petroleum Technology* (April 1964), 441.

Jones, L.G., Blount, E.M. and Glaze, O.H.: “Use of Short Term Multiple Rate Flow Tests to Predict Performance of Wells Having Turbulence,” paper SPE 6133, presented at the SPE Annual Technical Conference and Exhibition, New Orleans, Louisiana, USA (October 3–6, 1976).

Jones, L.G. and Watts, J.W.: “Estimating Skin Effect in a Partially Completed Damaged Well,” paper SPE 2616, *Journal of Petroleum Technology* (February 1971), 249–252.

Jones, L.G., Yeh, C.S., Yates, T.J., Bryant, D.W., Doolittle, M.W. and Healy, J.C.: “Alternate Path Gravel Packing,” paper SPE 22796, presented at the SPE Annual Technical Conference and Exhibition, Dallas, Texas, USA (October 6–9, 1991a).

Jones, R.R., Carpenter, R.B. and Conway, M.W.: “A Study of Formation Damage Potential During Cementing Operations,” paper SPE 22777, presented at the SPE Annual Technical Conference and Exhibition, Dallas, Texas, USA (October 6–9, 1991b).

Kalfayan, L.J. and Watkins, D.R.: “A New Method for Stabilizing Fines and Controlling Dissolution During Sandstone Acidizing,” paper SPE 20076, presented at the SPE California Regional Meeting, Ventura, California, USA (April 4–6, 1990).

Kawanaka, S., Park, S.J. and Mansoori, G.A.: “Organic Deposition from Reservoir Fluids: A

Thermodynamic Predictive Technique,” paper SPE 17376, *SPE Reservoir Engineering* (May 1991), 185.

Keelan, D.K. and Koepf, E.H.: “The Role of Cores and Core Analysis in Evaluation of Formation Damage,” paper SPE 5696, *Journal of Petroleum Technology* (May 1977), 482–490.

Keeney, B.R. and Frost, J.G.: “Guidelines Regarding the Use of Alcohols in Acidic Stimulation Fluids,” paper SPE 5181, *Journal of Petroleum Technology* (May 1975), 552–554.

Keese, J.A. and Oden, A.L.: “A Comparison of Jet Perforating Services: Kern River Field,” paper SPE 5690, presented at the SPE Symposium on Formation Damage Control, Houston, Texas, USA (January 29–30, 1976).

Kennedy, D.K., Kitziger, F.W. and Hall, O.E.: “Case Study on the Effectiveness of Nitrogen Foams and Water-Zone Diverting Agents in Multistage Matrix Acid Treatments,” paper SPE 20621, *SPE Production Engineering* (May 1992), 203.

Khatib, Z.I., Hirasaki, G.J. and Falls, A.H.: “Effects of Capillary Pressure on Coalescence and Phase Mobilities in Foams Flowing Through Porous Media,” *SPE Reservoir Engineering* (August 1988), 919.

Khilar, K.C. and Fogler, S.H.: “Water Sensitivity of Sandstones,” paper SPE 10103, presented at the SPE Annual Technical Conference and Exhibition, San Antonio, Texas, USA (October 5–7, 1981); also in *Journal of Petroleum Technology* (February 1983), 55–64.

Kibodeaux, K.R., Zeilinger, S.C. and Rossen, W.R.: “Sensitivity Study of Foam Diversion Processes for Matrix Acidization,” paper SPE 28550, presented at the SPE Annual Technical Conference and Exhibition, New Orleans, Louisiana, USA (September 25–28, 1994).

King, G.E., Anderson, A. and Bingham, M.: “A Field Study of Underbalance Pressures Necessary to Obtain Clean Perforations Using Tubing-Conveyed Perforating,” paper SPE 14321, presented at the SPE Annual Technical Conference and Exhibition, Las Vegas, Nevada, USA (September 22–25, 1985).

King, G.E. and Hollingsworth, H.F.: “Evaluation of Diverting Agent Effectiveness and Cleanup Charac-

teristics Using a Dynamic Laboratory Model—High Permeability Case,” paper SPE 8400, presented at the SPE Annual Technical Conference and Exhibition, Las Vegas, Nevada, USA (September 23–26, 1979).

King, G.E. and Lee, R.M.: “Adsorption and Chlorination of Mutual Solvents Used in Acidizing,” paper SPE 14432, *SPE Production Engineering* (May 1988), 205–209.

Kline, W.E.: “The Catalyzed Dissolution of Silicate Materials by Hydrofluoric Acid,” PhD dissertation, University of Michigan, Michigan, USA (1980).

Kline, W.E. and Fogler, H.S.: “Dissolution Kinetics: The Nature of the Particle Attack of Layered Silicates in HF,” *Chem. Eng. Sci.* (1981a) 36, 871–884.

Kline, W.E. and Fogler, H.S.: “Dissolution of Silicate Minerals by Hydrofluoric Acid,” *Ind. Eng. Chem. Fundam.* (1981b) 20, 155–161.

Klotz, J.A., Krueger, R.F. and Pye, D.S.: “Maximum Well Productivity in Damaged Formations Requires Deep, Clean Perforations,” paper SPE 4792, presented at the SPE Symposium on Formation Damage Control, New Orleans, Louisiana, USA (February 7–8, 1974).

Knobloch, T.S., Farouq Ali, S.M. and Diaz, M.J.T.: “The Role of Acid-Additive Mixtures on Asphaltene Precipitation,” paper SPE 7627, presented at the SPE Eastern Regional Meeting, Washington, D.C., USA (November 1–3, 1978).

Kovscek, A.R. and Radke, C.J.: “Fundamentals of Foam Transport in Porous Media,” *Foams: Fundamentals and Applications in the Petroleum Industry*, L.L. Schramm (ed.), ACS Advances in Chemistry Series, American Chemical Society, Washington, D.C., USA (1994) 3.

Krause, D.C.: “Solids-Free Brines: Efficient Displacement Techniques Can Save You Money,” paper SPE 14830, presented at the SPE Symposium on Formation Damage Control, Lafayette, Louisiana, USA (February 26–27, 1986).

Krueger, R.F.: “An Overview of Formation Damage and Well Productivity in Oil Field Operations,” paper SPE 10029, *Journal of Petroleum Technology* (February 1986), 131–152.

Krueger, R.F.: “An Overview of Formation Damage and Well Productivity in Oilfield Operations: An Update,” paper SPE 17459, presented at the SPE California Regional Meeting, Long Beach, California, USA (March 23–25, 1988).

Krueger, R.G., Vogel, L.C. and Fischer, P.W.: “Effect of Pressure Drawdown on Clean-Up of Clay- or Silt-Blocked Sandstone,” paper SPE 1605, *Journal of Petroleum Technology* (March 1967), 397–403.

Kular, G.S., Lowe, K. and Coombe, D.: “Foam Application in an Oil Sands Steamflood Process,” paper SPE 19690, presented at the Annual Technical Conference and Exhibition, San Antonio, Texas, USA (October 8–11, 1989).

Kunze, K.R. and Shaughnessy, C.M.: “Acidizing Sandstone Formations with Fluoboric Acid,” paper SPE 9387, *SPE Journal* (February 1983), 65–72.

Kuo, C.H.: “On the Production of Hydrogen Sulfide-Sulfur Mixtures from Deep Formations,” *Journal of Petroleum Technology* (September 1972), 1142–1146.

Kutasov, I.M. and Bizanti, M.S.: “Fluid Losses While Drilling,” paper SPE 13963 (1985).

Labrid, J.C.: “Stimulation Chimique: Etude Theorique et Experimentale des Equilibres Chimiques Decrivant l’Attaque Fluorhydrique d’un Gres Argileux,” *Revue d’Institut Français du Pétrole* (October 1971) 26, No. 10, 855–876.

Labrid, J.C.: “Thermodynamic and Kinetic Aspects of Argillaceous Sandstone Acidizing,” paper SPE 5165, *SPE Journal* (April 1975), 117–128.

Lambert, M.E.: “A Statistical Study of Reservoir Heterogeneity,” MS thesis, The University of Texas at Austin, Austin, Texas, USA (1981).

Lauritzen, S.E., Odling, N. and Petersen, J.: “Modeling the Evolution of Channel Networks in Carbonate Rocks,” presented at the Eurock Conference (September 1992).

Lea, C.-M., Hill, A.D. and Sepehrnoori, K.: “Effect of Fluid Diversion on the Acid Stimulation of a Perforation,” paper SPE 22853, *SPE Production & Facilities* (May 1993), 131.

Lee, H.O., Heller, J.P. and Hoofer, A.M.W.: “Change in Apparent Viscosity of CO<sub>2</sub> Foam with Rock

Permeability," paper SPE 20194, *SPE Reservoir Engineering* (November 1991), 421–428.

Lejon, K., Thingvoll, J.T., Vollen, E.A. and Hammonds, P.: "Formation Damage Due to Losses of Ca-Based Brine and How It Was Revealed Through Post Evaluation of Scale Dissolver and Scale Inhibitor Squeeze Treatments," paper SPE 30086, presented at the SPE European Formation Damage Conference, The Hague, Netherlands (May 15–16, 1995).

Leon, L.: "The Role of the Service Company in Minimizing and Reducing Formation Contamination," paper SPE 4660, presented at the SPE Annual Meeting, Las Vegas, Nevada, USA (September 30–October 3, 1973).

Leontaritis, K.J.: "Asphaltene Deposition: A Comprehensive Description of Problem Manifestations and Modeling Approaches," SPE 18892, presented at the SPE Production Operations Symposium, Oklahoma City, Oklahoma, USA (March 13–14, 1989).

Leontaritis, K.J., Amaefule, J.O. and Charles, R.E.: "A Systematic Approach for the Prevention and Treatment of Formation Damage Caused by Asphaltene Deposition," paper SPE 23810, presented at the SPE International Symposium on Formation Damage Control, Lafayette, Louisiana, USA (February 26–27, 1992).

Leontaritis, K.J. and Mansoori, G.A.: "Asphaltene Flocculation During Oil Production and Processing: A Thermodynamic Colloidal Model," paper SPE 16258, presented at the SPE International Symposium on Oilfield Chemistry, San Antonio, Texas, USA (February 4–6, 1987).

Levich, V.G.: *Physicochemical Hydrodynamics*, Englewood Cliffs, New Jersey, USA, Prentice Hall (1962).

Li, Y., Sullivan, R.B., de Rozières, J., Gaz, G.L. and Hinkel, J.J.: "An Overview of Current Acid Fracturing Technology with Recent Implications for Emulsified Acids," paper SPE 26581, presented at the SPE Annual Technical Conference and Exhibition, Houston, Texas, USA (October 3–6, 1993).

Liétard, O., Bellarby, J. and Holcomb, D.: "Design, Execution, and Evaluation of Acid Treatments of Naturally Fractured Carbonate, Oil Reservoirs of the

North Sea," paper SPE 30411, presented at the Offshore Europe Conference, Aberdeen, Scotland (September 5–8, 1995).

Liétard, O. and Daccord, G.: "Acid Wormholing in Carbonate Reservoirs: Validation of Experimental Growth Laws Through Field Data Interpretation," presented at the 195th National Meeting of the American Chemical Society, Toronto, Ontario, Canada (June 5–11, 1988).

Lieu, V.T., Miller, S.G. and Miller S.: "Chemical Reactions with Reservoir Sand in the Recovery of Petroleum by Alkaline Flooding," paper SPE 12561 (1983).

Lissant, K.J.: *Emulsions and Emulsion Technology*, part 1, New York, New York, USA, Dekker, Inc. (1974).

Lissant, K.J. and Mayhan, K.G.: "A Study of Medium and High Internal Phase Ratio Water/Polymer Emulsions," *J. Colloid and Interface Science* (January 1973), 201–208.

Locke, S.: "An Advanced Method for Predicting the Productivity Ratio of a Perforated Well," paper SPE 8804, *Journal of Petroleum Technology* (December 1981), 2481.

Lund, K. and Fogler, H.S.: "Acidization V. The Prediction of the Movement of Acid and Permeability Fronts in Sandstone," *Chemical Engineering Science* (1976) 31, No. 5, 381–392.

Lund, K., Fogler, H.S. and McCune, C.C.: "Acidization I: The Dissolution of Dolomite in Hydrochloric Acid," *Chemical Engineering Science* (1973) 28, 691–700.

Lund, K., Fogler, H.S., McCune, C.C. and Ault, J.W.: "Acidization II—The Dissolution of Calcite in Hydrochloric Acid," *Chemical Engineering Science* (1975) 30, 825–835.

Lybarger, J.H. and Gates, H.R.: "SGMA Performance, Design—Part 1: New Acidizing System Yields Sustained Production Increase," *Oil & Gas Journal* (October 16, 1978a), 59–64.

Lybarger, J.H. and Gates, H.R.: "SGMA Performance, Design—Part 2: Proper Reservoir Choice, Fluid Design Keys to SGMA Success," *Oil & Gas Journal* (October 23, 1978b), 137–142.

- Mahajan, N.C. and Barron, B.M.: "Bridging Particle Size Distribution: A Key Factor in the Designing of Non-Damaging Completion Fluids," paper SPE 8792, presented at the SPE Symposium on Formation Damage Control, Bakersfield, California, USA (January 28–29, 1980).
- Maly, G.P.: "Close Attention to the Smallest Job Details Vital for Minimizing Formation Damage," paper SPE 5702, presented at the SPE Symposium on Formation Damage Control, Houston, Texas, USA (January 29–30, 1976).
- Manlowe, D.J. and Radke, C.J.: "A Pore-Level Investigation of Foam/Oil Interactions in Porous Media," paper SPE 18069, *SPE Reservoir Engineering* (November 1990), 495.
- Maya, L.: "Fluoroboric Acid and Its Hydroxy Derivatives—Solubility and Spectroscopy," *J. Inorg. Nucl. Chem.* (1977) 39, 225–231.
- McClaflin, G.G. and Whitfill, D.L.: "Control of Paraffin Deposition in Production Operations," paper SPE 12204, presented at the SPE Annual Technical Conference and Exhibition, San Francisco, California, USA (October 5–8, 1983).
- McCorriston, L.L., Demby, R.A. and Pease, E.C.: "Study of Reservoir Damage Produced in Heavy Oil Formations Due to Steam Injection," paper SPE 10077, presented at the SPE Annual Technical Conference and Exhibition, San Antonio, Texas, USA (October 5–7, 1981).
- McCune, C.C., Fogler, H.S., Lund, K., Cunningham, J.R. and Ault, J.W.: "A New Model of the Physical and Chemical Changes in Sandstone During Acidizing," paper SPE 5157, *SPE Journal* (October 1975), 361–370.
- McDougall, L.A.: "Corrosion Inhibitors for High Temperature Applications," *Mater. Protection* (August 1969), 31–32.
- McElhiney, J.E., Schalge, A.L., McKnight, R.S. and Robinson, J.R. 1978: "Coreflood Acidization: Model, Measurement, and Methodology," paper SPE 7891, presented at the SPE International Symposium on Oilfield and Geothermal Chemistry, Houston, Texas, USA (January 22–24, 1979).
- McKinney, L.K. and Azar, J.J.: "Formation Damage Due to Synthetic Oil Mud Filtrates at Elevated Temperatures and Pressures," paper SPE 17162, presented at the SPE Formation Damage Control Symposium, Bakersfield, California, USA (February 8–9, 1988).
- McLeod, H.O. Jr.: "The Effect of Perforating Conditions on Well Performance," paper SPE 10649, *Journal of Petroleum Technology* (January 1983), 21.
- McLeod, H.O. Jr.: "Matrix Acidizing," paper SPE 13752, *Journal of Petroleum Technology* (December 1984) 36, 2055–2069.
- McLeod, H.O. and Coulter, A.W.: "The Use of Alcohol in Gas Well Stimulation," paper SPE 1663, presented at the SPE Eastern Regional Meeting, Columbus, Ohio, USA (November 10–11, 1966).
- McLeod, H.O. Jr. and Coulter, A.W. Jr.: "The Stimulation Treatment Pressure Record—An Overlooked Formation Evaluation Tool," paper SPE 2287, *Journal of Petroleum Technology* (August 1969) 71, No. 8, 951–960.
- McLeod, H.O. Jr., Ledlow, L.B. and Till, M.V.: "The Planning, Execution and Evaluation of Acid Treatments in Sandstone Formations," paper SPE 11931, presented at the SPE Annual Technical Conference and Exhibition, San Francisco, California, USA (October 5–8, 1983).
- McLeod, H.O. Jr. and Minarovic, M.J.: "Monitoring and Analysis of Gravel-Packing Procedures to Explain Well Performance," paper SPE 27356, presented at the SPE International Symposium on Formation Damage Control, Lafayette, Louisiana, USA (February 9–10, 1994); also in *Journal of Petroleum Technology* (October 1994), 878–883.
- Meehan, D.N. and Schell, E.J.: "An Analysis of Rate-Sensitive Skin in Gas Wells," paper SPE 12176, presented at the SPE Annual Technical Conference and Exhibition, San Francisco, California, USA (October 5–8, 1983).
- Methven, N.E. and Kemick, J.G.: "Drilling and Gravel Packing with an Oil Base Fluid System," *Journal of Petroleum Technology* (June 1969), 671–679.
- Millhone, R.S.: "Completion Fluids for Maximizing Productivity—State of the Art," paper SPE 10030, *Journal of Petroleum Technology* (January 1983), 47.
- Milne, A.: "Horizontal Well Completion & Stimulation Technology," Schlumberger Dowell (1991).



- Monger, T.G. and Fu, J.C.: "The Nature of CO<sub>2</sub>-Induced Organic Deposition," paper SPE 16713, presented at the SPE Annual Technical Conference and Exhibition, Dallas, Texas, USA (September 27–30, 1987).
- Monger, T.G. and Trujillo, D.E.: "Organic Deposition During CO<sub>2</sub> and Rich-Gas Flooding," paper SPE 18063, *SPE Reservoir Engineering* (February 1991), 17.
- Montgomery, C.T., Jan, Y.-M. and Niemeyer, B.L.: "Development of a Matrix Acidizing Stimulation Treatment Evaluation and Recording System," paper SPE 26579, presented at the SPE Annual Technical Conference and Exhibition, Houston, Texas, USA (October 3–6, 1994); also in *SPE Production & Facilities* (November 1995) 10, No. 6, 219.
- Montgomery, M.: "Discussion of the Drilling Mud Dilemma—Recent Examples," paper SPE 14481, *Journal of Petroleum Technology* (July 1985), 1230.
- Moore, E.W., Crowe, C.W. and Hendrickson, A.R.: "Formation, Effect and Prevention of Asphaltene Sludges During Stimulation Treatments," paper SPE 1163, *Journal of Petroleum Technology* (September 1965), 1023–1028.
- Morales, R.H., Brown, E., Norman, W.D., DeBonis, V., Mathews, M., Park, E.I. and Brown, D.: "Mechanical Skin Damage on Wells," paper SPE 30459, presented at the SPE Annual Technical Conference and Exhibition, Dallas, Texas, USA (October 22–25, 1995).
- Morgenthaler, L.N.: "Formation Damage Tests of High-Density Brine Completion Fluids," paper SPE 13811, *SPE Production Engineering* (November 1986), 432.
- Morita, N., Gray, K.E., Srouji, F.A.A. and Jogi, P.N.: "Rock Property Change During Reservoir Compaction," paper SPE 13099, presented at the SPE Annual Technical Conference and Exhibition, Houston, Texas, USA (September 16–19, 1984).
- Mostofizadeh, B. and Economides, M.J.: "Optimum Injection Rate from Radial Acidizing Experiments," paper SPE 28547, presented at the SPE Annual Technical Conference and Exhibition, New Orleans, Louisiana, USA (September 25–28, 1994).
- Muecke, T.W.: "Formation Fines and Factors Controlling Their Movement in Porous Media," *Journal of Petroleum Technology* (February 1979), 144–150.
- Muhr, A.H. and Blanchard, J.M.V.: "Diffusion in Gels," *Polymer* (July 1982 Suppl.) 23, 1012–1026.
- Mungan, N.: "Permeability Reduction Due to Salinity Changes," *J. Can. Pet. Tech.* (July–September 1968), 113–117.
- Muskat, M.: *Physical Properties of Oil Production*: New York, New York, USA, McGraw-Hill Book Company (1949), 242.
- NACE International: Standard Recommended Practice: Handling and Proper Usage of Inhibited Oilfield Acids, NACE Standard RP0273-95, Item No. 21009 (1995).
- Nancollas, G.H. and Sawada, K.: "Formation of Scales of Calcium Carbonate Polymorphs: The Influence of Magnesium Ion and Inhibitors," paper SPE 8992, *Journal of Petroleum Technology* (March 1982), 645.
- Newberry, M.E.: "Chemical Effects on Crude Oil Pipeline Pressure Problems," paper SPE 11561, *Journal of Petroleum Technology* (May 1984), 779.
- Newberry, M.E., Addison, G.E. and Barker, K.M.: "Paraffin Control in the Northern Michigan Niagaran Reef Trend," paper SPE 12320, *SPE Production Engineering* (May 1986), 213.
- Newberry, M.E. and Barker, K.M.: "Formation Damage Prevention Through the Control of Paraffin and Asphaltene Deposition," paper SPE 13796, presented at the SPE Production Operations Symposium, Oklahoma City, Oklahoma, USA (March 10–12, 1985).
- Newman, G.H.: "The Effect of Water Chemistry on the Laboratory Compression and Permeability Characteristics of Some North Sea Chalks," paper SPE 10203, *Journal of Petroleum Technology* (May 1983), 976.
- Nierode, D.E. and Kruk, K.F.: "An Evaluation of Acid Fluid Loss Additives, Retarded Acids and Acidized Fracture Conductivity," paper SPE 4549, presented at the SPE Annual Meeting, Las Vegas, Nevada, USA (September 30–October 3, 1973).
- Nierode, D.E. and Williams, B.B.: "Characteristics of Acid Reactions in Limestone Formations," paper SPE 3101, presented at the SPE Annual Meeting,

Houston, Texas, USA (October 4–7, 1970); also in *SPE Journal* (December 1971), 406–418.

Nitters, G. and Hagelaars, A.M.P.: “Careful Planning and Sophisticated Support: The Key to Improved Acidisation Results,” paper SPE 20967, presented at Europec 90, The Hague, Netherlands (October 22–24, 1990).

Nougaro, J. and Labbé, C.: “Etude des Lois de L’Acidification dans le Cas d’un Calcaire Vacuolaire,” *Rev. Fran. Pet.* (1955) 10, No. 5, 354.

Oddo, J.E., Smith, J.P. and Tomson, M.B.: “Analysis of and Solutions to the  $\text{CaCO}_3$  and  $\text{CaSO}_4$  Scaling Problems Encountered in Wells Offshore Indonesia,” paper SPE 22782, presented at the SPE Annual Technical Conference and Exhibition, Dallas, Texas, USA (October 6–9, 1991).

Odeh, A.S.: “Steady-State Flow Capacity of Wells with Limited Entry to Flow,” paper SPE 1797, *SPE Journal* (March 1968), 43–51.

Ogino, K. and Onishi, M.: “Interfacial Action of Natural Surfactants in Oil/Water Systems,” *J. Colloid and Interface Science* (September 1981) 83, No. 1, 18–25.

Oudeman, P., ter Avest, D., Grodal, E.O., Asheim, H.A. and Meissner, R.J.H.: “Bull Heading to Kill Live Gas Wells,” paper SPE 28896, presented at the SPE European Petroleum Conference, London, UK (October 25–27, 1994).

Oyenenin, M.B., Peden, J.M., Hosseini, A. and Ren, G.: “Factors to Consider in the Effective Management and Control of Fines Migration in High Permeability Sands,” paper SPE 30112, presented at the SPE European Formation Damage Conference, The Hague, Netherlands (May 15–16, 1995).

Paccaloni, G.: “Field History Verifies Control, Evaluation,” *Oil & Gas Journal* (November 26, 1979a) 77, No. 46, 61–65.

Paccaloni, G.: “New Method Proves Value of Stimulation Planning,” *Oil & Gas Journal* (November 19, 1979b) 77, No. 45, 155–160.

Paccaloni, G.: “A New, Effective Matrix Stimulation Diversion Technique,” paper SPE 24781, presented at the SPE Annual Technical Conference and Exhibition, Washington, D.C., USA (October 4–7, 1992); also in *SPE Production & Facilities* (August 1995), 151–156.

Paccaloni, G. and Tambini, M.: “Advances in Matrix Stimulation Technology,” paper SPE 20623, presented at the SPE Annual Technical Conference and Exhibition, New Orleans, Louisiana, USA (September 23–26, 1990).

Paccaloni, G., Tambini, M. and Galoppini, M.: “Key Factors for Enhanced Results of Matrix Stimulation Treatments,” paper SPE 17154, presented at the SPE Formation Damage Control Symposium, Bakersfield, California, USA (February 8–9, 1988).

Paktinat, J.: “Reduced Adsorption and Emulsion Tendencies in Sandstone Formation Through the Use of Ethoxylates,” paper SPE 21011, presented at the SPE International Symposium on Oilfield Chemistry, Anaheim, California, USA (February 20–22, 1991).

Parlar, M., Nelson, E.B., Walton, I.C., Park, E. and DeBonis, V.: “An Experimental Study on Fluid-Loss Behavior of Fracturing Fluids and Formation Damage in High-Permeability Porous Media,” paper SPE 30458, presented at the SPE Annual Technical Conference and Exhibition, Dallas, Texas, USA (October 22–25, 1995).

Parlar, M., Parris, M.D., Jasinski, R.J. and Robert, J.A.: “An Experimental Study of Foam Flow Through Berea Sandstone with Applications to Foam Diversion in Matrix Acidizing,” paper SPE 29678, presented at the SPE Western Regional Meeting, Bakersfield, California, USA (March 8–10, 1995).

Patton, J.T. and Phelan, P.F.: “Well Damage Hazards Associated with Conventional Completion Fluids,” paper SPE 13800, presented at the SPE Production Operations Symposium, Oklahoma City, Oklahoma, USA (March 10–12, 1985).

Paul, J.R. and Plonka, J.H.: “Solids Free Completion Fluids Maintain Formation Permeability,” paper SPE 4655, presented at the SPE Annual Meeting, Las Vegas, Nevada, USA (September 30–October 3, 1973).

Persoff, P., Pruess, K., Benson, S.M., Wu, Y.S., Radke, C.J. and Witherspoon, P.A.: “Aqueous Foams for Control of Gas Migration and Water Coning in Aquifer Gas Storage,” *Energy Sources* (1990) 12, 479–497.

Persoff, P., Radke, C.J., Pruess, K., Benson, S.M. and Witherspoon, P.A.: “A Laboratory Investigation of Foam Flow in Sandstone at Elevated Pressure,” *SPE Reservoir Engineering* (August 1991), 365–372.

- Perthuis, H., Touboul, E. and Piot, B.: "Acid Reactions and Damage Removal in Sandstones: A Model for Selecting the Acid Formulation," paper SPE 18469, presented at the SPE International Symposium on Oilfield Chemistry, Houston, Texas, USA (February 8–10, 1989).
- Petitjean, L., Couet, B., Abel, J.C., Schmidt, J.H. and Ferguson, K.R.: "Well Productivity Improvement Using Extreme Overbalance Perforating and Surging—Case History," paper SPE 30527, presented at the SPE Annual Technical Conference and Exhibition, Dallas, Texas, USA (October 22–25, 1995).
- Phelps, G.D., Stewart, G., Peden, J.M. and Heriot-Watt, U.: "The Analysis of the Invaded Zones Characteristics and Their Influence on Wireline Log and Well-Test Interpretation," paper SPE 13287, presented at the SPE Annual Technical Conference and Exhibition, Houston, Texas, USA (September 16–19, 1984).
- Pichler, T., Frick, T.P., Economides, M.J. and Nittmann, J.: "Stochastic Modeling of Wormhole Growth in Carbonate Acidizing with Biased Randomness," paper SPE 25004, presented at the SPE European Petroleum Conference, Cannes, France (November 16–18, 1992).
- Piro, G., Barberis Canonico, L., Galbariggi, G., Bertero, L. and Carniani, C.: "Experimental Study on Asphaltene Adsorption onto Formation Rock: An Approach to Asphaltene Formation Damage Prevention," paper SPE 30109, presented at the SPE European Formation Damage Conference, The Hague, Netherlands (May 15–16, 1995).
- Pittaway, K.R., Albright, J.C., Hoover, J.W. and Moore, J.S.: "The Maljamar CO<sub>2</sub> Pilot: Review and Results," paper SPE 14940, *Journal of Petroleum Technology* (October 1987), 1256.
- Place, M.C. Jr. and Smith, J.T.: "An Unusual Case of Salt Plugging in a High-Pressure Sour Gas Well," paper SPE 13246, presented at the SPE Annual Technical Conference and Exhibition, Houston, Texas, USA (September 16–19, 1984).
- Plummer, L.N., Wigley, T.M.L. and Parkhurst, D.L.: "The Kinetics of Calcite Dissolution in CO<sub>2</sub>-Water Systems at 5° to 60°C and 0.0 to 1.0 atm CO<sub>2</sub>," *Am. J. Sci.* (February 1978) 278, 179–216.
- Porter, K.: "An Overview of Formation Damage," paper SPE 19894, *Journal of Petroleum Technology* (1989), 780.
- Potter, G.F.: "Formation Damage of Brine Corrosion Inhibitors," paper SPE 12495, presented at the Formation Damage Control Symposium, Bakersfield, California, USA (February 13–14, 1984).
- Priisholm, S., Nielsen, B.L. and Haslund, O.: "Fines Migration, Blocking, and Clay Swelling of Potential Geothermal Sandstone Reservoirs, Denmark," *SPE Formation Evaluation* (June 1987), 168.
- Prouvost, L. and Economides, M.J.: "Real-Time Evaluation of Matrix Acidizing Treatments," *Pet. Sci. and Eng.* (November 1987), 145–154.
- Prouvost, L. and Economides, M.J.: "Applications of Real-Time Matrix-Acidizing Evaluation Method," paper SPE 17156, *SPE Production Engineering* (November 1989) 4, No. 6, 401–407.
- Pye, D.S., Gallus, J.P. and Kemp, J.D.: "Placement Control Boosts Well-Stimulation Results," *Oil & Gas Journal* (November 9, 1970), 76–80.
- Quinn, M.A.: "Designing Effective Sandstone Acidizing Treatments Through Geochemical Modeling," MS thesis, The University of Texas at Austin, Austin, Texas, USA (1994).
- Radke, C.J. and Gillis, J.V.: "A Dual Gas Tracer Technique for Determining Trapped Gas Saturation During Steady Foam Flow in Porous Media," paper SPE 20519, presented at the SPE Annual Technical Conference and Exhibition, New Orleans, Louisiana, USA (September 23–26, 1990).
- Raleigh, J.T. and Flock, D.L.: "A Study of Formation Plugging with Bacteria," *Journal of Petroleum Technology* (February 1965), 201–206.
- Recommended Practices for Laboratory Testing of Surface Active Agents for Well Stimulation (RP 42)*, second edition, Dallas, Texas, USA, American Petroleum Institute (January 1, 1977).
- Records, L.R.: "Drilling Practices that Affect Formation Damage," paper SPE 5714, presented at the SPE Symposium on Formation Damage Control, Houston, Texas, USA (January 29–30, 1976).
- Records, L.R. and Ritter, J.E.: "Results of Field Use of Very Low Water Loss Oil Well Cements for Better Production Capability of Oil and Gas Wells,"

paper SPE 7010, presented at the SPE Symposium on Formation Damage Control, Lafayette, Louisiana, USA (February 15–16, 1978).

Reed, M.G.: “Gravel Pack and Formation Sandstone Dissolution During Steam Injection,” *Journal of Petroleum Technology* (June 1980), 941–949.

Reid, P.: “Formation Damage,” *Drilling Fluids*, E. Potts (ed.), Elsevier (1996).

Ridwan, A. and Cannan, W.: “Well Stimulation Review for the Arun Limestone Reservoir,” paper OSEA-90140 (1990).

Rike, J.L.: “The Relationship Between Clean Fluids and Effective Completions,” paper SPE 9426, presented at the SPE Annual Technical Conference and Exhibition, Dallas, Texas, USA (September 21–24, 1980).

Rike, J.L. and Pledger, T.M.: “Clean Fluids Improve Completion Results,” paper SPE 9752, presented at the SPE Production Operation Symposium, Oklahoma City, Oklahoma, USA (March 1–3, 1981).

Robert, J.A. and Mack, M.G.: “Foam Diversion Modeling and Simulation,” paper SPE 29676, presented at the SPE Western Regional Meeting, Bakersfield, California, USA (March 8–10, 1995).

Roberts, L.D. and Guin, J.A.: “The Effect of Surface Kinetics in Fracture Acidizing,” paper SPE 4349, *SPE Journal* (August 1974), 385–396; also in *Trans., AIME* 257.

Rogers, B.A., Burk, M.K. and Stonecipher, S.A.: “Designing of Remedial Acid Treatment for Gulf of Mexico Deepwater Turbidite Sands Containing Zeolite Cement,” paper SPE 39595, presented at the SPE International Symposium on Formation Damage Control, Lafayette, Louisiana, USA (February 18–19, 1998).

Rogers, E.B. Jr.: “Successful Well Stimulation Program Has Revitalized a California Oil Field,” *Journal of Petroleum Technology* (December 1976), 1420–1426.

Rosen, M.J.: *Surfactants and Interfacial Phenomena*, second edition, John Wiley and Sons (1989), 207.

Rossen, W.R.: “Theory of Minimum Pressure Gradient of Flowing Foams in Porous Media. I. Incompressible Foam, II. Effect of Compressibility,

III. Asymmetric Lamella Shapes,” *J. Colloid and Interface Sci.* (1990) 136, 1, 17, 38 and (1990) 139.

Rossen, W.R.: “Foams in Enhanced Oil Recovery,” *Foams: Theory, Measurements and Applications*, R.K. Prud’homme and S. Khan (eds.), New York, New York, USA, Marcel Dekker (in press).

Rossen, W.R. and Zhou, Z.H.: “Modeling Foam Mobility at the Limiting Capillary Pressure,” *SPE Advanced Technology Series* (1995) 3, 146.

Rowan, G.: “Theory of Acid Treatment of Limestone Formations,” *J. Inst. Pet.* (November 1959) 45, No. 431, 321.

Ryan, D.F., Browne, S.V. and Burnham, M.P.: “Mud Clean-Up in Horizontal Wells: A Major Joint Industry Study,” paper SPE 30528, presented at the SPE Annual Technical Conference and Exhibition, Dallas, Texas, USA (October 22–25, 1995).

Saidikowski, R.M.: “Numerical Simulations of the Combined Effects of Wellbore Damage and Partial Penetration,” paper SPE 8204, presented at the SPE Annual Technical Conference and Exhibition, Las Vegas, Nevada, USA (September 23–26, 1979).

Samuelson, M.L.: “Alternatives to Aromatics for Solvency of Organic Deposits,” paper SPE 23816, presented at the SPE International Symposium on Formation Damage Control, Lafayette, Louisiana, USA (February 26–27, 1992).

Sands, E.E. Jr.: “Good Communications, a Tool for the Prevention of Formation Damage,” paper SPE 4657, presented at the SPE Annual Meeting, Las Vegas, Nevada, USA (September 30–October 3, 1973).

Sanner, D.O. and Azar, J.J.: “Alteration of Reservoir Rock Wettability and Its Flow Properties Caused by Oil-Based and Water-Based Drilling Muds,” paper SPE 27354, presented at the SPE International Symposium on Formation Damage Control, Lafayette, Louisiana, USA (February 7–10, 1994).

Saucier, R.J. and Lands, J.F.: “A Laboratory Study of Perforations in Stressed Formations,” paper SPE 6758, *Journal of Petroleum Technology* (September 1978) 30, 1447–1353.

Saxon, A., Chariag, B. and Rahman, M.R.A.: “An Effective Matrix Diversion Technique for Carbonate

Formations,” paper SPE 37734, presented at the SPE Middle East Oil Conference and Exhibition, Manama, Bahrain (March 17–20, 1997).

Schantz, S.S. and Stephenson, W.K.: “Asphaltene Deposition: Development and Application of Polymeric Asphaltene Dispersants,” paper SPE 22783, presented at the SPE Annual Technical Conference and Exhibition, Dallas, Texas, USA (October 6–9, 1991).

Schechter, R.S.: *Oil Well Stimulation*, Englewood Cliffs, New Jersey, USA, Prentice Hall (1992).

Schechter, R.S. and Gidley, J.L.: “The Change in Pore Size Distribution from Surface Reactions in Porous Media,” *AIChE J.* (May 1969) 15, No. 3, 339–350.

Scheuerman, R.F.: “A Buffer-Regulated HF Acid for Sandstone Acidizing to 550°F,” paper SPE 13563, *SPE Production Engineering* (February 1988), 13.

Schiabbe, D.F., Akpan, B. and Ayoub, J.A.: “Identification, Evaluation, and Treatment of Formation Damage, Offshore Louisiana,” paper SPE 14820, presented at the SPE Symposium on Formation Damage Control, Lafayette, Louisiana, USA (February 26–27, 1986).

Schramm, L.L. (ed.): *Foams: Fundamentals and Applications in the Petroleum Industry*, ACS Advances in Chemistry Series, Washington, D.C., USA, American Chemical Society (1994) 3, No. 242.

Schramm, J.L. and Novosad, J.J.: “The Destabilization of Foams for Improved Oil Recovery by Crude Oils: Effect of Nature of the Oil,” *J. Petr. Sci. Eng.* (1992) 7, 77–90.

Seanard, K.C.: “Underbalanced Perforating in a Closed System,” paper SPE 14828, presented at the SPE Symposium on Formation Damage Control, Lafayette, Louisiana, USA (February 26–27, 1986).

Sengupta, S.K., Hayatdavoudi, A., Tiab, J.O., Kalra, S.K., LeBlanc, J.L. and Schluntz, E.K.: “Effect of Flow Rate and Rheology on Shear Strength of Migrating Formation Fines Due to Flow of Pseudoplastic Fluids,” paper SPE 10669, presented at the SPE Formation Damage Control Symposium, Lafayette, Louisiana, USA (March 24–25, 1982).

Settari, A.: “Modeling of Acid-Fracturing Treatments,” paper SPE 21870, presented at the SPE Rocky Mountain Regional/Low Permeability Reservoirs Symposium, Denver, Colorado, USA (April 15–17, 1991); also in *SPE Production & Facilities* (February 1993) 8, No. 1, 30–38.

Sevougian, S.D., Lake, L.W. and Schechter, R.S.: “A New Geochemical Simulator to Design More Effective Sandstone Acidizing Treatments,” paper SPE 24780, presented at the SPE Annual Technical Conference and Exhibition, Washington, D.C., USA (October 4–7, 1992).

Sharma, B.G. and Sharma, M.M.: “Polymerizable Ultra-Thin Films: A New Technique for Fines Stabilization,” paper SPE 27345, presented at the SPE International Symposium on Formation Damage Control, Lafayette, Louisiana, USA (February 7–10, 1994).

Sharma, M.M., Yortsos, Y.C. and Handy, L.L.: “Release and Deposition of Clays in Sandstones,” paper SPE 13562, presented at the International Symposium on Oilfield and Geothermal Chemistry, Phoenix, Arizona, USA (April 9–11, 1985).

Shaughnessy, C.M. and Kline, W.E.: “EDTA Removes Formation Damage at Prudhoe Bay,” *Journal of Petroleum Technology* (October 1983), 1783–1792.

Shaughnessy, C.M. and Kunze, K.R.: “Understanding Sandstone Acidizing Leads to Improved Field Practices,” paper SPE 9388, *Journal of Petroleum Technology* (July 1981), 1196–1202.

Shaw, R.C. and Rugg, F.E.: “Clean Fluids Lead to Better Completions,” paper SPE 4778, presented at the SPE Symposium on Formation Damage Control, New Orleans, Louisiana, USA (February 7–8, 1974).

Sherman, P. (ed.): *Emulsion Science*, London, England, Academic Press (1968).

Shuchart, C.E. and Ali, S.A.: “Identification of Aluminum Scale with the Aid of Synthetically Produced Basic Aluminum Fluoride Complexes,” paper SPE 23812, presented at the SPE International Symposium on Formation Damage Control, Lafayette, Louisiana, USA (February 26–27, 1992).

Shuchart, C.E. and Gdanski, R.D.: "Improved Success in Acid Stimulation with a New Organic-HF System," paper SPE 36907, presented at the SPE European Petroleum Conference, Milan, Italy (October 22–24, 1996).

Shuler, P.J., Baudoin, D.A. and Weintritt, D.J.: "Diagnosis and Prevention of NORM at Eugene Island 341-A," paper SPE 29711, presented at the SPE/EPA Exploration & Production Environmental Conference, Houston, Texas, USA (March 27–29, 1995).

Simon, D.E., Kaul, F.W. and Culbertson, J.N.: "Anadarko Basin Morrow-Springer Sandstone Stimulation Study," paper SPE 6757, *Journal of Petroleum Technology* (June 1979), 683.

Simpson, J.P.: "Drilling Fluid Filtration Under Simulated Downhole Conditions," paper SPE 4779, presented at the SPE Formation Damage Control Symposium, New Orleans, Louisiana, USA (February 7–8, 1974).

Simpson, J.P.: "Author's Reply to Discussion of The Drilling Mud Dilemma—Recent Examples," paper SPE 14527, *Journal of Petroleum Technology* (July 1985a), 1230.

Simpson, J.P.: "The Drilling Mud Dilemma—Recent Examples," paper SPE 13927, *Journal of Petroleum Technology* (February 1985b), 201–206.

Singhal, H.K., Sahai, G.C., Pundeer, G.S. and Chandra, K.: "Designing and Selecting Wax Crystal Modifier for Optimum Field Performance Based on Crude Oil Composition," paper SPE 22784, presented at the SPE Annual Technical Conference and Exhibition, Dallas, Texas, USA (October 6–9, 1991).

Sjöberg, E.L. and Rickard, D.T.: "Calcite Dissolution Kinetics: Surface Speciation and the Origin of the Variable pH Dependence," *Chem. Geol.* (1984) 42, 119.

Sloan, J.P., Brooks, J.P. and Dear, S.F. III: "A New, Nondamaging, Acid-Soluble Weighting Material," paper SPE 4782, *Journal of Petroleum Technology* (January 1975), 15–20.

Smith, C.F., Crowe, C.W. and Nolan, T.J. III: "Secondary Deposition of Iron Compounds Following Acidizing Treatments," paper SPE 2358, *Journal of Petroleum Technology* (September 1969), 1121–1129.

Smith, C.F., Dollarhide, F.E. and Byth, N.J.: "Acid Corrosion Inhibitors—Are We Getting What We Need?," paper SPE 5644, *Journal of Petroleum Technology* (May 1978), 737–747.

Smith, C.F. and Hendrickson, A.R.: "Hydrofluoric Acid Stimulation of Sandstone Reservoirs," paper SPE 980, *Journal of Petroleum Technology* (February 1965), 215–222.

Smith, C.F., Ross, W.M. and Hendrickson, A.R.: "Hydrofluoric Acid Stimulation—Developments for Field Application," paper SPE 1284, presented at the SPE Annual Meeting, Denver, Colorado, USA (October 3–6, 1965).

Smith, C.L., Anderson, J.L. and Roberts, P.G.: "New Diverting Techniques for Acidizing and Fracturing," paper SPE 2751, presented at the SPE Annual California Regional Meeting, San Francisco, California, USA (November 6–7, 1969).

Sparlin, D.D.: "Sand and Gravel: A Study of Their Permeabilities," paper SPE 4772, presented at the SPE Symposium on Formation Damage Control, New Orleans, Louisiana, USA (February 7–8, 1974).

Sparlin, D.D. and Hagen, R.W.: "SPE Short Course on Formation Damage Prevention," International Completion Consultants, Inc. (1983).

Stadlman, J.R., Novotny, R.J. and Houchin, L.R.: "Understanding Changing Wellbore Pressures Improves Sand Control Longevity," paper SPE 14160, presented at the SPE Annual Technical Conference and Exhibition, Las Vegas, Nevada, USA (September 22–25, 1985).

Stein, N. and Hilchie, D.W.: "Estimating the Maximum Production Rate Possible from Friable Sandstones Without Using Sand Control," paper SPE 3499, *Journal of Petroleum Technology* (September 1972), 1157–1160.

Stein, N., Odeh, A.S. and Jones, L.G.: "Estimating Maximum Sand-Free Production Rates from Friable Sands for Different Well Completion Geometries," paper SPE 4534, *Journal of Petroleum Technology* (October 1974), 1156–1158.

Stewart, B.R., Mullen, M.E., Howard, W.J. and Norman, W.D.: "Use of Solid-Free Viscous Carrying Fluid in Fracturing Applications: An Economic and Productivity Comparison in Shallow Completions," paper SPE 30114, presented at the SPE European

Formation Damage Conference, The Hague, Netherlands (May 15–16, 1995).

Strickland, F.G.: “Reasons for Production Decline in the Diatomite, Belridge Oil Field: A Rock Mechanics View,” paper SPE 10773, *Journal of Petroleum Technology* (March 1985) 37, No. 3, 521–526.

Suman, G.O. Jr.: “Perforations—A Prime Source of Well Performance Problems,” paper SPE 3445, *Journal of Petroleum Technology* (April 1972), 399–411.

Sumotarto, U.: “Sandstone Acidizing Simulation: Development of an Expert System,” PhD dissertation, The University of Texas at Austin, Austin, Texas, USA (1995).

Sutton, G.D. and Roberts, L.D.: “Paraffin Precipitation During Fracture Stimulation,” paper SPE 4411, *Journal of Petroleum Technology* (September 1974), 997–1006.

Svetgoff, J.: “Paraffin Problems Can Be Resolved with Chemicals,” *Oil & Gas Journal* (February 27, 1984), 79–82.

Taha, R., Hill, A.D. and Sepehrnoori, K.: “Simulation of Sandstone Matrix Acidizing in Heterogeneous Reservoirs,” paper SPE 13218, *Journal of Petroleum Technology* (July 1986), 753.

Taha, R., Hill, A.D. and Sepehrnoori, K.: “Sandstone Acidizing Design with a Generalized Model,” paper SPE 16885, *SPE Production Engineering* (February 1989), 49–55.

Takhar, S., Ravenscroft, P.D. and Nicoll, D.C.A.: “Prediction of Asphaltene Deposition During Production—Model Description and Experimental Details,” paper SPE 30108, presented at the SPE European Formation Damage Conference, The Hague, Netherlands (May 15–16, 1995).

Takulpakdee, S.: “Flow and Reaction of Weak Acids in Carbonate Porous Media,” MS thesis, Chulalongkorn University, Bangkok, Thailand (1998).

Tambini, M.: “An Effective Matrix Stimulation Technique for Horizontal Wells,” paper SPE 24993, presented at the European Petroleum Conference, Cannes, France (November 16–18, 1992).

Tariq, S.M.: “Evaluation of Flow Characteristics of Perforations Including Nonlinear Effects Using

Finite-Element Method,” paper SPE 12781, presented at the SPE California Regional Meeting, Long Beach, California, USA (April 11–13, 1984).

Templeton, C.C., Richardson, E.A., Karnes, G.T. and Lybarger, J.H.: “Self-Generating Mud Acid,” paper SPE 5153, *Journal of Petroleum Technology* (October 1975), 1199.

Tetelman, A.S.: “Recent Developments in Classical (Internal) Hydrogen Embrittlement,” *ASM Symposium Series on Hydrogen in Metals* (1973).

Thawer, R., Nicoll, D.C.A. and Dick, G.: “Asphaltene Deposition in Production Facilities,” paper SPE 18473, *SPE Production Engineering* (November 1990), 475.

Thomas, D.C.: “Selection of Paraffin Control Products and Applications,” paper SPE 17626, presented at the SPE International Meeting on Petroleum Engineering, Tianjin, China (November 1–4, 1988).

Thomas, R.L., Ali, S.A., Robert, J.A. and Acock, A.M.: “Field Validation of a Foam Diversion Model: A Matrix Stimulation Case Study,” paper SPE 39422, presented at the SPE International Symposium on Formation Damage Control, Lafayette, Louisiana, USA (February 18–19, 1998).

Thomas, R.L. and Crowe, C.W.: “Matrix Treatment Employs New Acid System for Stimulation and Control of Fines Migration in Sandstone Formations,” paper SPE 7566, presented at the SPE Annual Technical Conference and Exhibition, Houston, Texas, USA (October 1–3, 1978); also in *Journal of Petroleum Technology* (August 1981), 1491–1500.

Thomas, R.L. and Milne, A.: “The Use of Coiled Tubing During Matrix Acidizing of Carbonate Reservoirs,” paper SPE 29266, presented at the SPE Asia Pacific Oil and Gas Conference, Kuala Lumpur, Malaysia (March 20–22, 1995).

Thompson, K.E. and Fogler, H.S.: “Modeling Flow in Disordered Packed Beds from Pore-Scale Fluid Mechanics,” *AIChE J.* (1997) 43, No. 6, 1377.

Thompson, K.E. and Gdanski, R.D.: “Laboratory Study Provides Guidelines for Diverting Acid with Foam,” paper SPE 23436, *SPE Production & Facilities* (November 1993), 285.



- Tippie, D.B. and Kohlhaas, C.A.: "Variation of Skin Damage with Flow Rate Associated with Sand Flow or Stability in Unconsolidated-Sand Reservoirs," paper SPE 4886, presented at the SPE Annual California Regional Meeting, San Francisco, California, USA (April 4–5, 1974).
- Tuttle, R.N.: "High-Pour-Point and Asphaltic Crude Oils and Condensates," paper SPE 10004, *Journal of Petroleum Technology* (June 1983), 1192–1196.
- Tuttle, R.N. and Barkman, J.H.: "New Nondamaging and Acid-Degradable Drilling and Completion Fluids," paper SPE 4791, *Journal of Petroleum Technology* (November 1974), 1221–1226.
- Tyler, T.N., Metzger, R.R. and Twyford, L.R.: "Analysis and Treatment of Formation Damage at Prudhoe Bay, Alaska," paper SPE 12471, *Journal of Petroleum Technology* (June 1985), 1010–1018.
- Vaidya, R.N. and Fogler, H.S.: "Fines Migration and Formation Damage: Influence of pH and Ion Exchange," paper SPE 19413, presented at the SPE Formation Damage Control Symposium, Lafayette, Louisiana, USA (February 22–23, 1990); also in *SPE Production Engineering* (November 1992), 325.
- Van Ditzhuijzen, P.J.D. and de Waal, J.A.: "Reservoir Compaction and Surface Subsidence in the Central Luconia Gas Bearing Carbonates, Offshore Sarawak, East Malaysia," paper SPE 12400, presented at the Offshore South East Asia Conference, Singapore (February 21–24, 1984).
- Van Everdingen, A.F. and Hurst, W.: "The Application of the Laplace Transformation to Flow Problems in Reservoirs," *Trans., AIME* (1949) 186, 305–324.
- Ventresca, M.L., Betancourt, J., Castillo, J., Ciguela, S. and Azuaje, C.: "Chemical System for Treating Formation Damage Induced by Inverted Oil Muds," paper SPE 30125, presented at the SPE European Formation Damage Conference, The Hague, Netherlands (May 15–16, 1995).
- Vetter, O.J. and Kandarpa, V.: "Prediction of  $\text{CaCO}_3$  Scale Under Downhole Conditions," paper SPE 8991, presented at the SPE International Symposium on Oilfield and Geothermal Chemistry, Stanford, California, USA (May 28–30, 1980).
- Vetter, O.J.G. and Phillips, R.C.: "Prediction of Deposition of Calcium Sulfate Scale Under Down-Hole Conditions," *Journal of Petroleum Technology* (October 1970), 1299–1308.
- Vitagliano, V. and Lyons, P.A.: "Diffusion in Aqueous Acetic Acid Solutions," *J. Am. Chem. Soc.* (1956) 78, 4538.
- Walsh, M.P., Lake, L.W. and Schechter, R.S.: "A Description of Chemical Precipitation Mechanisms and Their Role in Formation Damage During Stimulation by Hydrofluoric Acid," paper SPE 10625, presented at the SPE Symposium on Formation Damage Control, Lafayette, Louisiana, USA (March 24–25, 1982); also in *Journal of Petroleum Technology* (September 1982), 2097–2112.
- Wamser, C.A.: "Hydrolysis of Fluoboric Acid in Aqueous Solution," *J. Am. Chem. Soc.* (March 1948), 1209–1215.
- Wang, Y.: "Existence of an Optimum Rate in Carbonate Acidizing and the Effect of Rock Heterogeneity on Wormholes Patterns," PhD dissertation, The University of Texas at Austin, Austin, Texas, USA (1993).
- Wang, Y., Hill, A.D. and Schechter, R.S.: "The Optimum Injection Rate for Matrix Acidizing of Carbonate Formations," paper SPE 26578, presented at the SPE Annual Technical Conference and Exhibition, Houston, Texas, USA (October 3–6, 1993).
- Wat, R.M.S., Sorbie, K.S., Todd, A.C., Ping, C., Ping, J. and Heriot-Watt, U.: "Kinetics of  $\text{BaSO}_4$  Crystal Growth and Effect in Formation Damage," paper SPE 23814, presented at the SPE International Symposium on Formation Damage Control, Lafayette, Louisiana, USA (February 26–27, 1992).
- Weeks, S.G.: "Formation Damage or Limited Perforating Penetration? Test-Well Shooting May Give a Clue," *Journal of Petroleum Technology* (September 1974), 979–984.
- Weingarten, J.S. and Perkins, T.K.: "Prediction of Sand Production in Gas Wells: Methods and Gulf of Mexico Case Studies," paper SPE 24797, presented at the SPE Annual Technical Conference and Exhibition, Washington, D.C., USA (October 4–7,



1992); also in *Journal of Petroleum Technology* (July 1995), 596.

Wendorff, C.L.: "New Solids-Free, High Density Brines Solve Many Workover and Completion Problems," paper SPE 4788, presented at the SPE Symposium on Formation Damage Control, New Orleans, Louisiana, USA (February 7–8, 1974).

Williams, B.B.: "Hydrofluoric Acid Reaction with Sandstone Formations," *J. Eng. for Ind.* (February 1975), 252–258.

Williams, B.B., Gidley, J.L., Guin, J.A. and Schechter, R.S.: "Characterization of Liquid-Solid Reactions: Hydrochloric Acid–Calcium Carbonate Reaction," *Ind. Eng. Chem. Fund.* (1970) 9, No. 4, 589.

Williams, B.B., Gidley, J.L. and Schechter, R.S.: *Acidizing Fundamentals*, Monograph Series, Richardson, Texas, USA, Society of Petroleum Engineers (1979) 6.

Wilson, M.D. and Pittman, E.D.: "Authigenic Clays in Sandstones: Recognition and Influence on Reservoir Properties and Paleoenvironmental Analysis," *Journal of Sedimentary Petrology* (March 1977) 47, No. 1.

Woodroof, R.A. Jr. and Anderson, R.W.: "Synthetic Polymer Friction Reducers Can Cause Formation Damage," paper SPE 6812, presented at the SPE Annual Technical Conference and Exhibition, Denver, Colorado, USA (October 9–12, 1977).

Yeager, V.J.: "Investigation of Gravel Pack Damage Due to HF Acidizing," paper SPE 19406, presented at the SPE Formation Damage Control Symposium, Lafayette, Louisiana, USA (February 22–23, 1990).

Zeilinger, S.C., Wang, M., Kibodeaux, K.R. and Rossen, W.R.: "Improved Prediction of Foam Diversion in Matrix Acidization," paper SPE 29529, presented at the SPE Production Operations Symposium, Oklahoma City, Oklahoma, USA (April 2–4, 1995).

Zerhoub, M., Ben-Naceur, K., Touboul, E. and Thomas, R.: "Matrix Acidizing: A Novel Approach to Foam Diversion," paper SPE 22854, presented at the SPE Annual Technical Conference and Exhibition, Washington, D.C., USA (October 4–7, 1992); also Zerhoub, M., Touboul, E., Ben-Naceur, K. and Thomas, R.L., in *SPE Production & Facilities* (May 1994), 121–126.

Zhou, Z.H. and Rossen, W.R.: "Applying Fractional-Flow Theory to Foams for Diversion in Matrix Acidization," paper SPE 24660, presented at the SPE Annual Technical Conference and Exhibition, Washington, D.C., USA (October 4–7, 1992); also in *SPE Production & Facilities* (February 1994) 9, 29.

Zhou, Z.H. and Rossen, W.R.: "Applying Fractional-Flow Theory to Foam Processes at the 'Limiting Capillary Pressure,'" *SPE Advanced Technology Series* (1996) 3, No. 1, 154.

# Nomenclature

$a$	Prats' relative capacity parameter	$b$	channel width
$a$	Archie constant	$b$	linear regression constant
$a$	ellipse axis, ft, m	$b$	slope of log-log plot of net pressure versus time
$a$	viscosity degradation coefficient	$b_{fD}$	dimensionless fracture width
$a$	intermediate area, ft <sup>2</sup> , m <sup>2</sup>	$b_{lf}$	linear flow fracture width
$a_c$	length scale characteristic	$b_M$	Mayerhofer <i>et al.</i> (1993) method intercept
$a_{sH,max}$	horizontal axis of the maximum damaged ellipse, ft, m	$b_N$	Nolte method intercept
$a_{sH,min}$	horizontal axis of the minimum damaged ellipse, ft, m	$b_s$	damage extent normal to the fracture plane, ft, m
$a_{sV,max}$	vertical axis of the maximum damaged ellipse, ft, m	$B$	formation volume factor, RB/STB, res-ft <sup>3</sup> /scf, res-m <sup>3</sup> /m <sup>3</sup>
$a_{sV,min}$	vertical axis of the minimum damaged ellipse, ft, m	$B$	Skempton pore pressure coefficient
$a_X$	chemical activity of species $X$	$B$	ratio of the inner cup radius to bob radius
$A$	area, ft <sup>2</sup> , acre, m <sup>2</sup>	$B_g$	formation volume factor for gas, res-ft <sup>3</sup> /scf, res-m <sup>3</sup> /m <sup>3</sup>
$A_{BL}$	representative formation property in the boundary layer	$B_o$	formation volume factor for oil, RB/STB, res-m <sup>3</sup> /m <sup>3</sup>
$A_c$	acid capacity number	$B_w$	formation volume factor for water
$A_e$	area at the end of an interval	$c_f$	fracture compliance
$A_{elas}$	elastic area	$c_f$	pore compressibility, psi <sup>-1</sup> , bar <sup>-1</sup>
$A_{etch}$	acid-etched area	$c_g$	compressibility of gas, psi <sup>-1</sup> , bar <sup>-1</sup>
$A_f$	fracture face surface area, ft <sup>2</sup> , m <sup>2</sup>	$c_o$	compressibility of oil, psi <sup>-1</sup> , bar <sup>-1</sup>
$A_{fso}$	fracture area at screenout, ft <sup>2</sup> , m <sup>2</sup>	$c_o$	borate foam viscosity adjustment factor
$A_{ik}$	influence function	$c_t$	total compressibility, psi <sup>-1</sup> , bar <sup>-1</sup>
$A_L$	leakoff area	$c_{tf}$	fracture compressibility, psi <sup>-1</sup> , bar <sup>-1</sup>
$A_{PZ}$	representative formation property in the pay zone	$c_w$	compressibility of water, psi <sup>-1</sup> , bar <sup>-1</sup>
$A_T$	critical transitional pore size	$C$	wellbore storage, bbl/psi, m <sup>3</sup> /bar
$b$	y-axis intercept for spurt	$C$	proppant concentration, ft <sup>3</sup> /ft <sup>3</sup> , m <sup>3</sup> /m <sup>3</sup>
		$C$	chemical concentration, mol/L
		$C$	constrained modulus, psi, bar, Pa

$C$	discharge coefficient	$C_{pfl}$	fluid heat capacity
$C$	rock type and grain size constant	$C_{pi}$	product concentration at the solid/liquid interface, mol/L
$C$	shape factor accounting for wellbore curvature	$C_R$	general reservoir-controlled leakoff coefficient, ft/min <sup>1/2</sup> , m/s <sup>1/2</sup>
$C^*$	critical overlap concentration, lbm/1000 gal, dL/g	$C_{RD}$	dimensionless reservoir conductivity
$C_A$	reservoir geometric shape factor	$C_t$	combined fluid-loss coefficient, ft/min <sup>1/2</sup> , m/s <sup>1/2</sup>
$C_A$	acid concentration	$C_v$	viscosity-controlled leakoff coefficient, ft/min <sup>1/2</sup> , m/s <sup>1/2</sup>
$C_c$	compressibility control leakoff coefficient, ft/min <sup>1/2</sup> , m/s <sup>1/2</sup>	$C_{ve}$	effective filtrate-controlled leakoff coefficient, ft/min <sup>1/2</sup> , m/s <sup>1/2</sup>
$C_{ce}$	effective reservoir-controlled fluid-leakoff coefficient, ft/min <sup>1/2</sup> , m/s <sup>1/2</sup>	$C_w$	wall or filter-cake fluid-loss coefficient, ft/min <sup>1/2</sup> , m/s <sup>1/2</sup>
$C_{CO}$	total interface concentration of carbonate species	$C_W$	acid concentration at solid/liquid interface
$C_{cv}$	combined leakoff coefficient, ft/min <sup>1/2</sup> , m/s <sup>1/2</sup>	$C_{wall}$	surface acid concentration
$C_d$	dimensionless discharge coefficient	$C_{wcv}$	total leakoff coefficient, ft/min <sup>1/2</sup> , m/s <sup>1/2</sup>
$C_D$	dimensionless wellbore storage coefficient	$C_0$	acid concentration at capillary inlet
$C_{div}$	concentration of diverter particles, lbm/gal, kg/m <sup>3</sup>	$C_1$	external phase constant
$C_{div}'$	net concentration of diverter particles after dissolution effects, lbm/gal, kg/m <sup>3</sup>	$CF$	concentration factor
$C_{drag}$	drag coefficient	$d$	diameter, in., m
$C_{dyn}$	dynamic constrained modulus, psi, bar, Pa	$d$	distance, ft, in., m
$C_{eqm}$	equilibrium concentration	$d_{prop}$	proppant particle diameter, in., m
$C_{fD}$	dimensionless fracture conductivity	$d_{sol}$	solid particle diameter, in., m
$C_{fDapp}$	apparent dimensionless fracture conductivity	$d_{tbg}$	tubing diameter, in., m
$C_{fD,opt}$	optimal dimensionless fracture conductivity	$D$	diameter, in., m
$C_{fDtrue}$	actual dimensionless fracture conductivity	$D$	distance, ft, in., m
$C_{gel}$	gel mass concentration in fluid	$D$	turbulence coefficient
$C_H$	shape factor	$D$	diffusion constant, cm <sup>2</sup> /s
$C_{HF}$	concentration of hydrofluoric acid	$D_A$	molecular diffusion coefficient, cm <sup>2</sup> /s
$C_i$	reactant concentration at the solid/liquid interface, mol/L	$D_e$	effective acid diffusion coefficient, cm <sup>2</sup> /s
$C_L$	leakoff or fluid-loss coefficient, ft/min <sup>1/2</sup> , m/s <sup>1/2</sup>	$D_{eff}$	effective acid diffusion coefficient, ft <sup>2</sup> /s, m <sup>2</sup> /s
$C_o$	rock cohesion, psi, bar, Pa	$D_H$	hydraulic diameter, in., m
$C_o$	initial reactant concentration	$D_p$	pipe inner diameter, in., m
$C_p$	product concentration	$D_p$	perforation diameter, in., m
		$D_{pe}$	effective diffusion coefficient for reaction products, cm <sup>2</sup> /s

$D_w$	wire diameter, in., m	$F_L$	linear flow function
$Da$	Damköhler number	$F_{meas}$	fracture development function for measured data
$Da_{mt}$	mass-transfer-limited Damköhler number	$F_{sim}$	fracture development function for simulated data
$Da_{rxn}$	reaction-rate-limited Damköhler number	$F_0$	surface flux at time zero
$De$	Deborah number	$g$	acceleration of gravity, ft/s <sup>2</sup> , m/s <sup>2</sup>
$DR$	damage ratio	$g(\Delta t_D)$	dimensionless fluid-loss volume function
$E$	Young's modulus, psi, bar, Pa	$g_f$	fracture gradient, psi/ft, Pa/m
$E'$	plane strain modulus, psi, bar, Pa	$g_0$	fluid-loss volume function
$E_{av}$	average Young's modulus, psi, bar, Pa	$G$	shear modulus, psi, bar, Pa
$E_{dyn}$	dynamic Young's modulus, psi, bar, Pa	$G(\Delta t_D)$	dimensionless fluid-loss time function
$E_f$	reaction rate constant	$G^*$	corrected value of $G$ -function at closure
$E_n$	effect of all previous time steps	$G'$	elastic storage modulus, psi, bar, Pa
$E_s$	secant Young's modulus, psi, bar, Pa	$G''$	viscous loss modulus, psi, bar, Pa
$E_t$	tangent Young's modulus, psi, bar, Pa	$G_c$	fluid-loss time function $G(\Delta t_D)$ at fracture closure
$E_t$	Young's modulus of a plastic material, psi, bar, Pa	$G_{dyn}$	dynamic shear modulus, psi, bar, Pa
$f$	friction factor	$G_e$	strain energy release rate
$f$	elastic influence function	$GR_{API}$	gamma ray value
$f_{aL}$	apparent length fraction	$h$	height, ft, m
$f_d$	drag coefficient	$h$	formation or reservoir thickness, ft, m
$f_{fL}$	ratio of fracture to loss volume during injection	$h$	hardening parameter
$f_{LS}$	volume fraction lost to spurt	$h$	heat transfer coefficient
$f_p$	pad volume fraction	$h_{cp}$	height at the center of perforations, ft, m
$f_{pad}$	pad volume fraction	$h_D$	dimensionless height
$f_s$	slurry volume fraction	$h_f$	fracture height, ft, m
$f_v$	volume fraction	$h_{fD}$	ratio of the leakoff area to the characteristic length
$f_w$	water fractional flow	$h_{fo}$	initial fracture height, ft, m
$f_\kappa$	spurt fraction	$h_L$	permeable or fluid-loss height, ft, m
$F$	fill fraction	$h_{pay}$	height of the pay zone, ft, m
$F$	formation factor	$h_s$	penetration into bounding layer, ft, m
$F$	force, lbf, N	$h_{wD}$	dimensionless completion thickness
$F$	fracture development function	$H$	depth, ft, m
$F_b$	ratio of wellbore width or net pressure	$i$	injection rate
$F_c$	critical load		
$F_i$	surface flux at the $i$ th time step		

$i$	interest rate	$k_{pf}$	perforation friction proportionality constant
$I$	diffusion flux	$k_r$	relative permeability, md
$I$	influence function	$k_r$	reservoir permeability, md
$I_{ani}$	index of horizontal-to-vertical permeability anisotropy	$k_r$	surface reaction rate constant, cm/s
$J$	acid flux	$k_{r,app}$	apparent reservoir permeability, md
$J$	pseudosteady-state productivity index	$k_{rg}$	gas relative permeability, md
$J_F$	fractured well productivity index	$k_{ro}$	oil relative permeability, md
$J_H$	pseudosteady-state productivity index of horizontal well	$k_{rw}$	water relative permeability, md
$J_{ideal}$	ideal productivity index	$k_s$	damaged permeability, md
$J_o$	initial productivity index	$k_{sph}$	spherical permeability, md
$J_{real}$	real productivity index	$k_V$	vertical permeability, md
$J_V$	pseudosteady-state productivity index of vertical well	$k_{Vs}$	damaged vertical permeability, md
$k$	permeability, md	$k_w$	water effective permeability, md
$k_c$	damaged zone permeability, md	$k_x$	maximum permeability directed parallel to the principal permeability axis, md
$k_{cake}$	filter or diverter cake permeability, md	$k_x$	permeability in the x direction, md
$k_d$	dissociation constant	$k_y$	minimum permeability directed perpendicular to the principal permeability axis, md
$k_f$	fracture permeability, md	$k_y$	permeability in the y direction, md
$k_{fD}$	dimensionless fracture permeability	$k_z$	vertical permeability, md
$k_{fil}$	relative permeability of the formation to filtrate, md	$k_0$	reaction rate constant at the reference temperature
$k_{fl}$	thermal conductivity of a fluid	$K$	bulk modulus, psi, bar, Pa
$k_{foam}$	foam permeability, md	$K$	mass-transfer coefficient, cm/s
$k_{fs}$	fracture permeability in the near-well skin effect zone, md	$K$	equilibrium constant
$k_g$	gas effective permeability, md	$K$	coefficient of earth stress, dimensionless
$k_h$	thermal conductivity, BTU/hr ft°F, J/s m°C	$K$	empirical kinetic constant
$k_H$	horizontal permeability, md	$K$	Mark-Houwink coefficient, dL/g
$k_{Hs}$	damaged horizontal permeability, md	$K$	power law fluid rheology consistency coefficient, lbf-s <sup>n</sup> /ft <sup>2</sup>
$k_i$	initial permeability, md	$K'$	power law effective consistency coefficient, lbf-s <sup>n</sup> /ft <sup>2</sup>
$k_{near\ wellbore}$	near-wellbore friction proportionality constant	$K_a$	equilibrium constant of acid
$k_o$	oil effective permeability, md	$K_{ads}$	equilibrium constant of the exothermic adsorption of molecules at surface reactive sites
$k_o$	initial permeability, md	$K_c$	conditional equilibrium constant

$K_c$	$G$ -plot slope correction factor for pressure-dependent leakoff	$L$	horizontal well length, ft, m
$K_d$	dissociation constant	$L_{app}$	apparent of equivalent fracture penetration, ft, m
$K_{dyn}$	dynamic bulk modulus	$L_e$	length to tip, ft, m
$K_{eq}$	effective equilibrium constant	$L_p$	productive length, ft, m
$K_{foam}$	consistency coefficient for the foam phase	$L_t$	length of the fracture tip region, ft, m
$K_g$	mass-transfer coefficient	$L_v$	length of filtrate-invaded zone, ft, m
$K_I$	stress intensity factor, psi/in. <sup>1/2</sup> , bar/m <sup>1/2</sup>	$m$	slope on semilogarithmic straight line, psi/cycle (oil), psi <sup>2</sup> /cycle or psi <sup>2</sup> /cp/cycle (gas)
$K_{Ic}$	critical stress intensity factor, psi/in. <sup>1/2</sup> , bar/m <sup>1/2</sup>	$m$	Archie constant
$K_{Ic}^{eff}$	effective fracture toughness, psi/in. <sup>1/2</sup> , bar/m <sup>1/2</sup>	$m$	linear regression constant
$K_{Ic}^{lag}$	critical stress intensity factor in the fluid lag region, psi/in. <sup>1/2</sup> , bar/m <sup>1/2</sup>	$m$	reaction rate order
$K_{Ic-apparent}$	apparent fracture toughness, psi/in. <sup>1/2</sup> , bar/m <sup>1/2</sup>	$m$	power law turbulence factor
$K_{II}$	stress intensity factor at bottom fracture tip, psi/in. <sup>1/2</sup> , bar/m <sup>1/2</sup>	$m_{bf}$	bilinear flow slope, psi/hr <sup>1/4</sup> , bar/hr <sup>1/4</sup>
$K_{Iu}$	stress intensity factor at top fracture tip, psi/in. <sup>1/2</sup> , bar/m <sup>1/2</sup>	$m_c$	early-time slope used to compute the wellbore storage coefficient $C$
$K_o$	coefficient of earth pressure at rest, dimensionless	$m_{cf}$	linear flow slope in an elongated reservoir
$K_{pipe}$	consistency index for pipe flow, lbf-s <sup>n</sup> /ft <sup>2</sup>	$m_{epr}$	early pseudoradial flow slope
$K_r$	reaction rate	$m_G$	slope of the $G$ -plot, psi, bar, Pa
$K_r$	temperature-dependent reaction rate constant	$m_{Gc}$	slope of the $G$ -plot at fracture closure, psi, bar, Pa
$K_s$	bulk modulus of the solid constituents, psi, bar, Pa	$m_{hl}$	linear flow slope of a horizontal well
$K_s$	solubility constant	$m_{lf}$	linear flow slope, psi/hr <sup>1/2</sup> , bar/hr <sup>1/2</sup>
$K_{slot}$	consistency index for slot flow, lbf-s <sup>n</sup> /ft <sup>2</sup>	$m_M$	Mayerhofer <i>et al.</i> (1993) method slope
$K_v$	consistency index for a concentric cylinder viscometer, lbf-s <sup>n</sup> /ft <sup>2</sup>	$m_n$	straight-line slope
$l$	length, ft, in., m	$m_N$	Nolte method slope
$l$	diverter cake thickness, ft, m	$m_p$	match pressure, psi, bar, Pa
$l_d$	length of damaged zone, ft, m	$m_{pp}$	spherical flow slope
$l_p$	perforation channel length, ft, m	$m_{rf}$	radial flow slope, psi, bar, Pa
$L$	length, ft, m	$m_{3/4}$	slope of the $G$ -plot at the $3/4$ point, psi, bar, Pa
$L$	fracture half-length, ft, m	$M_{acid}$	moles of acid per unit rock face area
		$M_{gel}$	specific density of gel mass in the fluid
		$M_v$	viscosity average molecular weight, g/mol
		$MW$	molecular weight, g/mol
		$n$	number or order
		$n$	index of time step

$n$	power law fluid rheology behavior index, dimensionless	$p_{D,up}$	dimensionless pressure for a uniform-pressure, fixed-length fracture
$n'$	power law effective index, dimensionless	$p_e$	constant outer reservoir pressure, psi, bar, Pa
$n_e$	index of time step after shut-in	$p_f$	fissure or fracture pressure, psi, bar, Pa
$n_f$	power law exponent of the filtrate	$p_f$	fracturing fluid pressure, psi, bar, Pa
$n_{perf}$	number of perforations	$p_f$	far-field pore pressure, psi, bar, Pa
$N_{DH}$	dimensionless cumulative recovery from a longitudinally fractured horizontal well	$p_{fc}$	formation capacity
$N_{DV}$	dimensionless cumulative recovery from a fractured vertical well	$p_{fo}$	fissure opening pressure, psi, bar, Pa
$N_p$	oil cumulative production, bbl, m <sup>3</sup>	$p_h$	hydrostatic pressure, psi, bar, Pa
$N_{Re}$	Reynold's number	$p_{head}$	hydrostatic head of wellbore fluid, psi, bar, Pa
$N_{Sc}$	Schmidt number	$p_i$	initial reservoir pressure, psi, bar, Pa
$N_{Sh}$	Sherwood number	$p_{if}$	breakdown pressure for fracture initiation, psi, bar, Pa
$N_\phi$	coefficient of passive stress	$p_{inj}$	injection pressure, psi, bar, Pa
$p$	pressure, psi, bar, Pa	$p_{ISI}$	instantaneous shut-in pressure, psi, bar, Pa
$p$	reservoir pressure, psi, bar, Pa	$p_{it}$	wellhead injection pressure, psi, bar, Pa
$p_b$	bubblepoint pressure, psi, bar, Pa	$p_{iw}$	bottomhole injection pressure, psi, bar, Pa
$p_{bh}$	borehole pressure, psi, bar, Pa	$p_m$	microannulus pressure, psi, bar, Pa
$p_c$	constant confining pressure, psi, bar, Pa	$p_m$	mud pressure in the wellbore, psi, bar, Pa
$p_c$	closure pressure, psi, bar, Pa	$p_{meas}$	measured pressure, psi, bar, Pa
$p_c$	capillary pressure, psi, bar, Pa	$p_{net}$	net pressure, psi, bar, Pa
$p_{cf}$	casing friction pressure, psi, bar, Pa	$p_{net,crit}$	critical net pressure, psi, bar, Pa
$p_{corr}$	pressure corrected for non-plane-strain contribution, psi, bar, Pa	$p_{net,fo}$	net pressure required for fissure opening, psi, bar, Pa
$p_{cp}$	pressure at center of the perforations, psi, bar, Pa	$p_{net,max}$	maximum net pressure, psi, bar, Pa
$p_D$	dimensionless pressure	$p_{net,si}$	net pressure at shut-in, psi, bar, Pa
$p_D'$	dimensionless pressure derivative	$p_{net,so}$	net pressure at screenout, psi, bar, Pa
$p_{DLs}$	dimensionless pressure difference for pressure-dependent leakoff	$p_o$	wellbore pressure, psi, bar, Pa
$p_{dr}$	downstream restriction pressure, psi, bar, Pa	$p_p$	far-field reservoir pressure, psi, bar, Pa
$p_{dsc}$	pressure downstream of the surface choke, psi, bar, Pa	$p_{pf}$	perforation friction, psi, bar, Pa
$p_{dsv}$	pressure downstream of the safety valve, psi, bar, Pa	$p_{pipe\ friction}$	pipe friction pressure, psi, bar, Pa
		$p_{pwD}$	dimensionless pseudopressure
		$p_r$	reservoir pressure, psi, bar, Pa

$p_s$	pressure at the outer bound of the damaged zone, psi, bar, Pa	$q_D$	dimensionless flow rate
$p_{sc}$	standard condition pressure, psi, bar, Pa	$q_{DND}$	dimensionless non-Darcy flow rate
$p_{sep}$	separator pressure, psi, bar, Pa	$q_e$	flow at tip
$p_{sim}$	simulated pressure, psi, bar, Pa	$q_f$	volume rate of storage in a fracture
$p_{surf}$	surface pressure, psi, bar, Pa	$q_g$	gas production rate, Mscf/D, m <sup>3</sup> /d
$p_{tf}$	tubing flowing pressure, psi, bar, Pa	$q_i$	injection rate, B/D, bbl/min, m <sup>3</sup> /d, m <sup>3</sup> /s
$p_{tip}$	net pressure at fracture tip for extension, psi, bar, Pa	$q_{i,max}$	maximum injection rate, B/D, bbl/min, m <sup>3</sup> /d, m <sup>3</sup> /s
$p_{ur}$	upstream restriction pressure, psi, bar, Pa	$q_L$	rate of fluid loss, B/D, bbl/min, m <sup>3</sup> /d, m <sup>3</sup> /s
$p_{usv}$	pressure upstream of the safety valve, psi, bar, Pa	$q_{last}$	last flow rate, B/D, bbl/min, m <sup>3</sup> /d, m <sup>3</sup> /s
$p_{vapor}$	fluid vapor pressure, psi, bar, Pa	$q_{L,C}$	rate of fluid loss for reservoir-controlled leakoff, B/D, bbl/min, m <sup>3</sup> /d, m <sup>3</sup> /s
$p_w$	wellbore pressure, psi, bar, Pa	$q_n$	leakoff rate from one wing through two faces, B/D, m <sup>3</sup> /s
$p_{wD}$	dimensionless wellbore pressure	$q_o$	initial flow rate, B/D, m <sup>3</sup> /s
$p_{wf}$	bottomhole flowing pressure, psi, bar, Pa	$q_o$	oil production rate, B/D, m <sup>3</sup> /s
$p_{wf,ideal}$	ideal bottomhole flowing pressure, psi, bar, Pa	$q_{o,max}$	maximum oil production rate at two-phase flow, B/D, m <sup>3</sup> /s
$p_{wf,real}$	real bottomhole flowing pressure, psi, bar, Pa	$q_{perf}$	flow entering a perforation
$p_{wfs}$	wellbore sandface flowing pressure, psi, bar, Pa	$q_{RT}$	total reservoir production rate, B/D, m <sup>3</sup> /d
$p_{wh}$	wellhead flowing pressure, psi, bar, Pa	$q_s$	damaged flow rate
$p_{ws}$	bottomhole shut-in pressure, psi, bar, Pa	$q_T$	total injection rate
$p_{1\ hr}$	pressure on extension of semilogarithmic straight line at $t = 1$ hr, psi, bar, Pa	$q_{tot}$	constant total injection rate
$p_{3/4}$	pressure at the $G$ -plot $3/4$ point, psi, bar, Pa	$q_w$	water production rate, B/D, m <sup>3</sup> /d
$Pe$	Peclet number	$Q_p$	cumulative production, B/D, m <sup>3</sup> /d
$PI$	productivity index, B/D/psi (oil), Mscf/D/psi (gas), m <sup>3</sup> /d/bar	$r$	radial distance, ft, m
$PI_s$	damaged productivity index, B/D/psi (oil), Mscf/D/psi (gas), m <sup>3</sup> /d/bar	$r$	reaction rate
$PV_{BT}$	number of pore volumes to breakthrough	$r_A$	rate of reactant consumption, mol/cm <sup>2</sup> /s
$PV_{inj}$	number of pore volumes injected	$r_{ac}$	stimulation radius, ft, m
$q$	flow rate, B/D (oil), Mscf/D (gas), m <sup>3</sup> /d	$r_b$	acid bank radius, ft, m
$q_{app}$	apparent flow rate, B/D, bbl/min, m <sup>3</sup> /d, m <sup>3</sup> /s	$r_{bob}$	bob radius
$q_{ave}$	average flow rate, B/D, bbl/min, m <sup>3</sup> /d, m <sup>3</sup> /s	$r_{cup}$	cup radius
$q_c$	flow rate in capillary pores	$r_D$	rate of surface reaction, mol/cm <sup>2</sup> /s
$q_c$	injection rate into core face	$r_e$	reservoir radius, ft, m
		$r_{eH}$	radius of horizontal drainage ellipse formed around a horizontal well, ft, m



$r_f$	radial extent of foam bank, ft, m	$R_{so}$	solution-gas/oil ratio
$r_{feldspar}$	reaction rate of feldspar, mol feldspar/cm <sup>2</sup> /s	$R_{sw}$	solution-gas/water ratio
$r_{HF}$	radial penetration of hydrofluoric acid, ft, m	$R_t$	true formation resistivity, ohm-m
$r_{hyd}$	hydraulic radius	$R_w$	resistivity of formation water, ohm-m
$r_i$	specific reaction rate of mineral $i$	$R_{xo}$	resistivity of the flushed zone, ohm-m
$r_i$	inner radius	$R_0$	filter-cake resistance, s·m <sup>-1</sup>
$r_o$	outer radius	$R_{0,app}$	apparent filter-cake resistance, s·m <sup>-1</sup>
$r_p$	ratio of permeable area to fracture area	$s$	skin effect, dimensionless
$r_p$	probe radius	$s$	reactive surface area
$r_{pD}$	dimensionless ratio of permeable area to fracture area	$s_c$	skin effect from partial penetration, dimensionless
$r_{perf}$	perforation radius, in., m	$s_c + \theta$	skin effect due to partial penetration and slant, dimensionless
$r_{quartz}$	reaction rate of quartz, mol quartz/cm <sup>2</sup> /s	$s_{cake}$	temporary skin effect due to diverter cake, dimensionless
$r_s$	radius of damaged or displaced section, ft, m	$s_d$	skin effect due to damage, dimensionless
$r_v$	fraction of well drainage volume occupied by the crest at water breakthrough	$(s_d)_o$	perforation skin effect in openhole, dimensionless
$r_w$	wellbore radius, ft, m	$(s_d)_p$	perforation skin effect due to perforations terminating outside the damaged zone, dimensionless
$r_w'$	effective or apparent wellbore radius, ft, m	$s_e$	vertical eccentricity skin effect, dimensionless
$r_{wD}'$	dimensionless effective wellbore radius	$s_f$	skin effect while flowing at pseudoradial conditions, dimensionless
$r_{wh}$	wormhole radius	$s_f$	fracture stiffness, ft/psi/m
$R$	pore radius	$s_f$	skin effect due to a fracture, dimensionless
$R$	reaction rate	$s_{foam}$	foam skin effect, dimensionless
$R$	universal gas constant, psi ft <sup>3</sup> /mol °R, bar m <sup>3</sup> /mol K	$s_{fs}$	fracture face damage skin effect, dimensionless
$R$	fracture radius, ft, m	$s_H$	plane-flow skin effect, dimensionless
$R_A$	rate of appearance of reactant	$s_o$	initial skin effect, dimensionless
$R_{At}$	rate of reactant consumption at the tip	$s_o$	constant skin effect, dimensionless
$R_B$	rate of mineral dissolution	$s_p$	skin effect due to perforations, dimensionless
$R_{cake}$	diverter cake resistance, m <sup>-1</sup>	$s_t$	total skin effect, dimensionless
$R_{eff}$	effective radius, ft, m	$s_V$	vertical skin effect, dimensionless
$R_f$	radial fracture radius, ft, m	$s_{wb}$	wellbore skin effect, dimensionless
$R_i$	overall reaction rate of mineral $i$	$s_x$	vertical effects skin effect, dimensionless
$R_{mf}$	resistivity of the mud filtrate, ohm-m	$s_\theta$	skin effect due to slant, dimensionless
$R_o$	resistivity of 100% water-saturated formation, ohm-m		
$R_p$	pressure-difference curve, dimensionless		

$S$	surface area	$t_{Dr_w'}$	dimensionless time referenced to the effective wellbore radius $r_w'$
$S_F$	surface area per unit volume of solids for fast-reacting minerals	$t_{Dx_f}$	dimensionless fracture time
$S_g$	gas-phase fluid saturation, fraction	$t_e$	time at end of pumping or injection, min, s
$S_i$	reactive surface area of mineral $i$	$t_{end}$	time of the end of dual-porosity behavior
$S_o$	oil-phase fluid saturation, fraction	$t_{exp}$	time of fracture opening and initial fluid exposure
$S_{oi}$	initial oil saturation, fraction	$t_i$	injection time
$S_{or}$	residual oil saturation, fraction	$t_i$	time at the end of the $i$ th step
$S_p$	spurt-loss coefficient, gal/ft <sup>2</sup> , m <sup>3</sup> /m <sup>2</sup>	$t_{knee}$	knee time for the crossing of pressure derivatives
$S_{RE}$	rock embedment strength	$t_{min}$	minimum time
$S_S$	surface area per unit volume of solids for slow-reacting minerals	$t_n$	time at the end of step $n$ , s
$S_w$	water saturation, fraction	$t_{on}$	time of onset of dual-porosity behavior
$S_{wc}$	connate water saturation, fraction	$t_p$	producing time, hr
$S_{wi}$	irreducible water saturation, fraction	$t_p$	pumping or injection time, hr
$t$	time, day, hr, min, s	$t_P$	compressional wave arrival time
$t^*$	reduced time	$t_{pss}$	time to pseudosteady state, hr
$t_a$	pseudotime	$t_r$	time at reference point $r$
$t_{aD}$	dimensionless pseudotime	$t_S$	time of tip screenout or injection without screenout
$t_{BT}$	time of water breakthrough, hr	$t_S$	shear wave arrival time
$t_c$	closure time, min	$t_{so}$	time at screenout
$t_{cD}$	dimensionless closure time	$t_{sp}$	spurt time
$t_D$	dimensionless time	$t_0$	reference time
$t_{DA}$	dimensionless time referenced to reservoir drainage area	$t_{\alpha D}$	dimensionless ratio of time to pumping time
$t_{Dbf}$	dimensionless time at start of formation linear flow regime	$T$	temperature, °F, °C, K
$t_{Debf}$	dimensionless time at end of bilinear flow regime	$T$	absolute temperature, °R, K
$t_{Defl}$	dimensionless time at which fracture linear flow behavior ends	$T$	dimensionless time for after-closure analysis
$t_{Delf}$	dimensionless time at which formation linear flow behavior ends	$T$	constant for tectonic effects on stress
$t_{dep}$	time of departure from flow regime trend	$T$	wire tension, lbf/ft
$t_{D,knee}$	dimensionless knee time for the pressure derivatives	$T_d$	dead weight, lbf
		$T_D$	dimensionless temperature
		$T_f$	flowing temperature, °F, °C
		$T_{fl}$	fluid temperature, °F, °C
		$T_i$	fluid temperature at the fracture mouth, °F, °C

$T_{inlet}$	temperature at inlet, °F, °C	$V$	volume, ft <sup>3</sup> , m <sup>3</sup>
$T_{knee}$	dimensionless knee time for after-closure analysis	$V_{ac}$	acid volume injected, ft <sup>3</sup> , m <sup>3</sup>
$T_o$	offset temperature, °F, °C	$V_f$	fracture volume, ft <sup>3</sup> , m <sup>3</sup>
$T_o$	tensile strength, psi, bar, Pa	$V_f$	fluid volume
$T_p$	dimensionless time at the end of pumping for after-closure analysis	$V_F$	volume of fast-reacting minerals
$T_r$	reservoir temperature, °F, °C	$V_{fp}$	fracture volume at the end of pumping, ft <sup>3</sup> , m <sup>3</sup>
$T_{ref}$	reference temperature, °F, °C	$V_{fso}$	fracture volume at screenout, ft <sup>3</sup> , m <sup>3</sup>
$T_s$	wire strength, lbf/ft	$V_{HC}$	volume of hydrocarbons, ft <sup>3</sup> , m <sup>3</sup>
$T_{sc}$	standard condition temperature, °F, °C, K	$V_{HCl}$	volume of hydrochloric acid, ft <sup>3</sup> , m <sup>3</sup>
$TR$	tool response	$V_{HF}$	volume of hydrofluoric acid, ft <sup>3</sup> , m <sup>3</sup>
$u$	velocity, ft/s, cm/s	$V_i$	volume of fluid injected, bbl, gal, m <sup>3</sup>
$u$	acid flux	$V_{iso}$	fluid volume injected at screenout, bbl, gal, ft <sup>3</sup> , m <sup>3</sup>
$u_g$	volumetric flux of gas	$V_L$	leaked-off fluid volume, bbl, gal, m <sup>3</sup>
$u_L$	leakoff velocity, ft/s, cm/s	$V_{L,C}$	volume of fluid lost due to filtration, bbl, gal, m <sup>3</sup>
$u_P$	$P$ -wave velocity, ft/s, m/s	$V_{Lp}$	leaked-off volume during pumping, bbl, m <sup>3</sup>
$u_r$	rising velocity of spherical particles in a fluid, ft/s, cm/s	$V_{Lp,C}$	volume of fluid lost due to filtration at the end of pumping, bbl, gal, m <sup>3</sup>
$u_S$	$S$ -wave velocity, ft/s, m/s	$V_{Ls}$	volume of fluid lost during shut-in, bbl, gal, m <sup>3</sup>
$u_{sol}$	solid particle velocity, ft/s, cm/s	$V_{L,S}$	fluid-loss component due to spurt, bbl, gal, m <sup>3</sup>
$u_t$	terminal settling velocity, ft/s, m/s	$V_{Ls,C}$	volume of fluid lost due to filtration during shut-in, bbl, gal, m <sup>3</sup>
$u_{tip}$	fracture tip velocity, ft/s, cm/s	$V_M$	molar volume
$u_w$	volumetric flux of water	$V_{mineral}$	volumetric fraction of a mineral
$u_{\infty}$	terminal proppant settling velocity, ft/s, m/s	$V_p$	pore volume, ft <sup>3</sup> , m <sup>3</sup>
$v$	flow velocity, ft/s, cm/s	$V_{prop}$	bulk proppant volume injected
$\hat{v}$	specific volume of foam	$V_{rp}$	relative proppant volume, lbm/md-ft <sup>3</sup>
$v_{A,x}$	Fick's law for the velocity of species A	$V_S$	volume of slow-reacting minerals
$v_c$	damaged zone velocity, ft/s, cm/s	$V_S$	volume of fluid lost to spurt, gal/100 ft <sup>2</sup>
$v_{fall}$	settling rate, ft/s, cm/s	$V_{wall}$	volume of fluid leaked off at the fracture wall
$\hat{v}_l$	specific volume of the base liquid	$w$	width, ft, m
$v_L$	fluid-loss velocity, ft/min	$w$	fracture width, ft, in., m
$v_L$	specific fluid-loss volume	$w_e$	average fracture width at end of pumping, ft, m
$v_m$	matrix velocity, ft/s, cm/s		
$v_x$	average fluid velocity along the fracture length, ft/s, cm/s		

$w_{etch}$	acid-etched width, ft, m
$w_f$	fracture width, ft, m
$w_L$	leakoff width, ft, m
$w_{lost}$	proppant volume lost to the fracture width
$w_{max}$	maximum width, ft, m
$w_{max,p}$	maximum fracture width at the end of pumping, ft, m
$w_{max,si}$	maximum fracture width immediately after shut-in, ft, m
$w_n$	average fracture width at time step $n$ , ft, m
$w_o$	wellbore width, ft, m
$w_p$	propped width, ft, m
$w_{p-eff}$	effective propped width, ft, m
$w_{so}$	width at screenout, ft, m
$w_w$	width at the wellbore, ft, m
$W_{elas}$	elastic energy stored in a solid
$W_{ext}$	potential energy of exterior forces
$W_i$	weighting factors
$W_{kin}$	kinetic energy
$W_s$	energy dissipated during propagation of a crack
$x$	linear distance, ft, m
$x_e$	well drainage dimension, ft, m
$x_{e,opt}$	optimal well spacing, ft, m
$x_f$	productive fracture half-length, ft, m
$x_{fa}$	apparent fracture half-length, ft, m
$x_{feldspar}$	feldspar volume fraction of a sandstone
$x_s$	half-length of the skin effect zone, ft, m
$X$	volumetric dissolving power
$X_C$	dissolving power of acid
$X_{HCl}$	bulk rock fraction dissolved by hydrochloric acid
$y$	vertical linear distance, ft, m
$z$	linear distance, ft, m
$z_{TVD}$	true vertical depth, ft, m
$z_w$	elevation from reservoir bottom, ft, m

$z_w$	standoff from oil-water contact, ft, m
$z_w$	elevation of midpoint of perforations from the bottom of the reservoir, ft, m
$z_{wD}$	dimensionless completion elevation
$Z$	gas deviation factor, dimensionless

## Symbols

$\alpha$	Forscheimer equation coefficient
$\alpha$	Biot poroelastic constant
$\alpha$	proportionality constant
$\alpha$	specific diverter cake resistance, m/kg
$\alpha$	exponent of fracture area growth, dimensionless
$\alpha$	order of reaction
$\alpha_{bf}$	bilinear flow constant
$\alpha_c$	wellbore storage constant
$\alpha_{cf}$	elongated reservoir constant
$\alpha_f$	sealing fault constant
$\alpha_g$	geometry coefficient
$\alpha_{hl}$	linear flow to a horizontal well constant
$\alpha_{lf}$	linear flow constant
$\alpha_p$	dimensionless pressure constant
$\alpha_{pp}$	partial penetration constant
$\alpha_t$	dimensionless time constant
$\alpha_T$	linear thermal expansion coefficient
$\alpha_0$	lower bound of area exponent, dimensionless
$\alpha_1$	upper bound of area exponent, dimensionless
$\alpha_\theta$	perforation-phase-dependent variable
$\beta$	dissolving power coefficient related to acid strength
$\beta$	stiffness
$\beta$	ratio of average to wellbore net pressure or width
$\beta$	Forscheimer equation coefficient
$\beta$	non-Darcy flow rate coefficient
$\beta_p$	net pressure or width ratio during injection

$\beta_s$	net pressure or width ratio during shut-in	$\Delta p_{friction}$	friction pressure ratio with and without solids
$\gamma$	shear strain		
$\gamma$	channel factor	$\Delta p_h$	hydrostatic pressure drop, psi, bar, Pa
$\gamma$	$G$ -plot slope correction factor for pressure-dependent leakoff	$\Delta p_{int}$	difference in the pressure intercept, psi, bar, Pa
$\gamma$	specific gravity	$\Delta p_{misalign}$	perforation misalignment friction, psi, bar, Pa
$\gamma$	shear rate, $s^{-1}$	$\Delta p_{near\ wellbore}$	near-wellbore pressure loss, psi, bar, Pa
$\gamma_{ab}$	interaction energy per unit surface area between liquids a and b	$\Delta p_{nf}$	pressure difference due to near-face leakoff effects, psi, bar, Pa
$\gamma_b$	shear rate at the bob, $s^{-1}$	$\Delta p_{pf}$	friction through the perforation, psi, bar, Pa
$\gamma_F$	fracture surface energy		
$\gamma_{fluid}$	specific gravity of fluid	$\Delta p_{piz}$	pressure drop across a polymer-invaded zone, psi, bar, Pa
$\gamma_g$	specific gravity of gas	$\Delta p_r$	pressure drop in the reservoir, psi, bar, Pa
$\gamma_I$	interfacial tension	$\Delta p_R$	total pressure increase in the reservoir beyond the filtrate invasion region, psi, bar, Pa
$\gamma_{prop}$	specific gravity of proppant		
$\gamma_v$	volume-averaged shear rate, $s^{-1}$	$\Delta p_{RC}$	pressure increase in the reservoir beyond the filtrate region due to Carter-based leakoff, psi, bar, Pa
$\Gamma$	foam quality, fraction	$\Delta p_{RS}$	pressure increase in the reservoir beyond the filtrate region due to spurt, psi, bar, Pa
$\Gamma(d)$	Euler gamma function		
$\Gamma(x)$	gamma function		
$\delta$	dip of the formation (angle with the horizontal), degree	$\Delta p_{safe}$	pressure safety margin, psi, bar, Pa
$\Delta$	rate of deformation tensor	$\Delta p_T$	total pressure difference between the fracture pressure and initial reservoir pressure, psi, bar, Pa
$\Delta C$	change in concentration	$\Delta p_{tort}$	tortuosity component of pressure, psi, bar, Pa
$\Delta E$	activation energy, kcal/mol	$\Delta p_{total}$	difference between fracture pressure and far-field reservoir pressure, psi, bar, Pa
$\Delta H$	heat of reaction	$\Delta p_v$	pressure drop across the filtrate-invaded zone, psi, bar, Pa
$\Delta MD$	change in measured depth, ft, m	$\Delta p_w$	difference in wellbore pressure, psi, bar, Pa
$\Delta p$	pressure difference or gradient, psi, bar, Pa	$\Delta p_\mu$	viscous pressure contribution, psi, bar, Pa
$\Delta p_c$	pressure drop between filtrate/reservoir interface and far-field reservoir, psi, bar, Pa	$\Delta t$	time difference, hr
$\Delta p_{cake}$	pressure drop across the filter cake, psi, bar, Pa	$\Delta t$	sonic transit time in the formation
$\Delta p_{ct}$	total pressure drop, psi, bar, Pa		
$\Delta p_{departure}$	pressure departure, psi, bar, Pa		
$\Delta p_{entry}$	fracture entry pressure, psi, bar, Pa		
$\Delta p_{face}$	pressure drop across fracture face dominated by filter cake, psi, bar, Pa		

$\Delta t$	shut-in time, hr, min, s	$\eta$	efficiency
$\Delta t_{ae}$	effective pseudotime	$\eta$	diffusivity constant
$\Delta t_c$	closure time	$\eta_C$	efficiency including spurt loss
$\Delta t_C$	compressional wave traveltime	$\eta_f$	fracture hydraulic diffusivity
$\Delta t_{cD}$	dimensionless closure time	$\eta_{fD}$	dimensionless fracture hydraulic diffusivity
$\Delta t_D$	dimensionless time difference	$\eta_p$	efficiency at end of pumping
$\Delta t_D$	dimensionless shut-in time	$\eta_{so}$	efficiency at screenout
$\Delta t_{Dso}$	dimensionless time after a screenout	$\theta$	angle, degree
$\Delta t_e$	effective time	$\theta$	fluid-loss exponent
$\Delta t_{ma}$	sonic transit time in the rock matrix	$\theta$	dimensionless time
$\Delta t_S$	shear wave traveltime	$\kappa$	opening-time distribution factor
$\Delta t_{so}$	time following screenout	$\kappa$	ratio of fracture-opening stress to minimum stress
$\Delta t_{sup}$	superposition time function	$\kappa$	spurt effect factor
$\Delta T_{surf}$	temperature change at the surface, °F, °C	$\kappa$	thermal diffusivity
$\Delta TBT$	change in true bed thickness, ft, m	$\kappa$	overall dissolution rate constant, cm/s
$\Delta TVD$	change in true vertical depth, ft, m	$\kappa_{so}$	spurt correction at screenout
$\Delta V$	change in volume	$\lambda$	interporosity constant
$\Delta \rho$	density difference, lbm/ft <sup>3</sup> , g/cm <sup>3</sup>	$\lambda$	experimental coefficient for the tortuosity reorientation of a fracture path
$\Delta \phi_{max}$	difference in maximum porosity	$\lambda$	apparent time multiplier
$\Delta \sigma$	stress difference, psi, bar, Pa	$\lambda$	characteristic relaxation time
$\Delta \$ _n$	incremental revenue	$\lambda_{rt}$	total mobility
$\varepsilon$	introduced error	$\lambda_t$	multiphase mobility
$\varepsilon$	ratio of closure time to the time interval	$\Lambda$	length scale corresponding to pore size
$\varepsilon$	longitudinal strain	$\mu$	viscosity, cp
$\varepsilon_a$	axial strain	$\mu_a$	apparent viscosity, cp
$\varepsilon_e$	elastic strain	$\mu_{base}$	viscosity of base fracturing fluid, cp
$\varepsilon_f$	acid front position divided by the linear flow core length	$\mu_{eff}$	effective viscosity, cp
$\varepsilon_h$	minimum tectonic strain	$\mu_{fil}$	viscosity of fracturing fluid filtrate, cp
$\varepsilon_H$	maximum tectonic strain	$\mu_{fluid}$	fluid viscosity, cp
$\varepsilon_p$	plastic strain	$\mu_g$	gas viscosity, cp
$\varepsilon_r$	radial strain	$\mu_{gi}$	gas viscosity at initial reservoir pressure and temperature, cp
$\varepsilon_S$	specific volume expansion ratio	$\mu_i$	intrinsic viscosity, cp
$\varepsilon_V$	volumetric strain		
$\eta$	poroelastic stress coefficient		

$\mu_{inh}$	inherent viscosity, cp	$\rho_r$	ratio of slurry density to fluid density
$\mu_o$	oil viscosity, cp	$\rho_{rock}$	rock density, lbm/ft <sup>3</sup> , g/cm <sup>3</sup>
$\mu_r$	viscosity ratio	$\rho_s$	slurry density, lbm/ft <sup>3</sup> , g/cm <sup>3</sup>
$\mu_r$	viscosity of reservoir fluid, cp	$\rho_{sol}$	solid particle density, lbm/ft <sup>3</sup> , g/cm <sup>3</sup>
$\mu_r$	relative viscosity, cp	$\sigma$	stress, psi, bar, Pa
$\mu_{slurry}$	slurry viscosity, cp	$\sigma'$	effective stress, psi, bar, Pa
$\mu_{sp}$	specific viscosity, cp	$\sigma_a$	axial stress, psi, bar, Pa
$\mu_w$	water viscosity, cp	$\sigma_{BL}$	stress acting on a bounding layer, psi, bar, Pa
$\mu_0$	zero-shear viscosity, cp	$\sigma_c$	uniaxial compressive strength, psi, bar, Pa
$\mu_{100}$	viscosity at 100°F [40°C], cp	$\sigma_c$	closure pressure or stress, psi, bar, Pa
$\mu_\infty$	high-shear-limiting viscosity, cp	$\sigma_c'$	effective confining stress, psi, bar, Pa
$\nu$	Poisson's ratio	$\sigma_f$	normal stress across a fissure, psi, bar, Pa
$\nu$	stoichiometric ratio of reactants to products	$\sigma_{failure}'$	effective ultimate strength, psi, bar, Pa
$\nu_{CaCO_3}$	stoichiometric coefficient of CaCO <sub>3</sub>	$\sigma_h$	minimum horizontal stress, psi, bar, Pa
$\nu_{dyn}$	dynamic Poisson's ratio	$\sigma_h'$	minimum effective horizontal stress, psi, bar, Pa
$\nu_{HCl}$	stoichiometric coefficient of hydrochloric acid	$\sigma_H$	maximum horizontal stress, psi, bar, Pa
$\nu_u$	undrained Poisson's ratio	$\sigma_{H,max}$	maximum horizontal stress, psi, bar, Pa
$\xi$	fluid-loss term	$\sigma_{h,min}$	minimum horizontal stress, psi, bar, Pa
$\xi$	dimensionless area or position	$\sigma_m$	mean stress, psi, bar, Pa
$\xi_f$	forward rate constant	$\sigma_{min}$	minimum stress or minimum principal stress, psi, bar, Pa
$\xi_r$	reverse rate constant	$\sigma_n$	normal stress component, psi, bar, Pa
$\rho$	density, lbm/ft <sup>3</sup> , g/cm <sup>3</sup>	$\sigma_n'$	effective normal stress, psi, bar, Pa
$\rho_a$	mass of diverter cake per unit area of available sandface, g/cm <sup>3</sup>	$\sigma_o$	equal-stress constant, psi, bar, Pa
$\rho_A$	density of reactant, g/cm <sup>3</sup>	$\sigma_{pay}$	stress of the pay zone, psi, bar, Pa
$\rho_b$	bulk density, lbm/ft <sup>3</sup> , g/cm <sup>3</sup>	$\sigma_{PZ}$	stress acting on the pay zone, psi, bar, Pa
$\rho_{brine}$	brine density, lbm/ft <sup>3</sup> , g/cm <sup>3</sup>	$\sigma_r$	radial stress, psi, bar, Pa
$\rho_C$	density of acid solution	$\sigma_{ref}$	constant state of stress, psi, bar, Pa
$\rho_{CaCO_3}$	density of calcium carbonate, lbm/ft <sup>3</sup> , g/cm <sup>3</sup>	$\sigma_{r\theta}$	shear stress, psi, bar, Pa
$\rho_{div}$	density of diverter particles, kg/m <sup>3</sup>	$\sigma_v$	vertical stress, psi, bar, Pa
$\rho_f$	fluid density, lbm/ft <sup>3</sup> , g/cm <sup>3</sup>	$\sigma_v'$	effective vertical stress, psi, bar, Pa
$\rho_l$	liquid density, lbm/ft <sup>3</sup> , g/cm <sup>3</sup>	$\sigma_1$	maximum principal stress, psi, bar, Pa
$\rho_{ma}$	density of matrix components, lbm/ft <sup>3</sup> , g/cm <sup>3</sup>	$\sigma_1'$	maximum principal effective stress, psi, bar, Pa
$\rho_o$	oil density, lbm/ft <sup>3</sup> , g/cm <sup>3</sup>		
$\rho_p$	proppant or particle density, lbm/ft <sup>3</sup> , g/cm <sup>3</sup>		

$\sigma_2$	intermediate principal stress, psi, bar, Pa	$\phi_{cake}$	diverter cake porosity, fraction
$\sigma_2'$	intermediate principal effective stress, psi, bar, Pa	$\phi_D$	porosity from density, fraction
$\sigma_3$	minimum principal stress, psi, bar, Pa	$\phi_{eff}$	effective porosity, fraction
$\sigma_3'$	minimum principal effective stress, psi, bar, Pa	$\phi_f$	fracture porosity, fraction
$\sigma_\theta$	tangential stress, psi, bar, Pa	$\phi_i$	initial porosity, fraction
$\sigma_{\theta\theta}$	circumferential stress, psi, bar, Pa	$\phi_N$	porosity from neutron, fraction
$\tau$	shear stress, psi, bar, Pa	$\phi_p$	proppant pack porosity, fraction
$\tau$	time of fracture opening	$\phi_S$	porosity from sonic, fraction
$\tau$	dimensionless slurry time	$\phi_{total}$	total porosity, fraction
$\tau_c$	characteristic time for fracture propagation, dimensionless	$\varphi$	angle, degree
$\tau_o$	foam yield stress, lbf/ft <sup>2</sup> , bar, Pa	$\Phi$	channel flow function
$\tau_{oct}$	octahedral shear stress, psi, bar, Pa	$\psi$	change of angle, degree
$\tau_w$	wall shear stress, lbf/ft <sup>2</sup> , bar, Pa	$\Psi$	dimensionless hydrofluoric acid concentration
$\tau_{yp}$	yield point, lbf/ft <sup>2</sup> , bar, Pa	$\Psi$	dimensionless rock dissolution rate
$\phi$	porosity, fraction	$\omega$	angular velocity, rad/s, rpm
$\phi$	angle of internal friction, degree	$\omega$	storativity ratio
		$\Omega$	stoichiometric coefficient